Geofluids

Mechanism and Control of Geological Disasters in Deep Engineering Under High Temperature, Ground Stress and Water Pressure 2021

Lead Guest Editor: Wen Zhijie
Guest Editors: Yongzheng Wu and Zhang Hualei

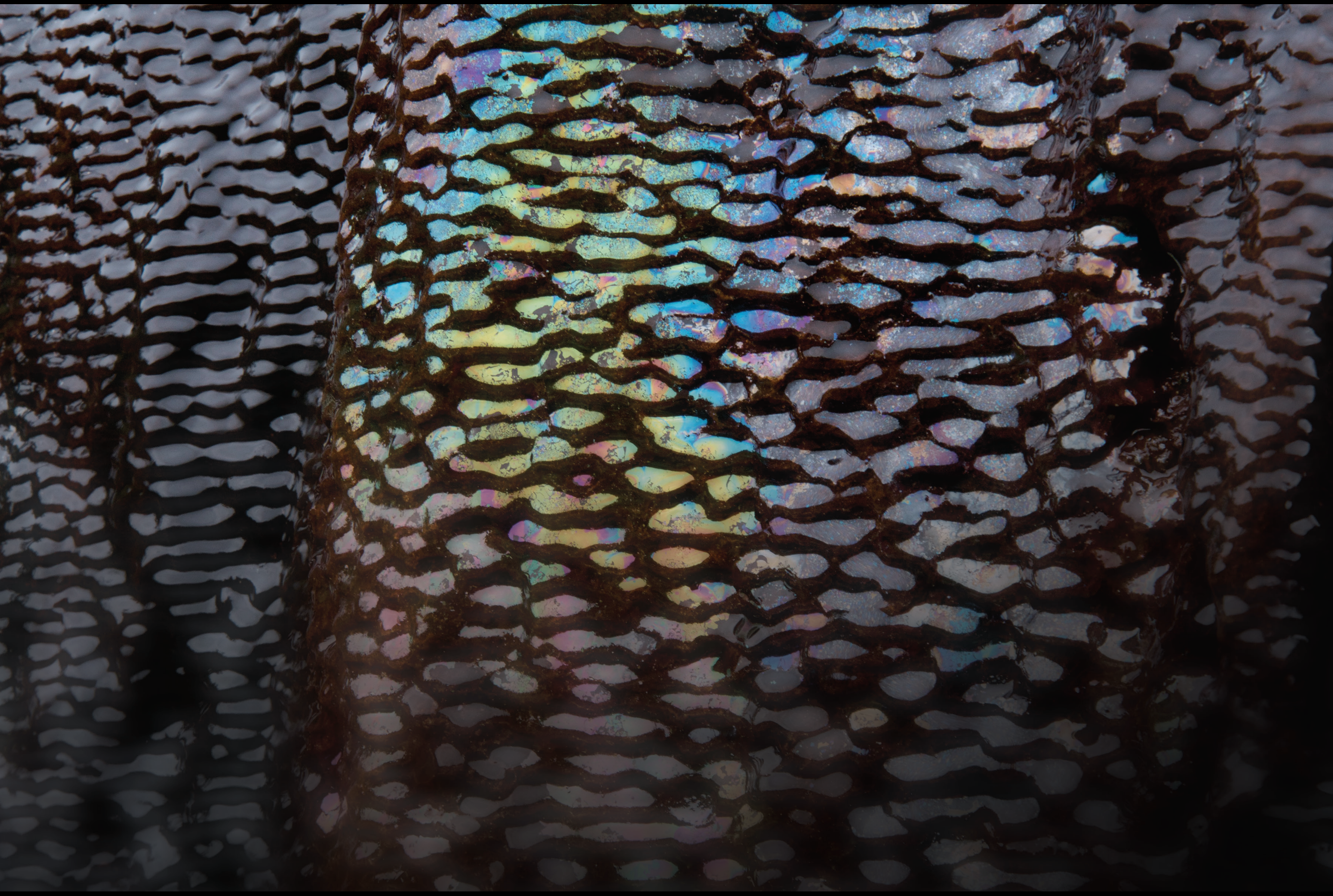

Mechanism and Control of Geological Disasters in Deep Engineering Under High Temperature, Ground Stress and Water Pressure 2021

Geofluids

Mechanism and Control of Geological Disasters in Deep Engineering Under High Temperature, Ground Stress and Water Pressure 2021

Lead Guest Editor: Wen Zhijie
Guest Editors: Yongzheng Wu and Zhang Hualei

Contents

Dynamic Response Analysis of Roadway Surrounding Rock Induced by Dynamic Load under the Action of Hard and Thick Rock Stratum
Kaihua Liang, Quansen Wu, Quanlin Wu, Xiang Shi, Hong Zhao, Fuwu Ma, and Zhaomin Zhang
Research Article (23 pages), Article ID 1750844, Volume 2023 (2023)

Roof Water Damage Prediction and Evaluation of Sand-Mud Sedimentary Tectonic Strata
Pengfei Jiang, Fumin Zhuge, Suolin Jing, Zongkai Li, Peng Xiao, and Yuguang Lv
Research Article (10 pages), Article ID 2243885, Volume 2023 (2023)

Risk Assessment of Water and Sand Inrush in Mining under Thick Loose Layer Based on Comprehensive Weight-Cloud Model
Wenquan Zhang, Xintao Wu, Xunan Wu, Yu Lei, Jianli Shao, and Zaiyong Wang
Research Article (12 pages), Article ID 1181284, Volume 2023 (2023)

Experiment and Numerical Simulation of Strength and Stress Distribution Behaviors of Anchored Rock Mass in a Roadway
Honghui Zhao, Haijian Su, Xiaofeng Qin, Kai Zhang, Yu Jiang, and Wenbo Wang
Research Article (14 pages), Article ID 9311206, Volume 2023 (2023)

Evolution Mechanism and Control of Floor Heave in the Deep Roadway with Retained Bottom Coal
Peng Li, Yonglu Suo, Peilin Gong, Xingping Lai, Kang Yi, Chao Su, and Chang Liu
Research Article (16 pages), Article ID 3658141, Volume 2023 (2023)

Study on the Bearing Mechanism and Stability of Surrounding Rock in Original Roadway Filling and Nonpillar Tunneling
Wenbao Shi, Jucai Chang, Yan Li, Dong Li, and Ru Hu
Research Article (12 pages), Article ID 2545442, Volume 2023 (2023)

Roadway Instability Mechanism of Weakly Consolidated Soft Rocks and Support Technologies
Jinlong Cai, Min Tu, Luxiu Chai, Fengyan Qin, and Zhengfeng Shen
Research Article (12 pages), Article ID 3492686, Volume 2023 (2023)

A New Method to Predict Shock-Type Coal-Gas Outburst Disaster and Its Application
Pengfei Lyu, Tan Li, and Xuehua Chen
Research Article (8 pages), Article ID 6957653, Volume 2023 (2023)

Research on Stability Control Technology of Mining Roadway Based on Energy Transformation
Guohua Zhang, Yanwei Duan, and Tao Qin
Research Article (17 pages), Article ID 8938807, Volume 2023 (2023)

Effect of Cyclic Loading and Unloading on the Deformation and Damage Properties of Sandstone from Beizao, a Coal Mine underneath the Bohai Sea in China
Yan Chen, Gaofei Wang, Lei Zhou, Guolong Zhang, Jiangfan Yang, and Meiheng Li
Research Article (11 pages), Article ID 9654025, Volume 2022 (2022)

Study on Roof Presplitting Mechanism and Deformation Control of Reused Roadway in Compound Soft Rock by Roof Presplitting Approach
Fuzhou Qi, Dangwei Yang, Xinming Li, Bin Li, Yingying Zhai, and Shuisheng Yu
Research Article (23 pages), Article ID 9144937, Volume 2022 (2022)

Quantitative Identification of Grouting Effect of Working Face Floor with Multifactor Set
Zhenwei Yang, Junchao Yue, Xinyi Wang, and Shuitao Guo
Research Article (9 pages), Article ID 2734122, Volume 2022 (2022)

Characterization of Acoustic Emission Parameters during Fracture Process of Siltstone with Prefabricated Void
Xiaorong Liu, Lulin Zheng, Hengyi He, Qing Qiu, Ziqi Liu, Xuefeng Li, Lin Yan, and Gang Huang
Research Article (9 pages), Article ID 6188833, Volume 2022 (2022)

Predicting Time-to-Failure of Red Sandstone by Temporal Precursor of Acoustic Emission Signals
Ansen Gao, Chengzhi Qi, Renliang Shan, and Chunlai Wang
Research Article (11 pages), Article ID 8063469, Volume 2022 (2022)

Research on Permeability Enhancement Model of Pressure Relief Roadway for Deep Coal Roadway Strip
Zhonghua Wang, Jianjun Cao, Jun Liu, and Chengcheng Li
Research Article (11 pages), Article ID 1342592, Volume 2022 (2022)

Analysis on Evolution Law of Small Structure Stress Arch and Composite Bearing Arch in Island Gob-Side Entry Driving
Shunjie Huang, Xiangqian Wang, Yingming Li, Lei Wang, Gang Liu, Fukun Xiao, and O. V. Bashkov
Research Article (12 pages), Article ID 4303681, Volume 2022 (2022)

Roof-Breaking Characteristics and Ground Pressure Behavior in Deep Jurassic Coal Seams: A Thick-Plate Model and Field Measurements
Wei Zhang, Yandong Zhang, Weisheng Zhang, Liang Chen, Fanjia Li, and Kaidi Xie
Research Article (15 pages), Article ID 6307522, Volume 2022 (2022)

Study on Energy Distribution Law and Numerical Simulation of Mining Roadway Surrounding Rock
Guohua Zhang, Chao Ju, Yanwei Duan, Yiwei Wang, Tao Qin, and Chengjia Wu
Research Article (12 pages), Article ID 7598831, Volume 2022 (2022)

A Prediction Method for Floor Water Inrush Based on Chaotic Fruit Fly Optimization Algorithm–Generalized Regression Neural Network
Zhijie Zhu, Chen Sun, Xicai Gao, and Zhuang Liang
Research Article (11 pages), Article ID 9430526, Volume 2022 (2022)

Contents

Petrogenesis, Magma Source, and Geodynamics of Paleogene Mafic Rocks, Huimin Sag, Jiyang Depression, Eastern China
Lihua Gao, Zhigang Song, Chao Han, Mei Han, Chenlin Zhu, Di Xia, Zuozhen Han, and Shuangjian Li
Research Article (18 pages), Article ID 1571066, Volume 2022 (2022)

Analysis Deformation Failure Characteristics and the Energy Evolution of Varying Lithologies under Cyclic Loading
Jianqiang Liu, Guangpeng Qin, Jing Cao, and Minghua Zhai
Research Article (13 pages), Article ID 7984910, Volume 2022 (2022)

Natural Frequency of Coal: Mathematical Model, Test, and Analysis on Influencing Factors
Jianping Wei, Junzhao Zhang, Zhihui Wen, Libo Zhang, Yongjie Ren, and Leilei Si
Research Article (13 pages), Article ID 7891894, Volume 2022 (2022)

Effects of Real-Time High Temperature and Loading Rate on Deformation and Strength Behavior of Granite
YiFeng Zhang, Fan Zhang, Ke Yang, and ZhengYu Cai
Research Article (11 pages), Article ID 9426378, Volume 2022 (2022)

Simulation Study of the Velocity Profile and Deflection Rate of Non-Newtonian Fluids in the Bend Part of the Pipe
Defeng Wang, Zhanbo Cheng, Qingwen Shi, Jinhai Zhao, and Helmut Mischo
Research Article (11 pages), Article ID 7885556, Volume 2022 (2022)

Effect of Water on Mechanical Properties of Coal Measures Mudstone Using Nanoindentation
Wenshuai Li, Bangyou Jiang, and Shitan Gu
Research Article (16 pages), Article ID 9032572, Volume 2022 (2022)

Research on Crack Propagation of Deep Geologic Mass Disturbed by Excavation Based on Phase Field Method
Ningdong Chang, Jinan Wang, and Fei Li
Research Article (13 pages), Article ID 5791006, Volume 2022 (2022)

Deformation Characteristics and Control Technology of Roadway in Water-Rich Soft Rock
Weiguo Lin, Jianliang Cheng, Dalei Li, and Haibo Dang
Research Article (8 pages), Article ID 2234334, Volume 2022 (2022)

Study on the Migration Law of Overlying Strata on the Working Surface of Large Mining Height in Y.C.W Coal Mine
Hongtao Liu, Tianhong Huo, Yang Liu, Zhou Han, Zijun Han, and Wanliang Liang
Research Article (13 pages), Article ID 6292783, Volume 2022 (2022)

The Investigation of Strata Control for Ultrasoft Coal Seam Mining
Chuanqi Zhu, Lei Wang, and Shaobo Li
Research Article (15 pages), Article ID 8130555, Volume 2022 (2022)

Mechanical Mechanism Analysis of Roof Fracture Evolution in Stope with Variable Length Based on Elastic-Plastic Structure Theory
Xinfeng Wang, Mingyuan Lu, Rui Wei, Zhaofeng Wang, and Shan Li
Research Article (19 pages), Article ID 2475021, Volume 2022 (2022)

Field Pull-Out Test and Analysis of Fiberglass Anchors in Sanshandao Gold Mine
Qingbiao Wang, Zhongjing Hu, Hongyue You, Haolin Xu, Lujie Bai, Shanghuan Yang, Ming Zhang, and Zhenyue Shi
Research Article (8 pages), Article ID 5160876, Volume 2022 (2022)

Effect of Strong Mining on the Fracture Evolution Law of Trick Rise in the Mining Field and Its Control Technology
Zhaolin Li, Lianguo Wang, and Ke Ding
Research Article (8 pages), Article ID 3953650, Volume 2022 (2022)

Research on Pressure Relief Method of Close Floor Roadway in Coal Seam Based on Deformation and Failure Characteristics of Surrounding Rock in Deep Roadway
Jianjun Cao, Benqing Yuan, Siqian Li, Zunyu Xu, Qihan Ren, and Zhonghua Wang
Research Article (16 pages), Article ID 5820228, Volume 2022 (2022)

Effect of Rheological Mesoparameters on Shear Mechanical Behavior of Joints
Kefeng Zhou, Sheng Liu, and Yanhui Cheng
Research Article (10 pages), Article ID 3512507, Volume 2022 (2022)

Study on the Dynamic Instability Mechanism of the Rock Formation in the Multifault Structure Zone of the Stope
Hanxiao Guo, Weijian Yu, Yong Liu, Zongtang Zhang, and Xiangtao Kang
Research Article (13 pages), Article ID 8382493, Volume 2022 (2022)

Study on the Failure Mechanism of Lower Cambrian Shale under Different Bedding Dips with Thermosolid Coupling
Wentao Wang, Zhonghu Wu, Huailei Song, Hengtao Cui, Yili Lou, Motian Tang, and Hao Liu
Research Article (15 pages), Article ID 1976294, Volume 2022 (2022)

Jianghui He, Wenping Li, Wei Qiao, Qiqing Wang, Zhi Yang, and Liangning Li
Research Article (19 pages), Article ID , ()

Pressure Relief and Permeability Enhancement Mechanism of Short-Distance Floor Roadway in Deep Coal Roadway Strip
Benqing Yuan, Min Tu, Jianjun Cao, and Xiang Cheng
Research Article (12 pages), Article ID 7430025, Volume 2022 (2022)

Contents

Study on the Law of Subsidence of Overburden Strata above the Longwall Gob
Yujiang Zhang, Caiyi Du, Guorui Feng, Honghui Yuan, Xiaogang Deng, Ronggang Zhang, Renle Zhao, and Yuxia Guo
Research Article (10 pages), Article ID 6321031, Volume 2022 (2022)

Feasibility of Water Injection on the Coal Wall of Loose Thick Coal Seam to Prevent Rib Spalling and Its Optimal Moisture Content
Jian Sun, Bin Li, Ruofei Zhang, and Zhou Huang
Research Article (8 pages), Article ID 5733695, Volume 2022 (2022)

Application and Research of Gangue Partial-Filling Mining Method in Preventing Water Inrush from Floor
Zhenzhong Pang, Xinguo Zhang, Juntao Chen, and Feifan Li
Research Article (19 pages), Article ID 6464564, Volume 2022 (2022)

Determination of Reasonable Width of Filling Body for Gob-Side Entry Retaining in Mining Face with Large Cutting Height
Shijiang Pu, Guiyi Wu, Qinzhi Liu, Yuliang Wang, Qiang Li, and Yu Xiong
Research Article (11 pages), Article ID 1774110, Volume 2022 (2022)

Dynamic Monitoring and Research on the Evolution of the Damage of Weakly Consolidated Coal Floor under Dynamic Pressure Using Distributed Optical Fiber
Chang Liu, Pingsong Zhang, Duoxi Yao, Yutong Tian, and Yuanchao Ou
Research Article (16 pages), Article ID 9552210, Volume 2022 (2022)

Structural Characteristics of Regenerated Roof and Distribution Law of Overburden Porosity in Downward Mining of a Bifurcated Coal Seam
Ru Hu, Jiwen Wu, Xiaorong Zhai, Wenbao Shi, and Kai Huang
Research Article (17 pages), Article ID 6914746, Volume 2022 (2022)

Study on the Precursors of Coal-Rock Fracture Based on the Maximum Lyapunov Exponent of Acoustic Emission Parameters
Guoqiang Cheng, Xiaohui Sun, and Jiangong Li
Research Article (10 pages), Article ID 3280185, Volume 2022 (2022)

Effect Of Open-Pit Blasting Vibrations on a Hanging-Wall Slope: A Case Study of the Beizhan Iron Mine in China
Yong-gang Xiao, Jie Cao, Xiao-min Liu, and Chang-hong Li
Research Article (10 pages), Article ID 6943834, Volume 2022 (2022)

The Coal Pillar Width Effect of Principal Stress Deflection and Plastic Zone Form of Surrounding Rock Roadway in Deep Excavation
Ji Li, Rongguang Zhang, and Xubo Qiang
Research Article (17 pages), Article ID 1007222, Volume 2022 (2022)

Floor Failure Characteristics in Deep Island Longwall Panel: Theoretical Analysis and Field Verification
Pengpeng Wang, Yixin Zhao, Qingshan Ren, Yaodong Jiang, Cun Zhang, and Yirui Gao
Research Article (14 pages), Article ID 1851899, Volume 2022 (2022)

A Coal Bump Risk Assessment and Prediction Model Based on Multiparameter Indices
Tao Luo, Gangwei Fan, Shizhong Zhang, Shang Ren, Yibo Fan, and Ruiliang Shen
Research Article (10 pages), Article ID 2090809, Volume 2022 (2022)

Study on the Effect of Rock Strength on the Macro-Meso Shear Behaviors of Artificial Rock Joints
Yujing Jiang, Sunhao Zhang, Hengjie Luan, Qinglin Shan, Baocheng Li, Dong Wang, and Chuanyang Jia
Research Article (15 pages), Article ID 1968938, Volume 2022 (2022)

Stress Evolution Mechanism and Control Technology for Reversing Mining and Excavation under Mining-Induced Dynamic Pressure in Deep Mine
Jiyu Wang, Fangtian Wang, and Xigui Zheng
Research Article (17 pages), Article ID 4133529, Volume 2022 (2022)

Research on Gas Extraction Technology of Directional Long Borehole in Ultrathick Coal Seam
Yaobin Li, Tao Jiang, and Xin Guo
Research Article (12 pages), Article ID 6957896, Volume 2022 (2022)

Experimental Study of Seepage Characteristics of Filling Structures in Deep Roadway
Shaoshuai Shi, Xiangxiang Zhu, Zhiguo Cao, Lin Bu, Zhijie Wen, Zongqing Zhou, Weidong Guo, and Ruijie Zhao
Research Article (13 pages), Article ID 9517011, Volume 2022 (2022)

Erosion Effect on Non-Darcy Hydraulic Characteristics of Limestone and Mudstone Mixture
Chong Li and Sifeng He
Research Article (13 pages), Article ID 8781289, Volume 2022 (2022)

Genesis of the Daping Gold Deposit in the Middle Xuefeng Mountain Area, Southern China: Constraints from Geochemistry, Fluid Inclusion, and H-O-S Isotope
Xu Kong, Wen-Tian Mi, Xue-Yuan Qi, Shu-Jun L#, Yu-Jun Dong, and Jie Xin
Research Article (22 pages), Article ID 6416174, Volume 2022 (2022)

Study on the Synchronous Instability Mechanism of the Coal Wall and Direct Roof of High Soft Coal Seam
Baojie Fu, Jiawen Li, Min Tu, and Ningping Jin
Research Article (11 pages), Article ID 4703957, Volume 2022 (2022)

Mechanism and Control of Rockburst Induced by Draining Spatial Islands and Squaring
Yunhai Cheng, Fenghui Li, Xiufeng Zhang, Gangwei Li, and Le Xu
Research Article (10 pages), Article ID 5633861, Volume 2022 (2022)

Contents

Experimental Study on Seepage Characteristics of Fractured Rock Mass under Different Stress Conditions
Ma Haifeng, Yao Fanfan, Niu Xin'gang, Guo Jia, Li Yingming, Yin Zhiqiang, and Li Chuanming
Research Article (11 pages), Article ID 6381549, Volume 2021 (2021)

The Effects of Precrack Angle on the Strength and Failure Characteristics of Sandstone under Uniaxial Compression
Shuai Zhang, Jinhai Xu, Liang Chen, Hideki Shimada, Mingwei Zhang, and Haiyang He
Research Article (11 pages), Article ID 7153015, Volume 2021 (2021)

Study on Influence of Joint Distribution on Surrounding Rock Failure of an Underground Tunnel
Wanrong Liu, Chao Peng, and Baoliang Zhang
Research Article (12 pages), Article ID 3621040, Volume 2021 (2021)

Organic Geochemical Characteristics of Mudstone and Marl from Western Hoh Xil Basin of Tibet
Wentian Mi, Xueyuan Qi, Yan Shang, Xu Kong, and Zifu Hu
Research Article (15 pages), Article ID 2235555, Volume 2021 (2021)

Study on the Reinforcing Effects of the FRP-PCM Method on Tunnel Linings for Dynamic Strengthening
Xiaoshan Wang, Lin Wei, Zaiquan Wang, Yujing Jiang, Liming Zhang, Fanzhen Meng, and Yu Cong
Research Article (13 pages), Article ID 8926423, Volume 2021 (2021)

A Study of Support Characteristics of Collaborative Reinforce System of U-Steel Support and Anchored Cable for Roadway under High Dynamic Stress
Qizhou Wang, Haiwang Ye, Ning Li, Xiuwen Chi, Wenbing Xie, Dongfang Chen, Shengguo Jing, and Tao Lei
Research Article (12 pages), Article ID 9881280, Volume 2021 (2021)

Study on Influence of Cavity and Water Mist on Flame Propagation of Gas Explosion in a Pipeline
Shicheng Gu, Shujie Yuan, Zhuo Yan, and Xiaoxue Xu
Research Article (8 pages), Article ID 2530909, Volume 2021 (2021)

Geological Structure Exploration of Karst Collapse Column and Evaluation of Water Insulation Properties of the Mud Part
Shijian Yu, Jiyang Liu, Peng Bai, Hongtao Xu, Runshan He, Yongshen Wang, and Dawei Yin
Research Article (9 pages), Article ID 2071333, Volume 2021 (2021)

Effect of Fly Ash and Cement on the Engineering Characteristic of Stabilized Subgrade Soil: An Experimental Study
Partab Rai, Wenge Qiu, Huafu Pei, Jihui Chen, Xufeng Ai, Yang Liu, and Mahmood Ahmad
Research Article (11 pages), Article ID 1368194, Volume 2021 (2021)

Influence of Mine Earthquake Disturbance on the Principal Stress of the Main Roadway near the Goaf and Its Prevention and Control Measures
Penghui Guo, Jiazhuo Li, Xiqing Hao, Heng Cui, Lihua Tian, Wenhao Xie, and Jiaqi Chu
Research Article (13 pages), Article ID 1968846, Volume 2021 (2021)

Prevention of Water Inrushes in Deep Coal Mining over the Ordovician Aquifer: A Case Study in the Wutongzhuang Coal Mine of China
Huichao Yin, Bin Xu, Shangxian Yin, Wuzi Tian, Hui Yao, and Haopeng Meng
Research Article (13 pages), Article ID 5208670, Volume 2021 (2021)

Research on the Reasonable Strengthening Time and Stability of Excavation Unloading Surrounding Rock of High-Stress Rock Mass
Wensong Xu, Wentao Xu, and Yunhai Cheng
Research Article (13 pages), Article ID 3508661, Volume 2021 (2021)

Roof Fracture Characteristics and Strata Behavior Law of Super Large Mining Working Faces
Guozhen Zhao, Baisheng Zhang, Lihong Zhang, Chao Liu, and Shuai Wang
Research Article (12 pages), Article ID 8530009, Volume 2021 (2021)

Research on Optimization of Coal Pressure Relief Borehole Parameters under High-Stress Conditions
Heng Zhang, Tie Li, Zhenhua Ouyang, Su Liu, and Haiyang Yi
Research Article (13 pages), Article ID 4673152, Volume 2021 (2021)

Mechanical Properties and Damage Behavior of Rock-Coal-Rock Combined Samples under Coupled Static and Dynamic Loads
Jinzheng Bai, Linming Dou, Piotr Małkowski, Jiazhuo Li, Kunyou Zhou, and Yanjiang Chai
Research Article (18 pages), Article ID 3181697, Volume 2021 (2021)

An Analysis of the Impact of Deviatoric Stress and Spherical Stress on the Stability of Surrounding Rocks in Roadway
Liu Rui and Zhu Quanjie
Research Article (13 pages), Article ID 3095690, Volume 2021 (2021)

The Integrated Development Strategy of Coastal Industrial Areas and City Based on Underground Space Development
Feng Shao, Pingyang Shi, Yusheng Ding, and Ce Dong
Review Article (9 pages), Article ID 4336163, Volume 2021 (2021)

Numerical Simulation on the Progressive Failure Processes of Foundation Pit Excavation Based on a New Particle Failure Method
Guojin Zhu, Shuyang Yu, Yu Ning, Xuhua Ren, Peng Wei, and Yu Wu
Research Article (10 pages), Article ID 7374363, Volume 2021 (2021)

Contents

Modified Stochastic Petri Net-Based Modeling and Optimization of Emergency Rescue Processes during Coal Mine Accidents
Xiao Li, Yongkui Shi, Zaiyong Wang, and Wenquan Zhang
Research Article (13 pages), Article ID 4141236, Volume 2021 (2021)

An Experimental Research on Surrounding Rock Unloading during Solid Coal Roadway Excavation
Hongjun Guo, Ming Ji, Dapeng Liu, Mengxi Liu, Gaofeng Li, and Jingjing Chen
Research Article (9 pages), Article ID 5604642, Volume 2021 (2021)

Characterization of Discontinuity and Mechanical Anisotropy of Shale Based on Continuum Damage Mechanics
Qinglin Shan, Peng Yan, Hengjie Luan, Yujing Jiang, and Sunhao Zhang
Research Article (12 pages), Article ID 5714547, Volume 2021 (2021)

Investigation on the Movement and Fracture Characteristics of an Extra-Thick Hard Roof during Longwall Panel Extraction in the Yima Mining Area, China
Hongwei Wang, Daixin Deng, Ruiming Shi, Guozhen Yang, Shuo Xu, and Yaodong Jiang
Research Article (18 pages), Article ID 4092242, Volume 2021 (2021)

Operating Environment Assessment of the Coalface in Underground Coal Mining Based on Analytic Hierarchy Process (AHP) and Matter-Element Theory (MET)
Jianghui He, Shiliang Liu, Wenping Li, Wei Qiao, Zhi Yang, and Qiqing Wang
Research Article (8 pages), Article ID 9083547, Volume 2021 (2021)

Study on Deformation and Failure Characteristics of Surrounding Rock of Overlying Roadway under Upward Mining in the Deep Mine
Teng-Gen Xiong, Ju-Cai Chang, Kai He, Ya-Feng Su, and Chao Qi
Research Article (14 pages), Article ID 5667183, Volume 2021 (2021)

Experimental Study of the Influence of Moisture Content on the Mechanical Properties and Energy Storage Characteristics of Coal
Nan Liu, Chuanming Li, Ruimin Feng, Xin Xia, and Xiang Gao
Research Article (12 pages), Article ID 6838092, Volume 2021 (2021)

Hindawi
Geofluids
Volume 2023, Article ID 1750844, 23 pages
https://doi.org/10.1155/2023/1750844

Research Article

Dynamic Response Analysis of Roadway Surrounding Rock Induced by Dynamic Load under the Action of Hard and Thick Rock Stratum

Kaihua Liang,[1,2] Quansen Wu,[3] Quanlin Wu,[3,4] Xiang Shi,[1,2] Hong Zhao,[1,5,6] Fuwu Ma,[1,2] and Zhaomin Zhang[1,2]

[1]*Engineering Laboratory of Deep Mine Rockburst Disaster Assessment, Shandong Province, Jinan 250100, China*
[2]*Shandong Province Research Institute of Coal Geology Planning and Exploration, Jinan 250100, China*
[3]*Jining University, Qufu 273100, China*
[4]*Yankuang Energy Group Company Limited, Zoucheng 273500, China*
[5]*Physical Exploration and Survey Team of Shandong Bureau of Coal Geology, Jinan 250100, China*
[6]*Shandong Taishan Resources Prospecting Group Ltd., Taian 271000, China*

Correspondence should be addressed to Quansen Wu; 2401392747@qq.com and Quanlin Wu; jnxywql@163.com

Received 24 March 2022; Revised 22 June 2022; Accepted 13 July 2022; Published 30 April 2023

Academic Editor: Yong-Zheng Wu

In the process of coal seam mining, there are often hard thick key layers in the overlying strata. Due to the high strength and good integrity of the hard thick key layer, after the hard thick key layer is broken, the overlying strata will collapse and lose stability in a large area, which is very easy to induce dynamic disasters such as rock burst, mine earthquake, coal wall caving, and roof slab caving. Aiming at the hard and thick key layer overlying the working face, the dynamic response of the mine under the strong mine earthquake induced by the breaking of the main key layer of high-level magmatic rock is numerically simulated and analyzed by using FLAC2D numerical simulation software, and the variation laws of the stress field, displacement field, and velocity field of the coal seam roadway under different boundary conditions and different focal heights are studied. The research shows that the roof of solid coal roadway is prone to vibration in a small range, and the displacement increases and decreases with the disturbance. The displacement of the floor and two sides of the solid coal roadway and the top floor and two sides of the roadway along the goaf continues to increase in the initial stage of the disturbance, and the displacement will remain stable with the continuation of the disturbance. The displacement of both sides and roof and floor of gob roadway can reach stability in the later stage of disturbance, and with the increase of the number of adjacent goaf, the longer it takes for the displacement of surrounding rock to reach stability. When the focal height is lower than 90 m, the variation of surrounding rock response increases sharply with the decrease of focal height. When a strong earthquake occurs in the low rock stratum, the impact damage of roadway surrounding rock is almost inevitable. The influence degree of strong earthquake on the stability of roadway surrounding rock is arranged as follows: gob-side roadway (mined out on one side) > solid coal roadway (mined out on both sides) > solid coal roadway (mined out on one side). The evolution process also shows that the working face boundary conditions have an important influence on the energy propagation of mine earthquake. With the increase of the number of adjacent goafs, the faster the energy attenuation rate of mine earthquake propagation is. The research results have important reference significance for the safe mining of working face under similar geological conditions.

1. Introduction

With the continuous increase of mining depth and in-situ stress, mine dynamic phenomena or disasters such as mine earthquake, rock burst, coal and gas outburst, and support dynamic load are becoming more and more serious [1–6]. Relevant studies show that the range of overburden movement and stress field related to dynamic disasters in deep mining has exceeded the range of traditional basic roof in the longitudinal direction. In particular, when the overburden of the working face has a hard and thick key layer, due to the good integrity of the hard and thick key layer and the large first breaking span, under the bearing and shielding effect of the hard and thick key layer, the abutment pressure concentration of the working face before the breaking of the super thick key layer is high and the separation space under the key layer is large. When the suspension span length of the hard thick key layer reaches the limit suspension span length, the key layer will break [7–9]. Due to a large amount of separation space under the hard thick key layer, the broken magmatic rock block sinks rapidly, generates intense instantaneous kinetic energy, releases a large amount of energy, and produces mine earthquakes. When the energy is large enough, there are even produce strong earthquakes [10, 11]. The combined action of mine earthquake and highly concentrated static load of working face is easy to cause coal wall caving and roof caving and even induce rockburst. Hard and thick key layers are distributed in most mining areas in China, such as Huaibei coalfield, Yanzhou coalfield, and Datong coalfield [12–14]. For example, the 400–800 m thick conglomerate overlying Huafeng coal mine has abnormal abutment pressure and rock burst from time to time. Since 1992, the impact has occurred tens of thousands of times rock burst, and the maximum magnitude is as high as 2.9. The number of rock burst that caused damage to the working face reached 108 times, forcing the working face to stop production for 12 times, resulting in 43 serious injuries and many deaths, and resulting in countless times of roadway maintenance, which had an adverse impact on social and economic benefits. There is 94.27 m thick medium sandstone in the upper 91 m of the third coal layer in the second mining area of Baodian coal mine. The extremely thick medium sandstone is cut by Machang fault outside the stopping line of 2310, 2311, and 2312 working faces. After the 2310, 2311, and 2312 working faces are mined out, the huge thick medium sandstone cut is suspended in a large area and is in a dynamic equilibrium state, and the huge thick medium sandstone is prone to large-area movement. On September 6, 2004, a rock burst accident occurred in no. 1 air inlet connection lane of 2310 working face of Baodian coal mine, and the seal was broken, resulting in two deaths and six injuries. According to the analysis, the accident was caused by the mining earthquake caused by the large-area movement of the huge thick medium sandstone on the upper part of the goaf. The shock wave generated by the mining earthquake destroyed the closed wall, and the impact spread to the thrown closed bricks, resulting in casualties. The rockburst is serious under the condition of high-level huge thick conglomerate in Huafeng coal mine and Qianqiu Coal Mine. The rock burst and coal and gas outburst in Haizi coal mine and Yangliu Coal Mine are related to the fracture of high-level magmatic rock overburden. Through the above dynamic disaster analysis, it can be seen that when the working face is covered with hard thick rock stratum, the dynamic disaster caused by the breaking of hard thick rock stratum seriously threatens the safe and efficient production of coal mine. Therefore, people must pay great attention to the dynamic disaster caused by the breaking of hard and thick rock strata in the mining process of the working face.

At present, many well-known scholars have done a lot of research on the occurrence mechanism of mining dynamic disasters under hard and thick key layers, the change characteristics of overburden structure, and the characteristics of stress evolution by using the methods of theoretical analysis, numerical simulation, and field observation [13, 15–20]. He [21] and others adopted the key layer theory of rock movement and obtained through analysis that the mine pressure reaches the maximum when the key layer of overburden is broken, which is very easy to lead to strong mine earthquake and rockburst. Jiang [10] and others used the method of theoretical analysis to deduce the fracture calculation method of hard and thick key layers and verified the calculation method through field dynamic response observation. Hu [22] and others established a numerical model of mining under similar geological conditions by using FLAC3D numerical simulation and simulated and analyzed the causes of dynamic load disasters induced by hard and thick strata. Jiang et al. used FLAC3D numerical simulation calculation method to study the movement law, mining stress evolution characteristics, energy distribution characteristics of overlying strata under hard thick igneous rocks, and the influence of igneous rock occurrence horizon and thickness on the movement law, stress distribution, and energy distribution of overlying strata [23]. Wu et al. took the 103 upper 02 working face of Baodian coal mine as an engineering example, studied the breaking law of overlying hard thick sandstone caused by working face mining according to the field measured microseismic data, and explained the relationship between microseismic data and rock movement [24]. Ning et al. carried out microseismic monitoring on the existing hard and thick rock strata covered on the working face, studied the relationship between the fracture of hard and thick rock strata and microseismic data by using the microseismic distribution law, and put forward prevention and control measures [25]. Yang et al. comprehensively used similar material test, theoretical analysis, and numerical simulation methods to study the deformation and failure of overlying super thick key layer and the variation characteristics of working face bearing pressure and analyzed the mechanism and manifestation mode of working face rock burst induced by the failure of super thick key layer [26]. To sum up, the existing research results play an important role in the prediction and prevention of mining dynamic disasters under hard and thick strata, but they mostly stay in the stage of static load, ignoring the dynamic load effect in the process of coal mining after hard and thick strata are broken.

Based on this, aiming at the occurrence of hard and thick igneous rocks overlying the working face, this paper uses FLAC2D numerical simulation software, numerically simulate and analyze the dynamic response of the mine under the strong mine earthquake induced by the breaking of the main key layer of high-level magmatic rock, and study the variation laws of the stress field, displacement field, and velocity field of the coal seam roadway under different boundary conditions and different focal height. The second part is the description of numerical model. The third part studies the influence law of boundary conditions on roadway

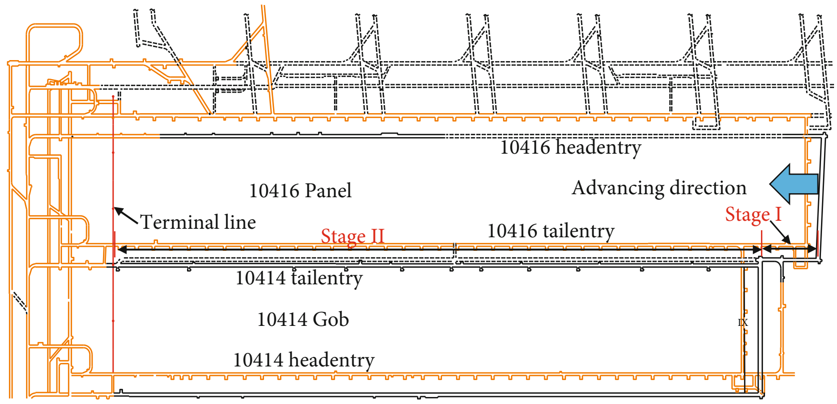

Figure 1: The plane layout of the working face.

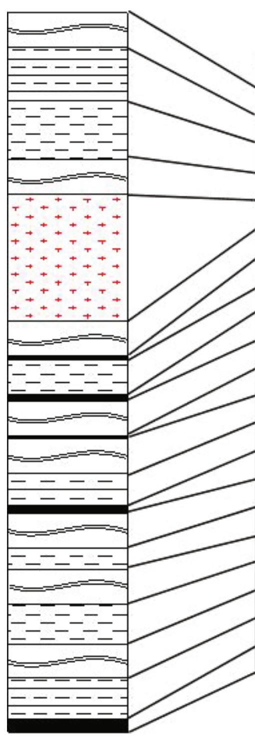

Rock thickness (m)	Depth (m)	Lithology
12.62	394.04	
15.43	409.46	Mudstone
17.13	426.59	Siltstone
14.88	441.47	
43.60	485.07	Igneous rock
2.81	487.88	
1.16	489.04	Coal seam $\#7_1$
7.62	496.66	Siltstone
1.6	499.38	Coal seam $\#7_2$
1.89	501.27	
0.82	502.09	Coal seam $\#8_1$
3.07	505.15	
9.26	514.41	Sandstone
2.23	516.64	Coal seam $\#8_2$
2.25	518.89	
6.30	525.19	Siltstone
28.57	553.76	
11.45	565.76	Siltstone
10.09	575.30	
11.60	589.90	Mudstone
3.54	590.90	Coal seam $\#1_0$

Figure 2: The borehole histogram.

dynamic response. The fourth part is the influence of focal height on roadway dynamic response. The fifth part verifies the correctness of the research through the field data measurement. The research results of this paper have important guiding significance for safe and efficient mining of working face under similar geological conditions.

2. Model Description

2.1. General Engineering Geology Conditions. Taking the geological conditions of 10416 working face in Yangliu Coal Mine as the engineering background, a numerical calculation model is established. The northeast of the working face is the solid coal of mining area 106, and the southwest is the goaf of working face 10414. A 5 m section of protective coal pillar is reserved. The inclined length of the working face is 180 m, the average thickness of the coal seam is 3.5 m, the average inclined angle is 4°, and the buried depth is -570–-610 m. There are two layers of magmatic rocks in the upper part of 10416 working face, which intrude along the roof of 5_2 coal seam and 7_2 coal seam, respectively. The average thickness of the magmatic rock in the roof of coal seam 5_2 is 31.5 m, the average thickness of the magmatic rock in the roof of coal seam 7_2 is 43.5 m, and the average distance between the magmatic rock in the roof of coal seam 5_2 and the magmatic rock in the roof of coal seam 7_2 is 116 m. The plane layout of the working face is shown in Figure 1, and the borehole histogram is shown in Figure 2 [11].

2.2. Establishment of Numerical Model. In this paper, two numerical calculation models are established. The model size, rock composition, and mechanical parameters are the same. When simulating the mining of working face, the mechanical boundary conditions of working face are different.

Table 1: Mechanical parameters and strata of model.

Lithology	Density/kg•m^{-3}	Bulk modulus/GPa	Shear modulus/GPa	Cohesion/MPa	Tensile strength/MPa	Friction angle/°
Coal	1350	4.8	3.6	1	0.8	28
Sandstone	2530	26.4	20.7	4.3	3.8	37
Magmatic rock	3000	38.7	29.7	6.2	7.5	42
Fine sandstone	2530	12.3	8.3	3.4	3.2	35
Siltstone	2530	15.2	9.4	2.8	2.4	30
Mudstone	2340	7.1	5.1	1.2	2.4	25

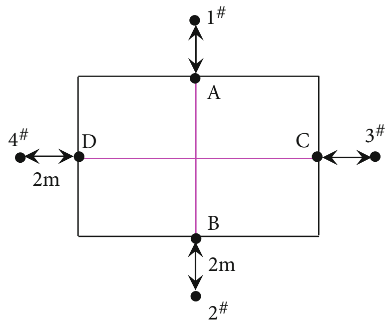

Figure 3: Layout of monitoring points.

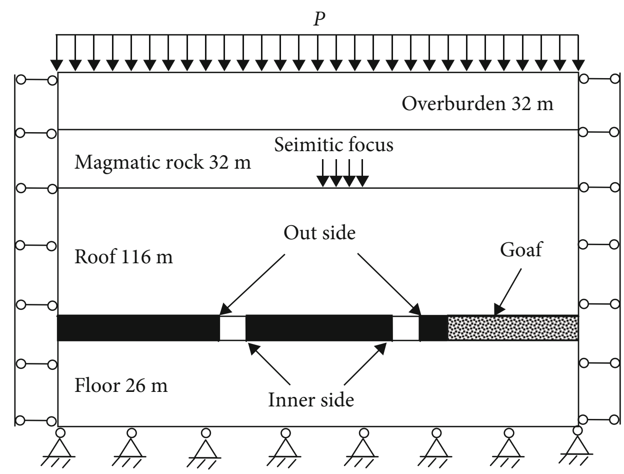

Figure 4: Numerical calculation model.

The first model is the mining of solid coal face on both sides. The second model is the working face mining with one side of solid coal and one side of goaf. According to the research content of this paper, two identical numerical models are established, and the model size is 660 m (length) × 208 m (height), roadway size 5 m (width) × 3 m (high), the buried depth of the simulated coal seam is 600 m, and the vertically uniformly distributed load of 10.75 MPa is applied on the top of the model. The composition and mechanical parameters of model rock stratum can be seen in Table 1.

The calculation process of the two numerical models is divided into 5 steps. Step 1: establish the model and initialize the stress field. Step 2: excavate two roadways in the working face (model 1), and excavate one side of the working face into a goaf (model 2). Step 3: static field balance. Step 4: the displacement and velocity of static field are cleared. Step 5: apply disturbance load and monitor the mechanical response of roadway surrounding rock.

2.3. Numerical Simulation Scheme. Four displacement monitoring points A, B, C, and D are arranged at the midpoint of the roadway top and floor and two sides of the working face (the side of the working face is called the inner side, and the side of the roadway far away from the working face is called the outer side), and 1#, 2#, 3#, and 4# four stress monitoring points are arranged 2 m outside the displacement monitoring points (as shown in Figure 3) to monitor the stress field, displacement field, and the variation law of velocity field and acceleration field.

(1) During the mining process of the working face, strong earthquake events have occurred at the bottom of magmatic rock for many times. In view of this, apply strong disturbance at the bottom of magmatic rock in models 1 and 2 (116 m away from the coal seam) and monitor the dynamic response law of roadway surrounding rock

(2) For models 1 and 2, apply strong disturbances are at 50 m, 70 m, and 90 m above the coal seam to analyze the dynamic response law of roadway surrounding rock under different focal heights

The strong earthquake distance M_0 above the working face is 1.0×10^{13} N · m, converted into Richter scale $M_L = 2.56$ and vibration energy $E = 4.55 \times 10^6$ J, dominant frequency $f_0 = 50$ Hz. The dynamic calculation time is set to 1.0 s, and the static boundary setting and Rayleigh damping are adopted. The model adopts plane strain analysis, the calculation and analysis criterion adopts Mohr Coulomb strength criterion, and the goaf and working face roadway are simulated by empty element. The schematic diagram of the model (taking model 2 as an example) is shown in Figure 4.

3. Influence of Boundary Conditions on Dynamic Response of Roadway

3.1. Solid Coal on Both Sides of Working Face

(1) Dynamic response of roadway surrounding rock

Figure 5 reflects the dynamic response characteristics of roadway surrounding rock under the condition that the focal

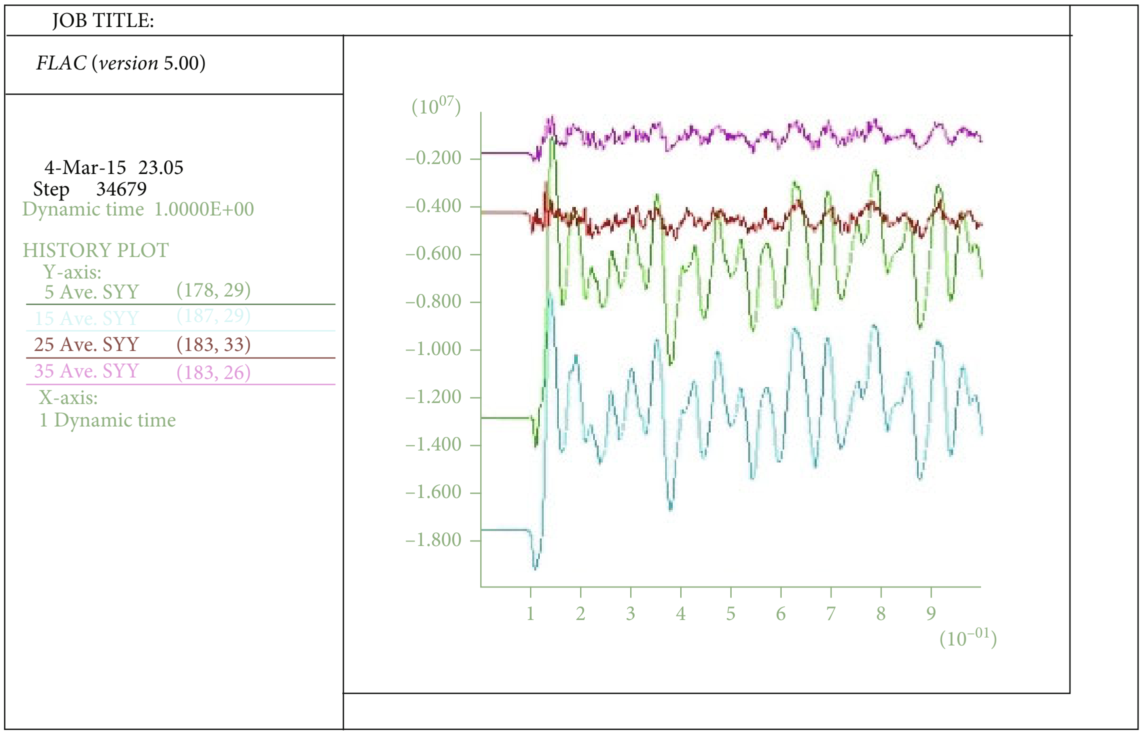

(a) Vertical stress variation of roadway roof, floor, and two sides

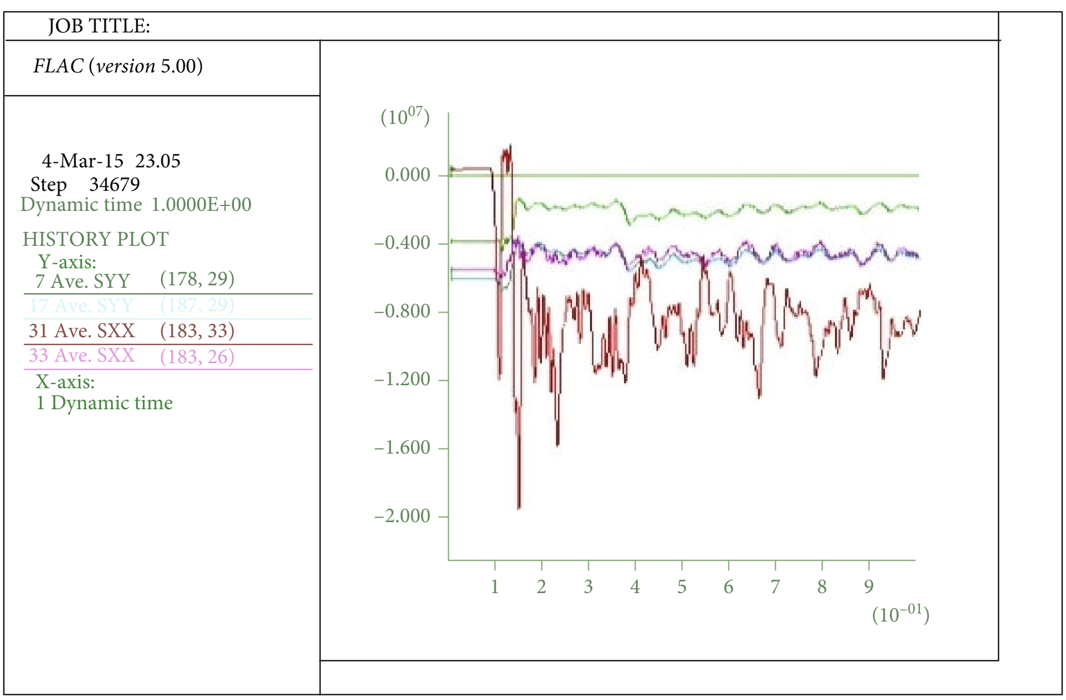

(b) Horizontal stress variation of roadway roof, floor, and two sides

Figure 5: Continued.

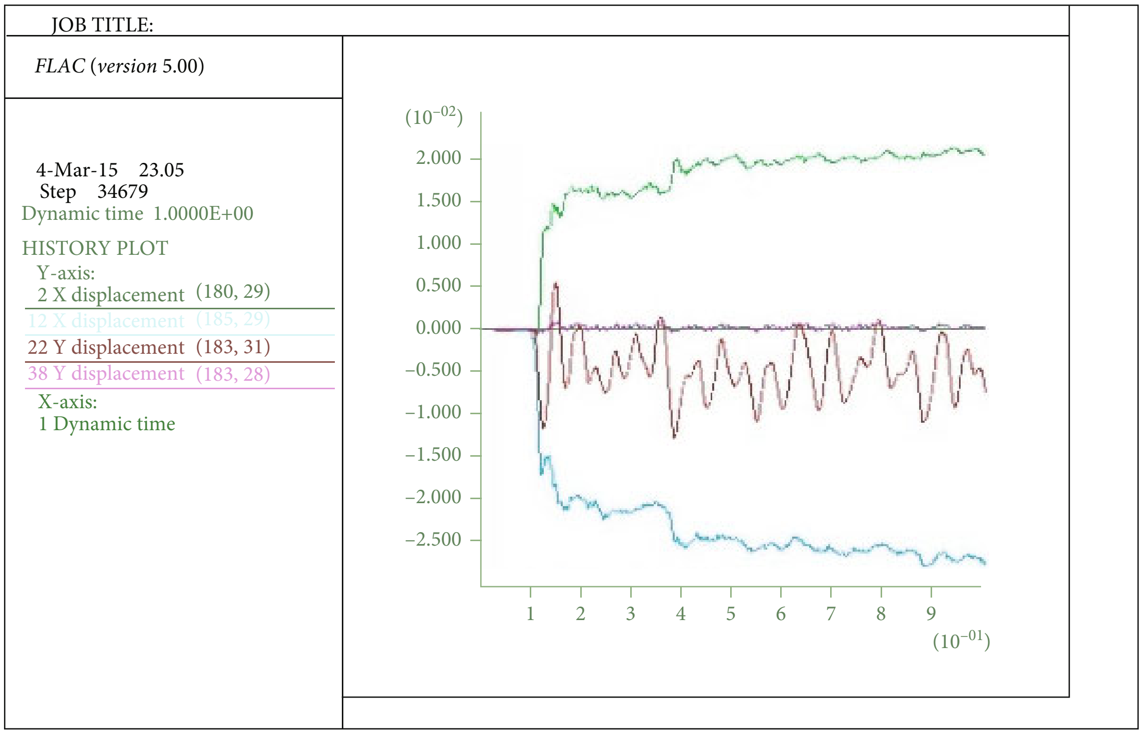

(c) Displacement of roof, floor, and two sides of roadway

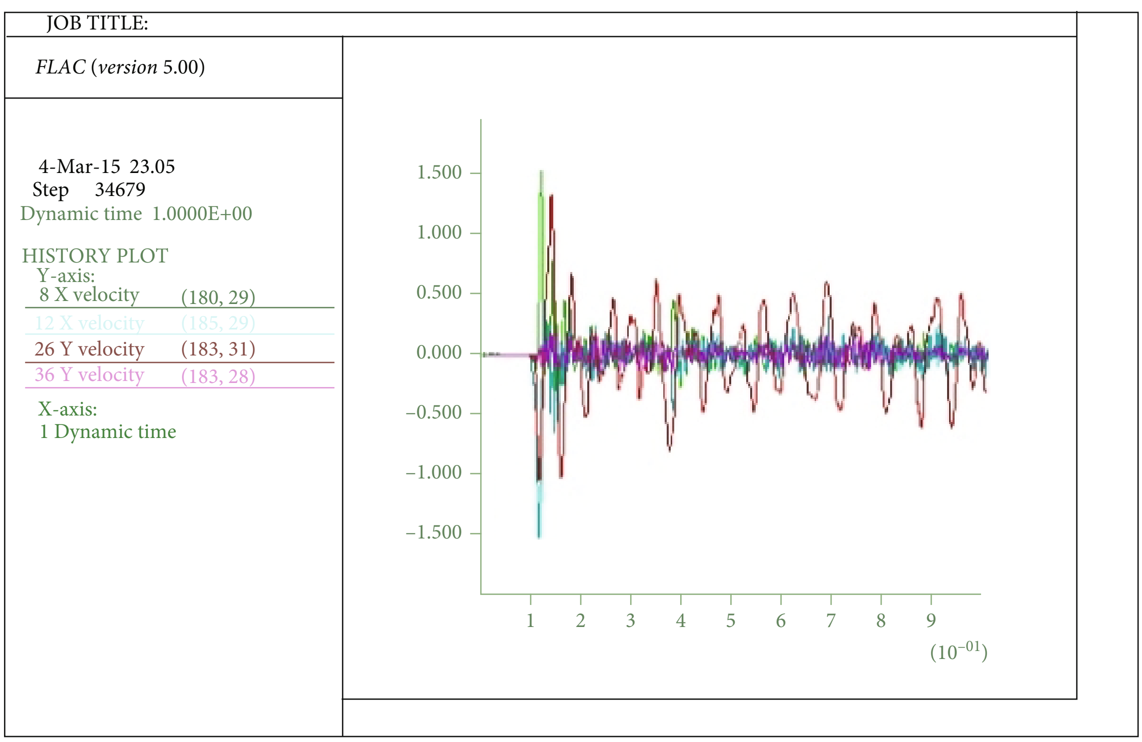

(d) Displacement speed of roadway roof and floor and two sides

FIGURE 5: Continued.

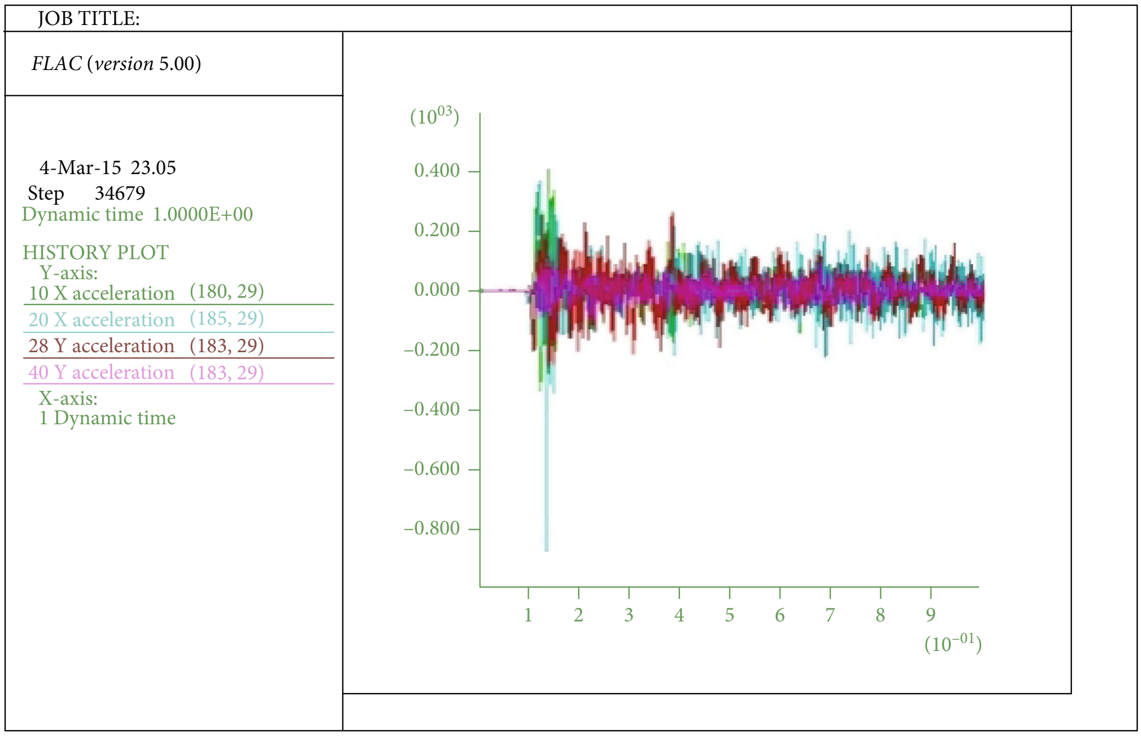

(e) Displacement acceleration of roadway roof and floor and two sides

Figure 5: Dynamic response of roadway surrounding rock under the condition of solid coal on both sides.

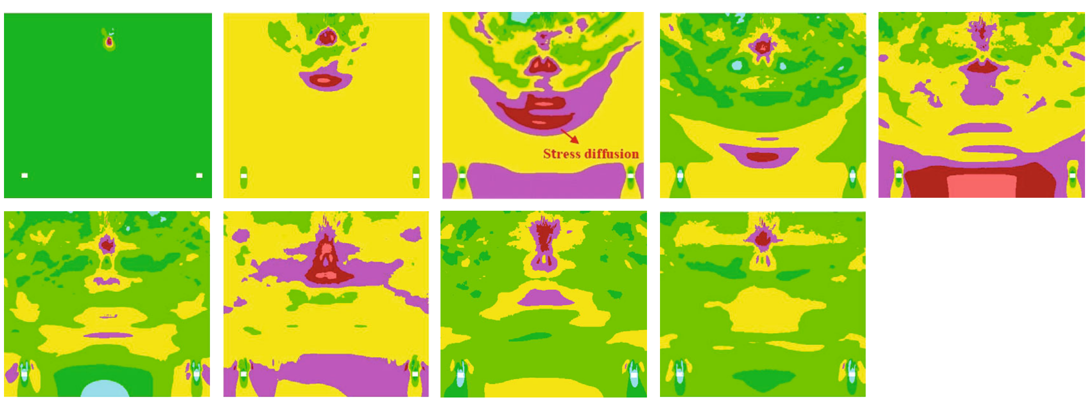

Figure 6: Temporal and spatial evolution law of vertical stress field of roadway surrounding rock under strong earthquake disturbance.

point is located at the bottom of magmatic rock and solid coal on both sides of the working face. It can be seen from Figure 5 that under the influence of strong earthquake, the horizontal stress, vertical stress, and displacement of surrounding rock of roadway have changed, but there are significant differences in change sensitivity.

In terms of stress, the influence of mine earthquake on stress is mainly reflected in the horizontal stress of roof and the vertical stress of inner wall. After 0.11 s disturbance, the vertical stress of the inner wall instantly reaches 19.36 MPa, and the inner wall compresses sharply and then decreases to 8.01 MPa. In the process of sharp increase and decrease of stress, the energy is released rapidly, which is easy to form dynamic phenomena such as rock burst and microseism. After 0.38 s of disturbance, the peak value of vertical stress in the inner wall decreases and fluctuates between 9.3 and 15.4 MPa. The stress change trend of the outer wall is the same as that of the inner wall. The vertical stress of the top and bottom plate is at a low level, and the stress level basically reaches a stable state after 0.15 s disturbance. For the horizontal stress, when the disturbance is 0.15 s, the horizontal stress of the top plate reaches the maximum value of 20.62 MPa. After 0.23 s, the horizontal stress decreases greatly and fluctuates between 4.98 and 13.6 MPa. After 0.36 s, the horizontal stress of the bottom plate and two sides is basically stable.

In terms of displacement, the deformation of both sides of the roadway is greater than that of the roof and floor, and the floor deformation is basically not affected by disturbance. For the upper part, the displacement of the upper part

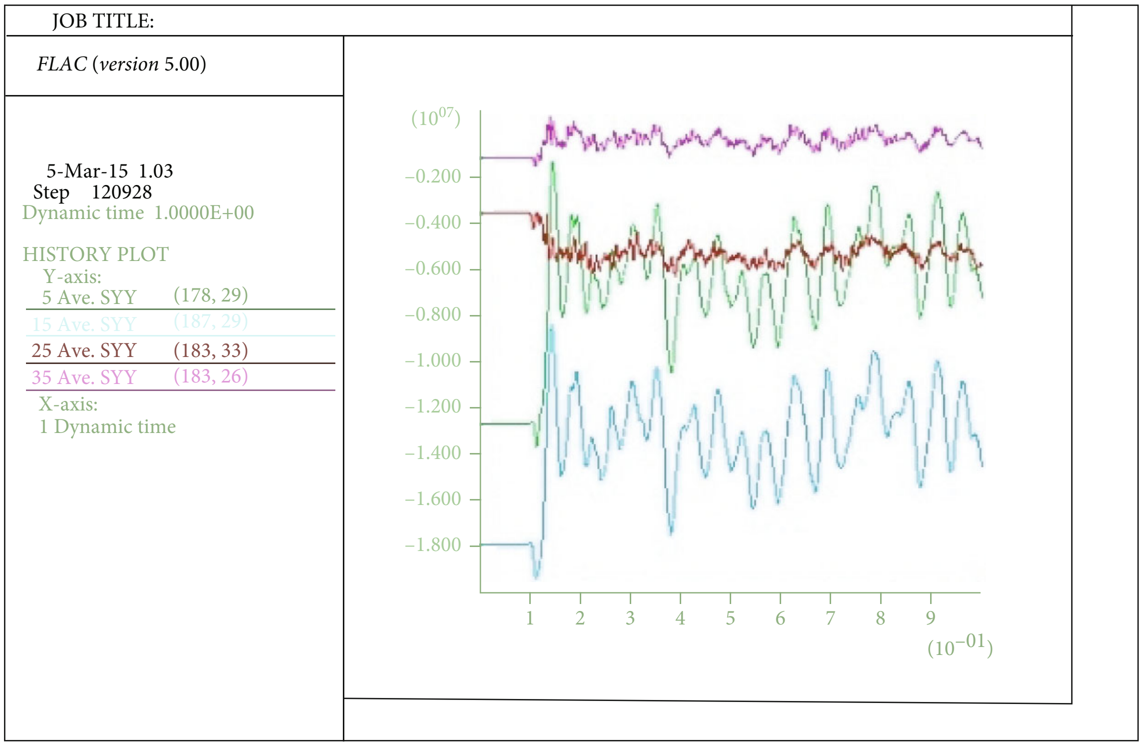

(a) Vertical stress variation of roadway roof, floor, and two sides

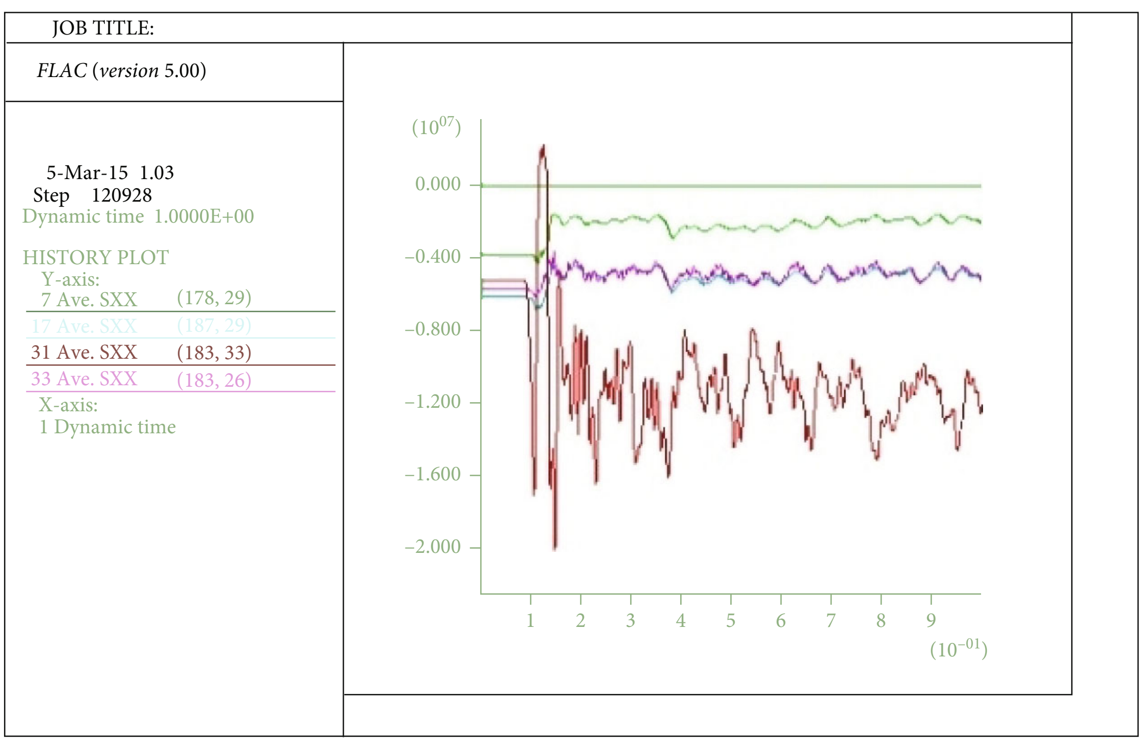

(b) Horizontal stress variation of roadway roof, floor, and two sides

Figure 7: Continued.

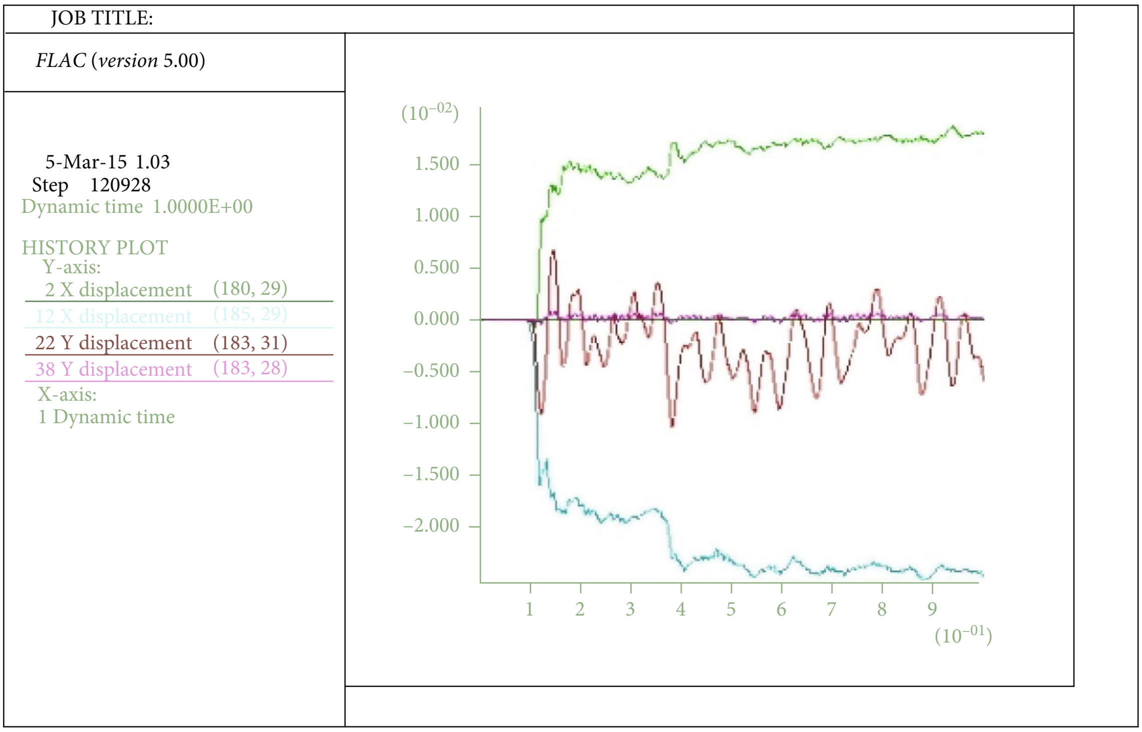

(c) Displacement of roof, floor, and two sides of roadway

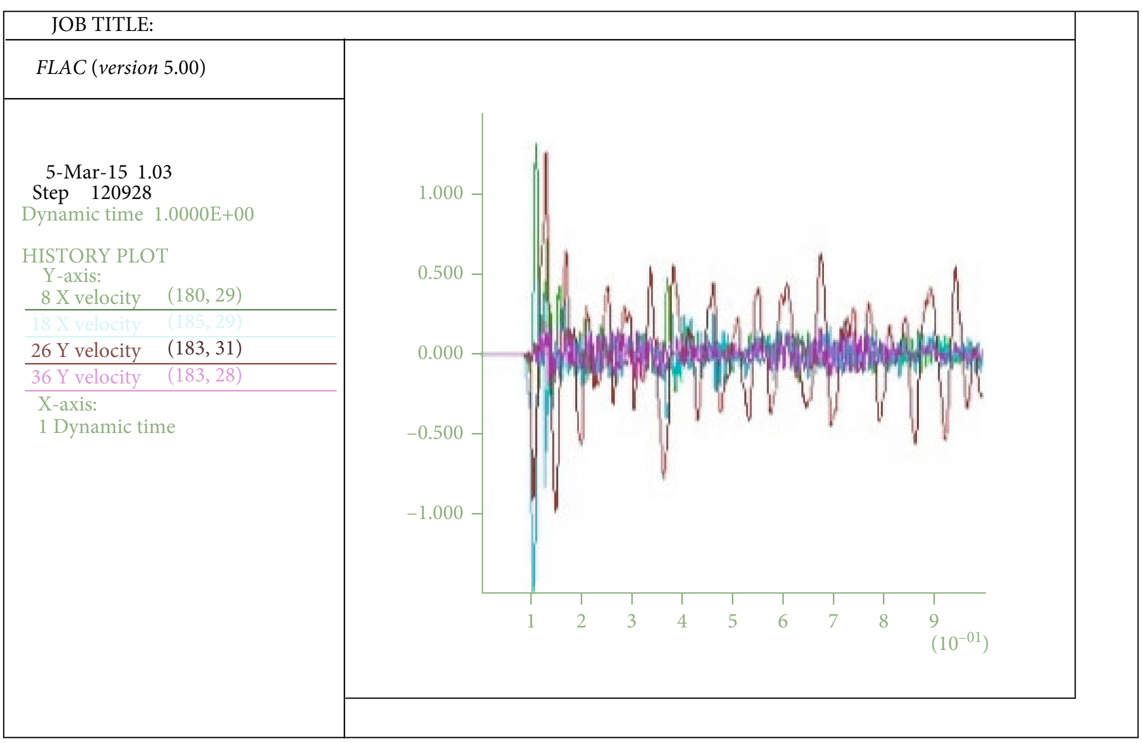

(d) Displacement speed of roadway roof and floor and two sides

FIGURE 7: Continued.

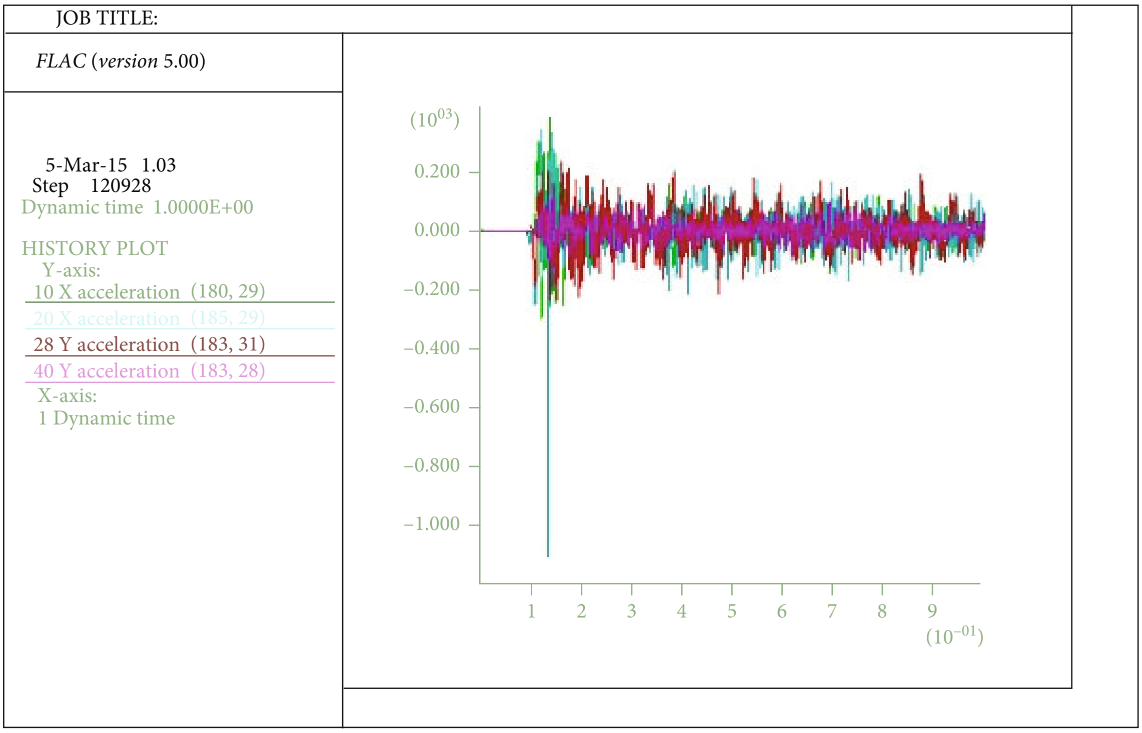

(e) Displacement acceleration of roadway roof and floor and two sides

Figure 7: Dynamic response of surrounding rock in solid coal roadway.

increases linearly during the disturbance of 0–0.11 s. After 0.38 s of disturbance, the displacement is basically stable. Finally, the maximum displacement of the outer side reaches 21.05 mm, and the displacement of the inner side reaches 27.28 mm. For the roof, the displacement fluctuates in a small range, which will cause roof vibration.

In terms of deformation speed, there is little difference between the maximum displacement speed of the two sides of the roadway and the roof, which are 1.53 m/s for the outer side, 1.54 m/s for the inner side, and 1.33 m/s for the roof, respectively, and the maximum displacement speed of the floor is only 0.19 m/s. In terms of deformation acceleration, the displacement acceleration of the two sides is very different, which are 404 mm/s^2 for the outer side and 887.07 mm/s^2 for the inner side. The deformation acceleration of the roof and floor is small, which are 261 m/s^2 for the roof and 94 m/s^2 for the floor.

Generally speaking, under the condition of solid coal on both sides, the damage degree of the two sides of the roadway after strong earthquake disturbance is greater than that of the roof and floor, and the damage degree of the inner side is greater than that of the outer side.

(2) Spatial evolution characteristics of impact failure of roadway caused by strong earthquake

In order to more vividly show the impact damage effect of strong earthquake on roadway surrounding rock, the movie function of FLAC2D software is used to record the evolution characteristics of roadway surrounding rock stress field in detail according to a certain time step, as shown in Figure 6.

It can be seen from Figure 6 that after the strong earthquake disturbance, the stress wave rapidly propagates downward and attenuates in a spherical manner. During the propagation process, the radiation range of the stress wave continues to expand. When $t = 1500$ time steps, it reaches the direct top of the coal seam, and then the inner wall stress of the roadway in the working face increases significantly. As the simulation continues, the roadway will be significantly deformed. By comparing the vertical stress distribution characteristics under different time steps, it can be seen that the stress propagation takes the middle of the working face as the axis of symmetry and presents a symmetrical distribution shape, and the stress level of the inner side of the roadway is higher than that of the outer side.

3.2. One Side Gob Face Working Face

3.2.1. Dynamic Response of Roadway Surrounding Rock. Figures 7 and 8 reflect the dynamic response characteristics of roadway surrounding rock under the condition that the seismic focus is located at the bottom of magmatic rock and the goaf on one side of the working face. It can be seen from Figure 7 that the mechanical response law of surrounding rock of solid coal roadway in working face under the condition of one side goaf is similar to that of solid coal roadway on both sides, with only slight differences in value and stability time. When the disturbance is 0.15 s, the horizontal stress of the roof reaches the maximum value of

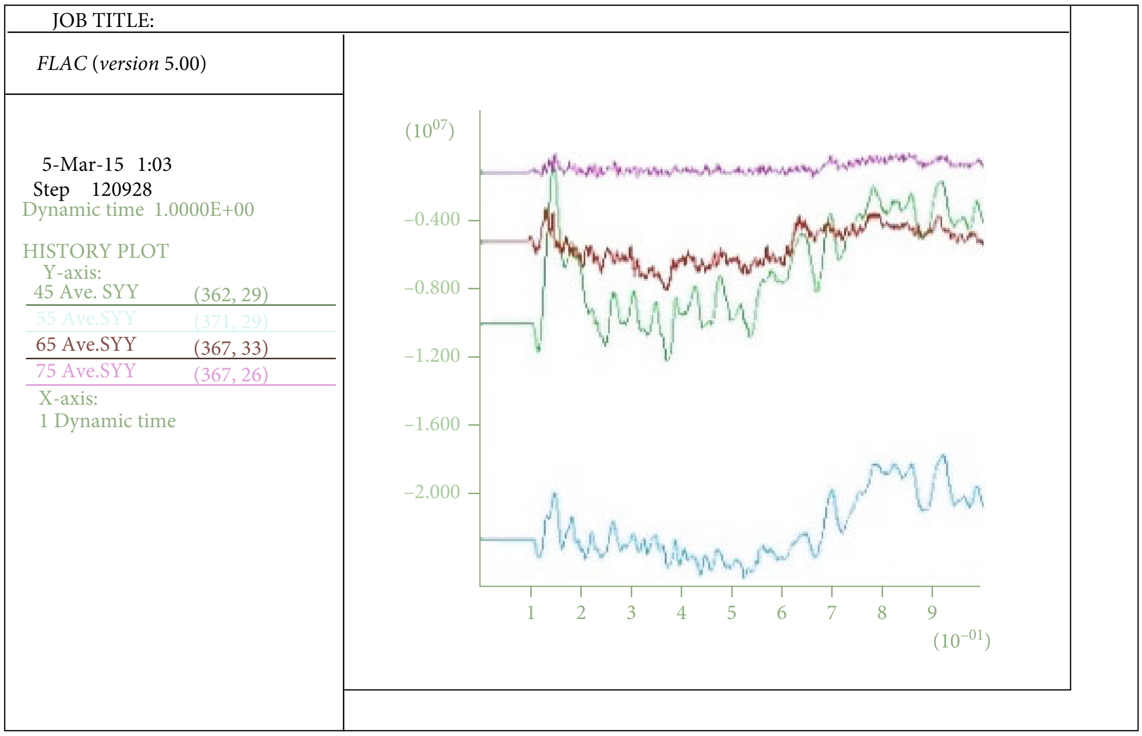

(a) Vertical stress variation of roadway roof, floor, and two sides

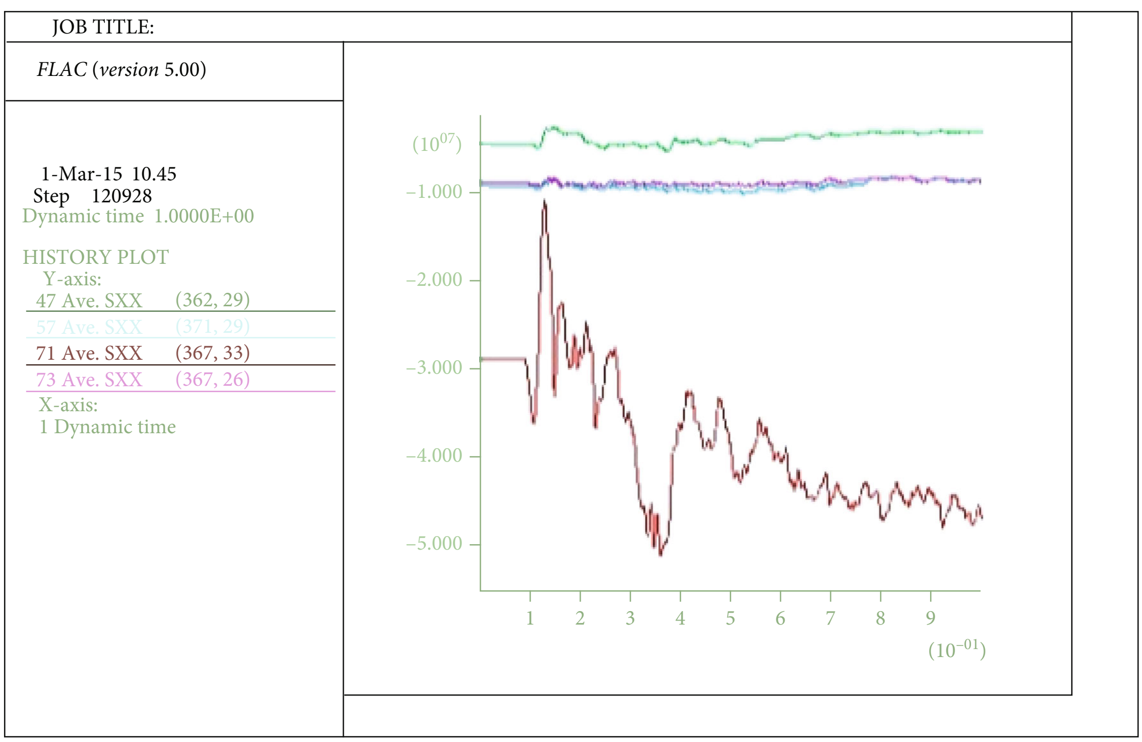

(b) Horizontal stress variation of roadway roof, floor, and two sides

FIGURE 8: Continued.

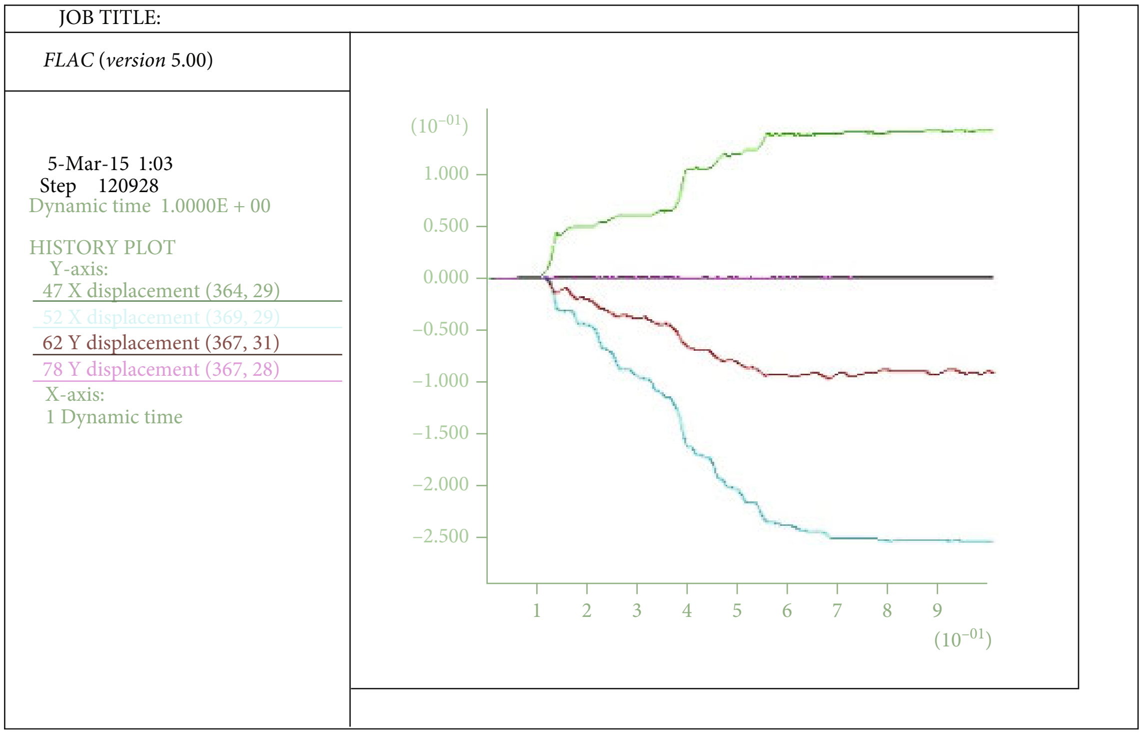

(c) Displacement of roof, floor, and two sides of roadway

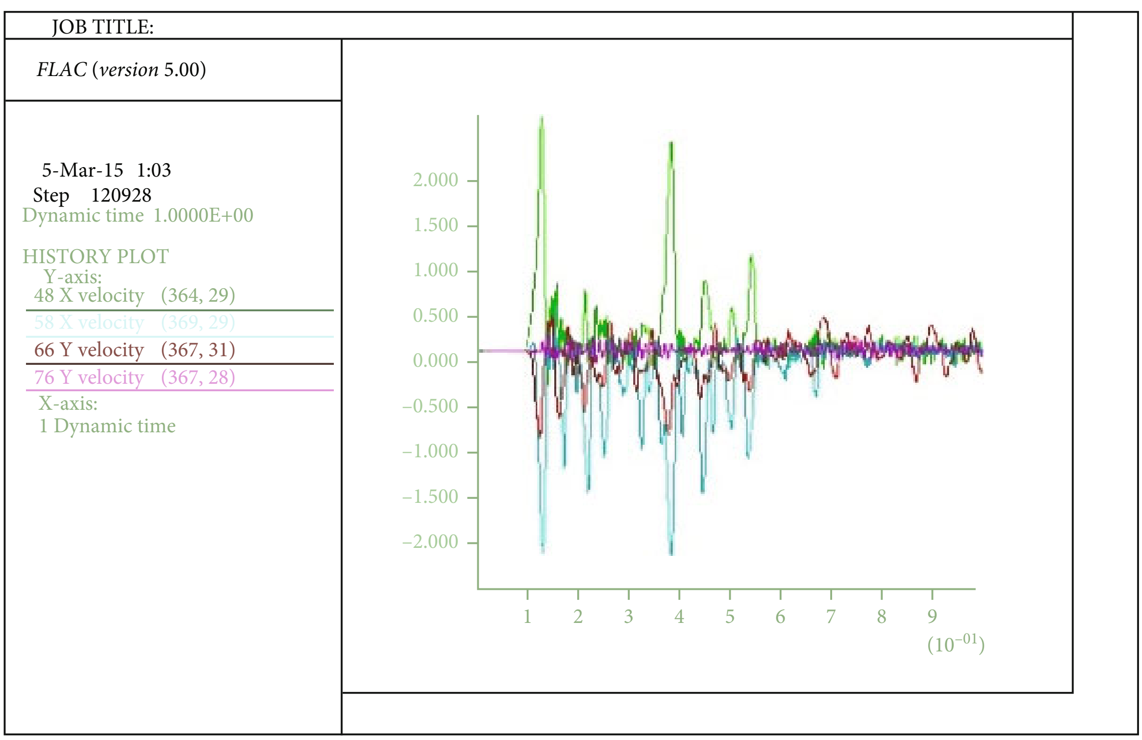

(d) Displacement speed of roadway roof and floor and two sides

Figure 8: Continued.

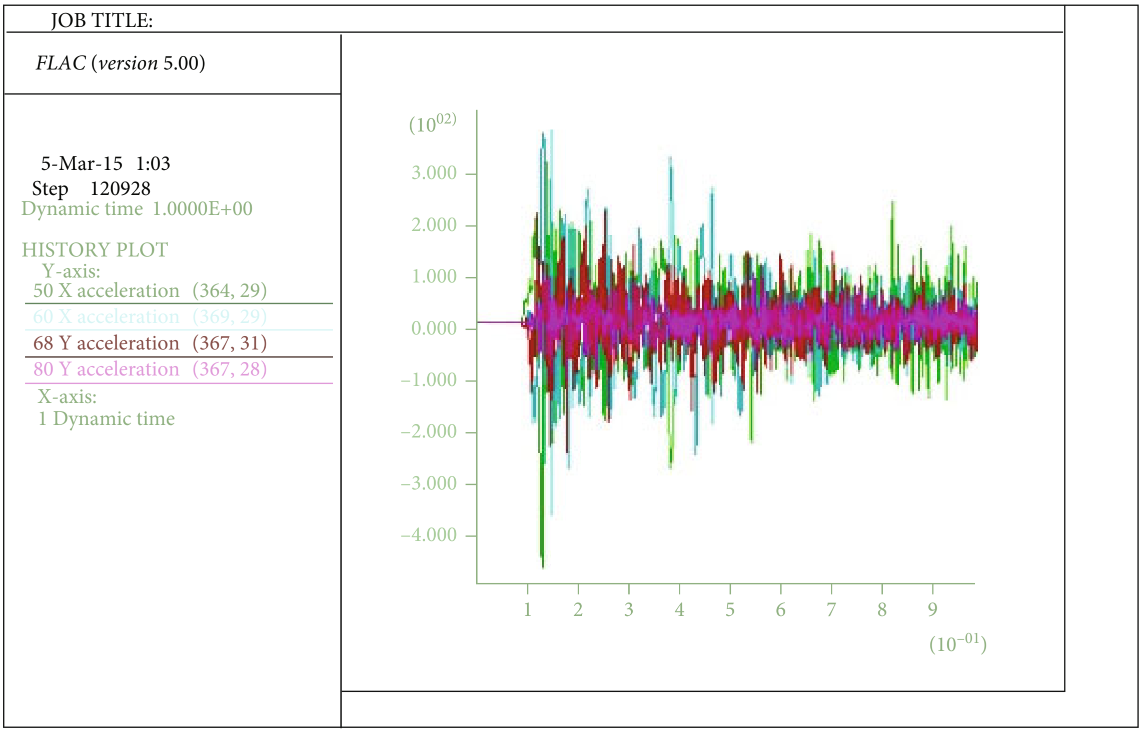

(e) Displacement acceleration of roadway roof and floor and two sides

Figure 8: Dynamic response of surrounding rock of the gob-side roadway.

21.52 MPa. After 0.5 s, the variation range of the stress decreases, and the horizontal stress fluctuates up and down around 9–16 MPa. The horizontal stress state of both sides and floor is less affected by mine earthquake, and the stress basically reaches a stable state after 0.4 s disturbance. The vertical stress of the top and bottom plate is at a low level, which is basically stable after 0.4 s disturbance. The evolution law of approach velocity and acceleration is generally consistent with the solid coal conditions on both sides. The approach of the two sides basically reaches a stable state after 0.6 s disturbance.

It can be seen from Figures 7 and 8 that under the dual influence of lateral abutment pressure and disturbance in goaf, the dynamic response degree of the gob-side roadway is significantly higher than that of solid coal roadway.

In terms of stress, the vertical stress of the outer side (23.2 MPa) is higher than that of the inner side (12.34 MPa), but the change of the vertical stress of the outer side is relatively gentle compared with that of the inner side. In the process of strong earthquake disturbance, the horizontal stress of the roof of the roadway along the goaf has been in a high stress state, and the maximum value has reached 55.28 MPa. The probability of shear failure of the roof has been significantly strengthened. Compared with solid coal roadway, the vertical stress and horizontal stress of the gob-side roadway have been fluctuating, which is difficult to achieve stability.

In terms of displacement, the convergence of surrounding rock of the gob-side roadway is significantly greater than that of solid coal roadway, and the convergence of two sides is more obvious. The stability of the outer upper is poor and the degree of stress concentration is high, resulting in the maximum approach of the outer upper reaches 250.53 mm. The displacement of the inner upper also increased significantly, reaching 139.58 mm. The roof subsidence reached 91.81 mm. Therefore, under the influence of strong earthquake, the risk of side caving, roof separation, or caving of roadway along goaf increases significantly. However, the time required for the displacement of the two sides to reach stability is the same as that of the solid coal roadway, both of which are 0.6 s.

In terms of deformation velocity and acceleration, the deformation velocity and acceleration of the inner side are greater than those of the outer side, and the maximum deformation velocity and deformation acceleration of the inner side reach 2.43 m/s and 469.23 m/s^2, respectively. However, the time when the velocity of the outer side is greater than 1 m/s is significantly higher than that of the inner side, so that the final deformation of the external side is greater than that of the inner side. Compared with the solid coal roadway, the roof displacement of the gob side roadway shows a continuous increasing trend, and the roof does not shock.

According to the dynamic response characteristics of the gob-side roadway and the solid coal roadway, the deformation amount and deformation velocity of the gob-side roadway are greater than those of the solid coal roadway, and the rock burst is more likely to occur in the gob side roadway under the disturbance of strong earthquake. Therefore, it is necessary to predict and judge the breaking and migration of magmatic rock in time during the mining process of the working face and strengthen the support strength of the roadway in the broken area.

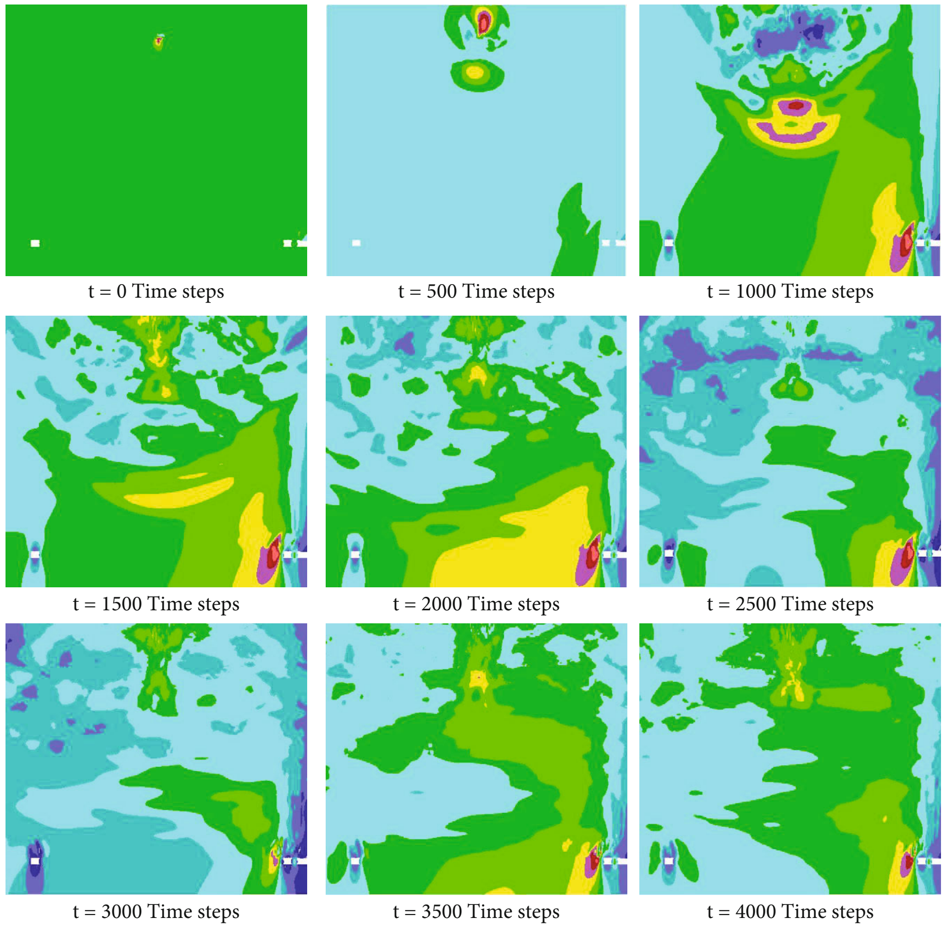

FIGURE 9: Temporal and spatial evolution law of vertical stress field of roadway surrounding rock under strong earthquake disturbance.

TABLE 2: Dynamic response of roadway surrounding rock under different boundary conditions.

Boundary condition			Dynamic response Peak value of vertical stress/MPa	Peak value of horizontal stress/MPa	Deformation of surrounding rock/mm	Deformation velocity/m/s	Deformation acceleration/m/s^2
Solid coal face on both sides	Solid coal roadway	Outer side	14.02	4.62	21.05	1.53	404
		Inner side	19.36	7.42	27.28	1.54	366
		Roof	4.89	20.62	10.58	1.33	261
		Floor	2.13	6.25	0.67	0.19	94
One side gob face working face	Solid coal roadway	Outer side	13.76	4.26	18.16	1.32	386.27
		Inner side	19.18	7.06	24.54	1.47	1107.63
		Roof	6.67	21.52	9.63	1.25	236.96
		Floor	2.11	6.33	0.61	0.21	191.03
	Gob-side roadway	Outer side	23.2	8.44	250.53	2.11	369.69
		Inner side	12.34	3.02	139.58	2.43	469.23
		Roof	8.87	55.28	91.81	0.91	248.38
		Floor	3.14	7.83	0.2	0.17	110.65

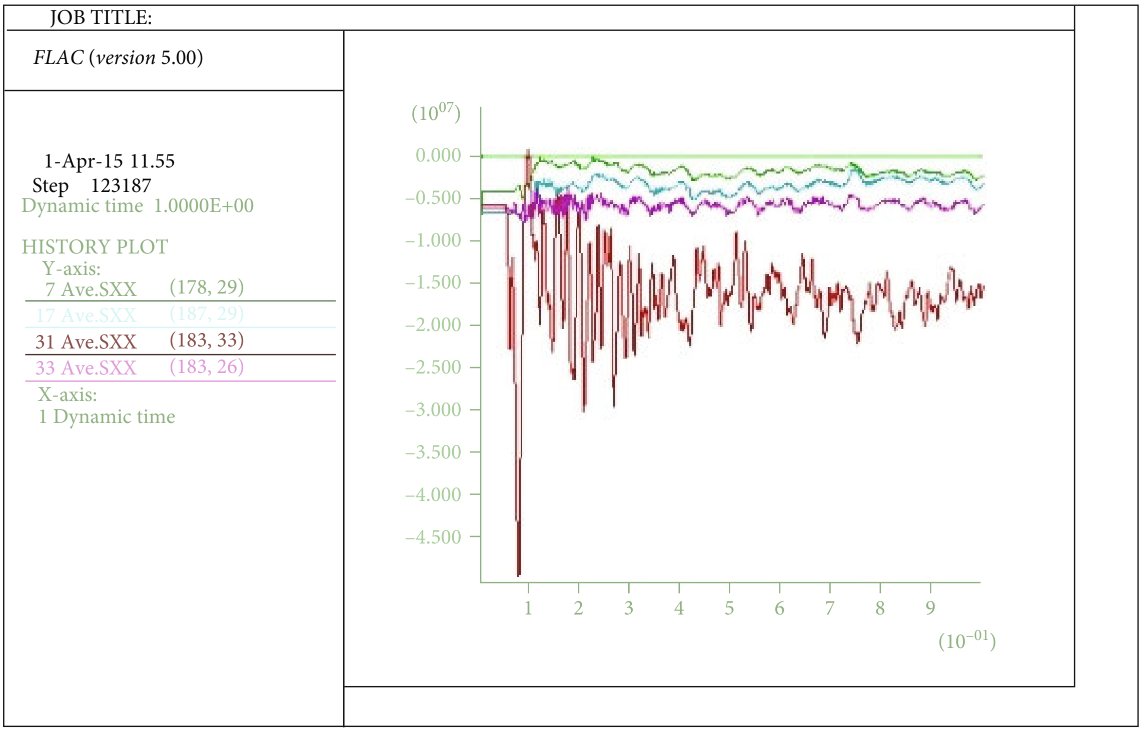

(a) Horizontal variation of roadway floor and roof stress

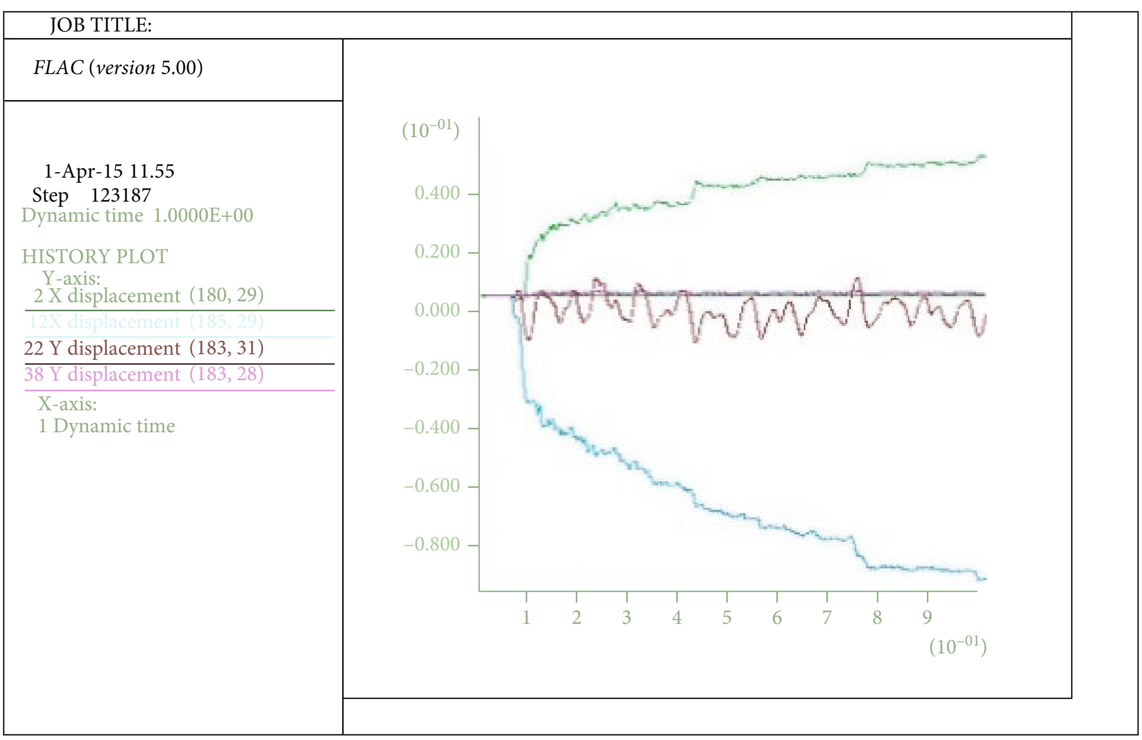

(b) Displacement of roof, floor, and two sides of roadway

Figure 10: Continued.

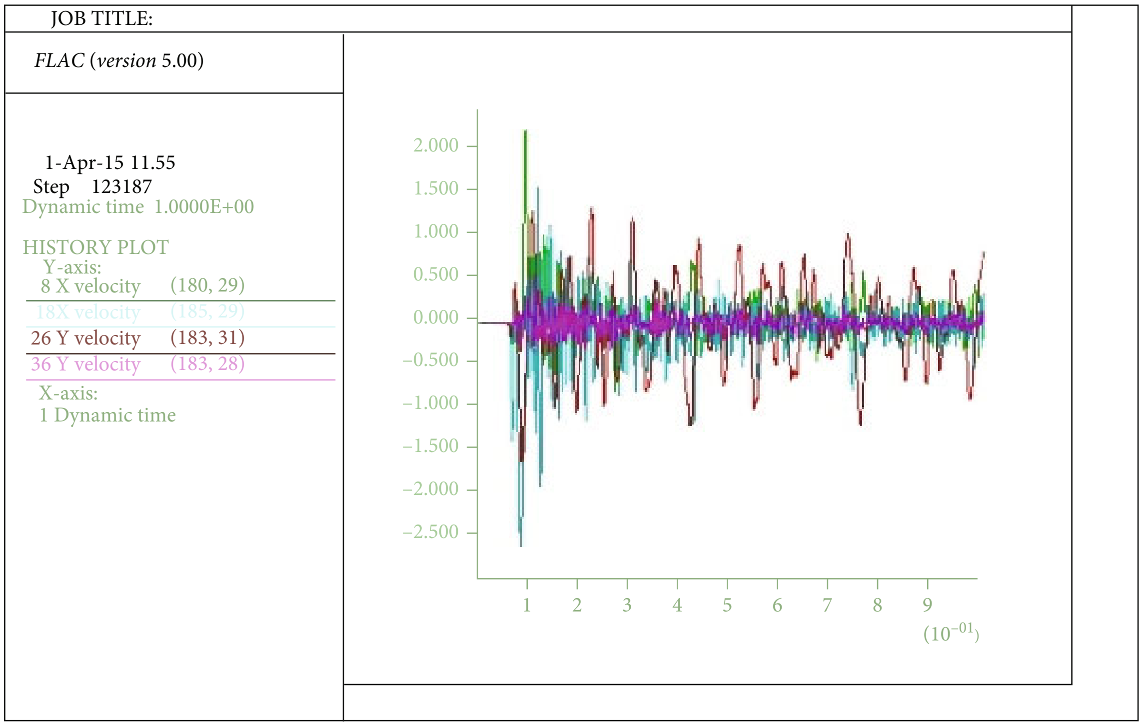

(c) Displacement speed of roadway roof and floor and two sides

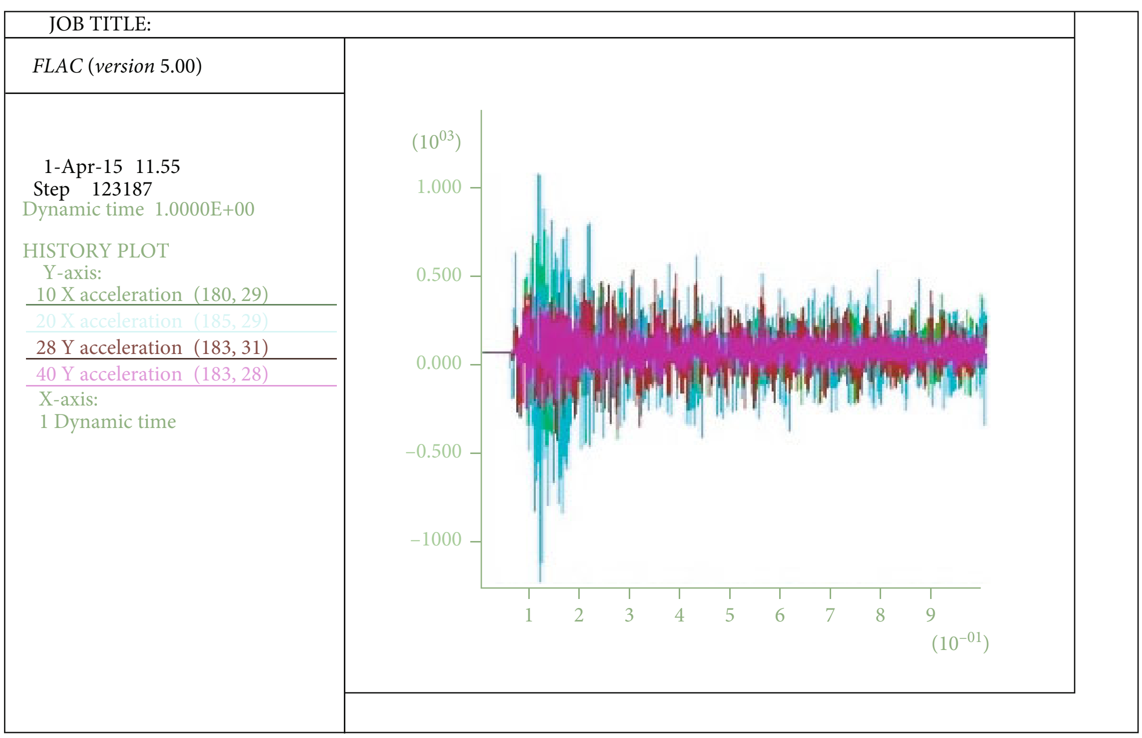

(d) Displacement acceleration of roadway roof and floor and two sides

Figure 10: Dynamic response of surrounding rock of solid coal roadway when the seismic focus height is 50 m.

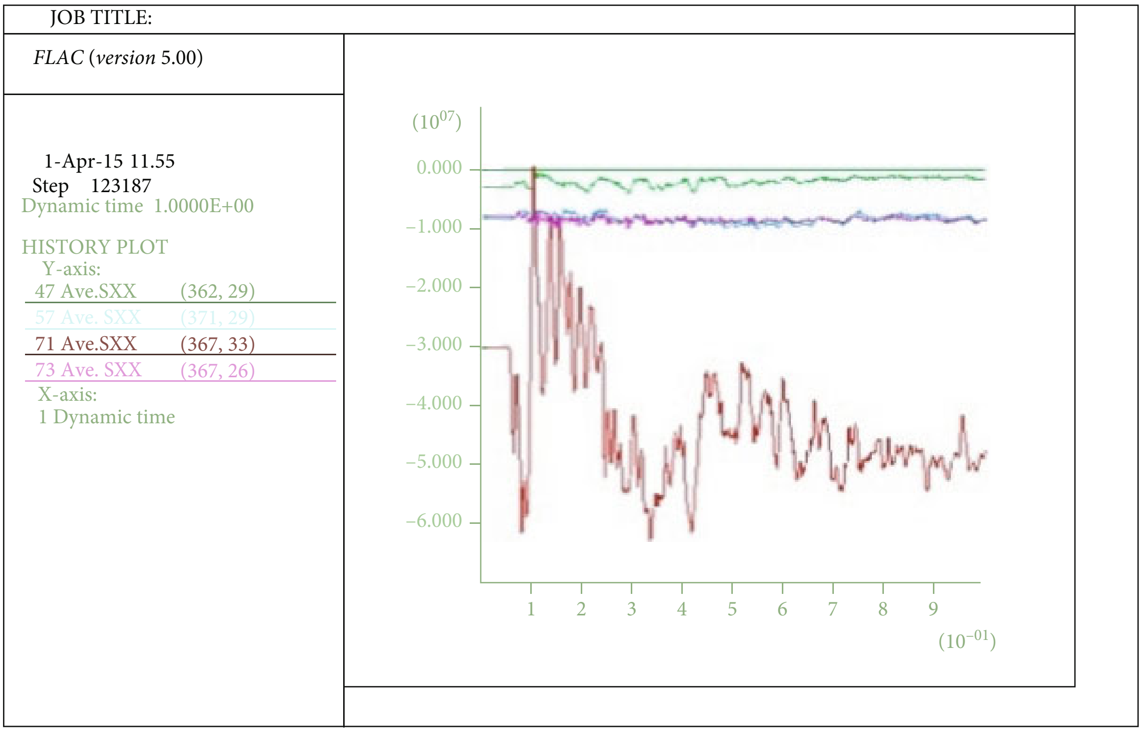

(a) Horizontal variation of roadway floor and roof stress

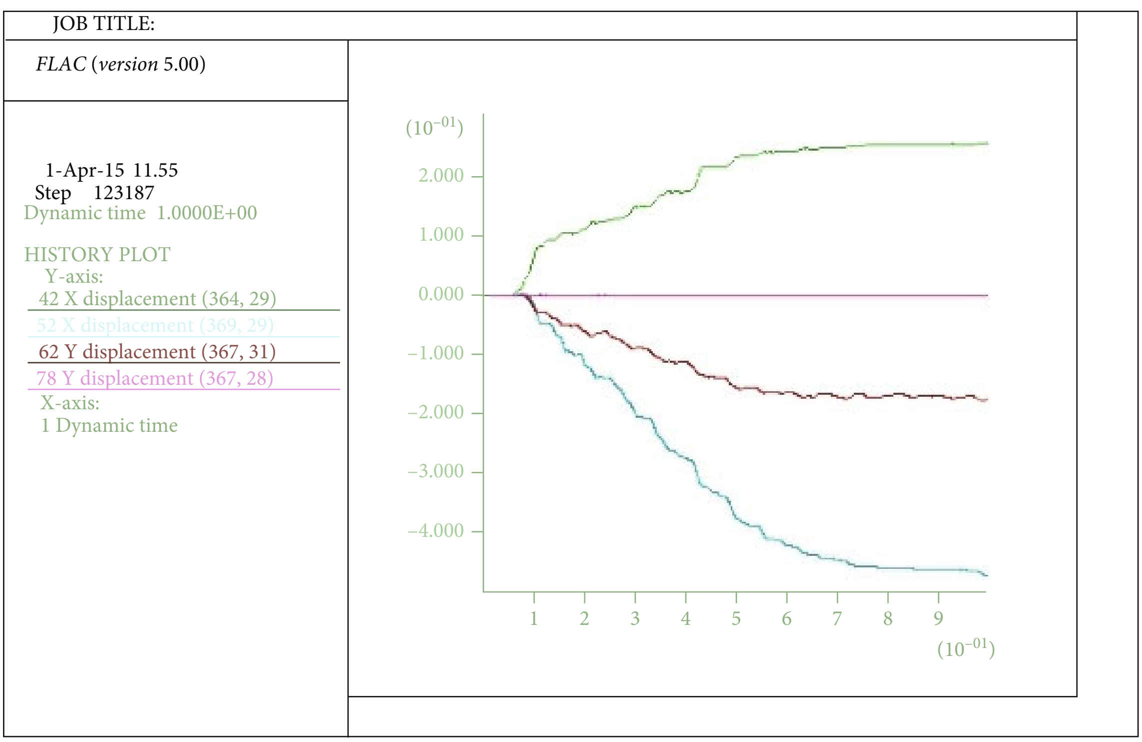

(b) Displacement of roof, floor, and two sides of roadway

Figure 11: Continued.

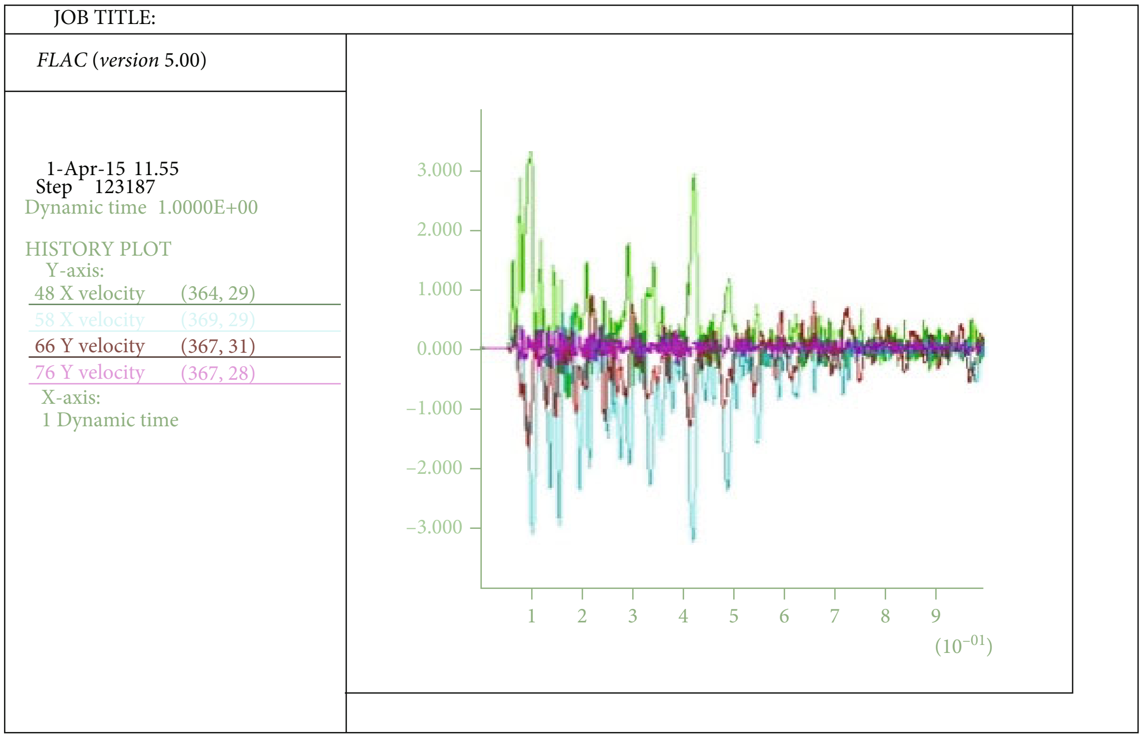

(c) Displacement speed of roadway roof and floor and two sides

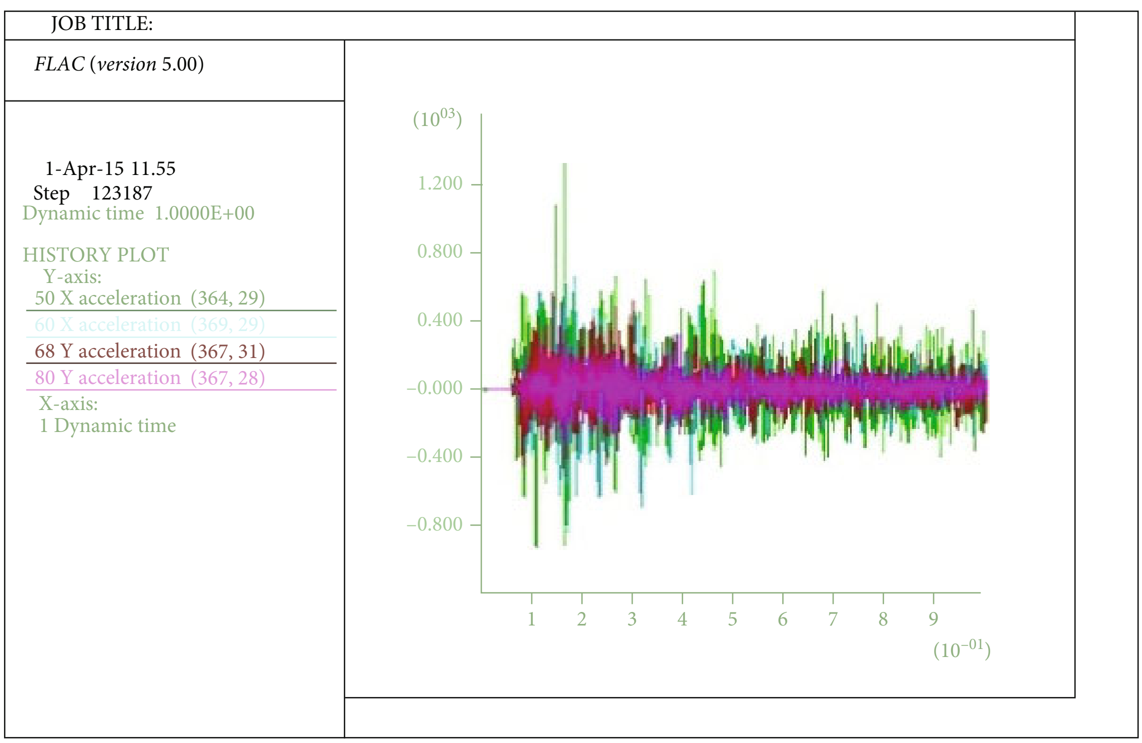

(d) Displacement acceleration of roadway roof and floor and two sides

Figure 11: Dynamic response of surrounding rock of gob roadway when the seismic focus height is 50 m.

Table 3: Dynamic response of surrounding rock of roadway with different seismic focus height under the condition of solid coal on both sides.

Seismic focus height		Dynamic response				
		Peak value of vertical stress/MPa	Peak value of horizontal stress/MPa	Deformation of surrounding rock/mm	Deformation velocity/m/s	Deformation acceleration/m/s^2
113 m	Outer side	14.02	4.62	21.05	1.53	404
	Inner side	19.36	7.42	27.28	1.54	887.07
	Roof	4.89	20.62	10.58	1.33	261
	Floor	2.13	6.25	0.25	0.19	94
90 m	Outer side	13.77	4.49	28.67	1.09	346.02
	Inner side	20.02	7.52	46.24	1.53	760.31
	Roof	8.03	35.95	20.25	0.96	382.94
	Floor	2.51	6.78	0.81	0.27	180.49
70 m	Outer side	13.37	4.32	29.48	0.966	646.18
	Inner side	19.16	7.34	54.91	1.95	783.97
	Roof	7.20	25.2	15.28	1.31	339.99
	Floor	2.48	6.64	0.96	1.01	213.98
50 m	Outer side	14.19	4.88	51.73	2.19	910
	Inner side	19.06	7.44	115.17	2.58	2344.1
	Roof	6.56	44.77	16.1	1.41	601.85
	Floor	3.46	7.82	1.82	0.57	474.55

4. Spatial Evolution Characteristics of Impact Failure of Roadway Caused by Strong Earthquake

Figure 9 reflects the temporal and spatial evolution characteristics of the stress field of roadway surrounding rock under strong earthquake disturbance. It can be seen from Figure 9 that after the source is applied, the stress also diffuses rapidly in a spherical manner, but the attenuation speed of the stress wave is greater than that of the solid coal on both sides under the goaf condition on one side, and the diffusion of the stress wave tends to the goaf side. Under the combined action of the lateral abutment pressure and disturbance in the goaf, and the stability of the surrounding rock on the goaf side is worse than that of the solid coal, the deformation of the roadway along the goaf side increases rapidly, while the solid coal side is relatively slow.

4.1. Comparative Analysis of Dynamic Response of Roadway Surrounding Rock under Different Boundary Conditions under Strong Earthquake Disturbance. The dynamic response characteristics of roadway surrounding rock under different boundary conditions under the same focal conditions are shown in Table 2. It can be seen from Table 2 that for the same source disturbance, the dynamic response of surrounding rock is obviously different under different roadway boundary conditions, and the failure effect increases with the increase of the number of adjacent goafs, especially the horizontal stress of roof and the horizontal displacement of two sides. For the horizontal stress of the roof, the peak value of the horizontal stress of the roof under the conditions of goaf on both sides and goaf on one side is 3.39 and 2.68 times of the horizontal stress of the roof under the conditions of solid coal on both sides, respectively. The shear instability of the roof support is easy to occur. Therefore, for the mine with hard or even extremely thick key layers on the working face, the isolated working face should be avoided. For the displacement of the side wall, the displacement of the roadway along the goaf is significantly greater than that of the solid coal roadway. Therefore, for the roadway along the goaf, the support of the side wall should be strengthened to prevent the instability of the side wall. Under strong earthquake disturbance, the damage effect of solid coal roadway is low, and the risk caused by strong earthquake is controllable.

5. Influence Law of Seismic Focus Height on Roadway Dynamic Response

Magmatic rocks with different heights from the coal seam lead to the change of the seismic focus height of strong earthquakes. In order to study the influence of the seismic focus height on the dynamic response of roadway, strong seismic disturbance was applied at 50 m, 70 m, and 90 m above the coal seam, respectively.

Taking one side as solid coal and the other side as goaf working face, the seismic focus height is 50 m as an example, and the dynamic response law of roadway surrounding rock under strong earthquake disturbance is studied. Figure 10 reflects the dynamic response characteristics of surrounding rock of solid coal roadway under the condition that one side of the working face is mined out when the focal height is 50 m. It can be seen from Figures 7 and 10 that under the same focal intensity and boundary conditions, when the focal height is 50 m, the seismic damage effect is stronger than that when the focal height is 116 m. Take

Table 4: Dynamic response of roadway surrounding rock with different focal height under one side goaf condition.

Seismic focus height			Dynamic response: Peak value of vertical stress/MPa	Peak value of horizontal stress/MPa	Deformation of surrounding rock/mm	Deformation velocity/m/s	Deformation acceleration/m/s^2
116 m	Solid coal roadway	Outer side	13.76	4.26	18.16	1.32	386.27
		Inner side	19.18	7.06	24.54	1.47	1107.63
		Roof	6.67	21.52	9.63	1.25	236.96
		Floor	2.11	6.33	0.61	0.21	191.03
	Gob-side roadway	Outer side	23.2	8.44	250.53	2.11	369.69
		Inner side	12.34	3.02	139.58	2.43	469.23
		Roof	8.87	55.28	91.81	0.91	248.38
		Floor	3.14	7.83	0.2	0.17	110.65
90 m	Solid coal roadway	Outer side	13.64	4.43	33.79	0.94	499.36
		Inner side	19.37	7.59	46.61	1.6	1137.5
		Roof	10.97	29.08	20.45	1.3	322.88
		Floor	2.52	6.8	1.12	0.29	234.14
	Gob-side roadway	Outer side	24.04	9.67	283.65	2.26	464.1
		Inner side	12.56	3.84	198.58	2.57	461.93
		Roof	8.75	61.35	130.89	1.09	376.37
		Floor	3.52	9.04	0.6	0.33	253.52
70 m	Solid coal roadway	Outer side	13.57	4.47	28.5	1.1	602.05
		Inner side	19.52	7.58	49.05	2.12	1245.01
		Roof	7.41	44.92	14.05	1.45	333.4
		Floor	2.25	6.89	0.96	0.25	207.75
	Gob-side roadway	Outer side	24.44	9.41	348.63	2.72	543.54
		Inner side	12.19	3.65	187.39	2.11	738.51
		Roof	9.6	62.03	148.54	1.32	437.73
		Floor	3.64	9.19	0.61	0.22	161.47
50 m	Solid coal roadway	Outer side	14.31	4.97	47.37	2.27	768.42
		Inner side	20.06	7.5	96.42	2.63	1466.62
		Roof	6.82	49.01	16.37	1.62	573.02
		Floor	3.29	7.71	1.55	0.56	401.76
	Gob-side roadway	Outer side	24.84	9.91	471.88	3.29	861.36
		Inner side	12.86	4.03	257.16	3.29	1323.45
		Roof	9.13	63.11	176.67	1.73	564.41
		Floor	4.05	10.28	0.92	0.48	407.03

the horizontal stress of roadway surrounding rock and the approach amount of roadway surrounding rock as an example.

The horizontal stress of roadway roof increases greatly, with the maximum value of 49.01 MPa, which is 2.27 times higher than that under the condition of seismic focus height of 116 m. As a result, the spalling failure of roof is almost inevitable, and the mechanical environment of surrounding rock worsens sharply. The maximum displacement of the outer slope and the inner slope reaches 47.37 mm and 96.42 mm, respectively. The displacement of the surrounding rock is significantly enhanced, which is easy to cause support instability and serious slope, and the vibration amplitude of the roof is also strengthened accordingly.

Figure 11 reflects the dynamic response characteristics of surrounding rock of gob-side roadway under the condition of goaf on one side of the working face when the seismic focus height is 50 m. It can be seen from Figure 11 that after the focal height is reduced, the influence of disturbance on the roadway along the goaf is also significantly strengthened. The maximum horizontal stress of roof reaches 63.11 MPa, and the horizontal stress during disturbance is basically above 33 MPa. The movement of roof, floor, and two sides is also at a high level. The maximum movement of roof is 176 mm, the movement of inner side is 256.41 mm, and the movement of outer side is 471.88 mm, which is 1.9 times of the movement of outer side along the roadway when the seismic focus height is 116 m.

To sum up, when the focal height is 50 m, the vibration effect of gob-side roadway is more intense, and the gob-side roadway becomes the key prevention area of rock burst during the breaking and migration of hard and thick key layer. The support strength of roof and two sides should be increased to reduce the risk of impact.

In order to better reflect the influence of seismic focus height on roadway dynamic response, the variation characteristics of roadway surrounding rock dynamic response at different focal height are counted, as shown in Tables 3 and 4. It can be seen from Tables 3 and 4 that under the condition of the same seismic focus intensity, when the focal point is 116 m above the coal seam, the vibration effect of roadway surrounding rock is relatively small. As the focal height decreases, the damage degree of roadway surrounding rock increases and the stability of surrounding rock becomes worse.

Taking one side gob condition as an example, the influence of seismic focus height on the stability of roadway surrounding rock is analyzed. It can be seen from Table 4 that with the continuous decrease of seismic focus height, the disturbance effect of strong earthquake on roadway continues to strengthen, but there is a significant difference in strengthening rate. When the focal height decreases from 116 m to 90 m, the horizontal stress of the roof, the displacement of the side and roof, the approaching velocity, and the approaching acceleration begin to increase, but the increment is small. When the seismic focus height decreases from 90 m to 50 m, the increment increases rapidly in a nearly linear manner. Taking the horizontal approach of the outer wall of the roadway along the goaf as an example, when the seismic focus height is reduced from 116 m to 90 m, the approach increases by only 33.12 mm, while when the seismic focus height is reduced from 90 m to 50 m, the approach increases by 188.23 mm. In addition, with different roadway boundary conditions, the influence degree of focal height on roadway is also different. The influence degree of horizontal stress of solid coal roadway roof is much greater than that of goaf roadway. Regardless of the boundary conditions, the vertical stress of the roadway slope is less affected by the focal height.

To sum up, when a strong earthquake occurs in the lower position, the dynamic response degree of the roadway is much greater than that in the higher position, and the influence degree of the goaf side is greater than that of the solid coal side. In addition, when the seismic focus height is the same, the influence degree of strong earthquake on the stability of roadway surrounding rock under different boundary conditions is also significantly different. Basically, the influence degree can be arranged as follows: gob-side roadway (mined out on one side) > solid coal roadway (mined out on both sides) > solid coal roadway (mined out on one side). The strong earthquake tends to the goaf side in the transmission process, resulting in the energy of solid coal roadway under the goaf condition on one side is lower than that under the solid condition on both sides, and resulting in the dynamic response of solid coal roadway under the goaf condition on one side is weaker than that under the solid coal condition on both sides. Combined with the roadway stress level before dynamic load disturbance, under the condition of high static load, the stability of roadway surrounding rock is more obviously affected by dynamic load. The greater the static load level is, the worse the stability of surrounding rock is, that is, the higher the static load level is, the more obvious the coupling effect with dynamic load is.

6. Conclusion

Using the dynamic calculation function of FLAC2D software, this paper analyzes the dynamic response of roadway surrounding rock under strong earthquake disturbance when it is covered with hard and thick key layer, studies the influence of roadway boundary conditions on the dynamic response of surrounding rock under strong earthquake disturbance and the effect of the seismic focus height on the impact damage degree of roadway, and simulates and reproduces the dynamic evolution process of roadway degeneration damage. The main conclusions are as follows:

(1) Under the influence of strong earthquake, the stress level of gob-side roadway is higher than that of solid coal roadway, especially the horizontal stress of roof, which is easy to lead to the instability of roof support. The stress level of the outer side of the gob-side roadway is higher than that of the inner side. The gob coal pillar is in a high stress state, and the coal pillar is easy to lose stability

(2) Under the influence of strong earthquake, the roof of solid coal roadway is easy to vibrate in a small range, and the displacement increases and decreases with the disturbance. The displacement of the floor and two sides of the solid coal roadway and the top floor and two sides of the roadway along the goaf continues to increase in the initial stage of the disturbance, and the displacement will remain stable with the continuation of the disturbance. The displacement of both sides and roof and floor of gob-side roadway can reach stability in the later stage of disturbance, and with the increase of the number of adjacent goaf, the longer it takes for the displacement of surrounding rock to reach stability

(3) There is a close correlation between the seismic focus height and the dynamic response of roadway surrounding rock. The magnitude of stress field, displacement field, velocity field, and acceleration field of roadway surrounding rock is negatively correlated with the seismic focus height. When the seismic focus height is lower than 90 m, the variation of surrounding rock response increases sharply with the decrease of the seismic focus height. When a strong earthquake occurs in the low rock stratum, the impact damage of roadway surrounding rock is almost inevitable

(4) The influence degree of strong earthquake on the stability of roadway surrounding rock is arranged as follows: gob-side roadway (mined out on one side) > solid coal roadway (mined out on both sides) > solid coal roadway (mined out on one side). According to the dynamic response degree of surrounding rock under different boundary conditions, the greater the static load level

before strong earthquake disturbance, the more obvious the coupling effect with dynamic load

(5) The spatial evolution of roadway impact failure caused by strong earthquake shows that the working face boundary conditions have an important influence on the energy propagation of mine earthquake. When there is solid coal on both sides of the working face, the energy basically propagates to the two lanes of the working face in a symmetrical way. When one side of the working face is mined out, the energy transfer is biased to the side of the goaf. The evolution process also shows that with the increase of the number of adjacent goafs, the faster the attenuation rate of mine earthquake propagation energy

Data Availability

The data used to support the findings of this study are included within the article.

Conflicts of Interest

The authors declare that there are no conflicts of interest related to the publication of this paper.

Acknowledgments

This research was funded by the Natural Foundation of Shandong Province (Grant no. ZR2020QE121), the Postdoctoral Innovation Project of Shandong Province (Grant no. 202003090), the Postdoctoral Science Foundation of China (Grant no. 2020M682267), Engineering Laboratory of Deep Mine Rockburst Disaster Assessment Open Project (LMYK002), and the Jining key research and development plan (Grant no. 2020JNZC002).

References

[1] D. Chlebowski, A. Zorychta, Z. Burtan, and M. Cała, "Location of opening-out cross-cuts in relation to rockburst hazard conditions along the face in the light of model testing," *Archives of Mining Sciences*, vol. 62, no. 1, pp. 121–130, 2017.

[2] L. S. Jiang, P. P. Zhang, L. J. Chen et al., "Numerical approach for goaf-side entry layout and yield pillar design in fractured ground conditions," *Rock Mechanics and Rock Engineering*, vol. 50, no. 11, pp. 3049–3071, 2017.

[3] Y. Y. Wen, Z. L. Mu, E. B. Yi, H. Wang, and Z. J. Liu, "The response features of roadway surrounding rock in different hardness coal seams under dynamic disturbance," *Journal of Mining and Safety Engineering*, vol. 30, no. 4, pp. 555–559, 2013.

[4] A. Sainoki and H. S. Mitri, "Simulating intense shock pulses due to asperities during fault-slip," *Journal of Applied Geophysics*, vol. 103, pp. 71–81, 2014.

[5] G. Mutke, J. Dubiński, and A. Lurka, "New criteria to assess seismic and rock burst hazard in coal mines / nowe kryteria dla oceny zagrożenia sejsmicznego I tąpaniami W kopalniach węgla kamiennego," *Archives of Mining Sciences*, vol. 60, no. 3, pp. 743–760, 2015.

[6] A. Mortazavi and F. T. Alavi, "A numerical study of the behavior of fully grouted rockbolts under dynamic loading," *Soil Dynamics and Earthquake Engineering*, vol. 54, pp. 66–72, 2013.

[7] C. P. Lu, Y. Liu, H. Y. Wang, and P. F. Liu, "Microseismic signals of double-layer hard and thick igneous strata separation and fracturing," *International Journal of Coal Geology*, vol. 160-161, pp. 28–41, 2016.

[8] L. Wang, Y. P. Cheng, C. Xu, F. H. An, K. Jin, and X. L. Zhang, "The controlling effect of thick-hard igneous rock on pressure relief gas drainage and dynamic disasters in outburst coal seams," *Natural Hazards*, vol. 66, no. 2, pp. 1221–1241, 2013.

[9] W. J. Guo, Y. Y. Li, D. W. Yin, S. C. Zhang, and X. Z. Sun, "Mechanisms of rock burst in hard and thick upper strata and rock-burst controlling technology," *Arabian Journal of Geosciences*, vol. 9, no. 10, p. 561, 2016.

[10] Q. S. Wu, L. S. Jiang, Q. L. Wu, Y. C. Xue, and G. Bing, "A study on the law of overlying strata migration and separation space evolution under hard and thick strata in underground coal mining by similar simulation," *DYNA-Ingeniería e Industria*, vol. 93, no. 1, pp. 175–181, 2018.

[11] J. L. S. Jiang, Q. S. Wu, Q. L. Wu, P. Wang, Y. C. Xue, and G. Bing, "Fracture failure analysis of hard and thick key layer and its dynamic response characteristics," *Engineering Failure Analysis*, vol. 98, pp. 118–130, 2019.

[12] A. Y. Cao, L. L. Zhu, F. C. Li, L. M. Dou, Y. L. Zhao, and Z. L. Zhang, "Characteristics of T-type overburden structure and tremor activity in isolated face mining under thick-hard strata," *Journal China Coal Sciences*, vol. 39, no. 2, pp. 328–335, 2014.

[13] W. Wang, Y. P. Cheng, H. F. Wang, W. Li, and L. Wang, "Coupled disaster-causing mechanisms of strata pressure behavior and abnormal gas emissions in underground coal extraction," *Environment and Earth Science*, vol. 74, no. 9, pp. 1–9, 2015.

[14] W. Wang, Y. P. Cheng, H. F. Wang et al., "Fracture failure analysis of hard-thick sandstone roof and its controlling effect on gas emission in underground ultra-thick coal extraction," *Engineering Failure Analysis*, vol. 54, pp. 150–162, 2015.

[15] J. Wang, J. G. Ning, and J. Q. Jiang, "Research on the energy criterion for rockbursts induced by broken hard and thick rock strata and its application," *Geotechnical & Geological Engineering*, vol. 35, no. 2, pp. 1–16, 2016.

[16] F. Ju, M. Xiao, Z. He, P. Ning, and P. Huang, "Study on fracture and stress evolution characteristics of ultra-thick hard sandstone roof in the fully mechanized mining face with large mining height: a case study of Xiaojihan coal mine in western China," *Engineering*, vol. 10, pp. 1–12, 2018.

[17] J. L. Xu and M. G. Qian, "Method to distinguish key strata in overburden," *Journal of China University of Mining and Technology*, vol. 29, pp. 463–467, 2000.

[18] S. Zhou, K. Wu, D. Zhou, L. Li, and Y. Xu, "Experimental study on displacement field of strata overlying goaf with sloping coal seam," *Geotechnical and Geological Engineering*, vol. 34, no. 6, pp. 1–10, 2016.

[19] J. L. Xu, M. G. Qian, and W. B. Zhu, "Study on influences of primary key stratum on surface dynamic subsidence," *Chinese Journal of Rock Mechanics and Engineering*, vol. 24, no. 5, pp. 787–791, 2005.

[20] Q. S. Wu, Q. L. Wu, Y. C. Xue, and G. Bing, "Analysis of overlying strata movement and disaster-causing effects of coal

mining face under the action of hard thick magmatic rock," *Processes*, vol. 6, no. 9, p. 150, 2018.

[21] H. He, L. M. Dou, and S. Y. He, "Rock burst rules induced by cracking of overlying key stratum," *Chinese Journal of Geotechnical Engineering*, vol. 32, no. 8, pp. 1221–1241, 2010.

[22] M. J. Hu, L. G. Wang, S. S. Zhu, X. Sun, and G. Zhang, "Reasons and prevention measures for rock burst caused by extremely thick igneous rock," *Mining Research and Development*, vol. 33, pp. 54–57, 2013.

[23] J. Q. Jiang, Q. S. Wu, Q. L. Wu, W. Pu, and B. Gong, "Study on distribution characteristics of mining stress and elastic energy under hard and thick igneous rocks," *Geotechnical and Geological Engineering*, vol. 2, pp. 3451–3466, 2018.

[24] Q. S. Wu, J. Q. Jiang, Q. L. Wu, Y. C. Xue, and B. Gong, "Study on the fracture of hard and thick sandstone and the distribution characteristics of microseismic activity," *Geotechnical and Geological Engineering*, vol. 1, pp. 1–17, 2018.

[25] J. G. Ning, J. Wang, L. S. Jiang, X. S. Liu, and J. Q. Jiang, "Fracture analysis of double-layer hard and thick roof and the controlling effect on strata behavior: a case study," *Engineering Failure Analysis*, vol. 81, pp. 117–134, 2017.

[26] P. J. Yang, Y. He, and W. B. Guo, "Disaster-causing mechanism and control measures of extremely thick and hard magmatic rock above working face," *Journal of China Coal Society*, vol. 38, no. 12, pp. 2106–2112, 2013.

Hindawi
Geofluids
Volume 2023, Article ID 2243885, 10 pages
https://doi.org/10.1155/2023/2243885

Research Article

Roof Water Damage Prediction and Evaluation of Sand-Mud Sedimentary Tectonic Strata

Pengfei Jiang[1], **Fumin Zhuge**[1], **Suolin Jing**[1], **Zongkai Li**[2], **Peng Xiao**[1] **and Yuguang Lv**[3]

[1]*College of Energy and Mining Engineering, Shandong Province (Shandong University of Science and Technology), Qingdao 266590, China*
[2]*Shandong Dongshan Wanglou Coal Mine Co., Ltd., Jining 272000, China*
[3]*Inner Mongolia Shanghaimiao Mining Co., Ltd., Ordos 016299, China*

Correspondence should be addressed to Fumin Zhuge; 303035697@qq.com and Suolin Jing; jslsdkj@163.com

Received 31 August 2021; Revised 7 October 2021; Accepted 16 October 2021; Published 13 April 2023

Academic Editor: Andri Stefansson

The prediction and control of roof water disaster has been one of the key problems in the mining process of coal resources. With the increase of mining depth in the western mining area, the roof caving and communicating to the overlying water-bearing strata have led to an increasing number of roof water inrush accidents and deterioration of production environment of the working face. Aiming at the problem of roof water disaster prediction of sandy-argillaceous structural strata in Shanghaimiao mining area in China, firstly, the mechanical structure model of roof water inrush was built according to the parameters in the advance of the working face, and the thickness of the sandstone was used as the main controlling geological factor; the formula was derived for calculating the water-rich intensity F_{zh} of the overlying strata in the mining area. Secondly, starting from the height of the "Breakage-arch" development disturbance by combining the mechanical structure model of roof water inrush, the relative positional relation of the "Breakage-arch" and the water-bearing strata was analyzed, and a new method for judging the risk coefficient T_W of roof water inrush was proposed. Finally, according to the geological drilling histogram and the field conditions of #111084 working face of the no. 1 mine in Shanghaimiao mine area, the water-rich index and water inrush risk coefficient of overlying water-bearing strata were obtained by means of discriminant analysis, and the water inrush risk of #111084 working face was evaluated and predicted quantitatively. The water-rich property evaluation of water-bearing strata under the condition of low degree of hydrogeological exploration was evaluated accurately and reasonably, and a new evaluation method of the water disaster during mining was proposed.

1. Introduction

Chinese Jurassic recoverable coal resources account for more than 67% of the total coal reserves, which are mainly distributed in Western China. In the early stage, coal resource mining was mainly shallow mining [1, 2]. With the increase of coal mining depth, there are more and more accidents that roof caving communicates with the overlying aquifer, resulting in roof inrush disaster or deteriorating the production environment of the working face [3–5]. Facing the increasingly severe situation of roof water inrush disaster, many scholars have carried out a lot of research and made great progress in the prediction and treatment of roof water inrush disaster. Including Academician Wu's "three maps-two predictions method" for quantitative evaluation of roof water inrush conditions [6]. Li et al. and Zhang et al. [7, 8] established the mathematical model of indirect prediction of roof water disaster according to the multi-information composite analysis method of geographic information system (GIS). The concept of the water inrush possibility coefficient of the loose aquifer was proposed by Meng et al. and Gao [9, 10]. Fan et al. [11] comprehensively divided the risk of water inrush and sand break in the Yushenfu mining area and evaluated the risk of water inrush and sand break in the mining area. Yi et al. [12] predicted the roof water inrush possibility area of the working face based on the discrimination results of the position of the main key strata of the overburden. Based on the influence of key strata position on the development height of the water diversion fracture zone, Xu et al. [13, 14] proposed a new method for predicting the height of the water diversion zone.

However, the conditions and mechanism of roof water inrush are complex. It is obviously not comprehensive to consider only whether the height of the water-conducting fracture zone induced by coal seam mining touches the roof aquifer. When the water-conducting fracture zone fails to reach the aquifer, the mining strata will break under the influence of secondary disturbance, and the disturbance range of the water-conducting fracture zone will change accordingly. Therefore, this paper considers the influencing factors of water-bearing sandstone thickness. According to the spatial relationship between overburden failure and overlying aquifer affected by mining, a discrimination method of roof water inrush possibility coefficient T_W is proposed, which is verified in a working face in Shanghaimiao mining area, China.

2. Spatial Structure Model of Roof Water Inrush

In the process of advancing the working face of coal mining, the fracture and fragmentation of the overlying strata are in continuous movement and development, and the relative positional relationship between the aquifer and the water-conducting fracture zone is regular; that is, it is determined by the strata movement. Therefore, the research on water inrush from coal seam roof should focus on the rock movement and focus on the damage range of overlying rock movement in the process of stope advancement and the spatial relationship between this range and the aquifer.

The rock stratum above the coal seam can be divided into two parts: overburden spatial structure and outer part of overburden spatial structure [15]. The outer part of the overburden spatial structure is the rock stratum without obvious movement outside the "Breakage-arch," which has little impact on the water permeability of the stope roof. With the advancement of the working face, the hanging space of the stope is increasing, the overlying strata are breaking, and the fracture positions are staggered from bottom to top, forming a "Breakage-arch" that has a direct impact on the water permeability of the stope roof (as shown in Figure 1). The moving rock structure in the "Breakage-arch" is called overburden spatial structure. In general, it can be considered that the development height of a "Breakage-arch" is the height of the water diversion fracture zone [16]. As for the relative position relationship between the "Breakage-arch" and the aquifer, the "Breakage-arch" communicates with an aquifer, and water inrush occurs immediately.

Some scholars believe that the key to the prevention of water inrush disaster is to clarify the location of water-bearing rock strata and the scope of the water-rich area [17, 18]. By adjusting the length of the working face and the position relationship of the open cut hole relative to the water-rich area, it is ensured that the fractured rock strata are interrupted during the advancement of the working face and do not spread to the water-bearing rock strata. Even if the fractured rock stratum does not affect the water-bearing rock stratum, there is a possibility of water inrush in the roof according to the separation catchment and hydrostatic water inrush [19].

3. Numerical Simulation of Development Law of "Breakage-Arch"

In the process of advancing the working face, the overburden is disturbed by mining, and the "Breakage-arch" continues to develop and expand upward, resulting in a large number of network fractures, which is very easy to induce water inrush in the stope. In order to study the relationship between the length of the working face and the development height of "Breakage-arch," combined with the field peeping borehole observation results and exploration borehole data in Shanghaimiao mining area, a FLAC^{3D} numerical simulation model was established (as shown in Figure 2). Model size is long × wide × height = 500 m × 300 m × 300 m, the model contains 121875 grid elements and 146256 nodes, and the excavation dimensions of the simulated working face are 150 m, 180 m, 210 m, and 240 m, respectively. The M-C constitutive model is used to describe the mechanical response of overburden under tension failure and instability. The vertical stress and horizontal stress applied in the model are $\sigma_{zz} = 20$ MPa, $\sigma_{yy} = 16$ MPa, and $\sigma_{xx} = 16$ MPa. The mechanical parameters of coal and various rocks are shown in Table 1. After the model calculation reaches the initial equilibrium, the working face is excavated according to the dimensions of 150 m, 180 m, 210 m, and 240 m and calculated to the default equilibrium state of the software to obtain the development characteristics of the plastic zone as shown in Figure 3.

The numerical simulation results show that the development height of the plastic zone increases with the increase of the width of the working face. After measurement and comparison, the development height of the plastic zone is about 1/2 of the width of the working face.

4. Discriminant Analysis of Roof Water Inrush Possibility

The water yield of the aquifer is measured by the specific yield. The greater the specific yield, the stronger the water yield of the aquifer and vice versa. Therefore, the specific yield can directly reflect the water abundance of the aquifer. According to the engineering practice, the degree of hydrogeological exploration in most coal mining areas in China is low, the number of pumping (drainage) test is limited, the data of unit water inflow can be obtained is less, the water abundance of the aquifer cannot be fully reflected, and the high-precision evaluation and prediction of water abundance of the aquifer cannot be realized. Therefore, based on previous studies, the author puts forward a new method to distinguish the risk of roof water inrush.

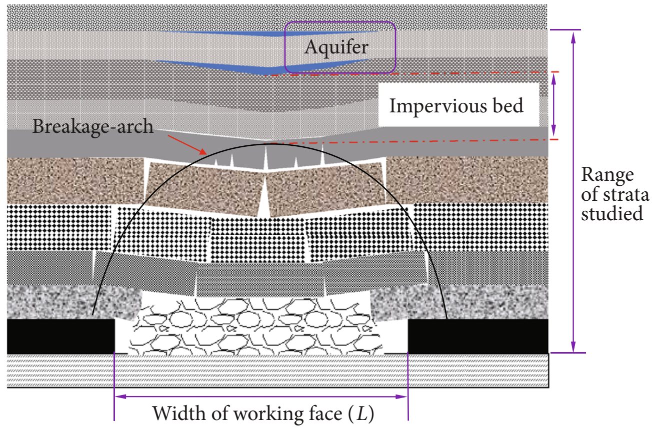

FIGURE 1: Spatial structure model of water inrush.

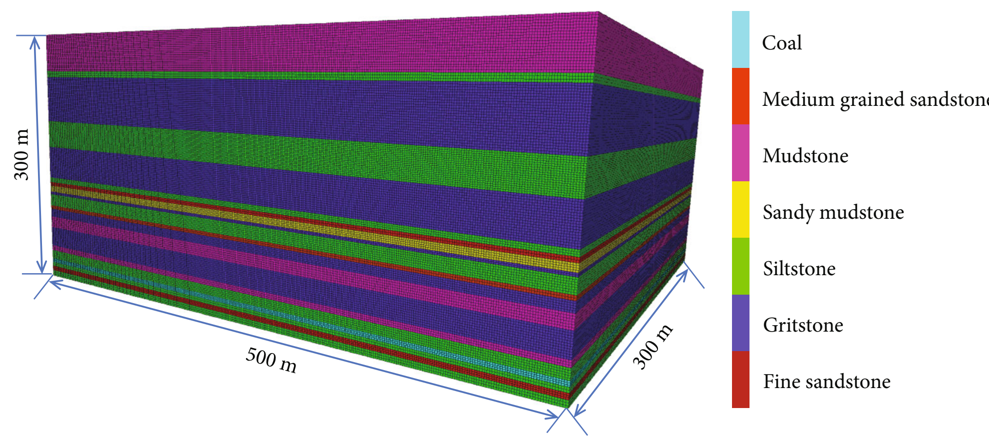

FIGURE 2: Numerical simulation model.

TABLE 1: Properties of coal and rock mass used in the numerical model.

Rock character	Poisson's ratio	Density (kg·m^{-3})	Cohesion (MPa)	Internal friction angle (°)	Bulk modulus (GPa)	Shear modulus (MPa)	Tensile strength (MPa)
Mudstone	0.25	2470	1.78	25	2.41	4.13	0.70
Siltstone	0.22	2602	3.10	33	7.21	2.80	0.80
Gritstone	0.32	2700	6.20	34	4.80	2.20	3.00
Fine sandstone	0.20	2590	3.96	50	6.98	2.80	1.35
Sandy mudstone	0.27	2490	1.79	26	2.44	4.23	0.75
Coal	0.31	1347	1.21	30	2.13	1.35	0.12

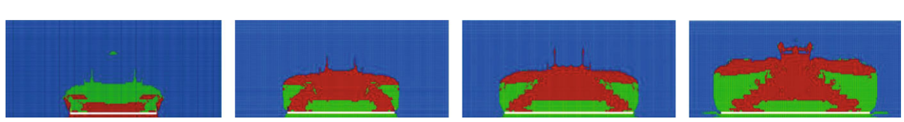

FIGURE 3: Development law of plastic zone under different working face width.

4.1. Water Rich Index. The lithology of sandy-argillaceous sedimentary structures can be divided into two categories: (1) conglomerate rocks, coarse sandstone, and fine sandstone are called sandy rocks (or brittle rocks) because of their coarse particles and high brittleness; (2) siltstone, mudstone, sandy mudstone, and carbonaceous mudstone are called argillaceous rocks (or plastic rocks) because of their fine particles and strong plasticity. Sandy rocks have large primary porosity and are prone to produce a large number of fractures, which are the main water storage space. Because there are certain differences in mechanical properties among strata in the stratum, the conditions for forming the separation layer are met. During the formation of the separation layer, the fissure water in the sandstone strata will continue to collect into the separation layer. With the increase of collected water, the separated strata water will exert pore water pressure and load on its lower rock stratum. This leads to the fracture and instability of the lower rock stratum and the formation of water inrush in the working face. However, there are argillaceous strata with fine particles and strong plasticity in sandy-argillaceous sedimentary structural strata. It can withstand a certain tension failure, is not easy to produce cracks, can curb the expansion of water storage space, and hinders the collection of pore fissure water to the separation strata. Therefore, taking the adjacent argillaceous rock overlying the key strata as the top boundary and the interval between the top boundary and the roof of the working face as the effective research interval, the proportion of the cumulative thickness of brittle rock within the effective research interval can reflect the water yield in the overlying strata.

$$F_Z = \frac{\sum D_i}{H_y} \times 100\%, \tag{1}$$

where F_Z is the water abundance index (dimensionless) $\sum D_i$ is the cumulative thickness of sandy rock strata within the effective study interval (m), and H_y is the vertical distance between the adjacent argillaceous rock above the key strata and the roof of the working face (m).

4.2. Water Inrush Possibility Coefficient. The risk of water inrush from the roof is determined by the height of the "Breakage-arch" and the water content of the roof. The larger the scope of disturbing and damaging the aquifer and the stronger the water abundance, the risk of water inrush is relatively high. In order to quantitatively evaluate the possibility of water inrush into the stope of indirectly water-filled aquifer, the water inrush possibility coefficient is introduced here. The probability of water inrush in stope is evaluated by measuring the safe distance between the water-conducting fracture and the upper aquifer. Without considering other factors, the calculation formula is [20]

$$T_{\mathrm{wy}} = \frac{H_{\mathrm{gs}} - H_{\mathrm{fs}}}{H_{\mathrm{fs}}}, \tag{2}$$

where T_{wy} is the water inrush possibility coefficient of predecessors (dimensionless), H_{gs} is the thickness of the water-resisting strata, i.e., the distance between the coal seam roof and the upper aquifer (m), and H_{fs} is the theoretical calculation value of water-resisting coal (rock) pillar (m).

There are differences in physical and mechanical properties in the strata of sandy-argillaceous sedimentary structures, which determine that the subsidence process of overburden must be uncoordinated movement. Therefore, the separation space was generated, which provided physical space development conditions for water inrush dangerous water bodies, and the main separation strata were developed below the key strata. During the advancement of the working face, the overburden on the main roof was broken, rotated, and sunk. The main roof continuously evolves dynamically in space, forming a "Breakage-arch" structure in a two-dimensional plane, resulting in a large number of water diversion fractures. This increases the possibility of connecting the aquifer with the water-conducting fracture zone.

Regardless of the hulking sex of the overburden above the main roof, the fracture and bending of the overburden from the main roof to the key strata have similar morphology. In the calculation of deformation, it can be regarded as a multistrata ring with the same center, as shown in Figure 4.

According to the geometric relationship in Figure 4,

$$|OA_1| = H_C + H_{\mathrm{zj}}\text{-}\mathrm{K_C} H_{zj}, \tag{3}$$

$$|A_1 A_n| = \cos^{-1}\theta \sum_{i=1}^{n} D_i, \tag{4}$$

$$H_l = |OA_1| + |A_1 A_n|, \tag{5}$$

where A_i (i ranges from 1 to n) is the maximum settlement point of the overburden except the direct roof, D_i is the thickness of overburden of strata i (m), θ is the turning angle of overburden (°), H_C is the height of coal mining (m), H_{zj} is the thickness of the direct roof (m), K_C is the residual crushing expansion (dimensionless), and H_l is the development height of the lowest point of separation strata (m).

With the development of the separation space, the pore water and fissure water of adjacent sandy strata are continuously collected in the separation layer (as shown in Figure 5). The collected water exerts an additional load on the lower unbroken barrier strata. When the applied load exceeds the tensile strength of the impervious bed (σ_t), it is very easy to induce the instability of barrier strata and finally leads to water inrush in the working face. Therefore, according to the spatial relationship between the water of the abscission layer and the "Breakage-arch," the ratio of the development height of the "Breakage-arch" to the lowest point height of the catchment separation strata is taken as the discrimination basis. At the same time, the discrimination formula of water inrush possibility is obtained by combining the position of key strata and the tensile strength of the impervious bed:

(1) Judging from the geometric relationship:

$$T_{W1} = \frac{H}{H_l} \times 100\%, \tag{6}$$

$$H = kL. \tag{7}$$

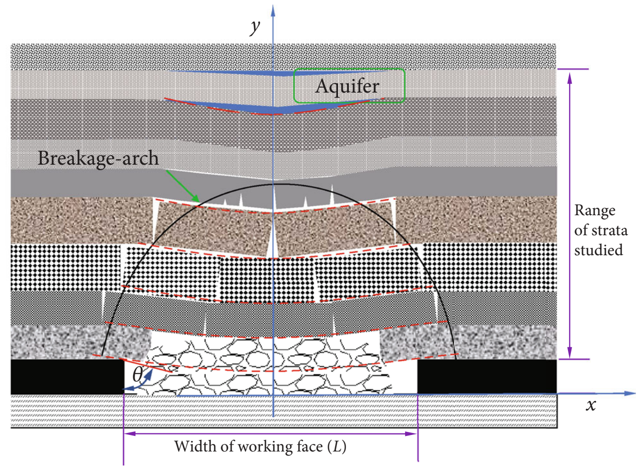

(a)

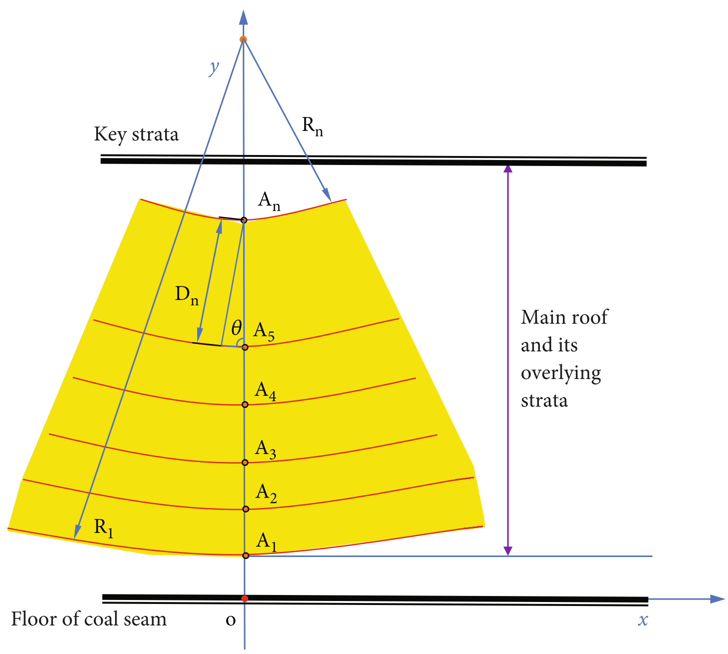

(b)

FIGURE 4: Schematic diagram of final position state of upper strata fracture and subsidence.

(2) Judging from the stress state:

$$T_{W2} = \frac{\rho g\left(H_g - H_l\right)}{\sigma_t} \times 100\%, \quad (8)$$

where T_W is the water inrush possibility coefficient (dimensionless), H_l is the height of the lowest point of separation (m), H is the development height of "Breakage-arch" (m), H_g is the height of key strata (m), L is the width of the working face (m), k is the proportionality coefficient, $k = 0.5 \sim 0.7$ (dimensionless), σ_t is the tensile strength of the rock as the impervious bed (Pa), ρ is the density of water in the separation strata (kg/m^3), and g is the gravitational acceleration (about 9.8 m/s^2).

The greater the value of T_W, the greater the risk of water inrush in the working face. When T_W approaches 100%, it indicates that the spatial position of the "Breakage-arch" and the aquifer is infinitely close (as shown in Figure 6). The impervious bed was infinitely close to the breaking instability state, which was very easy to induce water inrush in the working face.

5. Engineering Verification

5.1. Geological Conditions of the Project. Shanghaimiao no. 1 coal mine is located in etokeqian banner, Inner Mongolia. The total amount of coal resources is about 14.3 billion tons. The mining area is a typical geological structure of sandy argillaceous sedimentary formation, and the geological profile is shown in Figure 7. The Jurassic Yan'an Formation

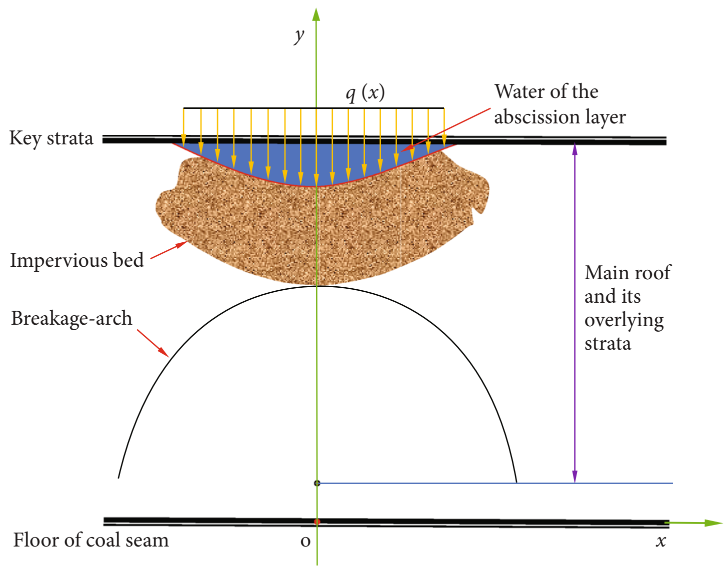

Figure 5: Mechanical model of roof structure when water inrush was about to occur.

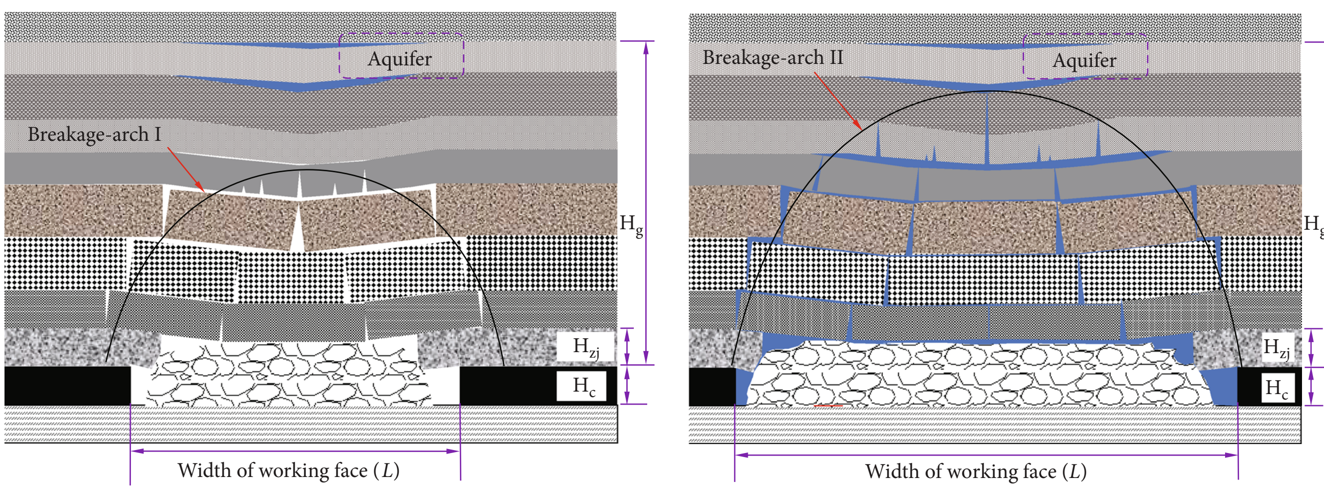

Figure 6: The relationship between the development height of "Breakage-arch" and water-bearing strata.

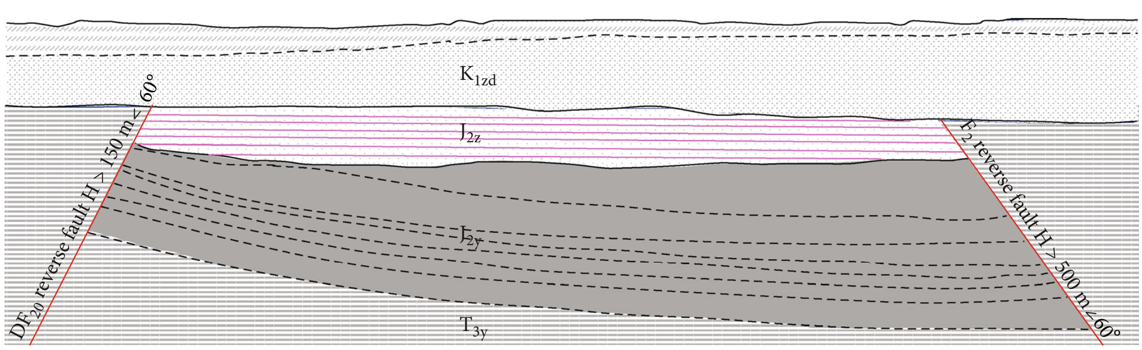

Figure 7: Geological profile of minefield.

(J_{2y}) is a coal-bearing formation, which is overlaid by Jurassic Zhiluo Formation (J_{2z}), Cretaceous Zhidan group (K_{1zd}), and underlying by Triassic Yanchang Formation (T_{3y}).

5.2. Aquifer and Water Yield. The main aquifers of Shanghaimiao no. 1 coal mine are the Cretaceous conglomerate aquifer, Jurassic Yan'an Formation sandstone aquifer, and Jurassic Zhiluo Formation sandstone aquifer.

(1) The average thickness of the aquifer section of Jurassic Zhiluo Formation sandstone was 41.0 m, the elevation of water level was +1220~+1252 m, the

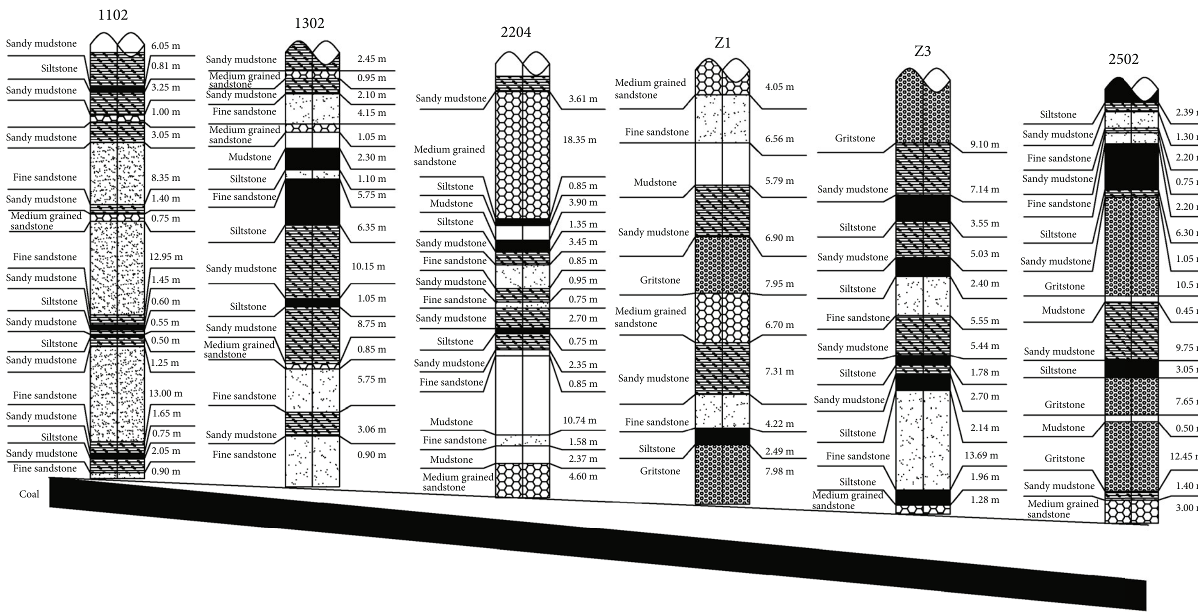

FIGURE 8: Part of borehole column of "Qilizhen sandstone" in Zhiluo Formation.

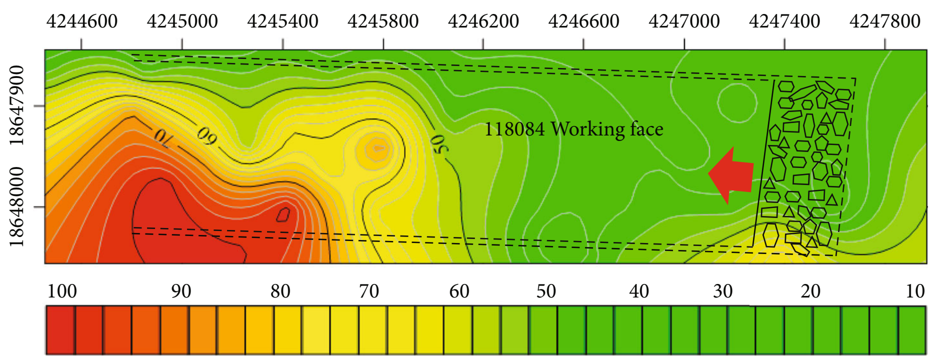

FIGURE 9: Contour map of the water-rich index of #111084 working face.

permeability coefficient was 0.05~0.35 m/d, and the specific yield was 0.017~0.015 L/(s·m)

(2) The average thickness of the Cretaceous conglomerate aquifer was 64.5 m, the elevation of water level was +1240~+1269 m, the permeability coefficient was 0.049~0.341 m/d, and the specific yield was 0.047~0.341 L/(s·m)

(3) The aquifer group of Jurassic Yan'an Formation sandstone is pore (fissure) water, the permeability coefficient was 0.0029~0.1970 m/d, and the specific yield was 0.0027~0.0281 L/(s·m)

The maximum mining height of coal seam #8 is 3.8 m, the length of the working face is 220 m, and the maximum thickness of the waterproof safety coal (rock) pillar is 20 m. According to the drilling data (Figure 8 shows some drilling data) and the calculation formula of water yield index (1), the contour map of the water-rich index of #111084 working face is obtained (as shown in Figure 9).

5.3. Water Inrush Possibility of Roof in Working Face. Taking the geological conditions of #111084 working face as an example, the water level change of #z1 hydrological observation wells near the water inrush position of the working face is measured, as shown in Figure 10.

(1) During the water storage in the separation space: the water level of Zhiluo Formation decreased by 13.59 m after being advanced by 0~110 m (data from July 13 to July 31)

(2) During the formation of the bend zone: the advance was 110~140 m, the overburden subsidence occurred, and the water level rose by 0.972 m (data from July 31 to August 5)

(3) Water inrush: when advancing to 141 m, the water diversion fissure destroys the separation closed space above the working face and water inrush occurs. The maximum water volume is 2000 m^3/h, and the water level drops by 29.12 m

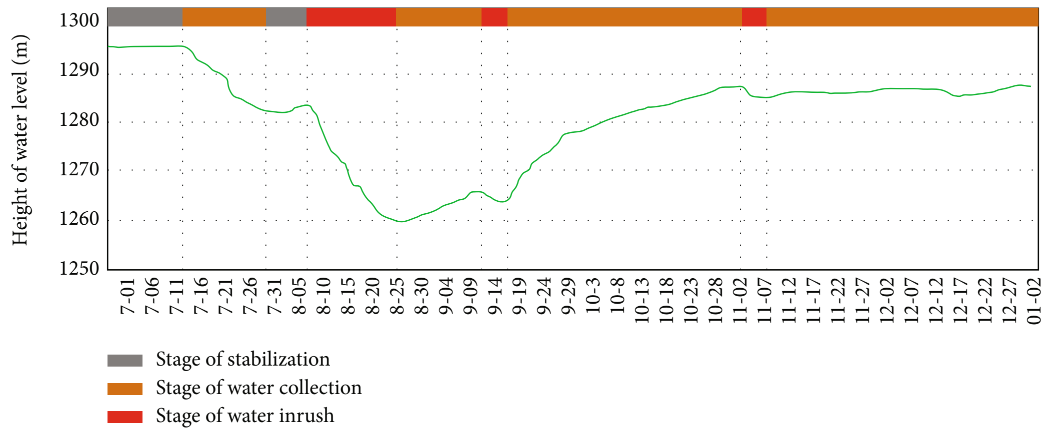

Figure 10: Water level change map of Z1 hydrological observation hole in #111084 working face.

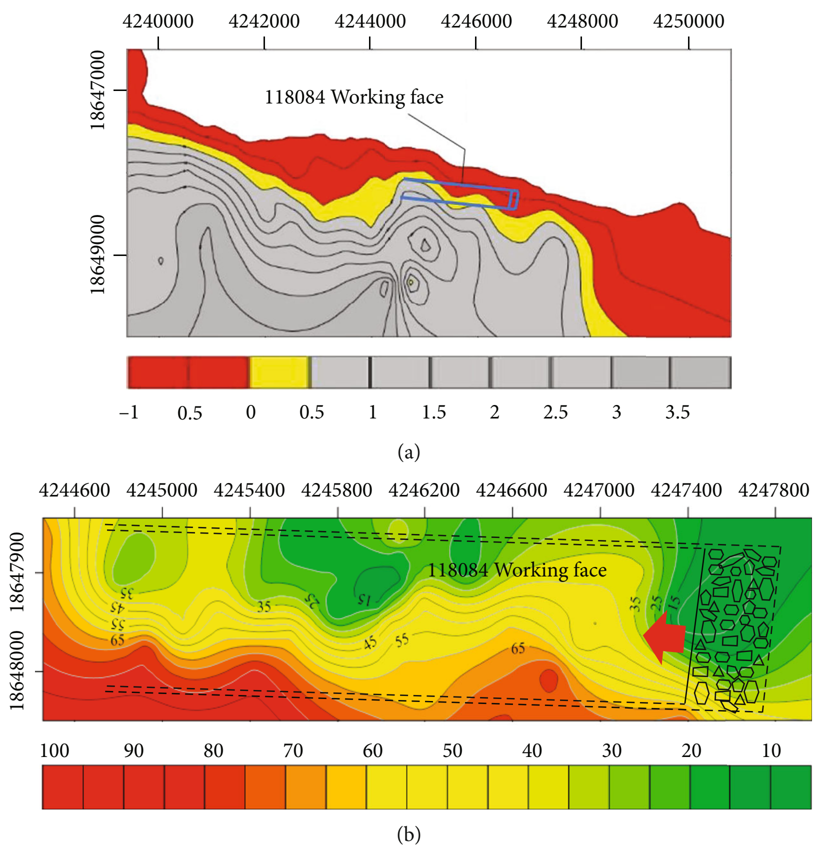

Figure 11: Contour map of water inrush possibility of #111084 working face.

According to the observed data on site, #111084 working face has the conditions for water inrush, and it is necessary to predict the possibility of water inrush in the unmined area.

The position of the key strata and the thickness of the immediate roof were determined according to the geological borehole histogram. Combined with the water-rich index and using the discriminant Equations (6) and (8) of the water inrush possibility coefficient, the water inrush possibility of the overlying aquifer during mining in the 111084 working face of no. 1 mine in Shanghaimiao mining area was evaluated. Due to the difference of lithology of immediate roof, the value range of crushing expansion coefficient fluctuates between 1.15 and 1.4 [21]. The calculated water inrush possibility coefficient and coordinates were imported into surfer 12.0 to obtain the contour map (as shown in Figure 11) of water inrush possibility coefficient. The contour map was filled with gradient colors based on numerical intervals. Among them, the red-filled part indicates that there was a great possibility of “Breakage-arch” contacted the aquifer in this area. The green-filled area indicates that the possibility of a "Breakage-arch" contacting the aquifer was very small. Referring to the "three-line" method of ponding in goaf, the area ($35 < T_W \leq 65$) was filled with yellow, which belongs to the warning range.

Compared with the existing results [20], this paper mainly modifies the discrimination method of the water-rich index and the possibility of water inrush in the working face. When the mining parameters of coal seam were included, the predicted coefficients were positive, the fluctuation range of coefficients was 10~80+, the accuracy of prediction results is high, and the variable range of coefficients is large. When having the same geographical coordinates, Figure 11(a) is the contour map of prediction results drawn by using the water inrush possibility index method before correction, and Figure 11(b) is the contour map of prediction results drawn by using discriminant Equation (2) and Equation (3) in this paper. The comparison shows that the modified discrimination method proposed in this paper has good prediction accuracy and improves the practicability of water inrush possibility prediction zoning.

6. Conclusion

(1) The water abundance in sandy argillaceous sedimentary structural strata is uneven. The proportion of the thickness of sandy strata in the whole overburden is taken as the main index to evaluate the water abundance. Combined with the parameters of the working face and the overburden structure model of water inrush, the evaluation method of water yield was established

(2) In view of the evaluation and prediction of water damage to the roof of the working face under the condition of sandy argillaceous sedimentary structural stratum, the damage range of the "Breakage-arch" to the aquifer and the water yield strength of the aquifer are comprehensively considered. Combined with the parameters of the working face and the residual dilatancy coefficient of the direct roof, the discrimination formula of the possibility coefficient of water inrush was proposed

(3) According to the new discrimination formula proposed in this paper, the water-rich index of overburden and the possibility coefficient of water inrush are obtained, and the possibility of water inrush in #111084 working face was quantitatively evaluated and predicted. It realized the scientific evaluation of water abundance and water inrush possibility of sandy argillaceous sedimentary structural strata under the condition of low degree of hydrogeological exploration

Data Availability

The data used to support the findings of this study are available from the corresponding authors upon request.

Conflicts of Interest

The authors declare no conflicts of interest.

Acknowledgments

We are grateful for the financial support from the National Natural Science Foundation of China (51974174), Shandong Excellent Youth Fund (ZR2019YQ26), university key scientific research program project (science and technology) of Shandong Province (J18K2010), Source Innovation Programme (No. 18-2-2-68-jch), and Natural Science Foundation of Shandong Province (No. ZR2018MEE001).

References

[1] S. Chen, Y. Wang, W. Yuezhong, Z. Wang, and W. J. Zhang, "Coal resources and development potential in Northwest China," *Northwestern Geology*, vol. 39, no. 4, pp. 40–56, 2006.

[2] H. Li and X. Tian, "Comprehensive evaluation and analysis of exploitation potential of coal resource in northwest of China," *Coal Geology & Exploration*, vol. 26, no. S1, pp. 1–4, 1998.

[3] E. Brunetti, J. P. Jones, M. Petitta, and D. L. Rudolph, "Assessing the impact of large-scale dewatering on fault-controlled aquifer systems: a case study in the Acque Albule basin (Tivoli, central Italy)," *Hydrogeology Journal*, vol. 21, no. 2, pp. 401–423, 2013.

[4] S. Kerang, "Numerical study identifying the factors causing the significant underestimation of the specific discharge estimated using the modified integral pumping test method in a laboratory experiment," *Journal of Contaminant Hydrology*, vol. 180, no. 9, pp. 1–11, 2015.

[5] A. T. Tizro, K. Voudouris, and Y. Basami, "Estimation of porosity and specific yield by application of geoelectrical method-a case study in western Iran," *Journal of Hydrology*, vol. 454-455, pp. 160–172, 2012.

[6] W. Qiang, "Dynamic visualization and prediction for water bursting on coal roof based on "three maps method"," *Journal of China Coal Society*, vol. 41, no. 12, pp. 2968–2974, 2016.

[7] K. Li, Y. Zeng, and Y. Shang, "The application of "three maps-two predictions" method based on GIS," *Coal Geology & Exploration*, vol. 43, no. 2, pp. 58–62, 2015.

[8] H. Zhang, R. Zhou, D. Guo, and P. Du, "Investigation on predicting roof water gush in coal mines based on multi-factor analysis," *Journal of China University of Mining& Technology*, vol. 34, no. 1, pp. 115–119, 2005.

[9] Z. Meng, Y. Gao, L. Aihong, R. Wa, X. Qi, and C.-Y. Hu, "Water inrush risk evaluation of coal mining under quaternary alluvial water and reasonable design method of waterproof coal pillar," *Journal of Mining and Safety Engineering*, vol. 30, no. 1, pp. 23–29, 2013.

[10] Y. Gao, "Four-zone model of rock mass movement and back analysis of dynamic displacement," *Journal of China Coal Society*, vol. 21, no. 1, pp. 51–56, 1996.

[11] L. Fan, X. Ma, H. Jiang, and S. Cheng, "Risk evaluation on water and sand inrush in ecologically fragile coal mine," *Journal of China Coal Society*, vol. 41, no. 3, pp. 531–536, 2016.

[12] M. Yi, W. Zhu, L. Li, Z. Xu, and X. Jia-lin, "Water inrush mechanism and prevention for fourth panel roof in Bulianta coalmine," *Journal of China Coal Society*, vol. 33, no. 3, pp. 241–245, 2008.

[13] X. Jialin, W. Zhu, and X. Wang, "New method to predict the height of fractured water-conducting zone by location of key strata," *Journal of China Coal Society*, vol. 37, no. 5, pp. 762–769, 2012.

[14] X. Jialin, M. Qian, and H. Jin, "Study and application of bed separation distribution and development in the process of strata movement," *Chinese Journal of Geotechnical Engineering*, vol. 24, no. 5, pp. 632–636, 2004.

[15] Z. Wen, *Study on Key Technologies and Mechanical Model of Gob-Side Retaining Entry*, Shandong University of science and technology, 2011.

[16] Z. Wen, S. Jing, Z. Song et al., "Study on coal face spatial structure model and control related dynamic disasters," *Coal Science and Technology*, vol. 47, no. 1, pp. 52–61, 2019.

[17] A. F. Diogo and M. C. Oliveira, "A simplified approach for the computation of steady two-phase flow in inverted siphons," *Journal of Environmental Management*, vol. 166, pp. 294–308, 2016.

[18] A. M. Sape, "A head loss model for slurry transport in the heterogeneous regime," *Ocean Engineering*, vol. 106, pp. 360–370, 2015.

[19] W. Qiao, W. Li, and X. Li, "Mechanism of "hydrostatic water inrush" and counter measures for water inrush in roof bed separation of a mining face," *Journal of Mining & Safety Engineering*, vol. 28, no. 1, pp. 96–104, 2011.

[20] Y. Lv, H. Li, and Y. Xia, "Prediction and evaluation study on coal seam roof water inrush based multi-type four-double method," *Coal Science and Technology*, vol. 47, no. 9, pp. 219–228, 2019.

[21] X. Chen, S. Chengdong, X. Tang, and W. Guo, "Experimental study of effect of water-saturated state on compaction property of crushed stone from coal seam roof," *Chinese Journal of Rock Mechanics and Engineering*, vol. 33, no. S1, pp. 3318–3326, 2014.

Hindawi
Geofluids
Volume 2023, Article ID 1181284, 12 pages
https://doi.org/10.1155/2023/1181284

Research Article

Risk Assessment of Water and Sand Inrush in Mining under Thick Loose Layer Based on Comprehensive Weight-Cloud Model

Wenquan Zhang,[1,2] **Xintao Wu**,[1,2] **Xunan Wu**,[1,2] **Yu Lei**,[1,2] **Jianli Shao**,[1,2] **and Zaiyong Wang**[1,2]

[1]*College of Energy and Mining Engineering, Shandong University of Science and Technology, Qingdao 266590, China*
[2]*State Key Laboratory of Strata Intelligent Control and Green Mining Co-founded by Shandong Province and the Ministry of Science and Technology, Qingdao 266590, China*

Correspondence should be addressed to Wenquan Zhang; wenquanzhang415@163.com

Received 15 July 2021; Revised 29 April 2022; Accepted 27 May 2022; Published 13 April 2023

Academic Editor: Andrea Brogi

Many deep mining mines in southwestern Shandong Province of China are covered with thick loose layers. When mining near the loose layers, there is a risk of water and sand inrush, which threatens the personal safety of miners. The prediction of sudden water and sand inrush is difficult due to the comprehensive influence of many factors, and the influencing factors are fuzzy and random. To solve this problem, in this paper, a new risk assessment method of water and sand inrush based on comprehensive weight and cloud model was proposed. Seven factors are selected as indexes: the aquifer thickness, the thickness ratio of sand layer to clay layer, the thickness of bottom clay layer, the coal seam thickness, the percentage of core recovery, the geological structure, and the bedrock thickness. The assessment index system is established, and the index is divided into three grades. A comprehensive weighting method, which combines analytic hierarchy process (AHP), entropy weight method (EWM), and minimum entropy principle, is used to reasonably assign the weight of index. Based on the cloud generator equation, the membership function is obtained. The assessment result of the assessment object is obtained by combining the membership degree and the weight of index. The comprehensive weight-cloud model assessment method is applied to the risk assessment of water and sand inrush in the 6311-2 working face in the sixth mining area of Baodian Coal Mine. According to the assessment results, the following conclusions can be drawn: (1) the bedrock thickness and the coal seam thickness are the main factors of water and sand inrush under loose layer mining; (2) the assessment results obtained by the comprehensive weight-cloud model method are consistent with the actual situation. The assessment method can provide scientific reference for the safe mining under the thick loose layer in the deep mines of southwest Shandong.

1. Introduction

Water and sand inrush is a kind of mine geological disaster that water and sand mixed fluid with high sand content bursts into underground working face and causes property damage and casualties [1]. Some coalfields in North China are covered with thick loose layers, especially in deep mining mines in southwest Shandong Province. When mining near the loose layers, the upper water-rich sand layer is prone to water and sand inrush under the disturbance of mining activities, which affects the normal production of the mine and causes casualties [2, 3]. In order to reduce the occurrence of water and sand inrush disasters and take timely and effective measures, it is necessary to put forward a more accurate assessment method of water and sand inrush disasters under loose layer mining [4, 5].

Experts and scholars studied the problem of water and sand inrush by various methods [6–13]. Zhong et al. used software PFC^{3D} and software GID to simulate the whole process of water and sand inrush in precast ideal fracture with different opening widths and dip angles in overlying rock strata. Their analysis shows that the opening widths and dip angles of fracture change the flow patterns of water-sand flow inrush and have great impact on the contact force of the fracture channel, flow velocity of water, and the time of mixed water-sand flow [14]. Zhao et al. studied the overlying stratum fracture development and distribution characteristics of water-sand inrush channel through the simulation experiment. They divided the development process of water-inrush channels into three stages: the stage of gradual development, the stage of penetration linking channel formation, and the stage of water-sand inrush, and divided the area of the overlying rock fracture and water-sand inrush into three sections: the zone of overburden fracture gradual development, the zone of water-sand intrusion, and the zone of water-sand-intrusion blocking [15]. Peng et al. made a comprehensive analysis on the mechanism of water and sand inrush disaster from many aspects such as channel, water source, water storage space, power source, and geological structure. They found out that the cause of water and sand inrush disaster under thick overlying bedrock is that the water flowing fractured zone generated by mining causes water to enter the separated cavity between rock formations. The water in the separated cavity penetrates into the loose geological body and breaks into the working face instantly along the concentrated channel generated by cutting the working face, resulting in the occurrence of water and sand inrush disaster [16]. Zhang et al. established the mechanics model of sand inrush in fractures and analyzed the limit equilibrium condition of water and sand inrush in fractures. Through experiments, they quantitatively analyzed the characteristics of water and sand migration and correlation changes of physical parameters in different stages of water and sand inrush and divided the whole process of water and sand inrush in fractures into four stages, namely, start-up stage, continuous outburst stage, silt blockage stage, and outburst equilibrium stage [17]. Ma et al. established a water-sediment flow resistance model in fractures based on the two-phase flow theory and verified it through laboratory-scale test [18]. Using the LBM-DEM coupling simulation method, Pu et al. studied the problem of the water and sand two-phase migration in the single-fracture opening channel model. They compared the changes of section flow rate and sand inrush rate under different boundary pressures, fracture opening widths, and sand layer thickness [19].

As mentioned above, researchers have made many achievements in the mechanism of water and sand inrush. However, the prediction of sudden water and sand inrush is difficult due to the comprehensive influence of many factors, and the influencing factors are fuzzy and random. To solve this problem, a risk assessment method of water and sand inrush is proposed based on comprehensive weight and cloud model in this paper. The membership degree function transformed from the normal cloud generator equation is used to calculate the membership degree of the index. Combine analytic hierarchy process, entropy weight method, and minimum entropy principle to calculate the comprehensive weight of the index. Based on the membership degree and the comprehensive weight, the risk of water and sand inrush of the assessment object is evaluated, hoping it can provide new ideas and methods for the prevention and control of water and sand inrush disasters. The assessment process is shown in Figure 1.

2. Overview of the Study Area

The sixth mining area of Baodian Coal Mine is selected as the study area. The range and location of boreholes near the sixth mining area are shown in Figure 2. Baodian Coal Mine is located in Yanzhou District, Jining City, Shandong Province. The sixth mining area is located in the west of Baodian Coal Mine. The structure is controlled by Yanzhou syncline, and the axial direction is NEE, inclining to the northeast. There is a small south lake syncline in the north of the sixth mining area. The southern development range was Baochang anticline. Fault strike is mostly northeast.

The sixth mining area is a fully concealed North China Carboniferous Permian coalfield. The strata from old to new are Ordovician (O_2), Carboniferous (C), Permian (P), Jurassic (J_3), and Quaternary (Q). The following is a detailed description:

(1) Middle and lower Ordovician ($O_{2,\ 1}$): it is the basement of coal measure strata, which is composed of gray and gray-white limestone

(2) Carboniferous (C): the Taiyuan formation of upper Carboniferous is composed of dark gray-grayish black mudstone, bauxite mudstone, siltstone, and medium-coarse sandstone, with 0-11 layers of limestone. Among them, the thickness of the tenth lower limestone and the third limestone is large and the horizon is stable, which is the auxiliary marker layer of the sixth mining area

(3) Permian (P): Shanxi formation is the main coal-bearing strata in the sixth mining area. It is thick in the north but thin in the south. It is composed of gray-white medium, coarse sandstone, gray siltstone, mudstone, bauxite mudstone, and coal seam. Among them, No. 3 coal seam is the main minable coal seam, which has complete contact with the underlying strata

(4) Jurassic (J_3): the upper member is gray-green, purple-gray medium-fine sandstone. The middle member is loose red sandstone. The next section is brownish-red siltstone. It is distributed within a very small range in the eastern part of the sixth mining area. It is in angular unconformity contact with underlying coal measures

(5) Quaternary (Q): thin in the east and thick in the west, thin in the south, and thick in the north. It is composed of sandy clay, clay sand, clay layer, and medium and coarse sand layers

In all strata, the main coal-bearing area is the Carboniferous strata and Permian strata of Shanxi and Taiyuan formation, which belongs to the type of coal-bearing rock series in North China. The main coal seam is the No. 3 coal seam, with a thickness of about 7.86~10.02 m and an average

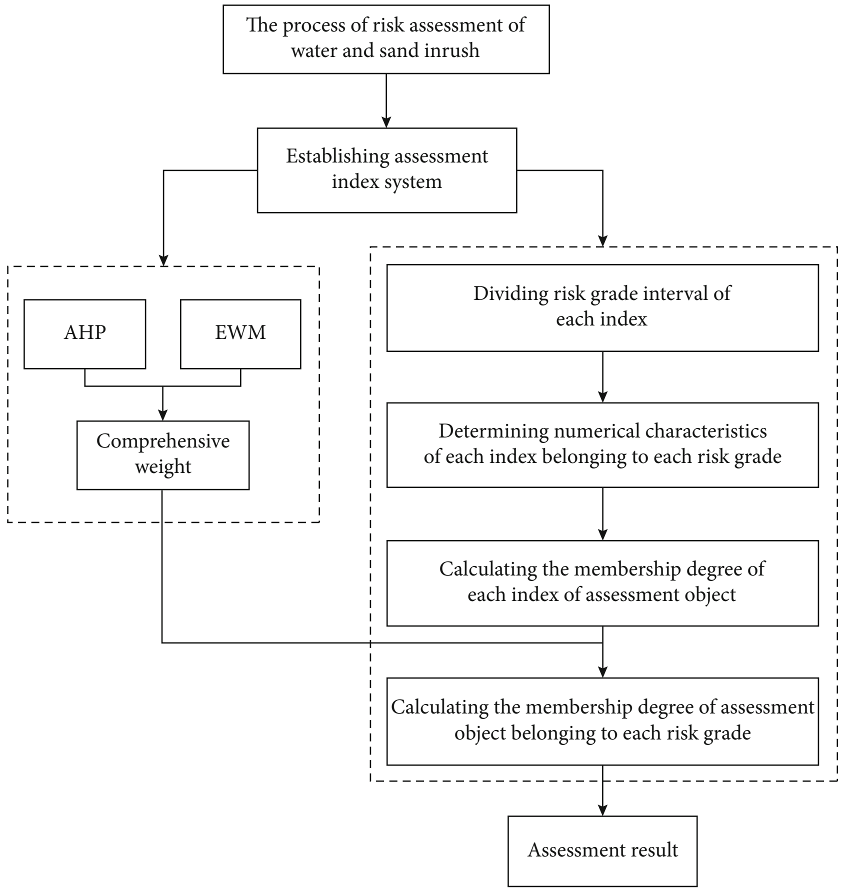

Figure 1: The process of using the comprehensive weight-cloud model method to assess the risk of water and sand inrush during mining under loose layers.

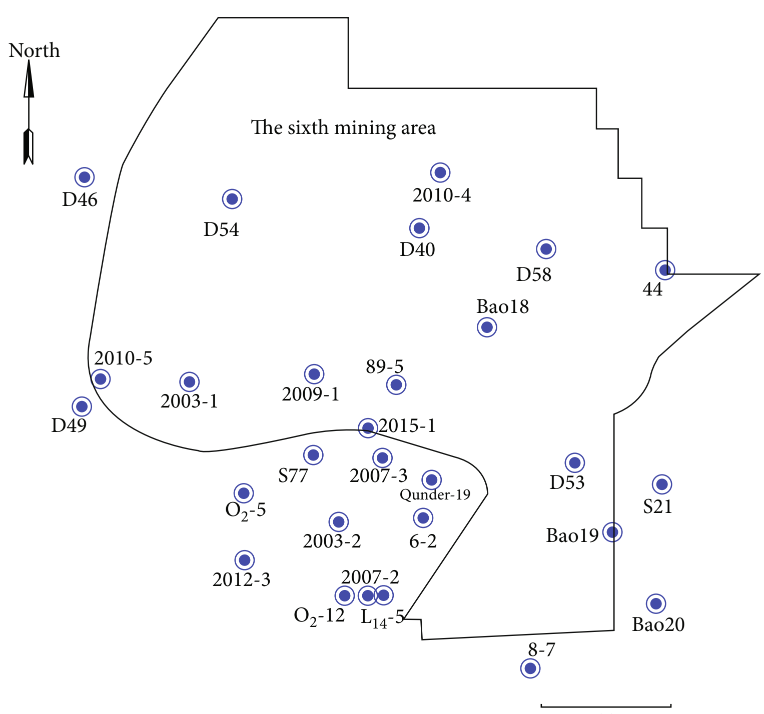

Figure 2: The scope and borehole location of the sixth mining area of Baodian Coal Mine.

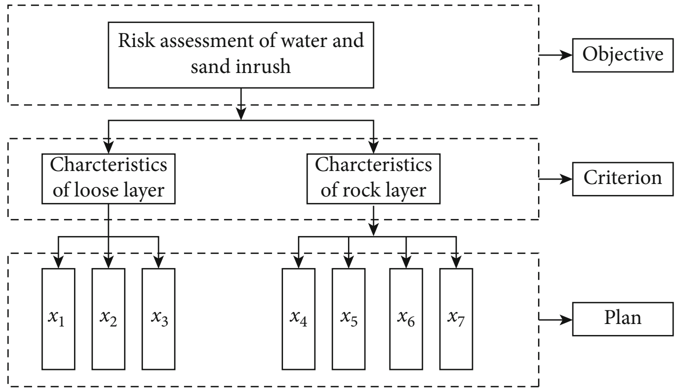

FIGURE 3: Hierarchical structure system of water and sand inrush index for mining under loose layers.

TABLE 1: Risk grade interval of water and sand inrush risk assessment index.

Index	Risk grade interval I	II	III
x_1 (m)	0~15	15~30	>30
x_2 (-)	0~1	1~3	>3
x_3 (m)	>10	5~10	0~5
x_4 (m)	0~3.5	3.5~8	>8
x_5 (%)	80~100	60~80	0~60
x_6 (-)	0~0.4	0.4~0.6	0.6~1.0
x_7 (m)	>40	20~40	0~20

thickness of about 9.00 m. The thickness of the coal seam is stable, and the buried depth of coal seam is about 200~390 m.

The main aquifers affecting the production of the No. 3 coal seam in the sixth mining area from top to bottom are the gravel aquifer in the Quaternary upper group, the gravel aquifer in the Quaternary lower group, and the sandstone aquifer at the roof and floor of the No. 3 coal seam. Among them, the direct water-filled aquifer of coal seam mining is the sandstone aquifer at the roof and floor of the No. 3 coal seam and the gravel aquifer in the Quaternary lower group, and the indirect water-filled aquifer is the gravel aquifer in the Quaternary lower group (when the sandstone aquifer at the roof of the No. 3 coal seam is the direct water-filled aquifer). Except for the gravel aquifer in the Quaternary upper group, the remaining aquifers are mainly static reserves, and the recharge, runoff, and discharge conditions are poor. With the development of mining activities, the water level of the sand layer in the Quaternary lower group decreased slowly year by year, and the water level of the sandstone at the roof of the No. 3 coal seam decreased significantly.

3. Assessment Methods

3.1. Analytic Hierarchy Process. American operational researcher Saaty put forward the famous analytic hierarchy process (AHP) in the early 1970s. The analytic hierarchy process is a decision-making method which decomposes the elements related to decision-making into objective, criterion, plan, and other levels and, on this basis, makes qualitative and quantitative analysis [20].

As a weight determination method, the analytic hierarchy process is commonly used in the field of mine water disasters, such as water abundance assessment and floor water inrush risk assessment [21–23]. In this paper, the improved analytic hierarchy process with three scales is used to calculate the weight.

The traditional AHP needs to check the consistency of the judgment matrix. In this paper, the improved three-scale AHP is used for weight calculation, and the traditional AHP is optimized by using the properties of the optimal transfer matrix, so that it naturally satisfies the consistency. It can greatly reduce the number of iterations and make the subjective factors analytic, thereby reducing the system error.

Supposing there are N lower-level indexes under a certain upper-level index, the importance of each index at the same level is compared according to expert consultation, and the comparison matrix $\mathbf{A} = \{a_{ij}\}_{N\times N}$ is established through the following equation:

$$a_{ij} = \begin{cases} -1 & (\text{index } j \text{ is more important than } i), \\ 0 & (\text{index } i \text{ is as important as index } j), \\ 1 & (\text{index } i \text{ is more important than } j), \end{cases} \tag{1}$$

$$t_{ij} = \frac{1}{n}\sum_{k=1}^{N}\left(a_{ik} - a_{jk}\right) = \frac{1}{n}\sum_{k=1}^{N}\left(a_{ik} + a_{kj}\right), \tag{2}$$

$$d_{ij} = \exp\left(t_{ij}\right). \tag{3}$$

Since matrix $\mathbf{A}$ satisfies $a_{ij} = -a_{ji}$ and $a_{ij} = a_{ik} - a_{jk}$, it is an antisymmetric matrix; then, according to the principle of optimal transfer matrix, the optimal transfer matrix $\mathbf{T}$ of matrix $\mathbf{A}$ should conform to Equation (2).

According to the Equations (2) and (3), the judgment matrix $\mathbf{D} = \{d_{ij}\}_{N\times N}$ is obtained.

Due to the properties of the optimal transfer matrix, no consistency check is required. The equation of the weight

Table 2: Index data of boreholes.

Number	Borehole ID	x_1 (m)	x_2 (-)	x_3 (m)	x_4 (m)	x_5 (%)	x_6 (-)	x_7 (m)
1	Q_{under}-19	12.93	4.92	0.00	9.10	83.69	0.30	39.57
2	6-2	15.05	2.10	0.00	9.01	93.15	0.50	10.13
3	Bao19	4.96	1.65	0.00	8.91	94.33	0.30	144.95
4	2015-1	20.00	3.43	0.00	9.01	92.35	0.70	51.36
5	2003-1	26.65	4.76	0.00	8.38	90.50	0.30	66.4
6	2003-2	16.80	11.42	0.00	8.70	71.79	0.10	14.28
7	2010-5	10.99	1.19	0.00	8.10	88.43	0.50	56.66
8	O_2-5	17.37	6.22	3.39	8.02	88.01	0.10	22.68
9	O_2-12	13.80	5.75	0.00	9.00	94.50	0.70	3.57
10	L_{14}-5	13.20	2.73	1.50	8.46	87.42	0.50	70.39
11	2007-2	13.35	3.13	1.39	11.82	87.40	0.90	55.38
12	2007-3	19.26	4.13	0.00	9.16	89.19	0.10	39.65
13	D49	13.50	1.43	1.45	8.60	89.55	0.30	42.83
14	D53	6.5	1.48	4.23	8.39	92.63	0.50	111.89
15	2012-3	34.07	10.88	1.25	2.10	84.84	0.10	2.1
16	89-5	14.15	2.36	10.86	8.07	90.37	0.30	73.4
17	2009-1	41.88	5.88	0.00	5.66	86.48	0.50	19.43
18	2010-4	6.98	1.16	0.00	9.00	90.56	0.30	122.73
19	D40	11.87	1.50	12.15	9.19	91.57	0.30	108.29
20	D46	13.68	1.44	4.12	9.14	88.93	0.30	26.7
21	D54	18.78	4.38	0.00	8.73	89.15	0.10	102.24
22	Bao18	8.05	1.14	0.00	8.84	91.51	0.10	115.9
23	8-7	19.35	2.15	2.00	8.73	86.73	0.10	107.4
24	Bao20	3.82	0.51	0.00	5.87	96.35	0.10	163.93
25	S77	24.20	8.36	2.50	7.70	83.37	0.10	36.73
26	D58	5.14	1.22	2.00	7.96	93.61	0.10	147.29
27	S21	7.80	1.17	3.75	9.46	97.38	0.10	152.34
28	44	8.20	3.24	1.95	9.03	92.34	0.10	171.18

Table 3: Weights determined by the analytic hierarchy process, the entropy weight method, and the comprehensive weight method.

Weight vector	x_1	x_2	x_3	x_4	x_5	x_6	x_7
$\mathbf{W}_1$	0.1513	0.0399	0.0777	0.2018	0.1224	0.0742	0.3327
$\mathbf{W}_2$	0.1362	0.1311	0.1730	0.1649	0.1092	0.1332	0.1524
$\mathbf{W}_3$	0.1504	0.0758	0.1215	0.1911	0.1211	0.1042	0.2359

w_i of the index i is as follows:

$$w_i = \frac{\sqrt[N]{\prod_{j=1}^{N} d_{ij}}}{\sum_{i=1}^{N}\left(\sqrt[N]{\prod_{j=1}^{N} d_{ij}}\right)} \quad (i = 1, 2, \cdots, N). \tag{4}$$

Finally, according to Equation (4), the weight of the plan level to the criterion level and the weight of the criterion level to the objective level are calculated, respectively, and then, the weight vector $\mathbf{W}_1 = \{w_{1i}\}_{1\times n}$ of the plan level to the objective level is obtained, where n is the index number in the plan level.

3.2. Entropy Weight Method. As a weight calculation method, entropy weight method (EWM) has been well applied in the weight calculation of multifactor indexes [24–27].

Assuming that there are m samples and each sample has n indexes, the original matrix $\mathbf{R} = \{R_{ij}\}_{m\times n}$ can be constructed, where R_{ij} represents the data of index j of the sample i.

Then, according to the original matrix $\mathbf{R}$, the normalized matrix $\mathbf{r} = \{r_{ij}\}_{m\times n}$ is calculated.

For the positive indexes that the greater the better indexes, the calculation equation is as follows:

$$r_{ij} = \frac{R_{ij} - \min\left\{R_{1j,} R_{2j}, \cdots, R_{mj}\right\}}{\max\left\{R_{1j,} R_{2j}, \cdots, R_{mj}\right\} - \min\left\{R_{1j,} R_{2j}, \cdots, R_{mj}\right\}}. \tag{5}$$

For negative indexes that the smaller the better indexes, the calculation equation is as follows:

$$r_{ij} = \frac{\max\left\{R_{1j,} R_{2j}, \cdots, R_{mj}\right\} - R_{ij}}{\max\left\{R_{1j,} R_{2j}, \cdots, R_{mj}\right\} - \min\left\{R_{1j,} R_{2j}, \cdots, R_{mj}\right\}}. \tag{6}$$

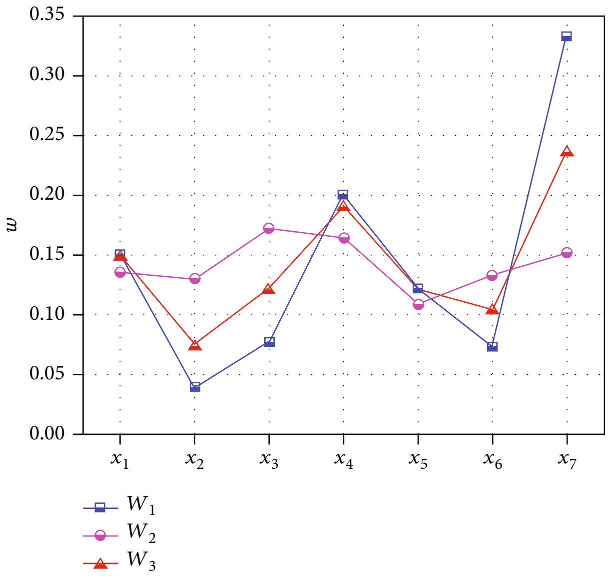

Figure 4: Comparison of weights determined by the analytic hierarchy process, the entropy weight method, and the comprehensive weight method.

Table 4: Numerical characteristics of each index belonging to each risk grade.

Index	Numerical characteristics I	II	III
x_1	(7.5, 6.369, 0.5)	(22.5, 6.369, 0.5)	(37.5, 6.369, 0.5)
x_2	(0.5, 0.425, 0.05)	(2, 0.849, 0.05)	(9.5, 5.520, 0.05)
x_3	(12.5, 2.123, 0.2)	(7.5, 2.123, 0.2)	(2.5, 2.123, 0.2)
x_4	(1.75, 1.486, 0.1)	(5.75, 1.911, 0.1)	(10, 1.699, 0.1)
x_5	(90, 8.493, 1)	(70, 8.493, 1)	(30, 25.478, 1)
x_6	(0.2, 0.170, 0.001)	(0.5, 0.085, 0.001)	(0.8, 0.170, 0.001)
x_7	(108, 57.325, 1)	(30, 8.493, 1)	(10, 8.493, 1)

According the normalized matrix $\mathbf{r} = \{r_{ij}\}_{m\times n}$, calculate the proportion p_{ij} of the j index data of the i sample:

$$p_{ij} = \frac{1 + r_{ij}}{\sum_{j=1}^{n}\left(1 + r_{ij}\right)}. \tag{7}$$

Then, calculate the entropy of all index, and the calculation equation for the entropy value H_j of the index j is

$$H_j = \frac{\sum_{j=1}^{m} p_{ij} \ln p_{ij}}{\ln m}. \tag{8}$$

Calculate the entropy weight of all index, and the calculation equation for the entropy weight w_j of the index j is

$$w_j = \frac{1 - H_j}{\sum_{j=1}^{n}\left(1 - H_j\right)}. \tag{9}$$

Finally, get the weight vector $\mathbf{W}_2 = \{w_{2i}\}_{1\times n}$.

3.3. Comprehensive Weight. Each weight calculation method has its own scope of application, and sometimes, it is often necessary to use a variety of methods to measure the weight of the same data, so that the comprehensive weight has higher performance and can reflect the real characteristics of the data. According to the minimum entropy principle, this paper processes the weight vector $\mathbf{W}_1$ determined by the analytic hierarchy process and the weight vector $\mathbf{W}_2$ determined by the entropy weight method to determine the comprehensive weight vector $\mathbf{W}_3$ [28, 29]. The calculation process is as follows:

$$w_{3j} = \frac{\sqrt{w_{1j} \times w_{2j}}}{\sum_{j}^{n}\sqrt{w_{1j} \times w_{2j}}}, \tag{10}$$

$$\mathbf{W}_3 = \left(w_{31} w_{32} \cdots w_{3n}\right). \tag{11}$$

3.4. Cloud Model. Cloud model is an uncertain cognitive model based on fuzzy set theory and probability concept, which was proposed by Liu et al. [27]. The cloud model can be used to deal with the uncertain conversion between qualitative concepts and quantitative description and has been widely used in algorithm improvement, simulation, risk assessment, geological prediction, excavation, and other fields [30–33]. In the conversion process from quantitative data (influencing factors data) to qualitative concepts (risk grade), the cloud model can better handle the effects of randomness and ambiguity, thus making the evaluation results more scientific and accurate.

Normal cloud is an important cloud model based on normal distribution and Gaussian membership function. Since the expected value curves of influencing factors in natural science are mostly normal distribution or seminormal distribution [34], the normal cloud model is used in this paper to evaluate the risk of water and sand inrush.

Supposing the set $X = \{x\}$ is a domain, the qualitative concept on the domain is defined as Y. For any x belonging to X, there exists a random number $u(x)$ belonging to Y. The set of $u(x)$ is called the membership degree of x belonging to Y, if $u(x)$ satisfies

$$u(x) = \exp\left(-\frac{(x - \mathrm{Ex})^2}{2\mathrm{En}'2}\right). \tag{12}$$

If x satisfies $x \sim N(\mathrm{Ex}, \mathrm{En}'2)$ and $\mathrm{En}' \sim N(\mathrm{En}, \mathrm{He}^2)$, the distribution of x on X is called a normal cloud, and each x is called a cloud drop. Ex, En, and He are the numerical characteristics of a qualitative concept, where Ex represents expectation, En represents entropy, and He represents hyperentropy. If the three numerical characteristics of the qualitative concept are known, the normal cloud generator can be used to generate the normal cloud. The process is as follows:

Step 1. Generate a normal random number En′ with an expected value of En and a standard deviation of He.

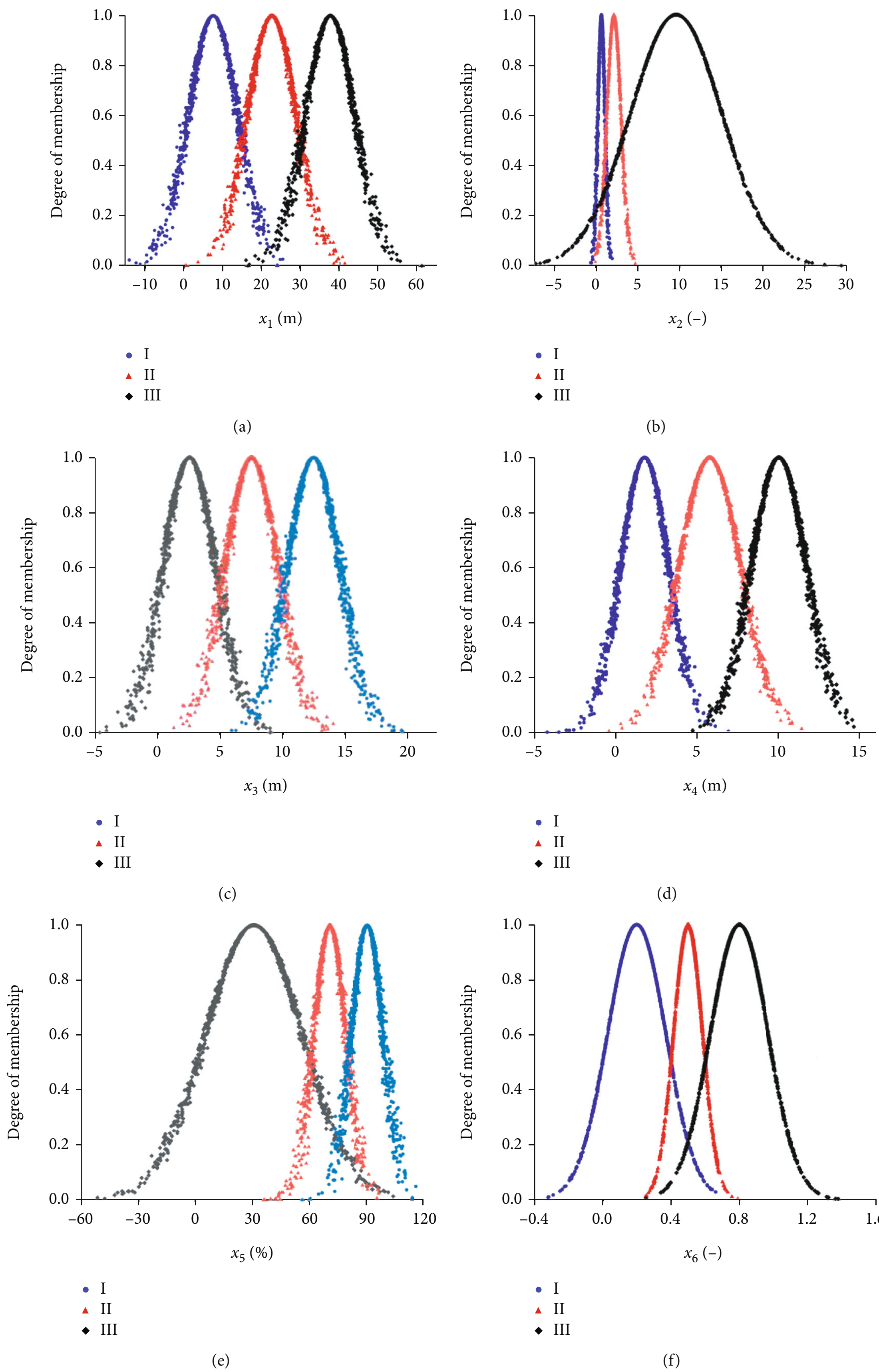

Figure 5: Continued.

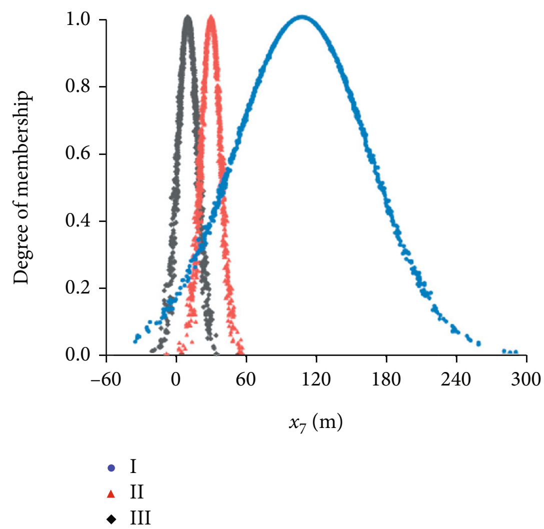

(g)

FIGURE 5: Normal cloud of each index belonging to each risk grade.

TABLE 5: Working face index data.

Name of working face	x_1 (m)	x_2 (-)	x_3 (m)	x_4 (m)	x_5 (%)	x_6 (-)	x_7 (m)
6311-2	26.90	3.81	0.00	8.64	89.15	0.30	53.51

TABLE 6: Membership degree of working face belonging to each risk grade.

Name of working face	Membership degree I	Membership degree II	Membership degree III	Comprehensive weight-cloud model	Actual situation
6311-2	0.3610	0.2086	0.2912	I	I

Step 2. Generate a normal random number x with an expected value of Ex and a standard deviation of abs(En′).

Step 3. Calculate $u(x)$ through Equation (12), and a cloud drop x with a membership degree of $u(x)$ for the qualitative concept is generated.

Step 4. Repeat Step 1–Step 3 until the number of cloud drops meets the requirements.

The calculation of the numerical characteristics (Ex_{ij}, En_{ij}, and He_{ij}) and of the index i belonging to the risk grade j is as follows.

Assuming that the upper and lower boundary values of the index i belonging to the risk grade j are x_{ij}^1 and x_{ij}^2, then

$$\mathrm{Ex}_{ij} = \frac{\left(x_{ij}^1 + x_{ij}^2\right)}{2}. \quad (13)$$

Since the boundary value is from one grade to another and should belong to both grades [32], so

$$\mathrm{En}_{ij} = \frac{\left(x_{ij}^1 - x_{ij}^2\right)}{2.355}. \quad (14)$$

The size of He_{ij} is determined according to the fuzziness and randomness of the specific case, and the value is about 0.1 times of En_{ij} [35].

Some scholars use the cloud model to obtain the membership degree by using the cloud generator to randomly generate cloud drops and then obtain the average membership degree [33]. The membership degree obtained by this method has a certain degree of volatility, resulting in the same calculation process which may not be able to obtain the same assessment results. In order to obtain a stable membership degree, the membership function is obtained based on Equation (12). The membership function is shown below:

$$u_{ij} = \exp\left(-\frac{\left(x_i - \mathrm{Ex}_{ij}\right)^2}{2\mathrm{En}_{ij}}\right), \quad (15)$$

where x_i represents the value of the index i and u_{ij} represents the membership degree of the index i belonging to the risk grade j.

The membership degree matrix $\mathbf{U} = \{u_{ij}\}_{n\times l}$ of the assessment object is obtained, where n is the number of indexes, and l is the number of risk grades.

In order to find out the membership degree of the assessment object to a risk grade, it is necessary to multiply the membership degree of index of the assessment object corresponding to the risk grade by the index weight and add them, so as to obtain the membership degree of the assessment object to the risk grade.

The comprehensive weight vector $\mathbf{W}_3$ is combined with the membership matrix $\mathbf{U}$ of the assessment object to obtain the matrix $\mathbf{B}$.

$$\mathbf{B} = \mathbf{W}_3\mathbf{U} = (b_1, b_2, \cdots, b_n), \tag{16}$$

$$b_j = \sum_{i=1}^{n} w_i u_{ij} \quad (j = 1, 2, \cdots, l). \tag{17}$$

In Equation (17), b_j represents the membership of the assessment object to the risk grade j. Then, according to the principle of maximum membership degree, the risk grade $j_{\max}$ corresponding to the maximum membership degree $b_{j\max}$ is the water inrush risk grade of the assessment object.

4. Preparation of Assessment

4.1. Index Selection. The occurrence of water and sand inrush in the mining under the loose layer depends on the combined effect of various influencing factors. According to the hydrogeological data in the sixth mining area of Baodian Coal Mine, this paper selects seven influencing factors, namely, the aquifer thickness (x_1), the thickness ratio of the sand layer to clay layer (x_2), the thickness of the bottom clay layer (x_3), the coal seam thickness (x_4), the percentage of core recovery (x_5), the geological structure (x_6), and the bedrock thickness (x_7), as index. These factors can be categorized into the characteristics of loose layer and the characteristics of rock layer. The hierarchical structure system of water and sand inrush index for mining under loose layer in the mining under the loose layer is shown in Figure 3.

(1) The aquifer thickness (x_1). Generally speaking, the aquifer in the loose layer is mainly sand layer. Thicker aquifer can store more groundwater, and under the influence of mining, there is a greater possibility of water and sand inrush [36]

(2) The thickness ratio of the sand layer to clay layer (x_2). The sand layer with fractures has strong water storage and water conductivity, while the clay layer has certain water and sand resistance. The thickness ratio of the sand layer to clay layer in the loose layer of the Quaternary lower group determines the risk of water and sand inrush

(3) The thickness of the bottom clay layer (x_3). The clay layer at the bottom of the loose layer is a powerful barrier that directly hinders the downward seepage and inrush of water and sand in the upper aquifer. The thicker the clay layer at the bottom is, the more likely it will reduce the possibility of water and sand inrush in the exploitation of coal resources [36]

(4) The coal seam thickness (x_4). The height of the roof fall zone and fracture zone caused by coal seam mining is related to the cumulative mining thickness of the coal seam. Generally speaking, the greater the cumulative mining thickness of the coal seam, the greater the height of the caving zone and fracture zone of the roof. In mining, it is necessary to set sand-prevention coal and rock pillars to avoid excessive water and sand inrush due to the excessive height of the caving zone and fracture zone. Since No. 3 coal is the main mineable coal seam in the sixth mining area, this paper uses the thickness of the No. 3 coal seam instead of the cumulative mining thickness as the index [37]

(5) The percentage of core recovery (x_5). The integrity of the core taken during drilling is related to the degree of rock fragmentation. The core of the bedrock is relatively complete, indicating that the bedrock has a low degree of fragmentation and is an effective water-blocking layer. The possibility of water and sand inrush is low when mining [38]

(6) The geological structure (x_6). The development degree of geological structure can be expressed by density of faults, fault drop, density of joints, etc. The area with developed geological structures has high risk of water and sand inrush. Based on the actual mining experience and geological data, the degree of geological structure development is divided, and the equation is as follows [39]:

$$x_6 = \begin{cases} 0.1, & \text{not developed}, \\ 0.3, & \text{less developed}, \\ 0.5, & \text{more developed}, \\ 0.7, & \text{developed}, \\ 0.9, & \text{very developed}. \end{cases} \tag{18}$$

(7) The bedrock thickness (x_7). The bedrock is thick and stable, the fracture zone cannot develop to the aquifer, and the risk of water and sand inrush is low. If the bedrock is thin or missing, the fracture zone develops to the aquifer, and the risk of water and sand inrush is high [33, 40]

4.2. Risk Grade. The risk of water and sand inrush is divided into three grades, namely, low risk (I), medium risk (II), and high risk (III). The corresponding situation of grade I is that the aquifer at the bottom of the loose layer has little influence on the mining of the working face, and the water and sand inrush will not occur in the mining process. The corresponding situation of grade II is that the aquifer at the bottom of the loose layer has a certain influence on the mining of the working face. For example, the roof of the working face often shows the phenomenon of water leaching, and the water inflow of the working face changes greatly; mining process, sudden water, and sand inrush may occur. The corresponding situation of grade III is that the aquifer at the bottom of the loose layer has a great impact on the mining of the working face. When the roof comes to pressure, the water inflow of the working face changes greatly, and there is a great possibility of sudden water and sand inrush in the mining process. According to the engineering experience, each index is divided into intervals according to the risk grade, as shown in Table 1.

4.3. Weight Calculation. Based on the analysis and statistics of hydrogeological data and borehole data in the study area, 28 borehole data are collected as samples, as shown in Table 2, and the borehole locations are shown in Figure 2.

After consulting and analysis, this paper argues that for the occurrence of water and sand inrush, in the criterion level, the characteristics of the rock layer are greater than the characteristics of loose layer. For the characteristics of loose layer, the index weights in descending order are the aquifer thickness (x_1), the thickness of the bottom clay layer (x_3), and the thickness ratio of the sand layer to clay layer (x_2). For the characteristics of the rock layer, the index weights in descending order are the bedrock thickness (x_7), the coal seam thickness (x_4), the percentage of core recovery (x_5), and the geological structure (x_6). The comparison matrix $\mathbf{A}_1$ of criterion level and the comparison matrices $\mathbf{A}_2$ and $\mathbf{A}_3$ of plan level are obtained as follows:

$$\mathbf{A}_1 = \begin{bmatrix} 0 & -1 \\ 1 & 0 \end{bmatrix},$$
$$\mathbf{A}_2 = \begin{bmatrix} 0 & 1 & 1 \\ -1 & 0 & -1 \\ -1 & 1 & 0 \end{bmatrix}, \tag{19}$$
$$\mathbf{A}_3 = \begin{bmatrix} 0 & 1 & 1 & -1 \\ -1 & 0 & 1 & -1 \\ -1 & -1 & 0 & -1 \\ 1 & 1 & 1 & 0 \end{bmatrix}.$$

The weight vector $\mathbf{W}_1$ is calculated according to Equation (4). According to the data in Table 2, the weight vector $\mathbf{W}_2$ is determined by the entropy weight method, and then, the comprehensive weight vector $\mathbf{W}_3$ is obtained by Equation (10). Analyzing the weight vector $\mathbf{W}_2$, the thickness of the bottom clay layer (x_3), the coal seam thickness (x_4), and the bedrock thickness (x_7) have a greater impact on the risk of water and sand inrush. Among the weight vector $\mathbf{W}_3$, the aquifer thickness (x_1), the coal seam thickness (x_4), and the bedrock thickness (x_7) are larger. Combining the weights determined by the three methods, it can be concluded that the coal seam thickness (x_4) and the bedrock thickness (x_7) are the main influencing factors of water and sand inrush. The index weights of the three methods are shown in Table 3 and Figure 4.

4.4. Numerical Characteristics. Based on the risk grade range and borehole sample data (Table 2), by using Equations (13) and (14), the numerical characteristics (Ex, En, and He) of each index belonging to risk grades I, II, and III are determined, as shown in Table 4.

According to the normal cloud generation process and the numerical characteristics, the normal cloud of each index belonging to each risk grade is generated (Figure 5). The number of the cloud drops for each normal cloud is 1000. The normal cloud can represent the distribution of the membership degree of the index belonging to a certain risk grade.

As can be seen from Figure 5, Ex determines the position of the center point of the risk grade normal cloud; En determines the range of the risk grade normal cloud. The larger the En, the larger the risk level normal cloud range. He determines the discreteness of the normal cloud of risk grades. When the ratio of He to En is small, the distribution of the normal cloud tends to a curve with a normal distribution. When the ratio of He to En is large, the dispersion of the normal cloud is large.

5. Verification via the Application

The 6311-2 working face is located in the west of Baodian Coal Mine, and the south of the working face is close to the outcrop area of the No. 3 coal seam aeolian oxidation zone in the sixth mining area. The No. 3 coal seam is mined at the working face, the thickness of the coal seam is about 8.12~9.16 m, and the average is about 8.64 m. The Quaternary lower group is composed of gray-green, gray-yellow, and gray-white clay; clay-bearing gravel; and sand. The main aquifers of the lower group are clay gravel and gravel layers.

The coal seam of the working face is a monoclinic structure and belongs to the north wing of the Baojiachang anticline. Small secondary wide and gentle folds are developed in the working face. The maximum water inflow of the 6311-2 working face during mining is 24 m^3/h, and it is 18.9 m^3/h under normal conditions. The water inflow of the working face is basically the water inflow after mining and the water inflow during production. The working face did not show excessive water inrush locally and at intervals, and no water and sand inrush disaster occurred.

According to the corresponding geological report, the index data of the working face was determined (Table 5), by using Equations (15)–(17) to calculate the membership degree of the working face belonging to each risk grade according to the index data of the working face. According to the calculation results (Table 6), the maximum membership degree of the 6311-2 working face is 0.3610, and the water and sand inrush risk grade corresponding to the maximum membership degree is grade I, which means that water and sand inrush will not occur in mining. The actual mining process of this working face did not appear to have water and sand inrush, which is consistent with the prediction of the comprehensive weight-cloud model assessment method proposed in this paper. This result illustrates the feasibility of this method.

6. Conclusions

To reduce the randomness and ambiguity of the influencing factors in the prediction of the risk of water and sand inrush and to better assess the risk of water and sand inrush in short-distance mining under thick loose layers of coal mines, this paper proposes a new risk assessment method of water and sand inrush based on the comprehensive weight and cloud model. The method is applied to the risk assessment of water and sand inrush in the 6311-2 working face in the sixth mining area of Baodian Coal Mine. The following conclusions are drawn from the research:

(1) Analyzing the weights determined by the analytic hierarchy process, the entropy weighting method, and the comprehensive weighting method, the weight of the bedrock thickness and the coal seam thickness are all ranked in the top three of the three weights. It can be considered that among the seven indicators that affect the risk of water inrush and sand inrush, the bedrock thickness and the coal seam thickness have a greater influence on the risk of water inrush and sand inrush and are the main influencing factors

(2) The comprehensive weight-cloud model method is applied to assess the risk of water and sand inrush in the working face, and the assessment result is consistent with the actual situation. It shows that the comprehensive weight-cloud model method has good prediction performance and can provide scientific reference for safe mining under thick loose layer in deep mines in southwest Shandong

(3) The comprehensive weight-cloud model method is based on the existing sample data. The number of samples, the selection of indexes, and the division of risk grade interval will have a certain impact on the assessment results of the method. In view of the complexity of water and sand inrush in close-distance mining under thick loose layer, in order to obtain more accurate prediction results, it is necessary to collect more engineering examples and sample data, so as to improve the accuracy of the method

Data Availability

All data, models, or codes generated or used during the study are available from the corresponding author by request.

Conflicts of Interest

The authors declare no conflicts of interest.

Acknowledgments

The authors of the paper would like to extend grateful thanks to the National Natural Science Foundation of China (Grant No. 51774199) for its support and Baodian Coal Mine for providing relevant geological data.

References

[1] W. H. Sui, Y. K. Liang, G. L. Zhang, Q. H. Dong, and B. B. Yang, "Study status and outlook of risk evaluation on water inrush and sand inrush mechanism of excavation and mining," *Coal Science and Technology*, vol. 39, no. 11, pp. 5–9, 2011.

[2] Z. H. Li, X. P. Ding, and Z. H. Cheng, "Research on fractal characteristics of overlying strata crack evolution in coal seam with thin bedrock," *Journal of Mining & Safety Engineering*, vol. 27, no. 4, pp. 576–580, 2010.

[3] W. H. Sui, D. D. Wang, Y. J. Sun, W. F. Yang, Z. M. Xu, and L. Feng, "Mine hydrogeological structure and its responses to mining," *Journal of Engineering Geology*, vol. 27, no. 1, pp. 21–28, 2019.

[4] H. Q. Lian, X. X. Xia, W. Ran, and T. Yan, "Possibility analysis of water and sand inrush at shallow buried coal seam with unconsolidated formation and thin bedrock," *Safety in Coal Mines*, vol. 46, no. 2, pp. 168–171, 2015.

[5] F. Wang, C. Zhang, X. Zhang, and Q. Song, "Overlying strata movement rules and safety mining technology for the shallow depth seam proximity beneath a room mining goaf," *International Journal of Mining Science and Technology*, vol. 25, no. 1, pp. 139–143, 2015.

[6] B. Chen, S. C. Zhang, Y. Y. Li, and J. P. Li, "Experimental study on water and sand inrush of mining cracks in loose layers with different clay contents," *Bulletin of Engineering Geology and the Environment*, vol. 80, no. 1, pp. 663–678, 2021.

[7] G. Fan, D. Zhang, S. Zhang, and C. Zhang, "Assessment and prevention of water and sand inrush associated with coal mining under a water-filled buried gully: a case study," *Mine Water and the Environment*, vol. 37, no. 3, pp. 565–576, 2018.

[8] H. Li, J. Li, L. Li, H. Xu, and J. Wei, "Prevention of water and sand inrush during mining of extremely thick coal seams under unconsolidated Cenozoic alluvium," *Bulletin of Engineering Geology and the Environment*, vol. 79, no. 6, pp. 3271–3283, 2020.

[9] Q. Liu and B. Liu, "Experiment study of the failure mechanism and evolution characteristics of water-sand inrush geo-hazards," *Applied Sciences*, vol. 10, no. 10, p. 3374, 2020.

[10] Y. Xu, Y. Luo, J. Li, K. Li, and X. Cao, "Water and sand inrush during mining under thick unconsolidated layers and thin bedrock in the Zhaogu No. 1 Coal Mine, China," *Mine Water and the Environment*, vol. 37, no. 2, pp. 336–345, 2018.

[11] W. Yang, L. Jin, and X. Zhang, "Simulation test on mixed water and sand inrush disaster induced by mining under the thin bedrock," *Journal of Loss Prevention in the Process Industries*, vol. 57, pp. 1–6, 2019.

[12] D. Ma, H. Duan, X. Li, Z. Li, Z. Zhou, and T. Li, "Effects of seepage-induced erosion on nonlinear hydraulic properties of broken red sandstones," *Tunnelling and Underground Space Technology*, vol. 91, article 102993, 2019.

[13] D. Ma, H. Duan, J. Zhang, X. Feng, and Y. Huang, "Experimental investigation of creep-erosion coupling mechanical properties of water inrush hazards in fault fracture rock masses," *Chinese Journal of Rock Mechanics and Engineering*, vol. 40, no. 9, pp. 1751–1763, 2021.

[14] J. C. Zhong, H. W. Zhou, Y. F. Zhao, Y. Q. Liu, H. Y. Yi, and D. J. Xue, "The two-phase flow of water-sand inrush under shallow coal seam mining: a coupled numerical study," *Engineering Mechanics*, vol. 34, no. 12, pp. 229–238, 2017.

[15] Q. F. Zhao, N. Zhang, C. L. Han et al., "Simulation experiment of water-sand inrush during the mining of the shallow coal seam under roof aquifer with thin bedrock," *Journal of Mining & Safety Engineering*, vol. 34, no. 3, pp. 444–451, 2017.

[16] T. Peng, X. H. Feng, L. L. Long, Y. Wang, C. Niu, and Y. F. Liu, "Study on mechanism of water inrush and sand inrush in mining of coal seam with thick overlying bedrock," *Coal Science and Technology*, vol. 47, no. 7, pp. 260–264, 2019.

[17] S. C. Zhang, Y. Y. Li, J. P. Li, W. H. Yang, G. L. Wang, and Z. J. Wen, "Experimental studies on variation characteristics of physical parameters during water and sand burst through mining fractures," *Journal of China Coal Society*, vol. 45, no. 10, pp. 3548–3555, 2020.

[18] D. Ma, H. Duan, W. Liu, X. Ma, and M. Tao, "Water–sediment two-phase flow inrush hazard in rock fractures of overburden strata during coal mining," *Mine Water and the Environment*, vol. 39, no. 2, pp. 308–319, 2020.

[19] H. Pu, S. R. Guo, D. J. Liu, J. C. Xu, and J. Wang, "Study on laws of water inrush and sand burst migration based on LBM-DEM coupling method," *Coal Science and Technology*, vol. 49, no. 2, pp. 206–216, 2021.

[20] X. Deng, J. M. Li, H. J. Zeng, J. Y. Chen, and J. F. Zhao, "Analysis and application research on the weight calculation method of AHP," *Mathematics in Practice and Theory*, vol. 42, no. 7, pp. 93–100, 2012.

[21] Y. S. Bi, J. W. Wu, X. R. Zhai, S. H. Shen, R. Hu, and Q. D. Ju, "Evaluation of coal mine aquifer water-richness based on AHP and independent weight coefficient method," *Journal of China Hydrology*, vol. 40, no. 4, pp. 40–45, 2020.

[22] Q. Li and W. H. Sui, "Risk evaluation of mine-water inrush based on principal component logistic regression analysis and an improved analytic hierarchy process," *Hydrogeology Journal*, vol. 29, no. 3, pp. 1299–1311, 2021.

[23] J. X. Wang, H. S. Liu, and M. Qiu, "FDAHP-TOPSIS model for evaluation of the water inrush risk from coal floors," *Journal of Mining and Strata Control Engineering*, vol. 3, no. 2, pp. 104–115, 2021.

[24] X. Y. Fan, Z. X. Jia, X. L. Bai, T. J. Yang, and Y. Liu, "Classification of extremely soft rock tunnels using comprehensive evaluation model of entropy-weighted fuzzy," *Journal of Engineering Geology*, vol. 27, no. 6, pp. 1236–1243, 2019.

[25] X. B. Gu, S. T. Wu, X. Ji, and Y. H. Zhu, "The risk assessment of debris flow hazards in Banshanmen gully based on the entropy weight-normal cloud method," *Advances in Civil Engineering*, vol. 2021, Article ID 8841310, 11 pages, 2021.

[26] J. Y. Li, Q. M. Liu, Y. Liu, and H. C. Chai, "Risk assessment of water inrush from coal seam roof based on GIS and entropy method," *Coal Engineering*, vol. 51, no. 8, pp. 115–119, 2019.

[27] W. T. Liu, Q. Sun, and B. C. Xu, "Risk evaluation of water inrush from coal seam floor based on GIS and principal component analysis-entropy weight method," *Mining Research and Development*, vol. 40, no. 11, pp. 83–88, 2020.

[28] W. Q. Zhang, Z. Y. Wang, J. L. Shao, X. X. Zhu, W. Li, and X. T. Wu, "Evaluation on the stability of vertical mine shafts below thick loose strata based on the comprehensive weight method and a fuzzy matter-element analysis model," *Geofluids*, vol. 2019, Article ID 3543957, 15 pages, 2019.

[29] H. Bai, F. Feng, J. Wang, and T. Wu, "A combination prediction model of long-term ionospheric foF2 based on entropy weight method," *Entropy*, vol. 22, no. 4, p. 442, 2020.

[30] D. Y. Li, H. J. Meng, and X. M. Shi, "Membership cloud and membership cloud generator," *Journal of Computer Research and Development*, vol. 32, no. 6, pp. 15–20, 1995.

[31] X. T. Wang, S. C. Li, X. Y. Ma, Y. G. Xue, J. Hu, and Z. Q. Li, "Risk assessment of rockfall hazards in a tunnel portal section based on normal cloud model," *Polish Journal of Environmental Studies*, vol. 26, no. 5, pp. 2295–2306, 2017.

[32] K. G. Li, M. L. Li, and Q. C. Qin, "Research on evaluation method of rock burst tendency based on improved comprehensive weighting," *Chinese Journal of Rock Mechanics and Engineering*, vol. 39, no. S1, pp. 2751–2762, 2020.

[33] X. T. Wang, S. C. Li, Z. H. Xu, J. Hu, D. D. Pan, and Y. G. Xue, "Risk assessment of water inrush in karst tunnels excavation based on normal cloud model," *Bulletin of Engineering Geology and the Environment*, vol. 78, no. 5, pp. 3783–3798, 2019.

[34] X. J. Chen, L. J. Chen, Y. Song, and P. Y. Bi, "Prediction and analysis of karst collapse with entropy-normal cloud model," *Journal of Engineering Geology*, vol. 27, no. 6, pp. 1389–1394, 2019.

[35] Z. Y. Chen and Z. H. Dai, "Improved cloud model for stability evaluation of reservoir slopes," *Journal of Engineering Geology*, vol. 28, no. 3, pp. 619–625, 2020.

[36] W. Zhang, Z. Wang, X. Zhu, W. Li, B. Gao, and H. Yu, "A risk assessment of a water-sand inrush during coal mining under a loose aquifer based on a factor analysis and the Fisher model," *Journal of Hydrologic Engineering*, vol. 25, no. 8, 2020.

[37] W. T. Liu, J. X. Li, and W. Q. Zhang, "Fuzzy mathematical method for roof water inflow grade evaluation," *Journal of China Coal Society*, vol. 26, no. 4, pp. 399–403, 2001.

[38] Y. D. Ji, "The risk assessment of roof water inrush based on cluster analysis and fuzzy comprehensive evaluation," *Mining Safety & Environmental Protection*, vol. 46, no. 4, pp. 68–72, 2019.

[39] W. Q. Zhang, G. P. Zhang, W. Li, and X. Hu, "A model of Fisher's discriminant analysis for evaluating water inrush risk from coal seam floor," *Journal of China Coal Society*, vol. 38, no. 10, pp. 1831–1836, 2013.

[40] B. Li, W. Q. Zhang, and L. Ma, "Influencing factors and prediction of mine water inrush disaster under thick unconsolidated layers and thin bedrock," *Journal of Shandong University of Science and Technology (Natural Science)*, vol. 36, no. 6, pp. 39–46, 2017.

Hindawi
Geofluids
Volume 2023, Article ID 9311206, 14 pages
https://doi.org/10.1155/2023/9311206

Research Article

Experiment and Numerical Simulation of Strength and Stress Distribution Behaviors of Anchored Rock Mass in a Roadway

Honghui Zhao,[1,2] Haijian Su ,[1] Xiaofeng Qin,[1] Kai Zhang ,[1] Yu Jiang,[1] and Wenbo Wang[1]

[1]*State Key Laboratory for Geomechanics and Deep Underground Engineering, China University of Mining and Technology, Xuzhou 221116, China*
[2]*East China Environmental and Geotechnical Engineering Branch, China National Petroleum Corporation, Qingdao 266000, China*

Correspondence should be addressed to Haijian Su; hjsu@cumt.edu.cn

Received 24 February 2022; Revised 31 May 2022; Accepted 24 November 2022; Published 12 April 2023

Academic Editor: Chao-Zhong Qin

Due to the influence of the ground stress, mining disturbance, and other factors, the roadway surrounding rock in deep underground engineering such as mines, tunnels, and underground caverns is prone to looseness and deformation with the excavation of roadways. In such engineering, the bolt support is frequently employed to stabilize the surrounding rock. In this work, a part of the anchor and the surrounding rock were taken as a simplified model of the anchorage rock mass, and the laboratory compression test was performed on the similitude model. Then, the FLAC3D software was used to simulate varying numbers of bolts and different lateral pressure conditions, and the peak stress, the maximum principal stress field, and the anchor stress field distribution of the anchorage rock mass were obtained. The influence of bolt pretightening force and row spacing on the stability of surrounding rock was discussed using the combined arch theory. The results show that increasing the number of bolts and lateral pressure in the anchorage rock mass can significantly improve the stress value and distribution range of the maximum principal stress field and the anchorage stress field. The fluctuation of the anchorage stress field at different anchorage distances can be lessened by increasing the number of bolts (bolt density). When the lateral pressure exceeds 3 MPa, the anchorage mechanical characteristics of the anchorage rock mass tend to remain stable. The coverage of the effective anchorage stress field and the thickness of the surrounding rock anchorage composite arch can be increased by increasing the bolt pretightening force and decreasing row spacing, consequently improving the anchorage mechanical characteristics of the anchorage rock mass. The research results can be used as a theoretical reference for choosing appropriate bolt support parameters for the roadway surrounding rock.

1. Introduction

The surrounding rock of the roadway in deep engineering such as mines, tunnels, and underground caverns is prone to deformation due to the high ground stress, mining disturbance, and other factors [1, 2]. The excessive deformation of the surrounding rock structure may cause the floor heave, rib spalling, roof leakage, roof fall, and other phenomena [3–5], which manifests as the formation of a loose fracture structure with fully developed fractures in the rock mass around the roadway [6]. To ensure that roadways can be used normally, timely support is required from the start of excavation to limit deformation and displacement of the surrounding rock. It is critical to effectively strengthen the bearing capacity of the surrounding rock structure and the stability of the surrounding rock after support.

Bolt support, the most commonly used support measure in rock engineering, may effectively stabilize the surrounding rock by improving and making full use of the bearing capacity of the rock mass. Currently, research on bolt support can be roughly divided into three categories according to the main focus: (i) study on the effects of the properties of the anchored rock mass (surrounding rock), such as the lithology of the surrounding rock, the strength of the surrounding rock, joints, cracks, and weak interlayer [7–10]; (ii) study on the effects of external load, that is, considering the stress state (tension, compression, shear), loading, unloading, and the creep of the bolt according to the engineering site [11, 12]; (iii) study on the effects of the nature of the bolt itself, such as type, size (diameter, length), row spacing, pretightening force, and the spatial distribution position of multiple bolts [13–18]. Some contributed results have been obtained: in terms of the bolting mechanisms, Kang [19, 20] considered that the main function of bolt support on surrounding rock is to control the separation, sliding, cracking, and dilatancy deformation of rock mass in the anchorage zone and put forward the corresponding key bearing ring theory. Cao et al. [21] investigated the load transfer mechanism of the bolt support system, deduced the two-stage failure mode of the bolt anchorage system, and discussed the failure mode of the bolt by using a bond strength model and the iterative method. Song and Mu [22] discussed the theoretical calculation of the bearing capacity and supporting load of the bolt combination arch, the reasonable thickness of the combined arch, and the reasonable length of the anchor bolt and put forward relevant reasonable calculation formulas, based on the analysis of bolt-shotcrete support mechanism and failure characteristics of soft rock. In terms of anchorage mechanical properties, Guo et al. [23] established the mechanical model (considering the tray effect) of anchorage surrounding rock based on the elastic theory, believing that the influence of the tray on the stress of the surrounding rock supported by the bolt axis can be ignored except near the surface of the surrounding rock. Based on the self-developed test system of the composite bolt-rock bearing structures, Zhang et al. [24] investigated the influence of bolt support density on the bearing characteristics of anchor composite bearings, obtained the strength and failure characteristics of anchor composite bearings, and found the variation law of central stress and surrounding rock displacement of the composite bolt-rock bearing structure. Zong et al. [25] found that the number of bolts and the pretightening force would affect the failure mode. The failure mode of fractured sandstone changes from the tensile failure to tensile-shear mixed failure with the increase in bolts. The pretightening force can inhibit the formation and evolution of the tensile crack, delay the failure process of fractured sandstone under anchorage, and promote its transformation from the brittle failure to plastic failure. Du et al. [26] studied the effect of bolts on the stress redistribution of roadway surrounding rock and believed that the bolt could improve the strength of the roadway by increasing the minimum main force around the roadway. A comprehensive ground arch that is crucial to the stability of the roadway will be formed around the roadway under appropriate supporting conditions.

With the excavation of the roadway, the stress environment of the surrounding rock changes, and the plastic zone forms in the surrounding rock of the roadway. The stress is redistributed, and large stress appears in the roadway side area, which often causes the two sides to break and swell. The role of the bolt support is to keep the broken rock mass from separating, sliding, cracking, and deforming. Therefore, this work took the bolt support of the roadway surrounding rock in Gubei coal mine as the background. The surrounding rock of the roadway sidewall area under the anchorage effect of the bolt was taken as the research area (Figure 1), which was simplified as the model of the anchorage rock mass. Laboratory tests and FLAC3D numerical simulation tests were carried out to study the mechanical properties of the surrounding rock anchorage under varied bolt numbers (bolt density) and different lateral pressures. In addition, the influence of bolt pretightening force and bolt row spacing on the anchorage effect of the surrounding rock was discussed based on the combined arch theory.

2. Experimental Study of Anchorage Effect of Surrounding Rock Mass

2.1. Experimental Method and Procedure. A similitude model was poured according to the real mechanical properties of the surrounding rock mass in the Gubei coal mine, Huainan mining area, China. To simulate the anchorage rock mass in line with the actual state of the site to a large extent, the aggregate of the pouring model (the aggregate gradation was 8~10 cm) was picked from the rock of the actual roadway site in the test process. Quartz sand, cement, and gypsum combined with a certain amount of water were selected as the anchorage rock mass model cementing materials. Through many comparative tests, the mass ratio of the quartz sand, cement, gypsum, and water was chosen as 0.5 : 1 : 0.2 : 0.6. The size of the rock specimen is frequently chosen as large as feasible in the rock mechanics tests using a physical similarity model, and the ideal state is to construct a model that is close to the real size, because the larger the rock sample size, the more accurately the test findings can reflect the actual engineering properties. However, the test devices and other factors limit the size of the specimen. After careful consideration of the above issues, the actual anchored surrounding rock mass was adequately simplified. The cubic anchorage rock mass specimen with a size of 200 mm* 200 mm* 200 mm was poured in this work utilizing the above ingredients and ratios, as indicated in Figure 2(a) [27, 28]. After pouring in the mold, the specimen was left for 24 hours in its natural state and then removed. Then, the specimen was put into the maintenance water tank at a constant temperature for 7 days and, finally, made it naturally air dried and wrapped with preservative film to maintain moisture content. At the same time, the specimens without bolt reinforcement were also prepared for comparative analysis.

The anchor bolt was placed after the anchorage rock specimen was poured, as shown in Figure 2(b). First, a 12 mm diameter prefabricated bolt hole was bored in the center of the specimen. Then, the bolt was mounted, as illustrated in Figure 2(c), with bolts, pallets, nuts, and gaskets as its primary components. A torsion wrench was used to apply a pretightening force of 15.59 kN to the bolt. The 7075-T6 aluminum alloy rod with a diameter of 10 mm was chosen to simulate the body of the anchor bolt. To determine the mechanical properties of the anchor bolt, a tensile test of the aluminum alloy metal rod was performed prior to the

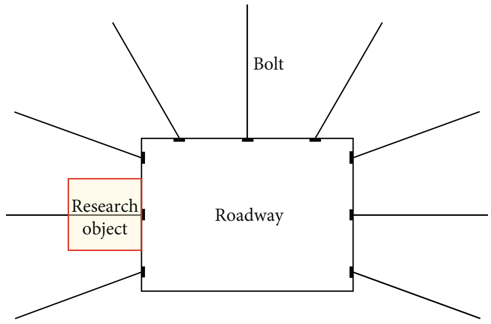

Figure 1: Research object of surrounding rock mass in a roadway.

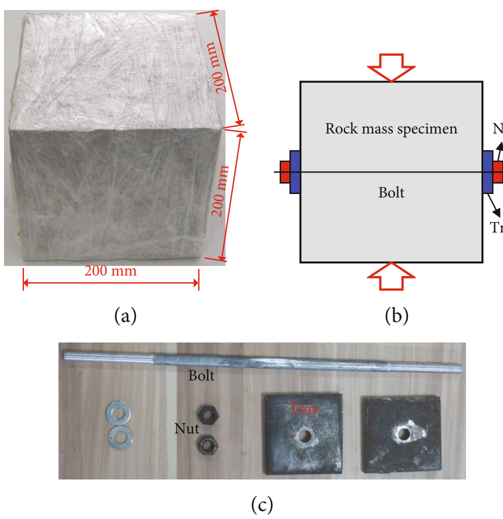

Figure 2: (a) Rock mass specimen, (b) schematic diagram of anchorage method, and (c) bolt and auxiliary appliances.

start of the test. The elastic modulus, yield strength, yield strain, and peak stress of the aluminum alloy metal rod were 70.65 GPa, 426.59 MPa, $7.69^{*}10^{-3}$, and 559.9 MPa, respectively. The tray was a square steel plate with a size of 70 mm*70 mm*10 mm and a middle hole diameter of 12 mm.

The YNS2000 servo test system, with a maximum test force of 2000 kN, was used to perform the compression tests. During the loading operation, the test system will automatically collect data on the axial displacement and axial force of the loaded specimen. In the test, a loading rate of 0.5 mm/min was used. Before the test, a reasonable amount of Vaseline was evenly placed over the upper and lower ends of the specimen to reduce the influence of end-face friction on the test findings.

2.2. Experimental Result and Analysis. Figure 3 shows the axial stress-strain curves of the anchored and unanchored rock mass model specimens. The compaction stage (*oa*), the linear elastic growth stage (*ab*), the plastic deformation stage (*bc*), and the strain softening stage (*cd*) are all found in the axial loading curves of the two models, according to the test results. The peak strength and elastic modulus of the specimen after anchorage have increased by 36.65% and 28.33%, respectively, from 9.25 MPa and 1.20 GPa to 12.64 MPa and 1.54 GPa. Furthermore, following anchorage, the residual strength of the surrounding rock model specimen is much higher than that before anchorage.

Three states (the initial failure state, axial stress peak state, and final state) of the specimen were chosen to compare the failure characteristics of the anchored and unanchored rock mass model specimens, as shown in Figure 4. Compared with the anchored, the broking degree of the unanchored surrounding rock model sample is relatively lower. The number of cracks propagating on the surface of the specimen is noticeably lower at the peak state and final state, and the specimen is eventually destroyed by multiple massive cracks. When the anchorage surrounding rock model specimen ultimately breaks, many cracks appear inside the specimen, and the degree of fracture is substantially greater than that of the model specimen without anchorage. In summary, the surrounding rock interacts with the bolt to generate an anchorage rock mass under the action of bolt support. The bolt has strong supporting ability, which can effectively improve the bearing capacity of the surrounding rock while reducing deformation and failure [29, 30].

3. Numerical Simulation of Anchorage Mechanical Properties of Surrounding Rock Mass

3.1. Establishment of the Numerical Model. The numerical calculation method has been widely and rapidly applied in the study of geotechnical engineering problems with the rapid development of computer technology, which tremendously promotes the development of geotechnical mechanics. It is becoming increasingly significant in numerous domains of modern science and technology due to its remarkable benefits of high reproducibility, fast cycle time, and low cost. FLAC3D is a three-dimensional fast Lagrangian analysis program developed by Itasca in the United States that can better simulate the mechanical behavior of geological materials when reaching the strength or yield limit and makes complex geotechnical engineering or mechanical problems easy to simulate [31, 32]. Due to the influence of test conditions and other factors, it is difficult to obtain the distribution characteristics of parameters such as the stress field in the physical model. Therefore, this work used the FLAC3D numerical software to study and analyze the surrounding rock anchorage model.

As shown in Figure 5, the FLAC3D numerical model was built as a cube with a side length of 200 mm, which mainly includes the model body, anchor bolt, and tray (70 mm*70 mm*10 mm) based on the physical model test of the surrounding rock anchorage. The center of the model was symmetrically arranged and positioned at the origin of the coordinates. The model contained 64784 units and 70271 nodes after meshing. To better understand the interaction mechanism between nearby bolts, the internal stress distribution of the anchorage model was obtained by numerical model experiments with various bolt densities. On the basis of controlling the tray size of the model, five numerical simulation models with anchor density of 0, 1, 2, 3, and 4 are established. As illustrated in Figure 5(a), each bolt was

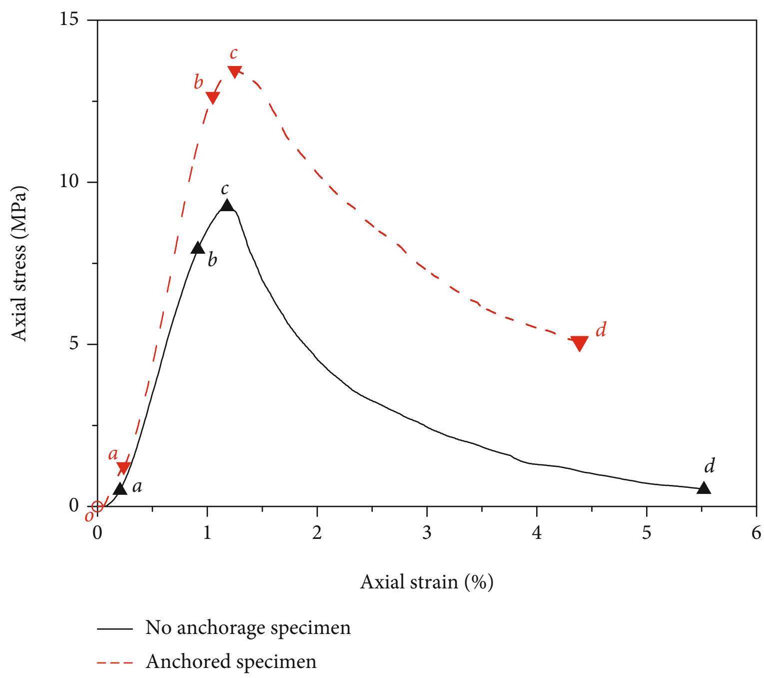

Figure 3: Axial stress vs. axial strain curve of rock mass specimen under uniaxial compression.

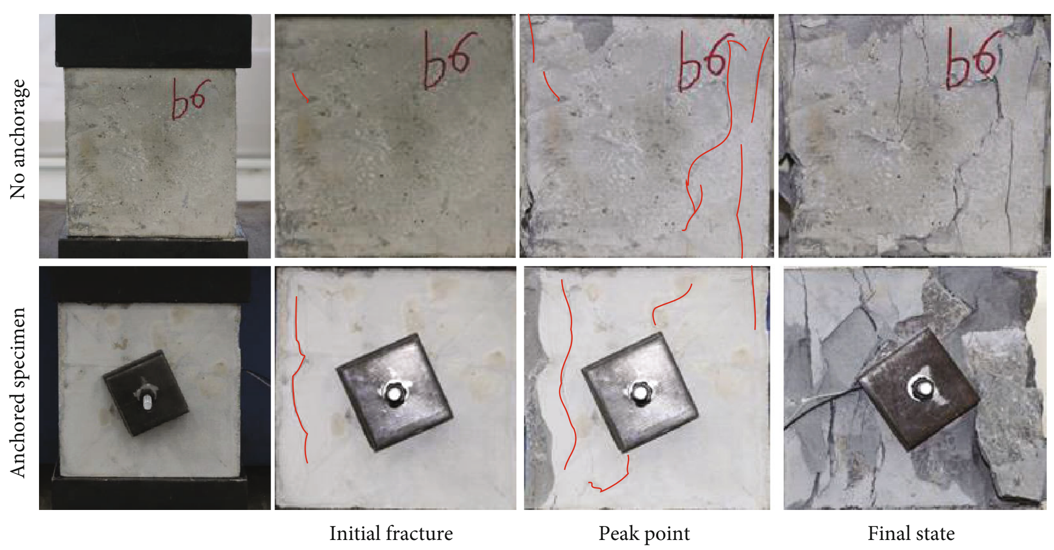

Figure 4: Fracture process of rock mass specimen during uniaxial compression.

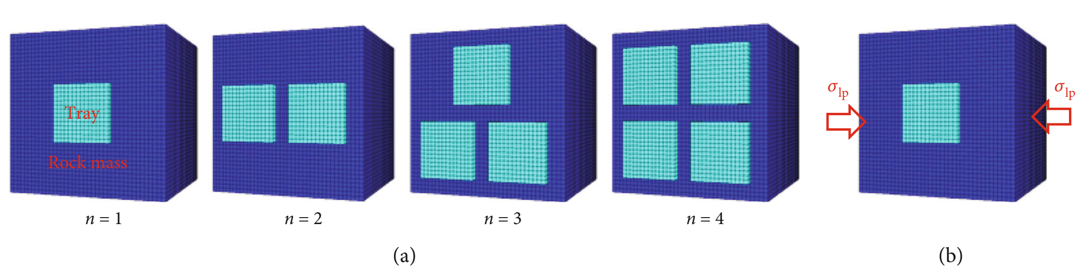

Figure 5: Numerical simulation mode of rock mass specimen with different (a) bolt number and (b) lateral pressure, respectively.

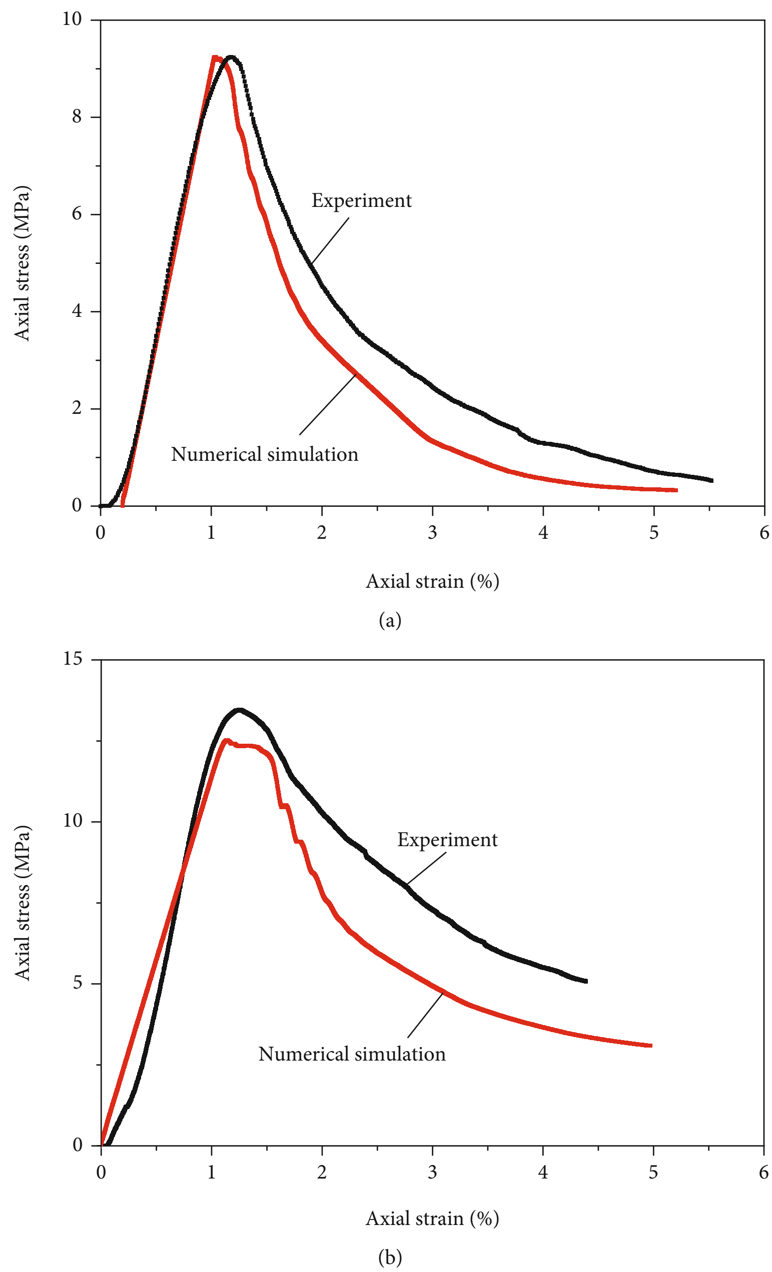

Figure 6: Axial stress vs. axial strain curve comparison between experiment and numerical simulation results of rock mass specimen with (a) no bolt and (b) one bolt reinforced, respectively.

preloaded at 15 kN. The front and back sides of the model were configured as free surfaces (vertical x direction), and varied lateral pressure could be added to the simulation to simulate the lateral restricting pressure of the actual surrounding rock mass. As indicated in Figure 5(b), the left and right sides of the model were anchorage surfaces (vertical y direction), whereas the upper and bottom sides were displacement loading surfaces (vertical z direction). The quantitative test findings revealed that when deformation increased in the post-peak loading stage, the mechanical properties of rock materials deteriorated gradually, exhibiting strain softening characteristics, which was consistent with the physical model test results in Section 2.2. Therefore, combined with the characteristics of the constitutive relations in the numerical simulation software, the strain softening constitutive relation was picked for the simulation calculation. The selection of the basic mechanical parameters of the model: the prepeak linear elastic stage parameters of the model were determined by the previous laboratory physical model test. The postpeak strain softening parameters of the model were investigated by comparing the stress-strain curves of the physical model with those determined by the inversion method. As illustrated in Figure 6, the axial stress-strain curves of the specimens of unanchored and anchored with a single anchor obtained through numerical simulation were compared to those acquired from the physical model test in Section 2.2. The peak strength and elastic modulus of the unanchored model were 9.25 MPa, 1.20 GPa (laboratory test results) and 9.25 MPa, 1.19 GPa

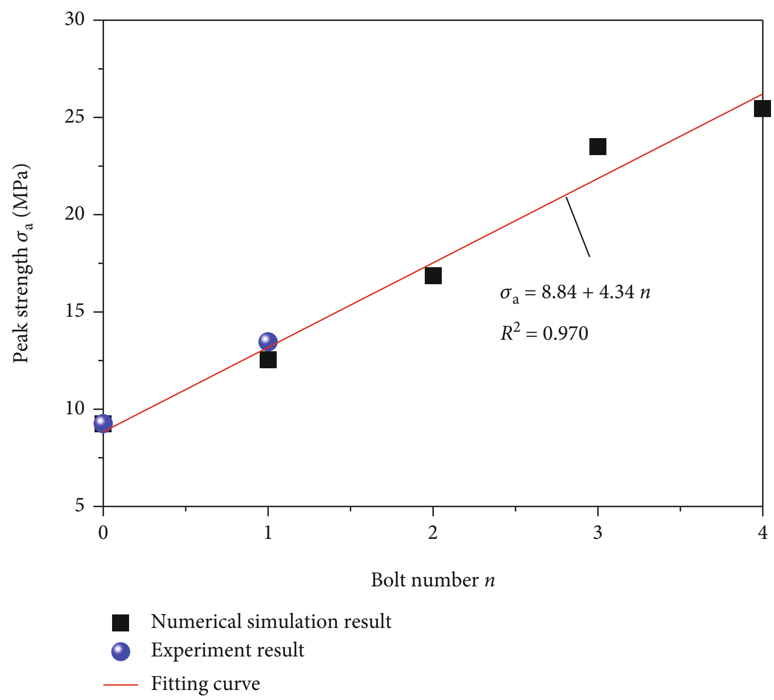

FIGURE 7: Relationship between peak strength and bolt number of rock mass specimen.

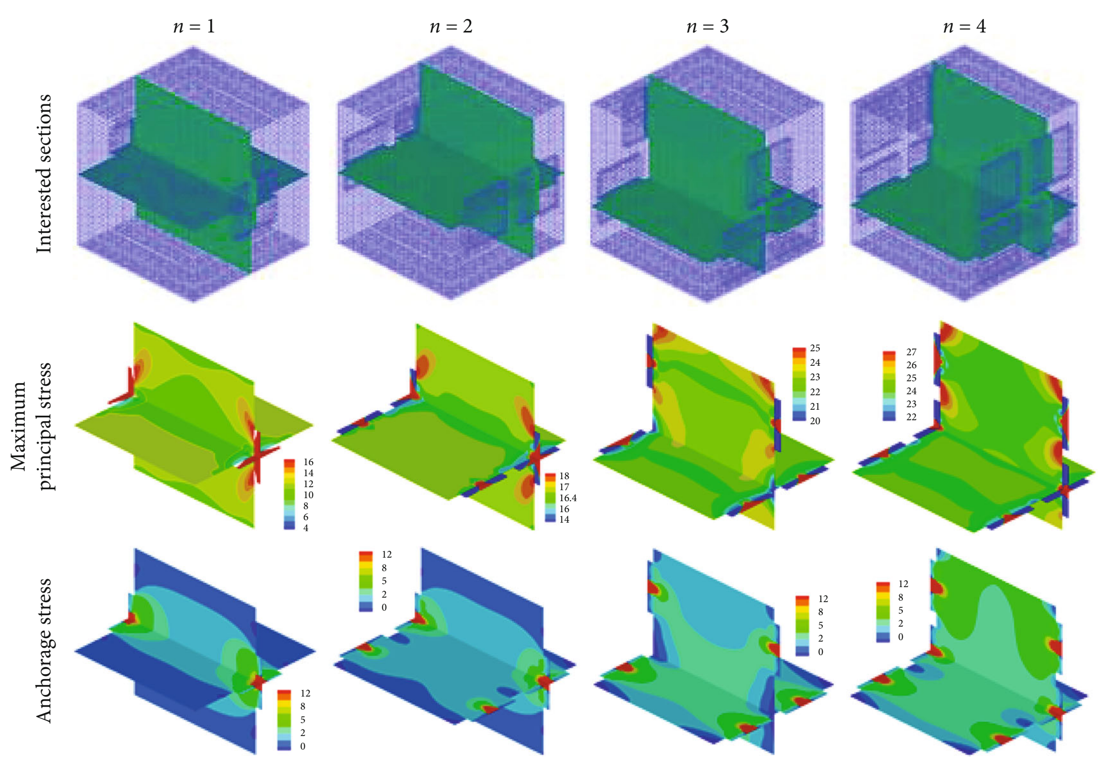

FIGURE 8: Maximum principal stress and anchorage stress distributions of rock mass specimen with different bolt numbers.

(numerical simulation results), respectively, and the values after anchorage were 12.64 MPa, 1.54 GPa (laboratory test results) and 12.53 MPa, 1.51 GPa (numerical simulation results), respectively. The fitting degree of the surrounding rock mass model's axial stress-strain curve was high in both the prepeak and postpeak stages, regardless of whether the surrounding rock was anchored or not, implying that the selected model's postpeak strain softening parameters were well in line with the test requirements, ensuring the reliability of the subsequent test results.

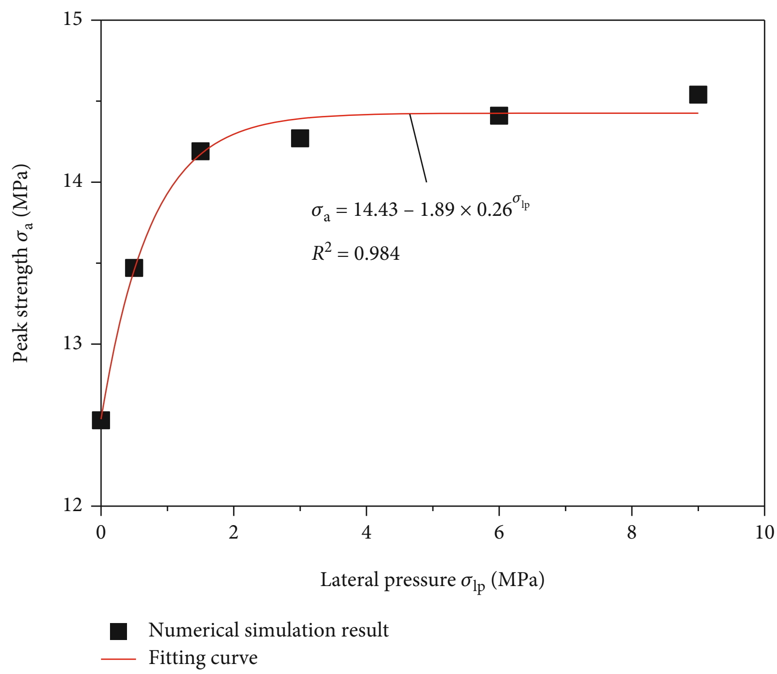

FIGURE 9: Relationship between peak strength and lateral pressure of rock mass specimen.

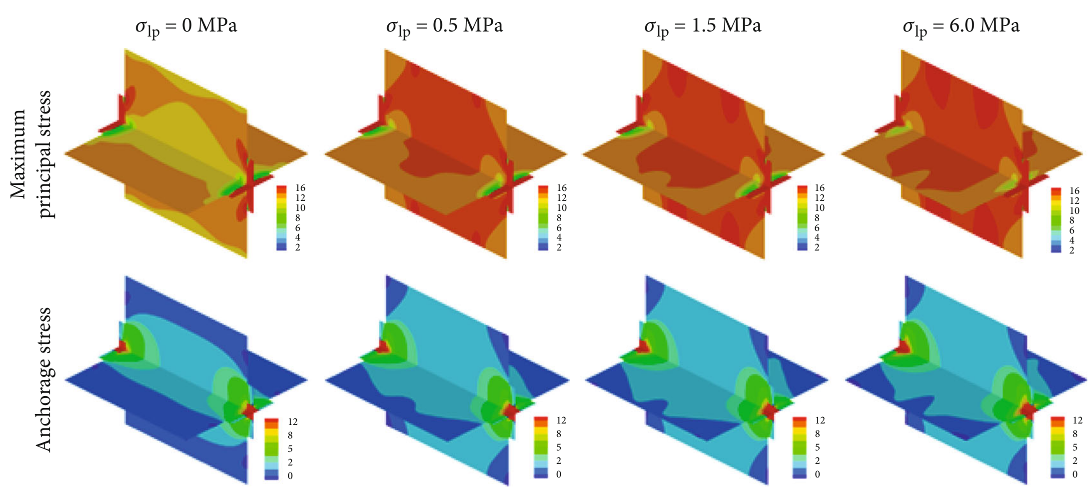

FIGURE 10: Maximum principal stress and anchorage stress distributions of rock mass specimen with different lateral pressures.

3.2. Influence of Bolt Number on the Mechanical Behaviors of Rock Mass. According to the axial peak strength of specimens under different bolt numbers calculated by numerical simulation, the relationship between axial peak strength and the bolt number was obtained, as shown in Figure 7. It can be seen that the peak strength and bolt number show a significant positive linear relationship. As the bolt number changes from 0 to 1, the peak strength of the model rises from 9.25 MPa to 12.53 MPa, with a change extent of 35.46%. As the bolt number increases, the axial peak strength of the surrounding rock anchorage model sample gradually rises. In the bolt number range of 0~3, the axial peak strength of the model sample increases by about 36.49%. When the bolt number increases from 3 to 4, the increasing rate is 8.29% of the axial peak strength, and the increasing rate decreases significantly. It can be discovered that a reasonable density of the bolt provides the optimal stability control effect on the rock mass.

Figure 8 depicts the model's internal maximum primary stress field at peak time as well as the anchorage stress field. The maximum primary stress, which was commonly stated as the vector sum of normal and shear stresses, was a widely used metric for assessing the stability of a structure's interior parts. Two mutually perpendicular planes were selected as monitoring planes in the model to explore the stress features of internal space and the action mechanism of the bolt with varying bolt numbers in the loading process of the anchorage surrounding rock mass model. For the single bolt anchorage surrounding the rock mass model, there was a noticeable stress rise zone from the connection between the bolt and the tray along the *z* direction of compression to the inclined direction of the two loading ends. In the

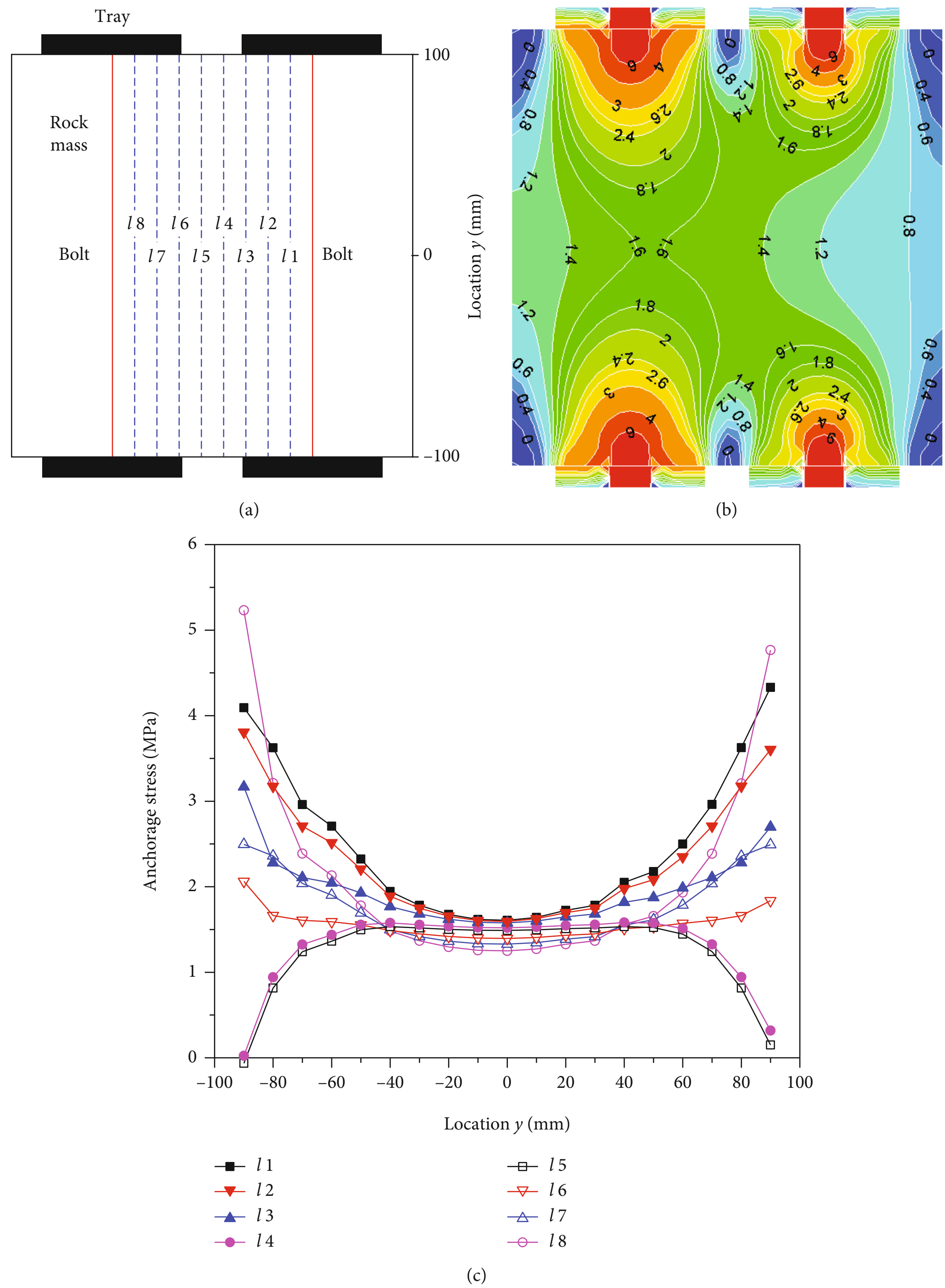

Figure 11: (a) Interested section and line, (b) anchorage stress distribution of interested section of rock mass specimen with two bolts reinforced, and (c) anchorage stress distribution in the interested lines.

multibolt anchorage surrounding rock mass model, the side of the bolt facing the loading end also showed this clear inclined stress rise zone. The difference is that, for the multibolt anchorage surrounding rock mass model, in the z direction, the stress rise zone is also formed in the area between bolts. It is noteworthy that the opposite stress reduction zone is formed in the area between bolts in the x direction. The same is that, whether in the x direction or in the z direction, the maximum principal stress is relatively small in the vicinity of the bolt.

The bolt primarily enhances the mechanical properties of the anchorage rock mass through anchorage stress. Therefore, the stress field of bolt action is a key indicator for analyzing the effect of the bolt. The anchorage stress and the

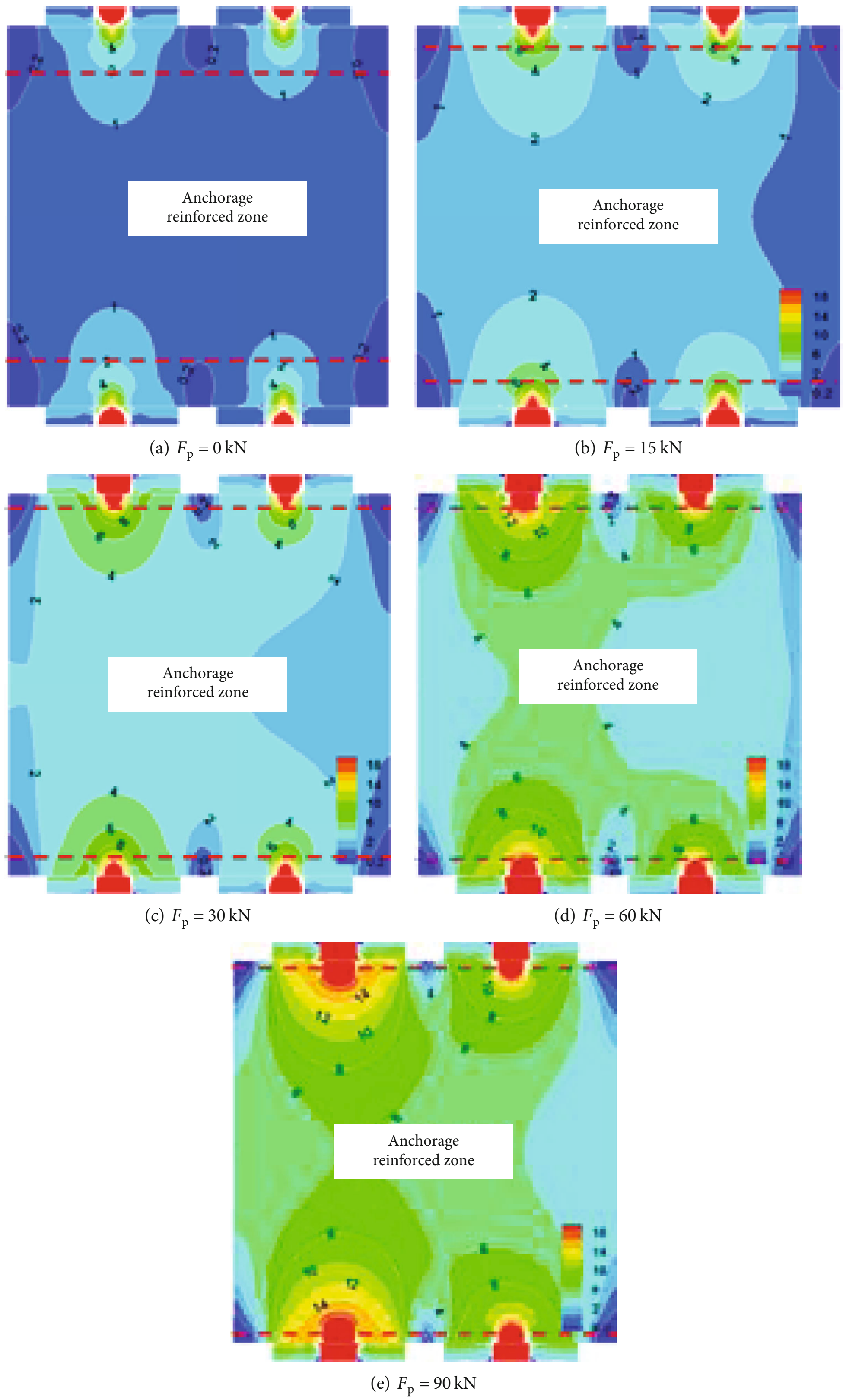

Figure 12: Anchorage stress distribution of rock mass specimen with different pretightening forces.

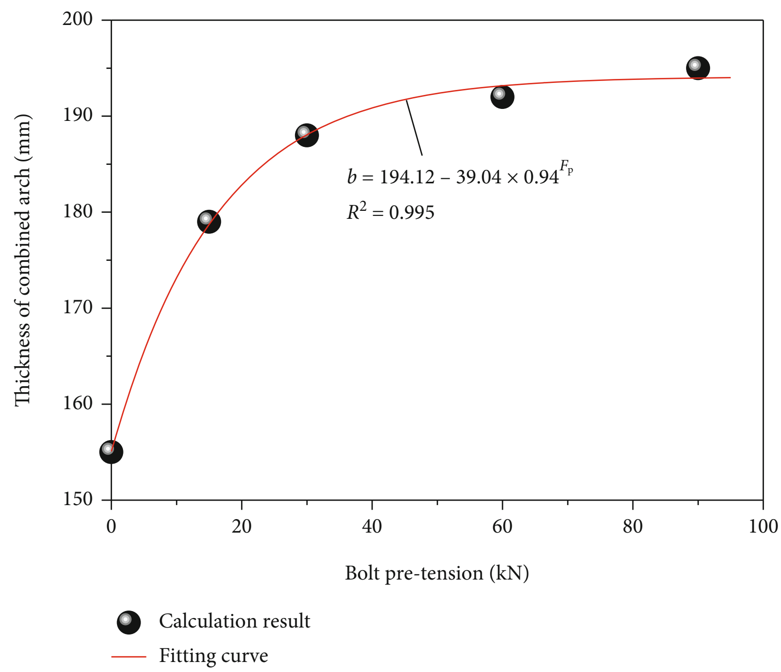

Figure 13: Effect of pretightening force on the thickness of combined arch.

distribution range of the anchorage stress in the anchorage model rise dramatically when the bolt number increases, as shown in Figure 8. In other words, the anchorage model's mechanical characteristics continue to rise as the bolt density rises. Furthermore, the anchorage stress between bolts of the multibolt anchorage surrounding rock mass model significantly decreases in the x direction.

3.3. Influence of Lateral Pressure on the Mechanical Behaviors of Rock Mass. Affected by the geological tectonic movement, the distribution laws of ground stress are complicated and changeable, and high-level tectonic stress exists in some regions. Therefore, a variety of model tests with varied lateral pressures (0 MPa, 0.5 MPa, 1.5 MPa, 3 MPa, 6 MPa, and 9 MPa) were carried out, and the effect of lateral pressure on the mechanical properties of the anchorage model and internal stress distribution was studied. The relationship between the peak strength and varied lateral pressures in the anchorage surrounding rock mass model is shown in Figure 9. As the lateral pressure level rises, the peak strength of the model shows a gradual increasing trend, but the reduction extent gradually decreases. When the lateral pressure level changes from 0 MPa to 3 MPa, the peak strength of the model increases dramatically. However, when the lateral pressure is greater than 3 MPa, the peak strength of the model rises slowly with the increase in the lateral pressure. The nonlinear relationship between the axial peak strength and the lateral pressure in the anchorage model is obtained by nonlinear fitting. As shown in Figure 9, the fitting results are accurate, which can provide a useful basis for future research.

Four lateral pressure conditions were designed in this experiment to investigate the impact rule of lateral pressure on the internal spatial stress distribution characteristics in the anchorage surrounding rock mass model: 0 MPa, 0.5 MPa, 1.5 MPa, and 6 MPa. Two mutually perpendicular planes were chosen as monitoring planes for the model in each working state. The maximum principal stress and the anchorage stress distributions on the monitoring plane for each working state under the peak strength are shown in Figure 10. The maximum principal stress around the bolt is relatively low for the anchorage rock mass model without lateral pressure. The stress in the middle part of the bolt rises in the model, and the size of this region grows gradually as the lateral pressure increases. The area with large stress expands in the x direction as the lateral pressure increases, from the central area where anchorage stress increases to the two ends where lateral pressure is applied. From the loading end to the bolt region, an obvious stress concentration zone exists in the z direction, and the stress concentration zone grows as the confining pressure rises. The anchorage stress and the maximum principal stress have similar distribution characteristics: the anchorage stress is higher in the vicinity of the bolt, and the area connected between the bolt and the tray has a noticeable stress increase zone. The area of the stress field around the bolt in the peak period gets bigger as the lateral pressure increases.

4. Discussion

According to previous research, the stress field analysis of the bolting support is an important tool for understanding bolt action processes. The peak states of anchorage models with two bolts were chosen to explore the variation law of the anchorage stress field (*syy*) in the anchorage rock mass model quantitatively, as shown in Figure 11. Considering the symmetry, the monitoring plane was chosen to be in the center of the model (over the coordinate origin, vertical

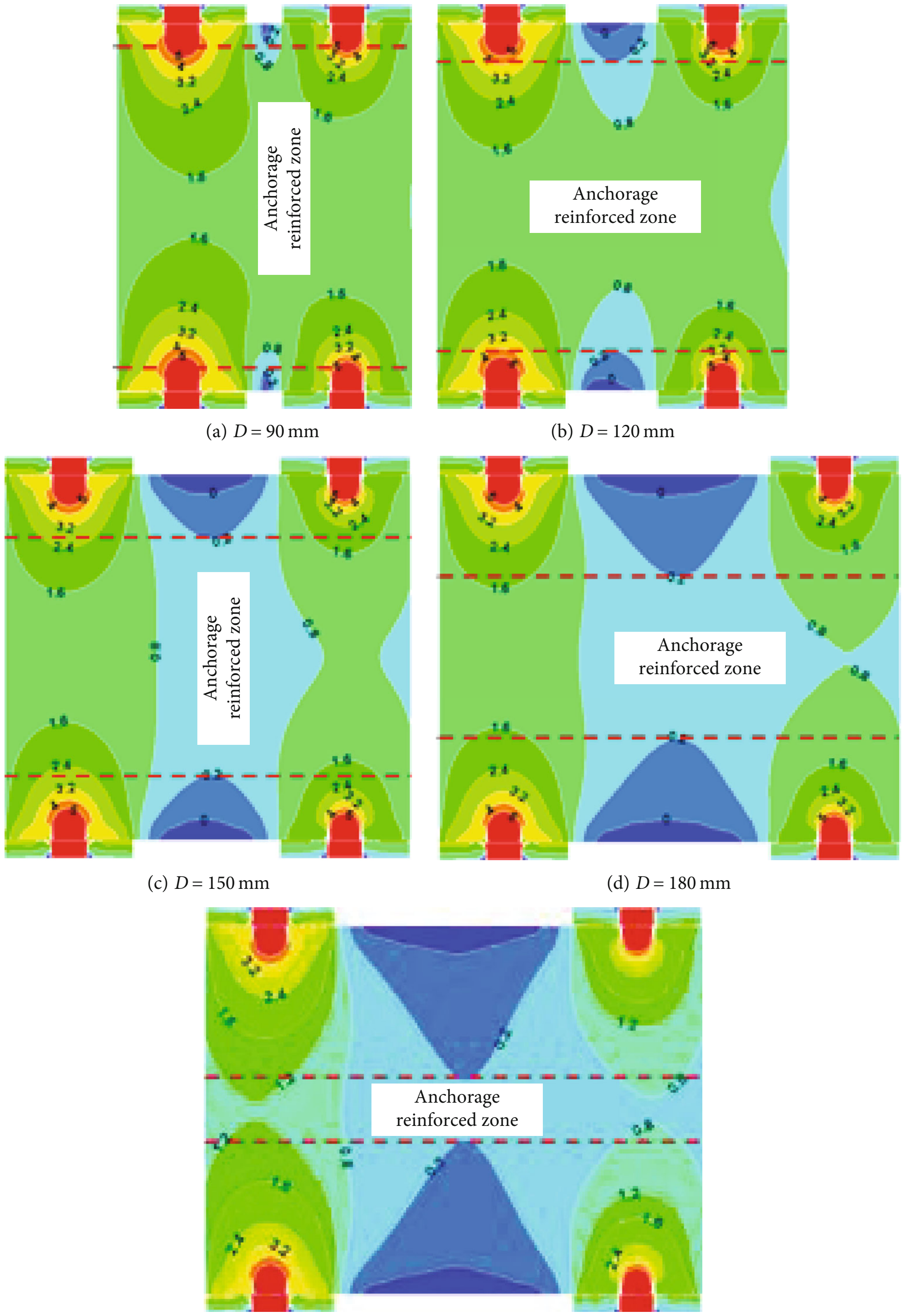

(a) $D = 90$ mm (b) $D = 120$ mm (c) $D = 150$ mm (d) $D = 180$ mm (e) $D = 200$ mm

Figure 14: Anchorage stress distribution of rock mass specimen with different bolt spacings.

z axis, and in the same plane as the bolt), as illustrated in Figure 11(a). Eight monitoring lines ($l1$~$l8$) were uniformly distributed across the middle plane of two bolts, with 19 monitoring points spread on each monitoring line. As illustrated in Figure 11(b), the area connected between the bolt and the tray has a noticeable stress concentration zone of the anchorage stress. The anchorage stress decreases slowly along its route, whereas the anchorage stress perpendicular to the bolt's direction decreases rapidly. The changing law of *syy* stress on the monitoring line in the axial direction

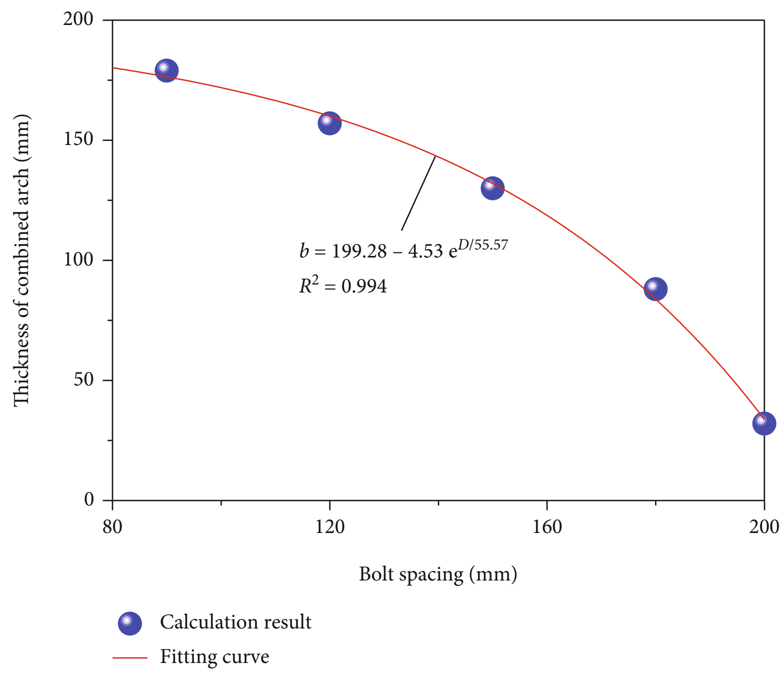

Figure 15: Effect of bolt spacing on the thickness of combined arch.

of the bolt at peak state is depicted in Figure 11(c). When the monitoring line is close to the bolt ($l1$~$l3$ and $l6$~$l8$), the *syy* stress of the monitoring points changes from dropping to increasing in the direction of the bolt. However, the *syy* stress on the monitoring lines $l4$ and $l5$ displays the change characteristics of a "crest shape" with a symmetrical increase from both ends to the middle.

According to the composite arch theory [33, 34], a single bolt can squeeze the surrounding rock and create a conical compression zone on both sides of the bolt under pretightening force. When the bolts are suitably spaced, the compression zones formed by each individual bolt can be layered on top of one another, resulting in a homogeneous compression zone of a definite thickness. Bolt reinforcement forms a combined reinforcement arch with a defined thickness around the roadway. The arch has a high bearing capacity and compressibility, allowing it to sustain the roadway well. The thickness of a rock-soil anchored composite arch is frequently linked to the bolting support parameters, according to a substantial quantity of study expertise. Therefore, the numerical simulation method was utilized to investigate the stress distribution in the anchorage rock mass and its influence on the thickness of the composite arch under different pretightening forces and bolt row spacings.

Figure 12 shows the distribution of the internal anchorage stress field in the model with five different pretightening forces (0, 15, 30, 60, and 90 kN). Based on the fluctuation of peak strength with lateral pressure in Section 3.3, the 0.2 MPa criteria were defined, implying that the anchorage area is recognized as the area where the anchorage stress is greater than 0.2 MPa. In the model, the anchorage stress field (middle symmetry plane) is shown under various pretightening forces. As the pretightening force increases, the anchorage strengthening area steadily rises, and the stress value in the anchorage strengthening region also climbs drastically. The axial force of the bolt causes the surrounding rock to convert from a uniaxial compression state before anchorage to a triaxial compression state. Thus, the lateral compressive strength of the surrounding rock is improved, and the rock is compacted and reinforced.

The variation of the thickness of the composite arch with the bolt pretightening force is obtained (in Figure 13). When the pretightening force rises from 0 kN to 15 kN, the thickness of the composite arch in the model increases from 155 mm to 179 mm, which is an increase of 15.48%. As the pretightening force changes from 15 kN to 30 kN, the thickness of the composite arch in the model changes from 179 mm to 188 mm, with a change extent of 5.03%. With the pretightening force raised from 30 kN to 60 kN, the thickness of the composite arch in the model increased by 2.13%, from 188 mm to 192 mm. When the pretightening force changes from 60 kN to 90 kN, the thickness of the composite arch in the model changes from 192 mm to 195 mm, which is increased by 1.56%. As the pretightening force increases, the thickness of the composite arch between bolts steadily increases. When the pretightening force exceeds 30 kN, the thickness of the composite arch is drastically reduced, indicating that there is a reasonable bolt pretightening force to achieve the required anchorage effect.

Figure 14 depicts the distribution of the internal anchorage stress field in the model for five different bolt row spacings (90, 120, 150, 180, and 200 mm). When the bolt row spacing is increased, the anchorage reinforcement area gradually shrinks, and the stress value in the anchorage reinforcement region also decreases considerably. Simultaneously, as the bolt row spacing rises, the area with insufficient anchorage stress between bolts grows, and the area has a conical symmetric distribution. As shown in Figure 15, the variation of the thickness of the composite arch with the bolt row spacing is obtained. When the bolt row spacing changes from 90 mm to 120 mm, the thickness of the composite arch in the model decreases from 179 mm to 157 mm, which is reduced by 12.29%. As the bolt row spacing rises from 120 mm to 150 mm, the thickness of the composite arch in the model changes from 157 mm to 130 mm, with a change extent of 17.20%. The thickness of the composite arch in the model reduces by 32.31%, from 130 mm to 88 mm, when the bolt row spacing changes from 150 mm to 180 mm. The thickness of the composite arch in the model decreases from 88 mm to 32 mm as the bolt row spacing increases from 180 mm to 200 mm, with a change extent of 63.64%. As the bolt row spacing is increased, the thickness of the composite arch between bolts steadily decreases. The anchorage strengthening area of bolts and the thickness of the composite arch are reduced when the bolt row spacing exceeds 150 mm, indicating that the recommended maximum bolt row spacing should be specified to enable efficient anchorage in actual engineering.

5. Conclusions

This work, which was based on the bolting support of roadway surrounding rock at Gubei coal mine, simplified the sidewall region of the roadway's surrounding rock influenced by the bolt anchorage to the anchorage rock mass model. The mechanical properties (such as peak strength, the principal stress, and the anchorage stress) of the anchorage rock mass under various bolt numbers (bolt density) and lateral pressures were determined using laboratory compression tests and the FLAC3D numerical simulation tests. The impacts of pretightening force and bolt row spacing on the total anchorage effect of bolts were explored using the composite arch theory. The following are the primary conclusions:

(1) The internal anchorage stress field of the specimen shows the following law as a whole: the near-point anchorage stress in the end area of the bolt is large, and the far-point anchorage stress is small. The near-point anchorage stress is small, and the far-point anchorage stress is large in the middle area of bolt. As the number of bolts (bolt density) in the anchorage rock mass model grows, the anchorage stress and distribution range increase considerably. The fluctuation of the anchorage stress field at different distances can be decreased by increasing the bolt number (bolt density)

(2) The maximum principal stress field stress of the anchorage rock mass improves as lateral pressure increases, the coverage region with larger stress expands, and the anchorage stress field expands as well. The anchorage mechanical properties of the anchorage rock mass, on the other hand, tend to be stable when the lateral pressure level is greater than 3 MPa

(3) Increased pretightening force and decreased bolt row spacing can improve the coverage range of the anchorage stress field and the thickness of the anchorage rock mass composite arch within a reasonable range. Thus, the appropriate pretightening force and bolt row spacing can improve the mechanical properties of the anchorage rock mass, making it more stable

Data Availability

The data used to support the findings of this study are available from the corresponding author upon request.

Conflicts of Interest

The authors declare that they have no conflicts of interest.

Acknowledgments

This study is financed by the National Natural Science Foundation of China (no. 42077240).

References

[1] Y. X. Sun, "Research on the deformation mechanism of mining roadway stratiform surrounding rock with nonuniform stress field," *Shock and Vibration*, vol. 2021, Article ID 6624045, 19 pages, 2021.

[2] Y. L. Hai, G. W. Zhi, L. Ji, and B. Lang, "Coal seam roadway bolt support design method based on the supporting theory of broken rock zone," *Advanced Materials Research*, vol. 734-737, no. 734-737, pp. 535–539, 2013.

[3] G. Y. Guo, H. P. Kang, D. Y. Qian, F. Q. Gao, and Y. Wang, "Mechanism for controlling floor heave of mining roadways using reinforcing roof and sidewalls in underground coal mine," *Sustainability*, vol. 10, no. 5, p. 1413, 2018.

[4] C. X. Zhao, Y. M. Li, G. Liu, and X. R. Meng, "Mechanism analysis and control technology of surrounding rock failure in deep soft rock roadway," *Engineering Failure Analysis*, vol. 115, article 104611, 2020.

[5] S. S. Yu and J. Z. Li, "Pre-reinforcement technology in broken roof side condition," *Applied Mechanics and Materials*, vol. 215-216, no. 215-216, pp. 681–684, 2012.

[6] J. K. Xu, R. Zhou, D. Z. Song, N. Li, K. Zhang, and D. Y. Xi, "Deformation and damage dynamic characteristics of coal-rock materials in deep coal mines," *International Journal of Damage Mechanics*, vol. 28, no. 1, pp. 58–78, 2019.

[7] W. X. Zhu, H. W. Jing, L. J. Yang, B. Pan, and H. J. Su, "Strength and deformation behaviors of bedded rock mass under bolt reinforcement," *International Journal of Mining Science and Technology*, vol. 28, no. 4, pp. 593–599, 2018.

[8] S. X. Ding, H. W. Jing, K. F. Chen, G. A. Xu, and B. Meng, "Stress evolution and support mechanism of a bolt anchored in a rock mass with a weak interlayer," *International Journal of Mining Science and Technology*, vol. 27, no. 3, pp. 573–580, 2017.

[9] Y. L. Chen, J. Y. Teng, R. A. Bin Sadiq, and K. Zhang, "Experimental study of bolt-anchoring mechanism for bedded rock mass," *International Journal of Geomechanics*, vol. 20, no. 4, 2020.

[10] S. C. Li, H. T. Wang, Q. Wang et al., "Failure mechanism of bolting support and high-strength bolt-grouting technology

for deep and soft surrounding rock with high stress," *Journal of Central South University*, vol. 23, no. 2, pp. 440–448, 2016.

[11] Y. M. Zhao, N. Zhang, and X. G. Zheng, "Experimental study of axial stress distribution and transfer along the bolt rods in an underground coal mine," *Arabian Journal of Geosciences*, vol. 9, no. 1, 2016.

[12] B. Wang, X. X. Guo, H. Jin, F. H. Li, and Y. Song, "Experimental study on degradation behaviors of rock bolt under the coupled effect of stress and corrosion," *Construction and Building Materials*, vol. 214, pp. 37–48, 2019.

[13] W. L. Zhang, L. Huang, and C. H. Juang, "An analytical model for estimating the force and displacement of fully grouted rock bolts," *Computers and Geotechnics*, vol. 117, article 103222, 2020.

[14] C. H. Liu and Y. Z. Li, "Predicting the shear resistance contribution of passive fully grouted bolts to jointed rock," *International Journal of Geomechanics*, vol. 20, no. 2, article 04019174, 2020.

[15] S. L. Yang, M. Li, G. F. Song, Y. Yang, and F. Xie, "Optimization of face flexible bolting and grouting technology for longwall face support under difficult geological conditions," *Energy Science and Engineering*, vol. 8, no. 4, pp. 1260–1270, 2020.

[16] H. W. Jing, J. Y. Wu, Q. Yin, and K. Wang, "Deformation and failure characteristics of anchorage structure of surrounding rock in deep roadway," *International Journal of Mining Science and Technology*, vol. 30, no. 5, pp. 593–604, 2020.

[17] H. P. Kang, J. H. Yang, and X. Z. Meng, "Tests and analysis of mechanical behaviours of rock bolt components for China's coal mine roadways," *Journal of Rock Mechanics and Geotechnical Engineering*, vol. 7, no. 1, pp. 14–26, 2015.

[18] Y. Li, C. Li, L. Zhang, W. S. Zhu, S. C. Li, and J. Liu, "An experimental investigation on mechanical property and anchorage effect of bolted jointed rock mass," *Geosciences Journal*, vol. 21, no. 2, pp. 253–265, 2017.

[19] H. P. Kang, "Support technologies for deep and complex roadways in underground coal mines: a review," *Internal Journal of Coal Science and Technology*, vol. 1, no. 3, pp. 261–277, 2014.

[20] H. P. Kang, "Analysis on load bearing ring in surrounding rock of roadway," *Rock and Soil Mechanics*, vol. 17, no. 4, pp. 84–88, 1996, (In Chinese).

[21] C. Cao, N. Jan, T. Ren, and A. Naj, "A study of rock bolting failure modes," *International Journal of Mining Science and Technology*, vol. 23, no. 1, pp. 79–88, 2013.

[22] H. W. Song and B. S. Mu, "Research on load capability and rational thickness of a reinforced broken rock arch," *Journal of China University of Mining and Technology*, vol. 26, no. 2, pp. 33–35, 1997, (In Chinese).

[23] X. Q. Guo, X. B. Mao, C. Ma, and J. L. Huang, "Bolt support mechanism based on elastic theory," *International Journal of Mining Science and Technology*, vol. 23, no. 4, pp. 469–474, 2013.

[24] Y. D. Zhang, L. Cheng, and J. F. Yang, "Bearing characteristic of composite rock-bolt bearing structure under different bolt support density," *Journal of Mining and Safety Engineering*, vol. 32, no. 2, pp. 305–309, 2015, (In Chinese).

[25] Y. J. Zong, L. J. Han, Q. Tao, and S. Q. Yang, "Mechanical properties and failure characteristics of fractured sandstone with grouting and anchorage," *Mining Science and Technology*, vol. 24, no. 2, pp. 165–170, 2014.

[26] Z. Du, B. Qin, and F. Tian, "Numerical analysis of the effects of rock bolts on stress redistribution around a roadway," *International Journal of Mining Science and Technology*, vol. 26, no. 6, pp. 975–980, 2016.

[27] H. J. Su, H. W. Jing, H. H. Zhao, L. Y. Yu, and Y. C. Wang, "Strength degradation and anchoring behavior of rock mass in the fault fracture zone," *Environmental Earth Sciences*, vol. 76, no. 4, p. 179, 2017.

[28] Q. Yin, H. W. Jing, H. J. Su, and H. H. Zhao, "Experimental study on mechanical properties and anchorage performances of rock mass in the fault fracture zone," *International Journal of Geomechanics*, vol. 18, no. 7, article 04018067, 2018.

[29] Z. J. Zhang, Q. L. Han, S. W. Liu, and Y. M. Li, "Roof bolts broken mechanism and their reasonable construction structures," *Key Engineering Materials*, vol. 306-308, no. 1-2, pp. 37–42, 2006.

[30] J. C. Chang, K. He, D. D. Pang, D. Li, C. M. Li, and B. J. Sun, "Influence of anchorage length and pretension on the working resistance of rock bolt based on its tensile characteristics," *International Journal of Coal Science and Technology*, vol. 8, no. 6, pp. 1384–1399, 2021.

[31] T. G. Sitharam, V. B. Maji, and A. K. Verma, "Practical equivalent continuum model for simulation of jointed rock mass using FLAC3D," *International Journal of Geomechanics*, vol. 7, no. 5, pp. 389–395, 2007.

[32] H. Wang, Z. X. Chen, and D. M. Zhang, "Rock slope stability analysis based on $FLAC^{3D}$ numerical simulation," *Applied Mechanics and Materials*, vol. 170-173, pp. 375–379, 2012.

[33] W. Hoek and E. T. Brown, *Underground Excavations in Rock*, The Institution of Mining and Metallurgy, 1980.

[34] H. Y. Yang, Y. B. Liu, Y. Li et al., "Research on the support of larger broken gateway based on the combined arch theory," *Geomechanics and Engineering*, vol. 23, no. 2, pp. 93–102, 2020.

Hindawi
Geofluids
Volume 2023, Article ID 3658141, 16 pages
https://doi.org/10.1155/2023/3658141

Research Article

Evolution Mechanism and Control of Floor Heave in the Deep Roadway with Retained Bottom Coal

Peng Li,[1,2] **Yonglu Suo**,[1] **Peilin Gong**,[3] **Xingping Lai**,[1] **Kang Yi**,[4,5] **Chao Su**,[3,5] **and Chang Liu**[5]

[1]*Energy School Xi'an University of Science and Technology, Xi'an 710054, China*
[2]*Department of Mining Engineering, Shanxi Institute of Energy, Jinzhong 030600, China*
[3]*College of Mining Technology, Taiyuan University of Technology, Taiyuan 030024, China*
[4]*School of Energy & Mining Engineering, China University of Mining and Technology (Beijing), Beijing 100083, China*
[5]*Mining and Designing Branch, China Coal Research Institute, Beijing 100013, China*

Correspondence should be addressed to Yonglu Suo; shiya@xust.edu.cn and Peilin Gong; plgong@126.com

Received 21 May 2021; Revised 31 July 2021; Accepted 23 September 2021; Published 22 March 2023

Academic Editor: Yong-Zheng Wu

Roadways with retained bottom coal are common in thick coal seam mining, and floor heaving is a prominent problem. In this study, based on the interaction between the floor and two sides of the roadway-surrounding rock, a Winkler elastic foundation beam model is established to analyze the floor heave problem. A 3DEC model was used to analyze the failure range, failure mode, and migration law of the floor-surrounding rock with different bottom coal thicknesses and coal body strengths. The results show that (1) an increase in the thickness of the bottom coal results in a decrease in the stiffness of the roadway side coal body (the foundation of the supporting rock layer) and an increase in the bending deformation range, the amount of floor rock beam deformation, and the extrusion force. This leads to an expansion in the range of the sides of the coal body that are squeezed by the floor rock layer, resulting in additional failure and deformation of the coal body sides. Therefore, the damage to the floor rock layer is extended and increased. (2) The expansion of the floor pressure-bearing arch and surrounding rock in the arch are the causes of floor heave in the deep coal roadway with retained bottom coal. (3) Because of an increase in the thickness of the bottom coal and a decrease in the coal body strength, the floor pressure-bearing arch expands to the deeper part; thus, the range of surrounding rock in the arch with deformation and failure increases, resulting in an increase in floor heave. The field practice indicates that the support strategy of the "high prestressed strong rock bolt (cable) supporting two sides and bottom corners in time" can effectively control the floor heave of a roadway with retained bottom coal.

1. Introduction

With the development of deeper coal resources in recent years [1–3], the buried depth of roadways has been increasing. Deep roadways account for 30% of the roadways excavated every year in China, of which 70% need to be repaired due to large deformations, greatly increasing production costs [4]. Compared to the roof and two sides, the roadway floor usually exhibits greater deformation because it often lacks support [5, 6]. Roadways with retained bottom coal are often used in thick coal seam mining, and their weak floor can result in very serious floor heave [7].

There are two main factors that cause floor heaving in coal mine roadways. The first factor, in situ stress, is the local stress resulting from roadway excavation. Radial unloading and shear loading are the main causes of deformation and failure in the surrounding rock [8–10]. For the floor, an increase in horizontal in situ stress—as the initial value of tangential stress—aggravates the deformation and failure of the rock mass [11, 12]. Roadway floor heave is also induced by the mining stress from coal mining activities [13, 14]. The second factor includes the characteristics of the floor rock mass; a high elastic modulus and strength of the floor rock mass both reduce the amount of floor heave. Whereas, an increase in floor rock mass discontinuity leads to an increase in floor heave [7, 15]. The floor rock mass also deteriorates as water from the floor and roadway passes through the fault fracture zone [16, 17], further increasing floor heave [18].

Control of roadway floor heave should start with the two factors listed above [19, 20]. The first is stress control. Optimizing the mining layout and implementing slotting in the floor can reduce the stress level of the floor rock mass, thus controlling floor heave [21]. Alternatively, floor heave can also be reduced by strengthening the floor rock mass. The strength of the floor rock mass can be improved by installing floor bolts [22–24], constructing a concrete inverted arch [25, 26], or modifying floor grouting [27, 28].

Most of the papers referenced above focus only on the floor itself. However, the floor and the surrounding rock should be understood as a single unit. Therefore, the deformation and failure of the roof and roadway sides also affects the floor [29]. Additionally, it is difficult to strengthen the floor by drilling holes to install bolts or by modifying floor grouting, and constructing a concrete inverted arch is expensive and time consuming. Therefore, the mechanism of floor heave should be further studied to develop more efficient support methods.

The accumulated floor heave was more than 2 m before mining in No. 020202 roadway of the Qingyun coal mine, Jiexiu, Shanxi Province. The roadway floor heave was controlled by removing the bottom coal and adding bolts and cables to the bottom corners of the roadway.

This study uses theoretical analysis, physical similarity simulation, and field observation to comprehensively evaluate the evolution mechanism and control of floor heave in a deep roadway with retained bottom coal. This study establishes a mechanical model to evaluate the influence of bottom coal on the deformation and failure of floor rock using the No. 020202 tailgate of the Qingyun mine as the research subject. The evolution mechanism of floor heave caused by the floor expansion of a roadway with retained bottom coal is studied using numerical simulations. A new support method and parameters are proposed based on the deformation and migration of floor rock strata. Field practice confirms that roadway floor heave is controlled using the new support method.

2. Project Background

The 020202 working face of the Qingyun coal mine was mining the No. 2 coal seam. There were no mining activities or goafs around the working face, as shown in Figure 1. The No. 020202 tailgate of the Qingyun mine had a buried depth of 792–810 m, classifying it as a deep roadway [30]. The roadway was excavated along the roof of the No. 2 coal seam with a width of 4.5 m and a height of 3.8 m. A rock bolting system was adopted, including rock bolts with a length of 3000 mm, a diameter of 20 mm, a preload of about 10-20 kN, and a row spacing of 800 mm (11 rock bolts per row), as well as cables with a diameter of 17.8 mm, a length of 6200 mm, a preload of about 50-60 kN, and a row spacing of 1600 mm (8 cables per row). The physical and mechanical properties of the rock surrounding the roadway are listed in Table 1.

Before mining, the deformation of the No. 020202 tailgate was serious, with large displacements on the two sides of the roadway and serious floor heave. However, the roof was complete, and its displacement was small. The cumulative floor heave was more than 2 m, as shown in Figure 2, seriously restricting safe production.

The thickness of the floor coal of roadway No. 020202 was 1.3 m. The floor heave caused by floor coal crushing was only 0.26 m with a crushing expansion coefficient of 1.2, far less than the cumulative floor heave of the roadway. Therefore, the deformation and failure of the floor rock of the roadway was inevitable. The floor heave was not only related to the deformation of the floor itself but was also related to the deformation of the two sides. The low strength of the surrounding rock on the two sides also increased floor heave.

3. Deformation and Failure Mechanism of the Floor in the Deep Roadway with Retained Bottom Coal

3.1. Reverse Foundation Model of Roadway Floor. When the roadway was excavated, the floor rock beam bent under the action of ground stress from the roadway. Therefore, an elastic foundation beam model was used to analyze the deformation of the roadway floor, as shown in Figure 3. The coal body on the two sides of the roadway was the elastic foundation (the roof was hard and anchored, so it can be assumed that the roof deformation was small). The rock beam and foundation used in the elastic foundation model were elastic bodies. To simplify the conditions for semiquantitative analysis, the elastic modulus of the coal body in the plastic zone of the roadway side was approximated.

Assuming that the rock and coal in the floor conform to the Winkler foundation hypothesis [31], the vertical force p in the coal body satisfies the following conditions:

$$p = -ky, \tag{1}$$

where p is the vertical force in the coal seam, k is the foundation coefficient of the coal seam, and y is the deformation of the coal seam induced by p.

According to Timoshenko's solution, the differential equations that describe the floor rock beam bending deformation are [32] as follows:

$$\mathrm{EI}y'''' + Ny'' = q_z \text{ for} - (l + b_1) \le x < -b_1, \tag{2}$$

$$\mathrm{EI}y'''' + Ny'' = q_1(x) - k_1 y \text{ for}(-b_1 \le x < 0), \tag{3}$$

$$\mathrm{EI}y'''' + Ny'' = q_2(x) - k_2 y \text{ for}(0 \le x < b_2), \tag{4}$$

where EI is the stiffness of the floor rock stratum, k_2 is the foundation coefficient of the complete coal body, k_1 is the coefficient of the parallel foundation between the coal body with support and the bottom coal without support, q_z is the load of the exposed floor rock beam, q_0 is the load of

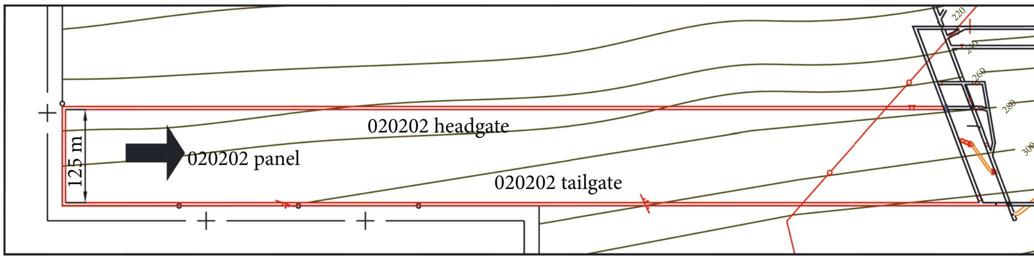

FIGURE 1: Layout of the No. 020202 panel of Qingyun coal mine.

TABLE 1: Physical and mechanical properties of the surrounding rock.

Stratum lithology	The average thickness (m)	Bulk modulus (GPa)	Shear modulus (GPa)	Tensile strength (MPa)	Cohesion (MPa)	Frictional angle (°)
Compound roof	18.5	13.6	3.7	3.5	12.1	27
Siltstone	3.7	10.3	3.1	3.7	9.2	26
Mudstone	2.3	7.9	2.1	1.1	3.2	23
Siltstone	2.9	16.2	5.3	3.3	7.2	26
Medium sandstone	2.3	13.2	3.7	5.2	13.1	29
No. 2 coal	5.1	3.7	1.3	0.6	2.3	27
Sandy mudstone	5.7	8.8	3.6	2.5	3.2	21
No. 4 coal	0.9	3.7	1.3	0.6	2.3	27
Siltstone	1.9	12.7	3.1	3.2	6.7	26
Fine-grained sandstone	3.3	12.9	2.6	2.1	3.3	23
Compound floor	18.0	9.7	2.6	2.7	3.1	27

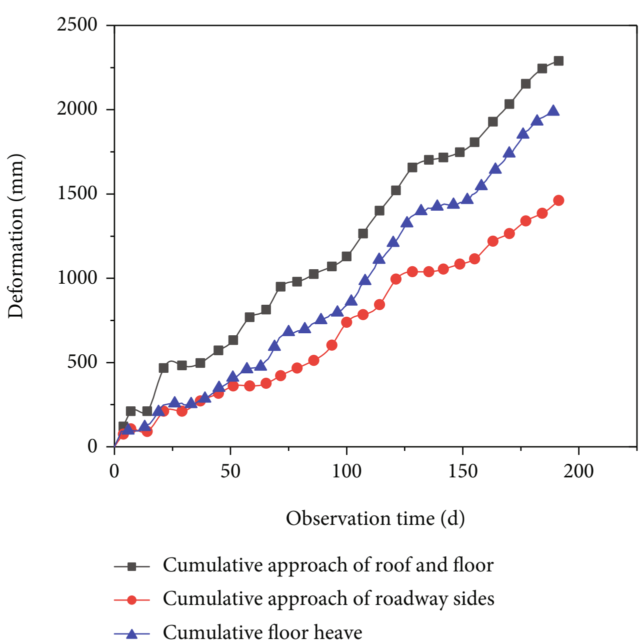

FIGURE 2: Deformation of the No. 020202 tailgate of Qingyun mine with the original support.

the exposed floor rock beam, q_v is the load of the exposed floor rock beam, $q_{1(x)}$ is the function formula of the stress in the floor rock beam, $q_{2(x)}$ is the function formula of the stress in the floor rock beam, y is the deformation of the coal seam, l is one-half of the width of the roadway, b_1 is the plastic zone width of the roadway, and b_2 is the stress increased zone width of the roadway. When the entire rigid displacement load is not considered, the load can be calculated as follows:

$$q_2(x) = \frac{b_2 - x}{b_2}(q_0 - q_v), \tag{5}$$

$$q_1(x) = \frac{q_0 - q_z - q_v}{b_1}x + q_0 - q_v. \tag{6}$$

The expression $y(x)$ can be obtained using the differential equation.

When the elastic foundation beam model is adopted, it must be assumed that the plastic zones on both sides of the roadway $-b_1 \le x < 0$ obey the law of elastic deformation. The foundation coefficient is k_2 in the elastic zone and k_1 in the plastic zone, as follows:

$$k_1 = \frac{k_{11}k_{12}}{k_{11} + k_{12}}, \tag{7}$$

where k_{11} is the foundation coefficient after the installation of the bolt support, and k_{12} is the foundation coefficient of the bottom coal in the plastic zones of the two sides of the roadway without bolt support. It should be noted that the

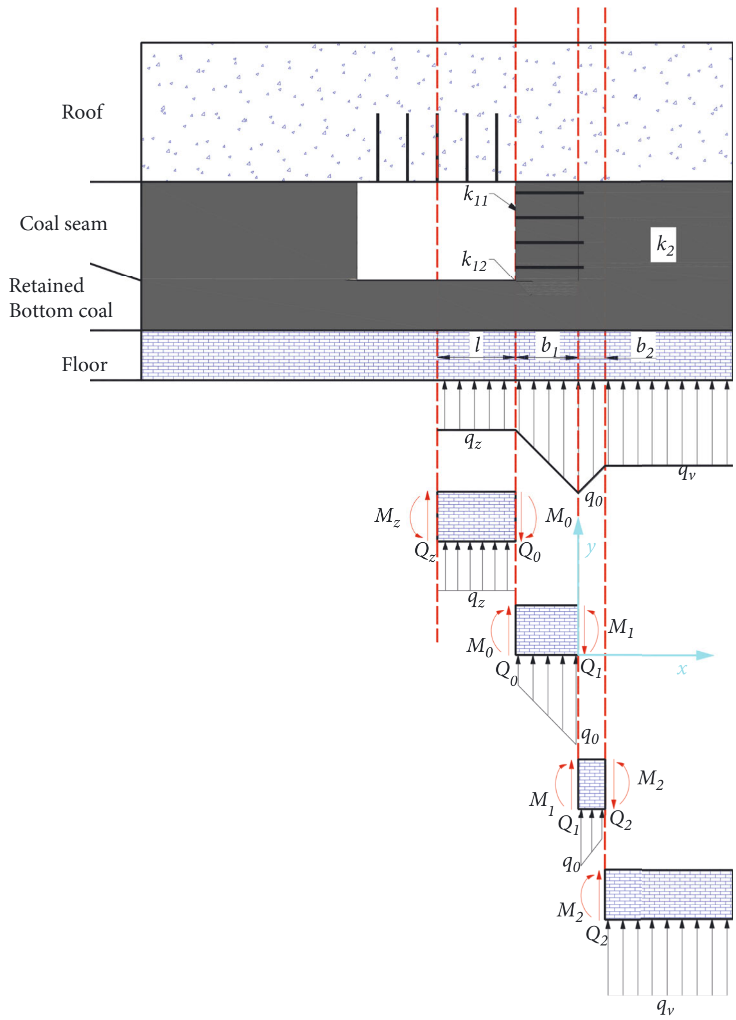

FIGURE 3: Reverse foundation model of the roadway floor.

value of the foundation coefficient k_{12} of the coal wall in the plastic zone is expressed by an average empirical value smaller than the foundation coefficient k_2 of the complete coal body.

Generally,

$$k = \frac{E}{h}, \tag{8}$$

where h is the thickness of the foundation, E is the elastic modulus of the foundation, and the equivalent elastic modulus of the coal body supported by the bolt can be calculated according to the following formula [33–35]:

$$E_{11} = E_{12} + \frac{\pi {d_b}^2 E_b}{4 S_\theta S_r}, \tag{9}$$

where d_b is the diameter of the bolt, E_b is the stiffness of the bolt, and S_θ and S_r are the radial and axial bolt spacings, respectively.

In equation (9), the equivalent elastic modulus is composed of the elastic modulus of coal in the plastic zone and the stiffness of the bolt support. If the bolt support is implemented before plastic deformation of the surrounding rock, then the plastic deformation of the two sides of the coal body can be effectively limited. As a result, the elastic modulus of the coal body increases, better controlling the deformation of the surrounding rock.

When $x \geq 0$, there is no support and no plastic failure in the coal. The displacement of the semi-infinite foundation beam under the unknown moment and shear force, M_1 and Q_1, at $x = 0$ is as follows:

$$y_b(x) = \frac{2\beta_2}{k_2}\left[Q_1\theta(x) + \beta_2 M_1 \psi(x)\right], \tag{10}$$

where $\psi(x)$, $\theta(x)$, $\varphi(x)$, and $\xi(x)$ are function formulas and β_2 is a constant, as described here:

$$\begin{aligned} \varphi(x) &= e^{-\beta_2 x}[\cos \beta_2 x + \sin \beta_2 x], \\ \psi(x) &= e^{-\beta_2 x}[\cos \beta_2 x - \sin \beta_2 x], \\ \theta(x) &= e^{-\beta_2 x} \cos \beta_2 x, \\ \xi(x) &= e^{-\beta_2 x} \sin \beta_2 x. \end{aligned} \tag{11}$$

$$\beta_2 = \sqrt[4]{\frac{k_2 b}{4\mathrm{EI}}}. \tag{12}$$

As shown in Figure 3, the displacement of the semi-infinite beam under a distributed load should also be considered.

When $x \geq b_2$, it is

$$y_2(x) = \frac{2\beta_2}{k_2}\left[Q_1\theta(x) + \beta_2 M_1 \psi(x)\right] + \frac{q_0 - q_v}{4k\beta_2 b_2}\left[\psi(x\text{-}b_2) - 2\xi(b_2)\theta(x) - \varphi(b_2)\psi(x)\right]. \tag{13}$$

When $0 \leq x < b_2$, it is

$$y_1(x) = \frac{2\beta_2}{k_2}\left[Q_1\theta(x) + \beta_2 M_1\psi(x)\right] + \frac{q_0 - q_v}{4k\beta_2 b_2} \cdot \left[4\beta_2(b_2 - x) + \psi(b_2 - x) - 2\xi(b_2)\theta(x) - \varphi(b_2)\psi(x)\right]. \tag{14}$$

When $-b1 \leq x < 0$, the coal body is strengthened by bolt support, the bottom coal is plastic damaged, the foundation coefficient of the coal body changes, and the displacement of the floor strata can be calculated as a finite-length foundation beam as follows:

$$\begin{aligned} y_0(x) = {} & y_a F_1(x) - \frac{\theta_a}{\beta_1}F_2(x) + \frac{M_a}{{\beta_1}^2\mathrm{EI}}F_3(x) + \frac{Q_a}{{\beta_1}^3\mathrm{EI}}F_4(x) \\ & - \frac{M_0}{{\beta_1}^2\mathrm{EI}}F_3(x + \mathrm{b}_1) - \frac{Q_0}{{\beta_1}^3\mathrm{EI}}F_4(x + \mathrm{b}_1) \\ & - \frac{1}{{\beta_1}^3\mathrm{EI}}\int_0^{-x}\left[\frac{q_0 - q_z - q_v}{b_1}\mathrm{t} + (q_z - q_v)\right]F_4(x + \mathrm{t})dt, \end{aligned} \tag{15}$$

where y_a, θ_a, M_a, and Q_a are the transition parameters for displacement, rotation angle, bending moment, and shear force, respectively, at $x = 0$ when there is no other external force, and

$$\begin{aligned} F_1(x) &= ch(\beta_1 x)\cos(\beta_1 x), \\ F_2(x) &= \frac{1}{2}\left[ch(\beta_1 x)\sin(\beta_1 x) + sh(\beta_1 x)\cos(\beta_1 x)\right], \\ F_3(x) &= \frac{1}{2}sh(\beta_1 x)\cos(\beta_1 x), \\ F_4(x) &= \frac{1}{4}\left[ch(\beta_1 x)\sin(\beta_1 x) - sh(\beta_1 x)\cos(\beta_1 x)\right]. \end{aligned} \tag{16}$$

When $-l - b1 \leq x < -b1$, the foundation coefficient is zero, and the bending moment of the rock deformation is

$$M(x) = M_z + \frac{1}{2}q_z(l + x)^2, \tag{17}$$

where q_z calculates the load of exposed floor rock beam.

By using $\mathrm{EI}y^{(2)} = M$ and the deformation compatibility conditions at $x = -l - b_1$ in the middle of the beam and $x = -b1$ and $x = 0$ at the ends of the beam, the deformation curve and bending moment equation of the floor can be calculated.

Based on the physical and mechanical parameters of the surrounding rock and in situ stress of the roadway, the deformation and bending moment of the floor rock without failure in the roadway were calculated when the bottom coal thicknesses were 0 m, 2 m, and 4 m, and where the vertical stress of the roadway is $q_v = \gamma H = 21.87$MPa. The stress concentration factors on the two sides of the roadway were both 1.5. As the roadway was excavated, the roof load was $q_z = 5$ MPa. The widths of the plastic zone and stress reduction zone were calculated to be 2 m and 4 m, respectively. The elastic moduli of the floor rock, coal body, and plastic zone of the coal body are 10 GPa, 3.7 GPa, and 1.1 GPa, respectively. The increase in the elastic modulus of the coal after the addition of supports was calculated using equation (9) and reference [36].

3.2. Influence of Different Bottom Coal Thickness on Crossfeed Action between Floor and Two Sides. By excavating the roadway to obtain different bottom coal thicknesses, the deformation and bending moment of the floor rock could be calculated. As the bottom coal thickness increases from 0 m to 4 m, the bending deformation and maximum bending moment of the floor rock increases significantly, as shown in Figure 4. Compared to the maximum deformation and maximum bending moment with a bottom coal thickness of 0 m, the maximum deformation of the floor rock bottom coal with thicknesses of 2 m and 4 m increases by 45% and 83%, respectively, and the maximum bending moment of the floor rock increases by 24% and 29%, respectively.

As shown in Figure 4(a), the zone $x > -2$ is the coal body zone on the roadway side. The deformation range of the roadway floor is below the roadway and 6–10 m from the roadway side. When the bottom coal thickness is 0 m, 2 m, and 4 m, the extended depth of the floor deformation range from the roadway side to the deep surrounding rock is 8.94 m, 9.86 m, and 10.57 m, respectively, and the deformation accounts for 89%, 90%, and 91% of the total deformation, respectively. Combined with Figure 5, it can be observed that, after the excavation of the roadway, the floor coal strength is at its lowest, and no support is applied. Because of the high stress of the deep surrounding rock, the floor coal fails first, and the floor rock is then unloaded. The floor rock bends under the action of in situ stress and bulges into the roadway. The deformation of the floor rock squeezes the bottom coal on both sides. If the support is not applied in time, the coal in the plastic zone of the two sides will further deteriorate, expand, and migrate into the roadway. This, in turn, weakens the bearing foundation of the floor rock, reduces the “span increasing” effect of the equivalent rock beam, causes the floor rock to further bend, aggravates the damage of the floor rock, and converts a larger range of rock into a plastic failure state.

As shown in Figure 4(b), the bending moment of the floor rock increases with an increase in the thickness of the

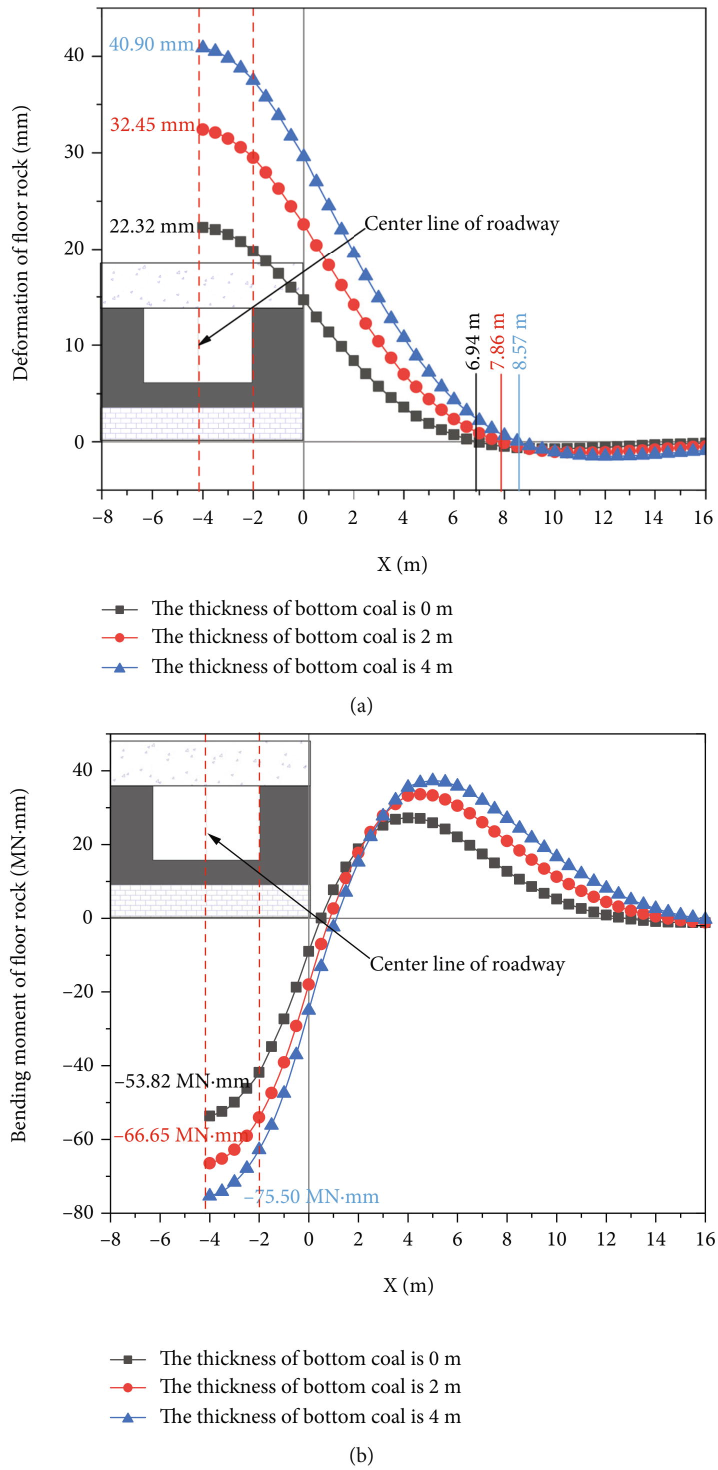

Figure 4: Deformation and bending moment of the floor rock under different thicknesses of the bottom coal. (a) Deformation of the floor rock. (b) Bending moment of the floor rock.

bottom coal, eventually causing the floor rock to break, first in the middle, and then at the end, forming a broken rock block.

As shown in Figure 4, an increase in the thickness of the bottom coal decreases the stiffness of the coal body (the foundation of the supporting rock layer), while the bending deformation range, deformation of the floor rock layer, and extrusion force all increase. This leads to an expansion in the range of the sides of the coal body that are squeezed by the floor rock layer, resulting in additional failure and deformation of the two sides of the coal body. Consequently, the damage to the floor rock layer is extended and increased. With an increase in the range of rock mass in the plastic failure state, roadway floor heave significantly increases.

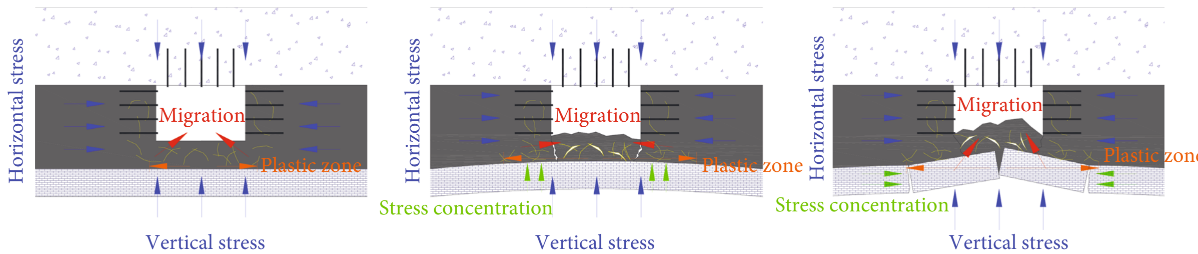

Figure 5: Migration evolution of floor-surrounding rock.

3.3. Influence of Different Support Strategies on Crossfeed Action between Floor and Two Sides. Figure 6 shows the deformation and bending moment of the roadway floor strata when the bottom coal thickness is 2 m while applying different support strategies. When close support is adopted, it is assumed that the plastic zone of the two sides is effectively controlled, and the elastic modulus of the coal in the plastic zone is the same as the elastic modulus of the coal body that is not damaged. The increase in the elastic modulus of the coal body with prestressed and non-pre-stressed supports is determined according to equation (9) and reference [36]. The foundation coefficients of the two sides of the coal body before and after the bottom corner support is installed are calculated according to equation (7) and equation (8).

Compared to the nontimely and non-pre-stressed support of the roadway side without supporting the bottom angle, the maximum deformation and bending moment of the floor rock with timely and prestressed support of the roadway side and the addition of a bottom angle support were reduced by 33% and 36%, respectively, while the maximum deformation and bending moment of the floor rock with timely and prestressed support of the roadway side but without the bottom angle support were both reduced by 13%. Therefore, supporting the bottom angle can effectively control the floor rock deformation of the roadway with retained bottom coal.

The maximum deformation and maximum bending moment of the floor rock with timely prestressed support of the roadway side and installed bottom angle support were reduced by 27% and 32%, respectively, compared to untimely prestressed support of the roadway side and with bottom angle supports installed. Conversely, when timely prestressed support of the roadway side is applied, but a supporting bottom angle is not used, the maximum deformation and bending moment of the floor rock are both reduced by 13% compared to untimely prestressed support of the roadway side without the bottom angle support installed. Therefore, timely support can effectively reduce the deformation and stress of the floor rock after roadway excavation.

The timely application of prestressed two-side support and bottom angle support after the excavation of a roadway with retained bottom coal can effectively improve the stiffness of the two sides of the roadway, reduce the damage range of the floor rock, and reduce the damage to the surrounding rock.

4. Evolution Mechanism of Floor Heave in the Deep Roadway with Retained Bottom Coal

Using the elastic foundation beam model, the induced effect of bottom coal on the deformation and failure of the floor rock and the two sides of the roadway are analyzed. Because the failure deformation of the floor rock is not equal to floor heave, it is necessary to study the mechanism of floor heave evolution caused by surrounding rock migration after the failure of the floor rock and floor sides.

4.1. Establishment of the Numerical Model. According to geological data and optical observation results in the borehole of the Qingyun mine, a plane model was established. The model size is $x = 64.5$ m in the direction of the roadway width and $z = 64$ m in the direction of the roadway height. To reduce the error, the model boundary was set 30 m from the roadway boundary. Because a continuous medium is conducive to applying more accurate boundary conditions, whereas a discrete medium is more suitable for simulating large deformations (because large deformations of deep roadway-surrounding rock are discontinuous and structural [37], many studies have adopted this method [38, 39]), the plane model was divided into two parts: the discrete medium is within 10 m of the roadway (greater than the range of significant deformation of the surrounding rock), and the rest is a continuous medium. To tailgate floor heave, the sandy mudstone floor with a thickness of 5.7 m was divided into 12 different colored layers (the physical and mechanical properties of the 12 layers are the same). The Mohr-Coulomb model was used to analyze and calculate the rock blocks and joints in the model. Considering gravitational acceleration $g = 9.81\ \mathrm{m/s^{-2}}$, the bottom of the model was fixed, the normal displacement of the side of the model was limited, and the stress boundary condition was used at the top of the model to replace the overburden weight. When the distribution law of rock joints is unknown, the rock block and joint surface in the 3DEC model were assigned a uniform strength and stiffness, representing the allowable cracking position in the model [40].

In this study, the influence of bottom coal on the movement of surrounding rock in the roadway was simulated to determine the influence of coal strength and bottom coal thickness. In the Mohr-Coulomb model, the strength of the coal seam and floor primarily depends on the cohesion and internal friction angle. However, in this instance, the amount of change in the internal friction angle was small.

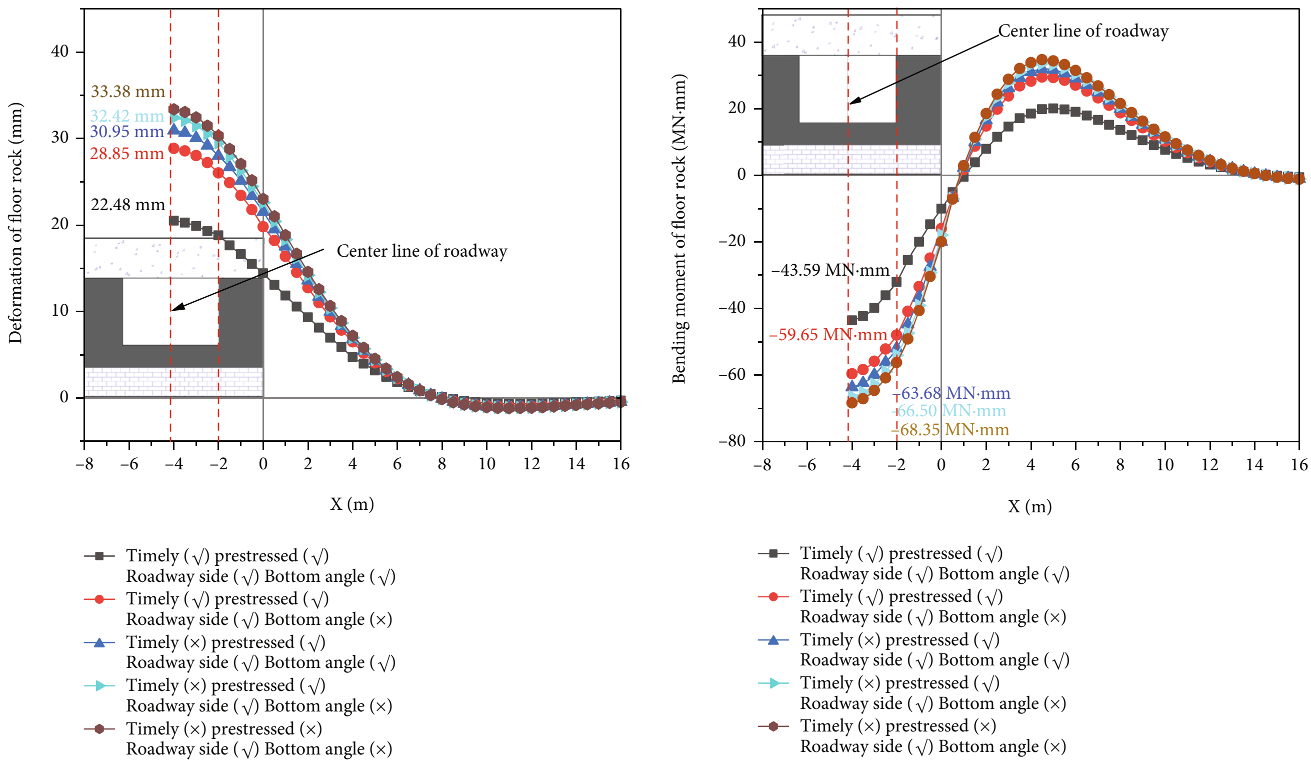

Figure 6: Deformation and bending moment of the floor rock under different support strategies.

Therefore, we simplified the model by assuming that the coal seam and floor strength were only influenced by cohesion. Based on the geological conditions of the No. 020202 tailgate of the Qingyun coal mine, three parameters were set for each factor in the range of common values: the thickness of the bottom coal was 0 m, 2 m, and 4 m; the cohesion of the coal body was 1 MPa, 3 MPa, and 5 MPa; and other mechanical parameters of the surrounding rock were set according to Table 1. Five simulation schemes were used in this study. Taking the bottom coal thickness of 0 m as an example, the numerical model is shown in Figure 7.

4.2. Expansion Law of the Bottom Arch in the Roadway with Retained Bottom Coal. Because the stress environment of the roadway floor is similar to that of the roadway roof, no difference was observed when comparing the deformation and failure of the floor-surrounding rock to that of the roof-surrounding rock. Therefore, it can be assumed that a bearing arch—similar to the one that formed when the roof-surrounding rock was destroyed—was also formed on the floor [41]. The floor rock mass did not collapse, but floor heave did occur. The numerical simulation results shown in Figure 8 better demonstrate this point. The evolution of the stress tensor with numerical steps in the surrounding rock of the retained bottom coal roadway is shown in Figure 9. When the roadway was excavated, the stress of the surrounding rock was redistributed, and stress deflection occurred at the shoulder angle and bottom angle of the roadway, forming the bearing arch. Stress was transferred to the arch foot through the bearing arch.

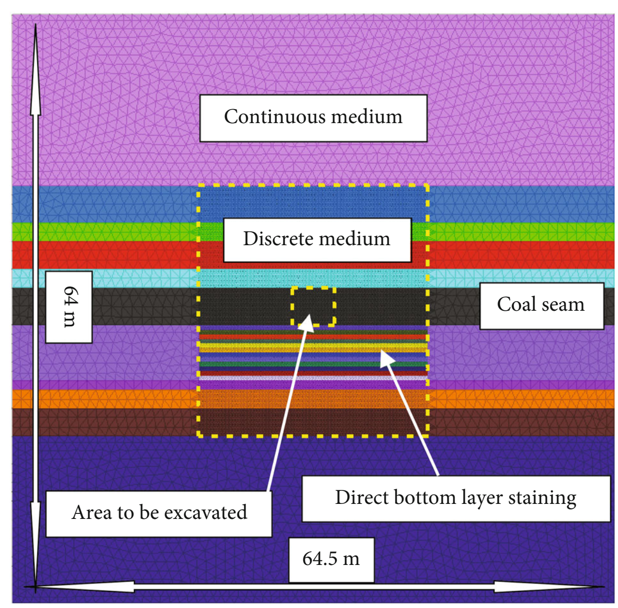

Figure 7: Numerical model.

The movement of the arch foot position in the horizontal and vertical directions with numerical time steps seen in Figure 9 was recorded, and the results are shown in Figures 10 and 11. With an increase in the thickness of the bottom coal, the position of the arch foot moved farther away from the roadway. When the thickness of the bottom coal was 0 m, 2 m, and 4 m, the position of the arch foot moved away from the roadway by 3 m, 3.5 m, and 4 m

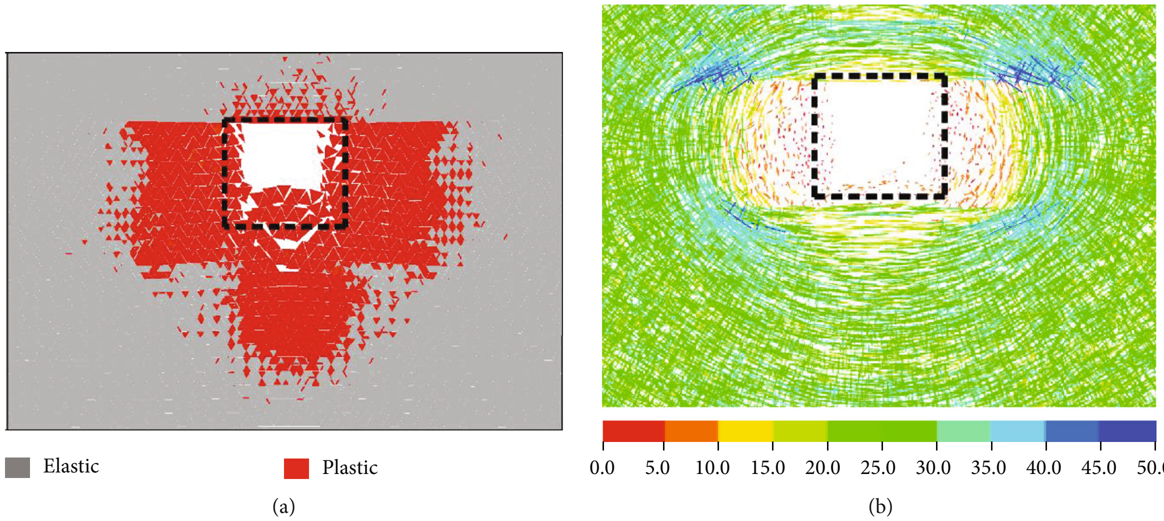

Figure 8: Reverse arching mechanism of the roadway floor. (a) Plastic zone and (b) stress tensors (MPa, colored by σ_1).

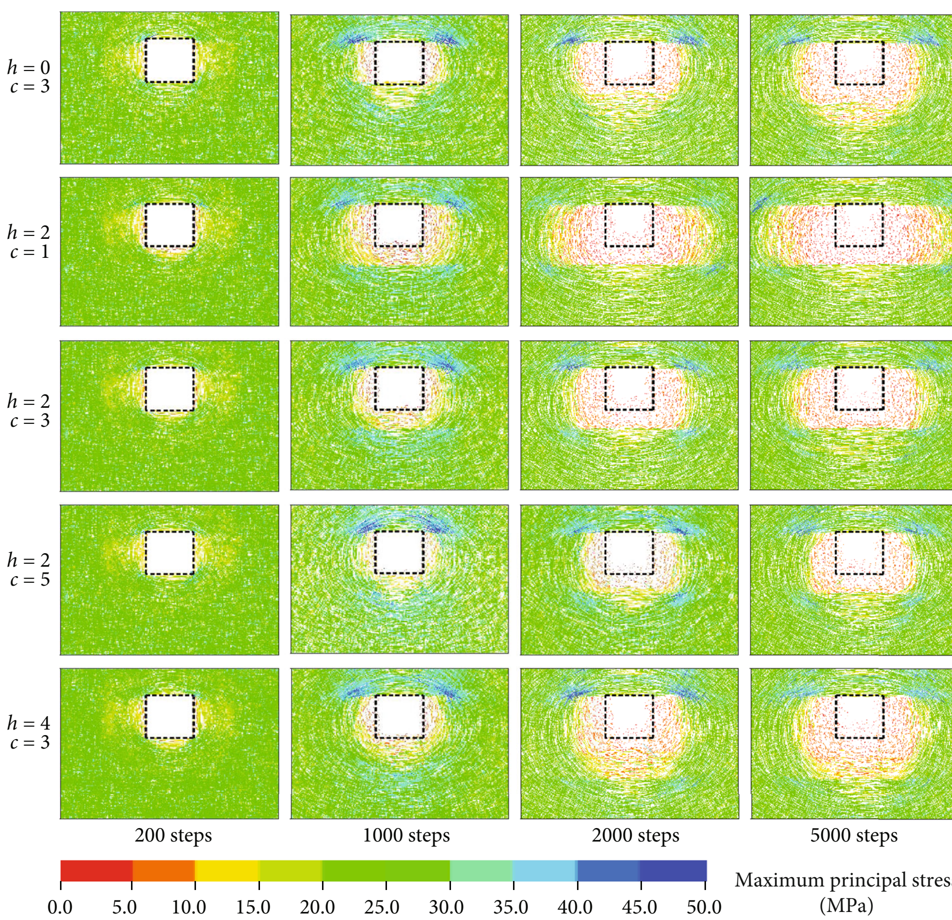

Figure 9: Time-varying evolution of stress tensor of the surrounding rock in the retained bottom coal roadway. Here, h = bottom coal thickness (m) and c = coal cohesion (MPa), the same as in Figures 10–13.

horizontally, and 1.7 m, 2.2 m, and 3.5 m vertically, respectively. With a decrease in coal strength, the position of the floor arch foot also moved away from the roadway. When the coal cohesion was 5 MPa, 3 MPa, and 1 MPa, the position of the arch foot moved away from the roadway 2 m, 2.3 m, and 2.3 m horizontally, and 2.8 m, 3 m, and 5.6 m vertically, respectively. The range and boundary shape of the surrounding rock failure was estimated based on the distance between the arch foot, the roadway side, and the arched structure of the floor.

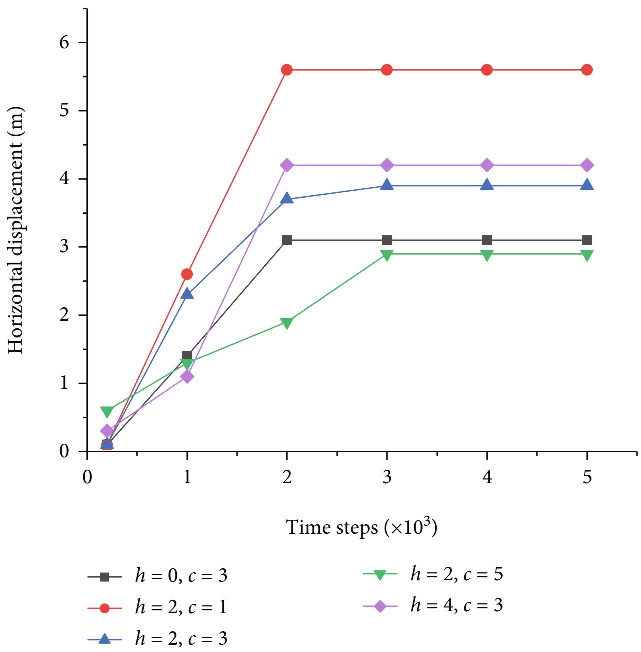

Figure 10: Horizontal displacement of the arch foot.

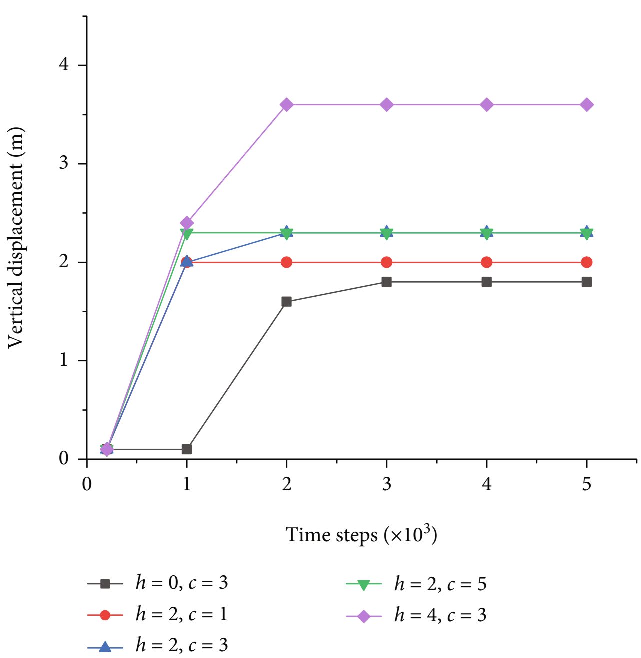

Figure 11: Vertical displacement of the arch foot.

Figures 12 and 13 show that the curve of the floor heave and displacement of the two sides of the roadway increased with time. The floor heave and displacement of the two sides of the roadway were consistent with the movement of the arch foot. The floor heave and displacement of the two sides of the roadway increased both with an increase in the thickness of the bottom coal and with a decrease in the strength of the coal body. The deformation of the two sides of the roadway and the floor stopped immediately when the arch foot stopped moving. The outward movement of the arch foot position implies that the failure range of the rock surrounding the floor arch increased, leading to an increase in the deformation of the roadway.

The stress concentration occurred on the surface of the roadway after excavation. Because of the unloading of the roadway surface, the surrounding rock in the shallow part was destroyed quickly, transferring concentrated stress to the deep part of the surrounding rock until it reached a balance with the strength of the surrounding rock. The induced effect of bottom coal on floor heave was that an increase in bottom coal thickness and a decrease in coal strength reduced the strength of the surrounding rock near the roadway surface, which was more likely to be destroyed under the action of concentrated stress. The concentrated stress was transferred deeper until a balance was reached with the deep surrounding rock of the roadway. Finally, both the depth of deformation and failure of the floor, as well as the width of the failure of the surrounding rock increased.

The shape of the failure boundary of the rock surrounding the floor was determined using the above simulation. The support of the roadway depended on the bearing capacity of the surrounding rock. The anchor cable should be anchored to the stable surrounding rock outside the floor arch. The support length of the anchor cable can be estimated using the arch foot positions shown in Figures 10 and 11. For example, when a bottom angle support is applied to the bottom coal of the roadway with a thickness of 2 m and cohesion of 3 MPa, the vertical and horizontal depths should not be less than 2.2 m and 3 m, respectively.

4.3. Migration Law of the Surrounding Rock of the Floor Arch of the Roadway with Retained Bottom Coal. In addition to the range and boundary shape of the floor rock failure, it was also necessary to investigate the deformation and migration of the surrounding rock in the arch to determine a reasonable support scheme.

Figure 14 shows the simulation results of the strata, plastic zone, and displacement of the five simulation schemes. Figures 15 and 16 present the layout of the four measuring points and their moving curves along the horizontal and vertical directions on the floor of the roadway with retained bottom coal.

As shown in Figure 15, following the excavation of the roadway, the measuring points on the floor moved significantly in the horizontal direction, with a maximum horizontal movement of 0.6 m. When the thickness of the bottom coal was 0 m, measuring points 2 and 3 were in the shallow part, which had horizontal displacement. In other cases, no horizontal displacement occurred at measuring points 2 and 3. However, the horizontal movement of measuring points 1 and 4 in the shallow part was significant. The horizontal movement of measuring point 4 was always the largest, approximately 0.3–0.6 m. Thus, the horizontal displacement of the floor rock generally occurred in the shallow part of the roadway rock. Therefore, the shear displacement of the shallow surrounding rock should be considered when setting the anchor cable support at the bottom corner, and the anchor cable support system should have a certain shear strength. Additionally, the horizontal displacement of

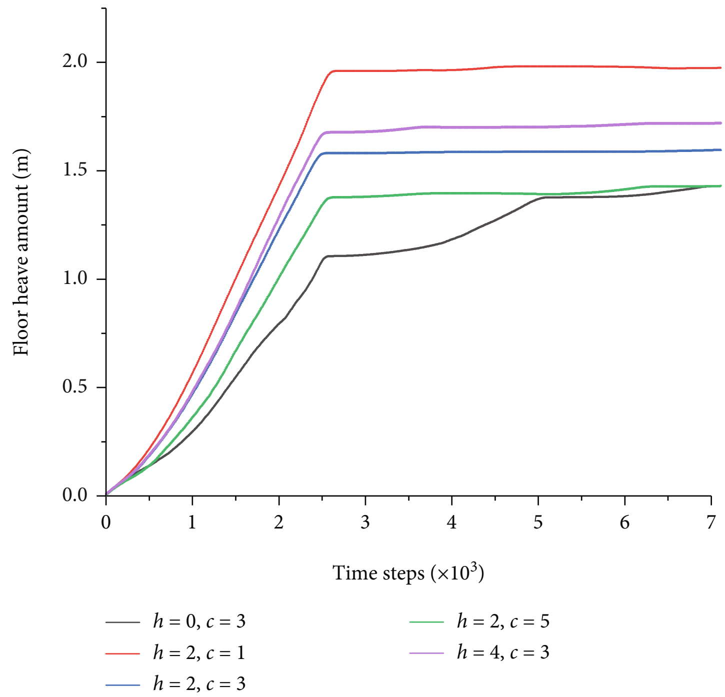

Figure 12: Floor heave amount.

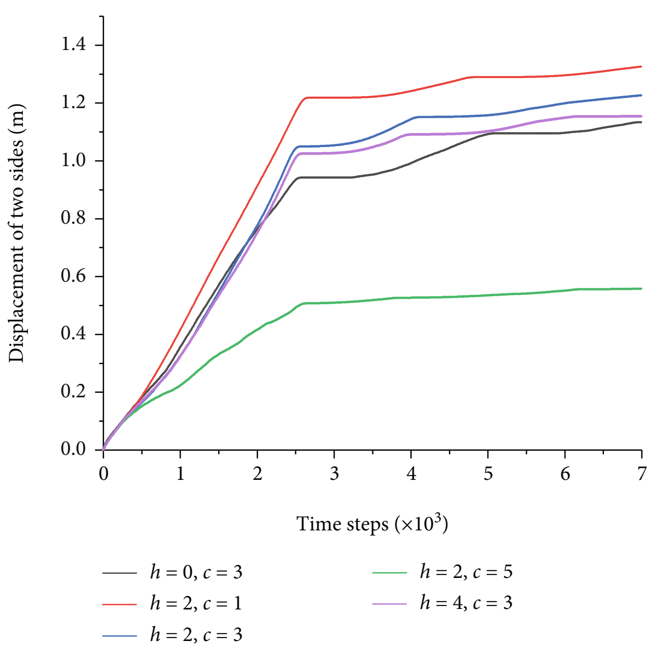

Figure 13: Displacement of two sides.

measuring point 1 first decreased, and then it increased, with time. The analysis shows that the surrounding rock at measuring point 1 moved to the two sides first, then to the middle line of the roadway. This finding is consistent with the conclusion from Section 4.2 that, under horizontal stress, the floor-surrounding rock first breaks in the middle of the roadway, moves to the two sides, then moves to the middle of the roadway. As shown in Figure 15(d), increasing the strength of the bottom coal can effectively control the horizontal displacement of the floor rock.

As shown in Figure 16, following the excavation of the roadway, the measuring points in the floor moved significantly in the vertical direction. The maximum vertical movement of measuring point 1 was approximately 0.9–1.4 m. The vertical movement of measuring points 3 and 4 under the two sides of the roadway was small, approximately 0.1–0.2 m. In Figure 16(a), measuring point 2 was in the shallow part of the surrounding rock and had a deformation of about 0.5 m. With an increase in the thickness of the bottom coal, the deformation of measuring point 2 decreased significantly to 0.2 m or less. Therefore, the shallow floor can be supported by an anchor or short anchor cable with a length of approximately 2 m.

In summary, the deformation of the floor-surrounding rock of the roadway with retained bottom coal mainly occurred in the shallow surrounding rock (approximately 2 m) close to the roadway surface. The floor-surrounding rock mainly migrated in the horizontal direction, whereas the roadway floor mainly moved in the vertical direction. The horizontal movement of the surrounding rock can be limited by setting an inclined anchor cable at the bottom angle, improving the shear capacity of the support with an anchor cable at the bottom angle, improving the strength of the surrounding rock at the bottom, or controlling the vertical movement of the floor with an anchor cable or short cable at the bottom angle.

4.4. Floor Heave Mechanism of the Roadway with Retained Bottom Coal. Because the supporting force provided by the supporting components is much smaller than the in situ stress in the surrounding rock, the existing supporting concept resists the in situ stress using the bearing arch structure of the surrounding rock in the roadway roof support. As

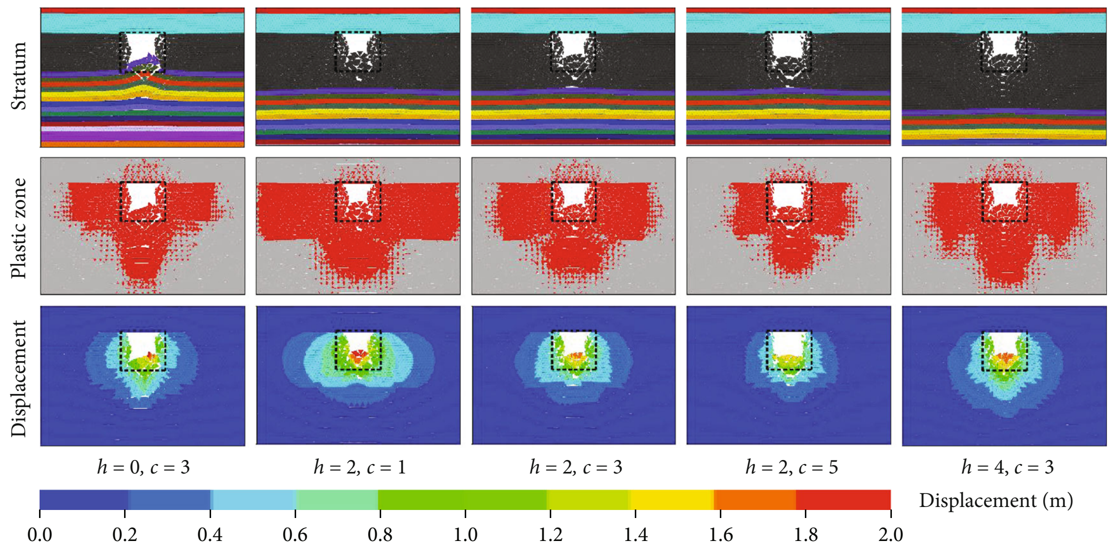

FIGURE 14: Simulation results of surrounding rock deformation of the roadway with retained bottom coal.

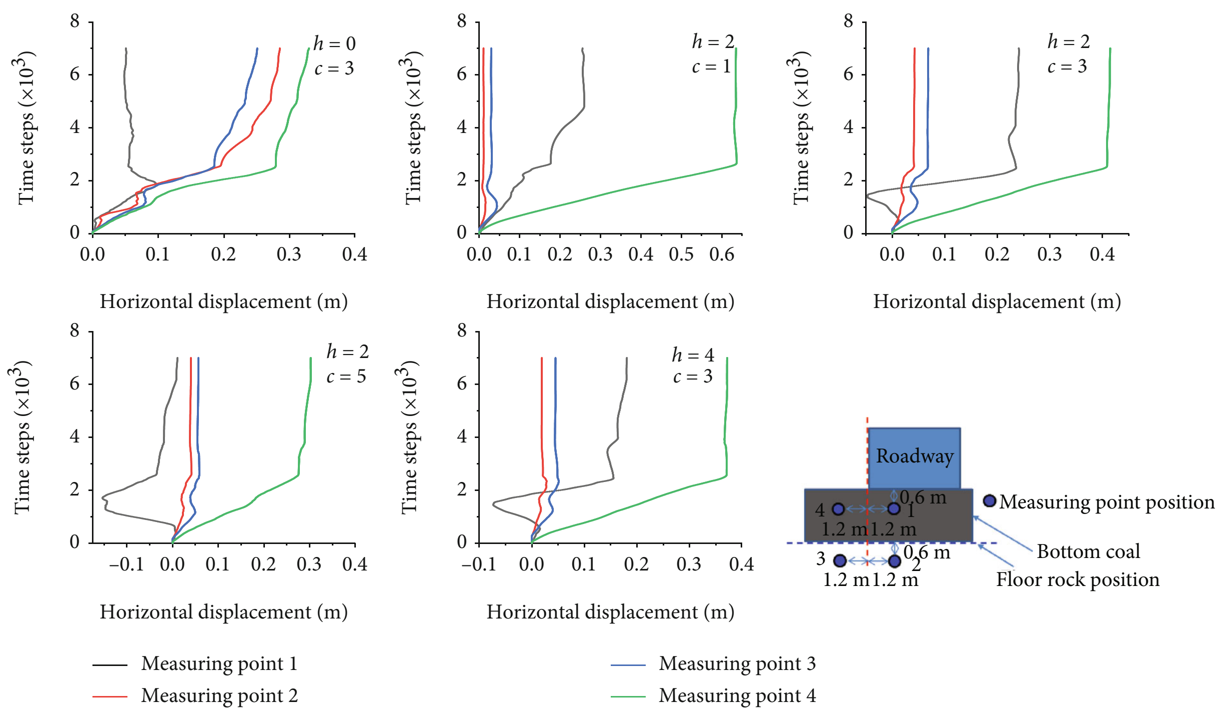

FIGURE 15: Curve of measuring point moving along the horizontal direction in the roadway floor.

mentioned above, the deformation and failure law of the floor under the action of in situ stress is similar to that of the roof, and, as shown in Figure 17, a floor arch structure is formed.

Under the condition of deep high stress, the plastic zone of the unsupported floor arch expands gradually until the stress and strength of the surrounding rock reach equilibrium. Compared to the arch of the supported roof, the floor arch, which is not constrained by the support system, expands outward significantly. The broken surrounding rock in the floor arch exhibits discontinuous deformation and moves toward the roadway. The larger the expansion range of the floor arch, the larger the expansion deformation of the surrounding rock in the arch, and, thus, the more significant the floor heave. Therefore, the unsupported floor is the main cause of floor heave in the deep coal roadway.

5. Engineering Practice

Based on this theoretical calculation and the numerical simulation, the supporting strategy of "high prestressed strong rock bolt (cable) supporting two sides and bottom corners in time" was proposed [42]. The supporting mode of the

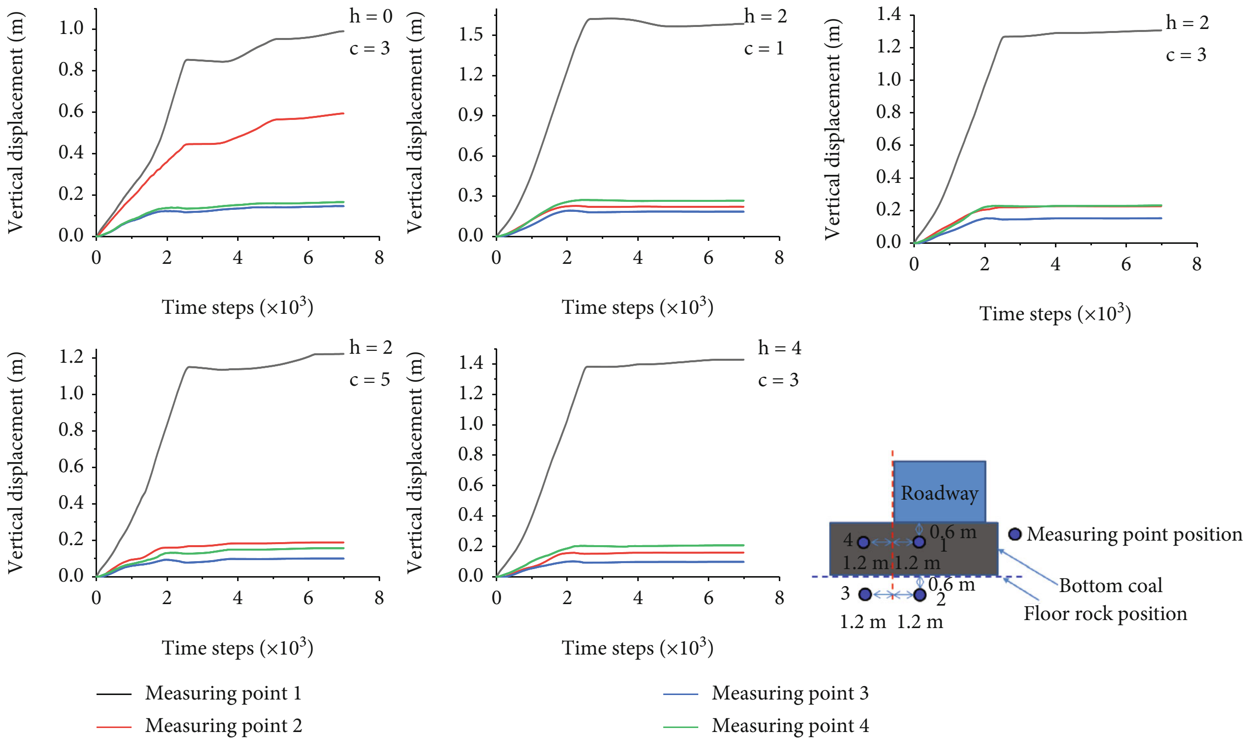

FIGURE 16: Curve of measuring point moving along the vertical direction in the roadway floor.

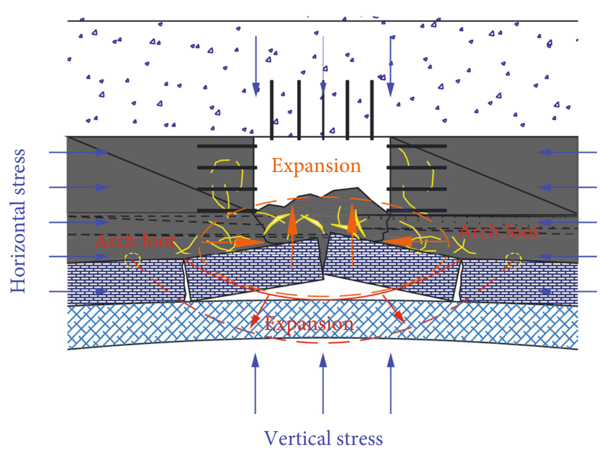

FIGURE 17: Evolution mechanism of the reverse arch expansion.

No. 020202 tailgate in the Qingyun mine was designed, and an industrial test was carried out in a new 100 m excavation section. The support strategy is illustrated in Figure 18. The support includes MG500 screw steel rock bolts with a length of 3000 mm, a diameter of 22 mm, and a preload of 70 kN, as well as cables with a 1 × 19 structure, a diameter of 21.8 mm, and a length of 6200 mm. The preload of the cables on the roof and the two sides was 300 kN and was 200 kN on the bottom corners. The cable support was used to limit the horizontal displacement at the bottom corners, and the rock bolt support was used to resist the horizontal shear displacement of the rock stratum; a W-type steel strip with a width of 280 mm was used for the roof, and a W-type steel guard plate with a width of 280 mm was used for the two sides.

As shown in Figure 19, the field test showed that both the displacement and the damage of the two sides of the No. 020202 tailgate were significantly reduced by strengthening the support of the two sides, increasing the bottom angle support, and adopting the timely prestressed anchor cable support. The maximum floor heave during the service period of the roadway was not more than 0.6 m (considering the cost, the economical and reasonable support scheme is designed on the premise that the roadway section meets the requirements of production and safety, although the deformation is still considerable), and there was no bottom lifting, confirming the feasibility of the support design.

6. Discussion

Floor heave is a complex engineering problem, especially for roadways with retained bottom coal. This paper analyzes this problem by establishing a Winkler elastic foundation beam model, and gives the floor heave mechanism and its influencing factors. It should be noted that the shallow part of the surrounding rock has entered the plastic stage, which is contrary to the assumption of the Winkler elastic foundation beam model. A lower foundation coefficient in the plastic zone than in the elastic zone is adopted to solve this problem, but errors exist. Then, the evolution mechanism of the roadway floor rock mass is analyzed by a discrete element numerical method, but the grid dependence is ignored. Finally, based on the laws obtained by the theoretical

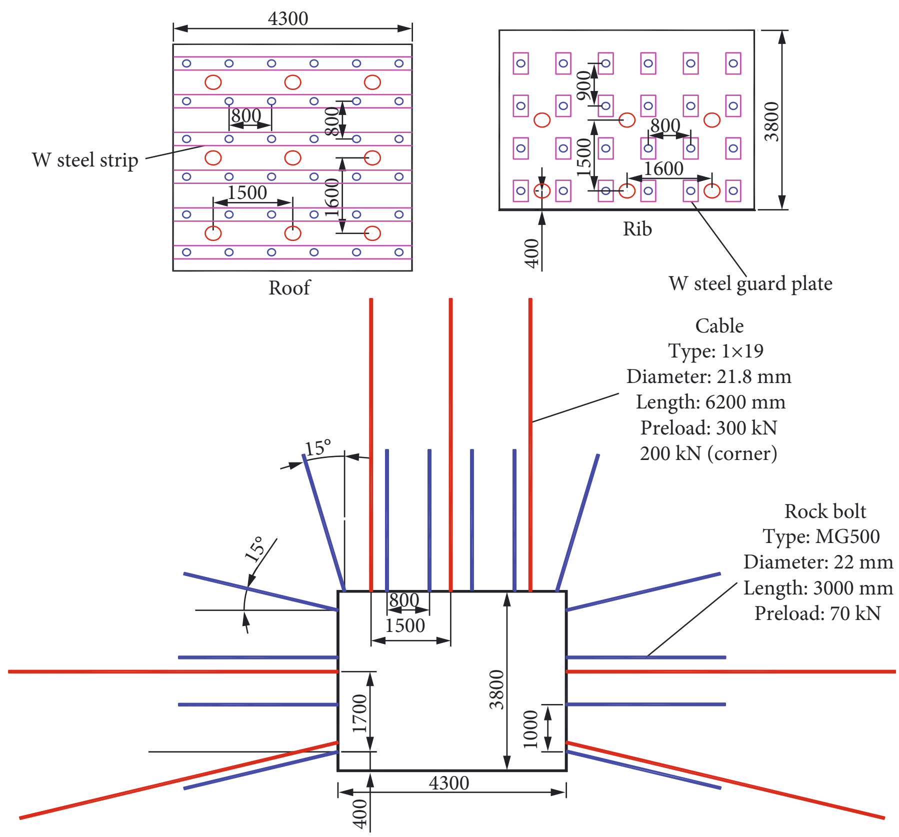

Figure 18: Support plan (mm).

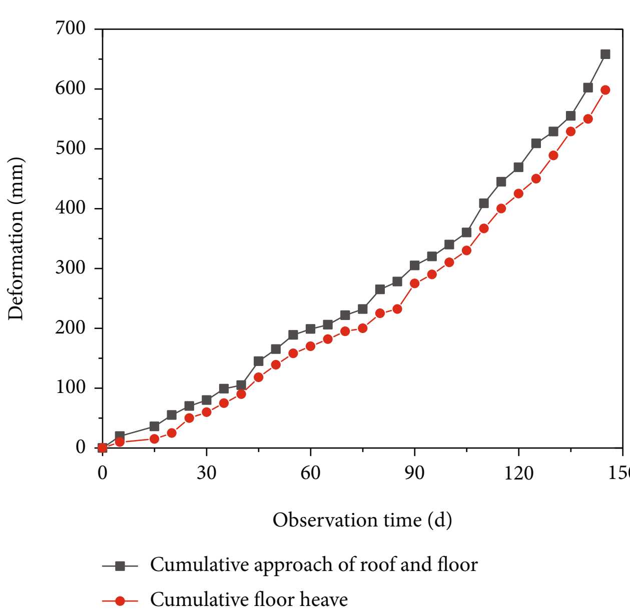

Figure 19: Deformation of No. 020202 tailgate in industrial test section during the service period (mm).

analysis and numerical simulation, a support scheme suitable for the No. 020202 tailgate in the Qingyun coal mine is put forward, which can provide reference for roadway support with similar geological conditions.

7. Conclusion

With an increase in the thickness of the bottom coal, the rigidity of the coal body (the foundation of the supporting rock layer) decreases, while the bending deformation range of the floor rock layer increases. This leads to an expansion in the range of the two sides of the coal body being squeezed by the floor rock layer, resulting in additional failure and deformation of the coal body sides. Therefore, the damage to the floor rock layer is extended and increased.

An increase in the bottom coal thickness and a decrease in the coal strength will decrease the surrounding rock strength near the roadway surface, which is more easily destroyed under a more concentrated stress. Thus, the concentrated stress should be transferred to the deeper part of the surrounding rock to achieve a balance with the unloaded surrounding rock in the deep part of the roadway. Finally, the depth of the floor deformation and failure increases, and the width of the failure surrounding the rock increases. The floor heave of the deep roadway is caused by expansion of the floor arch and surrounding rock. The increase in bottom coal thickness aggravates the expansion of the floor arch and causes greater floor heave deformation.

The support strategy of “high prestressed strong rock bolt (cable) supporting two sides and bottom corners in time” was proposed. After the excavation of the roadway, the prestressed strong rock bolt (cable) supporting the two sides of the roadway was applied in time, the inclined cable was applied to the bottom corner of the roadway to limit the horizontal movement of the surrounding rock, and the bottom corner rock bolt was applied to improve the shear capacity of the bottom corner. Practice shows that this support scheme effectively controlled floor heave, and the feasibility of the support scheme was verified.

Data Availability

The data used to support the findings of this study are available from the corresponding authors upon request.

Conflicts of Interest

The authors declare no conflict of interest.

Acknowledgments

This research was funded by the National Key Research and Development Program of China (grant number 2017YFC0603003), the Applied Basic Research Project of Shanxi Province (grant number 201901D111049), and the Key Research and Development Projects of Shanxi Province (grant number 201903D321080).

References

[1] H. Kang, Y. Wu, F. Gao, J. Lin, and P. Jiang, "Fracture characteristics in rock bolts in underground coal mine roadways," *International Journal of Rock Mechanics and Mining Sciences*, vol. 62, pp. 105–112, 2013.

[2] M. Wang, N. Zhang, J. Li, L. Ma, and P. Fan, "Computational method of large deformation and its application in deep mining tunnel," *Tunnelling and Underground Space Technology*, vol. 50, pp. 47–53, 2015.

[3] Z. Wang, S. Yang, G. Xu, and Z. Wen, "Ground response and mining-induced stress in longwall panel of a kilometer-deep coal mine," *Shock and Vibration*, vol. 2021, Article ID 6634509, 14 pages, 2021.

[4] S. Yang, M. Chen, H. Jing, K. Chen, and B. Meng, "A case study on large deformation failure mechanism of deep soft rock roadway in Xin'An coal mine, China," *Engineering Geology*, vol. 217, pp. 89–101, 2017.

[5] D. Fan, X. Liu, Y. Tan, L. Yan, S. Song, and J. Ning, "An innovative approach for gob-side entry retaining in deep coal mines: a case study," *Energy Science and Engineering*, vol. 7, no. 6, pp. 2321–2335, 2019.

[6] Y. Jiang, Y. Zhao, W. Liu, and Q. Li, "Research on floor heave of roadway in deep mining," *Chinese Journal of Rock Mechanics and Engineering*, vol. 23, pp. 2396–2401, 2004.

[7] S. Mo, H. L. Ramandi, J. Oh et al., "A new coal mine floor rating system and its application to assess the potential of floor heave," *International Journal of Rock Mechanics and Mining Sciences*, vol. 128, 2020.

[8] K. Yi, Z. Liu, Z. Lu, J. Zhang, and S. Dong, "Effect of axial in-situ stress in deep tunnel analysis considering strain softening and dilatancy," *Energies*, vol. 13, no. 6, p. 1502, 2020.

[9] G. Zhao and S. Yang, "Analytical solutions for rock stress around square tunnels using complex variable theory," *International Journal of Rock Mechanics and Mining Sciences*, vol. 80, pp. 302–307, 2015.

[10] X. G. Zhao and M. Cai, "Influence of plastic shear strain and confinement-dependent rock dilation on rock failure and displacement near an excavation boundary," *International Journal of Rock Mechanics and Mining Sciences*, vol. 47, no. 5, pp. 723–738, 2010.

[11] K. Yi, Z. Liu, Z. Lu, J. Zhang, and Z. Sun, "Transfer and dissipation of strain energy in surrounding rock of deep roadway considering strain softening and dilatancy," *Energy Science and Engineering*, vol. 9, no. 1, pp. 27–39, 2021.

[12] X. Sun, F. Chen, M. He, W. Gong, H. Xu, and H. Lu, "Physical modeling of floor heave for the deep-buried roadway excavated in ten degree inclined strata using infrared thermal imaging technology," *Tunnelling and Underground Space Technology*, vol. 63, pp. 228–243, 2017.

[13] S. Mo, K. Tutuk, and S. Saydam, "Management of floor heave at Bulga Underground Operations—a case study," *International Journal of Mining Science and Technology*, vol. 29, no. 1, pp. 73–78, 2019.

[14] S. Liu, J. Bai, X. Wang, B. Wu, and W. Wu, "Mechanisms of floor heave in roadways adjacent to a goaf caused by the fracturing of a competent roof and controlling technology," *Shock and Vibration*, vol. 2020, 17 pages, 2020.

[15] Z. Ma, X. Liang, G. Fu, Y. Zou, A. Chen, and R. Guan, "Experimental and numerical investigation of energy dissipation of roadways with thick soft roofs in underground coal mines," *Energy Science and Engineering*, vol. 9, no. 3, pp. 434–446, 2021.

[16] S. B. Tang and C. A. Tang, "Numerical studies on tunnel floor heave in swelling ground under humid conditions," *International Journal of Rock Mechanics and Mining Sciences*, vol. 55, pp. 139–150, 2012.

[17] Y. Xu, E. Zhang, Y. Luo, L. Zhao, and K. Yi, "Mechanism of water inrush and controlling techniques for fault-traversing roadways with floor heave above highly confined aquifers," *Mine Water and the Environment*, vol. 39, no. 2, pp. 320–330, 2020.

[18] K. Yi, H. Kang, W. Ju, Y. Liu, and Z. Lu, "Synergistic effect of strain softening and dilatancy in deep tunnel analysis," *Tunnelling and Underground Space Technology*, vol. 97, p. 103280, 2020.

[19] J. Yang, G. Song, Y. Yang, and Z. Yang, "Application of the complex variable function method in solving the floor heave problem of a coal mine entry," *Arabian Journal of Geosciences*, vol. 11, no. 17, 2018.

[20] Q. Zhao, Y. Wang, Y. Liu, H. Li, J. Shi, and L. Shi, "The controlling techniques on floor heave of large cross section mining roadway with complicated surrounding rock," *Coal Engineering*, pp. 231–236, 2014.

[21] A. Ilinets, A. Sidorenko, and Y. G. Sirenko, "Computer modelling of a floor heave in coal mines," *In International Conference: Information Technologies in Business and Industry*, vol. 1333, p. 032028, 2019.

[22] L. Shi, H. Zhang, and P. Wang, "Research on key technologies of floor heave control in soft rock roadway," *Advances in Civil Engineering*, vol. 2020, 13 pages, 2020.

[23] C. Wang, G. Li, A. Gao, F. Shi, Z. Lu, and H. Lu, "Optimal preconditioning and support designs of floor heave in deep roadways," *Geomechanics and Engineering*, vol. 14, pp. 429–437, 2018.

[24] Y. Zhang, J. Shao, P. Chen, X. Li, and Z. Kan, "Development and application of mechanized control equipment for roadway

floor heave in coalmine," in *In Proceedings of the 2017 2nd Joint International Information Technology, Mechanical and Electronic Engineering Conference*, vol. 62, pp. 287–290, 2017.

[25] C. Liu, J. Ren, B. Gao, and Y. Song, "Support design and practice for floor heave of deeply buried roadway," *Iop Conference*, vol. 64, p. 12032, 2017.

[26] W. Zheng, Y. Zhao, and Q. Bu, "The coupled control of floor heave based on a composite structure consisting of bolts and concrete antiarches," *Mathematical Problems in Engineering*, vol. 2018, 14 pages, 2018.

[27] X. Zhang, T. Li, G. Chen, H. Liu, and P. Destech, "Study of floor heave mechanism in deep soft rock roadway," in *In 3rd Asian Pacific Conference on Energy, Environment and Sustainable Development*, pp. 164–167, 2017.

[28] X. Kang, D. Guo, and Z. Lu, "Mechanism of roadway floor heave controlled by floor corner pile in deep roadway under high horizontal stress," *Advances in Civil Engineering*, vol. 2021, 10 pages, 2021.

[29] G. Guo, H. Kang, D. Qian, F. Gao, and Y. Wang, "Mechanism for controlling floor heave of mining roadways using reinforcing roof and sidewalls in underground coal mine," *Sustainability*, vol. 10, no. 5, p. 1413, 2018.

[30] H. Xie, H. Zhou, D. Xue, H. Wang, R. Zhang, and F. Gao, "Research and consideration on deep coal mining and critical mining depth," *Journal of China Coal Society*, vol. 37, pp. 535–542, 2012.

[31] L. Wang and T. Ishihara, "A study of the effects of foundation uplift on the seismic loading of wind turbine tower and shallow foundation using a new dynamic Winkler model," *Engineering Structures*, vol. 219, 2020.

[32] G. Zhang, Y. Qu, X. Gao, and F. Jin, "A transversely isotropic magneto-electro-elastic Timoshenko beam model incorporating microstructure and foundation effects," *Mechanics of Materials*, vol. 149, p. 103412, 2020.

[33] L. Jiang, P. Zhang, P. Kong et al., "Rib-control support principle based on the foundation rigidity of coal mine roadways," *Journal of China Coal Society*, vol. 44, pp. 1020–1029, 2019.

[34] A. Bobet, "Elastic solution for deep tunnels. application to excavation damage zone and rockbolt support," *Rock Mechanics and Rock Engineering*, vol. 42, no. 2, pp. 147–174, 2009.

[35] A. Bobet and H. H. Einstein, "Tunnel reinforcement with rockbolts," *Tunnelling and Underground Space Technology*, vol. 26, no. 1, pp. 100–123, 2011.

[36] Z. Qin, *The Anchoring Mechanism of High-Strength Pressed Anchor and Time-Dependent Deformation Analysis of Bolted Rock Mass*, Institute of Rock and Soil Mechanics the Chinese Academy of Sciences, Wuhan, 2007.

[37] B. Huang, N. Zhang, H. Jing et al., "Deformation and failure characteristics and control technology of roadway surrounding rock in deep coal mines," *Journal of the China Coal Society*, vol. 2020, pp. 1–15, 2020.

[38] F. Gao and D. Stead, "Discrete element modelling of cutter roof failure in coal mine roadways," *International Journal of Coal Geology*, vol. 116-117, pp. 158–171, 2013.

[39] F. Gao, D. Stead, H. Kang, and Y. Wu, "Discrete element modelling of deformation and damage of a roadway driven along an unstable goaf—a case study," *International Journal of Coal Geology*, vol. 127, pp. 100–110, 2014.

[40] K. Yi, P. Gong, and C. Liu, "Overlying strata structures and roof control of working face under thin topsoil and thin bedrock in shallow seam," *Journal of China Coal Society*, vol. 43, pp. 1230–1237, 2018.

[41] S. S. Peng, *Coal Mine Ground Control*, John Wiley & Sons. Inc., New York, 2008.

[42] J. Chen, S. Yang, H. Zhao, J. Zhang, F. He, and S. Yin, "The analytical approach to evaluate the load-displacement relationship of rock bolts," *Advances in Civil Engineering*, vol. 2019, 15 pages, 2019.

Hindawi
Geofluids
Volume 2023, Article ID 2545442, 12 pages
https://doi.org/10.1155/2023/2545442

Research Article

Study on the Bearing Mechanism and Stability of Surrounding Rock in Original Roadway Filling and Nonpillar Tunneling

Wenbao Shi[1] **Jucai Chang**[1] **Yan Li**[2] **Dong Li**[1] **and Ru Hu**[1]

[1]Key Laboratory of Safe and Effective Coal Mining, Ministry of Education, School of Mining Engineering, Anhui University of Science and Technology, Huainan 232001, China
[2]School of Mechanical and Electrical Engineering, Huainan Normal University, Huainan 232038, China

Correspondence should be addressed to Yan Li; 1960526430@qq.com and Ru Hu; 1595036962@qq.com

Received 23 August 2021; Revised 14 September 2021; Accepted 28 September 2021; Published 13 March 2023

Academic Editor: Dan Ma

This study is focused on the problem that with the increase of coal seam mining depth, it is difficult to continuously replace mining due to complex roadway layout and unreasonable stope layout. By taking the mining geological conditions of the 62210 fully mechanized mining face of Xinzhuangzi Coal Mine in Huainan mining area, China, as the background, it explores the stress characteristics of the original roadway filling body as well as the stress distribution and deformation characteristics of roadway surrounding rock in original roadway filling and nonpillar tunneling (ORFNPT) through theoretical analysis and numerical simulation. The following findings are obtained. The required strength for the filling body is primarily determined by two factors, i.e., the span of the hanging roof that lies over the filling body and the width of the filling body. The span of the hanging roof is positively correlated with the required strength of the filling body. However, when the width of the filling body reaches a certain value, its further increase fails to change the required strength of the filling body. Compared with gob-side entry driving with small coal pillars, when the ORFNPT technology is applied to the lower-section roadway, the peak stress position in the solid coal on the lower side of the roadway is closer to the roadway sides, and the filling body is of a much higher stress than the small coal pillars. Besides, the roadway surrounding rock undergoes milder deformation. According to the on-site application and measurement data, the roof-to-floor convergence and side-to-side displacement amounts of the roadway are about 89 mm and 58 mm during tunneling of the 62310 working face, and the two amounts are about 910 and 1,290 mm during recovery of the 62310 working face, respectively. This tunneling method achieves an excellent roadway control effect.

1. Introduction

With the rapid economic development in China, the depth of coal mining is increasing year by year, and mining areas in eastern China have successively stepped into the stage of deep mining [1, 2]. In deep mining, the roadway surrounding rock is affected by complex stress fields such as high ground stress and intensive mining, which causes difficulties to the maintenance of roadway, thus hindering continuous mining of the stope [3, 4]. For old mining areas, stope replacement is faced with more difficulties induced by the increase in mining depth, the complex layout of mine roadway, and the unreasonable layout of stope [5]. Moreover, the retention of various coal pillars during coal mining not only notably affects the coal recovery rate but also leads to a large waste of resources.

At present, the commonly used section roadway protection methods can mainly be classified into two categories: gob-side entry driving with small coal pillars (GSEDSCP) [6, 7] and gob-side entry retaining (GSER) [8, 9]. The former often leads to stress concentration in the underlying coal seams, which may induce geological disasters (such as large deformation, rock burst, and coal and gas outburst) in the surrounding rock of gob-side roadway during underlying coal seam recovery [10]. The latter is influenced by tunneling once and by mining twice, and generally, the roadway is barely functioning when used for the second time as a result of fast and serious surrounding rock deformation

[11]. In order to ensure the stability of roadway in deep coal recovery, scholars have attached importance to the research on the support strength and deformation stress characteristics of the filling body in GSER in recent years. Kong et al. [12] deduced a calculation formula for the width of the roadway-side support. Qi et al. [13] and Huang et al. [14] studied the bearing characteristics of underground filling body and the support strength of working face and analyzed the technical difficulties and key points in the construction of solid filling mining support. Khaldoun et al. [15] investigated the movement process and deformation characteristics of roadway roof strata in a deep mine, determined a design principle for the support resistance of the filling body, and established a mathematical model for the support resistance and compression of the filling body. Chen et al. [16, 17] classified roadway roofs into three typical types, namely, thick immediate roof, thin immediate roof, and no immediate roof. Besides, they obtained formulae to calculate the support resistance of gob-side roadway for the above three types by superimposing the continuous layer model and considering the bearing effect of the coal on the retained roadway sides and the factors inducing roof collapse. Cheng et al. [18] analyzed the influence of the width of filling body and material characteristics on the stability of surrounding rock in fully mechanized caving roadways based on the key technology of surrounding rock control in such roadways and put forward measures to improve the deformation resistance capacity of the filling body. Feng and Zhang and Guo et al. [19, 20] simplified the deep coal seam roof as a rectangular "superimposed layer" without interlayer bonding force, analyzed the law of roadway roof activity in different periods, established a mechanical model of the relationship between roadway "surrounding rock and support" with the aid of elastic-plastic mechanical theory, and obtained a formula to calculate the support resistance. Kong et al. [21] analyzed the factors influencing roadway surrounding rock deformation in fully mechanized caving face, conducted in-depth analysis on the interaction mechanism between surrounding rock and filling body, and obtained a formula to calculate the support resistance of the filling body, which provided a theoretical basis for the on-site application of working face roadway. To solve the problem of gas accumulation in the upper corner of high-gas mines, Ma et al. [22, 23] proposed the secondary roadway technology, established a mechanical model of the key blocks at the ends, and obtained theoretical formulae to calculate the support resistance and the width of the filling body. Meng et al. and Mo et al. [24, 25] put forward a roadway technology of "concrete filling on the roadway sides + anchor-net-cable combined support in the roadway + anchor-cable reinforcement on the roadway sides" based on the activity law and deformation characteristics of roadway roof strata in a deep mine. Furthermore, they analyzed the relationship between roof separation and roof deformation and obtained the critical value of roof separation. Zhu et al. [26] established a mechanical model of the key block and the immediate roof and analyzed the mechanism of interaction between the key block and the roadway surrounding rock. The results revealed that the width of the filling body had a great influence on the stability of the gob-side roadway. Sun et al. [27] studied the deformation characteristics of fully mechanized caving roadways through similar simulation tests, concluding that the filling body should be of both a certain strength and a certain deformation resistance capacity. Seryakov [28] analyzed the deformation and stress distribution characteristics of roadway surrounding rock and proposed a design principle for deep roadway filling support by analyzing on-site mine pressure monitoring data. In summary, previous studies were focused on the bearing characteristics of the filling body of GSER as well as the interaction between the filling body and the surrounding rock. Constructing the filling body can effectively improve the stress state of the surrounding rock in the entire roadway and provide more support for the surrounding rock in the roadway roof. The research results serve as important reference for the application of the new method for recovery roadway tunneling, i.e., the original roadway filling and non-pillar tunneling (ORFNPT) technology.

In this study, a mechanical model for original roadway filling under the influence of roof structure was established based on the basic law of roof stratum fracture and the key stratum theory. Next, the stress distribution and deformation characteristics of surrounding rock of ORFNPT were analyzed theoretically and numerically. Finally, on-site application was conducted in the 62210 working face of Xinzhuangzi Coal Mine.

2. Geological Overview

Xinzhuangzi Coal Mine is located in the west of Huainan City, China, and at the east foot of Bagong Mountain. The mine field stretches from the north side of Huaihe River to the south side of it. The 62210 fully mechanized working face of the mine, whose elevation ranges from -660 m to -770 m, has an average strike length of 1,285 m, an average dip length of 194 m, and an area of 249,290 m^2. The average coal seam thickness is 1.0 m, and the coal seam dip angle lies in the range of 21°-30°, with an average of 25°. The corresponding overlying B11 and B8 coal seams have not been mined yet. The immediate roof belongs to sandy mudstone with a thickness of 2-12 m, and it is a fragile dark-gray thin layer. The main roof is fine sandstone with a thickness of 0-6 m. The immediate floor is fine sandstone with a thickness of 1-3.5 m, and it is a fragile gray thick layer. The main floor belongs to mudstone with a thickness of 1-4 m. The schematic diagram of geological overview of the working face is given in Figure 1.

3. Force Analysis on the Filling Body in ORFNPT

3.1. Force Calculation on the Filling Body in Original Roadway Filling. The support resistance of the filling body in the gob-side roadway is usually calculated with the superimposed continuous layer model which considers the separation and dislocation between layers. In the model, each layer can be regarded as an independent continuous layer structure, and the layers are connected by distributed loads, so this model is faithful to the actual situation of stratum

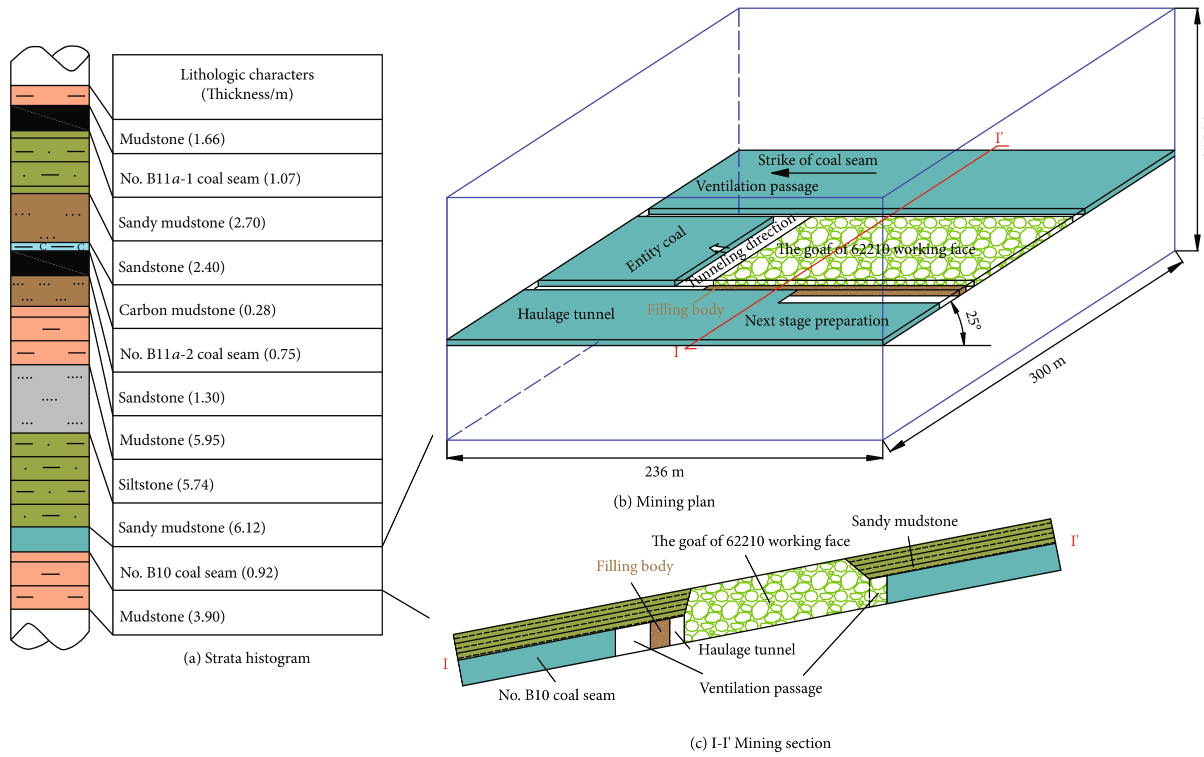

Figure 1: Schematic diagram of geological overview of the 62210 working face.

occurrence [29]. In addition, a mechanical structure model of the filling body support and roof was established with reference to the basic law of roof stratum fracture and the key stratum theory [30]. The support resistance of the filling body in the original roadway was studied through the block mechanical balance method. Figure 2(a) is the roof structure model with four sides supported, and Figure 2(b) is the one with three sides supported and one side free. During the first weighting, the roof in the fully mechanized mining face belongs to the model with four sides supported. q is the uniformly distributed load of roof; the load on ABCD surface after division by strip only concentrates on sections AB and CD, and the support resistance is Q.

The calculation of the required strength of the filling body starts from the last stratum of the overlying strata. According to Figure 2(a), the required strength of the filling body under a single overlying stratum is calculated as follows:

$$\begin{gathered}\sum F_y = 0,\\ \text{Section AB}: \; aq_1 \cos\eta + F_{A1} - Q_1 a - F_{O1} = 0,\\ \therefore F_{O1} = q_1(a + L_1) - Q_1 a,\end{gathered} \tag{1}$$

where a is the width of the filling body (m), b is the span of immediate hanging roof above the filling body (m), η is the dip angle of coal seam, F_{A1} is the shear force generated downward by the fracture block at the rock fracture, and $F_{A1} = q_1 L_1$.

During periodic weighting of the working face roof, the roof belongs to the roof structure model with three sides supported and one side free. For the above two models, a slat with unit width and a large load in the gob-side roadway is taken as the calculation unit (Figures 3(a) and 3(b)).

$$\begin{gathered}\sum M = 0,\\ \text{Section OA}: \; M_{p1} - M_{01} + \frac{1}{2} q_1 \cos\eta (a+b)^2\\ + q_1 \cos\eta L_1 (a+b) - \frac{1}{2} Q_1 a^2 = 0,\end{gathered} \tag{2}$$

where $q_1 = \gamma_1 \cdot h_1 \cos\eta$. Then, q_1 is substituted in the expression of Q_1:

$$Q_1 = \frac{2M_{p1} - 2M_{01} + (a+b)^2 L_1 \gamma_1 h_1 \cos\eta + (a+b) L_1 2\gamma_1 h_1 \cos\eta}{a^2}, \tag{3}$$

where M_{p1} is the ultimate bending moment of strata (kN·m), M_{01} is the bending moment of strata (kN·m), F_{A1} is the downward shear force generated by the rock fracture block of point A (kN), Q_1 is the roof cutting strength (MPa), q_1 is the rock mass concentration (MPa), γ_1 is the bulk density of the first stratum above the filling body, h_1 is the depth of the first stratum above the filling body (m), and L_1 is the fracture characteristic size of the first stratum (m).

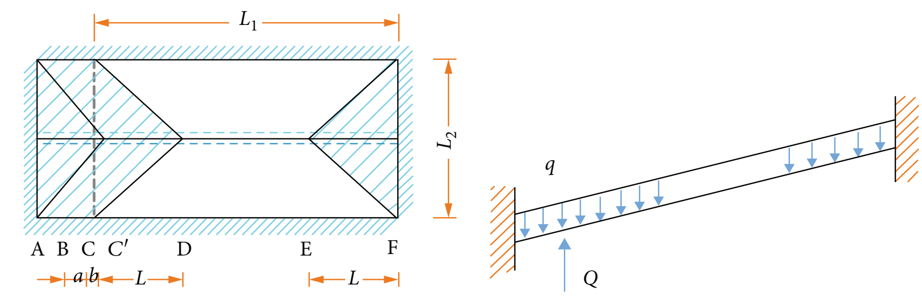

(a) Roof mechanical model for first weighting (b) Roof radial strip mechanical model

Figure 2: Calculation model of support strength of the filling body in the roadway.

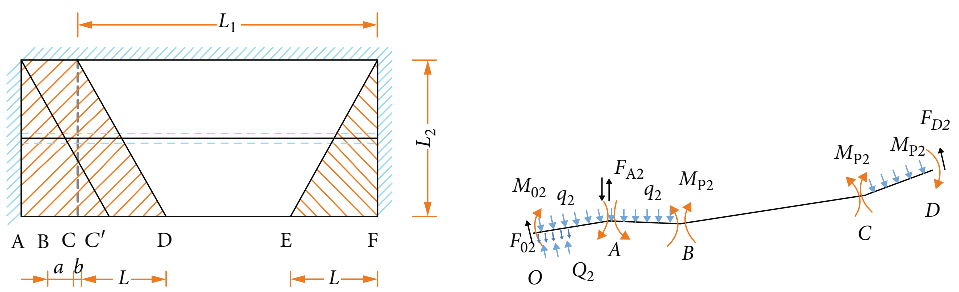

(a) Mechanical model of roof during periodic weighting (b) Schematic diagram of the mechanical model of roof

Figure 3: Calculation model of support strength of the filling body during periodic weighting.

Under the second stratum fracture, the required strength of the filling objects is Q_2, and the mechanical analysis on the stress state of the filling body is as follows:

$$\begin{aligned}
\sum M &= M_{01} + M_{02} + \frac{1}{2} Q_2 a^2 \\
&= M_{p2} + \frac{1}{2}\gamma_2 h_2 (a + b + h_1 \tan\theta_1)^2 \cos\eta \\
&\quad + \frac{1}{2}\gamma_1 h_1 (a + b)^2 \cos\eta + F_{A2}(a + b + h_1 \tan\theta_1) \\
&\quad + F_{A1}(a + b)\frac{1}{2} Q_2 a^2 \\
&= \left[\frac{1}{2}\gamma_2 h_2 (a + b + h_1 \tan\theta_1)^2 + \frac{1}{2}\gamma_1 h_1 (a + b)^2 \right. \\
&\quad \left. + \gamma_1 h_1 L_1 (a + b) + \gamma_2 h_2 L_2 (a + b + h_1 \tan\theta_1)\right] \cos\eta \\
&\quad + M_{p2} - M_{01} - M_{02} \\
&= \frac{1}{2}\sum_{i=1}^{2} \gamma_1 h_1 \left(a + b + \sum_{j=0}^{i=1} h_j \tan\theta_j\right)^2 \cos\eta \\
&\quad + \sum_{i=1}^{2} F_{Ai}\left(a + b + \sum_{j=0}^{i=1} h_j \tan\theta_j\right) + M_{p2} - \sum_{i=1}^{2} M_{0i}.
\end{aligned} \tag{4}$$

The strengths of the filling body under one layer or two layers of overlying strata are obtained through mechanical analysis on the first and second layers of the overlying strata of the filling body. Similarly, the required strength Q_m of the filling body under the fracture of the m -th stratum above the filling body can be obtained as follows:

The m-th layer of roof:

$$\begin{aligned}
Q_m &= \frac{\sum_{i=1}^{m} \gamma_i h_i \left(a + b + \sum_{j=0}^{i=1} h_j \tan\theta_j\right)^2 \cos\eta}{a^2} + \frac{2M_{pm}}{a^2} \\
&\quad - \frac{2\sum_{i=1}^{m} M_{0i}}{a^2} + \frac{2\sum_{i=1}^{m} F_{Ai}\left(a + b + \sum_{j=0}^{i=1} h_j \tan\theta_j\right)}{a^2} \\
&= \sum_{i=1}^{m} \gamma_i h_i \left(1 + \frac{b}{a} + \frac{1}{a}\sum_{j=0}^{i=1} h_j \tan\theta_j\right)^2 \cos\eta \\
&\quad + \sum_{i=1}^{m} F_{Ai}\left(\frac{1}{a} + \frac{b}{a^2} + \frac{1}{a^2}\sum_{j=0}^{i=1} h_j \tan\theta_j\right) \\
&\quad + \frac{2M_{pm}}{a^2} - \frac{2\sum_{i=1}^{m} M_{0i}}{a^2},
\end{aligned} \tag{5}$$

where M_{pm} is the ultimate bending moment under the fracture in the m -th stratum (kN·m), θ_j is the fracture angle of roof strata, and F_{Ai} is the shear force generated downward by fracture block of overlying strata (kN).

It can be seen from Equation (5) that under certain geological conditions of the working face, the required strength (Q) of the filling body is inversely proportional to the width of the filling body (a), and the larger the width of the filling body is, the lower the required strength is. In addition, the required strength of the filling body is proportional to the span of the hanging roof (b) that lies over the filling body. A larger span of the roof needs a higher required strength

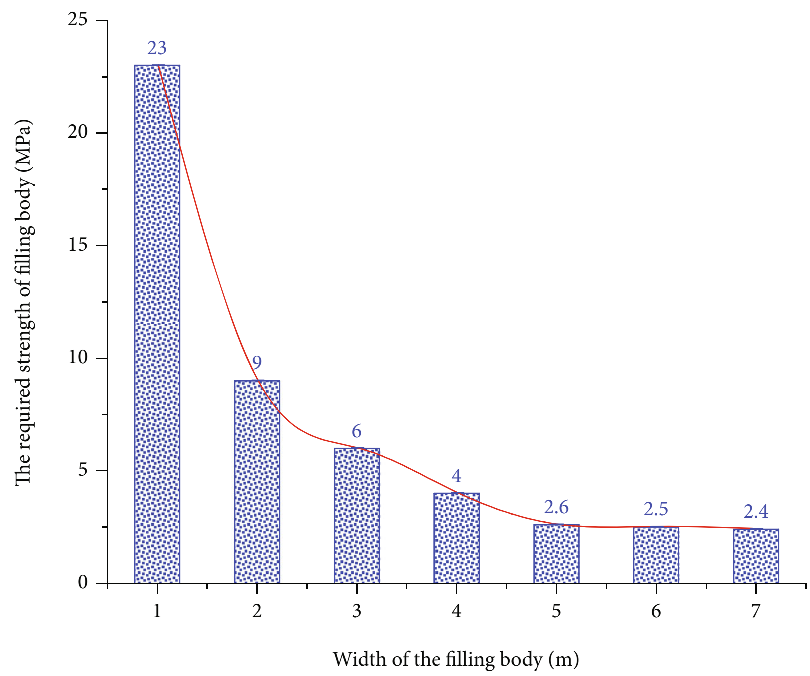

Figure 4: Stress variation curves of the filling body at different widths.

of the filling body. When the surrounding rock and the supporting structure jointly form a stable support bearing system, the filling body is able to support the load of the overlying strata, thereby reducing the load on the filling body.

3.2. Engineering Example Calculation. With the geological conditions of the 62210 working face in Xinzhuangzi Coal Mine of Huainan mining area taken as the background, the stress characteristics of the original roadway filling body were calculated under the widths of 1 m, 2 m, 3 m, 5 m, and 7 m, respectively.

According to on-site investigation, the immediate roof of the 62210 working face is sandy mudstone with a thickness of 6 m. The specific parameters are as follows: the bulk density (γ) is 25,100, and the fracture angle of strata is about 25° (measured on site). Under the limit conditions, the ultimate bending moment of strata is considered equal to the bending moment of the strata, i.e., $M_{01} = M_{P1}$. The working resistance of the filling body can be calculated by Equation (4) under different widths of the filling body. Figure 4 shows the relationship between the width of the filling body and the required strength of it.

Figure 4 reveals the following phenomenon: as the width of the filling body increases from 1 m to 2 m, the required strength plunges dramatically at a high rate. From 2 m to 3 m, the required strength continues to drop at a high rate. From 3 m to 7 m, the required strength corresponds to a low decline rate. The width of the filling body plays an important role in the required strength of them. Considering the technical and economic benefits, the reasonable width of original roadway filling in the 62210 working face is 3 m. Therefore, the filling materials and filling process can be selected according to the required strength.

4. Study on the Stability of Recovery Roadways

4.1. Tunneling Method of the B10 Coal Recovery Roadway. The B10 coal seam, which serves as the key protective seam of Xinzhuangzi Coal Mine, is mined for the purpose of relieving the pressure and protecting the overlying B11 coal seam and the underlying B8 coal seam. Therefore, in the mining process, the retention of large coal pillars for roadway protection should be minimized to avoid the influence of stress concentration on the underlying coal seam. Conventionally, the roadway layout often adopts GSEDSCP or GSER. GSEDSCP reduces the width of coal pillar, but it still induces stress concentration to the underlying coal seam. GSER does not involve the retention of coal pillars, but the retained roadway is barely functioning when used for the second time because it has suffered the disturbance of tunneling once and mining twice. On-site practice has also proved the poor stability of surrounding rock and a high maintenance cost when the GSER method is applied to roadway layout. Hence, according to the mine production and geological conditions, the ORFNPT technology is proposed here to arrange roadways in the stope.

4.2. Numerical Analysis. To analyze the stability characteristics of surrounding rock in ORFNPT and solve practical problems, a calculation model was established through large-scale finite difference software FLAC3D by taking the 62210 working face as the background. Some parameters of the model are listed as follows: strike length 320 m, dip length 230 m, height 248 m, and average coal seam thickness 1 m. The four sides and bottom of the model were fixed. Besides, a 13.8 MPa vertical stress was applied to the top of the model to simulate the mass of the overlying strata, and

Table 1: Mechanical parameters of coal rock involved in the simulation.

Rock	Rock thickness (m)	Elastic modulus E (GPa)	Poisson's ratio μ	Cohesion C (MPa)	Internal friction angle φ (°)	Tensile strength σ_T (MPa)	Density d (kg/m^3)
Mudstone	1.66	22.5	0.22	3.21	39	1.52	2660
B11a coal	1.07	5.13	0.33	1.15	33	0.14	1387
Sandy mudstone	2.7	5.45	0.147	2.16	36	1.3	2520
Sandstone	2.4	13.7	0.13	2.02	40	1.03	2497
Carbon mudstone	0.28	8.85	0.26	1.2	30	0.605	2461
B11 coal	0.75	4.91	0.34	1.35	33	0.132	1355
Sandstone	1.3	13.7	0.13	2.03	40	1.03	2497
Mudstone	5.95	16.8	0.22	2.22	33	1.51	2484
Siltstone	5.74	1.81	0.232	2.51	37	1.22	2465
Sandy mudstone	6.12	5.45	0.15	2.26	36	1.23	2533
B10 coal	1	5.5	0.24	1.52	33	1.23	1465
Mudstone	5.1	16.8	0.22	2.22	33	1.51	2484
Sandy mudstone	7.67	5.45	0.147	2.16	36	1.3	2520

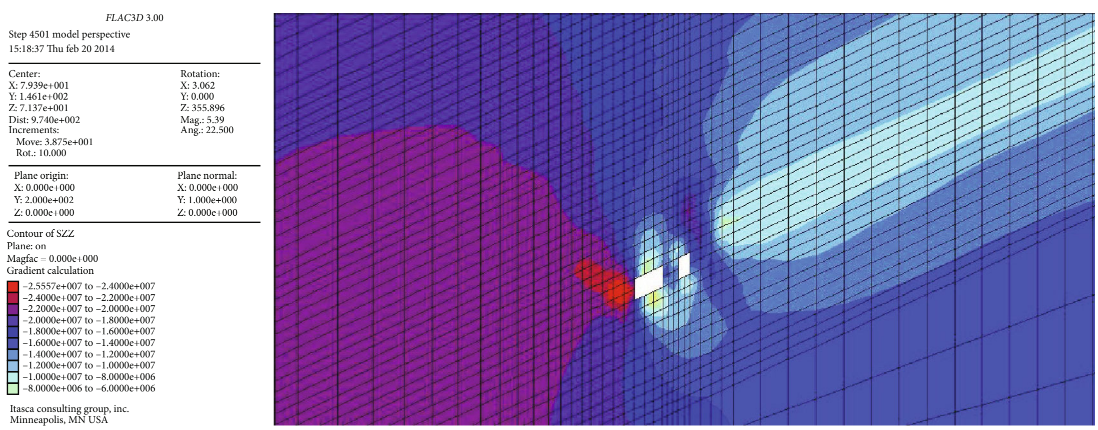

Figure 5: Nephogram of vertical stress distribution of surrounding rock in ORFNPT along the coal seam dip.

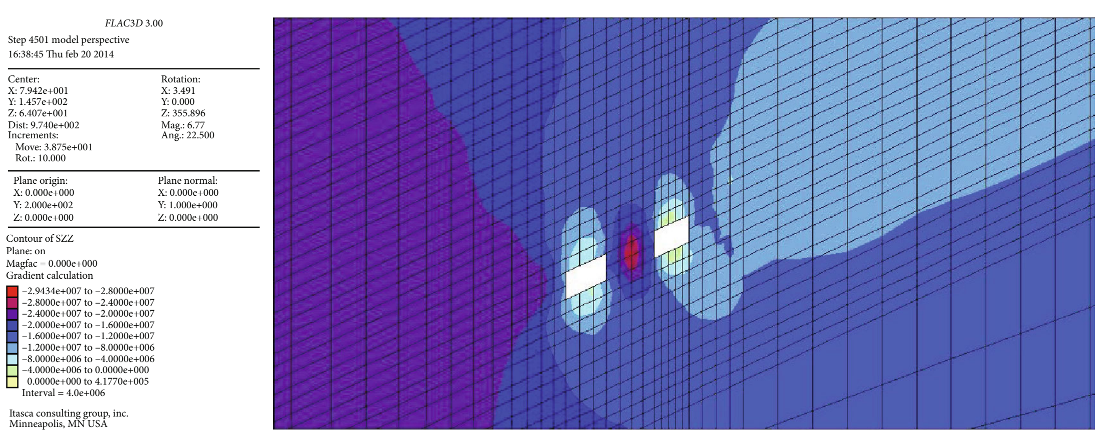

Figure 6: Nephogram of vertical stress distribution of surrounding rock in GSEDSCP along the coal seam dip.

the lateral pressure coefficient was 1.0. The mechanical parameters of coal rock are given in Table 1.

The four sides of the model were only a horizontal displacement boundary, and the floor was a fixed boundary. The simulated buried depth of the coal seam ranged from -660 m to -770 m, and a uniformly distributed load was applied to the top boundary of the model. The constitutive relation of roadway surrounding rock followed the modified Mohr-Coulomb criterion. The numerical simulation included two parts: (1) the vertical stress distribution characteristics of

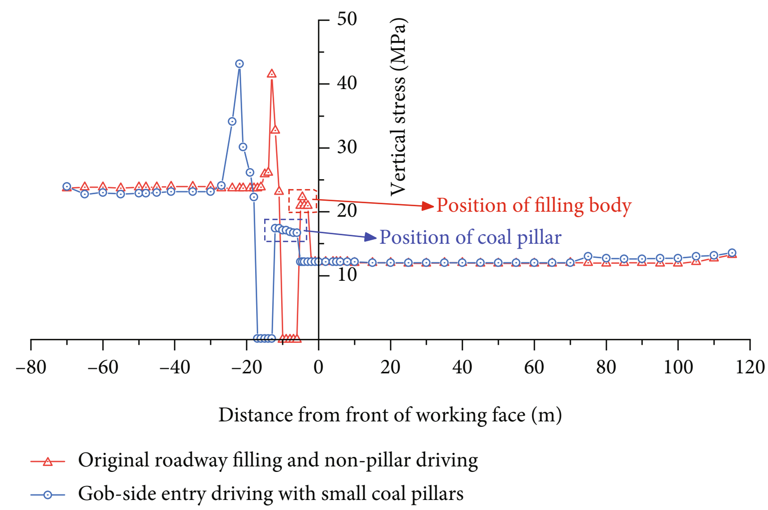

Figure 7: Stress distribution curves of roadway surrounding rock along the coal seam dip.

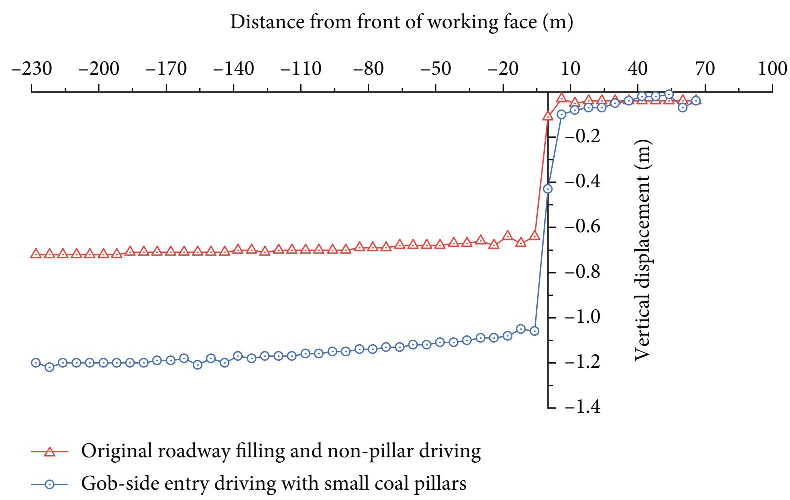

(a) Variation curves of vertical displacement

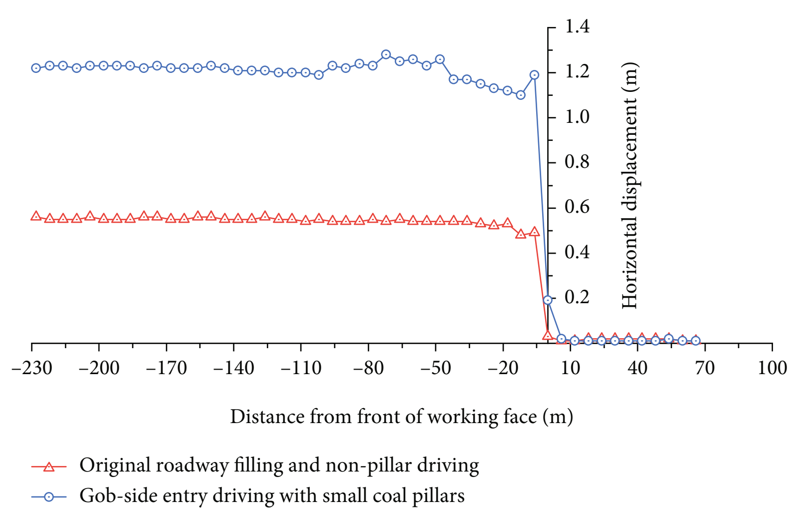

(b) Variation curves of horizontal displacement

Figure 8: Distribution characteristics of roadway surrounding rock displacement in ORFNPT and GSEDSCP along the coal seam dip.

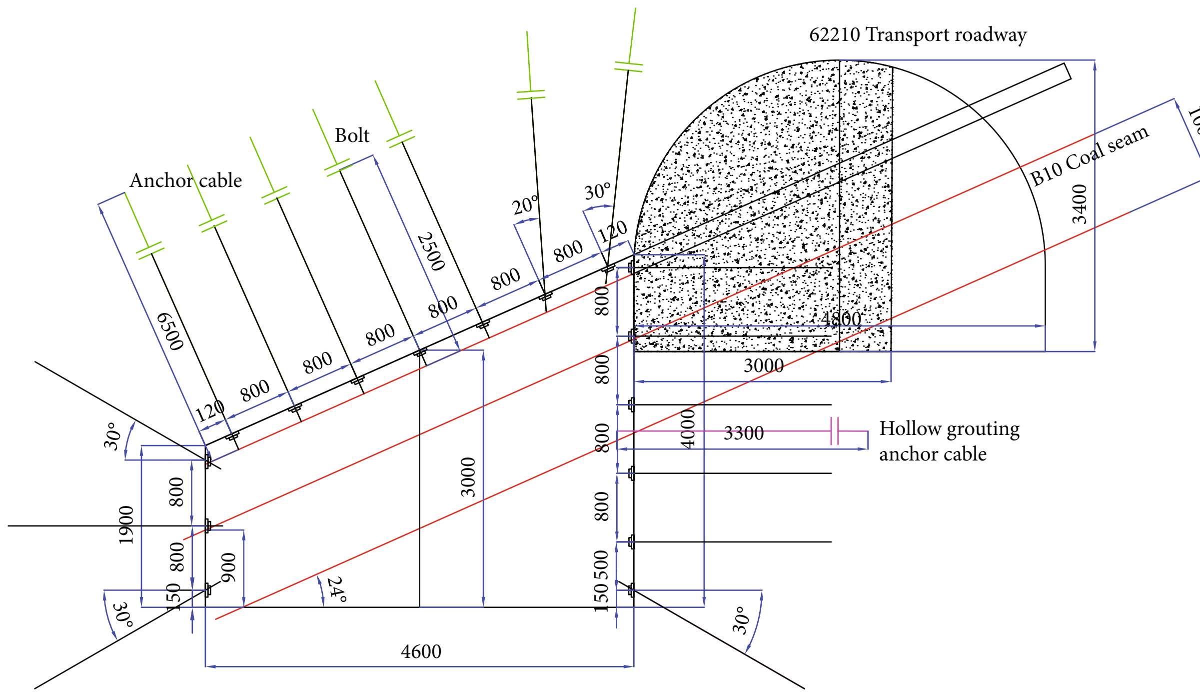

Figure 9: Support design in ORFNPT.

roadway surrounding rock in ORFNPT and GSEDSCP and (2) the deformation and displacement characteristics of roadway surrounding rock in ORFNPT and GSEDSCP.

The simulation was conducted using single-factor analysis. For ORFNPT, the width and strength of the filling body were 3 m and 6.6 MPa, respectively. For GSER, the width of the coal pillar was 7 m.

4.2.1. Stress Distribution Law of Roadway Surrounding Rock in Lower-Section Tunneling. The stress state of roadway surrounding rock is an important indicator to evaluate the stability of roadway, yet the stress characteristics of the coal rock for roadway protection in the gob-side roadway are more crucial for the success of the retained gob-side roadway. Therefore, numerical simulation was conducted on the above two tunneling methods. The yielded stress distribution nephograms is given in Figures 5 and 6, and the stress variation curves are displayed in Figure 7. It can be known that under the same geological conditions, for different tunneling methods, the distribution characteristics of the roadway surrounding rock of the excavated roadway differ notably. For ORFNPT, the peak stress of the solid coal side is located at the position of about 3 m in the coal; the peak stress is about 41.5 MPa; the stress concentration coefficient is about 1.74, and the stress on the filling body is about 21 MPa. For GSEDSCP, the stress peak in the solid coal on the lower side of the roadway is about 4.25 m in the coal; the stress peak is around 43.2 MPa; and the stress concentration coefficient is 1.82. Besides, a stress concentration core (range about 1 m and stress peak about 17.2 MPa) exists in the small coal pillar. Compared with GSEDSCP, ORFNPT can protect the roadway tunneling in the lower section more effectively. Its peak stress of the solid coal on the lower side of the roadway is closer to the roadway sides, and the stress of the filling body is much higher than that of the small coal pillar, indicating that the filling body can support the overlying roof better and can bear more load from the overlying strata.

4.2.2. Deformation and Displacement Distribution of Roadway Surrounding Rock in Lower-Section Tunneling. The displacement variations of roadway surrounding rock of the two tunneling methods were monitored (Figure 8). For ORFNPT, the maximum displacement of the roof is 0.63 m; the maximum heave of the floor is about 0.35 m; and the horizontal displacement on the solid coal side is about 0.51 m. For GSEDSCP, the maximum displacement of the roof is about 1.21 m; the maximum heave of the floor is about 0.48 m; and the maximum horizontal displacement on the solid coal side is about 1.22 m.

The comparison in Figure 7 suggests that the stress field and displacement field of roadway surrounding rock differ under different strength of the filling body. Under a high strength of the filling body, the stress is more likely to be concentrated on the filling body and less likely to be concentrated on the roadway surrounding rock. Accordingly, the roof-to-floor convergence will be smaller, and the damage to the surrounding rock will be slighter. These data indicate that ORFNPT is of a milder roadway surrounding rock deformation than GSEDSCP and is thus more conducive to the maintenance and stability of the lower-section roadway.

5. Engineering Application and Effect

5.1. Design of Roadway Support Parameters [31]. The 62310 return airway, in which no coal pillars are retained, is a

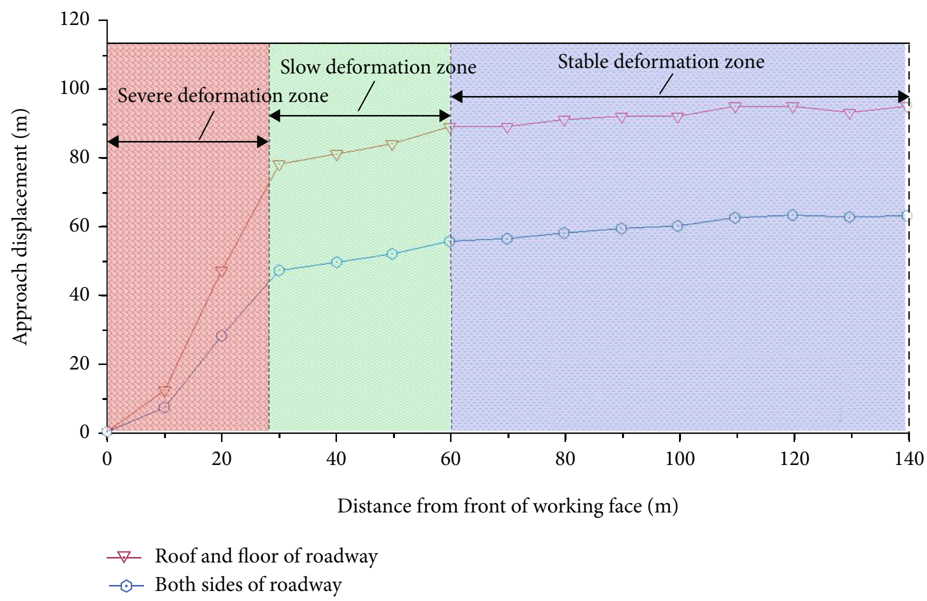

Figure 10: Variation curves of surface displacement in the 62310 return airway during tunneling.

newly excavated roadway along the filling body in the upper section. Considering the influence of roadway section and coal seam dip angle, the section of the 62310 return airway is designed into an inclined rectangular section. Such a design could effectively avoid roof instability in the upper and lower roadway clamping area. The specific support design is given in Figure 9.

(1) The inclined roof was high-strength left-handed special deformed steel bolt without longitudinal reinforcement (ϕ22 mm × 2500 mm), with 7 bolts per row and spacing of 800 mm × 1,600 mm. The first bolt on the high side of the inclined roof was arranged at 30° with the normal direction of the roof; the adjacent bolt was arranged at 20° with the normal direction of the roof; and other bolts were arranged perpendicular to the inclined roof. Three Z2560 new full-length resin anchoring agents were used for full-length anchoring. Anchor cables were high-strength low-relaxation prestressed steel strands (ϕ22 mm, 1 × 19 strands); the length was 6,500 mm; anchor cables were arranged by 7-0-7 and spacing of 800 × 1,600 mm. The first anchor cable near the high side of the roof was arranged at 30° with the normal direction of the roof; the adjacent anchor cable was arranged at 20° with the normal direction of the roof; other anchor cables were arranged perpendicular to the roof, and the anchor cables were installed on the W4-280 steel bands and staggered with bolts. 4,900 mm long W4-280 steel bands were used for roof protection

(2) The high-strength left-handed special deformed steel bolt without longitudinal reinforcement (ϕ22 mm × 2,500 mm) was used in the side. Six anchors were used in the high side, and the spacing was 800 mm × 800 mm. The anchor near the floor was arranged at 30° in the horizontal direction; other bolts were set perpendicular to the roadway sides. Three bolts were used in the low side, and the spacing was 800 mm × 800 mm. The bolts close to the floor and roof were arranged at 30° in the horizontal direction. W4-280 steel bands were used for roof protection. The length of the low side was 1,800 mm, and the high side was composed of two strips, one being 1800 mm long and the other being 2,250 mm long. Reinforcement support was applied to the high side in the following way: two hollow grouting anchors (ϕ22 mm and length 3,300 mm) were arranged in every two rows of anchors (arrangement mode 2-0-2). The anchor cable near the floor was downward arranged at 30° with horizontal direction, and the other anchor cable was arranged in the middle of bolt 3 and bolt 4

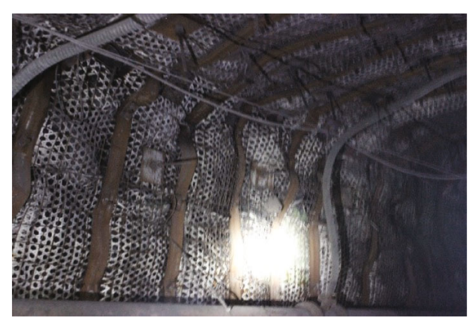

Figure 11: Support effect of the high side in the 62310 return airway.

5.2. Surface Deformation of the 62310 Return Airway. To further explore the application effect of the ORFNPT technology in the mining process of the B10 coal seam in

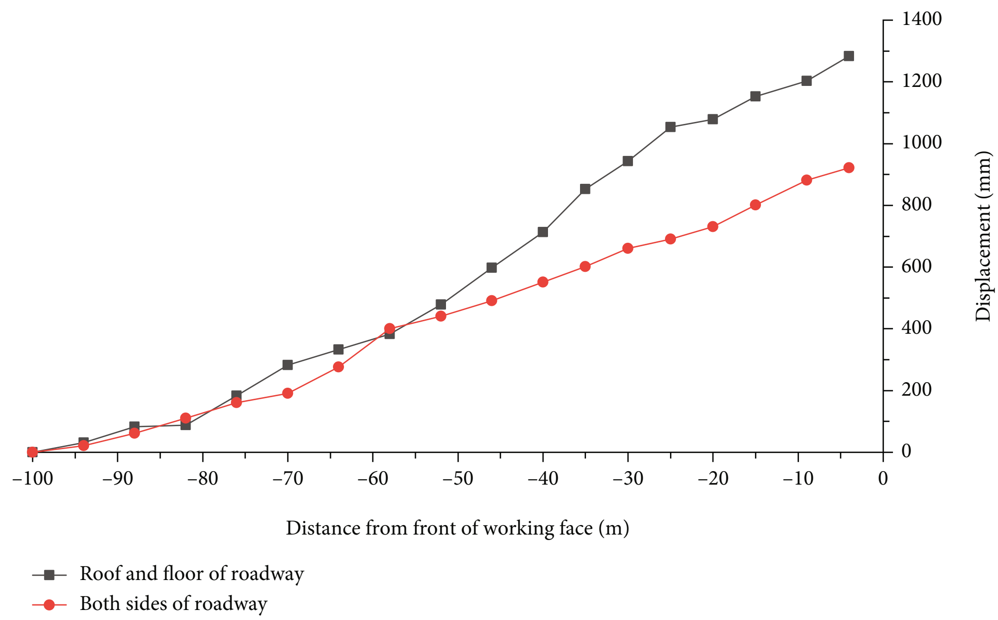

Figure 12: Variation curves of surface displacement amount in the 62310 return airway during recovery.

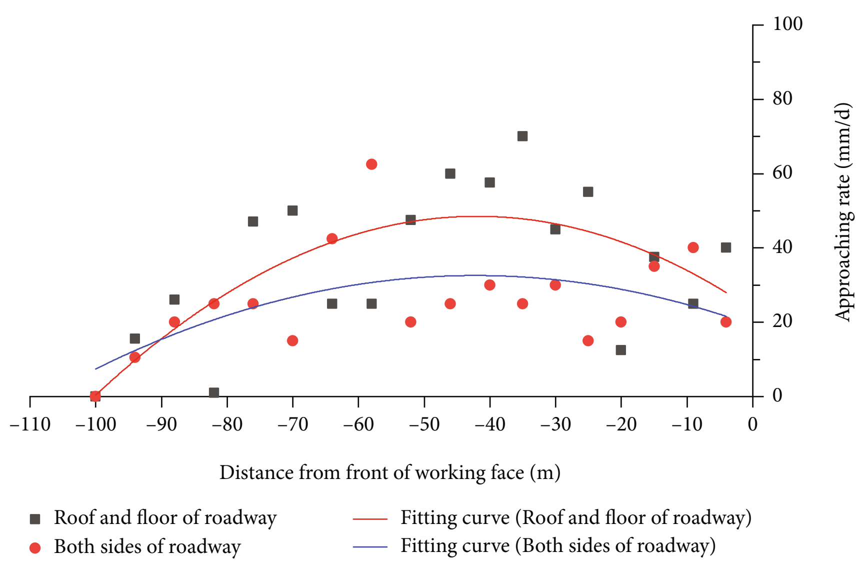

Figure 13: Variation curves of surface displacement rate in the 62310 return airway during recovery.

Xinzhuangzi Coal Mine, roof-to-floor convergence and side-to-side displacement of the 62310 return airway were monitored continuously during both tunneling and recovery. According to the monitoring results, during tunneling along the original roadway filling body in the upper section, the roadway gradually stabilizes at the position of about 27 m behind the excavation working face. Roof-to-floor convergence (about 89 mm) is greater than side-to-side displacement (about 58 mm), as illustrated in Figure 10. The on-site application effect is shown in Figure 11. During the recovery of the 62310 working face, roof-to-floor convergence and side-to-side displacement of the return airway start to increase continuously at about 100 m away from the working face, and the deformation rate of roadway surrounding rock reaches the maximum at about 40 m away from the working face. The rates of roof-to-floor convergence and side-to-side displacement for the return airway are about 29 mm/d and 50 mm/d, respectively (Figures 12 and 13), and their maximum amounts are about 910 mm and 1,290 mm, respectively (due to the continuous deformation of the roadway, floor dinting and flitching were carried out on the roadway. The deformation of the recovery roadway includes the amount of roadway repair, in which the floor dinting amount is about 500-600 mm and the flitching amount is about 300-400 mm). Clearly, the full-cycle displacement rates and amounts of the surrounding rock of the 62310 return airway satisfy the requirements for stability control of the coal mine roadway, indicating that the

ORFNPT technology for stope roadway layout meets the needs for safe mining and realizes the continuous replacement of the stope without coal pillars.

6. Conclusions

Difficulty in continuous mining replacement caused by complex layout of roadways and unreasonable layout of stope is a significant problem that perplexes coal mining. Aiming at solving the problem, this study analyzed the stress characteristics and design parameters of the original roadway filling body based on the theoretical study on gob-side roadway and verified the stability of roadway surrounding rock in ORFNPT through numerical simulation and on-site monitoring of roadway surrounding rock deformation. The main conclusions are as follows:

(1) The superimposed continuous layer theory was adopted to establish the stress model of the original roadway filling body and obtain the expression of the working resistance of the original roadway filling body. The required strength for the filling body is primarily determined by two factors, i.e., the span of the hanging roof that lies over the filling body and the width of the filling body. The span of the hanging roof is positively correlated with the required strength of the filling body. However, when the width of the filling body reaches a certain value, its further increase fails to change the required strength of the filling body

(2) The finite element calculation software FLAC3D was used to comparatively analyze the stability of roadway in ORFNPT and GSEDSCP. The stress distribution characteristics of the surrounding rock of the roadway are obviously different. When ORFNPT is applied to the lower-section roadway, the peak stress position in the solid coal on the lower side of the roadway is closer to the roadway sides, and the filling body is of a much higher stress than the small coal pillars. Besides, the roadway surrounding rock undergoes milder deformation, and the roadway excavated in the lower section is more stable

(3) As the 62210 transportation roadway of Xinzhuangzi Coal Mine belongs to a straight wall semicircular section, the 62310 return airway adopts an inclined roof trapezoidal section. The hollow grouting anchor cable is used to strengthen the support for the higher side of the roadway. In this way, surrounding rock deformation in ORFNPT is controlled. According to the on-site monitored data, roadway surrounding rock deformation in the 62310 return airway is well controlled during both tunneling and recovery

Data Availability

The experimental data used to support the findings of this study are included within the manuscript.

Conflicts of Interest

The authors declare that they have no conflicts of interest.

Acknowledgments

This work was supported by the National Natural Science Foundation of China (52104117, 52174103, 52174105, 51874006, and 51774009); Anhui Provincial Natural Science Foundation (2008085QE226); Scientific Research Foundation of the Higher Education Institutions of Anhui Province, China (KJ2021A0969); and School Level Scientific Research and Innovation Team of Huainan Normal University (XJTD202009).

References

[1] D. Z. Kong, S. J. Pu, Z. H. Cheng, G. Y. Wu, and Y. Liu, "Coordinated deformation mechanism of the top coal and filling body of gob-side entry retaining in a fully mechanized caving face," *International Journal of Geomechanics*, vol. 21, no. 4, pp. 1943–5622, 2021.

[2] J. F. Lou, F. Q. Gao, J. H. Yang et al., "Characteristics of evolution of mining-induced stress field in the longwall panel: insights from physical modeling," *International Journal of Coal Science and Technology*, vol. 8, pp. 1–18, 2021.

[3] Q. J. Cao, *Coupling Bearing Analysis and Control of Backfill Body and Surrounding Rock in Gob-Side Entry Retaining [Ph.D. thesis]*, China University of Mining and Technology, 2018.

[4] M. C. He, Y. B. Guo, J. Yang, and W. L. Gong, "An innovative approach for gob-side entry retaining in thick coal seam longwall mining," *Energies*, vol. 10, no. 11, pp. 1785–1795, 2017.

[5] M. C. He, X. G. Ma, F. L. Niu, J. Wang, and Y. X. Liu, "Adaptability research and application of rapid gob-side entry retaining formed by roof cutting and pressure releasing with composite roof and medium thick coal seam," *Chinese Journal of Rock Mechanics and Engineering*, vol. 37, no. 12, pp. 2641–2654, 2018.

[6] J. Yang, H. Y. Wang, Y. J. Wang, B. H. Liu, S. L. Hou, and Y. Cheng, "Stability analysis of the entry in a new mining approach influenced by roof fracture position," *Sustainability*, vol. 11, no. 22, pp. 6349–6369, 2019.

[7] X. J. Yang, Y. Sun, E. Y. Wang, and W. B. Mao, "Study and application of gob-side entry retaining formed by roof cutting and pressure relief in medium-thickness coal seam with hard roof," *Geotechnical and Geological Engineering*, vol. 38, no. 4, pp. 3709–3723, 2020.

[8] F.-T. Zhang, X.-Y. Wang, J.-B. Bai, G.-Y. Wang, and B.-W. Wu, "Post-peak mechanical characteristics of the high-water material for backfilling the gob-side entry retaining: from experiment to field application," *Arabian Journal of Geosciences*, vol. 13, no. 11, pp. 386–398, 2020.

[9] G. C. Zhang, Y. L. Tan, S. J. Liang, and H. G. Jia, "Numerical estimation of suitable gob-side filling wall width in a highly gassy longwall mining panel," *International Journal of Geomechanics*, vol. 18, no. 8, pp. 401–412, 2018.

[10] J. Zhang and Y. Li, "The stability of gob-side entry retaining in a high-gas-risk mine," *Advances in Civil Engineering*, vol. 2019, Article ID 7540749, 769 pages, 2019.

[11] C. Q. Zhu, X. X. Miao, and Z. Liu, "Mechanical analysis on deformation of surrounding rock with road-in packing of gob-side entry retaining in fully-mechanized sub-level caving face," *Journal of Coal Science and Engineering (China)*, vol. 14, no. 1, pp. 24–28, 2008.

[12] D. Kong, S. Pu, S. Zheng, C. Wang, and Y. Lou, "Roof broken characteristics and overburden migration law of upper seam in upward mining of close seam group," *Geotechnical and Geological Engineering*, vol. 37, pp. 3193–3203, 2019.

[13] W. Qi, J. Zhang, N. Zhou, Z. Wu, and J. Zhang, "Mechanism by which backfill body reduces amount of energy released in deep coal mining," *Shock and Vibration.*, vol. 2019, no. 1, pp. 1–14, 2019.

[14] Z. Huang, L. Zhang, and Z. Ma, "Study on the mechanical relationship among the backfilling mining support, roof rock beam, and gangue filling body in comprehensive mechanized filling mining process," *Advances in Civil Engineering*, vol. 2020, Article ID 8824735, 15 pages, 2020.

[15] A. Khaldoun, L. Ouadif, K. Baba, and L. Bahi, "Valorization of mining waste and tailings through paste backfilling solution, Imiter operation, Morocco," *International Journal of Mining Science and Technology.*, vol. 26, no. 3, pp. 511–516, 2016.

[16] Y. Chen, J. B. Bai, S. Yan, Y. Xu, X. Y. Wang, and S. Q. Ma, "Control mechanism and technique of floor heave with reinforcing solid coal side and floor corner in gob-side coal entry retaining," *International Journal of Mining Science and Technology*, vol. 22, no. 6, pp. 841–845, 2012.

[17] Y. L. Chen, Q. B. Meng, G. Xu, H. S. Wu, and G. M. Zhang, "Bolt-grouting combined support technology in deep soft rock roadway," *International Journal of Mining Science and Technology*, vol. 26, no. 5, pp. 777–785, 2016.

[18] Z.-B. Cheng, L.-H. Li, and Y.-N. Zhang, "Laboratory investigation of the mechanical properties of coal-rock combined body," *Bulletin of Engineering Geology and the Environment*, vol. 79, no. 4, pp. 1947–1958, 2020.

[19] X. Feng and N. Zhang, "Position-optimization on retained entry and backfilling wall in gob-side entry retaining techniques," *International Journal of Coal Science & Technology*, vol. 2, no. 3, pp. 186–195, 2015.

[20] P. F. Guo, X. H. Zhang, Y. Y. Peng, M. C. He, C. R. Ma, and D. J. Sun, "Research on deformation characteristic and stability control of surrounding rock during gob-side entry retaining," *Geotechnical and Geological Engineering*, vol. 38, no. 3, pp. 2887–2902, 2020.

[21] D.-Z. Kong, Z.-B. Cheng, and S.-S. Zheng, "Study on the failure mechanism and stability control measures in a large-cutting-height coal mining face with a deep-buried seam," *Bulletin of Engineering Geology and the Environment*, vol. 78, no. 8, pp. 6143–6157, 2019.

[22] Q. Ma, Y. L. Tan, Z. H. Zhao, Q. Xu, J. Wang, and K. Ding, "Roadside support schemes numerical simulation and field monitoring of gob-side entry retaining in soft floor and hard roof," *Arabian Journal of Geosciences*, vol. 11, no. 18, pp. 563–572, 2018.

[23] X. G. Ma, M. C. He, J. Guo, and C. X. Zhang, "Entry deformation law in the full life cycle under entry retaining with roof cutting," *Geotechnical and Geological Engineering*, vol. 37, no. 5, pp. 4365–4379, 2019.

[24] Q. B. Meng, L. J. Han, W. G. Qiao, D. G. Lin, and J. D. Fan, "Support technology for mine roadways in extreme weakly cemented strata and its application," *International Journal of Mining Science and Technology*, vol. 24, no. 2, pp. 157–164, 2014.

[25] J. Mo, J. Yang, W. Ma, F. Chen, and S. Zhang, "Numerical simulation and field experiment study on onboard dust removal technology based on airflow–dust pollution dispersion characteristics," *Environmental Science and Pollution Research*, vol. 27, no. 2, pp. 1721–1733, 2020.

[26] G. L. Zhu, R. L. Sousa, M. C. He, P. Zhou, and J. Yang, "Stability analysis of a non-pillar-mining approach using a combination of discrete fracture network and discrete-element method modeling," *Rock Mechanics and Rock Engineering*, vol. 53, no. 1, pp. 269–289, 2020.

[27] D. Sun, Q. Wu, X. Li et al., "Sensitivity analysis and numerical simulation study on main controlling factors of surface movement and deformation in strip filling mining under thick unconsolidated layers," *Geofluids*, vol. 2021, Article ID 6615937, 10 pages, 2021.

[28] V. M. Seryakov, "Calculating stresses in support and sidewall rocks in stagewise face drivage in long excavations," *Journal of Mining Science*, vol. 51, no. 4, pp. 673–678, 2015.

[29] X. S. Shi, H. W. Jing, J. G. Ning, Z. L. Zhao, and J. F. Zhu, "Stability control of gob-side entry retaining in fully mechanized caving face based on a compatible deformation model," *Computer Modeling in Engineering and Sciences*, vol. 124, no. 1, pp. 315–343, 2020.

[30] S. Xiao-ming, L. Gan, S. Peng et al., "Application research on gob-side entry retaining methods in no. 1200 working face in Zhongxing mine," *Geotechnical and Geological Engineering*, vol. 37, pp. 185–200, 2018.

[31] W. Yu, K. Li, Z. Liu, B. An, P. Wang, and H. Wu, "Mechanical characteristics and deformation control of surrounding rock in weakly cemented siltstone," *Environmental Earth Sciences*, vol. 80, no. 9, pp. 1–15, 2021.

Hindawi
Geofluids
Volume 2023, Article ID 3492686, 12 pages
https://doi.org/10.1155/2023/3492686

Research Article

Roadway Instability Mechanism of Weakly Consolidated Soft Rocks and Support Technologies

Jinlong Cai,[1,2] Min Tu,[2] Luxiu Chai,[1] Fengyan Qin,[1] and Zhengfeng Shen[1]

[1]*School of Architecture and Civil Engineering, West Anhui University, Lu'An, Anhui 237012, China*
[2]*Key Laboratory of Safe and Effective Coal Mining, Ministry of Education, Anhui University of Science and Technology, Huainan, Anhui 232001, China*

Correspondence should be addressed to Min Tu; mtu@aust.edu.cn

Received 4 April 2022; Revised 15 September 2022; Accepted 12 October 2022; Published 3 March 2023

Academic Editor: Mohammed Fattah

During tunneling in weakly consolidated soft rock strata, lithology, joints, and fractures of rock strata play an important role in controlling overall roof stability of the roadway. A case study based on weakly consolidated soft rock roadway in Bojianghaizi mine was conducted to address disasters caused by sudden changes and collapse as well as difficulties in maintenance of weakly consolidated soft rock roadway. First, physical and mechanical properties of weakly consolidated soft rocks were investigated by X-ray diffraction mineral component analysis and scanning electron microscopy. Second, failure characteristics and instability mechanism of the roadway were analyzed by combining field survey and theoretical analysis. A mechanical model of fracture development on the composite roof of the roadway was built, and the initiation angle and critical stress for fracture development were deduced. The instability criteria of cracks based on cracking angle (θ_0) were established. Moreover, the instability mechanism caused by roof falling was disclosed. Fractures were formed upon shear failure at vertex angle of the roadway. The fracture belt extended to the soft bedding plane of the separation stratum along the fracture propagation angle and connected with it, thereby inducing roof falling. On this basis, a high-strength and high-preload "inverted trapezoidal" anchoring mesh-beam string supporting structure + arched roadway cross-section with vertical walls + full-section guniting coupling control technology was proposed, which achieved good site application effects.

1. Introduction

With the gradual exploitation of coal resources in mideastern China, the coal resource exploitation center has gradually shifted to the midwestern region. Owing to squeezing influences by the Qinghai–Tibet subplate, North China plate, and Tarim plate against coal-measure strata in midwestern China, extensive weakly consolidated soft rock strata exist in the local coal-measure strata [1–3], which are mainly manifested by low strength of surrounding rocks, poor cementing properties, weathering swelling upon water, and easy development of separation stratum among different rock strata. In these geological conditions, the excavated roadway is characterized by great deformation, high deformation rate with a long duration, which increases the difficulties in roadway support.

During tunneling in weakly consolidated strata, relatively high development of fractures and joints occurs during the advancing and follow-up service periods. When the roadway roof bears stresses, a great tensile stress occurs in the lower part, which can easily cause uneven subsidence. Moreover, weak interlayer adhesive forces exist due to the complicated roof structure, which easily develops an extreme separation stratum. The space domain of this separation stratum shifts quickly from progressive extension to sudden changes and roof falling-induced disasters, thereby causing accidents on weakly consolidated soft rock roadways [4, 5]. Many experts and scholars in China and other countries have conducted theoretical and experimental studies to address sudden changes and roof falling-induced disasters of weakly consolidated soft rock roadways as well as difficulties in maintenance control. For example, Zhang and Jiang

[6], Zhang et al., Zhao et al, and Jia et al. [7–9] studied bending-induced instability mechanism of stratified roof separable strata in a coal roadway and pointed out that it could easily cause shearing stress concentration at the vertex angle due to stratified roof separation and bending, which further extended to the upper hard rock strata and intensified the risks of roof falling. Zhang et al., Guo et al., and Cao et al. [10–12] established the systematic mechanical model of the rock composite system, which contains interlayers to disclose the failure and instability mechanism of surrounding rocks in roadways with interlayer rocks and determine judgment indexes for surrounding rock stability. Research results provided references for the control design of stratified rock stability. Considering the stratified roof structural characteristics of full-coal roadway with a large cross-section, Zhang et al. [13, 14] investigated the deformation characteristics of the separation layer on a stratified roof after tunneling by using state nonlinear simulation method of interlayer contact surfaces. Based on analysis of the deformation failure characteristics of soft rock roadway, Meng et al. [15–17] studied the deformation failure mechanism of surrounding rocks in weakly consolidated soft rock roadway; they also investigated and supervised surrounding rock evolution laws in the roadway as well as optimized support design. Li et al. [18] analyzed the deformation failure process of rectangular roadway of weakly consolidated soft rocks and compared simulation results with field supervision results. Some suggestions in cross-section shape selection and roadway support were provided. Li and Hou [19] pointed out that a semicircle arched roadway with vertical walls and anchoring mesh-beam spraying supporting structure could improve the physical and mechanical properties of surrounding rocks effectively and increase the bearing capacity of surrounding rocks.

Although relevant experts and scholars have investigated the deformation failure characteristics and mechanism of the soft rock roadway, the deformation failure characteristics of the weakly consolidated soft rock roadway are different from those of the ordinary soft rock roadways. This is still in the exploration stage at present. Based on mineral composition, space characteristics, and microscopic structure of weakly consolidated soft rocks, this study further explores the internal deformation instability mechanism of the roadway and established theoretical criteria of roof instability. Research conclusions provided theoretical references to the design of the roof support scheme of a weakly consolidated roadway.

2. Engineering Overview and Lithologic Characteristics

2.1. Engineering Overview. The Bojianghaizi coal mine is located in Dongsheng District, Inner Mongolia. The first working face was 113101, which was advanced by 2603 m. The surface length and mining area were 200 m and 520,600 m^2, respectively. Coal seam #3-1 was stable and belonged to a uniclinal and approximately horizontal structure. The thickness of this coal seam was 3.2–6.4 m, averaging at 5.4 m. The basic roof was medium-coarse sandstone, and the average thickness was 7.07 m. The direct bottom was sandy mudstone, and the old bottom was 5 m thick siltstone. The geological location is shown in Figure 1.

The working face 113101 has been the site of roof falling accidents. The length and maximum height of the roof falling section were 14.6 m and 10.2 m, respectively. The roof falling region resembles an upside-down bowl and is narrow in the upper part and wide at the bottom. Four holes were drilled on the roof in this region by using a SGZ-IIIA drill for roof detection. The profiles of field drilling and survey diagram are shown in Figure 2.

According to comprehensive analysis, the roadway roof was composed of crushed rock section (0–3 m), grouting section (3–6 m), empty roof section (6–10.2 m), and hard roof (>10.2 m). Therefore, the maximum height of roof failing was 10.2 m, and the maximum distance of the empty roof was 7.2 m. Comprehensive analysis of drilling shows that lithology in the section of the roof falling zone from the upper part to the bottom is coal, thin mudstone layer with coal lines, fine sandstone, and sandy mudstone. The lithology is brittle, and the full section is generally horizontal. The cable anchoring section is basically made up of sandy sandstones. Obvious fracture surfaces and buried structures exist in the falling roof. Vertical fracture developments are on the sides, which lead to poor shaping of the roadway before and after the roof falling and serious wall caving. In particular, the maximum wall caving at the shoulder reaches as high as 1.5 m. In view of field drilling detection on the roof, the roof falling thickness is in the 6–6.5 m range. In other words, the weak strata or interlayers fall completely except for the effective supporting scope of anchoring cables.

2.2. Analysis of Lithologic Characteristics. The minable seams mainly distribute in Jurassic and Cretaceous strata. The average uniaxial compressive strengths of fine siltstone and sandy mudstone in surrounding rocks of the roadway are 29.9 MPa and 24.1 MPa, respectively. The average uniaxial compressive strength of the sandy mudstone changes to 7.8 MPa after softening by water absorption, and the softening coefficient reaches 0.32.

Four rock samples were collected from the roof and floor of coal seams, which were sandstone and sandy mudstone. XRD analysis was conducted on all rock samples. The XRD spectra of the sandstone and sandy mudstone are shown in Figure 3. Quartz, feldspar, illite, kaolinite, and chlorite are major mineral components. In view of the microstructural characteristics of rocks under SEM (Figure 4), sand structures form porous cementation and the skeleton structure is a characteristic of porous, stacking, and loosing. Fine clays are arranged randomly, which are off-white and have moderate roundness. They present subangular and semiround shapes and have uneven sizes and clear edges.

In other words, the microstructures of weakly consolidated rocks are cellular, with uneven particles stacking together. A large number of pores bring good connectivity. The whole structure is relatively weak and exhibits low rock strength. Clay minerals are dominant, and kaolinite accounts for the highest proportion, which is characterized by easy swelling and disintegration in water.

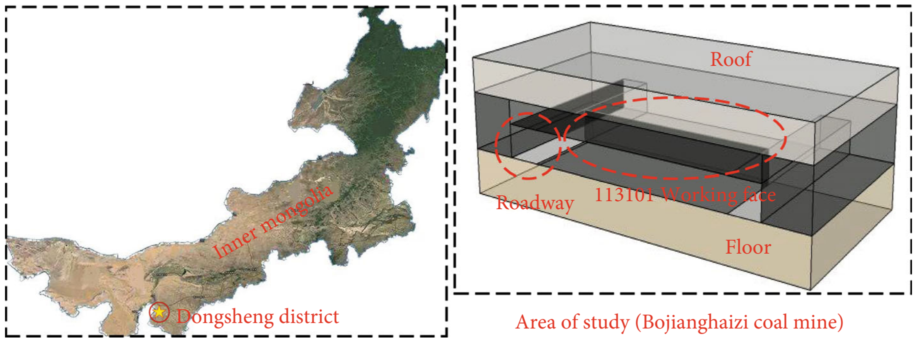

Figure 1: Roadway research geographical location.

3. Instability Mechanism and Mechanical Analysis of Weakly Consolidated Soft Rocks

Stresses in the upper roof strata are released after tunneling. Due to collaborative action of compressive, tensile, and shear stresses, different strata have varying deformations. Evident separation is developed between any two strata, and the roof is further bent. Fractures are formed at the vertex angle of the roadway.

3.1. Stress Field Analysis at Fracture Tip

3.1.1. Stress Distribution and Strength Factor at the Tip of Compression Shear Fracture. Figure 5 shows that the initial fracture is 2a long. Influenced by a combination of the vertical stress (σ_y) and horizontal stress (σ_x), normal and tangential stresses on the fracture surface can be obtained as follows:

$$\begin{cases} \sigma_n = \sigma_y \sin^2\beta + \lambda\sigma_y \cos^2\beta, \\ \sigma_n = -\sigma_y(1-\lambda)\sin\beta\cos\beta, \end{cases} \tag{1}$$

where σ_n and τ_n are positive stress and tangential stress on the fracture surface, respectively, and λ is the lateral pressure coefficient.

In this case, the stress strength factor at the crack tip is [20]

$$\begin{cases} K_{\mathrm{I}} = -\sqrt{\pi a}\sigma_y\left(\sin^2\beta + \lambda\cos^2\beta\right), \\ K_{\mathrm{II}} = \sqrt{\pi a}\sigma_y(1-\lambda)\sin\beta\cos\beta. \end{cases} \tag{2}$$

3.1.2. Stress Distribution and Strength Factor at the Tip of Tensile Shear Fracture. As the practical loads on the roof rock beam are usually uneven, strength factor could be calculated by the integral method under these circumstances [20]. Results are shown in Figure 6.

In this case, the stress strength factor at the tip of cracks is

$$\begin{cases} K_{\mathrm{I}} = \dfrac{1}{2\sqrt{\pi}}\displaystyle\int_{-a}^{a} p(x)\sqrt{\frac{a+x}{a-x}}d(x) + \frac{1}{2\sqrt{\pi}}\left(\frac{k-1}{k+1}\right)\int_{-a}^{a} q(x)d(x), \\ K_{\mathrm{II}} = \dfrac{1}{2\sqrt{\pi}}\displaystyle\int_{-a}^{a} q(x)\sqrt{\frac{a+x}{a-x}}d(x) - \frac{1}{2\sqrt{\pi}}\left(\frac{k-1}{k+1}\right)\int_{-a}^{a} p(x)d(x), \end{cases} \tag{3}$$

where

$$k = \begin{cases} \dfrac{3-\nu}{1+\nu}, & \text{Plane stress}, \\ 3-\nu, & \text{Plane strain}, \end{cases} \tag{4}$$

where ν is Poisson's ratio.

(1) Horizontally, the rock beam at the upper position of the roadway bears upward and downward linear positive stresses, as shown in Figure 7

At this moment, the strength factor could be calculated as follows:

$$\begin{cases} K_{\mathrm{I}} = \dfrac{\sigma_x}{2}\sqrt{\pi a}\cos^2\beta, \\ K_{\mathrm{II}} = \dfrac{\sigma_x}{2}\sqrt{\pi a}\sin\beta\cos\beta. \end{cases} \tag{5}$$

(2) Vertically, the rock beam at the upper position of the roadway bears leftward and rightward linear shear stresses. In this case, the stress analysis of inclined cracks is shown in Figure 8

Thus, the stress strength factor can be obtained as follows:

$$\begin{cases} K_{\mathrm{I}} = \dfrac{2\tau_{\max} a(\pi-2)}{\sqrt{\pi a}}\sin\beta\cos\beta, \\ K_{\mathrm{II}} = \dfrac{\tau_{\max} a(\pi-2)}{\sqrt{\pi a}}\cos 2\beta. \end{cases} \tag{6}$$

3.1.3. Composite Fractures under Collaboration of Multiple Stresses. Unit blocks in the rock beam of the rectangular roadway roof are subordinated to the collaborative effect of multiple stresses. According to stress superposition principle [21], the strength factor of composite fracture was calculated by using the stress superposition method (Figure 9).

According to literature [22], then the tensile stress acts on the crack surface; the initial cracks are damaged by tensile stress and then become extensive cracks. According to the

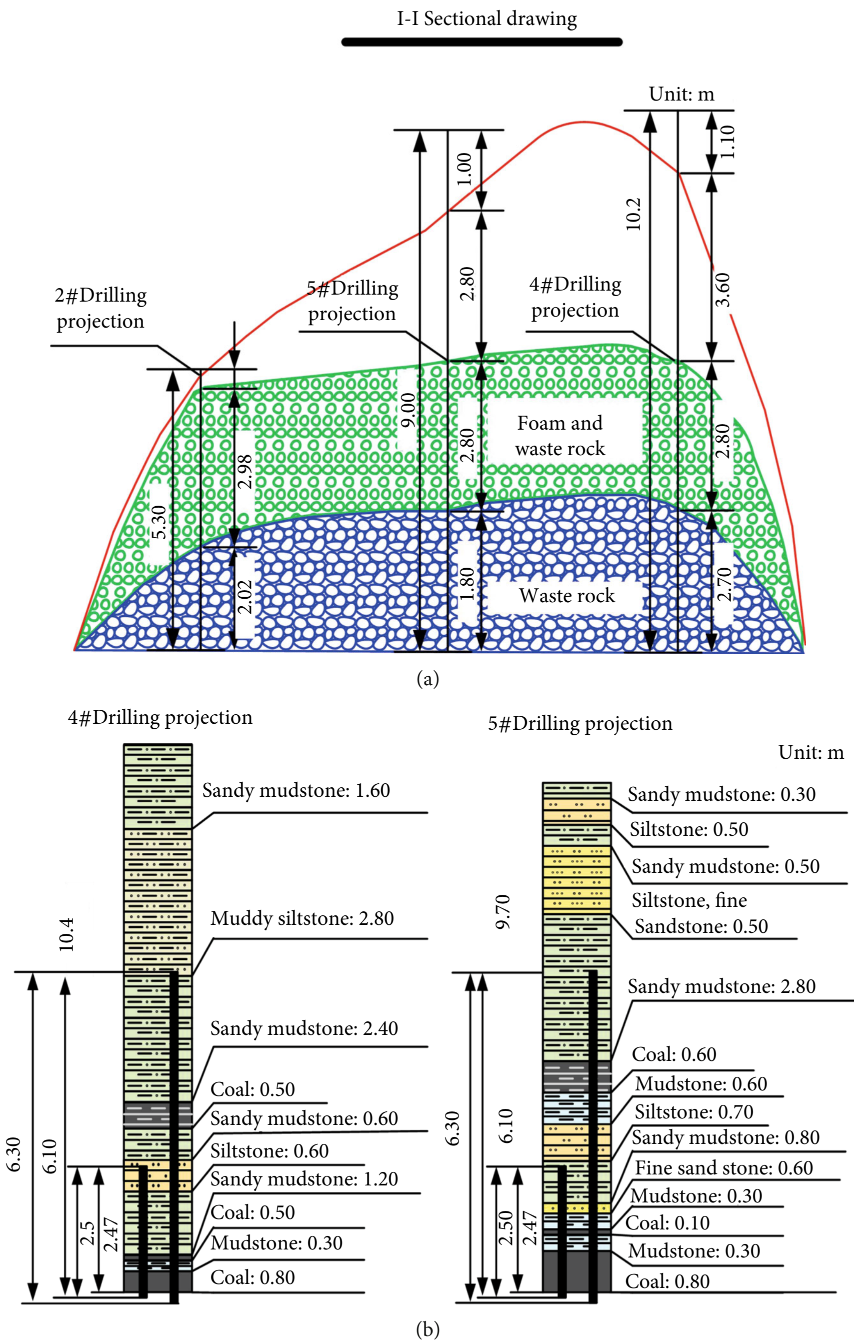

FIGURE 2: The diagrammatic cross-section of caving zone: (a) the schematic diagram of drilling section; (b) the columnar section of investigation.

preceding analysis results, Equations (2), (5), and (6) were combined to calculate the composite strength stress factor:

$$\begin{cases} K_{\mathrm{I}} = \dfrac{\sigma_{\max}}{2}\sqrt{\pi a}\cos^2\beta + \dfrac{2\tau_{\max}a(\pi-2)}{\sqrt{\pi a}}\sin\beta\cos\beta, \\ K_{\mathrm{II}} = \dfrac{\sigma_{\max}}{2}\sqrt{\pi a}\sin\beta\cos\beta + \sqrt{\pi a}\sigma_y(1-\lambda)\sin\beta\cos\beta - \dfrac{\tau_{\max}a(\pi-2)}{\sqrt{\pi a}}\cos 2\beta. \end{cases} \tag{7}$$

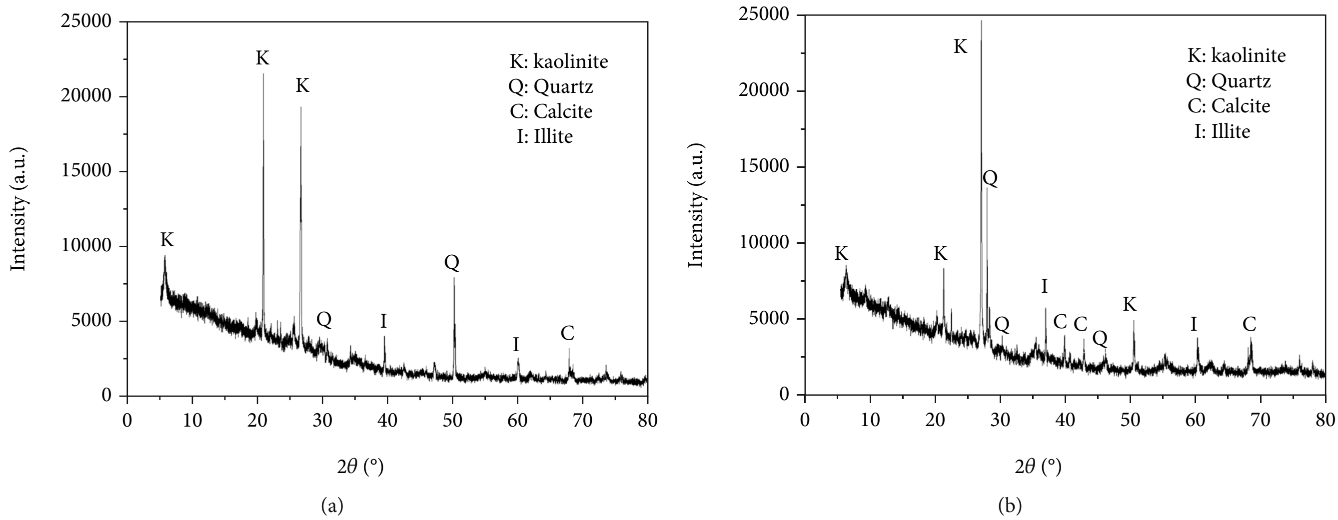

Figure 3: The results of XRD: (a) medium sandstone; (b) sandy sandstone.

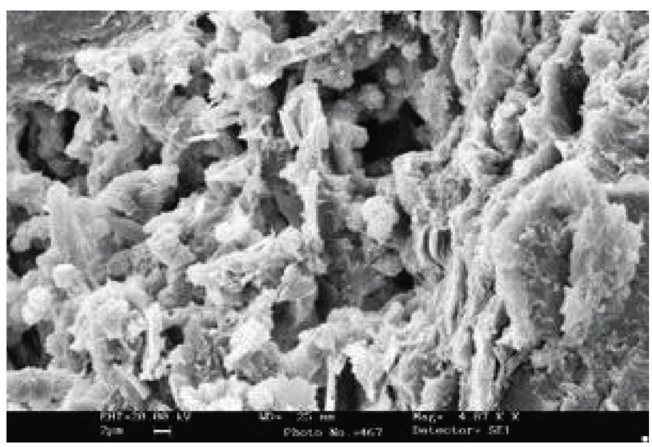

Figure 4: Microstructure of rock.

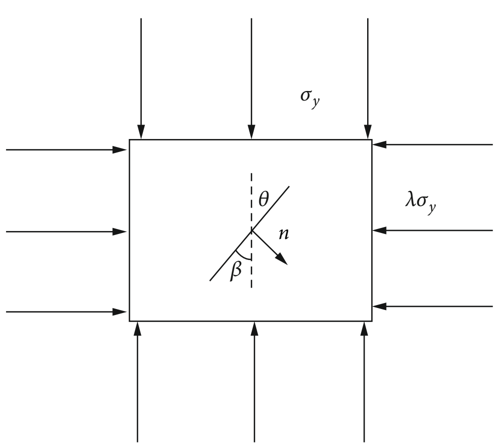

Figure 5: Schematic diagram of expansion of compression shear crack tip.

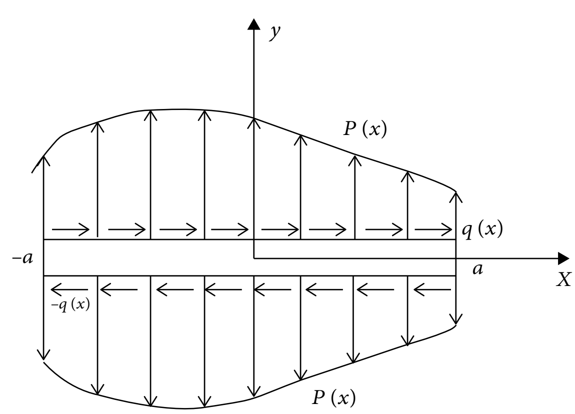

Figure 6: Schematic diagram of expansion of compression tensile shear crack tip.

According to mechanical related knowledge of materials, $\sigma_{\max}$ and $\tau_{\max}$ can be expressed as follows:

$$\begin{cases} \sigma_{\max} = \dfrac{M'}{W_z} = \dfrac{6\left(M + (ql/2)x - (1/2)qx^2 + p\omega\right)}{bh^2}, \\ \tau_{\max} = \dfrac{3F_s}{2bh}. \end{cases} \tag{8}$$

Equations (7) and (8) were combined as follows:

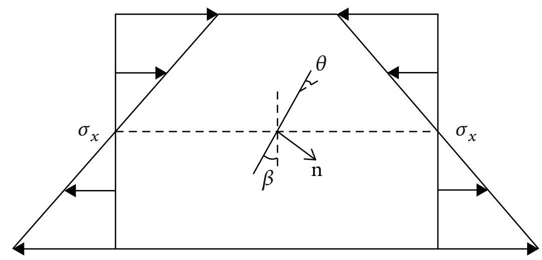

FIGURE 7: Schematic diagram of fracture tip expansion in horizontal direction of rock beam.

$$\begin{cases} K_{\mathrm{I}} = \dfrac{3\left(M + (ql/2)x - (q/2)x^2 + p\omega\right)}{bh^2} \sqrt{\pi a} \cos^2\beta + \dfrac{3F_s}{bh} \dfrac{a(\pi - 2)}{\sqrt{\pi a}} \sin\beta \cos\beta, \\ K_{\mathrm{II}} = \dfrac{3\left(M + (ql/2)x - (q/2)x^2 + p\omega\right)}{bh^2} \sqrt{\pi a} \sin\beta \cos\beta + \sqrt{\pi a}\sigma_y(1-\lambda) \sin\beta \cos\beta - \dfrac{3F_s}{2bh} \dfrac{a(\pi - 2)}{\sqrt{\pi a}} \cos 2\beta. \end{cases} \tag{9}$$

3.2. Composite Breakage Criteria. In practical engineering, almost all fractures are composite type. Many experts and scholars in China and other countries have conducted numerous studies on the judgment of crack expansion direction and critical loads of expansion. Among them, the maximum circumferential stress criteria are used mostly [23], which posit the following:

(1) When $(\sigma_\theta)_{\max}$ reaches the critical value σ_c, cracks begin to propagate

(2) The propagation direction of composite crack is the direction when σ_θ is the maximum

Based on the aforementioned criteria, the initiation angle θ_0 of cracks is

$$\theta_0 = \arcsin \frac{1}{\sqrt{(K_1/K_2)^2 + 9}} - \arctan \frac{3K_{\mathrm{II}}}{K_{\mathrm{I}}}. \tag{10}$$

The critical value of maximum circumferential stress $(\sigma_\theta)_c$ is

$$(\sigma_\theta)_c = \frac{K_{\mathrm{IC}}}{\sqrt{2\pi a}} = \frac{\cos(\theta_0/2)\left[K_{\mathrm{I}} \cos^2(\theta_0/2) - (3/2)K_{\mathrm{II}} \sin\theta_0\right]}{\sqrt{2\pi a}}. \tag{11}$$

3.3. Analysis of Fracture Propagation Parameters on Roadway Roof. The composite roof of weakly consolidated soft rock roadway in the first working face of the Bojianghaizi mine was used in the case study. The breakage criteria applied the maximum circumferential stress criteria. The first working face of the Bojianghaizi mine was at 540 m underground, and the net section size of the rectangular roadway was $b = 5.6$ m in width and $h = 3.6$ m in height. According to the primary stress and experimental test, vertical stress, lateral pressure coefficient, Poisson's ratio of rocks, initial cracking angle of rock beams, and uniformly distributed loads on beams were $\sigma_y = 14$ MPa, $\lambda = 0.8$, $\mu = 0.25$, $\beta = 5°$, and $q = 500$ kPa, respectively. The above numerical values were brought into Equations (10) and (11), which lead to the data in Figures 10–14.

Figure 10 shows that with the increase of strata thickness, the positive and shear stresses on the fractures decrease gradually. The fracture development angle in the strata decreases, and the fractures present small-angle development. Under this circumstance, the critical stress of fracture development also declines. When the lithology of the upper rock beam of the roadway is relatively weak, the bending and sinking rock beam thickens and the direct roof of the roadway easily develops connected fractures, thereby leading to roof falling accidents. Thus, a supporting structure has to be designed reasonably to prevent fracture propagation.

Figure 11 shows that with the increase of distance to the ends of rock beams, the fracture propagation angle decreases and the critical stress increases. In other words, fractures at the ends of the rock beam are easier to propagate toward large angles. Thus, an inclined anchor rod or cable has to be applied at two ends of the roadway roof to prevent crack propagation.

Figure 12 shows that with the increase of distance to the ends of rock beams, the fracture propagation angle decreases and the critical stress increases. In other words, fractures at the ends of the rock beam are easier to propagate toward large angles. Thus, an inclined anchor rod or cable has to be applied at two ends of the roadway roof to prevent crack propagation.

As shown in Figure 13, the fracture development angle increases gradually with the increase of the lateral pressure coefficient, while the critical stress declines gradually. This result reveals that with the increase of horizontal stress, the risk of high-angle falling of the rock beam also increases.

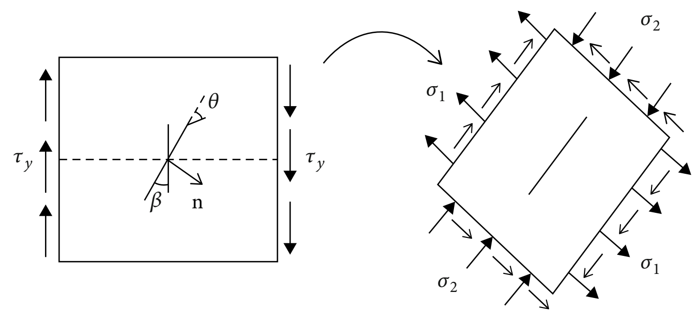

FIGURE 8: Schematic diagram of fracture tip expansion in level direction of rock beam.

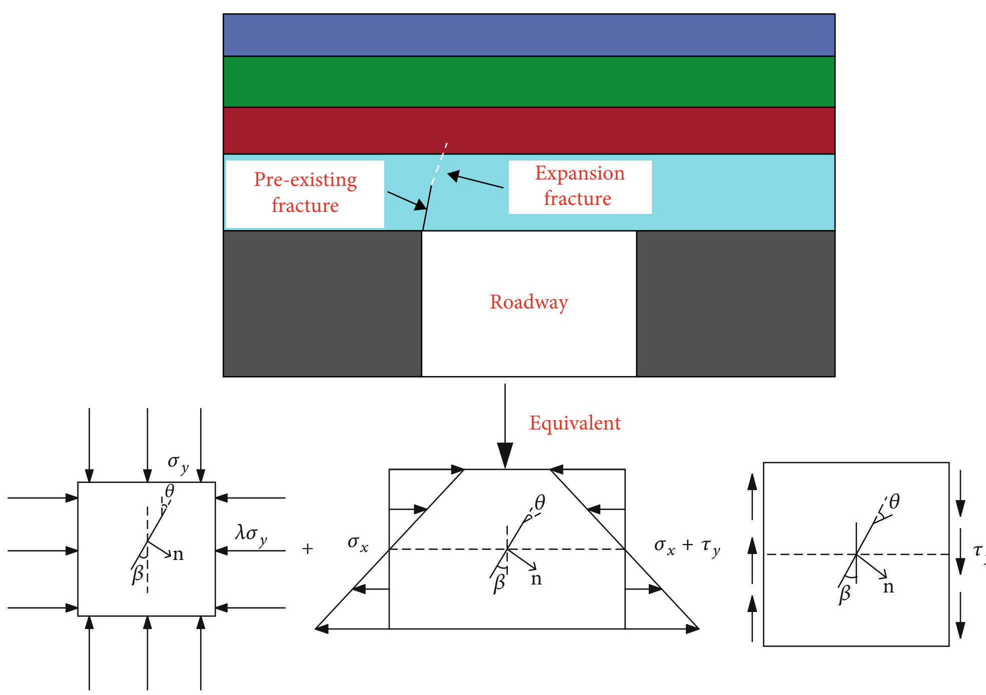

FIGURE 9: Equivalent diagram of composite fracture strength factor.

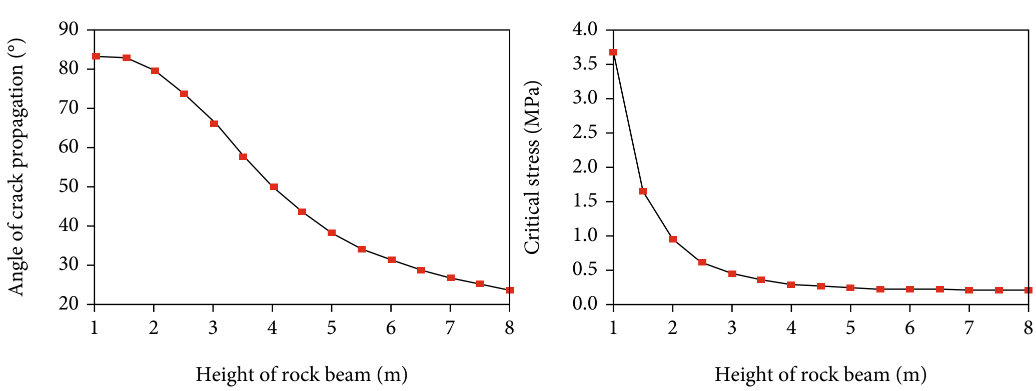

FIGURE 10: Sensitivity analysis of crack propagation angle and critical stress and rock beam height.

4. Instability Mechanism Analysis of Roadway Roof

The weakly consolidated roof has thin layers, and the interlayer cohesive force is weak. The roof begins to bend and sink in response to the gravity of overlying stones and horizontal stresses, thereby generating a shear force. Shear dislocation occurs between layers when the shear force is larger than the interlayer shear resistance. When the flexural rigidity of the lower rock strata is higher than that of the upper rock strata, it maintains coordinated movement and the layer separation is not obvious; otherwise, the layers are

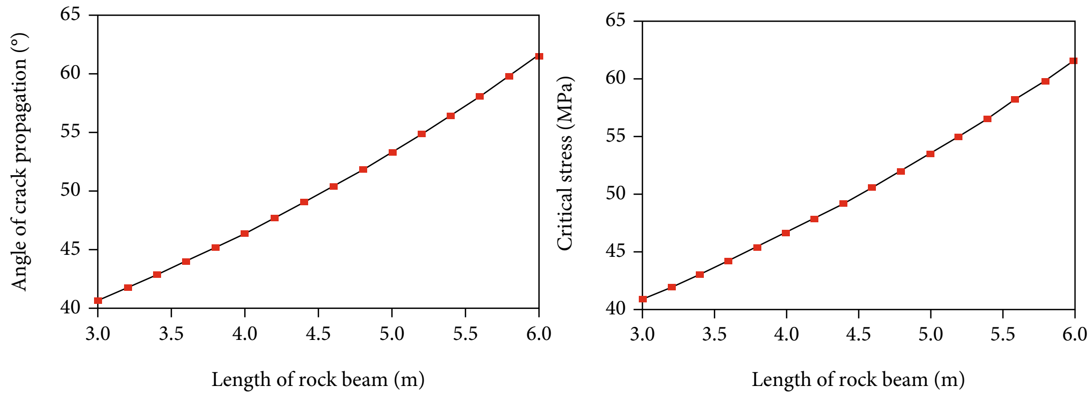

Figure 11: Analysis of crack propagation angle and critical stress and length of rock beam.

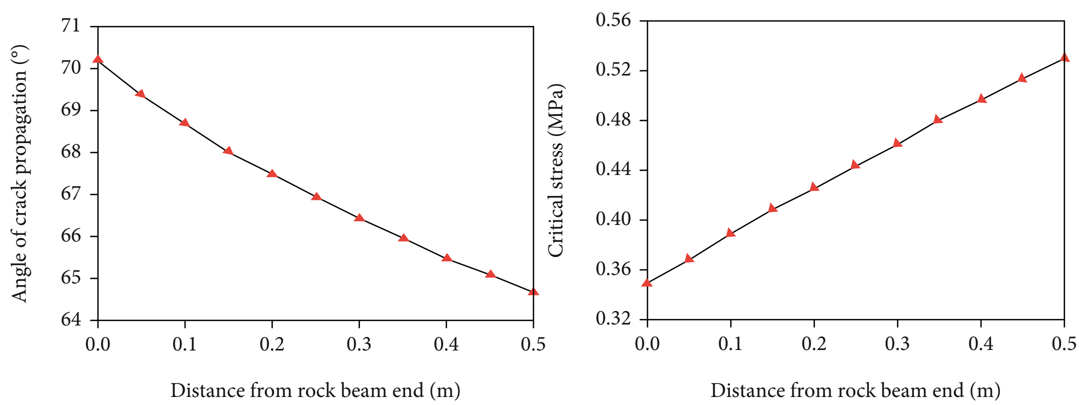

Figure 12: Analysis of crack propagation angle and critical stress and sensitivity of distance beam end.

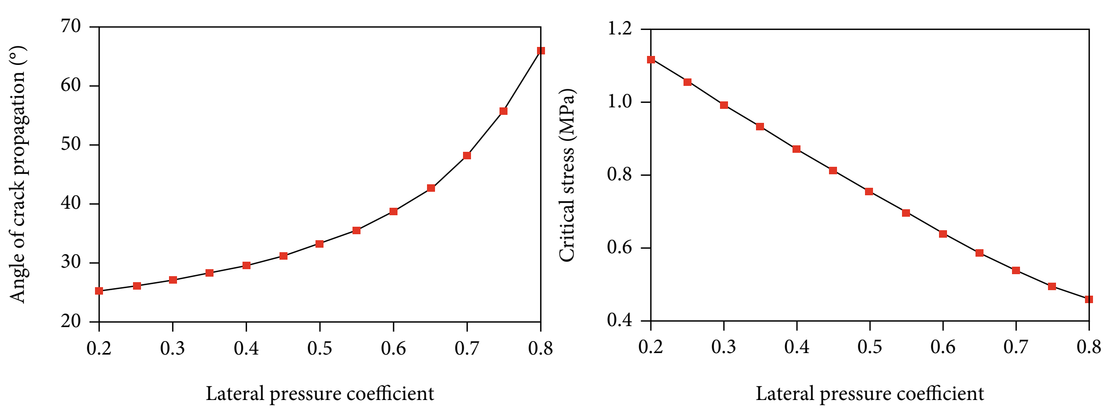

Figure 13: Sensitivity analysis of crack propagation angle and critical stress and lateral pressure coefficient.

separated. With the increase of layer separation, the roof is further bent and great shear stress is easily generated at the vertex angle of the roadway. Shearing failure occurs when this shear stress exceeds the shear strength of the rocks on the roof. When the shear failure forms cracks at the vertex angle of the roadway, this crack belt extends upward at an angle to the deep rock strata. Subsequently, the crack belt connects with the soft bedding plane of the separation stratum or soft weak interlayer, thus inducing roof falling. This process is shown in Figure 14.

According to instability mechanism analysis, the thin-layered roof is bent and deformed due to the dual actions of dead loads and horizontal stress of the roadway, thereby generating shear stress concentration at the vertex angle and causing shear failure. Cracks are formed at the vertex angle of the roadway. This crack belt extends upward along the fracture propagation angle to the soft bedding plane of the separation stratum of the soft weak interlayer and then connects with them, finally causing roof falling.

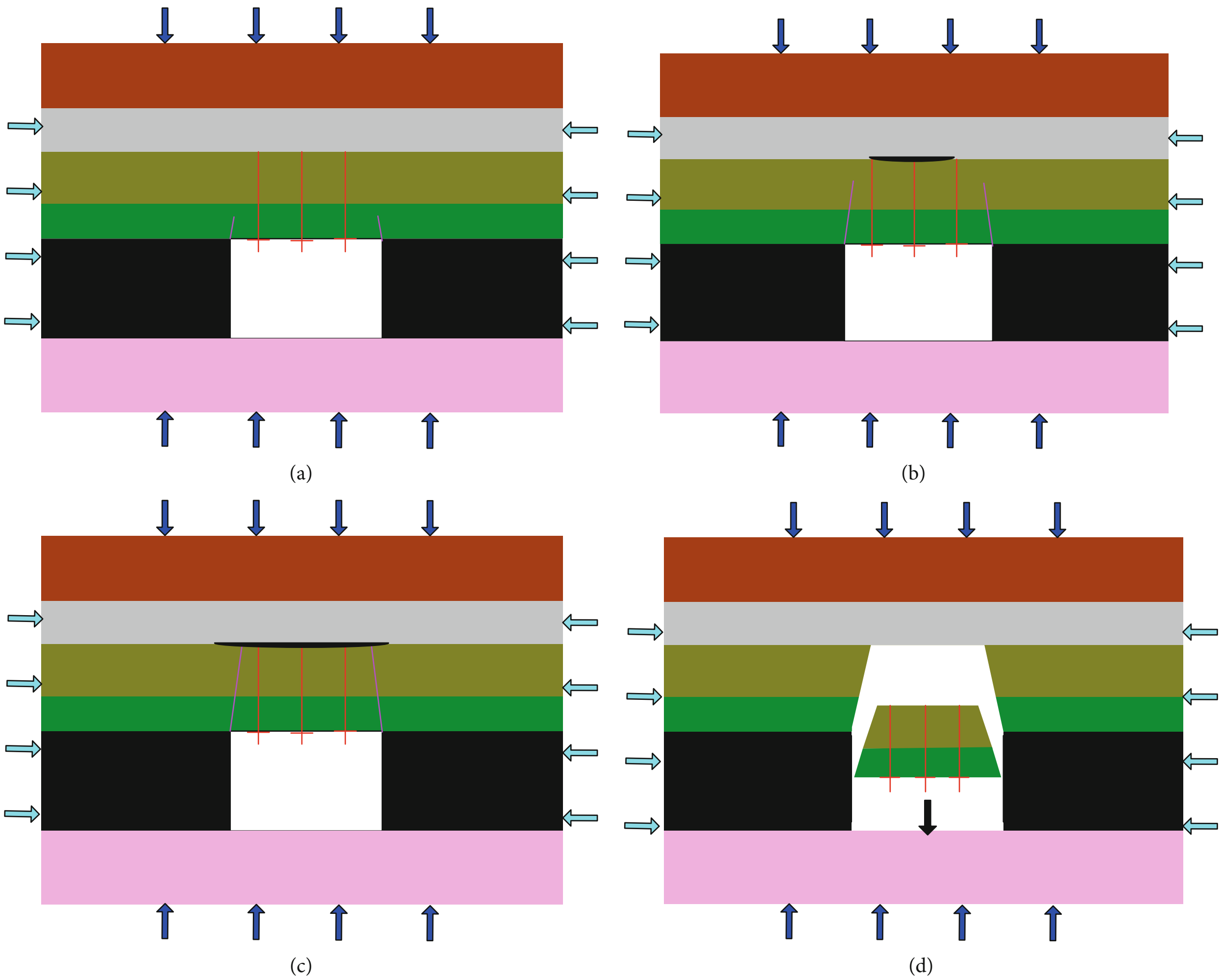

Figure 14: Evolution process of roof caving: (a) crack produce; (b) crack development; (c) fracture penetration; (d) roof caving.

5. Surrounding Rock Control and Engineering Applications

5.1. Roadway Control Technology. Due to the collaborative influences of primary deposit and diagenesis of weakly consolidated soft rock roadway, the degree of consolidation of rock strata is low, accompanied with poor cementation or rocks and weak interlayer adhesive force. Rocks have low compressive and tensile strengths. Due to tectonic lifting effect in the late stage, vertical and tensile fractures are extensively developed in rock strata, thus making rocks brittle and easy to crash. Based on the preceding analysis, the key to control deformation and instability of weakly consolidated soft rock roadways is to maintain the continuity of rock beams on the stratified roof and prevent softening of the weak interlayer or bedding plane above the anchoring body, controlling the separation layers and inhibiting the vertex angle failures of the roadway.

To overcome the deformation failures of weakly consolidated soft rock roadway, this study proposes a high-strength and high-preload "inverted trapezoidal" anchoring mesh-beam string supporting structure + arched roadway cross-section with vertical walls + full-section guniting coupling optimization support structure (Figure 15). The self-bearing capacity of surrounding rocks is used fully, which not only allows deformation of surrounding rocks but also restricts deformation. The roof becomes increasingly stable in the process of collaborative action of surrounding rocks and anchoring supporting structure.

5.2. Engineering Applications. To verify the reliability of supporting technology after the optimization, this study examines the applications of this technology during field experiment in the return roadway of working face #113102 in coal seam #3-1. To further elaborate the effects of optimized supporting scheme in the separation and deflection control of the roof, the internal structure of the roadway roof was studied by using a TS-C0601 drill imager after the roadway was advanced for 10 months. Results are shown in Figure 16.

Through the drill imaging, white cracks were detected near 1.6 m in the upper position of the roof, which were separation layers. The separation layer size was approximately 6–7 mm. Furthermore, an annular black zone within a certain scope occurred on the porous wall, which is 6.2 m near the upper position of the roof, and the separation layer size

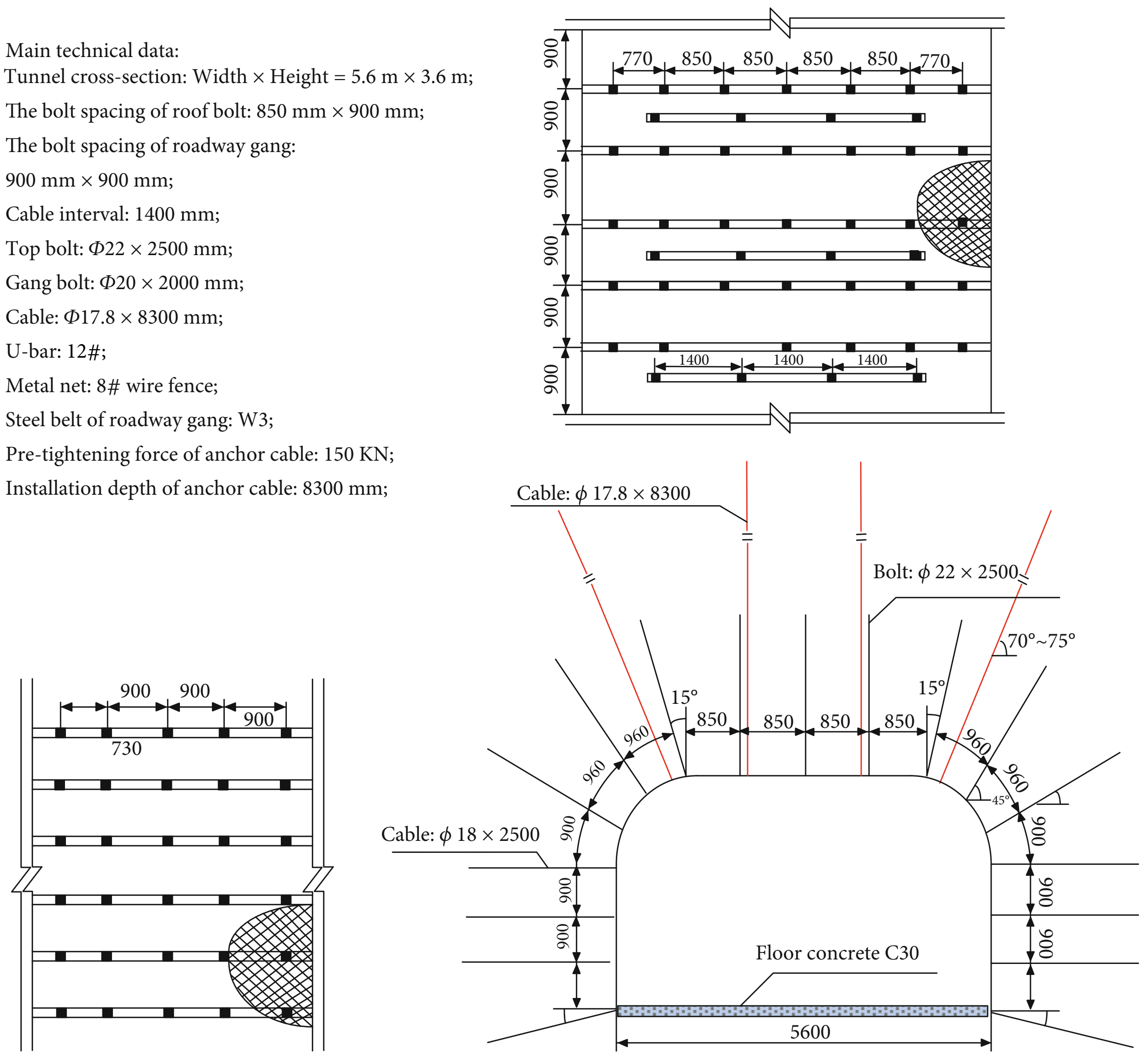

Figure 15: The new support parameter of the soft-rock coal roadway.

(a) (b)

Figure 16: Roof borehole peep view: (a) 1.6 m; (b) 6.2 m.

was approximately 7–10 mm. In the experimental section, surrounding rocks on the roadway roof were relatively integrals, without evident opening bedding and the separation value of the roof was small. Cracks were not connected yet, which further proved that the optimized supporting structure could effectively control the separation layers, fracture development, and roof connection, thereby improving the overall structure of the roof.

6. Conclusions

(1) According to the laboratory test of mineral composition and structural analysis of the roof, the weakly consolidated rocks generally form a weak structure and have low rock strength. Moreover, clay minerals are the major mineral components. Kaolinite accounts for the highest proportion and is a characteristic of swelling and disintegration in water

(2) The mechanical model of fracture development in the composite roof of the roadway is constructed, thereby obtaining the initiation angle and critical stress of fracture development. The critical cracking angle (θ_0) of the roof is obtained according to the strain energy density factor of crack propagation

(3) Through an engineering case study, relations of rock beam height, span of roadway, and fracture development angles at the ends of rock beams with fracture development trend and critical stress of crack propagation are disclosed. On this basis, the instability mechanism of roof falling in the roadway is summarized. Shear failure occurs at the vertex angle of the roadway, thereby forming cracks. The crack belt extends along a certain angle to the soft bedding plane of the separation stratum or weak bedding plane and finally connects with them, which leads to roof falling

(4) A high-strength and high-preload "inverted trapezoidal" anchoring mesh-beam string supporting structure + arched roadway cross-section with vertical walls + full-section guniting coupling optimized supporting structure is proposed to solve the deformation failure of weakly consolidated soft rock roadway. According to field test results, this optimized supporting structure can effectively control the separation and deformation of the roadway, thereby significantly increasing the stability of surrounding rocks

Data Availability

The data used to support the findings of this study are included within the article.

Conflicts of Interest

The authors declare that there is no conflict of interest regarding the publication of this article.

Acknowledgments

This research was funded by the Open Research Fund Project of Key Laboratory of Safety and High-Efficiency Coal Mining of Ministry of Education of the People's Republic of China (JYBSYS2021202), the research start-up fees for high-level talents of West Anhui University (WGKQ2021071), the Domestic Study Visit and Training Project for Outstanding Young Backbone Teachers in Colleges and Universities in Anhui Province (gxgnfx2020096), and the Provincial Quality Engineering Project of colleges and universities of Anhui Provincial Department of Education (2020jyxm2153 and 2020szsfkc0953).

References

[1] H. B. Jia, L. J. Su, and Z. Qin, "Ground stress numerical inversion of roadways with weakly cemented strata," *Chinese Journal of Shandong University of Science and Technology (Natural Science)*, vol. 30, no. 5, pp. 30–35, 2011.

[2] Q. B. Meng, L. J. Han, W. G. Wei, D.-G. Lin, and J.-D. Fan, "Evolution of surrounding rock in pioneering roadway with very weakly cemented strata through monitoring and analyzing," *Chinese Journal of Coal Society*, vol. 38, no. 4, pp. 572–579, 2020.

[3] W. M. Wang, L. Wang, and C. Q. Dai, "Frozen wall deformation analysis in weakly cemented soft rock based on layered calculation of strength," *Chinese Journal of Rock Mechanics and Engineering*, vol. 30, no. 5, pp. 4110–4116, 2011.

[4] Q. F. Zhao, N. Zhang, G. Z. Li, and R. Peng, "Similarity simulation experimental study on abrupt collapse of roof separation in large cross-section argillaceous roadway," *Chinese Journal of Mining & Safety Engineering*, vol. 35, no. 6, pp. 1107–1115, 2018.

[5] N. Zhang and L. Yuan, "Control principle of separating and broken roof rock strata in roadway," *Chinese Journal of Mining & Safety Engineering*, vol. 23, no. 1, pp. 34–38, 2006.

[6] N. Zhang and Y. Jiang, "Theoretical estimation of loosening pressure on tunnels in soft rocks," *Chinese Journal of Tunneling and Underground Space Technology*, vol. 16, no. 2, pp. 99–105, 2001.

[7] N. Zhang, Z. C. Zhang, J. B. Bai, W. J. Wang, and H. Wu, "Mechanical analysis of roof separation within and outside anchorage zone above backfill area of gob-side entry retaining and its engineering application," *Chinese Journal of Mining & Safety Engineering*, vol. 35, no. 5, pp. 893–901, 2018.

[8] Z. H. Zhao, N. J. Ma, H. T. Liu, and J. C. Feng, "Mechanism and early-warning methods of roadway roof fall in coal seam," *Chinese Journal of Coal Society*, vol. 43, no. 2, pp. 369–376, 2018.

[9] H. S. Jia, G. S. Li, L. Y. Wang, and A. Z. Qiao, "Characteristics of stress-field environment and roof falling mechanism of mining influenced roadway," *Chinese Journal of Mining & Safety Engineering*, vol. 34, no. 4, pp. 707–714, 2019.

[10] D. L. Zhang, Y. H. Wang, T. Z. Qu, and W. K. Li, "Influence analysis of inter band on stability of stratified rockmass," *Chinese Journal of Rock Mechanics and Engineering*, vol. 19, no. 2, pp. 140–144, 2000.

[11] F. L. Guo, D. L. Zhang, J. Su, and X. K. Liu, "Change of strength of surrounding rock system induced by weak interlayer,"

Chinese Journal of Geotechnical Engineering, vol. 31, no. 5, pp. 720–726, 2009.

[12] L. Q. Cao, D. L. Zhang, and Q. Fang, "Semi-analytical prediction for tunnelling-induced ground movements in multi-layered clayey soils," *Chinese Journal of Tunneling and Underground Space Technology*, vol. 102, no. 5, article 103446, 2020.

[13] B. S. Zhang, Y. G. Yan, L. X. Kang, and C. R. Yu, "Application of the contact element method in analyzing the separation and deformation of the stratified roof," *Chinese Journal of Coal Society*, vol. 33, no. 4, pp. 387–392, 2008.

[14] B. S. Zhang, L. X. Kang, and S. S. Yang, "Numerical simulation on roof separation and deformation of full seam roadway with stratified roof and large section," *Chinese Journal of Mining & Safety Engineering*, vol. 23, no. 3, pp. 264–267, 2016.

[15] Q. B. Meng, L. J. Han, W. G. Qiao, D. G. Deng, and S. Y. Wen, "Deformation failure characteristics and mechanism analysis of muddy weakly cemented soft rock roadway," *Chinese Journal of Mining & Safety Engineering*, vol. 33, no. 6, pp. 1015–1022, 2016.

[16] Q. B. Meng, L. J. Han, W. G. Qiao et al., "The deformation failure mechanism and control techniques of soft rock in deep roadways in Zhaolou mine," *Chinese Journal of Mining & Safety Engineering*, vol. 30, no. 2, pp. 165–172, 2013.

[17] Q. Meng, L. Han, W. Qiao, D. Lin, and J. Fan, "Support technology for mine roadways in extreme weakly cemented strata and its application," *International Journal of Mining Science and Technology*, vol. 24, no. 2, pp. 157–164, 2014.

[18] T. C. Li, L. Zhen, J. Z. Liu, and Q. X. Ma, "Deformation and failure process analysis of rectangular roadway in muddy weakly cemented soft rock strata," *Rock and Soil Mechanics*, vol. 35, no. 4, pp. 1077–1083, 2014.

[19] Q. Li and J. Hou, "Research on deformation mechanism and support technology of coal roadway with weakly cemented rock strata in Yangjiacun mine," *Chinese Journal of Coal Engineering*, vol. 48, no. 7, pp. 40–48, 2016.

[20] T. Y. Fan, *Theoretical Basis of Fracture*, Science Press, Beijing, China, 2018.

[21] Z. H. Zhou, *Crack Propagation Mechanism of Fractured Rock under Static-Dynamic Loading and Seepage Water Pressure*, Central South University, Changsha, Hunan, China, 2014.

[22] F. Erdogan and G. C. Sih, "On crack extension in plates under plane loading and transverse shear," *International Journal of Basic Engineering*, vol. 5, no. 4, pp. 512–517, 1963.

[23] R. J. Nuismer, "An energy release rate criterion for mixed mode fracture," *International Journal of Fracture*, vol. 11, no. 2, pp. 245–250, 1975.

Hindawi
Geofluids
Volume 2023, Article ID 6957653, 8 pages
https://doi.org/10.1155/2023/6957653

Research Article

A New Method to Predict Shock-Type Coal-Gas Outburst Disaster and Its Application

Pengfei Lyu[1], **Tan Li**[1], **and Xuehua Chen**[2]

[1] *Institute of Mining and Coal, Inner Mongolia University of Science and Technology, Baotou, Inner Mongolia Autonomous Region 014010, China*
[2] *College of Mining, Liaoning Technical University, Fuxin, Liaoning Province 123000, China*

Correspondence should be addressed to Pengfei Lyu; 2018930@imust.edu.cn

Received 18 April 2022; Revised 28 June 2022; Accepted 25 November 2022; Published 30 January 2023

Academic Editor: Hualei Zhang

Coal-gas outburst is the one of most serious coal mine dynamic disasters which affects safety mining, with 39 deaths reported during 2019 in China. The mechanism of coal-gas outbursts is complex, and the prediction methods are immature at present. This article was based on previous research results. Firstly, the occurrence mechanism of coal-gas outburst disasters was summarized. It is clear that the occurrence of coal-gas outburst disasters is jointly affected based on the stability of the static structure of coal-rock, the gas parameters, and the release intensity of shock stress. Secondly, the stability evaluation models of coal-rock static structure, gas parameters, and shock stress release intensity were built, respectively, based on the influence factors. Then they were coupled and supposed to form a new prediction model. Finally, the prediction method was applied to the Ji_{15}-17200 working face of No.12 coal mine in Pingmei company. The working face was divided into three danger levels including weak outburst danger area, medium outburst danger area, and strong outburst danger area. The accuracy of the predicted results was analyzed based on the actual mining condition of the Ji_{15}-17200 working face. The results show that prediction accuracy is high, and it can be used for actual applications. The research results are of guiding significance to better prevent and control coal-gas outburst accidents and ensure safe production in coal mines.

1. Introduction

Coal is the main source of energy in China. With the yearly increase of coal mining depth, the coal seam gas pressure and the in situ stress are also increasing, and the danger of mine dynamic disaster is increasing especially coal-gas outburst [1–6]. At present, the requirements of coal precision and intelligent mining pose more difficult challenges to the effective prevention and control of dynamic disasters such as coal-gas outburst [7–15]. Therefore, it is imperative to research coal-gas outburst prediction methods with high accuracy and suitable for engineering applications.

Domestic and foreign scholars have carried out a lot of research results on coal-gas outburst predictions, forming a series of commonly used coal-gas outburst danger prediction technology, such as drilling cuttings method [16], drilling gas inrush initial velocity method [17], etc. Meanwhile, geophysical methods have been gradually applied to coal-gas outburst prediction in recent years, such as the acoustic emission method [18], microseismic method [19], and electromagnetic radiation method [20]. In addition, according to the time series feature of coal-gas outburst, prediction indexes can be divided into dynamic prediction and static prediction, and critical value was often used to judge the danger of coal-gas outburst in static prediction; for dynamic prediction, the method based on the change characteristics of precursory information of monitoring indexes was used to determine the danger of coal-gas outburst. Lama and Bodziony [21] studied coal-gas outburst risk prediction technology and prevention and control measures based on management system, decision-making, and risk analysis; safety mining process of outburst coal seam was put forward. Cyrul [22] used data mining technology to study the prediction method of outburst coal seam in Poland and has got good application results. The development of data mining technology provides more theoretical support for the prediction of coal-gas outburst danger, such as the neural network method [23], fuzzy comprehensive evaluation [24], gray theory method [25], and extreme learning machine method [26]. Song and Zhang [27, 28] predicted and visualized the coal-gas outburst area based on geographical information system technology. Zhang et al. [29–31] studied a new prediction method of coal-gas outburst based on the η parameter that was put forward on the basis of experimental study, and its dangerous level was divided into five categories; the method was compared with other traditional methods at the same time. Liu et al.'s physical simulation system for large coal-gas outburst had been developed, and the occurrence mechanism of coal-gas outburst was analyzed from the perspective of energy, which laid a theoretical foundation for the accurate prediction of coal-gas outburst disasters.

Some typical coal-gas outburst prediction methods were listed above, and most of them use precursor information or data mining technology to judge the possibility of outburst, few studies on constructing prediction criteria of outburst disasters from the perspective of outburst disaster mechanism. In this article, we first elaborated the coal-gas outburst disaster occurrence principle, and the prediction method was constructed based on the outburst principle; finally, the instance prediction and effect test are carried out, and a new prediction method of coal-gas outburst disaster is formed; it provides new approaches for the accurate prediction of such disasters.

2. Shock-Type Coal-Gas Outburst Occurrence Principle

According to relevant theories [32, 33], as shown in Figure 1, the stress source of shock-type coal-gas outburst disaster includes static stress of coal-rock, dynamic load stress induced by mining, and gas pressure in cracks of coal-rock. Higher static stress of coal-rock near mining working face, the corresponding gas pressure, and ultimate strength are low. The mechanism of coal-gas outburst is in the final analysis that the combined load of coal-rock exceeds its bearing strength and destroys. When mining induced dynamic load superimposed to the adjacent working face area and meets the critical load of coal-rock dynamic disaster that will induce coal-gas outburst disaster; the stress formula is shown in

$$\sigma_s + \sigma_d + \sigma_g \geq \sigma_{b\ min}, \tag{1}$$

where σ_s is the static load stress of coal-rock, σ_d is the dynamic load stress induced by mining, σ_g is the gas pressure in fissure of coal-rock, and $\sigma_{b\ min}$ is the critical load of coal-gas outburst.

It can be known that when the sum of static load, dynamic load, and gas pressure exceeds the critical load of dynamic disaster, the dynamic disaster will occur, as shown in Figure 2. Therefore, it is considered that the prediction of shock-type stress release coal-gas outburst disaster should be carried out from three aspects: stability of static excavation structure of coal-rock, gas parametric strength, and shock-type stress release strength.

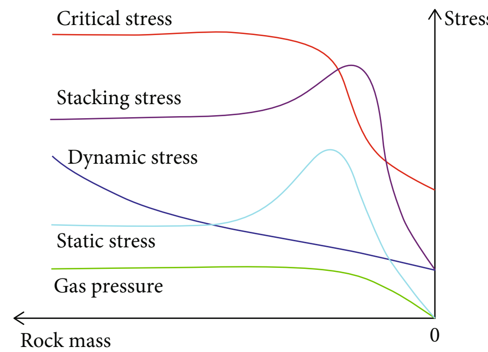

Figure 1: Critical condition of shock-type coal and gas outburst disaster.

3. New Method to Predict Shock-Type Coal-Gas Outburst

3.1. Evaluation of Static Structure Stability. The complex coal-gas outburst coal-rock structures are formed by the geological conditions in the coal mining area and the underground mining activities. The coal-rock structures of shock-type coal-gas outburst are mainly controlled by the coupling of geological conditions and mining activities. Geological conditions mainly include coal seam and roof-floor lithologic characters and geological structure. After roadway excavation or working face mining, coal-rock might form a permanent or temporary static structure. When the coal-rock structure is disturbed by external vibration, it is easy to cause sudden stress distribution imbalance, to trigger instability of coal-rock structure, and combined with gas pressure effect, the shock-type stress release coal-gas outburst disaster occurs. Therefore, the prediction method of coal-gas outburst based on shock-type stress release includes four aspects: static coal-rock structure stability evaluation technology, gas parameter strength evaluation technology, working face disturbance strength evaluation technology, and classification prediction criterion establishment. The detailed description is as follows. The evaluation indexes of coal-rock static structure stability mainly include mining depth, ground stress level, coal-rock properties, geological structure, and change of coal seam thickness.

3.1.1. Mining Depth. The mining depth of coal seam is an important index for predicting coal-gas outburst disasters and evaluating the static structure of coal-rock. According to the analysis of mining depth and the latest comprehensive index method [34, 35], the mining depth index is defined to evaluate the stability of the static structure of coal-rock as follows: when H (the mining depth) > 1000 m, the stability index of the static structure of coal-rock is 4; when $700 < H \leq 1000$ m, the stability index of coal-rock static structure is 3; when $400 < H \leq 700$ m, the stability index of coal-rock static structure is 2; when $H \leq 400$ m, the stability index of coal-rock static structure is 1.

3.1.2. In Situ Stress. Coal-gas outburst is a dynamic phenomenon of rapid release of stress and energy. Therefore, the in

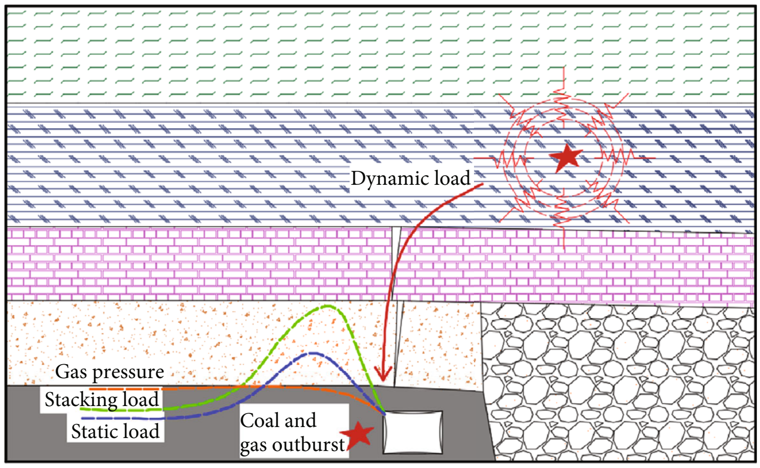

Figure 2: Model of shock-type coal and gas outburst disaster.

situ stress of coal mining area is an important index to evaluate the static structure of coal-rock. The in situ stress evaluation used in this paper includes two indexes of original rock stress and mining stress, maximum principal stress index is used in original rock stress, and stress concentration coefficient index is used in mining stress. When the maximum principal stress $\sigma_1 > 30$ MPa, the static structural stability index of coal-rock is 4; when $24 < \sigma_1 \leq 30$ MPa, the stability index of static structure of coal-rock is 3; when $18 < \sigma_1 \leq 24$ MPa, the stability index of static structure of coal-rock is 2; when σ_1 is less than 18 MPa, the stability index of the static structure of coal-rock is 1. When the stress concentration factor $k > 2.8$, the static structure stability index of coal-rock is 4; when $2.3 < k \leq 2.8$, the stability index of static structure of coal-rock is 3; when $1.7 < k \leq 2.3$, the stability index of coal-rock static structure is 2; when $k \leq 1.7$, the stability index of the static structure of coal-rock is 1.

3.1.3. Coal-Rock Mass Attribute. Coal-gas outburst and static structure formation are also controlled by coal-rock properties. The index evaluation of the impact tendency of coal seam and roof is adopted. The static structural stability index of coal-rock corresponding to strong impact tendency of coal seam and roof is 4, the static structural stability index of coal-rock corresponding to medium impact tendency of coal seam and roof is 3, the coal-rock static structural stability index corresponding to the weak impact tendency of coal seam and roof is 2, and the static structural stability index of coal-rock corresponding to nonimpact tendency of coal seam and roof is 1.

3.1.4. Geological Structure. Coal mining in geological structure area and nongeological structure area has great difference in forming static structure of coal-rock, because geological structure is difficult to quantify, so according to the geological structure, severity is strong, general, weak, and no geological structure classification; the corresponding static structural stability indexes of coal-rock are 4, 3, 2, and 1, respectively.

3.1.5. Variation of Coal Seam Thickness. The practice shows that the stability of regional coal-rock structure is poor when the coal thickness changes sharply. And coal-gas outbursts occur frequently, which may be due to unbalanced stress transfer. The change degree of coal thickness is summarized into four categories: severe change, relatively severe change, stable change, and almost no change; the corresponding static structural stability indexes of coal-rock are 4, 3, 2, and 1, respectively.

Based on the above coal static structure stability evaluation index and index determination, evaluation results of static structural stability of coal-rock *Sta* are shown in

$$Sta = \frac{S_1 + S_2 + L + S_n}{n}, \quad (2)$$

where S_1, S_2, and S_n are the indexes of n indexes for evaluating stability of coal-rock static structure.

3.2. Evaluation of Gas Parameters. The gas parameter strength of working face is mainly controlled by gas pressure, gas content, absolute gas emission rate, and initial velocity of gas release.

3.2.1. Gas Pressure. Original gas pressure in coal seam is the key factor of coal-gas outburst disaster. The normal case, multipoint gas pressure measurement in working face of coal-gas outburst mine. But in general case, the part of gas pressure parameters in the prediction unit can be collected. The remaining uncollected unit grid gas pressure parameters are calculated by interpolation method, calculation method of interpolation method without detailed description. Dividing gas pressure into four grades is as follows: when the gas pressure is $P \leq 0.2$ MPa, the corresponding gas reflection strength index is 1; when the gas pressure is $0.2 < P \leq 0.4$ MPa, the corresponding gas reflection strength index is 2; when the gas pressure is $0.4 < P \leq 0.74$ MPa, the corresponding gas reflection strength index is 3; when the gas pressure is $P > 0.74$ MPa, the corresponding gas reflection strength index is 4.

TABLE 1: Disturbance intensity index of shock-type coal and gas outburst by hard roof.

Serial number	Thickness, m	Compressive strength, MPa	Distance between hard rock and coal seam, m	Disturbance intensity index
1	≥30	≥60	<20	6
2	15~30	≥60	<20	5
3	<15	≥60	<20	4
4	≥30	≥60	20~40	5
5	15~30	≥60	20~40	4
6	<15	≥60	20~40	3
7	≥30	≥60	≥40	4
8	15~30	≥60	≥40	3
9	<15	≥60	≥40	2
10	≥30	35~60	<20	5
11	15~30	35~60	<20	4
12	<15	35~60	<20	3
13	≥30	35~60	20~40	4
14	15~30	35~60	20~40	3
15	<15	35~60	20~40	2
16	≥30	35~60	≥40	3
17	15~30	35~60	≥40	2
18	<15	35~60	≥40	1

3.2.2. Gas Content. Coal seam gas content is also the key factor of coal-gas outburst disaster. The normal case multipoint gas pressure measurement in working face of coal-gas outburst mine, but general case the part of gas pressure parameters in the prediction unit can be collected, the remaining uncollected unit grid gas pressure parameters are calculated by interpolation method, calculation method of interpolation method without detailed description. Dividing gas content into four grades is as follows: when the gas content is $Q \le 5\,\mathrm{m^3/t}$, the corresponding gas reflection strength index is 1; when the gas content is $5 < Q \le 12\,\mathrm{m^3/t}$, the corresponding gas reflection strength index is 2; when the gas content is $12 < Q \le 20$ $\mathrm{m^3/t}$, the corresponding gas reflection strength index is 3; when the gas content is $Q > 20\,\mathrm{m^3/t}$, the corresponding gas reflection strength index is 4.

3.2.3. Absolute Gas Emission Rate. Absolute gas emission rate has a great effect on coal-gas outburst disaster. If the absolute gas emission is not measured in the predicted grid unit, the interpolation method is also used for calculation. Dividing absolute gas emission rate into three grades is as follows: when the absolute gas emission rate is $U \le 10\,\mathrm{m^3/min}$, the corresponding reflection strength of gas parameters is 1; when the absolute gas emission rate is $10 < U \le 30\,\mathrm{m^3/min}$, the corresponding reflection strength of gas parameters is 2; when the absolute gas emission rate is $U > 30\,\mathrm{m^3/min}$, the corresponding reflection strength of gas parameters is 3.

3.2.4. Initial Velocity of Gas Release. Initial velocity of gas release is also an important index of coal-gas outburst disaster. Interpolation method is also used to predict weak grid cell without this index. Dividing absolute gas emission rate into three grades is as follows: when the absolute gas emission rate is $q \le 2.5\,\mathrm{L/min}$, the corresponding reflection strength of gas parameters is 1; when the absolute gas emission rate is $2.5 < q \le 4.5\,\mathrm{L/min}$, the corresponding reflection strength of gas parameters is 2; when the absolute gas emission rate is $q > 4.5\,\mathrm{L/min}$, the corresponding reflection strength of gas parameters is 3.

TABLE 2: Static structure calculation process of coal and rock.

	S_1	S_2	S_3	S_4	S_5	S_6	*Sta*
1	2	4	1	2	1	1	1.83
2	2	4	1	2	1	1	1.83
3	2	4	1	2	1	1	1.83
4	2	4	1	2	1	1	1.83
5	2	4	1	2	1	1	1.83
6	2	4	1	2	1	1	1.83
7	2	4	1	2	1	1	1.83
8	2	4	1	2	1	1	1.83
9	2	4	2	2	1	1	2
10	2	4	2	2	1	1	2

Based on the above gas parameter strength evaluation index and index determination, the gas parameter strength evaluation result *Sta* is shown in

$$Gas = \frac{G_1 + G_2 + L + G_n}{n}, \tag{3}$$

where G_1, G_2, and G_n are the indexes of n indicators for evaluating the static structural stability of coal-rock.

3.3. Evaluation of Vibration Stress Release Intensity. The disturbance strength of working face is mainly affected based on the mining thickness of coal seam, degree of fault activation, stability of residual coal pillar, and activity strength of hard roof and the filling degree.

3.3.1. Coal Seam Thickness. The thickness of coal seam in working face has great influence on roof caving and its shock disturbance. Therefore, the mining thickness of coal seam is regarded as an important index to evaluate the disturbance strength of coal-rock. According to field observation and practical experience, when the coal seam mining thickness $h > 6\,\mathrm{m}$ was drafted, the coal-rock disturbance strength index was 4; when $4 < H \le 6\,\mathrm{m}$, the coal-rock disturbance strength index was 3; when $2 < H \le 4\,\mathrm{m}$, the coal-rock disturbance strength index was 2; when $H \le 2\,\mathrm{m}$, the coal-rock disturbance strength index was 1.

3.3.2. Fault Activation Degree. Working face mining results in the activation of faults near the face. The fault activation would easily induce high energy shock disturbance near the working face. According to relevant research results [36] judge the disturbance strength index of the fault to the shock-type stress release coal-gas outburst. When the

Table 3: Gas parameter strength calculation process.

	G_1	G_2	G_3	G_4	*Gas*
1	3	2	1	2	2
2	3	2	1	2	2
3	3	2	1	2	2
4	3	2	1	2	2
5	3	2	1	3	2.25
6	3	2	1	3	2.25
7	2	1	1	3	1.75
8	2	1	1	3	1.75
9	2	1	1	3	1.75
10	2	1	1	3	1.75

Table 4: Disturbance strength calculation process.

	D_1	D_2	D_3	D_4	D_5	D_6	*Dis*
1	3	0	3	2	5	2	2.5
2	3	0	3	2	5	2	2.5
3	3	0	3	2	5	2	2.5
4	3	0	3	2	5	2	2.5
5	3	0	3	2	5	2	2.5
6	3	0	3	2	5	2	2.5
7	3	0	3	2	5	2	2.5
8	3	0	3	2	5	2	2.5
9	3	0	3	2	5	2	2.5
10	3	0	3	2	5	2	2.5

Table 5: Coal and gas outburst risk index.

	Sta	*Gas*	*DIS*	ODI
1	1.83	2	2.5	6.33
2	1.83	2	2.5	6.33
3	1.83	2	2.5	6.33
4	1.83	2	2.5	6.33
5	1.83	2.25	2.5	6.58
6	1.83	2.25	2.5	6.58
7	1.83	1.75	2.5	6.08
8	1.83	1.75	2.5	6.08
9	2	1.75	2.5	6.25
10	2	1.75	2.5	6.25

coal wall is 62~39 m away from the fault, the coal-rock disturbance strength index is 2; when the coal wall is 40~18 m away from the fault, the coal-rock disturbance strength index is 3; when the coal wall is 18~0 m away from the fault, the coal-rock disturbance strength index is 4; when the coal wall crosses the fault 0~40 m, the coal-rock disturbance strength index is 2; when the coal wall crosses the fault 40~80 m, the disturbance strength index is 1.

3.3.3. Mining Speed. Mining speed is also a key factor affecting the occurrence of high energy shock. The increase of mining speed will induce the violent activity of roof, and the frequency and energy of mine earthquakes will increase. According to the corresponding relationship between mining speed and the occurrence of high energy mine earthquake, the disturbance strength index of shock-type stress release coal-gas outburst caused based on proposed mining speed is as follows: when the mining speed is greater than 6 m/d, the coal-rock disturbance strength index is 4; when the mining speed is 4~6 m/d, the coal-rock disturbance intensity index is 3; when the mining speed is 2~4 m/d, the coal-rock disturbance strength index is 2; when the mining speed is less than 2 m/d, the coal-rock disturbance strength index is 1.

3.3.4. Residual Coal Pillar Stability. Coal mining in working face, the residual coal pillars near the working face for various reasons. The residual coal pillar causes higher degree of stress concentration. Therefore, the index of disturbance strength of shock-type stress release coal-gas outburst caused based on the coal pillar size is proposed. When the coal pillar width is greater than 80 m, the coal-rock disturbance strength index is 1; when the coal pillar width is 60~80 m, the disturbance strength index is 2; when the coal pillar width is 40~60 m, the disturbance strength index is 3; when the coal pillar width is 20~40 m, the disturbance strength index is 4; when the coal pillar width is 10~20 m, the disturbance strength index is 3, when the coal pillar width is 0~10 m, the disturbance strength index is 2.

3.3.5. Hard Roof Activity Strength. The fracture of hard roof is another key factor to induce high energy shock. But the disturbance effect of hard roof is the result of three indexes including the distance between hard rock and coal seam. The thickness of hard rock and the compressive strength of hard rock. The disturbance intensity index caused by the comprehensive effects of the three indexes is shown in Table 1.

3.3.6. Goaf Filling Degree. After the working face is mined, the roof caving above the gob with different conditions will occur to different degrees. The disturbance strength exerted on the static structure of coal-rock based on different degrees of caving is bound to be different. The filling degree of gob after roof caving is divided into four categories: complete filling, basic filling, few filling, and basically no filling; the corresponding coal-rock disturbance strength index is 1, 2, 3, and 4, respectively.

Based on the above shock-type stress release coal-gas outburst disturbance strength index and index determination, the disturbance strength index evaluation result *Dis* is shown in

$$Dis = \frac{D_1 + D_2 + L + D_m}{m}, \tag{4}$$

where D_1, D_2, and D_n are the indexes of m indicators for disturbance intensity evaluation.

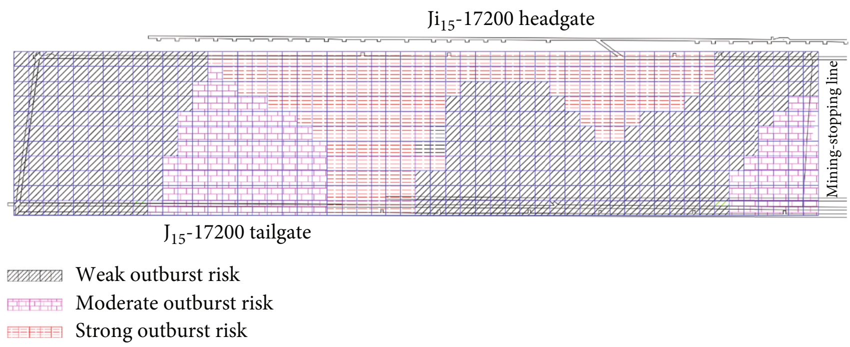

Figure 3: The classification prediction result of coal and gas outburst risk of the Ji_{15}-17200 working face.

3.4. Prediction Criterion. According to the above analysis results, the static structural stability of coal-rock, the strength of gas parameters, and the strength of coal-rock disturbance in a certain area of working face can be dynamically evaluated; the superposition of the three evaluation results can constitute the danger evaluation index ODI of shock-type stress release coal-gas outburst, namely:

$$ODI = Sta + Gas + Dis. \tag{5}$$

The criteria for classification of prominent risk levels are defined as follows: when ODI is <2.8, for no outstanding danger; when $2.8 \leq \text{ODI} < 5.0$, for weak outburst danger; when $5.0 \leq \text{ODI} < 7.2$, for moderate outburst danger; when $7.2 \leq \text{ODI}$, for strong protruding danger.

Shock-type stress release coal-gas outburst danger classification prediction process is as follows:

(1) The prediction area is divided into 5 m, 10 m, or 20 m grid cells as required

(2) According to the actual situation, the coal-rock static structure stability index, gas parameter strength index, and disturbance strength index are filled in each grid unit

(3) The *Sta* index, *Gas* index, and *Dis* index in each grid cell were calculated, and then the shock-type stress release coal-gas outburst danger index ODI was calculated

(4) Classification of outburst hazards based on calculation results, complete classification prediction of coal-gas outburst

4. Engineering Application and Its Validation

4.1. Basic Information of Coal Face. The No.12 coal mine of Pingmei company is a typical coal and gas outburst mine in Henan, China, which is south adjacent gob of the working face Ji_{15}-17200, untapped areas in the north, east adjacent to downhill, west adjacent well field boundary. The ground elevation of the working face is +170~+220 m, elevation of working face -483 m~-574 m. The average dip angle is 19°, the inclination length is 225.3 m, the strike length 762.5 m, the coal seam thickness 2.2~3.7 m, the gas content 15.256 m^3/t, the gas pressure 1.5 MPa, the relative gas emission 7.8~11.9 m^3/t, and the absolute gas emission rate 4.47~8.8 m^3/min. Siltstone with thickness of 2.45~4.11 m and 0.76~1.95 m at direct top and bottom, respectively, the basic roof is medium sandstone with a thickness of 11.51~16.82 m, the basic bottom is 7.83~11.52 m flour fine sandstone. A total of 7 typical faults were exposed in the tunneling process of transportation and return air along the working face; faults are FD35 ($H = 0 \sim 8$ m), FD36 ($H = 0 \sim 10$ m), LF10 ($H = 1.1$ m), LF11 ($H = 2.5$ m), LF12 ($H = 3.0$ m), LF13 ($H = 1.9$ m), and LF14 ($H = 2.6$ m).

4.2. Prediction Results and Its Analysis. Based on the above prediction method of coal-gas outburst disaster, combined with the actual geological condition of the Ji_{15}-17200 working face in the No.12 coal mine in Pingmei company. And the risk of coal and gas outburst during the working face mining is classified and predicted. Firstly, the Ji_{15}-17200 working face was divided into a square grid with a side length of 20 m. Secondly, the parameter data from each grid was collected on site. Thirdly, the static structural stability index of coal-rock in each grid was calculated, respectively, as gas parameter strength index and disturbance strength index. Then the coal-gas outburst danger index of each grid was calculated according to the prediction criterion. Because of the large amount of data, only some grid data are enumerated in the calculation process, as shown in Tables 2–5. In Table 2, $S_1 \sim S_6$ represent the indexes which affect the static structure of coal-rock, respectively, which are coal seam mining depth, maximum principal stress, stress concentration coefficient, coal seam impact tendency, geological structure strength degree, and coal thickness change degree. In Table 3, $G_1 \sim G_4$ represents gas pressure, gas content, absolute gas emission rate, and initial velocity of gas release. In Table 4, $D_1 \sim D_6$ represent the indexes that affect the disturbance strength of coal-rock, respectively, which are the thickness of coal seam once stopping, degree of fault activation, mining speed, remaining coal pillar, hard roof, and filling degree of gob. Figure 3 is the classification prediction results of coal-gas outburst danger in the Ji_{15}-17200 working face of No.12 coal mine in Pingmei company. Comparing the prediction results with coal-gas outburst in actual mining, serious crown drill occurred when mining to strong outburst danger area during mining of the Ji_{15}-17200 working face, and drill cuttings increased significantly compared with other areas. The possibility of coal-gas outbursts has greatly increased. It shows that the prediction result has a certain accuracy, and it can be used for field practical applications.

5. Conclusions

Based on the principle of coal-gas outburst occurrence, a new prediction method of coal-gas outburst disaster was developed and has been applied on the No.12 coal mine in Pingmei company, China. The actual application effects were well. The main conclusions are as follows:

(1) The principle of shock-type coal-gas outburst disaster was expounded. It was considered that the prediction of shock-type coal-gas outburst disasters should be considered from three aspects: static structure of coal-rock, gas parametric strength, and disturbance strength.

(2) The prediction of shock-type coal-gas outburst was divided into three aspects: static structure evaluation of coal-rock, gas parameter strength evaluation, and disturbance strength evaluation. The corresponding evaluation criteria were constructed, respectively. Finally, the prediction criterion of shock-type stress release coal-gas outburst was proposed

(3) Based on the shock-type coal-gas outburst prediction method, the actual prediction was carried out in the Ji_{15}–17200 working face of the No.12 coal mine in Pingmei company, China. The prediction results were verified and analyzed; the results show that the prediction method has good accuracy and can be popularized and applied

Data Availability

The data used to support the findings of this study are available from the corresponding author upon request.

Conflicts of Interest

The authors declare that they have no conflicts of interest.

Acknowledgments

The study of this paper is support by the Natural Science Foundation of Inner Mongolia Autonomous Region (2019LH05005) and the Innovation Foundation of Inner Mongolia University of Science and Technology (2019QDL-B32).

References

[1] C. Zhang, J. Xu, G. Yin, S. Peng, Q. Li, and Y. Chen, "A novel large-scale multifunctional apparatus to study the disaster dynamics and gas flow mechanism in coal mines," *Rock Mechanics and Rock Engineering*, vol. 52, no. 8, pp. 2889–2898, 2019.

[2] A. E. Hatem, M. L. Cooke, and K. Toeneboehn, "Strain localization and evolving kinematic efficiency of initiating strike- slip faults within wet kaolin experiments," *Journal of Structural Geology*, vol. 101, pp. 96–108, 2017.

[3] P. Lyu, F. Ma, and X. Bao, "Experimental study on pore microstructure and methane occurrence characteristics of shale of marine-continent transition phase," *Fresenius Environmental Bulletin*, vol. 30, no. 1, pp. 330–337, 2021.

[4] R. S. Michael and J. Thomas, "Fault induced rock bursts and micro-tremors - experiences from the Gotthard base tunnel," *Tunnelling and Underground Space Technology*, vol. 81, pp. 358–366, 2018.

[5] B. Orlic and B. B. T. Wassing, "A study of stress change and fault slip in producing gas reservoirs overlain by elastic and viscoelastic caprocks," *Rock Mechanics and Rock Engineering*, vol. 46, no. 3, pp. 421–435, 2013.

[6] C. C. Xue, A. Y. Cao, W. H. Guo et al., "Mechanism and energy evolution characteristics of coal burst in mining thick, deep, and large inclined coal seams: a case study from a Chinese coal mine," *Geofluids*, vol. 2022, Article ID 7704226, 18 pages, 2022.

[7] P. F. Lyu and X. K. Cui, "Mechanism of vibration energy action on dynamic instability of shock-type rockburst carrier system," *Shock and vibration*, vol. 2020, Article ID 6663269, 10 pages, 2020.

[8] A. Y. Cao, L. M. Dou, C. B. Wang, X. X. Yao, J. Y. Dong, and Y. Gu, "Microseismic precursory characteristics of rock burst hazard in mining areas near a large residual coal pillar: a case study from Xuzhuang coal mine, Xuzhou, China," *Rock Mechanics and Rock Engineering*, vol. 49, no. 11, pp. 4407–4422, 2016.

[9] A. Sainoki and H. S. Mitri, "Dynamic modelling of fault slip induced by stress waves due to stope production blasts," *Rock Mechanics and Rock Engineering*, vol. 49, no. 1, pp. 165–181, 2016.

[10] Z. H. Zhi-Kang, W. A. Lian-Guo, and D. A. Ren-Liang, "Support technology of high resistant and yielding property for deep roadway under dynamic pressure," *Journal of Mining and Safety Engineering*, vol. 29, no. 1, pp. 33–37, 2012.

[11] L. Zhang, M. Q. Huang, J. H. Xue, M. X. Li, and J. H. Li, "Repetitive mining stress and pore pressure effects on permeability and pore pressure sensitivity of bituminous coal," *Natural Resources Research*, vol. 30, no. 6, pp. 4457–4476, 2021.

[12] L. Zhang, M. Q. Huang, M. X. Li et al., "Experimental study on evolution of fracture network and permeability characteristics of bituminous coal under repeated mining effect," *Natural Resources Research*, vol. 31, no. 1, pp. 463–486, 2022.

[13] L. Zhang, J. H. Li, J. H. Xue, C. Zhang, and X. Q. Fang, "Experimental studies on the changing characteristics of the gas flow capacity on bituminous coal in CO_2-ECBM and N_2-ECBM," *Fuel*, vol. 291, article 120115, 2021.

[14] D. Tuncay, I. B. Tulu, and T. Klemetti, "Investigating different methods used for approximating pillar loads in longwall coal mines," *Inernational Journal of Mining Sciences and Technology*, vol. 31, no. 1, pp. 23–32, 2021.

[15] W. T. Hou, H. P. Wang, L. Yuan, W. Wang, Y. Xue, and Z. W. Ma, "Experimental research into the effect of gas pressure, particle size and nozzle area on initial gas-release energy during gas desorption," *International Journal of Mining Science and Technology*, vol. 31, no. 2, pp. 253–263, 2021.

[16] P. F. Lyu, J. B. Lu, E. Y. Wang, and X. H. Chen, "The mechanical criterion of activation and instability of normal fault induced by the movement of key stratum and its disaster-causing mechanism of rockburst in the hanging wall mining," *Advances in Civil Engineering*, vol. 2021, Article ID 6618957, 11 pages, 2021.

[17] A. Manouchehrian and M. Cai, "Numerical modeling of rockburst near fault zones in deep tunnels," *Tunnelling and Underground Space Technology*, vol. 80, pp. 164–180, 2018.

[18] P. F. Lyu, X. H. Chen, G. B. Chen, and L. Qiu, "Experimental study on dynamic mechanical responses of coal specimens under the combined dynamic-static loading," *Arabian Journal of Geosciences*, vol. 13, no. 18, article 935, 2020.

[19] K. Ma, F. Z. Yuan, D. Y. Zhuang, Q. S. Li, and Z. W. Wang, "Study on rules of fault stress variation based on microseismic monitoring and numerical simulation at the working face in the Dongjiahe Coal Mine," *Shock and Vibration*, vol. 2019, Article ID 7042934, 12 pages, 2019.

[20] Y. Y. Di and E. Y. Wang, "Rock burst precursor electromagnetic radiation signal recognition method and early warning application based on recurrent neural networks," *Rock Mechanics and Rock Engineering*, vol. 54, no. 3, pp. 1449–1461, 2021.

[21] R. D. Lama and J. Bodziony, "Management of outburst in underground coal mines," *International Journal of Coal Geology*, vol. 35, no. 1-4, pp. 83–115, 1998.

[22] T. Cyrul, "A concept of prediction of rock and gas outbursts," *Geotechnical and Geological Engineering*, vol. 10, no. 1, pp. 1–17, 1992.

[23] J. Y. Zhang, Z. B. Ai, L. W. Guo, and X. Cui, "Research of synergy warning system for gas outburst based on entropy-weight Bayesian," *International Journal of Computational Intelligence systems*, vol. 14, no. 1, pp. 367–385, 2021.

[24] J. R. Fan, C. C. An, X. Y. Zhang, X. Li, and J. J. Tan, "Hazard assessment of glacial lake outburst floods in Southeast Tibet based on RS and GIS technologies," *International Journal of Remote Sensing*, vol. 40, no. 13, pp. 4955–4979, 2019.

[25] T. X. Wen, F. E. Yu, and L. S. Shao, "Probabilistic neural network prediction model of coal and gas outburst based on grey relational entropy," *Application Research of Computers*, vol. 35, no. 11, pp. 3326–3329, 2018.

[26] X. Wang, T. J. Chen, and H. Xu, "Thickness distribution prediction for tectonically deformed coal with a deep belief network: a case study," *Energies*, vol. 13, no. 5, p. 1169, 2020.

[27] W. H. Song and H. W. Zhang, "Visualization research on regional prediction of coal and gas outburst based on GIS," *Journal of Liaoning Technical University*, vol. 27, no. 33, pp. 337–339, 2008.

[28] J. X. Kou and W. H. Song, "Secondary prediction of working face dynamic disasters based on relational grade analysis," *Safety in Coal Mines*, vol. 45, no. 12, pp. 223–226, 2014.

[29] C. L. Zhang, E. Y. Wang, J. Xu, and S. J. Peng, "Research on temperature variation during coal and gas outbursts: implications for outburst prediction in coal mines," *Sensors*, vol. 20, no. 19, p. 5526, 2020.

[30] C. L. Zhang, E. Y. Wang, J. Xu, and S. J. Peng, "A new method for coal and gas outburst prediction and prevention based on the fragmentation of ejected coal," *Fuel*, vol. 287, article 119493, 2021.

[31] C. L. Zhang, E. Y. Wang, J. Xu, and S. J. Peng, "Experimental investigation on mechanics and seepage characteristics of tectonic and intact coal containing gas," *Applied Sciences Basel*, vol. 10, no. 20, p. 7290, 2020.

[32] Y. B. Liu, H. T. Sun, B. Wang, L. C. Dai, and J. Cao, "Experimental accuracy and stability of gas outburst experimental system," *Geofluids*, vol. 2021, Article ID 6678608, 9 pages, 2021.

[33] L. M. Dou, X. Q. He, T. Ren, J. He, and Z. Y. Wang, "Mechanism of coal-gas dynamic disasters caused by the superposition of static and dynamic loads and its control technology," *Journal of China University of Mining & Technology*, vol. 47, no. 1, pp. 48–59, 2018.

[34] B. Zhou, J. Xu, S. J. Peng et al., "Effects of geo-stress on the dynamic response of multi-physical field parameters during coal and gas outbursts under true triaxial stress," *International Journal of Rock Mechanics and Mining Sciences*, vol. 142, article 104759, 2021.

[35] C. J. Fan, H. O. Wen, S. Li, G. Bai, and L. J. Zhou, "Coal seam gas extraction by integrated drillings and punchings from the floor roadway considering hydraulic-mechanical coupling effect," *Geofluids*, vol. 2022, Article ID 5198227, 10 pages, 2022.

[36] P. F. Lyu, X. Y. Bao, G. Lyu, and X. H. Chen, "Research on fault activation law in deep mining face and mechanism of rockburst induced by fault activation," *Advances in Civil Engineering*, vol. 2020, Article ID 8854467, 13 pages, 2020.

Hindawi
Geofluids
Volume 2023, Article ID 8938807, 17 pages
https://doi.org/10.1155/2023/8938807

Research Article

Research on Stability Control Technology of Mining Roadway Based on Energy Transformation

Guohua Zhang, Yanwei Duan, and Tao Qin

Key Laboratory of Mining Engineering of Heilongjiang Province College, Heilongjiang University of Science and Technology, Harbin 150022, China

Correspondence should be addressed to Yanwei Duan; 1354070597@qq.com

Received 26 November 2021; Revised 22 April 2022; Accepted 13 June 2022; Published 19 January 2023

Academic Editor: Zhijie Wen

The process of roadway surrounding rock deformation and instability is always accompanied by energy changes, and the energy transformation of surrounding rock directly drives its deformation and failure. In order to realize the stability control of mining roadway, the distribution of elastic strain energy and plastic strain energy of surrounding rock was analyzed by using FLAC^{3D} numerical simulation software on the basis of the energy transformation law of sandstone under different confining pressures revealed by indoor triaxial compression test. Based on this, combined with the energy transformation, the principle of roadway surrounding rock stability control technology is proposed. One is to reduce the elastic strain energy of surrounding rock, that is, by increasing the extension of support body, part of the roadway energy is transferred to the support body, so as to improve the energy release of surrounding rock, or by optimizing the layout of roadway to reduce the energy accumulation of surrounding rock. The second is to increase the plastic strain energy of surrounding rock, that is, to increase the energy dissipation of surrounding rock by setting weak structure. The above research results are applied to the surrounding rock control of the right second transport roadway in the 91st coal of Xinjian coal mine. After the optimization of support measures, the roadway surface displacement and its increase rate decreased significantly, roof subsidence decreased from 247 mm to 62 mm, floor heave decreased from 120 mm to 26 mm, and the right rib shrinkage decreased from 292 mm to 94 mm, that is, the floor heave control effect was particularly obvious. The deformation of surrounding rock gradually stabilized after 45 days.

1. Introduction

The rapid development of China's economy is inseparable from energy. Coal accounts for about 70% of the primary energy consumption structure. Therefore, the safe production of coal mines is of great significance to economic development [1–3] in coal mine safety accidents, the accidents caused by deformation and instability of surrounding rock account for a large proportion [3]. Ensuring the stability of surrounding rock is the premise of coal mine production. In the study of surrounding rock stability, scholars often analyzed the surrounding rock stability from the perspective of mechanics, but the complex geological conditions (large buried depth, faults, soft rock, etc.) often made the mechanical analysis process become complicated [4–8]. In fact, the deformation and failure process of surrounding rock is a process with energy changes from local deformation to overall damage and finally failure. Due to energy accumulation caused by roadway excavation, the energy may be higher than its energy storage limit, which causes deformation of the surrounding rock, and this part of energy will be released concentratedly, resulting in the failure of the surrounding rock. Energy change is the external performance of material physical change, and the great change will cause material damage. Therefore, energy transformation directly drives deformation and failure of surrounding rock, from the perspective of energy interpretation of surrounding rock can reflect its essence [9–11].

For the study of surrounding rock stability related to energy, scholars have done a lot of research from laboratory experiments and numerical simulation. On the one hand, laboratory experiments are mainly conducted to explore the characteristics and laws of rock energy evolution through rock mechanics experiments under different stress paths. From the perspective of energy, Xu et al. [12] analyzed the deformation and damage process of sandstone under the action of circulating pore water pressure, and discussed the evolution law of energy absorption and release in this process. Zhao et al. [13] carried out three confining pressure unloading tests under different unloading paths to study the energy evolution characteristics and evolution rate of rock under unloading conditions. By carrying out triaxial cyclic loading and unloading experiments, Yang et al. [14] discussed the energy evolution characteristics of postpeak stress drop stage and postpeak residual stress stage. Liu et al. [15] studied the energy evolution law and linear storage law of red sandstone in the creep process by conducting uniaxial graded creep test and uniaxial cyclic loading and unloading test after creep. Meng et al. [16] carried out triaxial cyclic loading and unloading tests of limestone under six kinds of confining pressures, revealing the confining pressure effect of energy evolution process and distribution law of loaded rock samples.

On the other hand, the numerical simulation mainly carries out the energy characteristics of surrounding rock under different working conditions. Hao et al. [17] used FLAC^{3D} to simulate the advance process of working face, analyzed the morphological characteristics and energy distribution characteristics of roadway plastic area within 100 m of the front working face when the advance was 400 m, and revealed the relationship between the morphological distribution and energy of roadway plastic area. By using discrete element simulation software PFC, Yu et al. [18] analyzed the energy and dynamic acoustic emission evolution law of roadway excavation, and discussed the influence of different vertical stresses and lateral pressure coefficients on roadway excavation energy evolution. Shi et al. [19] used FLAC^{3D} to simulate the process of working face, analyzed the energy evolution and release law of surrounding rock in stope, and pointed out that the roof and the front of coal wall were the key areas of energy accumulation or release. Wang et al. [20] used FLAC^{3D} simulation software to analyze the evolution law of elastic energy of the roof, two ribs and driving face under different driving speeds, which was used as the basis for establishing the evolution mechanism of rock burst energy zoning. Huang et al. [21] used FLAC^{3D} to simulate the stress distribution before and after filling gangue in goaf, and then obtained the distribution of elastic strain energy before and after filling. Ma et al. [22] used UDEC to analyze the energy evolution law of roadway surrounding rock under roof of different thickness, and optimized roadway support parameters according to the simulation results, effectively solving the problem of large deformation of roadway.

Based on the analysis of the above studies, the study of surrounding rock stability related to energy mainly focuses on the laboratory study of rock energy evolution law and the numerical simulation study of surrounding rock energy characteristics, while the study of roadway surrounding rock stability control based on energy characteristics is relatively insufficient. In this paper, the mining roadway of Xinjian coal mine is taken as the engineering background. Triaxial compression tests were carried out in the laboratory to reveal the energy evolution law of sandstone under different confining pressures. FLAC^{3D} numerical simulation software was used to analyze the distribution law of elastic strain energy and plastic strain energy of roadway surrounding rock. Based on this, combined with the energy transfromation, the principle of roadway surrounding rock stability control technology is proposed. The monitoring results showed that the roadway surface displacement and its increasing speed decreased obviously after the optimization of support measures, which effectively solved the roadway control problem and provided reference for roadway surrounding rock stability control under similar conditions.

2. Energy Evolution Characteristics of Rock Deformation and Failure Process

2.1. Test Scheme. In order to obtain the characteristics of energy evolution during the deformation and failure of the rock specimens, the conventional triaxial loading test was conducted on the sandstone samples from Xinjian Coal Mine in Qitaihe in China with TOP INDUSTRIE Rock 600-50 automatic servo rock rheometer (see Figure 1). The rock specimen was a standard cylinder (50 mm in diameter and 100 mm in height). Axial pressure was applied at a rate of 0.1 mm/min and confining pressure was applied at a rate of 0.05 MPa/s. The predetermined confining pressure was 5 MPa, 10 MPa, 15 MPa, and 20 MPa.

2.2. Energy Calculation Method Based on Test Data. The loading process of the rock specimens is always accompanied by the storage and dissipation of energy. Both of the variables representing the energy storage and dissipation inside rock are elastic energy and dissipated energy. In the experiment, these two variables cannot be recorded in real time. Therefore, they are calculated through stress-strain curves that are easily accessible. Figure 2 shows the calculation method. The shaded area denotes the elastic strain energy (U^{e}) stored by the deformation of the rock specimens, and E^{u} denotes the unloading modulus of the rock specimens. The dissipated energy (U^{d}) is the area constrained by the unloading modulus, the stress-strain curve and the horizontal axis.

According to the first law of thermodinamics, supposing the experiment system is a closed system ignoring the thermal energy dissipation in the experiment, the total energy U generated by the work done by external force is [23–27]

$$U = U^e + U^d = \int \sigma_1 \mathrm{d}\varepsilon_1 = \sum_{i=0}^{n} \frac{1}{2} \left(\varepsilon_{1i+1} - \varepsilon_{1i}\right)\left(\sigma_{1i} + \sigma_{1i+1}\right), \quad (1)$$

where U^{e} is elastic strain energy, U^{d} is dissipated energy and $\sigma_{1\mathrm{i}}$, $\varepsilon_{1\mathrm{i}}$, $\sigma_{3\mathrm{i}}$, and $\varepsilon_{3\mathrm{i}}$ are axial stress, axial strain, circumferential stress, and circumferential strain, respectively.

Figure 1: TOP INDUSTRIE Rock 600-50 automatic servo rock rheometer.

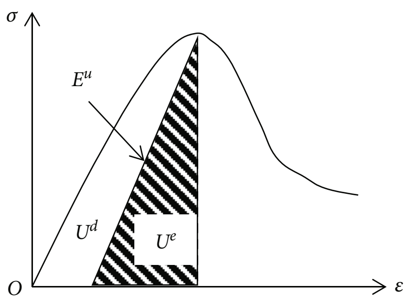

Figure 2: Energy calculation method.

The expression of triaxial compression elastic energy is

$$U^{\mathrm{e}} = \frac{1}{2E_u}\left[\sigma_1{}^2 + 2\sigma_3{}^2 - 2\mu(2\sigma_1\sigma_3 + \sigma_2\sigma_3)\right], \tag{2}$$

where E_{u} is unloading modulus and μ is about 50% ~60% of the peak strength [28–30].

2.3. Characteristic Law of Rock Energy Evolution. It is assumed that the loading system is a closed system with no heat exchange with the external environment. In the loading system, external load input mechanical energy is absorbed by rock specimens, the rock specimens elastic deformation occur in the form of elastic strain energy stored within rock specimens. As the load goes on, the elastic strain energy stored by the rock specimens become less and less, and the energy absorbed at this time is mainly used to produce microcracks inside the rock specimens, namely, the part of energy is dissipated. In order to compare and analyze the law of energy evolution corresponding to different stages of stress-strain curves, axial strain is used as the horizontal axis, axial stress as the left axis, and energy density as the right axis. The energy evolution curves of the conventional triaxial compression test sandstone under different confining pressures are shown in Figure 3.

It can be seen that the energy evolution process can be divided into prepeak stage and postpeak stage according to the stress-strain curve in Figure 3 and that different energy evolution curves under different confining pressures have similar characteristics.

(1) As axial strain increases, total energy U increased exponentially before the axial stress peak and the growth rate decreased slightly after the stress peak. The growth rate is correlated with the properties of stress and strain. The maximum of U varied under different confining pressures. It increased with the increase of confining pressure

(2) Elastic strain energy U^e indicates the releasable energy stored in the rock specimens, the evolution law is consistent with the stress-strain curve. In the prepeak stage, the difference between U^e and U was not great. After reaching the peak, U^e dropped rapidly. Also, the difference increased as the axial strain increased. The law of U^e is consistent with the stress-strain curve, which is positively associated with the confining pressure

(3) Dissipated energy U^d indicates the energy consumed by the rock specimens during plastic deformation, crack expansion and energy release, which is irreversible. The evolution trend of U^d was slow growth before the peak but rapid growth after the peak. It grew almost exponentially and quickly became a major component of energy. The maximum of U^d varied under different confining pressures and increased with the increase in confining pressure. After the peak, the growth rate of U^d also increased slightly with the increase in confining pressure

To study the transformation of the energy in different stages, the corresponding energy characteristics of each stage are drawn in the bar graphs, and Figure 4 shows the energy distribution characteristics of different stages.

As can be seen in Figure 4(a), the energy absorbed in the prepeak stage was mainly converted to elastic strain energy, accounting for about 72% ~80% of the total energy, while dissipated energy remained 18% to 20%. As confining pressure increased, the amount of the stored elastic strain energy became larger. The elastic strain energy was 464 kJ·m^{-3} when confining pressure was 5 MPa, and when the confining pressure increased to 20 MPa, the elastic strain energy was 1102.6 kJ·m^{-3}, with an apparent confining pressure effect. At this stage, the elastic strain energy generated by rock specimen's deformation can be continuously stored, while energy is consumed for the closure of cracks inside the rock specimens and the initiation and propagation of microcracks. As can be seen From Figure 4(b), the vast majority of the energy absorbed in the postpeak stage was transferred to dissipated energy, accounting for about 87% of the total energy. As the confining pressure increased, dissipated energy also increased. When confining pressure was 5 MPa, dissipated energy was 787 kJ·m^{-3}. When confining pressure

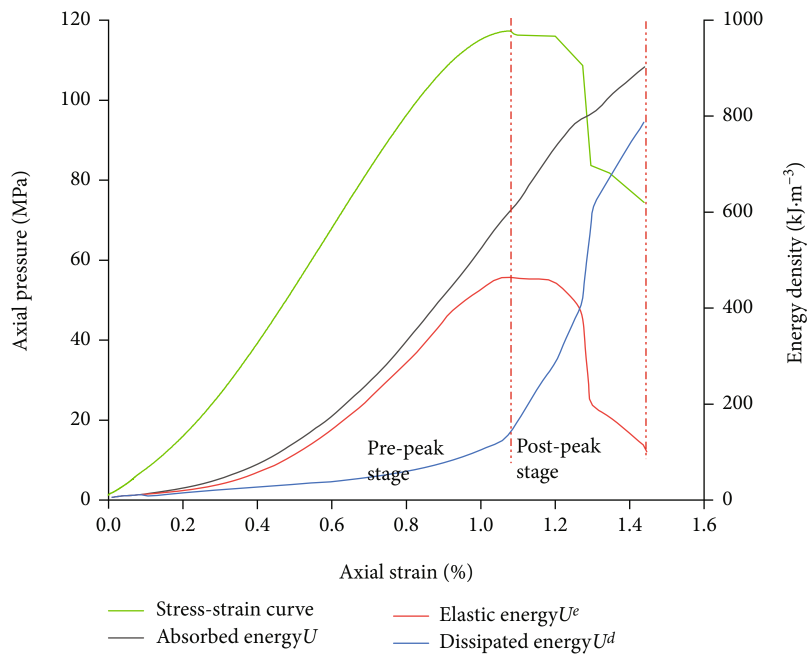

(a)

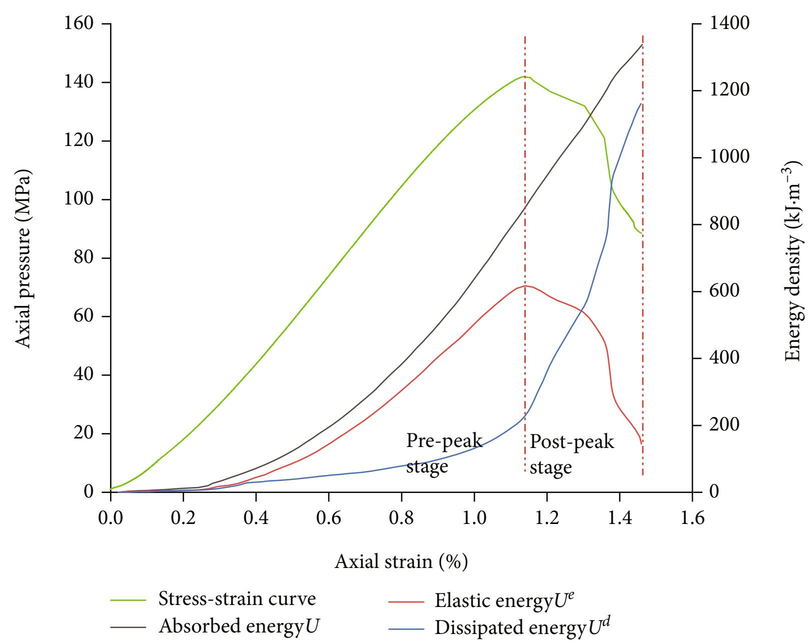

(b)

Figure 3: Continued.

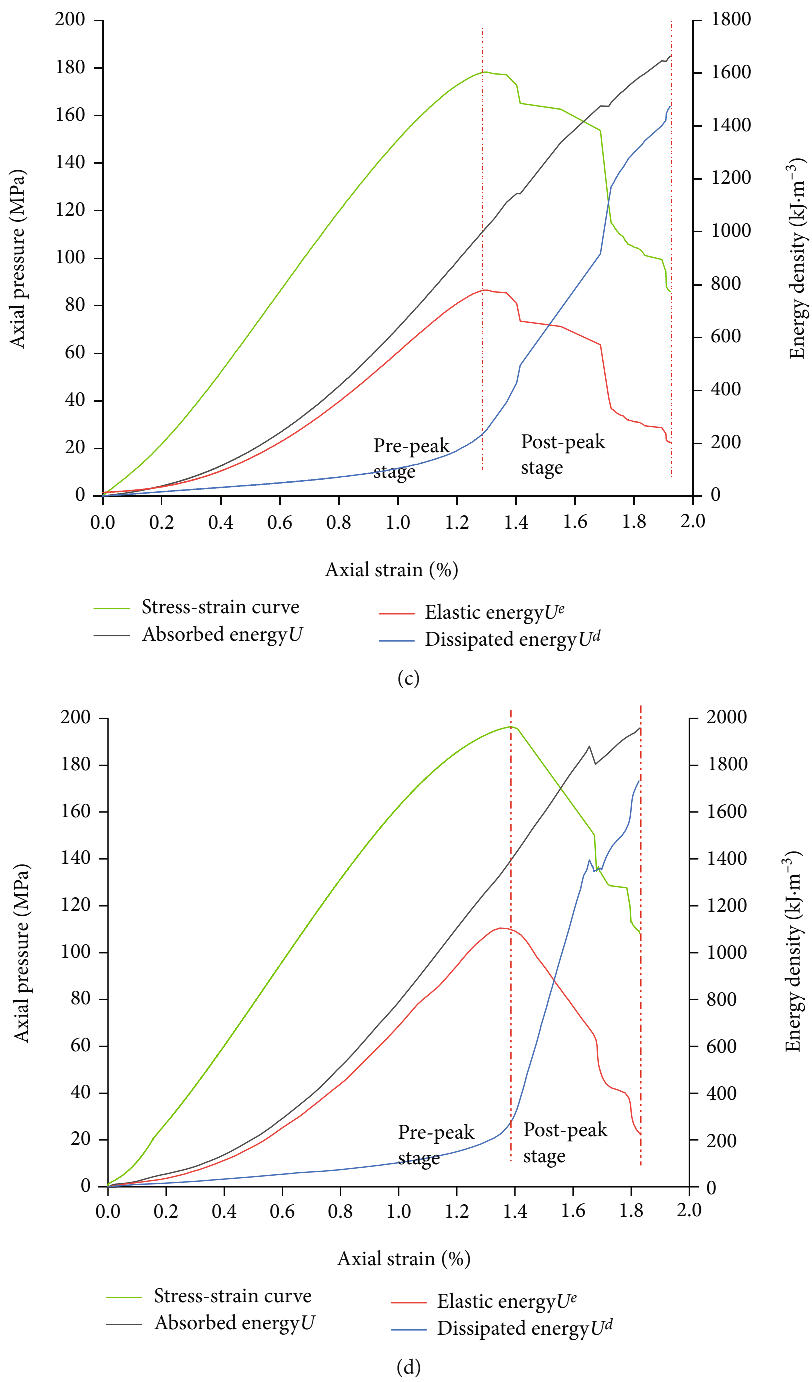

FIGURE 3: Energy evolution curve of sandstone under different confining pressure. (a) Confining pressure 5 MPa. (b) Confining pressure 10 MPa. (c) Confining pressure 15 MPa. (d) Confining pressure 20 MPa.

increased to 20 MPa, elastic strain energy was 1733 kJ·m^{-3}. Elastic strain energy only accounted for a very small proportion. In this stage, a large number of macroscopic cracks form in the rock specimens and the total energy is mainly used for the formation and penetration of the macroscopic cracks. However, due to the existence of confining pressure, the rock specimens have certain residual strength, so a small amount of elastic strain energy can still be stored.

3. Energy Transformation of Roadway Surrounding Rock Numerical Simulation Method and Its Implementation

3.1. Energy Model of Roadway Surrounding Rock. Figure 5 shows the mechanical model diagram of the roadway surrounding rock. Figure 5(a) is the schematic diagram of the roadway excavation, Q_1 represents the underground space; Q_2 represents roadway surrounding rock; and Q_3 is

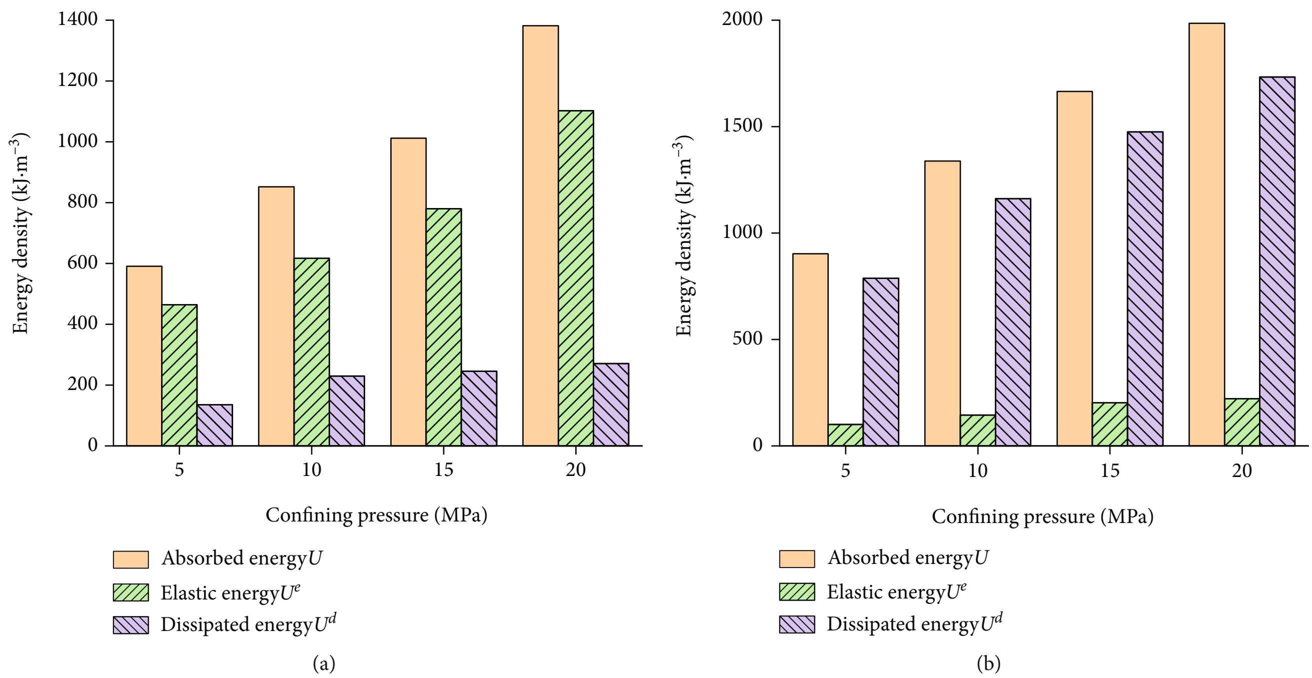

Figure 4: Energy distribution characteristics at different stages. (a) Prepeak stage. (b) Postpeak stage.

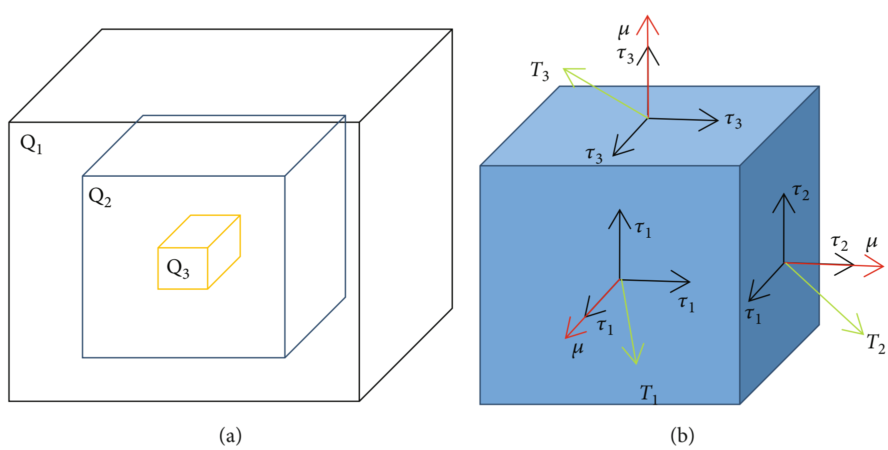

Figure 5: Mechanical model of roadway surrounding rock. (a) Schematic diagram of roadway surrounding rock. (b) The stress state of any point of surrounding rock.

roadway. The stress state of arbitrary point of surrounding rock is shown in Figure 5(b), which is represented by the stress component of the three orthogonal faces of the unit body. T_i indicates the stress component on arbitrary side. τ_{ij} is the stress state of the surface, μ_j is the normal unit vector of the surface, and the relationships among the three satisfies $T_i = \mu_j \tau_{ij}\ (i, j = 1, 2, 3)$.

Supposing the stable state before the roadway excavation is State I, and the stable state of the roadway surrounding rock after the stress adjustment is State II. The energy transformation process of roadway surrounding rock from State I to State II is shown in Figure 6. Energy input consists of two parts. One part is the work done by underground space Q_1 on surrounding rock Q_2, which is called the external force work. The other part is the work done by physical strength in the unit body of surrounding rock Q_2, which is called internal work. Energy accumulation consists of elastic strain energy, and the main source is the difference between the elastic strain energy before and after the excavation, namely, the difference between U_{I} and U_{II}. Energy dissipation consists of two parts. The first part is elastic strain energy U_{m} stored in the excavated part of roadway surrounding rock Q_2 and the second part is the plastic energy generated by the plastic deformation of surrounding rock.

3.2. The Energy Model in FLAC^{3D}. In FLAC^{3D} the elastic strain energy and the dissipated plastic energy of the

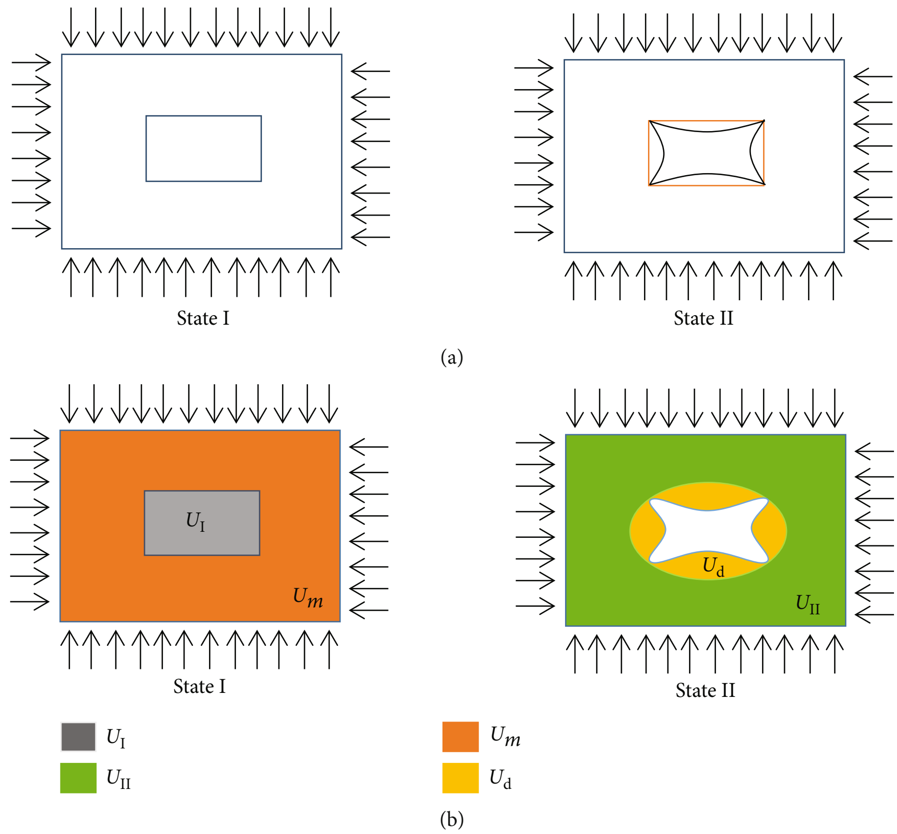

FIGURE 6: Schematic diagram of surrounding rock energy evolution. (a) Schematic diagram of energy input. (b) Schematic diagram of energy accumulation and dissipation.

unit body containing mechanical model can be calculated. The whole process is solved incrementally: the motion equation of grid points and the stress strain of the region are solved in each time step. In the process where the system reaches equilibrium, the increment of the energy component can be determined by the stress-strain equation [31–33]. Elastic strain energy W_e of the unit body can be expressed as

$$W_e = \frac{V}{2}\left(\frac{\sigma_{ij}^{d}\sigma_{ij}^{d}}{2G} + \frac{\bar{\sigma}}{K}\right), \tag{3}$$

where V is volume, $\sigma d\,ij$ is partial stress, $\bar{\sigma}$ is mean stress, and G and K are bulk modulus and shear modulus, respectively.

Elastic strain energy increment ΔW_e is the difference between the elastic energy in successive time steps, which can be divided into shear elastic energy increment ΔW_{es} and volume elastic energy increment ΔW_{ev}. The expression is as follows:

$$\Delta W_e = W_e{}' - W_e = \Delta W_{\mathrm{es}} + \Delta W_{\mathrm{ev}}. \tag{4}$$

Total shear strain energy increment ΔW_{Ts} and total volume strain energy increment ΔW_{Tb} can be obtained through average stress, respectively

$$\begin{aligned} \Delta W_{Ts} &= \frac{V}{2}\left[\left(\sigma_{ii} + \sigma_{ii}'\right)e_{ii} + 2\left(\sigma_{ij} + \sigma_{ij}'\right)e_{ij}\right], \\ \Delta W_{Tv} &= \frac{3V}{2}\left(\bar{\sigma} + \bar{\sigma}'\right)\bar{e}. \end{aligned} \tag{5}$$

Plastic strain energy increment ΔW_p can be divided into shear plastic energy increment ΔW_{ps} and volume plastic energy increment ΔW_p, which is the difference between total strain energy and elastic strain energy. The expression is shown as follows:

$$\Delta W_p = \Delta W_{\mathrm{ps}} + \Delta W_{\mathrm{pv}} = (\Delta W_{\mathrm{Ts}} - \Delta W_{\mathrm{es}}) + (\Delta W_{\mathrm{Tv}} - \Delta W_{\mathrm{ev}}). \tag{6}$$

The above energy formula is edited and transferred in the fish language built in FLAC^{3D} so as to obtain such energy evolution characteristics of roadway surrounding rock as elastic strain energy and plastic strain energy.

3.3. Case of Study. Take the left fourth coal ventilation roadway in the 93rd coal of Xinjian coal mine as an example. A

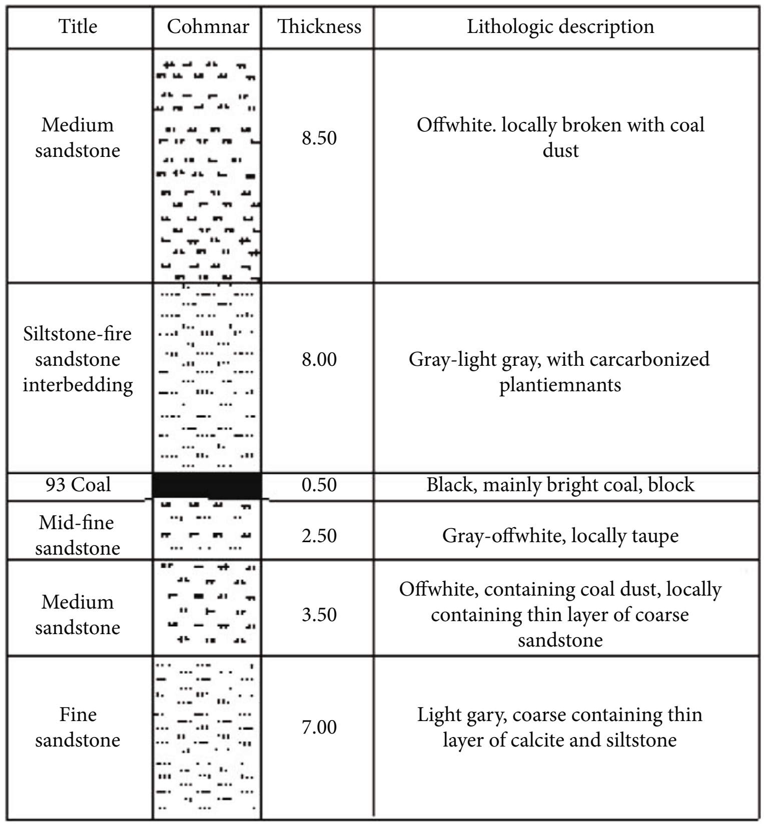

Title	Cohmnar	Thickness	Lithologic description
Medium sandstone		8.50	Offwhite. locally broken with coal dust
Siltstone-fire sandstone interbedding		8.00	Gray-light gray, with carcarbonized plantiemnants
93 Coal		0.50	Black, mainly bright coal, block
Mid-fine sandstone		2.50	Gray-offwhite, locally taupe
Medium sandstone		3.50	Offwhite, containing coal dust, locally containing thin layer of coarse sandstone
Fine sandstone		7.00	Light gary, coarse containing thin layer of calcite and siltstone

Figure 7: Histogram of coal strata.

calculation model is established. In order to ensure the accuracy of the model, the stratigraphic parameters are appropriately simplified. The histogram of each stratum is shown in Figure 7. The left fourth coal ventilation roadway is a rectangular roadway which is 3 m in width and 2 m in hight. The dimensions of the model are

$x \times y \times z = 35\,\text{m} \times 20\,\text{m} \times 30\,\text{m}$. The x-axis direction is trend, the y-axis direction is inclination, and the z-axis direction is gravity. There are 57576 nodes and 52400 unit bodies.

The constitutive relationship of the model adopts Mohr-Coulomb criterion. Displacement constraints are made on the four sides and bottom surface of the model. According to the stress test report and other data, $\sigma_z = 10.34$ MPa and $\sigma_x = 12.36$ MPa are applied to the model. Model schematic and boundary conditions is shown in Figure 8. The mechanical parameters of surrounding rock are shown in Table 1.

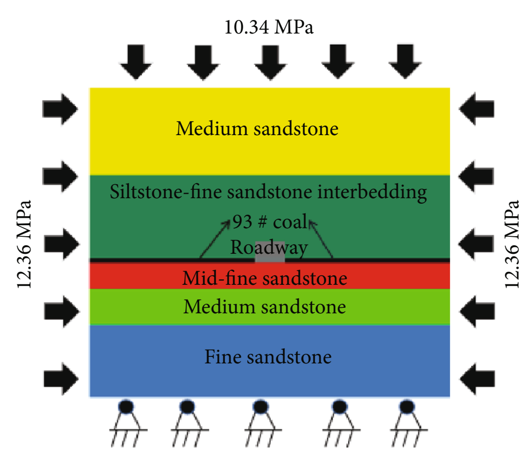

Figure 8: Model schematic and boundary conditions.

Figure 9 shows the nephogram of the distribution of the rock plastic zone of roadway surrounding rock. The shear failure of the two ribs and the top and bottom corner of the roadway appeared in different degrees and distributed roughly symmetrically. Compared with top corners, the destructed range on bottom corners was larger. That is because the stress on the two ribs of roadway is transferred to the bottom corners, causing worse shear damage to bottom corners.

In the process of roadway excavation, the initial stress state of surrounding rock changes and the energy also changes accordingly. Figure 10 is energy distribution nephogram of surrounding rock. As can be seen from Figure 10(a), the elastic strain energy of surrounding rock spreaded around the boundary of roadway. The spread range on the roof and floor was longer, which was roughly in the shape of strip with round ends. Both of ribs spreaded roughly in a circular way. The maximum of elastic strain energy density was 68.5 kJ·m^{-3}, located in the position 1.2 m away from the two ribs of the roadway. As can be seen in Figure 10(b), the distribution range of plastic strain energy was consistent

Table 1: Mechanical parameters of surrounding rock.

Rock formation	Bulk modulus/GPa	Shear modulus/GPa	Cohesion/MPa	Internal frictional angle/°	Tensile strength/MPa	Density/kg·m^{-3}
Medium sandstone	7.2	5.4	4.46	32	3.09	2568
Siltstone-fine sandstone interbedding	8.5	6.3	3.54	31	3.03	2640
93# coal	5.3	3.1	2.36	28	1.68	1395
Midfine sandstone	10.3	7.8	3.25	32	2.62	2608
Medium sandstone	9.5	7.3	3.89	30	4.20	2568
Fine sandstone	9.8	6.2	4.02	32	2.89	2614

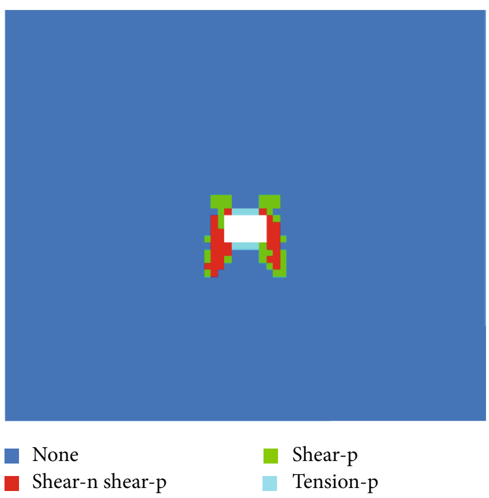

Figure 9: Plastic distribution nephogram of surrounding rock.

with plastic failure area, mainly distributing on the two ribs of the roadway, in the shape of semicircle, with a slightly larger bottom corners. Plastic strain energy spreaded from the both of ribs of the roadway. The spread range was about 1.2 m. The maximum of plastic strain energy density was 15.2 kJ·m^{-3}, located in the boundary position of the two ribs. In fact, energy distribution of the roadway surrounding rock corresponds to plastic zone, which arises after surrounding rock reaches the yield state. This shows that, under those geological conditions, two ribs are the main sources of energy accumulation and dissipation.

Figure 11 shows energy characteristic change curve of the roadway ribs. The elastic strain energy density located within 1.2 m from the roadway surface was in the increase stage, rapidly increasing from 16.6 kJ·m^{-3} to 68.6 kJ·m^{-3}. As the distance from the two ribs increased, elastic strain energy density decreased rapidly. When the distance increased to 6 m, the trend became stable gradually. Within the range 1.2 m from the surface of the roadway, plastic strain energy density decreased rapidly from 15.1 kJ·m^{-3} to about zero. That is because plastic deformation of the roadway arises on the two ribs. The range of plastic zone was roughly 1.2 m from the roadway surface. Plastic deformation of the roadway arose in this area, generating larger elastic strain energy and plastic strain energy. The deformation of surrounding rock outside the plastic zone decreased gradually and the elastic strain energy decreased gradually while the plastic strain energy was zero.

4. Roadway Surrounding Rock Control Technology Based on Energy Transformation

Roadway is in a stable state before excavation, while stress distribution of roadway is adjusted after excavation. Stress concentration may occur in some positions, where a lot of energy may accumulate. According to the energy balance law [34–36], the accumulated energy is released substantially; plastic failure may arise in surrounding rock. The energy in this process is irreversible. The internal energy conversion of the fully elastic rock mass can be expressed as

$$W_c + U_m = U_c + W_r, \tag{7}$$

where W_c is the work done on rock mass by roadway excavation stress. U_m is the strain energy generated from the excavated rock mass; U_c is the strain energy accumulated for roadway excavation; and W_c is the elastic energy released by roadway excavation.

In the incompletely elastic roadway, W_r is approximate constant and U_m and U_c are fixed values, which are related to the geological conditions of roadway surrounding rock. Therefore, the internal energy transformation of incompletely elastic rock mass can be expressed as

$$U_m = U_c + W_r + W_n + W_f, \tag{8}$$

where U_c is the strain energy accumulated by the incompletely elastic roadway excavation, W_n is the energy released when the roadway is damaged and W_f is the energy absorbed by the support.

Based on the energy characteristics and rock energy evolution process, the control technology principle of roadway surrounding rock stability is proposed, as is shown in Figure 12. The first is reducing the elastic strain energy of surrounding rock. (1) By increasing the extension amount of the support. Part of the roadway energy is transferred to the support body, thus improving the energy release of surrounding rock; (2) By optimizing the layout of the roadway. Select the positions with good geological conditions for roadway construction, try to avoid the areas with such stress

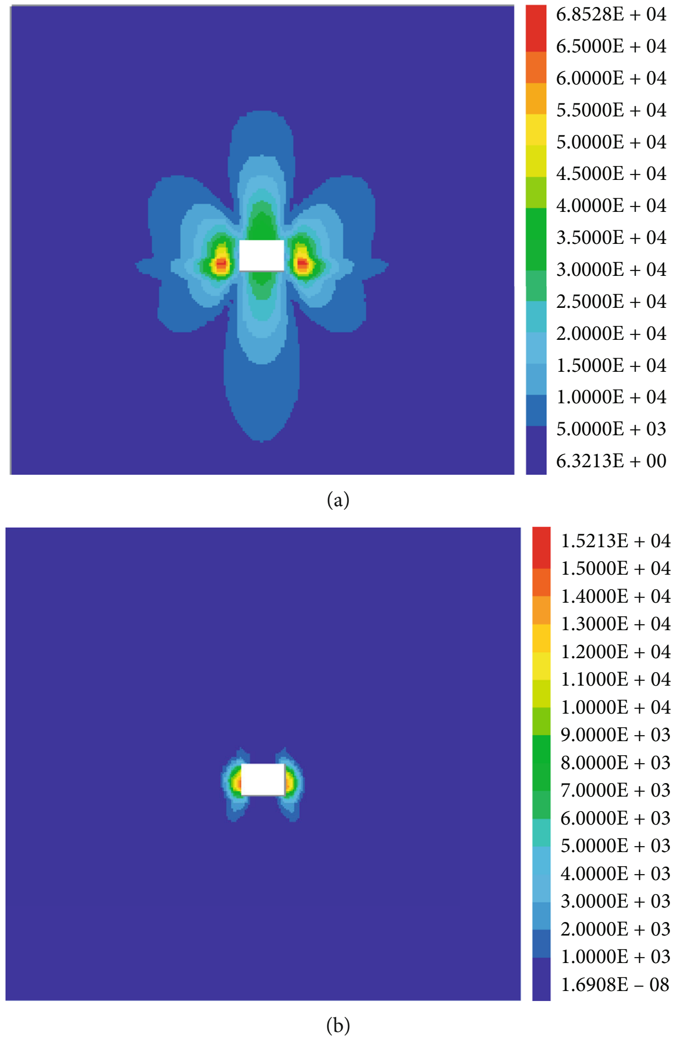

Figure 10: Energy density nephogram of roadway surrounding rock. (a) Elastic strain energy. (b) Plastic strain energy.

concentration as faults and geological structures to avoid stress concentration, thus reducing the energy accumulation of surrounding rock. The second is increasing the plastic strain energy of surrounding rock by setting weak structures, such as borehole pressure relief and other measures, to consume part of the energy in the coal body, thus improving the energy dissipation of surrounding rock.

5. Industrial Tests

5.1. Project Overview. The strike length of the right second working surface of the 91st coal of Xinjian coal mine is 800 m in depth, and the average dip length is 130 m. The average thickness of the coal seam is 1.4 m and the mean obliquity is 11°. Obliquity changes less and it tends to become larger from the east to the west. The occurrence of coal seam is stable and the coal type is 1/3 coking coal, which has stable structure and clear layer structure. The roof and floor is sandstone, which is gray and has high hardness.

The cross section of the transport roadway is trapezoidal, 4.0 m wide and the central axis height of 3.2 m. Joint anchor bolt-cable support is adopted. The anchor cable is 5.0 m long, the diameter is 17.8 mm and the row spacing is 2.0 m × 1.2 m. The bolt is 2.4 m long, with a 20.0 mm diameter and 1.0 m × 1.2 m row spacing. The section support diagram is shown in Figure 13.

5.2. Stability Control Scheme of Roadway Surrounding Rock. In the actual roadway engineering, the optimization of roadway layout is greatly limited by the geological conditions and excavation influence, which is only applicable to the initial stage of roadway construction. It is difficult to set weak structures for construction, which has high requirements for the size, height, and angle of weak structures. The energy release in roadway surrounding rock is mostly released in the form of deformation energy. For the roadway with specific geological conditions, the total amount of released energy is certain. Energy can be released on the support to reduce the energy amount on surrounding rock. Therefore,

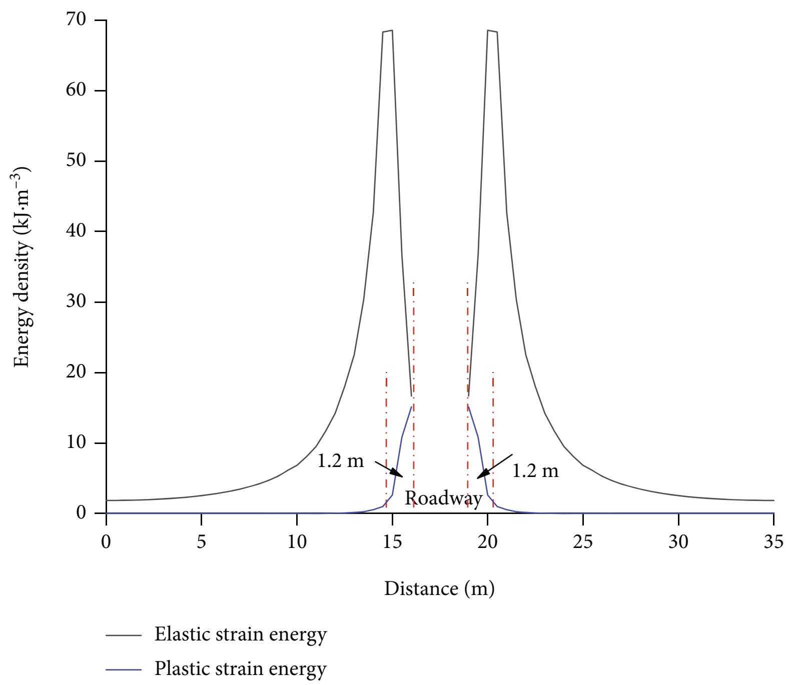

Figure 11: Energy change curve of ribs of roadway.

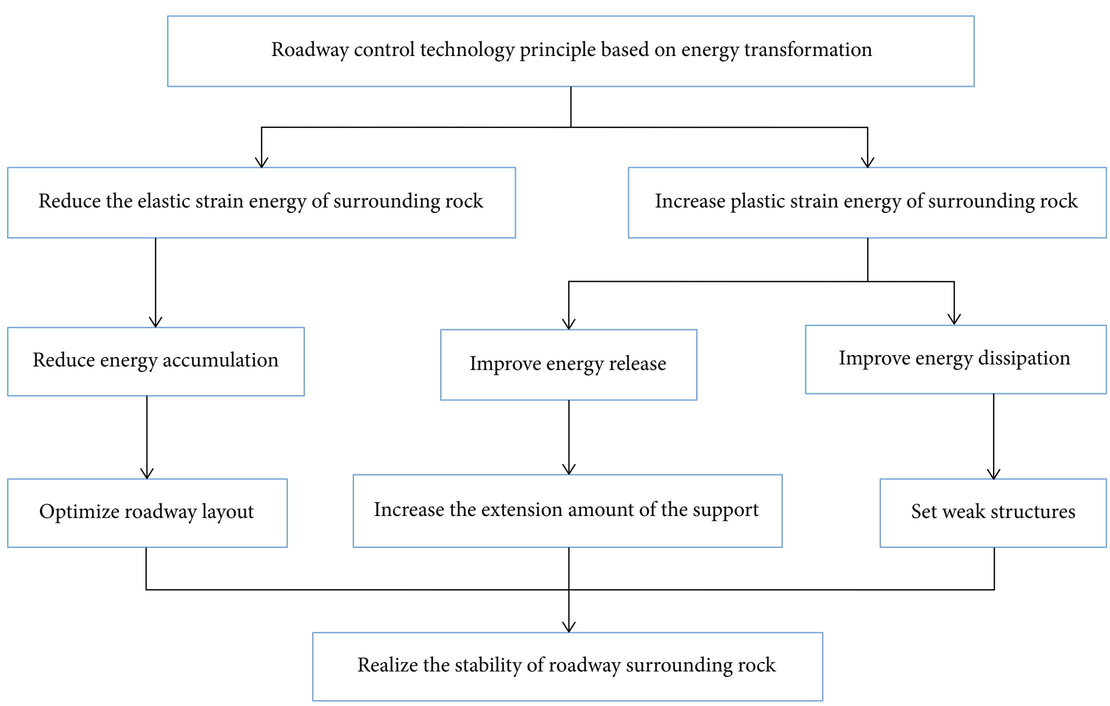

Figure 12: Roadway control technology principle based on the energy transformation.

roadway stability control is conducted mainly in terms of improving the energy release of surrounding rock.

5.2.1. Roadway Support Measures. (1) Control roof stability with high-density long anchor cable. On the basis of the original support, adjust the parameters of the support, strengthen the supporting role of the anchor cable, and improve the integrity of surrounding rock so that the surrounding rock and the support body can form a complete bearing structure. Adopt high density long anchor cable, 7300 mm long, with a diameter of 21.8 mm, whose row spacing is 1000 mm × 1000 mm, arranged alternatively with

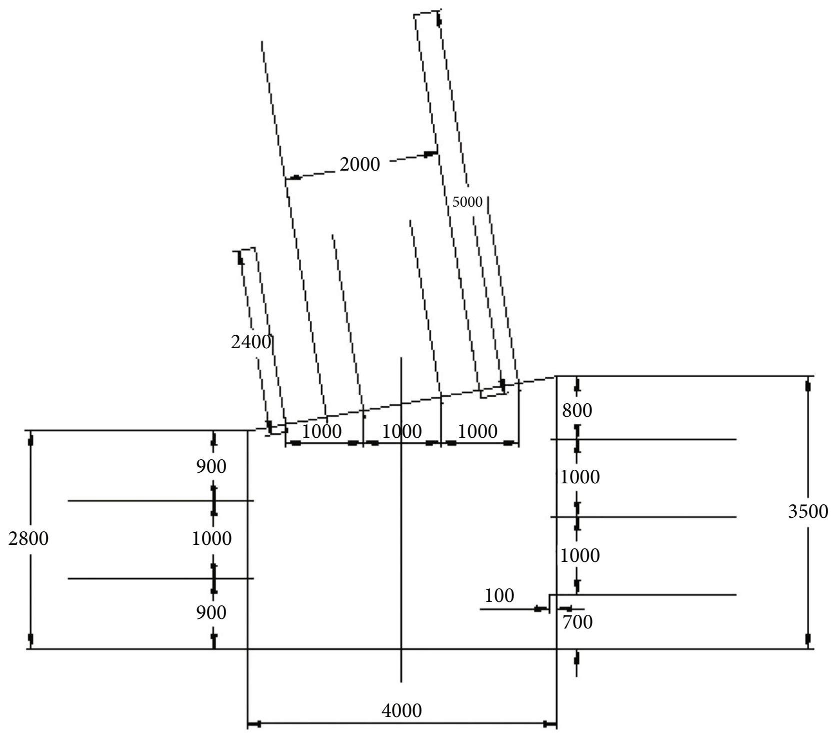

Figure 13: Roadway section support map.

bolts. (2) Replace the ribs bolt with the short anchor cable with a large diameter. Due to the limitation of length, the control range to the two ribs of the ordinary bolt is limited. The ordinary short bolt is replaced with the short anchor cable with a large diameter. Its length is greater than the ordinary short bolt, which can increase the control range of the surrounding rock on the ribs. The pretightening force of the large-diameter anchor cable is higher than the ordinary anchor cable, which can effectively control the loosening and destruction of the surrounding rock on the ribs. The short anchor cable is 3000 mm long and its diameter is 21.8 mm and row spacing is 1000 mm × 1000 mm

According to the above support measures, the support parameters are designed. The support map of the optimized roadway section is shown in Figure 14.

5.2.2. Analysis of Support Optimization. Take the ventilation roadway in the 91st coal of Xinjian Coal Mine as the engineering background. According to the data of the mine, a calculation model is established. In order to ensure the accuracy of the model, the strati parameters are appropriately simplified. The roadway is 4.0 m wide and the central axis is 3.2 m high. The dimensions of the model are $x \times y \times z = 40\,\mathrm{m} \times 20\,\mathrm{m} \times 30\,\mathrm{m}$. The constitutive model adopts the Mohr-Coulomb criterion. Displacement constrains are conducted on the four sides and the bottom of the model. According to the geological data, *in suit* stress $\sigma_z = 10.34\,\mathrm{MPa}$, $\sigma_x = 11.63\,\mathrm{MPa}$, $\sigma_y = 7.15\,\mathrm{MPa}$ is applied to the model. The mechanical parameters of the surrounding rock are shown in Table 2.

Figure 15 shows the energy nephograms before and after the support optimization. The energy distribution of the roof and floor of roadway was relatively uniform, and the energy distribution range of the roof was slightly greater than floor. The high energy area connection of the roadway ribs was roughly the same as the seam inclination, and the high energy area on the right rib was larger. Before and after the support optimization, the maximum of elastic strain energy decreased significantly and the maximum of elastic strain energy of the two ribs decreased from 193.3 kJ·m^{-3} to 159.0 kJ·m^{-3}, and the maximum of elastic strain energy on the roof and floor decreased from 114.2 kJ·m^{-3} to 95.3 kJ·m^{-3}, decreasing 17.7% and 16.5%, respectively. After the support optimization, the extension amount of the support increased, and the energy of roadway surrounding rock can be transferred to the support body. Thus, the energy release of roadway surrounding rock improves and the elastic strain energy is also reduced.

5.3. Validation of Effect. In order to verify the rationality of the supporting parameters, monitoring points were selected on the right rib, roof, and floor of the roadway to monitor the deformation amount. They were monitored every 3 to 5 days, which lasted 60 days. The displacement change curve of the surface before and after the roadway was optimized is shown in Figure 16. The surface displacement amount of the roadway before and after the optimization dropped apparently. Before the optimization, the displacement amount of the roadway surface showed a growth trend. The floor had an obvious slowing trend while the roof and the right rib still

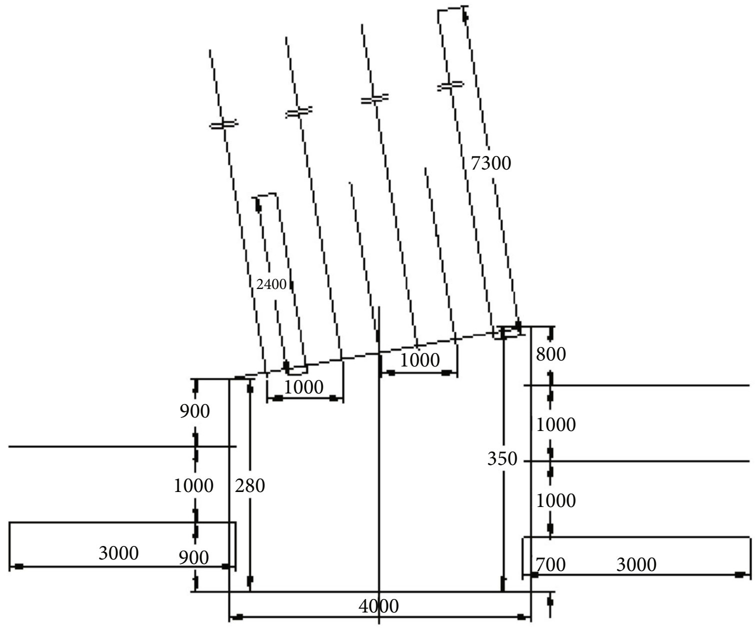

Figure 14: Optimized roadway section support map.

Table 2: Mechanical parameters and thickness of surrounding rock.

Rock formation	Bulk modulus/GPa	Shear modulus/GPa	Cohesion/MPa	Internal frictional angle/°	Tensile strength/MPa	Density/kg·m^{-3}	Thickness/m
Fine sandstone4	17.2	10.4	4.46	32	2.18	2568	2.35
Siltite2	18.5	11.3	3.54	31	2.35	2640	1.09
Middle sandstone3	19.8	12.1	2.36	28	1.98	1395	4.55
Fine sandstone3	10.3	9.8	3.25	32	2.62	2608	3.2
Siltite1	19.5	11.3	3.89	30	3.20	2568	1.38
91Coal	7.4	3.5	2.38	25	1.68	1398	1.35
Middle sandstone 2	19.8	12.1	2.36	28	1.98	1395	1.56
Fine sandstone 2	10.5	9.5	3.25	32	2.62	2608	2.2
90 coal	7.3	3.4	2.19	26	1.52	1396	0.85
Middle sandstone 1	19.8	12.1	2.36	28	1.98	1395	1.0
Fine sandstone 1	10.2	9.3	3.25	32	2.62	2608	5.95

had a growth trend. The maximum of roof subsidence, floor heave and shrinkage of the right rib were 247 mm, 120 mm, and 292 mm, respectively. After the optimization, the increase rate of roadway surface displacement became slow on the whole, and the effect of floor was particularly obvious, which gradually became stable after 45 days. Each displacement amount decreased apparently: roof subsidence decreased to 62 mm, floor heave dropped to 26 mm, and right rib shrinkage dropped to 94 mm.

6. Discussion

In this paper, based on elastic strain energy and plastic strain energy, the evolution law of sandstone energy characteristics and roadway surrounding rock energy evolution law were obtained, respectively, through laboratory test and numerical simulation, and the stability control technology principle of roadway surrounding rock based on energy transformation is proposed. According to the geological conditions, the stability control of roadway surrounding rock was carried out. It shows that the technique principle is suitable for surrounding rock stability control, and the technique of surrounding rock stability control is a supplement to mechanics from the perspective of energy, and has a good application prospect.

In the process of rock deformation and failure under external force, the energy changes all the time. In this paper, the energy evolution law of rock specimens in the process of failure is studied by elastic strain energy and dissipation energy, ignoring energy characteristic parameters such as

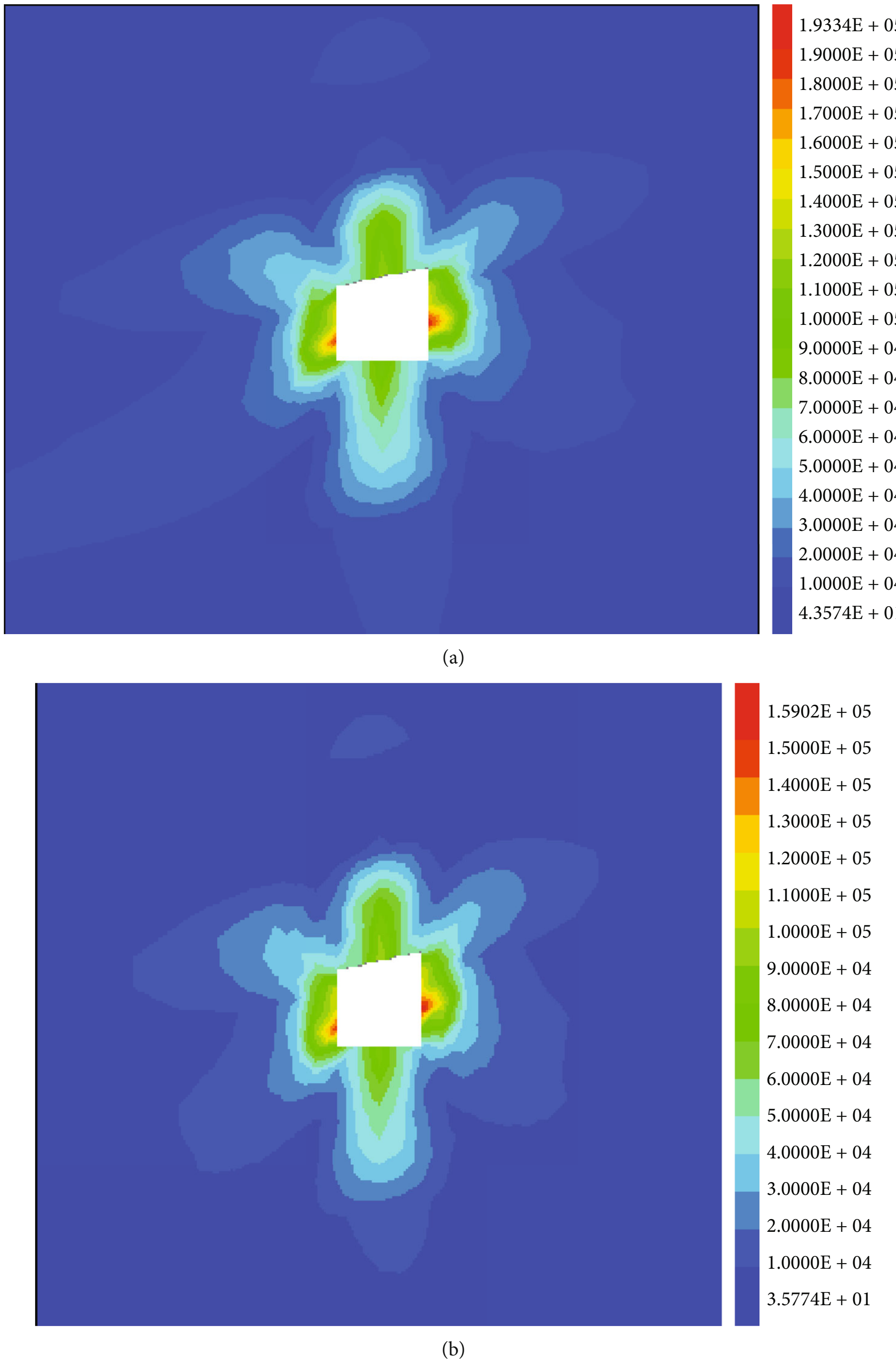

Figure 15: Elastic strain energy nephogram before and after optimization. (a) Original support. (b) After optimization.

frictional dissipation energy used between cracks in the process of energy evolution, thus there are some errors in the description of energy evolution in the whole process of deformation and failure.

The stability of roadway surrounding rock can be reflected by the energy transformation of surrounding rock. The numerical model of roadway surrounding rock energy established in this paper is based on the elastic strain energy and plastic strain energy of surrounding rock, which has good application effect, but lacks the verification of field application. Therefore, the energy of roadway surrounding rock can be quantified by combining seismological principle.

From the perspective of energy transformation, the principle of roadway surrounding rock stability control technology is put forward. Due to the limitation of geological conditions, this paper only carried out field construction aiming at improving the energy release principle of

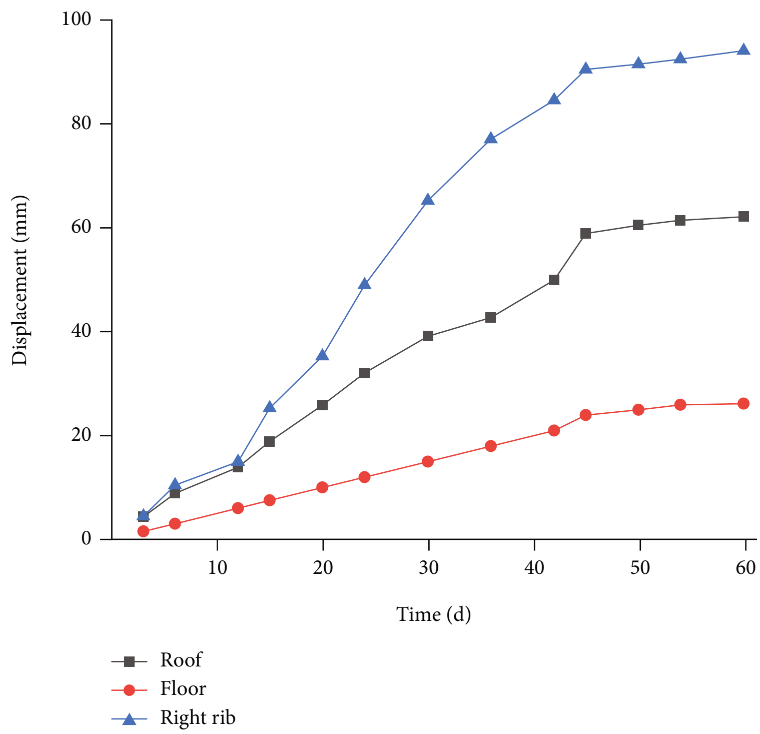

(a)

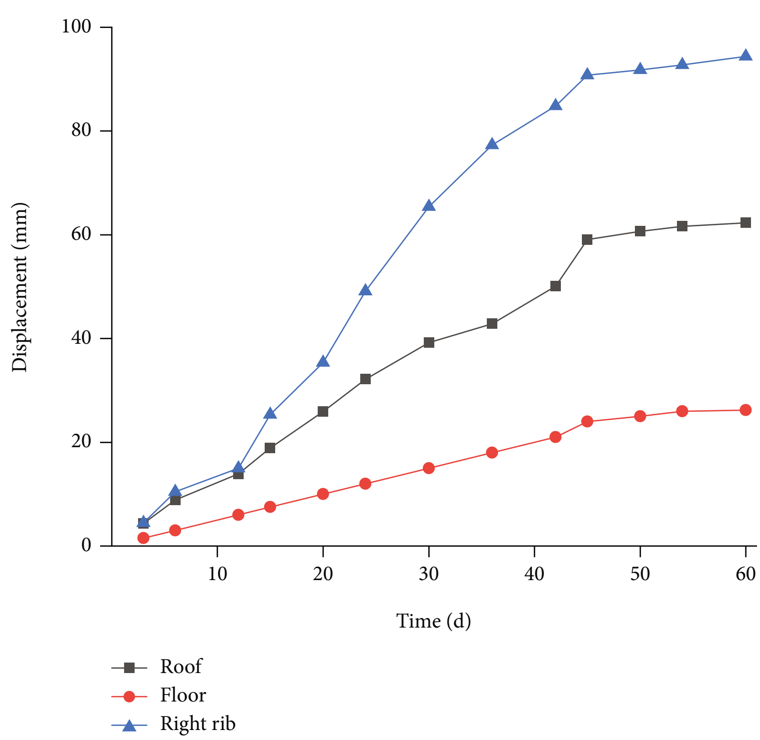

(b)

Figure 16: Surface displacement curve of roadway. (a) Before the optimization. (b) After the optimization.

surrounding rock, and achieved good application effect. The effect of improving the energy dissipation of surrounding rock, reducing the energy accumulation, and the synergistic effect of each other have not been verified in the field, so corresponding research should be carried out.

7. Conclusion

In this paper, based on the research of the energy evolution regularity of sandstone samples, the surrounding rock energy numerical model was established, and then the principle of roadway surrounding rock stability control technology is put forward. Field industrial test results show that the control effect is good. The main conclusions are as follows:

(1) In the process of rock deformation and failure, the total energy increased exponentially before the axial stress peak, mainly transferred to elastic strain energy, accounting for about 72% ~80% of the total energy and the dissipated energy remained 18% ~20%. The total energy growth rate decreased slightly in the postpeak stage. The vast majority of energy was transferred to dissipated energy, accounting for about 87% of the total energy

(2) Combined with energy transformation, put forward the principle of roadway surrounding rock stability control technology: one is to reduce the elastic strain energy of surrounding rock. On the one hand, by increasing the extension amount of support body, part of roadway energy is transferred to support body, thus improving the energy release of surrounding rock. On the other hand, by optimizing roadway layout, stress concentration is avoided and energy accumulation of surrounding rock is reduced. The second is to increase the plastic strain energy of surrounding rock, that is, to increase the energy dissipation of surrounding rock by setting weak structure

(3) After the optimization of support measures, the roadway surface displacement and its increase rate decreased significantly, roof subsidence decreased from 247 mm to 62 mm, floor heave decreased from 120 mm to 26 mm, and the right rib shrinkage decreased from 292 mm to 94 mm, that is, the floor heave control effect was particularly obvious. The deformation of surrounding rock gradually stabilized after 45 days

Data Availability

The data used to support the study is available within the article.

Conflicts of Interest

The authors declare that they have no conflicts of interest.

Acknowledgments

This study was supported by the National Natural Science Foundation of China (51774122), Outstanding Young Talents Project supported by the Central Government for The Reform and Development of Local Universities (2020YQ13), and the Natural Science Foundation of Heilongjiang Province (LH2019E087).

References

[1] Q. L. Zou, H. Liu, Z. H. Cheng, T. C. Zhang, and B. Q. Lin, "Effect of slot inclination angle and borehole-slot ratio on mechanical property of pre-cracked coal: implications for ECBM recovery using hydraulic slotting," *Natural Resources Research*, vol. 29, no. 3, pp. 1705–1729, 2020.

[2] X. L. Li, Z. H. Li, E. Y. Wang et al., "Pattern recognition of mine microseismic and blasting events based on wave fractal features," *Fractals*, vol. 26, no. 3, article 1850029, 2018.

[3] X. L. Li, Z. Y. Cao, and Y. L. Xu, "Characteristics and trends of coal mine safety development," *Energy Sources, Part A: Recovery, Utilization, and Environmental Effects*, vol. 11, pp. 1–9, 2020.

[4] H. P. Kang, P. F. Jiang, B. X. Huang et al., "Roadway strata control technology by means of bolting-modi- fication-destressing in synergy in 1000 m deep coal mines," *Journal of China Coal Society*, vol. 45, no. 3, pp. 845–864, 2020.

[5] W. J. Wang, C. Yuan, W. J. Yu et al., "Stability control method of surrounding rock in deep roadway with large deformation," *Journal of China Coal Society*, vol. 41, no. 12, pp. 2921–2931, 2016.

[6] X. X. Chen and J. P. Wu, "Study on the mechanism and control technology of large deformation of roadway surrounding rock in the fault fracture zone," *Journal of Mining & Safety Engineering*, vol. 35, no. 5, pp. 885–892, 2018.

[7] P. Peng, D. L. Zhang, and Z. Y. Sun, "Deformation characteristics of surrounding rock and reinforcement parameter design of weak interlayer tunnels," *Chinese Journal of Rock Mechanics and Engineering*, vol. 40, no. 11, pp. 2260–2272, 2021.

[8] H. S. Jia, K. Pan, D. F. Li et al., "Roof fall mechanism and control method of roof with weak interlayer in mining roadway," *Joural of China University of Mining & Technology*, vol. 51, no. 1, pp. 67–76, 2022.

[9] H. P. Xie, R. D. Peng, and Y. Jv, "Energy dissipation of rock deformation and fracture," *Chinese Journal of Rock Mechanics and Engineering*, vol. 23, no. 21, pp. 3565–3570, 2004.

[10] H. P. Xie, R. D. Peng, Y. Jv, and H. W. Zhou, "Preliminary study on energy analysis of rock failure," *Chinese Journal of Rock Mechanics and Engineering*, vol. 24, no. 15, pp. 2603–2608, 2005.

[11] H. P. Xie, Y. Jv, and L. Y. Li, "Criteria for strength and structural failure of rocks based on energy dissipation and energy release principles," *Chinese Journal of Rock Mechanics and Engineering*, vol. 24, no. 17, pp. 3003–3010, 2005.

[12] J. Xu, Y. Zhang, H. W. Yang, and J. N. Wang, "Energy evolution law of deformation and damage of sandstone under cyclic pore watwe pressures," *Chinese Journal of Rock Mechanics and Engineering*, vol. 30, no. 1, pp. 141–148, 2011.

[13] G. Y. Zhao, B. Dai, L. J. Dong, and C. Yang, "Energy conversion of rocks in process of unloading confining pressure under different unloading paths," *Transactions of Nonferrous Metals Society of China*, vol. 25, no. 5, pp. 1626–1632, 2015.

[14] X. B. Yang, H. M. Cheng, and Y. Y. Pei, "Study on the evolution characteristics of rock deformation and post-peak energy under different loading methods," *Chinese Journal of Rock Mechanics and Engineering*, vol. 39, no. S2, pp. 3229–3236, 2020.

[15] Z. X. Liu, G. M. Zhao, X. R. Meng et al., "Analysis of creep energy evolution of red sandstone based on linear energy storage law," *Journal of Central South University (Science and Technology)*, vol. 52, no. 8, pp. 2748–2760, 2021.

[16] Q. B. Meng, C. K. Wang, B. X. Huang et al., "Rock energy evolution and distribution law under triaxial cyclic loading and unloading conditions," *Chinese Journal of Rock Mechanics and Engineering*, vol. 39, no. 10, pp. 2047–2059, 2020.

[17] Z. Hao, L. F. Guo, X. D. Zhao, G. X. Chen, and G. H. Zhang, "Analysis of burst failure energy characteristics of mining roadway surrounding rock," *Journal of China Coal Society*, vol. 45, no. 12, pp. 3995–4005, 2020.

[18] H. Yu, X. J. Zhang, B. Y. Li, and F. J. Chu, "Macro-micro mechanical response and energy mechanism of surroundin-grock under excavation disturbance," *Journal of China Coal Society*, vol. 45, no. S1, pp. 60–69, 2020.

[19] H. Y. Shi, N. J. Ma, J. J. Shi, N. Li, and G. W. Tan, "Simulation study on energy evolution and release of surrounding rock in stope," *Coal Science and Technology*, vol. 48, no. 3, pp. 106–111, 2020.

[20] S. W. Wang, W. J. Ju, J. F. Pan, and C. Lu, "Mechanism of energy partition evolution of excavation roadway rockburst in coal seam under tectonic stress field," *Journal of China Coal Society*, vol. 44, no. 7, pp. 2000–2010, 2019.

[21] P. Huang, S. Spearing, F. Ju, K. V. Jessu, Z. W. Wang, and P. Ning, "Control effects of five common solid waste back filling materials on in situ strata of gob," *Energies*, vol. 12, no. 1, 2019.

[22] Z. Q. Ma, C. M. Tao, Y. J. Zuo, G. Y. Wu, and P. Liu, "Supporting technology of roadways with thick and soft roof based on energy balance theory," *Journal of Mining and Safety Engineering*, vol. 35, no. 3, pp. 496–502, 2018.

[23] R. D. Peng, Y. Jv, F. Gao, H. P. Xie, and P. Wang, "Energy analysis on damage of coal under cyclical triaxial loading and unloading conditions," *Journal of the China Coal Society*, vol. 39, no. 2, pp. 245–252, 2014.

[24] S. Gao, L. M. Zhang, Z. Q. Wang, and Y. Cong, "Study of deformation and energy properties of marble unloading failure," *Chinese Journal of Rock Mechanics and Engineering*, vol. 33, no. S1, pp. 2808–2813, 2014.

[25] T. Qin, Y. W. Duan, H. R. Sun, H. L. Liu, and L. Wang, "Energy evolution and acoustic emission characteristics of sandstone specimens under unloading confining pressure," *Shock and Vibration*, vol. 2019, Article ID 1612576, 9 pages, 2019.

[26] X. J. Dong, A. Karrech, H. Basarir, M. Elchalakani, and A. Seibi, "Energy dissipation and storage in underground mining operations," *Rock Mechanics and Rock Engineering*, vol. 52, no. 1, pp. 229–245, 2019.

[27] T. Qin, Y. W. Duan, H. R. Sun, L. Wang, and H. L. Liu, "Mechanical characteristics and energy dissipation characteristics of sandstone under triaxial stress conditions," *Journal of the China Coal Society*, vol. 45, no. S1, pp. 255–262, 2020.

[28] Z. Z. Zhang and F. Gao, "Confining pressure effect on rock energy," *Chinese Journal of Rock Mechanics and Engineering*, vol. 34, no. 1, pp. 1–11, 2015.

[29] Z. Y. Li, G. Wu, T. Z. Huang, and Y. Liu, "Variation of energy and criteria for strength failure of shale under traixial cyclic loading," *Chinese Journal of Rock Mechanics and Engineering*, vol. 37, no. 3, pp. 662–670, 2018.

[30] B. Dai, G. Y. Zhao, H. Konietzky, and P. L. P. Wasantha, "Experimental investigation on damage evolution behaviour of a granitic rock under loading and unloading," *Journal of Central South University*, vol. 25, no. 5, pp. 1213–1225, 2018.

[31] J. Q. Guo, X. R. Liu, J. B. Wang, and Z. H. Huang, "Strength criterion of rock based on elastic strain energy," *Rock and Soil Mechanics*, vol. 37, no. S2, pp. 129–136, 2016.

[32] Q. Sun, S. C. Li, X. D. Feng, W. T. Li, and C. Yuan, "Study of numerical simulation method of rock fracture based on strain energy density theory," *Rock and Soil Mechanics*, vol. 32, no. 5, pp. 1575–1582, 2011.

[33] Itasca Consulting Group Inc, *FLAC3D 5.0 manual*, ICG, Minneapolis, 2010.

[34] W. L. Gong, D. Y. Zhu, J. Wang, M. C. He, and D. L. Wang, "Deformation and energy equation verification of NPR anchor cable support roadway based on model test," *Journal of Mining and Safety Engineering*, vol. 37, no. 5, pp. 918–927, 2020.

[35] G. Y. Cui, B. H. Song, M. N. Wang, D. Y. Wang, and X. G. Wu, "Study on the anti-breaking design method of tunnel across active fault based on the energy balance method," *China Civil Engineering Journal*, vol. 53, no. S2, pp. 309–314, 2020.

[36] T. B. Zhou, Y. P. Qin, Q. F. Ma, and J. Liu, "A constitutive model for rock based on energy dissipation and transformation principles," *Arabian Journal of Geosciences*, vol. 12, no. 15, p. 492, 2019.

Hindawi
Geofluids
Volume 2022, Article ID 9654025, 11 pages
https://doi.org/10.1155/2022/9654025

Research Article

Effect of Cyclic Loading and Unloading on the Deformation and Damage Properties of Sandstone from Beizao, a Coal Mine underneath the Bohai Sea in China

Yan Chen,[1,2] Gaofei Wang,[1] Lei Zhou,[1] Guolong Zhang,[1] Jiangfan Yang,[1] and Meiheng Li[1]

[1]*School of Energy Science and Engineering, Henan Polytechnic University, Jiaozuo 454000, China*
[2]*Collaborative Innovation Center of Coal Work Safety and Clean High Efficiency Utilization, Henan Polytechnic University, Jiaozuo 454000, China*

Correspondence should be addressed to Yan Chen; chenyan@hpu.edu.cn

Received 14 March 2022; Revised 8 September 2022; Accepted 12 September 2022; Published 24 September 2022

Academic Editor: Dan Ma

Mining under the sea is a challenging task in China. Affected by blasting, tunneling, and other engineering disturbance, surrounding rock is often in a state of cyclic loading and unloading stress. In this study, in order to investigate the effect of cyclic loading and unloading on the deformation and damage characteristics of sandstone underneath the Bohai Sea, the GCTS test machine is used to conduct cyclic loading and unloading tests on sandstone. The results show that under cyclic loading and unloading compression, the stress-strain curves of sandstone form a hysteresis loop. The axial residual deformation first decreases, then increases with the increase of cycle number and unloading stress level. Both the circumferential residual strain and volumetric residual strain decrease with the increase of cycle number and unloading stress level. The axial elastic deformation increases with the increase of the cyclic number and cyclic load. The volume deformation first increases, then decreases, and the circumferential strain gradually decreases. In the process of cyclic loading and unloading, the loading elastic modulus gradually increases. Affected by damage, the unloading stress difference of sandstone initially increases with the increase of cycles. Next, the effects of cycle number and unloading stress level on the damage parameters of sandstone are analyzed. Before brittle failure of the specimen, the absolute damage parameters of axial, circumferential, and volume show an increasing trend, and the increase rates of circumferential damage parameters and volume damage parameters suddenly increase, which is also the precursor of the sandstone specimen's instability failure.

1. Introduction

In the process of underground coal mining, the surrounding rock of roadway of the working face is mostly affected by various mining-induced stresses. Some accidents, including rock burst and environmental problems, have been caused by underground coal mining [1–5]. In addition, its deformation behavior, strength characteristics, and failure mode are essentially different from those under conventional uniaxial and triaxial loading [6, 7]. Affected by mining and blasting, roadway surrounding rock is often in a state of cyclic loading and unloading stress. For these reasons, exploring the change of rock mechanical parameters under cyclic loading and unloading is of great significance for safe and efficient coal mining and mine disaster prevention.

Cyclic loading and unloading tests are typically used to study the fatigue and damage characteristics of materials. The existing experimental research has confirmed that the mechanical properties of rocks under cyclic loading and unloading differ significantly from those under monotonic loading [8–11]. Zoback and Byerlee [12] conducted cyclic loading and unloading tests on Westerly granite and observed that the dilatancy point of rock was not affected by the number of cycles under the confining pressure of 50 to 200 MPa. Elliott and Brown [13] studied recoverable deformation and unrecoverable deformation of rock under cyclic loading and unloading and distinguished elastic and plastic components of rock. Singh [14] studied the fatigue characteristics and strain hardening phenomenon of sandstone and found that when the fatigue stress amplitude was reduced, the fatigue life of rock increased, and the higher the number of cycles, the greater the proportion of strain hardening. Yoshinaka et al. [15] carried out cyclic loading and unloading tests on Ohya tuff, Yokohama sandstone and mudstone, and Kobe mudstone and sandstone. They also analyzed the deformation behavior, and dilatancy characteristics of these four soft rocks were analyzed. It was found that the deformation modulus was exponentially related to plastic strain, and the relationship model between internal friction angle and dilatancy angle and plastic strain was given. Li et al. [16] studied the fatigue damage characteristics of frozen rock containing cracks, obtained the fatigue failure law of frozen rock, and pointed out that the fatigue effect of rock containing cracks is stronger than that of intact rock under freezing conditions. Bagde and Petroš [17] carried out uniaxial cyclic loading and unloading tests on sandstone and studied the influence of loading frequency on mechanical parameters. It is considered that Young's modulus, secant modulus, and uniaxial compressive strength increase with the increase of loading frequency. Zhou et al. [18] studied the mechanical properties of red sandstone under cyclic loading and found that the fatigue life of red sandstone decreased first and then increased with the increase of loading frequency and lower limit load ratio. It can be seen that cyclic loading has a significant effect on the damage of rock.

In terms of rock deformation and strength characteristics under cyclic loading and unloading, Fuenkajorn and Phueakphum [19] carried out cyclic loading and unloading tests on rock salt and analyzed the influence of cycle times on the strength and elastic behavior of rock salt. The results showed that the compressive strength of rock salt decreased with the increase of cycle times. In the early cycle, the elastic modulus first decreased, then remained basically unchanged until failure. Liu et al. [20] studied the deformation and failure characteristics of sandstone under cyclic loading and unloading. The test results showed that the axial strain of sandstone under cyclic loading and unloading was larger than that under static loading when dilatancy occurred. The sandstone mainly underwent shear failure. Compared with static loading, the local failure shear band under cyclic loading was wider. Using triaxial cyclic loading and unloading tests, Wang et al. [11] studied the mechanical properties of granite. In the volumetric compression stage, axial residual strain and volumetric residual strain decreased with the increase of cycles, while the deformation modulus gradually increased. However, in the volumetric dilatancy stage, with the increase of cycles, the axial residual strain and volumetric residual strain gradually increased, and the deformation modulus gradually decreased. Qiu et al. [21] studied the damage characteristics of marble based on irreversible deformation and considered that the damage increased with the increase of confining pressure unloading increment. Zhang et al. [22] carried out triaxial cyclic loading and unloading tests on mudstone with different bedding angles and analyzed the influence of plastic deformation on the inelastic deformation of anisotropic mudstone. They considered that the elastic modulus was negatively correlated with the cumulative plastic strain, while Poisson's ratio was opposite. Yang et al. [23, 24] carried out triaxial cyclic loading and unloading tests on sandstone and marble, respectively. They found that the strength of sandstone under cyclic loading and unloading was higher than that under monotonic loading at low confining pressure, and the strength was basically equal when the confining pressure exceeded 20 MPa. Before the peak, the axial damage was larger than the circumferential damage, while after the peak, the circumferential damage was larger than the axial damage. They also found that with the increase of cycles, the elastic strain of marble first increased, then decreased, and the plastic strain showed a nonlinear growth trend. Meng et al. [25] carried out uniaxial cyclic loading and unloading tests on red sandstone and analyzed the acoustic emission and energy characteristics. It was found that the number of acoustic emissions reached the maximum at each peak of cyclic stress, and the energy density increased with the increase of loading stress. Song et al. [26, 27] studied the deformation field and damage evolution of sandstone under cyclic loading and unloading by the digital image correlation method. The results showed that the damage of rock can be reflected by the maximum tensile strain on the surface of the sample. When the cyclic load reached the critical value, the cumulative damage of rock would evolve into a high local damage area corresponding to the macroscopic failure crack of rock, resulting in rock failure. Wang et al. [28] investigated the characteristics of rock deformation and failure under cyclic loading and unloading and found that compared with the uniaxial compression test, cyclic loading and unloading had a certain strengthening effect on the strength of the rock samples.

In summary, many studies have focused on the deformation, damage, and strength characteristics of rock under cyclic loading and unloading and have achieved good results. However, there have been few studies on mechanical properties of surrounding rock in seabed mining. Based on this, in this study, taking sandstone as the research object, the failure mechanics test of sandstone under cyclic loading and unloading is carried out by the GCTS testing machine, and the deformation damage characteristics of sandstone under cyclic loading and unloading are analyzed. The research conclusions provide theoretical reference for the failure behavior and stability analysis of surrounding rock in seabed mining.

2. Test Overview

2.1. Test Sample. The rock used in the test is sandstone, which is taken from the Beizao Coal Mine in the Longkou Mining Area, Shandong Province. The buried depth is approximately 400 m. The sandstone in the roof of coal 4 is layered light gray and white, with an average thickness of 68.02 m. According to X-ray diffraction test results, the sandstone material is composed of 33.97% quartz, 24.28% albite, 5.290% white mica, 16.98% dolomite, 2.100% calcite,

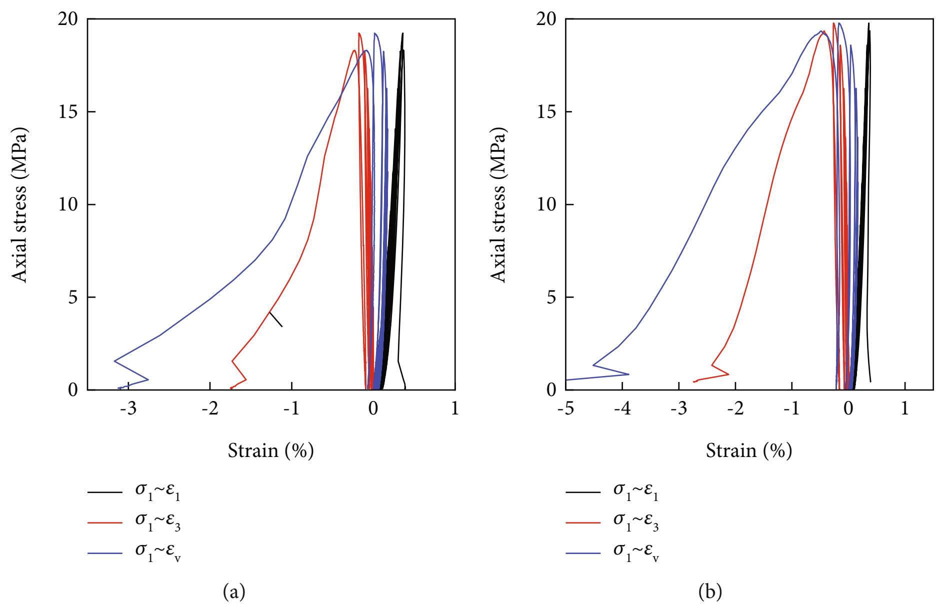

Figure 1: Complete stress-strain curves of sandstone under cyclic loading: (a) UC-C-1; (b) UC-C-2.

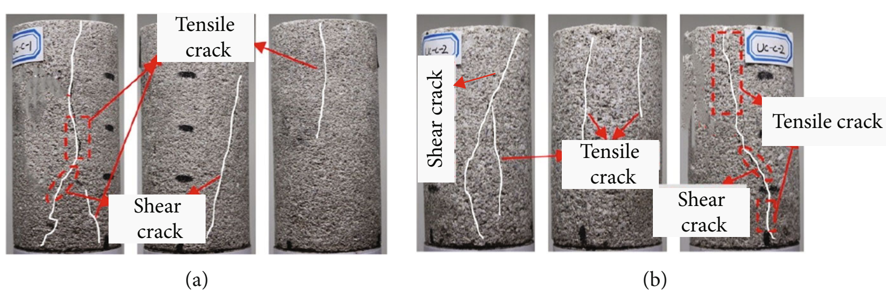

Figure 2: Failure modes of the sandstone specimens: (a) UC-C-1; (b) UC-C-2.

and 17.38% kaolinite. The porosity of the sandstone material is approximately 9.1%, with a coarse grain size varying from 0.25 to ~1 mm.

After drilling, sawing, and grinding, the sandstone was processed into a cylinder sample with a diameter of 50 mm and a height of 100 mm. In the machining process, it was ensured that the two ends of the sample are parallel and smooth without large scratches. The nonparallel degree of the two ends is greater than 0.01 mm, and the diameter deviation of the two ends is not greater than 0.02 mm, so as to make the two ends of the sample meet the requirements of the measurement method. The basic mechanical properties of the sandstone have been investigated in Ref. [29]. The respective uniaxial compressive strength and elastic modulus of the sandstone are approximately 23.35 MPa and 8.32 GPa.

2.2. Test Scheme. The test equipment adopts the GCTS RTR-1000 rock triaxial test system of the State Key Laboratory of Coal Resources and Safety Mining of China University of Mining and Technology (Beijing). The GCTS RTR-1000 rock triaxial test system is a closed-loop digital servo control device, which can be used for simple and rapid uniaxial loading test and seepage test of rock samples. The stress-strain curve of rock and a series of mechanical parameters such as elastic modulus, Poisson's ratio, and compressive strength can be measured. The maximum axial load is 1000 kN, the stiffness is 1750 kN/mm, the maximum confining pressure is 140 MPa, and the resolution is 0.01 MPa. The pressurization device is a double piston pressurization system. The axial and circumferential deformations of the rock samples are tested by a 5 mm extensometer.

The axial strain control is used in the process of cyclic loading and unloading, and the loading and unloading rates are 0.02%/min. The interval between each cycle is controlled by strain, which is 0.03%. The loading and unloading scheme is as follows: 0→0.03%→0→0.06%→0→0.09%… until failure is reached.

3. Test Results

3.1. Stress-Strain Curves of Sandstone under Cyclic Loading. The stress-strain curves of the sandstone under uniaxial cyclic loading and unloading are shown in Figure 1. It can be seen from the axial stress-axial strain curve that the post-peak curve of sandstone has no obvious strain softening stage, thus forming a typical type II curve. Figure 2 shows the failure modes of sandstone specimens under uniaxial cyclic loading and unloading compression. Compared with

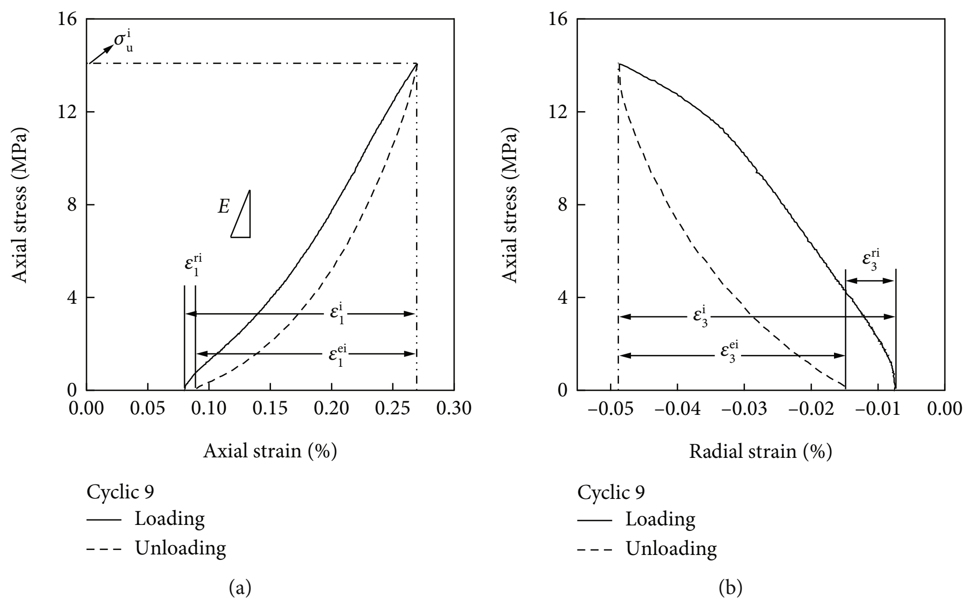

FIGURE 3: Calculation method of deformation parameters of sandstone under cyclic loading: (a) axial strain; (b) radial strain.

the failure modes of the sandstone under conventional uniaxial and triaxial compression in Ref. [30], under the cyclic loading and unloading compression, the cracks of the sandstone specimens increase obviously.

The calculation method of deformation parameters of sandstone is shown in Figure 3. Figure 3(a) shows the ninth cycle of the axial stress-axial strain curve of sandstone UC-C-1, while Figure 3(b) shows the ninth cycle of the axial stress-radial strain curve of sandstone UC-C-1. It can be seen from Figure 4 that each cyclic sandstone forms a hysteresis loop, which is mainly due to the internal microcracks. The distance between the loading starting point and unloading end point is an irreversible strain, namely, residual strain. Among them, ε_1^{ri} and ε_3^{ri} are the axial and circumferential residual strains, respectively. The deformation under the unloading curve is recoverable deformation, namely, elastic strain, where ε_1^{ei} and ε_3^{ei} are the axial and circumferential elastic strains, respectively. The sum of the residual strain and elastic strain is the deformation under the loading curve under this cycle, namely, the total strain, where ε_1^{i} and ε_3^{i} are the axial and circumferential total strains under this cycle, respectively. The elastic modulus is the slope of the straight line of the loading and unloading curve. The elastic moduli of loading and unloading are expressed by E_L^i and E_U^i , respectively.

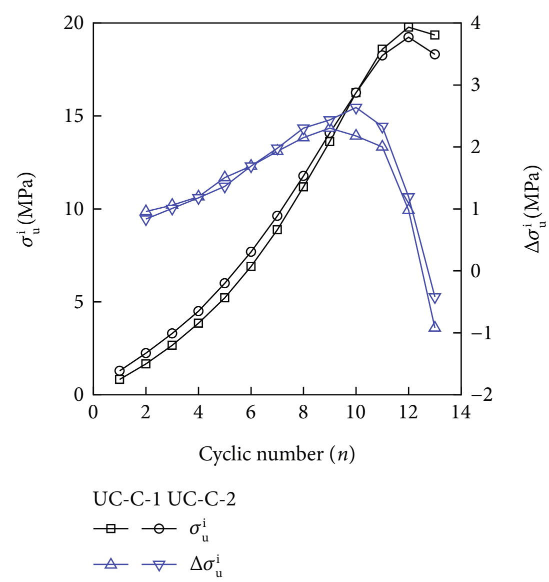

FIGURE 4: Unloading stress level and its difference of sandstone under cyclic loading.

4. Discussion

4.1. Effect of Cycles on Sandstone Deformation

4.1.1. Relationship among Residual Strain, Elastic Strain, and Number of Cycles. The residual deformation and elastic deformation of sandstone under different cycles are shown in Figure 5. Figure 5(a) shows the relationship between residual strain and cycles, while Figure 5(b) shows the relationship between elastic strain and cycles. The total strain of sandstone under each cycle is the sum of the cyclic elastic strain and residual strain. The ratios of residual strain, elastic strain, and total strain are shown in Figures 5(c) and 5(d), where R_1^r and R_1^e are the ratios of axial residual strain and axial elastic strain to total strain, respectively. The ratios of circumferential residual strain and circumferential elastic strain to total strain can be expressed as R_3^r and R_1^e.

It can be seen from Figure 5(a) that the axial residual strain first decreases and then increases with the increase of cycles. The residual strains of specimens UC-C-1 and UC-C-2, respectively, reach the minimum values at the tenth and seventh cycles, namely, 0.042×10^{-3} and 0.062×10^{-3}. Both the circumferential residual strain and volumetric residual strain decrease with the increase of cycles. With the continuous increase in the number of cycles, the

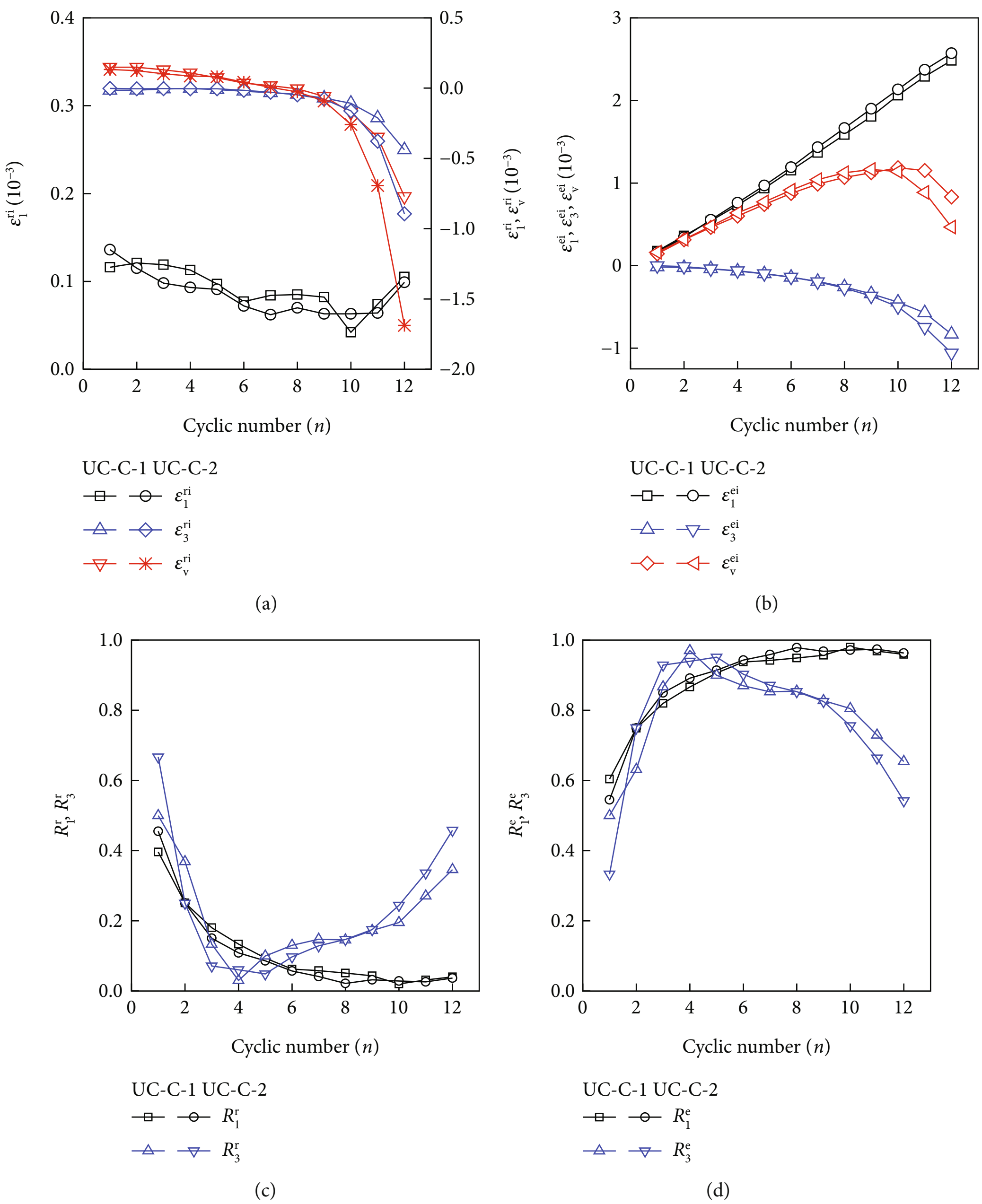

FIGURE 5: Residual (elastic) strain and their ratios of sandstone under uniaxial cyclic loading-unloading compression: (a) residual strain, (b) elastic strain, (c) proportion of residual strain, and (d) proportion of elastic strain.

microcracks in the sandstone first produce a closure effect, resulting in the axial residual strain gradually decreasing. Then, with the continuous increase in the graded load, the stress concentration occurs at the tip of the microcracks; then, the crack initiation and propagation occur, thus resulting in the gradual increase of the irreversible deformation.

It can be seen from Figure 5(b) that with the increase of cycles, the axial elastic strain showed a linear growth trend before the peak. The circumferential elastic strain decreases with the increase of the number of cycles, and the decreasing rate increases gradually. In the first six cycles, the volumetric elastic strain of sandstone increases linearly with the number of cycles. Then, with the number of cycles, the increase rate of volumetric elastic strain gradually decelerates. The bulk elastic strain of UC-C-1 and UC-C-2 samples reaches the maximum value after the tenth and ninth cycles, namely, 1.185×10^{-3} and 1.165×10^{-3}, respectively. Then, with the increase of cycles, the volume elastic deformation gradually decreases.

Figure 5(c) illustrates the relationship among the R_1^r, R_3^r, and cycle times of specimens UC-C-1 and UC-C-2. It can be seen that, with the increase of cycle times, the R_3^r decreases gradually. For example, specimen UC-C-1 sample reaches the minimum in the tenth cycle and then increases gradually with each cycle. The relationship between R_3^r and cycle times first decreases, then increases. Among them, specimens UC-

C-1 and UC-C-2 reach the minimum at the fourth and fifth cycles, respectively, and then gradually increase. Figure 5(d) shows the relationship among R_1^e, R_3^e, and the number of cycles. It can be seen that R_1^e increases gradually with the increase of cycles. On the contrary, R_3^e first increases, then decreases.

During the cyclic loading and unloading process, due to the gradual closure of the primary crack, the axial residual strain gradually decreases, and the ratio of residual strain to total strain gradually decreases. Then, with the increase of the cyclic load, the stress concentration occurs at the tip of the original crack, and the crack initiation occurs, resulting in the increase of the axial residual strain.

4.1.2. Relationship between Loading and Unloading Elastic Modulus and Cycles. The relationship between the loading and unloading elastic modulus of sandstone and the number of cycles under cyclic loading and unloading is shown in Figure 6. It can be seen from the figure that, with the increase of cycles, the loading elastic modulus increases gradually. Specimen UC-C-1 reaches the maximum value of 8.965 GPa at the tenth cycle, while specimen UC-C-2 reaches the maximum value of 10.48 GPa at the eleventh cycle, then begins to decrease.

The loading elastic modulus gradually increases. This is mainly because, in the process of cyclic loading, the microcracks inside the rock gradually close, and the rock matrix bears large deformation, resulting in the elastic modulus gradually increasing. In the early stage of loading, the unloading elastic modulus of specimen UC-C-1 gradually decreases, but overall, the relationship between the unloading elastic modulus and the number of cycles is not obvious, and its value changes little.

4.2. Effect of Unloading Stress Level on Deformation. The unloading stress level refers to the starting point when each cyclic stress begins unloading. The unloading stress difference refers to the difference between the unloading stress level of this cycle and that of the previous cycle, which is expressed as follows:

$$\Delta\sigma_u^i = \sigma_u^{i+1} - \sigma_u^i. \tag{1}$$

In the formula, σ_u^{i+1} is the unloading stress level of the $i+1$-th cycle, σ_u^i is the unloading stress level of the i-th cycle, $\Delta\sigma_u^i$ is unloading stress difference, and i is the number of cycles. The magnitude of unloading stress difference can reflect the damage degree of rock samples during cyclic loading and unloading. The unloading stress difference gradually decreases, indicating that the rock continues to undergo damage. The smaller the unloading stress difference, the greater the damage will be.

The unloading stress level and unloading stress difference of sandstone in each cycle are shown in Figure 4. It can be seen from the figure that, with the increase of the number of cycles, the unloading stress level increases gradually. The UC-C-1 and UC-C-2 samples reach the maximum value in the 12th cycle, which are 19.23 MPa and 19.78 MPa, respectively. Then, the failure occurs in the 13th cycle, and the peak values are 18.31 MPa and 19.36 MPa. The unloading stress difference of specimens UC-C-1 and UC-C-2 initially increases with the increase of cycles and reaches the maximum value at the ninth and tenth cycles, respectively, i.e., 2.303 MPa and 2.635 MPa. After that, with the continuous action of the cyclic load, the unloading stress difference gradually decreases, reaching a negative value in the 13th cycle.

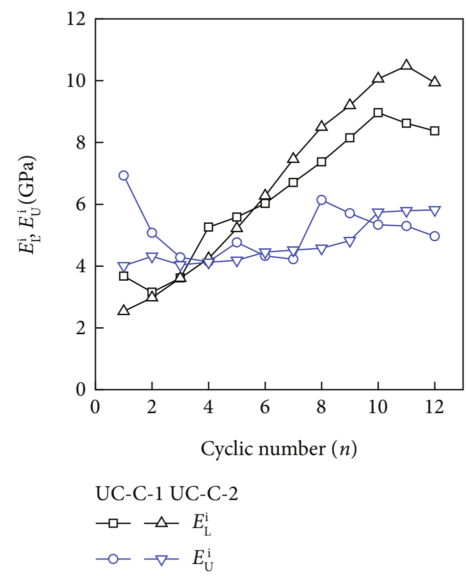

Figure 6: Loading and unloading moduli of sandstone under cyclic loading.

Figure 7 illustrates the relationship between the unloading stress level and deformation parameters of sandstone under cyclic loading and unloading. It can be seen from Figure 7(a) that, with the increase of the unloading stress level, the axial residual strain gradually decreases. Then, when the unloading stress levels of UC-C-1 and UC-C-2, respectively, reach 16.25 MPa and 18.58 MPa, the axial residual strain begins to increase. The circumferential residual strain and volume residual strain decrease with the increase of the unloading stress level, and the decrease rate increases gradually. With increase of the cyclic number, the stress unloading level increases and the damage of the sandstone will be more server. And it produces more internal cracks in the sandstone. These cracks are residual deformation. Therefore, with the increase of the cyclic number, circumferential and volume deformations increase.

The influence of the unloading stress level on the axial elastic strain is shown in Figure 7(b). It can be seen that the axial elastic strain is positively correlated with the unloading stress level. With the increase of the unloading stress level, the circumferential elastic strain gradually decreases, and the reduction rate gradually increases.

4.3. Damage Evolution Law of Sandstone under Cyclic Loading and Unloading. Damage refers to the deterioration process of materials or structures caused by mesostructural defects, which is manifested as the weakening of cohesion of materials and even the destruction of volume elements

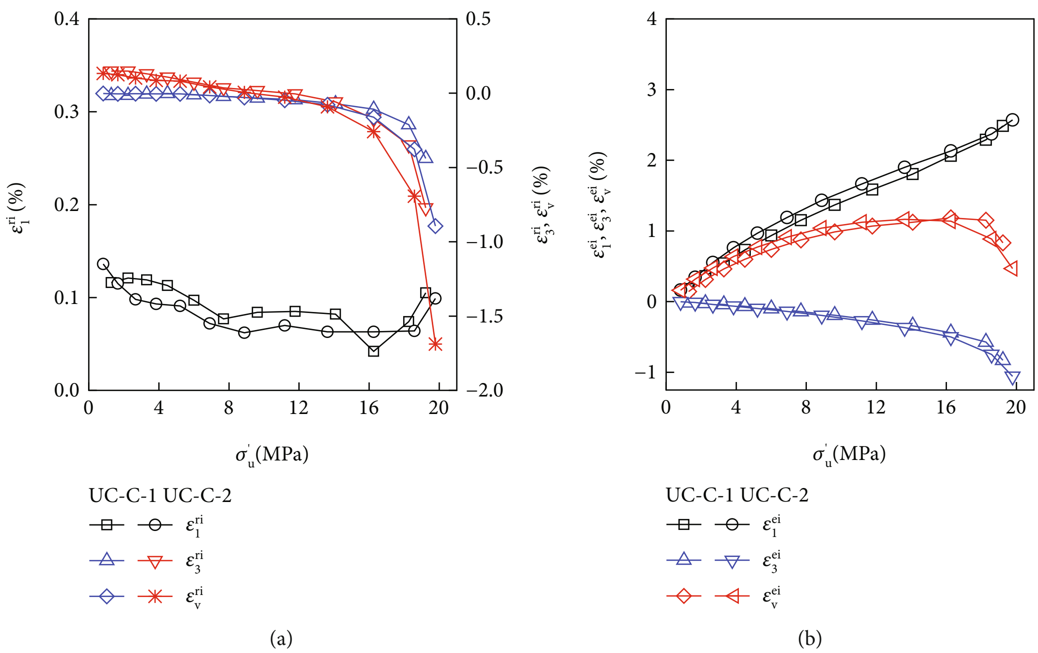

FIGURE 7: Relationship between unloading stress level and deformation: (a) residual strain; (b) elastic strain.

under external loads. It is an irreversible process of energy dissipation. Eberhardt et al. [31] proposed the following method for calculating damage parameters suitable for the cyclic loading and unloading process:

$$\omega_{ax} = \frac{\varepsilon_1^{ri}}{\sum_{i=1}^{n} \varepsilon_1^{ri}},$$
$$\omega_{lat} = \frac{\varepsilon_3^{ri}}{\sum_{i=1}^{n} \varepsilon_3^{ri}}, \quad (2)$$
$$\omega_{vol} = \frac{\varepsilon_v^{ri}}{\sum_{i=1}^{n} \varepsilon_v^{ri}},$$

where ω_{ax}, ω_{lat}, and ω_{vol} are the axial, circumferential, and volumetric strain damage parameters, respectively, which are the absolute damage parameters under each cycle, and n is the number of loading and unloading cycles.

The relationship between the damage parameters of sandstone and unloading stress level under cyclic loading and unloading is shown in Figure 8. In the figure, T_{ax}, T_{lat}, and T_{vol} are the axial, circumferential, and volume cumulative damage parameters, respectively. Their values are the sum of all the absolute damage parameters under a certain cycle. For example, the cumulative damage parameters of the sixth cycle are the sum of the absolute damage parameters of these six cycles. Taking UC-C-1 as an example, it can be seen from Figures 8(a) and 8(c) that, with the increase of the unloading stress level, the axial absolute damage parameter ω_{ax} of sandstone first decreases gradually, reaches the minimum value after about 16 MPa, then increases. The circumferential absolute damage parameter ω_{lat} of sandstone first gradually decreases, reaches the minimum value after 4 MPa, then gradually increases, and the increase rate is accelerated, indicating that the sandstone will soon fail. The volume absolute damage parameter ω_{vol} of sandstone first decreases, then increases with the increase of the unloading stress level. When the unloading stress level is about 12 MPa, it reaches the minimum, then increases, and the increase rate gradually accelerates. The absolute damage parameters of sandstone specimen UC-C-2 are similar to those of specimen UC-C-1. Based on the same phenomenon of sandstone specimens UC-C-1 and UC-C-2, it can be considered that during the cyclic loading and unloading, the absolute damage parameters (including axial, circumferential, and volume) of sandstone first decrease and gradually increase with the increase of unloading stress level, and the increase rate gradually increases. The main reason for this is that the rock itself undergoes initial damage, including a large number of primary cracks or pores and other defects. In the early stage of loading, the load bears a compaction effect on the microcrack inside the rock. The cracks gradually close, and the initial damage decreases; thus, the absolute damage parameter of the rock first decreases. Then, with the gradual increase of the graded load, the stress concentration occurs at the tip of the microcracks inside the rock, after which the crack initiation and propagation occur. The damage to the rock increases; thus, the absolute damage parameter of the rock begins to increase before the failure.

It can be seen from Figures 8(b) and 8(d) that with the increase of the unloading stress level, the cumulative damage parameters of specimens UC-C-1 and UC-C-2 have similar laws. Taking specimen UC-C-1 as an example, the axial cumulative damage parameter T_{ax} of sandstone increases with the increase of the unloading stress level, but the increase rate first increases, then decreases. The relationship between the circumferential cumulative damage parameter T_{lat} of sandstone and the unloading stress level exhibits

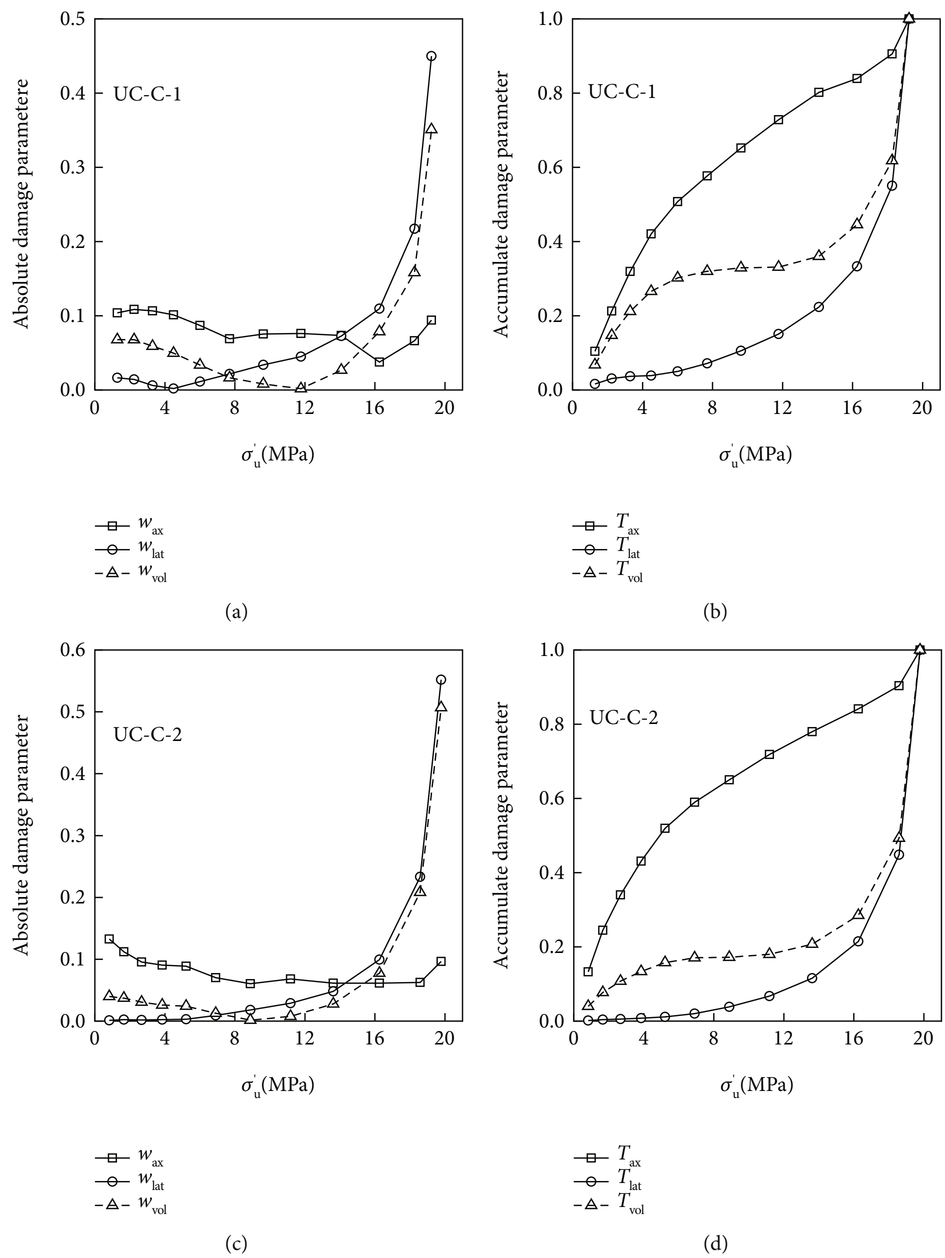

Figure 8: Damage parameters of sandstone with different unloading stress levels: (a) absolute damage parameter of UC-C-1; (b) accumulated damage parameter of UC-C-1; (c) absolute damage parameters of UC-C-2; (d) accumulated damage parameters of UC-C-2.

obvious nonlinearity; i.e., with the increase of the unloading stress level, T_{lat} increases nonlinearly. With the increase of the unloading stress level, the variation of cumulative damage parameter T_{vol} of sandstone can be divided into three stages. The first is the slow growth stage, the cycle number of which is 1~5, and T_{vol} gradually increases, but the increase rate gradually decelerates. The second stage is stationary, and T_{vol} basically remains unchanged with the increase of the number of cycles, which are 0.32 (UC-C-1) and 0.17 (UC-C-2); the third stage is the accelerated damage stage, in which, with the increase of the unloading stress level, the increase rate of T_{vol} gradually increases and almost increases vertically.

The relationship between the absolute damage parameters and cumulative damage parameters of sandstone under cyclic loading and unloading and the number of cycles is shown in Figure 9. It can be seen from the figure that the damage parameters of UC-C-1 and UC-C-2 are basically consistent with the evolution trend of cycles. The axial absolute damage parameter ω_{ax} of sandstone first shows a decreasing trend with the increase of cycles, but the decrease is not obvious; then, it begins to increase. The circumferential absolute damage parameter ω_{lat} of sandstone increases with the increase of cycles, thus indicating that the circumferential residual deformation increases with the loading and unloading cycles. With the increase of cycles, the

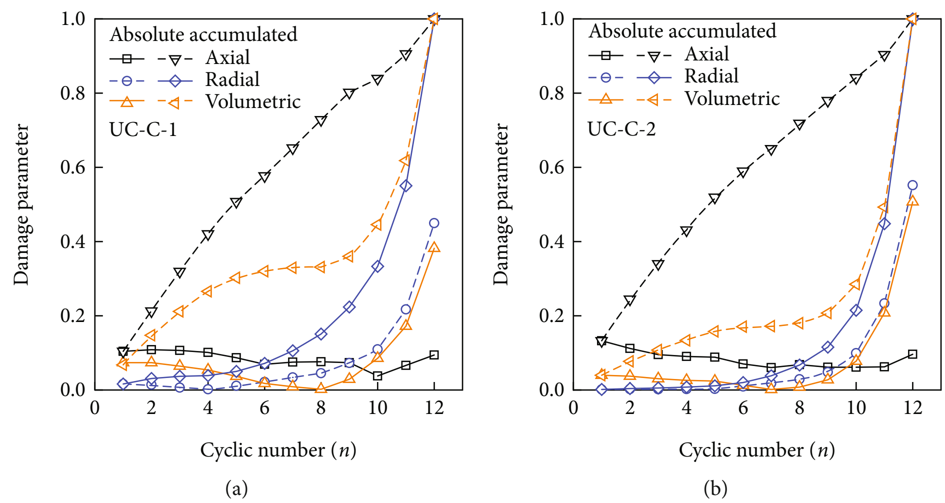

FIGURE 9: Damage parameters of sandstone with different cyclic numbers: (a) UC-C-1; (b) UC-C-2.

variation law of the absolute volume damage parameter ω_{vol} of sandstone can be divided into two stages. The first is the gradual decrease stage, at which time the ω_{vol} gradually decreases with the increase of the cycle number. Among them, specimen UC-C-1 reaches the minimum in the eighth cycle, while specimen UC-C-2 reaches the minimum in the seventh cycle; the respective values are 0.0019 and 0.0015. Then, ω_{vol} gradually increases with the increase of cycles, and the respective maximum absolute volume damage parameters of UC-C-1 and UC-C-2 are 0.381 and 0.507.

Comprehensively viewing Figures 8 and 9, it can be seen that the absolute and cumulative damage parameters of the axial, circumferential, and volume show increasing trends before brittle failure occurs. In addition, the increase rate of circumferential damage parameters and volume damage parameters suddenly increases, which is also the precursor of instability failure of the sandstone specimens. In the underground coal mine, the instability failure of surrounding rock may induce roof fall, rock burst, coal bump, or other accidents. Therefore, we must figure out the cyclic loading properties of the sandstone to give some references for supporting the roadway.

5. Conclusions

(1) Under cyclic loading and unloading, the cyclic stress-strain curve forms a hysteresis loop due to the influence of microcracks in sandstone. In the early stage, due to the closure of microcracks in sandstone, the axial residual deformation decreases with the increase of the number of cycles and unloading stress level. Then, with the increase of the grading load, the stress concentration at the tip of the primary crack occurs, and the crack initiation occurs, resulting in the axial residual deformation gradually increasing. The circumferential residual strain and volume residual strain bear a decreasing trend with the increase of the cycle number and unloading stress level; i.e., with the increase of the cycle number and unloading stress level, the circumferential residual deformation and volume residual deformation gradually increase. The axial elastic deformation increases with the increase of the cyclic number and cyclic load. The volume deformation first increases, then decreases, and the circumferential strain gradually decreases

(2) During the cyclic loading process, the microcracks inside the rock gradually close, and the rock matrix undergoes large deformation. Therefore, during the cyclic loading and unloading process, the loading elastic modulus gradually increases. Affected by damage, the unloading stress difference of sandstone initially increases with the increase of cycles. The effects of the cycle number and unloading stress level on the damage parameters of sandstone are analyzed. Prior to the brittle failure of the specimen, the absolute damage parameters of axial, circumferential, and volume exhibit an increasing trend, and the increase rates of circumferential damage parameters and volume damage parameters suddenly increase, which is also the precursor of instability failure of the sandstone specimen

Data Availability

The data used to support the findings of this study are available from the corresponding author upon request.

Conflicts of Interest

No potential conflict of interest is reported by the authors.

Acknowledgments

Financial supports from the National Natural Science Foundation of China (51904092), Key Scientific Research Project of Higher Education Institutions in Henan Province (20B580002), Fundamental Research Funds for the

Universities of Henan Province (NSFRF210454), Young Backbone Teachers Funding Program of Henan Polytechnic University (2022XQG-01), and Doctor Fund supported by Henan Polytechnic University (B2019-21) are gratefully acknowledged.

References

[1] Y. D. Jiang, Y. X. Zhao, H. W. Wang, and J. Zhu, "A review of mechanism and prevention technologies of coal bumps in China," *Journal of Rock Mechanics and Geotechnical Engineering*, vol. 9, no. 1, pp. 180–194, 2017.

[2] H. He, L. M. Dou, S. Y. Gong, J. He, Y. L. Zheng, and X. Zhang, "Microseismic and electromagnetic coupling method for coal bump risk assessment based on dynamic static energy principles," *Safety Science*, vol. 114, pp. 30–39, 2019.

[3] P. Wang and H. J. Luan, "Size effect analysis of remaining coal pillar on rock burst caused by fault," *Bulletin of Engineering Geology and the Environment*, vol. 81, no. 3, pp. 1–15, 2022.

[4] D. Ma, J. Zhang, H. Duan et al., "Reutilization of gangue wastes in underground backfilling mining: overburden aquifer protection," *Chemosphere*, vol. 282, p. 128400, 2021.

[5] D. Ma, S. Kong, Z. Li, Q. Zhang, Z. Wang, and Z. Zhou, "Effect of wetting-drying cycle on hydraulic and mechanical properties of cemented paste backfill of the recycled solid wastes," *Chemosphere*, vol. 264, p. 131163, 2021.

[6] E. Eberhardt, "Numerical modelling of three-dimension stress rotation ahead of an advancing tunnel face," *International Journal of Rock Mechanics and Mining Sciences*, vol. 38, no. 4, pp. 499–518, 2001.

[7] X. Huang, Q. Liu, B. Liu, X. Liu, Y. Pan, and J. Liu, "Experimental study on the dilatancy and fracturing behavior of soft rock under unloading conditions," *International Journal of Civil Engineering*, vol. 15, no. 6, pp. 921–948, 2017.

[8] M. Rao and Y. V. Ramana, "A study of progressive failure of rock under cyclic loading by ultrasonic and AE monitoring techniques," *Rock Mechanics and Rock Engineering*, vol. 25, no. 4, pp. 237–251, 1992.

[9] G. C. He, W. Y. Wu, Y. Wang, Y. M. Xue, B. Dai, and Z. J. Zhang, "Fracture Characteristics and fatigue damage of noncoplanar fractured rocklike specimens under uniaxial graded cyclic loading and unloading," *Geofluids*, vol. 2021, Article ID 9993195, 13 pages, 2021.

[10] M. J. Heap, S. Vinciguerra, and P. G. Meredith, "The evolution of elastic moduli with increasing crack damage during cyclic stressing of a basalt from Mt. Etna volcano," *Tectonophysics*, vol. 471, no. 1–2, pp. 153–160, 2009.

[11] Z. Wang, S. Li, L. Qiao, and J. Zhao, "Fatigue behavior of granite subjected to cyclic loading under triaxial compression condition," *Rock Mechanics and Rock Engineering*, vol. 46, no. 6, pp. 1603–1615, 2013.

[12] M. D. Zoback and J. D. Byerlee, "The effect of cyclic differential stress on dilatancy in westerly granite under uniaxial and triaxial conditions," *Journal of Geophysical Research*, vol. 80, no. 11, pp. 1526–1530, 1975.

[13] G. M. Elliott and E. T. Brown, "Further development of a plasticity approach to yield in porous rock," *International Journal of Rock Mechanics and Mining Sciences & Geomechanics Abstracts*, vol. 23, no. 2, pp. 151–156, 1986.

[14] S. K. Singh, "Fatigue and strain hardening behaviour of graywacke from the flagstaff formation, New South Wales," *Engineering Geology*, vol. 26, no. 2, pp. 171–179, 1989.

[15] R. Yoshinaka, T. V. Tran, and M. Osada, "Non-linear, stress- and strain-dependent behavior of soft rocks under cyclic triaxial conditions," *International Journal of Rock Mechanics and Mining Sciences*, vol. 35, no. 7, pp. 941–955, 1998.

[16] N. Li, P. Zhang, Y. Chen, and G. Swoboda, "Fatigue properties of cracked, saturated and frozen sandstone samples under cyclic loading," *International Journal of Rock Mechanics and Mining Sciences*, vol. 40, no. 1, pp. 145–150, 2003.

[17] M. N. Bagde and V. Petroš, "The effect of machine behaviour and mechanical properties of intact sandstone under static and dynamic uniaxial cyclic loading," *Rock Mechanics and Rock Engineering*, vol. 38, no. 1, pp. 59–67, 2005.

[18] Z. L. Zhou, Z. B. Wu, X. B. Li, X. Li, and C. D. Ma, "Mechanical behavior of red sandstone under cyclic point loading," *Transactions of Nonferrous Metals Society of China*, vol. 25, no. 8, pp. 2708–2717, 2015.

[19] K. Fuenkajorn and D. Phueakphum, "Effects of cyclic loading on mechanical properties of Maha Sarakham salt," *Engineering Geology*, vol. 112, no. 1–4, pp. 43–52, 2010.

[20] E. Liu, S. He, X. Xue, and J. Xu, "Dynamic properties of intact rock samples subjected to cyclic loading under confining pressure conditions," *Rock Mechanics and Rock Engineering*, vol. 44, no. 5, pp. 629–634, 2011.

[21] S. L. Qiu, X. T. Feng, J. Q. Xiao, and C. Q. Zhang, "An experimental study on the pre-peak unloading damage evolution of marble," *Rock Mechanics and Rock Engineering*, vol. 47, no. 2, pp. 401–419, 2014.

[22] J. C. Zhang, S. H. Zhou, L. G. Fang, and X. H. Xu, "Effects of axial cyclic loading at constant confining pressures on deformational characteristics of anisotropic argillite," *Journal of Central South University*, vol. 20, no. 3, pp. 799–811, 2013.

[23] S. Q. Yang, P. G. Ranjith, Y. H. Huang et al., "Experimental investigation on mechanical damage characteristics of sandstone under triaxial cyclic loading," *Geophysical Journal International*, vol. 201, no. 2, pp. 662–682, 2015.

[24] S. Q. Yang, W. L. Tian, and P. G. Ranjith, "Experimental investigation on deformation failure characteristics of crystalline marble under triaxial cyclic loading," *Rock Mechanics and Rock Engineering*, vol. 50, no. 11, pp. 2871–2889, 2017.

[25] Q. Meng, M. Zhang, L. Han, H. Pu, and T. Nie, "Effects of acoustic emission and energy evolution of rock specimens under the uniaxial cyclic loading and unloading compression," *Rock Mechanics and Rock Engineering*, vol. 49, no. 10, pp. 3873–3886, 2016.

[26] H. Song, H. Zhang, D. Fu, and Q. Zhang, "Experimental analysis and characterization of damage evolution in rock under cyclic loading," *International Journal of Rock Mechanics and Mining Sciences*, vol. 88, pp. 157–164, 2016.

[27] H. Song, H. Zhang, Y. Kang, G. Huang, D. Fu, and C. Qu, "Damage evolution study of sandstone by cyclic uniaxial test and digital image correlation," *Tectonophysics*, vol. 608, no. 6, pp. 1343–1348, 2013.

[28] T. Wang, C. Wang, F. Xue, L. Wang, B. H. Teshome, and M. Xue, "Acoustic emission characteristics and energy evolution of red sandstone samples under cyclic loading and unloading," *Shock and Vibration*, vol. 2021, Article ID 8849137, 15 pages, 2021.

[29] Y. Chen, J. Zuo, Z. Li, and R. Dou, "Experimental investigation on the crack propagation behaviors of sandstone under different loading and unloading conditions," *International Journal of Rock Mechanics and Mining Sciences*, vol. 130, p. 104310, 2020.

[30] Y. Chen, *Study on deformation failure behaviors and nonlinear models for rocks under the influence of mining disturbance*, Doctoral Dissertation, China University of Mining and Technology, Beijing, 2018.

[31] E. Eberhardt, D. Stead, and B. Stimpson, "Quantifying progressive pre-peak brittle fracture damage in rock during uniaxial compression," *International Journal of Rock Mechanics and Mining Sciences*, vol. 36, no. 3, pp. 361–380, 1999.

Hindawi
Geofluids
Volume 2022, Article ID 9144937, 23 pages
https://doi.org/10.1155/2022/9144937

Research Article

Study on Roof Presplitting Mechanism and Deformation Control of Reused Roadway in Compound Soft Rock by Roof Presplitting Approach

Fuzhou Qi,[1] **Dangwei Yang**,[2,3] **Xinming Li**,[1] **Bin Li**,[1] **Yingying Zhai**,[1] **and Shuisheng Yu**[1]

[1]*School of Civil & Architecture Engineering, Zhongyuan University of Technology, Zhengzhou, 450007 Henan, China*
[2]*Pingdingshan University, Pingdingshan, 467000 Henan, China*
[3]*Pingdingshan Coal No. 10 Mine, Pingdingshan, 467000 Henan, China*

Correspondence should be addressed to Dangwei Yang; ydw15162171009@163.com

Received 27 December 2021; Accepted 11 July 2022; Published 1 August 2022

Academic Editor: Hualei Zhang

Based on the compound soft rock movement law, the rock formation structural features for a mining roadway were examined. Furthermore, the presplitting, extension, and coalescence mechanism of rock formation and the engineering needs for reusing an abandoned underground roadway were studied. According to engineering and geological conditions, an analytic expression of the inertial force, the moment of inertia, and the vertical stress acting on the breakage are obtained by constructing a structural mechanical model of the overlying strata. The transfixion law, the tensile shear failure characteristics, the release rate in the fracture expansion process of presplitting fissures, and the evolution law of the plastic zone in reused roadway surrounding rock on conditions of 0 m, 0.5 m, 1 m, 1.5 m, and 2 m fissure intervals are analyzed by creating a three-dimensional numerical model. The stress distribution and deformation laws of the roadway under mining disturbance are obtained. The results show that when the fissure interval is 1 m, the peak value of the horizontal stress reaches 10~12 MPa, and the stress concentration factor is 1.8~2.2, which promotes fracture expansion and transfixion and controls plastic damage development on both sides of a fracture. The elastic strain energy of the reused roadway is reduced to 32.7% of the peak value. The deformation of the roof is coordinated and deformed. It is helpful for the compound soft rock strata to fall and plug the area, forming a stable composite reused roadway surrounding the rock structure. A 1 m presplitting fissure interval is adopted for field testing, and the monitoring results show that 0~3.0 m behind the mining face, presplitting fissures will be connected and begin to fall. Moreover, 3.0~6.0 m behind the mining face, compound soft rock strata will fall and plug the area fully, forming a reused roadway structure. Severe deformation of reused roadway was reduced, and the stability of surrounding rock was improved by implementing the roof presplitting approach.

1. Introduction

In China, coal resources are dominated by underground mining and result in large abandonment problems in underground spaces such as roadways or underground chambers. These areas are of widespread concern while satisfying the rapid development of social economy requirements. Abandoned underground spaces waste resources and bring hidden dangers such as water bursts, gas outbursts, and strong mine pressures [1–3]. For the resource development of adjacent areas, a series of environmental problems such as ground subsidence may also occur. Therefore, it is undoubtedly the best solution to solve the above problems by taking full advantage of existing abandoned underground spaces according to local conditions to perform afterheat reuse of the abandoned underground spaces [4, 5]. The abandoned underground spaces of mines include two parts: the leftover and abandoned roadways of the production mine and the underground mine chamber. Mines are equipped with production systems such as transport, aeration, and pedestrian conditioning systems. Use of the abandoned underground space will more effectively take full advantage of the service functions of every mine production system on the basis of good production and safety. The abandoned roadway and chamber systems in the last mining section can be used as a warehouse for storing production materials or a provisional substation, and water storage increases the use ratio of resources and the length of mine service and reduces environmental pollution. Reused roadways are different from the general mining roadways in that one side lateral wall of the reused roadway is coal-rock mass, while another side is gob, which includes large deformations in the surrounding rock. The superimposed stress of double roadway mining and the adjacent slope is held up by the gob, supporting tremendous mine ground pressure, and is extremely complicated engineering technology [6, 7]. The stability of the surrounding reused roadway rock depends on the degree of stress concentration during mining, and the stress concentration also depends on factors such as the top and bottom mining coal seam slate structure and its mechanical properties and the roof structure after caving. To ensure the stability of the surrounding reused roadway rock, the supporting design and high safety factor and the size and strength enhancing the support inside or adjacent to the roadway are generally adopted [8]. The expected effect is hard to achieve due to the influence of normal production and safety, and they cause unnecessary economic losses [9]. Meanwhile, coal seams with a compound soft roof are widely found; each rock formation is small in thickness with joint and fracture development. There are weak bond forces and low overall strength among rock formations and lower overall strength, so separation rock formations become larger under the surrounding rock pressure. The pressure could easily cause inbreak, and it is hard to form a bearing structure. Thus, there are greater stability requirements for the surrounding reused roadway rock [10, 11].

To solve the above problems, automatic broken roof stowboard technology is developed from compound soft rock, which simplifies the retained roadway technique, improves the retained roadway efficiency, and provides reliable technical support for taking full advantage of the remaining abandoned underground space. In the above technical system, the advance presplitting of the roof formation is an important step [12, 13], since continuous advanced presplitting of the roof on one side of the roadway along with the mining side is required, and the length of the presplitting fissure is up to 1,000 meters. Meanwhile, the influence on mining must be taken into consideration. Thus, there are stringent requirements on the time and structure of advanced presplitting. As a key parameter of roof presplitting, the presplitting fissure intervals have a significant influence on the stress distribution of the roadway surrounding rock, the roof cutting result, and the falling position and state [14]. The intervals become a key factor of whether the reused roadway plays a normal role. In the paper, the 5# coal seam with a compound soft rock roof of the mining area in Linfen, Shanxi, was selected to study the propagation and coalescence effect of rock presplitting fissure and the stress and deformation law of surrounding rock. Additionally, the plastic zone distribution characteristics of the reused roadway presplitting rock fissure under different presplitting rock fissure intervals were analyzed to provide a basis for the stability of the surrounding reused roadway rock.

2. Study on the Reused Roadway Stratum Structure

2.1. Engineering Background. The coal seam 5# at a mine has an average thickness of 2 m, belonging to medium-thickness coal seams. As shown in the geology columnar Figure 1, the immediate roof stratum of the coal seam is black mudstone with the average thickness of 3.3 m, weak carrying capacity, and crushing and abscission of strata are liable to occur. The main roof stratum is sandy mudstone with the average thickness of 3.1 m, with good stability, and having direct impact on the roadway pressure. The main roof stratum has sandy mudstone with the average thickness of 7.7 m at the top. The overlying rock of coal seam 5# is the thick-stratum soft compound rock strata, mainly mudstone strata and sandy mudstone strata. It has low strength and weak carrying capacity. Under the effect of mining disturbance, fracture development and severe deformation may occur (Figure 2), so the roadway is hard to maintain. In order to make full use of abandoned roadway in the 5203 mining face, the air return roadway of the 5203 mining face as air return roadway is near the 5205 working face, and the transport roadway for the production material storage warehouse is in 52 mining section.

2.2. Analysis of Presplitting Structure of Composite Soft Rock Strata. The gob side of the compound soft rock roof is broken to cut the connection of the roadway roof and the overlying rock on the gob side. This process also shortens the hanging length of the roof rock beam at the roadway gob and weakens the superimposed pressure caused by mining disturbances. Meanwhile, under the effect of its own gravity, the overlying rock pressure, and the mining disturbance, the compound soft rock strata will be cut along the presplitting fracture. Using the bulking collapsed rock characteristics, the roadside gob is filled to form the retained roadway of the gangue wall, and contact is made with the overlying stable rock. The bearing structure is formed at the area of gob side to support the overlying rock pressure and form a coordinated control structure of the roadway surrounding rock by "roof breaking+pressure releasing+filling with collapsed rock," as shown in Figure 3.

The roof presplitting will weaken the boundary constraint of A, as shown in Figure 3(a).

The curvature of the compound soft rock formation group axis after deformation appeared as follows [15]:

$$\frac{1}{\rho} = \frac{M_0}{EI_z}. \tag{1}$$

M_0 is the bending moment of the compound soft rock under the mine pressure effect, E refers to the rock formation elasticity modulus, and I_z is the rock formation inertia

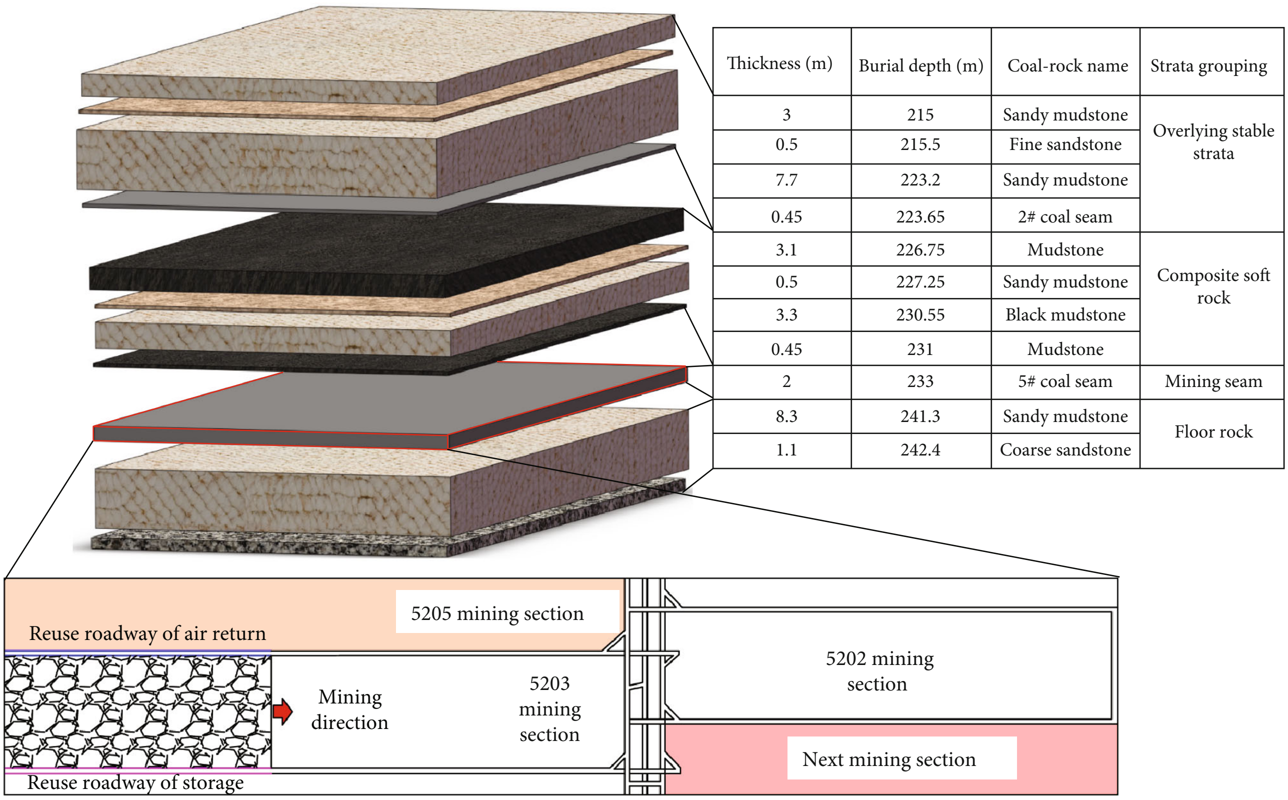

Thickness (m)	Burial depth (m)	Coal-rock name	Strata grouping
3	215	Sandy mudstone	Overlying stable strata
0.5	215.5	Fine sandstone	
7.7	223.2	Sandy mudstone	
0.45	223.65	2# coal seam	
3.1	226.75	Mudstone	Composite soft rock
0.5	227.25	Sandy mudstone	
3.3	230.55	Black mudstone	
0.45	231	Mudstone	
2	233	5# coal seam	Mining seam
8.3	241.3	Sandy mudstone	Floor rock
1.1	242.4	Coarse sandstone	

Figure 1: Geological structure of strata.

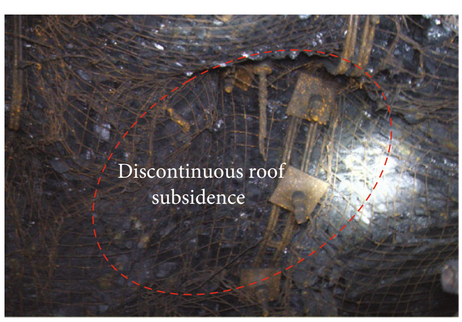

(a) Roof subsidence

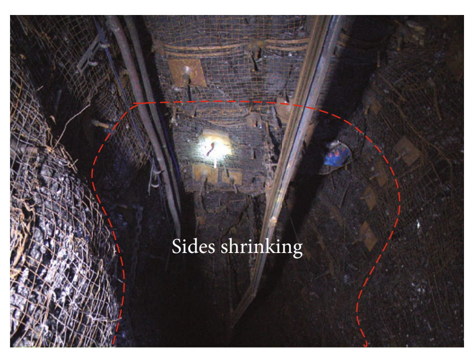

(b) Side shrinking

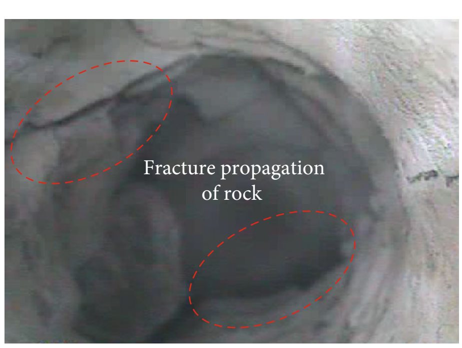

(c) Rock fracture

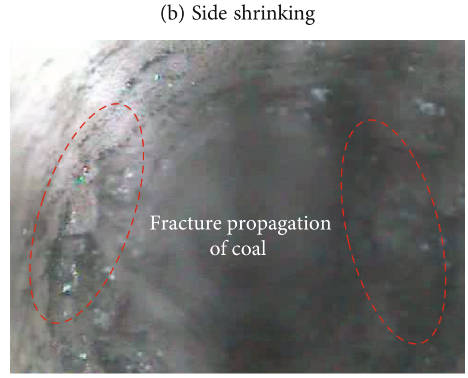

(d) Coal fracture

Figure 2: Failure mode of soft roadway.

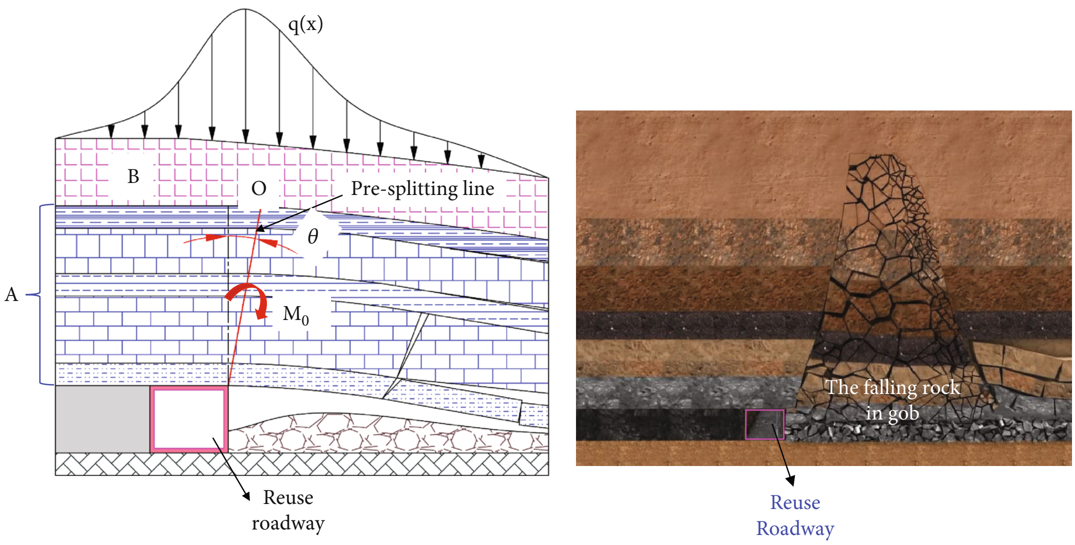

(a) Before roof presplitting

(b) After roof presplitting

Figure 3: Mechanical model of the presplitting structure of compound soft rock strata.

moment; among them, EI_z is the flexural rigidity of the rock formation. At the time of rock formation presplitting, the roof flexural rigidity EI_z reaches a maximum; as the presplitting fissure interval decreases, the controlling effects of the surrounding rock formation on the gob roof formation diminish, the sinking bending becomes obvious, the curvature increases, and when the presplitting fissure interval is 0, that is, when the presplitting fissure is mutually connected, the flexural rigidity is minimal. If the weakening degree of the rock formation flexural rigidity after presplitting is large, M_0 drops rapidly, and compound soft rock will undergo drastic bending, subsidence, and reversal falling. The lower rock formation as well as the overlying and comparatively complete rock formation cannot deform synchronously and coordinately, or the dynamic loading effect will occur and threaten the surrounding roadway rock stability. If the weakening degree of the rock formation flexural rigidity after presplitting is small, the compound soft rock cannot break along the fissure in time, the roof exposed area increases, the stress concentration occurs on the solid coal-rock side of the roadway, and the plastic damage scope of the surrounding rock increases. Hence, the optimizing fissure width parameter can control the rock formation structure, the caving position, and the presplitting roof state; improve stress conditions of the roadway surrounding rock; and ensure the stability of the reused roadway.

The compound soft rock strata fall along the presplitting fissure and form the supporting structure in the gob side of the reused roadway, as shown in Figure 2(b). The upper stable rock B will rotate and bend at point O, and the support strength of the filling support structure for the high top plate B is as follows [16, 17]:

$$E \cdot (l - a) \cdot \sin \theta = P_0, \tag{2}$$

where E is the caving gangue supporting elasticity modulus; P_0 is the loose gangue strength; θ is the upper rock formation angle; l is the suspended roof length, basically being the same as that of the periodic fracture of the rock stratum and could be monitored on field; and a is the roadway width. It is known from Equation (2) that when the angle is larger, the holding power borne by the filled rubble is larger, and the cantilever beam caves easily on the kerf after presplitting, which effectively reduces the acting force of the upper rock formation bending deformation on the caving support and enhances the stability of the reused roadway surrounding rock structure.

I_B is the moment of inertia of the upper stable rock B. l_B is the hanging length of rock B on the gob side. α_0 is the rotational acceleration of rock B. The inertia force F_B and inertia moment of couple M_B acting on the base point O are [18, 19]

$$\begin{aligned} F_B &= m\alpha_0 = m\frac{l_B}{2}\alpha, \\ M_B &= J_B\alpha = \frac{1}{3}ml_B^2\alpha, \end{aligned} \tag{3}$$

where$\alpha_o = (L/2)\alpha$and$q(x)$is the equation of vertical load distribution for rock$B$and is the vertical shear stress of the key block$B$at the gob side. According to the force balance in the vertical direction, the vertical force F_O acting on B at O point is

$$F_O = f_o + \int_0^l q(x)dx + mg - \frac{\alpha m l_B}{2}. \tag{4}$$

Therefore, when the compound soft rock strata are falling, the dynamic pressure of the upper strata B causes the rapid pressurization of the support structure collapse and is one of the key factors affecting the stability of surrounding rock of the reused roadway.

2.3. Determination of Roof Breaking Height. The height of rock stratum caving after compaction will depend on the bulking coefficientK_p of the rock. The rock caving at the roof soft rock caving zone in the working face is irregular. After recompaction, the loosening coefficient is low and the residual breaking expansion coefficient K_p is taken as 1.2 [20]. When the caving thickness of the overlying rock stratum is $\sum h$, the accumulation height after caving is $K_p\sum h$. The possible gap remaining with the overlying stable rock stratum is [21, 22]

$$\Delta = \sum h + M - K_p \sum h = M - \sum h(K_p - 1), \quad (5)$$

where M is the mining height, taken as 2 m, and K_p is the residual bulking coefficient of rock, taken as 1.2.

According to Equation (5), when$M = \sum h(K_p - 1)$, $\Delta = 0$, i.e., the falling overlying rock will fill up the gob to support the load of overlying rock. Thus, the required thickness of the overlying rock to fill up the gob is

$$\sum h = \frac{M}{K_p - 1}. \quad (6)$$

The parameters are entered into Equation (6) to obtain $\sum h$. For the 5203 panel, the coal seam mining height is 2 m, and the height of the caved zones is 9.9 m based on field measurement. According to above equation, the bulking coefficient is 1.2 and the fracturing height of the roof strata is 10 m.

3. Analysis of the Presplitting Fissure Extension and Presplitting Roof Stability

3.1. Model Establishment. According to the field monitoring results, the effective fracture length is 2 m. In order to study the migration law and the presplitting effect of the roof rock under different presplitting fissure intervals, the continuous element numerical model is established for the presplitting fissure intervals of 0, 0.5 m, 1 m, 1.5 m, and 2 m, respectively. Ahead of the presplitting with the mining at the same time, the establishment of the model is shown in Figure 4.

m,n,φ, and$h$, respectively, are for the resplitting length, intervals, deflection angle, and height. The direction of m, n is consistent with the mining direction of the 5203 working face in the numerical model.

The size of model is 85 m × 45 m × 37 m. The equivalent load is applied to the upper boundary of the model. The lateral displacement of the model is limited, and the vertical movement is restricted by the bottom surface. The Mohr-Coulomb strength criterion is used to judge the yielding state of coal and rock mass [23, 24]:

$$f_s = \sigma_1 - \sigma_3 \frac{1 + \sin\varphi}{1 - \sin\varphi} + 2C\sqrt{\frac{1 + \sin\varphi}{1 - \sin\varphi}}, \quad (7)$$

where σ_1 and σ_3 are the maximum and minimum main stress, respectively.C and φ are the bonding force and frictional angle of the rock, respectively. When$f_s > 0$, the material will experience shear failure, according to the law of tensile strength ($\sigma_3 \geq \sigma_t$) to analyze whether there is rock tensile deformation. See Table 1 for the physical and mechanical parameters of the rock stratum. In the numerical model, before extraction of the 5203 panel, a roof presplitting line is arranged in the roof strata of reused roadway. This was performed by adopting null element representing the roof fracturing line.

3.2. Distribution Horizontal Stress Characteristics. The presplitting fissure is an opening-type fracture that induces the roof rock formation to extend and cut along the predetermined direction. The superimposed stress caused by mining disturbance plays a leading role on the presplitting fissure extension [25]. Under static-dynamic loading, the fissure tip stress is concentrated. When the horizontal stretching stress of the rock formation on both sides of the fissure exceeds the extension strength of the rock formation, the rock formation will break along the fissure tip and the compound soft roof on the gob side will experience large horizontal displacement. The bearing capacity of the sandy mudstone at 0.5-3.5 m above the reused roadway is strong, which is close to the roadway and has a strong control effect on the caving of the compound soft rock formation. The average breaking distance period of intact rock formations is 25-30 m. The slice at 3 m above the reused roadway is taken as the main object of study in the model, and the survey line is set at 2 m away from the presplitting fissures in the roadway. Figure 5 shows the horizontal stress nephogram for both sides of the presplitting fissures and the horizontal stress curve at the survey line.

The development and coalescence of the presplitting fissure are accompanied by the stress evolution of rock mass around the fracture. Figure 5 shows a presplitting interval of 0 m, and the presplitting fissures coalesced in the initial section of the retained roadway. When mining 0-6 m, the rock with presplitting fissures is in an unstable state because the roof loses the binding force on one side. The surrounding horizontal stress is then concentrated in the ends of the fracture, and the horizontal stresses reaches 8-12 MPa, while the stress concentration factor is 1.45-2.18. When mining to 6-9 m, the horizontal tensile stress is drastically attenuated from the peak and remains stable. The average horizontal tensile stress is kept at 1 MPa. If the slope of the stress curve is large, fissures dramatically occur and spread horizontally in a short time, effects that are not beneficial for the stability control of the rocks with presplitting fissures.

Figures 5(b) and 5(c) show that the presplitting fissure intervals are 0.5 m and 1 m, which are short in distance. When mining to 0-6 m, the rock is weakened under the cutting action of rock formation. The presplitting fissures are not penetrated, so there is no momentary instability and the stress concentration is eased; stress around the presplitting fissures is 6-7 MPa, and its concentration factor is reduced to 1.1-1.3, which is better to ensure the integrity of its surrounding rock and fully engage the self-bearing rock capacity. When mining to 6-9 m, the tension stress among rocks in fractures overlaps to form an "O" ring with

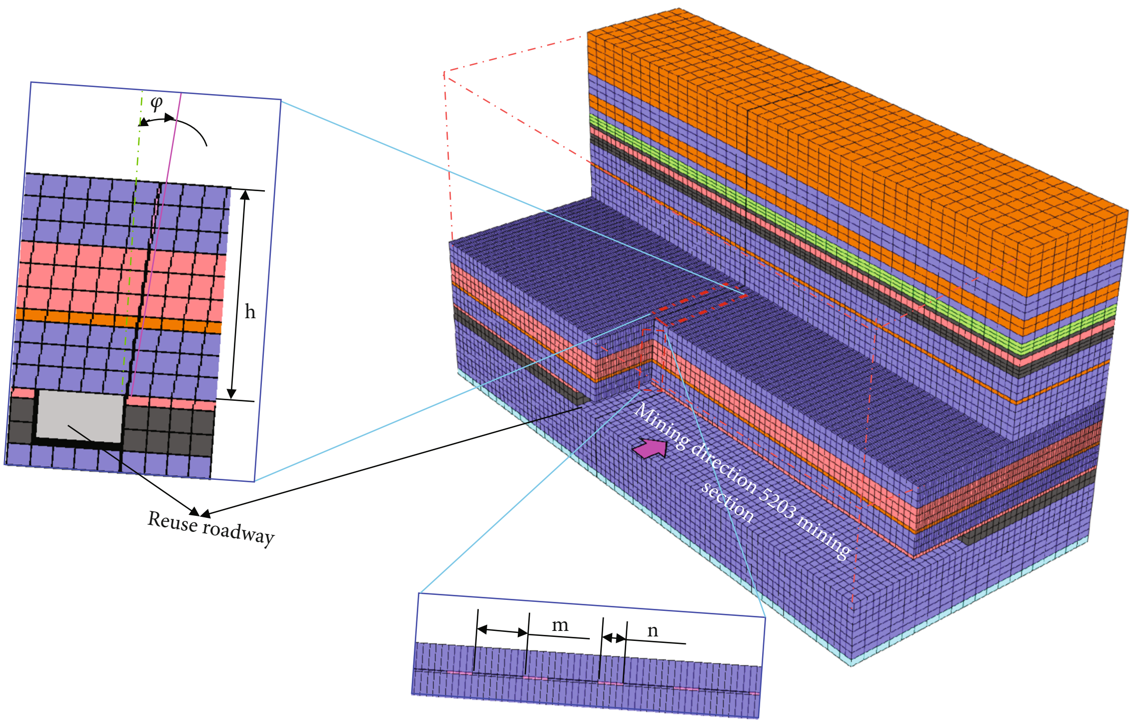

Figure 4: Numerical model of reused roadway.

Table 1: Physical and mechanical parameters of rock stratum.

Parameters	Bulk (GPa)	Shear modulus (GPa)	Tension (MPa)	Cohesion (MPa)	Friction (°)	Density (kg·m^{-3})
Sand mudstone	12	8.6	2.1	1.2	32	2600
5# coal seam	1.5	2.0	1.2	0.9	24	2450
Mudstone	4.3	8.6	1.7	1.4	30	2200
Fine sandstone	36	12.6	7.2	1.45	31.5	2600
Siltstone	25	4.6	3.6	1.0	33	2500
2# coal seam	1.5	2.0	1.2	0.9	24	2450

a radius of 0.5-1 m. The horizontal stress peak of rocks in the fissure interval reaches 10-12 MPa, and expansion and coalescence occur in the ends of the presplitting fissures. When mining to 9-12 m, the horizontal tensile stress starts to become stable, and the stability remains between 6 and 6.5 MPa. A large displacement occurs on the presplitting fissure in the short range, which benefits the timely caving of the compound soft rock formation, plugging of the gob side of the reused roadway, and rapid building of the reused roof cutting stowboard structure.

Figures 5(d) and 5(e) illustrate that the presplitting fissure intervals are 1.5 m and 2 m, and the distance between presplitting fissure interval rocks increases. When mining to 0-9 m, the control forces on both sides of the presplitting fissure become stronger. The horizontal tension stresses of both sides increase to 8-10 MPa, and the concentration factors are 1.45-1.8. The stress of the fractured interval rock is elliptical, and the stress concentrations at the fissure ends do not overlap. The central position of the horizontal tensile stress peak decreased to 8-9 MPa. When mining to 10-15 m, the horizontal displacement reaches its peak value, and the slope of the stress curve is small and represents a cyclical fluctuation. The timely cutting effects of caving and plugging into the gob of the compound soft rock formation are not ensured, which influences the quick roadway construction effect.

3.3. Plastic Damage Evolution Law of Presplitting Fissure Zones. As shown in Figure 6, in the vicinity of the fracture tip, the plastic zone is formed due to stress concentration and relaxation. Under mining disturbance action, the damage plastic zone is distributed along the axial direction of the reused roadway, the rock mass around the fracture decreased, and the plastic zone expanded.

As shown in Figure 6(a), the reused roadway is reserved and set as 0-9 m. Both sides of the fissure and the roof at the gob side are mainly shear damage. If 9-27 m is reserved, the shear stress is drastically attenuated from the peak, and frictional slip occurs between the fractures. Dilatancy displacement is restricted by the side, and the secondary fissure development is induced, which exacerbates the damage range of the fissure sidewall. In Figures 6(b) and 6(c), 0-

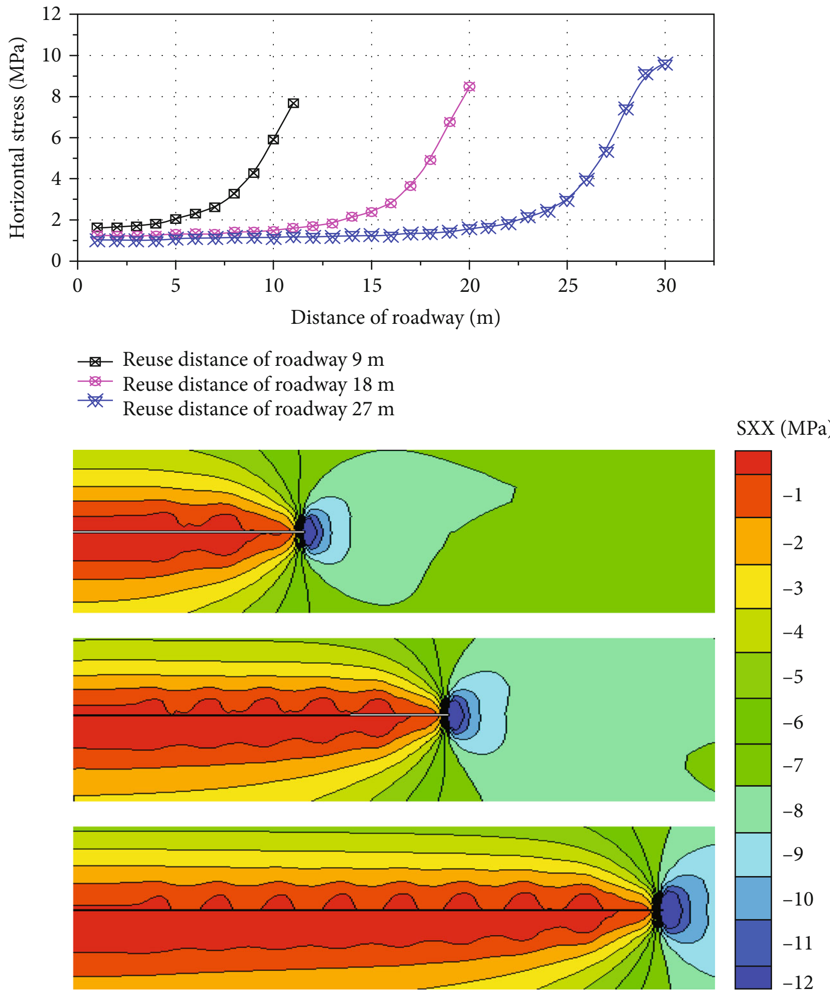

(a) Presplitting interval 0 m

Figure 5: Continued.

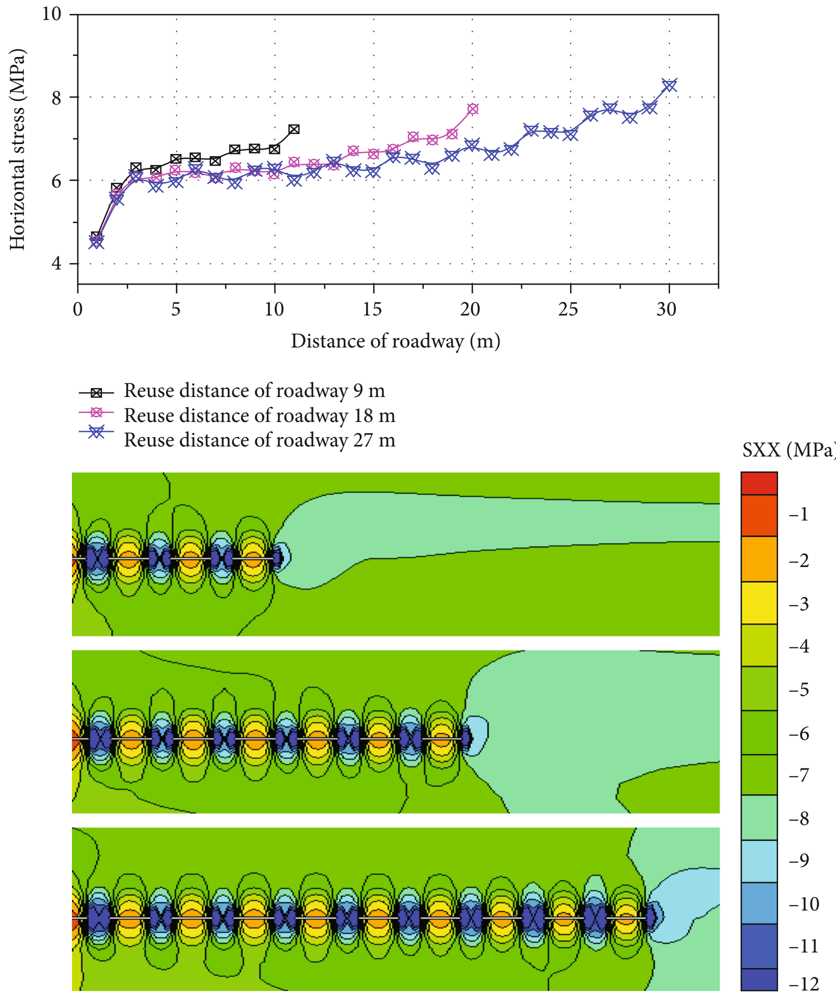

(b) Presplitting interval 0.5 m

Figure 5: Continued.

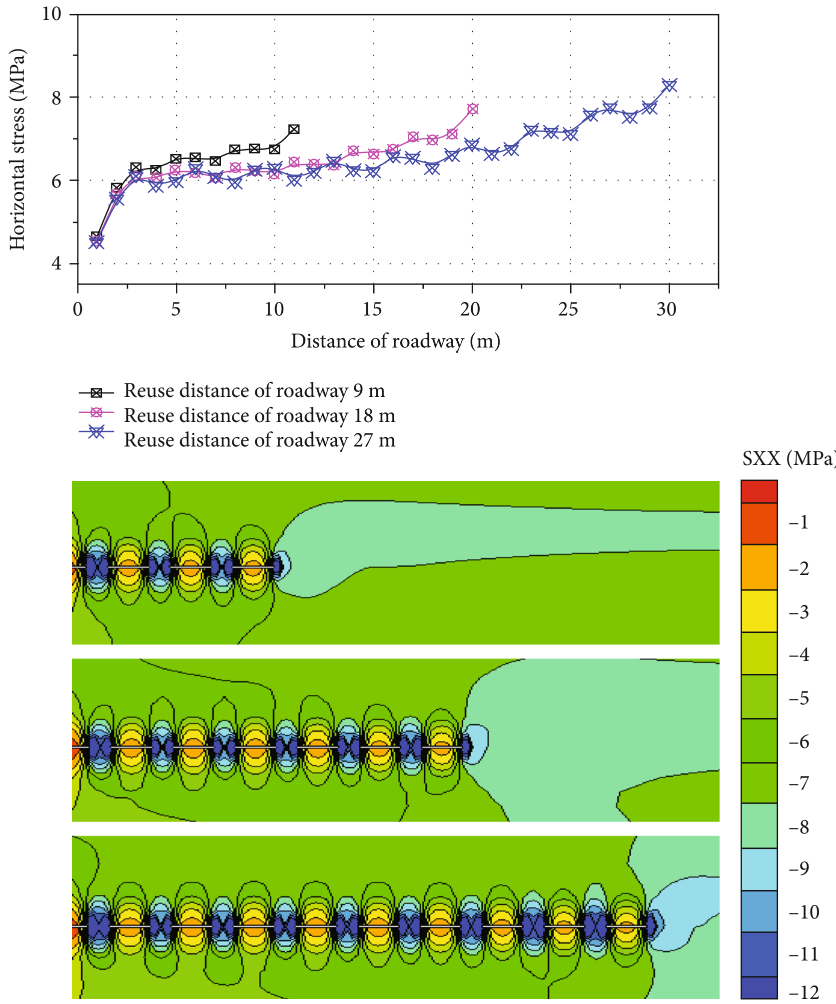

(c) Presplitting interval 1 m

FIGURE 5: Continued.

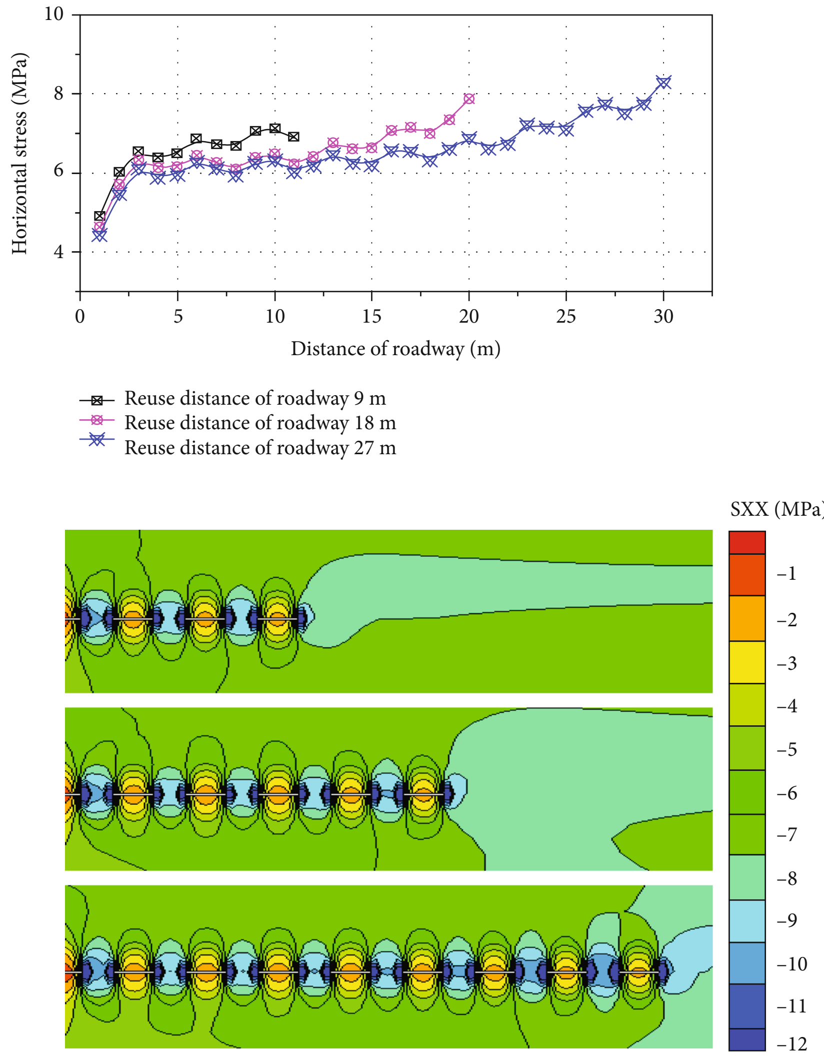

(d) Presplitting interval 1.5 m

Figure 5: Continued.

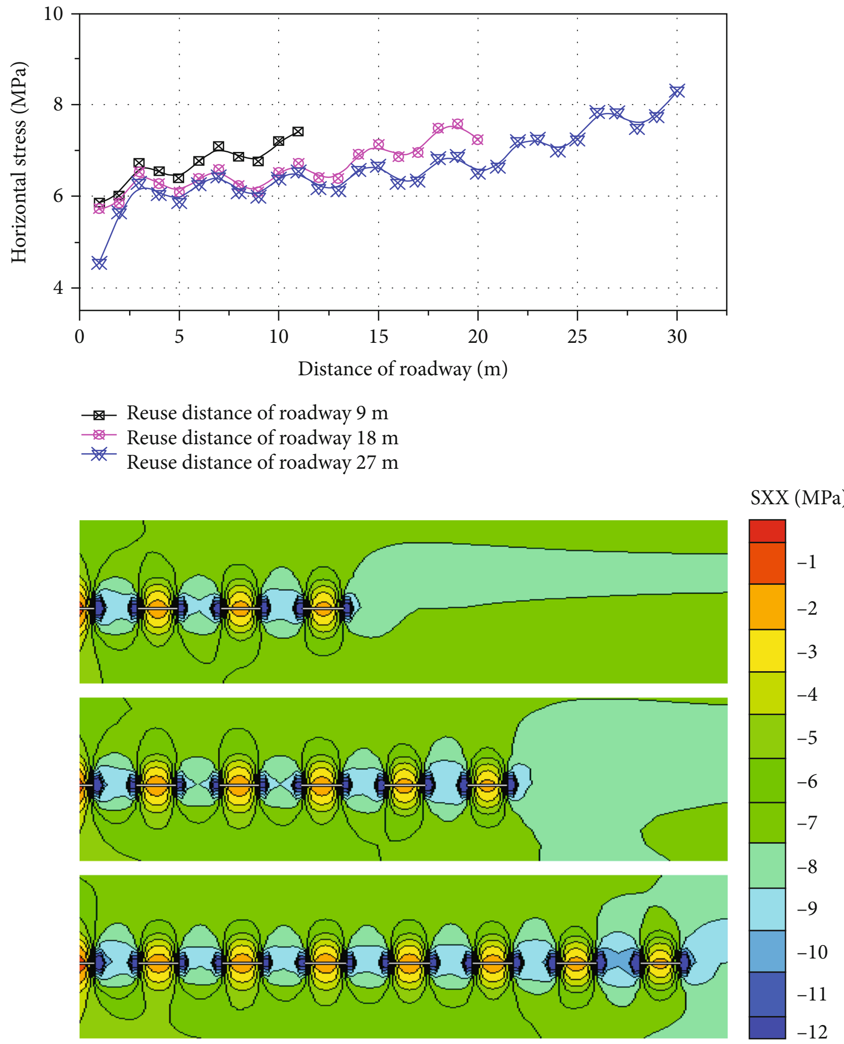

(e) Presplitting interval 2 m

Figure 5: Horizontal tensile stress curve and stress nephogram of the presplitting zone.

9 m is reserved in the reused roadway, and both sides of the fracture show damage. Due to the roof suspension area increase, the roof at the gob side is bent and sunken under the upper overlying stratum pressure and mining disturbance actions; the segregated rock is mainly subject to shear, and dilatant plastic damage occurs. When 0-18 m is reserved, the plastic area at both sides of the presplitting fissure has a sustainable development within 10 m from the initial end of the roadway. The force of the roof is from the shear stress to tension stress, the tensile and plastic damage areas increase, and the fissure interval accelerates the expanding and coalescence. The plastic areas are also connected to each other afterwards. When 27 m is reserved, the above evolution process proceeds in the roof presplitting fissures at the gob side; therefore, the expansion and coalescence cycle of its presplitting fissure is 8-10 m. In Figures 6(d) and 6(e), the fracture expansion is further limited when the presplitting fissure enlarges, and 0-18 m is reserved in the roadway. The suspension rock formation at the gob side does not experience large shear damage except in the small area where shear dilation as well as tensile and plastic damages occurs; the presplitting fissure does not show an expansion trend. The retained roadway is 27 m. It reaches the intact cycle caving distance of the roof rock, and the overburden pressure is transferred to the compound soft rock formation. The roof shows dramatic bending, subsidence, instability, and collapse, and the presplitting fissure has large expansion and coalescence as well as shear dilation at the gob side. The tension and plastic damage areas intermingle. The presplitting fissure does not have a better control effect on the caving of the compound soft rock formation, and the expansion and coalescence cycle of the fissure reaches 18-25 m.

3.4. Energy Dissipation of Presplitting Fissure Features. Coal bump occurs in a very short period of time, and there is no sign before it occurs. In order to eliminate the occurrence of coal bump, many researches on the strain energy distribution characteristics were conducted. Energy is considered the internal variable through the presplitting fissure opening

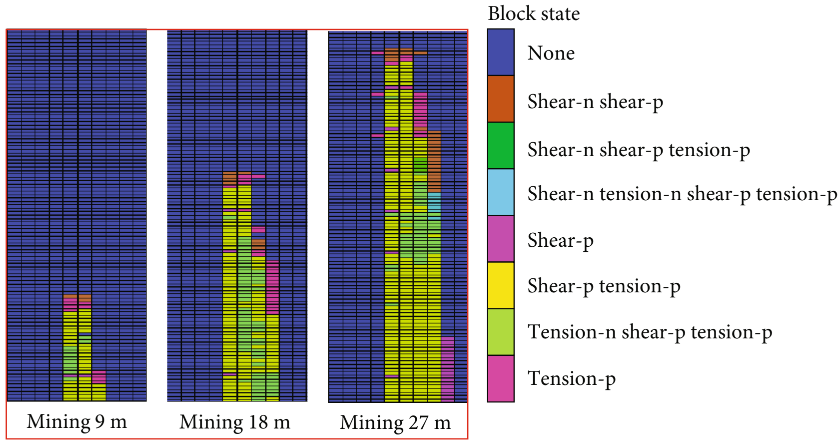

(a) Presplitting interval 0 m

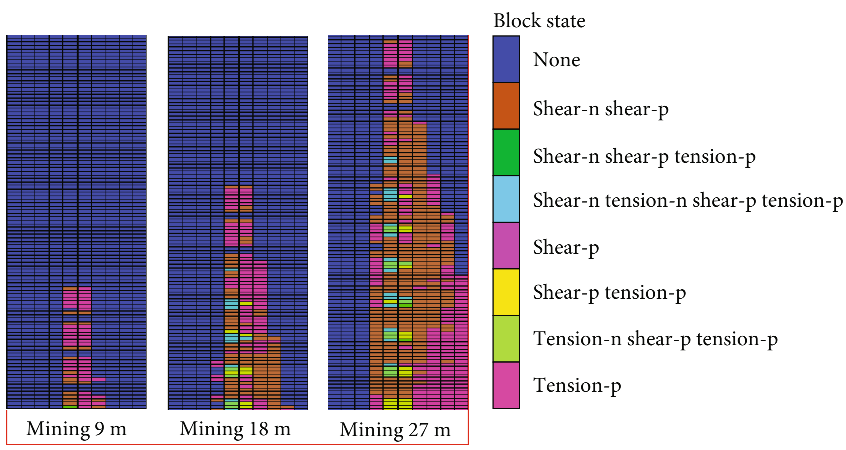

(b) Presplitting interval 0.5 m

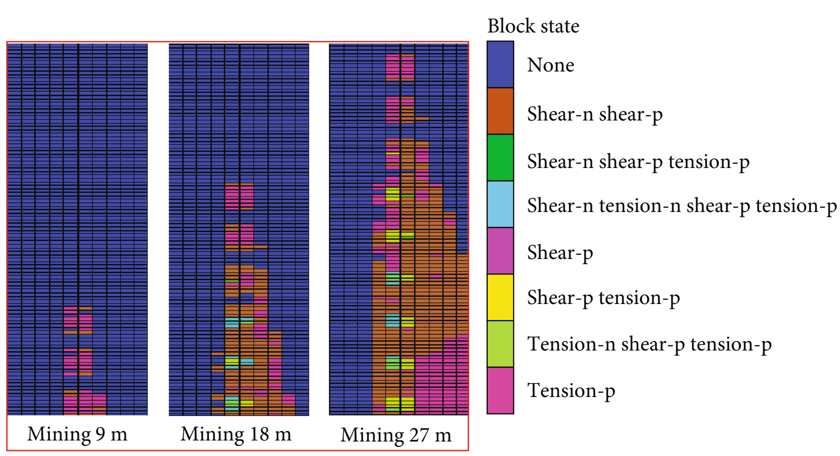

(c) Presplitting interval 1 m

Figure 6: Continued.

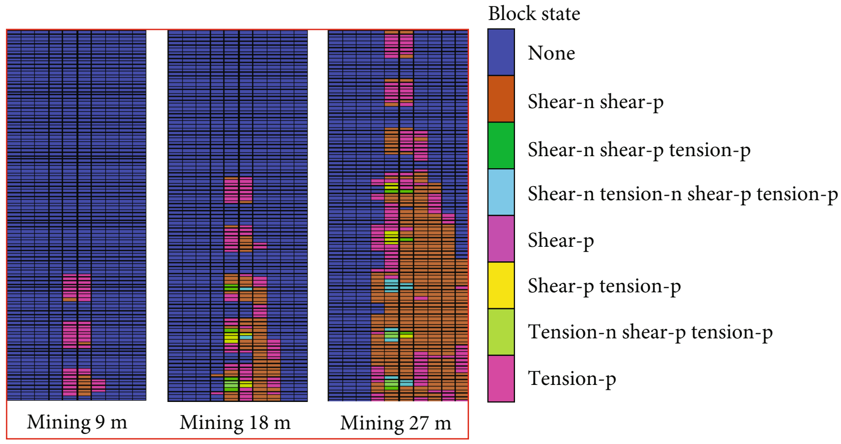

(d) Presplitting interval 1.5 m

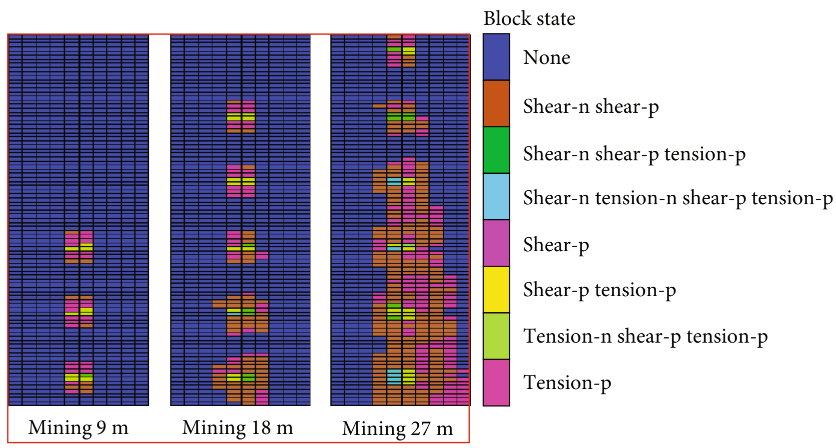

(e) Presplitting interval 2 m

Figure 6: Plastic damage evolution process of rock mass in the presplitting area.

and spreading. The damage process of the surrounding rock damage and the evolution process can thus reflect the presplitting effect [26]. In the fracture propagation process, the energy is released at the fracture tip, part of which will be used to form a new fracture area, and the other produces plastic deformation. The energy release rate G of the presplitting fissure end region is greater than the surface free energy γ_s of the interval rock mass against fracture propagation, i.e., $G > \gamma_s$; the presplitting fissure will continue to expand and cross. According to the energy balance theory, the crack energy release rate G is as follows [27, 28]:

$$G = \frac{1}{2B}\frac{d(W-U)}{da}, \tag{8}$$

where W is external work done on the presplitting fissure structure, U is stored strain energy, B is thickness of the presplitting strata, and a is length of the presplitting fissure. According to Equation (8), when the strain energy U, the thickness of presplitting strata B, and the length of the presplitting fissure are certain, the presplitting fissure is subjected to the work W of the mining disturbed rock mass in the horizontal direction as

$$W = \int_l p(x)s(x)dx. \tag{9}$$

Monitoring lines are set in the gob side from the prefabricated fissure as 3 m. The horizontal tensile stress distribution $p(x)$ and the horizontal displacement $s(x)$ are fit into the polynomial equation and integrated into Equation (9), as shown in Figure 7. The dispersion curves of the strain energy dissipation in the horizontal direction of the fracture zone are then obtained.

The expansion and coalescence of a presplitting fissure are the exchange process of energy absorption, transformation, and release. As shown in Figure 7(a), when the retained roadway is 9 m, the slope of the curve becomes larger with the side roof of the gob cutting down along the fissure, and the sliding energy accelerates to release with a value of 1172.5 kJ. When the retained roadway is 18 m and 27 m, respectively, the curve changes from index variation to linear variation. The overlapping range of the upper and lower surfaces increases, which leads to the dilatancy effect. Large amounts of friction are created in

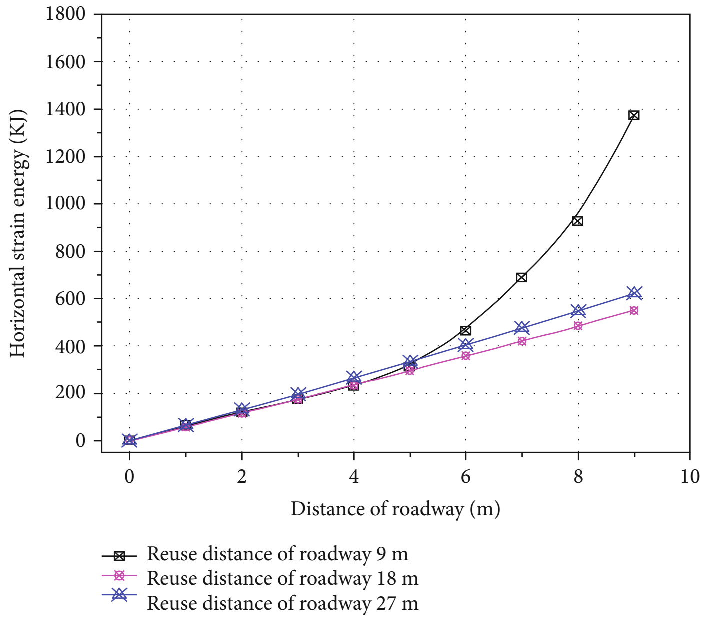

(a) Presplitting interval 0 m

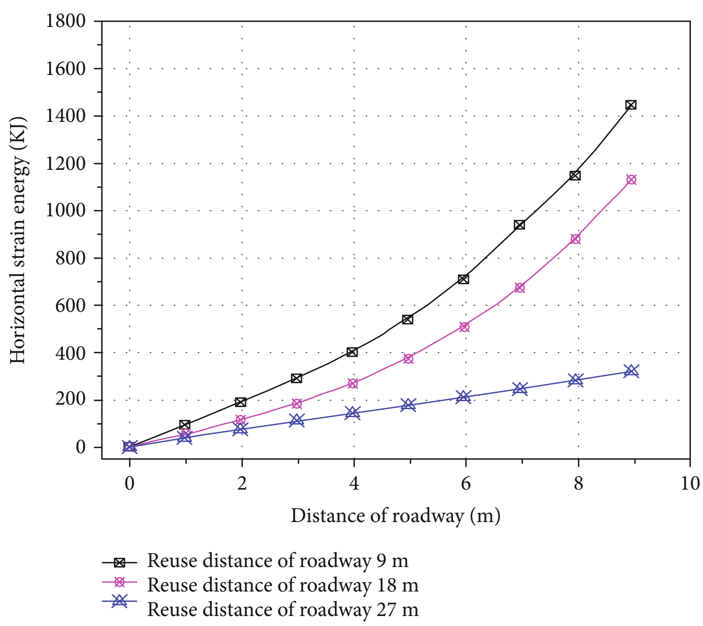

(b) Presplitting interval 0.5 m

Figure 7: Continued.

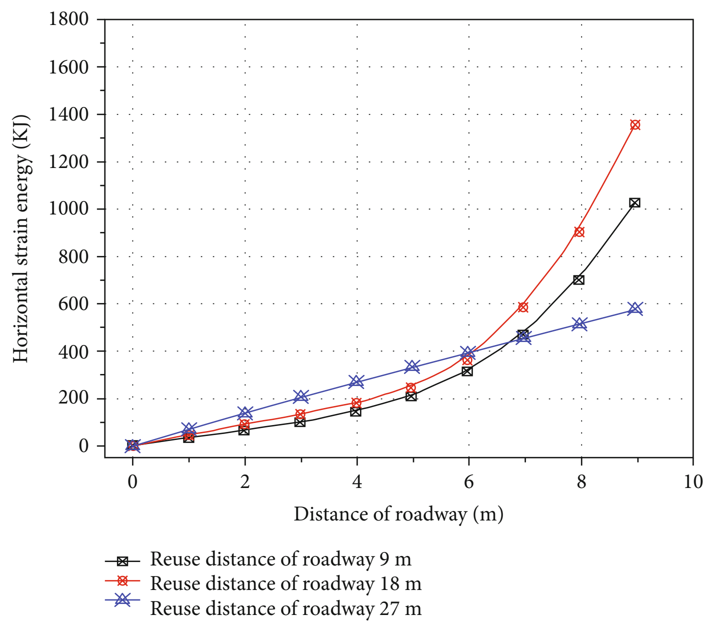

(c) Presplitting interval 1 m

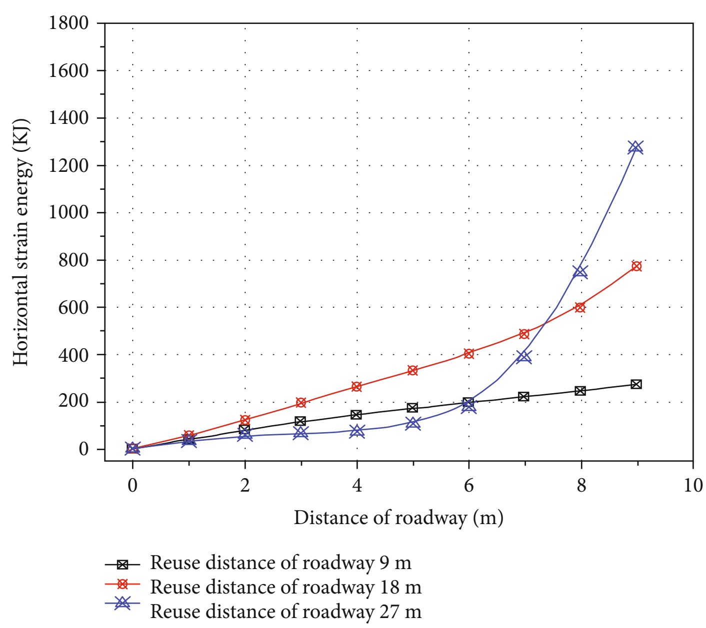

(d) Presplitting interval 1.5 m

Figure 7: Continued.

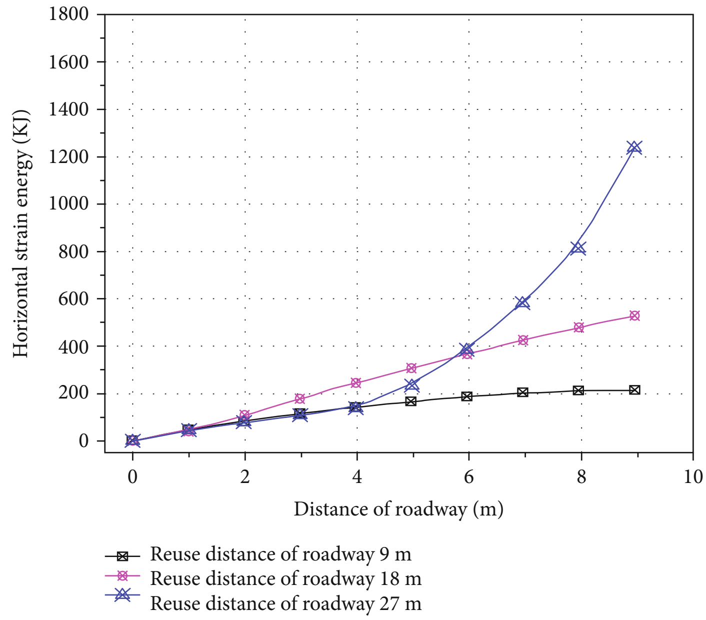

(e) Presplitting interval 2 m

FIGURE 7: Strain energy accumulation and dissipation curve of presplitting fissure propagation.

the gap interfaces, and the energy consumption rate decreases to 550 kJ, which is 47% of the initial rate. In Figures 7(b) and 7(c), the retained roadway is 0-18 m, and the presplitting fissure remains in a stable expansion stage while the elastic strain energy release curve presents an exponential form and steady growth. The strain energy of the rocks around the presplitting fissure has sustainable growth, and the average peak value reaches 1,650 kJ when the retained roadway is 9-18 m. At this point, the accumulated ability of the elastic strain energy release reduces because the initial fissure occurs. When the retained roadway is 27 m, the fissures continually expand and link, so the energy consumption rate of the surface shows a linear increase. Meanwhile, the peak values decrease to 319 kJ and 576 kJ, which are 19.3% and 32.7% of the peak, respectively, and the shear friction weakens and quickly achieves that of the stowboard. In Figures 7(d) and 7(e), no cutting downward or sinking occurs along the presplitting fissure of the soft rock formation at the gob side. However, the overall bending subsidence occurs based on the solid roadway rock. When the retained roadway is 9 m, the plastic deformation of the solid rock is large, the strain energy rapidly accumulates, the broken rock zone of the surrounding roadway rock is enlarged, and the elastic strain energy release decreases to a peak value of 1,100 kJ. Compared with the presplitting fissure intervals of 0.5 m and 1 m, the slope of the curve flattens and decreases greatly to 66%, seriously weakening the fracture expansion capacity. When the retained roadway is 9-27 m, the elastic strain energy curve presents a linear variation, of which the mean peak value is 360 kJ. The energy consumption rate decreases, and the linkage cycle period is prolonged, causing difficulties in achieving quick stowboard after mining.

4. Analysis on the Stability of Roadway

4.1. Deformation and Plastic Damage Characteristics of Surrounding Roadway Rock. Rocks have strain softening and dilatancy characteristics. The failure zone of the surrounding rocks is the cause of increased pressure and deformation of the surrounding rock [29, 30]. In reused roadways, during the initial excavation process, the medium-term mining disturbance, and the latter part of the maintenance and reuse process, the elasticity, plasticity, and rupture of the surrounding rock have an evolutionary process. The occurrence, development, and stability generally cause an unstable state of destruction. The larger the damage area is, the greater the amount of convergence deformation is [31]. Therefore, the size of the surrounding rock damage rupture zone is a measure of the degree of instability of the surrounding rock key factors.

As shown in Figure 8, the presplitting fissure interval is 0 m and 0.5 m, since the lateral diastrophism limit of the compound soft rock formation is greatly weakened, and the fissure interfaces overlap during collapse, the rock integrity is destroyed, and the bearing capacity is weakened. The friction action between the interfaces enlarges the shear and plastic damage around the fissures, which easily leads to a rapid collapse due to the sudden instability on the side rock mass of the reused roadway. The upper stable rock suddenly loses the support of the lower rock to create a stress concentration and a large range of tension damage occurs. The 1 m presplitting fissure weakens the flexural rigidity of the roadway soft rock mining side as a tensile fracture. The falling rock formation inversion alleviates the dilation friction between fractures. Meanwhile, the plastic zone of the roadway gob side soft rock formation has a wedge distribution with a large end towards the bottom, which is advantageous

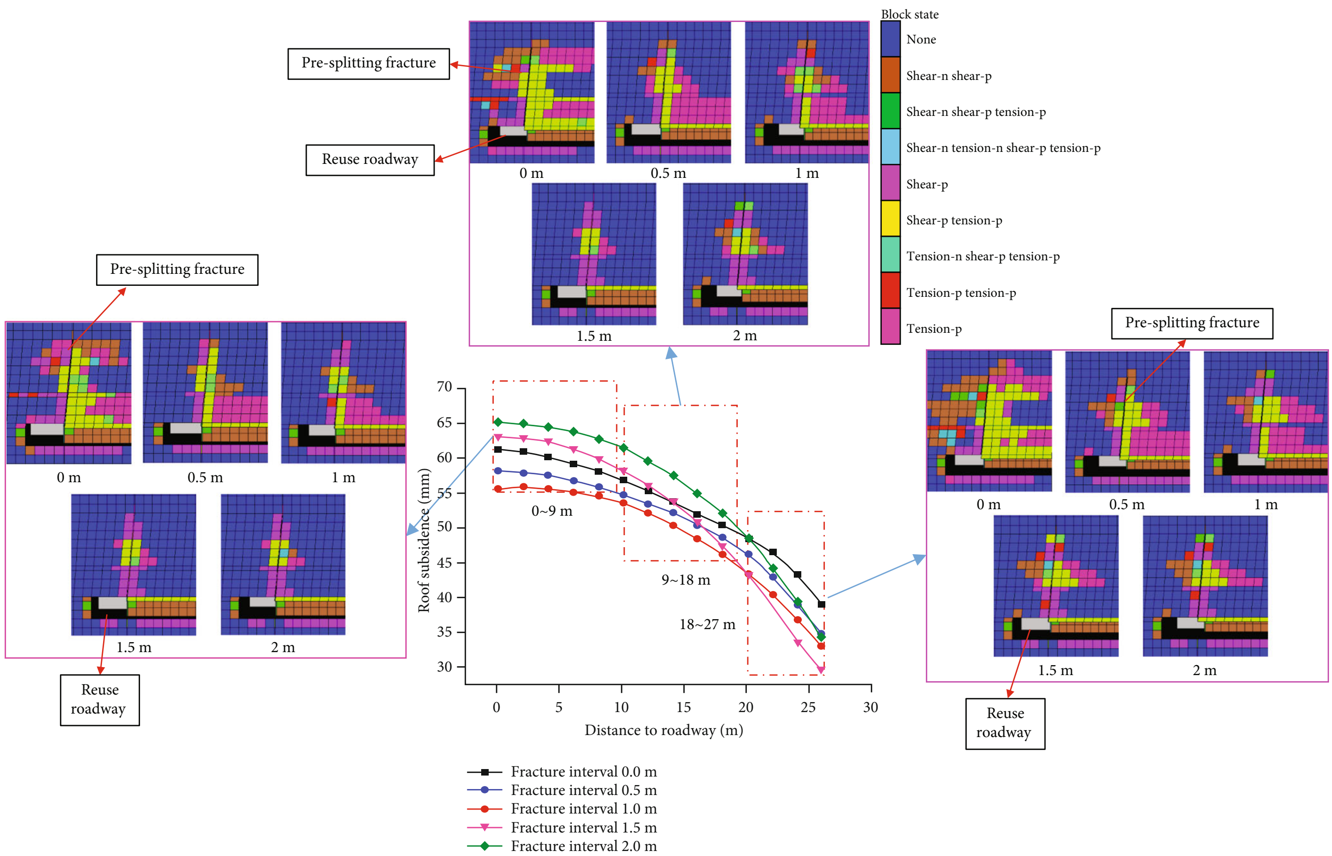

Figure 8: Deformation curves and plastic damage distribution characteristics of surrounding reused roadway rock.

for the successive, coordinated caving of low and median rock formations. A stable supporting structure at the gob side of roadway is then formed. In the case of presplitting fissure intervals of 1.5 m or 2 m, the fracture effect will slightly weaken the flexural rigidity of the rock formation, with the roofs of both sides being sidewise limited. The compound rock formation is not easily cut downwards along the presplitting fissure, resulting in the whole roadway tiling down sharply and going against the stability of surrounding rocks.

4.2. Study on the Roadway Roof Stratum Stability. One side of the reused roadway is the solid coal, and the other side is the filling body. The roof deformation is asymmetric, so the roof to the gob side rotation subsides, and the roof above the gob produces a wide range of shear failure. Thin, weak, soft rocks exist in the overlying roadway strata, the stratum movement is severe, and the shear slip range and tear propagation increase [32]. The roof separation and separation stratum increases cause the bearing capacity of the rock stratum to be greatly reduced, which threatens the stability of the surrounding rock. The upper roadway section of 10 m is the cut-off section of the presplitting fracture. The distribution range of the composite soft rock, the presplitting cracks on the upper reused roadway at 10 m, and the composite soft rock distribution influence the stability of the surrounding rock. As shown in Figure 8, the distribution curve of the upper 3 m, 6 m, and 9 m shows vertical stress.

Different interrock formation properties including the stiffness, intensity, and joint development occur in the structural plane and are prone to separation under high stress. According to the comprehensive geological histogram, the upper sections that are 3 m and 6 m higher than the roadway are composed of thick and well-bearing sandy mudstone and mudstone; sections 9 m higher than the road are close to the upper section of the compound soft rock, which is adjacent to the upper stable rock. Upper, lower, and middle rocks are mingled with several types of soft rock strata, making it prone to separation and instability. Figures 9(a) and 9(b) show that with an increase in retained roadway distance, the 3 m and 6 m high rock formations are close to the gob side. The vertical slope of the vertical stress curve increases, and the sloping deformation is obvious on the gob side; the shear slippage on the structural plane is intense. The shear stress increases as its distance away from the solid coal seam of roadway increases, resulting in an increase in local curvature and the formation of an isolated instability zone. A vertical stress of 9 m high rock appears high in the middle and bottom of both ends. Deflection appears when bending, and the maximum vertical stress reaches 10.3 MPa and 7.6 MPa at the gob side. The rock section is in a nonlinear state of rotation, buckling, etc., which leads to the separation and instability of the upper stable roadway rock. In Figure 9(c), the average change in the vertical stress range of the 3 m, 6 m, and 9 m high rocks is smaller. The deformation deflection remains consistent, and coordinated roof deformation

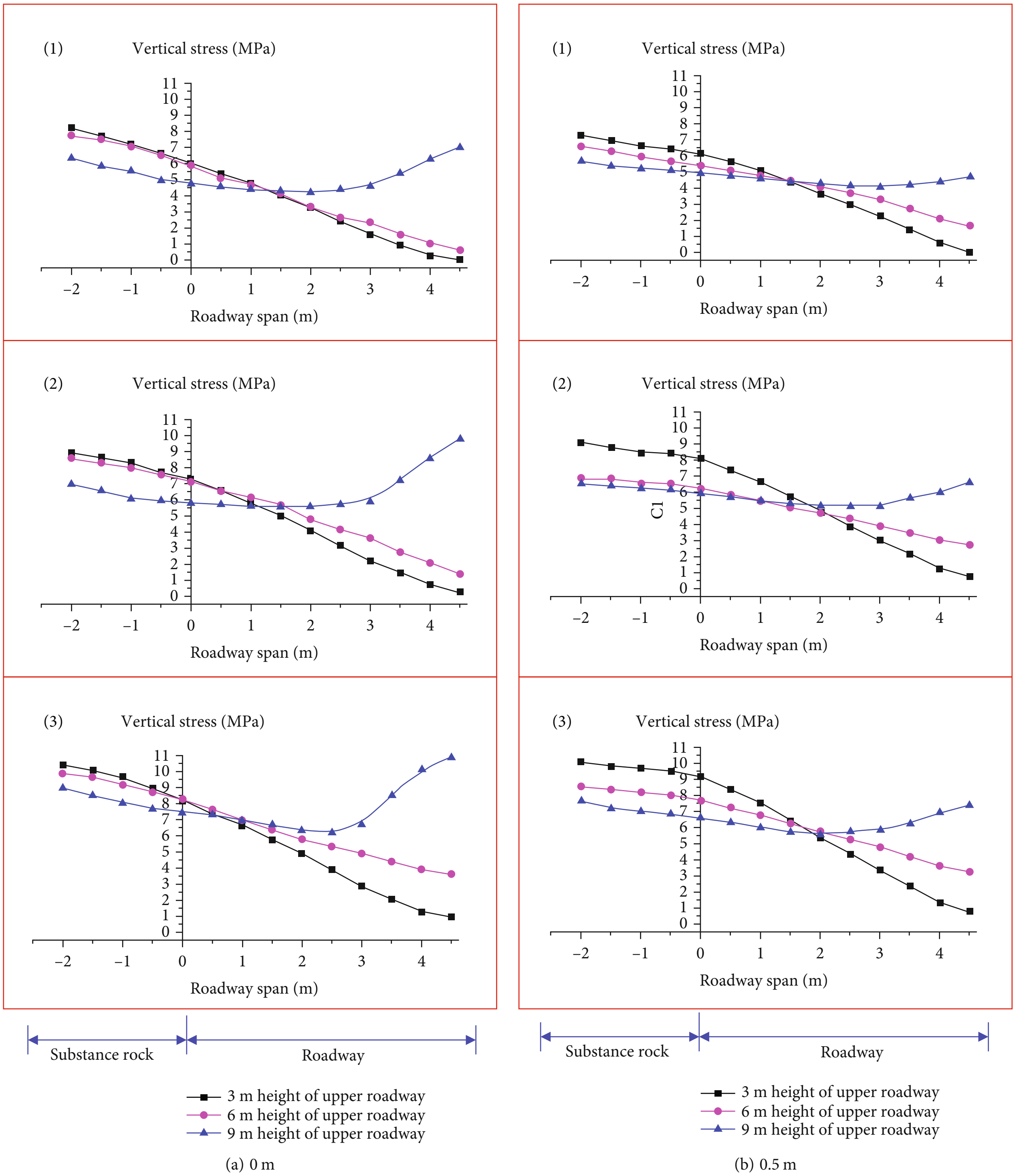

Figure 9: Continued.

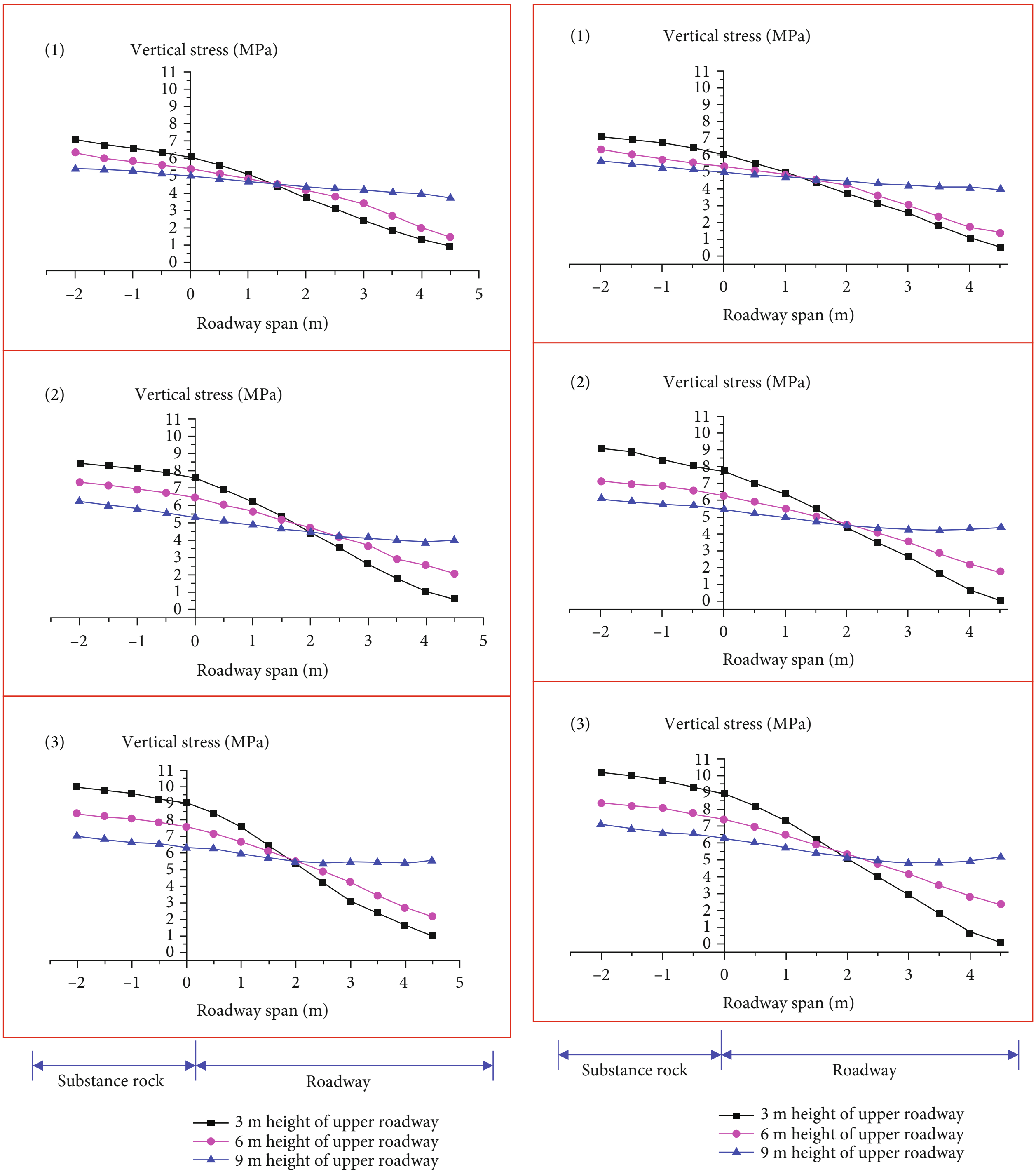

(c) 1 m

(d) 1.5 m

Figure 9: Continued.

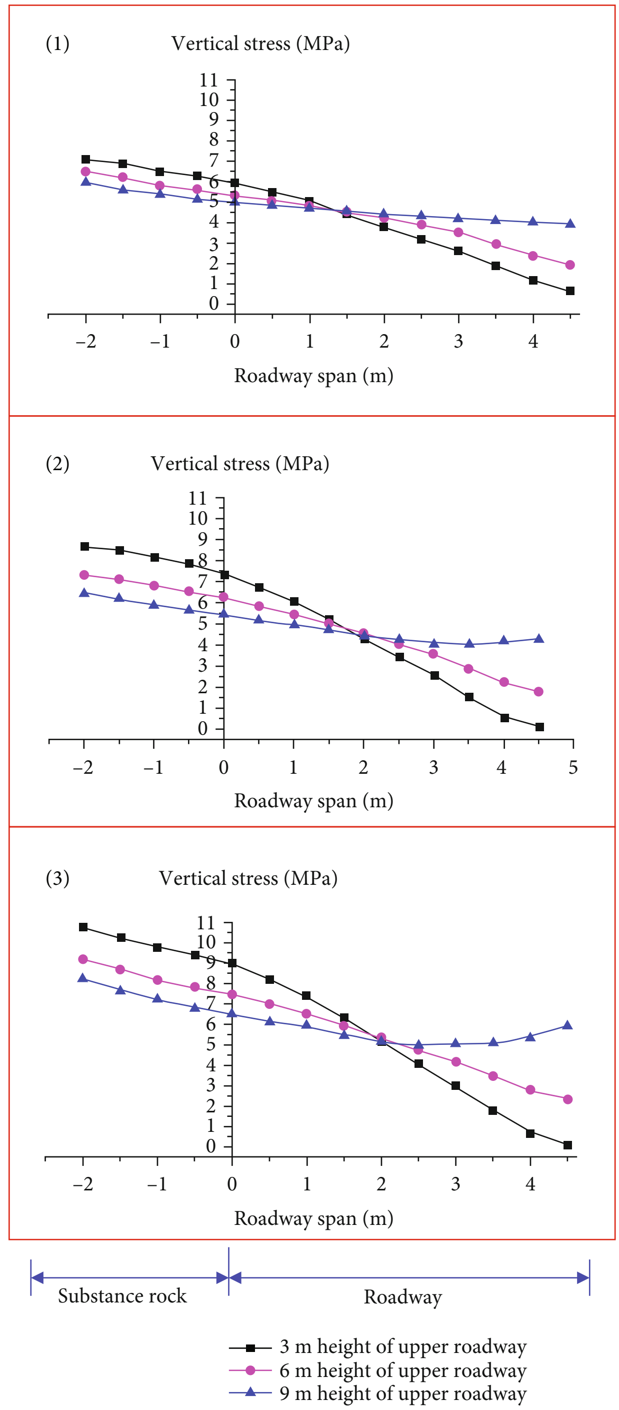

(e) 2 m

FIGURE 9: Stress distribution of the Reused roadway roof at the heights of (1) 9 m, (2) 18 m, and (3) 27 m.

develops, restricting the separation and dislocation of the rock formation surface and assuring the integrity of the compound soft rock and the stability of the surrounding roadway rocks. Therefore, the stress concentration weakened, and the pressure change eased. In Figures 9(d) and 9(e), the vertical stresses of the gob and solid coal-rock sides of the 3 and 6 m high rock formations decrease and increase, respectively; as increasing gap of the retained roadway increases, the vertical stress difference on both sides increases sharply, and the roadway roof stress concentration coefficient is larger, increasing the shear slip and immediately tearing the fissure growth at the two ends of the 9 m rock formation and structural plane The separation range of the middle section of the structural plane is enlarged and is prone to local separation and instability, making it, difficult to maintain the surrounding roadway rock.

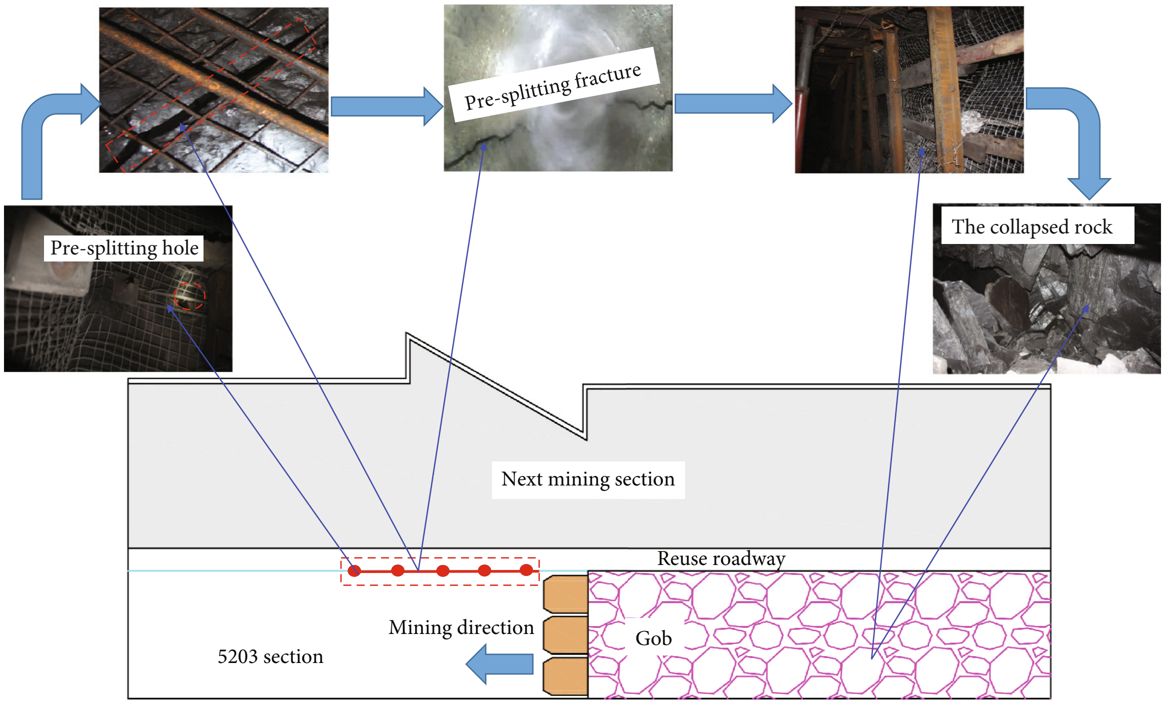

FIGURE 10: Expansion and penetration field test of roof presplitting fractures.

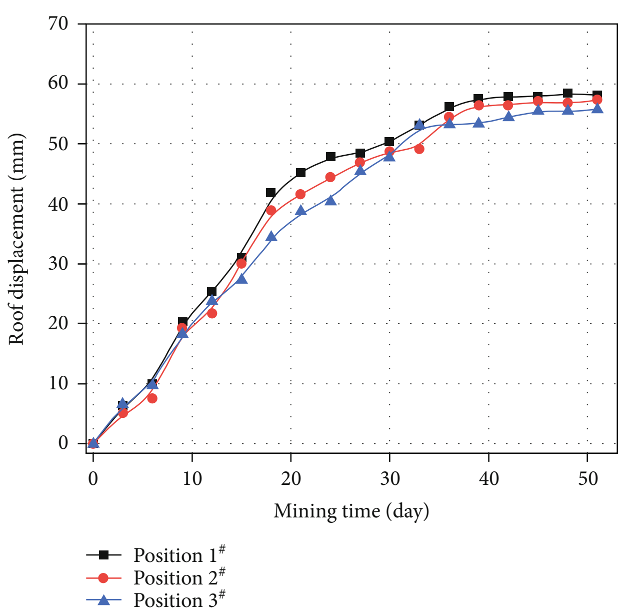

FIGURE 11: Deformation law of roadway roof.

FIGURE 12: The stable reused roadway surrounding rock after roof presplitting.

5. Field Test

Based on the simulation results, the optimal presplitting interval of roof is 1 m. In field test, the roof presplitting line could be arranged at about 1 m from the presplitting side of the roadway roof and the purpose is to facilitate the construction of drilling equipment. At the same time, it is also convenient to maintain the integrity of reused roadway surrounding rock. The presplitting interval 1 m of roof fracture is implemented in the field test, as shown in Figure 10. The whole process of the formation, development of the presplitting cracks, and the deformation of the overlying strata is observed by the method of drilling.

In front of the mining work, the roof of the reused roadway is presplitting fractures. Behind the mining working face of 0~3.0 m, the fractures appear on the roof of the roadway and finally connect each other and begin to fall. Behind the mining working face of 3.0~6.0 m, the upper strata show coordinated deformation. Compound soft rock strata fall and plug fully at the gob side to form the reused roadway structure. Through drilling observation, there is no obvious separation and dislocation; the roof rock is more complete. Three deformation monitoring stations are arranged in the roadway, each 50 m apart. After mining face for 40 days, the deformation of roadway roof is effectively controlled and surrounding rock tends to be stable, as shown in Figures 11 and 12.

6. Conclusions

(1) Based on the engineering needs of compound soft rock, the characteristics of overlying stratum mechanisms, presplitting, extension, and coalescence of rock formation are examined. The compound soft rock stratum breaking and falling process is established, and the dynamic pressure of the upper strata causes the rapid pressurization and collapse of the support structure. This is one of the key factors affecting the stability of the surrounding rock of reused roadways

(2) A three-dimensional model with fissure interval conditions of 0 m, 0.5 m, 1 m, 1.5 m, and 2 m is established to analyze the horizontal stress around the presplitting fissure, the plastic damage evolution rule, and energy dissipation features associated with fissure extension. In the case of presplitting fissure intervals of 0.5 m and 1 m, the stress concentration of the initial section of the retained roadway is removed, and the presplitting fissure is expanded and cut through, effectively controlling the dilatancy and damage of the surrounding rock mass and the energy dissipation process. This control is also beneficial to the coordinated caving of rock formations

(3) When the presplitting fissure interval is 1 m, the stress transfer caused by mining disturbance is obstructed and the flexural rigidity of side soft rock formation of roadway mining side is weakened. By avoiding the dilatancy friction, the plastic zone of the roadway gob side weak strata has a wedge distribution with the big end down, which is advantageous for the successive, coordinated caving of low and median rock formations. This type of caving limits the separation and dislocation of the roadway roof rock surface and helps to form a stable supporting structure on the gob side of the roadway and increases the self-bearing capacity of the upper rocks

(4) A 1 m presplitting fissure interval is adopted to be used in field test and on the monitoring surface: if the reused roadway is reserved and set as 3-6 m, the presplitting fissures will connect. If the reused roadway is reserved and set as 9-12 m, the roadways will be constructed after being plugged and cut downwards along the coalescence fractured from top to bottom. After mining 40 days, the surrounding rock deformation of reused roadway tends to be steady

Data Availability

The data used to support the findings of this study are included within the article.

Conflicts of Interest

The authors declare that they have no conflicts of interest.

Acknowledgments

This study was supported by the National Natural Science Foundation of China (No. 52104157) and Funding Program of Research Projects in Henan Province (No. 222102320239).

References

[1] S. Q. Yang, M. Chen, G. Fang et al., "Physical experiment and numerical modelling of tunnel excavation in slanted upper-soft and lower-hard strata," *Tunnelling and Underground Space Technology*, vol. 82, pp. 248–264, 2018.

[2] B. Lin, F. Yan, C. Zhu et al., "Cross-borehole hydraulic slotting technique for preventing and controlling coal and gas outbursts during coal roadway excavation," *Journal of Natural Gas Science and Engineering*, vol. 26, pp. 518–525, 2015.

[3] J. Ning, J. Wang, X. Liu, K. Qian, and B. Sun, "Soft-strong supporting mechanism of gob-side entry retaining in deep coal seams threatened by rockburst," *International Journal of Rock Mechanics and Mining Sciences*, vol. 24, no. 6, article S2095268614001463, pp. 805–810, 2014.

[4] J. Wang, J. Zhang, and Z. Li, "A new research system for caving mechanism analysis and its application to sublevel top-coal caving mining," *International Journal of Rock Mechanics and Mining Sciences*, vol. 88, pp. 273–285, 2016.

[5] W. S. Xu, W. T. Xu, and Y. H. Cheng, "Research on the reasonable strengthening time and stability of excavation unloading surrounding rock of high-stress rock mass," *Geofluids*, vol. 2021, Article ID 3508661, 2021.

[6] B. Wang, F. Dang, S. Gu, R. Huang, Y. Miao, and W. Chao, "Method for determining the width of protective coal pillar in the pre-driven longwall recovery room considering main roof failure form," *International Journal of Rock Mechanics and Mining Sciences*, vol. 130, p. 104340+11, 2020.

[7] Y. L. Tan, F. H. Yu, J. G. Ning, and T. B. Zhao, "Design and construction of entry retaining wall along a gob side under hard roof stratum," *International Journal of Rock Mechanics and Mining Sciences*, vol. 77, article S1365160915000842, pp. 115–121, 2015.

[8] J. X. Yang, C. Y. Liu, B. Yu, and F. F. Wu, "The effect of a multi-gob, pier-type roof structure on coal pillar load-bearing capacity and stress distribution," *Bulletin of Engineering Geology and the Environment*, vol. 74, no. 4, article 685, pp. 1267–1273, 2015.

[9] Y. Fan, W. Lu, Y. Zhou, P. Yan, Z. Leng, and M. Chen, "Influence of tunneling methods on the strainburst characteristics during the excavation of deep rock masses," *Engineering Geology*, vol. 201, pp. 85–95, 2016.

[10] H. Zhu, B. Ye, Y. Cai, and F. Zhang, "An elasto-viscoplastic model for soft rock around tunnels considering overconsolidation and structure effects," *Computers and Geotechnics*, vol. 50, pp. 6–16, 2013.

[11] Y. J. Wang, Y. B. Gao, E. Y. Wang, M. He, and J. Yang, "Roof deformation characteristics and preventive techniques using a novel non-pillar mining method of gob-side entry retaining by roof Cutting," *Energies*, vol. 11, no. 3, pp. 627–630, 2018.

[12] D. W. Yang, Z. G. Ma, F. Z. Qi et al., "Optimization study on roof break direction of gob-side entry retaining by roof break and filling in thick-layer soft rock layer," *Geomechanics and Engineering*, vol. 13, pp. 195–215, 2017.

[13] R. Gu and U. Ozbay, “Numerical investigation of unstable rock failure in underground mining condition,” *Computers and Geotechnics*, vol. 63, pp. 171–182, 2015.

[14] X. L. Yang, J. S. Xu, Y. X. Li, and R. M. Yan, “Collapse mechanism of tunnel roof considering joined influences of nonlinearity and non-associated flow rule,” *International Journal of Geomechnics Engineering*, vol. 10, no. 1, pp. 21–35, 2016.

[15] Y. Yong, S. Tu, X. Zhang, and L. Bo, “Dynamic effect and control of key strata break of immediate roof in fully mechanized mining with large mining height,” *Shock and Vibration*, vol. 2015, Article ID 657818, 11 pages, 2015.

[16] X. Li, M. Ju, Q. Yao, J. Zhou, and Z. Chong, “Numerical investigation of the effect of the location of critical rock block fracture on crack evolution in a gob-side filling wall,” *Rock Mechanics and Rock Engineering*, vol. 49, no. 3, pp. 1041–1058, 2016.

[17] H. G. Ji, H. S. Ma, J. A. Wang, Y. H. Zhang, and H. Cao, “Mining disturbance effect and mining arrangements analysis of near-fault mining in high tectonic stress region,” *Safety Science*, vol. 50, no. 4, pp. 649–654, 2012.

[18] X. Li and W. Li, “Numerical investigation on fracturing behaviors of deep-buried opening under dynamic disturbance,” *Tunnelling and Underground Space Technology*, vol. 54, pp. 61–72, 2016.

[19] Y. Li, D. Zhang, Q. Fang, Q. Yu, and L. Xia, “A physical and numerical investigation of the failure mechanism of weak rocks surrounding tunnels,” *Computers and Geotechnics*, vol. 61, pp. 292–307, 2014.

[20] B. X. Huang, Q. Y. Cheng, X. L. Zhao, W. Xue, and M. Scoble, “Using hydraulic fracturing to control caving of the hanging roof during the initial mining stages in a longwall coal mine: a case study,” *Arabian Journal of Geosciences*, vol. 11, no. 20, pp. 603–618, 2018.

[21] F. Z. Qi and Z. G. Ma, “Investigation of the roof presplitting and rock mass filling approach on controlling large deformations and coal bumps in deep high-stress roadways,” *Latin American Journal of Solids and Structures*, vol. e190, pp. 1–24, 2019.

[22] B. X. Huang, Y. Z. Wang, and S. G. Cao, “Cavability control by hydraulic fracturing for top coal caving in hard thick coal seams,” *International Journal of Rock Mechanics and Mining Sciences*, vol. 74, pp. 45–57, 2015.

[23] C. Periasamy and H. V. Tippur, “Measurement of crack-tip and punch-tip transient deformations and stress intensity factors using Digital Gradient Sensing technique,” *Engineering Fracture Mechanics*, vol. 98, pp. 185–199, 2013.

[24] J. B. Bai, W. L. Shen, G. L. Guo, X. Y. Wang, and Y. Yu, “Roof deformation, failure characteristics, and preventive techniques of gob-side entry driving heading adjacent to the advancing working face,” *Rock Mechanics and Rock Engineering*, vol. 48, no. 6, pp. 2447–2458, 2015.

[25] W. L. Tian and S. Q. Yang, “Experimental and numerical study on the fracture coalescence behavior of rock-like materials containing two non-coplanar filled fissures under uniaxial compression,” *Geomechanics and Engineering*, vol. 12, no. 3, pp. 541–560, 2017.

[26] G. F. Wang, S. Y. Gong, Z. L. Li, L. M. Dou, W. Cai, and Y. Mao, “Evolution of stress concentration and energy release before rock bursts: two case studies from Xingan coal mine, Hegang, China,” *Rock Mechanics and Rock Engineering*, vol. 14, pp. 1–9, 2016.

[27] H. Zhou, C. K. Qu, D. W. Hu et al., “In situ monitoring of tunnel deformation evolutions from auxiliary tunnel in deep mine,” *Engineering Geology*, vol. 221, article S0013795217302247, pp. 10–15, 2017.

[28] N. Falaknaz, M. Aubertin, and L. Li, “Numerical analyses of the stress state in two neighboring stopes excavated and backfilled in sequence,” *International Journal of Geomechnics*, vol. 15, no. 6, p. 04015005, 2015.

[29] H. Yan, F. He, T. Yang, L. Li, S. Zhang, and J. Zhang, “The mechanism of bedding separation in roof strata overlying a roadway within a thick coal seam: a case study from the Pingshuo Coalfield, China,” *Engineering Failure Analysis*, vol. 62, pp. 75–92, 2016.

[30] G. R. Feng, P. F. Wang, and Y. P. Chugh, “Stability of gate roads next to an irregular yield pillar: a case study,” *Rock Mechanics and Rock Engineering*, vol. 52, no. 8, pp. 2741–2760, 2019.

[31] W. Feng, R. Huang, and T. Li, “Deformation analysis of a soft-hard rock contact zone surrounding a tunnel,” *Tunnelling and Underground Space Technology*, vol. 32, pp. 190–197, 2012.

[32] S. Zhang, D. S. Zhang, H. Z. Wang, and S. S. Liang, “Discrete element simulation of the control technology of large section roadway along a fault to drivage under strong mining,” *Journal of Geophysics and Engineering*, vol. 15, no. 6, pp. 2642–2657, 2018.

Hindawi
Geofluids
Volume 2022, Article ID 2734122, 9 pages
https://doi.org/10.1155/2022/2734122

Research Article

Quantitative Identification of Grouting Effect of Working Face Floor with Multifactor Set

Zhenwei Yang[1,2] **Junchao Yue**[1,2] **Xinyi Wang**[1,2] **and Shuitao Guo**[3]

[1]*Institute of Resources & Environment, Henan Polytechnic University, Jiaozuo 454000, China*
[2]*Collaborative Innovation Center of Coal Work Safety and Clean High Efficiency Utilization, Jiaozuo 454100, China*
[3]*Jiaozuo Coal Industrial (Group) Co., Ltd., Jiaozuo 454002, China Guhanshan Mine*

Correspondence should be addressed to Xinyi Wang; wangxy@hpu.edu.cn

Received 27 March 2022; Accepted 28 June 2022; Published 28 July 2022

Academic Editor: Hualei Zhang

The deep coal mining in the North China type of coalfield is generally threatened by the underlying limestone water of Taiyuan Formation and Ordovician. The occurrence of water inrush can be avoided effectively by applying grouting reinforcement technology to the coal floor. However, the reinforcement treatment of the coal floor belongs to underground concealment engineering, and it is of great significance for the safe production of the coal mine by scientifically and comprehensively evaluating the technical method of the grouting effect on the working face floor. In this study, the optimal transfer matrix is used to construct the judgment matrix that meets the consistency requirements; the analytic hierarchy process is improved; and the grouting effect of the working face floor is evaluated by fuzzy comprehensive evaluation based on several factors of the grouting effect. Taking the grouting engineering of the 15092 working face of the Guhanshan Mine as an example, the evaluation of the grouting effect based on four evaluatory indices have been refined: dynamic hydrological features, grout amount, grouting inspection hole, and geophysical prospecting have been refined. Based on the improved analytic hierarchy process (AHP), the result of the grouting effect can be divided into four levels: distinction, good, average, and poor. The study would play a very important role in the evaluation of the grouting reinforcement of the working face floor and the practice of coal mine production safety.

1. Introduction

With complex hydrogeological conditions, the coal-bearing strata in the North China type of coalfield are mainly the Permian Shanxi Formation and the Lower Shihezi Formation [1]. As coal resources in the shallow part of coalfields are exhausted, the threat to the mining of lower coal groups threatened by confined karst aquifers is increasing, and the danger of mine water inrush is gradually increasing [2, 3]. The mining of the lower coal seams of the Shanxi Formation is generally seriously threatened by the limestone water of the underlying Taiyuan Formation and the Ordovician limestone water [4–6]. The Ordovician water pressure on the coal seam floor of many mines has exceeded 10 MPa, and the risk of Ordovician limestone inrush into the coal seam floor is increasing [7]. In order to mine the lower coal group safely, the coal seam floor must be grouted and reinforced, which can increase the thickness of the effective water-resistant layer and eliminate or reduce accidental karst water inrush accidents [8, 9]. However, grouting on the coal seam floor is an underground concealed project. Furthermore, grouting mainly considers the weak water content within the water barrier, the depth of bottom plate mining damage, and the development of bottom plate fissures, but the premise ensures that the water control by-laws are within the safety factor of water burst, and cannot be measured by the head pressure size alone. The scientific and effective evaluation of the grouting effect is related to the success or failure of the grouting project [10–13]. Therefore, it is of great significance to carry out grouting effect evaluation research.

In recent years, the evaluation of the grouting effect on the coal floor has mainly focused on various detecting methods, including water quantity, water temperature, post-grouting pressure, water absorption, *P-Q* curve analysis, coring inspection, and geophysical exploration results. Based on the fact that the permeability and mechanical strength of the rock mass are important parameters reflecting the grouting effect of the rock mass, Liu et al. [14] proposed the high-pressure water pressure test method for the quantitative evaluation of the grouting effect of plugging the Taiyuan formation limestone. On the basis of carrying out the single-hole water discharge experiment, Li et al. [15] combined it with the dominant surface theory of water inrush to put forward the floor classification grouting technology. Based on the data set of grouting drilling, Xie et al. studied the case of water inrush in the grouting reinforcement of the working face and the data at the point of mine water inrush and combined it with the study of factors such as geological structures, hydraulic pressure of underlying water, floor water-conducting properties, and grouting amounts, and established the risk evaluation for floor water inrush in the grouted working face [16–18]. The novel technique of evaluating grouting techniques such as the artificial neural network (ANN) is also used for consolidation grouting quality assessment of dam foundation [19]. But the evaluation system of dam foundation is different from grouting of the working face floor. There is a certain limitation to the grouting effects evaluatory methods because these evaluatory methods were either based on a single evaluatory factor [3, 5] or did not contain the different evaluatory factors which covered the whole of grouting engineering [9]. Even though a combination of several factors is used, if the weight of each factor is not settled scientifically, it will lead to a low reliability of the overall evaluation as a result. It is dangerous to make a decision concerning coal mine production based on a wrong or an incomplete grouting evaluatory result.

Fuzzy comprehensive evaluation is a fuzzy concept with multiple indicators and levels, which is an effective way for evaluating targets affected by multifactor. It has been widely used in many fields, such as the safety management of petrochemical company, medicine, construction, urban development. and the environment, quality supervision, water quality assessment, and feed safety assessment. The analytic hierarchy process (AHP) is a decision analysis method that combines qualitative and quantitative methods. It is good at solving complex problems with multiple goals. The weight of each evaluatory factor can be calculated by the analytic hierarchy process method, and the comment set and evaluatory results can be gotten by fuzzy concepts [20, 21]. By combining the two methods, more scientific and reliable evaluatory results can be obtained.

In order to overcome the shortcomings of evaluating the grouting effect by a single index, this paper classifies major evaluatory indices of the grouting effect. With the improved analytic hierarchy process, the fuzzy comprehensive evaluation method for the evaluation of the grouting effect of the working face floor is studied. The grouting effect of the 15092 working face floor of the Guhanshan Mine of the Coking Coal Group has been evaluated by the studied method, and the science and validity of the studied method have been verified.

2. Calculation Method and the Study Area

2.1. Improved AHP Method. The analytic hierarchy process (AHP) is a practical multischeme or multiobjective system analysis and decision-making method which was proposed by Professor Thomas L. Saaty, an operations researcher at the University of Pittsburgh in the United States. AHP method combines qualitative and quantitative analyses. The goal of the combined weight of each level is calculated through the establishment of a hierarchical structure or model, the construction of a judgmental matrix, single-level ordering, total level ordering, a consistency check, etc. and is a systematic method of objective and optimized decision-making [22–24].

The consistency of the judgmental matrix established by the analytic hierarchy process must be tested. There are some difficulties in the consistency test of the judgmental matrix, and the standard CR < 0.1 for testing lacks a scientific basis. In order to solve the problem, this research improves the method of constructing the judgment matrix and uses complementary ideas for its construction, which can automatically meet the consistency requirements of the judgment matrix.

2.2. Constructing a Complementary Judgment Matrix. Constructing a complementary judgment matrix Q based on the importance of impact factors, that is,

$$Q = \begin{bmatrix} q_{11} & q_{12} & \cdots & q_{1m} \\ q_{21} & q_{22} & \cdots & q_{2j} \\ \cdots & \cdots & \cdots & \cdots \\ q_{m1} & q_{m2} & \cdots & q_{mn} \end{bmatrix}. \quad (1)$$

The elements in matrix Q meet the following condition:

$$q_{mn} = q_{mk} - q_{nk} + 0.5, \quad (2)$$

where m represents the number of factors involved in the evaluation, $0 \le q_{mn} \le 1$, $q_{mn} + q_{nm} = 1$, q_{mn} represents the importance of membership that the factor q_m has when compares to q_n. The higher the q_{mn} shows that q_m is more important than q_n. q_m and q_n have the same importance when q_{mn} equals 0.5.

2.3. Calculating the Complementary Consistent Judgmental Matrix. Fuzzy complementary matrix $Q = (q_{ij})_{n\times n}$, summed by line, marked as

$$b_i = \sum_{k=1}^{n} q_{ik}, i = 1, 2, \cdots, n, \quad (3)$$

then the following further transformation

$$b_{ij} = \frac{b_i - b_j}{a} + 0.5, \quad (4)$$

where $a = 2 * (n-1)$ and $B = (b_{ij})_{n\times n}$ is the complementary consistent judgmental matrix.

2.4. Weighting Calculation. Weighting calculation formula:

$$w_i = \frac{\beta^{(1/n)\sum_{j=1}^{n} r_{ij}}}{\sum_{k=1}^{n} \beta^{(1/n)\sum_{j=1}^{n} r_{kj}}}, \tag{5}$$

where w represents weight and β is the parameter used for adjusting the resolution. The value is a positive integer greater than 1, and the larger the value of β, the higher the resolution of the weight calculated by formula (5).

In the general analytic hierarchy process (AHP) method, when constructing the pairwise comparison judgmental matrix, the fuzziness of human judgment is usually not considered. Experts often give some fuzzy amount, so the fuzzy comprehensive evaluation theory is introduced.

2.5. Fuzzy Comprehensive Evaluation Method. The fuzzy mathematics theory is the basis of fuzzy comprehensive evaluation, applying the principle of fuzzy relationship synthesis, quantifying some difficult quantitative factors, and comprehensively evaluating the status of the evaluated affairs by multiple factors.

2.6. Determining the Domain of Factors of the Evaluated Object. According to the evaluatory research of the grouting effect, the evaluatory factors $U = \{$dynamic hydrological characteristics of grouting holes, grouting characteristics, inspection holes, geophysical prospecting$\}$.

2.7. Determining the Comment Set. Determining the comment set is essential to the grade division of the grouting effect, which can generally be divided into four grades. The comment set is $V = \{$distinction, good, average, poor$\}$.

2.8. Constructing the Fuzzy Complementary Consistent Judgmental Matrix. Since the judgmental matrix is not complementary and consistent, the fuzzy complementary consistent judgmental matrix B is further established by formula (4):

$$B = \begin{pmatrix} b_{11} & b_{12} & \cdots & b_{1n} \\ b_{11} & b_{22} & \cdots & b_{2n} \\ \cdots & \cdots & \cdots & \cdots \\ b_{m1} & b_{m2} & \cdots & b_{mn} \end{pmatrix}, \tag{6}$$

where $b_{ij} (i = 1, 2, \cdots, m\,; j = 1, 2, \cdots, n)$ represents the degree of membership of b_i to b_j.

(1) Determining the fuzzy weight vector of the evaluatory factor

Using the weight calculation formula (3), the weight factor $w_i\ (i = 1, 2, \cdots, m)$ is calculated based on the judgmental matrix, w_i meets the conditions, which are $w_i \geq 0$ and $\Sigma w_i = 1$. The weight set W consists of a fuzzy set of weights. With the second-level weight vector and the single-factor evaluatory matrix, the second-level evaluation matrix E can be obtained.

(2) Fuzzy comprehensive evaluation by multifactor

The fuzzy synthesis operator of the matrix is used to synthesize the first-level weight factor W and the second-level evaluatory matrix E. The fuzzy comprehensive evaluatory vector can be calculated by

$$A = W \circ E = (w_1, w_2, \cdots, w_m) \begin{pmatrix} e_{11} & e_{12} & \cdots & e_{1n} \\ e_{21} & e_{22} & \cdots & e_{2n} \\ \cdots & \cdots & \cdots & \cdots \\ e_{m1} & e_{m1} & \cdots & e_{mn} \end{pmatrix} = (a_1, a_2, \cdots, a_n). \tag{7}$$

In formula (7), $^\circ$ is a fuzzy operator, and a_j represents the degree of membership of the rated object to the fuzzy subset element v_j of the evaluatory level as a whole. The principle of maximum degree of membership is adopted to process the fuzzy comprehensive evaluatory vector, that is, if the fuzzy comprehensive evaluation result vector $A = (a_1, a_2, \cdots, a_n)$, if $a_r = \max_{1\leq j\leq n}\{a_j\}$, the evaluating result is the rth level as a whole.

2.9. Geological Profile. The Guhanshan Mine is located in the eastern section of the Jiaozuo Coalfield and is under the jurisdiction of Xiuwu County, Jiaozuo City, 15 km south of Xiuwu County, and 42 km east of Huixian City. The minefield is 15 km south of the Xinjiao Railway, and the mine is connected to the Daiwang Station of the Xinjiao Line by the special coal mine railway. The transportation is convenient, and the regional geological structure is complex. The large faults around the minefield include the Jiulishan Fault, the Mafangquan Fault, and the Fenghuangling Fault, which are shown in Figure 1.

The main mining strata of the Guhanshan Mine is the II_1 coal in the lower part of the Shanxi Formation. The coal thickness is 2.79-9.13 m, with an average of 4.86 m. The roof is gray to dark gray mudstone, sandy mudstone, and fine-grained sandstone or partial siltstone. The floor is gray-black to dark gray mudstone, sandy mudstone, or siltstone. According to the bed thickness, lithology, water-bearing conditions, and water yield properties, the aquifers in the study area could be divided into three types: (1) The Ordovician limestone aquifer is the sedimentation base of the coal measure strata. The osmotic coefficient of the aquifer is 1-30 m/d. (2) The Carboniferous limestone aquifer, which is mainly composed of the Taiyuan Formation limestone and the L_2 and L_8 limestone. The osmotic coefficient is 1-3 m/d. The thickness of the aquiclude between the aquifer and the II_1 coal seam is relatively stable, with an average of 35.55 m. There is an aquiclude (aluminous mudstone) between the Ordovician limestone and L_2 aquifers. The direct water-filled rock layer on the floor is the L_8 limestone fissure-karst aquifer in the upper part of the Carboniferous Taiyuan Formation. The L_2 limestone and Ordovician

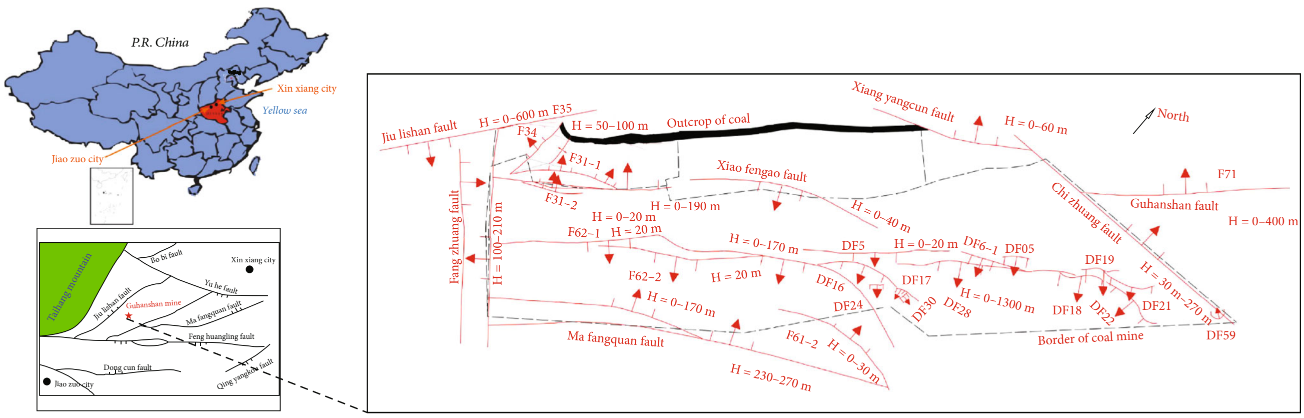

Figure 1: Regional tectonic profile and sketch of mine geological structure.

limestone karst water aquifers in the lower part of the Carboniferous Taiyuan Formation are indirect water-filled aquifers mined in the II_1 coal seam, with strong water-bearing aquifers, as shown in Figure 2. Due to the thin layer of the L_8 aquifer and the long-term regional drainage effect, it is not harmful to the coal mining of the II_1 coal seam. If the lower L_2 limestone aquifer is recharged, the risk of water inrush will increase. (3) the Quaternary porous aquifer is mainly consist of the sandy gravel layer or fine sand layer. The supply sources of the water are atmospheric precipitation and infiltration from canals and rivers.

The 15092 working face has a strike length of 984 m, an inclination width of 127.7 m, a coal seam strike of 50°, an inclination of 140°, an inclination angle of 12-15°, an average of 13°, an average coal thickness of 2 m, and a recoverable reserve of 396,000 tons. The geological conditions of the 15092 working face are relatively simple. The coal seams are stable and fold in a wide and gentle manner. The occurrence of the strata changes slightly under the influence of faults. The hydrogeological conditions of the working face are simple.

3. Evaluation of Grouting Effect on the Working Face Floor

3.1. Index System Construction. The impact indicator of the grouting effect evaluatory grade is complex are interrelated but poorly correlated. Therefore, based on the analysis of the influence of each factor on the effect evaluation, combined with the characteristics and construction requirements during the grouting construction period, the grouting effect evaluatory hierarchy is established, as shown in Figure 3. In this paper, a comprehensive evaluation of the grouting at the working face of the Jiaozuo coalfield is carried out, and four first-level index evaluatory systems, namely, $U = \{u_1, u_2, u_3, u_4\}$, are constructed for the dynamic hydrological characteristics of grouting holes, grouting characteristics, inspection holes, and geophysical prospecting, respectively.

According to the requirement of coal mine production safety, the grouting effect evaluatory level is divided into four evaluatory sets: distinction, good, average, and poor. The grouting effect evaluation set is shown in Table 1.

4. Factor Weight Determination

Weight is a measure of the relative importance or contribution of a specific evaluatory factor in determining the set of reviews. In the fuzzy comprehensive evaluation, the weight has an important influence on the final evaluatory result, and different weights will even lead to completely different conclusions. At present, the main methods for determining weights are the weighted average method, the analytic hierarchy process, the expert survey method, the eigenvalue method, etc. The analytic hierarchy process has the characteristics of strong objectivity and strong reliability of the evaluatory results, which ensure the judgmental matrix. In this study, the improved analytic hierarchy process was used to determine the weight of the evaluatory factor. The weight setting is shown in Table 2.

5. Determination of the Weight of the Primary Evaluation Factor

First-level evaluation factor set $U = \{u_1, u_2, u_3, u_4\} = \{$ dynamic hydrological characteristics of grouting hole, grouting feature, inspection hole, geophysical prospecting$\}$, considering that the weight difference of the first-level evaluation factor should not be too large, take $\alpha = 810$, $\beta = 100$, from Table 2 and considering the importance membership degree between factors, the judgment matrix is obtained:

$$Q = \begin{pmatrix} 0.5 & 0.6035 & 0.7675 & 0.7906 \\ 0.3965 & 0.5 & 0.7403 & 0.7675 \\ 0.2325 & 0.2597 & 0.5 & 0.664 \\ 0.2094 & 0.2325 & 0.336 & 0.5 \end{pmatrix}. \quad (8)$$

Based on Q, constructing a fuzzy complementary consistent judgment matrix according to formula (4):

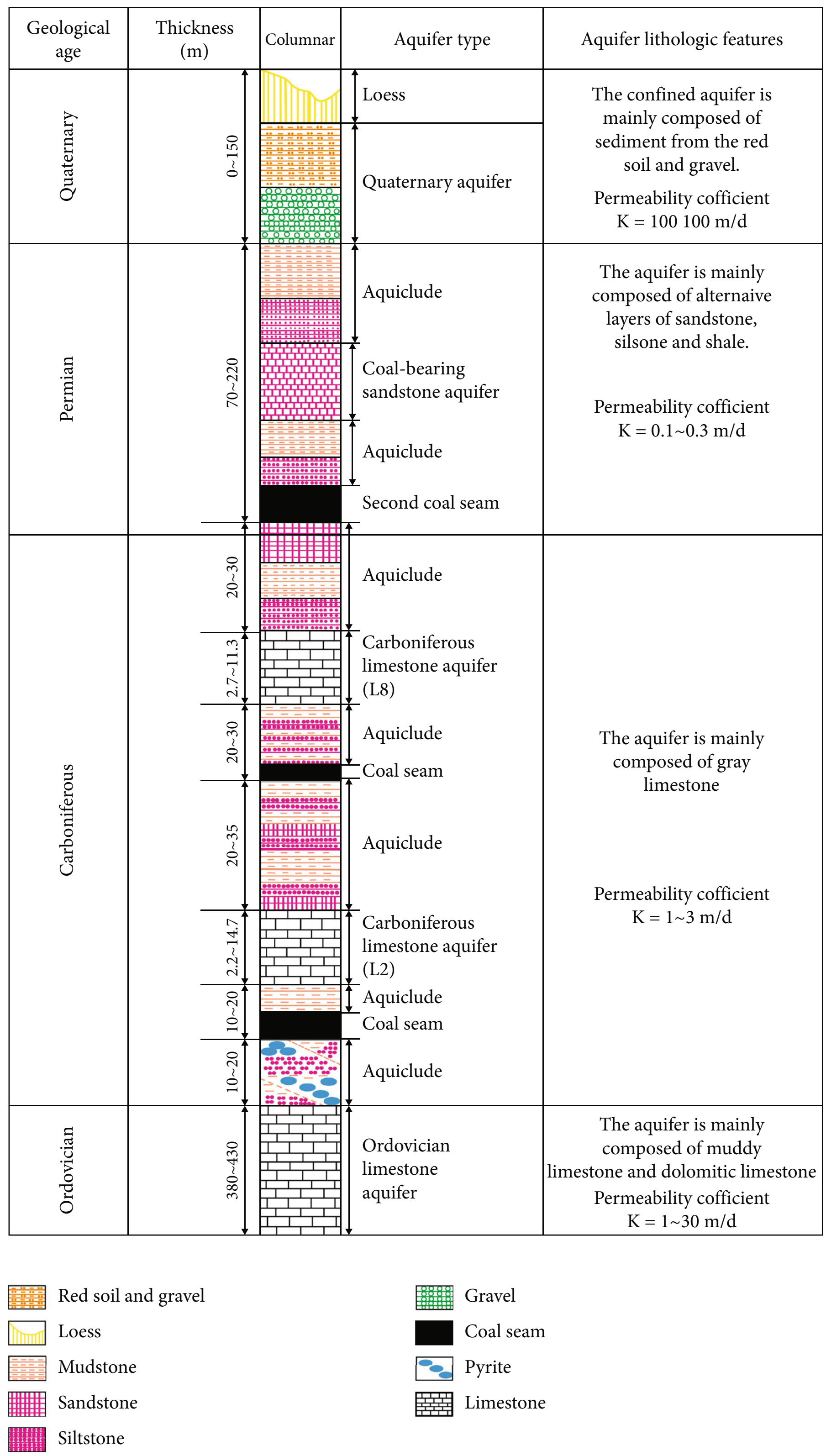

Figure 2: Stratigraphic histogram of the upper Ordovician.

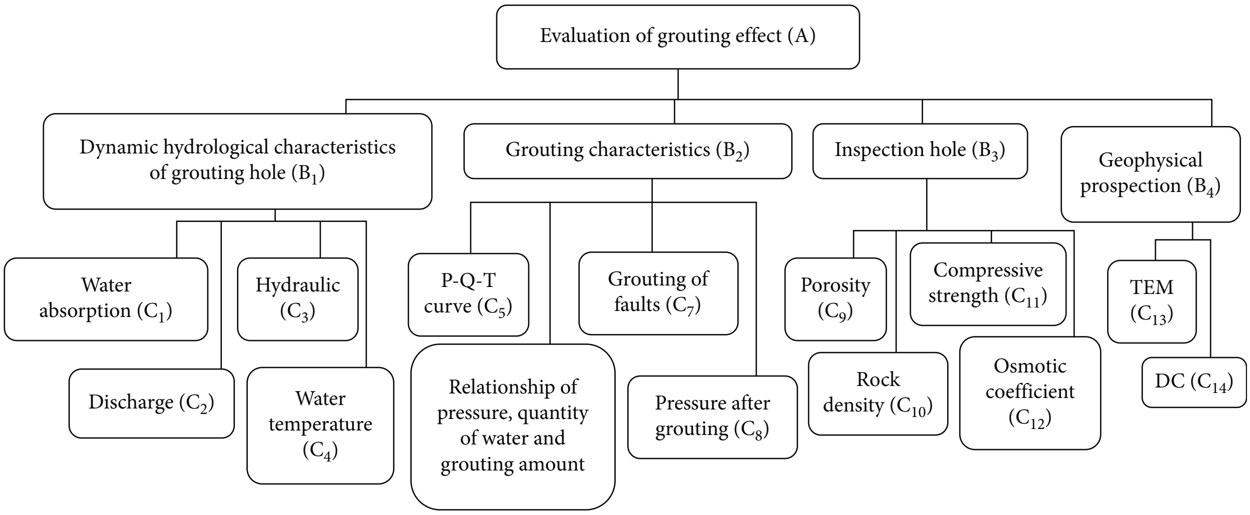

Figure 3: Architecture of multilayered evaluatory factors.

Table 1: Fuzzy comment set.

Level	Distinction	Good	Average	Poor
Value	$0 < v \leq 0.25$	$0.25 < v \leq 0.5$	$0.5 < v \leq 0.75$	$0.75 < v \leq 1$

$$B = \begin{pmatrix} 0.5 & 0.5429 & 0.6676 & 0.7306 \\ 0.4571 & 0.5 & 0.6246 & 0.6877 \\ 0.3324 & 0.3753 & 0.5 & 0.5631 \\ 0.2694 & 0.3123 & 0.437 & 0.5 \end{pmatrix}. \quad (9)$$

From the calculation formula of the weight vector, the resolution of the combined factor, the β value is 100, then the weight of each factor:

$$W = (0.38, 0.31, 0.18, 0.13). \quad (10)$$

6. Determination of the Weight of Secondary Evaluation Factors

The secondary evaluation factor of the judgmental matrix of the calculation process and the fuzzy complementary consistent judgmental matrix is omitted. Due to limited space, the result of the fuzzy complementary consistent judgmental matrix is directly given. The calculation process and parameter settings are the same as the primary evaluation factor.

The evaluatory matrix of the dynamic hydrological characteristics of the grouting hole is

$$B_1 = \begin{pmatrix} 0.5 & 0.5072 & 0.4861 & 0.6448 \\ 0.4928 & 0.5 & 0.4789 & 0.6376 \\ 0.5139 & 0.5211 & 0.5 & 0.6587 \\ 0.3552 & 0.3624 & 0.3413 & 0.5 \end{pmatrix}. \quad (11)$$

Weight vector $W_1 = (0.28, 0.27, 0.30, 0.15)$.

The evaluatory matrix of grouting characteristics is

$$B_2 = \begin{pmatrix} 0.5 & 0.5791 & 0.5413 & 0.3797 \\ 0.4209 & 0.5 & 0.4622 & 0.3006 \\ 0.4587 & 0.5378 & 0.5 & 0.3384 \\ 0.6204 & 0.6994 & 0.6616 & 0.5 \end{pmatrix}. \quad (12)$$

The weight vector of the grouting feature $W_2 = (0.23, 0.16, 0.20, 0.41)$.

The evaluatory matrix of the inspection hole is

$$B_3 = \begin{pmatrix} 0.5 & 0.5134 & 0.3597 & 0.3107 \\ 0.4867 & 0.5 & 0.3463 & 0.2973 \\ 0.6403 & 0.6537 & 0.5 & 0.451 \\ 0.6894 & 0.7027 & 0.549 & 0.5 \end{pmatrix}. \quad (13)$$

The weight vector of the inspection hole $W_3 = (0.16, 0.15, 0.31, 0.38)$.

The evaluatory matrix of the geophysical method is

$$B_4 = \begin{pmatrix} 0.5 & 0.436 \\ 0.564 & 0.5 \end{pmatrix}. \quad (14)$$

The weight vector of the geophysical method $W_4 = (0.43, 0.57)$.

7. Evaluation of Grouting Effect

7.1. Constructing Single-Factor Evaluatory Matrix. Based on the actual grouting data of the 15092 working face of Guhanshan Mine, multiple experts independently voted on each index of evaluating the grouting effect. The number of

Table 2: The meaning of membership degree of fuzzy uniform matrix and its comparison table.

Degree of membership	Definition	Semanteme
0.5	Equal importance	The importance of two index to the goal is equal
$\log_{\alpha}3 + 0.5$	Slight importance	The importance of two index to the goal is that index 1 is slight importance to index 2
$\log_{\alpha}5 + 0.5$	Obvious importance	The importance of two index to the goal is that index 1 is obvious importance to index 2
$\log_{\alpha}7 + 0.5$	Strong importance	The importance of two index to the goal is that index 1 is strong importance to index 2
$\log_{\alpha}9 + 0.5$	Extreme importance	The importance of two index to the goal is that index 1 is extreme importance to index 2
$\log_{\alpha}i + 0.5, i = 2, 4, 6, 8$	Compromise value of adjacent scale	Represents the degree of membership when adjacency factor compromising
The degree of membership of the above is complementary	Complementation	The degree of membership of scheme A_i to scheme A_j is r_{ij}, otherwise $1 - r_{ij}$

experts' votes for each index is used as the evaluation of the factor, as shown in Table 3.

7.2. Single-Factor Evaluatory Matrix. Combining the voting results of the experts in Table 3, the normalized value of the votes obtained by each secondary evaluatory factor is used as the element in the corresponding single-factor evaluatory matrix. Thus, the single-factor evaluatory matrix of four first-level evaluation factors $u_1, u_2, u_3,$ and u_4 can be obtained as

$$
\begin{aligned}
E_1 &= \begin{pmatrix} 0.3 & 0.4 & 0.2 & 0.1 \\ 0.5 & 0.3 & 0.1 & 0.1 \\ 0.4 & 0.4 & 0.1 & 0.1 \\ 0.3 & 0.3 & 0.3 & 0.1 \end{pmatrix}, \\
E_2 &= \begin{pmatrix} 0.3 & 0.4 & 0.2 & 0.1 \\ 0.4 & 0.3 & 0.2 & 0.1 \\ 0.3 & 0.3 & 0.3 & 0.1 \\ 0.4 & 0.3 & 0.2 & 0.1 \end{pmatrix}, \\
E_3 &= \begin{pmatrix} 0.4 & 0.5 & 0.0 & 0.1 \\ 0.2 & 0.4 & 0.2 & 0.2 \\ 0.3 & 0.3 & 0.1 & 0.3 \\ 0.4 & 0.3 & 0.1 & 0.2 \end{pmatrix}, \\
E_4 &= \begin{pmatrix} 0.3\,0.3\,0.2\,0.2 \\ 0.4 \quad 0.2 \quad 0.2 \quad 0.2 \end{pmatrix}.
\end{aligned} \tag{15}
$$

7.3. Single-Factor Evaluation. According to the improved analytic hierarchy process, using the fuzzy evaluatory theory to calculate the weight of the secondary evaluation factor is

$$
\begin{aligned}
W_1 &= (0.28, 0.27, 0.30, 0.15), \\
W_2 &= (0.23, 0.16, 0.20, 0.41), \\
W_3 &= (0.16, 0.15, 0.31, 0.38), \\
W_4 &= (0.43, 0.57).
\end{aligned} \tag{16}
$$

The fuzzy operator $F(\cdot, \oplus)$ is used to get the secondary evaluatory matrix:

$$
E = \begin{pmatrix} W_1 \circ E_1 \\ W_2 \circ E_2 \\ W_3 \circ E_3 \\ W_4 \circ E_4 \end{pmatrix} = \begin{pmatrix} 0.384 & 0.358 & 0.158 & 0.1 \\ 0.357 & 0.323 & 0.22 & 0.1 \\ 0.339 & 0.347 & 0.099 & 0.215 \\ 0.357 & 0.243 & 0.2 & 0.2 \end{pmatrix}. \tag{17}
$$

7.4. First-Level Comprehensive Evaluation. The weights of the first-level evaluatory factors $u_1, u_2, u_3,$ and u_4 are

$$
\begin{aligned}
A &= W \circ E = (a_1, a_2, a_3, a_4) = (0.38, 0.31, 0.18, 0.13) \\
&\circ \begin{pmatrix} 0.384 & 0.358 & 0.158 & 0.1 \\ 0.357 & 0.323 & 0.22 & 0.1 \\ 0.339 & 0.347 & 0.099 & 0.215 \\ 0.357 & 0.243 & 0.2 & 0.2 \end{pmatrix} \\
&= \begin{pmatrix} 0.37 & 0.33 & 0.17 & 0.13 \end{pmatrix}.
\end{aligned} \tag{18}
$$

Finally, the first-level evaluation vector is obtained: $(0.37, 0.33, 0.17, 0.13)$.

According to the criterion of the maximum degree of membership, the largest of the comprehensive evaluatory vector A is the final evaluation result, that is, the grouting effect of the 15092 working face of the Guhanshan Mine is good.

Table 3: The weight of the grouting evaluation on the 15092 coal workface of Guhanshan mine.

Evaluation factor of first level	Weight	Evaluation factor of second level	Weight	Distinction	Good	Average	Poor
Dynamic hydrological characteristics of grouting hole	0.38	Water absorption	0.28	3	4	2	1
		Water inflow	0.27	5	3	1	1
		Water pressure	0.30	4	4	1	1
		Water temperature	0.15	3	3	3	1
Grouting characteristics	0.31	Curve of P-Q-T	0.23	3	4	2	1
		Dynamic relationship of water pressure, quantity of water, and grout amount	0.16	4	3	2	1
		Grouting characteristics of fault	0.19	3	3	3	1
		Pressure after grouting	0.40	4	3	2	1
Inspection hole	0.18	Porosity	0.16	4	5	0	1
		Rock mass density	0.15	2	4	2	2
		Compressive strength	0.31	3	3	1	3
		Osmotic coefficient	0.38	4	3	1	2
Geophysical prospecting	0.13	TEM	0.43	3	3	1	2
		DC	0.57	4	2	2	2

8. Conclusion

(1) The method of judgmental matrix construction of the analytic hierarchy process has been improved. The evaluatory result is divided into four grades: distinction, good, average, and poor. According to the method, the grouting effect of the coal floor in the 15092 working face of Guhanshan Mine in the Jiaozuo Coalfield was evaluated and classified

(2) The evaluation of the grouting effect of the working floor is an important issue for the safety of coal mine production. The use of the fuzzy evaluatory method to quantitatively study the grouting effect is an active attempt in the evaluation of the grouting effect. Compared to single-factor or multifactor qualitative evaluation, this evaluatory method is simple, easy to implement, and convenient to guide the practice of grouting effect evaluation. The coal mining production shows that the evaluatory result is reliable

(3) This study has extracted four first-level evaluation factors and fourteen second-level evaluatory factors from the grouting effect evaluation indicators. The scientific nature of the weight setting of the corresponding index factors needs to be further verified by more engineering practices

Data Availability

The data used to support the findings of this study are included within the article.

Conflicts of Interest

The authors declare no competing interests.

Authors’ Contributions

Zhenwei Yang and Junchao Yue designed the evaluation project. Xinyi Wang and Shuitao Guo devised the evaluation method and collected the grouting data. Zhenwei Yang analyzed the data and wrote the main manuscript text.

Acknowledgments

This work was financially supported by the National Natural Science Foundation of China (Grants 41672240 and 41972254), Natural Science Foundation of Henan Province (Grant 202300410179), Key Scientific Research Projects of Higher Education Institutions of Henan Province (19A170005), and Fundamental Research Funds for the Universities of Henan Province (NSFRF200337 and NSFRF200103).

References

[1] Q. Wu, K. Tu, Y. F. Zeng, and S. Q. Liu, “Discussion on the main problems and countermeasures for building an upgrade version of main energy (coal) industry in China,” *Journal of China Coal Society*, vol. 44, no. 6, pp. 1625–1636, 2019.

[2] Q. B. Zhao, “Ordovician limestone karst water disaster regional advanced government technology study and application,” *Journal of China Coal Society*, vol. 39, no. 6, pp. 1112–1117, 2014.

[3] S. N. Dong, H. Wang, and W. Z. Zhang, “Judgement criteria with utilization and grouting reconstruction of top Ordovician limestone and floor damage depth in North China,” *Journal of China Coal Society*, vol. 44, no. 7, 2019.

[4] J. C. Wang, Y. C. Yang, D. Z. Kong, and W. D. Pan, “Failure mechanism and grouting reinforcement technique of large mining height coal wall in thick coal seam with dirt band during topple mining,” *Journal of mining and safety engineering*, vol. 31, no. 6, pp. 831–837, 2014.

[5] Z. Z. Guo and J. Z. Wang, “Methods of estimating surface subsidence-reducing effect by separated- bed grouting and their precision,” *Journal of China University of Mining and Technology*, vol. 31, no. 4, pp. 384–387, 2002.

[6] X. Jin, T. X. Wang, K. K. Yu, Y. Luo, and P. F. Zuo, “Effect assessment of sodium silicate self- permeated grouting in intact loess,” *Journal of Xi'an university of architecture & technology (Natural science edition)*, vol. 48, no. 4, pp. 516–521, 2016.

[7] Z. B. Yang and S. N. Dong, “Study on quantitative evaluation of grouting effect by water pressure test,” *Journal of China Coal Society*, vol. 43, no. 7, pp. 2021–2028, 2018.

[8] Y. L. Peng, X. W. Hu, D. G. Song, L. Zhang, Y. X. Zheng, and M. H. Sun, “Inspection method for grouting effect in treating large complicated cavities due to ming,” *Journal of Engineering Geology*, vol. 38, no. 5, pp. 38–48, 2011.

[9] X. L. Wang, Z. G. Ji, and W. Q. Luo, “Comprehensive evaluation technology and application of grouting reinforcement effect for broken coal and rock mass,” *Coal geology & exploration*, vol. 47, no. 6, pp. 92–97, 2019.

[10] K. Makantasis, K. Karantzalos, A. Doulamis, and N. Doulamis, “Deep supervised learning for hyperspectral data classification through convolutional neural networks,” in *Geoscience and Remote Sensing Symposium (IGARSS)*, pp. 4959–4962, IEEE International, 2015.

[11] J. B. Lan, Y. Xu, L. G. Huo, and J. Z. Liu, “Research on the priorities of fuzzy analytical hierarchy process,” *Systems Engineering - Theory & Practice*, vol. 26, no. 9, pp. 107–112, 2006.

[12] N. Srivastava, G. Hinton, A. Krizhevsky, I. Sutskever, and R. Salakhutdinov, “Dropout: a simple way to prevent neural networks from overfitting,” *Journal of Machine Learning Research*, vol. 15, pp. 1929–1958, 2014.

[13] Q. Liu, W. Z. Chen, J. Q. Yuan, Y. X. Wang, and H. Wan, “Evaluation of grouting reinforcement effect for karst filling medium based on seepage-erosion theory,” *Chinese Journal of Rock Mechanics and Engineering*, vol. 39, no. 3, pp. 1–7, 2020.

[14] S. D. Liu, J. Liu, Y. Cao, and R. Q. Lv, “Applied technologies and new advances of parallel electrical method in mining geophysics,” *Journal of China Coal Society*, vol. 44, no. 8, pp. 2336–2345, 2019.

[15] H. F. Li, Z. Q. Luo, X. Y. Zhang, and C. Y. Xie, “Inspection and evaluation of reinforcement effect of collapse zone by grouting in a metal mine,” *Mining and metallurgical engineering*, vol. 39, no. 5, pp. 22–26, 2019.

[16] Z. G. Xie, Q. M. Liu, H. C. Chai, Q. D. Ju, J. Y. Li, and J. J. Rao, “Prediction of water inrush from hidden collapse column at coal seam floor and evaluation of grouting reinforcement before mining,” *Journal of safety science and technology*, vol. 15, no. 5, pp. 105–110, 2019.

[17] Z. P. Zhang, X. Liu, H. M. Xu, and J. S. Yang, “Experimental studies on grouting quality examination of gob of coalmine,” *Chinese journal of geotechnical engineering*, vol. 27, no. 5, pp. 604–606, 2005.

[18] D. W. Zhang, S. D. Chen, Z. L. Mao, and K. Liang, “Induced surface displacement and evaluation method of grouting for railway embankment in karst region,” *Journal of southeast university (Natural science edition)*, vol. 48, no. 6, pp. 1094–1101, 2018.

[19] J. Zadhesh, F. Rastegar, F. Sharifi, H. Amini, and H. M. Nasirabad, “Consolidation grouting quality assessment using artificial neural network (ANN),” *Indian geotech J*, vol. 45, no. 2, pp. 136–144, 2015.

[20] H. L. Zhang, M. Tu, H. Cheng, and Y. Tang, “Breaking mechanism and control technology of sandstone straight roof in thin bedrock stope,” *International Journal of Mining Science and Technology*, vol. 30, no. 2, pp. 259–263, 2020.

[21] Z. J. Wen, P. F. Jiang, S. L. Jing, Z. G. Cao, and Y. T. Guan, “Development and verification of simulation testing system for floor seepage in coal mine underground reservoir,” *Journal of China Coal Society*, vol. 46, no. 5, pp. 1487–1497, 2021.

[22] B. Y. Sun, P. S. Zhang, and M. R. Fu, “Comparative study on the “optic-electric” monitoring method for the deformation and failure of surrounding rock in stopes,” *Natural Hazards*, vol. 110, no. 1, pp. 407–427, 2022.

[23] P. H. Huang and X. Y. Wang, “Piper-PCA-Fisher recognition model of water inrush source: a case study of the Jiaozuo mining area,” *Geofluids*, vol. 2018, 10 pages.

[24] X. Y. Wang, F. Li, Q. Wang, B. Chen, Y. Zou, and B. Zhang, “Quantitative identification of the water resistance capacity of composite strata in mining coal seam floors,” *Geofluids*, vol. 2021, 14 pages, 2021.

Hindawi
Geofluids
Volume 2022, Article ID 6188833, 9 pages
https://doi.org/10.1155/2022/6188833

Research Article

Characterization of Acoustic Emission Parameters during Fracture Process of Siltstone with Prefabricated Void

Xiaorong Liu, Lulin Zheng, Hengyi He, Qing Qiu, Ziqi Liu, Xuefeng Li, Lin Yan, and Gang Huang

Mining College, Guizhou University, Guizhou, Guiyang 550025, China

Correspondence should be addressed to Lulin Zheng; llzheng@gzu.edu.cn

Received 21 March 2022; Accepted 15 June 2022; Published 27 July 2022

Academic Editor: Zhijie Wen

Due to the transfer of Lannigou gold mining from shallow to deep, a series of stability problems of surrounding rock have been caused. The drilling pressure relief technology has unique advantages in the control of mine pressure in high-stress roadways. In order to explore the damage effect of borehole pressure relief technology on rock, uniaxial compression and acoustic emission tests were carried out on siltstone specimens with borehole diameters of 8 mm, 12 mm, and 16 mm, respectively, and the acoustic emission signals of the whole process were collected simultaneously to explore the uniaxial compression of siltstone specimens with prefabricated holes in this paper. According to the statistical characteristics of acoustic emission, the damage law of siltstone specimens with prefabricated holes was explored from the microscopic point of view and the damage effect of drilling on siltstone specimens reflected by the acoustic emission phenomenon was revealed. The research results show that there are multiple stress drops before the deformation and failure of the rock sample with prefabricated drill holes; there is a positive correlation between the diameter of the drill hole and the power law index of the stress drop distribution; the acoustic emission activity of the rock during the deformation and failure process can be indirectly reflected the evolution of microfractures; the energy probability density function under different borehole diameters conforms to the power law distribution; the critical exponent obtained by the maximum likelihood estimation has an optimal plateau value, which can accurately characterize the power exponent of the energy distribution; the launch waiting time and aftershock sequence have a good power-law distribution in logarithmic coordinates. The research results provide a certain theoretical basis for the application of drilling pressure relief technology in southwestern Guizhou.

1. Introduction

The geological structure of the southwestern Guizhou region is complex, which makes the Lannigou gold mine show the characteristics of high in situ stress when it is gradually mined to the deep. With the increase of mining depth, the in situ stress of the Lannigou gold mine will reach 30 MPa, which leads to frequent occurrence of dynamic disasters such as the roof falling of the roadway. The mechanical environment of surrounding rock in high-stress roadways is more complex, showing a series of engineering response problems such as discontinuity, noncoordinated large deformation, and large-scale instability and damage [1]. For some high-stress roadways that are difficult to maintain, pressure relief technology can achieve better mine pressure control effect than strengthening support and surrounding rock reinforcement [2, 3]. Compared with other pressure relief technologies, drilling pressure relief technology has its unique advantages. Compared with blasting pressure relief, drilling pressure relief does not require charging. Compared with water injection pressure relief, drilling pressure relief saves a lot of water resources. The construction process is simple, and pressure relief effect is good [4, 5].

However, the drilling pressure relief technology will weaken the strength of the surrounding rock mass. The application of the drilling pressure relief technology in underground engineering does not consider this damage effect, resulting in problems such as unsatisfactory drilling parameters design. Acoustic emission technology, as a nondestructive testing method [6], can monitor the deformation and failure process of rocks in real time, dynamically, and continuously, thus reflecting the development of internal fractures in rocks [7]. Since the absolute energy of acoustic emission and the number of acoustic emission events can span multiple orders of magnitude, some scholars have introduced statistical theory and used statistical methods such as histogram method, least square method, and maximum likelihood estimation to study acoustic emission signals, so as to reversely understand compression failure characteristics of rock materials [8–10]. The moment tensor of major events can be obtained by the full waveform inversion of the acoustic emission signal, which can be used to evaluate the tunnel ground vibration caused by underground mines and study the focal mechanism of large earthquakes [11, 12]. At present, the research on the statistical characteristics of acoustic emission signals mainly focuses on the rock material and the stress environment. In terms of rock materials, there are mainly sandstone [13], granite [14], calcareous shale [15], goethite [16], and coal and sandstone combination rocks [17]. In terms of stress environment, scholars' research mainly focuses on uniaxial compression [18], triaxial compression [19], triaxial shearing [20], and wetting-drying cycle [21].While the above studies mostly focus on intact rocks, there are few studies on the statistical characteristics of acoustic emission signals during the deformation and failure of rocks with prefabricated cavities.

Therefore, it is of great significance to study the deformation and failure characteristics and acoustic emission characteristics of rocks with prefabricated holes for the rational design of drilling parameters to achieve a good pressure relief effect. Based on avalanche dynamics and acoustic emission as a monitoring method, this paper studies the statistical characteristics of acoustic emission of siltstone specimens with prefabricated cavities in the process of uniaxial compression. The influence of borehole diameter on the stress drop and avalanche dynamic activity of siltstone specimens with prefabricated cavities is investigated from a microscopic perspective. The stress drop of the specimen and the influence law of avalanche dynamic activity reveal the instability and failure mechanism of rock with prefabricated boreholes reflected by the acoustic emission phenomenon. This research reveals the instability failure mechanism of rock with prefabricated boreholes reflected by acoustic emission phenomenon.

2. Test Overview

2.1. Geological Background. It can be seen from Figure 1, Lannigou gold mine, as the largest fault-controlled Carlin-type gold deposit in a triangular district of the junction of Yunnan, Guizhou, and Guangxi Provinces in southwestern China, has a complex geological structure and complex ore body shape. The ore-hosting rock and surrounding rock are mainly sandstone and siltstone, which have the engineering characteristics of being weak and broken, easily weathered and argillized by water. Now it has been mined to -200 m horizontal elevation. Due to the influence of high ground stress, the surrounding rock of the deep roadway has challenges such as large deformation and difficulty in supporting [22]. For this purpose, nine rock samples were collected in the tunnel. Due to the influence of mineralization (silicification) alteration, the rock samples are dense and hard in texture. In order to more accurately identify the lithology, the collected rock samples were observed and identified by microscope. The magnification of the scanning electron microscope is 100 times. As shown in Figure 2, the particle size of the debris in the rock is generally between 0.1 and 0.4 mm. And the debris has high roundness and sphericity, good sorting. The debris is cemented by silica. It is thus determined that the lithology is siltstone.

2.2. Sample Processing. The siltstone with good homogeneity in the Lannigou gold mine was selected as the test material. After cutting and grinding, it was processed into a cuboid specimen of 50 mm × 50 mm × 100 mm. A round hole with a diameter of D was cut on the top. The parameters are shown in Table 1. Each group of tests used 3 specimens. The processed specimens are shown in Figure 3.

2.3. Test Plan. The test adopts the servo medium control system to carry out the uniaxial compression test on the sample. The loading method adopts displacement loading. The loading rate is 0.01 mm/min.

In the process of uniaxial compression, the DISP type acoustic emission system is used to simultaneously collect the whole process acoustic emission signal of the specimen during the loading process. Parameter setting: the monitoring threshold is 40 dB, the peak definition time is 50 μs, the bump definition time is 200 μs, the bump blocking time is 300 μs, and the acquisition frequency is 140 kHz. To ensure the reliability of the acoustic emission test data, two acoustic emission probes were arranged symmetrically in the middle of the left and right sides of the cuboid specimen during the test. Vaseline was smeared between the probe and the specimen to enhance the coupling effect between the two.

3. Results and Discussion

3.1. Mechanical and Failure Characteristic Analysis. According to Figure 4, when the borehole diameter is 8 mm and 12 mm, with the increase of the axial stress, the axial stress-strain curve shows multiple stress drops, and there are two obvious stress drops. When the first obvious stress drop occurs, the specimen still has a certain bearing capacity, indicating that the specimen has no overall instability and failure. There is a certain time interval between two obvious stress drops in the axial stress-strain curve. When the borehole diameter is 16 mm, the axial stress-strain curve also shows multiple stress drops, but there is no obvious stress drop phenomenon. When the borehole diameter is 16 mm, the rock transforms from brittle failure to ductile deformation, and no stress drop or significant stress drop occurs at this time. Stress drop is a range of individual variations, the brittle-ductile transition state. At the same time, the higher the strength of the rock fracture, the greater the stress drop, the lower the strength, and the smaller the stress drop [24]. The specimen exhibits plastic flow characteristics by comparing and analyzing the stress and strain corresponding to the peak

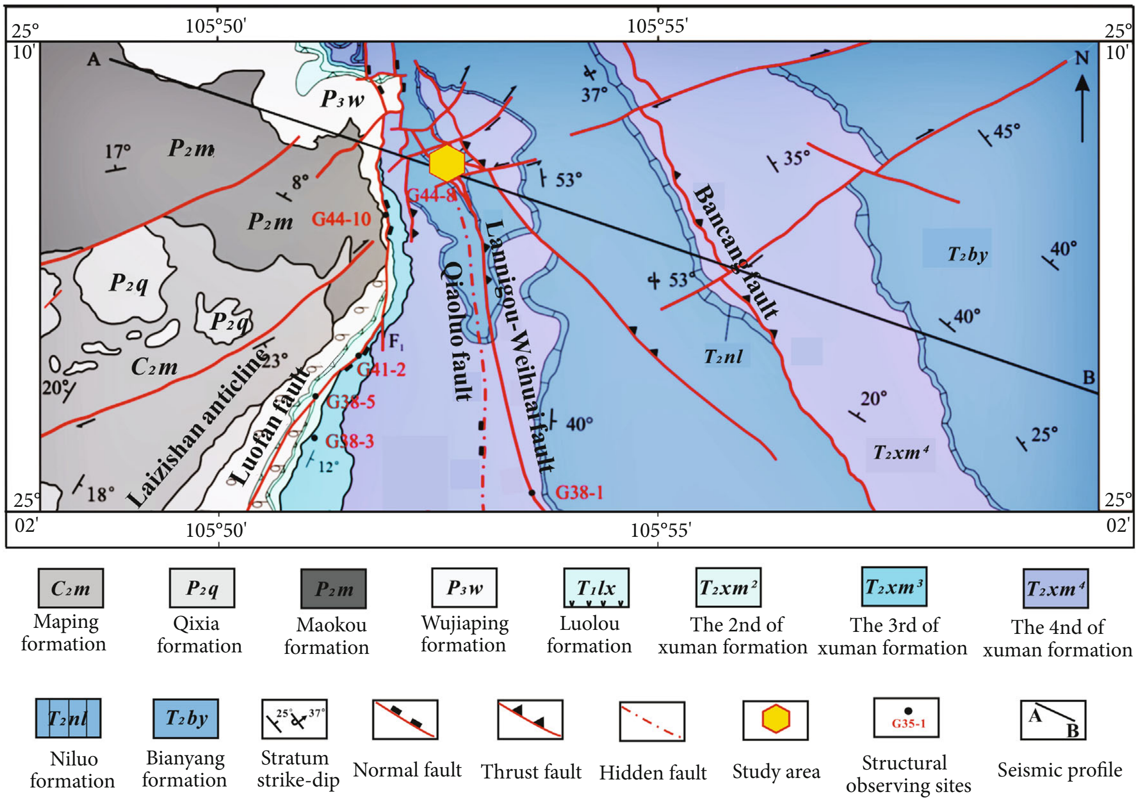

Figure 1: Regional structural geological map [23].

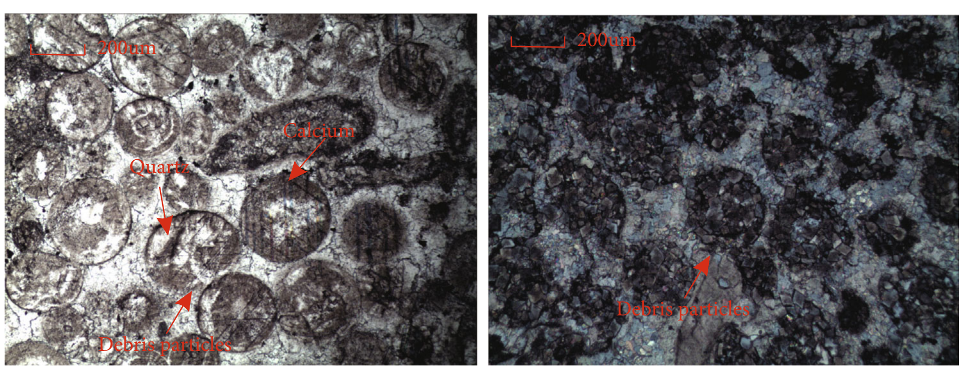

Figure 2: Micrograph of siltstone.

Table 1: Geometry parameters of samples.

Sample no.	L (mm)	W (mm)	H (mm)	D (mm)
1-1	50.0	50.1	100.0	8
1-2	50.2	50.0	100.1	8
1-3	50.0	50.2	100.1	8
2-1	50.0	50.1	100.0	12
2-2	50.1	50.2	100.1	12
2-3	50.1	50.0	100.2	12
3-1	50.0	50.2	100.1	16
3-2	50.0	50.1	100.1	16
3-3	50.1	50.0	100.2	16

point 1 and the peak point 2 of the stress drop phenomenon, it is found that with the increase of the borehole diameter, the stress difference and strain between the two peak points gradually increase. The stress of peak point 1 is 98.6% and 94% of the stress of peak point 2, respectively, and the strain of peak point 1 is 98% and 93% of the strain of peak point 2, respectively. The fast propagation point of the rock crack gradually moves away from the peak strength. This means that the likelihood of rock instability occurring increases with borehole diameter.

The stress drop of rock specimen under the action of force can be used as avalanche signal [25]. To further understand the stress drop phenomenon of rock compression failure with prefabricated boreholes, the probability

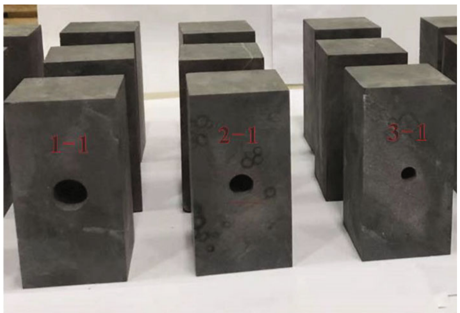

FIGURE 3: The processed siltstone specimen.

density of stress drop obtained during the whole process of compression failure of prefabricated borehole specimens was statistically analyzed. The statistical results of the probability density of the stress difference are shown in Figure 5. In Figure 5, $\Delta\sigma$ is the adjacent axial stress difference, and $P(\Delta\sigma)$ is the probability density function of the adjacent stress difference. Its expression is as follows:

$$\Delta\sigma = \sigma_{1i} - \sigma_{1i+1}. \quad (1)$$

Among them, $\Delta\sigma$ needs to satisfy the relation of $\Delta\sigma > 0$; σ_{1i}, $i = 1, 2, 3, \cdots, n$ is the observed value of axial stress.

According to Figure 5, the probability density map of the adjacent axial stress difference has a good linear relationship in the double logarithmic coordinate. This result shows that the distribution law of the stress drop phenomenon obtained during the compression failure process of the prefabricated drilled specimen follows the power law distribution. At the same time, as the borehole diameter increased from 8 mm to 16 mm, the power-law exponents of the stress drop distribution were -1.00, -0.81, and -0.72, respectively. It can be seen that there is a positive correlation between the borehole diameter and the power law exponent of the stress drop distribution.

The occurrence of stress drop phenomenon usually means the initiation or unstable propagation of macroscopic cracks. In this paper, the probability density statistics method is used to obtain that the distribution law of the stress drop phenomenon follows the power law distribution, which directly proves that the deformation and failure of the rock with prefabricated boreholes need to go through a gradual process from instability to failure.

3.2. Basic Characteristics of Acoustic Emission Energy. The intensity of an acoustic emission event is related to the amount of energy released. The absolute energy of acoustic emission is defined as the integral over the duration of the square of the acquired signal voltage. Its expression is as follows:

$$E = \frac{1}{R}\int_{t_i}^{t_j} U^2(t)dt. \quad (2)$$

Among them, t_i is the time when the acoustic emission event signal starts, t_j is the time when the acoustic emission signal ends; R is the internal resistance value; the unit of absolute energy is aJ.

It can be seen from Figure 6 that the overall trend of the $\sigma - t$ curve for different borehole diameters is relatively consistent. The energy signal is disordered and spans multiple orders of magnitude over time. As the borehole diameter increases, the number of acoustic emissions decreases. Especially when the hole diameter is 16 mm, the number of acoustic emissions is greatly reduced and the strength to the specimen is significantly reduced. The reason may be that when the borehole diameter is 16 mm, the weakening effect of the drilling technology on the strength of the rock specimen is obvious, which greatly reduces the strength of the rock, and which greatly shortens the fracture process of the specimen and reduces the acquisition of acoustic emission signal collection time. The whole process can be divided into the following stages.

Combined with the number of acoustic emission events reflected in the rock and the corresponding energy, each loading stage has different acoustic emission characteristics. In the fracture compaction stage, the acoustic emission events are less and more sparse and the energy value is relatively stable. This is mainly due to the end effect and the closure of the initial internal microcracks. In the linear elastic stage, the acoustic emission energy is briefly in a quiet period. At this time, the microcracks inside the sample have been compacted, and there are not new cracks generated. In the stage of microcrack generation and propagation, as the stress increases, microcracks begin to appear inside the sample. The crack gradually expands, and high-energy acoustic emission events increase. When the loading reaches the failure stage, the crack continues to expand violently, the energy accumulated inside is released, and the number of acoustic emission events increases sharply. The energy value of the acoustic emission event expands rapidly and is densely distributed, spanning multiple orders of magnitude. Due to the continuous accumulation of energy, the peak intensity of the specimen is reached and rupture occurs. At this time, the acoustic emission energy value is the largest, the event frequency is the largest, and the stress drops instantly. According to Figure 6, the evolution law of the acoustic emission energy of the rock during the deformation process with time reflects the change trend of its stress with time to a certain extent. This feature is not affected by the change of the diameter of the borehole, which indirectly proves that the acoustic emission activity can reflect the microfracture evolution activity.

3.3. Statistical Characteristics of Acoustic Emission Energy. Since both the AE energy and the AE event number span multiple orders of magnitude, they can be expressed in logarithmic coordinates. For acoustic emission signals spanning multiple orders of magnitude, it is an appropriate and effective analysis method to introduce avalanche theory and use statistical methods to study.

(1) Gutenberg-Richter law

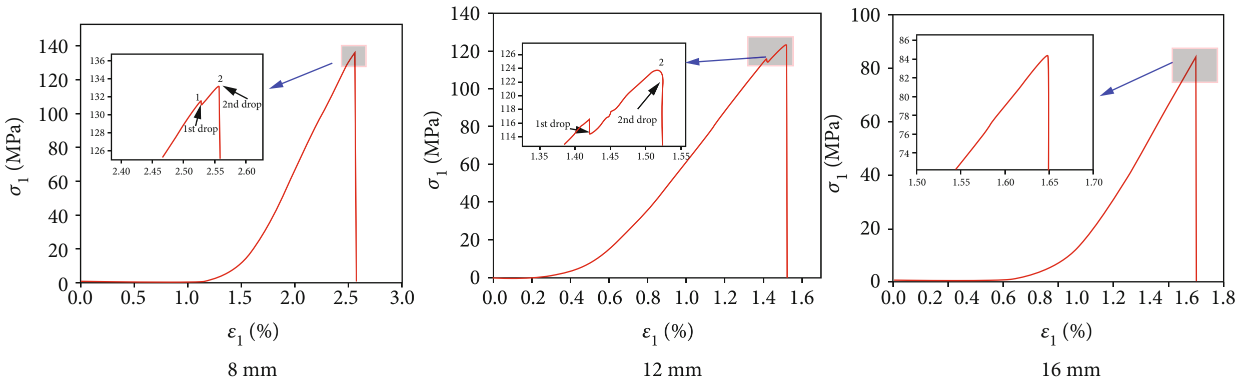

FIGURE 4: Stress-strain curve of culvert prefabricated drilled specimen under uniaxial compression.

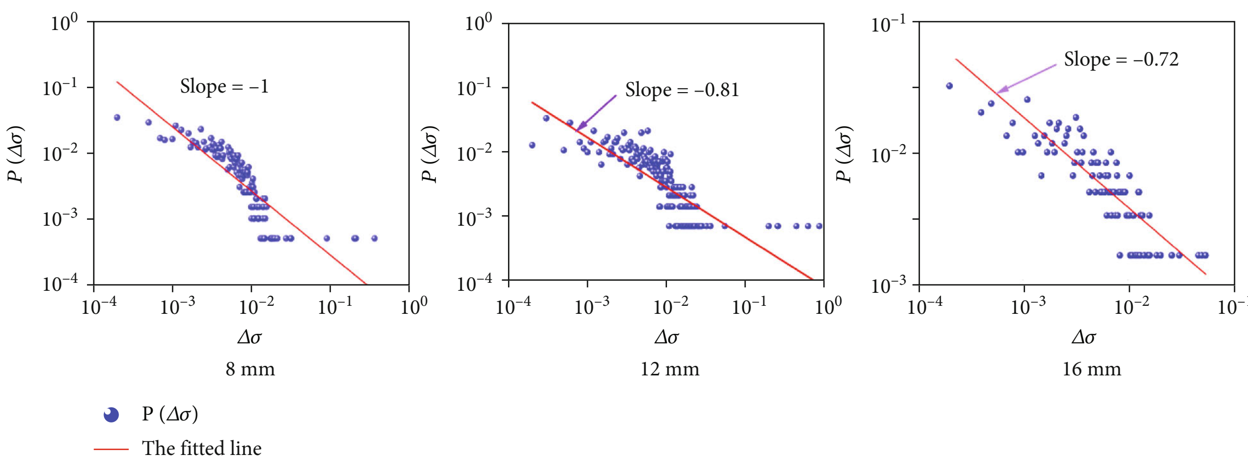

FIGURE 5: Stress drop probability density map.

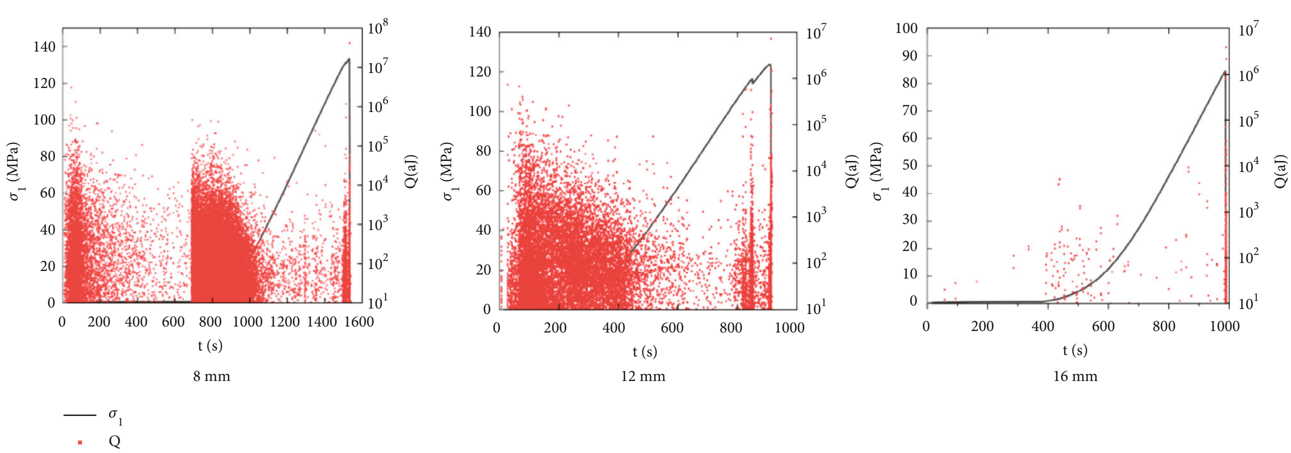

FIGURE 6: Relationship between acoustic emission energy and stress with time.

The acoustic emission energy data obtained during the whole process of compression failure of the specimen with prefabricated drilling holes were counted by the histogram method, and the acoustic emission energy probability density map of the specimen was obtained. The result is shown in Figure 7. The acoustic emission energy of the specimen with prefabricated holes obeys a power-law distribution [26]:

$$p(x) = \frac{x^{-r}}{\tau(r, x_{\min})}. \tag{3}$$

In the formula, r is the critical exponent characterizing the entire probability density distribution; τ is the Huiwiz-zeta function.

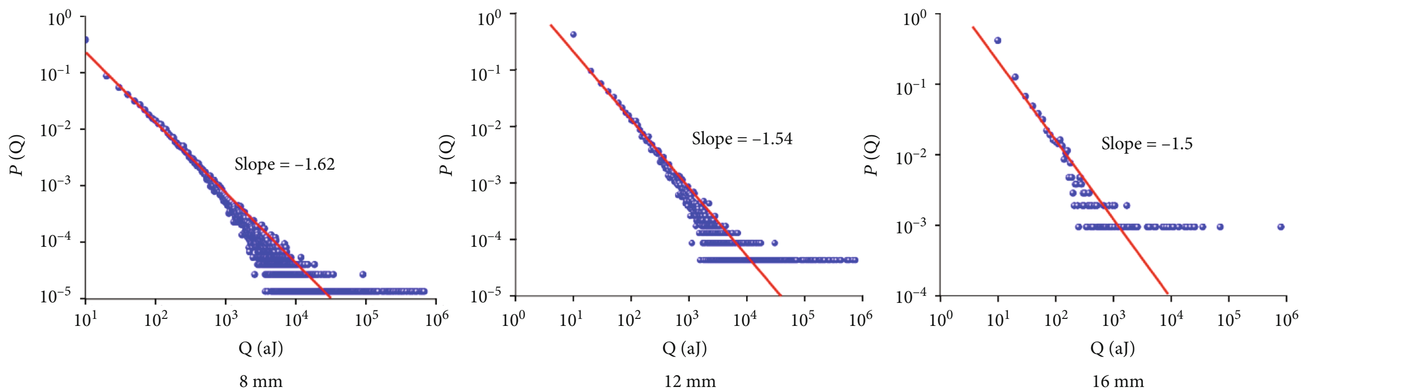

FIGURE 7: Acoustic emission energy probability density diagram of the specimen with drilled hole.

It can be seen from Figure 7 that the acoustic emission energy probability density map has a good linear relationship in the double logarithmic coordinate, and the inherent property of the acoustic emission energy distribution follows a power-law distribution and is not affected by the change of the borehole diameter. The absolute value of the slope of the fitted straight line in Figure 7 can be expressed as the magnitude of the power-law exponent of the acoustic emission energy. The power exponent can reflect that the damage of rock originates from the development process [27].

When using maximum likelihood estimation, the distribution index r of the absolute energy of acoustic emission can be expressed as [28]

$$r_{(x_{\min})} = 1 + n\left(\sum_{i=1}^{n} \ln \frac{x_i}{x_{\min}}\right)^{-1}, \tag{4}$$

where x_i, $i = 1 \cdots n$ are all observations that satisfy the inequality $x_i \geq x_{\min}$.

It can be seen from equation (4) that the number of critical exponent r and histogram units is independent of the length. There are not artificial parameters introduced in the whole calculation, and the result is only related to its own data structure.

However, using different energy intervals as the estimation basis will result in different power exponents r, that is, the power exponent as a function of the energy interval $r = f([X_{\text{low}}, X_{\text{high}}])$. Therefore, each different sample interval $[X_{\text{low}}, X_{\text{high}}]$ can get a power exponent estimate $r^{'}$. Sample interval is selected according to the following rules. In the case of fixed X_{high}, the corresponding power exponent is estimated by sliding X_{low}. Research shows (J.BAR), when $X_{\text{high}} = X_{\max}$, the distribution of the power exponent r corresponding to different sample intervals is the most concentrated by sliding X_{low}. Therefore, by setting $X_{\text{high}} = X_{\max}$, a more accurate power exponential dynamic distribution curve can be obtained by changing the size of the sample interval.

The maximum likelihood method is used to calculate and analyze the absolute energy of acoustic emission generated by the specimen in the process of compression failure by using MATLAB software. The calculation results are shown in Figure 8.

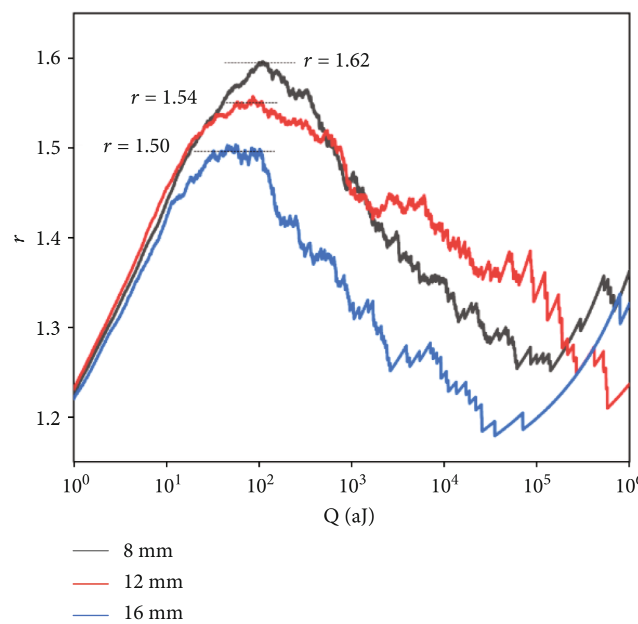

FIGURE 8: Maximum likelihood estimation of acoustic emission energy power law exponent.

According to Figure 8, the plateau value of the power-law exponential curve can represent the best estimate of the power-law of the probability density curve. The power-law exponent r at this stage can well represent the energy distribution of the entire process. For 8 mm, 12 mm, and 16 mm different drill hole diameters, the value range of the power law index is $r_{8\text{mm}} = 1.62 \pm 0.05$, $r_{12\text{mm}} = 1.54 \pm 0.05$, and $r_{16\text{mm}} = 1.5 \pm 0.05$. The absolute energy of acoustic emission generated during the compression failure process of rock specimens with prefabricated cavities can better satisfy the G-R law. The power-law exponent decreases gradually as the borehole diameter increases. The trend of negative correlation is between borehole diameter and absolute energy power law exponent of acoustic emission. The

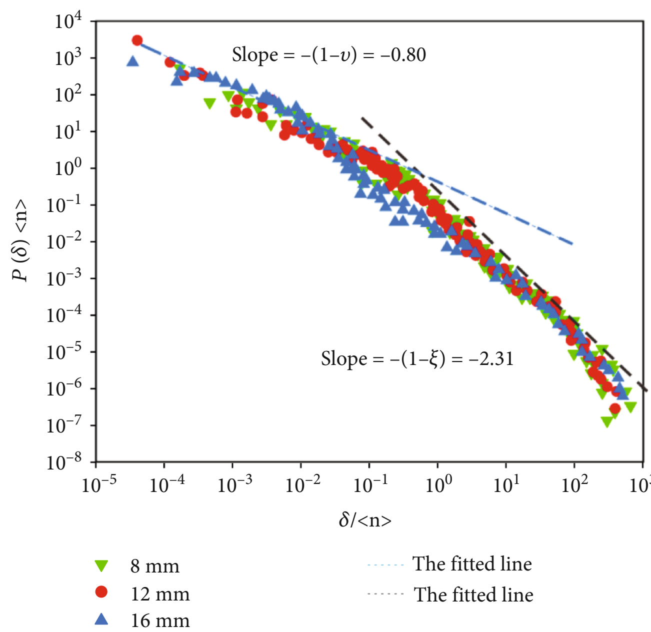

Figure 9: Distribution of waiting time of specimens with different borehole diameters.

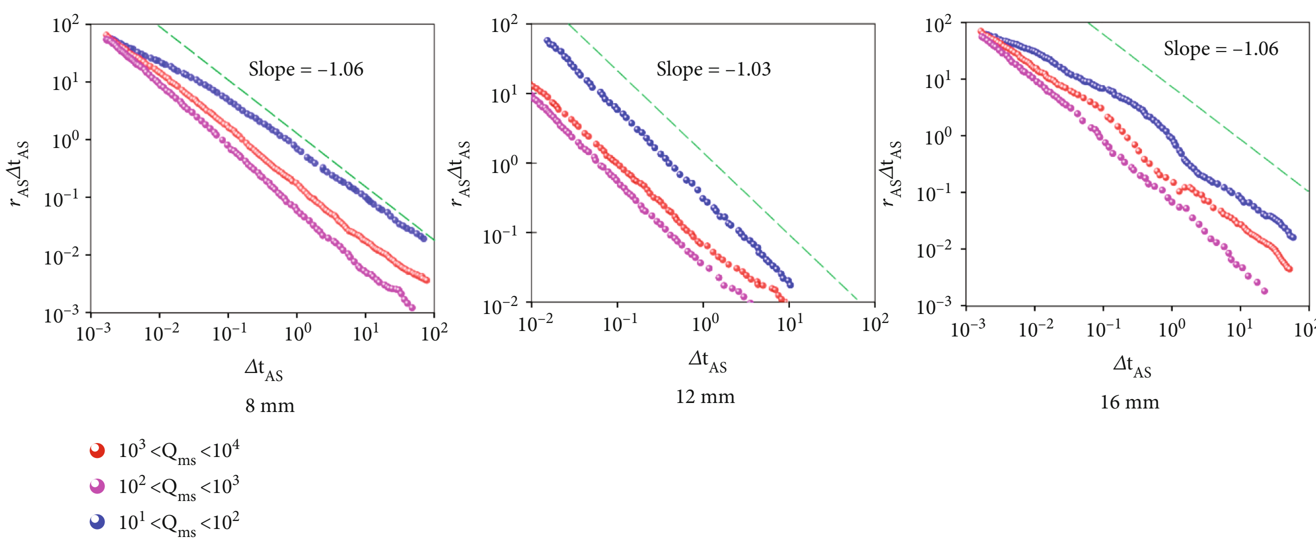

Figure 10: Distribution of aftershock sequences of specimens with different diameters.

acoustic emission energy power-law index obtained by the maximum likelihood method is roughly the same as the acoustic emission energy power-law index obtained by the histogram method. Therefore, the absolute energy power-law index of acoustic emission obtained in this study has high reliability.

(2) Distribution of waiting time

The time interval between adjacent acoustic emission events is regarded as the waiting time, denoted by the symbol δ.

For the compression failure of rock materials, the calculation results are shown in Figure 9 through statistical analysis of the waiting time of adjacent acoustic emission events. In Figure 9, $P(\delta)$ represents the probability density function of the waiting time of adjacent acoustic emission, δ represents the waiting time of adjacent acoustic emission events, and $<n>$ represents the unit time of the absolute energy of acoustic emission under the diameter of the borehole average number of acoustic emission events. For acoustic emission events with waiting time less than 0.1 s, the power critical exponent is $1-\nu$, while the power critical exponent for acoustic emission with waiting time greater than 0.1 is

$2+\zeta$. According to Figure 9, it can be seen that the waiting time distribution of the three specimens with different borehole diameters shows a good power-law distribution in the double logarithmic coordinate. The waiting time distribution of the siltstone specimens with the three borehole diameters is basically the same, which shows that the time distribution of AE signal generation is not affected by the diameter of the borehole.

(3) Distribution of aftershock sequences

The relationship between the main shock and aftershocks can be described by Omori's law, that is, the number of aftershocks decreases exponentially with the time from the main shock [29]. For the data analysis of Omori's law, artificially divided energy intervals 10^1 aJ~102 aJ, 10^2 aJ~103 aJ, and 10^3 aJ~104 aJ are used, and the main shock is selected in the above energy interval. Count the frequency r_{AS} of aftershocks in the time interval Δt_{AS} from the main shock.

Figure 10 shows the statistical results of aftershock sequences for sandstone specimens with three borehole diameters. For the sandstone specimens with three different borehole diameters, their aftershock sequences show good power-law distribution in the above three orders of magnitude, and the aftershock frequency attenuation coefficients are all about 1 in the double logarithmic coordinate. Thus, the distribution of aftershock sequences of sandstone specimens with three borehole diameters satisfies a power-law distribution, and the distribution index is close to the seismic statistics in the case of uniaxial compression. The power-law similarity of the three mainshock energy intervals reflects the scale-free characteristics of Omori's law, that is, the selection of mainshock energy does not affect the attenuation coefficient of aftershock frequency and the law of aftershock frequency attenuation over time. The data for the sandstone specimen with a borehole diameter of 16 mm is not as linear in logarithmic coordinates as for the sandstone specimens with a borehole diameter of 8 mm and 12 mm. The reason may be related to the fact that the amount of acoustic emission data of the 16 mm sandstone specimen is far less than that of the other two groups of specimens.

4. Conclusion

In this paper, the uniaxial compression acoustic emission test is carried out on siltstone specimens with different borehole diameters, and the acoustic emission signals of the whole process are collected simultaneously.

(1) The prefabricated drilled rock has multiple stress drops before deformation and failure, but when the diameter of the drilled hole is 16 mm, the stress drop is small. The rock failure occurs after a certain stress drop $\Delta\sigma$. The evolution law of the acoustic emission energy of the rock during the deformation process reflects the change trend of its stress with time to a certain extent, which indirectly proves that the acoustic emission activity can reflect the microfracture evolutionary activity

(2) The acoustic emission energy obeys the power-law distribution in multiple orders of magnitude, and the change of the borehole diameter does not change. The two methods of the histogram method and the maximum likelihood estimation method also confirm that the critical exponent of the acoustic emission energy probability density has a high reliability

(3) The larger the absolute value of the slope is, the steeper the probability density curve is, which is reflected in the figure as the increase in the rate density $P(E)$ of the low-energy acoustic emission signal. The change of the slope reflects the deterioration of the rock by the drilling technology. The changing behavior of the critical index can characterize the damage

(4) The distribution of acoustic emission waiting time of siltstone specimens with different borehole diameters. The distribution of aftershock sequences have similar power-law distributions in double logarithmic coordinates. The waiting time distribution of the specimens has the same power-law exponent, and the aftershock attenuation coefficient p is close to 1

(5) As the borehole diameter increases, the weakening of rock strength increases significantly. Therefore, on the premise of obtaining a good pressure relief effect, the diameter of the drill hole should be selected as small as possible to prevent the instability of the rock mass

Data Availability

The experimental data used to support the findings of this study are available from the corresponding author upon request.

Conflicts of Interest

The authors declare that there is no conflict of interest regarding the publication of this paper.

Acknowledgments

This work was supported by the Guizhou Province Science and Technology Support Program Project (grant number QIANKEHE Support [2021] General 516), the National Natural Science Foundation of China (grant numbers 41962008, 52164006, and 51964007), and Scientific and Technological Innovation Talents Team in Guizhou Province (grant number [2019] 5619).

References

[1] C. Pan, B. Xia, Y. Zuo, B. Yu, and C. Ou, “Mechanism and control technology of strong ground pressure behaviour induced by high-position hard roofs in extra-thick coal seam mining,” *International Journal of Mining Science and Technology*, vol. 32, no. 3, pp. 499–511, 2022.

[2] B. Ma, *Research on Prevention and Control of Rockburst by Drilling Pressure Relief*, General Research Institute of Coal Science, 2018.

[3] J. Ma, *Research on the Application of Pressure Relief Method in the Safety and Stability Control of Impact-Type Deep Well Mining Roadway*, Shanghai University of Applied Sciences, 2020.

[4] S. Zhang, Y. Li, B. Shen, X. Sun, and L. Gao, “Effective evaluation of pressure relief drilling for reducing rock bursts and its application in underground coal mines,” *International Journal of Rock Mechanics and Mining Sciences*, vol. 114, pp. 7–16, 2019.

[5] C. Wang, A. Cao, G. Zhu, G. Jing, J. Li, and T. Chen, “Mechanism of rock burst induced by fault slip in an island coal panel and hazard assessment using seismic tomography: a case study from Xuzhuang colliery Xuzhou China,” *Geosciences Journal*, vol. 21, no. 3, pp. 469–481, 2017.

[6] Y. Xiao, L. Wang, X. Jiang, T. M. Evans, A. W. Stuedlein, and H. Liu, “Acoustic emission and force drop in grain crushing of carbonate sands,” *Journal of Geotechnical and Geo environmental Engineering*, vol. 145, no. 9, 2019.

[7] S. Li and H. Tang, “Acoustic emission characteristics of rock material fracture process under different loading conditions,” *Chinese Journal of Geotechnical Engineering*, vol. 31, no. 1, pp. 147–152, 2010.

[8] L. Girard, J. Weiss, and D. Amitrano, “Damage-cluster distributions and size effect on strength in compressive failure,” *Physical Review Letters*, vol. 108, no. 22, article 225502, 2012.

[9] E. K. H. Salje, A. Planes, and E. Vives, “Analysis of crackling noise using the maximum-likelihood method: power-law mixing and exponential damping,” *Physical Review E*, vol. 96, no. 4, article 042122, 2017.

[10] G. Chen, X. Sun, J. Wang, D. Wang, and Z. Zhu, “Detection of cracking behaviors in granite with open precut cracks by acoustic emission frequency spectrum analysis,” *Arabian Journal of Geosciences*, vol. 13, no. 6, p. 258, 2020.

[11] J. Ma, L. Dong, G. Zhao, and X. Li, “Focal mechanism of mining-induced seismicity in fault zones: a case study of Yongshaba mine in China,” *Rock Mechanics and Rock Engineering*, vol. 52, no. 9, pp. 3341–3352, 2019.

[12] J. Ma, L. Dong, G. Zhao, and X. Li, “Qualitative method and case study for ground vibration of tunnels induced by fault-slip in underground mine,” *Rock Mechanics and Rock Engineering*, vol. 52, no. 6, pp. 1887–1901, 2019.

[13] D. Jiang, H. Yue, X. Zhang, K. Xie, and X. Jiang, “Sandstone uniaxial compression acoustic emission and fiber bundle model simulation,” *Rock and Soil Mechanics*, vol. 38, no. 2, 2017.

[14] J. Davidsen, G. Kwiatek, E. M. Charalampidou et al., “Triggering processes in rock fracture,” *Physical Review Letters*, vol. 119, no. 6, article 068501, 2017.

[15] K. Xie, D. Jiang, X. Jiang et al., “Energy distribution and criticality characteristics analysis of shale Brazilian splitting test,” *Journal of China Coal Society*, vol. 42, no. 3, pp. 613–620, 2017.

[16] E. K. H. Salje, G. I. Lampronti, D. E. Soto-Parra, J. Baro, A. Planes, and E. Vives, “Noise of collapsing minerals: predictability of the compressional failure in goethite mines,” *American Mineralogist*, vol. 98, no. 4, pp. 609–615, 2013.

[17] H. Liu, L. Jin, D. Jiang, K. Xie, and X. Jiang, “Experiment and maximum likelihood theory of acoustic emission statistical effect of coal and sandstone composite rocks,” *Chinese Journal of Coal Society*, vol. 44, no. 5, pp. 1544–1551, 2019.

[18] D. Jiang, K. Xie, X. Jiang, J. Chen, and X. Yuan, “Statistical analysis of acoustic emission energy distribution during uniaxial compression failure of shale,” *Chinese Journal of Rock Mechanics and Engineering*, vol. 35, no. 2, pp. 3822–3828, 2016.

[19] G. Hou, J. Liang, H. Jing et al., “Acoustic emission characteristics of small surrounding rock specimens under triaxial action during unloading process,” *Rock and Soil Mechanics*, vol. 40, no. 12, pp. 4564–4572, 2019.

[20] Y. Zhao, H. Liu, K. Xie, E. K. H. Sajie, and X. Jiang, “Avalanches in compressed sandstone: crackling noise under confinement,” *Crystals*, vol. 9, no. 11, p. 582, 2019.

[21] K. Xie, D. Jiang, Z. G. Sun, J. Chen, W. Zhang, and X. Jiang, “NMR, MRI and AE statistical study of damage due to a low number of wetting-drying cycles in sandstone from the three gorges reservoir area,” *Rock Mechanics and Rock Engineering*, vol. 51, no. 11, pp. 3625–3634, 2018.

[22] L. Zheng, L. Zheng, Y. Zuo et al., “Study on mesoscale damage evolution characteristics of irregular sandstone particles based on digital images and fractal theory,” *Advances in Materials and Engineering*, vol. 2021, article 6552847, 14 pages, 2021.

[23] S. Zheng, Y. Hu, S. Guan, and X. Li, “Structural deformation and evolution of the Lannigou gold orefield in southwestern Guizhou,” *Geological Review*, vol. 66, no. 5, pp. 1431–1445, 2020.

[24] S. Zang, “Seismic stress drop and rock fracture stress drop,” *Acta Seismologica Sinica*, vol. 6, no. 2, pp. 182–184, 1984.

[25] W. Hu, G. Scaringi, Q. Xu, and R. Huang, “Acoustic emissions and micro-seismicity in granular slopes prior to failure and flow-like motion: the potential for early warning,” *Geophysical Research Letters*, vol. 45, no. 19, pp. 406–410, 2018.

[26] P. O. Castillo-Villa, J. Baro, A. Planes et al., “Crackling noise during failure of alumina under compression: the effect of porosity,” *Journal of Physics: Condensed Matter*, vol. 25, no. 29, article 292202, 2013.

[27] X. Jiang, H. L. Liu, I. G. Main, and E. K. H. Sajie, “Predicting mining collapse: superjerks and the appearance of record-breaking events in coal as collapse precursors,” *Physical Review E*, vol. 96, no. 2, article 023004, 2017.

[28] A. Clauset, C. R. Shalizi, and M. E. J. Newman, “Newman M E J. Power-law distributions in empirical dataPower-Law Distributions in Empirical Data,” *SIAM Review*, vol. 51, no. 4, pp. 661–703, 2009.

[29] T. Utsa, “The centenary of the Omori formula for a decay law of aftershock activity,” *Journal of Physics of the Earth*, vol. 43, no. 1, pp. 1–33, 1995.

Hindawi
Geofluids
Volume 2022, Article ID 8063469, 11 pages
https://doi.org/10.1155/2022/8063469

Research Article

Predicting Time-to-Failure of Red Sandstone by Temporal Precursor of Acoustic Emission Signals

Ansen Gao[1] **Chengzhi Qi**[1,2,3] **Renliang Shan**[1] **and Chunlai Wang**[4]

[1]*School of Mechanics and Civil Engineering, China University of Mining and Technology (Beijing), Beijing 100083, China*
[2]*School of Civil and Transportation Engineering, Beijing University of Civil Engineering and Architecture, Beijing 100044, China*
[3]*Beijing Advanced Innovation Centre for Future Urban Design, Beijing University of Civil Engineering and Architecture, Beijing 100044, China*
[4]*School of Energy and Mining Engineering, China University of Mining and Technology (Beijing), Beijing 100083, China*

Correspondence should be addressed to Ansen Gao; gaoansen@163.com and Chengzhi Qi; buceaqcz@163.com

Received 18 March 2022; Accepted 8 June 2022; Published 18 July 2022

Academic Editor: Zhijie Wen

The evolution pattern of rock damage is a progressive failure process of rock materials. It is the basis for predicting failure time of rock materials. By theoretical and experimental analysis, the acoustic emission (AE) precursor characteristics of rock fracture and the gradual evolution pattern of rock damage were analyzed detailedly. Then, the time-to-failure of red sandstone was predicted and compared by several different methods. The results demonstrated that the failure process of red sandstone can be divided into the stable deformation stage and the critical acceleration failure stage. In the critical acceleration failure stage, the AE precursor of rock failure was easy to be observed, and the AE event rate occurred as jump-like increase phenomenon. Moreover, the gradual evolution pattern of rock damage obeyed an exponential function, and the damage acceleration phenomenon existed in the critical failure stage. Furthermore, the higher values of the average of rock damage was, the more obvious linear evolution pattern will be, which was beneficial to improve the prediction accuracy of time-to-failure of rocks. Clearly, the linear prediction results of rock failure time, after taking average values of five rock damage variables, had more higher accuracy when damage variable exceeded $D = 0.5$. The predicting result of specimen R1 was 0.2 s ahead of its actual failure time, and the predicting result of specimen R6 was 8.1 s ahead of its actual failure time. Therefore, this method is meaningful and it can be used for the early warning of rockburst.

1. Introduction

The crack initiation to rock fracture is accompanied by acoustic emission (AE) phenomenon. It is very useful for revealing the failure mechanism of rock materials [1], and it is particularly effective for monitoring the physics precursor of natural events such as earthquake and rockburst. Typically, the accelerating phenomenon of AE monitoring signals is observed before the failure of rock materials [2–5]. It means that there is a critical failure stage of rocks, and it is very important to make full use of the critical AE precursor to elucidate the failure mechanism of rock materials. Therefore, it is an important challenge to present a quantitative method for forecasting time-to-failure of rocks.

Rockburst always occurs in the excavation process of tunneling and mining, which seriously endangers the safety of engineering structures [6, 7]. In many cases, the precursor of seismic activity showed acceleration phenomenon which can be used as a robust precursor of volcanic eruptions [8]. Meanwhile, many rockbursts were preceded by increases of AE monitoring signals [2–5, 9]. A range of different models have been proposed to relate the evolution of AE monitoring signals to the onset time of rockburst. Fukuzuno [10] used an empirical power law to model the evolution of surface displacements prior to slope failure. Later on, Voight [8] proposed a general material failure law to characterize the evolution pattern of rock deformation and AE signals. Nevertheless, Voight's model required that the failure pattern of materials must conform to a power-law relationship, which was not friendly to the non-power-law evolution pattern of rock failure. Boué et al. [11] presented an approach for real-time monitoring volcano-seismic precursors. It can forecast the eruption time before it erupting. However, the time scale of this method was relatively large and inaccurate, and the accuracy of predicting time-to-failure of rock materials was still unclearly.

Rock fracture is driven by the stress and the time-dependent cracking process [12]. The time-dependent fracture behavior is particularly important for rock engineering structures for long-term stability [13]. However, the turning point of the stable and unstable deformation stage of rocks has not been quantitatively distinguished [13]. The time series of daily seismic event rate for Kilauea Volcano from 1959 to 2000 was analyzed by Chastin et al. [14]. It showed that an accelerating behavior of the mean seismic event rate emerged 10-15 days before the eruption. Still, the predicting time scale was measured in days, and it was relatively large and fuzzy [14]. The determined accelerating behavior of average seismic events seems to give us some insights for the time-to-failure of sudden disasters such as volcanic eruption and rockburst. The onset time of acceleration phenomenon is the better evaluation indicator for materials failure prediction [15]. Despite the widespread interest in predicting failure time of rocks, the starting point of damage acceleration was not reliably identified. This usually resulted in a lag in predicting time-to-failure of rock materials. It can decrease the possibility of false alarms of rockburst by accurately identifying the starting point of rock damage acceleration stage [2–5, 9]. Therefore, a credible method is still required to identify the starting point of damage acceleration process for predicting time-to-failure of rocks.

The AE signals monitoring technology has been verified as an effective, nondestruction, and real-time monitoring tool, which reliably reflects the nucleation and propagation of irreversible microcracks before rock failure. In this study, we focused on methods for forecasting the time-to-failure of a forthcoming rockburst based on damage accelerating phenomenon of AE signals. Firstly, the internal damage evolution model of rocks was revealed by theoretical derivation. Then, the red sandstone specimens were subjected to the uniaxial compression test. The AE precursor of rock failure and the evolution pattern of rock damage were analyzed based on AE event rate. Moreover, the time-to-failure of rocks was further predicted and compared by linear and exponential function methods.

2. Theoretical Basis

The damage acceleration behavior exists in the critical failure stage of rock materials, and it is very meaningful for better identifying the damage evolution pattern and predicting time-to-failure of rock materials [15]. Before analyzing and calculating rock damage variables, the following assumptions are made for simplification: (i) rock materials are isotropic, homogenous, continuous, and brittle materials with preexisting microcracks on a macroscale; (ii) the elastic damage constitutive law is applicable to each mesoscopic element; (iii) rock damage is continuously developed and gradual accumulation in mesoscopic elements; (iv) the strength of mesoscopic elements is observed following Weibull distribution function [16–18].

$$P(F) = \begin{cases} \dfrac{m}{F_0}\left(\dfrac{F}{F_0}\right)^{m-1} \exp\left[-\left(\dfrac{F}{F_0}\right)^{m}\right] & F > 0, \\ 0 & F \leq 0, \end{cases} \tag{1}$$

where F is an elemental strength parameter or stress level, F_0 is its mean value, and m is the shape parameter (Weibull modulus) or a homogeneous index of rock materials which measures the concentration of F.

Then, let N denotes the number of all mesoscopic elements, and N_f denotes the number of all failed mesoscopic elements. The damage variable (D) can be directly defined as the following equation.

$$D = \frac{N_f}{N}. \tag{2}$$

When the stress level F increases to $F + dF$, the number of failed mesoscopic elements increases by $NP(F)dF$. If external force increases from zero to F, from equation (1), the total number of failed mesoscopic elements is calculated by the following equation.

$$N_f(F) = \int_0^F NP(y)dy = N\left\{1 - \exp\left[-\left(\frac{F}{F_0}\right)^{m}\right]\right\}. \tag{3}$$

Then, from equations (2) and (3), the following equation can be obtained.

$$D = 1 - \exp\left[-\left(\frac{F}{F_0}\right)\right]^{m}. \tag{4}$$

It is assumed that the ultimate principal stress for rock failure meets the Hoek-Brown strength criterion [19].

$$F(\sigma) = n\sigma_c \frac{I_1^*}{3} + 4J_2^* \cos^2\theta_\sigma + n\sigma_c\sqrt{J_2^*}\left(\cos\theta_\sigma + \frac{\sin\theta_\sigma}{\sqrt{3}}\right) = s\sigma_c^2, \tag{5}$$

where σ_c is the uniaxial compressive strength, n and s are the material constants, θ_σ is Lode's angle, I_1^* is the first invariant of effective stress, and J_2^* is the second invariant of effective stress deviators.

For the uniaxial compression, $\sigma_2 = \sigma_3 = 0$, $\theta_\sigma = 30°$, there are the following determinate relationships.

$$I_1^* = E\varepsilon_1, \tag{6}$$

$$\sqrt{J_2^*} = \frac{E\varepsilon_1}{\sqrt{3}}, \tag{7}$$

where E is the modulus of elasticity and ε_1 is the axial strain.

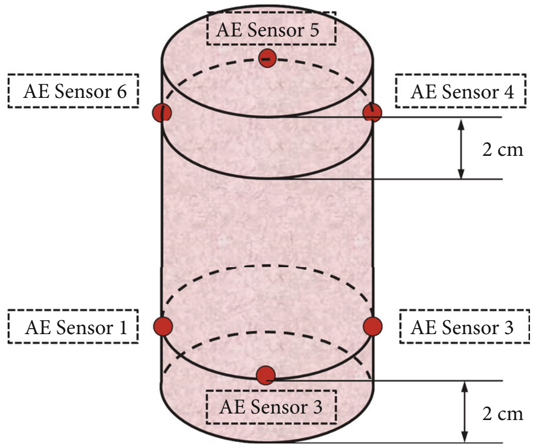

Figure 1: Schematic diagram of AE sensors distribution.

Substituting equations (6) and (7) into (5), the following equation can be obtained.

$$F(\sigma) = n\sigma_c E\varepsilon_1 + (E\varepsilon_1)^2. \tag{8}$$

According to equations (4) and (8), the mechanical damage (D) caused by the compression stress is as the following equation.

$$D = 1 - \exp\left\{-\left[\frac{n\sigma_c E\varepsilon_1}{F_0} + \frac{E^2\varepsilon_1^2}{F_0}\right]^a\right\}. \tag{9}$$

This is the damage evolution equation of mesoscopic elements in the statistical constitutive model of rock materials. Equation (9) can be simplified as the following equation.

$$D = 1 - \exp\left[-\left(\alpha\varepsilon_1 + \beta\varepsilon_1^2\right)^a\right], \tag{10}$$

where $\alpha = n\sigma_c E/F_0$ and $\beta = E^2/F_0$.

Then, assuming that rock materials have no initial damage, the cumulative number of AE events is N_{AW} when rock is completely broken. For any deformation time t, the cumulative number of AE events is $N_A(t)$. Then, the following damage equation can be defined by AE events.

$$D = \frac{N_A(t)}{N_{AW}}. \tag{11}$$

3. Experimental Investigation

3.1. Experimental Equipment. The Instron 5985 compression testing machine was used in this study, which had a maximum load capacity of 250 kN and the minimum loading rate of 0.0001 mm/min. The AE monitoring equipment employed PCI-II, which was an AE signals acquisition and analysis system. To improve the spatial positioning accuracy of AE events, six AE sensors were used in this test and they were placed 20 mm away from both ends of rock specimens, as shown in Figure 1. In addition, the AE sensors were distributed at an angle of 90° to ensure they were not coplanar. The threshold value of the AE monitoring system was set to 45 dB, the preamplifier gain was set to 40 dB, and the sampling frequency was set to 1 MHz.

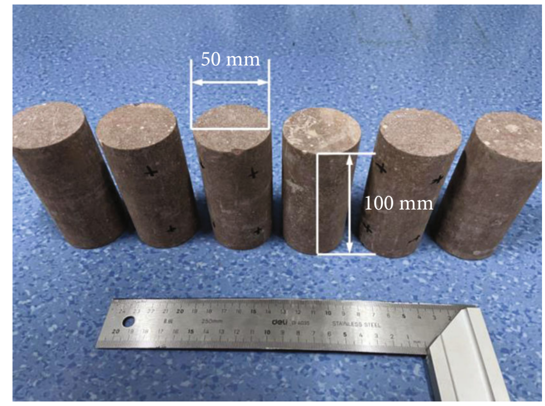

Figure 2: The prepared red sandstone specimens.

3.2. Specimen Preparation. The same raw rock sample was used for preparing rock specimens to ensure the physical and mechanical parameters of specimens had the same level of magnitude. Then, the specimens were prepared as cylinder with a height-diameter ratio of 2 : 1 (with the size of 100 : 50 mm). After preliminary preparation, the specimens were carefully polished to ensure both ends were ground flat without significant damage, as shown in Figure 2.

3.3. Experimental Method. For verifying the rationality of the damage evolution model and the method of predicting time-to-failure of rocks, six red sandstone specimens were used for this study. For specimens R1~R3, their loading rate was 0.1 mm/min, and for specimens R4~R6, their loading rate was 0.03 mm/min. The loading process was monitored synchronously with AE signals monitoring process. Beyond peak stress, the loading process was stopped after the stress dropped to 80% of its peak value to ensure rock specimens had been completely destroyed. In particular, the representative results of specimens R1 and R6 were used to analyze in this study.

4. Results

4.1. The Evolution Characteristics of AE Signals of Red Sandstone. Figure 3 shows the evolution characteristics of AE events with the increasing axial loading. To illustrate, Figure 3(a) is the result of specimen R1, and Figure 3(b) is the result of specimen R6. The results showed that the failure process of red sandstone needed to experience stable elastic deformation firstly, the stress increased steadily, and the stress curve was smooth. Subsequently, rock specimens entered the critical fracture stage, the stress was fluctuating and unstable, and the peak stress will be reached in a short time. Then, the stress decreased slightly in steps which was followed by the complete penetration of cracks. During the elastic deformation stage (Stage I), the AE events had relatively lower values and fewer numbers, and its variation was relatively stable and smooth. In the critical acceleration

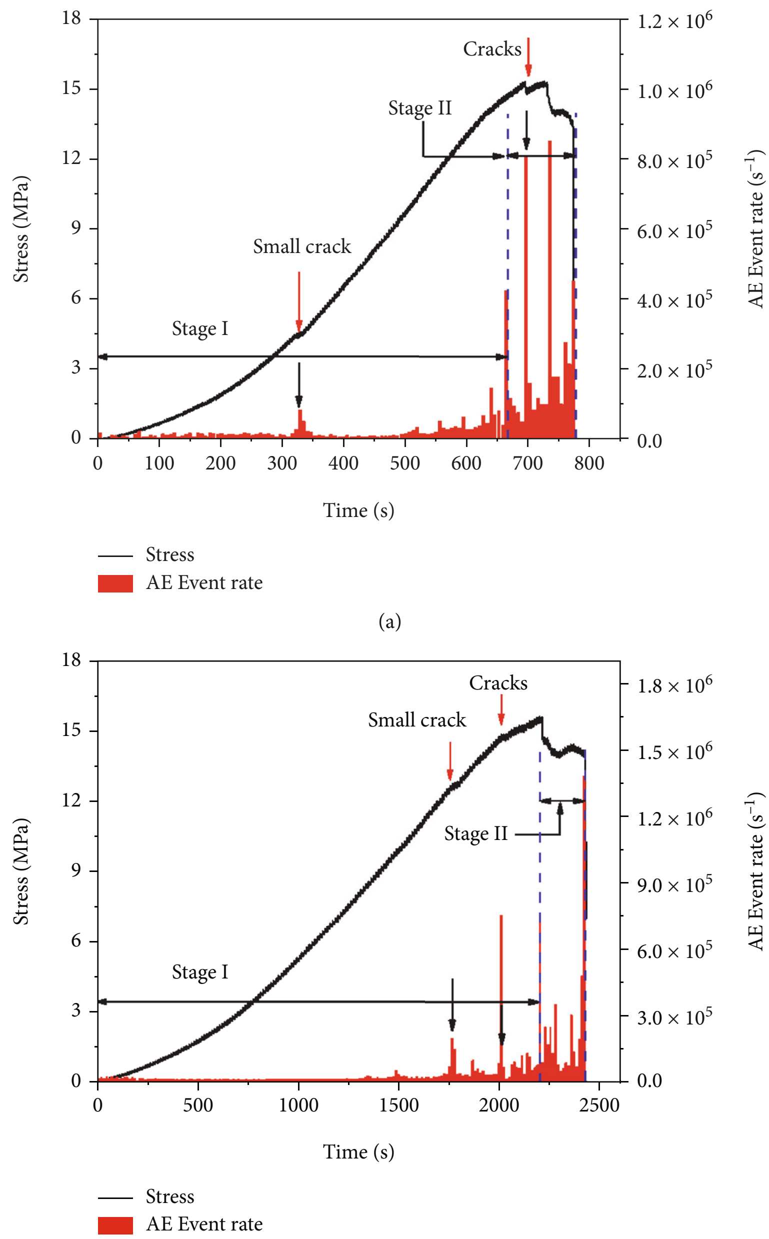

(a)

(b)

FIGURE 3: The evolution characteristics of AE signals. (a) The result of specimen R1. (b) The result of specimen R6.

failure stage (Stage II), the evolution characteristics of AE events were obviously different from the previous stage. The jumping spurt of AE events occurred with each large fracture (crack) inside rocks. Due to the frequent occurrence of rock fractures, the AE events increased with multiple jumps. Moreover, AE events had relatively larger values, larger numbers, and more frequent fluctuation. Due to different characteristics of AE events in Stage I and Stage II, Stage I was defined as the stable deformation stage, and Stage II was defined as the accelerated failure stage. In addition, an obvious acceleration phenomenon for cumulative AE events, generated from microcrack propagation, was clearly observed nearby the failure point. The typical evolution pattern of AE events can be used as a precursor for rock failure.

Figure 4 shows the localization of AE events inside rocks in the critical failure stage, and Figure 4(a) is the result of specimen R1 when $D = 0.5$, Figure 4(b) is the result of specimen R6 when $D = 0.5$, Figure 4(c) is the result of specimen R1 when $D = 1$, and Figure 4(d) is the result of specimen R6 when $D = 1$. Moreover, the corresponding failure time is 655 s for specimen R1 in Figure 4(a), and the corresponding failure time is 2018 s for specimen R6 in Figure 4(b). It can be seen that before the critical acceleration failure stage, the high-energy AE events inside rocks were relatively few and scattered. It demonstrated that the main cracks inside

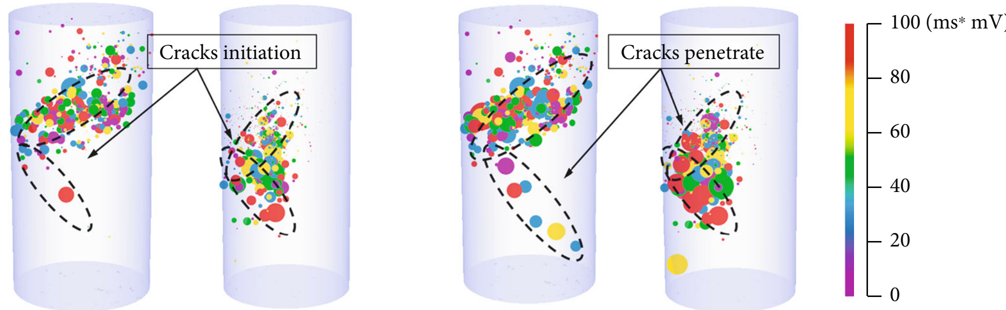

(a) (b) (c) (d)

Figure 4: The fracture characteristic of red sandstone by AE events. (a) The result of specimen R1 when $D = 0.5$. (b) The result of specimen R6 when $D = 0.5$. (c) The result of specimen R1 when $D = 1$. (d) The result of specimen R6 when $D = 1$.

rock specimens had not penetrated. When rocks were completely destroyed, the distribution and morphology of main fractures (cracks) can be clearly observed. It indicated that the fracture behavior was more frequent and significant in the critical acceleration failure stage.

4.2. Identification of the Damage Acceleration Point of Red Sandstone. From equation (10), it can be seen that the damage evolution pattern of rocks is in line with the growth pattern of exponential function. Based on equation (11), the damage evolution curve of rock specimen can be calculated and plotted by AE events. Since it had been assumed that the growth pattern of rock damage obeyed the exponential law, the function ($D = y_0 + A \exp(-x/t_1)$) was used as the fitting function to analyze the damage evolution pattern of rock specimens. The fitting results indicated that this function can accurately characterize the damage evolution pattern of rocks. Furthermore, rock damage had a low-rate steady growth stage and an accelerated growth stage. From Figure 5 (Figure 5(a) is the result of specimen R1, and Figure 5(b) is the result of specimen R6), it can be known that there is a significant difference for damage growth of rock specimens before and after $D = 0.375$. Before this damage point, rock damage growth rate was relatively low and rock specimen was still in the stable deformation stage. After this damage point, rock damage growth rate began to accelerate significantly, and the damage curve became steeper. Therefore, the damage point ($D = 0.375$) can be taken as the first turning point of rock damage curve, since the turning point of stable deformation stage and the critical acceleration failure stage occurred at damage variable reaching 0.5 ($D = 0.5$). This also can be confirmed by the AE precursor in Figures 3 and 4. Therefore, for further distinguishing the evolution characteristics of rock damage, the second damage point ($D = 0.5$) can be taken as another turning point of rock damage curve. In fact, the second damage point ($D = 0.5$) was the turning point of accelerating deformation rather than the accelerating turning point of damage variables.

4.3. The Method for Predicting Time-to-Failure of Red Sandstone. As shown in Figure 5, it can be learned that rock damage has accelerated behavior in the critical failure stage. From Figure 6 (Figure 6(a) is the result of specimen R1, and Figure 6(b) is the result of specimen R6), the damage evolution characteristics, from $D = 0.375$ and $D = 0.5$ to rock failure, were further analyzed detailedly in the critical failure stage. It can be found that rock damage approximately conformed to the linear growth in the critical acceleration failure stage. Certainly, from $D = 0.375$ and $D = 0.5$ to the complete failure of rocks, the accuracy degree of linear fitting of rock damage was different. The results demonstrated that the linear evolution pattern of rock damage was more obvious and clearly when the fitting data from $D = 0.5$ to rock failure. From Figure 6, it can be seen that rock damage is not uniform, but it is grouped in several intervals. Since there are many groups of damage variables from $D = 0.375$ to rock failure, the distribution of rock damage variables was relatively discrete. Therefore, for improving the effect of linear fitting, rock damage variables were averaged from $D = 0.5$ to rock failure.

Based on the method of ordinary least squares [20], the linear fitting equation for predicting time-to-failure of rocks can be obtained. The linear fitting equation ($y = a + bx$) was used to fit the evolution curve of rock damage. For specimen R1, its actual failure time is 787.2 s ($D = 1$) in this study. For specimen R6, its actual failure time is 2432.0 s ($D = 1$) in this test. To illustrate, the negative data indicated the forecast time was advanced than the actual failure time, and the positive data indicated the forecast time was lagging behind the actual failure time. The precision of the slope for the fitting curve was only accurate to 4 digits after decimal point. Although these two fitting curves had the same slope after approximation (Figure 7(a), Line 1 and Line 2), the slopes of these two fitting curves were actually slightly different.

Table 1 compares the prediction results, by different fitting equations, with the actual failure time ($D = 1$), and it can distinguish the prediction accuracy of time-to-failure of rocks. It can be known that the fitting equations (1)~(4) (Nos. 1~4) are the results of specimen R1 and equations (5)~(8) (Nos. 5~8) are the results of specimen R6. Obviously, the fitting result of specimen R1 was better than specimen R6. The exponential growth pattern of specimen R1 was more obvious and matched, and its predicted time-to-failure of rocks was only advanced 0.7 s than the actual failure time. However, the predicted time-to-failure of specimen R6 was quite different from the actual failure time,

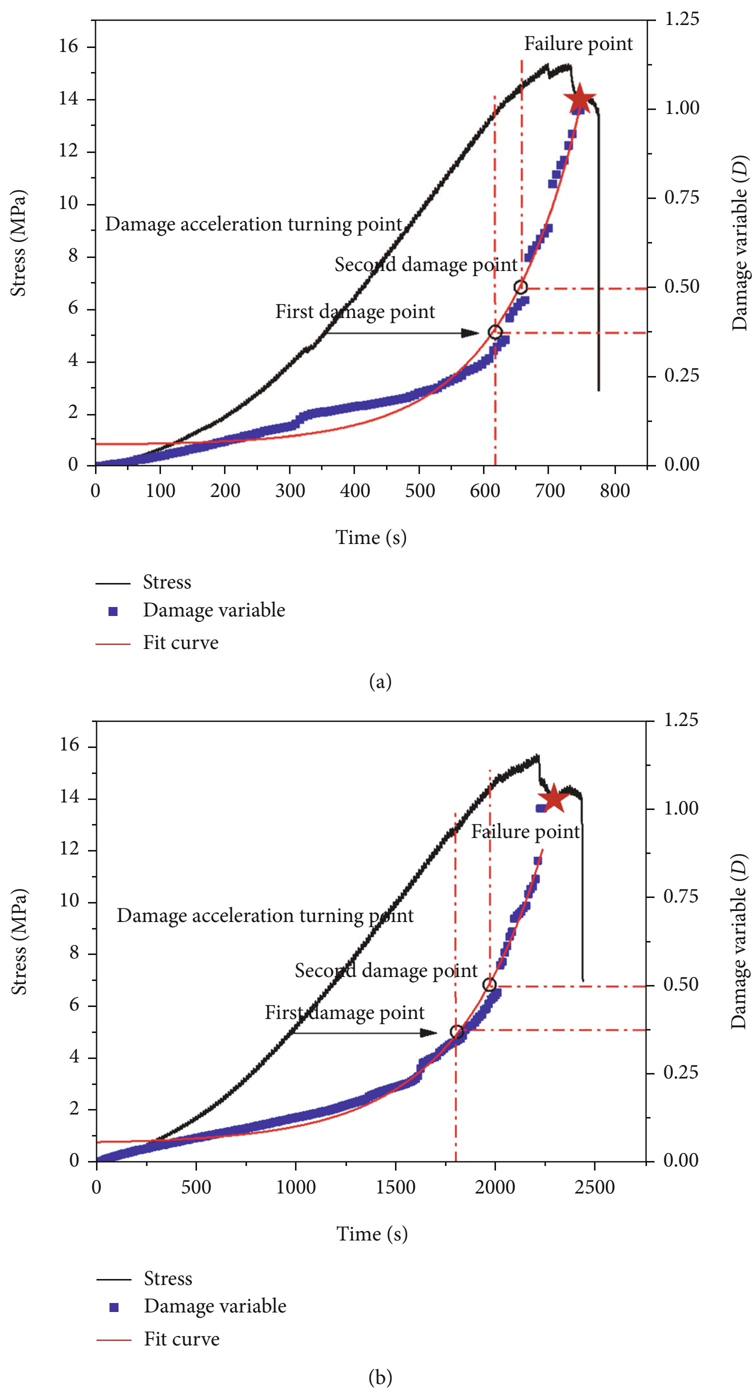

Figure 5: The damage evolution curve of red sandstone under compression. (a) The result of specimen R1. (b) The result of specimen R6.

approximately delayed 70.7 s. It demonstrated that the accuracy of predicting time-to-failure of rocks by the exponential fitting function was unstable. Then, compared with $D = 0.5$ to rock failure, the distribution of damage variables (from $D = 0.375$ to rock failure) was more scattered, and they were grouped obviously in several intervals. Then, the prediction accuracy of rock failure time was mainly analyzed from $D = 0.5$ to rock failure. Fitting equations (2) (No. 2) and (6) (No. 6) were the linear fitting equations for specimens R1 and R6 from $D = 0.5$ to rock failure, respectively. Therefore, it can be seen that the linear evolution characteristics of rock damage (from $D = 0.5$ to $D = 1$) were more obvious and clearly.

Subsequently, two different damage processing methods were used to fit damage variables, and the predicting accuracy of time-to-failure of rocks was compared. In Figure 7 (Figure 7(a) is the result of specimen R1, and Figure 7(b) is the result of specimen R6), the blue line (Line 1) was obtained by taking average of each two original damage variables. Similarly, the red line (Line 2) was obtained by taking

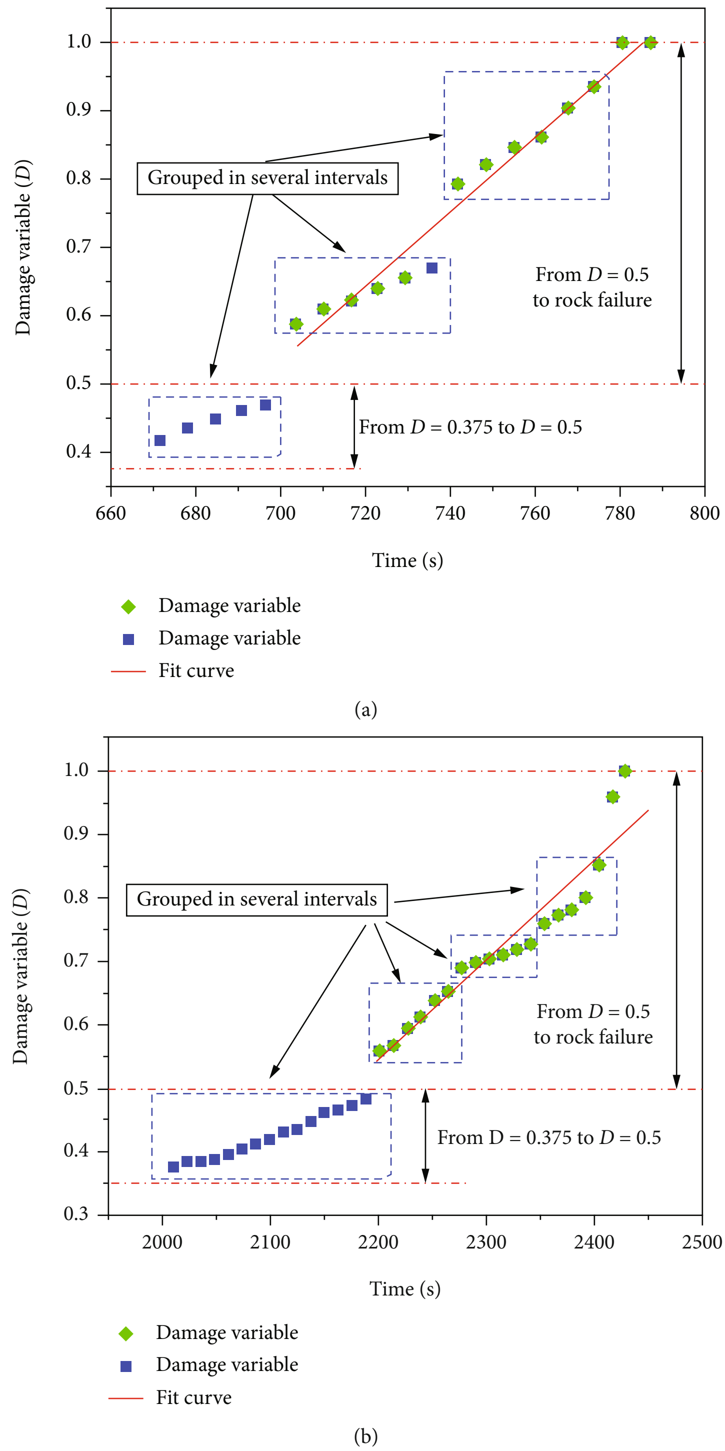

FIGURE 6: The damage evolution characteristic from $D = 0.375$ and $D = 0.5$ to rock failure. (a) The result of specimen R1. (b) The result of specimen R6.

average of each five original damage variables. This processing method, by taking the average values of different numbers of damage variables, can reduce the volatility of damage variables and it can improve its stationarity and accuracy of the fitting equation.

In Figure 7(a), the fitting equation for Line 1 is $y = 0.0054x - 3.24$, and its R-square is 0.9923. Likewise, the fitting equation for Line 2 is $y = 0.0053x - 3.23$, and its R-square is 0.9985. Comparing the fitting effect, it can be seen that the fitting effect of Line 2 was slightly better than Line 1. In Figure 7(b), the fitting equation for Line 1 is $y = 0.0019x - 3.90$, and its R-square is 0.9904. The fitting equation for Line 2 is $y = 0.0021x - 4.26$, and its R-square is 0.9972. For specimen R1, the fitting effect of fit equation (4) (No. 4) is

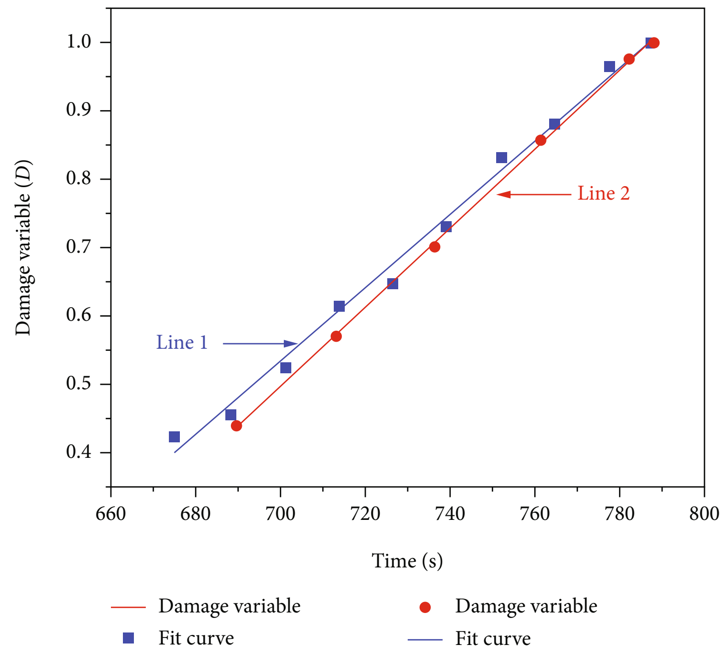

(a)

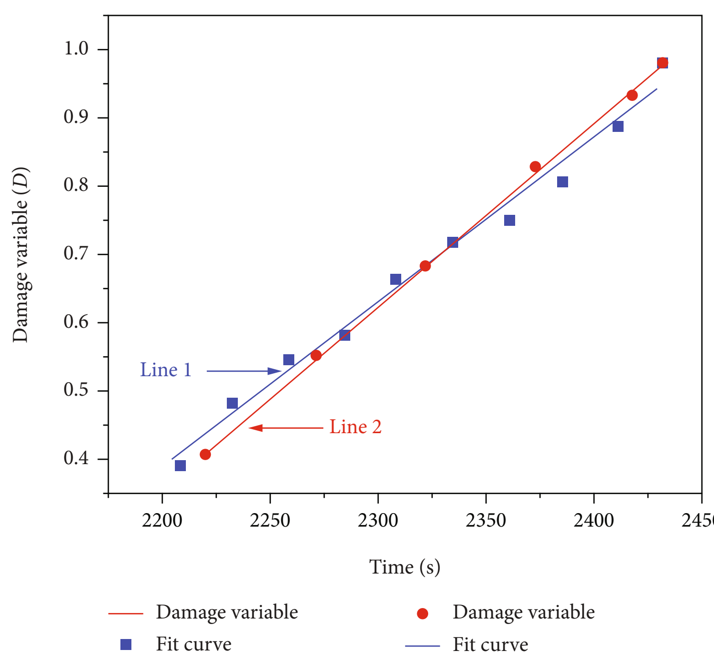

(b)

Figure 7: The damage fitting curve by different methods. (a) The result of specimen R1. (b) The result of specimen R6.

better than fit equation (3) (No. 3), and the predicted time-to-failure of specimen R1 can be advanced by 0.2 s than the actual failure time. For specimen R6, the fitting effect of fit equation (8) (No. 8) is better than fit equation (7) (No. 7), and the predicted time-to-failure of specimen R6 can be advanced by 8.1 s than the actual failure time. Hence, from $D = 0.5$ to rock failure, the predicting results of the linear function, based on the average treatment of five damage variables, were better than the predicting results of the average treatment of two damage variables. Moreover, the fitting effect of the linear function, based on averaging five damage variables, was better than the exponential function.

5. Discussions

It can be seen from Figures 3 and 4 that the evolution process of AE signals has stable deformation stage and critical acceleration failure stage. For the stable deformation stage, AE events were relatively gentle and quiet due to the overall weak damage of rocks. For the accelerated failure stage, AE

Table 1: The results of predicting time-to-failure of rocks. Nos. 1~4 are the results of specimen R1. Nos. 5~8 are the results of specimen R6.

No.	Fit data	Fit equation	R-square	Prediction time (s)	Error (s)
1	Figure 5(a)	$y = 0.063 + 0.0021 \exp(x/128.92)$	0.9725	786.5	-0.7
2	Figure 6(a)	$y = 0.0054x - 3.27$	0.9787	790.7	3.5
3	Figure 7(a), Line 1	$y = 0.0054x - 3.26$	0.9923	788.9	1.7
4	Figure 7(a), Line 2	$y = 0.0054x - 3.25$	0.9985	787.0	-0.2
5	Figure 5(b)	$y = 0.054 + 0.0049 \exp(x/475.52)$	0.9824	2502.7	70.7
6	Figure 6(b)	$y = 0.0013x - 2.25$	0.9737	2500.0	68.0
7	Figure 7(b), Line 1	$y = 0.0019x - 3.71$	0.9904	2478.9	46.9
8	Figure 7(b), Line 2	$y = 0.0021x - 4.09$	0.9972	2423.8	-8.1

events fluctuated greatly with a small fluctuation of stress, which indicated that a large number of cracks had been initiated inside specimens, and the damage increased rapidly. It had entered a critical failure stage. It meant that large amounts of macroscopic fractures will occur without a large stress increasing. The dynamic fluctuation of AE events also indicated that some relatively large-sized cracks were penetrated and connected. Consequently, this was an AE precursor to the impending destruction of rocks. Therefore, the rock deformation stage was very important for its damage evaluation. Then, according to the evolution characteristics of AE events, the damage state can be distinguished, and the appropriate damage evolution equation can be selected to quantitatively characterize the damage evolution pattern of rocks. Subsequently, the first damage point ($D = 0.375$) was defined and determined based on the turning point of damage variables. Based on the mutation of AE events, the second damage point ($D = 0.5$) was also defined and determined. Absolutely, it was known as the start point of the critical failure stage. Therefore, it is helpful for the prediction of time-to-failure of rocks and the early warning of rockburst.

The damage variable is an indicator for evaluating fracture and damage state of rocks. It can reflect the evolution characteristics of cracks inside rock materials. Through theoretical analysis, it can be learned that the damage evolution curve of rock specimens followed the exponential function law, as shown in Figure 5. By fitting the damage variables with an exponential function, the critical accelerated failure phenomenon can be clearly characterized, and the quantitative evaluation of rock damage can be realized. This provides the basis for realizing the mathematical characterization of rock damage and predicting time-to-failure of rocks. Therefore, based on the damage evolution curve, the first damage point ($D = 0.375$) was defined and determined. Before this point, the damage evolution rate was slow and gradual. After this point, the damage evolution rate grew rapidly. Thus, the first damage point can be used to distinguish differences of damage evolution growth for rocks. Then, according to the actual fracture situations of rocks, the second damage point ($D = 0.5$) was also defined and determined. Correspondingly, the second damage point ($D = 0.5$) can be used to distinguish the stable deformation stage and the critical acceleration failure stage. It can be confirmed by the evolution pattern of AE signals, especially the AE precursor of rock failure occurred after this point, which verified the rationality of the defined second damage point. Accordingly, by defining different damage turning points, the predicting accuracy of rock failure time can be improved.

Based on the first damage point, the damage evolution state of rocks was distinguished, and by the second damage point, the fracture evolution state of rocks was distinguished. No matter from the first damage point to rock failure or from the second damage point to rock failure, the damage state of rocks was in an accelerated growth stage. Moreover, from these two damage points to rock failure, the damage variables roughly showed a linear rapid growth trend. Therefore, it seems possible to predict the failure time of rocks by linear fitting equations. Consequently, based on the damage evolution characteristics, from the second damage point to rock failure, the time-to-failure of rocks was calculated by linear fitting equations, as shown in Figure 7. Moreover, it can be seen that the fitting results were fitted better. This demonstrated that it was reasonable and reliable to fit rock damage evolution pattern by linear equation. Obviously, the results of the fitting equation, from the second damage point to rock failure, had a better linear fitting effect, and the predicted time-to-failure of rocks was more accurate. The damage state and fracture state can be distinguished by the first damage point and the second damage point, which narrowed the data range of the linear fitting of rock damage. However, the deformation of rocks was unstable in the critical failure stage, and the evolution trend of damage variables was unstable. This reduced the prediction accuracy of time-to-failure of rocks due to the local dispersion of damage variables. Therefore, for improving the prediction accuracy, it is necessary to average the damage variables to reduce the predicting errors for time-to-failure of rocks which is caused by the discrete damage variables.

Due to the discontinuity of rock fracture, the average treatment of damage variables can reduce the prediction errors caused by data concentration and unevenness to some extent. It can improve the prediction accuracy by homogenizing and smoothing the discrete data. From the fitting results of Line 1 and Line 2 in Figure 7, it can be seen that the fitting effect of Line 2, with the average of five damage variables, is better than that of Line 1, with the average of two damage variables. It should be noted that this method has a better fitting effect on processing data with larger discreteness than the data with a more concentrated distribution. For improving the predicting accuracy, a phased calculation method can be used for the early warning of rockburst. The results showed that the predicting time-to-failure of rocks by exponential function will make the results unstable and inaccurate due to the discreteness of damage variables. However, the linear evolution pattern of rock damage can be achieved by averaging damage variables, which had a good effect on improving the prediction accuracy. In fact, it will contribute to the early warning of rock dynamic disasters.

6. Conclusions

Based on the AE signals monitoring experiment and the uniaxial compression test, the time-to-failure of red sandstone was studied and analyzed, and the following conclusions can be obtained.

(1) The red sandstone had stable deformation stage and accelerated failure stage under uniaxial compression. In the stable deformation stage, the stress grew relatively smoothly and AE events were relatively quiet with lower values. In the acceleration failure stage, the stress increased slightly and AE events showed a jump-increase phenomenon with large fluctuation. From the positioning results of AE events, it can be known that the crack penetration mainly occurred in the critical failure stage.

(2) Rock damage obeyed the growth pattern of exponential function under axial loading, and rock damage variables had the steady increase stage and the accelerated increase stage. Moreover, different damage acceleration turning points will affect the linear characterization of acceleration damage stage, and it can further affect the predicting accuracy of rock failure time.

(3) Based on different damage acceleration turning points, the linear fitting effect will be quite different. The linear fitting effect from $D = 0.5$ to rock failure will be better than $D = 0.375$ to rock failure. The averaging processing method of damage variables (from $D = 0.5$ to rock failure) can improve the linear fitting effect and the accuracy of predicting time-to-failure of rocks.

Data Availability

The data used to support the findings of this study are included within the article.

Conflicts of Interest

The authors declare that they have no conflicts of interest.

Acknowledgments

This study was supported by the National Natural Science Foundation of China (Grant Nos. 12172036 and 51774018).

References

[1] X. Lei, K. Kusunose, M. V. M. S. Rao, O. Nishizawa, and T. Satoh, "Quasi-static fault growth and cracking in homogeneous brittle rock under triaxial compression using acoustic emission monitoring," *Journal of Geophysical Research: Solid Earth*, vol. 105, no. B3, pp. 6127–6139, 2000.

[2] A. F. Bell, J. Greenhough, M. J. Heap, and I. G. Main, "Challenges for forecasting based on accelerating rates of earthquakes at volcanoes and laboratory analogues," *Geophysical Journal International*, vol. 185, no. 2, pp. 718–723, 2011.

[3] A. F. Bell, M. Naylor, and I. G. Main, "The limits of predictability of volcanic eruptions from accelerating rates of earthquakes," *Geophysical Journal International*, vol. 194, no. 3, pp. 1541–1553, 2013.

[4] A. F. Bell, "Predictability of landslide timing from quasi-periodic precursory earthquakes," *Geophysical Research Letters*, vol. 45, no. 4, pp. 1860–1869, 2018.

[5] J. Vasseur, F. B. Wadsworth, Y. Lavallée, A. F. Bell, I. G. Main, and D. B. Dingwell, "Heterogeneity: the key to failure forecasting," *Scientific Reports*, vol. 5, no. 1, article 13259, 2015.

[6] X. L. Li, S. J. Chen, Q. M. Zhang, X. Gao, and F. Feng, "Research on theory, simulation and measurement of stress behavior under regenerated roof condition," *Geomechanics and Engineering*, vol. 26, no. 1, pp. 49–61, 2021.

[7] X. L. Li, S. J. Chen, S. M. Liu, and Z. H. Li, "AE waveform characteristics of rock mass under uniaxial loading based on Hilbert-Huang transform," *Journal of Central South University*, vol. 28, no. 6, pp. 1843–1856, 2021.

[8] B. Voight, "A method for prediction of volcanic eruptions," *Nature*, vol. 332, no. 6160, pp. 125–130, 1988.

[9] M. J. Heap, P. Baud, P. G. Meredith, A. F. Bell, and I. G. Main, "Time-dependent brittle creep in Darley Dale sandstone," *Journal of Geophysical Research*, vol. 114, no. B7, article B07203, 2009.

[10] T. Fukuzuno, "A method to predict the time of slope failure caused by rainfall using the inverse number of velocity of surface displacement," *Landslides*, vol. 22, no. 2, pp. 8–13_1, 1985.

[11] A. Boué, P. Lesage, G. Cortés, B. Valette, and G. Reyes-Dávila, "Real-time eruption forecasting using the material failure forecast method with a Bayesian approach," *Journal of Geophysical Research: Solid Earth*, vol. 120, no. 4, pp. 2143–2161, 2015.

[12] N. Brantut, M. J. Heap, P. G. Meredith, and P. Baud, "Time-dependent cracking and brittle creep in crustal rocks: a review," *Journal of Structural Geology*, vol. 52, pp. 17–43, 2013.

[13] Z. T. Bieniawski, "Time-dependent behaviour of fractured rock," *Rock Mechanics*, vol. 2, no. 3, pp. 123–137, 1970.

[14] S. F. M. Chastin and I. G. Main, "Statistical analysis of daily seismic event rate as a precursor to volcanic eruptions," *Geophysical Research Letters*, vol. 30, no. 13, article 1671, 2003.

[15] R. R. Cornelius and P. A. Scott, "A materials failure relation of accelerating creep as empirical description of damage accumulation," *Rock Mechanics and Rock Engineering*, vol. 26, no. 3, pp. 233–252, 1993.

[16] W. Weibull, “A statistical distribution function of wide applicability,” *Journal of Applied Mechanics*, vol. 18, no. 3, pp. 293–297.

[17] Z. L. Wang, Y. C. Li, and J. G. Wang, “A damage-softening statistical constitutive model considering rock residual strength,” *Computers & Geosciences*, vol. 33, no. 1, pp. 1–9, 2007.

[18] J. B. Keats, F. R. Lawrence, and F. K. Wang, “Weibull maximum likelihood parameter estimates with censored data,” *Journal of Quality Technology*, vol. 29, no. 1, pp. 105–110, 2018.

[19] E. Hoek and E. Brown, *Underground Excavation in Rock, Institution of Mining and Metallurgy*, CRC Press, Taylor & Francis Group, London, 1980.

[20] G. D. Hutcheson, *Ordinary Least-Squares Regression*, The Multivariate Social Scientist, SAGE Publications Ltd, London, 1999.

Hindawi
Geofluids
Volume 2022, Article ID 1342592, 11 pages
https://doi.org/10.1155/2022/1342592

Research Article

Research on Permeability Enhancement Model of Pressure Relief Roadway for Deep Coal Roadway Strip

Zhonghua Wang[1,2,3] **Jianjun Cao,**[2,3] **Jun Liu,**[2,3] **and Chengcheng Li**[2,3]

[1]*College of Energy and Mining Engineering, Shandong University of Science and Technology, Qingdao 266590, China*
[2]*China Coal Technology Engineering Group Chongqing Research Institute, Chongqing 400037, China*
[3]*State Key Laboratory of gas Disaster Monitoring and Emergency Technology, Chongqing 400037, China)*

Correspondence should be addressed to Zhonghua Wang; 564478818@qq.com

Received 9 January 2022; Accepted 5 June 2022; Published 30 June 2022

Academic Editor: Chao-Zhong Qin

Aiming at the problem of permeability enhancement in deep coal roadway strip, it proposed a pressure relief roadway permeability enhancement model, and the model was verified through experiments, theoretical calculations, and field tests. The experiment reveals that the unloading of gas-containing coal can achieve the effect of permeability enhancement. Theoretical calculation shows that with the increase of the distance from the coal seam, the overlying coal seam's permeability enhancement multiple and the width of the significant permeability enhancement zone gradually decrease, and the width of the general permeability enhancement zone gradually increases and then stabilizes. Field tests show that the pressure relief roadway is arranged 9 m directly below the coal seam; the overlying coal strata has a significant pressure relief and permeability enhancement effect. This research can provide reference value for the high-efficiency permeability enhancement in the deep coal roadway strip.

1. Introduction

With the increase of coal mining depth, most of the deep coal seams have the characteristics of low gas permeability [1–4], which has seriously affected the gas drainage of deep coal seams, especially in the coal and gas outburst areas of coal roadways. Gas drainage is difficult [5–8], long time for drainage to reach the standard [9, 10], and low drainage efficiency [11, 12]. For this reason, domestic and foreign studies have successively proposed hydraulic flushing [13–16], hydraulic slitting [3, 17, 18], hydraulic fracturing [19, 20], CO_2 fracturing [21–23], and high-pressure gas blasting [24]; these permeability enhancement technologies can increase the permeability of the coal seam, but there are still some shortcomings. For example, deep hole loosening blasting has disadvantages such as complex technology, hydraulic fracturing, which is prone to local stress concentration, and hydraulic slitting with a small pressure relief range. Therefore, it is an urgent to realize high-efficiency coal seam drainage and effective outburst prevention research on pressure relief and permeability enhancement in deep coal seams with high ground stress and low permeability.

In recent years, scholars at home and abroad have conducted a large number of studies on the failure characteristics of deep surrounding rocks through field investigation [25, 26], theoretical analysis [27–31], laboratory experiments [32, 33], numerical simulation [34–37], and other methods and found that deep surrounding rocks will appear zonal disintegration [38, 39], and studies have shown that the damage range of the zonal disintegration of the deep roadway surrounding rock is much larger than that of the shallow. From the perspective of roadway surrounding rock control, the damage and deformation of surrounding rock should be minimized. From the perspective of deep coal seam permeability enhancement, the regional fracture characteristics of deep surrounding rock not only have the effect of reducing the in-situ stress of the coal rock, but also can play a role permeability enhancement in the coal.

Therefore, the author proposes to arrange the coal roadway to be excavated within the pressure relief influence range of the pressure relief roadway. So it can relieve the overlying coal and rock layer the ground stress and increase the coal seam permeability in advance. It is expected to provide a reference for the permeability enhancement of coal roadway strip.

2. Permeability Enhancement Model of Pressure Relief Roadway

2.1. Model Principle. Coal roadway strip area generally uses floor rock roadway to gas drainage to prevent coal and gas outburst. Traditional floor rock roadways are usually arranged internally and externally horizontal distance 20~30 m below the coal roadway to be excavated (the internal and external horizontal distance is generally 15~25 m). It cannot be formed with a pressure relief and permeability enhancement effect to the overlying coal seam. Studies have shown that the surrounding rock of deep roadway will have zonal disintegration, and the fracture zone of surrounding rock in shallow roadway is only the first fracture zone of zonal disintegration in deep roadway, that is, the range of deep surrounding rock fracture is obviously larger than that of shallow [40–42].

Based on this, the author proposes to change the layout of the traditional floor rock roadway, arrange it directly under the coal roadway to be excavated, and appropriately reduce the distance between the pressure relief roadways and coal roadway. So it not only can relieve the pressure of the overlying coal seam, but also can increase the gas permeability of the coal seam. Floor rock roadway arranged in such a way is called "pressure relief roadways." After undergoing mechanical action by the excavation of the pressure relief roadway, it can reduce the stress of the surrounding rock over the pressure relief roadway and increase the gas permeability of the overlying coal seam. The author proposes that the surrounding rock stress that decreases more than 5% is called the surrounding rock stress relief zone, and the area where the coal seam permeability coefficient increases is called the coal seam pressure relief and permeability enhancement zone. According to the degree of coal fracture and the increase of coal seam permeability, the coal seam pressure relief and permeability enhancement zone can be divided into significant permeability enhancement zone X_1 and general permeability enhancement zone X_0.

Therefore, the author proposes the permeability enhancement model of pressure relief Roadway for deep coal roadway strip (shown in Figure 1). It is to study the impact range and effect of permeability enhancement on the overlying coal seam, when the pressure relief roadway is different distance from the seam. It is expected that the pressure relief roadway can be used to relieve pressure and increase the permeability of the coal seam in the coal roadway strip area. It can provide a new method for safe, economical, and efficient permeability enhancement and drainage in the deep coal road strip area.

2.2. Model Parameters

2.2.1. Location of the Pressure Relief Roadway. Figure 2 shows the calculation model of the surrounding rock plastic zone after the pressure relief roadway and coal roadway are excavated successively. H_y and h_m are the failure depths of the rock mass after the pressure relief roadway and coal roadway are excavated successively. After the pressure relief roadway and the coal road have been excavated successively, the overlying coal and rock layers have been subjected to twice pressure relief. In order to ensure the stability of the surrounding rock of the roadway and prevent coal and gas outburst, the pressure relief roadway and the upper coal seam should be prevented from forming a through failure zone. Then, the reasonable formula of the distance between the pressure relief roadway and the coal seam is

$$\Delta h \geq h_y + h_m. \tag{1}$$

After sorting out, the calculation formula changes to

$$\begin{cases} h_y = \delta \cdot R_y - (M - H) \\ h_m = \delta \cdot R_m - \dfrac{M}{2} \end{cases}. \tag{2}$$

In Formula (2), δ is the superposition coefficient of the secondary pressure relief effect, which can be calculated through on-site monitoring statistical analysis or simulation calculation. R_y is the plastic zone radius of the pressure relief roadway, m. R_m is the plastic zone radius of the coal roadway, m.

Combining Formulas (1) and (2), the criterion for the reasonable distance between the pressure relief roadway and the coal seam can be obtained as

$$\Delta h \geq \delta \cdot \left(R_y + R_m\right) - \left(\frac{3}{2}M - H\right). \tag{3}$$

2.2.2. Scope of the Permeability Enhancement Zone. Figure 3 shows the zoning characteristics of the surrounding rock formation of the roadway after the excavation of the pressure relief roadway, that is, the surrounding rock can be divided into the fracture zone, the plastic zone, the elastic zone, and the original rock stress zone.

Assuming that the radius of the stress relief zone is r' (that is, the radius of the area where the stress reduction is not less than 5%), it can be seen from Figure 3 that when the stress reduction of the coal seam is 5%, it is located in the elastic zone. In polar coordinates, the vertical stress calculation formula is

$$\sigma_r = p_0 - \left(p_0 - \sigma_R^p\right)\left(\frac{R_p}{r'}\right)^2 = 0.95 p_0. \tag{4}$$

In Formula (4), σ_r is the vertical stress in polar coordinates. R_p is the radius of the plastic zone. P_0 is the original

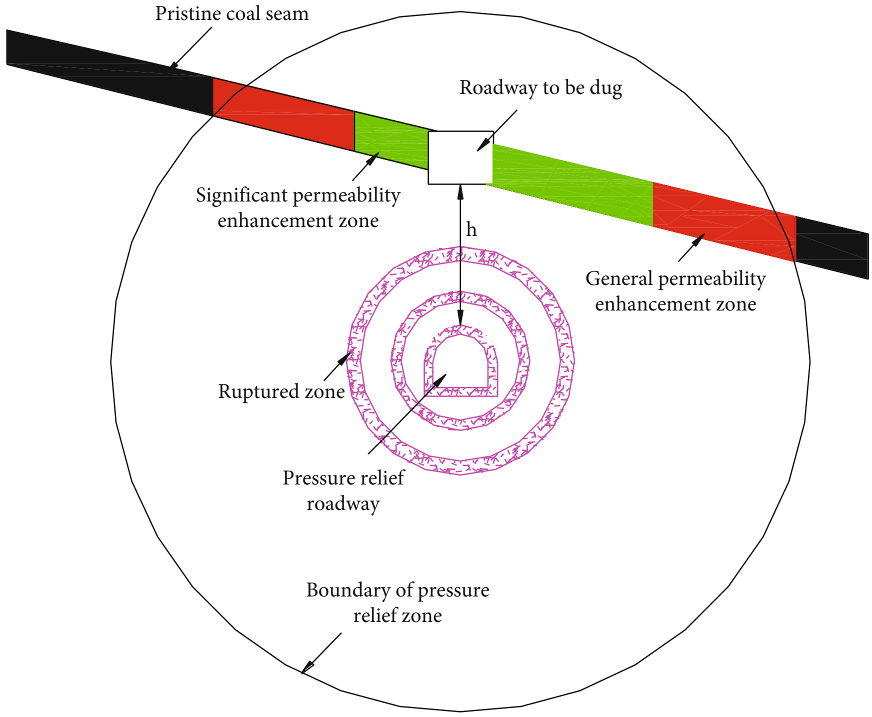

Figure 1: The model of pressure relief roadway for deep coal roadway strip.

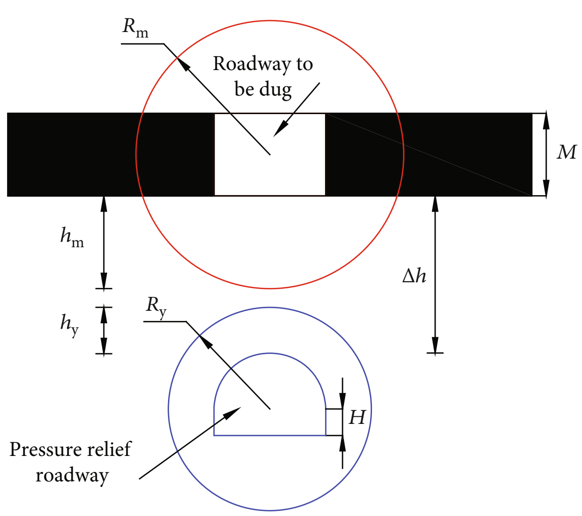

Figure 2: Calculation model of pressure relief roadway position.

rock stress. σ_R^p is the vertical stress in the plastic zone.

$$r' = 2\sqrt{5}R_p\sqrt{1 - \frac{\sigma_R^p}{p_0}}. \tag{5}$$

Combining the stress calculation formula and geometric relationship, the vertical stress calculation formula in the Cartesian coordinate system is

$$\sigma_y = p_0 - \frac{\left(p_0 - \sigma_R^p\right)R_p^2}{\left(h^2 + x^2\right)^2}\left(h^2 - x^2\right). \tag{6}$$

In Formula (6), h is the normal distance from the coal seam floor to the center of the roadway, m. x is the distance in the horizontal direction, m. φ is the angle between the radius r and the vertical direction, °. σ_y is the vertical stress in the Cartesian coordinate system, MPa.

After the excavation of the pressure relief roadway, the adsorbed gas becomes free gas in the upper coal seam and increases the gas stress in the coal seam. According to the coal sample unloading experiment, it can be seen that as the coal gas content increases, its uniaxial compressive strength will decrease. Its relationship conforms to the following formula:

$$\sigma_c = A_2 + B_2 \cdot p. \tag{7}$$

In Formula (7), σ_c is the uniaxial compressive strength. A_2 and B_2 are parameters related to coal.

From the unified strength criterion:

$$\frac{\alpha_c}{1+b}\left(\sigma_x + b\sigma_z\right) - \sigma_y = \alpha\sigma_c. \tag{8}$$

In Formula (8), α is the ratio of the tensile strength of the rock. b is the influence coefficient of the intermediate principal stress. σ_x, σ_y, and σ_z are the stresses in the X, Y, and Z directions, respectively, MPa.

Substituting Formulas (6) and (7) into Formula (8), and substituting pressure relief roadway layout conditions and related parameters of the overlying coal seam, it can obtain the width of the significant coal seam permeability enhancement zone X_1 and the width of the general coal seam permeability enhancement zone X_0.

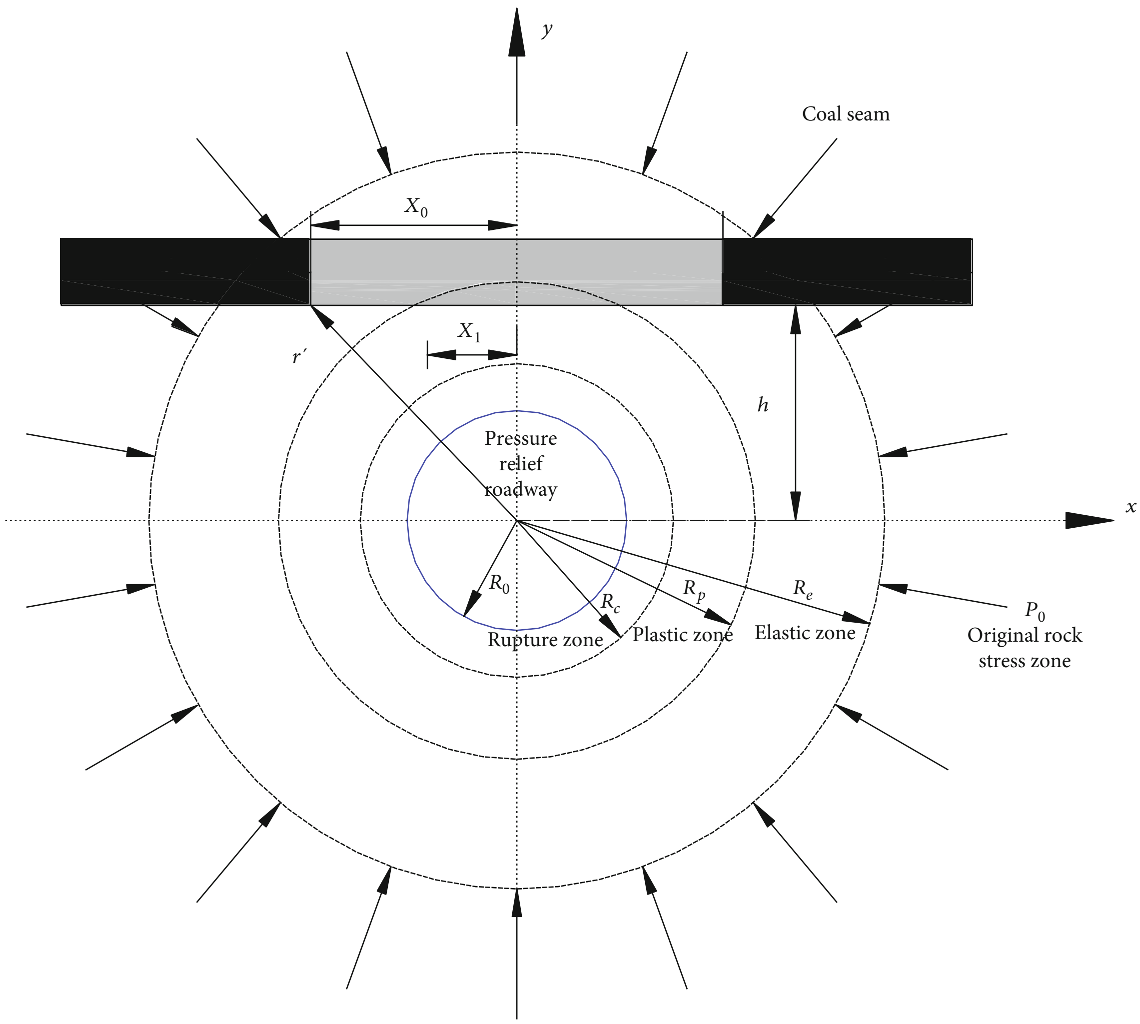

Figure 3: Calculation model of coal seam permeability enhancement.

(a) Press-formed test piece

(b) Glued test piece

Figure 4: Physical image of rectangular coal briquette specimen.

Figure 5: Diagram of gas-solid coupling experiment device.

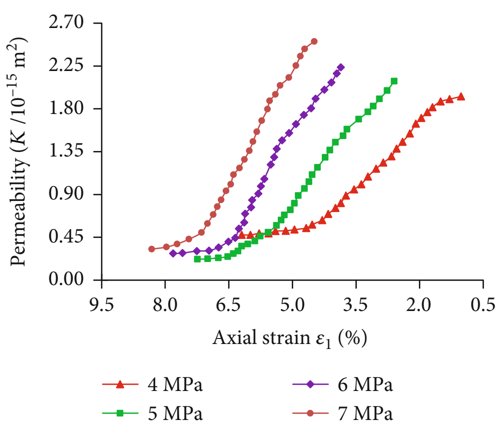

Figure 6: Axial unloading mechanics-permeability characteristic curves of different confining pressure specimens.

Table 1: The permeability enhancement effect of coal seams with different Δh.

Distance from the center of the roadway $\triangle h$/m	Significant permeability enhancement zone X_1/m	General permeability enhancement zone X_0/m	Gas permeability increase multiple
7	4.3	12.1	11.1~239.3
9	3.5	15.4	6.7~89.2
12	1.2	20.5	3.6~37.1
15	0.3	20.7	2.4~9.1
18	0	20.5	1.2~5.5
21	0	20.4	0.8~1.6

3. Model Verification

According to the principle of the model, the location of the pressure relief roadway and the range of the permeability enhancement zone are the main parameters of the model. Therefore, it proposed a method for determining the location of the pressure relief roadway and the range of the permeability enhancement zone, which provides a theoretical basis for the model.

3.1. Unloading Seepage Experiment of Gas-Containing Coal. In the unloading seepage experiment of gas-containing coal, it adopts the steady-state method to test the pressure relief and the change law of permeability in the cuboid standard coal sample, when the gas pressure of 1.5 MPa and different confining pressures ($\sigma_2 = \sigma_3 = 4$ MPa, 5 MPa, 6 MPa, and7 MPa).

The experimental raw coal was taken from coal seam B_4 of Qujiang Coal Mine in Fengcheng City, Jiangxi Province, China. There are three steps in coal sample preparation. First, the fresh coal sample of B_4 coal seam in Qujiang Coal Mine is pulverized and ground on a pulverizer, screened out the same amount of 20-40 mesh and 40-80 mesh coal powder sample base material, mixed with water evenly, and placed into the sample forming device. Secondly, it is pressed on a 100 t press for 30 minutes to form a rectangular parallelepiped standard coal specimen with a size of 100 mm × 100 mm × 200 mm (as shown in Figure 4). Thirdly, put it in a drying oven at 80 °C and dry it for 24 hours and then wrap it with insurance film for later use.

The experiment used 0.01 N/s to continuously apply axial pressure to 80% of the coal sample's compressive strength and then unload the axial pressure at 0.01 N/s until the coal body was damaged. Figure 5 is a diagram of the gas-solid coupling experiment device. Figure 6 shows the axial pressure unloading mechanics-permeability characteristic curves of different confining pressure specimens.

It can be seen from Figure 6 that during the process of fixed confining pressure and axial stress unloading, when the confining pressure increases from 4 MPa to 7 MPa, the permeability of the coal sample gradually increases, but the increase rate decreases, and the permeability K increases from 1.93×10^{-15} m^2 to 2.51×10^{-15} m^2, the increase rate is 30.05%. Experiments show that with the increase of

Figure 7: Geographical location of Qujiang Coal Mine.

Table 2: Test content and test method.

Test content	Test parameter	Drilling diameter (mm)	Drilling depth (m)	Test method	Remarks
Effect of surrounding rock relief	Destruction	32	9	YTJ20 rock detection recorder	6 test points per drill hole
	Displacement	32	9	DW-6 multipoint displacement meter	
Effect of gas extraction	Coal permeability	75	9~21	Radial flow method [44]	Compare with the original coal seam
	Excavation diameter	75	9~21	Statistical analysis [45]	

confining pressure, the axial pressure unloading permeability increases significantly, revealing that unloading can effectively increase the permeability of coal samples.

3.2. Theoretical Calculation of Coal Seam Permeability Enhancement Effect

3.2.1. Calculation Method. According to the axial stress unloading experiment of the gas-containing coal sample under the conditions of 4 MPa confining pressure and 1.5 MPa gas pressure, it obtained the fitting formula of gas permeability K and $\sigma_1 - \sigma_3$:

$$K = A_3 \cdot e^{B_3 \cdot (\sigma_1 - \sigma_3)}. \quad (9)$$

In the formula, A_3 and B_3 are parameters related to coal body, stress and gas.

From the surrounding rock stress analysis, when $x < h$, the first principal stress is σ_x, and the third principal stress is σ_y; when $x > h$, the first principal stress is σ_y, and the third principal stress is σ_x. Therefore, the formula for permeability

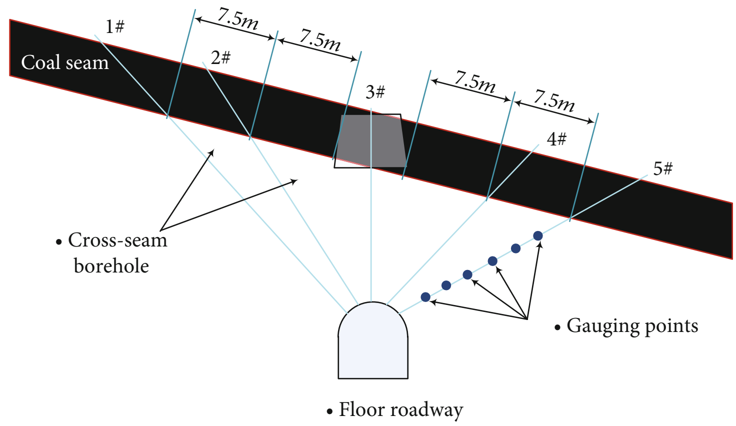

FIGURE 8: Test scheme.

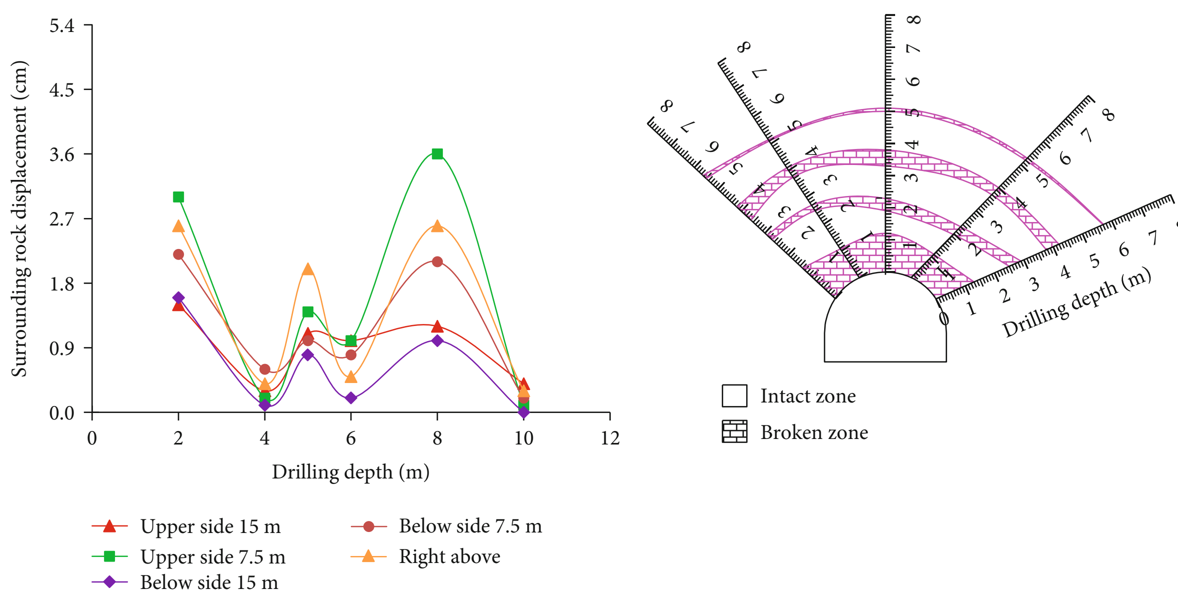

(a) Displacement

(b) Surrounding rock failure

FIGURE 9: Pressure relief effect of surrounding rock in 213 pressure relief roadway.

K and $\sigma_1 - \sigma_3$ can be sorted as

$$\begin{cases} K = A_3 \cdot e^{\left(2B_3 \cdot \left(p_0 - \sigma_R^p\right)\left(h^2 - x^2\right) R_p^2\right) / \left(\left(h^2 + x^2\right)^2\right)}, x < h \\ K = A_3 \cdot e^{-\left(2B_3 \cdot \left(p_0 - \sigma_R^p\right)\left(h^2 - x^2\right) R_p^2\right) / \left(\left(h^2 + x^2\right)^2\right)}, x > h \end{cases}. \tag{10}$$

The gas permeability of a coal seam is usually expressed by the gas permeability coefficient of the coal seam, and the relationship between the gas permeability coefficient of the coal seam and the permeability of a confined coal sample is as follows [43]:

$$\lambda = \frac{K}{2\rho p_n}. \tag{11}$$

In Formula (11), λ is the coal seam permeability coefficient, $m^2/(MPa^2 \cdot d)$; ρ is the absolute viscosity of gas (CH_4), 1.08×10^{-8} $N \cdot s/cm^2$; and P_n is a standard atmospheric pressure, 0.1013 MPa.

Substituting Formula (10) into Formula (11), the relationship between the coefficient of coal seam permeability and the change in stress conditions can be obtained as

$$\begin{cases} \lambda = \dfrac{A_3}{2\rho p_n} \cdot e^{\left(2B_3 \cdot \left(p_0 - \sigma_R^p\right)\left(h^2 - x^2\right) . R_p^2\right) / \left(\left(h^2 + x^2\right)^2\right)}, x < h \\ \lambda = \dfrac{A_3}{2\rho p_n} \cdot e^{-\left(2B_3 \cdot \left(p_0 - \sigma_R^p\right)\left(h^2 - x^2\right) . R_p^2\right) / \left(\left(h^2 + x^2\right)^2\right)}, x > h \end{cases}. \tag{12}$$

3.2.2. Enhancement Effect of Coal Seam Permeability. Assuming that the coal seam confining pressure is 4 MPa and the gas pressure becomes 2 MPa after pressure relief,

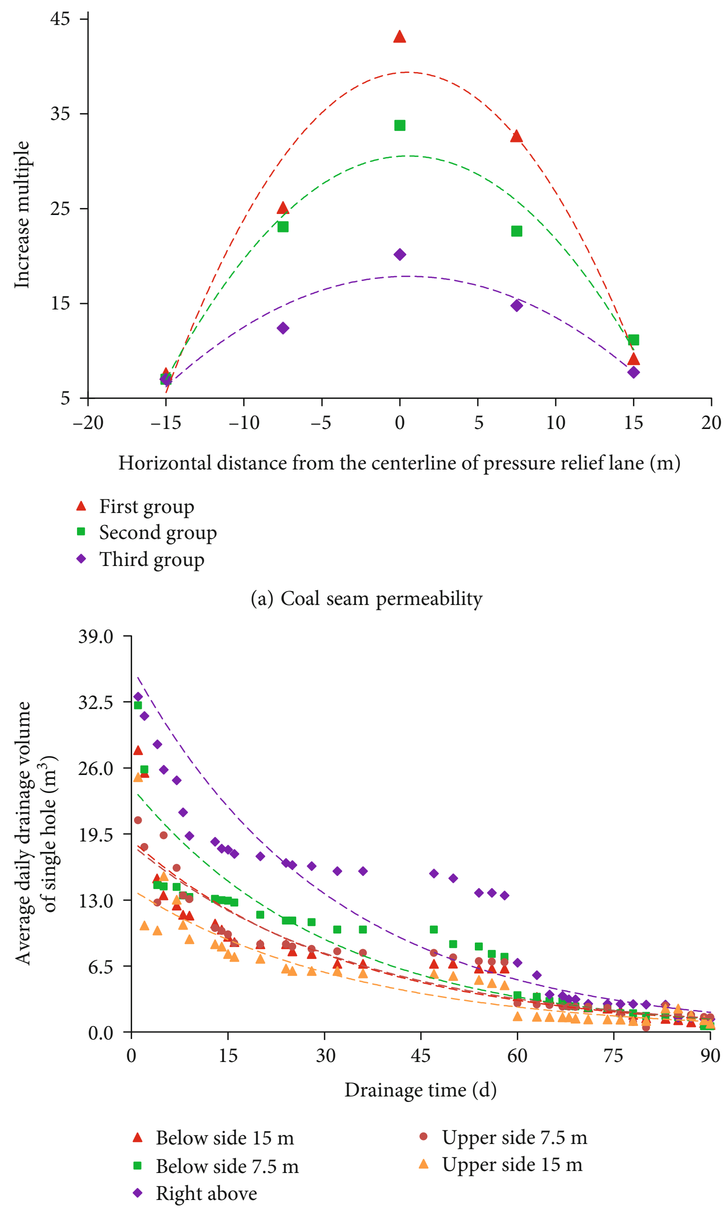

(a) Coal seam permeability

(b) Single hole daily average drainage

FIGURE 10: The permeability enhancement effect of the overlying coal seam above 213 pressure relief roadway.

regardless of the rheological effect of pressure relief of the roadway, substituting the rock formation conditions and the relevant parameters the 213 pressure relief roadway of Qujiang Coal Mine into the relevant formula, it can obtain σ_R^P=7.72 MPa⊠$K_0 = 2.4407 \cdot e^{-0.089\cdot(\sigma_x-\sigma_y)}$. It can obtain the effective pressure relief distance and the effect of increasing the permeability of the upper coal seam, when the distance between the coal seam and the floor roadway center is different Δh. It is shown in Table 1.

It can be seen from Table 1 that as the distance between the pressure relief roadway and the coal seam increases, the width of the significant enhancement zone and the coal seam permeability enhancement multiple are gradually reduced, and the width of the general enhancement zone gradually increases and then stabilizes.

When the layer spacing is 7 m, the maximum widths of the significant and general permeability enhancement zones are 12.1 m and 4.3 m, respectively, which are 5.4 times and 1.9 times the radius of the roadway; the maximum widths of the significant and general permeability enhancement zones are coal seam permeability enhancement multiples which are, respectively, 239.3 times and 11.1 times that of the original coal seam.

When the interlayer spacing is 18~21 m, the significant coal seam permeability enhancement zone is 0, the general coal seam permeability enhancement zone is 9.1 times the radius of the roadway, and the maximum coal seam permeability enhancement multiples of the significant coal seam permeability enhancement zone and the general coal seam permeability enhancement zone are 5.5 times and 1.6 times of the original coal seam, that is, the overlying coal seam's permeability enhancement effect is not significant.

3.3. Field Test of the Coal Seam Permeability Enhancement

3.3.1. Test Scheme. Based on the abovementioned experiments and theoretical calculations, field tests were carried out. It tests the effect of permeability enhancement of the overlying coal seam. The test site is also the Qujiang Coal Mine in Fengcheng City, Jiangxi Province, China. Figure 7 shows the geographical location of the Qujiang Coal Mine. The 213 pressure relief roadway is arranged 9 m directly below the roadway to be excavated, which is about 1000 m in ground buried depth. The measured coal seam permeability coefficient of the test area is $0.002\,m^2/MPa^2{\bullet}d$, which is a deep low-permeability coal seam.

The test content is the pressure relief effect of the surrounding rock and the permeability enhancement effect of the coal seam. The test area is 15 m from the upper and lower sides of the overlying coal rock above the 213 pressure relief roadway. As shown in Table 2. Figure 8 shows the layout of the test boreholes, with 5 test boreholes arranged for each parameter.

3.3.2. Enhancement Effect of Coal Seam Permeability. Figure 9 is the pressure relief effect of the overlying strata above the 213 pressure relief roadway. Figure 10 is the coal seam's permeability enhancement effect above the 213 pressure relief roadway. It can be seen from Figure 9(a) that the maximum displacement of the surrounding rock of the roadway is 3.6 cm, and the displacement of the surrounding rock shows the phenomenon of "wave crest" and "wave trough" alternately. The same law is also obtained in laboratory physical simulation [46, 47]. It can be seen from Figure 9(b) that the surrounding rock of the roadway appears divided into zones, that is, four fracture zones appear from the outside to the inside of the roadway, and the maximum influence range of the fracture zone is 5.7 m. It can be seen from Figure 10(a) that the permeability coefficient of the pressure relief coal seam is 7.0-43.2 times higher than that of the original coal seam. It can be seen from Figure 10(b) that the maximum single-hole daily average drainage is $31.1\,m^3/d$, which is 3 times larger than the original coal seam (maximum $7.7\,m^3/d$). It shows that the overlying coal and rock layers of the 213 pressure relief roadway have a significant effect on pressure relief and permeability enhancement. The test results are consistent with the aforementioned research rules (although there are other objective factors in the test area), verifying that the model is feasible and effective for pressure relief and permeability enhancement.

4. Discussion

Based on the zonal disintegration of the surrounding rock in the deep roadway, it is proposed to arrange the pressure relief roadway directly under the coal roadway to be excavated to increase the pressure relief of the overlying coal seam. The coal seam pressure relief and permeability enhancement model is carried out at the appropriate position directly below the roadway, which realizes the safe, economical, and efficient permeability enhancement of the deep seam coal roadway strip area. However, the research still needs to be improved. First, there is a time rheological effect in the pressure relief zone of the pressure relief roadway [48], so the time rheology effect on the overlying coal roadway needs further study. Second, this model only studies the experimental results under specific conditions, and the pressure relief and permeability enhancement effects under different gas geological conditions (such as coal seam dip, coal thickness, lateral pressure coefficient, buried depth, and geological structure) need further research. Third, this model only studies the pressure relief and permeability enhancement effects of single factors such as ground stress and gas, and the coupling effect of the two needs to be further studied.

5. Conclusion

(1) Based on the zonal disintegration of the surrounding rock in the deep roadway, the area is defined as the stress relief area of the surrounding rock above the pressure relief roadway, where the stress reduction is more than 5%. It is defined the pressure-relief and permeability enhancement area of the overlying coal seam. It constructed a permeability enhancement model of pressure relief roadway for the of deep coal roadway strip, which provides a new method for deep coal roadway strip pressure relief and permeability enhancement

(2) The unloading seepage experiment of gas-containing coal shows that unloading can effectively increase the permeability of the coal sample. Calculations show that with the increase of the distance from the coal seam, the overlying coal seam's permeability enhancement multiple and the significant permeability zone width gradually decrease and the width of the permeability enhancement generally zone gradually increases and then tends to be stable. When the pressure relief road is 7 m away from the coal seam, the widths of the significant and general enhancement zones are, respectively, 5.4 and 1.9 times the radius of the roadway. When the pressure relief roadway is 18-21 m away from the coal seam, the widths of the significant and general enhancement zones are 0 times and 9.1 times the radius of the roadway, respectively. It provides a theoretical basis for the location of the pressure relief roadway

(3) Field tests show that when the pressure relief roadway is located 9 m directly below the coal seam, the overlying coal strata has a significant pressure relief and permeability enhancement effect. The maximum displacement is 3.6 cm of the surrounding rock of the pressure relief roadway, the maximum influence range of the fracture zone is 5.7 m, and the coal seam permeability coefficient is increased by 7.0~43.2 times, and the maximum daily average drainage volume of a single hole has increased by 3 times. It has

realized safe, economical, and efficient permeability enhancement and drainage in the deep coal seam strip area, which provides a certain reference for the permeability enhancement of the coal road strip area in similar coal seams

Data Availability

All data included in this study are available upon request from the corresponding author.

Conflicts of Interest

The authors declared that they have no conflicts of interest to this work.

Acknowledgments

This research was financially supported by Technological Innovation and Entrepreneurship Fund Special Project of Tiandi Technology Co., Ltd. (2021-2-TD-ZD008), general project of Chongqing Research Institute Co., Ltd. (2020YBXM22 and 2020YBXM23), and Chongqing Natural Science Foundation General Project (cstc2021jcyj-msxmX1149).

References

[1] Y. Liu, Z. Zhang, B. Deng, and M. Li, "Liquid carbon dioxide fracturing application and its effect on gas drainage in low permeability coal seams of underground coal mine," in *Energy Sources, Part A: Recovery, Utilization, and Environmental Effects*, pp. 1–13, Taylor & Francis, 2019.

[2] R. Zhang, Y. Cheng, and L. Yuan, "Study on the stress relief and permeability increase in a special low-permeability thick coal seam to stimulate gas drainage," *Energy Sources, Part A: Recovery, Utilization, and Environmental Effects*, vol. 42, no. 8, pp. 1001–1013, 2020.

[3] G. Si, S. Durucan, J. Q. Shi, A. Korre, and W. Cao, "Parametric analysis of slotting operation induced failure zones to stimulate low permeability coal seams," *Rock Mechanics and Rock Engineering*, vol. 52, no. 1, pp. 163–182, 2019.

[4] Q. Liu, Y. Cheng, W. Haifeng et al., "Numerical assessment of the effect of equilibration time on coal permeability evolution characteristics," *Fuel*, vol. 140, pp. 81–89, 2015.

[5] Y. Zhang, Q. Zou, and L. Guo, "Air-leakage model and sealing technique with sealing-isolation integration for gas-drainage boreholes in coal mines," *Process Safety and Environmental Protection*, vol. 140, pp. 258–272, 2020.

[6] R. Zhang, Y. Cheng, L. Yuan, H. Zhou, L. Wang, and W. Zhao, "Enhancement of gas drainage efficiency in a special thick coal seam through hydraulic flushing," *International Journal of Rock Mechanics and Mining Sciences*, vol. 124, p. 104085, 2019.

[7] B. Lin, H. Song, Y. Zhao, T. Liu, J. Kong, and Z. Huang, "Significance of gas flow in anisotropic coal seams to underground gas drainage," *Journal of Petroleum Science and Engineering*, vol. 180, pp. 808–819, 2019.

[8] C. Huang, Y. Zhang, J. He, Y. Luo, and Z. G. Sun, "Permeability improvements of an outburst-prone coal seam by means of presplitting and blasting with multiple deep boreholes," *Energy Science & Engineering*, vol. 7, no. 5, pp. 2223–2236, 2019.

[9] Y. Li, S. Wu, B. Nie, and Y. Ma, "A new pattern of underground space-time tridimensional gas drainage: a case study in Yuwu coal mine," *China. Energy Science & Engineering*, vol. 7, no. 2, pp. 399–410, 2019.

[10] S. V. Serdyukov, M. V. Kurlenya, L. A. Rybalkin, and T. V. Shilova, "Hydraulic fracturing effect on filtration resistance in gas drainage hole area in coal," *Journal of Mining Science*, vol. 55, no. 2, pp. 175–184, 2019.

[11] Y. Zhang, "Improvement of gas drainage efficiency of low-permeability coal seams using ultra-high pressure hydraulic cutting technique," *MS & E*, vol. 472, no. 1, article 012084, 2019.

[12] G. Yue, M. Li, L. Wang, and W. Liang, "Optimal layout of blasting holes in structural anisotropic coal seam," *Plo S one*, vol. 14, no. 6, article e0218105, 2019.

[13] T. Liu, B. Lin, X. Fu, Y. Zhao, Y. Gao, and W. Yang, "Modeling coupled gas flow and geomechanics process in stimulated coal seam by hydraulic flushing," *International Journal of Rock Mechanics and Mining Sciences*, vol. 142, p. 104769, 2021.

[14] Y. Ma, X. Mao, K. Yang, J. Liu, and A. Zhao, "Improvement on gas drainage of soft gassy coal seam with underground hydraulic flushing and fracturing: a case study in Huainan," *Arabian Journal of Geosciences*, vol. 13, no. 4, p. 178, 2020.

[15] D. Chen, W. He, S. Xie, F. He, Q. Zhang, and B. Qin, "Increased permeability and coal and gas outburst prevention using hydraulic flushing technology with cross-seam borehole," *Journal of Natural Gas Science and Engineering*, vol. 73, article 103067, 2020.

[16] X. Gao, M. Dong, and Y. Fan, "Application of borehole hydraulic flushing while drilling in low-permeability coal seam gas antireflective [J]," *Coal Mine Machinery*, vol. 40, no. 1, pp. 122–124, 2019.

[17] Y. Zhao, B. Lin, T. Liu, J. Kong, and Y. Zheng, "Gas flow in hydraulic slotting-disturbed coal seam considering stress relief induced damage," *Journal of Natural Gas Science and Engineering*, vol. 75, p. 103160, 2020.

[18] J. Zhong, Z. Ge, Y. Lu, Z. Zhou, and J. Zheng, "New mechanical model of slotting–directional hydraulic fracturing and experimental study for coalbed methane development," *Natural Resources Research*, vol. 30, no. 4, pp. 1–18, 2020.

[19] X. Wang, Q. Hu, and Q. Li, "Investigation of the stress evolution under the effect of hydraulic fracturing in the application of coalbed methane recovery," *Fuel*, vol. 300, no. 3, p. 120930, 2021.

[20] X. Su, F. Li, L. Su, and Q. Wang, "The experimental study on integrated hydraulic fracturing of coal measures gas reservoirs," *Fuel*, vol. 270, p. 117527, 2020.

[21] L. Zhou, X. Zheng, Y. Lu, H. Li, and M. Feng, "Fracture pattern and caprock integrity analyses via hydraulic fracturing for CO_2 enhanced coal bed methane," *Engineering Fracture Mechanics*, vol. 228, p. 106894, 2020.

[22] Y. Zhou, H. Ni, Z. Shen, and X. Teng, "Key issues in the application of supercritical carbon dioxide fracturing in unconventional gas well," in *In IOP Conference Series: Earth and Environmental Science*, Wuhan, Hubei, China, 2020, AugustIOP Publishing.

[23] Y. Zhang, Y. Lou, C. Mou, J. Bai, and J. Jia, "Effects of supercritical carbon dioxide fracturing on rock mechanics characteristics of tight sandstone gas reservoirs," *Oil Drilling & Production Technology*, vol. 41, no. 2, pp. 242–248, 2019.

[24] F. Y. Zeng, X. J. Zeng, and Q. Liu, "Study Influence High Pressure Gas Blasting to Simulated Coal Seam Permeability [J]," *Coal Mining Technology*, vol. 23, no. 1, pp. 78–80+26, 2018.

[25] X. T. Feng, H. S. Guo, C. X. Yang, and S. J. Li, "In situ observation and evaluation of zonal disintegration affected by existing fractures in deep hard rock tunneling," *Engineering Geology*, vol. 242, pp. 1–11, 2018.

[26] Z. Tian, C. Tang, Y. Liu, and Y. Tang, "Zonal disintegration test of deep tunnel under plane strain conditions," *International Journal of Coal Science & Technology*, vol. 7, no. 2, pp. 337–349, 2020.

[27] Q. Y. Zhang, "The zonal disintegration mechanism of surrounding rock around deep spherical tunnels under hydrostatic pressure condition: a non-euclidean continuum damage model," *Acta Mechanica Solida Sinica*, vol. 26, no. 4, pp. 373–387, 2013.

[28] J. Li, M. Y. Wang, N. Zhang, and P. X. Fan, "Basic problems for dynamic deformation and fracture of deep rock mass," *Engineering Sciences*, vol. 15, no. 5, pp. 71–79, 2013.

[29] X. Zhou and Q. Qian, "Zonal disintegration mechanism of the microcrack-weakened surrounding rock mass in deep circular tunnels," *Journal of Mining Science*, vol. 49, no. 2, pp. 210–219, 2013.

[30] C. Z. Qi, K. R. Li, J. P. Bai, A. I. Chanyshev, and P. Liu, "Strain gradient model of zonal disintegration of rock mass near deep-level tunnels," *Journal of Mining Science*, vol. 53, no. 1, pp. 21–33, 2017.

[31] H. Chen, C. Qi, S. Wang, and M. Wang, "A simple gradient model for zonal disintegration of the surrounding rock around a deep circular tunnel," *Tunnelling & Underground Space Technology*, vol. 91, no. SEP., p. 103006, 2019.

[32] S. Wu, L. Chen, and Z. Cheng, "Macro and meso research on the zonal disintegration phenomenon and the mechanism of deep brittle rock mass," *Engineering Fracture Mechanics*, vol. 211, pp. 254–268, 2019.

[33] X. R. Zeng, S. H. You, F. Li, and B. Rahmani, "An analytical research on stress-wave propagation and comparison of experiments and theory of zonal disintegration in rock masses around deep tunnels," *Forum*, vol. 980, pp. 333–345, 2020.

[34] J. Bi and P. Z. Xiao, "Numerical simulation of zonal disintegration of the surrounding rock masses around a deep circular tunnel under dynamic unloading," *International Journal of Computational Methods*, vol. 12, no. 3, p. 1550020, 2015.

[35] X. Wang, Y. Pan, and Z. Zhang, "A spatial strain localization mechanism of zonal disintegration through numerical simulation," *Journal of Mining Science*, vol. 49, no. 3, pp. 357–367, 2013.

[36] L. Z. Tang, Y. Y. Chen, C. Liu, and F. Shen, "Numerical simulation of zonal disintegration of surrounding rock based on strain rate damage constitutive model," *Journal of Yangtze River Scientific Research Institute*, vol. 37, no. 7, p. 82, 2020.

[37] X. Zhu, Y. Wang, and Y. Ren, "Numerical simulation to research on the fracture mechanism of the surrounding rock in deep tunnels," *Geotechnical and Geological Engineering*, vol. 38, no. 1, pp. 319–327, 2020.

[38] H. P. Xie, "Research review of the state key research development program of China: deep rock mechanics and mining theory," *Journal of China Coal Society*, vol. 44, no. 5, pp. 1283–1305, 2019.

[39] M. Y. Wang, H. X. Chen, J. Li, and X. P. Li, "Theoretical research on zonal disintegration of rock masses around deep tunnels and comparisons with in-situ observations," *Chinese Journal of Rock Mechanics and Engineering*, vol. 37, no. 10, pp. 2209–2218, 2018.

[40] Q. Gao, Q. Zhang, and W. Xiang, "Mechanism of zonal disintegration phenomenon (zdp) around deep roadway under dynamic excavation," *Geotechnical & Geological Engineering*, vol. 37, no. 1, pp. 25–41, 2019.

[41] Q. Zhang, X. Zhang, Z. Wang, W. Xiang, and J. Xue, "Failure mechanism and numerical simulation of zonal disintegration around a deep roadway under high stress," *International Journal of Rock Mechanics and Mining Sciences*, vol. 93, pp. 344–355, 2017.

[42] S. Q. Lu, Y. P. Cheng, H. F. Wang, L. Wang, W. Li, and J. H. Mou, "Numerical simulation research on the Hongling coal mine's minimum mining thickness of upper protective layer," *Journal of China Coal Society*, vol. 37, no. S1, pp. 43–47, 2012.

[43] Y. Bufan, *Technical Manual of Coal Mine Gas Disaster Prevention and Utilization (Revised Edition)*, Coal Industry Press, Beijing, 2005.

[44] R. Feng, S. Chen, S. Bryant, and J. Liu, "Stress-dependent permeability measurement techniques for unconventional gas reservoirs: review, evaluation, and application," *Fuel*, vol. 256, p. 115987, 2019.

[45] B. Tang, C. F. Si, and X. Z. Meng, "Determination method for gas extraction radius from coal seam by boreholes and practice," *Mining Safety and Environmental Protection*, vol. 39, pp. 43–48, 2012.

[46] Q. Zhang, X. Chen, B. Lin, D. Liu, and N. Zhang, "Study of 3d geomechanical model test of zonal disintegration of surrounding rock of deep roadway," *Chinese Journal of Rock Mechanics & Engineering*, vol. 28, pp. 1757–1766, 2009.

[47] Y. Xu and P. Yuan, "Model test of zonal disintegration in deep rock under blasting load," *Chinese Journal of Rock Mechanics & Engineering*, vol. 34, pp. 3844–3851, 2015.

[48] J. J. Cao, *Research on the Method of Coal and Gas Outburst Prevention by Floor Roadway Pressure Relief and Gas Dranage in Deep Coal Seam Roadway Strip*, Anhui University of Science and Technology, 2020.

Hindawi
Geofluids
Volume 2022, Article ID 4303681, 12 pages
https://doi.org/10.1155/2022/4303681

Research Article

Analysis on Evolution Law of Small Structure Stress Arch and Composite Bearing Arch in Island Gob-Side Entry Driving

Shunjie Huang,[1,2] Xiangqian Wang,[1,2] Yingming Li,[1,2] Lei Wang,[3] Gang Liu,[4] Fukun Xiao,[4] and O. V. Bashkov[5]

[1]*State Key Laboratory of Mining Response and Disaster Prevention and Control in Deep Coal Mines, Anhui University of Science and Technology, Huainan 232001, China*
[2]*School of Mining Engineering, Anhui University of Science and Technology, Huainan, Anhui 232001, China*
[3]*Mining Products Safety Approval and Certification Center Co., Ltd., Beijing 100013, China*
[4]*Heilongjiang Ground Pressure and Gas Control in Deep Mining Key Laboratory, Heilongjiang University of Science and Technology, Harbin 15002, China*
[5]*Komsomolsk-na-Amure State Technical University, Komsomolsk-na-Amure 681013, Russia*

Correspondence should be addressed to Xiangqian Wang; 1203259514@qq.com

Received 11 November 2021; Revised 3 May 2022; Accepted 14 May 2022; Published 23 June 2022

Academic Editor: Zhijie Wen

At present, the theory of supporting the surrounding rock small structure of gob-side entry driving has been widely used, but there is no specific quantitative analytical formula for the bearing strength and bearing characteristics of the structure. Construct a small structural stress arch mechanical model based on the arch axis equation, and divide the width of coal pillars (fractured zone-plastic softening zone-plastic hardening zone) and small structural stress arch height. According to the relationship between the stress arch height and the size of the roadway, the anchor cable length is determined to be 7.3 m, and the "anchor mesh + ordinary long anchor cable + grouting anchor cable" coordinated support plan is proposed: anchor net support is used for the first support, and long anchor cable and grouting anchor cable are used for the second support. Combined with the supporting parameters, a mechanical model of the surrounding rock composite bearing stress arch is proposed, and the composite bearing stress arch structure is derived using elastoplastic mechanics to obtain the ultimate bearing strength relationship expression. The results show that the ultimate bearing capacity of the haulage gateway of 17236 island working-face in the north of Zhangji coal mine can reach 29.193 MPa after the composite bearing stress arch support. The feasibility of the supporting scheme is verified, and field monitoring showed that the deformation zone of the surrounding rock of the transportation haulage gateway is stable after being supported by the composite bearing stress arch structure, the maximum shrinkage of the top and bottom of the roadway is 287 mm, and the distance between the two sides is 640 mm.

1. Introduction

At present, many mines have entered the residual mining stage due to the rapid decline of recoverable reserves of coal resources due to high tension coal mining, in order to improve the recovery rate of coal resources and prolong the production and service life of mines, and gob-side entry has become the first choice for island working-face [1–4]. Under the action of side abutment pressure of gob-side entry in isolated island working-face, the roof pressure is big, the degree of coal fragmentation is high, the difficulty of roadway support is improved, and the roadway damage is serious due to mining influence and geological structure [5–9].

Therefore, the support of gob roadway is particularly important for island face mining. Wang et al. [10] analyzed the deformation mechanism and the stress state of gob-side entry driving heading adjacent to the advancing working-face (HAWF) roof structure and proposed a roof failure criterion to examine the roof flexure deformation pattern. Zhang et al. [11] analyzed the distribution law of lateral support stress near the working-face, discussed the relationship between coal pillar stress distribution and coal pillar deformation, roadway surrounding rock stress distribution, roadway surrounding rock deformation, and coal pillar width, and verified the feasibility of coal pillar width through the field. Ma and Zhong [12] established the "three zone" failure similarity simulation experimental model of surrounding rock and deduced the action mode of surrounding rock stress structure, but there is no theoretical and numerical simulation analysis and lack of theoretical basis. Hou and Li [13] analyzed the mechanical properties of arc triangular key blocks of the main roof, put forward the stability principle of big and small structures, and provided a theoretical basis for the application of bolt support. Yang et al. [14] regard the broken rock mass near the roadway opening as a small ground structure and the deep stable rock mass as a big ground structure through numerical simulation software experiments and proposed support technology of interconnecting the big and small structures, based on high-strength bolts, high-stiffness shotcrete layer plugging water, and strengthening the small structure with deep-hole grouting. Wu et al. [15] established the three-dimensional structural mechanics model of deep stope, put forward the "big and small structure theory" of coal pillar free mining, and found a new method to control the two tunnel dynamic disasters of "given deformation" and "finite deformation." Zhang et al. [16] proposed a new joint support technology in the soft rock roadway of Gubei Coal Mine in Huainan, China. The on-site monitoring results show that the combined support technology is satisfactory. Li and Hua [17] put forward a supporting concept of enhancing the support strength and realizing the cutting roof and designed three roadside support schemes of gob-side entry for a soft floor and hard roof.

Most of the current research results focus on the "big-structure" of gob-side entry driving; however, the research on the small structure of surrounding rock of gob side roadway with isolated coal pillar mostly ignores the arch height of small-structure stress and the bearing strength of roadway support structure. Zhao et al. [18] analyzed the evolution of stress arch through theoretical and numerical simulation, and a zoning asymmetric coupling control technology named narrow flexible-formwork wall with steel bar reinforcement along single prop wall + strong double-row single props + high-strength and high-preloading asymmetric anchor cable is proposed. For the small structure of surrounding rock of roadway along working-face of isolated island coal pillar, the arch height of small structure stress and the bearing strength of roadway support structure are mostly ignored. Therefore, according to the structural characteristics of surrounding rock of gob driving roadway, the coal pillar failure area is divided into fractured zone-plastic softening zone-plastic hardening zone [19–37] and according to the total stress-strain curve. Taking the gob driving roadway of isolated island working-face of the north of Zhangji coal mine as the research background, the anchor cable support parameters and the bearing strength of "composite bearing stress arch" structure formed by the support structure and surrounding rock are calculated through theoretical analysis. The corresponding support scheme is adopted for field industrial test, and the reliability of the support scheme is verified.

2. Background

2.1. Geological Conditions. The schematic diagram of 17236 working-face in the north of Zhangji coal mine of Huaihe Energy Coal Industry Company is shown in Figures 1 and 2. It is located between 17226 working-face and 17246 working-face. The mine able strike length of 17236 island working-face is 1580 m (horizontal range), and the elevation of the working-face is -519.6~-630.0 m. A narrow coal pillar of 8 m is reserved along the edge of 17246 working-face. The design section of the roadway is rectangular, with a net section zone of 18.7 m^2, an average dip angle of 4.5°, and an average thickness of 4.2 m. The direct top is sandy mudstone with an average thickness of 3.8 m, and the direct bottom is silty fine sandstone with an average thickness of 1 m; the surrounding rock column diagram is shown in Figure 3.

2.2. The Failure Characteristics of Gob-Side Entry Driving. The stress field of the transportation trough of 17236 island working-face based on lateral bearing pressure and advance bearing pressure in Zhangji North Mine was found through field study. The rock pressure appeared mainly shows the failure forms of roadway: bolt and anchor cable fractured, steel belt broken and cracked, and steel beam bent and deformed, which seriously affects the safety and stability of roadway. The failure characteristics of roadway are shown in Figure 4.

And four roadway section monitoring points (each monitoring point is 40 m away and 3#, 4# measuring points are located in the abnormal fault development zone) are selected in the haulage gateway 158 m from the cutting hole. The monitoring results are shown in Figure 5. The results show that the displacement of roadway's two side is big, especially at the 3# and 4# measuring points in the abnormal zone. The deformation degree is the biggest, and the maximum deformation rate can reach 47 mm/d. At the same time, the roof shrinkage is serious.

(1) Composition of surrounding rock. The surrounding rock of the roadway is mainly silty fine sandstone, sandy mudstone, and fine sandstone. The rock strength test is carried out on the samples taken from the top and bottom plates. It can be seen that the compressive strength of fine sandstone and sandy mudstone is 26.6 MPa and 15.8 MPa, respectively, and the compressive strength of silty fine sandstone is 23.9 MPa. The rock mass has low load resistance. Under the condition of high stress intensity, the surrounding rock fissures develop violently, and the expansion deformation is big

(2) Mining depth. The buried depth of the haulage gateway is 653 m, with big in situ stress and unstable surrounding rock

(3) Mining method. When the skip mining method is adopted for mining, the surrounding rock is disturbed, resulting in the deterioration of the integrity and bearing capacity of the roadway surrounding rock, leading to the advance of the crushing range

FIGURE 1: Location of the north of Zhangji coal mine.

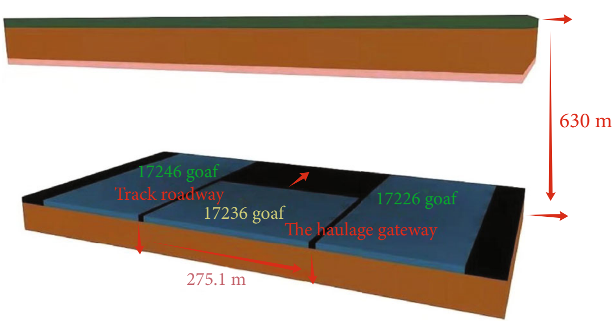

FIGURE 2: Schematic diagram of position relationship of 17236 working-face.

Lithology	Columnar	Thickness (m)
Mudstone		1.7
Coal line		0.5
Sandy mudstone		2.1
Fine sandstone		2.8
Sandy mudstone		3.8
6 coal		4.2
Siltstone		1
Coal line		0.4
Siltstone		1.6
Medium grained sandstone		4.1

FIGURE 3: Synthesis column map of the surrounding rock.

of the working-face, affecting the transportation channel, and increasing the instability of the roadway

(4) The superposition of excavation disturbance and residual mining stress has a serious impact. Due to the big buried depth of the roadway and the superposition of the vertical stress and the residual mining

FIGURE 4: Deformation and failure characteristics of roadway surrounding rock.

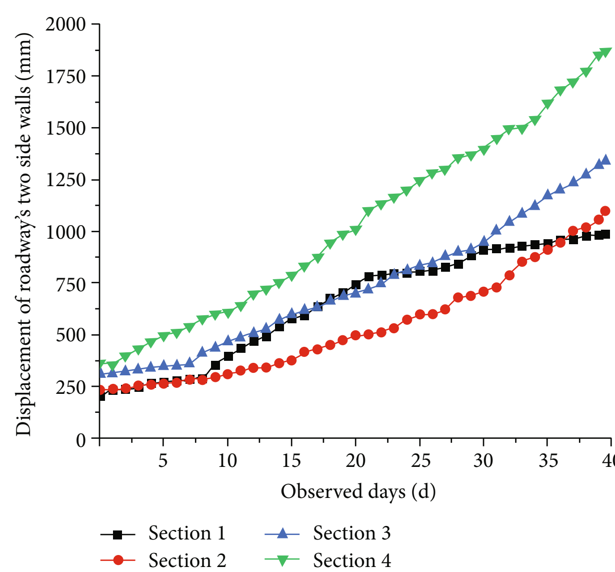

FIGURE 5: Convergence of the haulage gateway.

stress in the working-face, the peak strength of the coal body is low

According to the above analysis, in order to solve the problem that the roof separation and roadway side deformation become the core of the support technology, the bolt group is generally used for intensive support in the early stage, which can provide great support resistance within the anchorage range, but the surrounding rock outside the bolt length will still produce separation, resulting in roof caving. Therefore, only by improving the support structure and strengthening the support technology can the roadway deformation be minimized.

Therefore, in order to better act the nonanchored rock mass load and the expansion energy generated by the broken rock mass on the bolt in the early stage of the roadway, the metal mesh can be added to the original bolt support mode to control the deformation of the nonanchored rock mass and prevent the collapse of the broken rock mass. At the same time, in order to further improve the service life of roadway and the bearing capacity of narrow coal pillar, in the later stage, in order to mobilize the bearing energy of deep surrounding rock and narrow coal pillar, grouting anchor cable and long anchor cable can be added for joint support, improve the stress state of surrounding rock, and effectively control the deformation of roadway surrounding rock.

3. Stability Analysis of Overburden Stress Arch along Gob-Side Entry in Isolated Island Working-Face

3.1. Mechanical Model of Overburden Stress Arch along Gob-Side Entry in Isolated Island Working-Face. With the completion of the previous excavation working face, the overlying rock on the roof of the goaf collapses, and the rock blocks after the periodic rupture of the basic roof or the old roof will follow the direction or inclination of the working face, and the overlying rock in the goaf will inevitably form a large structure. Among them, the artificial support has little effect on the large structure, but the artificial support mainly controls the stability of the small structure under the large structure.

After the mining disturbance of the gob-side roadway, the overlying rock mass structure will be stable in the form of stress arch (the arch line trajectory belongs to the distribution law of the envelope curve under the Moore-Coulomb criterion strength) and form a "large-small" structure to protect the coal and rock below body and roadway. The large structure is a large-scale surrounding rock structure with coal pillars and arc-shaped triangular blocks as the main centers, but the small structure usually takes the roadway as the center point and the "support-surrounding rock" system becomes a small bearing structure. Among them, the small structure is under the large structure, and the arch foot is close, the stability of the large structure determines the stability of the small structure, and at the same time, the stability of the small structure affects the stability of the arch foot, thus affecting the stability of the large structure; "small" structures interact and influence each other. The schematic diagram of the "big-small" structure is shown in Figure 6. Since the key block with the greatest influence on the stability of the gob-side roadway is block B, this chapter studies the influence of block B on the small structure of the gob-side roadway after stabilization [15–19].

The small structure of the gob-side entry is an arch structure [20–22]. The arch foot of the arch is located on both sides of the solid coal and the coal pillars, and the apex of the arch is located at the point of stress concentration. For better analysis of the stress arch height, referring to the solution method of literature [23] for analysis, the internal stress distribution of the coal pillar is analyzed separately, and it will correspond to the whole stress-strain curve. The failure area of the arch foot is from the flow zone of the coal pillar (close to the working-face side) and the plastic softening zone to the junction of plastic hardening zone and elastic zone (K is the stress concentration factor of coal pillar; γ is the unit weight of overburden (kN/m^3); H is the mining depth of coal seam (m); x_f is the width of fractured zone (m); x_s is the width of plastic softening zone (m); x_e is the width of plastic hardening zone (m)).

According to the above, the arch foot is located at the junction of the flow zone and the plastic softening zone. Therefore, the arch axis mechanical model is established. In order to facilitate the analysis, the following assumptions are made for the model: (1) given deformation of curved triangle block B and the block is stable; (2) the arch structure can be approximately regarded as a horizontal semicircular arch, and the arch thickness remains unchanged; (3) the stress arch apex is vertically corresponding to the roadway center point; the arch foot is horizontally symmetrical; (4) the rock mass still has cohesion after excavation; (5) arch structures only bear compressive stress but not tensile stress, and the mechanical model is shown in Figure 7.

Set the arch axis equation as:

$$\frac{x^2}{(S)^2} + \frac{y^2}{\left(H_g\right)^2} = 1, \qquad S = 2r + 2x_e. \tag{1}$$

In the formula, S is the arch span (m); P_0 is the gravity of overlying strata (MPa); H_g is the arch height (m); F_{Ax}, F_{Ay}, F_{BX}, and F_{By} are the reaction force (MPa) of arch foot at two points A (solid coal) and B (coal pillar); G_X is the horizontal force of the right half arch to the left half arch (MPa); R is the distance from the roadway center to a certain point of surrounding rock (m).

From the model of mechanical equilibrium equation in the Y direction, it can be obtained:

$$F_{Ay} = F_{By} = \frac{P_0 S}{2}. \tag{2}$$

From formula (3), it can be seen that the arch foot bears a great load in the vertical direction. In order to meet the stability of the arch foot in the vertical direction, the plastic

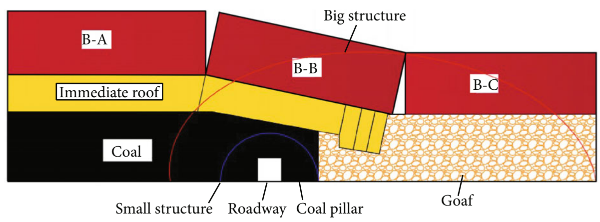

FIGURE 6: Schematic diagram of big and small structure of surrounding rock in gob-side entry driving.

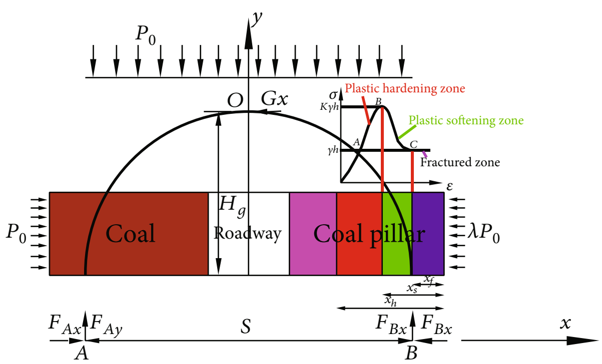

FIGURE 7: Mechanical model of stress arch (small-structure).

softening zone, plastic hardening zone, and elastic zone are arch feet. According to the literature [24, 25], the results are as follows.

The width of the fractured zone is:

$$x_f = \frac{2h\left[\tan^2(45^\circ - (\varphi_e^*/2)) - (P_0/\gamma H)\right]}{(\tan \varphi_{eu}^* + \tan \varphi_{ed}^*)}. \tag{3}$$

The width of the coal gang destruction zone is:

$$x_s = \frac{2h\left[\tan^2(45^\circ - (\varphi_{se}^*/2)) - (P_0/\gamma H)\right]}{(\tan \varphi_{su}^* + \tan \varphi_{sd}^*)}. \tag{4}$$

The width of the limit equilibrium zone is:

$$x_h = \frac{L\lambda}{2\tan\varphi^*} \ln\left(\frac{K\gamma H + (c_0/\tan\varphi^*)}{(c_0/\tan\varphi^*) + (P_0/\lambda)}\right). \tag{5}$$

From the above formula, c_0 is the comprehensive cohesion of stress arch bearing structure (MPa); φ^* is the comprehensive internal friction angle of stress arch bearing structure (°); L is the roadway side height (m); $\varphi^*{}_e$ is the friction angle in the coal seam in the fractured zone (°); $\varphi^*{}_{se}$ is the comprehensive internal friction angle of coal seam in fractured zone and plastic softening zone (°); $\varphi^*{}_{eu}$ is the angle of internal friction between the coal seam and the roof in the fracture zone (°); $\varphi^*{}_{su}$ is the integrated internal friction angle between the coal seam and the roof in the fracture zone and plastic softening zone(°); $\varphi^*{}_{ed}$ is the angle of internal friction between the coal seam and the base plate in the fractured zone (°); $\varphi^*{}_{sd}$ is the integrated angle of internal friction between the coal seam and the base plate in the fractured zone, plastic softening zone (°).

Within the plastic softening zone $[x_f, x_s]$, the stress is distributed as follows:

$$\sigma_{y1} = \gamma H - \frac{x - x_f}{x_s - x_f}(1-K)\gamma H. \tag{6a}$$

Similarly, within the plastic hardening zone $[x_s, x_h]$, the stress is distributed as follows:

$$\sigma_{y2} = \gamma H - \frac{x_h - x}{x_h - x_s}(1-K)\gamma H. \tag{6b}$$

The derivation of the integral for each partition range of Equations (6a) and (6b) above gives:

$$\left.\begin{aligned} F_{Ay1} &= \frac{(x_s - x_f)(K+1)\gamma H}{2} \\ F_{Ay2} &= \frac{(x_h - x_s)(K+1)\gamma H}{2} \end{aligned}\right\}. \tag{7}$$

Taking the left half-arch as the object of study and taking the moment formula for the rotation axis O, we can obtain:

$$-H_g F_{Ax} - \frac{1}{2}\left(\frac{S}{2}\right)^2 P_0 - \frac{H_g^2}{2}\lambda P_0 + \frac{L_s}{2}F_{Ay} = 0. \tag{8}$$

According to the Morh-Coulomb, the shear stress between the top and bottom slab and the coal body is:

$$\tau_x = c_0 + \sigma_y \tan\varphi^*, \tag{9}$$

where c_0 is the cohesive force at the interface between the roof and floor and the coal seam(MPa); φ^* is the angle of internal friction at the interface between the roof and floor and the coal seam (°).

From Equation (10), it can be seen that the shear stress τ_x is related to the size of the coal pillar stress φ_y, so the coal pillar stress φ_y satisfies:

$$\sigma_y = F_{y1} + F_{y2}. \tag{10}$$

At the same time, simultaneously, Equations (6a), (6b), (9), and (10) into Equation (11), the result is the horizontal friction force F_f at the foot of the arch:

$$F_f = \int_{x_f}^{x_h} \tau_x dx. \tag{11}$$

Simultaneous Equations (7)~(11), the analytical expression of stress arch structure height H_g is as follows:

$$H_g = \frac{\left(-2F_f + \sqrt{4F_f^2 + \lambda[SH\gamma]^2}\right)}{2\lambda H\gamma}. \tag{12}$$

From Equation (12) it can be seen that horizontal friction force F_f, measurement coefficient λ, appearance density γ, and burial depth H all have an influence on the stress arch height. And the horizontal friction force at the arch foot is located in the coal pillar plastic zone (as shown in Figures 5 and 6), the stress value here is the biggest, and the plastic softening zone and plastic hardening zone of coal pillar are superimposed on the plastic zone formed by roadway surrounding rock of roadway, the extent of rock mass failure continues to increase over time, while the failure range of rock mass is within the height of the stress arch. Therefore, it is necessary to select the optimal supporting parameters to effectively and reasonably control the development of the damage zone.

3.2. Example Analysis of Test Roadway. In order to verify the above theoretical analysis, according to the actual occurrence of surrounding rock along the 17236 transport channel in Zhangjibei Coal Mine and the rock mechanical test results, the experimental result is arch span $S = 21.5$ m, mining depth $H = 653$ m, stress concentration factor $K = 2.8$ and measurement coefficient $\lambda = 0.3$, overlying rock capacity = 25 kN/m^3, overlying strata load P0 = 18 MPa, comprehensive cohesion $c0 = 1.8$ MPa, combined internal friction angle $\varphi^* = 25°$, and $\varphi^*{}_e = 20°$, $\varphi^*{}_{eu} = 19°$, $\varphi^*{}_{ed} = 22°$, $\varphi^*{}_{se} = 16°$, $\varphi^*{}_{su} = 15°$, and $\varphi^*{}_{sd} = 17°$, the above parameters are substituted into Equations (3)~(5), (7)~(8), (10), and (13) to obtain the partition width of gob-side entry and the stress arch height along the roadway.

3.3. Selection of Roadway Support Parameters. According to Table 1, it can be concluded that the fractured zone is 2.22 m, plastic softening zone is 2.39 m, and plastic hardening zone is 2.49 m of the coal column in the original support. The stress arch height is 10.738 m, and the thickness of the arch structure is 7.338 m. So, according to the relationship between the arch height of the stress arch and the size of the roadway, the length of the roadway anchor cable is 7.3 m, and it is proposed that the roadway is supported by anchor nets for the first time. The anchor bar is made of left-hand screw steel with length of 2500 mm, diameter of 20 mm, and the spans and rows are both 800 mm, metal mesh protects roadway's roof (5200 × 1000 mm), and metal mesh protects roadway's two side walls (3400 × 1000 mm). The secondary support uses ordinary anchor cable with a length of 7300 mm and diameter of 21.8 mm, and the spans are 1100 mm, and the rows are 800 mm, and grouting anchor cable with a length of 4300 mm, diameter of 22 mm, 17 anchors per row, and 7 anchor cables (two sides are grouting anchor cables) are arranged to suppress the expansion of deformation along the groove side of the track. Single-liquid cement slurry is used for consolidation grouting, with water-cement ratio of 0.6~0.8 : 1 and grouting pressure of 3~8 MPa; the support time node of pillars and roadway solid coal-side can be used as the optimal time for reinforcing roadways by grouting when the initial support roadway deformation is close to the threshold value. The roadway section support diagram is shown in Figure 8.

Table 1: Partition and stress arch height of coal pillar in transportation channel.

Partition category	Thickness/m
Fractured zone	2.22
Plastic softening zone	2.39
Width of coal slope failure zone	4.61
Plastic hardening zone	2.49
Width of limit equilibrium zone	7.1
Arch height (small structure height)	10.738

4. Rational Analysis of Supporting Structure Strength of Test Roadway

4.1. The Structural Strength of Theoretical Analysis. Because the stress area in the arch is mainly composed of the tension stress area of the anchor cable support and the compression stress area of the anchor bar-anchor cable and interacts with the surrounding rock to form the anchor composite bearing body to maintain the roadway stability, in order to verify the rationality of supporting parameters, the structural strength of anchor composite bearing stress arch should be analyzed, and the following assumptions are made in combination with the field geological data of 17236 island working-face:

(1) The surrounding rock of the roadway after support is isotropic and homogeneous, and the anchored composite bearing body is in the broken state of the surrounding rock

(2) The composite bearing structure is completely in contact with the external surrounding rock, and the external load is evenly distributed on the surface of the bearing body

(3) The surrounding rock of the roadway after support is the elastic-plastic medium, and the rock mass follows the Mohr-Coulomb strength criterion

Before the gob-side entry driving excavation, the surrounding rock was already in the nonisocompressive stress field. With the increasing excavation depth, the stress state of the nearby surrounding rock changes from three direction to two direction, and the shallow surrounding rock enters the crushing and plastic state. Through the initial reinforcement of the anchor rod, the anchor area and the surrounding rock combine to form. Before the roadway excavation, the surrounding rock is in the original rock stress field. With the increasing excavation depth, the stress state of the nearby surrounding rock changes from three direction to two direction, and the shallow surrounding rock enters the crushing and plastic state. Through the initial reinforcement of the anchor rod, the anchor anchoring area couples with the surrounding rock to form a secondary bearing layer, which plays a role in supporting the fractured surrounding rock. With the rapid growth of surrounding rock deformation, the surrounding rock is in tension or compression shear state due to the insufficient bolt support strength. When

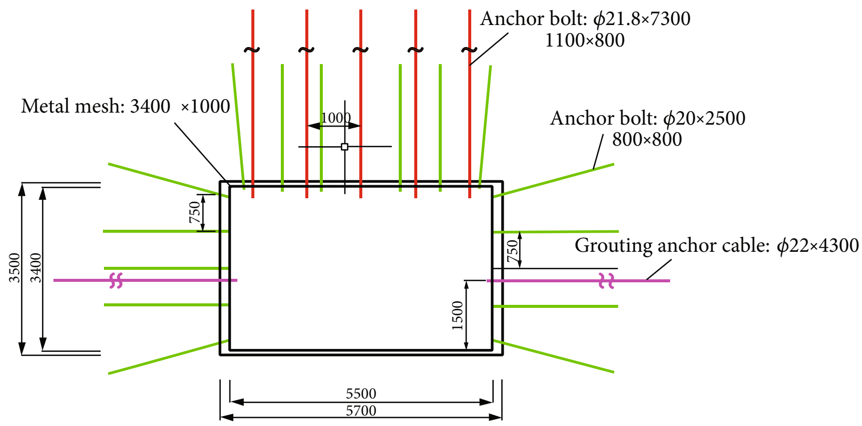

Figure 8: Diagram of roadway support section.

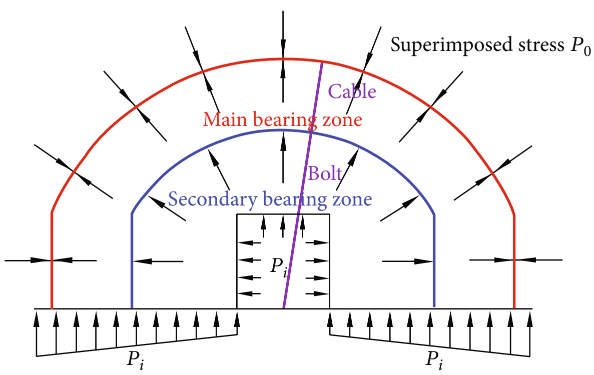

Figure 9: Mechanical model diagram of composite bearing stress arch structure.

the external load exceeds the bearing capacity, the crack initiation and breakthrough appear of the surrounding rock, the anchor structure tends to be broken, and the surrounding rock deformation energy is also released rapidly to inhibit the development of harmful deformation of surrounding rock. The deformation increases gradually, and the surrounding rock surface cracks and heaves, and then sloughs. At this time, the anchor cable can form a new bearing stress structure—main bearing structure in the deep surrounding rock of the roof. In the whole bearing stress structure, the secondary bearing layer formed by the anchor blot groups is connected with the deep surrounding rock through the suspension effect of the anchor cable, to enhance the support effect of the secondary bearing structure and also mobilize the bearing capacity of the main bearing layer, so as to control the deformation of the surrounding rock. The mechanical model diagram of composite bearing stress arch structure is shown in Figure 9.

According to the analysis of the above assumptions, under the limit equilibrium condition of the composite bearing stress arch structure, the surrounding rock after support still follows the Mohr-Coulomb criterion of strength:

$$\sigma_1 = \sigma_3 \frac{1 + \sin \varphi_b}{1 - \sin \varphi_b} + \frac{2c_b \cos \varphi_b}{1 - \sin \varphi_b}, \tag{13}$$

where σ_1, σ_3 is the maximum and minimum principal stress in surrounding rock (MPa); c_b is the cohesion of bearing structure (MPa); φ_b is the internal friction angle of bearing structure (°); therefore, the stress state of a certain point of surrounding rock in the bearing structure meets Equation (14), indicating that the bearing structure is in failure state at this time. Assuming that the surrounding rock stress in the bearing structure is equal to the support resistance, there can be $\sigma_3 = P$, and the support resistance P is:

$$P = {P_1}^* + {P_2}^* + {P_3}^* + {P_4}^*, \tag{14}$$

where P is the total support resistance (MPa) in support structure and the force in its structure is: ${P_1}^*$ is the primary support resistance of anchor bolt (MPa); ${P_2}^*$ is the secondary support resistance of common anchor cable (MPa); ${P_3}^*$ is the support resistance of metal mesh (MPa); ${P_4}^*$ is the support resistance of grouting anchor cable (MPa). By substituting the above formula into Equation (14):

$$\sigma_1 = \left({P_1}^* + {P_2}^* + {P_1}^* + {P_2}^*\right) \cdot \frac{1 + \sin \varphi_b}{1 - \sin \varphi_b} + \frac{2c_b \cos \varphi_b}{1 - \sin \varphi_b}. \tag{15}$$

It can be seen from the above formula that the support resistance affects the maximum principal stress σ_1, the support resistance increases with the principal stress σ_1 increase and become bigger. In order to consider the influence of support parameters on the composite bearing stress arch structure, the underground stress analysis of a certain point of surrounding rock in the bearing structure can be obtained from the static balance equation along the vertical direction of the roadway:

$$F_n = b\sigma_1 + \int_0^b F_{(x)} \mathrm{d}x, \tag{16}$$

where F_n is the bearing force on the arch structure with composite bearing stress (MPa); b is the thickness of composite bearing stress arch structure (m); $F_{(x)}$ is the vertical

Table 2: Physical and mechanical parameters of rock.

Lithology	Density	Bulk modulus (GPa)	Shear modulus (GPa)	Tensile strength (MPa)	Cohesion (MPa)	Friction angle (°)
Mudstone	2382	5.93	4.74	2.74	3.52	28
Sand mudstone	2447	6.68	5.27	3.58	3.2	27
Mudstone	2382	5.93	4.74	2.74	3.52	28
Coal line	1421	3.8	1.63	0.6	1.9	27
Sand mudstone	2312	5.3	4	2.4	2.8	25
Fine sandstone	2335	4.15	3.2	1.5	3.6	34
Sand mudstone	2270	4.76	3.85	1.35	2.5	21
6-coal	1390	4.33	1.77	0.8	1.8	25
Siltstone	2210	6.1	4.79	2.68	3.25	28
Coal line	1265	4.6	3.54	1.13	2.1	26
Siltstone	2286	6.38	5.6	3.26	4.5	31
M-granted sandstone	2080	5.4	4.1	1.89	4.7	35
Sand mudstone	2312	5.3	4	2.4	2.8	25

component function of the radial uniformly distributed load along the composite stress bearing arch structure, that is $F_{(x)} = kx$.

According to the simultaneous Equations (14) (16), the bearing force Fn outside the composite bearing stress arch is:

$$F_n = b\left[(P_1^* + P_2^* + P_1^* + P_2^*) \cdot \frac{1+\sin\varphi_b}{1-\sin\varphi_b} + \frac{2c_b\cos\varphi_b}{1-\sin\varphi_b}\right] + \frac{kb^2}{2}. \tag{17}$$

Assuming that the composite bearing stress arch is in the limit equilibrium state at this time, $F_n = P$, and considering the symmetry of the bearing arch, that is:

$$\begin{aligned} 2F_n &= \int_0^{\beta} qR\sin\gamma\, d\gamma - PB, \\ \beta &= 2\arcsin\left(\frac{(B/2)+b}{R}\right), \end{aligned} \tag{18}$$

where R is the outer boundary radius of composite bearing stress arch structure (m); β is the center angle differential element corresponding to the arc segment d_s.

$$q = \frac{2b[(P_1^* + P_2^* + P_1^* + P_2^*) \cdot (1+\sin\varphi_b/1-\sin\varphi_b) + (2c_b\cos\varphi_b/1-\sin\varphi_b)]}{R(1-\cos\beta)} + \frac{kb^2}{R(1-\cos\beta)} + \frac{PB}{R(1-\cos\beta)}. \tag{19}$$

Among them, the support strength of anchor bolt (anchor cable) is mainly through the axial action and the use of confining pressure to improve the peak strength and residual strength of surrounding rock, so as to enhance the support strength of rock mass in the anchorage zone.

Therefore, the relationship between the support resistance of anchor blot, anchor cable, and metal mesh and other support parameters [16] is as follows.

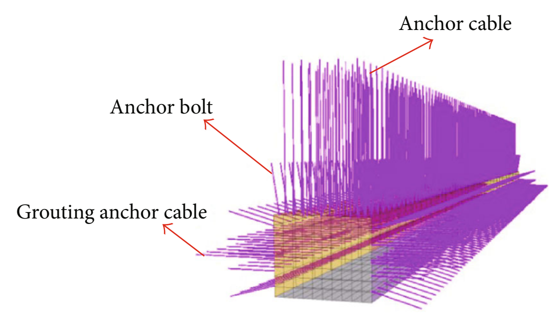

Figure 10: The support structures in numerical model.

The support resistance of anchor blot $P_1{}^*$ is:

$$P_1^* = \frac{P_1}{et}. \tag{20}$$

The support resistance of anchor cable $P_2{}^*$ is:

$$P_2^* = \frac{P_2}{e^* t^*}, \tag{21}$$

where P_1 and P_2 are the axial load of anchor blot and anchor cable (MPa). e and t are the spans and rows of anchor blot (m); e^* and t^* are the spans and rows of anchor cable (m).

The support resistance of metal mesh $P_3{}^*$ is:

$$P_3^* = \frac{2\tau_3 S_3}{2B\cos(\pi - 2\varphi_b/4)\beta_3}, \tag{22}$$

where τ_3 is the shear strength of the material (MPa); β_3 is the material shear angle (°); S_3 is the cross-sectional area of the metal mesh in the radial direction of the roadway (m^2).

The bearing strength of the composite bearing stress arch structure is obtained from the analysis of Equations (20)~(22), and the structural strength is calculated in combination with the indoor uniaxial compression test and the field geological conditions, The bearing strength of the composite bearing stress arch structure is obtained from the

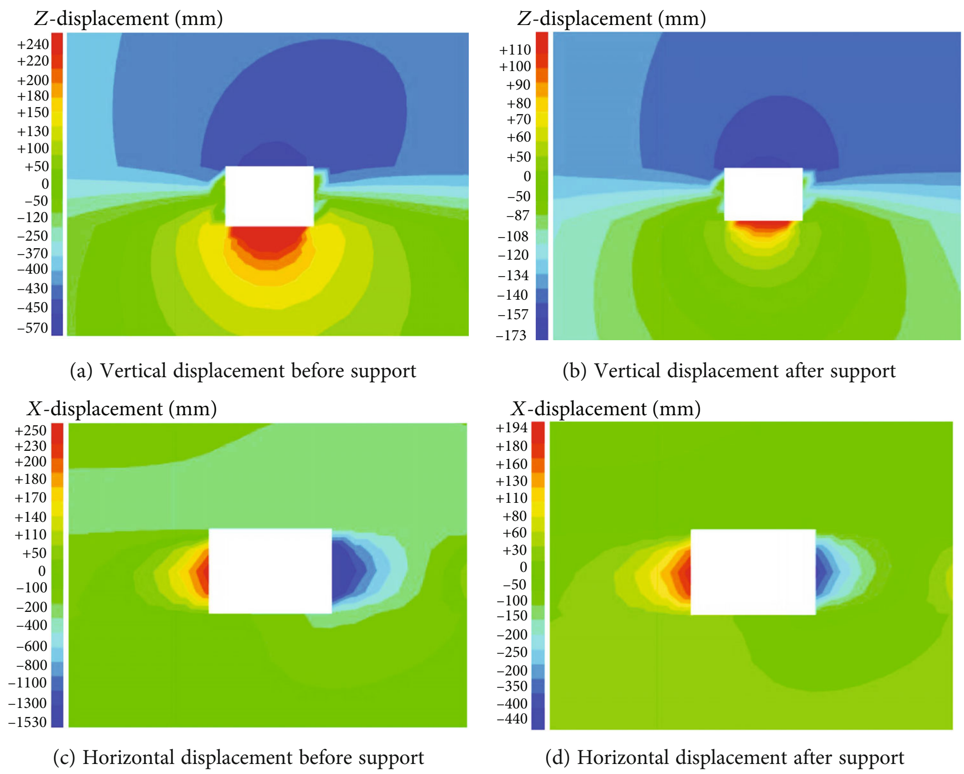

(a) Vertical displacement before support

(b) Vertical displacement after support

(c) Horizontal displacement before support

(d) Horizontal displacement after support

Figure 11: Displacement of roadway before and after support. (a) Vertical displacement before support. (b) Vertical displacement after support. (c) Horizontal displacement before support. (d) Horizontal displacement after support.

analysis of Equations (20)~(22), and the structural strength is calculated in combination with the indoor uniaxial compression test and the field geological conditions, through the calculation of each support structure, the total support resistance $P = 8.63$ MPa, the thickness B of the composite bearing stress arch structure is 7.338 m, the cohesion after support is 2.6 MPa, and the internal friction angle is 30°. By substituting the parameters of rock mass and bearing structure into the above formula, the ultimate bearing capacity of the composite bearing stress arch structure formed after 17236 transportation along the channel support in Zhangji north coal mine is $q = 29.193$ MPa, which is greater than the superimposed stress of 25 MPa, which proves that the composite bearing stress arch structure can maintain the stability of the roadway.

4.2. Numerical Simulation Verification. In order to better verify the reliability of the bolt-anchor cable stress distribution law in the theoretical analysis, the three-dimensional numerical simulation software FLAC3d is used to simulate and verify the geological conditions of the transportation channel in Zhangjibei Coal Mine. The physical and mechanical parameters of the roof and floor of the roadway are shown in Table 2. The surrounding rock is mainly composed of fine sandstone, argillaceous sandstone, and silt fine sandstone. A numerical simulation model is established by the simulation calculation software FLAC3D; the size of the numerical model in X direction, Y direction, and Z direction are 274 m, 300 m, and 100 m; the numerical simulation adopts the Mohr-Coulomb criterion; and the tunnel section

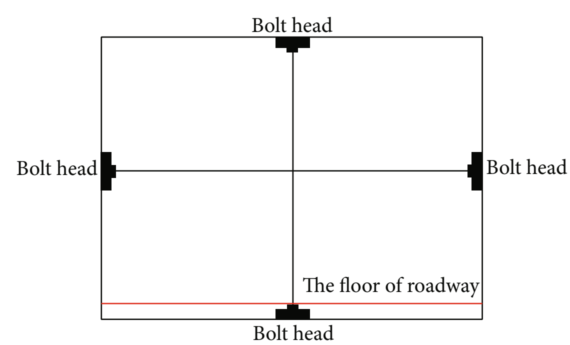

Figure 12: Full section monitoring points of haulage gateway.

Figure 13: Construction site diagram of roadway after support.

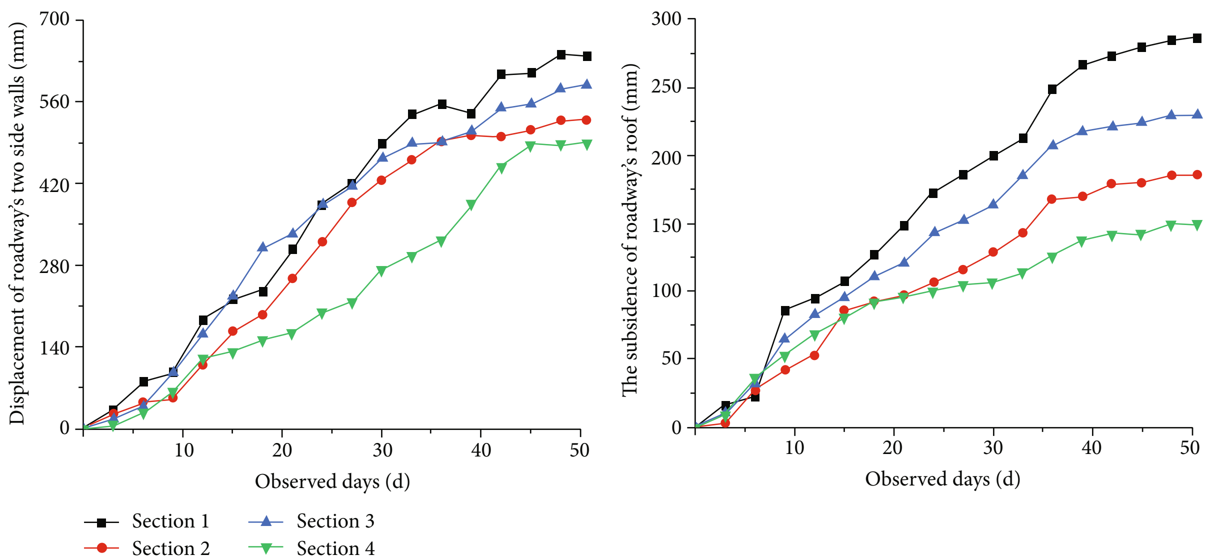

(a) Displacement of roadway's two side walls

(b) The subsidence of roadway's roof

Figure 14: Roadway surface displacement monitoring results.

is rectangular, with a height of 4 m and a width of 5 m. Since the simulated depth of the roadway is 630 m, the average density of the surrounding rock mass is 2500 kg/m^3. Therefore, the ground stress is 15.75 MPa. After the initial stress is balanced, after the working-face is excavated and stabilized, the actual parameters of the roadway are installed with bolts, ordinary anchor cables, and grouting anchor cables. The numerical model diagram of the supporting structure is shown in Figure 10.

The vertical and horizontal displacements of the roadway before and after the support are shown in Figure 11. Due to the influence of the composite stress field, the maximum subsidence of the roof before the support is 817 mm, the maximum displacement of the two sides is 1780 mm, and the bottom heave is seriously damaged. The vertical displacement of the surrounding rock at the two vertex corners exceeds 700 mm; the maximum subsidence of the top and bottom after support is 285 mm, and the displacement of the two sides is 640 mm. Comparing the effect before and after the support, the subsidence of the roof after the support is reduced by 80%, the maximum displacement of the two sides has been reduced by 65%. Therefore, it can be seen that the properties of the surrounding rock are improved after the support, and the overall strength of the surrounding rock is increased as a whole, which effectively suppresses the deformation of the two sides of the roadway and is beneficial to the stability of the surrounding rock of the roadway.

5. Industrial Test

Because it is found that the effect of supporting haulage gateway is good, and in order to analyze the deformation law of surrounding rock and verify the rationality of composite bearing stress arch structure theory, relevant industrial tests are carried out. The roadway monitoring arrangement is "cross-point method," which means that anchor measuring points are buried on two-sides and the roof and floor of the roadway, and the distance change between the two points is measured by monitoring equipment. The comprehensive monitoring station (30 m away from each monitoring station) is arranged at 200 m from the opening of the transportation chute to observe the convergence deformation of the surrounding rock. It is found that the support effect is good, and the deformation of the surrounding rock of the roadway is effectively controlled. The layout of the monitoring points is shown in Figure 12, and construction site diagram of roadway after support is shown in Figure 13.

As shown in Figure 14 that the roadway deformation and surface displacement after support are observed for 36 days, and a total of 4 monitoring points (no. 1#, 2#, 3#, and 4#) are carried out, each data collection is carried out after mining; among them, the maximum convergence deformation of the two side walls of the roadway is 640 mm, and the maximum convergence deformation of the roof and floor of the roadway is 287 mm, and the initial deformation increases and gradually tends to be stable after reaching the maximum value. After the roadway is supported by anchor bolt and anchor cable, the integrity of surrounding rock is strengthened, the bulge of roadway side is effectively controlled, and the control effect of steel beam on roof is not obvious. It shows that the anchor bolt and anchor cable support parameters are reasonable, the surrounding rock control is remarkable, and the support system is good.

6. Conclusions

(1) With the collapse stability of working-face, after roadway excavation, the narrow coal pillar can be divided into three failure zones: fractured zone, plastic softening zone, and plastic hardening zone. A small structural stress arch mechanical model based on arch axis is established. Through the analysis of theoretical mechanical model and field actual

conditions, it is found that reasonable support methods can be selected to control the development of roadway plastic failure zone

(2) According to the site geological conditions, the stress arch height of the small structure of the surrounding rock of the transportation channel is determined to be 10.738 m, and the length of the anchor cable is determined to be 7.3 m according to the relationship between the stress arch height and the roadway size, and the twice support technology is selected to ensure the stability of the roadway. Among them, the anchor mesh support is used for the primary support, and the ordinary long anchor cable and grouting anchor cable are used for the secondary support

(3) In order to verify the rationality of the support parameters and the strength of the composite bearing stress arch structure, a mechanical model of the composite bearing stress arch structure of surrounding rock is proposed. The elastic-plastic mechanics is used to deduce the composite bearing stress arch structure, and the expression of the relationship between the ultimate bearing strength is obtained. After the transportation channel support of 17236 island working-face in the north of Zhangji coal mine is calculated, the support resistance of the support structure reaches 8.36 MPa. The ultimate bearing capacity of the bearing structure can reach 29.193 MPa

(4) The field monitoring results show that after the support of composite bearing stress arch structure, the deformation area of surrounding rock along the transportation channel is stable, the maximum shrinkage of roadway top and bottom is 287 mm, and the displacement of two sides is 640 mm. With the increase of monitoring time, the deformation is gradually stable, which is conducive to the long-term stability of the transportation channel

Data Availability

The data used to support the findings of this study are available from the corresponding author upon request.

Conflicts of Interest

The authors declare that there are no conflicts of interest regarding the publication of this paper.

Acknowledgments

This research was supported by the National Natural Science Foundation of China (nos. 51874002 and 52174102), China Scholarship Council (no. 202108340064), and Natural Science Foundation of Heilongjiang Province (no. LH2019E087).

References

[1] M. C. He, H. P. Xie, S. P. Peng, S. P. Peng, and Y. D. Jiang, "Study on rock mechanics in deep mining engineering," *Chinese Journal of Rock Mechanics and Engineering*, vol. 24, no. 16, pp. 2803–2813, 2005.

[2] G. Wu, W. J. Yu, J. Zuo, and S. Du, "Experimental and theoretical investigation on mechanisms performance of the rock-coal-bolt (RCB) composite system," *International Journal of Mining Science and Technology*, vol. 30, no. 6, pp. 759–768, 2020.

[3] J. H. Xue and Q. S. Liu, "Surrounding rock stability control theory and support technique in deep rock roadway for coal mine," *Journal of the China Coal Society*, vol. 36, no. 4, pp. 535–543, 2011.

[4] J. B. Bai, W. L. Shen, G. L. Guo, X. Y. Wang, and Y. Yu, "Roof deformation, failure characteristics, and preventive techniques of gob-side entry driving heading adjacent to the advancing working face," *Rock Mechanics and Rock Engineering*, vol. 48, no. 6, pp. 2447–2458, 2015.

[5] M. Wang, J. B. Bai, X. Y. Wang, Y. Xu, Y. H. Guo, and J. L. Cao, "The surrounding rock deformation rule and control technique of the roadway driven along goaf and heading for adjacent advancing coal face (in Chinese)," *Mining Safety Engineering*, vol. 29, pp. 197–202, 2012.

[6] J. M. Xi, J. H. Mao, G. S. Yang, and J. F. Wang, "Method for determining rational pillar width in mining roadway along working-face," *Mining Safety Engineering*, vol. 25, no. 4, pp. 400–4003, 2008.

[7] F. K. Qi, Y. J. Zhou, Z. H. Cao, Q. Zhang, and N. Li, "Width optimization of narrow coal pillar of roadway driving along working-face in fully mechanized top coal caving face," *Mining Safety Engineering*, vol. 33, no. 3, pp. 475–480, 2016.

[8] J. P. Yang, "Rational width of narrow coal pillar and control technology of surrounding strata at roadway driven along working-face," *Journal of Liaoning Technical University: Natural Science*, vol. 32, no. 1, pp. 39–43, 2013.

[9] M. S. Gao, N. Zhang, and L. Cheng, "The reasonable coal pillar width determined of roadway driving along working-face," *Mine Press Ceil Manage*, vol. 3, pp. 4–7, 2004.

[10] J. Wang, H. Huang, X. Xie, and B. Antonio, "Void-induced liner deformation and stress redistribution," *Tunnelling and Underground Space Technology*, vol. 40, pp. 263–276, 2014.

[11] S. Zhang, X. Wang, G. Fan, D. Zhang, and C. Jianbin, "Pillar size optimization design of isolated island panel gob-side entry driving in deep inclined coal seam——case study of Pingmei no. 6 coal seam," *Journal of Geophysics and Engineering*, vol. 15, no. 3, pp. 816–828, 2018.

[12] Y. Ma and S. Zhong, "Study on the relationship between hydraulic support on the working face with large mining height and surrounding rock," *Advanced Materials Research*, vol. 328-330, pp. 1671–1674, 2011.

[13] C. J. Hou and X. H. Li, "Stability principle of big and small structures of rock surrounding roadway driven along working-face in fully mechanized top coal caving face," *Journal of China Coal Society*, vol. 26, 2001.

[14] R. Yang, Y. Li, D. Guo, L. Yao, T. Yang, and T. Li, "Failure mechanism and control technology of water-immersed roadway in high- stress and soft rock in a deep mine," *International Journal of Mining Science and Technology*, vol. 27, no. 2, pp. 245–252, 2017.

[15] W. Wu, H. Zhu, J. S. Lin, X. Zhuang, and G. Ma, "Tunnel stability assessment by 3D DDA-key block analysis," *Tunnelling & Underground Space Technology*, vol. 71, pp. 210–214, 2018.

[16] N. Zhang, L. Yuan, C. Han, J. Xue, and J. Kan, "Stability and deformation of surrounding rock in pillarless gob-side entry retaining," *Safety Science*, vol. 50, no. 4, pp. 593–599, 2012.

[17] Y. F. Li and X. Z. Hua, "Mechanical analysis of stability of key blocks of overlying strata for gob-side entry retaining and calculating width of roadside backfill," *Rock and Soil Mechanics*, vol. 33, no. 4, pp. 1134–1140, 2012.

[18] M. S. Zhao, K. M. Wei, Z. K. Wen, and Y. L. Fang, "Study on the response of surrounding rock for gob-side entry retaining under the mining," *Applied Mechanics & Materials*, vol. 448, pp. 3879–3883, 2013.

[19] C. Q. Zhu, X. X. Miao, and Z. Liu, "Mechanical analysis on deformation of surrounding rock with road-in packing of gob-side entry retaining in fully-mechanized sub-level caving face," *Journal of Coal Science and Engineering (China)*, vol. 14, no. 1, pp. 24–28, 2008.

[20] Z. J. Wen, M. Rinne, Z. Z. Han, Z. Song, and Y. K. Shi, "Structure model of roadway with big deformation and its basic research into engineering theories," *Tehnicki Vjesnik*, vol. 21, no. 5, pp. 1065–1071, 2014.

[21] Q. Ma, Y. Tan, Z. Zhao, Q. Xu, J. Wang, and K. Ding, "Roadside support schemes numerical simulation and field monitoring of gob-side entry retaining in soft floor and hard roof," *Arabian Journal of Geosciences*, vol. 11, no. 18, pp. 1–13, 2018.

[22] S. Xie, E. Wang, D. Chen et al., "Failure analysis and control mechanism of gob-side entry retention with a 1.7-m flexible-formwork concrete wall: a case study," *Engineering Failure Analysis*, vol. 117, p. 104816, 2020.

[23] P. Yang, *Evolution Characteristics of Surrounding Rock Deformation of Gob-Side Entry Retaining in Deep Mine and Its Control Measures*, Anhui University of Science and Technology, 2018.

[24] L. Xuehua, *Surrounding Rock Stability Control Principle and Technology of Gob Side Entry Driving in Fully Mechanized Top Coal Caving*, China University of mining and Technology Press, 2008.

[25] B. Jianbiao, *Surrounding Rock Control of Gob Side Entry Driving*, China University of mining and Technology Press, 2006.

[26] H. Chaojiong and L. Xuehua, "Stability principle of big and small structures of rock surrounding roadway driven along working-face in fully mechanized top coal caving face," *China Coal Society*, vol. 26, pp. 1–6, 2001.

[27] W. Q. Xu, E. Y. Wang, R. X. Shen, D. Z. Song, and J. M. Zhang, "Distribution pattern of front abutment pressure of fully-mechanized working face of soft coal isolated island," *International Journal of Mining Science and Technology*, vol. 22, no. 2, pp. 279–284, 2012.

[28] W. J. Yu, G. S. Wu, B. An, and P. Wang, "Experimental study on the brittle-ductile response of a heterogeneous soft coal rock mass under multifactor coupling," *Geofluids*, vol. 2019, 15 pages, 2019.

[29] A. J. Das, P. K. Mandal, C. N. Ghosh, and A. Sinha, "Extraction of locked-up coal by strengthening of rib pillars with FRP - a comparative study through numerical modelling," *Mining Science and Technology*, vol. 27, no. 2, pp. 261–267, 2017.

[30] W. Li, J. Bai, S. Peng, X. Wang, and Y. Xu, "Numerical modeling for yield pillar design: a case study," *Rock Mechanics and Rock Engineering*, vol. 48, no. 1, pp. 305–318, 2015.

[31] M. C. He, H. S. Yuan, and H. W. Jing, *Theory and Practice of Bolt Supporting of Coal Mines in China*, Science Press, Beijing, 2004.

[32] Y. Zang, Z. J. Wan, F. C. Li et al., "Stability of coal pillar in gob-side entry driving under unstable overlying strata and its coupling support control technique," *International Journal of Mining Science and Technology*, vol. 23, no. 2, pp. 193–199, 2013.

[33] J. P. Zhang, L. M. Liu, J. Shao, and Q. H. Li, "Mechanical properties and application of right-hand rolling-thread steel bolt in deep and high-stress roadway," *Metals (Basel)*, vol. 9, no. 3, p. 346, 2019.

[34] G. X. Xie, J. Z. Li, L. Wang, and Y. Z. Tang, "Mechanical characteristics and time and space evolvement of stress shell in stope floor stratum," *Journal of the China Coal Society*, vol. 43, pp. 52–61, 2018.

[35] R. Pan, Q. Wang, B. Jiang et al., "Failure of bolt support and experimental study on the parameters of bolt- grouting for supporting the roadways in deep coal seam," *Engineering Failure Analysis*, vol. 80, pp. 218–233, 2017.

[36] X. X. Zhai, G. S. Huang, C. Y. Chen, and R. B. Li, "Combined supporting technology with bolt-grouting and floor pressure-relief for deep chamber: an underground coal mine case study," *Energies*, vol. 11, no. 1, p. 67, 2018.

[37] F. Xiao, G. Liu, Z. Zhang, Z. Shen, F. Zhang, and Y. Wang, "Acoustic emission characteristics and stress release rate of coal samples in different dynamic destruction time," *Mining Science and Technology*, vol. 26, no. 6, pp. 981–988, 2016.

Hindawi
Geofluids
Volume 2022, Article ID 6307522, 15 pages
https://doi.org/10.1155/2022/6307522

Research Article

Roof-Breaking Characteristics and Ground Pressure Behavior in Deep Jurassic Coal Seams: A Thick-Plate Model and Field Measurements

Wei Zhang,[1,2] Yandong Zhang ,[2] Weisheng Zhang,[3] Liang Chen,[1,2] Fanjia Li,[4] and Kaidi Xie[2]

[1]*State Key Laboratory of Coal Resources and Safe Mining, China University of Mining and Technology, Xuzhou 221116, China*
[2]*School of Mines, China University of Mining and Technology, Xuzhou 221116, China*
[3]*Zhengzhou Coal Mining Machinery Group Co., Ltd, Zhengzhou 450016, China*
[4]*School of Information and Control Engineering, China University of Mining and Technology, Xuzhou 221116, China*

Correspondence should be addressed to Yandong Zhang; zhangyandong@cumt.edu.cn

Received 29 July 2021; Accepted 17 September 2021; Published 23 June 2022

Academic Editor: Hualei Zhang

Roof-breaking characteristics and ground pressure behavior of the coalface are instrumental in guiding deep Jurassic coal seam mining, in particular in the Shaanxi and Inner Mongolia regions of China. A thick-plate mechanical model (TPMM) of the main roof was developed and applied to the case study of 21102 first-mined coalface (FMC) of the Hulusu Coal Mine (HCM) in the Hujirt Mining Area (HMA), China. A theoretical analysis performed via the developed model revealed that the first and periodic breaking intervals of the main roof were 40.6 and 25.0 m, respectively. The roof failure occurred in the tensile mode, was controlled by the internal stress σ_x in the rock strata, and started from the center of the long side with the fixed support in the goaf. The field measurement of roof weighting was also performed for the coalface advance from zero to 400 m. The measurement results showed that the first weighting average interval was 41.4 m, and the average interval of periodic weighting was 22.0 m, which agreed with the theoretical calculation and proved the proposed model's feasibility. Finally, the frequency distribution features of the hydraulic support working resistance in the FMC were analyzed statistically. The results showed that the ZY10000-16/32D supports could adapt to the mining geological conditions of the FMC. However, the margin of the rated working resistance of supports was still small. Thus, roof management enhancement during the mining process was strongly recommended. These research findings could offer theoretical guidance for safe and high-efficiency production in the coal mines under similar geological conditions.

1. Introduction

In recent years, the development of coal resources in China has rapidly shifted to Northwestern China, especially the Inner Mongolia Autonomous Region [1]. From January to December 2020, China's northwestern coal mining areas accounted for about 70% of the total national coal output and became a forepost of China's coal industry upgrading [2–5]. A good example is the Ordos City in the Inner Mongolia Autonomous Region, in which coal production in 2018, 2019, and 2020 amounted to 616, 679, and 640 million tons, respectively.

The Dongsheng Coalfield in the Ordos City extends for about 100 km in the north-south direction and has the largest width in the east-west direction of 100 km, covering an area of about 8790 km^2 [6, 7]. The main coal-bearing seams in the Dongsheng Coalfield belong to the Middle Jurassic Yanan Formation, which lithology consists primarily of medium sandstone, siltstone, mudstone, and coal seam [8]. The coal seam's burial depth generally drops from north to south but increases from east to west. The coal seams mined at an early stage are generally typical shallow-buried (below 300 m) with simple geological conditions, which have been investigated theoretically and subjected to field studies. Abundant reports have been published concerning roof-breaking characteristics, mining-induced fissure development, and ground pressure behavior [9–18]. These findings lay a theoretical foundation and offer ready technologies for the safe and high-efficiency mining of shallow-buried coal seams at an early stage. However, due to the variabilities of the burial depth of the coal seam and strata structure, the first-mined coal seams in some newly developed large-scale coal bases in the Dongsheng Coalfield have already entered the stage of deep mining [19]. One example of this is the HMA, a state planning mining area located in the midwestern part of the Dongsheng Coalfield. The main coal seams in the HMA are #2 and #3 coal seams in the upper Jurassic Yanan Formation, with a depth above 600 m. The available roof-breaking characteristics and ground pressure behavior in mining shallow-buried coal seams can no longer offer guidance for deep coal resource development in this region. It is necessary to carry out in-depth investigations into the occurrence conditions of the Jurassic deep-buried coal seam in this mining area.

The HMA is located on the border of Inner Mongolia and Shaanxi. The total planning area is about 2161 km^2. According to preliminary planning, this mining area is subdivided into seven mine fields, two exploration areas, and one prospective area. The total planning area is 63 Mt/a. HCM, located in the mid-southern part of the mining area, is one of the first developed in this region and has a design production capacity of 13.0 Mt/a. The burial depth of the mined coal seam is 650-900 m. The HCM is a typical newly built deep coal mine in Inner Mongolia and Shaanxi. The increased mining scope was accompanied by a series of problems: large intensity of overburdened rock activities in the stope, intense ground pressure at the coalface, and large deformation of the roadway-surrounding rocks [20]. However, there are only a few studies on roof breaking and ground pressure in this mining area [21–25].

Given this, we elaborated a TPMM for the main roof breakage in the 21102 FMC of the HCM in the HMA under the actual geological conditions. A theoretical analysis of the main roof's first and periodic breaking was performed using the established model. On this basis, we conducted a field measurement to study ground pressure behavior at the FMC. The applicability of the hydraulic supports used for this FMC was evaluated. Our research findings offer theoretical guidance for the normal mining of other coalfaces in the HCM. Moreover, these results can be utilized to guide the safe and high-efficiency coal production under similar geological conditions in the HMA.

2. Mining Technical Conditions for the FMC

The 21102 coalface of the HCM, the FMC in the entire mine field, is located in the first panel of the #2-1 coal seam. There are three roadways on the east wing of the mine north of the coalface. In the south, there is the fifth panel of the coal seam. The length of the coalface along the dip direction is 320 m, and that along the strike direction is 4150 m. The stoping area is 1,327,900 m^2. The ground surface above the coalface is hilly sand land, with an elevation of +1304 to +1328 m. The elevation of the underground coal seam roof is +673 to +694 m. The burial depth of the coalface is 626.17 to 647.91 m. The coalface under study is a typical deep-lying coalface in this region. The coal seam mined in the coalface is the #2-1 coal seam of the Jurassic Yanan Formation, with a density of about 1.31 t/m^3. The coal seam thickness is 1.7-3.0 m, with an average of 2.55 m, indicating a medium thickness. The coal seam is of a simple structure with slight undulation and a dip angle of 1°-3°. This coal seam is near-horizontal.

The geological structure of this coalface is also simple. The false roof of the coal seam is mainly composed of sandy mudstone, with a thickness of 0.2-0.5 m. The immediate roof comprises sandy mudstone and silty sandstone, with a thickness of 2.43-7.8 m. The main roof is composed of fine sandstone and medium sandstone, with a thickness of 13.30-23.3 m. The immediate floor comprises sandy mudstone and silty sandstone, with a thickness of 3.4-8.9 m. The stratigraphic synthesis column of the study area is shown in Figure 1. In this coalface, the full-thickness longwall mining method along the strike (with an average mining height of 2.55 m) is performed. The goaf roof is managed by using the full caving method. The hydraulic supports used in the coalface are ZY10000-16/32D two-column shield-type hydraulic supports manufactured by China Coal Beijing Coal Mining Machinery Co., Ltd. The rated working resistance of the supports is 10,000 kN, and the distance between the centers of the two supports is 1.75 m.

3. Mechanical Analysis of Breaking Characteristics of the Thick Sandstone Main Roof in the FMC

A goaf is formed along with the constant advance of the coalface from the open-off cut. The first breaking and weighting of the main roof occur when the roof overhang is too big. As the coalface continues to advance after the first breaking, the periodic weighting of the main roof occurs. Since the main roof of the FMC is composed of hard thick sandstone, the conventional beam model may not apply to the theoretical analysis of the roof-breaking characteristics [26]. According to the field measurement of ground pressure in the deep-buried mine near the HCM, we considered the influence of internal transverse shear stress of the plate based on the judgment criteria of the plate model. We developed the Reissner thick-plate model for the breaking of the thick sandstone main roof and performed a theoretical analysis of stress distribution in the main roof at different mining stages in the coalface. The inducing factors of the first and periodic breaking of the main roof were determined. The first and periodic weighting intervals were calculated for this coalface.

3.1. Establishment of the TPMM for Main Roof Breaking. Since the 21102 coalface is the FMC, the main roof can be simplified into a thick rectangular plate that has fixed support on the four sides upon the moment of the first breaking. Under this assumption, we built the TPMM for the first breaking of the main roof, as shown in Figure 2(a). After the first breaking of the main roof, broken rock masses in the goaf form a three-hinged arch. At this moment, the main roof can be reduced to a thick rectangular plate with simple support on one side and fixed support on the other three sides. Thus, the TPMM for periodic breaking of the main roof was

Overlying strata	Thickness (m)	Depth (m)	Lithology
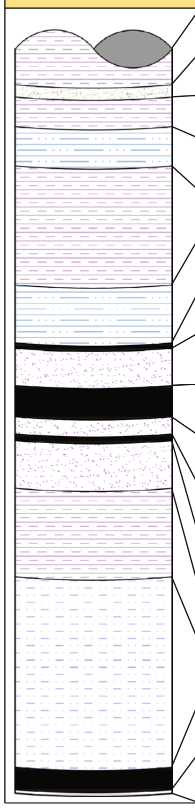	4.50	603.40	Sandy mudstone
	1.30	604.70	Silty sandstone
	2.60	607.30	Sandy mudstone
	3.70	611.00	Fine sandstone
	10.70	621.70	Sandy mudstone
	5.34	627.04	Fine sandstone
	0.30	627.34	Coal seam
	3.46	630.80	Silty sandstone
	2.90	633.70	#2-1 coal seam
	0.70	634.40	Silty sandstone
	0.50	634.90	Coal seam
	5.30	640.20	Silty sandstone
	7.50	647.70	Sandy mudstone
	17.80	665.50	Medium sandstone
	2.00	667.50	Coal seam
	0.30	667.80	Sandy mudstone

Figure 1: The stratigraphic synthesis column of study area.

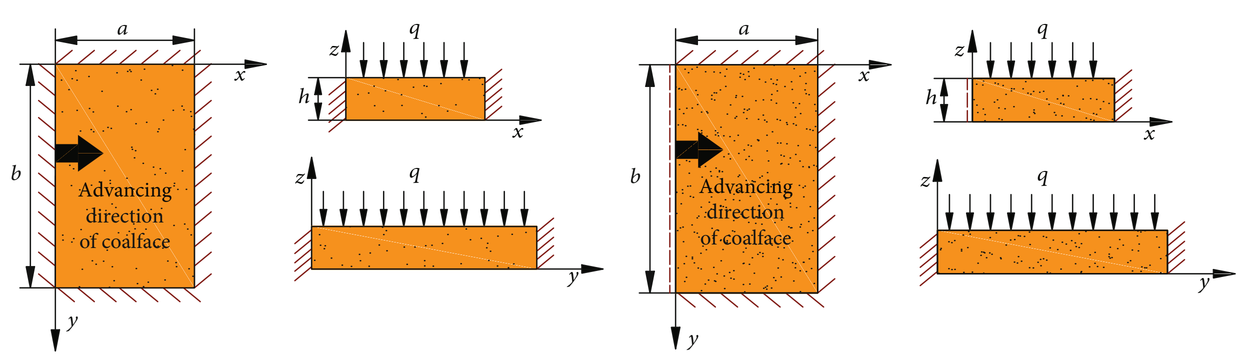

Figure 2: TPMM of the main roof breaking: (a) first breaking model and (b) periodic breaking model.

built, as shown in Figure 2(b), where a and b are the short and long sides of the thick rectangular plate, respectively; h is its thickness; and q is the load acting on the upper part of the thick rectangular plate.

According to the Reissner plate theory, the basic equations can be written as follows [27–29]:

$$D\nabla^2\nabla^2\omega = q(x, y) - \frac{(2-\mu)}{(1-\mu)}\frac{h^2}{10}\nabla^2 q(x, y), \tag{1}$$

$$\nabla^2\phi - \frac{10}{h^2}\phi = 0, \tag{2}$$

where D is the bending stiffness of the main roof, $D = Eh^3/[12(1-\mu^2)]$ (N·m), E is the elastic modulus of the main roof (GPa), ω is the deflection of the main roof (m), ∇ is the Laplace operator, $q(x, y)$ is the loading acting on the upper part of the main roof (MPa), μ is Poisson's ratio of the main roof, h is the main roof thickness (m), and φ is the stress function within the main roof.

The expressions of the shear stress Q and the bending moment M for the main roof can be derived as follows:

$$Q_x = -D\frac{\partial}{\partial x}\nabla^2\omega - \frac{(2-\mu)}{(1-\mu)}\frac{h^2}{10}\frac{\partial q}{\partial x} + \frac{\partial \phi}{\partial y}, \quad (3)$$

$$Q_y = -D\frac{\partial}{\partial y}\nabla^2\omega - \frac{(2-\mu)}{(1-\mu)}\frac{h^2}{10}\frac{\partial q}{\partial y} + \frac{\partial \phi}{\partial x}, \quad (4)$$

$$M_x = -D\left(\frac{\partial^2\omega}{\partial x^2} + \mu\frac{\partial^2\omega}{\partial y^2}\right) + \frac{h^2}{5}\frac{\partial Q_x}{\partial x} - \frac{\mu}{1-\mu}\frac{qh^2}{10}, \quad (5)$$

$$M_y = -D\left(\frac{\partial^2\omega}{\partial y^2} + \mu\frac{\partial^2\omega}{\partial x^2}\right) + \frac{h^2}{5}\frac{\partial Q_y}{\partial y} - \frac{\mu}{1-\mu}\frac{qh^2}{10}. \quad (6)$$

3.2. *Mechanical Analysis of the First Breaking Characteristics of the Main Roof*

3.2.1. A Theoretical Analysis of the Mechanical Model Describing the First Breaking of the Main Roof. The governing equations for the fixed support of the four sides before the first breaking of the main roof in the FMC have the following forms:

$$\begin{cases} \omega\big|_{x=0,x=a} = 0, \\ \dfrac{\partial\omega}{\partial x}\Big|_{x=0,x=a} = 0, \\ \omega\big|_{y=0,y=b} = 0, \\ \dfrac{\partial\omega}{\partial y}\Big|_{y=0,y=b} = 0. \end{cases} \quad (7)$$

Using the fixed support boundary conditions for the four sides of the main roof, the following deflection equation that satisfied the boundary conditions was derived:

$$\omega = c\left(x^2 - ax\right)^2\left(y^2 - by\right)^2. \quad (8)$$

Substituting Equation (8) and q_0 (the uniformly distributed load applied to the upper part of the main roof) into Equation (1), we can calculate the coefficient c by the Matlab software program:

$$c = \frac{49q_0}{8D\left(7a^4 + 4a^2b^2 + 7b^4\right)}. \quad (9)$$

Substituting Equation (9) into Equation (8), we obtain the deflection function under the fixed support boundary conditions for the four sides of the main roof:

$$\omega = \frac{49q_0\left(x^2 - ax\right)^2\left(y^2 - by\right)^2}{8D\left(7a^4 + 4a^2b^2 + 7b^4\right)}. \quad (10)$$

Substituting Equation (10) into Equations (3)–(6), the shear stress function and the bending moment function of the main roof are derived as follows:

$$\begin{aligned}
Q_x &= 2k\left[(6x-3a)\left(y^2-by\right)^2 + \left(x^2-ax\right)(2x-a)\left(6y^2-6by+b^2\right)\right],\\
Q_y &= 2k\left[(6y-3b)\left(x^2-ax\right)^2 + \left(y^2-by\right)(2y-b)\left(6x^2-6ax+a^2\right)\right],\\
M_x &= k\left\{\left(y^2-by\right)^2\left(6x^2-6ax+a^2+\frac{12}{5}h^2\right) + \left(6y^2-6by+b^2\right)\right.\\
&\quad\left.\cdot\left[\mu\left(x^2-ax\right)^2 + \frac{2h^2\left(6x^2-6ax+a^2\right)}{5}\right]\right\} - \frac{\mu q_0 h^2}{10(1-\mu)},\\
M_y &= k\left\{\left(x^2-ax\right)^2\left(6y^2-6by+b^2+\frac{12}{5}h^2\right) + \left(6x^2-6ax+a^2\right)\right.\\
&\quad\left.\cdot\left[\mu\left(y^2-by\right)^2 + \frac{2h^2\left(6y^2-6by+b^2\right)}{5}\right]\right\} - \frac{\mu q_0 h^2}{10(1-\mu)},
\end{aligned} \quad (11)$$

where $k = -49q_0/4(7a^4 + 4a^2b^2 + 7b^4)$.

According to the theory of elasticity and thick-plate theory, the stress σ in the main roof is related to the bending moment M as $\sigma = 6M/h^2$. From this, we can derive the stress function of the main roof:

$$\begin{aligned}
\sigma_x &= \frac{6k}{h^2}\left\{\left(y^2-by\right)^2\left(6x^2-6ax+a^2+\frac{12}{5}h^2\right) + \left(6y^2-6by+b^2\right)\right.\\
&\quad\left.\cdot\left[\mu\left(x^2-ax\right)^2 + \frac{2h^2\left(6x^2-6ax+a^2\right)}{5}\right]\right\} - \frac{3\mu q_0}{5(1-\mu)},\\
\sigma_y &= \frac{6k}{h^2}\left\{\left(x^2-ax\right)^2\left(6y^2-6by+b^2+\frac{12}{5}h^2\right) + \left(6x^2-6ax+a^2\right)\right.\\
&\quad\left.\cdot\left[\mu\left(y^2-by\right)^2 + \frac{2h^2\left(6y^2-6by+b^2\right)}{5}\right]\right\} - \frac{3\mu q_0}{5(1-\mu)}.
\end{aligned} \quad (12)$$

3.2.2. First Breaking Interval of the Main Roof and Its Mechanical Characteristics. According to the stress function calculated in Section 3.2.1, at $(x, y) = (0, b/2)$ and $(x, y) = (a, b/2)$, both σ_x and σ_y reach their peak negative values (that is, $\sigma_{x\ max}$ and $\sigma_{y\ max}$ are tensile stresses, $\sigma_{x\ max} > \sigma_{y\ max}$). Both are located at the centers of the long sides in the TPMM. $\sigma_{x\ max}$ and $\sigma_{y\ max}$ are given, respectively, as follows:

$$\begin{aligned}
\sigma_{x\ max} &= \frac{6k}{h^2}\left[\frac{b^4}{16}\left(a^2 + \frac{12}{5}h^2\right) - \frac{1}{5}a^2b^2h^2\right] - \frac{3\mu q_0}{5(1-\mu)},\\
\sigma_{y\ max} &= \frac{6k}{h^2}\left(\frac{1}{16}\mu a^2b^4 - \frac{1}{5}a^2b^2h^2\right) - \frac{3\mu q_0}{5(1-\mu)}.
\end{aligned} \quad (13)$$

If $\sigma_{x\ max}$ in the main roof reaches the tensile strength R_T (i.e.,$\sigma_{x\ max} = R_T$), the long side with fixed support in the TPMM undergoes the first tensile failure. According to the geological conditions for the FMC, the basic parameters R_T = 4.24 MPa, h = 13.3 m, q_0 = 0.554 MPa, μ = 0.22, and b =

320 m are substituted into the above formulas to estimate the first breaking interval of the main roof as $a = 40.6$ m.

Below, we analyze the mechanical characteristics of the main roof upon first weighting in the FMC by plotting the deflection and stress distribution of the main roof upon the first breaking using the Matlab software program based on the parameters calculated above. The results are shown in Figures 3–5.

As shown in Figure 3, the deflection of the main roof under fixed support on the four sides had a symmetric distribution about the goaf center. The largest deflection occurred in the center, and the deflection decreased gradually towards the periphery. The largest defection at the center of the goaf $(a/2, b/2)$ reached 1.25 mm.

As shown in Figure 4, the stress σ_x in the main roof under the condition of fixed support on the four sides had an axisymmetric distribution about the goaf center with coordinates $(a/2, b/2)$, where the stress σ_x in the main roof reached its maximum ($\sigma_{x\ \max} = 0.7$ MPa), indicating the largest compressive stress at this position. At the centers of the two long sides in the goaf, that is, at $(0, b/2)$ and $(a, b/2)$, the stress σ_x in the main roof reached the peak negative value ($\sigma_{x\ \max} = 4.24$ MPa), indicating the largest tensile stress in this position. Besides, the tensile stress σ_x already reached the ultimate tensile strength of the main roof. Therefore, tensile failure of the main roof occurred at the centers of the goaf's long sides.

As shown in Figure 5, stresses σ_y and σ_x in the main roof under the boundary condition of fixed support on four sides also had an axisymmetric distribution about the goaf center. At the center of the goaf $(a/2, b/2)$, the stress σ_y in the main roof reached the largest positive value ($\sigma_{y\ \max} = 0.28$ MPa), indicating the largest compressive stress at this position. At the centers of the two long sides in the goaf, i.e., $(0, b/2)$ and $(a, b/2)$, the stress σ_y in the main roof reached the largest negative value ($\sigma_{y\ \max} = 0.82$ MPa), indicating the largest tensile stress in this position. However, the tensile stress σ_y did not reach the ultimate tensile strength of the main roof. Given the above, the failure of the main roof was not caused by the stress σ_y.

3.3. Mechanical Analysis of the Periodic Breaking Characteristics of the Main Roof

3.3.1. Theoretical Analysis of the Mechanical Model for the Periodic Breaking of the Main Roof. The governing equation for the boundary condition of fixed support on three sides and simple support on one side before the periodic breaking of the main roof in the FMC can be written as follows:

$$\begin{cases} \omega\big|_{x=0,x=a} = 0, \\ \dfrac{\partial^2\omega}{\partial x^2}\Big|_{x=0} = 0, \\ \dfrac{\partial\omega}{\partial x}\Big|_{x=a} = 0, \\ \omega\big|_{y=0,y=b} = 0, \\ \dfrac{\partial\omega}{\partial y}\Big|_{y=0,y=b} = 0. \end{cases} \tag{14}$$

Under the boundary condition of fixed support on three sides and simple support on one side, we derive the following deflection equation that satisfies the boundary conditions:

$$\omega = cx\left(x^2 - a^2\right)^2\left(y^2 - by\right)^2. \tag{15}$$

Substituting Equation (15) and q_0 into Equation (1), we can calculate the coefficient c by the Matlab software program:

$$c = \frac{8085q_0}{128Da\left(336a^4 + 176a^2b^2 + 165b^4\right)}. \tag{16}$$

Substituting Equation (16) into Equation (15), we can derive the deflection function under the condition of fixed support on the three sides and simple support on one side for the main roof:

$$\omega = \frac{8085q_0x\left(x^2 - a^2\right)^2\left(y^2 - by\right)^2}{128Da\left(336a^4 + 176a^2b^2 + 165b^4\right)}. \tag{17}$$

Substituting Equation (17) into Equations (3)–(6), we can derive the shear stress function and the bending moment function of the main roof as follows:

$$\begin{aligned} Q_x &= k\left[\left(30x^2 - 6a^2\right)\left(y^2 - by\right)^2 + \left(x^2 - a^2\right)\left(5x^2 - a^2\right)\left(6y^2 - 6by + b^2\right)\right], \\ Q_y &= 2k\left[x\left(x^2 - a^2\right)^2(6y - 3b) + \left(10x^3 - 6a^2x\right)\left(y^2 - by\right)(2y - b)\right], \\ M_x &= k\left\{\left(y^2 - by\right)^2\left(10x^3 - 6a^2x + 12h^2x\right) + \left(6y^2 - 6by + b^2\right)\right. \\ &\quad \left.\cdot\left[\mu x\left(x^2 - a^2\right)^2 + \frac{4h^2\left(5x^3 - 3a^2x\right)}{5}\right]\right\} - \frac{\mu q_0h^2}{10(1 - \mu)}, \\ M_y &= k\left\{x\left(x^2 - a^2\right)^2\left(6y^2 - 6by + b^2 + \frac{12}{5}h^2\right) + \left(5x^3 - 3a^2x\right)\right. \\ &\quad \left.\cdot\left[2\mu\left(y^2 - by\right)^2 + \frac{4h^2\left(6y^2 - 6by + b^2\right)}{5}\right]\right\} - \frac{\mu q_0h^2}{10(1 - \mu)}, \end{aligned} \tag{18}$$

where $k = -8085q_0/64a(336a^4 + 176a^2b^2 + 165b^4)$.

Substituting the abovementioned bending moment function into $\sigma = 6M/h^2$, we can obtain the corresponding stress function:

$$\begin{aligned} \sigma_x &= \frac{6k}{h^2}\left\{\left(y^2 - by\right)^2\left(10x^3 - 6a^2x + 12h^2x\right) + \left(6y^2 - 6by + b^2\right)\right. \\ &\quad \left.\cdot\left[\mu x\left(x^2 - a^2\right)^2 + \frac{4h^2\left(5x^3 - 3a^2x\right)}{5}\right]\right\} - \frac{3\mu q_0}{5(1 - \mu)}, \\ \sigma_y &= \frac{6k}{h^2}\left\{x\left(x^2 - a^2\right)^2\left(6y^2 - 6by + b^2 + \frac{12}{5}h^2\right) + \left(5x^3 - 3a^2x\right)\right. \\ &\quad \left.\cdot\left[2\mu\left(y^2 - by\right)^2 + \frac{4h^2\left(6y^2 - 6by + b^2\right)}{5}\right]\right\} - \frac{3\mu q_0}{5(1 - \mu)}. \end{aligned} \tag{19}$$

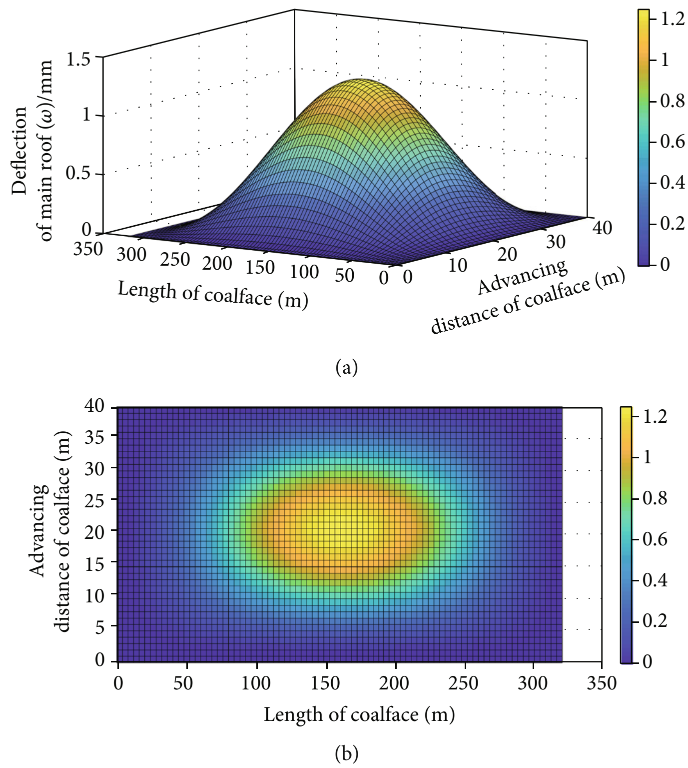

FIGURE 3: Deflection distribution of the main roof upon the first breaking: (a) three-dimensional distribution and (b) planar distribution.

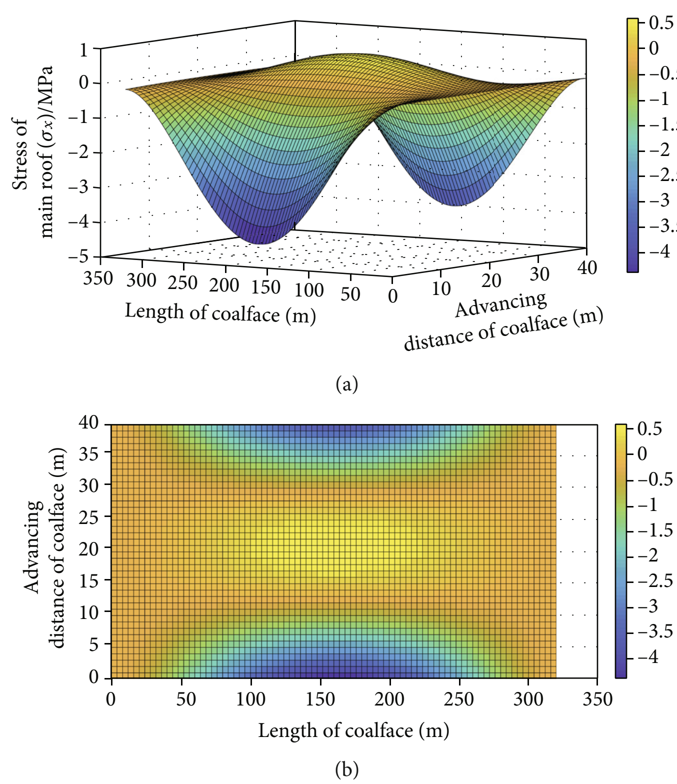

FIGURE 4: Distribution characteristics of the stress σ_x upon the first breaking of the main roof: (a) three-dimensional distribution of the stress σ_x and (b) planar distribution of the stress σ_x.

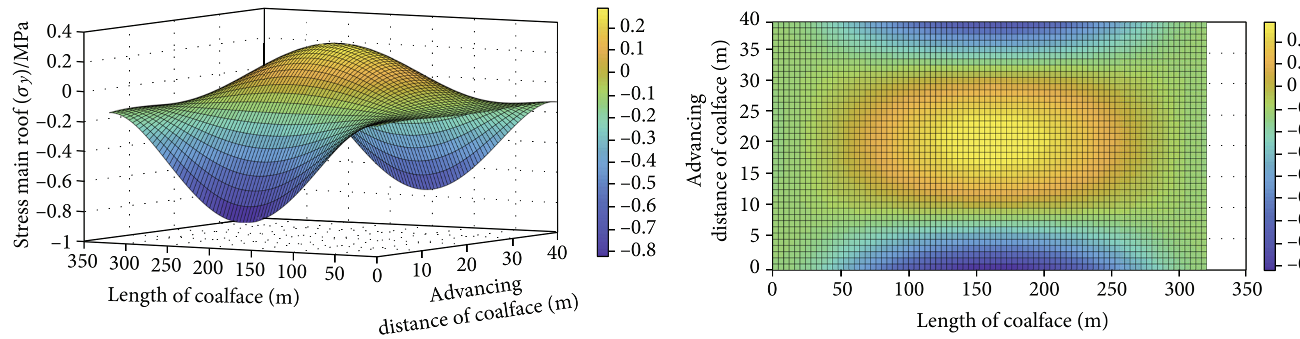

(a) (b)

FIGURE 5: Distribution characteristics of stress σ_y upon the first breaking of the main roof: (a) three-dimensional distribution of the stress σ_y and (b) planar distribution of the stress σ_y.

3.3.2. Periodic Breaking Interval of the Main Roof and Its Mechanical Characteristics. According to the stress function calculated in Section 3.3.1, at $(x, y) = (a, b/2)$, both σ_x and σ_y both reach the largest negative value (that is, $\sigma_{x\ \max}$ and $\sigma_{y\ \max}$ are tensile stresses, $\sigma_{x\ \max} > \sigma_{y\ \max}$), indicating that both are located at the centers of the long sides with fixed support in the TPMM. Values of $\sigma_{x\ \max}$ and $\sigma_{y\ \max}$ are derived as follows:

$$\sigma_{x\ \max} = \frac{6k}{h^2}\left[\frac{ab^4(a^2+3h^2)}{4} - \frac{4h^2a^2b^2}{5}\right] - \frac{3\mu q_0}{5(1-\mu)},$$
$$\sigma_{y\ \max} = \frac{6k}{h^2}a^3b^2\left(\frac{\mu b^2}{4} - \frac{4h^2}{5}\right) - \frac{3\mu q_0}{5(1-\mu)}. \tag{20}$$

Thus, when $\sigma_{x\ \max}$ in the main roof reached the tensile strength R_T (i.e.,$\sigma_{x\ \max} = R_T$), tensile failure occurred periodically at the long sides with fixed support in the TPMM. By substituting the basic parameters of the FMC into the above equations, we estimated the periodic breaking interval of the main roof as $a = 25.0$ m.

Similarly, we plotted the deflection and stress distributions of the main roof upon periodic breaking using the Matlab software program (Figures 6–8). Then, the mechanical characteristics of the main roof upon periodic weighting in the FMC were analyzed.

As shown in Figure 6, the deflection of the main roof had an axisymmetric distribution about the goaf center ($y = b/2$) under the boundary condition of fixed support on the three sides and simple support on one side. We observed the largest deflection at the center, with a gradual decrease towards the periphery. In the position ($\sqrt{5}a/5$, $b/2$) in the goaf, the main roof deflection reached a maximum of 0.36 mm.

As shown in Figure 7, the stress σ_x in the main roof had an axisymmetric distribution about the goaf center ($y = b/2$) under the boundary condition of fixed support on the three sides and simple support on one side. At the center of the long side with fixed support in the goaf $(a, b/2)$, the stress σ_x in the basic stress reached the peak negative value ($\sigma_{x\ \max} = 4.24$ MPa), indicating the largest tensile stress in this position. At this moment, the tensile stress σ_x already reached the ultimate tensile strength of the main roof. Therefore, tensile failure of the main roof occurred at the centers of the long sides with fixed support in the goaf.

As shown in Figure 8, both stresses σ_y and σ_x in the main roof had an axisymmetric distribution about the goaf center ($y = b/2$) under conditions of fixed support on the three sides and simple support on one side. At ($\sqrt{5}a/5$, $b/2$) in the goaf, stress σ_y reached the largest positive value ($\sigma_{y\ \max} = 0.12$ MPa), indicating the largest compressive stress in this position. At the center of the goaf long side $(a, b/2)$, the stress σ_y in the main roof reached the largest negative value ($\sigma_{y\ \max} = 0.58$ MPa), indicating the largest tensile stress in this position. However, the tensile stress σ_y did not reach the ultimate tensile strength in the main roof at this moment. It could be inferred that the stress σ_y caused no failure in the main roof.

4. Field Measurement of Ground Pressure Behavior in the FMC

In this section, the working resistance of hydraulic supports in the FMC was studied during the stoping period. The working resistance variations of the hydraulic supports were characterized. We analyzed the first and periodic weighting patterns in the coalface and verified the feasibility of the proposed TPMM for the main roof breaking. On this basis, we evaluated the applicability of the hydraulic supports used in the coalface, offering valuable clues for roof management in the coalface.

4.1. Field Measurement Plan for Ground Pressure. A total of 25 measurement stations were installed along the dip direction of the coalface to analyze ground pressure behavior at different positions in the roof (Figure 9). The measurement stations were located at the following hydraulic supports: #4, #8, #15, #23, #30, #38, #46, #53, #60, #68, #76, #83, #92, #98, #106, #113, #120, #128, #136, #143, #150, #158, #166, #174, and #183. The YHY60W(A) support pressure gauges for mines developed by the Xuzhou Shengneng

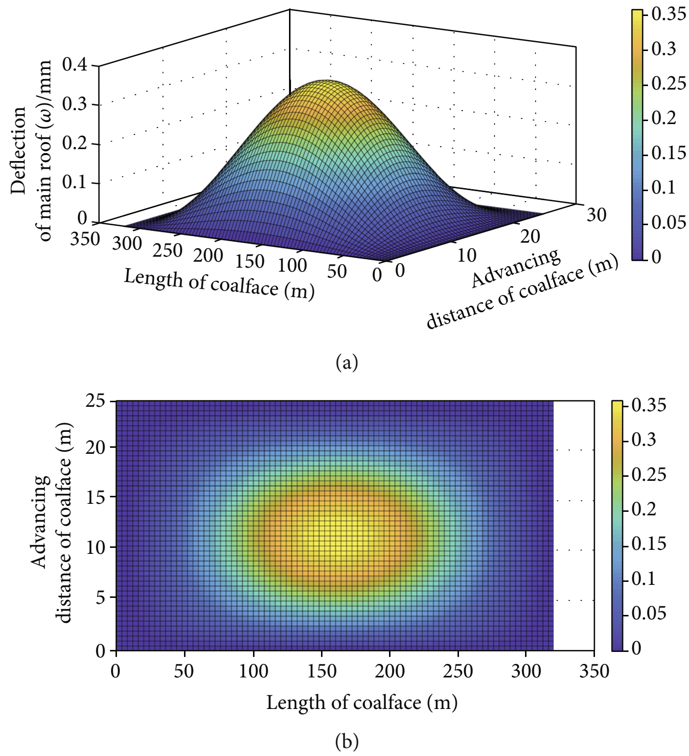

FIGURE 6: Characteristics of deflection distribution of the main roof upon periodic breaking: (a) three-dimensional distribution and (b) planar distribution.

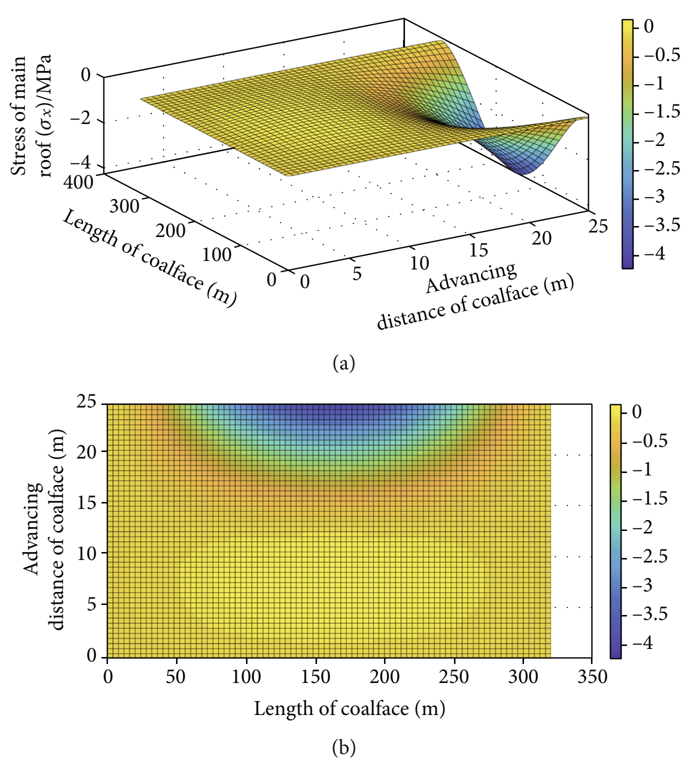

FIGURE 7: Distribution characteristics of stress σ_x in the main roof upon periodic breaking: (a) three-dimensional distribution of the stress σ_x and (b) planar distribution of stress σ_x.

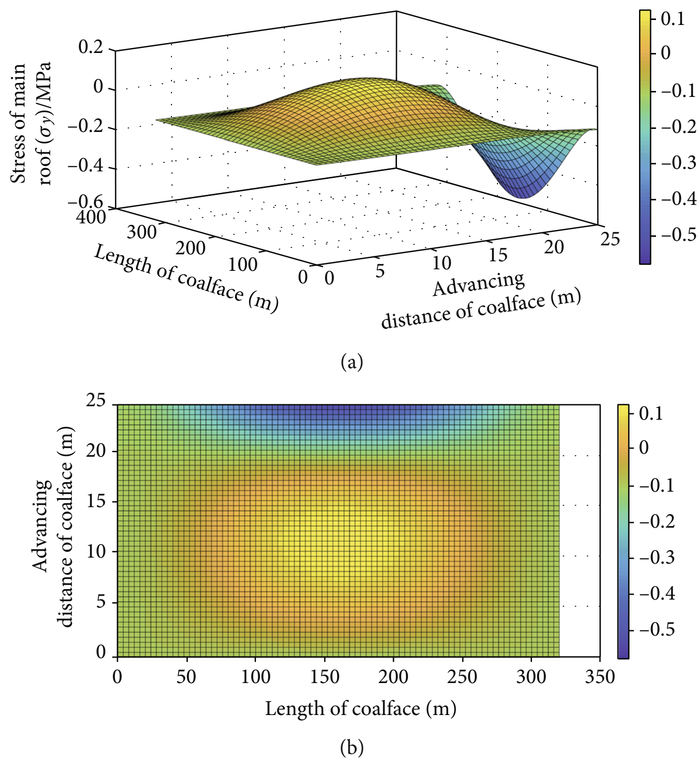

FIGURE 8: Distribution characteristics of stress σ_y in the main roof upon periodic breaking: (a) three-dimensional distribution of the stress σ_y and (b) planar distribution of the stress σ_y.

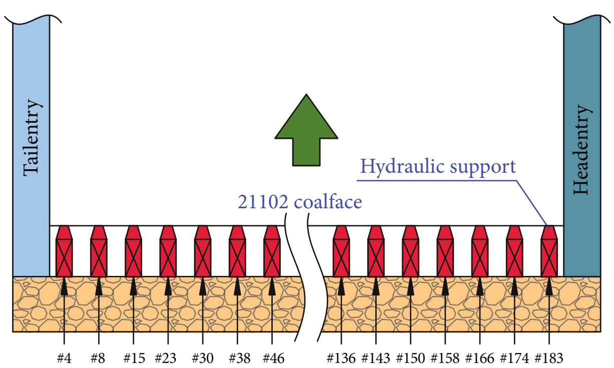

FIGURE 9: The layout of the measurement stations in the coalface.

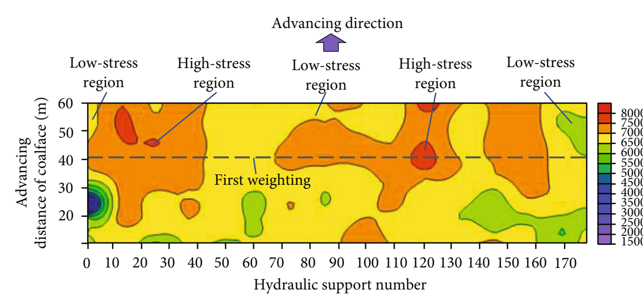

FIGURE 10: Distribution characteristics of the daily average working resistance of hydraulic supports during primary mining.

Technology Co., Ltd. were installed in the corresponding measurement stations for continuous monitoring of the working resistance of hydraulic supports.

4.2. Analysis of the First Weighting Characteristics in the Coalface. Generally speaking, weighting in the coalface can be more accurately performed using the circulation terminal resistance (CTR) of hydraulic supports. However, after installing and debugging the special ground pressure-monitoring system, the FMC had already advanced by 140 m. Therefore, the CTR could not be timely and accurately captured by the electrohydraulic control system embedded in the hydraulic supports. For this reason, we analyzed the first weighting of the main roof in the coalface according to the actual roof caving, time-weighted resistance (TWR) of the hydraulic supports, and daily maximum resistance (DMR) of the hydraulic supports.

During the primary mining of the FMC, when the coalface advanced from the open-off cut for about 12 m, the immediate roof in the middle of the coalface collapsed. As the coalface further advanced to 20 m, the entire immediate roof had collapsed, filling the goaf. When the coalface advanced to about 40 m, clear breaking sounds could be heard from the main roof. Thus, the occurrence of the first weighting of the coalface was confirmed. During the primary mining of the coalface, the overall distribution of the daily average working resistance of the hydraulic supports is monitored and plotted in Figure 10. From the coalface's head to its tail, the low-stress region, high-stress region, low-stress region, high-stress region, and low-stress region appeared successively. This was a saddle-shaped distribution, which was typical of the ultralong coalface.

Table 1: Judgment criteria for the first weighting in some hydraulic supports.

No.	$\bar{P}_t$	σ_t	P_t	$\bar{P}_{\max}$	$\sigma_{\max}$	$P_{\max}$
#8	6765	348	7113	7922	379	8301
#46	6680	290	6970	7694	271	7965
#92	6805	310	7115	7783	289	8072
#120	7150	500	7650	8019	395	8414
#174	6850	230	7080	7894	231	8125

$\bar{P}_t$: value of TWR; σ_t: standard deviation of TWR; P_t: JCTWR; $\bar{P}_{\max}$: mean value of DMR; $\sigma_{\max}$: standard deviation of DMR; $P_{\max}$: JCDMR.

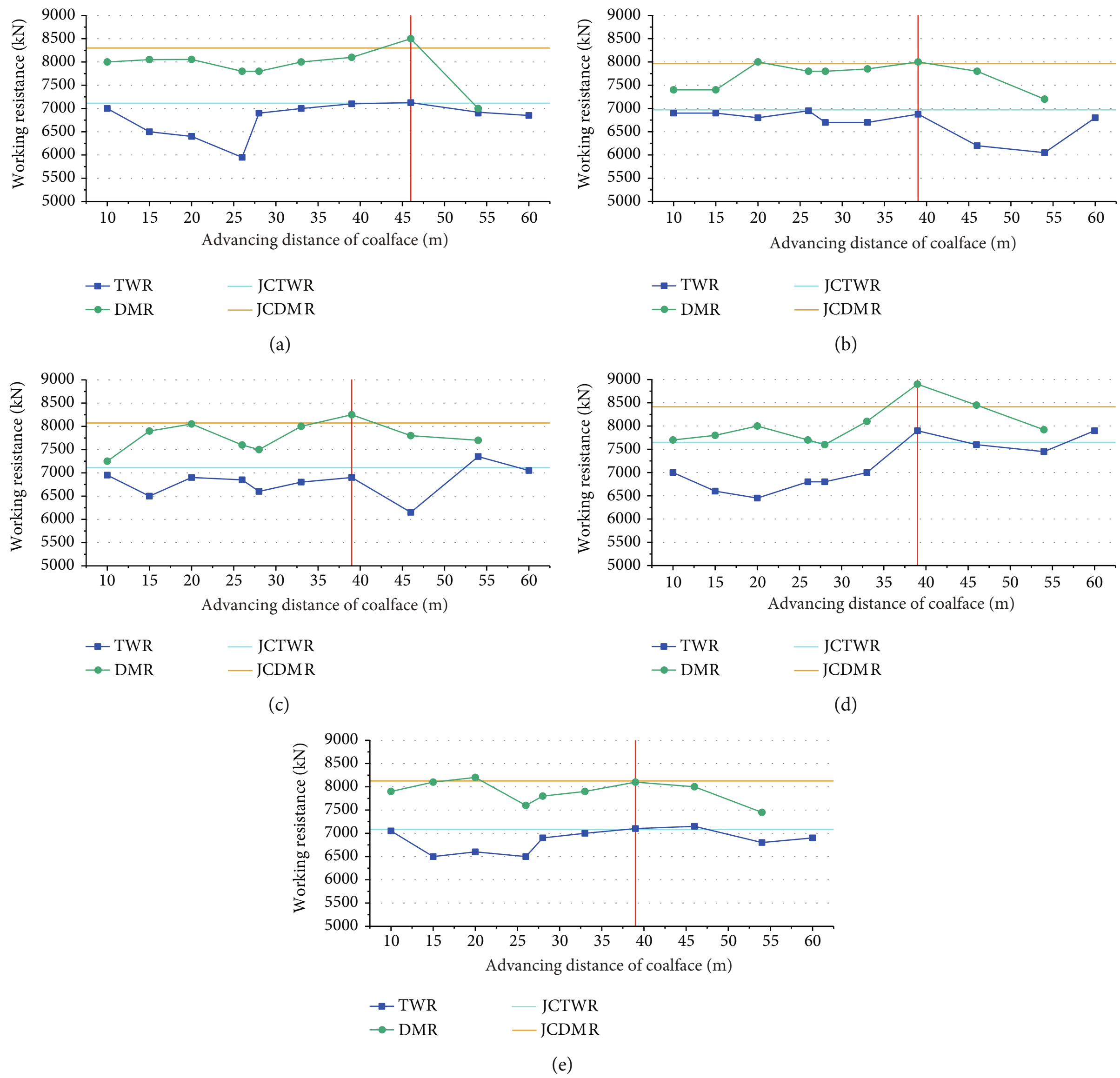

Figure 11: Variation curves of working resistance in some hydraulic supports upon first weighting: (a) #8 hydraulic support, (b) #46 hydraulic support, (c) #92 hydraulic support, (d) #120 hydraulic support and (e) #174 hydraulic support.

The judgment criteria of time-weighted resistance (JCTWR) and the judgment criteria of daily maximum resistance (JCDMR) of some hydraulic supports in the coalface were calculated for the first weighting, as shown in Table 1. The variation curves of the working resistance of hydraulic supports are presented in Figure 11 (the red vertical line indicates the position of the first weighting in the coalface).

According to Table 1 and Figure 11, the first weighting interval of the main roof in the FMC was 38.5-45.9 m, with an average of 41.4 m, which agreed with the field

Table 2: Judgment criteria for periodic weighting in some hydraulic supports.

No.	$\bar{P}_t$	σ_t	P_t	$\bar{P}_m$	σ_m	P_m
#4	7635	680	8315	8794	663	9457
#15	8537	534	9071	9502	508	10010
#30	8999	520	9519	9810	573	10383
#46	8905	434	9339	9731	473	10204
#60	8957	475	9432	9873	633	10506
#83	8840	379	9219	9729	448	10177
#92	8552	708	9260	9547	486	10033
#98	8893	363	9256	9695	365	10060
#113	8844	436	9280	9676	505	10181
#128	8595	591	9186	9516	442	9958
#136	9259	667	9926	10245	783	11028
#150	8664	561	9225	9614	590	10204
#166	7590	543	8133	8652	687	9339
#174	7419	830	8249	8169	690	8859

$\bar{P}_m$: mean value of CTR; σ_m: standard deviation of CTR; P_m: JCCTR.

observation. The main roof of the FMC was composed of hard and thick sandstone. Deep-hole presplit blasting has been performed for the open-off cut roof to prevent roof disaster caused by the extensive roof overhang. Therefore, the first weighting of the coalface had low intensity, and the safety valves of the hydraulic supports did not open extensively. The dynamic load factor of the hydraulic supports during the first weighting of the coalface was 1.04-1.18, with an average of 1.08, which values were relatively small.

4.3. Analysis of the Periodic Weighting Characteristics in the Coalface. Field measurement data were collected from the special ground pressure monitoring system installed in the hydraulic supports. Periodic weighting was analyzed as the coalface advanced from 140 to 400 m. The judgment criteria of time-weighted resistance (JCTR) and the judgment criteria of circulation terminal resistance (JCCTR) of some hydraulic supports were calculated; the results are shown in Table 2. The variation curves of the working resistance of some hydraulic supports are shown in Figure 12 (the red vertical line indicates the position of the periodic weighting in the coalface).

As shown in Table 2 and Figure 12, as the FMC advanced from 140 to 400 m (i.e., by a distance of 260 m), 10-13 events of periodic weighting occurred in total. The minimum, average, and maximum weighting intervals were 11.6, 22.0, and 38.7 m. The dynamic load factor of the hydraulic supports during the periodic weighting of the coalface was 1.03-1.09, with an average of 1.06. This dynamic load factor was relatively small.

4.4. Applicability Evaluation of the Hydraulic Supports Used. The operational resistance data of the hydraulic supports were analyzed as the FMC advanced from 0 to 400 m. The distribution of the daily average working resistance of the hydraulic supports is shown in Figure 13. From the head to the tail of the coalface, hydraulic supports' daily average working resistance presented a "saddle-shaped" distribution similar to the primary mining of the coalface (low-stress region, high-stress region, low-stress region, high-stress region, and low-stress region). Along the advanced direction of the coalface, there were three types of regions, classified by their daily average working resistance, namely, low-stress region, transition region, and high-stress region.

(1) *Low-Stress Region (0-100 m)*. The overburden failure in the coalface was extremely insufficient within this region. The daily average working resistance of hydraulic supports was generally below 7000 kN and changed little. No significant coal wall spalling was observed during the coalface advance.

(2) *Transition Region (100-300 m)*. Within this region, the degree of overburden failure in the coalface grew with the coalface advance. The daily average working resistance of hydraulic supports gradually increased.

(3) *High-Stress Region (Beyond 300 m)*. The overburden failure in the coalface already became sufficient within this region. The daily average working resistance of hydraulic supports was generally above 8000 kN. Significant coal wall spalling was observed during the coalface advance.

The frequency distribution of working resistance usually characterizes the operational performance of hydraulic supports. A reasonable working resistance distribution of hydraulic supports is a near-normal distribution [30]. A higher share of low working resistance usually indicates a lower efficiency of the hydraulic supports. Besides, the rated working resistance margin is large under the above situation. By contrast, a higher share of the high working resistance indicates that the hydraulic supports mostly work at a high load. The rated working resistance is lower and cannot meet the actual support demand on-site. The frequency distribution of the working resistance of hydraulic supports was analyzed statistically as the FMC advanced from 0 to 400 m. It

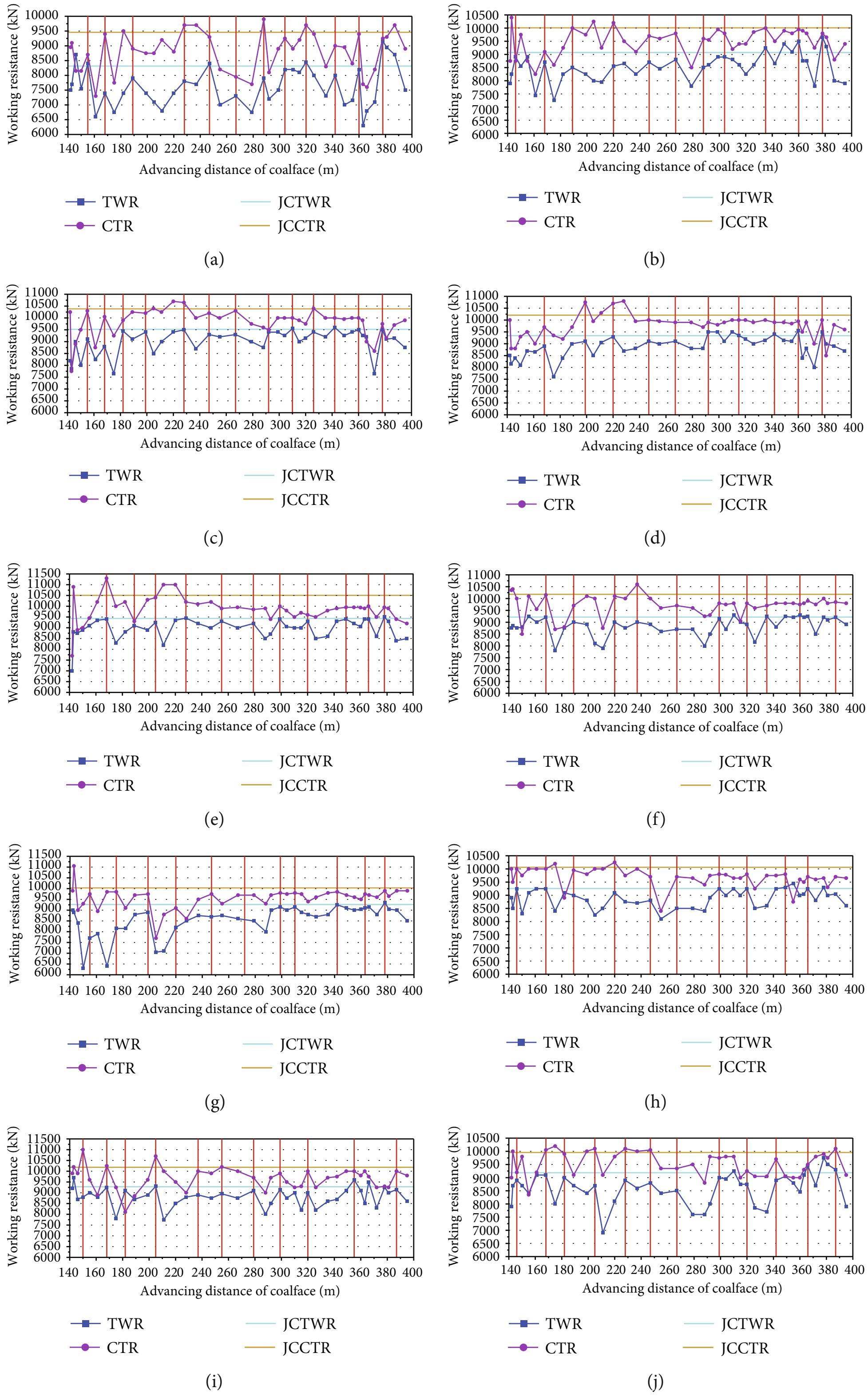

Figure 12: Continued.

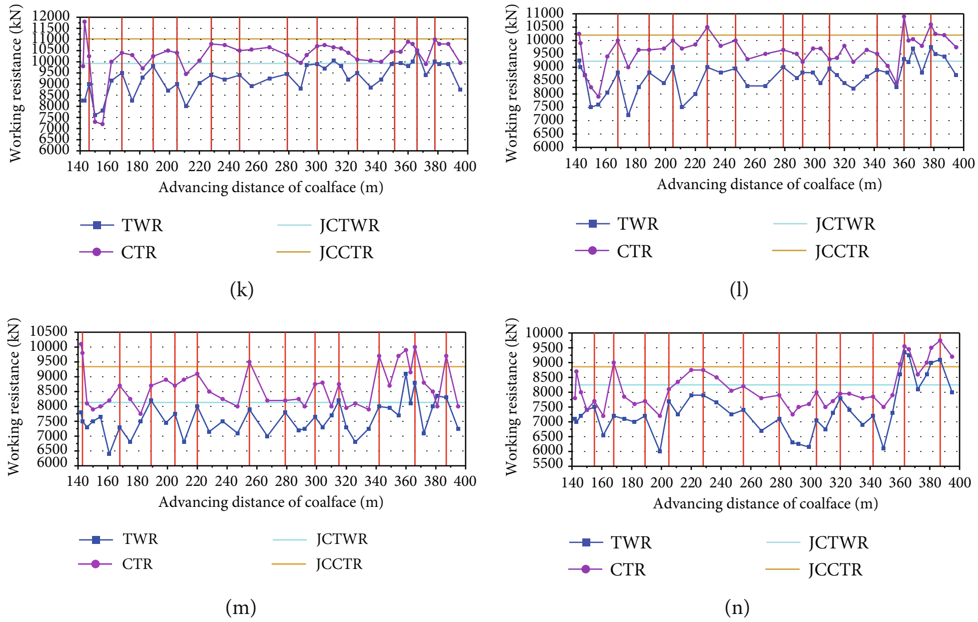

Figure 12: Variation curves of working resistance of some hydraulic supports upon periodic weighting: (a) #4 hydraulic support, (b) #15 hydraulic support, (c) #30 hydraulic support, (d) #46 hydraulic support, (e) #60 hydraulic support, (f) #83 hydraulic support, (g) #92 hydraulic support, (h) #98 hydraulic support, (i) #113 hydraulic support, (j) #128 hydraulic support, (k) #136 hydraulic support, (l) #150 hydraulic support, (m) #166 hydraulic support, and (n) #174 hydraulic support.

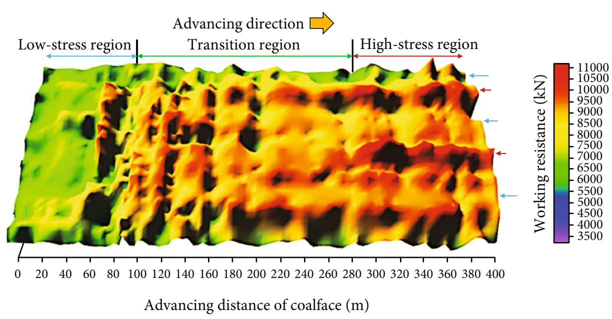

Figure 13: Distribution characteristics of the daily average working resistance of hydraulic supports.

yielded 0.4% for the 0-2000 kN interval, 0.2% for the 2000-4000 kN interval, 1.1% for the 4000-6000 kN interval, 28.2% for the 6000-8000 kN interval, 65.3% for the 8000-10000 kN interval, and 4.8% for the interval above 10000 kN. According to these results, high working resistance (above 8000 kN) had the dominating share of 70.1%. This indicated that the hydraulic supports generally worked at high loads with a small margin of the rated working resistance.

5. Conclusions

(1) The proposed TPMM of the main roof breaking predicted that the first and periodic weighting intervals of the main roof caused by the internal stress σ_x in the rock strata were 40.6 and 25.0 m, respectively. The tensile failure first started in the goaf from the center of the long side with fixed support

(2) Field measurements of ground pressure showed that the first weighting interval of the main roof in the FMC was 38.5-45.9 m, with an average of 41.4 m. The periodic weighting interval was 11.6-38.7 m, with an average of 22.0 m. The discrepancy between the model predictions and field data was quite small. The above results indicated that the TPMM was applicable to the particular geological conditions of the FMC

(3) The estimation of the daily average working resistance of hydraulic supports exhibited a saddle-shaped pattern along the coalface dip direction, with the following sequence order: low-stress region, high-stress region, low-stress region, high-stress region, and low-stress region, judging by the daily average working resistance. This saddle-shaped distribution was typical of the ultralong coalface. Along the advanced direction of the coalface, the daily average working resistance could be classified into three types of regions by the low-stress region, transition region, and high-stress region

(4) Analysis of the working resistance frequency distribution revealed that the ZY10000-16/32D two-column shield-type hydraulic supports could adapt to the geological conditions under which the FMC was mined. However, the hydraulic supports generally experienced high loads, with an insufficient margin of the rated working resistance (i.e., 10000 kN). Therefore, enhanced roof management in the presence of special geological structures (e.g., faults and goaf passages) during the coalface mining is strongly recommended

Data Availability

The data used to support the findings of this study are included within the article.

Conflicts of Interest

The authors declare that there are no conflicts of interest regarding the publication of this paper.

Acknowledgments

This work was financially supported by the National Natural Science Foundation of China (No. 51874278), the "Six Talent Peaks" Project of Jiangsu Province (No. JNHB-087), the Postgraduate Research and Practice Innovation Program of Jiangsu Province (Nos. KYCX21_2339 and KYCX21_2247), and the Independent Research Project of State Key Laboratory of Coal Resources and Safe Mining (No. SKLCRSM2020X04). We wish to thank the HCM in HMA, China, for supporting field help to conduct this important study.

References

[1] D. S. Zhang, W. P. Li, X. P. Lai, G. W. Fan, and W. Q. Liu, "Development on basic theory of water protection during coal mining in northwest of China," *Journal of China Coal Society*, vol. 42, no. 1, pp. 36–43, 2017.

[2] D. L. Jiang and H. Cheng, "Medium and long term forecast and prospect of coal consumption in China," *Coal Economic Research*, vol. 40, no. 7, pp. 16–21, 2020.

[3] M. D. Woodworth, "Disposable Ordos: The making of an energy resource frontier in western China," *Geoforum*, vol. 78, no. 1, pp. 133–140, 2017.

[4] W. Z. Liu, Z. P. Guo, S. W. Niu, J. F. Hou, F. Y. Zhang, and C. Q. He, "Mechanical properties and damage evolution behavior of coal-fired slag concrete under uniaxial compression based on acoustic emission monitoring technology," *Journal of Materials Research and Technology*, vol. 9, no. 5, pp. 9537–9549, 2020.

[5] Q. Ma, Y. L. Tan, X. S. Liu, Q. H. Gu, and X. B. Li, "Effect of coal thicknesses on energy evolution characteristics of roof rock-coal-floor rock sandwich composite structure and its damage constitutive model," *Composites Part B: Engineering*, vol. 198, 2020.

[6] H. G. Nie, F. C. Dong, W. K. Zhao, and Z. Xi, "Coal-Tbearing strata sequence stratigraphic fatures and coal accumulation pattern analysis in Dongsheng coalfield -a case study of Abuhai exploration area in Dongsheng coalfield," *Coal Geology of China*, vol. 23, no. 2, pp. 10–16, 2011.

[7] X. M. Wang, X. M. Wang, S. D. Pan et al., "Occurrence of analcime in the middle Jurassic coal from the Dongsheng Coalfield, northeastern Ordos Basin, China," *International Journal of Coal Geology*, vol. 196, no. 1, pp. 126–138, 2018.

[8] Y. Q. Jiao, S. M. Wang, L. M. Fan, L. Q. Wu, H. Rong, and F. Zhang, "Key elements and framework model of groundwater system in Jurassic coal measures of Ordos Basin," *Journal of China Coal Society*, vol. 45, no. 7, pp. 2411–2422, 2020.

[9] Q. X. Huang, *Strata Control of Shallow Coal Seam Longwall Mining*, Science Press, Beijing, 2019.

[10] S. S. Peng, H. M. Li, Y. Zhou et al., *Study on Strata Control in Shendong and Junggar Mining Areas*, Science Press, Beijing, 2015.

[11] D. S. Zhang, G. W. Fan, X. F. Wang, W. Zhang, and H. L. Liu, *Study on Overburden Activity Law and Its Control Technology of Shallow Coal Seam Mining in Gully-Growth-Wide Mining Area*, China University of Mining and Technology Press, Xuzhou, 2014.

[12] S. G. Cao, H. J. Jiang, and Y. Zhang, *Study on the Breaking and Control of Key Strata under Short-Wall Mining in Shallow Seam*, China University of Mining and Technology Press, Xuzhou, 2019.

[13] Y. H. Zhao and X. M. Song, "Stability analysis and numerical simulation of hinged arch structure for fractured beam in super-long mining workface under shallow seam," *Rock and Soil Mechanics*, vol. 37, no. 1, pp. 203–209, 2016.

[14] J. G. Ning, X. S. Liu, Y. L. Tan, M. Zhang, and L. S. Zhang, "Fracture structure model of weakly cemented roof in shallow seam," *Journal of Mining & Safety Engineering*, vol. 31, no. 4, pp. 569–574, 2014.

[15] G. X. Xie, H. Fan, and L. Wang, "Evolution law and engineering application of surrounding rock force chain in shallow coal seam working face," *Journal of China Coal Society*, vol. 44, no. 10, pp. 2945–2952, 2019.

[16] X. W. Yin, "Cutting block structure model of overburden with shallow buried coal seam and ultra-large mining height working face," *Journal of China Coal Society*, vol. 44, no. 7, pp. 1961–1970, 2019.

[17] B.-F. Wa, L. Bing, K.-M. Su et al., "Research on overlying strata response and control during typical shallow coal seam longwall mining," *Rock and Soil Mechanics*, vol. 38, no. 9, pp. 2693–2700, 2017.

[18] J. C. Wang and Z. H. Wang, "Stability of main roof structure during the first weighting in shallow high-intensity mining face with thin bedrock," *Journal of Mining & Safety Engineering*, vol. 32, no. 2, pp. 175–181, 2015.

[19] C. S. Di, X. Ding, and H. Huang, "Practice of exploration and discharge technology of roof water in deep Jurassic coal seam: with Hulusu coal mine in Hujiert mine area as example," *Coal Geology & Exploration*, vol. 44, no. 6, pp. 96–100, 2016.

[20] S. J. Su, "Research on technology of preventing mine rock burst of roadways near gob when fully-mechanized over anticlinal structure," *Coal Science and Technology*, vol. 48, no. 3, pp. 120–125, 2020.

[21] J. Sun, "Study on deep coal roof Qilizhen sandstone aquifer water yield property in Hujiert mining area," *Coal Geology of China*, vol. 33, no. 4, pp. 62–67, 2021.

[22] Q. Wu, Y. Z. Liu, W. F. Zhou et al., "Evaluation of water inrush vulnerability from aquifers overlying coal seams in the Menkeqing coal mine, China," *Mine Water and the Environment*, vol. 34, no. 3, pp. 258–269, 2015.

[23] J. Wang, J. Ning, L. Jiang, J. Q. Jiang, and T. Bu, "Structural characteristics of strata overlying of a fully mechanized longwall face: a case study," *Journal of the Southern African Institute of Mining and Metallurgy*, vol. 118, no. 11, 2018.

[24] G. L. Ding, X. H. Lu, S. G. Wu, and Y. Q. Liu, "Sturdy on ground pressure law and support adaptability of deep-buried and ultra-long fully-mechanized longwall mining face," *Coal Science and Technology*, vol. 49, no. 3, pp. 43–48, 2021.

[25] W. Zhang, X. Qu, C. Li et al., "Fracture analysis of multi-hard roofs based on microseismic monitoring and control

techniques for induced rock burst: a case study," *Arabian Journal of Geosciences*, vol. 12, no. 24, 2019.

[26] S. L. Yang, J. C. Wang, and L. H. Li, "Deformation and fracture characteristics of key strata based on the medium thick plate theory," *Journal of China Coal Society*, vol. 45, no. 8, pp. 2718–2727, 2020.

[27] B. L. Fu and W. F. Tan, "The reciprocal theorem method for solving bending problems of thick rectangular plates," *Applied Mathematics and Mechanics*, vol. 16, no. 4, pp. 367–379, 1995.

[28] E. Reissner, "The effect of transverse shear deformation on the bending of elastic plates," *Journal of Applied Mechanics*, vol. 12, no. 2, pp. A69–A77, 1945.

[29] V. L. Salerno and M. A. Goldberg, "Effect of shear deformations on the bending of rectangular plates," *Journal of Applied Mechanics*, vol. 27, no. 1, pp. 54–58, 1960.

[30] W. H. Zha, X. Z. Hua, J. C. Wang, H. F. Zheng, N. G. Wang, and X. Liu, "Study on strata movement rules and hydraulic support selection for fully-mechanized working face with large mining height of extra," *Journal of Safety Science and Technology*, vol. 10, no. 8, pp. 75–80, 2014.

Hindawi
Geofluids
Volume 2022, Article ID 7598831, 12 pages
https://doi.org/10.1155/2022/7598831

Research Article

Study on Energy Distribution Law and Numerical Simulation of Mining Roadway Surrounding Rock

Guohua Zhang, Chao Ju, Yanwei Duan, Yiwei Wang, Tao Qin, and Chengjia Wu

Key Laboratory of Mining Engineering, Heilongjiang Universities, Heilongjiang University of Science and Technology, Harbin 150022, China

Correspondence should be addressed to Yanwei Duan; 1354070597@qq.com

Received 14 January 2022; Accepted 24 May 2022; Published 23 June 2022

Academic Editor: Zhijie Wen

In underground engineering, the deformation and failure process of the surrounding rock of the roadway is always accompanied by the occurrence of energy. The study of the energy distribution law of the surrounding rock of the roadway plays an important role in its stability. This paper first theoretically analyzes the stress and energy distribution law of the surrounding rock of the roadway, then with the help of numerical simulation method, combined with the existing physical and mechanical parameters, based on the existing support parameters of Dongrong No. 2 Mine, gradually compares and analyzes the distribution of vertical stress and energy under the three support methods of no support, original support, and combined support, and the results found that the vertical stress distribution law under the three support methods is basically the same. High-stress areas appear on the two ribs of the roadway, and low-stress areas appear on the roof and floor. The range of high-stress areas from no support to combined support continues to decrease and becomes more evenly distributed. The energy distribution pattern is basically the same. The overall energy of the coal seam is high. There are high-energy areas at 2 m left and right of the roadway, and the roof and floor energy of the roadway is the smallest. The low energy area extends 5 m up and down, respectively. The range of high-energy areas from no support to combined support is shrinking, and the energy distribution is more uniform.

1. Introduction

In underground engineering, the rock mass is in equilibrium before excavation. After excavation, the stress on the surrounding rock of the roadway changes from the original three-way stress state to an approximately two-way stress state, changing the stress environment. In order to achieve a new equilibrium state, part of the energy is transferred to the deep part of the roadway, part is deformed, and part is stored. When the energy storage limit of the rock is reached, the energy is released in the form of deformation and failure. In addition, the occurrence of energy always accompanies the deformation and failure process of the roadway. The practice and theoretical research of roadway support in coal mine indicate that [1–5] the stress of the surrounding rock of the roadway is mainly borne by the surrounding rock itself, and the supporting structure only bears a small part of the stress, but the support plays a crucial role in maintaining the stability of the surrounding rock of the roadway. Moreover, the supporting structure can change the mechanical state of the surrounding rock and absorb part of the energy that causes the deformation and failure of the surrounding rock to reach balance and stability.

At present, a large number of literature from the perspective of energy, supporting theory, and technology conducted in-depth theory research and field application. On the one hand, it mainly focuses on the prevention and treatment of rock burst. Based on the energy balance theory, Gao et al. [6] deduced and analyzed the energy criterion for the instability of roadway surrounding rock structure under impact disturbance, improved roadway support parameters, and achieved good field results. Based on the energy theory of rock burst, Ju [7] proposed the energy checking design method of rock burst roadway and checked the support system from the perspective of energy. Based on the principle of energy conservation and considering the impact release level, failure characteristics of surrounding rock, and mechanical characteristics of supporting equipment, Wang et al. [8] proposed a method to determine the parameters of three-stage energy-absorbing support. Pan et al. [9] considered that the starting stress condition of rock burst under roadway support was that the stress in the far-field was greater than the critical stress, and the stopping energy condition was that the absorption energy of surrounding rock in the near-field and the absorption energy of support was greater than the release energy in the far-field, and put forward the three-level support theory and technology of roadway rock burst in coal mine.

On the other hand, it focuses on the stability of surrounding rock of mining roadway. For existing projects, Gong et al. [10] conducted similar simulation experiments to study the working principle of NPR anchor cable from the perspective of energy transformation, so as to guide the roadway support design. Shan et al. [11] adopted the energy analysis method to deduce the energy constitutive equation of the yielding anchor bolt and the energy equation under the action of surrounding rock, which were applied to the on-site support and achieved good results. Lin et al. [12] proposed the support scheme with high strength and stable resistance and analyzed the stability of roadway surrounding rock under different support schemes through FLAC^{3D} simulation, so as to determine the reasonable size of reserved coal pillar. Ma et al. [13] studied the control of the surrounding rock in the roof of the roadway with different thicknesses of soft rock formations through UDEC and field monitoring. It is considered that the roadway support scheme is designed based on the energy balance, so that the roadway deformation can be effectively controlled.

The above research provides solid support theory and rich support technology experience from the perspective of energy, but the support research based on energy distribution is relatively insufficient. In this paper, firstly, the stress and energy distribution law of roadway surrounding rock is analyzed theoretically. Then, based on the existing support parameters of Dongrong No. 2 Mine, the stress and energy distribution situation under different support modes is compared and analyzed by numerical simulation, combined with the existing physical and mechanical parameters, and the optimization scheme is proposed. Through on-site verification, the support problem is effectively solved. It provides a solution for similar engineering problems.

2. Engineering Background

2.1. Project Profile. The average buried depth of the coal seam in the third working face of the 17th layer in the fourth south mining area of Dongrong No. 2 Mine is 450 m, with a coal thickness of 2.80~3.39 m, an average thickness of 3.15 m, and an average dip angle of 17°. The coal seam is stable in deposition, simple in structure, and joints are not developed. The direct roof is fine sandstone with an average thickness of 2.28 m, and the direct floor is siltstone with a thickness of 6.81 m. The roof and floor histogram of coal seam is shown in Figure 1.

2.2. Support Status and Evaluation. The ventilation roadway of the third working face of the 17th layer in the fourth south mining area of Dongrong No. 2 Mine is driven along the roof of coal seam, which is supported by "anchor, net, and belt." There are four rows of roof bolts with a row spacing of 1200 mm × 1000 mm and three rows of right rib bolts with a row spacing of 1200 mm × 1000 mm, all using Φ22 mm × 2500 mm type bolts. The roadway adopts trapezoidal section, the net width of the roadway is 4.2 m, the net middle height is 2.65 m, and the sectional area is 11.13m^2.

The deformation and failure characteristics of the roadway in Dongrong No. 2 Mine are as follows: the roadway support is difficult, the support cost is high, and the efficiency is low. The roadway will be affected by its special geological and stress conditions such as faults during tunneling. The stress concentration degree in the surrounding rock is large, the roadway convergence is obvious, and the surrounding rock deformation is large. The overlying rock layer on the working face has large overlying strata and fractured zone heights.

The peak values of the working face of abutment pressure are high, and the influence range is also large, which will cause serious disturbance to the stability of the front mining roadway. With the mining of the working face, the structural state and stress state of the roadway continue to change, which further intensifies the difficulty to support.

At present, the existing support design of the roadway is based on the experience data of the adjacent roadway that has been constructed, that is, the engineering analogy method is used for the roadway support design. The overall effect of this supporting method is mediocre, and bolt and metal mesh support is used in some broken areas. Most of the roadway roofs and both ribs have the coal body falling along with the excavation, and the surface of the roadway partially shows the characteristics of irregularity and unevenness. In terms of support conditions, most roadways have different degrees of instability of the roof and two ribs.

3. Theoretical Analysis of Roadway Surrounding Rock Energy Distribution

3.1. Mechanical Model of Roadway Surrounding Rock. Figure 2 is taken as the mechanical model of the roadway surrounding rock, assuming that the surrounding rock is a homogeneous and isotropic medium, the in situ rock stress is set to P_0, and the lateral pressure coefficient is 1. After the roadway is excavated, the surrounding rock is divided into plastic zone, elastic zone, and in situ rock stress zone from the center of the circle. The radius of the plastic zone of surrounding rock is R_p, and the radius of roadway is R_0. The elastic zone of the surrounding rock is denoted by the superscript "e", and the plastic zone is indicated by the superscript "p."

Histogram	Lithology	Thickness(m)	Lithologic description
	Siltstone	4.15	Dark grey, rich in plant debris, argillaceous cement
	Siltstone fine sandstones interbedded	2.10	Gray, mainly fine sandstone, siltstone to this end, with wavy horizontal bedding
	Coarse sandstone	10.75	Grayish white, poor sorting, containing trace gravel, hard cementation
	Siltstone	1.60	Dark grey, with more fossil plant clasts in abrupt contact with the overburden
	17 coal	3.15	Black, block, mainly bright coal, good quality
	Siltstone	3.15	Dark gray, argillaceous cement, dense, complete core
	Fine sandstone	2.70	Dark gray, dense, locally containing tuff, solid ratio of significant
	Siltstone	10.60	Dark gray, argillaceous content increased, with thin layers of coarse sandstone and a small amount of tuff, upper core intact, lower core broken

Figure 1: Composite strata histogram.

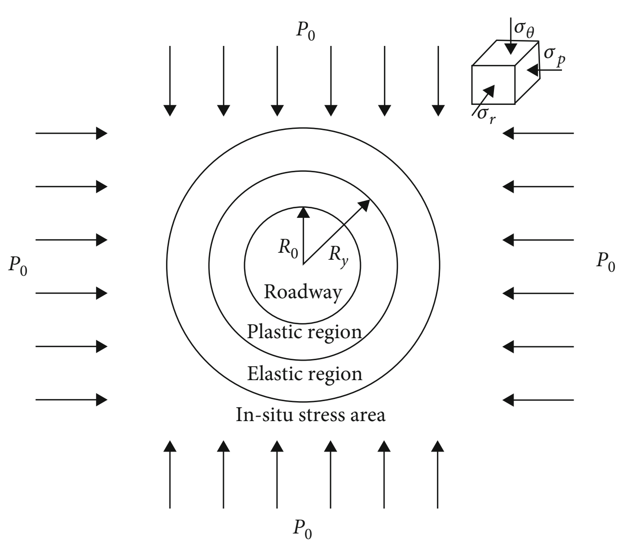

Figure 2: Partition map of roadway surrounding rock.

In order to analyze the mechanical characteristics of the surrounding rock of roadway, the surrounding rock should meet the following conditions [2, 3]:

3.1.1. Yield Function.

$$F = \sigma_\theta - \frac{1 + \sin \phi}{1 - \sin \phi} \phi_r - \frac{2c \sin \phi}{1 - \sin \phi} = 0, \quad (1)$$

where σ_θ and σ_r are the radial stress and tangential stress of the surrounding rock, respectively; φ is the internal friction angle of rock; and c is the cohesion of the rock.

3.1.2. Differential Equations of Equilibrium.

$$\frac{d\sigma_r}{dr} + \frac{\sigma_r - \sigma_\theta}{r} = 0, \quad (2)$$

where r is the distance from the research point to the center of the roadway circle.

3.1.3. Geometric Equations.

$$\begin{cases} \varepsilon_r = \dfrac{1 - \mu^2}{E} \left[\left(\sigma_r - p_0 \right) - \dfrac{\mu}{1 - \mu} \left(\sigma_\theta - p_0 \right) \right], \\ \varepsilon_\theta = \dfrac{1 - \mu^2}{E} \left[\left(\sigma_\theta - p_0 \right) - \dfrac{\mu}{1 - \mu} \left(\sigma_r - p_0 \right) \right], \end{cases} \quad (3)$$

where ε_r and ε_θ are the radial strain and tangential strain of the surrounding rock, respectively; μ is the Poisson's ratio of the rock.

Regardless of the elastic displacement caused by in situ rock stress before tunnel excavation, the constitutive equation is

$$\begin{cases} \varepsilon_r = \dfrac{du}{dr}, \\ \varepsilon_\theta = \dfrac{u}{r}, \end{cases} \tag{4}$$

where E is the elastic modulus of the rock; u is the radial displacement of the surrounding rock.

3.2. Stress Distribution of Roadway Surrounding Rock. After the excavation of the roadway, under the condition of supporting reaction force p_1, the stress in the elastic zone [2, 3, 14, 15]

$$\begin{cases} \sigma_r^e = p_0 - (c\cos\phi + p_0\sin\phi)\left[\dfrac{(p_0 + c\cot\phi)(1-\sin\phi)}{p_1 + c\cot\phi}\right]^{1-\sin\phi/\sin\phi}\left(\dfrac{R_0}{r}\right)^2, \\ \sigma_\theta^e = p_0 + (c\cos\phi + p_0\sin\phi)\left[\dfrac{(p_0 + c\cot\phi)(1-\sin\phi)}{p_1 + c\cot\phi}\right]^{1-\sin\phi/\sin\phi}\left(\dfrac{R_0}{r}\right)^2. \end{cases} \tag{5}$$

The stress of the plastic zone

$$\begin{cases} \sigma_r^{\mathrm{p}} = (p_1 + c\cot\phi)\left(\dfrac{r}{R_0}\right)^{2\sin\phi/1-\sin\phi} - c\cot\phi, \\ \sigma_\theta^{\mathrm{p}} = (p_1 + c\cot\phi)\left(\dfrac{1+\sin\phi}{\sin\phi}\right)\left(\dfrac{r}{R_0}\right)^{2\sin\phi/1-\sin\phi} - c\cot\phi. \end{cases} \tag{6}$$

The radius of the plastic zone

$$R_p = R_0\left[\frac{(p_0 + c\cot\phi)(1-\sin\phi)}{(p_1 + c\cot\phi)}\right]^{1-\sin\phi/\sin\phi}. \tag{7}$$

Therefore, the stress variation law of the surrounding rock of the roadway in the elastic-plastic state is shown in Figure 3.

3.3. Energy Distribution of Roadway Surrounding Rock

3.3.1. Energy Expression of the Elastic Region. The elastic strain energy in the surrounding rock of the roadway is a measure of how much work done by internal and external forces in a certain range is stored by the surrounding rock mass. The elastic strain energy density refers to the elastic strain energy per unit volume, which is a function of strain. The following formula is used for calculation [15–17]:

$$v_\varepsilon = \int \varepsilon_i d\sigma_i. \tag{8}$$

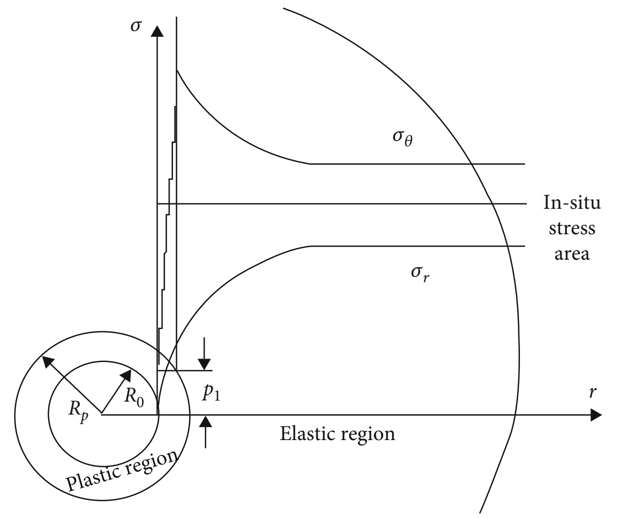

Figure 3: Stress variation law of the surrounding rock of the roadway.

The equations of physics can be expressed as

$$\begin{cases} \varepsilon_1 = \dfrac{[\sigma_1 - \mu(\sigma_2 + \sigma_3)]}{E}, \\ \varepsilon_2 = \dfrac{[\sigma_2 - \mu(\sigma_3 + \sigma_1)]}{E}, \\ \varepsilon_3 = \dfrac{[\sigma_3 - \mu(\sigma_1 + \sigma_2)]}{E}. \end{cases} \tag{9}$$

By substituting Equation (9) into Equation (8), the expression of elastic strain energy density under the elastic state of surrounding rock can be obtained:

$$v_z^e = \frac{[\sigma_1^2 + \sigma_2^2 + \sigma_3^2 - 2\mu(\sigma_1\sigma_2 + \sigma_2\sigma_3 + \sigma_1\sigma_3)]}{2E}. \tag{10}$$

3.3.2. Energy Expression of the Plastic Zone. Using the equal area principle [18–20], the trapezoidal roadway is equivalent to a circular roadway with a radius of 1.88 m. According to Equation (7), the radius of the plastic zone is calculated to be 3.95 m. Combined with the strata histogram, it can be seen that the lithology within this zone is coal seam, siltstone, and coarse sandstone. From the stress-strain curve, the ratio of plastic energy to elastic energy k can be calculated, and the strain energy density in the plastic zone of the surrounding rock of the roadway is

$$v_z^p = k v_z^e. \tag{11}$$

4. Numerical Simulation of Roadway Surrounding Rock Stability

4.1. Establish Model and Select Parameter

4.1.1. Selection of Numerical Calculation Software. FLAC^{3D}, as one of the most important numerical analysis software of finite difference method in the field of geotechnical

Table 1: Mechanical parameters and thickness of layers.

Lithology	Bulk modulus (GPa)	Shear modulus (GPa)	Cohesion force (MPa)	Friction angle (°)	Tensile strength (MPa)	Density ($g\cdot cm^{-3}$)
Siltstone	15.6	10.8	27.25	27	1.17	4.15
Siltstone fine sandstones interbedded	24.3	8.2	39.36	30	4.8	2.1
Coarse sandstone	19.67	9.34	25.47	19	10.14	10.75
Siltstone	15.6	10.8	27.25	27	1.17	1.6
17 coal seam	4.24	1.11	1.51	20	1.90	3.15
Siltstone	15.6	10.8	27.25	27	1.17	3.15
Fine sandstone	20.67	10.10	43.47	19	10.14	2.7
Siltstone	15.6	10.8	27.25	27	1.17	10.6

engineering [21, 22], can simulate the mechanical properties of failure of geological materials when the ultimate strength or yield limit is reached and can simulate a variety of structural forms, such as rock mass and soil. Moreover, it can also simulate artificial structures, such as support, anchor cable, and other geotechnical engineering mechanic problems. Through its embedded FISH language, users can write command flows to achieve more simulation functions, such as customizing the constitutive model, obtaining the stress and strain curves of a certain gridpoint, and extracting the data of a certain zone node. The distribution of elastic strain energy density of the surrounding rock in different areas of the roadway deduced above is realized by FISH language embedded in FLAC^{3D}, and subsequent analysis is carried out.

4.1.2. Modeling. The model takes the inclination as the x-axis, the strike direction as the y-axis, and the gravity direction as the z-axis. The lengths along the x, y, and z axes are 50 m, 40 m, and 50 m, respectively. The cross-section width of the roadway is 4.2 m, and the middle line height is 2.65 m. The principle of grid division is that the area near the roadway is dense and the distance is sparse. Considering the influence range of the rock strata, the upper and lower strata are simplified, and the mechanical parameters of each layer are shown in Table 1. The model has a total of 40,116 nodes and 35,080 units. The model and the conditions of each rock layer are shown in Figure 4.

4.1.3. Initial Stress. Before the excavation of the roadway, the rock mass is in the in situ stress that has not been disturbed by the engineering, which is also called the initial stress. From the measured in situ stress, it can be seen that the initial stress field should not be underestimated to the underground engineering and is the source of deformation and failure to the rock mass surrounding the roadway. Meanwhile, the roadway excavation will produce disturbance to the initial stress field, which will redistribute the initial stress and produce high stress several times higher than the initial stress, so the simulation is combined with the initial stress field on site. According to the in situ stress test report, vertical stress is 10.34 MPa and the lateral pressure coefficient is 1.2.

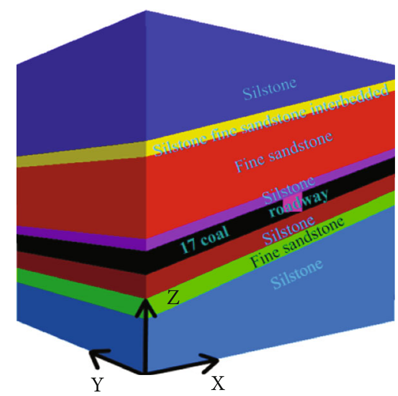

Figure 4: 3D mode diagram.

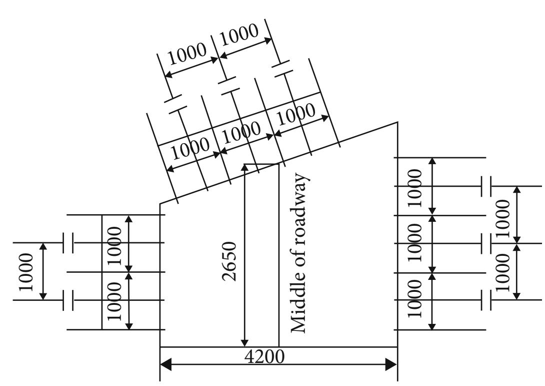

Figure 5: Combined support.

4.1.4. Boundary Conditions. The simulation uses the Mohr-Coulomb model to impose constraints on the boundaries by controlling the displacement. Vertical constraints are applied to the bottom of the model, horizontal constraints are applied to the left and right boundaries, and the top of the model is a free surface without any constraints. In addition, stress boundary conditions are applied according to the in situ stress.

4.2. Supporting Scheme. According to the parameters of the existing roadway section, the no support, original support, and combined support models are established, respectively. The combined support is shown in Figure 5. The roof adopts

Table 2: Mechanical parameters of bolt (anchor cable) anchorage.

Supporting artifacts	Diameter (mm)	Length (mm)	Elasticity modulus (GPa)	Tensile strength (MPa)	Pretightening force (kN)
Anchor cables	21.6	10000	200	200	60
Bolts	22	2500	190	250	80

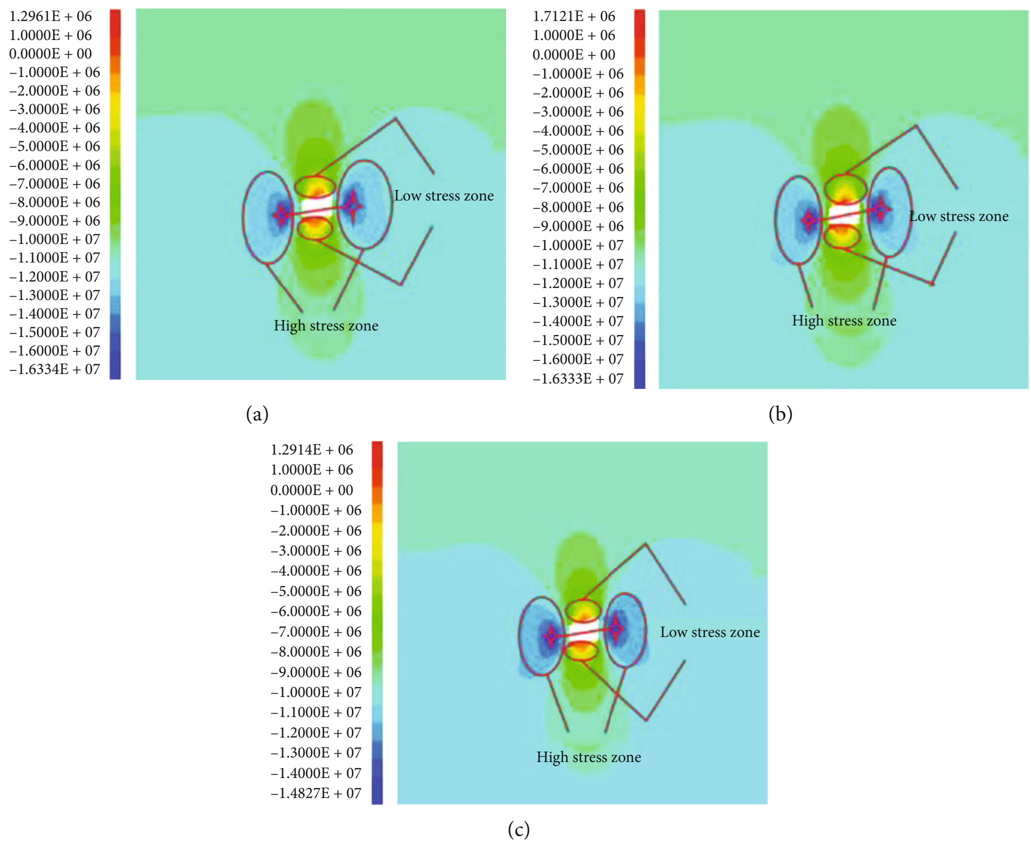

Figure 6: Vertical stress nephogram under different support methods. (a) No support. (b) Original support. (c) Combined support.

the combined support scheme of anchor mesh belt and anchor cable beam. The roof bolt uses $\Phi 22\text{mm} \times 2500$ mm high-strength bolt, the row distance between the bolts is 1000 mm × 1000 mm, the size of the roof anchor cable is Φ 21.6 mm × 10000 mm, and the row distance is 1000 mm × 1200 mm. The wall is supported by the anchor mesh belt. The bolt is $\Phi 22\text{mm} \times 2500$ mm type high-strength bolt, the row distance between bolts is 1000 mm × 1000 mm, the cable size is $\Phi 21.6$ mm × 10000 mm, and the row distance is 1000 mm × 1200 mm. Cable element is adopted in bolt (anchor cable) in FLAC^{3D}, and mechanical parameters of bolt (cable) are shown in Table 2.

4.3. Stress Distribution Law. In order to eliminate the interference of the boundary, the vertical stress distribution of the surrounding rock of the roadway at $y = 20$ m is selected. The distribution of vertical stress under different support methods is shown in Figure 6.

It can be seen from Figure 6 that after the roadway excavation, high stress concentration zones appear on the two ribs of the roadway, and the direction of the connection between the two stress concentration zones is consistent with the coal seam tendency. The roof and floor of the roadway are all low-stress zones, and the floor has a small-scale tensile stress zone. This is because the roof and floor will release pressure and transfer to the two ribs after the excavation of the roadway, resulting in stress concentration on the two ribs. With the increase of the distance from the center of roadway, the vertical stress tends to be stable and close to the in situ rock stress. Overall, the vertical stress above the roof is slightly less than other positions. By comparing the vertical stress field under three different support methods, from no support to combined support, it can be seen that the high-stress areas on the two ribs of the roadway are obviously shrinking, the change of the roof is small, and the stress concentration area at the floor corner of the floor is significantly reduced. The vertical stress concentration range of the surrounding rock of the roadway is significantly decreased after the support, the combined support effect is better, and the vertical stress distribution is more uniform, indicating that the combined support is more conducive to the stability of the roadway.

In order to study the variation of the vertical stress around the roadway, starting from the roadway boundary,

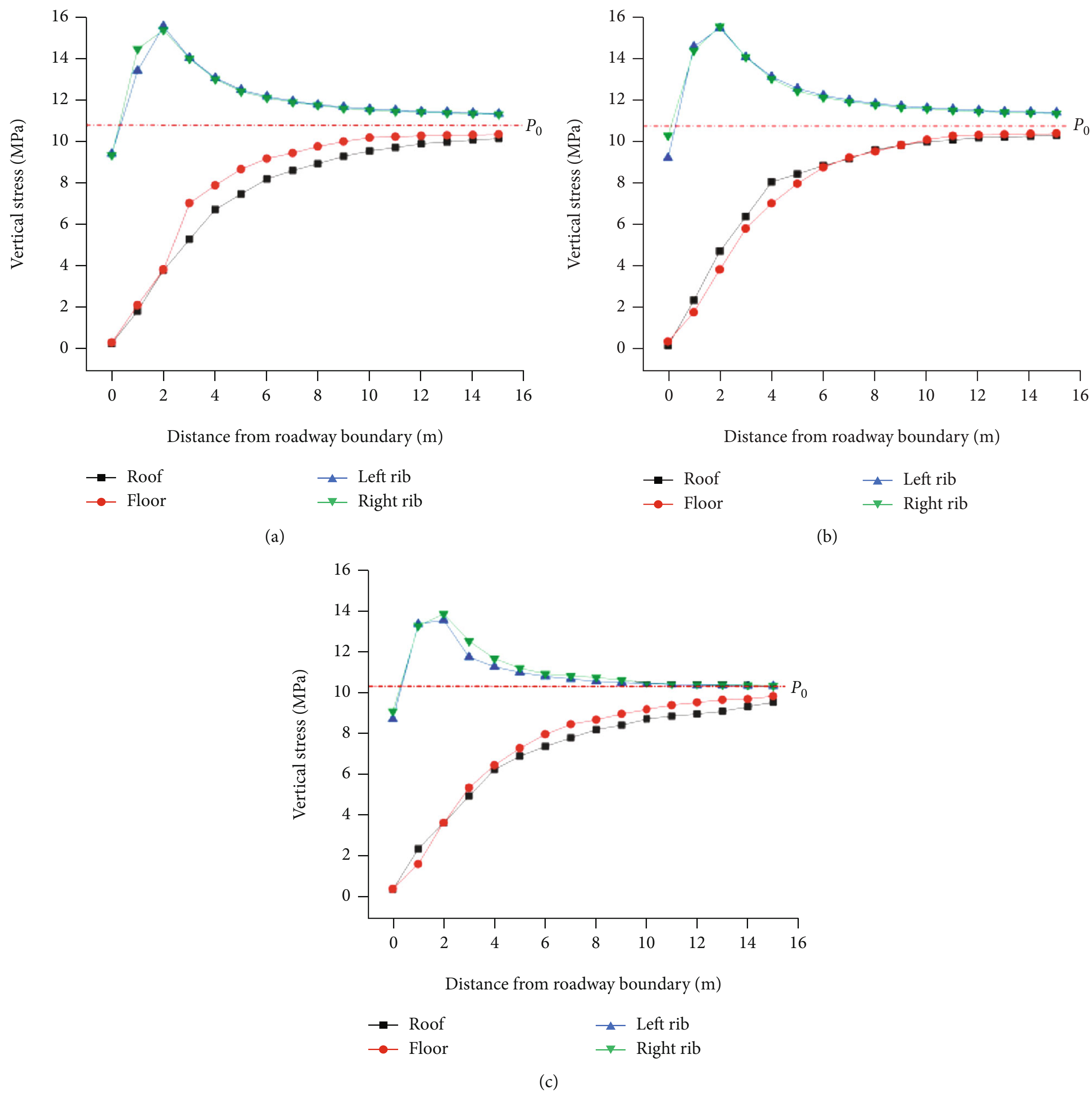

Figure 7: Vertical stress change curve under different support methods. (a) No support. (b) Original support. (c) Combined support.

measuring points are arranged within 15 m perpendicular to the roof, floor, and left and right ribs of the roadway, and the vertical stress values are recorded every 1 m. The vertical stress changes of the roof, floor, and right rib under different support methods are shown in Figure 7.

It can be seen from Figure 7 that the variation trend of vertical stress under different support methods is basically the same. The variation trend of vertical stress of the two ribs increases first and then decreases, gradually tends to be stable, close to the in situ rock stress. The vertical stress variation trend of the roof and floor is always increasing and finally tends to a stable value, which is close to the in situ rock stress. As can be seen from Figure 7(a), in the absence of support, the vertical stresses on the left and right ribs reach the maximum values of 15.55 MPa and 15.44 MPa at 2 m, respectively. In the range of 2~5 m, the vertical stress drops rapidly. After 5 m, the descending speed slows down and the vertical stress basically tends to be stable at 9 m, remaining at 11.3 MPa. The vertical stress grows rapidly in the range of 0 to 5 m in the roof and floor; in the range of 5 to 9 m, the growth rate becomes slower; at 9 m, it basically remains stable at 11.4 MPa and 11.37 MPa, respectively.

It can be seen from Figure 7(b) that under the original support condition, the vertical stresses on the left and right ribs reach the maximum of 15.42 MPa and 15.37 MPa at 2 m, which are slightly smaller than those without support. In the range of 2~5 m, the vertical stress drops rapidly. After 5 m, the descending speed becomes slower, and the vertical

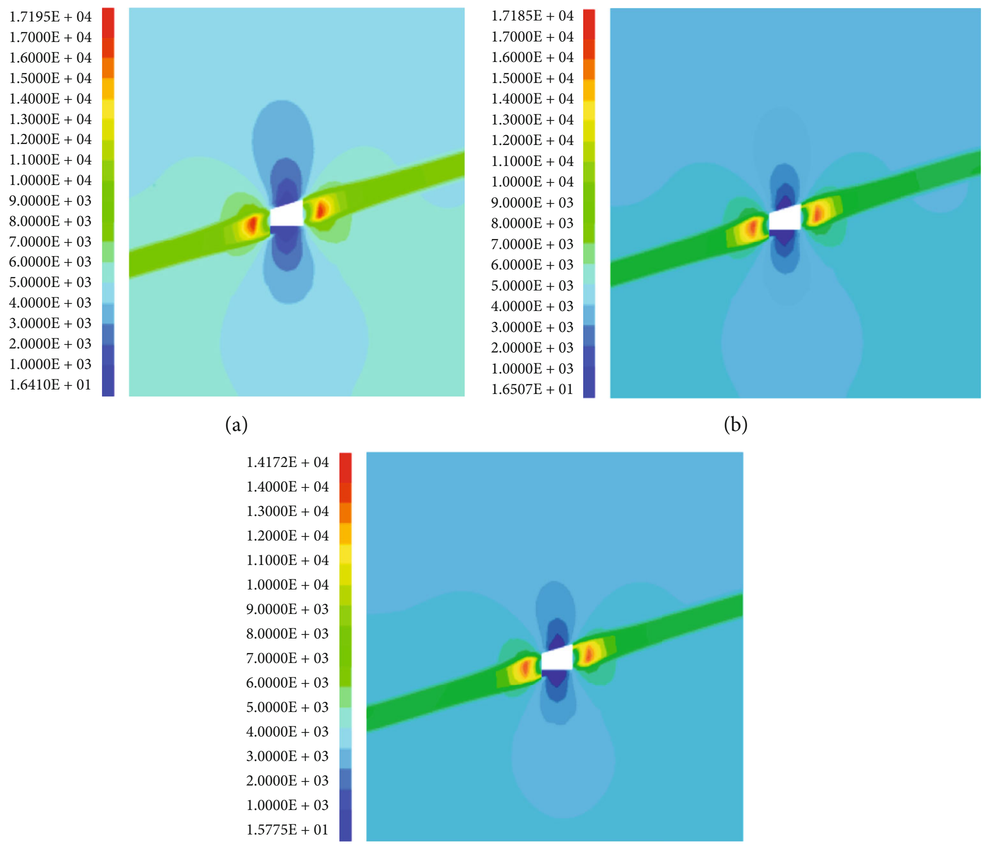

Figure 8: Energy density distribution nephogram of the three scheme. (a) No support. (b) Original support. (c) Combined support.

stress basically tends to be stable at 8 m, remaining at 11.3 MPa. The roof and the floor show a large difference in the range of 0 to 5 m. The vertical stress in the roof grows faster relative to the floor; in the range of 5 to 9 m, the growth rate becomes slower; at 9 m, it basically remains stable at 10.24 MPa and 10.15 MPa, respectively.

From Figure 7(c), it can be seen that the stress difference between the left and right ribs decreases significantly, and the change trend becomes significantly slower, which means that the stress concentration degree decreases significantly, and the stress peaks are 13.94 MPa and 13.88 MPa, respectively. The variation trend of the roof and the floor is basically the same and finally close to the in situ rock stress.

4.4. Law of Energy Distribution. Figure 8 shows the nephogram of energy distribution under different support methods, from which it can be seen that the overall energy of the coal seam is high, and a high energy zone appears at the position of about 2 m to the left and right of the roadway, which corresponds to the vertical stress high stress area. The energy of the roof and floor of the roadway is the smallest, extending 5 m up and down, respectively, to the low energy area. The rest of the locations have uniform energy distribution, and the overall energy of the lower part is greater than that of the upper part. This is because after the excavation of the roadway, the stress of the surrounding rock is redistributed. The elastic strain energy is concentrated near the surrounding rock of the roadway for the fine adjustment and tiny movement of a large number of surrounding rock particles. The energy at the position of the two ribs of the roadway and the junction of the floor and the two ribs is the largest, and the elastic deformation energy stored in the floor surrounding rock is the least, and the energy reduction is the largest. It means that after excavation, the floor of the roadway has been released and the stored energy has been reduced, and most of the elastic deformation energy has been turned into plastic dissipation energy, which is gradually reduced along the radial direction, corresponding to the vertical stress distribution. Comparing the energy density distribution nephogram under different support methods, it can be found that the range of high energy density in both ribs of the roadway after support has been reduced, and the low energy density area in the roof and the floor has been reduced and distributed more evenly.

Figure 9 shows the change curve of energy density under different supports. As can be seen from Figure 9(a), the overall variation trend of energy density is consistent with that of the vertical stress. The left and right ribs reach the maximum at 2 m, which are 15895.8 J/m^3 and 15637.4 J/m^3, respectively. In the range from 2 to 7 m, the energy density decreases rapidly. After 7 m from the roadway boundary, the energy density decreases slowly and gradually stabilizes,

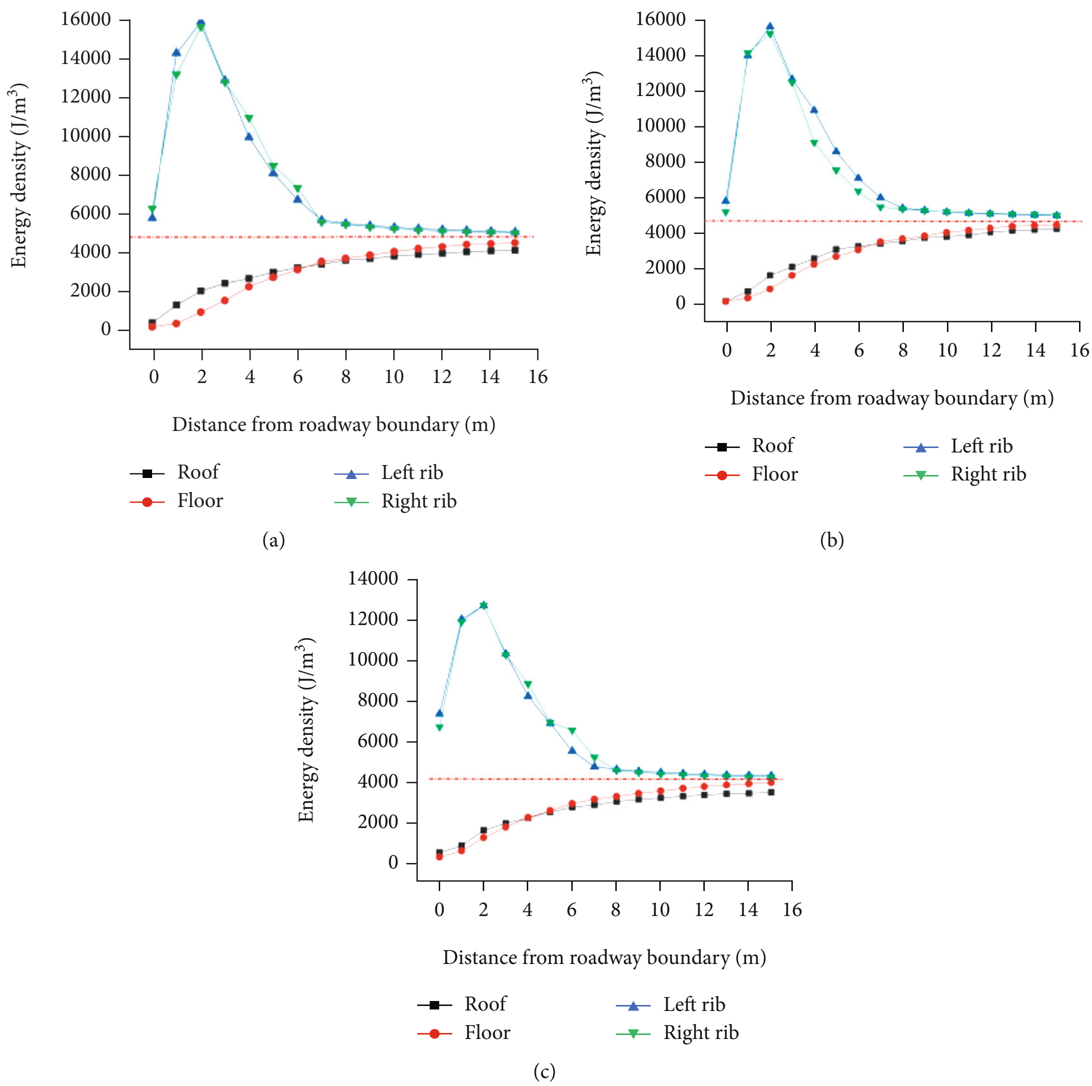

FIGURE 9: Energy density change curve under different support methods. (a) No support. (b) Original support. (c) Combined support.

basically remaining at about 4490 J/m^3. The roof and floor show a fast and then slow growth trend, and gradually stabilize after 7 m from the roadway boundary, and finally remain at about 4490 J/m^3. As can be seen from Figure 9(b), the left and right ribs reach the maximum at 2 m, which are 15679 J/m^3 and 15479 J/m^3, respectively. In the range of 2~7 m, the energy density of the left and right ribs varies, and the right rib is slightly smaller than the left rib, which is due to the support role to resist part of the deformation. After 7 m from the roadway boundary, the energy density decreases slowly and gradually stabilizes, basically keeping at about 4485 J/m^3. Compared with the condition without support, the growth trend of roof and floor is more uniform, and the energy density finally stays around 4485 J/m^3. It can be seen from Figure 9(c) that under the combined support condition, the peak energies of the left and right ribs are 12617 J/m^3 and 12632 J/m^3 respectively, which is lower than the first two cases and the overall energy difference is small. The energy density of the roof and floor is basically the same, and the energy of the floor is slightly larger than that of the roof.

5. Engineering Application Effect

Three roadway surface displacement stations are arranged in the original support and combined support roadway. The measuring stations are arranged by the “cross” point layout method, and the distance between the stations is 30~50 m. The data are further organized to get the amount of roof subsidence, floor heave, and right rib offset at the location of each measurement station and to compare and analyze the deformation of the original support and combined support of the roadway.

According to the monitoring data, the roadway surface displacement curves of the original support and the combined support were obtained through further processing and analysis. The roof subsidence, floor heave, and right rib offset of the roadway in different stages were compared, and the most representative group of curves was selected as shown in Figure 10.

From the roadway roof subsidence curve in Figure 10(a), it can be seen that the maximum roof subsidence of the floor heave in the original supporting roadway is about 247 mm, and the trend of continuous increase is obvious. The

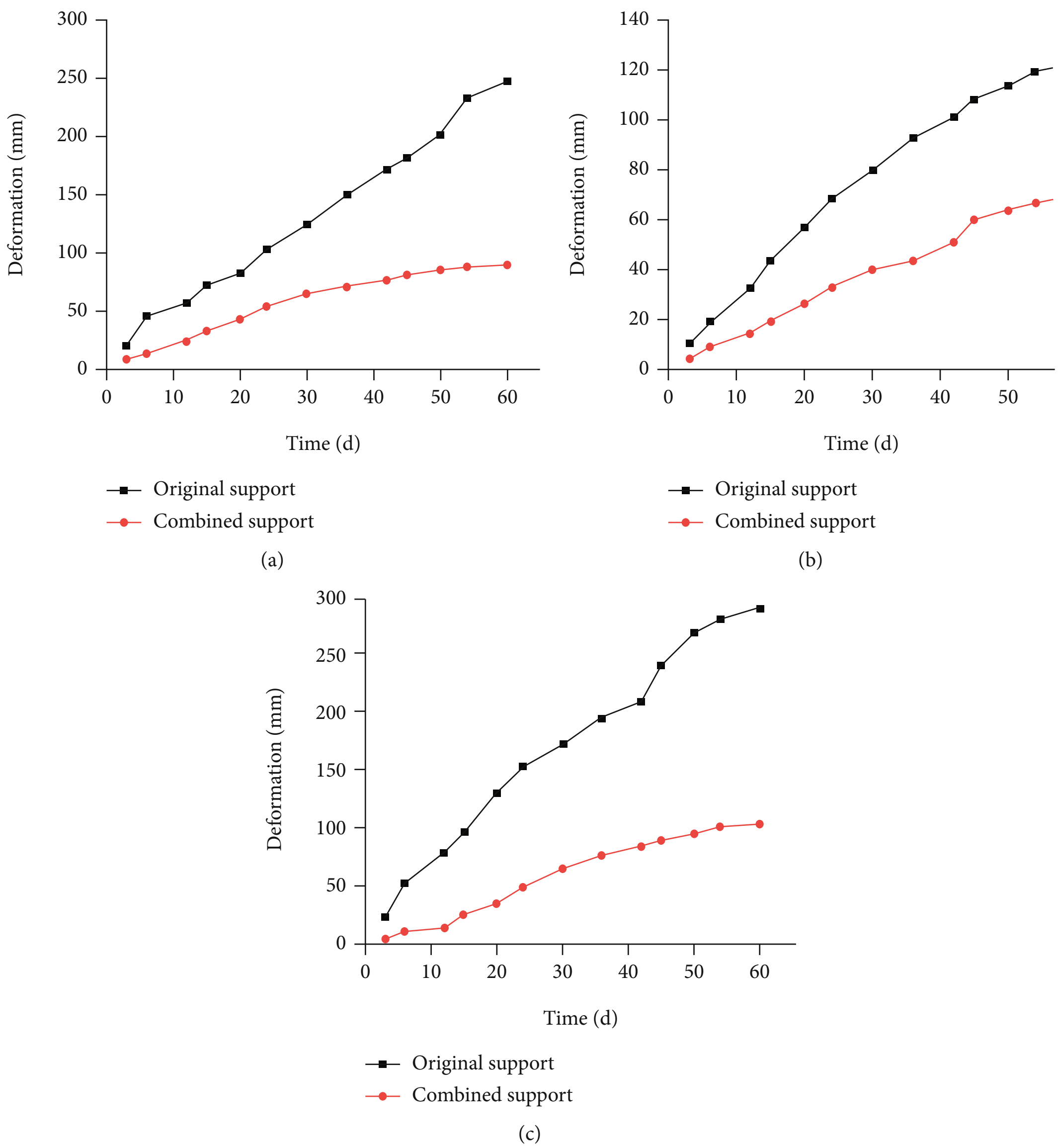

FIGURE 10: Roadway surface deformation curve. (a) Roof Subsidence. (b) Floor Heave. (c) Right Side Offset.

maximum roof subsidence in the combined support is about 90 mm, and the deformation is decreased by 63.56%, and the curve gradually stabilizes. From Figure 10(b), it can be seen that the floor heave maximum of the original support roadway is about 120 mm, the curve does not slow down, and the roadway floor heave will continue to increase. The floor heave maximum of roadway with combined support is 68 mm, and the deformation is reduced by 43.33%. Moreover, the curve starts to slow down when the monitoring time is about 45d, and the floor heave of the roadway gradually tends to be stable. As shown from Figure 10(c), the right rib offset maximum of the original supporting roadway is about 292 mm, which obviously shows a trend of continuous increase. The maximum right rib offset of the combined support roadway is about 104 mm, and the deformation is decreased by 64.38% and gradually tends to be stable. Through the above comparative analysis, it is obvious that after the roadway adopts the combined support technology, the roadway surrounding rock deformation is controlled, the overall stability of the roadway surrounding rock is improved, and the application effect of the technology is remarkable.

6. Conclusion

Based on the existing support parameters of Dongrong No. 2 Mine, this paper makes a comparative analysis of vertical stress and energy distribution under three support modes: no support, original support, and combined support and draws the following conclusions:

(1) After roadway excavation, the two sides of roadway are high stress areas, and the line direction is consistent with the tendency of coal seam. The roof and floor of the roadway are both low stress areas, and the floor appears in a small range of tensile stress area

(2) The variation trend of vertical stress under different support methods is consistent, and the variation trend of vertical stress on both ribs increases first and then decreases, gradually approaching the in situ rock stress. The vertical stress of roof and floor increases all the time and finally approaches the in situ rock stress. From no support to combined support, the area of high stress on both ribs of roadway is obviously reduced, the change of roof is small, and the stress concentration area of floor corner is obviously reduced. The vertical stress concentration range of roadway surrounding rock is obviously decreased after the support, and the combined support is more effective, and the vertical stress distribution is more uniform

(3) After the roadway excavation, the overall energy of the coal seam is high, and a high energy zone appears at about 2 m of the roadway, corresponding to the high vertical stress zone. The energy of the roof and floor of the roadway is the smallest, extending 5 m upward and downward to the low energy area. The rest of the positions have uniform energy distribution, and the overall energy of the lower part is larger than that of the upper part

(4) The variation trend of energy under different support methods is consistent with that of vertical stress. The variation trend of energy on both ribs increases first and then decreases. The variation trend of energy in the roof and floor is always increasing and finally tends to be stable. From no support to combined support, the high energy zone on both ribs of the roadway is obviously reduced. The energy concentration range of the roadway surrounding rock decreases after the support, the combined support effect is better, and the energy distribution is more uniform

(5) After the roadway adopts the combined support technology, the roof, floor, and right rib deformations are reduced by 63.56%, 43.33%, and 64.38%, respectively. The deformation of surrounding rock is controlled, and the overall stability of the surrounding rock is improved

Data Availability

The rock mechanical parameters in this paper are all measured in the laboratory, and the status quo of roadway support and on-site monitoring data are all obtained through on-site investigation.

Conflicts of Interest

The authors declare that they have no conflicts of interest.

Acknowledgments

The research presented in this paper has been supported by the Central Government for the Reform and Development of Local Universities (2020YQ13).

References

[1] D. J. Liu, J. P. Zuo, H. Y. Liu, Z. J. Hong, J. H. Wen, and Y. Shi, "Development and present situation of support theory and technology in coal mine roadway in China," *Journal of Mining Science and Technology*, vol. 5, no. 1, pp. 22–33, 2020.

[2] G. M. Zhao, X. B. Zhang, C. Wang, and X. R. Meng, "Mechanical analysis and numerical simulation for deep and shallow bearing structures of soft and broken roadway surrounding rock," *Journal of China Coal Society*, vol. 41, no. 7, pp. 1632–1642, 2016.

[3] Q. B. Meng, L. H. Kong, L. J. Han et al., "Stability control technology for deep soft and broken composite roof in coal roadway," *Journal of China Coal Society*, vol. 42, no. 10, pp. 2554–2564, 2017.

[4] S. Mehmet, "Two-and three-dimensional stability analysis of underground storage caverns in soft rock (Cappadocia, Turkey) by finite element method," *Journal of Mountain Science*, vol. 19, no. 4, pp. 1182–1202, 2022.

[5] P. Xu, R. S. Yang, J. J. Zuo et al., "Research progress of the fundamental theory and technology of rock blasting," *International Journal of Minerals, Metallurgy and Materials*, vol. 29, no. 4, pp. 705–716, 2022.

[6] M. S. Gao, N. Zhang, L. N. Dou, K. Wang, and J. G. Kan, "Study of roadway support parameters subjected to rock burst based on energy balance theory," *Journal of China University of Mining and Technology*, vol. 36, no. 4, pp. 426–430, 2007.

[7] W. J. Ju, "Energy checking design method of roadway with rock-brust danger," *Coal Mining Technology*, vol. 16, no. 3, pp. 81–83, 2011.

[8] A. W. Wang, D. W. Fan, Y. S. Pan et al., "Determination of three-level energy absorbing support parameters in rock burst roadway based on energy calculation," *Coal Science and Technology*, vol. 49, no. 6, pp. 72–81, 2021.

[9] Y. S. Pan, Q. X. Qi, A. W. Wang et al., "The theory and technology of three-level support for coal mine rockburst roadway," *Journal of China Coal Society*, vol. 45, no. 5, pp. 1585–1594, 2020.

[10] W. L. Gong, D. Y. Zhu, J. Wang, M. C. He, and D. L. Wang, "Deformation and energy equation verification of NPR anchor cable support roadway based on model test," *Journal of Mining & Safety Engineering*, vol. 37, no. 5, pp. 918–927, 2020.

[11] R. L. Shan, H. Yang, H. Zhong, and Y. Tao, "Design of support parameters and energy constitutive model yielding anchor blot," *Journal of China University of Mining & Technology*, vol. 43, no. 2, pp. 241–247, 2014.

[12] J. K. Lin, Y. Zhang, and Y. Hao, "Reasonable coal pillar size supported by high strength energy-absorbing rock bolt," *Coal Engineering*, vol. 53, no. 3, pp. 40–45, 2021.

[13] Z. Q. Ma, C. M. Tao, Y. J. Zuo, G. Y. Wu, and P. Liu, "Supporting technology of roadways with thick and soft roof based on energy balance theory," *Journal of Mining & Safety Engineering*, vol. 35, no. 3, pp. 496–502, 2018.

[14] F. T. Wang, J. J. Shang, B. Zhao, Q. H. Cao, and T. C. Niu, "Strengthened anchor cable support mechanism and its parameter optimization design for roadway's dynamic pressure section," *Journal of China University of Mining & Technology*, vol. 51, no. 1, pp. 56–66, 2022.

[15] H. X. Chen, M. Y. Wang, C. Z. Qi, and J. Li, "Mechanism of energy adjustment and balance of rock masses near a deep circular tunnel," *Chinese Journal of Geotechnical Engineering*, vol. 42, no. 10, pp. 1849–1857, 2020.

[16] Z. Hao, L. F. Guo, X. D. Zhao, G. X. Chen, and G. H. Zhang, "Analysis of burst failure energy characteristics of mining roadway surrounding rock," *Journal of China Coal Society*, vol. 45, no. 12, pp. 3995–4005, 2020.

[17] H. Y. Shi, N. J. Ma, J. J. Shi, N. Li, and G. W. Tan, "Simulation study on energy evolution and release of surrounding rock in stope," *Coal Science and Technology*, vol. 48, no. 3, pp. 106–111, 2020.

[18] J. W. Zheng, W. J. Ju, Z. Zhang et al., "Equivalent section supporting theory and its applications," *Journal of China Coal Society*, vol. 45, no. 3, pp. 1036–1043, 2020.

[19] J. W. Zheng, W. J. Ju, X. D. Sun et al., "Differentiation response characteristic of roadway deformation and rock supporting analysis," *Journal of Mining and Strata Control Engineering*, vol. 3, no. 3, pp. 13–20, 2021.

[20] D. P. Ma, Y. J. Yang, J. S. Cao, and L. Y. Xing, "Optimization design of cross section shape of deep roadways based on characteristics of energy release," *Journal of Central South University (Science and Technology)*, vol. 46, no. 9, pp. 3354–3360, 2015.

[21] Y. M. Chen and H. L. Liu, "Development and implementation of Duncan-Chang constitutive model in FLAC^{3D}," *Rock and Soil Mechanics*, vol. 28, no. 10, pp. 2123–2127, 2007.

[22] M. Wang, Z. F. Song, D. J. Zheng, W. L. Shen, P. F. Gou, and S. J. Wei, "Development and application of rock energy dissipation model in FLAC^{3D}," *Journal of China Coal Society*, vol. 46, no. 8, pp. 2565–2573, 2021.

Hindawi
Geofluids
Volume 2022, Article ID 9430526, 11 pages
https://doi.org/10.1155/2022/9430526

Research Article

A Prediction Method for Floor Water Inrush Based on Chaotic Fruit Fly Optimization Algorithm–Generalized Regression Neural Network

Zhijie Zhu,[1,2] Chen Sun,[1] Xicai Gao,[2] and Zhuang Liang[3]

[1]*School of Mining, Liaoning Technical University, Fuxin, China*
[2]*State Key Laboratory of Coal Resources in Western China, Xi'an University of Science and Technology, Xi'an, China*
[3]*Research Centre, Ministry of Emergency Management, China*

Correspondence should be addressed to Zhijie Zhu; zhuzhijie@lntu.edu.cn

Received 30 March 2022; Revised 10 May 2022; Accepted 8 June 2022; Published 20 June 2022

Academic Editor: Zhijie Wen

The research was aimed at predicting floor water-inrush risk in coal mines and forewarn of such accidents to guide safe production of coal mines in practice. To this end, a prediction method for floor water inrush combining the chaotic fruit fly optimization algorithm (CFOA) and the generalized regression neural network (GRNN) is proposed. Floor water inrush is predicted by virtue of the robust nonlinear mapping capability of the GRNN. However, because the prediction effect of the GRNN is influenced by the smoothing factor, the CFOA is adopted to optimize this factor. In this way, influences of human factors during parameter determination of the GRNN prediction model are decreased, and the prediction accuracy and applicability of the model are improved. Results show that the CFOA–GRNN prediction model has an accuracy of 93.2% for whether floor water inrush will occur or not. Compared with the BPNN, RNN, and GRU network prediction model, the CFOA–GRNN model is superior in the prediction accuracy and generalization, and it can more accurately predict floor water inrush.

1. Introduction

With the increasing depletion of shallow coal resources and the increasing intensity of coal mining, more and more coal mines will encounter deep mining issues [1–5]. Compared with shallow coal mining, deep rock mass is in a typical complex mechanical environment of "three highs and one disturbance" (high ground stress, high karst water pressure, high ground temperature, and strong mining disturbance), showing large deformation and uncoordinated deformation and impact deformation [6–15]. Due to the characteristics of deep rock mechanics that are significantly different from those of shallow rock mechanics, coupled with the complexity of the occurrence environment, a series of catastrophic accidents in deep resource mining have greatly increased in frequency, intensity, and scale. Coal-rock dynamic disasters such as pressure appearance, floor water inrush, mine earthquake, rock burst, and coal and gas outburst become more frequent, and the disaster mechanism will become more complex [16]. In recent years, several major accidents in coal mines in my country are mostly secondary disasters, which have caused the expansion of accidents and increased the catastrophic nature of accidents. For example, in 2005, Fuxin Sunjiawan Coal Mine caused coal and gas outbursts due to rock bursts, and then, a huge gas explosion occurred, killing 214 people and injuring 30 people. During the mining of the 4th coal seam in Huafeng Coal Mine, due to the frequent occurrence of rock bursts, a large amount of water from the roof abscission flowed into the working face. As mining depths increase, coal seams bear increasing karst aquifer pressure, and therefore, the floor water-inrush risk increases: this has been one of the greatest hidden dangers for safe production of coal mines in China. In such context, predicting floor water-inrush risk is important in preventing accidents arising from such disasters in coal mines and ensuring safe mining above high-pressure aquifers.

Much theoretical analysis and numerical simulation has been conducted on the principle and prediction of water inrush from coal floors. For examples, Hu et al. [17] built a physical model with similar materials of the fracture zone in the synclinal axis above a confined aquifer and studied the mechanism of floor water inrush under the combined effect of a confined aquifer and a fracture zone. Numerous scholars also evaluated the influences of confining pressure and permeation pressure on water inrush from coal floors and obtained the mechanism of water inrush from coal floors under the coupled effect of seepage field and stress field [18–21], studied the effects of faults on stability of the aquifuge of coal floors, deduced the critical water pressure formula for failure of the aquifuge under influences of the fault, and proposed the corresponding mechanical criterion for floor water inrush. Li and Wang [22] reproduced the formation and evolution process of water-inrush channels through numerical simulation using FLAC (3D), which provides insights into formation and evolution characteristics of water-inrush channels in coal floors under high pressure. Ma et al. [23] combined theoretical analysis and numerical simulation with rock failure process analysis and microseismic monitoring to study failure characteristics and damage depth of coal floors above a confined aquifer. The method overcomes the limitations of a single method in previous research and also provides a reference for solving the water-inrush problems in roadways and selection of proper reinforcement measures. Shao et al. [24] proposed a catastrophe prediction model for floor water inrush in coal mines and deduced formulae for critical stress and energy release at failure of the floor system, providing a new theoretical approach for predicting water inrush from coal floors. By using the Mohr–Coulomb criterion and theory of fracture mechanics, Zhang et al. [25] studied the failure mechanism of floor water inrush and found that the higher the breaking energy of fractures, the more significant the floor water-inrush risk in coal mines. Existing theoretical formulae for floor water inrush generally only consider a few influencing factors and therefore are inapplicable to other coal mines. In addition, laboratory tests simplify the mining conditions, so the results are only of reference significance in prediction. Although numerical calculation method develops apace, it is still unable to simulate the complex geological and hydrogeological conditions encountered in deep mining.

In recent years, several risk evaluation methods and prediction models from multiple aspects have been proposed based on nonlinear statistical theory. Zhang and Yang [26] proposed a dynamic GRU (gated recurrent unit) neural network prediction model, the model is able to predict water inrush from coal floor with high accuracy. Zhang et al. [27] established a MFIM-TOPSIS variable weight model, which combines a multifactor interaction matrix (MFIM) and the technique for order performance by similarity to ideal solution (TOPSIS) to implement the risk assessment of floor water inrush in coal mines. Zhang et al. [28] presented a mathematical assessment method for coal-floor water-inrush risk integrating the hierarchy-variable-weight model (HVWM) with collaboration-competition theory (CCT). Zhao et al. [29] proposed a novel and promising assessment model for water inrush based on random forest (RF), which was more practicable to assess the water-inrush risk than PNN. Dong et al. [30] combined the Fisher feature extraction and support vector machine (SVM) methods, and this new combined model was more accurate and efficient in discriminating water-inrush sources than the traditional SVM model. Wang et al. [31] established PCA- (principal component analysis-) BP (Back Propagation) neural network classification model which can effectively identify coal mine water inrush. These methods have been applied in practical work, while still showing certain drawbacks. For instance, the distance discriminant analysis correlates the discriminant distance with units of indices and considers various different indices and variables equally, which sometimes fails to meet the actual requirements, thus leading to less accurate predictions. The SVM does not provide general solutions to nonlinear problems, so it needs to be further improved. The BP neural networks have shortcomings that the BP neural network needs a large number of data samples for training and also has too many optimized parameters [32].The generalized regression neural network (GRNN) is a kind of radial basis function neural network proposed by Specht, which has a strong ability for nonlinear mapping [33]. Compared with the BPNN and the SVM, the GRNN has fewer adjustment parameters, does not easily fall into local minima, and is good at processing large-scale training samples. The generalized regression neural network (GRNN) is highly superior in approximation capability, learning rate, and prediction accuracy, and it can reduce computation complexity and better predict floor water-inrush risk [34, 35].

On this basis, the GRNN model is established to predict floor water inrush based on the theory of nonlinear regression by combining relevant water-inrush data of numerous working faces. At the same time, the chaotic fruit fly optimization algorithm (CFOA) is used to optimize the smoothing factor of the GRNN. The novelty of CFOA-GRNN model includes the following three aspects: (a) The fruit fly optimization algorithm achieves the goal of finding the global optimal solution of complex functions in space by simulating the competition and cooperation behavior of fruit fly individuals. The algorithm has the advantages of simple calculation process and fast convergence speed. (b) Generalized regression neural network (GRNN) has the advantages of strong nonlinear mapping ability, single setting parameters, high fault tolerance, and robustness and has high prediction accuracy and stability. (c) The GRNN algorithm is easy to fall into the shortcoming of local optimum. The CFOA algorithm can find the global optimal solution for complex functions in space, and the CFOA algorithm is combined with the GRNN prediction model to make up for the shortcomings of the GRNN algorithm that is easy to fall into local optimality, quickly find the global optimal solution, and improve the prediction efficiency. And accuracy can be greatly improved. The prediction results can provide reference for prediction of floor water inrush and safe production of working faces.

2. Influencing Factors of Floor Water Inrush in Coal Mines

2.1. Aquifer Pressure. Head pressure of confined aquifers below coal floors is the precondition and power for floor water inrush. To cause floor water inrush, the head pressure of underlying aquifers should be large enough. Under the same conditions of the aquifuge for coal floors, the confined water pressure below coal floors is directly proportional to the probability of occurrence of water inrush. Particularly, when the aquifuge is affected by mining activities or encounters a fault, the water pressure exerts significant influences on water inrush. Therefore, aquifer pressure is an important basis from which to study floor water inrush.

2.2. Aquifuge Thickness. An aquifuge for coal floors is an intact stratum between a coal floor and the top of an aquifer. The aquifuge exerts influences different from other factors and plays a critical role in preventing groundwater of a confined aquifer from entering the mining space of a mine. It is the only inhibiting factor for floor water inrush and forms a safety barrier for mining above confined aquifers.

Aquifuges can obstruct floor water inrush, and the capability depends on aquifuge thickness, mechanical strength of rock, and integrity of aquifuges. When keeping other conditions unchanged, the thicker and the stronger the aquifuge, the lower the probability of water inrush, and *vice versa* [15]. According to statistical analysis of 343 water-inrush records in typical mining areas in China, the relationship between the aquifuge thickness and the number of water inrush is revealed (Table 1).

2.3. Dip Angle of Coal Seams. According to dip angles, coal seams can be classified into nearly horizontal, gently inclined, inclined, deeply inclined, and steeply inclined, separately corresponding to dip angles of less than 8°, between 8~25°, 25~45°, and 35~65°, and greater than 45°. Previous research has shown that when the dip angle of faults is small, shear failure is likely to occur during coal mining, which induces fractures in aquifers and finally water-inrush accidents. Numerous engineering cases have proven that deeply inclined coal seams are more likely to encounter water-inrush accidents.

2.4. Fault Throw. Damage of faults to coal and rock mass is mainly manifest as increased fractures and pores in, and greatly decreased strength of, coal and rock mass nearby a fault. Different fault throws may produce different contact relationships between coal seams and aquifers in two plates of a fault. Analysis shows that the larger the fault throw and the deeper the cut, the greater the influences of faults and the greater the probability of floor water inrush.

Mining conditions such as mining height and mining methods also affect the initial stress state of the coal and rock mass and the damage depth of coal floors and further influence floor water inrush. Six factors including water pressure (MPa), mining height (m), aquifuge thickness (m), fault throw (m), dip angle of coal seams (°), and distance from a fault to a working face (m) are taken as main influencing factors of floor water inrush. The original data selected are listed in Table 2. The sample data is obtained from the statistics of some mines in my country, mainly including the water-inrush data from the working face and floor of the typical large-water mining areas, such as Hebei Fengfeng, Jinglong, Hebi Hebi, and Shandong Zibo, and the measured data of normal mining.

Table 1: Relationship between aquifuge thickness and number of water inrush in typical mining areas.

Aquifuge thickness (m)	Number of water-inrush events	Proportion (%)
>40	23	7
32-40	34	10
25-32	96	28
20-25	77	22
<20	113	33

3. Principles Underpinning Various Algorithms

3.1. CFOA. Fruit flies can accurately locate distant food sources because of their special sense organs. The fruit fly optimization algorithm (FOA) is an algorithm deduced for searching for the optimal results based on foraging behaviors of fruit flies. FOA simulates the optimization process of fruit flies according to their foraging behavior and then finds the optimal solution. It is characterized by advantages including understandable logic, no need to adjust data and parameters, and rapid convergence [36–38]. When searching in a complex environment, FOA is likely to be trapped in local extremums and leads to a large deviation between the results and reality. FOA has been applied in neural network training [39], financial distress model solving [40], power load forecasting [41], multidimensional knapsack problem [42], web auction logistics service [43], and so on [44–46].

Chaos theory is universal in its applicability to such problems, and its methods can avoid being trapped in local extrema. Therefore, the CFOA is used to compensate for the drawback of the FOA. The steps are briefly described as follows:

Step 1. The initial location (InitX, InitY) of a fruit fly is randomly determined.

Step 2. Random directions and distances are assigned to fruit flies to search for food.

$$X_i = \mathrm{InitX} + \mathrm{Random\ value},$$
$$Y_i = \mathrm{Inity} + \mathrm{Random}. \tag{1}$$

Step 3. The distance (Dist) of a fruit fly to the origin is estimated, and then, the judgment value of smell concentration (S) is calculated, which is the reciprocal of the distance.

$$\mathrm{Dist} = \sqrt{x^2 + y^2},$$
$$S = \frac{1}{\mathrm{Dist}}. \tag{2}$$

Step 4. The judgment value of smell concentration (S) is substituted into the judgment function of smell

Table 2: Original data pertaining to influencing factors.

Serial no.	Water pressure (MPa)	Mining height (m)	Aquifuge thickness (m)	Fault throw (m)	Dip angle of coal seams (°)	Distance from a fault to a working face (m)	Water-inrush level
1	1.82	0.8	26.39	4	12	16	I
2	1.65	1.6	25.85	50	17	90	II
3	1	0.9	22.33	2	13	16	II
4	2.88	1	17.68	1.3	20	0	II
5	2.01	8	28	0.6	18	10	III
6	1.91	8	43	1.5	11	2	III
7	1.33	0.85	36.28	0.8	7	62	I
8	0.95	1.45	26.89	1	6	55	I
9	0.92	1.4	33.61	0.5	8	0	I
10	0.34	0.9	32.65	22	6	6	I
11	1.06	2	27.79	0.46	7	21	I
12	0.83	2.85	26.56	0.7	12	6	I
13	2	2.81	30	1.5	18	12	IV
14	1.8	1.9	23	0	15	17	IV
15	1.7	2.8	10	5	17	10	II
16	0.6	1.1	17	2	19	6	I
17	2.1	1.6	59.5	3.5	10	39	I
18	2.8	2.75	69.17	11.7	12	36	I
19	2.8	2.55	66.11	16	12	29	I
20	1.3	1.7	30	4.9	5	21	II
21	1.08	0.9	16.5	3.2	7	7	II
22	1.01	0.9	16.5	3.2	14	75	II
23	2.01	8	28	0.6	18	10	II
24	1.91	8	43	1.5	11	2	I
25	2.55	8	50	4	13	10	I
26	2.35	2	50	100	16	153	I
27	0.69	3.85	42	32	12	19	III
28	1.68	5	35.3	7	16.7	20	II
29	1.67	5	35.4	7	16.4	12.4	II
30	1.82	5	34.5	7	16.5	0	II
31	1.75	5	34.6	7	13	6	II
32	1.7	5	34.8	7	12.5	12	IV
33	1.77	5	35	8	12	95	I
34	1.67	5	35.3	8	10	96	I
35	1.62	5	36	8	9	103	I
36	1.74	5	34.1	7	20	27	II
37	1.75	5	33.7	7	13	24	II
38	1.82	5	33.6	7	13.4	32	II
39	1.87	5	33.6	7	11	44	I
40	1.84	5	33.8	7	11	55	I
41	1.79	5	34	8	11.5	53	III
42	1.77	5	34.2	8	10.7	45	III
43	1.75	5	34.5	8	10.5	44.8	II
44	1.7	5	34.8	8	13	51	II
45	1.82	5	33.1	7	12	77	I
46	1.87	5	32.6	7	17	74	II
47	1.94	5	32.6	7	15.5	81	II
48	1.97	5	32.8	7	9.5	93	III

Table 2: Continued.

Serial no.	Water pressure (MPa)	Mining height (m)	Aquifuge thickness (m)	Fault throw (m)	Dip angle of coal seams (°)	Distance from a fault to a working face (m)	Water-inrush level
49	1.1	1.6	20	15	11	16	I
50	4.06	2.75	65.86	10	10	11	II
51	3.11	2.61	44.3	3.5	11	12	II
52	2.7	2.55	66.97	16	12	31	II
53	2.3	1.5	46.91	1	11	24	III
54	1.91	1.5	43.11	1.1	8	130	III
55	1.45	1.5	38.9	3	13.5	27	IV
56	1.5	1.5	38.9	1.2	13.5	7	IV
57	1.78	1.5	38.9	11	14	36	II
58	0.74	7.5	65	79	11	63	I
59	1.37	8	50	15	14	15	I
60	1.45	8	46	2.5	15	9	II

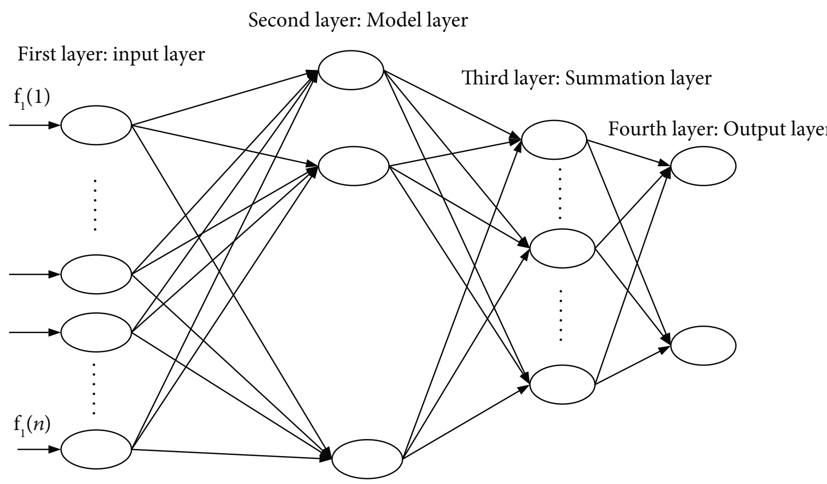

Figure 1: GRNN structure.

concentration to calculate smell concentration (smell) at the individual locations of each fruit fly.

Step 5. The fruit fly with the highest smell concentration in the population is found.

Step 6. The location of the fruit fly with the optimal smell concentration is retained, to which the fruit fly population flies.

Step 7. Iterative optimization is conducted, and Steps 2~5 are repeated. Whether the smell concentration is better than the previous iteration or not is judged. If yes, Step 6 is performed; otherwise, the prediction results are output.

Chaos Fruit Fly Optimization Algorithm (CFOA) is the optimal position of each generation obtained in the iterative optimization process of the fruit fly optimization algorithm, adding chaotic disturbance and performing secondary optimization, which can make the population jump out of the local optimal solution, implementing global search. Other variants of FOA often fall into local extrema when searching for complex environments, which affects the computational accuracy and efficiency.

3.2. GRNN. GRNN is based on the nonparametric kernel regression and allows nonparametric estimation taking sample data as the verification condition of posterior probability, so it has favorable learning ability. The most prominent advantage of GRNN is the setting of network parameters which is so convenient that its network performance can be adjusted only by setting the smoothing factor in the kernel function. The first layer of the GRNN is an input layer, on which the number of neurons is same as the dimensions of the input vectors of learning samples and each neuron is a simple distributed network unit. These neurons directly transfer the input variables into the hidden layer. GRNN uses sample data as the verification condition for posterior probability and nonparametric estimation. Finally, to obtain the regression of dependent variables relative to independent variables, the correlation density function between

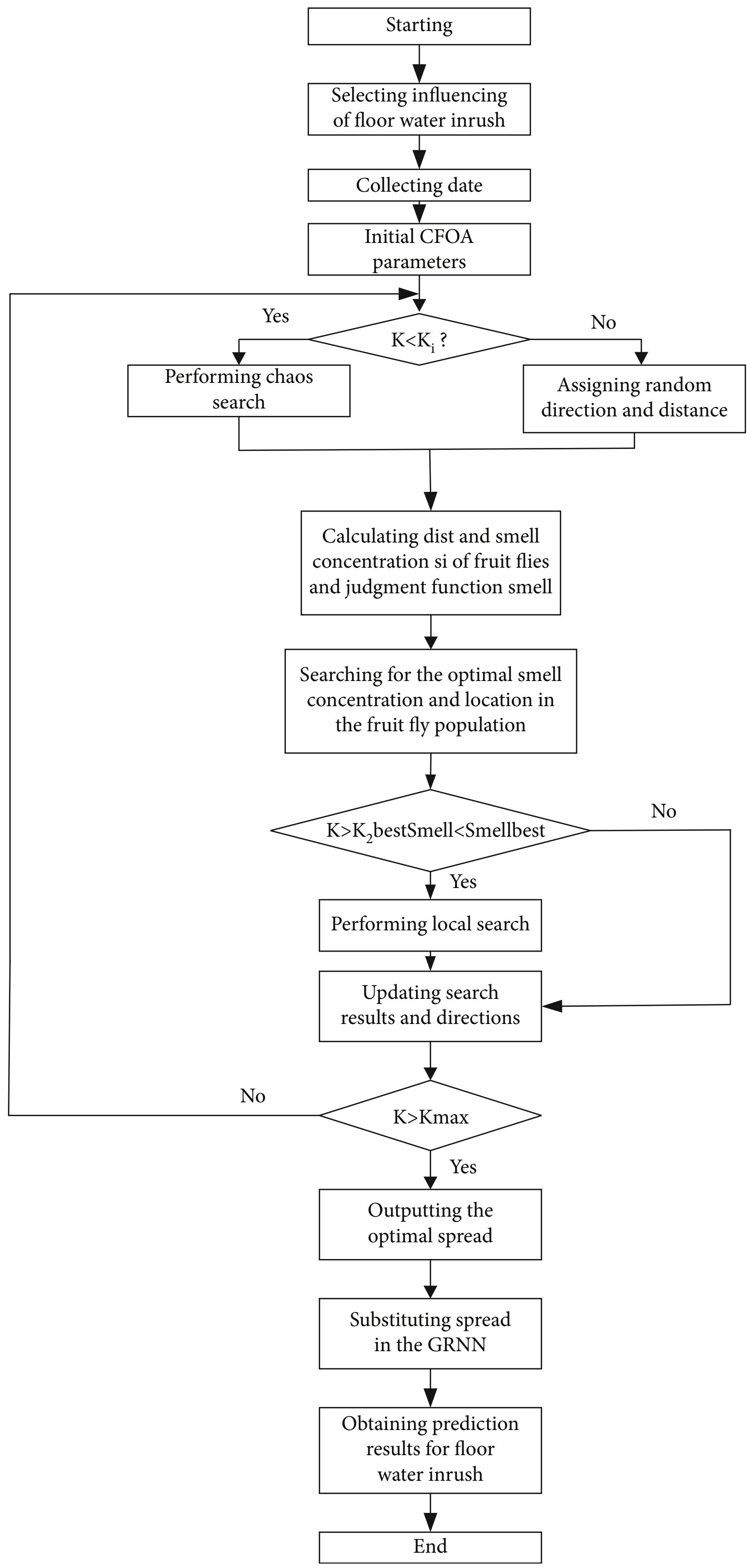

Figure 2: Flowchart of the CFOA–GRNN prediction model.

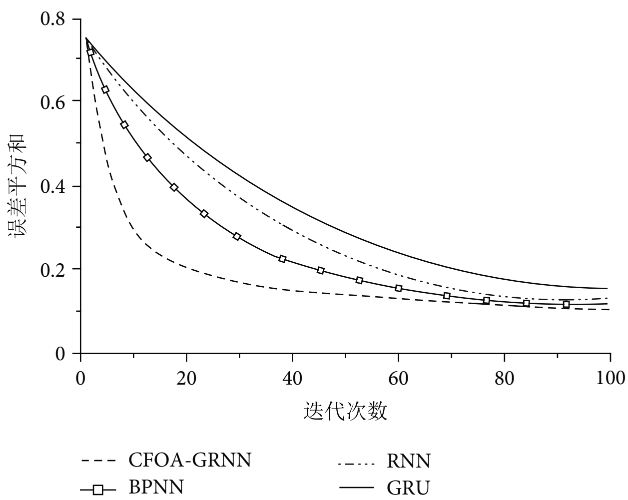

Figure 3: Network training error curve.

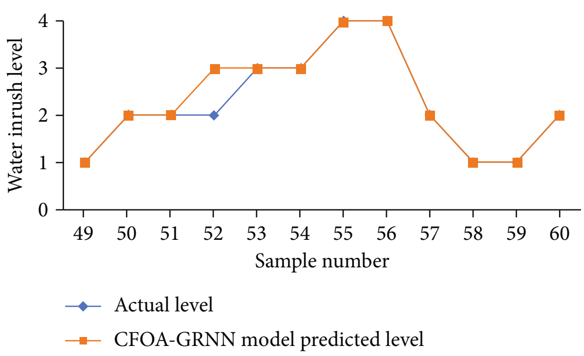

Figure 4: Prediction results of the CFOA-GRNN model.

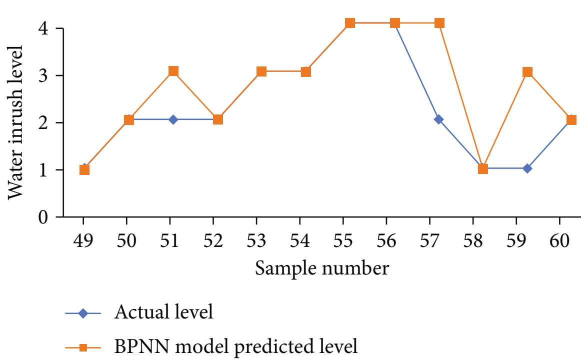

Figure 5: Prediction results of the BPNN model.

dependent variables and independent variables in the GRNN is calculated using the training samples. The calculation formula is shown as follows:

$$\bar{Y} = E(Y/X) = \frac{\int_{-\infty}^{+\infty} y f(X,Y)dY}{\int_{-\infty}^{+\infty} f(X,Y)dY}. \tag{3}$$

For an unknown probability density function $f(X, Y)$,

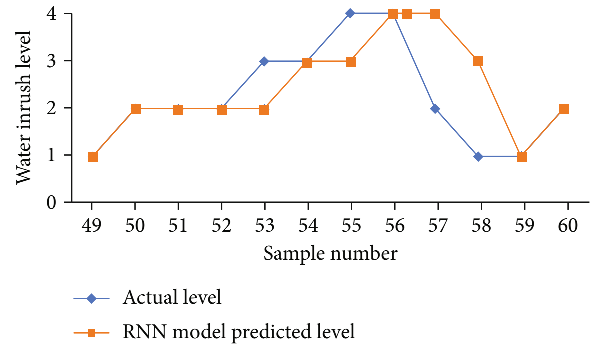

Figure 6: Prediction results of the RNN model.

the following formula is obtained through nonparametric estimation:

$$\bar{f}(X,Y) = \frac{1}{(2\pi)^{(p+1/2)}\delta^{(p+1)}n} \times \sum_{i=1}^{n} \exp\left[-\frac{(X-X_i)^T(X-X_i)}{2\delta^2}\right] \exp\left[-\frac{Y-Y_i}{2\delta^2}\right], \tag{4}$$

where X_i and Y_i separately refer to the observed values of random variables X and Y, δ is a smoothing factor, and n and p separately denote the sample size and dimension of x. The following can be attained according to Formulae (3) and (4):

$$\bar{Y} = \frac{\sum_{i=1}^{n} Y_i \exp\left[-\left((X-X_i)^T(X-X_i)\right)/2\delta^2\right] \int_{-\infty}^{+\infty} y \exp\left[-(y-Y_i)^2/2\delta^2\right] dy}{\sum_{i=1}^{n} Y_i \exp\left[-(X-X_i)^T(X-X_i)/2\delta^2\right] \int_{-\infty}^{+\infty} \exp\left[-(y-Y_i)^2/2\delta^2\right] dy}. \tag{5}$$

This can be simplified to

$$\bar{Y} = \frac{\sum_{i=1}^{n} Y_i \exp\left[-(X-X_i)^T(X-X_i)/2\delta^2\right]}{\sum_{i=1}^{n} \exp\left[-(X-X_i)^T(X-X_i)/2\delta^2\right]}. \tag{6}$$

Formula (6) is the expression for the final output of the GRNN. Based on the calculation formula, the output error of the GRNN is mainly dependent on its smoothing factor δ. When the smoothing factor is very large, $\bar{Y}$ tends to the mean of dependent variables of all samples; on the contrary, if the smoothing factor tends to 0, $\bar{Y}$ is approximated to the training samples. Dependent variables of all samples can be considered only when δ is set to a moderate value, thus obtaining favorable results. Therefore, satisfactory results can be obtained by simply adjusting the smoothing factor of the prediction model. The structure of the GRNN is illustrated in Figure 1.

4. Establishment and Analysis of the Model for Floor Water Inrush Based on CFOA–GRNN

4.1. Model Establishment. CFOA features excellent search capability, which is used to optimize the GRNN model. The basic idea of optimizing GRNN with CFOA is to

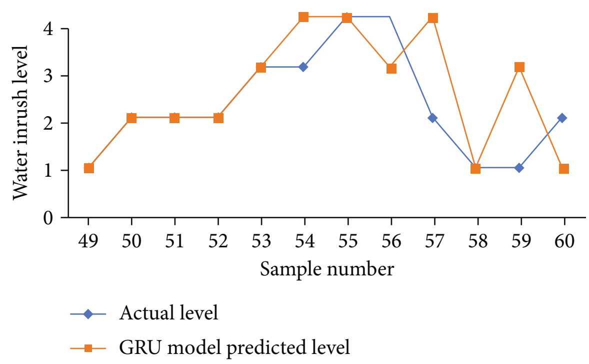

Figure 7: Prediction results of the GRU model.

Table 3: Comparison of the evaluation results of each model.

Parameters	RNN	BPNN	GRU	CFOA-GRNN
OA/%	66.7	75	58.3	91.7
LA(1)/%	66.7	66.7	66.7	100
LA(2)/%	80	60	60	80
LA(3)/%	50	100	50	100
LA(4)/%	50	100	50	100
Tm/s	5.1	4.66	4.8	3.78

convert the distance between a fruit fly and the origin into the smoothing factor (through use of the neural network toolbox in MATLAB™); through training of the GRNN model, the output samples are attained; the prediction error of GRNN is used as the judgment function of smell concentration to find the location of the individual with the lowest error corresponding to all smoothing factors; the above operation is repeated until the condition of convergence is met or the maximum number of iterations is reached. The specific steps are shown as follows:

(1) Influencing factors are selected and data collected

(2) The initial position (Init$X$,Init$y$) of a fruit fly is set at random, which searches within the range (X min, Xmax), (Y min, Ymax). After adding chaotic disturbance C, searched locations of the fruit fly can be obtained on the X and Y-axes

$$\begin{aligned} X_{\text{axis}} &= \text{Init}X(i) + C(\bullet) \\ Y_{\text{axis}} &= \text{Init}Y(i) + C(\bullet) \end{aligned} \tag{7}$$

(3) The distance $D(i)$ between the fruit fly and the origin is calculated according to coordinates of the fruit fly

$$D(i) = \sqrt{x^2 + y^2} \tag{8}$$

(4) The calculation function of smell concentration is determined using the distance function $D(i)$, and the optimal fitness function is searched. The fitness function is updated, and the variable values are optimized. Then, the local optimal location of the fruit fly is sought in accordance with the chaotic sequences

$$\begin{aligned} X(i) &= X\text{axis}c + (2\ \text{rand}\ () - 1)C(\bullet) \\ Y(i) &= Y\text{axis}c + (2\ \text{rand}\ () - 1)C(\bullet) \end{aligned} \tag{9}$$

(5) After finishing the iterative loop, the location of the fruit fly with the largest coverage is recorded, and the maximum smell concentration is retained

$$\begin{cases} X\text{axis}c = X(\text{bestindex}) \\ Y\text{axis}c = Y(\text{bestindex}) \\ \text{Smellbest} = \text{bestSmell} \end{cases} \tag{10}$$

(6) Search of the CFOA is stopped when the number of iterations K is bigger than K max; otherwise, the operation returns to Step 2 to collect the spread of GNRR

(7) The GRNN model is established, and the optimized spread is used to train the network

The specific prediction steps are shown in Figure 2.

4.2. Model Analysis. The first 48 sample data are selected as the training data for the CFOA–GRNN prediction model for floor water inrush and late 12 data as the samples for prediction. The fruit flies are initially at [0,1], and the fruit fly population is 25. The number of maximum iterations and the disturbance factor Dist are set to 150 and 0.5313, respectively. After 98 iterations, the root-mean-square error (RMSE) is 0.0636, and the optimal spread of the CFOA is 0.0076. The obtained optimal spread is substituted in the GRNN to predict floor water-inrush risk. In order to verify the superiority of the performance of the CFOA-GRNN model, the training and prediction effects of the FOA-GRNN model, BPNN model, RNN model, and GRU model are compared with it. Figure 3 shows the training error curves of each model. As can be seen from Figure 4, compared with the other three models, the CFOA-GRNN prediction model has a faster optimization and convergence speed, and the prediction error is relatively stable.

Water-inrush level of the 12 groups of data that occurred last in the sample set, that is, the 49th-60th group of sample data, was selected for testing. Establish CFOA-GRNN, BPNN, RNN, and GRU network prediction models, and compare the prediction results with the real situation, see Figures 4–7 for details.

For the analysis of the evaluation results, the following evaluation indicators can be used to evaluate the feasibility and pros and cons of the model.

(1)Overall accuracy (OA) refers to the proportion of the number of correctly classified samples to the total number of samples, which reflects the accuracy of the model's prediction of all levels. The expression is as follows:

$$\mathrm{OA} = \frac{N_c}{N_t} \times 100\% \tag{11}$$

In the formula, N_t is the total number of test samples, and N_t is the number of samples whose predicted level is equal to the original level of the Nc model.

(2)Local accuracy (LA) refers to the ratio of the number of correctly classified samples of the ith level to the total number of samples of the $i$level, reflecting the accuracy of the model's prediction of a certain level, and its expression is as follows:

$$\mathrm{LA}(i) = \frac{N(i)_c}{N(i)_t} \times 100\%, \ (i = 1, 2, 3, 4) \tag{12}$$

In the formula, $\mathrm{LA}(i)$ is the accuracy of water-inrush level i, $N(i)_t$ is the number of test samples with water-inrush level i, and $N(i)_c$ is the number of samples at level i equal to the original level.

(3)Operation time T: it reflects the operation speed of the model

The prediction results of the model are evaluated using the above evaluation indicators, and the evaluation results are shown in Table 3. In terms of overall accuracy, the overall accuracy of the CFOA-GRNN model is 16.7% higher than that of the BPNN model, 25% higher than that of the RNN model, and 33.4% higher than that of the GRU model. From the perspective of local accuracy, the introduction of CFOA can effectively improve the local accuracy of the neural network model for the prediction of water inrush at each level and greatly improve the prediction accuracy of the water inrush from the floor. In terms of operation time Tm, the operation time of the CFOA-GRNN model is 18.9% less than that of the BPNN model, 25.9% less than that of RNN, and 21.3% less than that of GRU. Therefore, in summary, the introduction of CFOA can greatly improve the accuracy of the GRNN neural network prediction model for water inrush from the bottom of the model and also significantly reduce the computing time.

Compared with the prediction results of the other three algorithms, it can be seen that the overall accuracy of the other three prediction models is not high. The overall accuracy of the BPNN neural network prediction model, the RNN neural network prediction model, and the GRU (gated recurrent unit) neural network prediction model is 75%, 66.7%, and 58.3%, while the overall accuracy of the CFOA-GRNN neural network prediction model is 91.7%. From the perspective of $\mathrm{LA}(i)$, the local accuracy of the CFOA-GRNN neural network prediction model introduced with the chaotic fruit fly optimization algorithm is also significantly improved compared with the other three neural network prediction models. The superiority of the proposed prediction model is confirmed from the three aspects of overall accuracy, local accuracy, and computation time. The prediction result of CFOA-GRNN model on whether water inrush occurs in actual engineering is very close to the actual situation, and its accuracy is significantly higher than that of the other three models. This result shows that the CFOA-GRNN model is reliable in predicting whether there is a risk of water inrush from the floor in actual engineering.

5. Conclusion

In order to solve the floor water-inrush issue, CFOA-GRNN model is established to predict floor water inrush based on the theory of nonlinear regression by combining relevant water-inrush data of numerous working faces and derived the following conclusions:

(1) The prediction effect of GRNN is affected by the smoothing factor, so the CFOA is used to optimize the smoothing factor, which reduces influences of human factors on the parameter determination in the GRNN prediction model and improves the prediction accuracy and applicability of the model

(2) By comprehensively analyzing causes of floor water inrush, six main factors are selected to construct the CFOA–GRNN prediction model for floor water inrush

(3) The accuracy of the CFOA–GRNN prediction model is 91.7%, the established prediction model has a high accuracy, and the prediction results are in agreement with reality, so it can be used to predict floor water inrush in coal mines in China to guide safe production

(4) In the established CFOA-GRNN model, it is found that the fruit fly search function has a great influence on the convergence of the prediction results. In future research, the optimization of the fruit fly search function will be explored in depth to reduce the prediction error caused by the change of the search function

Data Availability

The original contributions presented in the study are included in the article, and further inquiries can be directed to the corresponding author.

Conflicts of Interest

The authors declare that they have no conflicts of interest.

Acknowledgments

The authors acknowledge the State Key Laboratory of Coal Resources in Western China (SKLCRKF1913), the Basic Scientific Research Projects of Universities in Liaoning Province (LJKZ0343), and State Key Laboratory of Coal Mining and Clean Utilization (2021-CMCU-KF016).

References

[1] B. Zhao, G. Wen, J. Nian et al., "Numerical simulation study on the multi-physical field response to underground coal and gas outburst under high geo-stress conditions," *Minerals*, vol. 12, no. 2, p. 151, 2022.

[2] Z. Wen, E. Xing, S. Shi, and Y. Jiang, "Overlying strata structural modeling and support applicability analysis for large mining-height stopes," *Journal of Loss Prevention in the Process Industries*, vol. 57, pp. 94–100, 2019.

[3] X. Li, Q. Guo, and S. Liu, "Influence of steel fiber on durability performance of concrete under freeze- thaw cycles," *Advances in Materials Science and Engineering*, vol. 2021, Article ID 5460844, 12 pages, 2021.

[4] X. Li, Z. Cao, and Y. Xu, "Characteristics and trends of coal mine safety development," *Energy Sources Part a-Recovery Utilization and Environmental Effects*, pp. 1–19, 2020.

[5] C. Fan, H. Wen, S. Li, G. Bai, and L. Zhou, "Coal seam gas extraction by integrated drillings and punchings from the floor roadway considering hydraulic-mechanical coupling effect," *Geofluids*, vol. 2022, Article ID 5198227, 10 pages, 2022.

[6] B. Zhao, G. Wen, Q. Ma, H. Sun, F. Yan, and J. Nian, "Distribution characteristics of pulverized coal and stress–gas pressure–temperature response laws in coal and gas outburst under deep mining conditions," *Energy Science & Engineering*, pp. 1–19, 2022.

[7] K. Xiao, Z. Zhang, R. Zhang et al., "Anisotropy of the effective porosity and stress sensitivity of coal permeability considering natural fractures," *Energy Reports*, vol. 7, pp. 3898–3910, 2021.

[8] Z. Wen, S. Jing, Y. Jiang et al., "Study of the fracture law of overlying strata under water based on the flow- stress-damage model," *Geofluids*, vol. 2019, 12 pages, 2019.

[9] X. Wang, Z. Wen, Y. Jiang, and H. Huang, "Experimental study on mechanical and acoustic emission characteristics of rock-like material under non-uniformly distributed loads," *Rock Mechanics and Rock Engineering*, vol. 51, no. 3, pp. 729–745, 2018.

[10] S. Liu, X. Li, D. Wang, and D. Zhang, "Investigations on the mechanism of the microstructural evolution of different coal ranks under liquid nitrogen cold soaking," *Energy Sources Part a-Recovery Utilization and Environmental Effects*, pp. 1–17, 2020.

[11] X.-l. Li, S.-j. Chen, S.-m. Liu, and Z.-h. Li, "AE waveform characteristics of rock mass under uniaxial loading based on Hilbert-Huang transform," *Journal of Central South University*, vol. 28, no. 6, pp. 1843–1856, 2021.

[12] X. Li, S. Chen, Q. Zhang, X. Gao, and F. Feng, "Research on theory, simulation and measurement of stress behavior under regenerated roof condition," *Geomechanics and Engineering*, vol. 26, no. 1, pp. 49–61, 2021.

[13] Z. Jia, H. Xie, R. Zhang et al., "Acoustic emission characteristics and damage evolution of coal at different depths under triaxial compression," *Rock Mechanics and Rock Engineering*, vol. 53, no. 5, pp. 2063–2076, 2020.

[14] C. Fan, L. Yang, G. Wang, Q. Huang, X. Fu, and H. Wen, "Investigation on coal skeleton deformation in CO_2 injection enhanced CH4 drainage from underground coal seam," *Frontiers in Earth Science*, vol. 9, pp. 1–11, 2021.

[15] T. Ai, S. Wu, R. Zhang et al., "Changes in the structure and mechanical properties of a typical coal induced by water immersion," *International Journal of Rock Mechanics and Mining Sciences*, vol. 138, article 104597, 2021.

[16] Z. Zhu, Y. Wu, and J. Han, "A prediction method of coal burst based on analytic hierarchy process and fuzzy comprehensive evaluation," *Frontiers in Earth Science*, vol. 9, pp. 1–12, 2022.

[17] Y. Hu, W. Li, Q. Wang, S. Liu, and Z. Wang, "Evolution of floor water inrush from a structural fractured zone with confined water," *Mine Water and the Environment*, vol. 38, no. 2, pp. 252–260, 2019.

[18] Z. Ji, H. Tian, Z. Yang, T. Liu, and S. Bandara, "Mechanism of water inrush from coal seam floor based on coupling mechanism of seepage and stress," *Journal of Intelligent & Fuzzy Systems*, vol. 34, no. 2, pp. 965–974, 2018.

[19] S. Zhang, W. Guo, and Y. Li, "Experimental simulation of water-inrush disaster from the floor of mine and its mechanism investigation," *Arabian Journal of Geosciences*, vol. 10, no. 22, p. 503, 2017.

[20] S. Zhang, W. Guo, Y. Li, W. Sun, and D. Yin, "Experimental simulation of fault water inrush channel evolution in a coal mine floor," *Mine Water and the Environment*, vol. 36, no. 3, pp. 443–451, 2017.

[21] S. C. Li, J. Wu, Z. H. Xu, and W. M. Yang, "Mechanics criterion of water inrush from the coal floor under influence of fault and its engineering application," *International Journal of Geomechanics*, vol. 19, no. 5, pp. 1–9, 2019.

[22] T. Li and C. Wang, "Numerical simulation study on formation and evolution process of water-inrush channel in floor under high water pressure," *Geotechnical and Geological Engineering*, vol. 37, no. 4, pp. 3007–3012, 2019.

[23] K. Ma, X. Y. Sun, C. A. Tang, F. Z. Yuan, S. J. Wang, and T. Chen, "Floor water inrush analysis based on mechanical failure characters and microseismic monitoring," *Tunnelling and Underground Space Technology*, vol. 108, article 103698, 14 pages, 2021.

[24] A. J. Shao, J. P. Peng, Q. X. Meng, and Y. Huang, "Catastrophic model of water inrush from coal mine floor," *Applied Mechanics and Materials*, vol. 316-317, pp. 1106–1111, 2013.

[25] Z. Feng-da, S. H. Bao-hong, and K. A. Yong-hua, "Water inrush failure mechanism of mining floor under unloading effect," *Rock and Soil Mechanics*, vol. 37, no. 2, pp. 431–438, 2016.

[26] Y. Zhang and L. Yang, "A novel dynamic predictive method of water inrush from coal floor based on gated recurrent unit model," *Natural Hazards*, vol. 105, no. 2, pp. 2027–2043, 2021.

[27] G.-d. Zhang, Y.-g. Xue, C.-h. Bai, M.-x. Su, K. Zhang, and Y.-f. Tao, "Risk assessment of floor water inrush in coal mines based on MFIM-TOPSIS variable weight model," *Journal of Central South University*, vol. 28, no. 8, pp. 2360–2374, 2021.

[28] J. Zhang, Q. Wu, W. Mu, Y. du, and K. Tu, "Integrating the hierarchy-variable-weight model with collaboration-competition theory for assessing coal-floor water-inrush risk," *Environmental Earth Sciences*, vol. 78, no. 6, pp. 50–55, 2019.

[29] D. Zhao, Q. Wu, F. Cui et al., "Using random forest for the risk assessment of coal-floor water inrush in Panjiayao Coal Mine, northern China," *Hydrogeology Journal*, vol. 26, no. 7, pp. 2327–2340, 2018.

[30] D. Dong, Z. Chen, G. Lin, X. Li, R. Zhang, and Y. Ji, "Combining the fisher feature extraction and support vector machine methods to identify the water inrush source: a case study of the Wuhai mining area," *Mine Water and the Environment*, vol. 38, no. 4, pp. 855–862, 2019.

[31] Y. Wang, M. R. Zhou, P. C. Yan, C. Y. He, and D. Liu, "Identification of coalmine water inrush source with PCA-BP model based on laser-induced fluorescence technology," *Spectroscopy and Spectral Analysis*, vol. 37, no. 3, pp. 978–983, 2017.

[32] B. Wu, L. Wang, S. Wang, and Y. R. Zeng, "Forecasting the U.S. oil markets based on social media information during the COVID-19 pandemic," *Energy*, vol. 226, pp. 120403–120420, 2021.

[33] G. E. Lee and A. Zaknich, "A mixed-integer programming approach to GRNN parameter estimation," *Information Sciences*, vol. 320, pp. 1–11, 2015.

[34] J. Zhao, H. Guan, C. Lu, and Y. Zheng, "Evaluation of teachers' educational technology ability based on fuzzy clustering generalized regression neural network," *Computational Intelligence and Neuroscience*, vol. 2021, Article ID 1867723, 10 pages, 2021.

[35] L. Wang, T. J. Lee, J. Bavendiek, and L. Eckstein, "A data-driven approach towards the full anthropometric measurements prediction via generalized regression neural networks," *Applied Soft Computing*, vol. 109, article 107551, 2021.

[36] R.-Y. Wang, P. Hu, C. C. Hu, and J. S. Pan, "A novel fruit fly optimization algorithm with quasi-affine transformation evolutionary for numerical optimization and application," *International Journal of Distributed Sensor Networks*, vol. 18, no. 2, 2022.

[37] L. Wang, Y. Xiong, S. Li, and Y. R. Zeng, "New fruit fly optimization algorithm with joint search strategies for function optimization problems," *Knowledge-Based Systems*, vol. 176, pp. 77–96, 2019.

[38] S.-X. Lv, Y.-R. Zeng, and L. Wang, "An effective fruit fly optimization algorithm with hybrid information exchange and its applications," *International Journal of Machine Learning and Cybernetics*, vol. 9, no. 10, pp. 1623–1648, 2018.

[39] P.-W. Chen, W. Y. Lin, T. H. Huang, and W. T. Pan, "Using fruit fly optimization algorithm optimized Grey model neural network to perform satisfaction analysis for E-business service," *Applied Mathematics & Information Sciences*, vol. 7, no. 2L, pp. 459–465, 2013.

[40] W.-T. Pan, "A new fruit fly optimization algorithm: taking the financial distress model as an example," *Knowledge-Based Systems*, vol. 26, pp. 69–74, 2012.

[41] H. Li, S. Guo, H. Zhao, C. Su, and B. Wang, "Annual electric load forecasting by a least squares support vector machine with a fruit fly optimization algorithm," *Energies*, vol. 5, no. 11, pp. 4430–4445, 2012.

[42] L. Wang, X.-l. Zheng, and S.-y. Wang, "A novel binary fruit fly optimization algorithm for solving the multidimensional knapsack problem," *Knowledge-Based Systems*, vol. 48, pp. 17–23, 2013.

[43] S.-M. Lin, "Analysis of service satisfaction in web auction logistics service using a combination of fruit fly optimization algorithm and general regression neural network," *Neural Computing & Applications*, vol. 22, no. 3-4, pp. 783–791, 2013.

[44] L. Wu, Q. Liu, X. Tian, J. Zhang, and W. Xiao, "A new improved fruit fly optimization algorithm IAFOA and its application to solve engineering optimization problems," *Knowledge-Based Systems*, vol. 144, pp. 153–173, 2018.

[45] S. Kanarachos, J. Griffin, and M. E. Fitzpatrick, "Efficient truss optimization using the contrast-based fruit fly optimization algorithm," *Computers & Structures*, vol. 182, pp. 137–148, 2017.

[46] Z. He, H. Qi, Y. Yao, and L. Ruan, "Inverse estimation of the particle size distribution using the fruit fly optimization algorithm," *Applied Thermal Engineering*, vol. 88, pp. 306–314, 2015.

Hindawi
Geofluids
Volume 2022, Article ID 1571066, 18 pages
https://doi.org/10.1155/2022/1571066

Research Article

Petrogenesis, Magma Source, and Geodynamics of Paleogene Mafic Rocks, Huimin Sag, Jiyang Depression, Eastern China

Lihua Gao [1,2] **Zhigang Song,** [1,3] **Chao Han,** [1] **Mei Han,** [1] **Chenlin Zhu,** [1] **Di Xia,** [1] **Zuozhen Han** [1,4] **and Shuangjian Li** [5]

[1]*College of Earth Science and Engineering, Shandong University of Science and Technology, Qingdao 266590, China*
[2]*Key Laboratory of Coalbed Methane Resources & Reservoir Formation Process, Ministry of Education, China University of Mining and Technology, Xuzhou 221008, China*
[3]*Key Laboratory of Gold Mineralization Processes and Resource Utilization, MNR, Shandong Provincial Key Laboratory of Metallogenic Geological Process and Resource Utilization, Shandong Institute of Geological Sciences, Jinan 250013, China*
[4]*Laboratory for Marine Mineral Resources, Qingdao National Laboratory for Marine Science and Technology, Qingdao 266071, China*
[5]*Key Laboratory of Deep Geology and Resources, Sinopec, Beijing 102206, China*

Correspondence should be addressed to Zuozhen Han; hanzuozhen@sdust.edu.cn

Received 9 September 2021; Revised 29 March 2022; Accepted 20 April 2022; Published 8 June 2022

Academic Editor: Andri Stefansson

A suite of Paleogene mafic rocks was collected from boreholes in the Huimin Sag of the Jiyang Depression with the aim of investigating the petrogenesis and nature of mantle source for these rocks and further providing insights into the characteristic of related mantle plume. Whole-rock geochemical data indicate that the mafic rocks have relatively lower SiO_2 (42.93%–48.57%) contents and similar characteristics to alkaline basalt and belong to transitional calc-alkaline series. These samples were clearly enriched in LREEs and depleted in HREEs and were also characterized by the enrichment of LILEs, incompatible elements, and HFSEs, similar to those of the Ocean Island Basalt (OIB). In addition, they exhibited Pb enrichment; Y, Pr, and Yb depletion; absence of Nb-Ta anomalies; high Hf and low Zr; and Rb/Yb ratios exceeding 1.0, indicating characteristics of intraplate rift-type alkaline basalt. The samples exhibited $(Th/Ta)_{PM}$ and $(La/Nb)_{PM}$ ratios less than 1 and plotted within the OIB, EMI, and EMII fields, indicating that crustal components had no role in the generation of the rocks. With the exception of individual samples that have a distinctive range of ε_{Nd} values, the majority of samples have complex ε_{Nd} values of -1.15 to 5.56, indicating a mixture of different sources, which was also apparent in the $\delta^{18}O$-$^{87}Sr/^{86}Sr$ diagram, in which the samples plot close to the downward nonlinear curve. Based on the isotopic and trace elemental analyses, these igneous rocks are intraplate rift-type alkaline basalt and are of mantle plume origin. The variations in $^{87}Sr/^{86}Sr$, $^{143}Nd/^{144}Nd$, ε_{Nd} values, LREEs, and HFSEs were probably due to the different locations of the mantle plume for different samples. The primary magma of the rocks likely originated from the melting of a mantle plume and the further metasomatism of lithospheric mantle, continental, or oceanic crust.

1. Introduction

The impact of mantle plumes on mineralization involves all stages of the Earth's evolution. Some geologists have suggested that most intracontinental deposits formed during the Precambrian–Phanerozoic were all related to mantle hotspots [1–3] and proposed mantle plume metallogenic systems [4, 5]. Evidence from P-wave velocity, lithospheric discontinuity, thinning and transformation, a rise of asthenosphere with a mushroom cloud structure, and large igneous province suggests that mineralization and petroleum accumulation in eastern China during the Mesozoic–Cenozoic were tectonically controlled by submantle plumes [6–10].

The submantle plume of North China Craton (NCC) consists of Luxi, Jiaodong, Liaoxi, and Jibei mantle branches, which possess different deposits that are distributed spatially or in groups [9]. Over the past three decades, some researchers have proposed that the Bohai Bay Basin (BBB), which is the largest basin in the Eastern Block of the NCC, has close correlation with a mantle plume, on the basis of seismic data and physical simulation [11–14]. Liu et al. [11] concluded that five mantle plume uplifts, including Bozhong, Bohai Bay, Miaoxi, Liaodong Bay, and Kenli uplifts, existed in the BBB, according to studies on gravity and magnetic fields, geothermal heat flow, and high conductivity layers in the upper mantle. Zhu [14] suggested that mantle plume activities have occurred since the Jurassic and controlled the basin's tectonic evolution during the Late Cretaceous and established a mantle plume evolution model based on tectonic-sedimentation regularity, seismic section, paleostress, and paleoflow direction. Xiao et al. [12] thought that a mantle plume in the Songliao region, formed during the Late Jurassic–Late Cretaceous, moved to the Beijing-Tianjin-Bohai Bay regions and formed the BBB because of the northward movement of the NCC, based on regional seismic and sedimentary data and electron microprobe analysis. Ye and Wang [13] considered that the regular distribution of geological and geophysical characteristics of Jiyang Depression was caused by the difference of subduction angle of the Western Pacific plate from south to north, as well as tectonic migration of mantle plume from south to north.

Though some researchers have done research on various aspects (e.g., sedimentary strata, structural patterns, and tectonic evolutions), systematic studies focused on Cenozoic igneous rocks that are well developed in the BBB are still limited [15–20]. As a consequence, the petrogenesis and source of the igneous rocks deduced by those studies are still controversial. Liu et al. [15] suggested that the Tertiary basaltic rocks in the BBB are typical intraplate basalts that have a mantle source that was free from crustal contamination. Shen et al. [17] proposed that Tertiary basalts from the Jiyang Depression were formed by mixing of DMM and EMI, to varying degrees, with a minor contribution from EMII based on Sr-Nd isotopic analysis. Liu and Xie [16] argued that the magmas of Tertiary mafic intrusive and volcanic rocks in the Jiyang Depression were sourced from the upper mantle. The Tertiary basaltic rocks in the Huanghua Depression, investigated by Zhang et al. [19], have Sr-Nd isotopic characteristics similar with OIB, indicating an asthenospheric mantle magma source. Wang [18] argued that the Paleogene basaltic volcanic rocks from eastern depression of Liaohe Basin have OIB-Continental Flood Basalt (CFB) characteristics and probably sourced from a depleted mantle which were mixed by enriched components.

In this study, a suite of igneous samples was collected from five drilling wells from the Xia 38, Xia 39, Xia 381, Xia 382, and Shang 745 fault blocks of Huimin Sag, Jiyang Depression. We report petrological observations, whole-rock geochemical and Sr-Nd-O isotopic data for these rocks. These new data provide great significances for the study of the petrogenesis and nature of mantle source for the Cenozoic igneous rocks of BBB.

2. Geological Background and Petrological Characteristics

The BBB is a Meso-Cenozoic superimposed petroliferous basin located in the Eastern Block of the NCC. It is surrounded by four uplifted massifs, the Taihang Massif to the west, the Yanshan Massif to the north, the Jiaoliao Massif to the east, and the Luxi Massif to the south. The Huimin Sag is a NEE-trending sub-half-graben tectonic basin, located to the west of the Jiyang Depression in the BBB (Figure 1(a)). Its neighbours are Chengning Uplift to the north, Luxi Uplift to the south, Linqing Depression to the west, and Dongying Depression to the east. The Huimin Sag has a complex fracture system and faulted structures that were controlled by the north-dipping Xiakou Fault and south-dipping Linshang Fault. Many Cenozoic igneous rocks are developed in the Huimin Sag, especially near the conjunct parts of faults in the Linnan Sag and Yangxin Sag (Figure 1(b)). The Cenozoic igneous rocks in this region are more than 1000 m thick and were proposed to be divided into several eruption cycles (Figure 2). The collected igneous rock samples belong to the middle section of the third member, the upper section of the third member–lower section of the second member, and the first member of the Shahejie Formation (Figure 2). The collected igneous rocks are mainly mafic intrusive rocks and volcanic rocks of overflow facies; the petrography of which is described as follows.

2.1. Intrusive Bodies. The intrusive rock samples from Xia 38, Xia 381, and Xia 39 wells in the study area are greyish green and black-green in colour and have a dense massive structure and poikilitic and ophitic textures (Figures 3(a)–3(f)). These samples are mainly composed of augite (~45%), plagioclase (~40%), amphibole-biotite-sericite (~10%), and other opaque minerals (~5%). The augites are pink, Ti-enriched, and characterized by positive high protuberance, obvious pleochroism, and the highest interference colour of second order blue-to-green. The plagioclases are mainly euhedral plate-prismatic with polysynthetic twins, positive low protuberance, and the highest interference colour of first order grey-to-white. Amphiboles are mainly hornblende and barkevicite, with some replaced by biotite. The products of alteration of the intrusive rocks are mainly chlorite, sericite, and saponite.

2.2. Volcanic Rocks. The volcanic rock samples from Xia 382 well in this study are greyish green and black-green in colour with tiny holes and cracks. They have a porphyritic texture, and the groundmass has intergranular and intersertal textures (Figures 3(g)–3(l)). The phenocrysts are mainly augite and plagioclase. Minor hornblende and pyrite are also observed in the volcanic rocks (Figures 3(g) and 3(i)). The products of alteration of the volcanic rocks are mainly chlorite, sericite, and saponite.

3. Analytical Methods

Fifteen magmatic core samples for this study were collected from 5 wells, Xia 38, Xia 39, Xia 381, Xia 382, and Shang

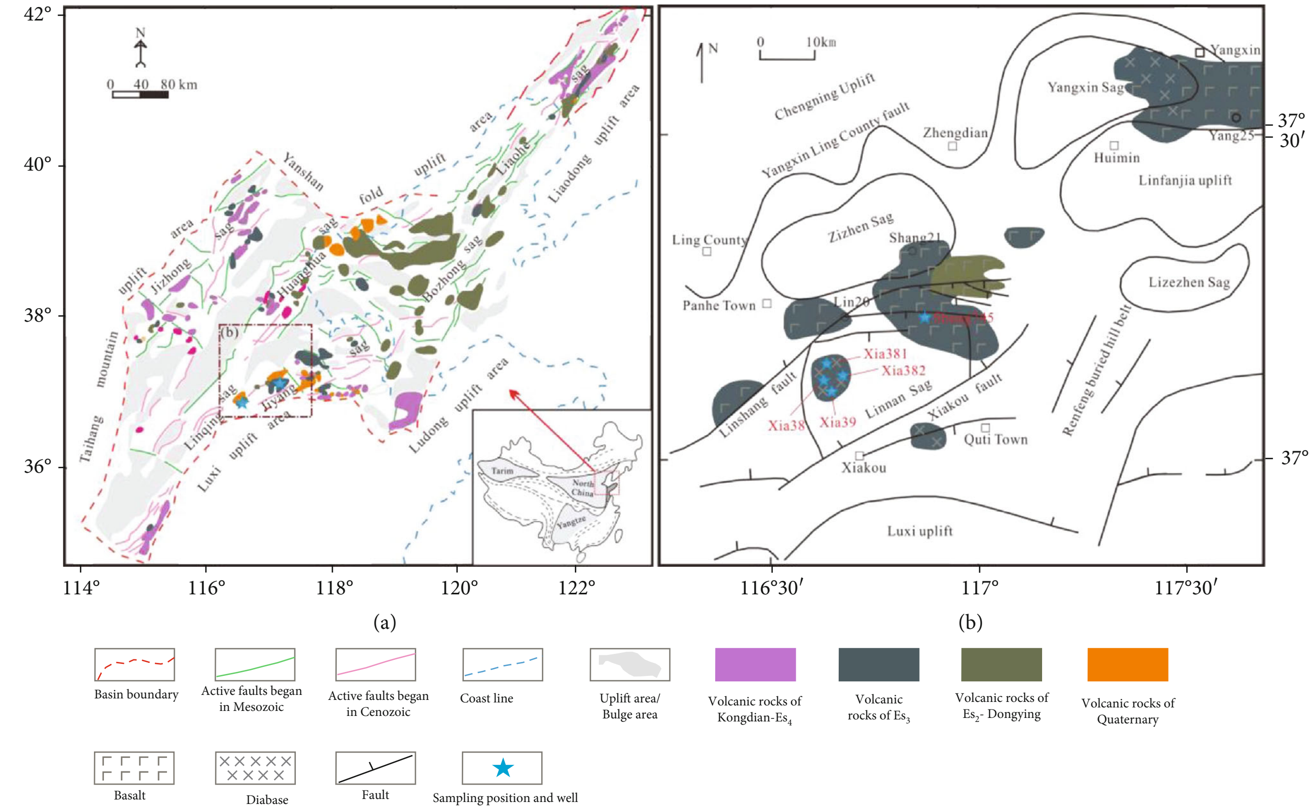

FIGURE 1: (a) Distribution of Cenozoic igneous rocks in the Bohai Bay Basin [55]. (b) A simplified structural map of the Huimin Sag.

745, including 7 intrusive rock samples (from wells of Xia 38, Xia 39, Xia 381, and Xia 382, collected from upper Es3 submember) and 8 volcanic rock samples (from the Shang 743 and Shang 745 wells, collected from the middle Es3 submember). Samples were first crushed, cleaned, soaked, dried, and then ground to a powder. The major elements, trace elements, rare earth elements, oxygen isotopes, and strontium-neodymium isotopes were analysed at the Geological Analysis and Testing Research Center of the Nuclear Industry. Major elements were analysed by Axios Max X-ray fluorescence spectrometer (Axios mAX) using fused glass disks according to the Chinese national standard (GB/T14506.14-2010). Trace elements were determined using a NexION 300D inductively coupled plasma mass spectrometer (ICP-MS) according to the Chinese national standard (GB/T14506.30-2010). Analytical results for Chinese standards (GBW07104 and GBW07312) indicate an analytical precision of >95% for both major and trace elements. Oxygen isotopes were determined using a Finnigan MAT 253 instrument with an accuracy exceeding 0.2% indicated by the Chinese standards GB04416 and GB04417. Strontium and neodymium isotopes were analysed using an IsoProbe-T thermal surface ionization mass spectrometer. During the collection of isotopic data, repeated analysis of the Nd isotopic standard JNdi-1 [21] gave an average $^{143}Nd/^{144}Nd$ value of 0.512098 ± 0.000007 $(n = 3)$, and the strontium NBS SRM 987 isotopic standard gave an average $^{87}Sr/^{86}Sr$ value of 0.710248 ± 0.000008 $(n = 3)$. Further details of the analytical methods are given in Lu et al. [22].

4. Analytical Results

4.1. Major and Trace Elements. The presence of a certain amount of secondary minerals and the moderate to high loss on ignition (LOI, 2.55–5.98) imply that the studied rocks have undergone varying degrees of hydrothermal alteration or metamorphism, to which some elements (such as Rb, Ba, Sr, Na, and K) are sensitive [23–25]. Therefore, the elements that are considered immobile during alteration, such as high field strength elements (HFSEs) and some transition metals, are chosen to describe the primary chemical features of the samples in this study. The igneous rocks in the Huimin Sag exhibited relatively concentrated major elements (Table 1), with SiO_2 ranging from 42.93% to 48.57%, with an average of 46.11%. They have relatively higher TiO_2, P_2O_5, FeO, and total alkaline (K_2O+Na_2O) and lower CaO/TiO_2 and Al_2O_3/TiO_2 values, with TiO_2 contents ranging from 1.62% to 2.79% (average 2.07%, which was significantly higher than the value of 0.85% for active continental margin basalts) (Table 1). All the samples show transitional to alkaline Nb/Y ratios and plot in the alkaline basalt field on a Zr/Ti versus Nb/Y diagram (Figure 4(a), [26]). In addition, they were plotted onto the Y versus Zr diagram exposing characteristics of transitional to calc-alkaline series rocks (Figure 4(b), [27]).

The basic igneous rocks in this study exhibited total rare earth elements (ΣREE) of 85.27 to 297.31 ppm (average 154.36 ppm) (Table 2). The light rare earth elements (LREEs) ranged from 69.77 to 272 ppm (average 134.25 ppm), whereas the heavy rare earth elements

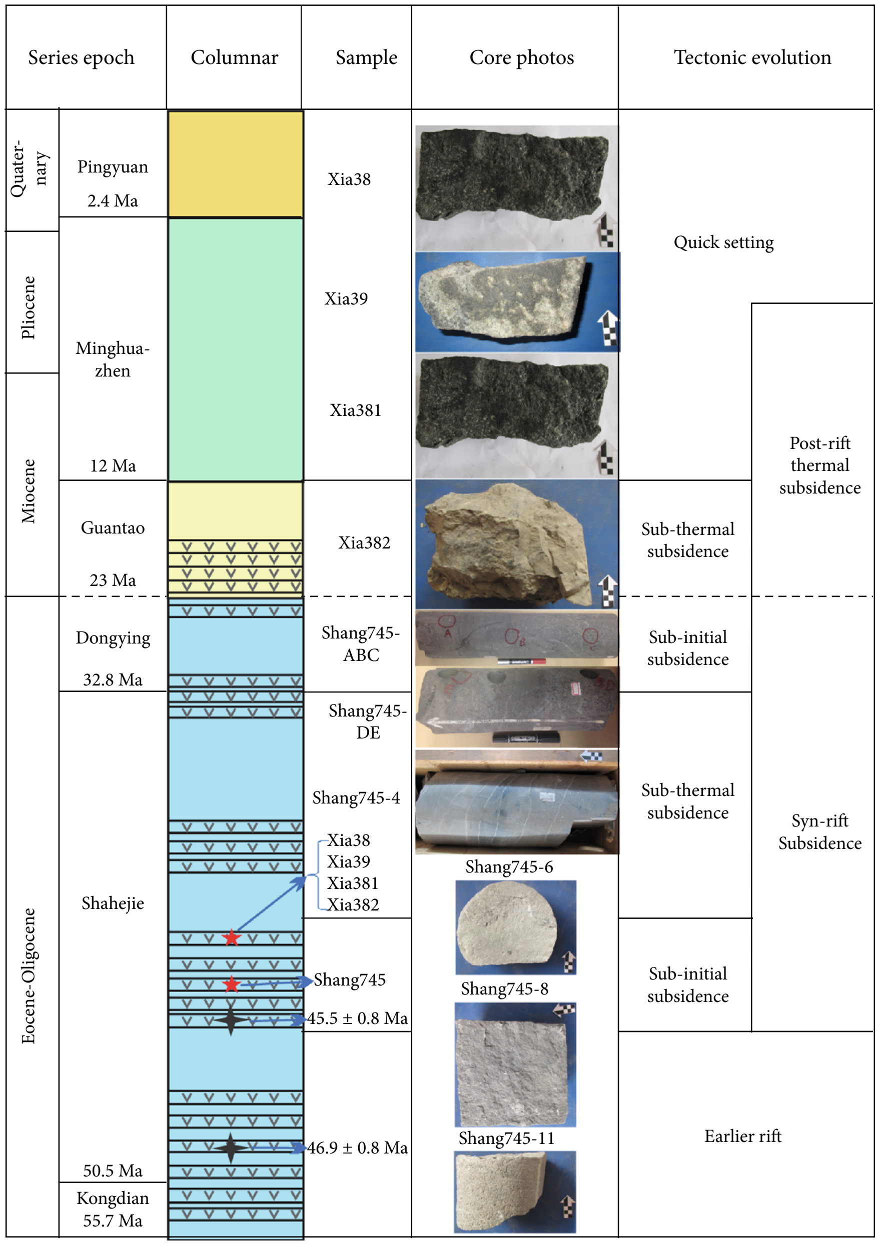

Figure 2: Cenozoic strata column of the Bohai Bay Basin with summary of the tectonic evolution and ^{40}Ar-^{39}Ar age data for basalts from the Shahejie Formation in the Jiyang Depression (modified after [56]), showing sample locations.

(HREEs) ranged from 15.38 to 27.50 ppm (average 19.77 ppm). The samples were relatively enriched in LREEs and depleted in HREEs (Figures 5(a) and 5(b)). In the primitive mantle-normalized trace element spider diagrams (Figures 5(c) and 5(d)), all samples were relatively enriched in large ion lithophile elements (LILEs, e.g., Ba, Pb, Sr, U, and K), incompatible elements (Rb, Ba, Th, U, and K), and some high field strength elements (HFSEs, e.g., Nb, Ta, Zr, and Hf).

4.2. Sr-Nd and O Isotopes. The Sr-Nd and O isotopic compositions of Paleogene igneous rocks from the Huimin Sag are given in Tables 3 and 4. The $^{87}Sr/^{86}Sr$ ratios varied from 0.7046 to 0.7098 (average 0.7078), whereas the $^{143}Nd/^{144}Nd$ ratios varied from 0.5117 to 0.5129 (average 0.5126). The ε_{Nd} values ranged from -17.71 to 5.56 (average -0.75), while the ε_{Sr} values ranged from -1.99 to 71.49 (average 41.8822). The $\delta^{18}O$ values ranged from 5.4‰ to 10.4‰, with an average of 7.9‰.

5. Discussion

5.1. Petrogenesis of the Mafic Rocks

5.1.1. Fractional Crystallization. It is noticed that the studied mafic rocks from the Huimin Sag have variable MgO, Cr, and Ni contents. In the variation diagrams of MgO versus selected major and trace elements (Figure 6), with the exception of Fe_2O_3+FeO, which was not correlated with MgO, the SiO_2, K_2O+Na_2O, TiO_2, Al_2O_3, and CaO concentrations

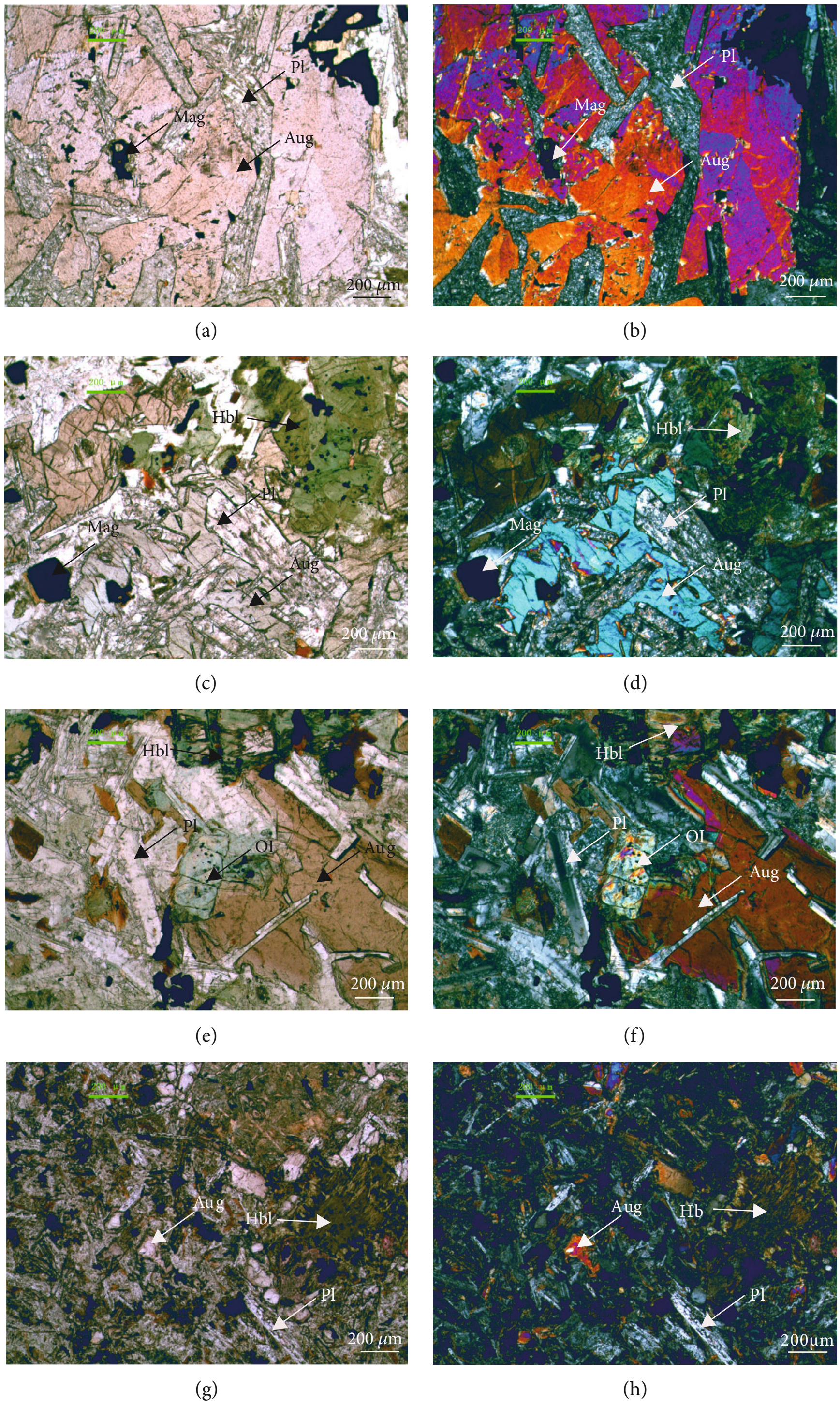

Figure 3: Continued.

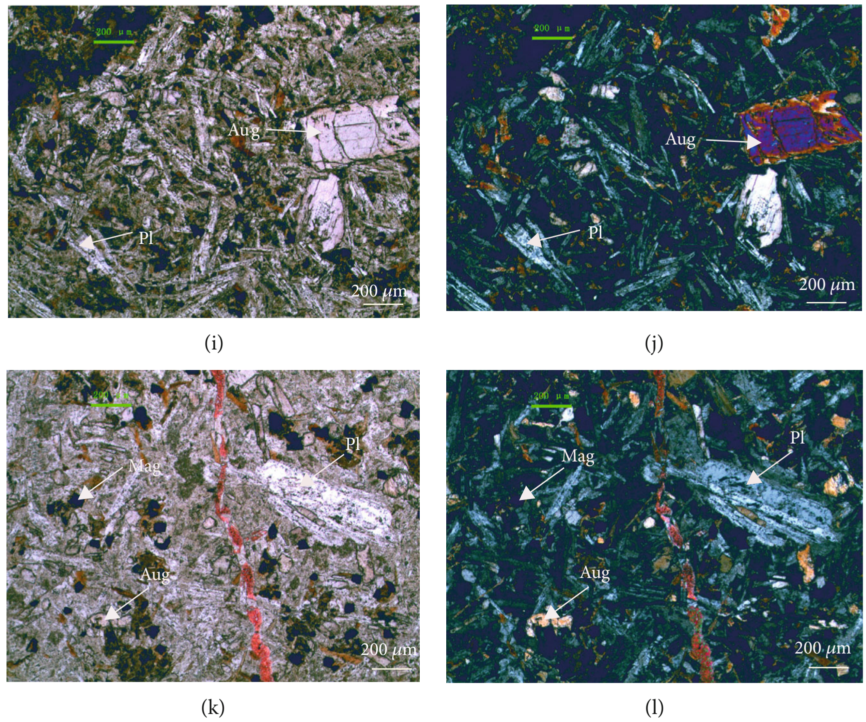

Figure 3: Microphotographs for Paleogene mafic rocks in Huimin Sag. (a, b) Intrusive rock from Xia 38 well, 3830.4 m. This sample is mainly composed of plagioclase and augite, with minor amphibole and magnetite and has a poikilitic texture. Corrosion of amphibole and sericitization of plagioclase can be seen. (c, d) Intrusive rock from Xia 38 well, 3668.5 m. This sample is mainly composed of plagioclase and augite and has a poikilitic texture. The augite shows latticed corrosion and obvious chloritization. The plagioclase experienced severe dissolution, and the dissolved pores were filled with asphaltic components. (e, f) Intrusive rock from Xia 381 well, 4006.1 m. This sample is mainly composed of plagioclase, augite, and olivine with minor amphibole and magnetite and has an ophitic texture. The augite and plagioclase were severely dissolved, and the pores were filled with asphaltic components. (g, h) Volcanic rock from Shang 745 well, 3215.2 m. This sample has a porphyritic texture with the matrix showing intergranular and interseptal textures. The phenocrysts are mainly plagioclase and augite, whereas the matrix is composed of subdirectionally distributed fine lath plagioclase, pyroxene, and glass, with a small amount of hornblende. (i, j) Volcanic rock from Shang 745 well, 3200.2 m. This sample has an interseptal texture and is mainly composed of randomly distributed long strip plagioclase, the spaces of which filled with granular pyroxene and glass that experienced devitrification, as well as a small amount of large pyroxene particles, with some of which have been saponified. (k, l) Volcanic rock from Shang 745 well, 3200.2 m. This sample has an interseptal texture, with a locally intersertal texture. It is mainly composed of randomly distributed long strip plagioclase, the spaces of which filled with granular pyroxene and magnetite. Structural fractures that filled with calcite can be seen. Pl—plagioclase; Hbl—hornblende; Ol—olivine; Aug—augite; Mag—magnetite.

were negatively correlated with MgO, whereas Cr and Ni concentrations were positively correlated with MgO. These data suggest that the geochemical differences of different samples may be attributed to the fractional crystallization of olivine and/or clinopyroxene. In addition, the TiO_2 (1.62%–2.79%) contents of the samples are relatively consistent, implying that the fractionation of Fe-Ti oxides did not occur. Moreover, no obvious Eu anomalies (0.92–1.17) have been observed in the studied samples, reflecting no significant fractionation of plagioclase.

5.1.2. Crustal Contamination. The petrological observation and geochemical analysed results imply a mantle source for the magma of studied rocks from the Huimin Sag. Thus, it is important to understand the effects of crustal contamination on the mafic rocks, which is a potential process during the ascent and evolution of mantle-derived magmas [28, 29]. It is widely accepted that minor crustal contamination could produce positive Zr-Hf anomalies of mantle-sourced rocks [24]. However, the Paleogene igneous rocks from the Huimin Sag have no positive Zr-Hf anomalies (Figures 5(c) and 5(d)), ruling out the possibility of crustal contamination. This hypothesis can be further evidenced by the lower Th (1.58 ppm–4.76 ppm) and U (0.79–2.31) contents of these samples relative to the upper crust (e.g., Th = 10.5 ppm and U = 2.7 ppm) [30]. Moreover, the Paleogene igneous rocks from the Huimin Sag had ε_{Nd} values of -17.71 to 5.56 and were mostly within the range of mantle plume-derived CFB, with the exception of samples Xia 382-1 and Shang 745-11, which had negative ε_{Nd} values and $^{143}Nd/^{144}Nd$ of 0.5117 and 0.5122, respectively, close to that of average continental crust (0.5119), reflecting the lithospheric mantle or crustal contamination [31]. Samples Shang 745-A, Shang 745-B, Shang 745-C, Shang 745-D, and Shang 745-8 exhibited high positive $^{143}Nd/^{144}Nd$ and ε_{Nd} values of 0.5127 to 0.5128 and 1.80 to 3.22, respectively, implying an upper depleted mantle source. The remaining samples had ε_{Nd} values of -1.15 to 0.62, consistent with the CHUR evolution curve (Figure 7), implying that

Table 1: Major element (%) compositions for Paleogene igneous rocks in Huimin Sag.

Sample no.	Lithology	SiO_2	AI_2O_3	TFe_2O_3	MgO	CaO	Na_2O	K_2O	MnO	TiO_2	P_2O_5	FeO	Loss
X38-2	Intrusive rock	47.57	15.94	10.80	4.52	9.98	3.65	1.02	0.145	2.12	0.327	7.73	3.88
X38-3	Intrusive rock	47.45	14.27	12.89	4.73	7.67	4.44	2.13	0.207	2.79	0.456	3.4	2.96
X39-1	Intrusive rock	46.94	15.56	11.97	6.62	8.02	3.47	1.37	0.174	2.03	0.3	2.75	3.48
X381-1	Intrusive rock	45.02	12.22	13.41	13.16	6.57	2.36	0.918	0.18	1.73	0.266	5.07	4.07
X382-1	Volcanic rock	46.38	14.47	12.28	8.05	8.43	3.22	0.866	0.169	1.96	0.291	9.03	3.78
X382-5	Volcanic rock	47.54	14.05	12.31	8.37	5.42	4.41	0.658	0.179	1.86	0.29	3.53	4.85
S745-4	Intrusive rock	47.64	15.07	11.84	5.38	8.39	3.71	1.69	0.192	2.03	0.302	4.05	3.23
S745-6	Intrusive rock	48.57	14.06	13.25	4.63	8.11	3.94	1.7	0.192	2.59	0.403	5.27	2.56
S745-8	Volcanic rock	47.17	15.25	10.25	7.52	6.86	4.44	1.28	0.135	1.67	0.557	7.7	4.85
S745-11	Intrusive rock	48.08	13.63	13.22	4.62	8.91	4.32	1.35	0.191	2.68	0.437	9.35	2.55
S745-A	Volcanic rock	44.6	15.27	10.21	5.64	10.94	3.77	1.39	0.151	1.74	0.565	8.15	5.73
S745-B	Volcanic rock	44.66	14.9	11.78	7.32	8.49	3.54	1.57	0.177	1.62	0.573	9.48	5.33
S745-C	Volcanic rock	42.97	15.74	11.26	7.01	10.64	3.17	0.848	0.175	1.63	0.58	8.78	5.98
S745-D	Volcanic rock	42.93	15.65	11.04	6.4	11.82	2.77	1.02	0.159	1.74	0.565	8.69	5.89
S745-E	Volcanic rock	44.08	13.51	12.93	4.5	11.36	3.62	0.512	0.161	2.46	0.37	8.45	5.49
Deccan	Continental basalt	50.18	13.70	3.72	6.58	11.44	1.70	0.73	0.21	2.20	—	9.08	
Siberia	Continental basalt	48.58	15.88	2.80	6.48	9.98	2.10	1.02	0.13	1.23	0.10	8.74	
Mount Emei	Continental basalt	44.75	7.70	13.25	17.95	9.00	1.18	0.71	0.18	2.24	0.20	—	
Hawaii Haleakala	OIB	46.46	10.85	—	17.65	8.07	1.93	0.39	0.16	2.06	0.22	12.20	
Hawaiian Islands	OIB	50.29	12.92	1.48	8.07	10.84	2.26	0.46	0.14	3.03	0.36	9.77	

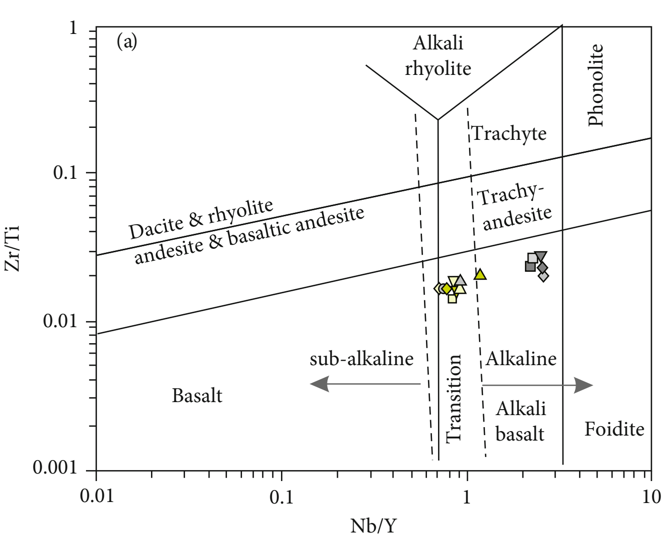

(a)

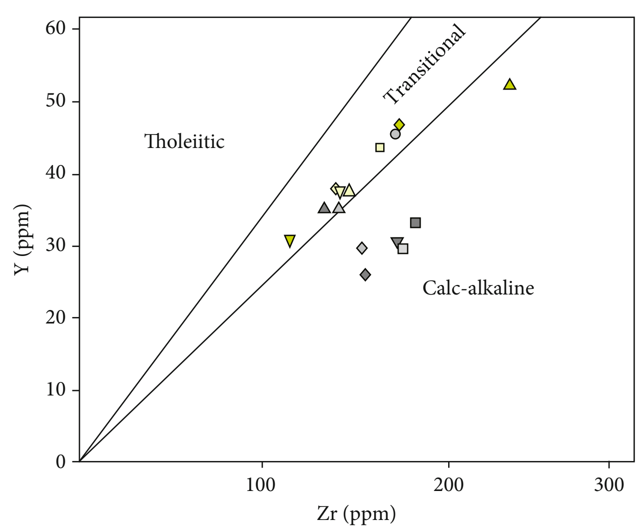

(b)

Figure 4: (a) Nb/Y vs. Zr/Ti and (b) Y vs. Zr discriminations for the Paleogene igneous rocks from the Huimin Sag. The boundary lines in (a) and (b) are from Pearce [26] and Miyashiro [27], respectively.

the magma was derived from different degrees of mixture of mantle plume and lithosphere.

Ratios of O isotopes and incompatible elements have been proposed to identify crustal contamination [32]. In the $\delta^{18}O$-$^{87}Sr/^{86}Sr$ diagram (Figure 8), the studied igneous rock samples plot within or close to the area of source contamination, also ruling out the significant impact of crustal contamination. $(Th/Ta)_{PM}$ was close to 1.0 and $(La/Nb)_{PM}$ exceeded 1.0 when lower crustal materials were involved, whereas the above ratios exceeded 2.0. The $(Th/Ta)_{PM}$ and $(La/Nb)_{PM}$ ratios of the Paleogene igneous rocks from the Huimin Sag were 0.54–0.79 and 0.55–0.72, respectively, suggesting that the upper crustal component had no role in the generation of the rocks.

5.1.3. Mantle Sources and Lithospheric Interaction. During mantle melting and metasomatism, Ti, P, and K can be easily enriched or depleted, as they are strongly incompatible

Table 2: Trace element (ppm) compositions for Paleogene igneous rocks in Huimin Sag.

Sample no.	X38-2	X38-3	X39-1	x381-1	x382-1	x382-5	S745-4	S745-6	S745-8	S745-11	S745-A	S745-B	S745-C	S745-D	S745-E
Sr	703.00	490.00	589.00	280.00	386.00	267.00	1479.00	568.00	631.00	389.00	313.00	530.00	482.00	437.00	200.00
Ba	320.00	452.00	895.00	218.00	224.00	307.00	926.00	463.00	665.00	302.00	775.00	637.00	283.00	391.00	64.10
Cr	96.80	31.30	251.00	467.00	291.00	336.00	125.00	81.70	232.00	46.50	214.00	196.00	228.00	212.00	84.60
V	233.00	259.00	216.00	181.00	198.00	199.00	195.00	249.00	178.00	250.00	183.00	149.00	164.00	182.00	237.00
Li	29.00	11.70	25.10	36.50	25.30	40.00	22.30	24.90	24.80	20.80	27.90	33.50	35.90	31.40	21.40
Be	1.17	1.76	1.10	0.77	1.21	1.68	0.91	1.34	2.45	1.08	2.62	1.85	3.66	4.15	1.84
Sc	30.00	27.00	26.60	21.90	25.10	22.90	26.20	31.70	22.60	32.00	21.60	18.80	20.40	22.50	30.00
Co	33.90	32.90	42.70	67.50	44.60	54.60	35.10	34.60	41.00	31.60	36.30	31.70	38.50	37.20	33.80
Ni	41.50	26.10	91.30	314.00	127.00	185.00	46.30	24.50	104.00	20.70	88.90	87.60	99.90	91.50	25.60
Cu	92.30	75.60	68.70	65.40	67.10	76.00	59.50	76.70	63.80	74.90	39.90	42.70	34.70	38.50	71.20
Zn	118.00	155.00	130.00	137.00	142.00	139.00	129.00	161.00	112.00	154.00	142.00	109.00	131.00	125.00	151.00
Ga	20.70	22.80	20.40	16.00	19.40	23.70	16.20	19.80	18.80	18.70	23.30	18.80	25.50	25.30	20.20
Rb	24.60	37.10	26.50	17.50	16.20	12.90	33.70	27.20	25.60	25.10	30.60	25.90	16.60	21.20	12.80
Y	30.30	42.20	30.10	25.10	28.50	28.40	30.60	37.70	24.70	35.30	24.10	21.00	24.00	26.90	36.80
Zr	146.00	233.00	141.00	114.00	140.00	133.00	139.00	173.00	172.00	163.00	153.00	155.00	175.00	182.00	171.00
Nb	26.70	50.60	26.20	22.10	25.40	26.20	22.50	30.00	64.90	30.40	65.00	56.30	61.90	64.30	28.20
Mo	2.96	7.59	3.86	2.05	2.60	2.19	6.24	5.22	6.23	4.43	6.42	5.24	5.26	5.61	5.29
Cd	0.19	0.21	0.15	0.14	0.21	0.09	0.19	0.16	0.11	0.15	0.18	0.18	0.21	0.18	0.27
Cs	0.77	6.69	1.94	1.85	0.51	0.37	0.95	0.49	1.44	0.59	1.37	1.08	1.22	1.63	1.65
La	18.40	26.90	16.00	13.10	15.50	15.80	15.70	19.10	39.10	20.40	41.20	36.70	41.50	39.40	18.00
Ce	36.00	51.80	32.10	26.20	30.30	31.10	31.40	39.30	69.90	39.80	73.00	63.20	70.90	68.00	36.40
Pr	4.68	6.84	4.30	3.42	3.89	4.15	4.49	5.45	8.25	5.42	8.53	7.27	8.03	8.00	4.99
Nd	19.90	28.80	18.30	14.50	17.00	17.60	20.40	24.90	30.40	24.30	32.10	27.20	30.40	31.00	22.90
Sm	5.20	7.07	4.72	3.65	4.64	4.64	5.32	6.65	6.09	6.50	6.25	5.05	6.02	6.15	6.14
Eu	1.71	2.07	1.76	1.30	1.63	1.44	1.83	2.02	1.87	1.90	2.20	1.64	1.99	2.19	1.75
Gd	4.90	6.74	4.78	3.80	4.50	4.47	4.82	6.07	5.27	5.97	5.30	4.74	5.24	5.46	5.42
Tb	0.98	1.35	0.99	0.76	0.95	0.90	1.00	1.15	0.89	1.16	0.88	0.80	0.89	0.95	1.08
Dy	6.11	8.42	5.80	4.68	5.67	5.74	6.01	7.32	5.12	7.15	4.99	4.28	4.81	5.22	6.87
Ho	1.15	1.53	1.17	0.87	1.08	1.07	1.14	1.38	0.88	1.30	0.88	0.79	0.84	0.93	1.36
Er	3.03	4.11	3.07	2.27	2.80	2.78	3.03	3.69	2.28	3.29	2.38	2.05	2.28	2.53	2.44
Tm	0.53	0.68	0.52	0.40	0.52	0.47	0.52	0.58	0.39	0.55	0.41	0.35	0.38	0.40	0.59
Yb	2.97	4.08	3.07	2.38	2.93	2.81	3.18	3.75	2.43	3.57	2.50	2.10	2.32	2.63	3.63
Lu	0.43	0.59	0.44	0.33	0.41	0.40	0.42	0.49	0.34	0.46	0.35	0.28	0.30	0.33	0.49
Hf	3.95	6.30	3.92	3.20	3.88	3.77	3.94	4.79	4.86	4.67	4.33	4.52	4.76	4.85	4.65
Ta	1.58	2.91	1.60	1.30	1.55	1.57	1.32	1.80	4.20	1.76	4.12	3.55	3.90	3.96	1.61
W	0.42	0.66	0.41	0.21	0.51	1.90	0.49	0.45	7.25	0.54	1.09	0.75	0.79	0.81	0.87
Pb	4.76	20.30	5.30	6.13	22.00	15.60	3.00	5.51	8.39	14.40	17.70	8.37	11.00	7.78	4.90
Th	2.60	3.80	2.20	1.58	2.09	2.26	2.02	2.21	4.68	2.19	4.76	4.12	4.57	4.53	2.10
U	1.34	1.90	1.34	0.79	1.13	1.07	1.26	1.12	1.72	1.41	2.31	1.58	1.56	1.79	1.27
∑REE	112.79	172.78	104.92	85.27	100.22	101.97	101.36	126.95	207.71	127.88	213.87	185.54	207.40	206.49	117.35
LREE	92.69	145.28	85.08	69.77	81.36	83.33	81.24	102.52	190.11	104.42	196.18	170.16	190.34	188.04	95.48
HREE	20.10	27.50	19.84	15.50	18.86	18.64	20.12	24.43	17.60	23.46	17.69	15.38	17.06	18.45	21.87
LREE/HREE	4.61	5.28	4.29	4.50	4.31	4.47	4.04	4.20	10.80	4.45	11.09	11.06	11.16	10.19	4.37
La_N/Yb_N	4.44	4.73	3.74	3.95	3.79	4.03	3.54	3.65	11.54	4.10	11.82	12.54	12.83	10.75	3.56
δEu	1.04	0.92	1.13	1.07	1.09	0.97	1.10	0.97	1.01	0.93	1.17	1.02	1.08	1.16	0.93
δCe	0.95	0.94	0.95	0.96	0.96	0.94	0.92	0.94	0.95	0.93	0.95	0.95	0.95	0.94	0.94

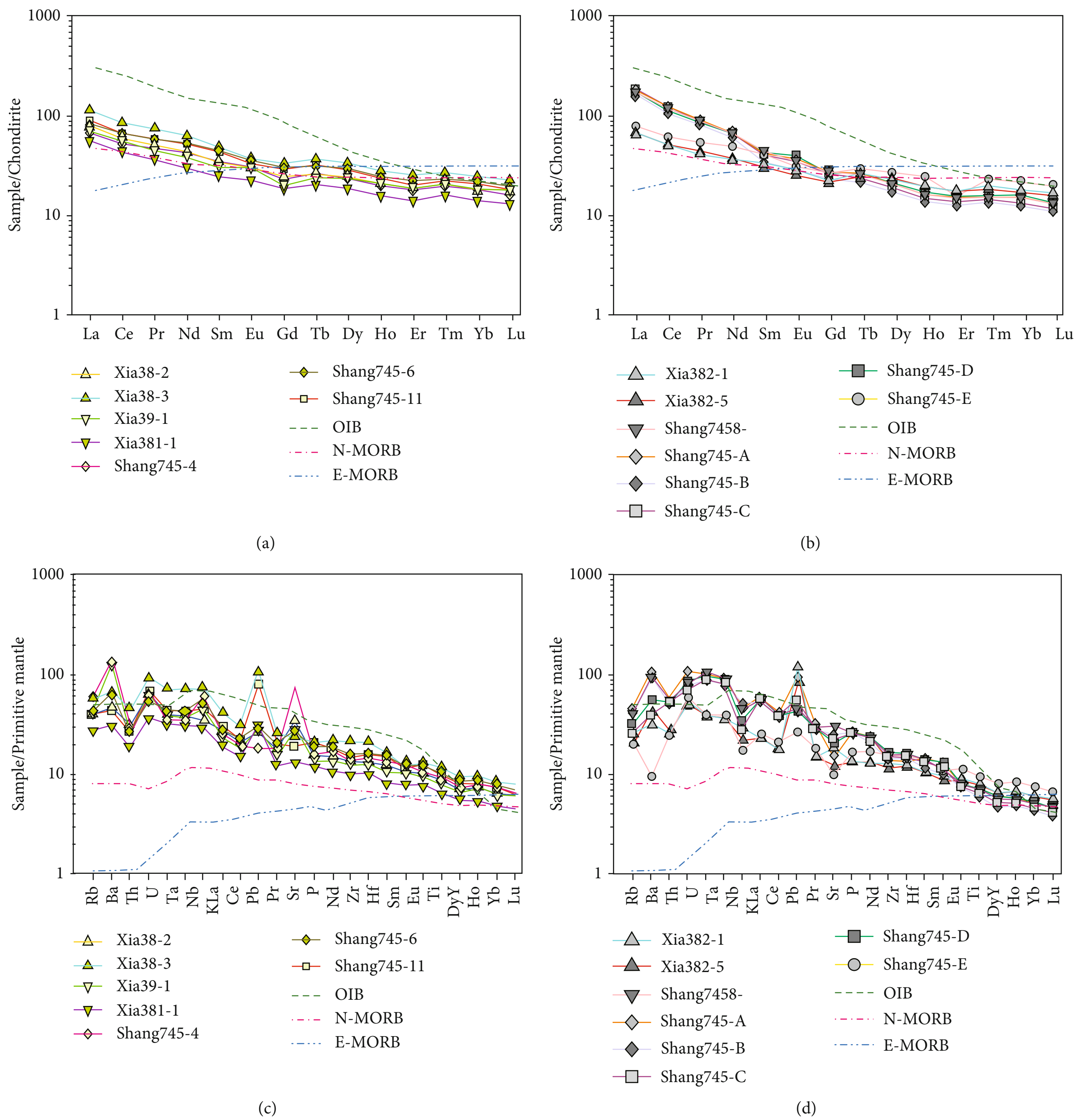

Figure 5: (a, b) Chondrite-normalized REE patterns and (c, d) primitive mantle (PM) normalized trace element diagrams for the Paleogene igneous rocks in Huimin Sag. The values of chondrite and PM are from Sun and McDonough [57].

elements. The high contents of Ti, P, and K of the Paleogene igneous rocks from the Huimin Sag are consistent with those of mantle plume-derived basalts, indicating a mantle plume source. In addition, the ΣREE contents (average 154.36 ppm) of these rocks are clearly higher than those of basalts (average 85 ppm) in eastern China [33], showing the characteristics of mantle plume-derived basalt, which are usually enriched in LREEs (e.g., the Emeishan basalts, Kerguelen mantle plume volcanic rocks, and Iceland volcanic rocks) [5, 34, 35]. The igneous rocks of the present study were characterized by enrichment of LILEs (e.g., Ba, Pb, Sr, U, and K), incompatible elements (Rb, Ba, Th, U, and K), and HFSEs, (e.g., Nb, Ta, Zr, and Hf), similar to those of the mantle-plume-related OIB (e.g., Hawaii basalt of Pacific Plate and Kerguelen basalt of Indian Ocean Plate) or CFB (e.g., Emeishan, Siberia, Deccan, and African continental basalts) [5]. Furthermore, the remarkable Pb enrichment and slightly depleted Y, Pr, and Yb indicate that the Cenozoic mafic rocks in the study area are intraplate rift-type alkali basaltic rocks, which display the characteristics of upper mantle sources. This view is further

Table 3: Sr-Nd-O isotopic compositions of Paleogene igneous rocks in Huimin Sag.

Sample no.	$^{87}Sr/^{86}Sr$	Std err	$^{143}Nd/^{144}Nd$	Std err	εSr	εNd	$\delta^{18}O$ (‰)
X38-2	0.708209	0.000016	0.512579	0.000015	49.08	-1.15	9.5
X38-3	0.706001	0.000009	0.512670	0.000010	17.75	0.62	8.3
X39-1	0.706680	0.000016	0.512670	0.000013	27.39	0.62	5.5
X381-1	0.704610	0.000016	0.512651	0.000010	-1.99	0.25	5.4
S745-4	0.708250	0.000013	0.512605	0.000010	49.66	-0.64	—
S745-6	0.708224	0.000011	0.512657	0.000010	49.29	0.37	—
S745-11	0.708823	0.000009	0.512652	0.000016	57.79	-9.23	—
X382-1	0.706250	0.000016	0.511730	0.000008	21.82	-17.71	8.5
X382-5	0.709788	0.000008	0.512620	0.000006	71.49	-0.35	10.4
S745-8	0.708294	0.000012	0.512783	0.000009	50.29	2.83	—
S745-A	0.708671	0.000012	0.512803	0.000009	55.64	3.22	—
S745-B	0.708346	0.000016	0.512730	0.000008	51.03	1.80	—
S745-C	0.708308	0.000013	0.512743	0.000010	50.49	2.05	—
S745-D	0.708127	0.000008	0.512751	0.000010	47.92	2.20	—
S745-E	0.708378	0.000013	0.512622	0.000005	51.48	-0.31	—

Table 4: Comparison of trace element ratios of Paleogene igneous rocks in Huimin Sag and crust and different mantle members (data of different mantle end members are from [22, 38]).

Element ratio	Primitive mantle	Depleted mantle	Crust	HIMU	EMI	EMII	Volcanic rock in study area
Zr/Nb	14.8	30	16.2	2.7~5.5	3.5~13.1	4.4~7.8	2.35~6.18 (4.42)
La/Nb	0.94	1.07	2.2	0.64~0.82	0.78~1.32	0.79~1.19	0.53~0.70 (0.63)
Ba/Nb	9.0	4.3	54	4.7~6.9	9.1~23.4	6.4~13.4	2.27~41.16 (13.48)
K/Nb	323	296	1341	66~187	207~523	203~378	109.21~623.33 (279.96)
Th/Nb	0.117	0.07	0.44	0.07~0.12	0.09~0.13	0.10~0.17	0.07~0.10 (0.08)
Th/La	0.125	0.07	0.2	0.10~0.16	0.09~0.15	0.11~0.18	0.11~0.14 (0.12)
Ba/La	9.6	4	25	6.2~9.36	11.3~19.1	7.3~13.5	3.56~58.98 (21.39)
$^{87}Sr/^{86}Sr$		0.7022		0.7028	0.7053	0.7078	0.7046~0.7098 (0.7078)
$^{143}Nd/^{144}Nd$		0.5133		0.5128	0.5124	0.5126	0.5117~0.5129 (0.5126)

supported by the Rb/Yb ratios (>1), high Hf and low Zr contents, and the absence of Nb-Ta anomalies in the samples [16, 36]. In the primitive mantle-normalized trace element spider diagrams (Figures 5(c) and 5(d)), the samples plot between the OIB and N-MORB, but closer to the OIB. The concentrations of compatible elements of Cr and Ni for the studied samples were 31.3–467 ppm and 20.7–314, respectively, consistent with those of the basaltic magma derived from primary mantle [37].

The average $^{87}Sr/^{86}Sr$ and $^{143}Nd/^{144}Nd$ ratios of the Paleogene igneous rocks from the Huimin Sag were 0.7078 and 0.5126, respectively, consistent with those of EMII ($^{87}Sr/^{86}Sr = 0.7078$, $^{143}Nd/^{144}Nd = 0.5126$), close to those of EMI ($^{87}Sr/^{86}Sr = 0.7053$, $^{143}Nd/^{144}Nd = 0.5124$) and HIMU ($^{87}Sr/^{86}Sr = 0.7028$, $^{143}Nd/^{144}Nd = 0.5128$), and higher than those of depleted mantle ($^{87}Sr/^{86}Sr = 0.7022$, $^{143}Nd/^{144}Nd = 0.5133$). The average Zr/Nb, La/Nb, Ba/Nb, K/Nb, Th/Nb, Th/La, and Ba/La ratios for the samples were 4.42, 0.63, 13.48, 279.96, 0.08, 0.12, and 21.39, respectively, distributed in the enriched mantle EMII, EMI, and HIMU fields [22, 38]. In the $^{87}Sr/^{86}Sr$-$^{143}Nd/^{144}Nd$ diagram, samples Xia 38-3, Xia 381-1, and Xia 39-1 plot in the OIB field, sample Xia 382-1 plots in the EMI field, sample Shang 745-11 plots in the ancient lithospheric mantle field close to the EMII, and the remaining samples plot close to the OIB, indicating a mantle source, which is further supported by the positive ε_{Nd} values of most samples (Figure 7(a)). Most samples plot in, or close to, the mantle source field, except samples Xia 382-1 and Shang 745-11, which plot in the EMI field and upper crust field, respectively (Figure 7(b)). The $^{87}Sr/^{86}Sr$ ratios of the igneous rocks in the study area varied from 0.7046 to 0.7098, similar to those of the OIB and CFB (<0.710) formed by mantle plume magmatism (e.g., mantle plume-derived basalts of Emeishan, Hawaii, Iceland, and Siberia), showing characteristics of typical mantle plume-derived basalt and deep mantle source [5].

The samples examined in the present study exhibited $\delta^{18}O$ values of 5.4‰ to 10.4‰, with an average of 7.93‰, similar to those of the continental tholeiite (5.0‰ to 7.5‰) and continental mafic lava (4.9‰ to 8.0‰), as well as clinopyroxene in the Emeishan mantle plume-derived basalt (6.2‰ to 7.86‰), but higher than those of the OIB (5.4‰) [39, 40].

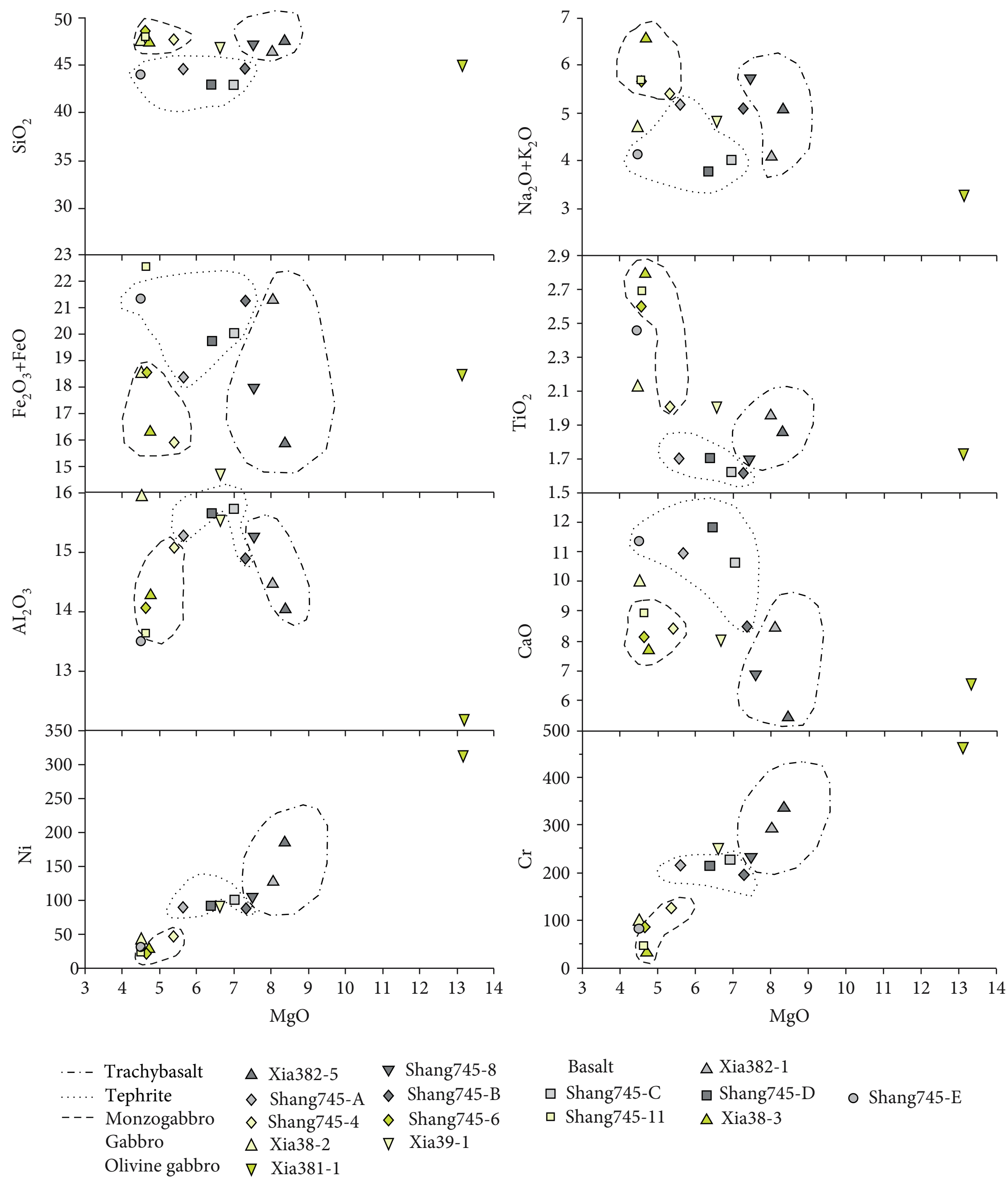

Figure 6: Various oxides and Cr, Ni plotted against MgO for the Paleogene igneous rocks in Huimin Sag with literature data for comparison.

However, the $\delta^{18}O$ values of the samples were slightly higher than those of the mantle, which was probably caused by contamination of crustal materials and source mixing, as the O isotopes were obtained by whole rock analysis. Enrichment of incompatible elements can be caused by the partial melting of an overlying mantle wedge, if the mantle source was influenced by fluids released by the subduction plate. Some researchers suggested that Sr and other incompatible elements can reflect the characteristics of the subduction plate, whereas O isotopes and other elements represent the characteristics of the overlying mantle wedge [39]. In the $\delta^{18}O$-$^{87}Sr/^{86}Sr$ diagram, the igneous rocks in the study area plot close to the downward nonlinear curve, indicating that the isotopic characteristics resulted from source mixing (Figure 8).

To sum up, the Sr-Nd-O isotopic and trace elemental characteristics described above were similar to those of the enriched OIB, indicating a mantle plume source and the existence of components from ancient subduction oceanic crust in the source region (Figures 7 and 9) [41]. The characteristic trace element ratios were consistent with those of the HIMU, EMI, and EMII OIB, which are represented by Mangaia, Pitcairn, and Society, respectively. Samples Shang

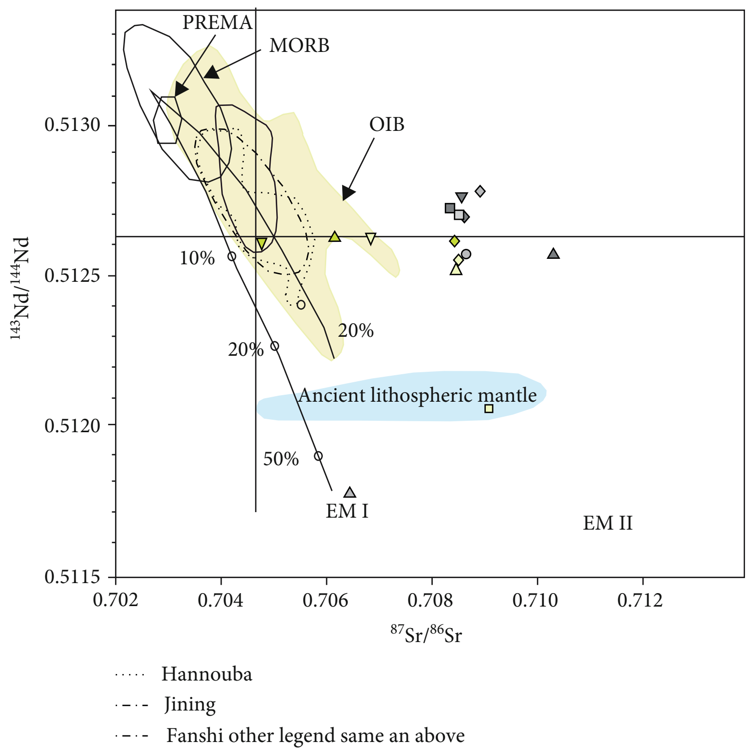

(a)

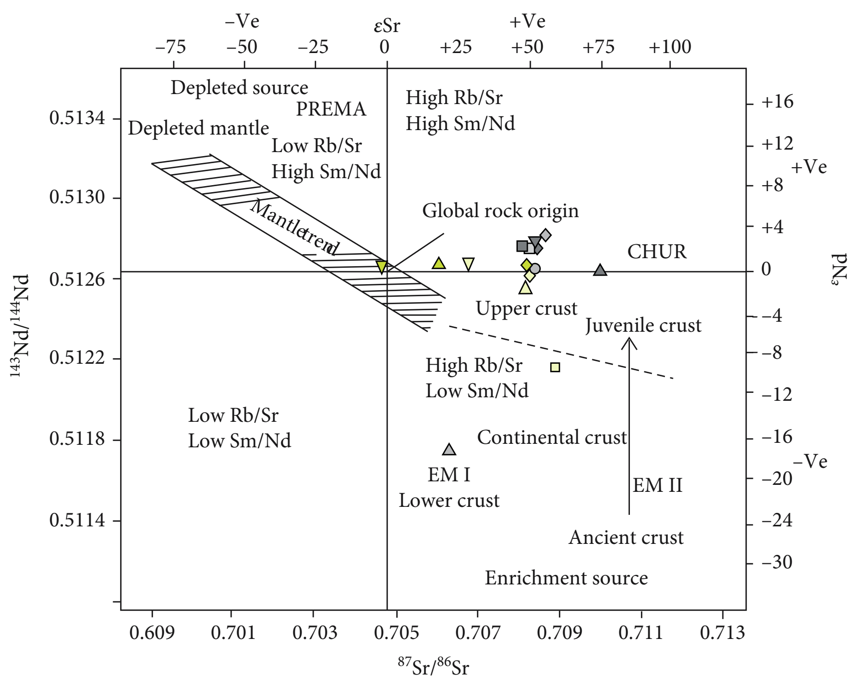

(b)

Figure 7: ^{87}Sr/^{86}Sr vs. ^{144}Nd/^{143}Nd costing point of Paleogene igneous rocks in Huimin Sag. Data sources in (a): Hannuoba basalts [58–60], MORB, OIB, EMI, EMII, and PREMA [61]; data source in (b): EMI, EMII, and PREMA are after Zindler and Hart [61] and Xia [62]. Symbols are as in Figure 5.

745-8, Shang 745-A, Shang 745-B, Shang 745-C, and Shang 745-D plot within the HIMU OIB field and the Ontong Java field, represented by oceanic platform basalt, whereas the remaining samples plot within the EMI and EMII fields, represented by Pitcairn and Society, respectively (Figure 9(a)). The enrichment of subduction-related materials suggests that there were heterogeneous source rocks of the magmatic rocks, which probably originated from different positions or

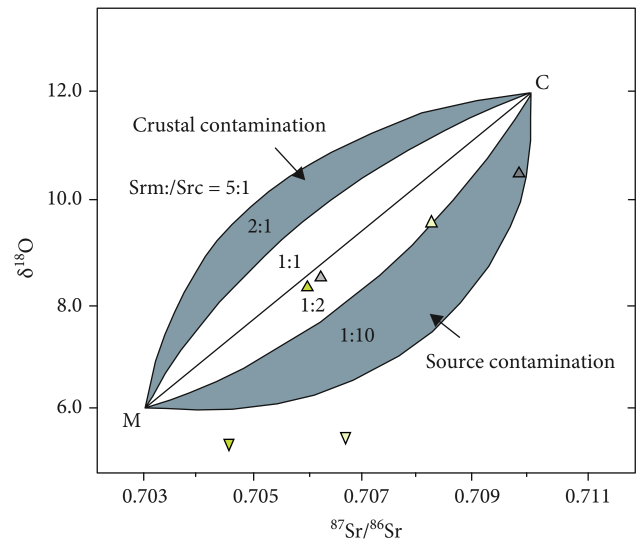

Figure 8: Variation of $\delta^{18}O$ vs. $^{87}Sr/^{86}Sr$ for the mixing of crustal and mantle components of Paleogene igneous rocks in Huimin Sag [39]. Symbols are as in Figure 5.

stages of the mantle plume. The $^{143}Nd/^{144}Nd$ ratios of the samples plot within the field close to the Society OIB (EMII), implying that a recycled oceanic crust that contains a small amount (i.e., a few percent) of terrigenous sediments was involved in the source (Figure 9(b)) [42, 43]. They distribute within the continental lithospheric mantle and crustal contamination fields, represented by Society and Siberia (Figure 9(b)).

The EMII enriched units have been proposed as being related to crustal derived material or recycled oceanic crust [44], whereas the HIMU are related to subducted ancient metamorphic oceanic crust [45]. The EMI are widely accepted to be formed in the lithosphere mantle, asthenosphere, mantle plume, and metasomatic lithosphere mantle by subducted ancient crust [46]. Based on the isotopic and trace elemental analyses discussed above, we suggest that the Paleogene igneous rocks from the Huimin Sag were sourced from the mantle rather than the crust. The primary magma of the rocks likely originated from the melting of a mantle plume and the further metasomatism of lithospheric mantle and continental or oceanic crust.

5.2. Mantle End Member. Based on the Sr-Nd-O isotopic and trace elemental analyses discussed above, three end members in the study area can be proposed. The characteristics of the samples are similar to HIMU, EMI, and EMII, which are represented by those of Mangaia, Pitcairn, and Society, respectively (Figure 9). Samples Shang 745-8, Shang 745-A, Shang 745-B, Shang 745-C, and Shang 745-D, which have high $^{143}Nd/^{144}Nd$ ratios, plot within the HIMU and Ontong Java OIB fields, whereas other samples plot within the EMI and EMII fields close to the Society field, suggesting the involvement of subduction-related materials. The analyses presented above suggest that the three mantle plume end members of the study area are as follows.

First is the low $^{143}Nd/^{144}Nd$ region represented by samples Xia 382-1 and Shang 745-11. Samples Xia 382-1 and Shang 745-11 have $^{143}Nd/^{144}Nd$, $^{87}Sr/^{86}Sr$, and ε_{Nd} of 0.5117 and 0.5122 (average of 0.5119), 0.7063 and 0.7088 (average of 0.7075), and -17.71 and -9.23, respectively, and plot within the EMI and ancient lithospheric mantle fields (Figure 7). These characteristics, in conjunction with the high Y contents and Rb/Sr ratios and low LREEs and HFSE contents and Sm/Nd ratios, indicate that the primary magma experienced crustal remelting and mixing of multiple sources.

Because Zr/Nb and La/Nb ratios can be slightly influenced by fractionation, they are considered to represent those of the mantle-derived rocks [41]. The Zr/Nb and La/Nb ratios of primary mantle and Ontong Java were 15.96 and 0.98 and 17.65 and 1.03, respectively, suggesting that the Ontong Java experienced a higher degree of melting (Figure 9(a)). Samples Xia 382-1 and Shang 745-11 exhibited relatively low Zr/Nb and La/Nb ratios of 5.118 and 0.610 and 5.362 and 0.671, respectively, close to those of Pitcairn and Society (7). They plot in the HIMU field and the boundary between Pitcairn and Society fields, which are not exactly the same as typical OIB, implying the influence of mixing of multiple sources [43]. The Th/Nb and Nb/U ratios of samples Xia 382-1 and Shang 745-11 were 0.082 and 22.488 and 0.072 and 21.56, respectively, and the samples plot within the Ontong Java field; the Th/Nb and Nb/U ratios of which were 0.082 and 35.15 (Figure 9(b)). They exhibited Rb/Sr ratios of 0.042 and 0.065, respectively, close to those of the Ontong Java (0.069) and plot within the OIB (Figure 9(c)). They exhibited La/Sm and Sm/Yb ratios of 3.341 and 1.584 and 3.138 and 1.821, respectively, and plot within the Siberia field, between the CLM and BCC (Figure 9(d)). They exhibited average Nb/Y and Zr/Y ratios of 0.966 and 4.906, respectively, and plot within the OIB field (Figure 9(e)).

Second is the high $^{143}Nd/^{144}Nd$ region represented by samples Shang 745-8, Shang 745-A, Shang 745-B, Shang 745-C, and Shang 745-D. These samples displayed $^{87}Sr/^{86}Sr$ of 0.7081 to 0.7087 (average of 0.7083) and the highest $^{143}Nd/^{144}Nd$ of 0.5127 to 0.5129 (average of 0.5128); they plot in a cluster close to the OIB (Figure 7). They also exhibited positive ε_{Nd} values, implying a depleted mantle source, high LREEs, HFSEs, Rb/Sr and Sm/Nd, and low Y contents. These samples had low Zr/Nb and La/Nb ratios of 2.70 and 0.62, respectively, plotting within the HIMU OIB field (Figure 9(a)). They exhibited relatively lower average Th/Nb and higher average Nb/U ratios of 0.074 and 36.493, respectively, close to those of the Ontong Java (0.082 and 5.15) and plot within the Mangaia and Ontong Java fields, which represent the HIMU OIB and oceanic platform basalt (Figure 9(b)). They displayed an average Rb/Sr ratio of 0.057, close to the Ontong Java (0.069) and plot within the BCC field (Figure 9(c)). These samples had the highest average La/Sm and Sm/Yb ratios (6.58 and 2.52, respectively) of all the studied samples, implying that the magma experienced no crustal contamination (Figure 9(d)). They exhibited average Nb/Y and Zr/Y ratios of 0.937 and 4.866, respectively, and plot within the OIB field (Figure 9(e)).

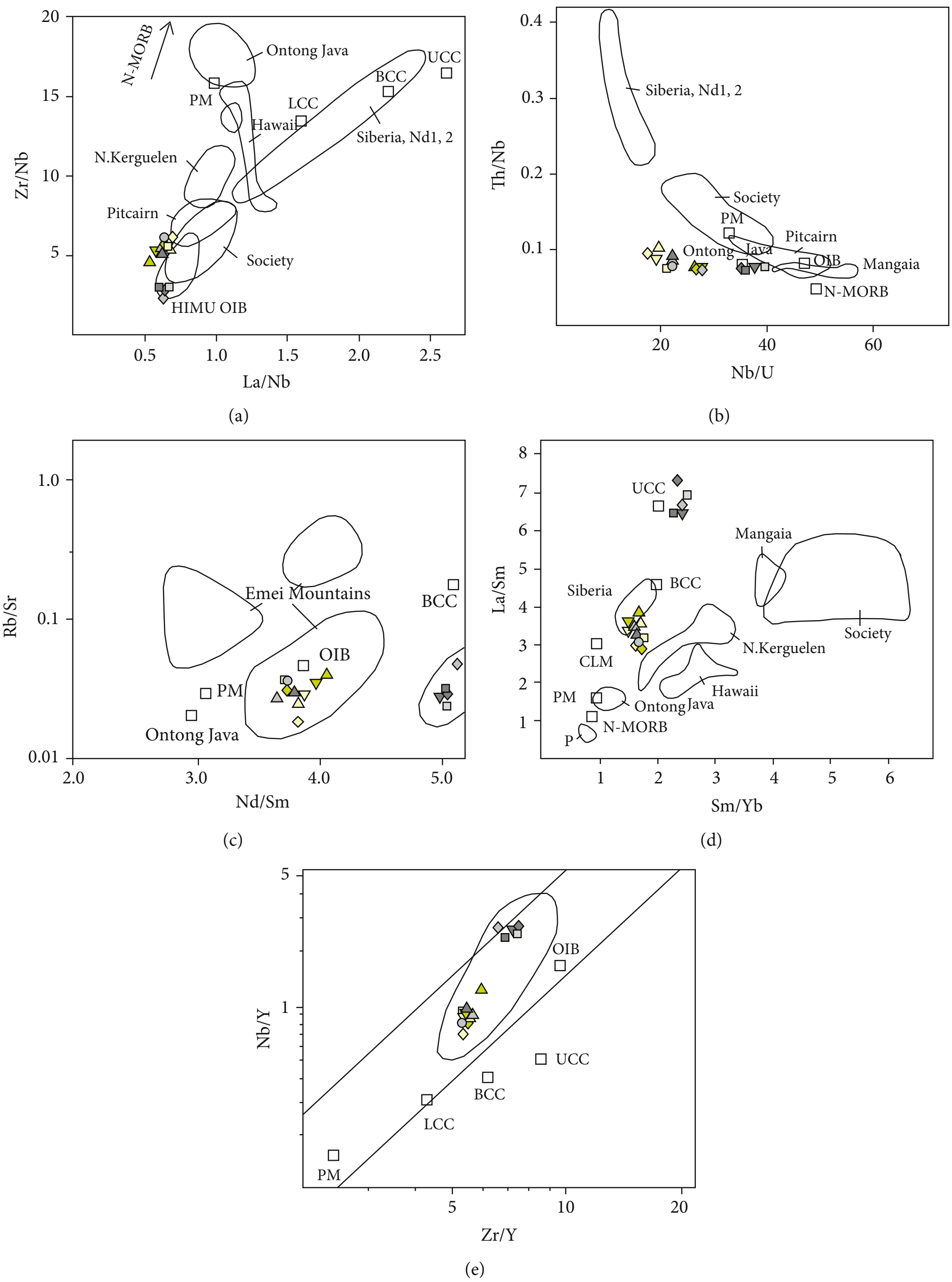

Figure 9: Trace element ratios of Paleogene igneous rocks in Huimin Sag. (a) Zr/Nb vs. La/Nb, (b) Th/Nb vs. Nb/U, (c) Rb/Sr vs. Nd/Sm, (d) La/Sm vs. Sm/Yb, and (e) Nb/Y vs. Zr/Y diagrams for the Paleogene igneous rocks from the Huimin Sag. Data sources are as follows: PM refers to primitive mantle values [63]; UCC, BCC, and CC mark the upper continental crust, whole continental crust, and average compositions of bulk, respectively [64]. HIMU OIB [65]; Pitcairn [66]; Society [43]; Ontong Java [67]; N. Kerguelen [68]; Hawaii [69]. Siberia, Nd1, 2 represent crustal contamination lavas typically [70]. The arrow points to the average MORB values: Zr/Nb = 31.76, La/Nb = 1.07 [57]. The values for OIB are from Sun and McDonough [57]. Composition of continental lithospheric mantle (CLM) is from McDonough [71]. Parallel lines mark the upper and lower bounds of the Iceland basalt data [72], All the symbols are the same as in Figure 5.

Third is the moderate $^{143}Nd/^{144}Nd$ region, represented by samples Xia 381-1-a, Xia 38-3, Xia 39-1, Shang 745-6, Xia 38-2, Shang 745-4, Shang 745-E, and Xia 382-5. These samples exhibited $^{87}Sr/^{86}Sr$ of 0.7046 to 0.7098 (average of 0.7075) and $^{143}Nd/^{144}Nd$ of 0.5126 to 0.5127 (average of 0.5126). The samples plot within the area close to the OIB and the

CHUR line and had moderate Rb/Sr and Sm/Nd, low LREEs and HFSEs, and high Y contents, implying an ancient rock source. These samples had average Zr/Nb and La/Nb ratios of 6.178 and 0.698, respectively, close to those of Pitcairn and Society (7) and plot in the HIMU field and the boundary between Pitcairn and Society fields (Figure 9(a)), which are not exactly the same as typical OIB, implying the influence of mixing of multiple sources. The average Th/Nb and Nb/U ratios of the samples were 0.097 and 27.975, respectively, consistent with those of the Ontong Java (0.082 and 35.15), and they plot within the Ontong Java, Pitcairn, and Society fields (Figure 9(b)). They had average Rb/Sr, Nb/Y, and Zr/Y ratios of 0.042, 0.795, and 4.649, respectively, and plot within the OIB field (Figures 9(c) and 9(e)). The average La/Sm and Sm/Yb ratios of the samples were 3.073 and 1.722, respectively, and they plot within the Siberia field, between the CLM and BCC (Figure 9(d)).

5.3. Characteristics of Mantle Plume Magmatism. Mantle plumes usually have a very large spherical head and a narrow tail, along which fluids can move upward rapidly [5, 47]. However, the nature of the reactions between mantle plume and lithosphere remains controversial. Campbell and Griffiths [47] suggested that the head of a mantle plume is a mixture of source materials and materials from the sides of magma channels. Because of the different sizes and depths of different mantle plumes, the representative magmatic products of a mantle plume head are alkaline rocks, due to crystallization differentiation, metasomatism, and contamination when the spherical head moves up and leads to the melting of the local lithosphere, as well as involvement of mantle mixed sources with different degrees of enrichment [5, 48]. The narrow and long mantle plume tail can provide channels for the ascent of high temperature and low viscosity mantle materials. The melting of a mantle plume tail and agglutination and ascent of magma provide the heat source and volatile components that enhance further mantle rock melting. The rocks formed by the mantle plume tail exhibit OIB-like geochemical characteristics, including low Yb contents and high LREEs and HFSEs (Ti, P, and Nb) contents [5]. The remelting of ascending mantle materials in the mantle plume channels caused by abnormal heat can form picrite and picritic basalt, whereas the magmatic products of a mantle plume tail are ultrabasic rocks. The OIB are extremely geochemically enriched and were usually considered to be related to hotspots or mantle plumes [49–51]. The samples examined in the current study have generally low $^{87}Sr/^{86}Sr$ ratios (mostly >0.710) and plot in the OIB field (Figures 5–7 and 9(a)–9(e)), showing the characteristics of a deep mantle source, which suggest that the genesis was the mantle plume. The Sr-Nd-O isotopic and geochemical characteristics of the studied samples indicate that the mantle plume in the study area consists of a head, a tail, and a middle section.

The mantle plume head: the EMI end member was formed by metasomatism and melting of mantle materials, which corresponds approximately to the MORB, and the subducting oceanic crust, whereas the EMII end member is formed by metasomatism of crust-mantle-derived fluids of crustal components from the descending ancient slab or oceanic crust [45, 52]. The early formed magma of the mantle plume has large proportions of crustal and lithosphere mantle materials because of contamination and involvement of fertile mantle (EMI and EMII) during ascent. The mantle plume head usually has mixed characteristics of two sources, as the magma forms in the magma chamber of shallow crust and experiences contamination and fractional crystallization. Samples from Xia 382-1 and Shang 745-11 wells have the lowest ε_{Nd} values of -17.71 and -9.23, respectively, significantly lower than those of the OIB (-4.1 to 8.0) and MORB (6.9 to 11.9) [53]. In the $^{87}Sr/^{86}Sr$-$^{143}Nd/^{144}Nd$ diagram, the samples plot in the EMI, EMII, and ancient lithospheric mantle fields (Figure 7). The lowest $^{143}Nd/^{144}Nd$ values of 0.5117 and 0.5122, as well as the depletion of LREEs, HFSEs (Ti, P, and Nb), and Nb-Ta, indicate that the lithospheric mantle that was previously metasomatized by crustal materials has experienced a low degree of homogenization.

The mantle plume tail: this section of mantle plume was formed by the eruption of high-energy mantle materials that experienced no crustal contamination. Rocks formed in the mantle plume tail are mainly ultrabasic rocks, which have high $^{143}Nd/^{144}Nd$ ratios, ε_{Nd} values, LREEs, HFSEs (Ti, P, and Nb), and low Yb contents. Samples Shang 745-A, Shang 745-B, Shang 745-C, Shang 745-D, and Shang 745-8 have high $^{143}Nd/^{144}Nd$ ratios (0.5127 to 0.5128), LREEs, and HFSEs (except sample Xia 381-1), as well as other geochemical and isotopic characteristics of typical OIB. We therefore consider that they were formed in the mantle plume tail. Furthermore, the samples exhibited the highest positive ε_{Nd} values of 1.80 to 3.22 consistent with those of the OIB (-4.0 to 8.0), suggesting a mantle source [53].

The middle section: rocks formed in the middle section of mantle plume represented by samples Xia 38-2, Xia 38-3, Xia 381-1, Shang 745-4, Shang 745-6, Xia 39-1, and Shang 745-E which are formed by magmas that experienced a low degree of melting [54], crustal contamination, as well as involvement of lithospheric material. They have moderate $^{143}Nd/^{144}Nd$ ratios, ε_{Nd} values, LREEs, and HFSEs (Ti, P, and Nb) contents. The moderate $^{143}Nd/^{144}Nd$ ratios (0.5126 to 0.5127), ε_{Nd} values (-1.15 to 0.62), LREEs, and HFSEs of these samples are lower than those of the mantle plume tail but higher than those of the mantle plume head. The ε_{Nd} values are distributed around zero and close to the CHUR line, consistent with those of the OIB (-4.0 to 8.0) [53].

6. Conclusions

The high Ti, P, and K contents of the studied igneous rocks are consistent with those of mantle plume-derived basalts. They are relatively enriched in LREEs and depleted in HREEs and have patterns of REE similar to OIB. The enrichment of LILEs (Ba, Pb, Sr, U, and K), incompatible elements (Rb, Ba, Th, U, and K), and HFSEs (Nb, Ta, Zr, and Hf) is similar to that of the mantle plume-derived OIB. The ε_{Nd} values and $^{87}Sr/^{86}Sr$ ratios of the rocks were -17.71 to 5.56 and 0.7046 to 0.7098 (mostly less than 0.710), respectively, and mostly plot within the OIB field, with a few samples within the ancient lithospheric mantle field close to the EMI and EMII, typical characteristics of mantle plume.

The mantle plume in the study area consists of a head, a tail, and a middle section. The mantle plume head was represented by samples Xia 382-1 and Shang 745-11, which had low ε_{Nd}, LREEs, HFSEs, Nb, and Ta contents and mixed characteristics of two sources. The mantle plume tail was represented by samples Shang 745-A, Shang 745-B, Shang 745-C, Shang 745-D, and Shang 745-8, which have the highest ε_{Nd}, LREEs, and HFSEs and typical isotopic and trace elemental characteristics of OIB. The remaining samples represent the middle section of the mantle plume and had ε_{Nd} values of approximately zero and close to the CHUR line.

Trace elemental and isotopic characteristics suggest that the studied rocks were similar to the HIMU, EMI, and EMII OIB, represented by the Mangaia, Pitcairn, and Society, respectively. The samples Shang 745-8, Shang 745-A, Shang 745-B, Shang 745-C, and Shang 745-D of the high $^{143}Nd/^{144}Nd$ region plot within the HIMU and OIB fields, whereas the remaining samples plot within the EMI and EMII fields close to the Society field, indicating enrichment by subduction-related materials.

The $(Th/Ta)_{PM}$ and $(La/Nb)_{PM}$ ratios of the samples were both less than 1.0, suggesting that the upper crust had no role in the generation of the rocks. The O isotopes plot close to the downward nonlinear curve, also indicating the absence of crustal contamination. The ε_{Nd} values of the sample ranged from -17.71 to 5.56, similar to those of the mantle plume-derived CFB. Based on the isotopic and trace elemental analyses discussed herein, we suggest that the Paleogene igneous rocks from the Huimin Sag were sourced from the mantle, rather than the crust. The primary magma of the rocks likely originated from the melting of a mantle plume, followed by further metasomatism of lithospheric mantle and continental or oceanic crust.

Data Availability

All data in the article is presented in the form of tables and graphs. All the data in this article is accessible to readers.

Conflicts of Interest

The authors declared that they have no conflicts of interest.

Acknowledgments

This study was financially supported by the Key Laboratory of Coalbed Methane Resources and Reservoir Formation Process of the Ministry of Education (China University of Mining and Technology) (Grant no. 2021-008), the National Natural Science Foundation of China (Grant no. U19B6003), the Natural Science Foundation of Shandong Province (Grant nos. ZR2019PD001 and ZR2020QD028), and the Geological Exploration Project of Shandong Province (Grant nos. LKZ (2020) 7 and LKZ (2021) 7).

References

[1] M. E. Barley and D. I. Croves, “Supercontinent cycles and the distribution of metal deposits through time,” *Geology*, vol. 20, no. 4, pp. 291–294, 1992.

[2] R. Kerrich, “Continents ring the changes,” *Nature*, vol. 358, no. 6381, pp. 16-17, 1992.

[3] F. J. Sawkins, “Metal deposits related to intracontinental hotspot and rifting environments,” *The Journal of Geology*, vol. 84, no. 6, pp. 653–671, 1976.

[4] Z. Q. Hou and H. Y. Li, “Atentative discussion on the mantle plume tectonics and metallogenic system as exemplified by the Sanjiang Tethyan metaliogenic domain,” *Mineral Deposits*, vol. 17, no. 2, pp. 97–113, 1998.

[5] H. Y. Li, S. Y. Niu, L. F. Wang, and Y. F. Gao, *Plume Tectonics*, Seismological Press, Beijing, 2002.

[6] S. P. Pei and Y. S. Chen, “Tomographic structure of East Asia: I. no fast (slab) anomalies beneath 660 km discontinuity,” *Earthquake Science*, vol. 23, no. 6, pp. 597–611, 2010.

[7] T. Wan, *The Tectonics of China: Data, Maps and Evolution*, Higher Education Press and Springr, Dordrecht Heidelberg, 2011.

[8] T. F. Wan and Q. I. Zhao, “The genesis of tectono-magmatism in eastern China,” *Science China: Earth Science*, vol. 55, no. 3, pp. 347–354, 2012.

[9] C. G. Wen, Y. Q. Zhen, H. Qiao, Q. Diao, and Z. Chen, “Interrelation of plate tectonics and mantle plume tectonics: in case of Mesozoic and Cenozoic ore control factor in East China,” *Contributions to Geology and Mineral Resources Research*, vol. 30, no. 1, pp. 1–15, 2015.

[10] S. H. Zhang, R. Gao, H. Y. Li et al., “Crustal structures revealed from a deep seismic reflection profile across the Solonker suture zone of the Central Asian Orogenic Belt, northern China: an integrated interpretation,” *Tectonophysics*, vol. 612-613, no. 613, pp. 26–39, 2014.

[11] L. Guangxia, Z. Wenjun, and L. Zhixiong, “Geophysical analysis on the tertiary Rift Valley expanding of Bohai Sea,” *Northwestern Seismological Journal*, vol. 18, no. 3, pp. 18–24, 1996.

[12] L. Xiao, F. Z. Wang, H. Wang, and F. Pirajno, “Mantle plume tectonics constraints on the formation of Songliao and Bohaiwan basins,” *Earth Science: Journal of China University of Geosciences*, vol. 29, no. 3, pp. 283–292, 2004.

[13] X. S. Ye and W. F. Wang, “Plate Subduction Contrains on the Formation of Jiyang Depression,” *Earth Science—Journal of China University of Geosciences*, vol. 33, no. 2, pp. 235–242, 2008.

[14] X. Q. Zhu, *The Mantle Plume Model for the Evolution of Bohai Bay Basin*, China University of Petroleurm (East China), Qingdao, 2009.

[15] Z. Y. Liu, S. B. Xiao, and Z. X. Jiang, “Volcanic rocks of Bohai Bay Basin in tertiary and their genesis,” *Journal of the University of Petroleum China*, vol. 25, no. 1, pp. 22–26, 2001.

[16] H. M. Liu and Z. H. Xie, “Analysis on the petrochemical characteristics and geneses of the tertiary igneous rock in the Jiyang Depression, the Bohaiwan Basin,” *Petroleum Geology & Experiment*, vol. 25, no. 4, pp. 385–389, 2003.

[17] W. Z. Shen, L. Z. Zhao, and M. Zhao, “Study on Nd-Sr isotopic compositions of Tertiary basalts from Jiyang depressional basin,” *Acta Petrologica Sinica*, vol. 18, no. 1, pp. 47–58, 2002.

[18] Y. Q. Wang, *Paleogene Volcanic Rocks in Eastern Depression of Liaohe Basin: From Petrogenesis to Exploration*, Jilin University, Changchun, 2016.

[19] C. Zhang, C. Q. Ma, and Q. A. Liao, "Formation of non-expandable 7 Å halloysite during Eocene-Miocene continental weathering at Djebel Debbagh, Algeria: a geochemical and stable-isotope study," *Acta Petrologica Sinica*, vol. 217, no. 1-4, pp. 140–153, 2009.

[20] C. Zhang, C. Q. Ma, Q. A. Liao, J. Y. Zhang, and Z. B. She, "Implications of subduction and subduction zone migration of the Paleo-Pacific Plate beneath eastern North China, based on distribution, geochronology, and geochemistry of Late Mesozoic volcanic rocks," *International Journal of Earth Sciences*, vol. 100, no. 7, pp. 1665–1684, 2011.

[21] T. Tanaka, S. Togashi, H. Kamioka et al., "JNdi-1: a neodymium isotopic reference in consistency with LaJolla neodymium," *Chemical Geology*, vol. 168, no. 3-4, pp. 279–281, 2000.

[22] J. J. Lu, L. Q. Wu, H. F. Ling et al., "The origin of the Huangpi-Zhangguangying diabase dykes in the Xiazhuang uranium ore district of northern Guangdong province: evidence from trace elemenst and Nd-Sr-Pb-O isotopes," *Acta Petrologica Sinica*, vol. 22, no. 2, pp. 397–406, 2006.

[23] Z. Z. Han, J. J. Li, Z. G. Song et al., "Geochemistry and zircon U-Pb-Hf isotopes of metamorphic rocks from the Kaiyuan and Hulan tectonic mélanges, NE China: implications for the tectonic evolution of the Paleo-Asian and Mudanjiang oceans," *Minerals*, vol. 10, no. 9, p. 836, 2020.

[24] Z. G. Song, Z. Z. Han, L. H. Gao et al., "Permo-Triassic evolution of the southern margin of the Central Asian Orogenic Belt revisited: insights from Late Permian igneous suite in the Daheishan Horst, NE China," *Gondwana Reaerch*, vol. 56, pp. 23–50, 2018.

[25] Z. G. Song, C. Han, H. Liu et al., "Early-middle Ordovician intermediate-mafic and ultramafic rocks in central Jilin Province, NE China: geochronology, origin, and tectonic implications," *Mineralogy and Petrology*, vol. 113, no. 3, pp. 393–415, 2019.

[26] J. A. Pearce, "A user's guide to basalt discrimination diagrams," in *Trace Element Geochemistry of Volcanic Rocks: Applications for Massive Sulphide Exploration. Short Course Notes*, A. H. Bailes, E. H. Christiansen, A. G. Galley, G. A. Jenner, J. D. Keith, R. Kerrich, D. R. Lentz, C. M. Lesher, S. B. Lucas, J. N. Ludden, J. A. Pearce, S. A. Peloquin, R. A. Stern, W. E. Stone, E. C. Syme, H. S. Swinden, and D. A. Wyman, Eds., vol. 12, pp. 79–113, Geological Association of Canada, 1996.

[27] A. Miyashiro, "Volcanic rock series in island arcs and active continental margins," *American Journal of Science*, vol. 274, no. 4, pp. 321–355, 1974.

[28] D. J. Depaolo and G. J. Wasserburg, "Petrogenetic mixing models and Nd-Sr isotopic patterns," *Geochimica et Cosmochimica Acta*, vol. 43, no. 4, pp. 615–627, 1979.

[29] Z. C. Zhang and F. S. Wang, "Sr, Nd and Pb isotopic characteristics of Emeishan Basalt Province and discussion on their source region," *Earth Science: Journal of China University of Geosciences*, vol. 28, no. 4, pp. 431–439, 2003.

[30] R. L. Rudnick and S. Gao, "Composition of the continental crust," in *Treatise Geochem*, D. H. Heinrich and K. T. Karl, Eds., vol. 3, pp. 1–64, Pergamon, Oxford, 2003.

[31] D. J. Depaolo, "A neodymium and strontium isotopic study of the Mesozoic calc-alkaline granitic batholiths of the Sierra Nevada and Peninsular Ranges, California," *Journal of Geophysical Research: Solid Earth*, vol. 86, no. B11, pp. 10470–10488, 1981.

[32] Z. Z. Peng, J. J. Mahoney, P. R. Hooper, C. Harris, and J. Beane, "A role for lower continental crust in flood basalt genesis? Isotopic and incompatible element study of the lower six formations of the Western Deccan Traps," *Geochimica et Cosmochimica Acta*, vol. 58, no. 1, pp. 267–288, 1994.

[33] J. X. Qiu, *Application of Magmatic Petrology*, China University of Geosciences Press, Beijing, 1991.

[34] Z. Q. Hou, J. R. Lu, and H. Y. Li, "Tectonic evolution of the Tethys in southwestern China is controlled by plume tectonics," *Acta Geoscientia Sinica*, vol. 17, no. 4, pp. 439–453, 1996.

[35] J. Zhu, *A Study of Mantle Plume Dynamics and Its Environmental Effect in the Emeishan Large Igneous Province*, China University of Geosciences (Beijing), Beijing, 2019.

[36] J. A. Pearce, "Trace element characteristics of lavas from destructive plate boundaries," in *Andesite*, R. S. Thorpe, Ed., pp. 525–548, Wiley, Chichester, 1982.

[37] T. Zhou, J. H. Wu, and C. H. Ai, "Petrogenesis of alkali olivine basalt from Guangfeng basins in Jiangxi Province: SHRIMP zircon U-Pb dating and element, Sr-Nd-Pb isotope constraints," *Journal of East China University of Technology (Natural Science)*, vol. 39, no. 2, pp. 108–117, 2016.

[38] B. L. Weaver, "The origin of ocean island basalt end-member compositions: trace element and isotopic constraints," *Earth and Planet Science Letter*, vol. 104, no. 2-4, pp. 381–397, 1991.

[39] L. Xiao, Y. G. Xu, and B. He, "Emei mantle plume-subcontinental lithosphere interaction: Sr-Nd and O isotopic evidences from low-Ti and high-Ti basalts," *Geological Journal of China Universities*, vol. 9, no. 2, pp. 207–217, 2003.

[40] Y. F. Zheng, *Stable isotope geochemistry*, Science Press, Beijing, 2000.

[41] Z. Q. Hou, J. R. Lu, and S. Z. Lin, "The axial zone consisting of pyrolite and eclogue in the Emei mantle plume major, trace element and Sr-Nd-Pb isotope evidence," *Acta Geologica Sinica*, vol. 79, no. 2, pp. 200–216, 2005.

[42] A. W. Hofmann, "Mantle geochemistry: the message from oceanic volcanism," *Nature*, vol. 385, no. 6613, pp. 219–229, 1997.

[43] W. M. White and R. A. Duncan, "Geochemistry and geochronology of the Society Island: new evidence for deep mantle recycling," in *Earth Processes: Reading The Isotopic Code*, A. Basu and S. R. Hart, Eds., vol. 95 of Union, Geophysical Monograph Series, pp. 183–206, 2013.

[44] A. Glazner and L. Farmer, "Production of isotopic variability in continental basalts by cryptic crustal contamination," *Science*, vol. 255, no. 5040, pp. 72–74, 1992.

[45] M. A. Menzies, "Archacan, Proterozoic and Phanerzoic lithospheres," in *Cont Inental Mantle*, M. A. Menzies, Ed., pp. 67–86, Oxford Science Publications, Oxford, 1991.

[46] M. Tatsumoto, A. R. Basu, W. K. Huang, W. Junwen, and X. Guanghong, "Sr, Nd, and Pb isotopes of ultramafic xenoliths in volcanic rocks of eastern China: enriched components EMI and EMII in subcontinental lithosphere," *Earth and Planetary Science Letters*, vol. 113, no. 1-2, pp. 107–128, 1992.

[47] I. H. Campbell and R. W. Griffiths, "Implications of mantle plume structure for the evolution of flood basalts," *Earth and Planetary Science Letters*, vol. 99, no. 1-2, pp. 79–93, 1990.

[48] Z. Q. Hou, Y. X. Mo, Q. W. Zhu, and S. Shangyue, "Mantle plume in the Sanjiang Paleo-Tethyan region, China evidence from Ocean-Island basalts," *Acta Geoscientia Sinica*, vol. 17, no. 4, pp. 343–361, 1994.

[49] Y. An, Q. Yang, and W. F. Chen, “The revelation of big data: differences between N-MORB, E-MORB and OIB and their possible causes,” *Chinese Journal of Geology*, vol. 52, no. 3, pp. 727–742, 2017.

[50] A. W. Hofmann and C. Hémond, “The origin of E-MORB,” *Geochimica et Cosmochimica Acta*, vol. 70, no. 18, article A257, 2006.

[51] Y. L. Niu, “Some basic concepts and problems on the petrogenesis of intra-plate Ocean Island basalts,” *Chinese Science Bulletin*, vol. 2009, no. 54, pp. 4148–4160, 2009.

[52] B. T. Zhang, J. Q. Wu, H. F. Ling, and P. P. Chen, “Geochemical evidence of element and Sr-O-Nd-Pb isotopes for petrogenesis of the Huichang Early Cretaceous shoshonite, southern Jiangxi province,” *Acta Geologica Sinica*, vol. 82, no. 7, pp. 986–997, 2008.

[53] E. Ito, W. M. White, and C. Göpel, “The O, Sr, Nd and Pb isotope geochemistry of MORB,” *Chemical Geology*, vol. 62, no. 3-4, pp. 157–176, 1987.

[54] Y. G. Xu and S. L. Zhong, “The Emeishan large igneous province: evidence for mantle plume activity and melting conditions,” *Geochimica*, vol. 30, no. 1, pp. 1–9, 2001.

[55] X. Mao, L. Luo, X. Wang, and D. B. Guo, “Distribution characteristics of Cenozoic volcanic rocks and its geothermal exploration potential in Bohai Bay Basin,” *Geoscience*, vol. 34, no. 4, pp. 858–864, 2020.

[56] H. Y. Li, X. L. Huang, and H. Guo, “Geochemistry of Cenozoic basalts from the Bohai Bay Basin: implications for a heterogeneous mantle source and lithospheric evolution beneath the eastern North China Craton,” *Lithos*, vol. 196-197, pp. 54–66, 2014.

[57] S. S. Sun and W. F. McDonough, “Chemical and isotopic systematics of oceanic basalts: implications for mantle composition and processes,” *Geological Society, London, Special Publication*, vol. 42, no. 1, pp. 313–345, 1989.

[58] Y. Song, F. A. Frey, and X. C. Zhi, “Isotopic characteristics of Hannuoba basalts, eastern China: implications for their petrogenesis and the composition of subcontinental mantle,” *Chemical Geology*, vol. 88, no. 1-2, pp. 35–52, 1990.

[59] L. Ye, J. J. Liu, Y. L. Niu, P. Y. Guo, P. Sun, and H. X. Cui, “Mantle sources and petrogenesis of the Cenozoic basalts in Fanshi, Shanxi Province: geochemical and Sr-Nd-Pb-Hf isotopic evidence,” *Acta Petrologica Sinica*, vol. 31, no. 1, pp. 161–175, 2015.

[60] X. C. Zhi, Y. Song, F. A. Frey, J. Feng, and M. Zhai, “Geochemistry of Hannuoba basalts, eastern China: constraints on the origin of continental alkalic and tholeiitic basalt,” *Chemical Geology*, vol. 88, no. 1-2, pp. 1–33, 1990.

[61] A. Zindler and S. R. Hart, “Chemical geodynamics,” *Annual Review of Earth and Planetary Sciences*, vol. 14, no. 1, pp. 493–571, 1986.

[62] D. Xia, *Effect of Intrusive Rocks on the Evolution of Organic Matter and Geochemical Characteristics of Surrounding Rocks in Linnan Sag*, Shangdong University of Science and Technology, Qingdao, 2017.

[63] W. F. McDonough and S. S. Sun, “The composition of the earth,” *Chemical Geology*, vol. 120, no. 3-4, pp. 223–253, 1995.

[64] M. G. Barth, W. F. McDonough, and R. L. Rudnick, “Tracking the budget of Nb and Ta in the continental crust,” *Chemical Geology*, vol. 165, no. 3-4, pp. 197–213, 2000.

[65] T. Kogiso, Y. Tatsumi, G. Shimoda, and H. G. Barsczus, “High μ (HIMU) Ocean Island basalts in southern Polynesia: new evidence for whole mantle scale recycling of subducted oceanic crust,” *Journal of Geophysical Research*, vol. 102, no. B4, pp. 8085–8103, 1997.

[66] J. D. Woodhead and C. W. Devey, “Geochemistry of the Pitcairn seamounts, I: source character and temporal trends,” *Earth and Planetary Science Letters*, vol. 116, no. 1-4, pp. 81–99, 1993.

[67] R. S. White and D. P. McKenzie, “Mantle plumes and flood basalts,” *Journal of Geophysical Research Atmospheres*, vol. 100, no. B9, pp. 17543–17585, 1995.

[68] H. J. Yang, F. A. Frey, D. Weis, A. Giret, D. Pyle, and G. Michon, “Petrogenesis of the flood basalts forming the northern Kerguelen archipelago: implications for the Kerguelen plume,” *Journal of Petrology*, vol. 39, no. 4, pp. 711–748, 1998.

[69] M. D. Norman and M. O. Garcia, “Primitive magmas and source characteristics of the Hawaiian plume: petrology and geochemistry of shield picrites,” *Earth and Planetary Science Letters*, vol. 168, no. 1-2, pp. 27–44, 1999.

[70] J. L. Wooden, G. K. Czamanske, V. A. Fedorenko et al., “Isotopic and trace-element constraints on mantle and crustal contributions to Siberian continental flood basalts, Noril'sk area, Siberia,” *Geochimica et Cosmochimica Acta*, vol. 57, no. 15, pp. 3677–3704, 1993.

[71] W. F. McDonough, “Constraints on the composition of the continental lithospheric mantle,” *Earth and Planetary Science Letters*, vol. 101, no. 1, pp. 1–18, 1990.

[72] J. G. Fitton, A. D. Saunders, M. J. Norry, B. S. Hardarson, and R. N. Taylor, “Thermal and chemical structure of the Iceland plume,” *Earth and Planetary Science Letters*, vol. 153, no. 3-4, pp. 197–208, 1997.

Hindawi
Geofluids
Volume 2022, Article ID 7984910, 13 pages
https://doi.org/10.1155/2022/7984910

Research Article

Analysis Deformation Failure Characteristics and the Energy Evolution of Varying Lithologies under Cyclic Loading

Jianqiang Liu,[1,2] **Guangpeng Qin**,[1,2,3] **Jing Cao**,[4] **and Minghua Zhai**[3]

[1]*College of Resource, Shandong University of Science and Technology, Tai'an, Shandong 271000, China*
[2]*National Engineering Laboratory for Coalmine Backfilling Mining, Shandong University of Science and Technology, Tai'an, Shandong 271000, China*
[3]*Shandong Energy Group Co., Ltd., Ji'nan, Shandong 250100, China*
[4]*College of Finance and Economics, Shandong University of Science and Technology, Tai'an, Shandong 271000, China*

Correspondence should be addressed to Guangpeng Qin; skd992807@sdust.edu.cn and Jing Cao; skd993798@sdust.edu.cn

Received 22 March 2022; Revised 16 May 2022; Accepted 17 May 2022; Published 6 June 2022

Academic Editor: Yong-Zheng Wu

Deep underground engineering often utilizes cyclic loading. To understand the deformation and damage characteristics of rock under cyclic loading conditions, cyclic loading tests of three different specimens with varying lithology were performed. The dissipated energy method was used to analyze the magnitude of damage and rock failure characteristics during the energy evolution process of cube specimens. The results indicated that the modulus of elasticity of three lithologies were stable prior and subsequent to cyclic loading. While the cyclic loading profile improved the rock's resistance to deformation, it increased the internal mesostructure defects. Rock damage caused by the cyclic loading reduced the uniaxial compression strength. This was especially true for coal samples. For coal samples, these observations were consistent with internal coal damage calculated by analysis. Under the same lithology and different loading modes, rock damage was caused by cyclic action, and the elastic strain energy released by instantaneous unloading of rock samples with significant damage was reduced. The rupture magnitude for cyclic loading was observed to be less than that of uniaxial compression. Under cyclic loading and varying different lithologies, sandstone absorbed the most energy, resulting in a larger final fracture magnitude compared to other lithologies.

1. Introduction

With the acceleration of industrialization, near-surface resources are being gradually exhausted, and the development and utilization of deep mineral resources has become essential [1]. Due to the significant depth to access deep mineral resources, roadways to access such resources are surrounded by rock in a variable geological environment. The presence of the tunnel containing the roadway has a direct impact on the stability of the surrounding rock. This is consequence of the tunnel's structural characteristics, the strength and mechanical properties of the surrounding rock, and the impact of excavation unloading. In addition, related support disturbance, propagating up to three support heights into surrounding rock, is a key factor for the deformation and failure of rock surrounding a deep tunnel [2, 3, 4]. In the engineering activities such as deep coal mining, the excavation of roadway tunnels was processed with forward excavation support, chamber, and tunnel excavation. During these processes, the surrounding rock experiences cyclic loading and unloading. The cyclic load will cause the mechanical properties of the surrounding rock to deteriorate and induce secondary failures. Such processes are more serious for deep roadway excavation.

Scholars globally have characterized the stress and energy evolution under cyclical loading conditions. In addition, damage characteristics have also been characterized. Research in these area includes Meifeng et al. [5], Li et al. [6], and Wu et al. [7]. From the perspective of thermodynamics, instable rock destruction is the factor driving energy conversion, accumulation, dissipation, and other similar processes. There is a connection between the expansion and development of rock internal microcracks, energy evolution law, and destructive morphology. Consequently, there is important theoretical significance to characterizing the destructive rock behavior from the perspective of energy evolution. Based on damage mechanics, Lei et al. [8] established a shear damage evolution model for joints which considered freeze-thaw cycles and joint persistence. Kai-Nan et al. [9] conducted Brazil splitting tests for shale and characterized the sample energy distribution characteristics. Yao and Wang [10] studied the energy variation rule for granite experiencing uniaxial compression failure and concluded that there was a linear relationship between energy and confining pressure in the failure process. Li et al. [11] conducted compression tests for coal at different loading rates and studied the relationship between energy conversion of coal and lumpiness after crushing. Ping et al. [12] conducted compression damage experiments on white sandstone under uniaxial conditions with different loading rates along with triaxial loading experiments with varying confining pressures and different control modes. In addition, Li et al. [11] discussed the relationship between the loading rate and both the final failure form and the ultimate strength of white sandstone. Loading rate was also related to confining pressure, loading control, and unloading control. Meng et al. [13] performed uniaxial compression tests on red sandstone with varying sizes and strain rates. It was found that the higher the absorption energy of red sandstone, per unit volume, in the compression process, the larger the magnitude of the final rupture. Liu et al. [14], Xu et al. [15], and Zhizhen and Feng [16] conducted cyclic loading tests under uniaxial compression for sandstone, characterized the relationship between load and elastic energy and dissipated energy, and analyzed sandstone rock burst propensity using the elastic energy index. Li et al. [17] calculated a preliminary estimate of the spatter velocity of broken rock particles based on the principle of energy conservation and provided a set of steps and methods for preliminary analysis of the overall failure mode together with the state and strength of rock mass structure from the perspective of an energy budget. Guo et al. [18] studied the mechanical properties and deformation characteristics of rock under uniaxial cyclic loading and characterized the stress-strain curve under each cyclic loading. The stress-strain curve formed a hysteresis loop which translated in the direction of increasing strain. Yang et al. [19] conducted uniaxial and cyclic tests on a coal-rock assemblage and found that dissipative energy accumulated had experienced sudden changes. In addition, it was indicated that rock fracture is caused by the release of elastic strain energy. Liu et al. [20] and Cheng and Xiao [21] used normalized dissipative energy to characterize rock damage. Zhang et al. [22–23] studied the fragmentation process of granite through acoustic emission observations and studied the law of total elastic strain energy change at different times. In addition, acoustic emission events under different stress conditions were studied. In addition, research regarding rock damage has also been a research topic receiving considerable attention. Chuang et al. [24] established damage variable expression based on residual strain principles and Yang et al. [25] established damage variable expression based on energy principles. Residual deformation accumulation is an external manifestation of internal damage. It is a qualitative rather than quantitative indicator. Energy is the internal cause of driving damage. The damage model based on energy principles may objectively reflect the damage evolution during rock deformation. In terms of rock uniaxial compression, Zhao et al. [26] conducted quasistatic and dynamic uniaxial compression tests on cylindrical thick-walled granite specimen with different clay filling volumes to understand the dynamic characteristics of rock in a mud-water environment. Fan et al. [27] conducted uniaxial compression tests on samples with a single nonpenetrating defect and presented the crack growth behavior and fracture characteristics of sandstone specimens with nonpenetrating fractures during uniaxial loading.

Most of the mentioned studies were based on the loading of rocks or with lower limit stresses, which did not fully reflect the cumulative effect of energy-induced fatigue damage and the nature of the rock damage processes. Based on this study's context, utilizing the rock destruction theory of energy change, the load cycle addition and unloading of different rock tests are developed to provide a theoretical basis for geotechnical engineering practice.

2. Materials and Methods

2.1. Engineering Background. Shandong Energy Zaozhuang Mining Group's Fucun Mine 1009 contains a working surface material roadway which utilizes tunnel arm excavation after the use of anchor parallel operation technology. The parallel operation of the tunnel construction area is divided into a header cutting area and an anchor operation area. The front of the header and the header behind the anchor operation division operate in parallel. The working area contains the roadway hydraulic support, back circulation support, and hydraulic door support. The working principle utilizes auxiliary support lifting the front of the manipulator roadway door hydraulic support from the support area. This support method is equivalent to a roof. Such an area which contains two cycle loading effects may cause surrounding rock strength deterioration and induce secondary failures. This risk is suggested by the working principle utilized by door hydraulic support and the indoor tests of loading and unloading. See Table 1 for material lithologic characteristics of the 1009 working face and see Figure 1 for hydraulic portal support.

Verification of the effectiveness of the hydraulic temporary support for improving stability of the rock surrounding the new roadway tunnel is vital. Also, characterizing the deformation and failure characteristics of rock surrounding the roadway when subjected to the installation of an advanced temporary support structure is very important for fast and safe roadway excavation. According to the actual geological situation of the roadway surrounding rock and the working principle of hydraulic portal support, cyclic loading and unloading tests related to sandstone, mudstone, and coal are carried out, combined with uniaxial compression test, to analyze the deformation and damage

Table 1: Comprehensive histogram of working face conditions.

No.	Thickness (m)	Depth (m)	Formation	No.	Thickness (m)	Depth (m)	Formation
1	1.85	52.66	Medium sandstone	6	5.5	82.46	Coal seam
2	9.0	61.66	Fine sandstone	7	0.3	82.76	Mudstone
3	10	71.66	Medium sandstone	8	5.12	87.88	Siltstone
4	5	76.66	Siltstone	9	0.15	88.03	Sandy mudstone
5	0.3	76.96	Mudstone				

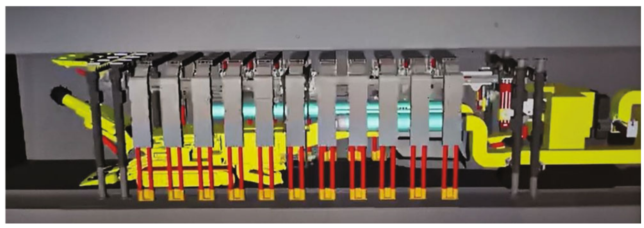

(a)

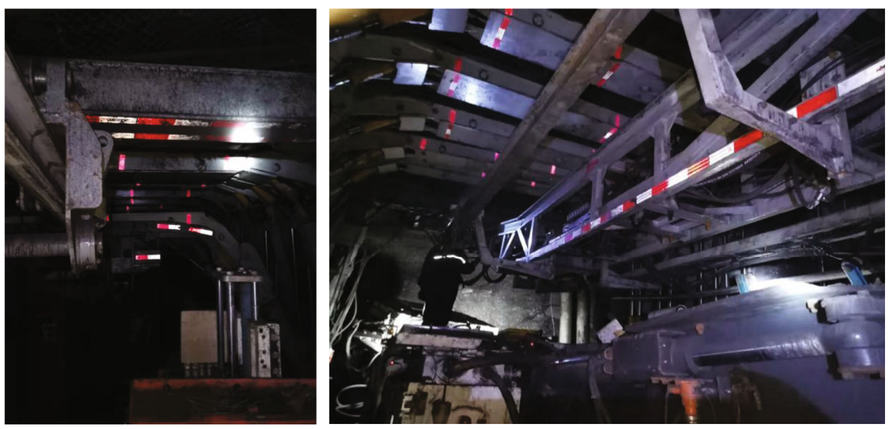

(b)

Figure 1: Hydraulic door bracket. (a) Renderings of hydraulic door-type bracket. (b) Photo of the hydraulic gate bracket.

characteristics and energy evolution law of the roadway surrounding rock.

2.2. Test Process

2.2.1. Sample Preparation. The large coal block and roof slab rock block were collected at the site and analyzed in the laboratory. During this analysis, three rock samples including sandstone, mudstone, and coal were utilized. These samples characterized the site lithological conditions. After cutting, grinding, and processing into a standard $70 \times 70 \times 70$ mm sample, the flatness and verticality of the processed test sample were verified to satisfy the rock test specification standard. The equipment used included a cutter (DQ-6) and grinder (SHM-200) shown in Figure 2(a), while the resulting sample is shown in Figure 2(b).

2.2.2. Test Scheme. Specimen combinations including rock, sandstone, mudstone, and coal were used and analyzed. Prior to cyclic loading, an uniaxial compression test was conducted on each lithology sample. In order to minimize measurement error, three samples were selected for duplicate testing test to determine the average compressive strength of varying lithologies. In addition, to magnify the failure characteristics and energy evolution law for varying lithologies, the loading was as much as 40% of the compressive material strength, which was subsequently unloaded. This was to model the hydraulic portal support's working principle. A loading speed of 0.2 mm/min was utilized. Uniaxial cycle loading adopted stress control. The cycle loading and loading rate was 0.1 MPa/s and there were four cycles. After the cycle loading, the loading continued until the specimen ruptured and experienced instability. The test process was completed in the ROCK600-50 rock test system according to the set control procedure. Figure 3 shows the ROCK600-50 rock test system. The cycle loading method is shown in Figure 4.

2.3. Results and Discussion

2.3.1. Basic Mechanical Properties. Table 2 contains an average for mechanical parameters for different lithological samples and the testing processes. One should note that after the

(a)

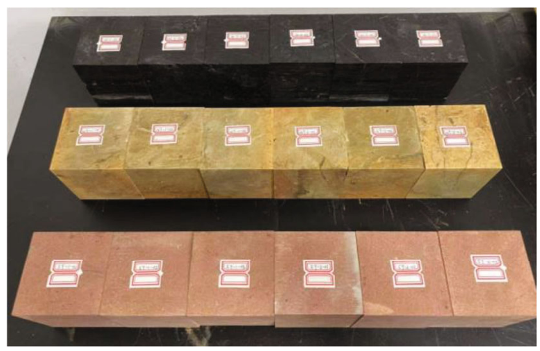

(b)

Figure 2: Processing instruments and produced rock samples. (a) Rock sample processing instrumentation and (b) resulting test sample.

Figure 3: ROCK600-50 testing system.

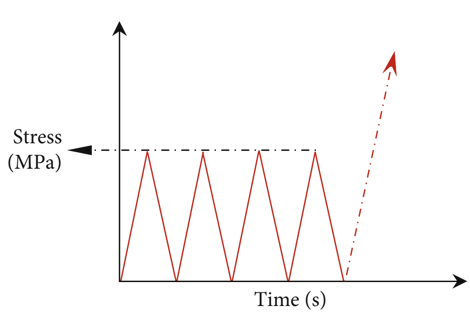

Figure 4: Cyclic loading mode. The compressive strength of rock sample is 40% and the loading/unloading slope is $k = \pm 0.1$ MPa/s.

cyclic loading, loading was continued until the specimen fractured and became unstable. The sandstone, mudstone, and coal strength limits decreased, with the coal strength limit decreased significantly by 15.42 MPa. At 40% cyclic loading and unloading, the average elastic modulus of mudstone and coal was greater than that of uniaxial compression. The sandstone elastic modulus was reduced but not significantly. The test indicated that the elastic modulus for the three rocks did not change significantly after four cycles of loading and unloading. The cyclical loading improved rock deformation resistance but produced defects within the fine visual structure inside the rock (such as microcracks and microholes). The above conclusions can be explained by examining the energy evolution and magnitude of rock damage.

2.3.2. Deformation Characteristics Analysis. During loading and unloading, elastic deformation and plastic deformation will continuously occur. The elastic deformation will be completely recovered after the removal of the stress, while the plastic deformation will accumulate and increase continuously during each cycle of loading and unloading. Such deformation is referred to as residual strain. Figure 5 shows the stress-strain curves of uniaxial compression and cyclic loading for different lithologies. Under cyclic loading, the stress-strain curves of different lithologies are similar to the uniaxial compression curves, which are divided into compaction, elastic, plastic, failure, and residual stages.

Each cycle produces plastic deformation, which results in a constant shift to the right for the hysteresis curve. Because the pore cracks in the initial cycle are not compacted by the test piece, the first residual strain generated by the initial cycle is larger than that of later cycles. The strain difference under different cycles and the residual strain difference are shown in Figure 6. The unrecoverable strain generated when the stress is unloaded is the residual

Table 2: Table of varying lithologic mechanical parameters.

	Lithology	The specimen number	Strength of limit (MPa)	Average intensity (MPa)	Modulus of elasticity (GPa)	Average elastic modulus (GPa)
Uniaxial compression	Sandstone	SY-1-01	58.58	56.04	4.173	3.861
		SY-1-02	52.48		3.490	
		SY-1-03	57.06		3.920	
	Mudstone	NY-1-01	12.29	10.89	1.099	0.981
		NY-1-02	9.24		0.704	
		NY-1-03	11.13		1.139	
	Coal	M-1-01	13.09	30.31	1.228	1.296
		M-1-02	32.33		1.420	
		M-1-03	28.29		1.241	
Cyclic loading and unloading	Sandstone	SY-2-01	55.39	50.34	3.582	3.665
		SY-2-02	45.29		3.748	
	Mudstone	NY-2-01	12.00	9.96	0.896	1.030
		NY-2-02	7.92		1.164	
	Coal	M-2-01	13.90	14.89	1.256	1.364
		M-2-02	15.87		1.472	

strain. However, in the stress-strain curve, with increasing stress, the difference between the two adjacent loading curves increases. This indicates that the corresponding strain difference at a given stress state is greater than the residual strain generated by a given cycle. This implies that some of the irreversible deformation under high stress is restored at low stress conditions. This portion of recoverable deformation may a result of the microelement rebound of rock, the recovery of microdefects, and other similar factors. This portion of the recoverable deformation may result in the illusion of large irreversible strain under a load threshold.

One may observe from the above data that the residual strain difference of the first coal cycle is larger than that of other lithologies, which indicates that there are many cracks and holes in the coal body resulting in large unrecoverable deformation. The sandstone interior itself contains comparatively fewer defects; consequently, the unrecoverable deformation is small. Mudstone has the lowest elastic modulus, low deformation resistance, significant deformation ability, and good recovery ability. Consequently, the residual deformation produced by the first cycle addition and unloading is less than other lithologies.

2.3.3. Analysis of Macrodestruction Characteristics. Three different lithological cubes loaded to fracture are shown in Figure 7. These specimens include three lithologies. The sandstone specimen shows principally tapered damage, and the mudstone specimen principally exhibits shear failure at angles of 45°. For the coal specimens, failure is generally tapered with some shear failure along angles of 45° along with split failure. For these fracture conditions, a theoretical study of 45° shear failure and cone failure is performed.

(1) Shear Failure. When the test block is in a state of uniaxial compressive stress, the mechanical model of the shear belt with a point of its force is shown in Figure 8. According to the mechanical model for the uniaxial stress state, the stresses along the oblique m-n plane are analyzed. The axial pressure is decomposed into components parallel, τ_n, and orthogonal to the m-n direction, σ_n. Using the Moore-Coulen criterion principle, the following formulas are obtained.

$$\sigma_n = \frac{1}{2}\sigma_1 + \frac{1}{2}\sigma_1 \cos 2\beta = \sigma_1 \cos^2\beta, \tag{1}$$

$$\tau_n = \frac{1}{2} \sin 2\beta = \sigma_1 \sin \beta \cos \beta. \tag{2}$$

Here, τ_n is the "sliding force" that causes shear damage, and σ_n improves the sliding friction resistance on the rupture surface. The value of the angle β affects the magnitude of τ_n and σ_n. The oblique section τ_n has the largest shear stress when β is 45°, but the shear resistance at the oblique section of 45° is the minimum. The surface generally ruptures at the section with the largest difference between the shear stress and the shear strength. The failures for the specimens with the three types of lithology generally occur on surfaces oriented at angles of 45° from the applied load.

According to the Moore-Coulen criterion, the shear strength τ_f at an angle β can be expressed as

$$\tau_f = c + \mu\sigma_n. \tag{3}$$

Here, c is the cohesive force (MPa), and μ is the friction coefficient on the inclined section, which is related to the roughness of the inclined section. $\mu = \tan\varphi$, where φ is the internal friction angle of the rock sample.

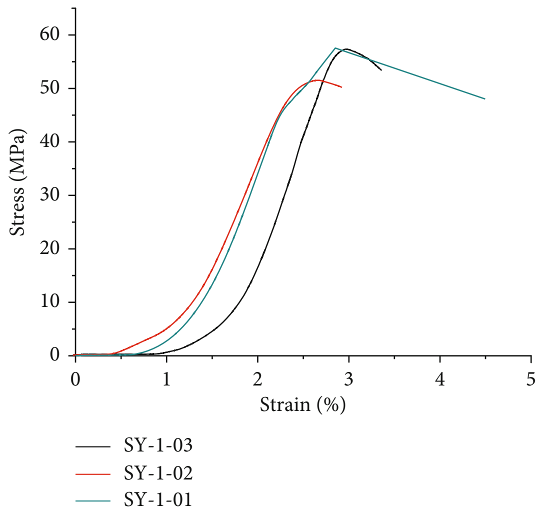

(a)

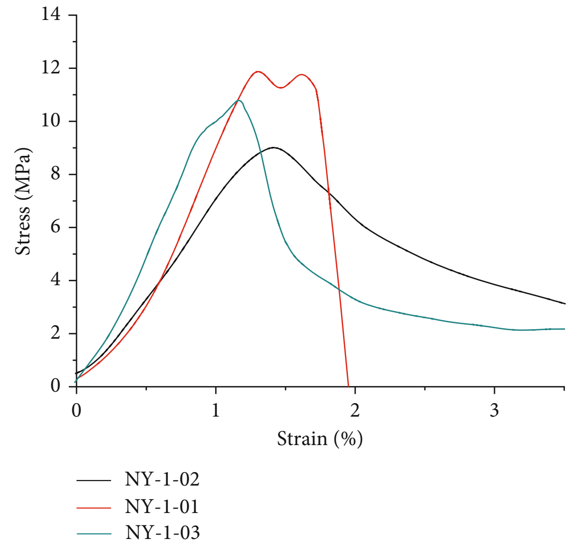

(b)

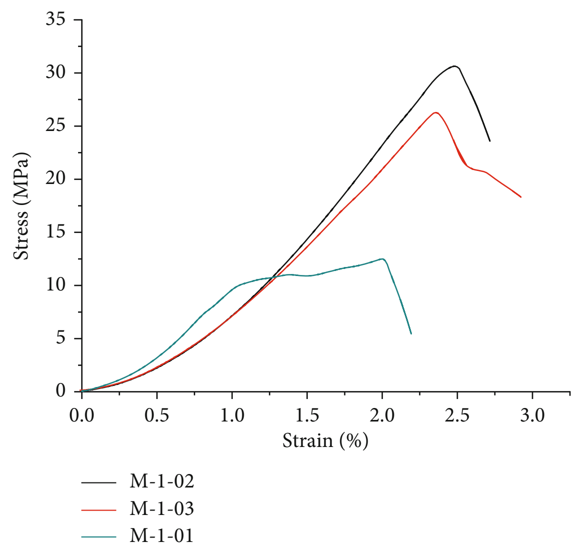

(c)

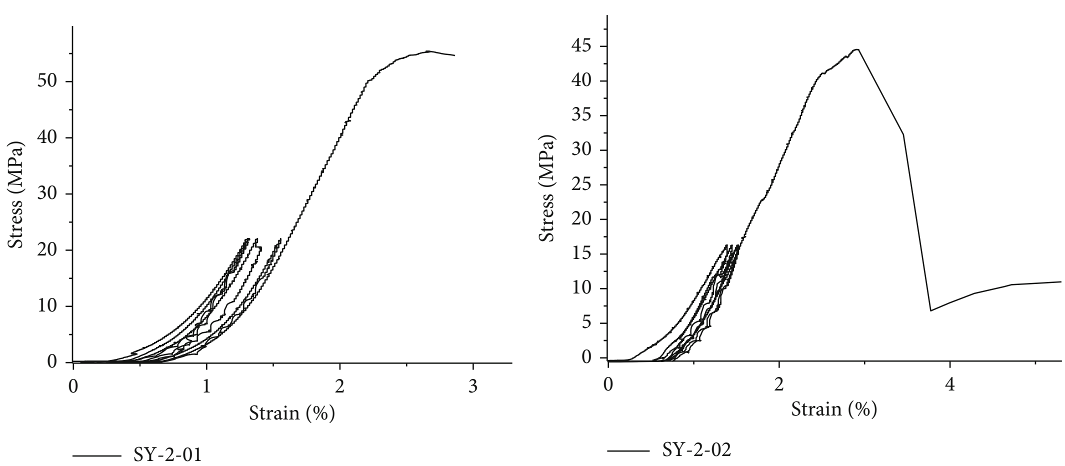

(d)

Figure 5: Continued.

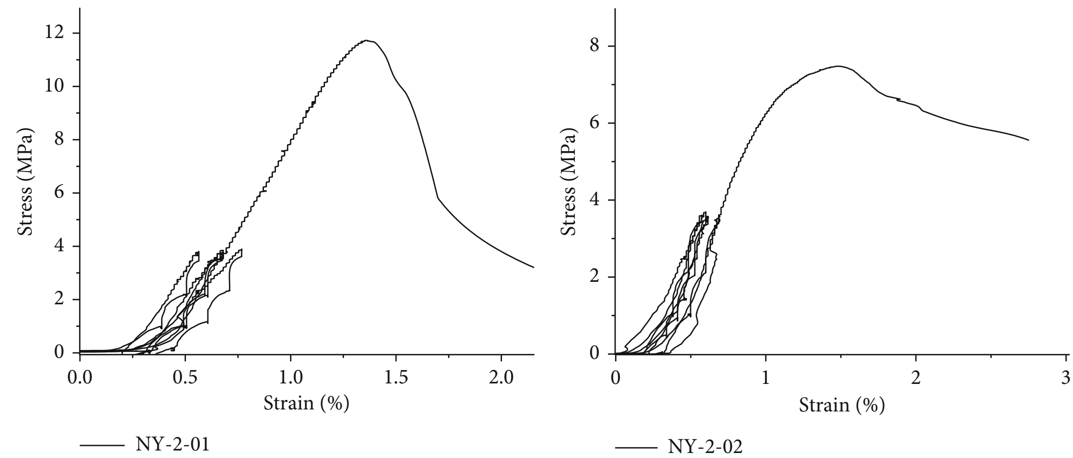

(e)

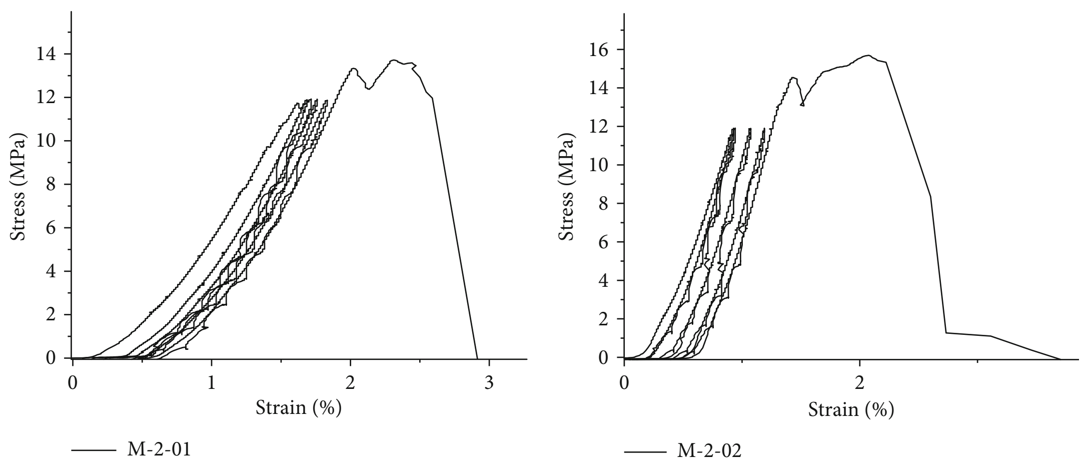

(f)

FIGURE 5: Total stress-strain curves. (a) Uniaxial compression for the SY lithology. (b) Uniaxial compression for the NY lithology. (c) Uniaxial compression for the M lithology. (d) Cyclic loading for the SY lithology. (e) Cyclic loading for the NY lithology. (f) Cyclic loading for the M lithology.

When the coaxial pressure is greater than a threshold value, the shear stress, τ_n, exceeds the shear strength τ_f, and fracture occurs along the oblique β surface. The oblique β cross section is the most probable rupture surface with the rock sample. The equation for τ_n at oblique angle β at the limit of instability balance is

$$\tau_n \geq \tau_n = c + \mu\sigma_n. \tag{4}$$

Substituting equations (1) and (2) into equation (4) yields

$$\frac{1}{2}\sigma_1 \sin 2\beta \geq c + \mu\sigma_1 \cos^2\beta. \tag{5}$$

One may observe that shear damage occurs under the conditions indicated previously. In addition, provided the strength parameters for lithology, c, μ, and σ_1, are known, the rupture angle range and the most probable fracture angle can be utilized to mitigate fraction risk.

(2) Cone Destruction. The cone disruption is caused by the end-surface effect and shear. The test machine places pressure on the sample face oriented toward the end face's center of the friction. Consequently, the transverse deformation of the sample face is constrained, which restricts the lateral deformation of the test sample and has a role similar to the peripheral pressure. In the process of sample transition from plastic deformation to fracture, specimen expansion becomes more significant. The end surface effect has a more important role as the loading continues. Friction with the rigid loading plate restricts movement to two specimen sides. Farther from the upper and lower specimen surfaces, where the friction effect is less, the largest lateral displacement occurs. This is approximately near the middle of the rock sample. The observed and calculated damage agree well near the middle of the outward bulge, which is shown in Figure 9.

Prior to fracture, the specimen "collapse zone" (near the specimen exterior at axal locations close the maximum deformation) generally fractures and falls from the sample.

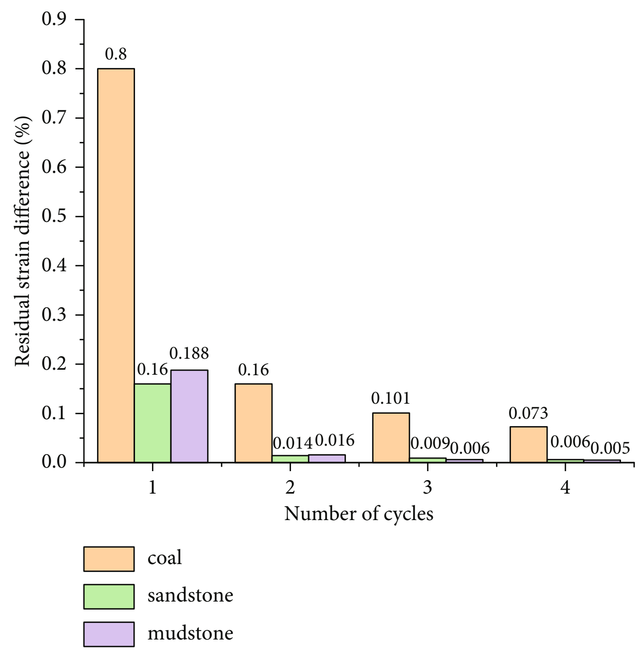

Figure 6: Residual strain difference of different lithologies with number of cycles.

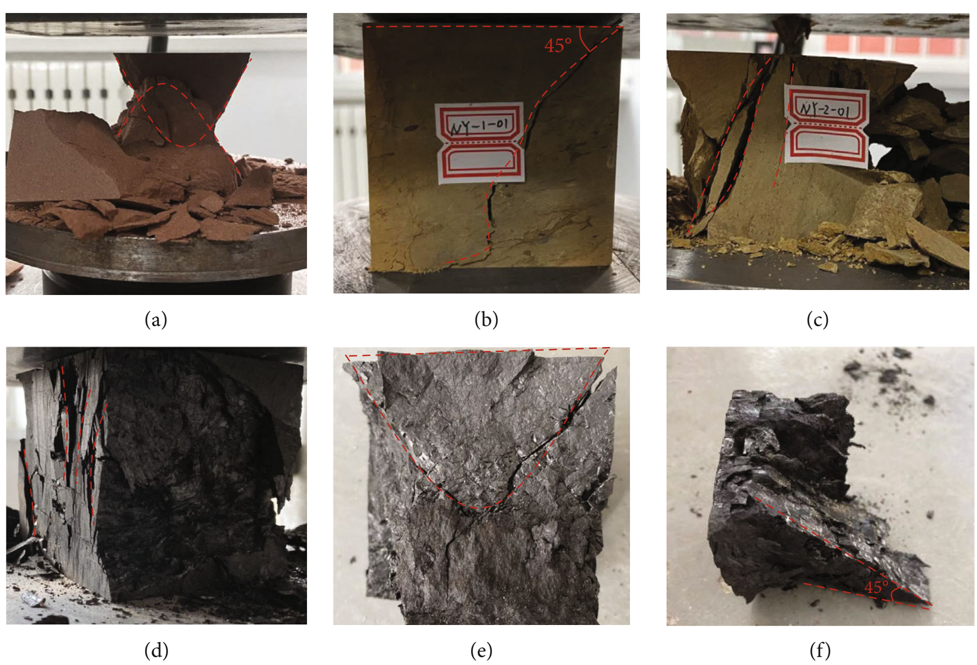

Figure 7: Typical fracture patterns for different lithological specimens. (a) Sandstone (cone damage). (b) Mudstone (45° shear damage). (c) Mudstone (crack break). (d) Coal (split break). (e) Coal (tapered damage). (f) Coal (45° shear damage).

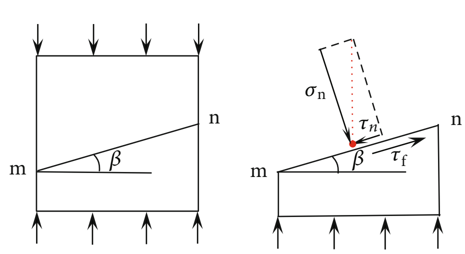

Figure 8: Stress components during axial loading.

The "thrust area" (areas of the sample influenced by the deformation constraints introduced by loading) thrust zone has a tendency to penetrate into the cube. With increasing pressure, two intersecting shear planes are formed inside the rock sample. With increased loading, the thrust zone is crushed into the collapse zone. The outer surface begins to collapse. Finally, a pair of "core," damaged surfaces, which are approximately symmetric, results from the loading. This process is summarized in Figure 10.

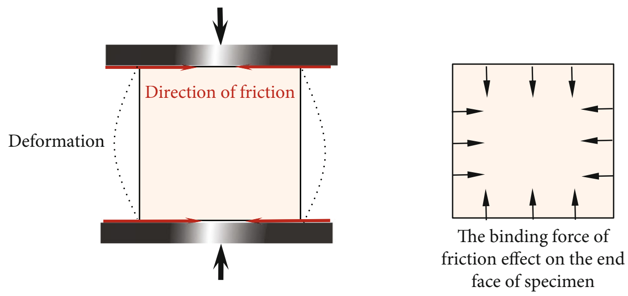

Figure 9: Deformation produced by friction at the specimen top and bottom faces.

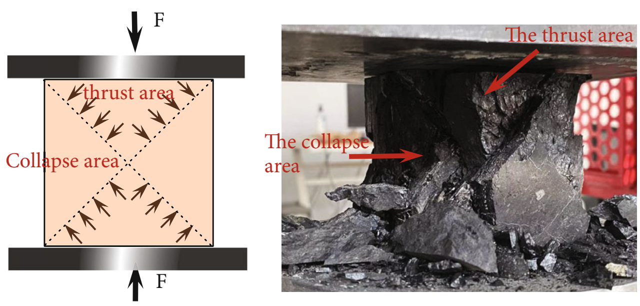

Figure 10: Shear slip surface under upper and lower constraints.

(3) Cleavage Breakdown. The mudstone and coal specimens showed cleavage failure. The probability of cleavage failure for mudstone was greater than that of coal, while sandstone did not show cleavage failure. The nature of splitting failure is that the rock tensile strength is significantly less than the compressive strength, and the mudstone and coal specimens reach their tensile strength before reaching their compressive strength. This resulted in tensile cracks within the rock samples. Under cyclic loading, tensile cracks grew and eventually formed splitting failure surfaces. The compressive strength of the three lithologies was in the order sandstone > coal > mudstone. The sandstone specimen's compressive strength was much greater than that of coal or mudstone. Specimens with small compressive strength were subjected to small compressive pressure by the pressing plate. Regarding the neglecting of the end faces' friction coefficient, the friction effect of the end face can be reduced by using a specimen with low compressive strength. This low compressive strength was also a reason for the specimen splitting failure.

(4) Energy Analysis and Rock Damage under Cycle Loading and Unloading. Rock damage is a deterioration process of material or structure caused by fine structure defects (such as microcracks and microholes), under the action of external loading and environmental factors. Energy is the driving force driving the development of fine structural defects; consequently, the rock deformation and fracture processes must be accompanied by capacity transformation. It is feasible to analyze the energy transformation characteristics of the rock deformation and rupture process to characterize the magnitude of rock damage.

The process of rock cycle loading and unloading results in the external force constantly performing work on the

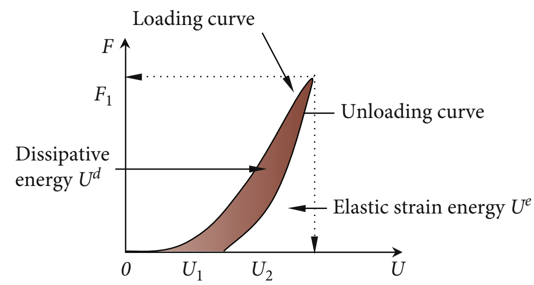

Figure 11: Calculated areas and the interrelationship of elastic strain energy and dissipation energy.

specimen. The external force is converted into elastic strain and dissipation energy. Using the principles of thermodynamics, energy transformation is the essential process by which the energy state of the specimen changes, as manifested by the rock deformation. Ultimately, the destruction of the specimen is an instability driven by changes of internal energy. According to the conservation of energy,

$$U = U^e + U^d. \tag{6}$$

Here, U is pressure performing work on the rock, specifically, the strain energy stored within the rock lattice. U^d is the dissipative energy transferred to the rock's lattice during the loading process. U^e is the elastic strain energy transferred to the rock's lattice during the loading process.

During rock loading, a portion of the transferred energy is absorbed by the rock's lattice is consumed to drive plastic deformation and damage, such as the formation and development of cracks. The other portion of transferred energy is stored in the lattice rock as elastic strain energy. This energy is completely recovered when the rock sample is unloaded. In cyclic loading, the elastic strain energy and dissipation energy are numerically equal to the area enclosed by the corresponding full stress-strain curve and the coordinate axis, as shown in Figure 11.

Based on basic principles and methods of energy analysis, cumulative dissipated energy is proposed to be indicative of energy dissipation after different cycles. The magnitude of damage is defined as the ratio of cumulative total strain energy to that at the cycle of specimen failure. The calculation of cumulative dissipated energy is shown in equations (7)–(9). The full stress-strain curve data of different lithology cube specimens were decomposed, and the area of each cycle was calculated by using the integral function provided in Origin software.

$$U^d(i) = \sum_{k=1}^{i} U_k^d, \tag{7}$$

where $U^d(i)$ is the cumulative dissipated energy in cycle i and U_k^d is the dissipated energy during cycle k.

$$U(i) = U^e(i) + U^d(i), \tag{8}$$

Table 3: Changes of various energy parameters for cycle loading and unloading.

(a)

Lithology	Coal			
Number of loading and unloading cycles	Cumulative dissipation energy U^d (kJ·m^{-3})	Cumulative strain energy U (kJ·m^{-3})	Degree of damage D (%)	Mean degree of damage (%)
1	1.016	4.098	3.16	3.23
	0.982	4.048	3.30	
2	1.949	7.549	6.06	6.26
	1.923	7.392	6.45	
3	2.740	10.973	8.52	8.86
	2.741	10.689	9.20	
4	3.356	14.335	10.44	10.85
	3.352	14.062	11.25	
The final cycle		32.156	100.00	
		29.799		

(b)

Lithology	Mudstone			
Number of loading and unloading cycles	Cumulative dissipation energy U^d (kJ·m^{-3})	Cumulative strain energy U (kJ·m^{-3})	Degree of damage D (%)	Mean degree of damage (%)
1	0.720	1.088	3.36	3.21
	0.590	1.326	3.05	
2	1.055	1.877	4.93	4.78
	0.892	2.503	4.62	
3	1.451	2.684	6.78	6.53
	1.211	3.744	6.27	
4	1.935	3.624	9.04	8.45
	1.519	4.974	7.86	
The final cycle		21.40	100	
		19.32		

(c)

Lithology	Sandstone			
Number of loading and unloading cycles	Cumulative dissipation energy U^d (kJ·m^{-3})	Cumulative strain energy U (kJ·m^{-3})	Degree of damage D (%)	Mean degree of damage (%)
1	2.261	7.730	1.71	2.10
	3.314	7.269	2.48	
2	3.663	14.919	2.76	3.18
	4.810	12.681	3.60	
3	5.791	21.787	4.37	4.93
	7.312	19.338	5.48	
4	6.629	28.809	5.00	6.17
	9.788	26.047	7.33	
The final cycle		132.539	100.00	
		133.449		

where $U(i)$ is the cumulative total strain energy during cycle i and $U^e(i)$ is the cumulative elastic strain energy during cycle i.

$$D(i) = \frac{U^d(i)}{U(t)} * 100\%, \quad (9)$$

where $D(i)$ is the magnitude of rock damage when loading to cycle i and $U(t)$ is the cumulative total strain energy at the failure cycle.

After the conversion of the strain, the test results are shown in Table 3.

Based on test data, the cumulative energy dissipation and rock damage trends are shown in Figure 12.

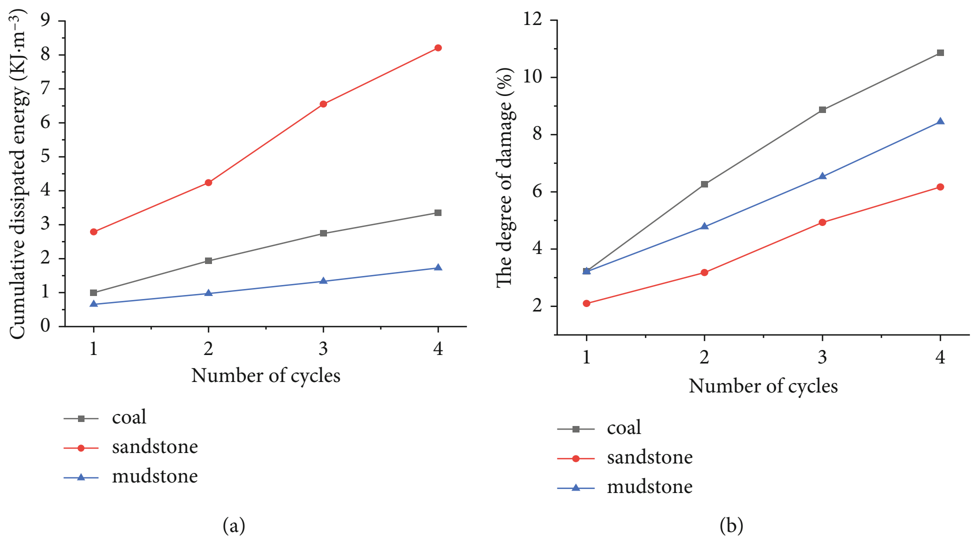

Figure 12: (a) Average cumulative dissipated energy. (b) Average degree of rock damage.

(a) (b)

Figure 13: (a) Uniaxial compression failure state. (b) Cyclical loading final failure state.

Using the data presented, one can arrive at the following conclusions. First, compared with the other two lithologies, sandstone has the highest cumulative dissipation energy, but after four loading cycles, its damage is the lowest at only 6.17%. This reflects the property of sandstone to have superior antifatigue ability compared with that of coal and mudstone. Second, the cumulative dissipated energy of coal is inferior to that of sandstone, but the magnitude of damage for coal is the highest of the studied lithologies. After four loading cycles, the damage is 10.85%. This conforms with its deformation characteristics, and the strength limit of coal decreases the most of the considered lithologies, with a decrease of 15.42 MPa. The deformation characteristics and energy and magnitude damage verify each other. This infers that the test results are reasonable. Third, for mudstone, the cumulative dissipation energy after four loading cycles is the minimum of the considered lithologies. This indicates significant elastic deformation for mudstone in addition to a significant internal deformation energy of total strain energy. This results in low energy dissipation, which is similar to the low residual strain of mudstone. Fourth, under different lithological cycle loading modes, loud sounds were emitted during rock damage. This was accompanied by the ejection of rock debris. The sandstone absorbs the most energy of the considered lithologies. It stores the most elastic strain energy, and the rupture magnitude is greater than other considered lithologies.

During the test procedure, both coal and sandstone suffered burst damage when the uniaxial compression reached the ultimate compressive strength. The damaged area, fragmentation, and fragment speed were all “violent” than the state caused by cyclic loading. This was mainly due to the energy evolution difference between uniaxial compression and cyclic loading. This is shown in Figure 13 for sandstone.

The observed behavior, including magnitude of damage, of different rocks can be explained by the energy evolution process. Studies have explained the principal reasons for rock damage using energy conversion. Any rock stress state corresponds to an energy state, from elastic and plastic deformation to failure. Energy is always exchanged with the surroundings, to maintain dynamic balance. Before the rock mass reaches the ultimate stress, it primarily absorbs energy from the surroundings. After the rock reaches the ultimate stress, it releases this energy back to the surroundings. The dynamic failure of rock is the result of the rapid accumulation and release of internal elastic energy in the failure state. For the coal and sandstone, which exhibited significant burst damage, the cyclic loading and magnitude fracture can be analyzed from the perspective of energy conservation. The same analysis can be performed for fragment ejection velocity being less than that of uniaxial compression. With an increasing of the number of loading cycles, the dissipative energy accumulated continuously, promoting the continuous formation and development of cracks. Finally, through theoretical calculation, the magnitude of damage for of coal and sandstone were 10.85% and 6.17%, respectively. This indicated that these rock samples were in the "plastic state." When the rock sample reached the ultimate strength failure, the elastic strain energy released by instantaneous unloading was less for the cyclic loading than for simple uniaxial loading.

3. Conclusions

It was demonstrated that the modulus of elasticity of the three lithologies did not change significantly after four loading cycles. The loading cycles improved the rock's antideformation ability but caused material defects (such as microcracks and microvoids) in the internal rock mesostructure. The magnitude of damage degree was the greatest for coal. It was also found that the ultimate strength decreased the most for coal, decreasing by 15.42 MPa. The magnitude of damage degree calculated by theory is consistent with the mechanical properties observed in the test.

There are many defects, such as fissures and holes, with in the coal body. This resulted in large, unrecoverable deformation. Mudstone had the smallest elastic modulus, but it had significant deformation and recovery ability; consequently, the residual deformation produced by the first cyclic loading was small. Comparing the failure modes of the three cubic lithologies, except the mudstone and coal specimens which generally failed by splitting failure, the specimens generally failed by shear and conical failure.

Under the same lithology and different loading modes, rock damage was caused by cyclic action, and energy evolution was different between the specimens. The transient unloading with significant previous damage may release less elastic strain energy. The cyclic loading and had a smaller fracture damage than that of uniaxial compression. Under different cyclic loading modes for different lithologies, sandstone absorbed the most energy, stored the most elastic strain energy, and had the largest magnitude of rupture destruction compared to other lithologies.

Data Availability

The data used to support the findings of this study are available from the corresponding author upon request.

Conflicts of Interest

The authors declare no conflicts of interest.

Acknowledgments

This study was sponsored by the Shandong Provincial Key R&D Plan of China (Grant No. 2019SDZY034-1), the Engineering Laboratory of Deep Mine Rock Burst Disaster Assessment Open Project (LMYK2020007), and the National Natural Science Foundation of China (Grant Nos. 51504145 and 51804182). The authors are grateful for their support.

References

[1] H. P. Xie, F. Gao, Y. Ju et al., "Quantitative definition and investigation of deep mining[J]," *Journal of China Coal Society*, vol. 40, no. 1, pp. 1–10, 2015.

[2] K. Hongpu, "Stress distribution characteristics and strata control technology for roadways in deep coal mines[J]," vol. 41, no. 9, pp. 12–17, 2013.

[3] L. Fuqiang, Q. Guangpeng, L. Yonggang, W. Qichen, W. Ying, and H. Fengjun, "Study on the mechanism of gas ignition by friction effect of hard quartz sandstone instability," *Geofluids*, vol. 2020, 17 pages, 2020.

[4] H. P. Xie, F. Gao, and Y. Ju, "Research and development of rock mechanics in deep ground engineering[J]," *Chinese Journal of Rock Mechanics and Engineering*, vol. 34, no. 11, pp. 2161–2178, 2015.

[5] C. Meifeng, H. Manchao, and L. Dongyan, *Rock Mechanics and Engineering[M]*, Science Press, Beijing, 2012.

[6] T. Li, X. Pei, D. Wang, R. Huang, and H. Tang, "Nonlinear behavior and damage model for fractured rock under cyclic loading based on energy dissipation principle," *Engineering Fracture Mechanics*, vol. 206, pp. 330–341, 2019.

[7] Z. Wu, X. Ji, Q. Liu, and L. Fan, "Study of microstructure effect on the nonlinear mechanical behavior and failure process of rock using an image-based-FDEM model," *Computers and Geotechnics*, vol. 121, p. 103480, 2020.

[8] D. Lei, H. Lin, and Y. Wang, "Damage characteristics of shear strength of joints under freeze–thaw cycles," *Archive of Applied Mechanics*, vol. 92, no. 5, pp. 1615–1631, 2022.

[9] X. I. E. Kai-Nan, D. Y. Jiang, and J. I. A. N. G. Xiang, "Energy distribution and criticality characteristics analysis of shale Brazilian splitting test[J]," *Journal of China Coal Society*, vol. 42, no. 3, pp. 613–620, 2017.

[10] J. Yao and Z. Wang, "Mechanical behavior and damage evolution for granite subjected to cyclic loading," *Huashan granite[J].Hydro-Science and Engineering*, vol. 2018, pp. 1–10, 2018.

[11] Y. Y. Li, S. C. Zhang, Z. J. Wen et al., "Energy conversion and fragment distribution characteristics of coal sample under uniaxial cyclic loading[J]," *Journal of China Coal Society*, vol. 44, no. 5, pp. 1411–1420, 2019.

[12] W. Ping, Z. Yongjian, F. Tao, and Y. Weijian, "Test and analysis of sandstone damage-weakening under loading-unloading-loading[J]," *Journal of China Coal Society*, vol. 41, no. 12, pp. 2960–2967, 2016.

[13] Q. B. Meng, L. J. Han, H. Pu, S. Y. Wen, H. Li, and H. Li, "Experimental on the effect of strain rate and size on the energy accumulation and dissipation of rock[J]," *Journal of China Coal Society*, vol. 40, no. 10, pp. 2386–2398, 2015.

[14] J. F. Liu, J. Xu, Q. S. Li, and G. L. Li, "Experimental research on damping parameters of rock under cyclic loading[J]," *Chinese Journal of Rock Mechanics and Engineering*, vol. 29, no. 5, pp. 1036–1041, 2010.

[15] J. Xu, Y. Zhang, H. W. Yang, and J. N. Wang, "Energy evolution law of deformation and damage of sandstone under cyclic pore water pressures[J]," *Chinese Journal of Rock Mechanics and Engineering*, vol. 30, no. 1, pp. 141–148, 2011.

[16] Z. Zhizhen and G. Feng, "Research on nonlinear characteristics of rock energy evolution under uniaxial compression[J]," *Chinese Journal of Rock Mechanics and Engineering*, vol. 31, no. 6, pp. 1198–1207, 2012.

[17] L. Y. Li, Y. Ju, Z. W. Zhao, L. Wang, J. F. Lu, and X. Ma, "Energy analysis of rock structure under static and dynamic loading conditions[J]," *Journal of China Coal Society*, vol. 34, no. 6, pp. 737–740, 2009.

[18] H. Guo, M. Ji, D. Liu, M. Liu, and W. Zhao, "The influence of fracture strain energy on the burst tendency of coal seams and field application," *Advances in Civil Engineering*, vol. 2021, 10 pages, 2021.

[19] L. Yang, F. Q. Gao, X. Q. Wang, and J. Z. Li, "Energy evolution law and failure mechanism of coal-rock combined specimen[J]," *Journal of China Coal Society*, vol. 44, no. 12, pp. 3894–3902, 2019.

[20] Y. Liu, F. Dai, L. Dong, N. Xu, and P. Feng, "Experimental investigation on the fatigue mechanical properties of intermittently jointed rock models under cyclic uniaxial compression with different loading parameters," *Rock Mechanics and Rock Engineering*, vol. 51, no. 1, pp. 47–68, 2018.

[21] C. H. E. N. G. Cheng and L. I. Xiao, "Cyclic experimental studies on damage evolution behaviors of shale dependent on structural orientations and confining pressures," *Energies*, vol. 11, no. 1, p. 160, 2018.

[22] Y. Zhang, X. T. Feng, C. Yang, X. Zhang, M. Sharifzadeh, and Z. Wang, "Fracturing evolution analysis of Beishan granite under true triaxial compression based on acoustic emission and strain energy," *International Journal of Rock Mechanics and Mining Sciences*, vol. 117, pp. 150–161, 2019.

[23] Y. Zhang, X. T. Feng, X. Zhang, Z. Wang, M. Sharifzadeh, and C. Yang, "A novel application of strain energy for fracturing process analysis of hard rock under true triaxial compression," *Rock Mechanics and Rock Engineering*, vol. 52, no. 11, pp. 4257–4272, 2019.

[24] Z. H. A. O. Chuang, W. U. Ke, L. I. Shu-cai, and Z. Jiangang, "Energy characteristics and damage deformation of rock subjected to cyclic loading[J]," *Chinese Journal of Geotechnical Engineering*, vol. 35, no. 5, pp. 890–896, 2013.

[25] X. B. Yang, Y. P. Qin, and F. Ye, "Damage constitutive relation of sandstone considering residual stress[J]," *Journal of China Coal Society*, vol. 40, no. 12, pp. 2807–2811, 2015.

[26] Y. Zhao, L. Chang, Y. Wang, H. Lin, J. Liao, and Q. Liu, "Dynamic response of cylindrical thick-walled granite specimen with clay infilling subjected to dynamic loading," *Archive of Applied Mechanics*, vol. 92, no. 3, pp. 643–648, 2022.

[27] X. Fan, H. Yu, Z. Deng, Z. He, and Y. Zhao, "Cracking and deformation of cuboidal sandstone with a single nonpenetrating flaw under uniaxial compression," *Theoretical and Applied Fracture Mechanics*, vol. 119, p. 103284, 2022.

Hindawi
Geofluids
Volume 2022, Article ID 7891894, 13 pages
https://doi.org/10.1155/2022/7891894

Research Article

Natural Frequency of Coal: Mathematical Model, Test, and Analysis on Influencing Factors

Jianping Wei,[1,2,3] Junzhao Zhang,[1,2] Zhihui Wen,[1,2,3] Libo Zhang,[1,2] Yongjie Ren,[1,2] and Leilei Si[1,2,3]

[1]*School of Safety Science and Engineering, Henan Polytechnic University, Jiaozuo 454000, China*
[2]*State Key Laboratory Cultivation Base for Gas Geology and Gas Control (Henan Polytechnic University), Jiaozuo 454000, China*
[3]*Collaborative Innovation Center of Coal Work Safety and Clean High Efficiency Utilization, Jiaozuo 454000, China*

Correspondence should be addressed to Zhihui Wen; wenzhihui@hpu.edu.cn

Received 30 August 2021; Revised 6 October 2021; Accepted 15 October 2021; Published 31 May 2022

Academic Editor: Zhijie Wen

The difficulty in enhancing the low permeability of deep coal seams is the key problem restricting gas extraction. The technology of coal rock resonance and permeability enhancement excited by vibration wave is hailed as a new technology to enhance coal seam permeability. In particular, the effect of resonance and permeability enhancement is remarkable when the excitation frequency is exactly the same as the natural frequency of coal. In order to promote the application of the technology, the first step is to explore the variation characteristics of coal natural frequency and its influencing factors. In this study, two mathematical models of coal natural frequency were established, and the variations and influencing factors of coal natural frequency were discussed through an experiment on the natural frequency of coal. The results show that coal vibration has multiorder natural frequency which grows with the increase of the order. In addition, the natural frequency of coal is closely related to its elastic modulus, density, size, mass, stiffness, and other physical and mechanical parameters. The larger the coal size and mass are, the lower the natural frequency would be. The natural frequency parallel to the bedding plane is higher than that perpendicular to the bedding plane. For the saturated coal sample, moisture changes its density and reduces its elastic modulus. Consequently, its natural frequency is lower than that of the dried coal sample. The difference of organic matter and mineral content coal of different rank affects the physical and mechanical properties of coal, which leads to the difference in natural frequency of different-rank coals. The natural frequencies of different-rank coal show bituminous > anthracite > lignite. The natural frequencies of coal samples under different influencing factors are all tens of Hz. Thus, the vibration excitation of coal under the low-frequency condition is the focus of future research. The study can provide a theoretical basis for the technology of coal resonance and permeability enhancement excited by vibration wave.

1. Introduction

The ground stress and gas pressure in coal seams increase as coal mining continues to deepen, which brings difficulty to gas extraction. Coal, as an organic matter containing unconventional natural gas resources, forms different types of pores during coalification [1]. Pore is the main place to store coalbed methane and fracture system is the main way of gas migration in coal seam. The abundance of micro-nano pore determines the permeability and gas adsorption capacity of coal seam, which directly affects the extraction of coalbed methane [2]. In addition, the permeability of coal is also affected by effective stress, matrix shrinkage and expansion, and gas slippage [3]. This shows that the mechanical properties of coal also affect the production of coalbed methane. Therefore, aiming at low-permeability coal seam, seeking a scientific new technology to improve the permeability of coal seam is the key to the success of coalbed methane exploitation.

Yuan [4] proposed that it is necessary to carry out research on the mechanism of modified anti-reflection of deep low-permeability coal seam to realize the large-scale anti-reflection of coal seam. The technology of permeability enhancement excited by mechanical wave vibration can not only disturb the coal seam and increase pores and cracks in coal but also modify coal seam gas adsorption/desorption to promote gas desorption and seepage. The technology has become a hot spot of the research on the permeability enhancement of low-permeability coal seams by means of an external physical field.

In the prevention and control of coal mine gas disaster, permeability enhancement mechanisms such as vibration-induced coal and gas outburst [5, 6], deep-hole blasting [7–9], CO_2 presplitting [10, 11], hydraulic fracturing [12–15], and acoustic or ultrasonic vibration [16, 17] are related to the theories of coal rock excitation by vibration wave. As a new technology, vibration wave excitation boasts great potential in improving the permeability of coal rock. Scholars have carried out extensive researches on gas desorption and coal rock crushing excited by vibration wave.

In terms of gas desorption excited by vibration wave, Chen et al. [18, 19] studied the influence of vibration on gas desorption diffusion in granular coal and drew the following conclusions: (1) With the increase of vibration frequency, gas desorption of coal samples first increased and then decreased. (2) Mechanical vibration could generate shear force in adsorbed gas to promote its desorption. (3) A larger vibration amplitude is conducive to gas desorption. Jiang et al. [20] proved that sound field can improve the desorption volume of methane, and the desorption volume increases with the increase of sound intensity. According to the above studies, vibration can promote gas desorption in coal, but the gas desorption effect varies greatly under different vibration frequencies.

In terms of coal rock crushing excited by vibration wave, Li et al. [21] proved that with the increase of excitation frequency, the drilling speed of rock increased and reached the maximum value at the natural frequency of rock. Yin et al. [22] found that the natural frequency of high-density hard rock ranged from 20 kHz to 38 kHz. Li et al. [23] adopted a large-scale vibration test device, and it is concluded that the coal body accelerates rupture when resonance occurs. Li et al. [24] put forward the theory of rock modal analysis and concluded that the cracks inside the rock would lead to the decrease of its natural frequency. The theory and practice [25, 26] show that the permeability enhancement is the best when the frequency of vibration wave is the same as the natural frequency of coal and rock. The study confirmed that the natural frequency of coal rock was related to the mass and stiffness of the system. The natural frequency of soft rock and coal, which generally ranged from tens of Hz to hundreds of Hz, belonged to low-frequency vibration. At the same time, the natural frequency of coal rock decreases with the fracturing of coal rock.

The technology of coal rock resonance and permeability enhancement excited by vibration wave (hereafter referred to as the RPEEVW technology) works in the following way. When the frequency of vibration wave is close to the natural frequency of coal, the amplitude of coal rises after forced resonance, so that pores and cracks in coal expand significantly. Obviously, the realization of this technology is closely related to the natural frequency and vibration characteristics of coal. However, compared with rock, coal has a more complex and its natural frequency is affected by more factors. Therefore, the study on the variations of coal natural frequency and its influencing factors is the premise and basis for the implementation of the RPEEVW technology.

In this study, considering the working requirements for permeability enhancement excited by vibration wave in low-permeability coal, the mathematical models of natural frequency of coal were established based on theoretical analysis on the natural frequency of coal. Moreover, an experiment was performed on the variations of the natural frequency of coal. In this way, the influences of factors such as coal bedding, size, coal rank, and moisture on the natural frequency of coal were explored. The research results can provide a theoretical basis for the RPEEVW technology.

2. Models of Natural Frequency of Coal

Natural frequency is a kind of inherent property of structural specimen, coal, and rock materials that have their own natural frequency. In this paper, it is assumed that coal is isotropic and homogeneous. On the premise of ignoring the influences of pressure and temperature on coal vibration, the vibration system of coal body is simplified according to the relevant vibration theories [27]. Based on the physical model of single-degree-of-freedom coal, the entire mass of coal is concentrated on the particle m, and all of its elasticity is concentrated in the equivalent spring. In this case, the stiffness k of the coal is the equivalent stiffness of the equivalent spring. All the damping existing in the coal is equivalent to a damper represented by c (Figure 1).

When the coal is in a static equilibrium position, the generated velocity $\dot{x}$ and acceleration $\ddot{x}$ are both functions of time t. According to Newton's Second Law, the free vibration differential equation of single-degree-of-freedom coal is:

$$m\ddot{x} + c\dot{x} + kx = 0, \tag{1}$$

where m is the mass of coal, kg; c is the damping of coal, dimensionless; k is the stiffness of coal, N/m; x is the displacement of coal relative to the equilibrium position, m.

Eq. (1) is a linear homogeneous second-order differential equation with constant coefficients. Let $\omega_n = \sqrt{k/m}$, $\xi = (c)/(2\sqrt{km})$. The initial conditions are:

$x(0) = x_0$ and $\dot{x}(0) = \dot{x}_0$. Laplace transformation was conducted on both sides of Eq. (1) to obtain the solution of the differential equation of vibration frequency of single-degree-of-freedom coal:

$$x(t) = e^{-\xi\omega_n t} B \sin(\omega_d t + \varphi), \tag{2}$$

where $B = \sqrt{x_0^2 + (\dot{x}_0 + \xi\omega_n x_0/\omega_d)^2}$, $\xi = c/2\sqrt{km}$, $\omega_d = (1 - \xi^2/2\pi)\sqrt{k/m}$, $\varphi = tg^{-1}(x_0\omega_d/\dot{x}_0 + \xi\omega_n x_0)$;

B is the amplitude, m/s^2; ξ is damping ratio, dimensionless; ω_d is the natural frequency of coal, Hz; φ is the phase angle, rad. Assuming that coal is an elastic medium, then its stiffness can be obtained from the stiffness equation of

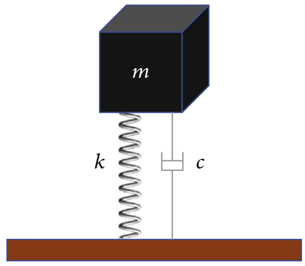

Figure 1: Vibration model of single-degree-of-freedom coal.

elastic material [28, 29]:

$$k = \frac{EA}{L}, \tag{3}$$

where E is the elastic modulus of coal, N/m; A is the cross-sectional area of coal, m^2; L is the length of coal, m.

By substituting Eq. (3) into ω_d in Eq. (2), the calculation equation of coal natural frequency can be obtained:

$$\omega_d = \frac{1-\xi^2}{2\pi}\sqrt{\frac{EA}{mL}}. \tag{4}$$

When the coal is a cube or cylinder, its natural frequency can be expressed as:

$$\omega_d = \frac{1-\xi^2}{2\pi}\sqrt{\frac{E}{\rho L^2}}, \tag{5}$$

where ρ is the density of coal, kg/m^3.

It is concluded that the natural frequency of macroscopic coal is not only related to the damping ratio and size of coal but also closely related to the physical and mechanical parameters such as density and elastic modulus of coal. Among them, the damping ratio of coal and rock is generally much less than 10%, so the influence of damping ratio on the natural frequency of coal can be ignored.

In fact, as a special continuous elastic body, the internal structure of coal is quite complex. Coal contains not only pores and fractures but also cleft bedding structure. The interaction between adjacent cleats and beddings can be assumed as free vibration between homogeneous blocks. Therefore, when the damping is ignored, the interaction between coal cleats and beddings can be represented by the physical model of the multi-degree-of-freedom system (Figure 2).

According to D'Alembert's principle, the differential equation of free vibration of multi-degree-of-freedom coal is:

$$M\ddot{X} + KX = 0. \tag{6}$$

In Eq. (6), M is the mass matrix of adjacent bedding coal; K is the stiffness matrix of adjacent bedding coal; X is the displacement vector of coal.

The coal itself has n degrees of freedom due to the free vibration between coal matrix blocks, and its vibration natural frequency can be expressed by the n-dimensional matrix or the column vector:

$$\begin{cases} \left(K-\omega^2 M\right)\phi = 0 \\ X(t) = \phi \sin(\omega t + \theta) \end{cases}, \tag{7}$$

where ϕ is the n-dimensional column vector; ω is the natural frequency of multi-degree-of-freedom coal, Hz; θ is the phase angle, rad.

Conditions for the non-zero solution of Eq. (7) are as follows:

$$\left|K-\omega^2 M\right| = 0. \tag{8}$$

The solution of Eq. (8) yields n values which can be arranged in an ascending order:

$$0 < \omega_1 \le \omega_2 \cdots \le \omega_n, \tag{9}$$

where $\omega_i (i = 1, 2, 3, \cdots n)$ is the i-th natural frequency of coal vibration.

In the multi-degree-of-freedom coal vibration model, the natural frequency of coal is closely related to the distribution, mass, and stiffness of bedding, and the vibration of coal has multiorder natural frequency, which increases with the increase of the order.

Based on the above established natural frequency vibration models on single-degree-of-freedom and multi-degree-of-freedom coals, it can be seen that coal vibration has multiorder natural frequency which grows with the increase of the order. In addition, the natural frequency of coal is directly determined by the physical and mechanical parameters such as elastic modulus, density, size, bedding, mass, and stiffness.

Taking coal as a whole specimen, the single-degree-of-freedom vibration model of coal is established. The single-degree-of-freedom vibration model of coal is used to illustrate the macroscopic influence factors of natural frequency. However, any continuous structure can be regarded as composed of infinite number of micro-rigid bodies. From the microscopic point of view, the interaction between adjacent cleft bedding inside coal can be considered the free vibration between homogeneous blocks. The multi-degree-of-freedom vibration model of coal body closely links the stiffness matrix and mass matrix with the macroscopic physical parameters such as elastic modulus, density, and size of the specimen. It lays a foundation for the industrial analysis of coal samples, the test of physical and mechanical parameters, and the analysis of natural frequency experimental results.

3. Experiment on Coal Natural Frequency

In order to further study the change characteristics of coal natural frequency, typical experimental coal samples with different rank of high, middle, and low coal were collected and prepared. Furthermore, an experiment was performed on the variations of coal natural frequency with the aid of

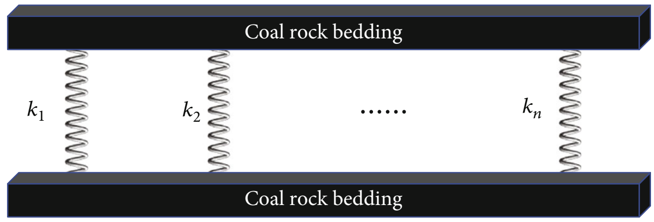

FIGURE 2: Vibration model of multi-degree-of-freedom coal.

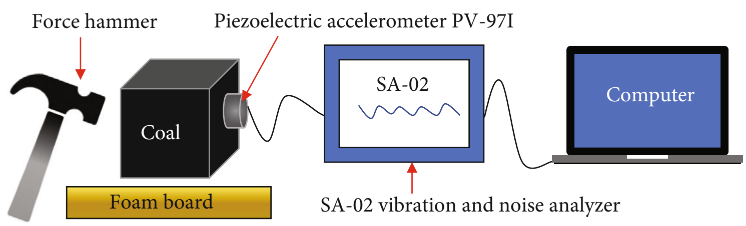

(a) Schematic diagram

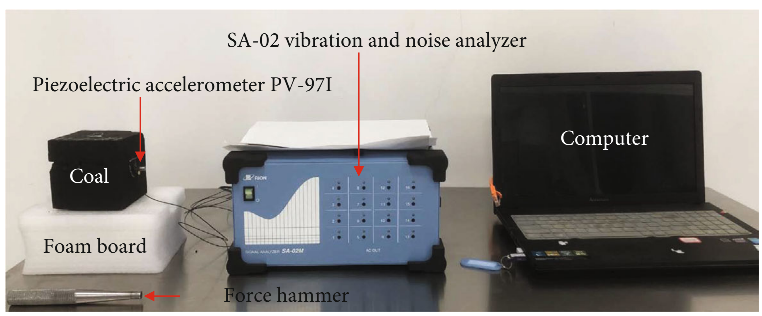

(b) Physical map

FIGURE 3: Testing device of coal natural frequency.

the experimental system setup using the relevant equipment of the State Key Laboratory Cultivation Base Forgas Geology and Gas Control relying on Henan Polytechnic University.

3.1. Test Principle and Device

(1) Test principle

Natural frequency is the inherent property of coal and rock material. When the coal body is subjected to external excitation, it will vibrate freely at a specific frequency, which is called the natural frequency of the coal body [23]. In this paper, instantaneous hammering method is used to test the natural frequency of coal. The specific operation is as follows: firstly, the acceleration sensor is installed on the surface of the cube coal sample to be tested by means of vaseline adhesive; secondly, using force hammer for instantaneous percussion hammer of coal samples, coal sample under a vibration shock pulse, the specimen will be its own inherent low order natural frequency of free vibration; finally, the frequency domain curve of the coal sample was obtained by applying fast Fourier transform (FFT) to the collected vibration signal, and the frequency corresponding to the acceleration peak, namely, the natural frequency of coal, was found on the curve.

(2) Test device

The test device of coal natural frequency comprises a force hammer, a foam board, the experimental coal sample, a vibration sensor, a vibration parameter detector, and a computer. The schematic diagram and photo of the test device are shown in Figure 3.

The vibration sensor used in the experiment is a three-direction piezoelectric accelerometer PV-97I sensor produced by RION, Japan. The sensor has a frequency measurement range of 1-10,000 Hz and a maximum test acceleration of 500 g. Since the natural frequency of coal is below 100 Hz, the sampling frequency in this experiment is set to 1-200 Hz, and the sampling number is 1,024. In addition, in order to avoid the influence of external medium on the vibration signal acquisition of acceleration sensor to the greatest extent, the foam board was used to support the coal sample for testing.

The vibration parameter detector is a SA-02 vibration noise analyzer produced by RION, Japan. The analyzer boasts the function of multichannel vibration signal acquisition and analysis. The analysis software that matches the vibration noise analyzer, i.e., the exclusive SA-02BASE vibration noise signal analysis system produced by RION, Japan, can conduct FFT analysis on the vibration signal data obtained and calculate the natural frequency of coal vibration.

3.2. Vibration Signal Processing

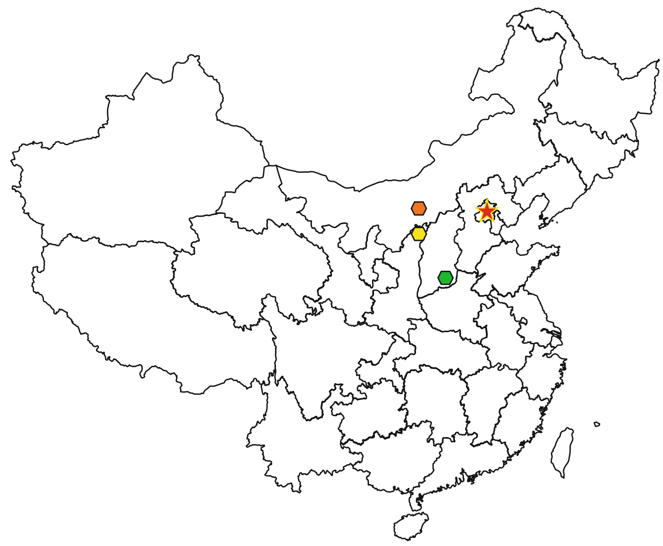

Figure 4: Sampling locations of experimental coal samples.

Table 1: Proximate analysis results of coal samples.

Type of coal	Proximate (wt%)			
	M_{ad}	A_{ad}	V_{ad}	FC_{ad}
Lignite	5.82	9.56	35.88	48.74
Bituminous	3.71	11.30	27.17	57.82
Anthracite	1.72	8.06	15.73	74.49

Note: M_{ad}: moisture content in the experimental coal sample; A_{ad}: ash content on an air: dried basis; V_{ad}: volatile matter content on an air: dried basis; FC_{ad}: fixed carbon content on an air-dried basis.

Table 2: Mechanical parameters of dried coal samples.

Type of coal	Elasticity modulus (GPa)	Poisson's ratio	Uniaxial compressive strength (MPa)
Lignite	1.11	0.32	9.36
Bituminous	3.16	0.29	18.69
Anthracite	2.67	0.30	14.73

(1) FFT transform

The original signal obtained by the signal acquisition system is the time-domain signal that changes with time. The vibration noise analysis software SA-02 BASE can be used to collect the time-domain signal for fast Fourier transform (FFT) to get the frequency domain signal, in the frequency domain diagram to determine the natural frequency of the sample. The formula of FFT transform is as follows [27]:

$$X(f) = \int_{-\infty}^{\infty} x(t) e^{-j2\pi f t} dt, \tag{10}$$

where $X(f)$ is the frequency domain representation of the signal; $x(t)$ is the time-domain representation of the signal.

(2) Signal interception

Because the time-domain signal we collected is of finite time length, so it is necessary to intercept the signal before FFT transformation. The time-domain weighting function used for intercepting signals is called window function. The selection of window function depends on the purpose of analysis and the type of vibration signal, which is generally selected according to the following principles: (1) If the truncated signal is a periodic signal, there is no leakage and no window is needed. (2) If the signal is a random signal or there are multiple frequency components in the signal, and the test focuses on the frequency point rather than the energy size, Hanning window should be selected. (3) For calibration, accurate amplitude is required and flat-top window can be selected.

Combined with the selection principle of the above window function, the natural frequency of the coal sample is the focus of the analysis when the "Instantaneous Hammering method" is used to test the natural frequency of the coal body. Therefore, Hanning window is selected for signal interception in this paper.

(3) Frequency domain average

In order to improve the reliability of the test results, after collecting the time-domain data of the specified test times, the vibration and noise analysis software SA-02 BASE is used. Firstly, the time-domain signal data collected each time are transformed by FFT to obtain the corresponding frequency domain data. Then, the acceleration amplitudes of the same frequency points in the frequency domain signal are automatically summed and averaged, and the final spectrum diagram with dominant frequency is obtained.

3.3. Experimental Coal Samples. Experimental lignite coal with a low metamorphic degree from Dongsheng Coal Mine

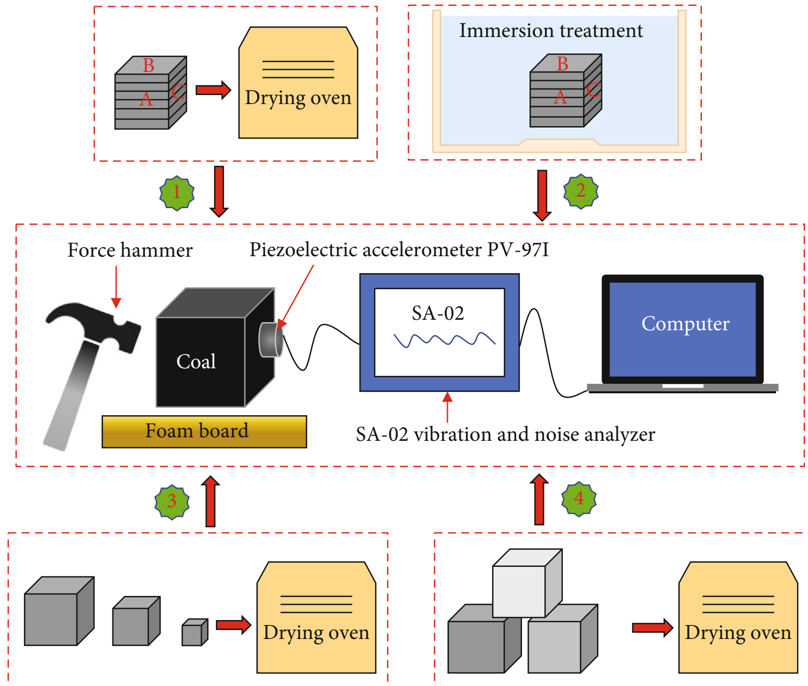

Figure 5: Experimental schemes and flowchart.

in Inner Mongolia, bituminous coal with a medium metamorphic degree from Daliuta Coal Mine in Shenmu City, Shaanxi Province, and anthracite coal with a high metamorphic degree in Chengzhuang Coal Mine in Shanxi Province, China, were selected as experimental coal samples. The sampling locations are displayed in Figure 4.

Proximate analysis was conducted on the three experimental coal samples to determine four indexes including moisture, ash, volatile matter, and fixed carbon. The determination results are given in Table 1, and the mechanical parameters of dried coal samples are exhibited in Table 2.

The lignite with the original structure was processed into cubes with sizes of 30 mm × 30 mm × 30 mm, 50 mm × 50 mm × 50 mm, and 100 mm × 100 mm × 100 mm based on the experimental needs. The bituminous coal and anthracite coal were processed into 100 mm × 100 mm × 100 mm cubes. Then, the experimental coal samples were put into an incubator at 55°C to be dried for 24 h. After the coal samples cooled to room temperature, they were put into a dryer for sealing and preservation for later use.

3.4. Test Schemes. In the hope of investigating the influences of bedding, moisture, size, and coal rank on the natural frequency of coal, four experimental schemes were developed. The experimental schemes and flowchart are exhibited in Figure 5.

(1) The influence of bedding on the natural frequency of coal: Among three adjacent faces of the 100 mm × 100 mm × 100 mm cubic dried lignite coal sample with an obvious bedding structure, the face parallel to the bedding was marked as Face B, and the two faces perpendicular to the bedding were labeled as Faces A and C; the faces corresponding to these three faces were marked as Faces a, b and c, respectively. Twenty natural frequency tests were carried out on each side, and the frequency domain signals of the six planes were obtained by the aforementioned "frequency domain average" method, and then the influence law of bedding on the natural frequency of coal was analyzed

(2) The influence of moisture on the natural frequency of coal: The 100 mm × 100 mm × 100 mm cubic lignite coal sample in Scheme (1) was soaked in water to obtain the saturated coal sample. The natural frequency of the saturated coal sample was tested and analyzed for the Faces A, B, and C, respectively. The results were compared with those measured in Scheme (1).

(3) The influence of size on the natural frequency of coal: The 30 mm × 30 mm × 30 mm, 50 mm × 50 mm × 50 mm, and 100 mm × 100 mm × 100 mm cubic dried lignite coal samples, ignoring the influence of bedding, were selected for obtaining frequency domain signals of different-size coal samples for the Face A according to the method in Scheme (1). Next, the values of natural frequencies of the coal samples for the Face A were used for analyzing the influence of size on natural frequency

(4) The influence of coal rank on the natural frequency of coal: Cubic dried lignite, bituminous coal, and anthracite coal with the size of 100 mm × 100 mm × 100 mm, ignoring the influence of bedding, were selected for obtaining frequency

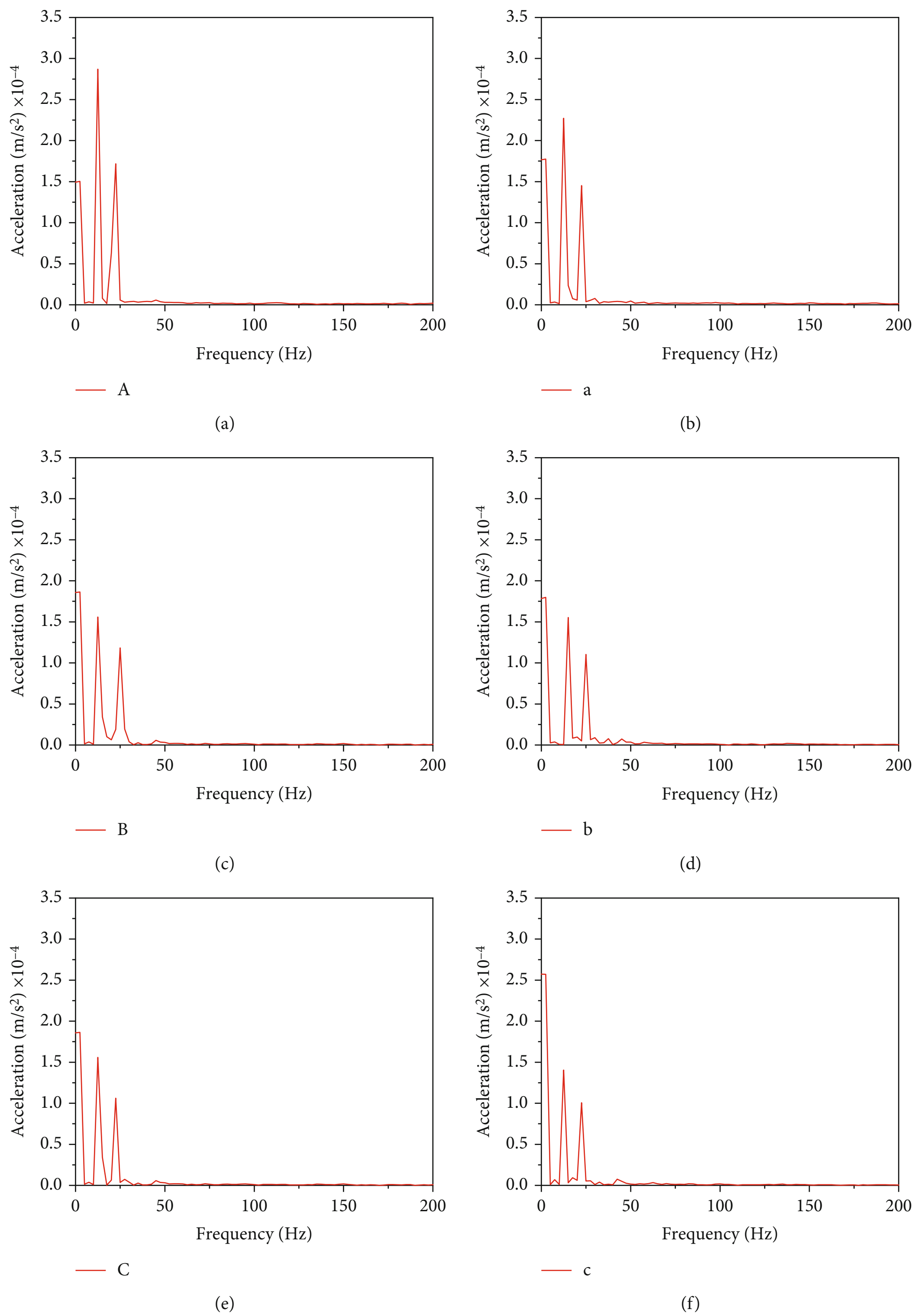

FIGURE 6: Frequency domains for the six faces of the dried lignite coal sample.

domain signals for the Face A of different-rank coal samples according to the method in Scheme (1). Next, the values of natural frequencies of the coal samples for the Face A were used for analyzing the influence of coal rank on natural frequency

4. Analysis and Discussion on the Experimental Results

4.1. Influence of Bedding. To analyze the influence of bedding on the natural frequency of coal, the frequency domains for

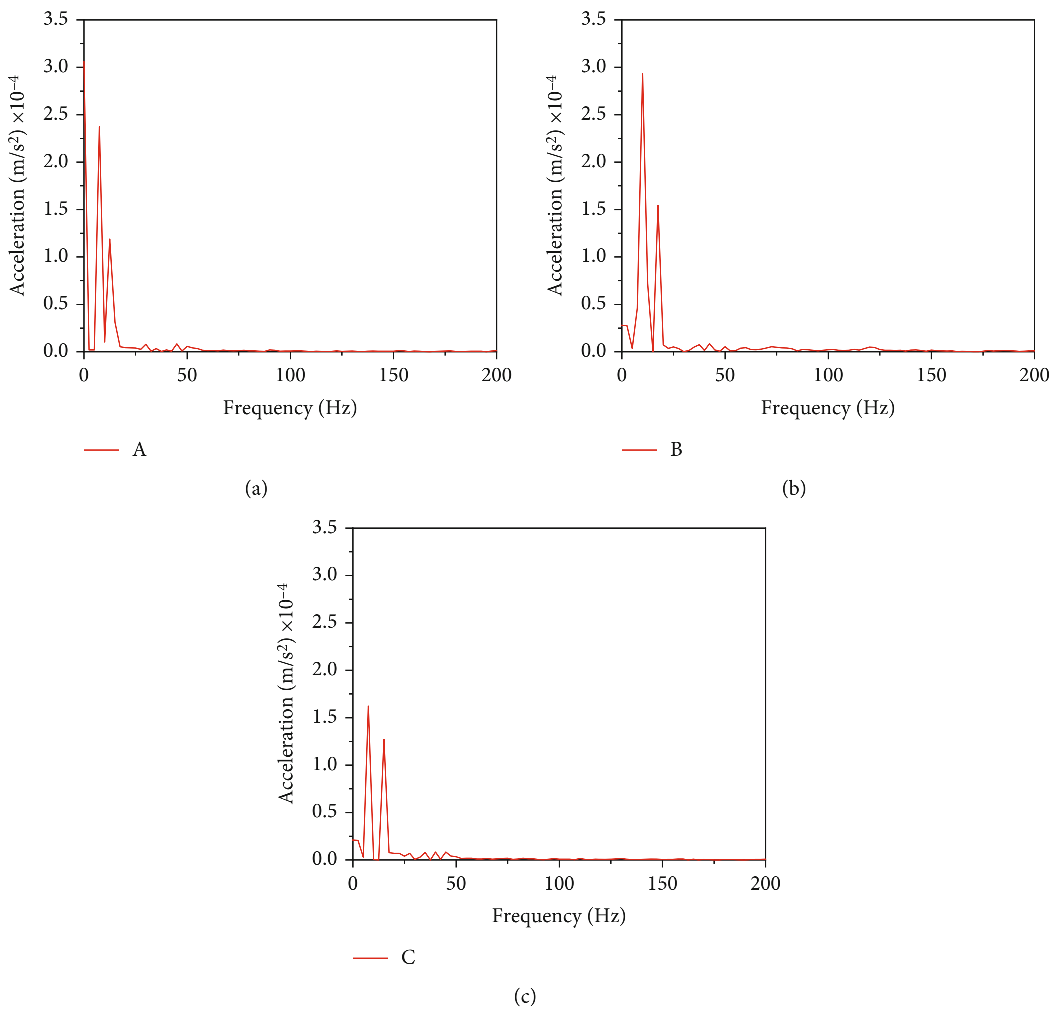

Figure 7: Frequency domains for the three adjacent faces of the saturated lignite coal sample.

Table 3: Mechanical parameters of dried and saturated lignite coal samples.

State of coal sample	Elasticity modulus (GPa)	Poisson's ratio	Uniaxial compressive strength (MPa)
Dried	1.11	0.30	9.36
Saturated	0.95	0.27	7.69

the six faces of the 100 mm × 100 mm × 100 mm cubic dried lignite coal sample were obtained according to Scheme (1) in Section 3.3. The test results are displayed in Figure 6.

The following findings are obtained from the frequency domain diagrams for the six faces of the dried lignite coal sample:

(1) The amplitudes of acceleration signals for different faces are not the same. This is because when the natural frequency of the coal sample is measured by the instantaneous hammering method, it was difficult to ensure that the intensity of each percussion is exactly the same. The amplitude of acceleration signals represents the magnitude of the percussion force to a certain extent, but this does not affect the test and analysis on the natural frequency of coal.

(2) Obvious natural frequencies of the first two orders, whose values lie in the range of 0-30 Hz, are excited for all the faces of the coal sample. Among them, the first-order and second-order natural frequencies for Faces A and a are both 12.5 Hz and 22.5 Hz; those for Faces B and b are both 15 Hz and 25 Hz; those for Faces C and c are both 12.5 Hz and 22.5 Hz. This indicates that the measured results of natural frequencies of coal samples conform to the reciprocity theorem. In other words, in the case of single excitation, the response remains unchanged when the positions of the excitation port and the response port are exchanged.

(3) For all the faces of the coal sample, the second-order natural frequency is higher than the first-order natural frequency, which agrees with the conclusion that the natural frequency of the coal sample increases with the rise of the order described in the multi-degree-of-freedom theoretical model.

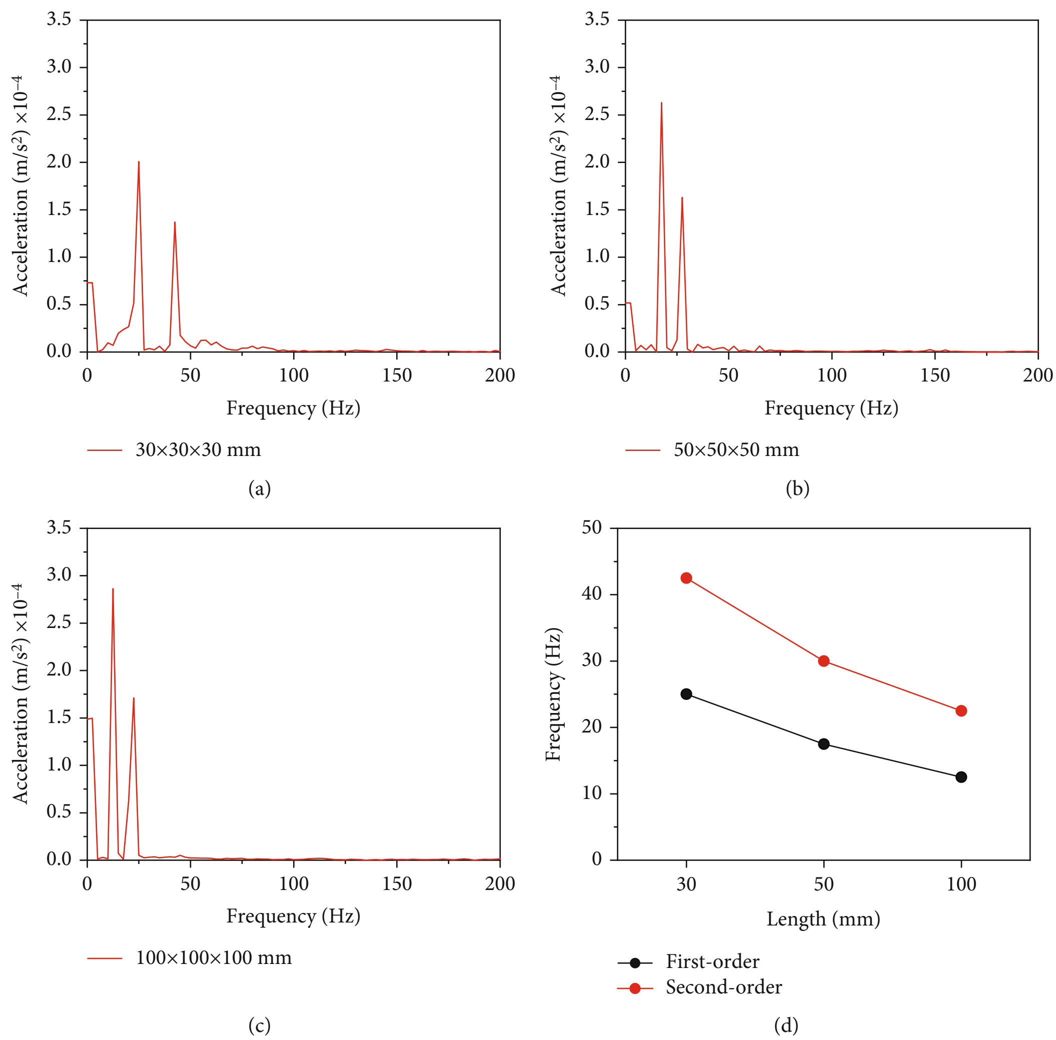

FIGURE 8: Frequency domain diagrams and natural frequency variation pattern diagram of different-size dried lignite coal samples.

(4) The first-order and second-order natural frequencies for Faces B and b are higher than those for Faces A, a, C, and c, mainly because the complexity of the internal structure of the coal sample results in the discrepancy of the direction of its internal mechanical properties.

In the literature [30], the influence of anisotropy on the mechanical response characteristics of coal was expounded in detail. The uniaxial compressive strength and peak strength parallel to the Faces of bedding are higher than those perpendicular to the Faces of bedding. The directional distribution characteristics of microstructures in the coal sample cause regular changes in mechanical properties. Therefore, the natural frequencies measured for faces parallel to the bedding are higher than those measured perpendicular to the bedding.

4.2. Influence of Moisture. Microscopically, coal has a porous structure of pores and cracks, and its molecular structure is rich in oxygen-containing functional groups, showing strong hydrophilicity [31]. The change of coal natural frequency is an external expression of its internal structural parameters. The influence of moisture erosion on coal natural frequency cannot be ignored.

According to Scheme (2) in Section 3.3, the natural frequencies for the six faces of the saturated coal sample were measured. The natural frequency of coal satisfied the reciprocity theorem based on the analysis in Scheme (2) in Section 4.1. Hence, the frequency domain diagrams for the three adjacent Faces A, B, and C of the saturated coal sample were plotted (Figure 7).

From the frequency domain diagrams for the three adjacent faces of the saturated lignite coal sample, it can be concluded that:

(1) When it comes to the saturated lignite coal sample, the first-order and second-order natural frequencies for Face A are 7.5 Hz and 15 Hz; those for Face B are 10 Hz and 17.5 Hz; those for Face C are 7.5 Hz and 15 Hz, respectively. Compared with the test results of the Faces A, B, and C of dried lignite samples in Section 4.1, the natural frequencies of saturated water coal sample are significantly reduced

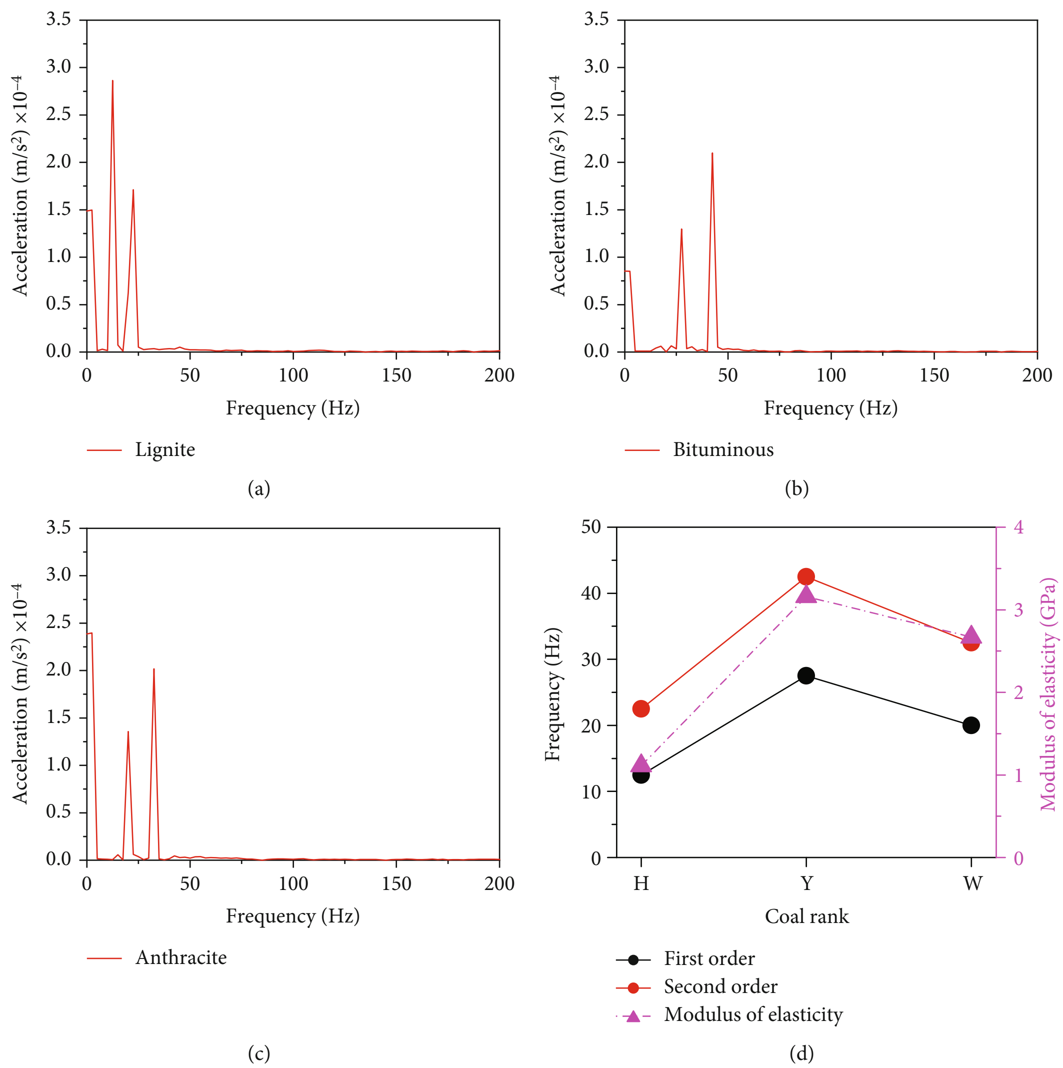

Figure 9: Frequency domain diagrams and natural frequency variation pattern diagram of different-rank dried lignite coal samples.

(2) Under water erosion, the natural frequencies for Face B are still higher than those for Faces A and C even of the same coal sample, which further verifies the influence of bedding structure on the natural frequency of coal

(3) The density of the coal sample increases after saturation treatment. According to Eq. (5) of the mathematical model of natural frequency of coal in section 2, the increase of coal sample density is bound to induce the reduction of natural frequency

(4) The moisture content of coal also exerts a significant effect on its mechanical parameters. The elastic modulus and uniaxial compressive strength of coal samples after saturated treatment are significantly reduced, which leads to the decrease of natural frequency of coal samples. The comparative test results of some mechanical parameters of dried and saturated lignite coal samples are listed in Table 3

4.3. Influence of Size. Due to the limitations of coal damping and vibration wave propagation energy, the size of coal also considerably influences on its natural frequency in the range of vibration wave transmission. A relevant study discloses that the strength of rock decreases monotonously and tends to approach its minimum strength value with the increase of its size [32]. In order to reveal the influence of size on the natural frequency of coal, frequency domain diagrams for Face A of dried lignite coal samples with the sizes of 30 mm × 30 mm × 30 mm, 50 mm × 50 mm × 50 mm, and 100 mm × 100 mm × 100 mm were obtained according to Scheme (3) in Section 3.3 (Figure 8).

From the frequency domain diagrams and natural frequency variation pattern diagram of different-size dried lignite coal samples, the following conclusions can be drawn:

(1) The first-order and second-order natural frequencies for Face A of the 30 mm × 30 mm × 30 mm dried lignite coal sample are 25 Hz and 42.5 Hz; those for Face A of the 50 mm × 50 mm × 50 mm dried lignite

coal sample are 17.5 Hz and 30 Hz; those for Face A of the 100 mm ×100 mm ×100 mm dried lignite coal sample are 12.5 Hz and 22.5 Hz, respectively. Under the same condition, the natural frequency decreases with the increase of coal sample size

(2) When the elastic modulus, density, moisture, bedding, and other conditions of coal remain constant, the natural frequency of coal is inversely proportional to its size. That is, the larger the coal size is, the lower the natural frequency will be. Through formula (5), the experimental results agree well with the theoretical model

Hence, the size effect of coal should be considered when using vibration wave for permeability enhancement excitation. Low-frequency vibration excitation should be applied to large-size coal for the purpose of achieving resonance and permeability enhancement effect.

4.4. Influence of Coal Rank. For different-rank coals, pores and cracks are distributed in different ways and the contents of organic matters and minerals also differ notably, which directly determines and affects the mechanical properties [33, 34]. In order to explore the influence of coal rank on the natural frequency of coal, frequency domain diagrams for Face A of the 100 mm ×100 mm ×100 mm typical dried coal samples of high, middle, and low rank were obtained according to Scheme (4) in Section 3.3 (Figure 9).

The following conclusions can be drawn from the frequency domain diagrams and natural frequency variation pattern diagram of different-rank dried lignite coal samples:

(1) Natural frequencies of different-rank coal samples are significantly different. The first-order and second-order natural frequencies of lignite are 12.5 Hz and 22.5 Hz; those of bituminous coal are 27.5 Hz and 42.5 Hz; those of anthracite coal are 20 Hz and 32.5 Hz. Under the conditions of identical bedding, size, and moisture, the first-order and second-order natural frequencies of different-rank coals follow the order: bituminous coal > anthracite coal > lignite

(2) The main frequency of signal refers to the frequency with the greatest response energy under the same impulse excitation. The main frequencies of signals generated by different-rank coal samples also differ. The main frequency of signals generated by lignite coal is located at the first-order natural frequency, while those of bituminous coal and anthracite coal are at the second-order natural frequency. Such a result suggests that the coal samples have multiple orders of natural frequencies, but the response degrees of different frequencies differ under the same impulse excitation

(3) A comparison of the relevant parameters of different-rank coal samples in Tables 1 and 2 demonstrates that the ash contents (one of the main parameters of mineral content) in the three coal samples follow the order: bituminous> anthracite > lignite. Besides, minerals fill the pores and cracks in coal, strengthen the compressive strength of the matrix skeleton, and improve the mechanical strength and elastic modulus. In the corresponding dry coal samples of the same size, the elastic modulus and uniaxial compressive strength of bituminous coal are the largest, followed by anthracite and lignite. According to the single-degree-of-freedom theoretical model, the larger the elastic modulus of the material is, the larger the natural frequency is. The physical and mechanical parameters of coal directly determine the natural frequency of coal samples of different rank

5. Conclusions

In this study, the natural frequency of coal was theoretically analyzed first. Based on the theoretical analysis, mathematical models of coal natural frequency were established, and an experiment was performed on the variations of coal natural frequency. Furthermore, the main factors influencing coal natural frequency were explored. The following conclusions were drawn:

(1) Based on the established natural frequency vibration models of coal, it is concluded that coal vibration has multiorder natural frequency which grows with the increase of the order. In addition, the natural frequency of coal is directly determined by the physical and mechanical parameters such as size, elastic modulus, density, bedding, mass, and stiffness

(2) The bedding structure characteristics of the experimental coal sample lead to regular variations of its mechanical properties, so that the natural frequency parallel to the bedding plane is higher than that perpendicular to the bedding plane. Besides, the size of the coal sample primarily exerts an influence on its mass. The larger the coal size and mass are, the lower the natural frequency would be

(3) For the saturated coal sample, moisture changes its the density and reduces its elastic modulus. Resultantly, its natural frequency is lower than that of the dried coal sample. Moreover, the physical and mechanical properties of different-rank dried coal samples are affected by the content of organic matter and minerals, which results in the difference of natural frequencies of different-rank dried coal samples. Thus, the natural frequencies of different-rank coal samples follow the order: bituminous >anthracite > lignite

(4) The experiment results indicate that the natural frequencies of coal samples under different influencing factors are all tens of Hz. Thus, in the application of the RPEEVW technology, attention should be paid to the vibration excitation under the low-frequency condition

Data Availability

The data used to support the findings of this study are included within the article.

Conflicts of Interest

The authors declare that they have no conflicts of interest.

Acknowledgments

This work was supported by the National Natural Science Foundation of China (Grant No.: 51974109), the Project funded by China Postdoctoral Science Foundation (2021M700132), the Program for Leading Talents in Scientific and Technological Innovation of Henan Province (Grant No.: 204200510032), the Scientific and Technological Projects of Henan Province (Grant No.: 202102310220), the Plan of Key Scientific Research Project of Colleges and Universities in Henan Province (Grant No.: 20A620001), the Fundamental Research Funds for the Universities of Henan Province (Grant No.: NSFRF210301), and the Doctoral Fund of Henan Polytechnic University (Grant No.: B2019-55).

References

[1] Y. Li, C. Zhang, D. Z. Tang et al., "Coal pore size distributions controlled by the coalification process: An experimental study of coals from the Junggar, Ordos and Qinshui basins in China," *Fuel*, vol. 206, pp. 352–363, 2017.

[2] Y. Li, J. H. Yang, Z. J. Pan, and W. Tong, "Nanoscale pore structure and mechanical property analysis of coal: an insight combining AFM and SEM images," *Fuel*, vol. 260, 2020.

[3] Y. Li, Y. B. Wang, J. Wang, and Z. J. Pan, "Variation in permeability during CO_2-CH_4 displacement in coal seams: Part 1 - Experimental insights," *Fuel*, vol. 263, 2020.

[4] L. Yuan, "Strategic thinking of simultaneous exploitation of coal and gas in deep mining," *Journal of China Coal Society*, vol. 41, no. 1, pp. 1–6, 2016.

[5] B. S. Nie and X. C. Li, "Mechanism research on coal and gas outburst during vibration blasting," *Safety Science*, vol. 50, no. 4, pp. 741–744, 2012.

[6] X. C. Li, B. S. Nie, and X. Q. He, "Mechanism of coal and gas bursts caused by vibration," *Journal of University of Science and Technology Beijing*, vol. 33, no. 2, pp. 149–152, 2011.

[7] P. Li, X. D. Zhang, and H. Li, "Technology of coupled permeability enhancement of hydraulic punching and deep-hole presplitting blasting in a "three-soft" coal seam," *Materials Technology*, vol. 55, no. 1, pp. 89–96, 2021.

[8] C. G. Huang, Y. B. Zhang, J. F. He, Y. Luo, and Z. G. Sun, "Permeability improvements of an outburst-prone coal seam by means of presplitting and blasting with multiple deep boreholes," *Energy Science & Engineering*, vol. 7, no. 5, pp. 2223–2236, 2019.

[9] Q. Ye, Z. Z. Jia, and C. S. Zheng, "Study on hydraulic-controlled blasting technology for pressure relief and permeability improvement in a deep hole," *Journal of Petroleum Science and Engineering*, vol. 159, pp. 433–442, 2017.

[10] H. D. Wang, Z. H. Cheng, Q. L. Zou et al., "Elimination of coal and gas outburst risk of an outburst-prone coal seam using controllable liquid CO_2 phase transition fracturing," *Fuel*, vol. 284, article 119091, 2021.

[11] H. D. Chen, Z. F. Wang, X. Chen, X. J. Chen, and L. G. Wang, "Increasing permeability of coal seams using the phase energy of liquid carbon dioxide," *Journal of CO_2 Utilization*, vol. 19, pp. 112–119, 2017.

[12] S. F. Yin, H. F. Ma, Z. H. Cheng et al., "Permeability enhancement mechanism of sand-carrying hydraulic fracturing in deep mining: a case study of uncovering coal in cross-cut," *Energy Science & Engineering*, vol. 7, no. 5, pp. 1867–1881, 2019.

[13] S. Gehne and P. M. Benson, "Permeability enhancement through hydraulic fracturing: laboratory measurements combining a 3D printed jacket and pore fluid over-pressure," *Scientific Reports*, vol. 9, no. 1, pp. 1–11, 2019.

[14] Y. C. Feng, L. Chen, A. Suzuki et al., "Enhancement of gas production from methane hydrate reservoirs by the combination of hydraulic fracturing and depressurization method," *Energy Conversion and Management*, vol. 184, pp. 194–204, 2019.

[15] S. Li, Q. Lei, X. Wang, B. Cai, G. F. Liu, and L. Wang, "Permeability regain and aqueous phase migration during hydraulic fracturing shut-ins," *Scientific Reports*, vol. 9, no. 1, pp. 1–10, 2019.

[16] Y. D. Jiang, X. F. Xian, J. Yi, Z. F. Liu, and C. Y. Guo, "Experimental and mechanical on the features of ultrasonic vibration stimulating the desorption of methane in coal," *Journal of China Coal Society*, vol. 33, no. 6, pp. 675–680, 2008.

[17] Z. L. Ge, Y. Y. Lu, and D. P. Zhou, "Study on regular and mechanism of coal bed methane desorption experiment under sonic vibrating of cavitation water jets," *Journal of China Coal Society*, vol. 36, no. 7, pp. 1150–1155, 2011.

[18] X. X. Chen, L. Zhang, and M. L. Shen, "Experimental research on desorption characteristics of gas-bearing coal subjected to mechanical vibration," *Energy Exploration & Exploitation*, vol. 38, no. 5, pp. 1454–1466, 2020.

[19] M. L. Shen and X. X. Chen, "Influence rules and mechanisms of mechanical vibration at different frequencies on dynamic process of gas diffusion from coal particles," *Energy Exploration & Exploitation*, vol. 39, no. 6, pp. 1939–1957, 2021.

[20] Y. D. Jiang, X. Song, H. Liu, and Y. Z. Cui, "Laboratory measurements of methane desorption on coal during acoustic stimulation," *International Journal of Rock Mechanics and Mining Sciences*, vol. 78, pp. 10–18, 2015.

[21] W. Li, T. Yan, S. Q. Li, and X. N. Zhang, "Rock fragmentation mechanisms and an experimental study of drilling tools during high-frequency harmonic vibration," *Petroleum Science*, vol. 10, no. 2, pp. 205–211, 2013.

[22] S. Y. Yin, D. J. Zhao, and G. B. Zhai, "Investigation into the characteristics of rock damage caused by ultrasonic vibration," *International Journal of Rock Mechanics and Mining Sciences*, vol. 84, pp. 159–164, 2016.

[23] C. W. Li, X. Y. Sun, T. B. Gao, B. J. Xie, and X. M. Xu, "Coal and rock vibration failure and the characteristics of microseismic signals," *Journal of the China Coal Society*, vol. 40, no. 8, pp. 1834–1844, 2015.

[24] S. Q. Li, T. Yan, W. Li, and F. Q. Bi, "Simulation on vibration characteristics of fractured rock," *Rock Mechanics and Rock Engineering*, vol. 49, no. 2, pp. 515–521, 2016.

[25] M. S. Mullakaev, V. O. Abramov, and A. V. Abramova, "Development of ultrasonic equipment and technology for well stimulation and enhanced oil recovery," *Journal of Petroleum Science and Engineering*, vol. 125, pp. 201–208, 2015.

[26] Q. Sun, A. Retnanto, and M. Amani, “Seismic vibration for improved oil recovery: a comprehensive review of literature,” *International Journal of Hydrogen Energy*, vol. 45, no. 29, pp. 14756–14778, 2020.

[27] W. T. Thomson, *Theory of Vibration with Applications*, Taylor & Francis, London, UK, 1993.

[28] R. Denzer, F. J. Barth, and P. Steinmann, “Studies in elastic fracture mechanics based on the material force method,” *International Journal for Numerical Methods in Engineering*, vol. 58, no. 12, pp. 1817–1835, 2003.

[29] S. Q. Li, S. L. Tian, W. Li, T. Yan, and F. Q. Bi, “Research on the resonance characteristics of rock under harmonic excitation,” *Shock and Vibration*, vol. 2019, Article ID 6326510, 11 pages, 2019.

[30] H. H. Song, Y. D. Jiang, D. Elsworth, Y. X. Zhao, J. H. Wang, and B. Liu, “Scale effects and strength anisotropy in coal,” *International Journal of Coal Geology*, vol. 195, pp. 37–46, 2018.

[31] L. L. Si, H. T. Zhang, J. P. Wei, B. Li, and H. K. Han, “Modeling and experiment for effective diffusion coefficient of gas in water- saturated coal,” *Fuel*, vol. 284, 2021.

[32] B. C. Liu, J. S. Zhang, Q. Z. Du, and J. F. Tu, “A study of size effect for compression strength of rock,” *Chinese Journal of Rock Mechanics and Engineering*, vol. 17, no. 6, pp. 611–614, 1998.

[33] D. K. Wang, F. C. Zeng, J. P. Wei, H. T. Zhang, Y. Wu, and Q. Wei, “Quantitative analysis of fracture dynamic evolution in coal subjected to uniaxial and triaxial compression loads based on industrial CT and fractal theory,” *Journal of Petroleum Science and Engineering*, vol. 196, 2021.

[34] Z. H. Wen, Q. Wang, Y. P. Yang, and L. L. Si, “Pore structure characteristics and evolution law of different-rank coal samples,” *Geofluids*, vol. 2021, Article ID 1505306, 17 pages, 2021.

Hindawi
Geofluids
Volume 2022, Article ID 9426378, 11 pages
https://doi.org/10.1155/2022/9426378

Research Article

Effects of Real-Time High Temperature and Loading Rate on Deformation and Strength Behavior of Granite

YiFeng Zhang, Fan Zhang, Ke Yang, and ZhengYu Cai

School of Civil Engineering, Architecture and Environment, Hubei University of Technology, Wuhan 430068, China

Correspondence should be addressed to Fan Zhang; fanzhang@hbut.edu.cn

Received 16 March 2022; Revised 11 April 2022; Accepted 15 April 2022; Published 14 May 2022

Academic Editor: Zhijie Wen

Knowledge of deformation and strength behavior of rocks under high in situ temperature is highly important for the control of geological disasters in exploration of hot dry rock and mining in deep formation. In this study, uniaxial compression tests were carried out on granite under different real-time high-temperature conditions (25, 200, 300, 400, 500, 600, and 700°C) and loading rates (0.01, 0.1, and 0.5 mm/min). The effects of real-time high temperature and loading rate on the uniaxial compressive strength and elastic modulus of granite were studied, and the microscopic morphology of the fracture surface was analyzed. The results show that the uniaxial compressive strength and elastic modulus of granite increase first and then decrease with the increase of temperature. The uniaxial compressive strength clearly increases at 200°C and decreases gradually when the temperature exceeds 300°C. Under the same temperature conditions, the uniaxial compressive strength of granite decreases and the elastic modulus increases with increasing loading rate. When the temperature reaches 600°C, the effect of the loading rate on the uniaxial compressive strength and elastic modulus of granite decreases significantly. The test results are compared with the results of work performed on quenched granite. Under real-time high-temperature conditions, the thermal crack effect has a significant influence on the uniaxial compressive strength and elastic modulus of granite, without the thermal hardening effect of quenched granite. During hydraulic fracturing, the rock skeleton near the injection well is cooled and shrunk, as is the thermal hardening effect caused by high-temperature quenching. The formation of thermal equilibrium leads to the large-scale extension of fracture cracks along the weak plane structure, such as the effect of thermal cracks on granite under real-time high-temperature conditions.

1. Introduction

Hot dry rock (HDR) energy is a well-recognized clean and renewable green energy which has many advantages, such as stability and safety, high utilization rate, and low operating cost [1]. HDR is widely distributed in the granite at depths in the order of 5 to 6 km, temperatures varying from 150 to 650°C [2, 3]. At present, HDR development is mainly concentrated in the granite thermal reservoir. Therefore, it is important to investigate the effect of real-time high temperature on the physical properties and mechanical behavior of granite for the design, construction, and maintenance of enhanced geothermal system (EGS).

A large number of experimental studies have been performed to investigate the physical properties and mechanical behavior of rocks subjected to thermal treatment. Zhang et al. [4] investigated the changes in the physical behavior of granite and sandstone after heat treatment by the uniaxial compression test and showed that the loss of adhered water, bound water, and structural water has a great influence on the mechanical properties of rocks at high temperature. Wang et al. [5] investigated the acoustic emission (AE) characteristics of granite during uniaxial compression tests after thermal treatment, and the experimental results showed that AE energy increases with the increase of treatment temperature. Chen et al. [6] measured the macroscopic mechanical properties of granite using uniaxial compression test after high-temperature thermal treatment and found that the uniaxial compressive strength gradually decreases with increasing temperature. Liu et al. [7] studied the mechanical properties of granite after high-temperature thermal treatment by the uniaxial compression test, and the results showed that 600°C is the critical temperature of granite. Zhao et al. [8] and Sun et al. [9] found that high temperature causes prefabricated cracks in granite to continue to expand and even produce new cracks. As the temperatures increase, the number and width of the microcrack increase, and the granite transforms from brittle to ductile. David et al. [10] analyzed the relation of the evolution of the physical properties and the amount of damage induced and indicated that changes in mineral composition and fracture size are the reasons for the decline of granite strength. Heuze [11] studied the influence of the thermal expansion coefficient and the thermal diffusivity on the mechanical properties of granite. Chaki et al. [12] confirmed the strong influence of thermal damage on physical properties of granite and determined parameters for the characterization of connected porosity and overall damage.

Furthermore, the thermal stimulation method can be effectively utilized to improve flow performance in tight porous media with an induced thermal shock by inducing the thermal gradient for permeable cracks, thus achieving geothermal reservoir stimulation [13]. Kumari et al. [13, 14] conducted strength tests under unconfined conditions, Brazilian tensile strength tests, and permeability tests in quenched granite. The results showed that increasing temperature causes significant reductions in the permeability of granite due to the thermally induced volumetric expansion. The failure mechanism of granite transitions from a brittle to a quasibrittle state. Zhang et al. [15] studied the damage variables and pores of granite after thermal shock, and the results showed that thermal shock induced by rapid cooling can cause more damage to granite than that induced by slow cooling, leading to a larger size and number of internal pores. Weng et al. [16] utilized integrated acoustic emission (AE) and digital image correlation (DIC) techniques to study the micro/macrocracking characteristics of the granite sample upon different heating/cooling cycles. The results showed that surface cracks and internal microcracks (including intergranular and intragranular) in granite increase significantly with the number of heating/cooling cycles. Li et al. [17] observed the generation of granite cracks in the process of hydraulic fracturing using AE and indicated that the coalescence of microcracks is a key precursor to hydraulically induced cracking. Avanthi Isaka et al. [18] comprehensively investigated the influence of heating followed by cooling on the alteration of microstructural properties of granite. The analysis revealed considerable unstable deterioration of quartz and feldspar grains subjected to thermal stresses, while biotite minerals show the most stable behavior against thermal shock-induced microcracking. Shao et al. [19] studied the effect of the cooling rate on the mechanical behavior of heated granite through uniaxial compression tests, and the results showed that thermal cracks during the cooling treatment of the heated sample for higher temperatures are the main reason for the decrease of the mechanical characteristics.

Thermal cracking behavior of granite at high temperature and high pressure is the key to the performance of HDR geothermal energy extraction system. Yang et al. [20] evaluated the influence of thermal effect on strength and deformation behavior, and the results showed that crack damage and maximum axial deformation gradually increase with increasing temperature. Gautama et al. [21] measured the thermal physical properties of granite in the range of 25 to 250°C and found that the thermal expansion coefficient of granite increases with the increase of temperature, while the thermal conductivity, thermal diffusivity, and elastic wave velocity of granite decrease gradually with increasing temperature. Gu et al. [22] explored the mechanical properties of granite under heating conditions, and indicated that the ability of the rock to resist deformation gradually weakens under the effect of temperature. Zhao et al. [23] conducted permeability tests on granite at high temperature and high pressure, and the results showed that thermal cracks in granite are induced by intragranular and intergranular thermal stress, and the critical temperature of permeability change decreases with increasing confining pressure. Yin et al. [24] performed triaxial compression tests on granite at high temperature, and the results showed that the larger crystal particles and the extreme heterogeneity of the coarse-grained granite lead to larger thermal deformation and greater deterioration of the mechanical properties. Ranjith et al. [25] carried out the uniaxial compressive tests of sandstone at various temperatures and found that the mineralogical changes in the sandstone cement with heating temperature have a significant influence on changes in mechanical behavior.

The previous work is devoted to rock by investigating the influence of thermal treatment and high-temperature quenching treatments on the macroscopic mechanical properties of rock. The results of experimental studies performed on preheated samples at room temperature are insufficient to represent the essential characteristics of rocks at high temperature in geothermal applications. In addition, the mechanical testing of granite has rarely integrated the coupling effects of real-time high-temperature conditions and loading rates. For this, uniaxial compression tests were carried out under different real-time high-temperature conditions (25, 200, 300, 400, 500, 600, and 700°C) and loading rates (0.01, 0.1, and 0.5 mm/min). The present study investigated the coupled high in situ temperature and loading rate effects. Then, the effect of real-time high temperature on the thermal damage characteristics of granite was analyzed using scanning electron microscopy (SEM). These comprehensive experimental studies provided knowledge of the underlying mechanisms of thermally induced damage in the geothermal reservoir rocks. The results of the testing were compared to results obtained for similar work carried out on quenched granite, which highlights the variability in the response of granite to real-time high temperatures. The research results could be of great significance for understanding the thermal damage and mechanical behavior of HDR mining.

2. Test Preparation and Process

2.1. Rock Description and Sample Preparation. For the present study, granite samples were collected from Miluo Village of Hunan Province, China. Initial granite samples are uniform and complete, with uniform texture, and no visible

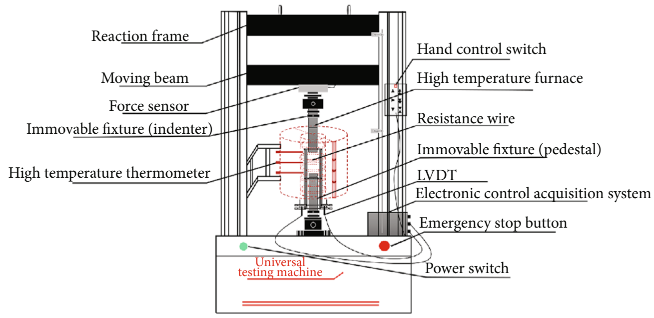

Figure 1: Microcomputer-controlled electronic universal testing machine.

defects were observed on the rock surface. The dimensions of the samples are 38 mm in diameter and 76 mm in length. The surface was polished smooth, and the height, diameter, and flatness all met the requirements. The parallelism was controlled within ±0.05 mm and the surface flatness was controlled within ±0.02 mm, which satisfied the standards of the International Society of Rock Mechanics and Rock Engineering (ISRM) [26]. The natural density and porosity of granite samples are 2.62 g/cm^3 and 0.92%, respectively. The mineral compositions were analyzed by X-ray diffraction, and the results show that the main mineral components are albite (34%), biotite (31%), potash feldspar (21%), quartz (13%), and plagioclase (1%).

2.2. Experimental Equipment and Testing Procedure. In this study, a computer-controlled universal testing machine was used to study real-time high-temperature uniaxial compression tests of granite. As shown in Figure 1, the test equipment is composed of a reaction frame, a high-temperature fixture, a high-temperature furnace, and two displacement sensors (LVDTs). The reaction frame is made of alloy steel and the system has an axial force capacity of 300 kN, which can ensure that the overall stiffness of the testing machine meets the test requirements. The high-temperature fixture is located in the high-temperature furnace with the maximum heating temperature of 1200°C. The granite sample was placed in the center of the high-temperature fixture to ensure that the center of the sample was under pressure. Granite samples were heated in the furnace at atmospheric pressure with a rate of 5°C/min until the prescribed temperature was reached. The heating temperature was held for 2 h to achieve stabilization of the temperature throughout the samples, in order to reduce the effect of the thermal gradient inside the samples and to ensure that the cracking process was induced merely by the temperature effect. Uniaxial compression tests of granite were carried out under the condition of constant target temperature. The granite sample was loaded using the displacement control method. The axial strain was measured by two displacement sensors (LVDTs). The difference between the two displacement sensor (LVDTs) measurements was not significant. This difference was mainly attributed toward that the sample was not completely parallel to the main direction of the axial stress at the time of installation. Installation errors were eliminated using average values. At least three samples were taken for each working condition to ensure the accuracy of the test.

3. Results and Discussion

3.1. Macroscopic Failure Mode. Figure 2(a) shows the macroscopic failure mode of granite after the uniaxial compression test at real-time high temperature. Granite exhibits an X-shaped conjugate inclined plane shear failure. The angle between the failure surface and the load axis is the conjugate shear fracture angle (β). Figure 2(a) also shows that the granite samples are thorough and serious. The area affected by the end effect of the granite sample has many minor extensile cracks at both ends of the sample and the junction of the shear cracks. The middle of the granite sample presents an X-type shearing fracture along the axial loading direction, and its macroscopic cracks are diagonally through [27, 28]. The damage surface is rough. The granite samples are broken down to a number of little pieces at the end of the tests. As shown in Figure 2(b), with the increase of temperature, the surface color of granite samples gradually changes from gray-blue to gray-white. The main reason for this color change is oxidation of biotite and K-feldspar minerals at high temperature. The obvious oxidation of ferrous compounds of these minerals is found in black mica and potassium feldspar minerals [13, 29, 30].

3.2. Microstructure of Fracture Surface. Figure 3 presents the microcrack morphology of the granite after uniaxial compression test under real-time high-temperature conditions by scanning electron microscope (SEM), and the red dotted line indicates the microcracks. Figure 3 shows that high temperature has a significant effect on the expansion of cracks in granite. At 25°C, a few initial cracks are observed in the fracture plane of the granite sample (Figure 3(a)), indicating that the fracture surface of the granite mineral grains in the initial state, the crystal grains remain in tight contact and have almost complete microstructure. When the temperature increases to 200°C, although a few initial grain boundaries and cracks can be observed, the relatively weak grain boundary cementation produces a small amount of grain boundary cracks with small length and small pore size. Most of the grain boundaries remain undivided in this temperature (Figure 3(b)). Below 300°C, no transgranular cracks occur

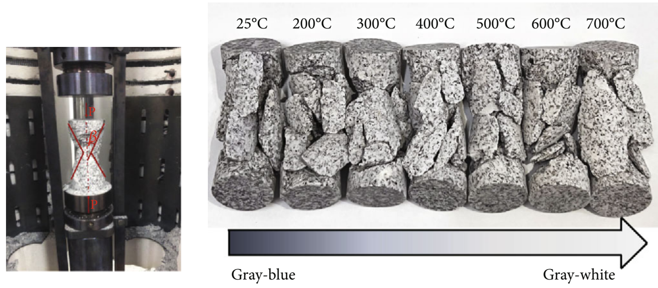

(a) (b)

Figure 2: Macroscopic failure morphology of granite samples. (a) Failure morphology of the granite sample in the uniaxial compression test. (b) Color change and failure morphology of granite samples under different real-time high temperatures.

in granite samples [20]. When the temperature exceeds 300°C, the number of grain boundary cracks increases gradually, the length and aperture of grain boundary cracks increase accordingly, and some grain boundary cracks begin to connect. At 400°C, the fracture aperture of intercrystalline cracks increases significantly (Figures 3(c) and 3(d)) [14, 31]. When the real-time temperature is 500°C, the length and width of intracrystalline cracks and intergranular cracks had been increasing as the temperature increases, and the transgranular cracks become increasingly obvious (Figure 3(e)). The quartz undergoes the transition in the crystal structure from α type to β type at 573°C [32]. At temperatures above 600°C, a large number of transgranular cracks appear on the fracture plane, and many crystals are segmented into small cellular structures by transgranular cracks (Figures 3(f) and 3(g)). The internal cracks in granite expand from intergranular cracks to transgranular cracks with the increase of temperature. Further, widely propagated larger cracks arise at the quartz-quartz and quartz-feldspar grain boundaries. The microfracture zone is composed of the main crack and intersecting branch cracks [33, 34]. Under the coupling effect of high temperature and stress, macroscopic cracks are formed, which led to the rapid deterioration of the macroscopic mechanical properties of granite.

3.3. Stress-Strain Curve. The typical stress–strain curves obtained from the real-time high-temperature uniaxial compression tests are shown in Figure 4. Figure 4 also shows that the stress-strain curves of the granite uniaxial compression test under real-time high temperature and different loading rates undergo the compaction stage, the linear elastic stage, the yield stage, and the failure stage [35]. In the initial compaction stage, the curve shows a "downward concave" nonlinear increase under the action of low load, and the microcracks in the granite gradually close under the action of pressure [36, 37]. As the temperature increases, the longer the compaction stage of the stress-strain curve [38–40]. In the linear elastic stage of the stress-strain curve, the microcracks expand stably, and the slope of the curve decreases with the increase of temperature. In granite from the yield phase of the curve to the failure phase of the curve, the granite changes from elastic deformation to plastic deformation with the increase of axial pressure, and the internal fissure expands continuously [41, 42]. In the failure stage, the stress-strain curves display the granite to reach the peak stress and then the stress suddenly decreases. Cracks develop rapidly, forming a macroscopic fracture surface, and the internal structure is destroyed and completely losing the bearing capacity. Between 25 and 500°C, the stress-strain curve shows that the failure mode of the granite is abrupt instability. Granite has typical brittle failure characteristics. The temperature increases from 600 to 700°C, and the plastic properties of granite increases, whereas the brittle properties decrease with increase in temperature. The stress-strain curves have obvious ductile deformation characteristics. For the granite sample, the strain variation increases from the yield point to peak pressure, and the time for the growth of internal cracks to breakdown gets longer. Figure 4 also shows that the process from the yield point to the peak strength is accompanied by an obvious nonlinear behavior. This is due to the high temperature causing the gradual transformation of quartz and feldspar in granite from brittle microcracks to a wider fragmented flow zone. The failure mode of granite becomes from brittle failure to ductile failure and presents the characteristics of semibrittle flow failure [42–44].

3.4. Uniaxial Compressive Strength (UCS). As shown in Figure 5, the UCS of granite shows a variation pattern of increasing and then decreasing with the increase of temperature. The UCS of granite increases significantly with increasing temperature from 25 to 200°C. The enhancement of biotite particles is the main reason for the reinforcement in mechanical properties under the effect of high temperature. At the same time, the mineral particles' volume expansion causes intergranular contact compaction, resulting in increased mutual attraction and cohesion between minerals [37, 45]. The UCS decreases continuously with increasing temperature between 300 and 600°C. This is due to the uneven thermal expansion of the mineral particles with different thermal expansion coefficients in granite, leading to the continuous expansion of cracks [32]. As the temperature rises, the cohesion continues to decrease [45]. Furthermore, the loss of adhered water, bound water, and structural water leads to the damage of mineral crystalline structure [46, 47]. At 573°C, the α-type to β-type transition

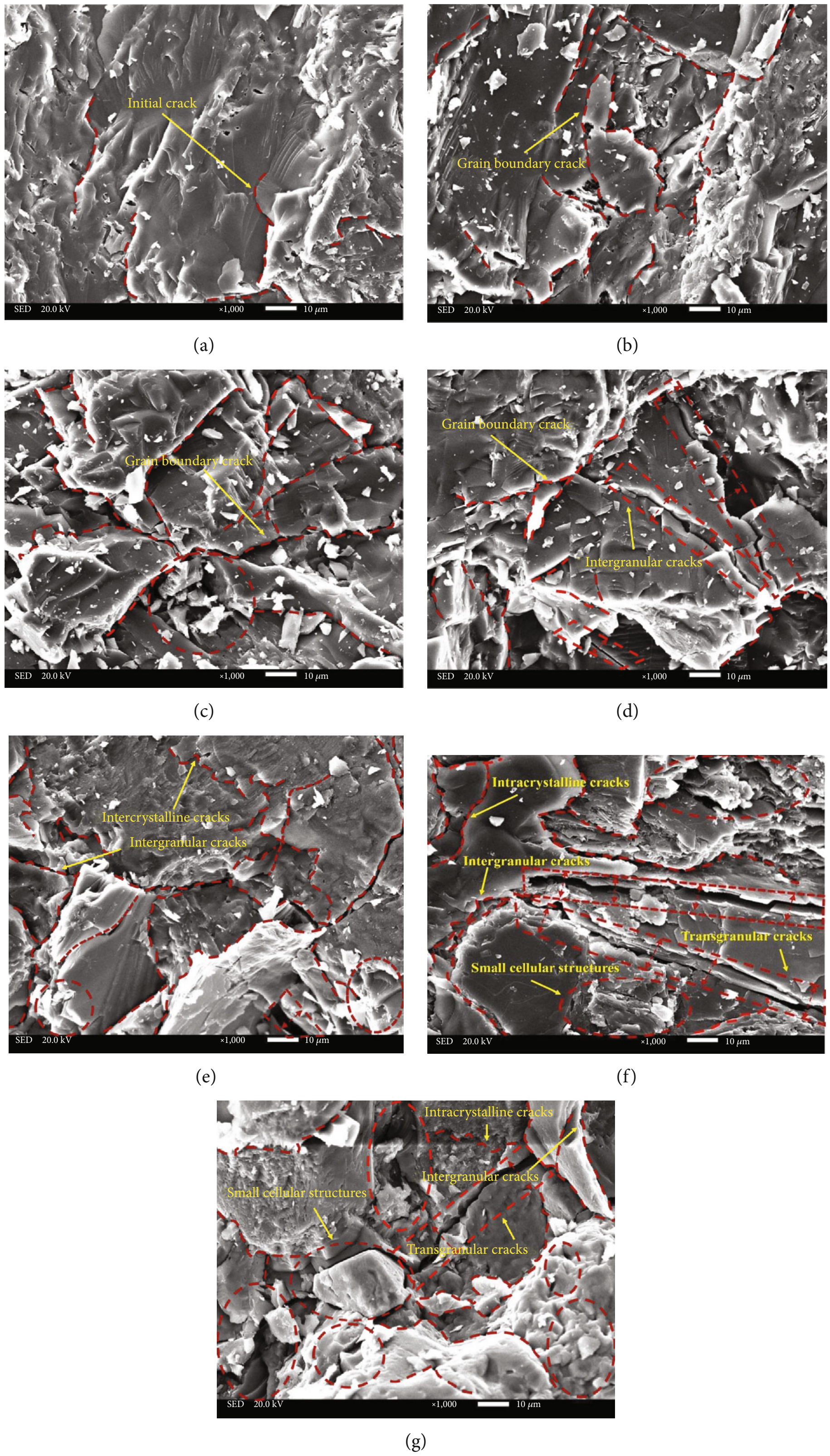

Figure 3: SEM images of the granite fracture surface at different real-time high temperatures: (a) 25°C; (b) 200°C; (c) 300°C; (d) 400°C; (e) 500°C; (f) 600°C; (g) 700°C.

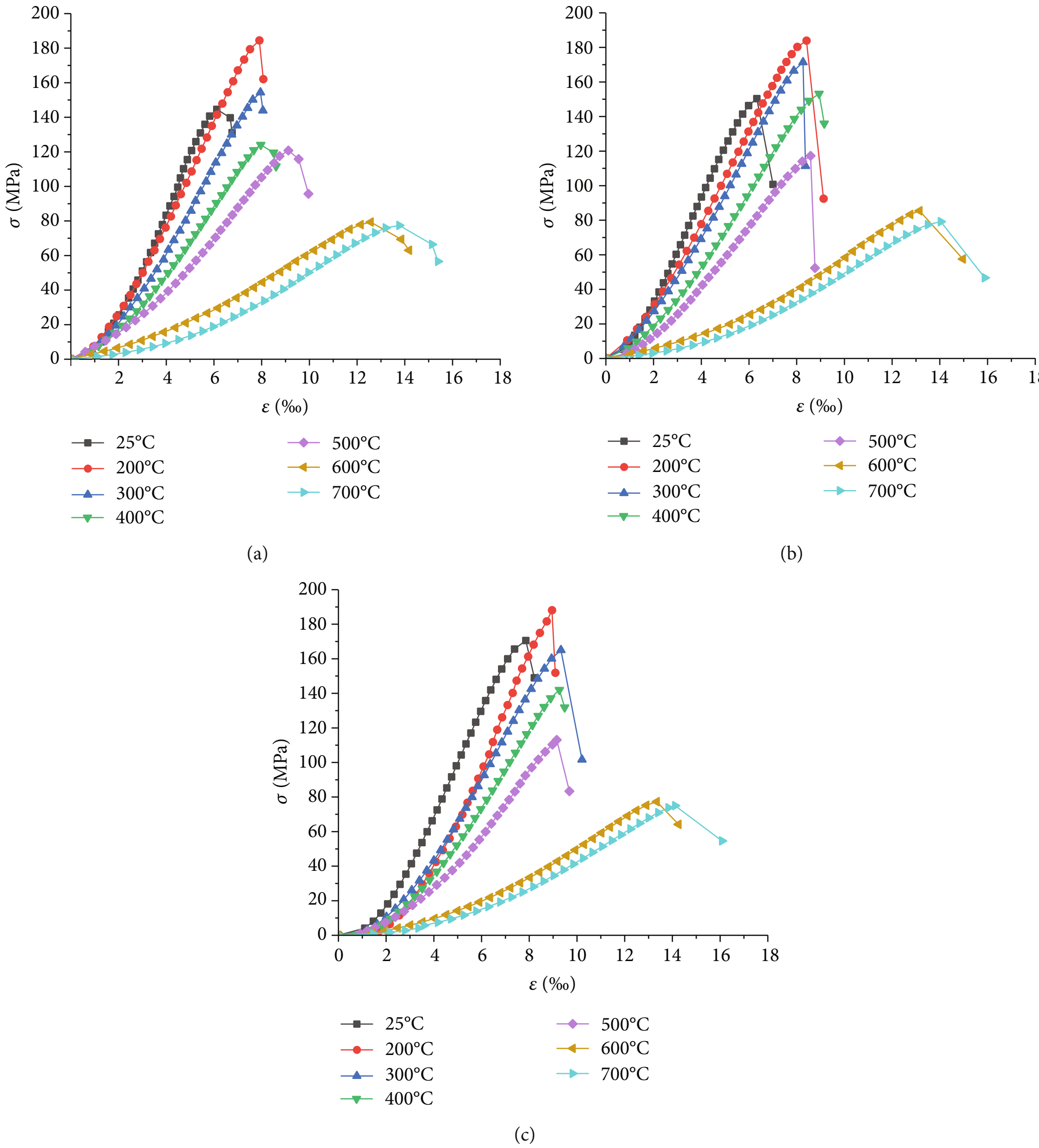

Figure 4: Stress-strain curves of granite under uniaxial compression at real-time high temperature: (a) 0.01 mm/min; (b) 0.1 mm/min; (c) 0.5 mm/min.

in the quartz crystal structure leads to microstructural rearrangement [48]. The extension of the crack in the quartz region increases significantly, forming a good crack network, leading to a rapid increase in structural failure [12, 49, 50]. Above 600°C, the number of cracks remains constant, without forming new cracks, and the length and width of the cracks gradually increase with continuous loading of the axial load [40]. The UCS of granite shows a slight decrease.

As shown in Figure 5, the UCS of granite for three different loading rates (0.01, 0.1, and 0.5 mm/min) shows the similar general trend with increasing temperature. The UCS of granite hardly changes with increasing loading rate, indicating that loading rate has not significantly influenced granite strength [33]. Compared to the other two loading rates (0.01 and 0.1 mm/min), at the loading rate of 0.5 mm/min, the UCS of granite is greater from 25 to 200°C, and the UCS is smaller in the range of 200 to 600°C. Between 600 and 700°C, a similar decreasing trend of UCS is observed for all three loading rates of granite. Under the loading rate of 0.5 mm/min, the UCS increases in the range of 25 to 200°C, which is due to the fact that the distance between individual mineral interfaces decreases more rapidly, resulting in the increase of cohesion. When the temperature exceeds 300°C, the higher the loading rate, the stronger the sliding of the various mineral particles, and the faster the

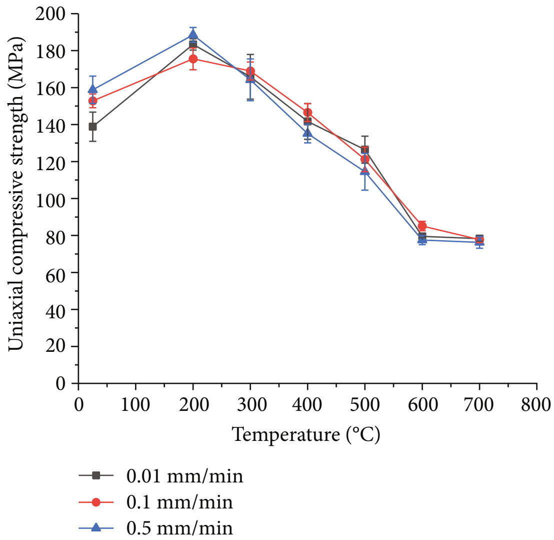

FIGURE 5: Relationship curves between uniaxial compression strength and temperature of granite under real-time high temperature.

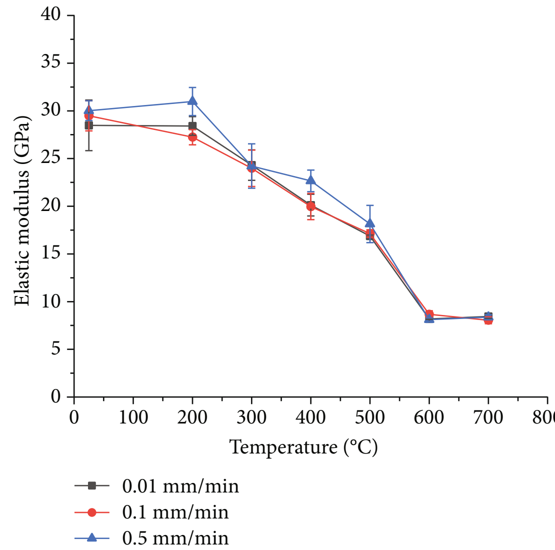

FIGURE 6: Relationship curves between elastic modulus and temperature of granite under real-time high temperature.

crack expansion produces secondary cracks and branches of the crack, accelerating the formation of internal defects [51]. As shown in Figures 3(d)–3(g), the length and width of intracrystalline and intercrystalline cracks in the granite increase greatly as the temperature increases from 400 to 700°C [52]. At 600°C, the amount of quartz has a significant effect on thermally induced microcracks due to the particularity of its thermal expansibility. Microcracks are growing into one other, creating a mesh of microcracks. Between 600 and 700°C, the brittle to plastic transition of granite occurs within this temperature range. Ductile properties dominate granite damage at high temperatures [53]. The increase in the loading rate has no obvious effect on crack propagation [54], and the UCS is almost unchanged.

3.5. Elastic Modulus. In this study, the tangent modulus in the elastic region of the stress–strain curve (approximately 40 to 60% of the peak strength in the experiments) is defined as the elastic modulus [22]. As shown in Figure 6, the elastic modulus of granite under real-time high temperature shows an overall decreasing trend with increasing temperature. In the range of 25 to 200°C, the mineral particles of granite are compacted, the microstructure is slightly damaged, and the elastic modulus hardly changes. The elastic modulus gradually decreases when the temperature is between 300 and 500°C, and the trend of the elastic modulus is similar to the trend of the UCS. When the temperature exceeds 600°C, microcracks are growing into one other, creating a mesh of microcracks, and the porosity continue to increase, resulting in no significant change in elastic modulus [30, 54].

Figure 6 shows that the elastic modulus variation with increasing temperature follows the similar tendency for all three different loading rates (0.01, 0.1, and 0.5 mm/min) of granites. Under the loading rate of 0.5 mm/min, the elastic modulus of granite increases in general. In the range of 25

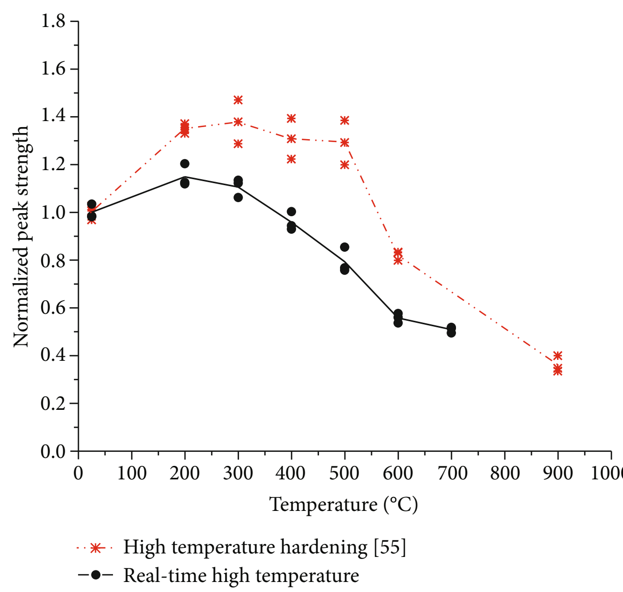

FIGURE 7: Normalized peak strength versus test temperature curves for granite at real-time high temperature and granite after high-temperature quenching.

to 500°C, the cracks in granite dominated by axial load have a lower degree of expansion and fewer numbers than those under low loading rate, resulting in an overall increase of elastic modulus. When the temperature exceeds 600°C, the increase in the loading rate has no effect on the elastic modulus.

4. Further Discussions

4.1. Comparison of Mechanical Properties of Real-Time High-Temperature Granite and Quenched Granite. Figure 7 shows the trend of normalized peak strength versus test temperature curves for granite at real-time high temperature and granite after high-temperature quenching. Between 25 and 200°C, the UCS of granite samples increases significantly with the increase of temperature. Between 200 and 500°C, the UCS decreases greatly with increasing temperature. When the temperature exceeds 600°C, the UCS decreases slightly with increasing temperature. The UCS increases significantly at 200°C. Beyond 300°C, the high temperature leads to uneven thermal expansion of the mineral particles and the thermal cracks gradually expand with increasing temperature [9]. At this time, the thermal crack creation has a significant effect on the UCS of granite samples. Compared with the granite samples after high-temperature quenching, there is no uneven stress field and cooling shrinkage [55]. Due to the propagation of the thermal cracks, the internal microstructure of granite is destroyed, leading to a gradual decrease in the UCS of granite samples within the temperature range of 300 to 500°C. Beyond 600°C, the UCS of granite samples decreases under real-time high-temperature conditions. This can be attributed toward the absence of thermal hardening effect in the granite, which results in a higher degree of crack expansion and a larger number of cracks [56], and the UCS decreases more clearly. After high-temperature quenching, the UCS of granite samples increases from 25 to 500°C. The UCS decreases significantly after the temperature reaches 500°C. Between 25 and 500°C, the strength of the outer surface of quenched granite increases rapidly, while the mineral particles do not cool synchronously with the outer surface of quenched granite. The strong temperature gradient results in high local thermal stress, resulting in the nonuniform local plastic strain field, which inhibits thermal crack propagation. The cohesion of granite samples increases, and the internal shrinkage occurs sharply, which has an obvious thermal hardening effect; the UCS of granite samples increases [15]. Above 500°C, a large number of thermal cracks occur and the cohesion of the material decreases significantly, resulting in a significant decrease in the UCS of granite samples.

Figure 8 shows the trend of normalized elastic modulus versus test temperature curves for granite at real-time high temperature and granite after high-temperature quenching. When the temperature is between 25 and 500°C, the elastic modulus of granite samples decreases greatly with increasing temperature. When the temperature reaches 500°C, the elastic modulus of granite samples decreases slightly under real-time high-temperature condition. The degree of propagation of cracks in granite under real-time high-temperature loading increases with increasing temperature, resulting in the destruction of microstructure and the decrease of elastic modulus. Compared with the granite sample after high-temperature quenching, there is no strong temperature gradient in the sample to inhibit the propagation of thermal crack [19]. The elastic modulus of granite samples after high-temperature quenching is similar to the trend of UCS. It increases rapidly between 25 and 500°C and decreases rapidly when the temperature reaches 500°C.

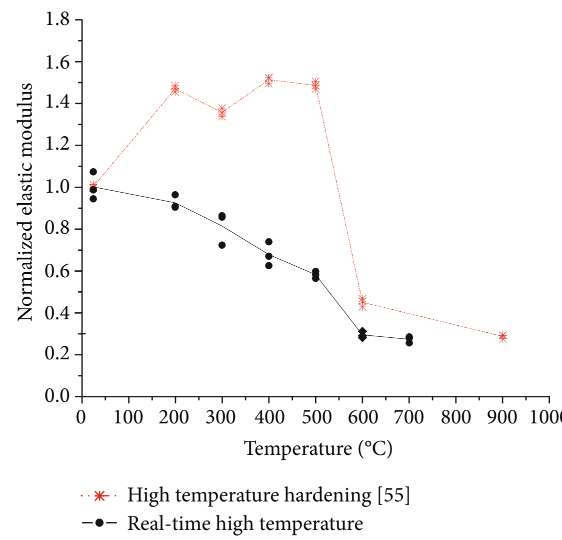

Figure 8: Normalized elastic modulus versus test temperature curves for granite at real-time high temperature and granite after high-temperature quenching.

4.2. Granite Fracturing Mechanism under Real-Time High Temperature. The thermal cracking behavior of granite at high temperature and high pressure is the key to the performance of HDR geothermal reservoir extraction system [23]. During hydraulic fracturing, the fracturing fluid is pumped into the wellbore to increase the pressure at the bottom of the well. With the injection of fracturing fluid, the pressure increases until the rock breaks and produces cracks, as shown in Figure 9(a). At the same time, the injection of fracture fluid causes the solid skeleton to shrink in both transverse and vertical directions. The cooling contraction strain increases over time and remains maximum near the injection well. This phenomenon is similar to the thermal hardening effect of quenched granite [23]. The coupled behavior of real-time high temperature and loading rate is controlled by the characteristic difference between the fluid and the rock matrix. Fluid heat transfer occurs in rock matrix and cracks by convection and conduction. The thermal depletion of the rock matrix is limited to the vicinity of the injection well. As the heat transfer between the fluid and the rock matrix completes, a thermal equilibrium state is formed that causes cracks to continue to grow along the weak interface [57]. Under real-time high-temperature conditions, thermal cracking occurs when the thermal stress exceeds the grain bearing capacity of the granite. Under low-pressure conditions, the difference in the thermal expansion of adjacent minerals is considered to be high-temperature thermal damage to granite. However, under high-temperature and high-pressure conditions, thermal cracking occurs both between adjacent grains (intergranular thermal stress) and within grains (intragranular thermal stress) [52]. According to the microscopic morphology of the granite fracture plane, fractured cracks can extend in a wide range along the weak plane structure, and the weak plane structure can form a natural and efficient water channel. It provides excellent geological conditions for the

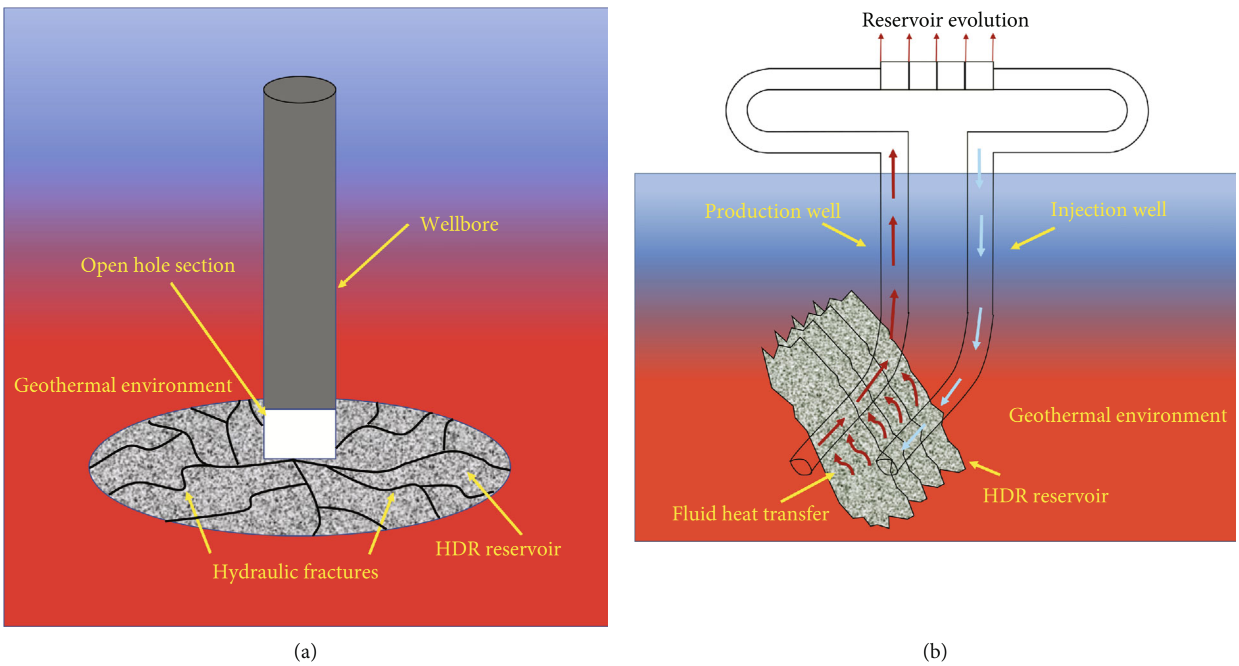

Figure 9: Granite fracturing mechanism under real-time high-temperature conditions [23, 33]: (a) hydraulic fracturing; (b) fluid heat transfer.

construction of large-volume artificial reservoir and effectively forms large-volume artificial geothermal reservoirs, as shown in Figure 9(b). However, previous studies have shown that the pumping rate during hydraulic fracturing has little effect on the formation of cracks in HDR geothermal formations. The main factors that affect the formation of cracks are geological characteristics such as stress and initial cracks [33]. This is consistent with the effect of the loading rate on the physical and mechanical properties of granite at the real-time high temperature.

5. Conclusions

In this study, uniaxial compression tests were carried out on granite at different real-time high-temperature conditions (25, 200, 300, 400, 500, 600, and 700°C) and loading rates (0.01, 0.1, and 0.5 mm/min). The tests showed that granite has significant thermal damage and mechanical behavior at real-time high temperature. It is found that microcracks occur in granite under real-time high temperature, grain boundary cracks gradually evolve into transgranular cracks, and the extension of microcracks is related to mineral composition and microstructure. The macroscopic cracks formed under the coupling effect of high temperature and stress can lead to rapid deterioration of the macroscopic mechanical behavior of granite. From 25 to 200°C, the UCS and elastic modulus of granite increase significantly. When the temperature is between 200 and 500°C, the thermal cracks continue to expand with increasing temperature, and the UCS and elastic modulus of granite gradually decrease with the increase of temperature. The UCS and the elastic modulus have no obvious changes after 500°C. Compared to the other two loading rates (0.01 and 0.1 mm/min), at the loading rate of 0.5 mm/min, from 25 to 200°C, the UCS and elastic modulus of granite are greater. In the range of 200 to 600°C, the UCS is smaller, and the elastic modulus is greater. Between 600 and 700°C, the UCS and elastic modulus of granite with three loading rates are basically similar. However, the tests showed that the UCS and elastic modulus of granite under real-time high temperature are weakly dependent on the loading rate overall. The results of the testing were compared to results obtained for work carried out on quenched granite; it is found that the UCS and elastic modulus are only affected by the thermal crack.

Data Availability

All the data used to support the findings of this study are included within the article.

Conflicts of Interest

The authors have declared that we have no financial and personal relationships with other people or organizations that can inappropriately influence our work.

Acknowledgments

This work was jointly supported by the National Natural Science Foundation of China (51979100) and Shandong Lunan Geological Engineering Exploration Institute Open Fund (LNY2020-Z08).

References

[1] E. Barbier, "Geothermal energy technology and current status: an overview," *Renewable and Sustainable Energy Reviews*, vol. 6, no. 1-2, pp. 3–65, 2002.

[2] K. Breede, K. Dzebisashvili, X. Liu, and G. Falcone, "A systematic review of enhanced (or engineered) geothermal systems: past, present and future," *Geothermal Energy*, vol. 1, no. 1, p. 4, 2013.

[3] A. C. Gringarten, P. A. Witherspoon, and Y. Ohnishi, "Theory of heat extraction from fractured hot dry rock," *Journal of Geophysical Research*, vol. 80, no. 8, pp. 1120–1124, 1975.

[4] W. Q. Zhang, Q. Sun, S. Q. Hao, J. S. Geng, and C. Lv, "Experimental study on the variation of physical and mechanical properties of rock after high temperature treatment," *Applied Thermal Engineering*, vol. 98, no. 8, pp. 1297–1304, 2016.

[5] Z. L. Wang, A. L. He, G. Y. Shi, and G. X. Mei, "Temperature effect on AE energy characteristics and damage mechanical behaviors of granite," *International Journal of Geomechanics*, vol. 18, no. 3, article 04017163, 2018.

[6] Y. L. Chen, S. R. Wang, J. Ni, R. Azzam, and T. M. Fernández-steeger, "An experimental study of the mechanical properties of granite after high temperature exposure based on mineral characteristics," *Engineering Geology*, vol. 220, pp. 234–242, 2017.

[7] S. Liu and J. Y. Xu, "An experimental study on the physico-mechanical properties of two post-high- temperature rocks," *Engineering Geology*, vol. 185, pp. 63–70, 2015.

[8] Z. H. Zhao, H. R. Xu, J. Wang, X. G. Zhao, M. Cai, and Q. Yang, "Auxetic behavior of Beishan granite after thermal treatment: a microcracking perspective," *Engineering Fracture Mechanics*, vol. 231, article 107017, 2020.

[9] Q. Sun, W. Q. Zhang, L. Xue, Z. Z. Zhang, and T. M. Su, "Thermal damage pattern and thresholds of granite," *Environmental Earth Sciences*, vol. 74, no. 3, pp. 2341–2349, 2015.

[10] C. David, B. Menéndez, and M. Darot, "Influence of stress-induced and thermal cracking on physical properties and microstructure of La Peyratte granite," *International Journal of Rock Mechanics and Mining Sciences*, vol. 36, no. 4, pp. 433–448, 1999.

[11] F. E. Heuze, "High-temperature mechanical, physical and thermal properties of granitic rocks– a review," *International Journal of Rock Mechanics and Mining Sciences & Geomechanics Abstracts*, vol. 20, no. 1, pp. 3–10, 1983.

[12] S. Chaki, M. Takarli, and W. P. Agbodjan, "Influence of thermal damage on physical properties of a granite rock: porosity, permeability and ultrasonic wave evolutions," *Construction and Building Materials*, vol. 22, no. 7, pp. 1456–1461, 2008.

[13] W. G. P. Kumari, P. G. Ranjith, M. S. A. Perera, and B. K. Chen, "Experimental investigation of quenching effect on mechanical, microstructural and flow characteristics of reservoir rocks: thermal stimulation method for geothermal energy extraction," *Journal of Petroleum Science and Engineering*, vol. 162, pp. 419–433, 2018.

[14] W. G. P. Kumari, D. M. Beaumont, P. G. Ranjith, M. S. A. Perera, B. L. Avanthi Isaka, and M. Khandelwal, "An experimental study on tensile characteristics of granite rocks exposed to different high-temperature treatments," *Geomechanics and Geophysics for Geo-Energy and Geo-Resources*, vol. 5, no. 1, pp. 47–64, 2019.

[15] F. Zhang, J. J. Zhao, D. W. Hu, F. Skoczylas, and J. F. Shao, "Laboratory investigation on physical and mechanical properties of granite after heating and water-cooling treatment," *Rock Mechanics and Rock Engineering*, vol. 51, no. 3, pp. 677–694, 2018.

[16] L. Weng, Z. J. Wu, and Q. S. Liu, "Influence of heating/cooling cycles on the micro/macrocracking characteristics of Rucheng granite under unconfined compression," *Bulletin of Engineering Geology and the Environment*, vol. 79, no. 6, 2020.

[17] B. Q. Li, B. Gonçalves da Silva, and H. Einstein, "Laboratory hydraulic fracturing of granite: acoustic emission observations and interpretation," *Engineering Fracture Mechanics*, vol. 209, pp. 200–220, 2019.

[18] B. L. Avanthi Isaka, P. G. Ranjith, T. D. Rathnaweera, M. S. A. Perera, and V. R. S. De Silva, "Quantification of thermally-induced microcracks in granite using X-ray CT imaging and analysis," *Geothermics*, vol. 81, pp. 152–167, 2019.

[19] S. S. Shao, P. L. P. Wasantha, P. G. Ranjith, and B. K. Chen, "Effect of cooling rate on the mechanical behavior of heated Strathbogie granite with different grain sizes," *International Journal Rock Mechanics and Mining Sciences*, vol. 70, pp. 381–387, 2014.

[20] S. Q. Yang, P. G. Ranjith, H. W. Jing, W. L. Tian, and Y. Ju, "An experimental investigation on thermal damage and failure mechanical behavior of granite after exposure to different high temperature treatments," *Geothermics*, vol. 65, pp. 180–197, 2017.

[21] P. K. Gautama, A. K. Verma, T. N. Singh, W. Hu, and K. H. Singh, "Experimental investigations on the thermal properties of Jalore granitic rocks for nuclear waste repository," *Thermochimica Acta*, vol. 681, article 178381, 2019.

[22] B. Gu, Z. Wan, Y. Zhang, Y. Ma, and X. B. Xu, "Influence of real-time heating on mechanical behaviours of rocks," *Advances in Civil Engineering*, vol. 2020, Article ID 8879922, 10 pages, 2020.

[23] Y. S. Zhao, Z. J. Feng, Y. Zhao, and Z. J. Wan, "Experimental investigation on thermal cracking, permeability under HTHP and application for geothermal mining of HDR," *Energy*, vol. 132, pp. 305–314, 2017.

[24] W. T. Yin, Z. J. Feng, and Y. S. Zhao, "Effect of grain size on the mechanical behaviour of granite under high temperature and triaxial stresses," *Rock Mechanics and Rock Engineering*, vol. 54, no. 2, pp. 745–758, 2021.

[25] P. G. Ranjith, R. V. Daniel, B. J. Chen, and M. S. A. Perera, "Transformation plasticity and the effect of temperature on the mechanical behaviour of Hawkesbury sandstone at atmospheric pressure," *Engineering Geology*, vol. 151, pp. 120–127, 2012.

[26] J. A. Franklin, U. W. Vogler, J. Szlavin, and J. M. Edmond, "Suggested methods for determining water content, porosity, density, absorption and related properties and swelling and slake-durability index properties : part 2: suggested methods for determining swelling and slake-durability index properties," *International Journal of Rock Mechanics and Mining Sciences & Geomechanics Abstracts*, vol. 16, no. 2, pp. 151–156, 1979.

[27] J. Liu, E. Y. Wang, D. Z. Song, S. H. Wang, and Y. Niu, "Effect of rock strength on failure mode and mechanical behavior of composite samples," *Arabian Journal of Geosciences*, vol. 8, no. 7, pp. 4527–4539, 2014.

[28] Y. Li, D. Huang, and X. A. Li, "Strain rate dependency of coarse crystal marble under uniaxial compression: strength, deformation and strain energy," *Rock Mechanics and Rock Engineering*, vol. 47, no. 4, pp. 1153–1164, 2013.

[29] M. Hajpal and A. Torok, "Mineralogical and colour changes of quartz sandstones by heat," *Environmental Geology*, vol. 46, no. 3-4, pp. 311–322, 2004.

[30] Z. H. Li, L. N. Y. Wong, and C. I. Teh, "Low cost colorimetry for assessment of fire damage in rock," *Engineering Geology*, vol. 228, pp. 50–60, 2017.

[31] V. G. Ruiz de Argandoña, L. Calleja, and M. Montoto, "Determinacion experimental del umbral de microfisuracion termica de la "roca matriz" o "intact rock"," *Trabajos de geología*, vol. 15, pp. 299–306, 2020.

[32] M. H. B. Nasseri, B. S. A. Tatone, G. Grasselli, and R. P. Young, "Fracture toughness and fracture roughness interrelationship in thermally treated westerly granite," *Pure Applied Geophysics*, vol. 166, no. 5-7, pp. 801–822, 2009.

[33] Z. Zhou, Y. Jin, Y. J. Zeng et al., "Investigation on fracture creation in hot dry rock geothermal formations of China during hydraulic fracturing," *Renewable Energy*, vol. 153, pp. 301–313, 2020.

[34] X. P. Zhou and X. Q. Zhang, "The 3D numerical simulation of damage localization of rocks using general particle dynamics," *Engineering Geology*, vol. 224, pp. 29–42, 2017.

[35] Z. N. Zhu, H. Tian, T. Kempka, G. S. Jiang, B. Dou, and G. Mei, "Mechanical behaviors of granite after thermal treatment under loading and unloading conditions," *Natural Resources Research*, vol. 30, no. 3, pp. 2733–2752, 2021.

[36] Y. J. Zong, L. J. Han, J. J. Wei, and S. Y. Wen, "Mechanical and damage evolution properties of sandstone under triaxial compression," *International Journal of Mining Science and Technology*, vol. 26, no. 4, pp. 601–607, 2016.

[37] R. D. Dwivedi, R. K. Goel, V. V. R. Prasad, and A. Sinha, "Thermo-mechanical properties of Indian and other granites," *International Journal Rock Mechanics and Mining Sciences*, vol. 45, no. 3, pp. 303–315, 2008.

[38] J. B. Walsh, "The effect of cracks on the compressibility of rock," *Journal of Geophysical Research*, vol. 70, no. 2, pp. 381–389, 1965.

[39] E. C. David, N. Brantut, A. Schubnel, and R. W. Zimmerman, "Sliding crack model for nonlinearity and hysteresis in the uniaxial stress- strain curve of rock," *International Journal Rock Mechanics and Mining Sciences*, vol. 52, pp. 9–17, 2012.

[40] L. Griffiths, M. J. Heap, P. Baud, and J. Schmittbuhl, "Quantification of microcrack characteristics and implications for stiffness and strength of granite," *International Journal for Numerical and Analytical Methods in Geomechanics*, vol. 100, pp. 138–150, 2017.

[41] F. Zhang, D. W. Hu, S. Y. Xie, and J. F. Shao, "Influences of temperature and water content on mechanical property of argillite," *European Journal Environmental and Civil Engineering*, vol. 18, no. 2, pp. 173–189, 2014.

[42] X. L. Xu, Z. X. Kang, M. Ji, W. X. Ge, and J. Chen, "Research of microcosmic mechanism of brittle-plastic transition for granite under high temperature," *Procedia Earth and Planetary Science*, vol. 1, no. 1, pp. 432–437, 2009.

[43] E. H. Rutter and K. H. Brodie, "Mechanistic interactions between deformation and metamorphism," *Geological Journal*, vol. 30, no. 3-4, pp. 227–240, 1995.

[44] J. Tullis and R. A. Yund, "Experimental deformation of dry westerly granite," *Journal of Geophysical Research*, vol. 82, no. 36, pp. 5705–5718, 1977.

[45] X. Ma, G. L. Wang, D. W. Hu, Y. G. Liu, H. Zhou, and F. Liu, "Mechanical properties of granite under real-time high temperature and three- dimensional stress," *International Journal Rock Mechanics and Mining Sciences*, vol. 136, article 104521, 2020.

[46] M. Nicco, E. A. Holley, P. Hartlieb, and K. Pfaff, "Textural and mineralogical controls on microwave-induced cracking in granites," *Rock Mechanics and Rock Engineering*, vol. 53, no. 10, pp. 4745–4765, 2020.

[47] K. Burlinson, "An instrument for fluid inclusion decrepitometry and examples of its application," *Rock Mechanics and Rock Engineering*, vol. 111, no. 3, pp. 267–278, 1988.

[48] B. J. Skinner, "Section 6: thermal expansion," in *Handbook of Physical Constants—Revised Edition*, pp. 75–96, The Geological Society of America Memoir, 1966.

[49] P. W. J. Glover, P. Baud, M. Darot et al., "A α/β phase transition in quartz monitored using acoustic emissions," *Geophysical Journal International*, vol. 120, no. 3, pp. 775–782, 1995.

[50] L. F. Fan, J. W. Gao, Z. J. Wu, S. Q. Yang, and G. W. Ma, "An investigation of thermal effects on micro-properties of granite by X-ray CT technique," *Applied Thermal Engineering*, vol. 140, pp. 505–519, 2018.

[51] J. Y. Wu, M. M. Feng, G. S. Han, B. Y. Yao, and X. Y. Ni, "Loading rate and confining pressure effect on dilatancy, acoustic emission, and failure characteristics of fissured rock with two pre-existing flaws," *Comptes Rendus Mecanique*, vol. 347, no. 1, pp. 62–89, 2019.

[52] X. P. Zhou, G. Q. Li, and H. C. Ma, "Real-time experiment investigations on the coupled thermomechanical and cracking behaviors in granite containing three pre-existing fissures," *Engineering Fracture Mechanics*, vol. 224, article 106797, 2019.

[53] S. S. Shao, P. G. Ranjith, P. L. P. Wasantha, and B. K. Chen, "Experimental and numerical studies on the mechanical behaviour of Australian Strathbogie granite at high temperatures: an application to geothermal energy," *Geothermics*, vol. 54, pp. 96–108, 2015.

[54] H. F. Wang, B. P. Bonner, S. R. Carlson, B. J. Kowallis, and H. C. Heard, "Thermal stress cracking in granite," *Journal of Geophysical Research*, vol. 94, no. B2, p. 1745, 1989.

[55] F. Zhang, Y. H. Zhang, Y. Y. Dong, D. W. Hu, and J. F. Shao, "Influence of cooling rate on thermal degradation of physical and mechanical properties of granite," *International Journal of Rock Mechanics and Mining Sciences*, vol. 129, article 104285, 2020.

[56] F. Zhang, Y. H. Zhang, D. W. Hu, and J. F. Shao, "Modification of poroelastic properties in granite by heating–cooling treatment," *Acta Geotechnica*, vol. 16, no. 7, pp. 2165–2173, 2021.

[57] R. Gelet, B. Loret, and N. Khalili, "Thermal recovery from a fractured medium in local thermal non-equilibrium," *International Journal for Numerical and Analytical Methods in Geomechanics*, vol. 37, no. 15, pp. 2471–2501, 2012.

Hindawi
Geofluids
Volume 2022, Article ID 7885556, 11 pages
https://doi.org/10.1155/2022/7885556

Research Article

Simulation Study of the Velocity Profile and Deflection Rate of Non-Newtonian Fluids in the Bend Part of the Pipe

Defeng Wang,[1] **Zhanbo Cheng**,[2] **Qingwen Shi**,[3] **Jinhai Zhao**,[4] **and Helmut Mischo**[1]

[1]*Institute of Mining and Special Civil Engineering, Technical University of Bergakademie Freiberg, Freiberg, 09599 Dresden, Germany*
[2]*School of Engineering, University of Warwick, Coventry CV47AL, UK*
[3]*West Virginia University, Morgantown 26505, USA*
[4]*College of Energy and Mining Engineering, Shandong University of Science and Technology, Huangdao District, 266590 Qingdao, China*

Correspondence should be addressed to Helmut Mischo; helmut.mischo@mabb.tu-freiberg.de

Received 30 October 2021; Accepted 16 April 2022; Published 12 May 2022

Academic Editor: Basim Abu-Jdayil

As resource extraction moves deeper underground, backfill mining has received a lot of attention from the industry as a very promising mining method that can provide a safe workplace for workers. However, the safe and efficient transport of fill slurry through pipelines still needs more exploration, especially in the bend section. In order to investigate the flow characteristics and velocity evolution of the slurry in the bend section of the pipe, a three-dimensional (3D) pipe model was developed using the computational fluid dynamics software Fluent, and nine sets of two-factor, three-level simulations were performed. Furthermore, a single-factor analysis was presented to investigate the effects of the two main influencing factors on the shifting of the maximum velocity of the slurry towards the distal side in the bend section, respectively. Then, the response surface analysis method was applied to the two-factor analysis of the maximum velocity shift and the weights of the two influencing factors were specified.

1. Introduction

Some of the world's biggest mining operations are currently at the stage of deep mining. For instance, the mining depth of coal resources has reached 1,500 m, the respective depth for the exploitation of geothermal resources has exceeded 3,000 m, and the mining depth of nonferrous metals has reached 4,350 m, while the exploitation of oil and gas resources has reached an astonishing depth of 7,500 m [1]. Based on forecasts made for the next ten to fifteen years, 50% of iron ore resources, 33% of nonferrous metal or mineral resources, and 53% of coal resources will be exploited at a mining depth of 1,000 m and below [2]. However, after the resource is mined out at such depths, significant geotechnical issues may increase. The vertical original rock stress caused by gravity and the tectonic stress generated by the addressed tectonic movement are basically exceeding the compressive level of the rock mass and the stress concentration level due to excavation, especially when large-scale mining activities take place. According to results of stress measurements in deep mining operations located in South Africa, at a depth ranging from 1 to 5 km, the ground stress can range from 50 to 135 MPa [3]. Other than that, according to surveys, in China alone, there are 1,600 coal gangue dumping fields, with a total volume of 4.5 billion tons, occupying a wide surface area [4].

The backfill mining method is a relatively new mining approach that can not only dispose of hazardous solid on the surface but also provide the operators underground a safe working space by supporting the adjacent rock mass or layers [5, 6]. In addition, a case study shows that the surface reclamation rate after filling and mining is up to 37.6% higher than that of other mining methods [7].

Therefore, with the further increase in environmental awareness, backfill mining has received unprecedented attention and many related practices were executed [8–10].

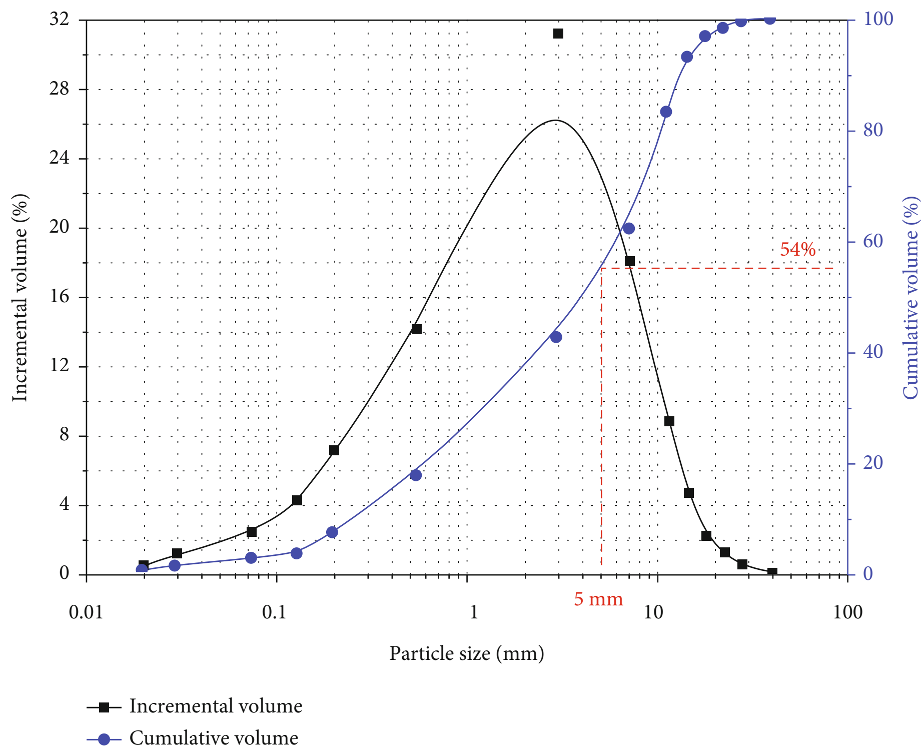

FIGURE 1: Coal gangue particle size distribution.

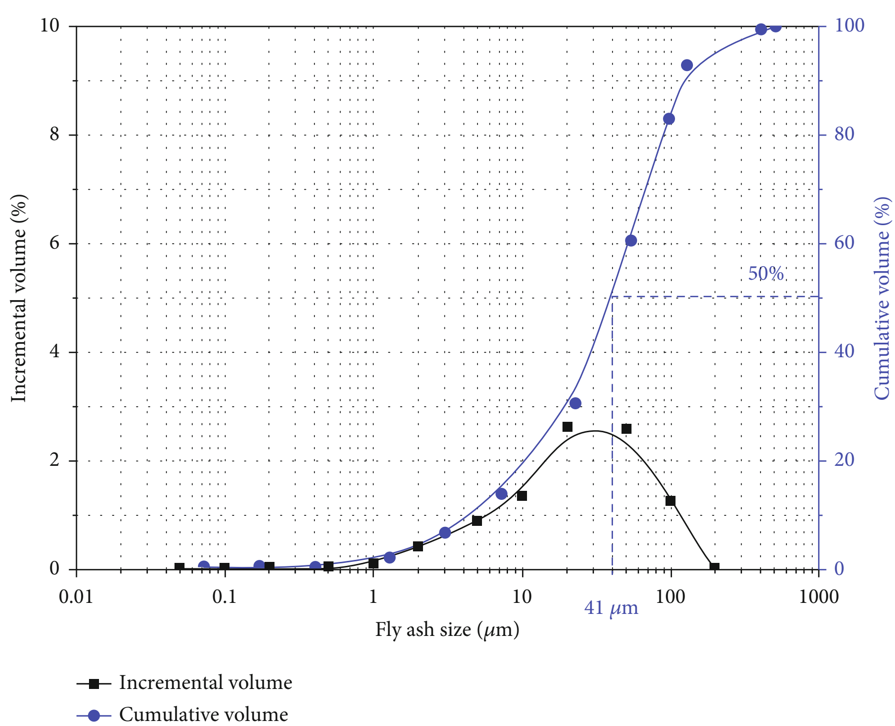

FIGURE 2: Fly ash particle size distribution.

Furthermore, the continuous transport capacity of the pipeline system makes itself a superior transportation method that is being applied broadly [11, 12]. Accordingly, an intensive investigation was conducted in this research field [13]. For instance, Zhang et al. [14] analyzed the factors that affect the backfilling pipeline resistance of the tailing slurry, in order to accurately calculate the pressure loss. In another experimental and modeling study done by Qi et al. [15],

Table 1: Chemical composition of coal gangue and fly ash.

Classification	Composition	Loss	SiO_2	Fe_2O_3	Al_2O_3	CaO	MgO	TiO_2	Na_2O	K_2O
Gangue	Percentage (%)	17.8	51.92	3.87	19.03	1.0	1.18	0.75	0.54	1.47
Fly ash	Percentage (%)	10.33	43.84	27.40	4.01	12.13	1.09	—	—	—

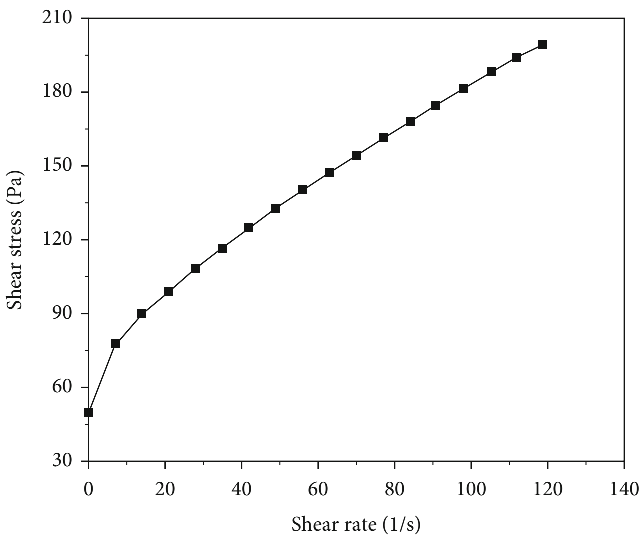

Figure 3: Rheological features of slurry.

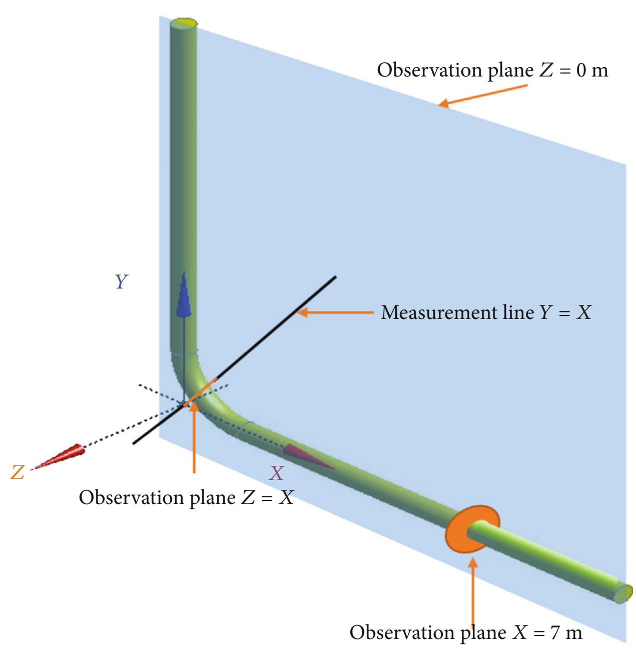

Figure 4: Geometry of the model.

the pressure evolution in pipe flow of cemented backfill is investigated. Liu et al. [16] compared experimental and simulation data in an effort to study the pipe flow characteristics of the cemented paste backfill slurry considering hydration effects.

In addition to the experimental study of the flow characteristics of fluids in pipes, many scholars adopted the numerical simulation method to reduce material and time costs [17–21]. In a research paper, Zhang et al. [22] predicted the erosion in a sharp bend geometry by applying a comprehensive CFD-based erosion prediction procedure, while Nuno and his colleagues [23] employed a computational fluid dynamics (CFD) model to analyze the laminar transients in pressurized pipes and proved that the strongest link between the wall shear stress and the axial component of the velocity occurs in the region close to the pipe wall as well as that the time shift between the wall shear stress and the local instantaneous flow acceleration increases significantly as time elapses.

The bend is an indispensable part of all pipeline transportation systems, and it is also the most easily worn or clogged place in the whole pipeline system. Although numerous experimental or simulation studies related to pipeline transportation are being carried out as described above, the velocity study of gangue fly ash high-concentration slurry in the bend part is still very limited. Thus, in this paper, computational fluid dynamics software was employed to reproduce the velocity characteristics of the slurry flowing through the bend part and to analyze how the influencing factors affect the offset of the velocity in the bend section of the pipe.

2. Material and Rheological Properties

The raw coal gangue used in this paper was collected from a coal mine located in Jining city, Shandong province, China. And after two stages of crushing, the processed coal gangue particle size is presented in Figure 1. From this figure, we can see that around 80% of the coal gangue particles are in sizes below 10 mm, and the particles smaller than 5 mm account for 54% of the total.

Fly ash (FA) is a byproduct produced during coal combustion in thermal power plants, with a large specific surface area and high adsorption activity. The particle size distribution of the fly ash being used in this paper is shown in Figure 2. And it is clear from this graph that the median particle diameter is 41 microns.

In addition to the size of the particles of the filling material which can have an influence on the properties of the slurry, the physical properties and chemical composition of the material are also factors that cannot be ignored. Nevertheless, the aforementioned properties of the filling material are not fixed; for example, the type of coal burned in a thermal power plant or even the manner and degree of burning of the coal can cause changes in the compounds of the fly ash particles. Hence, before preparing the filling material, the chemical composition of the particles needs to be specified in combination with an accurate measurement of the particle size distribution.

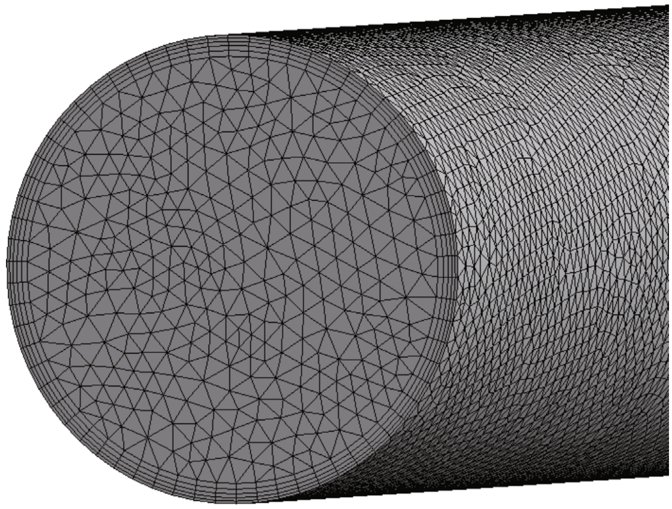

Figure 5: Mesh of the fluid domain.

Table 2: Model setting.

Diameter (m)	Velocity (m/s)	Concentration (%)
	2.0	
0.15	2.5	
	3.0	
	2.0	
0.18	2.5	76
	3.0	
	2.0	
0.21	2.5	
	3.0	

The physical and chemical properties of coal gangue and fly ash are shown in Table 1. The main phase of coal gangue is SiO_2, and the high content of SiO_2 indicates a decent compressive strength of the backfill mass. The content of the CaO in the fly ash accounts for 12.13%, and that defines the fly ash as a C type.

In the present study, fly ash and ordinary Portland cement (OPC) are mixed together as the binding agent in producing the backfill slurry, and the mixing ratio of FA and OPC by weight is 2 to 8, while the crushed coal gangue particles are used as aggregates.

After weighing the raw materials according to the planned proportion, the desired slurry with 76% solid concentration was mixed for 1 min at the speed of 100 r/min, then immediately transferred to rheological tests. The shear stress and shear rate relationships are demonstrated in Figure 3. However, the rheological curve shows a significant difference from that of a Newtonian flow; it is a nonlinear curve and needs critical stress to start the moving of the slurry flow. And according to some scholars' research, a suitable rheological model is the foundation that can achieve accurate prediction of flow characteristics [24–26]. Therefore, in this present paper, the Herschel-Bulkley model is adopted based on previous research studies [27–31].

3. Simulation Model

In order to reduplicate the flow characteristics of the CGFA slurry at the bend section of the pipeline, a 3D numerical model was developed as plotted in Figure 4. This model consists of three main parts (vertical section, bend section, and horizontal section), and the vertical section and the horizontal section were all set to be 10 m to ensure that a fully developed and stable slurry flow can be formed before or after passing through the bend section. The radius of the bend is 0.5 m. To facilitate the collection of fluid velocity information in the subsequent simulation experiments, a measurement line $Y = X$ was set up in the bend section. An observation plane at the measurement line position, as well as at the$X = 7$ mand$Z = 0$ mpositions, was set up.

An appropriate discretization is a foundation for the subsequent simulation; therefore, it is vital to have a fine mesh for the targeted computational domain [32]. There are three main types of adaptive mesh generation approaches that are most commonly used in engineering applications: the triangulation method [33], the advancing front method [34], and the quadtree/octree method [35, 36]. Among these three types of methods, the triangulation method is automatic, robust, and easy to control mesh density. When the triangulation method is applied, the computation convergence can be ensured and the meshing results are optimized greatly. For this reason, triangular prisms are used in this paper. The independence of the mesh was proven since simulated pressures no longer exhibit nonnegligible differences when changing the mesh density. Moreover, considering the more complex flow conditions of the boundary layer fluid, five inflation layers were deployed to capture the boundary layer effects accurately (see Figure 5).

In the present paper, we focus on the effect of the slurry transport velocity and pipe diameter on the maximum offset ratio. For that purpose, three-level experiments on the two main factors are performed in the CFD simulation software, and the detailed simulation scheme is presented in Table 2.

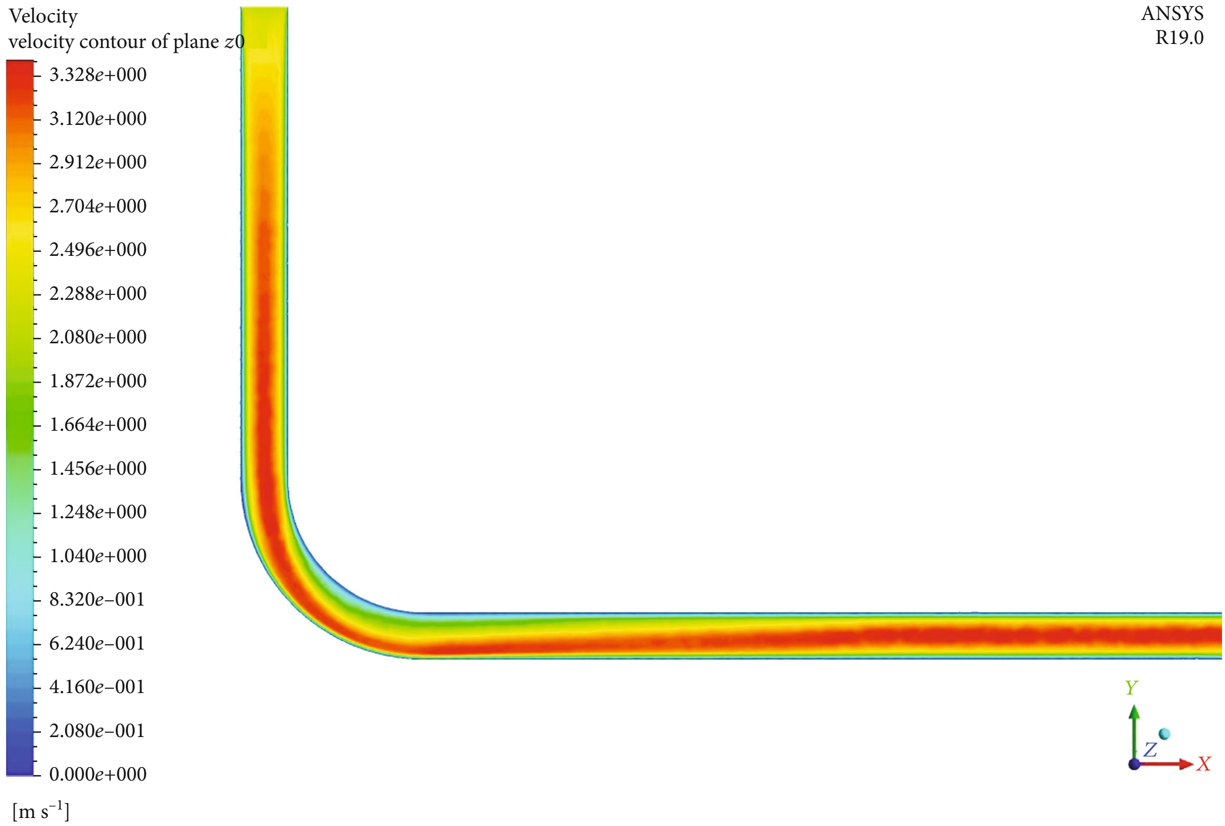

Figure 6: Velocity contour of the observation plane $Z = 0$ m.

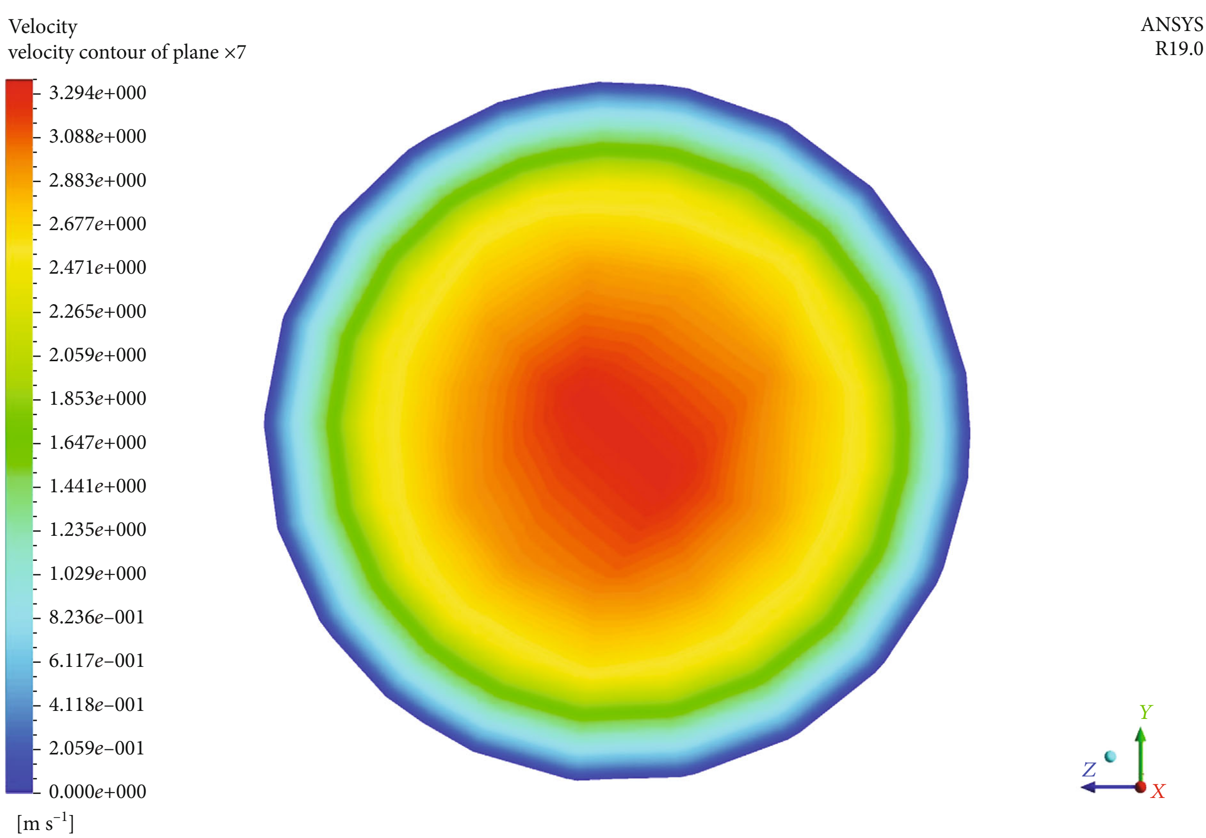

Figure 7: Velocity contour of the observation plane $X = 7$ m.

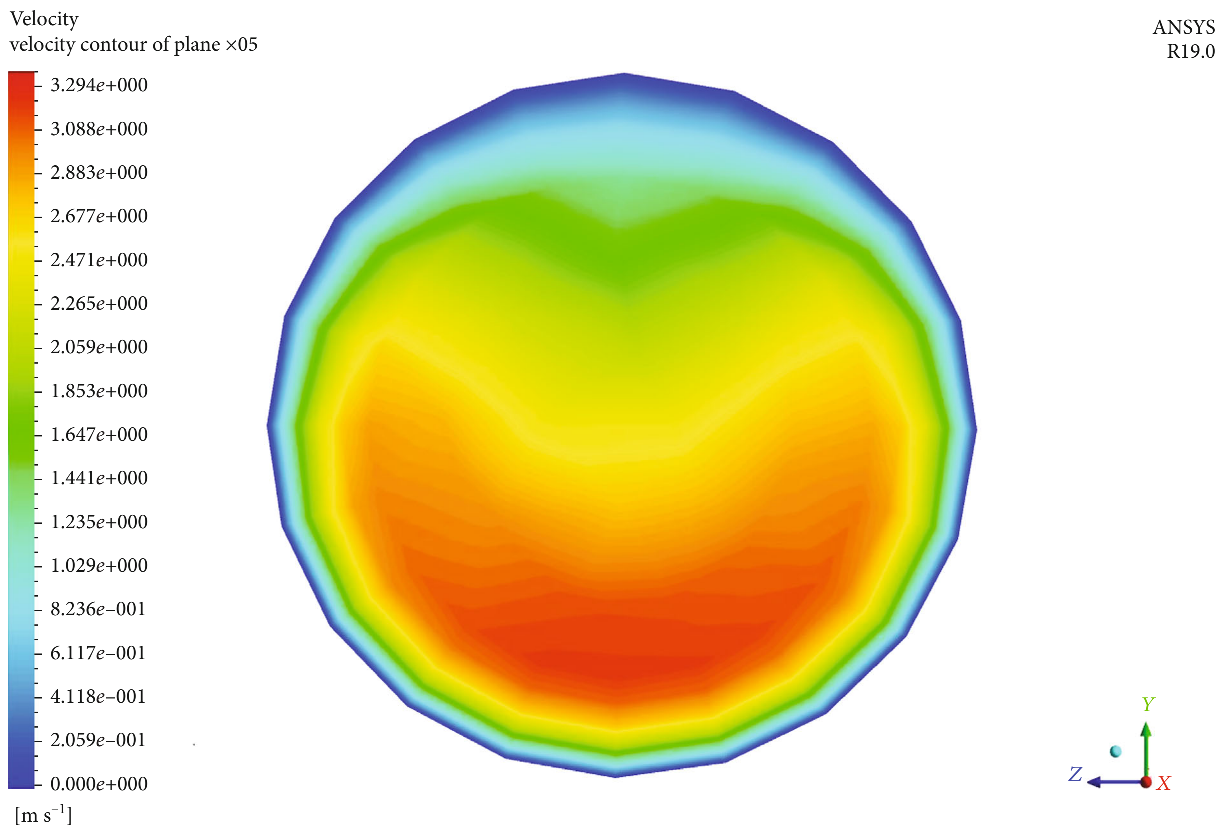

FIGURE 8: Velocity contour of the observation plane at the bend.

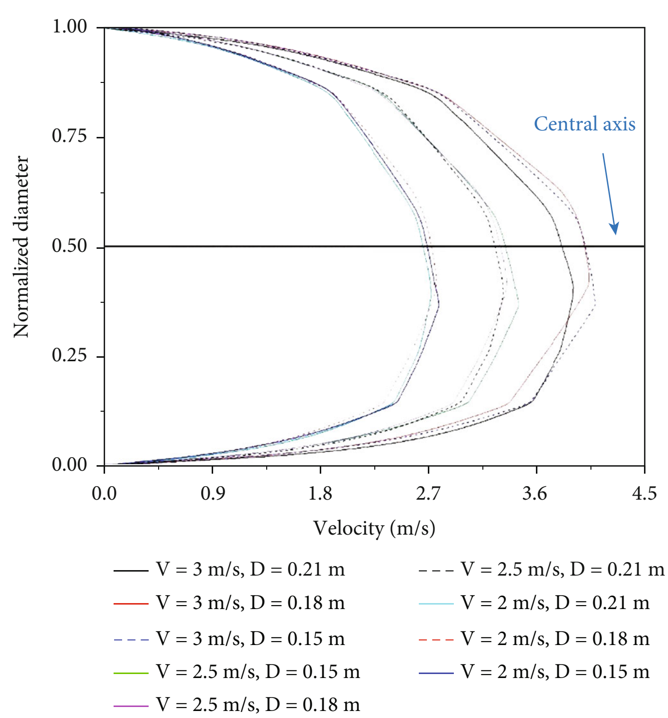

FIGURE 9: Velocity on the measurement line $X = Y$.

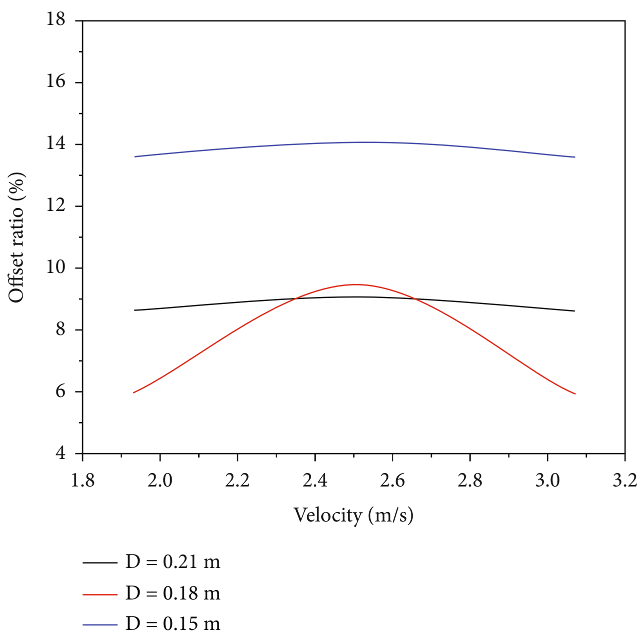

Figure 10: Offset ratio vs. velocity.

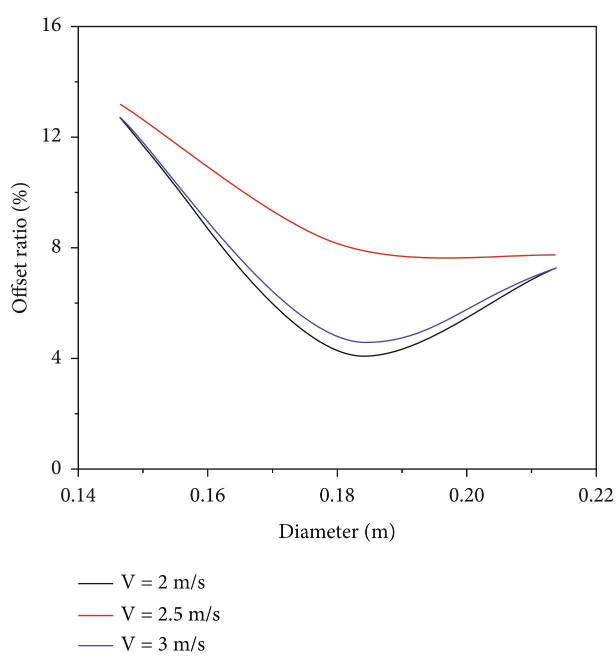

Figure 11: Offset ratio vs. diameter.

4. Results and Discussion

Following the setting of all parameters, the simulations are run, and hereinafter, the influence that the various pipe diameters and slurry flow velocities have on the velocity offset is analyzed. The velocity contours on the observation planes aforementioned are plotted to show the velocity evolution when the slurry flows through the bend section of the pipe. Then, a single-factor analysis and a two-factor combined analysis are used to show how the two main influencing factors change the flow pattern of the slurry.

Table 3: Coded run scheme.

Run	Factor 1: diameter	Factor 2: velocity	Response: offset ratio
1	0.000	1.000	7.5
2	-1.000	0.000	13.8
3	0.000	-1.000	7.1
4	-1.000	-1.000	13.4
5	-1.000	-1.000	13.4
6	-1.000	1.000	13.4
7	1.000	-1.000	9.3
8	0.000	0.000	10
9	1.000	0.000	9.7
10	0.000	0.000	10
11	0.000	0.000	10
12	1.000	1.000	9.3
13	0.000	1.000	7.5
14	-1.000	-1.000	13.4
15	1.000	0.000	9.7
16	0.000	0.000	10

Table 4: Fit summary.

Source	Sequential p value	Adjusted R^2	Predicted R^2	
Linear	0.0070	0.4621	0.2643	
2FI	0.7769	0.4213	0.0054	
Quadratic	*<0.0001*	*0.9163*	*0.7622*	*Suggested*
Cubic	0.9600	0.8964	-2.7962	Aliased

Since the distribution of velocity in the pipe and the tendency of deflection in the bend section are similar under different variables, in this paper, only the velocity contours are shown when the pipe diameter is 0.15 m and the slurry flow velocity is 2.5 m/s as demonstrated in Figures 6–8.

Figure 6 depicts a contour of velocities as the slurry flows through the pipe, from which we can clearly see the distribution of velocities and the large excursions that occur in the bend part of the pipe.

It can be seen that generally in the core section of the slurry flow, the velocity is larger than the margin layers close to the pipe wall. The reason behind this phenomenon is that, unlike in a Newtonian flow, the viscosity of the backfill slurry in the present study is relatively larger, and the slip velocity is positive near the pipe walls, whereas it is negative in the middle portion of the pipe cross-section. The same phenomenon was discussed in a study by Kumar et al. [37], in which they investigated the flow of highly concentrated iron ore slurry through a horizontal pipeline. Therefore, when the backfill slurry flows in a pipe, it forms a plug-like flow that has a special flow pattern with a distinguishing characteristic that the central section of the flow moves faster compared to its ambient flow section [38, 39]. And this velocity disparity is more intuitive and prominent in Figure 7.

Table 5: Coefficients in terms of coded factors.

Factor	Coefficient estimate	df	Standard error	95% CI low	95% CI high	VIF
Intercept	9.52	1	0.2953	8.86	10.18	
A: diameter	-2.19	1	0.2387	-2.72	-1.66	1.15
B: velocity	-0.0584	1	0.2387	-0.5903	0.4736	1.15
AB	0.0707	1	0.2983	-0.5940	0.7354	1.16
A^2	2.92	1	0.3568	2.12	3.71	1.13
B^2	-1.49	1	0.3568	-2.29	-0.6997	1.13

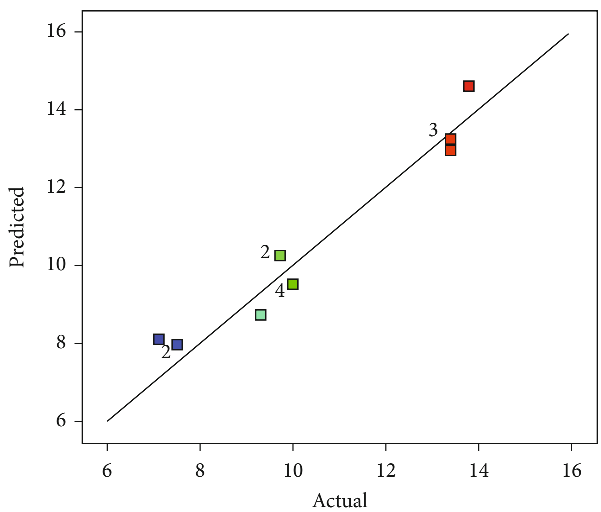

Figure 12: Predicted offset ratio vs. actual offset ratio.

When the slurry flows through the elbow section of the pipeline, the slurry flow direction changes 90°, which denotes from vertical negative to horizontal. During this process, despite the fact that the slurry flow generally follows the original flow pattern attributed to the dominating role that the inertial force plays, the velocity profile changes dramatically. The largest velocity moves from the central region of the slurry flow to the pipe bottom as illustrated in Figure 8. The large difference between Figures 7 and 8 represents a huge change in velocity in the bend section, and an in-depth study of the change in velocity in the bend section is of great significance for the pipeline transport of the slurry.

Figure 9 shows the velocity profile reproduced from the velocity information collected on the measurement line. The diameters were normalized to facilitate the comparison of the velocity offset under different pipe diameters. From this figure, it can be seen that the positions where the highest velocities occur in the slurry are shifted towards the distal side of the bend which is consistent with the velocity contours presented above (see Figure 8). However, the slurry deflections at different combinations of the flow velocity and pipe diameter show a marked difference.

The offset ratio of the maximum velocity position (OROMVP) varies with the conveying velocity, and the changing tendency between different investigated velocity-diameter combinations shows vast variance (see Figure 10). For instance, the OROMVP value of the slurry that flows in a pipe with a 0.15 m diameter is much larger than that of the other two counterparts. When the pipe diameter is 0.21 m or 0.15 m, the OROMVP reveals a gentle change with transport velocity, which implies that the maximum velocity of the slurry occurs at the same position when the slurry passes the bend section no matter what the transport velocity is. However, the OROMVP changes greatly with various flow velocities; when the pipe diameter is 0.18 m, it increases with the slurry conveying velocity until the conveying velocity reaches 2.5 m/s, and then the OROMVP decreases with the further increase of conveying speed.

Figure 11 demonstrates the effects of the pipe diameter on the OROMVP, and for all the three investigated groups, the largest OROMVP appears when the pipe diameter is 0.15 m. In terms of the slurry being transported at 2.5 m/s, the OROMVP decreases with the increasing conveying velocity although the speed of reduction becomes very slow when the pipe diameter exceeds 0.18 m. For the slurry that flows at 2 m/s, when the pipe diameter is in the interval of 0.15 m to 0.18 m, the OROMVP decreases with the rising pipe diameter, while when the pipe diameter is larger than 0.18 m, the OROMVP gradually increases with the increasing pipe diameter. And not only the tendency but also the values of the OROMVP of the slurry with a 3 m/s conveying velocity show a minor difference from that of the slurry with a 2 m/s conveying velocity.

A comparative analysis of Figures 10 and 11 shows that the 0.18 m diameter is special since, at this point, the OROMVP exhibits characteristics that clearly differ from other counterparts. Perhaps, designing the conveying system with a pipe diameter of about 0.18 meters can make the slurry velocity more stable when slurry flows through the bend section.

From the analysis in the previous section, it is clear that both the slurry transport velocity and the pipe diameter have a significant effect on the OROMVP, but it is not well explained how these two influences work together and what the respective weights of their contributions to the offset are. Therefore, the following parts will deal with this issue.

In order to determine the weights of the flow velocity and pipe diameter on OROMVP in the bend section, the response surface methodology (RSM) was adopted and run in a professional software program named Design-Expert (Stat-Ease Inc.). Response surface methodology [40] is a collection of mathematical and statistical techniques that can analyze all the dominant factors and how they influence

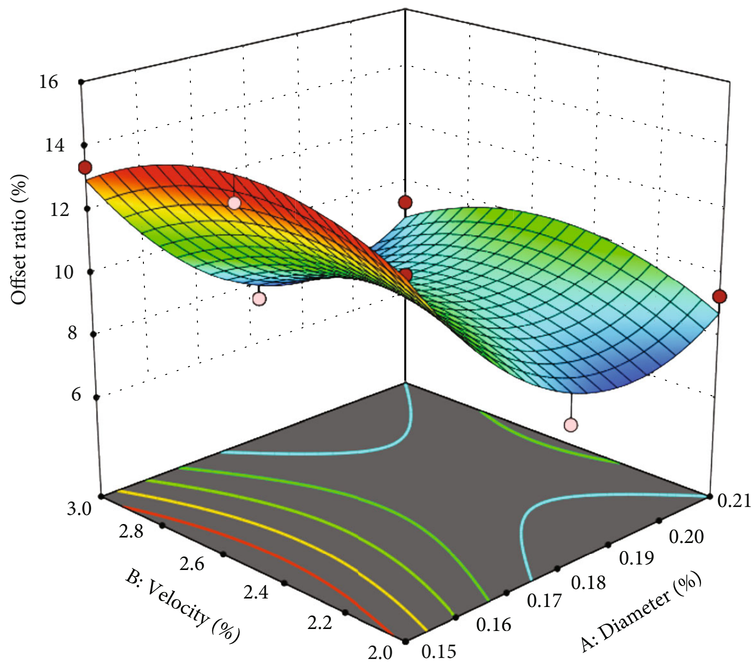

Figure 13: Response surface.

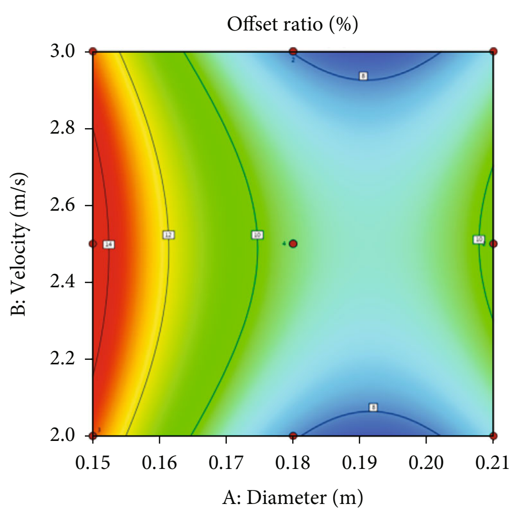

Figure 14: Two-dimensional projection of the response surface.

the dependent variables [41]. A central composite design with two independent variables (namely, the pipe diameter and slurry velocity) at three levels was performed by applying the Design-Expert 12.

The historical data RSM design and the response for this study can be found in Table 3. After 16 runs in total, the fit summary of different fitting models' accuracy and practicality is listed in Table 4, from which the most suitable model was automatically presented (denotes quadratic model in this present paper). And the adjusted R^2 and predicted R^2 indicate that the selected model has excellent accuracy.

The coefficient estimate represents the expected change in response per unit change in the factor value when all remaining factors are held constant while the intercept in an orthogonal design is the overall average response of all the runs. The coefficients are adjustments around that average based on the factor settings, and the coefficients of all the independent variables are documented in Table 5. Based on the value of the estimated coefficient, the weights of each independent variable on the response variable were determined and the pipe diameter has a much more notable influence on the OROMVP than flow velocity. And the most influencing term is A^2, namely, the diameter-square.

The accuracy of the regression model was also ascertained since the experimental data and the model response are evenly distributed around the diagonal line in Figure 12. The actual value of the offset ratio represents the measured result for each experimental run while the predicted value is evaluated from the independent variables in the regression model.

In this paper, the three-dimensional plots and the two-dimensional contour depicted in Figures 13 and 14 were studied to investigate the behavior of the OROMVP from the interactions of the two operational variables.

The 3D plot, overall, appears to have a smooth saddle shape showing the effect of the combination of the flow velocity and pipe diameter on the OROMVP. It can be inferred from this figure that the effect of the pipe diameter in adjusting OROMVP at the bend section overwhelms that of the flow velocity as the OROMVP reflects a more pronounced change under the influence of varying the pipe diameter. The minimum OROMVP always occurs at a pipe diameter close to 0.18 m, when the pipe diameter varies from 0.21 m to 0.15 m, regardless of the flow velocity. Correspondingly, among all two-factor combinations of the flow velocity and pipe diameter, the OROMVP of the combination at a flow velocity of 2.5 m/s has been maintained as the largest. In the present paper, among all the investigated flow velocity and diameter combinations, the OROMVP of the 0.15 m diameter and 2.5 m/s flow velocity group ranks the highest. When the pipe diameter is close to 0.19 m and the slurry transport velocity is more than 3 m/s or less than 2 m/s, the optimal OROMVP can be achieved. However, this conclusion was reached only considering the reduction of the OROMVP, and if more factors need to be included, such as filling efficiency or economics, a more comprehensive investigation is required.

5. Conclusion

Given the strong correlation between the velocity offset of the fluid flowing through the bend part and the damage to the bend, this paper focuses on the flow characteristics of the fluid in the bend part. In the present research, rheological parameters of the slurry were acquired by conducting a series of lab tests, and then the computational fluid dynamics simulation was operated to reproduce the fluid flow in the bend section, followed by an analysis of how the two influencing factors affect the OROMVP individually, and investigate how the two independent variables determine the OROMVP in the bend section by the response surface method. The following conclusions can be drawn:

(i) Although both the transport velocity and the pipe diameter have a significant effect on the OROMVP in the bend section, their weights differ significantly; in other words, the variation in the pipe diameter is more determinative

(ii) The critical conveying velocity for the slurry should be around 2.5 m/s since all the investigated samples show that conveying velocities above or below 2.5 m/s lead to a decrease in the OROMVP in the bend section. Therefore, in order to clarify the effect of conveying velocity on the OROMVP, further studies for the extended velocity range need to be conducted

(iii) The 3D response surface demonstrates the good performance of the 0.19 m diameter pipe in reducing the OROMVP of the slurry passing through the bend section. Therefore, under the premise of satisfying the mine filling efficiency, it is recommended to adopt 0.19 m pipes for slurry transportation to reduce damage such as abrasion of the pipe at the bend part

Data Availability

The data used to support the findings of this study are available from the first author upon request.

Conflicts of Interest

The authors declare no conflict of interest.

Acknowledgments

The research work was supported by the China Scholarship Council under Grant 201606430034, the Shandong Province Natural Science Foundation Project under Grant ZR2020QE12, and the National Natural Science Foundation of China under Grant 52104203. Open Access Funding by the Publication Fund of the TU Bergakademie Freiberg.

References

[1] H. P. Xie, F. Gao, and Y. Ju, "Research and development of rock mechanics in deep ground engineering," *Chinese Journal of Rock Mechanics and Engineering*, vol. 34, no. 11, pp. 2161–2178, 2015.

[2] H. P. Xie, "Research framework and anticipated results of deep rock mechanics and mining theory," *Advanced Engineering*, vol. 39, no. 2, p. 3, 2017.

[3] M. C. He, H. P. Xie, S. P. Peng, and Y. D. Jiang, "Study on rock mechanics in deep mining engineering," *Chinese Journal of Rock Mechanics and Engineering*, vol. 24, no. 16, pp. 2803–2813, 2005.

[4] B. N. Hu, "Backfill mining technology and development tendency in China coal mine," *Coal Science and Technology*, vol. 40, no. 11, p. 2, 2012.

[5] N. Sivakugan, R. Veenstra, and N. Naguleswaran, "Underground mine backfilling in Australia using paste fills and hydraulic fills," *International Journal of Geosynthetics and Ground Engineering*, vol. 1, no. 2, p. 18, 2015.

[6] H. A. Jati, N. Monei, G. Barakos, M. Tost, and M. Hitch, "Coal slurry pipelines: a coal transportation method in Kalimantan, Indonesia," *International Journal of Mining, Reclamation and Environment*, vol. 35, no. 9, pp. 638–655, 2021.

[7] Z. Q. Hu, W. Xiao, P. J. Wang, and Y. L. Zhao, "Concurrent mining and reclamation for underground coal mining," *Journal of China Coal Society*, vol. 38, no. 2, p. 301, 2013.

[8] D. J. Béket, L. Li, and P. Yang, "Experimental study of uniaxial compressive strength (UCS) distribution of hydraulic backfill associated with segregation," *Minerals*, vol. 9, no. 3, p. 147, 2019.

[9] H. Xu, D. B. Apel, J. Wang, C. Wei, and Y. Pourrahimian, "Investigation of backfilling step effects on stope stability," *Mining*, vol. 1, no. 2, pp. 155–166, 2021.

[10] D. F. Wang, G. Barakos, Z. Cheng, H. Mischo, and J. Zhao, "Numerical simulation of pressure profile of mining backfill fly-ash slurry in an L-shaped pipe using a validated Herschel-Bulkley model," *Journal of Sustainable Cement-Based Materials*, 2022.

[11] A. Lesmana and M. Hitch, "Heavy media coal hydro-transport in Malinau, Indonesia: a process study," *Journal of Mining and Mineral Engineering*, vol. 3, no. 1, pp. 1–15, 2011.

[12] H. A. Jati, N. Monei, G. Barakos, M. Tost, and M. Hitch, "Coal slurry pipelines: a coal transportation method in Kalimantan Indonesia," *Journal of Mining, Reclamation and Environment*, vol. 35, no. 9, pp. 638–655, 2021.

[13] S. Chandel, V. Seshadri, and S. N. Singh, "Effect of additive on pressure drop and rheological characteristics of fly ash slurry at high concentration," *Particulate Science and Technology*, vol. 27, no. 3, pp. 271–284, 2009.

[14] Q. Zhang, Z. Jiang, S. Wang, Q. Chen, Y. Zhu, and X. Hw, "Pipeline resistance model for the filling slurry transportation

with high concentration and superfine total tailing," *Science & Technology Review*, vol. 32, no. 24, pp. 51–55, 2014.

[15] C. Qi, Q. Chen, A. Fourie, J. Zhao, and Q. Zhang, "Pressure drop in pipe flow of cemented paste backfill: experimental and modeling study," *Powder Technology*, vol. 333, no. 2018, pp. 9–18, 2018.

[16] L. Liu, Z. Fang, C. Qi, B. Zhang, L. Guo, and K. I. I. L. Song, "Numerical study on the pipe flow characteristics of the cemented paste backfill slurry considering hydration effects," *Powder Technology*, vol. 343, pp. 454–464, 2019.

[17] X. Chen, J. Zhou, Q. Chen, X. Shi, and Y. Gou, "CFD simulation of pipeline transport properties of mine tailings three-phase foam slurry backfill," *Minerals*, vol. 7, no. 8, p. 149, 2017.

[18] A. X. Wu, Y. Yang, H. Y. Cheng, S. M. Chen, and Y. Han, "Status and prospects of paste technology in China," *Chinese Journal of Engineering*, vol. 40, no. 5, 525 pages, 2018.

[19] J. Singh, S. Kumar, J. P. Singh, P. Kumar, and S. K. Mohapatra, "CFD modeling of erosion wear in pipe bend for the flow of bottom ash suspension," *Particulate Science and Technology*, vol. 37, no. 3, pp. 275–285, 2019.

[20] S. Lahiri and K. C. Ghanta, "Regime identification of slurry transport in pipelines: a novel modelling approach using ANN & differential evolution," *Chemical Industry and Chemical Engineering Quarterly*, vol. 16, no. 4, pp. 329–343, 2010.

[21] M. Swamy, D. N. Gonzalez, and A. Twerda, "Numerical modelling of the slurry flow in pipelines and prediction of flow regimes," *WIT Transactions on Engineering Sciences*, vol. 89, pp. 311–322, 2015.

[22] J. Zhang, F. Darihaki, and S. A. Shirazi, "A comprehensive CFD-based erosion prediction for sharp bend geometry with examination of grid effect," *Wear*, vol. 430-431, pp. 191–201, 2019.

[23] M. C. Nuno, B. B. Martins, M. Silvia, M. R. Helena, and I. C. Dídia, "Efficient computational fluid dynamics model for transient laminar flow modeling: pressure wave propagation and velocity profile changes," *Journal of Fluids Engineering*, vol. 140, no. 1, 2018.

[24] N. Ratkovich, W. Horn, F. P. Helmus et al., "Activated sludge rheology: a critical review on data collection and modelling," *Water Research*, vol. 47, no. 2, pp. 463–482, 2013.

[25] J. Singh, M. Rudman, H. M. Blackburn, A. Chryss, L. Pullum, and L. J. W. Graham, "The importance of rheology characterization in predicting turbulent pipe flow of generalized Newtonian fluids," *Journal of Non-Newtonian Fluid Mechanics*, vol. 232, pp. 11–21, 2016.

[26] V. Khandelwal, A. Dhiman, and L. Baranyi, "Laminar flow of non-Newtonian shear-thinning fluids in a T-channel," *Computers and Fluids*, vol. 108, pp. 79–91, 2015.

[27] B. Bharathan, M. McGuinness, S. Kuhar, M. Kermani, F. P. Hassani, and A. P. Sasmito, "Pressure loss and friction factor in non-Newtonian mine paste backfill: modelling, loop test and mine field data," *Powder Technology*, vol. 344, no. 15, pp. 443–453, 2019.

[28] N. Gharib, B. Bharathan, L. Amiri, M. McGuinness, F. P. Hassani, and A. P. Sasmito, "Flow characteristics and wear prediction of Herschel-Bulkley non-Newtonian paste backfill in pipe elbows," *The Canadian Journal of Chemical Engineering*, vol. 95, no. 6, pp. 1181–1191, 2017.

[29] D. Mehta, A. Krishnan, T. Radhakrishnan, J. B. van Lier, and F. H. Clemens, "Assessment of numerical methods for estimating the wall shear stress in turbulent Herschel-Bulkley slurries in circular pipes," *Journal of Hydraulic Research*, vol. 59, no. 2, pp. 196–213, 2021.

[30] Y. Huang, W. Zheng, D. Zhang, and Y. Xi, "A modified Herschel–Bulkley model for rheological properties with temperature response characteristics of polysulfonated drilling fluid," *Energy Sources, Part A: Recovery, Utilization, and Environmental Effects*, vol. 42, no. 12, pp. 1464–1475, 2020.

[31] H. Taibi and F. Messelmi, "Effect of yield stress on the behavior of rigid zones during the laminar flow of Herschel-Bulkley fluid," *Alexandria Engineering Journal*, vol. 57, no. 2, pp. 1109–1115, 2018.

[32] L. Sun, G. Q. Zhao, and G. T. Yeh, "Automatic triangular and triangular-prism mesh generation for overland and subsurface water flow simulations," *Physics of Fluids*, vol. 32, no. 5, article 056602, 2020.

[33] L. Sun, G.-T. Yeh, F. P. Lin, and G. Zhao, "Automatic quadrilateral mesh generation and quality improvement techniques for an improved combination method," *Computational Geosciences*, vol. 19, no. 2, pp. 371–388, 2015.

[34] T. D. Blacker and M. B. Stephenson, "Paving: a new approach to automated quadrilateral mesh generation," *International Journal for Numerical Methods in Engineering*, vol. 32, no. 4, pp. 811–847, 1991.

[35] M. Yerry and M. Shephard, "A modified quadtree approach to finite element mesh generation," *IEEE Computer Graphics and Applications*, vol. 3, no. 1, pp. 39–46, 1983.

[36] L. Sun, G. Zhao, and X. Ma, "Quality improvement methods for hexahedral element meshes adaptively generated using grid-based algorithm," *International Journal for Numerical Methods in Engineering*, vol. 89, no. 6, pp. 726–761, 2012.

[37] N. Kumar, G. M. Kumar, and D. R. Kaushal, "Experimental investigations and CFD modeling for flow of highly concentrated iron ore slurry through horizontal pipeline," *Particulate Science and Technology*, vol. 37, no. 2, pp. 232–250, 2019.

[38] F. T. Pinho and J. H. Whitelaw, "Flow of non-Newtonian fluids in a pipe," *Journal of Non-Newtonian Fluid Mechanics*, vol. 34, no. 2, pp. 129–144, 1990.

[39] D. Picchi, A. Ullmann, and N. Brauner, "Modeling of core-annular and plug flows of Newtonian/non-Newtonian shear-thinning fluids in pipes and capillary tubes," *Journal of Multiphase Flow*, vol. 103, no. 1, pp. 43–60, 2018.

[40] I. M. Yusri, A. P. P. Abdul Majeed, R. Mamat, M. F. Ghazali, O. I. Awad, and W. H. Azmi, "A review on the application of response surface method and artificial neural network in engine performance and exhaust emissions characteristics in alternative fuel," *Renewable and Sustainable Energy Reviews*, vol. 90, pp. 665–686, 2018.

[41] K. S. Kazeem, O. A. Akeem, and D. A. Mohammed, "Application of response surface methodology for the modelling and optimization of sand minimum transport condition in pipeline multiphase flow," *Petroleum and Coal*, vol. 60, no. 2, pp. 339–348, 2018.

Hindawi
Geofluids
Volume 2022, Article ID 9032572, 16 pages
https://doi.org/10.1155/2022/9032572

Research Article

Effect of Water on Mechanical Properties of Coal Measures Mudstone Using Nanoindentation

Wenshuai Li,[1] **Bangyou Jiang**,[2] **and Shitan Gu**[2]

[1]*Shandong Key Laboratory of Civil Engineering Disaster Prevention and Mitigation, Shandong University of Science and Technology, Qingdao 266590, China*
[2]*College of Energy and Mining Engineering, Shandong University of Science and Technology, Qingdao 266590, China*

Correspondence should be addressed to Bangyou Jiang; jiangbangyou123@163.com and Shitan Gu; chinasdgst@163.com

Received 15 September 2021; Revised 26 February 2022; Accepted 5 March 2022; Published 6 May 2022

Academic Editor: Andrea Brogi

Mudstone rich in clay minerals exhibits an obvious water-induced weakening effect, and the mechanical properties of mudstone are significantly affected by the groundwater. To investigate the effect of water on mechanical characteristics of mudstone at microscale, a series of uniaxial compression and nanoindentation tests were conducted on mudstone specimens at different moisture contents. Microscale measurements are upscaled to estimate the corresponding magnitudes at the macroscale using the Mori-Tanaka method. The results showed that the indentation modulus varied significantly, from as low as 0.2 GPa to a quite high value of 125 GPa, indicating a strongly heterogeneous distribution of mudstone. The water illustrated a significant effect on the microscale mechanical properties of water-sensitivity minerals like clay minerals. The water-sensitivity minerals occupied the highest proportion of the mudstone and were believed to play an important role in the mechanical properties of mudstone. For water-bearing specimens, the comparison with elastic modulus data obtained from common method indicated similar values as those predicted by homogenization method. The results of this study indicated that nanoindentation technique is a feasible experimental technique to assess the macroscale mechanical properties of rock materials.

1. Introduction

In China, about 60% of identified coal reserves are located at depth of more than 800 m and about 53% at depth below 1000 m [1–3]. The deep roadways are often excavated in sedimentary rocks near the coal seams [4, 5], such as mudstone. For decades, most research has been focused on the mechanical properties of coal measures rocks, including strength, deformation, and failure characteristics [6–10]. Due to the heterogeneity of coal measures rocks, it is thus vital to understand the mechanical characteristics at microscale [11, 12].

Nowadays, nanoindentation is used to investigate the microscale mechanical properties of rocks. Nanoindentation is based on elastic contact theory allowing obtaining the mechanical parameters at microscale, such as indentation modulus and hardness. Oliver and Pharr [13] established an improved method to determine the modulus and hardness from nanoindentation load-depth curves, which has been widely used in rock-like materials [14, 15]. Afterward, many researchers studied the microscale mechanical properties (*e.g.*, deformation, modulus, and hardness) of coal [16–19], shale [20], and cement-based materials [21–24]. Furthermore, Scanning Electron Microscopy (SEM) and Atomic Force Microscope (AFM) were also used to investigate nanoscale detection of the pore distribution and mechanical properties of rock [25, 26]. With large numbers of indents that carried out on the specimen surface, the mechanical properties of material can be obtained exclusively. However, previous studies have mainly focused on the field of oil and gas exploitation (such as shale and coal) or construction materials. By contrast, the microscale mechanical properties of coal measures mudstone are still not fully understood [19].

Furthermore, the mechanical properties of coal measures mudstone do not only depend on mineral components but are significantly affected by the external environment, especially the groundwater [27–30]. Mudstone rich in clay

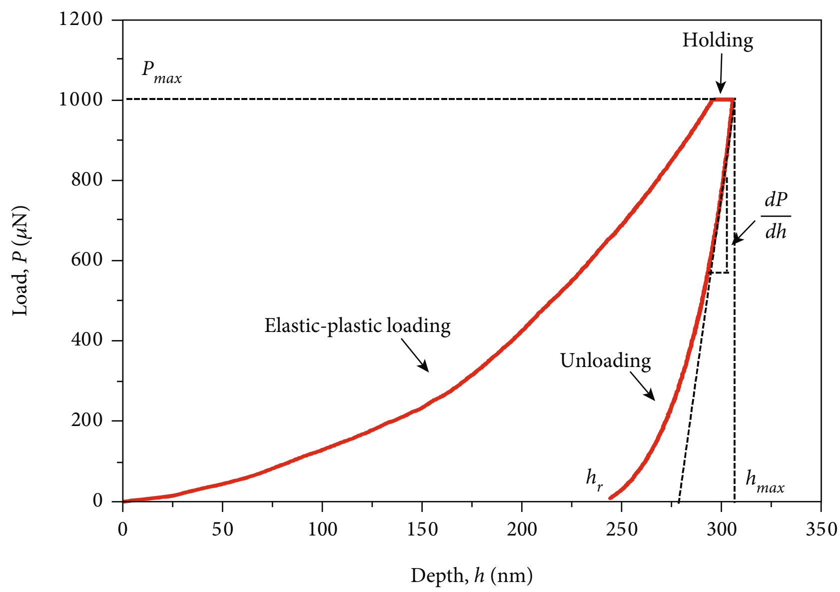

Figure 1: Typical load-depth curve obtained from nanoindentation.

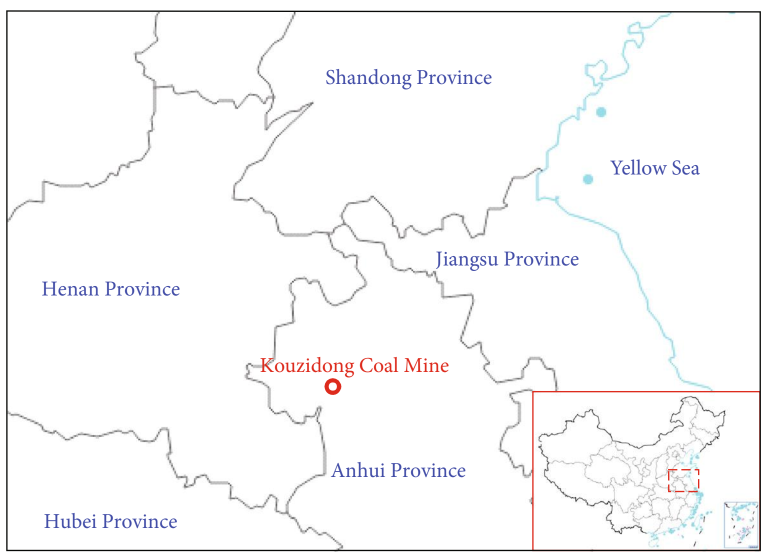

Figure 2: Sampling location map in Anhui, eastern China.

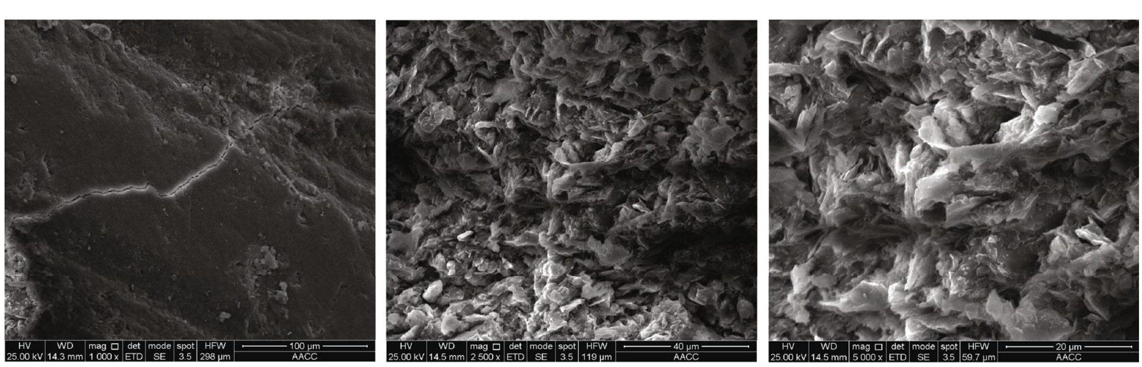

Figure 3: SEM photomicrographs of mudstone.

Table 1: Experimental scheme.

Uniaxial compressive test	Nanoindentation	Moisture content (%)
M-1	NM-1	~0.0
M-2	NM-2	~2.4
M-3	NM-3	~6.4

minerals exhibits an obvious water-induced weakening effect [31], and the increase in moisture content usually reduces the strength of rock [32]. However, due to the water sensitivity of argillite, it is generally a delicate task to investigate the mechanical properties in high moisture content mudstone by the specimens with standard size by bulk measurements (*e.g.*, acoustic emission, uniaxial compression, triaxial compression, and direct shear test) in some engineering fields. Thus, nanoindentation is a feasible experimental technique allowing for assessment of the mechanical properties of rock materials.

To the best of our knowledge, studies related to the effect of water on the microscale mechanical properties of coal measures mudstone are still lacking. Hence, nanoindentation was adopted to investigate the microscale mechanical properties of mudstone in this work. The effects of water on micro mechanical properties were analyzed, and the results were discussed.

2. Theory and Background

The principle of nanoindentation consisted of making contact between an indenter tip and the material surface. The changes in the applied load and penetration depth were measured simultaneously [33–35]. A typical indentation load-depth curve is shown in Figure 1. It consisted of three stages: loading, holding, and unloading. During the loading stage, the load increased as a function of the penetration depth, regarded as elastic-plastic loading. In the unloading stage, only elastic deformation was recovered and used to calculate the microscale mechanical properties of the specimen [36]. In Figure 1, $P_{\max}$ is the peak indentation load, $h_{\max}$ refers to the indentation depth at peak load, and h_f is the final depth of the contact impression after unloading.

From the load-depth curve, the initial unloading stiffness (S) can be expressed by Equation (1) [13].

$$S = \frac{dP}{dh} = \frac{2}{\sqrt{\pi}}\left(\frac{1}{E_r}\right)^{-1}\sqrt{A_c}, \tag{1}$$

where P is indentation load, h denotes the indentation depth, A_c is contact area of indenter at peak load, and E_r refers to the reduced modulus that can be determined by Equation (2).

$$\frac{1}{E_r} = \frac{1\text{-}\nu^2}{E} + \frac{1\text{-}\nu_i^{\,2}}{E_i}, \tag{2}$$

where E and ν are Young's modulus and Poisson's ratio of specimen, respectively. E_i and ν_i are Young's modulus and Poisson's ratio of indenter, respectively. A common Berkovich indenter was used in the present study, with Young's modulus $E_i = 1140$ GPa and Poisson's ratio $\nu_i = 0.07$.

Based on the principles of elastic contact theory, the modulus and hardness (H) of mudstone specimen can be calculated according to Equations (3) and (4).

$$E = \left(1\text{-}\nu^2\right)\left[\frac{1}{E_r} - \frac{1\text{-}\nu_i^{\,2}}{E_i}\right]^{-1}, \tag{3}$$

$$H = \frac{P_{\max}}{A_c}. \tag{4}$$

3. Experimental Material and Methods

3.1. Specimen Preparation. The mudstone was collected from the floor strata of a coal seam in Kouzidong coal mine located at Anhui in eastern China. Figure 2 shows the location where the mudstone was found. Figure 3 illustrates the SEM photomicrographs of the tested mudstone specimens. Loosed thin sheets were observed in the microstructure of the mudstone. According to the XRD results, the main mineral components of the mudstone were made of kaolinite (~52.2%), illite (~12.3%), chlorite (~28.1%), and quartz (~7.4%).

For uniaxial compression testing, the mudstone was cut into a series of cylindrical specimens with 50 mm in diameter and 100 mm in height. All specimens were fabricated from a large block of mudstone. The ends of the finished specimens were adjusted with a surface grinder to ensure nonparallelism and nonperpendicularity both less than 0.02 mm. The prepared specimens were tested by ultrasonic velocity measurements to select homogeneous specimens. In this study, specimens with three different moisture contents were prepared and the experimental scheme is summarized in Table 1. Three tests were repeated for each condition to minimize the dispersion of test results caused by the heterogeneity of the specimen.

After uniaxial compression tests, broken pieces were collected from the fractured specimens to prepare the specimens for nanoindentation, as shown in Table 1. For nanoindentation, it was based on the assumption of a perfectly smooth material surface since the smoothness was very important in obtaining reliable nanoindentation data [37, 38]. Before nanoindentation, the specimens were carefully ground and polished to achieve a smooth surface. The specimens were then cast in epoxy resin to create total stability for grinding and polishing during surface preparation. After solidification for 24 h, the specimens were ground using a grinder-polisher machine. An initial grinding and polishing of specimens were then conducted on silicon carbide papers with reduced gradation 52 μm, 35 μm, 22 μm, and 15 μm to expose the surface of each specimen. Preparation of specimens was completed after the final stage of grinding and polishing by diamond suspension with decreased size of 9 μm, 6 μm, 3 μm, 1 μm, and 0.05 μm on a polishing cloth. To avoid further change in the moisture content of mudstone, methanol-based liquids were used as

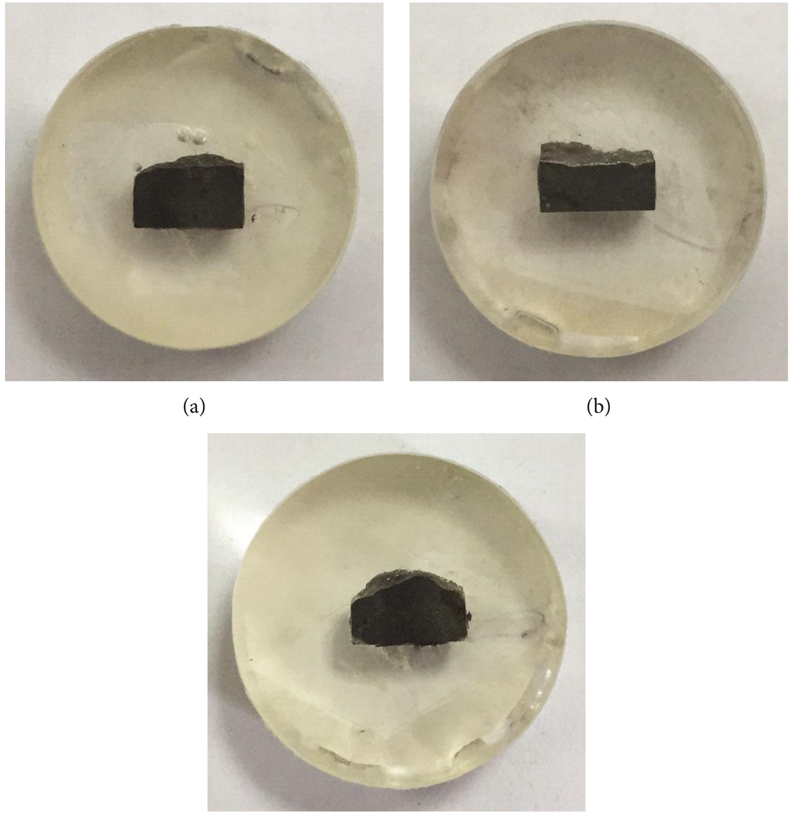

(a) (b) (c)

Figure 4: Well-prepared specimens: (a) NM-1, (b) NM-2, and (c) NM-3.

lubricants in the polishing process. The well-prepared specimens with smooth and flat surfaces used for nanoindentation are shown in Figure 4.

3.2. Nanoindentation. After polishing the specimens, a Hysitron T1 Premier (Figure 5) was used to investigate the microscale mechanical characteristics of all three mudstone specimens. A representative area of $100\,\mu\text{m} \times 100\,\mu\text{m}$ was selected for nanoindentation, as shown in Figure 6. A matrix of 100 indents was made on the surface, whereas the indent spacing was kept to $10\,\mu\text{m}$ in the vertical and lateral directions (Figure 6). In this study, a load control mode was adopted, and tests were programmed in such a way that the indenter came in contact with the specimen surface. Afterward, the load was increased at a constant rate of $200\,\mu\text{N/s}$ until reaching a maximum load value of $1000\,\mu\text{N}$. For the tested point, the maximum load of 1.0 mN here was determined so to respect on-average the scale separability condition and the 1/10 rule of thumb [39]. Next, the load was held at its maximum value for 2 s at the same loading rate before unloading to minimize the short-term creep and size effect [40, 41]. The movement protocol from one indent to the next was set as a constant direction mode. The unloading data were used to determine the indentation modulus and hardness values based on well-established equations.

Figure 5: Hysitron T1 Premier.

3.3. Statistical Analysis. The experimental data obtained by nanoindentation were used to estimate the elastic properties of different phases of mudstone specimens. Using a statistical Gaussian fitting method [14, 15, 42, 43], the microscale

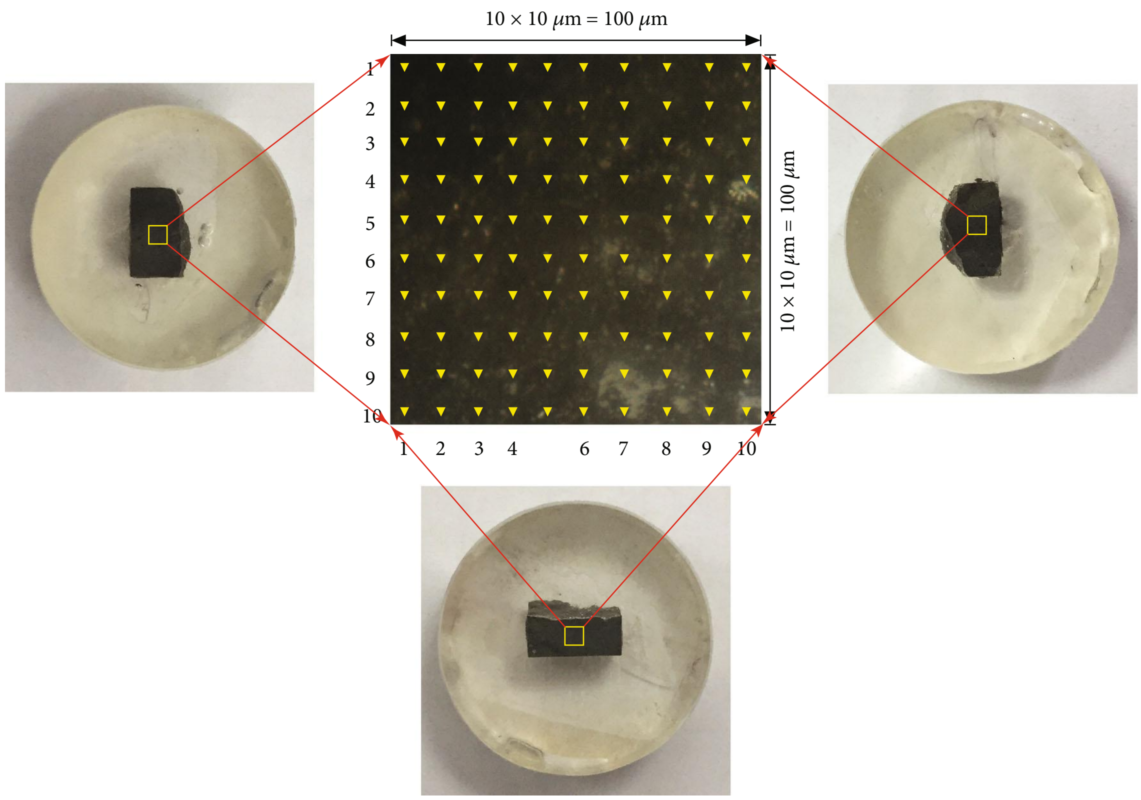

FIGURE 6: Indent arrangement on mudstone surface.

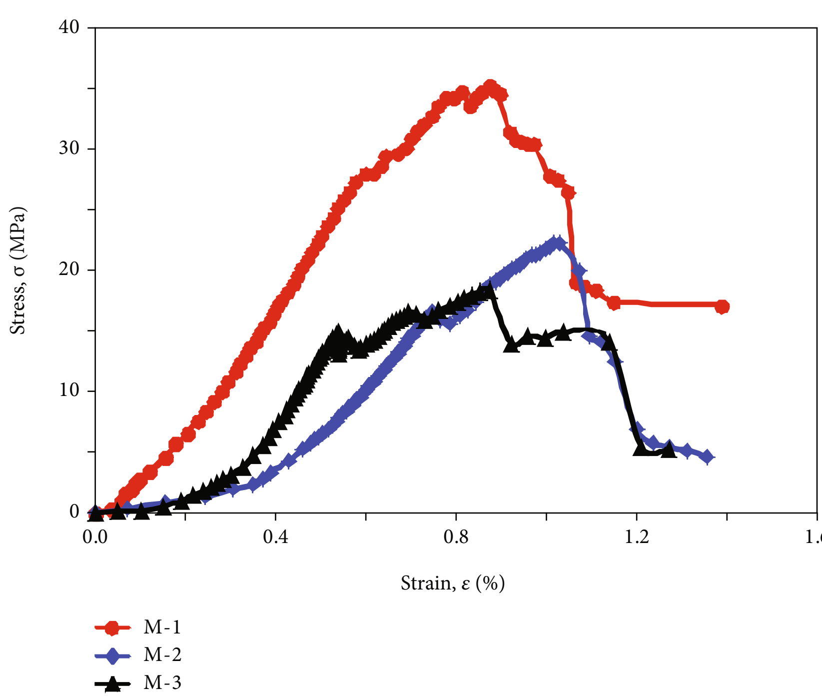

FIGURE 7: Uniaxial compression stress-strain curves of mudstone specimens: (a) M-1, (b) M-2, and (c) M-3.

Table 2: Mechanical properties of mudstone.

Rock types	Uniaxial compressive strength (MPa)		Young's modulus (GPa)	
	Experimental	Average	Experimental	Average
M-1	34.8	34.7	5.7	6.1
	34.8		5.6	
	34.6		6.9	
M-2	21.8	22.5	3.8	4.3
	24.1		4.9	
	21.7		4.2	
M-3	18.4	18.6	5.5	4.1
	17.8		3.6	
	19.6		3.2	

mechanical properties of different phases were analyzed statistically. The best model based on multimodal normal distribution curves (Gaussian distribution) was used to fit the experimental results following Equation (5).

$$f(x, \mu, \sigma) = \frac{1}{\sigma\sqrt{2\pi}} \exp\left[-\frac{(x-\mu)^2}{2\sigma^2}\right]. \quad (5)$$

The mean value μ and standard deviation σ of distribution can be extracted from each model fitting. When the number and distribution type of phases comprising a composite are known, the volume fraction for different phases can be estimated by the area under the normal distribution curve [15, 44].

4. Results and Discussion

4.1. Mechanical Behavior of Mudstone at Macroscale. The uniaxial compression tests were performed on mudstone specimens with different moisture contents, and typical stress-strain curves of the three specimens are shown in Figure 7. All three types of mudstone specimens exhibited similar mechanical behaviors. The values of uniaxial compressive strength and Young's modulus of different specimens are summarized in Table 2. Compared to specimen M-1, the average uniaxial compression strength of specimens M-2 and M-3 decreased by 35.2% and 46.4%, and Young's modulus declined by approximately 29.5% and 32.8%, respectively. Due to the water-weakening effect, the macroscale mechanical properties significantly decreased.

4.2. Nanoindentation Load-Depth Curves. To investigate the mechanical properties of mudstone at microscale, Figure 8 shows the typical load-depth curves of indented points in the tested areas of all three mudstone specimens. As shown in Figure 8, each loading and unloading cycle illustrated a deformation behavior of mudstone around the indented point.

The visual inspection of the load-depth curves revealed large differences in final depth values at the end of loading. Such different characteristic shapes represented the mechanical responses of various types of minerals induced by the heterogeneousity of mudstone. At the same maximum load (1000 μN), the final depths of left-most curves were much lower than in other curves, indicating strong resistance to external stress due to the existence of hard mineral grains in mudstone. The right-most curves with the largest final depth and clear creeping branch represented typical responses on the weakest mineral grains. When the maximum load was maintained for 2 s, the creep deformation of mudstone at the right-most curves was much larger than in left-most curves. Furthermore, the final depth of most curves observed from the mudstone specimens increased as a function of moisture content (Figure 8).

4.3. Mechanical Mapping of Indentation Modulus and Hardness. The indentation modulus and hardness of different tested points were calculated from the obtained load-depth curves using the Oliver-Pharr method. Figures 9–11 show the distribution of the indentation modulus and hardness in tested regions of three mudstone specimens. The color difference in the tested regions indicated a relatively complex and highly heterogeneous composition of mudstone. The blue area showing the lower modulus (hardness) represented the weak zones in mudstone, whereas the red area with a significantly higher modulus (hardness) displayed the rigid part. The other areas with the modulus (hardness) between the weak zones (shown in blue) and rigid part (shown in red) were exhibited in green or yellow. The elastic modulus of tested points in mudstone varied significantly, indicating a strongly heterogeneous distribution. This was caused by different mineral components in the rocks.

The general comparison of the mechanical properties maps (indentation modulus and hardness) showed considerable variations in different mudstone specimens. For specimen NM-1, the red area with higher indentation modulus accounted for a large proportion (Figure 9(a)) but decreased in specimens NM-2 (Figure 10(a)) and NM-3 (Figure 11(a)). Furthermore, the red area with highest modulus (100-120 GPa) still existed after water adsorption (Figure 11(a)).

Additionally, the tested points with higher indentation moduli corresponded to the elevated hardness values (Figures 9–11). The distribution map of indentation modulus and hardness looked similar in appearance. The correlation between indentation modulus and hardness of the three mudstone specimens is shown in Figure 12. The correlation between indentation modulus and hardness varied linearly with a positive slope.

4.4. Microcharacterization of Multiphase Structure in Mudstone. In multiphase (multimineral) materials like mudstone, nanoindentation could provide approximate information related to the microscale of each phase, as well as the role in the effective properties of multiphase systems [16]. Here, the contact surface area was around a few square microns, and different phases can be identified at a much finer scale. To distinguish different phases, Figure 13 shows a histogram of indentation moduli of different tested points in the three mudstone specimens. The distribution of

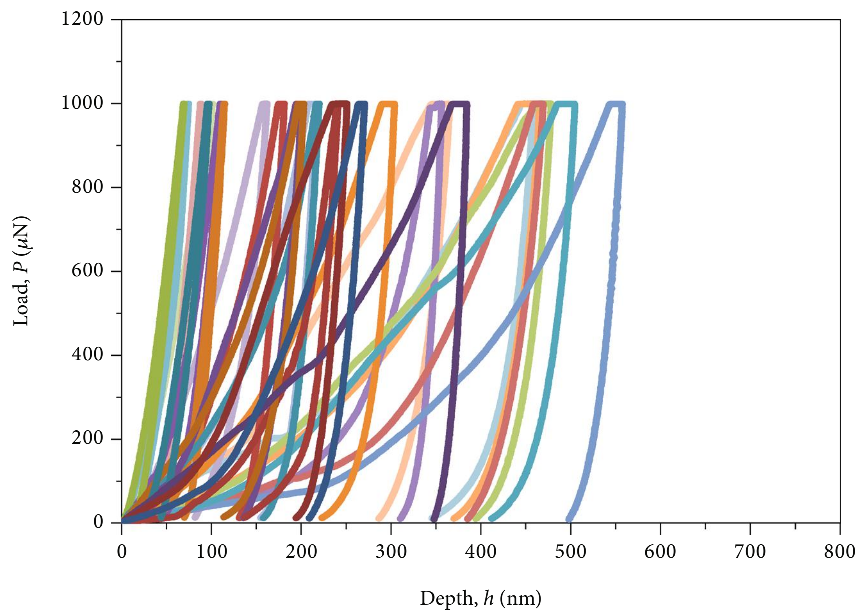

(a)

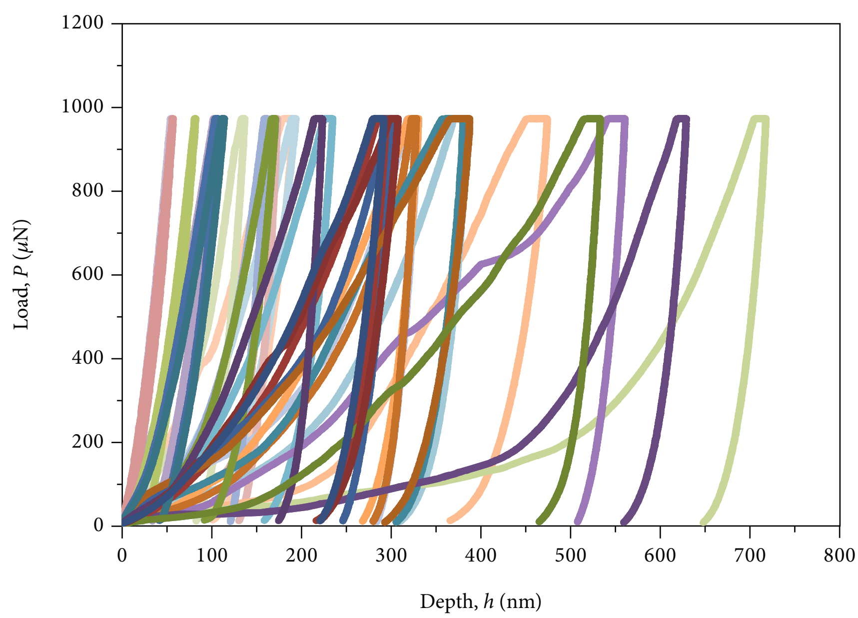

(b)

FIGURE 8: Continued.

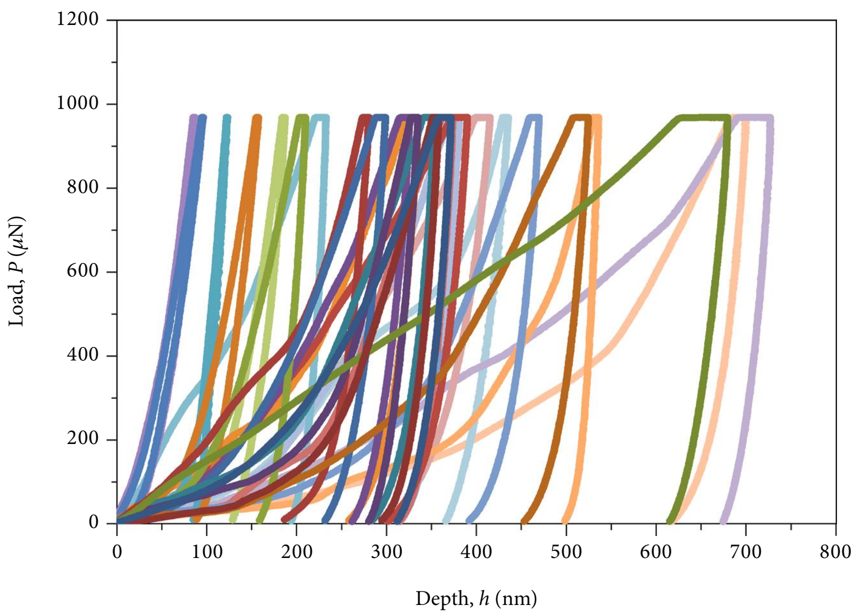

(c)

Figure 8: Typical load-depth curves of mudstone specimens obtained from nanoindentation: (a) NM-1, (b) NM-2, and (c) NM-3.

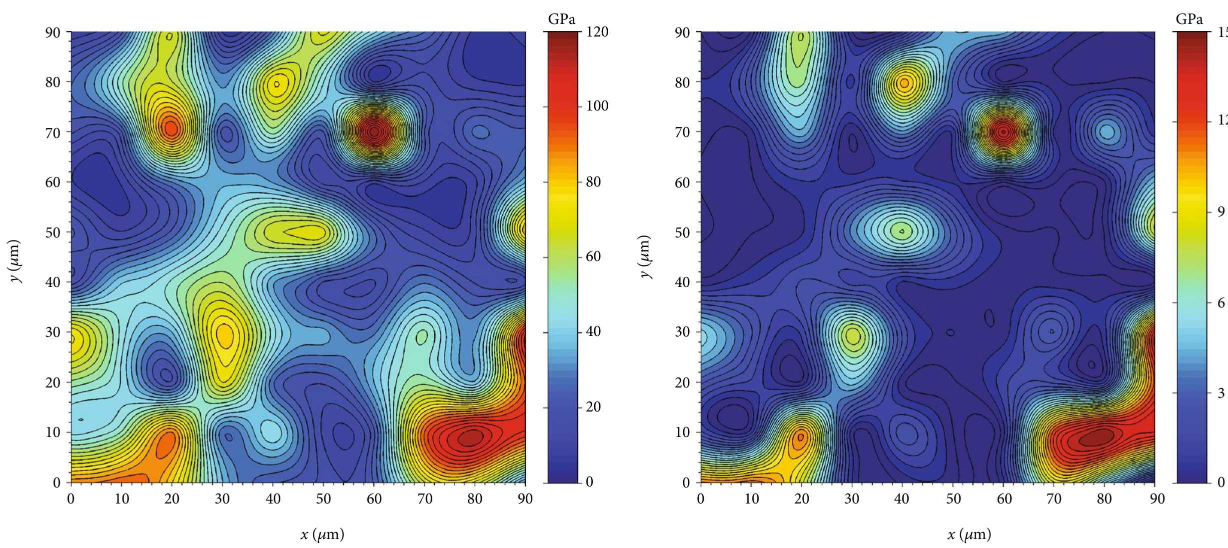

(a) (b)

Figure 9: Distribution of (a) indentation modulus and (b) hardness in the tested region of specimen NM-1.

indentation modulus was in a wide range from 0.2 GPa to 125 GPa. More than one peak can be observed in the indentation modulus histogram, indicating relatively heterogeneous characteristics. For each specimen, the indentation modulus concentrated on 0-60 GPa occupied the highest proportion.

For specimen NM-2 (Figure 13(b)), the frequency increased firstly with the increase in modulus from 0 GPa, until it reached a peak value between 3 GPa and 9 GPa. Afterward, the frequency decreased from 9 to 24 GPa. Note that the frequency between 0 and 24 GPa accounted for the largest proportion of 75.0%. As the modulus increased from 24 GPa to 63 GPa, the frequency exhibited an initial increase followed by a decrease. The modulus in the range of 24-63 GPa accounted for 16.0%. After a large discontinuity (63-84 GPa), the frequency of modulus at 84-115 GPa reached 9.0%.

After drying, the frequency distribution of indentation modulus of NM-1 (Figure 13(a)) was different from that of NM-2 and looked more uniform. The frequency of modulus at 5-45 GPa, 45-80 GPa, and 80-130 GPa was 62.0%, 25.0%, and 13.0%, respectively. For specimen NM-3 (Figure 13(c)), the frequency distribution of modulus was similar to that of specimen NM-2.

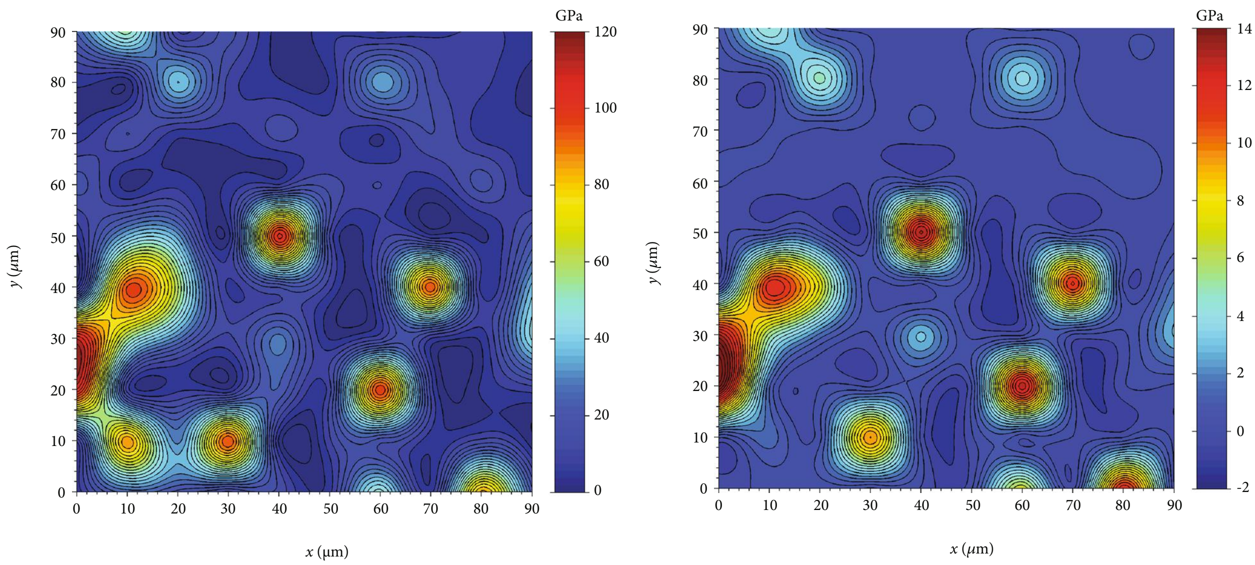

(a) (b)

FIGURE 10: Distribution of (a) indentation modulus and (b) hardness in the tested region of specimen NM-2.

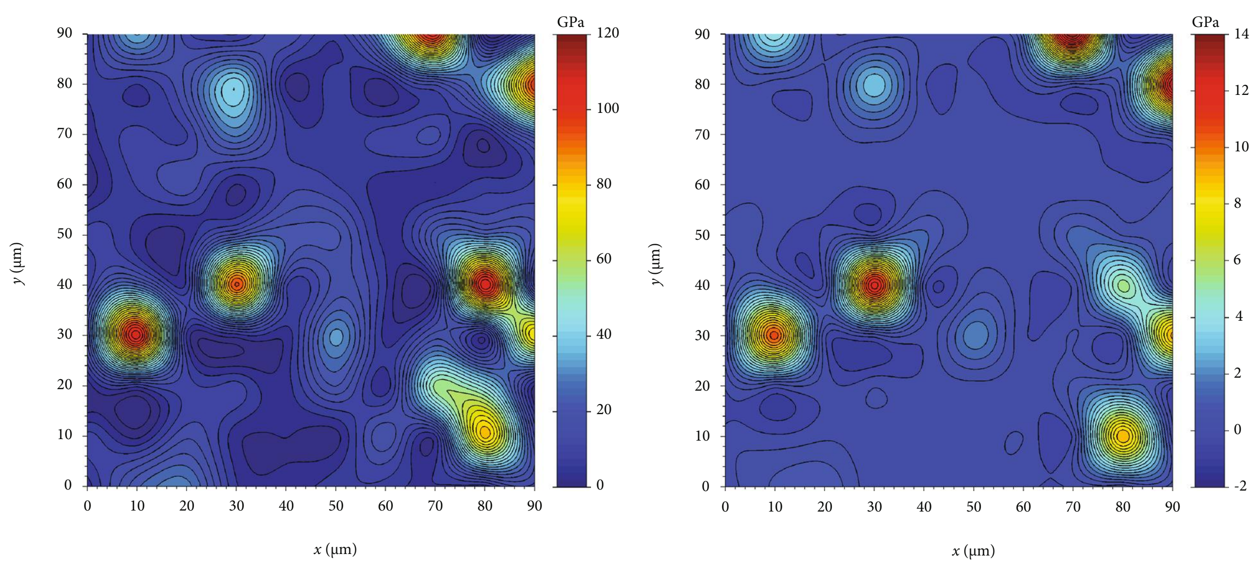

(a) (b)

FIGURE 11: Distribution of (a) indentation modulus and (b) hardness in the tested region of specimen NM-3.

4.5. Effect of Water on Microscale Mechanical Properties of Phases. In terms of microscale characterization, mudstone is a material composed of different phases. To further investigate the effects of moisture contents on the mechanical properties of mudstone specimens at microscale, Gaussian fitting was used to analyze the statistical results of mechanical properties. Figure 14 shows the experimental data and fractions of each Gaussian probability density of indentation modulus of all three mudstone specimens. In each figure, three model normal distribution curves were used to produce the best fit of the experimental data. Table 3 summarizes the modulus values extracted from the model fits of individual phases in different mudstone specimens. The volume fractions of different phases were also included in Table 3.

For clay minerals (kaolinite, etc.), Zhang et al. [45] reported that the modulus was less than 5.0 GPa in claystone, while Liu et al. [36] reported it was 22.3 GPa. Our results showed that indentation moduli of clay minerals (including kaolinite and illite) were in a range from 4.2 to 17.7 GPa. This difference in indentation moduli of clay minerals obtained from different studies may be caused by variable moisture contents in the specimens, and an explanation of this variation in indentation modulus values of clay minerals was the water-weakening effect or swelling effect, as previously reported [28, 46, 47].

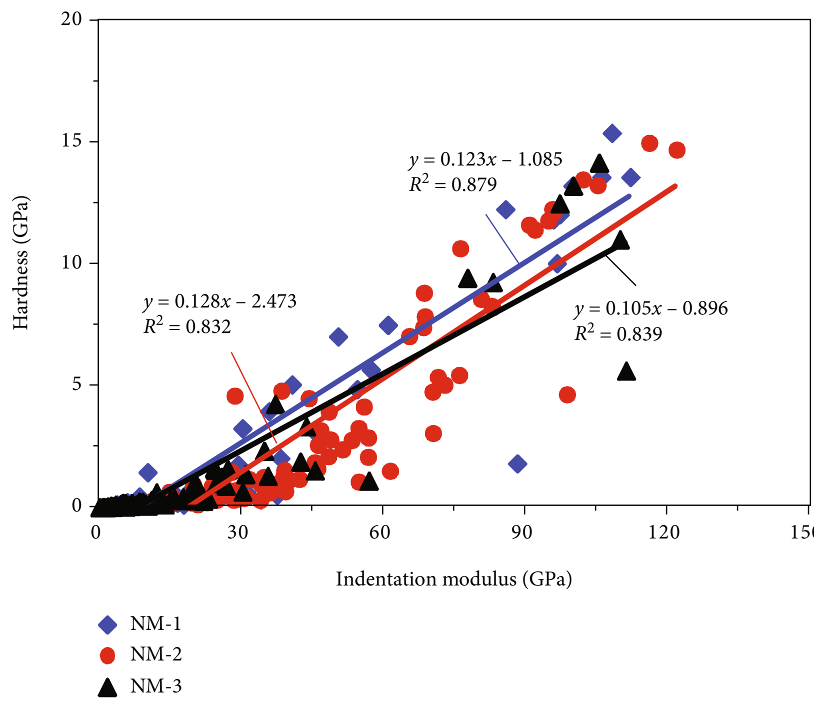

Figure 12: Correlation between indentation modulus and hardness of all three mudstone specimens.

From Table 3, it was apparent that the variation in indentation modulus looked relatively different for the dry specimen (NM-1) and water-bearing specimens (NM-2 and NM-3). For the same mineral composition (*e.g.*, clay minerals), the indentation modulus in NM-1 was larger than that in specimens NM-2 and NM-3. The swelling effect reduced the indentation modulus of kaolinite in specimen NM-2 to 4.67 GPa, while 17.68 GPa was recorded for specimen NM-1. With the increase in moisture content, the modulus of kaolinite decreased to 4.22 GPa (NM-3). Compared to the dry specimen (NM-1), the indentation moduli of kaolinite in specimens NM-2 and NM-3 decreased by approximately 73.6% and 76.1%, respectively. Also, the indentation moduli of chlorite diminished by approximately 39.8% and 52.1%, respectively. The difference in moisture content of all three mudstones led to variable mechanical properties of clay minerals (kaolinite, illite, and chlorite) at microscale.

The volume fractions of different phases were also analyzed. As shown in Table 3, the volumes of water-sensibility minerals of specimen NM-1 were estimated to 58.3% (kaolinite, etc.) and 27.2% (chlorite), respectively. By comparison, values of 80.7% (kaolinite, etc.) and 13.2% (chlorite) were obtained for specimen NM-2 and 77.7% and 18.0% for specimen NM-3, respectively.

For hard minerals (quartz), the indentation modulus of quartz ranged from 87 to 105 GPa. Zhu et al. [15] reported that the modulus of quartz in quartzite was 104.2 ± 5.9 GPa. Thus, the values for quartz determined in this study were reasonable. Compared to dry specimen NM-1, the statistical results of indentation modulus of quartz in specimens NM-2 and NM-3 increased by 11.0% and 18.6%, respectively.

Note that the indentation modulus may not represent the exact values for the pure phase due to unavoidable phase interactions. For example, the reported modulus of a specially prepared pure phase of quartz by nanoindentation was 117.26 ± 2.7 GPa [48]. This value was higher than those obtained in the present study or other reported ones [15, 36, 45]. Clearly, the complete separation of the mechanical performances of different individual phases was not possible from the measurement response. Though the characterization results were based on mechanically distinct phases instead of pure chemically distinct phases, they looked very well related.

4.6. Mechanical Properties at Macro- and Microscale. The average moduli obtained from uniaxial compression and nanoindentation tests were compared in Figure 15. The average moduli at macro- and microscale varied significantly, and the values obtained from nanoindentation looked much larger than those from macroscopic experiments. Compared to nanoindentation, the average modulus obtained from uniaxial compression tests decreased by approximately 80.0%.

The diversity in microscale mechanical properties of different phases rendered the average nanoindentation modulus unsuitable for characterizing the mechanical properties of specimens at macroscale. Therefore, the Mori-Tanaka method was used to link the nanoindentation data and macroscopic mechanical properties [49]. Based on homogenization scheme and nanoindentation data, Zhang et al. [45] and Liu et al. [36] determined the elastic properties of claystone and shale, respectively. The comparison with modulus data obtained from common method indicated similar values as those predicted by homogenization method.

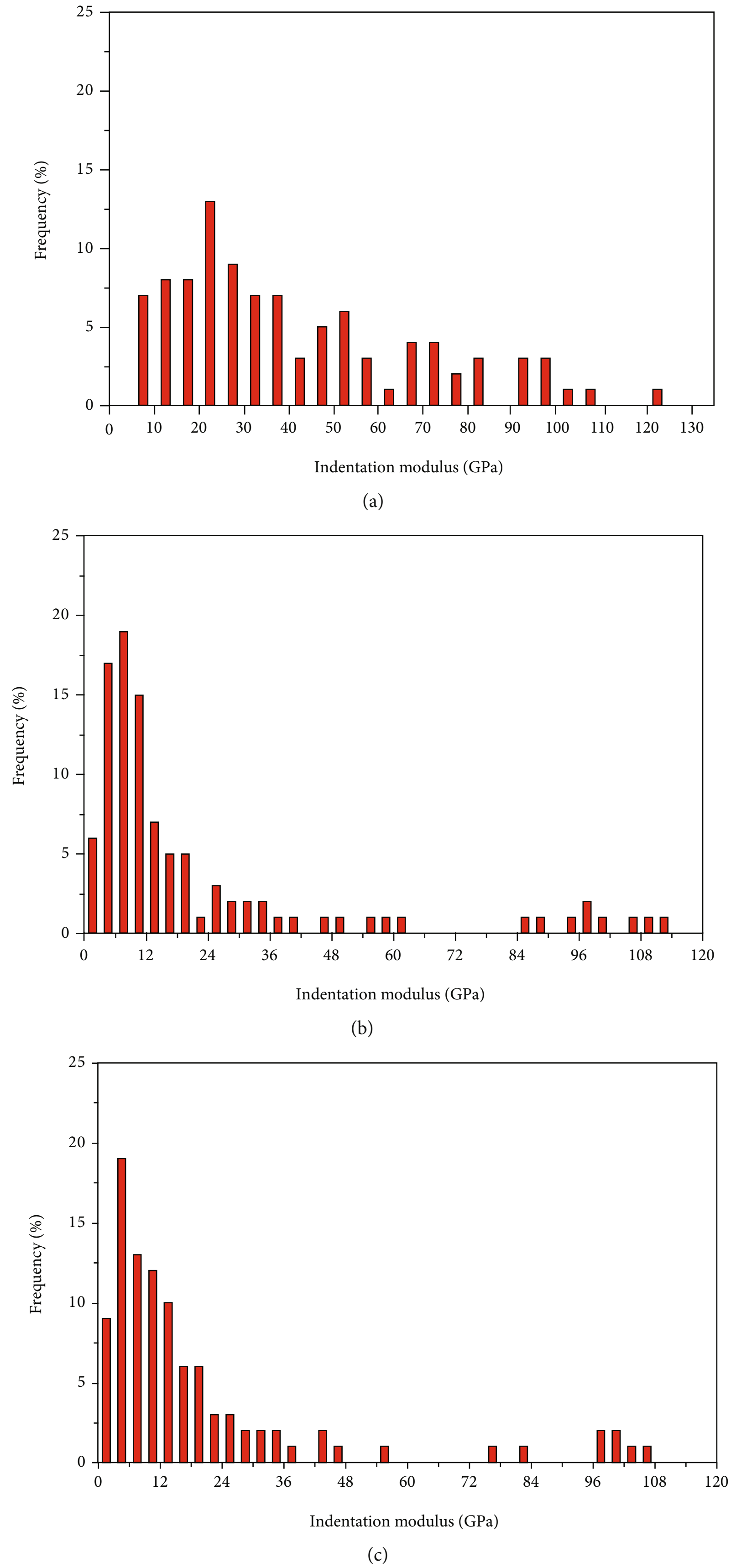

Figure 13: Histograms of indentation modulus of (a) NM-1, (b) NM-2, and (c) NM-3.

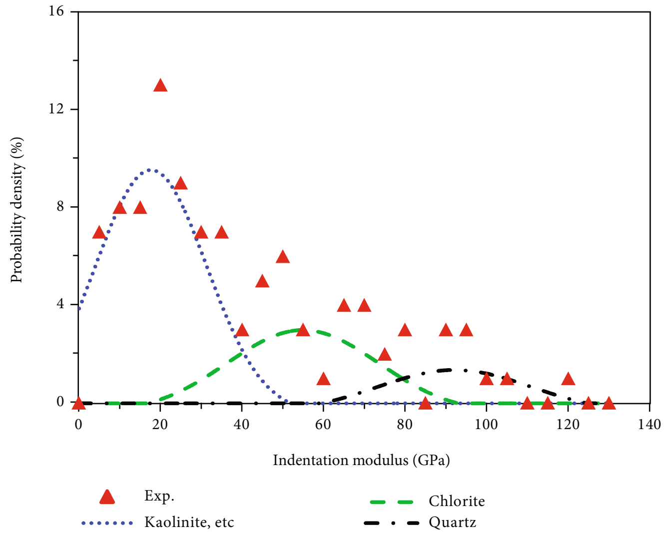

(a)

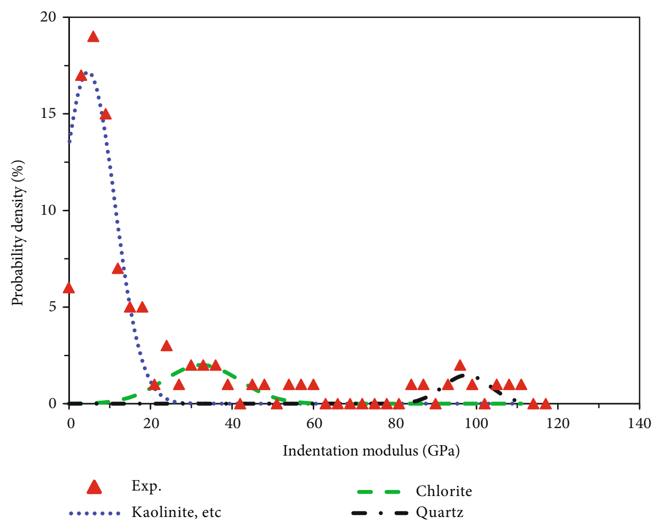

(b)

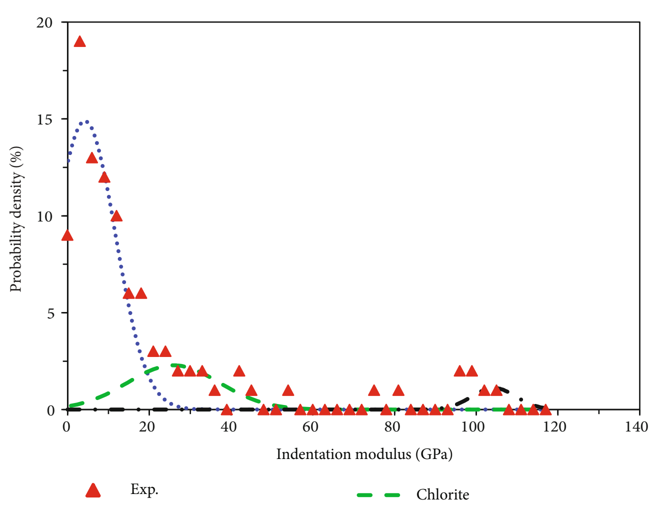

(c)

FIGURE 14: Fractions of each Gaussian probability density of indentation modulus of (a) NM-1, (b) NM-2, and (c) NM-3.

Table 3: Statistical results of indentation modulus for three mudstone specimens.

Rock types	Kaolinite, etc. Modulus (GPa)	Kaolinite, etc. V (%)	Chlorite Modulus (GPa)	Chlorite V (%)	Quartz Modulus (GPa)	Quartz V (%)
NM-1	17.68	58.3	54.08	27.2	87.96	14.5
NM-2	4.67	80.7	32.56	13.2	97.62	6.1
NM-3	4.22	77.7	25.90	18.0	104.30	4.3

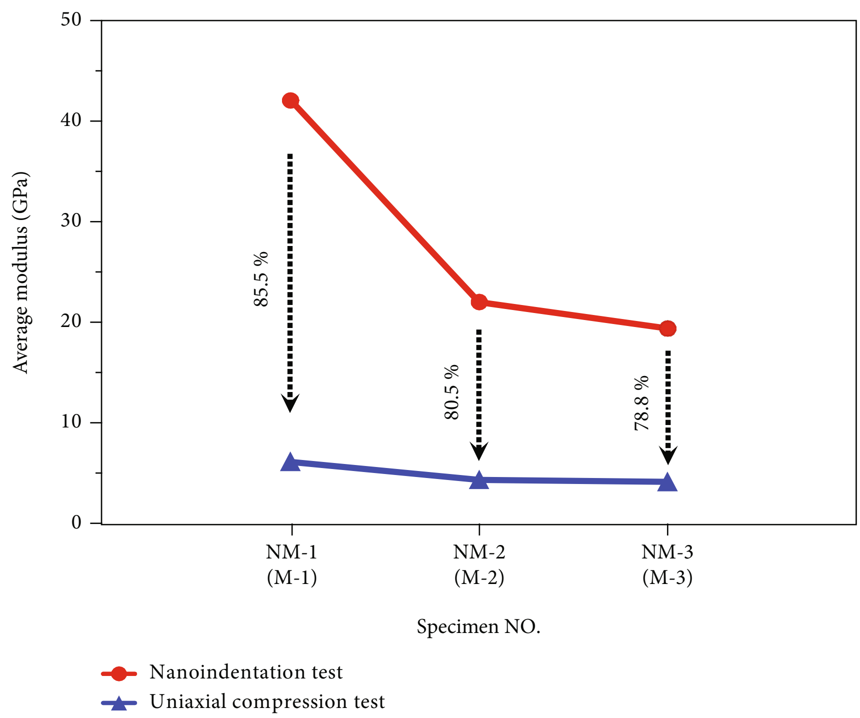

Figure 15: Comparison of average modulus of all specimens obtained from uniaxial compression and nanoindentation tests.

Table 4: Test results of homogenization and macroscopic experiments.

Rock types	Phases Name	E (GPa)	ν	V (%)	E_{macro} (GPa)	E_{micro} (GPa)	E_{hom} (GPa)	Error (%)
	Kaolinite, etc.	17.68	0.30	58.3	6.1	42.2	28.7	370.5
NM-1	Chlorite	54.08	0.25	27.2				
	Quartz	87.96	0.20	14.5				
	Kaolinite, etc.	4.67	0.30	80.7	4.3	22.0	6.4	48.8
NM-2	Chlorite	32.56	0.25	13.2				
	Quartz	97.62	0.20	6.1				
	Kaolinite, etc.	4.22	0.30	77.7	4.1	19.4	5.9	43.9
NM-3	Chlorite	25.90	0.25	18.0				
	Quartz	104.30	0.20	4.3				

Note: Error% = $(E_{hom} - E_{macro})/E_{macro}$.

In this study, linkages of the nanoindentation data and macroscopic mechanical properties were evaluated by homogenization scheme. Table 4 shows the input parameters of different phases of three specimens, as well as the homogenized elastic modulus (E_{hom}) values obtained by Mori-Tanaka method. The macroscopic experimental results (E_{macro}) and average indentation modulus (E_{micro}) were also included in Table 4. The Poisson's ratios associated with the clay minerals and quartz were obtained from literature [36, 45].

As shown in Table 4, the errors between the results obtained from the uniaxial compression test and homogenization method were estimated to about 45.0% for water-bearing specimens (NM-2 and NM-3). The evaluating results seemed reasonable, while for dry specimen of NM-1, the error was 370.5%. It seemed that the homogenization scheme cannot upscale the microscale mechanical properties of different phases to obtain data of the whole specimen at macroscale in dry specimen. After drying, the mechanical properties of water-sensitivity minerals increased significantly (Figure 13(a)), and the input parameters (Table 4) of different phases for dry specimens may not represent the actual value.

5. Conclusions

In this study, the effects of moisture contents on the macro- and microscale mechanical properties of mudstone were analyzed and the results were discussed. The following conclusions can be drawn:

(1) The load-depth curves, curve-based indentation modulus, and hardness were all obtained. The indentation modulus varied significantly from a low value of 0.2 GPa to a high value of 125 GPa, demonstrating a strongly heterogeneous distribution of different minerals in mudstone

(2) The moisture content showed a significant effect on the microscale mechanical properties of water-sensitivity minerals. The water-sensitivity minerals occupying the highest proportion of mudstone played a decisive role in the mechanical properties of mudstone

(3) The average moduli at macro- and microscale varied significantly, and the average elastic modulus values obtained from nanoindentation were much larger than those acquired by macroscopic experiments. The Mori-Tanaka method was used to link the nanoindentation data and macroscopic mechanical properties. The results of this study indicated that nanoindentation technique is a feasible experimental technique to assess the macroscale mechanical properties of rock materials

Data Availability

The data used to support the finding of this study are available from the corresponding author upon request.

Conflicts of Interest

The authors declare that there are no conflicts of interest.

Acknowledgments

This research is supported by the Natural Science Foundation of China (52004144), the Natural Science Foundation of Shandong Province, China (ZR2019BEE001), and the Project of Shandong Province Higher Educational Young Innovative Talent Introduction and Cultivation Team (Disaster prevention and control team of underground engineering involved in sea).

References

[1] Y. L. Lu, L. G. Wang, X. K. Sun, and J. Wang, "Experimental study of the influence of water and temperature on the mechanical behavior of mudstone and sandstone," *Bulletin of Engineering Geology and the Environment*, vol. 76, no. 2, pp. 645–660, 2017.

[2] S. Tao, S. D. Chen, and Z. J. Pan, "Current status, challenges, and policy suggestions for coalbed methane industry development in China: a review," *Energy Science & Engineering*, vol. 7, no. 4, pp. 1059–1074, 2019.

[3] S. Tao, Z. J. Pan, S. L. Tang, and S. D. Chen, "Current status and geological conditions for the applicability of CBM drilling technologies in China: a review," *International Journal of Coal Geology*, vol. 202, pp. 95–108, 2019.

[4] Y. Li, J. H. Yang, Z. J. Pan, S. Z. Meng, K. Wang, and X. L. Niu, "Unconventional natural gas accumulations in stacked deposits: a discussion of upper Paleozoic coal-bearing strata in the east margin of the Ordos Basin, China," *Acta Geologica Sinica-english Edition*, vol. 93, no. 1, pp. 111–129, 2019.

[5] Y. Li, D. Z. Tang, P. Wu et al., "Continuous unconventional natural gas accumulations of Carboniferous-Permian coal-bearing strata in the Linxing area, northeastern Ordos Basin, China," *Journal of Natural Gas Science and Engineering*, vol. 36, pp. 314–327, 2016.

[6] B. Y. Jiang, S. T. Gu, G. C. Zhang, and W. S. Li, "Strainburst process of marble in tunnel-excavation-induced stress path considering intermediate principal stress," *Journal of Central South University*, vol. 26, no. 4, pp. 984–999, 2019.

[7] M. Nicksiar and C. D. Martin, "Crack initiation stress in low porosity crystalline and sedimentary rocks," *Engineering Geology*, vol. 154, no. 2, pp. 64–76, 2013.

[8] M. Li, X. B. Mao, L. L. Cao, H. Pu, R. R. Mao, and A. H. Lu, "Effects of thermal treatment on the dynamic mechanical properties of coal measures sandstone," *Rock Mechanics and Rock Engineering*, vol. 49, no. 9, pp. 3525–3539, 2016.

[9] J. Ye, S. Tao, S. Zhao, S. Li, S. Chen, and Y. Cui, "Characteristics of methane adsorption/desorption heat and energy with respect to coal rank," *Journal of Natural Gas Science and Engineering*, vol. 99, p. 104445, 2022.

[10] Q. Feng, J. C. Jin, S. Zhang, W. W. Liu, X. X. Yang, and W. T. Li, "Study on a damage model and uniaxial compression simulation method of frozen-thawed rock," *Rock Mechanics and Rock Engineering*, vol. 55, no. 1, pp. 187–211, 2022.

[11] O. K. Mahabadi, B. S. A. Tatone, and G. Grasselli, "Influence of microscale heterogeneity and microstructure on the tensile behavior of crystalline rocks," *Journal of Geophysical Research Solid Earth*, vol. 119, no. 7, pp. 5324–5341, 2014.

[12] C. L. Sun, G. C. Li, M. E. Gomah, J. H. Xu, and H. Y. Rong, "Meso-scale mechanical properties of mudstone investigated by nanoindentation," *Engineering Fracture Mechanics*, vol. 238, p. 107245, 2020.

[13] W. C. Oliver and G. M. Pharr, "An improved technique for determining hardness and elastic modulus using load and displacement sensing indentation experiments," *Journal of Materials Research*, vol. 7, no. 6, pp. 1564–1583, 1992.

[14] G. Constantinides and F.-J. Ulm, "The effect of two types of CSH on the elasticity of cement-based materials: results from

nanoindentation and micromechanical modeling," *Cement and Concrete Research*, vol. 34, no. 1, pp. 67–80, 2004.

[15] W. Z. Zhu, J. J. Hughes, N. Bicanic, and C. J. Pearce, "Nanoindentation mapping of mechanical properties of cement paste and natural rocks," *Materials Characterization*, vol. 58, no. 11-12, pp. 1189–1198, 2007.

[16] G. Manjunath and B. Jha, "Nanoscale fracture mechanics of Gondwana coal," *International Journal of Coal Geology*, vol. 204, pp. 102–112, 2019.

[17] Y. H. Zhang, M. Lebedev, A. Al-Yaseri, H. Y. Yu, X. M. Xu, and S. Iglauer, "Characterization of nanoscale rockmechanical properties and microstructures of a Chinese sub-bituminous coal," *Journal of Natural Gas Science and Engineering*, vol. 52, pp. 106–116, 2018.

[18] H. Y. Yu, Y. H. Zhang, M. Lebedev et al., "Nanoscale geomechanical properties of Western Australian coal," *Journal of Petroleum Science and Engineering*, vol. 162, pp. 736–746, 2018.

[19] C. L. Sun, G. C. Li, M. E. Gomah, J. H. Xu, and Y. T. Sun, "Creep characteristics of coal and rock investigated by nanoindentation," *International Journal of Mining Science and Technology*, vol. 30, no. 6, pp. 769–776, 2020.

[20] G. Manjunath and R. R. Nair, "Microscale assessment of 3D geomechanical structural characterization of gondawana shales," *International Journal of Coal Geology*, vol. 181, pp. 60–74, 2017.

[21] A. R. Sakulich and V. C. Li, "Nanoscale characterization of engineered cementitious composites (ECC)," *Cement and Concrete Research*, vol. 41, no. 2, pp. 169–175, 2011.

[22] S. Barbhuiya and B. Caracciolo, "Characterisation of asphalt concrete using nanoindentation," *Materials*, vol. 10, no. 7, p. 823, 2017.

[23] H. Lee, V. Vimonsatit, and P. Chindaprasirt, "Mechanical and micromechanical properties of alkali activated fly-ash cement based on nano-indentation," *Construction and Building Materials*, vol. 107, pp. 95–102, 2016.

[24] W. Li, B. Jiang, S. Gu, X. Yang, and F. Shaikh, "Experimental study on the shear behaviour of grout-infilled specimens and micromechanical properties of grout-rock interface," *Journal of Central South University*, vol. 2022, pp. 1–14, 2022.

[25] Y. Li, J. H. Yang, Z. J. Pan, and W. S. Tong, "Nanoscale pore structure and mechanical property analysis of coal: an insight combining AFM and SEM images," *Fuel*, vol. 260, p. 116352, 2020.

[26] Y. Li, Z. S. Wang, Z. J. Pan, X. L. Niu, Y. Yu, and S. Z. Meng, "Pore structure and its fractal dimensions of transitional shale: a cross-section from east margin of the Ordos Basin, China," *Fuel*, vol. 241, pp. 417–431, 2019.

[27] Y. B. Liu, G. Z. Yin, D. M. Zhang et al., "Directional permeability evolution in intact and fractured coal subjected to true-triaxial stresses under dry and water-saturated conditions," *International Journal of Rock Mechanics and Mining Sciences*, vol. 119, pp. 22–34, 2019.

[28] Y. L. Lu and L. G. Wang, "Effect of water and temperature on short-term and creep mechanical behaviors of coal measures mudstone," *Environmental Earth Sciences*, vol. 76, no. 17, p. 597, 2017.

[29] L. P. Li, C. S. Shang, K. W. Chu et al., "Large-scale geomechanical model tests for stability assessment of super-large cross-section tunnel," *Tunnelling and Underground Space Technology*, vol. 109, p. 103756, 2021.

[30] K. E. Eang, T. Igarashi, M. Kondo, T. Nakatani, C. B. Tabelin, and R. Fujinaga, "Groundwater monitoring of an open-pit limestone quarry: water-rock interaction and mixing estimation within the rock layers by geochemical and statistical analyses," *International Journal of Mining Science and Technology*, vol. 28, no. 6, pp. 849–857, 2018.

[31] P. L. P. Wasantha and P. G. Ranjith, "Water-weakening behavior of Hawkesbury sandstone in brittle regime," *Engineering Geology*, vol. 178, no. 8, pp. 91–101, 2014.

[32] B. Vásárhelyi and P. Ván, "Influence of water content on the strength of rock," *Engineering Geology*, vol. 84, no. 1-2, pp. 70–74, 2006.

[33] X. H. Wang, S. Jacobsen, J. Y. He, Z. L. Zhang, S. F. Lee, and H. L. Lein, "Application of nanoindentation testing to study of the interfacial transition zone in steel fiber reinforced mortar," *Cement and Concrete Research*, vol. 39, no. 8, pp. 701–715, 2009.

[34] W. Da Silva, J. Němeček, and P. Štemberk, "Methodology for nanoindentation-assisted prediction of macroscale elastic properties of high performance cementitious composites," *Cement and Concrete Composites*, vol. 45, pp. 57–68, 2014.

[35] S. H. Zhao, Y. Li, Y. B. Wang, Z. T. Ma, and X. Q. Huang, "Quantitative study on coal and shale pore structure and surface roughness based on atomic force microscopy and image processing," *Fuel*, vol. 244, pp. 78–90, 2019.

[36] K. Q. Liu, M. Ostadhassan, B. Bubach, K. G. Ling, B. Tokhmechi, and D. Robert, "Statistical grid nanoindentation analysis to estimate macro-mechanical properties of the Bakken Shale," *Journal of Natural Gas Science and Engineering*, vol. 53, pp. 181–190, 2018.

[37] C. L. Hu and Z. J. Li, "A review on the mechanical properties of cement-based materials measured by nanoindentation," *Construction and Building Materials*, vol. 90, pp. 80–90, 2015.

[38] M. Miller, C. Bobko, M. Vandamme, and F.-J. Ulm, "Surface roughness criteria for cement paste nanoindentation," *Cement and Concrete Research*, vol. 38, no. 4, pp. 467–476, 2008.

[39] G. Constantinides and F.-J. Ulm, "The nanogranular nature of C–S–H," *Journal of the Mechanics and Physics of Solids*, vol. 55, no. 1, pp. 64–90, 2007.

[40] J. Němeček, "Creep effects in nanoindentation of hydrated phases of cement pastes," *Materials Characterization*, vol. 60, no. 9, pp. 1028–1034, 2009.

[41] J. Xu, D. J. Corr, and S. P. Shah, "Nanomechanical investigation of the effects of nanoSiO2 on C–S–H gel/cement grain interfaces," *Cement and Concrete Composites*, vol. 61, pp. 7–17, 2015.

[42] G. Constantinides, K. S. R. Chandran, F. J. Ulm, and K. J. V. Vliet, "Grid indentation analysis of composite microstructure and mechanics," *Materials Science and Engineering A*, vol. 430, no. 1-2, pp. 189–202, 2006.

[43] Y. Li, J. Chen, J.-H. Yang, J.-S. Liu, and W.-S. Tong, "Determination of shale macroscale modulus based on microscale measurement: a case study concerning multiscale mechanical characteristics," *Petroleum Science*, 2021.

[44] F. J. Ulm, M. Vandamme, C. Bobko, J. Alberto Ortega, K. Tai, and C. Ortiz, "Statistical indentation techniques for hydrated nanocomposites: concrete, bone, and shale," *Journal of the American Ceramic Society*, vol. 90, no. 9, pp. 2677–2692, 2007.

[45] F. Zhang, H. Q. Guo, D. W. Hu, and J. F. Shao, "Characterization of the mechanical properties of a claystone by nano-

indentation and homogenization," *Acta Geotechnica*, vol. 13, no. 6, pp. 1395–1404, 2018.

[46] Y. H. Zhang, M. Lebedev, A. Al-Yaseri et al., "Nanoscale rock mechanical property changes in heterogeneous coal after water adsorption," *Fuel*, vol. 218, pp. 23–32, 2018.

[47] X. G. Zhang, P. Ranjith, Y. Y. Lu, and A. Ranathunga, "Experimental investigation of the influence of CO_2 and water adsorption on mechanics of coal under confining pressure," *International Journal of Coal Geology*, vol. 209, pp. 117–129, 2019.

[48] M. E. Broz, R. F. Cook, and D. L. Whitney, "Microhardness, toughness, and modulus of Mohs scale minerals," *American Mineralogist*, vol. 91, no. 1, pp. 135–142, 2006.

[49] T. Mori and K. Tanaka, "Average stress in matrix and average elastic energy of materials with misfitting inclusions," *Acta Metallurgica*, vol. 21, no. 5, pp. 571–574, 1973.

Hindawi
Geofluids
Volume 2022, Article ID 5791006, 13 pages
https://doi.org/10.1155/2022/5791006

Research Article

Research on Crack Propagation of Deep Geologic Mass Disturbed by Excavation Based on Phase Field Method

Ningdong Chang[1], **Jinan Wang**[1,2] **and Fei Li**[1]

[1]*School of Civil and Resource Engineering, University of Science and Technology Beijing, Beijing 100083, China*
[2]*Key Laboratory of Ministry of Education for Efficient Mining and Safety of Metal Mines, Beijing 100083, China*

Correspondence should be addressed to Fei Li; lifei2016@ustb.edu.cn

Received 9 March 2022; Accepted 21 April 2022; Published 9 May 2022

Academic Editor: Zhijie Wen

In recent years, the phase field fracture model has been widely studied and applied. It has good convergence in crack propagation simulation. Comparing with other methods, the phase field method has advantages in simulating crack intersection, bifurcation, and three-dimensional propagation. Based on the phase field method, the influence of excavation disturbance on crack initiation of rock mass is realized in this paper. The phase field fracture variational model is built by using user-defined element interface (UEL) and user material subroutine (UMAT) in ABAQUS. Firstly, the prefabricated crack propagation simulation is carried out to verify the algorithm. The fracture initiates in a butterfly shape and then expands along the horizontal direction. The results show that the maximum support reaction decreases with the gradual increase of l, which is compared with the results obtained by Miehe et al. The result proved the correctness and reliability of the algorithm. In this paper, the phase field fracture model of a flat plate with a reserved small hole under the upper tension is established. The results show that the crack finally produces a crack in the lower left and upper right directions of the square hole and continues to extend to the model boundary, which proves the feasibility of crack independent initiation and propagation by the phase field method. The stress formed a butterfly region until the fracture occurs. And the butterfly stress distribution was still present at the end of crack propagation. The maximum vertical stress was 1.7×103 MPa. Based on the South-to-North Water Transfer Project, the simulation of tunnel crack propagation under excavation disturbance is realized for the first time, which is based on the phase field method. The results show that the influence area of excavation disturbance will increase after considering crack development. Comparing the simulation results without considering crack propagation with the simulation results considering crack propagation, it is found that the stress level in the excavation disturbance area around the tunnel is greatly affected by cracks. When the crack is not considered, the maximum vertical stress is 2.16×105 Pa, and the maximum horizontal stress is 9.35×105 Pa, which occurs at the waist of the tunnel on the horizontal axis. When the crack is considered, the maximum vertical stress is 2.53×105 Pa, and the maximum horizontal stress is 1.10×106 Pa. It shows that the stress at the dome increases greatly. The vertical stress reaches 3.68×105 Pa, and the horizontal stress is up to 3.07×103 Pa. For the rock mass far away from the excavation disturbance area, because part of the elastic strain energy is absorbed by the surface crack, the stress level considering the crack is lower than that without the crack. But it is basically similar, indicating the accuracy of the phase field fracture model. This paper realizes the simulation of crack propagation under excavation disturbance and provides a way for the application of phase field fracture model in rock mechanics. This paper proves that phase field method has broad prospects in simulating rock crack propagation and provides the possibility for the popularization of phase field method.

1. Introduction

In rock engineering, crack initiation and development are the main failure modes of rock. The crack development eventually leads to rock fracture [1, 2]. The crack development also leads to local stress disturbance. Therefore, numerical simulation of fracture is of great significance in the field of geotechnical engineering.

At present, finite element methods for crack propagation can be divided into two categories: One is geometric crack

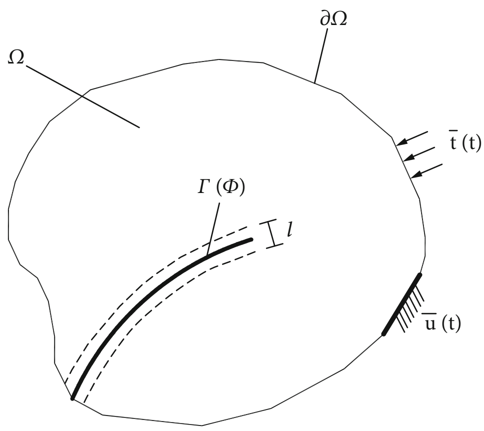

FIGURE 1: Crack described with a phase field mode.

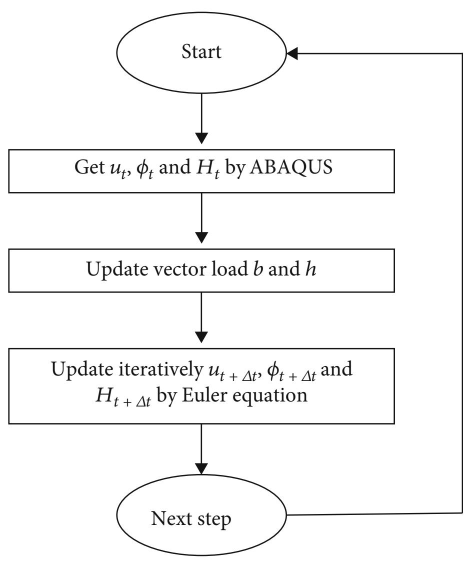

FIGURE 2: The process for solving phase field model.

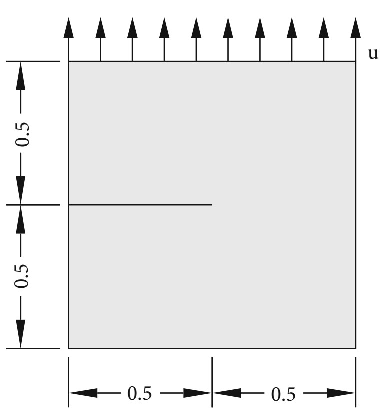

FIGURE 3: Geometric model and the location of crack (mm).

description method based on grid expansion, such as element deletion method [3] and interface element method. The element deletion method is a relatively simple method to describe the crack by discontinuous means. In this method, the stress of the element becomes 0 when it reaches the fracture critical [4]. The interface element method [5, 6] inserts cohesive interface elements between elements. When reached the critical condition of fracture, the interface element will be disconnected. The interface element method only allows the crack to expand on the boundary of the element [7]. This type of approach allows Raven to extend only at the boundaries of the cell. The other is the nongeometric description method, which is the diffusion crack model, such as the smooth particle hydrodynamics (SPH), the diffuse element method (DFM), the extended finite element method (XFEM), and phase field methods. Lucy and Gingold first applied the smooth particle hydrodynamics in the field of astrophysics [8, 9]. Nayrole et al. proposed the scatterer method in 1992 [10]. This method is collectively known as the meshless method. Although the meshless method does not need element structure, its crack propagation needs manual setting, and its computational efficiency is very low. Extended finite element method (XFEM) [11, 12] combined displacement field related parameters with variational function and test function by using the shape function. The fracture has nothing to do with the grid by using XFEM. The expansion of cracks can be achieved within the grid, but its calculation is limited to a few relatively simple bifurcation problems of crack. It is difficult to solve the three-dimensional model of crack propagation simulation [13, 14]. The phase field method [15] used the dispersed phase boundary to approximate the actual sharp boundary, which implemented a model describing fracture with continuous functions. By using phase field variables, the phase field method can explicitly track crack, instead of tracking the surface of crack. The propagation path of crack can be obtained by the evolution of order parameters. So, the phase field method of crack propagation simulation is not affected by meshing. Moreover, it has good convergence [16] and can also realize crack propagation in the grid.

In recent years, phase field model has been applied to fracture field. It has attracted extensive attention in this field. Emilio [17] realized the operation of phase field fracture model in user-defined unit interface (UEL) and user material subroutine (UMAT) of ABAQUS, but the model is simple. Hofacker [18, 19] established the evolution of complex crack mode for dynamic problems and applied interlacing algorithm to phase field simulation. He provided the basis for solving dynamic problems. Park [20] realized the refinement model of adaptive grid and carried out the simulation of cohesive cracks under dynamic loading. Liu Guowei [21] used ABAQUS platform to realize the step algorithm of phase field fracture model and analyzed the problem of two parallel air foil crack intersection. Cao Yakuo [22] studied the fracture process of elastic-plastic plate with holes at different spatial distances based on the elastic-plastic fracture theory of metal. It provided a thought for solving the elastic-plastic problem. Liu Jia [23] established a phase field model of hydraulic coupling based on porous elasticity theory and energy minimization theory. It solves the problem of phase field seepage.

The phase field fracture method describes the physical process of fracture through a series of differential equations, so as to avoid the tedious crack surface tracking. It has great advantages in simulating crack initiation, propagation, and

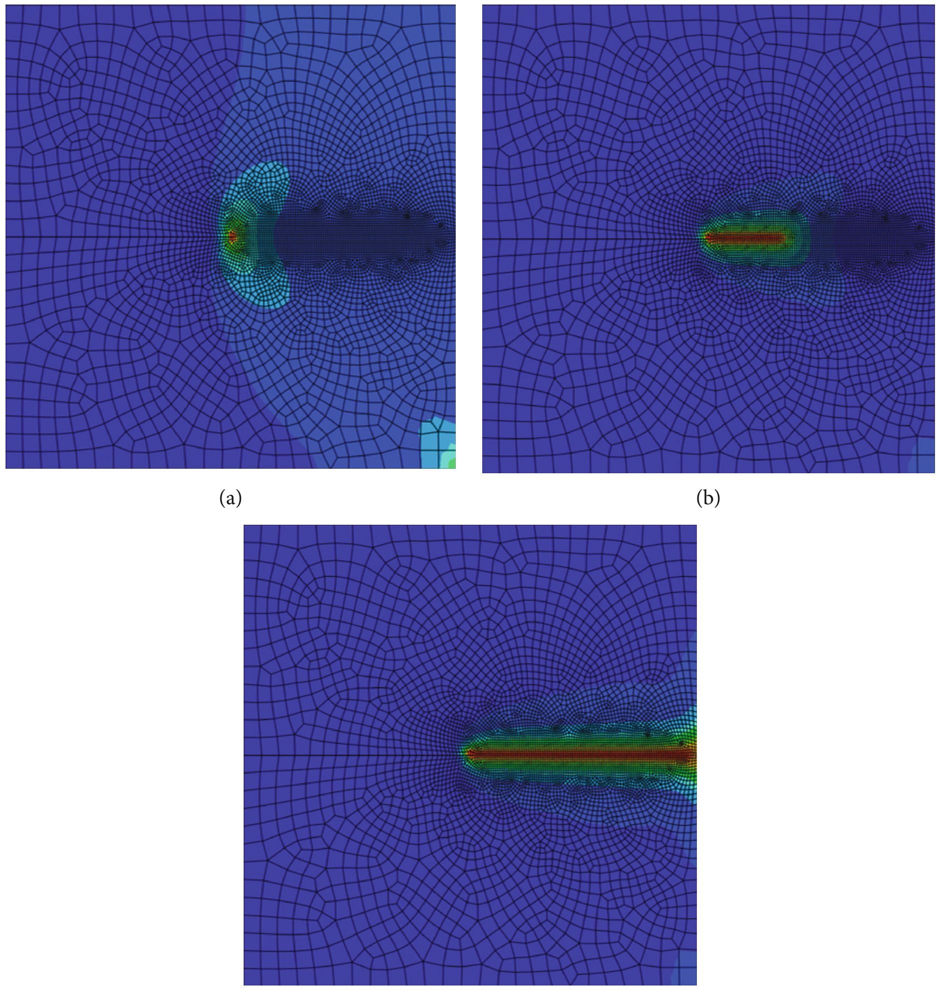

(a) (b) (c)

Figure 4: The propagation of crack when $l = 0.015$mm. (a) Crack initiation stage. (b) Crack development stage. (c) Crack penetration stage.

bifurcation. At present, most of the phase field method simulation is a two-dimensional simple model of single homogeneous material, and there is no correlation analysis of excavation disturbance. Based on the phase field method, this paper established a composite stratum model and realized the excavation simulation by element deletion.

In this paper, the user-defined element (UEL) of finite element software ABAQUS is used to calculate the propagation of prefabricated crack and the crack propagation of perforated plate during tensile, which verified the correctness of the code. The deep rock mass disturbed by excavation will crack on the excavation boundary, which will lead to local stress concentration of rock mass. Finally, rock mass will break and be instability. Therefore, it is of great significance to study the stress distribution of deep rock mass disturbed by excavation.

2. Phase Field Method Fracture Model

2.1. Fracture Variational Theory. The phase field method is based on Ginzburg-Laudau theory. Hakim and Karma proposed the phase field model [15], which defines the free energy of the fracture system as follows:

$$F(u, s) = \int \left\{ g(\phi)[\psi_0(\varepsilon(u)) - \psi_c] + V(\phi) + \frac{1}{2} D_\phi |\nabla\phi|^2 \right\} dx, \quad (1)$$

where ϕ is the order parameter; $g(\phi)$ is the interpolation function, $g(\phi) = \phi^{2+\alpha}$; ψ_0 is strain energy density; ψ_c is the critical strain energy density; $V(\phi)$ is the two potential well function, $V(\phi) = \phi^2(1-\phi^2)/4$; and D_ϕ is surface parameter. The first two terms are the body free energy term and the last term is the surface energy term.

In 1920, Griffith proposed Griffith energy theory based on energy [24], but this theory is suitable for simple model. It is difficult to analyze the complex crack model. In 1998, G. A. Francfor and J. J. Marigo proposed a variational method for fracture problems, which was based on the Griffith energy theory [25]. The total potential energy Π of elastomer Π can be divided into elastic energy of elastomer and

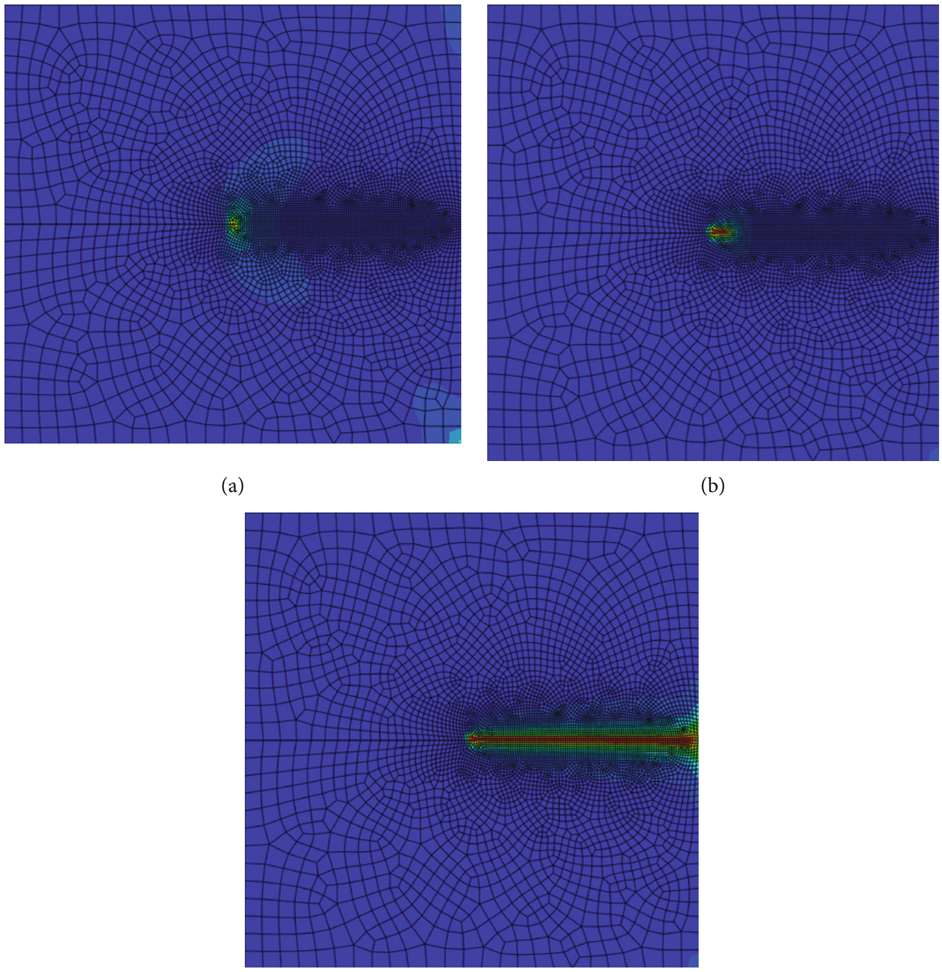

(a) (b) (c)

Figure 5: The propagation of crack when $l = 0.0075$mm. (a) Crack initiation stage. (b) Crack development stage. (c) Crack penetration stage.

surface energy of fracture:

$$\prod(u, \Gamma) = \int_{\Omega} \psi_e(\varepsilon(u)) d\Omega + \int_{\Gamma} G_c d\Gamma, \quad (2)$$

where ψ_e is the elastic energy density; $\varepsilon(u)$ is the strain tensor; and G_c is the critical energy release rate.

In the fracture variational model proposed by Francfor and Marigo, the crack propagation is controlled by the principle of minimum free energy. However, the boundary integral of surface energy in this method is not easy to deal with in the case of unknown crack boundary. In 2000, Bourdin and Francfort introduced the order parameter [26] and defined one in the interval [0, 1]. When $\phi = 0$, it means that the material is intact. When $\phi = 1$, it means that the material is completely fractured, as shown in Figure 1. The crack surface density can be expressed as

$$\gamma(\phi, \nabla\phi) = \frac{1}{2l}\phi^2 + \frac{l}{2}|\nabla\phi|^2, \quad (3)$$

where l is the characteristic length parameter and the time length parameter determines the diffusion degree of the crack. When $l \longrightarrow 0$, the characterization is closer to the tip crack. However, the size of L does not represent the actual width of crack diffusion.

Then, the total surface energy of cracks in the elastic body can be expressed as

$$\int_{\Gamma} G_c d\Gamma \approx \int_{\Omega} G_c \left[\frac{(\phi - 1)^2}{2l} + \frac{l}{2}|\nabla\phi|^2\right] d\Omega, \quad (4)$$

where G_c is the critical value of Griffith energy release rate of material per unit area.

To analyze the fracture phase field, the total energy function of the material can be expressed as

$$\Psi(u, \phi) = \Psi^b(u, \phi) + \Psi^s(\phi), \quad (5)$$

where $\Psi^b(u, \phi)$ is the elastic strain energy stored in the material and $\Psi^s(\phi)$ is the surface strain energy related to the crack.

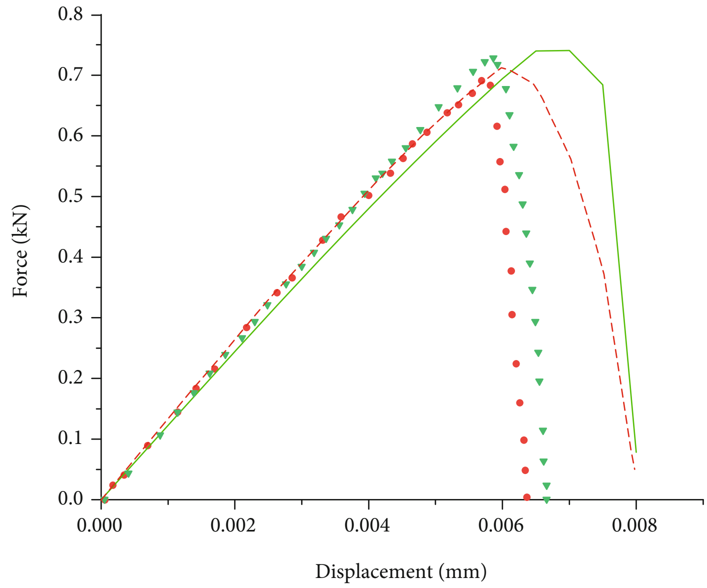

FIGURE 6: Comparison of load-displacement curves of different l.

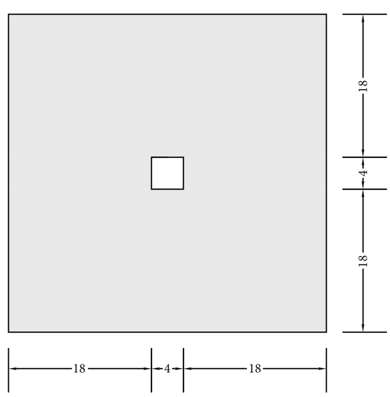

FIGURE 7: Prefabricated cavity plate model (m).

The elastic strain energy can be expressed by the elastic strain as

$$\Psi^b(u,\phi)=\int_\Omega \psi(\varepsilon(u),\phi)dV, \tag{6}$$

where u is the displacement of material; ϕ is the fracture phase field variable; energy storage function ψ of material per unit volume can be expressed as $\psi(\varepsilon,\phi)=g(\phi)\psi_0(\varepsilon)$; ψ_0 is the elastic strain energy density; $g(\phi)$ can be expressed as $g(\phi)=(1-\phi)^2+k$, and k is a very small constant.

Based on the above formula, the total energy function of materials can be expressed as

$$\Psi(u,\phi)=\int_\Omega\left\{\left[(1-\phi)^2+k\right]\psi_0(\varepsilon)+G_c\left[\frac{1}{2l}\phi^2+\frac{l}{2}|\nabla\phi|^2\right]\right\}dV, \tag{7}$$

2.2. Fracture Governing Equation by Phase Field Method. The energy of the system can be divided into external work generated by the application of load and internal work generated by deformation. The external energy increment δW_{ext} can be expressed as

$$\delta W_{\text{ext}}=\int_V b\delta u dV+\int_{\delta V} h\delta u\partial V, \tag{8}$$

where b is the body force per unit volume unit and h is the boundary surface force per unit area.

The change of internal potential energy increment is

$$\partial W_{\text{int}}=\partial\psi=\frac{\partial\psi}{\partial\varepsilon}\delta\varepsilon+\frac{\partial\psi}{\partial\phi}\delta\phi. \tag{9}$$

Combined with Equation (7), the internal potential energy increment can be expressed as

$$\partial W_{\text{int}}=\int_\Omega\left\{\boldsymbol{\sigma}\delta\varepsilon-2(1-\phi)\delta\phi\psi(\varepsilon)+G_c\left[\frac{1}{l}\phi\delta\phi+l\nabla\phi\cdot\nabla\delta\phi\right]\right\}dV, \tag{10}$$

where $\boldsymbol{\sigma}$ is Cauchy stress tensor,

$$\boldsymbol{\sigma}=\frac{\partial\psi}{\partial\varepsilon}=g(\phi)\boldsymbol{\sigma}_{\mathbf{0}}=\left[(1-\phi)^2+k\right]\boldsymbol{\sigma}_{\mathbf{0}}. \tag{11}$$

Assuming that the model is a quasi-static process, the virtual work done by the external force of the structure is equal to the virtual work done by the internal force of the

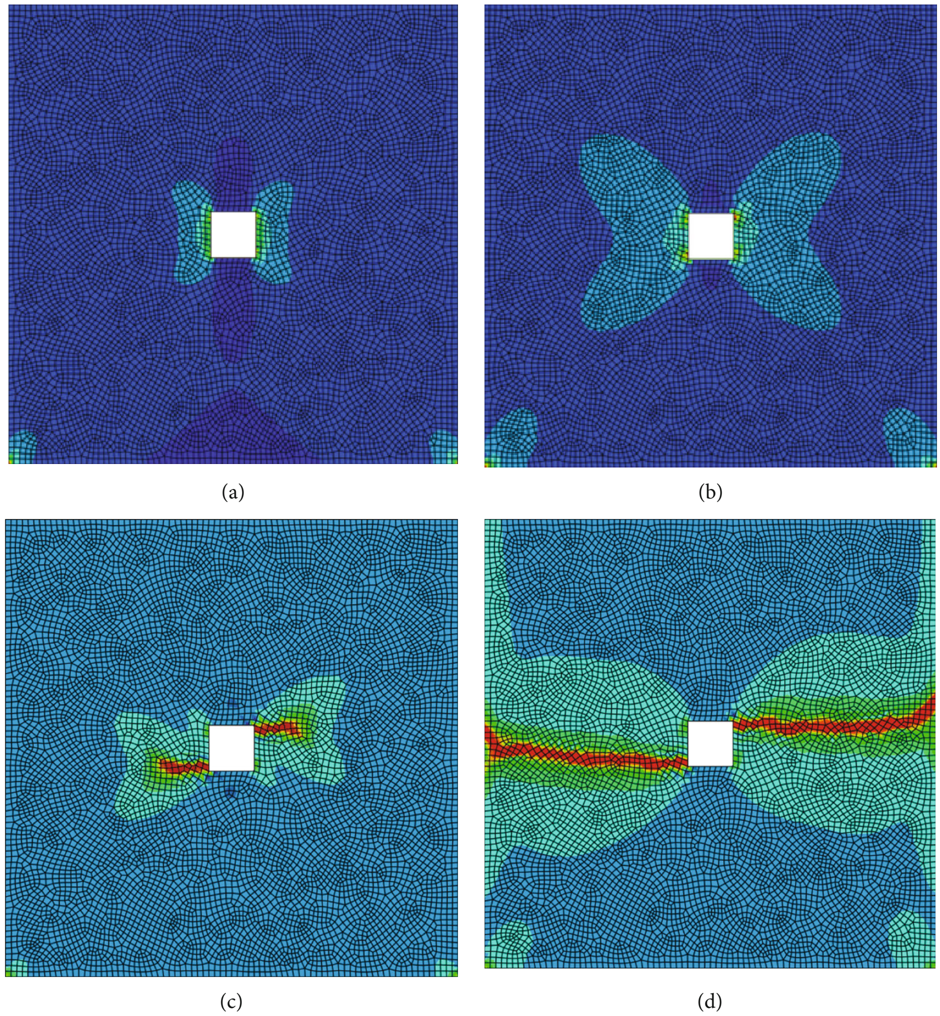

FIGURE 8: The result of crack propagation. (a) Crack initiation stage. (b) Crack initiation stage. (c) Crack development stage. (d) Crack penetration stage.

structure.

$$\partial W_{\mathrm{int}} - \partial W_{\mathrm{ext}} = 0. \tag{12}$$

Combining Equations (8) with Equation (10), Dirichlet boundary conditions are considered, and Gauss theorem is used to obtain

$$\begin{aligned}&\int_{\partial\Omega} [G_c l \nabla\phi \cdot \boldsymbol{n}] \cdot \delta\phi dA + \int_{\Omega} \\ &\left\{ -[Div[\boldsymbol{\sigma}] + \boldsymbol{b}] \cdot \delta\boldsymbol{u} - \left[2(1-\phi)\psi(\varepsilon) - G_c \left[\frac{1}{l}\phi + Div(l\nabla\phi) \right] \right] \delta\phi \right\} dV \\ &+ \int_{\partial\Omega_{\mathrm{h}}} [\boldsymbol{\sigma} \cdot \boldsymbol{n} - \boldsymbol{h}] \cdot \delta\boldsymbol{u} dA = 0,\end{aligned} \tag{13}$$

where n is the unit vector perpendicular to the plane.

Considering the Neumann boundary conditions $\boldsymbol{\sigma} \cdot \boldsymbol{n} = \boldsymbol{h}$ (on $\partial\Omega_{\mathrm{h}}$) and $\nabla\phi \cdot \boldsymbol{n} = 0$ (on $\partial\Omega$), the strong form of the governing equation of the phase field method fracture model is

$$\begin{cases} Div[\boldsymbol{\sigma}] + \boldsymbol{b} = 0, \\ G_c \left[\dfrac{1}{l}\phi + l\nabla\phi \right] - 2(1-\phi)\psi(\varepsilon) = 0. \end{cases} \tag{14}$$

3. Realize Fracture Finite Element by Using Phase Field Method

In order to solve the numerical solution of partial differential Equation (14), the weak form of the governing equation is solved by finite element method.

$$\begin{cases} \displaystyle\int_{\Omega} [\sigma\delta\varepsilon - \boldsymbol{b} \cdot \delta\boldsymbol{u}] \mathrm{d}V + \int_{\partial\Omega_{\mathrm{h}}} h \cdot \delta\boldsymbol{u} dA = 0, \\ \displaystyle\int_{\Omega} \left\{ -2(1-\phi)\delta\phi\psi(\varepsilon) + G_c \left[\frac{1}{l}\phi\delta\phi + l\nabla\phi \cdot \nabla\delta\phi \right] \right\} dV = 0. \end{cases} \tag{15}$$

Using the Voigt-notation method for discretization,

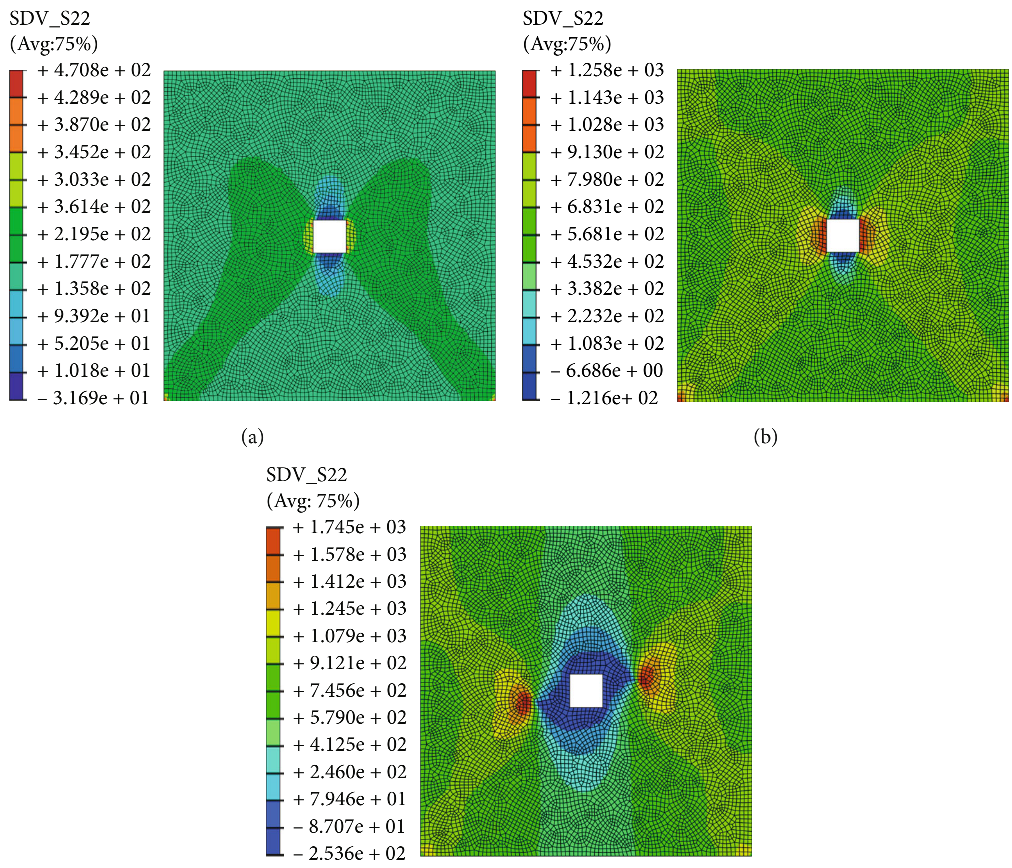

Figure 9: The vertical stress when the crack grows. (a) Crack initiation stage. (b) Crack initiation stage. (c) Crack development stage.

displacement field variables u and phase field variables ϕ on cell nodes I can be expressed as

$$\boldsymbol{u} = \sum_{i=1}^{n} N_i^u \boldsymbol{u}_i, \phi = \sum_{i=1}^{n} N_i^u \phi_i, \tag{16}$$

where n is the number of nodes on a cell; N_i is the corresponding shape function on the node I, and the shape function matrix in two-dimensional case is

$$N_i^u = \begin{bmatrix} N_i & 0 \\ 0 & N_i \end{bmatrix}. \tag{17}$$

Accordingly, the derivative of the form function can be discretized as

$$\boldsymbol{\varepsilon} = \sum_{i=1}^{n} \boldsymbol{B}_i^u \boldsymbol{u}_i, \nabla\phi = \sum_{i=1}^{n} \boldsymbol{B}_i^\phi \phi_i, \tag{18}$$

where $\boldsymbol{\varepsilon} = [\varepsilon_{xx}, \varepsilon_{yy}, \varepsilon_{xy}]^T$.

Strain-displacement matrix and phase field matrix are

$$\boldsymbol{B}_i^u = \begin{bmatrix} N_{i,x} & 0 \\ 0 & N_{i,y} \\ N_{i,y} & N_{i,x} \end{bmatrix}, \boldsymbol{B}_i^\phi = \begin{bmatrix} N_{i,x} \\ N_{i,y} \end{bmatrix}. \tag{19}$$

Then, the gradient of displacement variable and phase field variable can be expressed as

$$\delta\boldsymbol{\varepsilon} = \sum_{i=1}^{n} \boldsymbol{B}_i^{\delta u} \boldsymbol{u}_i, \nabla\phi = \sum_{i=1}^{n} \boldsymbol{B}_i^\phi \delta\phi_i. \tag{20}$$

To ensure that $\partial W_{\text{int}} - \partial W_{\text{ext}} = 0$ for any u and ϕ, and, therefore, to ensure balance, the residual of its equation can be expressed as

$$\begin{aligned} R_i^u &= \int_\Omega \left[(1-\phi)^2 + k\right] (\boldsymbol{B}_i^u)^T \sigma dV - \int_\Omega (N_i^u)^T b dV - \int_{\partial\Omega_h} (N_i^u)^T h dA, \\ R_i^\phi &= \int_\Omega \left\{-2(1-\phi) N_i \psi(\varepsilon) + G_c \left[\frac{1}{l} N_i \phi + l \left(\boldsymbol{B}_i^\phi\right)^T \nabla\phi\right]\right\} dV. \end{aligned} \tag{21}$$

In order to get the residual close to 0, Newton-Raphson

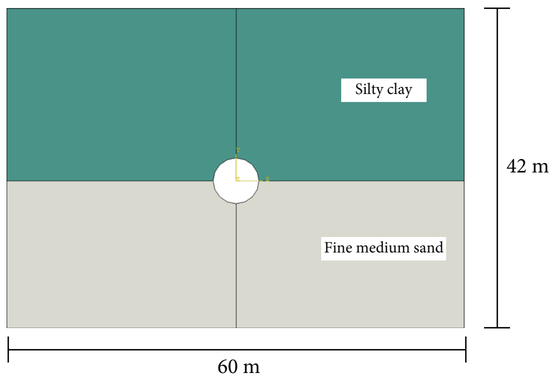

Figure 10: Initial model around pile No. 21+979.

Table 1: Parameters of geological model around pile No. 21+979.

Number	Stratum	Density (10^3kg/m^3)	Elasticity modulus (MPa)	Poisson's ratio
1	Silty clay	1.96	5.94	0.3
2	Fine medium sand	2.00	13.5	0.2

method is used for incremental iteration.

$$\begin{Bmatrix} u \\ \phi \end{Bmatrix}_{t+\Delta t} = \begin{Bmatrix} u \\ \phi \end{Bmatrix}_t - \begin{bmatrix} K^{uu} & K^{u\phi} \\ K^{\phi u} & K^{\phi\phi} \end{bmatrix}_t^{-1} \begin{Bmatrix} R^u \\ R^\phi \end{Bmatrix}_t. \tag{22}$$

The governing equation is a partial differential equation system composed of quasi-static equilibrium equation and phase field equation. However, in order to prevent crack closure when the elastic body is under pressure or unloading springback and ensure the irreversible process of crack evolution ($\phi_{t+\Delta t} \geq \phi_t$), a historical state variable H is introduced to realize the irreversible process.

$$H = \begin{cases} \psi(\varepsilon), \psi(\varepsilon) > H_t \\ H_t, \psi(\varepsilon) \leq H_t \end{cases}. \tag{23}$$

Therefore, after considering the historical state variables, the residual corresponding to phase field crack evolution is

$$R_i^\phi = \int_\Omega \left\{ -2(1-\phi)N_i H + G_c \left[\frac{1}{l} N_i \phi + l \left(\boldsymbol{B}_i^\phi \right)^T \nabla\phi \right] \right\} dV. \tag{24}$$

The residual of the displacement field is

$$R_i^u = \int_\Omega \left[(1-\phi)^2 + k \right] (\boldsymbol{B}_i^u)^T \sigma dV - \int_\Omega (N_i^u)^T b dV - \int_{\partial\Omega_h} (N_i^u)^T h dA. \tag{25}$$

The stiffness matrix gradually degenerates in the process of crack initiation and propagation, which will result in constant rearrangement of the stress field. The implicit solver

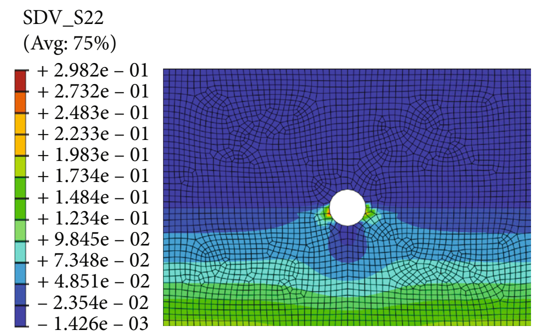

Figure 11: Crack propagation under the disturbance of excavation.

cannot be used to obtain a stable equilibrium solution. Therefore, the displacement field and phase field in Equation (14) are considered as coupling fields and solved separately. Considering the historical state variables, Equation (14) can be expressed as

$$G_c \left[\frac{1}{l} \phi + l \nabla\phi \right] - 2(1-\phi)H = 0. \tag{26}$$

By using the Newton-Raphson method for iteration, the Equation (23) can be expressed as

$$\begin{Bmatrix} u \\ \phi \end{Bmatrix}_{t+\Delta t} = \begin{Bmatrix} u \\ \phi \end{Bmatrix}_t - \begin{bmatrix} K^{uu} & 0 \\ 0 & K^{\phi\phi} \end{bmatrix}_t^{-1} \begin{Bmatrix} R^u \\ R^\phi \end{Bmatrix}_t, \tag{27}$$

where each stiffness matrix is

$$\begin{cases} K_{ij}^{uu} = \dfrac{\partial R_i^u}{\partial u_j} = \displaystyle\int_\Omega \left[(1-\phi)^2 + k \right] (\boldsymbol{B}_i^u)^T \boldsymbol{C}_0 \boldsymbol{B}_j^u dV, \\ K_{ij}^{\phi\phi} = \dfrac{\partial R_i^\phi}{\partial \phi_j} = \displaystyle\int_\Omega \left\{ \left[2H + \frac{G_c}{l} \right] N_i N_j + G_c l \left(\boldsymbol{B}_i^\phi \right)^T \boldsymbol{B}_j^\phi \right\} dV. \end{cases} \tag{28}$$

In this paper, ABAQUS is used to realize the phase field method fracture simulation. This research realized the phase field method model by using UEL of ABAQUS. The relevant stiffness matrix is updated in UEL. The specific process is shown in Figure 2. Due to the use of user element subroutine, the integral points defined by it cannot be visualized independently in ABAQUS postprocessing. However, the element stiffness matrix and stress-strain results on each node can be obtained. In order to realize the visualization of the results, this paper creates an auxiliary grid by using UMAT to define the relevant material parameters at each integral point of the auxiliary grid. Then, transmit the data of user unit subroutine to user material subroutine, and output SDV variables for final visualization. The stress component and stiffness matrix of the auxiliary virtual grid are zero, which have no influence on the solution result.

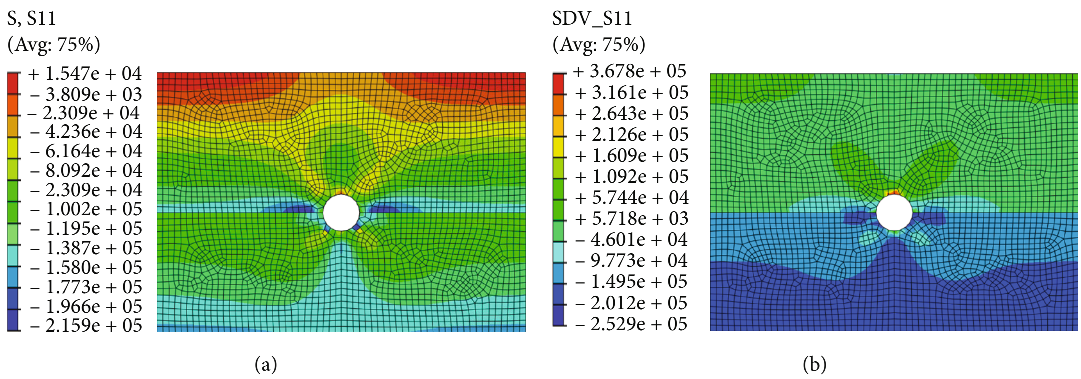

Figure 12: Horizontal stress distribution after excavation. (a) No cracks. (b) Consider cracks.

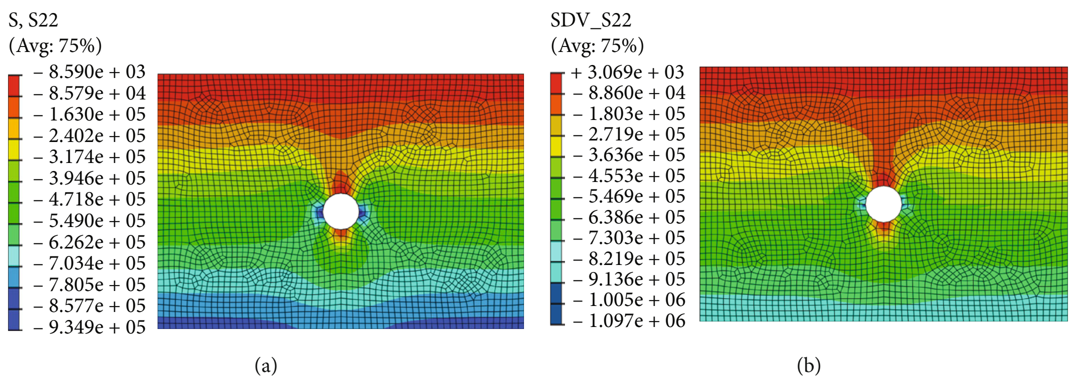

Figure 13: Vertical stress distribution after excavation. (a) No cracks. (b) Consider cracks.

4. Numerical Simulation Examples and Verification

4.1. A Case of Prefabricated Crack Propagation. To verify the correctness of the code, a square plate with prefabricated cracks on the left side was created. The specific size of the plate is shown in Figure 3. The lower boundary of the model was fixed. The upward displacement plate of 0.01 mm was applied to the upper boundary. The Young's modulus $E = 210GPa$. Poisson's ratio is $\mu = 0.3$. The critical energy release rate is $G_c = 2.7 \times 10^{-3} kN/mm$.

In this paper, the crack length parameters were, respectively, selected as $l = 0.015$mm and $l = 0.0075$mm. The crack propagation results are shown in Figures 4 and 5. In the figure, the blue area represented no failure, while the red area represented complete failure. The fracture initiates in a butterfly shape and then expands along the horizontal and vertical direction. Finally, the crack reaches the right side of the model.

Figure 6 shows the comparison between the reaction force and displacement curve calculated in this paper and Miehe [27]. At that time, the maximum support reaction force calculated was 0.71 kN, and the maximum support reaction force calculated was 0.74 kN. The calculation results were basically consistent with the crack growth and support reaction displacement curve obtained by Miehe. Although there is a small deviation on the curve, the maximum reaction force is basically similar, which is consistent with the results of Miehe. It is found that with the increase of l, while the maximum reaction force decreases. The result verifies the correctness of the phase field code.

4.2. A Case of Tensile Crack Propagation of Perforated Plate. A square plate with side length of 40 m was established. And a square hole with one side length of 4 m was established in the center of the plate, as shown in Figure 7. Young's modulus $E = 210GPa$, Poisson's ratio $\mu = 0.3$, and critical energy release rate $G_c = 2.7 \times 10^{-3} kN/mm$ were used to fix the lower boundary of the CPE4 unit model, and upward displacement was applied to the upper boundary of the model. The lower boundary of the CPE4 element model is fixed, and the upper boundary of the model is subjected to upward displacement.

Characteristic length $l = 0.04$m. The crack extension results are shown in Figure 8. The results showed that symmetrical butterfly-shaped microcracks appear around the hole in the initial stage. At this time, the structure damage was small. As the tension continued to be applied, the butterfly area expanded, eventually creating cracks in the upper right and lower left corners of the square hole. And the crack continued to expand and develops to the edge of the model, which proved the feasibility of crack initiation and self-propagation.

The variation of vertical stress with crack growth in this example is shown in Figure 9. The results showed that there was a great stress concentration at the four corners of the hole at the initial stage of crack development. And the stress distribution likes the butterfly. The maximum vertical stress was 4.7×102 MPa. The stress on both sides of the hole

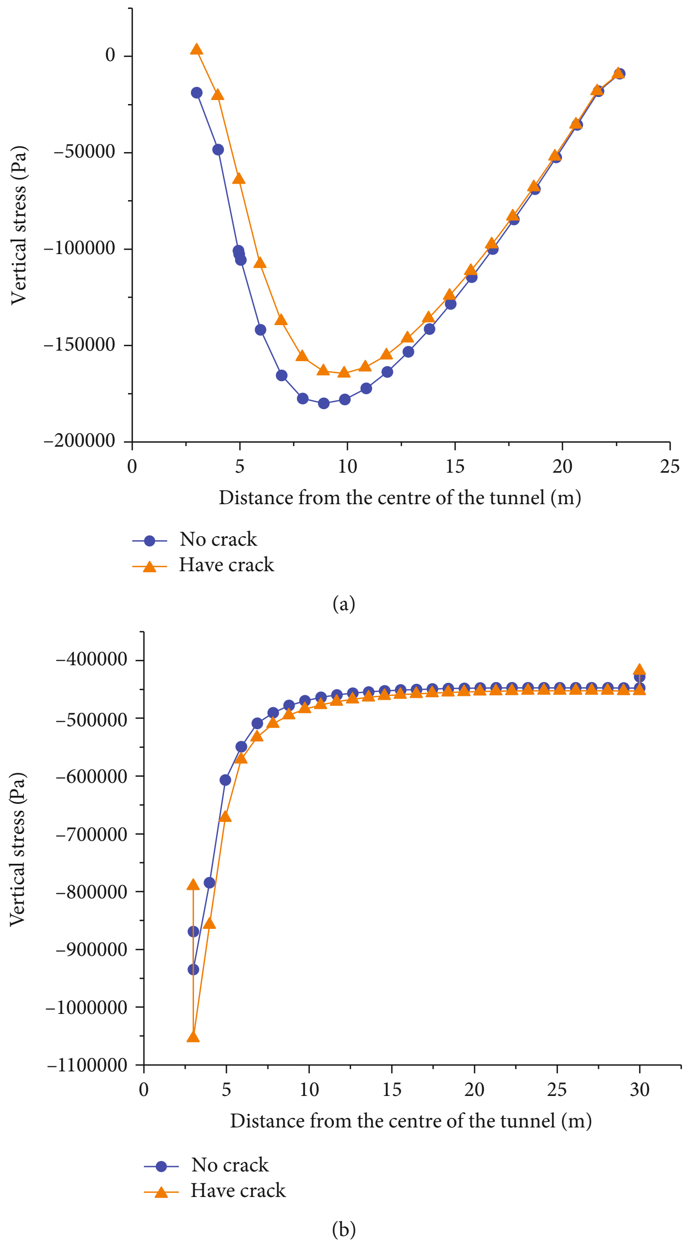

Figure 14: Comparison of vertical stress after excavation. (a) Above the vertical axis of the tunnel. (b) Right of horizontal axis of tunnel.

gradually increased and gradually formed a butterfly region until the fracture occurs. The stress on both sides of the hole is positive, and the stress above and below the hole is negative. The maximum vertical stress was 1.23×103 MPa. Crack propagation begins at this time. After that, the crack propagated gradually. And the butterfly stress distribution was still present at the end of crack propagation. At this time, the maximum vertical stress was 1.7×103 MPa.

4.3. A Case of Crack Propagation in Composite Stratum Disturbed by Excavation

4.3.1. Engineering Background. As a strategic project in China, the South-to-North Water Diversion Project is an extremely large infrastructure project to solve the serious shortage of water resources in the north and implement the optimal allocation of water resources. It plays a very important role in alleviating the bearing pressure of water resources and improving the water supply security and guarantee rate in Beijing.

Under the influence of excavation disturbance, some stress concentration occurs in the geological body of Eastern Canal in Beijing, which leads to lining damage and pipeline leakage. Therefore, the pile no. 21+979 and its surrounding area of Eastern Canal of the South-to-North Water Diversion Project were selected for the analysis. Crack propagation and stress disturbance were analyzed in this case. The left and right width of the numerical model near pile no.

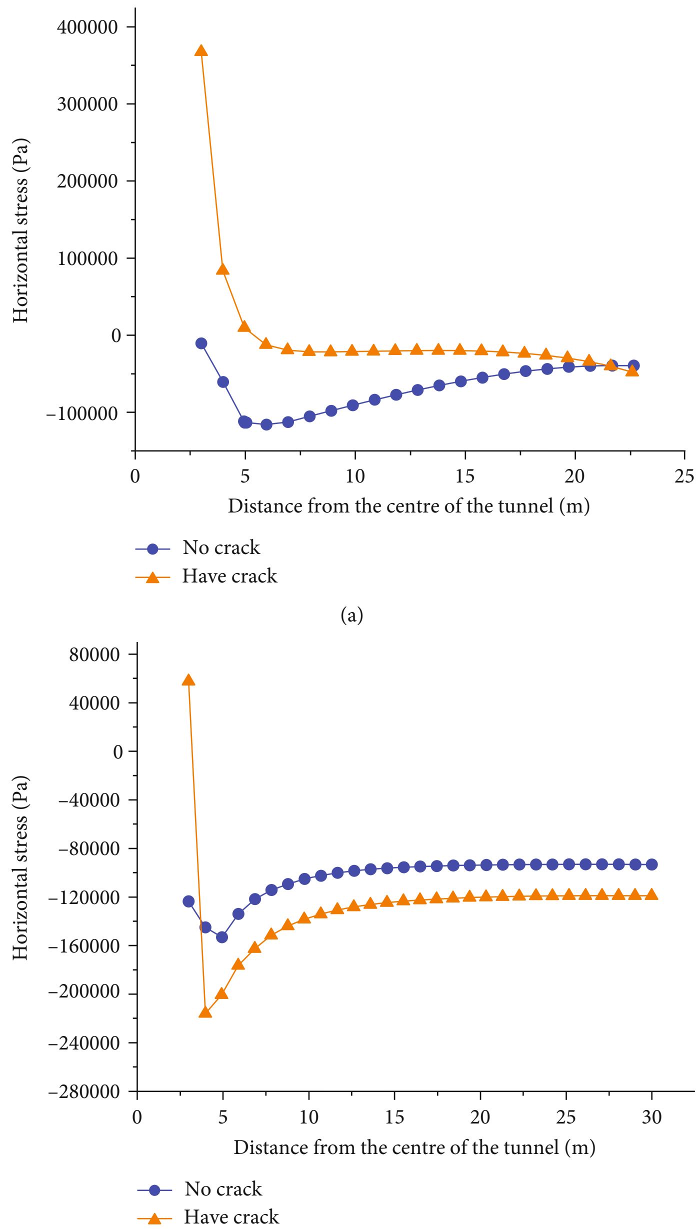

FIGURE 15: Comparison of horizontal stress after excavation. (a) Above the vertical axis of the tunnel. (b) Right of horizontal axis of tunnel.

21+979 is 60 m. The tunnel buried depth is 19.62 m. The depth below the axis of the tunnel is 22.38 m and the tunnel radius is 3 m.

According to the site geological survey data, the strata were simplified, and a composite stratum tunnel model was established. The tunnel size and stratum distribution are shown in Figure 10. The material parameters are shown in Table 1. Material critical energy release rate is $G_c = 2.7 \times 10^{-3} kN/mm$. Controlling the parameters of diffuse crack width is $l = 0.04$m.

4.3.2. Realization of Phase Field Method. In order to simulate the initial stress state of rock and soil mass, the ground stress balance was carried out first. Then, the excavation was carried out. The specific process of the excavation of rock and soil mass simulated based on the phase field method is as follows:

(1) Establish the initial composite formation model (without tunnel excavation). Fix the bottom boundary for the model, $u_x = 0$ and $u_y = 0$. The left and right boundaries of the model are fixed with normal displacement, $u_x = 0$. The initial geostress field of the model was obtained by the ground stress balance analysis step under the dead weight stress

(2) Delete some excavated units, renumber nodes and grids, and establish tunnel excavation model

(3) In the .inp file of ABAQUS, the fracture parameters related to the layer phase field method were defined and the virtual visualization grid was generated. Apply the initial in situ stress field calculated in the first step to the tunnel excavation model, and define the output variables to simulate the excavation of rock and soil mass, which considered the phase field method

Considering the crack growth, the crack growth is shown in Figure 11. After tunnel excavation, the cracks of the model are mainly distributed around the tunnel, and the weak links are on the horizontal sides of the tunnel. The crack initiation occurs firstly in horizontal direction and then gradually develops. After excavation, the stress of the tunnel is released, and the shape of tunnel is ellipse. Due to the maximum stress on both sides of the middle line of the tunnel, there is a large damage in this part. The crack begins to expand at the horizontal direction.

The horizontal stress cloud diagram after excavation is shown in Figure 12. Figure 12(a) is the horizontal stress result obtained without considering the phase field method, that is, without crack development; Figure 12(b) is the horizontal stress result obtained with crack development by using the phase field method. Both cases indicate that stress disturbance occurs in the surrounding area after tunnel excavation. When the crack is not considered, the maximum horizontal stress is 2.16×105 Pa, which occurs near the horizontal axis of the tunnel waist. When considering the crack, the maximum stress on the horizontal axis is 2.53×105 Pa, and it is found that the stress at the tunnel dome increases significantly, up to 3.68×105 Pa. It indicates that the crack development has a great influence on the stress.

The vertical stress cloud is shown in Figure 13. In situ stress is disturbed after excavation. When do not consider the crack, the maximum stress can reach 9.35×105 Pa. It occurs at the horizontal axis of the tunnel edge. When considering the crack development, the stress level around the tunnel increases due to the influence of the crack development. The maximum stress can reach 1.10×106 Pa. At the horizontal axis of the tunnel edge, the stress at the dome changes under the influence of the crack. It produces a vertical upward stress of 3.07×103 Pa.

After the phase field method is adopted to simulate the excavation, the stress around the tunnel changes greatly from considering the cracks, which is due to the development of cracks around the tunnel. In the area far away from the tunnel, it is less affected by the crack, as shown in Figures 14 and 15. However, its total stress level is reduced, which is due to part of the elastic energy into the surface energy of the crack. As the cracks developed along the horizontal axis, it can be found in Figure 14(b) and Figure 15(b) that when the distance from the center of the tunnel is 3 m (tunnel boundary), the stress level of the cracks is significantly different from that when the crack is not considered. The vertical stress reaches -7.90×105 MPa when the crack is considered. The vertical stress reaches -8.69×105 MPa when the crack is not considered. The horizontal stress is 5.76×104 MPa when the crack is considered and -1.24×105 MPa when the crack is not considered.

5. Conclusion

Based on ABAQUS platform, this paper realized the phase field method fracture model and simulated the crack growth of composite stratum under excavation disturbance. This paper realized the excavation simulation of composite stratum based on the phase field method. The main conclusions are as follows:

(1) By using UMAT/UEL of ABAQUS secondary development interface, prefabricated crack growth simulation, prefabricated hole crack growth simulation, and composite stratum crack growth simulation under excavation disturbance were carried out. Based on the previous phase field model, the simulation of various materials and the disturbance analysis of excavation to the model are realized in this paper

(2) The correctness and reliability of the phase field fracture model code were verified by comparing the results of prefabricated crack propagation simulation with those in other literature. It was found that the crack propagated in the upper right corner and the lower left corner of the hole through the tensile example of the perforated plate, which demonstrated the feasibility of the phase field method for the self-initiation and propagation of cracks. By comparing the crack growth model under excavation disturbance with the model without crack growth, it was found that the stress disturbance was great at the crack development. When considering the crack, the maximum stress on the horizontal axis was 2.53×105 Pa. It was found that the stress at the tunnel dome increased greatly, up to 3.68×105 Pa

(3) Based on the crack propagation model of composite strata established by phase field method, the crack distribution of rock mass after excavation disturbance and the fine in situ stress distribution around the tunnel are obtained. It provides an idea for simulating crack propagation in geotechnical engineering and lays a foundation for simulating in situ stress analysis in geotechnical excavation engineering

Data Availability

The data used to support the findings of this study are included within the article.

Conflicts of Interest

There is no conflict of interest regarding the publication of this paper.

Acknowledgments

The presented work has been financially supported by the National Key Research and Development Program of China (Grant No. 2017YFC1503104).

References

[1] H. Lin, H. Yang, Y. Wang, Y. Zhao, and R. Cao, “Determination of the stress field and crack initiation angle of an open flaw tip under uniaxial compression,” *Theoretical and Applied Fracture Mechanics*, vol. 104, p. 102358, 2019.

[2] H. Yang, H. Lin, Y. Chen et al., “Influence of wing crack propagation on the failure process and strength of fractured specimens,” *Bulletin of Engineering Geology and the Environment*, vol. 81, no. 1, 2022.

[3] R. Fan and J. Fish, “Thers-method for material failure simulations,” *International Journal for Numerical Methods in Engineering*, vol. 73, no. 11, pp. 1607–1623, 2008.

[4] J. Hallquist, *LS-DYNA Theoretical Manual*, Livemore Software Technology Corporation, USA, 1998.

[5] X. P. Xu and A. Needlemana, “*Numerical simulation of fast crack growth in brittle solids*,” *Journal of the Mechanics and Physics of Solids*, vol. 9, no. 42, pp. 1397–1434, 1994.

[6] G. Tcamacho and M. Ortiz, “Computational modelling of impact damage in brittle materials,” *International Journal of Solids and Structures*, vol. 33, no. 20-22, pp. 2899–2938, 1996.

[7] C. H. Sam, D. Katerina, and A. Stephen, “Obtaining initially rigid cohesive finite element models that are temporally convergent,” *Engineering Fracture Mechanics*, vol. 72, no. 14, pp. 2247–2267, 2005.

[8] L. B. Lucy, “A numerical approach to the testing of the fission hypothesis,” *The Astronomical Journal*, vol. 82, pp. 1013–1013, 1977.

[9] R. A. Gingold and J. J. Monaghan, “Smoothed particle hydrodynamics: theory and application to non-spherical stars,” *Monthly Notices of the Royal Astronomical Society*, vol. 181, no. 3, pp. 375–389, 1977.

[10] B. Nayroles, G. Touzot, and P. Villon, “Generalizing the finite element method: diffuse approximation and diffuse elements,” *Computational Mechanics*, vol. 10, no. 5, pp. 307–318, 1992.

[11] T. Belytschko and T. Black, “Elastic crack growth in finite elements with minimal remeshing,” *International Journal for Numerical Methods in Engineering*, vol. 45, no. 5, pp. 601–620, 1999.

[12] M. Nicolas, D. John, and B. Ted, “A finite element method for crack growth without remeshing,” *International Journal for Numerical Methods in Engineering*, vol. 46, no. 1, pp. 131–150, 1999.

[13] B. Ted, C. Hao, X. Jingxiao, and Z. Goangseup, “Dynamic crack propagation based on loss of hyperbolicity and a new discontinuous enrichment,” *International Journal for Numerical Methods in Engineering*, vol. 58, no. 12, pp. 1873–1905, 2003.

[14] J. H. Song, P. Areias, and B. Ted, “A method for dynamic crack and shear band propagation with phantom nodes,” *International Journal for Numerical Methods in Engineering*, vol. 67, no. 6, pp. 868–893, 2006.

[15] H. Vincent and K. Alain, “Laws of crack motion and phase-field models of fracture,” *Journal of the Mechanics and Physics of Solids*, vol. 57, no. 2, 2009.

[16] H. Zhang, J. D. Yu, and X. Y. Pei, “Development of phase field fracture methods,” *Chinese Journal of High Pressure Physics*, vol. 33, no. 3, pp. 128–139, 2019.

[17] M. P. Emilio, G. Alireza, and F. Christian, “A phase field formulation for hydrogen assisted cracking,” *Computer Methods in Applied Mechanics and Engineering*, vol. 342, pp. 742–761, 2018.

[18] M. Christian and L. M. Schänzel, “Phase field modeling of fracture in rubbery polymers. Part I: Finite elasticity coupled with brittle failure,” *Journal of the Mechanics and Physics of Solids*, vol. 65, pp. 93–113, 2014.

[19] M. Hofacker and C. Miehe, “A phase field model of dynamic fracture: robust field updates for the analysis of complex crack patterns,” *International Journal for Numerical Methods in Engineering*, vol. 93, no. 3, 2013.

[20] K. Park, G. Paulino, W. Celes, and R. Espinha, “Adaptive mesh refinement and coarsening for cohesive zone modeling of dynamic fracture,” *International Journal for Numerical Methods in Engineering*, vol. 92, no. 1, 2012.

[21] G. W. Liu, Q. B. Li, and Z. Zuo, “Implementation of phase field fracture model step algorithm in ABAQUS,” *Chinese Journal of Rock Mechanics and Engineering*, vol. 35, no. 5, pp. 1019–1030, 2016.

[22] Y. K. Cao, K. K. Sun, and S. X. Zhu, “Elastoplastic fracture simulation of a plate with holes based on phase field method,” *Ordnance Materials Science and Engineering*, vol. 44, no. 2, pp. 39–44, 2021.

[23] J. Liu, Y. Xue, and F. Gao, “Study on hydraulic fracture propagation of layered shale by phase field method,” *Chinese Journal of Geotechnical Engineering*, vol. 44, no. 3, pp. 1–9, 2021.

[24] A. Griffith, “The phenomena of rupture and flow in solids,” *Physical and Engineering Sciences*, vol. 221, no. 582-593, pp. 163–198, 1921.

[25] G. Afrancfort and J. Jmarigo, “Revisiting brittle fracture as an energy minimization problem,” *Journal of the Mechanics and Physics of Solids*, vol. 46, no. 8, pp. 1319–1342, 1998.

[26] Bourdin, *The Variational Approach to Fracture*, Springer, 2008.

[27] C. Miehe, F. Welschinger, and M. Hofacker, “Thermodynamically consistent phase-field models of fracture: variational principles and multi-field FE implementations,” *International Journal for Numerical Methods in Engineering*, vol. 83, no. 10, pp. 1273–1311, 2010.

Hindawi
Geofluids
Volume 2022, Article ID 2234334, 8 pages
https://doi.org/10.1155/2022/2234334

Research Article

Deformation Characteristics and Control Technology of Roadway in Water-Rich Soft Rock

Weiguo Lin, Jianliang Cheng, Dalei Li, and Haibo Dang

Ningxia Baofeng Energy Group Co., Ltd., Yinchuan, Ningxia 750001, China

Correspondence should be addressed to Dalei Li; 919091428@qq.com

Received 22 February 2022; Accepted 19 April 2022; Published 4 May 2022

Academic Editor: Zhijie Wen

Jurassic soft rocks are the main coal-bearing strata in western mining areas, which are rich in water and high in expansive minerals. The roof and floor of the coal seam are easily muddied and disintegrated when affected by water, and heave floor of roadway in soft rock has become one of the problems that restricts the safety and efficient production of coal mines in western mining areas. It is not ideal for the effect of the traditional roadway control theory on geological soft rock roadway support, and the deformation is difficult to control. Take the tailgate of 11506 working face of a coal mine in the western mining area as the research background. This surrounding rock conditions and the deformation characteristics of the roadway in tailgate of 11506 working face were analyzed systematically, and the optimization design of the support scheme of the water-rich soft rock roadway was carried out by using theoretical analysis and numerical simulation. The application of the support in the tailgate of 11506 working face was carried out. The results show that slip of the two sidewalls, support failure, stress concentration, and floor heave were failure characteristics in water-rich soft rock roadway. The optimization of the roadway section, thin guniting of the roadway surface, optimization of support components, and gradient support could effectively achieve the control of soft rock roadway deformation. The maximum floor heave during the roadway deformation monitoring period was 230 mm, which decreased about 75% compared with original support. The influence range of the advance abutment stress is 0~60 m, of which 0~30 m is the serious influence area. The research results have good engineering practice significance for the control of bottom bulge of the soft rock roadway in this coal mine and western mining area.

1. Introduction

Soft rock roadway support in Jurassic strata is influenced by the stress environment of the roadway, mining range, geological conditions, etc. The surrounding rock of roadway is dominated by muddy rock formations, which are more fragmented and easily disintegrated by water, and is a typical geological soft rock [1]. Mining in soft rock faces great challenges, and the problems caused by soft rock pose great hazards to mine production [2].

Aiming at the treatment of soft rock support in the western mining area, numerous studies and field practices have been conducted by many researchers. Controlling water environment and horizontal stress state in floor is the key to floor control [3]. Wang et al. [4] indicated that the greater the strength of the surrounding rock at the sidewalls, the smaller the amount of floor heave of the roadway, and the floor heave can be controlled by reinforcing the two sidewalls of the roadway; Hou et al. [5] believed that the weak position of the surrounding rock support is the first to be damaged under stress and the inverted arch can effectively control the floor heave; He et al. [6] proposed the surrounding rock synergistic control technology. Bai et al. [7] analyzed the deformation characteristics of the rock layer at the floor of the roadway under the action of mining-induced stress, summarized the stratum movement laws at different depths of the floor, and proposed a control scheme to reinforce the floor of the roadway; Kang et al. [8] used the method which is a combination of theoretical analysis and physical experiments to propose a mathematical expression for the amount of floor heave and unique measures which can prevent and control the floor heave; Wen et al. [9] established the floor heave mechanical model with corresponding floor heave control technology aiming at the technical difficulties of large deformation of soft rock in the district; Xie et al. [10] proposed the technology by using grouting bolt with concrete backfill to control the floor heave technology in deep roadways. The previous research has provided valuable experience for high water expansion weakly cemented soft rock roadway support. Yu et al. [11] investigated a combined optimized support method, which greatly improved the roadway stability and effectively controlled the roadway deformation. MO et al. [12] studied the mechanisms of floor heave by numerical models in roadways. Li et al. [13] considered that the stress field in the surrounding rock is important for the stability of roadway. Yang et al. [14] proposed a combined support to control large deformation of soft rock roadway. Water-rich soft rock in western mining area needs that the anchor cable used in the optimal control scheme has the characteristics of constant resistance and large deformation [15]. Jia and Liu [16] compared the two kinds of support by numerical simulation method and believed that the combined support of "steel mesh + full anchor cable + concrete floor" was effective for water-rich roadway. The support approaches for a water-rich soft rock roadway in tectonic stress areas were studied using UDEC software [17]. The tunnel deformation monitoring and measurement work can be used to grasp the dynamic evolution law of the surrounding rock [18]. Jing et al. [19] considered influence of the immersion softening phenomenon of the roadway floor and the self-supporting structure characteristics of the surrounding rock on the stability of the surrounding rock, and a new concept of the internal and external self-bearing structure was proposed. Aiming at soft rock ground support issues under conditions of high stress and long-term water immersion, Yang et al. [20] believed that the support technology focusing on cutting off the water, strengthening the small structure of the rock and transferring the large structure of the rock was effective. The key of supporting water-rich soft rock roadway is the protection of surrounding rock and the effectiveness of supporting. The meaningful work done by the researchers from the support technology can guide the development of this study.

The surrounding rock conditions and the deformation characteristics of the roadway were analyzed, and the optimization design of the water-rich soft rock roadway support scheme was carried out. The key points of roadway support in water-rich soft rock are pointed out. Engineering practice shows that the technology can effectively control the large deformation of the soft rock roadway and meet the requirements of an efficient production of working face.

2. Project Overview and Roadway Failure Characteristics

2.1. Project Overview. The 11506 working face is mining 5 coal seam with an average thickness of 2.62 m. It is a monoclinic structure inclined to the east, with an inclination angle of 6~9°. The surrounding rock of the roadway is soft rock; the lithology is mainly composed of mudstone, siltstone, and fine sandstone; and the rock is soft and easy to swell and become mudded when encountering water, mainly manifested as the floor heave of the roadway. There are no other large faults, folds, magma intrusion, and column collapse in the working face.

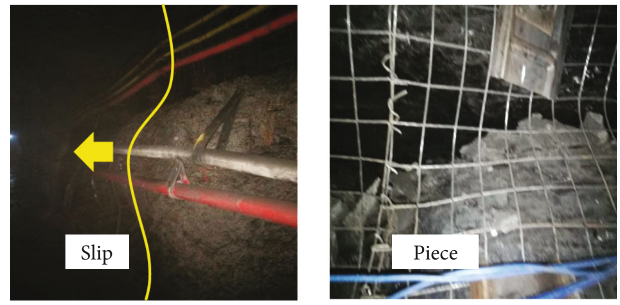

Figure 1: Slip of the sidewalls in site.

The 11506 working face is under the mining area in 2 coal seam and the coarse sandstone aquifer on the roof of the 2 coal seam, which may produce certain recharge to the sandstone aquifer on the roof of the 5 coal seam.

2.2. Roadway Failure Characteristics. According to the analysis of geological data of this coal mine and field observation, there are the following characteristics in the roadway of 11506 working face:

(1) Shallow buried depth and small stress

(2) False roof (mudstone) and immediate roof (siltstone and mudstone interlayer) swollen with water and poor cementation, making the support more difficult

(3) The roadway is drived along the roof, the lower part of the roadway is nearly 1 m high mudstone, and the floor of the roadway is 0.5 m thin coal seam. Due to the large amount of water causing the mudstone of the side to swell and weaken seriously, the mudstone interlayer between the coal seam is prone to weak surface slip when the roadway is loaded by the two sidewalls (Figure 1)

(4) Tailgate of 11506 working face is affected by mining 11502 working face and 12202 working face gob in 2 coal seam, which seriously affects the stability of the roadway bolt-mesh support system

Currently, there are mainly the following problems existing in the support of roadway in water-rich soft rock in the coal mine.

2.2.1. Slip of the Two Sidewalls. The roadway is drived along the roof, there are about 1 m high mudstone in the lower part of the roadway, and the bottom of the roadway is 0.5 m thin coal seam (Figure 2). Due to the large amount of water causing the mudstone of the side to be weakened seriously, the mudstone between the coal seam in sidewalls is prone to weak surface slip leading to the deformation of the sidewalls, affecting the normal work surface mining.

Two sidewall deformation can be divided into two types which are stress "weak face slip" and mudstone "weak face slip."

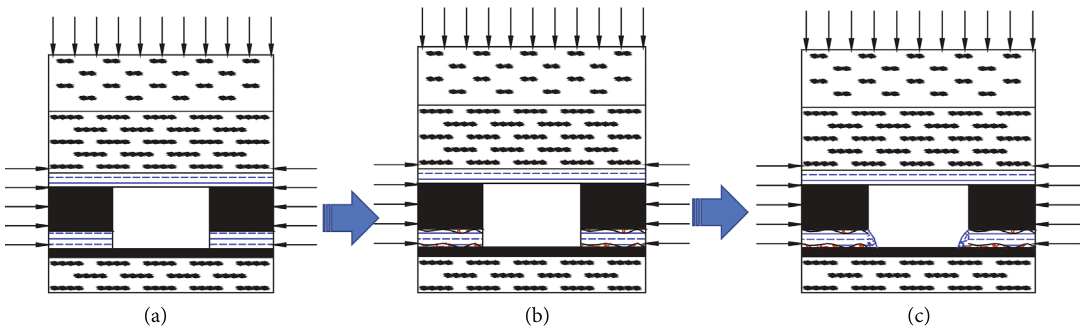

Figure 2: Sidewalls slip process of roadway in 11506 working face.

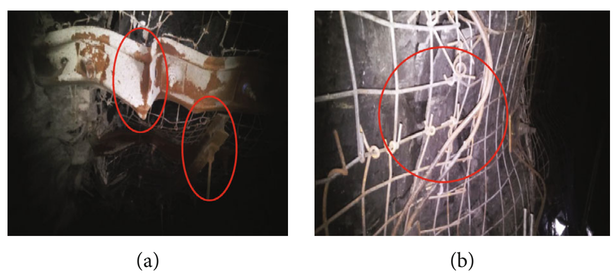

Figure 3: The failure of bolt-cable-mesh support: (a) steel belt bending and shear of anchor cable. (a) Failure of anchor net.

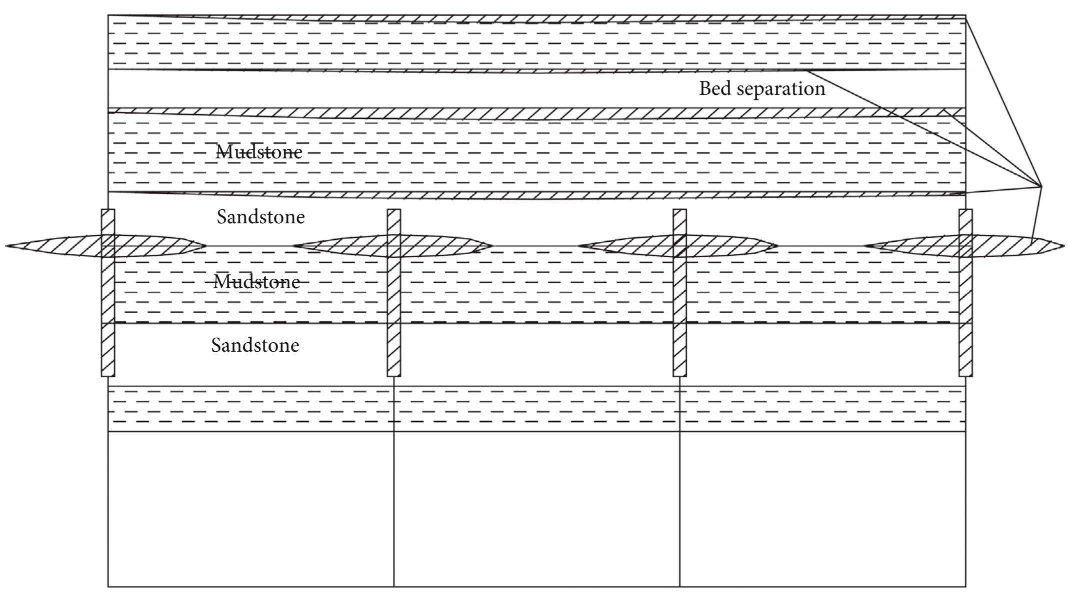

Figure 4: The diagram of composite roof separation.

With the increase of horizontal stress, due to the sliding contact between the mudstone and coal seams, the poor formation of the roadway at the intersection of different lithologies, and the poor control ability of the support to the surrounding rock, the weak surface (red part in Figure 2) is formed under the action of horizontal stress, and the horizontal slip of the two sidewalls occurs with the change of time.

Increasing the friction force at the intersection of coal and rock layers or taking measures to prevent the movement of the sidewalls can effectively control the deformation of the sidewalls. At the same time, undertaking timely surface blocking measures at the drenching place to avoid the contact between the surrounding rock and water will lead to the argillization of the surrounding rock and control the occurrence of the weak surface slip phenomenon.

2.2.2. Failure of Support. The main reasons for the failure of the support system are the unreasonable support and low efficiency of bolt and cable support, mainly manifested by

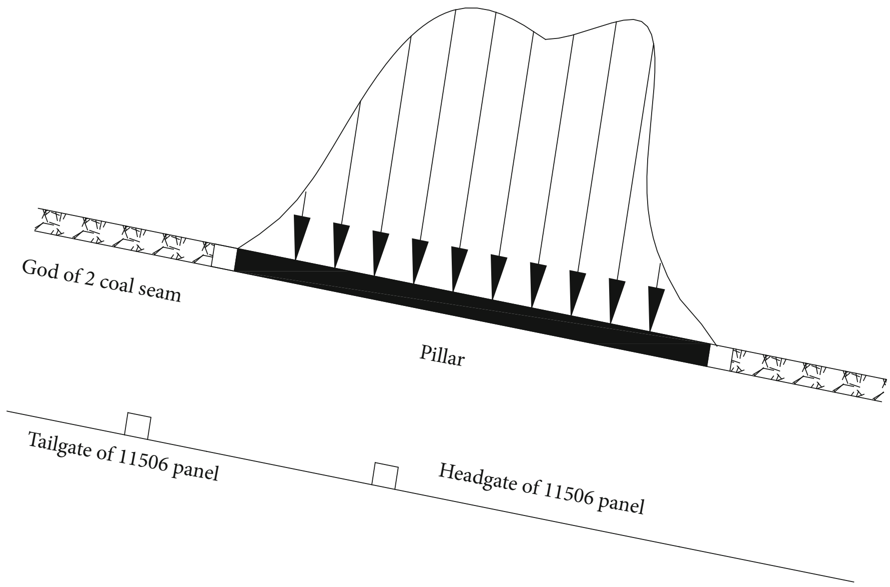

FIGURE 5: Roadway position relationship and stress field superposition.

the deformation of the steel belt shearing the bolt, the steel ladder obstructing the bolt force transfer, and the bolt beam shearing the anchor cable as shown in Figure 3.

The steel belt is deformed and stretched locally under stress causing the adjacent bolts to shear off, meanwhile, the stress of the steel ladder is linear, which is not conducive to the transmission of bolt preload and working resistance.. When the cable is stressed, the cable beam is twisted and deformed, and this results in the cable shearing off.

Under the condition of composite soft rock roof, there is obvious roof separation fracture distribution in the bolt section as shown in Figure 4, and the roof separation is beyond the control range of the bolt, which makes the bolt-cable support fail.

2.2.3. Stress Concentration. The tailgate of 11506 working face was arranged about 40 m below the coal pillar in the 2-coal mining interval, and the roadway was in the stress concentration area with significantly higher stresses as shown in Figure 5. At the same time, the tailgate of 11506 working face was influenced by mining disturbance by the adjacent working face.

2.2.4. Floor Heave. The floor is deformed and damaged under the influence of the stress of the two sidewalls and the lithology of the rock layer. It is necessary to build inverted arch to keep the roadway meet service requirement. If the design is not reached during the construction, the deformation of the roadway will be very violent. Figure 6 shows the damage of floor heave.

In summary, the overall slip of the two sidewalls of 11506 working face is large, which is nearly 1.5 m in local part. The existing support cannot effectively control the roadway deformation; therefore, the roadway support stability is not effectively guaranteed.

(a) (b)

FIGURE 6: The damage of floor: (a) floor heave. (b) Stress cracking of floor.

3. Support Design and Optimization Methods

3.1. Methods

3.1.1. Monitoring Measures. The roadway surface convergence monitoring can better judge the movement of surrounding rock and analyze whether the surrounding rock is in a stable state. Roadway surface convergence monitoring includes two sidewalls of the displacement monitoring, roof, and floor displacement monitoring. In site, the cross-point method is used to monitor the surface displacement of roadway, and the monitoring points are arranged on each monitoring section.

The aim of this study is to evaluate the effectiveness of the support scheme by monitoring roadway surface convergence.

3.1.2. Modeling. To simplify the simulation conditions, set the upper boundary as free and apply gravity (10 MPa), and set the remaining boundaries as fixed. The Mohr-Coulomb model was selected to simulate the condition. The rock parameters of main strata in the model are shown in Table 1. In FLAC3D, the cable structure elements are used to model the rock bolts and cables. The mainly mechanical and geometric parameters are listed in Table 2.

Table 1: Main rock parameters of main strata in the model.

Strata	Tensile strength (MPa)	Shear modulus (GPa)	Bulk modulus (GPa)	Cohesion (MPa)	Friction angle (°)
Overlying strata	0.55	3.66	5.31	1.43	41
Medium-fine sandstone	0.85	3.55	5.32	2.7	43
5 coal seam	0.23	1.45	4.97	0.68	24
Argillaceous siltstone	0.31	1.52	3.38	1.5	27
Fine sandstone	0.75	3.46	5.11	3.08	33

Table 2: Mechanical parameters of the blots [21].

Type	E (GPa)	C_g (N/m)	K_g (N/m)	ρ_g (m)	A (m^2)	F_t (N)
Rock bolt	200	4.7e5	5.6e9	8.79e-2	3.14e-4	1.6e5
Anchor cable	195	4.7e5	4.2e9	8.79e-2	2.49e-4	2.5e5
Introduction	Young's modulus	Grout cohesive strength per unit length	Grout stiffness per unit length	Grout exposed Perimeter	Cross-sectional area	Tensile yield strength

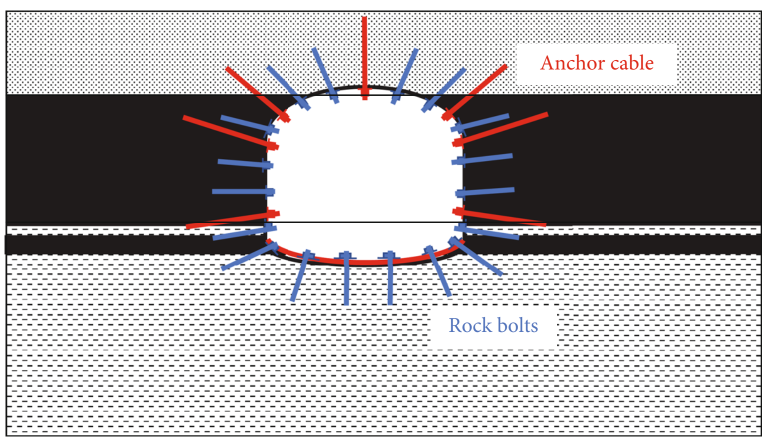

Figure 7: The diagram of cross-section support.

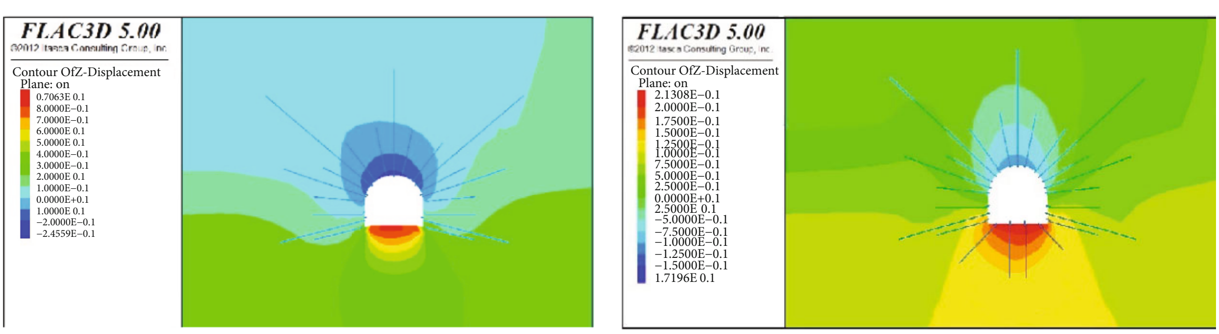

(a) Condition without floor bolts

(b) Condition with floor bolts

Figure 8: Numerical results of floor reinforcement.

3.2. Support Design and Optimization Principles and Scheme. In view of the problems in original support and the failure characteristics of roadway, the following supporting design and optimization principles were proposed..

3.2.1. Roadway Cross-Section Optimization. It is easy to cause stress concentration in the shoulder of the roadway with rectangular or trapezoidal shape, while the roadway driving forming effect is poor, which is not conducive to

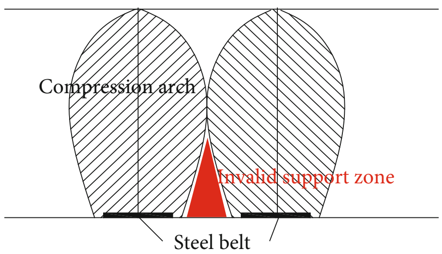

FIGURE 9: The relationship between bolt and surface support.

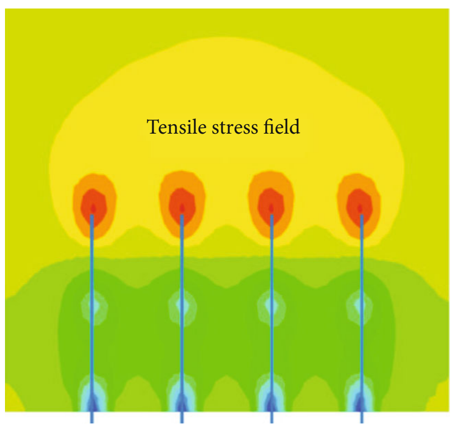

FIGURE 10: Bolt tensile stress field.

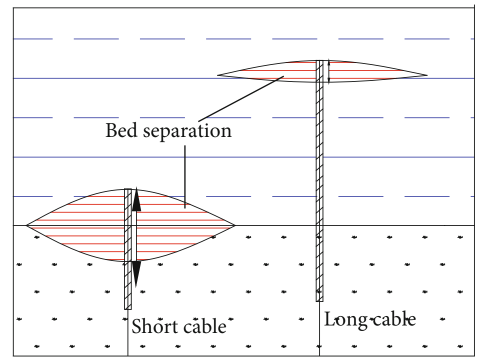

FIGURE 11: The diagram of "long+short cables" support.

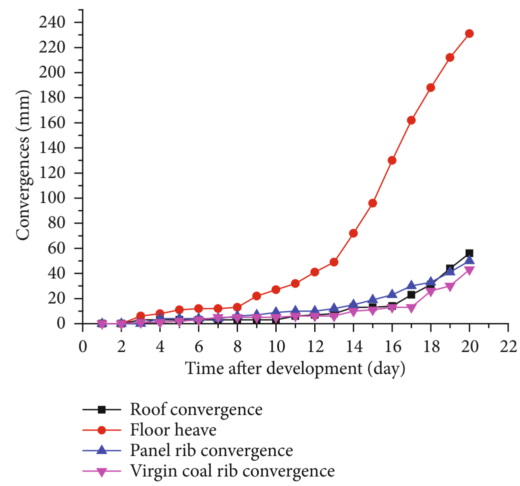

FIGURE 12: The relation between convergences and time.

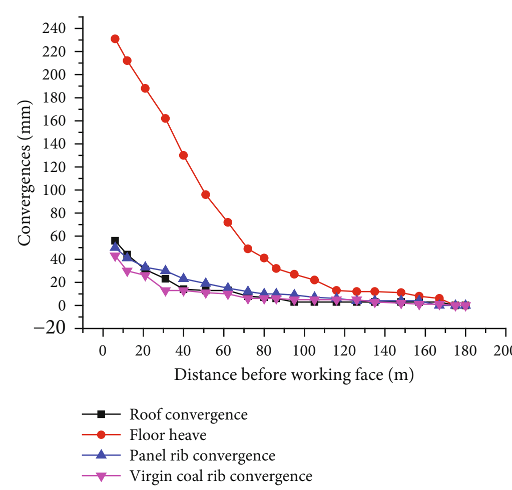

FIGURE 13: The relation between convergences and distance before working face.

the construction of bolt-mesh-cable support and the effect of the role. Therefore, the shape of the roadway was changed to straight wall arch with three-centered arch bottom section as shown in Figure 7, and the construction of the floor bolt was carried out along with the floor water impermeability treatment simultaneously.

Figure 8 shows the displacement of the floor with or without floor bolt support. The floor bolt support makes the laminated floor rock form a combined rock beam, which strengthens the integrity of the floor; meanwhile, it prevents the soft rock expansion, swelling, and the generation of new fissures.

3.2.2. Thin Guniting of Surrounding Rock. The purpose of thin guniting is to increase the surface sealing effect and slurry guniting speed while reducing the comprehensive cost of surface sealing. Effectively seal the spillage of harmful gases in the coal body, and isolate the mine air to produce oxidation to the coal body with the aim of providing fireproof, impermeable, anti-weathering, and anti-rusting function. The material has an elongation of 30%~50%, which can better adapt to the deformation of the roadway caused by mining.

3.2.3. Optimization of Surface Support. The surface support should not only have a certain surface area, but also have a certain strength and toughness. Surface support is to provide a certain compressive stress to the roadway surface through the tension of the bolt to the surface support body and to protect the surface (Figure 9).

3.2.4. Gradient Support. When the cables work, the bolting section and above a certain range of cables bolt is tensile stress (Figure 10). The composite soft rock roof interfacial bonding is poor, so the tensile stress area is very easy to make roof separation.

Figure 14: The result of roadway support optimization.

Therefore, the “long + short cables” are arranged alternately to strengthen the effective control of the composite soft rock roof slab in a targeted manner as shown in Figure 11.

4. Application and Result Analyses

The tailgate of 11506 working face was supported according to the support optimization design. Q500 high strength and high prestress bolts with snake shaped were used to reinforce the floor corner of the roadway. Blots for the floor corner are 20 mm in diameter and 2800 mm in length and that of the cables are 17.8 mm and 7000 mm. The size of steel belt guard is 450×280×4.75 mm (length×width×thickness) and that of the top bolt plate is 1 50×150×10 mm. The thin guniting be carried out with a thickness of 2~5 mm..

Four measuring points are arranged at 180 m in the advanced mining face, and the interval between the measuring points is 15 m. Typical measuring points are selected to analyze the relationship between surrounding rock deformation with time and mining distance. The relationship of the deformation of the surrounding rock ranging between the time and the pushing distance is analyzed in Figures 12 and 13, respectively.

The result shows that the deformation of the roadway is mainly floor heave. During the observation period, the maximum floor heave was 230 mm, and the roadway integrity was well (Figure 14). Compared to the maximum floor heave of 900 mm with origin support, the floor heave was reduced by about 75% after optimization.

After all the collected data were analyzed, it was concluded that the advanced abutment stress influence range of 11506 tailgate was 0~60 m, among which 0~30 m was the serious area.

5. Conclusion

(1) The failure in the tailgate of the 11506 working face is mainly the overall slip of the two sidewalls, the failure of the support system, the superposition of mining stress, and the floor heave

(2) The optimal support design methods of roadway deformation include “optimization of roadway section shape,” “rapid thin guniting of surrounding rock,” “improvement of surface support structure,” and “gradient support” in the water-rich soft rock roadway

(3) The deformation of the roadway is mainly floor heave. The maximum floor heave is 230 mm with the optimal support, which is reduced by about 75% compared with origin support. The advanced abutment stress influence range of 11506 tailgate was 0~60 m, among which 0~30 m was the serious area

The optimized support design avoids roadway reworking effectively, improves driving efficiency, reduces labor intensity, alleviates mining drifting, and achieves good social and economic benefits.

Data Availability

The tables, some figures, and data used to support the findings of this study are currently under embargo, while the research findings are commercialized. Requests for data six months after the publication of this article will be considered by the corresponding author.

Conflicts of Interest

The authors declare that they have no conflict of interest.

References

[1] B. T. Shen, “Coal mine roadway stability in soft rock: a case study,” *Rock Mechanics and Rock Engineering*, vol. 47, no. 6, pp. 2225–2238, 2014.

[2] J. L. Cai, *Research on deformation and instability mechanism and application research for Jurassic weak-cemented soft rock roadways*, Anhui University of Science and Technology, 2020.

[3] Yuyang Wang, Yong Liu, Chen Wang, Lianchang Han, and Guanghai Leng, “Mechanics of bottom bulge and control technology in deep mine soft rock roadway,” *Chinese Journal of Underground Space and Engineering*, vol. 17, no. S1, pp. 411–418, 2021.

[4] W. J. Wang and T. Feng, “Study on mechanism of reinforcing sides to control floor heave of extraction opening,” *Chinese Journal of Rock Mechanics and Engineering*, vol. 24, no. 5, pp. 808–811, 2005.

[5] C. J. Hou and L. H. Hou, “Reinforcing sidewalls and corners of gateway to control floor heave,” *Journal of China Coal Society*, vol. 20, no. 3, pp. 229–234, 1995.

[6] M. C. He, “Mechanics mechanism of soft rock deformation and supporting countermeasures in coal mine,” *Hydrogeology Engineering Geology*, vol. 24, no. 2, pp. 12–16, 1997.

[7] J. B. Bai, W. F. Li, X. Y. Wang, Y. Xu, and L. J. Huo, “Mechanism of floor heave and control technology of roadway induced by mining,” *Journal of Mining and Safety Engineering*, vol. 28, no. 1, pp. 1–5, 2011.

[8] H. P. Kang, *Mechanism of soft rock roadway floor heave and its prevention*, China Coal Industry Press, 1993.

[9] Z. J. Wen, J. Y. Lu, and Q. H. Xiao, “Failure mechanism of floor heave and supporting technology of soft rock roadway,” *Journal of China Coal Society*, vol. 44, no. 7, pp. 1991–1999, 2019.

[10] G. X. Xie and J. C. Chang, “Study on overcutting-bolting & grouting-backfilling concrete to control the floor heave of deep mine roadway,” *Journal of China Coal Society*, vol. 35, no. 8, pp. 1242–1246, 2010.

[11] K. P. Yu, F. Y. Ren, R. Puscasu, P. Lin, and Q. Meng, “Optimization of combined support in soft-rock roadway,” *Tunnelling and Underground Space Technology*, vol. 103, article 103502, 2020.

[12] S. Mo, P. Sheffield, P. Corbett et al., “A numerical investigation into floor buckling mechanisms in underground coal mine roadways,” *Tunnelling and Underground Space Technology*, vol. 103, article 103497, 2020.

[13] L. P. Li, C. S. Shang, K. W. Chu et al., “Large-scale geomechanical model tests for stability assessment of super-large cross-section tunnel,” *Tunnelling and Underground Space Technology*, vol. 109, article 103756, 2021.

[14] S. Q. Yang, M. Chen, H. W. Jing, K. F. Chen, and B. Meng, “A case study on large deformation failure mechanism of deep soft rock roadway in Xin'An coal mine, China,” *Engineering Geology*, vol. 217, pp. 89–101, 2017.

[15] T. B. Zhao, M. L. Xing, W. Y. Guo, C. W. Wang, and B. Wang, “Anchoring effect and energy-absorbing support mechanism of large deformation bolt,” *Journal of Central South University*, vol. 28, no. 2, pp. 572–581, 2021.

[16] H. C. Jia and Y. Liu, “Analysis on deformation and failure characteristics of surrounding rock in water-rich roadway and weakly cemented soft rock,” *China Energy and Environmental Protection*, vol. 44, no. 2, pp. 303–310, 2022.

[17] G. Z. Xue, C. Gu, X. Q. Fang, and T. Wei, “A case study on large deformation failure mechanism and control techniques for soft rock roadways in tectonic stress areas,” *China Energy and Environmental Protection*, vol. 11, no. 13, p. 3510, 2019.

[18] F. L. Chen, K. H. Zeng, X. J. Li, M. Xu, and H. Dai, “Construction monitoring and numerical simulation of water-rich tuff soft rock tunnel,” *IOP Conference Series-Earth and Environmental Science*, vol. 455, 2020.

[19] W. Jing, X. Wang, P. W. Hao, L. Jing, and W. Xue, “Instability mechanism and key control technology of deep soft rock roadway under long-term water immersion,” *Advances In Civil Engineering*, vol. 2021, Article ID 6670379, 13 pages, 2021.

[20] R. S. Yang, Y. L. Li, D. M. Guo, L. Yao, T. Yang, and T. Li, “Failure mechanism and control technology of water-immersed roadway in high-stress and soft rock in a deep mine,” *International Journal of Mining Science and Technology*, vol. 27, no. 2, pp. 245–252, 2017.

[21] K. Zhang, G. M. Zhang, R. B. Hou, Y. Wu, and H. Zhou, “Stress evolution in roadway rock bolts during mining in a fully mechanized longwall face, and an evaluation of rock bolt support design,” *Rock Mechanics and Rock Engineering*, vol. 48, pp. 333–344, 2015.

Hindawi
Geofluids
Volume 2022, Article ID 6292783, 13 pages
https://doi.org/10.1155/2022/6292783

Research Article

Study on the Migration Law of Overlying Strata on the Working Surface of Large Mining Height in Y.C.W Coal Mine

Hongtao Liu ,[1] Tianhong Huo ,[1] Yang Liu,[1,2] Zhou Han,[1] Zijun Han,[1] and Wanliang Liang[1]

[1]*School of Energy and Mining Engineering, China University of Mining and Technology (Beijing), Beijing 100083, China*
[2]*Ministry of Industry and Information Technology Talent Exchange Center, Beijing 100846, China*

Correspondence should be addressed to Tianhong Huo; cumtbhth@126.com

Received 9 September 2021; Accepted 29 March 2022; Published 25 April 2022

Academic Editor: Zhijie Wen

The migration law of overlying strata on working face is of great significance for safe mining of working face. In this paper, theoretical calculation, numerical simulation, and similar simulation are used to study the distribution characteristics, migration, and fracture law of key strata in the overlying strata of 130204 working face of Y.C.W coal mine and the relationship between the development height of water flowing fractured zone and the spatial position of weak aquifer. The theoretical calculation results show that there are "one main two sub" key strata in the overlying strata of 130204 working face, which play an important role in controlling rock movement. Numerical simulation and similar simulation results show that the first weighting step distance of the direct roof of 130204 working face is about 30-40 m. The initial weighting interval of the basic roof of the working face is about 70-80 m, and the periodic weighting interval is about 23.5-25 m. After the first weighting and multiple periodic weighting of the basic roof of the working face, the first subcritical layer is located in the caving zone, the second subcritical layer is located in the fracture zone, and the main key layer is finally located in the bending subsidence zone. The final height of the caving zone of the overlying strata is about 24 m, and the height of the water flowing fractured zone is about 130 m. Since the water-conducting fractured zone is connected and passes through the second subcritical layer with weak water-bearing property, it is possible for the water permeability accident of the working face. Therefore, in order to ensure the safety of the working face, the water should be detected and released in advance during the mining of the working face.

1. Introduction

Coal plays an important role in the development of national economy and society. Fully mechanized caving mining technology with large mining height in thick coal seam has been rapidly popularized and applied for its advantages of high recovery rate, high mechanization degree, safety, and high efficiency [1, 2]. Generally, the fully mechanized mining with mining height of 3.5~5.0 m is called large mining height, and the fully mechanized mining with mining height of more than 5.0 m is called extralarge mining height [3, 4]. At the same time, large mining height mining has more problems than normal mining height workings, such as the greater thickness of mining, the greater collapse height of the overlying strata after coal mining, and the stronger pressure on the roof of the working face. In order to study the stability and control technology of the surrounding rock under the conditions of large mining height, it is necessary to study the transport and failure law of the overlying rock layer on the large mining height working face.

Many domestic scholars have carried out constructive research work on the moving rule of roof and overburden structure characteristics of large mining height working face. Gong and Jin [5] and Peilin and Zhongming [6] applied the key stratum theory, and according to different strata structures of the immediate roof, the immediate roof of the large mining height is divided into three types, namely I, II, and III. Wen et al. [7] pointed out that accurately determining the position, thickness, and possible maximum ceiling span of overburden strata is the key to the roof control design and support selection calculation of large mining height mining face. Hao et al. [8] concluded that there is a balance structure in the overburden layer on the large mining height fully mechanized working face, which is higher than that of the upper rock layer but similar to that of the layered extraction, and the activity of this structure is a gradual change process.

Huang and Zhou [9, 10] and Huang and Tang [11] proposed that the immediate roof "short cantilever beam" structure and the basic roof key strata "high oblique step beam" structure model for the roof of large mining height working face revealed the mechanism of pressure coming from the large mining face. Fu et al. [12] concluded that the height of the roof caving zone and fracture zone showed a stepwise rise by similar simulation tests on the 5.5 m high working face of Shangwan coal mine in Shandong mining area. Yang and Liu [13] and Yang [14] obtained that the reason why the mining pressure is more intense than that of the ordinary mining height working face is that the mining intensity of the working face is high and the roof activity is violent, which leads to the single structure of the key layer, low occurrence layer, easy to slip and instability, and the overall breakage of the overlying roof. It is concluded that Yin [15] proposed a structural model of " cutting block " of overlying rock layer in shallow buried super-high working face and believed that the overburden layer of shallow buried coal seam is cut down and broken as a whole, forming an articulated structure mainly by slipping and destabilization. Pang et al. [16] considered that the peak stress, differential stress, and strength-stress ratio of sandstone in different horizons had very great difference and proposed the structure and stability control technology of "cantilever beam+masonry beam" for the roof rock fracture of ultra large mining height working face.

Xiang et al. [17] established the dynamic distribution equation of caving zone in different mining stages in the case of structural rock strata and no structure in the direct roof, revealing that the caving zone in overburden goaf of large mining height working face presents obvious dynamic change characteristics. Sun [18] obtained the progressive fall characteristics of overburden from bottom to top in the western weakly cemented strata and revealed the mechanism of overburden fracture eruption-development-penetration. Zhao et al. [19] divided the overlying strata of the stope into six regions according to the fracture development pattern after fully mining in the working face with 8.8 m ultralarge mining height. The fitting formula of fracture development height, mining height, and working face advancing distance was obtained by numerical simulation. Jin et al. [20] believed that the distribution law of advanced abutment pressure in front of the coal wall in deep working face with large mining height was not related to the mining depth but mainly depended on the mining face height and the composition structure of roof strata. Liang et al. [21] concluded that there are two structural patterns and six moving types of the key stratum in a fully mechanized mining face with large mining height, gave and verified the formation conditions of each structural form and movement pattern, and revealed the influence law of the six key layer movement types on the mine pressure in the mining site. Hu and Jin [22] established a mechanical model of large mining height working face through field mine pressure observation and made a preliminary study on the classification of the working face roof and the rationality of bracket selection. Sun et al. [23] used three technical methods, including loses of drilling fluid measuring, borehole wall observing by color TV, and transient electromagnetic method (TEM) geophysical exploration, to detect the height of "two zone" of the overlying rock layer in the goaf of large mining face. Wu [24] concluded that the overburden structure of large mining face in thick coal seam is "composite cantilever structure-nonarticulated roof structure-articulated roof structure." Yan et al. [25] and Yu et al. [26] pointed out that the frequency and energy of microseismic events have obvious periodicity and concluded that the roof of fully mechanized caving working face with large mining height is a structure of "cantilever beam and articulated rock beam."

Liu et al. [27, 28] studied the stress distribution law of bottom suction roadway and the reasonable position of bottom suction roadway and working face in Zhaogu No.2 mine; this provides theoretical guidance for preventing the occurrence of bottom water seepage accident in working face and at the same time presents a detailed comprehensive case study of strata movement in extraction of a long wall top coal caving panel of a composite coal seam with partings in the Baozigou coal mine. The caved zone and fractured zone development were captured through physical modeling by incorporating the digital image correlation method (DICM), universal distinct element code (UDEC) numerical modeling, and field observation with the method of high-pressure water injection. Zhang et al. [29] established a three-dimensional discrete element numerical model of soft overburden in high-intensity mining and analyzed that the maximum height of "two zones" of soft overburden in high-intensity mining increases with the increase of mining thickness, but it has no obvious relationship with the dip length and advance speed of high-intensity mining face. By using 3DEC discrete element numerical simulation software, Yu et al. [30] determined the key strata parameters and their control effects under the condition of fully mechanized caving with large mining depth. Li et al. [31] conducted similar simulation, numerical simulation, and theoretical research on the dynamic movement law of the roof in fully mechanized caving mining of steeply inclined extrathick coal seam and revealed that the roof in goaf will have regular alternate movement of "squeezing, sliding, and turning" in space with the advance of the working face.

To sum up, the domestic scholars use a variety of research methods of large mining height in upper strata in mining process of different forms of structure and movement; the "two belts" of overburden rock height were studied, which has achieved good results, but for large mining height under the condition of mining rock weak aquifer and water flowing fractured zone height between the spatial evolution, the law research is relatively small. After the mining of Yangchangwan coal mine with 130204 high mining height, there is a possibility that water gushing accident may occur in the working face due to the connection of water-conducting fracture zone with weak aquifer in overlying strata. Based on this, the author conducted in-depth research on the migration and breaking rule of overlying strata in the mining of 130204 high mining height working face, and the development height of water-conducting fracture zone.

2. Engineering Background and Determination of the Location of the Key Layer

Y.C.W coal mine is located in Ningdong Town, Lingwu City, Ningxia Hui Autonomous Region, with a north-south direction length of about 12.8 km and an east-west inclination width of about 9.8 km. The No. 2 coal seam mined in 130204 fully mechanized coal mining face with large mining height is a stable coal seam that can be mined in the whole region. The average buried depth of the working face is 508.9 m, the average dip angle of the coal seam is 9°, and the average thickness of the coal seam is 8 m. The comprehensive column diagram of the coal seam at the face is shown in Figure 1. The mining method of 130204 working face is large mining height and full height toward the long wall comprehensive mechanized backward caving mining method. Above 130202 working face mined-out area, the coal pillar of 35 m is left in the transportation groove with 130202. The lower part is the original coal seam without mining, so there is no mining activity affecting the mining of the working face. The geological data of working face tunneling show two normal faults, DF12 branches cross 130204 working face. The layout of fully mechanized working face is shown in Figure 2, in which the strike length of working face is 2531 m and the inclination length is 290 m.

The first task to study the breakage and transport law of overburden rock in the mining process of Y.C.W coal mine large mining face is to determine the location of the key strata in the overburden rock layer. Bay will be collected at the site of sheep field of roof overburden theory for the physical and mechanical parameters of the calculation; it is concluded that 130204 working face strata exist in the "one main and two subcritical layers," that is, one main key layer and two subkey layers as shown in Table 1, respectively, located in the 5 m above the roof of coal seam thickness of medium sandstone in 15 m for the subcritical layer. The coarse sandstone with a thickness of 51 m at 24 m away from the top of the roof is the second subkey layer, and the medium sandstone with a thickness of 48 m at 133 m above the roof of the coal seam is the main critical layer. Due to the distance between the main and inferior key strata, the second fault of the inferior key strata will cause a large range of migration of the overlying strata, and the fault distance of the main key strata will be greatly affected by the migration of the lower strata. The mining height of large mining face is relatively large. Therefore, the collapse range of the overlying rock layer is much larger than the collapse range during normal mining height. In addition, there is a possibility of forming an articulated link balance structure, and the

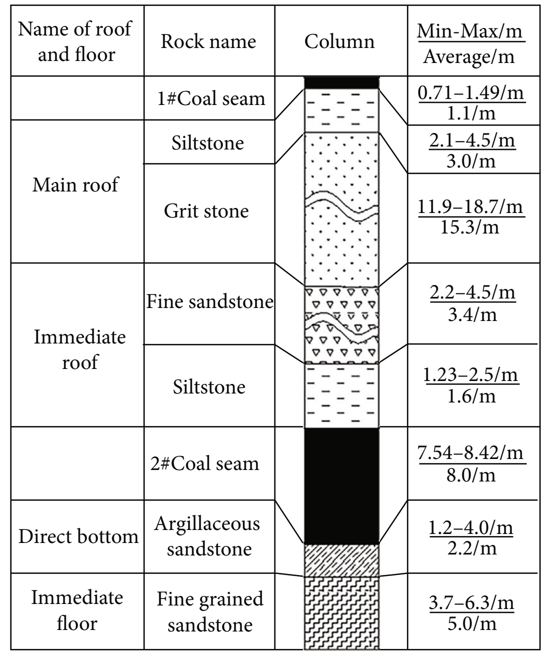

Figure 1: 130204 comprehensive column diagram of coal and strata in working face.

stable "masonry beam" structure may also have the structural form of "cantilever beam" and rotary collapse deformation due to excessive rotary volume, affected by the increase of mining height at the working face. The "masonry beam" structure is more likely to be formed in the higher rock seam above the coal seam.

Xu et al. proposed a height prediction method of water-conducting fracture zone based on the location of key layers [32], which is as follows: the specific methods and steps are as follows: first, according to the calculated location of the key stratum and the height of the mining coal seam, the identification of the key stratum broken fractures through. If the location of the key stratum is more than 7-10 M away from the height of the mining coal seam, the fracture fracture of the key stratum is not connected. If the location of the key stratum is less than 7-10 M from the height of the mining coal seam, the fracture fractures of the key stratum are connected, and the fracture fractures of the overlying strata controlled by the key stratum are also connected. Determine the height of the water-conducting fracture zone. When the main key stratum of overburden is within the critical height (7-10) M, the water-conducting fracture will develop to the top of bedrock, and the height of water-conducting fracture zone is equal to or greater than the thickness of bedrock. When the main key stratum of overburden is located beyond the critical height (7-10) M, the water-conducting fracture will develop to the bottom of the nearest key stratum above the critical height (7-10) M, and the height of the water-conducting fracture zone is equal to the height of the key stratum from the mining coal seam.

Based on the above theory and calculation method, further combined with the borehole bar chart of Y.C.W 130204 working face with large mining height and the determined key layer and location, it is concluded that the

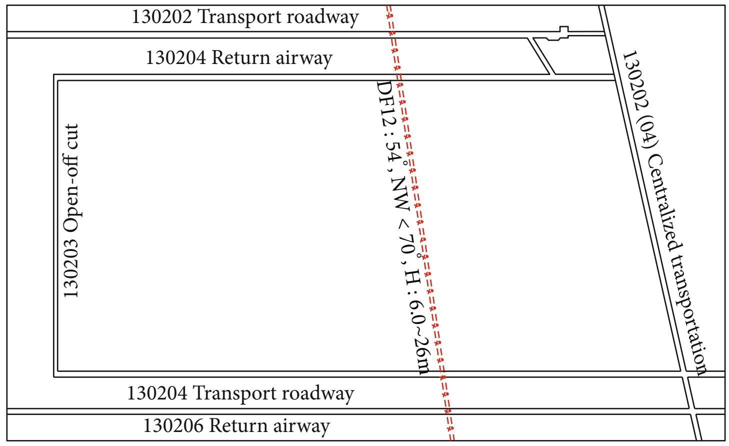

FIGURE 2: 130204 fully mechanized mining face layout.

TABLE 1: Mechanical parameters of overlying rock of working face and identification of key horizon.

No.	Rock name	Tensile strength (MPa)	Elastic modulus (GPa)	Poisson ratio	Cohesion (MPa)	Angle of internal friction (°)	Density (kg/m^3)	Thickness (m)	Depth (m)	Key strata location
1	Silty mudstone	2.64	1.14	0.22	4.27	39.2	2200	27	309	
2	Siltstone	2.4	1.39	0.22	9	42	2600	4	313	
3	Medium sandstone	3.12	0.85	0.22	7	39.2	2500	48	361	Main key stratum
4	Mudstone	1.5	0.78	0.34	6.89	24.7	2350	15	376	
5	Fine sandstone	3.86	1.44	0.23	4.83	52.4	2350	7	383	
6	Mudstone	1.15	0.56	0.34	6.89	24.7	2350	6	389	
7	Fine sandstone	3.51	1.52	0.23	4.83	52.4	2350	6	395	
8	Silty mudstone	2.64	1.14	0.22	4.27	39.2	2200	22	417	
9	Medium sandstone	3.12	0.82	0.23	7	39.7	2500	2	419	
10	Grit stone (with water)	3.27	1.46	0.23	4.66	46.7	2350	51	470	Inferior key strata II
11	1# coal seam	1.32	0.67	0.25	0.75	40.2	1500			
12	Siltstone	2.4	1.39	0.22	9	42	2600	1	471	
13	Medium sandstone	3.05	1.82	0.23	7	39.7	2500	3	474	
14	Fine sandstone	3.79	1.22	0.23	4.83	52.4	2350	15	489	Inferior key strata I
15	Siltstone	2.35	1.28	0.22	9	42	2600	3	492	
16	2# coal seam	1.35	0.71	0.25	0.75	40.2	1500	2	494	
17	Mudstone	1.57	0.68	0.34	6.89	24.7	2350	8	502	

fracture fracture of subkey layer 2 will be penetrated, while the fracture fracture of main key layer will not. The final development height of the water-conducting fracture zone is no more than 133 m. Therefore, the water-conducting fracture zone will run through the weak water-bearing strata above the working face. In order to ensure safe mining, water exploration and release work should be carried out in advance.

3. Numerical Simulation of Overlying Strata Migration Law on Working Face with Large Mining Height

3.1. Establishment of Numerical Model and Layout of Measuring Line. Based on geological conditions of 130204 working face with large mining height in Y.C.W coal mine and rock mechanical parameters measured in laboratory,

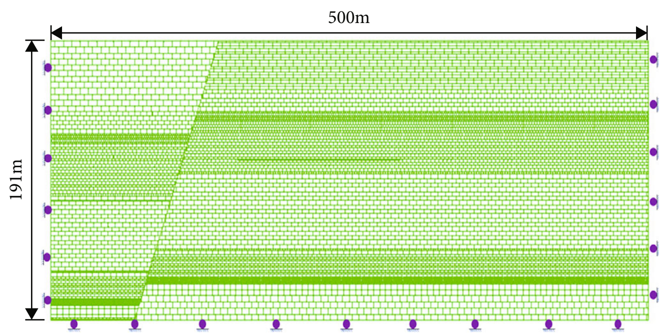

Figure 3: UDEC numerical model diagram of large mining height working face in Y.C.W coal mine.

considering the occurrence effect of DF12 fault, on the basis of reasonable simplification, the UDEC numerical model of Y.C.W coal mine working face with large mining height is established in two parts, as shown in Figure 3.

The size of the model is $X \times Y = 500\,\mathrm{m} \times 191\,\mathrm{m}$, the strike length of the model is 500 m, and the boundary influence area on both sides is 50 m. The left and right boundary is fixed by limiting the velocity and displacement in X and Y directions; thus, the boundary effect of the left and right models should be eliminated. The upper boundary of the model was fixed by applying 8.4 MPa overburden load in Y direction and setting stress gradient.

The model was calculated using the Coulomb criterion, and its physical and mechanical parameters are shown in Table 1. In 130204 working face, survey line 1 is arranged at the bottom of the direct roof of 2# coal seam; side line 2 is arranged at the boundary of the central strata of the direct roof 5 m above 2# coal seam; side line 3 is arranged at the bottom of the basic roof 20 m away from 2# coal seam roof. The model uses the method of multiple excavation, each excavation 5 m, continuous excavation 2 times, and recording data; namely, excavation of 10 m records a measuring point displacement and stress change data.

3.2. Numerical Simulation Analysis of Overlying Strata Migration Law. In the stress state of overlying strata in 130204 working faces of Y.C.W coal mine from 10 m excavation to 300 m advance, as shown in Figure 4, after the open-off cut, the overlying strata have a small bending due to the suspension. When the working face is pushed forward to 10 m (Figure 4(a)), the direct roof above the coal seam has the trend of subsidence, and the separation between the top and the basic top is formed. As the working face continues to advance to 30 m (Figure 4(b)), the distance between the direct roof and the basic roof increases gradually. The direct roof at the position of 30 m reaches the limit span, and the first collapse occurs. The collapse length is about 15 m and the height is 5 m. The first collapse of the direct roof falls behind with the advance of the working face, and the length of the basic roof is gradually increasing.

When the working face advances to 70 m (Figure 4(c)), a large area of collapse occurs after the basic roof reaches the ultimate breaking distance. The length of collapse is about 65 m and the height is about 20 m. The pressure of the working face is intense, and the strata above the basic roof also produce obvious cracks. When the working face advances to 95 m (Figure 4(d)), the basic roof breaks again. However, due to the support of the collapsed and broken rock strata to the overlying rock strata, the second subcritical layer after the broken rock blocks occluded each other to form a relatively stable articulated structure, which controlled the upper rock strata to sink obviously and produce a large separation layer. At this time, the basic roof breaking is periodic pressure, and the interval of periodic pressure step is 25 m. The analysis shows that the height of caving zone is about 24 m and the height of water flowing fractured zone is about 67 m.

When the working face advances to 120 m (Figure 4(e)), the third periodic fracture occurs on the main roof, and the periodic weighting step is 25 m. Because the caving broken rock strata fill the goaf sufficiently, the cracks formed above the goaf with the compaction of the overlying rock strata during the second cycle compaction of the coarse sandstone layer of the subkey 2 are closed. However, the water flowing fractured zone is further developed in the direction of the fracture angle of the strata before and after the mined-out area. At this time, the height of the caving zone is 24 m and the water flowing fractured zone is 98 m. When the working face advances to 300 m (Figure 4(f)), the overlying strata have undergone multiple periodic fractures. The periodic weighting step of the basic roof is about 25 m, and the maximum caving height is 24 m. At this time, the sandstone layer in the main key layer of the working face has been bent and sunk, and the development height of the water flowing fractured zone is 121 m. Compared with the results of the front mining, it is found that the development height of the water flowing fractured zone is no longer increasing with the expansion of the mined-out area, and the working face has entered the stage of full mining.

The measuring line 3 is placed in the basic roof 20 m away from the roadway roof, and 10 measuring points are arranged on the measuring line. From the cutting side, the measuring points are 10 to 1 along the mining direction, and the interval is 50 m. After extracting the data of the measuring points, the vertical displacement curve with the advancing process of the working face is obtained, as shown in Figure 5. With the mining face advancing to 30 m, the vertical displacement of monitoring point 9 and monitoring point 10 has changed obviously, and the direct roof of the working face has first collapsed. When the working face is mined to 70 m, the monitoring point 8 sank sharply, and the maximum subsidence

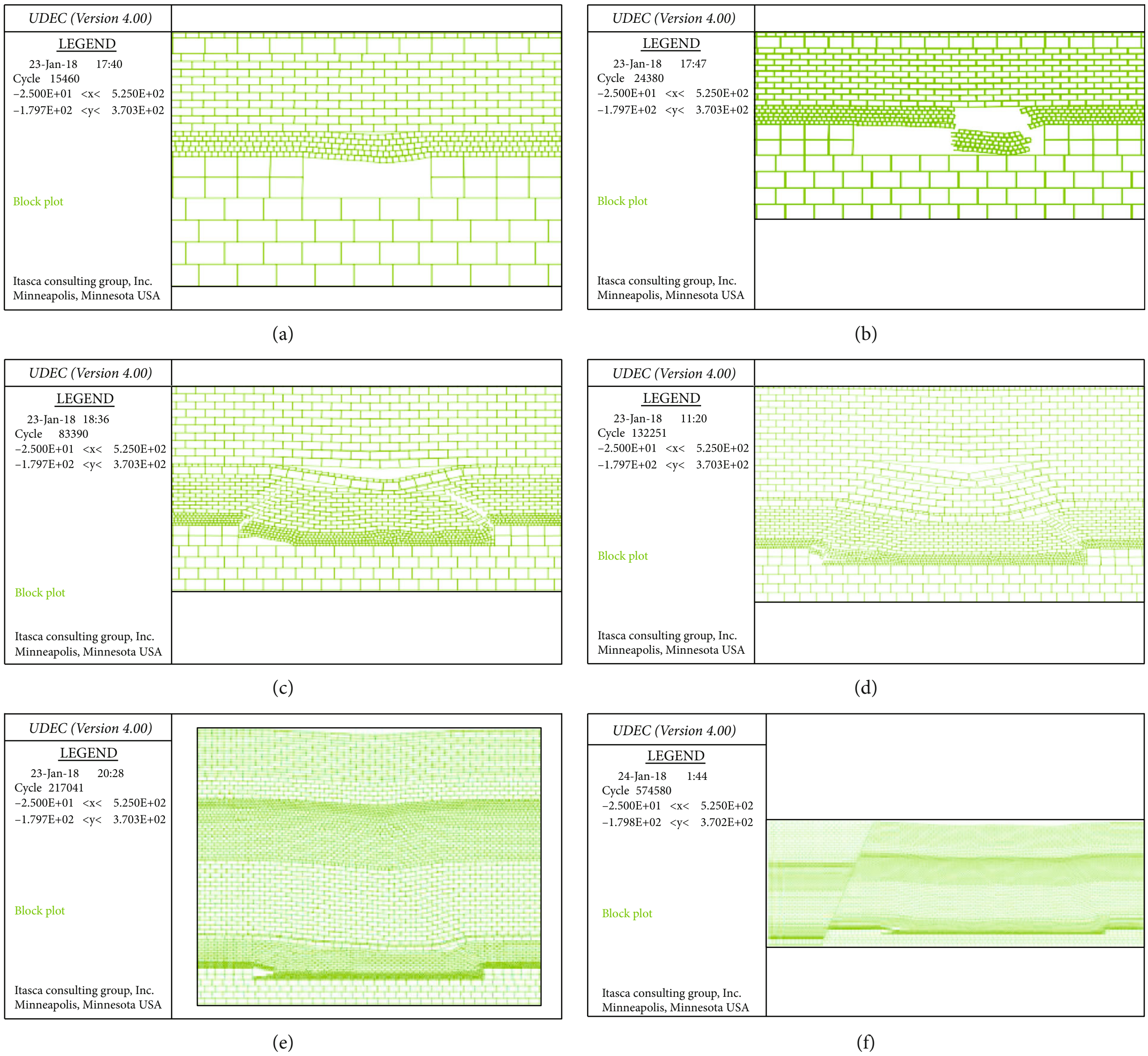

Figure 4: The migration change map of overlying strata under different distances of working face advancing, including (a) 10 m, (b) 30 m, (c) 70 m, (d) 95 m, (e) 120 m, and (f) 300 m.

reached 2.44 m. At this time, the primary roof collapsed and the roof collapsed in a large range. When the working face continues to stop at 95 m, the vertical displacement of monitoring point 7 continues to increase, and the maximum displacement increases to 3.49 m, and the vertical displacement of monitoring point 8 increases more. Therefore, the second periodic collapse of the basic roof of the working face occurred. By analyzing the maximum vertical displacement of 10 monitoring points in the mining process of the working face, when the vertical displacement of each monitoring point tends to be stable, the fully mining is achieved.

From Figure 6(a), it can be seen that the overlying strata on the working face have not broken and collapsed when the working face has not been mined after the opening and cutting of the working face, and the direct roof above the coal seam has subsided, but the subsidence is not large, but the shape of triangle-like cracks is produced in the interior of the direct roof and the bottom of the basic roof, and the height of the water-induced fracture zone is 9 m.

With the continuous advancement of the working face, the immediate roof above the mined-out area behind the working face continues to bend and sink, and a relatively obvious separation phenomenon occurs. The water flowing fractured zone continues to develop upward in a triangle shape. When advancing to 30 m, the direct roof breaks down for the first time, and the water-induced fracture zone rises further. At this time, the water-induced fracture zone develops to 33 m and develops into the weak aquifer of the second coarse sandstone in the subcritical layer. When the working face advances to 70 m and 95 m, the development heights of water flowing fractured zones are 45 m and 67 m. When the working face advances to 95 m, the longitudinal fractures develop upward in the shape of trapezoid. When the working face advances to 120 m, the basic roof

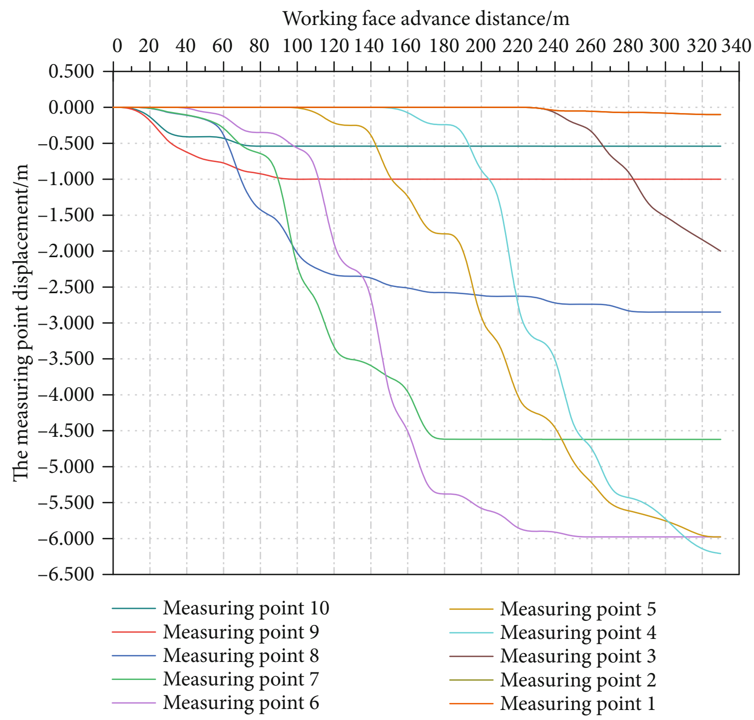

Figure 5: Measuring line 3 vertical displacement curve of each measuring point.

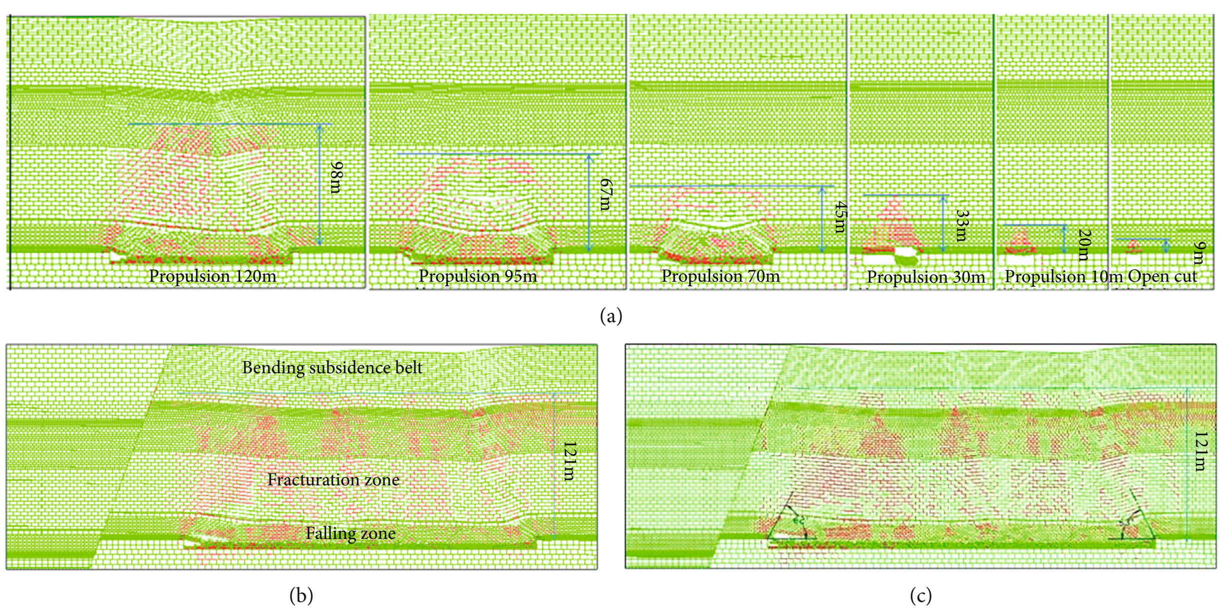

Figure 6: Variation of height of water flowing fractured zone with advancing distance of working face, including (a) 0, 10, 30, 70, 95, and 120 m and (b) 300 m and (c) stop mining line.

falls for the second time, and the water flowing fractured zone is still developed in a shape similar to the trapezoid with a development height of about 98 m.

When the working face advances to 300 m (Figure 6(b)), the overlying strata have reached full mining. At this time, the maximum development height of the water flowing fractured zone is 121 m. The fracture development is obvious in the overlying strata of the coal wall of 20 m in front of the working face, and a small range of longitudinal fractures also appear near the fault.

At the stop coal line position (Figure 6(c)), the height of the water flowing fractured zone did not continue to increase upward, still maintained at 121 m, but the fault activation was further obvious, and the cracks near the fault were further developed but did not connect with the water flowing fractured zone formed above the mined-out area, because

Table 2: Material ratio table of similar simulation test of Y.C.W mine 130204 working face.

Number right	Lithology	Model bulk density (g/cm^3)	Compressive strength of model (MPa)	Total thickness (cm)	Material ratio number	Total layered weight (kg)
16	Siltstone	1.63	0.07	4	855	1.97
15	Medium sandstone	1.56	0.06	21.5	755	10.14
14	Claystone	1.38	0.11	7.5	755	9.99
13	Fine sandstone	1.47	0.12	3.5	755	11.51
12	Claystone	1.38	0.11	3	755	10.05
11	Fine sandstone	1.47	0.12	3	855	10.25
10	Silty claystone	1.38	0.11	11	755	10.02
9	Medium sandstone	1.56	0.06	1	855	3.92
8	Grit sandstone (water)	1.47	0.08	25.5	755	14.86
7	One layer coal	0.94	0.04	0.5	873	2.09
6	Siltstone	1.63	0.07	1.5	855	6.3
5	Medium-grained sandstone	1.56	0.06	7.5	855	10.54
4	Fine sandstone	1.47	0.12	2	755	8.59
3	Siltstone	1.63	0.07	1	855	4.3
2	Two-layer coal	0.94	0.04	4	873	8.64
1	Silty claystone	1.38	0.11	7.5	755	10.85

Note: The material ratio number 873 indicates that the aggregate (sand) of the material accounts for 80%, the cement material accounts for 20%, and the cement material accounts for 70% lime and 30% gypsum.

it can be considered that the 40 m protective coal pillar left by the fault is reasonable, and the rock breaking angle at the cut is 63°, and the rock breaking angle at the stop mining of the working face is 62°.

4. Similar Simulation Study on Overburden Migration Law in Large Mining Height Working Face

4.1. Establishing Similar Simulation Model and Arranging Displacement Monitoring. Similarity simulation experiment has been widely used in the research of mining and rock mechanics because of its advantages such as easy to control, short test period, high efficiency, visual test results, and repeatable experiment process. On the basis of reasonable simplification, the similarity ratio between Y.C.W coal mine site and model is determined, which includes geometric similarity ratio 200 : 1, bulk density similarity ratio 1.6 : 1, and stress similarity ratio 320. At the same time, the motion of all corresponding points in the simulation is required to be similar to that of the entity; that is, the velocity, acceleration, and motion time of each corresponding point are required to be in a certain proportion, which is 14.1. The materials for similar simulation experiments are divided into aggregate and cementing material, in which fine sand is used for aggregate and lime and gypsum are used for cementing material, and the ingredients for each rock layer are finally obtained after several experiments and comparisons. The rock batching of similar simulation test of Y.C.W mine face 130204 is shown in Table 2. This experiment uses a laboratory table with dimensions of 1800 mm × 160 mm × 1300 mm. Since the second coal seam is a near horizontal coal seam, the dip angle of the coal seam is not considered too much in the lay-up experimental model, and the final completed lay-up model is shown in Figure 7.

The retraction channel was excavated in advance at 15 cm from the fault, and the open-off cut was excavated in advance at 15 cm from the right boundary. The mining height of the model was 4 cm, the model was retrieved every 14 minutes, and the mining length of the model was 140 cm. Since the theoretical calculation of the protective coal pillar of the fault is 40 m, the working face is pushed to stop mining at 40 m from the fault.

4.2. Analysis of the Overlying Rock Collapse Pattern of the Working Face Strike. The initial collapse process of the immediate roof is analyzed, as shown in Figure 8. When the advancing distance of the working face is less than 40 m (Figure 8(a)), there is no caving in the immediate roof. When the working face is pushed to 40 m, 60 m, and 78 m, the first collapse (Figure 8(b)), the second collapse, and the third collapse (Figure 8(c)) occur on the immediate roof, and the collapse lengths are 35 m, 18 m, and 15 m, respectively. Due to the relatively small bulking factor of the immediate roof, the broken rock between the goaf and the basic roof cannot fill the whole space. At this time, there are cracks between the basic roof strata and obvious bed separation phenomenon, and the lower layer is curved and deformed with obvious caving tendency. The lower layer is bent and deformed with obvious caving tendency. When the working face continues to advance to 80 m, the basic roof reaches the ultimate collapse distance (Figure 8(d)). The first weighting occurs with the pressure step of 80 m and the caving height of 5 m. The basic roof does not form a masonry beam structure after the first weighting fracture but forms a cantilever

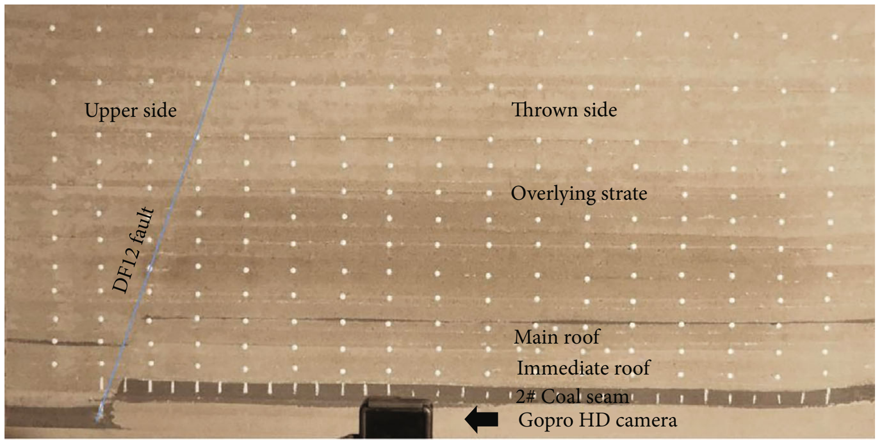

Figure 7: Similar simulation experiment layout.

beam structure. The caving height is 14 m, and the fracture development height is 4 m. The pressure of the working face is intense.

As the working face continued to excavate, the upper layer of the basic roof is broken and collapsed. Finally, when the working face is advanced to 105 m, the basic roof is completely collapsed (Figure 9(a)). The first weighting of the basic roof and the pressure step distance are 24 m, and the caving height is 17 m. The basic roof is separated from the overlying strata, and the longitudinal fracture development height is 26 m. However, the first periodic weighting of the basic roof is different from the first weighting breaking form. In the first weighting, the rock arch of the basic roof is an asymmetric rock arch structure. The thickness of the rock stratum at the right arch angle is thinner than that at the left side, and the bearing capacity is weak and the damage is serious. At this time, a relatively stable masonry beam structure is formed after the basic roof is weighting. The two ends of the beam are hinged on the rock strata that have not collapsed. The bending subsidence in the middle is the largest and acts on the caving zone. The broken rock in the caving zone is further compacted. At this time, the coarse sandstone 24 m above the coal seam is bending and sinking above the mining area, and longitudinal tension fissures are produced at the bottom of the seam, and off-layer fissures are also produced inside the seam, and the fissure zone development height is 28 m.

When the working face is advanced to 145 m (Figure 9(b)), the third periodic weighting of the basic roof and the pressure step distance are 20 m and the caving height is 22 m. The overlying strata continue to bend and sink. As the goaf is gradually filled, the overlying strata form a stable masonry beam structure under the support of the caving rock in the goaf. The maximum separation layer is located above the goaf 110 m behind the working face, and the height of the fracture zone is 62 m. As the working face continues to move forward to 175 m (Figure 9(c)), the fourth periodic weighting of the basic roof is 30 m, and the caving height is 19.5 m. However, the development height of the separation fracture and the longitudinal fracture does not change, and the development height of the fracture zone is 106 m at this time. When the working face is advanced to 185 m (Figure 9(d)), the working face is 60 m from the fault DF12, the fifth periodic weighting of the basic roof and the pressure step distance is 10 m, and the height of the caving zone is 14 m. There is no obvious migration change in the overlying strata, and the height of the fracture zone is still 106 m. When the working face advances to 195 m (Figure 9(e)), the working face is 50 m away from the fault DF12, the sixth periodic weighting of the basic roof and the pressure step distance is 10 m, the basic roof is cut off in large areas, and the caving height reaches 35 m. The overlying strata have undergone dramatic changes, resulting in a large number of separation fractures and longitudinal fractures. The maximum separation fracture develops to 125 m from the roof of the coal seam, and the height of the longitudinal fracture zone reaches 128 m.

When the working face advances to 205 m (Figure 9(f)), the working face is 40 m away from the fault DF12. Since the goaf is almost filled at this time, the extrusion between the rock seams is obvious, the overlying strata separation and longitudinal fracture zone continue to develop upward to 130 m above the roof of the coal seam, and many irregularly shaped fissure development areas appear. At this time, the breaking angle of the overburden at the open-off cut is 68°, and the breaking angle of the overburden at the stopping point of the working face is about 62°. It can be concluded from the collapse and fracture form of overburden roof in the whole process of working face that the goaf space of working face has relatively great influence on the collapse height of overburden roof. Because was not gob caving rock filling in time, so the permission of the overburden subsidence of space more than the limit between the broken blocks allow subsidence, resulting in in general can be formed under the condition of mining height are broken roof hinged structure breakage form, but due to mining under the condition of large mining height are broken down space is too large, lead to rupture rock cannot form the extrusion pressure. Finally, nonarticulated roof structure is applied to caving broken rock mass in goaf. Therefore, the overlying roof strata on the working face of 130204 large mining height in Y.C.W coal mine show the failure characteristics of "nonhinged roof structure-cantilever beam structure-hinged roof structure." In the process of working

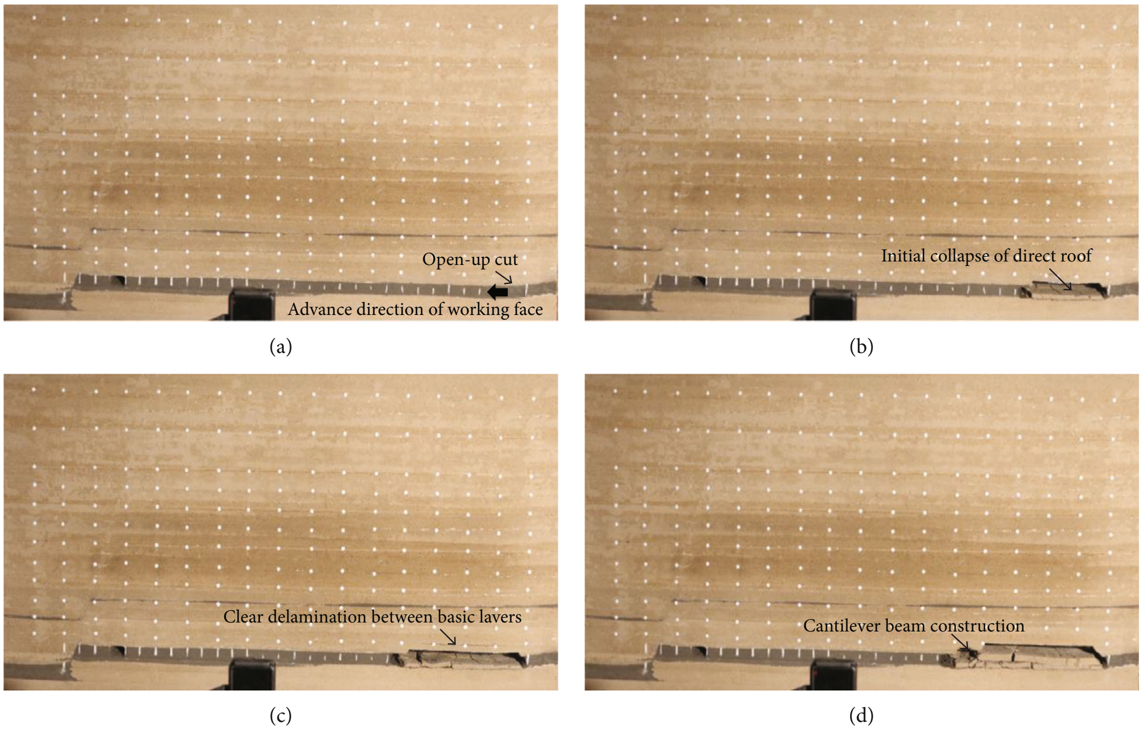

Figure 8: Immediate roof collapse diagram when the working face is advanced at different distances: (a) 0 m, (b) 40 m, (c) 78 m, (d) 80 m.

face advancing from the cut to DF12 fault, the periodic weighting interval of the main roof decreases from an average of 23.5 m to 10 m.

The relevant literature [33–37] shows that the macroscopic visible cracks in the model can be regarded as developed cracks. Therefore, based on the macroscopic visible cracks in the similar simulation experiment, the fracture development and distribution law of the overlying strata are studied. The variation curve of the development height of the water flowing fractured zone with the advance of the working face is shown in Figure 10.

It can be seen from the diagram that with the continuous advancement of the working face, the height of the caving zone increases first and then decreases, but the water flowing fractured zone is on the rise. When the working face advances to 125 m-180 m, the height of water flowing fractured zone develops fastest and reaches the maximum 130 m after the working face advances to the stop line.

Due to the large mining height of the working face, the stable hinge structure is not formed after the subcritical layer 1 reaches the limit breaking distance and enters the caving zone. Therefore, the height of the caving zone increases to 14 m after the first weighting of the basic roof, and the fracture zone also develops 4 m upward, which is shown as the first inflection point of the caving zone and the water flowing fracture zone in the figure. When the working face advances to 105 m, the basic roof continues to break in the form of a cantilever beam, and the overlying strata also break. At this time, the height of the caving zone further increases to 17 m, and the growth is small. The height of the water flowing fractured zone develops to 28 m, and the growth is large. When the working face advances to 125 m, the original hinge structure formed by the subcritical layer one has rotary deformation instability, which leads to its direct collapse, so the height of the caving zone increases rapidly. However, due to the existence of the subcritical layer two, the height of the water flowing fractured zone does not increase significantly, which is the second inflection point of the caving zone and the water flowing fractured zone in the diagram.

In the process of advancing the working face, the subcritical layer one enters the caving zone in the form of cantilever beam and masonry beam alternately, and the goaf space becomes smaller. The height of the caving zone is basically maintained at about 24 m. The bending and breaking subsidence of the subcritical layer two occurs, but due to the support of the broken rock in the goaf, it only enters the fracture zone. When the working face advances to 145 m and 165 m, the rock strata controlled above the bending fracture of the second subcritical layer also move downward, resulting in the development and penetration of internal fractures, and the height of water flowing fractured zone increases rapidly. The second subcritical layer and the overlying strata continue to move downwards, resulting in the formation of a stable masonry beam structure between the strata, which plays a supporting role in the main key layer above. The space under the main key layer is shrinking, and because the main key layer is thicker and stronger, in the process of advancing the working face to the stop line, only bending subsidence occurs, and the internal cracks are not penetrated. Therefore, when the working face reaches the stop line, the height of the water flowing fractured zone only develops to the bottom of the main key layer, and the final development height is 130 m.

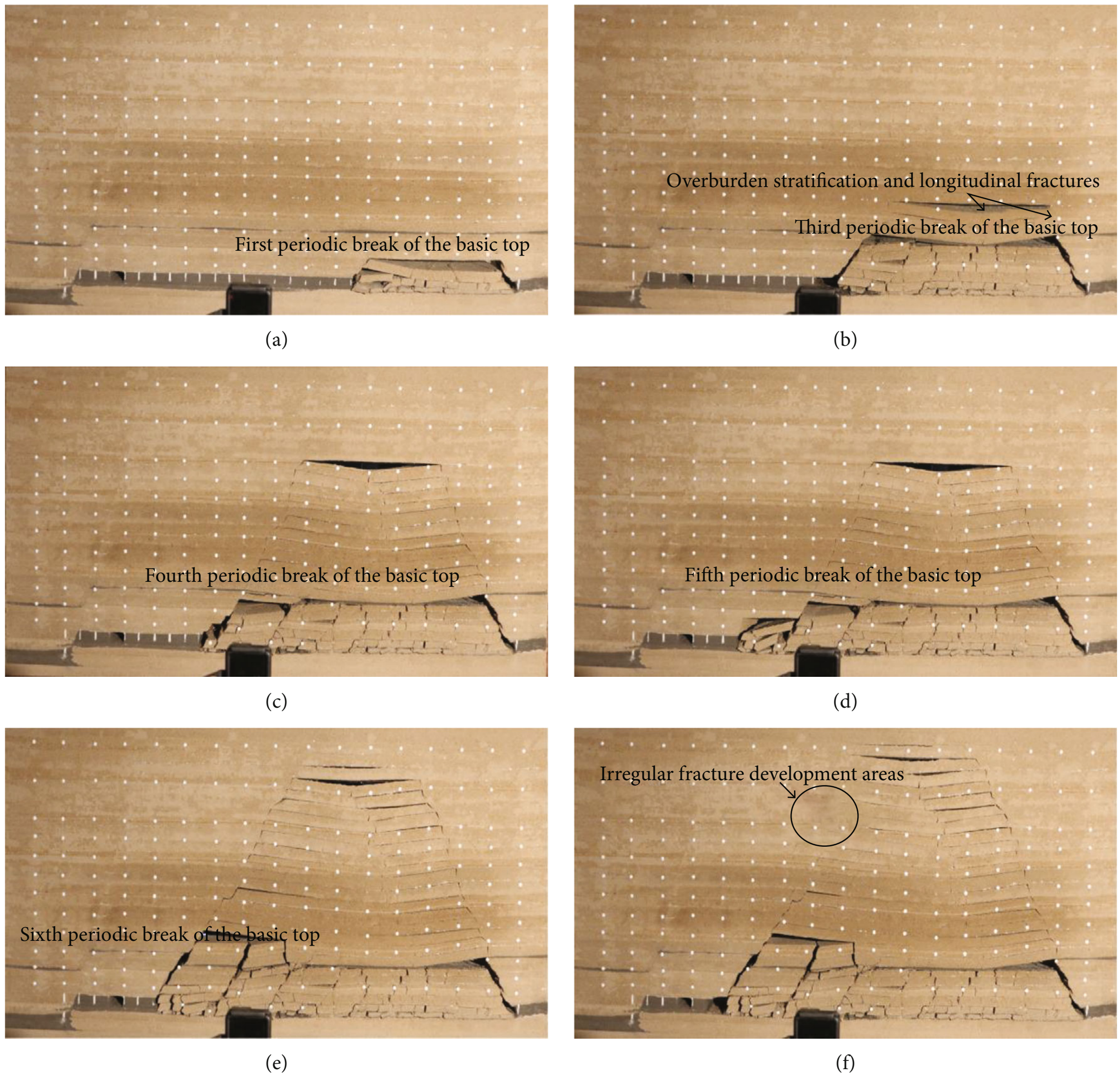

FIGURE 9: Periodic fracture diagram of basic roof under different distances of working face advancing, including (a) 105 m, (b) 145 m, (c) 175 m, (d) 185 m, (e) 195 m, and (f) 205 m.

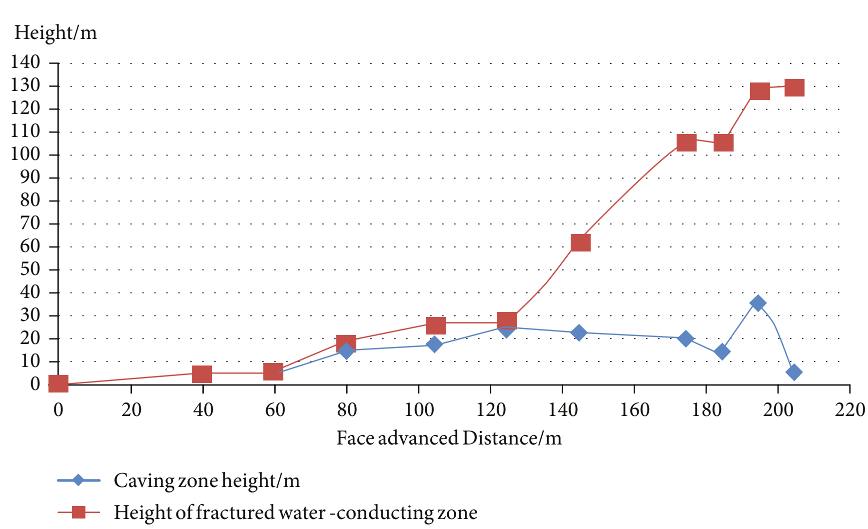

FIGURE 10: Curves of development height of water flowing fractured zone with working face advancing.

5. Conclusion

By means of theoretical analysis, similarity simulation, and numerical simulation, the migration law of overlying strata on the working face of large mining height in Y.C.W coal mine was studied. It is found that there are some deviations in the results obtained by the three research methods, but they are in line with the error range of engineering practice. Therefore, the maximum and minimum intervals of the three results are taken as the final conclusion. The main conclusions are as follows:

(1) The theoretical analysis results show that there are two subcritical strata and one main key strata in the strata above the direct roof, which are the subcritical strata of medium-grained sandstone with a thickness of 15 m above the coal seam roof. Coarse sandstone subcritical layer 2 with thickness of 51 m above the roof of coal seam is weak aquifer. Middle sandstone main key layer has a thickness of 48 m at 133 m above coal seam roof

(2) The roof of overlying strata on the working face of large mining height shows the failure characteristics of "nonhinged roof structure-cantilever beam structure-hinged roof structure." The initial caving step distance of the direct roof of the working face is about 30-40 m, and the initial caving step distance of the basic roof is about 70-80 m. When the working face is pushed to the DF12 fault greater than 60 m, the periodic weighting step distance is about 23.5-25 m. When the working face is pushed to the stop line position, the breaking angle of the overburden at the cutting hole is 63°-68°, and the breaking angle of the overburden at the stop line is about 62°

(3) With the working face continuous advancement, the overlying rock fractures continue to develop and the height of the water flowing fractured zone generally shows an upward trend. The development shape gradually changes from the initial triangle-like to trapezoid-like, and the final development height of the water flowing fractured zone is about 121-133 m. At the end of the mining, the height of the caving zone is developed to about 24 m. The water flowing fractured zone will lead to the overlying rock of the coarse sandstone weak aquifer above the working face, and the water should be detected and released in advance in the mining of the working face to ensure the safe and efficient mining of the working face

Data Availability

The data used to support the findings of this study are available from the corresponding author upon request.

Conflicts of Interest

The authors declare no conflict of interest.

Acknowledgments

This research has been supported by the National Natural Science Foundation of China (Grant No. 51774288) and the Fundamental Research Funds for the Central Universities (Grant No. 2021YJSNY20).

References

[1] B. Yu, W. B. Zhu, R. Gao, and J. R. Liu, "Strata structure and its effect mechanism of large space stope for fully mechanized sublevel caving mining of extremely thick coal seam," *Journal of China Coal Society*, vol. 41, no. 3, pp. 571–580, 2016.

[2] J. F. Ju, J. L. Xu, W. B. Zhu, Q. X. Wang, and X. J. Hao, "Strata behavior of fully-mechanized face with 7.0m height support," *Journal of Mining and Safety Engineering*, vol. 29, no. 3, pp. 344–356, 2012.

[3] H. Z. Zhao and Q. S. Song, "Development of hydraulic support for super great mining hight," *Journal of Mining and Safety Engineering*, vol. 24, no. 3, pp. 265–269, 2007.

[4] J. C. Wang, *Mining Theory and Technology of Thick Coal Seam*, Metallurgical Industry Press, Beijing, 2009.

[5] P. L. Gong and Z. M. Jin, "Study on the structure characteristics and movement laws of overlying strata with large mining height," *Journal of China Coal Society*, vol. 29, no. 1, pp. 7–11, 2004.

[6] G. Peilin and J. Zhongming, "Mechanical model study on roof control for fully-mechanized coal face with large mining height," *Chinese Journal of Rock Mechanics and Engineering*, vol. 27, no. 1, pp. 193–198, 2008.

[7] Z. Z. Wen, X. D. Zhao, L. M. Yin, and H. C. Xia, "Study on roof control model of large mining height and reasonable bearing capacity of support," *Journal of Mining and Safety Engineering*, vol. 27, no. 2, article 2550258, 2010.

[8] H. J. Hao, J. Wu, Y. Zhang, and Z. B. Yuan, "The balance structure of main roof and its action to immediate roof in large cutting height workface," *Journal of China Coal Society*, vol. 29, no. 2, pp. 137–141, 2004.

[9] Q. X. Huang and J. L. Zhou, "Roof weighting behavior and roof structure of large mining height longwall face in shallow coal seam," *Journal of China Coal Society*, vol. 41, supplement 2, pp. 279–286, 2016.

[10] J. L. Zhou and Q. X. Huang, "Stability analysis of key stratum structures of large mining height longwall face in shallow coal seam," *Chinese Journal of Rock Mechanics and Engineering*, vol. 38, no. 7, pp. 1396–1407, 2019.

[11] Q. X. Huang and P. F. Tang, "Roof structure analysis on large mining height longwall face in shallow coal seam," *Journal of Mining and Safety Engineering*, vol. 34, no. 2, pp. 282–286, 2017.

[12] Y. P. Fu, X. M. Song, P. W. Xing, and J. H. Zhang, "Study on simulation of caving and evolution law of roof strata of large mining height work face in shallow thick coal seam," *Journal of China Coal Society*, vol. 37, no. 3, pp. 366–371, 2012.

[13] J. Z. Yang and Q. J. Liu, "Analysis and measured of strata behavior law and mechanism of 8.8m ultra-high mining height working face," *Coal Science and Technology*, vol. 48, no. 1, pp. 69–74, 2020.

[14] J. Z. Yang, "Study on overlying strata breakage and strata behaviors law of 7.0 m mining height working face," *Science and Technology of Coal*, vol. 45, no. 8, pp. 1–7, 2017.

[15] X. W. Yin, "Cutting block structure model of overburden with shallow buried coal seam and ultra-large mining height working face," *Journal of China Coal Society*, vol. 44, no. 7, pp. 1961–1970, 2019.

[16] Y. H. Pang, G. F. Wang, J. H. Zhang, and H. L. Liu, "Overlying strata fracture structure and stability control technology for ultra large mining height working face," *Coal Science and Technology*, vol. 45, no. 11, pp. 45–50, 2017.

[17] P. Xiang, L. H. Sun, H. G. Ji, Y. Gao, Y. J. Liu, and Y. F. Wu, "Dynamic distribution characteristics and determination method of caving zone in overburden strata with large mining height," *Journal of Mining and Safety Engineering*, vol. 34, no. 5, pp. 861–867, 2017.

[18] L. H. Sun, "Structural evolution and rock pressure activity regularity of weakly cemented strata of the large mining height work face in Western China," *Chinese Journal of Rock Mechanics and Engineering*, vol. 36, no. 7, p. 1820, 2017.

[19] Y. X. Zhao, C. W. Ling, B. Liu, and X. He, "Fracture evolution and energy dissipation of overlying strata in shallow-buried underground mining with ultra-high working face," *Journal of Mining and Safety Engineering*, vol. 38, no. 1, pp. 9–18+30, 2021.

[20] Z. P. Jin, T. Qin, and J. W. Zhang, "Analysis of abutment pressure distribution characteristics and influencing factors of deep mining height face," *Coal Science and Technology*, vol. 46, supplement 1, pp. 97–99+134, 2018.

[21] Y. P. Liang, B. Li, Y. Yuan, Q. L. Zou, and L. X. Jia, "Moving type of key strata and its influence on ground pressure in fully mechanized mining face with large mining height," *Journal of China Coal Society*, vol. 42, no. 6, pp. 1380–1391, 2017.

[22] G. W. Hu and Z. M. Jin, "Study on mine pressure observation and its behavior law in fully mechanized mining face with large mining H8," *Journal of Taiyuan University of Technology*, vol. 37, no. 2, pp. 127–130, 2006.

[23] Q. X. Sun, Y. Mou, and X. L. Yang, "Study on "two-zone" height of overlying of fully-mechanized technology with high mining height at Hongliu coal mine," *Journal of China Coal Society*, vol. 38, Supplement 2, pp. 283–286, 2013.

[24] F. F. Wu, *Study on the Law of Roof Broken and Instability and the Control of Large Mining Height Fully Mechanized Mining in Thick Coal Seam*, China University of Mining and Technology, 2014.

[25] S. H. Yan, L. Yu, G. Xu, and Q. M. Liu, "Study on mining technology to further improve production in fully-mechanized coal mining face with large mining height," *Coal Science and Technology*, vol. 43, no. 8, pp. 1–6, 2015.

[26] L. Yu, S. H. Yan, D. B. Mao, Y. X. Xia, L. F. Zhu, and Z. Zhang, "Movement of roof strata of long wall with top coal caving with great mining height based on ARAMIS M/E microseismic monitoring," *Journal of China Coal Society*, vol. 36, Supplement 2, pp. 293–298, 2011.

[27] H. T. Liu, T. H. Huo, Y. E. Li, M. Luo, G. D. Zhou, and Z. J. He, "Numerical simulation study on the distribution law of deviatoric stress of floor under the influence of mining," *Geofluids*, vol. 2021, 14 pages, 2021.

[28] H. T. Liu, L. F. Guo, G. M. Cao et al., "Comprehensive study of strata movement behavior in mining a longwall top coal caving panel of a composite coal seam with partings," *Applied Sciences*, vol. 10, no. 15, pp. 5311–5315, 2020.

[29] G. Y. Zhang, Q. G. Yu, and G. B. Zhao, "Three-dimensional simulation of soft overburden "two-zone" height due to high intensity mining in Shajihai coal mine," *Journal of Mining and Strata Control Engineering*, vol. 3, no. 2, pp. 23–30, 2021.

[30] X. Y. Yu, S. S. Wang, Y. Yang, and X. W. Mao, "Numerical study on the movement rule of overburden in fully mechanized caving mining with thick depth and high mining height," *Journal of Mining and Strata Control Engineering*, vol. 3, no. 1, pp. 28–38, 2021.

[31] Y. P. Li, F. Cui, W. H. Yang, and X. Q. Y. Chi, "Dynamic migration law and its control of roof in fully mechanized top coal caving mining in extremely steep and thick coal seams," *Journal of Mining and Strata Control Engineering*, vol. 2, no. 4, pp. 30–37, 2020.

[32] J. L. Xu, W. B. Zhu, and X. Z. Wang, "New method to predict the height of fractured water-conducting zone by location of key strata," *Journal of China Coal Society*, vol. 37, no. 5, pp. 762–769, 2012.

[33] Z. Z. Feng and Y. S. Zhao, "Control effect of fissure scale on deformation and failure of rock mass," *Journal of Rock Mechanics and Engineering*, vol. 27, no. 1, pp. 78–83, 2008.

[34] Y. Wang, D. X. Nie, J. K. Zhang, and Q. Y. Lei, "Relation between development degree of joints and deformation parameters of rock mass," *Journal of Rock Mechanics and Engineering*, vol. 22, Supplement 2, pp. 2572–2574, 2003.

[35] H. Nan and Y. Zhou, "Effect of bulk density of analog simulation model on its strength," *Mining Research and Development*, vol. 27, no. 3, pp. 12-13, 2007.

[36] W. Liu and J. H. Gao, "Study on similar simulation of rock displacement," *Journal of Henan Polytechnic University (Natural Science Edition)*, vol. 28, no. 2, pp. 160–163, 2009.

[37] S. J. Liu, B. Q. Lin, J. Gao, Z. Y. Hao, Q. G. Li, and J. Meng, "Similar simulation of fracture deformation in overlying coal and rock in far-distance-lower-protective-layer mining," *Journal of Mining and Safety Engineering*, vol. 28, no. 1, pp. 51–55 +60, 2011.

Hindawi
Geofluids
Volume 2022, Article ID 8130555, 15 pages
https://doi.org/10.1155/2022/8130555

Research Article

The Investigation of Strata Control for Ultrasoft Coal Seam Mining

Chuanqi Zhu, Lei Wang, and Shaobo Li

State Key Laboratory of Mining Response and Disaster Prevention and Control in Deep Coal Mines, Anhui University of Science and Technology, Huainan 232001, China

Correspondence should be addressed to Chuanqi Zhu; cqzhu@aust.edu.cn

Received 31 May 2021; Revised 21 July 2021; Accepted 25 February 2022; Published 16 April 2022

Academic Editor: Zhijie Wen

Strata control of ultrasoft coal seam has been a critical problem for mining and geotechnical engineers in years. In this paper, the No. 66207 longwall panel at Xinzhuangzi coal mine, Anhui, China, was used as an example for study. A systematic approach using laboratory testing, numerical simulation, and field validation was implemented to investigate the influences of roadway layout and presplit blasting on mechanical properties of surrounding rock. Based on the results, an inward-stagger roadway layout with presplit blasting on roof was proposed for the regional strata control. The investigation on the relationship between angle of repose of ultrasoft coal and water content showed that the angle of repose first increased then decreased with increasing water content. The peak value was observed at 17.659% water content, suggesting water injection into ultrasoft coal seam can improve the coal mechanical properties and rib stability. The "high resistance, integral beam, two-stage rib+roof support system" was design to replace the traditional equipment, which can support the ultrasoft coal seam. The combination of this system and proposed "difference stepping" mining technique was capable of preventing roof and rib from failure, as well as mitigating the rockfall during moving hydraulic support. Based on the field validation, it was found that the stress concentration coefficient was relatively low during mining process. This was able to effectively manage the mining-induced stress while improving the productivity three times than without the technique. There was also no failure event observed during mining, such that the safety of mine workers was improved significantly.

1. Introduction

The occurrence conditions of Chinese coal resources are very complex, with soft coal seams widely distributed and extremely rich reserves. According to incomplete statistics, 53.3% of Chinese coal mines contains soft coal seams [1]. Huainan and Huaibei in Anhui, China, has significant high quality coal reserves, particularly in No. 7 and No. 8 areas. However, the mine site is under complex geological conditions, including various shapes of folds and densely distributed preexisting fractures, as displayed in Figure 1(a). Coal cut by the shearer is very loose and small, showing high porosity when it is stockpiled, as shown in Figure 1(b). Coal at the longwall face is extremely loose and fractured with low strength and almost zero cohesion, which can be broken by hands. When mining this type of ultrasoft coal seam, the longwall face collapses along with mining. At the same time, coal rib is rarely complete and competent, which in turn leads to roof failure, hydraulic support instability, and falling gangue. These hazardous events are harmful to the mine workers as well as production, especially for coal seams with high inclinations and high mining heights. Therefore, it is critical to investigate the strata control for this type of coal seams to ensure the safety and productivity.

In the study of coal and rock instability model Li et al. [2] established the coal instability risk analysis and prediction model by using the dynamic fuzzy logic method and tested the effectiveness and feasibility of the model. Based on 11224 working face of Panji No. 2 coal mine in Huainan Mining Area, Liu et al. [3] established the mechanical model of coal wall sliding instability and analyzed the characteristics of coal wall instability. Si et al. [4] put forward a new SVM algorithm

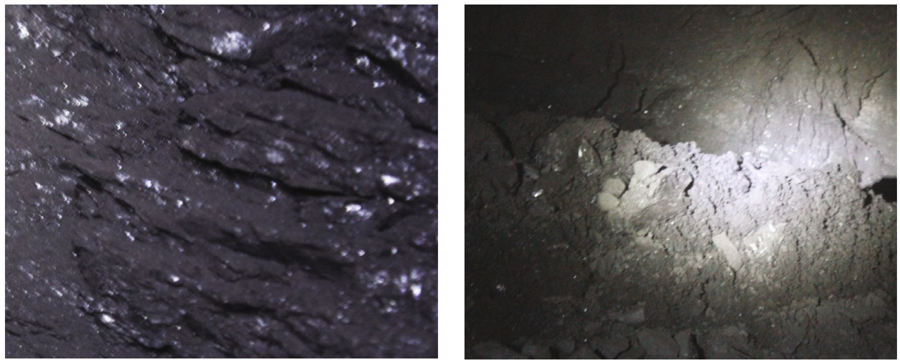

(a) (b)

Figure 1: Geological conditions of coal seam, (a) rib, and (b) loose coal.

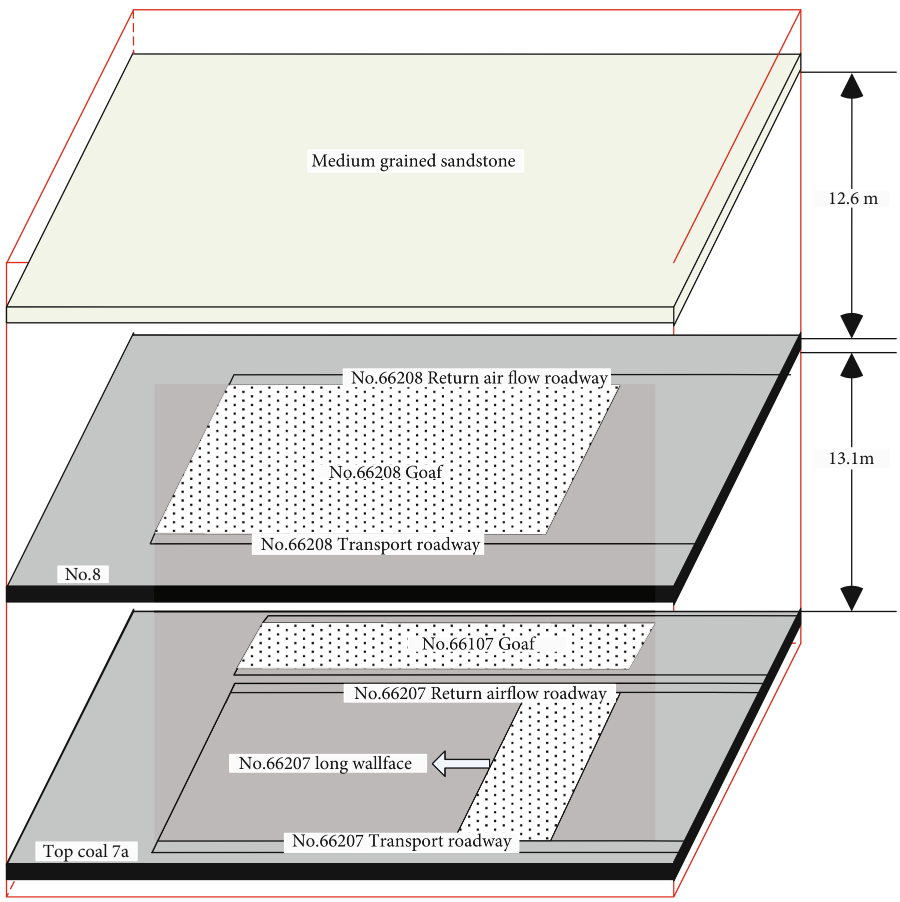

Figure 2: Location of No. 66207 seam.

for coal and rock instability disaster, established the coal and rock instability risk evaluation model, and verified the feasibility and superiority of the model. Li and Zhang [5] established the unloading field effect model of coal wall excavation according to the distribution characteristics of surrounding rock stress field of large mining height working face, analyzed the instability mechanism of coal wall under the action of unloading stress field, and put forward the prevention measures to improve the wall protection force, support initial support force, and coal cohesion. Li et al. [6] established the mechanical model of coal wall sliding instability, derived the analytical expression of the safety factor of each sliding surface, took 8102 working face of wulonghu coal mine as an example, solved the safety factors of different sliding surfaces, and obtained the critical sliding surface position and maximum sliding depth of coal wall. Yuan et al. [7] proposed a constitutive model for "wedge" sliding of coal rib and investigated the influential factors of rib stability. Yin et al. [8] developed constitutive models which describe the rib instability along slab tracing and weak inclusion. Thereby, a rib failure prediction tool for LTCC using C++ was proposed. Guo et al. [9] studied the interaction among coal wall, support, and roof

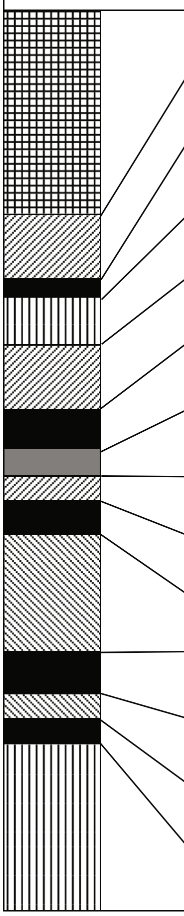

Comprehensive bar chart		Mechanical parameters of coal and rockmass								
Columnarsection	Lithology of columnar section	Thickness (m)	Bulk density (KN/m^3)	Elastic modulus (GPa)	Poisson's ratio	Cohesion (MPa)	Angle of internal friction (°)	Bulk modulus (GPa)	Shear modulus (GPa)	Tensile strength (MPa)
	Medium grained sandstone	11.0	28.20	25.33	0.23	3.35	39	9.96	8.62	1.59
	Sandy mudstone	3.8	26.65	23.21	0.17	2.61	41	11.72	9.92	1.21
	No.9	0.8	27.00	24.02	0.20	2.78	40	13.33	10.00	1.35
	Siltstone	3.0	26.65	23.21	0.17	2.61	41	11.72	9.92	1.21
	Sandy mudstone	4.5	24.61	8.81	0.26	1.2	30	6.08	3.47	0.61
	No.8	1.9	27.00	24.02	0.20	2.78	40	13.33	10.00	1.35
	Fine sandstone	1.5	25.49	14.41	0.24	1.78	34	9.23	5.81	0.88
	Sandy mudstone	1.5	24.61	8.81	0.26	1.2	30	6.08	3.47	0.61
	No.7b	1.1	13.7	5.13	0.32	1.25	32	4.72	1.93	0.13
	Mudstone	9.0	24.2	14.31	0.21	1.42	32	7.73	8.63	0.76
	Top coal 7a	2.7	13.7	5.13	0.32	1.25	32	4.72	1.93	0.13
	Mudstone	1.3	24.2	14.31	0.21	1.42	32	7.73	8.63	0.76
	Bottom coal 7a	1.0	13.7	5.13	0.32	1.25	32	4.72	1.93	0.13
	Siltstone	10.0	26.65	23.21	0.17	2.61	41	11.72	9.92	1.21

Figure 3: Mechanical properties of roof and floor.

by analyzing the mechanical model of support surrounding rock under different roof structures and put forward the control measures for the stability of deep hole static pressure pregrouting coal wall.

In the study of instability of surrounding rock, Yuan et al. [10] focused on the development, expansion and penetration of cracks on the coal wall of the working face in soft coal seam, and finally put forward the water injection prevention technology. In order to effectively control the surrounding rock instability accident of short wall coal seam with large mining height in soft thick coal seam, Yuan et al. [11] developed a drilling shearer and drilling mining technology and successfully applied them in 1305 working face of Zhaozhuang coal mine. Behera et al. [12] analyzed the key factors affecting the stability of coal and rock in Godavari Valley coalfield working face and put forward the damage criterion for quantifying the stability of coal wall in working face. Li G. S. et al. [13] studied the failure characteristics of coal wall spalling in thick coal seam with gangue, analyzed the morphology of coal wall spalling in different gangue positions, and found that coal seam with gangue is more prone to spalling at the gangue position. Yao et al. [14] comprehensively studied the supporting stress distribution in front of the working face under different mining dip angles and determined the main failure forms and positions of coal wall. Based on the propagation law of stress wave, Lu et al. [15] took the coal wall of deep working face as the research object and analyzed the dynamic damage and failure characteristics of coal wall from the perspective of dynamics. Tian et al. [16] analyzed the failure mechanism of rib under high mining height using the data from No. 4 coal seam at Longquan coal mine. Based on the investigation, the researchers obtained the relationship between rib failure and hydraulic support working resistance and determined the appropriate mining method which can prevent rib failure. Wang [17] studied the ultrasoft coal seam ribs and proposed a number of control technique, including Longwall Top Coal Caving (LTCC), improving hydraulic support resistance, water injection into coal seam, increasing mining rate, and reducing mining height. Based on the No.

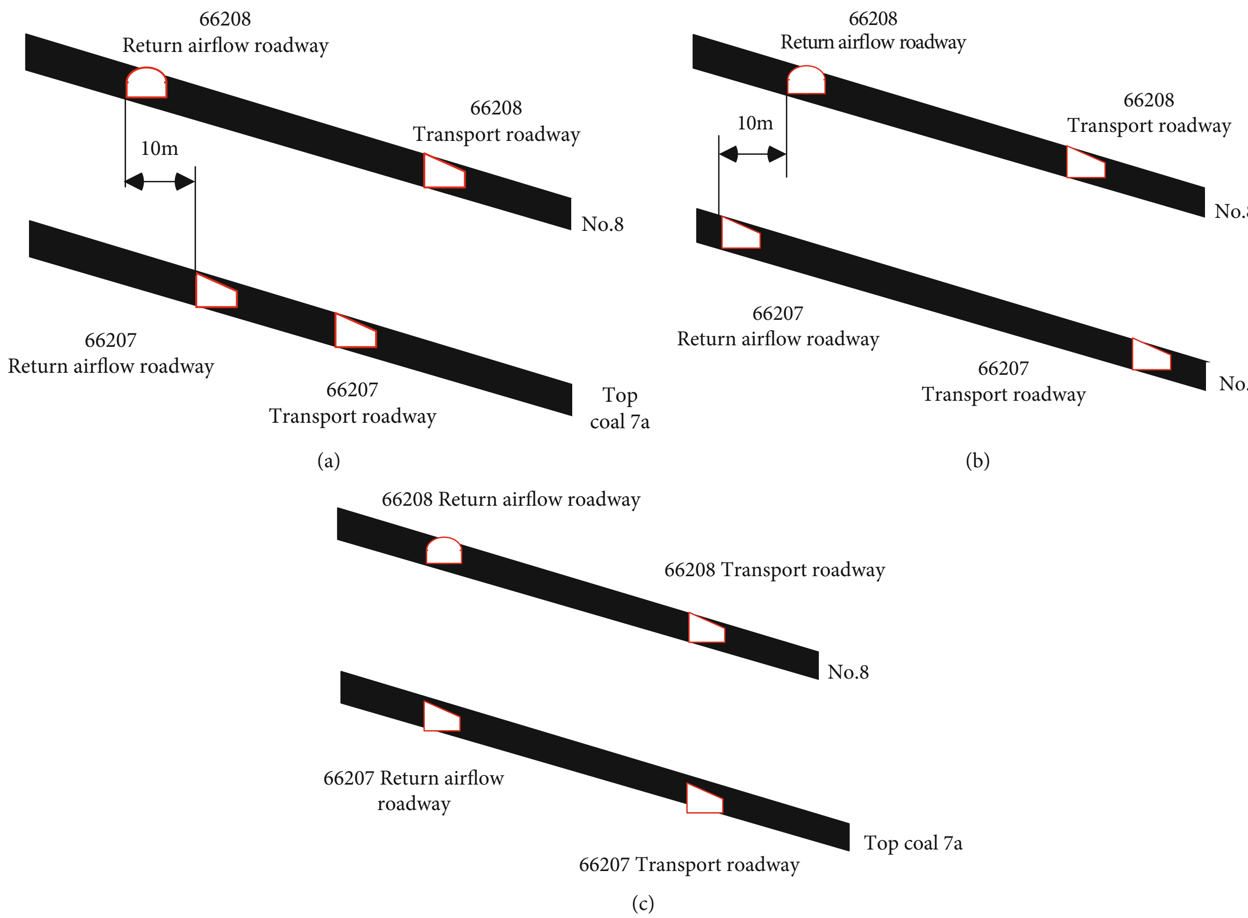

Figure 4: Different layouts for roadway. (a) 10 m inward-stagger layout, (b) 10 m outward-stagger layout, and (c) overlapping layout.

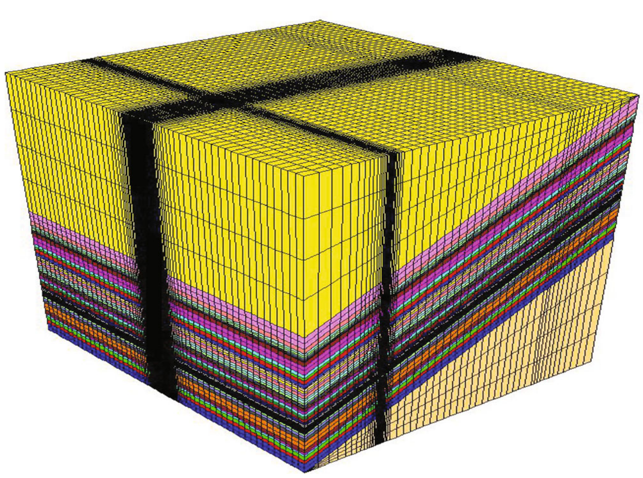

Figure 5: 3D simulation network.

1123 coal seam in Changzishan coal mine, Wu et al. [18] investigated the rib failure mechanism and characteristics and high risk areas under high inclination LTCC longwall face. Subsequently, the researchers suggested a comprehensive controlling technique. Huang and Liu [19] simulated the rib failure process under different mining heights for shallow coal seam via UDEC. Based on the results, the study suggested a series of control techniques, including improving roof support and increasing mining rate and rib support. Fang et al. [20] determined the supporting plan and parameters for Wuyang coal mine rib failure based on coal rib status and root cause as well investigated the stress distribution. Pang et al. [21] divided the rib failure process into two steps: (i) rib failure occurrence and (ii) rib instability and conducted sensitivity analysis on various parameters. Zhang and Wu [22] investigated the rib failure characteristics, influential parameters, and mechanisms under high inclination and high mining heights using monitoring data, numerical simulation, and theoretical analysis. Wang et al. [23] used similar approaches to investigate the stress and displacement distributions in ribs under various mining heights and found that the likelihood of rib failure increases with the increasing mining height. Yang et al. [24] discussed the rib failure mechanism of thick coal seam based on the Ruilong coal mine and conducted sensitivity analysis of controlling factors. According to the analysis, Yang et al. suggested that reducing mining height, improving support, and rib grouting are the effective measures of rib failure. Guo et al. [25] analyzed the relationship between rib failure and immediate roof failure when mining upwards. The paper subsequently defined the required hydraulic support and columns inclination angle. Xia et al. [26] investigated the relationship between longwall mining height and rib instability in LTCC

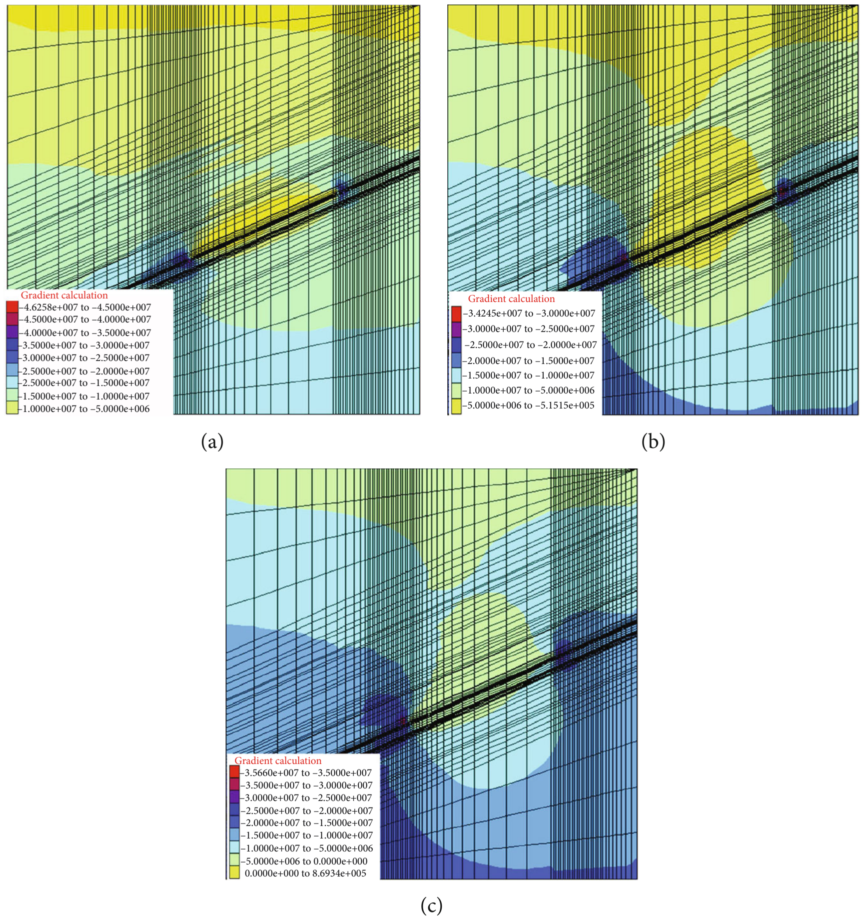

Figure 6: Cloud map of stress distribution along the inclined direction of coal seam, (a) inward-stagger, (b) outward-stagger, and (c) overlapping.

using FLAC3D. Results showed that increasing longwall mining height leads to rib deformation and fracture, which then results to rib failure and roof failure. Yang et al. [27] studied the rib stability of longwall face with gangue using laboratory investigation and theoretical analysis. Li et al. [28] analyzed the compressive shearing, sliding, splitting, or horizontal arching failures of coal rib based on Hetangou coal mine. Based on the analysis, Li et al. suggested to change the stress distribution in order to ensure rib stability. Zhang [29] analyzed the influences of stress distribution and rib characteristics on rib instability and proposed associated control techniques.

However, majority of previous studies focused on the instability of surrounding rock under high mining heights, whereas there is lack of attention for ultrasoft coal seams. Hence, this paper will investigate the instability of surrounding rock of ultrasoft coal seam based on the data collected from No. 66207 longwall face at Xinzhuangzi coal mine and propose the key equipment and techniques for strata control.

2. Engineering Background

2.1. Mechanical Properties of Coal. No. 7 mining area in Huainan contains dry and fractured coal (1.336% water content) with particle size less than 10 mm. There are 47.157% of particle size less than 2.5 mm, and the rock strength is extremely low, and the Platts coefficient is only 0.382.

2.2. Coal Reserve and Mining Conditions. No. 66207 longwall face has the maximum and minimum elevations of -721 m and -793 m. The coal seam thickness is between 1.7 and 4.8 m, with average thickness of 2.7 m. The inclination angle is 27°-34° with average angle of 30°. No. 7 seam has two subseams (No. 7 top and No. 7 bottom), and some parts converge into one seam. No. 7 top thickness is between 1 and 3.2 m, and the seam has average thickness of 2.7 m; whereas, No. 7 top thickness is between 0.7 and 1.7 m and the seam has an average thickness of 1 m. The interburden is between 0 and 1.7 m, with average thickness of 1.3 m.

Mining has completed at the last stage of No. 66107 and No. 66208 above, whereas mining at B6 seam beneath has not yet been commenced. Figure 2 shows the location of No. 66207 seam. This longwall face is between the F5-3 and F6 fault zones, where the north of longwall is close to F5-3. There is large change in the stratum with folds. The in situ stress is concentrated at the longwall face, and the surrounding geology is complex with noticeable faults.

2.3. Mechanical Properties of Roof and Floor. Based on the laboratory and field tests [30], the mechanical properties of

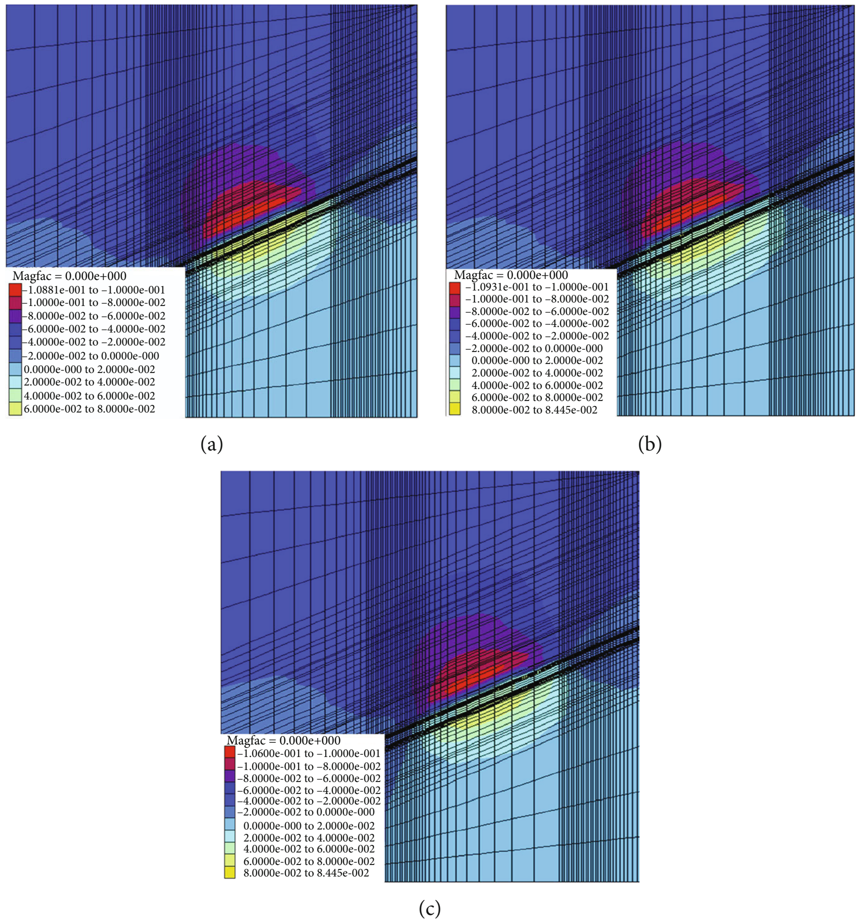

Figure 7: Cloud map of displacement distribution along the inclined direction of coal seam. (a) Inward-stagger, (b) outward-stagger, and (c) overlapping.

roof and floor were obtained, as shown in Figure 3. The immediate roof consists of 2-12 m mudstone, with average thickness of 9 m. The immediate floor is 6-19 m siltstone, with average thickness of 10 m.

Coal at No. 66207 is loose and fractures, which cannot self-sustain under high stress conditions. The distance between the seam and above seam is only 13.3 m. The residual pillars in above coal work (No. 8) caused stress concentration which will influence the safety of No. 66207. There is also medium-grained sandstone 12.6 m above the No. 8 with 11 m thickness. This strong rock layer will result in stress concentration at No. 66207 during mining, which can lead to macroscale instability.

3. Strata Control of Ultrasoft Coal Seam Mining

3.1. Preregional Control Technique via Mining Stress Reduction. FLAC3D was used to analyze the influence of various roadway layouts (inward- and outward- stagger and overlapping) on the stability of surrounding rock. Figure 4 shows the simulation of mechanical properties of surrounding rock under different layouts of No. 66207 longwall [31].

The model has the dimensions of 600 m × 550 m × 523.4 m. The horizontal displacement was constrained on side boundaries, whereas the vertical displacement was constrained on bottom boundary. Load was applied on the model vertically to simulate the overburden weight, see Figure 5. The mechanical properties of each strata is displayed in Figure 3.

Figures 6–8 show cloud maps of stress and displacement fields and fracture distribution of three layouts at No. 66207 longwall. Based on the figures, it can be seen that at the outward-stagger and overlapping layouts, the vertical stress was more concentrated, at 25 MPa and 20 MPa, respectively. Thereby, the vertical displacement was higher and there was some tensile and shear failures observed in the coal seam. On the other hand, 10 MPa vertical stress was observed in inward-stagger layout with maximum vertical displacement of 2 cm. Rock fracture and vertical stress concentration under this condition were not insignificant.

When the outward-stagger or overlapping layout was implemented, there was high stress concentration appeared at some regions along the dip direction of coal seam. Due to the pressure from longwall face, the deformation of surrounding rock gradually increased. This may lead to the likelihood of instability of surrounding rock. When the inward-stagger

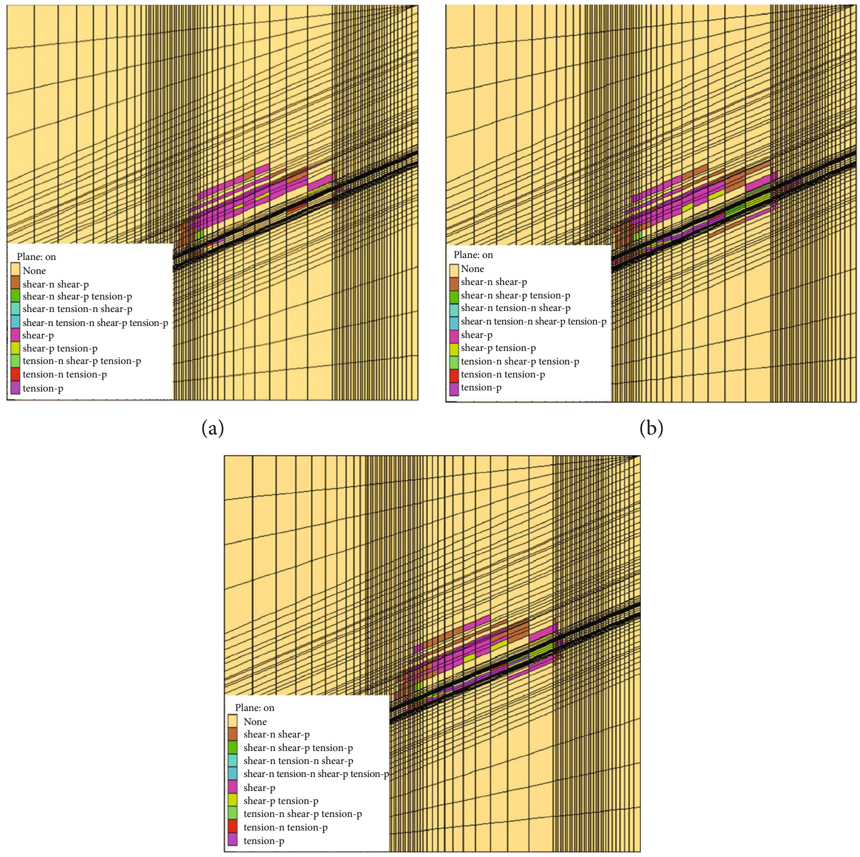

(a)

(b)

(c)

Figure 8: Cloud map of fracture distribution along the inclined direction of coal seam. (a) Inward-stagger, (b) outward-stagger, and (c) overlapping.

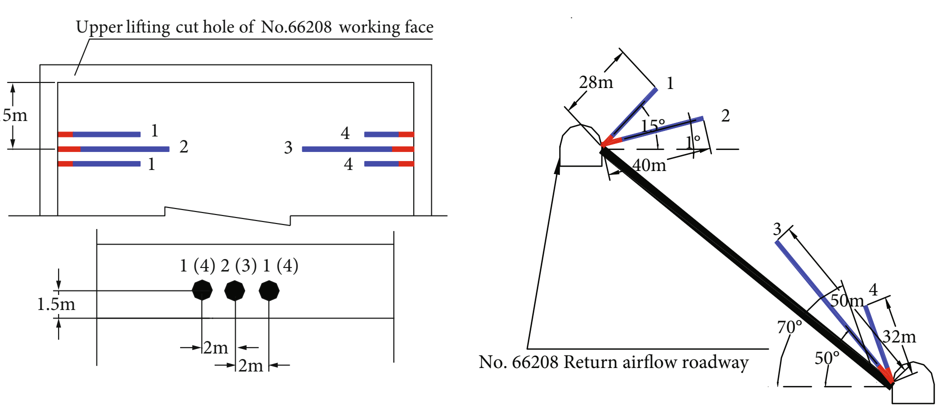

(a)

(b)

Figure 9: 1st set of blasting hole layout. (a) Plane view and (b) section view.

layout was setup, longwall face and roadway are under the stress relief zone of goaf area. This can effectively reduce the stress concentration while increasing the mining safety.

3.1.1. Stress Redistribution in Roof via Presplit Blasting

(1) Mechanical Properties of Surrounding Rock Prior and after Presplit Blasting. To reduce the stress concentration at the No. 66207 longwall face, the presplit blasting at immediate roof of No. 8 coal seam is considered. The numerical simulation schemes are as follows: The model is 600 m long along the strike, 500 m wide along the slope, and 456.36 m high. The model includes 7# coal, 8# coal, and the roof and floor strata. The average dip angle of the simulated coal seam in the model is 30°, which is consistent with the field.

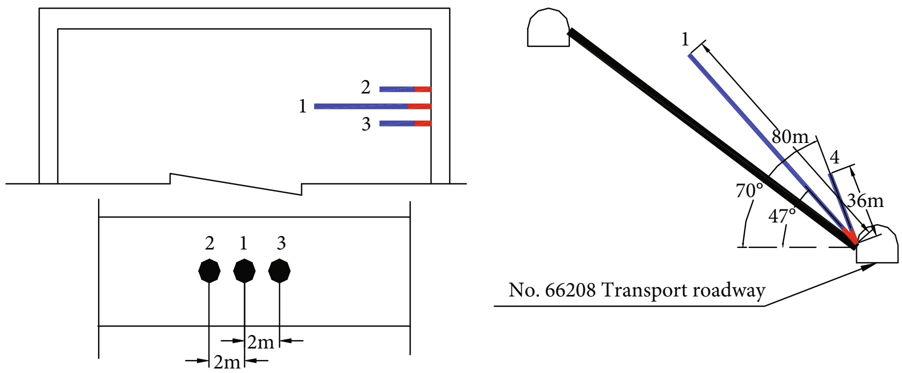

(a) (b)

Figure 10: 2nd to 5th set of blasting hole layouts. (a) Plane view and (b) section view.

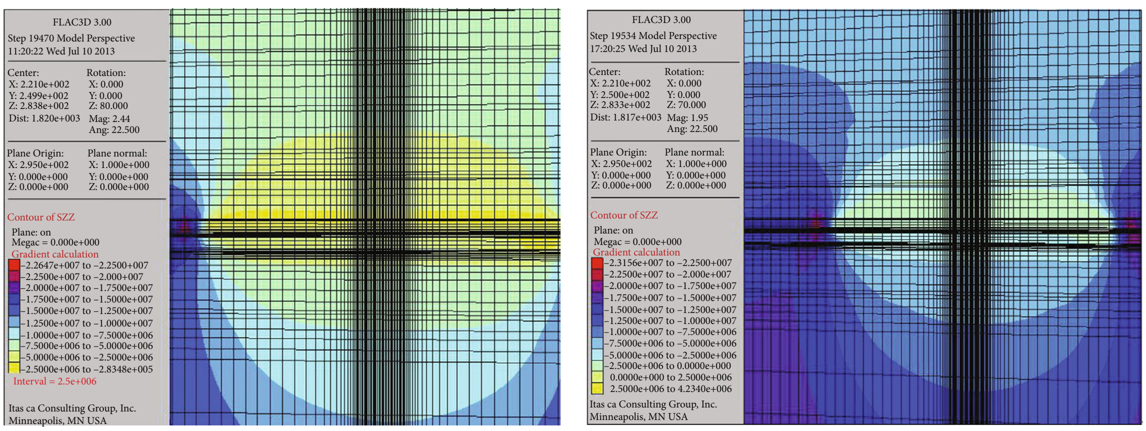

(a) (b)

Figure 11: Cloud map of cross-sectional stress distribution 5 m behind along the strike direction of coal seam. (a) Prior to presplit blasting and (b) after presplit blasting.

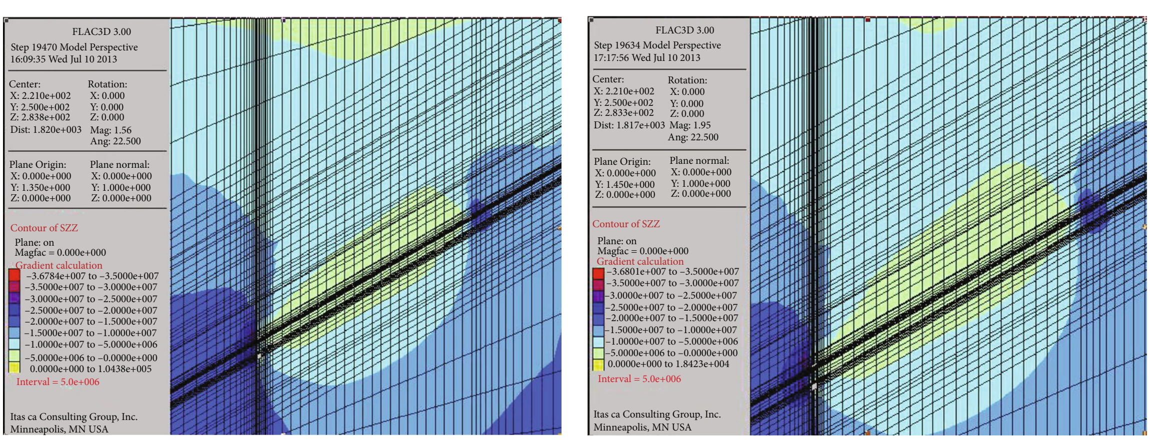

(a) (b)

Figure 12: Cloud map of cross-sectional stress distribution 5 m behind along coal seam inclined dip direction. (a) Prior to presplit blasting and (b) after presplit blasting.

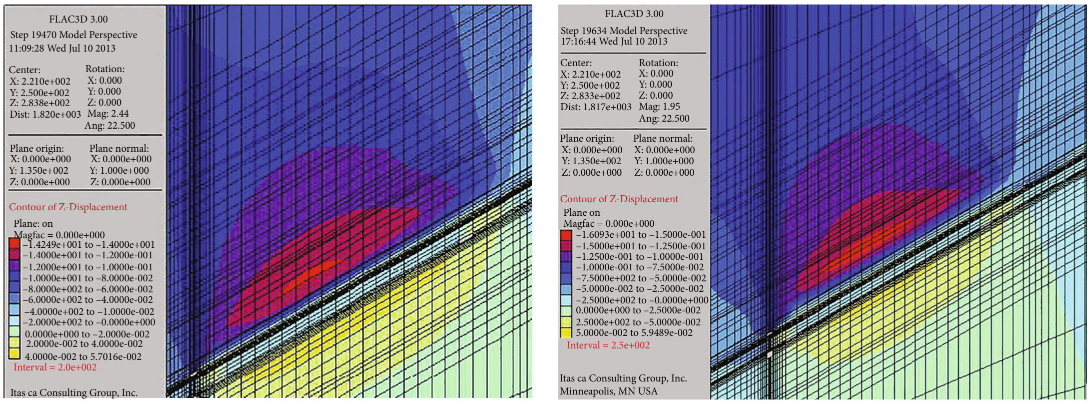

(a) (b)

FIGURE 13: Cloud map of cross-sectional displacement distribution 5 m behind along the inclined direction of coal seam. (a) Prior to presplit blasting and (b) after presplit blasting.

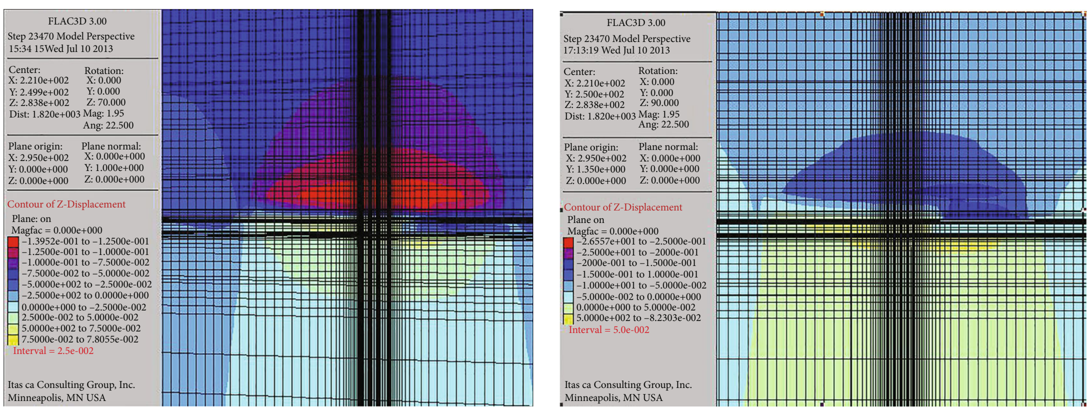

(a) (b)

FIGURE 14: Cloud map of cross-sectional displacement distribution 5 m behind along the strike direction of coal seam. (a) Prior to presplit blasting and (b) after presplit blasting.

The strength parameters of coal and rock mass around the blast hole are weakened to simulate presplitting blasting.

In deep hole presplit blasting parameters, when the deep hole blasting is used at the longwall face, the designed blasting height is 23 m. This enables the fracture development in the critical layer. There are 5 series of blasting planned, at 30 m interval. The 1st series uses simultaneous blasting at main gates and tail gates, in which the hole locations are shown in Figure 9. Figure 10 shows the hole locations for 2nd to 5th series.

Figures 11–16 provide the simulation results of stress, displacement, and rock fracture when the longwall face is at 70 m. According to the figures, it can be seen that the maximum vertical stress was 50–85 MPa from 90 m to 0 m ahead of the longwall face without presplit blasting, whereas the maximum vertical stress was 25–50 MPa from 90 m to 0 m ahead of the longwall face with presplit blasting.

Prior to presplit blasting, it is important to confirm that the vertical displacement should be within 250 mm from 10 m ahead of the face and majority of the roof is moving. After presplit blasting is implemented, the vertical displacement should be less than 50 mm in the same area.

The fracture was developed at 14 m above No. 8 coal seam prior to the implementation of deep hole presplit blasting, there would be a likelihood of roof rupture and result in increasing load from the roof weighting. This was unfavorable to the stability of surrounding rock. After the blasting, the fracture height above the coal seam was not further developed.

Prior the presplit blasting, the first weighting interval was 67.8 m and the periodic weighting interval was 41.3 m. After blasting, the first and periodic weighting intervals were 24.6 m and 21.9 m, respectively. The interval and time of weighting were reduced after presplit blasting. This led to reduction in load and frequency of weighting, which in turn result in less dynamic load and less pressure ahead of the longwall face. Presplit blasting disturbed the integrity of the strong roof and evenly distributed the stress while reducing the weighting magnitude, which is beneficial to the stability of No. 66207.

3.2. Reinforcement of Strata with Water Injection

3.2.1. The Influence of Water Content on Coal Stability. Firstly, granular coal with particle size in the range of 0.1-

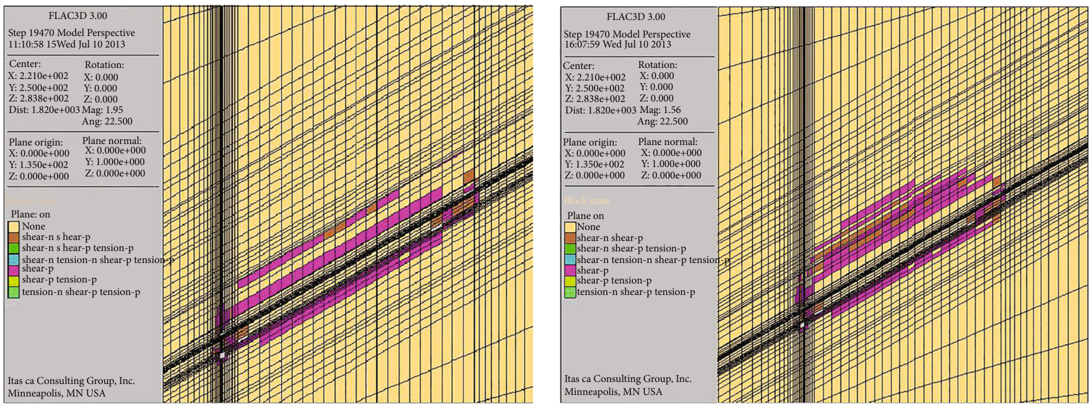

(a) (b)

Figure 15: Cloud map of cross-sectional fracture distribution 5 m behind along the inclined direction of coal seam. (a) Prior to presplit blasting and (b) after presplit blasting.

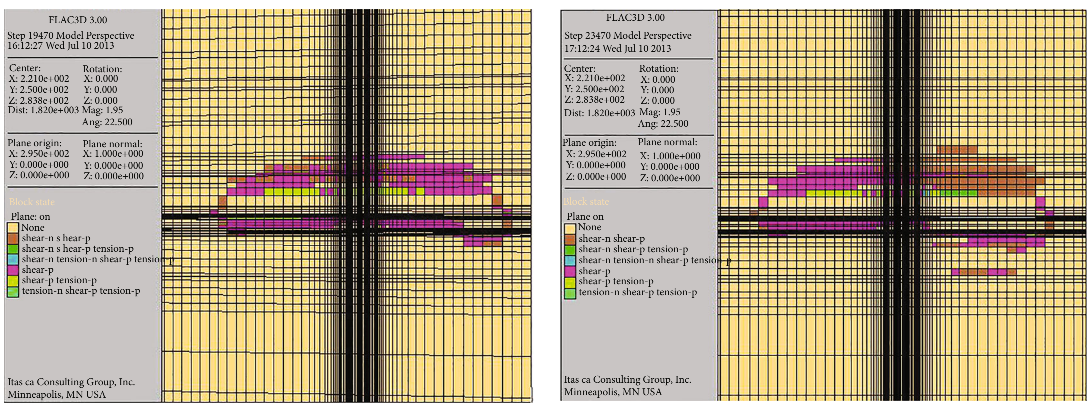

(a) (b)

Figure 16: Cloud map of cross-sectional fracture distribution 5 m behind along the strike direction of coal seam. (a) Prior to presplit blasting and (b) after presplit blasting.

0.25 mm was screened from the dried crushed coal. Then, eight wet pulverized coal samples with different moisture content were made of more than 1000 g granular coal and different qualities of pure water. There are three samples of each moisture content. Finally, the repose angle of wet pulverized coal samples was measured by stacking method, and each group of tests was carried out three times.

To investigate the influence of water content on coal stability, a series of tests on angle of repose of ultrasoft coal were conducted (see Figure 17). Figure 18 shows the relationship between angle of repose of coal and water content. Based on the figure, it can be seen that as the water content increases, the angle of repose decreases. The responding water content with regard to the peak value is 17.659%. This means water injection into the ultrasoft coal seam can change its mechanical properties and improve its stability.

3.2.2. Longwall Water Injection Technique and Parameters. In the field, water injection is conducted at the ribs of both roadways with deep holes (see Figure 19). The step-by-step procedures of deep hole (hole length > 80 m) is that water is injected at both roadways. The distance between hole at the tailgate and the roof should be below 0.8 m, and the hole should be at the center of the coal along the main gate. Water should be injected intermittently all day from 100 m to 20 m ahead of the longwall face. Shallow hole (hole length < 8 m) water injection should have holes 0.5–1 m from the roof. The holes should be drilled perpendicular of subperpendicular to the coal seam side of rib. Sealer should be place 1.5 m into the hole, and the water pressure should be around 2 MPa. Water injection takes place twice a day with at least three hours per injection.

3.3. Rigid-Flexi Active Support Technology. Surrounding rock at ultrasoft coal seam undergoes plastic deformation due to high stress concentration and continuous mining [32]. This would lead to instability of the longwall face and cause injury. To overcome the complex geological condition at No. 66207, ZZ7200/22/45 hydraulic support is selected, with the resistance force of 8800 kN. This equipment can redistribute stress along the roof while more effectively support rib and roof. The new hydraulic support uses an integral

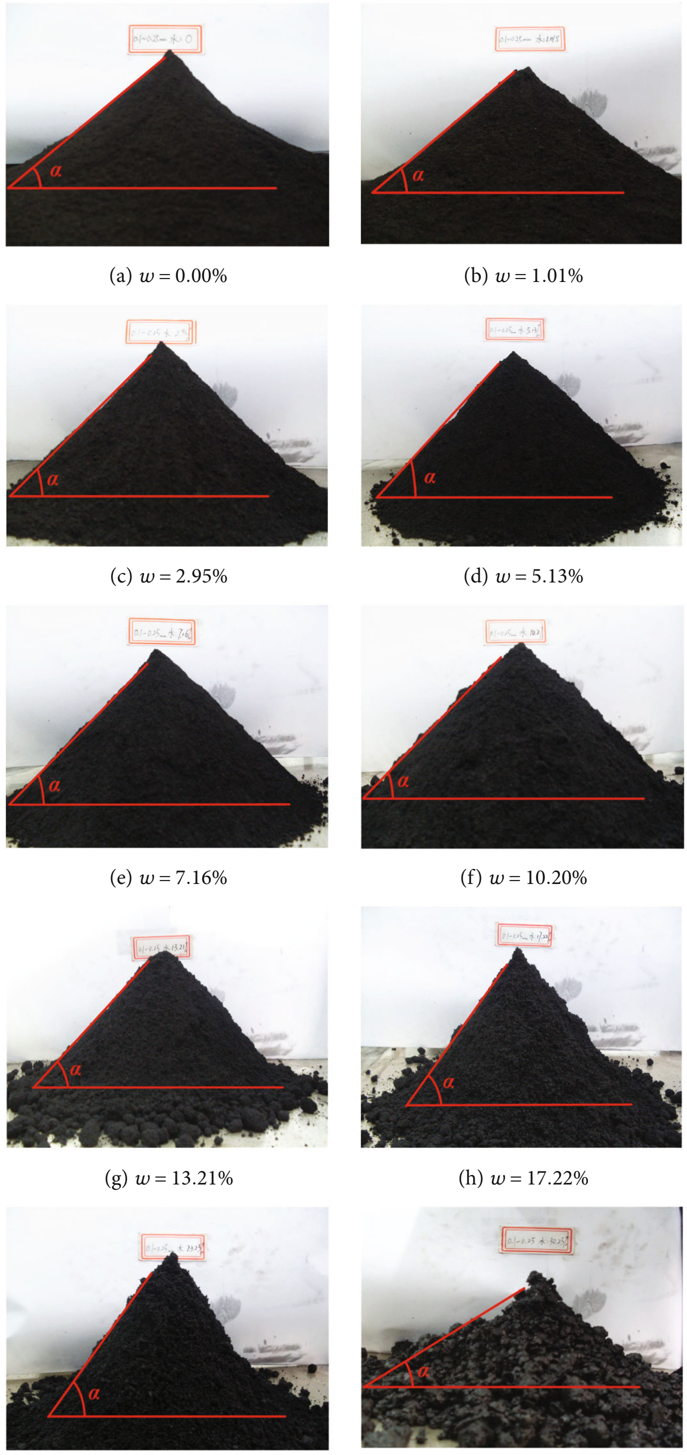

(a) $w = 0.00\%$
(b) $w = 1.01\%$
(c) $w = 2.95\%$
(d) $w = 5.13\%$
(e) $w = 7.16\%$
(f) $w = 10.20\%$
(g) $w = 13.21\%$
(h) $w = 17.22\%$
(i) $w = 23.23\%$
(j) $w = 30.25\%$

FIGURE 17: Accumulation state of coal particles with different water contents.

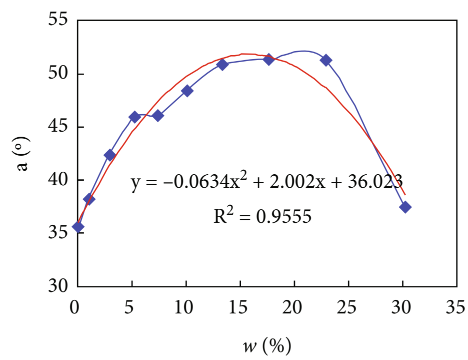

FIGURE 18: Change of angle of repose of coal with water content.

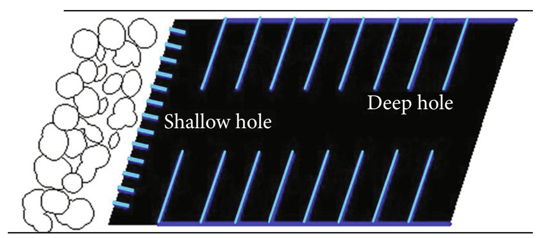

FIGURE 19: Schematic view of water injection in coal seam.

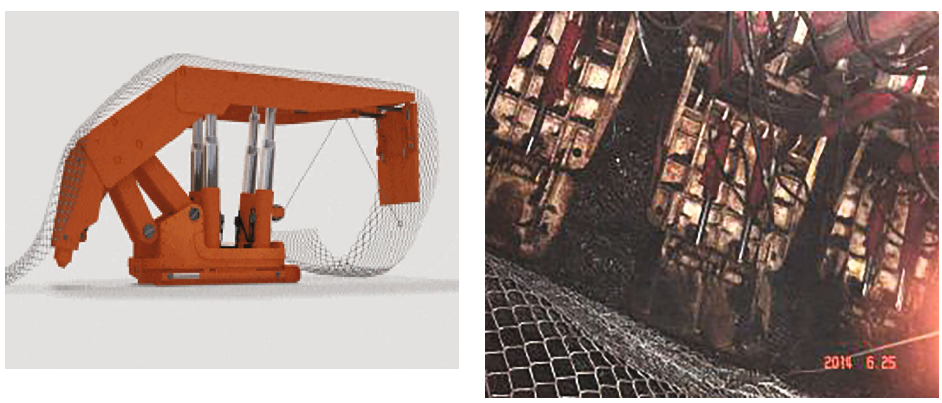

(a) (b)

FIGURE 20: "Rigid hydraulic support+flexible mesh" supporting system. (a) Support design and (b) support in place.

roof beam structure, which can reduce the disturbance to roof when moving the support. The long flexible beam and two-stage rib support can increase the supporting area and strength to exposed rib and roof, ensuring the integrity of rib and roof.

Figure 20 shows the combination of the hydraulic support and mesh. This approach forms as "high resistance, integral beam, two-stage rib+roof support system," which can effectively prevent the rib and roof from falling and enable the production. The mine operators can be protected in a safety roadway, and the surrounding rock can be hold stable.

3.4. "Difference Stepping" Mining Technology. As the ultra-soft coal seam is prone to rib instability and the interval between ribs at roadways is longer than that of the longwall face, the traditional "three machine" equal step equipment is not capable of preventing the partial failure. This may lead to large-scale failure of rib and roof and subsequently result in operation suspension. Hence, this study proposed "flexible beam length (1000 mm)>pushing length (800 mm)>cutting depth of shearer drum (600 mm)" method (see Figure 21). Hence, the selected equipment are ZZ7200/22/45 hydraulic support, MG500/1130-WD shearer, and SGZ800/1050 conveyor belt. Long flexible beam length can cover larger roof area when rib fails. Small shearer drum can reduce the rib and roof damage during cutting and enhance the integrity and stability of the roof and rib. Thereby, the combination between shallow cutting and long flexible beam can prevent drum from damaging the mesh.

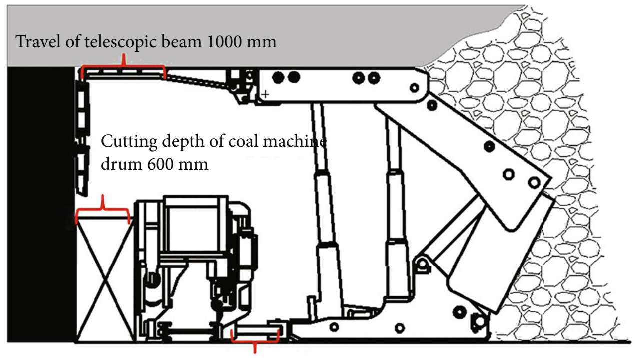

Figure 21: "Difference stepping" three machineries.

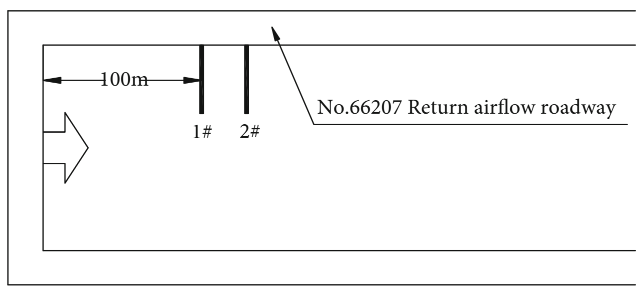

Figure 22: Stress measurement borehole location.

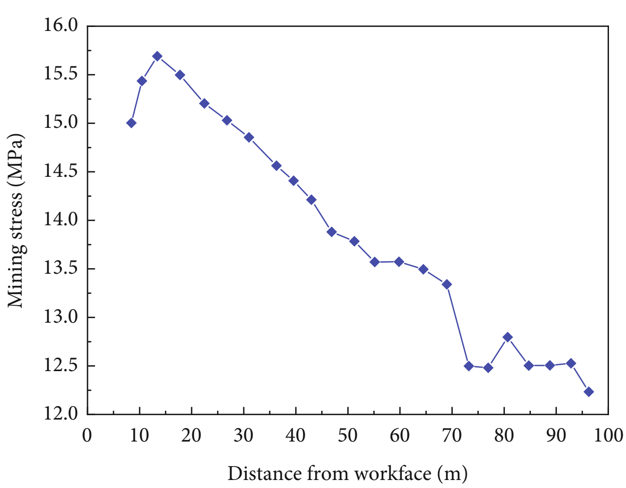

Figure 23: Stress distribution in the coal seam.

Pushing support column distance is greater than the drum cutting depth can increase the moving interval and better control the roof stability.

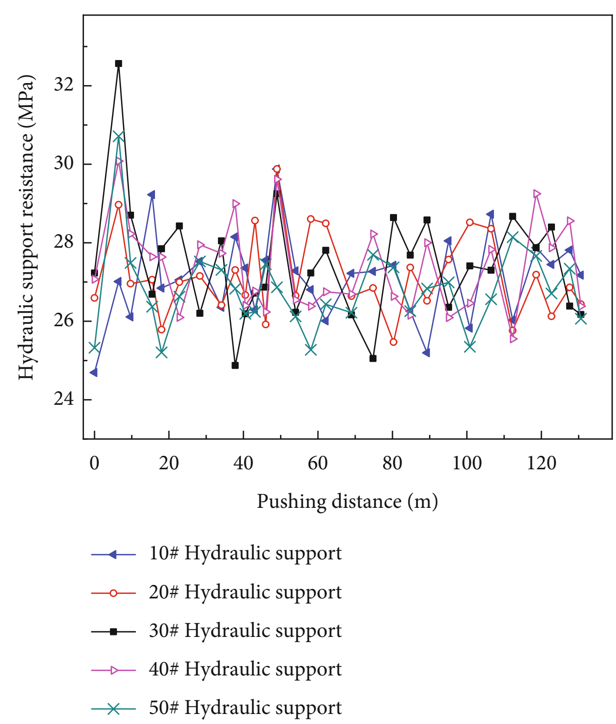

Figure 24: The relationship between hydraulic support resistance and pushing distance.

4. Engineering Applications

The stress distribution at No. 66207 longwall face was monitored to examine the effectiveness of proposed strata control technique. Two stress measurements were conducted using KSE-II-1 borehole stress measurement tool at 100 m from the tailgate. The measurement depth and interval were 10 m and 3 m, respectively (see Figure 22).

Figure 23 shows the stress distribution in the coal seam. It can be seen that as the longwall face approached the stress measurement location within 70 m, stress gradually increased and reached maximum when the distance is approximately 13.5 m. The magnitude of the maximum stress is 15.65 MPa with a stress concentration coefficient of 1.28. After that, stress gradually diminished. During the mining process, the stress concentration coefficient was relatively low and evenly distributed in the concentration area. The location of peak stress concentration is away from the coal rib, such that the excessive stress acting on the rib can be effectively managed.

Figure 24 shows the relationship between hydraulic support resistance and pushing distance. Based on the figure, it can be found that the stress acting on the hydraulic support is generally 26-28 MPa during mining. The hydraulic support is competent under this circumstance and can hold more pressure if needed. The periodic weighting was not obvious in this longwall panel with evenly distributed stress. The weighting interval is approximately 18-21 m with lower mining stress. There was no large scale weighing observed during the mining process.

By comparing the mining rate of No. 66207 longwall panel with the No. 66107 N panel which did not implement the proposed technique, the productivity of No. 66207 was three times of No. 66107 N. In No. 66207 longwall, the average mining rate is 4.35 m/day, with maximum rate at 7.2 m/day. On the other hand, the average mining rate and maximum rate of No. 66107 N were 1.43 m/day and 1.52 m/day. Thereby, there was less failure events occurred in No. 66207, indicating the proposed strata control technique was effective for ultrasoft coal seam.

5. Conclusion

In this study, a strata control technique was proposed for ultrasoft coal seam and it was examined at No. 7 coal seam in Huainan mining area. The technique comprises of mining stress reduction, rock mechanical properties modification of rock, and stability improvement of surrounding rock. The following conclusions were drawn from this study:

(1) Inward-stagger layout used in No. 66207 longwall panel was able to position the longwall face and main gate below the stress relief area of goaf, such that the mining stress concentration can be reduced. The presplit blasting on No. 8 roof was able to evenly distribute the incoming weighting while reducing the weighting intensity. The first weighting and periodic weighting intervals were 24.6 m and 21.9 m after presplit blasting. This technique can prevent weighting on large areas

(2) The investigation on the relationship between angle of repose of ultrasoft coal and water content showed that the angle of repose first increased then decreased with increasing water content. The peak value was observed at 17.659% water content, indicating water injection into ultrasoft coal seam can improve the coal mechanical properties and rib stability

(3) The "high resistance, integral beam, two-stage rib +roof support system" was design to replace the traditional equipment, which can support the ultrasoft coal seam. The combination of this system and proposed "difference stepping" mining technique was capable of preventing roof and rib from failure, as well as mitigating the rockfall during moving hydraulic support

(4) Once the technique was implemented, the stress concentration coefficient was relatively low during mining process. The stress was evenly distributed among the concentration area, and the peak concentration point was away from the longwall face. This was able to effectively manage the mining-induced stress while improving the productivity three times than without the technique. There was also no failure event observed during mining, such that the safety of mine workers was improved

Data Availability

The experimental results used to support the findings of this study are included within the article.

Conflicts of Interest

The authors declare that they have no conflict of interest.

Acknowledgments

The authors are grateful for the National Natural Science Foundation of China (No. 52004007), the Foundation of Educational Commission of Anhui Province (KJ2019A0130), and the Independent Research Foundation of the State Key Laboratory of Mining Response and Disaster Prevention and Control in Deep Coal Mines (SKLMRDPC19ZZ09).

References

[1] C. Liu, *Study on Mechanism and Controlling of Borehole Collapse in Soft Coal Seam [Ph.D. thesis]*, China University of Mining and Technology, Xuzhou, China, 2014.

[2] W. Li, Y. C. Ye, Q. H. Wang, X. H. Wang, and N.-Y. Hu, "Fuzzy risk prediction of roof fall and rib spalling: based on FFTA–DFCE and risk matrix methods," *Environmental Science and Pollution Research*, vol. 27, no. 8, pp. 8535–8547, 2020.

[3] S. Liu, K. Yang, T. Zhang, and C. A. Tang, "Rib spalling 3D model for soft coal seam faces with large mining Height in protective seam mining: theoretical and numerical analyses," *Geofluids*, vol. 2020, Article ID 8828844, 17 pages, 2020.

[4] L. Si, Z. B. Wang, X. H. Liu, C. Tan, and R. X. Xu, "Assessment of rib spalling hazard degree in mining face based on background subtraction algorithm and support vector machine," *Current Science*, vol. 116, no. 12, pp. 2001–2012, 2019.

[5] L. Li and F. Zhang, "Instability model of a coal wall with large mining height under excavation unloading conditions," *Advances in Civil Engineering*, vol. 2020, Article ID 8863602, 6 pages, 2020.

[6] C. Li, T. H. Kang, X. P. Li, L. G. Li, X. Y. Zhang, and R. X. Zhang, “Theoretical investigation of the sliding instability and caving depth of coal wall workface based on the bishop strip method,” *Advances in Civil Engineering*, vol. 2019, Article ID 3065930, 8 pages, 2019.

[7] Y. Yuan, S. H. Tu, X. T. Ma, L. L. Sui, and Q. S. Bai, “Study on stability and control of coal wall in fully mechanized face with ‘three soft’ and large mining height,” *Journal of Mining and Safety Engineering*, vol. 29, no. 1, pp. 21–25, 2012.

[8] S. F. Yin, F. L. He, and G. G. Cheng, “Study on criterion of rib spalling and safety evaluation system in fully mechanized top coal caving face with large mining height,” *Journal of China University of Mining & Technology*, vol. 44, no. 5, pp. 800–807, 2015.

[9] W. B. Guo, C. Y. Liu, G. W. Dong, and W. Y. Lv, “Analytical study to estimate rib spalling extent and support requirements in thick seam mining,” *Arabian Journal of Geosciences*, vol. 12, no. 8, pp. 1–12, 2019.

[10] Y. Yuan, S. H. Tu, X. G. Zhang, and A. X. Liu, “Mechanism and control technique of rib spalling disaster in fully-mechanized mining with large mining height in soft coal seam face,” *Disaster Advances*, vol. 6, no. 3, pp. 92–98, 2013.

[11] Y. Yuan, C. Zhu, H. M. Wei, C. F. Yuan, and Z. S. Chen, “Study on rib spalling control of shortwall drilling mining technology with a large mining height,” *Arabian Journal of Geosciences*, vol. 14, no. 3, pp. 1–12, 2021.

[12] B. Behera, A. Yadav, G. S. P. Singh, and S. K. Sharma, “A numerical modeling approach for evaluation of spalling associated face instability in longwall workings under massive sandstone roof,” *Engineering Failure Analysis*, vol. 117, article 104927, 2020.

[13] G. S. Li, Z. H. Li, F. Du, and Z. Z. Cao, “Study on the failure characteristics of coal wall spalling in thick coal seam with gangue,” *Advances in Civil Engineering*, vol. 2020, Article ID 6668458, 10 pages, 2020.

[14] Q. L. Yao, X. H. Li, B. Y. Sun et al., “Numerical investigation of the effects of coal seam dip angle on coal wall stability,” *International Journal of Rock Mechanics and Mining Sciences*, vol. 100, pp. 298–309, 2017.

[15] S. F. Lu, S. F. Liu, Z. J. Wan, J. Y. Cheng, Z. Z. Yang, and P. Shi, “Dynamic damage mechanism of coal wall in deep longwall face,” *Advances in Civil Engineering*, vol. 2019, Article ID 3105017, 10 pages, 2019.

[16] Q. Z. Tian, A. R. Zhang, Q. K. Lu, Y. F. Liu, and P. X. Li, “Study on coal wall stability of fully mechanized working face with large mining height in thick coal seam,” *Journal of Taiyuan University of Technology*, vol. 43, no. 1, 2012.

[17] J. C. Wang, “Rib spalling and prevention mechanism in extremely soft thick coal seam,” *Journal of China Coal Society*, vol. 32, no. 8, pp. 785–788, 2007.

[18] Y. P. Wu, D. Lang, and P. S. Xie, “Rib spalling mechanism and disaster mechanism of fully mechanized caving face in soft coal with large dip angle,” *Journal of China Coal Society*, vol. 41, no. 8, pp. 1878–1884, 2016.

[19] Q. X. Huang and J. H. Liu, “Analysis on pillar strip model of coal wall spalling in shallow mining face with large mining height,” *Journal of Mining and Safety Engineering*, vol. 32, no. 2, pp. 187–191, 2015.

[20] X. Q. Fang, J. He, and H. C. Li, “Study on the mechanism and prevention of the wall of soft coal fully mechanized caving face,” *Journal of China University of Mining & Technology*, vol. 38, no. 5, pp. 640–644, 2009.

[21] Y. H. Pang, G. F. Wang, and H. W. Ren, “Multi factor sensitivity analysis of coal wall spalling in large mining height face,” *Journal of Mining and Safety Engineering*, vol. 36, no. 4, pp. 736–745, 2019.

[22] H. Zhang and Y. P. Wu, “Rib spalling mechanism of longwall and high mining height stope in steep seam,” *Journal of Mining and Safety Engineering*, vol. 36, no. 2, pp. 331–337, 2019.

[23] H. W. Wang, Y. P. Wu, P. S. Xie, S. H. Luo, K. Z. Liu, and M. F. Liu, “Mining thickness effect of coal wall stability in longwall and large mining height working face of large inclined seam,” *Journal of Mining and Safety Engineering*, vol. 35, no. 1, pp. 64–70, 2018.

[24] S. L. Yang, D. Z. Kong, J. H. Yang, and H. Meng, “Coal wall stability and grouting reinforcement technology in fully mechanized top coal caving mining,” *Journal of Mining and Safety Engineering*, vol. 32, no. 5, pp. 827–839, 2015.

[25] W. B. Guo, Y. Lu, F. C. Huang, C. Y. Liu, M. S. Pei, and Y. S. Du, “Study on the stability and control of coal and rock at the end face of fully mechanized top-coal caving face in upward mining,” *Journal of Mining and Safety Engineering*, vol. 31, no. 3, pp. 406–412, 2014.

[26] Y. X. Xia, L. J. Kang, and Q. X. Qi, “Influence of coal cutting height on stability of coal wall in fully mechanized caving face with large mining height,” *Coal Science and Technology*, vol. 36, no. 12, 2008.

[27] J. X. Yang, C. Y. Liu, F. F. Wu, and Y. Yang, “The research on the coal wall stability mechanism in larger height coal seam with a stratum of gangue,” *Journal of Mining and Safety Engineering*, vol. 30, no. 6, pp. 856–862, 2013.

[28] J. G. Li, Q. Z. Tian, and S. S. Yang, “Coal wall spalling mechanism and control in fully mechanized coal caving mining face in Hetangou mine,” *Coal Science and Technology*, vol. 35, no. 12, pp. 73–75, 2003.

[29] X. H. Zhang, *Study on Mechanism Characteristics and Application of Fully Mechanized Top Coal Caving Mining with Great Mining Height in Very Thick Coal Seam, [Ph.D. thesis]*, AnHui University of Science and Technology, Huainan, China, 2012.

[30] M. Gao, J. Xie, Y. Gao et al., “Mechanical behavior of coal under different mining rates: a case study from laboratory experiments to field testing,” *International Journal of Mining Science and Technology*, vol. 31, no. 5, pp. 825–841, 2021.

[31] Y. Q. Xu, *Coal Mining*, China University of Mining and Technology Press, 2009.

[32] X. Wang, Z. J. Wen, Y. Jiang, and H. Huang, “Experimental study on mechanical and acoustic emission characteristics of rock-like material under non-uniformly distributed loads,” *Rock Mechanics and Rock Engineering*, vol. 51, no. 3, pp. 729–745, 2018.

Hindawi
Geofluids
Volume 2022, Article ID 2475021, 19 pages
https://doi.org/10.1155/2022/2475021

Research Article

Mechanical Mechanism Analysis of Roof Fracture Evolution in Stope with Variable Length Based on Elastic-Plastic Structure Theory

Xinfeng Wang,[1] Mingyuan Lu,[2] Rui Wei,[3] Zhaofeng Wang,[4] and Shan Li[5]

[1]College of Environment and Resources, Xiangtan University, Xiangtan, Hunan 411105, China
[2]College of Energy and Mining Engineering, China University of Mining and Technology (Beijing), Beijing 100083, China
[3]Wangjialing Coal Mine, China Coal Huajin Group Co., Ltd., Hejin, Shanxi 043300, China
[4]College of Safety Science and Engineering, Henan Polytechnic University, Jiaozuo, Henan 411105, China
[5]College of Qilu Transportation, Shandong University, Jinan, Shandong 250002, China

Correspondence should be addressed to Xinfeng Wang; wangxinfeng110@126.com

Received 15 November 2021; Accepted 15 March 2022; Published 4 April 2022

Academic Editor: Hualei Zhang

Stope with variable length is formed by length change of mining face due to the irregular distribution of geological rock pillars, which is a typical representative of complex coal seam mining. According to the geometric characteristics and mechanical boundaries of each mining stage of stope with variable length, the roof structure models with four boundary conditions were established and solved successively by using the small deflection thin plate bending theory. Combined with the simulated images of MATLAB and FLAC^{3D}, the fracture laws and corresponding engineering phenomena were analyzed. According to the characteristics of roof rock pressure zoning, the overburden structure pressure model of "three stopes, three areas, and three structures" is constructed. The research shows that the traditional "O-X" fracture occurs in the roof of small mining stope. For the cracks generated by prolonged "O-X" fracture and drift "O-X" fracture in mutative mining stope are similar to the crack development characteristics of large mining stope, so they are integrated into full-scale mining stope. The full-scale mining stope roof is broken in "X-O" shape, and the crack continues to develop to produce extended fracture, forming the roof fracture theory of "two stopes and two laws." The research conclusion strongly reveals the failure law of roof from tension instability to plastic fracture and abnormal ground pressure during mining in stope with variable length. It provides a basis for exploring the essence of overburden migration in stope with variable length and strengthening the roof prevention and control theory under the occurrence conditions of deep complex coal seams.

1. Introduction

As the shallow coal seams are gradually exhausted, the deep coal body located in sudden change of coal and rock structures becomes the key object of resource development. However, the mining problems such as complex geological conditions and "three highs and one disturbance" have been strongly affecting the continuity and safety of mining operations [1]. The phenomena of mining pressure are extremely abnormal in stope with variable length, especially when working face is approaching abrupt change of length. The irregular breaking of roof leads to the rapid migration of rock strata. The disturbance impact of hydraulic supports on both sides of working face has obvious spatiotemporal difference. After the sudden change of working face length, resistance of hydraulic supports continues to increase, and when the pressure step distance decreases, roof is broken seriously [2–4]. In addition, due to the influence of soft boundary conditions of the roof in roadway along goaf, coupling relationship between the space-time law of roof breakage and mining pressure is difficult to be characterized, which leads to great potential safety hazards in mining work, reducing resource recovery and utilization rate.

At present, there are two theoretical bases and corresponding methodologies for the study of roof fracture and overburden migration: beam structure and plate structure. The elastic-plastic deformation in coal body and the variation law of supporting pressure are demonstrated and summarized by analyzing the continuous dynamic fracture of beam structure, when studying disturbance characteristics about coal body caused by hinged fracture of basic roof. This method reflects dynamic migration characteristics and mechanical response mechanism of roof well [5–7]. However, the stope is a three-dimensional working space; beam structure is a one-dimensional model only containing length element, which cannot clearly explain the two-dimensional planar structure characteristics of the roof including width. Therefore, the thin plate theory gradually develops. The overlaying spatial structure engineering theory summarized by Jiang made use of microseismic positioning and monitoring technology that proposed the corresponding fracture forms of roof under different mining environments, thus strengthening the follow-up development of "O-X" fracture [8]. At the same time, in order to explore its specific evolution process in theory, a large number of scholars discussed the rules of roof breakage in stope by establishing a variety of thin plate models with rigid boundaries [9–12], deriving the "O-X" rule of fracture development with different sequences. However, in practical engineering, coal and roof are usually elastic when they are not disturbed and will be transformed into plastic after being disturbed. Therefore, in order to pursue higher precision roof fracture analysis and reveal the whole space-time disturbance characteristics, He, Chen, and Xie used the finite difference principle to build thin plate structure optimization models of elastic foundation boundaries and elastic-plastic foundation boundaries. Based on these, the first excavation of working face in the initial fracture and periodic fracture laws and influencing factors of the basic roof structure were obtained, deepening the roof fracture sequence theories [13–18]. The above theories greatly enrich the theoretical results of "O-X" breaking law under various square boundary conditions. However, when the geological coal and rock distribution are irregular, the roof boundaries of stope will be complicated, that is, the square boundary will change to polygonal boundary, which makes it more difficult to analyze [11]. What is more, the roadway along the goaf is in existence form in deep mining area, due to the influence of mining in adjacent section; the upper roof formed fracture edges. Resulting in the stress distribution of roof boundary and overburden are different from normal [19–24]. Therefore, considering complex boundary conditions, it is difficult to characterize the phenomenon of mining pressure and roof breakage in the stope with variable length, and the theory needs to be improved urgently. It is pressing to reveal the nature of overburden migration in deep stope and strengthen the roof prevention and control mechanism under the complex condition of deep coal seam.

2. Mechanical Model Analysis of Stope Roof with Variable Length

The mining geological characteristics of stope with variable length and the working face from short to long change law of stope are analyzed. Along the strike in turn, it can be divided into small mining, mutative mining, and large mining stope. As shown in Figure 1, coal seam strike per unit length is "a," and coal seam inclination per unit length is "b." The scope of small mining stope is "$2a \times b$," that of mutative mining stope is "$a \times 2b$," and that of large mining stope is "$3a \times 2b$."

Taking the initial mining of short working face as an example, in the deep mining area, in order to decrease the appearance of mining pressure and reduce the difficulty of roadway's maintenance, the roadway close to goaf is reserved as a goaf roadway. The plastic damage degree of the isolation coal pillar in this roadway is very high, resulting in a sharp decline in its clamping capacity for the roof. In addition, roof above the adjacent goaf had already been broken by mining influence of the upper section [18], so all the edges of lower side of the roof in stope with variable length are set as simply supported boundaries. The rest of the roof edges without disturbance and in the stable clamping state are set as fixed boundaries. As the working face advances from small mining stope to mutative mining stope and arrives at large mining stope, the underlying coal mass of the roof decreased, and the roof will be affected by load of the overlying strata and mining disturbance and subject to the corresponding boundary conditions, which lead to continuous fracture.

In view of the above roof boundary characteristics, small deflection thin-plate bending theory of elasticity [25] will be applied to establish the roof elastic model with three sides fixed and one simply supported (the simply supported side is the long side), one side fixed and three sides simply supported, one simply supported with three sides fixed (the simply supported side is the short side), and both sides fixed and both simply supported (the simply supported sides are adjacent). The bending moment numerical value and bending moment image of each stope roof will be obtained by solving the deflection equations using Galerkin method and Ritz method. The breaking laws of roof can be analyzed to reveal the migration nature of roof strata in deep stope with variable length.

2.1. Mechanical Model Analysis of Roof Fracture in Small Mining Stope. Lower boundary of roof in small mining stope has broken in goaf on the upper section, so set as simply supported boundary condition. Due to this stope was the first mining stope, other edges were clamped by strata and coal seam stability, which mechanical conditions were excellent, so set to fixed boundary conditions. Elastic model with three sides fixed and one side simply supported (the simply supported side is the long side) was formed, as shown in Figure 2. By approximate solving the deflection function and bending moment function of this model, the law of fracture evolution of small mining stope can be obtained.

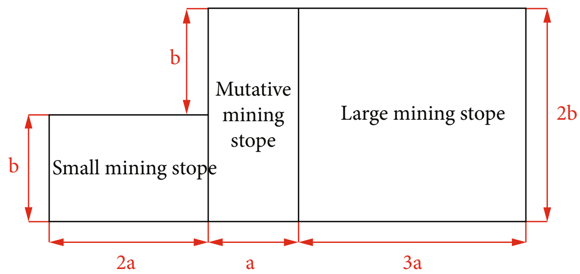

FIGURE 1: Zoning model of stope with variable length.

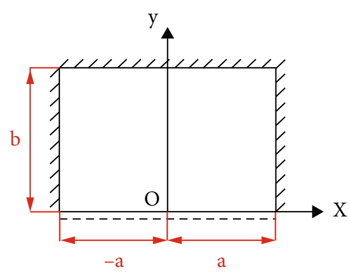

FIGURE 2: Mechanical model of small mining stope.

According to the condition,

$$\begin{aligned}(w)_{x=\pm a} &= 0, \left(\frac{\partial w}{\partial x}\right)_{x=\pm a} = 0,\\ (w)_{y=b} &= 0, \left(\frac{\partial w}{\partial y}\right)_{y=b} = 0,\\ (w)_{y=0} &= 0, \left(\frac{\partial^2 w}{\partial y^2}\right)_{y=0} = 0.\end{aligned} \tag{1}$$

In the equation, w is the deflection.

According to Galerkin's method, the deflection equation is

$$w = C_1 y\left(x^2 - a^2\right)^2\left(y^2 - b^2\right)^2. \tag{2}$$

In the equation, C_1 is constant, and C_2, C_3, and C_4 are the same.

Plug it:

$$\iint_A D\left(\nabla^4 w\right) w_m dxdy = \iint_A q w_m dxdy,$$

$$\Downarrow$$

$$\begin{aligned}&\int_0^b\int_{-a}^a DC_1 [120y\left(x^2 - a^2\right)^2 + 24y\left(y^2 - b^2\right)^2\\ &\quad + 2\left(20y^3 - 12b^2 y\right)\left(12x^2 - 4a^2\right)] y\left(x^2 - a^2\right)^2 \cdot \left(y^2 - b^2\right)^2 dxd\\ &= \int_0^b\int_{-a}^a qy\left(x^2 - a^2\right)^2\left(y^2 - b^2\right)^2 dxdy.\end{aligned} \tag{3}$$

In the equation, A is the integral interval; D is the bending stiffness of the plate, GPa·m; ∇^4 is the harmonic operator; w_m is the first-order deflection function; q is the load, MPa.

It can be calculated as follows:

$$C_1 = \frac{8085q}{2048\left(165a^4 b + 44a^2 b^3 + 21b^5\right)D}. \tag{4}$$

Then, we can get

$$w = \frac{8085qy\left(x^2 - a^2\right)^2\left(y^2 - b^2\right)^2}{2048\left(165a^4 b + 44a^2 b^3 + 21b^5\right)D}. \tag{5}$$

According to the internal force bending moment expression, we can get

$$\begin{aligned}M_x &= \frac{-8085q}{2048\left(165a^4 b + 44a^2 b^3 + 21b^5\right)}\\ &\quad \cdot \left[y\left(12x^2 - 4a^2\right)\left(y^2 - b^2\right)^2 + \mu\left(20y^3 - 12b^2 y\right)\left(x^2 - a^2\right)^2\right],\\ M_y &= \frac{-8085q}{2048\left(165a^4 b + 44a^2 b^3 + 21b^5\right)}\\ &\quad \cdot \left[\mu y\left(12x^2 - 4a^2\right)\left(y^2 - b^2\right)^2 + \left(20y^3 - 12b^2 y\right)\left(x^2 - a^2\right)^2\right].\end{aligned} \tag{6}$$

In the equation, μ is Poisson's ratio.

Assuming that $A = 37.5$ m, $B = 50$ m, $q = -15$ MPa, $D = 70.52$ GPa · m, and $\mu = 0.35$ (the same later) are substituted into the equation. The bending moment expression of this model is calculated by MATLAB to obtain its three-dimensional numerical image, as shown in Figure 3.

Through the analysis of bending moment numerical image, firstly, the bending moments reached its maximum in long fixed boundary midpoint of the plate, causing fixed boundary broke and became a new simply supported boundary. Due to the extreme value of two short fixed boundaries were close to long fixed boundary midpoint maximum, the breakage of short fixed boundaries will be slightly lagging behind long fixed boundary and becoming new simply supported boundaries. Secondly, with the continuous extension of fixed edge fracture, the fracture will be connected with old fracture boundary (the original long simply supported boundary) along the side of goaf roadway, forming an "O-type" fracture circle. Finally, bending moment will take the maximum value the in center of the plate. The fracture will appear in the center of the plate and extend into the "X-type" fracture, namely, the "O-X" fracture law. These are shown in Figure 4.

On the boundary conditions, deep mining stope that use goaf roadway is slightly different from a stope that do not use (three sides fixed and one simply supported/four sides fixed), but "O-X" fracture will occur in all of them. In the process of dynamic roof instability, the accompanying mining pressure phenomena are basically the same. Due to the factors of short length of working face and strike length,

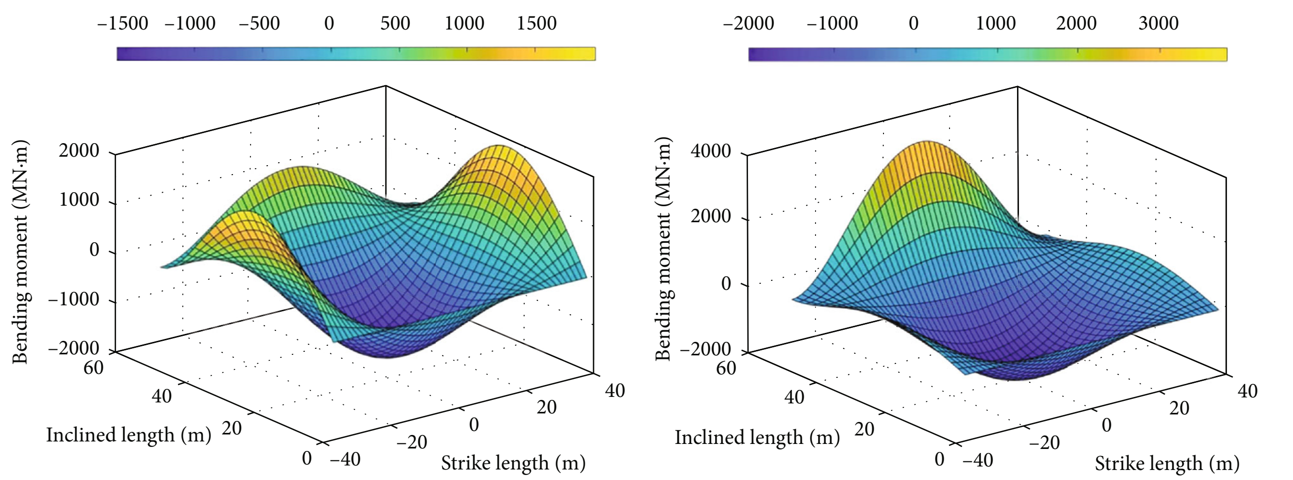

(a) Bending moment M_x

(b) Bending moment M_y

FIGURE 3: Bending moment of roof model with three sides fixed and one side simply supported (the simply supported side is the long side).

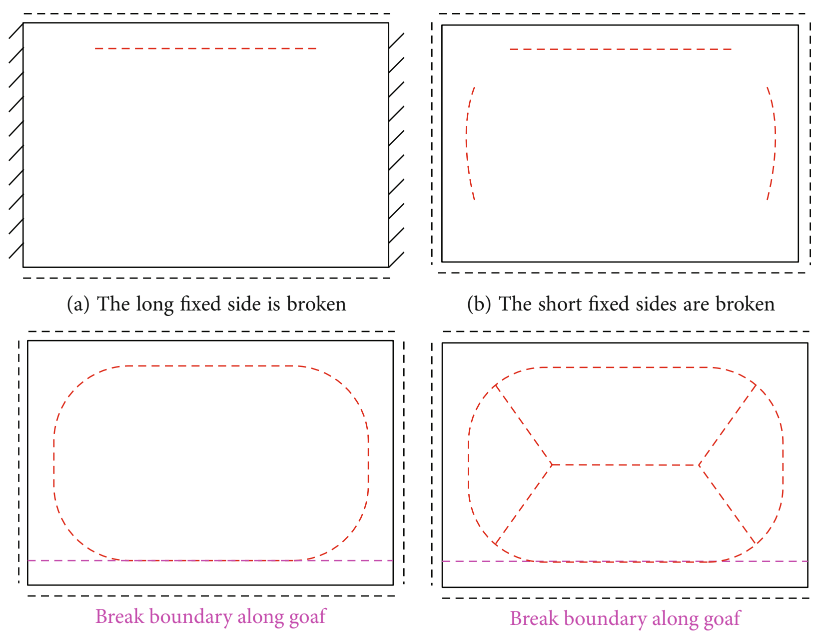

(a) The long fixed side is broken

(b) The short fixed sides are broken

(c) “O” fracture closure

(d) “X” fracture closure

FIGURE 4: Evolution process of “O-X” fracture in small mining stope.

the dynamic migration of overlying strata will happen moderately, and supporting pressure on the mining space is also small.

2.2. Mechanical Model Analysis of Roof Fracture in Mutative Mining Stope. When mining work of small mining stope was finished, the length of working face will be changing from short to long, entering mutative mining stope. As the working face continues to advance, initial pressure will be generating in mutative mining stope, and roof fracture line above this working face is the right boundary of the stope. In the elastic thin plate bending problems, mutative mining stope boundary for the lower part of 1/2 left side was small mining stope’s “O-X” breaking edge, setting it to simply supported boundary, and the left over 1/2 roof was clamped by rock pillars and overlying strata, so set it to fixed boundary. At this point, two kinds of boundary conditions appear on the same edge, which is difficult to effectively calculate and needs to be simplified according to the project situation.

According to the theory of the whole area disturbance characteristic caused by periodic rupture of roof structure, the basic roof fracture will cause the M-shaped or C-shaped rebound compression zone enveloping the working face in front of coal body [15]. Therefore, after completion of mining in small mining stope, a large roof pressure will be generated on basic roof in front of the leading coal wall, while the adjacent roof of leading coal wall will justly have little influence. Based on the above conditions, the lower half part of mutative mining stope's roof is in the rebound compression region, and considering the weak constraint of boundary conditions, this part can first reach the mechanical limit of fracture [12]. After fracture, stress will redistribute, and then, the second fracture of the upper half of roof will occur in mutative mining stope. This concept of overburden structure fracture with "drift" characteristics reasonably explains the engineering phenomenon of abnormal roof pressure and rapid step-by-step subsidence in narrow area of mutative mining stope.

To sum up, the mutative mining stope was divided into upper and lower parts based on the median line of long side. Just below the dividing line was the goaf, which cannot restrain the rotation deformation of the roof, so set it as simply supported boundary. The breaking order was from I to II. This is shown in Figure 5.

2.2.1. Mechanical Model Analysis of Roof Fracture in Mutative Mining Stope I. This plate's lower edge was the goaf roadway. The left side was broken edge of small mining stope, which was uniformly set as simply supported boundaries, and the right side was sandwich-supported roof between solid coal and overlying rock, which was set as fixed supported boundary, forming an elastic model with one side fixed and three sides simply supported, as shown in Figure 6.

According to the condition,

$$(w)_{x=\pm a/2} = 0, (w)_{y=\pm b/2} = 0, \left(\frac{\partial w}{\partial x}\right)_{x=a/2} = 0. \qquad (7)$$

According to Ritz method, let the deflection equation be

$$w = C_2\left(x+\frac{a}{2}\right)\left(x-\frac{a}{2}\right)^2\left(y^2-\frac{b^2}{4}\right). \qquad (8)$$

Plug it:

$$\begin{cases} V_\varepsilon = \dfrac{D}{2}\iint_A \left(\nabla^2 w\right)^2 dxdy, \\ \dfrac{\partial V_\varepsilon}{\partial C_2} = \iint_A q w_m dxdy, \end{cases}$$

$$\Downarrow$$

$$\begin{cases} V_\varepsilon = \dfrac{D}{2}\displaystyle\int_{-b/2}^{b/2}\int_{-a/2}^{a/2}\left[C_2(6x-a)\left(y^2-\frac{b^2}{4}\right)+2C_2,\right. \\ \left.\left(x+\dfrac{a}{2}\right)\left(x-\dfrac{a}{2}\right)^2\right]^2 dxdy, \\ \dfrac{\partial V_\varepsilon}{\partial C_2} = \displaystyle\int_{-b/2}^{b/2}\int_{-a/2}^{a/2} q\left(x+\frac{a}{2}\right)\left(x-\frac{a}{2}\right)^2\left(y^2-\frac{b^2}{4}\right)dxdy. \end{cases} \qquad (9)$$

In the equation, V_ε is deformation potential energy.

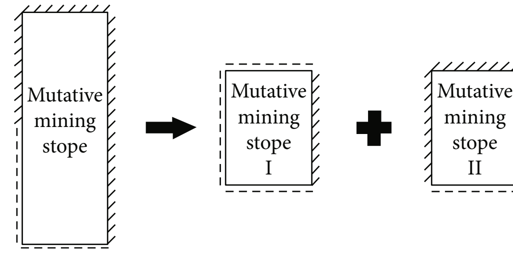

FIGURE 5: Mechanical model division of mutative mining stope.

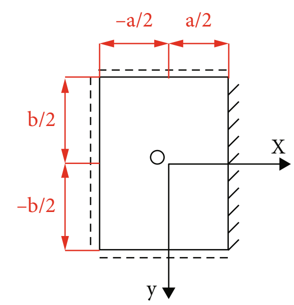

FIGURE 6: Mechanical model of mutative mining stope I.

It can be calculated as follows:

$$C_2 = \frac{-35ab^2q}{16\left(21b^4+6a^4+14a^2b^2\right)D}. \qquad (10)$$

Then, we can get

$$w = \frac{-35ab^2q(x+(a/2))(x-(a/2))^2\left(y^2-\left(b^2/4\right)\right)}{16\left(21b^4+6a^4+14a^2b^2\right)D}. \qquad (11)$$

According to the internal force bending moment expression, we can get

$$M_x = \frac{35ab^2q}{16\left(21b^4+6a^4+14a^2b^2\right)} \cdot \left[(6x-a)\left(y^2-\frac{b^2}{4}\right)+2\mu\left(x+\frac{a}{2}\right)\cdot\left(x-\frac{a}{2}\right)^2\right],$$

$$M_y = \frac{35ab^2q}{16\left(21b^4+6a^4+14a^2b^2\right)} \cdot \left[\mu(6x-a)\left(y^2-\frac{b^2}{4}\right)+2\left(x+\frac{a}{2}\right)\left(x-\frac{a}{2}\right)^2\right]. \qquad (12)$$

The bending moment expression of this model was calculated by MATLAB to obtain its three-dimensional numerical image, as shown in Figure 7.

In this model, the bending moment M_x obtained the extreme value at the center of long simply supported edge, and bending moment M_y obtained the extreme value at long

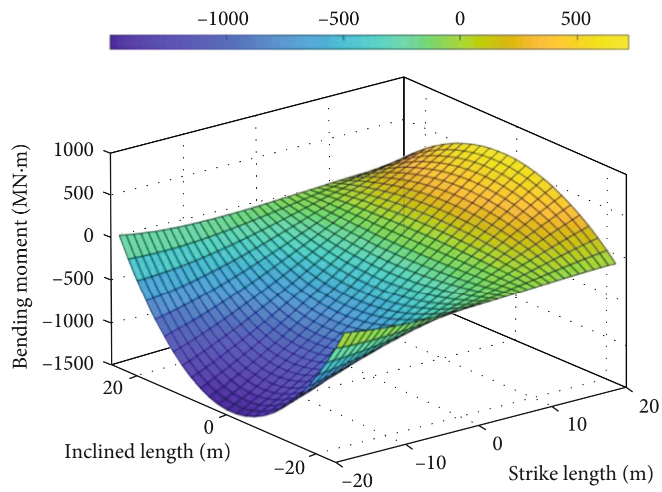

(a) Bending moment M_x

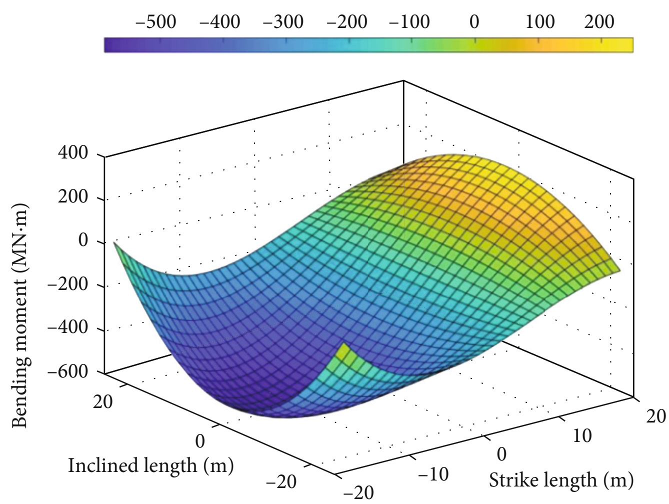

(b) Bending moment M_y

FIGURE 7: Bending moment of roof model with one side fixed and three sides simply supported.

simply supported edge near the center of plate. It can be concluded that mutative mining stope I broke at center of the long simple supported edge at first, and this boundary coexisted with the fracture boundary of the small mining stope. Then, the fracture will extend along the x-axis to inside of the plate and gradually get closer to fixed supported edge, thus causing instability failure of fixed supported boundary. When the fracture in the center of plate has connected with fixed supported fracture, it will expand to the two short simple supported edges and finally close, forming an "O-X" fracture with extension properties after the small mining stope, as shown in Figures 8 and 9.

2.2.2. Mechanical Model Analysis of Roof Fracture in Mutative Mining Stope II. The roof collapse of mutative mining stope I led to the redistribution of overburden pressure and then caused the roof instability of mutative mining stope II.

Lower boundary in this stope was the broken edge of mutative mining stope I. The middle of two stopes was connected by a hinged structure, so it can be set as simply supported boundary. The rest parts were supported by the stable clamping of rock layer, so they can be set as fixed supported boundaries, forming an elastic model with three sides fixed and one side simply supported (the simply supported side is the short side), as shown in Figure 10.

According to the condition,

$$\begin{gathered}(w)_{x=\pm\frac{a}{2}}=0,\ \left(\frac{\partial w}{\partial x}\right)_{x=\pm\frac{a}{2}}=0,\\ (w)_{y=b}=0,\ \left(\frac{\partial w}{\partial y}\right)_{y=b}=0,\\ (w)_{y=0}=0,\ \left(\frac{\partial^2 w}{\partial y^2}\right)_{y=0}=0.\end{gathered}\tag{13}$$

According to Galerkin's method, let the deflection equation be

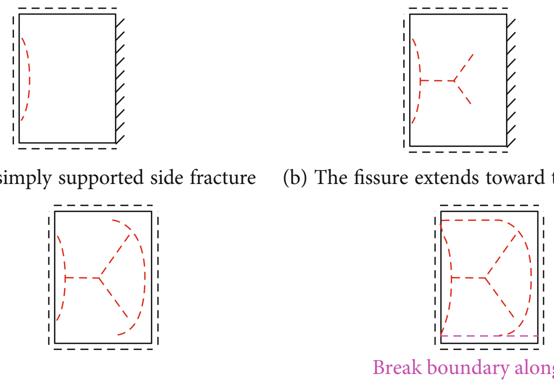

(a) The long simply supported side fracture (b) The fissure extends toward the center

(c) The fixed side breaks and closes (d) The two simply supported sides are through

Figure 8: Fracture evolution process of mutative mining stope I.

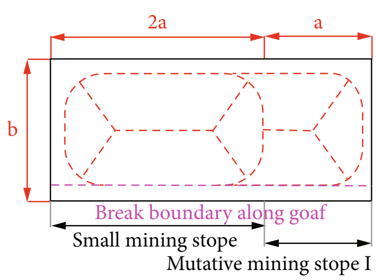

Figure 9: Prolonged "O-X" fracture of subsequent small mining stope.

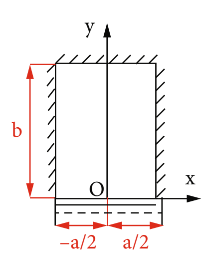

Figure 10: Mechanical model of mutative mining stope II.

$$w = C_3 y\left(x^2 - \frac{a^2}{4}\right)^2 \left(y^2 - b^2\right)^2. \tag{14}$$

Plug it:

$$\iint_A D\left(\nabla^4 w\right) w_m dxdy = \iint_A q w_m dxdy,$$

$$\Downarrow$$

$$\int_0^b \int_{-a/2}^{a/2} DC_3 \left[120y\left(x^2 - \frac{a^2}{4}\right)^2 + 24y\left(y^2 - b^2\right)^2 + 2\left(20y^3 - 12b^2y\right)\left(12x^2 - a^2\right)\right] y\left(x^2 - \frac{a^2}{4}\right)^2 \cdot \left(y^2 - b^2\right)^2 dxdy$$
$$= \int_0^b \int_{-a/2}^{a/2} qy\left(x^2 - \frac{a^2}{4}\right)^2 \left(y^2 - b^2\right)^2 dxdy. \tag{15}$$

It can be calculated as follows:

$$C_3 = \frac{8085q}{128\left(336b^5 + 176a^2b^3 + 165a^4b\right)D}. \tag{16}$$

Then, we can get

$$w = \frac{8085qy\left(x^2 - a^2/4\right)^2\left(y^2 - b^2\right)^2}{128\left(336b^5 + 176a^2b^3 + 165a^4b\right)D}. \tag{17}$$

According to the internal force bending moment expression, we can get

$$M_x = \frac{-8085q}{128\left(336b^5 + 176a^2b^3 + 165a^4b\right)} \cdot \left[y\left(12x^2 - a^2\right)\left(y^2 - b^2\right)^2 + \mu\left(20y^3 - 12b^2y\right)\left(x^2 - \frac{a^2}{4}\right)^2\right],$$

$$M_y = \frac{-8085q}{128\left(336b^5 + 176a^2b^3 + 165a^4b\right)} \cdot \left[\mu y\left(12x^2 - a^2\right)\left(y^2 - b^2\right)^2 + \left(20y^3 - 12b^2y\right)\left(x^2 - \frac{a^2}{4}\right)^2\right]. \tag{18}$$

The bending moment expression of this model was calculated by MATLAB to obtain its three-dimensional numerical image, as shown in Figure 11.

This model is compared with the small mining stope roof model with three sides fixed and one simply supported side (the simply supported side is the long side), and the inner part of plate bending moment greatly reduced and has a small cut with bending moment of fixed sides. But in general, bending moments of the maximum point still appear in long fixed side, and simply supported side has slight offset, which induce the initial rupture.

When the two long fixed sides of mutative mining stope II produced cracks, the constraint on bending moment transmission was reduced sharply. The fixed support will

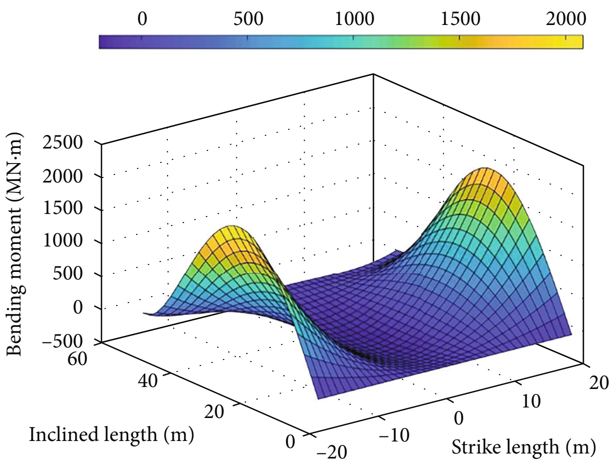

(a) Bending moment M_x

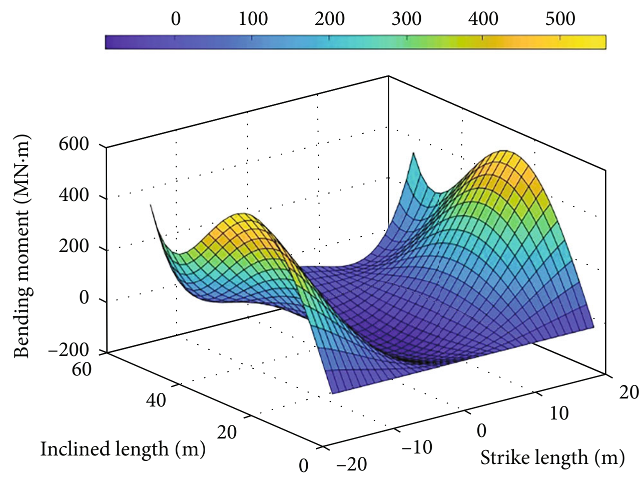

(b) Bending moment M_y

Figure 11: Bending moment of roof model with three sides fixed and one side simply supported (the simply supported side is the short side).

transform into simple support condition, and plate with three sides fixed and one side simply supported (the simple supported side is the short side) will transform into the plate with three sides simply supported and one side fixed, which is similar to mutative mining stope I, and then, the corresponding regularity of fracture can be generated. In other words, the crack in the center of initial simply supported edge will start to extend to the center of the plate and gradually get close to the short fixed supported edge to trigger fracture. Finally, it will close with simply supported edge on both sides to complete the secondary fracture of mutative mining stope, as shown in Figure 12.

In terms of the direction of open-off cut in small mining stope, the "O-X" fracture extending along the strike has drifted to inclined direction, as shown in Figure 13. This fracture law is consistent with the roof subsidence rule in the section of mutative mining stope in practical engineering. The law of prolongated "O-X" fracture and drifting "O-X" fracture produced in mutative mining stope is very complex. The entropy value of cutting roof control system is high, which is consistent with the phenomena in support engineering, such as short pressure step distance, high variable pressure strength, and difficult support of broken roof. As a whole, the temporal and spatial relationship between mining advancement and rock migration shows the drift of roof structure fracture, the continuity of rock structure instability, the migration of support pressure expansion, and the instantaneous increase of mining pressure phenomena.

2.3. Mechanical Model Analysis of Roof Fracture in Large Mining Stope. After the roof of mutative mining stope has broken twice, the phenomena of variable pressure and abnormal movement tend to be stable. It means that stope face enters large mining stope. Compared with small mining stope, the support space in the large mining stope is obviously expanded. It still has a trend of continuously increasing support pressure due to restriction of rock structure adjustment and the influence of residual energy release from mutative mining stope.

In engineering practice, when the length of working face reaches 100 m, the roof caving step is generally about 30 m [26]. According to calculated data simulated by MATLAB above, the inclined and strike lengths of roof model in large mining stope both exceed 100 m. In other words, when there is advanced unit distance on the$x$-axis, there will occur once basic roof period break, and there will be three times in total. However, after each break, boundary conditions and plate parameters will not change, and the breaking structure will not change either. Therefore, only the model range of "$a \times 2b$" was taken as the calculation boundary of single roof fracture. The left side and the lower side of model were the fracture roof edges of goaf, which can be set as simply supported boundary condition. The right side and the upper sides were the roof edge of coal layer clamped, which can be set as fixed boundary condition, forming an elastic model of two sides fixed and two sides simply supported (the simple support edges are adjacent), as shown in Figure 14.

According to the condition,

$$\begin{aligned}
(w)_{x=0} = 0, \left(\frac{\partial^2 w}{\partial x^2}\right)_{x=0} = 0, \\
(w)_{x=a} = 0, \left(\frac{\partial w}{\partial x}\right)_{x=a} = 0, \\
(w)_{y=0} = 0, \left(\frac{\partial^2 w}{\partial y^2}\right)_{y=0} = 0, \\
(w)_{y=2b} = 0, \left(\frac{\partial w}{\partial y}\right)_{y=2b} = 0.
\end{aligned} \tag{19}$$

According to Galerkin's method, let the deflection equation be

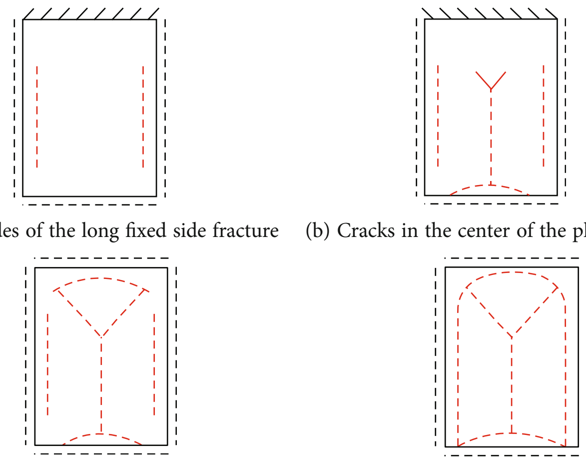

(a) Both sides of the long fixed side fracture (b) Cracks in the center of the plate extend

(c) The short fixed side breaks and closes (d) The two simply supported sides are through

Figure 12: Fracture evolution process of mutative mining stope II.

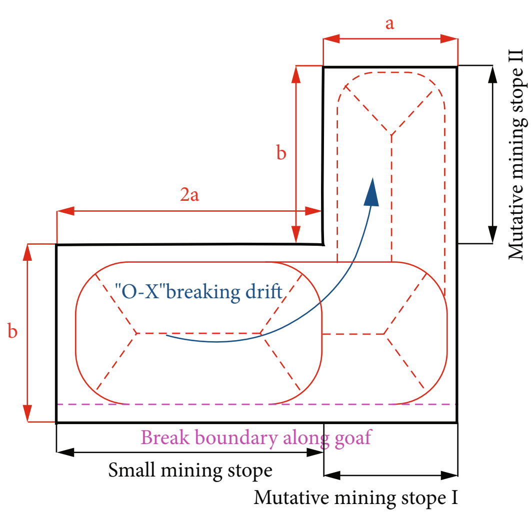

Figure 13: Drift-shaped "O-X" fracture of subsequent small mining stope.

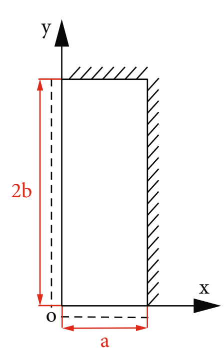

Figure 14: Mechanical model of large mining stope.

$$w = C_4 xy\left(x^2 - a^2\right)^2\left(y^2 - 4b^2\right)^2. \tag{20}$$

Plug it:

$$\iint_A D\left(\nabla^4 w\right) w_m dxdy = \iint_A q w_m dxdy,$$

$$\Downarrow$$

$$\begin{aligned}&\int_0^{2b}\int_0^a DC_4[120yx\left(x^2 - a^2\right)^2 + 120xy\cdot\left(y^2 - 4b^2\right)^2 \\ &\quad + 2\left(20y^3 - 48b^2y\right)20x^3 - 12a^2x]xy\left(x^2 - a^2\right)^2\left(y^2 - 4b^2\right)^2 dxdy \\ &= \int_0^{2b}\int_0^a qxy\left(x^2 - a^2\right)^2\left(y^2 - 4b^2\right)^2 dxdy.\end{aligned} \tag{21}$$

It can be calculated as follows:

$$C_4 = \frac{121275q}{65536\left(45a^5b + 176a^3b^3 + 720ab^5\right)D}. \tag{22}$$

Then, we can get

$$w = \frac{121275qxy\left(x^2 - a^2\right)^2\left(y^2 - 4b^2\right)^2}{65536\left(45a^5b + 176a^3b^3 + 720ab^5\right)D}. \tag{23}$$

According to the internal force bending moment expression, we can get

$$\begin{aligned}M_x &= \frac{-121275q}{65536\left(45a^5b + 176a^3b^3 + 720ab^5\right)} \\ &\quad\cdot\left[y\left(20x^3 - 12a^2x\right)\left(y^2 - 4b^2\right)^2 + \mu x\cdot\left(20y^3 - 48b^2y\right)\left(x^2 - a^2\right)^2\right], \\ M_x &= \frac{-121275q}{65536\left(45a^5b + 176a^3b^3 + 720ab^5\right)} \\ &\quad\cdot\left[\mu y\left(20x^3 - 12a^2x\right)\left(y^2 - 4b^2\right)^2 + x\cdot\left(20y^3 - 48b^2y\right)\left(x^2 - a^2\right)^2\right].\end{aligned} \tag{24}$$

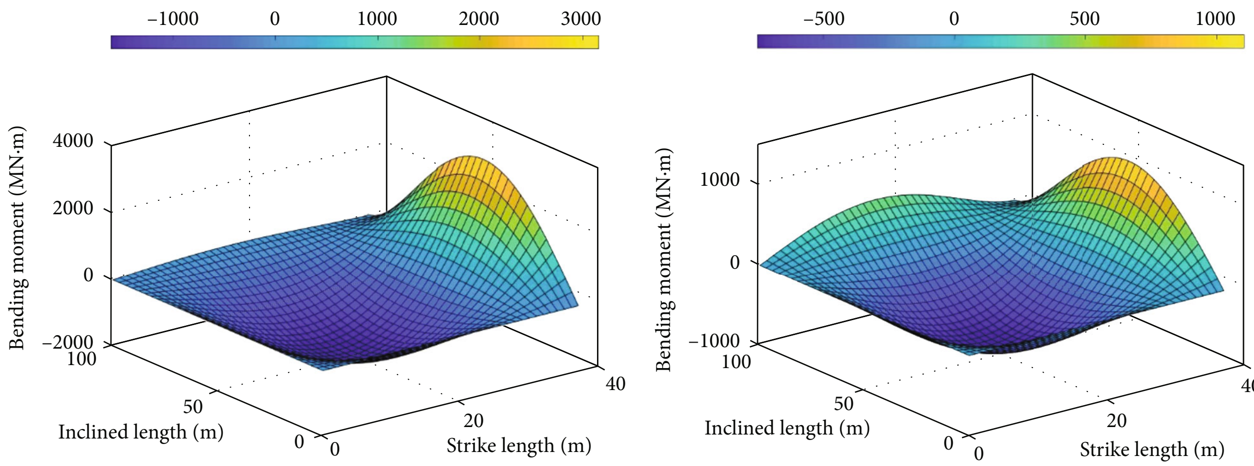

(a) Bending moment M_x

(b) Bending moment M_y

Figure 15: Bending moment of roof model with two sides fixed and two sides simply supported (simply supported sides are adjacent).

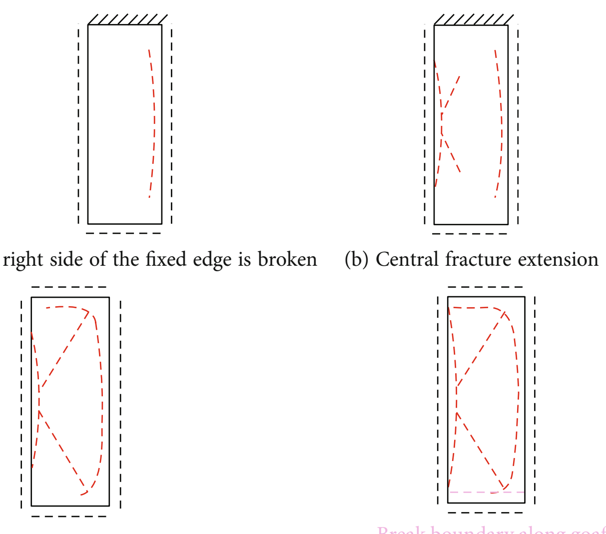

(a) The right side of the fixed edge is broken

(b) Central fracture extension

(c) The upper side of the fixed edge fracture and through

(d) Simply supported side through

Figure 16: Fracture evolution process of large mining stope.

The bending moment expression of this model was calculated by MATLAB to obtain its three-dimensional numerical image, as shown in Figure 15.

At the right side of large mining stope, the maximum bending moment was obtained on fixed edge. The roof model with both sides fixed and both sides simply supported (the simply supported sides are adjacent) will transform into a model with three sides simply supported and one side fixed, similar to the mutative mining stope I. Then, fracture will take place inside the plate close to long side of the simply supported. For the plate is relatively long and narrow, under the action of the corner effect, central crack will extend diagonally to the two corners and intersect with the right side of fixed edge cracks, which will promote upper fixed edge fracture and finally form closure, as shown in Figure 16.

Subsequent sections of large mining stope will form the same type of joint fracture. The stoping advance speed and support quality of this stope can be effectively controlled, and boundary conditions are continuous, so the fracture is regular. However, the length of working face is long, the roof control range is large, and the roof is broken regularly in a wide range, so the periodic pressure step distance is short, and space-time disturbance range caused by it is great. As a result, it has the characteristics of high dynamic pressure higher than the static pressure and will increase in a short time.

After calculation of four kinds of elastic bending thin plate theoretical models and the related numerical analysis, the roof broken whole structure of stope with variable length was finally formed, as shown in Figure 17, which is "small mining stope + mutative mining stope (I and II) + large mining stope."

2.4. Analysis of Integrated Model for Roof Fracture in Mutative Mining Stope and Large Mining Stope. In the

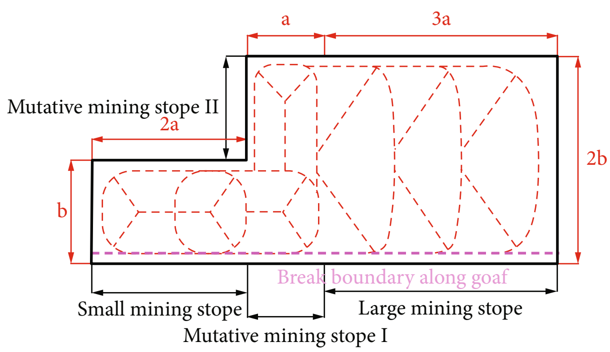

Figure 17: Overall broken structure of stope roof with variable length.

fracture analysis of mechanical model mentioned above, the stope with a working face length of 2b was divided into the mutative mining stope (I and II) and the large mining stope. This model can reasonably explain the complex roof disturbance breaking law, but dynamic evolution process is complicated. In the engineering field, after completion of mining in small mining stope, the working face advancement is still continuous and gradual. Although mutative mining stope has the most serious mining pressure, the most intensive roof movement, and the most difficult stope partition that is difficult to solve and deal with, the proportion of recoverable reserves and duration of mining and support work is the least. Considering factors such as working hours and efficiency and practical application of theory, it should be properly integrated with the larger mining stope with a larger proportion of stoping duration.

The theoretical model can be simplified by integrating the different fracture laws of mutative mining stope and large mining stope, which is beneficial to grasp the overall view of stope roof control theory. In following sections, mutative mining stope and large mining stope are collectively referred to as full-scale mining stope, as shown in Figure 18.

This model is an integrated stope by the strike length as the main guide. Through the overview analysis of fracture, the whole fracture law of full-scale mining stope can be obtained. At the lower part of left boundary of full-scale mining stope, there was an initial fracture generated by “O-X” fracture edge of small mining stope, which developed along the strike to inside of full-scale mining stope, and then, the upper part of left boundary fracture occurred and extended along the dip to inside of full-scale mining stope; finally, the two extended fractures converged. This was general law of mutative mining stope (I and II), in which the jumble fracture details were ignored and the “half-X-shaped” fracture was formed. The fracture of mutative mining stope I was the hypotenuse of lower part of the “half-X,” while the fracture of mutative mining stope II was the hypotenuse of upper part of the “half-X,” as shown in Figure 19.

Initial fracture occurred in long fixed side of the large mining stope, then cracks in the center of plate extended to the two sides and closed with long fixed side, and the two closed to short fixed side, finally causing it to break.

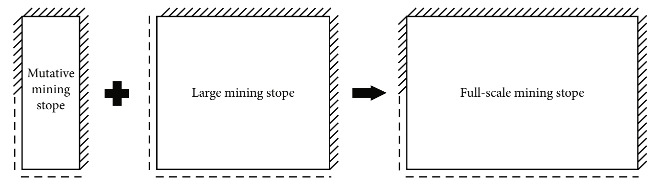

Figure 18: Full-scale mining stope model.

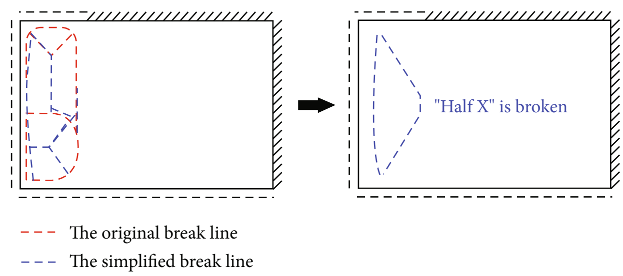

Figure 19: “Half X-shaped” fracture in full-scale mining stope.

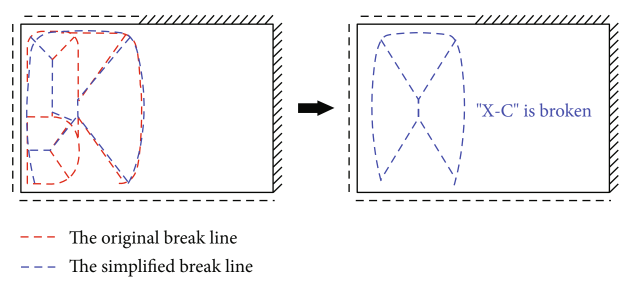

Figure 20: “X-C-shaped” fracture in full-scale mining stope.

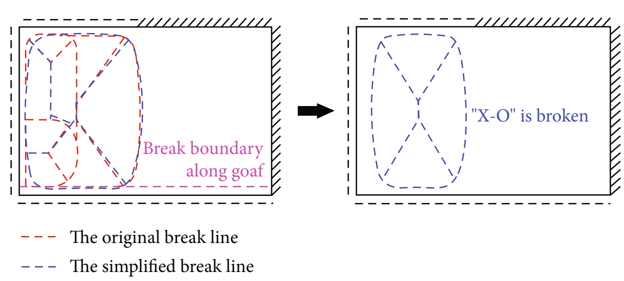

Figure 21: “X-O-shaped” fracture law in full-scale mining stope.

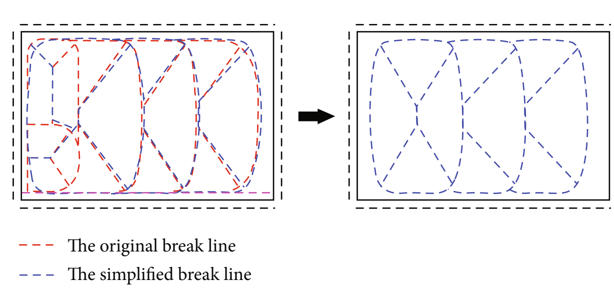

Figure 22: Fracture law of prolonged “X-O” fracture.

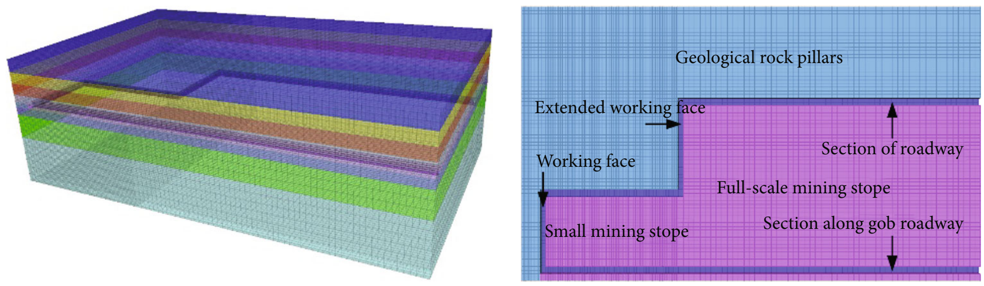

(a) Modeling figure (b) Top view of stope

Figure 23: FLAC^{3D} modeling schematic.

From the perspective of full-scale mining stope, fracture in the center of plate was further broken and expanded from "half X" to "full X" shape fracture, and all fixed sides became "∩" shape fracture, which can be called "C" shape for convenient description. To sum up, the second large-scale fracture of full-scale mining stope was "X-C" shape, as shown in Figure 20.

The "X-C-shaped" fracture was connected with the edge of goaf in the upper section at the lower part of full-scale mining stope, forming a "C-shaped" to "O-shaped" closure, as shown in Figure 21. The final occurrence of the roof in full-scale mining stope is similar to "O-X" fracture, but the development law of "X-O" fracture is slightly different, namely, from the traditional ① long fixed supported sides fracture ⟶ ② short fixed supported side fracture ⟶ ③ the "O" shape closed ⟶ ④ center fracture ⟶ ⑤ "X" shape closed ⟶ ⑥ "O-X" breakage form (form the "O" shape before forming an "X"). It is transformed into ① simple and fixed edge fracture ⟶ ② "half-X-shaped" fracture ⟶ ③ extension of long fixed edge and plate center fracture to induce short fixed side fracture ⟶ ④ "X-C-shaped" fracture ⟶ ⑤ "O-shaped" closure ⟶ ⑥ "X-O-shaped" fracture formation (first form "X" shape and then forming "O" shape).

As the working face continues to advance, the roof caving will occur periodically, and the fracture law is the same as the continuous fracture of large mining stope. The prolongated "X-O" fracture is formed with the roof in mutative mining stope, as shown in Figure 22.

3. Mechanical Characteristic Analysis of Roof Fracture Evolution in Stope with Variable Length

3.1. Establishment of Numerical Model. In order to verify the accuracy of mathematical model, explore the dynamic law of roof instability in stope with variable length, and consider universality of fracture theory in practical engineering problems. The following will use FLAC^{3D} software to establish corresponding coal seam and mining model, through the analysis of coal seam in multistage mining process of plastic zone development and change rules, to provide a strong support for fracture theory in this paper.

The cuboid model of 250 m × 150 m × 80 m was established, and Molar Coulomb model was adopted, fixing boundaries on the four sides and the bottom. An in situ stress of 15 MPa downward along the z-axis was applied on the top of model. The thickness of floor was 50 m, the thickness of coal seam was 3 m, and the thickness of roof was 27 m. The width of working face was 3 m, and the width of section roadway was 4 m. When section roadway was excavated in coal seam, strike length of small mining stope was 75 m and inclined length was 50 m. In this area, three stoping stages were simulated and grid was encrypted. The strike length of full-scale mining stope was 150 m, and the inclined length was 100 m. In this area, four stoping stages were calculated by simulation. The first stoping stage of full-scale mining stope was mutative mining stope zoning, and the last three stoping stages were large mining stope zoning, as shown in Figure 23.

3.2. Analysis of Mechanical Characteristics of Roof Fracture in Small Mining Stope. The small mining stope was divided into three mining calculations, and the roof plastic zone failure analysis was carried out once for every 25 m advancing average. The distribution characteristics of roof stress zone and plastic zone along with work progress are shown in Figures 24 and 25.

The lower part of roof boundary of small mining stope was the broken roof along the goaf. When the initial excavation of small mining stope advanced for 25 m, the stress concentration occurred in the lower part of the left and right sides of goaf. However, due to the short moment arm, the bending moment was not enough to cause roof to break. A wide shear plastic failure occurred to roof along the roadway strike, which conformed to the failure form of articulated point in the "S-R" instability theory of "masonry beam" [26]. The development of plastic zone in this roadway was mainly caused by mining disturbance in the upper section, so it was not included in analysis range of plastic zone in the stope with variable length. The roof near the open cut was undergoing shear failure, and the roof boundary on the upper side of goaf had undergone shear and tensile failure. Therefore, the two had a certain sequence in breaking time and space.

When 50 m was advanced, the range and value of shear stress on the upper side of the goaf gradually increased,

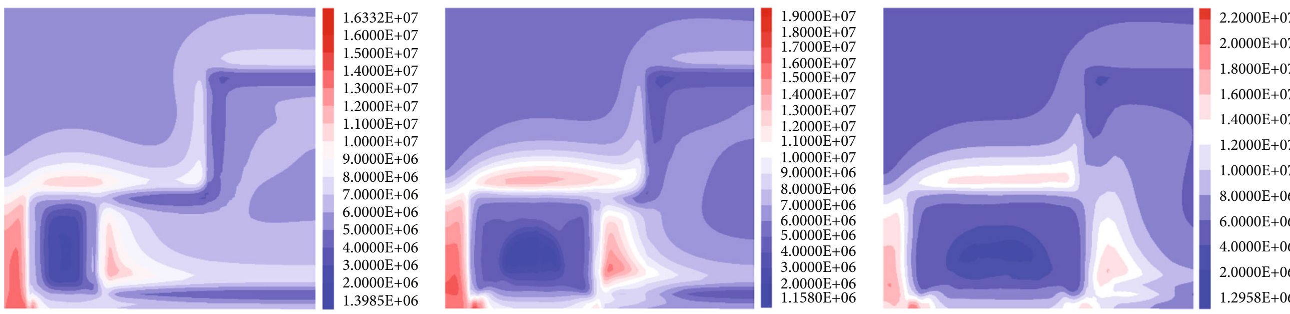

(a) Working face was advanced 25 m (b) Working face was advanced 50 m (c) Working face was advanced 75 m

Figure 24: Maximum shear stress of small mining stope.

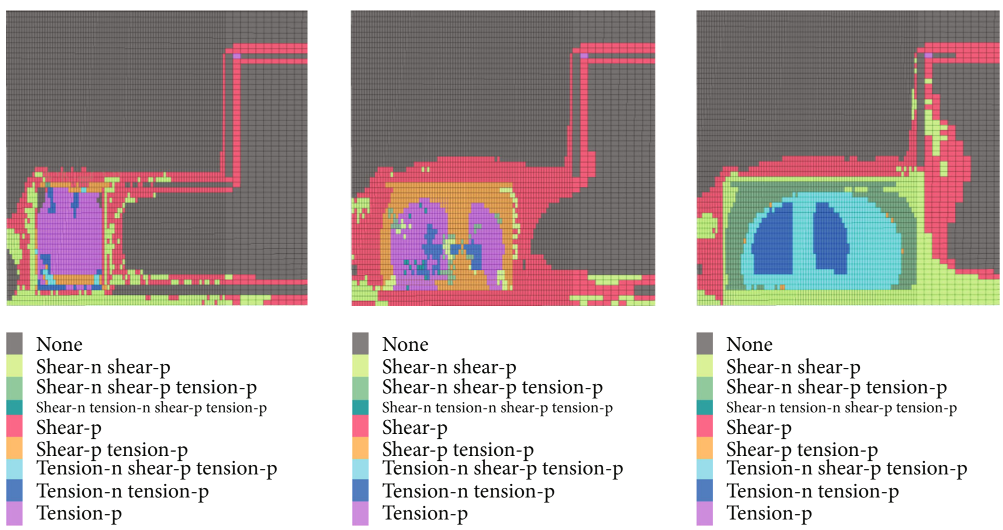

(a) Working face was advanced 25 m (b) Working face was advanced 50 m (c) Working face was advanced 75 m

Figure 25: Development of plastic zone in small mining stope.

and it was growing faster than the left and right sides. The main influence area of shear stress shifts to the long side of small mining stope. The roof above working face had a wide range of diffuse shear failure plastic zone and the goaf roof boundaries closed into an "O" shape, embedded shear and tensile failure plastic zone, the middle point exposed tensile failure plastic zone, in line with the "O-X" fracture in the roof center and the boundaries of their respective fracture characteristics. For the mechanical conditions of the lower boundary were very weak, the failure plastic zone in the middle was shifted downward.

When the working face was advanced 75 m, the shear stress range and bending moment of the goaf boundaries reached the maximum value, and the whole range of small mining stope roof was in dynamic activity stage of plastic failure. The "O-shaped" closure ring was dominated by dynamic shear failure, and the fracture in the center of the plate like an "X" shape was dominated by tensile failure; the shear and tensile mixed failure extended outwardly and blended with the plate boundaries, forming an "O-X" fracture.

To sum up, the upper boundary shear stress of small mining stope first reached the plate boundary breaking limit and shear failure occurred, and then, shear failure occurred at the left and right sides of the stope and formed "O-shaped" closure. Finally, the tensile failure occurred mainly in the center, and the shear and tensile failure extended outwards. When small mining stope was completely mined out, "O-X" plastic fracture will occur in the whole range. The broken law of the roof of small mining stope with three sides fixed and one side simply supported (the side simply supported is the long side) was verified.

3.3. Analysis of Mechanical Characteristics of Roof Fracture in Mutative Mining Stope. The first mining calculation of full-scale mining stope was the area of mutative mining stope. From the lengthening of the working face until the roof had obvious plastic zone, working face advance length was 40 m. The distribution characteristics of roof stress zone and plastic zone are shown in Figures 26 and 27.

In the lengthening stage of working face, the high stress concentration more than 25 MPa appeared at the right angle point of geological pillar. Shear stress range of roof near the working face ran through the whole length of working face, and the point stress concentration near roadway along goaf reached more than 25 MPa. The roof under such structural pressure will be prone to disaster.

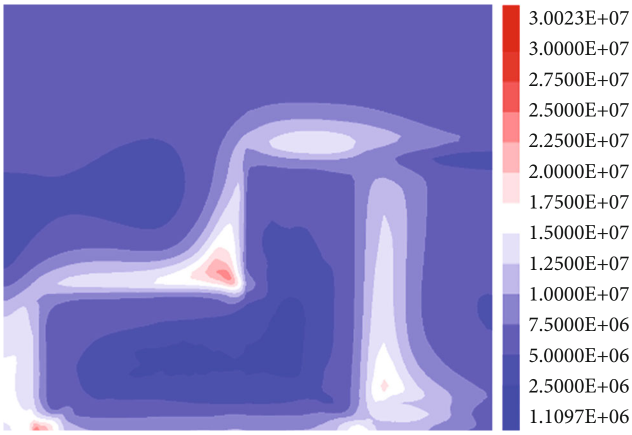

Figure 26: Maximum shear stress of mutative mining stope.

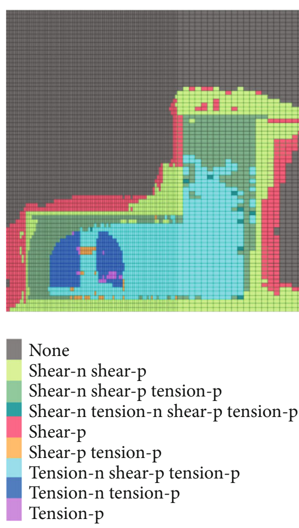

Figure 27: Development of plastic zone in mutative mining stope.

By comparison, the development degree of plastic zone of roof in mutative mining stope I and II was obviously different. Shear and tensile mixed plastic failure occurred in the whole roof of mutative mining stope I, which was the same as the failure form of goaf roof that adjacent small mining stope on the left. Moreover, both stopes have been surrounded by the “O” ring of the shear plastic zone, showing obvious continuity in the figure. Thus, the accuracy of the elongated “O-X” fracture was verified.

The plastic zone in the mutative mining stope II had a low degree of development, and shear and tensile mixed failure had occurred in the lower center position of roof and was connected with the plastic zone in mutative mining stope I. Considering that the depth of plastic zone along the strike of stope I was less than that along the inclined, it was sufficient to indicate that main development trend of plastic zone in mutative mining stope I was dip transfer to the II. Thus, the left “half-X-shaped” plastic fracture was formed, which verified the accuracy of the drift shape “O-X.”

The shear failure had occurred at the right and left boundaries of mutative mining stope II, and tensile shear mixed failure had occurred at the lower part of the center. Therefore, the roof failure took lead in the above three positions. The upper boundary of this stope was undergoing shear failure, indicating that this was the last roof fracture boundary. The breaking sequence can be summarized as ① the left and right long sides break ⟶ ② the center of the plate breaks towards the lower part ⟶ ③ the upper short side breaks. It was the same as the breaking law of roof model with three sides fixed and one side simply supported (the simply supported side is the short side) mentioned above, which provided corresponding evidence for it.

3.4. Analysis of Mechanical Characteristics of Roof Fracture in Large Mining Stope. The last three mining calculations of full-scale mining stope were the area of the large mining stope, and the advancing length of the working face was 40 m, 40 m, and 30 m. The distribution characteristics of roof stress zone and plastic zone are shown in Figures 28 and 29.

The range and value of shear stress at the boundaries of large mining stope increased with the expansion of goaf. The right side and the upper side of the goaf were both fixed boundaries, and the shear force value on right side was generally 8-10 MPa higher than upper side. Therefore, the criterion about right boundary of roof breaks first was more sufficient.

When the working face of large mining stope advanced 40 m (the mining of full-scale mining stope was 80 m), the tensile and shear failure plastic zone expanded in a large range. The area where the roof in stope with variable length had previously undergone plastic failure and stability was transformed from static to dynamic, a new round of plastic failure evolution occurs, the elastic residual energy releases, and the roof of goaf sank further. In this process, roof near working face had been shear broken; the location of fracture was consistent with shear stress concentration area in stress diagram. This boundary was the first to fracture, shear and tensile failure plastic zone was interluded in the middle of newly advanced 40 m goaf roof, and shear failure was occurring at the upper boundary. The development characteristics of plastic zone were in accordance with roof fracture law of roof plate with both sides fixed and both sides simply supported (the simply supported sides are adjacent).

When the working face advanced 80 m (the full-scale mining stope was mined 120 m), shear and tensile mixed linear fracture zone along the strike appeared in middle of large mining stope, which reflected the continuous fracture characteristics of large mining stope roof to a certain extent. At this time, the roof cycle pressure step distance was short and the pressure was intense. The coal wall fracturing, roof caving, coal wall scaling, floor heaving, and other mining pressure showed the most serious, and the timeliness is extremely complex, which promoted the support pressure of large mining stope to increase continuously.

When the working face was advanced 110 m (the full-scale mining stope was mined 150 m), all the stope with variable length was completed, and boundaries were dominated by shear failure and interior was dominated by tensile failure. The fracture pattern of goaf roof tended to be stable,

(a) Working face was advanced 40 m

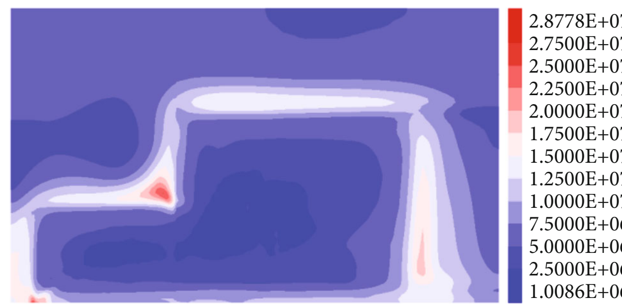

(b) Working face was advanced 80 m

(c) Working face was advanced 110 m

Figure 28: Maximum shear stress of large mining stope.

but the vigorous activities of the roof will not stop, and dynamic subsidence was still taking place in the whole area.

3.5. Analysis of Mechanical Characteristics of Roof Fracture in Full-Scale Mining Stope. As shown in Figure 27, in mutative mining stope I, due to the continuous development of the plastic zone in small mining stope, the "half-X" shape of the shear and tensile fracture plastic zone was not obvious. However, an obvious "half-X" shape was formed in mutative face stope II, which could be identified as the developmental characteristics of plastic zone of the drift-shaped "O-X" fracture based on small mining stope or as the initial plastic zone development characteristics of the "X-O" fracture based on full-scale mining stope. Figure 29 shows the shear tensile fracture plastic zone. In (a), the development form of shear tensile plastic failure had occurred in new goaf, which spread from the middle to the right corner and formed a "half-X" shape on the other side. At this time, the "X" shape has been fully developed, and shear failure has occurred at the left, right, and upper boundaries of the mutative mining stope and large mining stope, forming the "X-C" fracture. Finally, the "C-shaped" plastic zone and roof of the roadway along the goaf form plastic circle closured, namely, the "X-O" fracture. In (b), the upper part of stope, a shear and tensile mixed linear fracture zone along the strike has appeared, that is, the central fracture extension zone of the prolongated "X-O" fracture.

It can be seen that the plastic zone development characteristics of FLAC^{3D} numerical analysis are very consistent with the fracture theory mentioned above, which provides a powerful engineering simulation basis for the fracture theory.

4. Mechanical Model and Structural Evolution Law of Roof Fracture in Stope with Variable Length

By summarizing the movement law of overlying strata, corresponding geometric structure and mining pressure characteristics of each stope mentioned above, the different mining pressure characteristics and fracture laws of the stope with variable length can be obtained compared with the normal stope. There are three different development stages of working face advancing from small mining stope to mutative mining stope to large mining stope. In small mining stope, the stoping space is small, the working face length is short, and it belongs to the stable pressure structure. The relatively regular "O-X" fracture occurs in roof, and mining pressure appears to ease, so it is called the stably static pressure mining area. When entering mutative mining stope, the length of working face changes abruptly, which belongs to the sudden pressure structure. The boundary conditions of roof become complicated, the continuity instability of rock structure will occur, and fracture tends to transfer. The prolongated "O-X" fracture and drift "O-X" fracture appear in the roof, the mining pressure transient time changes abnormally, and the mining space is broken and difficult to support, so it can be called the suddenly alterant pressure mining area. When it is advanced to large mining stope, the period of pressing step interval is short, and the roof fracture is regular. It belongs to increasing pressure structure, and the prolongated "X-O" fracture appears. The rock structure readjusted, the elastic residual energy is fully released, and the whole roof of stope with variable length is transformed from static stability to dynamic failure. The support resistance of mining space is high and has a trend

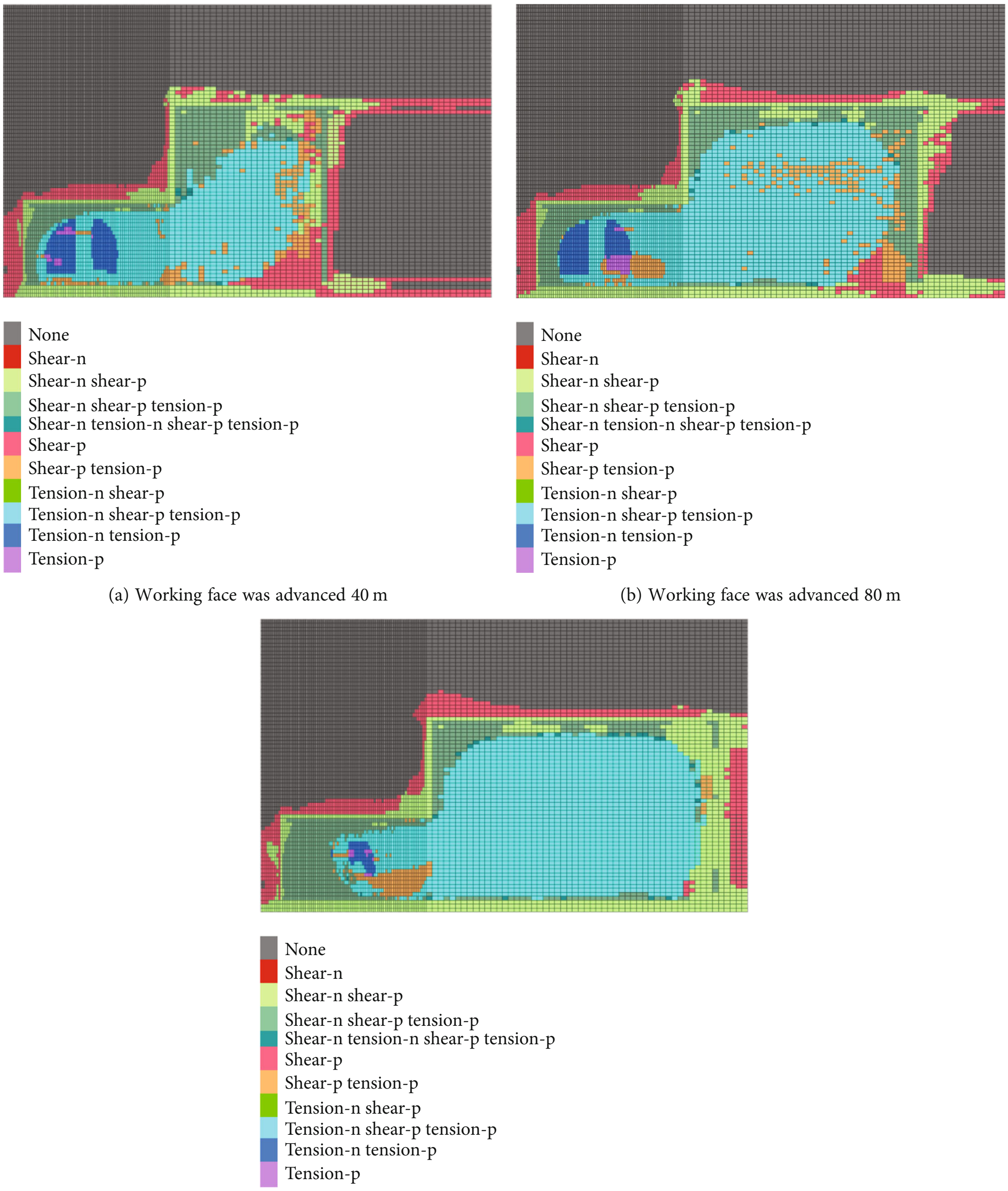

(a) Working face was advanced 40 m

(b) Working face was advanced 80 m

(c) Working face was advanced 110 m

FIGURE 29: Development of plastic zone in large mining stope.

of continuous growth, so it is called the increasingly dynamic mining area. The overburden structure pressure model of "three stopes, three areas, and three structures" is derived, as shown in Figure 30.

Mutative mining stope and large mining stope are integrated into full-scale mining stope, and the complex "half-X-shaped" fracture was developed from the irregular fracture in the center of mutative mining stope I and II. The fracture was combined with the central fracture of large mining stope to form an "X-shaped" fracture, and then, the peripheral fracture of full-scale mining stope was connected to form a "C-shaped" fracture, finally closed into the "X-O" form of breaking law. This is contrary to the traditional "O-X" form of fracture law in small mining stope, but it will occur with the advance of working face prolongated fracture. Thus, the roof breaking theory of "two stopes and two laws" in stope with variable length is derived, as shown in Figure 31.

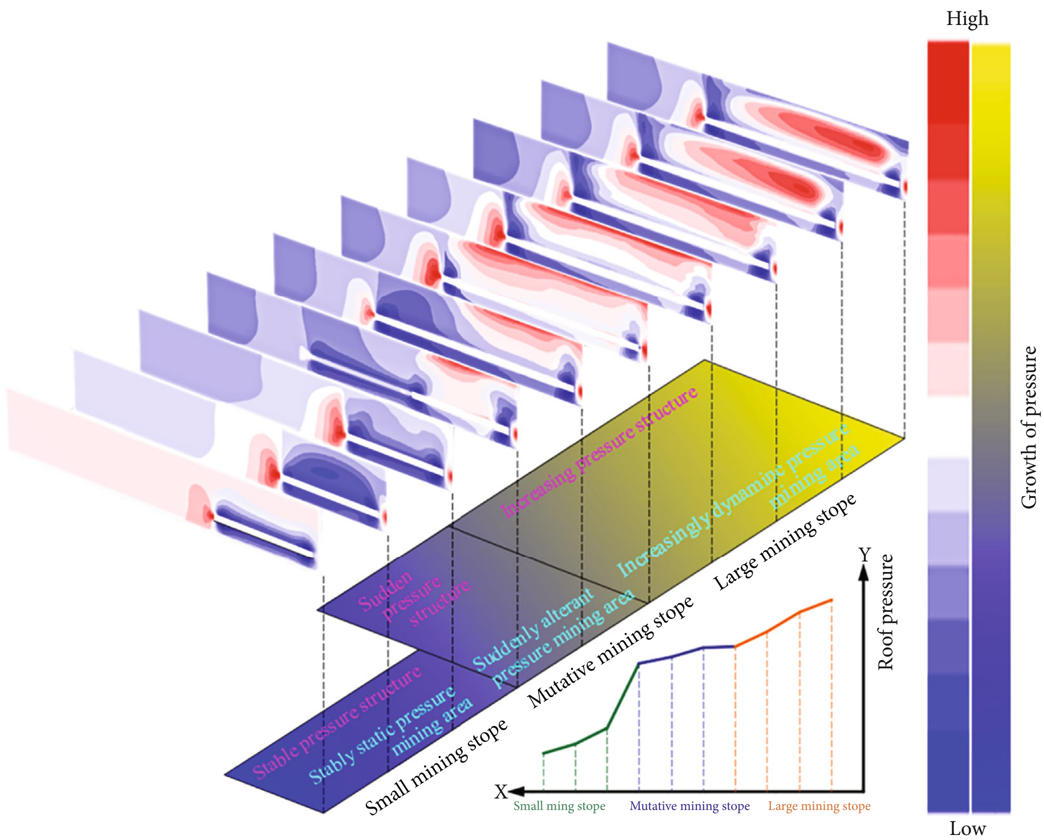

FIGURE 30: Pressure model of overburden structure of "three stopes, three areas, and three structures."

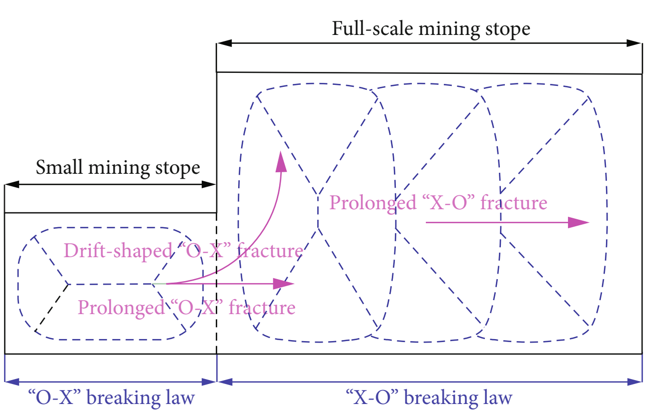

FIGURE 31: "Two stopes and two laws" roof fracture theoretical model.

It should be pointed out that, if the working face advances from full-scale mining stope to small mining stope, the overburden structural pressure and fracture law are also different, because of the different boundary conditions, so this theory is only applicable to process of advancing from small mining stope to full-scale mining stope at present.

5. Conclusions

(1) According to actual geological characteristics and working face layout characteristics of the stope with variable length, the theory of thin plate bending with small deflection of elasticity was applied to establish roof elastic model with three sides fixed and one simply supported (the simply supported side is the long side), one side fixed and three sides simply supported, one simply supported with three sides fixed (the simply supported side is the short side), and both sides fixed and both simply supported (the simply supported sides are adjacent). Through the roof breaking law of mathematical solution, the "O-X" fracture process of small mining stope, prolongated "O-X" fracture process, and drifting "O-X" fracture process of mutative mining stope, as well as the "X-O" fracture process and prolongated "X-O" fracture process of full-scale mining stope were deduced

(2) Using FLAC^{3D} to carry out engineering simulation, the evolution process of stress zone and plastic zone was obtained, which fully conformed to the calculation results of mathematical mechanics model. It provided a strong support for the breaking law of the stope with variable length, especially for the breaking law of the full-scale mining stope

(3) The roof "O-X" fracture rule of small mining stope is as follows: ① the long fixed side fracture on the upper part ⟶ ② the short fixed side fracture on both sides extending ⟶ ③ the "O-shaped" closure with the broken roof along the goaf ⟶ ④ the

central fracture ⟶ ⑤ "X-shaped" penetration → ⑥ "O-X" fracture law is formed. The roof "X-O" fracture law of the full-scale mining stope is as follows: ① left short simple and fixed side fracture ⟶ ② "half-X-shaped" fracture ⟶ ③ long fixed side and plate center fracture extension promote short fixed side fracture ⟶ ④ "X-C-shaped" fracture ⟶ ⑤ "O-shaped" closure formed by the broken roadway along the goaf ⟶ ⑥ "X-O" fracture law formed

(4) The causes and accompanying phenomena of mining pressure in small mining stope, mutative mining stope, and large mining stope were summarized, and the "three stopes, three areas, and three structures" overburden structure pressure model for stope with variable length was put forward. The roof fracture forms of small face stope and large face stope were summarized, and the theoretical model of "two stopes and two laws" roof fracture of stope with variable length was put forward (only applicable to the process of working face from short to long)

Data Availability

The data used to support the findings of this study are included within the article.

Conflicts of Interest

The authors declare that they have no conflicts of interest regarding the publication of this paper.

Acknowledgments

This work is supported by the National Natural Science Foundation of China (Grant No. 51904266), excellent youth project of Hunan Provincial Department of Education (Grant No. 21B0144), and Research Project on Teaching Reform of Colleges and Universities in Hunan Province in 2020 (Grant No. HNJG-2020-0231).

References

[1] M. C. He, H. P. Xie, S. P. Peng, and Y. D. Jiang, "Study on rock mechanics in deep mining engineering," *Chinese Journal of Rock Mechanics and Engineering*, vol. 24, no. 16, pp. 2803–2813, 2005.

[2] L. U. Bang-Wen, L. I. Chang-Wu, X. I. Hui, H. E. Tao, and W. A. Ding, "Law of overburden strata movement and mining roadway deformation under mining influence in the unequal length of working face," *Metal Mine*, vol. 45, no. 1, pp. 34–38, 2016.

[3] L. Yang-yang, Z. Shi-chuan, G. Li-qun, K. De-zhi, and K. He, "Mechanism and prevention of pressure burst in step region based on overburden strata movement of unequal length working face," *Rock and Soil Mechanics*, vol. 37, no. 11, pp. 3283–3290, 2016.

[4] X. F. Wang, *Slope Length Effect of Roof Fracture Mechanism and Stress Distribution Characteristics of Irregular Stope*, AnHui University of Science and Technology, Huainan, 2015.

[5] J. G. Ning, J. Wang, Y. L. Tan, and Q. Xu, "Mechanical mechanism of overlying strata breaking and development of fractured zone during close-distance coal seam group mining," *International Journal of Mining Science and Technology*, vol. 30, no. 2, pp. 207–215, 2020.

[6] Y. Y. Liu, X. M. Song, and D. F. Zhu, "Dynamic structural mechanical behavior and response characteristics of large key blocks," *Rock and Soil Mechanics*, vol. 41, no. 3, pp. 1019–1028, 2020.

[7] F. Cui, C. Jia, X. P. Lai, and J. Q. Chen, "Study on the evolution characteristics and stability of overburden structure in upward mining of short distance coal seams with strong burst tendency," *Chinese Journal of Rock Mechanics and Engineering*, vol. 39, no. 3, pp. 507–521, 2020.

[8] F. X. Jiang, "Viewpoint of spatial structures of overlying strata and its application in coal mine," *Journal of Mining and Safety Engineering*, vol. 23, no. 1, pp. 30–33, 2006.

[9] Y. Xue, T. Teng, and X. H. Wang, "Analysis of fracturing model and caving law of stope roof," *Science Technology and Engineering*, vol. 16, no. 7, pp. 156–161, 2016.

[10] H. Yu, *Study on the Movement of Upper Strata and the Pressure Behavior Law of Close Distance Coal Seams*, China University of Mining & Technology, Beijing, Beijing, 2015.

[11] W. A. Xin-Feng, G. A. Ming-Zhong, C. H. Yu-Xue, W. A. Jian-Jian, L. A. Xue-Qiang, and Z. H. An-Wei, "Analysis of fracturing characteristics of stope roof based on elastic thin plate theory," *Metals and Minerals*, vol. 50, no. 6, pp. 24–28, 2015.

[12] H. Wang, Z. Chen, Z. Du, and J. Li, "Application of elastic thin plate theory to change rule of roof in underground stope," *Chinese Journal of Rock Mechanics and Engineering*, vol. 25, no. S2, pp. 3769–3774, 2006.

[13] F. He, H. Wenrui, D. Chen, S. Xie, H. Li, and C. He, "First fracture structure characteristics of main roof plate considering elastic-plastic deformation of coal," *Journal of China Coal Society*, vol. 45, no. 8, pp. 2704–2717, 2020.

[14] D. D. Chen, S. R. Xie, and F. L. He, "Fracture rule of main roof thin plate with the elastic foundation boundary and long side coal pillar," *Journal of Mining & Safety Engineering*, vol. 35, no. 6, pp. 1191–1199, 2018.

[15] D. D. Chen, F. L. He, and S. R. Xie, "Time-space relationship between periodic fracture of plate structure of main roof and rebound in whole region with elastic foundation boundary," *Chinese Journal of Rock Mechanics and Engineering*, vol. 35, no. 6, pp. 1191–1199, 2018.

[16] Y. G. Wang, W. B. Guo, E. H. Bai et al., "Characteristics and mechanism of overlying strata movement due to high-intensity mining," *Journal of China Coal Society*, vol. 43, no. S1, pp. 28–35, 2018.

[17] W. A. Hong-sheng, L. I. Shu-gang, Z. H. Xin-zhi, W. U. Lin-zi, D. O. Yong-jian, and S. H. Hai-qing, "Analysis on stability of narrow coal pillar influenced by main roof fracture structure of gob-side roadway," *Coal Science and Technology*, vol. 42, no. 2, pp. 19–22, 2014.

[18] X. F. Wang, M. Y. Lu, Y. H. Gao, W. B. Luo, and W. G. Liu, "Structural mechanical characteristics and instability law of roof key block breaking in gob-side roadway," *Advances in Civil Engineering*, vol. 2020, Article ID 6682303, pp. 1–12, 2020.

[19] G. R. Feng and P. F. Wang, "Stress environment of entry driven along gob-side through numerical simulation

incorporateing the angle of break," *International Journal of Mining Science and Technology*, vol. 30, pp. 189–196, 2020.

[20] C. J. Hou, X. Y. Wang, J. B. Bai, N. K. Meng, and W. D. Wu, "Basic theory and technology study of stability control for surrounding rock in deep roadway," *Journal of China University of Mining and Technology*, vol. 50, no. 1, pp. 1–12, 2021.

[21] H. Wu, B. Dai, L. Cheng, R. Lu, G. Zhao, and W. Liang, "Experimental study of dynamic mechanical response and energy dissipation of rock having a circular opening under impact loading," *Mining, Metallurgy & Exploration*, vol. 38, no. 2, pp. 1111–1124, 2021.

[22] R. Cheng, Z. Zhou, W. Chen, and H. Hao, "Effects of axial air deck on blast-induced ground vibration," *Rock Mechanics and Rock Engineering*, vol. 55, no. 2, pp. 1037–1053, 2021.

[23] R. Cheng, W. Chen, and H. Hao, "A state-of-the-art review of road tunnel subjected to blast loads," *Tunnelling and Underground Space Technology*, vol. 112, p. 103911, 2021.

[24] F. Feng, S. J. Chen, Y. J. Wang, W. P. Huang, and Z. Y. Han, "Cracking mechanism and strength criteria evaluation of granite affected by intermediate principal stresses subjected to unloading stress state," *International Journal of Rock Mechanics and Mining Sciences*, vol. 143, p. 104783, 2021.

[25] Z. L. Xu, *Easticity*, Higher Education Press, Beijing, 2015.

[26] M. G. Qian, P. W. Shi, and J. L. Xu, *Mining Pressure and Strata Control*, China University of Mining and Technology Press, Xuzhou, 2010.

Hindawi
Geofluids
Volume 2022, Article ID 5160876, 8 pages
https://doi.org/10.1155/2022/5160876

Research Article

Field Pull-Out Test and Analysis of Fiberglass Anchors in Sanshandao Gold Mine

Qingbiao Wang,[1,2,3,4] Zhongjing Hu ,[1] Hongyue You,[5] Haolin Xu,[2] Lujie Bai,[2] Shanghuan Yang,[6] Ming Zhang,[7] and Zhenyue Shi [1]

[1]*College of Safety and Environmental Engineering (College of Safety and Emergency Management), Shandong University of Science and Technology, Qingdao 266590, China*
[2]*College of Resources, Shandong University of Science and Technology, Tai'an 271019, China*
[3]*National Engineering Laboratory for Coalmine Backfilling Mining, Shandong University of Science and Technology, Tai'an 271019, China*
[4]*State Key Laboratory of Mining Disaster Prevention and Control co-Founded by Shandong Provence and the Ministry of Science and Technology, Shandong University of Science and Technology, Qingdao 266590, China*
[5]*College of Civil Engineering and Architecture, Shandong University of Science and Technology, Qingdao 266590, China*
[6]*Sanshandao Gold Mine, Shandong Gold Mining (Laizhou) Co. Ltd., Laizhou 261400, China*
[7]*Xincheng Gold Mine, Shandong Gold Mining (Laizhou) Co. Ltd., Laizhou 261400, China*

Correspondence should be addressed to Zhenyue Shi; 201881010015@sdust.edu.cn

Received 14 October 2021; Revised 29 November 2021; Accepted 14 March 2022; Published 4 April 2022

Academic Editor: Chao-Zhong Qin

The Sanshandao gold mine is developed near the sea and has high-chloride ion content in the groundwater, resulting in serious corrosion of metal anchors and difficulty in maintaining metal anchors. To solve the corrosion problem of anchor rods in Sanshandao, the use of fiberglass anchor rods, instead of metal anchor rods, is proposed. To verify the feasibility of fiberglass anchor application, a fiberglass anchor (diameter: 27 mm) pulling test was conducted at the Sanshandao gold mine. The test results show that (1) the pull-out resistance of fiberglass anchor rods is better than those of metal pipe slit anchor rods and threaded anchor rods currently used in the Sanshandao gold mine; (2) the failure of fiberglass anchor rods is mainly because of the destruction of anchor washer discs and nuts, whose rods play only 69.90–77.7% of their performance and remain intact; (3) the fiberglass anchor rod was damaged to different degrees several times before the pulling failure, and the damage was accompanied by sound; (4) the fiberglass anchor continued to bear pressure after each damage until complete failure occurred; and (5) the anchor washer disc relative to the nut to allow the pressure effect can avoid nut pressure collapse and improve the pulling performance of the anchor rod to a certain extent simultaneously. Through the test, it was proved that the 27 mm fiberglass anchor can meet the support demand of the Sanshandao gold mine. It also provides an important reference for the promotion and application of fiberglass anchor rods in similar mines.

1. Introduction

The Sanshandao gold mine is located in Laizhou city, Shandong province, China. The mine site is adjacent to the sea, and its entrance is approximately 1.5 km from the coastline, as shown in Figure 1. Since the Sanshandao gold mine is close to the coastline, the mine's groundwater has a high-chloride ion content, which can easily lead to metal corrosion. Among them, metal anchors are seriously affected by corrosion, resulting in significant risk to the safety of underground rock support and increasing anchor maintenance costs.

To address the problem of corrosion of metal anchors, many scholars have conducted extensive research on anticorrosion and new materials. Wen et al. [1] comprehensively

Figure 1: Location of Sanshandao gold mine.

studied the instability mechanism and movement law of coal and rock mass. Li et al. [2] analyzed the failure mode of the tunnel support structure. Lin et al. [3] investigated the corrosion resistance of metal surface coatings on anchor rods. Zhu et al. [4] proposed an attractive waterborne epoxy that can provide good corrosion protection. Li et al. [5] studied the relationship between corrosion time and failure to grasp the failure node and then took maintenance measures in time. Cho et al. [6] investigated the corrosion protection effect of unbonded closure systems on anchor rods and anchor cables. Liao et al. [7] investigated a grouting corrosion protection method to compensate for the weakness of anchorage. Zou et al. [8] described the corrosion resistance of fiberglass anchor rods. Benmokrane et al. [9] reported that aramid and carbon-fiber-reinforced plastics have good corrosion resistance but they are expensive.

Research on the corrosiveness of anchors is reflected in three main areas: (1) the use of anticorrosive coatings for metal anchors, (2) use of unbonded protection or full-length bonded protection, and (3) replacement of anchors made of metal with corrosion-resistant materials. With the development of new material technology, the performance and cost of materials are increasingly converging with the needs of engineering applications, and thus, the development of new materials is a trend for the future. A fiberglass anchor is corrosion resistant and weighs approximately one-quarter of the weight of metal anchors, with a higher tensile strength than metal anchors [10]. Fiberglass anchors are more economical than carbon and aramid fiber anchors [11]. Therefore, in this study, we propose a support solution using fiberglass anchors, instead of metal anchors, to address the corrosion problem of metal anchors in Sanshandao.

Numerous studies on fiberglass have been conducted, and Kou et al. [12] studied the pull-out tests of fiberglass anchors as antifloating tools in weathered soils. Wang et al. [13] studied that an important method to improve the performance of concrete is to use alkali-resistant glass fiber (ARGF) as reinforcement. Ceroni et al. [14] and Ji [15] investigated the pull-out properties of glass-fiber reinforcement in combination with grouting materials. Shi et al. [16] studied that the addition of alkali-resistant glass fiber improved the compressive strength and tensile strength of grouting slurry. Wang et al. [17] investigated the pull-out performance of fiberglass anchor rods bonded to an anchor material interface using indoor tests. Sim et al. [18] studied the application of fiberglass anchors as permanent anchors in slope support through indoor tests, and the test results indicated that fiberglass anchors could replace metal anchors. Bai et al. [19] investigated the pull-out performance of fiberglass anchor rods using indoor tests. Huang et al. [20] investigated the structural damage mechanism of fiberglass anchor rods using field tests. Li et al. [21] investigated the load-bearing properties of fiberglass rods.

Numerous scholars have extensively studied fiberglass anchors, with the research results mainly focused on the interfacial bonding between fiberglass anchors and anchor solids and the tensile strength of fiberglass rods. There are many studies on laboratory tests, the field test was small. In the fiberglass pull-out test, there are more studies on the rod but the anchor role is a system that lacks field tests on the pull-out performance of the anchor rod, anchor washer disc, and nut supporting anchor system.

Therefore, the effectiveness of fiberglass anchors in supporting the Sanshandao gold mine and obtaining a scientific basis for future applications and promotions was determined. A field pull-out test was conducted at the Sanshandao gold mine. The results of the pull-out tests support the feasibility of the fiberglass material for application in the Sanshandao gold mine. It is also a reference value in similar mines where corrosion is severe.

2. Test Preparation

2.1. Test Material. The fiberglass anchor pull-out test material was supplied by Shandong SFT Industrial Co. Ltd. and comprised a fiberglass rod body, anchor washer disc, nut, and resin anchor fixation. A 27 mm diameter fiberglass rod was used for this test. The anchor washer disc, nut, and resin anchor fixations were matched to the rod specifications. The material parameters are shown in Table 1 and Figure 2.

2.2. Test Equipment

2.2.1. Anchor Construction and Installation Equipment. The hole-making equipment for this test was a TY-28 rock drill, as shown in Figure 3(a). The anchor installation equipment was a ZQS-50/1.9S air-coal drilling rig, as shown in Figure 3 (b). The mixer model matches the wind-coal drilling rig and anchor diameter, as shown in Figure 3(c).

2.2.2. Anchor Pull-Out Test Equipment. The anchor rod pull-out test was conducted using a KYG-20T-70 mm–34 mm manual hydraulic hollow jack, as shown in Figure 3(d). It can provide 0–20 T (0–200 kN) with a maximum cylinder stroke of 70 mm. The pressure gauge range of this equipment is 0–60 MPa, that is, when the pressure gauge is 60 MPa, the force value it provides is 20 T.

Table 1: Test materials and technical specifications (provided by the manufacturer).

Component	Anchor rod	Anchor washer	Nut	Resin anchor fixation
Technical requirement	Tensile strength ≥ 300 MPa	Bearing capacity ≥ 105 kN	Bearing capacity ≥ 105 kN	Gelation time 40–90 s

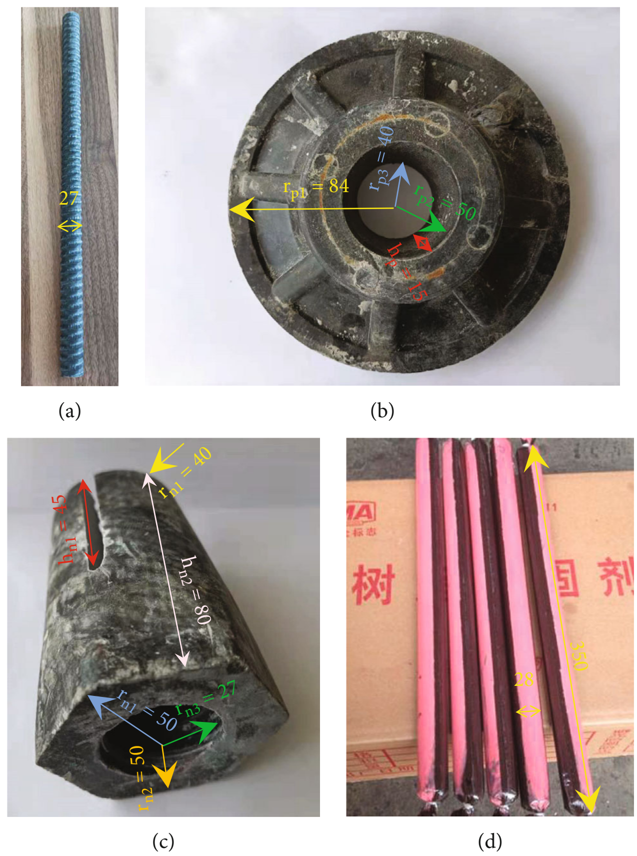

Figure 2: Test material (unit: mm). (a) Anchor rod. (b) Anchor washer. (c) Nut. (d) Resin anchoring agent.

3. Test Procedure

3.1. Test Location Selection. Considering construction safety, convenience, and typical features, the technical staff of Sanshandao operations recommended the test location to be chosen in the −330 m excavation tunnel of the Sanshandao gold mine, as shown in Figure 4. The surrounding rock at this location is mainly granite, the thickness of the rock layer is about 12.8~28.9 m, and the thickness of the aquifer is generally 11~43 m. The rock stores water in the form of fissures. The buried depth of the water level is 4.58~14.40 m, the water chemistry type is mainly Cl-Ca, and the salinity is 1.30~2.27 g/L. The tunnel surrounding rock is class III, with more obvious joints and fissures, relatively good rock integrity, and good control of light exploded in the surface surrounding rock, making it suitable for conducting basic tests.

3.2. Construction and Installation of Test Anchors

3.2.1. Anchor Layout and Drilling Construction. Three anchors were tested. Relatively flat surrounding rock conditions were selected by combining the site working face conditions, drilling, and anchor installation equipment. The feasibility of the application of fiberglass anchor rods in deep metal mines at sea was investigated by drawing the pull-out force-displacement curves of the three anchor rods through pull-out tests. The results of the three sets of anchor rod tests can be verified against each other, and the three anchor rods are named as no. 1, no. 2, and no. 3 anchor rods, respectively, as shown in Figure 5. The anchor spacing was 800 mm, and the anchor length was 2200 mm. The anchor diameter was 27 mm, and the drilling diameter was 34 mm. The distance between the tunnel face and the test site is 30 m. The test anchor holes were identified and drilled using a TY-28 rock drill.

3.2.2. Anchor Rod Installation. Two resin cartridges were placed in each hole, and the anchor rod was used to push the resin into the bottom of the hole. Adhesive cartridges are 28 mm in diameter and 350 mm in length. The stirrer was then tightened to the anchor rod body, and the air-coal drilling equipment was used to drive the rotation of the stirrer, which, in turn, drove the rotation of the anchor rod body, as shown in Figure 6. Simultaneous thrust was applied to the air-coal drill during the rotation of the rod,

Figure 3: Test equipment. (a) Rock drilling. (b) Air-coal drill. (c) Mixing head. (d) Pulling equipment.

Figure 4: Site photo of the test location.

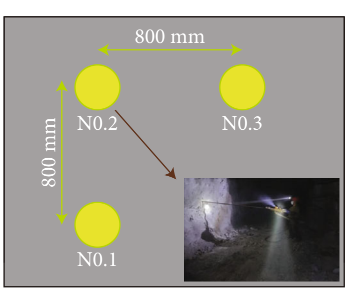

Figure 5: Location of test anchors and field tests.

causing the anchor rod to pierce the resin anchorant and agitate it at high speed. Stirring until the rod rotates with difficulty, the actual rotation time is approximately 60–70 s.

3.3. Anchor Pull-Out Test. When the construction of anchor rod no. 3 was completed, the anchor rod pull-out test was performed after waiting for half an hour. The actual test sequence was no. 2–no. 1–no. 3 anchor rods. During the test

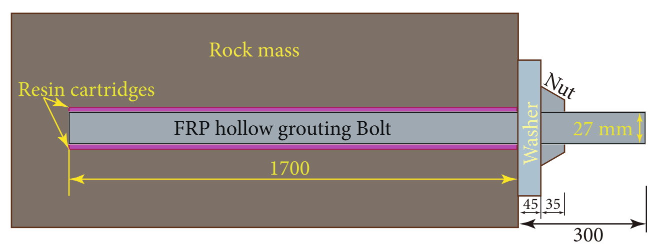

Figure 6: Schematic of anchor installation.

on anchor 2, the nut came into contact with the jack cylinder, resulting in premature damage to the nut. The test programme was temporarily adjusted on site, and two anchor washers were installed in contact, thus avoiding damage to the nut in contact with the cylinder. The specific test steps were as follows.

In step 1, the hollow jack is passed through the anchor rod body and the jack is in direct contact with the surrounding rock wall.

In step 2, the anchor washer and nut were sequentially fitted to the anchor rod.

In step 3, the jack is manually pressurised until the pressure drops suddenly. The pulling displacement of the anchor rod is measured by a vernier caliper, and the test time is timed by a stopwatch. Meanwhile, anchor damage is observed.

Anchor rods (that can continue to be pressurised) can be pressurised several times, recording the maximum pressure value for each pressure drop. The pressure value was used to calculate the load on the anchor rod, and the anchor

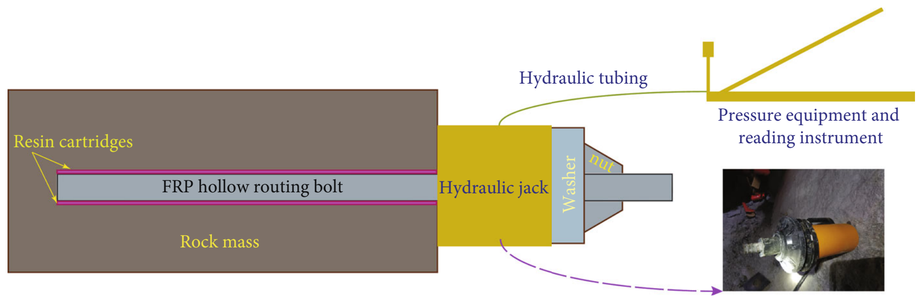

Figure 7: Installation view of the drawing equipment.

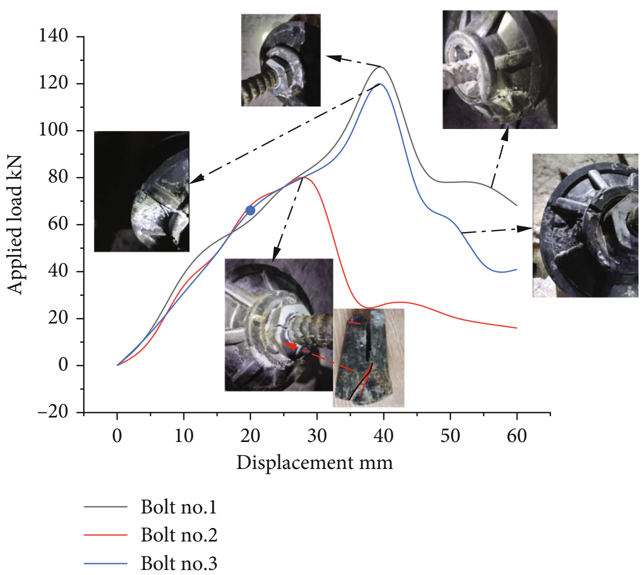

Figure 8: Anchor displacement-pulling force curve.

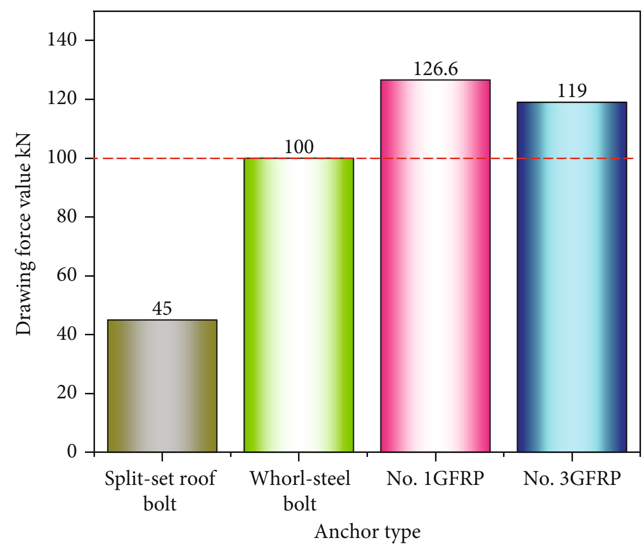

Figure 9: Comparison of pull-out values for different types of anchor bar.

rod and pulling equipment were installed, as shown in Figure 7.

4. Results and Discussion

The pull-out test on the anchor rods allows the values of the tensile force and displacement of the anchor head when the anchor rod is damaged. The experimental results were analyzed in relation to the anchor rod damage phenomenon. To facilitate the analysis, it was performed in the order of the actual tensioning of the anchor rods.

4.1. Analysis of Tensile Test Results of the Fiberglass Bolt. As shown in Figure 8, during tensioning, the displacement-drawing force curve for anchor no. 1 was approximately linear until the peak pulling force was reached. When the pull-out displacement was 30 mm and the pull-out force was 86 kN, a reverse bending point occurred, at which the slope of the displacement-draw-out force curve increased, reaching a peak stress of 126.6 kN at a displacement of 40 mm. After the peak pull-out force occurs, there is a sudden change in the pull-out force, but at this time, the anchor still has a certain load-bearing capacity. When the pull-out displacement was 50 mm, the anchor still had a pull-out resistance of 78 kN, and when the tray and bolt were completely damaged, the anchor lost its pull-out resistance.

During the test, a low-frequency friction sound was emitted at the pallet position as the hydraulic jack was pressurised. When the peak of the pulling force is reached, the pallet produces an explosive sound similar to the breaking of plastic. In the process of continuous loading, with the increase in pull-out displacement, the bolt and pallet are constantly embedded and compacted. When the peak pull-out force is reached, the bolt is subjected to a large circumferential pressure. The gap between the predetermined notches shrinks sharply, resulting in the breaking of the bolt ends and the explosion sound generated during the test. At this point, the pallet exhibited smaller cracks. As the load continued, the displacement changes were large. When the pull-out displacement was 50 mm, the change in the pull-out displacement slowed. At this point, the pallet and bolt cracks gradually expand until the pallet is destroyed and the anchor loses its pull-out force.

As shown in Figure 8, the peak stress of anchor rod no. 2 is similar to that of anchor rod nos. 1 and 3 during the loading process and it changes in an approximate line. The peak stress was reached when anchor no. 2 reached a pull-out displacement of 30 mm and a pull-out force of 75 kN; subsequently, the pull-out stress drops sharply and turns when

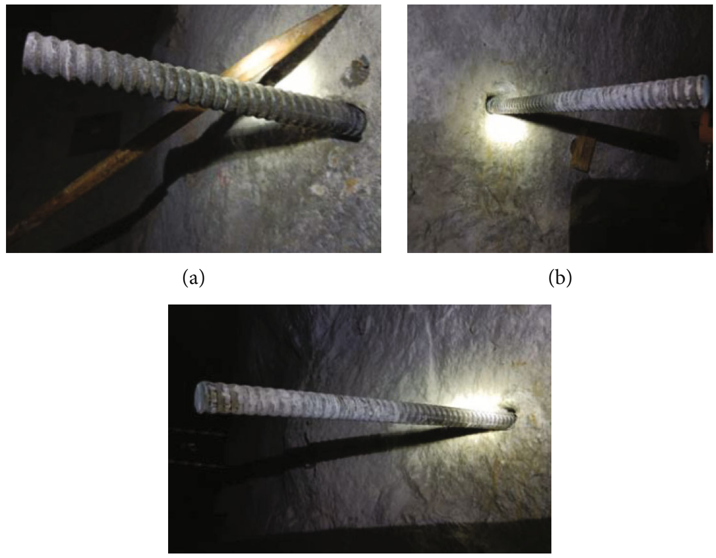

(a) (b) (c)

Figure 10: Condition of the rod after completion of the test. (a) Anchor rod no. 1. (b) Anchor rod no. 2. (c) Anchor rod no. 3.

the pull-out displacement is 40 mm and the pull-out force is 26 kN, after which the pull-out resistance of the anchor gradually decreases, but the anchor still has a certain pull-out resistance at this time.

Comparing the field tests of anchor nos. 1 and 2, anchor no. 1 was tested with two pallets while anchor no. 2 was tested with only one pallet. As there was only one pallet, the inner cylinder of the jack directly contacted the nut during tensioning, resulting in rigid damage to the nut and through cracks along the preopening joints and cracks on both sides of the preopening joints, resulting in a lower peak pulling force in the pulling test for anchor no. 2.

Combining the field test anchor rods no. 1 and 2, the pull-out test of anchor rod no. 3 was conducted. As shown in Figure 8, the trend of the pull-out displacement-draw out stress curve before and after the peak pull-out force during the pull-out test for anchor rod no. 3 was similar to that for anchor rod no. 1 and the location of the sound that occurred during the test was also similar. The pull-out displacement at the peak curve position of anchor no. 3 was 39.5 mm, and the pull-out force was 119 kN. The anchor nuts and pallets of anchor nos. 3 and 1 broke in a similar manner and at similar locations.

Three fiberglass anchor pull-out tests have shown that when the borehole is not perpendicular to the surrounding rock, the anchor washer will be unevenly stressed, damaging the anchor washer. The destruction of the anchor washer disc facilitated the movement of the nut, which, to some extent, acted as pressure relief such that no chipping of the nut occurred. Meanwhile, this let-down effect, on the contrary, increased the pull-out resistance of anchors, relative to anchor rod no. 1, by approximately 5% in this experiment.

4.2. Analysis of the Feasibility of Applying Fiberglass Anchors in the Deep Metal Roadway Near the Sea. Based on the abovementioned fiberglass anchor pull-out test results, a graph of the pull-out force versus displacement can be drawn, as shown in Figure 9. As can be observed from the graphs, the pulling of anchor nos. 1 and 3 was normal, except for the pulling of anchor no. 2, which failed. The first breakage displacements occurred at 40 mm and 39.5 mm, with pulling forces of 126.6 kN and 119 kN, respectively. The second breakage displacements occurred at 55 mm and 50 mm with pulling forces of 77 and 62 kN, respectively. Anchor no. 1 failed after two tensioning procedures owing to nut failure. After the 3rd tensioning, anchor no. 3 failed owing to the failure of the anchor washer disc when the hydraulic jack displacement was 55 mm and the maximum pulling force was 119 kN. The test results showed that the pulling effect of the fiberglass anchors was relatively constant.

Currently, pipe seam anchor rods and rebar anchor rods are used at the Sanshandao gold mine. Therefore, the fiberglass anchor rods were compared with both pipe seam anchor rods and rebar anchor rods and the results are shown in Figure 9. The pull-out requirement for the pipe slit anchor rod at the Sanshandao gold mine is 45 kN; the pull-out requirement for the threaded reinforcement anchor rod is 100 kN (this requirement is provided by the Sanshandao gold mine). The maximum pull-out values of the fiberglass anchor rods in the test were 126.6 kN and 119.0 kN for anchor rods no. 1 and 3, respectively. Consequently, the fiberglass anchor pulling effect meets the requirements of the Sanshandao gold mine support.

At the end of the pull-out test, the hydraulic jack was removed and found to be intact with only minor damage to the rod body, the rod body, and pallet and the nut bite position compared to other locations was white because, during the pull-out test, the nut pallet and rod bite provided tensile strength, as shown in Figure 10. According to the rod indoor pull-out test, the tensile strength of the rod is 300 MPa. It can be seen from the ratio of the peak value of the pull-out force failure in the field test to the peak value of the indoor tensile test of the anchor rod; the peak tensile strength of the anchor rod in the field pull-out test is only 69.90–77.7% of its performance. Consequently, there is still room to improve the matching anchor washer disc and nut for a 27 mm diameter fiberglass rod.

5. Discussion

This experiment is a field pull-out test based on an indoor test of 27 mm fiberglass anchors. The major difference between the field test and the indoor test is that the field test environment is complex and variable, involving various factors, such as temperature, humidity, lithology, and fissures [22–26].

Comparing the indoor tests with the field test data, the analysis of the anchor rod pull-out resistance shows that the fiberglass anchor rod is suitable for replacing metal anchor rods in deep metal mines in the sea [25]. Analysis of the field pull-out test results showed that the anchor rod damage was from the nut and pallet positions rather than the anchor rod body [27]. The next step in this research is to improve the performance of the nut and anchor washer disc in terms of structure and material, as well as to study the performance of fiberglass anchors under multifield coupling conditions through field tests for several aspects, such as high temperature, high ground pressure, and seawater erosion in deeper metal mines.

6. Conclusions

The test was conducted on an anchor rod comprising a 27 mm diameter fiberglass rod and its supporting components. The analysis of the pull-out test results shows that there are mutually mapped responses in terms of damage process, damage form, and damage response of the fiberglass anchor rod, with the following conclusions.

(1) The fiberglass anchor rod was damaged several times to varying degrees before pulling failure, mainly by cracking of the nut and anchor washer disc. Each time the fiberglass anchor was damaged, there was a sudden drop in pressure and audible noise. The fiberglass anchor rod can continue to be pressurised after each damage until it fails. According to the three sets of test results, the maximum pulling force when the nut is broken is 126.6 kN and the pulling displacement is 40 mm, and when the washer is broken, the pulling force is 78 kN and the pulling displacement is 50 mm

(2) The tensile performance of the fiberglass rod with a diameter of 27 mm was good, the rod remained intact during the test, and the performance of the rod was approximately 69.90–77.7%. The fiberglass anchor washer disc and nut are the weak links in the anchor support system and are prone to damage in the pull-out test

(3) The pressure of the anchor washer disc relative to the nut prevents the nut from collapsing under pressure and, to a certain extent, improves the pulling performance of the anchor rod

(4) The maximum drawing force of the 27 mm diameter fiberglass anchor is 126.6 kN and the drawing displacement is 40 mm, which meets the requirements of the Sanshandao gold mine with a minimum drawing force of 100 kN and a minimum drawing displacement of 50 mm

Data Availability

The data used to support the findings of this study are available from the corresponding author upon request.

Conflicts of Interest

The authors declare that they have no conflicts of interest.

Acknowledgments

This research was funded by the National Natural Science Foundation of China (NSFC), grant number 51778351, and SDUST Research Fund, grant number 2018TDJH101.

References

[1] Z. J. Wen, J. Huang, Y. J. Jiang, Y. J. Zuo, Z. W. Zhu, and P. Xiao, "Development and experiment of a coupled static-dynamic cyclic loading test system," *Journal of Central South University (Science and Technology)*, vol. 52, no. 8, pp. 2817–2827, 2021.

[2] L. Li, C. Shang, K. Chu et al., "Large-scale geo-mechanical model tests for stability assessment of super-large cross-section tunnel," *Tunnelling and Underground Space Technology*, vol. 109, p. 103756, 2021.

[3] N. Lin, H. Zhang, J. Zou, P. Han, Y. Ma, and B. Tang, "Improvements in wear and corrosion resistance of RB400 anchor rod steel by electroless Ni-P plating," *Journal of Engineering*, vol. 10, 372 pages, 2015.

[4] Q. S. Zhu, Y. X. Huang, Y. L. Li et al., "Aluminum dihydric tripolyphosphate/polypyrrole-functionalized graphene oxide waterborne epoxy composite coatings for impermeability and corrosion protection performance of metals," *Advanced Composites and Hybrid Materials*, vol. 4, no. 3, pp. 780–792, 2021.

[5] X. Y. Li, Z. B. Fan, T. Lu, T. Xiao, and L. M. Zhang, "A resilience model for engineered slopes subject to anchor corrosion," *Journal of Civil Engineering*, vol. 22, no. 3, pp. 887–895, 2018.

[6] A. S. Cho and T. H. K. Kang, "Load-carrying performance and hydrostatic tests of encapsulated anchor systems for unbonded post-tensioning single-strands," *International Journal of Concrete Structures and Materials*, vol. 12, no. 1, pp. 1–10, 2018.

[7] H. J. Liao, S. H. Cheng, C. C. Chen, and H. R. Chen, "Cement grouting to seal off voids below anchor head," in *5th International Conference on Grouting Deep Mixing and Diaphragm Walls*, vol. 287, pp. 303–313, Honolulu, HI, 2017.

[8] W. L. Zou, X. Q. Wang, and S. K. Vanapalli, "Experimental evaluation of engineering properties of GFRP screw anchors

for anchoring applications," *Journal of Materials in Civil Engineering*, vol. 28, no. 7, p. 04016029, 2016.

[9] B. Benmokrane, H. Xu, and I. Nishizaki, "Aramid and carbon fibre-reinforced plastic prestressed ground anchors and their field applications," *Canadian Journal of Civil Engineering*, vol. 24, no. 6, pp. 968–985, 1997.

[10] B. Benmokrane, B. Zhang, and A. Chennouf, "Tensile properties and pullout behaviour of AFRP and CFRP rods for grouted anchor applications," *Construction and Building Materials*, vol. 14, no. 3, pp. 157–170, 2000.

[11] O. Zabihi, M. Ahmadi, C. Liu et al., "A sustainable approach to the low-cost recycling of waste glass fibres composites towards circular economy," *Sustainability*, vol. 12, no. 2, p. 641, 2020.

[12] H. L. Kou, W. Guo, and M. Y. Zhang, "Pullout performance of GFRP anti-floating anchor in weathered soil," *Tunnelling and Underground Space Technology incorporating Trenchless Technology Research*, vol. 49, pp. 408–416, 2015.

[13] Q. B. Wang, H. X. Song, Y. Li et al., "Experimental study on the performance of graded glass fiber reinforced concrete (G-GRC) based on engineering application," *Materials*, vol. 14, no. 5, p. 1149, 2021.

[14] F. Ceroni, R. Cuzzilla, and M. Pecce, "Assessment of performance of steel and GFRP bars as injected anchors in masonry walls," *Construction and Building Materials*, vol. 123, pp. 78–98, 2016.

[15] H. S. Ji, "An experimental study on the pull-out behaviors of headed GFRP rebar in mortar," *Journal of Korea Academia-Industrial cooperation Society*, vol. 13, no. 6, pp. 2797–2803, 2012.

[16] Z. Shi, Q. Wang, and L. Xu, "Experimental study of cement alkali-resistant glass fiber (C-ARGF) grouting Material," *Material*, vol. 13, no. 3, p. 605, 2020.

[17] Y. Q. Wang, B. C. Wu, Y. Guo, and H. Yang, "Numerical research on the pullout failure of GFRP bolt," *Advances in Materials Science and Engineering*, vol. 2017, Article ID 3025804, 11 pages, 2017.

[18] J. S. Sim, T. S. Kang, Y. T. Lee, and H. J. Kim, "Analysis for mechanical behavior of GFRP rock bolt for permanent support of tunnel," *Journal of the Korea institute for structural maintenance and inspection*, vol. 14, no. 6, pp. 124–131, 2010.

[19] X. Y. Bai, M. Y. Zhang, H. Liu, and H. L. Kou, "Field test on bearing characteristics of fully threaded glass fiber reinforced polymer anti-floating anchor rods in weathered rock foundation," *Rock and Soil Mechanics*, vol. 35, no. 9, pp. 2464–2472, 2014.

[20] Z. H. Huang, G. W. Li, S. J. Wang, and W. C. Li, "Study on the failure mechanism of glass fiber reinforced plastic bolt structure under different surrounding rock conditions," *Chinese Journal of Rock Mechanics and Engineering*, vol. 5, pp. 1008–1018, 2008.

[21] G. W. Li, Z. H. Huang, and S. J. Wang, "Field test of load-bearing characteristics of glass fiber reinforced polymer bolts," *Chinese Journal of Rock Mechanics and Engineering*, vol. 11, pp. 2240–2246, 2006.

[22] Y. Chen and C. C. Li, "Performance of fully encapsulated rebar bolts and D-bolts under combined pull- and-shear loading," *Tunnelling and Underground Space Technology*, vol. 45, pp. 99–106, 2015.

[23] R. Giot, C. Auvray, S. Raude, and A. Giraud, "Experimental and numerical analysis of in situ pull-out tests on rock bolts in claystones," *European Journal of Environmental and Civil Engineering*, vol. 25, no. 12, pp. 2277–2300, 2021.

[24] M. Salcher and R. Bertuzzi, "Results of pull tests of rock bolts and cable bolts in Sydney sandstone and shale," *Tunnelling and Underground Space Technology*, vol. 74, pp. 60–70, 2018.

[25] I. Thenevin, L. Blanco-Martín, F. Hadj-Hassen, J. Schleifer, Z. Lubosik, and A. Wrana, "Laboratory pull-out tests on fully grouted rock bolts and cable bolts: results and lessons learned," *Journal of Rock Mechanics and Geotechnical Engineering*, vol. 9, no. 5, pp. 843–855, 2017.

[26] B. Benmokrane, M. Robert, H. M. Mohamed, A. H. Ali, and P. Cousin, "Durability assessment of glass FRP solid and hollow bars (rock bolts) for application in ground control of Jurong Rock Caverns in Singapore," *Journal of Composites for Construction*, vol. 21, no. 3, p. 06016002, 2017.

[27] J. P. Zhang, L. M. Liu, Q. H. Li et al., "Development of cement-based self-stress composite grouting material for reinforcing rock mass and engineering application," *Construction and Building Materials*, vol. 201, pp. 314–327, 2019.

Hindawi
Geofluids
Volume 2022, Article ID 3953650, 8 pages
https://doi.org/10.1155/2022/3953650

Research Article

Effect of Strong Mining on the Fracture Evolution Law of Trick Rise in the Mining Field and Its Control Technology

Zhaolin Li[1,2] **Lianguo Wang**[3] **and Ke Ding**[3]

[1]*School of Mines, China University of Mining and Technology, Xuzhou, Jiangsu 221116, China*
[2]*State Key Laboratory of Coal Resources and Safe Mining, China University of Mining and Technology, Xuzhou, Jiangsu 221116, China*
[3]*State Key Laboratory for Geomechanics and Deep Underground Engineering, China University of Mining and Technology, Xuzhou, Jiangsu 221116, China*

Correspondence should be addressed to Lianguo Wang; cumt_lgwang@163.com

Received 6 September 2021; Accepted 25 February 2022; Published 25 March 2022

Academic Editor: Hualei Zhang

This study investigates the law of stress field and fracture field of the surrounding rock at the trick rise of the mining area affected by strong mining. It is found that as the working face continues to approach, large-scale cracks occur in the surrounding rock on the track rise. In particular, when the working face crosses the track rise, the equivalent stress τ_{oct} concentration area expands, gradually intersecting with the surrounding rock concentration area of the roadway. It indicates that the working face advancement caused a dramatic change in the stress field of the roadway envelope, which will have an immediate adverse effect on the track rise. With comprehensive support costs, economic efficiency, and other factors, the working face will no longer cross the track rise, and the stopping line is roughly controlled at -20 m so that the track rise can serve other working faces for a long time. The reinforcement support scheme of "anchor mesh spray + grouting anchor" is proposed for the key areas such as arch shoulder. Through the analysis of the field monitoring of the roadway surface displacement, the deformation of the roadway surrounding rock showed a change trend of increasing first and then stabilizing with time, which indicates that the support effect was good and greatly improved the stability and safety of the roadway.

1. Introduction

There are many coal-forming periods in China [1], and the occurrence conditions are very complex [2]; among which most of them are mined by shaft, and the roadway is the lifeline of coal mine production [3]. Most of the excavation and preparation roadways in coal mines are arranged in the floor of coal seam [4]. Floor roadway is a kind of very common high stress roadway affected by coal seam strong mining [5]. When such roadways are affected by strong mining, the stress of roadway surrounding rock increases significantly [6], often exceeding or even several times the compressive strength of rocks [7]. This causes serious deformation of the surrounding rock during the service period of the roadway [8], so the roadway needs to be continuously maintained and repaired. The above strong mining and other effects caused by the roadway large deformation, difficult to support [9], not only support costs increased significantly and will cause difficulties in coal mining succession, seriously affecting the normal production of the mine [10]. Therefore, how to solve the support of this kind of roadway is one of the most complex engineering technical problems in the world of underground engineering [11] and also one of the key problems in underground resource exploitation [12].

Coal mining disrupts the original stress balance of the floor roadway [13], causing stress redistribution in the rock strata around the recovery space and transferring to the deep section of the floor [14], resulting in different degrees of damage to the floor [15]. Cheng et al. [16], Lu and Wang [17], and Xu et al. [18] grasp the law of the mining floor by studying the stress distribution and damage characteristics of the mining floor, which is of great significance for

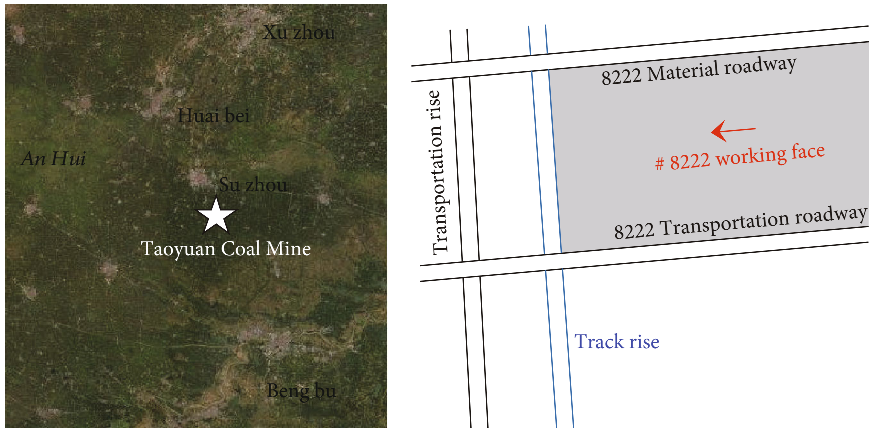

Figure 1: Location of the Taoyuan coal mine and the plane graph of mining face arrangement.

the layout and maintenance of the mining floor roadway [19].

In order to reduce the deformation of surrounding rock and ensure the normal use of roadway, a clear analysis of the failure mechanism of roadway surrounding rock is the premise of reasonable and effective support [20]. Many scholars have shown factors such as the lithology of the surrounding rock mass of the roadway, the vertical distance between the roadway and the working face [21], the horizontal distance between the roadway and the end of the working face [22], and the support method of the roadway [23]. Affected by mining, the mine pressure of the roadway appears drastically [24], resulting in the expansion of the range of the plastic zone of the surrounding rock, and the deformation of the surrounding rock is greatly increased [25]. As a result [26], the roadways exhibited large deformations and were difficult to maintain [27, 28]. More seriously, the original support system was seriously damaged, the surrounding rock extrusion was large, and the roadway rib spalling and floor heave were obvious. [29]. Therefore, it is of great theoretical and engineering significance to systematically analyze the rupture and evolution mechanism of the surrounding rock of the working face across the mining floor roadway under the influence of mining and to adopt effective local strengthening support technology [30].

In view of this, taking the track rise in the II2 mining area of Taoyuan coal mine as the engineering background [31], this study investigates the law of stress field and fracture field of the surrounding rock at the floor of the mining area affected by strong mining and proposes the reinforcement technology applicable to the reinforcement of the track rise in the mining area affected by strong mining pressure. This study has important theoretical significance and practical value for the effective control of the strong mining affecting the deformation and damage of the surrounding rock in the track rise of the mining area.

2. Engineering Background

Taoyuan coal mine is located in the southern suburb of Suzhou City, Anhui Province, China. The mine is located at the southeast edge of the Huaibei coalfield, which belongs to the Carboniferous Permian coalfield [32]. The 10# coal is the main mining seam, the thickness of the coal seam is 0~6.67 m, and the average thickness is 2.60 m. II2 mining area arranges four rise lanes, all of which are arranged in the floor of 8# coal and the roof of 10# coal. The four rise lanes, especially the track rise, have been affected by the mining of the lower 10# coal and the upper II8221 working face, resulting in serious deformation of the lanes. Worse still, the mining of the II8222 working face will cause a certain degree of mining impact on the four ascents (Figure 1).

II8222 working face is located in the first stage of the left flank in II2 mining area, the design elevation of the working face is -504.9 m~-604.2 m, and the average coal thickness of the coal seam is 2.0 m. Obviously, the mining of II8222 working face will have a serious impact on the safety of the track rise, so it is necessary to master the law of mine pressure appearing under the influence of mining, as well as the resulting deformation and damage mechanism of the surrounding rock, and put forward effective support countermeasures.

3. Numerical Model

In order to study the variation law of the stress field on the track rise induced by the advancing disturbance of the working face and the impact of the produced the fracture damage, the numerical modelling software ABAQUS (based on finite element method) is used to establish the numerical calculation model of the track rise in this study (Figure 2). The numerical calculation model uses a 64 m × 63 m × 15 m rectangular body, which is divided into 295,568 units. The roadway section is arched, with a width of 3.6 m, a straight wall height of 1.5 m, and a circular arch radius of 1.8 m. The model is simplified to three rock layers: roof strata, coal strata, and floor strata. The boundary conditions of the model are set as follows (in situ stress measurements): the bottom surface is constrained by vertical displacement, the height of the overlying rock layer of the model is 550 m, so it is loaded on the upper boundary of the model in the form of uniform load (14 MPa). The maximum horizontal stress is 17 MPa, along the direction of the roadway;

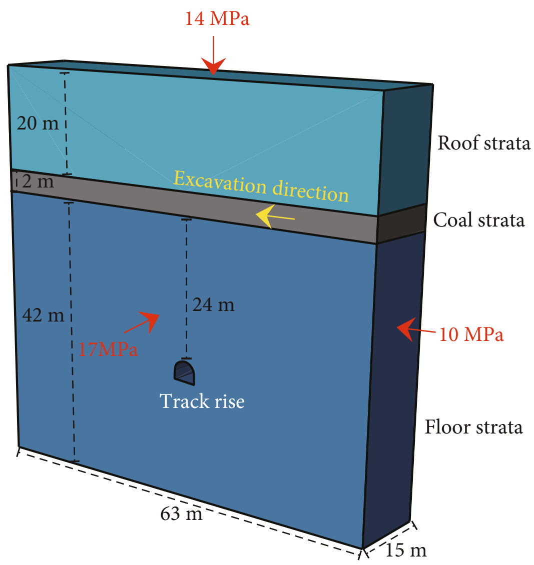

Figure 2: Numerical calculation model.

the minimum horizontal stress is 10 MPa, perpendicular to the direction of the roadway.

Based on the fact that natural rocks contain a large number of microdefects such as randomly distributed microfractures [33], a numerical model of rock damage rupture evolution with random distribution is developed using the secondary development subroutine USDFLD [34]. The total percentage of damaged units is n_0, and their basic mechanical parameters are about 1/2 of the intact units [35]. The Mogi-Coulomb strength criterion [36] is used to determine whether the unit is damaged or not, and the stiffness of the rock damage unit is degraded to 1/10~1/100 of the original initial stiffness [37]. The physical and mechanical parameters of each rock formation are shown in Table 1.

Figure 3 shows the rupture evolution law of the surrounding rock on the track rise during the working face advancement. When the working face advances to the horizontal distance of -20 m from the track rise (all the following are horizontal distance), the track rise has been affected by the previous excavation itself to appear fracture circle, and its rupture characteristics are consistent with the research results of other scholars [38]. As the working face continues to advance, the surrounding rocks of the track rise are gradually affected by the disturbance of the working face, and the rupture zone gradually appears to intersect. For example, when the working face is -12 m from the track rise, the local fissures in the surrounding rock appear to be conductive (similar to a fissure zone) because the surrounding rock adopts random damage distribution characteristics. The law is very obvious when the working face is -5 m from the track rise. The fracture zone is mainly generated by the fracture zone conduction near the two arched shoulders of the track rise and the floor of the working face. When the working face is 3 m away from the track rise, i.e., the working face crosses the track rise, the fracture area near its surrounding rock expands. It indicates that the track rise is strongly affected by the working face advancement and needs to be considered in the aspects of working face advancement and track rise support design.

Figure 4 shows the distribution characteristics of the support pressure coefficient of the track rise and the floor during the working face advancement. The maximum oversupport pressure coefficient of the floor is mostly 2.2, while 2.9 appears locally. The oversupport pressure of the surrounding rock in the two gangs of the track rise is higher, and the support pressure of the surrounding rock near the roof and floor is smaller (about 0.9). This provides the basis for further analysis of the influence of dynamic load on the track rise below.

4. Fracture Evolution Law of Track Rise under the Influence of Dynamic Loading

In the above text, the mining field advancement as a continuous process is simplified to 5 m working face advancement in each analysis time step, which is artificially divided by the actual engineering continuous excavation (infinitely small advancement distance in each analysis step) advancement process, which differs from the actual engineering. In order to further accurately analyze the evolution law of the fracture of the surrounding rock on the track under the influence of continuous mining, it is simplified to a mechanical model of the superposition of uniform load and triangular load (Figure 5) by combining the characteristics of the change law of oversupport pressure during the advance of the working face in the above paper. With the continuous advance [39] of the working face, the dynamic load changes accordingly.

As shown in Figure 5, according to the load distribution characteristics, the essence of the dynamic load change in the mechanical model is that the uniform load q remains unchanged, and the triangular load moves with the working face. The range of support pressure is ab (= $ac + cb$); o is the peak point of support pressure (kq, k is the maximum support pressure coefficient). Based on the above results, the maximum support pressure coefficient is $k = 2.9$. The basic dimensions and parameters of the model are shown in Table 2, and the physical and mechanical parameters of the floor rock are consistent with Table 1.

Figure 6 shows the characteristics of support pressure distribution and the law of large vertical deformation near the whole track rise surrounding rock affected by the advance of working face. The large vertical deformation contour is roughly circular in shape, and the specific shape characteristics are influenced by the support pressure coefficient and the action range [40].

Figure 7 shows the evolution of the rupture pattern of the track rise during the advance of the working face. When the working face is -30 m away from the track rise, the fracture circle of the track rise has been affected by the previous excavation itself, which is consistent with the above results; the working face advancement has not affected the surrounding rock of the roadway. When the working face is -20 m away from the track rise, the fracture circle of the surrounding rock on the track rise gradually expands. The rupture area of the surrounding rock of its right arch shoulder

Table 1: Numerical model parameters.

Parameters	Roof strata	Coal strata	Floor strata
Young's modulus, E	20 GPa	10 GPa	18 GPa
Poisson's ratio, μ	0.3	0.33	0.3
Internal cohesion, c	4.7 MPa	3.5 MPa	4.6 MPa
Internal frictional angle, φ	37°	28°	35°
The proportion of damaged elements, n_0	20%	25%	20%

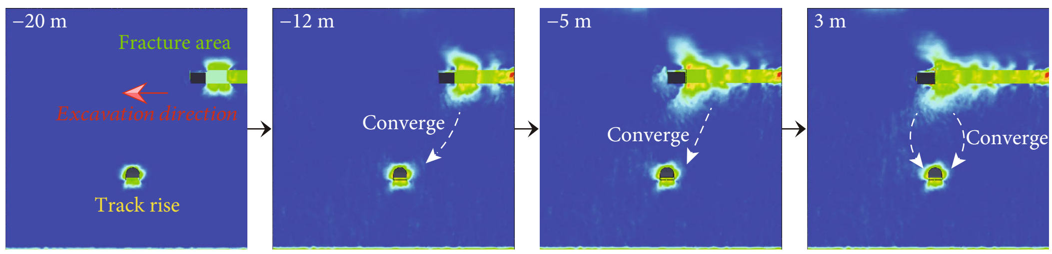

Figure 3: Variation pattern of fracture zone with the advance of working face.

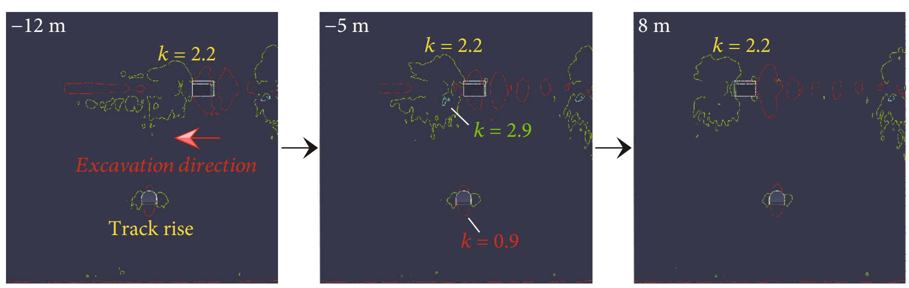

Figure 4: Contour of support pressure.

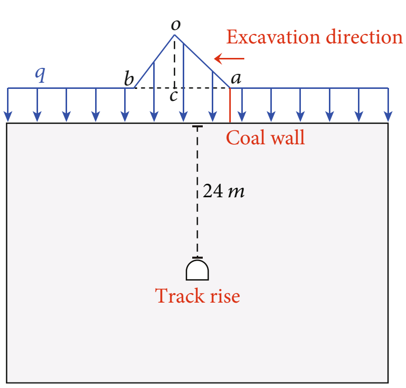

Figure 5: Numerical calculation model.

Table 2: Basic parameters of the numerical model.

Parameters	Values
Length of ac, L_{ac}	2.9 m
Length of cb, L_{cb}	3.2 m
Uniform load, q	14 MPa
Maximum support pressure coefficient, k	2.9

gradually has the tendency to expand to the rupture area of the floor, which indicates that the track rise starts to be obviously affected by the advance of the working face. When the working face is -8 m away from the track rise, the surrounding rock appears a large area of fracture and intersects with the fracture area of the floor. When the working face crossed the track hill 7 m, the whole floor and the surrounding rock of the track rise appeared a wide scale fracture area. It means that the track rise is greatly affected by the working face advance.

Since the computational model uses the Mogi-Coulomb intensity criterion, its calculation equation [41] is

$$\tau_{\text{oct}} = a + b\sigma_{m,2}, \tag{1}$$

$$\tau_{\text{oct}} = \frac{1}{3}\sqrt{(\sigma_1-\sigma_2)^2 + (\sigma_2-\sigma_3)^2 + (\sigma_1-\sigma_3)^2}, \tag{2}$$

$$\sigma_{m,2} = \frac{\sigma_1+\sigma_3}{2}. \tag{3}$$

Among them, the magnitude of the equivalent stress τ_{oct} has important directional significance for judging the rupture trend of the unit. Therefore, the equivalent stresses τ_{oct} are used in this study to quantify the fracture trend

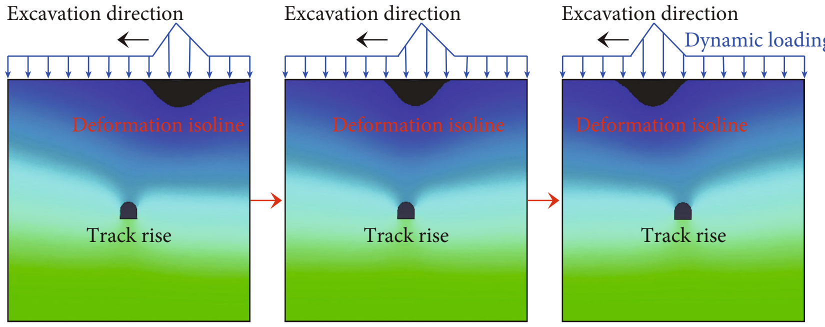

Figure 6: Regional characteristics of large vertical deformation.

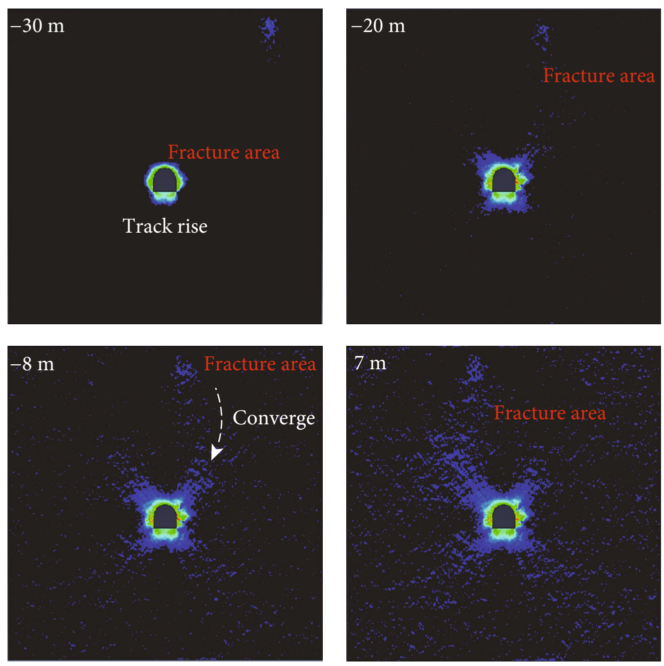

Figure 7: Variation pattern of fracture zone with the advance of working face.

triggered by the workface advancement process, as shown in Figure 8. When the working face is -30 m away from the track rise, the equivalent stress distribution is mainly concentrated near the working face and in the shallow surrounding rock area of the roadway, indicating that the working face has no impact on the roadway. As the working face continues to advance, the range of equivalent force concentration area expands and gradually intersects with the concentration area of the roadway surrounding rock. It indicates that the working face has a substantial impact on the roadway surrounding rock, resulting in a dramatic change in the stress field near its surrounding rock. In particular, in the process of -8 m~7 m from the working face to the track rise, a "waterfall-type" concentration area is formed near the arch shoulder of the track rise. This indicates that the track rise is affected by the disturbance of the working face, which also confirms the crack evolution law of the surrounding rock of the roadway in Figure 7. Therefore, with comprehensive support costs and economic benefits, the working face will no longer cross the track rise, and the stopping line is roughly controlled at -20 m so that the track rise can serve other stopes for a long time.

5. Surrounding Rock Control Technology

According to the rupture evolution characteristics of the track rise, it can be seen that the influence of the mining of II8222 working face is that the surrounding rock on the track rise is gradually destabilized and fractured. Unless effective support control is obtained, the roadway will be significantly deformed, resulting in destabilization of the track rise. Combined with the analysis of the previous study, the deformation and damage in the track rise are relatively heavy, and the key areas such as the arch shoulder are reinforced. The design adopts "anchor net and cable spray + - grouting anchor" reinforcement support scheme. The specific scheme is as follows (Figure 9).

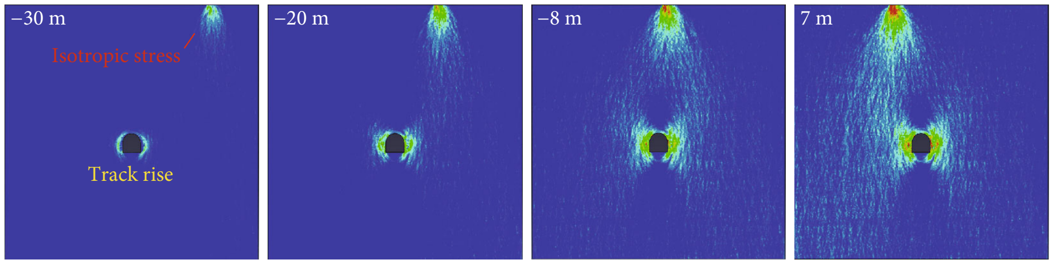

Figure 8: The variation pattern of the equivalent stress with the advance of the working face.

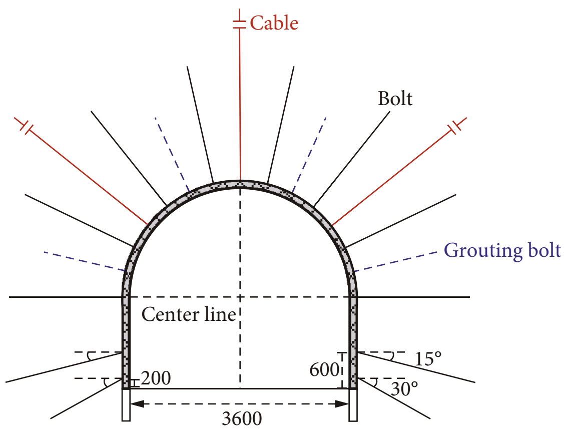

Figure 9: Supporting design of track rise.

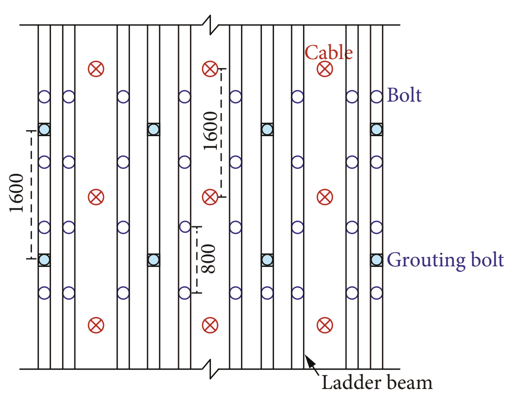

Figure 10: Arrangement of bolts and cables in the track rise.

The rebar bolts are GM22/3000-490 left-handed rebarless rebar anchor with equivalent strength. The interrow distance is 800 × 800 mm, 10 rows in a row, connected by ladder beam along the direction of the roadway. Hollow rebar grouting anchor rods with specifications $\Phi 25 \times 2500$ mm, interrow distance 1600 × 1600 mm, 6 pieces in a row, connected by ladder beam along the direction of the roadway (Figure 10).

The surface displacement observation section was set up in the anchor injection reinforcement section on the track rise. Four monitoring points were set up at the roof-to-floor plates and side-to-side of the section for observing the change of surface displacement of the track rise during the mining of the working face. The variation curves of the deformation of the track rise were obtained as shown in Figure 11.

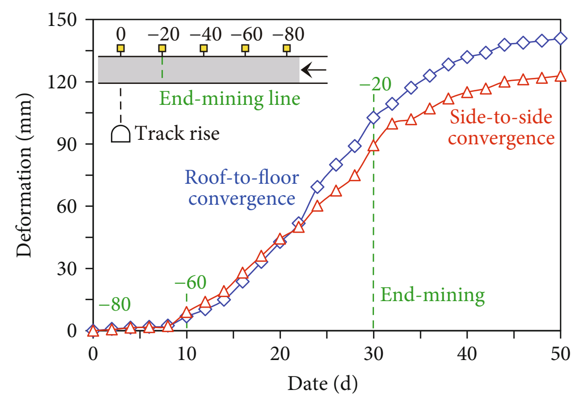

Figure 11: The variation in the convergence of roadway surface.

On the first day, the horizontal distance of II8222 working face from the track rise is 80 m, the track rise is less affected by the mining of the working face, and the amplitude and rate of roadway deformation are low. On the 10th day of the observation time (-60 m horizontal distance between II8222 working face and track rise), the impact of mining on the track rise became apparent, and the amplitude and rate of deformation of the roadway gradually increased. As the working face continued to advance, the track rise was gradually affected by the mining, and the deformation rate of the surrounding rock was accelerated. On the 30th day of the observation time (-20 m horizontal distance between II8222 working face and track rise), the working face stopped mining. The deformation of the roadway still increased, while the rate of deformation slowed down. It means that the influence of the track rise by the mining of II8222 working face gradually decreases. On the 50th day of the observation time, II8222 working face has stopped mining for 20 days, and the deformation of the roadway has stabilized. The amount of roof-to-floor convergence is stabilized at about 135 mm, and the side-to-side convergence is 120 mm. Through the analysis of the observation results, it can be seen that after strengthening the support of the roadway, the deformation of the surrounding rock is low, and the surrounding rock is effectively controlled, indicating that the support effect is good.

6. Conclusions

(1) Based on the random damage and Mogi-Coulomb strength theory, the variation rules of the stress field on the track rise induced by the workface advancement disturbance

and the resulting rupture damage impact were studied. It was found that the surrounding rocks near the track rise were gradually affected by the disturbance of the workface as the stope kept approaching in the process. In particular, when the working face crosses the track rise, the range of the surrounding rock fracture zone will be greatly increased, indicating that the track rise is strongly affected by the advancement of the working face. So the key considerations need to be given to the advancement of the working face and the design of the track rise support

(2) The fracture evolution law of the surrounding rock on the track under the continuous influence of the oversupport pressure (dynamic loading) during the advance of the working face was analyzed. As the working face continued to approach, large-scale cracks appeared in the surrounding rock on the track rise. The equivalent stress τ_{oct} concentration area expanded, gradually intersecting with the surrounding rock concentration area of the roadway. It indicates that the working face advancement caused a dramatic change in the stress field of the roadway envelope, which will have an immediate adverse effect on the track rise. Considering factors such as support costs and economic benefits, the working face will no longer cross the track rise, and the mining stop line will be roughly controlled at about -20 m so that the track rise will serve other stopes for a long time

(3) According to the influence of mining on the II8222 working face on the track rise, the surrounding rock rupture and evolution of the roadway is triggered. Therefore, the reinforcement support scheme of "anchor mesh spray + -grouting anchor" is proposed for the key areas such as arch shoulder. Based on on-site monitoring and analysis of the roadway surface displacement, the deformation of the surrounding rock of the roadway shows a trend of first increasing and then becoming stable over time. The deformation rate and deformation volume of the roadway enclosure are effectively controlled, which indicates that the support effect was good and greatly improved the stability and safety of the roadway

Data Availability

The data used to support the findings of this study are available from the corresponding author upon request.

Conflicts of Interest

The authors declare that there are no conflicts of interest regarding the publication of this paper.

Acknowledgments

We gratefully acknowledge the support provided by the Fundamental Research Funds for the Central Universities (Grant No. 2020QN42).

References

[1] Q. Feng, J. Jin, S. Zhang, W. Liu, X. Yang, and W. Li, "Study on a damage model and uniaxial compression simulation method of frozen–thawed rock," *Rock Mechanics and Rock Engineering*, vol. 55, no. 1, pp. 187–211, 2022.

[2] Y. L. Tan, W. Y. Guo, T. B. Zhao, F. H. Yu, B. Huang, and D. M. Huang, "Influence of fissure number on the mechanical properties of layer-crack rock models under uniaxial compression," *Advances in Civil Engineering*, vol. 2018, no. 4, 12 pages, 2018.

[3] W. Zhu, X. Qi, J. Ju, and J. Xu, "Mechanisms behind strong strata behaviour in high longwall mining face-ends under shallow covers," *Journal of Geophysics and Engineering*, vol. 16, no. 3, pp. 559–570, 2019.

[4] H. Wang, Y. Cheng, and L. Yuan, "Gas outburst disasters and the mining technology of key protective seam in coal seam group in the Huainan coalfield," *Natural Hazards*, vol. 67, no. 2, pp. 763–782, 2013.

[5] H. Liu, C. Xu, H. Wang, G. Li, and S. Fan, "Investigation on surrounding rock stability control technology of high stress roadway in steeply dipping coal seam," *Advances in Civil Engineering*, vol. 2021, no. 3, 11 pages, 2021.

[6] G. Wu, W. Chen, S. Jia et al., "Deformation characteristics of a roadway in steeply inclined formations and its improved support," *International Journal of Rock Mechanics and Mining Sciences*, vol. 130, article 104324, 2020.

[7] S. Wang, Z. Xiang, J. Deng, H. Yang, X. Yang, and S. Jin, "Analysis of cooperative control effect of pressure relief and long bolt support for deep roadway under strong mining disturbance of adjacent working face," *Geotechnical and Geological Engineering*, vol. 39, no. 3, pp. 2259–2268, 2021.

[8] F. Qi, D. Yang, Y. Zhang, and Y. Hao, "Analysis of failure mechanism of roadway surrounding rock under thick coal seam strong mining disturbance," *Shock and Vibration*, vol. 2021, 14 pages, 2021.

[9] S. Zhang, D. Zhang, H. Wang, and S. Liang, "Discrete element simulation of the control technology of large section roadway along a fault to drivage under strong mining," *Journal of Geophysics and Engineering*, vol. 15, no. 6, pp. 2642–2657, 2018.

[10] H. Yang, N. Zhang, C. Han et al., "Stability control of deep coal roadway under the pressure relief effect of adjacent roadway with large deformation: a case study," *Sustainability*, vol. 13, no. 8, pp. 4412–4414, 2021.

[11] G. A. Zhu, L. M. Dou, Z. L. Li, W. Cai, Y. Kong, and J. Li, "Mining-induced stress changes and rock burst control in a variable-thickness coal seam," *Arabian Journal of Geosciences*, vol. 9, no. 5, pp. 1–12, 2016.

[12] X. Xu, F. He, X. Li, and W. He, "Research on mechanism and control of asymmetric deformation of gob side coal roadway with fully mechanized caving mining," *Engineering Failure Analysis*, vol. 120, article 105097, 2021.

[13] M. Cai, "Influence of intermediate principal stress on rock fracturing and strength near excavation boundaries–insight from numerical modeling," *International Journal of Rock Mechanics and Mining Sciences*, vol. 45, no. 5, pp. 763–772, 2008.

[14] P. K. Kaiser, S. Yazici, and S. Maloney, "Mining-induced stress change and consequences of stress path on excavation stability – a case study," *International Journal of Rock Mechanics and Mining Sciences*, vol. 38, no. 2, pp. 167–180, 2001.

[15] Q. Zhao, B. Fu, and J. Yin, "Deformation mechanism and control technology of the surrounding rock of the floor roadway under the influence of mining," *Advances in Civil Engineering*, vol. 2020, 15 pages, 2020.

[16] Z. Cheng, Z. Ouyang, Q. Zou, Y. Lu, X. Zhao, and M. Li, "Characteristics of fracture field in different stress zones during multi-seam mining: quantification based on theoretical analysis and BBM-DEM accurate simulation method," *Energy Science & Engineering*, vol. 8, no. 5, pp. 1620–1633, 2020.

[17] Y. Lu and L. Wang, "Numerical simulation of mining-induced fracture evolution and water flow in coal seam floor above a confined aquifer," *Computers and Geotechnics*, vol. 67, pp. 157–171, 2015.

[18] Y. Xu, E. Zhang, Y. Luo, L. Zhao, and K. Yi, "Mechanism of water inrush and controlling techniques for fault-traversing roadways with floor heave above highly confined aquifers," *Mine Water and the Environment*, vol. 39, no. 2, pp. 320–330, 2020.

[19] Y. Peng and Q. Li, "Floor failure and roadway deformation induced by contiguous coal seams mining at Huopu Mine," *Arabian Journal of Geosciences*, vol. 13, no. 14, pp. 1–12, 2020.

[20] X. T. Feng, X. J. Hao, Q. Jiang, S. J. Li, and J. A. Hudson, "Rock cracking indices for improved tunnel support design: a case study for columnar jointed rock masses," *Rock Mechanics and Rock Engineering*, vol. 49, no. 6, pp. 2115–2130, 2016.

[21] G. A. Rui, B. Bya, and B. Xm, "Stress distribution and surrounding rock control of mining near to the overlying coal pillar in the working face," *International Journal of Mining Science and Technology*, vol. 29, no. 6, pp. 881–887, 2019.

[22] Y. Zhang, J. Yang, J. Zhang, X. Sun, and H. Xu, "Modeling the spatial and temporal evolution of stress during multiworking face mining in close distance coal seams," *Advances in Civil Engineering*, vol. 2021, no. 10, Article ID 5624972, 11 pages, 2021.

[23] Y. Du, G. Feng, Y. Zhang, X. Zhang, Y. Zhai, and J. Bai, "Pressure reduction mechanism and effect of working face passing through abandoned roadway by roof presplit," *Energy Science & Engineering*, vol. 8, no. 10, pp. 3502–3513, 2020.

[24] E. Eberhardt, "Numerical modelling of three-dimension stress rotation ahead of an advancing tunnel face," *International Journal of Rock Mechanics & Mining Sciences*, vol. 38, no. 4, pp. 499–518, 2001.

[25] Q. Jiang, Y. Shi, F. Yan, H. Zheng, Y. Kou, and B. He, "Reconstitution method for tunnel spatiotemporal deformation based on 3D laser scanning technology and corresponding instability warning," *Engineering Failure Analysis*, vol. 125, article 105391, 2021.

[26] B. Rahimi, M. Sharifzadeh, and X. Feng, "A comprehensive underground excavation design (CUED) methodology for geotechnical engineering design of deep underground mining and tunneling," *International Journal of Rock Mechanics and Mining Sciences*, vol. 143, article 104684, 2021.

[27] Z. Hu, J. Shen, Y. Wang, T. Guo, Z. Liu, and X. Gao, "Cracking characteristics and mechanism of entrance section in asymmetrically- load tunnel with bedded rock mass: a case study of a highway tunnel in southwest China," *Engineering Failure Analysis*, vol. 122, article 105221, 2021.

[28] W. Li, B. Jiang, S. Gu, X. Yang, and F. U. A. Shaikh, "Experimental study on the shear behaviour of grout-infilled specimens and micromechanical properties of grout-rock interface," *Journal of Central South University*, pp. 1–14, 2022.

[29] Z. Li, L. Wang, Y. Lu, W. Li, and K. Wang, "Effect of principal stress rotation on the stability of a roadway constructed in half-coal-rock stratum and its control technology," *Arabian Journal of Geosciences*, vol. 14, no. 4, p. 292, 2021.

[30] Y. F. Wang, Z. Q. Liu, and B. S. Jiang, "The stability control technology of crosscut while mining without coal pillar in steep seam," *Applied Mechanics & Materials*, vol. 90, pp. 2073–2079, 2011.

[31] Y. Guo, J. Wei, H. Gui, Z. Zhang, and M. Hu, "Evaluation of changes in groundwater quality caused by a water inrush event in Taoyuan coal mine, China," *Environmental Earth Sciences*, vol. 79, no. 24, pp. 1–15, 2020.

[32] Z. Lin, B. Zhang, and J. Guo, "Analysis of awater-inrush disaster caused by coal seam subsidence karst collapse column under the action of multi-field coupling in Taoyuan coal mine," *Computer Modeling in Engineering and Sciences*, vol. 126, no. 1, pp. 311–330, 2021.

[33] X. Li, Q. L. Liao, and J. M. He, "In-situ tests and a stochastic structural model of rock and soil aggregate in the three gorges reservoir area, China," *International Journal of Rock Mechanics & Mining Sciences*, vol. 41, no. 3, pp. 702–707, 2004.

[34] R. Pakzad, S. Y. Wang, and S. W. Sloan, "Numerical simulation of hydraulic fracturing in low-/high-permeability, quasi-brittle and heterogeneous rocks," *Rock Mechanics and Rock Engineering*, vol. 51, no. 4, pp. 1153–1171, 2018.

[35] T. Li, L. Li, C. Tang et al., "A coupled hydraulic-mechanical-damage geotechnical model for simulation of fracture propagation in geological media during hydraulic fracturing," *Journal of Petroleum Science and Engineering*, vol. 173, pp. 1390–1416, 2019.

[36] Z. Li, L. Wang, Y. Lu, W. Li, K. Wang, and H. Fan, "Experimental investigation on true triaxial deformation and progressive damage behaviour of sandstone," *Scientific Reports*, vol. 9, no. 1, pp. 442–455, 2019.

[37] L. N. Y. Wong, V. Maruvanchery, and G. Liu, "Water effects on rock strength and stiffness degradation," *Acta Geotechnica*, vol. 11, no. 4, pp. 713–737, 2016.

[38] J. Zuo, H. Liu, D. Liu, J. Wang, T. Zhang, and F. Xu, "Study on large deformation mechanism and concrete-filled steel tubular support technology for ventilation shaft roadway," *Bulletin of Engineering Geology and the Environment*, vol. 80, no. 8, pp. 6245–6262, 2021.

[39] U. Pillai, Y. Heider, and B. Markert, "A diffusive dynamic brittle fracture model for heterogeneous solids and porous materials with implementation using a user-element subroutine," *Computational Materials Science*, vol. 153, pp. 36–47, 2018.

[40] B. Fu and B. Wang, "An influence study of face length effect on floor stability under water-rock coupling action," *Geofluids*, vol. 2021, 13 pages, 2021.

[41] Z. Song, G. Yin, P. G. Ranjith, M. Li, J. Huang, and C. Liu, "Influence of the intermediate principal stress on sandstone failure," *Rock Mechanics and Rock Engineering*, vol. 52, no. 9, pp. 3033–3046, 2019.

Hindawi
Geofluids
Volume 2022, Article ID 5820228, 16 pages
https://doi.org/10.1155/2022/5820228

Research Article

Research on Pressure Relief Method of Close Floor Roadway in Coal Seam Based on Deformation and Failure Characteristics of Surrounding Rock in Deep Roadway

Jianjun Cao[1,2] **Benqing Yuan**[1,2,3] **Siqian Li,**[1,2] **Zunyu Xu,**[1,2] **Qihan Ren,**[1,2] **and Zhonghua Wang**[1,2,4]

[1]*CCTEG Chongqing Research Institute, Chongqing 400037, China*
[2]*State Key Laboratory of the Gas Disaster Detecting, Preventing and Emergency Controlling, Chongqing 400037, China*
[3]*Anhui University of Science and Technology, Huainan 232001, China*
[4]*Shandong University of Science and Technology, Qingdao 266590, China*

Correspondence should be addressed to Benqing Yuan; yuanbengqing3@163.com

Received 5 September 2021; Accepted 10 March 2022; Published 30 March 2022

Academic Editor: Mohammed Fattah

To solve the high-stress hazard faced in the process of deep mining process, the pressure relief characteristics of gas bearing coal and the deformation characteristics of surrounding rock in deep roadway are studied by means of laboratory test, similar simulation analysis, and field investigation. The investigation results and engineering application showed that the specimens could more easily reach the failure point due to the axial pressure relief under high confining pressure. In addition, the deformation and failure degree of the surrounding rock was higher due to the disturbance from the deep high-stress roadway. The scope of the height affected by the pressure relief of the overlying strata reached above 10 m. Moreover, the initial gas emission could reach 4.41–14.39 times that of the original coal seam by drilling a hole in the coal seam at 10 m from the roof. Thus, the short-distance floor roadway exerted an obvious pressure relief effect on the overlying coal seam.

1. Introduction

As the coal mining depth is increased and the gas permeability of deep coal seams is further degraded in China [1, 2], for the single outburst coal seam or coal seam group without exploitation of the protective layer, the coal roadway strips at the outburst coal seam will be initially exploited, and the outburst prevention measure is still mainly to drill crossing holes on the floor roadway for the gas preextraction [3–5]. The difficulty in the drilling construction under deep high ground stress condition is significantly aggravated, and the gas preextraction further enhances the ground stress-dominated dynamic danger [6–9]. Various pressure relief and permeability enhancement technologies, such as hydraulic flushing [10, 11], hydrofracturing [12, 13], hydraulic slotting [14, 15], presplitting blasting [16, 17], cumulative blasting [18, 19], and CO_2 presplitting blasting [20], have been successively proposed at home and abroad. Hydraulic reaming is carried out by conveying high-pressure water to the reaming drill pipe through an underground emulsion pump (31.5 MPa). Continuous reaming of high-pressure water jet along the radial direction of drilling hole is formed through reaming drill bit or jet device. However, the depth of reaming hole is limited due to the influence of high-pressure water resistance along the path, and the maximum depth is generally not more than 60 m. Hydraulic fracturing is performed by injecting high-pressure water into sealing boreholes through a fracturing pump set (40~70 MPa). The fracture was fractured by high-pressure water in the original coal body, but the uniformity was poor after fracturing, and there were obvious stress and gas rich areas. Currently, hydraulic fracturing pump sets are generally large in volume, high in failure rate, and poor in downhole applicability. Hydraulic slotting is separated by radial high-pressure water jet through ultrahigh pressure clean water pump (70~100 MPa) and high-pressure sealing drill pipe in slotting bit. The high pressure hydraulic slotting has good slotting effect on medium hard coal seam, but it cannot form flat disc slotting groove for soft coal seam, and the working pressure is high, so there is a certain safety hazard. The exposed area of coal seam in coal hole section is increased by mechanical cutting through secondary mechanical reaming. However, the increase of the overall reaming radius is limited. At present, the maximum aperture of reaming using equipment machinery is only 300 mm, which is easy to induce dynamic phenomenon for coal seam reaming with higher gas content and pressure, i.e., greater outburst risk, and brings certain security risks. Controlled presplitting blasting is to produce a large number of cracks around the blast hole through the blasting effect of explosives in the coal and rock stratum, increase the permeability of coal, and improve the extraction effect. However, for the deep soft coal seam, the hole forming effect is poor, the charging is difficult, and the blasting pressure relief and permeability enhancement effect is not ideal, which is easy to produce misfire and bring potential safety hazards.

Given the complex and diversified stress field evolution of surrounding rock in deep roadway, the large deformation and strong rheological properties of surrounding rock, the brittleness–ductility transformation of coal and rock mass, and the mutability of dynamic response [21, 22], a pressure relief and permeability enhancement method of short-distance floor roadway in deep coal seam was investigated and formed. The comprehensive study shows that in view of the high stress hazard of deep mine, the stress level of overlying coal rock mass can be reduced in advance by laying near floor roadway at a certain distance below the coal roadway to be excavated. The pressure relief method of near floor roadway proposed in this paper is feasible and can provide reference for the prevention and control of mine disasters under similar conditions.

2. Mechanical Characteristic Test of Pressure Relief in Gas-Bearing Coal

2.1. Testing System and Program

2.1.1. Testing System. The gas–solid coupling seepage system [23] used in the test was mainly composed of four major parts, namely, pressure loading chamber, hydraulic servo control system, gas seepage system, and data acquisition system. The test device is shown in Figure 1, which can test the coupling relationship between mechanical properties and seepage characteristics of coal under different stress paths.

The pressure chamber provides the required stress environment for the test. The frame system is composed of 4 columns and upper and lower supports. The true three-axis pressure chamber is embedded in the circular groove set by the lower support, the cylinder height is 494 mm, the inner diameter is 500 mm, and the "O" type sealing ring is installed at the joint. Three-way stress loading and unloading is controlled by hydraulic servo system and automatically controlled by constant speed and constant pressure

Figure 1: Physical diagram of gas–solid coupling coal seepage test system.

metering pump. It has two working modes of constant current and constant pressure. At the same time, it is equipped with touch-type keyboard and data display screen, which can easily set and intuitively display the operating status, pressure, and flow. It is through the standard data interface to ensure that the computer to pressure, flow, pump, or pump volume and other parameters can be real-time acquisition. The gas seepage system consists of high-pressure gas cylinders, gas guide pipes, pressure reducing valves, and flowmeters. The gas enters the pressure chamber through the pressure reducing valve, flows through the coal specimen, and then passes through the mass flowmeter. The pressure copper pipe of 6 mm is the gas guide pipe, which is connected with a conical head to ensure good air tightness of the seepage system. Three-way automatic control of stress loading and unloading parameters and stress path and continuous and automatic data acquisition ensure the reliability of data.

2.1.2. Testing Program. In this paper, the variation characteristics of stress, deformation, and permeability of coal under axial stress unloading path were studied. The gas-bearing coal was loaded to 80% of the compressive strength of the test coal mass. After the deformation and seepage of the coal mass became stable, the axial pressure or confining pressure was kept constant, and the axial pressure was unloaded at a rate of 0.01 N/s until the failure of coal specimen. The stress loading and unloading path is shown in Figure 2.

Given that the coal mass structure was soft, the raw coal specimen was difficult to fabricate with a low success rate; conversely, the differences among the coal specimens in their physical and mechanical parameters, such as compressive strength and tensile strength, were minor due to the standard fabrication process; the influence of specimen difference on the experimental results was basically eliminated, and the physical and mechanical properties of coal could be well reflected [24]. Hence, standard rectangular-shaped coal specimens were used in this test. Specifically, the fresh coal samples are ground and ground on the pulverizing machine, screened out the same amount of 20~40 mesh and 40~80 mesh coal sample preparation base material, mixed evenly with water, then put into the specimen forming device, and pressed on the 100 T press for 30 min into rectangular

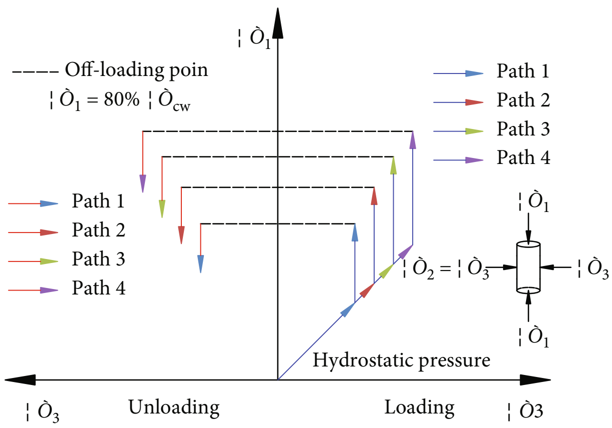

FIGURE 2: Schematic of stress loading/unloading path.

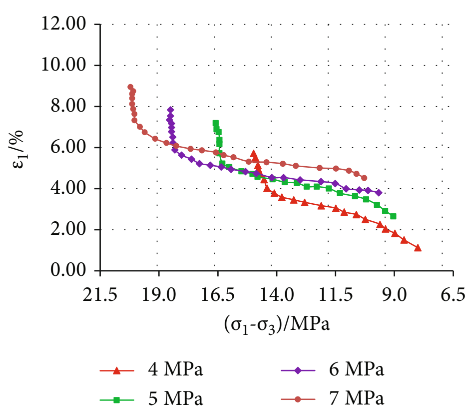

FIGURE 3: Mechanical characteristic curves in the axial pressure unloading of coal specimens under a constant atmospheric pressure of 1.5 MPa and different confining pressures.

standard briquette specimen with size of 100 mm × 100 mm × 200 mm. Place in a drying oven at 80°C for 24 hours and wrap it with insurance film for later use.

2.2. Axial Unloading Characteristics under Different Confining Pressures

2.2.1. Engineering Background. This paper takes Qujiang Coal Mine as the engineering background. The mine is located in Qujiang Town, Fengcheng City, Jiangxi Province. It is 9 km long from east to west and 4.8 km wide from north to south, covering an area of 39.5988 km^2, and the ground elevation is +20.1~+90.8 m. Qujiang Coal Mine is the main mine of Fengcheng Mining Area, with a designed production capacity of 900,000 t/a. The current production level is -850 m level, and the buried depth of coal seam exceeds 900 m, which belongs to deep mining.

The single B_4 coal seam mined in Qujiang Coal Mine is a gently inclined medium-thick coal seam with a dip angle of 12°~14° and an average coal thickness of 2.86 m. The roof of the coal seam is intermingled with fine sandstone and mudstone with a high proportion of sandstone and good sealing performance. The bottom plate is dominated by fine, medium fine, coarse, and medium sandstone. B_4 coal seam has high buried depth geostress, gas pressure and gas content (measured gas pressure $P_{max} = 9.2$ MPa and gas content $W = 13.5 \sim 25.3\ m^3/t$), soft structure (firmness coefficient $f = 0.29 \sim 0.8$), and extremely low permeability ($K = 1.7 \times 10^{-5} \sim 4.4 \times 10^{-5}\ m^2/MPa^2{\cdot}d$), it is difficult to extract gas, and it takes a long time for intensive drilling to reach the standard, and the extraction efficiency is low.

In view of the coal roadway belt, the regional predrainage gas outburst prevention measures are mainly implemented through the construction of dense drilling holes through the floor (the spacing between them is 3.0 m × 3.0 m). The gas drainage from drilling holes reduces the energy of gas outburst, but it is difficult to eliminate the harm of high in situ stress in deep mining. In the process of drilling construction, abnormal phenomena such as jet holes and drill clamping often occur.

2.2.2. Mechanical Characteristics. The axial pressure unloading test under the conventional triaxial stress condition with constant pressure and different confining pressure is conducted. The axial pressure and confining pressure are, respectively, loaded to different hydrostatic pressure levels (successively $\sigma_1 = \sigma_2 = \sigma_3 = 4$ MPa, 5 MPa, 6 MPa, and 7 MPa), and gas with pressure $P = 1.5$ MPa is introduced to keep the confining pressure unchanged. Continue to apply axial pressure to 80% of the compressive strength of coal samples under the same conditions in force control mode of 0.01 N/s, and then unload axial pressure in control mode of 0.01 N/s until coal failure occurs. The axial compressive stress–axial strain unloading curves of gas-bearing coal under constant gas pressure ($p = 1.5$ MPa) and different confining pressures ($\sigma_2 = \sigma_3 = 4, 5, 6,$ and 7 MPa) are shown in Figure 3.

Under different confining pressures, the axial strain decreases rapidly at first and then slowly during the unloading process of axial stress. However, with the increase of confining pressure, the axial strain at final failure shows an increasing trend (as shown in Figure 4). When the confining pressure was elevated from 4 MPa to 7 MPa, the strain ε_{final} was increased from 1.13% to 4.52% in case of coal failure, with the increase amplitude reaching 300%. That is, the higher the confining pressure is, the more easily the specimen under axial pressure relief will reach the failure point.

3. Simulation Analysis of Deformation Characteristics of Surrounding Rock in Deep Roadway

3.1. Similar Simulation Scheme and Parameter Determination

3.1.1. Testing System. A two-way four-plane load-adjustable multifunctional similar simulation testing device [25] was used to simulate deep underground engineering. This device mainly included a model steel truss, a constraining channel steel, a transparent organic glass viewing window (800 mm × 900 mm), and a loading system. The effective dimensions were 3,000 mm × 2,000 mm × 200 mm. A picture of this device is shown in Figure 5.

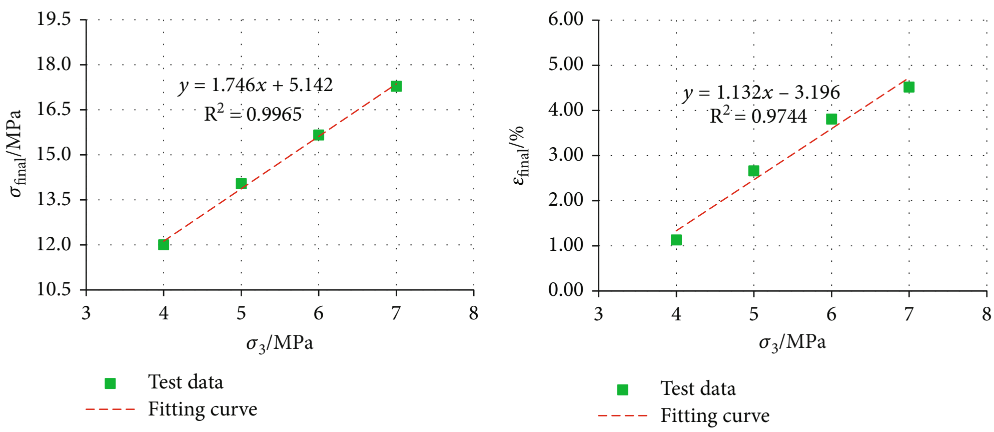

(a) Failure strength (b) Strain at failure point

Figure 4: Strength and strain change curves at the failure point in the axial pressure unloading of coal specimens under a constant atmospheric pressure of 1.5 MPa and different confining pressures.

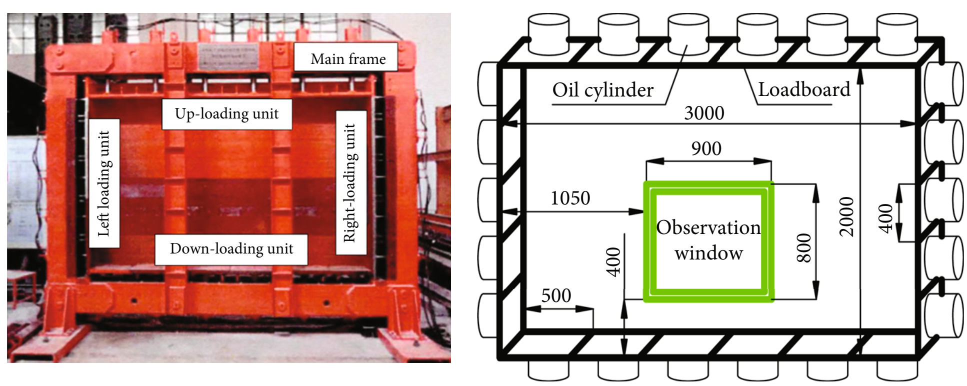

(a) Real figure (b) Parametric dimension diagram (mm)

Figure 5: Picture of the testing device for similar simulation.

3.1.2. Experimental Parameters. According to the literature [26], the geometric similarity ratio is generally 20–300 in the similar simulation of mining and 20–50 in the simulation of underground chamber and tunnel (roadway). By combining the size of the viewing window in the actual testing device for the similar simulation, the geometric similarity ratio was taken as $\alpha_l = 25 : 1$ in this study, and the roadway width and height were calculated as 160 mm and 120 mm, respectively.

The average density of field surrounding rock in the roadway was 2.5 g/cm^3, and that of similar material matched in the laboratory was 1.56 g/cm^3. Thus, the similarity ratio of the volume weight was $\alpha_r = 1.6$, that of stress was $\alpha_\sigma = \alpha_l \times \alpha_r = 40$, and that of Poisson's ratio was constantly 1. On the basis of the similar three theorems, the similarity ratio of time was obtained as $\alpha_t = (\alpha_l)^{0.5} = 5$, and it was taken as 6 to facilitate the time simulation. That is, 4 h simulation was equivalent to 24 h field operation.

According to the principle of similarity, 14 anchor bolts and 3 anchor cables shall be arranged in each row, with a total of 84 anchor bolts and 18 anchor cables. In consideration of ineradicable friction effect, supporting intensity, and density of front and rear baffles in the model, the support parameters were adjusted, 4 rows were arranged in the front and back, and 10 anchor bolts and 3 anchor cables were arranged in each row, with a total of 40 anchor bolts and 12 anchor cables.

The simulated aggregate is river sand with particle size of 0.2~0.5 mm brushed by 250 mesh sieve, the cementitious material is freshly burned lime and hydrated gypsum, and 40-mesh mica powders were applied on the bedding plane. On the basis of the corresponding matching number, the matching ratio of similar simulation materials was determined, as shown in Table 1.

3.1.3. Monitoring Method. A totally enclosed-type test rack was used in the simulation. The strain inside the surrounding rock was monitored with a distributed optical fiber. The distributed optical fiber monitoring equipment and measuring line layout are presented in Figure 6.

The surface displacement was observed by high-definition digital camera. To clearly observe the fracture and displacement development on the model surface, the observed surface at the viewing window part was uniformly whitewashed, the vertical crossing measuring lines were marked using ink lines, and the displacement measuring point layout in the viewing window is shown in Figure 7.

Table 1: Matching materials in similar simulation test and their use levels.

Serial number	Rock stratum name	Seam height/ mm	Proportion number	Amount/kg River sand	Lime	Gypsum	Total/ kg	Water quantity/kg	Remark
1	Gritstone	100	4 : 0.6 : 0.4	115.2	17.2	11.6	144.0	14.4	Pavement stratum
2	Sandy shale	100	6 : 0.7 : 0.3	123.6	14.4	6.0	144.0	14.4	
3	Fine sandstone	100	5 : 0.6 : 0.4	120.0	14.4	9.6	144.0	14.4	
4	Medium-fine grained sandstone	120	5 : 0.6 : 0.4	144.0	17.9	11.4	172.8	17.4	Layer of floor roadway
5	Sandy shale	300	6 : 0.7 : 0.3	370.2	43.2	18.6	432.0	43.2	Roof layer
6	Mudstone	100	7 : 0.7 : 0.3	126.0	12.6	5.4	144.0	14.4	
7	Coal seam	120	10 : 0.5 : 0.5	157.0	7.9	7.9	172.8	17.3	
8	Mudstone	100	7 : 0.7 : 0.3	126.0	12.6	5.4	144.0	14.4	
9	Fine sandstone	200	5 : 0.6 : 0.4	240.0	28.8	19.2	288.0	28.8	
10	Mudstone	130	7 : 0.7 : 0.3	163.8	16.4	7.0	187.2	18.7	
11	Fine sandstone	230	5 : 0.6 : 0.4	288.0	34.5	23.1	345.6	34.6	
12	Fine sandstone	200	5 : 0.6 : 0.4	252.0	30.2	20.2	302.4	30.2	
Accumulate		1,800	/	2,225.8	250.1	145.4	2,620.8	262.2	

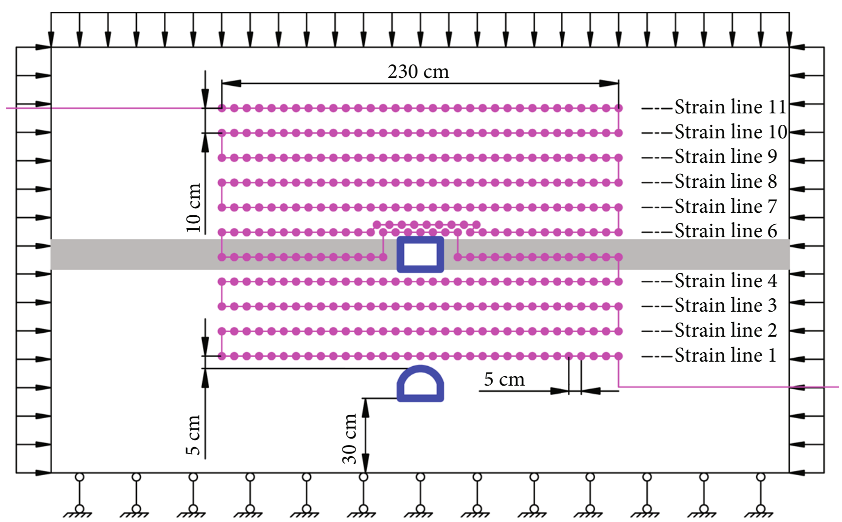

Figure 6: Strain measuring line and monitoring point layout plan of distributed optical fiber.

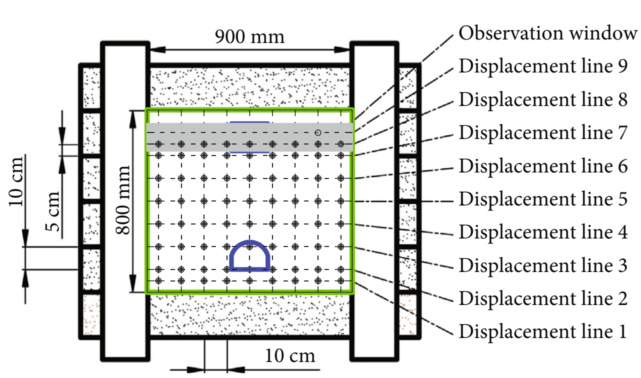

Figure 7: Displacement measuring line and monitoring point layout plan of viewing window.

During the pressurization process, the strain was acquired via a distributed optical fiber, the surface displacement was observed using a high-precision digital camera, and the failure was photographed synchronously. In the steady pressure phase, the strain data acquisition frequency was 4 h each time, and it was 1 h each time in other phases. The photographing frequency was 2 h each time in case of no obvious changes and 0.5 h each time in case of evident changes.

3.2. Deformation and Failure Characteristic Analysis of Overlying Strata after Floor Roadway Excavation

3.2.1. Displacement Evolution Characteristics of Overlying Strata. The vertical displacement changes on the model surface in different loading phases were collected through the near-view photographing technology of a high-definition digital camera, and the changes at some measuring lines

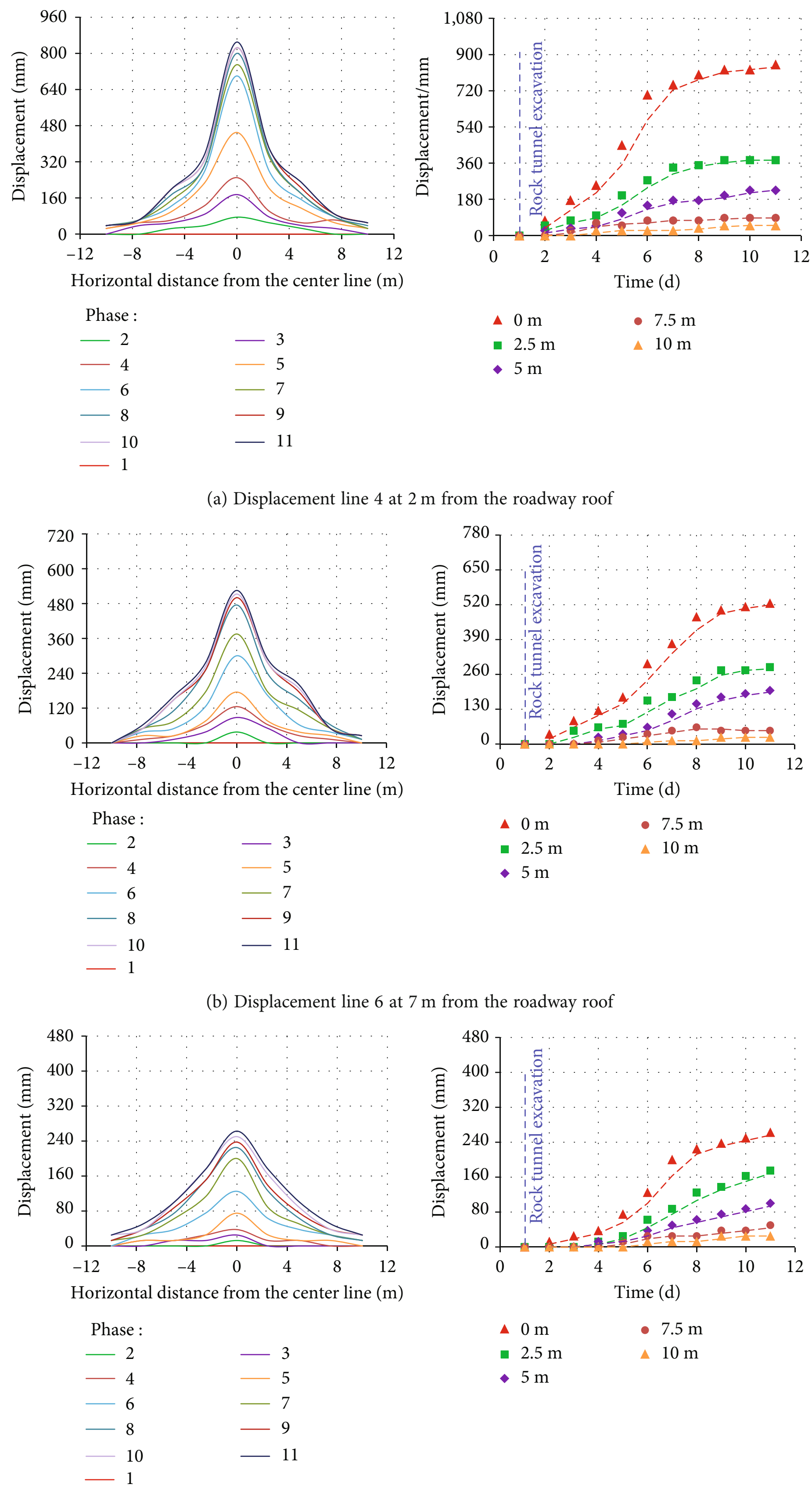

(a) Displacement line 4 at 2 m from the roadway roof

(b) Displacement line 6 at 7 m from the roadway roof

(c) Displacement line 9 at 12 m from the roadway roof (stratum of coal seam)

Figure 8: Roof displacement curves in different loading phases after floor roadway excavation.

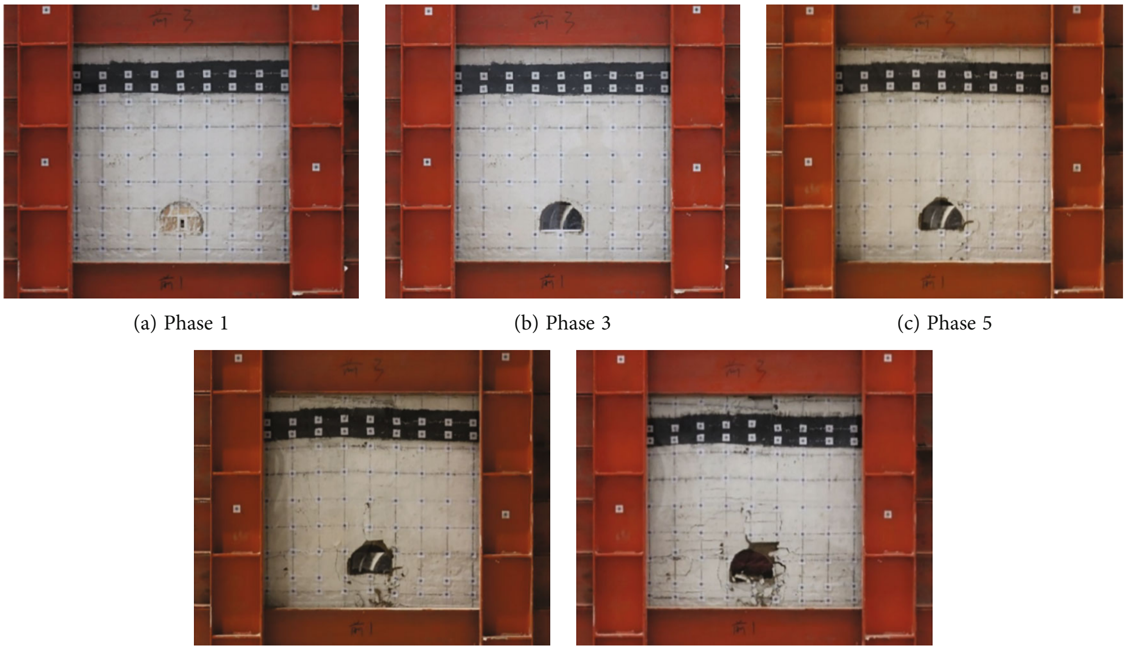

(a) Phase 1 (b) Phase 3 (c) Phase 5

(d) Phase 9 (e) Phase 11

Figure 9: Fracture development characteristics on the roadway surface in different loading phases.

are displayed in Figure 8 (the following related data were all the original sizes after conversion; the displacement field formed in loading phase 1 was taken as base point 0; the left side of the roadway center line was negative, whereas the right side was positive).

As shown in Figure 8, in the steady pressure phase (phase 1) and initial loading phase (phases 2–4), the subsidence of the roadway surface was minor, and the deformation basically presented the “?”-shaped symmetric distribution characteristic; as the load was increased (phases 2–5), the subsidence of the roadway surface was enlarged, and the deformation basically showed “V”-shaped symmetric distribution characteristics. That is, the subsidence displacement at the roof position, where the left and right sides of the same measuring line were equally distant from the roadway center line, was basically identical, presenting the axisymmetric laws. The more distant from the roadway center line was, the smaller the displacement would be. The maximum displacement appeared at the middle of the roadway, specifically as follows. After the roadway excavation, from loading phase 2 to phase 11 (1–11 d after the excavation), the surface subsidence displacement in the roadway center at 2 m from the roof was elevated from 75 mm to 850 mm, that in the roadway center at 7 m from the roof was increased from 37.5 mm to 525 mm, and that in the roadway center at 12 m from the roof (stratum of coal seam) was increased from 12.5 mm to 262.5 mm.

The observation line 9 of the horizon where the coal seam is located (within the range of 10~13 m above the floor roadway) is in the loading phase 11, and the corresponding subsidence at the distance of 2.5 m, 5 m, 7.5 m, and 10 m from the roadway center is 170 mm, 98 mm, 48 mm, and 24 mm, respectively. The comprehensive analysis indicated that the scope of influence of the floor roadway excavation under the effect of mine ground pressure reached above 10 m when the burial depth of Qujiang Coal Mine was 800 m.

3.2.2. Fracture Development Characteristics in Overlying Strata. With the increase in the load applied to the upper, lower, left, and right loading units, the appearance and development process of fractures around the roadway could be intuitively displayed through the high-definition camera. After the experimental preparations were made, the whole overlying strata movement and fracture development and evolution process during the loading process after the roadway excavation was completely recorded, as shown in Figure 9. The fractures at the roadway roof were continuously developing and propagating with the increase in the load applied. Relative to the three-phase evolution characteristics of the displacement of the surrounding rock, the fracture development at the roadway roof was also basically divided into three phases: initial phase nearly without fracture, slow development phase, and intense development phase.

In loading phases 1–4, the maximum pressure reached 5 MPa at the upper and lower loading units and that at the left and right loading units reached 4 MPa. In this period, the pressure load borne by the model was relatively small. Specifically, the fractures between the internal rock strata were continuously compacted, the overall rock strata at the roof subsided, and almost no fractures appeared.

In loading phase 5, the fractures that deviated from the arch corner to the floor at the roadway center were initially generated at the right arch corner of the roadway due to shear dislocation, with the extended length of about

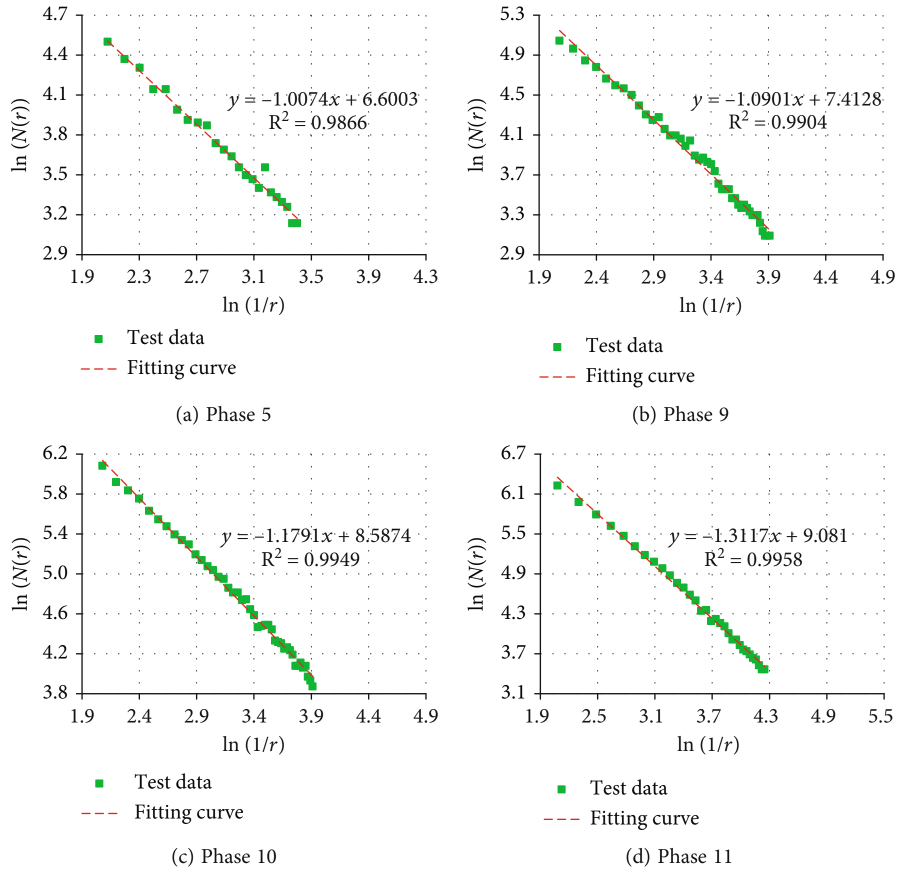

Figure 10: Curve chart of fractal dimension calculation for fractures in different loading phases.

2.5 mm. Almost at the same time, an inverse “L”-shaped fracture developed at the roadway roof from the roadway center, with the vertical length of about 2.4 m and transverse length of about 2.6 m. As the load was increased until phase 9, the original fractures within 3 m range at the roadway roof continuously developed, propagated, and extended. Moreover, multiple transverse and vertical fractures developed at the right side of the roadway center line due to the upper load without obvious detachment. Given the stress concentration, multiple vertical fractures and a small quantity of transverse fractures appeared within 5 range at the left wall of the roadway. Long fractures were generated within 1.5 m range from the roadway floor to the undersurface under the continuous squeezing effect of the surrounding rock, with the length reaching 4 m, and small-scale floor heaving started appearing.

In the 10~11 loading phases, the surrounding rock of the roadway began to be damaged, the existing cracks developed violently, some cracks formed through cracks, and the block fell off on the surface of the model. In the intense fracture development phase, as the compressive strength of the material was considerably greater than the tensile strength, the original fractures at the model strata, especially the roof strata, were continuously developing under the combined action of horizontal and vertical stresses. Moreover, a large number of vertical fractures were generated due to the Poisson’s effect, along with the rupturing phenomenon. The roof continuously subsided, the subsidence at the right side of the roof center could be evidently manifested from a macroscopic perspective, and a bulging phenomenon was prominent. Some rock strata experienced obvious shear dislocation, and the central subsidence was apparently larger than that of the rock mass at the two sides.

According to the literature, the fractal characteristics of fracture development were analyzed using box dimension in this study, and the calculation method is expressed as follows:

$$D = \lim_{r \longrightarrow 0} \left[\frac{\ln N(r)}{\ln (1/r)} \right], \tag{1}$$

where D is the fractal dimension value based on box dimension; r denotes the radius of nonempty subset, and $r > 0$; $N(r)$ represents the least number in the covered subset A_r; A_r is an arbitrary bounded subset in the domain.

The fracture development laws in the overlying rock strata of the roadway in different loading phases were quantitatively analyzed. The fracture pictures in different loading phases were selected, followed by the grey processing, to obtain the black and white bar graph used to calculate the fractal dimension. The fracture distribution graphs in different loading phases were transformed into sketch maps. Next,

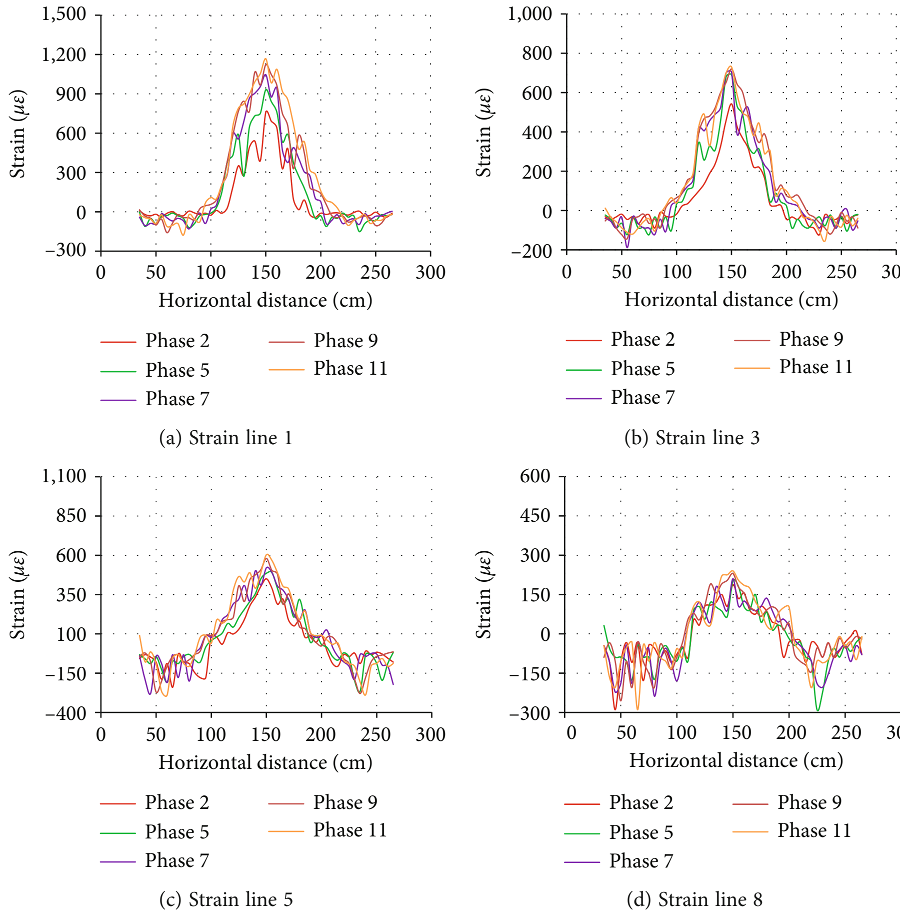

Figure 11: Strain curve chart of overlying strata in different loading phases after the floor roadway excavation.

the related parameters in Equation (1) were calculated via the Fractal Fox software, and the fractal dimension shown in Figure 10 was generated. In the figure, the fractal dimension in the fracture network in the mined rock mass was presented through a straight slope.

The occupation of fractures in two-dimensional space under different loading phases reflects the dynamic evolution law of fracture network distribution, and better reveals the variation characteristics of fractures with loading phase (buried depth). In the fractal dimension calculation for fractures in different loading phases after the floor roadway excavation, the fitting precision (R^2 value) was high (over 0.99), indicating that the fractal characteristics of the fracture network evolution in the floor roadway in different loading phases were regular. After the floor roadway excavation, the fractal dimension of fractures presented an overall increasing trend with the loading phase (namely, with the increase in the pressure), being basically divided into three phases: the phase almost without fractal dimension, phase with slow dimension increase, and phase with rapid dimension reduction, which basically corresponded to the fracture development characteristics in the previous section.

3.2.3. Strain Distribution Characteristics in Overlying Strata. The data acquisition interval at the distributed optical fiber strain points used in this study was 5 cm, the length of each measuring line was 230 cm, and the collected data size was 46. Given the overall large data size, the observed data of strain measuring lines 1, 3, 5 (stratum of coal seam), and 8 at 5, 25, 45, and 75 cm from the roadway roof were calculated to form the test results of strain measuring lines in different loading phases, as shown in Figure 11. The tensile strain was set positive, whereas the compressive strain was negative.

Figure 11 shows the strains at the coal and rock strata within a certain range at the left and right sides of the roadway center line. With the roadway center line taken as the center, the strains were basically symmetrically distributed, which was nearly identical with the characteristic curve of the displacement evolution in the surrounding rock, as aforementioned. The existence of tensile strain reflected that the coal and rock strata within this range were affected by the mining disturbance, with a certain subsidence displacement. In the zone with tensile strain, the coal and rock strata were under pressure relief state, and the greater the tensile strain was, the higher the pressure relief degree would be. Compressive strain existed in the other zones, indicating that they were almost not affected by the roadway excavation. Moreover, they were basically located at the terminal line of the fracture development.

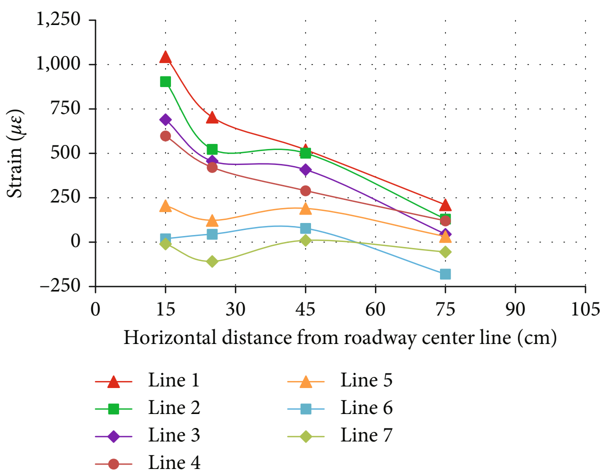

Figure 12: Curve chart of strain test results at different positions and measuring lines at the left side of the roadway center line (phase 7).

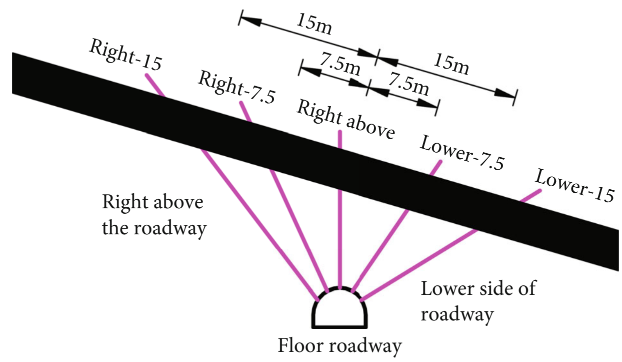

Figure 13: Drill hole layout plan.

Following the roadway excavation, the maximum tensile strain appeared nearby the roadway center. For example, the maximum tensile strains at strain measuring lines 1, 3, 5, and 8 were 1,167, 730, 603, and 240 $\mu\varepsilon$, respectively, indicating that these positions were greatly disturbed after the roadway excavation. With the increase in the distance from the roadway roof, the strain of overlying strata followed such laws. ① In the same loading phase, the tensile strain was gradually reduced. That is, the pressure relief was gradually weakened, and the strain test results at different positions and measuring lines in phase 7 are specifically shown in Figure 12. ② The ranges of tensile strain zones generated at measuring lines 1–5 were gradually enlarged. In phase 7, the ranges of tensile strain zones at measuring lines 1, 3, and 5 were 26.25, 30.00, and 31.25 m, respectively. However, the range of tensile strain zone at the coal seam roof was gradually shrunk, and that at measuring line 8 was only 23.75 m.

As the loading proceeded (i.e., the pressure applied was increased), the strain of the overlying strata basically presented the following laws. ① At the same measuring line, the range of tensile strain was gradually enlarged in phases 2–9, and that in phases 10 and 11 was almost unchanged. For example, the ranges of tensile strains at measuring line 3 in phases 2, 5, 7, 9, and 11 were 23.75, 26.25, 30.00, 31.25, and 31.25 m, respectively. ② The tensile strain value at the same measuring line was gradually enlarged. For instance, the tensile strains at measuring line 3 in phases 2, 5, 7, 9, and 11 were 542.0, 600.0, 704.0, 720.0, and 730.0 $\mu\varepsilon$, respectively.

The measuring line 5 of the coal seam is located at 11.25 m of the roadway roof. At the end of the 11th phase of loading, the tensile strain range is 31.25 m, that is, the tensile strain is generated within 15.6 m on both sides with the roadway centerline as the midpoint. Therefore, the coal seam within this range is in a pressure relief state after roadway excavation.

4. Engineering Application of Pressure Relief Method through Short-Distance Floor Roadway at Deep Coal Seam

4.1. Project Profile and Investigation Scheme for Application Effect. To further verify the previous study results, the outburst prevention method through the pressure–relief gas drainage in the floor roadway was applied in Fengcheng Mining Area, and the study object was 213 floor roadway in Qujiang Coal Mine. The single B_4 coal seam exploited in this mine was medium-thickness coal seam with a gentle dip. The dip angle of the coal seam was 12°–14°; the average coal thickness was 2.86 m; the coal seam roof was composed of fine sandstone and mudstone, where sandstone accounted for a high proportion with good sealing capacity; the floor was mainly composed of fine, medium, and coarse sandstone and medium sandstone. The B_4 coal seam was characterized by a large burial depth, high ground stress, gas pressure and gas content (measured gas pressure: $p_{\max} = 9.2$ MPa and gas content: $W = 13.5 - 25.3\,\mathrm{m}^3/\mathrm{t}$), loose and soft structure (firmness coefficient: $f = 0.29 - 0.8$), extremely low gas permeability ($k = 1.7 \times 10^{-5} - 4.4 \times 10^{-5}\,\mathrm{m}^2/\mathrm{MPa}^2 \cdot \mathrm{d}$), difficult gas extraction, long time consumed by the dense borehole drainage to reach the standard, and low extraction efficiency. Given that the geological structures were complicated in the Fengcheng Mining Area to reduce the safety risk induced by the mistaken coal uncovering, the 213 floor roadway was arranged at 10 m away from the coal seam floor in Qujiang Coal Mine, and the pressure–relief baseplates were overlapped up and down.

The pressure relief effect of the floor roadway was investigated mainly from two aspects: displacement and failure of the surrounding rock. The drill holes were arranged, as shown in Figure 13, and the investigation sites were designed, as shown in Table 2. The displacement and failure characteristics at different depths of the surrounding rock were investigated using DW-6 multipoint displacement meter and YTJ20 rock strata detection recorder, the diameter of all drill holes was Φ32 mm, and the real pictures of the instruments are displayed in Figure 14.

4.2. Investigation on Pressure Relief Effect in Overlying Strata of the Roadway

Table 2: Investigation sites of pressure relief effect.

Mine	Floor roadway number	Distance from investigation site to head-on/m			Diameter of drill hole/mm	Investigation content
		Group 1	Group 2	Group 3		
Qujiang	213	244	208	116	32	Displacement and failure of the surrounding rock and gas flow in the drill hole

(a) DW-6 multipoint displacement meter

(b) YTJ20 rock strata detection recorder

Figure 14: Real pictures of instruments used for investigating pressure relief effect.

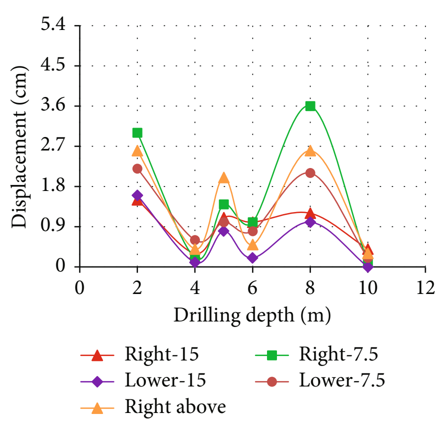

(a) Group 1 (244 m away from the tunneling head-on)

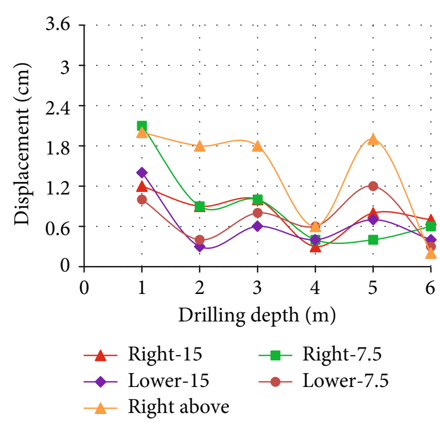

(b) Group 2 (208 m away from the tunneling head-on)

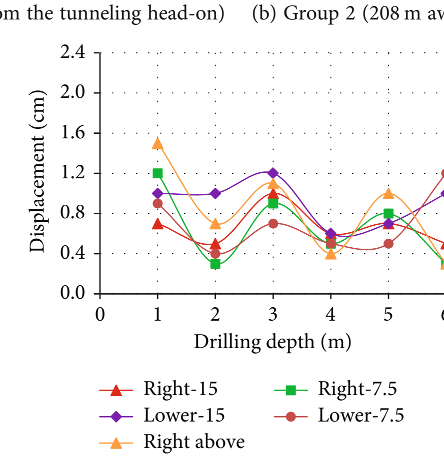

(c) Group 2 (116 m away from the tunneling head-on)

Figure 15: Displacement curve chart of surrounding rock in 213 floor roadway in Qujiang Coal Mine.

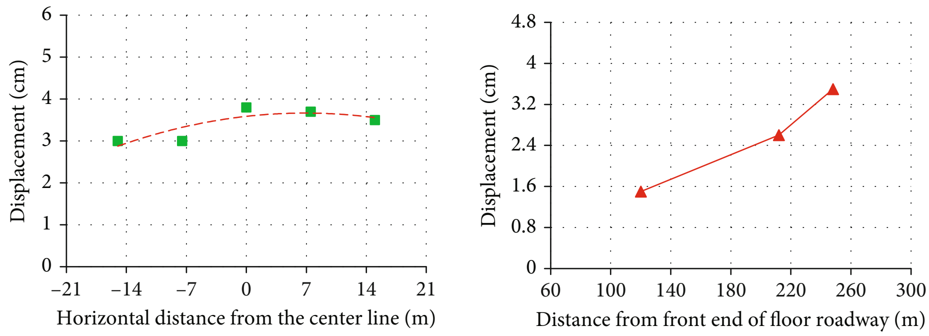

Figure 16: Curve chart of maximum displacement of surrounding rock in 213 floor roadway of Qujiang Coal Mine.

(a) Intact rock

(b) Fracture

(c) Crack

(d) Fractured

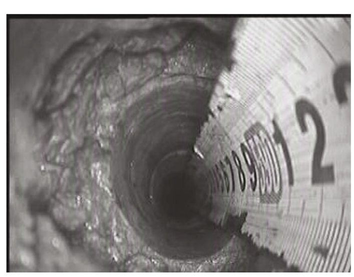

(e) Seriously fractured

(f) Gas dissipation

Figure 17: Peering video screenshots of drill holes.

4.2.1. Displacement Change of Overlying Strata. A total of six measuring points were arranged in each drill hole to investigate the displacement of the surrounding rock, and the investigation results are presented in Figure 15. The displacements at different depths of drill holes were characterized by the alternate change of crest and trough, which indicated the zonal disintegration inside the surrounding rock. The crest and trough represented the failure and nonfailure zones of the surrounding rock, respectively [27].

The maximum displacements on different investigated sections (sites) of the surrounding rock in the roadway were calculated, as shown in Figure 16, basically presenting the distribution characteristic of successive reduction from the roadway center line to the two sides. With the increase in the distance from the working face, the deformation of the surrounding rock in the roadway above the floor roadway became greater. In addition, the pressure relief of the surrounding rock was more sufficient, which accorded with the pressure relief law in the deep roadway and the theory of rheological effect.

4.2.2. Zonal Fracture of Surrounding Rock. The situation in the holes could be detected using a peering instrument, a steel measuring tape, and video transmission technology

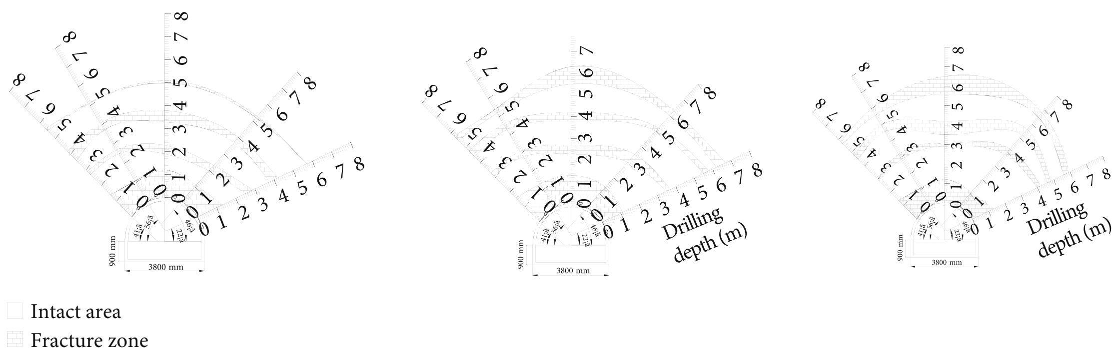

Figure 18: Zonal fracture of surrounding rock in 213 floor roadway of Qujiang Coal Mine.

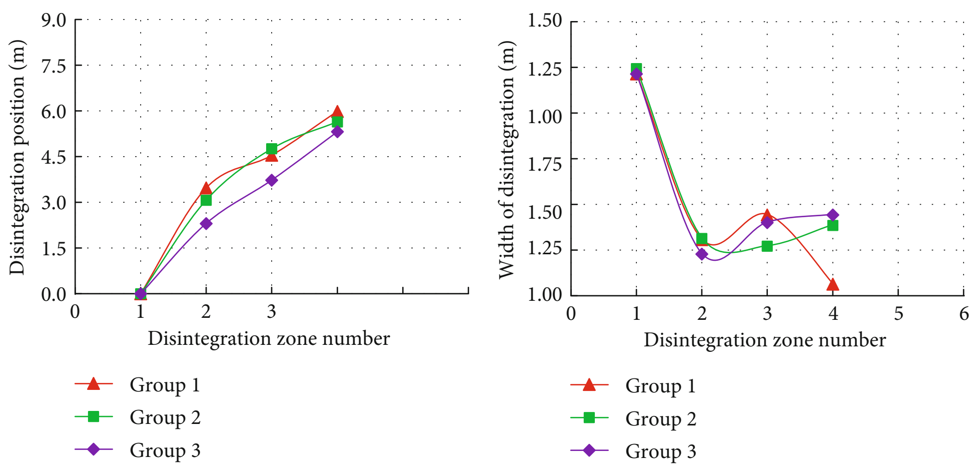

(a) Average initial fracture position (b) Average width of fracture zone

Figure 19: Distribution diagram of zonal fracture under confining pressure in 213 floor roadway of Qujiang Coal Mine.

[27]. The peering results of typical drill holes are shown in Figure 17. The fracture zones above 0.2 m of different drill holes on each investigated section in the 213 floor roadway of Qujiang Coal Mine were delineated, and their distribution is shown in Figure 18. The fracture zone on the roadway surface was traditional excavation damaged zone. Multiple fracture zones appear from the roadway surface to the interior of surrounding rock [28]. There existed generally 4–5 fracture zones in the surrounding rock on each roadway section, and the fractures were gradually reduced from the roadway center toward the two sides, which was consistent with the previous theoretical study results.

The average initial positions (distance from the roadway wall) of the fracture zones in the surrounding rock at different positions within 15 m range from the upper and lower walls of the surrounding rock above the test roadway, as well as the average width of the fracture zone, were further calculated. The fracture laws and distribution in the surrounding rock of 213 floor roadway in Qujiang Coal Mine are shown in Figure 19. The fracture zone basically presented a linear increase trend with the increase in the distance from the tunneling head-on (i.e., the fracture zone was enlarged with the pressure relief time), which coincided with the theory of rheological effect in the pressure relief of the roadway.

4.2.3. Initial Gas Flow in Drill Holes. The investigation results of gas flow in the drill holes arranged in the overlying coal seam of 213 floor roadway in Qujiang Coal Mine and the maximum increase amplitudes are shown in Figures 20 and 21, respectively.

The gas flow in the drill hole rightly above the floor roadway was the maximum, followed by those at 7.5 m and 15 m from the two sides of the roadway. The gas flow in the drill holes at the same position presented a gradual attenuation trend with the time. Therefore, the pressure relief effect of the coal seam above the floor roadway was gradually weakened from the center line to the two sides but strengthened as the pressure relief time was lengthened, which was identical with the previous study results. The initial gas flow per meter in the drill hole rightly above the pressure–relief floor roadway and those at 7.5 m and 15 m from the two sides were increased to 14.39, 9.90, and 4.41 times that in the original coal seam, respectively, fully manifesting that the pressure relief effect of floor roadway was significant.

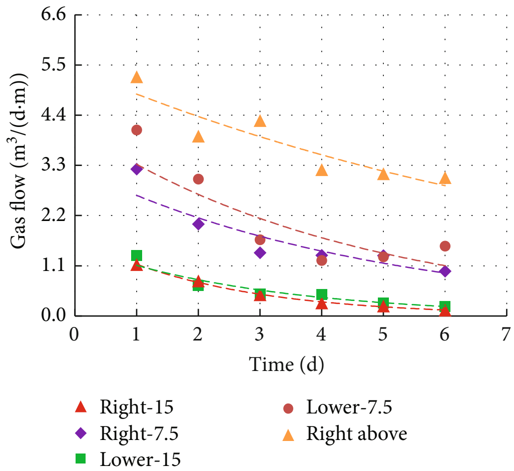

(a) Group 1

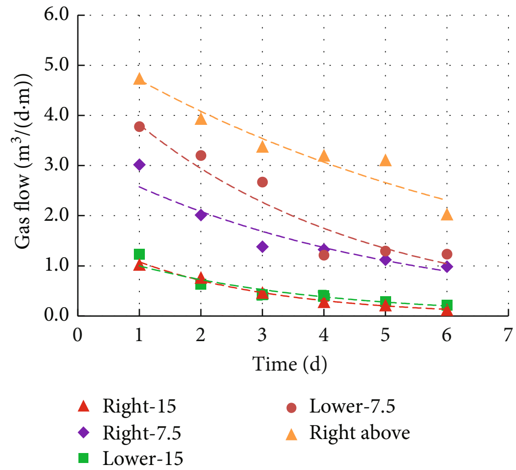

(b) Group 2

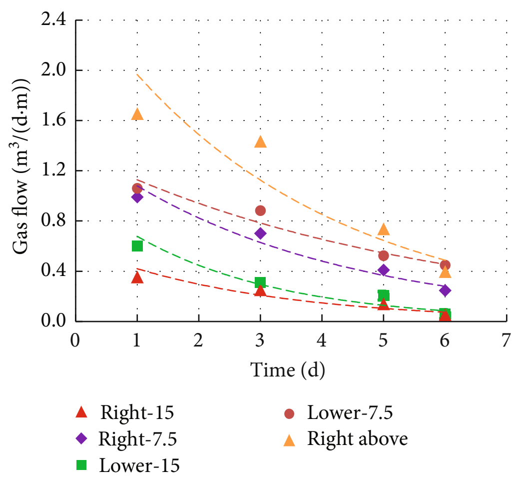

(c) Group 3

Figure 20: Variation diagram of gas flow in drill holes in 213 floor roadway of Qujiang Coal Mine.

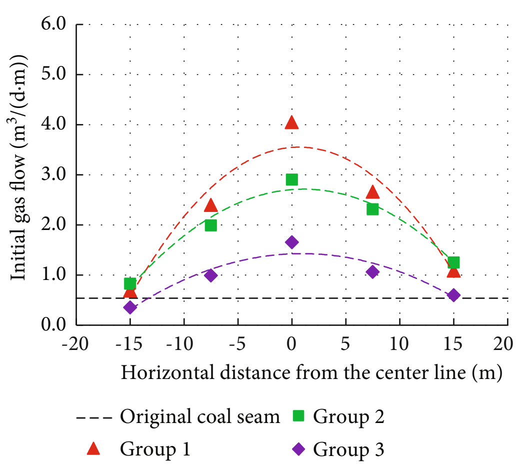

(a) Gas flow

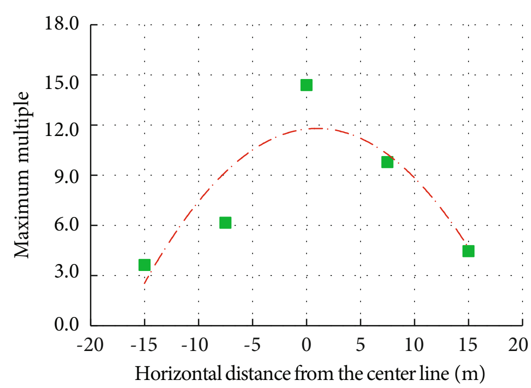

(b) Increase amplitude

Figure 21: Change curve chart of initial gas flow in drill holes in 213 floor roadway of Qujiang Coal Mine.

5. Main Conclusions

(1) The unloading test of gas-bearing coal shows that the axial strain declines slowly after the rapid reduction initially during the unloading process of axial stress. The higher the confining pressure is, the greater the axial stress and strain in case of specimen failure will be. Moreover, the specimen can more easily reach the failure point due to the axial pressure relief under a high confining pressure, and the disturbance-induced deformation and failure degree of surrounding rock is higher in a deep high-stress roadway

(2) According to the similar simulation test results, the subsidence displacement on the roadway surface experiences three phases—slow, rapid, and stable deformations—with the increase in the load, and the fractures are continuously generated and propagating at the roadway roof. The displacement is the maximum at the roadway center line. The more distant from the roadway center line is, the smaller the displacement will be, and the displacements will show the symmetric distribution laws. The scope of influence of floor roadway excavation on the pressure relief of overlying rock strata reaches over 10 m. The tensile strain is generated within 15.6 m range at the two sides of the coal seam at 11.25 m away from the roadway roof, and the pressure relief state is manifested within this range

(3) The investigation results of displacement and failure in the overlying strata of deep floor roadway imply that the displacements of surrounding rock at different positions above the floor roadway are featured by the alternate crest and trough variation. Zonal fracture takes place inside the surrounding rock, and the deformation of surrounding rock and fracture zones are the maximum at the roadway center line and gradually reduced at the two sides. Moreover, the pressure relief effect is better if the distance from the tunneling face is greater and the pressure relief time is longer. The initial gas emission in the drill holes rightly above the roadway and those at 7.5 m and 15 m from the two sides reach 14.39, 9.90, and 4.41 times that in the original coal seam, hinting a highly apparent roadway pressure relief effect

(4) The stress level in the overlying coal and rock strata can be reduced in advance by arranging a short-distance floor roadway beneath the coal roadway to be mined to prevent and control the high-stress induced hazards in the deep mine. Hence, the pressure relief method through the short-distance floor roadway proposed in this study is feasible, thereby providing reference for the hazard prevention and control in other mines with similar conditions

Data Availability

The known data in this paper come from practical engineering case data, which are reliable and available.

Conflicts of Interest

The authors declare that they have no conflicts of interest.

Acknowledgments

This work is financially supported by the Innovation and Development Joint Fund of National Natural Science Foundation of China (U21A20110), the General Project of Chongqing Natural Science Foundation (cstc2021jcyj-msxmX1149), and the State Key Laboratory Open Fund Project (SKLMRDPC20KF01).

References

[1] G. Cui, "Permeability improved technology of low permeability seams group in underground mine," *Coal Science and Technology*, vol. 44, no. 5, pp. 151–154, 2016.

[2] Y. Liu, Z. Zhang, B. Deng, and M. Li, "Liquid carbon dioxide fracturing application and its effect on gas drainage in low permeability coal seams of underground coal mine," *Energy Sources Part A Recovery Utilization and Environmental Effects*, vol. 106, pp. 1–13, 2019.

[3] C. J. Lian, C. M. Guo, Z. Y. Deng, and H. Y. Ma, "Spatial gas control technology and application of first mining protective layer of coal seam group with high gas outburst," *Coal Mining*, vol. 24, no. 1, pp. 124–127, 2019.

[4] X. Cheng, G. M. Zhao, Y. M. Li, X. R. Meng, C. L. Dong, and W. S. Xu, "Study on relief-pressure antireflective effect and gas extraction technology for mining soft rock protective seam," *Journal of Mining & Safety Engineering*, vol. 35, no. 5, pp. 1045–1053, 2018.

[5] M. J. Zhang, J. J. Shu, and J. T. Hua, "Anti-burst technology of gas strip in pre-extracted coal roadway with single coal seam floorway," *Coal Mine Safety*, vol. 42, no. 6, pp. 30–32, 2011.

[6] Z. Wang, *New Classification and Induced Transformation Conditions of Coal-Rock Gas Dynamic Disasters*, Chongqing University, 2010.

[7] L. Yuan, "Control of coal and gas outbursts in Huainan mines in China: a review," *Journal of Rock Mechanics and Geotechnical Engineering*, vol. 8, no. 4, pp. 559–567, 2016.

[8] D. J. Lei, C. W. Li, Z. M. Zhang, and Y. Zhang, "Coal and gas outburst mechanism of the "Three Soft" coal seam in western Henan," *Mining Science and Technology (China)*, vol. 20, no. 5, pp. 712–717, 2010.

[9] X. H. Sun and T. Li, *Theory and Technology for Preventing and Controlling Gas Dynamical Disasters of Compound Briquette and Rock in Deep Mines*, Science Press, Beijing, 2011.

[10] Z. J. Ren, "Application of hydraulic punching technology in seam gas drainage in Yuwu coal mine," *Coal Engineering*, vol. 51, no. 3, pp. 65–70, 2019.

[11] M. J. Liu, K. Cui, Y. W. Liu, Q. G. Deng, and Z. Liu, "Analysis on outburst prevention mechanism of borehole hydraulic flushing measures for deep and low permeability seam," *Coal Science and Technology*, vol. 40, no. 2, pp. 45–48, 2012.

[12] Q. B. Mou, Z. M. Yan, and J. Zhang, "High efficiency gas drainage technology of hydraulic fracturing with directional long drilling in underground coal mine," *Coal Science and Technology*, vol. 48, no. 7, pp. 296–303, 2020.

[13] S. G. Li, W. Z. Jiang, B. S. Jia, and R. S. Nie, "Application and prospect of fracturing and permeability enhancement

technology in low permeability coal seam," *Coal Science and Technology*, vol. 45, no. 6, pp. 35–42, 2017.

[14] J. J. Cao, "Application research on regional outburst prevention technology of ultra-high pressure hydraulic slot pressure in relief drainage area," *Coal Science and Technology*, vol. 48, no. 6, pp. 88–94, 2020.

[15] H. M. Yang, "Research status and development tendency of hydraulic cutting technology for pressure relief and permeability increasing of deep coal seam," *Safety in Coal Mines*, vol. 49, no. 6, pp. 147–151, 2018.

[16] Y. L. Li, Y. Liu, S. Wang, and Q. X. Wang, "Research and application of deep hole pre-splitting blasting technology for permeability enhancement in high gas and low permeability coal seam," *Journal of Safety Science and Technology*, vol. 16, no. 9, pp. 71–76, 2020.

[17] M. J. Gong, P. Chi, and M. J. Zhang, "Permeability increase with deep borehole controlled pre-cracking blasting technology in low permeability and high gassy seam," *Coal Science and Technology*, vol. 40, no. 10, pp. 69–72, 2012.

[18] W. L. Pu and Y. W. Bi, "Permeability improvement gas drainage technology with deep borehole accumulated energy hydraulic blasting of low permeability seam," *Coal Science and Technology*, vol. 42, no. 5, pp. 37–40, 2014.

[19] D. Y. Shang, L. Peng-fei, X. Y. YU, and H. J. Zhang, "Permeability improved technology and practices with deep borehole energy accumulation blasting in low permeability seam," *Coal Science and Technology*, vol. 40, no. 12, pp. 48–51, 2012.

[20] N. Jia, "Joint application research on screen pipe protection hole and CO^2 phase change fracturing technology in low permeability and soft coal seam," *Safety in Coal Mines*, vol. 49, no. 1, pp. 153–156, 2018.

[21] H. P. Xie, F. Gao, and Y. Ju, "Research and development of rock mechanics in deep ground engineering," *Chinese Journal of Rock Mechanics and Engineering*, vol. 34, no. 11, pp. 2161–2178, 2015.

[22] H. P. Xie, "Research review of the state key research development program of China: deep rock mechanics and mining theory," *Journal of China Coal Society*, vol. 44, no. 5, pp. 1283–1305, 2019.

[23] W. X. Li, G. Wang, W. Z. Du et al., "Development and application of a true triaxial gas-solid coupling testing system for coal seepage," *Rock and Soil Mechanics*, vol. 37, no. 7, pp. 2109–2118, 2016.

[24] G. Wang, Z. Y. Liu, P. F. Wang, W. R. Wang, C. Fan, and X. Song, "Experimental study on shear seepage characteristics of true triaxial coal body under the consideration of gas adsorption," *Journal of Mining and Safety Engineering*, vol. 36, no. 5, pp. 1061–1070, 2019.

[25] T. F. Xie, *Study of Mechanism and Control Technology of Floor Heave under High Stress in Deep Roadway*, AnHui University of Science and Technology, 2018.

[26] M. Yang, X. Z. Hua, Z. G. Liu, and Q. J. Liu, "A multifunctional test apparatus for deep mining engineering," *Safety in Coal Mines*, vol. 50, no. 5, pp. 126–129, 2019.

[27] Z. H. Wang, "Displacement failure of deep surrounding rock and optimization of sealing process of through holes," *China Coal*, vol. 41, no. 12, pp. 105–109, 2015.

[28] S. C. Li, H. P. Wang, Q. H. Qian et al., "In-situ monitoring research on zonal disintegration of surrounding rock mass in deep mine roadways," *Chinese Journal of Rock Mechanics and Engineering*, vol. 27, no. 8, pp. 1545–1553, 2008.

Hindawi
Geofluids
Volume 2022, Article ID 3512507, 10 pages
https://doi.org/10.1155/2022/3512507

Research Article

Effect of Rheological Mesoparameters on Shear Mechanical Behavior of Joints

Kefeng Zhou,[1] **Sheng Liu**,[1] **and Yanhui Cheng**[2,3]

[1]*School of Traffic and Transportation Engineering, Changsha University of Science and Technology, Changsha Hunan 410114, China*
[2]*School of Civil Engineering, Hunan City University, Yiyang, Hunan 413000, China*
[3]*School of Resource Safety Engineering, Central South University, Changsha, Hunan 410083, China*

Correspondence should be addressed to Kefeng Zhou; zkf1978@126.com

Received 2 January 2022; Accepted 14 March 2022; Published 30 March 2022

Academic Editor: Zhijie Wen

Under natural conditions, joint failure usually occurs after long-term loading rather than short-term loading. In order to prevent rock mass failure caused by creep behavior, bolt is widely used as a mature and effective reinforcement method. Therefore, it is necessary to consider the rheological effect of bolted joint. In this paper, the particle flow code (PFC) was used to study the effect of mesoparameters on the rheological shear mechanical behavior of joints without bolts and with bolts. The effects of mesoparameters such as Maxwell elastic coefficient E_m, Maxwell viscosity coefficient C_m, Kelvin elastic coefficient E_m, Kelvin viscosity coefficient C_m, and friction coefficient F_s were analyzed. The results show that E_m and F_s mainly affect the instantaneous shear displacement, but have little effect on the rheological shear displacement. However, C_m, E_k, and C_k have little effect on the instantaneous shear displacement, and the sensitivity is mainly reflected in the rheological shear displacement. E_m and F_s mainly affect the instantaneous shear displacement, but have little effect on the rheological shear displacement. However, C_m, E_k, and C_k have little effect on the instantaneous shear displacement, and the sensitivity is mainly reflected in the rheological shear displacement. Compared with the parameter sensitivity characteristics without bolt, the instantaneous shear displacement, shear stiffness, and steady rheological displacement under anchor condition are less affected by parameters, indicating that anchor can reduce the influence of joint parameters.

1. Introduction

The mechanical properties of joints are important factors affecting the stability of rock mass engineering [1–3]. Under natural conditions, joint failure usually occurs after long-term loading rather than short-term loading. Under the condition of constant external stress, the displacement and stress field of joint are constantly adjusted and reorganized with time, resulting in the creep phenomenon that the strain increases continuously with time, which leads to the failure of jointed rock mass [4–6]. In order to prevent rock mass failure caused by creep behavior, bolt is widely used as a mature and effective reinforcement method [7, 8]. The mechanical properties of bolted joints can be studied by experiment, theoretical analysis, and numerical simulation [9–13]. At present, numerical calculation methods have been widely used in the field of rock mechanics, forming a variety of numerical calculation methods, including finite element method, discrete element method, motion element method, and meshless method [14–16]. Each method has its own advantages and disadvantages, which can solve geotechnical engineering-related problems. In the process of joint shear, due to the fluctuation of rock rupture, the cracks will occur in the rock mass and lead to stress and strain change [17–19]. However, the numerical calculation method based on continuum cannot easily simulate crack development, joint shear slip of continuous deformation of the line. Therefore, it is necessary to consider the material discontinuity numerical calculation method, such as particle flow code (PFC) [20, 21]. In order to study the mesomechanical characteristics of bolted joints, some scholars adopted PFC to simulate the macroscopic mechanical response of bolted

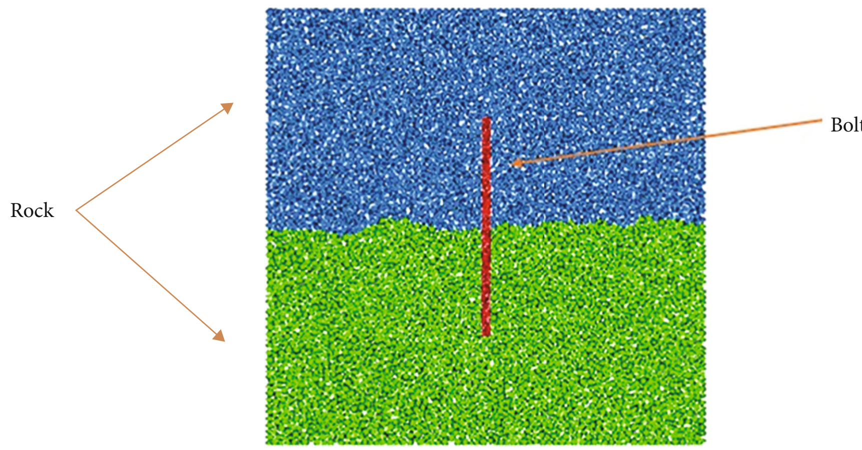

FIGURE 1: Numerical model of bolted joint subjected to rheological direct shear.

TABLE 1: Mesoscopic parameters of the numerical model.

Category	Microparameter (unit)	Value
Particle	Density (kg/m^3)	2500
	Radius (mm)	0.48-0.9
	f	5.0
	Krat (kn/ks)	0.5
	Porosity	0.16
	Emod (10^9)	0.425
Flat-joint contact model	fj_ten (10^6)	4.10
	fj_coh (10^6)	20.8
	fj_fa (°)	58.47
	fj_n	4
Burger contact model	bur_knm (10^9)	0.06
	bur_ksm (10^9)	0.06
	bur_cnm (10^9)	12.4
	bur_csm (10^9)	12.4
	bur_knk (10^9)	1.6
	bur_ksk (10^9)	1.6
	bur_cnk (10^9)	13.1
	bur_csk (10^9)	13.1
	bur_fs	0.6

joints through the interaction between mesoparticles. Shang et al. [22] established a numerical calculation model of discontinuous joints, studied the characteristics of joint mesoscopic parameters, and simulated the failure mode and strength characteristics of joints under equal normal stress and equal normal stiffness. The previous work mainly studied the shear mechanical properties of joints under conventional conditions, and the rheological effects of joint shear were seldom considered. Therefore, this paper adopts discrete element numerical calculation method to conduct rheological shear simulation tests on both anchored and unbolted joints and adopts control variable method in parameter sensitivity analysis. The effects of rheological mesoscopic parameters such as Maxwell body elastic coefficient E_m, Maxwell body viscosity coefficient C_m, Kelvin body elastic coefficient E_m, Kelvin body viscosity coefficient C_m, and friction coefficient F_s on shear mechanical behavior of joints were investigated.

2. Numerical Model

The numerical calculation model of joint was established using PFC, and the size of the model was 100 mm × 100 mm. Based on the established intact rock mass geometry model, the corresponding joint geometry is drawn in CAD. The geometry is imported into PFC by the geometry import command, and it is set to DFN fracture to establish the rock mass geometry model with joints. In the model, different particle parameters are set to simulate the bolt, as shown in Figure 1. In this paper, a flat-joint model is used to simulate the upper and lower rock blocks. Due to shear box in the rheological shear test parts in addition to a constant load, loading wall outside wall is consistent with the only wall loading rate of unconstrained free wall.

In the study of shear mechanical behavior, the experimental phenomenon at the moment of peak shear displacement is an important research object, and it is necessary to keep the simulated peak shear displacement consistent with the real test as much as possible [23–25]. Therefore, in this paper, the results of numerical simulation when normal stress is 1 MPa and laboratory test are the same as the standard, and the trial-and-error method is adopted to calibrate the mesoscopic parameters of rock. Firstly, a complete sample numerical model of flat joints is established to simulate the shear stress-shear displacement curve of flat joints. Finally, the mesoscopic parameters matching the actual situation are calibrated. The microscopic parameters of the numerical model are shown in Table 1. According to the bolt parameters in reference [26], a parallel bond model is used to describe the bolt. The friction coefficient is 0.5, which is smaller than that of rock. The tensile strength of bolt particles is 4.0 GPa, the bond force is 0.9 GPa, and the internal friction angle is 20°. Set a 5 cm long bolt with a diameter of 2 mm, as shown in Table 2 for specific parameters.

Table 2: Mesoscopic parameters of bolt.

Category	Mesoscopic parameters	Value
Particle	Density (kg/m^3)	7850
	Radius (mm)	0.18-0.3
	f	0.5
	Porosity P	0.16
	Normal stiffness kn	8e9
	Shear stiffness ks	2.286e9
Flat-joint contact model	Tensile strength pb_ten (GPa)	4.25
	Cohesion pb_coh (MPa)	900
	Friction angle pb_fa (°)	0
	Normal stiffness pb_kn	5.9e14
	Shear stiffness pb_ks	5.9e14

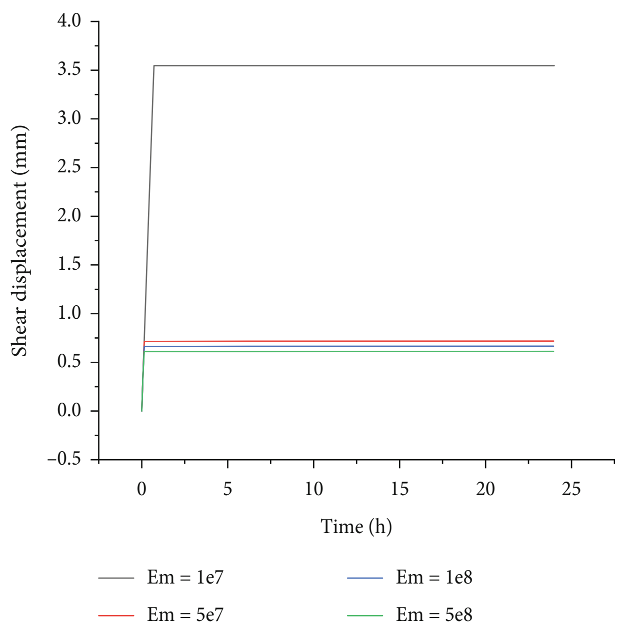

Figure 2: Shear displacement-time relation of unbolted joints under different E_m.

3. Calculation Results and Analysis

3.1. Relationship between Maxwell Elastic Coefficient and Macroscopic Shear Stiffness. In the rheological contact model, Maxwell volume elastic coefficient E_m controls the instantaneous displacement of intergranular contact. It is of important reference value to analyze the influence of E_m , the microscopic parameter of intergranular contact, on the macroscopic shear mechanical properties of joints. The control variable method was adopted, set to 1E7, 5E7, 1E8, and 5E8 (unit: Pa), respectively, to analyze the sensitivity of elastic coefficient E_m of Maxwell body. Shear displacement-time curves of bolt-free joints under different E_m conditions are shown in Figure 2. As can be seen from the figure, the instantaneous shear displacement decreases

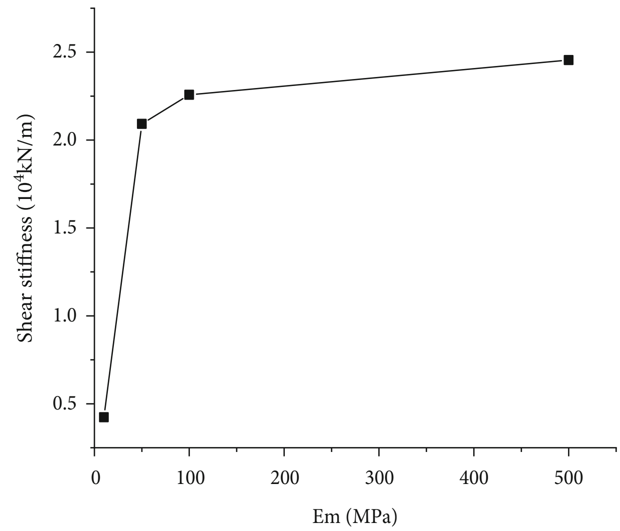

Figure 3: Relationship between E_m and macroscopic shear stiffness of joints without bolt.

with the increase of E_m, and E_m has a significant effect on the instantaneous shear displacement. Different E_m corresponds to the same rheological shear displacement, and E_m has no effect on the rheological shear displacement. By analyzing the elastic moduli corresponding to different E_m, the macroscopic shear stiffness K_s corresponding to different E_m is obtained, and the relationship between E_m and shear stiffness is shown in Figure 3. The shear stiffness is obtained from the curve of relation between shear stress and shear displacement; the curve slope represents the shear stiffness. It can be seen that there is a nonlinear relationship between E_m and macroscopic shear stiffness, and the shear stiffness changes greatly and converges to a value, indicating that E_m has a significant influence on macroscopic shear stiffness. The nonlinear expression is used to fit it, and the results are shown in Equation (1); R^2 is 0.98, indicating that the formula can well predict the macroscopic shear stiffness under different E_m conditions.

$$K_s = 3.1[1 - \exp(-0.04E_m)] - 0.719. \quad (1)$$

In the case of bolted joint, shear displacement-time curves under different E_m conditions were recorded, as shown in Figure 4. It can be seen that, similar to the case without bolt, the instantaneous shear displacement decreases with the increase of E_m, and E_m has a significant effect on the instantaneous shear displacement. Different E_m corresponds to the same rheological shear displacement, and E_m has no effect on the rheological shear displacement.

By analyzing the elastic moduli corresponding to different E_m, the macroscopic shear stiffness corresponding to different E_m is obtained, and the relationship between E_m and shear stiffness is shown in Figure 5. It can be seen that there is a nonlinear relationship between E_m and macroscopic shear stiffness, and the shear stiffness changes greatly and converges to a value, indicating that E_m has a significant influence on macroscopic shear stiffness. Nonlinear expression was used to fit them, and the results are shown in

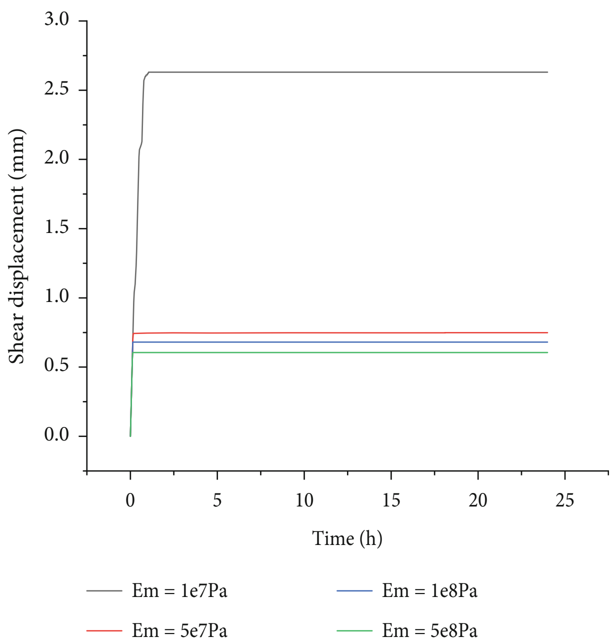

FIGURE 4: Shear displacement-time relation under different E_m with bolts.

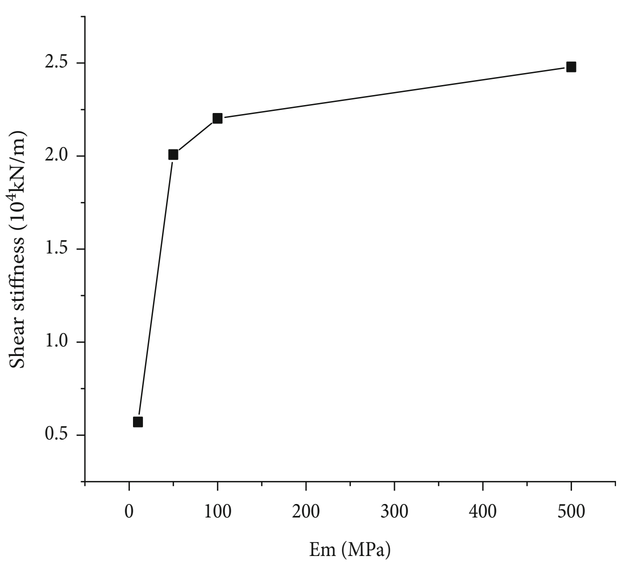

FIGURE 5: Shear stiffness of different E_m with bolt.

Equation (2). R^2 is 0.96, indicating that this formula can well predict the macroscopic shear stiffness under different E_m. Compared with Formula (1) without bolt, the shear stiffness with bolt is less affected by E_m, and the convergence value is also smaller, indicating that the bolt can reduce the influence brought by the change of joint parameters.

$$K_s = 2.6[1 - \exp(-0.03E_m)] - 0.207. \quad (2)$$

3.2. Influence of Maxwell Volume Viscosity Coefficient on the Relationship between Joint Shear Displacement and Time. In Burger's contact model, Maxwell viscosity coefficient C_m controls the creep displacement of interparticle contact,

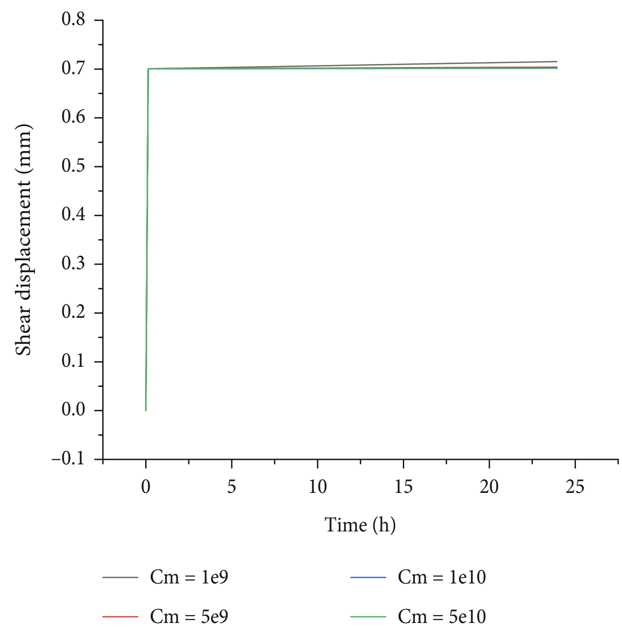

FIGURE 6: Shear displacement-time relation of unbolted joints under different C_m conditions.

and the displacement is closely related to time. Analyzing the microscopic parameter C_m of interparticle contact can effectively reflect the macroscopic mechanical characteristics of Burger's model parameters in the process of joint shear. The control variable method was adopted, set to 1E9, 5E9, 1E10, and 5E10, respectively, to analyze the sensitivity of Maxwell body viscosity coefficient C_m. The shear displacement-time curves of bolt-free joints under different C_m are shown in Figure 6. It can be seen that C_m has little influence on instantaneous shear displacement, but significant influence on rheological shear displacement. The larger C_m is, the smaller the rheological shear displacement is, and there is a negative correlation between the two. The rheological shear simulation results of unbolted joints obtained by changing C_m show that the adjustment of C_m has no significant effect on the joint numerical model displacement, crack. The results show that C_m affects the shear mechanical properties under rheological conditions, but the effect is small when no damage occurs. C_m is a factor affecting particle contact, but different from the displacement affected by E_m. The displacement affected by C_m is controlled by time. Therefore, when the time scale is not very large and C_m is not very small, the displacement affected by C_m is not particularly obvious.

In the case of bolted joint, shear displacement-time curves under different C_m conditions were recorded, as shown in Figure 7. It can be seen that C_m has little influence on instantaneous shear displacement, but significant influence on rheological shear displacement. The larger C_m is, the smaller the rheological shear displacement is, and there is a negative correlation between the two. Compared with Figure 6 without bolt, the discretization of shear displacements and time curves of different C_m in Figure 7 with bolt is smaller, indicating that anchor can reduce the influence of

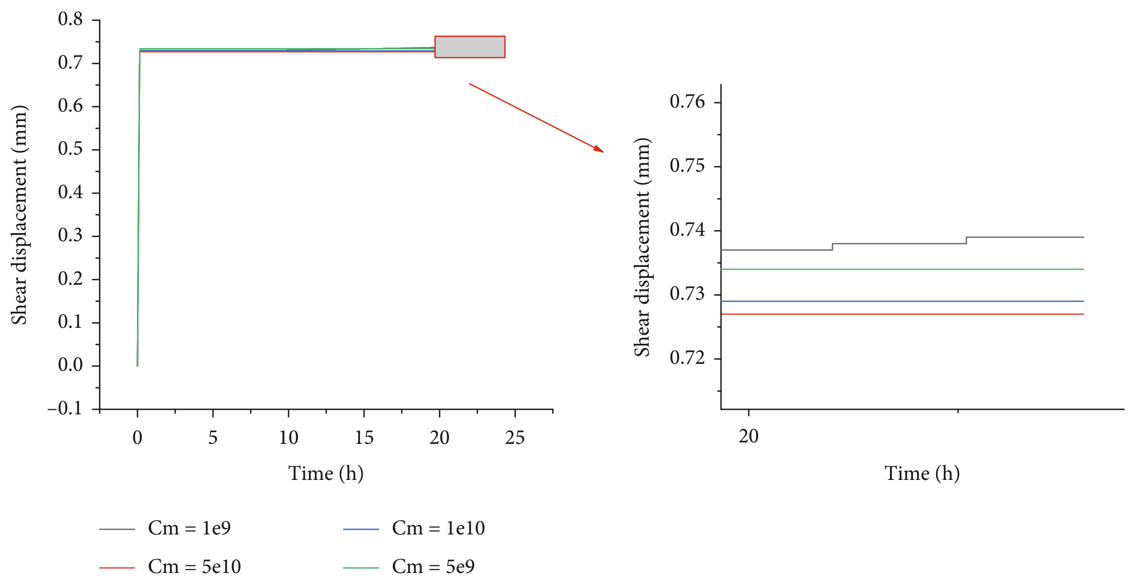

Figure 7: Shear displacement-time curves of bolted joints at different C_m.

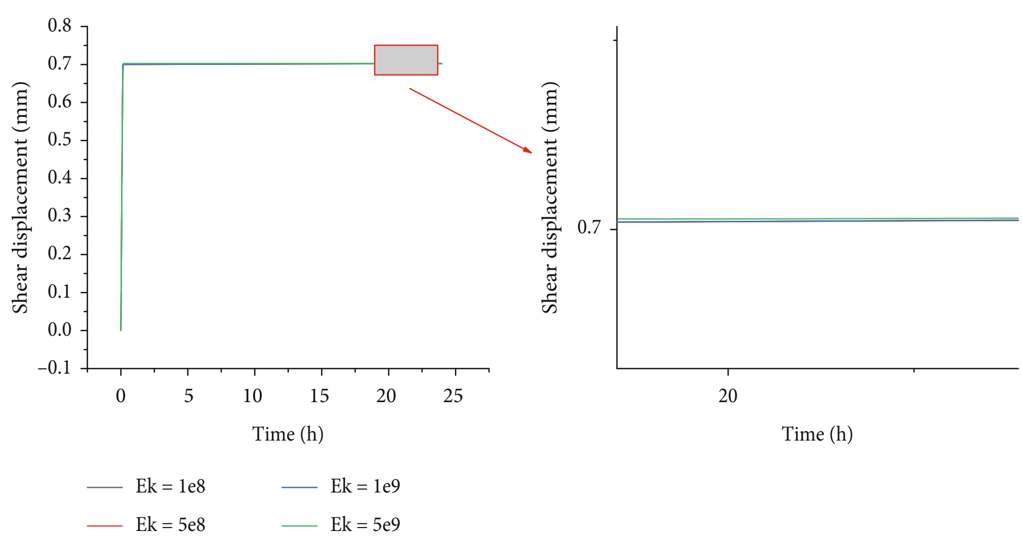

Figure 8: Shear displacement-time curves under different E_k conditions without bolt.

joint parameter C_m on joint aging deformation. The rheological shear simulation results of bolted joints obtained by changing C_m show that adjusting C_m has no significant effect on the joint numerical model displacement and crack. The results show that C_m affects the shear mechanical properties under rheological conditions, but the effect is small when no damage occurs. Compared with the condition without bolt, the influence of C_m on displacement is less obvious in the condition with bolt, and the influence of C_m on displacement can be weakened by bolt.

3.3. Influence of Nonlinear Kelvin Elastic Coefficient on Shear Mechanical Behavior of Joints. In the rheological contact model, the Kelvin elastic coefficient (E_k) affects the aging displacement of interparticle contact. The analysis of the micro parameter (E_k) of interparticle contact can effectively study the reflection of Burger's model parameters in macroscopic shear mechanical properties of joints. The control variable method was adopted, set to 1E8, 5E8, 1E9, and 5E9 (unit: Pa), respectively, to analyze the sensitivity characteristics of the elastic coefficient of Kelvin body E_k. The shear displacement-time curves of boltless joints under different E_k conditions are shown in Figure 8. It can be seen that E_k has little effect on the instantaneous shear displacement, but has an obvious effect on the rheological shear displacement. The larger E_k is, the smaller the rheological shear displacement is, and there is a negative correlation between them.

The rheological shear simulation results of unbolted joints obtained by changing E_k show that adjusting E_k has no obvious effect on the numerical model displacement, crack of the joints. The results show that E_k affects the shear mechanical properties under rheological conditions, but the effect is small when no damage occurs. E_k affects particle displacement, but the displacement is controlled by time.

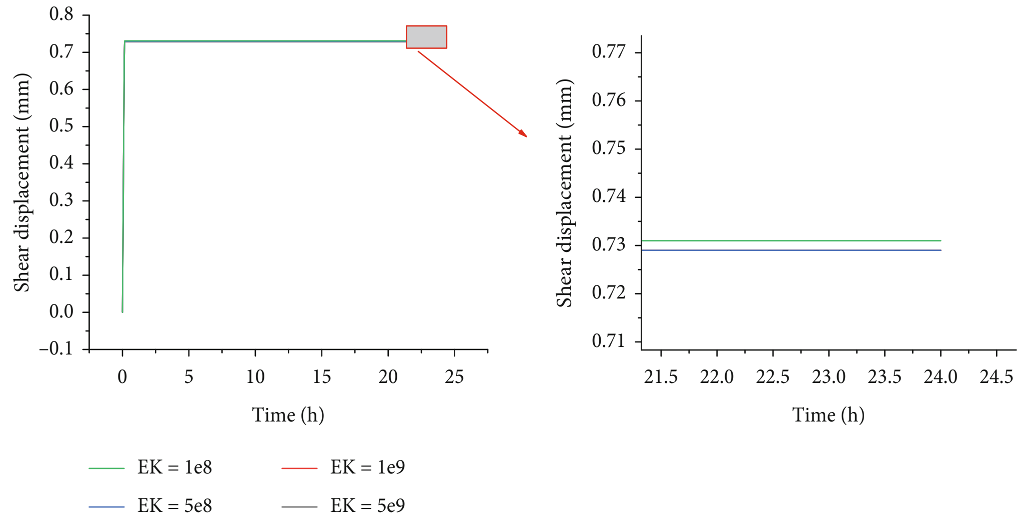

FIGURE 9: Shear displacement-time relation under different E_k conditions with bolt.

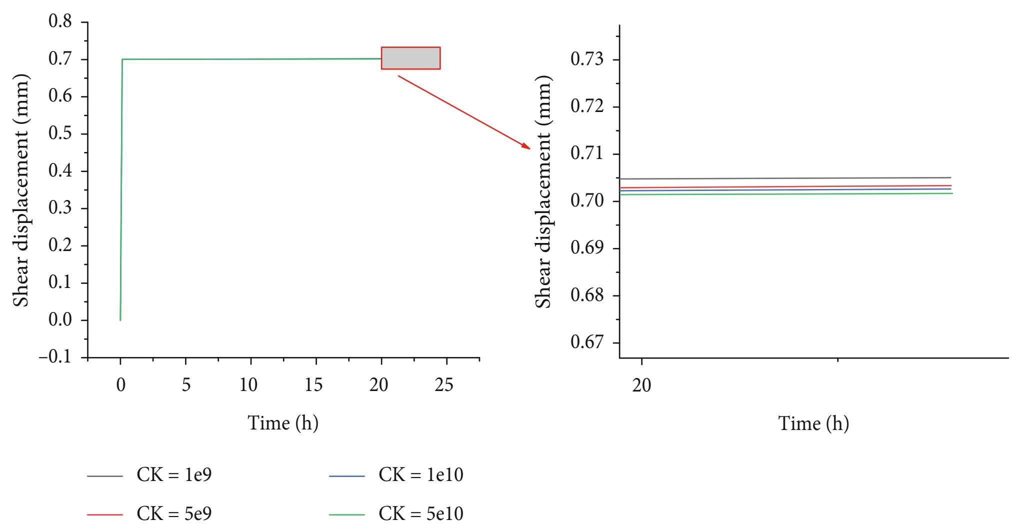

FIGURE 10: Shear displacement-time relation under different C_k.

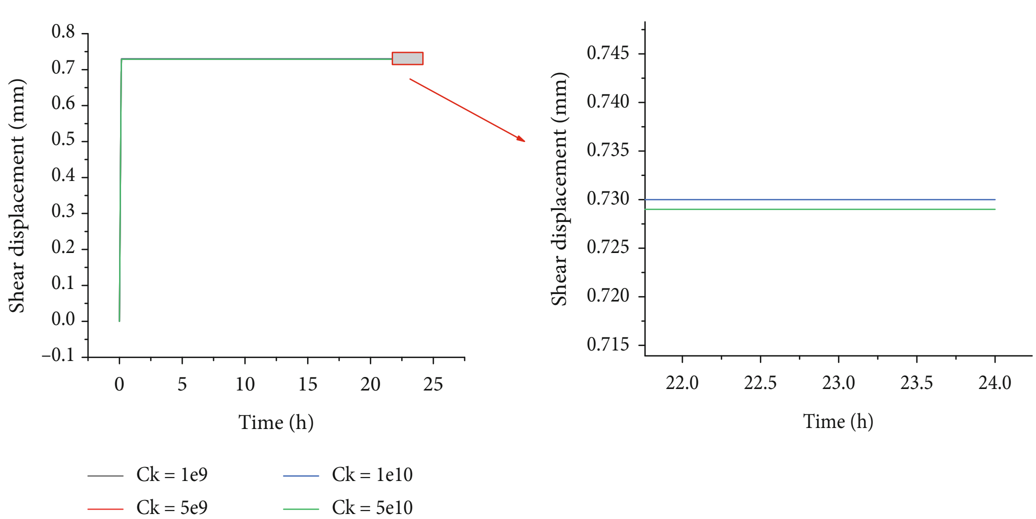

FIGURE 11: Shear displacement-time curves with bolts under different C_k conditions.

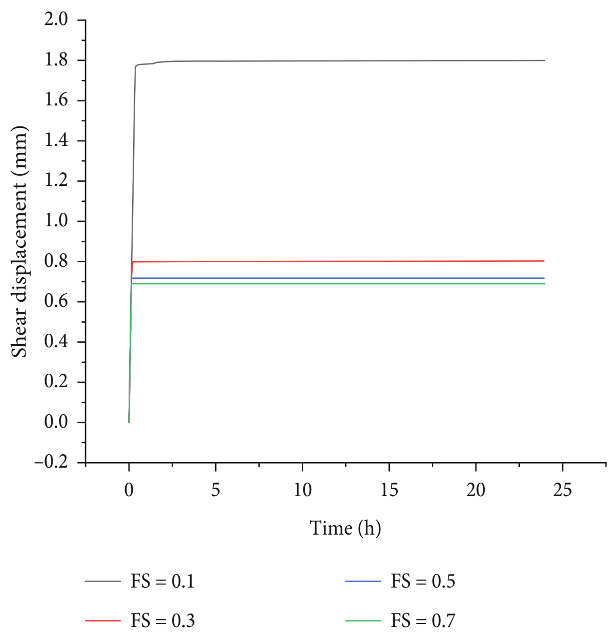

Figure 12: Shear displacement-time curves under different F_s conditions.

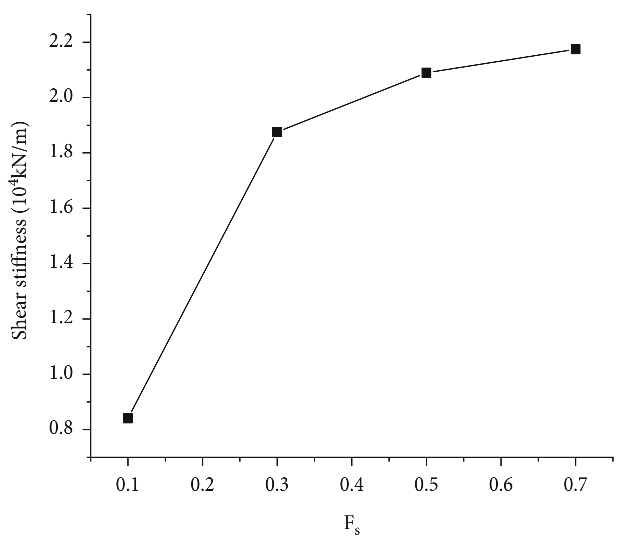

Figure 13: Relationship between F_s and shear stiffness.

Therefore, when the time range is not very large and E_k is not very small, the displacement affected by E_k is not particularly obvious. The relationship between shear displacement and time at different E_k was recorded, as shown in Figure 9. It can be seen from Figure 9 that E_k has little influence on instantaneous shear displacement, but has obvious influence on rheological shear displacement. The larger E_k is, the smaller the rheological shear displacement is, and there is a negative correlation between them. The rheological shear simulation results of bolted joints obtained by changing E_k show that adjusting E_k has no obvious effect on the numerical model displacement and crack of the joints. The results show that E_k affects the shear mechanical properties under rheological conditions, but the effect is small when no damage occurs. Compared with the condition without bolt, the rock mass displacement with bolt is less affected by E_k.

3.4. Relationship between Joint Shear Displacement and Time under Different Kelvin Body Viscosity Coefficients. The Kelvin viscosity coefficient C_k affects the aging displacement of the contact between particles. The analysis of the microscopic parameters C_k of the contact between particles can effectively study the reflection of the parameters of Burger's model on the macroscopic shear mechanical properties of joints. Control variable method was adopted, set as 1E9, 5E9, 1E10, and 5E10, respectively, to analyze the sensitivity characteristics of Kelvin body viscosity coefficient C_k. Shear displacement-time curves under different C_k conditions are shown in Figure 10. It can be seen that C_k has little influence on instantaneous shear displacement, but significant influence on rheological shear displacement. The larger C_k is, the smaller the rheological shear displacement is, and there is a negative correlation between the two.

The rheological shear simulation results of unbolted joints obtained by changing C_k show that adjusting C_k has no significant effect on the joint numerical model displacement, crack. The results show that C_k affects the shear mechanical properties under rheological conditions, but the effect is small when no damage occurs. C_k is a factor affecting particle contact, but different from the displacement affected by E_m, the displacement affected by C_k is controlled by time. Therefore, when the time scale is not very large and C_k is not very small, the displacement affected by C_k is not particularly obvious. Shear displacement-time curves of bolted joints under different C_k conditions are shown in Figure 11. It can be seen that C_k has little influence on instantaneous shear displacement, but significant influence on rheological shear displacement. The larger C_k is, the smaller the rheological shear displacement is, and there is a negative correlation. The rheological shear simulation results of bolted joints obtained by changing C_k show that adjusting C_k has no significant effect on the joint numerical model displacement and crack. The results show that C_k affects the shear mechanical properties under rheological conditions, but the effect is small when no damage occurs. Compared with the condition without bolt, the rock mass displacement with bolt is less affected by C_k.

3.5. Influence of Joint Friction Coefficient on Joint Mechanical Behavior. In the rheological contact model, the friction coefficient affects the contact force between particles, and the analysis of the friction coefficient can effectively study the reflection of the rheological model parameters on the macroscopic shear mechanical properties of joints. The control variable method was adopted, set to 0.1, 0.3, 0.5, and 0.7, respectively, to analyze the sensitivity characteristics of friction coefficient F_s. Shear displacement-time curves under different F_s conditions are shown in Figure 12. As can be seen from the figure, the instantaneous shear displacement decreases with the increase of F_s, and F_s has a significant impact on the instantaneous shear displacement. The rheological shear displacement corresponding to

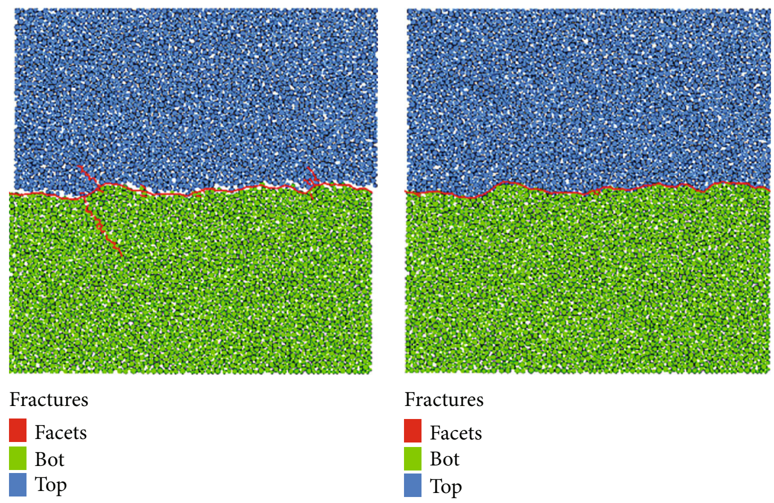

(a) $F_s = 0.1$ (b) $F_s = 0.7$

Figure 14: Number of sample cracks under different friction coefficients F_s.

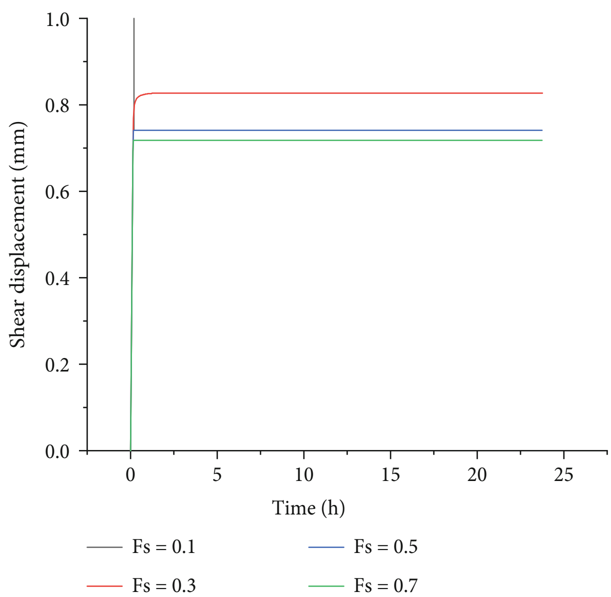

Figure 15: Shear displacement-time curves of different F_s with bolt.

different F_s is roughly the same, and F_s has no effect on the rheological shear displacement. By analyzing the elastic moduli corresponding to different F_s, the macroscopic shear stiffness corresponding to different F_s is obtained, and the relationship between F_s and shear stiffness is shown in Figure 13. It can be seen that there is a nonlinear relationship between F_s and the macroscopic shear stiffness, and the shear stiffness changes greatly, indicating that F_s has a significant impact on the macroscopic shear stiffness. The nonlinear expression is used to fit it, and the results are shown in Equation (3); R^2 is 0.99, indicating that the formula can well predict the macroscopic shear stiffness under different F_s conditions.

$$K_s = 2.77(1 - \exp(-7.3F_s)) - 0.59. \tag{3}$$

Respectively, change the interparticle friction coefficient of F_s, by calculation, the joint can be obtained corresponding crack number, displacement, as shown in Figure 14. It shows that, in the process of shearing, joint displacement and number of crack are significantly affected by F_s. The greater the shear displacement is smaller, the less crack. F_s has a negative relationship with shear displacement and crack number. In the rheological model, the shear strength is controlled by the normal stress and friction coefficient F_s. Therefore, the larger F_s is, the greater the static friction force to overcome under the condition of the same displacement caused by particle contact is, and it is less likely to produce sliding and cracks.

In the case of bolted joint, shear displacement-time curves under different F_s conditions are shown in Figure 15. As can be seen from the figure, the instantaneous shear displacement decreases with the increase of F_s, and F_s has a significant impact on the instantaneous shear displacement. The rheological shear displacement corresponding to different F_s is roughly the same, and F_s has no effect on the rheological shear displacement. By analyzing the elastic moduli corresponding to different F_s, the macroscopic shear stiffness corresponding to different F_s is obtained, and the relationship between F_s and shear stiffness is shown in Figure 16. It can be seen that there is a nonlinear relationship between F_s and the macroscopic shear stiffness, and the shear stiffness changes greatly, indicating that F_s has a significant impact on the macroscopic shear stiffness. The nonlinear expression is used to fit it, and the results are shown in Equation (4); R^2 is 0.99, indicating that the formula can well predict the macroscopic shear stiffness under different F_s conditions. Compared with Formula (3) without bolt, the shear stiffness with bolt is less affected by F_s, and the anchor can reduce the influence of joint parameter F_s on mechanical properties.

For bolted joints, F_s is changed separately, and it is found that the larger F_s is, the smaller the shear displacement is, the fewer the cracks are, and the less obvious the tension chain

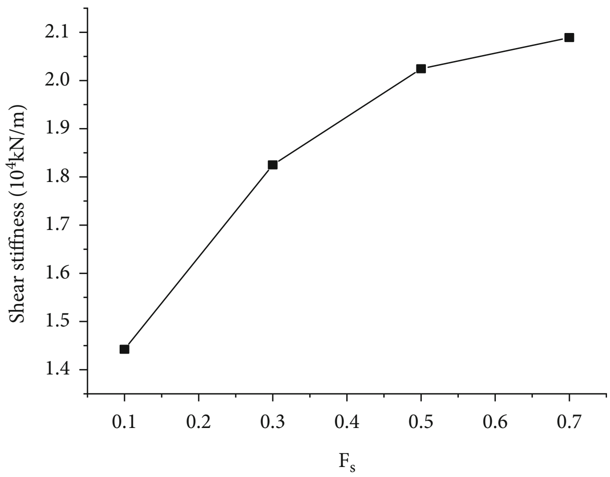

Figure 16: Relationship between F_s and shear stiffness.

concentration on the joints is. F_s has a negative relationship with shear displacement and crack number. Shear strength is controlled by normal stress and friction coefficient F_s and is proportional to F_s. Therefore, the larger F_s is, the more static friction force to be overcome under the condition of the same displacement caused by particle contact and the less prone to sliding and cracking of rock mass. However, the rock mass under the condition of anchor is less affected by F_s than that without bolt, and the anchor can reduce the influence brought by the change of rock mass mesoscopic parameters, which is conducive to enhancing the stability of rock mass.

$$K_s = 1.06[1 - \exp(-3.86F_s)] + 1.09. \quad (4)$$

4. Conclusions

(1) For unbolted joint, E_m and F_s mainly affect the instantaneous shear displacement, but have little effect on the rheological shear displacement. However, C_m, E_k, and C_k have little effect on the instantaneous shear displacement, and the sensitivity is mainly reflected in the rheological shear displacement

(2) For bolted joint, E_m and F_s mainly affect the instantaneous shear displacement, but have little effect on the rheological shear displacement. However, C_m, E_k, and C_k have little effect on the instantaneous shear displacement, and the sensitivity is mainly reflected in the rheological shear displacement. It should be noted that the instantaneous shear displacement, shear stiffness, and steady rheological displacement with bolt are less affected by parameters than the parameter sensitivity without bolt, indicating that the anchor can reduce the influence of joint parameters

Data Availability

The data used to support the findings of this study are available from the corresponding author upon request.

Conflicts of Interest

The authors declare no conflicts of interest.

References

[1] X. Zhang, H. Lin, Y. Wang, R. Yong, Y. Zhao, and S. Du, "Damage evolution characteristics of saw-tooth joint under shear creep condition," *International Journal of Damage Mechanics*, vol. 30, no. 3, pp. 453–480, 2021.

[2] S. Zare, S. Karimi-Nasab, and H. Jalalifar, "Analysis and determination of the behavioral mechanism of rock bridges using experimental and numerical modeling of non-persistent rock joints," *International Journal of Rock Mechanics and Mining Sciences*, vol. 141, p. 104714, 2021.

[3] Y. Tang, H. Lin, Y. Wang, and Y. Zhao, "Rock slope stability analysis considering the effect of locked section," *Bulletin of Engineering Geology and the Environment*, vol. 80, no. 9, pp. 7241–7251, 2021.

[4] H. Mansouri and R. Ajalloeian, "Mechanical behavior of salt rock under uniaxial compression and creep tests," *International Journal of Rock Mechanics and Mining Sciences*, vol. 110, pp. 19–27, 2018.

[5] X. Fan, H. Yu, Z. Deng, Z. He, and Y. Zhao, "Cracking and deformation of cuboidal sandstone with a single nonpenetrating flaw under uniaxial compression," *Theoretical and Applied Fracture Mechanics*, vol. 119, article 103284, 2022.

[6] Y. Zhao, Y. Wang, W. Wang, L. Tang, Q. Liu, and G. Cheng, "Modeling of rheological fracture behavior of rock cracks subjected to hydraulic pressure and far field stresses," *Theoretical and Applied Fracture Mechanics*, vol. 101, pp. 59–66, 2019.

[7] M. Zambrano, A. D. Pitts, A. Salama, T. Volatili, M. Giorgioni, and E. Tondi, "Analysis of fracture roughness control on permeability using SfM and fluid flow simulations: implications for carbonate reservoir characterization," *Geofluids*, vol. 2019, Article ID 4132386, 19 pages, 2019.

[8] E. Komurlu and A. Kesimal, "Experimental study on usability of friction rockbolts with plastic bodies," *International Journal of Geomechanics*, vol. 17, no. 9, p. 04017058, 2017.

[9] H. Lin, W. Xiong, Z. Xiong, and F. Gong, "Three-dimensional effects in a flattened Brazilian disk test," *International Journal of Rock Mechanics and Mining Sciences*, vol. 74, pp. 94–100, 2019.

[10] Z. Wen, E. Xing, S. Shi, and Y. Jiang, "Overlying strata structural modeling and support applicability analysis for large mining-height stopes," *Journal of Loss Prevention in the Process Industries*, vol. 57, no. 10-4, 2015.

[11] D. Han, K. Li, and J. Meng, "Evolution of nonlinear elasticity and crack damage of rock joint under cyclic tension," *International Journal of Rock Mechanics and Mining Sciences*, vol. 128, article 104286, 2020.

[12] D. Han, Y.-f. Leung, and J. Zhu, "Tensile strength and deformational behavior of stylolites and mineral healed joints subject to dynamic direct tension," *Rock Mechanics and Rock Engineering*, vol. 55, 2022.

[13] K. Li, Y. Cheng, Z. Y. Yin, D. Y. Han, and J. J. Meng, "Size effects in a transversely isotropic rock under Brazilian tests: laboratory testing," *Rock Mechanics and Rock Engineering*, vol. 53, no. 6, pp. 2623–2642, 2020.

[14] H. Yang, H. Lin, Y. Wang, R. Cao, J. Li, and Y. Zhao, "Investigation of the correlation between crack propagation process and the peak strength for the specimen containing a single

pre-existing flaw made of rock-like material," *Archives of Civil and Mechanical Engineering*, vol. 21, no. 2, p. 68, 2021.

[15] Y. Chen, H. Lin, X. Ding, and S. Xie, "Scale effect of shear mechanical properties of non-penetrating horizontal rock-like joints," *Environmental Earth Sciences*, vol. 80, no. 5, p. 1, 2021.

[16] J. Meng, J. Huang, S. Sloan, and D. Sheng, "Discrete modelling jointed rock slopes using mathematical programming methods," *Computers and Geotechnics*, vol. 96, pp. 189–202, 2018.

[17] J. Jin, P. Cao, Y. Chen, C. Pu, D. Mao, and X. Fan, "Influence of single flaw on the failure process and energy mechanics of rock- like material," *Computers and Geotechnics*, vol. 86, pp. 150–162, 2017.

[18] C. Zhang, Y. Wang, and T. Jiang, "The propagation mechanism of an oblique straight crack in a rock sample and the effect of osmotic pressure under in-plane biaxial compression," *Arabian Journal of Geosciences*, vol. 13, no. 15, p. 736, 2020.

[19] X. Fan, Z. Yang, and K. Li, "Effects of the lining structure on mechanical and fracturing behaviors of four-arc shaped tunnels in a jointed rock mass under uniaxial compression," *Theoretical and Applied Fracture Mechanics*, vol. 112, article 102887, 2021.

[20] V. Sarfarazi, S. Abharian, and E. Z. Ghalam, "Physical test and PFC2D simulation of the failure mechanism of echelon joint under uniaxial compression," *Computers and Concrete*, vol. 27, pp. 99–109, 2021.

[21] A. S. Tawadrous, D. Degagné, M. Pierce, and I. D. Mas, "Prediction of uniaxial compression PFC3D model micro-properties using artificial neural networks," *International Journal for Numerical and Analytical Methods in Geomechanics*, vol. 33, no. 18, pp. 1953–1962, 2009.

[22] J. Shang, Z. Zhao, and S. Ma, "On the shear failure of incipient rock discontinuities under CNL and CNS boundary conditions: insights from DEM modelling," *Engineering Geology*, vol. 234, pp. 153–166, 2018.

[23] X. Zhang, H. Lin, Y. Wang, and Y. Zhao, "Creep damage model of rock mass under multi-level creep load based on spatio-temporal evolution of deformation modulus," *Archives of Civil and Mechanical Engineering*, vol. 21, no. 2, p. 71, 2021.

[24] M. Behnia, B. Nateghpour, J. Tavakoli, and B. M. Sharifi, "Comparison of experimental and empirical methods for estimating the shear strength of rock joints based on the statistical approach," *Environmental Earth Sciences*, vol. 79, no. 14, p. 361, 2020.

[25] R. Hao, P. Cao, Y. Chen, J. Jin, H. Wang, and X. Fan, "Mechanical and propagating behaviors of single-flawed rock samples with hydraulic pressure and uniaxial compression conditions," *International Journal of Geomechanics*, vol. 18, no. 7, article 04018078, 2018.

[26] N. Che, H. Wang, and M. Jiang, "DEM investigation of rock/bolt mechanical behaviour in pull-out tests," *Particuology*, vol. 52, pp. 10–27, 2020.

Hindawi
Geofluids
Volume 2022, Article ID 8382493, 13 pages
https://doi.org/10.1155/2022/8382493

Research Article

Study on the Dynamic Instability Mechanism of the Rock Formation in the Multifault Structure Zone of the Stope

Hanxiao Guo,[1] Weijian Yu,[1,2] Yong Liu,[3] Zongtang Zhang,[4] and Xiangtao Kang[3]

[1]*School of Resource, Environment and Safety Engineering, Hunan University of Science and Technology, Xiangtan, Hunan 411201, China*
[2]*Hunan Provincial Key Laboratory of Safe Mining Techniques of Coal Mines, Hunan University of Science and Technology, Xiangtan, Hunan 411201, China*
[3]*College of Mining, Guizhou University, Guiyang, Guizhou 550003, China*
[4]*Hunan Provincial Key Laboratory of Geotechnical Engineering for Stability Control and Health Monitoring, Hunan University of Science and Technology, Xiangtan 411201, China*

Correspondence should be addressed to Weijian Yu; ywjlah@163.com

Received 21 August 2021; Accepted 24 February 2022; Published 29 March 2022

Academic Editor: Dan Ma

Under the influence of tectonism in geological activities, most fault structures appear in groups. Multiple fault structures can induce a variety of mine dynamic disasters, which significantly affect the safety of mine production. To study the dynamic instability mechanism of the strata in the multifault structure zone of the stope when mining, a numerical model of multiple fracture structures was established. At the same time, the mechanism of the dynamic instability of the rock formation in the multifault structure zone of the stope has been studied through similar simulation experiments and on-site data analysis. The research results show that the stress-affected areas of the faults in the multiple-fault structure area overlap, and the stress evolution law of the fault will distinguish its independent dynamic evolution model. The multifault structure area has a multifault overall evolution law model. In this model, there is a synergy between the fault layers, and the maximum value of stress concentration is diagonally distributed. Under the influence of mining, the fault structure will be activated to change the stress field distribution form of the stope. The two faults in multiple structural areas have a joint mechanism, which plays a key role in controlling the dynamic instability process of the surrounding rock of the stope. The first activated faults in the multiple-fault structure area will undergo secondary activation under the influence of subsequent fault activities. The evolution law of cracks in the overburden of similar simulation experiments confirms that the early active F1 fault will be affected by the subsequent F2 fault activity. The mine pressure data measured on-site verifies the reliability of the numerical simulation experiment and the similar simulation experiment.

1. Introduction

The fault is one of the important factors causing the mine dynamic disaster. Theoretical research on the mechanism of the impact of faults on coal mines is the research hotspot of mine dynamic disasters [1–4]. There are many mountainous structures in southwest China, which are affected by tectonic action in geological activities, and fault structures are developed and mostly appear in groups [5]. Therefore, it is of great significance to study the mechanism of mine dynamic disasters induced by multiple fault structures for mine production safety. Due to technical and economic constraints, most of the small faults are gradually excavated in the process of roadway excavation and mining. At the same time, the solutions are often proposed for the current fault problems, and the interaction mechanism of adjacent faults is rarely considered due to the timeliness of mining. The previous active fault will change the surrounding rock stress state and the active influence range of the adjacent fault. The activation of the second fault will amplify the influence and range of activity of the first fault. The rock mass affected by multiple fracture structures is broken and has low mechanical strength. At present, under the influence of in situ stress and mining disturbance, problems such as the deformation of surrounding rock of the mining roadway and the instability of the overlying rock layer have become more and more prominent. It makes the transportation and operation of mining equipment very difficult to deform and even causes roof fall accidents. Faults are one of the geological structures frequently encountered in mining activities. The existence of faults destroys the continuity and integrity of the rock formations. It is an important factor affecting the safety of coal mining. Many mine disasters such as rock shock, mine water inrush, and stepped subsidence of the ground are caused by the activation of faults caused by mining.

Han et al. [6] established a mechanical model of fault activation when mining on hang-wall and foot-wall mining based on the theory of key strata and deduced the criterion of fault slip and instability. The movement model of key strata is shown in Figure 1. Wang et al. [7] studied the crack areas of overlying strata affected by reverse faults and discovered the characteristics of easy slicing of coal walls in the areas affected by faults. Wu et al. [8] conducted a similar simulation, taking the coal pillar away from the fault as a variable, and concluded that the width of the coal pillar plays a key role in the stability of the surrounding rock of the fault. Li et al. [9] revealed the dynamic change indexes of displacement and stress after fault activation under similar simulation through the data recording of measuring points in the model. Zhang et al. [10] obtained the variation law of stability of faulted rock mass after failure by studying the process of rock mass expansion and dilatancy. Hudson et al. [11] found that the stress near the structural plane is caused by the joint action of the structural plane itself and the surrounding rock mass. Atsushi Sainoki et al. [12–14] studied the influence of joints on the activation of faults by means of simulations and obtained the law of action of different factors on the activities of mining over faults.

Xiao et al. [15] pointed out that the surrounding rock with a developed geological structure and loose and broken will suffer from strong tectonic stress when the coal seam is mined. The surrounding rock of the roadway is characterized by asymmetric deformation and failure, large floor heave deformation, and inner squeezing of two sides. Through field investigation, numerical simulation, and theoretical analysis, Yu et al. [16, 17] studied the action mechanism of fissures on roadway surrounding rock, which has an important guiding role in the study of the failure law of roadway surrounding rock in the fracture zone of fault. Gou et al. [18] simulated the instability process of overlying rock when mining on the fault zone to grasp the movement characteristics of the overlying strata near the fault mining roadway. The test results show that the fault activation is caused by the mining of coal seam, which makes the strata movement have discontinuity, and the roof separation occurs. When the mining roadway is close to the fault, vertical cracks appear on the roadway side, the failure depth of floor increases, the deformation of the roof is not coordinated, and the deformation of the boundary coal pillar is large. Wang et al. [19] found that large mining height, poor mechanical properties of coal and rock mass, and large roof load were important reasons for coal wall slicing near faults. At the same time, the internal mechanism of coal wall lamination in the working face is revealed, and the discriminant basis of coal wall lamination is established. Wang et al. [20] analyzed the top plate stress distribution law by establishing an elastic beam model including normal and inverse faults. Based on the Mohr-Coulomb criterion, the failure mechanism and mechanical mechanism of the roof under different roof loads, different support strengths, and different span-to-height ratios are revealed. Li et al. [21] analyzed the distribution characteristics of the in situ stress field in China's coal mining areas and the relationship between the in situ stress field and fault activity by using 219 groups of measured in situ stress data optimized by regression analysis. The conclusion indicates that 0.6 is the appropriate criterion for fault slip instability in the overall evaluation of fault stability in coal mining areas of China. Wei et al. [22] analyzed the layout of roadway preexcavation and the rationality of the technology when the working face passed through the fault by applying the theory of key strata. The characteristics of mine pressure in the preexcavation roadway at fault position are pointed out, and the optimal supporting parameters are selected by numerical simulation. Wang et al. [23, 24] obtained the failure law of surrounding rock under different confining pressures in the process of coal mining through experimental research, providing theoretical guidance for the failure form of surrounding rock under different confining pressures when mining across faults. Through experiments and theoretical analysis, Ma et al. [25–28] studied the fracture propagation form of overlying rock in stope and the water conduction law of the fracture, which provided an important theoretical basis for the study of fault fracture failure mechanism. Lai et al. [29] observed the microstructure and distribution of cracks (pores) of coal and rock samples adjacent to the fault and measured the physical and mechanical properties of the coal and rock mass. The effect of faults on dynamic pressure in stope was explored through the physical experiment and the numerical simulation. The analysis shows that the existence of fault blocks the continuity of the medium and causes energy to accumulate at the fault. When the work is advancing towards the fault area, the accumulated energy is released and transferred, resulting in the roof of the mining roadway being cut off, coal wall slicing, partial support fracture, and other phenomena.

Experts and scholars have carried out a lot of research work on rockburst under the influence of faults by means of physical experiments, theoretical derivation, and numerical simulation. A series of important indexes representing the relationship between fault and rockburst are revealed, which provides a useful reference for mine safety production [30–33]. As one of the important factors to induce the mining response of coal seam, fault poses a great threat to the safe mining of coal mines. Therefore, it is very important to know the development degree and distribution of faults. For a long time, relevant experts at home and abroad have attached great importance to the adverse effects of faults on the safe mining of coal mines, carried out a lot of research

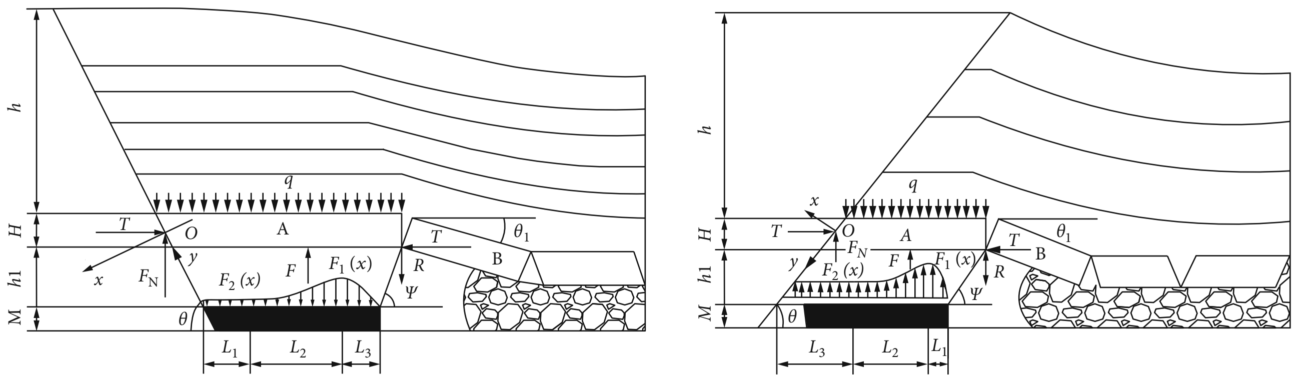

FIGURE 1: Movement of key strata when mining on hanging-wall and foot-wall [6].

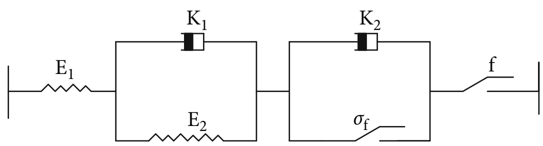

FIGURE 2: Comprehensive model diagram of rheological instability.

work on this, and achieved fruitful research results [34–37]. At present, most studies focus on a single fault, but few on the joint mechanism of multiple faults. Based on the actual conditions of the specific coal mine, this paper uses a combination of theoretical analysis, numerical simulation, similar simulation, and on-site measurement to study the overburden cracks and stress evolution laws caused by coal mining. The dynamic instability mechanism of rock strata was systematically revealed in the multifault structural area of the stope and provided a reference for the actual production activities.

2. Fault Activation Instability Model

It is rare for the faults to exist alone in nature, and faults often appear in groups during structural changes. Many faults of varying sizes are either almost parallel to each other or intersect or tend to intersect at a certain angle, forming a fault zone. Faults are generated and developed in the process of crustal tectonic changes. Faults are widely distributed in the world and in my country. It is not only an important geological phenomenon related to a series of theoretical issues in structural geology, seismology, and geodynamics. Moreover, it is closely related to the formation and distribution of mineral resources, the foundation stability of large-scale projects, the division of seismic danger zones, and earthquake prediction.

The southwestern region is one of the most widely distributed areas of faults in China. In order to study the dynamic instability mechanism of the strata in the multifault structure zone of the stope, the specific working face of the mining area in Liupanshui, Guizhou, was selected as the research object. By analyzing the mechanical effect of fault, it was found that the rheological instability comprehensive model can explain the activation phenomenon of fault rock well. The model consists of three parts, which can properly describe the viscoelastoplastic mechanical properties of rock. The first part is composed of spring E_1 in series with the Kelvin body, which is mainly manifested as viscoelastic deformation. The viscous element and the friction element are connected in parallel to form the second part and when $\sigma > \sigma_f$ exhibits viscoplastic deformation characteristics. The third part is composed of the friction element, which is used to simulate the phenomenon of sudden sliding when $\sigma > f$. Different rheological instable mechanical phenomena will appear when the σ_f and f values of the model are different. This is shown in Figure 2.

When $\sigma < \sigma_f < f$, the model satisfies the following stress-strain relationship:

$$\begin{cases} \sigma = E_1 \cdot \varepsilon_1, \\ \sigma = E_2 \cdot \varepsilon_2 + K_1 \cdot \varepsilon_2, \\ \varepsilon = \varepsilon_1 + \varepsilon_2. \end{cases} \tag{1}$$

The rheological equation can be obtained from equation (1) as follows:

$$\frac{K_1}{E_1} \cdot \sigma + \frac{E_1 + E_2}{E_1} \cdot \sigma = K_1 \dot{\varepsilon} + E_2 \cdot \varepsilon, \tag{2}$$

where σ and ε represent the differential of stress and strain with respect to time, respectively. When the stress is constant, the following can be obtained:

$$\sigma = \sigma_0 = \cos s \cdot t. \tag{3}$$

And set the initial conditions as $\varepsilon(0) = \varepsilon_0 = \sigma_0 / E_1 \ (t = 0^+)$. Then, the solution of rheological equation (2) can be changed to

$$\varepsilon(t) = \frac{\sigma_0}{E} + \frac{\varepsilon_0 - \sigma_0}{E} \cdot e^{-t/t_{\mathrm{ret}}}, \tag{4}$$

where $t_{\mathrm{ret}} = K_1 / E_2$ is the lag time, $E = E_1 \cdot E_2 / E_1 + E_2$.

In summary, when stress is constant, the strain increases with time. Assuming that the strain does not change, that is,

$$\varepsilon = \varepsilon_0 = \cos s \cdot t. \tag{5}$$

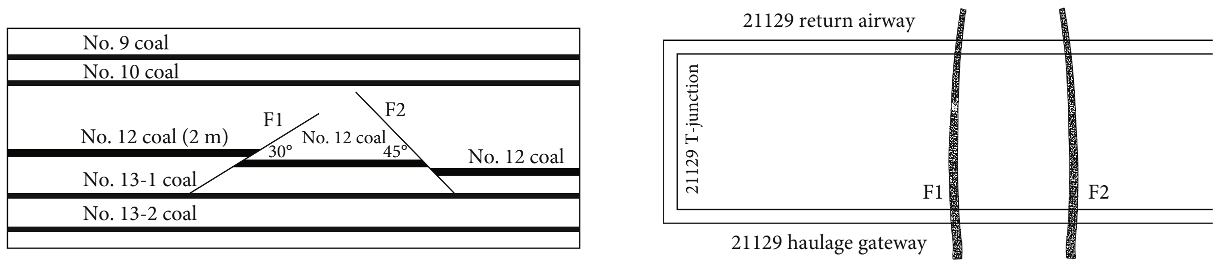

Figure 3: Sketch of the engineering drawing (flat and section).

Table 1: Rock mechanical parameters of each rock layer.

Rock name	Thickness (m)	Bulk (GPa)	Shear (GPa)	σ_{tension} (MPa)	Coh. (MPa)	Fric. (°)	Density (kN/m^3)
Siltstone	47	9.94	6.5	2.3	3.2	35	2460
No. 9 coal	1.5	3.22	1.0	0.23	0.6	22	1620
Fine sandstone	2	9.82	6.7	2.5	1.6	32	2660
Siltstone	2	9.94	6.5	2.4	3.2	30	2460
No. 10 coal	0.8	3.22	1.0	0.23	0.6	22	1620
Mudstone	1.5	3.68	3.1	1.8	0.56	20	0.23
Siltstone	4.5	9.94	6.5	2.4	3.2	30	2460
Fine sandstone	22	10.6	9.1	2.0	2.2	32	2200
No. 12 coal	2	4.36	1.2	0.2	0.6	22	1620
Silty mudstone	8	8.16	5.8	1.7	0.7	26	1980
No. 13-1 coal	2	3.22	1.0	0.23	0.6	25	1620
Silty mudstone	5	8.16	5.8	1.7	0.7	26	1980
Fine sandstone	4	10.6	9.1	2.0	2.2	32	2200
No. 13-2 coal	2	3.22	1.0	0.23	0.6	22	1620
Sandy mudstone	5	8.16	5.8	1.7	0.7	26	1980
Siltstone	49	9.94	6.5	2.4	3.2	35	2460

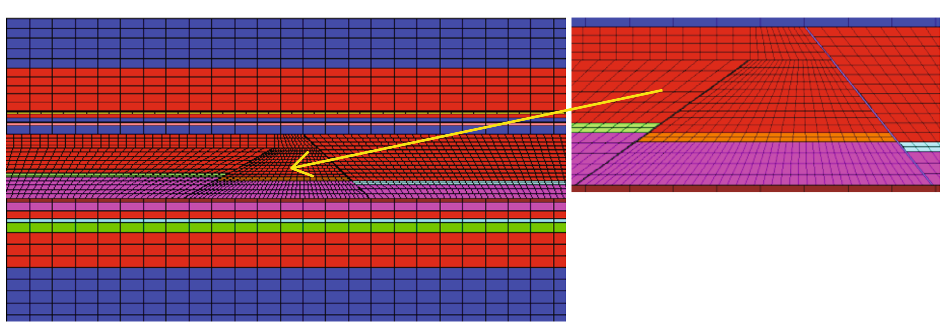

Figure 4: Model and local magnification of the fault.

Then the change of stress with time can be obtained by formula (2) as

$$\sigma(t) = \frac{E_1 \cdot E_2}{E_1 + E_2} \cdot \varepsilon_0 + \frac{E_1{}^2 \cdot \varepsilon_0}{E_1 + E_2} \cdot e^{-t/t_{\text{ret}}}, \tag{6}$$

where $t_{\text{ret}} = K_1/(E_1 + E_2)$ is the relaxation time, which decreases with the increase of time.

The mining of the working face will have a certain impact on the fault. When the support pressure in the above expression is sufficient, the fault will "activate" and slip. Due to the difficulty in selecting the rock mechanics parameters in the above formulas, the actual engineering calculation is huge. In this paper, numerical simulation and similar simulation are used to study the stress variation in the fault region.

3. Numerical Simulation Analysis of Multiple Fault Zones in Stope

3.1. Model Building. The numerical model established in this paper is based on the geological conditions of the 21 mining area of a coal mine in Guizhou. The average thickness of the No. 12 coal seam excavated by simulation is 2 m, the

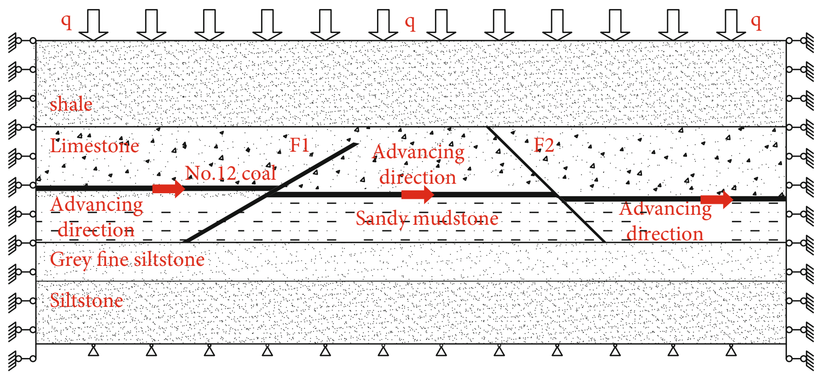

Figure 5: Schematic design of numerical model.

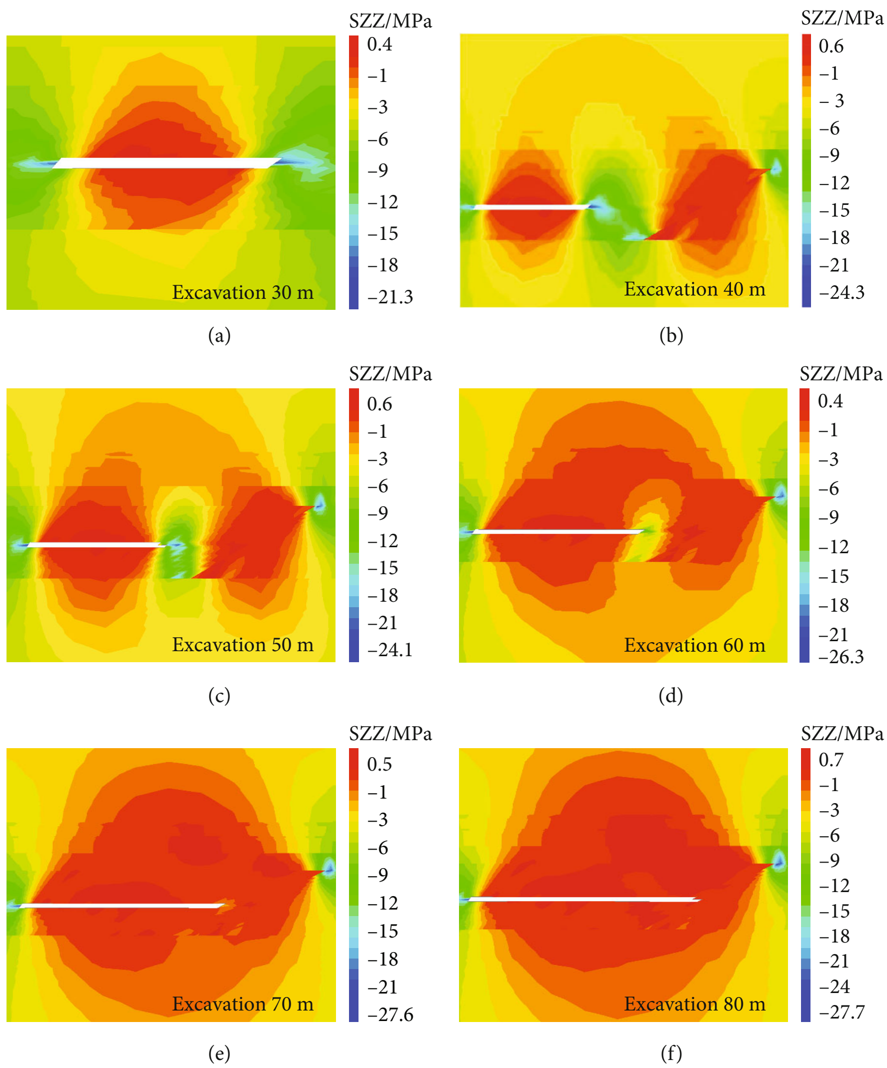

Figure 6: Stress distribution diagram.

inclination is 0°, and the average buried depth is 453 m. In the process of mining, the central part of the working face revealed multiple fault zones composed of F1 and F2 faults. F1 is a reverse fault (dip angle of 30°, drop 2 m), and F2 is a normal fault (dip angle of 45°, drop 2 m). The horizontal distance between the two faults is 62 m in the No. 12 coal seam. According to the measured data of the mine, the strike length, dip length, and height of the model are 340 m, 240 m, and 160 m. According to the measured data of the mine, the strike length, dip length, and height of the model

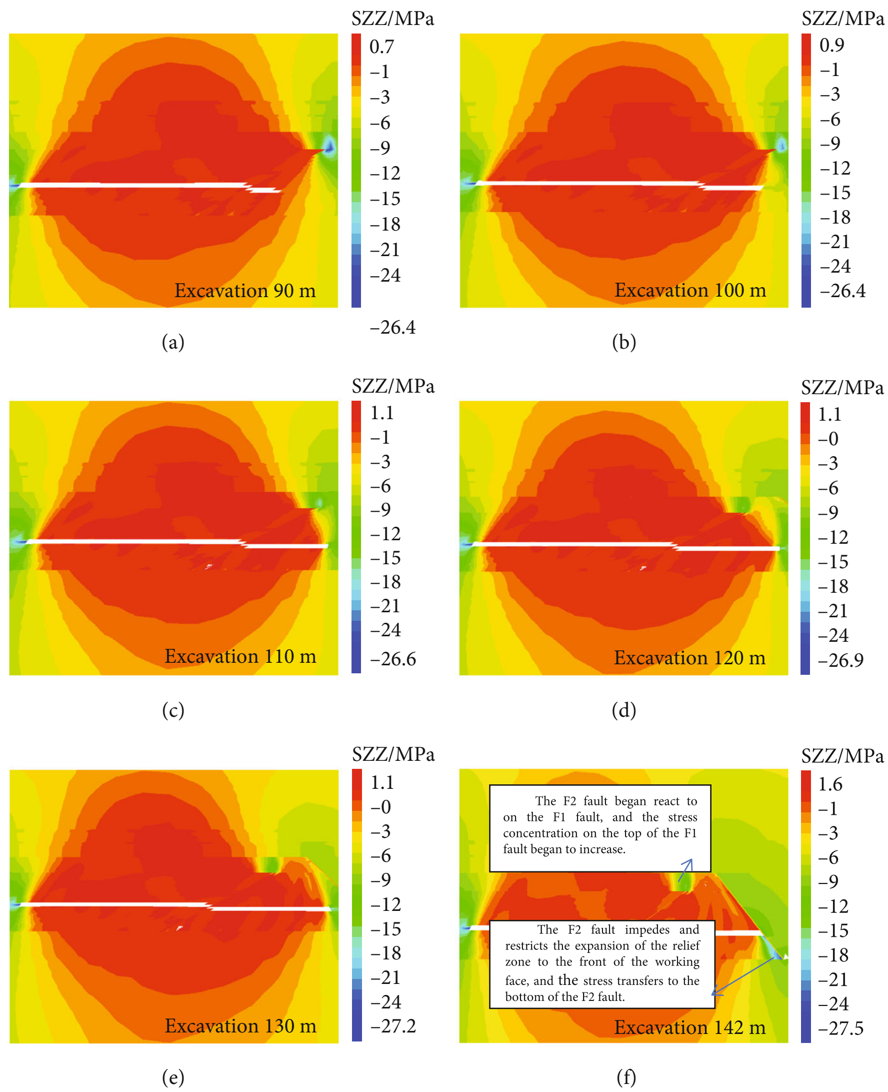

Figure 7: Stress distribution diagram.

are 340 m, 240 m, and 160 m. There is a fracture zone between the upper and footwall of the inverse and normal faults, and the average width of the fracture zone is 0.5 m. Each rock layer is set independently in different layers according to the actual situation. The engineering diagram of the model is shown in Figure 3.

In this model, the Moors-Coulomb model was adopted for rock mass, and the brick element was selected as the basis for modeling [38]. Boundary conditions and initial conditions or model boundary conditions are as follows: fix command is used to fix the velocity components of the boundary nodes in x, y, and z directions. The commands fix x range $x-0.1\ 0.1$ and fix x range $x\ 339.9\ 340.1$ fix the left and right boundaries of the model. The commands fix y range $y-0.1\ 0.1$ and fix y range $y\ 239.9\ 240.1$ fix the front and back boundaries of the model. The command fix z range $z-0.1\ 0.1$ fixes the bottom boundary of the model, and the top of the model is regarded as the free boundary.

The initial conditions of the model stress are as follows: the model height is 160 m, in which the thickness of the overburden of the No. 12 coal seam in the model is 81 m. The actual buried depth of No. 12 coal seam is 453 m, and the overburden pressure of 372 m needs to be compensated by simulation. Taking the bulk density of the rock layer as 28 kN/m^3, the pressure value of overlying rock at 372 m is 10.416 MPa. The horizontal stress coefficient is $\lambda = 1.66$, so the boundary pressure applied around the model is 17.29 MPa. The gravity acceleration $g = 9.8\ \text{m/s}^2$ should be considered in the whole model. The mechanical parameters of coal and rock mass in the study area are shown in Table 1.

3.2. Simulation Scheme. According to the measured data in the mining area, FLAC^{3D} was used to establish a three-dimensional model, as shown in Figure 4. The measured data and boundary conditions were input to simulate the excavation process. In the simulated 12# coal seam mining, the front and rear protective coal pillars are 40 m, and the left and right protective coal pillars are 50 m. The excavation distance is 10 m for each time. Continue to push forward

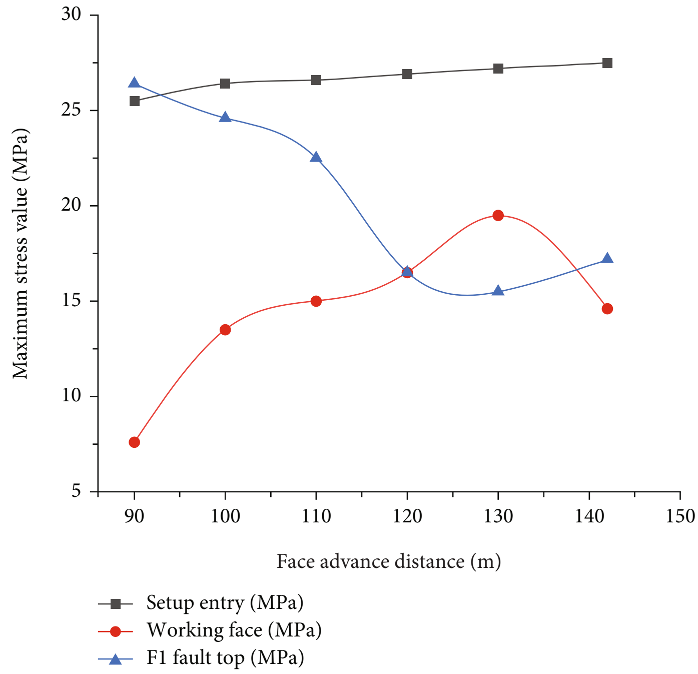

Figure 8: Vertical stress diagram.

after the operation is stable. The mining diagram is shown in Figure 5.

4. Numerical Simulation and Dynamic Analysis of Stope Stress

According to the vertical stress diagram obtained from the simulation, the change of mining stress is systematically described and analyzed.

Stage 1 is from setup entry to F1 (a reverse fault).

As shown in Figure 6(a), the simulated excavation is 30 m, and it is 50 m away from F1, and mining has no effect on the fault basically. The stress concentration appeared in the setup entry and the front of the working face, and their maximum stress values were 21.3 MPa and 20.6 MPa, respectively. The central part of the excavation area is under pressure relief, and the pressure relief height of the upper strata is 22 m.

As shown in Figure 6(b), the working face advances 40 m, and at this time, it is 40 m away from the F1, and the F1 fault begins to have an impact on the working face. The suspension distance of the overlying strata in the goaf reaches the limit span of the old roof fault. The present stress concentration area is formed in the setup entry and the front end of the working face. The stress value of the working face and the setup entry increased obviously, and the maximum stress value was 24.3 MPa and 23 MPa, respectively. The stress reduction zone is formed in the overlying strata of the excavation area, and the pressure relief effect is better at 26.5 m above the roof. At the same time, the stress change occurred in the reverse fault zone, and local pressure relief occurred in the middle part. The stress concentration zones appeared at the upper and lower ends, and the maximum values of the stress concentration zones at the upper and lower ends were 22.5 MPa and 17.5 MPa, respectively. The stress reduction zone appears in the upper-pressure relief zone of the goaf and above the pressure relief zone in the middle of the fault, and the two pressure relief zones are connected in series to form an "n"-shaped pressure relief zone.

As shown in Figure 6(c), the working face advances 50 m, and at this time, it is 30 m away from the F1, and the stress at fault appears to change. At this time, the maximum stress value of the setup entry and the stress concentration area at the front of the working face are 24.1 MPa and 23.7 MPa, respectively. With the increase of excavation range, the value of stress concentration area increases gradually, and the pressure relief area of overlying rock in goaf increases gradually.

As shown in Figure 6(d), the working face advances 60 m. It is 20 m away from F1, and the effect of reverse fault on the roof of the coal seam increases. The stress at the working face and the setup entry is significantly increased. At this time, the maximum stress value of the setup entry and the stress concentration area at the front of the working face are 26.3 MPa and 25.5 MPa, respectively. The roof pressure relief zone in the middle of the excavation area was further extended to 27.3 m above the roof. At the same time, the stress changes in the reverse fault zone, and the maximum values of the stress concentration zones at the upper and lower ends are 23.7 MPa and 17.4 MPa, respectively. The "n"-shaped connected relief zone of the two relief zones at the upper part increases. The "U"-shaped connected relief zones of the two relief zones at the lower part increase, and the two relief zones are connected at the lower part.

As shown in Figure 6(e), the working face advances 70 m, and it is 10 m away from F1. The reverse fault has a significant effect on the surrounding rock of the working

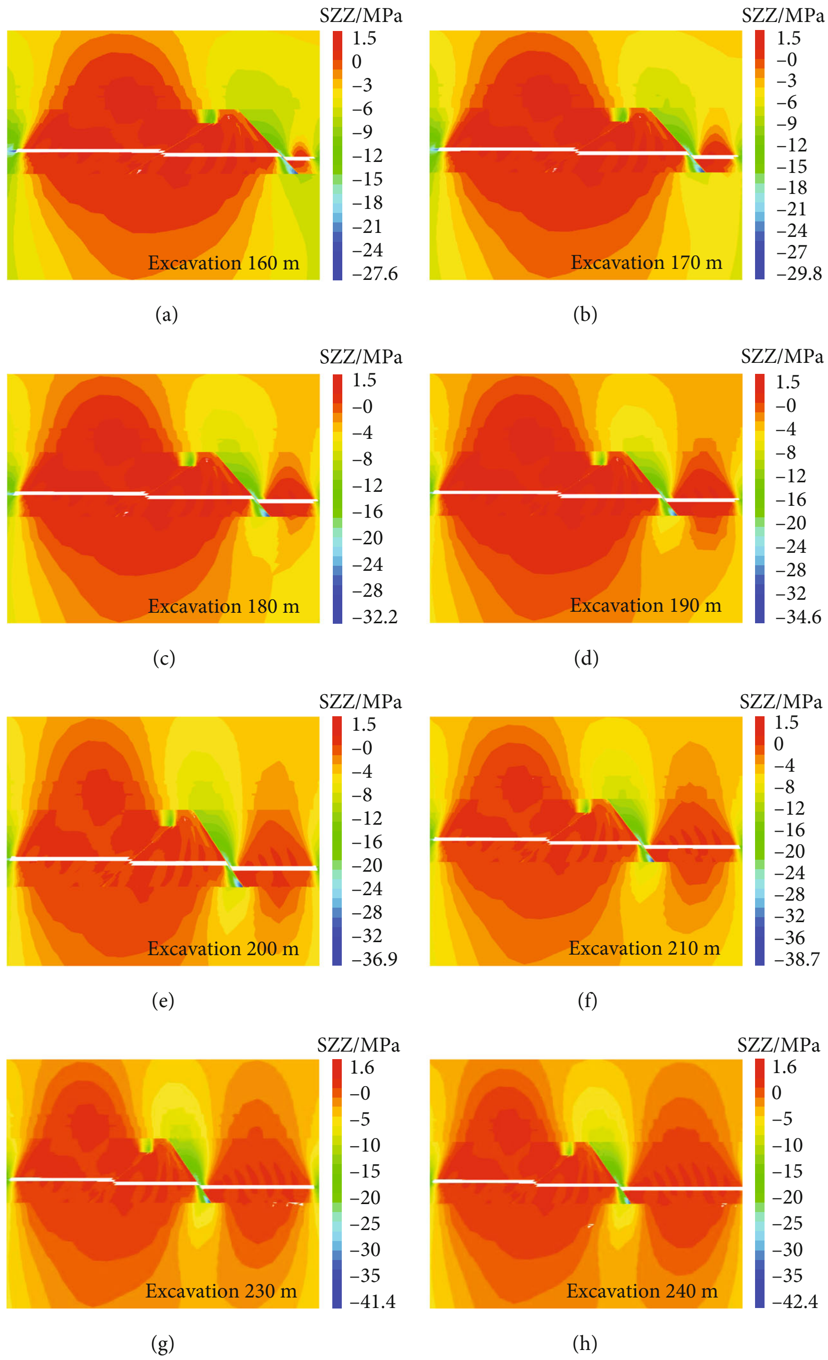

Figure 9: Stress distribution diagram.

face. The maximum stress concentration area at the setup entry is 27.7 MPa, and the stress concentration area at the front of the working face is reduced sharply. At this time, the pressure relief range of the upper strata of the goaf extends to 28.1 m above the roof. At the same time, the stress changes in the reverse fault zone, and local pressure relief occurs in the middle part. The maximum value of the stress concentration zone at the upper end increases to 24.6 MPa, and the lower end is in the pressure relief zone.

As shown in Figure 6(f), the working face advances 80 m, and it is 0 m away from F1 at this time. At this time, the maximum stress value of the setup entry and the stress concentration area at the front of the working face are 27.6 MPa and 5.6 MPa, respectively. At the same time, the maximum value of the stress concentration zone at the upper end of the reverse fault zone is 26.5 MPa, the lower end is in the relief zone, and the relief zone begins to increase in the middle of the fault. The pressure relief area above the goaf

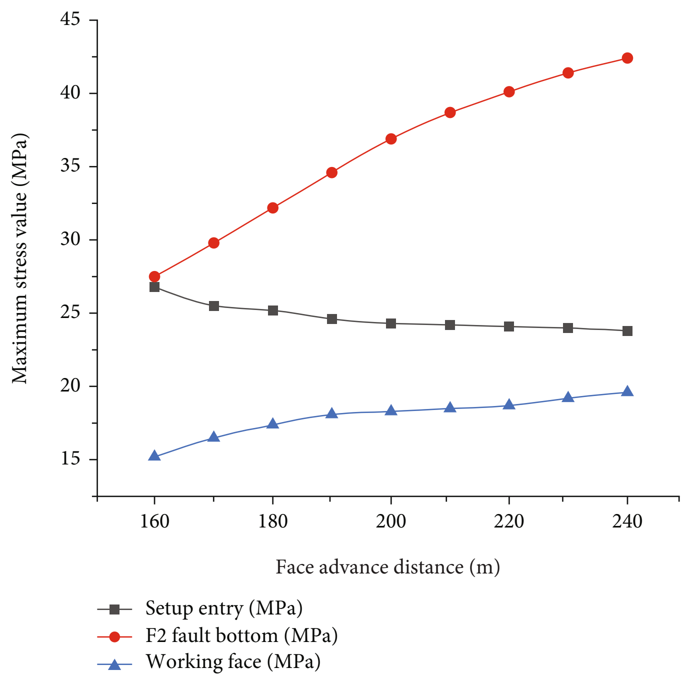

Figure 10: Vertical stress diagram.

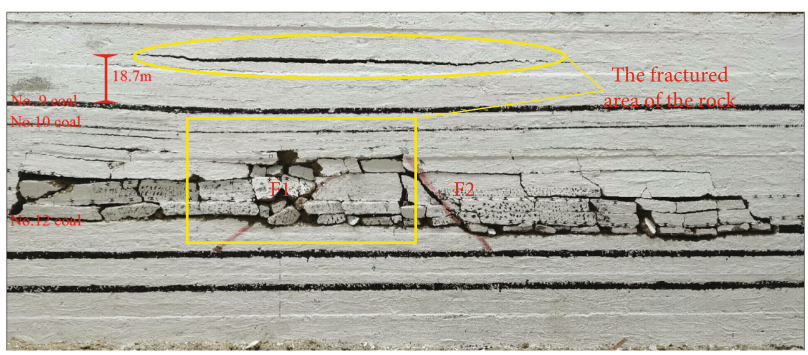

Figure 11: Fracture distribution diagram of similar simulation.

overlapped with the upper plate pressure relief area of F1, and the "n"-shaped pressure relief area above the stope disappeared. The lower pressure relief area of the goaf coincides with the bottom pressure relief area of F1, and the "U"-shaped pressure relief area under the stope disappears.

The second stage is from F1 (a reverse fault) to F2 (a normal fault).

As shown in Figure 7(a), the working face advances 90 m. It is 10 m past the F1 and 52 m away from the F2. F1 reverse fault has a significant influence on the working face, and its effect on the roof of coal seam increases, while normal fault has almost no influence on the working face. The maximum stress concentration area at the setup entry is 25.5 MPa, and there is no obvious stress concentration at the front end of the working face. The pressure relief zone of the goaf surrounding rock is further increased. At the same time, the stress concentration area at the end of the reverse fault zone increases, and the maximum value of stress is 26.4 MPa. The middle part and lower part are in the relief zone.

As shown in Figure 7(b), the working face advances 100 m. It is 20 m over F1 and 42 m away from F2. The F1 reverse fault has a significant influence on the working face, while the F2 normal fault has little influence on the working face. The maximum stress values of setup entry and stress concentration area in front of the working face are 26.4 MPa and 13.5 MPa, respectively. Meanwhile, the maximum value of the stress concentration area at the upper end of the reverse fault is 24.6 MPa.

From the above analysis, it can be seen that in the process of advancing from 80 m to 100 m, the F1 fault and the working face interact greatly, and the F2 fault area is basically stable.

As can be seen from Figures 7(c)–7(f), the advancing distance of the working face ranges from 110 m to 142 m. In this process, the working face is far away from the F1

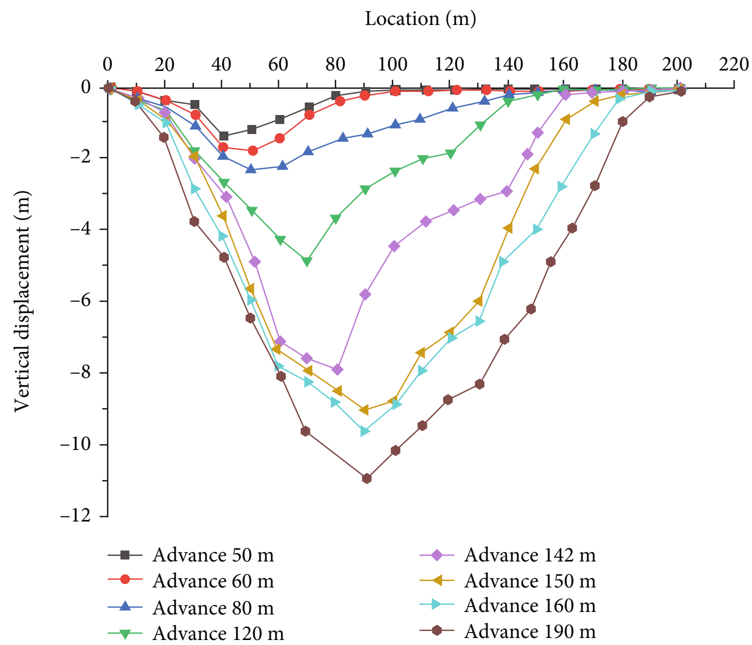

Figure 12: Overburden vertical displacement curve.

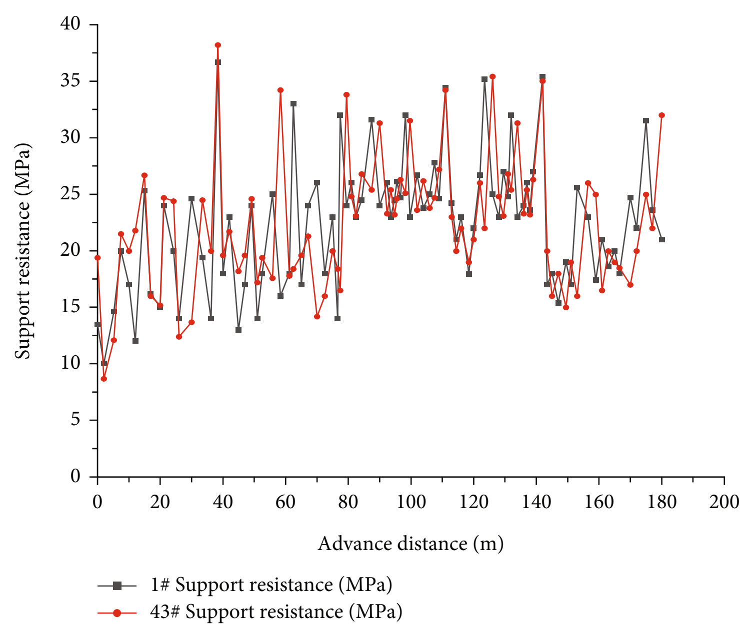

Figure 13: Working resistance curve of hydraulic support.

fault, and the distance from the F1 reverse fault is 30 m-62 m. The working face is close to the F2 fault and the distance from the F2 normal fault is 32 m-0 m. In this process, the influence of fault F1 on the working face gradually decreases, and the interaction between fault F2 and the working face begins to increase [39, 40].

It can be seen from Figure 8 that, within the range of 90 m-100 m, under the influence of the F1 fault, the stress values of the working face and the setup entry changed greatly. With the continuous advancement of the working face, the stress value at the setup entry increases with the increase of the mined-out area. When the advancing distance of the working face is 90 m-130 m, as the distance between the working face and F1 continues to increase, the interaction between F1 and the working face gradually becomes smaller, and the leading support pressure of the working face gradually increases. The F1 fault tends to be stable gradually, and the value of the stress concentration area at the top of the F1 fault decreases gradually. When the working face advances from 130 m to 142 m, the advance bearing stress of the working face suddenly increases from 19.5 MPa to 14.6 MPa, and the maximum stress at the top of the F1 fault increases from 15.5 MPa to 17.2 MPa. As can be seen from the data changes in Figure 8, the blocking effect of the F2 fault makes the surrounding rock at the front end of the working face at 142 m in the stress reduction zone. At the same time, the activity of the surrounding rock of the F2 fault has an influence on the F1 fault, which intensifies the activity of the F1 fault.

According to Figures 9(a) and 10, the working face advances 160 m. At this time, the working face is 80 m away from the F1 fault and 18 m away from the F2 fault. The stress concentration area is distributed in the setup entry, the lower part of F2, and the front end of the working face. The lower part of the F2 fault shares some of the overburden pressure, which reduces the value of the stress concentration area near the setup entry and the working face. The maximum stress at the cut hole reaches 26.2 MPa, and the maximum stress at the lower part of F2 reaches 27.6 MPa. The maximum stress at the working face is 15.2 MPa. As can be seen from Figures 9(a)–9(h), with the advance of the working face, the F1 fault tends to be basically stable. The value of the stress concentration area from the setup entry is decreasing gradually. The overburden pressure gradually transfers to the lower part of the F2 fault. The maximum stress concentration at the working face increases gradually. Multiple fault structures seriously destroy the continuity of surrounding rock and change the stress distribution of the stope. The multifault structure hinders the stress transfer of the overburdened strata to the working face, which makes the value of the leading abutment pressure of the working face low. Through numerical simulation research and analysis, the role of multiple fault structures in the energy transfer process of the surrounding rock of the stope is obtained. The multicracked structure severely damaged the continuity of the surrounding rock and changed the energy distribution of the surrounding rock. The transfer and concentration of the energy field to the F1 and F2 faults effectively reduce the energy value of the working face.

5. Stope Similarity Simulation Experiment and Field Measurement

As shown in Figure 11, fractures develop in the overlying strata of the goaf in the multifault structural area composed of F1 reverse fault and F2 normal fault, and the rock mass is broken. In particular, due to the multiple effects of mining and F2 fault, the surrounding rock activity in this area is intense, the overlying strata fractures are more developed, and the caving rock mass is more broken. The vertical displacement subsidence of overlying strata in the stope is larger than that of nondouble fault areas on both sides. The vertical displacement curve of overburden is shown in Figure 12. The analysis of the resistance monitoring data of the hydraulic support in the working face shows that the multiple fracture structures can be divided into "high-pressure zone" and "low-pressure zone." The surrounding rock stress in the "high-pressure area" and "low-pressure area" of the fault is abnormal, and the working resistance value of the support in the low-pressure area is higher than that in the nonfault affected area. The working resistance curve of the hydraulic support is shown in Figure 13.

6. Conclusion

By means of finite element numerical simulation software and similar simulation experiment, the movement law of overlying strata and the ore pressure behavior law are studied when 12# coal seam mining passes through multiple fault structure areas. The conclusions are as follows:

(1) The ore pressure behavior law of the surrounding rock of the stope crossing the multiple fault zone was analyzed by the finite element numerical simulation software. The study concluded the following: When the working face passes through the faulting area, the fault has a significant effect on the stress distribution of the surrounding rock. When the working face is 20 m past the F1 fault and advanced to the middle area of multiple fault structures, the pressure relief zone of the surrounding rock in the goaf becomes smaller. The increase of stress concentration area within 10 m in front of the working face is not conducive to the release of gas pressure in front of the working face

(2) During the advancing process of the working face from 80 m (F1 fault) to 142 m (F2 fault), the concentration area and numerical value of the stress at the top of the F1 fault experienced a process of increasing, maximal, decreasing, slowly decreasing, and increasing. The results show that the stress change of the F2 fault promotes the stress change of the F1 fault undermining

(3) When the working face advances to the F2 fault, there is no strong stress concentration in front of the working face due to the blocking effect of the fault. The stress concentration is transferred to the bottom of the F2 fault, which easily causes the floor heave of the working face

(4) Through the numerical analysis of finite element software, it is concluded that the multiple fracture structures will seriously cut the continuity of the surrounding rock and affect the stress distribution of the surrounding rock. Multiple fault structures will only change the energy distribution of the surrounding rock but will not increase the value of energy. The transfer and concentration of the energy field to the F1 fault and the F2 fault effectively reduced the energy value of the working face. This phenomenon provides a new possibility for the study of underground engineering

Data Availability

The experimental test data used to support the findings of this study are available from the corresponding author upon request.

Conflicts of Interest

The authors declare that there are no conflicts of interest regarding the publication of this article.

Acknowledgments

This study was supported by the National Natural Science Foundation of China (Grant Nos. 52174076, 51974117, 51964008, and 52064009), Hunan Provincial Natural Science Foundation of China (Grant No. 2020JJ4027), and Hunan Provincial Graduate Scientific Research Innovation Project (Grant No. CX20210984).

References

[1] Q. MG and S. PW, *Mine Pressure and Rock Formation Control*, China University of Mining and Technology Press, 2003.

[2] P. YS, L. ZH, and Z. MT, "Mechanism and prevention of rockbrust in China," *Chinese Journal of Rock Mechanics and Engineering*, vol. 22, no. 11, pp. 1844–1851, 2003.

[3] Y. D. P. Y. Jiang and J. FuX, "State of the art review on mechanism and prevention of coal bumps in China," *Journal of China Coal Society*, vol. 39, no. 2, pp. 205–213, 2014.

[4] F. Cui, S. Dong, X. Lai, J. Chen, C. Jia, and T. Zhang, "Study on the fracture law of inclined hard roof and surrounding rock control of mining roadway in longwall mining face," *Energies*, vol. 13, no. 20, p. 5344, 2020.

[5] H. FM, *Introduction to Fault Mechanics*, Seismological Press, 2013.

[6] H. KM, Y. QG, Z. HX, and L. FM, "Mechanism of fault activation when mining on hanging-wall and foot-wall," *Journal of China Coal Society*, vol. 45, no. 4, pp. 1327–1335, 2020.

[7] W. A. N. G. Chen, T. U. Shihao, T. U. Hongsheng, B. A. I. Qingsheng, and C. H. E. N. Guanshen, "Rock deformation and support bearing characteristics in reversed fault zone with strata pinchout," *Journal of Mining and Safety Engineering*, vol. 32, no. 2, pp. 182–186, 2015.

[8] J. W. Wu, H. S. Tong, S. J. Tong, and D. Q. Tang, "Study on similar material for simulation of mining effect of rock mass at fault zone," *Chinese Journal of Rock Mechanics and Engineering*, vol. 26, pp. 4170–4175, 2007.

[9] Z. H. Li, C. Z. Zhai, and L. F. Li, "Experimental study on water inrush mechanism due to floor faults activation in mining above confined aquifer," *Journal of Central South University*, vol. 46, no. 5, pp. 1806–1810, 2015.

[10] W. Q. Zhang, Q. Sun, S. Y. Zhu, and D. Q. Liu, "Analysis of roof reverse fault instability-reactivation mechanism under mining," *Coal Safety*, vol. 44, no. 3, pp. 179–182, 2013.

[11] A. HJ and P. HJ, *Engineering Rock Mechanics-An Introduction to the Principles*, Elsevier, 2000.

[12] H. G. Ji, H. S. Ma, J. A. Wang, Y. H. Zhang, and H. Cao, "Mining disturbance effect and mining arrangements analysis of near-fault mining in high tectonic stress region," *Safety Science*, vol. 50, no. 4, pp. 649–654, 2012.

[13] A. Sainoki and H. S. Mitri, "Dynamic behaviour of mining-induced fault slip," *International Journal of Rock Mechanics and Mining Sciences*, vol. 66, pp. 19–29, 2014.

[14] A. Sainoki and H. S. Mitri, "Effect of slip-weakening distance on selected seismic source parameters of mining-induced fault-slip," *International Journal of Rock Mechanics and Mining Sciences*, vol. 73, pp. 115–122, 2015.

[15] T. Q. Xiao, J. B. Bai, J. P. Li, X. Y. Wang, and S. Yan, "Stabilization mechanism of crushed surrounding rock in coal roadway with bolt support near fault," *Journal of Mining & Safety Engineering*, vol. 27, no. 4, pp. 482–486, 2010.

[16] W. Yu, K. Li, Q. Lu, and H. Guo, "Engineering characteristics and deformation control of roadways in fractured rock mass," *Journal of China Coal Society*, vol. 46, no. 11, pp. 1–12, 2021.

[17] W. Yu, G. Wu, and B. An, "Large deformation characteristics and stability control of roadway with fractured rock mass," *Journal of Mining and Safety Engineering*, vol. 36, no. 1, pp. 103–111, 2019.

[18] P. F. Gou and Y. G. Hu, "Effect of faults on movement of roof rock strata in gateway," *Journal of Mining & Safety Engineering*, vol. 23, no. 3, pp. 285–288, 2006.

[19] Z. H. Wang, J. H. Yang, and H. Meng, "Mechanism and controlling technology of rib spalling in mining face with large cutting height passing through fault," *Journal of China Coal Society*, vol. 40, no. 1, pp. 42–49, 2015.

[20] Q. Wang, S. C. Li, Z. Li et al., "Analysis of roof collapse mechanism and supporting measures in fault zone of coal roadway," *Rock and Soil Mechanics*, vol. 33, no. 10, pp. 3093–3102, 2012.

[21] L. P and M. SJ, "Analysis of the characteristics of in-situ stress field and fault activity in the coal mining area of China," *Journal of China Coal Society*, vol. 41, no. S2, pp. 319–329, 2016.

[22] L. W. Wei and D. S. Zhang, "Gateway pre-heading feasibility in fault of coal mining face and support parameter optimization," *Coal Science and Technology*, vol. 32, no. 4, pp. 57–60, 2004.

[23] W. Shao-feng, T. Yu, and W. Shan-yong, "Influence of brittleness and confining stress on rock cuttability based on rock indentation tests," *Journal of Central South University*, vol. 28, pp. 2786–2800, 2021.

[24] W. Shao-feng, T. Yu, L. Xi-bing, and D. Kun, "Analyses and predictions of rock cuttabilities under different confining stresses and rock properties based on rock indentation tests by conical pick," *Transactions of the Nonferrous Metals Society of China*, vol. 31, no. 6, pp. 1766–1783, 2021.

[25] D. Ma, S. Kong, Z. Li, Q. Zhang, Z. Wang, and Z. Zhou, "Effect of wetting-drying cycle on hydraulic and mechanical properties of cemented paste backfill of the recycled solid wastes," *Chemosphere*, vol. 282, p. 131163, 2021.

[26] D. Ma, J. Wanga, X. Cai et al., "Effects of height/diameter ratio on failure and damage properties of granite under coupled bending and splitting deformation," *Engineering Fracture Mechanics*, vol. 220, p. 106640, 2019.

[27] D. Ma, J. Zhang, H. Duan et al., "Reutilization of gangue wastes in underground backfilling mining: overburden aquifer protection," *Chemosphere*, vol. 264, p. 128400, 2021.

[28] H. Wu, D. Ma, A. J. S. Spearing, and G. Zhao, "Fracture reponse and mechanisms of brittle rock with different numbers of openings under uniaxial loading," *Geomechanics and Engineering*, vol. 25, pp. 481–493, 2021.

[29] X. Lai, J. Zheng, J. Chen, X. J. Jiang, B. Chang, and H. H. Zhao, "Comprehensive identification of rock-coal mass internal critical destabilization in fault influenced broken zone," *Journal of China Coal Society*, vol. 40, no. S1, pp. 1–5, 2015.

[30] Z. H. Li, L. M. Dou, Z. Y. Lu, X. W. Lu, and G. R. Wang, "Study of the fault slide destabilization induced by coal mining,"

Journal of Mining and Safety Engineering, vol. 27, no. 4, pp. 499–504, 2010.

[31] Y. X. Xia, J. H. Wang, and D. Mao, "Analysis of fault activation induced rock burst risk based on in-situ stress measurements," *Journal of China Coal Society*, vol. 41, no. 12, pp. 3008–3015, 2016.

[32] Y. Qiuge, Z. Huaxing, and D. Weinan, "Analysis of fault separation generation and its effect on mining zone transferring," *Journal of China Coal Society*, vol. 43, no. 12, pp. 3286–3292, 2018.

[33] L. G. Wang and X. X. Miao, "Numerical simulation of coal floor fault activation influenced by mining," *Journal of China University of Mining and Technology*, vol. 16, no. 4, pp. 385–388, 2006.

[34] B. E. Adler, "Tektonische Deformationszahl zur Gebirgsbeschreibung," *Glückauf*, vol. 114, no. 4, pp. 169–175, 1978.

[35] H. Kose, "Modeltheoretische Untersuchung der Gebirgsdruckverteilung beim Abbau," *Gluckauf-Forschungshefte*, vol. 48, no. 1, pp. 17–22, 1987.

[36] X. YC and H. MX, "GMDH-BP evaluation and prediction method of mine structure and its application," *Journal of China Coal Society*, vol. 22, no. 5, pp. 466–469, 1997.

[37] W. YJ and W. YM, "Influence and control of surrounding rock stress on roadway in fault fracture zone," *Coal Science & Technology*, vol. 2, pp. 35–37, 1999.

[38] P. WB, *FLAC3D Practical Tutorial*, China Machine Press, Beijing, 2007.

[39] J. P. Zuo, Z. H. Chen, H. W. Wang, X. P. Liu, and Z. P. Wu, "Experimental investigation on fault activation pattern under deep mining," *Journal of China Coal Society*, vol. 34, no. 3, pp. 305–309, 2009.

[40] Y. D. Jiang, T. Wang, Y. X. Zhao, and C. Wang, "Numerical simulation of fault activation pattern induced by coal extraction," *Journal of China University of Mining and Technology*, vol. 42, no. 1, pp. 1–5, 2013.

Hindawi
Geofluids
Volume 2022, Article ID 1976294, 15 pages
https://doi.org/10.1155/2022/1976294

Research Article

Study on the Failure Mechanism of Lower Cambrian Shale under Different Bedding Dips with Thermosolid Coupling

Wentao Wang,[1] Zhonghu Wu,[1,2,3] Huailei Song,[1] Hengtao Cui,[1] Yili Lou,[1] Motian Tang,[1] and Hao Liu[4]

[1]*College of Civil Engineering, Guizhou University, Guiyang 550025, China*
[2]*School of Qilu Transportation, Shandong University, Jinan 250002, China*
[3]*Geotechnical and Structural Engineering Research Center, Shandong University, Jinan 250061, China*
[4]*Mining College, Guizhou University, Guiyang, Guizhou 550025, China*

Correspondence should be addressed to Zhonghu Wu; wuzhonghugzu@163.com

Received 7 June 2021; Revised 10 September 2021; Accepted 15 October 2021; Published 26 March 2022

Academic Editor: Yong-Zheng Wu

To investigate the damage pattern and acoustic emission pattern of temperature on laminated shales, numerical experiments were carried out using the RFPA2D-Thermal numerical software under the effect of thermosolid coupling. During the tests, temperatures of 30°C, 60°C, and 90°C were controlled, and five sets of shales containing different laminar dips were numerically modeled at each temperature, with dips of 0°, 22.5°, 45°, 67.5°, and 90°. The test results show that (1) the increase in temperature reduced the linear elastic phase of the shale specimens in each group, with a significant reduction in the linear elastic phase of the shale at lamina dips of 22.5° and 45°. (2) The lamination effect decreased slightly as the temperature rose from 30°C to 60°C, and the most significant enhancement of the lamination effect on the shale occurred when the temperature reached 90°C. (3) The shale damage pattern is divided into five types (N, ʌ, v, slanted I-type, and cluttered-type), in which the lamina effect is stronger for high-angle lamina dips, and the lamina surface has a strong dominant effect on the entire shale crack expansion. At a temperature of 90°C, the lamina effect and temperature effect of the shale reached their maximum at the same time, and the thermal and load stresses inside the shale acted together causing the shale to show a complex damage mode. (4) The fractal dimension was used to analyze the damage pattern of the shale. The larger the fractal dimension was, the greater the crack rate of the specimen. The fractal dimension curve was flatter at a temperature of 60°C, while at 90°C, the fractal dimension rose rapidly, indicating the most favorable crack expansion in the shale at a temperature of 90°C.

1. Introduction

As the first country to develop shale gas, the United States has succeeded in reducing natural gas consumption and has seen a gradual increase in natural gas exports, contributing to the optimization of the US energy system [1–5]. In recent years, with the massive depletion of conventional energy sources, there has been an urgent need for a new q-energy source that can replace natural gas and oil, which has led to strong interest in shale gas from all corners of the world [6–13].

Currently, the commonly used technology in shale gas exploitation is hydraulic fracturing technology. In hydraulic fracturing technology, a series of rock mechanic problems are involved [14–20]. Hence, exploring the mechanical ability of shale is of outstanding importance for the evolution of reformed shale gas reservoirs. Shale gas is stockpiled in shale pores containing shale gas under high ambient stress and high-temperature conditions. Therefore, the exploitation of shale gas always includes the coupling of stress and temperature fields [21–23].

Inhomogeneous bedding has attracted the attention of scholars for a long time, but the temperature impact on the mechanical properties of shale rocks has only gradually received attention since the 1970s. Therefore, domestic and foreign researchers have acquired successful outcomes regarding the effect of temperature on the mechanical properties of shale rocks. Lou et al. [24] used numerical modeling experiments to probe the bedding effects of shale with different bedding dips and applied fractal dimensions to analyze the crack laws of shale. Wei et al. [25] created a thermal damage thermosolid coupling model, performed physical tests on granites, and found that the thermal effect caused changes in rock parameters thereby stimulating rock tensile-reduction damage. Zhou et al. [26] established compression, and the thermosolid coupling model of thermal expansion provided the thermosolid coupling equation for shale. Alm et al. [27] studied the effect of microcrack density on the elastic and mechanical properties of granite. After the granite was heated, the crack density of the rock was measured by scanning electron microscopy and other instruments, and finally, it was found that when the temperature exceeded 300°C, the crack density increased significantly. Lu et al. [28] carried out a large-scale triaxial compression test on shale. By controlling temperature variables, the relationship between temperature, peak strength of shale, Poisson's ratio, internal elastic modulus, and friction angle was found. Wang et al. [29] found that the fractality, connectivity and connectivity of parallel laminations were 1.31, 1.12, and 1.61 times higher than those of vertical ones by studying the coal rocks in the Fukang Mine area. Yao et al. [30] investigated the mechanical properties of outcrop shale under different laminar dip angles and found that the damage extension direction almost coincided with the laminar dip angle around 0~45°, and when the dip angle was 60~90°, only a small part of the fracture extension direction coincided with the laminar dip angle. Only a small part of the fracture extension direction coincides with the laminar dip angle.. Masri et al. [31] performed hydrostatic and conventional triaxial tests to explore the mechanical properties of the bedding angles of parallel and vertical bedding angles at different temperatures. As the temperature rose, the elastic modulus and compressive strength of the rock were weakened, but the overall deformation was strengthened. Gautam et al. [32] studied the deformation characteristics of sandstone at various temperatures. They observed that the stress-strain curve showed that sandstone underwent brittle deformation at 250°C, and plastic deformation occurred when the temperature exceeded 450°C. Ranjith et al. [33] performed uniaxial compression tests on Hawkesbury sandstone at different temperatures. The results showed that the maximum elastic modulus of Hawkesbury sandstone was a threshold value at 500°C, which explained the softening phenomenon of sandstone when the temperature exceeded 500°C. Lei et al. [34] used the MTS 815 MPa rock testing machine to monitor the microscopic failure process of sandstone during uniaxial compression testing. AE monitored the sandstone transition from brittleness to plasticity at approximately 600°C and found that the sandstone microscopic porosity decreased with increasing temperature. Mahanta et al. [35] conducted experiments on Manoharpur sandstone, Dholpur dolomite, and Bellary sandstone during these heating treatments. Their fracture strength increased by 40%, 25%, and 65%, respectively, within the range of 100°C. However, with temperature rising to 600°C, the fracture strength decreased by 59%, 36%, and 30%, respectively. Yang et al. [36] performed a dynamic compression test on shale rocks and controlled the temperature between 20 and ~220°C. Their conclusion was that there was a temperature threshold between 20 and 220°C, before which the compressive strength increased with temperature and beyond which the compressive strength decreased with increasing temperature. Currently, many achievements have been made regarding the mechanical properties of rocks at diverse temperatures, dip angles, and confining pressures. They have mainly focused on the rupture modes of rocks at various temperatures. However, there have been few reports on the failure processes and acoustic emission characteristics under thermosolid coupling at different dip angles of shale bedding and thermosettings. Therefore, it is of great practical significance to carry out numerical simulation experiments to explore the mechanisms of thermosolid coupling on the propagation of shale fracturing and restructuring.

This paper utilizes the Lower Cambrian Niutitang Formation shale as the research object in the northern Guizhou area, uses statistical methods to describe the correlation between the bedding dip and temperature in the shale, and uses RFPA2D-Thermal to establish a numerical model of 5 groups of shale samples that have different dips. A constant confining pressure and several temperature conditions are set to simulate the natural environment of shale under high temperature and high pressure. Simultaneously, shale is analyzed in detail, in which the shale contains compressive strength and cracking processes at various temperatures, and the evolution of acoustic emission signals during the process is studied.

2. Geological Characteristics of the Study Area

2.1. Geographical Location of the Feng'gang No. 3 Block, South China. Guizhou is located in southwestern China and has unique geographic advantages in shale gas storage. Most areas of Guizhou are within the tectonic unit of the Yangtze block, which is divided into four blocks. The third block of shale gas in Feng'gang, Guizhou (referred to as the research area in the text), is an important part of the national shale gas resource experiment, with abundant resources and a good geological environment. The geographic location of the study area is located in the southeastern part of Zunyi city in the northern part of Guizhou Province (see Figure 1). The administrative divisions are located in the subregions of Meitan County, Feng'gang County, and Sinan County of Tongren city and parts of Meitan-Feng'gang-Tongren Sinan County from Zhengjiashan in Sinan County to Zhangjiapo and Tianjiawan Line in the east, Liujiawuji-Liangshuijing-Huangnipo Line in Meitan County in the west, Jiangjiagou-Ranjiayuanzi-Houtang Line in Tan County, Meitan County in the south, and North to Feng'gang Xianglu Mountain-Qinggang Park-Loquat Bay line. The area coverage in the study area is approximately 1167.49 km^2. The study area has diverse terrain types that contain hills, midmountains, hills and dams interspersed with each other, and karst landforms with conventional landforms alternately spread in between. The terrain is generally mountainous and hilly. The western terrain is dominated by flat dams and hills. Most areas contain

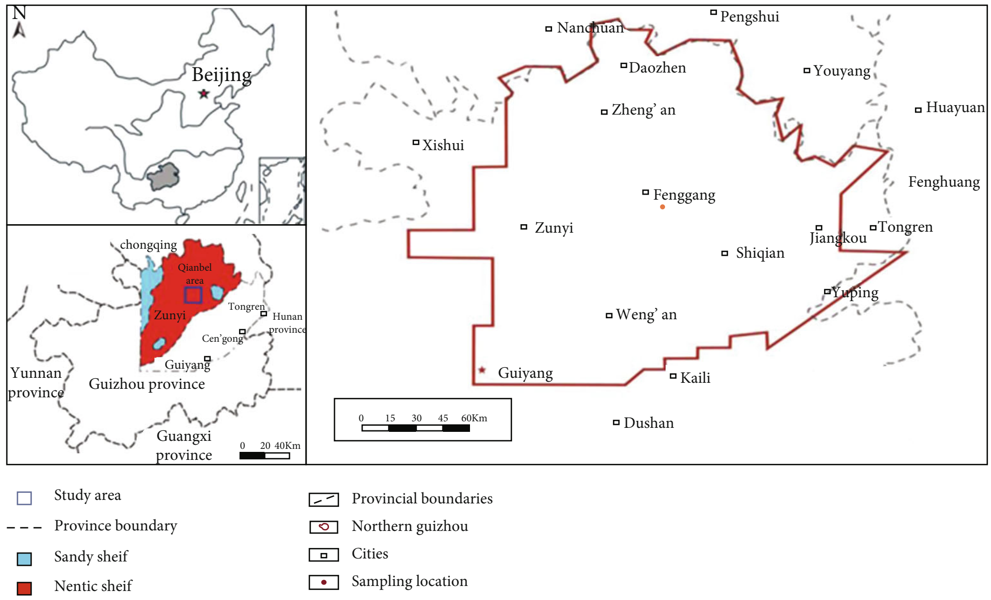

Figure 1: Detailed location map of the third district of the Feng'gang No. 3 block, Guizhou [37].

low hills and relatively flat valleys, with certain undulations. Some areas are cut by rivers (100~300 m), and the east is mountainous. The terrain is undulating, and the cut is deeper.

2.2. Influence of Folds and Fractures on Shale Temperature. The occurrence of folds and fractures caused the strata to no longer lie on the same plane during the same period, presenting a spatially scattered structure with a large depth decrease. Affected by structural compression and deformation, the Niutitang Formation in the study area is generally shallower in the southeast and northwest (approximately 1500 m and 500 m, respectively) and relatively deep in the middle (mainly 2000~4000 m); among them, the overall burial depth is between 1000 m and 3500 m, and the Meitan compound anticline is relatively shallow, with a burial depth of 500 m to 1500 m, while the Yachuan compound syncline contains Triassic strata, and the burial depth is at a maximum of 5000 m (see Figure 2). Near the study area, detailed logging data record the burial depth of the Niutitang Formation shale. The Niutitang Formation, which is located in Songtao Wuluo well ZK408 in the eastern part of the survey area, is present at a depth of 616.90~640.80 m. In the Deye 1 well in the northern part of the study area, the floor depth of the Niutitang Formation is at 1661.66~1752.20 m. In the drilling record of Well Fengshen 1, the Niutitang Formation is approximately 2500 m underground in Liujiazhai Village, Dangwan Township, Feng'gang County. The temperature of the stratum increases as depth increases. According to valid statistics, every time the depth increases by 100 meters, the temperature increases by 3°. The temperature at the Niutitang Formation in the study area is approximately 45°C~120°C. The amount of methane adsorption is greater at low temperature and low pressure, and the amount of free methane at high temperature and high pressure is greater. To approximate these real conditions, this study is conducted from 30°C to 90°C.

2.3. Pore Characteristics of Shale. Nanoscale pores are prevalent in shales, but the connectivity between pores is negligible. Shale gas is mainly stored in the micropores of shale. The size and connectivity of pores have a large impact on the ability of shale to adsorb shale gas and its storage performance. The degree of pore development in shale determines the permeability of shale and the degree of gas reservoir storage. Using nuclear magnetic resonance (NMR) technology, the pores of 5 groups of samples in the rock reservoirs in the study area are quantitatively tested, and the pore throat and pore size distributions are obtained [37].

Figure 3 shows that the pore throat and pore size distribution of each group of samples are approximately similar. Three peaks appear in the pore size distribution, indicating that the pore size range of shale is primarily concentrated at 0.001~0.1 μm and 0.01~0.4 μm, and a very small amount is distributed at 1~10 μm.

Through NMR analysis of the Lower Cambrian shale in the Feng'gang No. 3 block, it can be seen that the development of pores in the Lower Cambrian shale is advantageous to the storage of shale gas. This indicates that the development of shale gas in this area is economically important. It can also be seen from Figure 3 that although the micron-scale pores are well developed, the connectivity between the pores is not good, and increasing the temperature helps to increase the porosity and permeability of the shale. It is therefore important to study the mechanism of damage under thermosolid coupling for the extraction of shale gas.

3. Thermosolid Coupling Element Model

3.1. Element Thermal Damage Evolutionary Theory. At the microscopic scale of shale, an element is considered to be an elastic body at the initial failure stage, and the stress-strain curve of each element is linear. When the damage threshold is reached, the properties of the unit begin to change. When shale is compressed, stretched, or sheared,

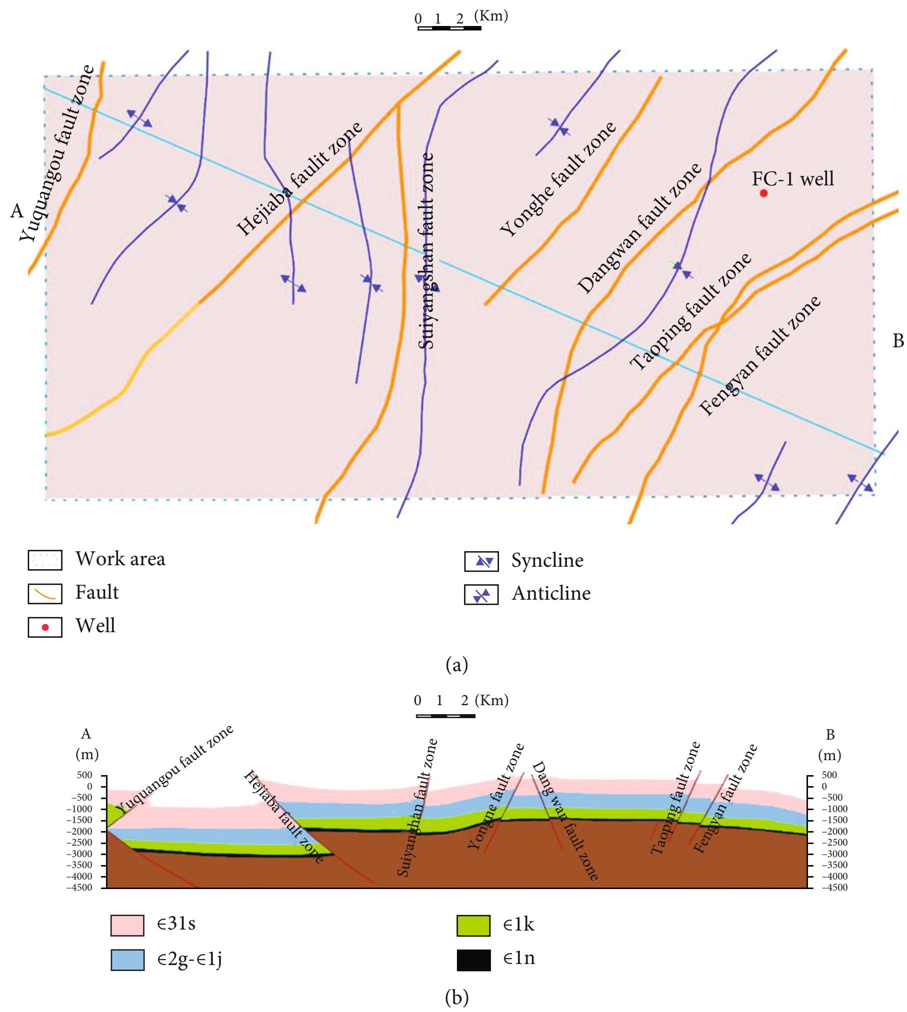

Figure 2: Geological formations in the study area. (a) Geological structural section view of the Feng'gang No. 3 block. (b) Basic structural feature map of the Feng'gang No. 3 block [37].

the tensile strength of shale is much smaller than the compressive strength, and tensile failure occurs, as shown in Equation (1). When shale reaches a critical state of stress, the shear stress exceeds the shear strength, and shear failure occurs, as shown in Equation (2) [38, 39].

$$F_1 \equiv \sigma_1 - f_{t0} = 0, \tag{1}$$

$$F_2 \equiv -\sigma_3 - \frac{1+\sin\varphi}{1-\sin\varphi}\sigma_1 - \mathrm{f}_{c0} = 0. \tag{2}$$

F_1 and F_2 are the two damage threshold functions, and σ_1 and σ_3 are the maximum principal stress and minimum principal stress, respectively. In terms of the sign, the compressive stress is positive, and the tensile stress is negative. In actual situations, f_{t0} in the formula is expressed in terms of uniaxial tensile strength. f_{c0} is the uniaxial compressive strength of shale, and φ is the internal friction angle of the material. In the case of uniaxial compression and uniaxial tension, $f_{c0/}f_{c0} = f_{c0}/f_{c0} = \lambda$ indicates that the formula is applicable.

3.2. Element Thermosolid Coupling Equation. Assuming that the shale is an elastic body, the constitutive relationship satisfies the generalized Hooke's law. The shale in the study area is at high temperature and high pressure. Under this condition, Wee et al. proposed that the relationship between temperature variables and shale under combined loading is expressed as follows [40]:

$$\sigma'_{ij} = 2G\left(\varepsilon_{ij} + \delta_{ij}\frac{\nu}{1-2\nu}\varepsilon_{kk}\right) - K'\alpha_T T\delta_{ij}. \tag{3}$$

$\sigma'_{ij} = \sigma_{ij} + \xi p \delta_{ij}$, δ represents the total stress tensor (symbol is positive for tension), δ_{ij} is the Kronecker symbol, G is the shear modulus of the material, ν is Poisson's ratio, $\xi(\leq 1)$ is the compressibility of the material $[\xi = 1 - (K'/K_S)]$, K_S is the shale material modulus of elasticity, and α is the volume expansion coefficient (K^{-1}). In this formula, the strain and stress caused by temperature changes are relative to the initial temperature; therefore, T is the temperature increase compared with the initial temperature.

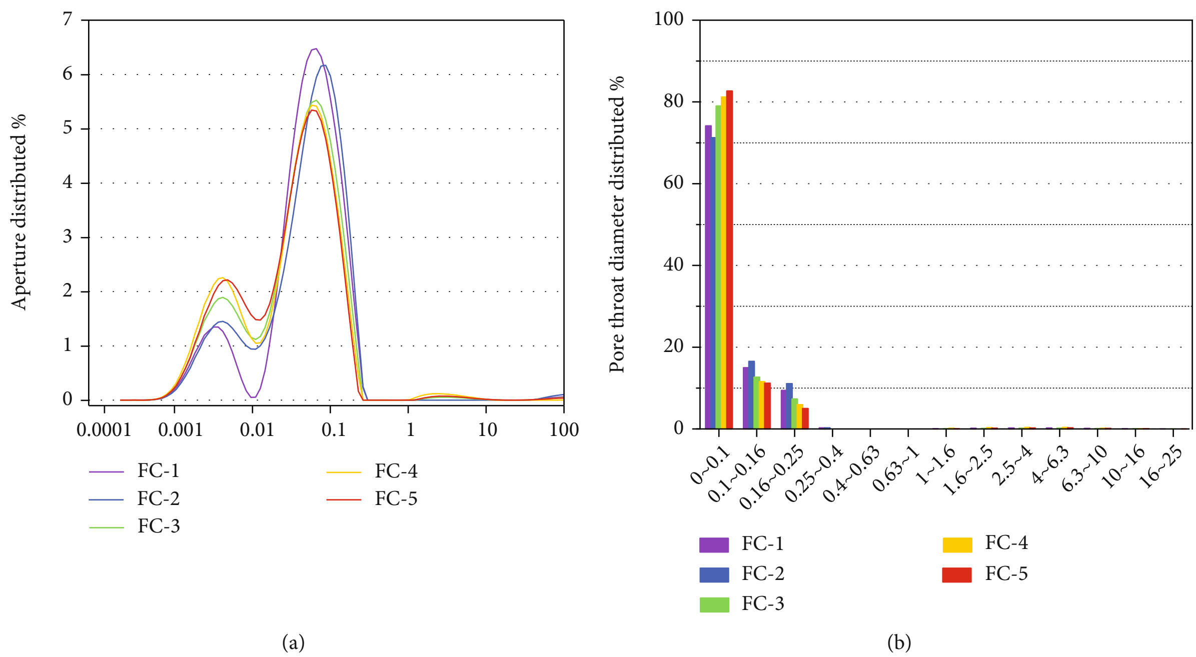

FIGURE 3: Distribution of pore size and pore throats. (a) Schematic diagram of shale aperture distribution/μm. (b) Pore throat diameter/μm [37].

During the research process, the interaction between mechanical energy and thermal energy is ignored. Based on the REV heat balance equation, it can be expressed as follows [26]:

$$(\rho_s C_s)\frac{\partial T}{\partial t} + (T_0 + T)K^{'}\alpha_T \frac{\partial \varepsilon_v}{\partial t} = \lambda_s \nabla^2 T. \tag{4}$$

In this formula, T_0 is the initial temperature (K) in the unstressed state, ρ_s is the density of the shale (kg/m^3), C_s is the specific heat capacity (J/kg·K), and λ_s is the heat transfer coefficient H of the shale (J/s·m·K). Equations (3) and (4) are a set of fully coupled nonlinear equations that control the thermosolid coupling of shale. This equation explains the evolution of heat transfer, compressibility, and thermal damage between shale materials under thermosolid coupling. The nonlinear differential equation is controlled by the second-order space partial derivative and the first-order time partial derivative. The nonlinear differential equation in the space and time domains is unsolvable.

3.3. Numerical Simulation. The RFPA temperature version software is used to study crack propagation under the thermosolid coupling of shale. RFPA is software that is based on the finite element, statistical damage theory, and Coulomb failure criterion. The deformation and failure of the rock are analyzed to obtain the true failure mode. This calculation method considers fully the randomness of the material distribution, such as rock heterogeneity and pores, and combines it with the statistical distribution assumption of material properties into the finite element algorithm. The division unit meets the given strength criterion; therefore, the rock under real conditions and the destruction process can be presented through numerical simulation. In actual situations, many difficult-to-implement problems can be solved. Figure 4 shows the schematic diagram of controlling the displacement of the model with bedding inclinations of 0°~90°.

The discretization unit of RFPA obeys the Weibull distribution. On this premise, the relationship between the microscopic conditions and the mechanical properties of the macroscopic medium is established, and the Weibull statistical distribution function is introduced to describe the following [41]:

$$\varphi(\alpha) = \frac{m}{\alpha_0} \cdot \left(\frac{\alpha}{\alpha_0}\right)^{m-1} \cdot e^{-(\alpha/\alpha_0)^m}, \tag{5}$$

where α is the mechanical property parameters of the primitive body, α_0 is the average value of the mechanical property parameters of the material, m is the parameter reflects the homogeneity of the material medium in a physical sense and is defined as the uniformity coefficient, and $\varphi(\alpha)$ is the statistical distribution density of the primitive property α.

In the RFPA temperature version, the temperature distribution function $T(x, y, z, t)$ is used to express the functional expression of the temperature change with time at each certain point in the rock.

In the calculation, the heat $q(x, y, z, t)$, $q = dQ/dt/S$, and Q per isothermal area are considered heat, t is time, and S is area, where q is proportional to the gradient of temperature function u, and the proportional coefficient H is the thermal conductivity.

$$q = -k\nabla T \tag{6}$$

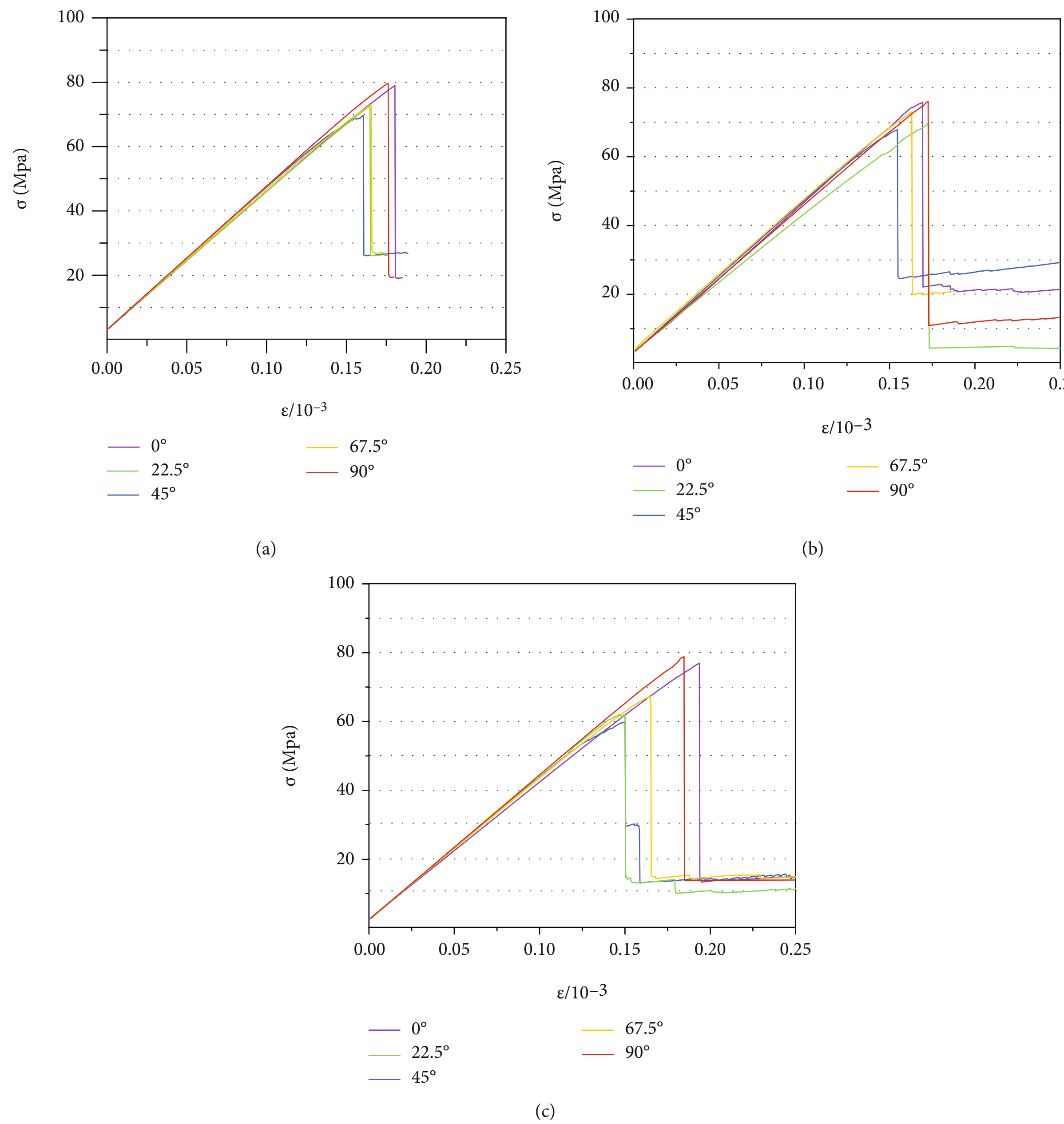

Figure 4: Stress-strain curves of different bedding inclination angles at (a) 30°C, (b) 60°C, and (c) 90°C.

Table 1: Numerical simulation parameters [24].

Material	Elastic modulus/ MPa	Mean degree	Compressive strength/MPa	Poisson ratio ν	Internal friction angle (°)	Compression tension ratio	Thermal capacity	Thermal expansion coefficient	Heat transfer coefficient
Shale substrate	51600	4	145	0.22	35	14	3.250	1.36	0.20
Bedding	30960	2	116	0.31	30	13	2.153	1.30	3.57

The numerical experimental model uses a two-dimensional model to simulate shale at different temperatures. The calculation range is 100 mm in width and 100 mm in height. The entire numerical simulation model is divided into 100×100 units, and the initial value of displacement is set to 0.001 mm. The loading method is displacement loading $\Delta S = 0.0003$ mm and fixed confining pressure $p_1 = 10$ MPa. A layered structure with a thickness of 3 mm and a spacing of

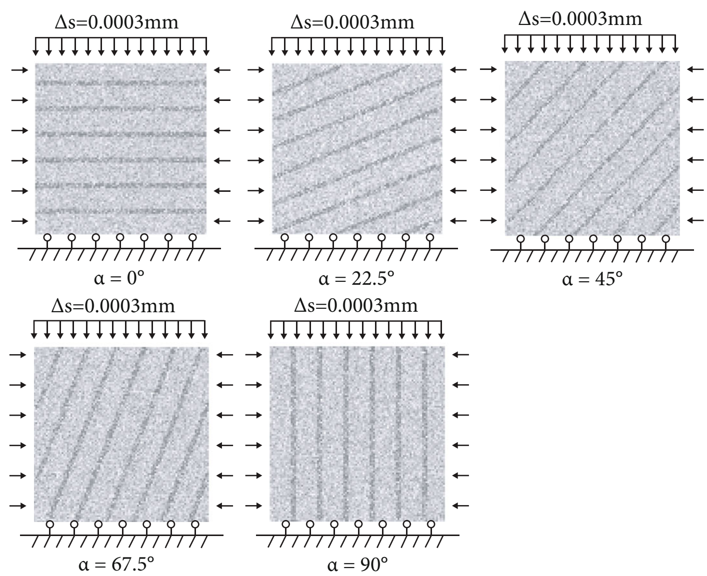

Figure 5: Schematic diagram of model loading.

15 mm is established in the model to simulate the layered structure of shale. The specific parameters in the model are shown (see Table 1) below.

The experimental study is a numerical model of shale with different bedding angles under the condition of gradually increasing temperature. The bedding angles in the model are set to 0°, 22.5°, 45°, 67.5°, and 90°. A schematic diagram of the model's overall conditions is shown in Figure 5. The fixed temperatures for the shale numerical model are 30°C, 60°C, and 90°C. The temperature boundary condition is set as the first type boundary condition (temperature is constant at 30°C, 60°C, and 90°C), and there is no heat flow between the shale matrix and outside world.

4. Analysis of Results

4.1. Analysis of Mechanical Characteristics of Shale Rupture. Figure 4 shows the stress-strain curves for shale at 30°C and dip angles of 0°, 22.5°, 45°, 67.5°, and 90° in a and 60°C and 90°C in (b) and (c). As seen from the graphs, the corresponding stress-strain curves for the shale change significantly with different inclinations, with temperature having less influence on the stress-strain curve than the effect of shale inclination. The damage of shale is broadly divided into four stages: the linear elastic stage, yielding stage, damage stage, and stability stage.

(1) The first stage is the linear elastic stage. In this stage, stress and strain have a linear relationship and exhibit good elastic properties. As seen in Figure 4, the linear elastic phase of the shale decreases significantly with increasing temperature and laminar dip angles of 22.5° and 45°. This indicates that the increase in thermal stress within the shale reduces the cementation between the shale matrix and laminae, and the softening effect becomes more pronounced as the lamina dip angle increases

(2) In the second stage of the yielding stage, influenced by the surrounding pressure and thermal stress, the temperature increase causes plastic deformation within the shale, and the shale stress-strain curve under the effect of thermosolid coupling shows a more obvious yielding stage

(3) The third stage is the failure stage. When the strength reaches its peak, the stress decreases sharply, and shale damage occurs. The graph shows that the failure strength of the shale decreases to a certain extent at each laminar dip angle after the temperature rises, especially at laminar dips of 22.5° and 45°. When the dip of the shale is the same and is accompanied by a decrease in temperature, the reduction in peak strength is due to the difference in the coefficient of thermal expansion between the bedding and shale matrix within the shale. When the particles are heated, they cause uneven expansion and uneven deformation of the shale. The particles squeeze each other so that a temperature-induced thermal stress is developed in the shale. As the temperature increases, the thermal stresses increase, resulting in thermal damage to the shale. More microfractures or primary fractures appear in the shale. On a macroscopic scale, the temperature of the shale increases. In this case, the strength decreases, which is consistent with the results of Yan et al., who studied mudstones [42]

(4) The fourth stage is the stabilization stage, where the tail end of the curve is smoothed. It can be seen from the graph that the stabilization phase at 30°C is shorter than that at 60°C and 90°C. At a temperature of 30°C, the damage mode of the shale mainly shows a brittle damage state. As the temperature increases, the properties of the shale change from brittle to plastic, showing an increase in the stability phase

Table 2: Simulation results of shale compressive strength.

Azimuth/ (°)	$t = 30°C$, compressive strength	$t = 60°C$, compressive strength	$t = 90°C$, compressive strength
0	78.98	75.81	76.91
22.5	72.69	68.67	62.34
45	69.64	67.79	59.79
67.5	72.65	72.86	67.20
90	79.61	74.98	78.79

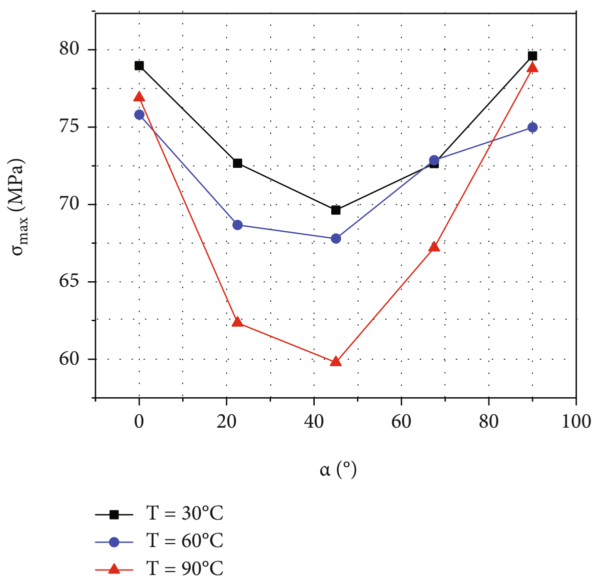

Figure 6: Shale peak intensity variation law.

Table 3: The bedding effect coefficient of the compressive strength of shale.

Azimuth/ (°)	$t = 30°C$, bedding effect coefficient	$t = 60°C$, bedding effect coefficient	$t = 90°C$, bedding effect coefficient
0	0	0	0
22.5	0.01	0.08	0.25
45	0.12	0.11	0.22
67.5	0.08	0.04	0.13
90	-0.01	0.01	-0.02

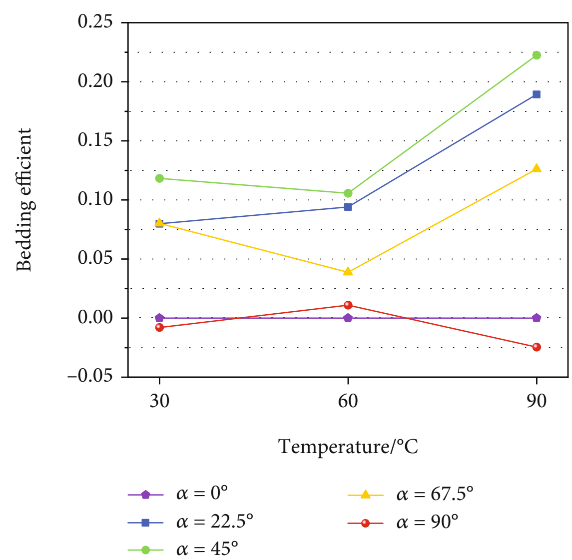

Figure 7: Variation law of the shale bedding effect at different temperatures and different dip angles.

Table 2 shows the compressive strength of shale with different bedding dip angles obtained by numerical simulation at 30°C, 60°C, and 90°C. The compressive strengths from Table 2 are plotted in Figure 6, from which it can be seen that the compressive strength of the shale reaches its maximum at 30°C, while the compressive strength decreases with increasing temperature. Additionally, temperature has a strong effect on the anisotropy of shale bedding, with increasing temperature leading to reduced cementation of the laminae to the shale matrix, and the effect is strongest at lamina dips of 22.5° and 45°. At temperatures of 30°C and 60°C, the compressive strength of the bedding inclination is greatest at 0° and least at 45°. As the azimuth of the bedding rises, the compressive strength of the shale shows a trend of first falling and then rising. When the temperature is 90°C, the compressive strength is greatest at a bedding azimuth of 90°. Alternatively, the compressive strength is lowest at 45° because of the weak cementation between the shale matrix and weak bedding surface. As the temperature increases, the thermal stress resulting from the incompatible expansion of the laminated particles and shale matrix gradually increases, and the compressive strength of the shale specimens decreases under the combined effect of the thermal stress and lamination effect.

As seen from the variation curve in Figure 6, the encrusted shale exhibits a strong lamina effect. To represent the effect of laminations on the mechanical properties of shale under thermosolid coupling, $S(\alpha)$ is used to characterize the structural effect of the laminations. The bedding effect is 1 minus the compressive strength at different inclination angles divided by the compressive strength measured at the inclination level. The expression is as follows [24]:

$$S(\alpha) = 1 - \frac{\theta(\alpha)}{\theta(0°)}. \tag{7}$$

In the formula, $S(\alpha)$ is the bedding effect coefficient, $\theta(\alpha)$ is the compressive strength of different bedding dips, and $\theta(0°)$ is the compressive strength of the shale when the bedding dip is 0°. According to the above formula, Table 3 shows the bedding effect coefficients of different shale dip angles. To observe the changes in bedding effect coefficients more intuitively, bedding effect diagrams of different bedding dip angles at 30°C, 60°C, and 90°C are drawn.

As shown in Figure 7, the shale lamina effect rises more slowly at 60°C with increasing temperature, with a significant effect at 90°C. The laminar effect is not evident for dips of 0° versus 90°, and temperature changes within 30°C to

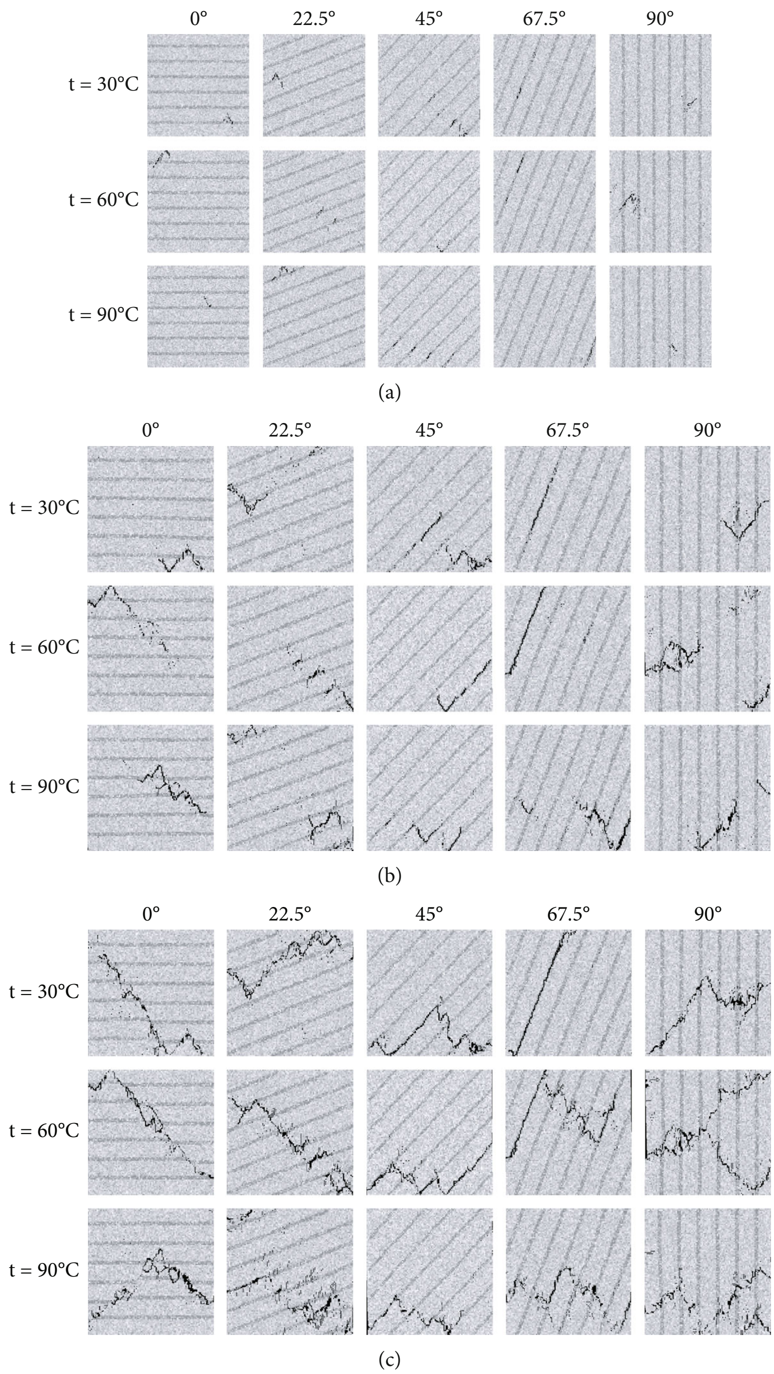

Figure 8: Continued.

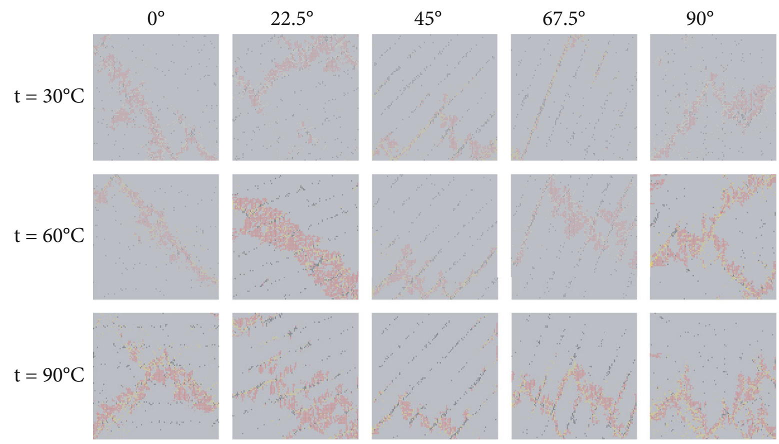

(d)

Figure 8: Fracture process and acoustic emission diagram of shale. (a) Crack initiation. (b) Crack propagation. (c) Instability mode. (d) Acoustic emission.

Table 4: Fractal dimensions at different temperatures and stress levels.

Stress level azimuth		10%	20%	30%	40%	50%	60%	70%	80%	90%	100%	Temperature
	D_s	0	0	0	0	0.129	0.278	0.411	0.572	0.771	0.978	30°C
0°	D_s	0	0	0	0	0.109	0.254	0.352	0.522	0.714	0.897	60°C
	D_s	0	0	0	0	0.327	0.532	0.667	0.796	0.916	1.063	90°C
	D_s	0	0	0	0	0.303	0.413	0.557	0.731	0.849	1.057	30°C
22.5°	D_s	0	0	0	0.231	0.385	0.551	0.717	0.82	0.916	1.091	60°C
	D_s	0	0	0	0	0.341	0.492	0.656	0.819	0.906	1.269	90°C
	D_s	0	0	0	0	0.128	0.451	0.626	0.769	0.872	1.037	30°C
45°	D_s	0	0	0	0	0.280	0.417	0.593	0.743	0.870	1.018	60°C
	D_s	0	0	0	0	0.261	0.461	0.609	0.720	0.874	1.1	90°C
	D_s	0	0	0	0	0.241	0.419	0.554	0.756	0.837	0.874	30°C
67.5°	D_s	0	0	0	0	0	0.409	0.575	0.719	0.852	0.977	60°C
	D_s	0	0	0	0	0.297	0.437	0.565	0.731	0.909	1.079	90°C
	D_s	0	0	0	0	0	0.054	0.520	0.631	0.772	0.897	30°C
90°	D_s	0	0	0	0	0	0.600	0.662	0.782	0.940	1.179	60°C
	D_s	0	0	0	0	0	0	0.428	0.591	0.734	1.286	90°C

90°C have little effect on the strength of the units divided within the shale, in the form of a smooth curve in the graph. The laminar effect curves for the 22.5°, 45°, and 67.5° shale specimens show a decreasing and then increasing pattern. The temperature rises to 90°C, the thermal stress from the uneven expansion of the particles within the shale rises sharply, and the shale matrix turns to plastic deformation between the shale and laminae, leading to a weakening of cementation; therefore, the lamina effect increases, and the fold line in the diagram shows a rapid rise.

4.2. Failure and Deformation Characteristics of Shale under Thermosolid Coupling. During the evolution of shale damage by thermosolid coupling, shale specimens reach peak strength followed by a sharp decrease in stress and sudden rupture. Figure 8 shows the damage process and the corresponding acoustic emission variation pattern for shales with different bedding dips at a fixed confining pressure. As seen from the diagram, the shale undergoes three stages: fracture initiation, fracture extension, and penetration. Figure 8(a) shows the fracture initiation phase of the shale damage process, Figure 8(b) shows the fracture extension and expansion phase, Figure 8(c) shows the final destabilization damage phase, and Figure 8(d) shows the acoustic emission map corresponding to the damage phase, where red represents tensile damage, yellow is shear damage, and the black area is the damaged unit. As seen in Figure 8(c), the damage pattern is significantly influenced by the lamination effect,

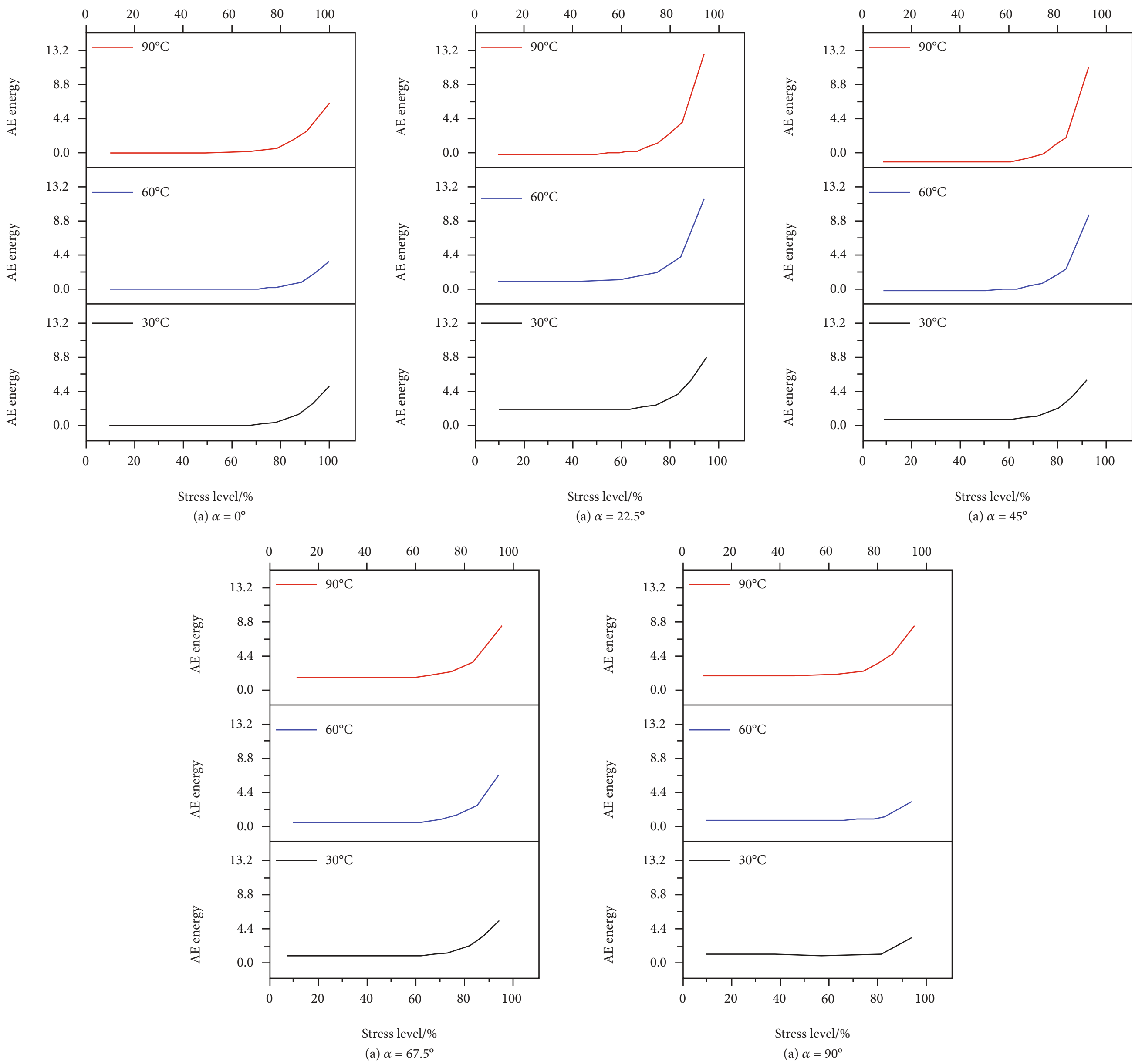

FIGURE 9: Plot of AE energy versus temperature and stress level.

with an increase in temperature having a definite effect on the change in damage pattern. The damage patterns of shales with different laminar dips at the three temperatures are classified into five damage patterns.

(1) *N-type* ($90^{\circ}_{30^{\circ}C}$, $67.5^{\circ}_{60^{\circ}C}$, $90^{\circ}_{60^{\circ}C}$ *and* $45^{\circ}_{90^{\circ}C}$). During the evolution of fractures in these groups of shale specimens, cracks first appear in the laminae. As loading progresses, the cracks extend through the laminae and eventually penetrate the shale matrix along a 45° or 135° dip to form an N-fracture. When the laminar inclination is at a high angle, temperatures below 60°C have less effect on the damage pattern, and temperatures of 90°C strengthen the laminar effect. The lamina effect is stronger at high angular lamina dips, and the laminae have a strong dominant effect on the overall shale integrity. As seen from the acoustic emission diagrams in Figure 8(d), these shale specimens are mainly distributed in tensile stresses during the final damage phase, but there are a number of shear stresses in the laminae, which can be judged to be a gradual increase in tensile stresses in the shale matrix after shear damage has occurred in the laminae.

(2) ⊠*-type* ($45^{\circ}_{30^{\circ}C}$ *and* $0^{\circ}_{90^{\circ}C}$). In both groups, the shale with a laminar dip of 45° at a temperature of 30°C cracks first in the laminae during damage, showing a strong lamina effect. In contrast, shales with a laminar dip of 0° at 90°C are cracked first in the shale

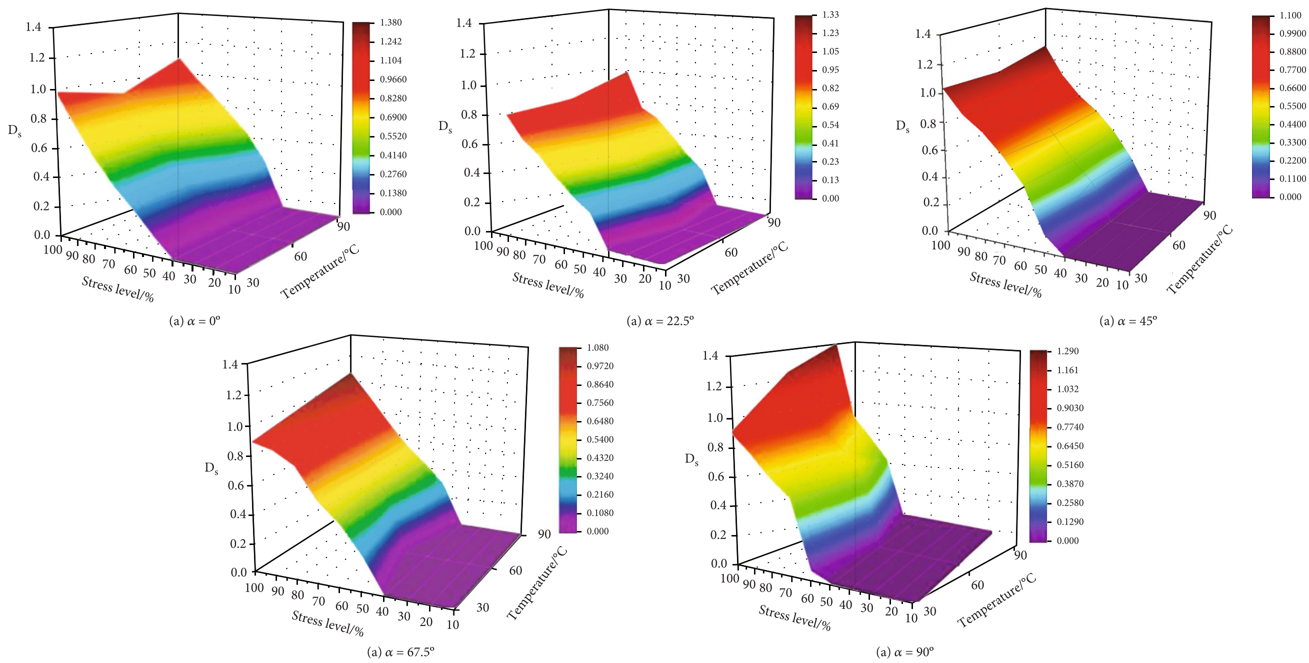

Figure 10: Relationships between different temperatures, stress levels, and fractal dimensions.

matrix, at which point the temperature effect manifests itself significantly. Shear damage occurs in the lamina section at a lamina dip of 45°, as seen in Figure 8(d), while shear damage occurs within the shale matrix at a lamina dip of 0°.

(3) *v-type* ($22.5^\circ_{30^\circ C}$ *and* $45^\circ_{60^\circ C}$). Shale specimens with a laminar dip angle of 22.5° at a temperature of 30°C show internal cracks in both the shale matrix and laminae, eventually forming v-shaped cracks along the laminae. Specimens with a lamina dip angle of 45° at a temperature of 60°C show a strong lamina effect, with cracks appearing in the lamina and then breaking along the lamina.

(4) *Slanted I-type* ($0^\circ_{30^\circ C}$, $67.5^\circ_{30^\circ C}$, $0^\circ_{60^\circ C}$ *and* $22.5^\circ_{60^\circ C}$). Damage to shale specimens at low laminar angles is primarily subject to tensile and shear stresses, when the surrounding pressure plays a major factor in preventing multiple cracks from forming. The specimen with a high angle of 67.5° at a temperature of 30°C is then subject to the effects of perimeter pressure and laminae, with cracks expanding along the laminae and the perimeter pressure preventing the formation of multiple cracks, resulting in an oblique I-shaped damage pattern.

(5) *Cluttered-type* ($22.5^\circ_{90^\circ C}$, $67.5^\circ_{90^\circ C}$ *and* $90^\circ_{90^\circ C}$). At the higher temperatures of the 90°C complex, irregular disorganized damage is more likely to occur. At a temperature of 90°C, the laminar and temperature effects of the shale reach their maximum at the same time, and thermal and loading stresses within the shale act together to cause the shale to exhibit a complex damage pattern.

According to the above analysis, the surrounding pressure at low angles of the shale laminae is the dominant factor in the damage pattern with simpler forms of damage and more complex damage occurring as the temperature rises. The lamina effect is stronger at high angles in shale laminae, where the lamina effect is the main controlling factor, mainly manifesting itself as damage occurring first along the laminae, with the lamina effect acting in conjunction with the temperature effect to produce a more complex damage pattern as the temperature rises. During hydraulic fracturing, hydraulic fractures may extend along high angular laminar dips, inhibiting the expansion of the fracture network, while higher temperatures contribute to the formation of complex fracture networks, thereby increasing shale gas production.

4.3. Quantitative Fractal Characterization of Shale Damage under Thermosolid Coupling. Analytical theory can be used to quantitatively describe irregular and complex matters in nature, including the evolution of damage to rocks. Shale converts its internal stored energy into elastic waves and releases them rapidly at the moment of destruction, a phenomenon known as acoustic emission [43, 44]. During shale damage, acoustic emission occurs for each unit that breaks down; therefore, acoustic emission has a fractal character. In this paper, images of acoustic emissions at different stress levels are grayed out by ImageJ and imported into a MATLAB calculation program to find their fractal dimension. The fractal dimension is solved by the following [45]:

$$D_s = -\lim_{1/r \longrightarrow 0} \frac{\log N(r)}{\log 1/r}, \tag{8}$$

where D_s is the adaptive fractal dimension of the damaged region, r is the side length of the square box, and $N(r)$ is the number of square boxes with side length r needed to cover the damaged region therein.

Table 4 shows the fractal dimension values. Figures 9 and 10 show the trends between AE energy, fractal dimension, laminar dip, temperature, and stress level. As shown in Figure 9, the AE energy generally shows an increase with increasing stress levels. At stress levels less than 50%, the AE energy of each group is almost zero, showing little or no damage. When the stress level is between 50% and 80%, the AE energy rises slowly at this stage, with a more pronounced rise in AE energy in low-angle shale specimens compared with high-angle shale. When stress levels exceed 80%, AE energy rises rapidly, and shale damage breaks down. 22.5°, 45°, and 67.5° show significant increases in AE energy, corresponding to the macroscopic damage forms, with high release energy representing intense shale damage and injury. An increase in energy is observed as the temperature rises, at which point the macroscopic damage intensifies, with an insignificant increase in energy at 60°C and a significant increase at 90°C, when the corresponding damage pattern becomes more complex. Figure 10 shows the fractal dimension as a function of laminar dip, temperature, and stress level, with the x-axis coordinates representing stress level and the y-axis coordinates representing temperature. It is clear from the graphs that the fractal dimension generally increases with increasing temperature, and at $\alpha = 22.5^\circ$, 67.5°, and 90°, the fractal dimension increases more with increasing temperature, indicating that temperature enhances the laminar effect of the three groups of shale dip specimens, and the macroscopic phenomenon shifts from simple oblique I or N damage to more complex heterogeneous damage. Conversely, smaller fractal dimensions correspond to simpler forms of destruction.

5. Conclusion

In this paper, the effect of temperature on the damage process of shales containing laminated shales with different dip angles is studied by establishing a coupled thermosolid model for shales of the Niutitang Formation, and the following laws are summarized:

(1) The temperature increase reduced the linear elastic phase of the shale specimens in each group, with a significant reduction in the linear elastic phase of shales with lamina dip angles of 22.5° and 45°. The elevated temperature causes partial plastic deformation within the shale, and the shale stress-strain curve under thermosolid coupling exhibits a more pronounced yielding phase

(2) When the temperature rises from 30°C to 60°C, it makes the unit swell leading to an increase in pore space, which further compacts the shale matrix with the laminae under displacement-controlled loading, and the lamina effect decreases to a small extent. And after the temperature reaches 90°C, the thermal stress generated by the uneven expansion of particles inside the shale rises sharply. The shale matrix and laminae turn to plastic deformation between them leading to weakening of cementation, and the strengthening effect of laminae in shale is most significant

(3) The shale damage patterns are grouped into five categories (N-Type, ʌ-Type, v-type, slanted I-type, and cluttered-type). Among them, the occurrence of N-type damage is mainly due to the strong dominant effect of high-angle laminae on the integrity of the whole shale, and the warming reinforces the lamina effect. The ʌ and v shapes mainly occur when the dip angle of the laminae is 45°. The sloping I-shaped damage occurs in shale specimens with low laminar dip, which are mainly subjected to tensile and shear stresses, when the surrounding pressure plays a major role in preventing the formation of multiple cracks. Heterogeneous damage occurs at a temperature of 90°C. The lamina effect and temperature effect of the shale reach a maximum at the same time, and the thermal and loading stresses inside the shale act together to give the shale a complex damage pattern

(4) The active role of temperature in shale damage is further quantified by the fractal dimension. The fractal dimension curve is relatively flat when the temperature is 60°C, while the fractal dimension rises rapidly by 90°C, indicating that the fractal extension of the shale is most favorable at a temperature of 90°C. At $\alpha = 22.5$, 67.5°, and 90°, the fractal dimension increases with increasing temperature, indicating that the laminar effect of the three groups of shale dip specimens is strongly influenced by temperature, and the macroscopic phenomenon shifts from simple oblique I- or N-shaped damage to more complex heterogeneous damage

Data Availability

The data used to support the study is available within the article.

Conflicts of Interest

The authors declare that they have no conflicts of interest.

Acknowledgments

This study was supported by the National Natural Science Foundation of China (Project Nos. 51774101, 51964007, and 52104080), the Guizhou Science and Technology Fund (Project No. [2021]401), the Guizhou Province Graduate Research Fund (YJSCXJH[2020]086 and [2020]087), and the Project: Scientific Research Project of Attached Rail Transit Line 2 Phase I Project (Project No. D2 (I)—FW—YJ—2019-001—WT), Guizhou Province, China [2021] 4023.

References

[1] J. Cooper, L. Stamford, and A. Azapagic, "Environmental impacts of shale gas in the UK: current situation and future scenarios," *Energy Technology*, vol. 2, no. 12, pp. 1012–1026, 2015.

[2] L. E. William, "Impacts of shale gas advancements on natural gas utilization in the United States," *Energy Technology*, vol. 2, no. 12, pp. 953–967, 2014.

[3] M. Zhang, W. Guo, and Z. Lei, "Patent analysis of shale gas technology in China and implications for its exploitation," *Energy Technology*, vol. 2, no. 12, pp. 1040–1045, 2015.

[4] S. S. Zhiltsov and I. S. Zonn, "Shale Gas Production in the USA," in *Shale gas: Ecology, politics, economy*, pp. 25–35, Springer, Cham, 2016.

[5] J. Cooper, L. Stamford, and A. Azapagic, "Shale gas: a review of the economic, environmental, and social sustainability," *Energy Technology*, vol. 4, no. 7, pp. 772–792, 2016.

[6] Y. Wang, Y. Zhu, S. Chen, and W. Li, "Characteristics of the nanoscale pore structure in Northwestern Hunan shale gas reservoirs using field emission scanning electron microscopy, high-pressure mercury intrusion, and gas adsorption," *Energy Fuels*, vol. 28, no. 2, pp. 945–955, 2014.

[7] L. Wang, Y. Guo, C. Yang, J. Xiao, C. Lu, and Y. Song, "Mechanical characterization of continental shale in Sichuan Basin of China and its potential impact on reservoir stimulation," *Journal of Natural Gas Science and Engineering*, vol. 79, p. 103346, 2020.

[8] Z. Li, S. Liu, W. Ren, J. Fang, and Z. Dun, "Multiscale laboratory study and numerical analysis of water-weakening effect on shale," *Advances in Materials Science and Engineering*, vol. 2020, Article ID 5263431, 14 pages, 2020.

[9] L. Li, B. Huang, Y. Li, R. Hu, and X. Li, "Multi-scale modeling of shale laminas and fracture networks in the Yanchang formation, Southern Ordos Basin, China," *Engineering Geology*, vol. 243, pp. 231–240, 2018.

[10] J. Liu, W. Ding, R. Wang et al., "Quartz types in shale and their effect on geomechanical properties: an example from the Lower Cambrian Niutitang Formation in the Cen'gong block, South China," *Applied Clay Science*, vol. 163, pp. 100–107, 2018.

[11] H. Song, Z. Wu, A. Wang, W. Sun, and Y. Zuo, "Study on the microscale tensile properties of Lower Cambrian Niutitang Formation shale based on digital images," *Geofluids*, vol. 2020, Article ID 8828965, 14 pages, 2020.

[12] M. Tang, Z. Wu, A. Wang, Y. Zuo, and W. Sun, "Study on the microscopic fracture process and acoustic emission of shale based on digital image," *Geofluids*, vol. 2021, Article ID 8874918, 14 pages, 2021.

[13] Y. Wu and Y. Yang, "The competition situation analysis of shale gas industry in China: applying Porter's five forces and scenario model," *Renewable and Sustainable Energy Reviews*, vol. 40, pp. 798–805, 2014.

[14] R. Wang, Y. Gu, W. Ding et al., "Characteristics and dominant controlling factors of organic-rich marine shales with high thermal maturity: a case study of the Lower Cambrian Niutitang Formation in the Cen'gong block, southern China," *Journal of Natural Gas Science and Engineering*, vol. 33, pp. 81–96, 2016.

[15] W. Ju, C. Wu, and W. Sun, "Effects of mechanical layering on hydraulic fracturing in shale gas reservoirs based on numerical models," *Arabian Journal of Geosciences*, vol. 11, no. 12, 2018.

[16] M. M. Nezhad, Q. J. Fisher, E. Gironacci, and M. Rezania, "Experimental study and numerical modeling of fracture propagation in shale rocks during Brazilian disk test," *Rock Mechanics & Rock Engineering*, vol. 51, no. 6, pp. 1755–1775, 2018.

[17] Y. Wang, X. Li, Y. X. Zhang, Y. S. Wu, and B. Zheng, "Gas shale hydraulic fracturing: a numerical investigation of the fracturing network evolution in the Silurian Longmaxi formation in the southeast of Sichuan Basin, China, using a coupled FSD approach," *Environmental Earth Sciences*, vol. 75, no. 14, 2016.

[18] H. Cui, Z. Wu, L. Li, J. Wang, and Y. Lou, "Numerical test study of the microscale failure modes and fractal analysis of Lower Cambrian shale based on digital images," *Advances in Civil Engineering*, vol. 2020, Article ID 8819711, 16 pages, 2020.

[19] N. Shrestha, G. Chilkoor, J. Wilder, V. Gadhamshetty, and J. J. Stone, "Potential water resource impacts of hydraulic fracturing from unconventional oil production in the Bakken shale," *Water Research*, vol. 108, pp. 1–24, 2017.

[20] Z. Wu, H. Song, L. Li, Z. Zhou, and Y. Lou, "Study on the damage evolution process and fractal of quartz-filled shale under thermal-mechanical coupling," *Geofluids*, vol. 2021, Article ID 8843120, 14 pages, 2021.

[21] C. Qin, Y. Jiang, Y. Luo, J. Zhou, and Y. Xie, "Effect of supercritical CO2 saturation pressures and temperatures on the methane adsorption behaviours of Longmaxi shale," *Energy*, vol. 206, p. 118150, 2020.

[22] T. F. Rexer, M. J. Benham, A. C. Aplin, and K. M. Thomas, "Methane adsorption on shale under simulated geological temperature and pressure conditions," *Energy & Fuels*, vol. 27, no. 6, pp. 3099–3109, 2013.

[23] D. H. Johnston, "Physical properties of shale at temperature and pressure," *SEG Technical Program Expanded Abstracts*, vol. 4, no. 1, 2012.

[24] Y. Lou, Z. Wu, W. Sun et al., "Study on failure models and fractal characteristics of shale under seepage-stress coupling," *Energy Science & Engineering*, vol. 8, no. 5, pp. 1634–1649, 2020.

[25] C. H. Wei, W. C. Zhu, Q. L. Yu, T. Xu, and S. Jeon, "Numerical simulation of excavation damaged zone under coupled thermal- mechanical conditions with varying mechanical parameters," *International Journal of Rock Mechanics & Mining Sciences*, vol. 75, pp. 169–181, 2015.

[26] Y. Zhou, R. K. N. D. Rajapakse, and J. Graham, "A coupled thermoporoelastic model with thermo-osmosis and thermal-filtration," *International Journal of Solids & Structures*, vol. 35, no. 34-35, pp. 4659–4683, 1998.

[27] O. Alm, L. L. Jaktlund, and K. Shaoquan, "The influence of microcrack density on the elastic and fracture mechanical properties of Stripa granite," *Physics of the Earth and Planetary Interiors*, vol. 40, no. 3, pp. 161–179, 1985.

[28] B. M. Lu, B. L. Tian, W. J. Liang, and M. M. Hong, "Experimental study on the influence of temperature on shale mechanical properties under conventional triaxial compression," *Advanced Materials Research*, vol. 250-253, pp. 1452–1455, 2011.

[29] Z. Wang, J. Pan, Q. Hou, B. Yu, M. Li, and Q. Niu, "Anisotropic characteristics of low-rank coal fractures in the Fukang mining area, China," *Fuel*, vol. 211, pp. 182–193, 2018.

[30] G. Yao, Q. Chen, H. Liu, Y. Tan, and L. Wang, "Experimental study on mechanical properties of lower silurian longmaxi

formation laminated shale in Southeast Yu," *Journal of Rock Mechanics and Engineering*, vol. 34, no. S1, pp. 3313–3319, 2015.

[31] M. Masri, M. Sibai, J. F. Shao, and M. Mainguy, "Experimental investigation of the effect of temperature on the mechanical behavior of Tournemire shale," *International Journal of Rock Mechanics & Mining Sciences*, vol. 70, pp. 185–191, 2014.

[32] P. K. Gautam, A. K. Verma, S. Maheshwar, and T. N. Singh, "Thermomechanical analysis of different types of sandstone at elevated temperature," *Rock Mechanics & Rock Engineering*, vol. 49, no. 5, pp. 1985–1993, 2016.

[33] P. G. Ranjith, D. R. Viete, J. C. Bai, and M. Perera, "Transformation plasticity and the effect of temperature on the mechanical behaviour of Hawkesbury sandstone at atmospheric pressure," *Engineering Geology*, vol. 151, pp. 120–127, 2012.

[34] R. Lei, Y. Wang, L. Zhang, B. Liu, and Y. K. Wang, "The evolution of sandstone microstructure and mechanical properties with thermal damage," *Energy Science & Engineering*, vol. 7, no. 6, pp. 3058–3075, 2019.

[35] B. Mahanta, T. N. Singh, and P. G. Ranjith, "Influence of thermal treatment on mode I fracture toughness of certain Indian rocks," *Engineering Geology*, vol. 210, pp. 103–114, 2016.

[36] G. Yang, J. Liu, X. Li, and J. Bi, "Effect of temperature on shale strength under dynamic impact loading," *Arabian Journal of Geosciences*, vol. 13, no. 12, 2020.

[37] Z. Wu, Y. Zuo, S. Wang et al., "Numerical study of multiperiod palaeotectonic stress fields in Lower Cambrian shale reservoirs and the prediction of fractures distribution: a case study of the Niutitang Formation in Feng'gang No. 3 block, South China," *Marine and Petroleum Geology*, vol. 80, pp. 369–381, 2017.

[38] W. C. Zhu and C. A. Tang, "Micromechanical model for simulating the fracture process of rock," *Rock Mechanics & Rock Engineering*, vol. 37, no. 1, pp. 25–56, 2004.

[39] W. C. Zhu, C. H. Wei, S. Li, J. Wei, and M. S. Zhang, "Numerical modeling on destress blasting in coal seam for enhancing gas drainage," *International Journal of Rock Mechanics and Mining Sciences*, vol. 59, pp. 179–190, 2013.

[40] A. Wcz, A. Chw, C. Jlb, B. Hyq, and D. De, "A model of coal—-gas interaction under variable temperatures - ScienceDirect," *International Journal of Coal Geology*, vol. 86, no. 2-3, pp. 213–221, 2011.

[41] C. A. Tang, H. Liu, P. K. K. Lee, Y. Tsui, and L. G. Tham, "Numerical studies of the influence of microstructure on rock failure in uniaxial compression – part I: effect of heterogeneity," *International Journal of Rock Mechanics and Mining Sciences*, vol. 37, no. 4, pp. 555–569, 2000.

[42] S. X. Yan, X. L. Wang, and Z. G. Liu, "Experimental study on bedding structure effect in mudstone drilling," *Industrial Minerals & Processing*, vol. 46, pp. 59–62, 2017.

[43] H. P. Xie, J. F. Liu, Y. Ju, J. G. Li, and L. Z. Xie, "Fractal property of spatial distribution of acoustic emissions during the failure process of bedded rock salt," *International Journal of Rock Mechanics and Mining Sciences*, vol. 48, 2011.

[44] S. W. Zhang, K. J. Shou, X. F. Xian, J. P. Zhou, and G. J. Liu, "Fractal characteristics and acoustic emission of anisotropic shale in Brazilian tests," *Tunnelling and Underground Space Technology*, vol. 71, pp. 298–308, 2018.

[45] R. Zhang, F. Dai, M. Z. Gao, N. W. Xu, and C. P. Zhang, "Fractal analysis of acoustic emission during uniaxial and triaxial loading of rock," *International Journal of Rock Mechanics and Mining Sciences*, vol. 79, pp. 241–249, 2015.

Hindawi
Geofluids
Volume 2022, Article ID 8978653, 19 pages
https://doi.org/10.1155/2022/8978653

Research Article

Establishment and Application of Bed-Separation Water Inrush Coefficient Method Considering Water Resistance of Fractured Rock Mass

Jianghui He,[1,2] Wenping Li,[3] Wei Qiao,[3] Qiqing Wang,[3] Zhi Yang,[4] and Liangning Li[3]

[1]*State Key Laboratory of Mining Response and Disaster Prevention and Control in Deep Coal Mines, Anhui University of Science and Technology, Huainan 232001, China*
[2]*School of Earth and Environment, Anhui University of Science and Technology, Huainan 232001, China*
[3]*School of Resources and Geosciences, China University of Mining & Technology, Xuzhou 221116, China*
[4]*School of Environment and Spatial Informatics, China University of Mining & Technology, Xuzhou 221116, China*

Correspondence should be addressed to Wenping Li; hjh@cumt.edu.cn

Received 6 September 2021; Accepted 24 February 2022; Published 25 March 2022

Academic Editor: Yong-Zheng Wu

Deep mining in Ordos Basin faces the threat of bed-separation water inrush (BWI), so it is necessary to carry out BWI risk assessment before mining. However, the existing BWI risk assessment methods fail to provide a universal risk classification standard. In this paper, taking three coal mines in Ordos Basin as research cases, the water resistance of fractured rock mass was analyzed, and a BWI coefficient (*BWIC*) method for BWI risk assessment was established. Firstly, by comparing the weight of each BWI-related factor, the formula for calculating the thickness of equivalent water-resisting layer of fractured rock mass was derived. The weight of each BWI-related factor was obtained by entropy weight method. Secondly, based on the stress arch theory, the overall *BWIC* in bed separation zone corresponding to different excavation lengths was obtained. *BWIC* was expressed by the ratio of the Cretaceous water pressure to the total thickness of the unbroken water-resisting layer and the equivalent water-resisting layer of the fractured rock mass. Finally, by comparing the value range of the overall *BWIC* in the bed separation zone corresponding to the excavation length with and without BWI, the standard of BWI risk classification was determined. The application results verified the scientificity of *BWIC* method and the universality of the BWI risk classification standard proposed in this paper.

1. Introduction

Bed separation is a layered cavity formed between adjacent strata due to uneven settlement of strata in overburden during underground coal mining [1–5]. When the water in the surrounding aquifer accumulates into the bed separation, bed-separation water is formed. Once the bed-separation water breaks through the water-resisting layer below it and flows into the mining site, it will cause bed-separation water inrush (BWI) [6]. BWI has the characteristics of large instantaneous water volume and strong destructiveness. Coal is still the most important fossil energy in China, and Ordos Basin has become China's main coal producing area [7, 8]. In underground coal mining, because China has the most complex geological conditions and the largest coal mining scale in the world, almost all accidents caused by BWI occur in China. For example, in 2016, a BWI occurred at Zhaojin coal mine in China, resulting in 11 deaths. Therefore, for those coal mines facing BWI threat in Ordos Basin, BWI risk assessment has important reference value for the formulation of safe mining scheme.

At present, mine engineers still have different views on the formation mechanism of BWI. Some views are that the power to induce BWI comes from the impact of the fracture of the rock stratum constituting the bed separation on the bed-separation water [9–11], while some views are that the bed-separation water pressure is the power to drive the bed-separation water to break through the aquiclude [12, 13]. In fact, in the overburden, the inrush of bed-separation water in the fracture zone should be caused by the fracture of rock stratum, but the inrush of bed-separation water above the fracture zone should be driven by bed-separation water pressure. Although BWI is not a new type of roof water hazards in coal mining in recent years, but due to the lack of attention, there are few research results on risk assessment of BWI. Multifactor-weighted superposition method is a mature risk assessment method, and it is often used in mine roof/floor water inrush risk assessment [14, 15]. However, in the multifactor-weighted superposition method, the result of data standardization processing will be affected by the value range of the data set, which will lead to the BWI risk may be wrongly evaluated and the boundary values between different risk levels changing with the change of evaluation area, for example, assuming that the values of one of the BWI-related factors in mining areas A and B are data set $A = \{a_1, a_2, \cdots, a_i, \cdots, a_m\}$ and data set $B = \{b_1, b_2, \cdots, b_j, \cdots, b_n\}$, respectively. The maximum and minimum values in data set A are $a_{\max}$ and $a_{\min}$, respectively, and the maximum and minimum values in data set B are $b_{\max}$ and $b_{\min}$, respectively. The value of the BWI-related factor at coordinate point X in mining area A is a_x, and the value of the BWI-related factor at coordinate point Y in mining area B is b_y, and $a_x = b_y$. If $a_{\max} = b_{\max}$ and $a_{\min} = b_{\min}$ cannot exist at the same time, the standardized values of a_x and b_y will not be equal, and the BWI risk at coordinate point X and coordinate point Y will be evaluated as unequal, which is not in line with the reality. The water inrush coefficient method, which was improved from the empirical formula suitable for floor water inrush risk assessment and suitable for roof water inrush risk assessment, has been used in BWI risk assessment [16]. However, the evaluation results were not convincing because the water-resisting capacity of the fractured Jurassic strata in Ordos Basin due to the fracture self-healing effect was not considered.

The above analysis shows that there is still a lack of practical methods suitable for BWI risk assessment in Ordos Basin. Moreover, the BWI risk corresponding to different excavation lengths cannot be obtained by using the existing BWI risk assessment methods, which is not conducive to guiding relevant disaster prevention and control. Therefore, the purpose of this paper is to analyze the role of BWI-related factors in BWI and establish a BWI risk assessment method that can provide water inrush risk corresponding to different excavation lengths and universal risk classification standard.

2. Engineering Geological Background of Coal Mining in Ordos Basin

Ordos Basin is the main coal producing area in China, and Jurassic coal seams are the main excavation objects. In the middle of the basin, a thick layer of Cretaceous strata is deposited above the Jurassic Anding Formation (Figure 1). The Cretaceous strata are mainly composed of thick sandstone with a small amount of sandy mudstone intercalation, which has good integrity (Figures 2 and 3(a)) and is not easy to deform, while the Jurassic Anding Formation is mainly composed of mudstone and sandy mudstone and has weathering zone inside, which is easy to deform (Figures 3(b) and 4). In the subsidence caused by underground mining, due to the asynchronous deformation between sandstone and sandy mudstone in Cretaceous and between Cretaceous and Jurassic Anding Formation, layered cavities (i.e., bed separations) appear in Cretaceous and the interface between Cretaceous and Jurassic Anding Formation (Figure 5). When the water in the aquifer around a bed separation converges into the bed separation, bed-separation water is formed, which can lead to the decline of the water level in the surrounding aquifer (Figure 6). When the bed-separation water suddenly burst into the mining area, BWI is formed. Due to the deformation of sandy mudstone intercalation in Cretaceous is clamped by its adjacent thick sandstone layers, bed separations in Cretaceous have smaller scale. On the contrary, because the overall antideformation ability of Cretaceous is greater than that of Jurassic Anding Formation, the deformation difference between Cretaceous and Jurassic Anding Formation is larger; bed separations at the interface of Cretaceous and Jurassic Anding Formation have larger scale. Therefore, the bed-separation water at the interface between Cretaceous and Jurassic Anding Formation is the focus of this study.

3. Methods and Materials

3.1. BWI-Related Factors and Their Quantification. As shown in Figure 5, BWI is caused by the breakthrough of the Jurassic protective layer by the Cretaceous bed-separation water above it. Therefore, the research objects directly involved in BWI process include the Cretaceous bed-separation water and the Jurassic protective layer. In the Jurassic protective layer, the upper part is the unbroken Jurassic strata (UJS), and the lower part is the fractured Jurassic strata (FJS). The water-resisting capacity of FJS is due to the closure of fractures in FJS under the action of water flow. Furthermore, the strata in FJS can be divided into fractured mudstone and fractured sandstone. The role and quantification of each BWI-related factor in BWI are described below.

(1) Bed-separation water pressure (P_b)

The bed-separation water pressure (P_b) provides the inducing power for the occurrence of BWI. Since the bed-separation water comes from the aquifer around the bed separation, when the bed separation is filled with water, P_b will gradually increase to be consistent with the water pressure in the aquifer around the bed separation. Since the bed separations at the interface between Cretaceous and Jurassic strata are the focus of this study, in this study, the Cretaceous P_b can be expressed by the water pressure in the aquifer at the bottom of Cretaceous.

(2) UJS thickness (T_U)

UJS is the key factor affecting BWI because it can prevent the release of bed-separation water. Because the integrity of UJS is not damaged, it has greater strength and

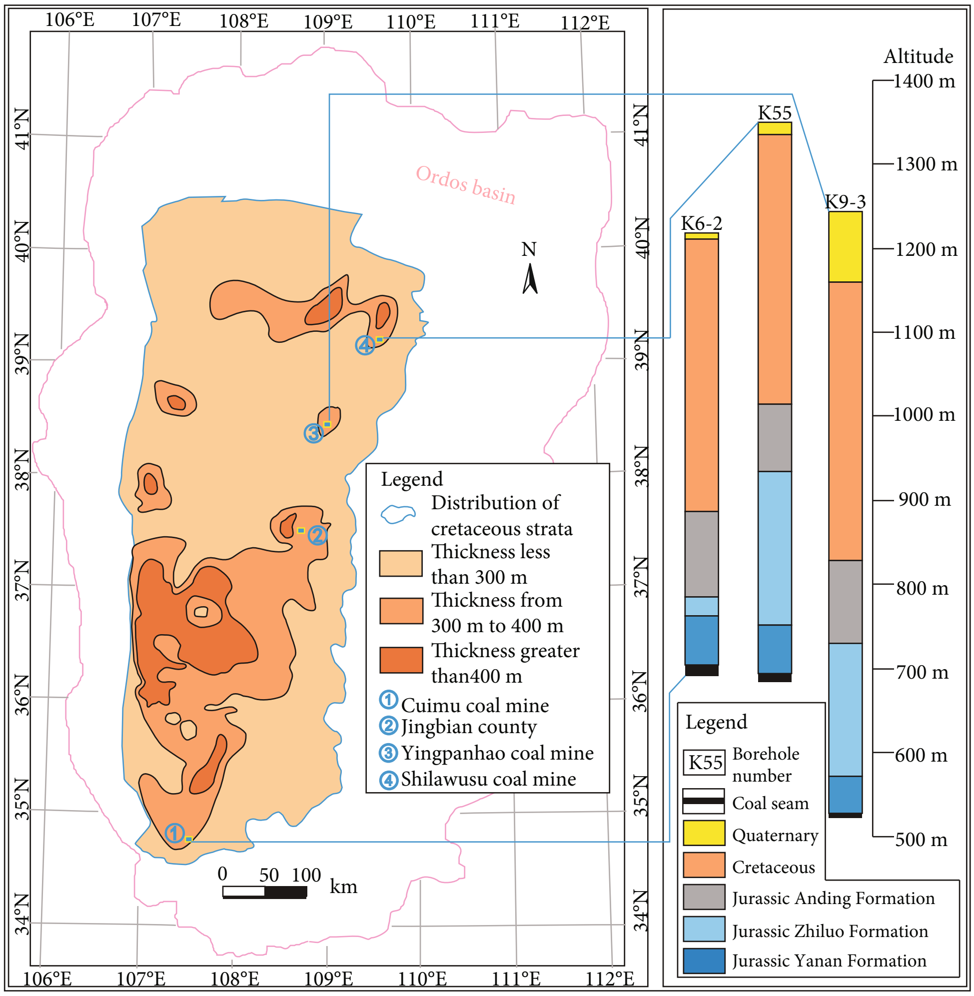

Figure 1: Engineering geological background in the study area.

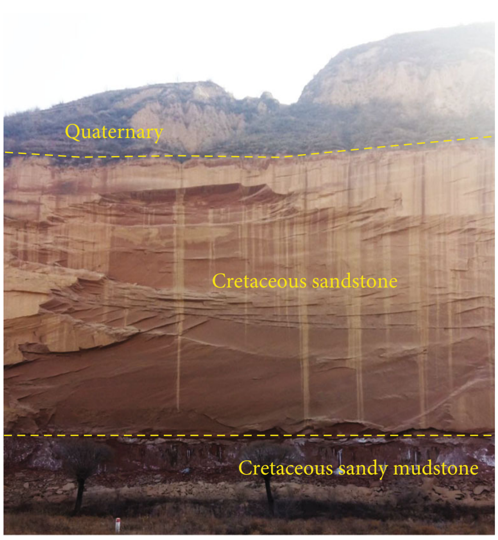

Figure 2: Outcrop of Cretaceous strata (December 2018, Jingbian, China).

better water-resisting capacity than FJS. The greater the thickness of UJS (T_U) is, the stronger its water-resisting capacity is. T_U can be calculated as follows:

$$T_U = T_J - T_F, \quad (1)$$

$$T_F = M * R_{FM}, \quad (2)$$

where T_J is the thickness of Jurassic strata between coal seam and Cretaceous (that is, the thickness of Jurassic protective layer); T_F is the thickness of FJS; M is the mining thickness; and R_{FM} is the ratio of T_F and M, which can be obtained through field monitoring.

(3) Closure potential of mudstone fractures in FJS (C_m)

Due to the low strength (with an average saturated uniaxial compressive strength of 4.75 MPa) and low softening coefficient (with an average softening coefficient of 0.34), the Jurassic mudstone can be easily argillated and deformed after encountering water (Figure 7), resulting in the self-healing effect of fractures in Jurassic mudstone under the action of water flow.

(a)

(b)

Figure 3: Rock cores drilled in the Yingpanhao mine of (a) Cretaceous strata and (b) the Jurassic Anding Formation.

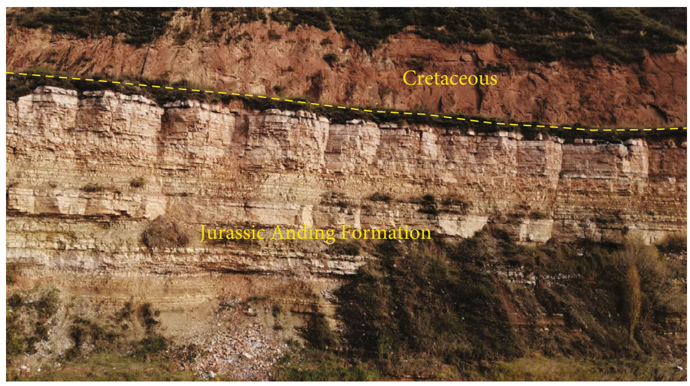

Figure 4: Outcrop of the interface between Cretaceous strata and the Jurassic Anding Formation in the Ordos Basin (October 2019, Jingbian, China).

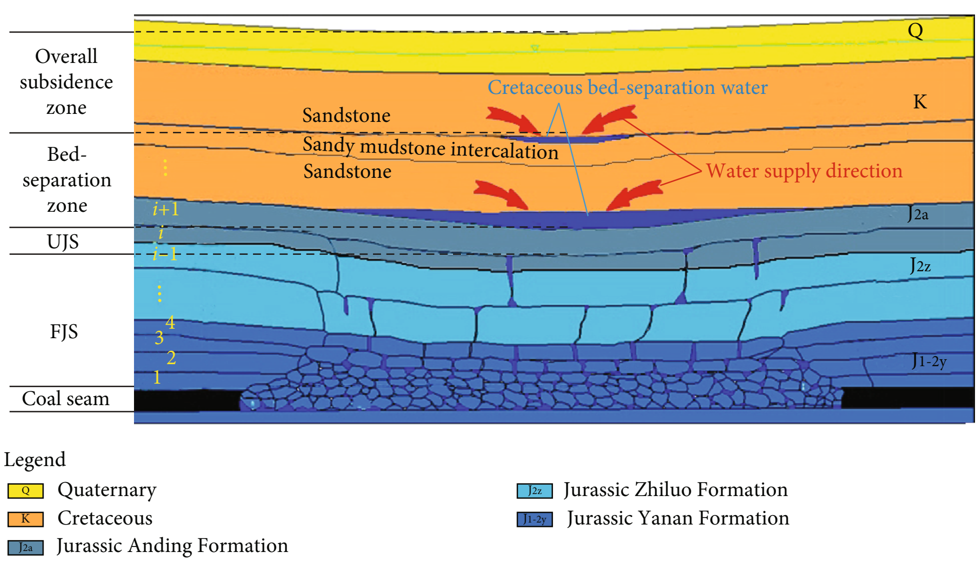

Figure 5: Schematic diagram of Cretaceous bed-separation water formation and mining disturbed overburden zoning during Jurassic coal seam mining: T_i: total thickness of all strata between the i^{th} layer and the coal seam.

In FJS, the better the closure effect of mudstone fractures, the stronger the water-resisting capacity of mudstone, and the smaller the probability of BWI. Here, the closure potential of mudstone fractures in FJS (C_m) was used to evaluate the closure effect of mudstone fractures. Because C_m is positively correlated with the volume of mudstone and the volume of mudstone is positively correlated with the mudstone thickness, C_m is positively correlated with the mudstone thickness. On the contrary, because C_m is negatively correlated with the opening degree of mudstone fractures, and the opening degree of mudstone fractures is positively correlated with the height of available subsidence space of mudstone before mudstone fracture, C_m is negatively correlated with the height of available subsidence space of

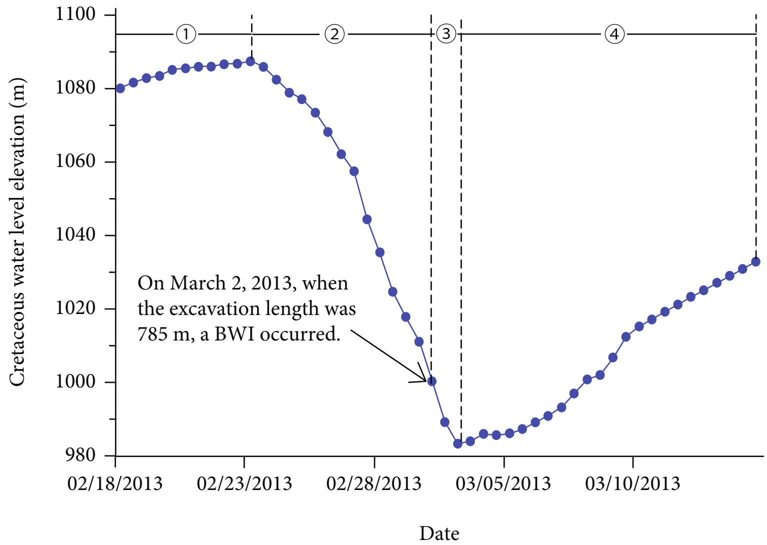

FIGURE 6: Changes of Cretaceous water level during the formation of a Cretaceous BWI in Cuimu coal mine. ①: natural recovery period of water level; ②: filling period of water in Cretaceous aquifer into bed separation; ③: bed-separation water inrush period; ④: water level recovery period after water inrush channel closure.

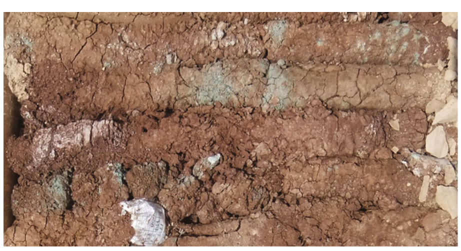

FIGURE 7: Argillization of Jurassic mudstone core after encountering water.

FIGURE 8: Disintegration of Jurassic sandstone core after encountering water.

mudstone before mudstone fracture. Therefore, C_m can be quantified by the following formula:

$$C_m = \sum_{i=1}^{n} c_{mi}, \tag{3}$$

$$c_{mi} = \frac{t_{mi}}{\Psi_{mi}} = \frac{t_{mi}}{M - T_{mi} * (\eta - 1)}. \tag{4}$$

where c_{mi}, t_{mi}, and Ψ_{mi} refer to the closure potential, thickness, and height of available settlement space of the i^{th} mudstone layer in FJS, respectively; η refers to the average expansion coefficient of the fractured rock mass, which can be obtained through field monitoring; and T_{mi} refers to the total thickness of all strata between the i^{th} mudstone layer in FJS and the coal seam.

(4) Closure potential of sandstone fractures in FJS (C_s)

Due to the low cementation degree, the Jurassic sandstone is easy to disintegrate after encountering water (Figure 8), and the fractures in the Jurassic sandstone are easy to be filled and closed by the disintegrated rock debris.

In FJS, the better the closure effect of sandstone fractures, the stronger the water-resisting capacity of sandstone, and the smaller the probability of BWI. Here, the closure potential of sandstone fractures in FJS (C_s) was used to evaluate the closure effect of sandstone fractures. Because C_s is positively correlated with the sandstone fracture length and the sandstone fracture length is positively correlated with the sandstone thickness, C_s is positively correlated with the sandstone thickness. On the contrary, because C_s is negatively correlated with the opening degree of sandstone fractures, and the opening degree of sandstone fractures is positively correlated with the height of available subsidence space of sandstone before sandstone fracture, C_s is negatively correlated with the height of available subsidence space of sandstone before sandstone fracture. Therefore, C_s can be quantified by the following formula:

$$C_s = \sum_{i=1}^{n} c_{si}, \tag{5}$$

$$c_{si} = \frac{t_{si}}{\Psi_{si}} = \frac{t_{si}}{M - T_{si} * (\eta - 1)}. \tag{6}$$

where c_{si}, t_{si}, and Ψ_{si} refer to the closure potential, thickness, and height of available settlement space of the i^{th} sandstone layer in FJS, respectively; and T_{si} refers to the total thickness

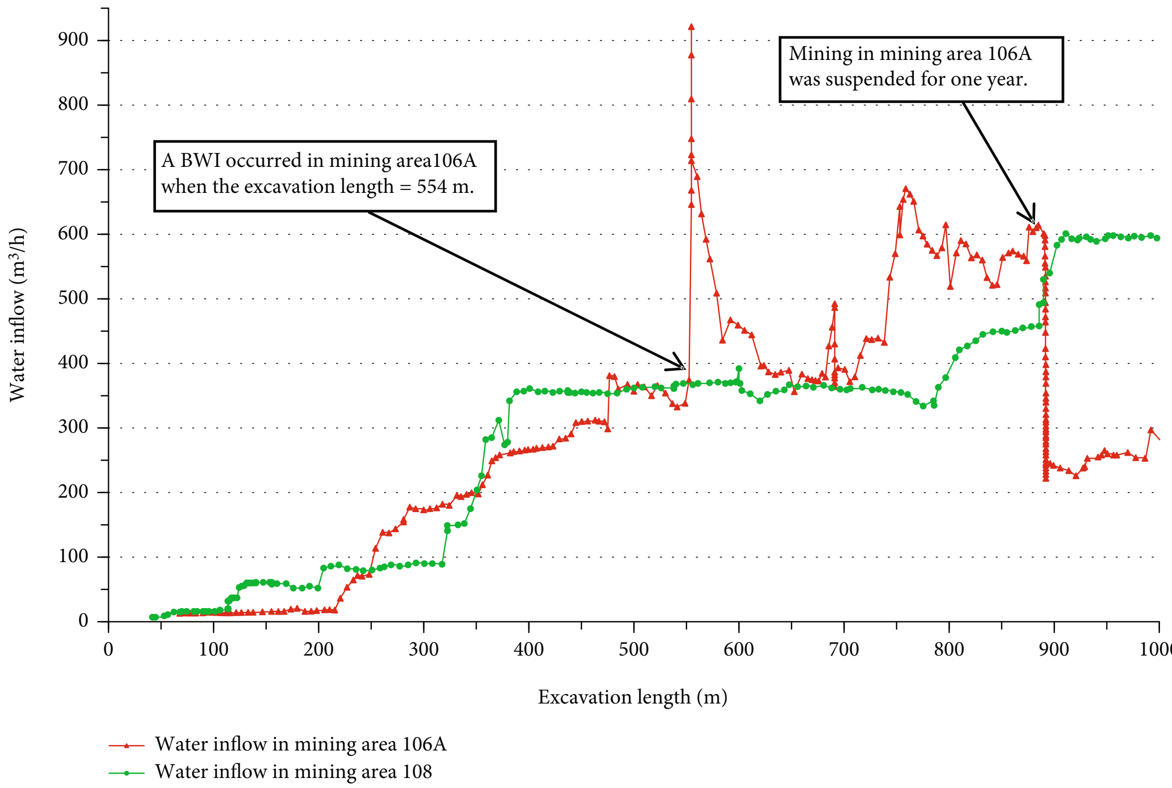

Figure 9: Comparison of water inflow in mining areas 106A and 108 in the Shilawusu coal mine.

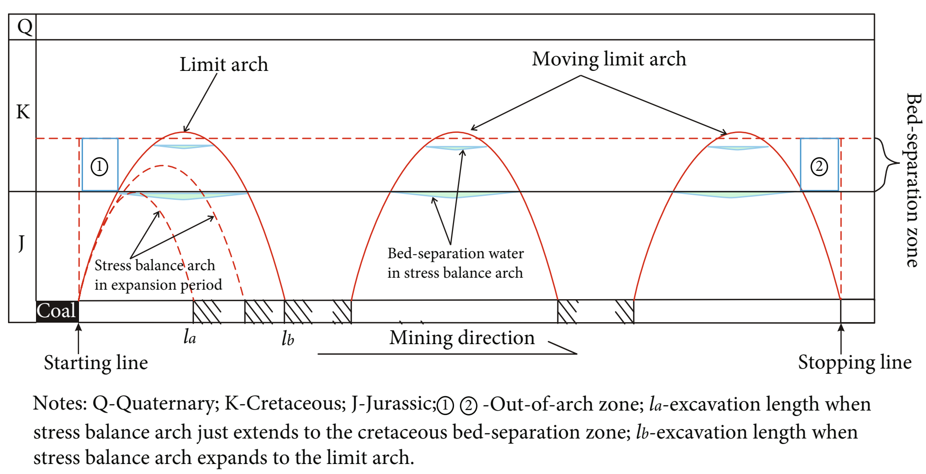

Figure 10: Schematic diagram of stress balance arches and bed separations in mining disturbed overburden.

of all strata between the i^{th} sandstone layer in FJS and the coal seam.

3.2. Bed-Separation Water Inrush Coefficient (BWIC) Method

3.2.1. Obtaining the BWI-Related Factors at Each Coordinate Point. According to the strata information revealed by each borehole, the values of BWI-related factors in each borehole are calculated. Then, through interpolation calculation, the values of each BWI-related factor at any coordinate point in the area to be evaluated can be obtained. Interpolation calculation can be realized by using a drawing software named Surfer.

3.2.2. Identifying the Weight of Each BWI-Related Factor. UJS with a certain thickness and the same water-resisting capacity as FJS was called the equivalent strata of FJS (E-FJS). In order to calculate the thickness of E-FJS, it is necessary to determine the weight of each BWI-related factor in BWI.

In this paper, the mining areas 106A and 108 in Shilawusu coal mine are taken as examples to explain how to obtain the weight of each BWI-related factor. Mining in

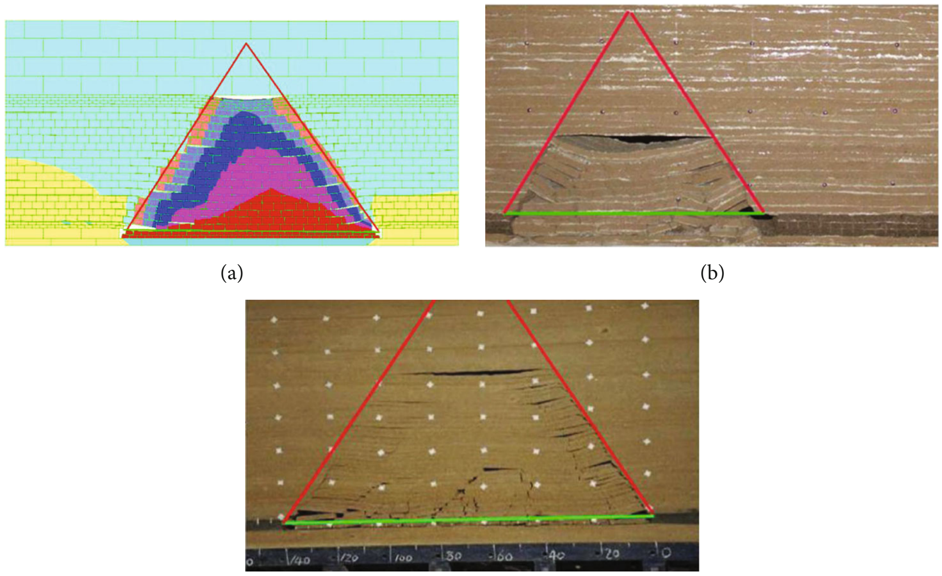

FIGURE 11: Stress balance arch and its simplification based on some coal seam mining experiments. (a) Numerical simulation experiment of coal seam mining in Cuimu coal mine; (b) similar material simulation experiment of coal seam mining in Buerdong coal mine; (c) similar material simulation experiment of coal seam mining in Daliuta coal mine.

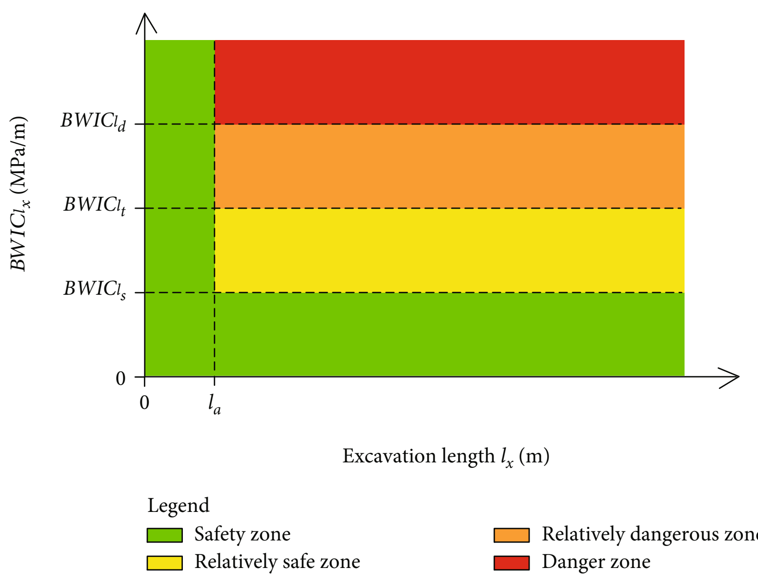

FIGURE 12: Principle of BWI risk classification based on *BWIC* method.

mining area 106A has been completed, mining in mining area 108 is still in progress, and 1000 m has been excavated. When the excavation length was 554 m, a BWI occurred in mining area 106A, but no BWI occurred in mining area 108 during mining. Because the total amount of water in a bed separation is limited, the water inflow in a BWI has the characteristics of rapid increase and rapid decrease (Figure 9). However, the instantaneous water inflow of BWI is very large, so BWI is very destructive.

Even though mining areas 106A and 108 have the same mining width, similar mining depth, and similar mining thickness, there are differences in BWI-related factors between the two mining areas, which eventually lead to differences in BWI risk between the two mining areas. Therefore, by comparing the differences of BWI-related factors between mining area 106A and mining area 108, the weight of each BWI-related factor in the formation of BWI can be obtained under the premise of excluding the influence of mining width, mining depth, and mining thickness on BWI. The principle of obtaining the weight of each BWI-related factor is consistent with the basic principle of entropy weight method. Therefore, in this paper, entropy weight method was used to obtain the weight of each BWI-related factor.

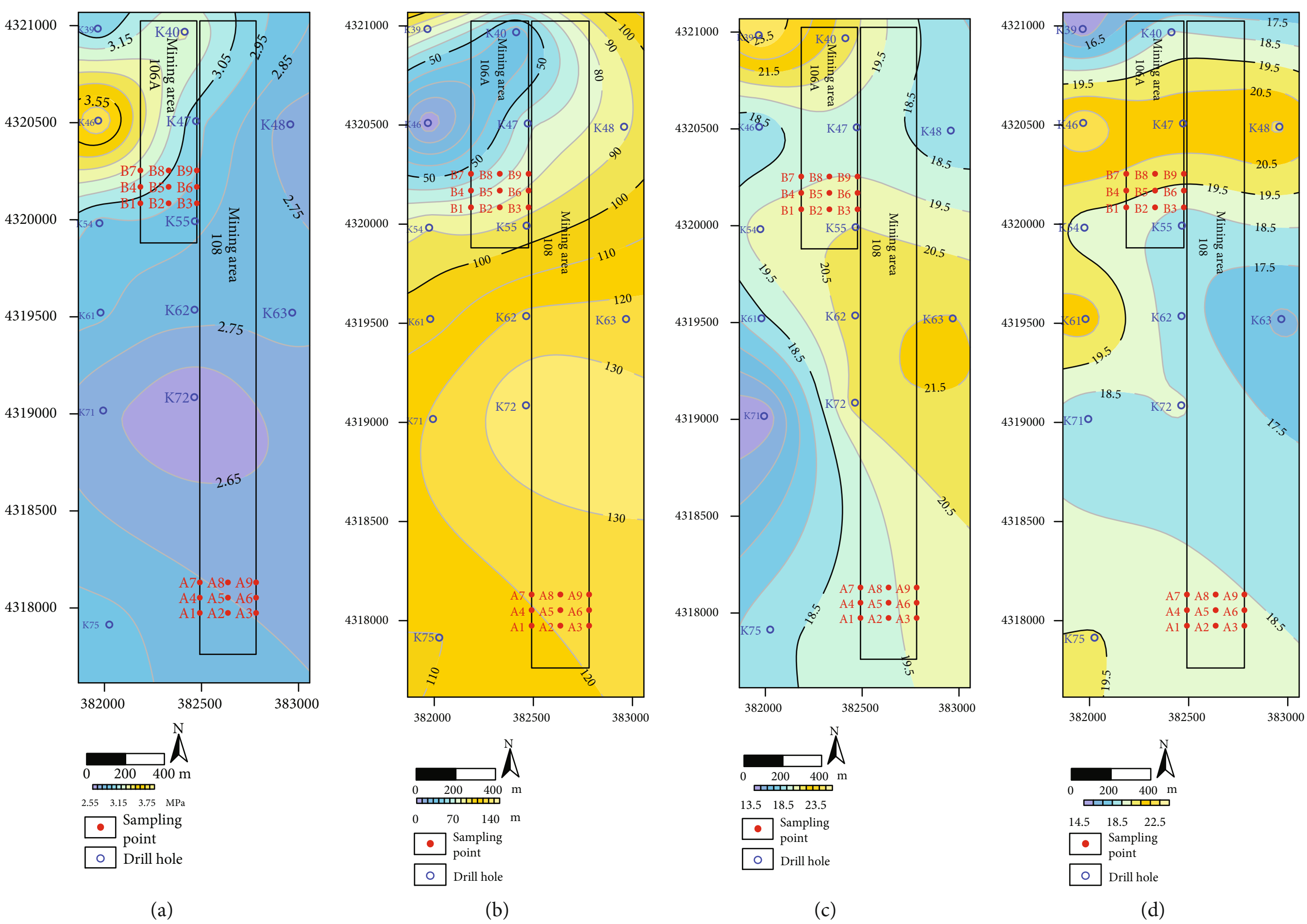

FIGURE 13: Distribution of (a) P_b, (b) T_U, (c) C_m, and (d) C_s in mining areas 106A and 108 in Shilawusu coal mine.

The data used for weight calculation obtained from m sampling points and n BWI-related factors is written as:

$$X = (x_{ij})_{m\times n} = \begin{pmatrix} x_{11} & \cdots & x_{1n} \\ \vdots & \ddots & \vdots \\ x_{m1} & \cdots & x_{mn} \end{pmatrix}. \tag{7}$$

After standardization, the following results can be obtained:

$$R = (r_{ij})_{m\times n} = \begin{pmatrix} r_{11} & \cdots & r_{1n} \\ \vdots & \ddots & \vdots \\ r_{m1} & \cdots & r_{mn} \end{pmatrix}, \tag{8}$$

where r_{ij} is the standardization value of the i^{th} sampling point for the j^{th} BWI-related factor. For the BWI-related factors positively correlated with BWI, r_{ij} is calculated as follows:

$$r_{ij} = \frac{x_{ij} - \min_j x_{ij}}{\max_j x_{ij} - \min_j x_{ij}}, \tag{9}$$

whereas for the BWI-related factors negatively correlated with BWI, r_{ij} is calculated as follows:

$$r_{ij} = \frac{\max_j x_{ij} - x_{ij}}{\max_j x_{ij} - \min_j x_{ij}}. \tag{10}$$

The information entropy of the j^{th} BWI-related factor (e_j) is defined as:

$$e_j = \frac{-1}{\ln m} \sum_{i=1}^{m} p_{ij} * \ln p_{ij}, \tag{11}$$

where p_{ij} is calculated as follows:

$$p_{ij} = \frac{r_{ij}}{\sum_{i=1}^{m} r_{ij}}. \tag{12}$$

Because when p_{ij} infinitely approaches 0, $p_{ij} * \ln p_{ij}$ approaches 0; here, when $p_{ij} = 0$, the value of $p_{ij} * \ln p_{ij}$ was

Table 1: Values of BWI-related factors at each sampling point.

Sampling points	P_b (MPa)	T_U (m)	C_m	C_s
A1	2.78	119.774	18.858	18.997
A2	2.761	121.818	19.128	18.875
A3	2.746	123.425	19.378	18.767
A4	2.768	120.75	18.829	18.922
A5	2.75	122.759	19.135	18.805
A6	2.737	124.304	19.411	18.699
A7	2.755	121.842	18.799	18.839
A8	2.739	123.791	19.146	18.73
A9	2.726	125.248	19.45	18.628
B1	3.019	77.908	20.419	19.315
B2	2.963	82.763	20.607	18.905
B3	2.898	88.448	20.76	18.539
B4	3.102	68.009	20.08	19.796
B5	3.014	75.583	20.285	19.449
B6	2.925	83.201	20.39	19.213
B7	3.191	57.792	19.726	20.319
B8	3.065	68.571	19.983	20.001
B9	2.95	78.299	20.078	19.832

Table 2: Index weight of BWI-related factors.

BWI-related factors	P_b	T_U	C_m	C_s
Index weight	0.354	0.390	0.158	0.098

Table 3: $T_{E-M-FJS}$ of mudstone at different locations in FJS.

Location	t_m (m)	T_m (m)	c_m	$T_{E-M-FJS}$ (m)	$T_{E-M-FJS}/t_m$
Top of FJS	1	229	0.374	0.763	76.3%
Bottom of FJS	1	0	0.1	0.204	20.4%

Table 4: $T_{E-S-FJS}$ of sandstone at different locations in FJS.

Location	t_s (m)	T_s (m)	c_s	$T_{E-S-FJS}$ (m)	$T_{E-S-FJS}/t_s$
Top of FJS	1	229	0.374	0.487	48.7%
Bottom of FJS	1	0	0.1	0.130	13.0%

set to 0. The entropy weight of the j^{th} BWI-related factor (w_j) can be calculated by the following formula:

$$w_j = \frac{1 - e_j}{n - \sum_{j=1}^{n} e_j}. \tag{13}$$

In this paper, there are four BWI-related factors, so $n = 4$, and w_1, w_2, w_3, and w_4 refer to the weight of P_b, T_U, C_m, and C_s, respectively.

3.2.3. Calculating the E-FJS Thickness (T_{E-FJS}). After calculating the weight of each BWI-related factor in BWI, the

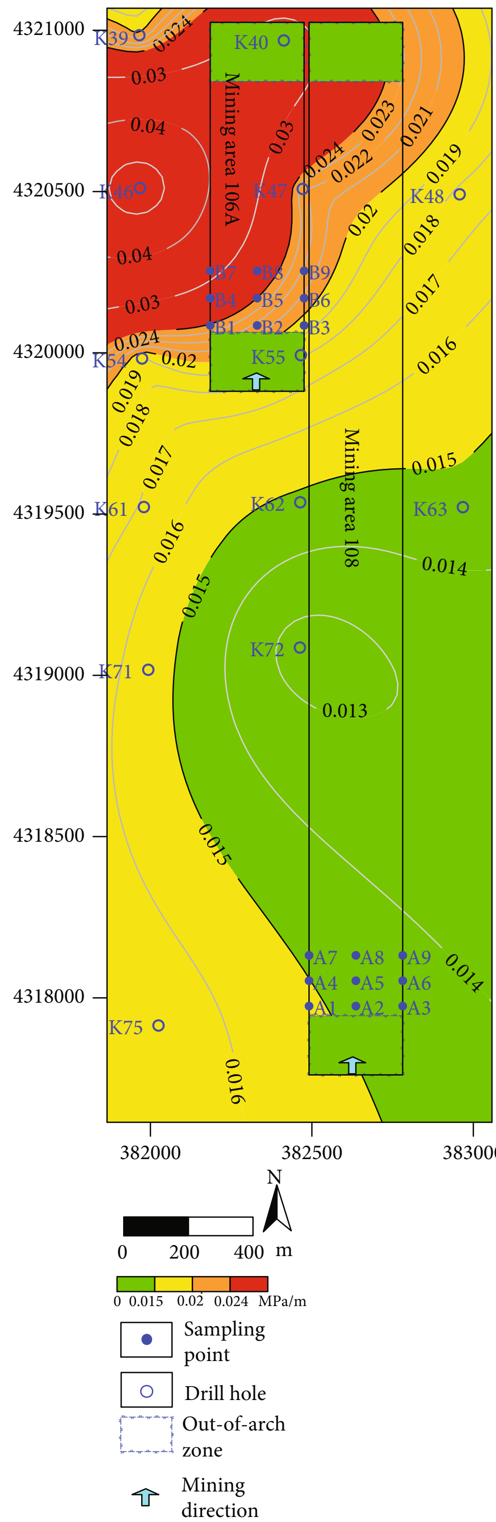

Figure 14: Distribution of *BWIC* in mining areas 106A and 108 in Shilawusu coal mine.

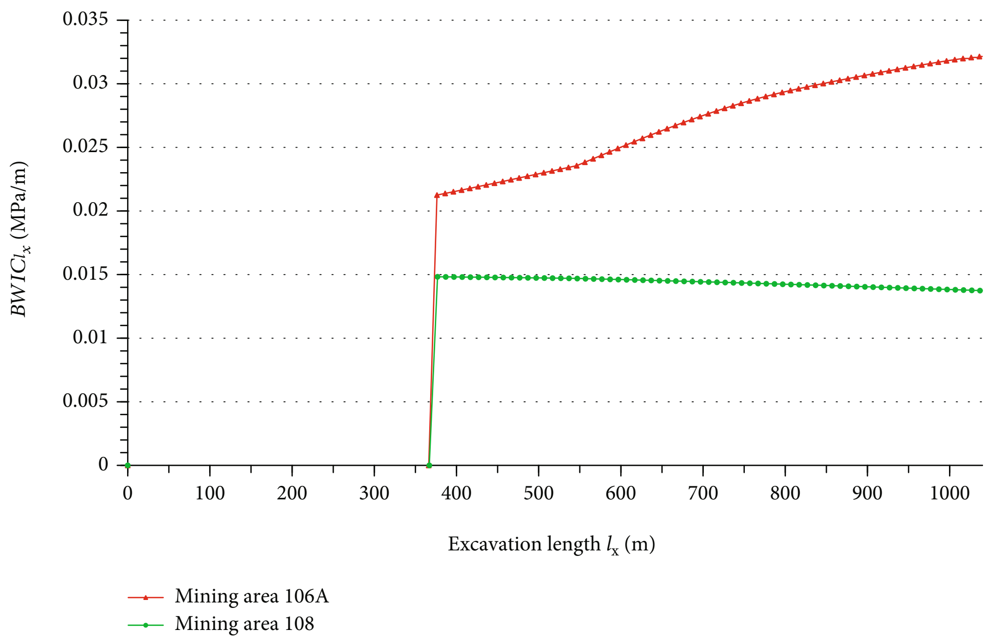

FIGURE 15: Overall *BWIC* corresponding to different excavation lengths in mining areas 106A and 108 in Shilawusu coal mine.

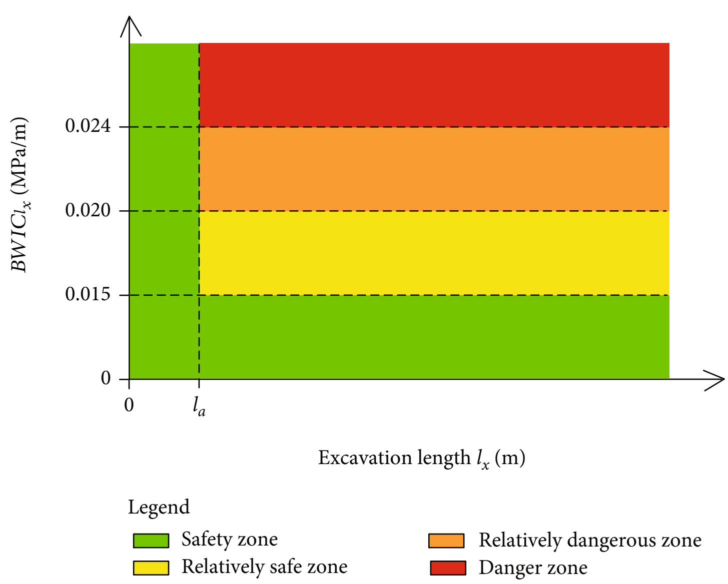

FIGURE 16: Discriminant diagram of BWI risk classification based on *BWIC* method.

water-resisting capacity index (V_i) of Jurassic protective layer at the i^{th} sampling point can be calculated by the following formula:

$$V_i = \frac{T_{Ui}}{\sum_{i=1}^{m} T_{Ui}} w_2 + \frac{C_{mi}}{\sum_{i=1}^{m} C_{mi}} w_3 + \frac{C_{si}}{\sum_{i=1}^{m} C_{si}} w_4. \quad (14)$$

Equation (14) can be transformed into:

$$V_i = T_{Ui} * k_1 + C_{mi} * k_2 + C_{si} * k_3, \quad (15)$$

where k_1, k_2, and k_3 are constants.

Assuming that the values of T_U, C_m, and C_s at the coordinate point A are T_{UA}, C_{mA}, and C_{sA}, respectively, and the values of T_U, C_m, and C_s at the coordinate point B are T_{UB}, C_{mB}, and C_{sB}, respectively, then according to Equation (15), the water-resisting capacity index of Jurassic protective layer at the coordinate points A and B can be shown as follows:

$$V_A = T_{UA} * k_1 + C_{mA} * k_2 + C_{sA} * k_3, \quad (16)$$

$$V_B = T_{UB} * k_1 + C_{mB} * k_2 + C_{sB} * k_3, \quad (17)$$

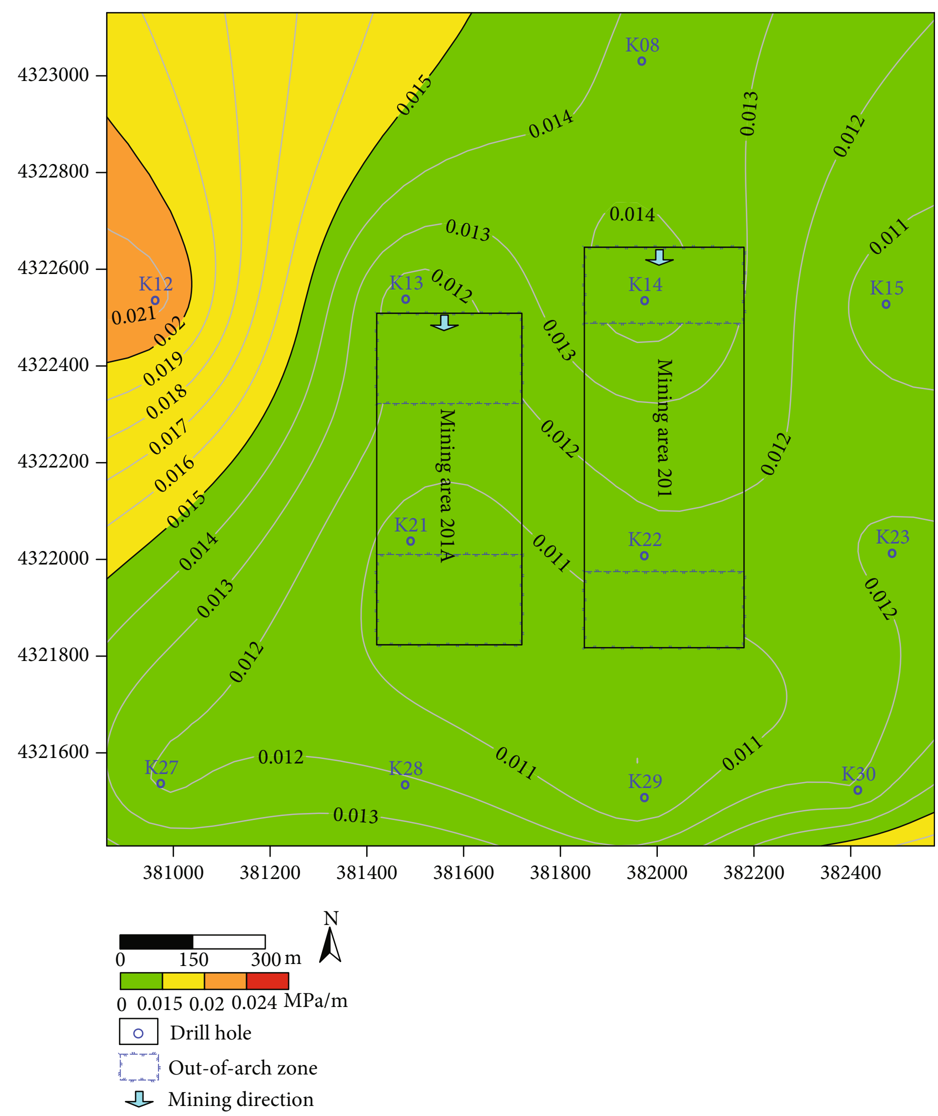

Figure 17: Distribution of *BWIC* in mining areas 201A and 201 in Shilawusu coal mine.

where V_{A} and V_{B} are the water-resisting capacity index of Jurassic protective layer at the coordinate points A and B, respectively. Then, the restriction conditions (18) and (19) were set as follows:

$$\begin{cases} V_{\mathrm{A}} = V_{\mathrm{B}}\,;\, C_{s\mathrm{A}} = C_{s\mathrm{B}}, \\ T_{U\mathrm{A}} \neq 0\,;\, T_{U\mathrm{B}} = 0, \\ C_{m\mathrm{A}} = 0\,;\, C_{m\mathrm{B}} \neq 0, \end{cases} \tag{18}$$

$$\begin{cases} V_{\mathrm{A}} = V_{\mathrm{B}}\,;\, C_{m\mathrm{A}} = C_{m\mathrm{B}}, \\ T_{U\mathrm{A}} \neq 0\,;\, T_{U\mathrm{B}} = 0, \\ C_{s\mathrm{A}} = 0\,;\, C_{s\mathrm{B}} \neq 0. \end{cases} \tag{19}$$

By synthesizing Equations (16) and (17) and restriction condition (18), the following equation can be obtained:

$$T_{U\mathrm{A}} * k_1 = \left(\frac{k_2}{k_1} * C_{m\mathrm{B}}\right) * k_1 = \left(k_m * C_{m\mathrm{B}}\right) * k_1, \tag{20}$$

where k_m is a constant and its value is the ratio of k_2 to k_1. From Equation (20), it can be concluded that:

$$T_{U\mathrm{A}} = k_m * C_{m\mathrm{B}}. \tag{21}$$

The physical meaning of Equation (21) can be expressed as when C_m is dimensionless and the unit of T_U is m, the water-resisting capacity of UJS with $T_U = k_m$ m is equal to that of one unit of C_m. UJS with a certain thickness and

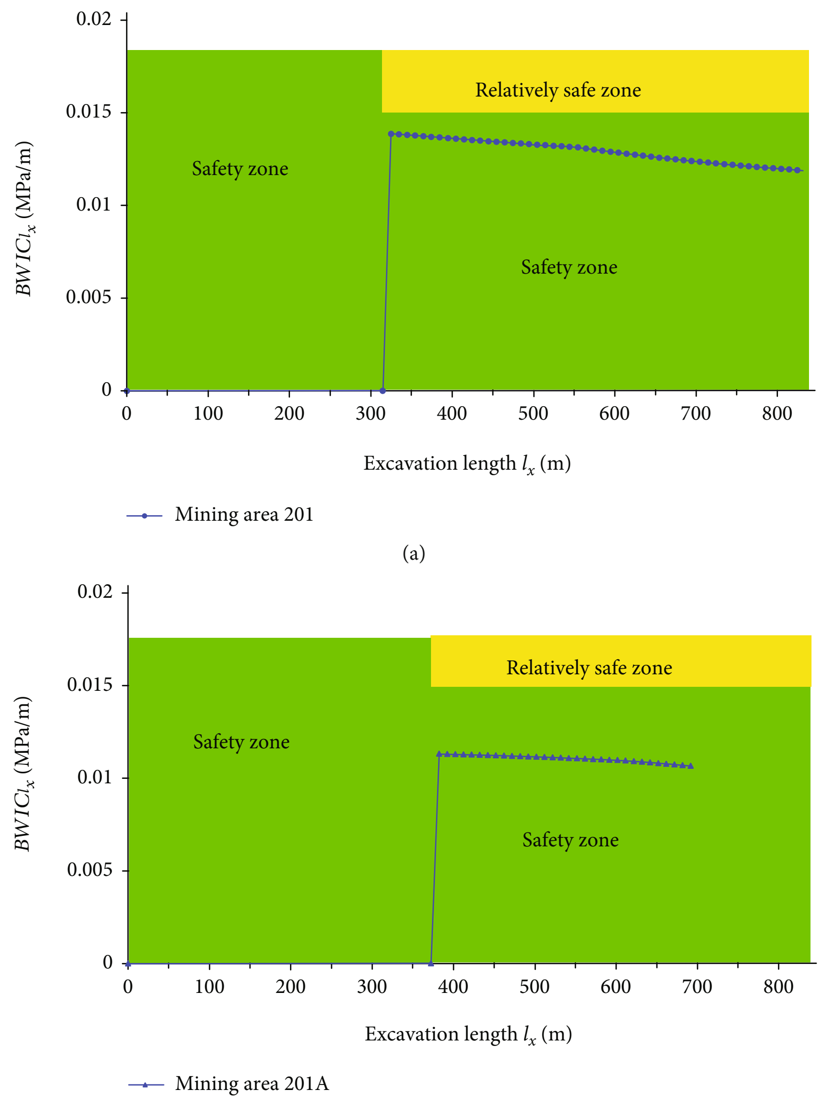

(a)

(b)

Figure 18: Overall *BWIC* corresponding to different excavation lengths in (a) mining area 201 and (b) mining area 201A in Shilawusu coal mine.

the same water-resisting capacity as mudstone in FJS was called equivalent strata of mudstone in FJS (E-M-FJS). Therefore, the E-M-FJS thickness ($T_{E-M-FJS}$) can be obtained as:

$$T_{E-M-FJS} = k_m * C_m. \quad (22)$$

By synthesizing Equations (16) and (17) and restriction condition (19), the following equation can be obtained:

$$T_{UA} * k_1 = \left(\frac{k_3}{k_1} * C_{sB}\right) * k_1 = (k_s * C_{sB}) * k_1, \quad (23)$$

where k_s is a constant and its value is the ratio of k_3 to k_1. From equation (23), it can be concluded that:

$$T_{UA} = k_s * C_{sB}. \quad (24)$$

The physical meaning of Equation (24) can be expressed as when C_s is dimensionless and the unit of T_U is m, the water-resisting capacity of UJS with $T_U = k_s$ m is equal to that of one unit of C_s. UJS with a certain thickness and the same water-resisting capacity as sandstone in FJS was called equivalent strata of sandstone in FJS (E-S-FJS). Therefore, the E-S-FJS thickness ($T_{E-S-FJS}$) can be obtained as:

$$T_{E-S-FJS} = k_s * C_s. \quad (25)$$

The relationship among T_{E-FJS}, $T_{E-M-FJS}$, and $T_{E-S-FJS}$ satisfies the following equation:

$$T_{E-FJS} = T_{E-M-FJS} + T_{E-S-FJS}. \quad (26)$$

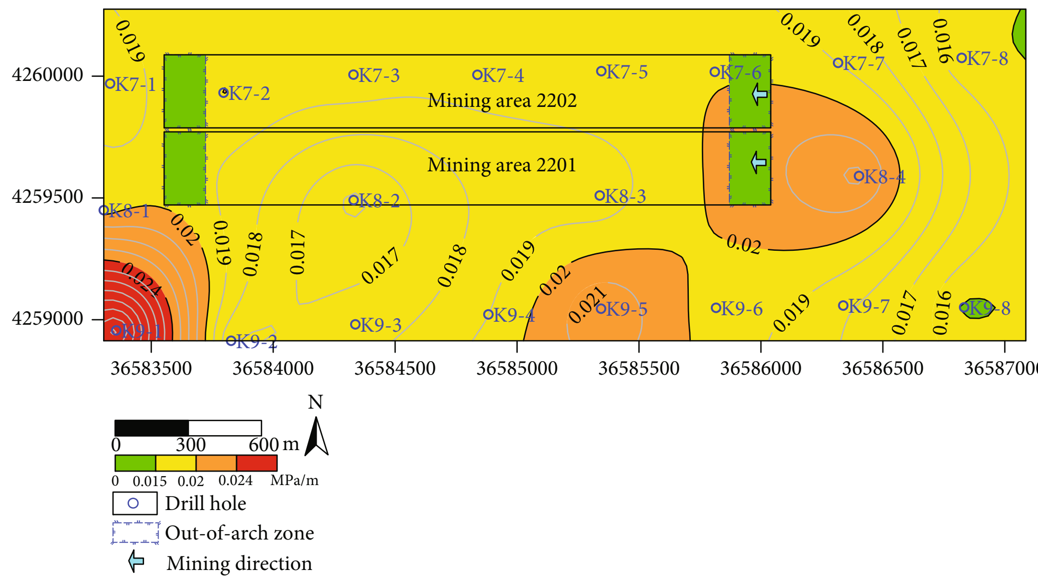

Figure 19: Distribution of *BWIC* in mining areas 2202 and 2201 in Yingpanhao coal mine.

According to Equations (22), (25), and (26), the formula for calculating T_{E-FJS} can be obtained as follows:

$$T_{E-FJS} = k_m * C_m + k_s * C_s. \tag{27}$$

3.2.4. Calculating the BWIC at Each Coordinate Point. The formula for calculating the *BWIC* at each coordinate point (x_i, y_i) can be obtained as follows:

$$BWIC_{(x_i,y_i)} = \frac{P_{b(x_i,y_i)}}{T_{U(x_i,y_i)} + T_{E-FJS(x_i,y_i)}}, \tag{28}$$

where $BWIC_{(x_i,y_i)}$, $P_{b(x_i,y_i)}$, $T_{U(x_i,y_i)}$, and $T_{E-FJS(x_i,y_i)}$, respectively, refer to the *BWIC*, P_b, T_U, and T_{E-FJS} at the coordinate point (x_i, y_i). According to Equation (27), Equation (28) can be transformed into:

$$BWIC_{(x_i,y_i)} = \frac{P_{b(x_i,y_i)}}{T_{U(x_i,y_i)} + k_m * C_{m(x_i,y_i)} + k_s * C_{s(x_i,y_i)}}, \tag{29}$$

where $C_{m(x_i,y_i)}$ and $C_{s(x_i,y_i)}$, respectively, refer to the C_m and C_s at the coordinate point (x_i, y_i).

3.2.5. Obtaining the Overall BWIC Corresponding to Different Excavation Lengths. Since any excavation length corresponds to a stress balance arch (Figure 10), the average *BWIC* in the bed separation zone in the stress balance arch corresponding to each excavation length was used as the overall *BWIC* corresponding to each excavation length. Therefore, the overall BWI risk when the excavation length is l_x can be expressed by the following formula:

$$BWIC_{l_x} = \frac{1}{z} \sum_{i=1}^{z} BWIC_{(x_i,y_i)}, \tag{30}$$

where $BWIC_{l_x}$ and z, respectively, refer to the overall *BWIC* and the number of selected coordinate points within the distribution range of bed separation zone when the excavation length is l_x. In this paper, for the convenience of calculation, z refers to the number of grid points after each bed separation zone distribution range was divided into squares with side length of 10 m.

With the increase of the excavation length, the size of the stress balance arch expands continuously. When the excavation length reaches a specific value, the size of the stress balance arch develops to the maximum, which is called the limit arch. The maximum height of limit arch is about 0.7 times of mining depth. Then, as the excavation continues, the stress balance arch exists in the form of moving arch, which has the same size as the limit arch [17, 18]. In order to observe the shape of the stress balance arch, some mining cases in Cuimu coal mine, Buerdong coal mine, and Daliuta coal mine in Ordos Basin were studied. The mining process of mining area 21301 in Cuimu coal mine was simulated by using the discrete element software UDEC. The results show that the deformed and broken rock strata are located in a triangular area as a whole, the two sides of the triangle are rock fracture lines, and the bottom of the triangle is the distribution range of goaf. In the triangular area, the deformation and fracture degree of the rock stratum below the bed separation is large, while the deformation of the rock stratum above the bed separation is small (Figure 11(a)). Similar material physical simulation experiments of mining cases in Buerdong coal mine and Daliuta coal mine also show that the rock strata that can deform and fracture are located in the triangular area surrounded by the two rock fracture lines and the distribution area of goaf (Figures 11(b) and 11(c)). Because the deformation and failure of overburden occur in the stress balance arch, the area surrounded by the triangle composed of rock fracture lines and goaf can be equivalent to the area in the stress balance arch, that is, the stress

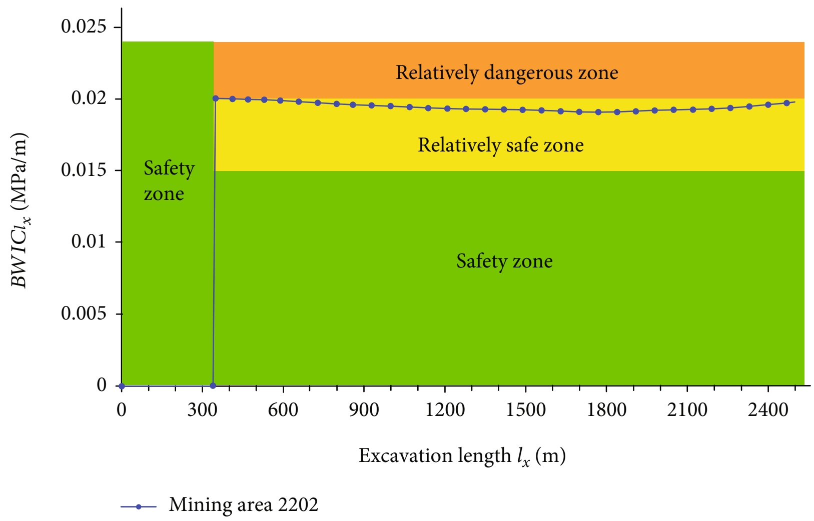

(a)

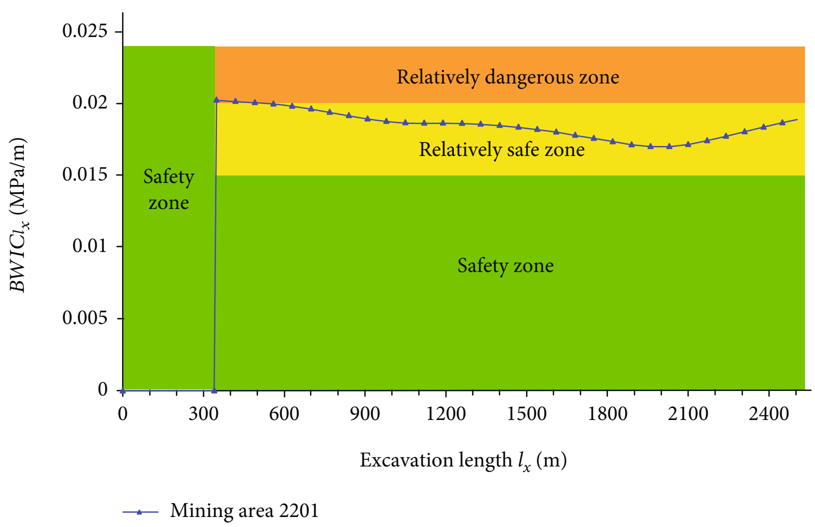

(b)

FIGURE 20: Overall *BWIC* corresponding to different excavation lengths in (a) mining area 2202 and (b) mining area 2201 in Yingpanhao coal mine.

balance arch can be simplified into a triangle with a base angle of about 60° [19, 20].

3.2.6. Grading BWI Risk. In actual mining, the excavation length with or without BWIs is called danger excavation length (l_d) and safety excavation length (l_s), respectively. The $BWIC_{l_x}$ corresponding to l_d and l_s are $BWIC_{l_d}$ and $BWIC_{l_s}$, respectively. $BWIC_{l_x}$ greater than $BWIC_{l_d}$ indicates a high risk of BWI, while $BWIC_{l_x}$ smaller than $BWIC_{l_s}$ indicates a low risk of BWI. Therefore, the risk level with $BWIC_{l_x}$ greater than $BWIC_{l_d}$ was identified as danger, the risk level with $BWIC_{l_x}$ smaller than $BWIC_{l_s}$ was identified as safety, and the risk level with $BWIC_{l_x}$ greater than $BWIC_{l_s}$ less than $BWIC_{l_d}$ was identified as transition. Further division of the transition can be achieved by means of the average value of $BWIC_{l_d}$ and $BWIC_{l_s}$. Here, the average value of $BWIC_{l_d}$ and BWIC_{l_s} was marked as $BWIC_{l_t}$. The risk level with $BWIC_{l_x}$ greater than $BWIC_{l_s}$ less than $BWIC_{l_t}$ was identified as relatively safe, and risk level with $BWIC_{l_x}$ greater than $BWIC_{l_t}$ less than $BWIC_{l_d}$ was identified as relatively dangerous. In addition, when the excavation length is less than l_a, the BWI risk was determined as safe because the stress balance arch has not expanded to the Cretaceous bed separation zone (Figure 10). The principle of BWI risk classification is shown in Figure 12.

4. Results and Discussion

Taking mining areas 106A and 108 in Shilawusu coal mine as examples, the establishment process of *BWIC* method was introduced.

4.1. Obtaining the BWI-Related Factors at Each Coordinate Point. The distribution of related factors in mining areas 106A and 108 in Shilawusu coal mine is shown in Figure 13.

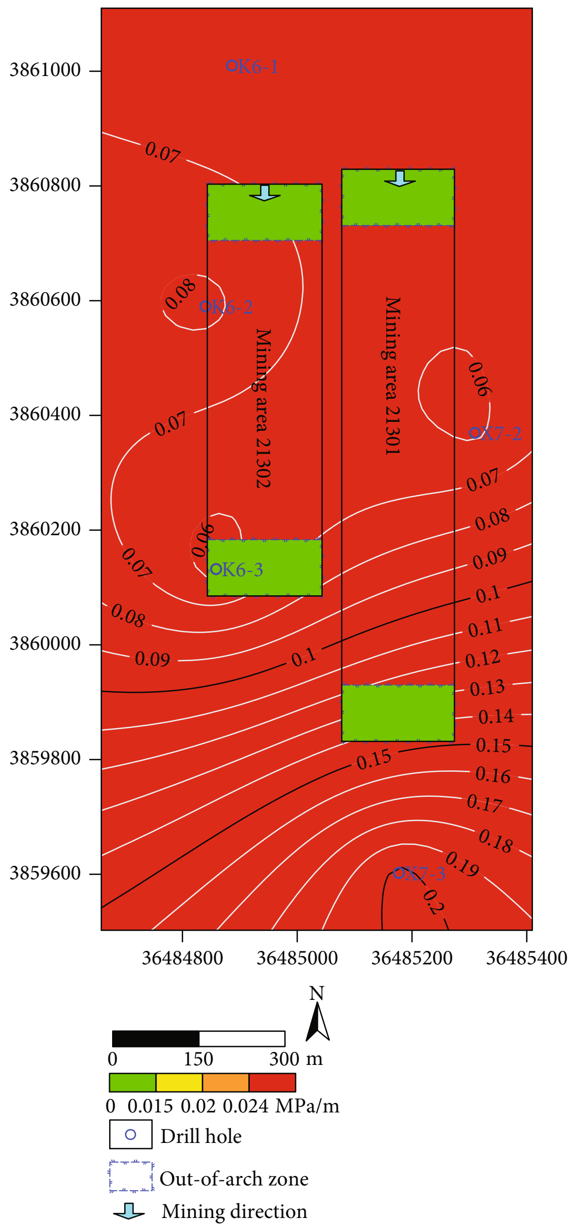

FIGURE 21: Distribution of *BWIC* in mining areas 21301 and 21302 in Cuimu coal mine.

4.2. Identifying the Weight of Each BWI-Related Factor. According to the analysis in Section 3.2, the entropy weight method can be used to determine the weight of BWI-related factors, and the sampling points in mining areas 108 and 106A should be located in the range of the bed separation zone corresponding to the excavation length of 554 m. Based on the triangle stress arch theory, it can be determined that when the excavation length is 554 m, the sampling points in mining area 108 are A1-A9, and the sampling points in mining area 106A are B1-B9 (Figure 13). The values of BWI-related factors at each sampling point are shown in Table 1.

By analyzing the data in Table 1 according to Equations (9)–(13), the weight of each BWI-related factor can be obtained (Table 2).

Because bed-separation water pressure is the power source of BWI, P_b has a large weight. As the integrity of UJS was not damaged, UJS plays an important role in preventing water inrush, so the weight of T_U should be the largest. Because the integrity of the rock strata in FJS has been destroyed, the water-resisting capacity of FJS is still weaker than that of UJS, so the weight of C_m and C_s is less than that of T_U. In addition, because the fracture closure degree of mudstone is relatively better than that of sandstone, the water-resisting capacity of mudstone in FJS is stronger than that of sandstone, so the weight of C_m is greater than that of C_s.

The above analysis results are obtained by reasonable inference based on the actual engineering geological conditions, which are consistent with the results in Table 2, indicating that the calculation results of the weights of BWI-related factors are in line with the reality.

4.3. Calculating the E-FJS Thickness (T_{E-FJS}). According to the weights of BWI-related factors in Table 2, Equation (15) can be expressed as:

$$V_i = 2.186 \times 10^{-4} T_{Ui} + 4.457 \times 10^{-4} C_{mi} + 2.844 \times 10^{-4} C_{si}. \tag{31}$$

It can be seen from Equation (31) that k_1, k_2, and k_3 are 2.186×10^{-4}, 4.457×10^{-4}, and 2.844×10^{-4}, respectively. Then, k_m and k_s can also be calculated, which are 2.039 and 1.301, respectively, and Equations (22) and (25) can be expressed as follows:

$$T_{E-M-FJS} = 2.039 C_m, \tag{32}$$

$$T_{E-S-FJS} = 1.301 C_s, \tag{33}$$

Taking mining area 106A in Shilawusu coal mine as an example, when M, R_{FM}, and η are 10 m, 23, and 1.032, respectively, the $T_{E-M-FJS}$ of mudstone with a thickness of 1 m at different locations in FJS was calculated by using Equations (4) and (32) (Table 3), and the $T_{E-S-FJS}$ of sandstone with a thickness of 1 m at different locations in FJS was calculated by using Equations (6) and (33) (Table 4).

Although the rock in FJS still have water-resisting capacity due to the closure of internal fractures, the restored water-resisting capacity is still weaker than that of the unfractured rock because the integrity of the fractured rock has been destroyed. This conclusion can also be obtained by analyzing the data in Table 3 and Table 4. It can be seen from Table 3 and Table 4 that the water resistance capacity of mudstone and sandstone in FJS is weaker than that of intact rock. Due to the larger opening and weaker closure of the fractures, the water-resisting capacity of the rock at the bottom of FJS is less than that of the rock at the top of FJS. In addition, in FJS, due to the self-healing effect of fractures in mudstone, the fractures in mudstone are easier to close than those in sandstone, so that the water-resisting capacity of mudstone at the same location is stronger than that of sandstone.

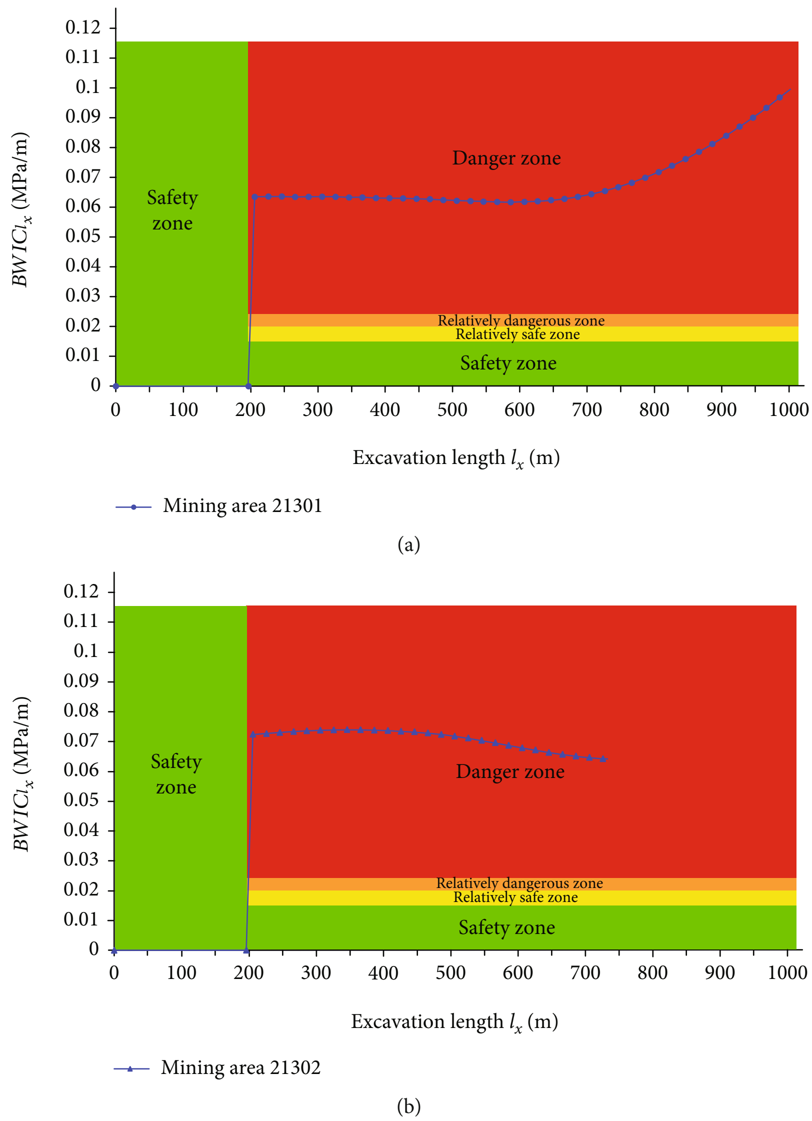

FIGURE 22: Overall *BWIC* corresponding to different excavation lengths in (a) mining area 21301 and (b) mining area 21302 in Cuimu coal mine.

The above analysis shows that the method of obtaining T_{E-FJS} determined in this paper is practical, and the formula for calculating T_{E-FJS} is as follows:

$$T_{E-FJS} = 2.039C_m + 1.301C_s. \tag{34}$$

4.4. Calculating the BWIC at Each Coordinate Point. Since k_m and k_s are 2.039 and 1.301, respectively, Equation (29) can be transformed into:

$$BWIC_{(x_i,y_i)} = \frac{P_{b(x_i,y_i)}}{T_{U(x_i,y_i)} + 2.039C_{m(x_i,y_i)} + 1.301C_{s(x_i,y_i)}}, \tag{35}$$

According to formula (35), the *BWIC* at each coordinate point in mining areas 108 and 106A can be obtained (Figure 14).

4.5. Obtaining the Overall BWIC Corresponding to Different Excavation Lengths. Based on the triangle stress arch theory, the overall *BWIC* corresponding to different excavation lengths can be obtained by using Equations (30) and (35) (Figure 15).

4.6. Grading BWI Risk. Because BWI occurred in mining area 106A when $l_x = 554$ m, but no BWI occurred in the completed 1000 m mining process in mining area 108, the $BWIC_{l_x}$ corresponding to the excavation length of 554 m in mining area 106A was regarded as $BWIC_{l_d}$, and the maximum value of $BWIC_{l_x}$ in mining area 108 was used as $BWIC_{l_s}$. According to Figure 15, $BWIC_{l_d} = 0.024$ MPa/m, $BWIC_{l_s} = 0.015$ MPa/m, so $BWIC_{l_t} = 0.020$ MPa/m. Therefore, Figure 12 can be improved to Figure 16.

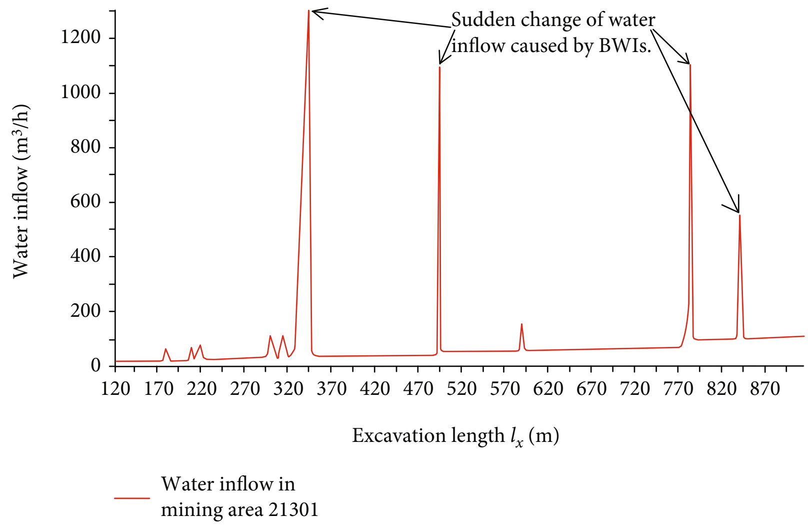

(a)

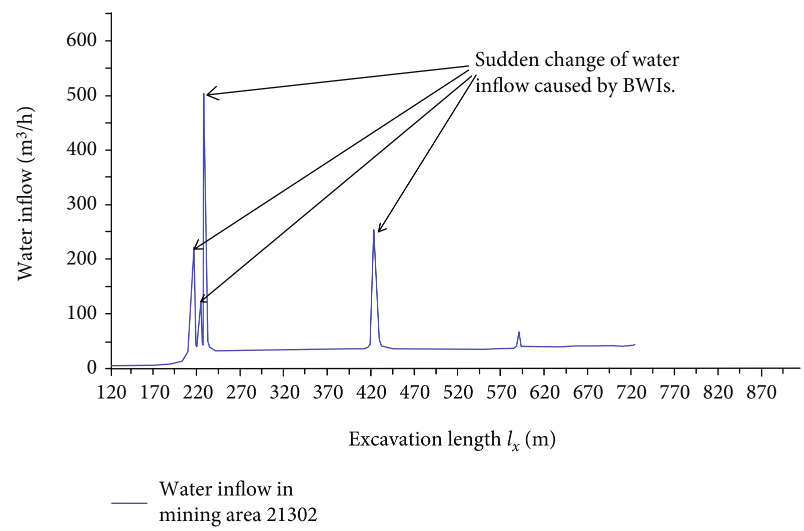

(b)

FIGURE 23: Water inflow in (a) mining area 21301 and (b) mining area 21302 in Cuimu coal mine.

5. Application and Validation

5.1. Shilawusu Coal Mine. According to formula (35), the *BWIC* at each coordinate point in mining areas 201 and 201A in Shilawusu coal mine can be obtained (Figure 17). Based on the triangle stress arch theory, the overall *BWIC* corresponding to different excavation lengths can be obtained by using Equations (30) and (35) (Figure 18). It can be seen from Figure 18 that the BWI risk in mining areas 201 and 201A during mining belongs to the "safety zone." In fact, the mining in mining areas 201 and 201A has been completed, and no BWI occurred during mining, which verifies the accuracy of the evaluation results shown in Figure 18.

5.2. Yingpanhao Coal Mine. According to formula (35), the *BWIC* at each coordinate point in mining areas 2202 and 2201 in Yingpanhao coal mine can be obtained (Figure 19). Based on the triangle stress arch theory, the overall *BWIC* corresponding to different excavation lengths can be obtained by using Equations (30) and (35) (Figure 20). It can be seen from Figure 20 that the BWI risk in mining areas 2202 and 2201 during mining belongs to the "relatively safe zone." In fact, mining has been completed in mining area 2201, and 1000 m excavation has been completed in mining area 2202. No BWI occurred during mining in these two mining areas, which verifies the accuracy of the assessment results shown in Figure 20.

5.3. Cuimu Coal Mine. According to formula (35), the *BWIC* at each coordinate point in mining areas 21301 and 21302 in Cuimu coal mine can be obtained (Figure 21). Based on the triangle stress arch theory, the overall *BWIC* corresponding to different excavation lengths can be obtained by using Equations (30) and (35) (Figure 22). It can be seen from Figure 22 that the BWI risk in mining areas 21301 and 21302 during mining belongs to the "danger zone." In fact, the mining in mining areas 21301 and 21302 has been completed, and BWIs occurred during mining (Figure 23), which verifies the accuracy of the evaluation results shown in Figure 22.

6. Conclusions

The objects directly involved in BWI process include the Cretaceous bed-separation water and the Jurassic protective layer. The bed-separation water pressure (P_b) provides the inducing power for the occurrence of BWI and can be expressed by the water pressure in the aquifer at the bottom of Cretaceous. In the Jurassic protective layer, the upper part is the unbroken Jurassic strata (UJS), and the lower part is the fractured Jurassic strata (FJS). The water-resisting capacity of FJS is due to the closure of fractures in FJS under the action of water flow.

The greater the UJS thickness (T_U) is, the stronger its water-resisting capacity is. In FJS, the closure potential of mudstone fractures (C_m) was used to evaluate the closure effect of mudstone fractures, and the closure potential of sandstone fractures (C_s) was used to evaluate the closure effect of sandstone fractures. C_m is positively correlated with the mudstone thickness and negatively correlated with the height of available subsidence space of mudstone before mudstone fracture. C_s is positively correlated with the sandstone thickness, and negatively correlated with the height of available subsidence space of sandstone before sandstone fracture. UJS with a certain thickness and the same water-resisting capacity as mudstone in FJS was called equivalent strata of mudstone in FJS (E-M-FJS). UJS with a certain thickness and the same water-resisting capacity as sandstone in FJS was called equivalent strata of sandstone in FJS (E-S-FJS). By comparing the weight of each BWI-related factor, the formulas for calculating the E-M-FJS thickness ($T_{E-M-FJS}$) and the E-S-FJS thickness ($T_{E-S-FJS}$) were derived. And the $T_{E-M-FJS}$ corresponding to one unit of C_m is 2.039 m, while the $T_{E-S-FJS}$ corresponding to one unit of C_s is 1.301 m. The weight of each BWI-related factor was obtained by entropy weight method. And the weights of P_b, T_U, C_m, and C_s are 0.354, 0.390, 0.158, and 0.098, respectively.

In bed-separation water inrush (BWI) risk assessment, the existing multifactor-weighted superposition method cannot provide a universal risk classification standard, and the existing water inrush coefficient method ignores the water separation capacity of FJS, so there is still a lack of scientific BWI risk assessment method. In this paper, three coal mines in Ordos Basin were taken as research cases, and a bed-separation water inrush coefficient ($BWIC$) method for BWI risk assessment was established. The value of $BWIC$ is the ratio of P_b to the sum of T_U, $T_{E-M-FJS}$ and $T_{E-S-FJS}$. Based on the stress arch theory, the overall $BWIC$ in bed separation zone corresponding to different excavation lengths ($BWIC_{l_x}$) was obtained. By comparing the value range of BWIC_{l_x} with and without BWI, the standard of BWI risk classification was determined. In the BWI risk classification discrimination diagram established based on $BWIC$ method, the area with $0\,\mathrm{MPa/m} < BWIC_{l_x} \leq 0.015\,\mathrm{MPa/m}$ was divided into safety zone, the area with $0.015\,\mathrm{MPa/m} < BWIC_{l_x} \leq 0.02\,\mathrm{MPa/m}$ was divided into relatively safe zone, the area with $0.02\,\mathrm{MPa/m} < BWIC_{l_x} \leq 0.024\,\mathrm{MPa/m}$ was divided into relatively dangerous zone, and the area with $BWIC_{l_x} > 0.024\,\mathrm{MPa/m}$ was divided into danger zone. The application results verified the scientificity of $BWIC$ method and the universality of the BWI risk classification standard proposed in this paper.

Data Availability

The authors confirm that the data supporting the findings of this study are available within the article.

Conflicts of Interest

The authors declare that they have no conflicts of interest.

Acknowledgments

The authors are grateful to the many people who assisted with this study. The study was jointly supported by the Scientific Research Start-Up Fund for High-Level Introduced Talents of Anhui University of Science and Technology (grant no. 2022yjrc21), the Key Projects of the Natural Science Foundation of China (grant no. 41931284), the China Postdoctoral Science Foundation (grant no. 2019M652015), and the Natural Science Foundation of Jiangsu Province (grant no. BK20190646).

References

[1] J. H. He, W. P. Li, Y. Liu, Z. Yang, S. L. Liu, and L. F. Li, "An improved method for determining the position of overlying separated strata in mining," *Engineering Failure Analysis*, vol. 83, pp. 17–29, 2018.

[2] V. Palchik, "Formation of fractured zones in overburden due to longwall mining," *Environmental Geology*, vol. 44, no. 1, pp. 28–38, 2003.

[3] V. Palchik, "Localization of mining-induced horizontal fractures along rock layer interfaces in overburden: field measurements and prediction," *Environmental Geology*, vol. 48, no. 1, pp. 68–80, 2005.

[4] S. S. Peng, *Longwall mining*, Science Press, Morgantown, 2006.

[5] X. L. Xu, N. Zhang, and S. C. Tian, "Mining-induced movement properties and fissure time-space evolution law in overlying strata," *International Journal of Mining Science and Technology*, vol. 22, no. 6, pp. 817–820, 2012.

[6] H. R. Gui and M. L. Lin, "Types of water hazards in China coalmines and regional characteristics," *Natural Hazards*, vol. 84, no. 2, pp. 1501–1512, 2016.

[7] S. L. Liu and W. P. Li, "Indicators sensitivity analysis for environmental engineering geological patterns caused by underground coal mining with integrating variable weight theory and improved matter-element extension model," *Science of the Total Environment*, vol. 686, pp. 606–618, 2019.

[8] S. L. Liu, W. P. Li, and Q. Q. Wang, "Zoning method for environmental engineering geological patterns in underground coal mining areas," *Science of the Total Environment*, vol. 634, pp. 1064–1076, 2018.

[9] H. J. Li, Q. T. Chen, Z. Y. Shu, L. Li, and Y. C. Zhang, “On prevention and mechanism of bed-separation water inrush for thick coal seams: a case study in China,” *Environmental Earth Sciences*, vol. 77, no. 22, article 759, 2018.

[10] X. Q. Li, *Study on the inrush mechanism of the water in bed separation due to repeated coal mining under hard rock*, China University of Mining and Technology, Xuzhou, 2011.

[11] R. Hu, J. W. Wu, X. R. Zhai, and W. Liu, “Recognition and prevention of bed-separation water: based on trapezoid platform model,” *Geofluids*, vol. 2021, Article ID 6626268, 10 pages, 2021.

[12] J. G. Xu, D. L. Zhao, and J. H. He, “Mechanism of water inrush in overlying strata of cretaceous thick sandstone,” *Safety in Coal Mines*, vol. 51, no. 2, pp. 58–63, 2020.

[13] S. N. Dong, Y. D. Ji, H. Wang et al., “Prevention and control technology and application of roof water disaster in Jurassic coal field of Ordos Basin,” *Journal of China Coal Society*, vol. 45, no. 7, pp. 2367–2375, 2020.

[14] Q. Y. Lu, X. Q. Li, W. P. Li, W. Chen, L. F. Li, and S. L. Liu, “Risk evaluation of bed-separation water inrush: a case study in the Yangliu coal mine China,” *Mine Water and the Environment*, vol. 37, no. 2, pp. 288–299, 2018.

[15] Q. Y. Lu, *Risk Prediction and Evaluation of Bed-Separation Water Inrush Caused by Breakage of Hard Overburden: a Case Studied in Yangliu Coal Mine*, China University of Mining and Technology, Xuzhou, 2019.

[16] K. F. Fan, W. P. Li, Q. Q. Wang et al., “Formation mechanism and prediction method of water inrush from separated layers within coal seam mining: a case study in the Shilawusu mining area, China,” *Engineering Failure Analysis*, vol. 103, pp. 158–172, 2019.

[17] Z. J. Su, *Research of Deformation Mechanism of Mining Overburden Separated Strata*, Liaoning Technical University, Fuxin, 2001.

[18] Z. J. Su, G. M. Yu, and L. Yang, “Numerical simulation on mechanism of deformation of separated strata in overburden,” *Chinese Journal of Rock Mechanics and Engineering*, vol. 22, no. 8, pp. 1287–1290, 2003.

[19] J. H. He, *Dynamic Evolution of Bed Separation in Coal Seam Mining and Assessment of Bed-Separation Water Hazards*, PhD He, China University of Mining and Technology, Chinese, 2018.

[20] J. H. He, W. P. Li, and W. Qiao, “A rock mechanics calculation model for identifying bed separation position and analyzing overburden breakage in mining,” *Arabian Journal of Geosciences*, vol. 13, no. 18, article 920, 2020.

Hindawi
Geofluids
Volume 2022, Article ID 7430025, 12 pages
https://doi.org/10.1155/2022/7430025

Research Article

Pressure Relief and Permeability Enhancement Mechanism of Short-Distance Floor Roadway in Deep Coal Roadway Strip

Benqing Yuan[1,2,3,4] **Min Tu**[1,3] **Jianjun Cao**[2,4] **and Xiang Cheng**[1]

[1]*State Key Laboratory of Mining Response and Disaster Prevention and Control in Deep Coal Mines, Anhui University of Science and Technology, Huainan 232001, China*
[2]*CCTEG Chongqing Research Institute, Chongqing 400037, China*
[3]*Key Laboratory of Safety and High-Efficiency Coal Mining of Ministry of Education, Anhui University of Science and Technology, Huainan 232001, China*
[4]*State Key Laboratory of the gas Disaster Detecting, Preventing and Emergency Controlling, Chongqing 400037, China*

Correspondence should be addressed to Benqing Yuan; bqyuan@aust.edu.cn, Min Tu; mtu@aust.edu.cn, Jianjun Cao; 108485815@qq.com, and Xiang Cheng; xcheng@aust.edu.cn

Received 20 September 2021; Accepted 24 February 2022; Published 24 March 2022

Academic Editor: Zhijie Wen

A pressure relief and permeability enhancement method through short-distance floor roadway was proposed to solve the difficult outburst prevention during the gas extraction at the coal roadway strips in deep outburst coal seams with high ground stress and low gas permeability. On the basis of an equivalent model of the surrounding rock in a deep roadway, the analytical solutions of deep roadway excavation to the stress and deformation of pressure relief at overlying short-distance coal roadway strips were obtained using the unified strength theory and nonassociated flow rules. Next, the criteria for determining the reasonable position of floor roadway were established, and a mechanical model of short-distance floor roadway for the pressure relief and permeability enhancement zone at the overlying coal seam was constructed. Finally, the scope of the zonal disintegration at the coal roadway strips in the elastic and elastic–plastic zones of the surrounding rock in the roadway, as well as the expression of gas permeability change, was given. The engineering trial calculation and practice showed that the stress and strain of the surrounding rock in the roadway were evidently influenced by the intermediate principal stress coefficient. Moreover, the vertical stress and vertical displacement of overlying coal seam were gradually reduced with the increase in the intermediate principal stress coefficient and vertical distance of the floor roadway. The minimum reasonable distance arranged for the 213 floor roadway in Qujiang Coal Mine was 6.21 m, and the effective pressure relief should be conducted within 10.6 m from the coal seam floor. When the pressure relief was located at 9.0 m from the coal seam floor, the investigation results were basically consistent with the theoretical analysis results, exerting obvious pressure relief and permeability enhancement effects on the overlying short-distance coal roadway strips.

1. Introduction

Coal is the basic energy source that guarantees the energy safety and stability in China. Coal resources are estimated to still account for over 50% of primary energy consumption by 2030 [1, 2]. China is also one of the countries with the most serious coal and gas outburst (hereinafter abbreviated as "outburst") in the world, and the main regional measures taken to prevent and control the outburst include the exploitation of the protective layer and gas preextraction at the coal seam. For the single outburst coal seam or coal seam group without exploitation of the protective layer, the coal roadway strips at the outburst coal seam will be initially exploited, and the outburst prevention measure is still mainly to drill the crossing holes on the floor roadway for the gas preextraction [3–5].

However, with the continuously increasing coal mining depth in China, the high ground stress and low gas permeability of outburst coal seams in most coal mines are more prominent. The difficulty in the drilling construction under deep high ground stress condition is significantly aggravated, and the gas preextraction further enhances the ground stress-dominated dynamic danger [6, 7], such as the ground stress-dominated dynamic disasters appearing in deep mines in provinces such as Anhui, Liaoning, and Jiangxi. Hence, pressure relief and permeability enhancement technologies, such as hydrofracturing, hydraulic reaming, and control of presplitting blasting, have been investigated in coal mines in China [8–14]. However, some shortcomings exist, such as large difference in the effect of pressure relief and permeability enhancement, failure to change the stress condition of surrounding rock in advance, and complex process.

Given the complex and diversified stress field evolution of the surrounding rock in deep roadways, the large deformation and strong rheological properties of surrounding rock, the brittleness–ductility transformation of coal and rock mass, and the mutability of dynamic response [15, 16], an elastic–plastic deformation model of the surrounding rock in deep roadway was constructed to study the mechanical mechanism of a preexcavated short-distance floor roadway for the pressure relief of the surrounding rock and the permeability enhancement of the overlying coal seam. Next, the proactive pressure relief and permeability enhancement method for the short-distance floor roadway at the coal roadway strips in the deep outburst coal seams with high ground stress and low gas permeability was established, expecting to provide a reference for the outburst prevention and control at the coal roadway strips in deep mines.

2. Deformation Analysis of Layered Surrounding Rock in Deep Roadway

2.1. Equivalent Model Construction for Overlying Layered Rock Strata in Roadway. In engineering practice, the deep surrounding rock in a roadway is kept stable under the load effect of the vertical strata at the roof, and the displacement and section rotation of rock beam at the roof are restricted by the clamping effect between the rock strata. Under this circumstance, the upper rock stratum of the roadway can be simplified into a mechanical constraint model of a simply supported beam (Figure 1).

As shown in Figure 1, the bending moment at the support x is

$$M_x = \frac{1}{2}\mathrm{ql}\mathrm{x} - \frac{1}{2}\mathrm{qx}^2 + \mathrm{p}\omega - M, \tag{1}$$

where l is the upper rock beam span of the roadway, m; p stands for the horizontal force at the fixed end, $p = \lambda q b_0 h$, MPa; λ is the lateral pressure coefficient of the rock beam; b_0 denotes the width of the rock beam, m; ω is the deflection of the rock beam; and M is the bending moment at the support.

According to the principle of static equilibrium, a differential equation can be listed as follows:

$$\omega'' + \frac{P}{\mathrm{EI}}\omega = -\frac{\mathrm{ql}}{2\mathrm{EI}}\mathrm{x} + \frac{q}{2\mathrm{EI}}\mathrm{x}^2 + \frac{M}{\mathrm{EI}}. \tag{2}$$

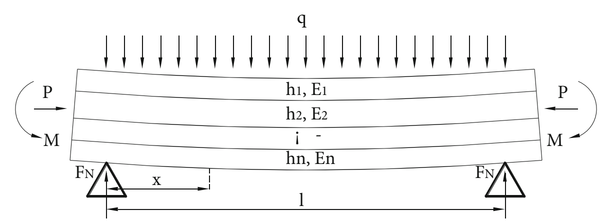

Figure 1: Hierarchical mechanical analysis chart of two-end simple support constraints.

$\mathrm{P/EI} = \beta^2$ is set, and the differential equation is solved to obtain

$$\omega = A\sin\beta x + B\cos\beta x + \frac{q}{2p}x^2 - \frac{\mathrm{ql}}{2p}\mathrm{x} + \frac{M_B}{p} - \frac{q}{p\beta^2}. \tag{3}$$

The boundary conditions $\begin{cases} x = 0 & \omega = 0 & \theta = 0 \\ x = 1 & \omega = 0 & \theta = 0 \end{cases}$ are substituted into the above equation to solve

$$\begin{cases} A = \left(\dfrac{q}{p\beta^2} - \dfrac{M}{p}\right)\tan\dfrac{\beta \mathrm{l}}{2} \\ B = \dfrac{q}{p\beta^2} - \dfrac{M}{p} \\ M_B = \dfrac{q}{\beta^2} - \dfrac{q\mathrm{l}}{2\beta}\cot\dfrac{\beta \mathrm{l}}{2} \end{cases}. \tag{4}$$

According to the deformation continuity condition in mechanics, the deformation of each rock stratum is continuous in the vertical direction, that is, the rock strata share the same deflection, that is, $\omega = \omega_1 = \cdots\cdots = \omega_{\mathrm{i}}$. In actual working conditions, the mutual bonding power between rock strata is extremely weak that it can be neglected. Then,

$$\omega_0 = \frac{q\mathrm{l}}{2p\beta}\tan\frac{\beta \mathrm{l}}{4} - \frac{q\mathrm{l}^2}{8p} = \omega_i = \frac{q_i l}{2p_i\beta_i}\tan\frac{\beta_i \mathrm{l}}{4} - \frac{q_i l^2}{8p_i}, \tag{5}$$

where ω_0 is the bending moment at the midspan of the rock beam; and q_i and p_i represent the vertical load and end horizontal acting force borne by the layer i, respectively, MPa.

Assume that the total height of the rock beam is h, and the horizontal acting force at the end of the rock beam of layer i is $p_i = (h_i/h)p$. For a specific rock stratum, Equation (5) can be simplified as follows:

$$\frac{4}{\beta}\tan\frac{\beta \mathrm{l}}{4} = \xi, \tag{6}$$

where ζ is the constant of a specific rock stratum.

Variable β cannot be separated from the left end of Equation (6), and its numerical solution can be solved through programming. According to $\mathrm{p/EI} = \beta^2, p = \lambda q b_0 h$, and the sectional inertia moment $I = b_0h^3/12$ of the rock beam, the overall equivalent elasticity modulus of the rock strata above the roadway is

$$E = \frac{12\lambda q}{h\beta^2}. \tag{7}$$

2.2. Elastic–Plastic Deformation Analysis of Surrounding Rock in Deep Roadway. The elastoplasticity and brittleness of the surrounding rock in roadway have been analyzed by most scholars using the Mohr–Coulomb criterion or Hoek–Brown criterion [17, 18], but the effect of intermediate principal stress has not been considered. As pointed out in literature [19, 20], given that the failure strength of a rock is strengthened due to the intermediate principal stress, an obvious disintegration zone with poor mechanical properties of rocks appears in the surrounding rock excavated in the deep roadway with high ground stress.

On this basis, the surrounding rock in a deep roadway was divided into elastic, plastic, and disintegration zones in this study based on the unified strength criterion and nonassociated flow rule to analyze the limiting equilibrium. To facilitate the calculation, a circular roadway was taken for example to establish a mechanical model (Figure 2) of the surrounding rock in this deep circular roadway, and the whole stress–strain curves of the rock were simplified, as shown in Figure 3.

The differential equation of the equilibrium that the stress in each zone should meet (body force unconsidered) is

$$\frac{d\sigma_r}{\mathrm{dr}} + \frac{\sigma_r - \sigma_\theta}{r} = 0. \tag{8}$$

The geometric equation is

$$\begin{cases} \varepsilon_r = \dfrac{\partial \mathrm{u}}{\partial \mathrm{r}} \\ \varepsilon_\theta = \dfrac{u}{r} \end{cases}. \tag{9}$$

The physical equation is expressed as follows:

$$\begin{cases} \varepsilon_r = \dfrac{1-\mu^2}{E}\left(\sigma_r - \dfrac{\mu}{1-\mu}\sigma_\theta\right) \\ \varepsilon_\theta = \dfrac{1-\mu^2}{E}\left(\sigma_\theta - \dfrac{\mu}{1-\mu}\sigma_r\right) \end{cases}, \tag{10}$$

where μ is Poisson's ratio.

Under the plain strain condition, the intermediate principal stress influence coefficient b $(0 \le b \le 1)$ reflects the influence degree of the intermediate principal stress on the rock failure. When the material is under yield and failure state, b is approximate to 1, and generally, $b = 1$. In this study, $b = 1$ was taken, and the unified strength criterion under the plane strain condition can then be obtained as follows:

$$\sigma_1 - A_{i,\varphi}\sigma_3 - B_{i,\varphi} = 0, \tag{11}$$

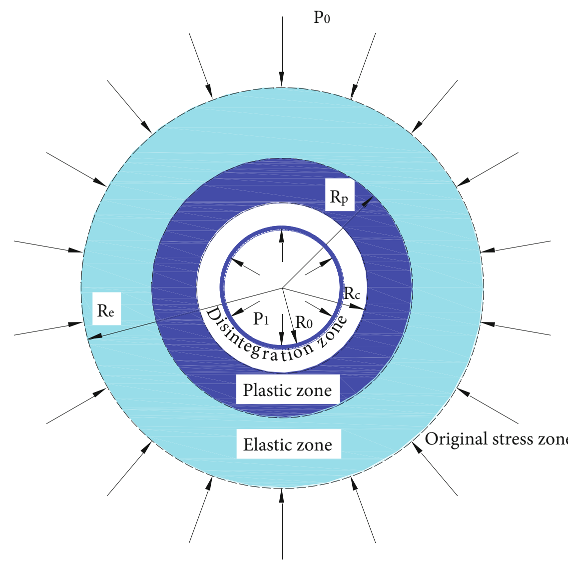

Figure 2: Mechanical model of circular roadway.

where $A_{i,\phi} = 2 + 2b - \alpha_{i\ \phi} b/\alpha_{i\ \phi}(2+b)$, σ_c is the compressive strength of rock, and $\alpha_{i,\varphi}$ is the compressive strength ratio of the rock.

Under the nonassociated flow rule, the stress boundary conditions and contact conditions are as follows:

$$\begin{cases} r \longrightarrow \infty & \sigma_r^e = p_0 & u_e = 0 \\ r = R_p & \sigma_r^e = \sigma_r^p & u_e = u_p \\ r = R_c & \sigma_r^p = \sigma_r^c & u_p = u_c \\ r = R_0 & \sigma_r^c = p_1 & \end{cases}. \tag{12}$$

Furthermore, through simultaneous Equations (8)–(10) and the different boundary conditions in Equation (12), the stress and deformation in the elastic, plastic, and disintegration zones, as well as the scopes of plastic and disintegration zones, can be solved by reference to literature [21].

3. Mechanical Response of Pressure Relief in Deep Roadway

3.1. Roadway Pressure Relief-Disturbed Zone Analysis of Surrounding Rock. Generally, the zone with a stress change of smaller than 5% is not affected by the excavation, and it is referred to as the stress zone of primary rock. The zone with the stress change of greater than 5%, which is affected by the excavation, is called the disturbed zone (the radius of the disturbed zone is r'), as shown in Figure 4.

r' is within the elastic zone, and the stress and radius of the disturbed zone are solved as follows:

$$\begin{aligned} \sigma_r^e &= p_0 - \left(p_0 - \sigma_R^p\right)\left(\frac{R_p}{r'}\right)^2 = 0.95p_0, \\ \mathrm{r}' &= 2\sqrt{5}R_p\sqrt{1 - \frac{\sigma_R^p}{p_0}}, \end{aligned} \tag{13}$$

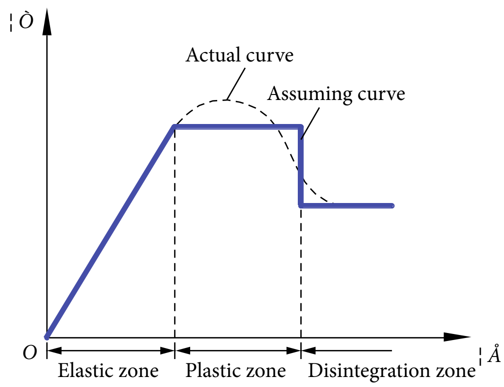

FIGURE 3: Stress–strain curves of rock deformation failure and zoning plan.

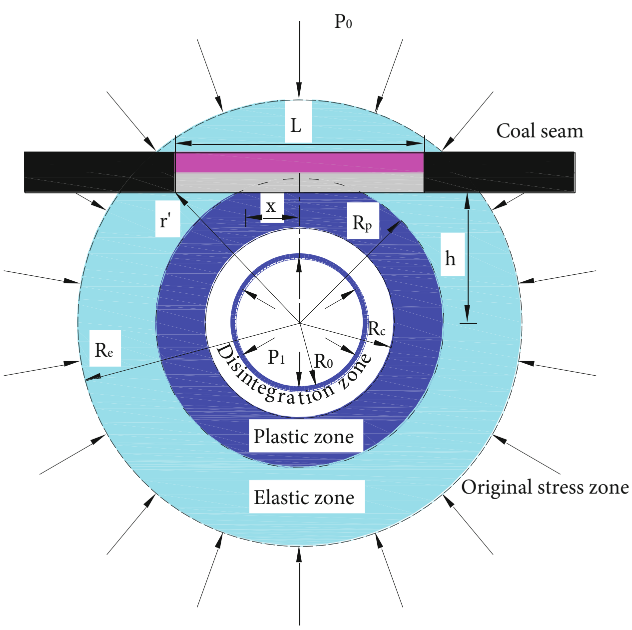

FIGURE 4: Pressure relief zoning model of floor roadway.

where $\sigma^p{}_R$ is the contact stress at the elastic–plastic interface, and it is calculated according to literature [21].

For the floor roadway in the outburst coal seam, its spacing with the overlying coal seam is generally greater than 7 m, that is, the coal seam is usually located within the elastic–plastic zone of the surrounding rock in the floor roadway. When $R_p < h < r^{'}$, the coal seam is located at the elastic zone and influenced by the roadway excavation; the horizontal stress change is as follows:

$$\begin{cases} \sigma_r^e = p_0 - \dfrac{\left(p_0 - \sigma_R^p\right) R_p{}^2}{h^2 + x^2} \\ \sigma_\theta^e = p_0 + \dfrac{\left(p_0 - \sigma_R^p\right) R_p{}^2}{h^2 + x^2} \end{cases}. \quad (14)$$

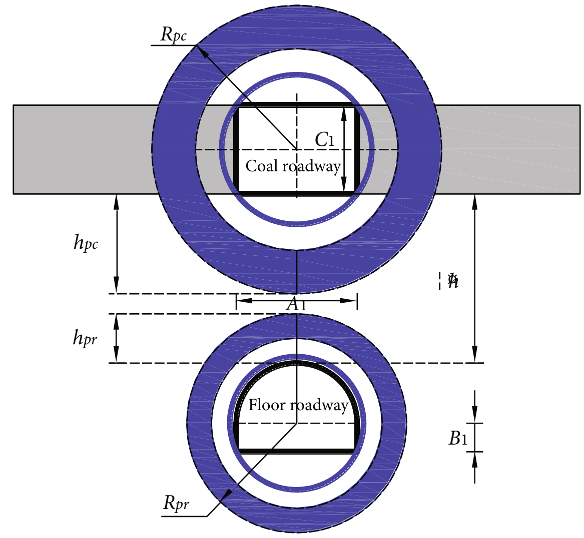

FIGURE 5: Schematic of surrounding rock deformation in double-roadway excavation.

When $R_c < h < R_p$, the coal seam is seated in the plastic and elastic zones. Under the influence of roadway excavation, the stress change in the horizontal direction is

$$\begin{cases} \sigma_r^p = \left(\sigma_R^p + D_p\right)\left(\dfrac{h^2 + x^2}{R_p{}^2}\right)^{\frac{A_{p\ \phi}-1}{2}} - D_p & \left(0 \le x \le \sqrt{R_p{}^2 - h^2}\right) \\ \sigma_\theta^p = A_p\left(\sigma_R^p + D_p\right)\left(\dfrac{h^2 + x^2}{R_p{}^2}\right)^{\frac{A_{p\theta\phi}-1}{2}} - D_p & \left(0 \le x \le \sqrt{R_p{}^2 - h^2}\right) \\ \sigma_r^e = p_0 - \left(p_0 - \sigma_R^p\right)\left(\dfrac{R_p{}^2}{h^2 + x^2}\right) & \left(\sqrt{R_p{}^2 - h^2} \le x \le \sqrt{r'^2 - h^2}\right) \\ \sigma_\theta^e = p_0 + \left(p_0 - \sigma_R^p\right)\left(\dfrac{R_p{}^2}{h^2 + x^2}\right) & \left(\sqrt{R_p{}^2 - h^2} \le x \le \sqrt{r'^2 - h^2}\right) \end{cases}, \quad (15)$$

where $D_p = B_{p\ \phi}/A_{p\ \phi} - 1$, and $A_{p,\psi} = 2 + 2b - \alpha_{p\ \psi} b/\alpha_{p\ \psi}(2 + b)$, which can be calculated according to literature [21].

When the coal seam is in the elastic and elastic–plastic zones, the minimum bottom stress is $\sigma 0_{0R}^{p} R_p/h^2{}_{rmin}$ and $\sigma_{Rp}^{p} h/R_p{}^{A_{p,\psi}-1}{}_{Prmin}$, respectively, and the horizontal disturbed area of the coal seam is $L = 2l = 2\sqrt{r'^2 - h^2}$.

3.2. Pressure Relief Mechanism of Short-Distance Floor Roadway for Coal Seam. The formulas for the vertical stress and displacement changes of the coal seam in the disturbed zone can be obtained through the coordinate transformation of elastic mechanics. For the axisymmetric problem, the coordinate transformation formula can be

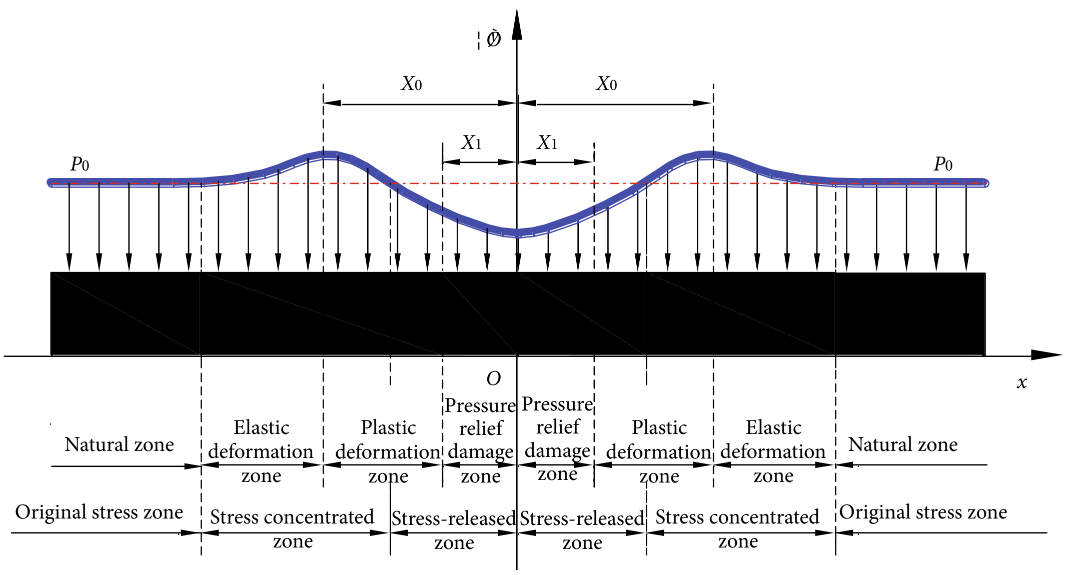

FIGURE 6: Mechanical model of pressure relief and permeability enhancement zones at coal seam.

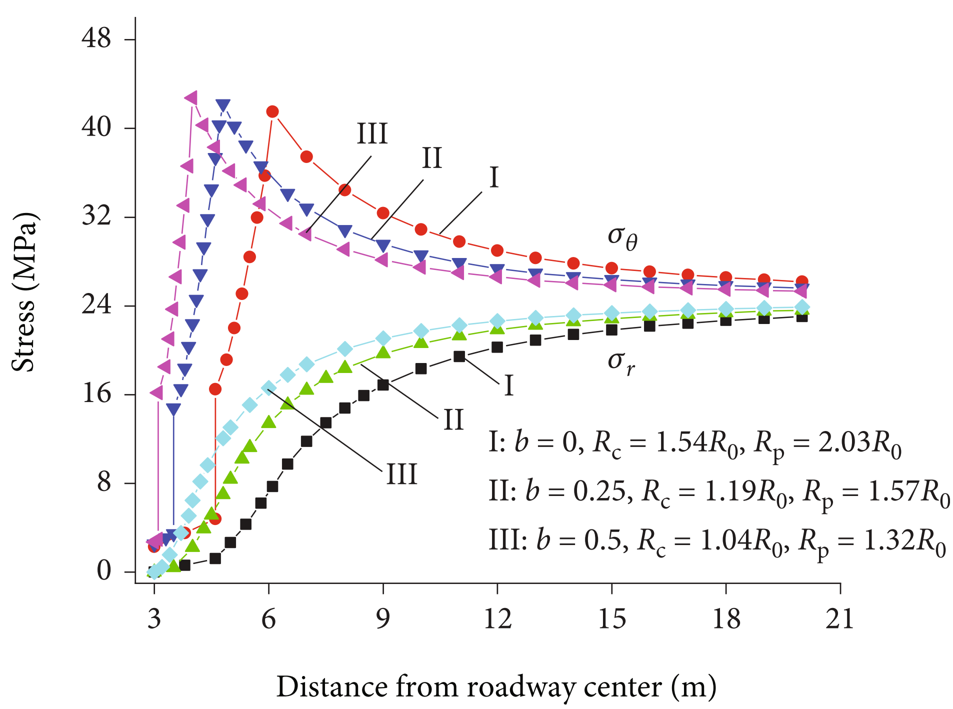

FIGURE 7: Stress distribution curve of surrounding rock in roadway.

simplified into the following form:

$$\begin{cases} \sigma_x = \sigma_r \sin^2\varphi + \sigma_\theta \cos^2\varphi \\ \sigma_y = \sigma_r \cos^2\varphi + \sigma_\theta \sin^2\varphi \\ u_x = u_r \sin\varphi \\ u_y = u_r \cos\varphi \end{cases}, \quad (16)$$

where φ is the included angle between the radius r and the vertical direction.

When the coal seam is in the elastic zone, Equation (14) is substituted into the above equation to solve the stress and displacement of the coal seam in the short-distance disturbed zone as follows:

$$\begin{cases} \sigma_x = p_0 + \dfrac{\left(p_0 - \sigma_R^p\right)R_p^2}{\left(h^2 + x^2\right)^2}\left(h^2 - x^2\right) \\ \sigma_y = p_0 - \dfrac{\left(p_0 - \sigma_R^p\right)R_p^2}{\left(h^2 + x^2\right)^2}\left(h^2 - x^2\right) \\ u_x = \dfrac{\left(p_0 - \sigma_R^p\right)R_p^2 x}{2G\left(h^2 + x^2\right)} \\ u_y = \dfrac{\left(p_0 - \sigma_R^p\right)R_p^2 h}{2G\left(h^2 + x^2\right)} \end{cases}. \quad (17)$$

3.3. Reasonable Position Criterion for Short-Distance Floor Roadway to Be Depressurized. After the overlying coal roadway of the floor roadway is excavated, the surrounding rock will experience secondary pressure relief. To prevent the outburst and guarantee the stability of surrounding rock, no through cracks should be formed at the rock pillar on the roadway roof, and the reasonable position model is shown in Figure 5.

As shown in Figure 5, the judgment criteria for the failure depths h_{pr} and h_{pc} of floor roadway and its overlying coal roadway for the rock mass, as well as the reasonable distance between the right-angular semicircular floor roadway and the coal seam, can be obtained as follows:

$$\begin{cases} h_{Pr} = \delta \cdot R_{Pr} - \left(C_1 - B_1\right) \\ h_{Pc} = \delta \cdot R_{Pc} - \dfrac{C_1}{2} \end{cases}, \quad (18)$$

$$\Delta h \geq \delta \cdot \left(R_{pr} + R_{pc}\right) - \left(\frac{3}{2}C_1 - B_1\right), \quad (19)$$

where δ is the superposition coefficient of the secondary pressure relief effect, which can be statistically analyzed through the field monitoring or calculated through the simulation.

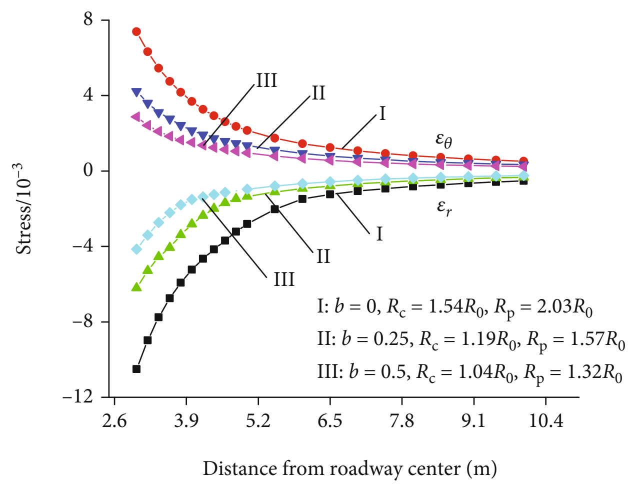

Figure 8: Strain distribution curve of surrounding rock in roadway.

4. Pressure Relief and Permeability Enhancement Mechanism of Floor Roadway at Deep Coal Roadway Strips

4.1. Pressure Relief and Zonal Disintegration Analysis of Floor Roadway at Coal Roadway Strips. After the short-distance floor roadway is excavated, the vertical stress at the coal seam rightly above the roadway is released. The original three-directional stress equilibrium of the coal mass is destructed, and the ultimate strength of the coal mass can be easily reached in the deep roadway, thereby leading to yield failure. Subsequently, the concentrated stress is transferred to the two sides to form a zoning model, as shown in Figure 6.

The vertical stress in the pressure relief damaged zone is obviously reduced. In this zone, the cracks are significantly developed in the coal mass, and it is called effective pressure relief zone, extending at the two sides X_1 of the center line in the roadway. The coal mass in the plastic deformation zone will experience minor deformation and cracking. Thus, the gas permeability coefficient is obviously enhanced, and it is called effective permeability enhancement zone, extending at the two sides X_0 of the center line in the roadway.

When the horizontal distance satisfies $x \leq h$, the first, second, and third principal stresses are σ_x, σ_z, and σ_y, respectively. Then,

$$\frac{\alpha_c}{1 + b}\left(\sigma_x + b\sigma_z\right) - \sigma_y = \alpha\sigma_c. \quad (20)$$

After the floor roadway is excavated, the original adsorbed gas in the upper coal seam is transformed into free gas, the gas stress in the coal seam will be increased, whereas the uniaxial compressive strength will be reduced, which conforms to the following relation [4]:

$$\sigma_c = A_2 + B_2 \cdot p, \quad (21)$$

where A_2 and B_2 are the parameters related to the coal mass.

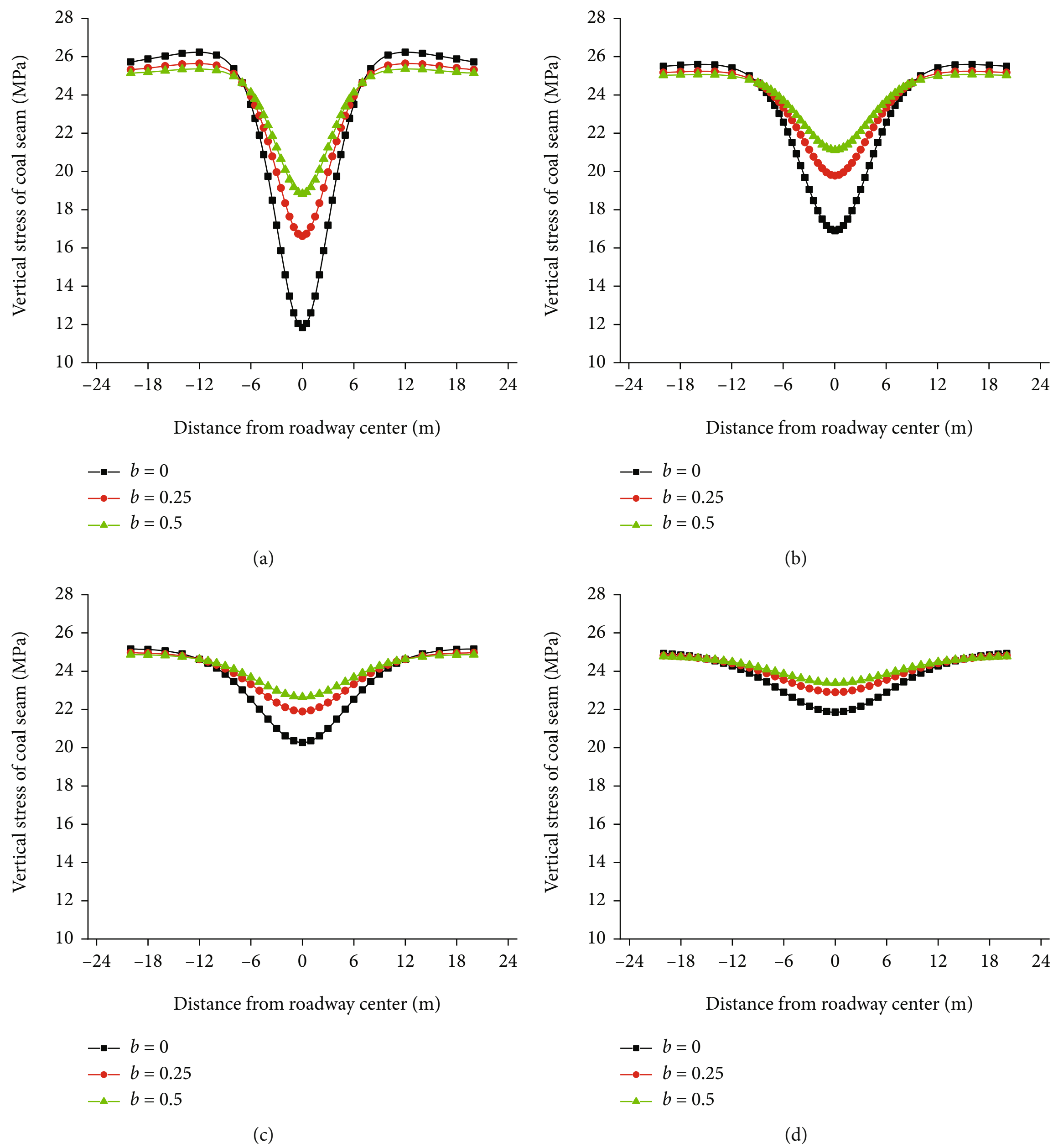

FIGURE 9: Continued.

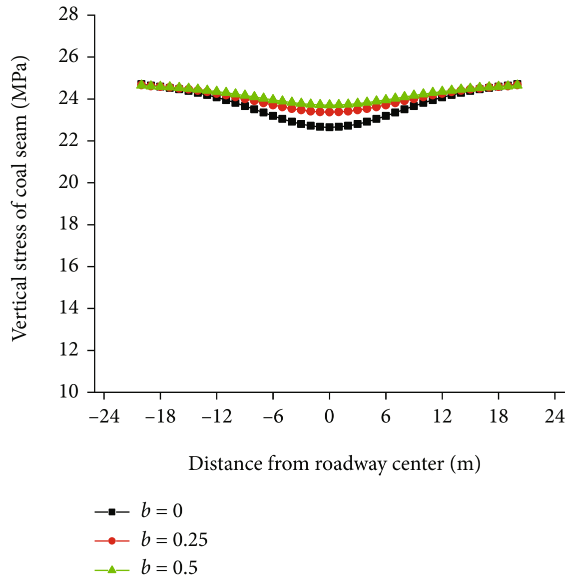

(e)

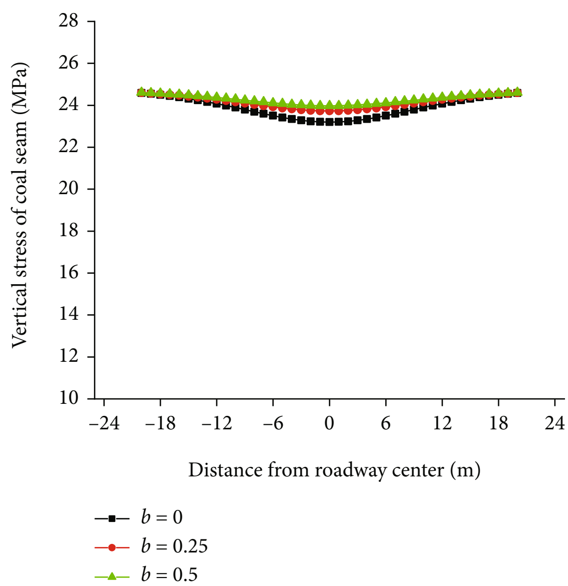

(f)

Figure 9: Vertical stress of coal seam during the excavation of floor roadways under different spacings.

Table 1: Pressure relief coefficients (%) at the center line of the roadway and coal seams at two sides.

b	Vertical distance h/m					
	7	9	12	15	18	21
0	52.0–4.6	31.4–5.0	17.7–4.7	11.3–4.9	7.8-2.7	5.8–2.3
0.25	32.6–2.9	19.7–3.2	11.1–2.7	7.1–3.1	4.9-2.2	3.6–2.0
0.5	23.6–2.1	14.3–2.2	8.0–2.2	5.1–2.2	3.6-2.0	2.6–1.9
Two sides	6 m	7 m	8 m	8 m	5 m	5 m

Table 2: Radius of plastic zone in the roadway under different principal stress coefficients.

Roadway name	Roadway shape	Equivalent radius R_0/m	Radius of plastic zone R_p/m		
			$b = 0$	$b = 0.25$	$b = 0.5$
Floor roadway	Right-angular semicircular arch	2.24	4.55	3.52	2.96
Overlying coal roadway	Rectangular	2.47	5.01	3.88	3.26

Table 3: Pressure relief effect of the overlying coal seam in the floor roadway at different positions.

h /m	Effective pressure relief zone $X1$/m	Effective permeability enhancement zone $X0$/m	Permeability enhancement ratio	Gas permeability enhancement ratio	Pressure relief effect
7	4.3	12.1	0.28–6.06	11.1–239.3	
9	3.5	15.4	0.17–2.26	6.7–89.2	Obvious
12	1.2	20.5	0.09–0.94	3.6–37.1	
15	0.3	20.7	0.06–0.23	2.4–9.1	
18	0	20.5	0.03–0.14	1.2–5.5	Unobvious
21	0	20.4	0.02–0.04	0.8–1.6	

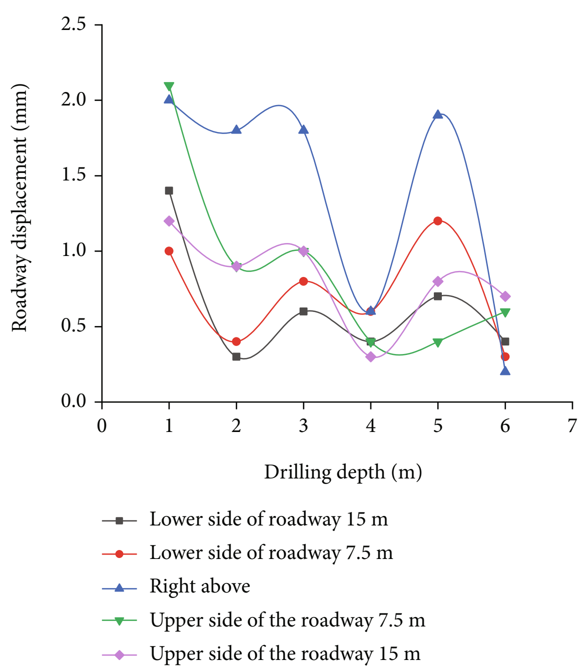

Figure 10: Displacement of surrounding rock in 213 floor roadway.

Substituting Equation (17) and (21) into Equation (20) yields the following:

$$\frac{1-\sin\varphi}{(1+b)(1+\sin\varphi)}\left[P_0+\frac{\left(P_0-\sigma_R^p\right)R_p^{\,2}}{\left(h^2+X_1^{\,2}\right)^2}\left(h^2-X_1^{\,2}\right)+b\sigma_z\right] - P_0+\frac{\left(P_0-\sigma_R^p\right)R_p^{\,2}}{\left(h^2+X_1^{\,2}\right)^2}\left(h^2-X_1^{\,2}\right)=\frac{1-\sin\varphi}{1+\sin\varphi}\left(A_2+B_2\cdot p\right). \tag{22}$$

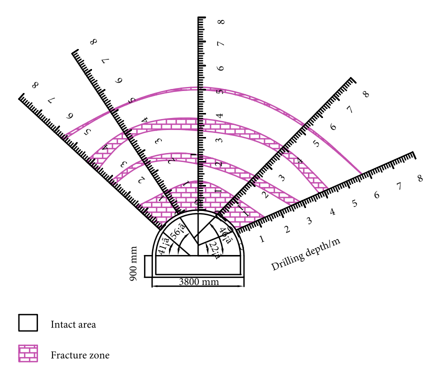

Figure 11: Failure of surrounding rock in 213 floor roadway.

According to the change laws of the uniaxial compressive strength of gassy coal seam, the width X_1 of the pressure relief damaged zone of short-distance floor for the overlying coal seam can be solved by combining the layout conditions of the floor roadway, the coal mass-related parameters at the overlying coal seam, and Equation (22).

The horizontal distance X_0 of the effective pressure zone is the horizontal distance when the vertical stress σ_y reaches the maximum value. As the analytical expression of σ_y in Equation (17) is complicated, the maximum value of σ_y and horizontal distance X_0 of effective pressure relief zone can be calculated via MATLAB.

4.2. Pressure Relief and Permeability Enhancement Mechanism of Floor Roadway at Coal Roadway Strips. According to the stress unloading experiment of gassy coal samples under constant confining pressure and atmospheric pressure, the fitting relation between permeability K and $\sigma_1-\sigma_3$ is as follows [4]:

$$K = A_3\cdot e^{B_3\cdot(\sigma_1-\sigma_3)}, \tag{23}$$

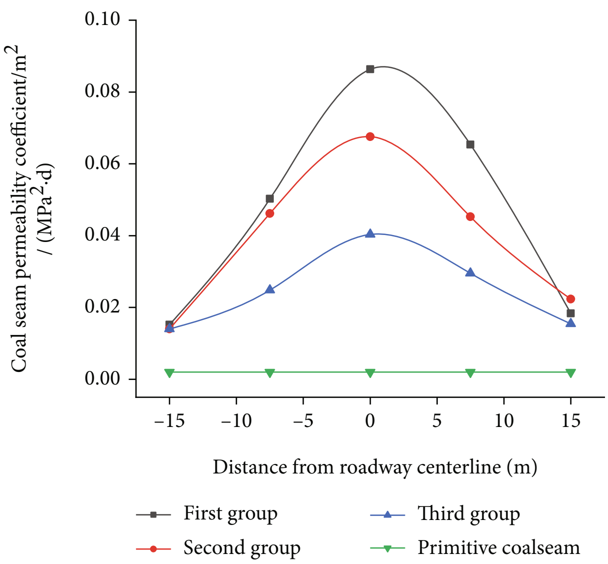

Figure 12: Gas permeability coefficient of overlying coal seam in 213 floor roadway.

where A_3 and B_3 are the parameters related to coal mass, stress, and gas.

As indicated by Equation (17) and the stress analysis of the surrounding rock, when $x < h$, the first and third principal stresses are σ_x and σ_y, respectively; when $x > h$, the first and third principal stresses are σ_y and σ_x, respectively. Therefore, the formulas of permeability K and $\sigma_1 - \sigma_3$ can be organized as follows:

$$\begin{cases} K = A_3 \cdot e^{2B_3 \cdot \left(p_0 - \sigma_R^p\right)\left(h^2 - x^2\right)R_p^2/\left(h^2 + x^2\right)^2} & x < h \\ K = A_3 \cdot e^{-2B_3 \cdot \left(p_0 - \sigma_R^p\right)\left(h^2 - x^2\right)R_p^2/\left(h^2 + x^2\right)^2} & x > h \end{cases}. \quad (24)$$

The difficulty of coal seam gas extraction is generally expressed by the gas permeability coefficient, which also characterizes the resistance formed by the coal seam to the gas flow. According to the relationship between the gas permeability coefficient of the coal seam and the permeability of the pressure-bearing coal sample [27], the relationship between the gas permeability coefficient of the coal seam and the stress change can be further acquired, as shown as follows:

$$\begin{cases} \lambda = \dfrac{A_3}{2\rho p_n} \cdot e^{2B_3 \cdot \left(p_0 - \sigma_R^p\right)\left(h^2 - x^2\right) \cdot R_p^2/\left(h^2 + x^2\right)^2} & x < h \\ \lambda = \dfrac{A_3}{2\rho p_n} \cdot e^{-2B_3 \cdot \left(p_0 - \sigma_R^p\right)\left(h^2 - x^2\right) \cdot R_p^2/\left(h^2 + x^2\right)^2} & x > h \end{cases}, \quad (25)$$

where ρ represents the absolute viscosity of gas, 1.08×10^{-8} N·s/cm^2; and P_n denotes a standard atmospheric pressure, 0.1013 MPa.

5. Pressure Relief and Permeability Enhancement Practice of Floor Roadway at Deep Coal Roadway Strips

5.1. Engineering Trial Calculation. The parameters used in the calculated example were the measured parameters of 213 floor coal rock stratum in Qujiang Coal Mine. The burial depth of 213 floor roadway was about 980 m, the roadway size was 4.0 m × 3.0 m, the wall height was 1.0 m, and the thickness of overlying B_4 coal seam was 3 m. According to the stress of the primary rock and the experiment, the vertical and horizontal stress components were 24.92 MPa and 24.35 MPa, respectively, and $P_0 = 24.6$ MPa; the Poisson's ratio, initial friction angle, initial cohesion, residual internal friction angle, and residual cohesion of rock were $\mu = 0.25$, $\varphi_p = 35°$, $c_p = 3$ MPa, $\varphi_c = 20°$, and $c_p = 0.8$ MPa, respectively, $\sigma_c = -1.576p + 24.77$ and $K_0 = 2.7191 \cdot e^{-0.09 \cdot (\sigma_1 - \sigma_3)}$.

The equivalent elasticity modulus of the rock and the equivalent excavation radius of the floor roadway were calculated as $E = 15.0$ GPa and $R_0 = 2.24$ m, respectively. When the intermediate principal stress coefficient b was taken as 0.75 and 1, the calculation results showed that no disintegration zone appeared in the roadway, which did not conform to the engineering practice. By combining literature [22], the stress, deformation, plastic zone, and permeability (Figures 7–9, Tables 1–3) were analyzed under $b = 0$, 0.25, and 0.5, respectively.

As shown in Figures 7–9, the circumferential stress of the surrounding rock in the roadway under different values of b was initially increased and then reduced, reaching the maximum value at the elastic–plastic interface. With the increase in the coefficient b, the circumferential stress reached the peak value at a closer distance from the roadway surface. Under different values of b, the radial stress presented a monotonic increasing trend and reached the stress of the primary rock at an infinite distance. At the same vertical distance in the elastic zone, the radial stress of the rock increased with coefficient b, whereas the circumferential stress showed an opposite trend. The absolute value of stain was gradually reduced with the distance; thus, the strain was obviously affected by coefficient b.

As shown in Figure 9 and Table 1, the pressure relief coefficient had the same change law as the vertical stress. The vertical stress of the coal seam was gradually reduced from the center line of the roadway toward the two sides, and it was also gradually reduced with the increase in the intermediate principal stress coefficient b and vertical distance h.

As shown in Table 2, the radius of the plastic zone in the roadway was gradually reduced with the increase in the intermediate principal stress coefficient b. $b = 0$ was taken to ensure the safety of distance arrangement. When $\delta = 1$, the minimum reasonable distance arranged in the floor roadway could be obtained as $\Delta h = 6.21$ m.

As shown in Table 3, with the increase in the distance from the floor roadway to the coal seam, the pressure relief effect was gradually weakened. When the distance reached

12 m, the pressure relief effect was not evident. By combining Equation (19), the pressure relief and permeability enhancement effect was significant when the roadway was arranged within 10.6 m from the coal seam.

5.2. Engineering Practice. Similarly, an engineering practice was performed in the 213 coal roadway of Qujiang Coal Mine. This floor roadway was arranged at 9.0 m away from the coal seam. The displacement of surrounding rock was measured using a DW-6 multipoint displacement meter. The failure status of surrounding rock was detected via YTJ20 rock strata detection recorder. The gas permeability coefficient of the coal seam was measured using a test drill hole, and the test results are displayed in Figures 10–12.

The field measurement showed that the "wave crest" and "trough" of the surrounding rock displacement in the roadway alternately appeared. An obvious pressure relief effect was achieved when the surrounding rock displacement was 1.2–2.1 cm and the expansion rate was 1.3‰–2.3‰. The zonal disintegration phenomenon occurred to the surrounding rock in the roadway. Four disintegration zones appeared inside the roadway from the wall, their maximum scope of influence was 5.7 m, and the investigation result was basically consistent with the theoretical analysis. The gas permeability coefficient in the coal seam under pressure relief was obviously enlarged in comparison to the original coal seam, being increased by 8.1–54.7 times in different zones. The permeability enhancement effect of short-distance floor roadway on the overlying coal roadway strip was significant, which highly coincided with the theoretical analysis.

6. Conclusion

(1) An equivalent mechanical model of the surrounding rock in deep roadway was established. The analytical solutions of deep roadway excavation to the pressure relief-induced stress and deformation at overlying short-distance coal roadway strips were obtained through the unified strength criterion and nonassociated flow rule. Next, the criterion for determining the reasonable position of floor roadway was constructed

(2) A mechanical model of short-distance floor roadway for the zonal pressure relief and permeability enhancement in the overlying coal seam was established. The expressions of stress and permeability changes at the coal roadway strips in the elastic and elastic–plastic zones of the surrounding rock in the roadway were given

(3) The engineering calculation example indicated that the intermediate principal stress coefficient exerted obvious effects on the stress and strain of the surrounding rock in the roadway. The vertical stress and vertical displacement of the overlying coal seam were gradually reduced with the increase in the intermediate principal stress coefficient and vertical distance of the floor roadway. The minimum reasonable distance arranged for the 213 floor roadway in Qujiang Coal Mine was 6.21 m, and the position of effective pressure relief should be located within 10.6 m from the coal seam floor

(4) The field practice manifested that the deep floor roadway exerted obvious pressure relief and permeability enhance effect on the overlying short-distance coal roadway strips. The investigation results were basically identical with the theoretical analysis results. Thus, the pressure relief and permeability enhancement method of short-distance floor roadway at deep coal roadway strips was feasible

Data Availability

The known data in this paper come from practical engineering case data, which are reliable and available.

Conflicts of Interest

The authors declare that they have no conflicts of interest.

Acknowledgments

This work is financially supported by the National Natural Science Foundation of China (Nos. 52074008, 52074007, and 52004005), the Anhui Provincial Natural Science Foundation (Nos. 2008085ME142 and 2008085QE222), the Anhui Collaborative University Innovation Project (GXXT-2020-056), the China Postdoctoral Science Foundation (2021 M691185), Open Research Fund Project of Key Laboratory of Safety and High-Efficiency Coal Mining of Ministry of Education (JYBSYS2019208), and the Independent Research Fund of The State Key Laboratory of Mining Response and Disaster Prevention and Control in Deep Coal Mines (Anhui University of Science and Technology, No. SKLMRDPC19ZZ012).

References

[1] L. Yuan, "Strategic thinking of simultaneous exploitation of coal and gas in deep mine," *Journal of China Coal Society*, vol. 41, no. 1, pp. 1–6, 2016.

[2] H. P. Xie, M. G. Qian, S. P. Peng, S. S. Hu, Y. Q. Cheng, and H. W. Zhou, "Sustainable capacity of coal mining and its strategic plan," *Engineering Science*, vol. 13, no. 6, pp. 44–50, 2011.

[3] C. J. Lian, C. M. Guo, Z. Y. Deng, and H. Y. Ma, "Spatial gas control technology and application of first mining protective layer of coal seam group with high gas outburst," *Coal Mining*, vol. 24, no. 1, pp. 124–127, 2019.

[4] X. Cheng, G. M. Zhao, Y. M. Li, X. R. Meng, C. L. Dong, and W. S. Xu, "Study on relief-pressure antireflective effect and gas extraction technology for mining soft rock protective seam," *Journal of Mining & Safety Engineering*, vol. 35, no. 5, pp. 1045–1053, 2018.

[5] M. J. Zhang, J. J. Hua, and J. T. Hua, "Anti-burst technology of gas strip in pre-extracted coal roadway with single coal seam floorway," *Coal Mine Safety*, vol. 42, no. 6, pp. 30–32, 2011.

[6] L. Yuan, "Control of coal and gas outbursts in Huainan mines in china: a review," *Journal of Rock Mechanics and Geotechnical Engineering*, vol. 8, no. 4, pp. 559–567, 2016.

[7] D. J. Lei, C. W. Li, Z. M. Zhang, and Y. G. Zhang, "Coal and gas outburst mechanism of the "Three Soft" coal seam in Western Henan," *Mining Science and Technology*, vol. 20, no. 5, pp. 712–717, 2010.

[8] C. H. Du and R. J. Feng, "Study on hydraulic creaming technology in low permeability and soft friable thick coal seam," *Coal Science and Technology*, vol. 47, no. 4, pp. 152–156, 2019.

[9] F. Cai and Z. G. Liu, "Simulation and experimental research on upward cross-seams hydraulic fracturing in deep and low-permeability coal seam," *Journal of China Coal Society*, vol. 41, no. 1, pp. 113–119, 2016.

[10] P. Li, K. Wang, Y. F. Jiang, and J. Q. Gou, "Applied study on hydraulic reaming technology of mining seam in Hongling Mine," *Coal Science and Technology*, vol. 43, no. 7, pp. 69–73, 2015.

[11] X. J. Jian and F. Cai, "Study on the technology of hydraulic fracturing strengthening and deepening in deep low permeability coal seam," *Safety in Coal Mines*, vol. 48, no. 10, pp. 76–79, 2017.

[12] J. F. Zhao, "Study on the technology of hydraulic punching strengthening and deepening in deep low permeability coal seam," *Coal Technology*, vol. 34, no. 1, pp. 179–181, 2015.

[13] Y. H. Zhou, X. R. Luo, L. L. Wu, and J. N. Xie, "Research status and new technology of anti-pressure and pressure relief of low permeability coal seam," *Mining Research and Development*, vol. 32, no. 1, pp. 23–25, 2012.

[14] F. Cai, Z. G. Liu, C. J. Zhang, and B. Q. Lin, "Numerical simulation of deep hole pre-splitting blasting in high gas permeability coal seam," *Journal of China Coal Society*, vol. 5, pp. 499–503, 2007.

[15] H. P. Xie, F. Gao, and Y. Ju, "Research and development of rock mechanics in deep ground engineering," *Chinese Journal of Rock Mechanics and Engineering*, vol. 34, no. 11, pp. 2161–2178, 2015.

[16] H. P. Xie, "Research review of the state key research development program of China: deep rock mechanics and mining theory," *Journal of China Coal Society*, vol. 44, no. 5, pp. 1283–1305, 2019.

[17] Q. Zhang, S. L. Wang, and X. R. GE, "Elastoplastic analysis of strain softening of surrounding rock of circular roadway," *Journal of Rock Mechanics and Engineering*, vol. 29, no. 5, p. 1035, 2010.

[18] B. S. Jiang, L. Yang, and L. P. Lin, "Stress analysis of fractured surrounding rock based on Hoek-Brown criterion," *Journal of Solid Mechanics*, vol. 32, no. S1, pp. 300–305, 2011.

[19] X. B. Zhang, G. M. Zhao, and X. R. Meng, "Plastic zone analysis of surrounding rock of circular roadway in non-uniform stress field based on the unified strength criterion of rock nonlinearity," *Journal of Safety and Environment*, vol. 13, no. 3, pp. 202–206, 2013.

[20] B. S. Jiang, Q. Zhang, Y. N. He, and L. J. Han, "Elastoplastic analysis of surrounding rock of deep circular roadway fracture," *Journal of Rock Mechanics and Engineering*, vol. 5, pp. 982–986, 2007.

[21] L. Chen, X. B. Mao, M. Li, and Y. L. Chen, "Elastoplastic analysis of cracked surrounding rock in deep roadway based on Drucker-Prager criterion," *Journal of China Coal Society*, vol. 42, no. 2, pp. 484–491, 2017.

[22] C. G. Zhang, C. L. Zhang, F. Zhou, and Q. Yan, "Study on the strength theory effect of elastoplastic analysis of circular tunnels," *Chinese Journal of Geotechnical Engineering*, vol. 40, no. 8, pp. 1449–1456, 2018.

Hindawi
Geofluids
Volume 2022, Article ID 6321031, 10 pages
https://doi.org/10.1155/2022/6321031

Research Article

Study on the Law of Subsidence of Overburden Strata above the Longwall Gob

Yujiang Zhang[1,2,3,4] **Caiyi Du**[1,4] **Guorui Feng**[1,4] **Honghui Yuan**[1,4] **Xiaogang Deng**[2] **Ronggang Zhang**[5] **Renle Zhao**[2] **and Yuxia Guo**[1,4]

[1]*College of Mining Engineering, Taiyuan University of Technology, Taiyuan 030024, China*
[2]*Shandong Energy Linyi Mining Group Co., Ltd., Linyi 276017, China*
[3]*Postdoctoral Centre, Shandong Energy Group Co., Ltd., Jinan 250014, China*
[4]*Shanxi Engineering Research Center for Green Mining, Taiyuan 030024, China*
[5]*Shaanxi Guohua Jinjie Energy Co., Ltd., Yulin 719000, China*

Correspondence should be addressed to Guorui Feng; fgr_tut@163.com and Honghui Yuan; yuanhonghui0583@link.tyut.edu.cn

Received 27 August 2021; Accepted 24 February 2022; Published 24 March 2022

Academic Editor: Hualei Zhang

In recent years, with the increase of depth and intensity of coal mining, geological disasters in deep engineering occur frequently. It is essential to study the law of subsidence of overburden after mining for analyzing the mechanism and control of geological disasters in deep engineering. However, the value of the subsurface subsidence factor and other overburden subsidence parameters could not be obtained easily. In this paper, the strata bulking of the caving zone, the bed separation of the fractured zone, and the dilatation of bending zone were considered a kind of expansion in the vertical direction uniformly. An assumption on vertical expansion value distribution of overburden strata above the longwall gob was proposed. Based on the assumption, a formula of the subsurface subsidence factor was deduced according to such parameters as the bulking factor, mining depth, mining height, and surface subsidence factor. Moreover, many field data were used to verify the correctness of the assumption by the data fitting method. The results show that the exponential function could well describe the expansion distribution characteristic of overburden strata and subsurface subsidence in the vertical direction. The parameter a in the deduced formula influences the shape of the subsurface subsidence curve; it is called the subsurface subsidence influence factor (SSIF). The SSIF, maximal vertical expansion value, and the mining depth-to-mining height (MD/MH) ratio influence the subsurface subsidence factor. The expansion distribution (E-D) factor is defined to describe the subsidence characteristic of overburden strata above the longwall gob by the surface subsidence factor and bulking factor of the caving zone. The E-D factor presents the logarithm relation with the MD/MH ratio, and the range of its maximum is 2.84~3.40. The case study demonstrates that the subsurface subsidence factor calculated by the proposed method has higher precision, and the mean errors between the calculated value and the measured value are less than 2%.

1. Introduction

The longwall working surface of coalmine distributes widely in the world. The overburden strata above the longwall working face are suspended in a large area, which is easy to cause coalmine disaster accidents such as rock bursts and a strong mine pressure. As is known to all, after excavated, the overburden strata above the longwall gob could be divided into such three zones as caving zone, fractured zone, and bending zone [1, 2]. Although the deformation and movement features among the "Three Zones" show the obvious difference, the fact that the surface subsidence value is less than the mining height indicates the expansion generality among them. The subsurface subsidence above the longwall gob has been used in many fields, including feasibility judgment and design for ascending mining [1, 3–6], mining of protective coal seam, depressurized mining for rock bursts and coal and gas outburst mine [1, 3–6], and destruction of coalmine roadway and chamber [7–9], surface waters protection [10, 11], and tunnel excavation above the longwall gob [12, 13]. Hence, the study on the subsurface subsidence can provide a vital fundamental basis for engineering works above the longwall gob.

Based on the motion features of overburden strata above the longwall gob, plenty of studies on the subsurface subsidence have been developed from such angles as surface subsidence and overburden strata structure, respectively. Many scholars have studied the relation between surface subsidence factor and subsurface subsidence factor according to the surface subsidence theory. Considering the hard rock proportion and overburden stratification, Luo et al. [10, 11] obtained the enhanced subsurface subsidence prediction model on the basis of the influence function method. The results of physical simulation tests [14] showed the quadratic relation between the surface subsidence factor and subsurface subsidence factor above the longwall gob:

$$q_z = q_0\left(a_1(z/H)^2 + a_2(z/H) + a_3\right), \tag{1}$$

where q_z and q_0 are the subsurface subsidence factor and surface subsidence factor, respectively, z and H are the depth away from the surface and the mining depth, the ratio of strata depth to mining depth (z/H) is called the depth level, and a_1, a_2, and a_3 refer to the parameters relevant to mining and geological conditions.

Based on Fangezhuang Coalmine's field data, Li [15] obtained the function relation between surface subsidence factor and subsurface subsidence factor as follows:

$$q_z = 1 - (1 - z/H)^n(1 - q_0), \tag{2}$$

where n refers to the parameters relevant to mining and geological conditions.

The above studies show the relation between surface subsidence and subsurface subsidence above the longwall gob to some extent. However, the influences of such geological and mining factors as mining depth, mining height, and strata collapse condition were not shown.

From the angle of overburden strata structure, the thick and hard strata in the fractured zone not only have major control significance for surrounding rock on the longwall working face but also play the control action on subsurface and surface subsidence [16, 17]. Qian and Miao [18] obtained voussoir beam's subsidence curve through a study on the voussoir beam theory. Xu and Qian [19] obtained the relation formula between the length of voussoir beam and the key strata subsidence with different breaking spans of the main roof by the UDEC software. This relation formula has better accuracy under the condition of a hard roof and lesser unconsolidated layers. Wu et al. and Zhou et al. [20, 21] monitored the vertical movements in internal rock with the borehole extensometer system and studied the density distribution of mining-induced fracture interspace above the longwall gob.

Many studies [22–25] show that the expansion decreases along with the increase of distance away from the gob. In the classical "Three Zones" theory, the bulking factors of "Three Zones" are 1.25-1.4, 1.05-1.15, and 1.01-1.02 successively from bottom to top [22]. Peng [26] and Deng et al. [27] discovered that the bulking factor decreases along with mining depth in certain disciplines in the vertical direction based on the method of statistics and physical simulation, respectively. Wang et al. [28] assumed that the vertical expansion value shows the linear change in the vertical direction to obtain the relation between the vertical expansion value and the ratio of bedrock thickness and mining height. Yavuz [29] proposed a method that the stress recovery distance in the gob and deems that the "Three Zones" have different strains, the caving zone's strain should follow Salamon's equation, the fractured zone's strain is about 0.4%, and the strain of bending zone does not change. Through this method, the surface subsidence value can be calculated, but not the subsurface subsidence.

Various methods have been adopted to investigate the relationship between subsurface subsidence factor and surface subsidence factor or overburden strata structure or bulking factor. Each parameter in the above studies is determined by a variety of factors, and the subsurface subsidence factor cannot be calculated accurately by any one of these parameters. And more, the mining and geological conditions' effects for subsurface subsidence have not been fully revealed. Thence, such parameters as mining depth, mining height, bulking factor, and surface subsidence factor should be considered to describe the subsurface subsidence above the longwall gob.

A method for determining subsurface subsidence based on overburden strata expansion above the longwall gob was proposed in this paper. In this method, the vertical expansion value in the overburden strata above the longwall gob is assumed to obey an exponential distribution in the vertical direction, and the relation between it and surface subsidence factor, mining depth, and mining height was deduced. On the base of the collection of a large number of field data, the correctness of this method was verified through parameter fitting and comparison with field data, and parameters of the distribution function of the subsurface subsidence factor were determined. Then the distribution discipline of the subsurface subsidence factor above the longwall gob was obtained. Finally, parameters of the distribution function of the subsurface subsidence factor were discussed and a case was analyzed.

2. Methods

2.1. Assumption. As shown in Figure 1, the bulking of the caving zone, the strata structure action of the fractured zone, and the bed separation and dilatation of the bending zone are uniformly considered a kind of expansion in the vertical direction. Moreover, the basic assumption is as follows.

(1) The vertical expansion value of strata could be described by the continuous function

(2) The study is based on the critical and supercritical longwall gob

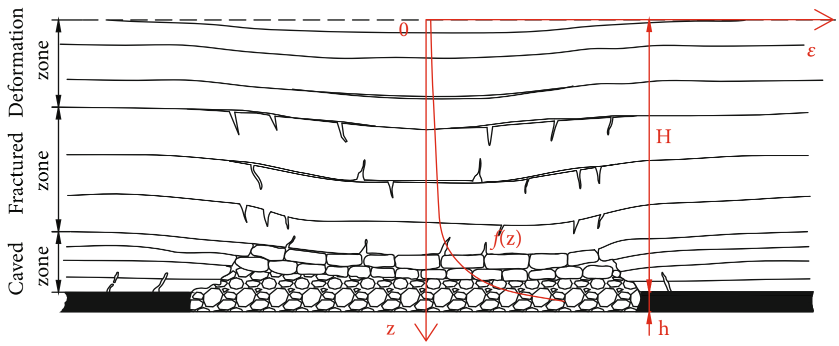

Figure 1: Distribution of "Three Zones" [26] and expansion distribution above the longwall gob.

(3) The coal seam is a nearly flat seam and gently inclined seam and the dip of a coal seam is assumed as $\alpha°$ (less than 25°)

(4) The vertical displacement of the floor in the gob is neglected

2.2. Model Establishment. Establish the rectangular plane coordinate system as shown in Figure 1. The vertical axis and horizontal axis refer to the depth from the ground and vertical expansion value of overburden strata, respectively. In Figure 1, $f(z)$ is the distribution function of vertical expansion value, and H and h are mining depth and mining height, respectively.

Based on relevant studies and numerous field experiences [22–24, 26–28], the vertical expansion value for overburden strata above the longwall gob is fiercer on change than the description by linearity and quadratic function. Thence, when a single coal seam is extracted, it is assumed that the change of vertical expansion value follows the exponential function:

$$f(z) = \lambda a^{(z-H)/h}, \tag{3}$$

where $f(z)$ is the distribution function of the vertical expansion value, z is depth, the parameters of λ and a are undetermined parameters, H is mining depth, and h is mining height.

The strata of caving zone are provided with maximal vertical expansion value, and according to the formula of maximum compression strain of bulked rock material [29], the maximal vertical expansion value could be expressed by the bulking factor of a caving zone:

$$\varepsilon_0 = \Delta l/l = (b_0 - 1)/1, \tag{4}$$

where ε_0 is the maximal vertical expansion value and b_0 is the bulking factor of a caving zone.

The equation of the vertical expansion value in the vertical direction is

$$\varepsilon(z) = \varepsilon_0 f(z) = \varepsilon_0 \lambda a^{(z-H)/h}. \tag{5}$$

The sum of surface subsidence value and accumulative vertical expansion value of overburden strata is equal to mining height. Therefore, the subsurface subsidence value W_z could be calculated by the following formula:

$$W_z = h - \int_H^z \varepsilon_0 f(z)dz = h - \frac{\lambda h \varepsilon_0}{\ln a}\left(a^{(z-H)/h} - 1\right). \tag{6}$$

Based on the relation between subsidence value and subsidence factor [30], the subsurface subsidence factor q_z is

$$q_z = 1 - \frac{\lambda \varepsilon_0}{\ln a}\left(a^{(z-H)/h} - 1\right). \tag{7}$$

When $z = 0$, the surface subsidence factor q_0 is

$$q_0 = 1 - \frac{\lambda \varepsilon_0}{\ln a}\left(a^{-(H/h)} - 1\right). \tag{8}$$

Through formulas (7) and (8), the relation between surface subsidence factor and subsurface subsidence factor could be obtained as follows:

$$q_z = 1 - (1 - q_0)\left(a^{(z/H-1)(H/h)} - 1\right)/\left(a^{-(H/h)} - 1\right). \tag{9}$$

3. Parameter Determination and Correctness Verification

3.1. Parameter Determination. Firstly, collect the data involved in the formula, including the surface subsidence factor, bulking factor of a caving zone, mining depth, and mining height. The working face in which the length of the panel is greater than 1.4 times of mining depth was selected and was considered a critical or supercritical working face [29]. Secondly, the transposition and arrangement were conducted for formula (8), and then the logarithm on both sides was taken to obtain the following form:

$$H/h = A \ln(1 + BT), \tag{10}$$

where $(1 - q_0)/\mathcal{E}_0 = T$ is defined as the expansion distribution factor (E-D factor), $A = -1/\ln a$, and $B = \ln a/\lambda$.

Finally, based on the collected data and formula (10), implement the regression fitting to obtain the value of λ and a and then determine the variation tendency of vertical expansion as well as the subsurface subsidence factor (q_z).

Table 1: Relevant parameters list of coalmines.

Mine	ε_0	q_0	h (m)	H (m)	$(1-q_0)/\varepsilon_0$	H/h
Qinghemen Mine	0.2	0.66	1.8	224	1.70	124.44
Taiji No.1 Mine	0.35	0.65	1.6	120	1.00	75.00
Baoan No.1 Mine	0.38	0.83	2.1	122	0.45	58.10
Fengfeng 0252	0.42	0.84	2.4	133	0.38	55.42
Zaozhuang 2042	0.58	0.76	1.45	61	0.41	42.07
Panxi Mine	0.58	0.68	2.2	91	0.55	41.36
Macun Mine	0.38	0.83	2.2	128	0.45	58.18
Pingdingshan No.10 Mine	0.39	0.80	2.0	115	0.51	57.50
Pingdingshan No.6 Mine	0.22	0.83	3.0	281	0.77	93.67
Dongzhuang Mine (107)	0.30	0.83	2.0	156	0.57	78.00
Quantai Mine	0.34	0.78	2.1	146.5	0.65	69.76
Hongshandian Mine	0.41	0.63	2.0	114.6	0.90	57.30
Gengcun Mine	0.53	0.60	3.0	146	0.75	48.67
Gengcun Mine	0.22	0.66	2.4	280	1.55	116.67
Wangjiayuan Longjiachong	0.21	0.62	1.5	195	1.81	130.00
Gaokeng Mine	0.19	0.63	1.05	170	1.95	161.90
Dongliang No.2 Mine	0.51	0.91	1.67	67	0.18	40.12
Wuyang Mine	0.39	0.72	3.0	213	0.72	71.00
Nantun Mine	0.17	0.78	2.9	284	1.29	97.93
Qinghemen No. 2 Mine	0.15	0.67	1.6	318.5	2.20	199.06
Fengfeng 0227	0.20	0.72	4.9	459	1.40	93.67
Dongzhuang Mine (113)	0.28	0.85	2.1	159.5	0.54	75.95
Baodian Mine	0.23	0.83	5.8	427	0.74	73.62
Xie'er Mine	0.41	0.77	6.6	288	0.56	43.64
Shizui Mine	0.31	0.86	4.7	268	0.45	57.02
Beisu Mine	0.08	0.80	0.92	305	2.50	331.52

3.2. Data and Processing. Many field data for coalmines' surface subsidence and basic parameters were collected in the reference [30]. Moreover, twenty-six coalmines with the critical and supercritical longwall gob were selected, whose detailed data are shown in Table 1. In the table, the maximal vertical expansion value $\mathcal{E}_0$ is calculated by formula (4), the E-D factor and MD/MH ratio are calculated by the form of $(1-q_0)/\mathcal{E}_0$ and H/h.

3.3. Correctness Verification. The data in Table 1 is used to verify the correctness of the assumption on vertical expansion distribution. According to formula (10) and the MD/MH ratio and the E-D factor in Table 1, the values of A and B were obtained by data fitting. The fitting result is as shown in Figure 2. In the figure, the x-coordinate is the E-D factor, and the y-coordinate is MD/MH ratio.

The calculated results are as follows: under the 95% confidence interval, $a = 1.0054$ (1.0046, 1.0066) and $\lambda = -0.01681$ (-0.02270, -0.01299). Therefore, the assumption that the vertical expansion value follows an exponential function along with depth change is available.

In order to evaluate the accuracy and adaptability of the method, surface subsidence factors of coalmines in Table 1 were calculated by the proposed method and Yavuz's method [29]. Moreover, the calculated value and field data were compared in Figure 3, in which the horizontal axis and vertical axis are the coalmines number and surface subsidence factor, respectively.

After eliminating a coarse error, the maximum relative error between the calculated two methods and measured values of surface subsidence factors are 20.1% and 18.8%. The average errors of the proposed method and Yavuz's 4method are 2.3% and 6.6%, and the standard deviation of the two methods are 9.9% and 9.1%. The complexity of geological and mining conditions leads to an approximate 20% maximum relative error with both methods. However, both methods have smaller average error and standard deviation. Thus, the correctness and accuracy of the proposed method are further verified by the comparison of surface subsidence.

4. Discussion

4.1. Influences on Subsurface Subsidence

4.1.1. Subsurface Subsidence Influence Factor. Considering that the parameter a influences the shape of the subsurface subsidence factor curve, it is called the subsurface subsidence influence factor (SSIF). Figure 4 shows the distribution

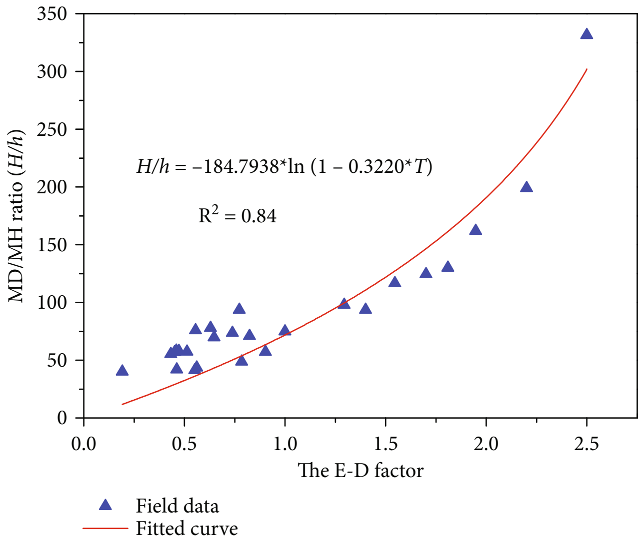

FIGURE 2: Relation curve between the E-D factor and MD/MH ratio.

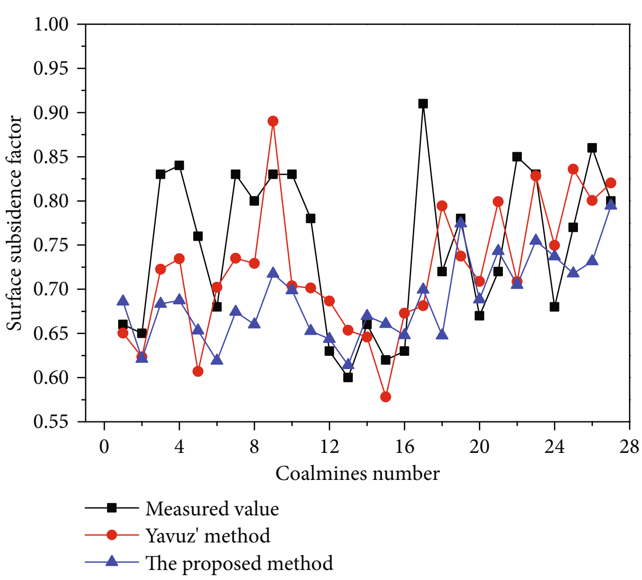

FIGURE 3: Comparison of the calculated and measured value of surface subsidence factor.

curves of the subsurface subsidence factor with different SSIF. The curves in Figure 4 were drawn based on formula (9). And the parameters with a mean 2.5 m mining height, 0.31 maximal expansion value, and maximal 460 m mining depth were selected from Table 1. The scattered points show the relationship between subsurface subsidence factor and depth level (z/H) after the normalization processing is conducted for surface subsidence factor and mining depth of mines in Table 1. In Figure 4, the vertical axis is the different depth levels (z/H), the horizontal axis is the subsidence factor, and the legend shows the fitted curves of the subsurface subsidence factor with different SSIF.

It could be known from the distribution scope of scattered points in Figure 4 that the value of SSIF should be

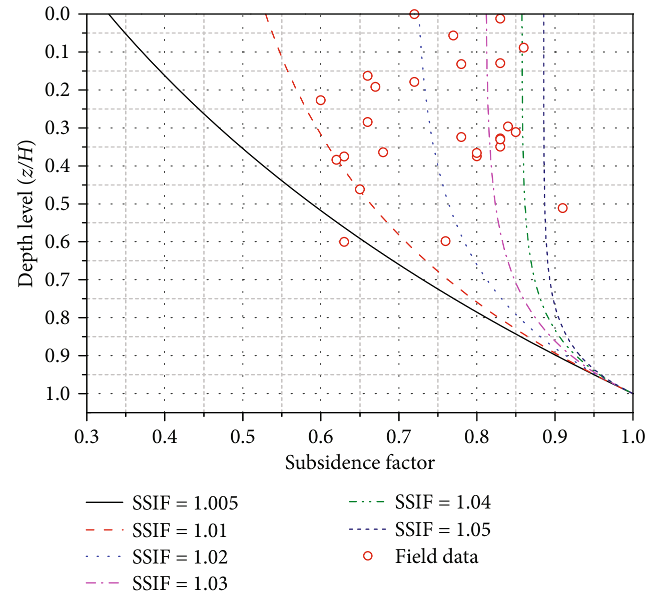

FIGURE 4: Curves of the subsurface subsidence factor with different SSIF.

greater than 1.0054. Since underground mining has a greater MD/MH ratio, and the MD/MH ratio in Table 1 exceeds 40, therefore, the SSIF of 1.0054 only embodies the change discipline of the subsurface subsidence factor on the section where the MD/MH ratio exceeds 40. On the section less than 40 times mining height, the change of the subsurface subsidence factor is greater and embodies a curve with greater curvature. Therefore, the SSIF should be greater, and the actual subsurface subsidence curve should have greater curvature on the section less than 40 times mining height.

As shown in Figure 4, the SSIF influences the distribution of the subsurface subsidence factor. The bending degree of the distribution curve for the subsidence factor increases along with the increase of the SSIF. The subsurface subsidence factor increases with the SSIF increase; however, the amplification decreases. When the SSIF is equal to 1.0054, the subsurface subsidence factor is small, and the decreasing velocity for the subsidence factor from the roof to the surface is great and uniform, which means that there is an expansion approaching the linearity [28]. When the SSIF increases, the surface and subsurface subsidence factors increase, the change rate of subsidence factor is small, and the expansion focuses on the roof area close to the coal seam (caving zone and fractured zone).

4.1.2. Maximal Vertical Expansion Value. When the values of SSIF are 1.015 and 1.05, respectively, Figure 5 shows the relation between maximal vertical expansion value and subsurface subsidence factor under different depth levels. In Figure 5, a mining depth of 400 m and a mining height of 2 m were adopted, and the horizontal axis and vertical axis are the maximal vertical expansion value and subsidence factor, respectively.

Along with the increase of maximal expansion value, the subsurface subsidence factor for each depth level linearly

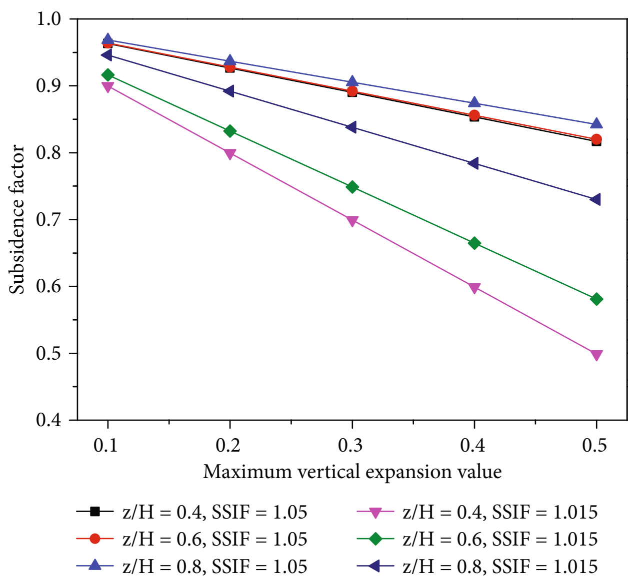

Figure 5: Relation between the subsurface subsidence factor and maximal vertical expansion value.

decreases. The decreased velocity of the subsurface subsidence factor with different depths is different, and it is much less on the depth level close to the coal seam. This shows that the influence degree of the maximal vertical expansion value for subsurface subsidence factor is far greater on the depth level approaching the gob than the surface. When the maximal expansion is identical, along with the depth increase, the difference value of the subsurface subsidence factor with equal depth intervals enlarges. This shows that the subsidence factor variation focuses on the deep section close to the gob. Meanwhile, the greater vertical expansion value means the fiercer subsidence factor variation for strata close to the gob. In addition, when the SSIF is different, the influence of expansion variation on the subsurface subsidence factor is weaker with the increase of the SSIF.

4.1.3. Mining Depth-to-Mining Height (MD/MH) Ratio. When the surface subsidence factor is definitive, different MD/MH ratios influence the subsurface subsidence factor with different depth levels. Figure 6 shows the relation between the subsurface subsidence factor with different depth levels and MD/MH ratio. The parameters that the surface subsidence factor is 0.8 and the MD/MH ratio is 50, 100, 150, 200, and 250, respectively, are adopted in Figure 6.

As shown in Figure 6, the subsurface subsidence factor decreases with the increase of MD/MH ratio. The greater MD/MH ratio means the greater expandable scope of strata, which causes the decrease of subsidence factor. However, the decrease of subsidence factor with the depth increase is nonlinear, the decreasing tendency of which is fast firstly and slow lately. The subsurface subsidence factor approaches certain values finally. When the SSIF is greater, the decreasing tendency of the subsurface subsidence factor along with the increase of MD/MH ratio is more obvious.

With the increase of the MD/MH ratio, the differences of the subsurface subsidence factor among different depth levels decrease. This shows that, under the condition of a great MD/MH ratio, the accumulative vertical expansion value above the fractured zone is very small, the further strata expansion more focuses on strata near gob. In comparison, the vertical expansion has a more uniform distribution under the condition of a small MD/MH ratio. For an identical MD/MH ratio and equal depth interval, the difference value of the subsurface subsidence factor near gob is far greater than that far away from gob. These show that the change of the subsurface subsidence factor is concentrated in the vicinity of the gob and is slow when close to the ground. The greater the SSIF, the more obvious the decreasing tendency for different values of the subsurface subsidence factor on the equal depth interval.

4.2. Expansion Distribution (E-D) Factor. The parameter q_0 is the surface subsidence; similarly, the form of $(1 - q_0)$ could be called the overburden expansion factor. Researchers agree that the maximal vertical expansion is the decisive factor of surface subsidence. And the E-D factor just reflects the relationship between the overburden expansion factor and maximal vertical expansion value. Formula (10) indicates the relation between the E-D factor and the MD/MH ratio. The E-D factor embodies the comprehensive characteristic of overburden strata induced by mining operations, while the MD/MH ratio reflects the mining factor. Both are dimensionless values, having generality.

Formula (10) is a logarithmic function, and its asymptote function is as follows:

$$T_{\max}\varepsilon = 1 - q_0. \tag{11}$$

Based on the field data in Table 1, the scope of the maximum of the E-D factor ($T_{\max}$) is (2.84, 3.40). The E-D factor has an ultimate value, which does not increase infinitively with the increase of the MD/MH ratio.

Two aspects of reason cause the ultimate value existence for E-D factor. On the one hand, a great MD/MH ratio corresponds to the less maximal vertical expansion value [28]. The greater MD/MH ratio means less mining height or greater mining depth. Under these two conditions, the maximal vertical expansion is less. This is because the greater vertical stress caused by greater mining depth decreases the maximal vertical expansion value, while the less mining height has less dropping space to decrease the maximal vertical expansion value [24, 29, 31]. On the other hand, the surface subsidence factor decreases, and the surface expansion factor increases with the growth of the MD/MH ratio [25]. Considering the limitation of coal seam thickness, when the mining depth reaches a certain degree, the surface expansion coefficient tends to one, while the maximal vertical expansion value tends to a constant value [28, 32]. Thence, the ultimate value exists for the E-D factor.

As shown in Figure 7, the relation between surface subsidence and maximal vertical expansion value could be obtained from formula (11). In the figure, the vertical axis is the surface subsidence factor and the horizontal axis is the maximal vertical expansion value.

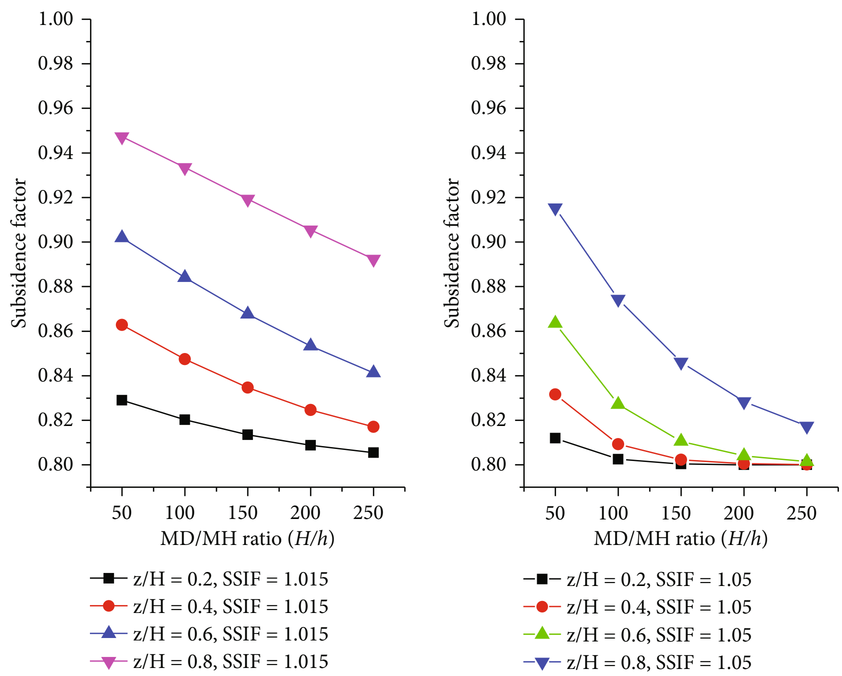

Figure 6: Relation between the subsurface subsidence factor and MD/MH ratio.

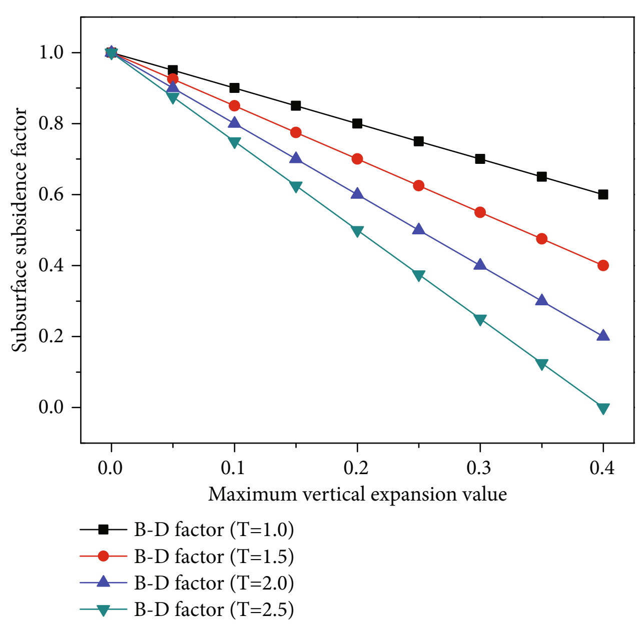

Figure 7: Relation between the surface subsidence factor and maximal vertical expansion value.

As shown in Figure 7, the surface subsidence factor linearly decreases along with the increase of maximal vertical expansion value. The decrease velocity of the surface subsidence factor with a less E-D factor is slower than that when the E-D factor is greater. In addition, along with the decrease of the E-D factor, the decreasing tendency of the surface subsidence factor is faster. This means that, for a condition of a great MD/MH ratio, the change of maximal vertical expansion coefficient has a greater influence on surface subsidence. This is because a great E-D factor corresponds to a greater MD/MH ratio and less surface subsidence factor [32], and the great MD/MH ratio represents the large scope of expansive strata. Thence, when maximal expansion value changes the identical percentage, the change of the surface subsidence factor with a large MD/MH ratio is greater.

5. Case Analyses

The subsurface subsidence was measured in the No. 94302 working face mined in Sihe No. 2 Coalmine, located in Shanxi Province, China [6]. The mining depth is 280-420 m. The mean value of the 9# coal seam in Sihe No. 2 Coalmine is 1.5 m of thickness, with 3° for dip angle of the coal seam.

As shown in Figure 8, the distance between 9# coal seam and 3# coal seam is 51 m. The multiple-position borehole extensometer was used for monitoring the subsidence of a roadway in 3# coal seam. And the monitoring borehole is located in the supercritical subsidence zone above the No. 94302 gob. Ten measuring points were arranged within the 2.3 m~47.5 m scope in the monitoring borehole.

The field data of the subsurface subsidence were analyzed with the two methods. The data were measured by borehole multipoint displacement meters. As shown in Figure 9, Li's method [15] and the proposed method were fitted to obtain the fitting curve and surface subsidence factor. The horizontal axis and vertical axis in the figure are depth level (z/H) and the subsidence factor.

As shown in Figure 9, the fitted value of SSIF and surface subsidence factor are, respectively, 1.06735 ± 0.02302 and 0.72247 ± 0.04039 through the proposed method. While

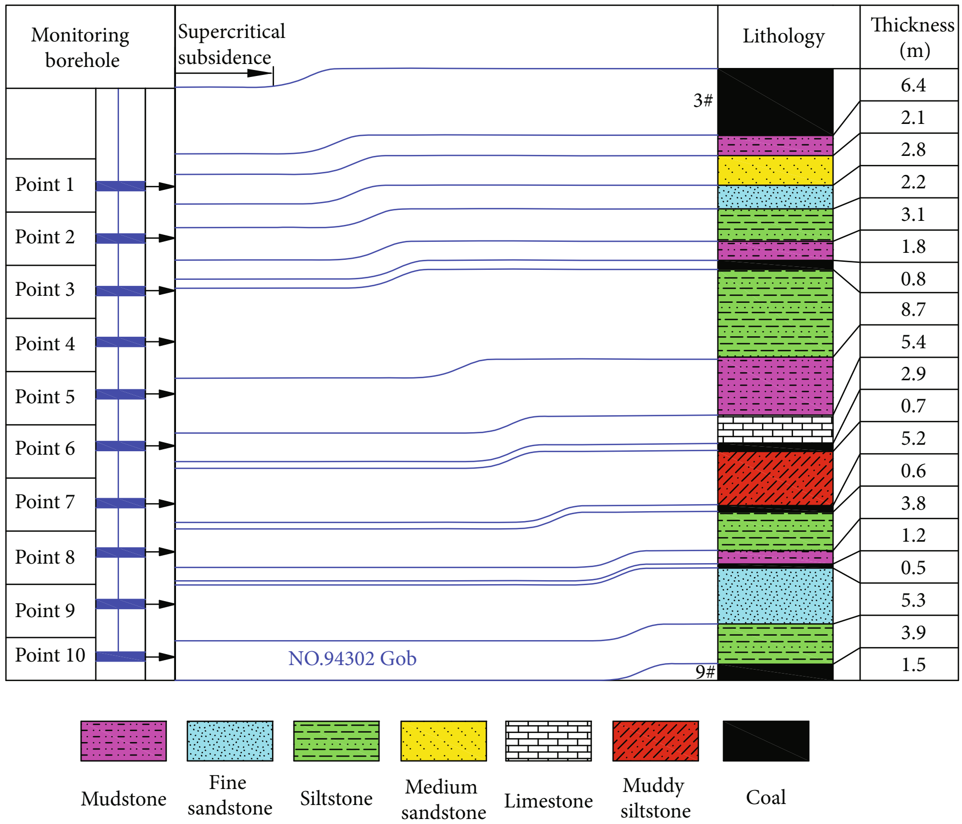

Figure 8: The geological condition and monitoring point arrangement.

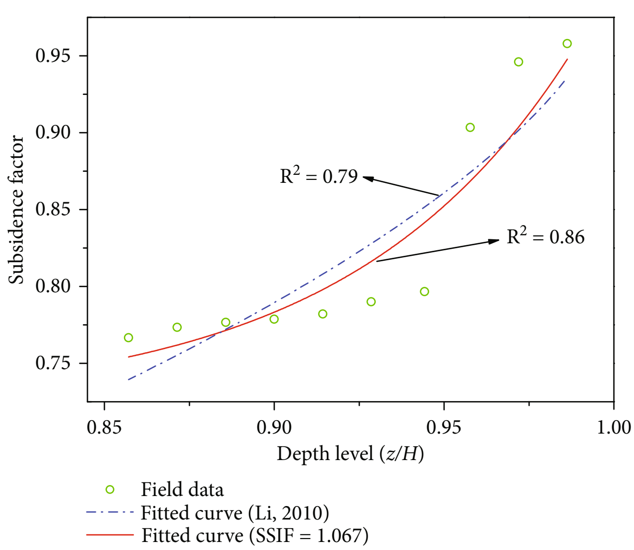

Figure 9: Curves of the subsurface subsidence factor fitted by different methods in Sihe No. 2 Coalmine.

the corresponding fitted values for Li's method are 0.59808 $\pm$ 0.13429 and 0.158 $\pm$ 0.267.

The mean and maximal values for relative error in this method are 0.13% and 5.7%, respectively, while the corresponding errors are 0.38% and 6.6% through Li's method. The smaller mean and maximum error show the higher precision of this method. The mean value and maximal value for relative error in this method are much lesser, showing that this method has higher precision.

It may be observed from the case that the mean error is less than 2%. However, the fitted value of the SSIF is farther greater than 1.0054 that was obtained via statistics. The chief reason is that underground coalmines have a great thickness of overburden strata and the MD/MH ratio exceeds 40. Thence, in practical application, the statistic for subsidence data of strata near the longwall gob is required to implement the fitting, or the parameters in the above-mentioned cases could be adopted to implement the rough estimate. In the next step, further study would be also required for the condition of multi-coal seam mining.

6. Conclusions

Such factors including the surface subsidence factor, maximal vertical expansion value, mining depth, and mining height were utilized to establish the distribution model of the subsurface subsidence factor above the longwall gob. Through data fitting, the correctness of the model is verified, and the conclusions as follows were obtained after analysis and discussion.

The assumption that the vertical expansion value for overburden strata above the longwall gob presents the exponential distribution along with a decrease from the gob to the ground is verified. The subsurface subsidence factor could be calculated by the formula $q_z = 1 - (1 - q_0)(a^{(z/H-1)(H/h)} - 1)/(a^{-(H/h)} - 1)$. In this formula, the SSIF could be obtained through parameter fitting and determine the distribution of the subsurface subsidence factor in the overburden strata. Different geological and mining conditions have different SSIF.

The SSIF, maximal vertical expansion value, and MD/MH ratio influence the subsurface subsidence factor. The greater SSIF means the less surface subsidence factor, and the distribution curve of the subsurface subsidence factor is more curve. The less the linearity for subsurface subsidence factor on each depth level decreases linearly with the increase of vertical expansion value. The influence degree of maximal vertical expansion value in strata approaching gob is farther greater than that in strata near the surface. The subsurface subsidence factor decreases with the increase of the MD/MH ratio. This is because the greater the MD/MH ratio means the greater expandable scope for strata and maximal vertical expansion value. When the SSIF, MD/MH ratio, and maximal vertical expansion value are greater, the strata expansion and subsidence furthermore focus on rock strata near the gob.

The expansion deformation (E-D) factor is defined as $(1 - q_0)/\mathcal{E}_0$ and is a dimensionless parameter, which embodies the relationship between subsurface expansion coefficient and maximal vertical expansion value and describes the comprehensive characteristic of overburden strata induced by mining operations. Based on the method proposed above, through the MD/MH ratio, the relation between surface subsidence and maximal vertical expansion value (bulking factor of a caving zones) is established under the condition of longwall mining. The MD/MH ratio and E-D factor follow the logarithmic relation. The E-D factor exists in the maximum, the range of which is (2.84, 3.40). Considering the limitation of coal seam thickness, when the mining depth reaches a certain degree, the surface expansion coefficient tends to one, while the maximal expansion value tends to a constant value. A study on the E-D factor shows that the surface subsidence factor with the greater MD/MH ratio is more sensitive to change of the maximal vertical expansion value.

The analysis for this case shows that the subsurface subsidence factor calculated by this method is provided with higher precision, and the mean error between the calculated value and measured value is less than 2%. Thence, in the practical application, it is necessary to correct the value of SSIF by adopting the data less than 40-time mining height or estimate roughly using the parameters in the above-mentioned cases.

Data Availability

The data used to support the findings of this study are included within the article.

Disclosure

The funders had no role in the design of the study; in the collection, analyses, or interpretation of data; in the writing of the manuscript; or in the decision to publish the results.

Conflicts of Interest

The authors declare no conflict of interest. The authors identify and declare no personal circumstances or interests that may be perceived as inappropriately influencing the representation or interpretation of reported research results.

Acknowledgments

This work was funded by the National Natural Science Foundation of China (No. 52004172), Distinguished Youth Funds of National Natural Science Foundation of China (No. 51925402), China Postdoctoral Science Foundation funded project (2020M682215), supported by Shanxi Science and Technology Major Project Funds (20201102004), Ten Thousand Talent Program of China for Leading Scientists in Science, Technology and Innovation, Science and Technology Innovation Project of Shanxi Colleges and Universities (2019L0181), Program for the “1331” Key Team of Scientific and Technology Innovation in Shanxi Province.

References

[1] K. Tajduś, “New method for determining the elastic parameters of rock mass layers in the region of underground mining influence,” *International Journal of Rock Mechanics and Mining Sciences*, vol. 46, no. 8, pp. 1296–1305, 2009.

[2] S. Chen, D. Yin, F. Cao, Y. Liu, and K. Ren, “An overview of integrated surface subsidence-reducing technology in mining areas of China,” *Natural Hazards*, vol. 81, no. 2, pp. 1129–1145, 2016.

[3] G. Feng, Y. Yan, S. Yang, B. Zhang, Y. Zhai, and L. Kang, “Analysis on damage zone of overlying strata and safety layer distance on the upward mining above the longwall goaf,” *Journal of China Coal Society*, vol. 8, pp. 1032–1036, 2009.

[4] G. Feng, X. Zhang, J. Li, S. Yang, and L. Kang, “Feasibility on upward mining of the left-over coal above goaf with pillar supporting method,” *Journal of China Coal Society*, vol. 6, pp. 726–730, 2009.

[5] X. Deng, J. Zhang, T. Kang, and X. Han, “Strata behavior in extra-thick coal seam mining with upward slicing backfilling technology,” *International Journal of Mining Science and Technology*, vol. 26, no. 4, pp. 587–592, 2016.

[6] Z.-Q. Xiong, C. Wang, N.-C. Zhang, and G.-M. Tao, “A field investigation for overlying strata behaviour study during protective seam longwall overmining,” *Arabian Journal of Geosciences*, vol. 8, no. 10, pp. 7797–7809, 2015.

[7] C. Wang, N. Zhang, Y. Han, Z. Xiong, and D. Qian, “Experiment research on overburden mining-induced fracture evolution and its fractal characteristics in ascending mining,” *Arabian Journal of Geosciences*, vol. 8, no. 1, pp. 13–21, 2015.

[8] X. Liu, S. Song, Y. Tan et al., “Similar simulation study on the deformation and failure of surrounding rock of a large section chamber group under dynamic loading,” *International Journal of Mining Science and Technology*, vol. 31, no. 3, pp. 495–505, 2021.

[9] X. Wu, J. Wang, J. Li et al., “The principle of invariant stress of the surrounding rock of the hole under the condition of equal pressure in the deep rock mass,” *Shock and Vibration*, vol. 2020, 10 pages, 2020.

[10] B. Qiu and Y. Luo, "Subsurface subsidence prediction model and its potential application for longwall mining operations," *J Xi'an Univ. Sci Tech*, vol. 31, pp. 823–829, 2011.

[11] Y. Luo and B. Qiu, "Enhanced subsurface subsidence," *Mining and Engineering*, vol. 64, no. 10, pp. 78–84, 2012.

[12] L. Tong, L. Liu, Y. Qiu, and S. Liu, "Tunneling in abandoned coal mine areas: problems, impacts and protection measures," *Tunnelling and Underground Space Technology*, vol. 38, pp. 409–422, 2013.

[13] Y. Guo, Y. Zhao, S. Wang, G. Feng, Y. Zhang, and H. Ran, "Stress-strain-acoustic responses in failure process of coal rock with different height to diameter ratios under uniaxial compression," *Journal of Central South University*, vol. 28, no. 6, pp. 1724–1736, 2021.

[14] C. Xu, J. Zhang, K. Wu, R. Chen, and Y. Chen, "Research on parameters in overlying rock of coal mine," *Safety in Coal Mines*, vol. 12, 2013.

[15] C. Li, "Prediction theory and experiment research of overburden and surface movement deformation evolution regulation," *China University of Mining & Technology (Beijing)*, 2010.

[16] J. Xu, G. Lian, W. Zhu, and M. Qian, "Influence of the key strata in deep mining to mining subsidence," *Journal of China Coal Society*, vol. 7, pp. 686–690, 2007.

[17] W. Zhu, J. Xu, X. Shi, X. Wang, and W. Liu, "Research on influence of overburden primary key stratum movement on surface subsidence with in-situ drilling test," *Chinese J.Rock Mech. Eng.*, vol. 2, pp. 403–409, 2009.

[18] M. Qian and X. Miao, "Theoretical analysis on the structural form and stability of overlying strata in longwall mining," *Chinese J.Rock Mech. Eng.*, vol. 2, pp. 97–106, 1995.

[19] J. Xu and M. Qian, "Study on the influence of key strata movement on subsidence," *Journal of China Coal Society*, vol. 2, pp. 122–126, 2000.

[20] K. Wu, J. Ge, L. Wang, and M. Zhou, *Unify Method of Mining Subsidence Prediction*, China University of Mining and Technology Press, Xuzhou, 1998.

[21] D. Zhou, K. Wu, X. Miao, and L. Li, "Combined prediction model for mining subsidence in coal mining areas covered with thick alluvial soil layer," *Bulletin of Engineering Geology and the Environment*, vol. 77, no. 1, p. 283, 2018.

[22] X. Jia, *Rock Mechanics and Strata Control*, China University of Mining and Technology press, Xuzhou, 2010.

[23] D. Munson and S. Benzley, "Analytic Subsidence Model Using Void-Volume Distribution Functions," in *in The 21st US Symposium on Rock Mechanics (USRMS)*, American Rock Mechanics Association, 1980.

[24] J. M. Listak, J. L. Hill, and J. C. Zelanko, *Direct Measurement of Longwall Strata Behavior: A Case Study*, vol. 9040, US Department of the Interior, Bureau of Mines, 1986.

[25] B. An, X. Miao, J. Zhang, F. Ju, and N. Zhou, "Overlying strata movement of recovering standing pillars with solid backfilling by physical simulation," *International Journal of Mining Science and Technology*, vol. 26, no. 2, pp. 301–307, 2016.

[26] S. S. Peng, *Coal Mine Ground Control*, 1978.

[27] K. Deng, M. Zhou, Z. Tan, and N. Xu, "Study on laws of rock mass breaking induced by mining," *Journsl China Univ. Min. Tech.*, vol. 3, pp. 43–46, 1998.

[28] Y. Wang, K. Deng, D. Zhang, and M. Zhou, "The study on the character of strata subsidence during repeat mining," *Journal of China Coal Society*, vol. 5, pp. 24–29, 1998.

[29] H. Yavuz, "An estimation method for cover pressure reestablishment distance and pressure distribution in the goaf of longwall coal mines," *International Journal of Rock Mechanics and Mining Sciences*, vol. 41, no. 2, pp. 193–205, 2004.

[30] S. C. I. Bureau, *Mining Rules of Coal Pillars Preservation of Main Roadway and Compressed Coal under Buildings, State Coal Industry Bureau, Editor*, China Coal Industry Publishing Home, Beijing, 2000.

[31] V. Palchik, "Bulking factors and extents of caved zones in weathered overburden of shallow abandoned underground workings," *International Journal of Rock Mechanics and Mining Sciences*, vol. 79, pp. 227–240, 2015.

[32] G. Zhang, F. Li, S. Li, and K. Deng, "Change of subsidence factor on the law of rock mass rupture," *J.China Coal Soc.*, vol. 6, pp. 977–981, 2013.

Hindawi
Geofluids
Volume 2022, Article ID 5733695, 8 pages
https://doi.org/10.1155/2022/5733695

Research Article

Feasibility of Water Injection on the Coal Wall of Loose Thick Coal Seam to Prevent Rib Spalling and Its Optimal Moisture Content

Jian Sun, Bin Li, Ruofei Zhang, and Zhou Huang

State Key Laboratory of Mining Response and Disaster Prevention and Control in Deep Coal Mines, School of Mining Engineering, Anhui University of Science and Technology, Huainan 232001, China

Correspondence should be addressed to Jian Sun; sj323@cumt.edu.cn

Received 20 May 2021; Accepted 2 March 2022; Published 21 March 2022

Academic Editor: Qingquan Liu

Rib spalling of loose thick coal wall seriously restricts the high yield, high efficiency of coal mine, affecting the safety production of coal mine. Based on the engineering background of water injection to control rib spalling of loose thick coal seam in the Luling Coal Mine of the Huaibei Mining Group, the mineral composition and microscopic morphology of III811 loose thick coal seam in Luling Coal Mine were analyzed by X-ray diffraction and scanning electron microscope. Through uniaxial compressive strength tests of coal samples with different moisture content, the relationship between uniaxial compressive strength, peak strain and moisture content, and their failure characteristics was studied. The results showed that the natural moisture content of III811 coal seam in Luling coal mine is low, and it contains a large amount of kaolinite (75.2%) belonging to clay mineral which is easy to absorb water and then expand, fully bond loose coal body and fill cracks to improve the integrity of coal body. These two factors provide feasibility for injecting water in workface to prevent rib spalling. The compressive strength of coal samples decreased slowly with the raise of moisture content, while the peak strain increased first and then decreased. The peak strain was the largest when the water content was 6.0%. The failure degree of coal samples intensifies with the increase of water content, and the failure form changes from tensile failure at low water content to shear failure at high water content. Considering the relationship between compressive strength, peak strain, and moisture content of coal samples, the optimal moisture content of III811 workface in loose thick coal seam is determined to be 4.5% ~6%.

1. Introduction

In recent ten years, in all coal mine accidents in China, the casualties due to roof accidents caused by rib spalling and roof caving account for 43% of all underground accidents. The rib spalling and roof caving pose a great threat to the production of workface and seriously affect advance speed and output of workface [1–4]. In the process of loose thick coal seam mining, because of the loose coal body and a higher workface mining height, the coal body fissure in front of the workface develops, and the rib spalling and roof caving are more serious [5, 6].

The stability of the coal wall can be enhanced by optimizing the advance speed of the workface, controlling the reasonable height of the workface and ensuring the reasonable support strength of the support, or changing the physical and mechanical parameters of the coal body by physical and chemical methods [7–10]. Due to the characteristics of loose coal seam, its compressive strength is low, and its bearing capacity is weak. It is particularly important to take physical and chemical methods to improve the mechanical properties and structure of coal body for the prevention of rib spalling [11, 12]. A large number of engineering practices showed that reasonable water injection in coal wall for soft coal seam with large mud content can effectively improve the cohesiveness, reduce the rib spalling and roof caving accidents. Cheng et al. [13] studied the stability of the surrounding rock of the workface after water injection. It shows that after water injection, the peak value of abetment pressure in front of the coal wall shifts to the deep, the pressure relief zone and plastic zone increase, the compression deformation of the coal body increases, and the water injection is beneficial to improve the stress state and enhance the stability of the coal wall. Wang et al. [14] analyzed the limit condition of coal wall failure and adopted FLAC^{3D} simulation to analyze the effect law of different water injection pressure on vertical stress distribution and compression of coal wall and coal body in front of workface. The results showed that water injection can increase the compression of coal wall and reduce the elastic energy of coal body. Yang et al. [15] used intermittent water injection technology to increase the moisture content of the coal seam from 4% to 5% ~6% and reduce the range of rib spalling from 50% ~70% to 10% ~30%. The problem of rib spalling is effectively solved by water injection. Yao et al. [16] conducted variable-angle shear test (compression-shear test) and research on the mechanism of crack propagation and strength weakening on coal samples with different moisture content in the 4-2 coal seam of the Meihuajing Coal Mine of Shenhua Ningxia Coal Industry. It showed that the main cracks of the dry coal samples exist along the shear plane, while the fracture surface of the saturated coal samples deviated from the shear plane and formed many irregular shear cracks. The shear strength, cohesion, and internal friction angle of the coal samples decreased linearly or exponentially with moisture content. Zhang et al. [17] conducted direct shear test on coal samples with different moisture content in Yiluo coal seam and used the X ray diffraction (XRD) to analyze the influence of different moisture content and clay minerals (kaolinite, montmorillonite, illite) to the bond strength of coal, and it showed that when the moisture content increased from 6.6% to 17.6%, bond strength increased and then decreased with increasing moisture content, determined that of 17.6% is the best moisture content to improve the stability of Yiluo coal seam. Zhou et al. [18] used extremely soft coal to make coal samples and conducted direct shear experiments under different moisture content and normal stress. The results showed that the cohesive of the coal samples increases first with the raise of the moisture content and reaches the optimum moisture content (about 17.64%), and the cohesive decreases with the raise of the moisture content; the moisture content has no obvious effect on the internal friction angle of the coal samples. Zhen et al. [19] used ultra-high speed digital image to analyze the influence of moisture content on the deformation trend and failure characteristics of extremely soft coal samples. It is shown that the dynamic stress-strain curve of coal samples consist of four stages. With the raise of moisture content, the brittleness of coal samples decreased and the plasticity increased. Wang et al. [20] carried out the uniaxial compression tests on coal samples with different moisture content. The results showed that with the raise of moisture content, the range of the stress-strain curve of coal samples increased in the compaction stage, decreased in the elastic stage, and became more significant in the yield stage. There was a negative linear relationship between compressive strength and moisture content, a positive linear relationship between peak strain and moisture content, and a negative exponential relationship between elastic modulus and moisture content.

The above researches are not accurate enough to influence factors of coal seam water injection, such as the feasibility of coal seam water injection and the optimal moisture content. In this paper, the water injection on the coal wall of loose thick coal seam to prevent rib spalling in the Luling Coal Mine of the Huaibei Mining Group was used as the engineering background, and the mineral composition and microscopic morphology of III811 loose thick coal seam in the Luling Coal Mine were analyzed by X-ray diffraction and scanning electron microscope. Through uniaxial compressive strength and shear strength tests, the relationship between uniaxial compressive strength, peak strain and moisture content of coal samples with different moisture contents, and their failure characteristics was studied. The research results are conducive to reveal the feasibility of water injection to prevent rib spalling and the optimum moisture content of coal seam in III811 workface of the Luling Coal Mine.

2. Feasibility of Water Injection on Loose Thick Coal Wall to Prevent Rib Spalling

2.1. Project Background. III811 workface in the Luling Coal Mine of the Huaibei Mining Group is located in one mining area in the east of the third level of the mine, mainly mining 8# and 9# coal seams. The thickness of 8# coal seam is 3.33~14.75 m with an average of 8.25 m, which belongs to stable coal seam. The thickness of 9# coal seam is 0 ~ 4.25 m, with an average of 1.21 m, which belongs to extremely unstable coal seam. III811 workface is mostly combined area of 8# and 9# coal seam, and inclination is 15° ~28° with an average of 20°, for gently inclined thick coal seam. The hardness coefficient of coal seam is 0.16~0.53, the whole coal seam is loose and extremely soft, and the joints are developed. The direct roof of III811 workface is mudstone with an average compressive strength of 14.92 MPa and tensile strength of 0.68 MPa. The direct floor is sandy mudstone with an average compressive strength of 15.07 MPa and with an average tensile strength of 1.04 MPa. The coal seam of III811 workface is a typical loose, extremely soft, thick coal seam, and the strength of the roof and floor strata is low.

In addition, in order to improve the recovery rate of coal resources, the III811 loose thick coal seam workface using a full high fully mechanized caving mining technology caused that the rib spalling of coal wall is serious in mining process, seriously affecting the safety of coal mine production and mining progress. Therefore, it is necessary to carry out the research of feasibility of water injection on the coal wall of loose thick coal seam to prevent rib spalling and its optimal moisture content, in order to achieve III811 loose thick coal seam workface of Luling Coal Mine safety, efficient mining.

2.2. Mineral Composition of Coal Seam

2.2.1. Test Coal Sample. Figure 1 shows the coal sample and test instrument for the mineral composition of coal seam. The test coal sample was taken from III811 workface of the Luling Coal Mine of the Huaibei Mining Group. The coal at III811 workface was ground into powder, and the coal

(a) Coal sample (b) X-ray diffractometer

Figure 1: Coal seam mineral component testing.

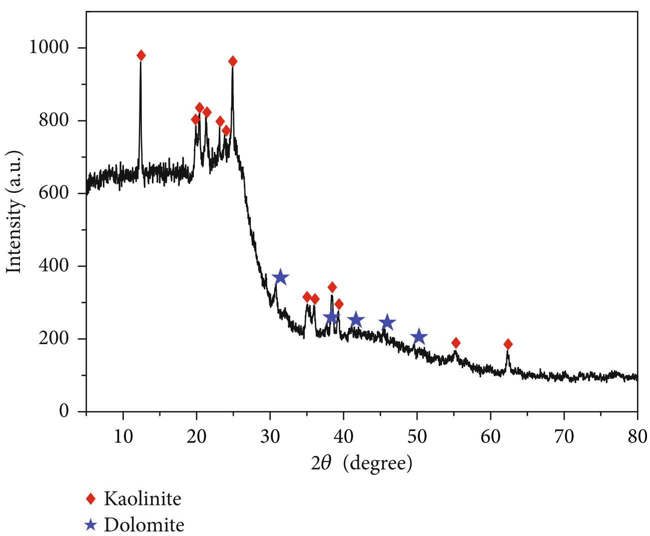

Figure 2: X-ray diffraction pattern of mineral components in coal sample.

sample (above 50 mg) was identified and analyzed by X-ray diffractometer. The principle is to compare the lattice plane spacing and diffraction intensity measured on the material with the diffraction data of the standard phase; so, the mineral composition of the coal seam at III811 workface can be determined.

2.2.2. Test Results. Figure 2 shows the X-ray diffraction pattern of mineral components in the test coal sample. It can be seen that the mineral composition of the coal seam at III811 workface of the Luling Coal Mine is mainly dolomite and clay mineral kaolinite. Kaolinite has a content of up to 75.2% in the test coal sample. It is characterized by soft quality, strong water absorption, and easy expansion in water absorption. It is easy to disperse and suspend in water and has good plasticity and high adhesion. The existence of large amounts of clay mineral kaolinite in the coal seam of the III811 workface provides the feasibility for preventing the rib spalling of coal wall by water injection in the Luling Coal Mine.

2.3. Microscopic Morphology of Coal Samples

2.3.1. Test Equipment. Figure 3 shows the microscopic morphology coal samples for testing and test equipment (scanning electron microscope). The test coal sample was taken from III811 workface of the Luling Coal Mine of the Huaibei Mining Group. The lump size of the test coal sample is 1 cm^3. FlexSEM 1,000 scanning electron microscope was used to observe the pore and crack structures and their distribution characteristics of the coal samples for testing. The principle is to scan the surface of the coal sample through the electron beam emitted and focused by the electron gun and stimulate the coal sample to produce various types of physical signals. After signal detection, video amplification, and signal processing, the scanning image that can reflect the surface characteristics of the coal sample can be read out on the fluorescent screen.

2.3.2. Test Results. Figure 4 shows the microcracks of the coal sample for testing at different magnification ratios. When the coal sample was magnified to 500 times, it can be seen that the coal sample is seriously damaged and attached with many crushed particles, as shown in Figure 4(a). When the coal sample was magnified to 5,000 times, a fine crack could be seen in the coal sample and the crack fracture was smooth, indicating that the coal sample was a brittle fracture, as shown in Figure 4(b).

Figure 5 shows the adhesion of coal sample particles under different magnifications. When the coal sample is magnified to 500 times, it can be seen that the integrity of the coal sample is poor, and a large number of tiny particles are attached, indicating that the coal sample is loose, as shown in Figure 5(a). When the coal sample is magnified to 5,000 times, it can be seen that the particle surface of the coal sample is smooth, indicating that the coal sample is prone to brittle fracture and has a low moisture content, as shown in Figure 5(b).

3. Optimum Moisture Content of Water Injection on Loose Thick Coal Wall to Prevent Rib Spalling

After injecting water into coal seam, the water molecules bound to the surface of coal will pull the particles closer and pick up it tighter in the loose coal seam through its connection effect which has a more obvious influence on the mechanical properties of the coal in the loose coal seam. However, if inject too much water, too high moisture content in this test which leads to the connecting force weakened, and friction reduced between loose coal particles because water plays a role of lubrication. The most hydrophilic rocks are clay minerals, and the rocks with more clay minerals are also most affected by water. Therefore, it is necessary to accurately control the moisture content and improve its ability of preventing rib spalling.

3.1. Preparation of Coal Samples with Different Moisture Contents. The coal samples were selected from III811 workface of the Luling Coal Mine. After being crushed by the

Figure 3: Test coal sample and scanning electron microscope.

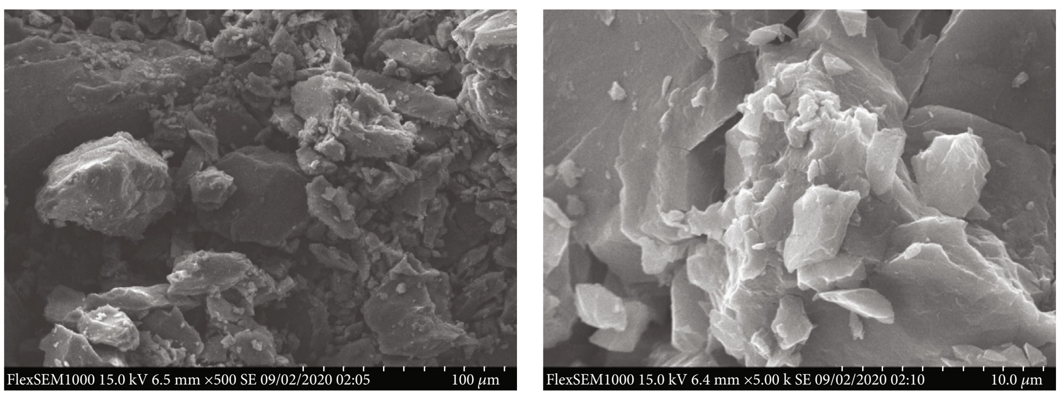

(a) 500 times

(b) 5,000 times

Figure 4: Microcracks in coal sample at different magnification ratios.

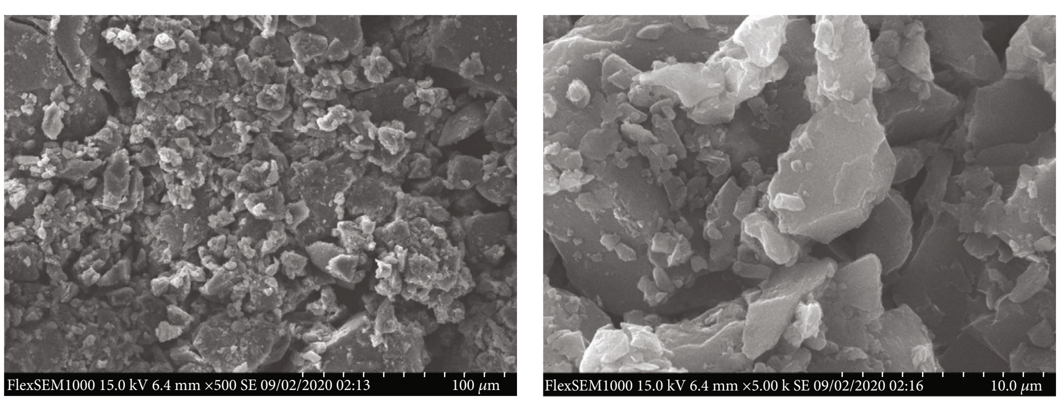

(a) 500 times

(b) 5,000 times

Figure 5: Particle attachment of coal sample under different magnification.

mill, pulverized coal particles of more than 0.25 mm and less than 1 mm were screened by classification and placed in a 105°C constant temperature drying box for drying. Mixed the water with the pulverized coal particles dried in a certain proportion and stir evenly and weighed mixture of a certain quality by using an electronic balance and put into the briquette pressing mold. Through a universal experimental machine (pressure 50 kN and maintain constant pressure 10 min), the mixture is pressed into $\Phi 50 \times 100$ mm, used for compressive strength test.

Figure 6 shows the variation curve of the moisture content of the coal sample with drying time. It can be seen that drying under the condition of constant temperature at 105°C, the moisture content of the coal sample decreased

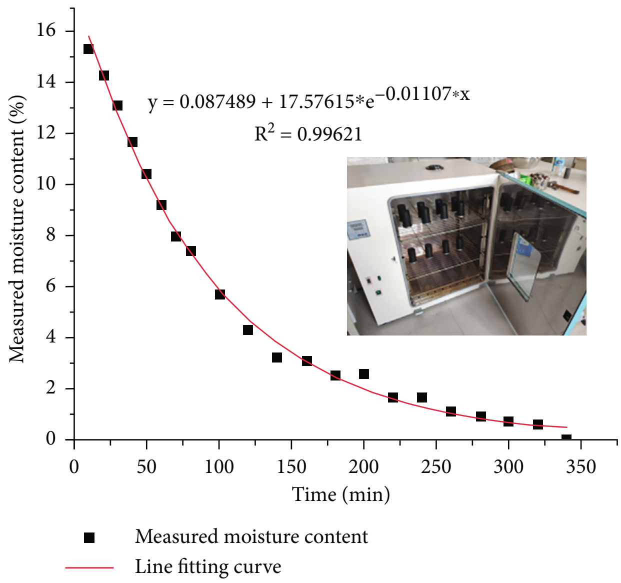

Figure 6: Variation curve of moisture content of coal sample with drying time.

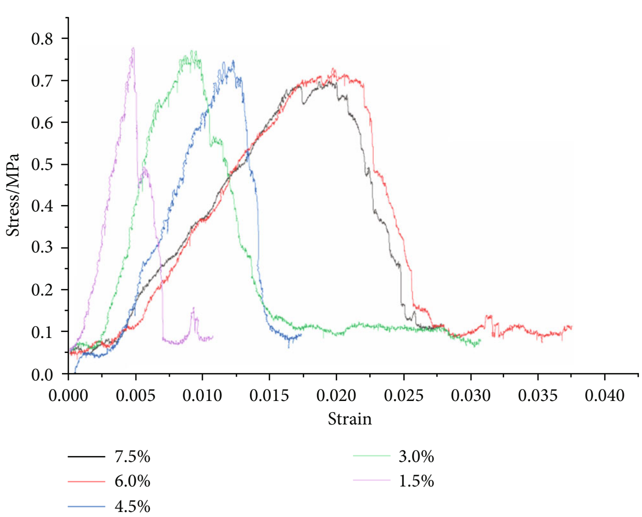

Figure 7: Total stress-strain process curves of coal samples with different moisture contents.

exponentially with the increase of drying time, especially in the early stage, and the moisture content decreased rapidly. In addition, it can be seen that the variation curve of the moisture content of the coal sample with drying time has a high fitting degree ($R^2 = 0.99621$). Therefore, coal samples with different moisture contents can provide reliable data support for compressive strength test and shear strength test. As can be seen from Figure 6, when drying for 345 minutes, the coal sample had the same weight twice as before and after; so, its moisture content can be considered to be 0. When the moisture content is 15%, the coal sample is considered to be in the state of saturation. According to the variation curve of moisture content with drying time (Figure 6), briquette with different moisture contents (1.5%, 3.0%, 4.5%, 6.0%, and 7.5%) can be obtained by drying the prepared briquette for different drying time, which can be used for compressive strength test.

3.2. Stress-Strain Curves of Coal Samples with Different Moisture Contents under Uniaxial Compression. Figure 7 shows the complete stress-strain process curves of coal samples with different moisture contents. It can be seen that in the process of uniaxial compression, coal samples with different moisture contents all go through four stages, including pore fracture compaction stage, elastic stage, yield stage, and postfracture stage. At the initial loading stage of coal samples with different moisture contents, there is a compaction stage, pulverized coal particles and tiny pores in the coal samples gradually close with the increase of load, and the stress of coal samples increases slowly with the increase of strain. After the compaction stage, the original microcracks of the coal samples had basically closed and began to enter the elastic stage. At this stage, the new cracks in the coal sample had not yet appeared, the overall structure was relatively stable, and the relationship between stress and strain shows a "linear growth." With the raise of axial stress, small cracks began to appear inside the coal samples. The development of cracks destroyed the stable state of the coal samples, and the coal samples entered the yield stage, in which the relationship between stress and strain presents a "nonlinear growth," and the increased rate of stress slows down. When the coal samples reach the peak strength, the internal structural failure occurred. After the coal samples passed the yield stage, the internal cracks developed rapidly, and many cracks appeared on its surface. After continuous loading, the coal samples did not fail and become unstable immediately, indicating that the loose coal still has a certain residual bearing strength after the peak strength. The water-bearing coal samples did not show obvious brittle failure after the peak strength but show certain ductility and plastic deformation in the complete stress-strain curve, that is the post-fracture stage.

By comparing the complete stress-strain curves of coal samples with different moisture contents, it is found that with the raise of moisture content, the compaction stage of coal samples gradually becomes longer and the elastic stage becomes longer, and the slope of stress-strain curve in the elastic stage also decreases; that is, the elastic modulus of coal samples decreases with the increase of moisture content. With the increase of moisture content, the yield stage of coal samples is gradually obvious, the peak strength decreases, and the peak strain increases gradually. Especially when the moisture content increases from 4.5% to 6.0%, the strain increases significantly and then decreases slightly (7.5%). After the peak strength, the deformation and failure characteristics of coal samples with different moisture content were similar, none of which showed obvious brittle failure, but obvious plastic failure, and there was a certain residual deformation. It should be noted that the coal samples with higher moisture content have strong compressive deformation resistance during the compression process and can withstand pressure for a long time to realize the overall expansion of the coal samples. The postpeak displacement is also large, which indicates that the maximum axial strain

Table 1: Mechanical parameters of coal samples with different moisture contents under uniaxial compression.

Moisture content/%	Coal samples	Compressive strength/MPa	Average/MPa	Elastic modulus/GPa	Average/GPa	Peak strain	Average
	1-1	0.77962		0.18690		0.00469	
1.5	1-2	0.77465	0.77656	0.18346	0.185	0.00478	0.00472
	1-3	0.77541		0.18464		0.00468	
	2-1	0.76758		0.13323		0.00908	
3.0	2-2	0.77082	0.77003	0.12809	0.132	0.00906	0.00907
	2-3	0.77169		0.13468		0.00907	
	3-1	0.74722		0.08045		0.01209	
4.5	3-2	0.74359	0.74599	0.07817	0.08	0.01214	0.01212
	3-3	0.74716		0.08138		0.01213	
	4-1	0.72881		0.04609		0.01966	
6.0	4-2	0.72347	0.72737	0.04546	0.046	0.01932	0.01956
	4-3	0.72983		0.04645		0.0197	
	5-1	0.69487		0.04503		0.01923	
7.5	5-2	0.69761	0.69707	0.04413	0.045	0.01934	0.01928
	5-3	0.69873		0.04584		0.01926	

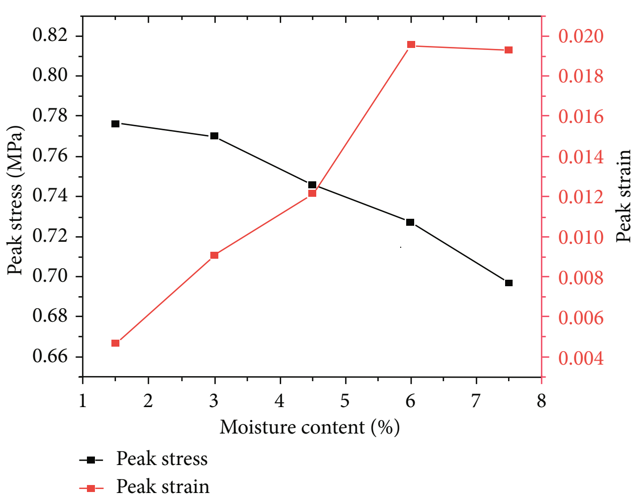

Figure 8: Relationship between compressive strength and peak strain of coal samples with different moisture contents.

of coal samples can increase with the raise of moisture content. Macroscopically, the plastic deformation of coal wall can increase with the raise of moisture content.

3.3. Uniaxial Compressive Strength of Coal Samples with Different Moisture Contents. Uniaxial compressive strength tests were carried out on 5 groups of coal samples with different moisture contents (1.5%, 3.0%, 4.5%, 6.0%, and 7.5%), with 3 test samples in each group and a total of 15 coal samples. During the uniaxial compression test, the universal testing machine adopts displacement control, and the loading rate is 3 mm/min. During the loading process, the failure characteristics of test coal samples are observed and obtain mechanical parameters (compressive strength, elastic modulus, and peak strain) of coal samples with different moisture contents under uniaxial compression load, as shown in Table 1.

As can be seen from Table 1, with the increase of moisture content, the uniaxial compressive strength of coal samples shows a slight downward trend, and the peak strain first increases and then decreases. When the moisture content is 6.0%, the peak strain is the largest. The elastic modulus decreases gradually with the increase of moisture content, and the rate of descent is the fastest when the moisture content is 6.0%, which is about 42.5% less than when the moisture content is 4.5%. When the moisture content is 7.5%, the rate of descent of elastic modulus becomes slow and only decreases by 2% compared with 6.0% moisture content. The elastic modulus refers to secant modulus. The elastic deformation before samples' failure increases gradually due to the binding effect of water on mineral particles, and the peak stress decreases slowly because the softening effect of water on samples is little. When the moisture content is exorbitant, the peak stress decreases further, and the elastic deformation before failure decreases gradually because the lubrication of water on mineral particles plays a dominant role.

Figure 8 shows the relationship between compressive strength, peak strain, and moisture content of coal samples with different moisture contents. It can be seen that the compressive strength of coal samples decreases slowly with the increase of water content, while the peak strain increases first and then decreases with the increases of moisture content. When the moisture content is 1.5%, the compressive strength of the coal sample is 0.77656 MPa, and the peak strain is 0.00472. When the moisture content is 4.5%, the compressive strength of the coal sample is 0.74599 MPa, and the peak strain is 0.01212. Compared with the moisture content of 1.5%, the compressive strength of the coal sample decreases by 3.93%, and the peak strain increases by 176.19%. The increase of moisture content greatly improves the plastic deformation of the coal samples. When the moisture content increases to 6.0%, the compressive strength of

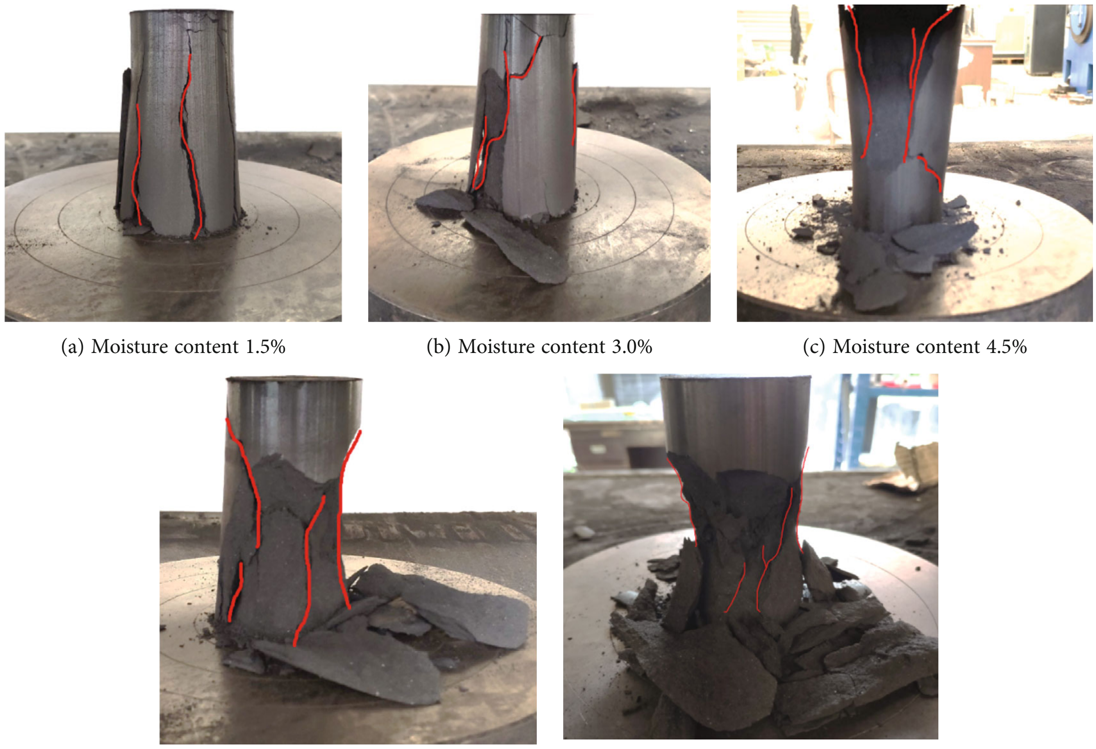

(a) Moisture content 1.5%
(b) Moisture content 3.0%
(c) Moisture content 4.5%
(d) Moisture content 6.0%
(e) Moisture content 7.5%

Figure 9: Failure characteristics of coal samples with different moisture contents.

the coal sample decreases slightly to 0.72737 MPa, while the peak strain increases to 0.01956, which is 60% higher than when the moisture content is 4.5%, and the peak strain reaches the maximum at this time. Therefore, considering the compressive strength and peak strain of coal samples, the optimal range of moisture content of coal seam is 4.5% ~6.0%, which can ensure that the coal wall of Luling Coal III811 workface has a certain compressive strength, and also provide maximum plastic deformation without damage.

3.4. Failure Characteristics of Coal Samples with Different Moisture Contents under Uniaxial Compression. Figure 9 shows the failure forms of coal samples with different moisture contents (1.5%, 3.0%, 4.5%, 6.0%, and 7.5%) under uniaxial compression. It can be seen that the failure degree of coal samples increases with the increasing of moisture content, and its failure form also changes. When the moisture content is 1.5% and 3.0%, the coal samples are mainly tensile failure, and there are two obvious tensile failure cracks. With the increase of water content (4.5%, 6.0%), the coal samples show x-shaped conjugate inclined plane shear failure, and the degree of breakage also increases. When the moisture content increases further (7.5%), the coal samples gradually become the main shear failure, and the degree of breakage is further intensified.

4. Conclusions

(1) The mineral composition and microscopic morphology of III811 loose thick coal seam in the Luling Coal Mine were analyzed by X-ray diffraction and scanning electron microscope. There is a large amount of clay mineral kaolinite (75.2%) in the coal seam of III811 workface. It has the characteristics of soft quality, strong water absorption, and easy expansion of water absorption. It has good plasticity and high adhesion. In addition, there are more small cracks in the coal seam and more pulverized coal particles, and the natural moisture content is low, which provides the feasibility for III811 loose thick coal seam workface through water injection to prevent and control the rib spalling of coal wall

(2) Through uniaxial compressive strength test of coal samples, the relationship between uniaxial compressive strength, peak strain, and moisture content of III811 loose thick coal seam in the Luling Coal Mine was studied. With the raise of moisture content, the compressive strength of coal samples decreases slowly, while the peak strain increases first and then decreases. When the moisture content is 4.5%, the compressive strength is 0.74599 MPa, and the peak strain is 0.01212. When the moisture content increases to 6.0%, the compressive strength decreases slightly to 0.72737 MPa, while the peak strain increases to 0.01956. At this time, the peak strain reaches the maximum, indicating that increasing the moisture content can increase the plastic deformation of the coal wall

(3) As the moisture content increases, the degree of coal samples' failure intensifies, and its failure form

changes accordingly. When the moisture content is 1.5% and 3.0%, the coal samples are mainly tensile failure. With the increase of water content (4.5%, 6.0%), the coal samples show x-shaped conjugate inclined plane shear failure, and the degree of breakage also increases. When the water content is further increased (7.5%), the coal sample gradually becomes the main shear failure, and the degree of breakage is further intensified

(4) Considering the compressive strength, peak strain, and moisture content of coal samples, the optimal range of water content of coal seam is determined to be 4.5% ~6.0%, which can guarantee the coal wall of Luling coal III811 loose thick coal seam workface with certain compressive strength and large plastic deformation

Data Availability

Without any supplementary materials for this study, all the data, table, and picture have been presented in the paper.

Conflicts of Interest

The authors declare that they have no conflicts of interest regarding the publication of this paper.

Acknowledgments

This study was supported by the National Natural Science Foundation of China (No. 51974010).

References

[1] W. Jiachen, "Mechanism of the rib spalling and the controlling in the very soft coal seam," *Journal of China Coal Society*, vol. 32, no. 8, pp. 785–788, 2007.

[2] W. Yongping, L. Ding, and X. Panshi, "Mechanism of disaster due to rib spalling at fully-mechanized top coal caving face in soft steeply dip-ping seam," *Journal of China Coal Society*, vol. 41, no. 8, pp. 1878–1884, 2016.

[3] W. Sheng, L. Liping, C. Shuai et al., "Study on an improved real-time monitoring and fusion prewarning method for water inrush in tunnels," *Tunnelling and Underground Space Technology*, vol. 112, article 103884, 2021.

[4] X. Yi, T. Teng, D. Faning, M. Zongyuan, W. Songhe, and X. Haibin, "Productivity analysis of fractured wells in reservoir of hydrogen and carbon based on dual-porosity medium model," *International Journal of Hydrogen Energy*, vol. 45, no. 39, pp. 20240–20249, 2020.

[5] T. Yuan Yong, M. X. Shihao, S. Lulu, and B. Qingsheng, "Coal wall stability of fully mechanized working face with great mining height in "Three soft" coal seam and its control technology," *Journal of Mining & Safety Engineering*, vol. 29, no. 1, pp. 21–25, 2012.

[6] Y. A. N. G. Ke, H. E. Xiang, L. I. U. Shuai, and L. U. Wei, "Rib spalling mechanism and control with fully mechanized longwall mining in large inclination "Three-soft" thick coal seam under closed distance mined gob," *Journal of Mining & Safety Engineering*, vol. 33, no. 4, pp. 611–617, 2016.

[7] H. Xinzhu and X. Guangxiang, "Coal wall spalling mechanism and control technology of fully mechanized high cutting longwall coal mining face," *Coal Science and Technology*, vol. 9, p. 1-3+24, 2008.

[8] X. Yongxiang, W. Guofa, X. Li Mingzhong, Z. C. Yajunl, and Z. Jinhu, "Mechanism of blabbed spalling failure of the coal face in fully mechanized caving face with super large cutting height," *Journal of Mining & Safety Engineering*, vol. 38, no. 1, pp. 19–30, 2021.

[9] Y. Ning, "Mechanism and control technique of the rib spalling in fully mechanized mining face with great mining height," *Journal of China Coal Society*, vol. 34, no. 1, pp. 50–52, 2009.

[10] Y. Xiwen, Y. Shaohong, and Y. An, "Characters of the rib spalling in fully mechanized caving face with great mining height," *Journal of Mining & Safety Engineering*, vol. 2, pp. 222–225, 2008.

[11] Y. Shengli and K. Dezhong, "Flexible reinforcement mechanism and its application in the control of spalling at large mining height coal face," *Journal of China Coal Society*, vol. 40, no. 6, pp. 1361–1367, 2015.

[12] Y. Jingjing, W. Fei, L. Yucheng, and G. Yabin, "A feasibility study of coal seam water injection processes: the effects of coal porosity and mass flow rates of injected water on wetting radii," *Energy & Fuels*, vol. 34, no. 12, pp. 16956–16967, 2020.

[13] C. Cai, *Study on Rule and Technological Parameters of Water Injection to Strengthen Stability of Soft Coal Wall*, China University of Mining and Technology, 2014.

[14] W. Jiaqi and L. Song, "Study on condition of coal wall spalling in large height mining and rising stability by water flooding," *Coal Technology*, vol. 36, no. 12, pp. 60–63, 2017.

[15] Z.-g. YANG, J.-h. TIAN, L.-y. ZHANG, J.-w. QIAO, and O. U. Ya-wei, "Dust prevention with deep borehole water injection and spalling prevention with grouting in unstable seam with soft roof, coal and floor," *Coal Science and Technology*, vol. 40, no. 9, pp. 60–63, 2012.

[16] Y. Qiangling, T. Chuanjin, X. Ze et al., "Mechanisms of failure in coal samples from underground water reservoir," *Engineering Geology*, vol. 267, article 105494, 2020.

[17] H. Zhang, Z. Wan, D. Ma, B. Zhang, and P. Zhou, "Coupled effects of moisture content and inherent clay minerals on the cohesive strength of remodelled coal," *Energies*, vol. 10, no. 8, p. 1234, 2017.

[18] Z. Peng and Z. Bo, "Experimental study on water sensitivity of shear strength of extremely soft coal seam," *Coal Science and Technology*, vol. 45, no. 5, pp. 103–108, 2017.

[19] Z. Wei, K. Yang, C. Xiaolou, X. He, Z. Xinyuan, and Z. Jiqaing, "Dynamic tensile properties, deformation, and failure testing of impact-loaded coal samples with various moisture content," *Scientific Reports*, vol. 11, no. 1, 2021.

[20] K. Wang, Y. F. Jiang, and C. Xu, "Mechanical properties and statistical damage model of coal with different moisture contents under uniaxial compression," *Chinese Journal of Rock Mechanics and Engineering*, vol. 37, no. 5, pp. 1070–1079, 2018.

Hindawi
Geofluids
Volume 2022, Article ID 6464564, 19 pages
https://doi.org/10.1155/2022/6464564

Research Article

Application and Research of Gangue Partial-Filling Mining Method in Preventing Water Inrush from Floor

Zhenzhong Pang,[1,2] Xinguo Zhang ,[3] Juntao Chen,[3] and Feifan Li[4]

[1]*Collage of Geoscience and Surveying Engineering, China University of Mining & Technology, Beijing 100083, China*
[2]*National Engineering Research Center of Coal Mine Water Hazard Controlling, Beijing 100083, China*
[3]*College of Energy and Mining Engineering, Shandong University of Science and Technology, Qingdao 266590, China*
[4]*Inner Mongolia Gucheng Mining Co., Ltd, Zhungeer Banner, 016215, China*

Correspondence should be addressed to Xinguo Zhang; pzz17864292900@163.com

Received 14 September 2021; Revised 7 November 2021; Accepted 24 February 2022; Published 21 March 2022

Academic Editor: Jianwei Cheng

Coal gangue produced during coal production not only poses a serious threat to the ground environment but also imposes serious economic burdens on the mine. The partial-filling mining (PFM) method proposed in this paper can make full use of coal gangue and is of great significance to the prevention and control of water disasters at the working face. The specific process used to implement this method is to first divide the working face into several narrow working faces and then fill the filling body into part of the goaf. The ability of PFM to restrain floor water inrush is analyzed by physical simulation, and the field application research is carried out at the No. 9211 mining face of Bucun Coal Mine in Shandong, China. The physical simulation results show that the failure depth of this layer is less than 5 m. The field measurements reveal that the maximum compression deformation of the filling body is 89.1 mm, and the maximum floor failure depth of the floor is only 8.6 m. Comparative analysis indicates that the floor failure depth of the No. 9211 working face with the local filling method is 4.6 m lower than that of the No. 9110 working face with the strip mining method. In addition, no water inrush accident occurs at the No. 9211 working face during mining. Therefore, PFM not only controls the floor damage depth effectively but also consumes coal gangue to protect the mine environment.

1. Introduction

In recent years, coal, as an important energy source, has made important contributions to China's economic development. However, due to the increasingly complex geological conditions encountered during coal resource excavation, there are many "secondary disasters" in mines, such as water inrush accidents, rock bursts, roof fall accidents, surface subsidence, and the creation of surface gangue hills [1–4]. These "secondary disasters" have had important impacts on continued mining development. In mining, mine water is not only a groundwater resource but also a potential threat that has become more important due to increases in mining depths and therefore the hydraulic pressures [5, 6]. More than 25 billion tons of coal resources are at risk of water inrush from the floor, especially in deep Permo-Carboniferous coal seams in the central and eastern parts of northern China [7–11]. Therefore, determining how to exploit resources threatened by a floor water inrush is an important main problem for scientific researchers and is important to continued mine development. The formation of water-conducting channels is the main cause of water inrush accidents under the premise of determining the water abundance and filling intensity of aquifers. Therefore, it is necessary to prevent and control the formation of water-conducting channels.

The formation of water-conducting channels is affected by many factors. The dynamic failure process and prevention measures have been investigated using the following approaches. First, several floor rock fracture evolution theories have been developed based on the theory of elastic-plastic mechanics. These include the under three-zone theory, the strong seepage theory, and the rock-water stress relationship theory [12–15].

Second, the formation and evolution of water-conducting channels under the combined action of rock pressure and confined water have been analyzed via numerical and physical simulations. For example, Cao et al. [16] established a numerical calculation model of roof collapse column water inrush using UDEC software and studied the influence of mining on roof collapse column water inrush. Lu and Wang [17] analyzed the control effects of propulsion distance, rock heterogeneity, and water pressure on inrushing water via numerical simulations. Liu et al. [18] proposed a new formation microscanning imaging method such that the results could directly reflect subtle changes in wellbore fractures. They used UDEC software to simulate the process by which water flow from fractured-zone height evolves. Zhang and Meng [19] analyzed coal seam floor failure using a self-developed simulation model of confined aquifer strata.

Third, geographic information systems and microseismic (MS) monitoring techniques have been used to predict and evaluate the dangerous parts of a water-conducting channel. For example, Chen et al. [20] used a geographic information system and an analytic hierarchy to forecast the areas at risk of a water inrush in the Qidong Coal Mine. This guided the safe mining of a coal seam. Gu et al. [21] established an evaluation model based on water blocking conditions and used two adjacent lower coal mining faces of the Yanzhou Xinglongzhuang coal mine as an example. The evaluation showed that the impermeability strength is a better index for measuring the water resistance capacity of a floor. Sun et al. [22] studied fault-zone occurrence using the electric couple method. Naghadehi et al. [23] established a fuzzy model by combining FAHP with AHP applying the method to the Jajarm bauxite mine in Iran and ranked the most suitable mining methods.

Finally, ground drilling, grouting, drainage or decompression, and curtain closure have been used to prevent the formation of water-conducting channels. Guo et al. [24] thought that plugging grouting is the most effective water inrush treatment scheme in the case of water inrush. Liu et al. [25] used concrete-based curtain grouting closures for mine flood prevention and control. Li et al. [6] applied rock beam theory to analyze the mechanism of grouting crack expansion caused by rock deformation during mining and proposed a new grouting casing model designed to prevent water inrush and therefore control floor rock deformation.

Thus, scientific researchers have performed detailed studies of dynamic damage due to diversion channels and the measures that might prevent the formation of these channels. These meaningful results are a useful reference for understanding water inrush mechanisms and for the application of appropriate measures to prevent and control water inrush. However, stress in the rock surrounding a roadway and the confined water pressure of an aquifer increase linearly with the mining depth. The water control measures used in mining a shallow coal seam may be inadequate for deep-water control. Moreover, the cost and difficulty of constructing such measures increase with depth, and the equilibrium between the groundwater and the ecosystem is destroyed [26–30]. Therefore, further in-depth research into methods of preventing and controlling water inrush into mines is needed.

In summary, there have been many detailed studies of dynamic failure among diversion channels and methods of preventing the formation of such channels. According to the "under three-zone" theory, controlling the heights of the floor failure and pressure conduction zones is an important step in improving the effective thickness of the complete rock strata. The empirical formula for the floor failure depth developed by domestic researchers indicates that reducing the inclined length of a working face can reduce the floor failure depth. Therefore, a short-wall mining face is important to reduce the floor damage depth. At the same time, as a green mining method, filling mining reduces not only the supporting stress around the excavation face but also the number of gangue hills, helping to protect the mine environment. Therefore, partial-filling mining (PFM), which is a combination of short-wall mining and filling mining, is proposed to prevent the formation of water diversion channels.

2. Engineering Geological Conditions

2.1. Engineering Geology Overview. The Bucun Coal Mine is located in Zhangqiu District, Jinan City, Shandong Province, China (Figure 1). The research object is 9211 working face in 921 mining area of 9-1 coal seam threatened by floor confined water. Seven faults were exposed in the 9211 working face tunneling process; no fault affects the working face during excavation. Thus, the influence of the fault structure on mining is not considered in this study. The 9211 working face coal seam thickness is 1.0 m–1.8 m, the average thickness is 1.5 m, the coal seam dip angle is 3°–14°, the average dip angle is 9.5°, the coal seam burial depth is 506 m–571.7 m, and the average burial depth is 538.9 m. The direct bottom of the 9-1 coal seam is fine sandstone, and the basic bottom is sandy shale. The layout of the working face in the mining area is shown in Figure 2.

2.2. Hydrological Conditions. The aquifers that affect mining of the 9211 working face mainly include the upper Carboniferous thin limestone IV(V) aquifer group, the middle Carboniferous Benxi Xujiazhuang limestone aquifer group, and the Ordovician limestone aquifer group. The upper Carboniferous thin limestone IV(V) aquifer group was drained during mining. Mining of the No. 9-1 coal seam is affected mainly by the Xujiazhuang limestone aquifer group in the Middle Carboniferous Benxi formation and Ordovician limestone aquifer group in the lower part of the coal seam. The Xujiazhuang limestone aquifer group is rich in water; some areas receive a vertical overflow recharge from the Ordovician limestone aquifer group. The average distance from the 9-1 coal seam is 58.01 m, the unit water inflow is 7.2 m^3/h–246 m^3/h, the water level is -128.3 m–46.8 m, and the water pressure is 4.11 MPa. The Ordovician limestone aquifer group is located in the basement of the coal measure strata and is the most important aquifer in this area, which is 88.87 m away from the 9-1 coal seam. According to the Ordovician limestone long observation data, the highest

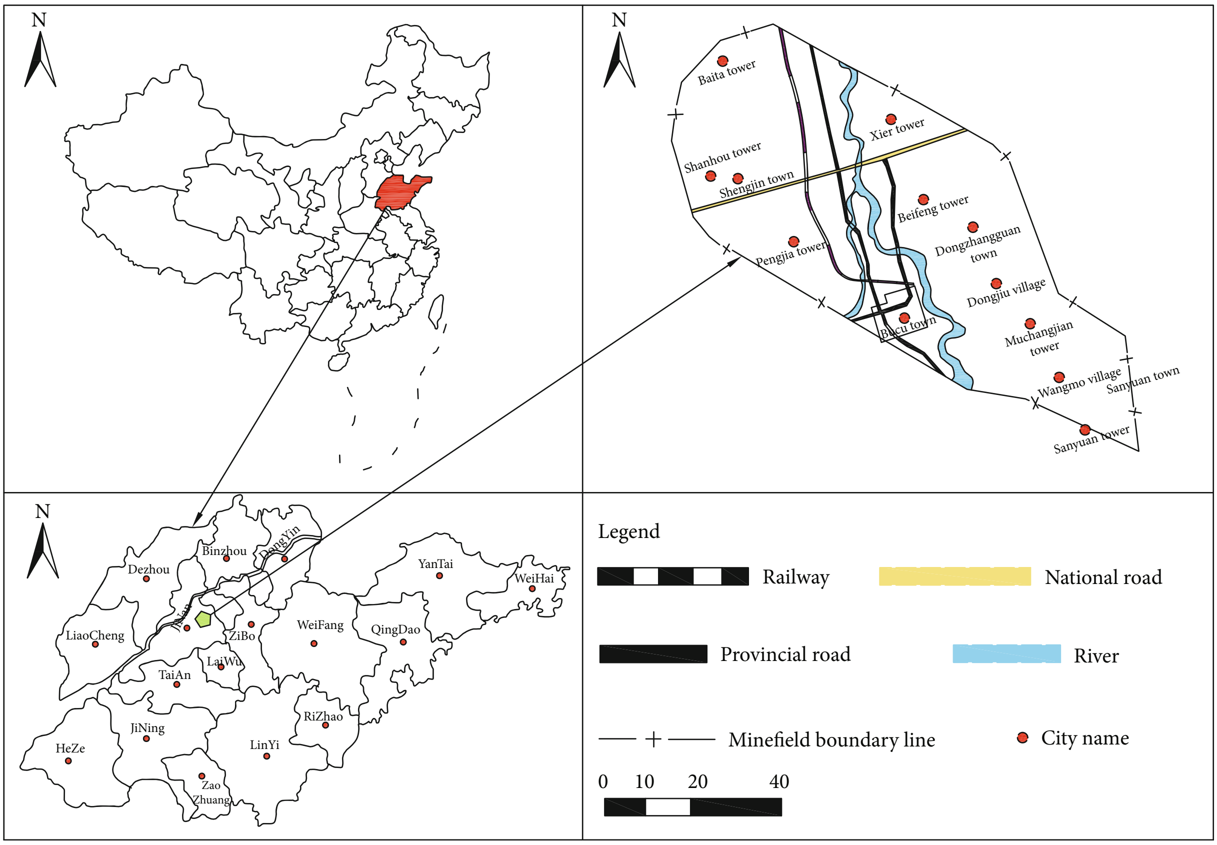

Figure 1: Location of the study area in Zhangqiu District, China.

water level is 78.34 m, the lowest water level is 47.82 m, and the Ordovician limestone water pressure is 4.87 MPa. The histogram is shown in Figure 3.

2.3. Analysis of a Water Inrush Accident. According to the analysis in Sections 2.1 and 2.2, the No. 9-1 coal seam is under threat of floor water inrush during mining. To reduce the floor damage depth at the working face, short-wall strip mining is adopted for the No. 9110 working face during coal seam mining. The mining width of the working face strip is 40 m. The working face advances along the trend of the coal seam. In order to determine the depth of floor failure when strip mining is adopted, the double-end water shutoff device observation method is used to measure the floor failure depth. On July 7, mining of the No. 9110 working face began in the Bucun Coal Mine. Deep observation of floor damage began on July 10. According to the summary of the mine pressure laws of other working faces provided by the field staff, it is believed that the initial pressure appears when the 9110 working face is pushed to July 27. However, according to the mine pressure theory, the initial pressure can cause flood accidents easily. In order to avoid potential personal injury from such an accident, observation work ended on July 27. According to the analysis of drilling leakage data, the failure depth of the working face floor reaches 13 m. It should be noted that this depth cannot represent the maximum failure depth of the floor as the working face advances. The depth continues to change as the working face advances. On July 31, the basic roof of the No. 9110 working face breaks and a water inrush accident occurs in the coal seam floor. The initial and maximum (stable) rates of water inflow are 150 m^3/h and 351.6 m^3/h, respectively. A map of the water inrush accident at the No. 9110 working face is shown in Figure 4.

Water prevention and control experts performed a detailed analysis of the factors that affected the water inrush accident at the No. 9110 working face. The results are as follows.

2.3.1. The Working Face Inclined Length. In order to prevent a water inrush accident from occurring at the working face, traditional long-wall mining was abandoned when working face 9110 was mined. The No. 9110 working face was mined using short-wall strip mining. However, water inrushes still occurred at the back of the goaf in the course of advancing. This shows that safe mining of the working face cannot be ensured when the inclined length of the working face is 40 m.

2.3.2. The Damage Depth of the Floor. The No. 9110 working face water inrush accident occurred during the initial pressure. The main reason for this is that the initial pressure increases the floor damage depth. The remaining undamaged floor thickness cannot resist the effect of the confined water pressure. Finally, the water inrush accident occurs at the working faces under the coupled effects of the initial pressure and the confined water pressure. Therefore, on

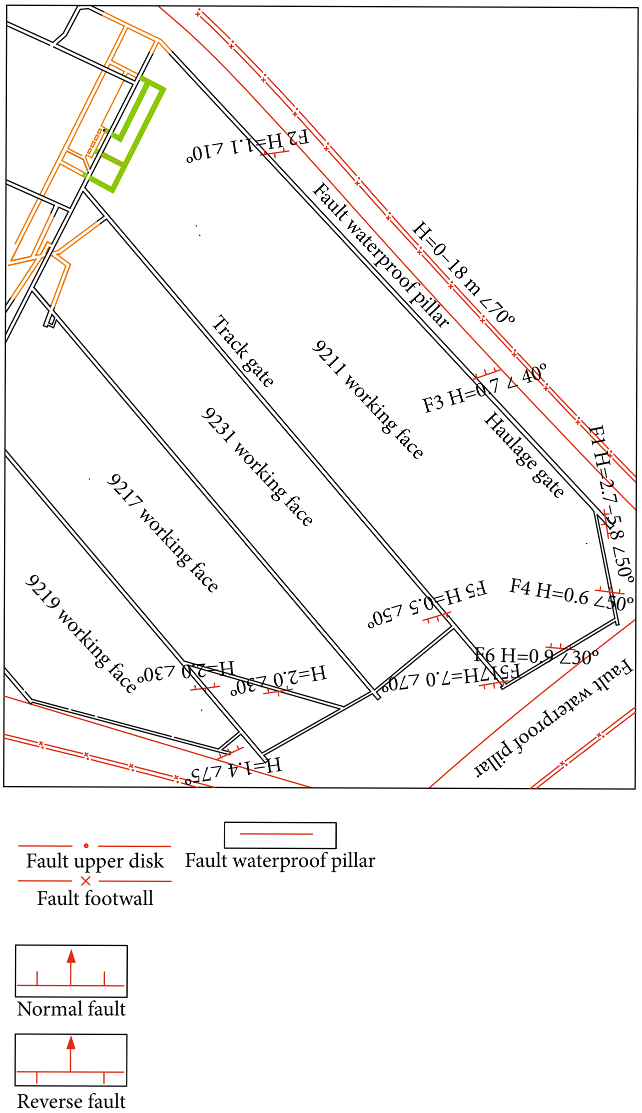

Figure 2: Working face layout in the Bucun Coal Mine.

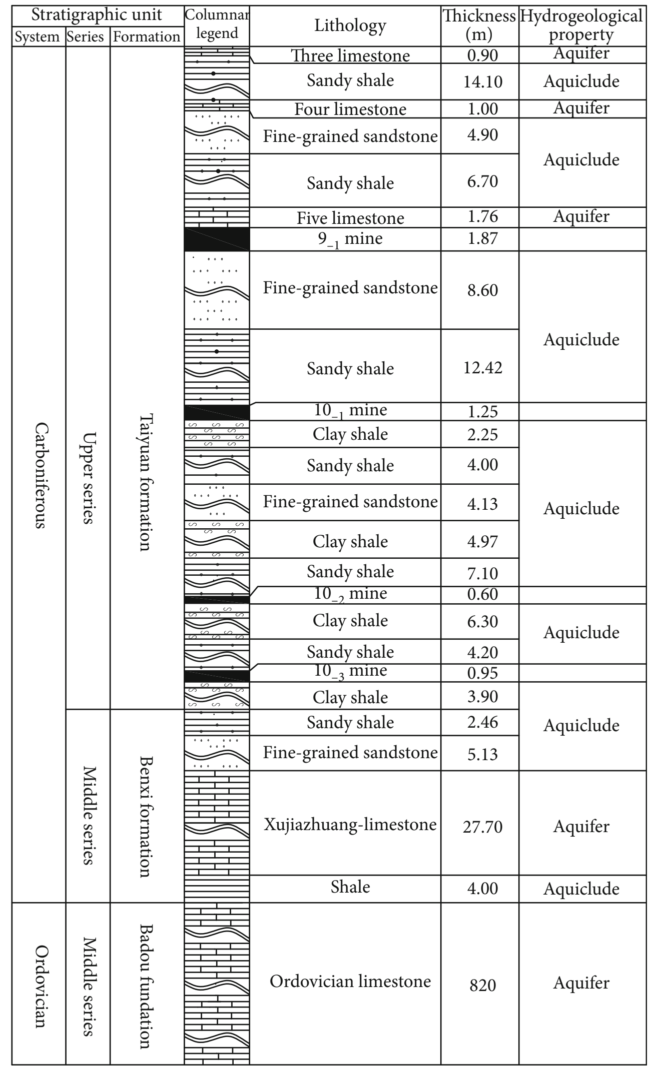

Figure 3: The histogram.

the premise of determining the thickness of floor aquifuge, reducing the depth of floor failure is required in order to prevent floor water inrush.

2.3.3. The Geological Structure. The borehole data shows that the geological structure in the lower part of the No. 9110 working face is well developed. Because faults and fault zones destroy aquifuge integrity, the water resistance capacity is reduced. At the same time, it is easy to change the hydraulic conductivity of the original fault via primary and periodic pressure. Therefore, under the premise of determining the geological structure of the coal seam floor, reducing the influences of the initial pressure and periodic pressure on the fault can help to control floor water inrush.

3. Methodology

3.1. Mining Methods and Filling Materials. According to the analysis of the water inrush at the No. 9110 working face in Section 2.3, selection of a reasonable mining method and working face inclined length is important to controlling the formation of a water inrush passage. These measures can reduce the occurrence of mine water inrush accidents. However, in coal seam mining, different mining methods have different destruction depths. PFM, which is a combination of short-wall mining and filling mining, may prevent the formation of a water-conducting channel. In this method, the pressure from the overlying strata is transferred to the floor. This prevents the floor from moving to the goaf via a composite support system comprised of the roof plus backfill plus a stratum. In short-wall mining, the working face is divided into narrow-strip faces with two safety exits. The distance between the strip faces must be less than the limit span of the roof stratum to ensure that the roof undergoes only bending deformation. In filling mining, the goaf of the working face is filled to ensure that the roof of the goaf does not subside.

Using PFM, the working face was first divided into narrow-strip faces with widths of 15 m along the coal seam strike after the coal mining system of the No. 9211 working

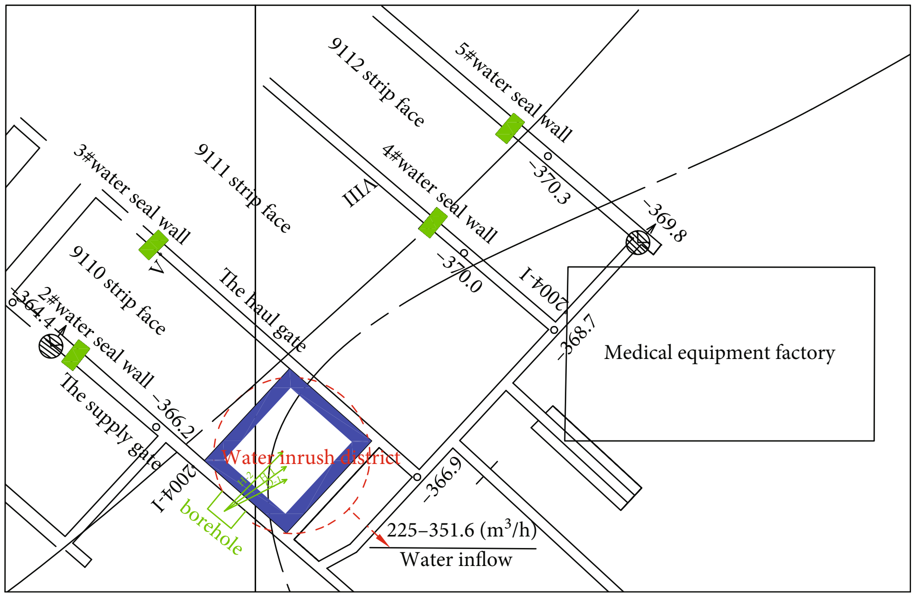

Figure 4: Map of the water inrush accident at the No. 9110 working face.

face was established. The narrow-strip faces were numbered from 1 to 15. The working face advanced along the coal seam tendency via blasting. Full negative pressure ventilation was adopted for the coalface. Figure 5 shows the PFM process, which is as follows:

(1) Face No. 1 was first extracted via blasting. Then, a preventing-grout wall was built at the upper and lower outlets of the narrow working face. When the preventing-grout wall was complete, the slurry was filled into the goaf via a pipeline from the upper exit of the strip face. This continued until all of the odd-numbered narrow-strip faces were excavated and filled

(2) When the compressive strength of the filling bodies was large enough, the coal pillars between the filling bodies were excavated in order

(3) The second cycle of PFM described above could also occur once the strength of the filling bodies in the first, third, and fifth zones was self-supporting, thus saving the process replacement time between the first and second cycles

The filling material used in the Bucun coal mine was composed mainly of aggregate, binders, and additives. The main aggregate was coal gangue. Fly ash and cement were binders. Lime, gypsum, and foaming agent were additives [28]. Since it took 40 min for the slurry to reach the far end of the underground filling face from the ground filling and mixing station, the slurry started to set after 60 min. The slurry reaction accelerated after another 50–70 min. After 8 h, the slurry completed its change from liquid to solid. Its compressive strength was then 1.15–2.12 MPa.

3.2. Physical Simulations. To avoid the influence of the F1 fault, the final position of the haulage gate was changed to that shown in Figure 2 when driving the No. 9211 working face. The fault drop was small, and the fault did not conduct water. Meanwhile, the four ash aquifers and five ash aquifers of the roof were drained during excavation. There was no water inrush accident at any time during the excavation process. Therefore, the effect of the fault was not considered in the physical simulation.

This study considered the effect of using PFM to restrain floor water inrush at working face 9211 of the Zhangqiu village coal mine in Shandong Province via physical simulation. The similarity ratio is the critical experimental parameter in simulation experiments that involve similar materials. Choosing a reasonable similarity ratio is an important step in producing valid experimental results. This simulation was based on similarity theory and actual geological conditions and was determined according to the test system. The main similarities were as follows:

(1) *Geometric Similarity*. Suppose that X', Y', and Z' are the three vertical dimensions of the prototype along x, y, z directions, respectively, and suppose X'', Y'', Z'' are the corresponding model sizes along x, y, z directions, respectively,

$$C_l = \frac{X'}{X''} = \frac{Y'}{Y''} = \frac{Z'}{Z''} = 200 \tag{1}$$

(2) *Time Similarity*.

$$C_t = \sqrt{C_l} = 10\sqrt{2} \tag{2}$$

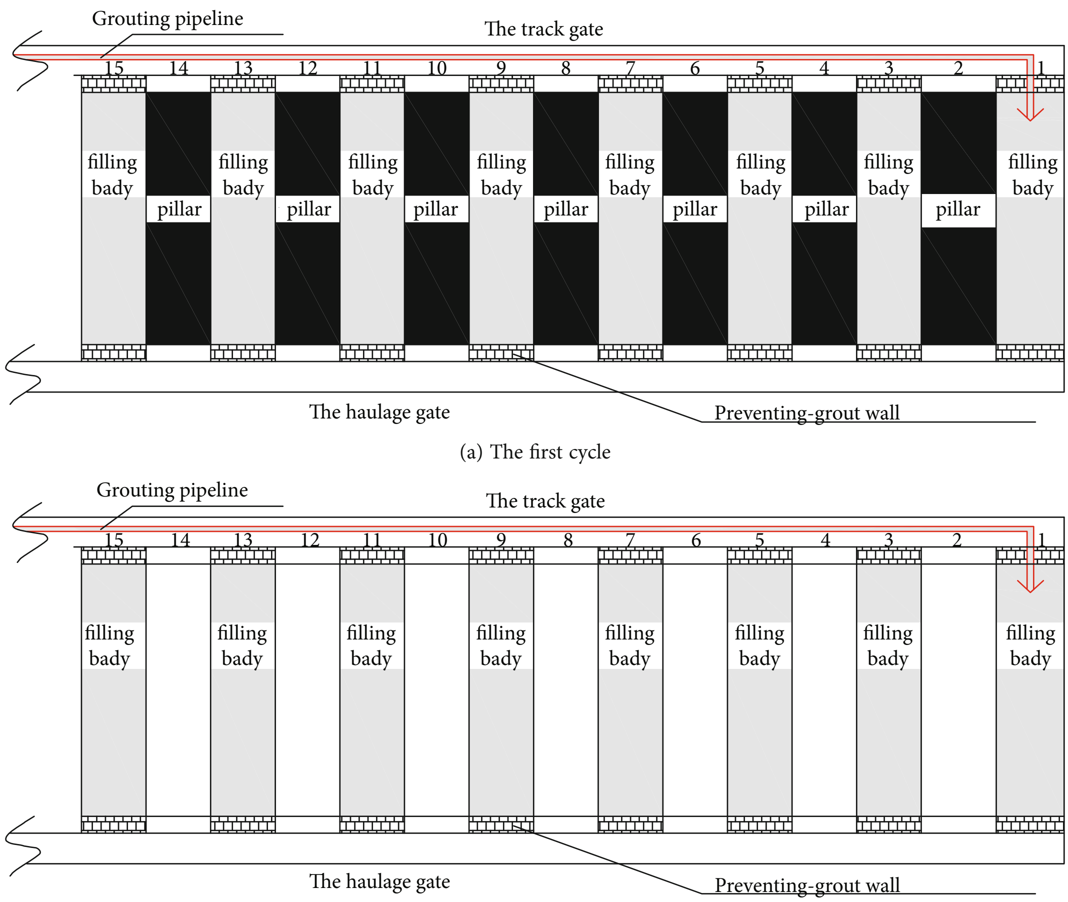

(a) The first cycle

(b) The second cycle

Figure 5: PFM process.

(3) *Bulk Density Similarity*. Let the rock bulk density at the ith layer in the prototype be γ', and the rock bulk density in the corresponding model is γ''. The bulk density similarity coefficient is as follows:

$$C_\gamma = \frac{\gamma'}{\gamma''} = 1.5 \tag{3}$$

(4) *Strength Similarity and Stress Similarity*.

$$C_P = C_l^* C_\gamma = 300 \tag{4}$$

(5) *The Permeability Coefficient Similarity*. Suppose the permeability coefficient is K and the fluid water used in the model is consistent with that in the prototype; therefore, $C_\lambda = 1$, and the permeability coefficient similarity ratio is

$$C_k = \frac{\sqrt{C_1}}{C_\lambda} = 10\sqrt{2} \tag{5}$$

The coal floor water inrush simulation system is composed mainly of a test bench, servo loading system, water pressure control system, and computer acquisition system. The test system is shown in Figure 6. The maximum horizontal load of the servo loading system is 300 kN, the maximum vertical load is 600 kN, the minimum loading rate is 0.01 kN/s, and the maximum loading rate is 100 kN/s. Hydraulic loading is performed mainly by a hydraulic control system. The designed maximum confined water pressure loading value of the system is 1.5 MPa, and the designed maximum flow rate is 0.015 m3/s. The water pressure control system is connected to the test bench water tank via a high-pressure hose. The plunger pump is connected to the water injection head via a high-pressure hose to inject the water from the water tank into the experimental cabin. At the same time, the EDC control system allows the model to achieve multistage, constant water flow control. After the model is prepared, water pressure is applied to it via the water pressure control system until the aquifer is saturated. The water pressure is adjusted automatically via the EDC

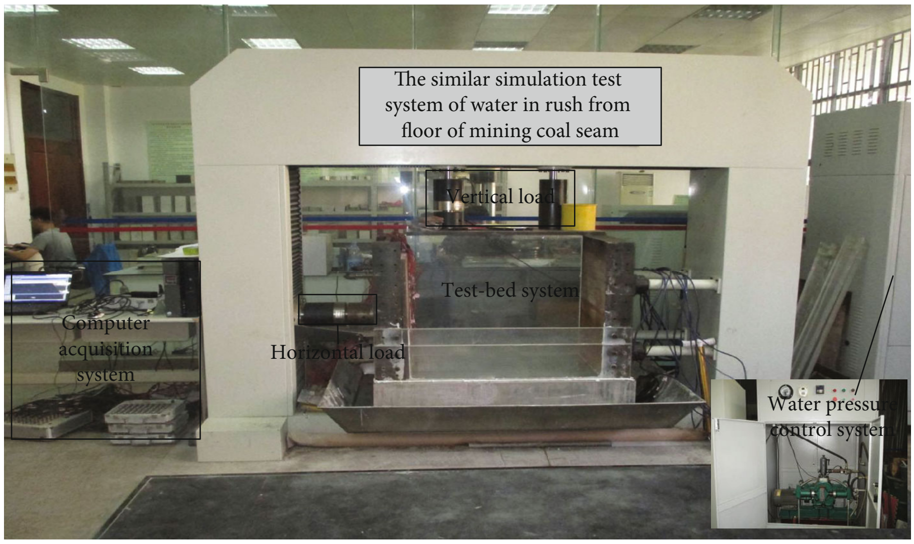

Figure 6: The physical simulation test rig.

Table 1: Physical and mechanical parameters of the strata used in the model.

Rock stratum		Thickness (cm)	Sand (kg)	Calcium carbonate (kg)	Gypsum (kg)	Vaseline (kg)	Paraffin (kg)	Water (kg)	Hydraulic oil (kg)	Actual strength (MPa)	Simulation strength (MPa)
Main roof	Limestone	0.45	20.79	2.376	0.594	0	0	2.376	0	62.7	0.209
	Sandy shale	3.5	13.376	1.0032	0.6688	0	0	1.5048	0	42.9	0.143
	Limestone	0.8	17.325	1.98	1.495	0	0	1.98	0	62.7	0.209
	Fine sandstone	2.5	12.474	0.891	0.891	0	0	1.4256	0	74.9	0.249
	Sandy shale	3.35	8.448	0.6336	0.4224	0	0	0.9504	0	42.9	0.143
Immediate roof	Limestone	0.85	14.08	1.056	0.4224	0	0	1.584	0	62.7	0.209
No. 9 coal seam		0.90	13.86	0.99	0.99	0	0	1.584	0	12.8	0.043
Water-resisting layer	Fine sandstone	4.3	8.1463	0.8689	0	0.3259	0.1629	0	0.9504	74.9	0.249
	Sandy shale	6.2	12.219	1.3034	0	0.4888	0.2444	0	1.4256	42.9	0.143
	No. 10-1 coal seam	0.6	13.86	0.99	0.99	0	0	1.584	0	12.8	0.043
	Clay shale	1.1	13.577	1.4482	0	0.5431	0.2715	0	1.584	32.7	0.109
	Sandy shale	2	10.862	1.1586	0	0.4345	0.2172	0	1.2762	42.9	0.143
	Fine sandstone	2.06	11.541	1.231	0	0.4616	0.2308	0	1.3464	74.9	0.249
	Clay shale	2.5	10.862	1.1586	0	0.4345	0.2172	0	1.6272	32.7	0.109
	Sandy shale	8.55	12.898	1.3758	0	0.5159	0.2580	0	1.5048	42.9	0.143
	Clay shale	3.15	10.183	1.0862	0	0.4073	0.2037	0	1.188	32.7	0.109
Aquifer	Sandstone	3.2	23.936	1.7952	1.0692	0	0	2.5344	0	69.8	0.233
	Limestone	4.1	28.413	1.7758	1.7758	0	0	3.2472	0	62.7	0.209

Figure 7: The construction process of the physical model.

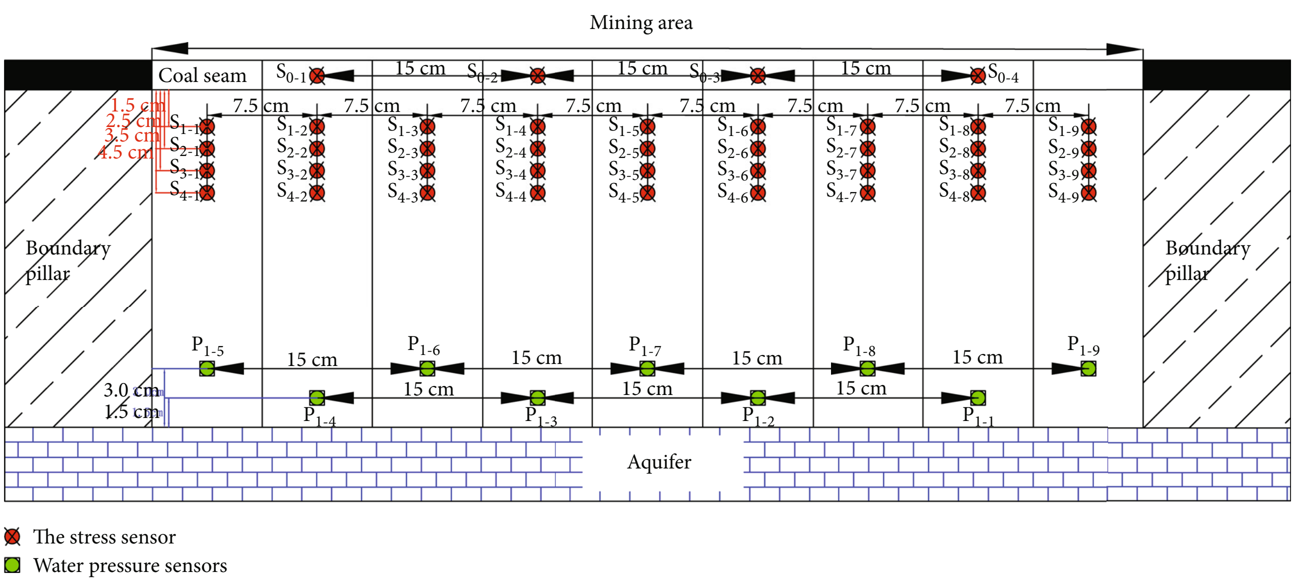

Figure 8: Front view of the monitoring point layout.

control system to ensure that the confined water pressure remains stable during mining.

Based on previous studies, the physical simulation used sand, gypsum, calcium carbonate, and water to simulate the macromotion failures of the overlying strata and the mining floor. The physical and mechanical strata parameters used in the model were determined via similarity theory (Table 1). Figure 7 shows the physical model construction process.

To monitor changes in the stress of the coal seam floor and the water pressure in the aquifer during PFM in real time, stress sensors were placed in the coal seam and in the floor, and water pressure sensors were placed above the aquifer. The arrangement of sensors used in the physical model is shown in Figure 8.

3.3. Test of Specimen Parameters. According to the similarity theory of fluid-solid coupling physical simulation, similar materials in solid-liquid coupling must meet similarity standards for solid deformation and permeability. Four different test schemes were designed in order to verify whether the standard sample of sandy shale prepared from sand, calcium carbonate, paraffin wax, Vaseline, and hydraulic oil could satisfy both the solid deformation and permeability requirements. The material was tested in the dry state and after soaking for 1 d, 2 d, and 3 d. Figure 9 shows the manufacturing processes used with various raw materials and standard samples.

3.3.1. Uniaxial Compressive Strength Test. Figure 10 shows the stress-strain curve of the specimen. The entire stress-

FIGURE 9: Raw materials and the production process.

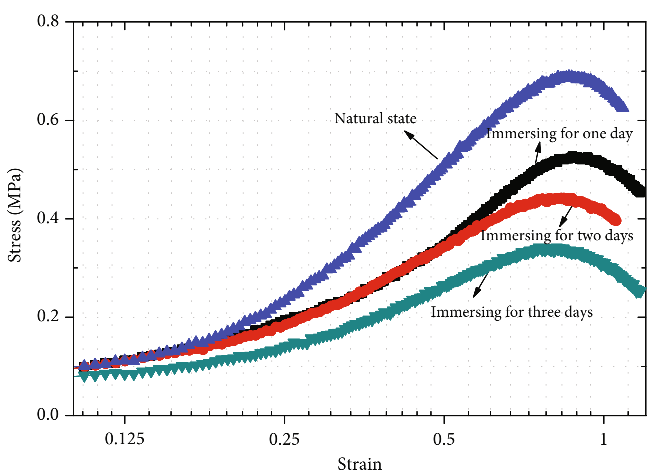

FIGURE 10: The stress-strain curve.

strain curve is similar to that of rock. However, the strength of the standard specimen decreases with the immersion time. The compressive strength of the hydrophilic specimen can exceed 75% of the specimen strength.

3.3.2. Permeability Coefficient Determination. The permeability coefficient K is one of the indexes that reflects the permeability of the coupling material. In this experiment, the permeability coefficient K of the coupling material is measured via the variable-head method. Diagrams of the test principle and test device are shown in Figure 11 [31]. The test instructions are as follows: first, put the saturated sample into a closed steel container for compaction; second, record the water head difference in the U-shaped pipe at the beginning of the test as Δh_1; third, record the water head difference in the U-shaped pipe after time t as Δh_2; fourth, calculate the permeability coefficient of the test piece according to Darcy's law. The formula for the permeability coefficient is

$$K = \frac{aL}{At} \ln \frac{\Delta h_1}{\Delta h_2}, \tag{6}$$

where K is the permeability coefficient, a is the cross-sectional area of the glass pipe, A is the cross-sectional area of the sample, L is the length of the sample, Δh_1 is the water head difference of the U-shaped pipe at time t_1, and Δh_2 is the water head difference of the U-shaped pipe at time t_2.

Coupling material permeability measurements performed using various proportions indicate that the permeability coefficient range is 4.55×10^{-4} to 1.48×10^{-7}. The permeability coefficient values of some materials are shown in Table 2.

3.4. Field Measurements. Field monitoring is an important way to verify the results of physical simulations and analyses. To verify the preventive effect of PFM with respect to floor water inrush accidents, stress and roof subsidence gauges were arranged in the filling area, transportation chute, and track chute of a narrow-strip working face. There were three pairs of measuring points in the filling area of the narrow-strip face. Roof subsidence gauges were placed along the transport and track chutes. The stress and roof subsidence gauges in the filling area of the narrow-strip working face were 25 m, 50 m, and 75 m from the No. 9211 haulage gate. The roof subsidence gauges in the transport and track grooves were 105 m away from the cutting hole of the working face. The sensor layout is shown in Figure 12.

The failure depth of the floor after coal seam mining was verified via the observation method using a double-end water shutoff device. The system has two pathways in the structure: the gas filling pathway and the water injection pathway. The inflatable pathway is composed of a high-pressure gas cylinder inflatable console and an in-hole blocking capsule; the water injection pathway is composed of high-pressure water, a water injection console, a water inlet push rod, and an in-hole water injection probe tube. First, gas is applied to the capsule at a certain pressure through the inflatable path so that the capsule expands and seals the two ends of the section where the hole is located. Then, constant-pressure water is injected into the blocked section of the capsule via the water injection path. The water

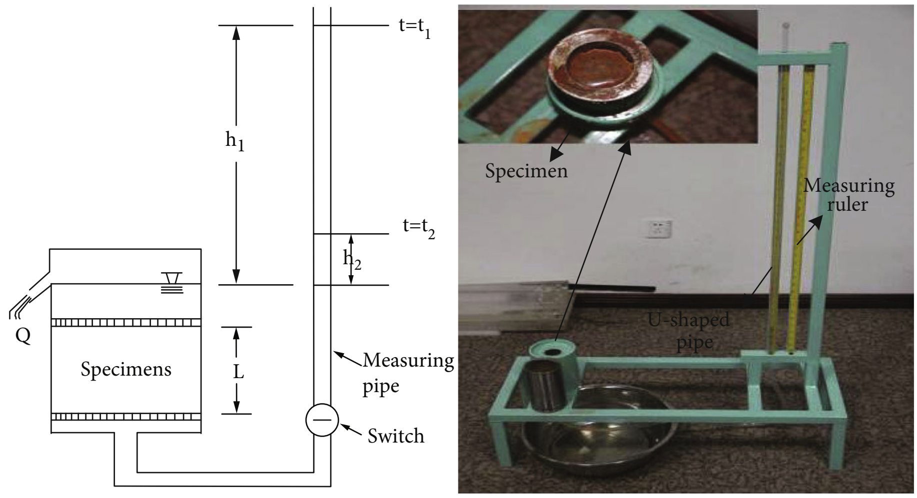

Figure 11: The permeability coefficients of some specimens.

Table 2: The permeability coefficients of some specimens.

Specimen number	K (cm/s)	Specimen number	K (cm/s)
1-3	5.86×10^{-5}	5-3	7.31×10^{-6}
2-3	4.75×10^{-4}	6-3	5.07×10^{-5}
3-3	6.02×10^{-5}	7-3	4.55×10^{-4}
4-3	4.56×10^{-6}	8-3	1.48×10^{-7}

pressure is controlled by the water injection console, and the water injection flow rate is monitored. The capsule of the blocker is depressurized after each hole section measurement. After contraction and depressurization, the procedure moves to the next measurement section and water injection observation continues until the leakage from each section of the entire borehole is measured, and the bottom plate fracture damage range is determined based on the change in leakage amount. A schematic diagram of water injection in the damaged floor area is shown in Figure 13 [32].

The water injection holes constructed before and after mining in the No. 9211 working face include one premining hole (hole No. 3) and two postmining holes (holes No. 1 and No. 2). Construction of and observations via the premining hole were performed without affecting mining. The drilling holes were protected when drilling the two postmining holes. Finally, the water lost into the pre- and postmining holes was measured using a double-end water shutoff device to determine the floor failure depth. Figure 14 shows the drilling elevation plan.

4. Results and Discussion

4.1. Physical Simulations. After the model was built, the vertical stress, horizontal stress, and confined water pressure were considered based on similarity theory. The model is maintained at room temperature for 4–5 days before excavation. To reduce the boundary effect, coal pillars 5 cm wide are retained on both sides of the model. The coal seam in the model is mined using PFM. The mining face and the pillar widths are both 7.5 cm. The working face is mined from the left end to the right end of the model. There are six periods of mining, each lasting 40 min. The goaf is filled 10 min after completion of each excavation. The pillars between fillings are extracted in turn from the left end of the model after mining of the working face is completed. In the physical simulation, mining of the coal seam uses manual drilling and the backfill body is foam. Figure 15(a) shows the initial physical model. Figures 15(b) and 15(c) show the first and second cycles of PFM, respectively.

In order to analyze the stress and water pressure variation laws relevant to simulated mining, data from stress monitoring points S1-3, S2-5, S3-5, and S4-5 and the data from pore water pressure monitoring points P1-4 and P1-8 are selected for analysis.

4.1.1. Evolution of the Stress Field during Mining. Data from stress sensor S1-3 are shown in Figure 16(a) for the first cycle of mining. The stress changes three times. The first change occurs during continuous excavation of the working face. The stress measured by the sensor at the lower 1.5 cm of the working face changes abruptly, increasing from 0 MPa to 0.031 MPa. This occurs mainly because the floor rock stratum in this area begins to move towards the goaf due to vertical stress and mine pressure after excavation of the working face. The rock stratum is in tension.

The second step change occurs during the filling step, after excavation of the working face has been completed. The stress in the rock floor gradually decreases to that of the rock floor mass without excavation. This change indicates that the weight of the roof rock stratum of the coal seam is beginning to transfer to the floor rock stratum through the filling body. This restrains the upward movement of the rock stratum.

The third step change occurs during compaction of the filler. The stress changes from 0 MPa to -0.01 MPa, indicating that the filling body in the goaf is in contact with the roof

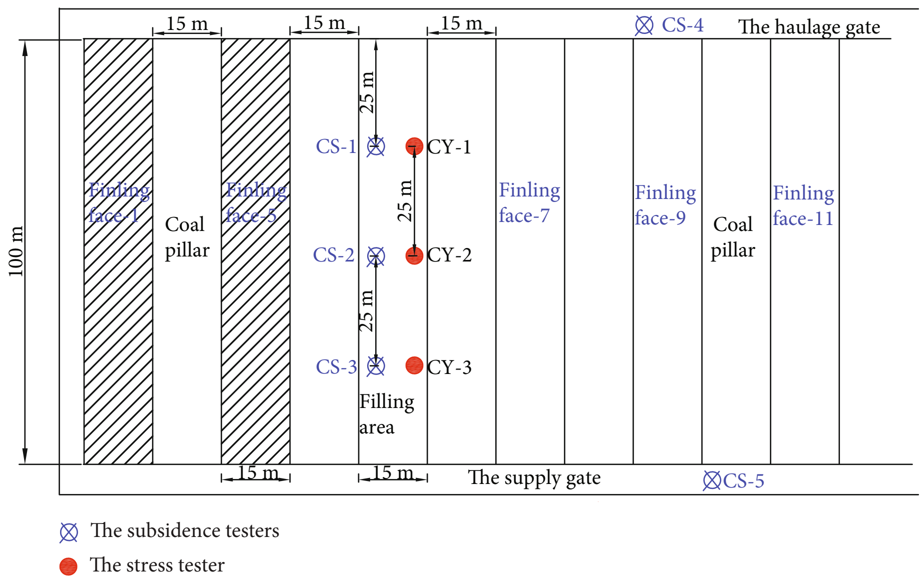

Figure 12: Layout of stress and subsidence gauges.

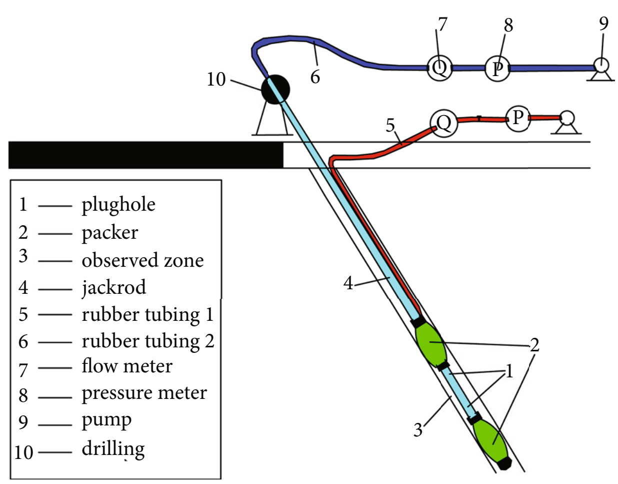

Figure 13: Schematic diagram of water injection in the damaged area of the mining floor.

and that the floor rock stratum is in compression again. This reduces the floor rock stratum failure depth.

In Figure 16(b), during the second mining cycle, the stress measured by the floor sensor 1.5 cm away from the coal seam indicates compression. The stress is higher than that at the end of the first excavation. This indicates that the floor rock layer is affected by excavation again.

The stress measured by sensor S2-5, which is 2.5 cm away from the coal seam, is always compressive during the first excavation period (Figure 17). The stress decreases during the second excavation. This occurs primarily because unloading occurs in the floor strata when the coal pillars are extracted. However, stress sensors S3-5 and S4-5 are always under pressure during the two rounds of excavation. Based on a similar material ratio of the laying model of 1 : 200, the floor failure depth would be less than 5 m during mining.

4.2. Evolution of the Pore Water Pressure during Mining. Data from water pressure sensor P1-4 (Figure 18) show that the initial water pressure increases from 0 MPa to -0.04 MPa during the two excavations. It then fluctuates between -0.03 and -0.04 MPa. This occurs mainly because the primary fissures in the rock strata open to form a water conduction channel under a sustained high confined water pressure. This produces a water flow that is measured by the water pressure sensor. Therefore, a water-conducting channel forms 1.5 cm above the aquifer due to the action of the confined water pressure.

Data from water pressure sensor P1-8 are shown in Figure 19. The sensor, which is 3.0 cm from the aquifer, is affected by the water pressure throughout PFM. The data from P1-8 show that under the action of high confined water and mine pressures, rock fractures develop to a height of 3.0 cm above the aquifer. This occurs mainly because the water pressure, as measured by the sensor, fluctuates continuously upwards and then falls to 0 MPa. This shows that the rock stratum is not completely broken.

The variation in the stress measured by water pressure sensors P1-4 and P1-8 shows that throughout mining of the No. 9211 working face, the height of the hydraulic conductivity lifting zone under long-term confined water pressure and mine pressure loads is less than 3.0 cm.

Layered demolition was used to measure the development and expansion of cracks in the upper aquifer of the floor during excavation. When the first, second, and third layers above the aquifer were dismantled, the fractures shown in Figures 20(a) and 20(b) appeared. This indicates that floor rock fractures expand during coal seam mining due to pressure from the mine and the confined water. The similarity ratio indicates that the height of the confined water conduction lifting zone would increase by less than 6 m.

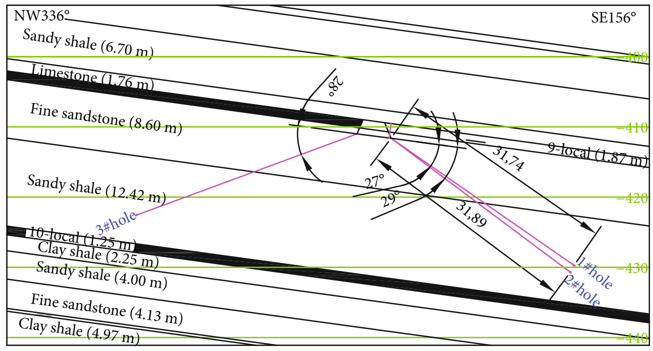

Figure 14: Drilling elevation plan.

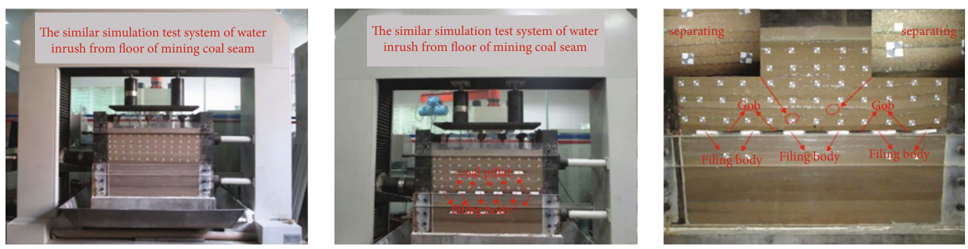

Figure 15: Excavation in the physical model.

4.3. Field Application

4.3.1. Compression Deformation of Filling Body in Mining. According to data from subsidence gauges CS-1, CS-2, and CS-3, compression of the filling body in the No. 9211 working face can be divided into two stages. The first stage is compressive deformation of the filling body (Figure 21). Compression of the high-water backfill in the No. 9211 working face is linear with time. The compressive deformation measured by CS-2, in the middle of the goaf, is the largest at 89.1 mm for the filling body. This occurs mainly because the early strength of the high-water backfill is relatively low and the support for the overlying strata is weak. This leads to subsidence of the rock strata and backfill compression. Therefore, the backfill compression is linear with time. The filling body is stable during the second stage. This is mainly because the strength of the filling body, which has high water content, increases. This increases support of the overlying strata and decreases the extent of strata settlement. Thus, compression of the filling body becomes stable.

The CS-5 and CS-4 subsidence gauges are in the track and transport chutes, respectively. Data from these sensors indicates that variation in compression can be divided into two stages (Figure 21). In the first stage, the compression increases, mainly because the roof stratum along the trough sinks is under mine pressure after the excavation of the coal body at the working face. The second stage is stable. The compression measured by CS-5 is larger than that measured by CS-4. This is mostly because CS-5 is on one side of a coal pillar.

4.3.2. Stress Evolution within the Filling Body during Mining. As shown in Figure 22, data from the CY-1, CY-2, and CY-3 pressure sensors in the goaf show that the pattern of stress in the filling body can be divided into two stages. Loading of the filling body increases during stage 1 but is stable during stage 2. The stress measured by sensor CY-2 is larger than that measured by the CY-1 and CY-2 sensors. This indicates that the filling body experiences a larger force in the middle of the goaf.

The depth of the No. 9211 working face is 430.26 m–484.96 m. Without considering the tectonic stress, the original rock stress is 4.61 MPa–5.20 MPa. The pressure on the filling body is 0.51 MPa in the middle of the working face and 0.32 MPa in the upper face. Therefore, the stress in a high-water filling body is less than the original rock stress of the working face. This indicates that movement of the rock strata above the working face is limited at this time. Therefore, PFM can inhibit the occurrence of strata breakage, thereby reducing the effect of the overlying strata pressure on the floor.

4.3.3. Floor Failure Depth during Mining. Using the drilling construction layout shown in Figure 14, floor damage depth observation was performed at the No. 9211 working face. The observation period was from July 15, 2013, to July 22, 2013. Water injection leakage results measured at various drilling depths during drilling are shown in Figure 23.

In Figure 14, the strata that the premining hole (S-3) passes through are mainly sandy shale and fine sandstone from the floor rock of the 9-1 coal seam. According to the water injection leakage diagram, the extent of leakage from the premining hole (S-3) decreases gradually from 11 m to 18 m. Leakage is maximized at a depth of 11 m, where the maximum leakage is 2.6 L/min and the corresponding rock

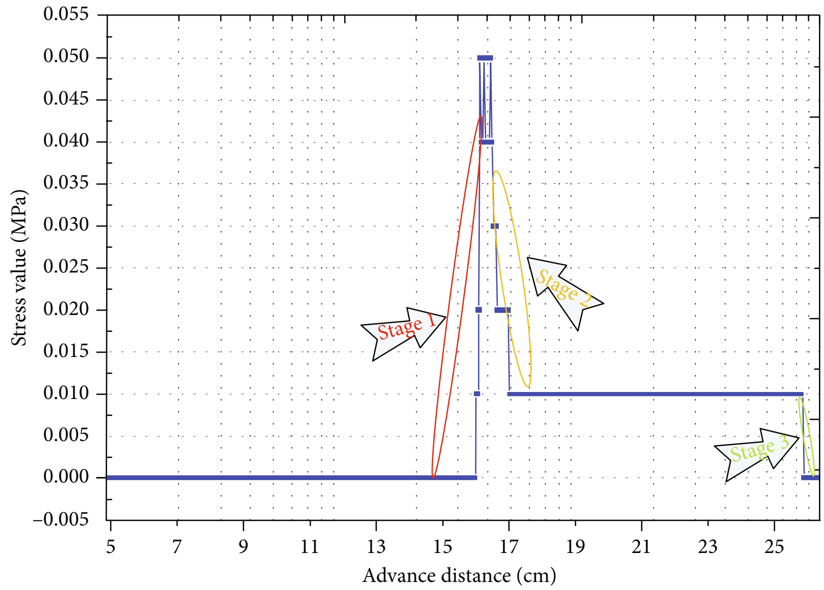

(a) The first cycle

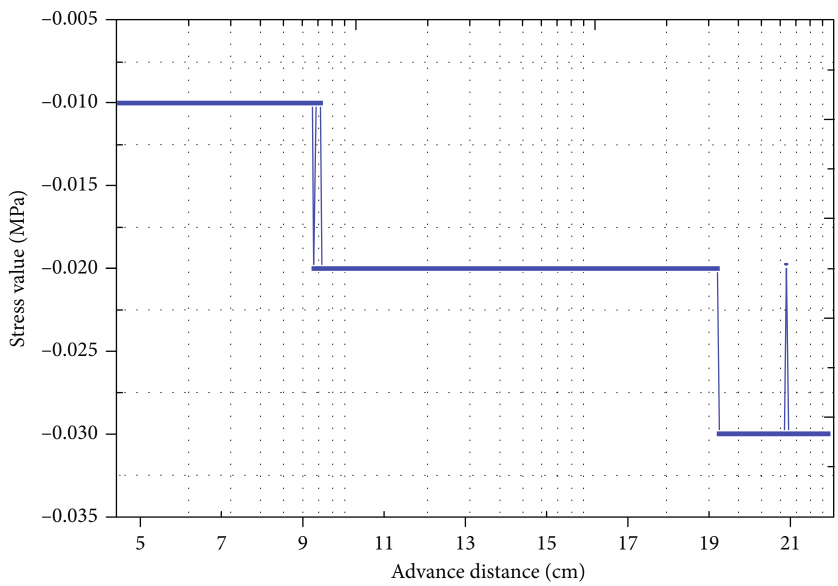

(b) The second cycle

Figure 16: Stress at monitoring point S1-3 vs. the distance advanced.

layer position of the fine floor sandstone is 5.16 m. The drilling depth ranges from 19 m to 31 m, and the corresponding rock layer is sandy shale. Due to the relatively complete rock stratum, the extent of leakage from the drilling section is stable within a relatively small range. The maximum leakage is 1.3 L/min. Across the borehole, the average leakage from the premining hole (S-3) is 1.39 L/min.

It can be seen from Figure 23 that drilling leakage from the postmining hole (S-1) between 8 m and 13 m is relatively stable at about 17.3 L/min. The maximum leakage of 18.0 L/min occurs at 13 m. The corresponding rock stratum at the maximum leakage location is 5.90 m of fine floor sandstone. From 14 m to 17 m, the corresponding strata are fine sandstone and sandy shale. The drilling leakage decreases from 18 L/min to 6.2 L/min, and the floor failure depth is 7.72 m. From 18 m to 30 m, the corresponding stratum is sandy shale, and the leakage is always less than 2 L/min. The average leakage across the entire borehole is 6.82 L/min.

The maximum leakage at S-2 between 8 m and 11 m is 18.3 L/min and occurs at 11 m. The corresponding rock stratum of the maximum leakage location is 5.33 m of fine floor sandstone. Between depths of 11 m and 17 m, leakage decreases from 18.3 L/min to 6.1 L/min. At depths of 17 m to 30 m, leakage is stable below 2 L/min. The average leakage across the entire borehole is 5.82 L/min.

According to the statistical analysis of water leakage at the three boreholes, the maximum and average leakage at the premining hole (S-3) are smaller than those at the

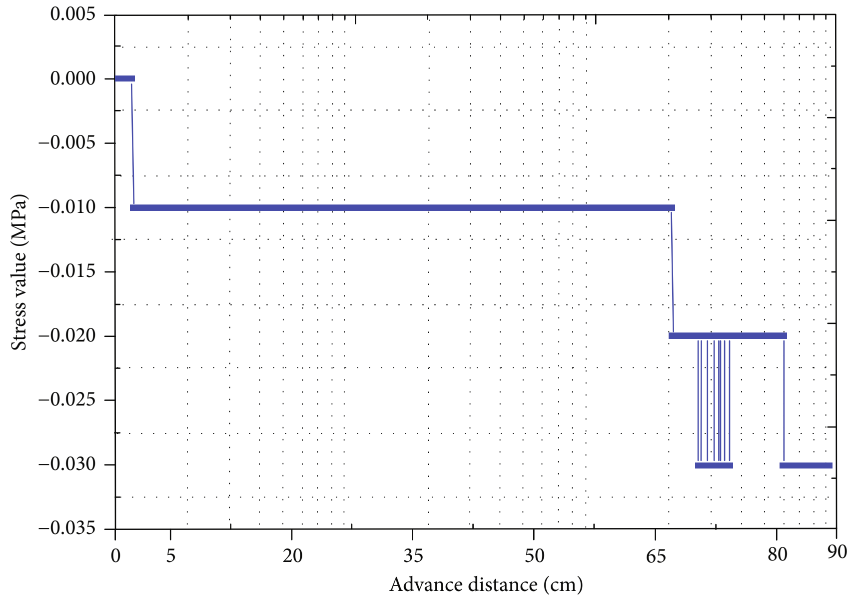

(a) The first cycle

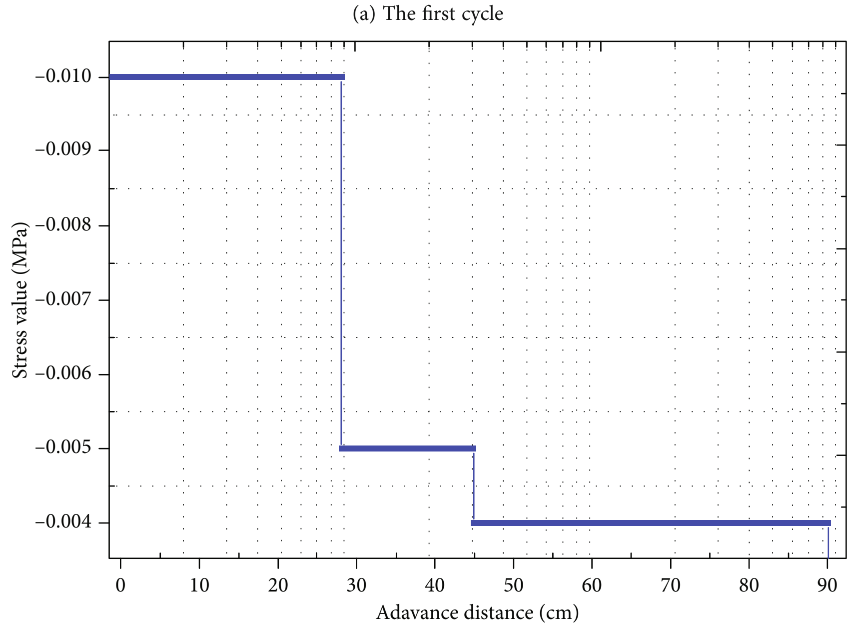

(b) The second cycle

Figure 17: Stress at monitoring point S2-5 vs. the distance advanced.

postmining holes (S-1 and S-2). In addition, analysis of the location of maximum leakage at the postmining holes (S-1 and S-2) and the drilling leakage attenuation process indicates that the fine floor sandstone is damaged and the sandy shale is nearly complete in the process of using PFM in 9211 working face.

4.4. Comparative Analyses. Analysis of the PFM mining process via the similar material simulation experimental method indicates that the overlying rock does not exhibit bubbling down during mining. The overlying rock layer develops microfractures and delamination from the top plate upward, and the fracture stops developing when it reaches approximately 6 times the mining height above the top plate. The overlying rock layer shows the overall bending and sinking phenomenon, and the open fissures formed by mining gradually close with bending and sinking of the rock layer. Therefore, the PFM process avoids formation of a large fissure channel in the roof plate that can cause roof aquifer water to gush into the mining area. At the same time, the laminar demolding method adopted at the end of the simulated excavation reveals that the coupled support system comprised of a top plate, filling body, and bottom plate formed by the PFM mining system transfers the pressure

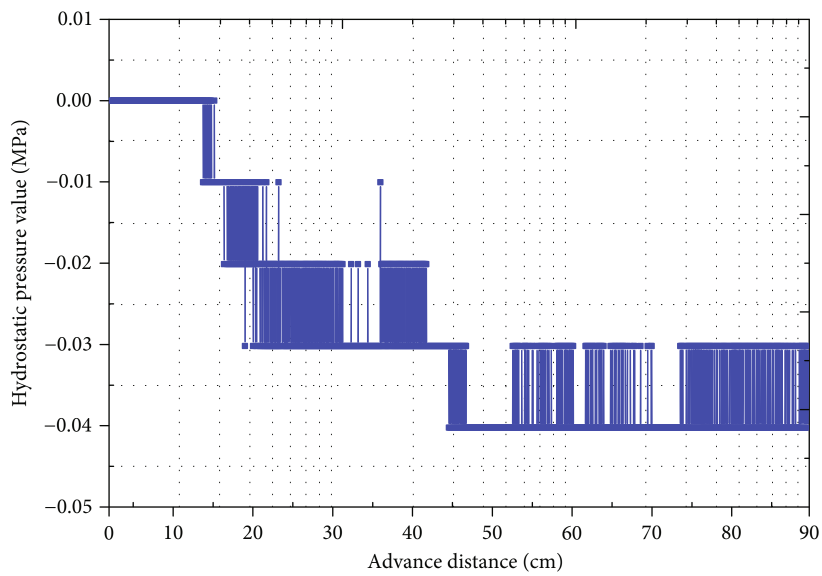

Figure 18: Pore water pressure at monitoring point P1-4 vs. the distance advanced.

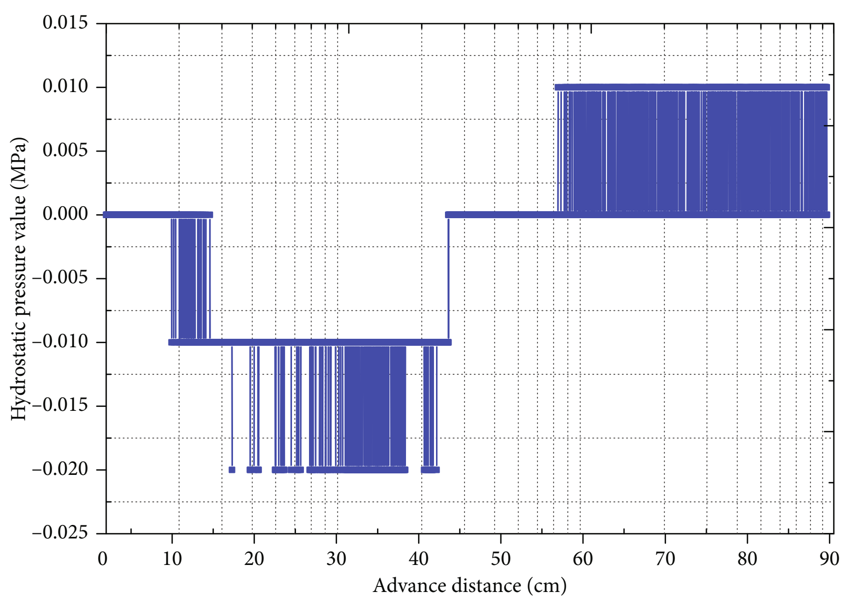

Figure 19: Pore water pressure at monitoring point P1-8 vs. the distance advanced.

of the overlying rock layer to the bottom plate via the filling body. This prevents the bottom plate rock layer from moving to the mining void area. The damage depth of the bottom plate is less than 5 m. Thus, the damage depth of the bottom plate rock layer is reduced, and the effective water barrier thickness of the bottom plate is increased.

In order to provide more accurate feedback on the effectiveness of the PFM method in preventing and controlling sudden bottom slab water, stress and top slab sinkage monitors were arranged in the filling area, transport chute, and track chute of the working face when the method was applied to working face 9211. The actual deformation of the top and bottom plates in the middle and end of the working face is approximately 80.8 mm and 57.4 mm, respectively. Based on the attenuation coefficient of the overlying rock layer, the actual surface deformation is expected to be approximately 56.6 mm and the surface building may be controlled within the Class I damage deformation. At the same time, it is known from the double-end plugger field measurement that the bottom slab damage depth range occurs within the siltstone. The lowest point of the bottom slab fracture development starts 8.95 m from the coal seam

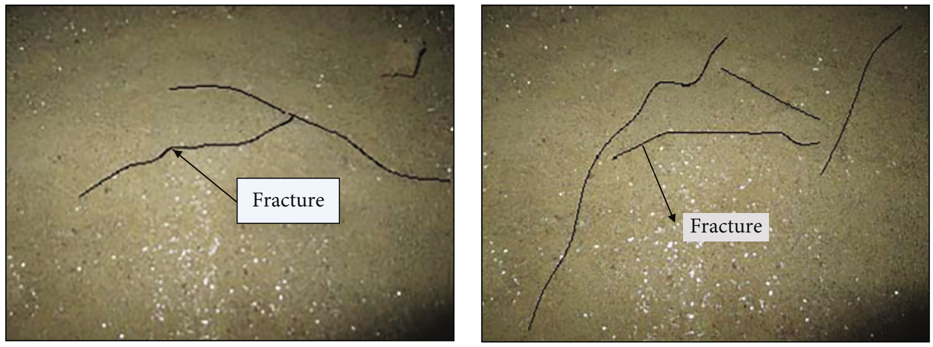

(a) The third layer (b) The second layer

Figure 20: Crack growth and expansion.

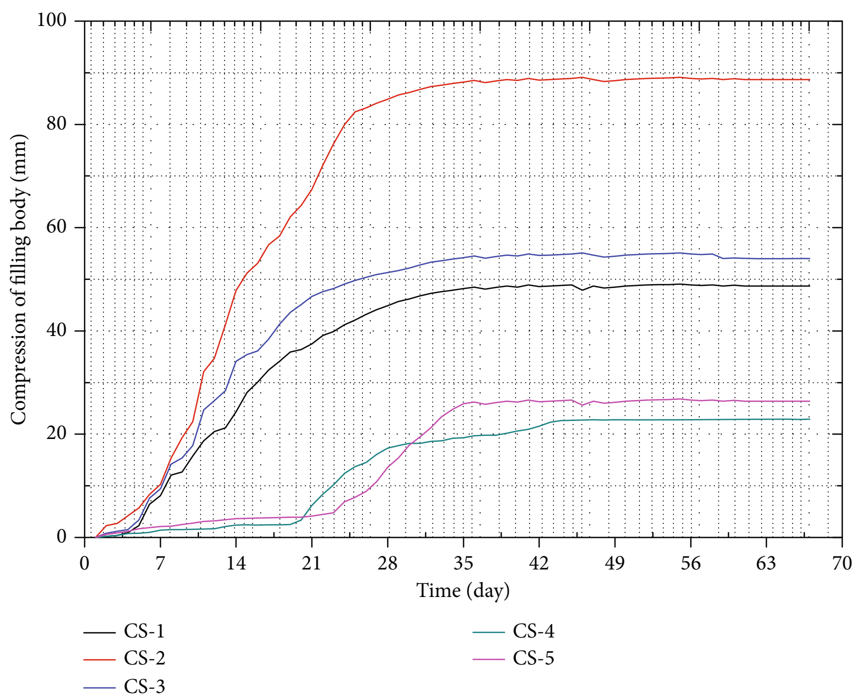

Figure 21: Compressive deformation of the paste backfill body vs. the curing age.

floor. However, according to the empirical formula (7) for the bottom slab damage zone used by the researchers, the bottom slab damage depth is 20.30 m when working face 9211 is mined via the conventional collapse method. Therefore, using this PFM method reduces the bottom slab damage depth by 11.35 m compared to the traditional collapse method. The hydrogeological conditions suggest that the effective water barrier thickness of the bottom slab of working face 9211 after completion of PFM mining is 50.85. According to formula (8), which uses the sudden water coefficient method, the sudden water coefficient is 0.08 MPa/m, which is less than 0.1 MPa/m and therefore safe. The effective water barrier thickness is 50.85:

$$h = 0.0085H + 0.1664\alpha + 0.1079L + 4.3597, \tag{7}$$

where H is the coal seam burial depth, which is taken to be 420 m in this paper; α is the coal seam dip angle, which is taken to be 9.5°; and L is the working face slope length, which is taken to be 100 m:

$$T = \frac{P}{M}, \tag{8}$$

where P is the bottom plate water barrier water pressure limit, which is taken to be 4.11 MPa, and M is the bottom plate water barrier effective thickness, which is taken to be 50.85 m.

In summary, the PFM method can not only effectively control the depth of bottom damage but also consume coal gangue to protect the mine environment and can be promoted and applied under similar conditions.

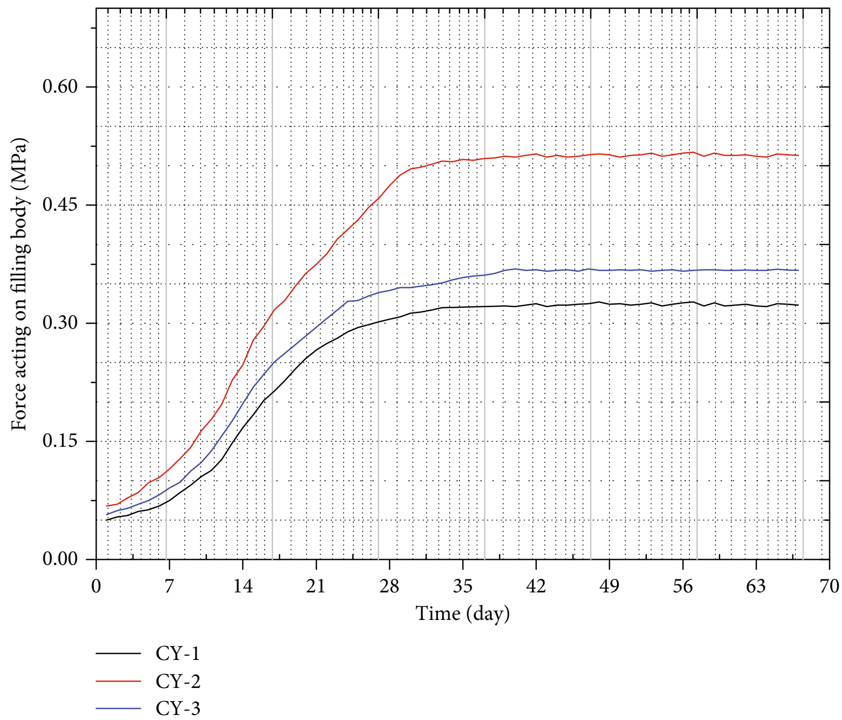

FIGURE 22: Force acting on the paste backfill body vs. the curing age.

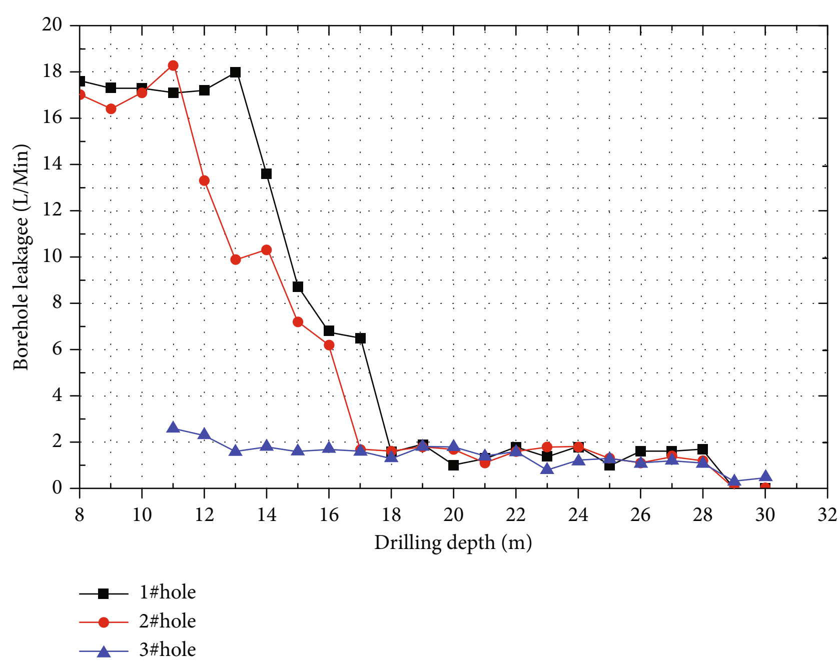

FIGURE 23: Amount of borehole water leakage.

5. Conclusions

Using the hydrogeological conditions of the No. 9211 working face of the Bucun Coal Mine, this paper presented PFM as a method of preventing water from inrushing from the floor. The feasibility of PFM was verified via indoor physical simulation tests and field application. Unlike the traditional water control method, this PFM method considers the relationship between the ground pressure and floor rock mass failure. In addition, coal gangue serves as the main aggregate and fly ash as the main cementing agent; they not only play the role of filling materials but also eliminate the negative impacts of fly ash and coal gangue on the environment. Therefore, this method can be used to prevent and control mine water disasters.

Data Availability

All data, models, and code generated or used during the study appear in the submitted article. For any questions or need for more detailed data, please contact the corresponding author of this article.

Conflicts of Interest

The authors declare that they have no conflicts of interest.

Acknowledgments

This study was supported by the National Natural Science Foundation of China (grants 51574159, 51428401, and 41702270), the Science and Technology Innovation and Entrepreneurship Fund Special Project of Tiandi Science and Technology Co., Ltd. (2019-td-ms004), the Youth Science Fund Project of National Natural Science Fund (51704161), the Shandong Province Natural Science Foundation (grant ZR2014EEM001), and a postdoctoral fund (grants 2015M572068 and 2016T90662).

References

[1] M. Christopher and G. Michael, "Evaluating the risk of coal bursts in underground coal mines," *International Journal of Mining Science and Technology*, vol. 26, no. 1, pp. 47–52, 2016.

[2] W. Y. Guo, T. B. Zhao, Y. L. Tan, F. H. Yu, S. C. Hu, and F. Q. Yang, "Progressive mitigation method of rock bursts under complicated geological conditions," *International Journal of Rock Mechanics and Mining Sciences*, vol. 96, pp. 11–22, 2017.

[3] G. N. Muriithi, L. F. Petrik, W. M. Gitari, and F. J. Doucet, "Synthesis and characterization of hydrotalcite from South African coal fly ash," *Powder Technology*, vol. 312, pp. 299–309, 2017.

[4] S. Vahab and T. Abdollah, "Numerical simulation of the influence of interaction between qanat and tunnel on the ground settlement," *Geomechanics and Engineering*, vol. 23, no. 5, pp. 455–466, 2020.

[5] S. N. Dong, H. Wang, and W. Z. Zhang, "Judgement criteria with utilization and grouting reconstruction of top Ordovician limestone and floor damage depth in North China coal field," *Journal of China Coal Society*, vol. 44, no. 7, pp. 2216–2226, 2021.

[6] S. C. Li, J. Wu, Z. H. Hu, and W. M. Yang, "Mechanics criterion of water inrush from the coal floor under influence of fault and its engineering application," *International Journal of Geomechanics*, vol. 19, no. 5, 2019.

[7] B. Fang, "Method for quickly identifying mine water inrush using convolutional neural network in coal mine safety mining," *Wireless Personal Communications*, 2021.

[8] S. L. Liu, W. T. Liu, and J. J. Shen, "Stress evolution law and failure characteristics of mining floor rock mass above confined water," *KSCE Journal of Civil Engineering*, vol. 21, no. 7, pp. 2665–2672, 2017.

[9] Z. P. Meng, G. Q. Li, and X. T. Xie, "A geological assessment method of floor water inrush risk and its application," *Engineering Geology*, vol. 143-144, pp. 51–60, 2012.

[10] W. C. Song and Z. G. Lian, "Theoretical and numerical investigations on mining-induced fault activation and groundwater outburst of coal seam floor," *Bulletin of Engineering Geology and the Environment*, vol. 76, no. 23, pp. 1–15, 2021.

[11] L. L. Xiao, Q. Wu, C. Niu et al., "Application of a new evaluation method for floor water inrush risk from the Ordovician fissure confined aquifer in Xiayukou coal mine, Shanxi, China," *Carbonates and Evaporites*, vol. 35, no. 3, 2020.

[12] J. W. Cheng, G. Zhao, G. R. Feng, and S. Y. Li, "Characterizing strata deformation over coal pillar system in longwall panels by using subsurface subsidence prediction model," *European Journal of Environmental and Civil Engineering*, vol. 24, no. 5, pp. 650–669, 2020.

[13] H. Karimi, E. Raeisi, and M. Bakalowicz, "Characterising the main karst aquifers of the Alvand basin, northwest of Zagros, Iran, by a hydrogeochemical approach," *Hydrogeology Journal*, vol. 13, no. 5-6, pp. 787–799, 2005.

[14] G. Panagopoulos, N. Lambrakis, C. Katagas, D. Papoulis, and P. Tsolis-Katagas, "Water–rock interaction induced by contaminated groundwater in a karst aquifer, Greece," *Environmental Geology*, vol. 49, no. 2, pp. 300–313, 2005.

[15] C. S. Wang, Y. J. Jiang, R. C. Liu, C. Wang, Z. Y. Zhang, and S. Satoshi, "Experimental study of the nonlinear flow characteristics of fluid in 3D rough-walled fractures during shear process," *Rock Mechanics and Rock Engineering*, vol. 5, no. 6, pp. 2581–2604, 2020.

[16] Z. Z. Cao, Y. L. Ren, Q. T. Wang, B. H. Yao, and X. C. Zhang, "Evolution mechanism of water-conducting channel of collapse column in karst mining area of southwest China," *Geofluids*, vol. 2021, 8 pages, 2021.

[17] Y. L. Lu and L. G. Wang, "Numerical simulation of mining-induced fracture evolution and water flow in coal seam floor above a confined aquifer," *Computers and Geotechnics*, vol. 67, pp. 157–171, 2015.

[18] S. L. Liu, S. Dai, W. P. Li, B. Han, B. He, and J. P. Luo, "A new monitoring method for overlying strata failure height in Neogene laterite caused by underground coal mining," *Engineering Failure Analysis*, vol. 117, article 104796, 2020.

[19] B. L. Zhang and Z. B. Meng, "Experimental study on floor failure of coal mining above confined water," *Arabian Journal of Geosciences*, vol. 12, no. 4, 2019.

[20] L. W. Chen, X. Q. Feng, D. Q. Xu, W. Zeng, and Z. Y. Zheng, "Prediction of water inrush areas under an unconsolidated, confined aquifer: the application of multi-information superposition based on GIS and AHP in the Qidong Coal Mine, China," *Mine Water and the Environment*, vol. 37, no. 4, pp. 786–795, 2018.

[21] Q. X. Gu, Z. Huang, S. J. Li, W. Zeng, Y. Wu, and K. Zhao, "An approach for water-inrush risk assessment of deep coal seam mining: a case study in Xinlongzhuang coal mine," *Environmental Science and Pollution Research*, vol. 27, no. 34, pp. 43163–43176, 2020.

[22] W. B. Sun, R. Malekian, J. C. Yu, X. H. Feng, and Z. X. Liu, "Electrical anisotropic response of water conducted fractured zone in the mining goaf," *IEEE Access*, vol. 4, pp. 6216–6224, 2016.

[23] M. Z. Naghadehi, R. Mikaeil, and M. Ataei, "The application of fuzzy analytic hierarchy process (FAHP) approach to selection of optimum underground mining method for Jajarm Bauxite Mine, Iran," *Expert Systems With Applacations*, vol. 36, no. 4, pp. 8218–8226, 2009.

[24] X. Guo, J. R. Chai, Y. Qin, Z. G. Xu, Y. N. Fan, and X. W. Zhang, "Mechanism and treatment technology of three water

inrush events in the Jiaoxi River Tunnel in Shaanxi, China," *Journal of Performance of Constructed Facilities*, vol. 33, no. 1, 2019.

[25] A. Li, Y. Liu, L. Mou, and K. Li, "Numerical analysis and case study on the mitigation of mining damage to the floor of no. 5 coal seam of Taiyuan Group by grouting," *Journal of the Southern African Institute of Mining and Metallurgy*, vol. 118, no. 5, pp. 461–470, 2018.

[26] E. Jaouhar, L. Li, and M. Aubertin, "An analytical solution for estimating the stresses in vertical backfilled stopes based on a circular arc distribution," *Geomechanics and Engineering*, vol. 15, no. 3, pp. 889–898, 2018.

[27] N. Jiang, C. X. Wang, H. Y. Pan, D. W. Yin, and J. B. Ma, "Modeling study on the influence of the strip filling mining sequence on mining-induced failure," *Energy Science and Engineering*, vol. 8, no. 6, pp. 2239–2255, 2020.

[28] M. G. Karfakis, C. H. Bowman, and E. Topuz, "Characterization of coal-mine refuse as backfilling material," *Geotechnical and Geological Engineering*, vol. 14, no. 2, pp. 129–150, 1996.

[29] Y. M. Qi, J. Y. Tian-Chyi, Y. C. Wu, M. Li, and Y. H. Hao, "Comparing control methods of water inrush disaster using mathematical programming: modelling, analysis and a case study," *Geomatics Natural Hazards and Risk*, vol. 8, no. 2, pp. 1869–1885, 2017.

[30] W. H. Sui, J. Y. Liu, S. G. Yang, Z. S. Chen, and Y. S. Hu, "Hydrogeological analysis and salvage of a deep coalmine after a groundwater inrush," *Environmental Earth Sciences*, vol. 62, no. 4, pp. 735–749, 2011.

[31] J. T. Chen, L. M. Yin, W. B. Sun, C. Lu, S. C. Zhang, and X. Z. Sun, "Development and application of new deep solid fluid coupling similar materials," *Chinese Journal of Rock Mechanics and Engineering*, vol. 34, no. 2, pp. 3956–3964, 2015.

[32] J. H. Zhao, J. T. Chen, X. G. Zhang, N. Jiang, and Y. Z. Zhang, "Distribution characteristics of floor pore water pressure based on similarity simulation experiments," *Bulletin of Engineering Geology and the Environment*, vol. 79, no. 9, pp. 4805–4816, 2020.

Hindawi
Geofluids
Volume 2022, Article ID 1774110, 11 pages
https://doi.org/10.1155/2022/1774110

Research Article

Determination of Reasonable Width of Filling Body for Gob-Side Entry Retaining in Mining Face with Large Cutting Height

Shijiang Pu,[1] **Guiyi Wu**,[2] **Qinzhi Liu**,[2] **Yuliang Wang**,[2] **Qiang Li**,[2] **and Yu Xiong**[2]

[1]*Faculty of Land Resources Engineering, Kunming University of Science and Technology, Kunming, Yunnan 650093, China*
[2]*Mining College of Guizhou University, Guiyang, Guizhou 550025, China*

Correspondence should be addressed to Guiyi Wu; 495881085@qq.com

Received 3 July 2021; Accepted 24 February 2022; Published 21 March 2022

Academic Editor: Hualei Zhang

When gob-side entry retaining is adopted in the mining face with large cutting height, due to large stope space, strong dynamic pressure, and other reasons, the filling body is usually broken and unstable due to improper width of filling body, and the stability of surrounding rock of a roadway is poor. Taking the actual project of Shaqu mine as the background, we analyze the stability factors of gob-side entry retaining with large mining height, and considering the lateral pressure and overlying load on the filling body, the mechanical model of a gob-side retaining roadway is established, the calculation method of the reserved width of the filling body is simplified, and the reasonable width of the filling body is obtained quantitatively. Through the monitoring results of numerical simulation and field test, the rationality of the calculation results of the reserved width of filling body is verified. The results show that if the width of the filling body is too small, it will not be able to bear the load of the overlying strata, resulting in the fragmentation of the filling body. The larger the width of the filling body, the greater the cutting resistance provided, which can reduce timely the stress on the roadway and above the filling body, and the more stable the retaining roadway is, but when the width increases to a certain value, the displacement of the surrounding rock of the roadway has changed little. When the width of the filling body is 4 m, the stability of gob-side entry retaining can be guaranteed.

1. Introduction

In recent years, in order to reduce the waste of resource, coal pillar-free mining technology is more and more popular in China, which is not only good for improving production rate of mining area, relieving the tension of replacement, resolving the problem of gas accumulation and so on but has also active effect on the prevention of coal spontaneous combustion, impact pressure [1, 2]. Gob-side entry retaining is generally used to mine coal pillar-free mining method; its main idea is to maintain a section of the roadway for using in the next section; according to the different roadway protection ways, roadway retention can be divided into the filling body of gob-side entry retaining and gob-side entry retaining by cutting roof; the two ways under different geological types have own advantages, usually according to different engineering backgrounds to choose the suitable way [3, 4]. Due to the characteristics of large stope space and strong dynamic pressure, many difficult support problems often appear when filling body of gob-side entry retaining in mining face with large cutting height [5–7]. In the case of unreasonable parameter setting of filling body in the early stage, the roof of the roadway is often prone to large-scale, and the number of renovations is more, which seriously hinders the working of coal mining face [8, 9]. The determination of filling body strength, width, and other factors has always been an important condition to be determined at the beginning of the project. Reasonable filling body retention can not only achieve higher economic benefits but also bring more stable bearing effect to the load-bearing system of filling body along the roadway, and it is also more favorable to the control of surrounding rock of the roadway [2, 10].

Based on this, many scholars carry out relevant research on gob-side entry retaining in mining face with large cutting height. It is generally believed that reasonable length width ratio of filling body can greatly increase the yield area and reduce the damage degree of the roadway. Different widths of filling body bear different compressive stress, and the compressive stress will tend to be stable when the width reaches a certain value [11–13]. Pu et al. [14] also studied the width of filling body in gob-side entry retaining in mining face with large cutting height and obtained the setting method of filling body width. The field test also fully verified the correctness of theoretical analysis and numerical simulation. This article was previously published as a preprint. Appropriate strength of filling body can not only relieve roof pressure and strong impact load but also increase support resistance and prevent filling from being crushed [15–18]. Zhang et al. [19] through uniaxial compression test and AE test compared the postpeak performance of high water content material samples and concrete samples, and the results showed that the internal damage of high water content material samples was very slow in the postpeak stage, and the damage was much smaller than that of concrete samples.

The above provides a lot of reference for setting the parameters of filling body in the initial stage of gob-side entry retaining. In terms of initial entry retention, many scholars have focused on the width and strength of the filling body to ensure the stability of gob-side entry retaining. When the strength material selection of the filling body has been determined, the width setting of filling has become a research hotspot. But according to the current research and practice, most scholars only qualitatively analyzed the relationship between the width of the filling body and the support resistance, indicating that the larger the width of the filling body is, the higher the support resistance can be provided, and the stress distribution around the roadway and the mechanical behavior of rock materials are summarized [20–23]. However, there is little research on the stress change of the filling body and the deformation law of the surrounding rock of the roadway. And the preliminary calculation of the width of the filling body should be set, through the tedious calculation formula which can only deduce a large range. Therefore, according to the engineering background of Shaqu mine, we established the mechanical model of gob-side entry retaining, quantitatively determined the minimum width of filling body, and numerically simulated the evolution law of displacement and stress distribution of the filling body with different widths by FLAC^{3D}. Finally, the gob-side entry retaining project in Shaqu coal mine is verified in order to provide reference for similar projects.

2. Working Face Profile

Shaqu mine is located in Lvliang City, Shanxi Province, China. Its main type of coal is coking coal, which is mined by a close coal seam group, as shown in Figure 1. The gas content of coal seam in Shaqu mine is high, the gas emission is large during coal mining, and the gas overrun phenomenon of coal mining face is frequent, which seriously threatens the safety production of mine. In order to implement Y-type ventilation roadway retention technology along a gob, reduce gas accumulation phenomenon at working face, and realize greater utilization of resources, it is decided to adopt the technology along gob roadway retention technology at 24207 working face to create good conditions for safe and efficient mining at working face. The test roadway is 24207 working face belt roadway. The average dip angle of the working face is 5°. The combined mining of 3 + 4# coal seam is between 3.85 m and 4.36 m with an average thickness of 4.17 m. The length of the belt roadway is 1692 m, the length of the track roadway is 1688 m, the length of the working face is 220 m, and the mineable length is 1548 m, as shown in Figure 2. The floor elevation of the working face is between 360 m and 450 m, and the overlying surface of the working face is a loess covered area with the ground elevation between 866 m and 1001 m. The pseudoroof of the working face is not developed, and there is 0.2 m mudstone locally. The immediate roof of the 3 + 4# coal is gray medium fine sandstone with a thickness of about 5 m; the main roof is coarse sandstone with a thickness of about 5.5 m and the black mudstone with a thickness of about 9 m. The immediate bottom of the 3#+4# coal seam is gray medium sandstone with lumpy pyrite, the main bottom is about 2.5 m sandy mudstone, and then, the immediate roof of the 5# coal seam is 0.6 m carbonaceous mudstone.

Figure 1: Geographical situation.

3. Analysis of Bearing Stability of Roadside Filling Body with Mining Face with Large Cutting Height

3.1. Analysis of Influence Factors of Stability. There are many factors affecting the stability of surrounding rock of the filling body of gob-side entry retaining. Gu et al. [24] and Wu et al. [25] conducted an experimental study on the roof of gob-side entry retaining and believed that the weak stability of surrounding rock supporting structure and the low lateral

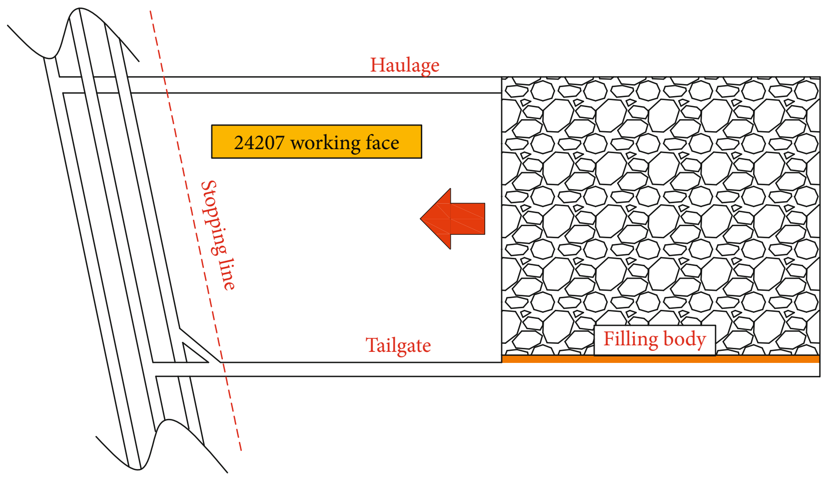

Figure 2: Working face layout.

cooperative bearing capacity of the roof were the subjective reasons for the deformation and failure of surrounding rock of gob-side entry retaining. In order to evaluate the adaptability of gob-side entry retaining, Yang et al. [26] analyzed the weight of each influencing factor under different conditions from geological factors such as coal seam dip angle, mining height, overburden thickness, immediate roof thickness, immediate roof lithology, and roof integrity and showed that mining height had a great influence on the stability of gob-side entry retaining. The overburden stratum at the mining height is a broken decision with activity space; the caving height and height are greater with the increase of mining height, which is a broken fissure zone and the support system on the force source of basic load from the fractured zone rock, so the requirements under the conditions of different mining heights are a broken lane beside the support system of the support resistance which is different also, with the increase of mining height which is broken, filling the pressure also increased significantly, when mining height is broken over after more than a certain value, the support resistance will increase significantly, and roof activity has more influence on the stability of surrounding rock. So for mining face with large cutting height, necessary for the carrying capacity of the filling body and roadway on the auxiliary support, higher requirements are put forward.

The main influencing factors of gob-side entry retaining are the geometric characteristics or geological conditions of the working face, which cannot be changed by humans. In terms of retention and performance of the filling body, reasonable support resistance can adapt to the severe deformation of gob-side entry retaining, and it also requires fast resistance increase speed and low filling cost. However, when the strength of the filling body material is low and the stiffness is small, the bearing capacity of the filling body is limited, and the load of the overburden is mainly borne by coal; then, the filling body has little influence on the lateral fracture law of the basic roof. When the filling materials on the strength and stiffness are bigger and have a certain width, overburden load is shared by the mass media and the roadway beside filling body and roof coal and the pack on the structure of the two supporting functions; key block B in the coal side fracture location will change with the change of the support resistance; when the immediate roof can be large enough to be transferred to the main roof, the support resistance on the key block B may even occur at the gob-side secondary fracture [27, 28]. In the case of different support resistances, the fracture positions of the main roof are mainly divided into the following three categories [29], as shown in Figure 3. Among them, according to different parameters of the filling body, the formation of the bearing structure within the support resistance is different; when the filling body of support resistance and the real bearing capacity of coal are reasonable, the solid coal with filling physical carrying overburden load and lateral cut overburden on the filling body, at this time of roadway stability, is best, as shown in Figure 3(c). The fracture position of the basic roof is not only related to lithology, coal seam dip angle, and other geological factors; on the other hand, a major factor determining the fracture position of the basic roof is the parameter setting of the filling body. Therefore, the setting of filling body width and strength plays a crucial role in the stability of gob-side entry retaining [30, 31].

3.2. The Determine of Reasonable Width of Filling Body. After screening the filling materials of the roadway, it was decided to adopt CHCT paste concrete filling material for retaining the roadway and then add 30 mm gravel. This method can increase the compressive strength of the filling material by about 30% and reduce the cost by about 15%. Therefore, after determining the filling material, the final parameter that determines the performance of the filling body is the width of the filling body. As shown in Figure 4, the mechanical model of load-bearing structure of gob-side entry retaining is established. The filling body beside the gob is mainly subjected to overburden load; friction force between the surrounding rock and lateral pressure is provided by gangue caving in the gob [32].

3.2.1. Lateral Stress Analysis of Filling Body. Assume the gob caving coal gangue on the pack on force F and caving waste rock and filling body above the force for uniform load Q; is the bending angle of roof; the friction angle between the

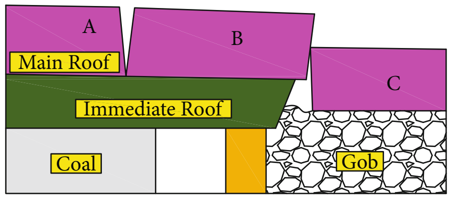

(a) The main roof fracture is above the solid coal body

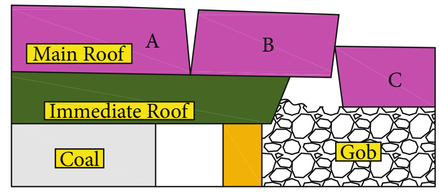

(b) The main roof fracture is above the roadway

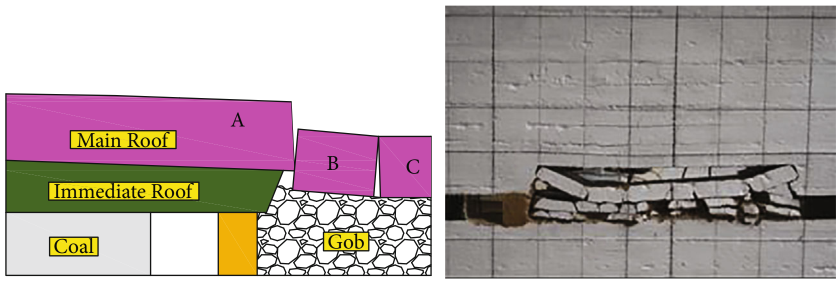

(c) The main roof fracture is located outside the filling body

Figure 3: Main top lateral fracture structure.

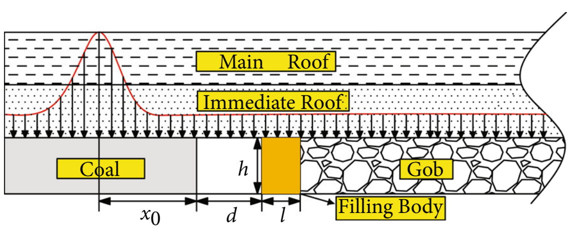

Figure 4: Mechanical model of bearing structure of gob-side entry retaining.

filling body and top coal gangue isδ. Under the condition of mining face with large cutting height, the mining space is large, the dynamic pressure is obvious, the immediate roof is easy to break, and the caving gangue at the bottom of the gob is easy to be compacted. Therefore, the gangue filling body can be approximately regarded as coarse-grain soil for calculation, and F can be regarded as the pressure on the surface of the filling body under the uniform distribution load of gangue. According to the geomechanical conditions, the force F exerted on the filling body at this time is equivalent to the active earth pressure. The Coulomb earth pressure theory is used to calculate [33], and then,

$$F = \frac{1}{2}\gamma h_1{}^2 K_a + h_1 K_a Q \sec\beta, \tag{1}$$

where γ is the average bulk density of filling gangue, h_1 is the height of filling body after compaction, K_a is the Coulomb active earth pressure coefficient, and its value is

$$K_a = \frac{\cos^2\varphi}{\cos\delta\left\{1 + \left[(\sin(\varphi+\delta)\sin\varphi)/\cos\delta\right]^{1/2}\right\}^2}, \tag{2}$$

$$h_1 = h - \Delta h, \tag{3}$$

$$\Delta h = (x_0 + d + l)\tan\beta, \tag{4}$$

where h is the filling height of the filling body and φ is the internal friction angle of the caved gangue. $\Delta h$is for compression deformation of gob side after filling compression;$d$and$l$are roadway width and filling body width, respectively; x_0 is the distance between the bending base point of roof rock beam and the side of gob roadway; and its value is [34]

$$x_0 = \frac{\lambda h}{2\tan\varphi_0}\ln\left[\frac{k\gamma H + (c_0/\tan\varphi_0)}{(c_0/\tan\varphi_0) + (p_0/\lambda)}\right], \tag{5}$$

where λ is the lateral pressure coefficient and 0.36 is taken according to Poisson's ratio; φ_0 and c_0 are the internal friction angle and cohesion of the interface between coal seam and roof and floor, respectively, taking 28° and 2 MPa; k is the stress concentration factor, which is 1.6; H is the buried depth of roadway, taking 529 m; p_0 is the coal support strength, and 2 MPa is taken.

For the filling body, if it is to be stable, its friction force f should meet the following requirements:

$$f \geq F h_1 \cos\delta. \tag{6}$$

The filling body is subjected to friction along the normal direction of the wall. In the case that the buried depth of the working face is large and the stress is large, the gravity action of the filling body can be ignored. Therefore, the friction force of the filling body can be approximated as

$$f = \mu(2Ql + F h_1 \sin\delta), \tag{7}$$

where μ is the friction coefficient between the filling body and the roof and floor.

Equations (1), (2), (6), (4), (5), and (7) are formulated together, and the function of filling body width under lateral

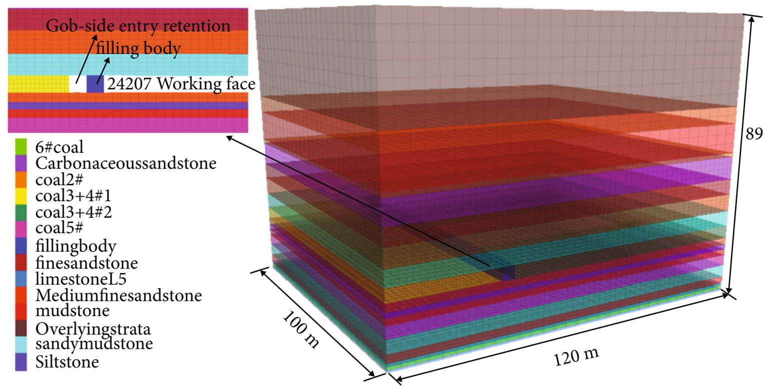

Figure 5: Numerical simulation model diagram.

Table 1: Mechanical parameters of rock mass.

Rock name	Density ($kg \cdot m^{-3}$)	Bulk modulus (Gpa)	Shear modulus (Gpa)	Cohesion (Mpa)	Tensile strength (Mpa)	Internal friction angle (°)
Mudstone	2 350	2.10	1.95	1.5	1.400	32
Fine-grained sandstone	2 600	1.89	1.20	8.3	1.252	35
Coal 2#	1 400	0.72	0.58	1.3	0.325	30
Sandy mudstone	2 600	1.34	1.00	8.2	1.025	36
Coal 3 + 4#	1 400	1.44	1.38	1.3	0.200	30
Siltstone	2 800	4.90	4.67	1.2	1.000	36
Coal 5#	1 400	1.44	1.38	1.3	0.200	30
Limestone L_5	2 730	1.21	1.20	6.3	1.119	40
Coal 6#	1 400	1.44	1.38	1.3	0.200	30
Medium sandstone	2 600	2.67	1.12	8.0	3.170	35
Carbonaceous sandstone	2 520	1.86	1.15	1.4	1.790	33
Filling body	2 950	2.60	1.70	3.0	1.650	34
Overlying strata	2 500	2.28	1.80	6.0	1.550	33

pressure should meet the following requirements:

$$l \geq \frac{Fh_1(\cos\delta - \mu\sin\delta)}{2\mu Q}. \tag{8}$$

The angle of β is related to the filling rate of the filling area. According to the field experience, the angle of β is set as 8°. According to the field investigation of Shaqu mine, relevant parameters can be obtained as follows: $h = 4.2$ m, $\delta = 30°$, $\varphi = 45°$, $Q = 3$ MPa, $\mu = 0.5$, and $d = 4$ m. The minimum width of filling can be obtained as 2.2 m when applied into equation (8).

3.2.2. Analysis of Overburden Load on Filling Body. When the overlying strata are bent and deformed, the load on the filling body is regarded as the weight of the roof strata of the filling body, the roadway, and the weak and broken part of the coal wall, which can be equivalent to the weight of $n = 4$~8 times of the mining height [35]. Therefore, for the filling body with strength q, there is a certain value

$$q \geq \frac{N(l + d + x_0)\gamma_0 h}{l}. \tag{9}$$

The results are as follows:

$$l \geq \frac{N(d + x_0)\gamma_0 h}{N\gamma_0 h - q}, \tag{10}$$

where γ_0 is the volumetric force of the immediate roof and q is the initial strength of the gob-side entry retaining filling body. According to the site conditions, q takes 2 MPa, N takes 4, and substituting formula (10) to get the minimum width of the filling body is 3.9 m.

To sum up, in addition to geological factors, the setting of filling body width and strength plays an important role in the stability of gob-side entry retaining. Whether the filling body can remain stable mainly depends on the friction force of filling body in the horizontal direction and the gravity load of overlying strata. Through comprehensive consideration of calculation, the minimum width of the filling body should be 3.9 m.

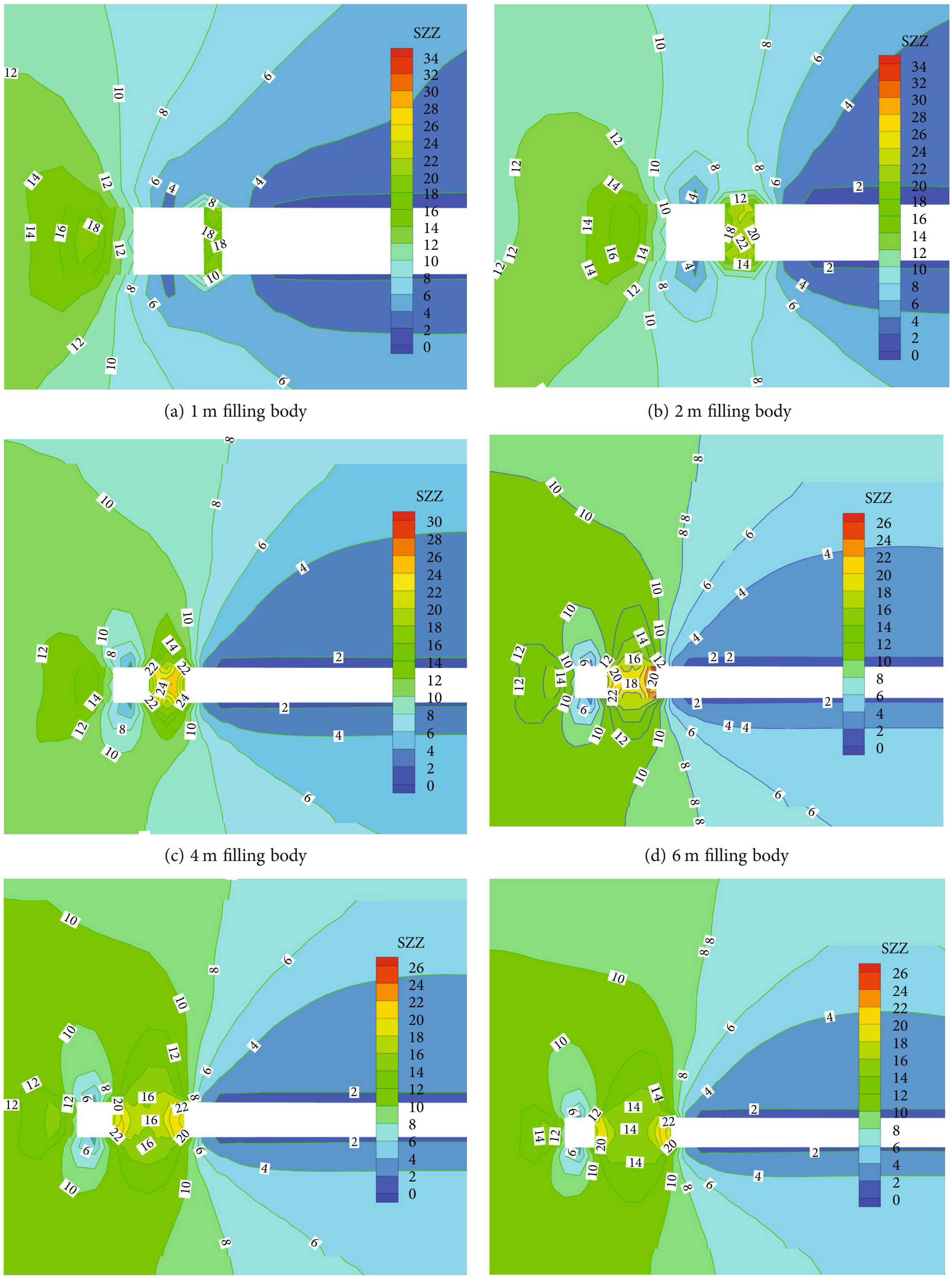

(a) 1 m filling body (b) 2 m filling body

(c) 4 m filling body (d) 6 m filling body

(e) 8 m filling body (f) 10 m filling body

Figure 6: Vertical stress distribution of different filling body widths.

4. Parameter Determination of Roadway Side Filling Body

According to the mechanical model of the bearing structure of gob-side entry retaining, it can be considered that the filling body has the same strength per unit length, and the pouring material of the filling body has been determined. Therefore, the final parameter determining the performance of the filling body is the width of the filling body. According to the actual situation of the 24207 working face, FLAC^{3D} is used to simulate the vertical stress, horizontal displacement, and plastic zone distribution when the filling body width is

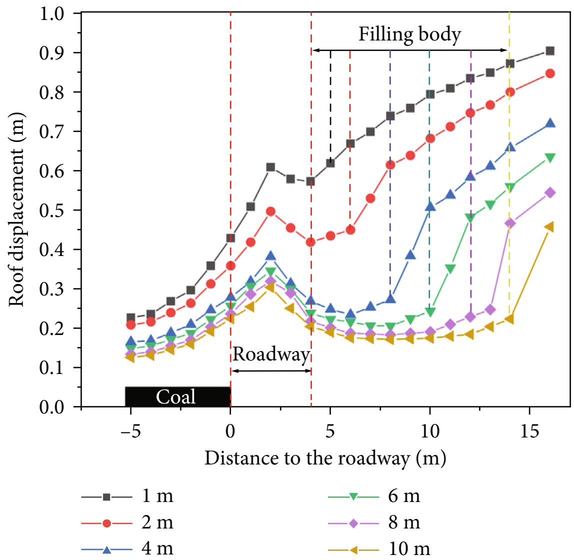

Figure 7: Vertical displacement distribution of the filling body with different widths behind the working face.

1 m, 2 m, 4 m, 6 m, 8 m, and 10 m, respectively. The calculation model as shown in Figure 5 is established, filling body is set in the model in advance, and roadway is excavated first, followed by the working face. The length, width, and height of the model are 120 m, 100 m, and 89 m, respectively. A total of 18 coal beds have been established. The coal seam is near horizontal, and the thickness of the coal seam is 4 m. The bottom boundary of the model is fixed; that is, the displacement of the bottom boundary in X, Y, and Z directions is zero. The top of the model is a free boundary, and the equivalent load is applied to the upper strata. The self-weight load is set in the z-axis direction, and its value is 8.2 MPa. The Molar-Coulomb criterion is used for calculation. By sampling the coal and rock mass of the roof and floor of the 24207 working face on site and testing the mechanical parameters of coal and rock mass in the laboratory, the mechanical parameters of coal and rock mass are obtained, as shown in Table 1.

4.1. Vertical Stress Analysis of Different Filling Body Widths. Figure 6 shows the vertical stress distribution diagram of the filling body with different widths. As can be seen from the figure, with the increase of the width of the filling body, the vertical stress of the filling body increases gradually, and the stress of the roof above and the floor below the filling body also increases gradually. When the filling body width is 6~10 m, the vertical stress of the filling body decreases with the increase of the filling body width, and the stress concentration area gradually changes from the symmetrical type when the filling body width is 1~4 m to the eccentric load type; that is, the stress concentration area changes from the middle part of the filling body when the filling body width is 1~4 m to the side of the filling body near the gob. This is because when the width of the filling body is too small, the resistance of the cutting top is too small to be a bearing body. The main roof breaks at the solid coal body side. Most of the force of the main roof when the main roof is rotated and sunk needs to be borne by the filling body. However, the overbroken filling body cannot play the bearing capacity, which leads to the sharp asymmetric subsidence of the roof and filling body of the roadway. When the filling body is 1 m, the filling body is the smallest, the overall maximum stress is only 18 Mpa, and the stress of roadway roof and floor is 4 MPa. At this time, it is very likely that the roadway roof has subsided violently and the filling body is seriously damaged. When the width of the filling body reaches a certain value, it can provide enough roof cutting resistance. At this time, the stress of the roof and floor of the roadway increases, and the filling body can cut off the roof of the gob side in time, so that the stress of the filling body decreases with the increase of the width, and the stress of the roof and floor of the roadway is normal.

4.2. Vertical Displacement Analysis of Different Filling Body Widths. Figure 7 shows the vertical displacement distribution diagram of the filling body with different widths behind the working face. As can be seen from the figure, roof subsidence decreases gradually with the increase of filling body width. When the width of filling body is 1 m, the maximum roof subsidence is 0.61 m, the serious roof subsidence has occurred, and the asymmetric distribution of roadway deformation is obvious. The side subsidence of the filling body is far greater than that of the solid coal body, and the side subsidence of the gob is also significantly greater than that of the roadway. Because the width of the filling body is too small to form an effective bearing body, the filling body is seriously damaged, and the roof and filling body sink sharply, which is consistent with the stress analysis, and the roof is basically broken on the side of the solid coal body. When the width of the filling body is 2 m, the roof subsidence of the roadway is still very large, the reason is the same as that when the width of the filling body is 1 m, and the roadway and the filling body also have asymmetric deformation. When the width of the filling body is 4 m, the roof subsidence decreases obviously compared with that of 1 m and 2 m. At this time, the subsidence of the roadway and the filling body appears to have obvious symmetrical distribution. The subsidence in the middle of the roadway is the largest, and the two sides are slightly smaller, and the maximum subsidence is 0.38 m. The subsidence in the middle of the filling body is the smallest, and the two sides are slightly larger, and the maximum subsidence of the filling body is 0.27 m. In the controllable range, it shows that the filling body provides the appropriate cutting resistance at this time, which can cut off the roof on the side of the filling body in time, which is conducive to the stability of the roadway and the filling body. When the width of the filling body is 6-10 m, the roof subsidence law is consistent with that of 4 m, but it is not obvious that the subsidence of the roadway and the roof above the filling body is reduced.

4.3. Distribution of Plastic Zone of Filling Body with Different Widths. As shown in Figure 8, the distribution of plastic zone of the filling body with different widths is shown. It can be seen from the figure that when the filling body width is 1 m or 2 m, the filling body has been completely damaged,

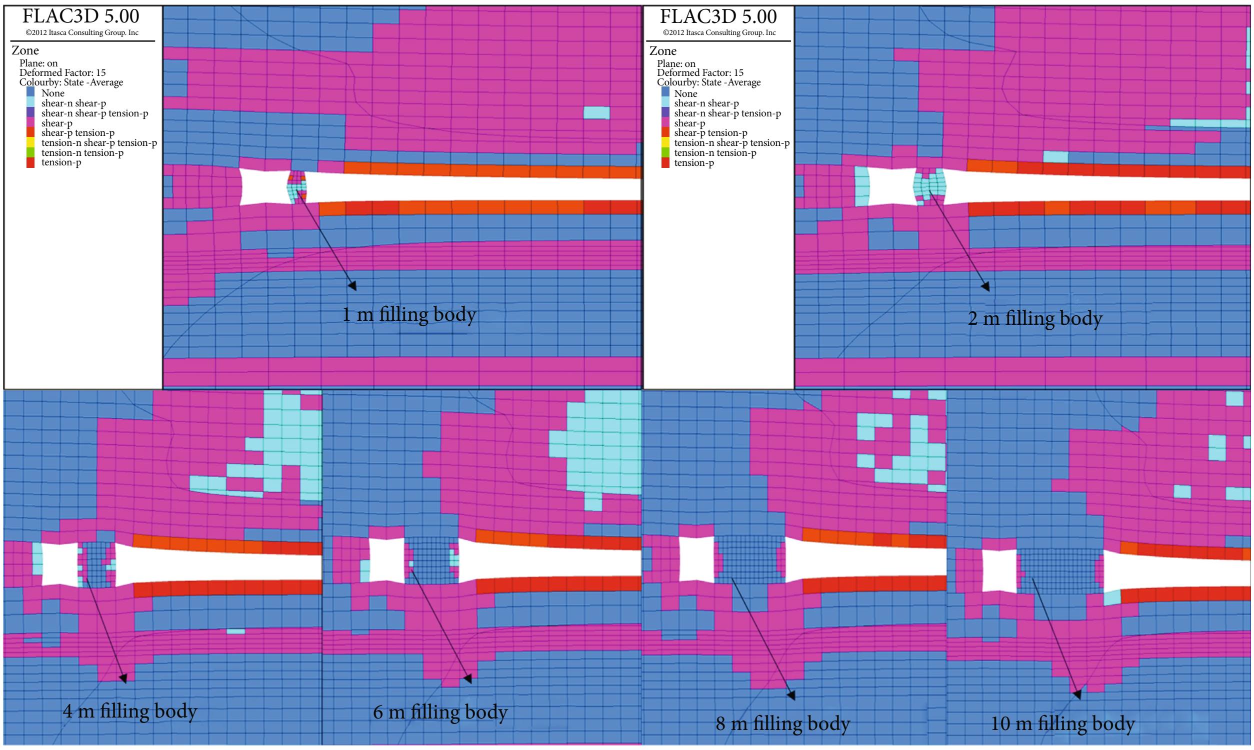

Figure 8: Distribution of plastic zone of different width filling bodies.

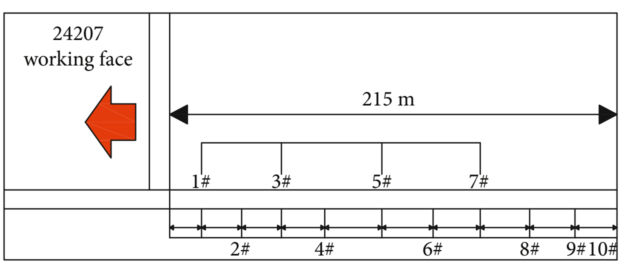

Figure 9: Layout of measuring station for 24207 gob-side entry retaining.

and the surrounding rock deformation of the roadway is serious. When the width of the filling body is 4 m, there is a small amount of plastic damage on both sides of the filling body, and most of the middle area is elastic area, which accounts for more than 80% of the whole filling body. When the width of the filling body is 4~6 m, it can be seen that with the increase of the width of the filling body, the plastic area of the filling body is less, which fully proves that the increase of the width of the filling body is conducive to the stability of the roadside bearing structure.

Therefore, through the analysis of the distribution of vertical stress, vertical displacement, and plastic zone in the working face, it can be concluded that if the width of the filling body is too small, the vertical stress of the filling body will be too small, and the vertical displacement of the roadway roof will be too large. This is because the filling body beside the roadway has been too broken to bear the load, which makes the roadway roof and filling body have serious asymmetric deformation. The larger the width of the filling body, the greater the cutting resistance, the more timely the roof of the gob side of the filling body can be cut off to reduce the stress on the roadway and above the filling body, and the more stable the retained roadway is. However, when the width of the filling body reaches a certain value, with the increase of the width of the filling body, the roof subsidence of the roadway has little change. Based on the above analysis and considering the economic cost, when the filling body width is 4 m, the roadway deformation is within the controllable range, and the plastic failure range of the filling body is less, which has little difference with the theoretical calculation, and the economic cost of this scheme is lower, so the filling body width is selected as 4 m.

5. Field Measurement

Monitoring the support effect of the filling body beside the roadway is an important means to check the success of roadway retaining. According to the above analysis, the survey station layout of the 24207 working face in Shaqu mine is carried out. The measuring station is arranged in the range of 0~260 m behind the working face. The observation work and mining are carried out simultaneously. When the filling length of the retained roadway reaches 220 m, it is installed uniformly and observed in time. As shown in Figure 9, from the working face to 215 m, the distance between 15 m and 30 m is not equal. A surface displacement measuring station is arranged, with 10 groups arranged, as shown in the figure; 1-10 # each surface displacement measuring station is arranged with a comprehensive station, as shown in Figures 1, 3, 5, and 7. The comprehensive measuring station

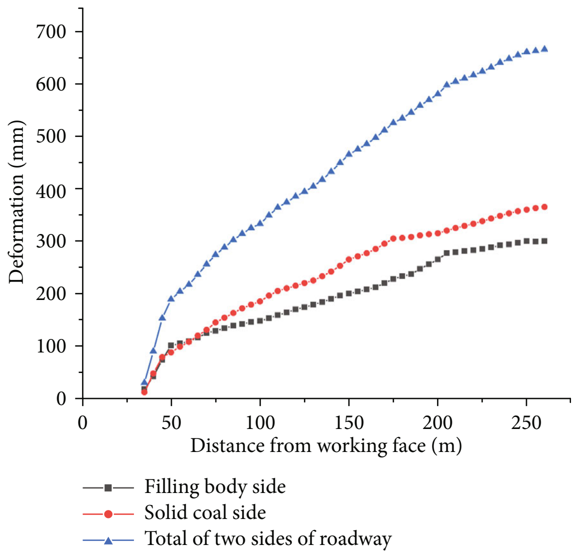

FIGURE 10: Deformation curve of two sides of 24207 gob-side entry retaining.

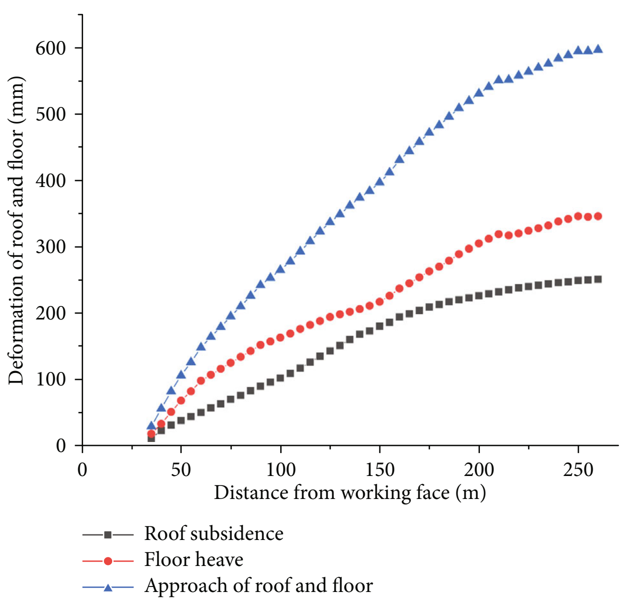

FIGURE 11: Curve of the roof and floor deformation of 24207 gob-side entry retaining.

includes one surface displacement measuring station, one roof off layer measuring station, and one filling body deformation station.

The displacement of the roof and two sides of the gob-side entry retaining of 4 m filling body at the 24207 working face were monitored, and the rationality of the filling body was verified by analyzing the monitoring data. The monitoring results are shown in Figures 10 and 11.

As shown in Figure 10, 24207 gob-side entry retaining two side deformation curves from the figure can be seen; with the farther away from the working face, the greater the deformation of roadway side. As shown in Figures 10, 24207 gob-side entry retaining two side deformation curves

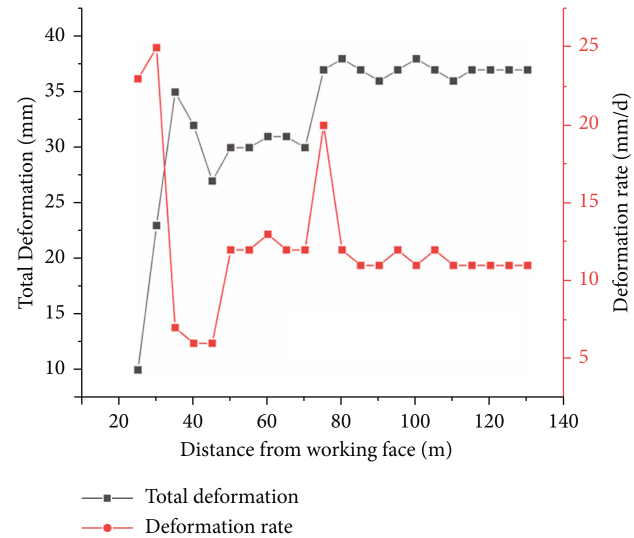

FIGURE 12: Relationship curve between deformation of filling body and distance from working face in 24207 gob-side entry retaining.

from the figure can be seen; with the farther away from the working face, the greater the deformation of roadway side. The deformation rate of the two sides is the fastest at about 30~60 m behind the working face and gradually decreases and tends to be stable after about 200 m behind the working face. The final deformation of the solid coal body side is 365 mm, the final deformation on the filling body side is 300 m, and the total deformation of the two sides is 665 mm. The deformation of the side of the solid coal body accounts for 55% of the total deformation of the two sides, which indicates that the filling body beside the roadway keeps good integrity, and the deformation is mainly affected by the revolving subsidence of the roof.

As shown in Figure 11, 24207 gob-side entry retains the roof and floor deformation curve. It can be seen from the figure that the deformation of the roof and floor is slightly lower than that of the two sides. With the increase of the distance from the working face, the deformation of the roof and floor is greater and then tends to be stable. The final subsidence of the roof is 251 mm, the final heave of the floor is 346 mm, and the final approach of the roof and floor is 597 mm. The deformation degree of the floor is greater than that of the roof, accounting for 58% of the total amount of the approach, which is in line with the deformation law of the surrounding rock of gob-side entry retaining. Moreover, the roof of the roadway has no severe subsidence and obvious cracking, and the floor has no excessive floor heave, indicating that the effect of roadway retaining is good.

As shown in Figure 12, the relationship between the deformation of the filling body and the distance from the working face in gob-side entry retaining is shown. In the figure, the left ordinate represents the cumulative deformation of the filling body (mm), and the right ordinate represents the deformation velocity of the filling body (mm/d). It can be seen from the figure that the filling body has a large deformation in a short time after filling solidification, and the cumulative deformation has reached 32 mm at 35 m behind the working face, and the cumulative deformation after that is only 7 mm. The deformation rate of the filling body has two large changes in the whole process. It shows that the filling body has two large deformations in a short time after filling and solidification. The filling body is greatly affected by the previous two periodic weighting of the working face, and then, the deformation of the wall is not obvious with the stability of the overlying strata.

In summary, it can be seen that the total deformation of the two sides of the roadway and the roof and floor of the roadway tended to be stable after 665 mm and 597 mm, respectively, and the deformation of the solid coal side accounted for 55% of the total deformation of the two sides, indicating that the filling body at the side of the roadway maintained a good integrity, and its deformation was mainly affected by the rotation and subsidence of the roof. The roof of the roadway did not appear to have sharp subsidence and obvious cracking, and the floor did not appear to have large floor heave. The effect of roadway retention was good.

6. Conclusion

(1) This paper analyzes the stability factors of gob-side entry retaining in mining face with large cutting height and obtains the setting of filling body width and strength, which plays an important role in the stability of gob-side entry retaining. Based on the lateral pressure and overlying load on the filling body, the mechanical model of the bearing structure of gob-side entry retaining is established. The minimum width of the filling body is 2.2 m in the lateral direction and 3.9 m in the vertical direction. Finally, the minimum width of the filling body is determined to be 3.9 m by theoretical calculation

(2) By using FLAC^{3D} numerical simulation software, the variation law of stress, displacement, and plastic zone of surrounding rock roadway with the width of filling body is obtained. When the width of the filling body is too small, the filling body has been over broken and cannot bear the bearing effect, resulting in serious asymmetric deformation of the roadway roof and the filling body, and the vertical displacement of the roadway roof is too large. The larger the width of the filling body is, the greater the cutting resistance is provided, the more timely the roof on the goaf side of the filling body can be cut off, the less the stress on the roadway and above the filling body, and the more stable the retained roadway is. Finally, when the filling body width is 4 m, it can ensure the stability of surrounding rock and reduce the economic cost, which has little difference with the theoretical calculation

(3) Through the observation of deformation of roof, two sides, and filling body of 24207 gob-side entry retaining, it is found that the total deformation of two sides and roof and floor tends to be stable after 665 mm and 597 mm, respectively, and the deformation of solid coal body side accounts for 55% of the total deformation of two sides, which indicates that the filling body beside the roadway maintains good integrity, the roadway roof does not appear to have severe subsidence and obvious cracking, and the floor does not appear to have excessive floor heave. The effect of retaining roadway is good, which shows that 4 m filling body can meet the needs of practical engineering and verifies the correctness of theoretical analysis and numerical simulation

Data Availability

All data, models, and codes generated or used during the study appear in the submitted article.

Conflicts of Interest

The authors declare that they have no conflicts of interest.

Authors' Contributions

Shijiang Pu and Guiyi Wu contributed equally to this work.

Acknowledgments

We acknowledge the financial support from the National Natural Science Foundation of China Youth Fund (No. 51904082) and the National Natural Science Foundation of China Regional fund (No. 52064005), the funding from Guizhou Science and Technology Plan Project (Qianke Science Foundation [2020] 1y214), and the funding from Key Laboratory Open Project of Shandong Province (MDPC202019).

References

[1] M. C. He, G. L. Zhu, and Z. B. Guo, "Longwall mining "cutting cantilever beam theory" and 110 mining method in China–The third mining science innovation," *Journal of Rock Mechanics and Geotechnical Engineering*, vol. 7, no. 5, pp. 483–492, 2015.

[2] Z. Zhang, X. Yu, and M. Deng, "Damage evolution of sandy mudstone mechanical properties under mining unloading conditions in gob-side entry retaining," *Geotechnical and Geological Engineering*, vol. 37, no. 4, pp. 3535–3545, 2019.

[3] H. Su, J. B. Bai, S. Yan, Y. Chen, and Z. Z. Zhang, "Study on gob-side entry retaining in fully-mechanized longwall with top-coal caving and its application," *International Journal of Mining Science and Technology*, vol. 25, no. 3, pp. 503–510, 2015.

[4] Y. B. Gao, Y. J. Wang, J. Yang, X. Y. Zhang, and M. C. He, "Meso- and macroeffects of roof split blasting on the stability of gateroad surroundings in an innovative nonpillar mining method," *Tunnelling and Underground Space Technology*, vol. 90, pp. 99–118, 2019.

[5] D. Z. Kong, Z. B. Cheng, and S. S. Zheng, "Study on the failure mechanism and stability control measures in a large-cutting-height coal mining face with a deep-buried seam," *Bulletin of Engineering Geology and the Environment*, vol. 78, no. 8, pp. 6143–6157, 2019.

[6] J. F. Lou, H. P. Kang, F. Q. Gao, J. H. Yang, and J. Z. Li, "Determination of large-height support resistance based on multi-factor analysis," *Journal of China Coal Society*, vol. 42, no. 11, pp. 2808–2816, 2017.

[7] J. F. Lou, F. Q. Gao, J. H. Yang et al., "Characteristics of evolution of mining-induced stress field in the longwall panel: insights from physical modeling," *International Journal of Coal Science & Technology*, vol. 8, no. 5, pp. 938–955, 2021.

[8] J. F. Lou, F. Q. Gao, J. Z. Li, J. H. Yang, X. Q. Wang, and S. Lei, "Research and application of stress (pressure) measurement system for physical modeling," *Journal of China Coal Society*, vol. 44, no. S1, pp. 31–40, 2019.

[9] Y. Xiong, D. Kong, Z. Cheng, G. Wu, and Q. Zhang, "The comprehensive identification of roof risk in a fully mechanized working face using the cloud model," *Mathematics*, vol. 9, no. 17, 2021.

[10] Q. L. Chang, W. J. Tang, Y. Xu, and H. Q. Zhou, "Research on the width of filling body in gob-side entry retaining with high-water materials," *International Journal of Mining Science and Technology*, vol. 28, no. 3, pp. 519–524, 2018.

[11] C. L. Han, N. Zhang, J. H. Xue, J. G. Kan, and Y. M. Zhao, "Multiple and long-term disturbance of gob-side entry retaining by grouped roof collapse and an innovative adaptive technology," *Rock Mechanics and Rock Engineering*, vol. 52, no. 8, pp. 2761–2773, 2019.

[12] Q. Sun, J. Zhang, Y. Huang, and W. Yin, "Failure mechanism and deformation characteristics of gob-side entry retaining in solid backfill mining: a case study," *Natural Resources Research*, vol. 2, 2020.

[13] Z. B. Cheng, L. H. Li, and Y. N. Zhang, "Laboratory investigation of the mechanical properties of coal-rock combined body," *Bulletin of Engineering Geology and the Environment*, vol. 79, no. 4, pp. 1947–1958, 2020.

[14] S. J. Pu, G. Y. Wu, Q. Z. Liu, Y. L. Wang, Q. Li, and Y. Xiong, "Determination of reasonable width of filling body for gob-side entry retaining in mining face with large cutting height," https://www.researchgate.net/publication/351054230.

[15] D. Z. Kong, S. J. Pu, Z. H. Cheng, G. Y. Wu, and Y. Liu, "Coordinated deformation mechanism of the top coal and filling body of gob-side entry retaining in a fully mechanized caving face," *International Journal of Geomechanics*, vol. 21, no. 4, 2021.

[16] J. G. Ning, J. Wang, X. S. Liu, Q. Kun, and B. Sun, "Soft-strong supporting mechanism of gob-side entry retaining in deep coal seams threatened by rockburst," *International Journal of Mining Science and Technology*, vol. 24, no. 6, pp. 805–810, 2014.

[17] B. Zhou, J. Xu, M. Zhao, and Q. Zeng, "Stability study on naturally filling body in gob-side entry retaining," *International Journal of Mining Science and Technology*, vol. 22, no. 3, pp. 423–427, 2012.

[18] S. R. Xie, H. Pan, D. D. Chen et al., "Stability analysis of integral load-bearing structure of surrounding rock of gob-side entry retention with flexible concrete formwork," *Tunnelling and Underground Space Technology*, vol. 103, pp. 103492–107798, 2020.

[19] F. T. Zhang, X. Y. Wang, J. B. Bai, G. Y. Wang, and B. W. Wu, "Post-peak mechanical characteristics of the high-water material for backfilling the gob-side entry retaining: from experiment to field application," *Arabian Journal of Geosciences*, vol. 13, no. 11, pp. 183–186, 2020.

[20] H. Wu and D. Ma, "Fracture phenomena and mechanisms of brittle rock with different numbers of openings under uniaxial loading," *Geomechanics and Engineering*, vol. 25, no. 6, pp. 481–493, 2021.

[21] H. Wu, B. Dai, L. Cheng, R. Lu, G. Y. Zhao, and W. Z. Liang, "Experimental study of dynamic mechanical response and energy dissipation of rock having a circular opening under impact loading," *Mining, Metallurgy & Exploration*, vol. 38, pp. 1111–1124, 2021.

[22] D. Kong, Y. Xiong, Z. Cheng, N. Wang, G. Wu, and Y. Liu, "Stability analysis of coal face based on coal face-support-roof system in steeply inclined coal seam," *Geomechanics and Engineering*, vol. 25, pp. 233–243, 2021.

[23] D. Kong, Q. Li, G. Wu, and G. Song, "Characteristics and control technology of face-end roof leaks subjected to repeated mining in close-distance coal seams," *Bulletin of Engineering Geology and the Environment*, vol. 80, no. 11, pp. 8363–8383, 2021.

[24] Q. Gu, W. Ru, Y. Tan, and Q. Xu, "Mechanical analysis of weakly cemented roof of gob-side entry retaining in fully-mechanized top coal caving mining," *Geotechnical and Geological Engineering*, vol. 37, no. 4, pp. 2977–2984, 2019.

[25] J. K. Wu, W. Zhou, H. Tao et al., "Research on failure characteristics and zoning control technology of thick- soft surrounding rock for deep gob-side entry retaining," *Shock and Vibration*, vol. 2020, Article ID 6613514, 14 pages, 2020.

[26] H. Y. Yang, S. G. Cao, S. Q. Wang, Y. C. Fan, S. Wang, and X. Z. Chen, "Adaptation assessment of gob-side entry retaining based on geological factors," *Engineering Geology*, vol. 209, pp. 143–151, 2016.

[27] X. W. Feng and N. Zhang, "Position-optimization on retained entry and backfilling wall in gob-side entry retaining techniques," *International Journal of Coal Science & Technology*, vol. 2, no. 3, pp. 186–195, 2015.

[28] W. Zheng and H. Duan, "Discussion on stability analysis and support technology of surrounding rock of gob-side entry retaining," *Journal of Vibroengineering*, vol. 21, no. 4, pp. 1058–1068, 2019.

[29] M. L. Zhang, *Study on mechanical characteristics of concrete filling body with large aspect ratio and stability of surrounding rock of gob-side entry retaining, [Ph.D thesis]*, School of Mines, China Univ. of Mining and Technology, Xuzhou, China, 2019, https://kns.cnki.net/kcms/detail/detail.aspx?FileName=1019603722.nh&DbName=CDFD2019.

[30] Y. F. Li and X. Z. Hua, "Mechanical analysis on the stability of surrounding rock structure of gob-side entry retaining," *Journal of China Coal Society*, vol. 42, no. 9, pp. 2262–2269, 2017.

[31] X. Sun, C. Zhao, G. Li, B. Zhang, J. Wang, and F. Cai, "Physical model experiment and numerical analysis on innovative gob-side entry retaining with thick and hard roofs," *Arabian Journal of Geosciences*, vol. 13, no. 23, pp. 1–16, 2020.

[32] X. Liu, X. Z. Ji, and K. J. Miao, "Stress characteristics and stability analysis of coal (rock) body in deep back-filling gob side entry," *Journal of Mining & Safety Engineering*, vol. 37, no. 1, pp. 32–39, 2020.

[33] G. X. Li, B. Y. Zhang, and Y. Z. Yu, *Soil Mechanics*, Tsinghua University Press, Beijing, 2013.

[34] C. J. Hou and X. H. Li, "Stability principle of large and small structure of surrounding rock in gob-side entry retaining in fully mechanized top coal caving face," *Coal Science and Technology*, vol. 26, no. 1, pp. 1–7, 2001.

[35] C. L. Han, N. Zhang, G. C. Li, B. Y. Li, and H. Wu, "Stability analysis of compound bearing structure of gob-side entry retaining with large mining height," *Chinese Journal of Geotechnical Engineering*, vol. 36, no. 5, pp. 969–976, 2014.

Hindawi
Geofluids
Volume 2022, Article ID 9552210, 16 pages
https://doi.org/10.1155/2022/9552210

Research Article

Dynamic Monitoring and Research on the Evolution of the Damage of Weakly Consolidated Coal Floor under Dynamic Pressure Using Distributed Optical Fiber

Chang Liu[1,2] **Pingsong Zhang**[1,2] **Duoxi Yao**[2] **Yutong Tian**[1,2] **and Yuanchao Ou**[1,2]

[1] *State Key Laboratory of Mining Response and Disaster Prevention and Control in Deep Coal Mines, Anhui University of Science and Technology, Huainan City, Anhui Province 232001, China*
[2] *School of Earth and Environment, Anhui University of Science and Technology, Huainan City, Anhui Province 232001, China*

Correspondence should be addressed to Pingsong Zhang; pszhang@aust.edu.cn

Received 9 September 2021; Accepted 24 February 2022; Published 19 March 2022

Academic Editor: Zhijie Wen

During the extraction of coal seam, the evolution pattern of the rock is an important element for controlling the rock seam and preventing water damage to mine. In order to obtain the deformation and damage of weakly cemented coal seam footings under dynamic pressure, the stability of the footings was studied using a combination of various methods, including rock mechanics testing, field testing, and numerical simulations. By sticking distributed optical fiber on the surface of rock samples, the degree and location of rupture on the surface of rock samples could be obtained using the strain response correlation for optical fiber. Two monitoring holes were arranged in the bottom plate of coal seam at 12307 working face of a mine in Ordos Basin, China. Moreover, a distributed optical fiber sensor was implanted in the hole. The results show that the failure depth was 16.5 m. On the other hand, the numerical simulation results show that the failure depth of the bottom plate was 16.0 m, which agreed well with the measured value. The distribution characteristics of the maximum principal stress of the bottom slab during the advancement of working face were obtained using three-dimensional (3D) numerical model. Based on the distributed optical fiber strain tests in the two boreholes in the same vertical profile and combined with the natural proximal interpolation method, the interhole strain increment distribution profile was obtained. The research results provide a reference for the safe mining of coal resources and the prevention and control of water damage in the mine floor.

1. Introduction

The stress concentration caused by coal seam mining can lead to the redistribution of regional rock stress, which in turn leads to changes in the stress state of the coal seam floor rock, deformation, damage, and movement [1]. In the hundreds of meters deep quarry space, the rock material has the characteristics of nonhomogeneity, irregularity, and anisotropy. Coupled with the complex geological conditions and hydrogeological conditions, the deformation and breakage of surrounding rock under dynamic pressure may result in the development of hydraulic fissures and the destabilization of the bottom water barrier to induce sudden water, which poses a great threat to safe and efficient mining of coal mines [2]. The distribution of stress-strain field and the deformation characteristics of the bottom slab rock are one of the primary conditions for studying the depth and extent of damage of the bottom slab. Therefore, monitoring the variations in the geophysical field of coal seam bottom slab and mastering the damage characteristics of bottom slab during coal mining are important elements of mine containment and water damage prevention [3].

At present, many scholars have conducted a lot of research on the evolution of mining damage in coal seam floor. Theoretical studies by Meng et al. [4] obtained the mechanical analytical correlation of any point of the bottom plate by establishing the mechanical model of the bottom plate. Wang et al. [5] considered the stress characteristics of the strike and tendency of the working face and established a spatial semi-infinite body model. They also deduced the iterative correlation for calculating the vertical stress of the bottom plate. Lu et al. [6] established the mechanical model under the joint action of mining and confined aquifer and obtained the distribution of vertical stress, horizontal stress, and shear stress along the strike of stope floor. Considering the influence of mining pressure and nonuniform hydraulic pressure, Liang et al. [7] proposed two-dimensional hydromechanical calculation model and key layer stability analysis model. By solving for the analytical solution, the methods could help in studying the failure depth and failure characteristics of coal seam mining floor. However, the stope environment is complex, under which, it is difficult to comprehensively consider all the factors. The analytical solution is helpful in studying the damage depth and damage characteristics of the coal seam mining floor. However, the complex environment of the mining site makes it difficult to consider all variables in a comprehensive fashion. Liu et al. [8] conducted numerical simulations on the failure characteristics of the floor of 3306 working face to determine the sensitivity of each major factor that contributes to the failure depth of the floor. Kmab et al. [9] used RFPA (rock failure process analysis) that considers the heterogeneity of the coal rock to simulate the progressive failure process of coal seam floor during mining. Zhang et al. [10] implanted distributed optical fiber sensors in the material model to detect the characteristics of the strain response during mining. Du et al. [11] implanted distributed optical fiber and FBG in the roof of the model and analyzed the deformation and failure of overburden according to the parameter response characteristics. Based upon customized confined water simulation equipment, Jiang et al. [12] conducted similar simulation tests on the fracture and instability characteristics of the roof and floor of the mining face above the aquifer and obtained the variation patterns of the stress of the roof and floor during the mining process. Compared with the field test, the similar model has the features of easy operation, short time consumption, and outstanding effect. Most of the existing similar models are mainly the two-dimensional models, whereas only a handful of three-dimensional models are developed due to the limitations of test equipment and sites. Field tests of the deformation damage of the quarry rock include seismic wave lamination method [13], microseismic monitoring method [14], high-density electrical method [15], and borehole television [16]. Field testing is the most direct testing method to capture the deformation of a rock and the damage under complex geological environment and variables.

In recent years, fiber optic sensing technology has found its way into geological hazard monitoring due to its high accuracy, insulation, and anti-interference features. The technology has been used to monitor the development of the fracture of surrounding rock and accurately reflect its deformation characteristics according to the correspondence between the fiber optic strain and the rock collapse movement [17, 18]. The related research only applies the distributed optical fiber sensing technology to the stope rock stratum test, which cannot be used to comprehensively study the response characteristics of strain to rock stratum deformation and fracture process. Based on distributed fiber, the rock mechanic test is used to compare the deformation and failure stages of rock samples with the fiber strain data. The results provide basis for the analysis and interpretation of field test data. Meanwhile, two one-dimensional borehole datasets in the same plane are combined, and the natural adjacent point interpolation method is used to obtain the two-dimensional strain profile between the layers, which provides a new method for optical fiber data processing. This paper takes the coal seam mining floor in 12307 working face of a coal mine in Ordos Basin (Figure 1) as the research object. Two floor drilling holes are arranged, and distributed optical fiber sensors are implanted in the holes. The disturbance characteristics of coal seam floor rock mass at different depths during the mining process are monitored by drilling distributed optical fiber sensors. Based on distributed optical fiber rock mechanics test, the measured data are analyzed to obtain the mining failure depth of the floor. Meanwhile, the finite difference software, FLAC^{3D} [8], is used to build a three-dimensional (3D) numerical model, whereas further analysis is carried out according to the regional distribution of plastic zone of coal floor.

2. Experiments

The rock uniaxial loading test was performed using the MTS 816 instrument [19]. Figure 2(a) shows the schematic of the testing system and includes loading device, optical fiber, distributed fiber demodulator, jumper, and lighting device. The rock sample was made up of sandstone and obtained from the field monitoring hole with the dimensions of 50 mm × 100 mm (diameter × height) (Figure 2(b)). The loading rate was 0.005 mm/s for strain dynamic testing of uniaxially loaded rock samples. Under indoor conditions, the variation in room temperature was very small, and the effect of temperature on the distributed fiber was negligible.

Figure 3(a) shows the axial strain record of MTS 816. During the first 214 s of loading, the rock sample underwent original pore compression and linear elasticity. When it was loaded to 214 s and the axial pressure became 141.9 kN, local cracks appeared on the surface of the rock sample. The first inflection point appeared in the time axial force curve. During the continuous pressurization of MTS 816, the local fractures were closed. Meanwhile, the rock sample continued to bear, and the bearing pressure continued to increase. When the pressure increased to 279 s and the axial pressure became 134.4 kN, the local cracks of the rock sample were penetrated. The fracture was formed, and the bearing capacity disappeared. The second inflection point appeared in the time axial force curve. The results presented in Table 1 show the whole process. Figure 3(b) shows the cloud diagram of distributed optical fiber test results. It can be seen that, before the formation of local fractures, the microstrain increment of rock sample became positive, and the optical fiber accumulated large tensile strain. After the local cracks were generated, the energy at the fracture position was released, and the strain value decreased. Based upon the previous high increment in strain, it suddenly dropped and even appeared to have negative value. After continuous pressurization, the fracture was closed, and the rock continued to

FIGURE 1: Geographical location of the study area.

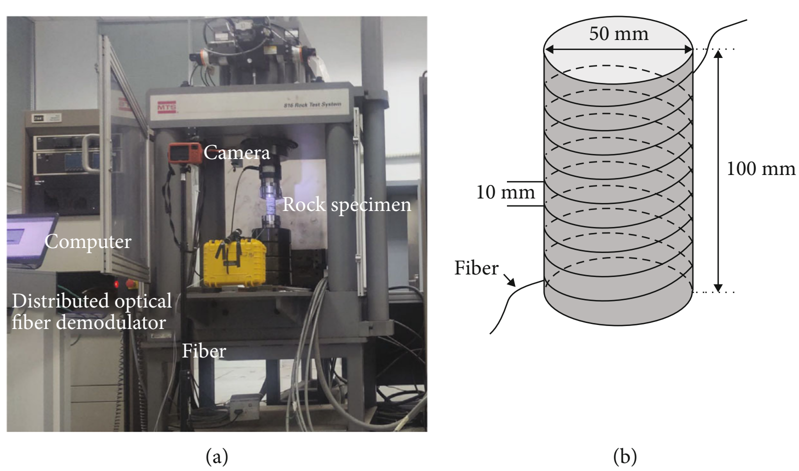

FIGURE 2: Schematic of the testing system (a) and rock sample and fiber winding method (b).

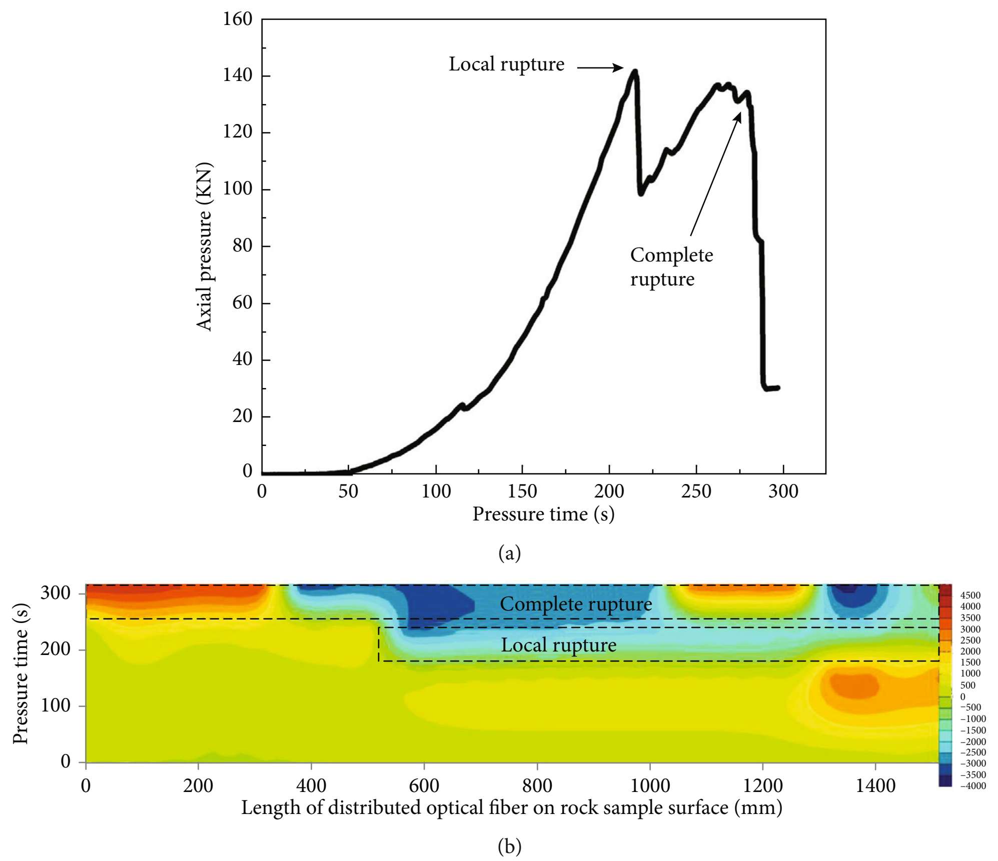

FIGURE 3: Pressure time-axial stress curve of MTS 816 (a) and strain evolution nephogram of axially pressurized distributed optical fibers (b).

TABLE 1: Loading process of the rock samples.

Loading time (s)	Axial pressure (kN)	Degree of rock sample damage
0 ~ 214	141.9	Initial pore compression and linear elasticity stages
214~279	98.8 ~ 134.4	Local fissures
>279	<134.4	Completely destroyed

bear until it was completely destroyed. At this time, the energy accumulated by the rock sample was completely released. Combined with the optical fiber strain increment nephogram, the strain increment had a second obvious change, indicating the characteristics of rock fracture.

The strain burst observed by distributed optical fiber corresponded clearly to the spatial spread of cracks on the specimen surface, which could reasonably circle the location of the area where rock damage occurred and sensitively capture the information of rock rupture precursors.

3. Numerical Simulation

3.1. Engineering Geology Overview. Figure 4 shows the spread of the mining area. Mining is mainly conducted in 3-1 coal seam, which belongs to the upper 3 coal group of the Jurassic Middle and Lower Eolian section. The geological conditions of the coal seam in this working face are relatively simple. The thickness of the coal seam in the working face varies greatly, and the average thickness of the coal seam mined in the retrieval range is about 2.2 m. It is a near-horizontal coal seam, and the dip angle of the stratum is $0 \sim 2^{\circ}$. The coal seam is black, with black-brown stripes and dull luster, dominated by dark coal and silk charcoal, and contains a small amount of bright coal with exogenous fissure development. The direct bottom of its bottom plate is sandy mudstone with more developed fissures, and the old bottom is siltstone. The substrate as a whole consists of weakly cemented rock layer. No large fractures and folding structures are found in the area. However, vertical microfissures are developed, which make the back mining face prone to sudden water threat.

3.2. Numerical Model. According to the stratigraphic division of the study area and the comprehensive bar chart of the borehole (Figure 4), the mechanical parameters of the bottom slab rock were obtained using indoor rock mechanics tests (Table 2). The numerical calculation model was

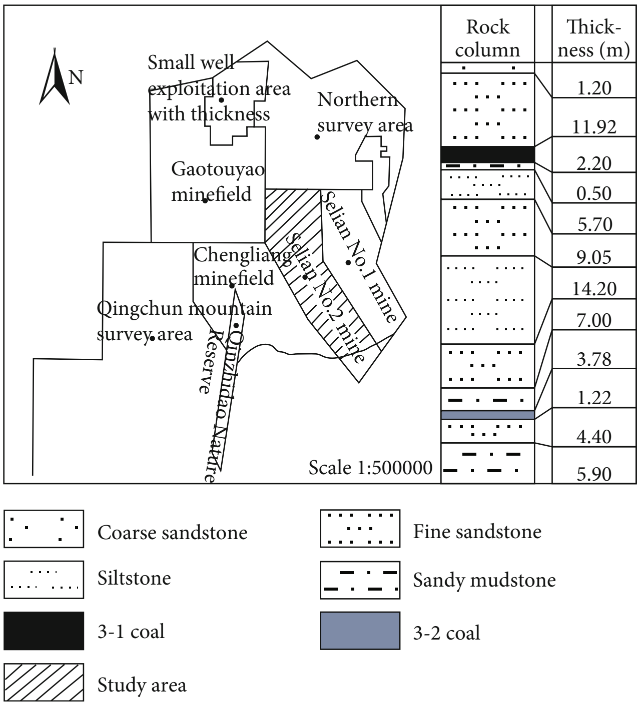

Figure 4: Location of the mining area and stratigraphic lithology histogram.

established, as shown in (Figure 5). Surrounding pressure was applied to the model, and all calculations were completed using the generalized Mohr-Coulomb damage criterion [20]. Mohr-Coulomb theory is more in line with the fracture mechanism of mine surrounding rock and can accurately reflect the mining failure depth of coal seam floor.

As shown in Figure 5, the model was 300 m long in the x-direction, 360 m wide in the y-direction, 80 m high in the z-direction, and 2.2 m thick in coal seam. The 3D model was divided into 206719 units and 194400 nodes. The mechanical boundary conditions of the model are as follows: the fully constrained boundary conditions are adopted at the bottom. The free boundary is adopted at the top of the model, and the surface force is applied to replace the rock stratum that cannot be simulated by the model. Free boundary condition is adopted for coal seam roof. The front, rear, left, and right boundaries of the model are fixed in X and Y directions.

3.3. Simulation Results and Analysis. By simulating the process of advancing the working face along the strike, the cloud diagram of the maximum principal stress distribution and the variation trend of the range of plastic zone affected by disturbance at different depths of the coal seam floor are studied. The variation patterns of deformation and damage to the bottom slab during mining are summarized. The simulation process and the corresponding results are shown in Figure 6.

As can be seen from Figure 6, with the advance of the working face, the maximum principal stress of the floor strata of coal seam was affected by abutment pressure, and the value of the maximum principal stress changed accordingly. The $0 \sim 10$ m in front of the work was significantly affected by the advance bearing pressure, and the surrounding rock appeared to undergo stress concentration, which is similar to the conclusion on the stress distribution in the front of the work obtained by Liang [21]. During the mining process, the maximum principal stress in the stress concentration area reached -22.1 MPa. The area below the goaf was a pressure relief area, and with the advancing of the working face, the pressure relief area gradually increased, and the rock stratum produced large deformation after unloading. There was a large range of tensile stress area in the floor of goaf, and the integrity of the rock stratum in the floor of goaf was damaged, which resulted in a continuous increase in the tensile stress area. The floor rock stratum in goaf changed from initial shear failure to tensile bending failure. With further intensification of stress concentration, the tension bending failure occurred in the floor strata of goaf. The distribution of maximum principal stress reflected the failure pattern of floor rock stratum to a certain extent [22].

Figure 7 shows the distribution of bottom plate's failure plastic areas with different excavation distances. It can be seen that, under the action of advance support pressure, the floor rock stratum mainly underwent compression shear plastic failure, and tension failure occurred in the front of the work. With the mining of the working face, the rock mass of the floor of the goaf underwent tensile failure under the action of unloading, forming a certain range of active plastic area. The mining fissures increased with the continuous advancement of the working face, and the failure range of the rock mass increased. There were positive and negative shear stress variation zones in the rock mass under the floor near the elastic-plastic junction at both the ends of the working face. The existence of the shear stress variation zones could promote crack propagation and form compression shear or tension shear failure. This is similar to the conclusion of floor damage obtained by Li [23]. The collapse of the upper strata of the coal seam and recompaction of the goaf weakened the unloading effect of the floor rock mass, so that the development of the floor fault zone slowed down until it completely stopped. At the end of the excavation, the results of plastic zone show that the maximum failure depth of the bottom plate was 16.0 m, while its failure boundary was shear failure mode.

4. Technology Principle

4.1. BOTDR Principles. Fiber optic sensing technology is a direct, continuous, real-time monitoring of the physical parameters at the location of the fiber and makes use of geometrically one-dimensional characteristics of the fiber and the Brillouin scattered optical power frequency shift with the measured temperature or strain parameters as a function of the fiber position length. The effect of strain and temperature on the Brillouin frequency shift can be expressed using Equation (1) [24].

$$V_B(\varepsilon, T) = V_B(0) + \frac{dV_B(\varepsilon)}{d\varepsilon}\varepsilon + \frac{dV_B(T)}{dT}T, \qquad (1)$$

where $V_B(\varepsilon, T)$ represents the Brillouin frequency shift value

Table 2: Mechanical parameters of rock mass in the model.

Lithology	Modulus of elasticity E (GPa)	Modulus of shear G (GPa)	Cohesion C (MPa)	Angle of internal friction ψ (°)	Tensile strength Rm (MPa)	Density Y (kg/m^3)
Coal	7.6	0.6	2.7	31.4	0.35	1460
Siltstone	15.6	2.5	3.1	35.2	1.45	2650
Fine sandstone	15.2	1.52	3.2	36.0	1.65	2675
Medium sandstone	13.7	4.3	3.0	35.4	1.6	2697
Coarse sandstone	12.7	5.8	2.8	34.9	1.55	2705
Sandy mudstone	10.2	2.56	2.9	37.5	1.3	2659

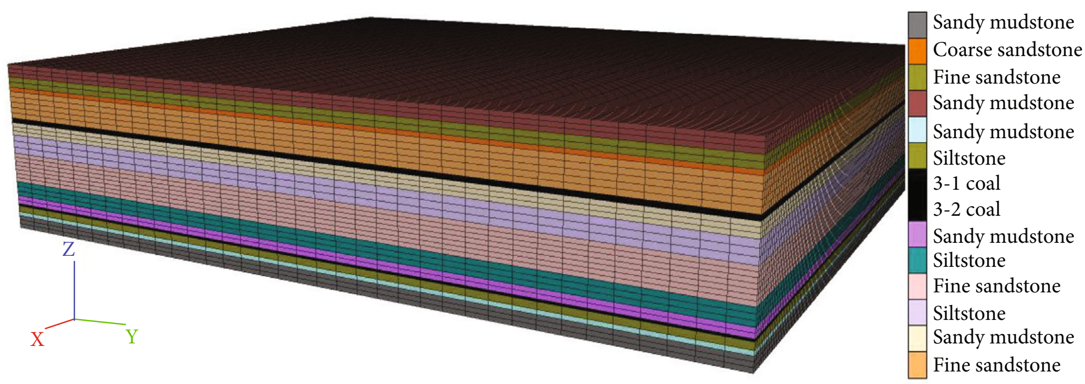

Figure 5: Three-dimensional numerical model.

under temperature and pressure, $V_B(\varepsilon)/d\varepsilon$ represents the Brillouin frequency shift-strain coefficient, $dV_B(T)/dT$ represents the Brillouin frequency shift-strain coefficient, T is the temperature (°C), and ε is the fiber axial micro strain ($\mu\varepsilon$). When the change in test temperature was less than 5°C, the Brillouin frequency shift due to the temperature change could be ignored; however, the Brillouin frequency shift of the fiber axial strain was considered. By measuring the Brillouin frequency shift of the stretched fiber (Figure 8), the strain of the fiber can be obtained by the linear relationship between the amount of change in the frequency shift and the strain of the fiber. Moreover, L represents the distance from the location where scattering occurred to the incident end of the pulsed light. The value of L can be calculated by Equation (2) using optical time domain analysis.

$$L = \frac{ct}{2n}, \tag{2}$$

where c denotes the speed of light in vacuum, n is the refractive index of the fiber, and t is the time interval between the emitted pulsed light and the received scattered light.

4.2. Fiber Optic Strain Test Base Rock Deformation Principle. The distributed monitoring of mining bottom deformation is to implant fiber optic cables in the coal seam and bottom rock. When any deformation occurs in the coal seam, the sensing optical fiber responds to the strain parameters of the bottom rock seam under different mining conditions at the working face. Based upon the results obtained using Equations (1) and (2), the strain value of each point along the sensing optical fiber is obtained. Furthermore, the stress-strain distribution information in the coal seam floor is continuously monitored to realize the dynamic monitoring of the deformation and damage of the floor rock with the progress in the mining process. Additionally, the stress-strain distribution helps in obtaining the state of the development of fracture of the floor or the failure depth of the rock, which provides a basis for mastering the evolutionary pattern of the actual working face floor damage. The outstanding advantage of this monitoring method is that it makes up for the shortage of point monitoring and can obtain continuous distribution information of the measurement in space and time, thus realizing the purposes of real-time, long-distance, and distributed monitoring.

5. Field Testing

5.1. Test Program. The optical fiber testing system was constructed with the help of rock borehole at the bottom of the coal seam. As shown in (Figure 9), the measurement boreholes were arranged at the working face's backwind chute towards the bottom of the roadway. The optical fiber sensors were arranged through the boreholes and drill boreholes downhole. The monitoring hole 1# was at an angle of 13.0°

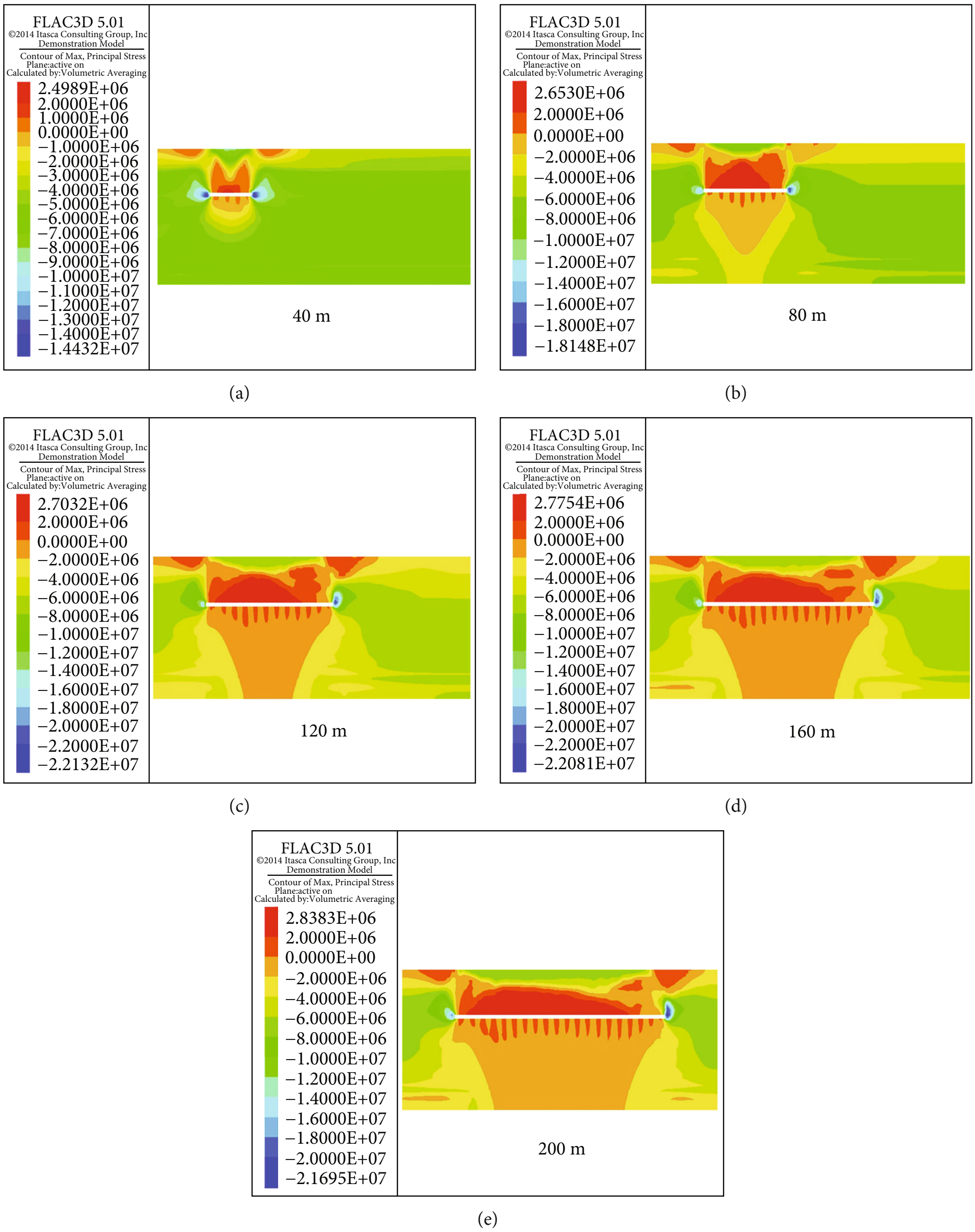

Figure 6: Cloud chart of maximum principal stress distribution at different propulsion distances (unit: MPa).

to the working face, with a depth of 78.0 m and a vertical depth of 17.5 m. The monitoring hole 2# was at an angle of 30.0° to the working face and had the depth and vertical depth of 68.0 m and 34.0 m, respectively. The stress characteristics of the coal seam before and after the mining process were studied, and the data were processed, imaged, and interpreted.

5.2. Analysis of the Results. The on-site data was collated and counted. The collected data from the distance of 97.6 m from the monitoring hole at the retreating footage of the back mining face was taken as the initial value. Furthermore, the variations in the increment in the strain of the optical fiber in holes 1# and 2# were plotted, as shown in Figure 10.

Drill hole 1# was relatively shallow and had a large horizontal length. It was affected by mining before drill hole 2#. There was an overriding effect of dynamic pressure on the rock formation, and the nonlinear response characteristics of rock deformation in the bottom slab were generally inversely related to the depth of the floor [25]. At the distance of 80 m from the orifice, a slight

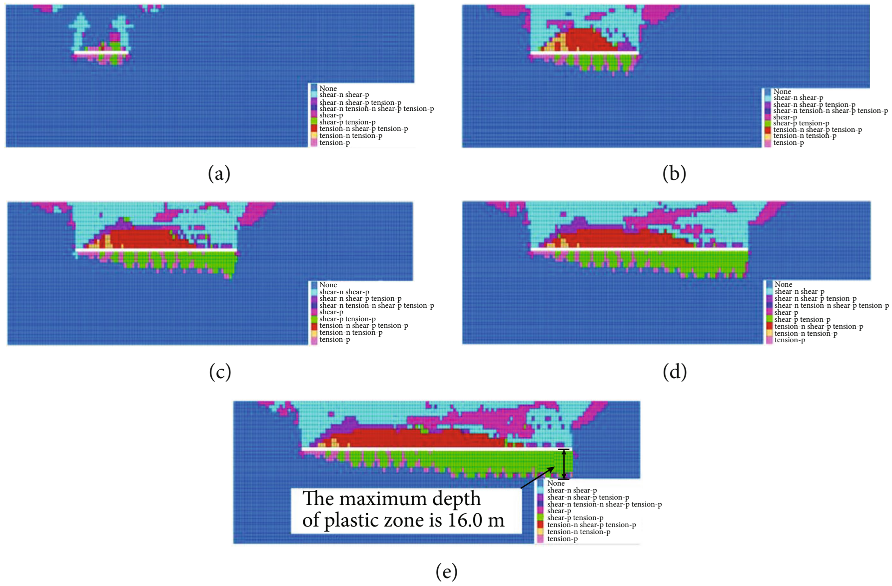

Figure 7: Distribution of plastic zone along the strike in the middle floor of the working face.

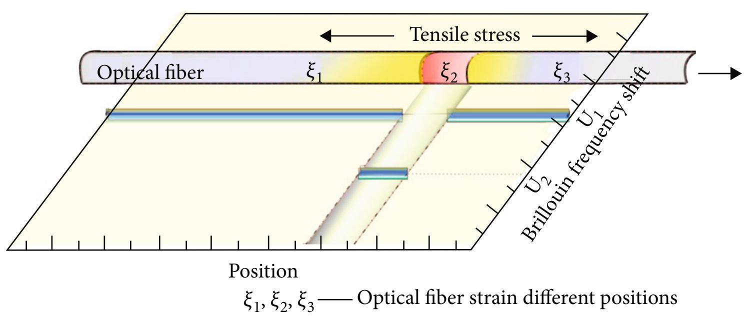

Figure 8: Measurement principle of the BOTDR system.

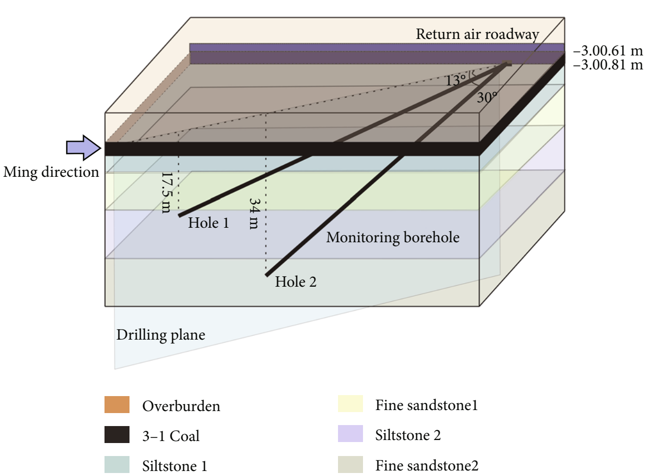

Figure 9: Layout of the monitoring holes.

strain change in the rock layer began to appear. At the distance of 50 m from the hole, the variation in the strain of the rock layer intensified and the local compressive stress of the rock layer increased significantly. Meanwhile, the rock layer started to produce microfractures. When the recovery face was located above the drill hole, the coal mining face showed an increase in the compressive strain, and the rock beneath the mining void showed an increase in the compressive strain. As shown in Figure 10(b), the optical fiber data fluctuated significantly at the hole depth of 33 m, which was analyzed as a rock breaking feature. During the whole process of recovery, when the recovery workface was 33.4 m away from the hole and was located at the vertical depth of -8.4 m in monitoring hole 1#, the maximum value of the pressure-strain increment of monitoring hole 1# was -1098 $\mu\varepsilon$. The tensile strain increased with the maximum value of 893 $\mu\varepsilon$, which is when the retrieval face was directly above the hole and was located at the vertical depth of -7.2 m in the 1# monitoring hole. The maximum value of the increase in pressure-strain in monitoring hole 2# was -2055 $\mu\varepsilon$. At this time, the retrieval face was 48.0 m away from the hole opening and was located at the vertical depth of -16.5 m in monitoring hole 2#. The maximum value of the increase in the tensile strain was 669 $\mu\varepsilon$. Meanwhile, the retrieval face was directly above the hole opening and located at the vertical depth of -15.2 m in monitoring hole 2#. Table 3 lists the maximum values of the distribution of the fiber strain.

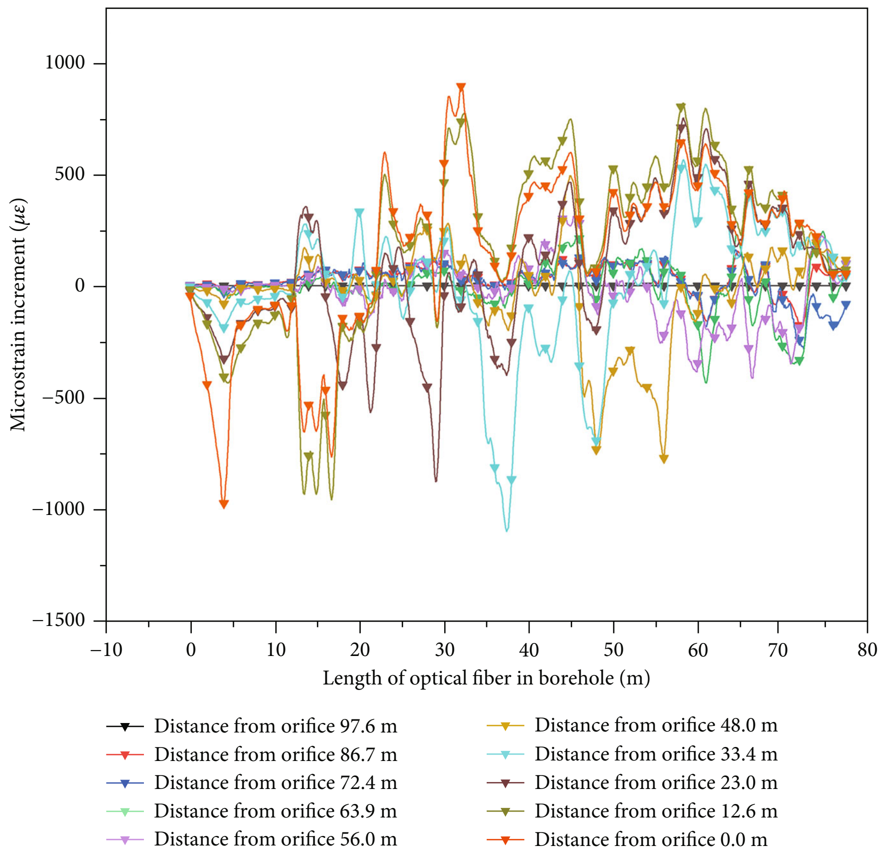

(a)

Figure 10: Continued.

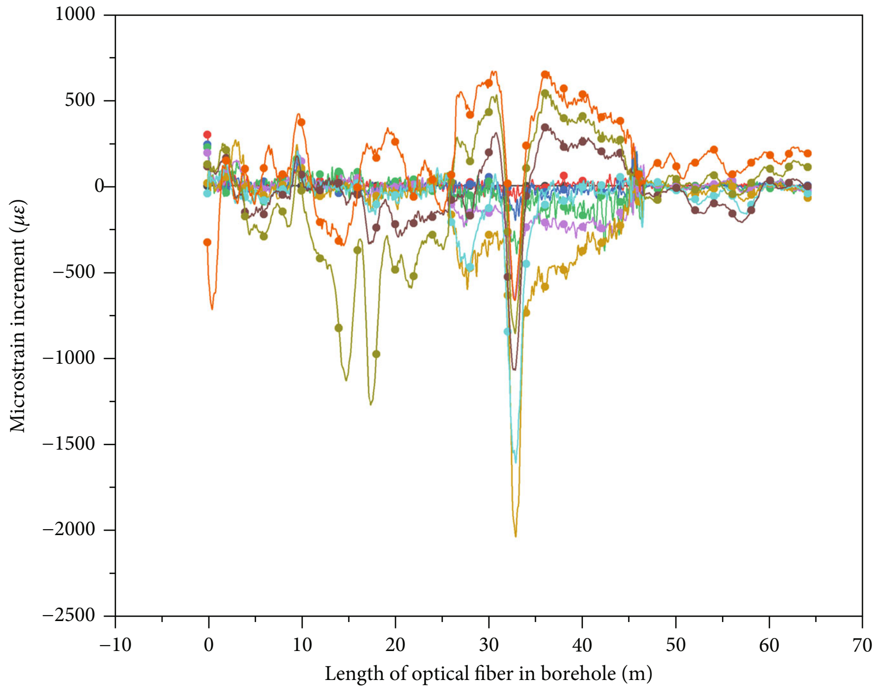

(b)

FIGURE 10: Optical fiber strain increment curve of hole 1# (a) and optical fiber strain increment curve of hole 2# (b).

TABLE 3: Distributed fiber strain maximum distribution.

Borehole	Extreme value of strain increment ($\mu\varepsilon$)	Floor vertical depth (m)	Layer	Distance between working face and orifice (m)
1#	-1098	-8.4	Fine sandstone	33.4
	893 $\mu\varepsilon$	-7.2	Fine sandstone	0
2#	-2055 $\mu\varepsilon$	-16.5	Siltstone	48.0
	669 $\mu\varepsilon$	-15.2	Siltstone	0

In order to further analyze the relationship between stress and deformation damage of the bottom slab rock, the relationship between the advancing distance of the working face and the maximum change in strain under different measurement points is shown in Figure 11.

Figure 11 shows the vertical depths of the monitoring points 1 ~ 5 in borehole 1#, which are at the distances of 10.7 m, 13.7 m, 16.2 m, 17.1 m, and 17.4 m, respectively. The monitoring point 1 was located in the middle of the fine sandstone, whereas the support pressure reached its maximum value when the working face was close to the hole opening (at the distance of 33.4 m). After that, the pressure strain value decreased due to the unloading of the mining area. The monitoring point 2 was further away from the hole than the monitoring point 1, and the peak bearing pressure was reached at 63.9 m near the hole, after which the tensile strain increased under the unloading effect of the mining area. The monitoring points 3 ~ 5 were less affected by the process of mining because of their relatively large burial depth, and the reason that their strain changes were relatively small. This indicates that the rock formation where monitoring points 3 ~ 5 were located was relatively stable. Figure 12 takes the vertical depths of monitoring points 6 ~ 10 in hole 2# as 10.5 m, 16.5 m, 18 m, 22.5 m, and 31.5 m, respectively. Except for monitoring points 7 and 10, the peak bearing pressure of monitoring points 6, 8, and 9 were 12.6 m, 23.0 m, and 48.0 m in front of the hole, respectively, which is consistent with the results reported

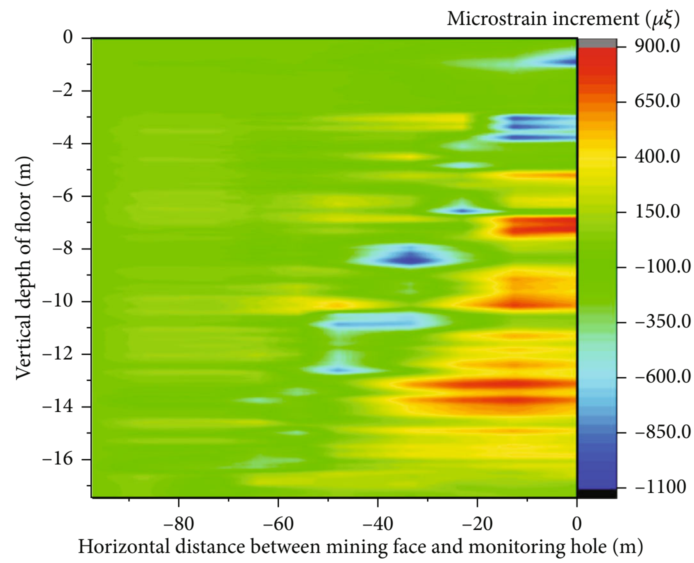

(a)

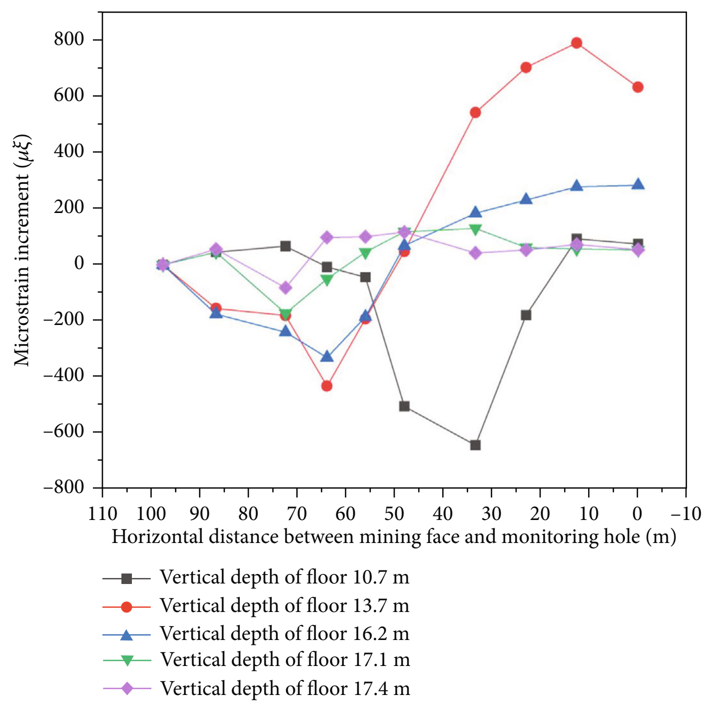

(b)

FIGURE 11: Strain cloud map of hole 1# (a) and strain curve of measuring point in hole 1# (b).

in some previous works [26, 27]. Under the effect of dynamic pressure, with the movement of "shell stress," the peak value of bearing pressure in front of the working face moved forward. This resulted in the peak value of the compressive stress in the borehole near the working face in the monitoring hole and the peak value of stress in the borehole far away from the monitoring point of the working face. The monitoring point 10 was located in the upper part of the fine sandstone formation with a vertical depth of 31.5 m, which remained almost unaffected by mining due to the deeper formation. The increase in peak strain at monitoring point 7 increased steeply from -641 $\mu\varepsilon$ to -2055 $\mu\varepsilon$ at 56.0 m before the hole opening, and the strain recovery under the subsequent unloading of the mining area was also very small, which is in line with the typical characteristics of rock damage that states that the strain changes drastically and in the shape of a "cliff." The strain cannot be recovered after unloading. It can be adjudged that the rocks in this formation had broken and lost their bearing capacity [28, 29].

Based upon a comprehensive analysis, the maximum failure depth of the bottom slab of working face 12307 was 16.5 m. The distributed optical fiber was sensitive to the change of disturbance displacement, had the accuracy of

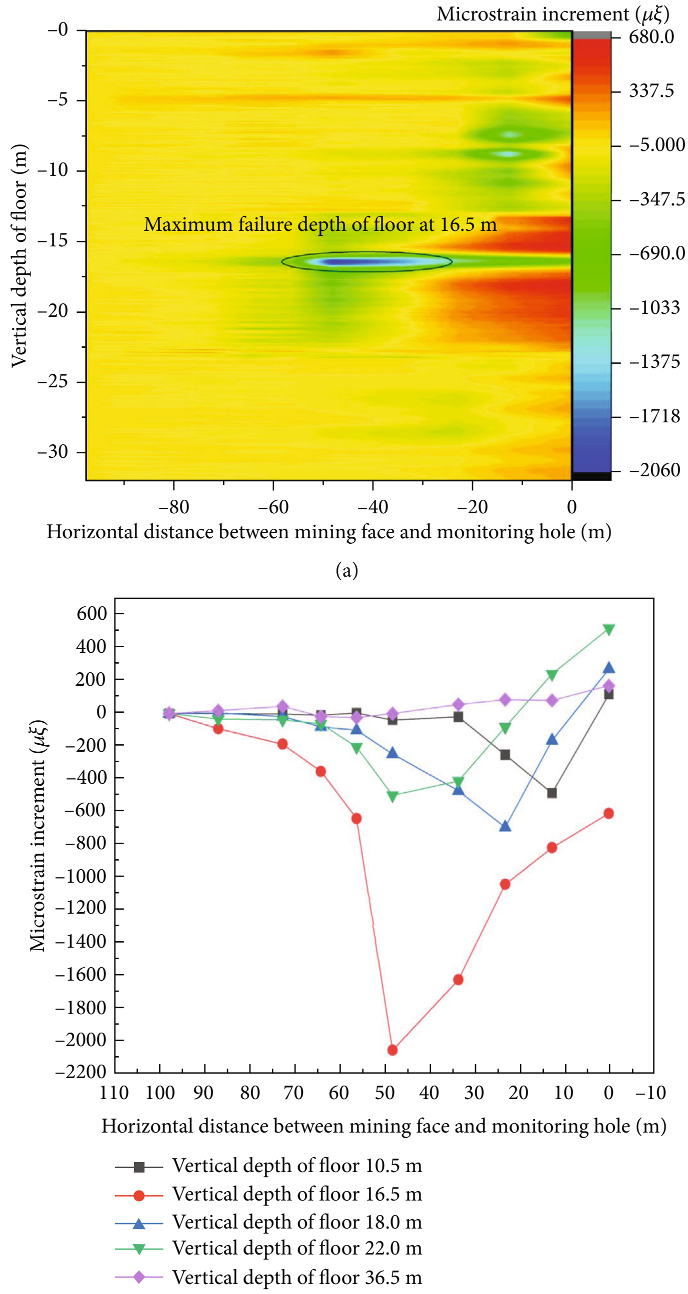

Figure 12: Strain cloud map of hole 2#(a) and strain curve of measuring point in hole 2# (b).

capturing strain data in the borehole, could restore the actual variation pattern of the increase in strain in the monitoring area, and had the capability of realizing the strain change situation of the rock formation in space.

The maximum depth of floor failure is 16.0 m in numerical simulation and 16.5 m in field monitoring, which are similar. According to the research results, key attention should be paid within 16.5 m of the coal seam floor of the working face. Strengthening the floor treatment within this depth range, increasing the number of monitoring boreholes, and reasonable grouting are effective means to maintain the safety of the floor.

6. Discussion

Natural neighbor interpolation (NNI) is one of the most common and effective methods in function approximation theory [30]. NNI is based on computational geometry that is used as the theoretical basis and fully reflects the geometric properties of Voronoi cells and Delaunay triangles and accurately expresses the discrete data [31] between local correlation between the discrete data. Let there be M natural neighbors of point x, which are $p_1, p_2, \ldots, p_M$. The interpolation correlation given by Equation (3) can be constructed. The interpolation results of the point are calculated

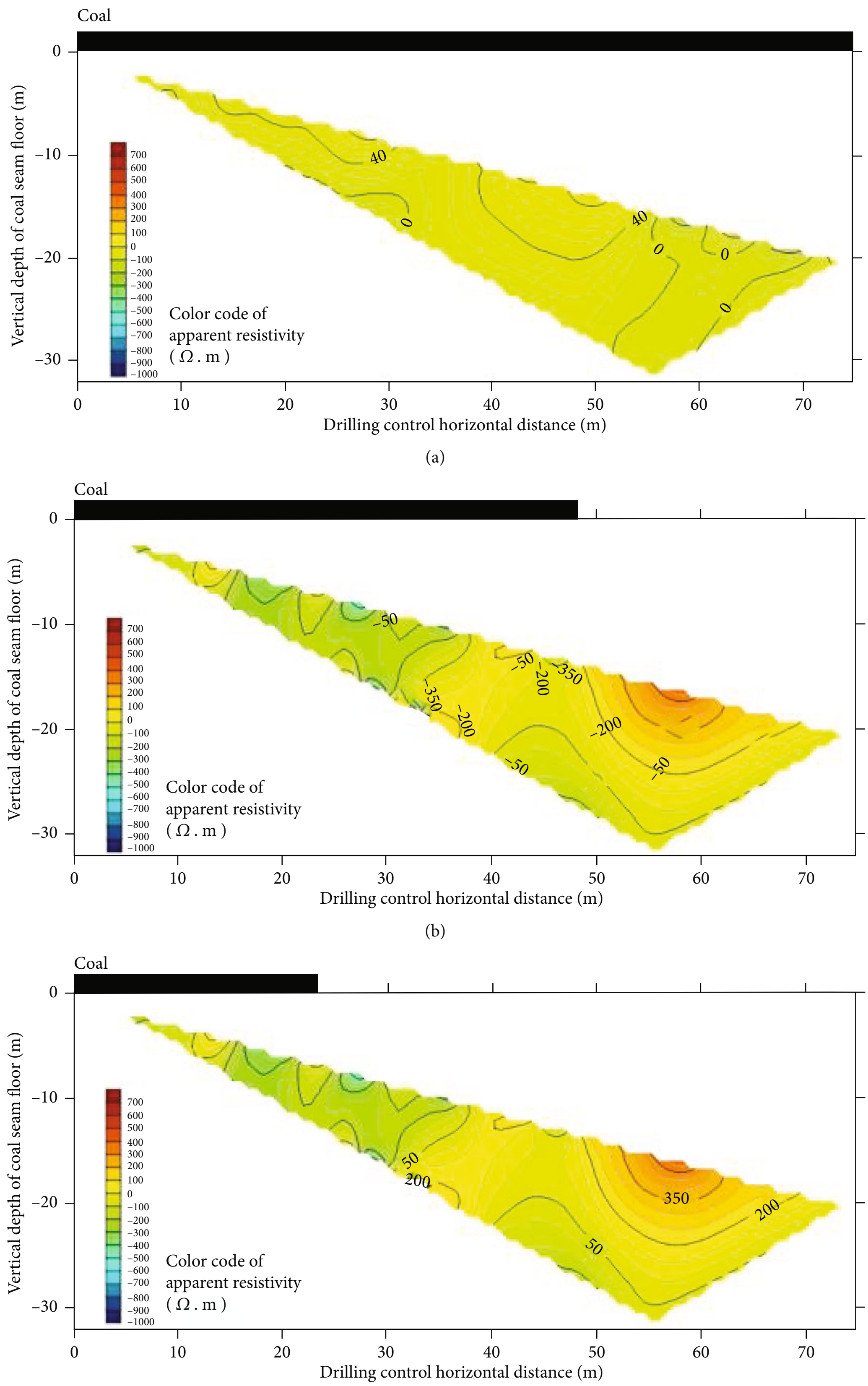

Figure 13: Continued.

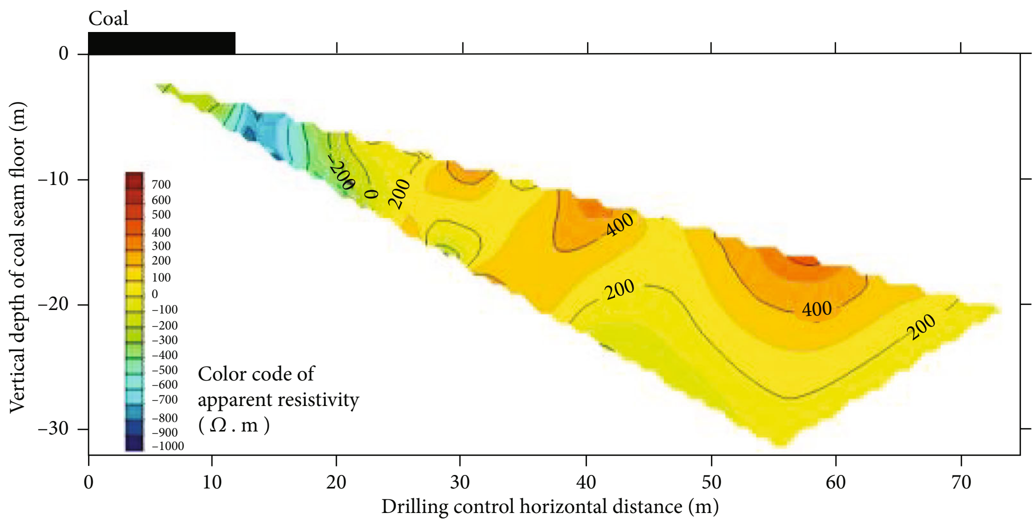

(d)

Figure 13: Working face is 86.7 m away from the orifice (a). Working face is 48.0 m away from the orifice (b). Working face is 23.0 m away from the orifice (c). Working face is 12.6 m away from the orifice (d).

according to the rate of contribution of each natural neighbor to point x to be interpolated. It is widely used in 3D geological models containing complex geological phenomena (such as folds, fluids, and force extrusion zones) constructed using boreholes as data sources.

$$f(\mathrm{x}) = \sum_{i=1}^{M} w_i f(p_i), \tag{3}$$

where $f(x)$ is the interpolation result at point x to be interpolated, $f(p_i)$ is the value at the natural neighbor p_i, and w_i represents the weight coefficient occupied by the natural neighbor p_i.

Figure 13 shows the strain data of monitoring holes 1# and 2# into a map using the natural neighbor interpolation method and reflects the distribution of inter-hole strain increment profiles. Initially, the strain in the hole increased slightly. When the mining workface was approaching, the recovery surface was directly above the hole. The compressive stress was concentrated in the bottom plate in front of the workface, whereas the tensile strain increased in the bottom plate below the extraction area. When the mining face was 23.0 m from the hole, the increment in the compressive strain increased significantly, and the rock layer below the working face received extrusion and was influenced by the disturbance. With the emergence of the mining hollow area, the support pressure moved forward. Meanwhile, the rock body in the data characteristics showed the transformation of tensile strain, while the compression and release of rock body under the action of force will result in the development of rock fissures, indicating that the formation of rock structure's deformation and damage. Meanwhile, the upper part of the coal seam collapsed and recompacted the mining hollow area. Furthermore, the unloading effect of the bottom rock body weakened. Therefore, the development of the bottom fracture zone slowed down until it stopped. The characteristics of the two-dimensional joint drilling profile could be a good analysis of the evolution of the bottom-slab rock damage. In the later work, the exploration and application of 3D compositions and new algorithms will be one of the few future research directions.

7. Conclusions

(1) The distributed optical fiber test system was constructed on the rock sample surface based on MTS 816. The cumulative pressurization was 268 s under the displacement control of 5×10^{-3} mm. The distributed strain response results of the whole process of pressurization were obtained. The high-precision strain test of distributed optical fiber sensitively captured the whole process starting from the generation of local fracture to the penetration of the local fracture of the rock. The obtained results provide reference for the analysis of field data

(2) By arranging two monitoring holes with different dip angles at the bottom plate of 12307 to monitor the evolution of the deformation field of the bottom plate under the influence of dynamic pressure, the failure depth of the bottom plate was 16.5 m, which was located near the partition interface of siltstone and fine sandstone. The result was close to the numerical simulation result of 16.0 m, whereas both the techniques adjudged that the failure depth of the coal seam mining floor was 16.5 m. This way, the two verify each other

(3) The three-dimensional numerical model calculated the distribution of the maximum principal stress of the bottom plate and the distribution of the plastic zone of the bottom plate under different excavation distances. The maximum principal stress of the

bottom plate reflected the depth and range of the bottom plate failure. The working face was subjected to stress concentration, and the stress in the goaf was unloaded within a certain range and transmitted to the depth of the bottom plate

(4) Two-dimensional nephogram of strain increment between the monitoring holes 1# and 2# was obtained using natural neighbor interpolation method. The algorithm has advantages in describing the irregular strain change in the floor rock layer, intuitively reflects the distribution characteristics of floor deformation and failure, and provides a novel idea for borehole optical fiber data analysis

Data Availability

The data used to support the findings of this study are available from the corresponding author upon request.

Conflicts of Interest

The authors declare that they have no conflicts of interest.

Acknowledgments

We gratefully acknowledge the financial support by the National Natural Science Foundation of China (Grant No. 41877268 and Grant No. 42074148), the Graduate Innovation Fund Project of the Anhui University of Science and Technology (Grant No. 2020CX2003), and Student Entrepreneurship Fund Support Project of Anhui University of Science and Technology in 2021. We are also grateful to Tian Yutong for her assistance in field testing and data processing.

References

[1] H.-p. Xie, F. Gao, and Y. Ju, "Research and development of rock mechanics in deep ground engineering," *Chinese Journal of Rock Mechanics and Engineering*, vol. 34, no. 11, pp. 2161–2178, 2015.

[2] L. Yuan, "Research progress of mining response and disaster prevention and control in deep coal mines," *Journal of China Coal Society*, vol. 46, no. 3, pp. 716–725, 2021.

[3] Y. Jiang, D. Zhang, K. Wang, and X. Zhang, "Mining-induced damage characteristics of floors during fully mechanized caving mining: a case study," *Advances in Materials Science and Engineering*, vol. 2018, Article ID 1513451, 2018.

[4] X.-r. Meng, C.-h. Xu, Z.-n. Gao, and X.-q. Wang, "Stress distribution and damage mechanism of mining floor," *Journal of China Coal Society*, vol. 35, no. 11, pp. 1832–1836, 2010.

[5] L.-g. Wang, M. Han, Z.-s. Wang, and S.-b. Ou, "Stress distribution and damage law of mining floor," *Journal of Mining & Safety Engineering*, vol. 30, no. 3, pp. 317–322, 2013.

[6] Z.-g. Lu, W.-j. Ju, X.-w. Yin, Z.-y. Sun, F.-d. Zhang, and C.-j. Han, "Mechanism of hard-roof rock burst control by the deep-hole blasting: numerical study based on particle flow," *Shock and Vibration*, vol. 2021, no. 8, p. 14, 2021.

[7] Z.-z. Liang, W.-c. Song, and W.-t. Liu, "Theoretical models for simulating the failure range and stability of inclined floor strata induced by mining and hydraulic pressure," *International Journal of Rock Mechanics and Mining Sciences*, vol. 132, article 104382, 2020.

[8] W. T. Liu, D. R. Mu, L. Yang, L. Y. Li, and C. H. Shi, "Calculation method and main factor sensitivity analysis of inclined coal floor damage depth," *Journal of China Coal Society*, vol. 42, no. 4, pp. 849–859, 2017.

[9] C. Kmab, B. Xysa, and B. Cata, "Floor water inrush analysis based on mechanical failure characters and microseismic monitoring," *Tunnelling and Underground Space Technology*, vol. 108, article 103698, 2020.

[10] D. Zhang, J. Wang, P. Zhang, and B. Shi, "Internal strain monitoring for coal mining similarity model based on distributed fiber optical sensing," *Measurement*, vol. 97, pp. 234–241, 2017.

[11] W.-g. Du, J. Chai, D. Zhang, and W. Lei, "Application of optical fiber sensing technology in similar model test of shallow-buried and thick coal seam mining," *Measurement*, vol. 181, article 109559, 2021.

[12] Z. Li, Z. Changzhi, H. Xie, and F. Yang, "Similar simulation test for breakage law of working face floor in coal mining above aquifer," *Chinese Journal of Rock Mechanics and Engineering*, vol. 30, no. 8, pp. 1571–1578, 2011.

[13] Z.-l. Mu, G.-j. Liu, J. Yang et al., "Theoretical and numerical investigations of floor dynamic rupture: a case study in Zhaolou Coal Mine, China," *Safety Science*, vol. 114, pp. 1–11, 2019.

[14] W.-l. Zhang, T.-h. Huo, C. Li, C.-w. Wang, X.-c. Qu, and C.-w. Xin, "Characteristics of valuable microseismic events in heading face of an underground coal mine using microseismic system," *Shock and Vibration*, vol. 2021, no. 1, p. 10, 2011.

[15] R.-x. Wu, Z.-a. Hu, and X.-w. Hu, "Principle of using borehole electrode current method to monitor the overburden stratum failure after coal seam mining and its application," *Journal of Applied Geophysics*, vol. 179, article 104111, 2020.

[16] J.-g. Chen, Z.-q. Xiong, H. Li et al., "Failure characteristics of floor under predssure inclined and extra thick coal seam in full-mechanized top coal caving faces," *Chinese Journal of Rock Mechanics and Engineering*, vol. 35, no. S1, pp. 3018–3023, 2016.

[17] Y. Ou, P. Zhang, M. Fu et al., "Geoelectric field response characteristics analysis of floor roadway surrounding rock fracture caused due to coal seam mining," *Scientific Reports*, vol. 11, no. 1, pp. 1–15, 2021.

[18] W.-l. Zhou, P.-s. Zhang, R.-x. Wu, and X.-y. Hu, "Dynamic monitoring the deformation and failure of extra-thick coal seam floor in deep mining," *Journal of Applied Geophysics*, vol. 163, pp. 132–138, 2019.

[19] P.-s. Zhang, C. Liu, Y.-c. Ou, B.-y. Sun, S.-a. Xu, and S.-l. Li, "Comprehensive testing research on floor damage characteristics of mining extra-thick seam in Jungar coalfield," *Coal Geology & Exploration*, vol. 49, no. 1, pp. 263–269, 2021.

[20] G.-j. Zhang and Y. Zhang, "Partition failure characteristics of rock material loading and unloading based on Mohr-Coulomb criterion," *Journal of China coal society*, vol. 44, no. 4, pp. 1049–1058, 2019.

[21] Z.-z. Liang and W.-c. Song, "Theoretical and Numerical Investigations of the Failure Characteristics of a Faulted Coal Mine Floor Above a Confined Aquifer," *Mine Water and the Environment*, vol. 40, pp. 456–465, 2021.

[22] G. X. Xie, J. Z. Li, L. Wang, and Y. Z. Tang, "Mechanical characteristics and time and space evolvement of stress shell in

stope floor stratum," *Journal of China Coal Society*, vol. 43, no. 1, pp. 52–61, 2018.

[23] A. Li, Q. Ma, Y. Lian, L. Ma, Q. Mu, and J. Chen, "Numerical simulation and experimental study on floor failure mechanism of typical working face in thick coal seam in Chenghe mining area of Weibei, China," *Environmental Earth Sciences*, vol. 79, no. 5, pp. 1–22, 2020.

[24] P. Lu, N. Lalam, M. Badar et al., "Distributed optical fiber sensing: Review and perspective," *Applied Physics Reviews*, vol. 6, 35 pages, 2019.

[25] H.-f. Duan, "Analysis on failure features and failure depth of coal seam floor during mining process," *Coal Science and Technology*, vol. 42, no. 5, pp. 17–20, 2014.

[26] J. Chai, Y.-l. Liu, Q. Yuan et al., "Theory-technology and application of optical fiber sensing ondeformation and failure of mine surrounding rock," *Coal Science and Technology*, vol. 49, no. 1, pp. 208–217, 2021.

[27] P.-s. Zhang, J.-w. Wu, and S.-d. Liu, "Study on dynamic observation of coal seam floor's failure law," *Chinese Journal of Rock Mechanics and Engineering*, vol. 2006, no. S1, pp. 3009–3013, 2006.

[28] L.-f. Zhang, D.-x. Yang, Z.-h. Chen, and A. Liu, "Deformation and failure characteristics of sandstone under uniaxial compression using distributed fiber optic strain sensing," *Journal of Rock Mechanics and Geotechnical Engineering*, vol. 12, no. 5, pp. 1046–1055, 2020.

[29] Y.-k. Sun, Q. Li, D.-x. Yang, C.-k. Fan, and A. Sun, "Investigation of the dynamic strain responses of sandstone using multichannel fiber-optic sensor arrays," *Engineering Geology*, vol. 213, pp. 1–10, 2016.

[30] Y.-j. Guo, M. Pan, and F. Yan, "Application of natural neighbor interpolation method in three-dimensional geological modeling," *Journal of PLA University of Science and Technology*, vol. 10, no. 6, pp. 650–655, 2009.

[31] W. Zhang, Q.-y. Qin, and X.-x. Jiang, "Natural neighbor interpolation and its application to 2D grid of irregular data," *Computing Techniques for Geophysical and Geochemical Exploration*, vol. 33, no. 3, p. 294, 2011.

Hindawi
Geofluids
Volume 2022, Article ID 6914746, 17 pages
https://doi.org/10.1155/2022/6914746

Research Article

Structural Characteristics of Regenerated Roof and Distribution Law of Overburden Porosity in Downward Mining of a Bifurcated Coal Seam

Ru Hu [1,2] Jiwen Wu [2] Xiaorong Zhai [2] Wenbao Shi [3] and Kai Huang [2]

[1]*State Key Laboratory of Mining Response and Disaster Prevention and Control in Deep Coal Mines, Anhui University of Science and Technology, Huainan 232001, China*
[2]*School of Earth and Environment, Anhui University of Science and Technology, Huainan 232001, China*
[3]*School of Mining Engineering, Anhui University of Science and Technology, Huainan 232001, China*

Correspondence should be addressed to Xiaorong Zhai; 616170984@qq.com

Received 15 October 2021; Revised 10 November 2021; Accepted 25 February 2022; Published 19 March 2022

Academic Editor: Yong-Zheng Wu

During downward mining of a bifurcated coal seam, the roof of the lower coal seam is relatively broken and difficult to control due to the mining influence of the upper coal seam. Roof accidents occur frequently during mining of the lower coal seam, reducing mining efficiency. How to ensure safe and efficient mining of the lower coal seam is a significant issue. In this paper, overlying strata migration and fracture characteristics of the lower coal seam, the structure and stability of the regenerated roof, and porosity and permeability characteristics of the overlying strata under the mining influence of the upper coal seam are studied by using similar simulation tests. Results show that the overburden structure of the lower coal seam is altered due to the mining influence of the upper coal seam, and the regenerated roof of the lower coal seam is divided into three structural types from top to bottom, namely: intact rock mass+block fracture rock mass+loose rock mass (type I structure); intact rock mass+block fracture rock mass+loose rock mass+cataclastic rock mass (type II structure); and intact rock mass+block fracture rock mass+loose rock mass+cataclastic rock mass+slab-rent rock mass (type III structure). The stability of each type of rock mass structure is evaluated, and the stability of three types of rock mass structures is III > II > I. The overburden porosity and slurry permeability coefficient are relatively large at the cutting hole and stopping line. The porosity of the caving zone within 70 m of the cut hole and stopping line is greater than 5%, and the permeability coefficient is greater than 0.1 m/s. Based on differences in the surrounding rock porosity and permeability characteristics, the grouting difficulty of overburden is divided into three types of areas: extremely easy grouting areas, easy grouting areas, and difficult grouting areas. The results of this paper can provide reference for the stability evaluation of the regenerated roof and the selection of grouting treatment parameters for the broken roof under similar conditions.

1. Introduction

In China, there are many reserves and wide distribution of coal resources under the condition of close storage [1, 2]. In recent years, with the depletion of easily mined coal resources, more and more close-distance coal seams with complex conditions are being mined. Bifurcated coal seams are one type of close-distance coal seam. Due to differences in interlayer thickness, the selection of mining technology for use in bifurcated coal seam stopes can be problematic, especially during layered mining of a coal seam in a bifurcated area, in which the roof of the lower coal seam is broken and difficult to control due to the mining influence of the upper coal seam, which seriously affects the safety and production efficiency of the working face [3–5]. Therefore, ensuring the safe mining of the lower coal seam is the primary concern when mining bifurcated coal seams.

Numerous scholars have conducted systematic research on the deformation and failure of rock surrounding a short-range coal seam stope [6–9], the distribution of stope spatial abutment pressure [10–15], roadway layout and support [16–20], and the stability of surrounding rock support [21–23], which has improved short-range coal seam mining theory and significantly improved the recovery rate of coal resources. However, there are few relevant studies on the stope of bifurcated coal seams as well as a lack of systematic research on the structural changes of the regenerated roof of the lower coal seam due to the mining influence. Mastering the structural characteristics of the regenerated roof is critical for effective treatment of the regenerated roof. At present, multiple effective and scientific technical treatment methods have been proposed for the broken roof, among which grouting reinforcement technology is primarily used for the treatment of broken rock mass [24–29]. Whether underground or surface grouting, for the whole grouting target area, the selection of grouting parameters is commonly based on production experience, without considering difference in the porosity and permeability of grouting target area caused by different overburden structures after mining. Such a lack of consideration may lead to grouting omission or material waste. Existing theoretical studies show that there are significant differences in porosity and permeability at different positions within overburden. Numerous scholars have conducted research regarding the porosity and permeability evolution of overburden. Adhikary and Guo et al. used a numerical simulation to calculate formation permeability due to the mining influence, producing results that are highly consistent with field test data [30]. Zhang et al. studied the compaction characteristics of the goaf caving zone, revealed the primary factors affecting the compaction process of the caving zone, and accurately calculated the compaction degree of the goaf using various methods [31]. Poulsen et al. proposed a numerical model to express the overburden fracture process induced by mining and estimated the permeability of overburden using the Kozeny-Carman permeability-porosity equation [32]. Ma et al. systematically studied the mechanical behavior and failure mechanism of rock mass in deep rock engineering and analyzed the hydraulic properties and deformation behavior of filling materials in filling mining through laboratory tests [33–36]. Existing research primarily focuses on water seepage within the overburden, goaf ventilation design, gas discharge, and natural ignition of the goaf [37–39]. Unfortunately, there are few studies on using differences in overburden porosity and permeability characteristics to guide the grouting of the broken roof. For coal seam stopes, current research methods primarily include similarity simulation [40, 41], numerical simulation [42, 43], field test [44–47], engineering analogy [48], theoretical analysis [49–51], and empirical formula calculation [52–54]. In terms of accuracy, field test results are more accurate, but field test implementation is difficult and costly. In contrast, simulations are easy to operate, low-cost, and accurate enough to meet production needs, making simulations more common than field studies. Most similar simulation tests are carried out around a single coal seam and close-distance coal seam stope. Few relevant studies on the mining conditions of bifurcated coal seams exist.

Based on the above analysis, this paper examines the bifurcated close coal seams in the Xutuan mining area of Anhui Province, specifically analyzing the regenerated roof of the lower coal seam. Through similar simulation experiments, this paper studies the deformation and fracturing of the surrounding rock during mining of the upper coal seam, divides the structural types of the regenerated roof, and analyzes the stability of different structural types of the regenerated roof during mining of the lower coal seam. According to differences in overburden porosity and permeability, the difficulty of grouting in the treatment area of the regenerated roof is determined, in order to provide a basis for the selection of grouting parameters for the broken roof in the lower coal seam.

2. Geological Overview of the Study Area

The no. 7 coal seam in the Xutuan mining area is the primary coal seam of the mine. The study area for this paper is located at the 72210 working face and the upper 71212 working face in the eighth mining area of the mine. The no. 7-1 and no. 7-2 coal seams are bifurcated and merged. The distance between the two coal seams is 0.7 m~9.0 m, with an average of 5.8 m. The spatial positions of no. 7-1 and no. 7-2 coal seams are shown in Figure 1.

The elevation of the 71212 working face is -500.0 m~-571.2 m, the strike length of the working face is 1366 m, and the inclined width is 168 m. The elevation of the 71212 working face is -500.0 m~-571.2 m, the strike length of the working face is 1366 m, the inclined width is 168 m, and the average thickness of the coal seam is 2 m. Strike long-arm mining is used to excavate coal seams. The elevation of the 72210 working face is -486.0 m~-593.5 m, the strike length of the working face is 2023 m, the inclined width is 184 m, and the average thickness of the coal seam is 3 m. The burial depth of the no. 7-1 coal seam in the study area is 550 m, and the thickness of the coal seam is 2 m. The dip angle of the no.7-2 coal seam along the strike profile is subhorizontal, and the dip angle of the no. 7-2 coal seam is 5°. For the in situ stress field in the study area, the maximum principal stress σ_1, minimum principal stress σ_3, and intermediate principal stress σ_2 are 13.51 MPa, 7.52 MPa, and 8.93 MPa, respectively. The included angle between the maximum principal stress direction and the vertical direction is about 23°, the direction of the minimum principal stress is consistent with the rock stratum trend, the direction of the middle principal stress is perpendicular to σ_1, and the maximum principal stress is about equal to the self-weight stress of the overburden. The plane layout of the working face is shown in Figure 2.

3. Simulation of Similar Materials in a Bifurcated Coal Seam Stope

The geological environment of the working face is complex, field tests are difficult to conduct, and the transportation of equipment and materials is difficult. According to similarity theory, the similarity transformation of the geological environment of the working face and the indoor similarity simulation test can not only achieve the research purpose but also are low-cost, which has become an important research means [55, 56].

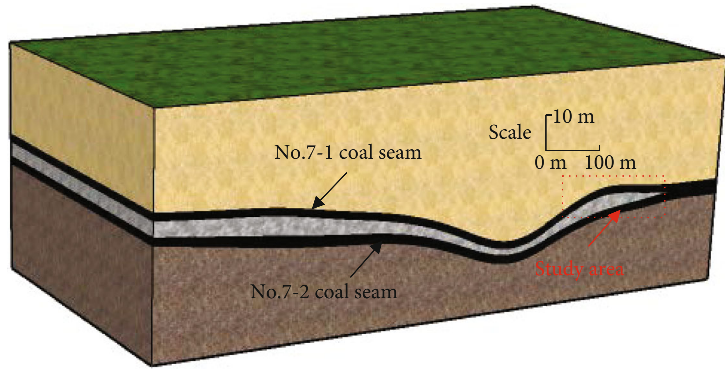

Figure 1: Schematic diagram of the no. 7-1 and no. 7-2 coal seams.

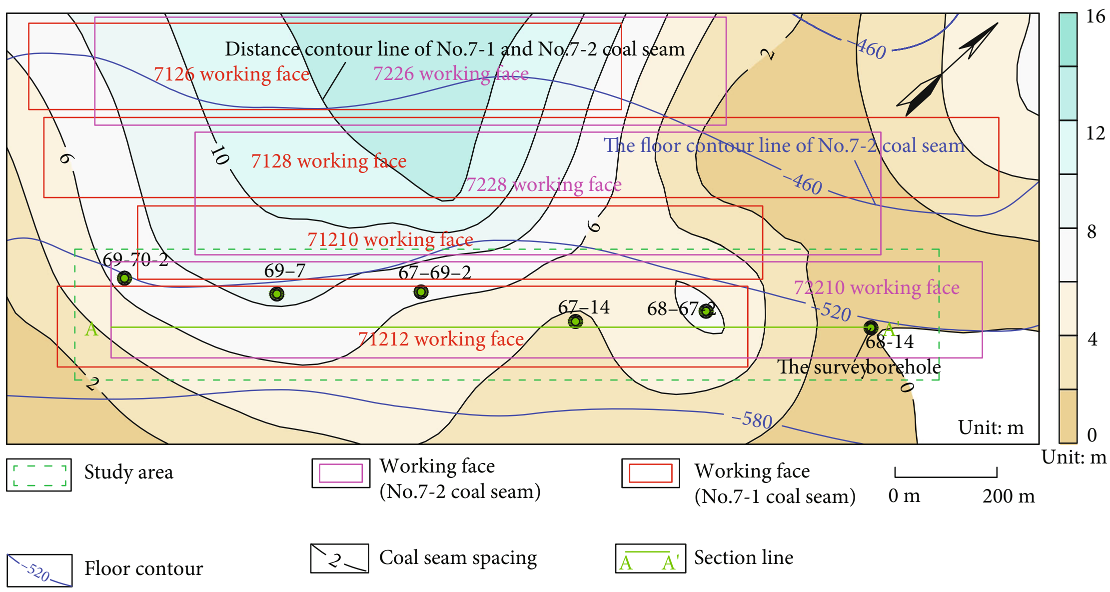

Figure 2: Plane layout of the working face.

3.1. Selection of Similar Simulation Test Parameters. According to the similarity principle, the selection of the similarity constant of the model is shown in Table 1(Table 1 is reproduced from Hu et al.) [40]. Combined with mechanical test results of the roof and floor rock mass of the working face, the material ratio orthogonal test can be carried out to determine the mechanical strength and ratio number of the model material. The detailed parameters and ratios are shown in Table 2.

The size of the similar model is 300 cm × 30 cm × 150 cm (length × width × height). In the process of model laying, the stress sensor (BW micro pressure box) is embedded and connected to the static resistance strain gauge (YJZA-32), the micro strain of overburden in the process of coal seam mining is obtained, and then the stress is further calculated through the formula, so as to achieve the purpose of stress monitoring. The conversion formula of stress and strain is as follows:

$$P = \mu\varepsilon \times K. \quad (1)$$

In formula (1), P is the pressure value (unit: KPa), $\mu\varepsilon$ is the strain, and K is the calibration coefficient (measured before delivery). The model and survey line layout are shown in Figure 3.

GetData Graph Digitizer software is used to postprocess the photos and extract the coordinate values of overburden displacement measuring points. Firstly, import the picture into the software, select O and A points that are not affected by mining horizontally as the x-axis control points, and O and A points are at the same horizontal line. Two points O and B in the vertical direction are selected as the y-axis control points, and the two points O and B are in the same vertical line. The three basic control points remain unchanged in each photo, and a two-dimensional plane coordinate system is established (Figure 4(a)). Secondly, the initial coordinate values of each displacement measuring point of overburden are obtained in the constructed two-dimensional coordinate system (Figure 4(b)). Finally, the coordinate values of overburden displacement measuring points during coal seam excavation are extracted and compared with the initial coordinate values to obtain the

Table 1: List of similar constants of the model.

Similarity constant	Model	Original rock
Similarity geometric ratio	1	100
Similarity bulk density ratio	0.608	1
Similarity elastic modulus ratio	0.00608	1
Similarity strength ratio	0.00608	1
Similarity Poisson ratio	1	1
Similarity time ratio	1	10

subsidence value of overburden (Figure 4(c)). During coal seam excavation, the displacement and stress of surrounding rock are monitored.

3.2. Analysis on Deformation and Failure Characteristics of Rock Mass in Upper Coal Seam Mining. When the working face advances to 90 m, the development heights of the caving zone and the fracture zone are 4.5 m and 19.3 m, respectively. The fracture angles of the overlying rock at the cut and the end of the working face are 54° and 49°, respectively. The surrounding rock of the stope forms an asymmetric trapezoidal failure mode along the fracture line. The overburden structure evolves from the original layered structure to the granular structure of the caving zone and fractured structure of the fracture zone (Figure 5(a)). When the working face advances to 165 m, affected by tectonic fissures in front of the working face, the overlying strata of the no.7–1 coal seam collapse along the tectonic fissure. A large crack appears at 19.5 m of the roof, and the crack width is about 1 m. Due to the rapid subsidence of the collapsed rock mass, the integrity is high, and the height of the caving zone is stable at 7.5 m. The maximum height of the fracture zone is 30.7 m. Thus far, the height of the two zones is stable (Figure 5(b)). When the working face advances to 220 m, mining of the 7-1 coal seam is completed, and the overburden fracture shape of the stope reaches a stable state. Due to the influence of tectonic fissures, compared with the degree of overburden fracture in front of tectonic fissure, after the coal seam pushes through tectonic fissure, and the overburden migration and fracture, the structure is obviously loose, the damage is more intense, and the pores are obviously large. The height of the collapse zone is 8 m, and the development height of the fracture zone is about 37 m (Figure 5(c)).

3.3. Stress Evolution Law of Roof and Floor Rock Mass. As the working face advances, the monitoring data at each measuring point on roof stress measuring line (monitoring line B) are recorded (Figure 6).

Monitoring line B is located 8 m from the roof of the no. 7-1 coal seam. Measuring point B5 shows the change in roof stress during advancement of the working face. During the advancing process, a stress concentration appeared in front of the coal wall, and the abutment pressure increased significantly. The influence range of the advance stress was 40 m–50 m, and the peak position of the abutment pressure was approximately 10 m away from the coal wall of the working face. When the working face passes through the measuring point, the roof is in a state of pressure relief, and the stress value decreases rapidly. As the overburden rock breaks and falls, it is gradually compacted, and the stress on rock mass in the upper part of the goaf is gradually restored. The stress recovery distance of the stress measuring point near the middle of the working face is 70 m~90 m as the working face advances (Figure 6). The stress value is stable 80 m away from the measuring point and is always slightly less than the original rock stress. The average breaking distance of the rock stratum is approximately 20 m. As stress increases, the fractured rock mass is gradually compacted, and the crack is closed (Figure 7).

The external reflection of overburden stress recovery is the compaction and closure of pores and fractures. When the working face advances to 90 m, transverse cracks appear behind the B4 measuring point. The stress value decreases rapidly to 0.0037 MPa after the working face passes the B4 measuring point (Figure 7). When advancing to 130 m, the stress value at B4 recovers to 0.0565 MPa, and the crack opening decreases significantly. When advancing to 170 m, the stress value of the measuring point is restored to 0.0641 MPa, which is close to the original rock stress value of 0.0822 MPa. With continuous advancement of the working face, the fracture opening closes and is stable. The roof stress recovery distance is 80 m, which is important for judging the compaction degree of the goaf rock mass and the boundary of stress zoning.

The C stress monitoring line is located at 28 m from the roof of the no. 7-1 coal seam. During the advancing process of the working face, the stress variation characteristics are consistent with those of survey line B (Figure 8). Next, take measuring point C3 as an example to illustrate the stress variation characteristics of rock mass in the fracture zone. Based on the stress recovery process of the C3 measuring point, the stress transmission is lagging; that is, after the fracture and migration of the overburden, the stress will not respond immediately but requires a certain transmission time. As the working face advances, the influence range of the advance abutment pressure in front of the working face is 40 m~50 m, and the peak position of abutment pressure is approximately 10 m from the coal wall of the working face. After the working face passes the stress measuring point 70 m~90 m, the stress is restored to the original rock stress.

The similar simulation test has difficulty observing the development of micro fractures in the model; therefore, the stress of the floor is primarily monitored during mining of the no. 7-1 coal seam. The failure depth of the No. 7-1 coal seam floor can be indirectly determined by analyzing the influence depth and transmission law of the floor stress. The monitoring data of A stress monitoring line are shown in Figure 9.

The A1~A5 sensor distance from the 7-1 coal seam is 1.75 m~8.75 m, and the A5 sensor distance from the no. 7-1 coal seam is 8.75 m. The stress change caused by 7-1 coal mining has obvious regularity in the transmission of the floor (Figure 9). With increasing burial depth, the variation trend line of peak stress peak at the A1~A10 stress sensors gradually becomes flat. When the distance between the stress sensor and the coal seam is greater than 8.75 m, the stress is

Table 2: Material parameters and mixing ratios.

Lithology	Original rock		Model					
	Stratum thickness (m)	Compressive strength (MPa)	Compressive strength (MPa)	Material ratio Sand : lime : gypsum	Weight of material (kg)			
					Sand	Lime	Gypsum	Water
Mudstone	2.0	20.40	0.124	12 : 3 : 7	27.9	0.7	1.6	3.0
Siltstone	4.0	43.44	0.264	10 : 7 : 3	55.0	3.8	1.6	6.0
Mudstone	1.0	18.50	0.112	12 : 3 : 7	14.0	0.3	0.8	1.5
Fine sandstone	2.0	52.80	0.460	8 : 7 : 3	26.9	2.4	1.0	3.0
Mudstone	2.0	18.40	0.112	12 : 3 : 7	27.9	0.7	1.6	3.0
Siltstone	2.0	41.70	0.264	10 : 7 : 3	27.5	1.9	0.8	3.0
Mudstone	3.0	17.30	0.112	12 : 3 : 7	41.9	1.0	2.4	4.5
Fine sandstone	4.0	71.80	0.460	8 : 7 : 3	53.8	4.7	2.0	6.0
Siltstone	2.0	35.70	0.264	10 : 7 : 3	27.5	1.9	0.8	3.0
Mudstone	9.0	20.50	0.112	12 : 3 : 7	125.6	3.1	7.3	13.6
Fine sandstone	4.0	65.00	0.460	8 : 7 : 3	53.8	4.7	2.0	6.0
Mudstone	5.0	19.20	0.112	12 : 3 : 7	69.8	1.7	4.1	7.6
5-1 coal	2.0	6.50	0.038	13 : 4 : 6	28.1	0.9	1.3	3.0
Mudstone	6.0	17.50	0.112	12 : 3 : 7	83.7	2.1	4.9	9.1
5-2 coal	1.0	7.30	0.038	13 : 4 : 6	14.0	0.4	0.6	1.5
Mudstone	9.0	18.30	0.112	12 : 3 : 7	125.6	3.1	7.3	13.6
Siltstone	3.0	29.50	0.264	10 : 7 : 3	41.2	2.9	1.2	4.5
Fine sandstone	1.0	55.80	0.460	8 : 7 : 3	13.4	1.2	0.5	1.5
Mudstone	3.0	19.40	0.112	12 : 3 : 7	41.9	1.0	2.4	4.5
Fine sandstone	16.0	76.50	0.460	8 : 7 : 3	215.0	18.8	8.1	24.2
Siltstone	11.0	45.90	0.264	10 : 7 : 3	151.2	10.6	4.5	16.6
Mudstone	6.0	15.50	0.112	12 : 3 : 7	83.7	2.1	4.9	9.1
Fine sandstone	5.0	60.30	0.460	8 : 7 : 3	67.2	5.9	2.5	7.6
Mudstone	5.0	16.80	0.112	12 : 3 : 7	69.8	1.7	4.1	7.6
7-1 coal	2.0	8.20	0.038	13 : 4 : 6	28.1	0.9	1.3	3.0
Mudstone	0 ~ 23	18.40	0.112	12 : 3 : 7	137.6	3.4	8.0	14.9
7-2 coal	3.0	7.50	0.038	13 : 4 : 6	42.2	1.3	1.9	4.5
Mudstone	3.0	23.36	0.142	12 : 3 : 7	38.9	1.0	2.3	4.2
Fine sandstone	11.0	75.60	0.460	8 : 7 : 3	148.4	13.0	5.6	16.7
Mudstone	2.0	45.07	0.274	10 : 7 : 3	26.7	1.9	0.8	2.9
8-2 coal	3.0	8.60	0.407	8 : 7 : 3	35.3	3.1	1.3	4.0
Mudstone	4.0	28.50	0.192	12 : 3 : 7	41.1	1.1	2.6	4.5
Siltstone	2.0	39.70	0.274	10 : 7 : 3	17.2	1.2	0.5	1.9
Fine sandstone	4.0	66.80	0.407	8 : 7 : 3	27.5	2.4	1.0	3.1
Mudstone	4.0	31.57	0.192	12 : 3 : 7	20.0	0.5	1.2	2.2

not affected by the abutment pressure in front of the working face, and the variation range is small. The stress peak monitored by the A5 stress sensor is less than that of A4 measuring point, and its stress peak is at the inflection point of the stress peak trend line. Therefore, the range of the strong failure zone in the floor formed by the stress change caused by mining is 5.00 m~8.75 m. The strata in this range are severely damaged due to the strong rock pressure, forming fractures. The crack development depth is 6 m (Figure 10). The development height of "two zones" of overburden and the failure depth of the floor are measured in the study area, which verifies the reliability of similar simulation results [40].

During mining, the floor of the working face is affected by the advance abutment pressure and is in a supercharging state. When the goaf is formed, the floor rock mass undergoes a high degree of pressure relief. With periodic collapse and gradual compaction of overburden, the floor stress begins to increase gradually until it becomes stable; however, the restored stress value is always slightly less than the initial stress, and the stress recovery distance is 70 m~90 m.

3.4. Structural Type Division and Stability Analysis of the Regenerated Roof. The rock mass in the caving zone is loose and is classified as either granular rock mass or block

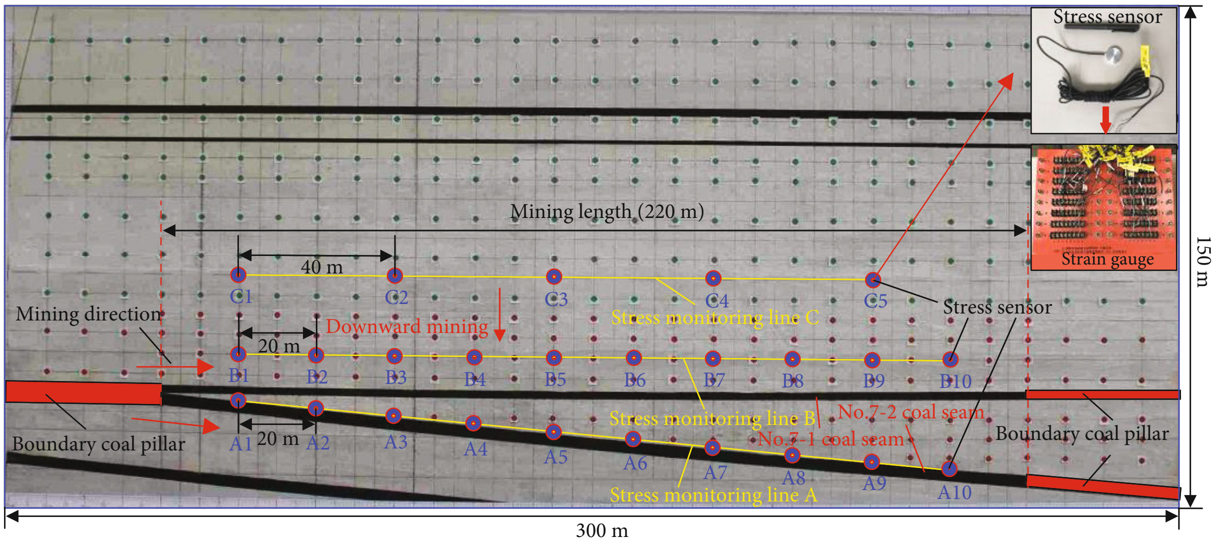

Figure 3: Schematic diagram of the monitoring line layout in the model.

fracture rock mass, which contains well-developed fractures. According to the stress transfer law of the floor, the floor is affected by mining forming a strong failure zone, and the rock mass in the strong failure zone is cut by mining fissures producing a cataclastic rock mass. The average depth of the strong failure zone of the floor is 6 m, and the rock mass in the lower part of the strong failure zone is less affected by mining (rock pressure disturbance zone), which can be considered staying in the original rock state and being a slab-rent rock mass. Based on the previous experience of mining bifurcated coal seams in the Xutuan coal mine as well as the results of similar simulation tests, when the coal seam spacing is less than 1 m, after mining the no. 7-1 coal seam, the top-down rock mass structure combination type of the no. 7-2 coal seam roof can be divided into intact rock mass+block fracture rock mass+loose rock mass (type I structure). When the coal seam spacing is between 1 m and 6 m, the rock mass structure combination type of the no. 7-2 coal seam roof can be divided into intact rock mass+block fracture rock mass+loose rock mass+cataclastic rock mass (type II structure). When the coal seam spacing is greater than 6 m, the rock mass structure combination type of the no. 7-2 coal seam roof can be divided into intact rock mass+block fracture rock mass+loose rock mass+cataclastic rock mass+slab-rent rock mass (type III structure) (Figure 11).

According to the above research results, the average failure depth of the strong failure zone of the floor of the no. 7-1 coal seam is 6 m. The stability of three regenerated roof structures is analyzed during mining of the no. 7-2 coal seam. The fracture form of roof rock mass when the no. 7-2 coal seam advances to 10 m, 50 m, and 70 m is shown in Figure 12.

When the working face advances to 10 m, the roof of coal seam 7-2 is directly covered with the caving zone of coal seam 7-1 (Figure 12(a)). During mining of the 7-2 coal seam, the loose rock mass in the caving zone of the no. 7-1 coal seam directly falls. Under the condition of this type of roof structure, the roof of the working face is relatively broken and difficult to control. Also, the roof leaks during mining, which poses a great threat to the safety of the working face. When the working face advances to 50 m, due to the gradual increase in interlayer distance, the interlayer strata of the no. 7-1 and 7-2 coal seams form a small-scale masonry beam structure, which plays a supporting role in the upper loose caving zone. As the mined area increases, the small-scale masonry beam structure rapidly becomes unstable, and the loose rock mass in the upper caving zone rapidly collapses (Figure 12(b)). When the working face advances to 70 m, the distance between the coal seams further increases, close to the depth (6 m) of the strong failure zone of the no. 7-1 coal seam floor, and the length of cantilever beam formed at the end of the working face gradually increases, which plays a significant supporting role for the upper rock stratum and prevents the downward movement of loose rock mass in the upper caving zone (Figure 12(c)). When the working face advances to 90 m, 165 m, and 220 m, the failure mode of surrounding rock is shown in Figure 13.

When the 7–2 coal seam advances to 90 m, the thickness of the interlayer rock at this position exceeded 6 m (Figure 13(a)). The cantilever beam structure formed at 70 m is broken and hinged with the collapsed rock mass behind it, forming a new masonry beam structure. With increasing thickness of the masonry beam structure, the breaking length of the rock mass increases significantly, and the stability of the masonry beam structure is enhanced. When the working face is advanced to 165 m, the length of the masonry beam continues to increase, and with increasing interlayer rock thickness, the thickness of masonry beam as well as the ultimate breaking distance of rock stratum at the end of the working face also increases, which will better support the upper rock mass before failure, which is conducive to successfully managing the working face roof (Figure 13(b)). When the working face advances to 220 m, with increasing interlayer distance, and when the interlayer thickness exceeds 6 m, the breaking length of cantilever rock

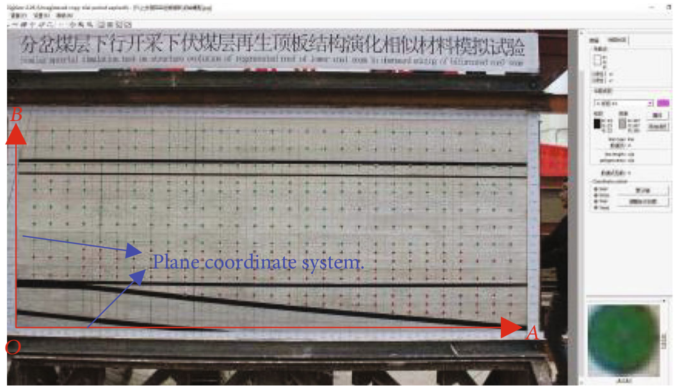

(a) Establish the two-dimensional plane coordinate system of the model

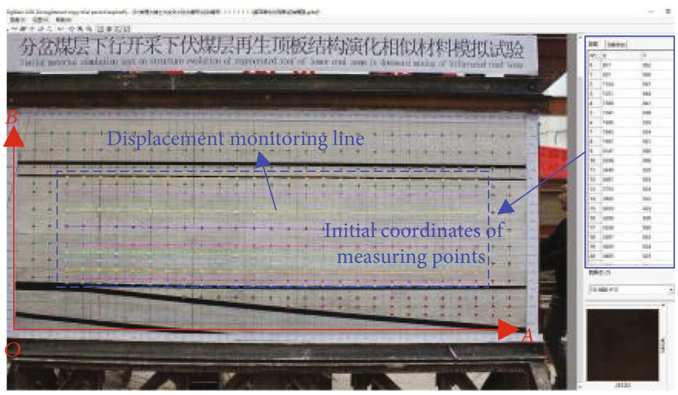

(b) Extract the initial coordinate value of the model measuring point

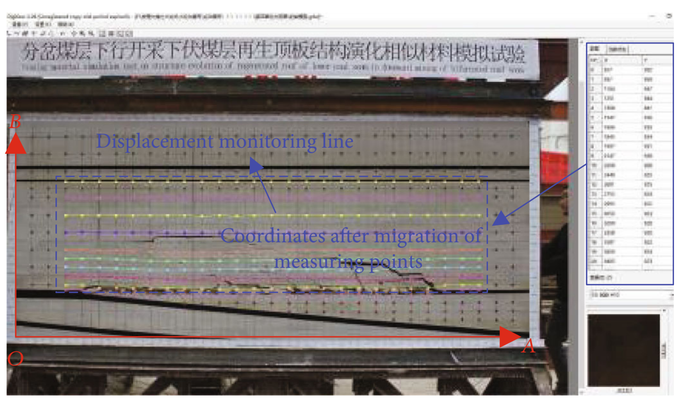

(c) Extract the coordinate values of measuring points after coal seam mining

Figure 4: Schematic diagram of measuring point displacement data extraction.

at the end of the working face gradually increases (Figure 13(c)). After breaking, they hinge with each other to form a masonry beam structure, so that mining of the no. 7-2 coal seam is not affected by mining of the no. 7-1 coal seam. In summary, when the coal seam spacing is less than 6 m, the rock mass structure of type I and type II roofs is relatively unstable, the interlayer structure is relatively loose, and the roof is broken, making it difficult to manage. When the interlayer distance is greater than 6 m, a stable masonry beam structure is formed between the layers, which can support the caving zone of the no. 7-1 coal seam. The stability of the three types of regenerated roof structure is III > II > I.

4. Study on Evolution Characteristics of Porosity and Permeability of Roof Overburden in the No. 7-2 Coal Seam

4.1. Distribution Characteristics of Porosity and Permeability Coefficient of Overburden. Through the analysis of the structural stability of various types of the regenerated roof, the rock mass structure of type I and II roofs is determined to be relatively unstable, and the interlayer structure is relatively loose, requiring that the broken rock mass be reinforced. The previous experience of mining the no. 7-2 coal seam in the Xutuan coal mine shows that when the coal seam spacing is less than 6 m and only support measures

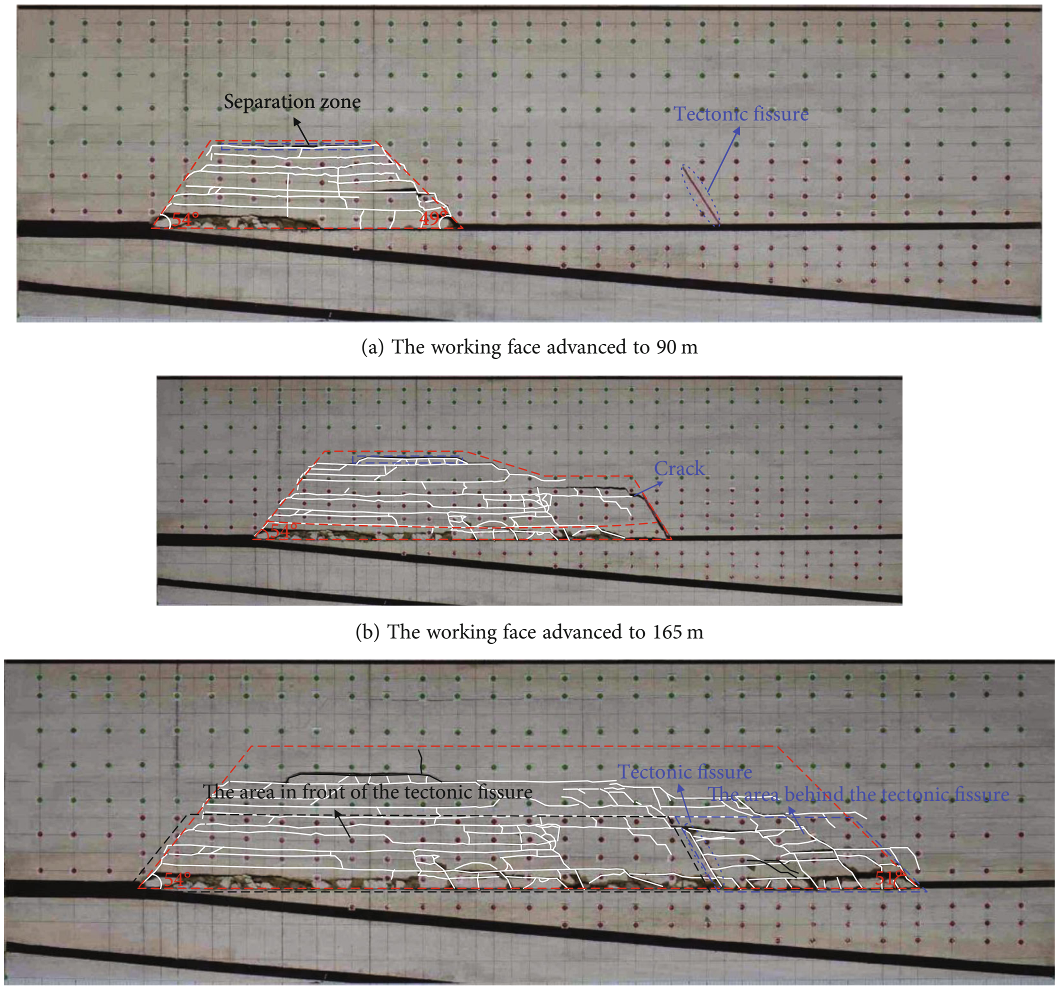

(a) The working face advanced to 90 m

(b) The working face advanced to 165 m

(c) The working face advanced to 220 m

Figure 5: Deformation characteristics of overburden during no. 7-1 coal seam mining.

are taken to strengthen the roof, the broken roof cannot be effectively controlled and the support effect is poor. Under this research background, the Xutuan coal mine attempted to reinforce broken roof by ground grouting. For the ground grouting engineering, the distribution characteristics of porosity and permeability of overburden are the key factors in the design of grouting parameters. The determination of grouting hole position, grouting pressure, single-hole grouting volume, and slurry diffusion radius is all affected by the porosity of overburden.

The volume changes and expansion coefficient of an actively mined rock mass can be determined using the ratio of volume before and after crushing [57, 58]:

$$K_{\mathrm{p}} = \frac{V_{\mathrm{h}}}{V_{\mathrm{q}}}. \tag{2}$$

In formula (2), V_{q} and V_{h} are the volume of the rock mass before and after mining.

According to the definition of porosity, the porosity n of broken rock mass due to the mining influence is the ratio of pore volume to total volume of the broken rock mass:

$$n = \frac{V_{\mathrm{h}} - V_q}{V_{\mathrm{h}}} = 1 - \frac{1}{K_{\mathrm{p}}}. \tag{3}$$

Summarizing the previous research results [59, 60], in the similar simulation experiment, with increasing vertical distance from the working face and considering the cumulative effect of the rock mass expansion coefficient, the average rock mass expansion coefficient in different height ranges can be calculated using the following formula:

$$K_{\mathrm{p}} = \frac{V_{\mathrm{h}}}{V_{\mathrm{q}}} = \frac{M + h - \Delta h}{h}. \tag{4}$$

In formula (4), K_{p} is the expansion coefficient of the rock mass. M is the thickness of the coal seam (unit: m). h is the distance between the roof measuring point and top interface

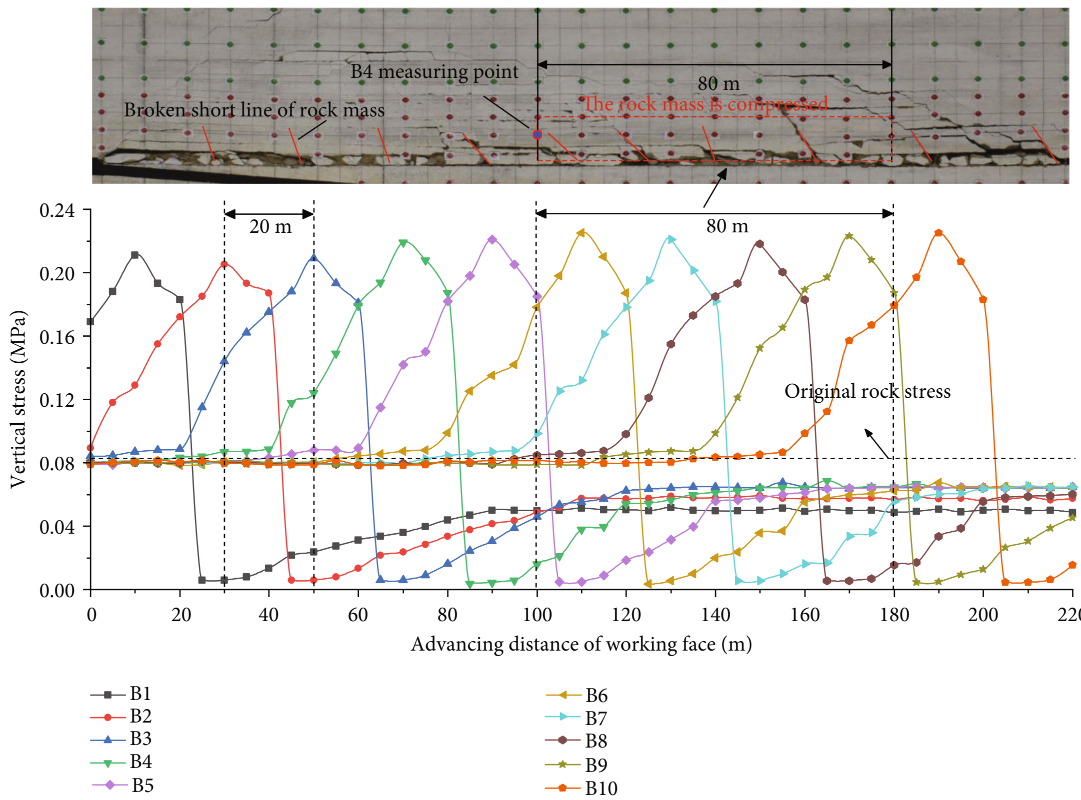

Figure 6: Stress variation diagram of overburden due to the mining influence (B monitoring line).

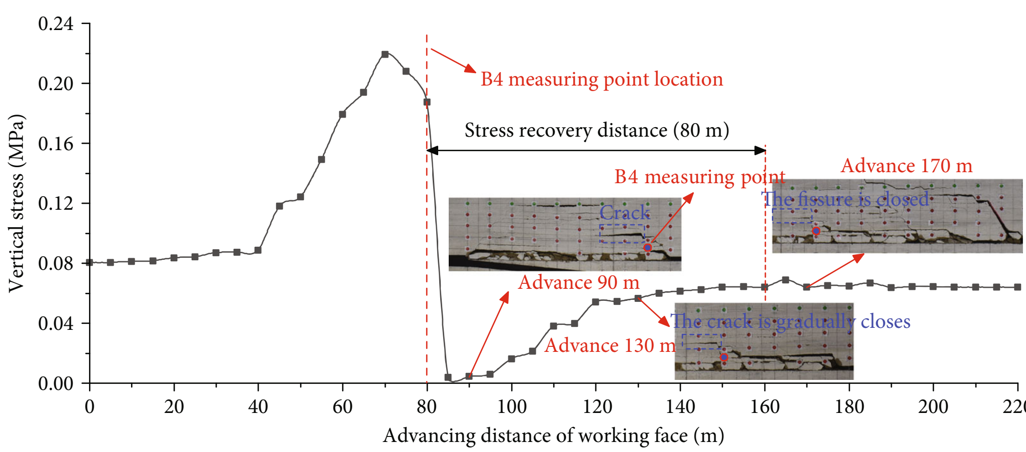

Figure 7: Relationship between stress recovery and dynamic evolution of crack morphology.

of the coal seam (unit: m). Δh is the subsidence of the measuring point (unit: m). The expression of porosity n is

$$n = \frac{V_{\mathrm{h}} - V_q}{V_{\mathrm{h}}} = 1 - \frac{1}{K_{\mathrm{p}}} = 1 - \frac{M + h - \Delta h}{h}. \tag{5}$$

Displacement measuring point data are used in equation (5) to calculate the porosity at different positions in overburden. According to the coordinate values of the measuring points in the model, import origin software to draw the plane porosity cloud map of the model. The distribution characteristics of overburden porosity of the no. 7-1 coal seam when the working face advances to 50 m, 110 m, and 220 m are shown in Figure 14.

When the working face advances to 50 m, the overburden directly collapses and fills the goaf (Figure 14(a)). The maximum porosity of the loose caving zone is 39.5% at the end of the working face and within 3 m of the roof. The sandstone layer at 8 m from the roof has not been broken, the rock deformation is weak, and the change in porosity is small. When the working face advances to 110 m, the support of the cantilever beam structure at the end of the working face hinders downward movement of the upper rock mass. There is a large space

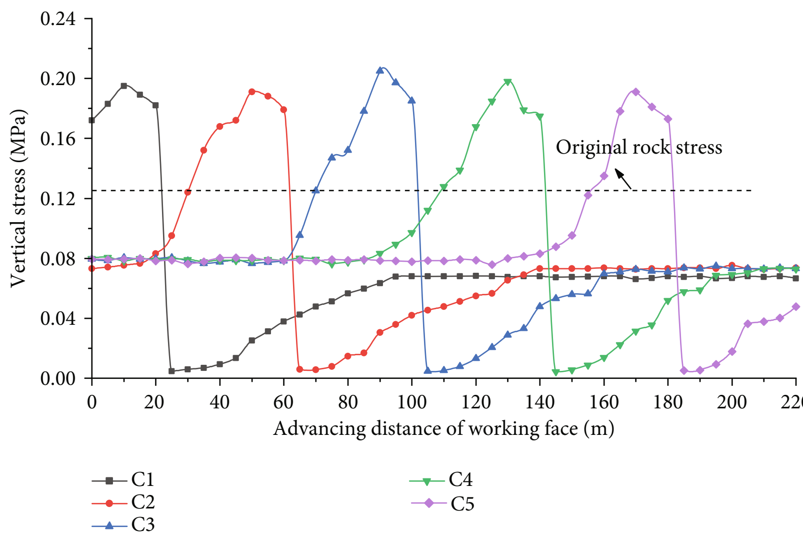

Figure 8: Stress variation diagram of overburden due to the mining influence (C monitoring line).

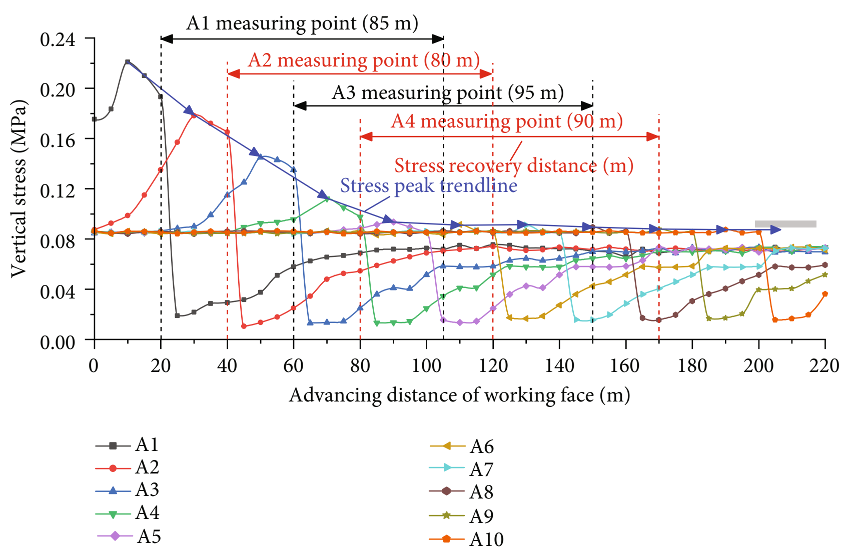

Figure 9: Transfer characteristics of floor stress during mining of the no. 7-1 coal seam.

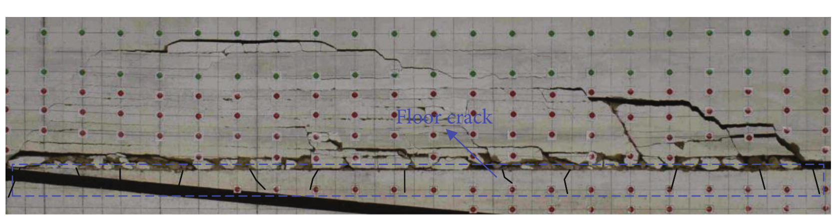

Figure 10: Schematic diagram of floor crack development due to the mining influence.

at the lower part of the cantilever beam, resulting in relatively large porosity of the overburden (Figure 14(b)). Within 8 m of the roof, the maximum porosity is 16.4%, and as the disturbed range of the overburden expands upward, the failure area of overburden increases, and the overburden porosity changes. In the horizontal direction, the maximum porosity of the rock mass in the collapse zone within 40 m of the cut hole is 34.3%, and the minimum porosity is 13.5%. Near the middle of the working face, the rock mass is gradually compacted due to stress recovery, and the porosity is 10%~12%. Vertically, the rock mass above the cut hole is broken upward along the fracture line. Within the separation area near the cut hole, the porosity of the rock mass is 12.0%~34.3%. The area above 33 m from the roof of the working face is relatively less affected by mining, and the porosity of the rock mass is not significantly affected. When the working face is mined to 220 m,

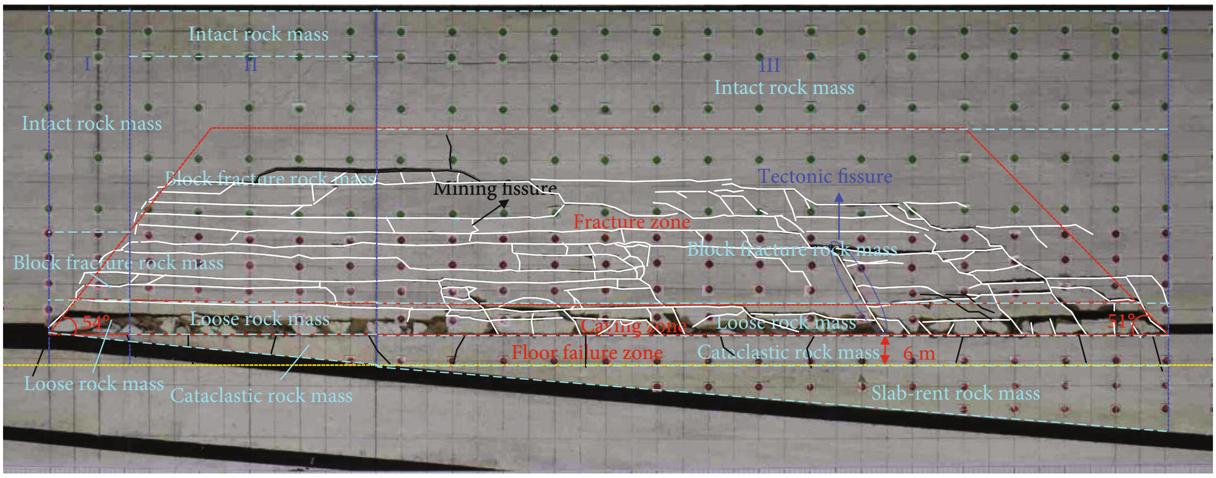

Figure 11: Schematic diagram of overburden structure division due to the mining influence.

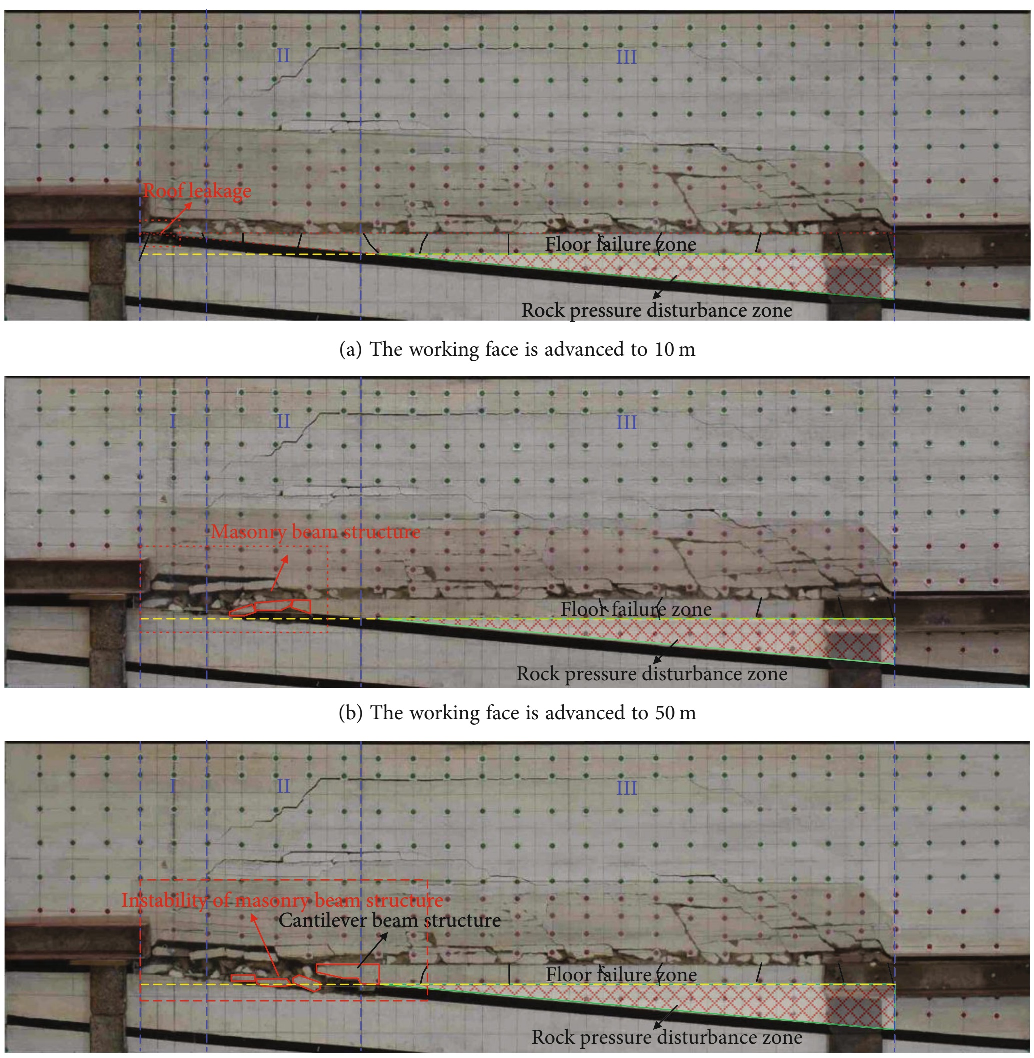

(a) The working face is advanced to 10 m

(b) The working face is advanced to 50 m

(c) The working face is advanced to 70 m

Figure 12: Schematic diagram of overburden fracture formation during 70 m advancement of the no. 7-2 coal seam.

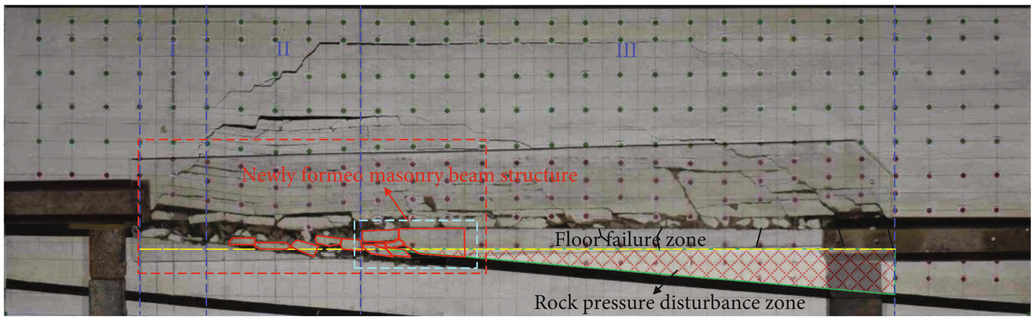

(a) The working face is advanced to 90 m

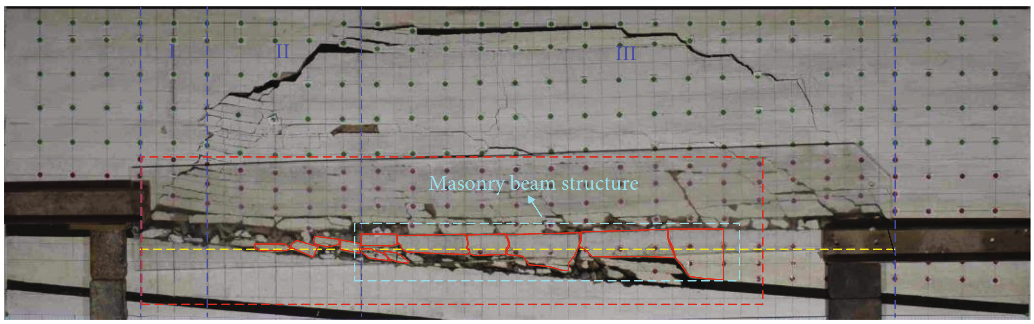

(b) The working face is advanced to 165 m

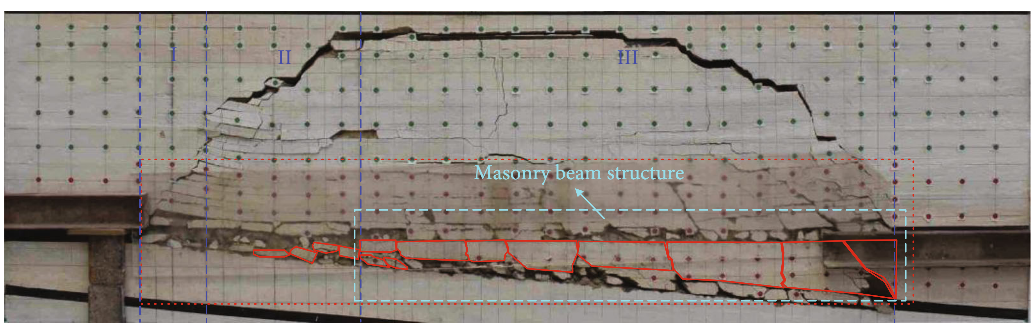

(c) The working face is advanced to 220 m

Figure 13: Schematic diagram of overburden fracture formation during advancement of the no. 7-2 coal seam to 90 m~220 m.

the maximum porosity of the surrounding rock near the cutting hole of the working face is 32.1%, and the maximum porosity of the surrounding rock near the stopping line of the working face is 32.6% (Figure 14(c)). The porosity gradually decreases away from both ends of the goaf to the middle. The middle compaction area ranges from 110 m to 190 m, at which point the porosity of the compaction area tends to be stable and less than 5%. The porosity of rock mass is greater than 5% within 70 m from the cut hole and stopping line. A strong disturbance zone is present within 33 m of the roof, and the porosity changes with movement and fracturing of the overburden. After stress recovery, the rock mass is gradually compacted. When the working face advances to 220 m, the compaction degree of overburden in the middle of goaf is significantly greater than that when the working face advances to 110 m. The porosity of overburden at the cut is affected by the separation space and masonry beam structure, and its influence range is 40 m~50 m in the transverse direction of the roof and 0 m~12 m in the longitudinal direction. The distribution characteristics of the porosity of the surrounding rock at the stopping line are similar to those at the cut hole.

The classic permeability porosity relationship Kozeny-Carman (KC) equation connects permeability K with porosity n. This equation is also widely used as the starting point of many permeability models [61–64]:

$$K = \frac{n^3}{(1-n)^2 c S^2}. \tag{6}$$

In formula (6), c is a constant, and the value is 5. S is the specific surface area. On this basis, the KC equation is further modified, and the permeability coefficient expression is [65, 66]

$$k = \frac{n^3 \rho g}{(1-n)^2 c S^2 \mu} = \frac{n^3 d^2 \rho g}{36 c (1-n)^2 \mu}. \tag{7}$$

The equation is commonly used to calculate the permeability coefficient of fluid in stope surrounding rock. In formula (7), k is the permeability coefficient (unit: m/s). n is the

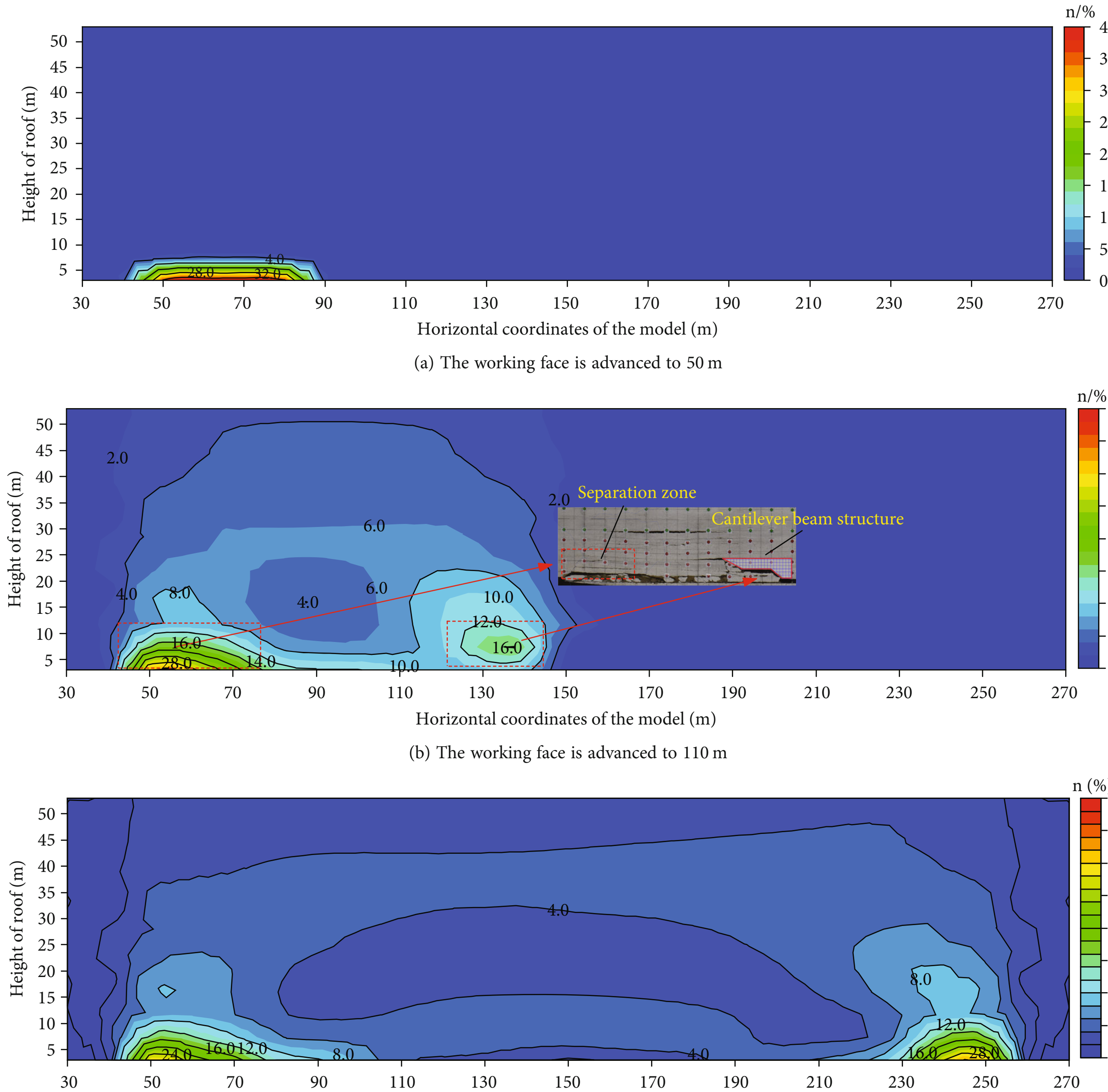

(a) The working face is advanced to 50 m

(b) The working face is advanced to 110 m

(c) The working face is advanced to 220 m

Figure 14: Distribution of overburden porosity during no. 7-1 coal seam mining.

porosity. d is the average diameter of the fractured rock mass, which is 0.5 m. ρ is the slurry density, with a value of 1309 kg/m^3. μ is the dynamic viscosity coefficient of slurry, which is 9×10^{-3} kg/(m $*$ s); g is the gravitational acceleration, taking 9.8 m/s^2.

The plane distribution law of permeability coefficient of slurry in overburden once mining of the 7-1 coal seam is completed is shown in Figure 15.

4.2. Division of Grouting Difficulty Degree in the Reconstruction Area of Broken Rock Mass with the Regenerated Roof. Based on the porosity difference in two rock mass zones, the surrounding rock at the cut of the caving zone and the stopping line is the primary space for slurry seepage and storage. According to the transverse distribution law of rock porosity and permeability coefficient in the goaf caving zone and the compaction characteristics of caving rock mass in goaf, the difficulty degree of overburden grouting is divided into different regions. The vertical plane of overburden is divided into an extremely easy grouting area, easy grouting area, and difficult grouting area (Figure 15) (Table 3).

(1) In the extremely easy grouting area, the caving rock mass in the goaf does not bear the abutment pressure

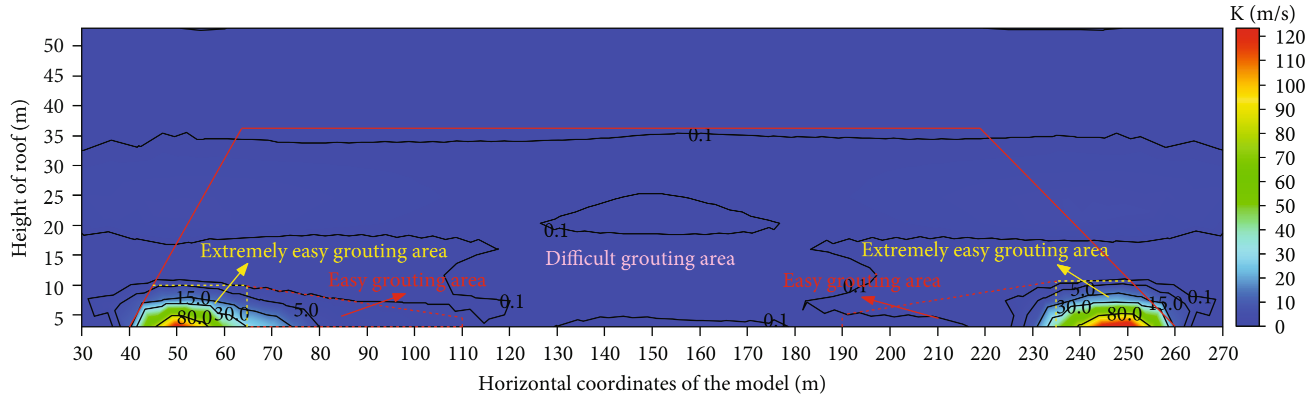

Figure 15: Regional division of grouting difficulty in overburden.

Table 3: Classification of grouting difficulty in overburden due to the mining influence.

Types	Distance from the coal wall (m)	Characteristics of caving rock mass	n (%)	Permeability coefficient (m/s)
Extremely easy grouting area	0 m~25 m	Rocks accumulate naturally	≥20	≥30
Easy grouting area	25 m~70 m	Rocks affected by load	$5 \leq n < 20$	$0.1 \leq k < 30$
Difficult grouting area	>70 m	The rock was compacted	$n < 5$	<0.1

and forms a natural accumulation state. The porosity of the caving rock mass is $n \geq 20\%$, and the permeability coefficient is $k \geq 30$ m/s. The slurry is flowing easily with this area, and grouting can be completed at low pressure. However, the area and seepage space are small, which are generally distributed on both sides of the coal wall of the roadway as well as within a certain range of the open cut and stopping line

(2) In the easy grouting area, the caving rock mass is under stress due to the action of the masonry beam structure of the overlying strata, and the caving rock mass is gradually compacted with increasing roof subsidence. The porosity range of the collapsed rock mass is $5\% \leq n \leq 20\%$, and the permeability coefficient is $0.1 \leq k \leq 30$ m/s

(3) In the difficult grouting area, the abutment pressure values in each area are relatively similar, and the caving rock mass is fully compacted and is stable. The porosity of the caving rock mass is $n < 5\%$, and the permeability coefficient is $k < 0.1$ m/s. The rock mass in this area requires grouting under high grouting pressure and is generally located in the central compaction area of the goaf

5. Conclusion

This paper reveals the structural characteristics of the regenerated roof of the lower coal seam after the mining of the upper coal seam in the bifurcated coal seam through the similar simulation test, divides the roof structure into types, and analyzes the stability of the roof of different structural types. Mining practice and similar simulation test results show that when the spacing of bifurcated coal seams is less than 6 m, the roof of the lower coal seam is relatively broken after mining of the upper coal seam, and a variety of support measures are taken, which is still difficult to control in the mining process of the lower coal seam. Under this background, the author studies the porosity and permeability characteristics of overburden under the mining influence of the upper coal seam and obtains the distribution law of porosity and permeability of overburden. The research results can provide reference for the parameter design of the ground grouting engineering of the regenerated roof. The main conclusions are as follows:

(1) After mining of the upper coal seam, the surrounding rock structure changes. Affected by interlayer distance, structural types of the regenerated roof of the lower coal seam can be primarily divided into three types from top to bottom, namely: intact rock mass+block fracture rock mass+loose rock mass (type I structure); intact rock mass+block fracture rock mass+loose rock mass+cataclastic rock mass (type II structure); and intact rock mass+block fracture rock mass+loose rock mass+cataclastic rock mass+slab-rent rock mass (type III structure)

(2) Through mining of the lower coal seam, the stability of three kinds of recycled roof structures is evaluated. Based on overburden migration and fracturing during mining of the lower coal seam, the stability of the three kinds of recycled roof structures is obtained: III > II > I

(3) Differences in porosity and permeability characteristics of overburden after mining of the upper coal

seam are analyzed. The porosity of the goaf and overburden at the cut hole and stopping line is significantly larger than that in the middle compaction area. Within 70 m of the coal wall, the rock mass porosity is greater than 5%, and the permeability coefficient of slurry in this range is greater than 0.1 m/s

(4) Based on porosity and permeability differences in the overburden, the difficulty degree of overburden grouting is divided into three areas: extremely easy grouting area, easy grouting area, and difficult grouting area

Data Availability

The data used for calculation in this paper can be obtained from the author.

Conflicts of Interest

The authors declare that they have no conflicts of interest.

Acknowledgments

The authors are grateful for the financial support provided by the Innovation Team Construction Project of University Scientific Research Platform in Anhui Province (2016-2018-24), the Anhui Province Natural Science Foundation (2008085QE226), and the National Natural Science Foundation of China (Grant nos. 41272278 and 52104117). We thank the School of Mining Engineering of Anhui University of Science and Technology for providing the site for this similar simulation test and thank the experimenter Bao Ming for his help in the process of the experiment. Finally, we would like to thank the authors of the references cited in this paper for their contributions in the field of mining.

References

[1] D. Y. Hao, Y. Z. Wu, H. J. Chen, X. W. Chu, and Y. Li, "Instability mechanism and prevention technology of roadway in close distance and extra thick coal seam under goaf," *Journal of China Coal Society*, vol. 44, no. 9, pp. 2682–2690, 2019.

[2] G. Y. Peng, M. Z. Gao, Y. C. Lv, and R. G. Zhang, "Investigation on mining mechanics behavior of deep close distance seam group," *Journal of China Coal Society*, vol. 44, no. 7, pp. 1971–1980, 2019.

[3] C. Y. Liu, J. X. Yang, B. Yu, and P. J. Yang, "Destabilization regularity of hard thick roof group under the multi gob," *Journal of China Coal Society*, vol. 39, no. 3, pp. 395–403, 2014.

[4] H. P. Kang, Z. Zhang, and Z. Z. Huang, "Characteristics of roof disasters and controlling techniques of coal mine in China," *Safety in Coal Mines*, vol. 51, no. 10, pp. 24–33, 2020.

[5] H. P. Kang, "Seventy years development and prospects of strata control technologies for coal mine roadways in China," *Chinese Journal of Rock Mechanics and Engineering*, vol. 40, no. 1, pp. 1–30, 2021.

[6] W. D. Wu, J. B. Bai, X. Y. Wang, Z. J. Zhu, and S. Yan, "Field investigation of fractures evolution in overlying strata caused by extraction of the Jurassic and Carboniferous coal seams and its application: case study," *International Journal of Coal Geology*, vol. 208, pp. 12–23, 2019.

[7] F. Cui, C. Jia, and X. P. Lai, "Study on deformation and energy release characteristics of overlying strata under different mining sequence in close coal seam group based on similar material simulation," *Energies*, vol. 12, no. 23, p. 4485, 2019.

[8] W. H. Sui, Y. Hang, L. X. Ma et al., "Interactions of overburden failure zones due to multiple-seam mining using longwall caving," *Bulletin of Engineering Geology and the Environment*, vol. 74, no. 3, pp. 1019–1035, 2015.

[9] J. Lu, C. B. Jiang, Z. Jin, W. Wang, W. Zhuang, and H. Yu, "Three-dimensional physical model experiment of mining-induced deformation and failure characteristics of roof and floor in deep underground coal seams," *Process Safety and Environmental Protection*, vol. 150, pp. 400–415, 2021.

[10] J. Wang, P. Q. Qiu, J. G. Ning, L. Zhuang, and S. Yang, "A numerical study of the mining-induced energy redistribution in a coal seam adjacent to an extracted coal panel during longwall face mining: a case study," *Energy Science & Engineering*, vol. 8, no. 3, pp. 817–835, 2020.

[11] H. Yan, M. Y. Weng, R. M. Feng, and W. K. Li, "Layout and support design of a coal roadway in ultra-close multiple-seams," *Journal of Central South University*, vol. 22, no. 11, pp. 4385–4395, 2015.

[12] X. J. Liu, X. M. Li, and W. D. Pan, "Analysis on the floor stress distribution and roadway position in the close distance coal seams," *Arabian Journal of Geosciences*, vol. 9, no. 2, pp. 4385–4395, 2016.

[13] W. Zhang, D. S. Zhang, D. H. Qi, W. Hu, Z. He, and W. Zhang, "Floor failure depth of upper coal seam during close coal seams mining and its novel detection method," *Energy Exploration & Exploitation*, vol. 36, no. 5, pp. 1265–1278, 2018.

[14] X. M. Sun, Y. Y. Liu, J. W. Wang, J. Li, S. Sun, and X. Cui, "Study on three-dimensional stress field of gob-side entry retaining by roof cutting without pillar under near-group coal seam mining," *PRO*, vol. 7, no. 9, p. 552, 2019.

[15] H. F. Shang, J. G. Ning, S. C. Hu, S. Yang, and P. Qiu, "Field and numerical investigations of gateroad system failure under an irregular residual coal pillar in close-distance coal seams," *Energy Science & Engineering*, vol. 7, no. 6, pp. 2720–2740, 2019.

[16] Y. Xiong, D. Z. Kong, Z. B. Cheng et al., "Instability control of roadway surrounding rock in close-distance coal seam groups under repeated mining," *Energies*, vol. 14, no. 16, p. 5193, 2021.

[17] Z. Y. Sun, Y. Z. Wu, Z. G. Lu, Y. Feng, X. Chu, and K. Yi, "Stability analysis and derived control measures for rock surrounding a roadway in a lower coal seam under concentrated stress of a coal pillar," *Shock and Vibration*, vol. 2020, Article ID 6624983, 12 pages, 2020.

[18] X. Gao, S. Zhang, Y. Zi, and S. K. Pathan, "Study on optimum layout of roadway in close coal seam," *Arabian Journal of Geosciences*, vol. 13, no. 15, 2020.

[19] Y. L. Xu, K. R. Pan, and H. Zhang, "Investigation of key techniques on floor roadway support under the impacts of superimposed mining: theoretical analysis and field study," *Environmental Earth Sciences*, vol. 78, no. 15, 2019.

[20] W. K. Ru, S. C. Hu, J. G. Ning et al., "Study on the rheological failure mechanism of weakly cemented soft rock roadway during the mining of close-distance coal seams: a case study," *Advances in Civil Engineering*, vol. 2020, Article ID 8885849, 20 pages, 2020.

[21] Y. L. Huang, J. X. Zhang, W. Yin, and Q. Sun, "Analysis of overlying strata movement and behaviors in caving and solid backfilling mixed coal mining," *Energies*, vol. 10, no. 7, p. 1057, 2017.

[22] K. Gao, P. Huang, Z. G. Liu, J. Liu, F. Wang, and C. M. Shu, "Pressure relief by blasting roof cutting in close seam group mining under thick sandstone to enhance gas extraction for mining safety," *PRO*, vol. 9, no. 4, p. 603, 2021.

[23] Q. H. Huang, Y. P. He, and L. B. Luo, "Study on the active structure of caved roof and support resistance in shallow buried and ultra-close coal seams mining," *Journal of Mining & Safety Engineering*, vol. 35, no. 3, pp. 561–566, 2018.

[24] Y. T. Sun, G. C. Li, N. Zhang, Q. Chang, J. Xu, and J. Zhang, "Development of ensemble learning models to evaluate the strength of coal-grout materials," *International Journal of Mining Science and Technology*, vol. 31, no. 2, pp. 153–162, 2021.

[25] D. Z. Kong, Z. B. Cheng, and S. S. Zheng, "Study on the failure mechanism and stability control measures in a large-cutting-height coal mining face with a deep-buried seam," *Bulletin of Engineering Geology and the Environment*, vol. 78, no. 8, pp. 6143–6157, 2019.

[26] K. Wang, L. G. Wang, and B. Ren, "Failure mechanism analysis and support technology for roadway tunnel in fault fracture zone: a case study," *Energies*, vol. 14, no. 13, p. 3767, 2021.

[27] J. P. Zhang, L. M. Liu, Q. H. Li et al., "Development of cement-based self-stress composite grouting material for reinforcing rock mass and engineering application," *Construction and Building Materials*, vol. 201, pp. 314–327, 2019.

[28] D. Y. Qian, N. Zhang, M. W. Zhang et al., "Application and evaluation of ground surface pre-grouting reinforcement for 800-m-deep underground opening through large fault zones," *Arabian Journal of Geosciences*, vol. 10, no. 13, 2017.

[29] Q. Wang, H. K. Gao, H. C. Yu, B. Jiang, and B. H. Liu, "Method for measuring rock mass characteristics and evaluating the grouting-reinforced effect based on digital drilling," *Rock Mechanics and Rock Engineering*, vol. 52, no. 3, pp. 841–851, 2019.

[30] D. P. Adhikary and H. Guo, "Modelling of longwall mining-induced strata permeability change," *Rock Mechanics and Rock Engineering*, vol. 48, no. 1, pp. 345–359, 2015.

[31] C. Zhang, S. H. Tu, and Y. X. Zhao, "Compaction characteristics of the caving zone in a longwall goaf: a review," *Environmental Earth Sciences*, vol. 78, no. 1, 2019.

[32] B. A. Poulsen, D. P. Adhikary, and H. Guo, "Simulating mining-induced strata permeability changes," *Rock Mechanics and Rock Engineering*, vol. 237, pp. 208–216, 2018.

[33] H. Wu and D. Ma, "Fracture phenomena and mechanisms of brittle rock with different numbers of openings under uniaxial loading," *Geomechanics and Engineering*, vol. 25, no. 6, pp. 481–493, 2021.

[34] D. Ma, J. J. Wang, X. Cai et al., "Effects of height/diameter ratio on failure and damage properties of granite under coupled bending and splitting deformation," *Engineering Fracture Mechanics*, vol. 220, p. 106640, 2019.

[35] D. Ma, J. X. Zhang, H. Y. Duan et al., "Reutilization of gangue wastes in underground backfilling mining: overburden aquifer protection," *Chemosphere*, vol. 264, no. 1, 2021.

[36] D. Ma, S. B. Kong, Z. H. Li, Q. Zhang, Z. Wang, and Z. Zhou, "Effect of wetting-drying cycle on hydraulic and mechanical properties of cemented paste backfill of the recycled solid wastes," *Chemosphere*, vol. 282, p. 131163, 2021.

[37] S. F. Wang, X. B. Li, and D. M. Wang, "Void fraction distribution in overburden disturbed by longwall mining of coal," *Environmental Earth Sciences*, vol. 75, no. 2, 2016.

[38] G. Y. Si, J. Q. Shi, S. Durucan et al., "Monitoring and modelling of gas dynamics in multi-level longwall top coal caving of ultra-thick coal seams, part II: numerical modelling," *International Journal of Coal Geology*, vol. 144-145, pp. 58–70, 2015.

[39] Z. P. Meng, X. C. Shi, and G. Q. Li, "Deformation, failure and permeability of coal-bearing strata during longwall mining," *Rock Mechanics and Rock Engineering*, vol. 208, pp. 69–80, 2016.

[40] R. Hu, J. W. Wu, W. B. Shi, X. Zhai, and K. Huang, "Study on evolution characteristics of regenerated roof structure in downward mining of bifurcated coal seam," *Advances in Materials Science and Engineering*, vol. 2021, Article ID 8226616, 13 pages, 2021.

[41] J. Chai, W. G. Du, Q. Yuan, and D. Zhang, "Analysis of test method for physical model test of mining based on optical fiber sensing technology detection," *Optical Fiber Technology*, vol. 48, pp. 84–94, 2019.

[42] G. W. Cheng, T. H. Yang, H. Y. Liu et al., "Characteristics of stratum movement induced by downward longwall mining activities in middle-distance multi-seam," *International Journal of Rock Mechanics and Mining Sciences*, vol. 136, p. 104517, 2020.

[43] W. T. Liu, L. F. Pang, B. C. Xu, and X. Sun, "Study on overburden failure characteristics in deep thick loose seam and thick coal seam mining," *Geomatics, Natural Hazards and Risk*, vol. 11, no. 1, pp. 632–653, 2020.

[44] T. Hu, G. Y. Hou, and Z. X. Li, "The field monitoring experiment of the roof strata movement in coal mining based on DFOS," *Sensors*, vol. 20, no. 5, p. 1318, 2020.

[45] J. J. Li, F. J. Li, M. S. Hu, X. Zhou, and Y. Huo, "Dynamic monitoring of the mining-induced fractured zone in overburden strata, based on geo-electrical characteristics," *Arabian Journal of Geosciences*, vol. 12, no. 14, 2019.

[46] J. G. Ning, J. Wang, Y. L. Tan, and Q. Xu, "Mechanical mechanism of overlying strata breaking and development of fractured zone during close-distance coal seam group mining," *International Journal of Mining Science and Technology*, vol. 30, no. 2, pp. 207–215, 2020.

[47] G. W. Cheng, T. H. Ma, C. A. Tang, H. Liu, and S. Wang, "A zoning model for coal mining-induced strata movement based on microseismic monitoring," *International Journal of Rock Mechanics and Mining Sciences*, vol. 94, pp. 123–138, 2017.

[48] W. Guo, G. Zhao, G. Lou, and S. Wang, "A new method of predicting the height of the fractured water-conducting zone due to high-intensity longwall coal mining in China," *Rock Mechanics and Rock Engineering*, vol. 52, no. 8, pp. 2789–2802, 2019.

[49] W. Y. Lu, C. C. He, and X. Zhang, "Height of overburden fracture based on key strata theory in longwall face," *PLoS One*, vol. 15, no. 1, 2020.

[50] T. Hu, G. Y. Hou, S. Bu et al., "A novel approach for predicting the height of water-conducting fracture zone under the high overburden caving strength based on optimized processes," *Process*, vol. 8, no. 8, p. 950, 2020.

[51] Y. P. Liang, B. Li, and Q. L. Zou, "Movement type of the first subordinate key stratum and its influence on strata behavior

in the fully mechanized face with large mining height," *Arabian Journal of Geosciences*, vol. 12, no. 2, 2019.

[52] Z. C. Ren and N. Wang, "The overburden strata caving characteristics and height determination of water conducting fracture zone in fully mechanized caving mining of extra thick coal seam," *Geotechnical and Geological Engineering*, vol. 38, no. 1, pp. 329–341, 2020.

[53] X. L. Wang, Q. R. Qin, and C. H. Fan, "Failure characteristic and fracture evolution law of overburden of thick coal in fully mechanized sub-level caving mining," *Journal of Engineering Geology*, vol. 46, no. 11, pp. 2041–2048, 2017.

[54] W. H. Sui, D. Y. Zhang, Z. C. Cui, Z. Wu, and Q. Zhao, "Environmental implications of mitigating overburden failure and subsidences using paste-like backfill mining: a case study," *International Journal of Mining, Reclamation and Environment*, vol. 29, no. 6, pp. 521–543, 2015.

[55] Q. X. Huang and J. B. Han, "Study on fracture evolution mechanism of shallow-buried close coal seam mining," *Journal of Mining & Safety Engineering*, vol. 36, no. 4, pp. 706–711, 2019.

[56] H. Z. Wang, Y. J. Ju, and K. K. Qin, "A comparative study on floor failure law in deep and short-distance coal seam mining," *Journal of Mining & Safety Engineering*, vol. 37, no. 3, pp. 553–560, 2020.

[57] C. D. Su, M. Gu, X. Tang, and W. B. Guo, "Experiment study of compaction characteristics of crushed stones from coal seam roof," *Chinese Journal of Rock Mechanics and Engineering*, vol. 31, no. 1, pp. 18–26, 2012.

[58] B. F. Wang, B. Liang, J. G. Wang, K. M. Sun, and H. B. Chi, "Experiment study on rock bulking of coal mine underground reservoir," *Rock and Soil Mechanics*, vol. 39, no. 11, pp. 4086–4092, 2018.

[59] K. Z. Deng, M. Zhou, and Z. X. Tan, "Study on laws of rock mass breaking induced by mining," *Journal of China University of Mining and Technology*, vol. 27, no. 3, pp. 261–264, 1998.

[60] L. H. Sun, H. G. Ji, H. Jiang, P. Zeng, and B. S. Yang, "Experimental study on characteristics of broken caving and regularity of compaction deformation of rocks in caving zone in the weakly cemented strata," *Journal of China Coal Society*, vol. 42, no. 10, pp. 2565–2572, 2017.

[61] P. C. Carman, "Permeability of saturated sands, soils and clays," *The Journal of Agricultural Science*, vol. 29, no. 2, pp. 262–273, 1939.

[62] P. C. Carman, "Book reviews: flow of gases through porous media," *Science*, vol. 124, pp. 1254-1255, 1956.

[63] J. Kozeny, "Ueber kapillare leitung des wassers im boden," *Sitzungsberichte der Kaiserlichen Akademie der Wissenschaften in Wien*, vol. 136, pp. 271–306, 1927.

[64] P. Xu and B. M. Yu, "Developing a new form of permeability and Kozeny-Carman constant for homogeneous porous media by means of fractal geometry," *Advances in Water Resources*, vol. 31, no. 1, pp. 74–81, 2008.

[65] J. Bear and B. M. Yu, *Dynamics of Fluid in Porous Media*, Elsevier, New York, 1972.

[66] M. Kaviany, *Principles of Heat Transfer in Porous Media*, Springer, New York, 1995.

Hindawi
Geofluids
Volume 2022, Article ID 3280185, 10 pages
https://doi.org/10.1155/2022/3280185

Research Article

Study on the Precursors of Coal-Rock Fracture Based on the Maximum Lyapunov Exponent of Acoustic Emission Parameters

Guoqiang Cheng,[1] **Xiaohui Sun**,[1] **and Jiangong Li**[2,3]

[1]*School of Energy and Mining Engineering, Shandong University of Science and Technology, Qingdao 266590, China*
[2]*State Key Laboratory of Gas Disaster Detecting, Preventing and Emergency Controlling, China Coal Technology Engineering Group Chongqing Research Institute, Chongqing 400039, China*
[3]*State Key Laboratory of Coal Mine Disaster Dynamics and Control, College of Resources and Environmental Sciences, Chongqing University, Chongqing 400030, China*

Correspondence should be addressed to Guoqiang Cheng; skd991928@sdust.edu.cn and Jiangong Li; flyljg@163.com

Received 16 August 2021; Accepted 24 February 2022; Published 18 March 2022

Academic Editor: Na Huang

In this paper, the relationship between acoustic emission (AE) parameters and coal-rock fracture is investigated by using the discrete element particle flow simulation software PFC. PFC is used to simulate the coal-rock uniaxial compression test for extracting the time series of AE event number, calculate the maximum Lyapunov exponent of the time series, and analyze the chaotic characteristics of AE event number. Combined with the relationship between the maximum point of the Lyapunov exponent and the peak point of the stress-strain curve, the coal-rock fracture precursor model was developed. The results indicate that during the uniaxial compression of coal-rock, the number of AE events first increases and then decreases, while the maximum point appears after the peak point of the stress-strain curve. The lower the coal-rock homogeneity, the earlier is the initial occurrence time of AE events. The AE event number has chaotic characteristics. In most cases, the chaotic characteristics of the number of AE events are the most evident before the specimen is completely destroyed. When the maximum Lyapunov exponent of AE event number time series mutates, it indicates that the specimen is about to be destroyed entirely, which can be used as a precursor criterion for coal-rock fracture.

1. Introduction

When rocks are deformed or damaged under external forces, strain energy is released as elastic waves, which is termed acoustic emission (AE). AE has been widely used in rock stability monitoring and predicting mines, slopes, and tunnels since it was discovered in the 1930s.

AE signals can not only reflect the failure process of the rock but also indicate the characteristic information of the internal structure of the rock. Over the years, many researchers have studied the relationship between AE signal parameters and rock fracture, further explaining the mechanism of rock fracture and putting forward reasonable precursor criteria for rock fracture. Shkuratnik et al. [1] studied the AE characteristics of coal-rock fracture under different loading methods. Liu et al. [2] developed a coal-rock damage model based on the AE characteristics of coal-rock under uniaxial compression to reveal the damage evolution of coal-rock under load. Cao et al. [3–5] conducted uniaxial compression tests on rock specimens, using ringing count, main frequency and entropy values of AE signals, and AE energy rate as main characteristic parameters to predict rock fracture. Wang et al. [6] examined the rock critical fracture criterion and precursor characteristics based on the uniaxial compression AE test of granite. The results obtained were used for monitoring and preventing the occurrence of coal-rock composite dynamic disasters. Li et al. [7, 8] used AE technology in No. 10 Coal Mine of Ping Coal Mine for monitoring and early warning of coal-rock dynamic disaster and proposed AE identification and early warning criteria for coal-rock gas dynamic disaster based on the ringing count and energy value.

In terms of numerical simulation, Tang [9] independently developed RFPA software based on the finite element method (FEM) and conducted a preliminary study on the numerical simulation of AE models. Subsequently, many researchers [10–12] used RFPA to conduct numerical simulations and explore the relationship between AE parameters and rock fracture.

Chaos system is sensitive to initial conditions. In recent years, many researchers have applied chaos theory to the study of coal-rock gas dynamic disasters [13–16], laying the foundational basis for the study of chaos theory in the early warning and prevention of coal-rock gas dynamic disasters.

In this paper, based on the discrete element method (DEM), the numerical simulation method to obtain the AE parameter is used. Based on AE parameter data, the nonlinear chaos theory is introduced for in-depth investigation of the chaotic characteristics of AE parameters and analyzed them. The relationship between the chaotic characteristics of AE parameters and coal-rock fracture was explored to put forward a new precursor criterion of rock fracture, which effectively avoids the error caused by data contingency.

2. PFC Simulation of Coal-Rock Uniaxial Compression Test

PFC is a particle flow numerical simulation software for material damage evolution, fracture mechanism, and deformation process from the mesolevel based on the DEM theory. It is used for simulating the uniaxial compression of coal-rock. It can reproduce the mechanical behavior obtained from field experiments and observe the changes in the whole process from a microscopic view. The generation and development of microcracks in coal-rock will produce an AE phenomenon. In the PFC simulation, each link bond fracture releases strain energy, and an AE signal is generated with each release of strain energy [17]. Therefore, the number of broken particle links is regarded as the number of AE events of coal-rock in this paper. As the elastic modulus of the parallel bond model gradually decreases in the cyclic loading and unloading simulation process, it can simulate the coal-rock damage in the loading process. Therefore, the parallel bond model is selected to simulate coal-rock and calibrate the mesoparameters in this paper [18]. The mesomechanical parameters of the specimen are given in Table 1.

In order to study the AE characteristics during uniaxial compression of coal-rock, the standard specimen with the same size as the laboratory test (50 mm diameter and 100 mm length) was adopted in the simulation, while the displacement loading method with the loading rate of 0.03 m/s was adopted.

3. Uniaxial Compression Test Results and Analysis of Coal-Rock

3.1. Numerical Simulation Characteristics. Figure 1 shows the stress-strain-AE event number variation curve of coal-rock. As can be seen from Figure 1, the curve can be divided into three parts. The first part is the elastic stage of the stress-strain curve. In this stage, there are no AE events at the beginning, but sporadic AE events occur as the loading progresses. The second part is the plastic stage of the stress-strain curve in which the number of AE events increases significantly, and the frequency of AE events accelerates. In the third part, at the postpeak stage of the stress-strain curve, the number of AE events increases sharply to the peak and then decreases sharply until the loading stops.

In Figure 1, the AE event distribution at six points, i.e., a, b, c, d, e, and f, is shown in Figure 2.

In Figure 2, the red parts are the broken particle link keys, namely, the AE events. As can be seen from Figures 2(a) and 2(b), the distribution of AE events in the elastic stage of the stress-strain curve of coal-rock is uniform, random or disordered, and without apparent stress concentration phenomenon. As the loading proceeds, the distribution of AE events appears disordered. However, the events are orderly and begin to show a trend of stress concentration. As shown in Figure 2(c), the AE events may exhibit stress concentration phenomena at 1, 2, 3, and 4, generating large through cracks. After the coal-rock is destroyed, the stress concentration becomes gradually noticeable, particularly in zone 1 and zone 2 in Figures 2(d) and 2(e); the stress concentration phenomenon is the most obvious, followed by zone 3, while in zone 4, it is the weakest. When loading is carried out to point F in Figure 1, as shown in Figure 2(f), only large through cracks in zones 1, 2, and 3 are generated.

3.2. Numerical Calculation Method of Maximum Lyapunov Exponent Based on Small Data Volume Method. The existence of chaos can be determined by the positive and negative properties of the Lyapunov exponent [19]. It is sufficient to look at the largest Lyapunov exponent λ_1 for the chaotic judgment of multidimensional dynamical systems. If $\lambda_1 > 0$, it means there is chaos. The larger the λ_1 value, the more obvious are the chaotic characteristics of the data. If $\lambda_1 = 0$, there is a limit cycle. If $\lambda_1 < 0$, there is a fixed point.

In this paper, the maximum Lyapunov exponent of chaotic time series is calculated using the small data volume method. Specific calculation steps are as follows:

(1) FFT transformation on the time series $\{x(t_i), i = 1, 2, \cdots, N\}$ is performed, and the average period P is calculated

(2) The C-C method is used to calculate the embedding dimension m and time delay τ

(3) Phase space $\{Y_i, i = 1, 2, \cdots, M\}$ is reconstructed based on time delay τ and embedding dimension m

(4) The nearest neighbor point $Y_{\hat{j}}$ of each point Y_j in the phase space is found, and the short separation

Table 1: Mesomechanical parameters of coal-rock specimens.

Minimum particle size (mm)	Grain diameter ratio	Contact modulus E (GPa)	Normal strength of bond σ (MPa)	Tangential strength of bond σ (MPa)	Coefficient of friction
0.3	1.6	0.7	1.105	3	0.8

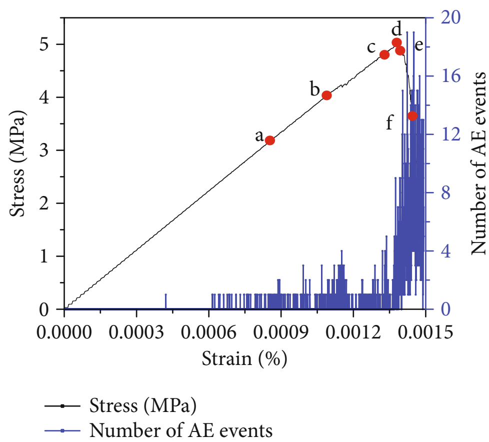

Figure 1: Stress-strain-AE event number variation curve of coal rock.

is limited, i.e.,

$$d_j(0) = \min_{\hat{j}} \left\| Y_j - Y_{\hat{j}} \right\|, \left| j - \hat{j} \right| > P \tag{1}$$

(5) For each point Y_j in the phase space, the distance $d_j(i)$ after i discrete time steps of the adjacent point pair is calculated

$$d_j(i) = \min_{\hat{j}} \left\| Y_{j+1} - Y_{\hat{j}+1} \right\|, \quad i = 1, 2, \cdots, \min\left(M - j, M - \hat{j}\right) \tag{2}$$

(6) The average y_i of all $\ln d_j(i)$ for each $\ln d_j(i)$ is determined:

$$y_i = \frac{1}{q\Delta t} \sum_{i=1}^{q} \ln d_j(i), \tag{3}$$

where q is the number of nonzero $d_j(i)$; $1/\tau \cdot d_j(i) \longrightarrow i$ point curve is drawn, and the regression line is made by the least-squares method; the slope of the line is the maximum Lyapunov exponent λ_1

3.3. Analysis of AE Characteristics Based on Maximum Lyapunov Exponent. During coal-rock uniaxial compression, the distribution of AE events is random. However, although the macrocracks formed in the end are different due to different microscopic parameters, the crack morphology presents a certain regularity, and the distribution process of AE events seems random and irregular. However, in fact, it is orderly, indicating the existence of chaos phenomenon in the process.

In this study, the recorded AE data is divided into groups of every 300 data points. The maximum Lyapunov exponent of each group of data is obtained by using the small-data volume method. The stress-strain-number of AE events-maximum Lyapunov exponent change relation is shown in Figure 3.

It can be seen from Figure 3 that the maximum Lyapunov exponent is greater than zero, indicating that the number of AE events during the coal-rock uniaxial compression has chaotic characteristics. In the elastic stage of the stress-strain curve, when the AE events start occurring, the maximum Lyapunov exponent of each data set cannot be calculated due to the weak continuity of AE events, i.e., there are no chaotic characteristics at this time. With the loading process, the frequency and continuity of AE events increase, and the maximum Lyapunov exponent of some time series can be calculated. The initial value of the maximum Lyapunov exponent fluctuates around zero, and chaos exists, but its characteristics are not prominent. Before the stress-strain curve reaches the peak point, the maximum Lyapunov exponent suddenly increases to the maximum value. At this time, the chaotic characteristics of AE events are the most apparent. In the postpeak stage of the stress-strain curve, the value of the maximum Lyapunov exponent is always smaller than the peak of the maximum Lyapunov exponent before the peak of stress-strain curve and gradually returns to zero, even though the number of AE events increases sharply and reaches the maximum value.

4. Simulation Validation and Analysis

AE is a kind of stress wave phenomenon produced during the deformation or damage of coal-rock under external force. The AE signal can not only reflect the internal structure of the specimens but also further extract the precursor information of the complete damage of the specimen, predict the occurrence of the specimen damage in advance, and then predict the occurrence of the coal-rock power disaster in advance.

If the maximum point of the maximum Lyapunov exponent of the time series of AE events shown in Figure 3 always appears in the stress-strain curve before peak point, then the maximum Lyapunov exponent of maximum points can be applied to warning specimens destroyed. In order to explore this idea, a simulation study on ten groups of coal-rock standard specimens is carried out in this paper. The mechanical

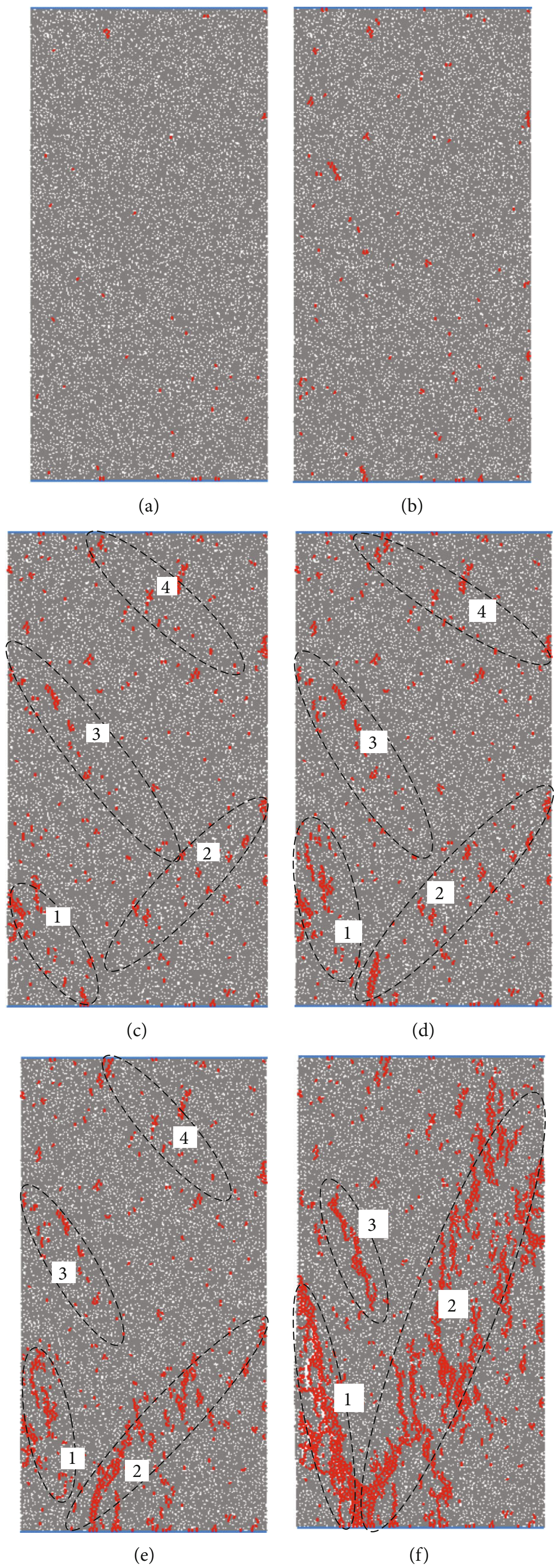

Figure 2: AE event distribution diagram.

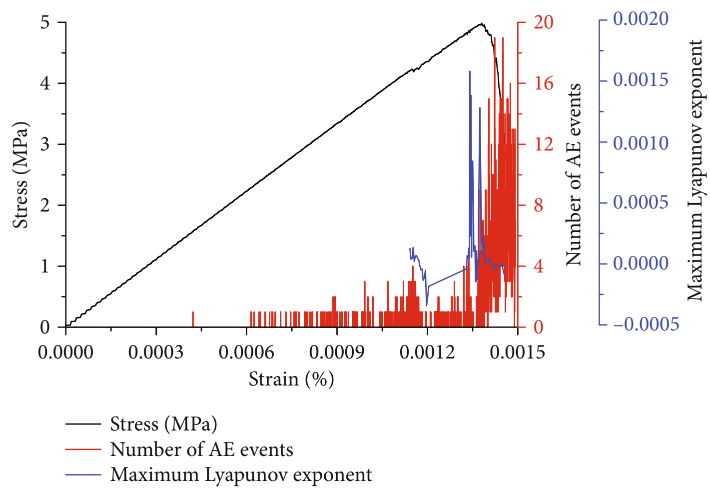

Figure 3: Coal-rock stress-strain-number of AE events-maximum Lyapunov exponential variation diagram.

Table 2: Summary of mechanical parameters of coal-rock standard specimens.

Specimen number	Peak stress (MPa)	Peak strain
1	4.983107832	0.001380257
2	4.25060345	0.001200344
3	2.543909411	0.000707774
4	6.694057265	0.001823883
5	2.976446791	0.00086566
6	8.223110102	0.002464985
7	3.151081825	0.000962933
8	8.619113876	0.002626044
9	3.169886512	0.001005317
10	3.169886512	0.001005317

Table 3: Summary table of maximum Lyapunov exponent.

Specimen serial number	Maximum initial Lyapunov exponent	Maximum Lyapunov exponent submaximum	Maximum Lyapunov exponent maximum
1	5.76×10^{-5}		1.70×10^{-3}
2	1.16×10^{-4}	7.27×10^{-4}	6.20×10^{-3}
3	-3.75×10^{-5}	9.34×10^{-4}	1.70×10^{-3}
4	1.34×10^{-4}		3.53×10^{-4}
5	3.06×10^{-5}		3.70×10^{-3}
6	1.46×10^{-4}	5.82×10^{-4}	1.30×10^{-3}
7	3.06×10^{-5}	5.98×10^{-4}	1.70×10^{-3}
8	1.43×10^{-4}	2.53×10^{-3}	4.28×10^{-3}
9	3.06×10^{-5}	7.66×10^{-4}	1.70×10^{-3}
10	3.06×10^{-5}	7.66×10^{-4}	1.70×10^{-3}

parameters of coal-rock standard specimens are enlisted in Table 2.

Table 3 is the summary table of the maximum Lyapunov exponent. The initial value of the maximum Lyapunov exponent is the first maximum Lyapunov exponent, and the submaximum value of the maximum Lyapunov exponent is the submaximum value before the occurrence of the maximum value of the maximum Lyapunov exponent. It is not the submaximum of all the maximum Lyapunov exponents.

It can be seen from Figures 4–13 that during coal-rock uniaxial compression, the variation pattern of AE events of all specimens is consistent with the scenarios shown in Figure 1, which generally shows a trend of first rising and then declining. In the initial stage of loading, no AE event occurred. As the loading progressed, sporadic AE events started appearing. When the stress-strain curve transitions into the plastic stage, the number of AE events increases significantly, and frequency is accelerated. When the specimen is near failure, the number of AE events increases sharply, and the maximum value appears after the peak point of the stress-strain curve. Subsequently, the number of AE events decreases sharply until the end of loading.

The homogeneity of coal-rock also influences the occurrence time of AE events. The lower the homogeneity of coal-rock, the smaller is the strain corresponding to the initial occurrence of AE events, i.e., the earlier is the initial occurrence time of AE events.

The maximum value of the maximum Lyapunov exponent in the time series of the number of AE events of specimens 1, 2, 3, 5, 7, 8, 9, and 10 appears before the peak of the stress-strain curve, i.e., before the specimen is completely destroyed, the chaotic characteristics of AE event number are the most obvious, which is consistent with the results shown in Figure 3. From Table 3, it can be seen that the maximum value of the largest Lyapunov exponent has a difference in magnitude compared with other values. Among these, there is an order of magnitude difference between specimen 2 and specimen 8, and two orders of magnitude difference between other specimens. However, the

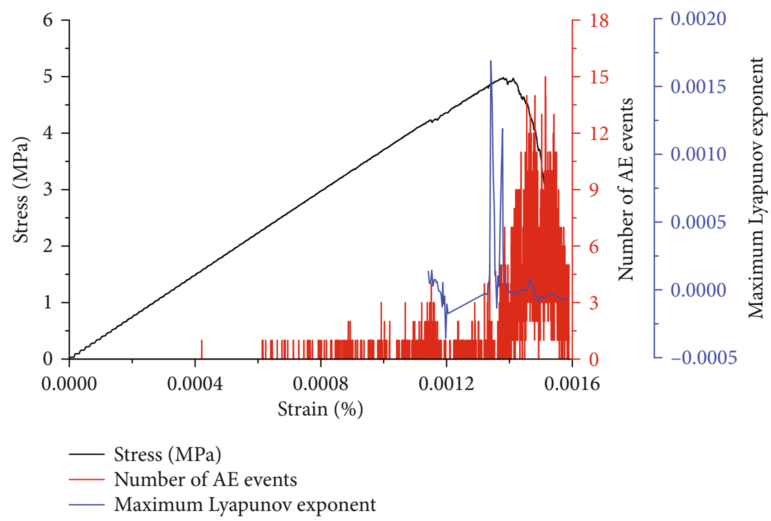

Figure 4: Stress-strain-number of AE events-maximum Lyapunov exponential variation diagram of specimen 1.

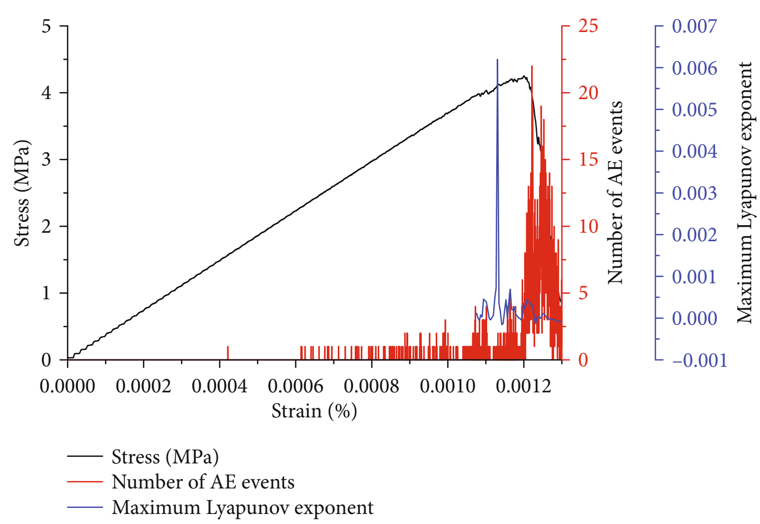

Figure 5: Stress-strain-number of AE events-maximum Lyapunov exponential variation diagram of specimen 2.

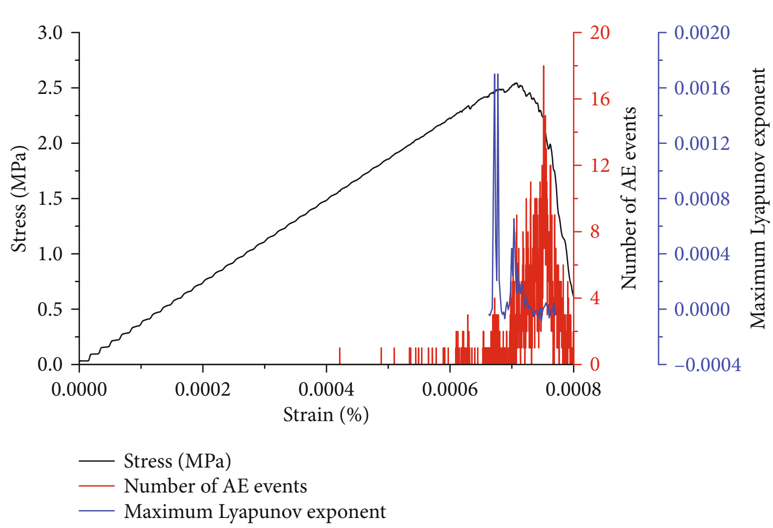

Figure 6: Stress-strain-number of AE events-maximum Lyapunov exponential variation diagram of specimen 3.

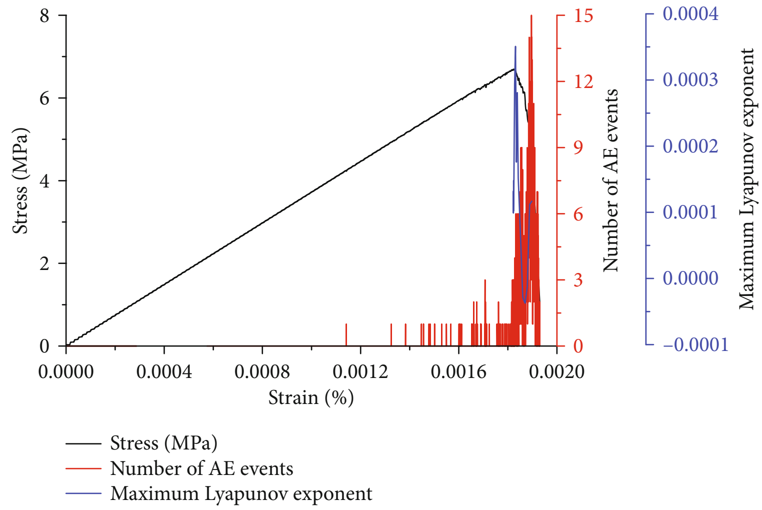

Figure 7: Stress-strain-number of AE events-maximum Lyapunov exponential variation diagram of specimen 4.

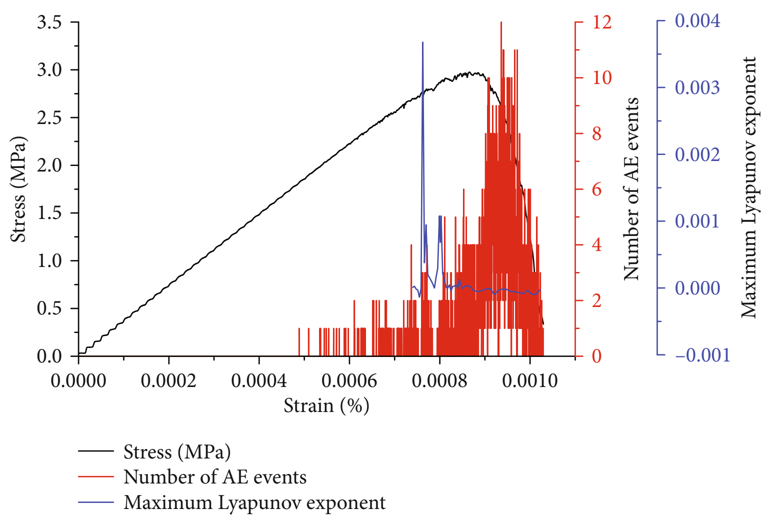

Figure 8: Stress-strain-number of AE events-maximum Lyapunov exponential variation diagram of specimen 5.

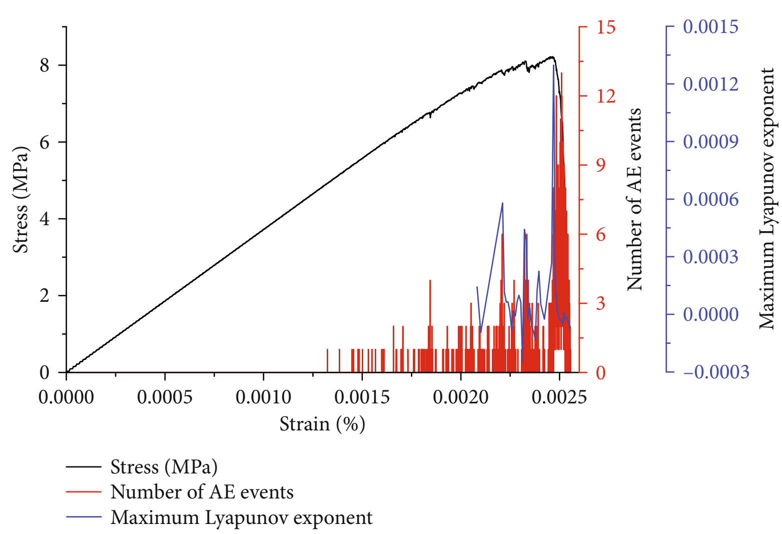

Figure 9: Stress-strain-number of AE events-maximum Lyapunov exponential variation diagram of specimen 6.

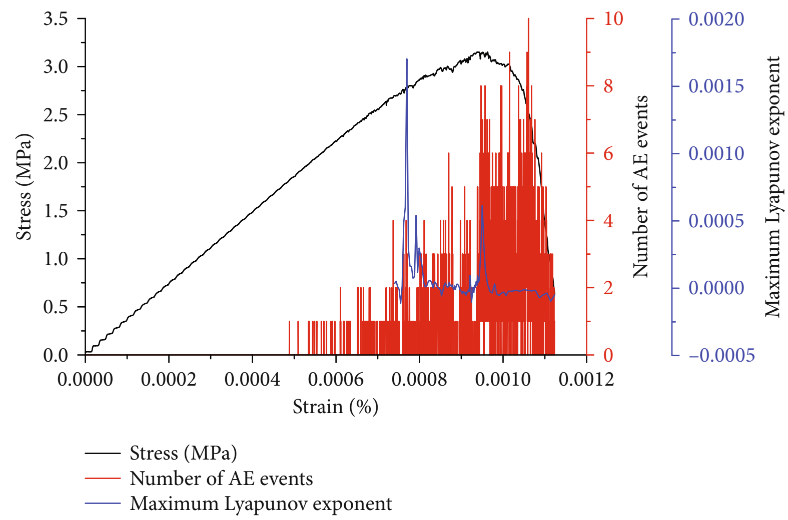

Figure 10: Stress-strain-number of AE events-maximum Lyapunov exponential variation diagram of specimen 7.

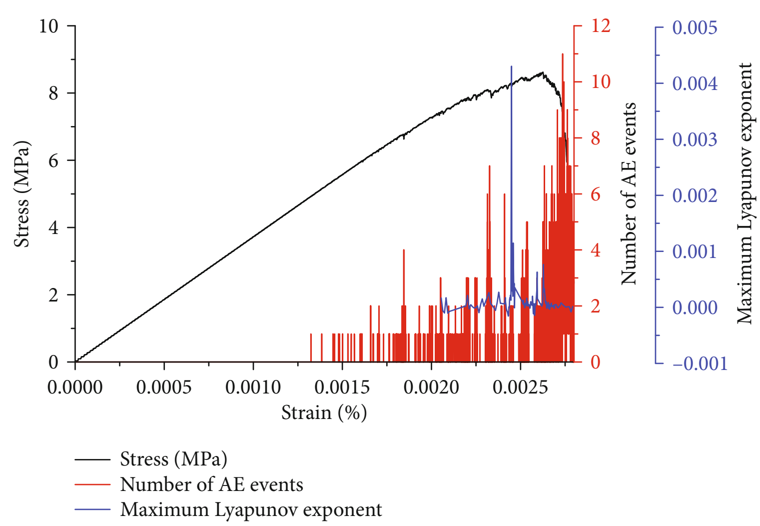

Figure 11: Stress-strain-number of AE events-maximum Lyapunov exponential variation diagram of specimen 8.

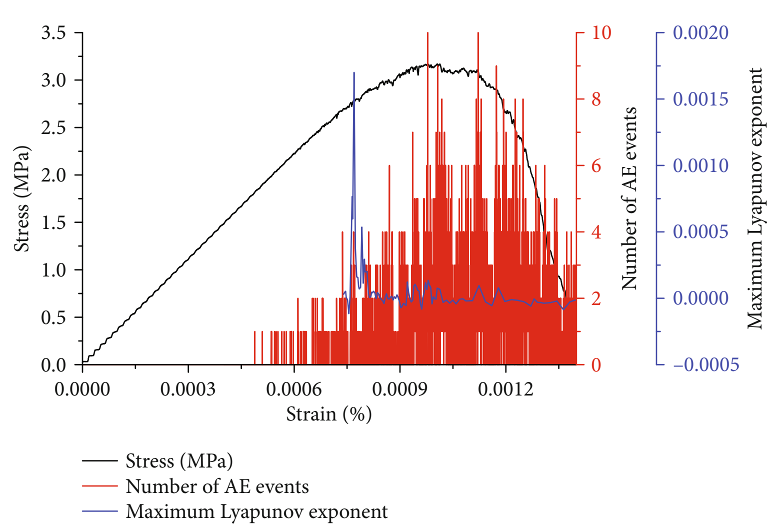

Figure 12: Stress-strain-number of AE events-maximum Lyapunov exponential variation diagram of specimen 9.

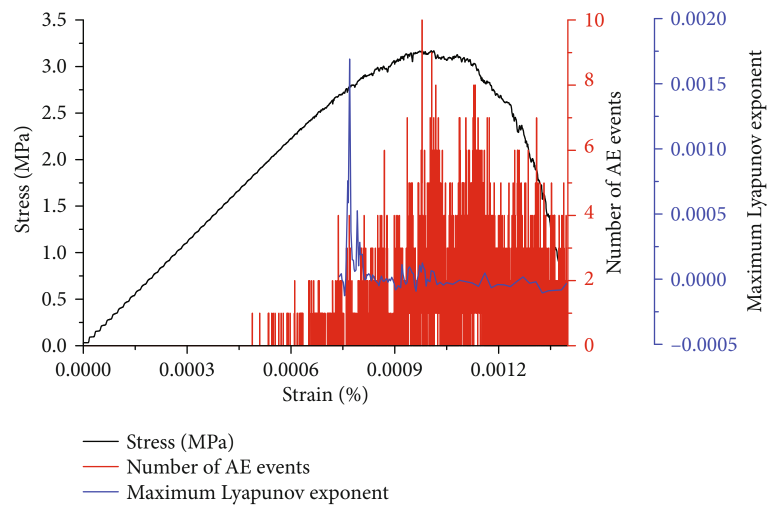

Figure 13: Stress-strain-number of AE events-maximum Lyapunov exponential variation diagram of specimen 10.

maximum value of the maximum Lyapunov exponent remains in the order of 10^{-3}.

In the AE event number time series of specimen 6, the maximum Lyapunov exponent and the peak value of the stress-strain curve appeared almost simultaneously, inconsistent with the results shown in Figure 3. However, it can be seen from Figure 9 that before the maximum point of the maximum Lyapunov exponent appears, there is a submaximum point whose value is greater than 5×10^{-4}.

The maximum Lyapunov exponent of the AE event number time series of specimen 4 appears almost simultaneously with the peak point of the stress-strain curve. However, it could be found that it is located behind the peak of the stress-strain curve, which is inconsistent with the situation shown in Figure 3.

The results of ten sets of simulation tests showed that before the specimens are destroyed, the maximum Lyapunov exponent in the AE event number time series of nine sets of simulation tests suddenly changed to the maximum (the maximum is 10^{-3}) or the submaximum (the submaximum is greater than 5×10^{-4}). This shows that the sudden change of the maximum Lyapunov exponent in AE event number time series can be used as a precursor to rock fracture.

5. Conclusions

In this paper, the relationship between acoustic emission (AE) parameters and coal-rock fracture is investigated by using the discrete element particle flow simulation software PFC. PFC is used to simulate the coal-rock uniaxial compression test for extracting the time series of AE event number, calculate the maximum Lyapunov exponent of the time series, and analyze the chaotic characteristics of AE event number. The following conclusions are drawn by analyzing the stress-strain-AE events-maximum Lyapunov exponent relationship curves of different coal-rocks in uniaxial compression:

(1) During coal-rock uniaxial compression, the variation of AE events generally shows a rising trend, which declines afterward. Before the specimen is near failure, the number of AE events increases sharply, and the corresponding frequency accelerates. The maximum number of AE events occurs after the peak point of the stress-strain curve

(2) The lower the homogeneity of coal-rock specimen, the smaller is the strain corresponding to the initial occurrence of AE events, i.e., the earlier the AE events occur

(3) The maximum Lyapunov exponent of the AE event number time series is high than zero, indicating that the AE event number has chaotic characteristics during coal-rock uniaxial compression

(4) The chaotic characteristics of the number of AE events are most prominent before the specimen is completely destroyed

(5) From the fact that the maximum Lyapunov exponent of the time series of AE events suddenly changes to the maximum (the maximum is of the order 10^{-3}) or the submaximum (the submaximum is greater than 5×10^{-4}) before the specimen is completely destroyed, it is feasible to use the maximum point of the maximum Lyapunov exponent of AE event number time series as the precursor criterion of rock fracture

(6) The maximum Lyapunov exponent of the AE event number time series appears before the maximum AE event number. Compared with the AE identification and warning criterion based on the AE parameters, the precursor criterion based on the chaotic characteristics of the number of AE events can effectively avoid the errors caused by parameter contingency. It can also early forewarn the occurrence of coal-rock damage and improve the accuracy of coal-rock gas dynamic disaster warnings

Data Availability

The data used to support the findings of this study are included within the article.

Conflicts of Interest

The authors declare that they have no conflicts of interest.

Acknowledgments

This work is supported by the National Natural Science Foundation (52074167) and the Graduate Education Quality Improvement Project of Shandong Province-Tensor Analysis (SDYKC21064).

References

[1] V. L. Shkuratnik, Y. L. Filimonov, and S. V. Kuchurin, "Experimental investigations into acoustic emission in coal samples under uniaxial loading," *Journal of Mining Science*, vol. 40, no. 5, pp. 458–464, 2004.

[2] B. X. Liu, J. L. Huang, Z. Y. Wang, and L. Liu, "Research on damage evolution and acoustic emission characteristics of coal and rock under uniaxial compression," *Chinese Journal of Rock Mechanics and Engineering*, vol. 28, no. S1, pp. 3234–3238, 2000.

[3] S. G. Cao, Y. B. Liu, and L. Q. Zhang, "Comprehensive analysis of acoustic emission characteristics of coal outburst deformation and failure," *Chinese Journal of Rock Mechanics and Engineering*, vol. S1, pp. 2794–2799, 2007.

[4] Y. B. Zhang, P. Liang, X. X. Liu, L. Shanjun, and B. Z. Tian, "Experimental study on precursors of rock failure based on dominant frequency and entropy of acoustic emission signals," *Chinese Journal of Rock Mechanics and Engineering*, vol. 34, no. S1, pp. 2959–2967, 2015.

[5] A. Q. Li, Q. Zhang, T. Ai et al., "Study on the spatial-temporal evolution behavior of acoustic emission during the whole process of uniaxial compression of granite and its precursors," *Chinese Journal of Geotechnical Engineering*, vol. 38, no. S1, pp. 306–311, 2016.

[6] C. Y. Wang, X. K. Chang, and Y. L. Liu, "Acoustic emission time-frequency domain signal characteristics and precursor identification information during the whole process of granite rupture," *Journal of Yangtze River Scientific Research Institute*, vol. 37, no. 3, pp. 82–89, 2020.

[7] J. J. Zhang, J. G. Li, and T. G. Zhu, "Application of acoustic emission technology in Pingmei no. 10 mine," *Coal Technology*, vol. 36, no. 3, pp. 212–214, 2017.

[8] J. G. Li, "Acoustic emission monitoring and early warning method for gas dynamic disaster of stress-dominated coal-rock in deep mine," *Journal of Shandong University of Science and Technology (Natural Science edition)*, vol. 39, no. 4, pp. 20–27, 2020.

[9] C. A. Tang, "Preliminary study on numerical simulation of rock acoustic emission law," *Chinese Journal of Rock Mechanics and Engineering*, vol. 4, pp. 75–81, 1997.

[10] Y. F. Fu and C. A. Tang, "Numerical simulation and experimental study on Kaiser effect of rock acoustic emission," *Mechanics and practice*, vol. 6, pp. 42–44, 2000.

[11] Y. Q. Rui and C. A. Tang, "Numerical simulation of rock fracture sliding process and its acoustic emission," *Journal of Engineering Geology*, vol. 4, pp. 357–361, 2001.

[12] T. Xu, C. A. Tang, Y. B. Zhang, and L. Yuan, "Parallel numerical simulation of peeling failure process of FRP concrete interface," *Journal of solid mechanics*, vol. 32, no. 1, pp. 88–94, 2011.

[13] H. H. Liu, "Application of chaos theory to prediction of coal mine gas concentration," *Shanxi Electronic Technology*, vol. 4, pp. 43-44, 2011.

[14] L. N. Shi, "Coal and gas outburst prediction research method based on chaos theory," *Computer Knowledge and Technology*, vol. 9, no. 28, 2013.

[15] L. Su, *Study on prediction of gas emission based on chaotic time series, [M.S. thesis]*, University of Science and Technology, Xi an, China, 2012.

[16] B. Wang and J. J. Han, "Chaotic time series prediction method of gas emission in a mine," *Modern Mining*, vol. 34, no. 8, pp. 206-207, 2018.

[17] Y. F. Wang, Z. J. Huang, and F. Cui, "Micromechanical damage evolution mechanism of coal rock failure process," *Journal of China Coal Society*, vol. 39, no. 12, pp. 2390–2396, 2014.

[18] Y. C. Yin, T. B. Zhao, Y. L. Tan, and F. H. Yu, "Reconstruction and numerical experiment of rock meso-model based on Otsu image processing," *Rock and Soil Mechanics*, vol. 36, no. 9, pp. 2532–2540, 2015.

[19] J. H. Lv, L. A. Lu, and S. H. Chen, *Chaos Time Series Analysis and Its Application*, Wuhan University Press, Wuhan, China, 2002.

Hindawi
Geofluids
Volume 2022, Article ID 6943834, 10 pages
https://doi.org/10.1155/2022/6943834

Research Article

Effect Of Open-Pit Blasting Vibrations on a Hanging-Wall Slope: A Case Study of the Beizhan Iron Mine in China

Yong-gang Xiao[1,2], Jie Cao[3], Xiao-min Liu[1], and Chang-hong Li[2]

[1]*China Construction Sixth Engineering Division Co. Ltd., Tianjin 300012, China*
[2]*School of Civil and Resource Engineering, University of Science and Technology Beijing, Beijing 100083, China*
[3]*Hebei Petroleum University of Technology, Chengde 067000, China*

Correspondence should be addressed to Jie Cao; caojieshiyou@163.com and Xiao-min Liu; 286237078@qq.com

Received 4 November 2021; Accepted 24 February 2022; Published 17 March 2022

Academic Editor: Yong-Zheng Wu

With the increase in the depth of large-scale open-pit mining, many mines have to face problems such as what is the effect of open-pit blasting on the rock slope and how to ensure the stability of a high-steep slope. The east slope of the Beizhan iron mine in Hejing County, Xinjiang, belongs to the typical open-pit high and steep slope of mined hanging-wall ore. To study the effect of open-pit blasting vibrations on hanging-wall slope stability, the intelligent blasting vibration detector was used to monitor the open-pit blasting wave of the Beizhan iron mine and the corresponding numerical model was established. We fitted the transmission law of slope blasting vibration by Sodev's regression formula and calculated stress, strain, and vibration velocity of the whole slope by numerical simulation. The result showed that the fitting functional relationship was correct and could be the basic rule of predicting the maximum charge amount per delay interval and minimum safe distance for this area. The estimated open-pit blasting charge weight was reasonable and blasting vibrations would have little effect on the hanging-wall slope. The research method and conclusions in this article have numerous reference values for studying the hanging-wall slope's kinetic stability.

1. Introduction

With the quickened pace of large-scale open-pit mining and open-pit mining depth increasing, more and more high-steep slopes are formed. Most mine slopes face problems such as the impact of open-pit blasting on hanging-wall ores and how to ensure the stability of high-steep slopes [1–3]. The hanging-wall ore is part of the ore body extending outside the open-pit boundary [4]. Large-scale blasting during open-pit mining caused great stress disturbance to the surrounding rock mass and stress concentration formed at the bottom of a pit and the foot of a slope. When the hanging-wall ore is mined, a more complex secondary stress field will be formed, causing further deformation and destruction of the surrounding rock of the slope and even engineering disasters such as landslides.

Given the influence of open-pit blasting on high and steep slopes, the commonly used research methods are blasting vibration tests and numerical simulation. The effect of controlled blasting on the stability of mine slopes was studied by Singh et al. [5] through presplit blasting tests. Hu et al. [6] analyzed the correlation between blasting damage depth and peak particle velocity and proposed a new damage-vibration coupling control method for high rock slopes. Yin et al. [7] and others monitored blasting vibration signals using different rock blasting scenes and studied the attenuation characteristic of blasting vibration waves transmitted in the joint rock slope. Rajmeny and Shrimali [8] monitored the sliding of the hanging wall caused by multiple blasting and fitted predictive equations for blast vibration at the Rampura Agucha Mine. Tao et al. [9] used remote monitoring and early warning system to continuously monitor a slope. The monitoring results showed that the open-pit mining technology of a “mechanical gun” instead of “blasting” had effectively reduced the impact of mining disturbance on the stability of the western slope. Bao and others [10]

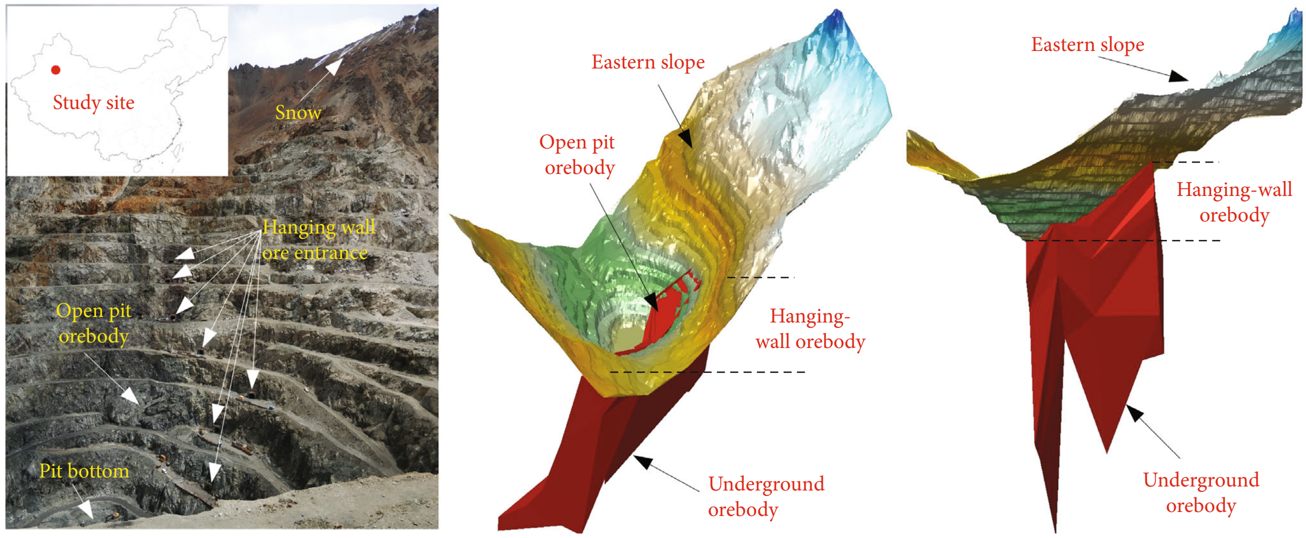

Figure 1: The morphological characteristics of the eastern slope with hanging-wall orebody.

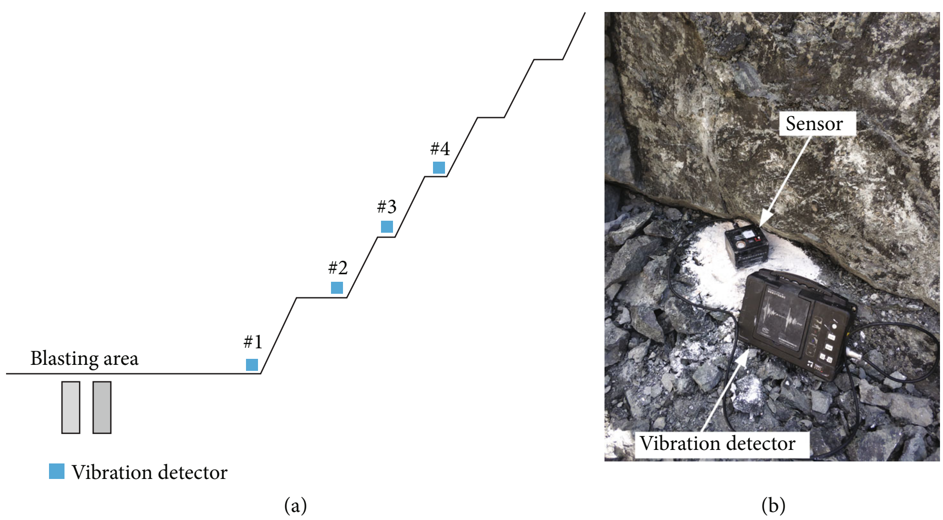

Figure 2: Schematic diagram of the relative positions of the vibration detector installation (a) and the field-installed vibration detector (b).

monitored an open-pit mine using a blasting vibration instrument and they found that the main influencing factors for slope stability were vibration velocity and duration. Xie et al. [11] monitored an open-pit mine slope using a blasting vibration system, and they found that changing the blasting order and direction could reduce blasting vibrations. Ma et al. [12] proved that presplitting blasting played a major role in absorbing blasting shock waves based on the blasting vibration testing of an open-pit mine slope. The numerical simulation analysis method is a common tool to solve mining rock mechanics problems. Hu et al. [13] proposed the relationship between peak vibration velocity and soil properties based on the improved Sodev equation. The classical Sodev empirical formula was improved by Ma et al. [14] to predict the vibration velocity of pipe explosions. A linear fitting model based on Sodev's empirical formula was developed, and blast vibration data from lighthouses near the blast area were monitored by Gu et al. [15]. Researchers used numerical simulation programs such as the finite element method (FEM) [16–22], discrete element method (DEM) [23–27], and finite difference method (FDM) [28–32] to study the dynamic response characteristics of blasting vibration to high and steep slopes. These response characteristics mainly included vibration velocity, displacement, amplification factor, frequency, stress, and strain of slope after blasting. Hu et al. used LS-DYNA software to study the effect of smooth blasting and presplitting blasting on rock high-slope damage and analyzed the spatial distribution of blasting damage [16, 33, 34]. Jiang et al. [35] used blasting excavation of Beijing Metro Line 16 as an example to monitor blasting vibration in the field. A three-dimensional numerical model was established to analyze the response

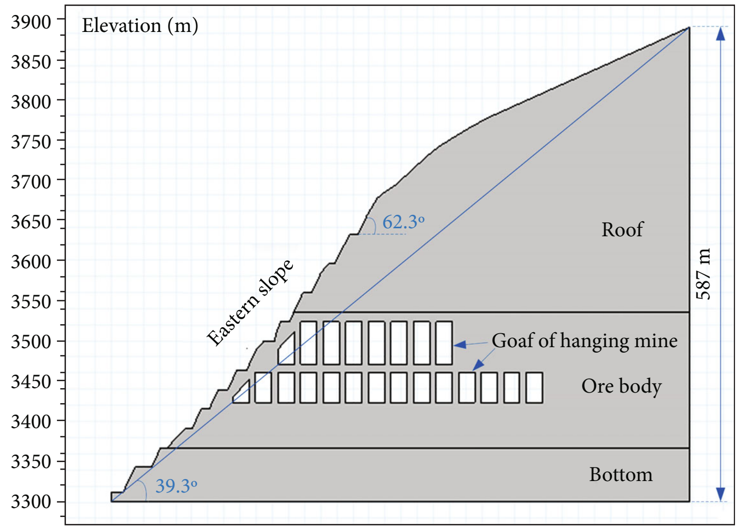

FIGURE 3: Numerical model of the slope with the hanging-wall ore slope.

TABLE 1: Statistic of the test results of physical and mechanical properties of rock strata.

Rock layer	Unit weight (kN/m^3)	Elasticity modulus (GPa)	Poisson's ratio	Cohesion (MPa)	Internal friction angle (°)
Roof	25.90	22.5	0.22	11.5	32.02
Orebody	24.80	34.2	0.16	9.8	35.1
Floor	27.10	50	0.17	10.23	31.6

characteristics of buried gas pipelines under the action of blasting vibration. Mohammadi Azizabadi et al. [36] simulated blast seismograms by monitoring single-hole blast vibrations. Then, the particle velocity time histories of blast vibrations in the mine wall were predicted using the universal distinct element code (UDEC). Chen et al. used the tensile-compression damage model to analyze the whole blasting process of the bedding rock slope for numerical simulation. In summary, there were many studies on the influence of open-pit blasting on a rock slope, while there were relatively few studies of the influence of the slope of the mined hanging-wall ore.

The hanging-wall ore mining and open-pit mining are carried out simultaneously in Beizhan's open-pit mine slope of Hejing County, Xinjiang. The mining adit of the hanging-wall mine and platform formed by open-pit mining were combined. The height of the benches was 12 m, and the height of parallel benches was 24 m/36 m. The stripping elevation was 3464 m~3596 m, and the lowest mining elevation was 3390 m. The open-pit benches above 3476 m have been steep. The top-down mining sequence was adopted hanging-wall mining. According to the mining stripping plan, the open-pit production can be continued for about 4 years. With the exploitation of hanging-wall mines and open-pit mines, the mines inside the slope are gradually mined out and the slope gradually becomes higher and steeper. It is necessary to study the influence of open-pit blasting vibration on the slope of the hanging-wall mine.

In this paper, vibration monitoring of Beizhan's open-pit mine slope was carried out by using NUBOX-6016 intelligent vibration monitors. According to the measured blasting vibration wave data, the propagation law of blasting seismic waves on high and steep slopes was studied. Then, the numerical model of the eastern slope of the Beizhan iron mine was established and the measured velocity time-history load at the bottom of the slope was input. Finally, the dynamic response characteristics such as stress, strain, and vibration velocity of high and steep slopes under open-pit blasting vibration were analyzed.

2. Methods

2.1. Geological Overview. The Beizhan iron mine is located in the northwest of Hejing County and the straight-line distance is about 130 km. It is 82 km from Baluntai town, Hejing County, and is under Bayingolin Mongol Autonomous Prefecture, Hejing County's jurisdiction. The mining area is located on the south slope of Yilianhabierga Mountain and west Tianshan Mountain which is a medium-high mountain area. The run of the mountain is nearly an east-west direction and the overall terrain is high in the southern part and low in the north part. The altitude is 3160–4575 m, relative altitude is 700–1000 m, general terrain slope is 25–35°. The ditch is deep and steep. It is a deep alpine landform. The altitude of the part where the orebody is located is 3450–3723 m. A few hundred meters south of the mine site is the ridge of Tianshan Mountain. With the continuous development of open-pit slope mining and under the action of slope excavation and frequent production blasting, the mining area in the south slope had suffered from different degrees of landslides. Especially after the double-step parallel mining, the single-step height reached 36 m, which was prone to instability. The strata in the mining area are mainly the Lower Carboniferous Dahalajunshan Formation, Akshake Formation, and Quaternary. The minimum mining elevation of the open-pit design is 3320 m. It has been mined to an elevation of 3390 meters, and open-pit mining is

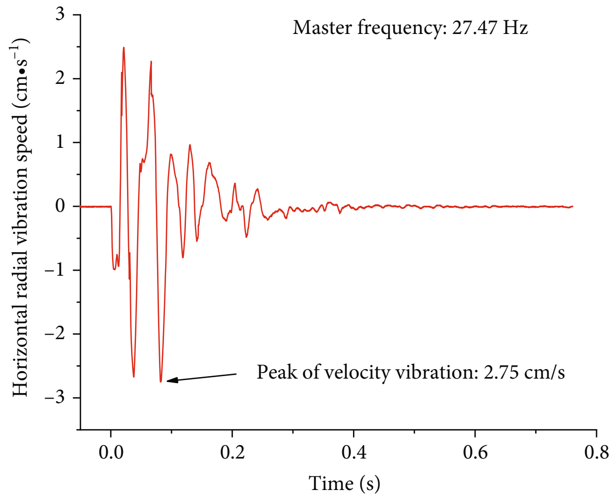

(a)

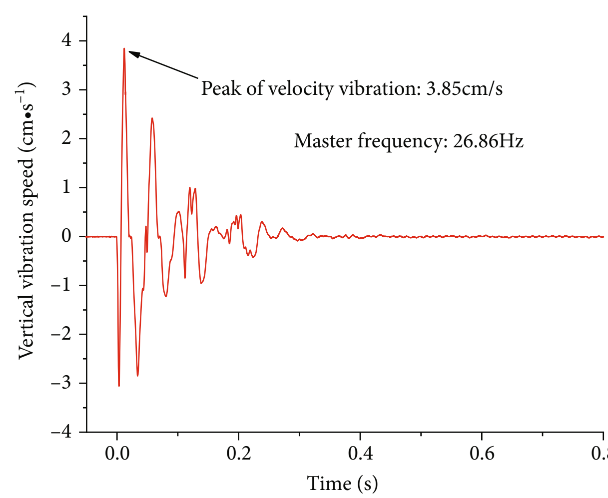

(b)

Figure 4: Velocity time history curves of no.1 measuring point in the open-pit blasting. (a) Horizontal radial and (b) vertical.

Table 2: The results of blast vibration monitoring.

Serial number	Maximum charge (kg)	Distance from the explosive center (m)	Horizontal radial		Horizontal tangent		Vertical		Combined vibration velocity (mm/s)
			Vibration velocity (mm/s)	Main frequency (Hz)	Vibration velocity (mm/s)	Main frequency (Hz)	Vibration velocity (mm/s)	Main frequency (Hz)	
1#	480	62	27.49	27.466	35.24	29.297	38.45	26.855	58.96
2#	480	84	41.41	21.362	14.96	28.076	32.15	19.531	54.52
3#	480	92	31.52	62.046	35.28	53.711	3.93	69.289	47.47
4#	480	121	12.87	26.855	0.27	35.368	1.42	52.472	12.95
5#	415	52	24.75	35.753	31.28	41.384	32.76	31.952	51.62
6#	415	79	18.83	31.928	27.86	48.358	25.83	38.261	42.40
7#	415	81	13.87	73.216	16.23	63.893	18.68	83.428	28.37
8#	415	159	10.28	52.467	0.83	83.138	2.73	121.438	10.67
9#	356	55	28.27	29.357	21.63	52.348	30.14	39.271	46.65
10#	356	88	23.64	36.339	19.27	45,773	27.44	38.621	41.03
11#	356	136	11.84	24.414	0.23	37.348	1.83	25.472	11.98
12#	356	152	7.47	14.038	2.27	12.817	1.97	14.038	8.05

coming to an end. In order to maintain the normal production of the mine and ensure the smooth transition from open-pit mining to underground mining, the hanging-wall ore is currently being mined. The present situation of open-pit slope mining and the morphological characteristics of hanging-wall ore are shown in Figure 1.

2.2. Blasting Vibration Test. The blasting area was located at the 3380 elevation mining area on the eastern slope of the pit. This blasting was for progressive mining down to a 3368 elevation. The blasting area was surrounded by buildings of 3404 flat caverns, pumping, and pumping pipes, which were close to the blasting area. The blasting area was all ore. The 3380 m steps were constructed from south to north undercut as required. The main borehole spacing was 2.5 m, the row spacing was 2.0 m, and the inclination angle was 80°. Millisecond delay blasting between rows was adopted in this blasting scheme. Blasting was launched from the west to east row by row in order to achieve the design purpose. The blasting sequence was rowed to row. The way of blasting was reverse initiation. That was, the detonating charge was located at the bottom of the hole and the direction of the energy accumulation hole of the detonator was towards the opening of the hole. The detonating network adopted an electronic-delay detonator. The delay time was set by the electronic detonator and the blasting was carried out from west to east in sections in order to achieve the purpose of blasting in sections and rows.

This test used the NUBOX-6016 intelligent vibration monitor produced by Sichuan Tuopu Measurement and Control Technology Company Ltd. The instrument is connected to a TP3V-4.5 3D velocity-type sensor through a special input signal cable. The first channel of the device is connected to the horizontal x-direction vibration signal,

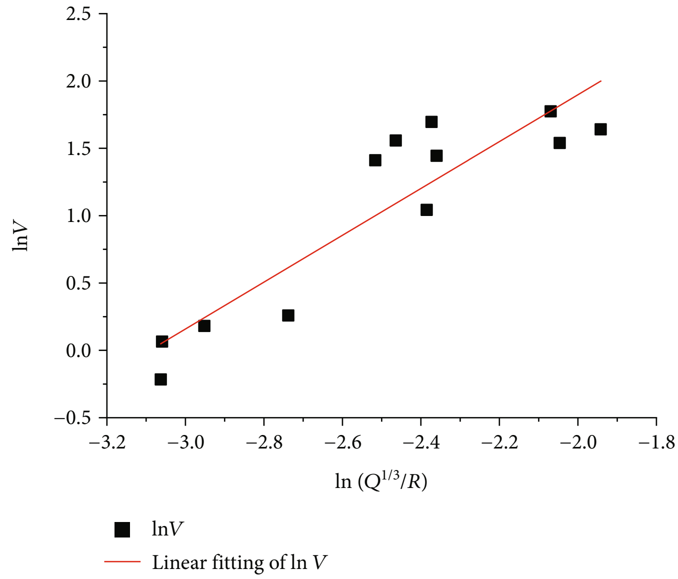

Figure 5: Decay regression line of blasting vibration.

the second channel to the horizontal y-direction signal, and the third channel to the vertical z-direction signal. The TP3V-4.5 three-dimensional velocity sensor is a practical vibration velocity measurement sensor that can simultaneously measure the velocity in the horizontal x, horizontal y, and vertical z directions. The measurement points are located at the foot of the slope. The relative positions of the measurement points and their installation on-site are shown in Figure 2.

2.3. Numerical Simulation of Blasting Vibration. The numerical simulation of blasting vibration would become true by the structural mechanics' module of COMSOL software. The horizontal x-direction and vertical z-direction vibration waves caused by blasting vibration have the greatest influence on the slope stability. Therefore, in the numerical simulation, the x- and z-direction vibration wave signals collected from the test were loaded into the finite element model of the slope at the same time for analysis.

The current slope profile of the hanging-wall ore in the Beizhan iron mine was selected for the study. A numerical model was established according to the shape of the slope and stratigraphic distribution (Figure 3). The model size was 587 m × 716 m, and the maximum step height was 36 m. In order to simulate the near slope blasting, the loading area of the blast load was located on the left boundary of the model, 14 m from the foot of the bottom step. The lithology of the magnetite ore body (layer) in the top and bottom parts is epidote skarn, diopside epidote skarn, tremolite skarn, and tremolite wollastonite skarn, which has great difference in rock integrity. The magnetite massive rock group is mainly composed of brecciated magnetite, disseminated magnetite, and massive magnetite. Its structure is tight, and the joints and fissures are not developed. The ore body has good structural solidity. The statistical values of the physical and mechanical properties of the slope rock test results are shown in Table 1.

This study adopted the low reflection boundary method. The slope surface adopted a free boundary and the rest adopted a low reflection boundary. By default, low reflection boundaries fetch data from adjacent domain materials. The nodes of low reflection boundary let the nonreflection waves flow out with the model to establish a perfect impedance matching for the P wave and S wave. Therefore,

$$\sigma \cdot \mathbf{n} = -\rho c_p \left(\frac{\partial \mathbf{u}}{\partial t} \cdot \mathbf{n} \right) \mathbf{n} - \rho c_s \left(\frac{\partial \mathbf{u}}{\partial t} \cdot \mathbf{t} \right) \mathbf{t}. \tag{1}$$

$\mathbf{n}$ and $\mathbf{t}$ were the unit normal vector and the tangent vector to the boundary, respectively. c_p and c_s were each represented longitudinal wave speed and transverse speed of the material, respectively. This method was most effective when the wave approaches the normal direction of the boundary.

In order to calculate the mechanical characteristics of the slope under different working conditions, three research steps were set up in this study. In the first step, the state of ground stress of the slope before the hanging gang mine was mined was calculated. In the second step, the stress state of the slope after mining was calculated based on the calculation results of the first step. In the third step, the impact of blasting on the slope of the hanging gang mine was calculated based on the first two steps and the response characteristics of the slope to blasting vibration were analyzed.

In general, the vertical and horizontal radial vibration rates have a greater impact on slope stability, while the horizontal tangential rate has a smaller impact on that. In order to avoid large errors in the calculation, this study choses the velocity time history curve that is near the measuring point of the blasting source in the production blasting when calculated as the blasting dynamic load. Only the horizontal radial and vertical vibration rates of this measurement point were selected. The selected time curves of vertical and horizontal radial vibration rates were shown in Figure 4.

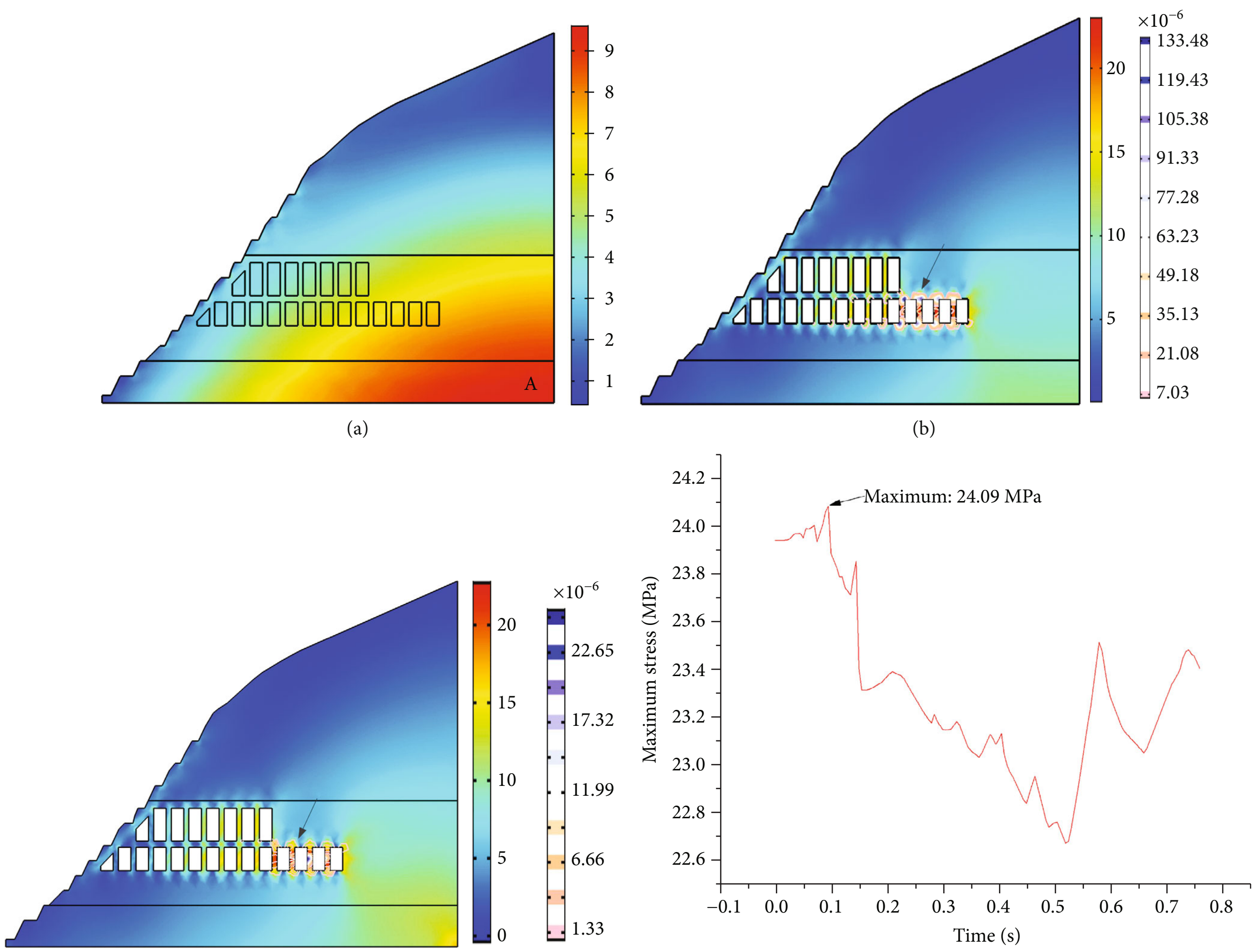

Figure 6: von Mises stress for 3 research steps; (a) before the exploitation of hanging-wall ore; (b) after the exploitation of hanging-wall ore; (c) after open-pit blasting; and (d) maximum stress value's changing law within the slope along with the blasting time.

3. Conclusion and Discussion

3.1. Results and Analysis of Blast Vibration Monitoring. Three blast vibrations in the open pit were monitored using NUBOX-6016 blast vibration detectors. Three monitoring layouts were similar, all along the direction away from the blast source of the 4 monitoring points arranged in turn (Figure 2). The sensor on the monitoring point has the function of monitoring the horizontal radial, horizontal tangential, and vertical direction vibration speed simultaneously. Blast vibration monitoring results are shown in Table 2.

Considering the influence of the maximum charge and the distance from the explosive center on the vibration speed according to *the blasting safety regulations*, the mathematical method of mathematical statistics was used to cope with the measured data by regression analysis. Sodev's regression formula is

$$V = k\left(\frac{Q^{1/3}}{R}\right)^{\alpha}. \tag{2}$$

In the formula, V stands for the maximum 3D synthesis velocity rate of the vibrating particle, cm/s; k and α are coefficients related to the topography and geological conditions between the blasting point and the protected object, respectively; Q is for the maximum single-section charge, kg; R is for the linear distance from the measuring point to the blasting source, m.

A least-mean-square linear regression operation was performed using Sadovsky's formula to fit a straight line (Figure 5). With this, to determine the regression equation, $k = 216.156$, $\alpha = 1.739$, and the correlation coefficient R value was 0.908. This equation can be used as the basis for predicting the maximum single-section charge and minimum safe distance at this site. So, the transmitted law formula of blasting vibration for east slope hanging-wall ore was

$$V = 216.156\left(\frac{Q^{1/3}}{R}\right)^{1.739}. \tag{3}$$

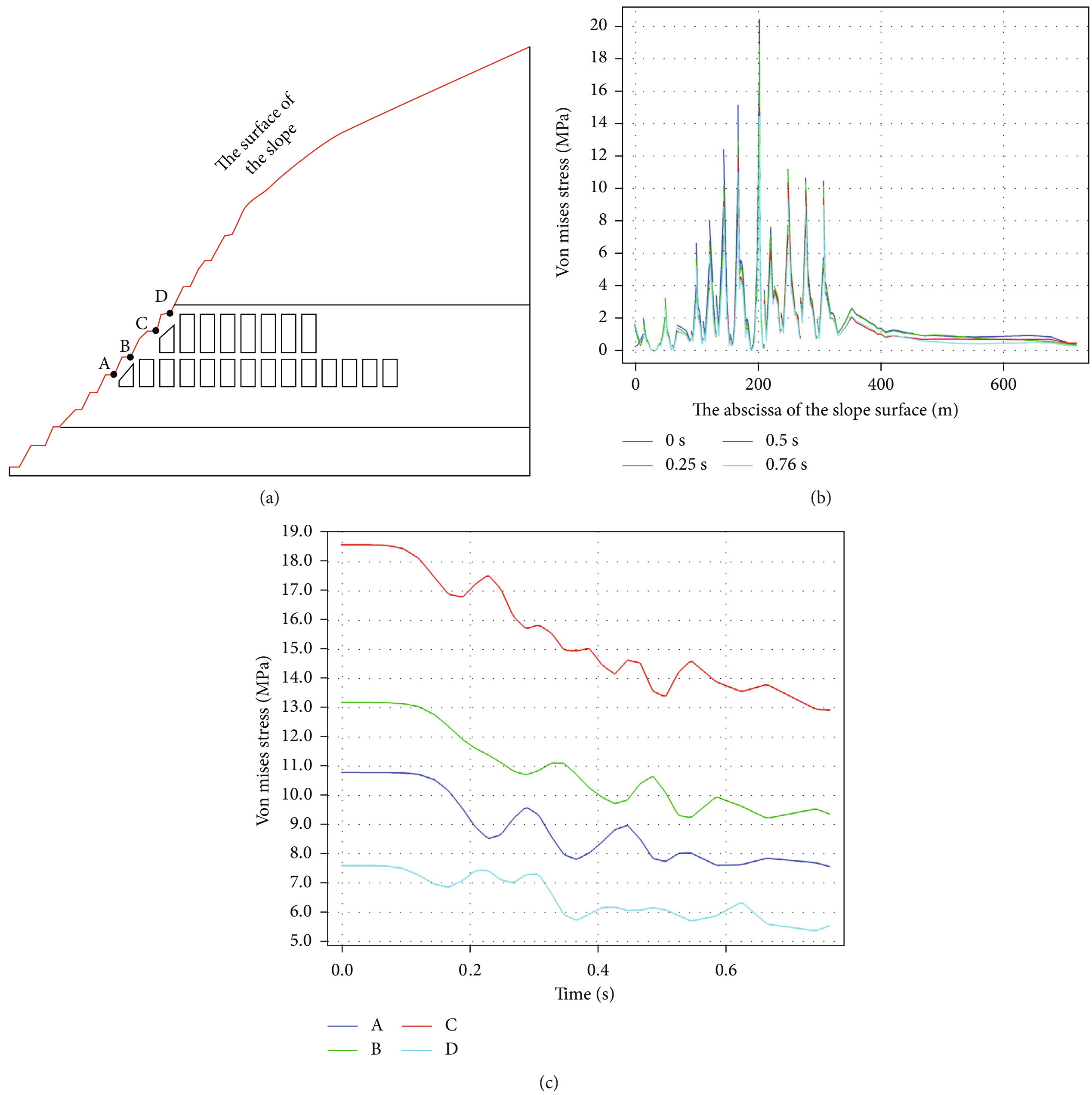

Figure 7: von Mises stress changing situation of the slope and hanging-wall ore mine under blasting vibration: (a) schematic diagram of calculated position of slope and hanging-wall ore mine; (b) von Mises stress changing law of slope surface with different blasting time; (c) von Mises stress changing law of points A, B, C, and D.

The previous experiments could tell that the maximum 3D synthetic velocity of blasting vibration in the toe of the slope was 5.986 cm/s. When the master frequency was greater than 10 Hz and less than 50 Hz according to the *blasting safety regulations*, the safety allowing the velocity range of particle vibration for a permanent rock high steep slope was 8~12 cm/s. The present blasting vibration of the open-pit mine had little impact on slope stability. The slope of the Beizhan iron mine had hanging-wall ore. However, there were no rules for safety allowing the velocity of particle vibration of such slope in *the blasting safety regulations*. Therefore, in order to study the effect of blasting vibration on this slope, a numerical simulation of this slope was established.

3.2. Result and Discussion of Numerical Simulation

3.2.1. Analysis of Stress and Strain. In order to analyze the effect of open-pit blasting on the slope, von Mises stress clouds were obtained from the simulation results before hanging-wall ore mining, after hanging-wall ore mining, and after open-pit blasting (Figure 6). In Figure 6(a), it can be seen that the stresses on the slope before the hanging-wall ore mining were caused by gravity. The

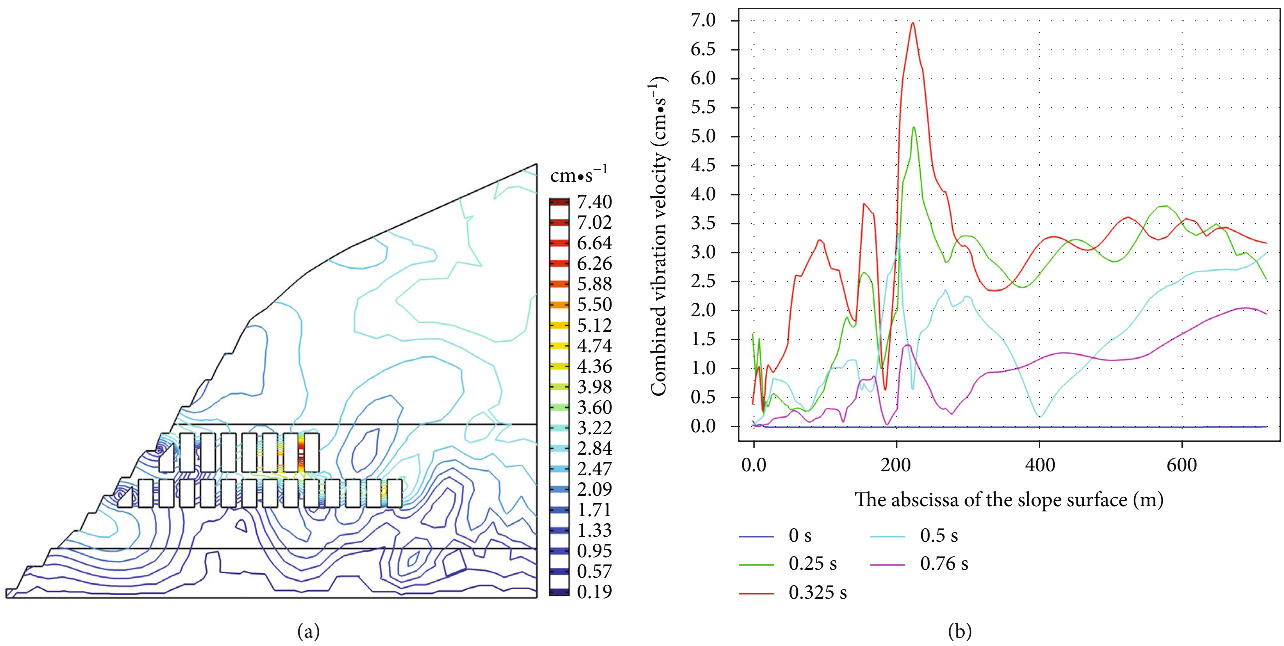

Figure 8: Combined vibration velocity caused by blasting vibration: (a) contour plot of slope combined vibration velocity when $t = 0.265$ s; (b) combined vibration velocity of the surface of the slope.

maximum value was 9.60 MPa in A. There was no plastic strain in the slope. In Figure 6(b), it can be seen that the hanging-wall ore mining caused the redistribution of internal stresses in the slope. The maximum value appears in region B with 23.95 MPa. The contour of the figure shows the plastic strain with a maximum value of 608 $\mu\varepsilon$. The greatest stresses were experienced at the location of the ore pillar in area B, and plastic deformation occurred. In Figure 6(c), it can be seen that blast vibration again causes the redistribution of internal stresses in the slope. The von Mises stress maximum occurred in the B region and varied with blasting time, as shown in Figure 6(d). Taking the calculated stress response into account in the second step, the maximum value was 23.95 MPa at 0 s. When the blasting finished at 0.76 s, the maximum value was 23.41 MPa. The peak maximum value was 24.09 MPa which happened at 0.095 s. The contour lines in Figure 6 (c) are plastic strain, located in the pillar at point B, and the maximum value is 47.6 $\mu\varepsilon$. Compared with the stresses after hanging-wall ore mining, the stress distribution pattern of the slope after open-pit blasting is not much different.

In order to analyze the effect of open blasting on the slope surface, the variation of von Mises stress on the slope surface was calculated. The red line in Figure 7(a) shows the slope surface, where points A, B, C, and D are the locations of the foot of the slope immediately adjacent to the hanging-wall ore. We assume that the horizontal coordinate of the location of the lowest foot of the slope is 0. Figure 7(b) shows the variation of von Mises stress on the slope surface at 0 s, 0.25 s, 0.5 s, and 0.76 s after open blasting. The figure shows that the stresses on the slope surface at different times after blasting are similar in magnitude and have the same change pattern. The larger values of stress are concentrated at the location of the foot of the slope immediately adjacent to the hanging-wall ore. Its maximum value is 20.39 MPa, which occurs at 0 s of open-pit blasting. Figure 7(c) shows the variation law of von mises stress in four points A, B, C, and D under the action of blast vibration wave. In Figure 7 (c), it can be seen that among the four points, the stress at point C is the largest, 18.5 MPa at 0 s and 12.9 MPa at 0.76 s. The remaining points also showed different degrees of reduction, with point A decreasing from 10.8 MPa to 7.6 MPa, point B decreasing from 13.1 MPa to 9.3 MPa, and point D decreasing from 7.6 MPa to 5.5 MPa. The pillar of the slope adjacent to the hanging-wall ore is the security pillar, which is the weak link in the whole hanging-wall ore slope system. The surface of the security pillar has the highest force among the whole slope surface after hanging-wall ore mining. As shown in Figure 7(c), the stress distribution pattern of the slope surface after open-pit blasting is not significantly different compared with the stress after hanging gang mining. This indicates that open-pit blasting did not increase the stresses on the slope surface of the security pillar.

3.2.2. Comparative Analysis of Vibration Speed. The combined vibration velocity of each moment could be collected after open-pit blasting by numerical simulation. Results show that the combined vibration velocity of the slope reached its maximum value when $t = 0.265$ s. The contour plot of the combined vibration velocity is shown in Figure 8(a). The combined vibration velocity of the slope surface reaches the maximum at $t = 0.325$ s. The contour plot of its combined vibration velocity is shown in Figure 8 (b).

As can be seen in Figure 8(a), the peak vibration velocity is located in the first row of the hanging-wall ore column, with a maximum value of about 7.40 cm/s. In Figure 8(b), it can be seen that the peak vibration velocity is located near position D and the maximum value is about 6.97 cm/s. According to *the blasting safety regulations*, when the main vibration frequency is greater than 10 Hz and less than 50 Hz, the safe allowable mass vibration velocity range for the mine tunnel is 18–25 cm/s. The safe allowable mass vibration velocity range for permanent rocky high slopes is 8 to 12 cm/s. It can be seen that the maximum peak value of particle vibration velocity of the slope under open blasting vibration is less than the safe allowable value of particle vibration velocity of the slope. It indicates that the current blasting vibration has little effect on this slope, which is stable under the joint action of dynamic and static loads.

4. Conclusions

According to the test data of blasting vibration wave monitoring on site, Sodev's formula was used to fit the blasting vibration propagation law of the east slope. The results of numerical simulation analysis showed that the current blasting vibration had little effect on this slope and the slope was stable under the combined action of dynamic and static loads. This can be used as the basis for predicting the maximum single-segment dose and minimum safe distance at this site.

It should be noted that in this paper, the focus was on the effect of open-pit blasting on the east slope of the Beizhan iron ore mine, ignoring the freeze-thaw action on the slope surface, anisotropy, and nonuniformity of the actual rock mass. We will take these factors into account for the next step of our research. The research methods and conclusions of this paper are good references for studying the dynamic stability of slopes with hanging-wall ore mines.

Data Availability

This study was approved and assisted by Hejing County Beizhan Mining Co. Ltd. The data used to support the findings of this study are included in the article.

Conflicts of Interest

The authors declare that they have no conflicts of interest regarding the publication of this paper.

Acknowledgments

This study was financially supported by the National Key R&D Program of China (Grant no. 2018YFC0808402). This financial support is gratefully acknowledged. Thanks are due to Hejing County Beizhan Mining Co. Ltd for the convenient conditions for blasting vibration detections.

References

[1] D. Q. Li, S. H. Jiang, Z. J. Cao, C. B. Zhou, X. Y. Li, and L. M. Zhang, "Efficient 3-D reliability analysis of the 530 m high abutment slope at Jinping I Hydropower Station during construction," *Engineering Geology*, vol. 195, pp. 269–281, 2015.

[2] C. A. Tang, L. C. Li, N. W. Xu, and K. Ma, "Microseismic monitoring and numerical simulation on the stability of high- steep rock slopes in hydropower engineering," *Journal of Rock Mechanics and Geotechnical Engineering*, vol. 7, no. 5, pp. 493–508, 2015.

[3] Y. K. Chen, J. H. Xu, X. H. Huo, and J. C. Wang, "Numerical simulation of dynamic damage and stability of a bedding rock slope under blasting load," *Shock and Vibration*, vol. 2019, 13 pages, 2019.

[4] B. H. Tan, F. Y. Ren, Y. J. Ning, R. X. He, and Q. Zhu, "A new mining scheme for hanging-wall ore-body during the transition from open pit to underground mining: a numerical study," *Advances in Civil Engineering*, vol. 2018, 17 pages, 2018.

[5] P. K. Singh, M. P. Roy, and R. K. Paswan, "Controlled blasting for long term stability of pit-walls," *International Journal of Rock Mechanics and Mining Sciences*, vol. 70, pp. 388–399, 2014.

[6] Y. G. Hu, M. S. Liu, X. X. Wu, G. Zhao, and P. Li, "Damage-vibration couple control of rock mass blasting for high rock slopes," *International Journal of Rock Mechanics and Mining Sciences*, vol. 103, pp. 137–144, 2018.

[7] Z. Q. Yin, Z. X. Hu, Z. D. Wei et al., "Assessment of blasting-induced ground vibration in an open-pit mine under different rock properties," *Advances in Civil Engineering*, vol. 2018, 10 pages, 2018.

[8] P. Rajmeny and R. Shrimali, "Use of radar technology to establish threshold values of blast vibrations triggering sliding of geological faults at a lead-zinc open pit mine," *International Journal of Rock Mechanics and Mining Sciences*, vol. 113, pp. 142–149, 2019.

[9] Z. Tao, C. Zhu, X. Zheng, and M. He, "Slope stability evaluation and monitoring of Tonglushan ancient copper mine relics," *Advances in Mechanical Engineering*, vol. 10, no. 8, 2018.

[10] D. R. Bao, Y. T. Gao, S. Xiao, and G. Kong, "Monitoring of blasting vibration and numerical simulation of a foreign open-pit mine slope," *Modern Mining*, vol. 12, pp. 121–125, 2015.

[11] C. Y. Xie, Z. Q. Luo, N. Jia, L. X. Xiong, and G. H. Cheng, "Dynamic effects of open blasting vibration on adjacent buildings and measures for vibration reduction," *Journal of Vibration & Shock*, vol. 32, no. 13, pp. 187–192, 2013.

[12] L. Ma, K. M. Li, S. S. Xiao, X. H. Ding, and S. Chordata, "Research on effects of blast casting vibration and vibration absorption of presplitting blasting in open cast mine," *Shock and Vibration*, vol. 2016, 9 pages, 2016.

[13] J. Hu, Y. Luo, and J. Xu, "Experimental and numerical analysis and prediction of ground vibrations due to heavy haul railway viaduct," *Mathematical Problems in Engineering*, vol. 2019, 15 pages, 2019.

[14] H. Ma, Y. Long, X. Li, M. Zhong, Q. Yin, and Q. Xie, "Attenuation and time-frequency characteristics of explosion ground vibration of shallow buried od1422-x80mm-12 MPa pipeline based on prototype experiment," *Journal of Performance of Constructed Facilities*, vol. 34, pp. 1–12, 2020.

[15] W. Gu, Z. Wang, J. Liu, J. Xu, X. Liu, and T. Cao, "Water-depth-based prediction formula for the blasting vibration velocity of lighthouse caused by underwater drilling blasting," *Shock and Vibration*, vol. 2017, 9 pages, 2017.

[16] Y. G. Hu, W. B. Lu, M. Chen, P. Yan, and J. H. Yang, "Comparison of blast-induced damage between presplit and smooth

blasting of high rock slope," *Rock Mechanics and Rock Engineering*, vol. 47, no. 4, pp. 1307–1320, 2014.

[17] N. Jiang, C. B. Zhou, S. W. Lu, and Z. Zhang, "Effect of underground mine blast vibrations on overlaying open pit slopes: a case study for daye iron mine in China," *Geotechnical and Geological Engineering*, vol. 36, no. 3, pp. 1475–1489, 2017.

[18] Y. T. Yang, G. H. Sun, H. Zheng, and Y. Qi, "Investigation of the sequential excavation of a soil-rock-mixture slope using the numerical manifold method," *Engineering Geology*, vol. 256, pp. 93–109, 2019.

[19] T. Bhandari, F. Hamad, C. Moormann, K. G. Sharma, and B. Westrich, "Numerical modelling of seismic slope failure using MPM," *Computers and Geotechnics*, vol. 75, pp. 126–134, 2016.

[20] M. Yilmaz, A. Ertin, S. Er, and A. Tugrul, "Numerical modelling of steep slopes in open rock quarries," *Journal of the Geological Society of India*, vol. 91, no. 2, pp. 232–238, 2018.

[21] Z. G. Qian, A. J. Li, A. V. Lyamin, and C. C. Wang, "Parametric studies of disturbed rock slope stability based on finite element limit analysis methods," *Computers and Geotechnics*, vol. 81, pp. 155–166, 2017.

[22] N. Jiang, C. B. Zhou, S. W. Lu, and Z. Zhang, "Propagation and prediction of blasting vibration on slope in an open pit during underground mining," *Tunnelling and Underground Space Technology*, vol. 70, pp. 409–421, 2017.

[23] N. Babanouri, H. Mansouri, S. K. Nasab, and M. Bahaadini, "A coupled method to study blast wave propagation in fractured rock masses and estimate unknown properties," *Computers and Geotechnics*, vol. 49, pp. 134–142, 2013.

[24] N. X. Xu, J. Y. Zhang, H. Tian, G. Mei, and Q. Ge, "Discrete element modeling of strata and surface movement induced by mining under open-pit final slope," *International Journal of Rock Mechanics and Mining Sciences*, vol. 88, pp. 61–76, 2016.

[25] H. Y. Liu, Y. M. Kang, and P. Lin, "Hybrid finite–discrete element modeling of geomaterials fracture and fragment muck-piling," *International Journal of Geotechnical Engineering*, vol. 9, no. 2, pp. 115–131, 2015.

[26] A. Haghnejad, K. Ahangari, P. Moarefvand, and K. Goshtasbi, "Numerical investigation of the impact of rock mass properties on propagation of ground vibration," *Natural Hazards*, vol. 96, no. 2, pp. 587–606, 2019.

[27] Z. Song, H. Konietzky, and M. Herbst, "Drawing mechanism of fractured top coal in longwall top coal caving," *International Journal of Rock Mechanics and Mining Sciences*, vol. 130, p. 104329, 2020.

[28] W. X. Li, D. L. Qi, S. F. Zheng, J. C. Ren, J. F. Li, and X. Yin, "Fuzzy mathematics model and its numerical method of stability analysis on rock slope of opencast metal mine," *Applied Mathematical Modelling*, vol. 39, no. 7, pp. 1784–1793, 2015.

[29] Y. Q. Liu, X. R. Liu, Y. M. Lu, X. W. Li, and P. Li, "Numerical analysis of evaluation methods and influencing factors for dynamic stability of bedding rock slope," *Journal of Vibroengineering*, vol. 19, no. 3, pp. 1937–1961, 2017.

[30] Z. Zhang, J. Han, and G. B. Ye, "Numerical investigation on factors for deep-seated slope stability of stone column-supported embankments over soft clay," *Engineering Geology*, vol. 168, pp. 104–113, 2014.

[31] I. Mehdipour, M. Ghazavi, and R. Z. Moayed, "Numerical study on stability analysis of geocell reinforced slopes by considering the bending effect," *Geotextiles and Geomembranes*, vol. 37, pp. 23–34, 2013.

[32] X. Y. Li, L. M. Zhang, and S. H. Jiang, "Updating performance of high rock slopes by combining incremental time-series monitoring data and three-dimensional numerical analysis," *International Journal of Rock Mechanics and Mining Sciences*, vol. 83, pp. 252–261, 2016.

[33] Y. Hu, Z. Yang, S. Huang, W. Lu, and G. Zhao, "A new safety control method of blasting excavation in high rock slope with joints," *Rock Mechanics and Rock Engineering*, vol. 53, no. 7, pp. 3015–3029, 2020.

[34] Y. Hu, W. Lu, M. Chen, P. Yan, and Y. Zhang, "Numerical simulation of the complete rock blasting response by sph-dam-fem approach," *Simulation Modelling Practice and Theory*, vol. 56, pp. 55–68, 2015.

[35] N. Jiang, T. Gao, C. Zhou, and X. Luo, "Effect of excavation blasting vibration on adjacent buried gas pipeline in a metro tunnel," *Tunnelling and Underground Space Technology*, vol. 81, pp. 590–601, 2018.

[36] H. R. Mohammadi Azizabadi, H. Mansouri, and O. Fouché, "Coupling of two methods, waveform superposition and numerical, to model blast vibration effect on slope stability in jointed rock masses," *Computers and Geotechnics*, vol. 61, pp. 42–49, 2014.

Hindawi
Geofluids
Volume 2022, Article ID 1007222, 17 pages
https://doi.org/10.1155/2022/1007222

Research Article

The Coal Pillar Width Effect of Principal Stress Deflection and Plastic Zone Form of Surrounding Rock Roadway in Deep Excavation

Ji Li,[1,2] Rongguang Zhang ,[1] and Xubo Qiang[1]

[1]*School of Energy, Xi'an University of Science and Technology, Xi'an 710054, China*
[2]*Key Laboratory of Western Mine and Hazard Prevention, Ministry of Education, Xi'an 710054, China*

Correspondence should be addressed to Rongguang Zhang; 20203226058@stu.xust.edu.cn

Received 9 September 2021; Accepted 24 February 2022; Published 18 March 2022

Academic Editor: Yong-Zheng Wu

In order to explore the influence of coal pillar width on the principal stress deflection and plastic zone form of surrounding rock in deep roadway excavation, taking 11030 working face transportation roadway of Zhaogu No. 2 Coal Mine as engineering background, theoretical analysis, numerical simulation, and field detection were used to study the effect of coal pillar width on principal stress deflection and plastic zone form and field detection and verification of plastic zone form of surrounding rock in 11030 transportation roadway. The results show that the maximum principal stress is deflected in the vertical direction, which in roadway surrounding rock excavation. The coal pillar width effect of principal stress deflection on both sides of roadway roof and floor and inside coal pillar are more obvious than that of middle roof and floor, coal pillar edge and coal wall position. The deflection of the principal stress affects the morphological distribution of the plastic zone of the surrounding rock, which led to the width effect of coal pillar in roof, and two sides plastic zone are more obvious than that in floor. The principal stress deflection of roadway surrounding rock is highly consistent with the maximum damage depth of plastic zone, and at the same time, the drilling peep results of surrounding rock are basically consistent with the form characteristics of plastic zone in numerical simulation. On this basis, the surrounding rock reinforcement support scheme of 11030 working face transportation roadway was proposed.

1. Introduction

With the increase of coal seam mining depth and mining intensity in China, and the comprehensive influence of production geological conditions and other factors, the deformation and damage of surrounding rock in deep roadways with different width of roadway protection coal pillars show different distribution characteristics. Under the influence of mining and coal pillar width, the stress field direction of roadway surrounding rock will deflect, resulting in the change of form distribution of surrounding rock plastic zone, and then affect the stability of roadway surrounding rock [1–3]. Therefore, the influence of roadway pillar width on principal stress deflection and plastic zone form of surrounding rock in deep roadway excavation is studied, which has important guiding significance for the stability control of surrounding rock in deep roadway.

By using the methods of theoretical analysis and numerical simulation, documents [4, 5] gave the calculation formula of failure width of supporting coal pillar under different failure criteria, revealed the stress distribution characteristics of working face and provided a new idea for retaining coal pillar width and roadway layout. Literature [6] studies showed that the larger the width of the reserved coal pillar, the smaller the proportion of plastic zone form, vertical stress, and horizontal deformation in the coal pillar, and the higher the stability of the coal pillar itself, which was helpful to maintain the stability of roadway surrounding rock. Literature [7] studied the variation law of vertical stress in the surrounding rock and coal pillar width along the open cut tunnel and combined with the limit equilibrium theory of coal body, and the optimized design of coal pillar width along the open cut tunnel was carried out. Literatures [8–10] studied an integrated detection system, established an ultrasonic model, and coupled it with a mechanical model, and the results of the research can predict whether the excavation damage zone, stress distribution, stress rotation, and ultrasonic velocity evolution of the roadway are consistent with the actual situation in the field. Literatures [11–13] proposed the characteristic radii of the plastic zone in the horizontal axis, longitudinal axis, and medial axis according to the damage boundary characteristics of the plastic zone of the roadway, through theoretical calculations and other research methods, in order to reflect the shape characteristics of the plastic zone, evaluate the potential hazard location of the roadway enclosure and the critical point of the roadway dynamic hazard evaluation based on the characteristic radii. The literatures [14, 15], based on mining rock mechanics, focused on the failure behavior and deformation mechanism of rocks with large burial depths and initially established the surrounding rock stress gradient failure theory and research results to provide the theoretical basis and technical support for the future development of deep mineral resources. The above results studied the influence law of coal pillar width on its own stability, roadway deformation, and the size of surrounding rock stress field and displacement field, respectively. However, the related research results on the deflection of the main stress and the form of the plastic zone in the surrounding rock of deep roadway excavation under different widths of coal pillars of the protection roadway are less. Therefore, this paper used numerical simulation to study the characteristics of main stress deflection and plastic zone form distribution of deep roadway excavation surrounding rocks under different widths of coal pillar protecting the roadway and discovered the coal pillar width effect of main stress deflection and plastic zone form and conducted theoretical analysis on the influence of coal pillar width effect on the stability of roadway surrounding rocks. On this basis, the detection and verification of the damage zone of the surrounding rock was carried out in the transporting roadway of 11030 working face of Zhaogu No. 2 Coal Mine, and the corresponding countermeasures for the control of the surrounding rock were proposed.

2. Deformation Characteristics of the Surrounding Rock in Deep Roadway Excavation under Different Coal Pillar Widths

2.1. Deformation Characteristics' Analysis of the Surrounding Rock. In order to study the deformation characteristics of the surrounding rock, which is in deep roadway under different widths of coal pillars of roadway protection, five roadways under different widths of coal pillars of roadway protection were selected through field research, and the deformation characteristics of the roadway surrounding rock after excavation were analyzed, as shown in Table 1.

Through the above case analysis, it can be seen that under different widths of coal pillar, the deformation of the roadway surrounding rock shows differential distribution characteristics, but the width of coal pillar and the amount of surrounding rock deformation does not show a direct correlation, that is, the larger the width of coal pillar, the smaller the amount of deformation of the roadway surrounding rock. And the deformation of the surrounding rock at different locations of the same roadway section shows nonuniform distribution characteristics. For example, in case 5, the maximum deformation of the roadway is 600 mm when 70 m coal pillar is left (two gang convergence), in case 1, the maximum deformation of the roadway is 45 mm when 5 m coal pillar is left (roof subsidence), and in case 2, the deformation of the roadway is different at different locations of the same section when 8 m coal pillar is left (maximum subsidence of roof is 428 mm, and maximum two gang convergence is 270 mm). The essence of the above phenomenon is that the width of the coal pillar will affect the distribution of the plastic zone of the surrounding rock in the roadway.

2.2. Factors Influencing the Deformation of the Surrounding Rock. The width of the coal pillar protecting the roadway is an important factor, which influencing the deformation and damage of the roadway excavation. The width of the coal pillar not only affects the size of the surrounding rock stress field but also deflects the direction of the surrounding rock stress field, which changes the form of the plastic zone of the surrounding rock (as shown in Figure 1) [16–19]. Under different pillar widths, the surrounding rock of mining roadway excavation presents differential deformation characteristics. The essence is that the surrounding rock forms different plastic zone. Therefore, this paper will focus on the deflection characteristics of the principal stress of the surrounding rock and the morphological distribution characteristics of the plastic zone under the condition of retaining different roadway pillar widths.

3. Effect of Coal Pillar Width on Deflection of Principal Stress and Plastic Zone Form of Surrounding Rock in Deep Roadway Excavation

3.1. Establishment of Numerical Model. According to the production geological conditions of transportation roadway in 11030 working face of Zhaogu No. 2 coal mine, FLAC^{3D} numerical simulation software was used to build a model with a length of 250 m, a width of 50 m, and a height of 42 m, with a model grid cell size of 0.5 m, as shown in Figure 2.

Displacement constraints were applied to the top and bottom of the model in the vertical direction, and displacement constraints in the horizontal direction were applied around the model, and the initial ground stresses were applied to the model based on the rock formation loads at a burial depth of 700 m, rock laboratory test, and the

Table 1: Deformation characteristics of surrounding rock in roadway excavation.

Roadway	General information	Scene photos	Deformation features
Wulihou coal mine lower group coal tape transport roadway	Average depth of coal seam 550 m; straight wall semi-circular arch roadway: 4.74 m and 4.3 m (net width and net height), wall height 2 m, arch height 2.3 m; 5 m coal pillar.		Maximum shifting in of the top and bottom plates is about 45 mm; the maximum shifting in of the two gangs is about 38 mm.
Transportation roadway of 11030 working face in Zhaogu No. 2 coal mine	Average depth of coal seam 700 m; rectangular roadway: 4.8 m and 3.3 m (width and height); 8 m coal pillar.	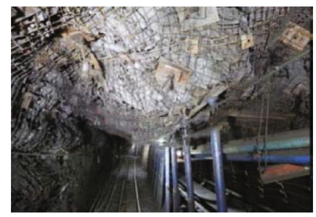	Maximum sinking of the roof is about 428 mm; maximum displacement of two sides is about 270 mm.
7608 return air roadway of Wuyang coal mine of Lu'an group	Average depth of coal seam 750 m; rectangular roadway: 5.4 m and 3.2 m (width and height); 15 m coal pillar.		Maximum sinking of the roof is about 200 mm; maximum displacement of two sides is about 700 mm.
Air return roadway in No. 9 mining area of Chensilou coal mine	Average depth of coal seam 900 m; straight wall semi-circular arch roadway: 4.2 m and 4.6 m (net width and net height), wall height 2.4 m, arch height 2.2 m; 13 m coal pillar.	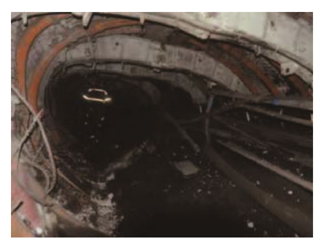	Maximum shifting in of the top and bottom plates is about 200 mm; the maximum shifting in of the two gangs is about 100 mm.
Transportation roadway in No. 7 mining area of Zhaolou coal mine	Average depth of coal seam 910 m; flat-topped domed roadway: 5 m and 4.5 m (net width and net height), upper arc height 2 m, flat top 3 m; 70 m coal pillar.		Maximum sinking of the roof is about 579 mm; maximum displacement of two sides is about 600 mm.

measured ground stresses in the adjacent mine area: 15.30 MPa for vertical stresses, 29.36 MPa (along the x-axis direction), and 16.82 MPa (along the y-axis direction) for horizontal stresses. The model is used Mohr-Coulomb, and the physical and mechanical parameters of each rock layer are shown in Table 2.

The plastic zone distribution characteristics of the roadway surrounding rock were simulated when the width of coal pillar was 4 m, 6 m, 8 m, 10 m, 12 m, 14 m, 16 m, 18 m, and 20 m, respectively, and the main stress direction measurement lines were arranged around the excavated roadway to study the main stress deflection characteristics. The length of each measurement line is 40 m, arranged along the tendency of coal seam, and the interval of measurement line is 0.5 m, and 31 measurement lines are arranged in total, as shown in Figure 3.

3.2. Coal Pillar Width Effect of Principal Stress Deflection of Roadway Surrounding Rock. According to the stress field imposed by numerical simulation, it is known that the maximum principal stress is 29.36 MPa, along the horizontal direction; the minimum principal stress is 15.30 MPa, along the vertical direction, and the following studies are analyzed by the angle between the maximum principal stress and the horizontal direction. Figure 4 shows the contour cloud of the maximum principal stress and the angle between the horizontal directions in the stress field of the roadway enclosure under different coal column widths. From the figure, it can

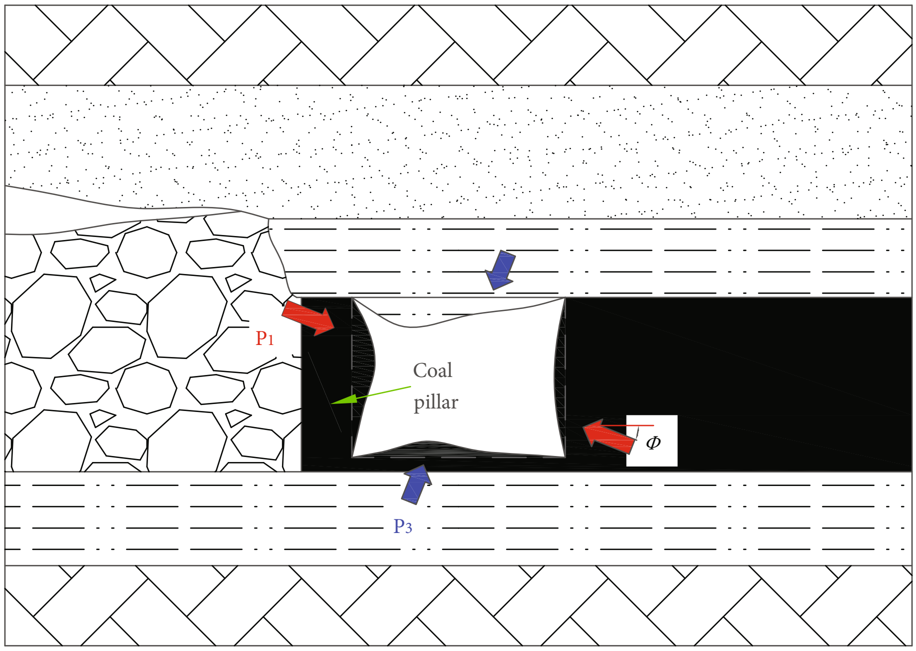

Figure 1: Deformation and failure mechanism of surrounding rock in roadway excavation.

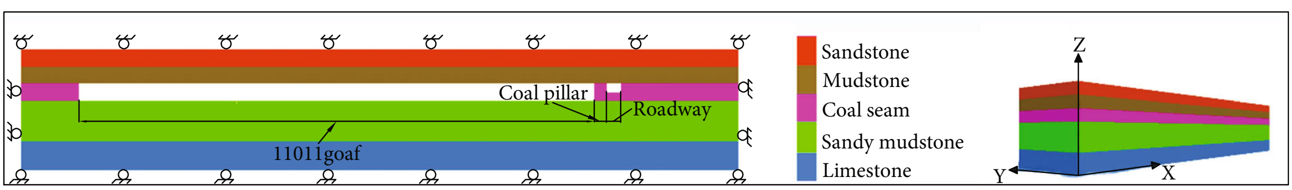

Figure 2: Numerical calculation model.

Table 2: Rock physical and mechanical parameters table.

Rock formation	Internal friction angle (°)	Cohesion (MPa)	Density (kg/m^3)	Shear modulus (GPa)	Bulk modulus (GPa)	Uniaxial tensile strength (MPa)
Sandstone	25	2.8	1500	4.8	5.4	1.5
Mudstone	30	5.24	2200	5.04	8.82	1.48
Coal seam	34	5.36	2500	4.54	10.44	2.6
Sandy mudstone	38	16	2700	9.0	10.2	7.5
Limestone	35	7.9	2300	5.3	8.9	8.71

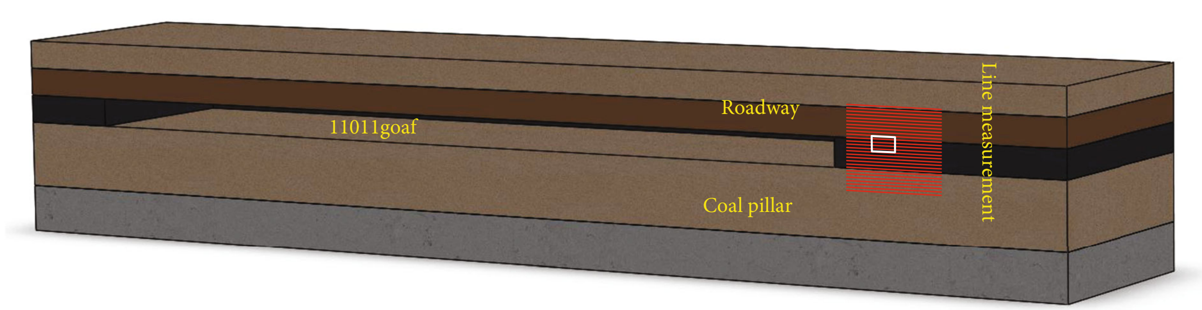

Figure 3: Layout of measuring line in principal stress direction of roadway surrounding rock.

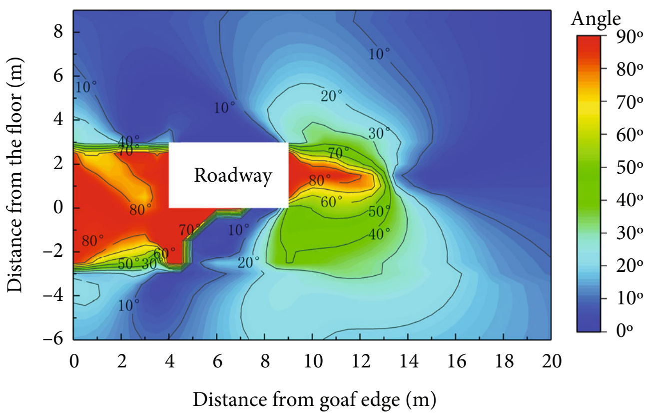

(a) 4 m coal pillar

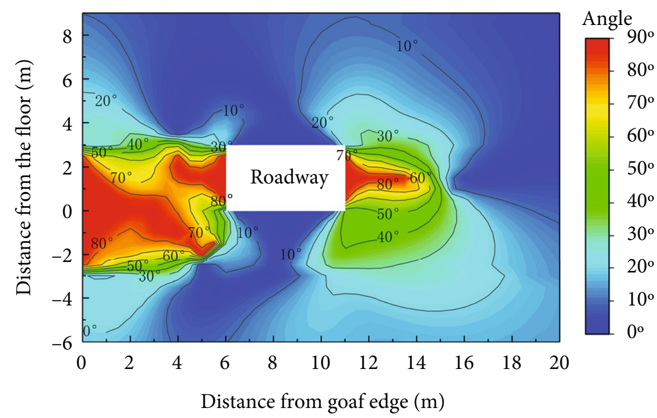

(b) 6 m coal pillar

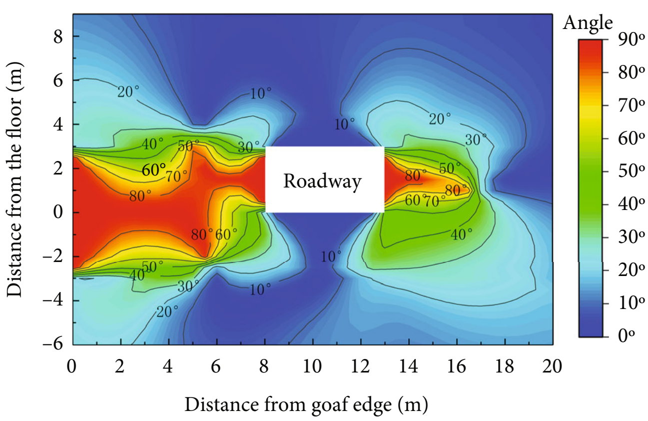

(c) 8 m coal pillar

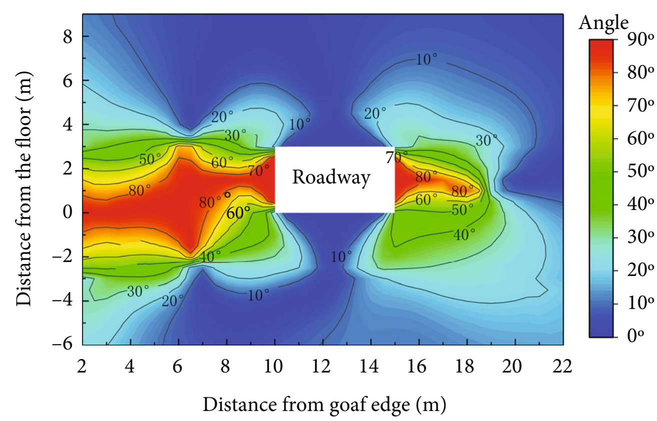

(d) 10 m coal pillar

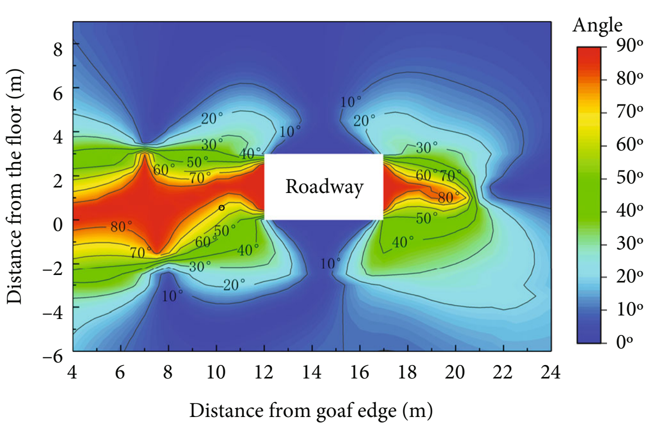

(e) 12 m coal pillar

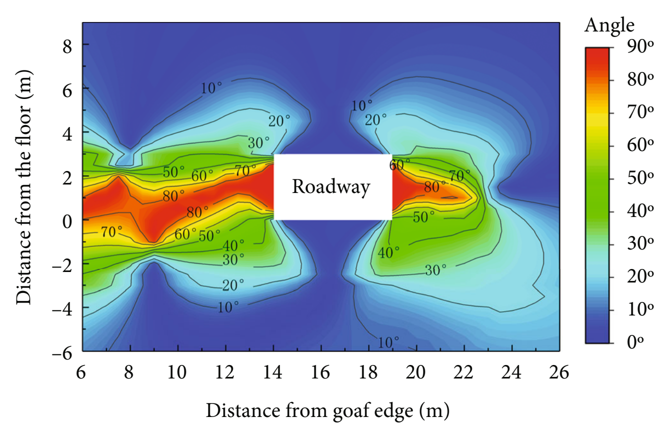

(f) 14 m coal pillar

Figure 4: Continued.

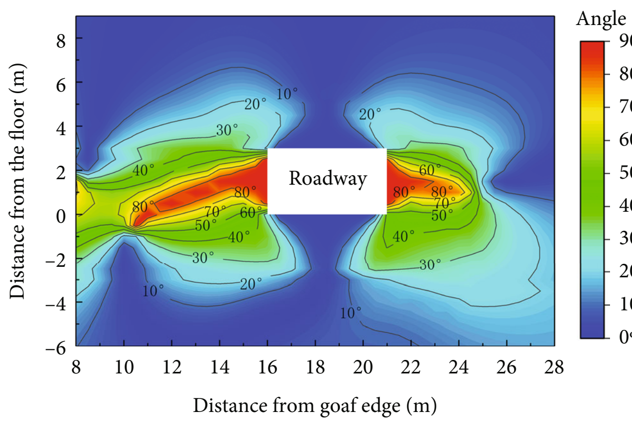

(g) 16 m coal pillar

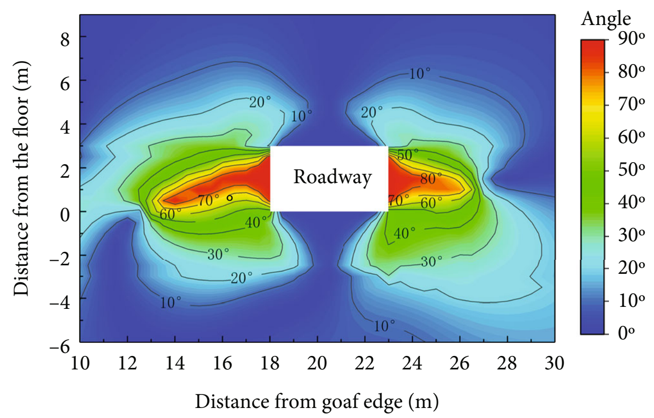

(h) 18 m coal pillar

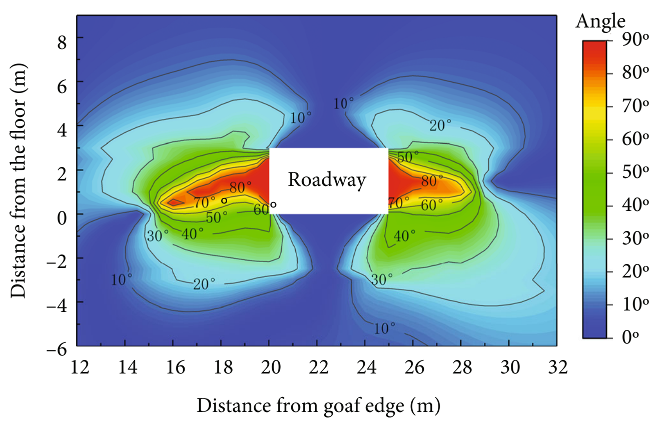

(i) 20 m coal pillar

Figure 4: Angle cloud chart of maximum principal stress and horizontal direction of surrounding rock. (left side is coal pillar, right side is coal wall).

be seen that the distribution characteristics of the maximum principal stress direction in the roadway surrounding rock change significantly under different coal column widths. For the roof, the maximum principal stress is mainly in the horizontal direction, and the minimum principal stress is mainly in the vertical direction; with the increase of the width of the coal pillar, the maximum principal stress of the overlying rocks near the coal pillar side and the coal wall side of the top slab has a tendency to deflect in the vertical direction, and the direction of the maximum principal stress of the overlying rocks in the middle of the top slab has no obvious deflection. For the coal pillar wall, with the increase of the width of the coal pillar, the direction of the maximum principal stress is obviously deflected, when the width of the coal pillar is 4 m~14 m, the maximum principal stress of the whole coal pillar is mainly in the vertical direction, and the minimum principal stress is mainly in the horizontal direction, when the width of the coal pillar is 16 m~20 m, the maximum principal stress within 4 m from the edge of the roadway is mainly in the vertical direction, and the maximum principal stress within 4~6 m from the edge of the roadway is mainly in the horizontal direction. For the coal wall, the maximum principal stress direction does not change significantly with the change of coal pillar width, and the maximum principal stress at the edge of the coal wall is mainly in the vertical direction, while the maximum principal stress at the deep part of the coal wall gang is mainly in the horizontal direction. For the floor, when the width of coal pillar is 4 m, the maximum principal stress is mainly in the vertical direction near the pillar side and in the horizontal direction near the coal wall side; when the width of coal pillar is 6 m~20 m, the maximum principal stress is mainly in the horizontal direction, and with the increase of the width of coal pillar, the direction of the maximum principal stress is not significantly deflected.

Figure 5 shows the curves of the maximum principal stresses, which are at different locations of road roof and floor and two surrounding rocks under different coal pillar widths with respect to the angle in the horizontal direction. From the above analysis, it can be seen that the 4 m and 6 m coal pillars are in plastic damage state, so no further analysis will be made here. By comparing the variation characteristics of the maximum principal stress direction in Figure 5 with the direction of the original rock stress field, it is obtained that the variation law of the maximum principal stress direction in the roadway surrounding rock area

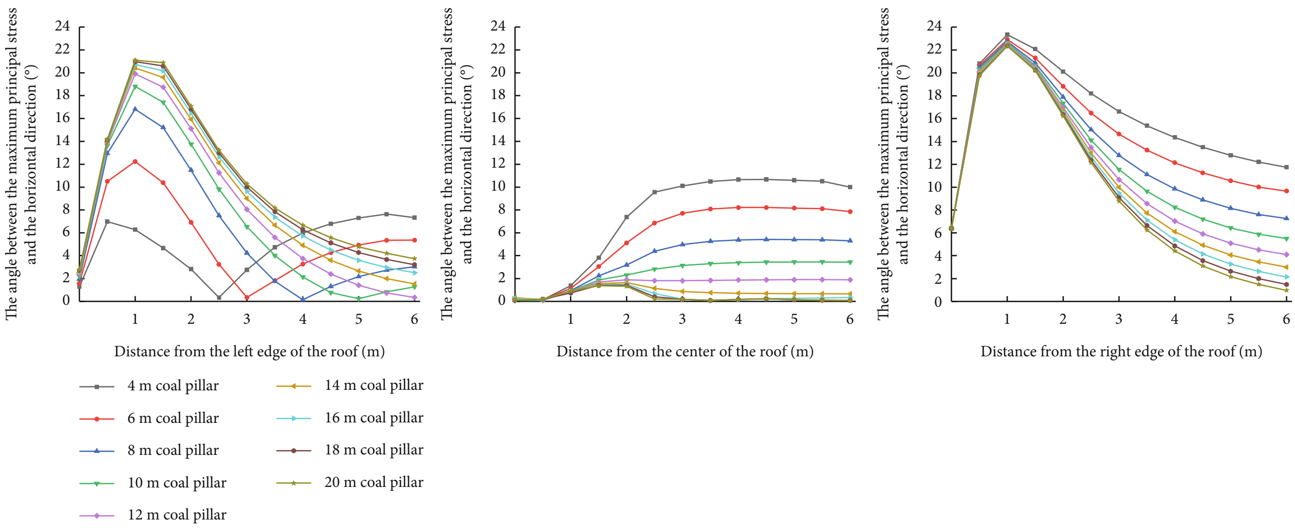

(a) roof

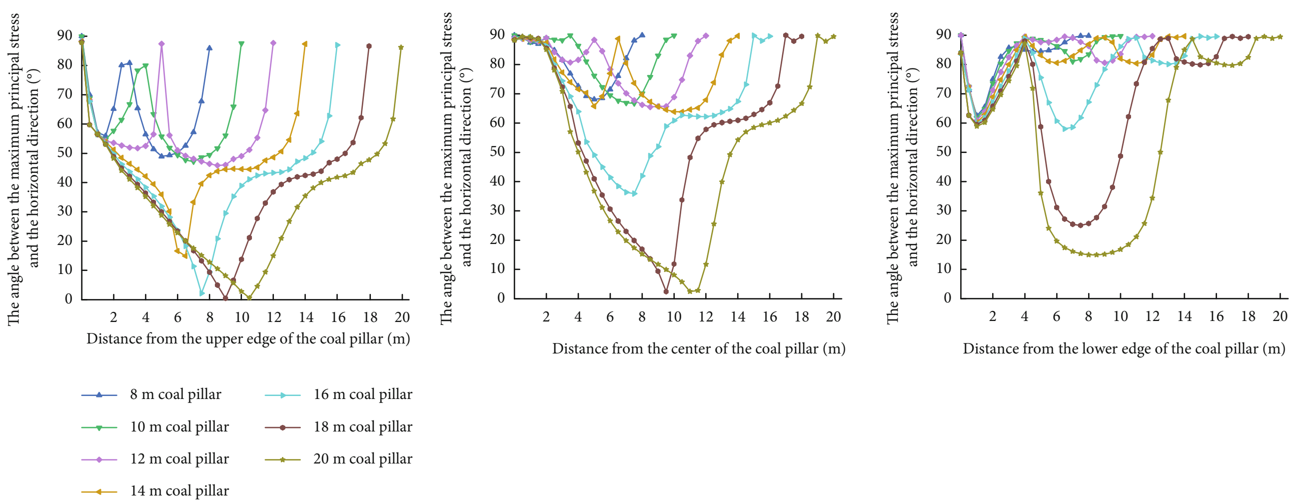

(b) coal pillar

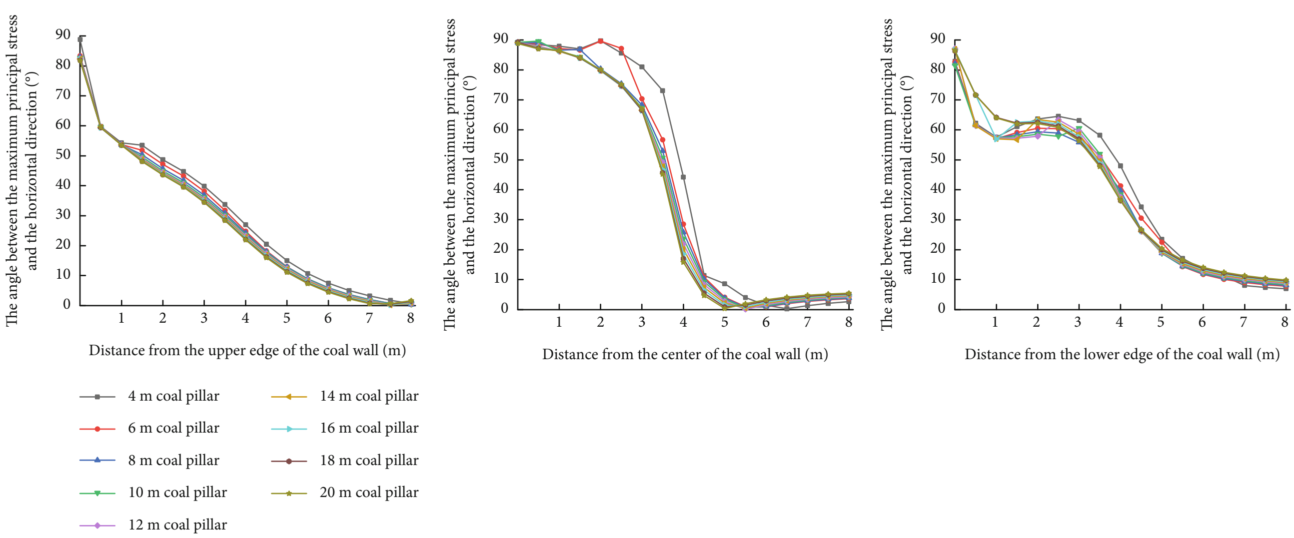

(c) coal wall

Figure 5: Continued.

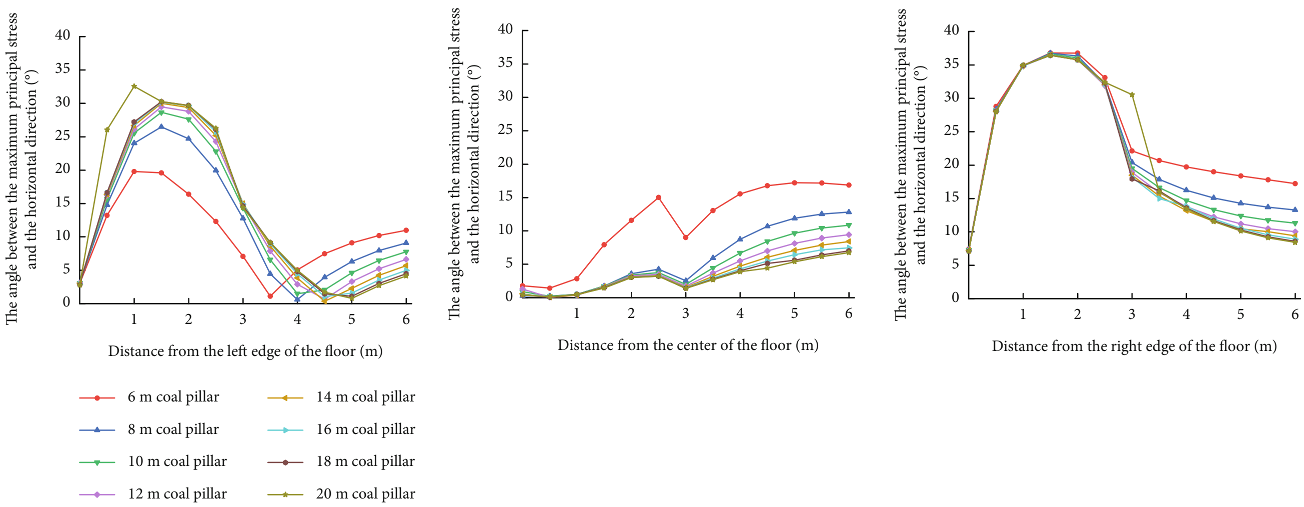

(d) floor

Figure 5: Variation curve of maximum principal stress direction of surrounding rock.

Table 3: The maximum principal stress deflection law of surrounding rock in roadway excavation.

Surrounding rock location	Deflection pattern
Roof	Continuous deflection in the vertical direction, but the degree of deflection is weak. Degree of deflection angle change: both sides of the roof > middle of the roof.
Coal pillar	The deflection is in the vertical direction, and the degree of deflection is decreasing. The degree of deflection from the edge of the coal pillar to the middle of the coal pillar shows "strong-medium-weak" transition. Degree of deflection angle change: middle of coal pillar > edge of coal pillar.
Floor	Continuous deflection in the vertical direction, with medium deflection at the position of 1.5 m~2 m under both sides of the floor, and weak deflection at other depth positions and the middle of the floor. Degree of deflection angle change: both sides of the floor > the middle of the floor.
Coal wall	All deflected in the vertical direction and the degree of deflection did not change significantly. The degree of deflection from the edge of the coal wall to the deep part of the solid coal shows "strong-medium-weak" transition. Degree of deflection angle change: middle of coal wall > edge of coal wall.

with the coal pillar width is shown in Table 3. (According to the deflection angle, three deflection degrees are defined: ① Weak: ≤30°; ② Medium: 30° ≤ 60°; and ③ Strong: ≥60°).

From the above analysis, it can be seen that the maximum principal stresses in the stress field of the roadway enclosure area are deflected in the vertical direction, but the deflection of the maximum principal stresses at different locations in the roadway enclosure has different sensitivities to the width of the coal pillar, resulting in the variability of the coal pillar width effect of the deflection of the principal stresses at different locations in the roadway enclosure.

(1) For the roof and floor, the sensitivity of the maximum principal stress deflection at the position of the roof and floor near the two sides of the roadway to the width of the coal column is stronger. With the increase of coal pillar width, the maximum principal stress deflection angle changes obviously (maximum change of 20°) on both sides of the roof and floor, and the change is smaller (maximum change of 8°) in the middle position. Therefore, the maximum principal stress deflection in the roof and floor near the edge of the two gangs has an obvious coal pillar width effect, while the coal pillar width effect in the middle position is weaker

(2) For the coal pillar, the sensitivity of the maximum principal stress deflection inside the coal pillar to the change of the coal pillar width is stronger. With the increase of coal pillar width, the change of maximum principal stress deflection angle inside the coal pillar is obvious (maximum change of 70°), and the change of edge position is relatively small (maximum change of 12°). Therefore, the maximum principal stress deflection inside the coal pillar has obvious coal pillar width effect, while the coal pillar width effect of edge position is weaker

(3) For the coal wall, the sensitivity of the maximum principal stress deflection of the coal wall to the coal pillar width is weaker. With the increase of coal pillar

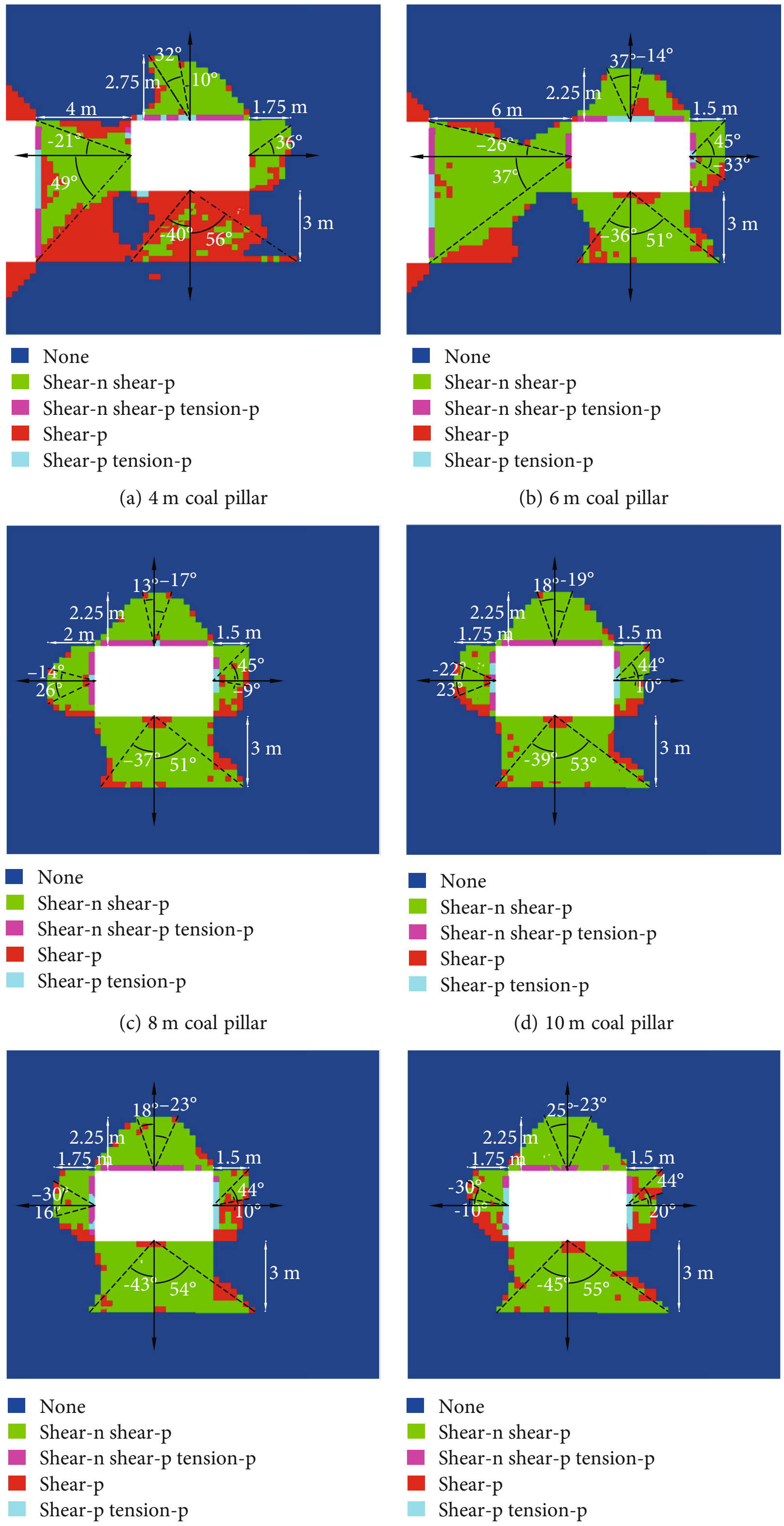

(a) 4 m coal pillar
(b) 6 m coal pillar
(c) 8 m coal pillar
(d) 10 m coal pillar
(e) 12 m coal pillar
(f) 14 m coal pillar

Figure 6: Continued.

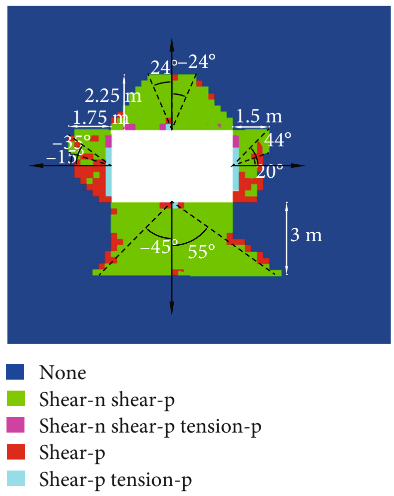

(g) 16 m coal pillar

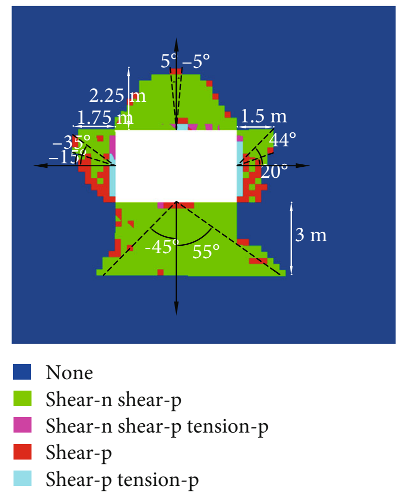

(h) 18 m coal pillar

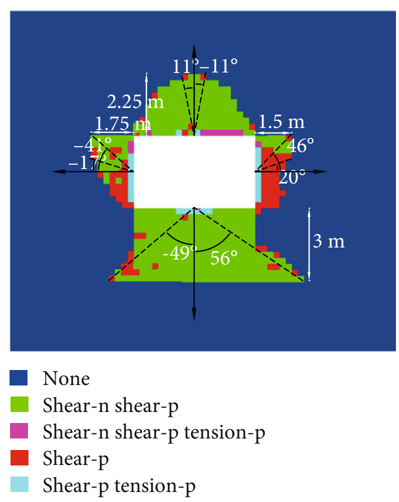

(i) 20 m coal pillar

Figure 6: The form distribution of plastic zone of roadway surrounding rock. (left side is coal pillar, right side is coal wall).

width, the change of coal wall maximum principal stress deflection angle is small (maximum change 15°). Therefore, the coal pillar width effect of coal wall maximum principal stress deflection is weaker

3.3. Coal Pillar Width Effect of Plastic Zone Form of Roadway Surrounding Rock. Figure 6 shows the distribution of the plastic zone form in the surrounding rock of the roadway under different coal pillar widths obtained by numerical simulation. For the convenience of analysis, two indicators, plastic zone maximum damage depth and plastic zone maximum damage depth location, are defined to characterize the plastic zone form, where the plastic zone maximum damage depth location is expressed by the angle between the plastic zone maximum damage depth boundary and the centerline of the top and bottom plates of the roadway and the two sides of the gang, and the counterclockwise direction is specified as positive. From Figure 6, it can be seen that with the increase of coal pillar width, the plastic zone form of the roadway surrounding rock changes to different degrees. For the roof, the maximum damage depth of plastic zone is 2.75 m, when the width of coal pillar is 4 m, and the position of the maximum damage depth (10°~32°) is close to the roof of coal pillar side. When the width of coal pillar is 6 m~20 m, the maximum damage depth of plastic zone decreases to 2.25 m and remains unchanged, but its position is deflected to clockwise direction (solid coal side) when the width of coal pillar is 6 m~14 m, and it is not deflected when the width of coal pillar is 16 m~20 m. The form of the plastic zone is symmetric about the centerline of the roof. For the coal pillar, when the width of coal pillar is 4 m~6 m, the whole coal pillar is in the plastic damage state; when the width of coal pillar is 8 m~20 m, the coal pillar is no longer in the plastic damage state completely, and the maximum damage depth of the plastic zone does not change significantly, which is about 1.75 m, but the position of the maximum damage depth of the plastic zone continues to deflect in the clockwise direction (roof direction) with the increase

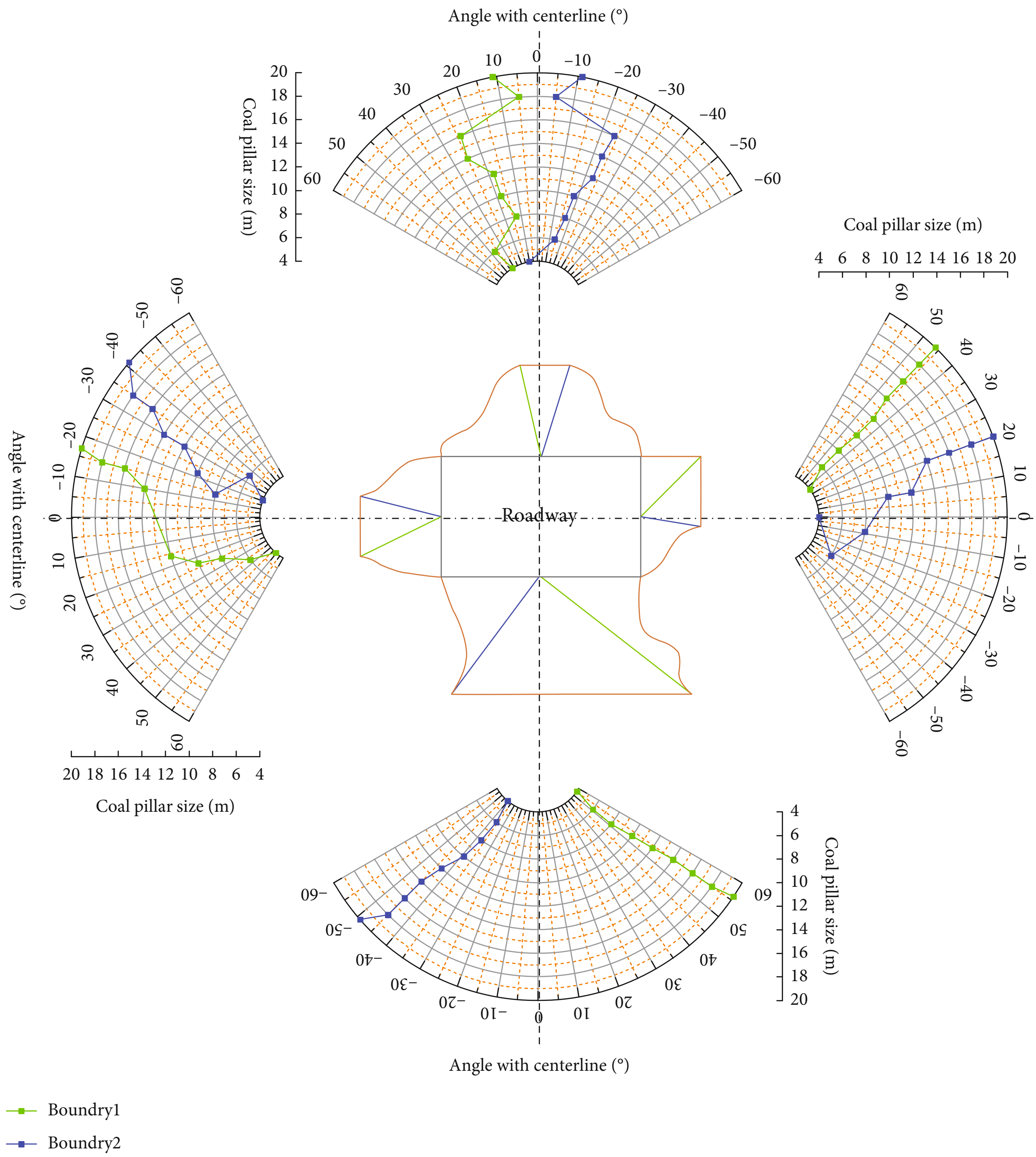

Figure 7: Location of maximum failure depth in plastic zone of roadway surrounding rock.

of the width of coal pillar. For the coal wall, when the width of coal pillar is 4 m, the maximum damage depth of plastic zone is 1.75 m, and the position of maximum break depth is 0°~36°. When the width of coal pillar is 6 m~14 m, the maximum damage depth of plastic zone decreases to 1.5 m and remains unchanged, but its position deflects significantly in the counterclockwise direction (roof direction). When the width of coal pillar is 16 m~20 m, the distribution of the plastic zone does not change significantly. For the floor, the maximum damage depth of the plastic zone does not change with the increase of coal pillar width, which is 3 m, and the location of the maximum damage depth also does not change significantly, and the form of the plastic zone is approximately symmetrical about the center line of the floor.

From the analysis of Figure 7 and Table 4, it can be seen that the form of plastic zone in different locations of the roadway surrounding rock shows different sensitivity to the change of coal pillar width, which leads to the variability of the coal pillar width effect of the form of plastic zone in different locations of the roadway surrounding rock.

From the above analysis, it can be seen that the plastic zone form at different locations of the roadway surrounding rock shows different sensitivities to the changes of coal pillar

Table 4: The variation law of the maximum failure depth position in plastic zone pillar.

	Width of coal pillar	Deflection direction	Deflection angle
Roof	4 m~8 m	Coal wall	10°~13.5°
	8 m~12 m	Coal wall	2°~2.5°
	12 m~16 m	Coal pillar	1°~1.5°
	16 m~20 m	No change	0°
	Width of coal pillar	Deflection direction	Deflection angle
Coal pillar	4 m~12 m	Roof	0.5°~8.5°
	12 m~16 m	Roof	10°~13°
	16 m~18 m	No change	0°
	18 m~20 m	Roof	4°
	Width of coal pillar	Deflection direction	Deflection angle
Floor	4 m~8 m	Coal pillar	0.5°~6.5°
	8 m~10 m	No change	0°
	10 m~14 m	Coal pillar	0.5°~1.5°
	14 m~20 m	No change	0°
	Width of coal pillar	Deflection direction	Deflection angle
Coal wall	4 m~6 m	Floor	12°
	6 m~10 m	Roof	10°~12°
	10 m~14 m	Roof	3°~5°
	14 m~20 m	No change	0°

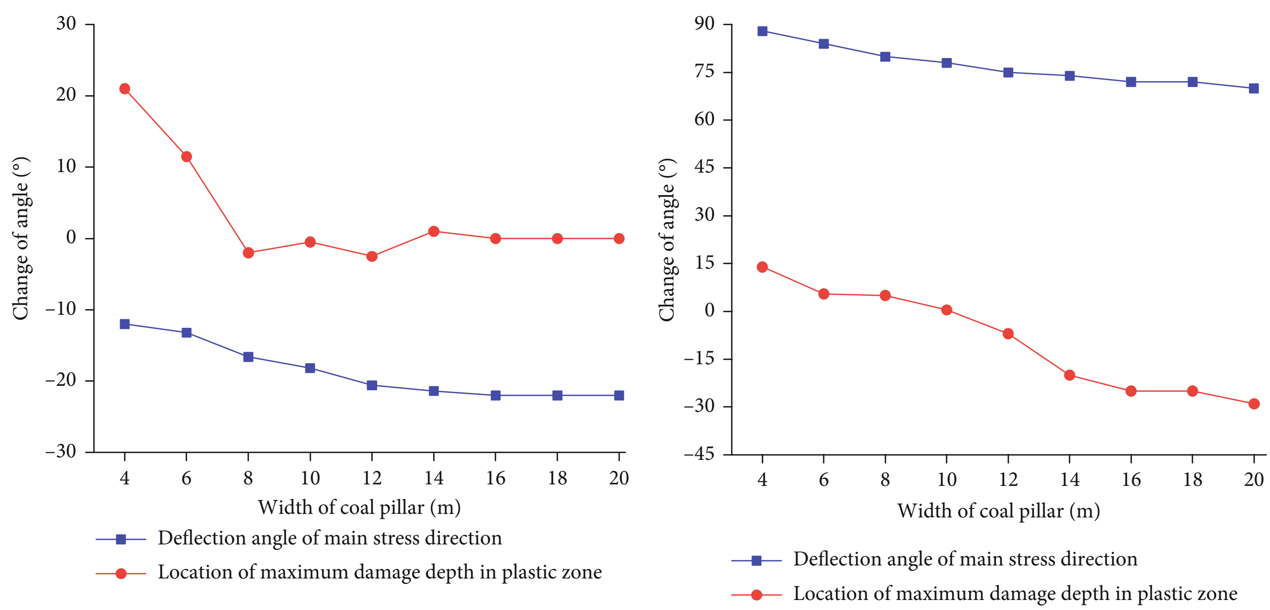

(a) roof

(b) coal pillar

Figure 8: Curve of maximum failure depth position and principal stress direction in plastic zone of roadway surrounding rock.

width, which leads to the variability of the coal pillar width effect of the plastic zone form at different locations of the roadway surrounding rock.

(1) For the roof, when the width of coal pillar is less than 8 m, the sensitivity of the top plastic zone form to the change of coal pillar width is stronger, and with the increase of coal pillar width, the maximum damage depth of plastic zone decreases significantly, and the position of the maximum damage depth of plastic zone continues to deflect toward the coal wall, and the top plastic zone form has obvious coal pillar width effect. When the width of coal pillar is greater than 8 m, the sensitivity of roof plastic zone form to coal pillar width change is weak, with the increase of coal pillar width, the maximum damage depth of

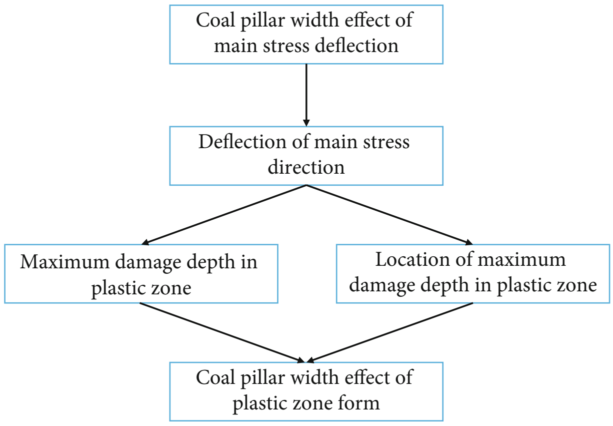

Figure 9: Formation mechanism of coal pillar width effect.

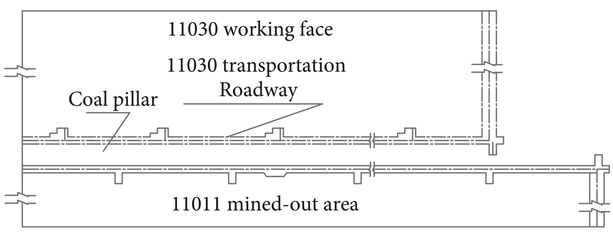

Figure 10: The layout plan of carrying roadway along 11030 working face.

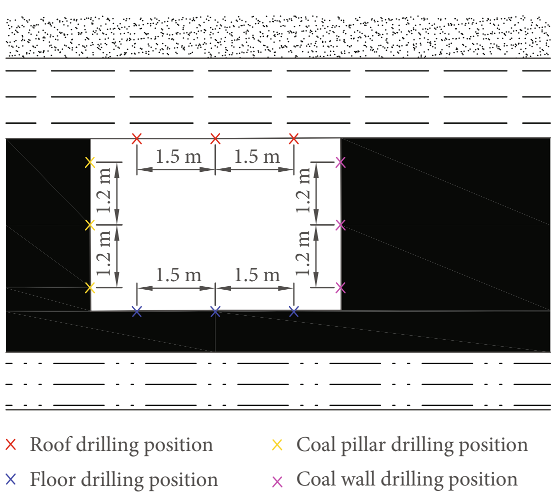

Figure 11: Borehole layout plan of transportation lane in 11030 working face.

plastic zone does not change obviously, its position change is small (maximum change 2.5°), and the coal pillar width effect of roof plastic zone form is weak

(2) For two sides of roadway, the form of plastic zone of two sides is sensitive to the change of coal pillar width. With the increase of coal pillar width, the maximum damage depth of plastic zone of coal pillar wall first decreases and then remains unchanged, and its position continues to deflect towards the roof. When the coal pillar width is less than 12 m, the maximum damage depth of the plastic zone of the coal wall first decreases and then remains unchanged, and its position first deflects to the floor direction and then to the roof direction. When the coal pillar width is greater than 12 m, the maximum damage depth and position of the plastic zone do not change significantly. The plastic zone form of two sides of roadway has obvious coal pillar width effect

(3) For the floor, the form of the plastic zone of the floor is less sensitive to the change of the coal pillar width. With the increase of the coal pillar width, the maximum damage depth of the plastic zone does not change significantly, and its position changes slightly (the maximum change is 6.5°), and the coal pillar width effect of the form of the plastic zone of the floor should be weak

4. Analysis of the Stability of the Surrounding Rock Based on the Coal Pillar Width Effect

4.1. Mechanism of Coal Pillar Width Effect Formation. For the stability of roadway surrounding rock, the key is to ensure the stability of roadway roof and coal pillar. Therefore, based on the previous research results, taking the roadway roof and coal pillar wall as the research object, the author analyzes the variation law of the deflection angle of the main stress direction of roadway surrounding rock and the position of the maximum failure depth of plastic zone under different coal pillar widths and reveals the formation mechanism of coal pillar width effect in the plastic zone of roadway surrounding rock. Figure 8 shows the curves of the change in the deflection angle of the main stress direction and the position of the maximum damage depth in the plastic zone of the roadway roof and coal pillar at different coal pillar widths (the counterclockwise direction is specified as positive). From the figure, it can be seen that the position of the maximum damage depth in the plastic zone of the roadway surrounding rock and the angle of deflection of the main stress direction have approximately the same changing trend. As the width of coal pillar increases, the position of maximum damage depth and the direction of main stress in the plastic zone of the floor and coal pillar are deflected in the clockwise direction.

The width effect of the main stress deflection of the surrounding rock after the roadway excavation will cause the obvious deflection of the main stress direction of the surrounding rock, which will cause the maximum damage depth and location of the surrounding rock plastic zone to change, which results in the difference distribution of the plastic zone form of the surrounding rock, and which results in the shape of the surrounding rock plastic zone having the width effect of the coal pillar, as shown in Figure 9.

4.2. The Influence of Coal Pillar Width Effect on the Stability of the Surrounding Rock. According to the above study, influenced by the coal pillar width effect, the principal stress direction and plastic zone form at different positions of surrounding rock after roadway excavation will change to

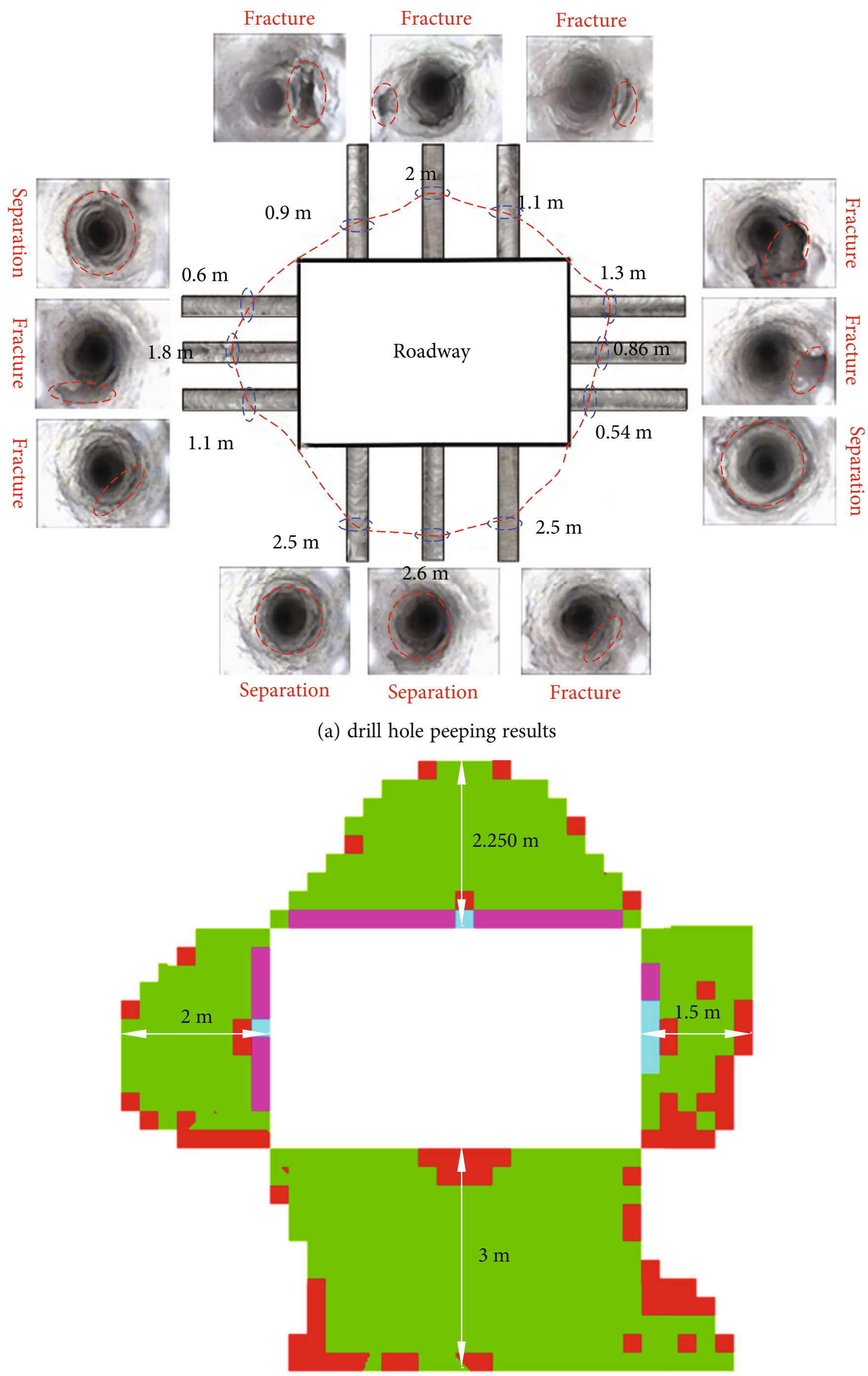

(a) drill hole peeping results

(b) numerical simulation results

Figure 12: Comparison of the damage range of surrounding rock in 11030 transportation lane with the results of numerical simulation.

different degrees. For the roof, the deflection degree of the principal stress direction near the two sides of the roof is significantly greater than that in the central position, and the damage depth of the plastic zone at different positions of the roof is quite different, resulting in the difference in the stability of the surrounding rock on both sides and in the central position of the roof. For the coal pillar side, the deflection degree of the principal stress direction in the middle position of the coal pillar is significantly greater than that in the upper and lower sides, and the damage depth of the plastic zone in different positions is also different, resulting in a large difference in the stability of the surrounding rock in the middle and upper and lower sides of the coal pillar. Therefore, for roadways with different coal pillar widths, it is necessary to adopt different control measures for different positions of roof and coal pillar to ensure the stability of surrounding rock. Taking the 11030 working face transportation roadway of Zhaogu No. 2 Mine as an example, the

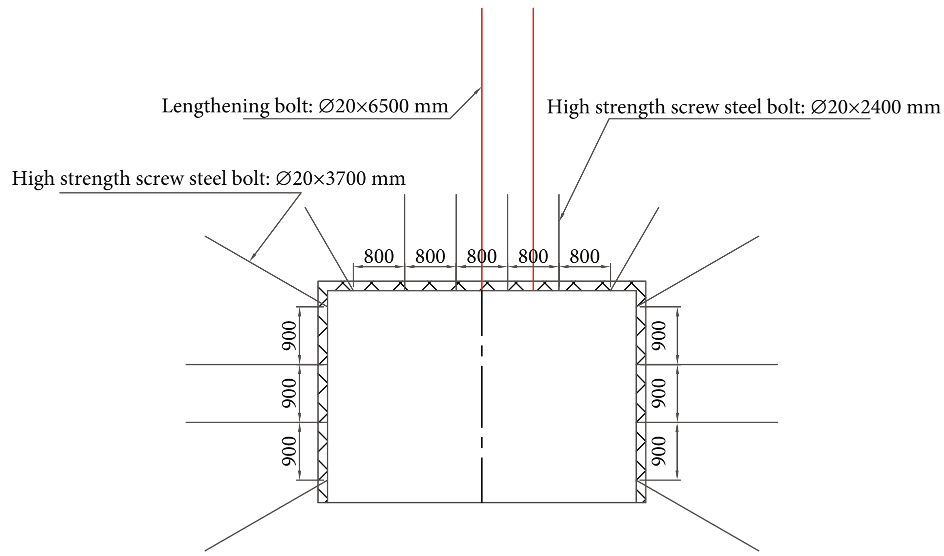

FIGURE 13: Section diagram of supporting design parameters for 11030 working face transportation roadway.

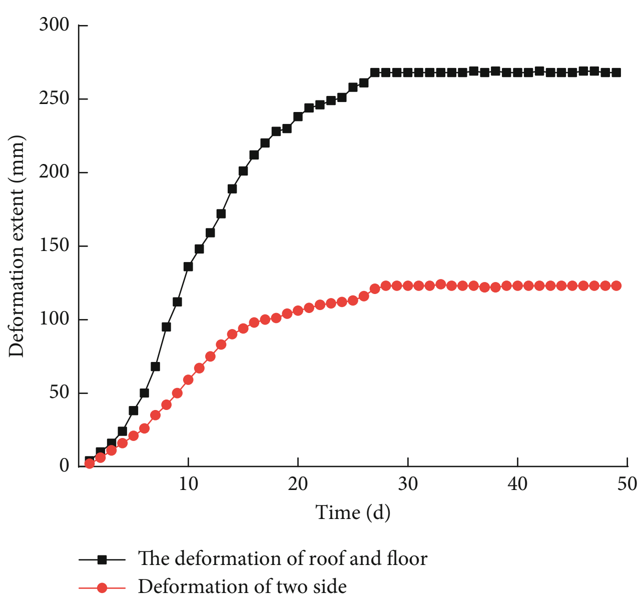

FIGURE 14: Change of surface displacement of roadway.

stability of roadway surrounding rock is analyzed combined with the width effect of coal pillar, which provides basic guidance for the stability control of roadway surrounding rock. For the roof, the maximum principal stress is mainly in the horizontal direction, but affected by the width effect of coal pillar, and the maximum principal stress on both sides of the roof tends to change in the vertical direction. And the maximum damage depth of plastic zone is located in the middle of roof. Therefore, the stability of the surrounding rock in the middle of the roof is poorer than that on both sides. In order to prevent the roof falling accident of the roadway, it is necessary to reinforce and support the middle position of the roadway roof after the roadway excavation is completed. For the coal pillar, the maximum principal stress is mainly in the vertical direction, but affected by the width effect of coal pillar, and the maximum principal stress at the upper and lower sides of coal pillar changes significantly in the horizontal direction. And the maximum damage depth of plastic zone deflects to the roof direction. The comprehensive analysis shows that the stability of the upper and middle sides of the coal pillar is worse than that of the lower side. In order to prevent the failure and instability of the coal pillar, it is necessary to reinforce the surrounding rock of the middle and upper sides of the coal pillar after the roadway excavation.

5. Engineering Case

The transportation roadway of 11030 working face in Zhaogu No. 2 Mine was excavated along the coal seam roof, and 8 m coal pillar was left between it and the 11011 mined-out area (Figure 10). The roadway was designed as a rectangular section of 4.8 m × 3.3 m (width × height). During the excavation of the roadway, the roadway surrounding rock had a nonuniform large deformation, the section contraction was serious, the maximum subsidence of roof was about 428 mm, and the maximum displacement of two sides was about 270 mm.

5.1. Detection of Rock Surrounding Damage Areas. In order to master the surrounding rock damage of 11030 working face transportation roadway and compare with the numerical simulation results (Figure 6(c)), the JL-IDOI (A) intelligent borehole TV imager was used to peep the surrounding rock damage of the roadway. Three boreholes were arranged at the roof and floor of the roadway and the two sides at 260 m from the opening of the roadway in 11030 working face. A total of 12 boreholes were arranged, as shown in Figure 11, the diameter of the borehole was 32 mm, and the depth of the borehole was 4 m.

Figure 12 shows the comparison between the borehole peeping results of surrounding rock of 11030 transportation roadway and the plastic zone form of numerical simulation. The damage area of roadway surrounding rock is asymmetric. The damage depth of rock stratum in the middle of roof is large, and the coal body in the middle of coal pillar is seriously broken. The damage depth of rock stratum near the roof of coal wall is the largest, and the distribution range of floor rock stratum is relatively uniform. The nonuniform morphological characteristics of plastic zone of roadway surrounding rock are basically consistent with the results of borehole peeping.

5.2. Roadway Support Design. Combined with the field peeping results and previous research results, it can be seen that the section convergence of 11030 transport roadway during excavation is serious, and the surrounding rock deformation of roadway shows obvious nonuniform characteristics. Therefore, considering the influence of mining activities in the later stage of the roadway, the middle roof is reinforced and supported by the length enable bolt and the high strength screw steel bolt to prevent the roof from falling [20–22]. Two sides, by patching high strength thread steel anchor, prevent two sides due to excessive deformation and cross. Specific design parameters are shown in Figure 13.

5.3. Support Effect. In order to verify the stability of the surrounding rock of the roadway after reinforcement support, a measuring station was arranged at 260 m from the opening of 11030 transportation roadway to monitor the change of the roadway surface displacement. The monitoring results show that the maximum deformation of the top and bottom plates from 0 to 28d after the roadway was reinforced and supported and is 268 mm, and the maximum deformation of the two sides is 123 mm; the displacement of the surrounding rock of the roadway remains basically the same after 28 d after the roadway was reinforced and supported, and there is no significant increase, indicating that the surrounding rock of the roadway tends to be stable. The monitoring results of the roadway surface displacement are shown in Figure 14.

6. Conclusion

(1) The deformation of the surrounding rock in the deep roadway under different widths of the coal pillar does not show a direct correlation between the width of the coal pillar and the deformation of the surrounding rock (the larger the width of the coal pillar, the smaller the deformation of the surrounding rock in the roadway), and the deformation of the surrounding rock at different locations in the same section of the roadway shows a nonuniform distribution

(2) The maximum principal stress deflects to the vertical direction in the stress field of the surrounding rock of deep roadway excavation, but the deflection of the maximum principal stress at different positions of the surrounding rock of roadway has different sensitivity to the width of the coal pillar. The coal pillar width effect of principal stress deflection on both sides of the roof and floor and inside the coal pillar is obvious, and the coal pillar width effect of principal stress deflection in the middle of the roof and floor and the edge of the coal pillar and the coal wall are weak

(3) The plastic zone form of surrounding rock of deep roadway after excavation will show differential distribution characteristics due to the change of coal pillar width, and the plastic zone form of surrounding rock at different positions of roadway has different sensitivities to the change of coal pillar width, resulting in obvious coal pillar width effect of plastic zone form of roadway roof and two sides, and weak coal pillar width effect of plastic zone form of floor

(4) The principal stress in the surrounding rock area of deep roadway excavation will deflect to varying degrees, which affects the form of the plastic zone of the surrounding rock. The position of the maximum damage depth of the plastic zone is approximately the same as the principal stress deflection, and the width effect of the coal pillar will have different degrees of influence on the stability of the surrounding rock at different positions of the roadway

Data Availability

The data used to support the findings of this study are available from the corresponding author upon request.

Conflicts of Interest

The authors declare that there are no conflicts of interest including any financial, personal, or other relationships with other people or organizations.

Acknowledgments

This paper was supported by the National Natural Science Foundation of China (Grant no. 51804243).

References

[1] H. P. Xie, F. Gao, and Y. Ju, "Research and development of rock mechanics in deep ground engineering," *Chinese Journal of Rock Mechanics and Engineering*, vol. 34, no. 11, pp. 2161–2178, 2015.

[2] A. H. Wilson, "The stability of underground workings in the soft rocks of the coal measures," *International Journal of Mining Engineering*, vol. 1, pp. 91–187, 1983.

[3] J. M. Galvin, B. K. Hebblewhite, and M. D. G. Salamon, "Australian coal pillar performance," *ISRM News Journal*, vol. 4, pp. 33–38, 1996.

[4] A. Jaiswal and B. K. Shrivastva, "Numerical simulation of coal pillar strength," *International Journal of Rock Mechanics and Mining Sciences*, vol. 46, no. 4, pp. 779–788, 2009.

[5] T. P. Medhurst and E. T. Brown, "A study of the mechanical behaviour of coal for pillar design," *International Journal of*

Rock Mechanics and Mining Sciences, vol. 35, no. 8, pp. 1087–1105, 1998.

[6] R. Wang, S. Yan, J. B. Bai, Z. Chang, and T. Zhao, "Theoretical analysis and study of the destabilization on damaged width of rib pillar in open-pit highwall mining," *Advances in Civil Engineering*, vol. 2019, no. 8, Article ID 6328702, p. 15, 2019.

[7] C. Xu, X. Li, K. Wang, C. Guo, Q. Fu, and Y. Ju, "Reasonable coal pillar width of protective layer during high-gas coal seams mining," *Journal of China University of Mining and Technology*, vol. 49, no. 3, pp. 445–452, 2020.

[8] L. S. Jiang, P. P. Zhang, L. J. Chen et al., "Numerical approach for goaf-side entry layout and yield pillar design in fractured ground conditions," *Rock Mechanics and Rock Engineering*, vol. 50, no. 11, pp. 3049–3071, 2017.

[9] H. J. Li, Q. T. Chen, Z. Y. Shu, L. Li, and Y. Zhang, "On prevention and mechanism of bed separation water inrush for thick coal seams: a case study in China," *Environmental Earth Sciences*, vol. 77, no. 22, p. ???, 2018.

[10] S. L. Yang, G. F. Song, and J. H. Yang, "An analytical solution for the geometric broken characteristics of the overlying strata and its physical modeling study in longwall coal mining," *Arabian Journal Of Geosciences*, vol. 13, no. 3, p. 139, 2020.

[11] X. Guo, Z. Zhao, X. Gao, X. Wu, and N. Ma, "Analytical solutions for characteristic radii of circular roadway surrounding rock plastic zone and their application," *International Journal of Mining Science and Technology*, vol. 29, no. 2, pp. 263–272, 2019.

[12] H. Basarir, I. F. Oge, and O. Aydin, "Prediction of the stresses around main and tail gates during top coal caving by 3D numerical analysis," *International Journal of Rock Mechanics and Mining Sciences*, vol. 76, pp. 88–97, 2015.

[13] Y. Li, N. Ma, and J. Ma, "Surrounding rock's failure characteristic and rational location of floor gas drainage roadway above deep confined water," *Journal of China Coal Society*, vol. 43, pp. 2491–2500, 2018.

[14] J. P. Zuo, J. T. Wang, and Y. Q. Jiang, "Macro/meso failure behavior of surrounding rock in deep roadway and its control technology," *International Journal of Mining Science and Technology*, vol. 6, no. 3, pp. 301–319, 2019.

[15] D. J. Xue, J. Zhou, Y. T. Liu, and L. Gao, "On the excavation-induced stress drop in damaged coal considering a coupled yield and failure criterion," *International Journal of Mining Science and Technology*, vol. 7, no. 1, pp. 58–67, 2020.

[16] J. Li, N. J. Ma, and Z. Q. Zhao, "Butterfly leaf type roof falling mechanism and control technology of mining gateway," *Coal Science and Technology*, vol. 45, no. 12, pp. 46–52, 2017.

[17] F. Pellet, M. Roosefid, and F. Deleruyelle, "On the 3D numerical modelling of the time-dependent development of the damage zone around underground galleries during and after excavation," *Tunnelling and Underground Space Technology*, vol. 24, no. 6, pp. 665–674, 2009.

[18] J. Li, X. B. Qiang, W. S. Wang, and F. Wang, "Distribution law of principal stress difference of deep surrounding rock of gob-side entry and optimum design of coal pillar width," *Tehnički Vjesnik*, vol. 26, no. 6, pp. 1743–1752, 2019.

[19] J. Li, "The coal pillar design method for a deep mining roadway based on the shape of the plastic zone in surrounding rocks," *Arabian Journal of Geosciences*, vol. 13, no. 12, p. 454, 2020.

[20] L. Giresini, M. L. Puppio, and F. Taddei, "Experimental pull-out tests and design indications for strength anchors installed in masonry walls," *Materials and Structures*, vol. 53, no. 4, p. 103, 2020.

[21] L. Ji, F. Jicheng, and Z. Shengkai, "Study on long and short bolt coordinate support technology of mine soft rock roadway," *Coal Science and Technology*, vol. 43, no. 3, pp. 17–21, 2015.

[22] W. Fei, L. Hongtao, and Z. Shengkai, "Yieldable technology of lengthened bolts for high-stress soft rock roadways," *Chinese Journal of Geotechnical Engineering*, vol. 36, no. 9, pp. 1667–1673, 2014.

Hindawi
Geofluids
Volume 2022, Article ID 1851899, 14 pages
https://doi.org/10.1155/2022/1851899

Research Article

Floor Failure Characteristics in Deep Island Longwall Panel: Theoretical Analysis and Field Verification

Pengpeng Wang,[1,2] Yixin Zhao,[1,2,3] Qingshan Ren,[1,2] Yaodong Jiang,[1,4] Cun Zhang,[1,2] and Yirui Gao[1,2]

[1]*Beijing Key Laboratory for Precise Mining of Intergrown Energy and Resources, China University of Mining and Technology (Beijing), Beijing 100083, China*
[2]*School of Energy and Mining Engineering, China University of Mining and Technology (Beijing), Beijing 100083, China*
[3]*State Key Laboratory of Coal Resources and Safe Mining, China University of Mining and Technology (Beijing), Beijing 100083, China*
[4]*School of Mechanics and Civil Engineering, China University of Mining and Technology (Beijing), Beijing 100083, China*

Correspondence should be addressed to Yixin Zhao; zhaoyx@cumtb.edu.cn

Received 12 October 2021; Accepted 24 February 2022; Published 17 March 2022

Academic Editor: Yong-Zheng Wu

Floor failure in deep coal mining above confined aquifers with high-water pressure may induce floor water inrush disasters. Considering the effects of mining stress and nonuniformly distributed water pressure, a mechanical calculation model of the island longwall panel in up-dip mining was established, and the stress distribution and floor failure characteristics were analyzed. The failure characteristics of the floor at NO. 2129 panel in Xingdong coal mine were detected by the borehole televiewer and microseismic monitoring system to validate the theoretical model. The results indicated that the floor failure characteristics along the strike and inclination of the island longwall panel in up-dip mining were "asymmetric inverted saddle-shaped" and "spoon-shaped," respectively. The maximum floor failure depths before and after roof hydraulic fracturing (RHF) were 45.7 m and 29.1 m, respectively. The theoretical calculation results of the maximum depths of floor failure were 45.1 m and 29.9 m, respectively. The theoretical failure characteristics were consistent with those measured on site. The stress concentration magnitude and floor failure depth on the side of the isolated coal pillar were greater than those of other areas, and the water-inrush-prone zones were concentrated on the side of the isolated coal pillar near the intersection of the working face and the roadway. The research results could provide a certain reference for floor failure and water inrush mechanisms under complex geological conditions in deep mining.

1. Introduction

With the increase of operational coal mining depth in China, the surrounding rock in deep mining is prone to large-scale destabilization or dynamic response damage [1]. Increased range of floor failure zone induced by the coupling of high-water pressure and ground stress as well as strong mining disturbances in deep coal mining [2–6]. Water inrushes occur when floor failure zones are connected with high water pressure aquifers in the overlying strata under the floor [7]. Therefore, it is essential to investigate the floor failure characteristics induced by mining and confined aquifers to manage floor water inrush.

Three methods of theoretical analysis, numerical calculation and on-site monitoring are generally applied to investigate the floor failure characteristics. In terms of theoretical analysis, according to the abutment pressure distribution around the working face, a mechanical model of coal seam floor failure under the abutment pressure induced by coal seam mining was established, and the stress distribution and the maximum failure depth of the coal seam floor during mining were also calculated [8–11]. Xue et al. [12]

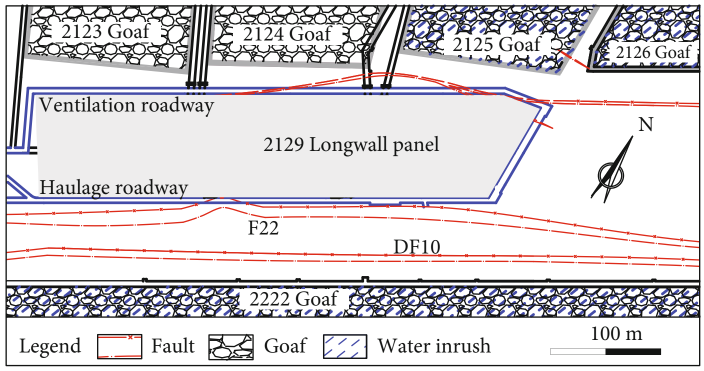

Figure 1: Location of the study area.

established a mechanical calculation model of the floor failure patterns in the strike and dip directions along the working face after mining to study the floor failure characteristics of roof cutting and gob side entry retaining in confined water. The floor rock mass was regarded as a transversely isotropic body and an analytical solution for the floor stress was derived [13–16]. A mechanical model for the floor failure depth in inclined coal seam mining was established to obtain the floor failure characteristics in inclined coal seams as "upper-small-lower-large" [17–19]. Song [19] and Liang et al. [20, 21] established a mechanical model under the combined action of water pressure and mining by considering the actions of high-water pressure and analyzed the stress field and failure characteristics. Ma et al. [5] proposed an improved theoretical model that considered the whole confined aquifer in the floor to analyze the stress distribution and failure zones.

On-site monitoring is a direct and effective method for understanding the extent of damage to the surrounding rock. Currently, the most commonly used field monitoring methods are the borehole water injection, borehole acoustic wave, and borehole imaging as well as borehole strain method [22–25]. In recent years, microseismic monitoring technology has been applied by many scholars to monitor floor damage and water inrush problems. Cheng et al. [26] adopted a microseismic monitoring system to identify the spatial location and formation process of water flow channels. Zhao et al. [27] proposed a set of rock mass seepage channel inversion methods based on microseismic data. Zhou et al. [28] presented a microseismic monitoring analysis method for evaluating potential seepage channels. Ma et al. [5] investigated the evolution characteristics and development pattern of floor failure during high thickness coal seam mining using microseismic monitoring. Cheng et al. [29] examined and calculated the floor disturbance depth through microseismic virtual reality visualization.

Scholars have conducted many investigations and yielded abundant findings in research on the failure characteristics of coal seam floor. Due to the inclination of the coal seam, the failure characteristics of the surrounding rock of the working face are obviously different from those of the horizontal and near horizontal coal seams [2, 30]. In addition, due to the superposition of high stress caused by nearby mined longwall panels, the high-stress concentration zone is formed in the surrounding rock [31]. The large deformation and large-scale failure of floor rock strata are induced by high-stress concentration. Water-conducting channels tend to be formed due to the large-scale and high-intensity stress disturbance induced by repeated mining [24, 32]. The risk of water inrush from coal seam floor in deep island longwall panel increases under deep complex hydrogeological conditions [16]. However, most previous scholars have investigated the floor failure characteristics of longwall mining faces along strikes, and few have addressed the floor failure characteristics of island longwall mining panels in up-dip mining. Therefore, the study of floor failure characteristics of the island longwall panel in up-dip mining above confined water are essential to propose a reasonable method to prevent and control floor water inrush in deep mining.

Therefore, a mechanical model of the island longwall panel in up-dip mining under the combined effect of high-water and mining pressure was established in this paper. The stress distribution in the mining floor rock mass was calculated, and then the floor failure characteristics were obtained based on the Mohr-Coulomb criterion. In addition, the floor failure characteristics before and after RHF were comparatively analyzed, and the results of on-site measurements verified the reasonableness of the theoretical model. The research results could provide a reference for studying the mechanism and prevention of floor water inrush under complex mining geological conditions.

2. Site Descriptions

The Xingdong coal mine is located in the northeastern Hanxing coalfield, Hebei Province, China. Figure 1 shows the general mining layout and the location of the study area. The mining depth of the longwall panel NO. 2129 at Xingdong coal mine is 1027–1125 m and 92.5 m wide, and the lengths of the ventilation and haulage roadways are 416 m and 367 m, respectively. The longwall panel NO. 2129 is an island longwall panel with a goaf on both sides. The ventilation roadway is adjacent to the goafs of longwall panels NOs. 2125–2127, and water inrush occurred in these panels. The ventilation roadway is also adjacent to the longwall panels NO. 2123 and NO. 2124 that do not have floor water inrushes. The average width of coal pillar between ventilation roadway and the goafs is 30 m, which is called narrow

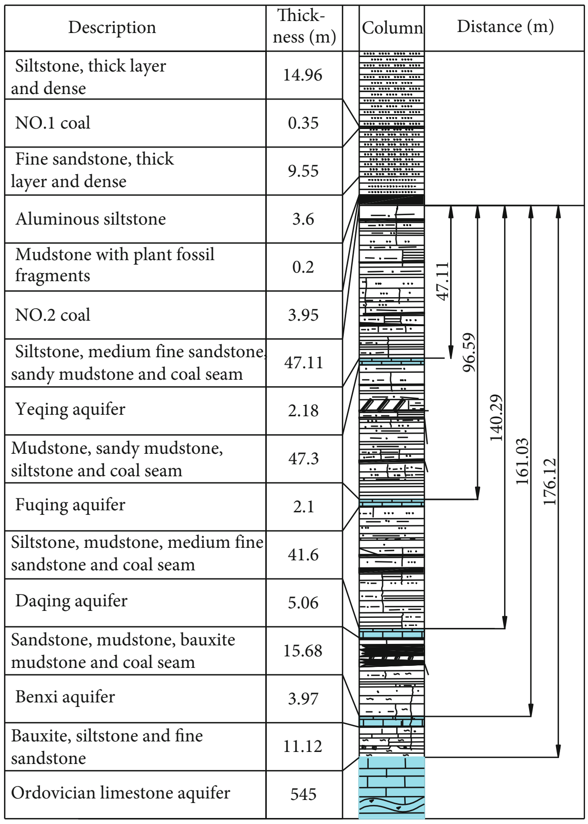

Figure 2: Stratigraphic column of seam, roof, and floor strata.

coal pillar. The haulage roadway is adjacent to longwall panel NO. 2222 with floor water inrush and the F22 and DF10 normal faults. The fault drops are 9–58 m and 8–40 m, respectively. The average width of the coal pillar between the haulage roadway and the goaf of longwall panel NO. 2222 is 74 m, which is called wide coal pillar. The up-dip longwall mining is adopted, and the roof is managed by the caving method. The average thickness of coal seam #2 is 3.95 m, dipping at an angle of 9°–14°, with an average of 11°. According to the stratigraphic column diagram of the Xingdong coal mine (Figure 2), the lithology of the overlying strata is fine sandstone, sandy mudstone, and siltstone, and the floor strata are fine sandstone and sandy mudstone. There are five aquifers in the floor of coal seam #2. The aquifers are the Yeqing, Fuqing, Daqing, Benxi, and Ordovician limestone aquifer, with average distances of 47.11 m, 96.59 m, 140.29 m, 161.03 m, and 176.12 m from the floor of the working face, respectively. The water pressure of the Ordovician limestone aquifer is 10–15 MPa. After regional grouting treatment, water inrush disasters from the coal seam floor in deep mining continue to occur frequently, which seriously restricts the safe production of the Xingdong coal mine.

3. Theoretical Analysis

3.1. Basic Principles. Based on the spatial semi-infinite body theory in elasticity [33] for the semi-infinite body bearing normal load or tangential load (Figure 3), the stress component of any point M (x, y) can be expressed by Equations (1) and (2), respectively.

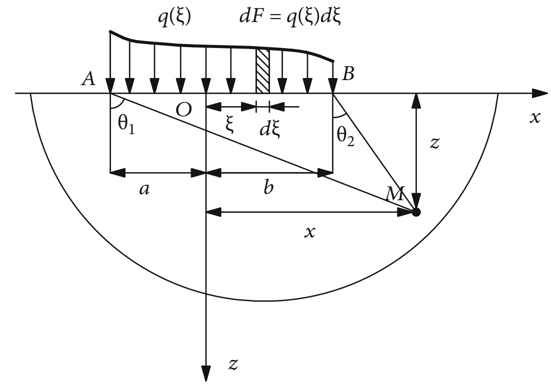

Figure 3: The mechanical models of a semi-infinite solid subjected to distributed load on the boundary.

$$\left.\begin{aligned}\sigma_z &= -\frac{2}{\pi}\int_{-a}^{b}\frac{q(\xi)z^3 d\xi}{\left[z^2+(x-\xi)^2\right]^2},\\ \sigma_x &= -\frac{2}{\pi}\int_{-a}^{b}\frac{q(\xi)z(x-\xi)^2 d\xi}{\left[z^2+(x-\xi)^2\right]^2},\\ \tau_{zx} &= -\frac{2}{\pi}\int_{-a}^{b}\frac{q(\xi)z^2(x-\xi) d\xi}{\left[z^2+(x-\xi)^2\right]^2}.\end{aligned}\right\} \tag{1}$$

$$\left.\begin{aligned}\sigma_{sz} &= -\frac{2}{\pi}\int_{-a}^{b}\frac{q'(\xi)z^2(x-\xi) d\xi}{\left[z^2+(x-\xi)^2\right]^2},\\ \sigma_{sx} &= -\frac{2}{\pi}\int_{-a}^{b}\frac{q'(\xi)(x-\xi)^3 d\xi}{\left[z^2+(x-\xi)^2\right]^2},\\ \tau_{szx} &= -\frac{2}{\pi}\int_{-a}^{b}\frac{q'(\xi)z(x-\xi)^2 d\xi}{\left[z^2+(x-\xi)^2\right]^2}.\end{aligned}\right\} \tag{2}$$

Assuming that

$$\left.\begin{aligned}x-\xi &= \rho\sin\theta,\\ z-\xi &= \rho\cos\theta,\\ d\xi &= \frac{\rho d\theta}{\cos\theta}.\end{aligned}\right\} \tag{3}$$

By substituting Equation (3) into Equations (1) and (2), the polar coordinate expression of vertical stress, horizontal stress, and shear stress can be obtained as shown in Equations (4) and (5).

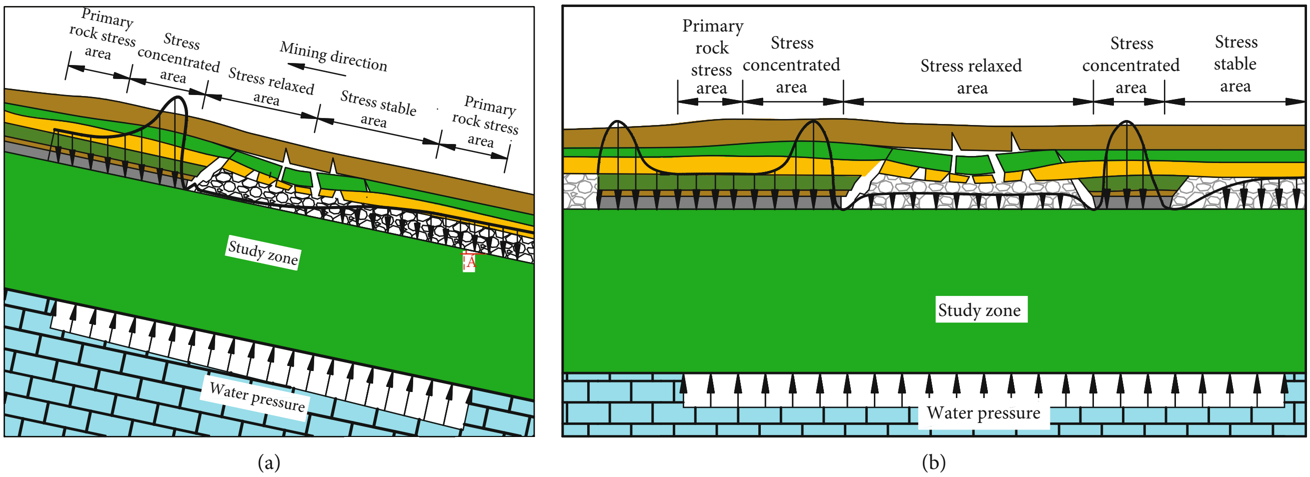

Figure 4: Schematic diagram of load on the floor under periodic weighting: (a) along the inclination; (b) along the strike.

$$\left.\begin{aligned} \sigma_z &= -\frac{2}{\pi}\int_{\theta_1}^{\theta_2} q(\xi)\cos^2\theta d\theta, \\ \sigma_x &= -\frac{2}{\pi}\int_{\theta_1}^{\theta_2} q(\xi)\sin^2\theta d\theta, \\ \tau_{zx} &= -\frac{2}{\pi}\int_{\theta_1}^{\theta_2} q(\xi)\sin\theta\cos\theta d\theta. \end{aligned}\right\} \quad (4)$$

$$\left.\begin{aligned} \sigma_{sz} &= -\frac{2}{\pi}\int_{\theta_1}^{\theta_2} q'(\xi)\sin\theta\cos\theta d\theta, \\ \sigma_{sx} &= -\frac{2}{\pi}\int_{\theta_1}^{\theta_2} q'(\xi)\frac{\sin^3\theta}{\cos\theta} d\theta, \\ \tau_{szx} &= -\frac{2}{\pi}\int_{\theta_1}^{\theta_2} q'(\xi)\sin^2\theta d\theta. \end{aligned}\right\} \quad (5)$$

3.2. Model Establishment. According to statistical analysis of floor water inrush disaster cases in deep mining, floor water inrush is frequently induced by strong mining pressure during periodic weighting [34, 35]. Therefore, it is of significant practical engineering to explore the redistribution of the floor stress and the floor failure range during periodic weighting [36]. Taking the longwall panel NO. 2129 at Xingdong coal mine as an example, the mining stress and the original rock stress are superimposed during the advancement of the working face. Figure 4 shows the general state of the floor rock mass of the island longwall panel in up-dip mining during periodic weighting based on the theory of ground pressure and strata control [37]. α is the dip angle of coal seam in Figure 4(a). Notably, compared with previous work, the dip angle of the mining direction and the goaf on both sides of the working face are considered, thereby enriching the investigation of floor stress and failure characteristics under different mining conditions.

Therefore, a mechanical model for the combination of the hydraulic pressure and mining pressure was constructed, as shown in Figure 5 and according to Figure 4. Both the mining pressure and the water pressure are simplified to a linear distribution in Figure 5. The water pressure is regarded as an uneven external force applied to the bottom of the aquifuge. In addition, the gravity of the floor strata is also considered. As shown in Figures 1 and 4(b), the width of coal pillar between longwall panels NO. 2129 and NO. 2222 is 74 m, and there is little effect of longwall panel NO. 2222 on the floor failure of longwall panel NO. 2129. Therefore, the stress in the mined area of longwall panel NO. 2222 is ignored in this paper.

In addition, the loads caused by the abutment pressure in Figure 5 are simplified to two triangular loads and decomposed accordingly into normal loads (q_1 and q_2) vertical to the floor and tangential loads ($q_1{'}$ and $q_2{'}$) parallel to the floor. The maximum value of them is determined by $(k_1 - 1)\gamma H cos\alpha$. k_1 represents stress concentration coefficient, γ is the average bulk density of the overlying strata, and H denotes burial depth of coal seam. The floor stress in the mined zone is considered a uniformly distributed rectangular load q_0, which is released to the free surface with the magnitude of $-\gamma H cos\alpha$. The stress recovery zone is gradually compacted by the overlying strata of the collapse zone, which is regarded as a triangular distribution load q_3 with the minimum value of $-\gamma H cos\alpha$ and the maximum value of 0. Since floor failure is mainly affected by the stress increment, the component of the stress increment zone parallel to the floor is considered, ignoring the component of the stress in the unloading zone.

In Figure 5, L_1 is the length of the elastic zone caused by advanced abutment pressure, L_2 is the length of the plastic zone caused by advanced abutment pressure, L_3 is the length of the crushing zone induced by advanced abutment pressure, L_4 is the length of the stress recovery zone, L_5 is the

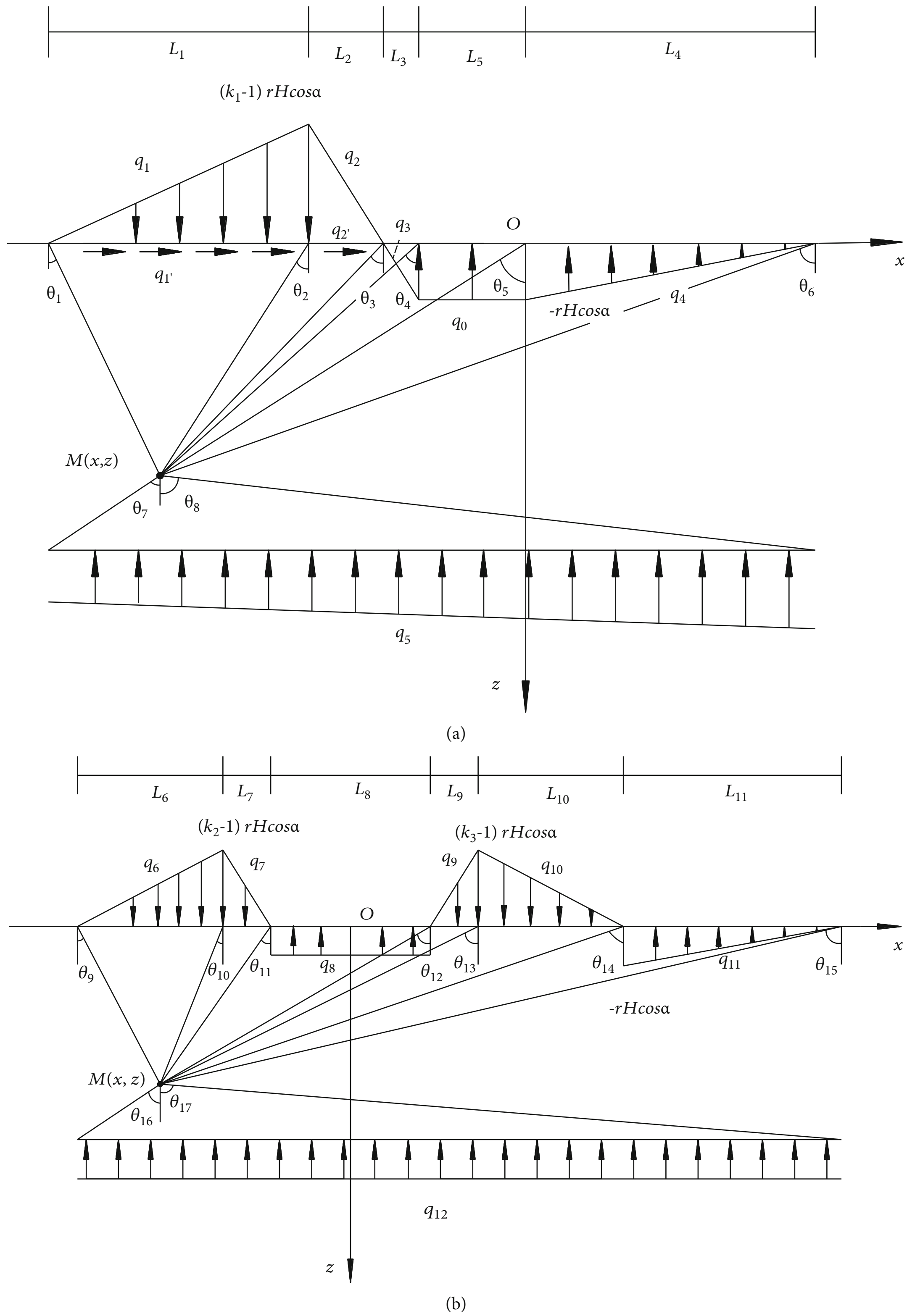

Figure 5: Mechanical models of floor stress in up-dip mining: (a) along the inclination; and (b) along the strike.

periodic weighting interval, L_6 and L_7 are the lengths of the plastic and elastic zones in the coal pillar along the strike, L_8 is the width of the working face, L_9 and L_{10} are the distances from the peak load point of the coal pillar to the boundary on both sides, and L_{11} is the distance of the stress recovery zone on the side of the isolated coal pillar.

The rock strata are assumed to be a continuous, intact, homogeneous, and an isotropic medium in the developed mechanical model, and the rock mass is assumed to apply the linear elastic constitutive model. According to the above assumptions, the stress components of M (x, z) can be derived by substituting the equations for all loads in Figure 5 into the corresponding Equations (4) and (5).

The calculation of stress components resulting from the triangular load q_1 are shown in Equation (6).

$$\left.\begin{aligned}
\sigma_{z1} &= \frac{(k_1-1)\gamma Hz\cos\alpha}{\pi L_1}\left[\tan\theta_1(\theta_1-\theta_2)-\frac{1}{2}\tan\theta_1\sin(2\theta_2)+\sin^2\theta_2\right],\\
\sigma_{x1} &= \frac{(k_1-1)\gamma Hz\cos\alpha}{\pi L_1}\left[\tan\theta_1(\theta_1-\theta_2)+\tan\theta_1\sin\theta_2\cos\theta_2+2\ln\frac{\cos\theta_1}{\cos\theta_2}-\sin^2\theta_2\right],\\
\tau_{zx1} &= \frac{(k_1-1)\gamma Hz\cos\alpha}{\pi L_1}\left[\tan\theta_1\left(\sin^2\theta_1-\sin^2\theta_2\right)+(\theta_2-\theta_1)+\frac{1}{2}(\sin(2\theta_1)-\sin(2\theta_2))\right].
\end{aligned}\right\} \tag{6}$$

As regards the stress components induced by the triangular load q_2, θ_1 and θ_2 in Equation (6) should be replaced by θ_3 and θ_2, respectively, and the corresponding distance by L_2. Similarly, the corresponding stress components for the triangular loads q_3, $q_4, q_6, q_7, q_9, q_{10},$ and q_{11} can be obtained.

The calculation of stress components resulting from the triangular load q_0 are shown in Equation (7).

$$\left.\begin{aligned}
\sigma_{z0} &= \frac{-\gamma H}{\pi}\left(\theta_4-\theta_5+\frac{1}{2}\sin 2\theta_4-\frac{1}{2}\sin 2\theta_5\right),\\
\sigma_{x0} &= \frac{-\gamma H}{\pi}\left[\theta_4-\theta_5-\frac{1}{2}\sin 2\theta_4+\frac{1}{2}\sin 2\theta_5\right],\\
\tau_{zx0} &= \frac{-\gamma H}{\pi}(\cos 2\theta_5-\cos 2\theta_4).
\end{aligned}\right\} \tag{7}$$

For the stress component induced by the rectangular load q_8, θ_4 and θ_5 in Equation (7) should be replaced by θ_{11} and θ_{12}, respectively. Similarly, the corresponding stress component for the rectangular load q_{12} can be obtained.

Equation (8) calculate the stress components caused by the load q_5.

$$\left.\begin{aligned}
\sigma_{z5} &= \frac{(H_z-z)\rho_w g\sin\alpha}{\pi}\left[\tan\theta_7(\theta_8-\theta_7)+\frac{1}{2}\tan\theta_7\sin(2\theta_8)-\sin^2\theta_8\right]\\
&+\frac{P_0}{\pi}\left(\theta_7-\theta_8+\frac{1}{2}\sin 2\theta_7-\frac{1}{2}\sin 2\theta_8\right),\\
\sigma_{x5} &= \frac{(H_z-z)\rho_w g\sin\alpha}{\pi}\left[\tan\theta_7(\theta_8-\theta_7)-\tan\theta_8\sin\theta_7\cos\theta_7-2\ln\frac{\cos\theta_8}{\cos\theta_7}+\sin^2\theta_8\right]\\
&+\frac{P_0}{\pi}\left[\theta_7-\theta_8-\frac{1}{2}\sin 2\theta_7+\frac{1}{2}\sin 2\theta_8\right],\\
\tau_{zx5} &= \frac{(H_z-z)\rho_w g\sin\alpha}{\pi}\left[\tan\theta_7\left(\sin^2\theta_8-\sin^2\theta_7\right)-(\theta_8-\theta_7)-\frac{1}{2}(\sin(2\theta_7)-\sin(2\theta_8))\right]\\
&+\frac{P_0}{\pi}(\cos 2\theta_8-\cos 2\theta_7).
\end{aligned}\right\} \tag{8}$$

The stress components caused by the load $q_1{}'$ can be obtained using Equation (9).

$$\left.\begin{aligned}
\sigma_{sz1} &= \frac{(k_1-1)\gamma Hz\sin\alpha}{\pi L_1}\left[\tan\theta_1\left(\sin^2\theta_2-\sin^2\theta_1\right)+\theta_1-\theta_2-\frac{1}{2}(\sin 2\theta_1-\sin 2\theta_2)\right],\\
\sigma_{sx1} &= \frac{(k_1-1)\gamma Hz\sin\alpha}{\pi L_1}\left[\tan\theta_1\left(\sin^2\theta_1-\sin^2\theta_2-2\ln\frac{\cos\theta_2}{\cos\theta_1}\right)+3(\theta_2-\theta_1)-2(\tan\theta_2-\tan\theta_1)-\frac{1}{2}(\sin 2\theta_2-\sin 2\theta_1)\right],\\
\tau_{szx1} &= \frac{(k_1-1)\gamma Hz\sin\alpha}{\pi L_1}\left\{\sin^2\theta_2-\sin^2\theta_1-2\ln\frac{\cos\theta_1}{\cos\theta_2}-\tan\theta_1\left[\theta_1-\theta_2-\frac{1}{2}(\sin 2\theta_2-\sin 2\theta_1)\right]\right\}.
\end{aligned}\right\} \tag{9}$$

For the stress component induced by the load $q_2{}'$, θ_1 and θ_2 in Equation (9) should be replaced by θ_3 and θ_2, respectively.

In Equations (6)–(9), H is the burial depth of the coal seam, α is the dip angle of the coal seam, k_1 is the concentration coefficient of advance abutment pressure, k_2 and k_3 are the concentration coefficient of abutment pressure on coal pillar at both ends of working face along the strike, γ indicates bulk density of the rock mass, ρ_w is density of confined water, P_0 denotes the hydraulic pressure of the confined aquifer, g is gravitational acceleration, and H_z is the distance between the coal seam floor and confined aquifer.

The angle in the above Equation can be calculated according to Equation (10).

$$\left.\begin{aligned}
\theta_1 &= \arctan\frac{x+L_1+L_2+L_3+L_5}{z},\\
\theta_2 &= \arctan\frac{x+L_2+L_3+L_5}{z},\\
\theta_3 &= \arctan\frac{x+L_3+L_5}{z},\\
\theta_4 &= \arctan\frac{x+L_5}{z},\\
\theta_5 &= \arctan\frac{x}{z},\\
\theta_6 &= \arctan\frac{x-L_4}{z},\\
\theta_7 &= \arctan\frac{x+L_1+L_2+L_3+L_5}{H_z-z},\\
\theta_8 &= \arctan\frac{x-L_4}{H_z-z},\\
\theta_9 &= \arctan\frac{x+L_6+L_7+1/2L_8}{z},\\
\theta_{10} &= \arctan\frac{x+L_7+1/2L_8}{z},\\
\theta_{11} &= \arctan\frac{x+1/2L_8}{z},\\
\theta_{12} &= \arctan\frac{x-1/2L_8}{z},\\
\theta_{13} &= \arctan\frac{x-1/2L_8-L_9}{z},\\
\theta_{14} &= \arctan\frac{x-1/2L_8-L_9-L_{10}}{z},\\
\theta_{15} &= \arctan\frac{x-1/2L_8-L_9-L_{10}-L_{11}}{z},\\
\theta_{16} &= \arctan\frac{x+L_6+L_7+1/2L_8}{H_z-z},\\
\theta_{17} &= \arctan\frac{x-1/2L_8-L_9-L_{10}-L_{11}}{H_z-z}.
\end{aligned}\right\} \tag{10}$$

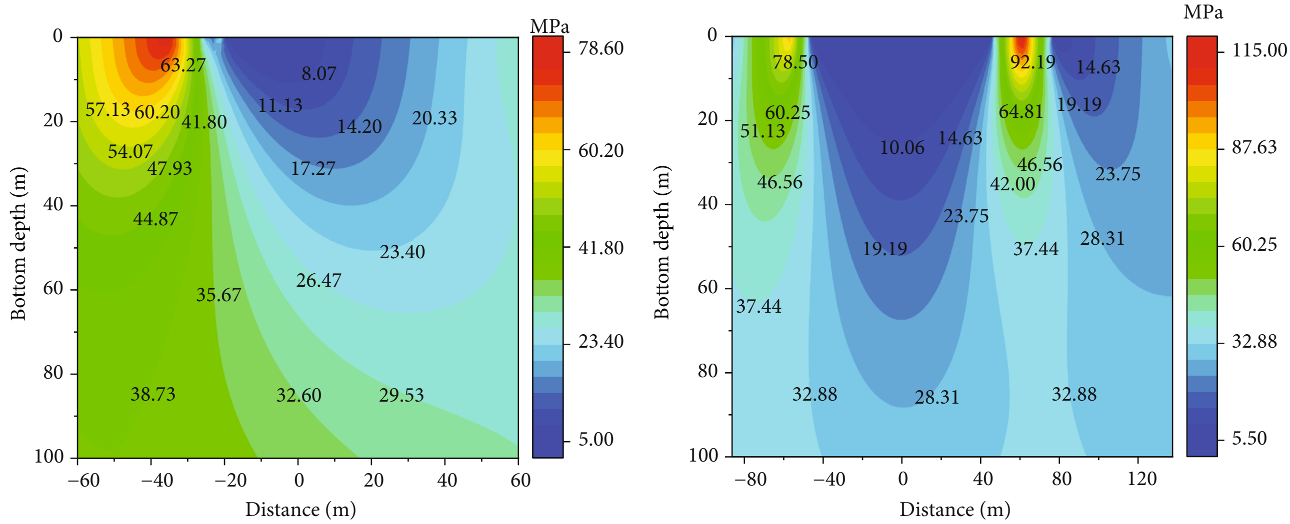

(a) (b)

Figure 6: The isoline of the vertical stress: (a) along the inclination; and (b) along the strike.

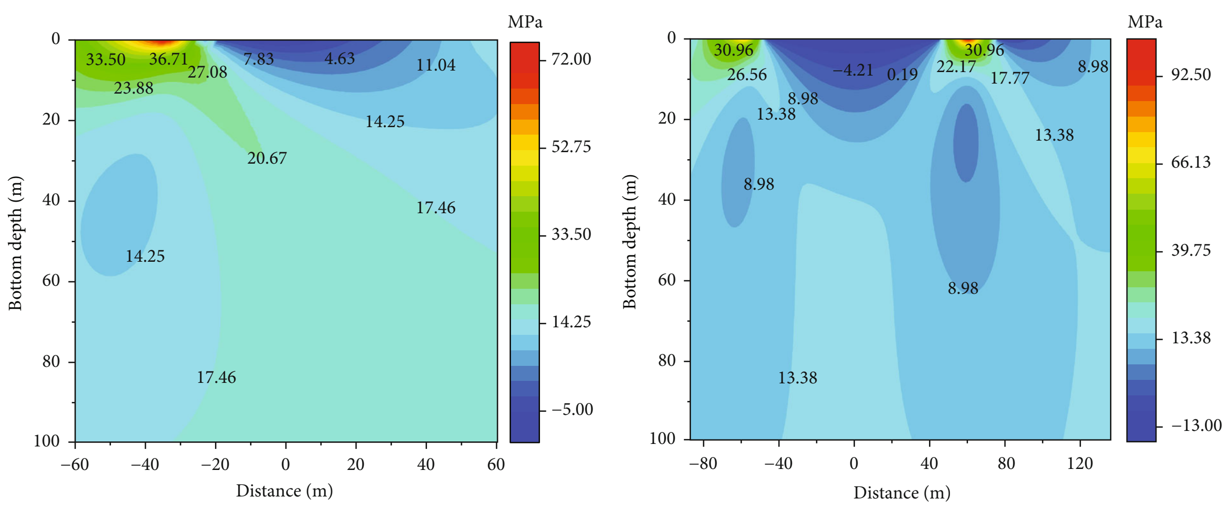

(a) (b)

Figure 7: The isoline of the horizontal stress: (a) along the inclination; and (b) along the strike.

3.3. Redistribution Law of Floor Stress. The total stress of M (x, z) in the floor can be obtained by summing the stress components induced by the abutment pressure, water pressure, and ground stress. According to the principle of stress superposition in elasticity theory, the vertical, horizontal, and shear stress at a point M (x, z) in the floor when the periodic weighting can be calculated as follows.

$$\left.\begin{aligned}\sigma_z &= \sigma_{z1}+\sigma_{sz1}+\sigma_{z2}+\sigma_{sz2}+\sigma_{z3}+\sigma_{z0}+\sigma_{z4}+\sigma_{z5}+\gamma(H+z),\\ \sigma_x &= \sigma_{x1}+\sigma_{sx1}+\sigma_{x2}+\sigma_{sx2}+\sigma_{x3}+\sigma_{x0}+\sigma_{x4}+\sigma_{x5}+\lambda\gamma(H+z),\\ \tau_{zx} &= \tau_{zx1}+\tau_{szx1}+\tau_{zx2}+\tau_{szx2}+\tau_{zx3}+\tau_{zx0}+\tau_{zx4}+\tau_{zx5}.\end{aligned}\right\} \tag{11}$$

$$\left.\begin{aligned}\sigma_x &= \sigma_{x6}+\sigma_{x7}+\sigma_{x8}+\sigma_{x9}+\sigma_{x10}+\sigma_{x11}+\sigma_{x12}+\gamma(H+z),\\ \sigma_z &= \sigma_{z6}+\sigma_{z7}+\sigma_{z8}+\sigma_{z9}+\sigma_{z10}+\sigma_{z11}+\sigma_{z12}+\lambda\gamma(H+z),\\ \tau_{zx} &= \tau_{zx6}+\tau_{szx7}+\tau_{zx8}+\tau_{szx9}+\tau_{zx10}+\tau_{zx11}+\tau_{zx12}.\end{aligned}\right\} \tag{12}$$

Where Equation (11) is the total stress component of the floor stress along the inclination and Equation (12) is the total stress component of the floor stress along the strike.

According to the site investigation, it is found that the roof of the coal seam #2 at Xingdong coal mine is difficult to cave in time, with a larger overhanging roof distance, which leads to a larger weighting interval, and the concentration degree of nearby abutment pressure will increase,

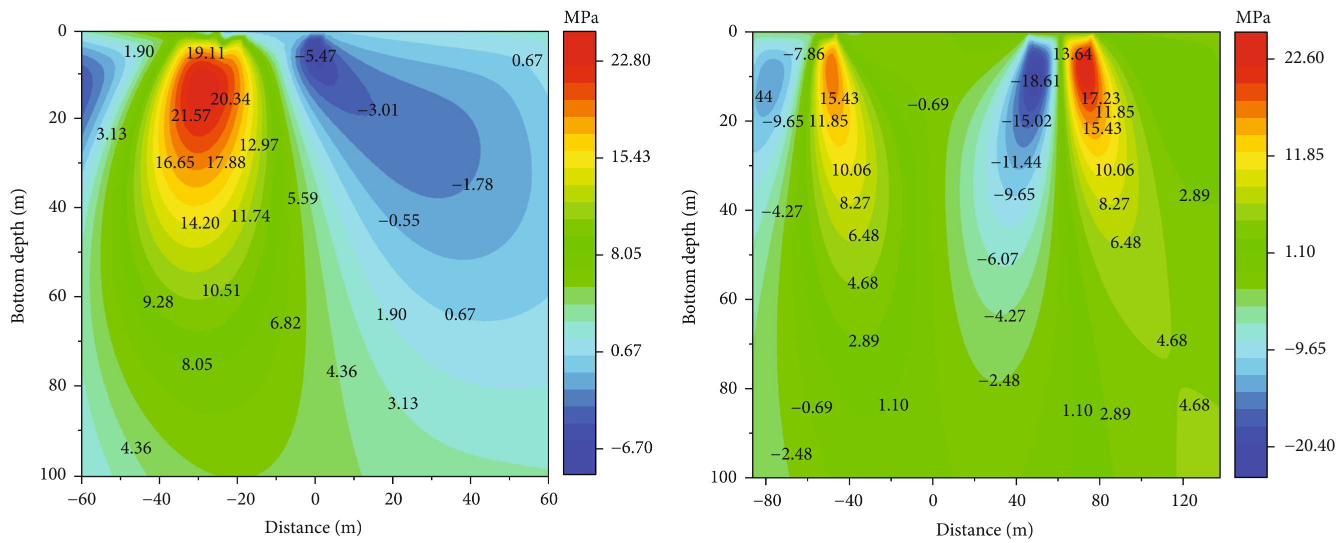

(a)

(b)

FIGURE 8: The isoline of the shear stress: (a) along the inclination; and (b) along the strike.

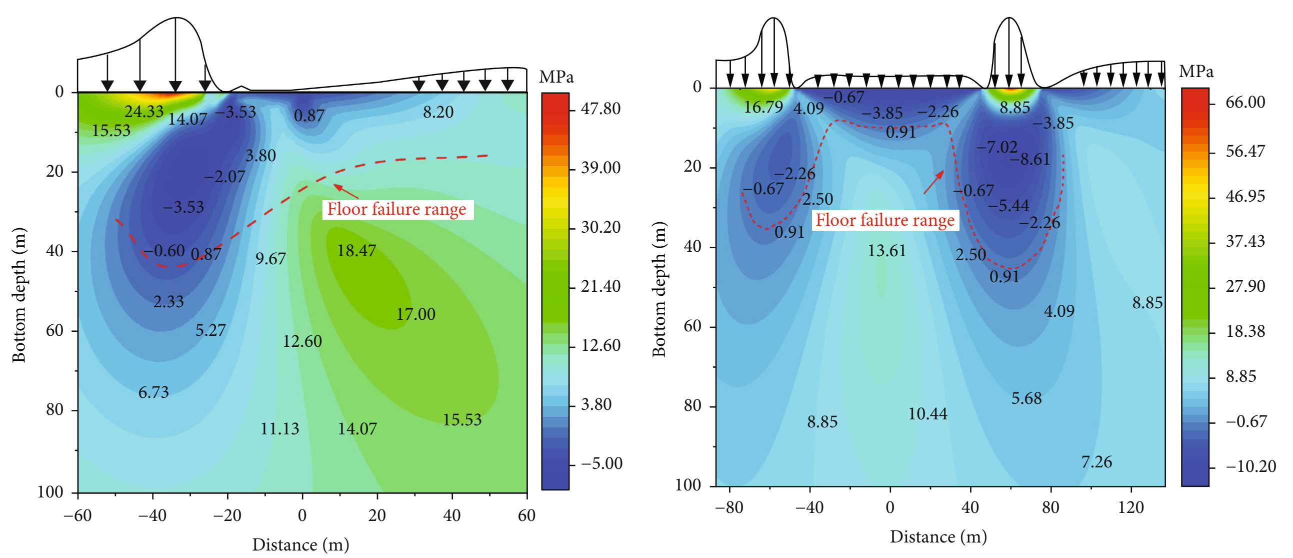

(a)

(b)

FIGURE 9: The floor failure zones: (a) along the inclination; and (b) along the strike.

especially when the stress concentration factor below the isolated coal pillar will be greater.

According to the geological survey report and field monitoring data of the longwall panel NO. 2129 at Xingdong coal mine, $L_1 = 50$ m, $L_2 = 10$ m, $L_3 = 5$ m, $L_4 = 60$ m, $L_5 = 20$ m, $L_6 = 30$ m, $L_7 = 10$ m, $L_8 = 92.5$ m, $L_9 = 15$ m, $L_{10} = 15$ m, $L_{11} = 60$ m, $k_1 = 3.5$, $k_2 = 2.5$, $k_2 = 3.5$, $P_0 = 10$ MPa, $\gamma = 25$ kN/m^3, $\rho_w = 1000$ kg/m^3, $g = 10$ N/kg, $H_z = 180$ m, $\alpha = 11^\circ$, and $H = 1000$ m. Substituting the above parameters into Equation (12), the floor stress component isoline under the combination of mining stress and water pressure can be obtained by using Python programming.

The vertical stress concentration is observed in the floor underlying the advanced abutment pressure zone along the inclination (Figure 6(a)). The maximum value of stress concentration is near the elastic-plastic bond of the coal seam, that is, near the peak of the advanced abutment pressure. The stress unloading zone is mainly located in the mined area, as well as the maximum degree of stress relief within the weighting interval (L_5). Along the strike direction, the vertical stress concentration in the floor below the isolated coal pillar due to the overhanging roof of the coal seam after mining is greater than that in other areas (Figure 6(b)).

Figure 7 shows that the variation of the horizontal stress is consistent with the distribution of the vertical stress. The degree of concentration and unloading and influence range of horizontal stress are significantly smaller than those of vertical stress. The influence range of horizontal stress

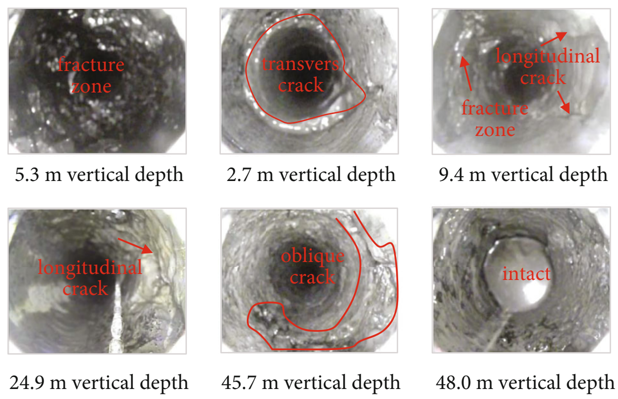

Figure 10: Floor failure depth measurement without RHF.

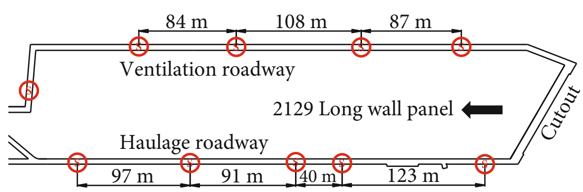

Figure 11: Layout of microseismic monitoring stations.

decreases rapidly as the depth increases. However, tensile stress is generated in the unloading zone along the inclination and along the strike.

The shear stress in the mined zone and the coal wall approximately presents a positive and a negative shear force couple along the inclination, forming a sharp shear stress variation zone (Figure 8(a)). The floor strata of this area are prone to compression shear or tension shear deformation damage, which is consistent with the vulnerable location around the stope on site. The maximum shear stress appears at the coal wall zones affected by advanced abutment pressure. The shear stress along the strike is also a positive and negative shear couple in the floor strata under the mined zones and the coal pillars, while the maximum shear stress appears on the side of the isolated coal pillar (Figure 8(b)).

3.4. Failure Characteristics of Floor Strata. Based on the Mohr-Coulomb failure criterion [38], the rock mass will be damaged when the maximum shear stress at a point in the floor rock strata equals or exceeds its shear strength. Equation (13) calculates the condition for shear failure to occur in the floor [17].

$$\frac{(\sigma_z + \sigma_x/2)\tan\varphi + c}{\sqrt{1+\tan^2\varphi}} \le \tau_{\max}, \tag{13}$$

where the maximum shear stress $\tau_{\max}$ is calculated as follows:

$$\tau_{\max} = \sqrt{{\tau_z}^2 + \left(\frac{\sigma_z - \sigma_x}{2}\right)^2}, \tag{14}$$

Substituting Equation (15) into Equation (13), we can construct the floor failure criterion Equation (15).

$$\mathrm{F}(x,z) = \frac{(\sigma_z + \sigma_x/2)\tan\varphi + c}{\sqrt{1+\tan^2\varphi}} - \sqrt{{\tau_z}^2 + \left(\frac{\sigma_z - \sigma_x}{2}\right)^2}, \tag{15}$$

where c and φ denote the cohesion and internal friction angle of the floor rock mass, respectively.

When $F(x, z) \le 0$, the floor strata fails. According to the laboratory test results, the weighted average method is used to determine the average friction angle $\varphi = 35.4^\circ$ and cohesive force $c = 4$ MPa and substituting into Equation (15). The $F(x, z)$ contour is obtained by using Python programming to calculate the theoretical floor failure characteristics of the island longwall panel in up-dip mining above confined aquifer during periodic weighting, as shown in Figure 9.

As seen in Figure 9(a), the floor failure characteristic along the inclination is spoon-shaped. Under the effect of advanced abutment pressure and high-water pressure, the maximum depth of floor failure reaches 43.2 m. The location of the maximum failure depth is in the floor of the stress concentration area of the coal wall in front of the working face. Tensile failure occurs within 10 m below the mined zone, resulting in floor heave. Shear failure occurs in the range of 10 m–43.2 m below the mined zone. With the increase of the floor failure depth, high-pressure confined water can easily rise from the shear failure zone to the bottom of the aquifuge, resulting in water inrush accidents.

Figure 9(b) shows that the floor failure range along the strike has an "asymmetric saddle shape." The maximum failure depth of the floor is 45.1 m, which is located on the side of the isolated coal pillar. Due to the abutment pressure of the two working faces on the side of the isolated coal pillar, the stress concentration factor increases, resulting in a large floor failure depth, and floor water inrush is likely to occur.

4. In Situ Measurement

To verify the feasibility of theoretical analysis, the borehole televiewer (BTV) and microseismic monitoring were used to detect the floor failure characteristics of the island longwall panel NO. 2129 before and after RHF.

4.1. Results of Borehole Televiewer Detection before RHF. The BTV is an effective means to visually analyze the failure range of the surrounding rock [39]. The evolution of internal fractures in the surrounding rock can be observed by a digital borehole television [40], which helps to determine the depth and range of fracture development induced by mining [41]. Therefore, to investigate the floor borehole, we examined the distribution of fractures in the sidewalls of the borehole by using a BTV (Figure 10). A CXK12(A) of BTV is equipped with a wide-viewing panoramic color camera with 1.34 million pixels, which can resolve cracks of 0.1 mm. According to the detection results, the floor fracture development demarcation point can be observed. The BTV image shows that the cracks are densely developed 0–45.7 m away from the borehole wall (Figure 10), but no cracks exceed this

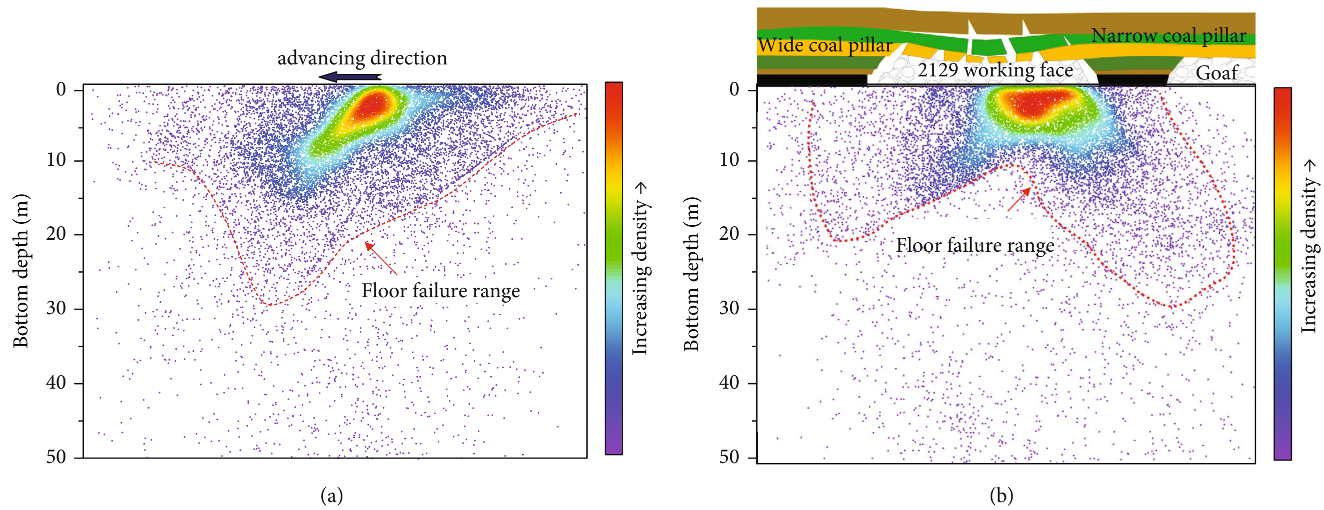

Figure 12: Microseismic monitoring results of floor failure range after RHF: (a) along the inclination; and (b) along the strike.

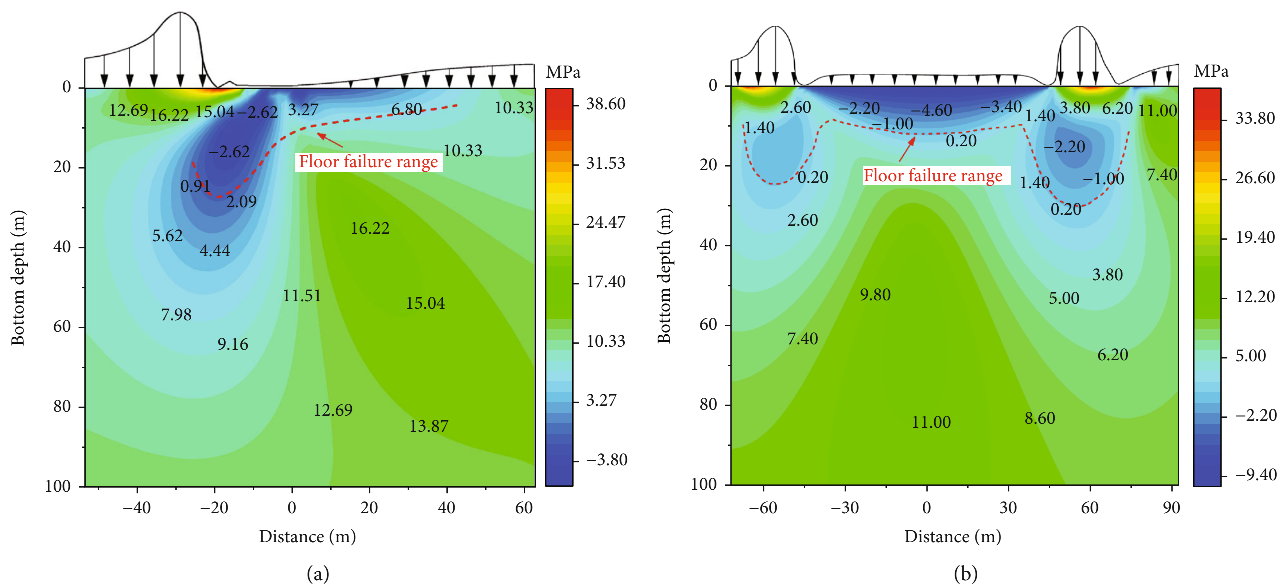

Figure 13: Theoretical calculation results of floor failure range after RHF: (a) along the inclination; and (b) along the strike.

area. The mining failure depth of the floor is 45.7 m, and the mining failure fractures will be connected with the Yeqing aquifer (47.1 m away from the coal seam floor on average).

According to theoretical calculations, the maximum failure depth of the floor before roof fracturing in the longwall panel NO. 2129 of the Xingdong coal mine is 45.1 m. The theoretical calculation results are consistent with the measurements taken from the site, indicating that the establishment of a mechanical model can accurately predict the floor failure depth. Under the superposition of high-water pressure and mining stress, the floor failure zone under the isolated coal pillar on one side of the island longwall panel easily connects with the Yeqing aquifer. The Yeqing aquifer is connected with Ordovician limestone through longitudinal water conducting fissures or structures, which can easily cause floor water inrush. Therefore, RHF is performed on site to break the hard roof of the working face and isolated coal pillar in advance to reduce the mining pressure and decrease the floor failure depth.

4.2. Results of Microseismic Monitoring after RHF. The formation process of the water conducting channels and the damage degree of the surrounding rock can be determined by using microseismic events [5, 26–28]. To monitor the development range of mining fractures in the floor after RHF, a microseismic monitoring system was installed in the roadway of the longwall panel NO. 2129 (Figure 11). A total of 10 microseismic sensors were installed in the ventilation roadway and haulage roadway, and the microseismic events were transmitted to the data processing center in real time through the collection substation. The sensors are ESG (Engineering Seismology Group) detectors. Three collection substations were installed with a sampling frequency of 5 kHz.

Figure 12 shows the distribution of microseismic monitoring events after roof fracturing. The abscissa is the position of the working face, and the ordinate is the depth of the coal seam floor. Figure 12(a) shows that the microseismic events in the floor are concentrated within 15 m of the floor, indicating that the shallow floor rock mass is first damaged under the action of mining stress. With increasing floor depth, the density of floor microseismic events decreases gradually. The distribution shape of the microseismic event density in the floor is a "spoon-shaped" along the advancing direction of the working face. According to the microseismic monitoring results, the maximum mining failure depth is 28.6 m (Figure 12(a)). Microseismic events are mainly concentrated on the floor of the goaf at the side of the isolated coal pillar along the strike. The floor failure range is also an "asymmetric inverted saddle-shaped," and the maximum failure depth is 29.1 m, located on the side of the isolated coal pillar (Figure 12(b)). No water inrush accident occurred during mining. The maximum floor failure depth of the working face along the strike or the inclined direction decreased significantly after RHF. The hard rock strata fractured and collapsed reducing the stress concentration in the isolated coal pillar and working face after hydraulic fracturing of roof.

The relevant parameters after RHF in the island longwall panel NO. 2129 are substituted into the theoretical model to obtain the corresponding floor failure characteristics. According to the on-site monitoring results, the measured values of various parameters after roof fracturing are $L_1 = 35\,\mathrm{m}$, $L_2 = 7\,\mathrm{m}$, $L_3 = 3\,\mathrm{m}$, $L_4 = 60\,\mathrm{m}$, $L_5 = 10\,\mathrm{m}$, $L_6 = 20\,\mathrm{m}$, $L_7 = 5\,\mathrm{m}$, $L_8 = 92.5\,\mathrm{m}$, $L_9 = 15\,\mathrm{m}$, $L_{10} = 15\,\mathrm{m}$, $L_{11} = 15\,\mathrm{m}$, $k_1 = 2.5$, $k_2 = 1.5$, $k_2 = 1.5$, $P_0 = 10\,\mathrm{MPa}$, $\gamma = 25\,\mathrm{kN/m^3}$, $\rho_w = 1000\,\mathrm{kg/m^3}$, $g = 10\,\mathrm{N/kg}$, $H_z = 180\,\mathrm{m}$, $\alpha = 11^\circ$, $H = 1000\,\mathrm{m}$, $\varphi = 35.4^\circ$, and $c = 4\,\mathrm{MPa}$. Substituting the above parameters into Equation (15), the floor failure depths along the inclination and the strike are 25.6 m and 29.9 m, respectively. The theoretical prediction values of the maximum failure depth and failure characteristics after roof fracturing are consistent with the microseismic monitoring results (Figure 13), indicating the feasibility and applicability of the theoretical model. The theoretical calculation results can provide a reference for the failure depth of the floor before mining.

5. Conclusion

A two-dimensional hydraulic calculation model was proposed to analyze the floor failure characteristics in deep island longwall panel using the up-dip mining method. The effects of mining stress and confined water pressure in the calculation model was considered in this paper. The floor failure depth and failure characteristics before and after RHF were discussed in association with the BTV and microseismic monitoring system, verifying the theoretical model. The main conclusions in this paper are as follows:

(1) The vertical stress in the floor is principally concentrated in the rock strata advanced the working face and under the coal pillar. The degree of concentration and unloading of the vertical stress are significantly greater than those of the horizontal stress. The shear stress distribution is approximately the coupling of positive and negative. Along the working face advance direction, the local stress concentration on the side of the coal pillar, and stress release on the side of the mined zone are observed. The stress concentration under the coal pillar is greater than that in other zones along the strike due to the stress superposition on the coal pillar

(2) The maximum floor failure depth before RHF is theoretically calculated to be 45.1 m, which is consistent with the 45.7 m depth detected by BTV. The theoretical calculation result of the floor failure depth after roof fracturing is 29.9 m, which is approximately equal to the microseismic monitoring result of 29.1 m

(3) The theoretical failure characteristics of the island longwall panel in up-dip mining along the inclination and the strike are approximately "spoon-shaped" and "asymmetric inverted saddle-shaped," respectively. The theoretical calculation of the floor failure characteristics and failure depth before and after roof fracturing are consistent with the measured on-site results, which verifies the rationality of the theoretical model

Data Availability

The data that support the findings of this study are available from the corresponding author upon reasonable request.

Conflicts of Interest

The authors declare that they have no known competing financial interests or personal relationships that could have appeared to influence the work reported in this paper.

Acknowledgments

This work was supported by the National Natural Science Foundation of China (Nos. U1910206, 51874312, and 51861145403), the Science and Technology Plant Project of Inner Mongolia Autonomous Region (No. 2019GG140), the Major Scientific and Technological Innovation Project of Shandong Province (No. 2019SDZY01), the Beijing Municipal Natural Science Foundation (No. 8184082), the Scientific and Technological Support Project of Guizhou Province: Qiankehe Support (2021) general 353, and the Scientific and Technological Support Project of Guizhou Province: Qiankehe Support (2021) general 514.

References

[1] C. Li, J. Zuo, Y. Shi et al., "Deformation and fracture at floor area and the correlation with main roof breakage in deep longwall mining," *Natural Hazards*, vol. 107, no. 2, pp. 1731–1755, 2021.

[2] W. Liu, D. Mu, X. Xie, L. Yang, and D. Wang, "Sensitivity analysis of the main factors controlling floor failure depth and a

risk evaluation of floor water inrush for an inclined coal seam," *Mine Water and the Environment*, vol. 37, no. 3, pp. 636–648, 2018.

[3] A. Vervoort, "Various phases in surface movements linked to deep coal longwall mining: from start-up till the period after closure.," *International Journal of Coal Science and Technology*, vol. 8, no. 3, pp. 412–426, 2021.

[4] S. Dong, H. Wang, X. Guo, and Z. Zhou, "Characteristics of water hazards in China's coal mines: a review," *Mine Water and the Environment*, vol. 40, no. 2, pp. 325–333, 2021.

[5] K. Ma, X. Y. Sun, C. A. Tang, F. Z. Yuan, S. J. Wang, and T. Chen, "Floor water inrush analysis based on mechanical failure characters and microseismic monitoring," *Tunnelling and Underground Space Technology*, vol. 108, article 103698, 2021.

[6] S. Dong, W. Zhang, W. Zhou et al., "Discussion on some topical issues of water prevention and control in coal mines," *Mine Water and the Environment*, vol. 40, no. 2, pp. 547–552, 2021.

[7] J. Zhang, "Investigations of water inrushes from aquifers under coal seams," *International Journal of Rock Mechanics and Mining Sciences*, vol. 42, no. 3, pp. 350–360, 2005.

[8] S. Zhu, Z. Jiang, K. Zhou, G. Peng, and C. Yang, "The characteristics of deformation and failure of coal seam floor due to mining in Xinmi coal field in China," *Bulletin of Engineering Geology and the Environment*, vol. 73, no. 4, pp. 1151–1163, 2014.

[9] S. Liu, W. Liu, and J. Shen, "Stress evolution law and failure characteristics of mining floor rock mass above confined water," *KSCE Journal of Civil Engineering*, vol. 21, no. 7, pp. 2665–2672, 2017.

[10] X. Meng, C. Xu, Z. Gao, and X. Wang, "Stress distribution and damage mechanism of mining floor," *Journal of China Coal Society*, vol. 35, no. 11, pp. 1832–1836, 2010.

[11] H. Zhang and L. Wang, "Journal of mining and safety engineering," *Journal of Mining and Safety Engineering*, vol. 28, no. 2, 2011.

[12] W. Xue et al., "Theoretical analysis and field measurement of floor failure in gob side entry of cutting roof in confined water mine area," *Journal of China Coal Society*, pp. 1–9, 2020.

[13] R. Yang, Y. Zhu, Y. Li, and W. Li, "Stress distribution and damage characteristics of roadway floor in layered rock mass," *Journal of China University of Mining and Technology*, vol. 49, no. 4, 2020.

[14] R. Yang, Y. Zhu, Y. Li, W. Li, and B. Xiao, "Stability analysis and control strategy of weakly cemented layered floor in mining affected roadway," *Journal China Coal Soc.*, vol. 45, no. 7, pp. 2667–2680, 2020.

[15] H. Lu, D. Yao, Y. Hu, and J. Sun, "Elasticity solution for failure depth of mining floor under water pressure," *Journal of Mining & Safety Engineering*, vol. 34, no. 3, pp. 452–458, 2017.

[16] C. Zhao, "Microseismic test and numerical simulation analysis of floor failure depth of isolated coal mining face," *Coal Geology and Exploration*, vol. 47, no. 4, pp. 110–116, 2019.

[17] J. Sun, L. Wang, and G. Zhao, "Stress distribution and failure characteristics for workface floor of a tilted coal seam," *KSCE Journal of Civil Engineering*, vol. 23, no. 9, pp. 3793–3806, 2019.

[18] W. Liu, D. Mu, X. Xie, W. Zhang, and D. Yuan, "Rules of stress distributions and failure characteristics in inclined coal seam floor due to mining," *Journal of Mining & Safety Engineering*, vol. 35, no. 4, pp. 756–764, 2018.

[19] W. Liu, J. Shen, and H. Jia, "Mining-induced stress evolution law and failure characteristics of floor in deep mine," *Journal of Mining & Safety Engineering*, vol. 33, no. 6, pp. 1045–1051, 2016.

[20] W. Song, Z. Liang, and C. Zhao, "Mechanical failure characteristics of mining floor along working face inclination above confined water," *Chinese Journal of Rock Mechanics and Engineering*, vol. 37, no. 9, pp. 2131–2143, 2018.

[21] Z. Liang, W. Song, and W. Liu, "Theoretical models for simulating the failure range and stability of inclined floor strata induced by mining and hydraulic pressure," *International Journal of Rock Mechanics and Mining Sciences*, vol. 132, article 104382, 2020.

[22] J. Chen, X. Zuqiang, and L. Hui, "Failure characteristics of floor under predssure inclined and extra thick coal seam in full-mechanized top coal caving faces," *Chinese Journal of Rock Mechanics and Engineering*, vol. 35, pp. 3018–3023, 2016.

[23] Y. Chen, S. Zhu, Z. Wang, and F. Li, "Deformation and failure of floor in mine with soft coal, soft floor, hard roof and varying thicknesses of coal seam," *Engineering Failure Analysis*, vol. 115, article 104653, 2020.

[24] H. Liu, P. Wang, W. Zhang, Q. Liu, and L. Su, "Comprehensive measurement of the deformation and failure of floor rocks: a case study of the Xinglongzhuang coal mine," *Geofluids*, vol. 2020, 14 pages, 2020.

[25] Y. Hu, W. Li, S. Liu, and Q. Wang, "Prediction of floor failure depth in deep coal mines by regression analysis of the multifactor influence index," *Mine Water and the Environment*, vol. 40, no. 2, pp. 497–509, 2021.

[26] G. Cheng, C. Tang, L. Li, X. Chuai, T. Yang, and L. Wei, "Micro-fracture precursors of water flow channels induced by coal mining: a case study," *Mine Water and the Environment*, vol. 40, no. 2, pp. 398–414, 2021.

[27] Y. Zhao, T. Yang, P. Zhang, H. Xu, and S. Wang, "Inversion of seepage channels based on mining-induced microseismic data," *International Journal of Rock Mechanics and Mining Sciences*, vol. 126, article 104180, 2020.

[28] J. R. Zhou, T. H. Yang, P. H. Zhang, T. Xu, and J. Wei, "Formation process and mechanism of seepage channels around grout curtain from microseismic monitoring: a case study of Zhangmatun iron mine, China," *Engineering Geology*, vol. 226, pp. 301–315, 2017.

[29] A. P. Cheng, Y. T. Gao, C. Liu, and J. F. Chai, "Microseismic monitoring and numerical simulation research of floor failure depth in extra-thick coal seam," *Advances in Materials Research*, vol. 881-883, pp. 1799–1804, 2014.

[30] S. Luo, Y. Wu, H. Wang, and P. Xie, "Asymmetric failure pattern and slip characteristics of floor of longwall face in steeply dipping seam mining," *Journal of China Coal Society*, vol. 43, no. 8, pp. 2155–2161, 2018.

[31] Y. Jiang, H. Wang, S. Xue, Y. Zhao, J. Zhu, and X. Pang, "Assessment and mitigation of coal bump risk during extraction of an island longwall panel," *International Journal of Coal Geology*, vol. 95, pp. 20–33, 2012.

[32] S. Zhu, Y. Feng, F. Jiang, and J. Liu, "Mechanism and risk assessment of overall-instability-induced rockbursts in deep island longwall panels," *International Journal of Rock Mechanics and Mining Sciences*, vol. 106, pp. 342–349, 2018.

[33] Z. Xu, *Concise Tutorial on Elasticity*, Higher Education Press, Beijing, China, 2002.

[34] E. Eberhardt, B. Stimpson, and D. Stead, "Effects of grain size on the initiation and propagation thresholds of stress-induced brittle fractures," *Rock Mechanics and Rock Engineering*, vol. 32, no. 2, pp. 81–99, 1999.

[35] J. Guo, L. Ma, and D. Zhang, "Management and utilization of high-pressure floor-confined water in deep coal mines," *Mine Water and the Environment*, vol. 38, no. 4, pp. 780–797, 2019.

[36] J. Sun, Y. Hu, and G. Zhao, "Relationship between water inrush from coal seam floors and main roof weighting," *International Journal of Mining Science and Technology*, vol. 27, no. 5, pp. 873–881, 2017.

[37] X. J. Qian and S. P. Minggao, *Mining Pressure and Strata Control*, China University of mining and Technology Press, Xuzhou, China, 2010.

[38] Z. Wen, S. Jing, Y. Jiang et al., "Study of the fracture law of overlying strata under water based on the flow- stress-damage model," *Geofluids*, vol. 2019, Article ID 3161852, 12 pages, 2019.

[39] K. Aoyagi and E. Ishii, "A method for estimating the highest potential hydraulic conductivity in the excavation damaged zone in mudstone," *Rock Mechanics and Rock Engineering*, vol. 52, no. 2, pp. 385–401, 2019.

[40] S. J. Li, X. T. Feng, C. Y. Wang, and J. A. Hudson, "ISRM suggested method for rock fractures observations using a borehole digital optical televiewer," *Rock Mechanics and Rock Engineering*, vol. 46, no. 3, pp. 635–644, 2013.

[41] Y. M. Zhao, X. T. Feng, Q. Jiang et al., "Large deformation control of deep roadways in fractured hard rock based on cracking-restraint method," *Rock Mechanics and Rock Engineering*, vol. 54, no. 5, pp. 2559–2580, 2021.

Hindawi
Geofluids
Volume 2022, Article ID 2090809, 10 pages
https://doi.org/10.1155/2022/2090809

Research Article

A Coal Bump Risk Assessment and Prediction Model Based on Multiparameter Indices

Tao Luo [1], Gangwei Fan [1,2], Shizhong Zhang [1], Shang Ren [1], Yibo Fan [1] and Ruiliang Shen [1]

[1] School of Mines, China University of Mining and Technology, No. 1 University Road, Xuzhou, Jiangsu 221116, China
[2] State Key Laboratory of Coal Resource and Safe Mining, China University of Mining and Technology, No. 1 University Road, Xuzhou, Jiangsu 221116, China

Correspondence should be addressed to Gangwei Fan; fangw@cumt.edu.cn

Received 10 October 2021; Accepted 24 February 2022; Published 16 March 2022

Academic Editor: Zhijie Wen

Coal bump, a common dynamic disaster in mining of deep coal resources, its assessing and predicting is an important component in safety management. This paper presents a model to assess and predict coal bump risk based on multiparameter indices. A new energy accumulation index S was proposed by considering acoustic emission and electromagnetic emission signal characteristics in mine shocks. Combined with indices E (energy of microseisms) and N (frequency of microseisms) of microseismic monitoring, a static and dynamic coal bump risk assessment and prediction model was established. We studied coal bump events that occurred during extraction in 311305 working face of Bayangale coal mine in Inner Mongolia, China. We obtained the acoustic emission and electromagnetic emission signal distribution and change law, using principal component analysis method and density ellipse to establish the index S. A typical precursory of coal bumps is that AE and EME strength has obvious fluctuation period of 3-4 days, index S showing an obvious decreasing trend, while the time-series curve of the microseismic energy is relatively stable, and the vibration frequency curve has a significant upward trend. After predict the potential coal bump risk and its area of occurrence, large diameter drilling (Φ150 mm) on-site was used to relief pressure concertation in coal seam and roof. The results demonstrate that this model based on multiparameter indices is capable of quantitatively prewarning rock burst risk.

1. Introduction

Coal bumps refers to the dynamic disaster of the instantaneous release of elastic energy accumulated in the coal and rock mass due to the severe instability of coal rock. As an extremely destructive hazard, coal bump can cause roadway deformation, support damage, and even casualties [1–3]. With the increasing demand for coal in China's economic development, the scale and strength of coal mining have improved significantly, and the mining depth has gradually increased. The research shows that the mining depth of coal mines in China extends to the deep at a speed of nearly 20 m per year [4–6]. With the increase of coal mining strength and average mining depth, the coal rock dynamic behavior induced by deep mining (such as coal bumps) is more frequent [7–9]. In the past ten years, more than 660 coal bump accidents occurred in coal mines with coal bump risk of China, and 224 deaths were caused in total [10, 11]. Figure 1 shows the relationship between China's coal production and the number of coal bump mines. As of February 2021, 138 mines with coal bump risk are still in production in China, which poses a great threat to coal mines production and the safety of miners.

The mechanism of coal bump has been expounded from the widely accepted theories, such as "strength theory", "energy theory", "stiffness theory," and "coal bump proneness theory" [13–19]. According to the strength theory, the failure of coal rock is not only affected by stress concentration but also closely related to the ratio of coal strength to rock strength. In the stiffness theory, it is believed that the necessary condition for coal bump is that the stiffness of rock mass structure is greater than that of the loading

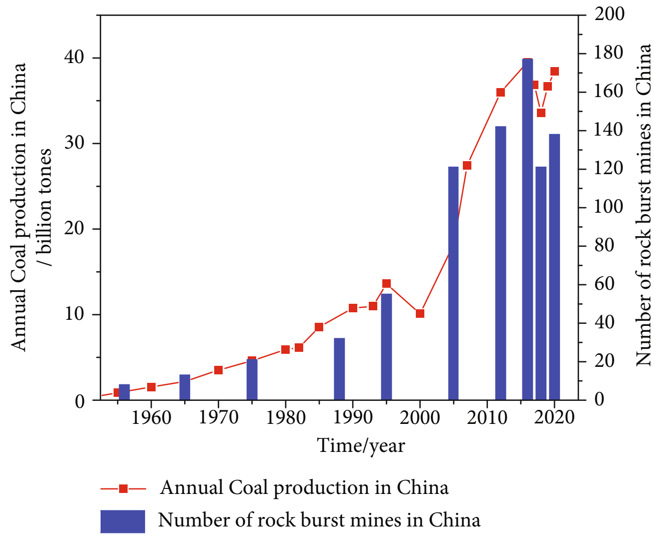

Figure 1: Annual coal production and the number of coal bump mines in China [12].

system. According to the energy theory, when the energy released by the mechanical equilibrium failure of the surrounding rock system is greater than the energy consumed in the system, the coal bump can be caused. In the coal bump proneness theory, it is claimed that the main condition of coal bump is that the tendency of coal rock is greater than its limit value. Based on the engineering practice, "coal bump strength weakening impact theory," "stress control theory," and "disturbance response instability theory" have also been proposed [20–22]. Besides, researchers have studied the impact failure of coal rock combination by laboratory test and numerical simulation and analyzed the dynamic failure process and failure mechanism of surrounding rock in the roadway under impact load [23–25]. Fan et al.'s [26] mechanism of roof shock in longwall coal mining under surface gully: the above researches reveal the initiation mechanism and disaster-causing process of coal bump from different angles. How successful application of the above results to the field of early warning on coal bumps has become the focus of current research.

At present, the main monitoring methods used in the early warning of coal bumps can be divided into drilling yield tests, acoustic emission and electromagnetic emission, microseismic monitoring, and seismic velocity tomography method [27–33]. Coal bump monitoring and early warning technology has a positive guiding role in the field of coal bump prevention and control in coal mines. However, Si et al. [34] proposed a single monitoring and early warning method which only describes the coal bump quantitatively from a specific aspect, due to the variability of coal mines occurrence conditions. The complexity of coal bump, which causes the diversity of coal bump precursor evolution characteristics. For example, the drilling cuttings method can be used to evaluate the coal bump risk and advance stress distribution characteristics of the working face according to the amount of coal powder, drilling depth, and dynamic effect. Nevertheless, this method has the disadvantages of a small monitoring range and poor applicability in the hard coal seam. As a regional monitoring method, acoustic emission (AE) and electromagnetic emission (EME) can be used to realize the monitoring and early warning by monitoring the charging index radiated to the outside space during the coal rock fracture (such as pulse number, amplitude, and frequency). However, this method is greatly affected by the field environment [10, 35–38]. Microseismic monitoring can obtain the occurrence time, duration, and energy field changes of coal bumps. However, He et al. [39] pointed out microseismic monitoring is mostly a postevent record, which is difficult to be used for coal bump prediction. Generally speaking, the early warning of coal bump is a multidimensional problem, and the formation, start-up, and disaster process of coal bump is hardly reflected in a comprehensive way by a single parameter [40, 41]. Comparative analysis of the early warning effectiveness between the new method and the original method used in the working face by the R-score method shows that the R values by the two methods are, respectively, 0.673 and 0.072, which indicates that the new method is far superior to the original method [42]. As a result, it is difficult to improve the accuracy of a single monitoring and early warning index in the field application. At present, the monitoring data of coal bump obtained by different monitoring and warning methods should be analyzed in depth, and the establishment of multiparameter, multilevel, and whole time-space coupling monitoring and early warning is one of the important research directions of coal bump.

Through the microseismic, AE, and EME on-site monitoring, the time-series evolution law of coal bump precursor signals was obtained in this study. The AE and EME parameter concentration index S was constructed by using covariance matrix and principal component analysis. Combined with the microseismic monitoring index, the static and dynamic coal bump risk assessment method was established and applied comprehensively in the subsequent mining of the working face 311305 in a coal mine of Inner Mongolia.

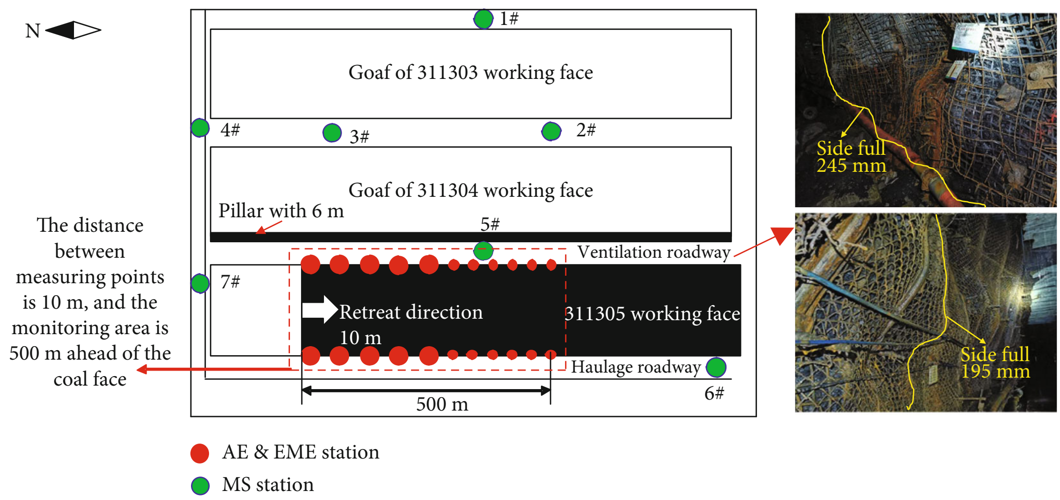

Figure 2: Position of the working face 311305 and layout of measuring points.

2. Geological and Mining Conditions

2.1. Introduction of the Working Face. The Bayangaole coal mine belongs to the Hujierte coalfield. It is located in the Inner Mongolia Autonomous Region, China. The coal-bearing strata were middle Jurassic coal layer. The average buried depth of the working face 311305 was 650 m, with the length of 2460 m and width of 300 m. It was adjacent to 311304 goaf in the east and entity coal in the west (see Figure 2); a coal pillar with a width of 6 m was reserved between the working face and the upper goaf. Extra-thick coal seam (3 No. coal seam) with average thickness of 5.80 m has dip angles ranging from 3° to 6°. The coal hardness coefficient f is $2 \sim 3$. Fully mechanized long wall mining method was used to extract the coal seam, and the gob-side entry retaining technology was adopted. The deformation of two sides in the ventilation roadway near the goaf was serious, and the side full was 195-245 mm. Figure 3 shows the comprehensive borehole columnar of the working face. The immediate roof of the coal seam was sandy mudstone with a thickness of 5.89 m, the uniaxial compressive strength of the immediate roof measured in the laboratory was 25.62 MPa, and the main roof was the fine sandstone with a thickness of 18.6 m.

2.2. Microseismic, AE, and EME Monitoring Scheme. The Seismological Observation System (SOS) microseismic monitor device imported from Poland was installed to monitoring seismicity continuously in the Bayangaole coal mine. This system can dynamically monitor the vibration waveform from a long distance in real-time and record the source position, energy level, and duration for subsequent analysis. The geophones are uniaxial with frequency of $1 \sim 600$ Hz, sampling rate of 500 Hz, maximum data transmission rate of 1 MB/s, and 16-bit A/D conversion. There are seven microseismic monitoring probes (green spots in Figure 2) in panel, which can well cover the target study area. The type YDD-16 acoustic emission and electromagnetic emission monitoring instrument for coal and rock dynamic disasters was used. The AE and EME measuring points (red points in Figure 2) were arranged in the ventilation roadway and haulage roadway, which was near the production side within 500 m ahead of the coalface; the distance between the two adjacent measuring points was 10 m. To minimize the impact of on-site production on the AE and EME signals, the monitoring time was set in the maintenance shift.

3. Analysis of Monitoring Results

3.1. MS Monitoring Results. Figure 4 shows the time-series curve of vibration energy and frequency monitored by the MS system of the working face 311305 from Aug 1 to Aug 31. The results of MS monitoring show that a strong coal bumps with the energy of more than 1.6×10^5 J occurred in the working face 311305 on August 7. Before the rock occurred, the time-series curve of the MS energy is relatively gentle, and the vibration frequency curve shows an upward trend. It indicates that before the occurrence of coal bump, the elastic energy accumulated in the coal rock is less exchanged with the external space, and the energy released by the microfracture in the coal rock is almost negligible compared with the originally accumulated elastic energy in the coal rock. However, the microfracture events in the coal rock gradually increase, and the microvibration is active. When the energy accumulation of coal rock exceeds the critical value needed for coal bump, the energy is released instantly, and the strong coal bump is caused. In active period, energy quiet existed and sustained $3 \sim 5$ days, but the seismic vibration frequency showed a remarkable rising trend, and rock burst/coal bumps always occurred after tremor number decrease.

On Aug 14, 20 and 29, coal bumps with energy over 1.2×10^5 J were detected. Before the occurrence of coal bumps, the microseismic energy curve and frequency curve show a similar fluctuation law as that on Aug 7. Before the microvibration in coal rock changing from active period to declining period, the vibration frequency is more than 15 times. Subsequently, strong coal bumps occur, vibration frequency decreases significantly, and the microseismic energy curve shows an obvious downward trend with the energy

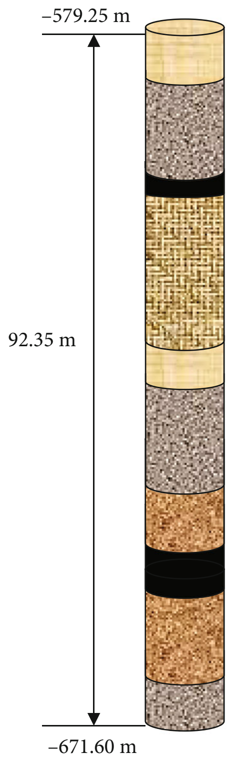

Lithology	Thickness (m)	Remarks
Siltstone	8.80	Dark grey, compact mass, phytolith rich.
Packsand	13.75	Grey to light grey, siliceous cement, rich of siderite stripes and dark grey siltstone stripes.
2# Coal	0.30	Black, semi-bright, stereoplasm, mainly consisting of lump coal.
Medium sandstone	23.00	Grey, mainly consisting of quartz, siliceous cement, harder.
Siltstone	4.61	Dark grey, compact mass, phytolith rich.
Packsand	18.60	Grey to light grey, siliceous cement, rich of siderite stripes and dark grey siltstone stripes.
Sandy mudstone	5.89	Gray, thin laminated, horizontal textured, hard
3# Coal	5.80	Black, semi-bright, stereoplasm, mainly consisting of lump coal.
Sandy mudstone	8.15	Gray, thin laminated, horizontal textured, hard
Packsand	3.45	Grey to light grey, siliceous cement, rich of siderite stripes and dark grey siltstone stripes.

Figure 3: Bore histogram: 311305 coal face.

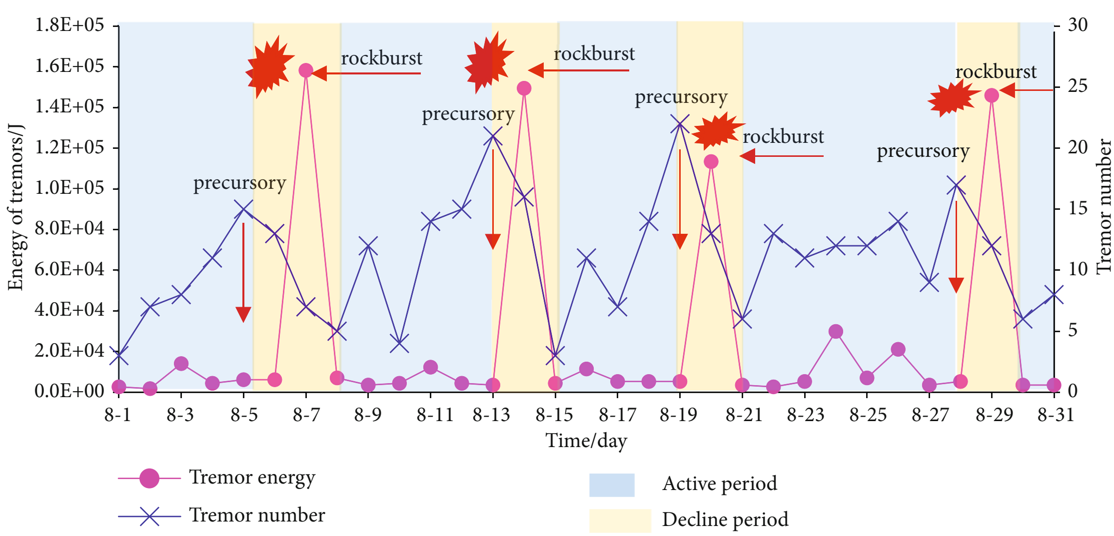

Figure 4: Time-series diagram of MS energy and frequency from Aug 1 to 31.

release. In general, when the vibration frequency curve is maintained at a high value (>15 times) and the total energy curve of the source appears a long stationary period (3 ~ 5d), there is a greater possibility of coal bumps in the working face.

3.2. AE and EME Monitoring Results. As shown in Figure 5, the time-series curve of AE and EME strength at 12 # measuring point, which was arranged ahead of the working face 311305. It can be seen that the AE and EM strength of this measuring point continues to rise within 3-4 days before the coal bump event on Aug 7, 14, 20, and Aug 29. The peak value of AE strength is 1.87-2.39 times of the average value, and the peak value of EME strength is 1.57-2.28 times of the average value. This process is called "active period of AE & EME signals." Subsequently, a strong coal bump occurs in the working face. After the coal bump, the strength of AE

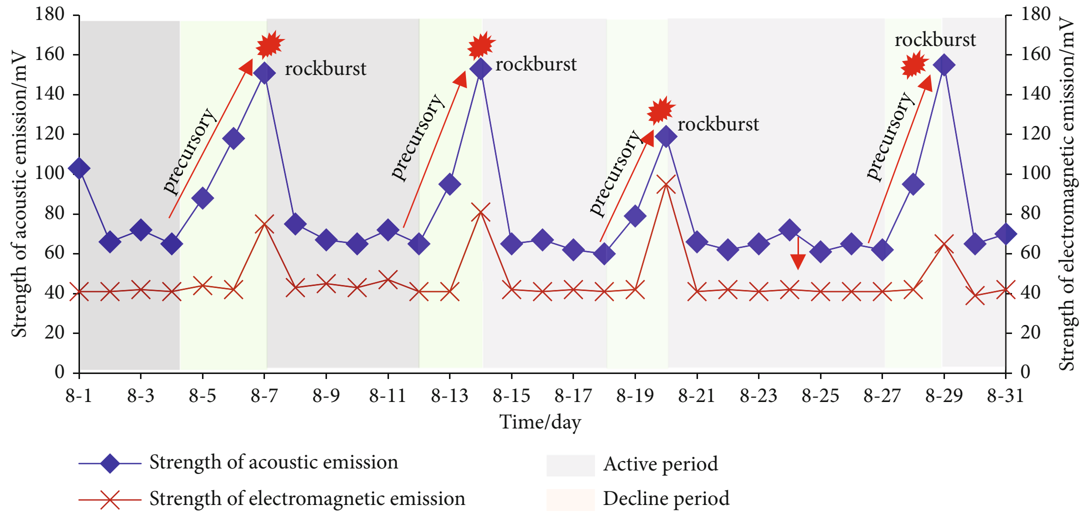

FIGURE 5: Time-series curve of AE and EME from Aug 1 to 31.

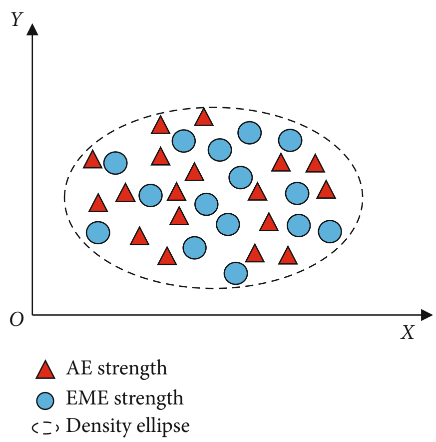

FIGURE 6: Schematic diagram of density ellipse.

and EME falls back to the normal value, and the time-series curve of AE and EME strength enters the "quiet period of AE & EME signals." Figure 5 also shown the EME strength curve is relatively stable on the whole, and the fluctuation is only observed before the occurrence of coal bump, while the AE strength curve fluctuates up and down with the increase of near-field stress concentration of coal rock and the occurrence of microfracture events. Therefore, the single use of AE strength or EME strength has certain limitations for the early warning of coal bump.

3.3. Multiparameter Coupling Analysis Method. Based on the above analysis, in the monitoring and early warning of coal bump, the energy dissipation and output of coal rock in the advanced area of mining face can be judged by the microseismic monitoring. The internal stress concentration of coal rock in the near field can be judged by the AE and EME signal analysis; then, a qualitative and quantitative evaluation of the risk of coal bump in the advanced area of the working face can be obtained.

Firstly, two measured physical quantities, AE strength and EME strength, are normalized. Assuming that the stress concentration and fracture degree of coal and rock increase in a certain area, the AE signals and EME signals generated in this area will also increase, and then a signal emission group will be formed [43]. The AE strength is represented by vector X, the EME strength is represented by vector Y, and the concentration C is used to describe the distribution of AE signals and EME signals in coal rock. In other words, the fracture area is taken as the center, and the measured X and Y are distributed around the center. The deviation from the center can be described by the covariance matrix, as shown in Eq. (1).

$$C = \begin{pmatrix} c_{11} & c_{12} \\ c_{21} & c_{22} \end{pmatrix}, \tag{1}$$

where

$$\begin{aligned} C_{11} &= E\{[X - E(X)^2]\}, \\ C_{12} &= E\{[X - E(X)][Y - E(Y)]\}, \\ C_{21} &= E\{[X - E(Y)][Y - E(X)]\}, \\ C_{22} &= E\{[Y - E(Y)^2]\}, \end{aligned} \tag{2}$$

and $E(X), E(Y)$ represents the mathematical expectation of vectors X and Y, respectively.

The concentration of acoustic and electrical signals cannot be quantitatively analyzed by the sole use of a covariance matrix. In this study, the principal component analysis method is used to solve the principal component and direction of the distribution of acoustic and electrical signals, and the density ellipse formed by acoustic and electrical signals is used to envelop the acoustic and electrical signals points (see Figure 6). The two principal axes and directions of the density ellipse are determined by the eigenvalues and eigenvectors of the covariance matrix. The larger the area of the density ellipse used for enveloping signals points, the more discrete the concentration of acoustic and electrical signals,

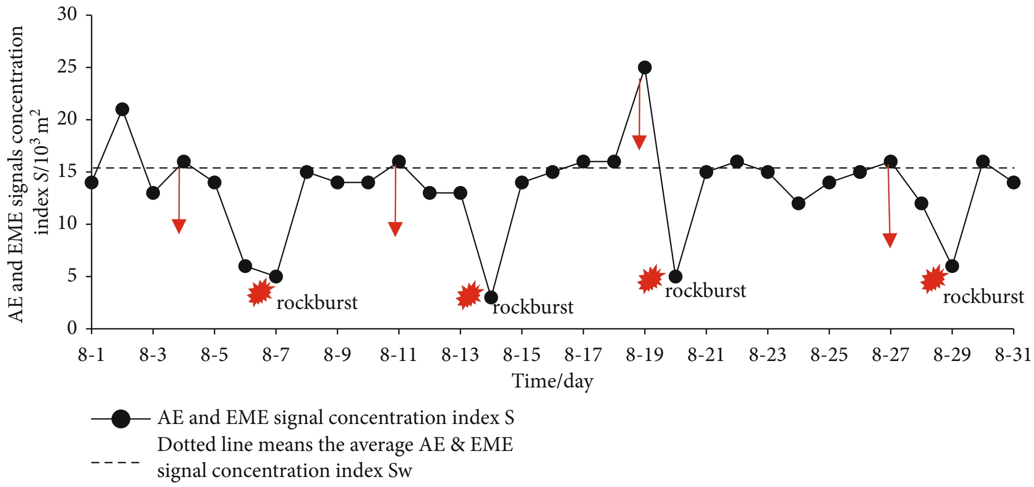

FIGURE 7: The concentration index S of the AE and EME strength from Aug 1 to 31.

TABLE 1: Static evaluation method of AE-EME-MS coupling monitoring.

Microseismic index	The concentration index S of acoustic and electrical signals No risk: level A $S > 1.1, S_w$	Weak risk: level B $1.1\ S_w < S < 0.8, S_w$	Medium risk: level C $0.5\ S_w < S < 0.8, S_w$	Strong risk: level D $S < 0.5, S_w$
E: <10^3J N: <5	A	A	B	C
E: 10^3-10^4 J N: <5	A	B	B	C
E: $1-5\times10^4$ J N: 5-10	B	C	D	D
E: $5-10\times10^4$ J N: 10-15	C	C	D	D
E: >1.6×10^5 J N: >15	D	D	D	D

Note: S refers to the concentration index of acoustic and electrical signals during mining, S_w is the average value of concentration index of acoustic and electrical signals, E is the total energy of microseisms, and N is the frequency of microseisms.

and vice versa. And the formula for calculating the area of the density ellipse is shown in Eq. (3).

$$S=\pi\sqrt{C_{11}C_{22}-C_{12}{}^{2}}, \tag{3}$$

where

$$\begin{aligned} C_{11}&=E\left\{\left[X-E(X)^{2}\right]\right\},\\ C_{12}&=E\{[X-E(X)][Y-E(Y)]\},\\ C_{22}&=E\left\{\left[Y-E(Y)^{2}\right]\right\}, \end{aligned} \tag{4}$$

Equation (3) is used to calculate the concentration index S of AE and EME signal concentration at 311305 working face. The time-series curve of concentration index S during mining in Aug is shown in Figure 7. Before the occurrence of coal bumps, the time-series curve of the concentration index S of AE and EME signals deviates significantly from the average concentration index S_w (S_w dotted line in Figure 7), showing an obvious decreasing trend. When the fracture occurs in the coal rock, the smaller the concentration index S of AE and EME signals, the more concentrated the area of AE and EME signals radiate outward. Accordingly, the higher the stress concentration in this area, the greater the possibility of coal bump. The concentration index S of the AE and EME signals can be used as a comprehensive index for coal bump AE and EME monitoring and early warning.

TABLE 2: Dynamic evaluation method of AE-EME-MS coupling monitoring.

Duration of continuous enhancement of microseismic activity	Static hazard level A	B	C	D
1d	A	B	C	D
2d	B	C	C	D
3d	B	C	D	D
More than 3d	Danger level is increased by 1 level			

Note: the enhancement of microseismic activity refers to the continuous increase of microseismic frequency.

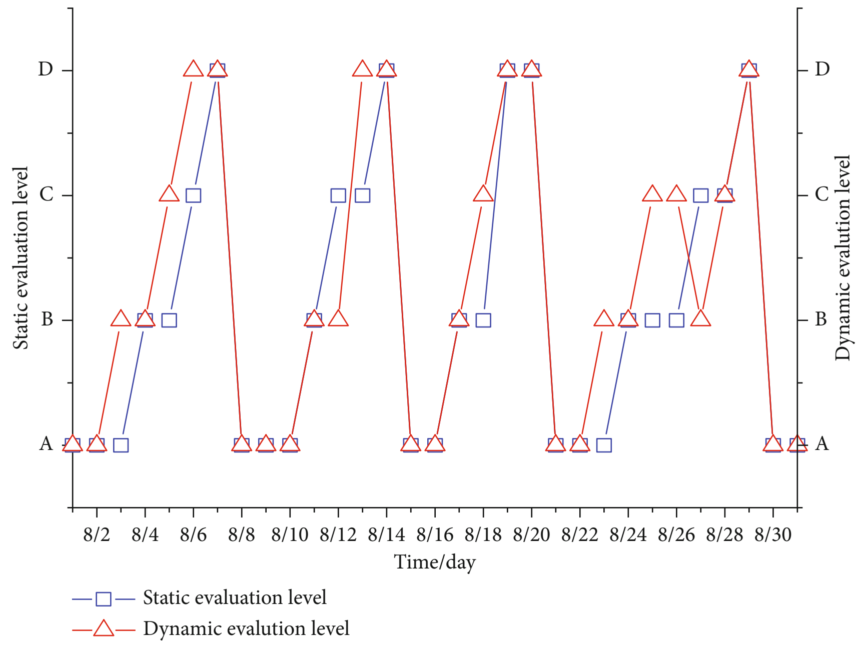

Figure 8: Coal bump risk assessment level from Aug 1 to 31.

Table 1 shows the static evaluation method of coal bump combined with the concentration index S of acoustic and electrical signals and microseismic monitoring index E and N, and Table 2 shows the dynamic evaluation method of AE-EME-MS coupling monitoring. The enhancement of microseismic activity means that the microseismic frequency monitored on the same day is higher than the average value of the microseismic frequency in the first 1-3 days. As shown in Figure 8, the time-series curves of coal bump risk assessment grade of the working face 311305 in Aug are obtained by the static method and dynamic method of the AE-EME-MS coupling monitoring in Tables 1 and 2. It can be seen that the near-field stress distribution, energy accumulation, and release of coal rock are considered simultaneously in the AE-EME-MS coupling monitoring method, and the risk of coal bump in situ can be effectively evaluated by the proposed monitoring method.

4. Discussion

The above research shows that the time-series curves of microseismic energy, microseismic frequency, and the concentration index of acoustic and electrical signals S can be used to characterize the coal bump risk in the working face. According to the time-series curve of AE and EME strength, the time-series curve of concentration index S, the time-series curve of microseismic energy, and the precursor characteristics of strong coal bumps can be determined as follows:

(1) Under the influence of mining stress, the state of the surrounding rock system will evolve to a new stable state over time. Therefore, the surrounding rock near the working face can be regarded as an open system, and the accumulated elastic potential energy, gravity potential energy, and tectonic stress are transmitted to the outside in the form of vibration, acoustic wave, and electromagnetic emission under the influence of mining. Therefore, when the time-series curves of vibration energy, vibration frequency, and AE and EME strength fluctuate violently, the stress concentration and fracture degree in coal rock increase correspondingly, which is the precursor of the strong mine earthquake

(2) When the energy output of the open system composed of surrounding rock near the working face is kept at a low level or has a certain downward trend, the working face has a strong risk of coal bump. Correspondingly, when the time-series curve of microseismic energy at the working face usually presents a stable period of energy fluctuation for 3 - 5 days or has a certain downward trend, and the microseismic frequency time-series curve is in the obvious rising stage and maintains at a high level (>15 times), then the working face has a strong coal bump risk

(3) The concentration index of acoustic and electrical signals deviates obviously from the average curve, showing a downward trend. The time-series curve of AE strength fluctuates obviously, which indicates that the microfracture in coal rock is concentrated in a small area at this time. The smaller the concentration index S, the greater the internal stress concentration in this area, and the higher possibility of a strong coal bumps occurring in the working face

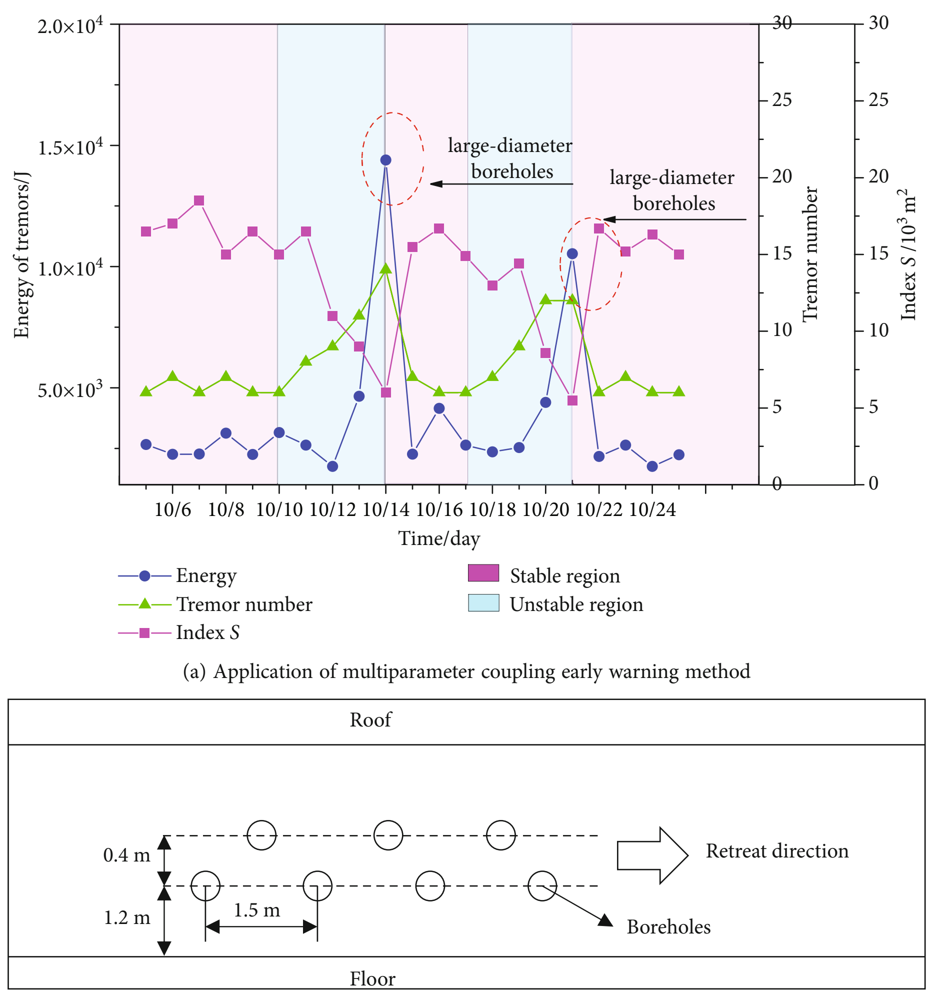

(a) Application of multiparameter coupling early warning method

(b) Main view of large-diameter boreholes layout

FIGURE 9: Application of multiparameter coupling monitoring from Oct 5 to 25.

5. Field Application and Prevention Measures for Coal Bumps

To test the applicability of the AE-EME-MS coupling monitoring method, during the mining period of the working face 311305 in Oct, AE and EME monitoring points were also arranged in the area 400 m ahead of the working face for continuous monitoring. The time-series curves of microseismic energy, vibration frequency, and concentration of acoustic and electrical signals were obtained, as shown in Figure 9(a). From Oct 10 to 13, the monitored time-series curve of microseismic energy on-site first decreased and then increased, the vibration frequency curve showed an obvious increasing trend, and the time-series curve of the concentration index S showed a downward trend. Combined with the monitoring and early warning methods of coal bump given in Tables 1 and 2, it was judged that there was a high probability of coal bump event in the working face 311305 near Oct 14. After that, the large-diameter boreholes were used in the coal seam in the nonproduction side of the transportation roadway 311305 for pressure relief (Figure 9 (b)). The diameter of boreholes was Φ150 mm, the borehole was arranged at a distance of 1.2-1.6 m from the bottom floor, the drilling depth was 15.0 m, and the row spacing was 1.5 m × 0.4 m. After the pressure relief measures were taken, the AE monitoring data was reduced to 65 mv, the EME monitoring data was reduced to 41 mV, and the microseismic energy monitoring data was reduced to 2263 J. According to the same early warning method, another early warning of coal bump was carried out on Oct 21. Through the above field practice, it can be seen that the multiparameter coupling monitoring and early warning method proposed in this study can make a good prediction of coal bump and significantly reduce the probability of coal bump accidents.

6. Conclusion

The occurrence of coal bump is the result of the accumulation and sudden release of elastic properties of coal rock. During the fracture process of coal rock, abundant acoustic and electrical signals can be observed, and the abnormal change of acoustic and electrical signals can be regarded as the precursor characteristics of coal bump.

Before the occurrence of coal bump, there are obvious precursors of acoustic emission and electromagnetic emission-microseism. Specifically, the total energy time-series curve of microseisms is at a low level and relatively stable; the vibration frequency time-series curve has an obvious upward trend; the AE strength time-series curve fluctuates obviously 3-4 days before the occurrence of coal bump, and the AE and EME strength is about 2 times of the normal value.

The area of density ellipse can be used to represent the area of acoustic and electrical signals emitted from coal rock; the covariance matrix and principal component analysis method can be used to construct the concentration index S of acoustic and electrical signals, which can effectively reflect the concentration change of acoustic and electrical signals of coal rock. The smaller concentration index S of acoustic and electrical signals indicates that the microfracture in coal rock is concentrated in a smaller area, and the corresponding stress concentration degree in this area is greater. When the time-series curve of the concentration index S of the acoustic and electrical signals of the working face shows an obvious downward trend and $S < 0.5S_w$, the working face will have a large probability of a strong mine earthquake.

Combined with the variation law of concentration index S of acoustic and electrical signals and microseismic monitoring index value (total energy and frequency of microseisms), the early warning method of AE-EME-MS multiparameter coupling monitoring is proposed. Combined with the pressure relief measures of large diameter borehole implemented in the field, the possibility of coal bump in thick coal seam with the hard roof is greatly reduced, and the effectiveness of the proposed methods with the static evaluation and dynamic early warning of coal bump is verified. This study provides an effective method for the subsequent mining of working face 311305 and early warning and prevention of coal bump on the succeeding working face.

Data Availability

The data of this manuscript is tested in the laboratory of State Key Laboratory of Coal Resources and Safe Mining, China University of Mining and Technology, which is available to authorized users.

Conflicts of Interest

The authors declare that they have no conflicts of interest.

Acknowledgments

We thank Dr. Huining Ni and Dr. Mingwei Chen for their fruitful discussions about this work and Huan Jiang and Xuyang Wang for their help in monitoring date analysis of this work. This work was supported by the National Natural Science Foundation of China (grant number 51774268), Key Research and Development Project of Shanxi Province (grant number 20201101009), and the Postgraduate Research and Innovation Projects of Jiangsu Province (grant number KYCX21_2334).

References

[1] L. Dou and X. He, "Theory and technology of rock burst prevention," University of mining and technology press, Xuzhou: China, 2001.

[2] M. C. He, H. P. Xie, S. P. Peng, and Y. D. Jiang, "Study on rock mechanics in deep mining engineering," *China Journal of Rock Mechanical and Engineering*, vol. 24, no. 16, pp. 2803–2813, 2005.

[3] Q. Qi and L. Dou, *Theory and Technology of Rock Burst*, University of mining and technology press, Xuzhou China, 2008.

[4] X. He, B. Nie, W. Chen et al., "Research progress on electromagnetic radiation in gas-containing coal and rock fracture and its applications," *Safety Science*, vol. 50, no. 4, pp. 728–735, 2012.

[5] Y. Jiang and Y. Zhao, "State of the art: investigation on mechanism, forecast and control of coal bumps in China," *Chinese Journal of Rock Mechanicals and Engineering*, vol. 34, no. 11, pp. 2188–2204, 2015.

[6] Y. Jiang, Y. Zhao, H. Wang, and J. Zhu, "A review of mechanism and prevention technologies of coal bumps in China," *Journal of Rock Mechanics and Geotechnical Engineering*, vol. 9, no. 1, pp. 180–194, 2017.

[7] C. Zhang, I. Canbulat, B. Hebblewhite, and C. R. Ward, "Assessing coal burst phenomena in mining and insights into directions for future research," *International Journal of Coal Geology*, vol. 179, pp. 28–44, 2017.

[8] F. Chen, A. Cao, Z. Liang, and Y. Liu, *A coal burst risk assessment model of seismic events based on multiple seismic source parameters: a case study of the Huating Coal Mine, Gansu Province, China*, Nature Resource Research, 2021.

[9] S. Zhang, G. Fan, D. Zhang et al., "Impacts of longwall mining speeds on permeability of weakly cemented strata and subsurface watertable: a case study," *Geomatics, Natural Hazards and Risk*, vol. 12, no. 1, pp. 3063–3088, 2021.

[10] W. Cai, L. Dou, G. Si, A. Cao, J. He, and S. Liu, "A principal component analysis/fuzzy comprehensive evaluation model for coal burst liability assessment," *International Journal of Rock Mechanics and Mining Sciences*, vol. 81, pp. 62–69, 2016.

[11] W. Cai, L. Dou, G. Si et al., "A new seismic-based strain energy methodology for coal burst forecasting in underground coal mines," *International Journal of Rock Mechanics and Mining Sciences*, vol. 123, article 104086, 2019.

[12] F. Cui, T. H. Zhang, and X. P. Lai, "Research on mining disturbance characteristics and productivity of rock burst mines under different mining intensities," *Journal of China Coal Society*, vol. 3, pp. 1–15, 2021.

[13] N. G. W. Cook, "A note on rockbursts considered as a problem of stability," *Journal of the Southern African Institute of Mining and Metallurgy*, vol. 65, pp. 437–446, 1965.

[14] J. A. Hudson, S. L. Crouch, and C. Fairhurst, "Soft, stiff and servo-controlled testing machines: a review with reference to rock failure," *Engineering Geology*, vol. 6, no. 3, pp. 155–189, 1972.

[15] S. P. Singh, "Burst energy release index," *Rock Mechanics and Rock Engineering*, vol. 21, no. 2, pp. 149–155, 1988.

[16] A. M. Linkov, "Rockbursts and the instability of rock masses," *International Journal of Rock Mechanics and Mining Sciences & Geomechanics Abstracts*, vol. 33, no. 7, pp. 727–732, 1996.

[17] J. Wang and H. D. Park, "Comprehensive prediction of rockburst based on analysis of strain energy in rocks," *Tunnelling and Underground Space Technology*, vol. 16, no. 1, pp. 49–57, 2001.

[18] A. Kidybinski, "Bursting liability indices of coal," *International Journal of Rock Mechanics and Mining Sciences*, vol. 18, no. 4, pp. 295–304, 1981.

[19] C. Zhang, I. Canbulat, F. Tahmasebinia, and B. Hebblewhite, "Assessment of energy release mechanisms contributing to coal burst," *International Journal of Mining Science and Technology.*, vol. 27, no. 1, pp. 43–47, 2017.

[20] L. Dou, C. Lu, Z. Mou, Y. Qin, and J. Yao, "Strength weakening theory for rockburst and its application," *Journal of China Coal Society.*, vol. 30, no. 6, pp. 690–694, 2005.

[21] Q. Qi, X. Li, and S. Zhao, "Theory and practices on stress control of mine pressure bumping," *Coal Science and Technology*, vol. 41, no. 6, pp. 1–5, 2013.

[22] Y. Pan, "Disturbance response instability theory of rockburst in coal mine," *Journal of China Coal Society*, vol. 43, no. 8, pp. 2091–2098, 2018.

[23] Y. S. Pan, Y. H. Xiao, L. I. Zhong-Hua, and K. X. Wang, "Study of tunnel support theory of rockburst in coal mine and its application," *Journal of China Coal Society*, vol. 39, no. 2, pp. 222–228, 2014.

[24] A. Sainoki and H. S. Mitri, "Dynamic behaviour of mining-induced fault slip," *International Journal of Rock Mechanics and Mining Sciences*, vol. 66, pp. 19–29, 2014.

[25] K. Yang, W. J. Liu, L. T. Dou, X. L. Chi, Z. Wei, and Q. Fu, "Experimental investigation into interface effect and progressive instability of coal-rock combined specimen," *Journal of China Coal Society*, vol. 45, no. 5, pp. 1691–1700, 2020.

[26] G. Fan, D. Zhang, and X. Wang, "Mechanism of roof shock in longwall coal mining under surface gully," *Shock and Vibration*, vol. 2015, 8 pages, 2015.

[27] S. T. Gu, C. Q. Wang, B. Y. Jiang, Y. L. Tan, and N. N. Li, "Field test of rock burst danger based on drilling pulverized coal parameters," *Disaster Advances*, vol. 5, no. 4, pp. 237–240, 2012.

[28] X. C. Qu, F. X. Jiang, Z. X. Yu, and H. Ju, "Rockburst monitoring and precaution technology based on equivalent drilling research and its applications," *Chinese Journal of Rock Mechanicals and Engineering*, vol. 30, no. 11, pp. 2346–2351, 2011.

[29] J. He, L. Dou, S. Gong, J. Li, and Z. Ma, "Rock burst assessment and prediction by dynamic and static stress analysis based on micro-seismic monitoring," *International Journal of Rock Mechanics & Mining Sciences*, vol. 93, pp. 46–53, 2017.

[30] V. Frid and K. Vozoff, "Electromagnetic radiation induced by mining rock failure," *International Journal of Coal Geology*, vol. 64, no. 1-2, pp. 57–65, 2005.

[31] E. Wang, X. He, X. Liu, Z. Li, C. Wang, and D. Xiao, "A non-contact mine pressure evaluation method by electromagnetic radiation," *Journal of Applied Geophysics*, vol. 75, no. 2, pp. 338–344, 2011.

[32] N. Hosseini, K. Oraee, K. Shahriar, and K. Goshtasbi, "Studying the stress redistribution around the longwall mining panel using passive seismic velocity tomography and geostatistical estimation," *Arabian Journal of Geosciences*, vol. 6, no. 5, pp. 1407–1416, 2013.

[33] L. M. Dou, W. Cai, S. Y. Gong, R. J. Han, and J. Liu, "Dynamic risk assessment of rock burst based on the technology of seismic computed tomography detection," *Journal of China Coal Society*, vol. 39, no. 2, pp. 238–244, 2014.

[34] G. Si, W. Cai, S. Wang, and X. Li, "Prediction of relatively high-energy seismic events using spatial–temporal parametrisation of mining-induced seismicity,Prediction of relatively high-energy seismic events using spatial–temporal parametrisation of mining-induced seismicity," *Rock Mechanics and Rock Engineering*, vol. 53, pp. 1–22, 2020.

[35] E. Y. Wang, X. F. Liu, X. Q. He, and Z. H. Li, "Acoustic emission and electromagnetic radiation synchronized monitoring technology and early-warning application for coal and rock dynamic disaster," *Journal of China University of Mining and Technology*, vol. 47, no. 5, pp. 942–948, 2018.

[36] Z. L. Li, X. Q. He, L. M. Dou, G. F. Wang, D. Z. Song, and Q. Lou, "Bursting failure behavior of coal and response of acoustic and electromagnetic emissions," *Chinese Journal of Rock Mechanics and Engineering*, vol. 38, no. 10, pp. 2057–2068, 2019.

[37] C. Lu, L. Dou, and X. Wu, "Pt catalyst supported on multi-walled carbon nanotubes for hydrogenation- dearomatization of toluene," *Chinese Journal of Rock Mechanics and Engineering*, vol. 28, no. 3, pp. 210–216, 2007.

[38] L. Dou, W. Cai, A. Cao, and W. Guo, "Comprehensive early warning of rock burst utilizing microseismic multi- parameter indices," *International Journal of Mining Science and Technology*, vol. 28, no. 5, pp. 767–774, 2018.

[39] H. He, L. Dou, S. Gong, J. He, Y. Zheng, and X. Zhang, "Microseismic and electromagnetic coupling method for coal bump risk assessment based on dynamic static energy principles," *Safety Science*, vol. 114, pp. 30–39, 2019.

[40] C. Wang, A. Cao, C. Zhang, and I. Canbulat, "A new method to assess coal burst risks using dynamic and static loading analysis," *Rock Mechanics and Rock Engineering*, vol. 53, no. 3, pp. 1113–1128, 2020.

[41] S. Li, G. Fan, D. Zhang et al., "Fracture propagation and hydraulic properties of a coal floor subjected to thick-seam longwalling above a highly confined aquifer," *Geofluids*, vol. 2021, Article ID 6668466, 12 pages, 2021.

[42] X. Tian, Z. Li, D. Song et al., "Study on microseismic precursors and early warning methods of rockbursts in a working face," *Chinese Journal of Rock Mechanics and Engineering*, vol. 39, no. 12, pp. 2471–2482, 2020.

[43] Y. A. N. G. Chundong, G. O. N. G. Siyuan, M. A. Xiaoping, and W. A. N. G. Guifeng, "Rock burst danger monitoring based on microseismic method," *Journal of Mining & Safety Engineering*, vol. 31, no. 6, pp. 863–868, 2014.

Hindawi
Geofluids
Volume 2022, Article ID 1968938, 15 pages
https://doi.org/10.1155/2022/1968938

Research Article

Study on the Effect of Rock Strength on the Macro-Meso Shear Behaviors of Artificial Rock Joints

Yujing Jiang,[1,2] Sunhao Zhang,[1,2] Hengjie Luan,[1,2] Qinglin Shan,[1,2] Baocheng Li,[1,2] Dong Wang,[1,2] and Chuanyang Jia[3]

[1] *State Key Laboratory of Mining Disaster Prevention and Control Co-founded by Shandong Province and the Ministry of Science and Technology, Shandong University of Science and Technology, Qingdao 266590, China*
[2] *College of Energy and Mining Engineering, Shandong University of Science and Technology, Qingdao 266590, China*
[3] *School of Civil Engineering and Architecture, Linyi University, Linyi 276000, China*

Correspondence should be addressed to Qinglin Shan; skd995946@sdust.edu.cn

Received 23 July 2021; Accepted 11 October 2021; Published 16 March 2022

Academic Editor: Bailu Teng

Understanding the shear properties of joints of rock masses is of great importance for engineering disaster prevention and control. In this paper, a systematic study of the macroscopic shear properties of joints of rock masses with different strengths is carried out using a combination of indoor tests and PFC^{2D} numerical simulations. The results show that (i) the shear stress curve of low-strength rock joints is strain-softening type, while high-strength rock joints are strain-hardening type, and high-strength rock joints are more sensitive to the change of roughness. (ii) With the increase of JRC, the damage mode of different strength rock joints gradually changes from "abrasion" to "abrasion + gnawing," and the damage characteristics of the surface of high-strength rock joints are more significant. (iii) The contact force between particles is mainly concentrated on the joints. At the beginning of shear, the contact force is mainly distributed on the second-order roughness and gradually concentrated on the first-order roughness as the shear progresses. Compared with the low-strength rock joints, the contact force on the high-strength rock joints is larger and more widely distributed. (iv) Due to the change of contact force, the cracks keep expanding and the particle rotation arc keeps changing. The particles with larger rotational arcs are consistent with the location of crack distribution, and the cumulative number of cracks on the joints of high-strength rock is higher. (v) The total input energy and dissipation energy increase continuously with the shear, and the elastic energy tends to increase at the beginning of shear and then starts to decrease and gradually tends to be constant near the peak of shear stress. The total input energy and dissipation energy of the joints of the high-strength rock are larger, while the peak elastic energy of it is smaller.

1. Introduction

As a universal discontinuous medium, rock masses contain various discontinuous surfaces such as fractures, joints, weak surfaces, and faults inside [1–3], which destroy the integrity of rock masses and lead to a significant reduction in their strength and stability. Numerous engineering practices have shown that shear deformation and slip of joints can lead to engineering instability problems, which seriously threaten the safety of people's lives and properties [4]. Therefore, the in-depth study of shear characteristics of rock joints is of great significance for engineering disaster prevention and control.

Since the 1860s, scholars at home and abroad have conducted a lot of researches on the shear properties of joints through indoor tests, theoretical analysis, and numerical simulations. Quite a number of research results have been obtained, mainly including the relationships between shear strength [5–8], surface damage characteristics [9–13], shear strength and surface morphology [14–16], and the influence pattern of rock type [17], boundary conditions [18–22], and loading methods [23, 24] and other factors on them. Since Patton [25] analyzed the influence of rock joint morphology on its shear mechanical behavior, the relationship between shear properties of rock joints and joint morphology has been a hot topic of research in the rock mechanics community in the past decades. Barton and Choubey [26] conducted a large number of experiments and summarized 10 JRC curves to predict the shear strength of joints. After that, many new methods have been proposed for the calculation of JRC [27–29]. Jiang et al. [22] developed an experimental system capable of constant normal stiffness loading (CNS) boundary conditions to compare and analyze the shear properties of rough joints under different boundary conditions. Liu et al. [30] further investigated the anisotropy of the shear properties of rough joints under different boundary conditions on this basis. With the rapid development of computer technology in recent years, numerical simulation methods have been widely used in engineering [31] and indoor experimental [20, 21] researches. Wang et al. [20] used PFC numerical simulation software to simulate the shearing process of rough joints under CNL and CNS boundary conditions and explored the damage process and the damage mechanism of rough joints under different boundary conditions from macroscopic and fine view perspectives, respectively. Zhang et al. [21] investigated the mechanism of shear deformation, damage, and energy dissipation of joints under CNL boundary conditions by indoor tests and PFC numerical simulations. Liu et al. [32, 33] also investigated the macroscopic and microscopic shear properties of through-shaped serrated joints containing first- and second-order rough bodies using a combination of indoor experiments and PFC numerical simulations. Ge et al. [34] investigated the evolution of joint roughness under CNL boundary conditions using indoor experiments and discrete element- (DEM-) based numerical simulations. Park and Song [35] used PFC^{3D} to simulate a series of joint direct shear experiments to investigate the effects of the geometrical features, and the microproperties of joints on its shear behavior were examined. Chen et al. [36] used PFC^{2D} to numerically calculate a series of nonpenetrating horizontal rock-like joints with different scales to investigate the size effect of shear mechanical properties of nonpenetrating horizontal rock-like joints. Zhang et al. [37] used PFC^{2D} to study the shear mechanical properties of joints under creep conditions.

However, most of the above studies have focused on the same strength rock conditions, and the shear characteristics exhibited by the joints are necessarily different for different joint rock strengths. For this reason, some scholars have also carried out relevant studies. Meng et al. [17] conducted shear tests under CNL boundary conditions on three different rock types and analyzed the strength characteristics and acoustic emission signal characteristics of joints of different rock types, and the results showed that rock type has a significant effect on the shear characteristics of joints. Fan et al. [38] carried out shear tests and corresponding PFC^{2D} numerical simulations of soft-hard joints with different strengths of the upper and lower joint faces and established a new peak shear strength model for soft-hard joints. Liu et al. [24] considered two typical forms of soft and hard interbedded rock joints, "soft + hard" and "hard + soft + hard," and carried out indoor shear tests and PFC^{2D} numerical simulations under CNL boundary conditions to investigate the shear properties. In the above studies, the shear properties of joints under different strength rock conditions were initially explored and some useful insights were obtained. However, the different shear properties of joints of different strength rock masses have not been compared and analyzed, and corresponding macroscopic studies have not been carried out to reveal the damage evolution process and degradation mechanism of joints of different strength rock masses.

In view of the above understanding, in order to study the macroscopic and fine shear properties of the joints of rocks of different strengths, this paper first carried out indoor one-way static direct shear tests under constant normal load (CNL) conditions on the joints of rocks of two strengths to study the macroscopic shear properties of rocks of different lithologies under different roughness conditions, which revealed the shear mechanical behavior and joint damage modes of joints of rocks with different strengths, etc. Then, the particle flow simulation software PFC^{2D} was used to dynamically simulate the whole process of shear on joints of different lithologies and to study the changes of particle contact force, number of microscopic cracks, arc of particle rotation, and microscopic damage energy on joints from the microscopic perspective and to compare the macroscopic damage evolution process of joints and their degradation mechanisms. The research results have enriched the theory of shear properties of joints and are of great significance for the prevention and control of engineering disasters caused by shear slip of joints.

2. Experimental Methods

2.1. Specimen Preparation. In order to analyze the shear characteristics of different strength rock joints, two types of rock joints with different strengths are used in the test. One is the low-strength rock on both sides of the joints (low-strength rock joints), and the other is the high-strength rock on both sides of the joints (high-strength rock joints).

In order to obtain rock joint samples of different strengths, two different material ratios were determined using materials such as cement, fine sand, and water and a method of orthogonal design. The low-strength rock joint samples were prepared using materials such as white cement, fine sand, water, and water-reducing agent and in the ratio $1:1:0.3:0.005$ [39], and the high-strength rock joint samples were prepared using materials such as grey cement, fine sand, water, and water-reducing agent and in the ratio $1:0.5:0.25:0.005$, respectively.

Meanwhile, to study the shear characteristics of joints of different lithologies under the influence of roughness, five steel molds representing different JRC (JRC of 0~2, 4~6, 8~10, 12~14, and 16~18, respectively) were fabricated based on Barton curves and using laser cutting techniques, and smooth joint samples of two strength rock masses and joint samples corresponding to the JRC represented by the molds ($200\,mm \times 100\,mm \times 100\,mm$) were prepared in combination with the above molds, respectively [40, 41].

2.2. Test Apparatus and Procedure. The JAW-600 rock shear seepage test system as shown in Figure 1 was used to conduct the direct shear test. This test system mainly consists of four parts: data collection and analysis system, vertical loading unit, horizontal loading unit, and its servo control system.

At the beginning of the test, a constant normal force of 1 MPa is first applied through the vertical loading unit, and then, the quasistatic shear load is applied through the horizontal loading unit at a shear rate of 0.01 mm/s after the normal stress reaches the target value. And this process continues until the end of the test. Since the shear displacement of the joint face can be considered as failure when it reaches a critical value, the critical value of the shear displacement is usually used as the basis for controlling the end of the test. In this paper, the critical value of shear displacement is 8 mm, i.e., the shear test is terminated when the shear displacement of the specimen reaches 8 mm. And the data collection and analysis system are used to record the shear stress and shear displacement values, respectively, during the whole test.

3. Results and Discussion

3.1. Characteristics of Shear Stress-Displacement Curve. In order to compare and analyze the macroscopic shear characteristics of different roughness joints under different strength rock conditions, the stress-shear displacement curves of shear obtained from shear tests on high-strength rock joints and low-strength rock joints under six different roughnesses are given in Figure 2.

From Figure 2, it can be seen that the stress-displacement curves of low-strength rock mass with different roughness of joint shear conform to the typical peak-type curve variation trend. And the shear stress-displacement curves of the joints of high-strength rock mass also conform to the typical peak variation trend when the roughness of the joints is low. However, when the roughness increases to 12~14, the shear stress gradually increases to a certain constant value with the shear test, and the strain hardening phenomenon occurs, and there is no obvious peak point, which is consistent with the strain-hardening type curve change trend. The shear displacement when the joints of low-strength rock reach the peak point is larger than that of the joints of high-strength rock. In other words, the high-strength rock is less susceptible to shear slip than the low-strength rock under the same boundary conditions, shear rate, and roughness, i.e., so it is more resistant to shear damage.

It can also be seen from Figure 2 that in the initial stage of shear, the stress-strain curve of the low-strength rock joints in shear is downwardly convex, i.e., the slope of the tangent line of the curve gradually increases, while the stress-strain curve of the high-strength rock joints in shear is upwardly convex, i.e., the slope of the tangent line of the curve gradually decreases. Because the slope of the tangent line at a point on the stress-displacement curve of shear represents the shear stiffness at that point, it can be seen from Figure 2 that the shear stiffness of the low-intensity rock surface gradually increases and the shear stiffness of the high-intensity rock surface gradually decreases in the initial stage of shear.

In the same lithology joint test, the change trend of stress-displacement curve of joint shear under different roughness is basically the same, that is, the increase of joint roughness has no obvious effect on the change trend of stress-displacement curve of joint shear of rock mass. With the increase of the roughness of the joints, the shear strength of the joints also increases significantly, and the growth rate shows an increasing trend.

3.2. Strength Characteristics. Table 1 shows the peak shear strengths of the joints of the two strengths at different roughness and the growth rates of the peak shear strengths relative to those at the previous level of roughness. Meanwhile, the peak shear strength values of the two strength rock joints at different roughness in Table 1 are fitted to obtain exponential fitting relations with fitting coefficients of 0.999 and 0.995, respectively, as shown in

$$\begin{gathered}\tau = 3.375 + 0.013 * \mathrm{JRC}^{1.848},\\ R^2 = 0.999,\\ \tau = 3.928 + 0.045 * \mathrm{JRC}^{1.498},\\ R^2 = 0.995.\end{gathered} \tag{1}$$

By plotting the above two fitted relational equations in a Cartesian coordinate system, two fitted relational curves can be obtained as shown in Figure 3.

As seen from Table 1 and Figure 3, the shear strength values of the joints of both strength rock masses grow in a power function relationship as the surface roughness of the joints increases, i.e., the shear strength of the joint face increases with the increase in roughness and the growth rate also increases.

Among them, the peak shear strength of the high-strength rock joints is larger than that of the low-strength rock joints as a whole, and the growth rate of the peak shear strength of the high-strength rock joints is also larger than that of the low-strength rock joints at the same roughness. This is because, with the increase of roughness, the meshing effect of high-strength rock joints is more significant compared with that of low-strength rock joints under the action of normal pressure.

As shown in Figure 4, the residual shear strength statistics of the two strength rock joints at different roughness are shown. It can be seen from the figure that the residual strength of the high-strength rock joints is larger, and the residual strength difference is the smallest when the JRC is 4~6, and the residual strength difference is the largest when the JRC is 8~10. On the whole, the difference between the residual strength of high-strength and low-strength rock joints is little when the JRC is small, and the difference between the residual strength of the two is obvious after the JRC exceeds 6. This is mainly due to the fact that the shear stress curves of high-strength rock joints and low-strength rock joints are displacement-softening type, and

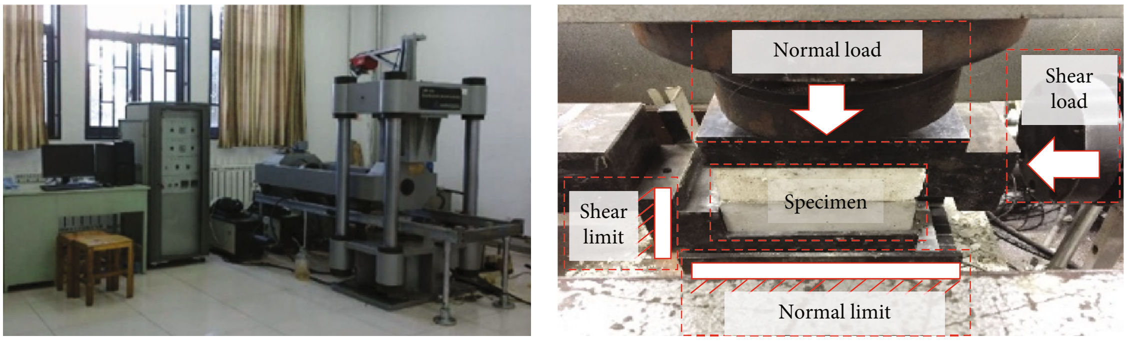

(a) (b)

Figure 1: Arrangement of the shear test [41]: (a) shear test system; (b) loading unit.

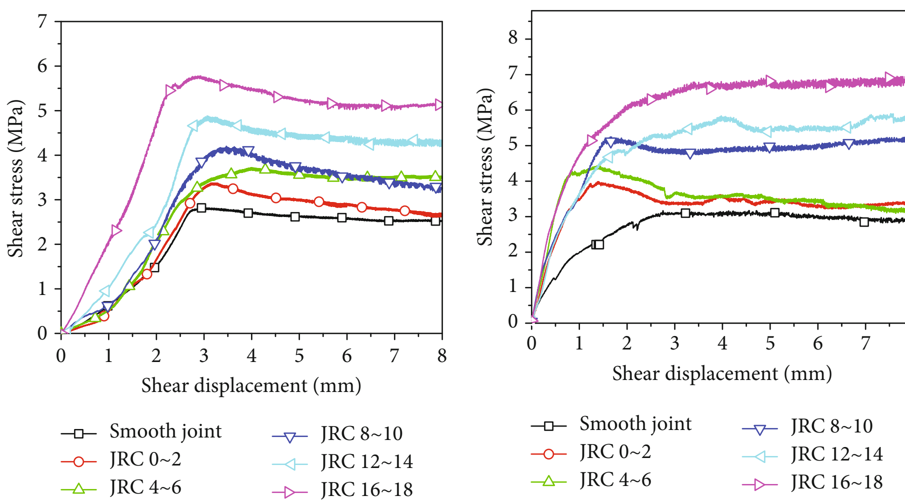

(a) (b)

Figure 2: Curves of shear stress vs. displacement of low-strength and high-strength rock joints: (a) low-strength rock joints; (b) high-strength rock joints.

Table 1: Shear strength of joint with different lithologies.

Joint surface type	Low-strength rock mass		High-strength rock mass	
	Peak strength (MPa)	Growth rate (%)	Peak strength (MPa)	Growth rate (%)
Smooth joint	2.83		3.17	
JRC 0~2	3.38	19.43	3.98	25.56
JRC 4~6	3.72	31.45	4.43	39.75
JRC 8~10	4.20	48.41	5.34	68.45
JRC 12~14	4.88	72.44	6.02	89.91
JRC 16~18	5.78	104.24	6.97	119.87

the shear stress decreases in the residual stage as the shear proceeds, so the difference in residual strength is not large. However, when the roughness increases to 8~10, the shear stress curve of high-strength rock joints changes to strain-hardening type. As the shear proceeds, the shear stress gradually increases in the residual phase, while the shear stress of the low-strength rock joints remains strain-softening type, and the shear stress gradually decreases in the residual phase, so the difference between the two residual shear stresses is significant.

3.3. Failure Characteristics. The damage after shearing of different roughness joints of the two strength rock masses is shown in Figures 5(a) and 5(b), respectively. From the figure, it can be seen that there is no obvious damage after shear for both low-strength and high-strength rock joints when they are endowed with smooth joints. When the JRC values of the joints of the two strengths are small (low-strength joints: 0~2 and 4~6; high-strength joints: 0~2), the shear damage characteristics are mainly shown in the form of raised wear on the joints. When the JRC values of the joints of both strengths are high (low-strength rock joints: JRC > 8 ~ 10; high-strength rock faces: JRC > 4 ~ 6), the shear damage characteristics of the joints are accompanied by a large amount of shearing of the joint projections in addition to the wear of the joint projections.

A comprehensive comparison of Figures 5(a) and 5(b) shows that the shear damage characteristics of the joints of the two strength rock masses after shearing are more

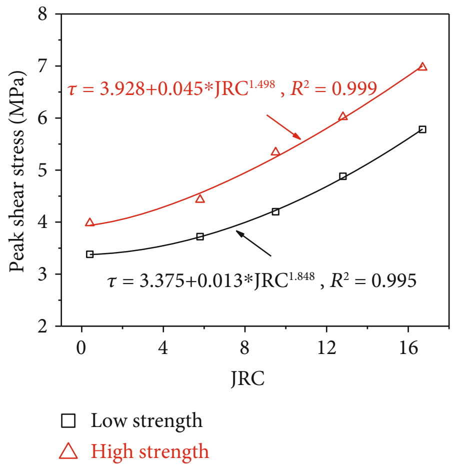

Figure 3: Relations between shear strength and JRC of joint.

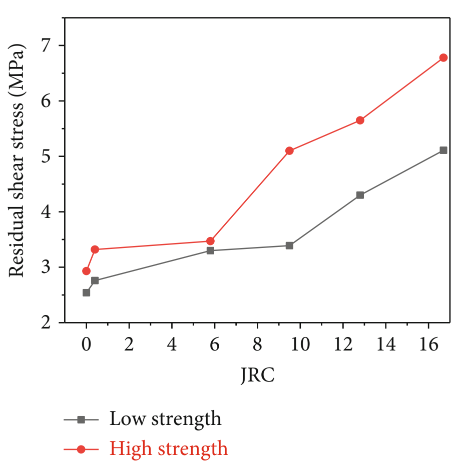

Figure 4: Residual shear strength of low-strength and high-strength rock joints with different JRC.

significant than those of the joints of the low-strength rock masses as the JRC increases, i.e., when the JRC of the joints of the two different strength rock masses are at the same level, the shear damage characteristics of the joint samples of the high-strength rock masses are more significant. This phenomenon indicates that the joints of high-strength rock still need to overcome a large frictional resistance after convex shearing and also explains the small reduction of shear stress in the postpeak phase of the shear curve of high-strength rock and the insignificant strain-softening phase.

4. Numerical Simulation of Shear Failure Mechanism

4.1. Numerical Simulation Scheme. In order to study the damage evolution process and degradation mechanism of the joints of the rock during shear, the numerical calculation model for typical working conditions (JRC of 12~14) was established by PFC^{2D} software based on the indoor tests. The dimensions of the established numerical model and the loading method are the same as those of the indoor test model. The numerical model of the rock joints was established according to the procedure shown in Figure 6. Firstly, the wall around the shear box is generated according to the specimen size, and secondly, the spheres are generated inside the wall according to the calibrated fine view parameters, and the contact model between the spheres is set to linear, as shown in Figure 6(a). Then, a certain circumferential pressure is applied to the specimen, and after the spheres are compacted, the contact model between the spheres is changed to linearpbond. The advantage of this step is to ensure that the cementation between all the spheres can be added (the pb-state is all displayed as "3"), as in Figure 6(b). After that, the joint profile is established and the spheres are grouped by importing the already drawn Barton curves, and the walls are regenerated according to the coordinates of the joint, as in Figure 6(c). The advantage of establishing the joint in this step is to ensure that the shape of the joints is the same as that of the joints of the experimental specimen and will not change during the modeling process due to the movement of the particles. In general, the joint model can be created by changing the contact properties of the particles on both sides of the joints, but due to the bump effect of the circular particles in the BPM model, the parameters of the created joints are high. Peter Cundall developed the smooth joint contact model for this purpose, which can avoid the bump effect of the particles and make the numerical simulation results more consistent with the actual results. Therefore, the contact model at the joints was changed to smooth joint, as shown in Figure 6(d).

The boundary conditions imposed in the numerical simulation are the same as those in the indoor test, limiting the horizontal displacements of wall_4 and wall_5 and the normal displacement of wall_3, controlling the vertical velocity of wall_6 by the servo function to achieve a constant normal stress (1 MPa) loading, and applying a constant horizontal velocity to wall_1, wall_2, and wall_3 (0.01 mm/s) to achieve unidirectional static shear load conditions. In PFC, the shear stress at the joint surface is derived mainly from the horizontal load between the particles and the wall, specifically: monitoring the horizontal load between the wall and the particle on the left side (wall_1 and wall_4) and the right side (wall_3 and wall_2) of the specimen, respectively, then taking the average of the left and right sides to obtain the shear load at the joint surface, and finally dividing by the joint surface length (200 mm) to get the shear stress on the joint surface. The monitoring of shear displacement is mainly achieved by monitoring the average horizontal displacement of the lower 3 sides of the specimen (wall_1, wall_2, and wall_3). After the model was established, the stress-shear displacement curves of the shear of two different strengths of the joints of the rock with JRC 12~14 at a constant normal stress of 1 MPa were used as calibration benchmarks to compare the simulation and indoor test results, and the numerical model was repeatedly calibrated using the "trial and error method" for the microscopic mechanical parameters [42]. The final obtained microscopic mechanical parameters are shown in Tables 2 and 3. The stress-shear displacement comparison curves of the numerical simulation and the shear of the indoor test are shown in Figure 7.

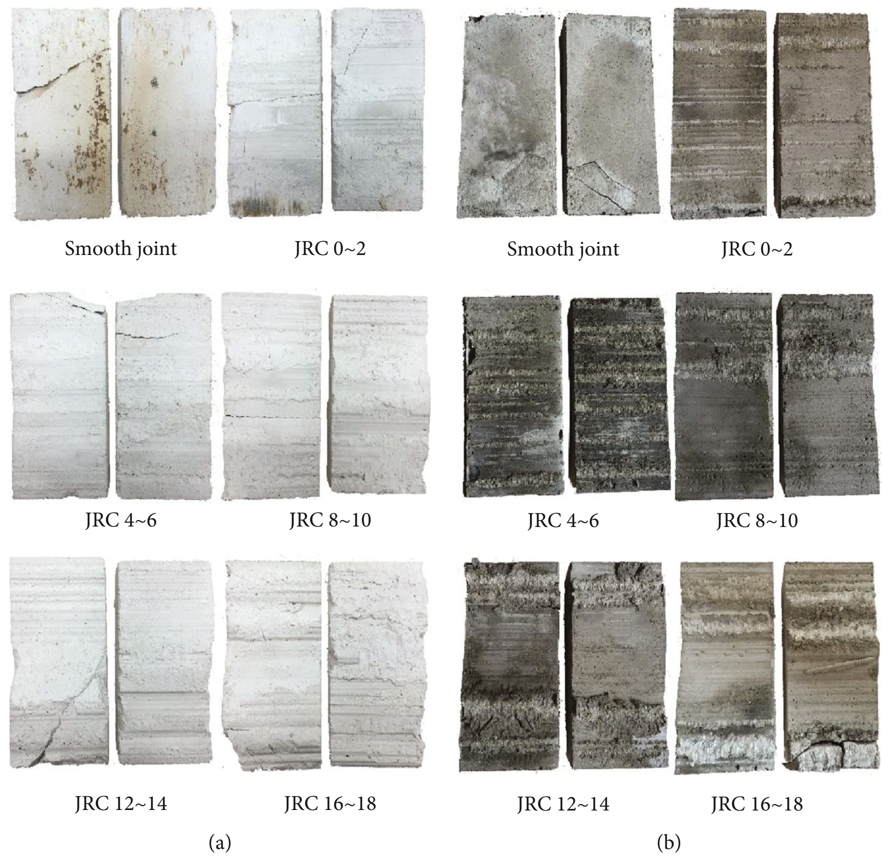

Figure 5: Shear failure model of low-strength rock joints and high-strength rock joints: (a) low-strength rock joint; (b) high-strength rock joints.

4.2. Cracking Process and Contact Force Evolution

4.2.1. Analysis of Interparticle Contact Force Evolution. During the shearing process of the rock mass, the upper and lower rock masses will be shear misaligned with each other, which makes the contact characteristics between the granules change continuously, and in turn, the contact force between the granules will also change continuously. Figure 8 shows the distribution and size evolution of the contact force detected at different shear displacements (1, 2, 3, 4, 5, 6, 7, and 8 mm) inside the rock mass, where different colors represent different contact forces. And the larger the contact force, the thicker the line. The larger the contact force between the particles, the more intense the extrusion between the particles, i.e., the size distribution of the interparticle contact force reflects the extrusion between the internal particles in the joints of the rock.

As shown in Figures 8(a) and 8(b), the distribution of contact force magnitudes between particles inside the rock during shearing of high-strength joint rocks and low-strength joint rocks is shown. As can be seen from the figures, the magnitude and orientation of the contact forces between the particles are changing as shearing proceeds. From the overall point of view, the contact force is larger at the projection of the joints during shear, and the contact force inside the rock is smaller. Generally, the joint roughness can be divided into first-order asperities (waviness) and second-order asperities (unevenness), and the two types of roughness jointly exert shear resistance during shear [25, 43]. In the early stage of shear, the contact forces on the structure surface are mainly concentrated on a few points, which are second-order rough bumps on the structure surface. As the shear proceeds, the contact force on these points gradually increases, causing the damage to this part of the projection to occur. Due to the destruction of the second-order bumps on the surface of the joints, the joint contact begins to redistribute and the points with higher contact forces begin to shift. With the further increase of shear displacement, the joint contact force is gradually concentrated to one place, i.e., the first-order rough bump.

Comparing Figures 8(a) and 8(b), it can be found that the joint contact force is greater for high-strength joint rocks under the same shear displacement conditions, and the contact force is concentrated on the first-order roughness within a smaller shear displacement. This indicates that the higher the force on the second-order roughness of the joints under the same conditions of the high-strength joint rock, the earlier and more serious the damage of the joint projection occurs. And it can also be found from the figure that the joint contact force is more widely distributed and the value is larger in the postpeak phase for high-strength joint rocks compared to low-strength joint rocks, which also explains why the shear stress curve of high-strength joint rocks is hardened while the shear curve of low-strength joint rocks is softened.

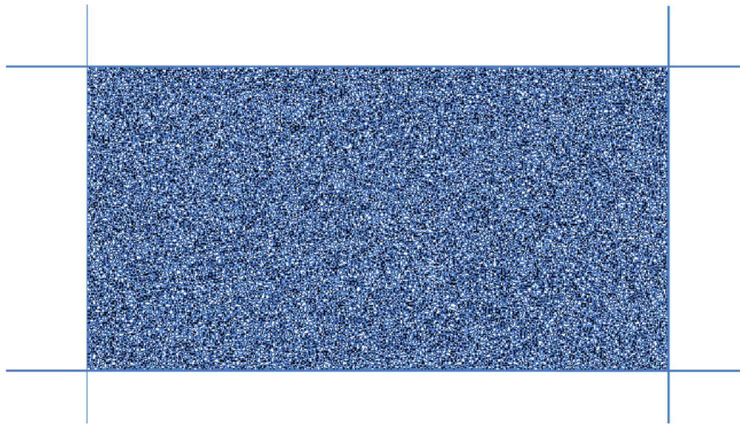

(a)

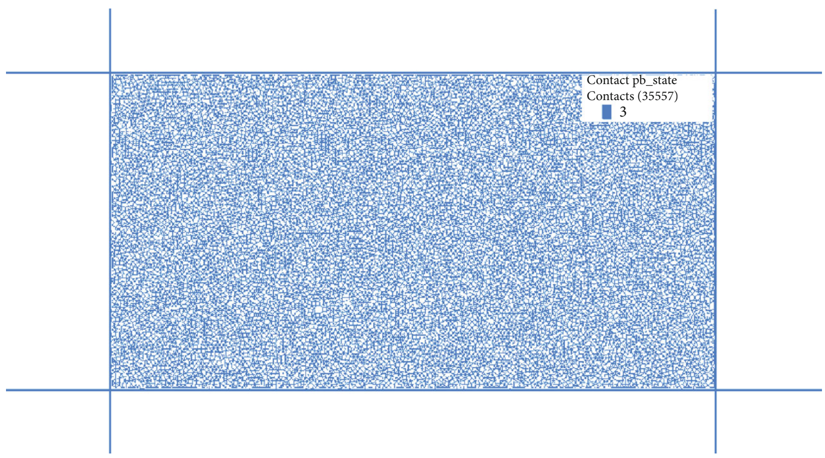

(b)

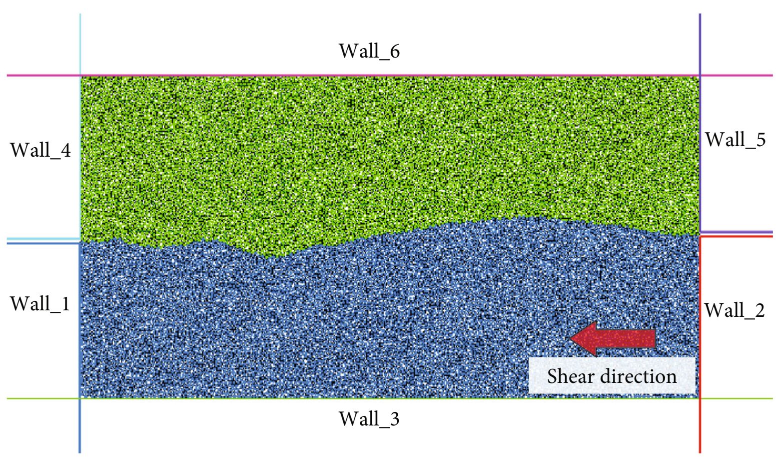

(c)

Figure 6: Continued.

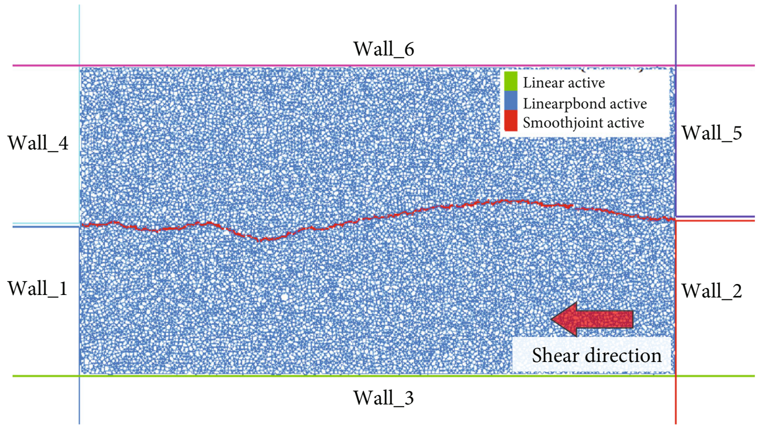

(d)

Figure 6: Construction process of anisotropic structure surface shear numerical model: (a) generation of particles; (b) change of contact model; (c) adding joints; (d) changing the joint contact model.

Table 2: Numerical calculation of microscopic mechanical parameters of low-strength rock joint.

Particle parameters	Value	Parallel bond parameters	Value	Smooth joint properties	Value
Young's modulus (GPa)	7.5	Young's modulus (GPa)	7.5	Normal stiffness (MPa/mm)	57
Ratio of normal to shear stiffness	1.0	Ratio of normal to shear stiffness	1.0	Tangential stiffness (MPa/mm)	14
Minimum particle radius (mm)	0.5	Normal strength (MPa)	31 ± 3.1	Friction coefficient	0.75
Radius ratio	1.66	Shear strength (MPa)	40 ± 4.1	Bond shear strength (MPa)	0
Density (kg/m^3)	2300			Bond normal strength (MPa)	0
Friction coefficient	0.5				

Table 3: Numerical calculation of microscopic mechanical parameters of high-strength rock joint.

Particle parameters	Value	Parallel bond parameters	Value	Smooth joint properties	Value
Young's modulus (GPa)	14	Young's modulus (GPa)	14	Normal stiffness (MPa/mm)	80
Ratio of normal to shear stiffness	1.5	Ratio of normal to shear stiffness	1.5	Tangential stiffness (MPa/mm)	80
Minimum particle radius (mm)	0.5	Normal strength (MPa)	41 ± 4.1	Friction coefficient	0.85
Radius ratio	1.66	Shear strength (MPa)	52 ± 5.1	Bond shear strength (MPa)	0
Density (kg/m^3)	2750			Bond normal strength (MPa)	0
Friction coefficient	0.6				

4.2.2. Analysis of Crack Growth Evolution. Figure 9 shows the numerical simulation evolution of the crack distribution inside the rock mass under different shear displacements in the shear process for the two strength rock joints. From the figure, it can be obtained that the crack development process of the two strength joints is similar. In order to better analyze the crack development law of the two strength joints, the number of cracks generated per unit time and the accumulated number of cracks in the joints during shear are counted, as shown in Figure 10. As can be seen from Figures 9 and 10, in the initial stage of shear (stage I), only a small number of cracks are generated at this stage because most of the interparticle contacts are in the linear elastic stage. After the elastic stage, the stress reaches the yield point and the specimen enters the stable rupture propagation stage, where the number of cracks starts to increase slowly and reaches the peak number of cracks at the peak shear stress. After the shear stress exceeds the peak point (stage II), the specimen enters the postpeak stage, and the number of cracks at this stage starts to gradually decrease and fluctuate, which is due to a large number of bumps on the joints being sheared and crushed, and the specimen shifts from the stable rupture propagation stage to the unstable rupture propagation stage, where the number of cracks fluctuates and penetrates the entire joints. Until entering stage III, the number of cracks tends to develop smoothly in general and is at a lower level, which is due to the fact that after the second-order roughness of the joints is sheared and crushed, the stress is gradually concentrated in the first-order roughness, and compared with the second-order

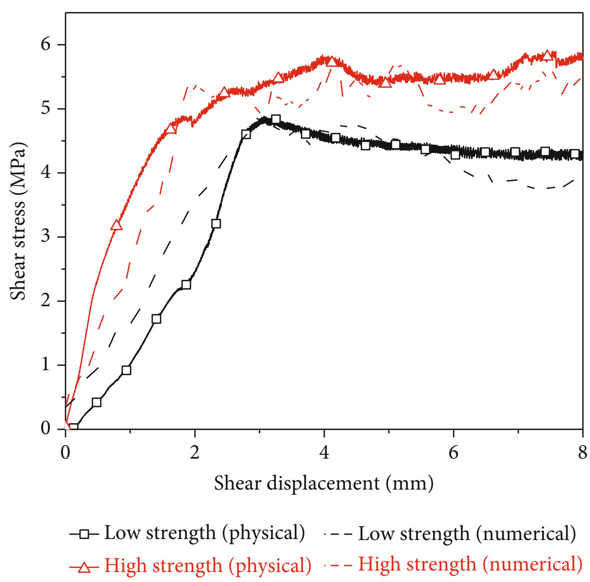

FIGURE 7: Shear stress-shear displacement curves of shear of indoor experiments and numerical simulations.

roughness, the first-order roughness is less prone to violent damage, and the joint resumes the development trend of stable rupture.

Comparing the crack development diagrams of joints of different lithologies, it can also be seen that the higher the strength of the joints, the earlier the maximum number of cracks in the joints appears and the larger the cumulative number of cracks. That is, it indicates that the damage of the joints becomes more serious at an earlier stage, which is consistent with the phenomenon observed in the indoor tests.

It can also be seen from Figure 9 that the number of tension cracks in the shear process is greater than the number of shear cracks, which is due to the fact that the internal contact force is dominated by pressure during the shear process on the joints of the rock, making the mutual extrusion between the particles resulting in the development of cracks mainly in tension cracks.

4.2.3. Analysis of Particle Rotation Radian Evolution. Figure 11 shows the evolution of the particle rotation arc inside the joints of the two strength rock masses when monitoring different shear displacements. From Figures 11(a) and 11(b), it can be seen that the shear misalignment of the rock mass causes the change of the internal rotational arc of the particle system, which in turn leads to the gradual evolution of the rotational arc of the particle body. In the initial stage of shear, the rotational arc of the particle body inside the rock mass is at a small level, and most of the particle rotational arcs are between -1 and 0, and only individual particles have slightly larger rotational arcs. Under the action of shear load, the compression density at the end of the rock body causes the particle body to rotate, so the rotation arc of the particles on the side of the applied shear stress (right side of the lower specimen) and the fixed side of the upper specimen (left side of the upper specimen) increases, and the rotation arc of the particles is mainly between 0 and 0.5. When the shear displacement further increases, the more particles with rotation arcs of 0 to 0.5 are gradually expanded from the two ends of the specimen to the lower left and upper right ends of the rock mass. The particles with high rotational arcs (i.e., rotational arcs of -600 to -1 and 1 to 600) are mainly distributed at the projections of the joint. And compared with the crack distribution, it can be found that these particles with high rotational arcs are mainly concentrated at the locations where cracks are generated. This is mainly the shear process in which the joint projection is the main bearing area. It is subjected to large normal stress and shear stress, so the granular body in this region is moving vigorously, accumulating more energy, and the rock is more prone to damage. It can be seen that the generation of cracks is related to the rotation of the particles, and the process of rock destruction is also a continuous redistribution of the internal particle rotation arc. Along with the continuous generation of cracks, it leads to the evolution of the rock mass from microscopic rupture to macroscopic failure.

To further analyze the evolution law of particle rotation arc during shearing, the proportion of the number of particles with particle rotation arcs of -600~-1, -1~0, 0~0.5, 0.5~1, and 1~600 was counted, as shown in Figure 11(c). As can be seen from the figure, the evolution process of particle rotational arcs on the joints of the two strength rock masses is roughly similar. Among them, particles with rotational arcs of 0.5~0 and 0~-1 account for the largest proportion. With the increase of shear displacement, the number of particles with rotational arcs of -1~0 shows an overall decreasing trend. In the initial stage of shear, the percentage changes less and tends to be smooth overall, while after the peak shear stress, the percentage decreases rapidly from 75% to about 50%. And after the shear displacement to 6 mm, the percentage tends to be smooth again roughly stabilized at about 50%. The proportion of particles with a rotational arc of 0.5 to 0 is on the whole on an upward trend from 20% to about 40%, and the growth trend of this proportion of particles is the opposite of the decreasing trend of the proportion of particles from -1 to 0. The percentage of particles with rotational arcs of 1~600, -1~-600, and 0.5~1 all show an increasing trend basically from 0% to about 3% slowly. Comparing the histograms of the joints of the two intensities, it is also clear that the decrease in the percentage of particles with rotational arcs of 0~-1 on the joints of the low-intensity rock is more continuous, while the joints of the high-intensity rock show a stepwise pattern, which is related to the damage pattern and range of the joints.

4.3. Evolution Characteristics of Energy

4.3.1. Determination of Dissipation Energy. The physical and mechanical change processes of rock are closely related to energy transformation, and its deformation and failure are instability phenomena driven by energy exchange [44].

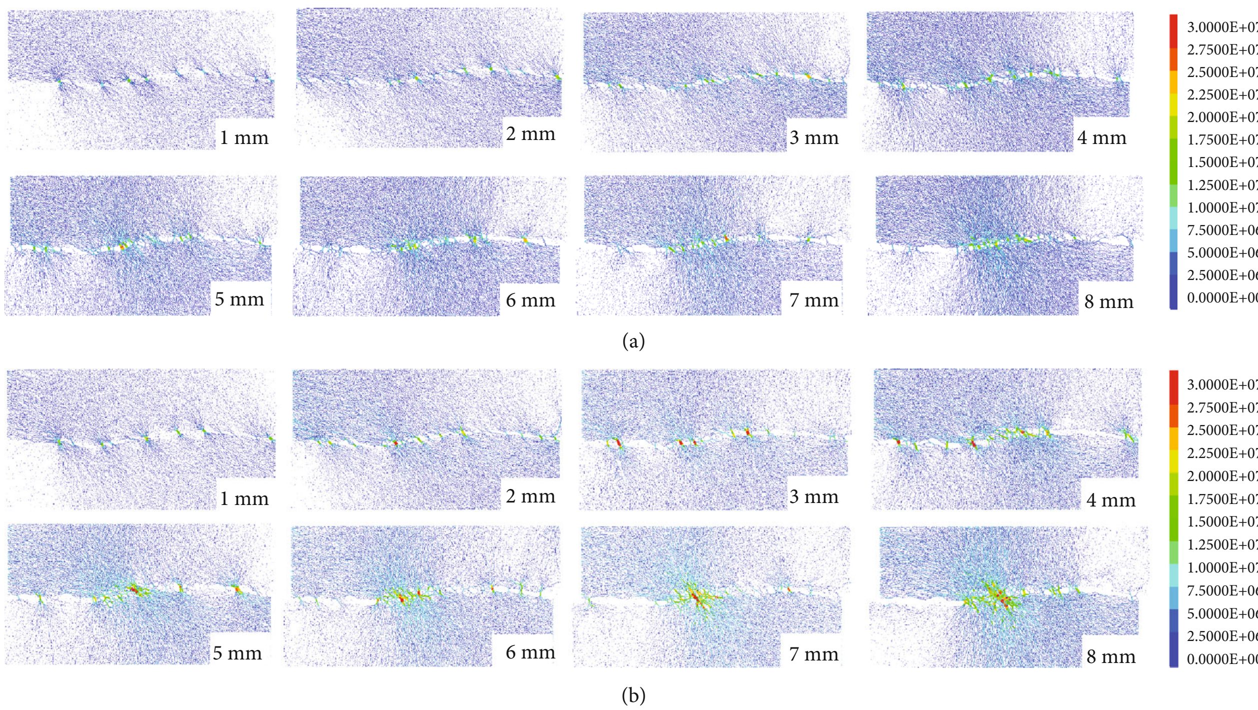

Figure 8: Evolution of contact force between particles during shearing: (a) low-strength rock joints; (b) high-strength rock joints.

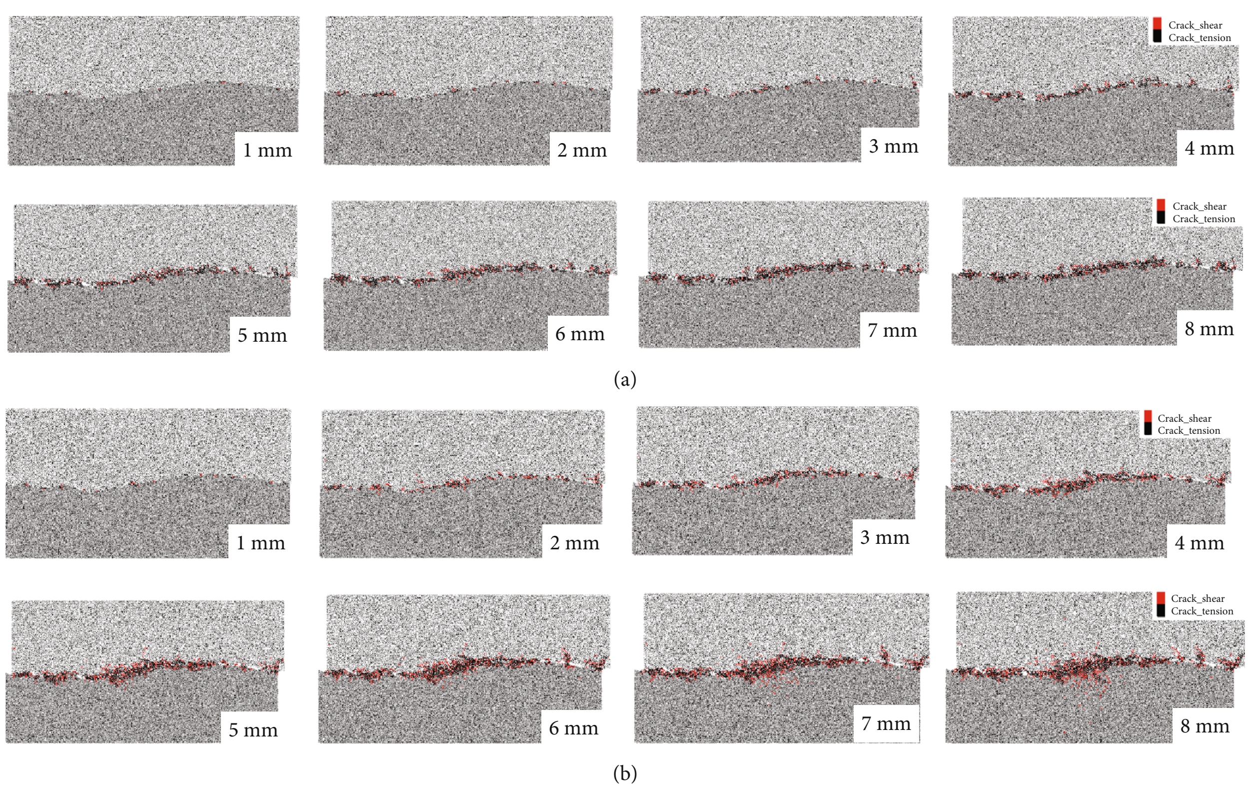

Figure 9: Evolution of microcracks during shearing: (a) low-strength rock joints; (b) high-strength rock joints.

Therefore, the energy dissipation can reflect the damage of the specimen, and the analysis of the energy evolution process of the joint of the rock body can also reveal the damage mechanism of the joint.

According to the law of energy conservation, the expression of total external energy U is as follows:

$$U = U_{\mathrm{e}} + U_{\mathrm{d}} + U_{\mathrm{k}}, \tag{2}$$

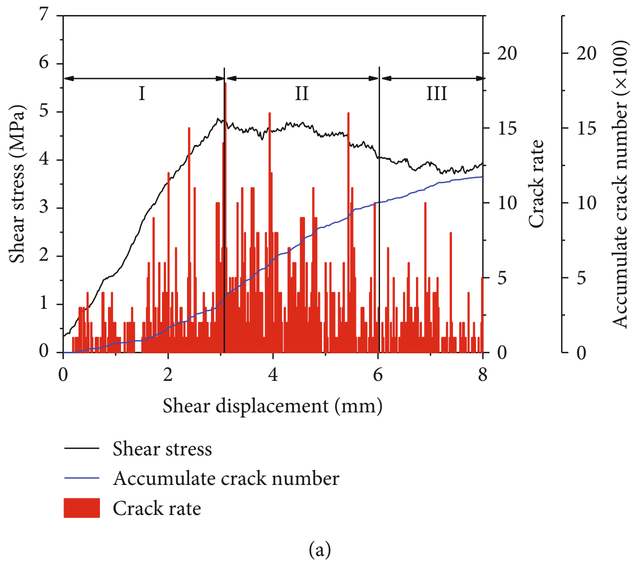

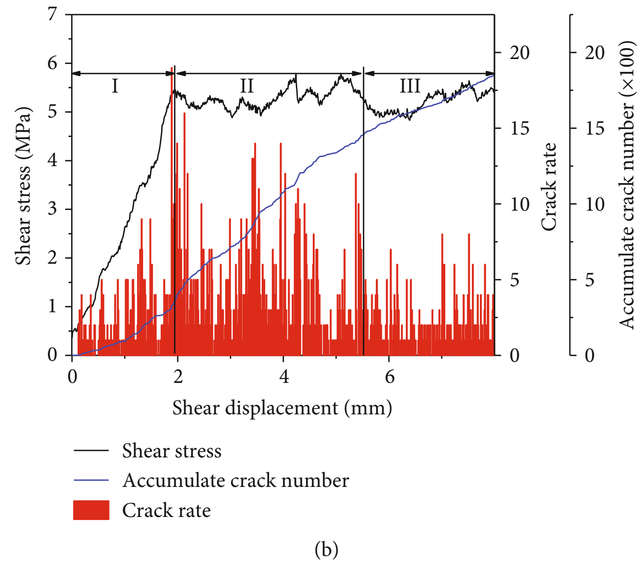

FIGURE 10: Number of cracks and cumulative number of cracks: (a) low-strength rock joints; (b) high-strength rock joints.

where U_e is the elastic energy, U_d is the dissipative energy, and U_k is the kinetic energy.

Since the shear speed is 0.01 mm/s during the whole simulated shear process, the kinetic energy is negligible, so the total energy expression can be simplified as

$$U = U_e + U_d. \quad (3)$$

In the PFC numerical simulation software, the total external input energy is Wall's boundary energy E_z. The elastic energy is mainly the linear elastic energy E_s and the gluing elastic energy E_b, as shown in the following:

$$U_e = E_s + E_b. \quad (4)$$

Among them, Wall's boundary energy E_z, linear elastic energy E_s, and gluing elastic energy E_b can be calculated by the self-contained function of the PFC numerical simulation software [45]; the equations are as follows:

$$\begin{aligned} E_z &= \sum_{N_w} (F_i d_i), \\ E_s &= \frac{1}{2}\left(\frac{(F_n^l)^2}{k_n} + \frac{\|F_s^l\|^2}{k_s}\right), \\ E_b &= \frac{1}{2}\left(\frac{F_n^2}{k_n A} + \frac{\|F_s\|^2}{k_s A} + \frac{\|M_b\|^2}{k_n I}\right), \end{aligned} \quad (5)$$

where N_w is the number of walls; F_i is the force exerted on the wall; d_i is the displacement of the wall; F_n^l is the linear normal force; F_s^l is the linear shear force; k_n is the linear normal stiffness; k_s is the linear shear stiffness. A is the cross-sectional area; I is the moment of inertia of the parallel bond cross-section; F_n is the normal force of parallel bond; F_s is the shear force of parallel bond; k_n and k_s are the normal and shear stiffness of parallel bond; M_b is the moment of parallel bond.

Dissipative energy is mainly generated by friction, damping dissipation, microrupture, and plastic deformation and can be obtained by subtracting the elastic energy from the total external energy, i.e.,

$$U_d = U - U_e. \quad (6)$$

4.3.2. Energy Evolution. As shown in Figure 12, the curves of the total external input energy, elastic energy, and dissipation energy changes during shear for the high-strength rock joints and low-strength rock joints are shown. As a whole, the energy evolution process of high-strength rock joints and low-intensity rock joints is similar. In the preshear stage, i.e., stage I, the total input energy increases rapidly with the increase of shear stress, shear displacement, and normal displacement. As the connection and cementation of most of the particles in the early stage of shear are still in the elastic stage, the elastic energy accumulates continuously as the shear proceeds. However, the analysis above shows that a small amount of cracks are generated in this stage and there is some damage, so some dissipation energy is also generated in this stage. And the dissipation energy is first at a small level and then starts to rise slowly. After the shear displacement exceeds a certain range, the rising rate increases rapidly, which is the same as the trend of the number of cracks accumulated on the joints during shear. The elastic energy reaches its peak by the time it reaches the peak of the shear stress, after which macroscopic damage occurs in stage II due to a large number of cracks on the joints. The elastic energy stored between the particle joints and between the glue junctions is consumed, causing the elastic energy curve to start decreasing. And the dissipation energy still keeps growing at a large rate. In stage III, the elastic energy remains basically the same, while the dissipation energy continues to increase. This is due to the fact that there are still a

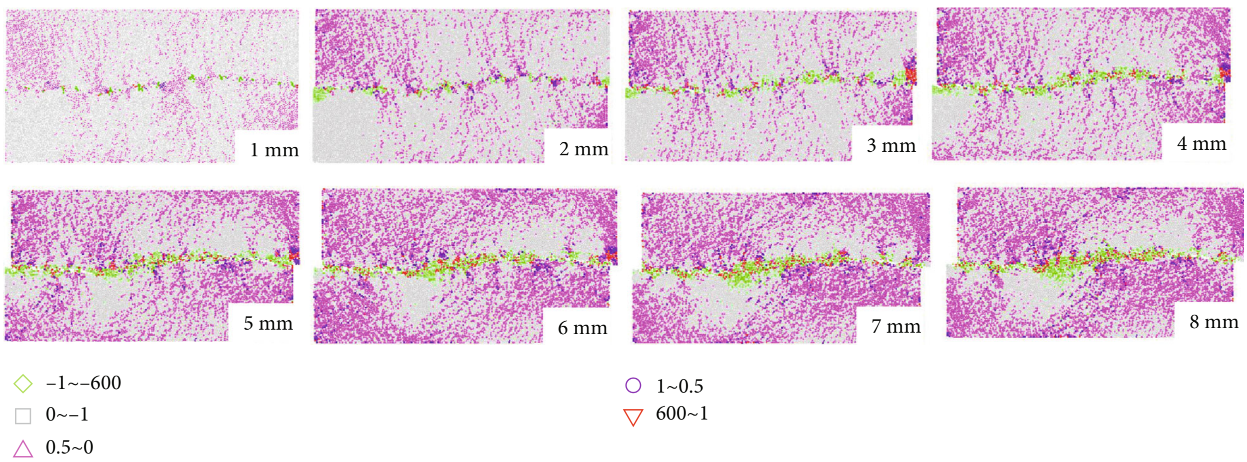

(a)

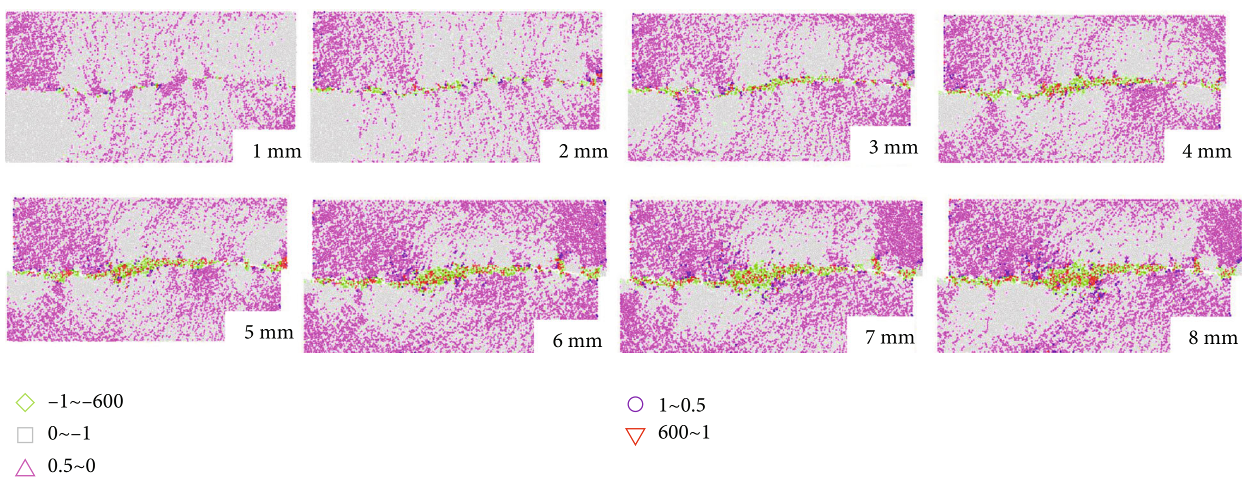

(b)

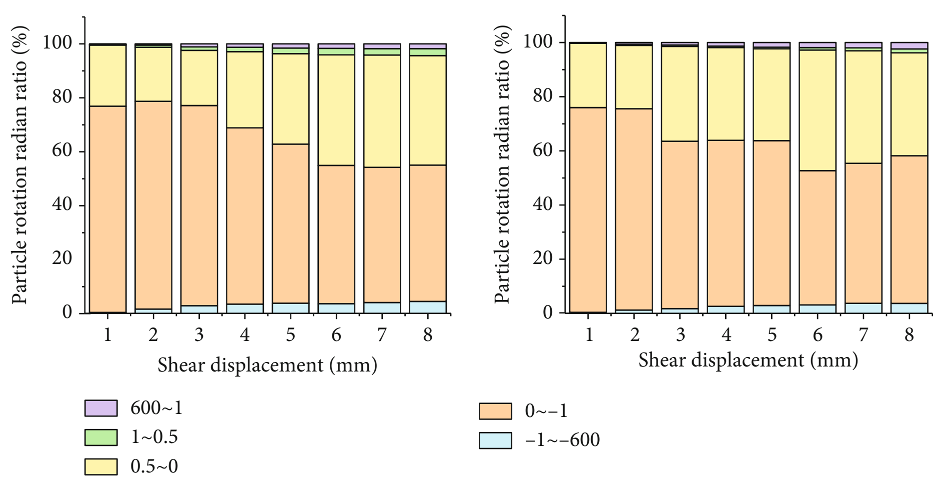

(c)

Figure 11: Evolution of particle rotation radian during shearing: (a) low-strength rock joints; (b) high-strength rock joints; (c) the percentage of particle rotation arc.

large number of cracks generated in this stage and the friction between particle contacts increases, so the frictional dissipation energy becomes the main energy dissipated.

Comparing the energy evolution curves of high-strength joint rocks and low-strength joint rocks, it can be seen that the high-strength joint rocks have greater total input energy,

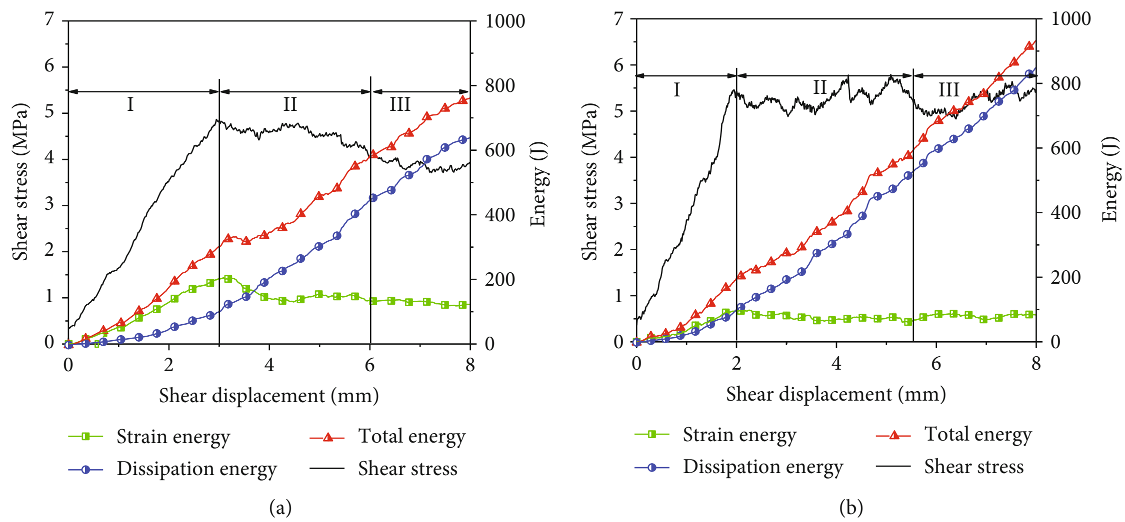

FIGURE 12: Variation curve of energy with shear displacement: (a) low-strength rock joints; (b) high-strength rock joints.

greater dissipation energy, and smaller peak elastic energy. This is due to the fact that the high-strength joint rock specimens have higher input shear stress and higher normal displacement during shear, which in turn results in higher total input energy. As shown in the above analysis, under the same conditions, the joint projections of high-strength joint rocks are damaged earlier and more severely than those of low-strength joint rocks, and a large number of cracks are produced at a smaller shear displacement. Therefore, the accumulated elastic energy is smaller, while the dissipation energy is larger.

5. Conclusion

In order to study the effect of rock mass strength on the macroscopic and microscopic shear properties of the joints, shear tests of rock specimens of two strengths were conducted in the laboratory and corresponding numerical simulations were carried out using PFC^{2D} numerical simulation software, and then, a systematic study of the shear properties of the joints of rock masses of different strengths was carried out from the macroscopic and microscopic perspectives, and the following conclusions were obtained:

(1) The shear stress curves of rock masses with different strengths tend to be different. High-strength rock masses tend to be hardened and low-strength rock masses tend to be softened. And comparing the test results under multiple roughness conditions, we can also find that the joints of high-strength rock masses are more sensitive to the change of roughness

(2) With the increase of JRC, the surface damage mode of the joints of both strength rock masses gradually changes from "abrasion" to "abrasion + gnawing". The damage range of high-strength joints is larger, which means that the high-strength joints are less susceptible to shear slip than the low-strength rock mass surface

(3) In the simulated shear process, the contact force is mainly concentrated on the joints, while the contact force inside the rock is smaller. And the contact force on the joints first acts on the second-order roughness and then gradually acts on the first-order roughness. Compared with the low-strength rock masses, the contact force on the joints of the high-strength rock masses is larger and more widely distributed

(4) At the early stage of shear, more rotations occurred in the end particle body, and only a small number of cracks occurred on the joints. With the increase of shear displacement, the number of particles and cracks with larger rotational arc increases rapidly, and the particle arc is mainly concentrated in the location where cracks occur. The cumulative number of cracks on the joints of the high-strength rock masses is more, and the particles with larger rotational arcs are distributed more widely

(5) As shearing proceeds, the total input energy continues to increase. At the beginning of shear, the elastic energy is greater than the dissipative energy. Near the peak of shear, the elastic energy reaches its peak and then begins to decrease and gradually tends to be constant. However, the dissipative energy keeps increasing and eventually becomes much larger than the elastic energy. The input energy and dissipation energy of the high-strength joint rock specimens are greater, while the peak elastic energy is smaller

Data Availability

The data used to support the findings of this study are available from the corresponding author upon request.

Conflicts of Interest

The authors declare no conflict of interest.

Acknowledgments

This work is supported by the National Natural Science Foundation of China (No. 52104093) and the Shandong Provincial Natural Science Foundation (Nos. ZR2019BEE065 and ZR2020QE120).

References

[1] Y. Su, F. Y. Zang, Y. Q. Li, Y. Q. Du, and W. Y. Wang, "Shear failure mode of anchored rock mass with through joints," *The Chinese Journal of Geological Hazard and Control*, vol. 31, no. 5, pp. 133–140, 2020.

[2] L. D. Wang, B. Y. Hao, and M. X. Liang, "Slurry diffusion of single fracture based on fluid-solid coupling," *Journal of Mining and Strata Control Engineering*, vol. 3, no. 1, pp. 104–112, 2021.

[3] J. K. Li and H. Wang, "Ground support of interbedded rock roof in a deep roadway with fully-anchored cables," *Journal of Mining and Strata Control Engineering*, vol. 2, no. 3, pp. 14–22, 2020.

[4] X. B. Yang, J. Zhou, Y. M. Song, and X. X. Han, "Evolution characteristics of sliding displacement of rock interface under cyclic loading," *Journal of China Coal Society*, vol. 44, no. 10, pp. 3041–3048, 2019.

[5] N. Barton, "The shear strength of rock and rock joints," *International Journal of Rock Mechanics and Mining Sciences & Geomechanics Abstracts*, vol. 13, no. 9, pp. 255–279, 1976.

[6] N. Barton, S. Bandis, and K. Bakhtar, "Strength, deformation and conductivity coupling of rock joints," *International Journal of Rock Mechanics and Mining Sciences & Geomechanics Abstracts*, vol. 22, no. 3, pp. 121–140, 1985.

[7] C. C. Xia, Z. C. Tang, W. M. Xiao, and Y. L. Song, "New peak shear strength criterion of rock joints based on quantified surface description," *Rock Mechanics and Rock Engineering*, vol. 47, no. 2, pp. 387–400, 2014.

[8] J. Yang, G. Rong, D. Hou, J. Peng, and C. B. Zhou, "Experimental study on peak shear strength criterion for rock joints," *Rock Mechanics and Rock Engineering*, vol. 49, no. 3, pp. 821–835, 2016.

[9] A. Karami and D. Stead, "Asperity degradation and damage in the direct shear test: a hybrid fem/dem approach," *Rock Mechanics and Rock Engineering*, vol. 41, no. 2, pp. 229–266, 2008.

[10] M. S. Asadi, V. Rasouli, and G. Barla, "A laboratory shear cell used for simulation of shear strength and asperity degradation of rough rock fractures," *Rock Mechanics and Rock Engineering*, vol. 46, no. 4, pp. 683–699, 2013.

[11] M. Bahaaddini, P. C. Hagan, R. Mitra, and M. H. Khosravi, "Experimental and numerical study of asperity degradation in the direct shear test," *Engineering Geology*, vol. 204, pp. 41–52, 2016.

[12] Z. H. Zhao, H. Peng, W. Wu, and Y. F. Chen, "Characteristics of shear-induced asperity degradation of rock fractures and implications for solute retardation," *International Journal of Rock Mechanics and Mining Sciences*, vol. 105, pp. 53–61, 2018.

[13] F. Z. Meng, H. Zhou, Z. Q. Wang et al., "Characteristics of asperity damage and its influence on the shear behavior of granite joints," *Rock Mechanics and Rock Engineering*, vol. 51, no. 2, pp. 429–449, 2018.

[14] G. Grasselli, "Shear strength of rock joints based on quantified surface description," At the Civil Engineering Department, EPF Lausanne, Switzerland, 2001.

[15] A. Fathi, Z. Moradian, P. Rivard, G. Ballivy, and A. J. Boyd, "Geometric effect of asperities on shear mechanism of rock joints," *Rock Mechanics and Rock Engineering*, vol. 49, no. 3, pp. 801–820, 2016.

[16] W. M. Xiao, C. C. Xia, W. Wang, S. G. Du, and R. G. Deng, "Contact algorithm for determining aperture evolution of rock fracture during shearing," *International Journal of Geomechanics*, vol. 16, no. 2, pp. 1–13, 2016.

[17] F. Z. Meng, H. Zhou, S. J. Li et al., "Shear behaviour and acoustic emission characteristics of different joints under various stress levels," *Rock Mechanics and Rock Engineering*, vol. 49, no. 12, pp. 4919–4928, 2016.

[18] G. J. Cui, C. Q. Zhang, H. C. Han, Z. Q. Zeng, H. Zhou, and J. J. Lu, "Experiment study on shear behavior of artificial joint under CNL and CNS boundary conditions," *Chinese Journal of Rock Mechanics and Engineering*, vol. 38, no. S2, pp. 3384–3392, 2019.

[19] Q. Yin, H. W. Jing, B. Meng, R. C. Liu, Y. J. Wu, and Y. J. Wu, "Macroscopic and microscopic shear mechanical properties of sandstone under CNL and CNS boundary conditions," *Journal of Mining & Safety Engineering*, vol. 38, no. 3, pp. 615–624, 2020.

[20] G. Wang, X. P. Zhang, Y. J. Jiang, B. Li, X. Z. Wu, and N. Huang, "Meso-mechanism research on shear failure of rock joint based on particle discrete element method," *Journal of Central South University*, vol. 46, no. 4, pp. 1442–1453, 2015.

[21] X. P. Zhang, Y. J. Jiang, G. Wang et al., "Mechanism of shear deformation, failure and energy dissipation of artificial rock joint in terms of physical and numerical consideration," *Geosciences Journal*, vol. 23, no. 3, pp. 519–529, 2019.

[22] Y. Jiang, J. Xiao, Y. Tanabashi, and T. Mizokami, "Development of an automated servo-controlled direct shear apparatus applying a constant normal stiffness condition," *International Journal of Rock Mechanics and Mining Sciences*, vol. 41, no. 2, pp. 275–286, 2004.

[23] W. C. Fan, P. Cao, and L. Long, "Degradation of joint surface morphology, shear behavior and closure characteristics during cyclic loading," *Journal of Central South University*, vol. 25, no. 3, pp. 653–661, 2018.

[24] X. R. Liu, B. Xu, X. H. Zhou, L. Yi, X. Zeng, and J. W. Wang, "Investigation on the macro-meso shear mechanical properties of soft-hard interbedded rock discontinuity," *Journal of China Coal Society*, vol. 40, no. 9, pp. 2895–2909, 2021.

[25] F. D. Patton, "Multiple modes of shear failure in rock," in *Proceedings of the 1st Congress of the International Society of Rock Mechanics*, pp. 509–513, Lisbon, Portugal, 1966.

[26] N. Barton and V. Choubey, "The shear strength of rock joints in theory and practice," *Rock Mechanics*, vol. 10, no. 1-2, pp. 1–54, 1977.

[27] G. C. Zhang, M. Karakus, H. M. Tang, Y. F. Ge, and L. Zhang, "A new method estimating the 2D joint roughness coefficient for discontinuity surfaces in rock masses," *International Journal of Rock Mechanics and Mining Sciences*, vol. 72, pp. 191–198, 2014.

[28] R. Tse and D. M. Cruden, "Estimating joint roughness coefficients," *International Journal of Rock Mechanics and Mining Sciences & Geomechanics Abstracts*, vol. 16, no. 5, pp. 303–307, 1979.

[29] Y. F. Ge, P. H. S. W. Kulatilake, H. Tang, and C. G. Xiong, "Investigation of natural rock joint roughness," *Computers and Geotechnics*, vol. 55, pp. 290–305, 2014.

[30] R. C. Liu, S. Lou, X. J. Li, G. S. Han, and Y. J. Jiang, "Anisotropic surface roughness and shear behaviors of rough-walled plaster joints under constant normal load and constant normal stiffness conditions," *Journal of Rock Mechanics and Geotechnical Engineering*, vol. 12, no. 2, pp. 338–352, 2020.

[31] E. K. Hou, T. Cong, X. S. Xie, and J. B. Wei, "Ground surface fracture development characteristics of shallow double coal seam staggered mining based on particle flow," *Journal of Mining and Strata Control Engineering*, vol. 2, no. 1, pp. 16–24, 2020.

[32] X. R. Liu, Z. Y. Deng, Y. Q. Liu, Y. M. Lu, S. L. Liu, and Y. F. Han, "Macroscopic and microscopic analysis of particle flow in pre-peak cyclic direct shear test of rock joint," *Journal of China Coal Society*, vol. 44, no. 7, pp. 2103–2115, 2019.

[33] X. R. Liu, B. Xu, J. H. Huang et al., "Macro-meso shear mechanical behaviors of coalescent rock joints with different morphologies," *Chinese Journal of Geotechnical Engineering*, vol. 43, no. 3, pp. 406–415, 2021.

[34] Y. F. Ge, H. M. Tang, M. A. M. Ez Eldin, L. Q. Wang, Q. Wu, and C. G. Xiong, "Evolution process of natural rock joint roughness during direct shear tests," *International Journal of Geomechanics*, vol. 17, no. 5, pp. 1–10, 2017.

[35] J. W. Park and J. J. Song, "Numerical method for the determination of contact areas of a rock joint under normal and shear loads," *International Journal of Rock Mechanics and Mining Sciences*, vol. 58, pp. 8–22, 2013.

[36] Y. F. Chen, H. Lin, X. Ding, and S. J. Xie, "Scale effect of shear mechanical properties of non-penetrating horizontal rock-like joints," *Environmental Earth Sciences*, vol. 80, no. 5, pp. 192–202, 2021.

[37] X. Zhang, H. Lin, Y. X. Wang, R. Yong, Y. L. Zhao, and S. du, "Damage evolution characteristics of saw-tooth joint under shear creep condition," *International Journal of Damage Mechanics*, vol. 30, no. 3, pp. 453–480, 2021.

[38] X. Fan, Z. Y. Deng, Z. M. Cui, Z. M. He, and H. Lin, "A new peak shear strength model for soft-hard joint," *Rock and Soil Mechanics*, vol. 42, no. 7, pp. 1–10, 2021.

[39] Y. J. Jiang, Y. Q. Chen, X. Z. Cheng et al., "Experimental study on shear behavior and acoustic emission characteristics of nonpersistent joints," *Geofluids*, vol. 2020, 10 pages, 2020.

[40] Y. J. Jiang, Y. H. Wang, P. Yan, H. Luan, and Y. Q. Chen, "Experimental investigation on the shear properties of heterogeneous discontinuities," *Geotechnical and Geological Engineering*, vol. 37, no. 6, pp. 4959–4968, 2019.

[41] X. Z. Cheng, H. J. Luan, Y. J. Jiang, S. H. Zhang, and C. Y. Jia, "Experimental study on shear behavior and failure mechanism of bolted heterogeneous rock joints under different anchorage conditions," *Geofluids*, vol. 2021, 14 pages, 2021.

[42] J. Yoon, "Application of experimental design and optimization to PFC model calibration in uniaxial compression simulation," *International Journal of Rock Mechanics and Mining Sciences*, vol. 44, no. 6, pp. 871–889, 2007.

[43] X. G. Liu, W. C. Zhu, Q. L. Yu, S. J. Chen, and K. Guan, "Estimating the joint roughness coefficient of rock joints from translational overlapping statistical parameters," *Rock Mechanics and Rock Engineering*, vol. 52, no. 3, pp. 753–769, 2019.

[44] Y. J. Jiang, P. Yan, Y. H. Wang, H. J. Luan, and Y. Q. Chen, "Numerical investigations on shear behavior and failure mechanism of non-persistent jointed rocks," *Geotechnical and Geological Engineering*, vol. 38, no. 2, pp. 1639–1651, 2020.

[45] Itasca Consulting Group Inc (ICG), *PFC2D Version 4.0: Theory and Background*, Itasca Consulting Group Inc, Minneapolis, 2008.

Hindawi
Geofluids
Volume 2022, Article ID 4133529, 17 pages
https://doi.org/10.1155/2022/4133529

Research Article

Stress Evolution Mechanism and Control Technology for Reversing Mining and Excavation under Mining-Induced Dynamic Pressure in Deep Mine

Jiyu Wang, Fangtian Wang, and Xigui Zheng

School of Mines, Key Laboratory of Deep Coal Resource Mining, Ministry of Education of China, China University of Mining & Technology, Xuzhou 221116, China

Correspondence should be addressed to Fangtian Wang; wangfangtian111@163.com

Received 4 November 2021; Accepted 24 February 2022; Published 15 March 2022

Academic Editor: Hualei Zhang

In order to alleviate the relationship between mining and roadway, the 3204 working face and the 3206 roadway in Shanxi Taitou coal mine are taken as an example, and the width of mining and the support parameters of mining while reversing mining and excavation under dynamic pressure are optimized. The research includes field investigations, theoretical analysis, numerical simulation, and field tests. Based on the characteristics of roof fracture and the distribution of coal pillar stresses that determine the coal pillar is 18.7 m wide, the control scheme of mining while reversing mining and excavation was developed; the stress of coal pillar and the characteristics of roadway deformation and failure are summarized. By means of FLAC^{3D} numerical simulation software, the influence of coal pillar widths and different mining positions on the stability of roadway surrounding rock are discussed. The asymmetric support structure of trapezoidal roadway is proposed as the core support, and the support scheme of dense bolts and anchor cables is proposed. The support of the 3206 return airway is composed of bolt, anchor cable, and anchor mesh, combined with M-shaped steel belt and steel beam. Through the research on the current situation of roadway support, the support scheme is optimized to make the 3206 return airway meet the production requirements, which provides a new breakthrough for roadway support under dynamic pressure in deep mines in China.

1. Introduction

With the rapid development of coal mining equipment and the rapid advancement of fully mechanized mining face, the replacement of mine face is becoming increasingly tense. In order to alleviate the tense situation of mining and roadway, some coal mines operate at the same time of adjacent working face mining and roadway excavation [1, 2]. The mining of the upper working face and the roadway excavation of the lower working face are operated at the same time, that is, the mining and excavation of the working face and roadway, as shown in Figure 1. Thus, the roadway excavation will be affected by multiple stresses, including its own excavation, the mining of the previous working face, and the dynamic pressure of the roof, which will bring great difficulties to roadway excavation and support [3–5]. Especially when the roadway and the working face are staggered, the roadway will be affected by the dynamic pressure as "stability-breaking-bending-stability" of the roof and goaf.

Based on the in-depth research on the coal pillar size and the characteristics of roadway deformation, relevant scholars put forward that the support technology plays a role in controlling the surrounding rock of roadway. Chen et al. [6] studied the stress distribution around the coal pillar, and the coal pillar widths of 5 m, 10 m, 20 m, and 30 m were designed for the layout of residual coal pillar mining roadway on this basis. Li et al. [7] studied the characteristics of stress distribution in surrounding rock of side mining roadway in goafs with different coal pillar widths. Zhang et al. [8] calculated the width of coal pillar, analyzed the distribution of stresses, and studied the relationship between coal pillar stresses. Gao [9] proposed a method of analyzing composite rock mass stability on the roof, floor, and coal pillar regarded

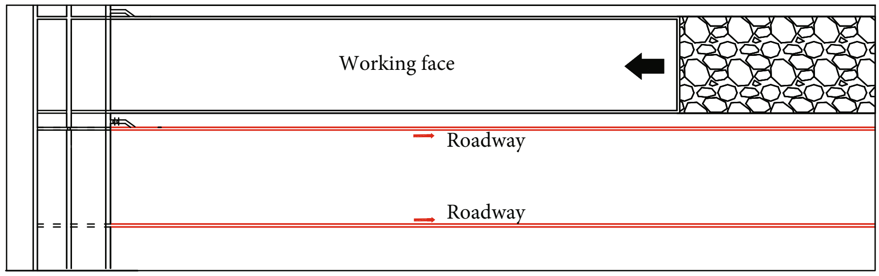

Figure 1: Schematic diagram of reverse mining and excavation.

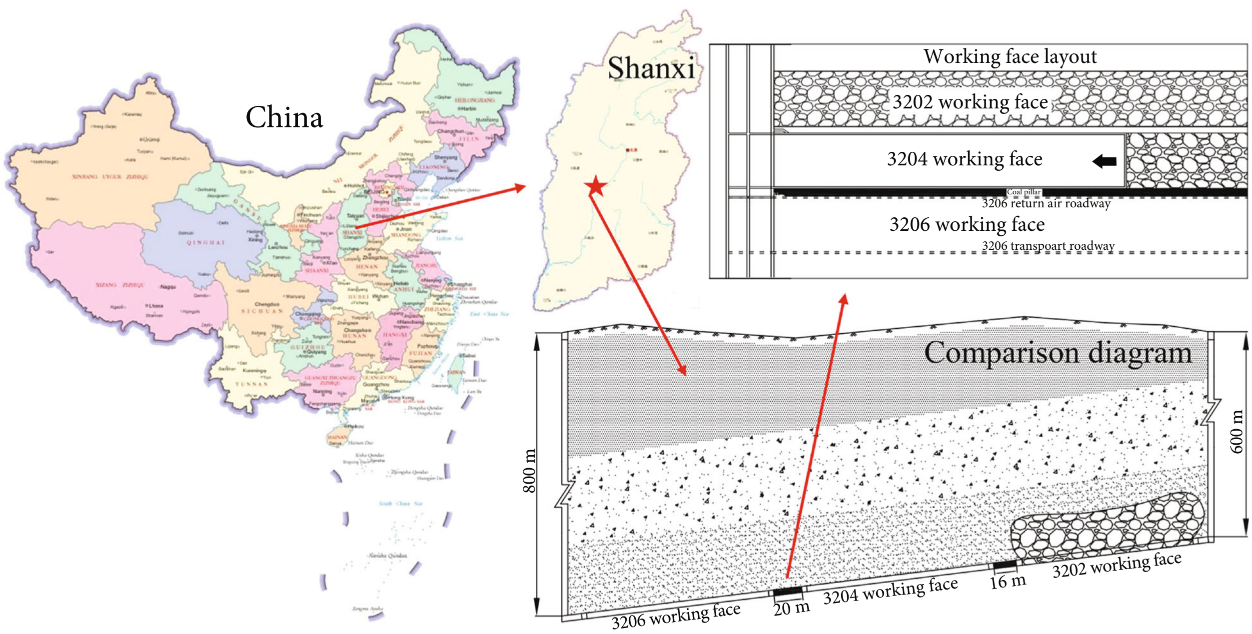

Figure 2: Layout of 3206 working face.

as layered composite rock mass and analyzed the influence of roof and floor on the coal pillar. Sun et al. [10] discussed the distribution of stresses in the mining of pillar roof cutting and retaining roadway in the goaf. In the large pillar mining and the small pillar mining, the peak stresses of pillars were reduced by 12-21% and 3-10%, respectively. Huang et al. [11] studied the impacts of different coal pillar distances on coal pillar stress concentration and formation fracture development. On this basis, the calculation formula of safe mining and reducing surface damage of shallow buried multicoal seam was established. Wang et al. [12], according to the distribution of acoustic wave velocities, put forward that the impact caused by mining activities could be extended about 40 m to the working face, and the stress peak concentration was found about 15 m ahead. Scholars have done a lot of researches on coal pillar, coal pillar reservation, and coal pillar size in the working face. Fan et al. [13] studied the formation and development of plastic zone and the creep and damage of rock mass and proposed the corresponding roadway support technology. Li et al. [14] deduced the elastic energy and dissipation energy in the process of rock burst by means of theoretical analysis and experimental technology. Yang et al. [15] utilized ANSYS/LS-DYNA software to implement an implicit solution to initial static stress and an explicit solution in dynamic analysis and then obtained the fracture behavior and energy evolution under coupled static and dynamic loads. Zhao et al. [16] studied the method of defining the reasonable width of coal pillar and roadway surrounding rock control technology. In consideration of roadway stability, safe and efficient mining, and other factors, the reasonable width of coal pillar was defined as 18 m. The combined support system of resin lengthened bolt and anchor cable reinforcement was proposed for roadway support. Qin et al. [17] proposed and applied a scheme of “anchor cable reinforcement to steel shed, floor pressure relief, deep, and shallow-hole composite grouting” for deep dynamic soft rock roadway. Klishin et al. [18] studied the joint deformation of roof rocks and analysed roof support with the finite element method. By this, a dedicated mobile roof support for underground coal mining was proposed. Ram et al. [19] presented a novel design of rock

Drill hole	Depth (m)	Thickness (m)	Geological formation	Lithology name	Lithological characteristics
Roof	563.7	14.0		Mudstone	Grayish black with plant fossils
	577.7	4.0		Mudstone	Grayish black, flat fracture, containing plant fossils
	582.7	5.0		Medium sandstone	Grayish white, argillaceous cementation
	587.7	3.0		Mudstone	Black, containing plant fossils, thin coal deposits can be seen locally
Coal	590.7	2.5		Coal	Black, asphalt glass luster, containing 1-2 layers of gangue
Floor	593.2	1.7		Mudstone	Black. High carbon content
	594.9	0.4		2_1 coal	Black, asphalt luster, blocky
	595.3	2.0		Mudstone	Gray dark gray, containing a large number of plant fossils
	597.3	3.5		Medium sandstone	Grayish white dark gray, argillaceous cementation

Figure 3: Geological formations.

bolts as goaf edge support. The relationship between the parameters affecting the estimation of rock load height at the edge of the goaf in the filling panel was established under the given geological mining conditions. Oliveira [20] studied the influence of anisotropy and brittle rock on the development of excavation disturbance area or softening height and made discussions on their significance in roof support design. However, few studies have been made on the width of coal pillar and roadway control scheme under the condition of mining while reversing mining and excavation.

This paper takes the deep excavation under dynamic pressure in the 3206 return airway in Taitou mine as the engineering background, analyzes the characteristics of roof fracture and the distribution of coal pillar stresses, determines the width of coal pillar, and develops the control scheme of mining while reversing mining and excavation. This study will solve the problems of excavation support for deep mining under dynamic pressure while reversing mining and excavation and the width of coal pillar in Taitou mine, which is of great significance to ensure the safe production of Taitou mine and to study the support of deep mining under dynamic pressure while reversing mining and excavation.

2. Engineering Background

2.1. Geological Conditions. The no. 2 coal seam of Shanxi Taitou coal mine is located in the lower part of Shanxi. The average distance between the upper part and no. 1 coal seam is 19.5 m, and the lower part is about 7.18 m from the sandstone. The thickness of the coal seam is 1.68-3.65 m, with an average thickness of 2.70 m. The roof consists of sandstone, sandy mudstone or mudstone, and the floor is composed of carbonaceous mudstone or mudstone, sandy mudstone, and asphaltic mudstone.

Due to the shortage of mining replacement, mining while reversing mining and excavation is carried out in the main return airway of the 3204 face and the 3206 face. The 3206 return airway is located in no. 2 coal seam and in the north of no. 3 mining area. The west part is solid coal seam, adjacent to the boundary of the third mining area in the north. The relative position of the 3204 working face and

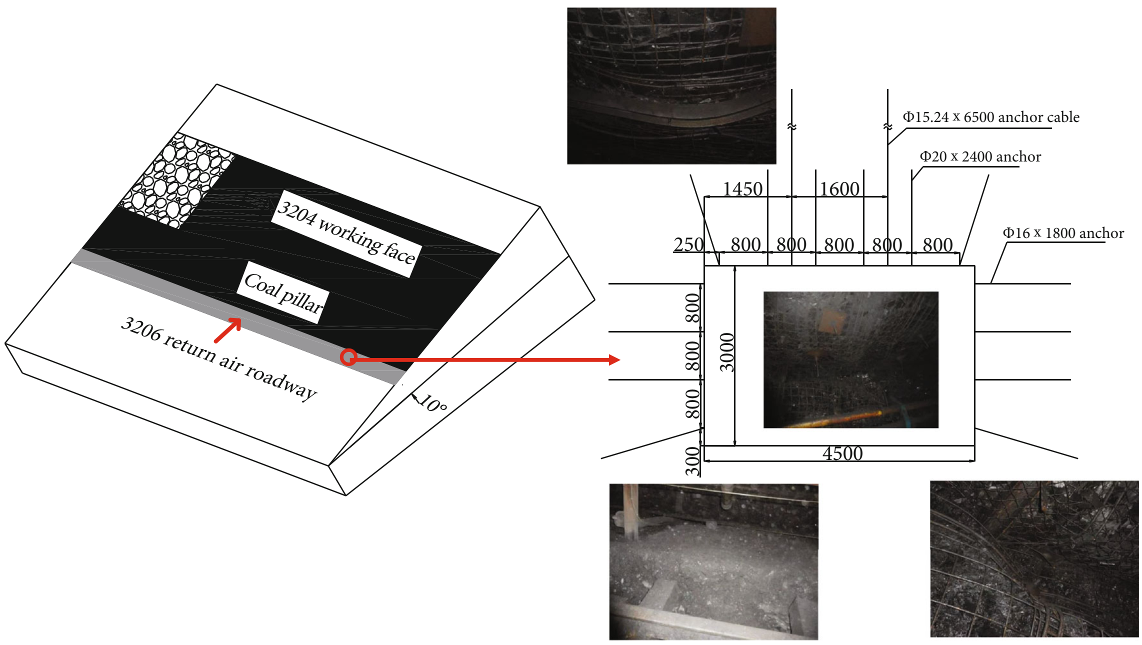

Figure 4: Schematic diagram of original support and failure (unit: mm).

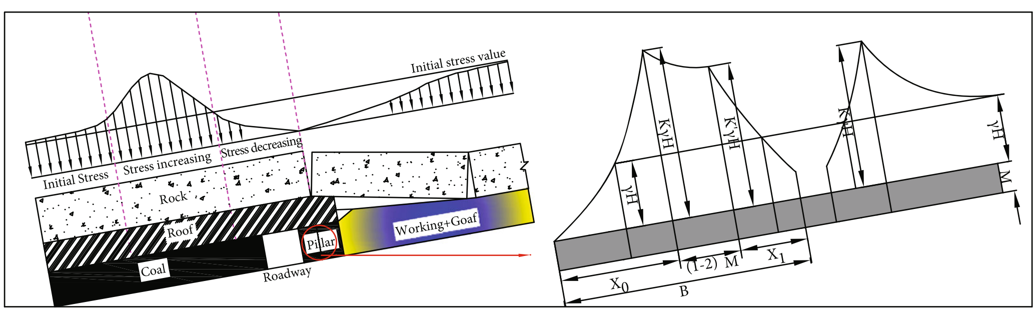

Figure 5: Elastic plastic deformation area and distribution of coal pillar stresses.

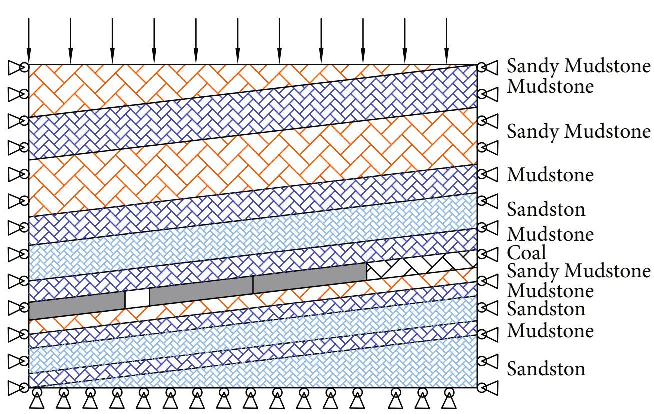

Figure 6: Numerical model.

the 3206 roadway and the comparison diagram of coal are shown in Figure 2.

2.2. Occurrence of Coal Seams. The direct roof of no. 2 coal seam is composed of mudstone with an average thickness of 3.1 m. The main roof is fine sandstone with a thickness of about 5.50 m, and the bottom plate is sandy mudstone. The compressive strength of the roof is 50.4-54.8 MPa, the tensile strength is 3.6-4.1 MPa, and the cohesion coefficient is 9. The compressive strength of the bottom plate is 15.2-

Table 1: Rock distribution and mechanical parameters.

Serial	Lithology	Thickness (m)	Density (kg/m^3)	Bulk modulus (GPa)	Shear modulus (GPa)	Cohesion (MPa)	Friction (°)	Tensile strength (MPa)
12	Sandy mudstone	1	2,500	3.6	1.89	1.35	29	6
11	Mudstone	6	2,400	2.88	1.53	1.17	26	4
10	Sandy mudstone	8	2,500	3.6	1.89	1.35	29	6
9	Mudstone	4	2,400	2.88	1.53	1.17	26	4
8	Sandstone	5	2,700	10.35	7.74	3.15	36	5
7	Mudstone	3	2,400	2.88	1.53	1.17	26	4
6	Coal	2.5	1,400	1.35	0.63	1.17	26	2
5	Sandy mudstone	2	2,500	3.6	1.89	1.35	29	6
4	Mudstone	2	2,400	2.88	1.53	1.17	26	4
3	Sandston	3.5	2,700	10.35	7.74	3.15	36	5
2	Mudstone	2	2,400	2.88	1.53	1.17	26	4
1	Sandston	36	2,700	10.35	7.74	3.15	36	5

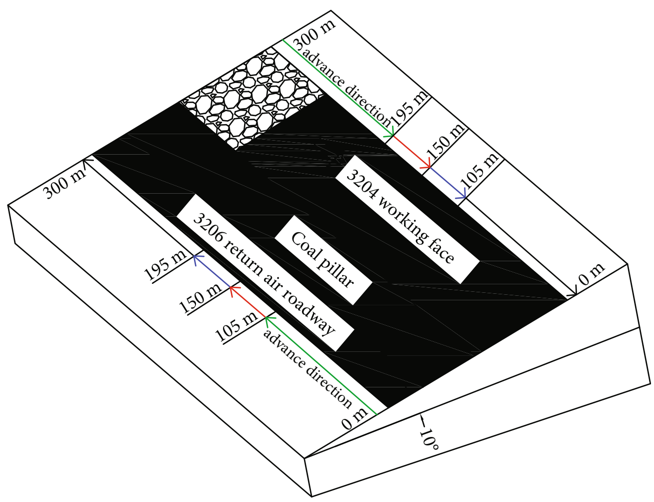

Figure 7: Schematic diagram of simulation.

16.8 MPa, the tensile strength is 0.4-0.6 MPa, and the cohesion coefficient is 3.1. The histogram of coal seam roof and floor is shown in Figure 3.

2.3. Roadway Support. The length of the 3206 return airway is 1350 m, and the mining length of the 3204 working face is 1263 m. When the 3204 working face and the 3206 return airway are about to meet and stagger, the 3206 return airway will be affected by the superposition of multiple dynamic pressures in this roadway excavation, the 3204 working face mining and unstable goaf, resulting in roadway deformation, i.e., floor heave, slope, and roof subsidence. In some areas, the roof and floor heaves are serious, and the deformation of roadway height is up to one meter. The specific deformation of the 3206 return airway is shown in Figure 4.

3. Theoretical Calculation of Coal Pillar

According to the elastic theory [21], when plastic deformation occurs on both sides of the roadway pillar, after the plastic deformation of X_0 and X_1, which can bear the influence of mining pressure and multiple dynamic pressures on the pillar, and given that the width of the elastic core is not less than twice the height of the pillar, the roadway pillar can remain stable, as shown in Figure 5.

The calculation formula of coal pillar width is:

$$B = X_0 + 2M + X_1, \tag{1}$$

where X_0 is the width of plastic zone of coal pillar in the side section of mining space, m; M is the coal cutting height of

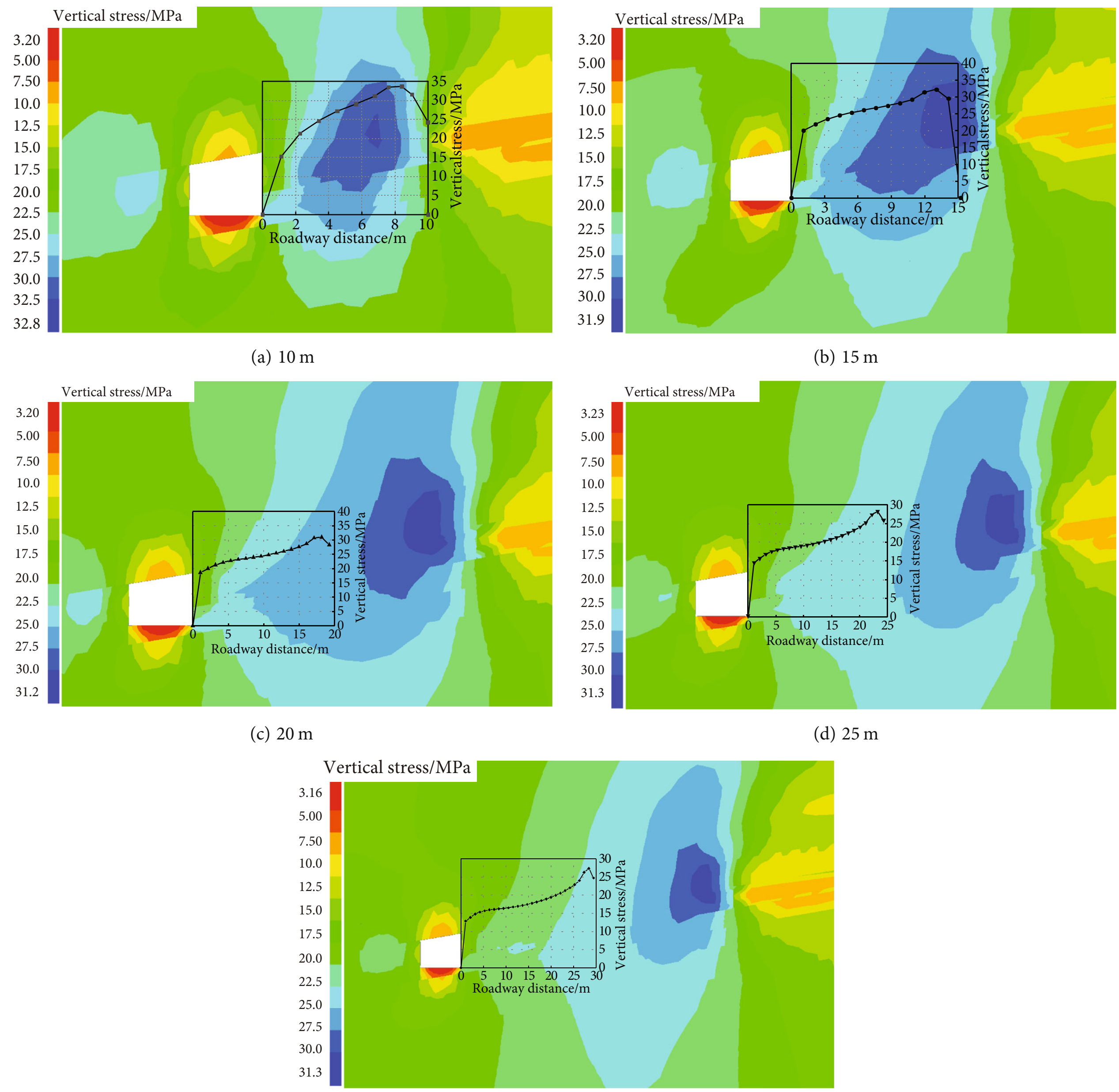

(e) 30 m

Figure 8: Vertical stress distribution in coal pillar with different widths.

the working face, m; and X_1 is the width of plastic zone of coal pillar in the mining preparation roadway, m.

According to the limit equilibrium theory [22, 23], the deformation width of the plastic zone of the coal pillar near the side of the mining space, the distance X_0 from the stress peak to the edge of the coal pillar is:

$$X_0 = \frac{M}{2\xi f} \ln \frac{K\gamma H + C \cot \varphi}{C \cot \varphi}, \tag{2}$$

where K is the stress concentration factor; γ is the average volume force of overburden, Kn/m^3; H is the mining depth, m; C is the cohesion of coal seam, MPa; φ is the internal friction angle, °; f is the friction coefficient; and ξ is the triaxial stress coefficient.

The width of coal pillar plastic zone in the mining preparation roadway is:

$$X_1 = r\left[\frac{(P + C + \cot \varphi)(1 - \sin \varphi)}{P_i + C + \cot \varphi}\right]^{(1-\sin \varphi/2 \sin \varphi)}, \tag{3}$$

where r is the roadway radius, m; P is the surrounding rock stress, MPa; and P_i is the resistance, MPa.

According to the geological engineering data and mechanical parameters in the rock experiment of Taitou mine, the mining height of the working face $M = 2.6$ m, the friction factor $f = 0.364$, the buried depth of the coal seam $H = 650$ m, the pressure concentration factor $K = 3$, the friction angle in the coal body $\varphi = 20°$, the cohesion of coal seam $C = 0.78$ MPa, the average volume force of overlying strata $\gamma = 25$ Kn/m^3, the roadway radius $r = 2.0$ m, the surrounding rock stress $P = 10$ MPa, and the resistance $P_i = 5$ MPa. The parameters above are brought into formula (2) and formula (3), and $X_0 = 5.5$ m, $X_1 = 2.5$ m, so the influence of mining $\lambda = 2$. If X_0 and X_1 are brought into formula (1), the coal pillar width $B = 5.5 \times 2 + 2 \times 2.6 + 2.5 = 18.7$m.

4. Numerical Simulation Analysis of Coal Pillar Stress

4.1. Model Establishment. According to the engineering cases of mining under dynamic pressure in a deep shaft in the 3204 working face and the 3206 return airway, the simulated size is $X \times Y \times Z = 200\,\text{m} \times 300\,\text{m} \times 75\,\text{m}$, as shown in Figure 6. In the simulation, the dip angle of the coal seam is 10°, the thickness of the coal seam is 2.5 m, the mining height of 3204 working face is 2.5 m, and the width is 90 m; the 3206 return airway is excavated along the roof, and the roadway section is trapezoidal. The roadway is 4.5 m long and 3.8 m high. This physical simulation model is the Mohr-Coulomb model.

The model boundary was constrained, the fixed boundary method was adopted for the bottom boundary, the left and right X-direction displacement is 0, and the front and rear Y-direction displacement is 0 [24–28]. The distance between the simulated upper boundary and the surface was calculated as 650 m, the vertical in situ stress was 16.25 MPa, the lateral pressure coefficient was selected as 1, and the gravity was applied to simulate the in situ stress field.

4.2. Physical and Mechanical Parameters of the Rock. The mechanical experiment was carried out in the laboratory with the on-site borehole sampling, and the physical and mechanical parameters of different lithologies were determined. The mechanical parameters of each rock stratum are shown in Table 1.

4.3. Numerical Simulation Scheme. When the 3204 working face advances from 300 m to 195 m, the 3206 return airway advances from 0 m to 105 m; when the 3204 working face advances from 195 m to 150 m, the 3206 return airway advances from 105 m to 150 m; when the 3204 working face advances from 150 m to 105 m, the 3206 return airway advances from 150 m to 195 m; when the 3204 working face advances from 105 m to 0 m, the 3206 return airway advances from 195 m to 300 m. The simulation process is shown in Figure 7.

The excavation under dynamic pressure in the 3204 working face and the 3206 return airway is divided into three periods, i.e., the periods before mining meets, when mining meets and after mining meets. The excavation in the 3206 return airway before mining meets was carried out in solid coal, which was not affected by the mining in the 3204 working face, and the roadway was stable and easy

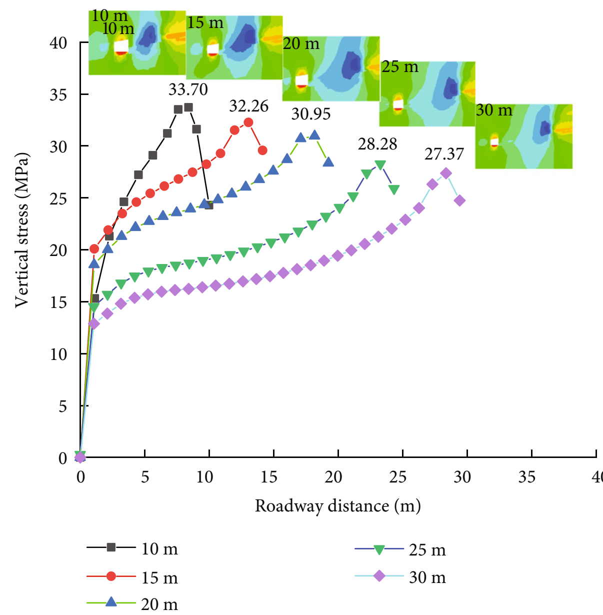

Figure 9: Distribution of vertical stresses on coal pillar with different widths.

to support. In the two time periods after mining encounter and mining stagger, the coal pillar was affected by multiple stresses such as the mining in the 3204 working face and the roof pressure of the goaf. Five different coal pillar widths were designed for simulation analysis, that is, 10 m, 15 m, 20 m, 25 m, and 30 m.

4.4. Analysis of Simulation Results When Mining Meets

4.4.1. Vertical Stress Distribution. When the widths of coal pillar were different, FLAC^{3D} was used to simulate the distribution in the mining state, and the distribution of vertical stresses in coal pillar was obtained, as shown in Figure 8.

On basis of Figure 9, when the coal pillar widths are different, the distribution of vertical stresses on coal pillar is compared. When the width of coal pillar is less than 10 m, the distribution of vertical stresses on the coal pillar is triangular, the peak value of vertical stress reaches 33.7 MPa, and the stress increase coefficient is 2.1. With the increase of the coal pillar width, the vertical stress peak decreases gradually, the stress concentration factor also decreases gradually, and the stresses present a trapezoidal distribution. There are two peaks near both sides of the coal pillar, but the stress near the goaf is larger. When the coal pillar width is 20 m, the peak stress is 30.95 MPa, and the stress increase coefficient is 1.9. The peak value of vertical stress decreases with the increase of coal pillar width, and the vertical stress on the coal pillar also decreases gradually. When the coal pillar width is greater than 20 m, the stress concentration area near the roadway side is basically 4-5 m away from the roadway. When the coal pillar width is equal to or greater than 20 m, the coal pillar stress is relatively large within a stable range.

Table 2: Surface displacement of roadway with different pillar widths.

Coal pillar width/m	Floor heave/mm	Coal pillar displacement/mm	Solid slope displacement/mm	Roof subsidence/mm
10	379	340	267	194
15	327	310	253	178
20	263	249	210	152
25	231	209	181	135
30	216	199	171	129

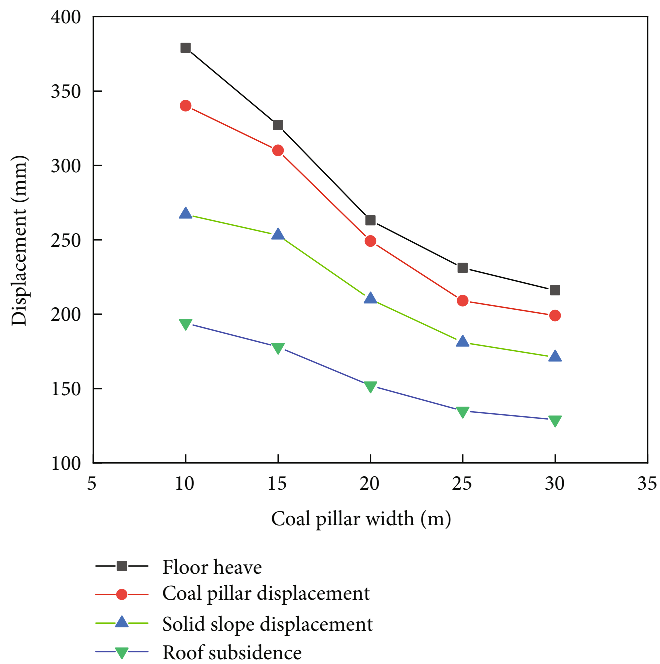

Figure 10: Deformation of roadway with different coal pillar widths.

4.4.2. Roadway Displacement. In the simulation process, measuring points were arranged in the roadway section, and the measuring points were placed in the middle of the roadway roof, floor, and the two sides of roadway. The monitoring results of surrounding rock variation in the roadway are shown in Table 2.

As shown in Table 2 and Figure 10, the change of coal pillar widths has a great impact on roadway deformation, especially on the change of floor heave and roof subsidence. As the width of coal pillar changes from 10 m to 20 m, the floor heave decreases from 379 mm to 263 mm. The reduction should not exceed 20 mm within each 5 m increase of coal pillar width, the general trend decreases with the increase of coal pillar width, and the range of reduction gradually decreases. When the coal pillar width increases from 15 m to 20 m, the displacement of coal pillar wall decreases by 91 mm, while the displacement of solid coal wall decreases by 57 mm. With the continuous increase of coal pillar width, the reduction of coal pillar displacement is less than 10 mm.

4.5. Analysis of Simulation Results after Mining Meets

4.5.1. Vertical Stress Distribution. The stress evolution when the dynamic pressure is 80 m away from different coal pillar widths is shown in Figures 11 and 12.

As shown in Figure 12, when the coal pillar width is less than 20 m, the vertical stress distribution on the coal pillar is triangular. When the coal pillar width is 10 m, the peak value of vertical stress reaches 46.7 MPa, and the stress increase coefficient is 2.9. When the coal pillar width increases to 20 m, the peak value of vertical stress reaches 43.1 MPa, and the stress increase coefficient is 2.7. The stresses present a trapezoidal distribution. With the increase of the coal pillar width, the impact on the surrounding rock of the roadway gradually decreases. When the coal pillar width is less than 20 m, the deformation on the two sides of roadway is obvious. The coal pillar width is greater than 20 m, and the deformation on both sides of the roadway decreases.

4.5.2. Roadway Displacement. The results of surrounding rock variation in the roadway are shown in Table 3.

According to Table 3 and Figure 13, when the width of coal pillar is 20 m, the deformation of the two sides decreases obviously. Compared with the 10 m coal pillar, the displacement of coal pillar is reduced from 510 mm to 411 mm. The displacement of solid roadway side is reduced from 486 mm to 372 mm, with a decrease of more than 20%. The deformation of roof and floor at the 20 m coal pillar is larger than that at coal pillars of other widths. Compared with the

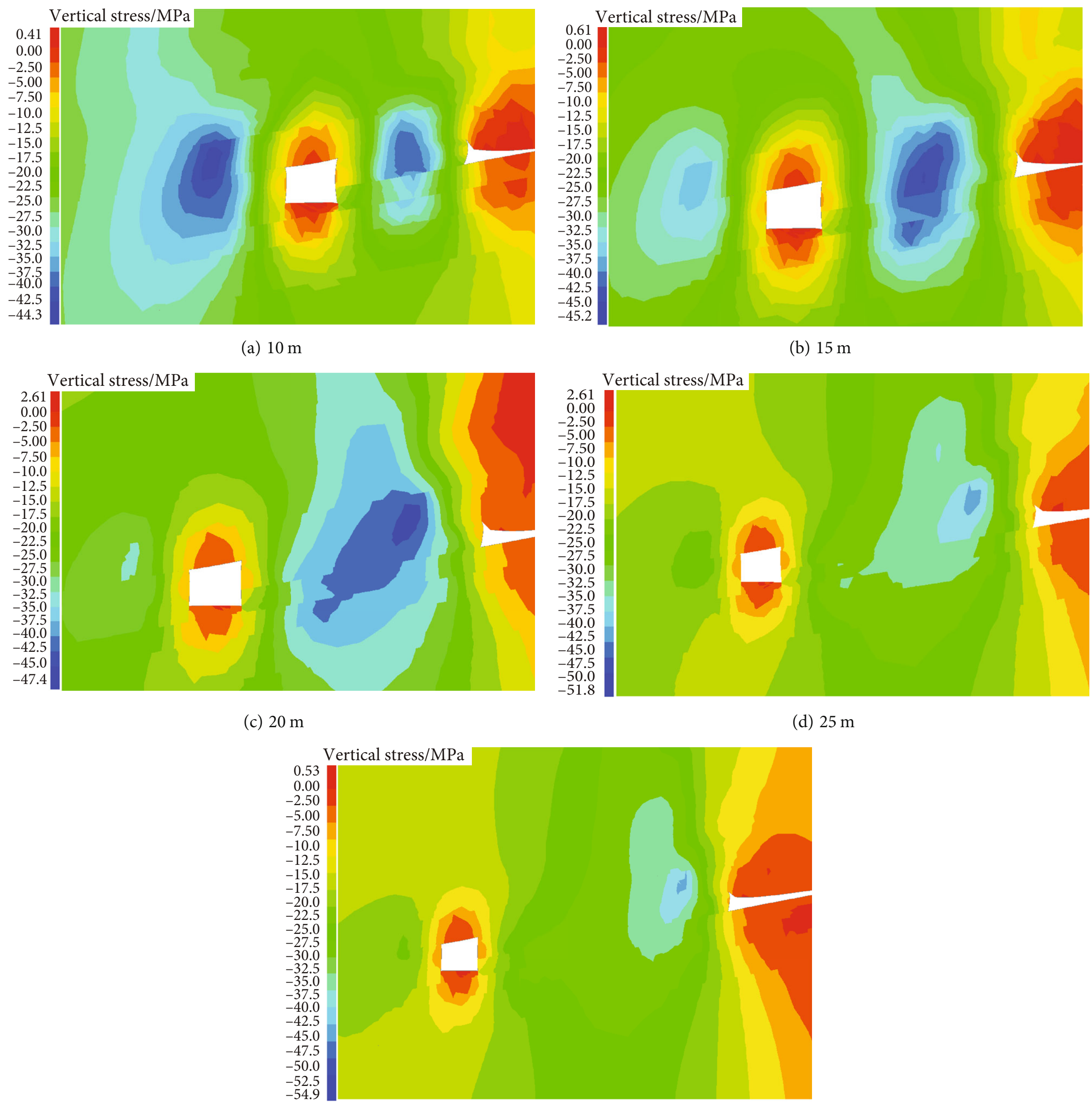

(a) 10 m

(b) 15 m

(c) 20 m

(d) 25 m

(e) 30 m

Figure 11: Stress distribution of coal pillars with different widths.

10 m coal pillar, the bottom heave is reduced from 457 mm to 324 mm, which is reduced by 133 mm, and the lower layer of the roof is reduced from 270 mm to 185 mm, which is reduced by 85 mm.

4.6. Stress and Depth of Coal Pillar. The vertical stress nephogram and vertical stress curve of coal pillar are obtained by slicing along the dip angle of coal seam. The position of coal pillar stress curve is selected from the working face to the heading face.

As shown in Figures 14 and 15, when the working face meets the roadway, the stress on the coal pillar increases as the buried depth becomes greater. The stress between 30 and 90 m behind the roadway heading face is relatively concentrated, and thus, the roadway support should be strengthened. When the buried depth is less than 500 m, the stress on the coal pillar changes little, and the curve is relatively flat. When the buried depth exceeds 500 m, the stress peak area appears in the coal pillar. With the increase of the buried depth, the influence range of the stress peak increases slowly, from about 20 m when the buried depth is 600 m to about 60 m when the buried depth is 900 m. The stress peak increases by 18.67 MPa, and the stress increase coefficient increases from 2 to 3.3. When the buried depth

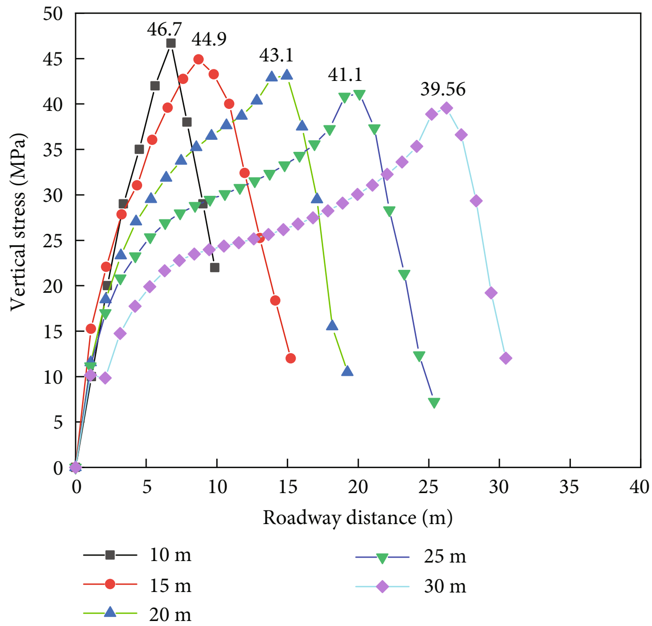

Figure 12: Stresses on coal pillar with different widths.

Table 3: Surface displacement of roadway with different pillar widths.

Coal pillar width/m	Floor heave/mm	Coal pillar displacement/mm	Solid slope displacement/mm	Roof subsidence/mm
10	457	510	486	270
15	399	475	445	238
20	324	411	372	185
25	276	373	326	156
30	249	345	291	143

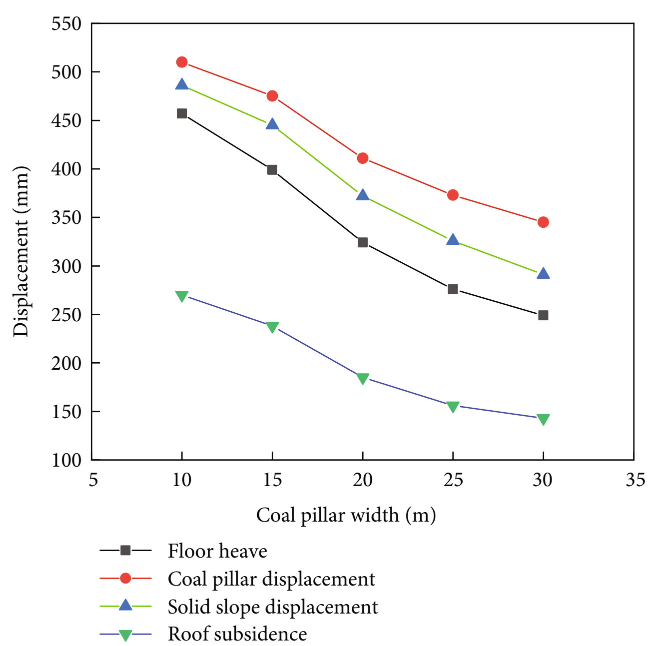

Figure 13: Deformation of surrounding rock in the roadway with different widths of coal pillars.

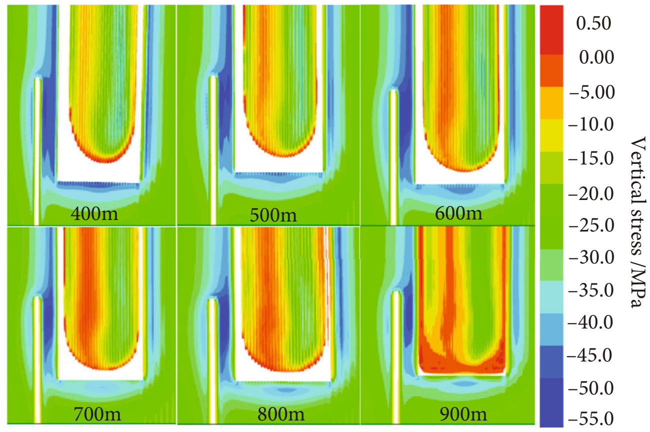

Figure 14: Vertical stress distribution with different buried depths.

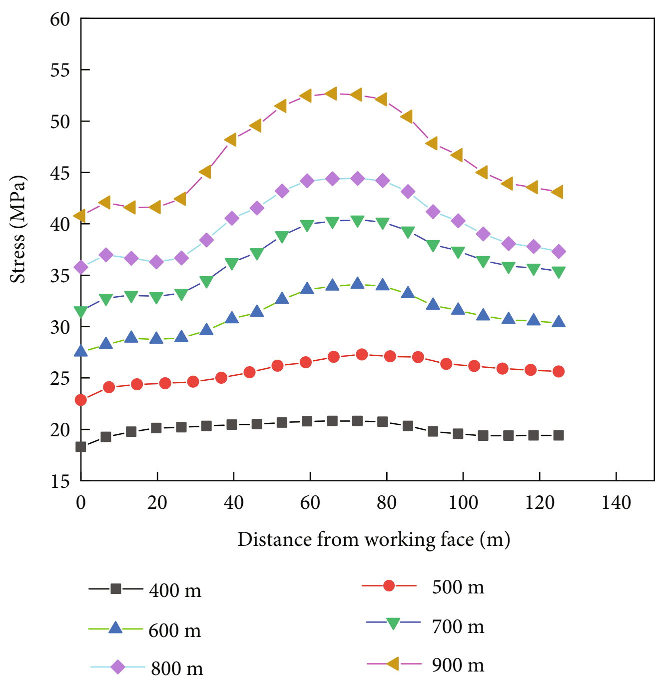

Figure 15: Vertical stress distribution curve on coal pillar with different buried depths.

increases from 600 m to 700 m and to 800 m, the stress of coal pillar increases from 33.91 MPa to 40.26 MPa and to 44.17 MPa; the stress increase coefficient increases from 2 to 2.5 and to 2.7.

5. Optimization and Industrial Test of Support Parameters

5.1. Parameter Optimization for Roadway Support Scheme. The support of the 3206 return airway is composed of bolt, anchor cable, and anchor mesh, combined with M-shaped steel belt and steel beam. The designed roadway section is trapezoidal, with an excavation width of 4,500 mm, a height of 3,000 mm, and a sectional area of 14.1 m^2. The overall support scheme is shown in Figure 16.

The $\Phi 22 \times 2{,}500$ mm anchors were used for the roof, of which the spacing is 800 mm, and the row spacing is 800 mm. The $\Phi 21.6 \times 6{,}800$ mm anchor cables were arranged along the roadway, with a spacing of 1.5 m and a row spacing of 0.8 m. Four anchor cables arranged in each row were supported with the 14# B-shaped channel steel. During the supporting process, the channel steel plane was in immediate contact with the anchor net, the processed steel plate tray was placed in the concave surface of channel steel, and the anchor cable lock was in contact with the tray through the self-aligning ball pad. The side bolt is $\Phi 22 \times 2{,}500$ mm, and the row spacing is 800 mm. The side anchor bolts were raised and lowered by 15 degrees, and the other anchor bolts should be constructed perpendicular to the roadway wall. The roof

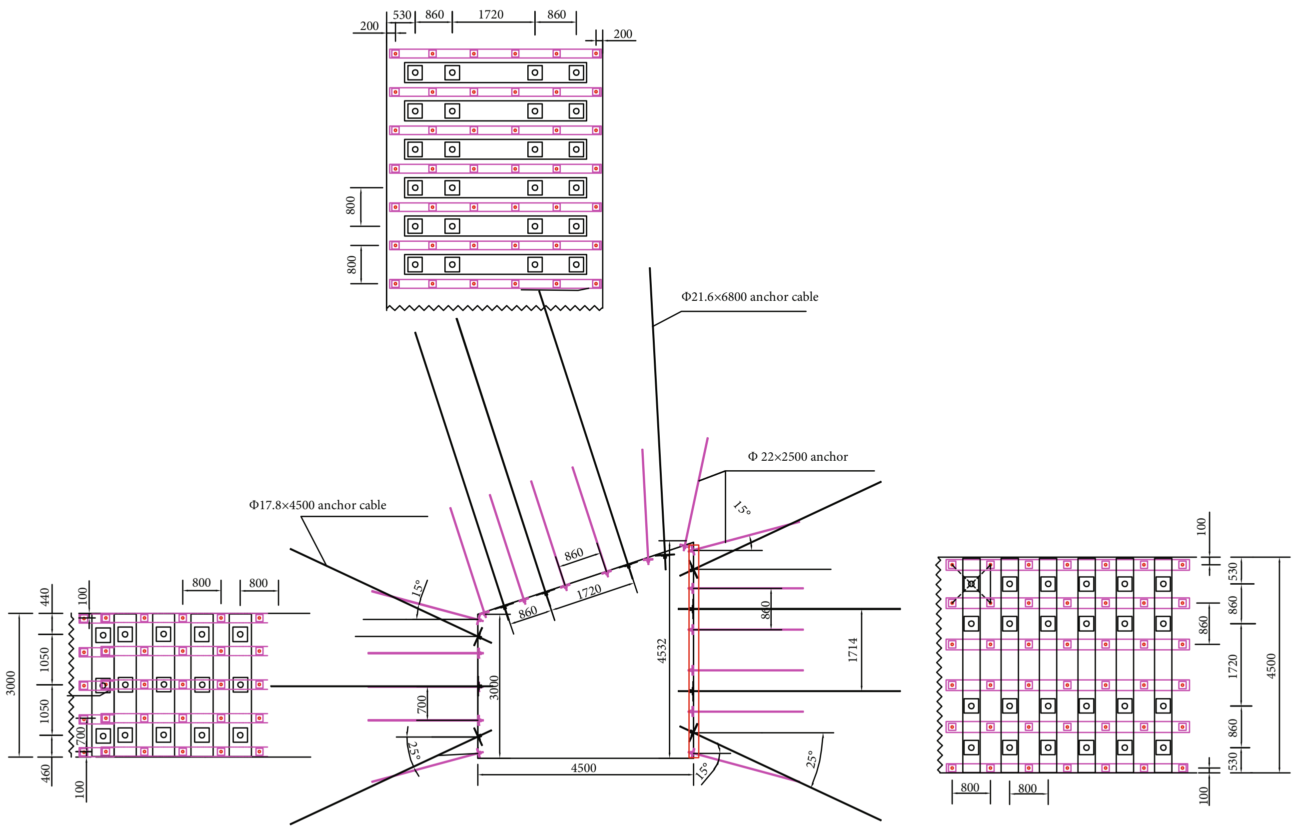

Figure 16: 3206 return airway support (unit: mm).

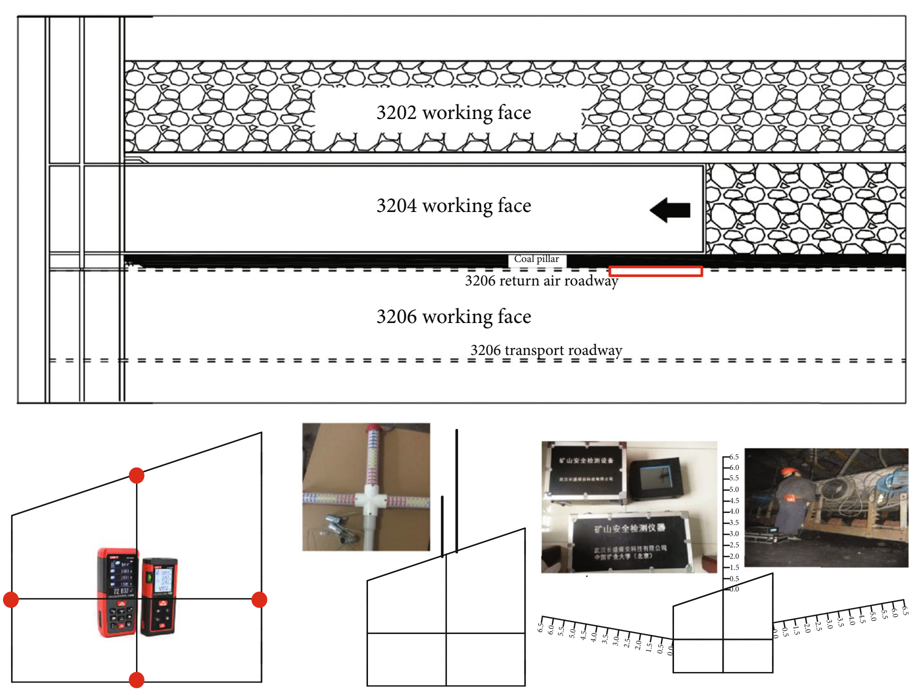

Figure 17: Monitoring of the roadway stability.

anchor cable is $\Phi 17.9 \times 4{,}500$ mm, with a row spacing of 800 mm and the exposed length of 150-250 mm. The anchor cables were arranged in each row and supported with the 14# B-shaped channel steel. Two 12 mm thick, 150 mm long, and 110 mm wide steel plates were used instead of dished trays.

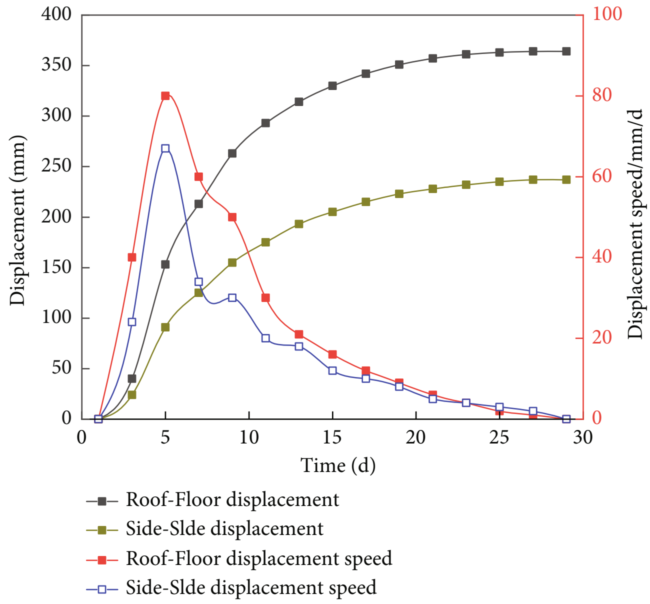

FIGURE 18: Deformation curve of roadway under dynamic pressure.

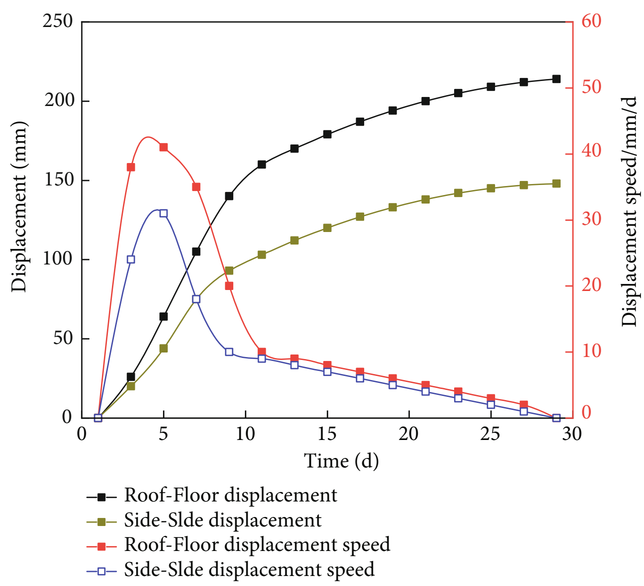

FIGURE 19: Deformation curve of roadway at the stage of stable stress.

TABLE 4: Maximum separations of roof.

No.	1	2	3	4	5	6	7	8	9	10
3.0 m	2 mm	3 mm	2 mm	9 mm	3 mm	2 mm	4 mm	2 mm	1 mm	2 mm
6.0 m	0	0	0	0	0	1 mm	0	0	0	0

5.2. Support Effect. In order to monitor the support effect, the deformation of the roadway should be measured and studied as shown in Figure 17. There are two methods to detect the roadway stability: the first is to detect the displacement of the roadway surface; the second is to detect the separation of roadway roof. In order to detect the roadway surface displacement, two measuring stations were set in the 3206 return airway, and the measuring station was set after the roadway was excavated to 550 m, which was measuring station 1. After the roadway was excavated to 650 m, station 2 was arranged. The displacement of the roof of the 3206 return airway, a roof separation instrument, was

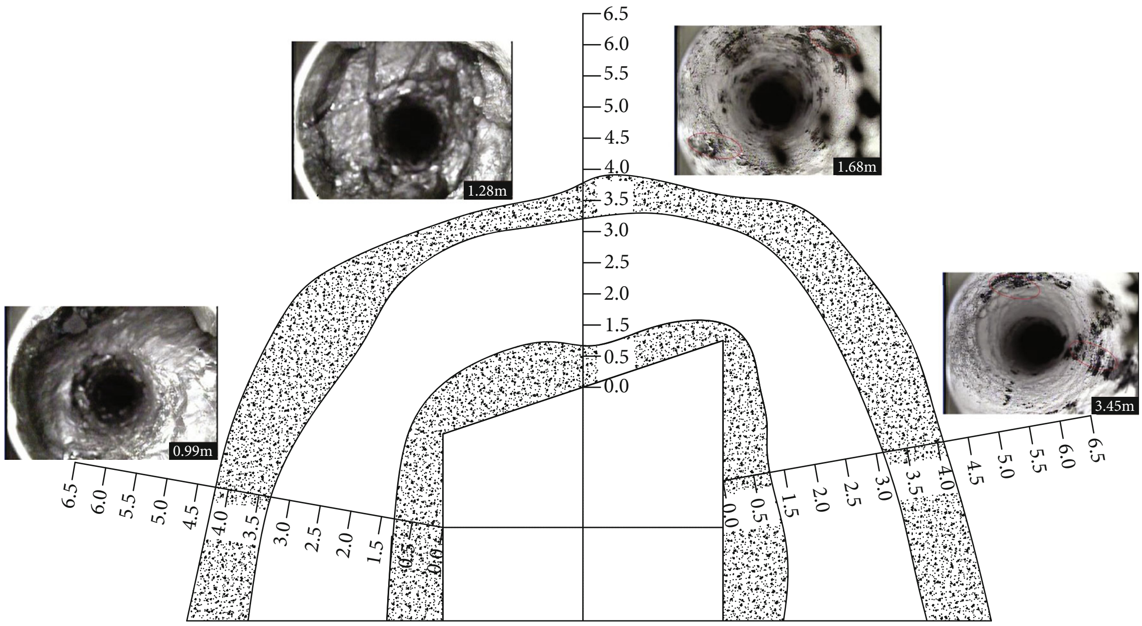

(a) Roof drilling at 600 m

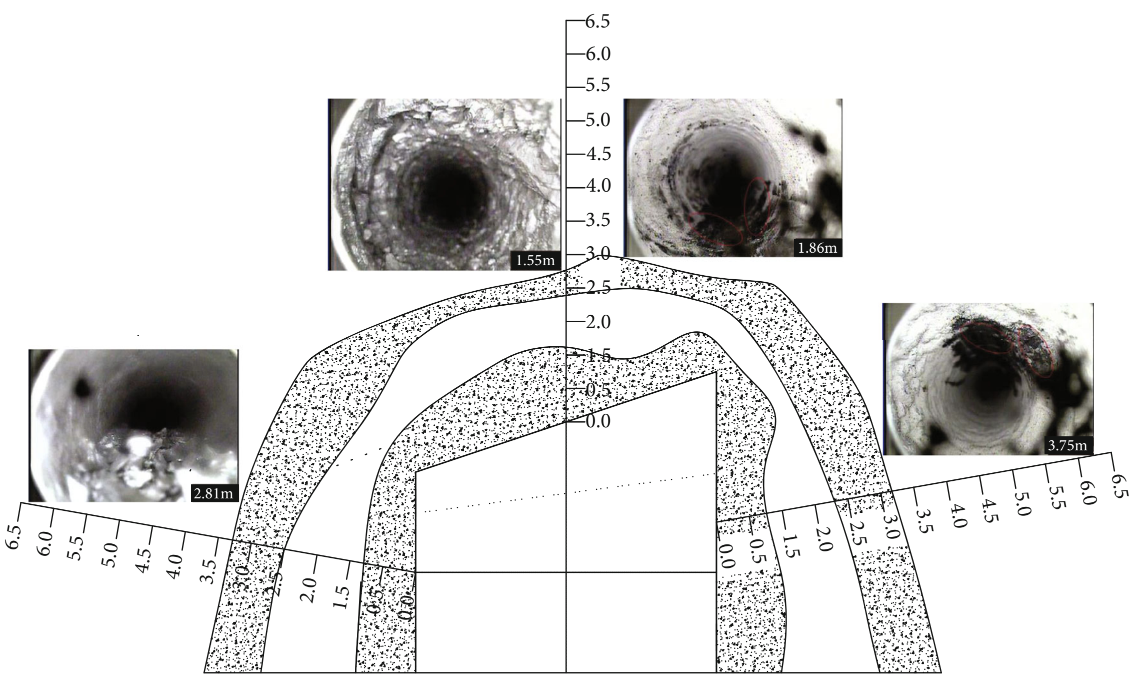

(b) Roof drilling at 650 m

Figure 20: Continued.

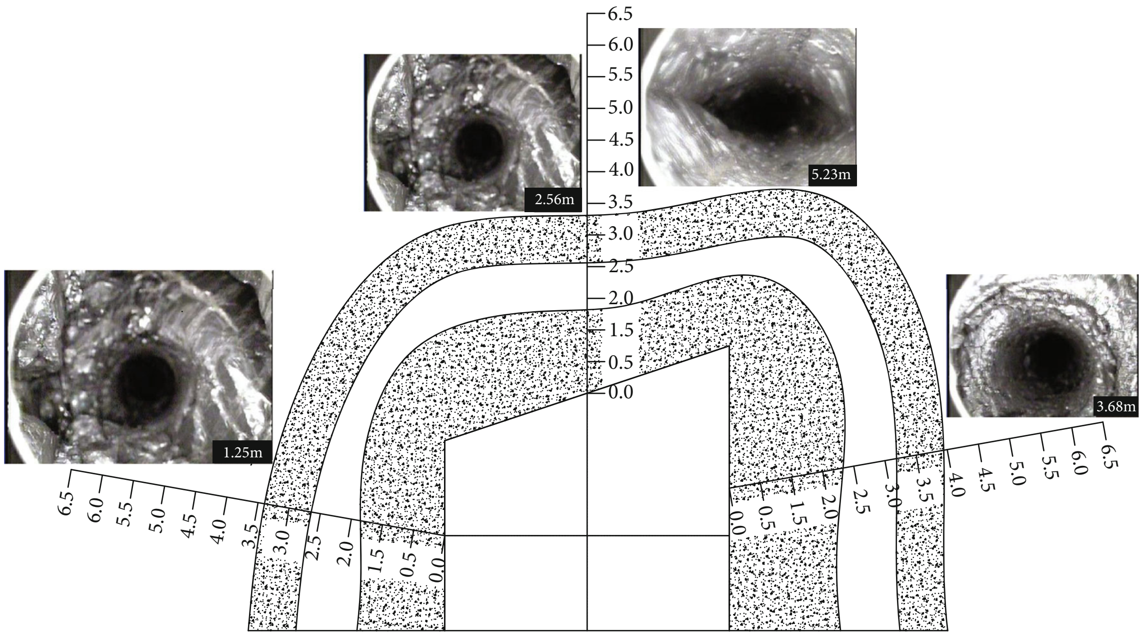

(c) Roof drilling at 700 m

Figure 20: 3206 return airway drilling.

installed in the middle of the roof of 3206 excavated roadway. The separation instrument spacing was 100 m, and the depths of the monitoring base points were 3 m and 6 m.

5.2.1. Surface Displacement. In monitoring the surface displacement of roadway, the cross-point method was adopted, and the roadway surface deformation was analyzed on basis of the displacement change and its change rate. The change of roadway surface displacement at the two stations is shown in Figure 18. Because the roof of the goaf is broken and unstable, the movements of the roof, floor, and the two sides of the roadway change the most. At this time, the movement of the two sides reaches 91 mm, the movement of the roof and floor reaches 153 mm, and the change rate reaches the maximum. The moving amount of the top and bottom plate and the moving amount of the two sides change slowly and gradually become stable. In this process, the maximum moving amount of the top and bottom plate is 364 mm, and the maximum speed is 80 mm/d. The maximum moving distance of the two sides is 237 mm, and the maximum moving speed is 67 mm/d.

As shown in Figure 19, the deformation of roadway surrounding rock mainly presents in the deformation of roof and floor. As time continues, the deformation gradually increases, but the speed lowers down. In this process, the maximum approach of roof and floor is 214 mm and the maximum approach speed is 41 mm/d. The maximum approach of the two sides is 148 mm, and the maximum approach speed is 31 mm/d.

5.2.2. Roof Separation. The deep and shallow roof separation in the roadway is recorded and analyzed below. The maximum roof separations are shown in Table 4.

In the roof of the 3206 return airway, the separation amount of 3 m shallow base point is about 2 mm, and the maximum separation amount is 9 mm; the 6 m deep base point basically has no separation, which shows that the roof of the 3206 return airway has good integrity under the control of anchor, with little separation and a small amount of lower layer of roof, as shown in Table 4.

5.2.3. Roof Drilling. In order to observe the development of cracks on the roof of the 3206 return airway after using optimized support, drill holes on the roadway roof were set for borehole peeping [29–31]. The equipment clearly distinguishes 0.1 mm cracks, and the diameter of peeping probe is φ 24 mm. The drill holes are 600 m, 650 m, and 700 m, respectively, away from the excavation face of the 3206 return airway. The drilling depths are 7 m, and the drilling diameter is φ 28 mm. The peeping process on site is shown in Figure 20.

Through the analysis of the borehole peeping view, the following results are obtained. The depth of the borehole at 650 m is 6 m, and the actual peeping depth is 5.8 m. There are obvious cracks at 4.1-4.6 m, and there are fine cracks in other sections. The roof rock is relatively complete, and the rock mass has great bearing capacity, indicating good support effect of the roadway roof. The drilling depth at 700 m is 7 m, and the actual peeping depth is 6.7 m. The rock integrity is poor in the range of 0.5-1.5 m. There are many fractures at different lengths. The rock integrity in other sections is good, with certain bearing capacity. The drilling depth at 750 m is 8 m, and the actual peeping depth is 7.6 m. There are fully developed fractures at 5.7-6.1 m. The roof rock mass in this section is relatively complete, and the roof rock mass has great bearing capacity, with good support effect of the roadway roof.

(a) Roadway roof

(b) Roadway side

Figure 21: Schematic diagram of support.

In the process of roadway support in the 3206 return airway, the roadway roof support presents good effect, and the results of roof rock mass are relatively intact in the anchor bolt anchorage section, anchor cable anchorage section, and deeper range. In the shallow range near the roof, the roof rock structure is relatively intact and has sufficient bearing capacity, indicating that the roadway roof support is effective, and the roadway is stable, as shown in Figure 21.

6. Conclusions

Based on the research background of the deep mining under dynamic pressure in the 3204 working face and the 3206 return airway while reversing mining and excavation in Taitou mine, this paper studies the support of the 3206 return airway. The research includes determining the appropriate size of coal pillar, the variation of surrounding rock stresses under dynamic pressure with different buried depths, with the parameters in the optimization of the 3206 return airway support, and with the combination of the theoretical analysis method, FLAC^{3D} numerical simulation analysis method, and field experimental observation method. Through research and analysis, the following conclusions are obtained:

(1) The calculation formula of coal pillar width is obtained by using elastic core theory. With the relevant data, it is calculated that the coal pillar width is 18.7 m. Combined with the actual situation of Taitou mine, the coal pillar width in the direct section of the 3204 working face and the 3206 return airway should comply with $B \geq 18.7$ m. On basis of FLAC^{3D} numerical simulation and coal pillar principle, the coal pillar width is finally determined as 20 m

(2) As the burial depth increases from 600 m to 700 m and to 800 m, the peak advance support pressure increases from 29.72 MPa to 32.27 MPa and to 37.63 MPa, and the stress increase coefficient increases from 1.82 to 2 and to 2.3

(3) According to the calculation of surrounding rock failure range, the calculation formula is established based on the parameters of bolt and anchor cable support. Aiming at the support strength and surface strength in the process of roadway support, the support parameters are optimized in three aspects: roadway section, support situation, and wall surface strength. By this, a new support scheme is formulated

(4) The research results have been implemented in the 3206 return airway of Taitou coal mine. The effect is remarkable and the deformation of roadway surrounding rock is reduced. The effect of roadway support reaches the standard for safety production, and remarkable benefits have been obtained

Data Availability

The data used to support the findings in this study are available from the corresponding authors upon request.

Conflicts of Interest

The authors declare that they have no conflicts of interest regarding the publication of this study.

Acknowledgments

This work was supported by the Fundamental Research Funds for the Central Universities (2019XKQYMS50). The authors gratefully acknowledge the financial support of the above-mentioned agencies.

References

[1] C. Qiao, C. H. Li, X. M. Wei, and Y. Y. Hu, “Numerical simulation study on the evolution law of mine pressure in deep mining,” *Arabian Journal of Geosciences*, vol. 13, no. 12, pp. 1–15, 2020.

[2] M. Najafi, A. Shishebori, and J. Gholamnejad, “Numerical estimation of suitable distance between two adjacent panels' working faces in shortwall mining,” *International Journal of Geomechanics*, vol. 17, no. 4, 2017.

[3] C. L. Dong, G. M. Zhao, X. Y. Lu, X. R. Meng, Y. M. Li, and X. Cheng, “Similar simulation device for unloading effect of deep roadway excavation and its application,” *Journal of Mountain Science*, vol. 15, no. 5, pp. 1115–1128, 2018.

[4] Y. Gao, Q. S. Zhang, S. C. Li, and Y. J. Jiang, "An experiment of temperature field of rock mass near water-bearing structure during roadway excavation," *Journal of Central South University*, vol. 45, no. 2, pp. 550–556, 2014.

[5] R. F. Zhang, G. G. Zhao, X. G. Meng et al., "Analysis on characteristics of surrounding rocks of roadway and bearing structure based on stress regulation," *Advances in Civil Engineering*, vol. 2021, 18 pages, 2021.

[6] Y. Chen, S. Q. Ma, and Q. J. Cao, "Extraction of the remnant coal pillar in regular and irregular shapes: a case study," *Journal of Loss Prevention in the Process Industries*, vol. 55, pp. 191–203, 2018.

[7] J. Li, X. B. Qiang, W. S. Wang, and F. Wang, "Distribution law of principal stress difference of deep surrounding rock of gob-side entry and optimum design of coal pillar width," *Tehnicki Vjesnik-technical Gazette*, vol. 26, no. 6, pp. 1743–1752, 2019.

[8] S. Zhang, X. F. Wang, G. W. Fan, D. S. Zhang, and J. B. Cui, "Pillar size optimization design of isolated island panel gob-side entry driving in deep inclined coal seam-case study of Pingmei No. 6 coal seam," *Journal of Geophysics and Engineering*, vol. 15, no. 3, pp. 816–828, 2018.

[9] W. GAO, "Influence of interaction between coal and rock on the stability of strip coal pillar," *Geomechanics and engineering*, vol. 16, no. 2, pp. 151–157, 2018.

[10] X. M. Sun, Y. Y. Liu, J. W. Wang, J. B. Li, S. J. Sun, and X. B. Cui, "Study on three-dimensional stress field of gob-side entry retaining by roof cutting without pillar under near-group coal seam mining," *PRO*, vol. 7, no. 9, pp. 552–559, 2019.

[11] Q. X. Huang, J. W. Du, J. Chen, and Y. P. He, "Coupling control on pillar stress concentration and surface cracks in shallow multi-seam mining," *International Journal of Mining Science and Technology*, vol. 31, no. 1, pp. 95–101, 2021.

[12] J. Wang, J. Q. Jiang, G. B. Li, and H. Hu, "Exploration and numerical analysis of failure characteristic of coal pillar under great mining height longwall influence," *Geotechnical & Geological Engineering*, vol. 34, no. 2, pp. 689–702, 2016.

[13] L. Fan, W. J. Wang, C. Yuan, and W. Q. Peng, "Research on large deformation mechanism of deep roadway with dynamic pressure," *Energy Science & Engineering*, vol. 8, no. 9, pp. 3348–3364, 2020.

[14] Q. W. Li, L. Chen, Z. L. Sui, L. P. Wang, and J. H. Dong, "Dynamic analysis and criterion evaluation on rock burst considering the fractured dissipative energy," *Advances in Mechanical Engineering.*, vol. 11, no. 1, pp. 9–21, 2019.

[15] C. Yang, K. P. Zhou, Z. C. Li, X. Xiong, Y. Lin, and Z. W. Luo, "Numerical modeling on the fracturing and energy evolution of large deep underground openings subjected to dynamic disturbance," *Energies*, vol. 13, no. 22, pp. 6102–6122, 2020.

[16] B. Zhao, F. T. Wang, N. N. Liang, and W. L. Wang, "Reasonable segment pillar width and its control technology for fully mechanized top-coal caving face with high stress," *Journal of Mining & Safety Engineering*, vol. 35, no. 1, pp. 19–26, 2018.

[17] D. D. Qin, X. F. Wang, D. S. Zhang, and X. Y. Chen, "Study on surrounding rock-bearing structure and associated control mechanism of deep soft rock roadway under dynamic pressure," *Sustainability.*, vol. 11, no. 7, pp. 1892–1907, 2019.

[18] V. I. Klishin, V. N. Fryanov, L. D. Pavlova, S. M. Nikitenko, and Y. V. Malakhov, "Rock mass-multifunction mobile roof support interaction in mining," *Journal of Mining Science*, vol. 57, no. 3, pp. 361–369, 2021.

[19] S. Ram, A. K. Singh, R. Kumar et al., "Design of rock bolt-based goaf edge support for conventional depillaring with stowing," *Arabian Journal of Geosciences.*, vol. 14, no. 21, pp. 361–369, 2021.

[20] D. Oliveira, "Application of a transversely isotropic brittle rock mass model in roof support design," in *Proceedings of the 12th Coal Operators Conference*, pp. 16–23, Xi'an, China, 2013.

[21] G. Asgari, G. Payganeh, and K. M. Fard, "Dynamic instability and free vibration behavior of three-layered soft-cored sandwich beams on nonlinear elastic foundations," *Structural Engineering & Mechanics*, vol. 3, no. 1, pp. 1–23, 2019.

[22] X. Q. Liu, Z. Sun, S. Tang, H. Y. Huang, and A. R. Liu, "A new calculation method for axial load capacity of separated concrete-filled steel tubes based on limit equilibrium theory," *Journal of Central South University*, vol. 20, no. 6, pp. 1750–1758, 2013.

[23] J. X. Yuan, Y. W. Yang, L. G. Tham, P. K. Kwong, and Y. Tsui, "New approach to limit equilibrium and reliability analysis of soil nailed walls," *International Journal of Geomechanics*, vol. 3, no. 2, pp. 145–151, 2003.

[24] C. Zhang, F. T. Wang, and Q. S. Bai, "Underground space utilization of coalmines in China: a review of underground water reservoir construction," *Tunnelling and Underground Space Technology*, vol. 107, 2021.

[25] H. Tang, Z. G. He, and H. B. Lian, "Numerical simulation analysis on stability of coal pillar of empty mine goaf in north of Shanxi Province," *Applied Mechanics & Materials*, vol. 470, pp. 205–210, 2013.

[26] F. T. Wang and C. Zhang, "Reasonable coal pillar design and remote control mining technology for highwall residual coal resources," *Royal Society Open Science*, vol. 6, no. 4, pp. 1–13, 2019.

[27] H. Wu, X. K. Wang, E. Wang, G. Peng, and Z. Z. Zhang, "Deformation characteristics and mechanism of deep subsize coal pillar of the tilted stratum," *Energy Science Engineering*, vol. 8, no. 2, pp. 544–561, 2020.

[28] F. T. Wang, J. J. Shang, B. Zhao, and Q. H. Chao, "Surrounding rock structural characteristics and anchor-cable strengthened support technology of the gob-side entry retaining with roof cutting and pressure releasing," *Chinese Journal of Rock Mechanics and Engineering*, vol. 40, no. 11, pp. 2296–2305, 2021.

[29] Y. L. He, M. S. Gao, D. Xu, and X. Yu, "Investigation of the evolution and control of fractures in surrounding rock under different pressure relief and support measures in mine roadways prone to rockburst events," *Royal Society Open Science*, vol. 8, no. 3, pp. 1–15, 2021.

[30] Z.-l. Li, X.-q. He, L.-m. Dou, D.-z. Song, and G.-f. Wang, "Numerical investigation of load shedding and rockburst reduction effects of top-coal caving mining in thick coal seams," *International Journal of Rock Mechanics and Mining Sciences*, vol. 110, pp. 266–278, 2018.

[31] N. Mohammad, D. J. Reddish, and L. R. Stace, "The relation between _in situ_ and laboratory rock properties used in numerical modelling," *International Journal of Rock Mechanics and Mining Sciences*, vol. 34, no. 2, pp. 289–297, 1997.

Hindawi
Geofluids
Volume 2022, Article ID 6957896, 12 pages
https://doi.org/10.1155/2022/6957896

Research Article

Research on Gas Extraction Technology of Directional Long Borehole in Ultrathick Coal Seam

Yaobin Li,[1,2] **Tao Jiang**,[2] **and Xin Guo**[2]

[1]*Joint National-Local Engineering Research Center for Safe and Precise Coal Mining, AnHui University of Science and Technology, Huainan, 232001 Anhui, China*
[2]*School of Safety Science and Engineering, Anhui University of Science and Technology, Huainan, 232001 Anhui, China*

Correspondence should be addressed to Tao Jiang; jt980804@163.com

Received 29 October 2021; Revised 1 December 2021; Accepted 24 February 2022; Published 14 March 2022

Academic Editor: Zhijie Wen

Gas extraction is an important way to control gas disasters. The effect of traditional gas extraction drilling on ultrathick coal seam is not well. In order to improve the rate of gas extraction, directional long drilling is used to replace conventional drilling for coal seam gas extraction. Through the combination of numerical simulation and field experimentation, the stress distribution around borehole is analyzed, and the influence of different time, different gas pressure, different negative pressure of extraction, and different permeability of coal body on directional borehole is simulated. According to the experimentation of Baode Mine, the data of gas drainage volume of conventional directional drilling are recorded and analyzed. The results indicate that the directional drilling is more suitable for Baode Mine 81306 working face of coal seam 8 gas extraction operation. Directional drilling is better than conventional drilling in work, with good drainage stability and large gas drainage volume, which can greatly reduce the outburst time and improve the gas drainage rate.

1. Introduction

According to data from the Ministry of Ecology and Environment of China, from 2010 to 2020, the proportion of coal consumption in China's primary energy consumption structure decreased from 69.2% to 56.8%. Although the proportion of coal consumption in China has decreased, coal still occupies a dominant position in China's primary energy consumption [1–3]. Even under the goal of low-carbon economy, China's demand for coal resources is still very large. Therefore, in a long period of time in the future, the importance of coal resources to China's economic development is self-evident [4, 5]. However, the geological conditions of coal seam occurrence in China are very complicated, and the permeability of coal seam is low, which leads to the emergence of many risk factors in the process of coal mining, among which the gas disaster is the most serious. The total number of coal and gas outburst events in China accounts for more than one-third of the total number of coal and gas outburst events in the world. Therefore, the elimination of a series of gas accidents such as coal mine gas explosion and gas outburst is an important issue in coal mine safety production at present [6–13]. Currently, gas extraction in coal mine is the main method to solve gas outburst, gas explosion, and other gas disasters. It has important significance for the development of coal industry to study coal mine gas drainage, improve existing gas drainage through borehole design, optimize borehole parameters, improve coal mine gas drainage rate, and reduce gas accidents [14–17].

At present, many studies have been carried out by researchers on gas extraction. Shi studied and analyzed the existing problems of gas treatment in recent years and solved the gas treatment problem of thick coal seam tunneling face by introducing the directional long drilling extraction process along the layer to preextract thick coal seam [18, 19]; Wang and Ma used directional long drilling holes in the roof to control the gas instead of high drainage roadway and proposed the coal gas drainage technology of "hole instead of roadway," which reduced the workload and the cost of gas drainage [20]; Zhang designed a directional long borehole predrainage roadway strip, which greatly reduced the time of gas extinction, and achieved good drainage effect [21, 22]; Wang conducted numerical simulation on directional long borehole of gas extraction in medium and hard coal seam, analyzed the influence degree of drilling length and spacing on gas extraction by drilling hole, and provided reference for the analysis of other influencing factors of gas extraction drilling [23–25]; Chen and Luo used long boreholes in bedding to prepump working face and transport pipeline, which saved the time of eliminating outburst and completed the technological innovation experiment project of "one borehole and two eliminating" in long drilling holes in bedding [26]; Zhang et al. studied the directional long drilling equipment at domestic and abroad, found out the problems existing in the application of RIGS drilling abroad under the geological conditions of coal seams in China, and put forward the corresponding opinions on optimization of compatibility [27].

However, most researches are aimed at the optimization of drilling design, and the research on the influencing factors of directional drilling is not sufficient. In view of this, this paper uses the method of combining numerical simulation and field measurement to analyze the influence of different factors on directional drilling and optimize the extraction process. Through the analysis of directional drilling and conventional drilling gas drainage CaiLiang, the advantages and disadvantages of the two kinds of drilling are analyzed, and the accuracy of the simulation is further verified. It is of great significance to further analyze the influence factors of directional drilling technology and also provides the basis for the design and optimization of directional drilling in Baode Mine.

2. Project Profile

The location of this test is the main air withdrawal channel of Baode Mine working face 81306, return air passage 81306, and glue transport passage 81306 of No. 8 coal seam of Baode Coal Mine. No. 8 coal seam is located above S3 sandstone at the bottom of Shanxi Formation (P1S). The coal seam is a gas coal with medium ash, high volatile content, low sulfur content, medium and high calorific value, good thermal stability, rich oil, and high ash content. Coal thickness is 2.15~10.50 m, with an average of 7.36 m; the thickness of pure coal is 3.19~8.84 m with an average of 6.01 m and with medium to extrathick coal seam, mainly thick coal seam. The structure of the coal seam is complex, including 0~8 layers of gangue, usually 3~4 layers, and the total thickness of gangue is 0.3~2.6 m, with an average thickness of 1.06 m. The roof is sandy mudstone or mudstone, part of which is coarse-grained sandstone; the bottom plate is mainly mudstone and secondary siltstone. There are 58 coal spots in the whole area, and all the coal thickness is recoverable. The mining index of coal seam is 1, and the coefficient of variation is 33%, which is a stable and recoverable coal seam in the whole area. The thickness of the coal seam is generally thick in the west and thin in the east, thick in the middle, and thin on both sides. The old coal seam is mostly coarse, medium, and fine grained sandstone with a thickness of 5~20 m and an average of 12.67 m. Most of the immediate roof is developed, the lithology is sandy mudstone, siltstone, mudstone, and thin sandstone, and the thickness is 0~16.13 m. It is mudstone and carbonaceous mudstone with thickness less than 0.5 m.

3. Stress Distribution and Gas Occurrence around Borehole

3.1. Borehole Stress Distribution. In the drilling process, the stress distance around the drilling hole is different from the drilling position, and there are broken zones and plastic zones. The borehole may collapse after stress change. In order to prevent the drilling collapse and deformation, it is necessary to explore the stress distribution around the drilling hole. As the drilling goes deeper, the buried depth of coal seam changes, the pressure changes, and the coal body change from elastic deformation to plastic deformation. When the drilling is finished, the stress distribution will keep balance again. If the initial gas pressure is greater than the surrounding rock mass, the coal body is in an elastic state; otherwise, the coal body becomes an elastic-plastic state [28, 29]. Assuming that the surrounding rock of the borehole is a continuous, homogeneous, and isotropic completely linear elastic body, any section of the borehole is taken for study:

3.1.1. Balance Equation.

$$\begin{aligned}&\frac{\partial \sigma_\rho}{\partial \rho}+\frac{1}{\rho}\frac{\partial \tau_{\rho\theta}}{\partial_\theta}+\frac{\sigma_\rho-\sigma_\theta}{\rho}+f_\rho=0,\\&\frac{\partial \tau_{\rho\theta}}{\partial \rho}+\frac{1}{\rho}\frac{\partial \sigma_\theta}{\partial_\theta}+\frac{2\tau_{\rho\theta}}{\rho}+f_\rho=0,\end{aligned}\tag{1}$$

where σ_ρ is the radial normal stress; σ_θ is the annular normal stress; $\tau_{\rho\theta}$ is the shear stress; ρ is the radial coordinates; θ is the toroidal coordinates; f_ρ is the radial force component; and f_θ is the circumferential force component.

3.1.2. Geometric Equations.

$$\begin{aligned}\varepsilon_\rho&=\frac{\partial u_\rho}{\partial \rho},\\\varepsilon_\theta&=\frac{u_\rho}{\rho}+\frac{1}{\rho}\frac{\partial u_\theta}{\partial \theta},\\\gamma_{\rho\theta}&=\frac{1}{\rho}\frac{\partial u_\rho}{\partial \theta}+\frac{\partial u_\theta}{\partial \rho}-\frac{u_\theta}{\rho},\end{aligned}\tag{2}$$

where ε_ρ is the radial linear strain; ε_θ is the circumferential linear strain; $\gamma_{\rho\theta}$ is the tangential strain; u_ρ is the radial displacement; and u_θ is the circumferential displacement.

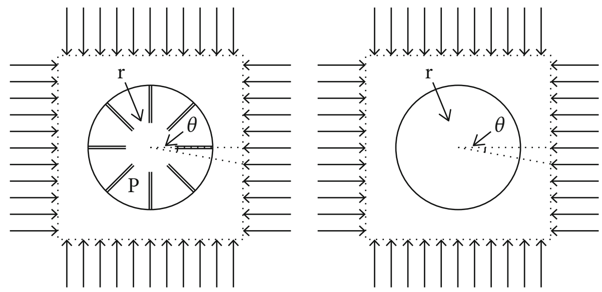

FIGURE 1: Stress analysis around borehole.

3.1.3. Constitutive Equation.

$$\varepsilon_\rho = \frac{1-\mu^2}{E}\left(\sigma_\rho - \frac{\mu}{1-\mu}\sigma_\theta\right),$$
$$\varepsilon_\theta = \frac{1-\mu^2}{E}\left(\sigma_\theta - \frac{\mu}{1-\mu}\sigma_\rho\right), \quad (3)$$
$$\gamma_{\rho\theta} = \frac{2(1+\mu)}{E}\tau_{\rho\theta,}$$

where E is the modulus of elasticity.

According to Saint Venant's Principle, a square boundary can be simplified to a circular boundary, which is regarded as a cylinder under pressure both inside and outside. In Figure 1(a), stress state of drilling hole is

$$\sigma_\rho = -\frac{R^2/\rho^2 - 1}{R^2/r^2 - 1}P - \frac{1 - r^2/\rho^2}{1 - r^2/R^2}\cdot\frac{\lambda+1}{2}\sigma_z,$$
$$\sigma_\theta = \frac{R^2/\rho^2 + 1}{R^2/r^2 - 1}P - \frac{1 + r^2/\rho^2}{1 - r^2/R^2}\cdot\frac{\lambda+1}{2}\sigma_z, \quad (4)$$
$$\tau_{\rho\theta} = 0,$$

where R is the radius of the cylinder.

Also according to Saint Venant's Principle, square boundary is simplified to circular boundary, and the stress state of Figure 1(b) is obtained by semi-inverse solution:

$$\sigma_\rho = -\frac{\lambda-1}{2}\sigma_z\left(1 + \frac{3r^4}{\rho^4} - \frac{4r^2}{\rho^2}\right)\cos 2\theta,$$
$$\sigma_\theta = \frac{\lambda-1}{2}\sigma_z\left(1 + \frac{3r^4}{\rho^4}\right)\cos 2\theta, \quad (5)$$
$$\tau_{\rho\theta} = \frac{\lambda-1}{2}\sigma_z\left(1 + \frac{2r^2}{\rho^2} - \frac{3r^4}{\rho^4}\right)\sin 2\theta.$$

The total stress state of drilling hole is

$$\sigma_\rho = -\frac{\left(R^2/\rho^2\right) - 1}{\left(R^2/r^2\right) - 1}P - \frac{1 - \left(r^2/\rho^2\right)}{1 - \left(r^2/R^2\right)}\cdot\frac{\lambda+1}{2}\sigma_z - \frac{\lambda-1}{2}\sigma_z\left(1 + \frac{3r^4}{\rho^4} - \frac{4r^2}{\rho^2}\right)\cos 2\theta,$$
$$\sigma_\theta = \frac{\left(R^2/\rho^2\right) + 1}{\left(R^2/r^2\right) - 1}P - \frac{1 + \left(r^2/\rho^2\right)}{1 - \left(r^2/R^2\right)}\cdot\frac{\lambda+1}{2}\sigma_z + \frac{\lambda-1}{2}\sigma_z\left(1 + \frac{3r^4}{\rho^4}\right)\cos 2\theta,$$
$$\tau_{\rho\theta} = \frac{\lambda-1}{2}\sigma_z\left(1 + \frac{2r^2}{\rho^2} - \frac{3r^4}{\rho^4}\right)\sin 2\theta. \quad (6)$$

The stress state at the hole wall $(\rho = R)$ is

$$\sigma_r = -P,$$
$$\sigma_\theta = \frac{R^2/r^2 + 1}{R^2/r^2 - 1}P - \frac{\lambda+1}{1 - \left(r^2/R^2\right)}\cdot\sigma_z + 2(\lambda-1)\sigma_z\cos 2\theta,$$
$$\tau_{r\theta} = 0. \quad (7)$$

3.2. Gas Occurrence State. In addition, the occurrence state of coal seam gas mainly includes adsorption and dissociation, which exist in a dynamic adsorption-desorption equilibrium state. The adsorbed gas generally accounts for 80%–90% of the total coal seam gas. Because the effective area of directional drilling on coal seam is large, the original stress distribution of coal body can be changed in a large range, and the dynamic equilibrium of adsorption and desorption can be broken, so that the gas is transformed from adsorption state to free state. After the coal body is drilled under the combined action of stress, gas pressure, and negative pressure, the free gas continues to flow into the borehole under the action of pressure gradient. The coal gas is effectively extracted and extracted, and the coal body shrinks and deforms. The permeability of the coal body increases, and the stress and gas pressure decrease. The influence radius of the gas extraction in the directional long borehole expands, and the gas extraction effect is significantly improved, so as to realize the large-scale effective extraction of coal seam gas [30].

4. Numerical Simulation

In order to further study the influencing factors of directional drilling in the working face 81306 of Baode Mine, combined with the geological conditions of the working face,

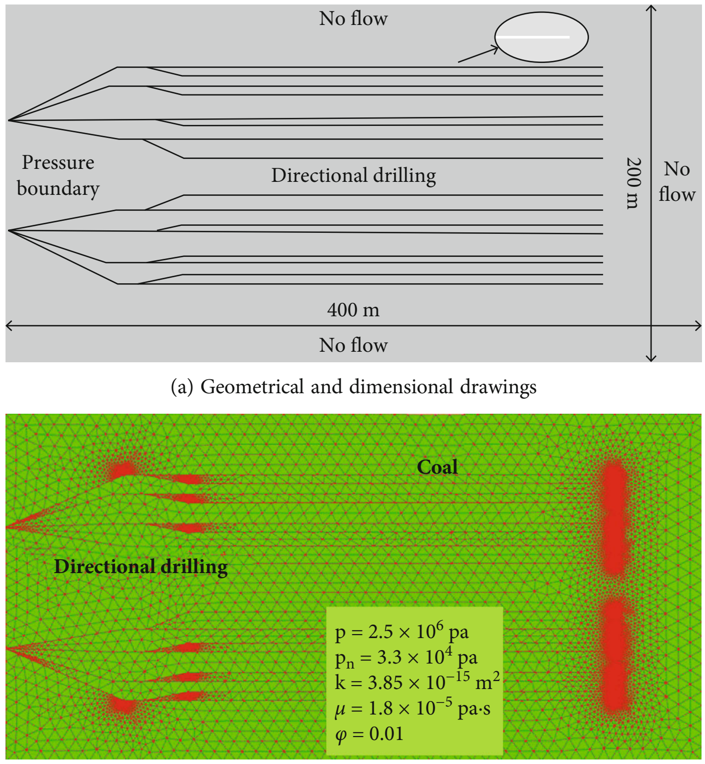

(a) Geometrical and dimensional drawings

(b) Grid drawing

Figure 2: Geometric diagram and grid diagram of gas extraction model in directional borehole.

a numerical model was established by COMSOL software to analyze the influence of different factors on directional drilling. The geometric model of gas extraction by directional drilling is shown in Figure 2(a), and the simulation grid is shown in Figure 2(b). The length and width of the model are $400\,\text{m} \times 200\,\text{m}$. The gas pressure of coal body is 2.5 Mpa, the negative pressure of extraction is 33 KPa, and the permeability is 3.85 mD. The simulation object is two groups of directional drilling holes, each group of drilling end consists of 8 branch holes, and the length of sealing hole section is 8 m. This model is used to study the effects of extraction time, gas pressure, negative pressure of extraction, and permeability of coal body on the extraction effect.

4.1. Different Extraction Time. Figure 3 shows the change of gas pressure in borehole after 10 d, 100 d, 200 d, 400 d, 600 d, and 800 d of drainage. It can be seen from the figure that in the initial stage of drainage, the influence radius of borehole is small, and the gas pressure around borehole basically maintains at about 2.5 Mpa. With the continuous pumping, the influence radius increases and the pressure value decreases. At the same time, the decrease of gas pressure in the early stage is larger than that in the later stage. After about 800 days of continuous pumping, the intermediate area between the two boreholes was effectively pumped. However, as shown in Figure 4, there are weak areas of extraction at the corner of the borehole and between the two boreholes with large spacing. These areas should be eliminated by increasing the extraction time or improving the borehole design to achieve effective extraction of all coal bodies.

4.2. Different Gas Pressure. The coal extraction process under three gas pressures (1.5 MPa, 2.5 MPa, and 3.5 MPa) was simulated and analyzed. Figure 5 shows the gas pressure changes on the pressure monitoring line under three different original pressures. It can be seen that on the one hand, the gas pressure around the borehole continues to decline with the progress of extraction. On the other hand, when the coal gas pressure is 1.5 Mpa, after a period of extraction, the area with pressure less than 0.74 Mpa around the borehole is the largest, followed by 2.5 Mpa coal body and 3.5 Mpa coal body. When the gas pressure of coal extraction is 1.5 Mpa after 400 days, most pressure values around the borehole are less than 0.74 MPa and after 800 days are less than 0.74 MPa. When the coal gas pressure is 2.5 Mpa, most of the pressure around the borehole is less than 0.74 Mpa after 800 days of extraction except for the most middle position of the monitoring line. When the gas pressure of coal body is 3.5 Mpa, after 800 days of extraction, the area with gas pressure less than 0.74 Mpa around the borehole is less than 2.5 Mpa. The above analysis shows that the higher the gas pressure of coal body, the longer the time required for extraction to reach the standard. When the gas pressure is high, it is suggested to take permeability enhancement measures to improve the permeability of coal body and shorten the extraction time.

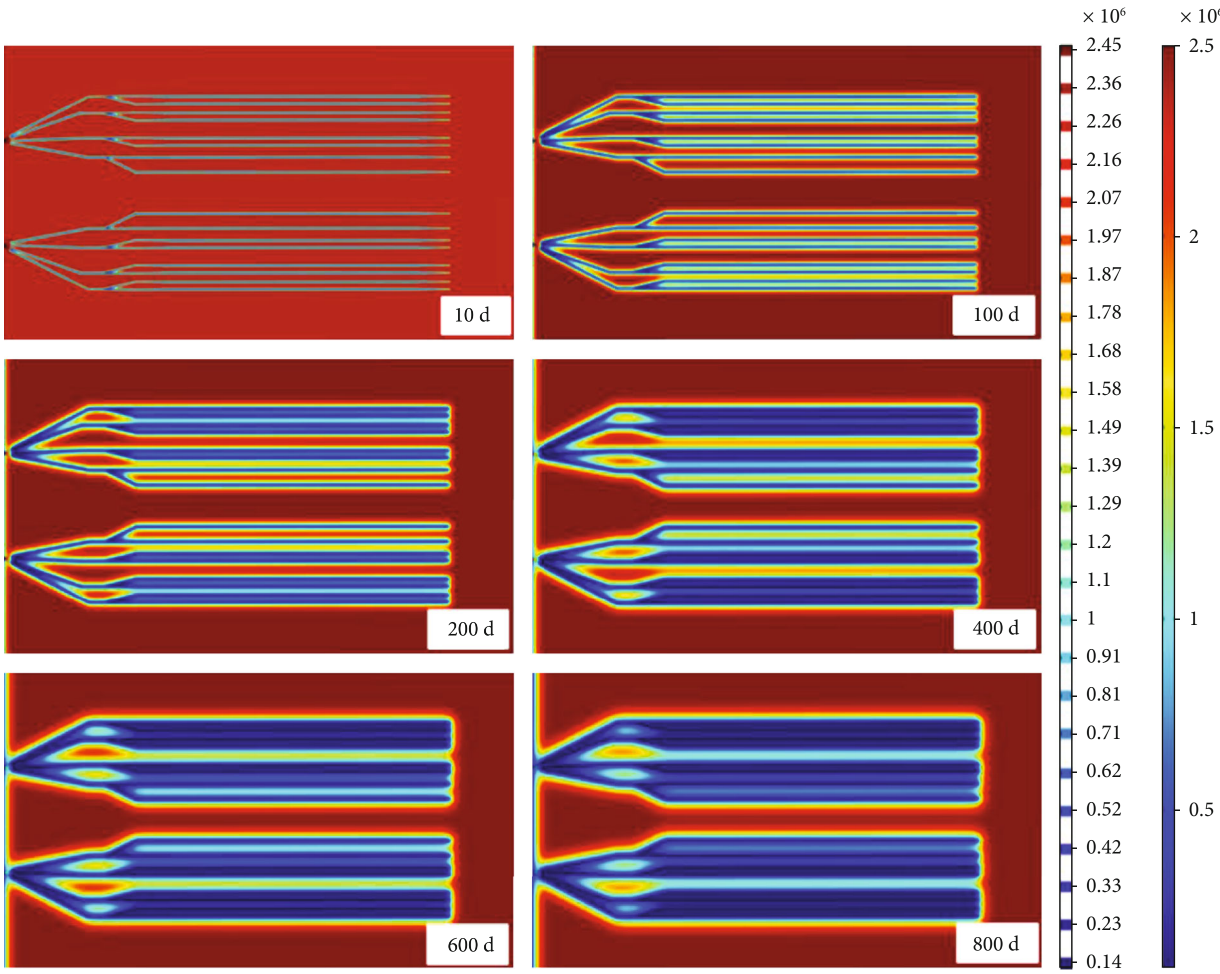

Figure 3: Borehole gas pressure variation under different extraction time.

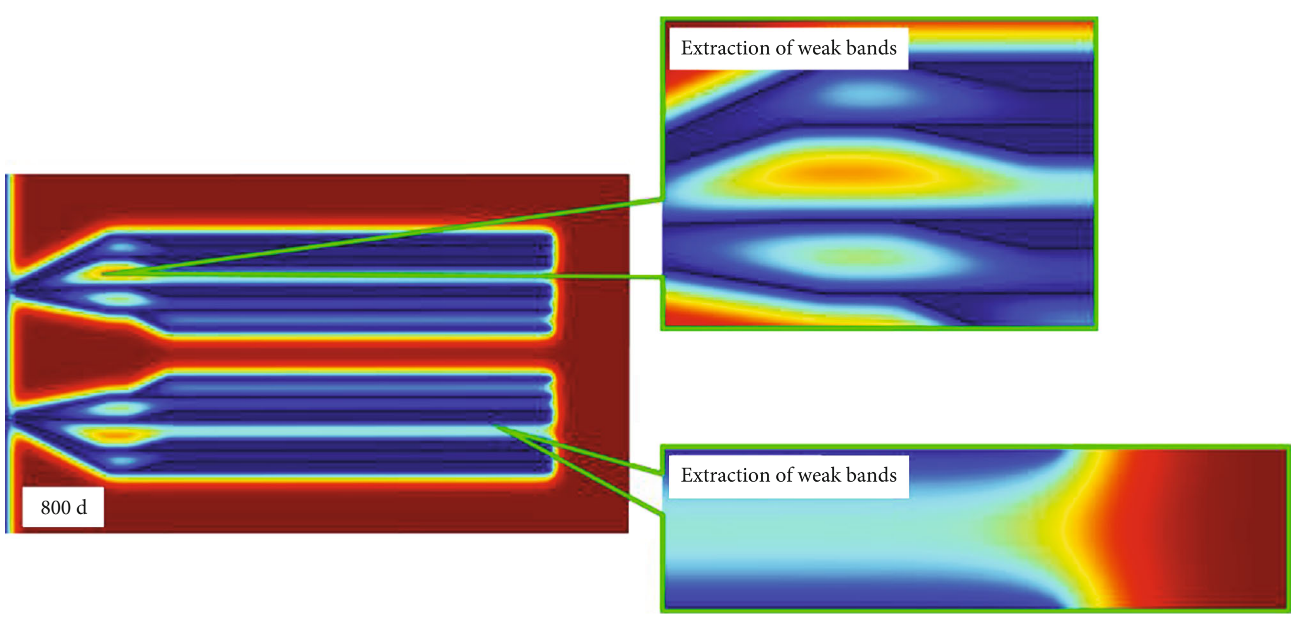

Figure 4: Weak zone of directional drilling extraction.

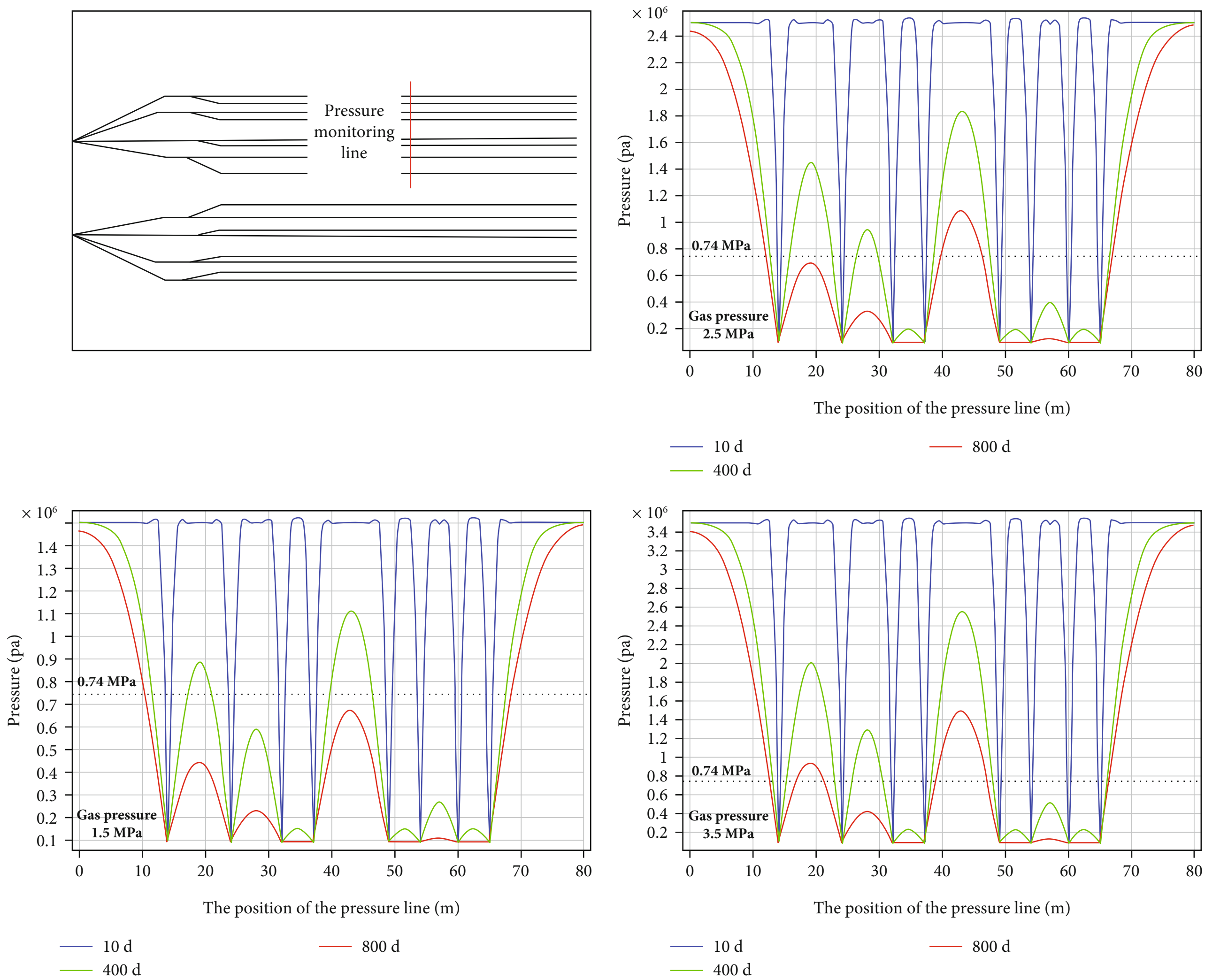

FIGURE 5: Comparison of extraction effects under different original gas pressures.

4.3. Different Suction Negative Pressure. At present, the negative pressure of drainage used in directional drilling in Baode Mine is about 33 KPa, and 13 KPa, 23 KPa, and 43 KPa are selected for comparative analysis. Figure 6 shows the gas pressure changes under different negative pressure conditions after 400 days of drainage. It can be seen that the increase of the negative pressure of drainage will make the gas pressure around the borehole decrease greatly. However, the above effects are limited, mainly because of the low permeability of coal seam itself. According to Darcy's Law, although the greater the negative pressure of extraction, the greater the differential pressure power of gas flow, the low permeability limits the positive effect of the increase of differential pressure on gas flow. At the same time, if the negative pressure value is too large, it will aggravate the degree of air leakage in the borehole sealing section and reduce the concentration and efficiency of gas extraction. So there is no need to increase the suction negative pressure excessively.

4.4. Different Coal Permeability. The gas extraction process of directional drilling was analyzed under three different coal permeability (0.385 mD, 3.85 mD, and 38.5 mD). Figure 7 shows the gas pressure changes after 100, 200, 400 and 800 days of extraction. It can be seen that the reduction range and degree of gas pressure around the borehole are positively correlated with the permeability value. When the permeability is 0.385 mD, the influence range of drainage is the smallest. Until 800 days after drainage, the drainage standard is still not achieved. However, when the permeability is 38.5 mD, the gas around the borehole decreased greatly, and the gas pressure decreases rapidly during the whole extraction process. After 800 days, the extraction standard is basically achieved, and the area of weak extraction area also drops to the lowest value. Therefore, for the coal body with high permeability, the design time of extraction can be appropriately shortened. For the coal body with low permeability, pressure relief and permeability enhancement measures such as hydraulic slit and loose blasting are needed to improve the pumping effect.

5. Field Test

81306 working face extraction boreholes include conventional boreholes and directional boreholes. This experiment

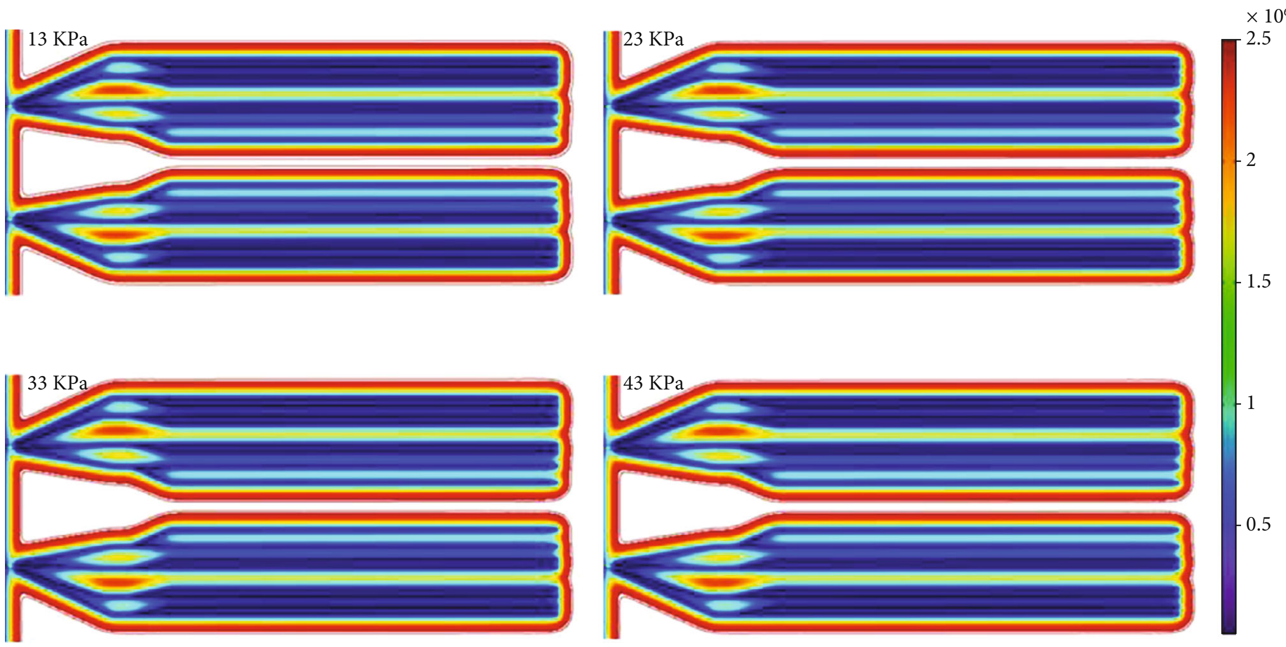

Figure 6: Gas pressure changes under different negative pressures (after 400 d).

mainly focuses on the comparative analysis of the drainage effect of two different hole distribution methods at the working face 81306 of Baode Mine. Figures 8 and 9, respectively, show the gas drainage diagram of directional borehole in the main drainage channel and the gas drainage diagram of conventional borehole in return air passage and glue transport passage. In the main air withdrawal channel, a 1000-meter directional borehole is adopted to extract gas. 81306 return air passage and 81306 glue transport passage are extracted by conventional boreholes. The extraction data of the two boreholes are collected and compared to analyze the advantages and disadvantages of the two boreholes.

A total of 30 months of gas extraction data from April 2011 to October 2013 were collected for analysis. The comparative analysis of the average extraction concentration and the pure extraction amount of the two boreholes is obtained:

5.1. Comparative Analysis of Average Extraction Concentration of Two Boreholes. The gas concentration extracted by directional drilling and conventional drilling in working face 81306 was compared and analyzed by drawing a contrast diagram as follows (Figure 10):

Directional drilling can be seen from the above; the average concentration of extraction in the extraction of gas in this period of time of attenuation is lesser, which can keep better extraction concentration. Even in the late state of extraction, extraction concentration remains at about 50%, while the return air and glue transported by conventional drilling along the through have different degrees of attenuation in the late stage of extraction. The extraction concentration of borehole in the No. 1 return air passage decreases rapidly, and the average extraction concentration in the later period decreases to about 10%. The extraction concentration of borehole in the glue transport passage also decreases significantly. It is found that the directional borehole has a better stability of extraction concentration and can still maintain a better extraction concentration in the later period of gas extraction. Therefore, under the condition of permitting, directional drilling is designed and constructed as much as possible for gas extraction.

5.2. Comparison and Analysis of 100 m Hole Extraction Pure Cumulative Quantity. The extraction effects of the two boreholes were compared through the comparative analysis of the 100-meter cumulative extraction pure amount of directional drilling and conventional drilling. The cumulative extraction purity of 100-meter boreholes in two boreholes is shown in the following (Figure 11):

From the above, we can see clearly that with the increasing number of extraction from drilling time, hundreds of meters drilling accumulative extraction from scalar are also increasing. However, compared with directional drilling and conventional drilling hundreds of meters total extraction from scalar, directional drilling still had better extraction effect. Compared with the conventional drilling, directional drilling has a more stable extraction concentration, Therefore, more pure gas can be extracted.

By preserved Baode Mine 81306 working face of the Lord from directional drilling and return air channel and glue along the trough of normal drilling analysis and comparison, normal drilling extraction concentration is generally lower than the directional drilling; only just started extraction, the draining directional borehole extraction and extraction of normal drilling concentration are higher than that of directional drilling, and conventional drilling attenuated rapidly. With the progress of drainage, the extraction concentration of conventional boreholes has been decreased. Just from the point of extraction concentration, if conditions are available, directional drilling can be used for gas

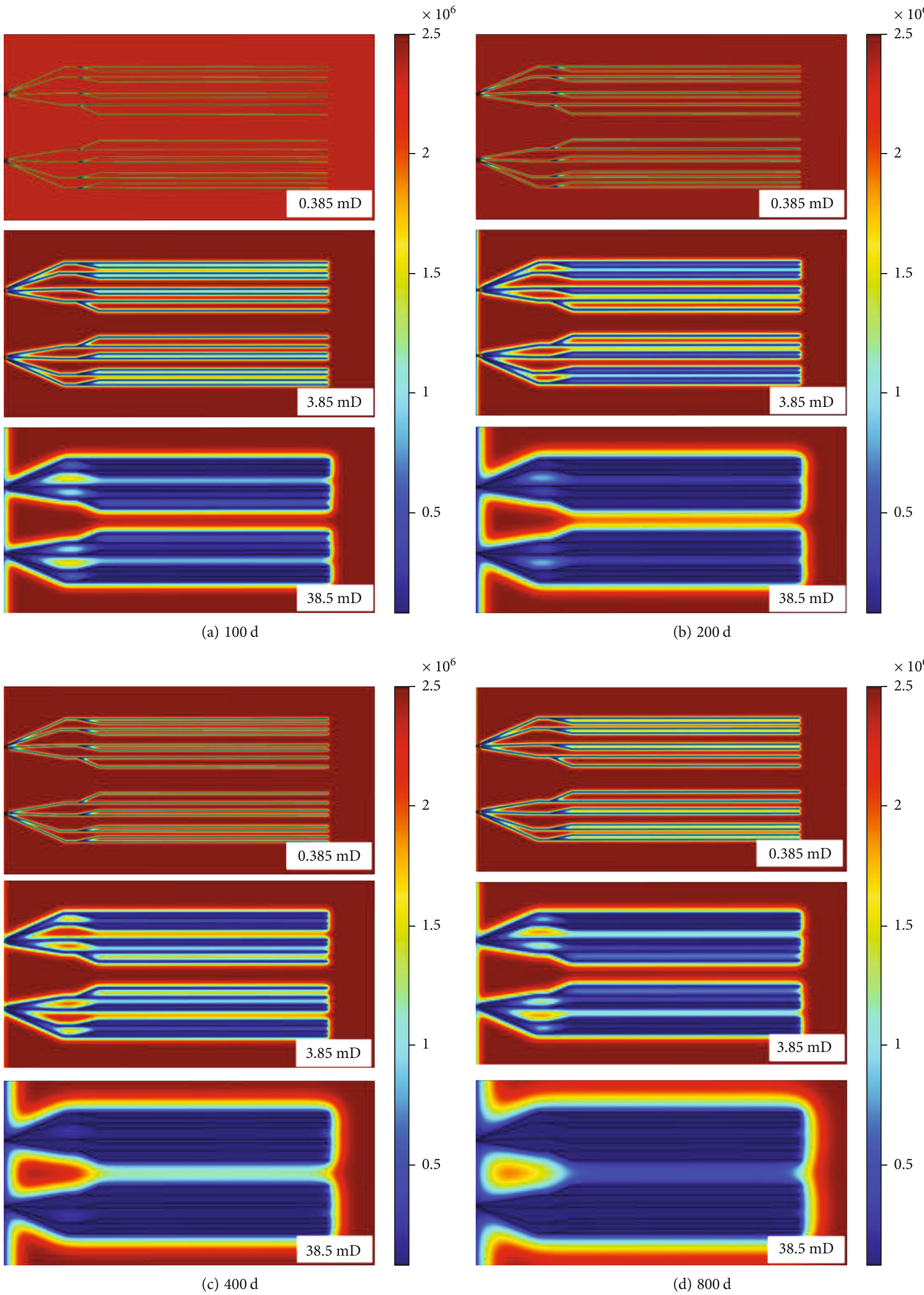

FIGURE 7: Gas extraction process diagram under different permeability.

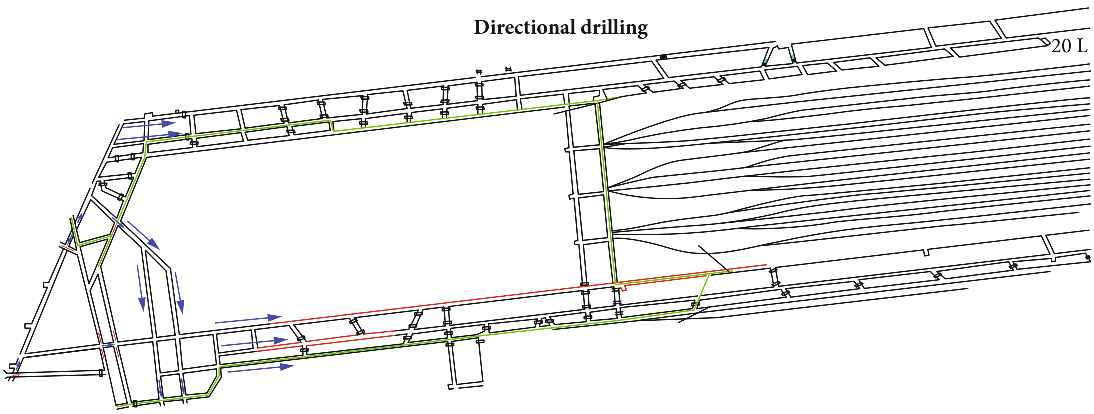

FIGURE 8: Gas drainage from directional boreholes in the main drainage channel.

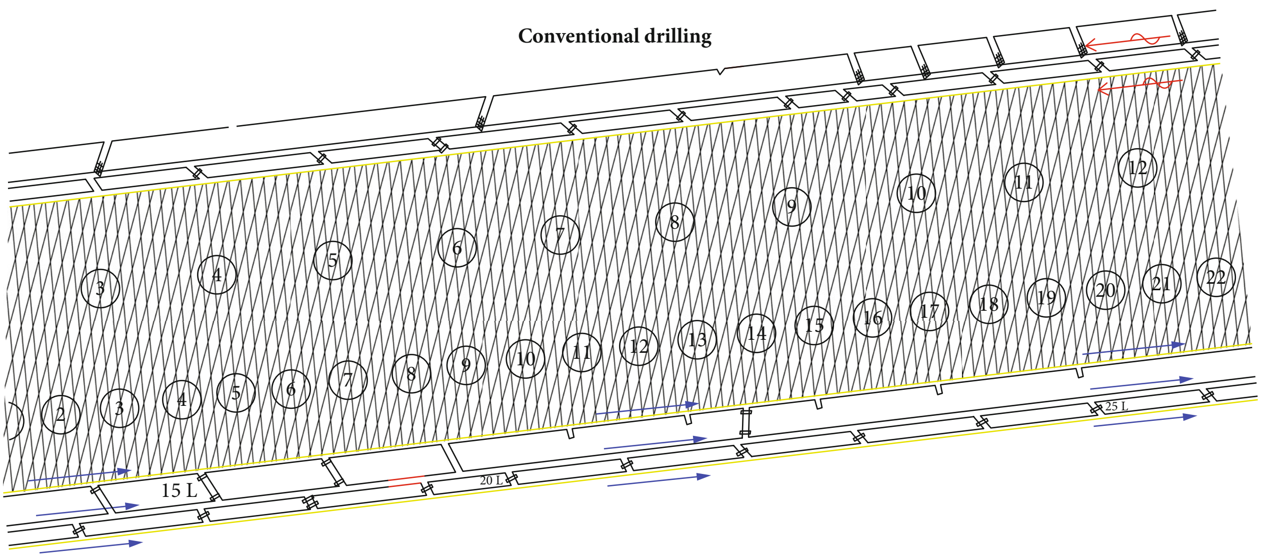

FIGURE 9: Conventional gas drainage from boreholes in the return air passage and glue transport passage.

preextraction as far as possible, so as to ensure good extraction effect. The reason why the cumulative pumping amount of directional drilling is larger than that of conventional drilling is that directional drilling has a deeper hole sealing depth and better hole sealing effect, which can maintain a good pumping concentration for a long time. At the same time, directional drilling can constantly adjust drilling angle according to the occurrence of coal seam, directional drilling can keep a high proportion of coal detection rate, and branch drilling can also continue to penetrate into the depth of coal seam gas extraction.

Directional drilling is generally superior to the extraction effect of normal drilling, but normal drilling also has its own advantages. Normal drilling rig is small, convenient to move, and easy to operate., The construction time of a drilling is shorter, and the problems of construction are easier to deal with. Some problems are relatively short in hole sealing distance of directional drilling, and the requirements for negative pressure of extraction are smaller. And directional drilling has some defects in these aspects, such as directional drilling, construction requires a relatively large space, drilling operation is more complex than conventional drilling, sealing hole length is generally longer than conventional drilling, and pumping negative pressure is about twice the conventional drilling. Therefore, the best drilling method should be selected according to the actual situation.

6. Conclusion

(1) Through the collection and comparison of field experimental data of 81306 working face, it is found that although directional drilling is more difficult to operate than conventional drilling and requires greater space and cost, directional drilling has better gas extraction stability than conventional drilling. The gas extraction concentration of the conventional boreholes in the return air passage and glue transport passage of the working face 81306 began to decline after 150 days of extraction and sharply decreased to less than 25% after 200 days, while the gas extraction concentration of the directional boreholes continued to increase. At 200 days, the gas

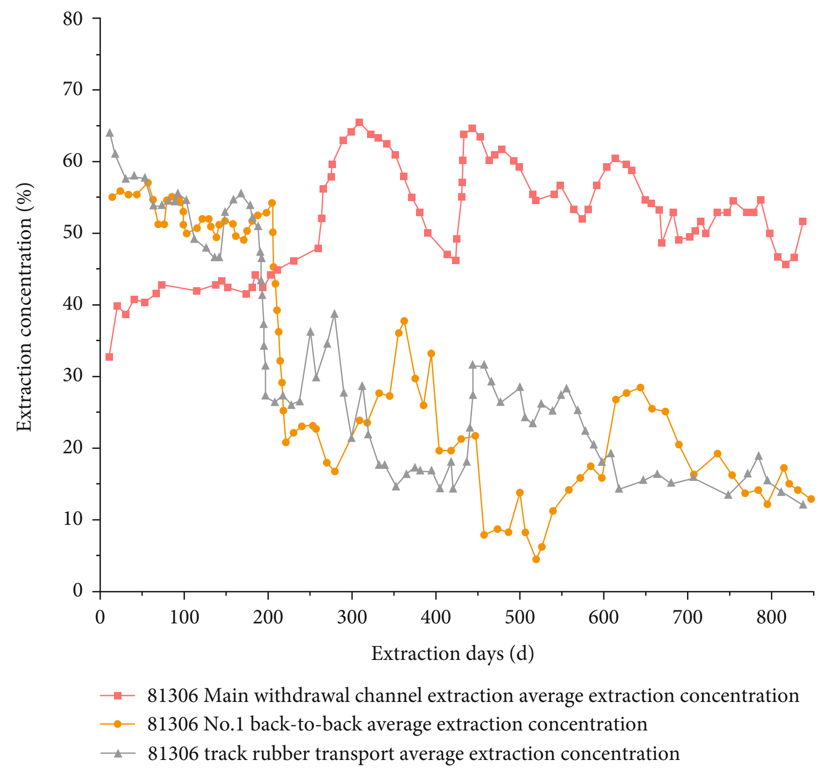

Figure 10: Comparison of extraction concentration between directional drilling and conventional drilling in working face 81306.

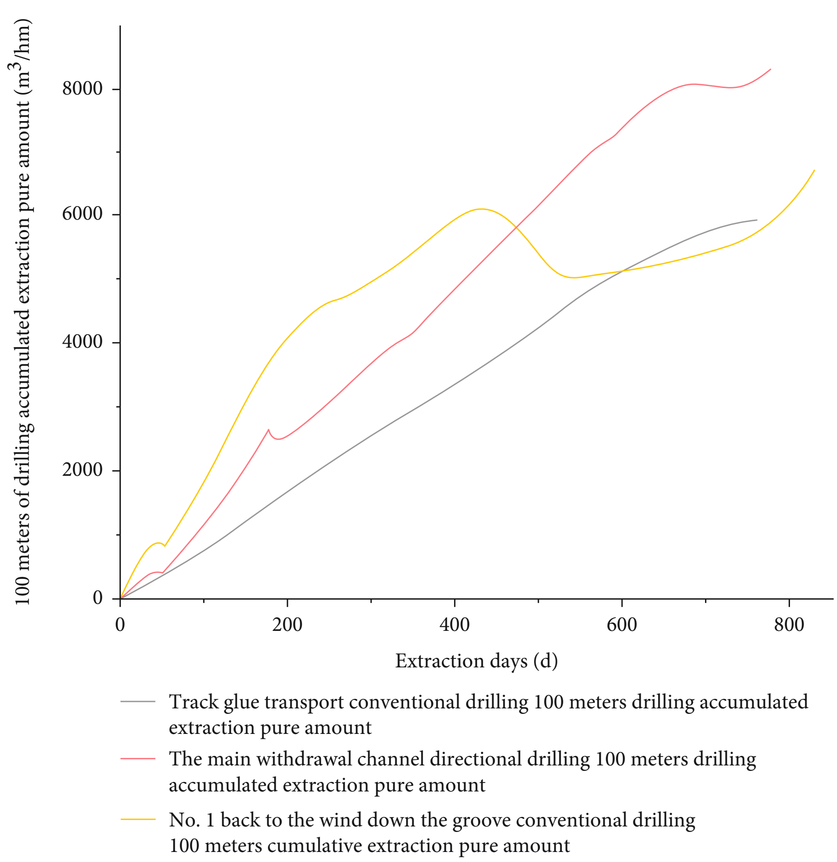

Figure 11: Comparison of cumulative pure extraction volume between directional drilling and conventional drilling on the working face 81306.

extraction concentration of directional drilling is about 44%, and at 350 days, the gas extraction concentration of directional drilling is about 61%. The gas extraction concentration was originally higher than that of conventional drilling in the same period. After 800 days of gas extraction, the gas extraction concentration of conventional drilling has decreased to about 14%, while the gas extraction concentration of directional drilling can still be maintained at about 50%. Compared with conventional drilling, directional drilling has longer service life, less attenuation of gas extraction concentration, higher stability, and better sealing effect. Even in the late stage of extraction, it can still maintain a good extraction concentration, greatly improve the extraction efficiency, and shorten the outburst elimination time. Compared with directional drilling, it has a more prominent advantage than conventional drilling

(2) The gas extraction effect under different extraction time, different gas pressure, different negative extraction pressure, and different coal permeability was analyzed. It was found that with the increase of extraction time, the influence range of directional drilling gradually increased and the pressure gradually decreased. After 800 days, the middle area of the two boreholes was basically effectively drained. However, there are weak areas in the corner of the borehole and between the two boreholes with large spacing. It is necessary to increase the extraction time or improve the borehole design to eliminate these areas so as to achieve effective extraction of all coal. In addition, the simulation analysis of coal extraction process under three kinds of gas pressure (1.5 MPa, 2.5 MPa, and 3.5 MPa) shows that when the gas pressure is 1.5 MPa, after a period of extraction, the area with pressure less than 0.74 MPa around the borehole is the largest, followed by 2.5 MPa coal and 3.5 MPa coal. Therefore, the higher the coal gas pressure, the longer the time required to reach the standard of extraction

(3) The negative pressure of extraction was analyzed by numerical simulation. The negative pressure of extraction used in directional drilling of Baode Mine is about 33 KPa, and 13 KPa, 23 KPa, and 43 KPa were selected for comparative analysis. The results show that the increase of negative drainage pressure will make the decrease range of gas pressure around borehole become larger, but because of the low permeability of coal seam itself, the above effect is limited, so there is no need to pursue excessively large negative drainage pressure. Meanwhile, the gas extraction process of directional drilling was simulated with three different coal permeability (0.385 mD, 3.85 mD, and 38.5 mD). When the permeability was 0.385 mD, the influence range of gas extraction was the smallest. Until 800 days after extraction, the gas extraction still failed to reach the standard. However, when the permeability is 38.5 mD, the gas around the borehole decreases greatly, and the influence range of extraction increases rapidly. Therefore, for the coal body with high permeability, the extraction time can be appropriately shortened

Data Availability

Data are available from the corresponding authors.

Conflicts of Interest

The authors declared no potential conflicts of interest with respect to the research, authorship, and/or publication of this article.

Acknowledgments

The project was supported by the Open Research Grant of Joint National-Local Engineering Research Center for Safe and Precise Coal Mining (Grant No.EC2021012) and entrusted by the China Coal Energy Research Institute Co., Ltd. (Contract No. ZMYHT*AJ-W-WSZNCC-02-21-090. This research was financially supported by the National Natural Science Foundation of China (Nos. 51934007 and 51904013) and Shandong Key S&T Innovation Engineering Project (2019JZZY020504).

References

[1] The Ministry of Ecology and Environment of the People's Republic of China, *Notice on Further Strengthening the Management of Environmental Impact Assessment for Coal Resources Development*, The Ministry of Ecology and Environment, China, 2020.

[2] Z. M. Jiang, "Thoughts on China's energy issues," *Shanghai Jiao Tong University*, vol. 2008, pp. 345–359, 2008.

[3] B. Q. Lin, X. Yao, and X. Y. Liu, "China's energy structure strategic adjustment under energy conservation and carbon emissions constraints," *Social Sciences in China*, vol. 31, no. 2, pp. 91–110, 2010.

[4] X. X. Miu and M. G. Qian, "Research status and prospect of green coal resources in China," *Mining and Safety Engineering Journal*, vol. 26, no. 1, pp. 1–14, 2009.

[5] C. Q. Ma, H. B. Chu, K. Li, and S. Q. Zhou, "Study on cointegration and error correction model of energy consumption and economic growth in China," *System Engineering*, vol. 2004, no. 10, pp. 47–50, 2004.

[6] H. P. Xie, H. W. Zhou, D. J. Xue, H. W. Wang, R. Zhang, and F. Gao, "Research and thinking on deep mining and extreme depth," *Coal Journal*, vol. 37, no. 4, pp. 535–542, 2015.

[7] M. G. Qian, "The scientific mining of coal," *Coal Journal*, vol. 35, no. 4, pp. 529–534, 2010.

[8] L. Yuan, "Scientific conception of accurate coal mining," *Coal Journal*, vol. 42, no. 1, pp. 1–7, 2017.

[9] L. Yuan, J. H. Xue, N. Zhang, and P. Lu, "Status and prospect of key technologies of coal seam gas extraction and coal and gas extraction," *Coal Science and Technology*, vol. 41, no. 9, pp. 6–11, 2013.

[10] L. Yuan, “Thoughts on the strategic strategy of deep coal and gas mining in China,” *Coal Journal*, vol. 41, no. 1, pp. 1–6, 2016.

[11] Y. P. Chen, J. H. Fu, and Q. X. Yu, “Development of China coal mine,” *Journal of Mining and Safety Engineering*, vol. 26, no. 2, pp. 127–139, 2009.

[12] Y. P. Chen, Q. X. Yu, H. X. Zhou, and H. F. Wang, “Practice and role of coal mining gas management of extraction before mining,” *Journal of Mining and Safety Engineering*, vol. 2006, no. 4, pp. 389–392, 2006.

[13] Q. X. Yu, Y. P. Chen, C. L. Jiang, and S. P. Zhou, “Principle and practice of high gas and unloading gas,” *Journal of China University of Mining and Technology*, vol. 2004, no. 2, pp. 3–7, 2004.

[14] X. Q. Zhou and G. X. Chen, “Probability analysis and revelation of major gas explosion accidents in coal mine,” *Coal Journal*, vol. 2008, no. 1, pp. 42–46, 2008.

[15] Z. F. Wang and J. Liu, “Problems and countermeasures of coal mine in China,” *Coal Mine Safety*, vol. 2005, no. 3, pp. 29–32, 2005.

[16] B. Q. Lin, J. H. Chang, and C. Zhai, “Analysis of coal mine safety status and countermeasures in China,” *Journal of Chinese Security Science*, vol. 2006, no. 5, pp. 42–46, 2006.

[17] D. Y. Ning, “Research progress and development direction of coal mine gas control technology in China,” *Coal Journal*, vol. 47, no. 2, pp. 161–165, 2016.

[18] Y. T. Shi, “Process and application of layer directional long drilling,” *Energy and Environmental Protection*, vol. 42, no. 6, pp. 8–11, 2020.

[19] Y. T. Shi, “Application of directional long drilling in working surface along thick coal seam,” *Mining Automation*, vol. 46, no. 6, pp. 76–80, 2020.

[20] Y. Wang and J. K. Ma, “Gas extraction technology,” *Mining Safety and Environmental*, vol. 46, no. 5, pp. 95–98, 2019.

[21] J. S. Zhang, “Study on gas testing of pre-pumped coal lane in directed long drilling,” *Coal Technology*, vol. 39, no. 9, pp. 102–105, 2020.

[22] J. S. Zhang, “Experimental study on the influence of gas pressure on coal body strength under adsorption conditions,” *Coal mine safety*, vol. 51, no. 1, pp. 26–29, 2020.

[23] G. H. Wang, “Numerical simulation study based on gas extraction by directional long boreholes,” *Mining Safety and Environmental*, vol. 48, no. 4, pp. 38–42, 2021.

[24] G. H. Wang, “Application of pre-extraction coal strip gas of directional long drilling,” *Energy and Environmental*, vol. 41, no. 7, pp. 25–28, 2019.

[25] G. H. Wang, “Application test of pre-extraction lane strip with directional long drilling technology,” *Energy and Environmental*, vol. 41, no. 5, pp. 1–4, 2019.

[26] J. Chen and Y. Luo, “Study of "one hole and two elimination" in long drilling,” *Mining Technology*, vol. 20, no. 5, pp. 48–50, 2020.

[27] Q. Zhang, Z. J. Shi, N. P. Yao, and H. L. Tian, “Analysis and suggestions of directional long drilling technology and equipment application in China,” *China CBM*, vol. 2007, no. 2, pp. 8–11, 2007.

[28] J. J. Wang, *Study on Strain and Stabilization Mechanism of Horizontal Directed Drilling Pressure*, Kunming University of Technology, China, 2008.

[29] Z. Y. Wei, *Study on Gas Gushing Rule and Extraction Mechanism of Long-Distance Directional Drilling*, Guizhou University, China, 2020.

[30] X. M. Ma, “Technology and application of deep hole in coal mine,” *Mining Automation*, vol. 47, no. 8, pp. 83–87, 2019.

Hindawi
Geofluids
Volume 2022, Article ID 9517011, 13 pages
https://doi.org/10.1155/2022/9517011

WILEY | Hindawi

Research Article

Experimental Study of Seepage Characteristics of Filling Structures in Deep Roadway

Shaoshuai Shi,[1,2,3] Xiangxiang Zhu,[2] Zhiguo Cao,[1] Lin Bu,[2] Zhijie Wen,[4] Zongqing Zhou,[2] Weidong Guo,[2] and Ruijie Zhao[2]

[1]*State Key Laboratory of water Resource Protection and Utilization in Coal Mining, Beijing 100011, China*
[2]*School of Qilu Transportation, Shandong University, Jinan 250061, China*
[3]*China Railway Economic and Planning Research Institute, Beijing 100083, China*
[4]*State Key Laboratory of Mining Disaster Prevention and Control Co-Founded by Shandong Province and Ministry of Science and Technology, Shandong University of Science and Technology, Qingdao 266590, China*

Correspondence should be addressed to Xiangxiang Zhu; zhuxiangxiang@mail.sdu.edu.cn and Zhijie Wen; wenzhijie@sdust.edu.cn

Received 6 September 2021; Revised 30 November 2021; Accepted 24 February 2022; Published 14 March 2022

Academic Editor: Richeng Liu

In order to study the seepage failure mechanism of roadway filling medium consisting of cohesive soil under complex hydrogeological conditions, a large-scale triaxial stress-seepage test system was utilized to investigate the influence of kaolin content and seepage loading rate on the seepage characteristics of filling medium. Through the analysis on the variation rules of sand loss and particle size distribution, the seepage characteristics and whole process of seepage instability of filling medium were explored in depth. It is concluded that (1) The seepage instability process of filling medium can be categorized into three stages: the initiation loss of fine clay, the accelerating loss of soil, and the stable status of soil loss. (2) The seepage failure process rate is proportional to the seepage loading rate and inversely proportional to the content of kaolin. (3) The kaolin and sand content of remaining mixture presented initial>bottom>middle>top status. The research results have guidance value for exploring the instability evolution mechanism of filling medium in deep roadway.

1. Introduction

Since the 21st century, especially with the implementation of the China Western Development and The Belt and Road Initiative, the focus of coal mining engineering or tunnel construction in China is gradually shifting to the western mountainous and karst areas with extremely complex terrain and geological conditions. Moreover, mine roof water inrush has been identified as one of the most serious dangers to mining safety and production in China [1–3]. Owing to various hydraulic and geological conditions and complex tectonic structures in deep coal mine roadway, causes and evolutionary mechanisms of mine water inrush vary significantly. [4, 5] The occurrence of mine water-mud inrush disasters in deep roadway has crypticity and burstiness, water-bearing structure(such as water-mud filling karst conduit) has the characteristics of large amount of water and sufficient water supply [6–9]. Mine water inrush disasters induced by water-bearing structures may cause casualties, economic losses, and project delay. If it is not effectively controlled, it is easy to induce environmental geological disasters such as water resources depletion and ground collapse, which seriously threatens social stability and economic development [10, 11].

At present, the key problem why mine water inrush disasters are difficult to forecast and control is that the geological conditions and catastrophic evolution process are extremely complex, which may cause that the catastrophic evolution mechanism of water inrush has not been systematically revealed. Through the case analysis of mine water inrush disasters in recent years, it is shown that the seepage instability of filling medium in fault, karst pipeline is one of the main causes of water-mud inrush disasters in coal mine [12–14] and most of them occur in the high permeability sandy-clay filling medium. Under the action of strong seepage, the continuous erosion of the filling medium makes the seepage channel appear, gradually extends then through, and the stability of the filling medium is constantly reduced, finally resulting in the occurrence of mine water inrush disasters [15, 16].

Previous studies on mine water inrush of deep roadway have focused on the water inrush mechanism and a large amount of research has been conducted through theoretical analysis, numerical simulation, and laboratory tests [17–20]. In terms of numerical simulation, Islam and Donnelly [21, 22] established a seepage-damage coupling model to reveal that mine water inrushes are related to the action of strong seepage and stress. Yang et al. [23] developed a flow erosion model for mine water inrush to reveal variation characteristics of the pressure field, velocity field, and porosity. In theoretical analysis, Yao et al. [24] established a deformation-seepage-erosion coupling model to explore the evolutionary rules of permeability characteristics of karst collapse columns in deep roadway. Li et al. [25] put forward stress-seepage-damage coupling equation before and after damage of filling medium to reveal the catastrophe evolution mechanism of mine water inrush in filling fault. However, the aforementioned research results could hardly simulate the actual water inrush process and elucidate the physical phenomenon.

In recent years, laboratory tests play a vital role in coal mining. Scholars around the world have gained plentiful and substantial achievements in the study of seepage characteristics of cohesionless soils by means of seepage instability tests. For example, Skempton and Brogan [26] carried out the experiments to reveal the critical hydraulic gradient of fine particle migration and instability in cohesionless soils under different particle size distributions. Su et al. [27], Tomlinson and Vaid [28], and Fannin and Moffat [29] have successively adopted large-scale permeameters to carry out the internal seepage test and studied the influences of particle size distribution, permeability, and confining pressure on the seepage instability process of cohesionless soil. However, the research results mentioned above were only limited to study on seepage characteristics of cohesionless soil and there are few large-scale experimental studies on seepage instability of cohesive soil. In order to explore evolutionary rules of internal erosion instability of cohesive soil, Bendahmane carried out seepage tests to analyze the influence of hydraulic gradient and clay content on the cohesive soil erosion mechanism [30–32]. Liang and Fan [33] investigated and analyzed the important reasons for the influence of pore size on clay seepage characteristics of tiny-particle clay. Richards and Reddy [34] conducted clay seepage erosion tests in a new true-triaxial pipeline test apparatus to explore three kinds of pipeline seepage failure modes under different fine particle contents and types. Mao and Akihiro [35] carried out the permeability test of cohesive soil, using a triaxial permeability tester to explore the influence of initial fine particle content on the seepage instability process. Meng et al. [36] employed the three-dimensional model test system of mine water inrush to analyze the structural instability characteristics and seepage laws of karst conduit fillings with different permeability coefficients. However, the aforementioned research results mainly focus on the study of the seepage characteristics of cohesiveless soil. Moreover, in terms of the seepage characteristics and evolution rules of cohesive soil, no in-depth studies have been conducted.

In this study, from the perspective of mine water inrush disaster characteristics of filling structures in deep roadway, a large-scale triaxial stress-seepage test system was utilized to carry out seepage instability test on filling medium. The effects of kaolin content and loading rate on seepage characteristics and the evolution rules of grain size distribution before and after seepage are investigated, so as to reveal the variation rules of permeability characteristics and seepage instability mechanism in filling medium.

2. Preparation of Similar Materials for Seepage Failure Test

2.1. Similar Materials of Surrounding Rock

2.1.1. Primary Components of Similar Materials of Surrounding Rock. In order to simulate factual evolution process of water-mud inrush induced by seepage instability of filling medium under the in situ stress state in deep roadway, similar materials consist of fine sand, calcium carbonate, iron powder, white cement, chlorinated paraffin, and silicone oil, which satisfy strength, deformation, and permeability of native rock. Then, a large amount of similar material ratio tests were conducted to select the ideal mix proportion of similar materials. Finally, the composition ratio of various ingredients is determined and the basic parameters of surrounding rock similar materials are obtained. The specific basic parameters are shown in Table 1.

In Table 1, S: Ca: Fe: Ce: Cp: So denote, respectively, sand: calcium carbonate: iron powder: white cement: chlorinated paraffin: silicon oil. ρ represents the density, σ_c represents the compressive strength, E represents the modulus of elasticity, k represents the permeability coefficient, and K represents the softening coefficient.

2.1.2. Preparation of Surrounding Rock Specimen. In this paper, the mold for the preparation of surrounding rock specimen is designed into a detachable iron mold. Rectangular blocks can meet the requirements of the precast rectangular structure in the specimen, providing convenience for sample processing. The outer diameter and height of the large-diameter specimen prepared by the mold can reach 300 mm and 300 mm, respectively. The rectangular piping-type disaster-causing structure is simplified and prepared by rectangular precast components to penetrate. The length and width of the rectangular section are both 80 mm.

The production of surrounding rock specimen is an important link of the test, which has significant influence on the test results. Therefore, in terms of physical, mechanical, and hydraulic properties, it is required that the specimen has stable properties, certain strength, low permeability, and is convenient for large-scale preparation at room

Table 1: Mix proportion of surrounding rock similar materials and its basic parameters.

S:Ca:Fe:Ce:Cp:So	ρ/(g·cm^{-3})	σ_c/(MPa)	E/(GPa)	k/(cm·s^{-1})	K
1 : 0.08: 0.07: 0.25: 0.1 : 0.02	2.48	0.92	0.10	3.55×10^{-6}	0.69

temperature. The basic components of surrounding rock similar materials are shown in Figure 1.

The preparation process is divided into five steps.

Step 1. The aggregate and cementing agent were prepared according to the ideal mix proportion of similar materials in Table 1.

Step 2. Four fine-grained materials including sand, calcium carbonate, iron powder, and cement were mixed evenly, and then, the appropriate amount of water was added into mixture by a mixer. Subsequently, the silicone oil and chlorinated paraffin were stirred in the mixture for 8-10 minutes.

Step 3. The stirred similar materials were added to the mold above and the single-layer cylindrical compaction was used to achieve a surrounding rock specimen.

Step 4. The specimen needed to be maintained at room temperature for 7 days, till then, the preparation of a large-diameter surrounding rock specimen containing disaster-causing structure was completed.

2.2. Similar Materials of Filling Medium

2.2.1. Primary Components of Filling Medium Similar Materials. With the water-bearing structures and unfavourable geological bodies exposed, the water-blocking structure consisting of cohesive soil, fine sand, and gravel is considered as the filling medium [25, 37]. Filling medium structure of deep roadways is the last barrier water-mud inrush disaster, the composition characteristics and mechanical properties are the key factors to affect its stability. However, the gushed filling medium is significantly different from initial fillings in physical and mechanical properties. Moreover, there are difficulties in sampling and maintaining for gushed filling medium, which is hard to apply to a large number of laboratory tests.

The penetration of filling medium induced by the continuous loss of clay and sand under seepage leads to the instability of filling medium structure and water-mud inrush disaster. Through the analysis of the samples of mud and sand gushed from the water-mud inrush cases, the gushed filling medium are mainly composed of gravel, fine sand, and clay. Therefore, the fine sand and clay with different grain compositions, used as filling particles of different grain sizes, are mixed uniformly to serve as filling material in the disaster-causing structure. Furthermore, the particles of which grain size is finer than 0.075 mm were replaced by kaolin.

2.2.2. Essential Properties of Filling Medium Similar Materials. The permeability and mechanical properties of filling medium play a key role and have a significant effect on the formation of internal seepage channel and instability evolution process. Therefore, in order to simulate the filling medium with different mechanical and permeability characteristics, three different mix proportions of filling medium similar materials were used to carry out seepage tests by adjusting the content of kaolin and sand. As is shown in Figure 2, the filling medium similar materials were prepared in this paper according to material composition and grain size distribution. The specific grain size distribution is shown in Table 2.

3. Test on Seepage Failures of Filling Medium

3.1. A Large-Scale Test System for Coupled Seepage and Triaxial Stress. As is shown in Figure 3, a self-developed large-scale triaxial stress-seepage test system was adopted to conduct permeability characteristics test on filling medium in rectangular disaster-causing structure. This test system consists of a visualization triaxial press chamber, particle loss collecting system, and a real-time data acquisition and monitoring system. Then, a visualization triaxial press chamber, which can truly simulate triaxial compression and hydraulic state of filling medium, includes confining pressure, axial pressure, and seepage pressure loading system. The pressure chamber, equipped with a real-time camera, adopts transparent acrylic material to realize high visual degree, which can meet the requirement of real-time monitoring of sample changes during test.

3.2. Test Scheme and Procedures

3.2.1. Design of Test Scheme. In order to explore the evolution rules of internal strength, permeability, and mechanical properties of fillings in the process of seepage instability, the tests focus on the influence of two parameters (kaolin content in the filling medium and seepage pressure loading rate) on the seepage instability of filling medium. As shown in Table 3, the tests are divided into six working conditions.

According to Table 2, the sand and kaolin are mixed together to prepare the corresponding gradation filling medium. As Tests 1, 3, and 5, the seepage pressure loading rate is fixed and the content of kaolin is adjusted. In rectangular cross-section karst pipeline of internal size 80 mm × 80 mm × 300 mm, the influence of kaolin content on the permeability of filling medium is analyzed under the condition of 100 kPa axial compression and 200 kPa confining pressure.

Meanwhile, the seepage rate has a great influence on the seepage failure of the filling medium, so it is vital to investigate the influence of seepage pressure loading rate on the seepage process in the experimental process. As Tests 1 and 2, filling medium with the same particle size distribution

Figure 1: Basic components of similar material of surrounding rock.

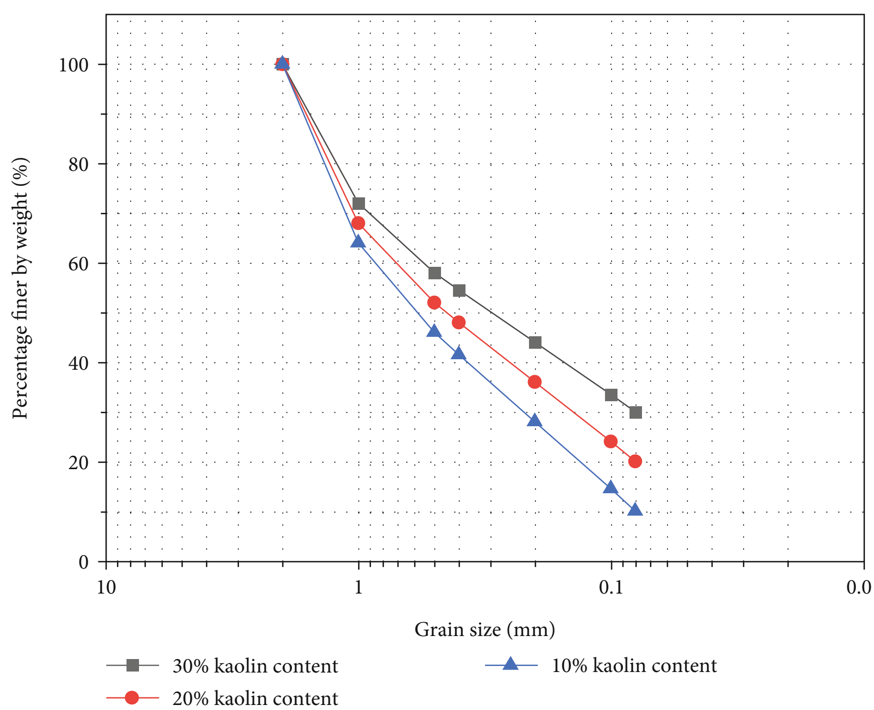

Figure 2: Grading curves of filling medium with different kaolin contents.

Table 2: Basic components of clay-sand-type filling medium.

Grain size composition						
Kaolin	Sand					
<0.08 mm	0.08-0.1 mm	0.1-0.2 mm	0.2-0.4 mm	0.4-0.5 mm	0.5-1 mm	1-2 mm
30.0%	3.5%	10.5%	10.5%	3.5%	14.0%	28.0%
20.0%	4.0%	12.0%	12.0%	4.0%	16.0%	32.0%
10.0%	4.5%	13.5%	13.5%	4.5%	18.0%	36.0%

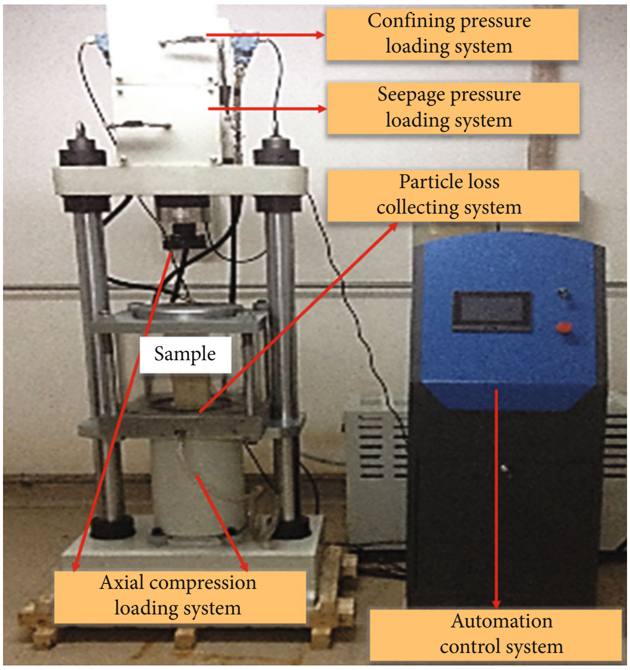

Figure 3: A large-scale triaxial stress-seepage test system.

Table 3: Test conditions.

Test number	Kaolin content %	Loading rate MPa/min
1	30	0.01
2	30	0.08
3	20	0.01
4	20	0.08
5	10	0.01
6	10	0.08

was prepared, by changing seepage pressure loading rates, the permeation characteristics of filling medium were going to be analyzed under the condition of 100 kPa axial compression and 200 kPa confining pressure. The loading schemes of permeability tests are shown in Table 4.

Having the seepage test completed, the remaining filling medium in the rectangular mold is analyzed. The top, middle, and bottom parts of the fillings are sampled, respectively, to analyze the changes of particle size distribution before and after the seepage failure of the filling medium.

3.2.2. Model Test Procedures. The permeability test process is summarized below.

Step 1. Preparation of test system. Firstly, the preparation of the triaxial stress-seepage test system is installed; then, a 2 mm filter is laid on a funnel-shaped particle loss collecting device. The sealing ring is placed around the large diameter of the rectangular base and the funnel to isolate the water and air in the confining pressure system and the specimens prepared by similar materials of surrounding rock are placed on the top.

Step 2. Construction of the filling material. The filling material is prepared on the basis of grain size composition in Table 2, and then, the filling material with uniform mixing is packed into the precasted structure in the light of 20-30 mm per layer. Each layer of filling medium is separately paved and compacted. When the filling medium height reaches 150 mm, Φ0.6 mm glass beads are laid at the top of the filling medium to form a uniform flow of injected water.

Step 3. Seal the test system. Subsequently, installing cover and round seal ring under it is to seal visual pressure chamber. In order to seal the whole device, the upper and lower cover plates are pressed by setting up four pull rod bolts. The automation control system is operated to load axial compression to design value, which completes the sealing of upper and lower cover plate and specimen.

Step 4. Saturate the specimen and sample. In order to make the specimen saturated, the water pressure loading system is adjusted to 10 kPa for some time to discharge air in the sample. When the sample is saturated, computer system is operated for loading confining pressure to the design value at a certain rate. The schematic diagram of a test system is shown in Figure 4.

Step 5. Loading of seepage pressure. So far, the preparation work in the early stage of the test is completed. Then, the permeability test of fillings for rectangular disaster-causing structure is conducted. The computer system is operated to start seepage pressure loading on the basis of loading scheme in Table 4. To ensure the seepage instability failure of the filling medium, the final pressure is set to 2 MPa.

Step 6. Collection and sampling of mixture. Water bottles are used to collect the sandy-clay mixture at the bottom of the device and replaced every minute to ensure that the mixture is collected at the same time interval. After completing the seepage test, the top, middle, and bottom parts of the filling medium are sampled, respectively.

4. Result Analysis of the Test

When the rectangle structure is filled with 10%, 20%, and 30% kaolin, the collected mixture condition is shown in Figure 5.

4.1. Effect of Kaolin Content on Permeability Characteristics

4.1.1. Sand and Clay Loss Analysis. In the process of permeability instability test on filling medium, water flowing from the bottom of the sample is collected every 60s, and the sandy-clay mixtures of the six groups of tests are loaded into transparent plastic bottles at the same time interval. Furthermore, in order to carry out wet and dry separation, the sand and clay effluent in each bottle is poured into disposable paper cup and then put into an oven adjusted to 50°C for

Table 4: Loading schemes of permeability tests.

Type of loading	Loading pressure (kPa/min)	Pressure type	Loading mode
Axial compression	14	Hydraulic fluid	Continuous loading to the design value
Confining pressure	30	Water hydraulic	Continuous loading to the design value
Seepage pressure	10/80	Water hydraulic	Gradually applied load to the failure of filling medium

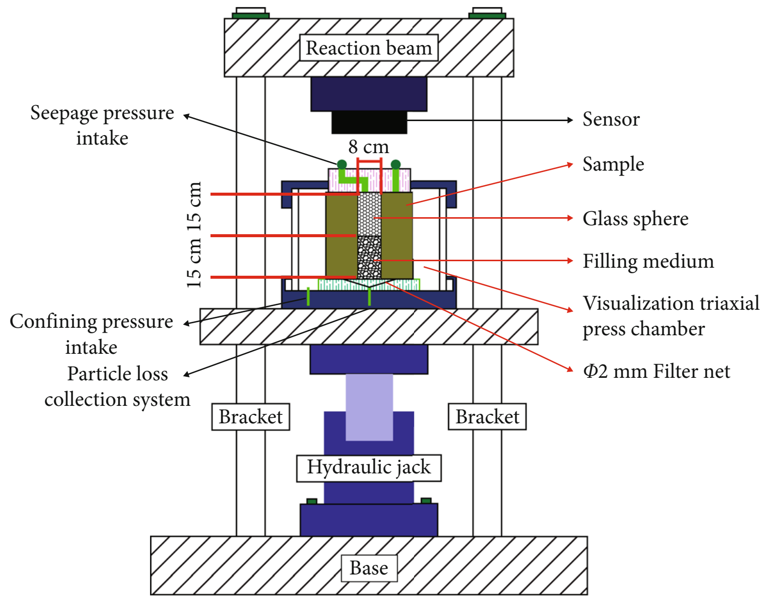

Figure 4: Schematic diagram of a test system.

24 h, to ensure that the water in the mixture has been completely removed and the mass of it in each stage is weighed. The specific amount of sandy-clay mixture is shown in Table 5.

Figure 6 shows the variation curves of cumulative sand inflow versus time for three kinds of kaolin content in the sandy-clay type filling medium. With the development of the seepage failure process of filling medium, the cumulative sand loss with the increasing of time shows "S" growth curve, and ultimately, the sand loss rate is reduced to zero. In terms of 20% or 30% kaolin content samples, in the first stage, some fine particles begin to flow out. Meanwhile, the sand inflow and growth rate are very low and the water quality is clear (see bottles 1 and 2 in Figures 5(a) and 5(b)). In the second stage, the cumulative sand-clay mixture loss shows a steep increase trend in 2 ~ 3 minutes. The water quality has changed from clear to turbid, as shown in bottles 3 and 4 in Figures 5(a) and 5(b). With a sandy-clay mixture inflow increasing sharply, the growth rate also becomes very large. The fine particles gush out of the filling medium with the flow, so as to decrease its permeability. Further, the larger particles inside filling medium began to slip, and the fine particles have been exhausted. In the third stage, the water quality gradually recovers from turbidity to clarity 4 minutes, as shown in bottles 5 to 8 in Figures 5(a) and 5(b). Compared with the high sand and clay loss rate in the initial stage, with the most fine sand and clay flowing out in the filling medium, only large skeleton sand is left. Eventually, the sand and clay loss rate decreases close to zero. The cumulative sand inflow curve of the water inrush process is close to the level, and the total amount of sand and clay loss tends to be stable. However, under the condition of kaolin content of 10%, the variation trend of cumulative sand inflow also presents the same trend, but the variation trend is not that obvious. As a result of low content of fine particles and large distance between soil particles, the interaction force is small, which slightly hinder the permeability process. Therefore, the filling medium in the structure is easy to be carried by the water to form a complete seepage channel, which leads to seepage instability and failure in advance.

Through comparative analysis, it can be concluded that the accumulative loss amounts of sandy-clay mixture in filling medium increase with the increase of time, and finally, the growth rate decreases close to zero. With the increase of kaolin content, the cumulative and ultimate amount of clay-sand increased in the same time period. With the decrease of kaolin content, the time point of sharp increase of sand and clay loss is advanced, which accelerates the process of seepage failure and destruction of filling medium.

4.2. Effect of Seepage Pressure Loading Rate on Permeability Characteristics

4.2.1. Sand and Clay Loss Analysis. Figure 7 shows the variation curve of cumulative sand-clay loss with time under two

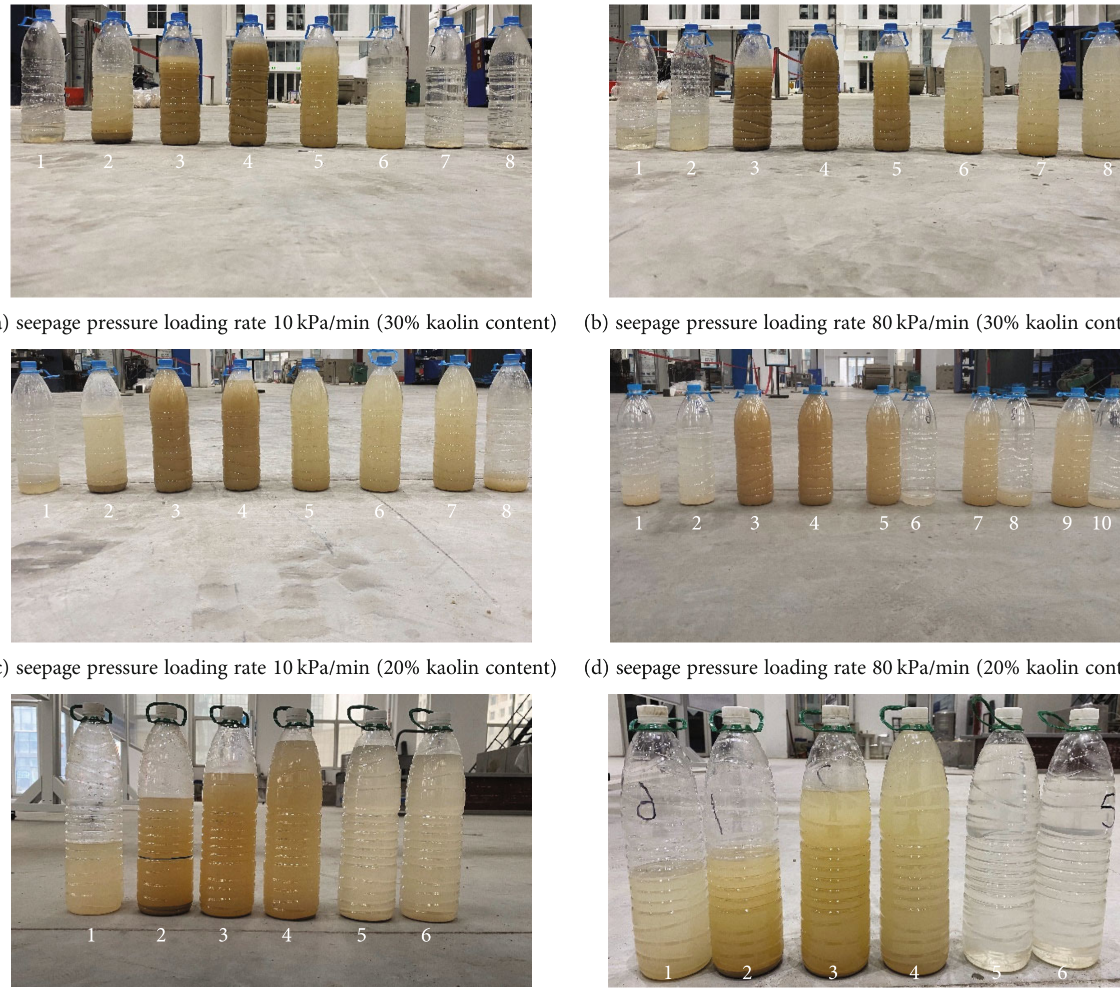

(a) seepage pressure loading rate 10 kPa/min (30% kaolin content) (b) seepage pressure loading rate 80 kPa/min (30% kaolin content)

(c) seepage pressure loading rate 10 kPa/min (20% kaolin content) (d) seepage pressure loading rate 80 kPa/min (20% kaolin content)

(e) seepage pressure loading rate 10 kPa/min (10% kaolin content) (f) seepage pressure loading rate 80 kPa/min (10% kaolin content)

Figure 5: Water quality condition during the process of water inrush from filling medium.

Table 5: Statistics of sand production in each bottle.

Test number	Seepage pressure loading rate MPa/min	Kaolin content %	Loss amounts of sandy-clay mixture g								Total amounts of sandy-clay mixture g
			1 min	2 min	3 min	4 min	5 min	6 min	7 min	8 min	
1	0.01	30	6.5	17.8	43.0	14.9	8.6	5.2	4.2	3.9	104.1
2	0.08	30	8.4	25.6	61.0	15.7	6.5	6.6	4.8	2.4	131.0
3	0.01	20	3.4	15.7	41.4	6.8	5.1	3.0	2.0	/	77.4
4	0.08	20	2.5	14.0	54.9	9.6	8.3	7.9	3.2	/	100.4
5	0.01	10	0.1	16.0	10.0	2.0	1.0	0.1	/	/	29.2
6	0.08	10	0.1	24.2	25.0	11.0	7.0	2.0	/	/	69.3

seepage pressure loading rates. The loading seepage pressure is comparatively small at 1 min, so the sand and clay loss remains at a very low level and only a few fine sand and clay gush out in the course of the test. It can be inferred that the finer particles are easier to reach the initial migration speed at the same seepage pressure loading rate. When the time is 2 min, as seepage pressure increases, the amount of gushing sand and clay begins to increase gradually. As fine particles continue to lose, the permeability increases, and the internal seepage channel begins to expand gradually; then, the relatively large particles begin to leave the filling medium, which represents the end of the first stage of the whole process. The second stage shows in 2-4 min that the sand and clay losses begin to accelerate significantly due to the expansion of seepage failure process. Meanwhile, the difference of cumulative sandy-clay mixture

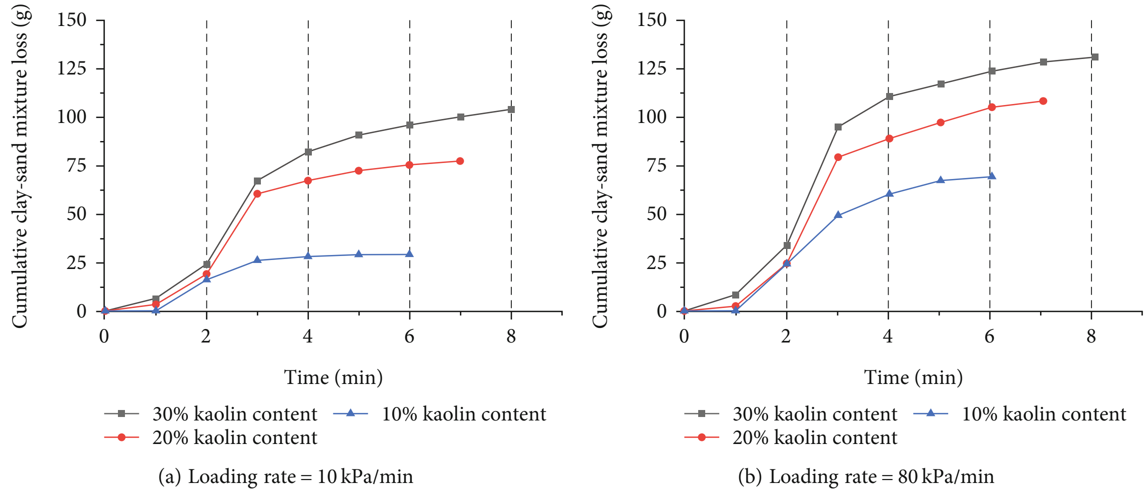

(a) Loading rate = 10 kPa/min

(b) Loading rate = 80 kPa/min

Figure 6: Variation curves of cumulative sandy-clay mixture loss for different kaolin contents.

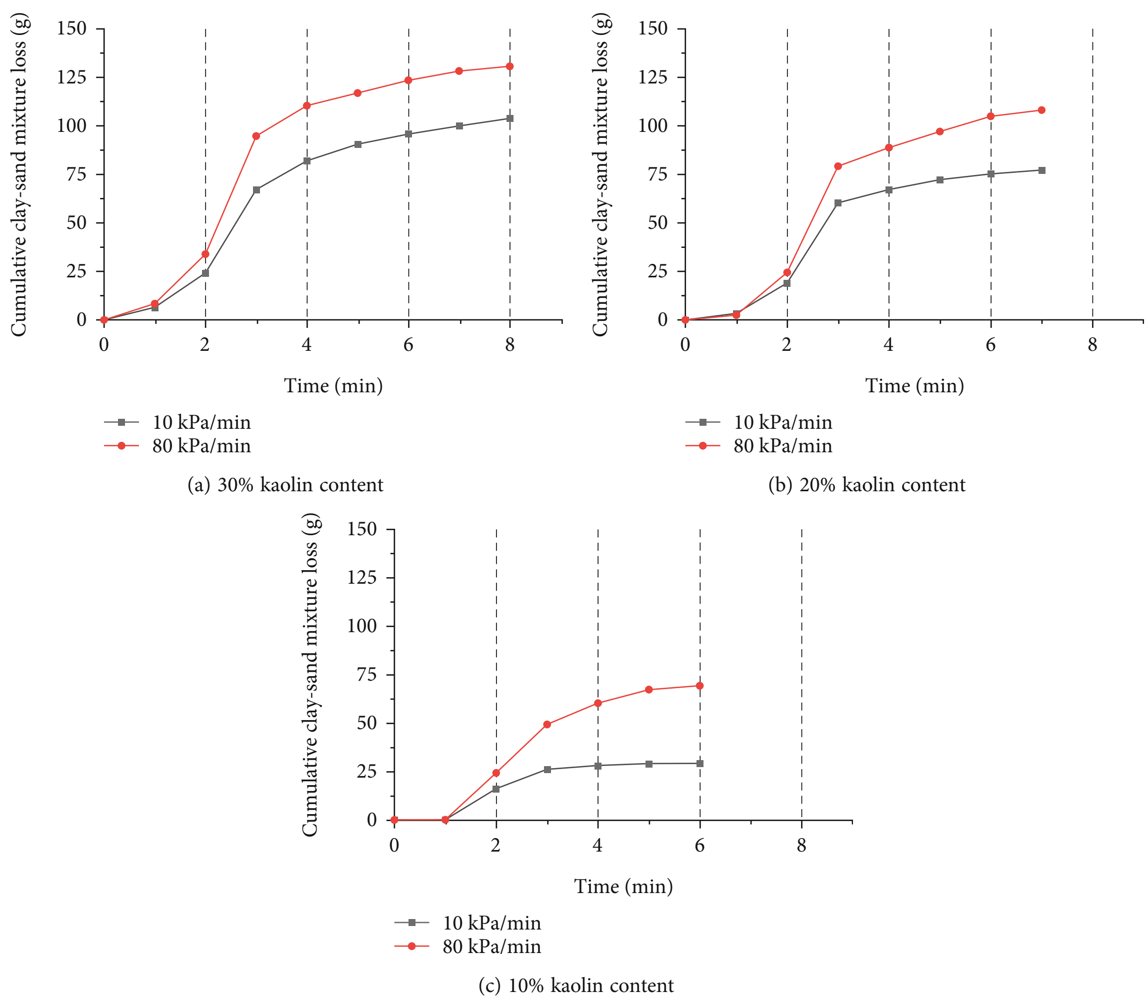

(a) 30% kaolin content

(b) 20% kaolin content

(c) 10% kaolin content

Figure 7: Variation curves of cumulative clay-sand mixture loss for different seepage pressure loading rates.

loss under different loading rates is expanding, which indicates that the seepage channel is gradually formed in filling medium. However, with the continuous loss of fine particles, the loss rate decreases sharply. Then, the third stage begins at 4 min, the sand and clay loss rate slowly decreases and the curve tends to be horizontal, which means the whole mixture of filling medium is lost except for large skeleton sand, a complete seepage channel network has formed.

Based on the analysis, the following conclusions can be drawn: firstly, with the increase of the seepage loading rate, the cumulative amount of mixture loss in the same period and the final state are greater; secondly, with the increase of seepage loading rate, the time point of sharp increase of mixture loss is advanced, which accelerates the process of seepage damage of filling medium.

4.3. Analysis on Particle Size Distribution of Filling Medium. Due to the migration of particles in the filling medium, the materials composed of still existing soil particles in the rectangular piping-type structure are called remaining mixture. At the end of the experiment, samples from remaining mixture of six tests are taken from the top, middle, and bottom of the structure. They are, respectively, put into disposable paper cups and then placed in the oven adjusted to 50°C for 24 hours to make sure the water is completely removed. Subsequently, the screening test is carried out on the dried sample. The pore sizes of sieve set are 0.08 mm, 0.1 mm, 0.2 mm, 0.4 mm, 0.5 mm, 1 mm, and 2 mm, respectively. After setting the sleeve into a shaker for 10 min, the weight of each sieve is to be weighed. The particle grading variation curves of remaining filling medium are shown in Figures 8–13. In this paper, the particle sizes (0 ~ 0.4 mm) are defined as fine particles and the particle sizes (0.4 ~ 2 mm) are defined as coarse particles. The content of particles represents weight percentage in a certain particle size range.

4.3.1. Analysis on Particle Size Distribution of Remaining Mixture with a 30% Kaolin Content. According to Figures 8 and 9, the particle gradation curves of the remaining mixture compared with those of initial status, the fine particle contents all decrease and the content of particles larger than 0.4 mm all increases.

When the seepage pressure loading rate is 10 kPa/min, the contents of particle sizes smaller than 0.08 mm, 0.08-0.1 mm, and 0.1-0.2 mm decrease, and the other particle size contents increase at the top, middle, and bottom parts of remaining mixture. As shown in Figure 8, the amount of particle size smaller than 0.08 mm in the top and middle of the filling medium decreases significantly. On the contrary, the contents of coarse particles apparently increase. The content of fine particles in the filling medium decreases slightly, which has little effect on the particle size composition of each part. When loading the seepage pressure at 80 kPa/min, similar to the loading rate of 10 kPa/min, the contents of particle size smaller than 0.2 mm also decrease and the other particle size contents increase as well. However, the difference is that the particle size of 0.4 mm-0.5 mm, 0.5 mm-1 mm, and 1-2 mm increase more dramatically than that of 10 kPa/min.

On the whole, the permeation process of filling medium with high clay content is most significantly affected by fine particles. In the initial stage of water seepage in filling medium, the clay and fine sands start to move in the pores shaped by coarse sand, leading to the reduction of the cohesion between particles. As more and more fine particle loss, the permeability and the pore water pressure increase, resulting in the expansion of the internal seepage channel of the filling medium. Migrated particles at the middle and bottom parts of the sample are fewer and relatively stable than the top part. The clay and fine sands in the top part are easier to lose under the action of seepage; hence, the loss amounts of migrated fine particle are the largest, which is contrary to coarse particles. Along with the gradual expansion of the seepage channel and water flow rate increases, the stability of the whole specimen is greatly weakened, making it more difficult to resist the seepage. Under the action of their own gravity and seepage, the fine particles at the top and middle parts of filling medium start moving to bottom part of kaolin-sand mixture and replace lost fine particles to form 'supplying-particles' at the bottom of filling medium. Except for a large number of fine particles, only a small number of coarse particles begin to gush out from the mixture and the seepage channel has formed. Therefore, the loss of fine particles in the top remaining mixture is the most, the coarse particles is the least, and the loss of fine particles in the lower part is the least.

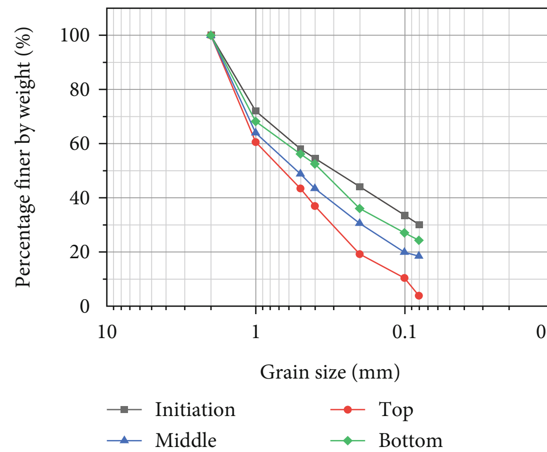

Figure 8: Test number 1 particle grading variation curves before and after seepage.

Through comparative analysis above, it can be summarized as follows: (1) Compared with the initial status of filling medium, the fine particle content of the remaining mixture decreases and the content of coarse particles increases. (2) With other conditions unchanged, when the seepage loading rate is greater, the content of coarse particles in each part is higher; conversely, the fine particle content is lower. (3) With the increase of loading rate, the seepage failure process of filling medium is aggravated. It can be inferred that the loss of fine particles leads to the decrease of internal cohesion and the loss of coarse particles is relatively increased. (4) With other conditions unchanged, contrary to 0.4-2 mm coarse particles, the change of fine particles content of remaining mixture presents initial>bottom>middle>top status.

4.3.2. Analysis on Particle Size Distribution of Remaining Mixture with a 20% Kaolin Content. According to

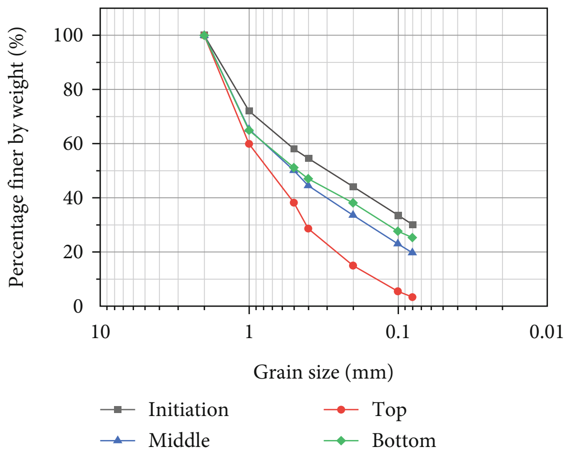

Figure 9: Test number 2 particle grading variation curves before and after seepage.

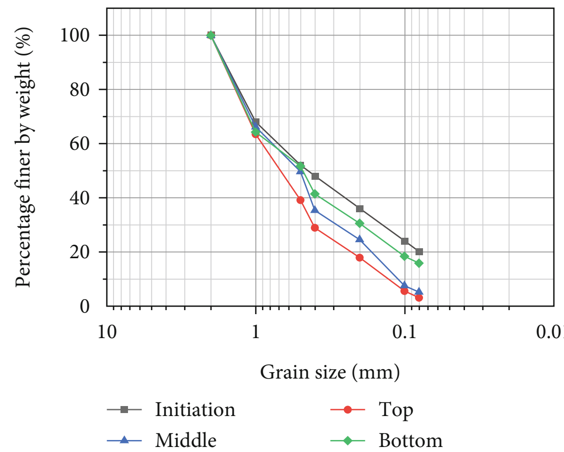

Figure 11: Test number 4 particle grading variation curves before and after seepage.

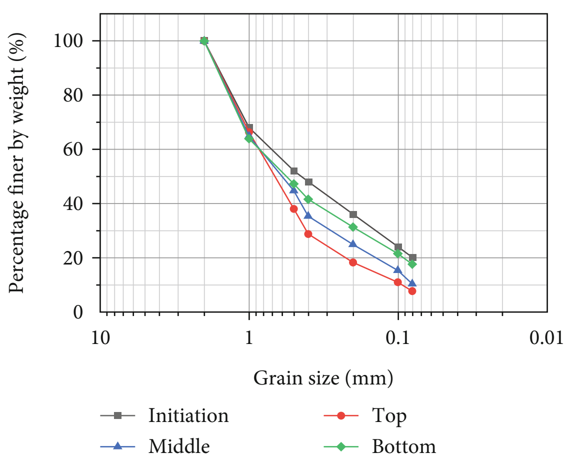

Figure 10: Test number 3 particle grading variation curves before and after seepage.

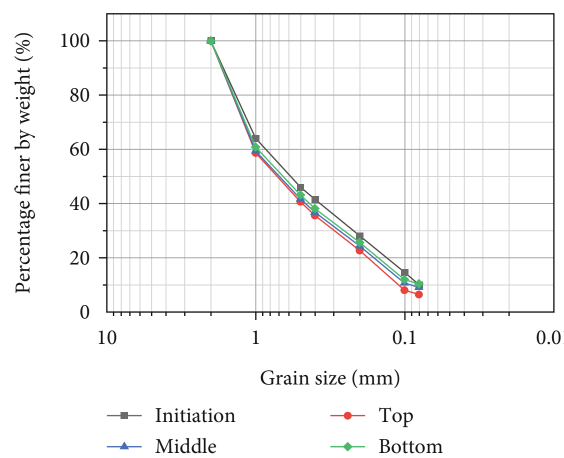

Figure 12: Test number 5 particle grading variation curves before and after seepage.

Figures 10 and 11, the particle gradation curves of the remaining mixture in tests 3 and 4, compared with those of initial status, the fine particles contents all decrease and the content of coarse particles all increases.

When the seepage pressure loading rate is 10 kPa/min, the contents of particle sizes smaller than 0.08 mm, 0.08-0.1 mm, 0.1-0.2 mm, and 0.2-0.4 mm all decrease and the other particle size contents increase at the top, middle, and bottom part of remaining mixture. As can be seen from Figure 10, the content of particle sizes smaller than 0.08 mm decreases dramatically and particle sizes of 0.4 mm-0.5 mm and 0.5 mm-1 mm are opposite at the top and middle of remaining mixture. When the seepage pressure is 80 kPa/min, similar to the loading rate of 10 kPa/min, the contents of particle size smaller than 0.2 mm also decrease and contents of coarse particles increase as well. The distinction is that the particle size smaller than 0.1 mm lower and 0.4 mm-0.5 mm, 0.5 mm-1 mm increases more dramatically than that of 10 kPa/min.

As can be seen from Figures 10 and 11, there is a crossover phenomenon in the particle gradation curves regarding to the top and middle remaining mixture, indicating that low seepage loading rate and the bonding effect between particles prevent initially internal fine particles from moving. With the increase of seepage loading rate, the seepage water fails to flow out from the seepage channels in time, which leads to local collapse of filling medium and block the original seepage channel. Hence, the seepage water with fine particles gushes out of the new seepage channel, resulting in the decrease of the content of fine particles, and consequently, the phenomenon above occurs.

Moreover, under the circumstance of local collapse of filling medium, particles of a certain size have been flushed with seepage water no matter how large they are. Consequently, gap-graded remaining mixtures have appeared in lack of particles of a certain size.

4.3.3. Analysis on Particle Size Distribution of Remaining Mixture with a 10% Kaolin Content. According to Figures 12 and 13, the particle gradation curves of the remaining mixture in Tests 5 and 6, compared with those

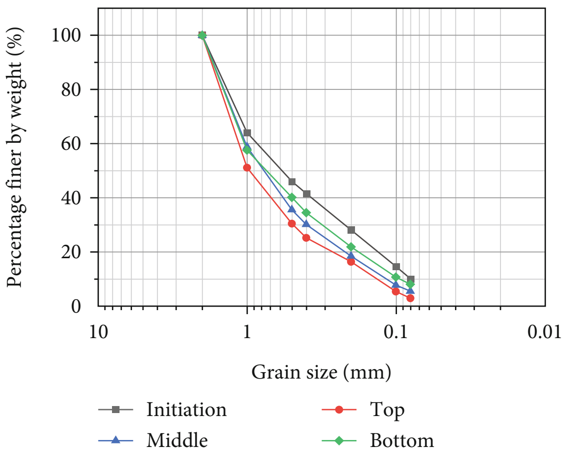

FIGURE 13: Test number 6 particle grading variation curves before and after seepage.

of initial status, the fine particle contents all decrease and the loss is more uniform. Similarly, the contents of particles larger than 0.5 mm all increase.

When the seepage pressure loading rate is 10 kPa/min, the contents of particle sizes smaller than 0.08 mm, 0.08-0.1 mm decrease and the contents of particle sizes 0.1-0.2 mm, 0.2-0.4 mm, and 0.4-0.5 mm show no significant change at the top, middle, and bottom part of remaining mixture. Furthermore, the contents of other particle size increase. Combined with Table 2, it can be inferred that the contents of particle sizes smaller than 0.1 mm reduce evenly and 1-2 mm rises dramatically. While loading rate is 80 kPa/min, the contents of fine particles all decrease, 0.4-0.5 mm has no significant change and the contents of other particle size increase.

Given the above, the fine particles of filling medium with low clay content have no significant influence on the seepage instability process. Due to the low kaolin content, the cohesion of filling medium with many large pores is comparatively small. Only a few fine particles gush out from the mixture, seepage channel has formed and seepage instability process is completed. Hence, compared with those of initial status, the tendency of particle size distribution curves of the top, middle, and bottom part of remaining mixture is basically consistent. Furthermore, the contents of particle size in each part have no significant changes.

Through comparative analysis above, it can be summarized as follows: (1) As the content of kaolin decreases, the content of fine particles in the remaining mixture also decreases and the distribution is more uniform. (2) The content of coarse particles drops more significantly as the content of kaolin decreases. (3) With the decrease of kaolin content, the effect of loading rate on particle size distribution is weakened. (4) With other conditions unchanged, contrary to coarse particles, the change of fine particles content of remaining mixture presents initial>bottom>middle>top.

5. Conclusions

A large-scale triaxial stress-seepage test system was utilized to conduct the seepage instability tests of filling-type disaster-causing structures. The changes of sand and clay loss and particle size distribution in the process of seepage instability were investigated in depth. The variation rules of seepage characteristics and the evolutionary process of seepage instability were revealed. Based on the aforementioned analysis, the results obtained in this paper can be summarized as follows.

(1) According to the evolution rules of clay-sand mixture loss, the seepage instability process of filling medium can be categorized into three stages: the initial seepage stage with very small number of fine particles loss, the accelerating seepage stage with large number of fine particles loss, and the stable stage with the whole sample collapse

(2) The effects of kaolin content and seepage pressure loading rate on the permeability of filling medium were investigated in depth. The seepage failure process rate is proportional to the seepage loading rate and inversely proportional to the content of kaolin

(3) The mutual promotion between stress-seepage erosion and particle loss is the internal cause of seepage instability. And the seepage instability process of filling medium with different kaolin contents is most significantly affected by fine particles. The change of fine particle contents of remaining mixture is consistent, presenting initial>bottom>middle>top status. Under higher seepage pressure loading rate, the lower kaolin content in the filling medium is , the more obvious phenomenon of fine particles loss in the remaining mixture is.

Data Availability

The data used to support the findings of this study are available from the corresponding author upon request.

Conflicts of Interest

The authors declare that they have no conflicts of interest.

Acknowledgments

This work was supported by the Open Fund of State Key Laboratory of Water Resource Protection andUtilization in Coal Mining(GJNY-18-73.3), Taishan Scholar Foundation of Shandong Province (Grant No.tsqn202103002), and the Key Research and Development Project of Shandong Province(Grant no.2019GSF111018).

References

[1] B. Hebblewhite, "Fracturing, caving propagation and influence of mining on groundwater above longwall panels-a review of

predictive models," *International Journal of Mining Science and Technology*, vol. 30, no. 1, pp. 49–54, 2020.

[2] H. B. Bai, D. Ma, and Z. Q. Chen, "Mechanical behavior of groundwater seepage in karst collapse pillars," *Engineering Geology*, vol. 164, pp. 101–106, 2013.

[3] B. Y. Zhang, H. B. Bai, and K. Zhang, "Seepage characteristics of collapse column fillings," *International Journal of Mining Science and Technology*, vol. 26, no. 2, pp. 333–338, 2016.

[4] W. J. Sun, Q. Wu, H. L. Liu, and J. Jiao, "Prediction and assessment of the disturbances of the coal mining in Kailuan to karst groundwater system," *Physics and Chemistry of the Earth*, vol. 89-90, pp. 136–144, 2015.

[5] Y. M. Qi, M. Z. Li, K. J. Li, and T. C. J. Yeh, "Spatiotemporal development of mine water inrush and its mechanism—a case study in Ganhe coal mine, Shanxi, China," *Arabian Journal of Geosciences*, vol. 10, no. 19, 2017.

[6] Q. H. Qian, "Challenges faced by underground projects construction safety and countermeasures," *Chinese Journal of Rock Mechanics and Engineering*, vol. 31, no. 10, pp. 1945–1956, 2012.

[7] S. C. Li, Y. H. Qi, Z. F. Li, H. Y. Li, and J. Zhang, "A novel treatment method and construction technology of the pipeline gushing water geohazards in karst region," *Tunnelling and Underground Space Technology*, vol. 113, p. 103939, 2021.

[8] H. B. Fan, Y. H. Zhang, S. Y. He, K. Wang, X. L. Wang, and H. Wang, "Hazards and treatment of karst tunneling in Qinling-Daba mountainous area: overview and lessons learnt from Yichang–Wanzhou railway system," *Environmental Earth Sciences*, vol. 77, no. 19, 2018.

[9] S. Alija, F. J. Torrijo, and M. Ouinta-Ferreira, "Geological engineering problems associated with tunnel construction in karst rock masses: the case of Gavarres tunnel (Spain)," *Engineering Geology*, vol. 157, pp. 103–111, 2013.

[10] S. C. Li, Z. H. Xu, X. Huang et al., "Classification, geological identification, hazard mode and typical case studies of hazard-causing structures for water and mud inrush in tunnels," *Chinese Journal of Rock Mechanics and Engineering*, vol. 37, no. 5, pp. 1041–1069, 2018.

[11] S. C. Li, S. S. Shi, L. P. Li, J. Chen, Z. H. Xu, and Z. Q. Zhou, "Control of water inrush in typical karst tunnels in three gorges reservoir area and its application," *Chinese Journal of Rock Mechanics and Engineering*, vol. 33, no. 9, pp. 1887–1896, 2014.

[12] S. S. Shi, L. Bu, S. Li et al., "Application of comprehensive prediction method of water inrush hazards induced by unfavourable geological body in high risk karst tunnel: a case study," *Geomatics, Natural Hazards and Risk*, vol. 8, no. 2, pp. 1407–1423, 2017.

[13] Y. G. Xue, F. M. Kong, S. C. Li et al., "Water and mud inrush hazard in underground engineering: Genesis, evolution and prevention," *Tunnelling and Underground Space Technology*, vol. 114, p. 103987, 2021.

[14] S. C. Li, K. Wang, L. P. Li, Z. Q. Zhou, S. S. Shi, and S. Liu, "Mechanical mechanism and development trend of water-inrush disasters in karst tunnels," *Chinese Journal of Theoretical and Applied Mechanics*, vol. 49, no. 1, pp. 22–30, 2017.

[15] Z. Q. Zhou, L. P. Li, S. S. Shi et al., "Study on tunnel water inrush mechanism and simulation of seepage failure process," *Rock and Soil Mechanics*, vol. 41, no. 11, pp. 3621–3631, 2020.

[16] L. P. Li, W. F. Tu, S. S. Shi, J. X. Chen, and Y. H. Zhang, "Mechanism of water inrush in tunnel construction in karst area," *Geomatics, Natural Hazards and Risk*, vol. 7, Supplement 1, pp. 35–46, 2016.

[17] P. Bukowski, "Water hazard assessment in active shafts in upper Silesian Coal Basin mines," *Mine Water and the Environment*, vol. 30, no. 4, pp. 302–311, 2011.

[18] N. Rapantova, S. Krzeszowski, A. Grmela, and C. Wolkersdorfer, "Quantitative assessment of mine water sources based on the general mixing equation and multivariate statistics," *Mine Water and the Environment*, vol. 31, no. 4, pp. 252–265, 2012.

[19] L. Surinaidu, V. Rao, and G. Ramesh, "Assessment of groundwater inflows into Kuteshwar limestone mines through flow modeling study, Madhya Pradesh, India," *Arabian Journal of Geosciences*, vol. 6, no. 4, pp. 1153–1161, 2013.

[20] K. Polak, K. Rozkowski, and P. Czaja, "Causes and effects of uncontrolled water inrush into a decommissioned mine shaft," *Mine Water and the Environment*, vol. 35, no. 2, pp. 128–135, 2016.

[21] L. J. Donnelly, "A review of coal mining induced fault reactivation in Great Britain," *Quarterly Journal of Engineering Geology and Hydrogeology*, vol. 39, no. 1, pp. 5–50, 2006.

[22] M. R. Islam, D. Hayashi, and A. B. M. Kamruzzaman, "Finite element modeling of stress distributions and problems for multi-slice longwall mining in Bangladesh, with special reference to the Barapukuria coal mine," *International Journal of Coal Geology*, vol. 78, no. 2, pp. 91–109, 2009.

[23] B. Yang, T. H. Yang, and J. Hu, "Numerical simulation of non-darcy flow caused by cross-fracture water inrush, considering particle loss," *Mine Water and the Environment*, vol. 40, no. 2, pp. 466–478, 2021.

[24] B. H. Yao, L. C. Wang, J. P. Wei, Z. H. Li, and X. J. Liu, "A deformation-seepage-erosion coupling model for water outburst of karst collapse pillar and its application," *Journal of China Coal Society*, vol. 43, no. 7, pp. 2007–2013, 2018.

[25] L. P. Li, S. C. Li, S. S. Shi, and Z. H. Xu, "Water inrush mechanism study of fault activation induced by coupling effect of stress-seepage-damage," *Chinese Journal of Rock Mechanics and Engineering*, vol. 30, pp. 3295–3304, 2011.

[26] A. W. Skempton and J. M. Brogan, "Experiments on piping in sandy gravels," *Geotechnique*, vol. 44, no. 3, pp. 449–460, 1994.

[27] B. Y. Su, M. L. Zhan, and Z. T. Zhang, "Experimental research of seepage characteristic for filled fracture," *Rock and Soil Mechanics*, vol. 15, no. 4, pp. 46–52, 1994.

[28] S. S. Tomlinson and Y. P. Vaid, "Seepage forces and confining pressure effects on piping erosion," *Canadian Geotechnical Journal*, vol. 37, no. 1, pp. 1–13, 2000.

[29] R. J. Fannin and R. Moffat, "Observations on internal stability of cohesionless soils," *Geotechnique*, vol. 56, no. 7, pp. 497–500, 2006.

[30] F. Bendahmane, D. Marot, and A. Alexis, "Experimental parametric study of suffusion and backward erosion," *Journal of Geotechnical and Geoenvironmental Engineering*, vol. 134, no. 1, pp. 57–67, 2008.

[31] D. Marot, F. Bendahmane, F. Rosquoet, and A. Alexis, "Internal flow effects on isotropic confined sand-clay mixtures," *Soil & Sediment Contamination*, vol. 18, no. 3, pp. 294–306, 2009.

[32] H. H. Nguyen, D. Marot, and F. Bendahmane, "Erodibility characterisation for suffusion process in cohesive soil by two types of hydraulic loading," *La Houille Blanche*, vol. 98, no. 6, pp. 54–60, 2012.

[33] J. W. Liang and Y. G. Fan, "Experimental study of seepage characteristics of tiny-particle clay," *Chinese Journal of Rock Mechanics and Engineering*, vol. 29, no. 6, pp. 1222–1230, 2010.

[34] K. S. Richards and K. R. Reddy, "Experimental investigation of initiation of backward erosion piping in soils," *Geotechnique*, vol. 62, no. 10, pp. 933–942, 2012.

[35] O. Y. Mao and T. Akihiro, "Influence of initial fines content on fabric of soils subjected to internal erosion," *Canadian Geotechnical Journal*, vol. 53, no. 2, pp. 299–313, 2016.

[36] Y. Meng, H. Jing, Q. Yin, and X. Wu, "Experimental study on seepage characteristics and water inrush of filled karst structure in tunnel," *Arabian Journal of Geosciences*, vol. 13, no. 12, 2020.

[37] M. X. Wang, W. M. Yang, Z. Q. Zhou et al., "Experimental research on the effect of particle migration of a filling medium in a fault during water and mud inrush," *Arabian Journal of Geosciences*, vol. 14, no. 21, 2021.

Hindawi
Geofluids
Volume 2022, Article ID 8781289, 13 pages
https://doi.org/10.1155/2022/8781289

Research Article

Erosion Effect on Non-Darcy Hydraulic Characteristics of Limestone and Mudstone Mixture

Chong Li [1,2] and Sifeng He [1]

[1]School of Mines, MOE Key Laboratory of Deep Coal Resource Mining, China University of Mining and Technology, Xuzhou, 221116 Jiangsu, China
[2]Jiangsu Laboratory of Mine Earthquake Monitoring and Prevention, China University of Mining & Technology, Xuzhou, 221116 Jiangsu, China

Correspondence should be addressed to Chong Li; lichong1923@cumt.edu.cn

Received 9 August 2021; Revised 1 September 2021; Accepted 13 September 2021; Published 10 March 2022

Academic Editor: Hualei Zhang

In order to study the water inrush mechanism of faulted rock mass, a series of erosion seepage experiments were carried out to test the non-Darcy hydraulic properties of a limestone and mudstone mixture. The test results are employed to verify and modify a classic permeability prediction model. Based on the evolution of mass loss rate, the erosion process can be divided into four stages, i.e., particle rearrangement, severe erosion, mild erosion, and stable seepage. During the erosion, the sample height decreases gradually, the water pressure at outlet grows first and then keeps stable, and the porosity and permeability decrease slightly first, then grow gradually and finally keep stable. The hydraulic properties show a more significant variation in the sample within high mudstone particle contents. Through the comparison of test results and the predicted results by the classic Carman-Kozeny model, it is found that the accuracy of the model is greatly affected by lithology. Based on this investigation, a revised model is proposed which introduces a proportional coefficient related to the rock composition, so as to increase the predicted precision in variable rock composition. The forecast accuracy of the revised model is much higher than the classical one in permeability although it decreases with the increase of mudstone content.

1. Introduction

Fault is a sort of common encountered geological body which is generated by tectonic movement [1]. The interior of a fault is composed of broken rock masses with different lithologies, and the rock stratum on both sides of this geological structure generally has large dislocations [2–4]. Faults create discontinuities in the stratum and are usually regarded as water channels that connected the aquifer and underground space. During the mining process, under the water pressure, and mining disturbance, the groundwater is prone to pass through the fault rocks and arrive in the working face, causing water inrush disasters [5–8]. In this process, a part of fine rock particles inside the fault rocks will migrate with the groundwater. This phenomenon is called the erosion behavior, which is catastrophic in underground construction: First, under the effect of erosion, rock particles and mud would enter the underground space, leading to equipment damage and personnel being buried [9, 10]. Second, the erosion effect causes the increase of rock mass porosity and permeability, leading to more groundwater influx [11, 12]; Last but not the least, the erosion effect reduces the strength of the fault rock mass, resulting in structural instability and damage [13, 14]. Therefore, it is of great significance to study the hydraulic characteristics of fault rock masses during the erosion process to prevent and control fault water inrush disasters [15, 16].

In the process of groundwater seepage, the fluid pressure gradient and the fluid velocity are considered to have a certain relationship. Back in the 19^{th} century, Darcy discovered that the fluid pressure gradient and the fluid velocity obey a linear relationship. Subsequently, this linear seepage law (Darcy's Law) has been widely applied in a variety of studies [17, 18]. However, Darcy's law assumes that the fluid regime is dominated by viscous resistance. When the fluid flows at a higher flow rate (e.g., when groundwater flows in a fractured rock mass), the inertial resistance can no longer be ignored, and the water pressure gradient and the flow velocity gradually shows a nonlinear relationship [19, 20]. In this case, doubling the water pressure can not obtain a doubled fluid velocity, which results in the inaccuracies of Darcy's law in the calculations and evaluations of water inrush [21, 22]. To end this, Darcy's law is usually replaced by Forchheimer equation when the seepage was researched in a high flow rate, which includes a quadratic term of fluid velocity, reflecting the effect of inertial resistance on the fluid regime [23, 24]. Many experimental studies [25–28] have verified the applicability of Forchheimer equation in different conditions, and the Forchheimer coefficient (the coefficient for the quadratic term) for various media forms (e.g., porous media and fractures) is also estimated.

From then on, based on the Forchheimer equation, a lot of scholars have conducted testing or numerical studies on the non-Darcy hydraulic properties of broken rocks. Through fluid testing of sandstone fractures, Zimmerman et al. [28] found that the fluid regime follows the Forchheimer equation when the Reynolds number is higher than 20. And this result is consistent with that of their high-resolution Navier-Stokes simulations. Zeng and Grigg [27] modified the Forchheimer coefficient and adopted this modified parameter as the standard for identifying non-Darcy seepage in porous media. Based on seepage experiments in three different rocks, the critical Forchheimer coefficient is calibrated. Zhou et al. [22] proposed a semiempirical prediction model for tunnel water inflow based on the Forchheimer equation. And the effectiveness of the semiempirical model is verified through numerical calculation results. Chen et al. [21] proposed a framework that combines the estimation of aquifer properties with numerical simulation to more accurately evaluate the flow rate and seepage erosion risk caused by tunnel construction in karst aquifers. This research results show that the predicted flow rate based on the Forchheimer equation agrees better with measured value than that in line with Darcy's law. Ma et al. [29] studied the nonlinear seepage characteristics of granular gangue during the filling process through laboratory and in situ tests and evaluated the reutilization of gangue in protecting overlying aquifers.

However, the above studies did not consider the erosion behavior during seepage. In fact, the erosion effect is a common encountered phenomenon during seepage. Since the 1980s, a series of experiments and numerical studies conducted in-depth research on the sand production phenomenon (oil and natural gas flows that drive the movement of fine particles in the rock mass) caused by the oil extraction stage [30, 31]. Vardoulakis et al. [32, 33] proposed an erosion model of broken rock mass based on the equivalent continuum theory. In this model, the broken rock mass is divided into three phases, which are rock skeleton, water, and fine rock particles. The skeleton particles do not shift during the seepage process, and the fine particles and water flow out at the same speed under the action of water pressure. After entering this century, the erosion problem in the process of underground water inrush has gradually attracted attention [34, 35]. In order to study the erosion phenomenon in the process of water inrush, Ma et al. [17, 36] developed a set of erosion seepage devices to realize the free migration of fine rock particles in the broken rock mass medium. The porosity and permeability of the rock increase rapidly and then gradually stabilize. Based on the test results, the influence mechanism of erosion on the nonlinear seepage characteristics of fluids is also analyzed. Yao et al. [37] studied the evolution characteristics of the water inrush channel under the influence of particle migration, and based on the established fluid-solid coupling control equation, predicted the water inrush time under different geological conditions.

Although there have been many studies simulating the process of water inrush from faults, most of these studies only study the erosion effect of a single kind of rock and do not research the hydraulic characteristics of the mixture by different lithology rocks. In fact, almost all fault rocks are composed of two or more lithologies [38, 39]. The interaction between different lithologies and water is very different, so the hydraulic characteristics of mixed lithologies will be different from that of single lithology [40].

In the no. 4 normal fault of the Buliangou mine, the fault rock mass is a mixture of mudstone and limestone (see Figure 1). This fault is in the northeast to southwest direction, with a dip angle of 60-70° and a drop range of 30-50 m. It is located in the middle of the mine field with an extended length of 815 m. In line with the previous research [41], the erosion effect of mudstone after encountering water is significantly stronger than that of limestone. Therefore, studying the influence of different rock components and their mixing ratios inside faults on their hydraulic characteristics is of great significance for preventing water inrush hazards that may occur in faults.

In this paper, limestone and mudstone mixtures in different proportions were selected as experimental materials to test the non-Darcy hydraulic evolution characteristics and porosity evolution of the samples under erosion. Based on the experimental results, a method for predicting the permeability of a limestone and mudstone mixture is proposed. The research results can provide a basis for the prevention and treatment of fault water inrush disasters.

2. Testing Methods

2.1. Testing Material. The test materials are limestone and mudstone sampled from Buliangou Mine. The dry density of limestone is 2.42-2.71 g/cm^3, and the dry density of mudstone is 2.35-2.61 g/cm^3. Since the difference in dry density between the two is small, we approximate both as 2.5 g/cm^3. Rocks are crushed into 0-20 mm crushed particles first and then divide the crushed particles into five groups by diameter, namely, Group A (0-2 mm), Group B (2-5 mm), Group C (5-10 mm), Group D (10-15 mm), and Group E (15-20 mm). Before the test, these particles are mixed according to the continuous gradation ratio (Equation (1)) and take into account the different ratios of the two rocks (denoted by the mass content of mudstone).

$$P_\alpha = \left(\frac{d_\alpha}{d_{\max}}\right)^\beta \times 100\%, \tag{1}$$

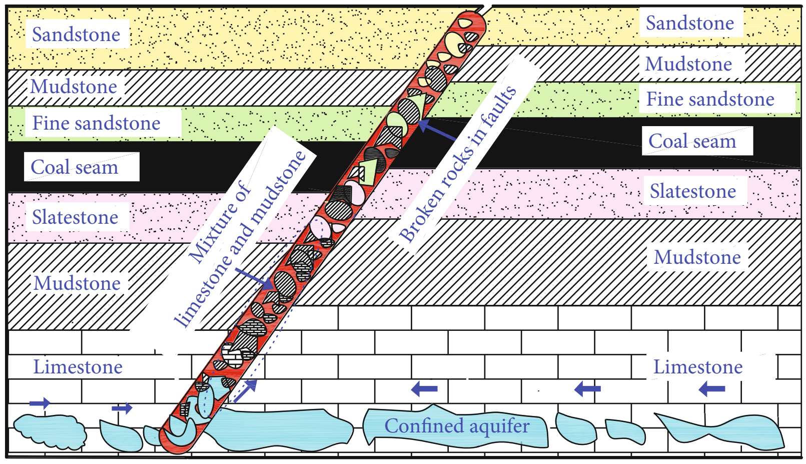

Figure 1: The diagram of limestone and mudstone mixture in no. 4 normal fault of Buliangou mine.

Table 1: Mixing scheme of LP and MP for different samples (LP: limestone particles; MP: mudstone particles).

Sample no.	Content of MP (%)	Weight of each particle group (g) A (0-2 mm) LP	A (0-2 mm) MP	B (2-5 mm) LP	B (2-5 mm) MP	C (5-10 mm) LP	C (5-10 mm) MP	D (10-15 mm) LP	D (10-15 mm) MP	E (15-20 mm) LP	E (15-20 mm) MP
1	0	1359.8	0	790.2	0	890.6	0	683.4	0	576.1	0
2	25	1019.8	339.9	592.7	197.6	667.9	222.6	512.5	170.8	432.1	144.0
3	50	679.9	679.9	395.1	395.1	445.3	445.3	341.7	341.7	288.0	288.0
4	75	339.9	1019.8	197.6	592.7	222.6	667.9	170.8	512.5	144.0	432.1
5	100	0	1359.8	0	790.2	0	890.6	0	683.4	0	576.1

where α is the group number of crushed particles, d_α is the largest particle diameter in the Group α, $d_{\max}$ is the largest diameter of all groups, P_α is the mass proportion of the groups which size is smaller than d_α, and β is gradation parameter denoting the gradation properties of mixed rock samples, which is set as 0.5 in this study.

The sample mass is set as 4300 g and the mixing scheme is shown in Table 1, and the continuous grading curve of the sample is shown in Figure 2.

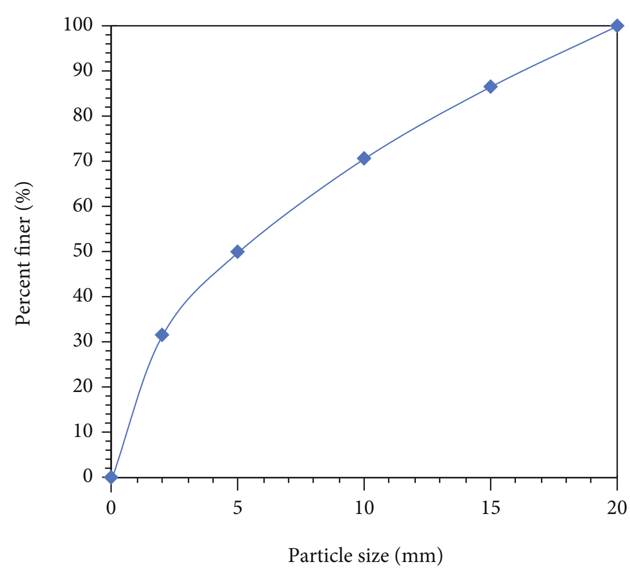

Figure 2: The gradation curve of the limestone and mudstone mixture.

2.2. Testing System. In order to carry out erosion tests on the limestone mudstone mixture, the following test system is designed to carry out experiments on the limestone mudstone mixture samples. As shown in Figure 3, the test system is composed of the fluid supply system, the data acquisition system, the particle collection system, and the seepage erosion unit.

2.2.1. Fluid Supply System. It is mainly composed of the oil pump, the water pump, the double-acting hydraulic cylinder, the connected pipelines and valves. The double-acting hydraulic cylinder consists of two cavities, and the volume of the cavities is controlled by the piston. Before the test, valve 1 is closed and valve 2 is opened, the water is injected into the lower cavity of the hydraulic cylinder through the water pump. After the test begins, valve 2 is closed and valve 1 is opened. When the oil pump is started, hydraulic oil is injected into the upper cavity, driving the piston to compress downward, so that provides stable water pressure to the erosion unit.

2.2.2. Erosion Unit. It comprises the piston, the cylinder, the upper and lower seepage plate, the conical bottom plate, the base and other parts. At the beginning of the test, the fluid supply device provided water pressure to the piston inlet.

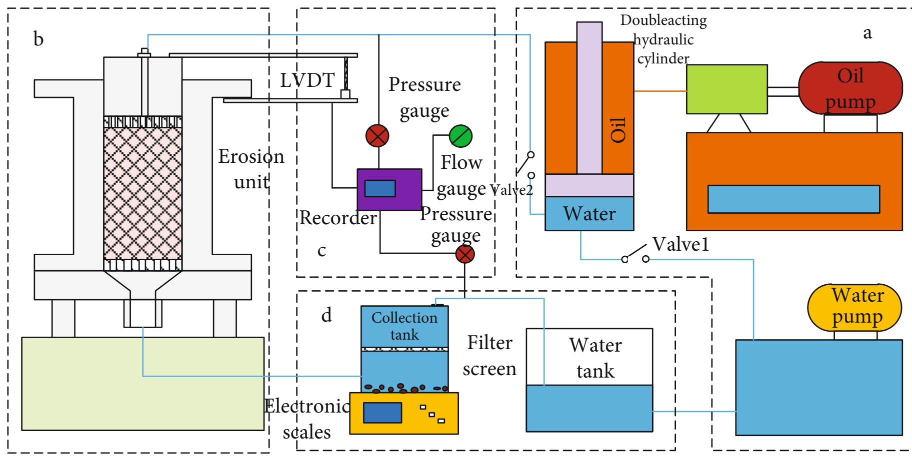

Figure 3: Test system. Note: (a) fluid supply system, (b) erosion unit, (c) data acquisition system, and (d) particle collection system.

Test preparation: First, the seepage pipeline is connected, and the data acquisition system is adjusted to make it work normally. After this, the double-acting hydraulic cylinder is filled with water. Then, the broken sample is put into the erosion unit, and the water is injected into the pipeline to exclude air in the pipeline and saturate the sample. Subsequently, the piston is placed and the initial height of the sample is recorded.

Procedure 1

Water pressure loading: the oil pump is started, and water is injected into the erosion unit, the data from the electronic scales in the particle collection system and the data measured by the acquisition system and are monitored.

Procedure 2

Posttest treatment: oil pump is turned off first, and then stop the water flow. Finally, the sample is taken out from the erosion unit.

Procedure 3

Small holes of 2 mm in diameter are arranged on the upper seepage plate to disperse the water flow. And small holes with a diameter of 10 mm are arranged on the lower seepage plate to facilitate the flow of broken rock particles with a diameter of less than 10 mm. The conical bottom plate can collect the fine particles from erosion outflow and then lead them to the particle collection system.

2.2.3. Data Acquisition System. It is composed of a linear variable differential transformer (LVDT), a water pressure gauge, a flow gauge, a recorder and a computer. LVDT is arranged at piston and floor to monitor the collapsed height of rock mass during erosion. Two water pressure gauges are arranged at the inlet and outlet of the erosion unit to monitor the water pressure at the water inlet and outlet, respectively. The flow meter is arranged at the entrance of the erosion unit to measure the fluid flow during the test. Each instrument is connected with the recorder and computer to record and output the measured data in real time.

2.2.4. Particle Collection System. It is composed of a particle collector, a filter screen, an electronic scale, and a water tank. This system can collect and weigh the fine particles flowing from the rock sample in real time. The reading of the electronic scale is zero at the beginning of the test, so the reading of the electronic scale records the mass change of the collection tank during the test. The fine particles will discharge the same volume of water when they flow into the collection tank. Because the density of fine particles is greater than the density of water, based on the mass change of the collection tank, we can calculate the volume of the fine particles by the density difference between the fine particles and the water.

2.3. Test Procedures. The test process can be divided into the following procedures:

2.4. Calculation of Non-Darcy Hydraulic Characteristics

2.4.1. Mass Loss Rate. The fine rock particles migrate into the particle collector under the action of water flow. The reading of electronic scale at time t_i is m_i. The volume of the fine particles collected at t_i time can be obtained as

$$V_i = \frac{m_i}{\rho_r - \rho_w}, \tag{2}$$

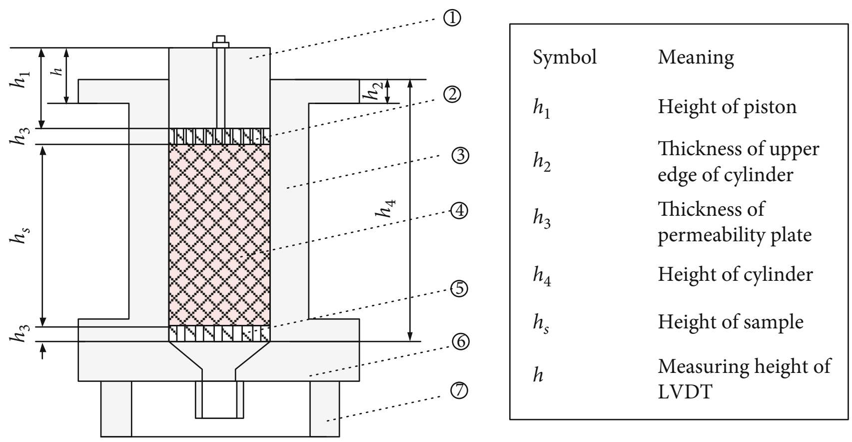

FIGURE 4: The structure of erosion unit. Note: ① piston, ② upper seepage plate, ③ cylinder, ④ sample, ⑤ lower seepage plate, ⑥ conical bottom plate, and ⑦ base.

where ρ_r is rock dry density, ρ_w is water density, and the accumulated mass loss is

$$M_i = \rho_r V_i = \frac{m_i \rho_r}{\rho_r - \rho_w}. \tag{3}$$

The mass loss at time interval i, ΔM_i, can be calculated by

$$\Delta M_i = M_i - M_{i-1}. \tag{4}$$

And the mass loss rate $\dot{M}_i$, which denotes the mass loss in unit time, can be acquired by the following equation:

$$\dot{M}_i = \frac{\Delta M_i}{\Delta t}. \tag{5}$$

2.4.2. Sample Height. As shown in Figure 4, the dimensions of each part of the test instrument are piston height $h_1 =$ 100 mm, cylinder upper edge thickness $h_2 = 15$ mm, permeability plate thickness $h_3 = 10$ mm, and cylinder height h_4 = 350 mm. According to the geometric relationship in Figure 4, we can get

$$h_s + 2h_3 + h_1 = h - h_2 + h_4, \tag{6}$$

where h_s is the sample height and h is the measured height through LVDT. Substituting the dimension data of each part, the sample height at time t_i can be obtained by the measured value of LVDT:

$$h_{si} = h_i + 215. \tag{7}$$

2.4.3. Porosity. Based on mass loss results, the porosity of sample at time i is

$$\phi_i = 1 - \frac{M_0 - M_i}{\pi r^2 \rho_r h_{si}}, \tag{8}$$

where M_0 is the initial sample mass and $M_0 = 4300$ g and r is the radius of the cylinder and $r = 50$ mm.

2.4.4. Permeability. According to the fluid flow Q measured by flow gauge, the flow velocity v can be calculated by the following equation:

$$v = \frac{Q}{\pi r^2}. \tag{9}$$

In line with Forchheimer's equation [27, 36], there is a well-known relationship between water pressure gradient and flow velocity:

$$-\nabla p = \frac{\mu}{k} v + \rho_w \beta v^2, \tag{10}$$

where μ is the viscosity of fluid, k is the permeability, and β is the non-Darcy factor.

Assuming that the water pressure is linearly distributed in the sample, the water pressure gradient can be expressed as

$$\nabla p = \frac{p_B - p_A}{h_s}, \tag{11}$$

where p_A and p_B are the water pressure at fluid inlet and outlet, respectively. According to the test principle, p_A is a constant and $p_A = 1.5$ MPa, and p_B is a variable changing with time, which can be measured by the pressure gauge. Combining Equations (10) and (11), there is

$$\frac{p_A - p_B}{h_s} = \frac{\mu}{k} v + \rho_w \beta v^2. \tag{12}$$

For each moment t_i, Equation (12) can be written as

$$\frac{p_A - p_{Bi}}{h_{si}} = \frac{\mu}{k_i} v_i + \rho_w \beta_i {v_i}^2. \tag{13}$$

According to previous studies [29, 42], the permeability at time interval i could be approximated to the average value of that at time interval i and $i+1$, so that the permeability

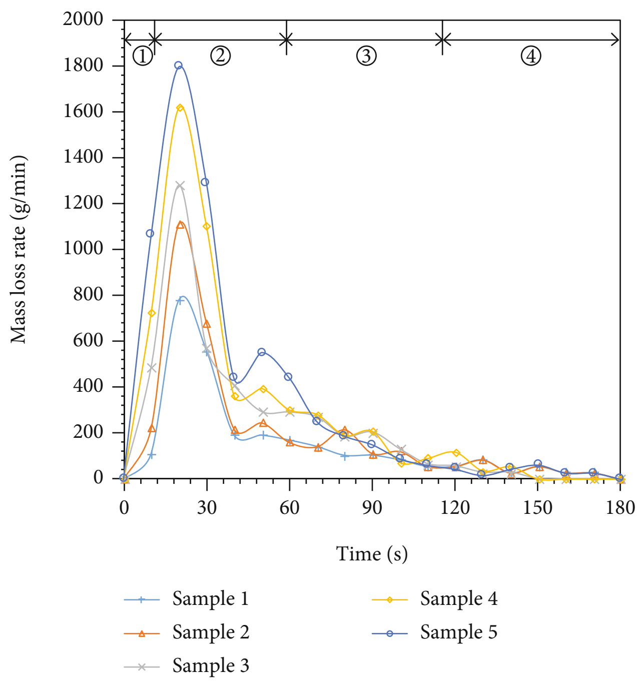

Figure 5: Evolution of mass loss rate during the erosion seepage.

can be calculated by Equation (14).

$$k_i = \frac{\mu v_i v_{i+1} h_{si} h_{si+1} (v_i - v_{i+1})}{(p_A - p_{Bi+1}) h_{si} v_i^2 - (p_A - p_{Bi}) h_{si+1} v_{i+1}^2}. \quad (14)$$

3. Test Results and Discussions

3.1. Variation of Non-Darcy Hydraulic Characteristics

3.1.1. Mass Loss Rate. The variation of the sample mass loss rate is shown in Figure 5. According to the variation trend of the mass loss rate, the entire erosion process can be divided into four stages, i.e., particle rearrangement, severe erosion, mild erosion, and steady seepage.

(1) Particle rearrangement: in the initial stage of the test, under the action of water flow, fine particles are dragged into the pores of large particles to form a more stable structure. At this stage, fewer particles are discharged. The amount of quality loss is small

(2) Severe erosion: in this stage, a large number of rock particles flow out of the sample under the action of water pressure, which is manifested as a rapid increase in mass loss

(3) Mild erosion: in this stage, only a small part of the rock particles migrate under the dragging action of water flow, and the mass loss fluctuates within a small range

(4) Stable seepage: at this stage, as all rock particles flow out, a stable seepage channel is formed in the rock mass, and the mass loss rate drops to 0

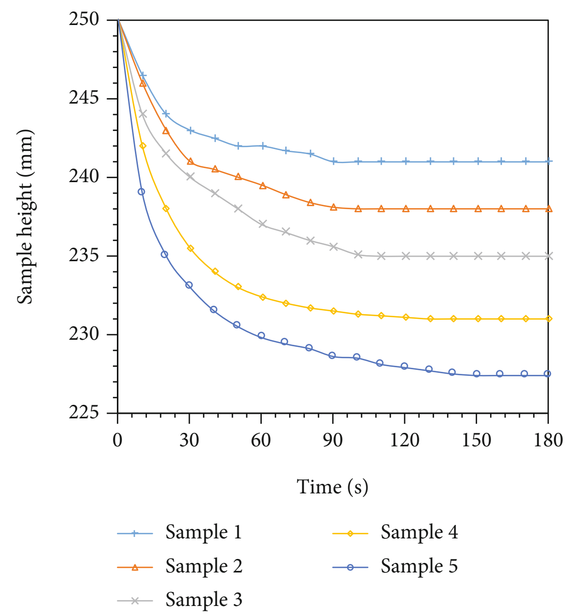

Figure 6: Evolution of sample height during the erosion seepage.

In the comparison of samples under different mudstone contents, it can be found that in samples with higher mudstone content, the particle rearrangement stage is shorter and the peak mass loss rate is more significant, and it enters the stable seepage stage soon after the severe erosion, which means there is a shorter mild erosion stage. This result manifests that the erosion effect of mudstone is stronger than that of limestone. Under the action of water flow, mudstone particles are more prone to migrate.

3.1.2. Sample Height. The evolution of the sample height during the seepage is shown in Figure 6. The height of all the samples has decreased under the action of erosion. The sample heights show a sharp decline in the early stage of the erosion test, which is because the rock particles are redistributed under the effect of water flow, and lots of fine particles are filled in the pores between the large particles, contributing to the rapid decreases in sample height. Then, the fine particles move and under the effect of the water flow, and finally flowed out from the bottom, so that the sample structure collapsed and the height declines. In these stages (severe erosion and mild erosion), the drop rate of the sample height gradually slows down. Finally, and sample height remained stable, which indicates that the erosion effect has terminated.

For the height before erosion, it can be observed that the heights of the samples with different rock composition ratios are the same. This shows that lithology has almost no effect on the natural accumulation height of the samples. As the erosion process progresses, it is found that the more mudstone content is, the height of the sample drops faster. This shows that under the action of water flow, the higher the mudstone content, the more significant rearrangement and erosion in the sample.

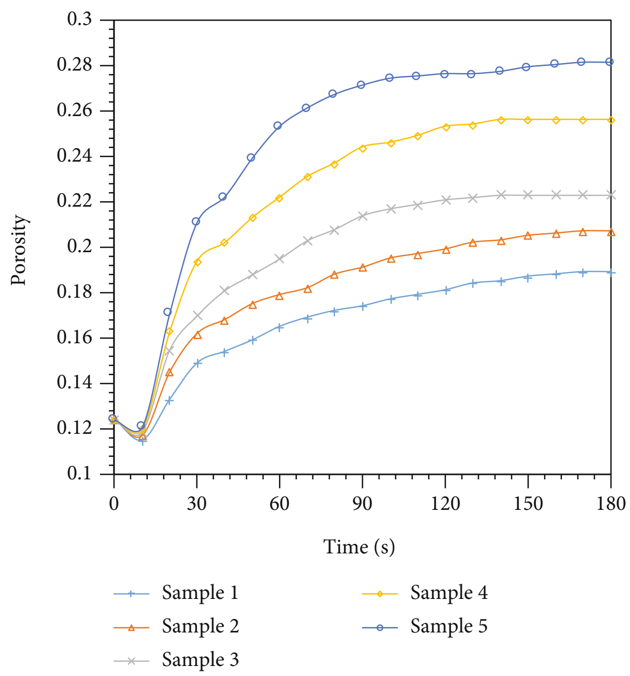

FIGURE 7: Evolution of sample porosity during the erosion seepage.

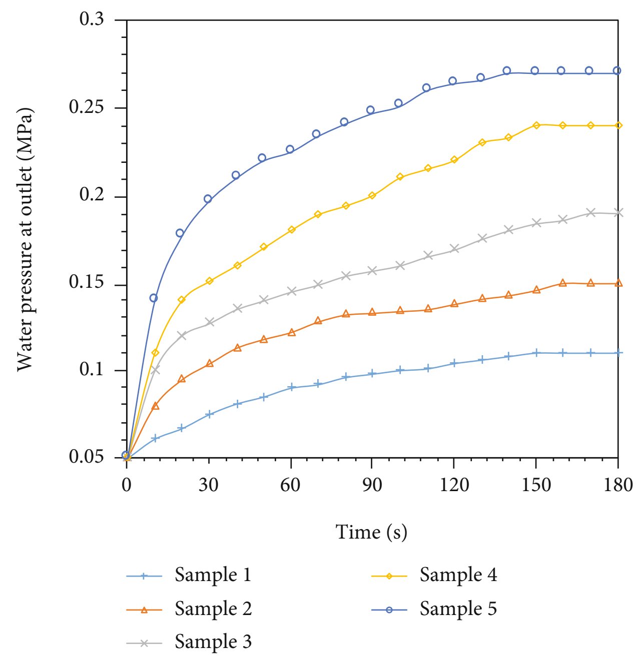

FIGURE 8: Evolution of water pressure at outlet during the erosion seepage.

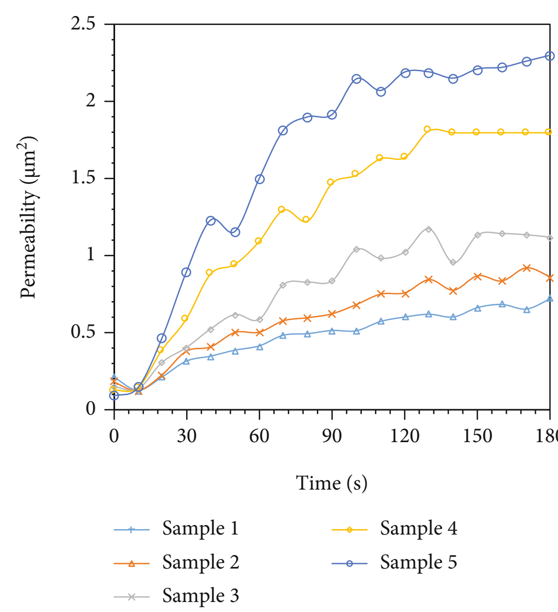

FIGURE 9: Evolution of sample permeability during the erosion seepage.

3.1.3. Sample Porosity. Figure 7 illustrates the porosity evolution of the sample. It can be found that in the first stage of erosion, i.e., the particle rearrangement stage, the porosity of the sample keeps stable or decreased slightly. This tiny decline in porosity is because there are a lot of small rock particles filled into the pore of large rock particles under the effect of water flow. In the second and third stages, a substantial increase in the porosity of samples can be observed. This corresponds to the phenomenon discussed earlier in which particles flow out of the sample in large quantities. Finally, the porosity of each sample has fallen into a stagnant stage, and the pore structure of the sample stays in a stable state, which indicates that most of the flowing particles have left the sample, and the migration of fine particles has not been observed. Comparing the porosity evolution curves of different samples, it is found that in samples with higher mudstone content the porosity has increased significantly, and the final porosity of the rock mass is also greater. This indicates that the erosion effect is stronger in these samples.

3.1.4. Water Pressure at the Outlet. The evolution curves of water pressure at the outlet are drawn in Figure 8. It is noted that in previous studies, the water pressure at the outlet of the sample is often regarded as connected to the atmospheric pressure and assumed to be 0. The results of this test show that the water pressure at the outlet of the sample is much greater than 0. Such an effect of water pressure at the outlet can not be ignored, especially when the water pressure at the inlet is small, improperly neglecting the hydraulic power at the outlet will harm the precision of the test results. In addition, the water pressure at the outlet is not a stable value: with the progress of the erosion, it can be found that all the samples have the phenomenon of rising water pressure at the outlet. This is because, under the erosion effect, the fine particles in the sample gradually flow out, and the resistance to the fluid decreases, resulting in a drop in the water pressure difference between the two ends of the sample. Comparing different samples, it can be found that although the outlet water pressure of each sample is almost the same at the initial moment; in the samples with more mudstone content, the outlet water pressure has increased on a larger scale. This is due to the more significant erosion effects that appear in these samples.

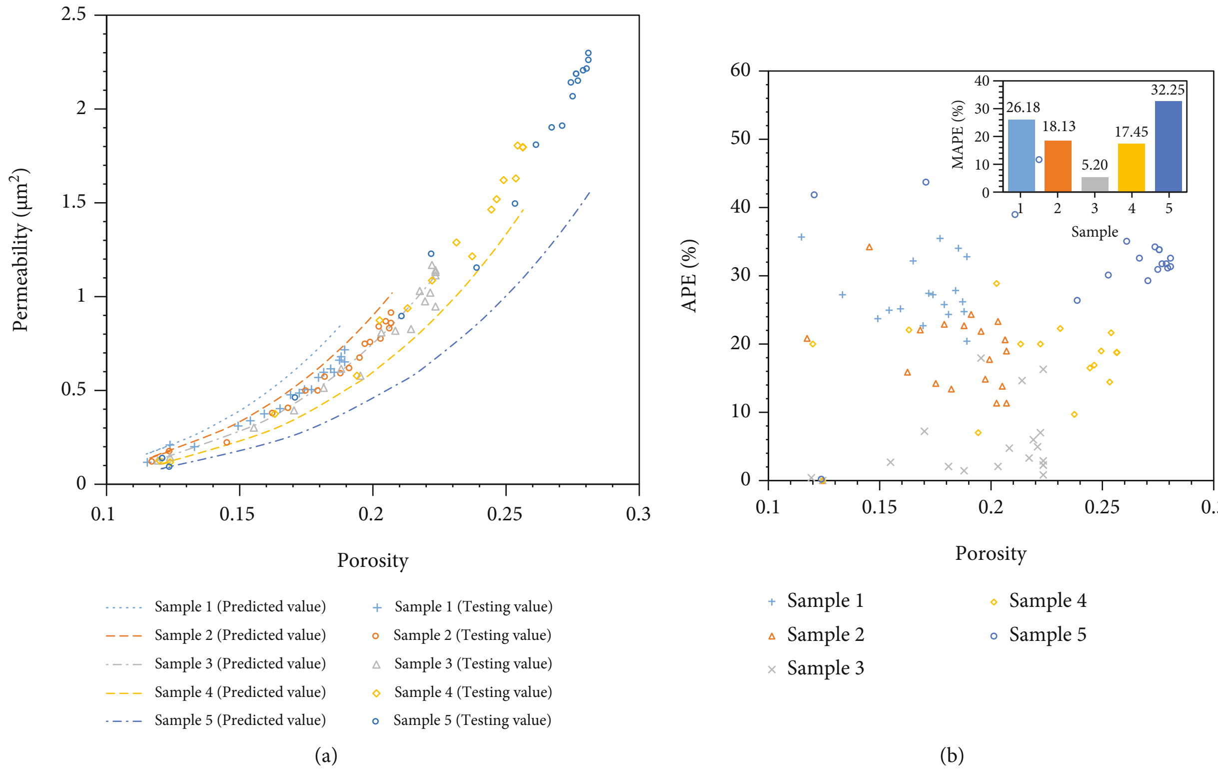

FIGURE 10: Comparison between testing results and predicted results by Carman-Kozeny model (a). Comparison of results (b) APE and MAPE.

3.1.5. Permeability. Figure 9 describes the variation in the permeability of the sample. It can be observed that the permeability of the sample has a similar variation trend comparing with the porosity of the sample, that is, the permeability of the sample decreases slightly with the progress of erosion, then gradually increases and finally trend plateau. The highest permeability can be observed in samples with higher mudstone content, and the time required for the increase in permeability in these samples is shorter than that in other samples, which means more severe permeability changes and a higher risk of water inrush.

3.2. Prediction Model of Permeability

3.2.1. Permeability Prediction Model Based on Porosity. In the process of underground water inrush, an important issue is to determine the permeability change of the rock mass. Unfortunately, due to the influence of the geological environment, direct measurement of permeability of fault broken rocks is a challenging task [43, 44]. Therefore, many previous studies have used other properties of the rock mass to indirectly predict its permeability [45, 46]. For example, in the well-known Carman-Kozeny model [47, 48], permeability is described as a cubic function of porosity. Based on this model, the permeability can be calculated when the porosity of the rock mass is obtained. On the basis of non-Darcy hydraulic characteristics of the limestone and mudstone mixture, the Carman-Kozeny model is employed to predict the permeability in this research, and the predicted results are compared with the testing results to verify the reliability of the equation.

The Carman-Kozeny model is as follows:

$$k = k_R \frac{\phi^3}{(1-\phi)^2}, \tag{15}$$

where k_R is constant, and in the initial time, there is

$$k_0 = k_R \frac{{\phi_0}^3}{(1-\phi_0)^2}. \tag{16}$$

If k_0 and ϕ_0 are known, combining Equations (15) and (16), we get

$$k = \frac{k_0 (1-\phi_0)^2}{{\phi_0}^3} \frac{\phi^3}{(1-\phi)^2}. \tag{17}$$

To evaluate the model's accuracy, the average percentage error (APE) is induced to describe the difference between testing and predicted values in each data point:

$$\mathrm{APE}_i = \frac{\left|k_i^p - k_i^t\right|}{k_i^t} \times 100\%, \tag{18}$$

where k_i^p and k_i^t are the testing and predicted values of the plot i $(i = 1, 2 \cdots n)$. And the mean average percentage error (MAPE) is employed to describe the mean difference between testing and predicted values in a certain sample.

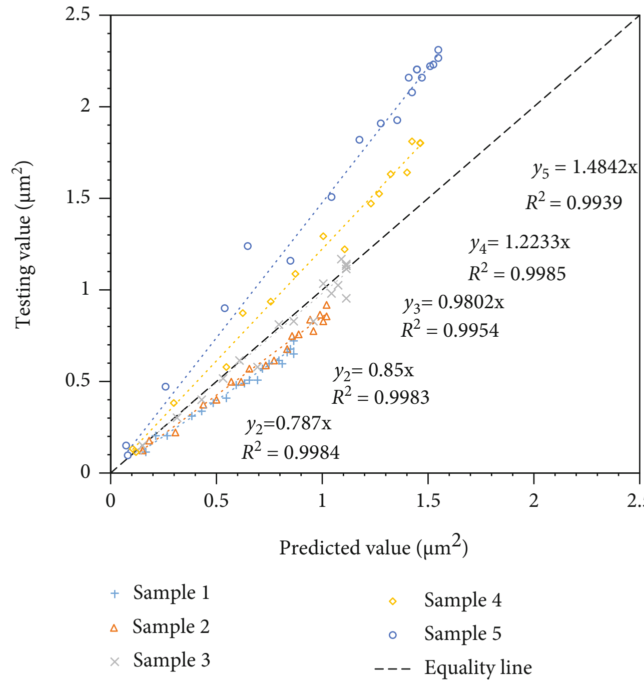

FIGURE 11: The linear relationship between the testing and predicted results of permeability by Carman-Kozeny model.

$$\text{MAPE} = \frac{1}{n}\sum_{i=1}^{n}\text{APE}_i. \tag{19}$$

Based on Equation (17), the predicted curves are obtained as shown in Figure 10. It is obvious that the trends of the predicted and measured results are semblable; that is, as the porosity increases, the permeability of the rock mass gradually increases. As the porosity increases, the prediction curve gradually deviates from the measured value point, which indicates that the prediction performance becomes worse when the porosity is large. By observing the APE distribution, the APE shows a high dispersion under different porosity conditions. According to the MAPE value of the model, it is indicated that the accuracy of the model is poor, the maximum MAPE value reached 32.25% (sample 5), which means that the model is not suitable for predicting permeability.

Comparing the predicted results in different samples (see Figure 10(b)), it is seen that in the sample with a 1 : 1 ratio of mudstone to sandstone, the prediction accuracy of the model is the highest, and the MAPE value is only 5.2%, while for samples with other mixed ratios, the MAPE is much higher. This phenomenon shows that the accuracy of the model is greatly affected by the lithology of the sample, and there is a certain relationship between the predictive performance of the model and the composition of the rock, which is worthy of further study.

3.2.2. Modified Prediction Model Based on Porosity and Mudstone Content. Based on the analysis in Section 3.2.1, to further study the relationship between the predictive performance of the model and the rock mixed ratios of the sample, the fitting lines between testing values and predicted values in different samples are drawn and shown in Figure 11. In Figure 11, the abscissa represents the predicted value, and the ordinate represents the testing value. When the predicted value is the same as the testing value, their fitted straight line is the equality line, and there is no error in the model at this time. When the fitted line deviates from the equality line, it means that the model has an error in this prediction, and the closer the fitting slope is to 1, the better the model's predictive effect. From this figure, it is clear that for samples with high mudstone content, the fitting line's slope exceeds 1, which means the predicted value is lower than the testing value and the model underestimates the testing results. On the contrary, in the samples containing more

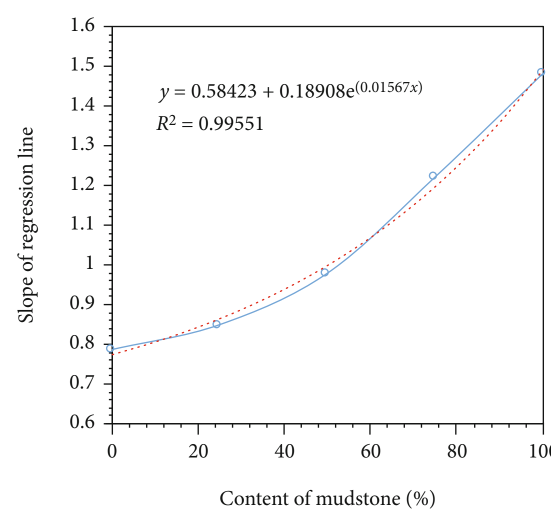

FIGURE 12: The relationship between the slope of fitting line and content of mudstone.

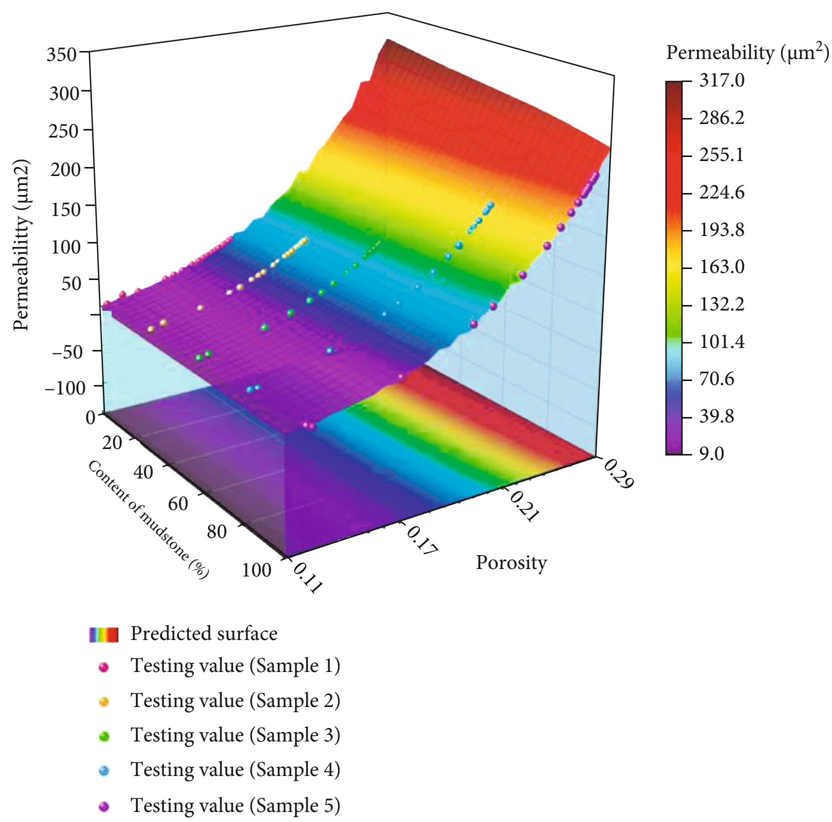

(a)

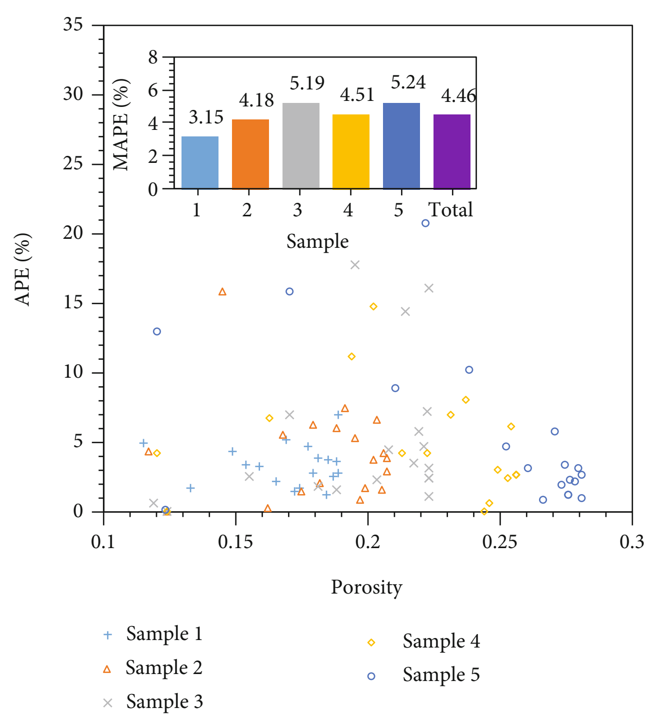

(b)

Figure 13: Comparison between testing results and predicted surface by mudstone content-based modified model (a). Comparison of results (b) APE and MAPE.

limestone, the fitting line's slope is lower than 1; that is, the model overestimated the experimental value. In addition, according to the R^2 value of fitting curves, it can be found that the fitting accuracy of each sample is high, indicating that the predicted value of the model and the experimental value present an obvious linear relationship.

Due to the linear relationship between the predicted value and the testing value, this research tries to add a scale factor to modify the Carman-Kozeny model. By introducing the variable of mudstone content, the modified model could consider the effect of variation in the proportions of different rock components on permeability prediction. Figure 12 shows the relationship between the slope of the fitting line ξ and the mudstone content c. It can be found that the slope of the fitted line and the mudstone content present an exponential distribution, and the fitting equation is given below:

$$\xi = 0.58423 + 0.18908e^{0.01567c}. \tag{20}$$

Based on the above discussion, we propose the following modified formula to predict the influence between permeability and porosity of limestone mudstone mixture:

$$k = \left(0.58423 + 0.18908e^{0.01567c}\right)\frac{k_0(1-\phi_0)^2}{{\phi_0}^3}\frac{\phi^3}{(1-\phi)^2}. \tag{21}$$

The above prediction equation fully considers the influence of mudstone content. According to the modified model (Equation (21)), we have predicted the permeability of the limestone mudstone mixture. In order to describe the accuracy of the predicted surface, the MAPE of the total sample is introduced and can be obtained by Equation (22):

$$\mathrm{MAPE}_{\mathrm{total}} = \frac{1}{5}\sum_{j=1}^{5}\mathrm{MAPE}_j, \tag{22}$$

where j is the number of samples.

The prediction results of the modified model are shown in Figure 13. In the comparison of the predicted value and the measured value, it can be found that the testing value point is very close to the predicted surface. Through the predicted surface, it is observed that as the porosity and the mudstone content increase, the permeability of the rock mass increases. As shown in Figure 13(b), although the dispersion of APE is still high, according to MAPE results, the accuracy of the modified model has been significantly improved. The MAPE of all samples is within 6%, and the MAPE of the total sample is 4.46%. Comparing the results of different rock samples, it can be found that as the mudstone content increases, the accuracy of the model gradually decreases (except when comparing samples 3 and 4). This may be due to the formation of more argillaceous material in the sample with higher mudstone content, which blocked the seepage channel, resulting in much higher uncertainty during the erosion process.

4. Conclusions

In this article, a series of erosion seepage experiments are carried out to investigate the non-Darcy hydraulic characteristics (e.g. mass loss rate, sample height, porosity, water pressure at the outlet, and permeability) of the limestone and mudstone mixture were studied. The test results are adopted to evaluate the accuracy of a classic permeability prediction model and then put forward a modified model considering the lithology of the medium. The main conclusions are as follows.

The erosion process can be divided into four stages: particle rearrangement, severe erosion, mild erosion, and stable seepage. The higher the mudstone content in the sample, the stronger the erosion effect in the sample. Under the action of erosion, the height of the sample decreases rapidly and then remains stable. The higher the mudstone content, the faster the height of the sample decreases under the effect of erosion, and the greater the decline. The porosity of the sample increases first and then remains stable. The higher the mudstone content, the more significant the increase in porosity. The water pressure at the outlet gradually increases with the erosion effect. The higher the mudstone content, the more obvious the increase. Permeability and porosity growth have a similar trend; that is, it increases first and then stabilizes under erosion. A higher porosity growth is observed in samples with high mudstone content.

Through the same test results and Carman-Kozeny model prediction results, it is found that the prediction performance of the classic model is unaccepted, the maximum MAPE is more than 32%, and the accuracy of the model is greatly affected by lithology. Further analysis of the model results shows that there is an obvious linear relationship between the predicted value and the test value. Based on this phenomenon, a proportional coefficient related to the rock composition is introduced to improve the Carman-Kozeny model. By comparing the test and calculation results, the prediction accuracy of the modified model is much higher than that of the classic one, and the MAPE values are within 6%. In addition, the predicted accuracy decreases with the increase of mudstone content. This phenomenon may be related to the clogging effect of muddy substances on the water conducting pathway.

Data Availability

The experimental data used to support the findings of this study are included in the article.

Conflicts of Interest

The authors declare no competing financial interest.

Acknowledgments

This research was financially supported by the National Natural Science Foundation of China (Grant No. 51874277).

References

[1] M. Niwa, K. Shimada, T. Ishimaru, and Y. Tanaka, "Identification of capable faults using fault rock geochemical signatures: a case study from offset granitic bedrock on the Tsuruga Peninsula, central Japan," *Engineering Geology*, vol. 260, article 105235, 2019.

[2] Z. Niu, Q. Li, X. Wei, X. Li, and J. Ma, "Numerical investigation of slippage characteristics of normal and reverse faults under fluid injection and production," *Environmental Earth Sciences*, vol. 76, no. 14, p. 502, 2017.

[3] A. Torabi, M. U. Johannessen, and T. S. S. Ellingsen, "Fault core thickness: insights from siliciclastic and carbonate rocks," *Geofluids*, vol. 2019, Article ID 2918673, 24 pages, 2019.

[4] S. Wang, X. Li, J. Yao et al., "Experimental investigation of rock breakage by a conical pick and its application to non-explosive mechanized mining in deep hard rock," *International Journal of Rock Mechanics and Mining Sciences*, vol. 122, article 104063, 2019.

[5] D. Ma, J. Wang, X. Cai et al., "Effects of height/diameter ratio on failure and damage properties of granite under coupled bending and splitting deformation," *Engineering Fracture Mechanics*, vol. 220, article 106640, 2019.

[6] S. Wang, L. Sun, X. Li et al., "Experimental investigation of cuttability improvement for hard rock fragmentation using conical cutter," *International Journal of Geomechanics*, vol. 21, no. 2, article 06020039, 2021.

[7] H. Yu, S. Zhu, H. Xie, and J. Hou, "Numerical simulation of water inrush in fault zone considering seepage paths," *Natural Hazards*, vol. 104, no. 2, pp. 1763–1779, 2020.

[8] S. Zhang, W. Guo, Y. Li, W. Sun, and D. Yin, "Experimental simulation of fault water inrush channel evolution in a coal mine floor," *Mine Water and the Environment*, vol. 36, no. 3, pp. 443–451, 2017.

[9] S. Li, R. Liu, Q. Zhang, and X. Zhang, "Protection against water or mud inrush in tunnels by grouting: a review," *Journal of Rock Mechanics and Geotechnical Engineering*, vol. 8, no. 5, pp. 753–766, 2016.

[10] Y. Xue, D. Wang, S. Li, D. Qiu, Z. Li, and J. Zhu, "A risk prediction method for water or mud inrush from water-bearing faults in subsea tunnel based on cusp catastrophe model," *KSCE Journal of Civil Engineering*, vol. 21, no. 7, pp. 2607–2614, 2017.

[11] W. Shi and T. Yang, "A coupled nonlinear flow model for particle migration and seepage properties of water inrush through broken rock mass," *Geofluids*, vol. 2020, Article ID 1230542, 14 pages, 2020.

[12] J. Wu, C. Jia, and L. W. Zhang, "Expansion of water inrush channel by water erosion and seepage force," *International Journal of Geomechanics*, vol. 21, no. 7, article 04021121, 2021.

[13] S. Li, C. Gao, Z. Zhou et al., "Analysis on the precursor information of water inrush in karst tunnels: a true triaxial model test study," *Rock Mechanics and Rock Engineering*, vol. 52, no. 2, pp. 373–384, 2019.

[14] D.-x. Liang, Z.-q. Jiang, S.-y. Zhu, Q. Sun, and Z.-w. Qian, "Experimental research on water inrush in tunnel construction," *Natural Hazards*, vol. 81, no. 1, pp. 467–480, 2016.

[15] Z. Huang, W. Zeng, and K. Zhao, "Experimental investigation of the variations in hydraulic properties of a fault zone in Western Shandong, China," *Journal of Hydrology*, vol. 574, pp. 822–835, 2019.

[16] Z. Huang, K. Zhao, X. Li, W. Zhong, and Y. Wu, "Numerical characterization of groundwater flow and fracture-induced water inrush in tunnels," *Tunnelling and Underground Space Technology*, vol. 116, article 104119, 2021.

[17] D. Ma, M. Rezania, H.-S. Yu, and H.-B. Bai, "Variations of hydraulic properties of granular sandstones during water inrush: effect of small particle migration," *Engineering Geology*, vol. 217, pp. 61–70, 2017.

[18] Y. Wang, F. Geng, S. Yang, H. Jing, and B. Meng, "Numerical simulation of particle migration from crushed sandstones during groundwater inrush," *Journal of Hazardous Materials*, vol. 362, pp. 327–335, 2019.

[19] B. Yu, Z. Chen, Q. Ding, and L. Wang, "Non-Darcy flow seepage characteristics of saturated broken rocks under compression with lateral constraint," *International Journal of Mining Science and Technology*, vol. 26, no. 6, pp. 1145–1151, 2016.

[20] W. Zhang, H. Zhou, and W. Guo, "Experimental study on seepage characteristics of fractured rock mass and its electrical response," *Journal of Hydrologic Engineering*, vol. 24, no. 7, article 04019017, 2019.

[21] Y.-F. Chen, Z. Liao, J. Q. Zhou et al., "Non-Darcian flow effect on discharge into a tunnel in karst aquifers," *International Journal of Rock Mechanics and Mining Sciences*, vol. 130, article 104319, 2020.

[22] J.-Q. Zhou, H.-B. Liu, C. Li, X.-L. He, H. Tang, and X.-J. Zhao, "A semi-empirical model for water inflow into a tunnel in fractured-rock aquifers considering non-Darcian flow," *Journal of Hydrology*, vol. 597, article 126149, 2021.

[23] A. Arianfar, A. Ramezanzadeh, and M. Khalili, "Numerical study of nonlinear fluid flow behavior in natural fractures adjacent to porous medium," *Journal of Petroleum Science and Engineering*, vol. 204, article 108710, 2021.

[24] C. Yao, Y. Shao, J. Yang et al., "Effects of non-darcy flow on heat-flow coupling process in complex fractured rock masses," *Journal of Natural Gas Science and Engineering*, vol. 83, article 103536, 2020.

[25] K. Chaudhary, M. B. Cardenas, W. Deng, and P. C. Bennett, "The role of eddies inside pores in the transition from Darcy to Forchheimer flows," *Geophysical Research Letters*, vol. 38, no. 24, 2011.

[26] Y.-F. Chen, J.-Q. Zhou, S.-H. Hu, R. Hu, and C.-B. Zhou, "Evaluation of Forchheimer equation coefficients for non-Darcy flow in deformable rough-walled fractures," *Journal of Hydrology*, vol. 529, pp. 993–1006, 2015.

[27] Z. Zeng and R. Grigg, "A criterion for non-Darcy flow in porous media," *Transport in Porous Media*, vol. 63, no. 1, pp. 57–69, 2006.

[28] R. W. Zimmerman, A. Al-Yaarubi, C. C. Pain, and C. A. Grattoni, "Non-linear regimes of fluid flow in rock fractures," *International Journal of Rock Mechanics and Mining Sciences*, vol. 41, no. 3, p. 384, 2004.

[29] D. Ma, J. Zhang, H. Duan et al., "Reutilization of gangue wastes in underground backfilling mining: overburden aquifer protection," *Chemosphere*, vol. 264, article 128400, 2021.

[30] H. Rahmati, M. Jafarpour, S. Azadbakht et al., "Review of sand production prediction models," *Journal of Petroleum Engineering*, vol. 2013, Article ID 864981, 16 pages, 2013.

[31] P. G. Ranjith, M. S. A. Perera, W. K. G. Perera, S. K. Choi, and E. Yasar, "Sand production during the extrusion of hydrocarbons from geological formations: a review," *Journal of Petroleum Science and Engineering*, vol. 124, pp. 72–82, 2014.

[32] E. Papamichos, I. Vardoulakis, J. Tronvoll, and A. Skjærstein, "Volumetric sand production model and experiment," *International Journal for Numerical and Analytical Methods in Geomechanics*, vol. 25, no. 8, pp. 789–808, 2001.

[33] I. Vardoulakis, M. Stavropoulou, and P. Papanastasiou, "Hydro-mechanical aspects of the sand production problem," *Transport in Porous Media*, vol. 22, no. 2, pp. 225–244, 1996.

[34] Y. Xue, F. Kong, S. Li et al., "Water and mud inrush hazard in underground engineering: genesis, evolution and prevention," *Tunnelling and Underground Space Technology*, vol. 114, article 103987, 2021.

[35] B. Yang, T. Yang, and J. Hu, "Numerical simulation of non-Darcy flow caused by cross-fracture water inrush, considering particle loss," *Mine Water and the Environment*, vol. 40, no. 2, pp. 466–478, 2021.

[36] D. Ma, H. Duan, X. Li, Z. Li, Z. Zhou, and T. Li, "Effects of seepage-induced erosion on nonlinear hydraulic properties of broken red sandstones," *Tunnelling and Underground Space Technology*, vol. 91, article 102993, 2019.

[37] B. Yao, Z. Chen, J. Wei, T. Bai, and S. Liu, "Predicting erosion-induced water inrush of karst collapse pillars using inverse velocity theory," *Geofluids*, vol. 2018, Article ID 2090584, 18 pages, 2018.

[38] F. Dellisanti, G. A. Pini, F. Tateo, and F. Baudin, "The role of tectonic shear strain on the illitization mechanism of mixed-layers illite–smectite. A case study from a fault zone in the northern Apennines, Italy," *International Journal of Earth Sciences*, vol. 97, no. 3, pp. 601–616, 2008.

[39] J. G. Solum, S. H. Hickman, D. A. Lockner et al., "Mineralogical characterization of protolith and fault rocks from the SAFOD main hole," *Geophysical Research Letters*, vol. 33, no. 21, 2006.

[40] D. Ma, S. Kong, Z. Li, Q. Zhang, Z. Wang, and Z. Zhou, "Effect of wetting-drying cycle on hydraulic and mechanical properties of cemented paste backfill of the recycled solid wastes," *Chemosphere*, vol. 282, article 131163, 2021.

[41] G. S. I. Onyenanu, G. J. Hampson, P. J. R. Fitch, and M. D. Jackson, "Effects of erosional scours on reservoir properties of heterolithic, distal lower-shoreface sandstones," *Petroleum Geoscience*, vol. 25, no. 2, pp. 235–248, 2019.

[42] J. Liu, W. Chen, W. Nie, J. Yuan, and J. Dong, "Experimental research on the mass transfer and flow properties of water inrush in completely weathered granite under different particle size distributions," *Rock Mechanics and Rock Engineering*, vol. 52, no. 7, pp. 2141–2153, 2019.

[43] L. N. Y. Wong, D. Li, and G. Liu, "Experimental studies on permeability of intact and singly jointed meta-sedimentary rocks under confining pressure," *Rock Mechanics and Rock Engineering*, vol. 46, no. 1, pp. 107–121, 2013.

[44] W. Yi and E. Wang, "Experimental research on measurement of permeability coefficient on the fault zone under coal mine in situ," *Arabian Journal of Geosciences*, vol. 9, no. 4, p. 253, 2016.

[45] S. Baziar, M. Tadayoni, M. Nabi-Bidhendi, and M. Khalili, "Prediction of permeability in a tight gas reservoir by using three soft computing approaches: a comparative study," *Journal of Natural Gas Science and Engineering*, vol. 21, pp. 718–724, 2014.

[46] R. F. Neumann, M. Barsi-Andreeta, E. Lucas-Oliveira et al., "High accuracy capillary network representation in digital rock reveals permeability scaling functions," *Scientific Reports*, vol. 11, no. 1, article 11370, 2021.

[47] D. Ma, H. Duan, J. Liu, X. Li, and Z. Zhou, "The role of gangue on the mitigation of mining-induced hazards and environmental pollution: an experimental investigation," *Science of the Total Environment*, vol. 664, pp. 436–448, 2019.

[48] P. Xu and B. Yu, "Developing a new form of permeability and Kozeny-Carman constant for homogeneous porous media by means of fractal geometry," *Advances in Water Resources*, vol. 31, no. 1, pp. 74–81, 2008.

Hindawi
Geofluids
Volume 2022, Article ID 6416174, 22 pages
https://doi.org/10.1155/2022/6416174

Research Article

Genesis of the Daping Gold Deposit in the Middle Xuefeng Mountain Area, Southern China: Constraints from Geochemistry, Fluid Inclusion, and H-O-S Isotope

Xu Kong,[1,2,3] **Wen-Tian Mi**,[1,4,5,6] **Xue-Yuan Qi**,[4] **Shu-Jun Lǚ**,[3] **Yu-Jun Dong**,[3] **and Jie Xin**[4]

[1]*Key Laboratory of Metallogenic Prediction of Nonferrous Metals and Geological Environment Monitoring (Central South University), Ministry of Education, Changsha 410083, China*
[2]*Department of Geology, Northwest University, Xi'an 710069, China*
[3]*No.407 Geological Team, Hunan Bureau of Geology and Mineral Exploration and Development, Huaihua 418000, China*
[4]*School of Mines, Inner Mongolia University of Technology, Hohhot 010051, China*
[5]*Key Laboratory of Geoscience Spatial Information of Land and Resources, Chengdu 610059, China*
[6]*Geomathematics Key Laboratory of Sichuan Province, Chengdu 610059, China*

Correspondence should be addressed to Xu Kong; konx163@163.com and Wen-Tian Mi; miwentian1982@imut.edu.cn

Received 22 August 2021; Revised 20 September 2021; Accepted 23 September 2021; Published 10 March 2022

Academic Editor: Yong-Zheng Wu

The medium-sized Daping gold deposit is located in the middle Xuefeng Mountain area of Southern China with gold ores hosted in sericite phyllite, sericitolite, and mylonite. The auriferous quartz-carbonate-sulfide veins and adjacent alteration rocks are structurally controlled within the NE (northeast) shear zone with NE, NNE (north-east-east), and NW (northwest) trending at high inclination angles. The petrogeochemistry analysis results show that the gold ores are characterized by high content values of SiO_2, S, and As and low content values of Al_2O_3 and Na_2O and display strong enrichment of LREE with δEu values ranging from 0.54 to 0.75. Four stages of mineralization/alteration were identified: the first stage has mineral assemblages of quartz+pyrite+arsenopyrite±carbonate minerals, the second stage has mineral assemblages of quartz+polymetallic sulfide minerals (pyrite, arsenopyrite, chalcocite, galena, chalcopyrite, tetrahedrite)±chlorite±carbonate minerals, the third stage has mineral assemblages of quartz and carbonate minerals, and the supergene stage is characterized by limonite±patina which were formed by the oxidation of metal sulfides. Among them, the first stage and the second stage are the main gold mineralization stages. The ore-forming fluid inclusions in quartz are mainly composed of liquid phase (H_2O) and gas phase (H_2O and CO_2), and based on the microthermometric analysis, the first metallogenic stage and second metallogenic stage yielded average homogenization temperature of 184.5 and 255.8°C and average salinity of 7.64 wt.% NaCl eqv. and 11.35 wt.% NaCl eqv., respectively. Thus, the ore-forming fluids belong to H_2O-CO_2-NaCl, medium-low temperature, and medium-low salinity fluid. The δD_{H_2O} and $\delta^{18}O_{H_2O}$ values of auriferous quartz are from -51‰ to 62‰ and from -1.44‰ to 5.42‰, respectively, indicating that the ore-forming fluids may belong to mixing fluids of the magmatic fluid and meteoric hydrothermal fluid. The values of $\delta^{34}S$ of metal sulfides range from -0.94‰ to 1.98‰ (-0.131‰ in average), implying that sulfur may source from the concealed granite and/or basement metamorphic strata. The Daping gold deposit formed in the Indosinian period under the tectonic environment of compression between the Cathaysian plate and Yangtze plate and may belong to orogenic gold deposits.

1. Introduction

As one of the crucial gold producers of south China, the Jiangnan Orogen Belt (JOB) has a total gold reserve of >970 tons [1] and thus attracted more and more attention from the metallogeny geologists. The middle Xuefeng Mountain which belongs to the western section of the Jiangnan Orogen is located in the transitional region between the Cathaysia plate and the Yangtze plate (Figure 1(a)) [1–8]. At present, 21 gold deposits (points) have been discovered, and among

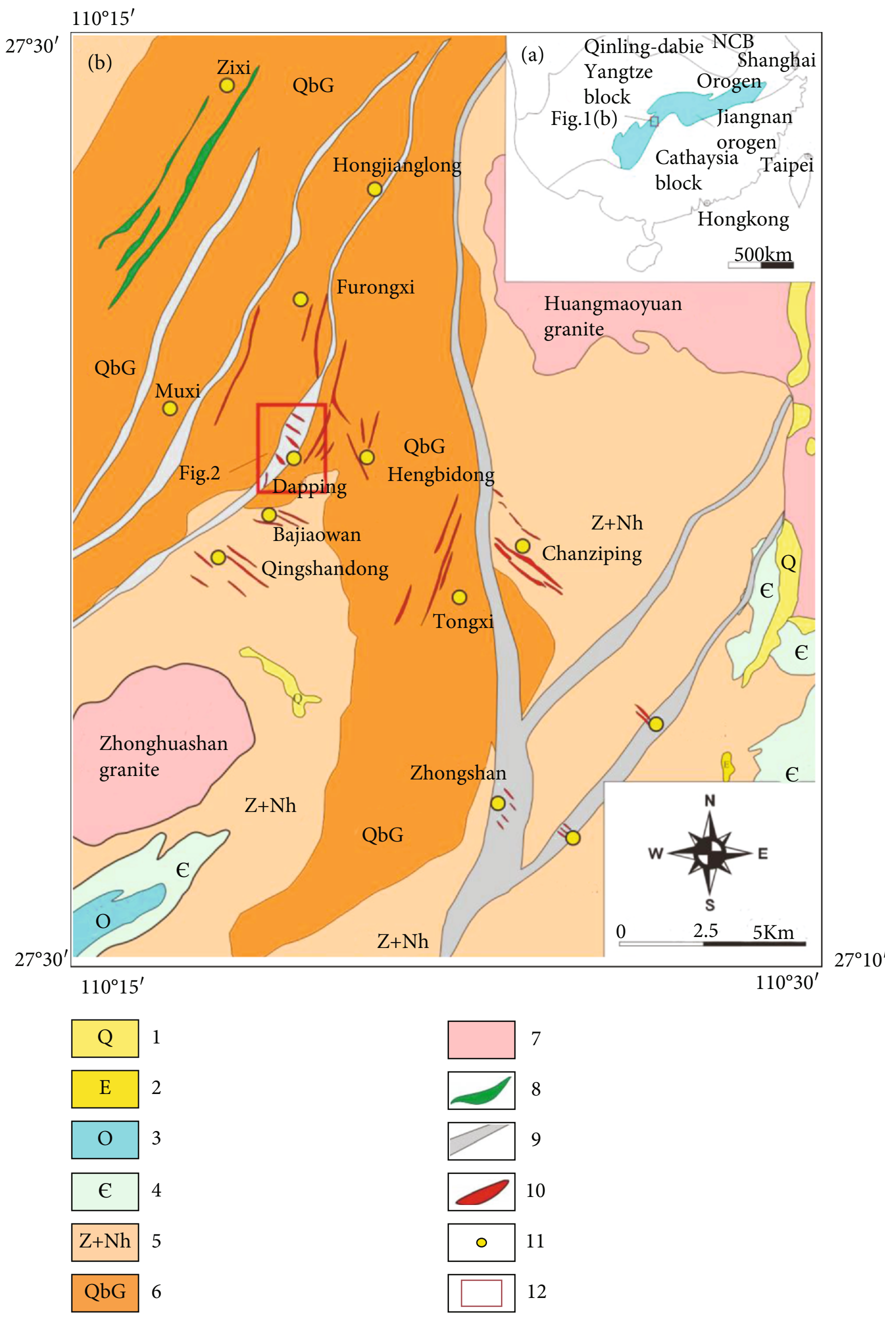

Figure 1: (a) Major tectonic blocks of China. (b) Regional geological sketch map of the middle Xuefeng Mountain (modified after [6–8]): 1: Quaternary (Q); 2: Palaeogene (E); 3: Ordovician (O); 4: Cambrian (Є); 5: Sinian and Nanhuan (Z+Nh); 6: Gaojian Group (QbG); 7: Early Triassic granite rocks; 8: Mafic-ultramafic rocks; 9: shear zone; 10: auriferous vein; 11: gold occurring spot; 12: study area.

them, the Chanziping gold deposit [9–13] and the Daping gold deposit [14] have a scale of large size and medium size, respectively. The exploration of the Daping gold deposit began in 1987 [15] and has proved gold reserves of more than 10 tons. Previous studies on the geological characteristics and metallogenic chronology indicate that the Daping gold deposit belongs to the shear zone type [16, 17] with ore-forming age of 204.8 Ma which belongs to Indosinian [18]. However, the ore-forming fluids, geochemical characteristics of the main and trace elements, rare earth elements, and isotopes of the deposit have not been systematically studied, and its metallogenic mechanism and process are still unknown.

This paper attempts to reveal the source of metallogenic materials, metallogenic mechanism, and deposit type of the Daping gold deposit by petrogeochemistry, H-O-S isotopes, and ore-forming fluids and provide more metallogenic information for further exploration and prediction of the Daping gold deposit and other similar gold deposits with the same metallogenic characteristics.

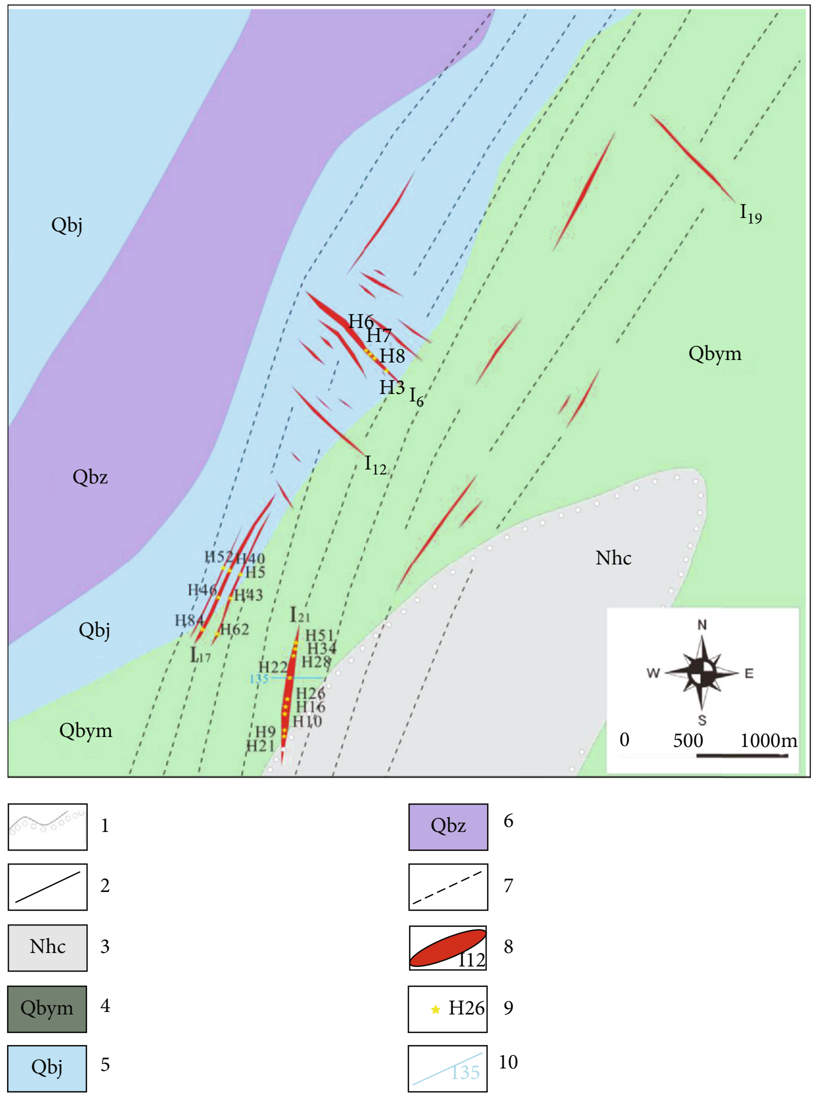

Figure 2: Geological sketch map of the Daping gold deposit (modified after [59]): 1: unconformity boundary; 2: conformity boundary; 3: Changan Formation (Nhc); 4: Yanmenzhai Formation (Qbym); 5: Jiajiantian Formation (Qbj); 6: Zhuanqiangwan Formation (Qbz); 7: ductile-brittle shear zone; 8: auriferous vein; 9: sample location; 10: prospecting line. Due to all the samples coming from diamond drills, only the horizontal positions are shown.

2. Regional Geological Setting

Daping gold deposit which is located in the transitional zone between Yangtze plate and Cathaysia plate belongs to the middle Xuefeng metallogenic belt (Figure 1(a)). The regional strata are composed of Quaternary, Palaeogene, Ordovician, Cambrian, Sinian, Nanhua System, and Gaojian Group of Qingbaikou System (Figure 1(b)). Among these strata, the Gaojian Group of the Qingbaikou System and the Nanhua Systems which belong to low-grade metamorphic greenschist facies clastic rocks with high gold-bearing background values are the main ore-bearing strata in the gold metallogenic belt of the middle Xuefeng Mountain [19]. Frequent acid magmatic activities occurred in this area during the Indosinian period (e.g., Zhonghuashan granite and Huangmaoyuan granite, Figure 1(b)). In addition, six NE-trending or NNE-trending ductile shear zones cross the middle Xuefeng Mountain gold field with length of 10–25 km and width of 0.5–2 km.

3. Geological Characteristics of Daping Gold Deposit

3.1. Deposit Features. The stratum of the Daping gold deposit is composed of the Gaojian Group of the Qingbaikou System and Changan Formation of the Nanhua System, and the gold-bearing faults are NE-trending, NW-trending [20, 21], and NNE-trending. Crossing through the middle part of the study area (Figure 2), the NE-trending ductile-brittle shear cleavage zone may serve as the ore-forming fluid passageways as well as auriferous host structures.

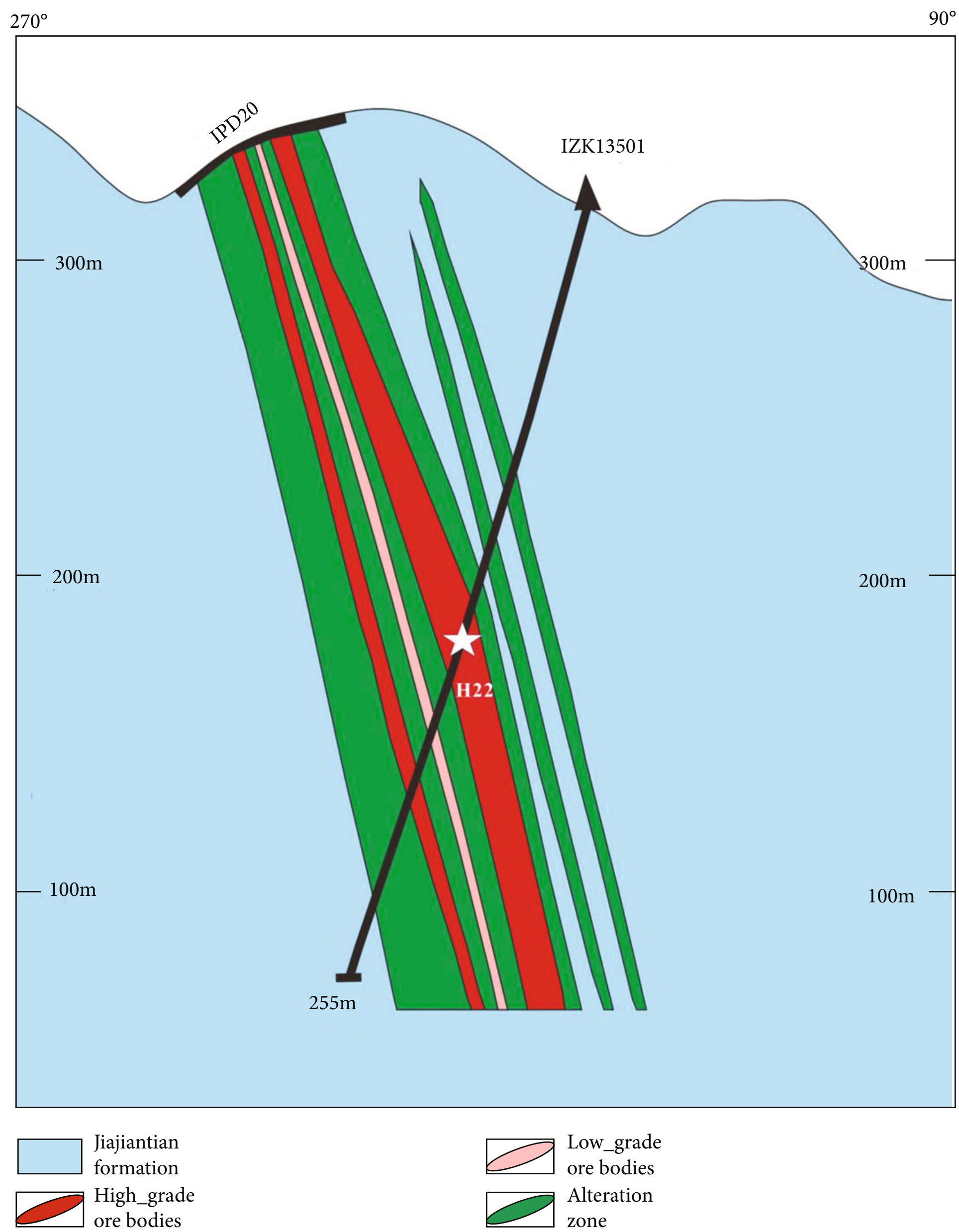

Figure 3: Geologic cross-section (prospecting line 135) of the Daping gold deposit (modified after [59]).

3.2. The Orebody Characteristics. At present, 23 auriferous veins were found out with a length of 120–2100 m and a width of 1.30–70 m. The auriferous veins which occurred in the ductile shear zone or adjacent fault segments are NW-trending of I_6, I_7, I_9, I_{12}, and I_{19} or NE-NNE-trending of I_{17}, I_{20}, I_{21}, and I_{26}. The NW-trending veins intersect the NE-trending vein at a large angle, and both the NE-trending and NW-trending auriferous veins have inclination angles of above 70° (Figure 3). At present, 38 ore bodies have been found out between the elevation of -40 m and 340 m, and among them, 7 main ore bodies have lengths of 170–470 m with an average thickness of 1.36–4.85 m and an average grade of 1.63–25.80 ppm. The alteration types of the Daping gold ores include silicification, sericitization, chloritization, carbonization, and clayization (Figures 4(a), 4(c), and 4(h)). The intensity of silicification, pyritization, and sericitization has positive relations with the intensity of gold mineralization.

3.3. Ore Characteristics. According to the differences of gold-bearing structures, the Daping gold ores can be divided into quartz vein type (gold mineralization mainly occurred in quartz veins and nearby metal sulfides), altered rock type (gold mineralization mainly occurred in alteration rocks), and tectonic breccia type (gold mineralization mainly occurred in tectonic breccia rocks) (Figure 5). The metal minerals of ores are composed of pyrite, arsenopyrite, chalcopyrite, galena, sphalerite, and stibnite, and among them,

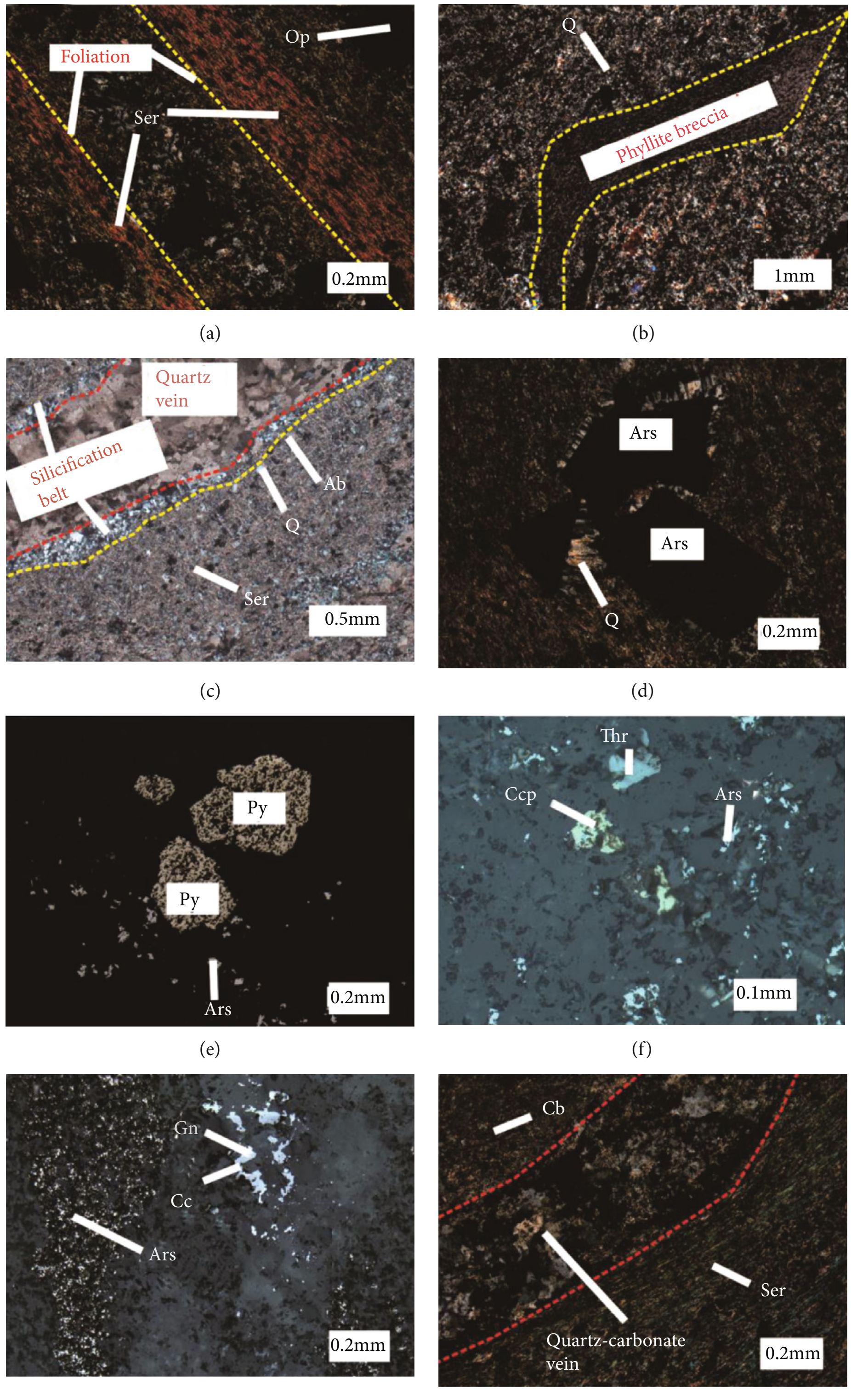

Figure 4: Photomicrographs and microstructures of the Daping gold deposit. (a) The schistose foliation formed by the orientation of sericite (cross-polarized light). (b) Tensile ductile deformation of the phyllite breccia (cross-polarized light). (c) The silicification belt around the quartz vein (plane-polarized light). (d) The pressure shadow (recrystallized quartz) formed by the arsenopyrite (cross-polarized light). (e) The quartz vein containing hypidiomorphic pyrite and xenomorphic arsenopyrite of the first stage of the metallogenic period (reflected light). (f) The quartz vein containing mineral assemblages of xenomorphic arsenopyrite, chalcopyrite, and tetrahedrite of the second stage of the metallogenic period (reflected light). (g) The quartz-carbonate vein of the third stage of the metallogenic period (cross-polarized light). Mineral abbreviation: Py: pyrite; Ars: arsenopyrite; Cc: chalcocite; Gn: galena; Ccp: chalcopyrite; Thr: tetrahedrite; Q: quartz; Ser: sericite; Ab: albite; Cb: carbonate mineral; Op: opaque mineral.

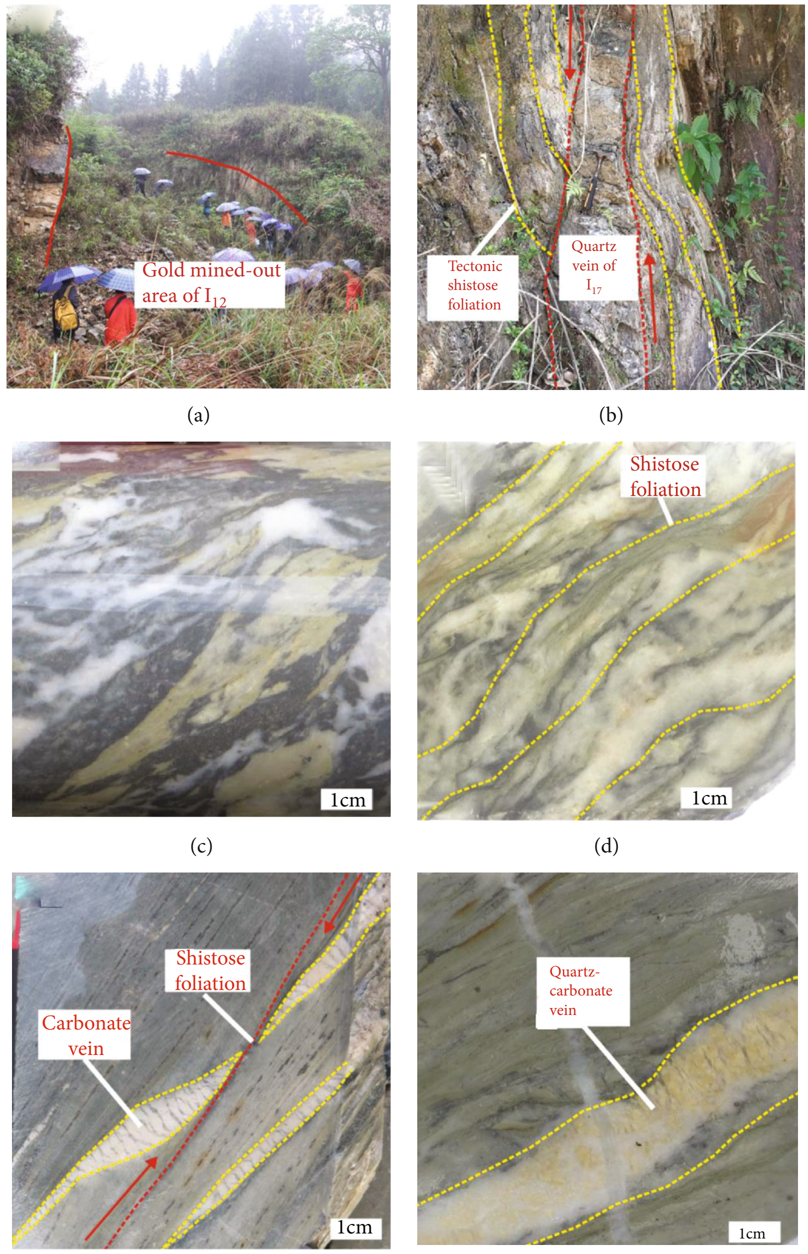

(a) (b) (c) (d) (e) (f)

Figure 5: Macroscopic images of auriferous veins and deformation characteristics of the Daping gold deposit. (a) Field image of the NW-trending veins of I_{12}. (b) Macroscopic image of the NE-trending veins of I_{17} shows distinct features of sinistral shear deformation. (c) Irregular quartz breccia and sericite slate breccia of I_{21} vein formed in the tectonic shearing environment. (d) The schistose foliation formed by the orientation of the sericite shows ductile deformation in the I_{21}. (e) The tensile-shearing space was filled by carbonate veins. (f) Quartz-carbonate veins show undulating edge of ductile deformation.

Table 1: Mineral assemblages of ore-forming stages and characteristics of the fluid inclusions.

Period	Stage	Mineral assemblages	Sample No.	Type of the fluid inclusions	Size of the fluid inclusions (μm)	Composition of liquid phase	Composition of gas phase	V/T (%) (20°C)
Metallogenic period	The first stage	Q+Py+Ars±Cb	H28-S1, H43-S1	Two-phase+liquid phase	4.1–12.5	H_2O	H_2O	14–28
	The second stage	Q+polymetallic sulfide minerals (Py, Ars, Cc, Gn, Ccp, Thr)±Chl±Cb	H10-S2, H21-S2, H28-S2, H43-S2	Two-phase+liquid phase+gas phase	2.5–17.8	H_2O	H_2O, CO_2	7–45
	The third stage	Q+Cb	H7-S3, H10-S3	Two-phase+gas phase	2.8–5.1	H_2O	H_2O, CO_2	5–20
Supergene period	Supergene stage	Limonite±patina						

Notes: Py: pyrite; Ars: arsenopyrite; Cc: chalcocite; Gn: galena; Ccp: chalcopyrite; Thr: tetrahedrite; Q: quartz; Chl: chlorite; Cb: carbonate minerals; V/T: vapor/total ratio of two-phase inclusions.

Table 2: Detail location and descriptions of the samples of the Daping gold deposit. The thickness and content of gold of the samples are from [59].

Sample	Auriferous vein	Sampling location	Thickness (m)	Content of gold (ppm)	Rock name
H3	I_6	ZK3201 drilling core 198 m	1.07	1.19	Sericite phyllite
H6	I_6	ZK2802 drilling core 210 m	0.89	0.84	Sericite phyllite
H7	I_6	ZK2802 drilling core 212 m	0.90	1.45	Sericite phyllite
H8	I_6	ZK2802 drilling core 214 m	1.02	0.26	Sericite phyllite
H5	I_{17}	ZK11701 drilling core 86 m	1.07	1.39	Sericite phyllite
H40	I_{17}	ZK11701 drilling core 191 m	0.94	2.94	Sericite phyllite
H52	I_{17}	ZK11701 drilling core 222 m	0.89	1.16	Sericite phyllite
H43	I_{17}	ZK12101 drilling core 211 m	1.16	1.11	Sericite phyllite
H46	I_{17}	ZK12101 drilling core 232 m	1.31	1.21	Sericite phyllite
H62	I_{17}	ZK12501 drilling core 232 m	0.84	1.13	Sericite phyllite
H84	I_{17}	ZK12501 drilling core 414 m	0.99	0.61	Sericite phyllite
H28	I_{21}	ZK13301 drilling core 238 m	1.10	6.78	Sericitolite
H34	I_{21}	ZK13301 drilling core 248 m	0.85	10.77	Sericitolite
H51	I_{21}	ZK13301 drilling core 290 m	1.16	1.86	Sericite phyllite
H22	I_{21}	ZK13501 drilling core 144 m	1.00	3.28	Sericite phyllite
H10	I_{21}	ZK13901 drilling core 138 m	1.35	8.21	Mylonite
H16	I_{21}	ZK13901 drilling core 152 m	1.18	1.47	Sericite phyllite
H26	I_{21}	ZK13902 drilling core 324 m	0.90	5.95	Sericite phyllite
H9	I_{21}	ZK14101 drilling core 211 m	1.08	2.93	Sericite phyllite

Table 3: Average content of the major elements of the Daping gold deposit (wt.%).

Sample	SiO_2	Al_2O_3	TFe_2O_3	CaO	MgO	K_2O	Na_2O	TiO_2	P_2O_5	MnO	SO_3	LOI	Total
H3	75.67	11.65	3.62	1.49	0.97	2.59	1.50	0.36	0.07	0.08	3.17	0.87	102.04
H5	73.11	13.14	2.32	1.22	0.60	1.44	4.78	0.33	0.04	0.05	0.23	2.41	99.67
H6	67.56	12.61	4.83	3.17	1.82	3.93	0.12	0.41	0.14	0.21	3.81	2.58	101.19
H7	67.45	13.31	5.94	2.00	1.37	2.07	3.62	0.40	0.09	0.14	5.92	1.33	103.64
H8	69.58	13.98	3.72	1.06	1.06	3.40	1.80	0.47	0.08	0.10	0.81	3.46	99.52
H26	71.68	10.23	6.30	1.86	1.31	2.61	0.87	0.40	0.03	0.09	3.54	0.96	99.88
H28	76.50	7.86	5.76	1.64	0.91	1.82	0.99	0.29	0.12	0.06	3.90	0.94	100.79
H34	67.98	12.09	7.88	0.88	0.96	2.86	1.50	0.47	0.05	0.06	5.46	0.55	100.74
H40	70.61	12.62	5.24	1.32	0.86	2.93	1.75	0.50	0.09	0.07	4.42	0.53	100.94
H43	65.89	17.06	4.73	1.24	1.14	4.18	2.23	0.65	0.14	0.12	1.17	1.86	100.41
H46	66.49	14.54	4.51	2.90	1.78	3.56	1.32	0.57	0.13	0.12	2.06	2.22	100.2
H51	64.79	15.53	5.86	1.77	1.57	3.68	1.76	0.66	0.08	0.12	1.43	1.81	99.06
H52	65.36	13.17	4.69	3.82	1.90	3.46	1.28	0.41	0.09	0.23	1.80	3.64	99.85
H62	65.75	14.32	4.31	3.41	1.80	3.85	1.22	0.50	0.08	0.19	1.12	3.46	100.01
H84	60.93	18.18	4.77	2.99	1.59	4.66	1.30	0.68	0.08	0.14	2.61	2.81	100.74
Average	68.62	13.35	4.97	2.05	1.31	3.14	1.74	0.47	0.09	0.12	2.76	1.96	

TABLE 4: Content of trace elements of the Daping gold deposit (ppm).

Sample	H3	H5	H6	H7	H8	H26	H28	H34	H40	H43	H46	H51	H52	H62	H84	Average
Li	20.40	7.20	14.60	9.50	12.40	6.10	6.40	6.00	6.30	9.40	13.40	10.50	6.60	9.40	11.10	9.95
Sc	8.00	9.70	9.40	10.10	11.00	8.60	6.00	9.30	10.70	14.10	11.80	14.60	9.90	10.50	13.50	10.48
V	27.00	17.00	30.00	28.00	56.00	50.00	36.00	57.00	51.00	68.00	59.00	77.00	36.00	50.00	69.00	47.40
Cr	35.00	8.00	21.00	24.00	35.00	31.00	34.00	33.00	25.00	25.00	32.00	40.00	13.00	18.00	26.00	26.67
Co	4.80	3.10	5.40	8.20	10.80	8.30	7.60	7.70	8.50	9.30	9.30	11.20	5.60	7.10	8.80	7.71
Ni	10.60	3.90	11.40	16.70	14.00	12.30	11.70	13.00	10.60	11.40	17.70	17.20	6.00	8.70	10.80	11.73
Cu	7.00	5.30	2.60	7.70	22.40	16.00	9.30	7.10	14.60	25.90	15.20	19.70	8.60	11.70	12.80	12.39
Zn	25.00	57.00	15.00	16.00	22.00	49.00	31.00	24.00	17.00	22.00	20.00	66.00	18.00	17.00	21.00	28.00
Ga	16.90	13.65	17.85	16.10	20.60	14.55	10.20	15.05	16.40	21.20	18.25	20.40	17.55	17.60	23.90	17.35
Rb	88.40	49.40	121.50	69.90	111.50	90.60	60.60	93.70	97.10	128.50	113.50	124.00	111.00	118.00	148.50	101.75
Sr	102.50	165.50	121.00	143.00	97.10	211.00	175.00	142.00	128.00	136.50	194.00	204.00	163.50	200.00	190.50	158.24
Nb	9.60	9.30	11.40	10.70	11.10	6.60	4.60	7.20	8.00	10.70	9.20	10.10	8.50	8.90	11.50	9.16
Cs	15.65	2.85	10.20	4.70	6.10	5.12	3.38	5.16	6.12	7.86	8.89	6.00	6.64	6.90	9.66	7.02
Ta	0.62	0.66	0.63	0.61	0.63	0.41	0.25	0.39	0.56	0.63	0.57	0.63	0.53	0.62	0.77	0.57
Tl	0.41	0.26	0.53	0.32	0.46	0.39	0.26	0.40	0.44	0.57	0.51	0.51	0.48	0.51	0.66	0.45
Bi	0.20	0.16	0.27	0.68	0.92	0.23	0.29	0.18	0.39	0.25	0.35	0.21	0.16	0.20	0.15	0.31
Th	6.52	9.02	8.01	7.99	9.01	5.57	4.34	6.37	6.99	9.77	9.17	8.87	7.47	9.49	11.30	7.99
U	1.40	1.97	1.95	1.77	1.98	0.99	0.79	1.17	1.36	1.84	1.72	1.68	1.58	1.95	2.14	1.62
Zr	194.00	234.00	213.00	191.00	212.00	125.00	96.00	145.00	177.00	242.00	218.00	195.00	209.00	205.00	262.00	194.53
Hf	5.80	7.20	6.30	5.80	6.50	3.70	2.90	4.40	5.20	7.20	6.40	5.80	6.10	6.00	7.90	5.81
$w(U)/w(Th)$	0.21	0.22	0.24	0.22	0.22	0.18	0.18	0.18	0.19	0.18	0.19	0.19	0.21	0.21	0.19	0.20
$w(Rb)/w(Sr)$	0.86	0.30	1.00	0.49	1.15	0.43	0.35	0.66	0.76	0.94	0.59	0.61	0.68	0.59	0.78	0.68
$w(Co)/w(Ni)$	0.45	0.79	0.47	0.49	0.77	0.67	0.65	0.59	0.80	0.82	0.53	0.65	0.93	0.82	0.81	0.68
$w(Zr)/w(Hf)$	33.45	32.50	33.81	32.93	32.62	33.78	33.10	32.95	34.04	33.61	34.06	33.62	34.26	34.17	33.16	33.47

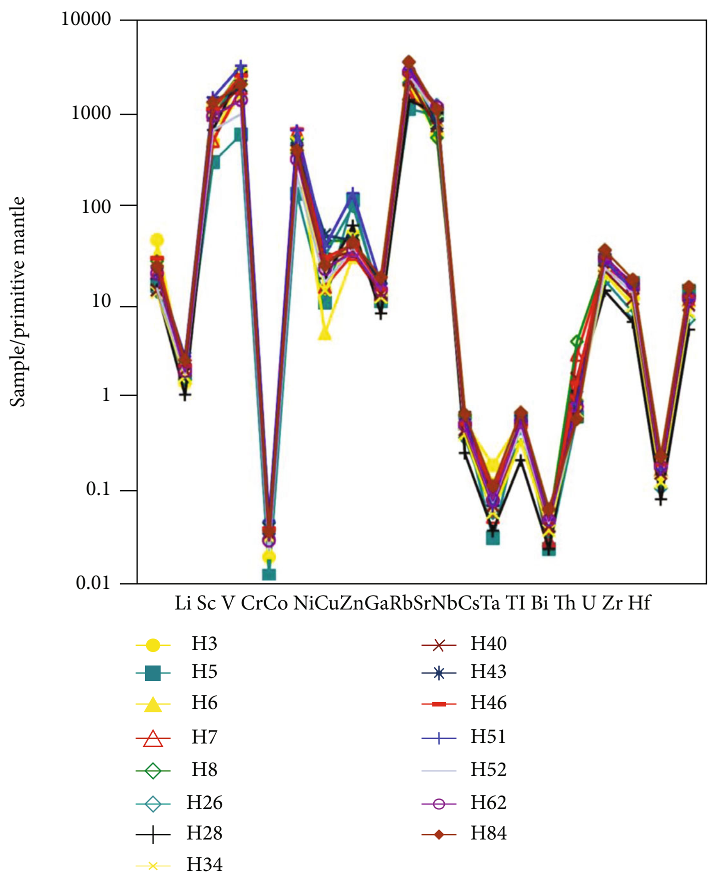

Figure 6: Primitive standard spider graph of trace elements of Daping gold deposit. The values for primitive mantle are from [62].

pyrite and arsenopyrite are the main gold-bearing minerals. The gangue minerals are mainly including quartz, carbonate minerals, albite, sericite, and muscovite.

According to the mineral assemblages, the metallogenic process of the Daping gold deposit can be divided into two periods (metallogenic period and supergene period) and four stages (Table 1, Figure 4). The first stage has mineral assemblages of quartz+pyrite+arsenopyrite±carbonate minerals and the second stage has mineral assemblages of quartz+polymetallic sulfide minerals (pyrite, arsenopyrite, chalcocite, galena, chalcopyrite, tetrahedrite)±chlorite±carbonate minerals which are the main gold mineralization stages. The third stage has mineral assemblages of quartz and carbonate minerals. The supergene stage is characterized by the mineral of limonite±patina which is formed by the oxidation of metal sulfides.

4. Sampling and Analytical Methods

4.1. Samples. The nineteen samples which were collected from drill holes are used for the geochemical and metallogenic study of the Daping gold deposit. Samples H3, H6, H7, and H8 from auriferous vein I_6 are sericite phyllite with gold content of 0.26–1.19 ppm. Samples H5, H40, H52, H43, H46, H62, and H84 from auriferous vein I_{17} are sericite phyllite with gold content of 0.61–2.94 ppm. Samples H28, H34, H51, H22, H10, H16, H26, and H9 from auriferous vein I_{21} are sericite phyllite, sericitolite, and mylonite with gold content of 1.47–10.77 ppm. For detailed sample information, see Table 2 and Figure 2.

4.2. Analytical Methods. The major elements and trace element of whole rock were tested in samples H3, H5, H6, H7, H8, H26, H28, H34, H40, H43, H46, H51, H52, H62, and H84. Hydrogen and oxygen isotopes of mineral quartz were tested in samples H28, H34, H22, H10, H16, H26, H9, and H46. Sulfur isotope of arsenopyrite and pyrite was tested in samples H34, H22, H16, H26, H7, and H46. The homogenization temperature, freezing temperature, and laser Raman spectra of the ore-forming fluid inclusions were tested in samples H7, H10, H21, H28, and H43.

The major elements, trace element, and isotopes of sulfur, hydrogen, and oxygen of the Daping gold ore samples were measured in the Australian Real Analysis Test (Guangzhou) Co., Ltd. The major elements were tested by the X-ray fluorescence instrument of ME-XRF26d with precision and accuracy better than ±5%. The trace elements and the rare earth elements are measured by instruments of M61-MS81, and the relative error is less than 10%. Sulfur isotope was measured by an instrument of S-ISTP01L with accuracy of better than 0.02%. Hydrogen isotope was tested by the instrument of H-ISTP01 with accuracy of better than 0.3%. The oxygen isotope was measured by the instrument of O-ISTP01 with accuracy of better than 0.03%. $\delta^{18}O_{H_2O}$ were

Table 5: Content of rare earth elements of the Daping gold deposit (ppm).

Sample	H3	H5	H6	H7	H8	H26	H28	H34	H40	H43	H46	H51	H52	H62	H84	Average
La	31.00	35.50	45.00	39.90	36.10	20.50	20.90	26.00	29.00	38.40	33.40	33.70	31.80	33.60	39.20	32.93
Ce	64.40	74.20	90.40	81.60	75.60	43.10	42.40	53.40	61.00	80.10	69.50	70.20	67.10	67.60	82.30	68.19
Pr	7.09	8.06	9.89	8.55	8.05	4.61	4.56	5.83	6.55	8.64	7.57	7.60	7.28	7.15	8.92	7.36
Nd	26.40	29.20	37.30	31.10	29.10	17.00	16.40	21.80	23.90	31.90	27.60	28.30	27.20	25.80	32.30	27.02
Sm	5.83	5.94	7.85	6.33	6.34	3.50	3.43	4.54	4.99	6.75	5.96	5.93	5.87	5.33	6.77	5.69
Eu	1.16	0.96	1.92	1.24	1.30	0.74	0.69	0.96	1.01	1.45	1.29	1.27	1.17	1.15	1.47	1.19
Gd	5.12	5.06	7.70	5.12	5.85	3.22	2.89	4.00	4.18	5.64	4.91	5.16	5.41	4.87	5.69	4.99
Tb	0.88	0.78	1.19	0.80	0.92	0.48	0.45	0.63	0.68	0.90	0.77	0.84	0.85	0.78	0.87	0.79
Dy	5.09	4.87	6.64	4.67	5.60	2.92	2.55	3.64	4.12	5.43	4.82	5.05	5.21	4.58	5.51	4.71
Ho	1.07	1.06	1.39	0.97	1.15	0.63	0.53	0.75	0.84	1.12	0.99	1.01	1.10	0.96	1.15	0.98
Er	3.27	3.14	4.06	3.01	3.40	1.83	1.48	2.16	2.38	3.25	2.89	2.98	3.14	2.82	3.31	2.87
Tm	0.49	0.49	0.63	0.48	0.53	0.27	0.23	0.33	0.38	0.50	0.45	0.45	0.47	0.42	0.52	0.44
Yb	3.28	3.23	4.14	3.22	3.77	1.92	1.47	2.18	2.53	3.40	2.88	3.11	3.21	2.86	3.37	2.97
Lu	0.47	0.49	0.65	0.52	0.57	0.29	0.22	0.33	0.38	0.50	0.45	0.48	0.48	0.43	0.53	0.45
Y	33.20	29.60	42.60	29.40	33.50	18.30	15.60	21.60	24.60	31.70	29.40	30.20	31.40	28.30	33.30	28.85
ΣREE	155.55	172.98	218.76	187.51	178.28	101.01	98.20	126.55	141.94	187.98	163.48	166.08	160.29	158.35	191.91	160.58
LREE	135.88	153.86	192.36	168.72	156.49	89.45	88.38	112.53	126.45	167.24	145.32	147.00	140.42	140.63	170.96	142.38
HREE	19.67	19.12	26.40	18.79	21.79	11.56	9.82	14.02	15.49	20.74	18.16	19.08	19.87	17.72	20.95	18.20
w (LREE)/w (HREE)	6.91	8.05	7.29	8.98	7.18	7.74	9.00	8.03	8.16	8.06	8.00	7.70	7.07	7.94	8.16	7.82
w (La) N/w (Yb) N	6.78	7.88	7.80	8.89	6.87	7.66	10.20	8.55	8.22	8.10	8.32	7.77	7.11	8.43	8.34	7.95
δEu	0.65	0.54	0.75	0.67	0.65	0.67	0.67	0.69	0.68	0.72	0.73	0.70	0.63	0.69	0.72	0.68
δCe	1.07	1.08	1.05	1.08	1.09	1.09	1.06	1.06	1.09	1.08	1.07	1.08	1.08	1.07	1.08	1.07

Table 6: Isotopic values of D and O of the Daping gold deposit. The values of the δO_{H_2O} are yielded by the equation: $\delta^{18}O_Q - \delta^{18}O_{H_2O} \approx 3.38 \times 10^6/T^2 - 3.40$ [22].

Sample	Mineral	δD (‰)	$\delta O_{V\text{-}SMOW}$ (‰)	δO_{H_2O} (‰)	T (°C)
H28-OH1	Quartz	-62	11.4	2.72	255.8
H34-OH1	Quartz	-59	14.1	5.42	255.8
H22-OH1	Quartz	-61	10.1	1.42	255.8
H10-OH1	Quartz	-60	11.3	-1.44	184.5
H16-OH1	Quartz	-53	12.9	0.16	184.5
H26-OH1	Quartz	-62	16	3.26	184.5
H9-OH1	Quartz	-61	13.6	0.86	184.5
H46-OH1	Quartz	-51	15.7	2.96	184.5

calculated according to the equation suggested by Clayton et al. [22]: $\delta^{18}O_Q - \delta^{18}O_{H_2O} \approx 3.38 \times 10^6/T^2 - 3.40$.

The homogenization temperature and freezing temperature testing of the ore-forming fluids were conducted by the instrument of LINKAMTHMSG600 in the Fluid Inclusion Laboratory of Chengdu University of Technology with temperature accuracy of ±0.1°C. The salinities of the metallogenic fluid inclusions were calculated by using the equation of [23]: $W = 0.00 + 1.78T_m - 0.042\,T_m{}^2 + 0.000557\,T_m{}^3$, where W is the weight percentage of NaCl (0–23.3% NaCl) and T_m is the freezing point depression (°C). The laser Raman spectra of single fluid inclusion were measured by the instrument of HORIBA LabRAM HR Evolution in the Raman Lab of Chengdu University of Technology with spatial resolution of 1 μm.

5. Analytical Results

5.1. Major Elements. The test results of the major elements illustrate that the Daping gold ores have a high content of SiO_2 and S and low content of Al_2O_3, TiO_2, CaO, Na_2O, MnO, and K_2O (Table 3). With the increasing of gold mineralization, the intensity of silicification alteration and sulfide mineralization increased significantly.

5.2. Trace Element. The trace element analysis results (Table 4) show that the samples have $w(\mathrm{U})/w(\mathrm{Th})$ ratios of 0.18–0.24 (0.20 in average), $w(\mathrm{Rb})/w(\mathrm{Sr})$ ratios of 0.35–1.15 (0.68 in average), $w(\mathrm{Co})/w(\mathrm{Ni})$ ratios of 0.45–0.93 (0.68 in average), and $w(\mathrm{Zr})/w(\mathrm{Hf})$ ratios of 32.50–34.26 (33.47 in average). The content values of U, Rb, and Co in the ores of Daping gold deposit are smaller than Th, Sr, and Ni. The content value of Zr is greater than Hf. The original mantle-standardized spider map shows that the elements of Li, Cr, Ni, Zn, Rb, Th, and Sr enriched obviously, and on the contrary, the elements of Sc, Co, Cu, Ga, Cs, Tl, and Zr were depleted (Figure 6).

5.3. Rare Earth Element. Rare earth elements are important indications for the analysis of the ore-forming material sources due to their stable chemical properties and the specificity of distribution [24]. REE testing results (Table 5) show that the total amount of rare earth element (ΣREE) of the Daping gold ores is 98.20–218.76 ppm (160.58 ppm in average), the total amount of LREE is 88.38–192.36 ppm (142.38 ppm in average), the total amount of HREE is 9.82–26.40 ppm (18.20 ppm in average), the ratio of $w(\mathrm{LREE})/w(\mathrm{HREE})$ is 6.91–9.00 (7.82 in average), and the ratio of $w(\mathrm{La})_N/w(\mathrm{Yb})_N$ is 6.78–10.20 (7.95 in average). The δEu values ranging from 0.54 to 0.75 and the δCe values ranging from 1.05 to 1.09 show positive Ce anomaly and negative Eu anomaly. All of the samples have a similar REE pattern of right-dip type indicating that they may have homologous origins (Figure 6) [25].

Table 7: Isotope values of δ^{34}S in the arsenopyrite or pyrite of the Daping gold deposit.

Sample	Mineral	δ^{34}S (‰)
H34-S1	Arsenopyrite	-0.94
H22-S1	Arsenopyrite	-1
H16-S1	Arsenopyrite	-0.76
H26-S1	Arsenopyrite	-0.67
H7-S1	Pyrite	1.98
H46-S1	Pyrite	0.23

5.4. Hydrogen and Oxygen Isotope. The hydrogen and oxygen isotope testing results (Table 6) of quartz mineral samples show that the value of δD_{H_2O} is from -51‰ to 62‰ (-58.6‰ in average), and the value of $\delta^{18}O_{H_2O}$ is from -1.44‰ to 5.42‰ (1.92‰ in average).

5.5. Sulfur Isotope. The sulfur isotope is important for studying the source of ore-forming materials [26, 27]. Six sulfur isotope samples of metal sulfides (pyrite or arsenopyrite) were tested, and the testing results (Table 7) show that the value of δ^{34}S is from -1.00‰ to 1.98‰ (-0.13‰ in average), which are close to the average S isotope of the magmatic hydrothermal deposit of 1.68‰ [28, 29].

5.6. Ore-Forming Fluid Inclusion Testing. According to the microscope observation, the ore-forming fluid inclusions are in the shape of circle, ellipse, or irregular. The metallogenic period of the Daping gold deposit can be divided into three stages. The inclusions of stage one are two-phase inclusions and liquid phase inclusions. The inclusions of stage

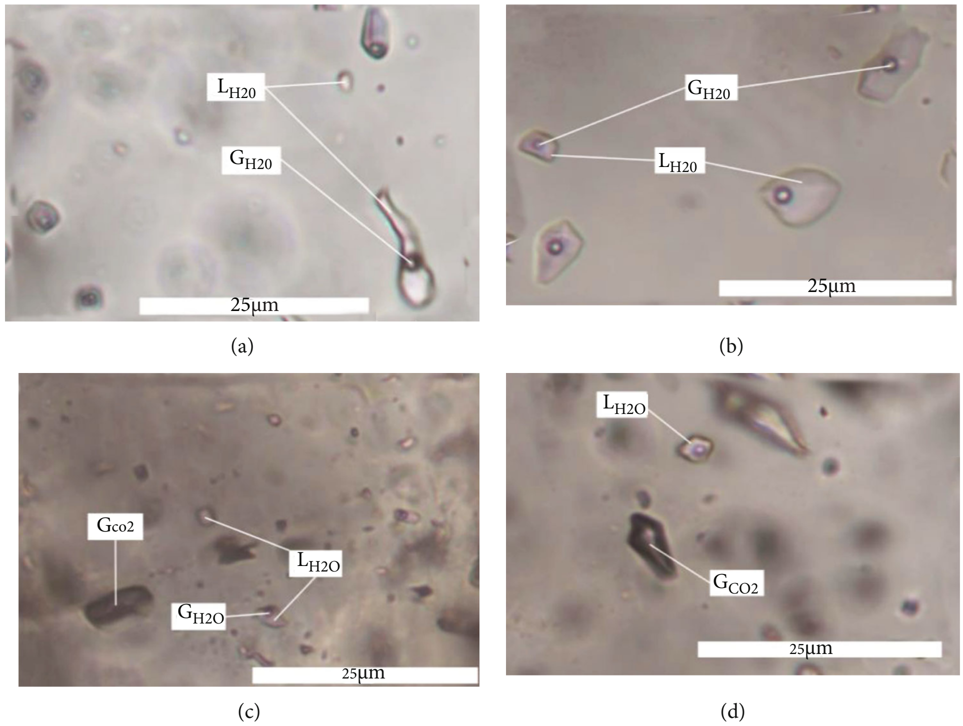

Figure 7: Photomicrographs of the typical fluid inclusions of the Daping gold deposit. (a) Two-phase and liquid phase of the first ore-forming stage. (b) Two-phase inclusions of the first ore-forming stage. (c) Two-phase, liquid phase, and gas phase inclusions of the second ore-forming stage. (d) Two-phase and gas phase inclusions of the third ore-forming stage. Abbreviation: L_{H_2O}: liquid H_2O; G_{H_2O}: vapor H_2O; G_{CO_2}: vapor CO_2.

two are two-phase inclusions, liquid phase inclusions, and gas inclusions. The inclusions of stage three are two-phase inclusions and gas phase inclusions. Based on the laser Raman spectra testing, the composition of the liquid phase inclusions is H_2O, and the composition of the gas phase inclusions is H_2O and CO_2. For detailed characteristics of the fluid inclusions, see Table 1 and Figures 7 and 8.

The first stage of the ore-forming fluid yielded homogenization temperature of 218.0–293.1°C (255.8°C in average) and salinity of 4.98–17.94 wt.% NaCl eqv. (11.35 wt.% NaCl eqv. in average). The second stage of the ore-forming fluid yielded homogenization temperature of 159.3–240.6°C (184.5°C in average) and salinity of 5.28–10.59 wt.% NaCl eqv. (7.64 wt.% NaCl eqv. in average). The third stage of the ore-forming fluid yielded homogenization temperature of 138.5–177.1°C (157.3°C in average) and salinity of 0.71–7.78 wt.% NaCl eqv. (4.82 wt.% NaCl eqv. in average). For details of the fluid inclusion testing, see Table 8 and Figure 9.

6. Discussion

6.1. Source of Ore-Forming Materials and Fluids. The Pre-Cambrian basement of the middle Xuefeng Mountain area is composed of Lengjiaxi Group, Gaojian Group, and Nanhua System which have average gold content of 19.46 ppb, 41.86 ppb, and 20.51 ppb, respectively [30–32]. The gold content of the base rocks is 6.5–14 times than the average bulk continental crust of 3.0 ppb [33] and thus can provide an abundant initial gold source for the formation of the gold deposits in the middle Xuefeng Mountain area.

Trace element studies show that the Daping gold ores enrich in Li, Cr, Ni, Zn, large ion lithophile elements of Rb and Sr, and high field strength element of Th and deplete in elements of Sc, Co, Cu, Ga, Cs, Tl, and Zr (Figure 6). The chondrite standard distributions of REE curves of gold ores have similar patterns of right-dip indicating that they probably have the same material sources and origins [25]. The rare earth elements of the gold ores are characterized by the strong enrichment of LREE (Figure 10). The δEu values range from 0.54 to 0.75 which show negative Eu anomaly, indicating that Daping gold deposit may form in the reducing environment [24, 34].

On the diagram of $\delta^{18}O_{H_2O}$ vs. δD_{H_2O} (Figure 11), auriferous quartz of the Daping gold ores is mainly located between the magmatic water and meteoric water and partly located at magmatic water, which indicates that the metallogenic fluids may be the mixing fluids of magmatic waters and meteoric water. Considering that the Zhonghuashan granite and Huangmaoyuan granite (belonging to Baimashan complex granites) (Figure 1) are only a few kilometers away from Daping gold deposit and have $\delta^{18}O$ value of 9.74–11.2‰ [35] which overlap partially with $\delta^{18}O$ value of 10.1–15.7‰ of the Daping gold-bearing quart, this indicates that the metallogenic fluids may partly come from the deep concealed granite with mixing of the meteoric water, which is similar to the Chanziping deposit (Figure 12). The $\delta^{34}S$‰ values of sulfide isotope from metal

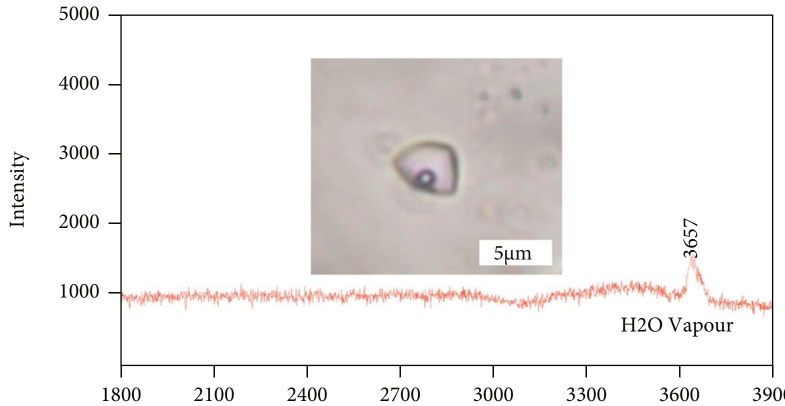

(a)

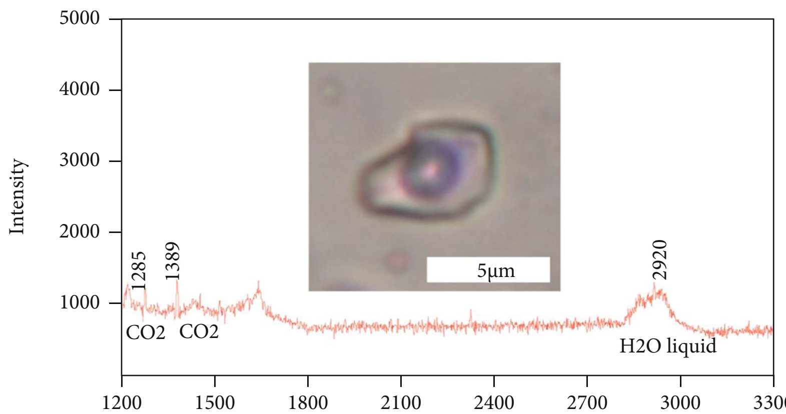

(b)

Figure 8: Microstructures and laser Raman spectra for fluid inclusions in Daping gold deposit.

Table 8: Microthermometric data of fluid inclusions of the metallogenic period in the Daping gold deposit.

Stage	Host mineral	Counts	T_h (°C)	Average T_h (°C)	T_m (ice) (°C)	Average T_m (ice) (°C)	Salinity (wt.% NaCl eqv.)	Average salinity (wt.% NaCl eqv.)
The first stage	Quartz	9	218.0–293.1	255.8	From -13.7 to -3.0	-7.6	4.98–17.94	11.35
The second stage	Quartz	39	159.3–240.6	184.5	From -7.0 to -3.2	-4.8	5.28–10.59	7.64
The third stage	Quartz	8	138.5–177.1	157.3	From -4.9 to -0.4	-2.9	0.71–7.78	4.82

T_h: homogenization temperature; T_m (ice): melting temperature of ice. The salinity and density of the fluid inclusions are calculated by the equation of [23].

sulfides of the Daping gold deposit range from -1 to 1.98, which are consistent with the granite; Gaojian Group (Figure 12) implied that both the granite and Gaojian Group may contribute to the sulfur sources.

Most granites in middle Xuefeng Mountain and adjacent regions belong to S-type granites [35–37] and have low gold contents (e.g., the Baimashan complex granites have average gold content of 1.25 ppb [38]). Considering that the magma source of the granites have gold contents of 19.46–41.86 ppb which are much higher than the 1.25 ppb of granites, thus, the gold element may aggregate in the magmatic hydrothermal fluids and may partly contribute to the formation of Mesozoic regional gold deposits.

6.2. Metallogenic Mechanism. Based on Rb-Sr dating of quartz, the Daping gold deposit and Chanziping gold deposit occurred in 204.8 Ma and 205.6 Ma, respectively [18]. Large-scale regional thrusting nappe structures and associated acid magma intrusion activities occurred at 225–201 Ma of the Indosinian period [18, 36, 37]. Thus, the

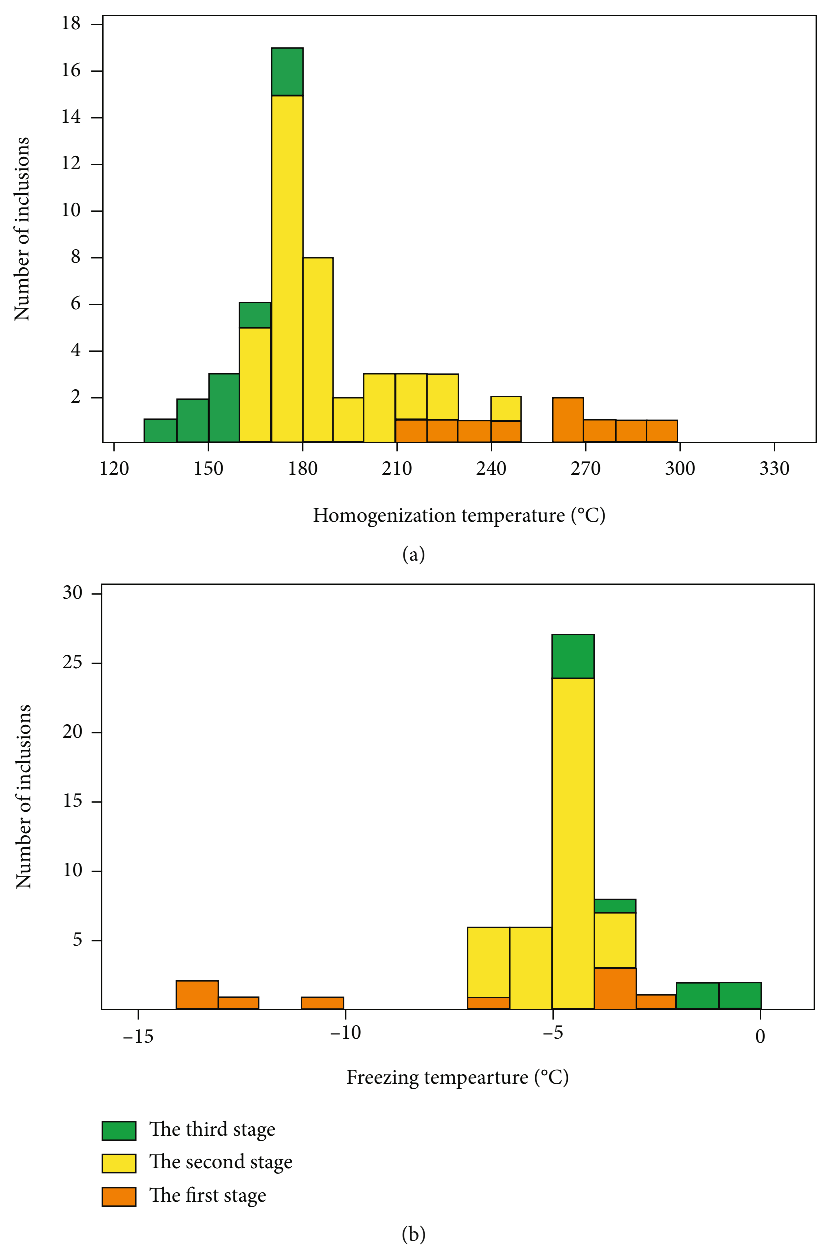

FIGURE 9: (a) Frequency histogram of the homogenization temperature of the Daping metallogenic fluids. (b) Frequency histogram of the freezing temperature of metallogenic fluids. The homogenization temperature data and freezing temperature data are from microthermometric analysis of the fluid inclusions (this study).

metallogenic epoch of regional gold mineralization is a little younger than the intrusion time of granites.

The tectonic schistose foliation developed in auriferous veins (for example, I_{17} and I_{21}) and ductile deformation of auriferous quartz veins (Figures 5(b), 5(d), and 5(e)) provides important evidence for the existence of brittle and ductile shear zones. The development of tectonic schistose foliation structure provides a migration channel for ore-forming fluids and serves as the main place for the precipitation and enrichment of ore-forming materials [39]. Driven by the thermal gradient of concealed granite, the gold metallogenic fluids migrate along the brittle and ductile shear zones, and in this process, the gold element of the adjacent stratum also adds to the fluids. When the ore-forming fluids reach the shallow stratum, and under the environment of depressurizing and fluid immiscibility, the thermodynamic equilibrium of CO_2 and oxygen fugacity were destroyed, and thus, the gold element precipitated in the quartz and metal sulfides to form the gold ores [16].

6.3. Ore Genetic Type. As an important type of gold deposits in the world, the orogenic gold deposits provide at least 30% of global gold reserves [40], and 17 giant gold deposits (>500 t Au) around the world belong to the orogenic gold type. Since the evolutionary history of the orogenic belt can be recorded in the formation of the orogenic gold

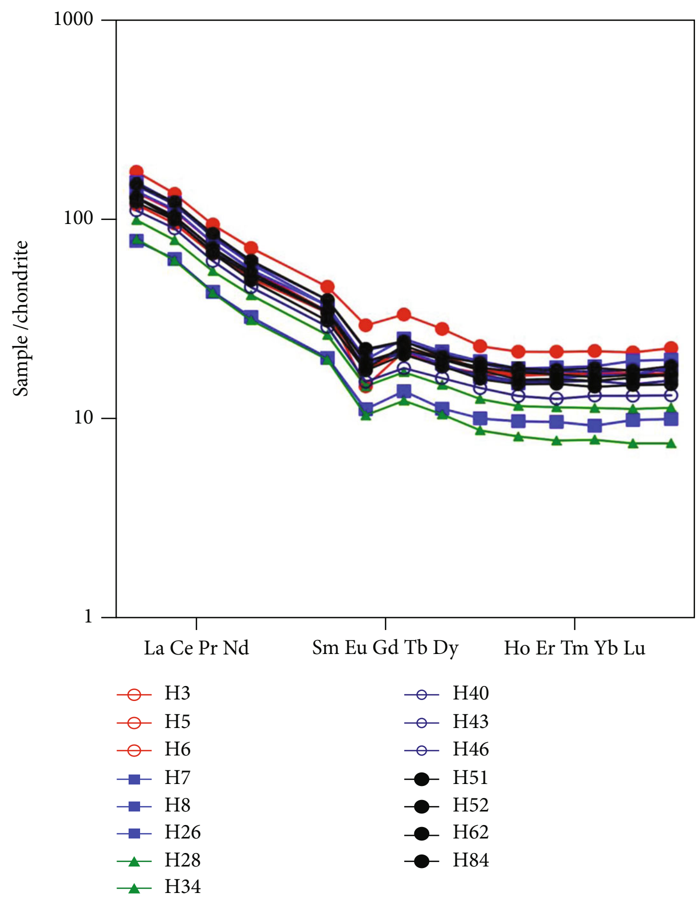

Figure 10: Chondrite meteorite standard distribution pattern of Daping gold deposit. The values for chondrite are from [63].

deposits [41], the study of the ore-forming process and genesis of the orogenic gold deposits can provide valuable information of metamorphism and uplift-erosion process of the orogenic belt and thus attracted more and more geologists to conduct research on such type of gold deposits. Before the jargon of orogenic gold deposits was proposed, the classification of the gold deposits which occurred in the orogenic belts or greenstone belts was in chaos. For instance, based on the differences of the surrounding rocks, the gold deposits were classified into green belt type, turbidite type, and BIF (banded iron formation) type [42]; based on the differences of mineralization characteristics, the gold deposits were classified into quartz vein type, altered rock type, and breccia type [43]; based on the differences of ore-controlling factors, the gold deposits were classified as shear zone type [44]. Groves et al. [45] proposed that the gold deposit formed in the tectonic environment of the squeezing or compression in the convergence region of the plates and has close genetic relationship with the orogenic process which can be classified as orogenic gold deposit, and thus, the gold types mentioned above should be classified as one type of orogenic gold deposit.

The middle Xuefeng Mountain area is located in the transition zone between Cathaysian plate and Yangtze plate and had undergone many periods of crustal tectonic movement and forms a large number of faults and folds as well as a series of ductile-brittle shear zone structures and multiple metallogenic episodes including Paleozoic (e.g., Zixi gold deposit of 425 Ma [46]) and Late Triassic (e.g., Chanziping and Daping gold deposit). In the Indosinian period, due to the strong NW-SE compression tectonic activities and the intrusion activities of regional acidic magmas, the magmatic hydrothermal fluids upwelled along the shear zone, and the gold elements in the stratum were activated, migrated, and gradually precipitated and enriched in the proper weak tectonic structures (for instance, ductile-brittle shear structures).

Similar Mesozoic gold deposits were also reported in the Jiangnan Orogen, e.g., Yanlinsi, Hengjiangchong, Wangu, Huangjindong, Jinjing, Mali, Fenshuiao, and Dayan [1, 4, 47–52]. And generally speaking, its gold mineralization has close spatial relations with regional granitic intrusions [1]. H–O–C–S–Pb isotopic data of ore-forming fluids indicate that its ore-forming materials mainly source from granitic magma and minor from basement metamorphic stratum ([1] and references therein). The ore-controlling structure of the shear zone of Daping gold deposit is similar to many world typical orogenic gold deposits [53–58]. In addition, the Daping gold deposit has many similar characteristics to the typical orogenic gold deposits (Table 9), for instance, the tectonic background of orogen, the ore-bearing rocks of semideep sea or deep sea sediments, the ore-type of quartz

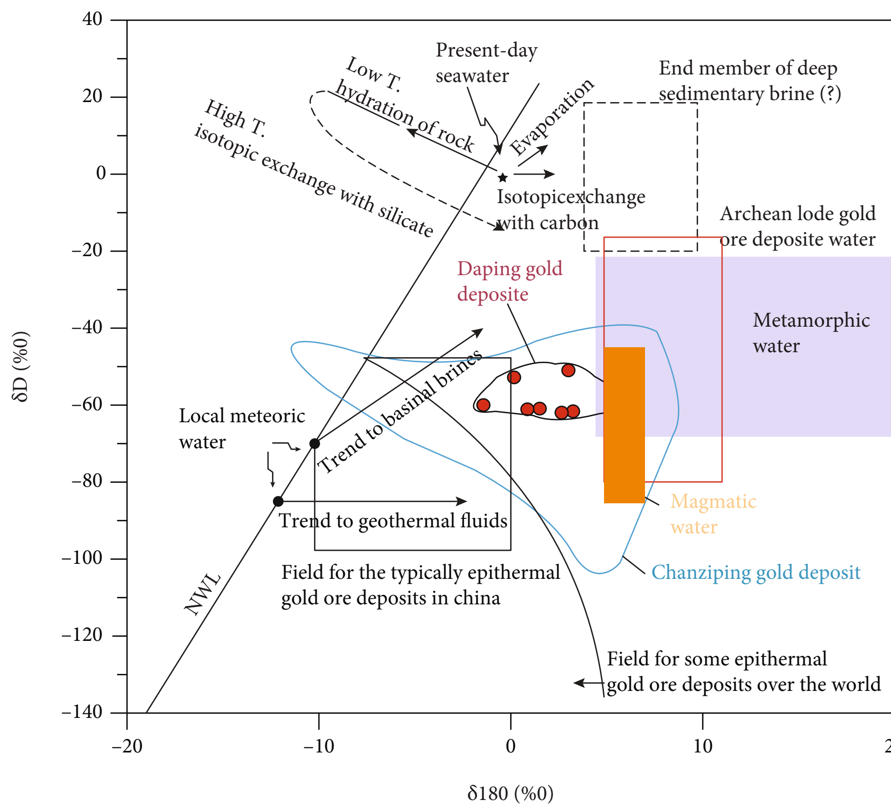

FIGURE 11: Plot of δD_{H_2O} versus $\delta^{18}O_{H_2O}$ of the metallogenic fluids in Daping gold deposit (modified after [1]). Primary magmatic and metamorphic water boxes and meteoric water line are from [64].

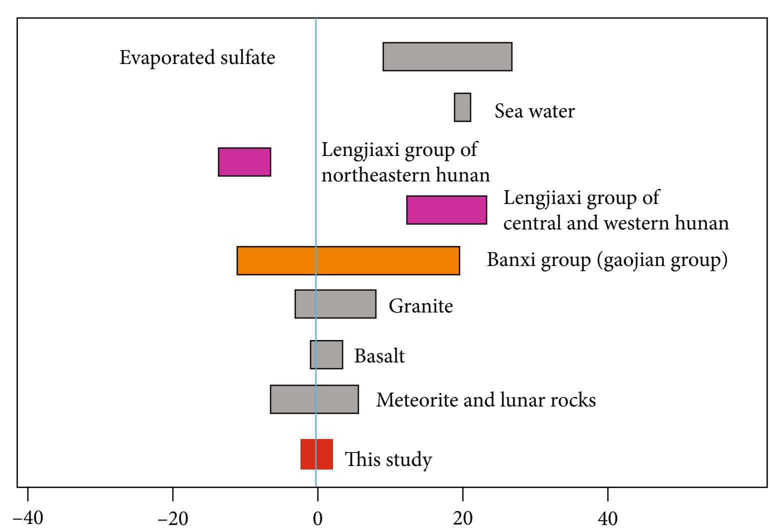

FIGURE 12: Sulfur isotope composition of ores in Daping gold deposit (modified after [46, 65–67]). Data of the Lengjiaxi Group and Banxi Group (Gaojian Group) are from Luo [68] and Liu et al. [69].

Table 9: The comparison of geological features between the Daping gold deposit and typical orogenic gold deposits.

Geological features	Typical orogenic gold deposits (Groves et al. [45]; Wang et al. [46]; Qiu et al. [60]; Xu et al. [1]; Lu et al. [61])	Daping gold deposit
Tectonic background	Tectonic compression environment of the orogenic belt	The Daping gold deposit is located in the transitional region of Xuefengshan orogenic belt between the Cathaysia plate and the Yangtze plate
Ore-bearing rocks	Most of the Archaean gold deposits occur in greenstone belts, and the ore-hosting rocks are mainly tholeiitic volcanic rocks. Phanerozoic gold deposits are mainly hosted in semideep sea or deep sea turbidite. The host rocks generally underwent shallow-medium metamorphism of greenschist facies and amphibolite facies	The wall rocks of the Daping gold ores are deep sea and semideep sea tuffaceous flysch formations of the Qingbaikou System with lithology assemblages mainly including slate, sandy slate, and sericite slate
Ore-controlling structure	The first-level fault is a large tectonic belt which cuts through the crust with a length of more than 100 km; the second-level fault has length of 1–10 km, and gold ore bodies are often located in the secondary level tectonic zones. The gold mineralization often occurred in the shear fracture and tension fracture	The Daping gold deposit is located in ca. 10 km southeast of the first-level deep fault of Anhua-Liping (about 350 km long). And second-level tectonics of the NE-trending ductile-brittle shear deformation zone of F8 (about 20 km long) cross through the Daping gold deposit from the middle. The mineralization structures are shear fracture of NW trend and tension fracture of the NE trend
Ore-type	The gold mainly occurred in the quartz veins with 3–5% metal sulfides	The gold mineralization mainly occurred in quartz veins and nearby metal sulfides, alteration rocks, and tectonic breccia rocks
Alteration type	K-feldspathization, silicification, sericitization, carbonization, and sulfidation	Silicification, sericitization, chloritization, carbonization, clayization, and sulfidation
Ore-forming fluids	Mantle-derived fluid, magmatic fluid, metamorphic fluid, and atmospheric water. The ore-forming fluids are characterized by CO_2-H_2O-NaCl±CH_4 and rich in CO_2	Magmatic fluid and atmospheric water. The ore-forming fluids are characterized by CO_2-H_2O-NaCl
Metallogenic temperature of the ore-forming fluids	150°C–700°C	157.3°C–255.8°C
Salinity of the ore-forming fluids	3–10 wt.% NaCl eqv.	4.57–10.93% (NaCl eqv.)
Assemblage of the metal elements	Au, Ag, ±As, Sb, Te, W, Bi	Au, As, ±Sb, ±Cu, ±Pb
Metallogenetic era	From the Neoarchaean to the Cenozoic era	The gold mineralization occurred in Indosinian era

vein with metal sulfides, the alteration of silicification and carbonization, and the ore-forming fluids of CO_2-H_2O-NaCl. In summary, the Daping gold deposit may belong to an orogenic type.

7. Conclusions

(1) The Daping gold ores have features of high content values of SiO_2, S, and As and low content values of Al_2O_3 and Na_2O and have intense alteration of silicification and sericitization. The gold ores are enriched in Li, Cr, Ni, Zn, Rb, Th, and Sr and depleted in Sc, Co, Cu, Ga, Cs, Tl, and Zr. The chondrite REE distribution patterns of the gold ores display strong enrichment of LREE with δEu values ranging from 0.54 to 0.75

(2) Four ore-forming stages were identified: the first stage has mineral assemblages of quartz+pyrite+arsenopyrite±carbonate minerals, the second stage has mineral assemblages of quartz+polymetallic sulfide minerals (pyrite, arsenopyrite, chalcocite, galena, chalcopyrite, tetrahedrite)±chlorite±carbonate minerals, the third stage has mineral assemblages of quartz and carbonate minerals, and the supergene stage is characterized by limonite±patina which were formed by the oxidation of metal sulfides. Among them, the first stage and the second stage are the main gold mineralization stages

(3) The ore-forming fluid inclusions from quartz are composed of liquid phase (H_2O) and gas phase (H_2O and CO_2). The main gold mineralization stages of the first stage and second stage yielded average homogenization temperature of 184.5 and 255.8°C and average salinity of 7.64 wt.% NaCl eqv. and 11.35 wt.% NaCl eqv., respectively. Thus, the ore-forming fluids may belong to H_2O-CO_2-NaCl, medium-low temperature, and medium-low salinity fluids

(4) The values of $\delta^{34}S$ of metal sulfides in Daping gold deposit range from -0.94‰ to 1.98‰ (-0.131‰ in average), the δD_{H_2O} and $\delta^{18}O_{H_2O}$ values of auriferous quartz are from -51‰ to 62‰ and from -1.44‰ to 5.42‰, respectively, indicating that the sulfur may source from the concealed granite and/or Gaojian Group, and the ore-forming fluids may belong to mixing fluids of the magmatic fluid and meteoric hydrothermal fluid

(5) The Daping gold deposit formed in Indosinian period under the tectonic environment of compression between the Cathaysian plate and Yangtze plate and has similar features of the ore-bearing rocks, ore-controlling structures, alteration, and mineralization styles with typical orogenic gold deposits

Data Availability

The data used to support the findings of this study are included within the article.

Conflicts of Interest

The authors declare that they have no conflicts of commercial or associative interest with the submitted paper.

Authors' Contributions

Wentian Mi and Xu Kong equally contributed to the work; they are joint first authors.

Acknowledgments

This research was financially supported by the Open Research Fund Program of Key Laboratory of Metallogenic Prediction of Nonferrous Metals and Geological Environment Monitoring (Central South University), Ministry of Education (Grant no. 2017YSJS06), Open Research Fund Program of Geomathematics Key Laboratory (Chengdu University of Technology) of Sichuan Province (Grant no. scsxdz201602), Science & Technology Research Project of Department of Natural Resources of Hunan Province (Grant nos. 2017-02 and 2019-03), Natural Science Foundation of Inner Mongolia (Grant nos. 2019LH04002, 2020MS04009, and 2021MS04010), Key Laboratory of Geoscience Spatial Information Technology of Land and Resources of Chengdu University of Technology (Grant no. KLGSIT2016-02), and Scientific study project for institutes of higher learning of Ministry of Education of Inner Mongolia (Grant no. NJZZ19067). Special thanks are due to Dr. Wang Cheng for his valuable help in improving the quality of this paper and to my dearly beloved Xiang Li for her lasting vigorous support.

References

[1] D. R. Xu, T. Deng, G. X. Chi et al., "Gold mineralization in the Jiangnan Orogenic Belt of South China: geological, geochemical and geochronological characteristics, ore deposit-type and geodynamic setting," *Ore Geology Reviews*, vol. 88, pp. 565–618, 2017.

[2] D. Y. Bai, B. Li, C. Zhou et al., "Gold mineralization events of the Jiangnan Orogen in Hunan and their tectonic settings," *Acta Petrologica et Mineralogica*, 2021.

[3] J. L. Cao, "Genesis and occurrence characteristics of Au-bearing shear zone gold ore vein along with Xuefengshan Mountain range," *Hunan Geology*, vol. 20, no. 3, pp. 189–192, 2001.

[4] J. Z. Huang, J. Sun, C. Zhou et al., "Metallogenic regularity and resource potential of gold deposits of Hunan area in the Jiangnan Orogenic Belt, South China," *Acta Geoscientica Sinica*, vol. 41, no. 2, pp. 230–252, 2020.

[5] S. Y. Liu, Z. A. Bao, and J. M. Bao, "Gold deposit features and metallogenic regularity of Precambrian in Hunan province, China," *Geology and Mineral Resources of South China*, vol. 29, no. 1, pp. 37–45, 2013.

[6] X. G. Meng, Z. Y. Chen, Z. G. Shao, and X. Y. Feng, "Ore-controlling structures and genesis in the Tongxi gold field in the central segment of the Xuefeng Mountains," *Regional Geology of China*, vol. 20, no. 4, pp. 404–410, 2001.

[7] J. G. Zhao, L. Shu, H. H. Fu, and W. G. Song, "Study on technique of producing potassium aurocyanide," *Gold*, vol. 24, no. 5, pp. 8–12, 2003.

[8] D. G. Zhu, X. G. Meng, J. P. Wang, X. J. Tian, X. X. Liu, and J. G. Zhao, "Tectonic features of the major fractural zones and their control of minerogenesis in the gold area of the mid-Xuefengshan mountain, Hunan province," *Journal of Geomechanics*, vol. 4, no. 1, pp. 65–73, 1998.

[9] L. Cao, Q. F. Duan, S. G. Peng, and Y. Zhou, "Characteristics and geological significance of stable isotopes in the Chanziping gold deposit of Xuefeng Mountains," *Geology and Mineral Resources of South China*, vol. 31, no. 2, pp. 167–175, 2015.

[10] Y. J. Cao, J. Li, F. Chen, C. J. Wang, and B. D. Liu, "On geological characteristics and ore prospecting indicators of Chanziping gold deposit in Hunan," *Journal of Geology*, vol. 38, no. 2, pp. 309–313, 2014.

[11] X. Q. Luo, "Mineralization and prospecting guide of Chanziping gold deposit in Hunan," *Hunan Geology*, vol. 15, no. 1, pp. 33–38, 1996.

[12] S. J. LYU, S. S. Liu, Y. D. Li, and X. Kong, "Geological characteristics and genesis of Chanziping gold deposit in Xuefengshan area, Hunan Province," *Geology and Mineral Resources of South China*, vol. 35, no. 3, pp. 325–336, 2019.

[13] J. G. Zhao and Q. C. Chen, "Integrated prospecting model of ore characteristics, geophysics and geochemistry in the Chanziping gold deposit," *Land & Resources*, vol. 3, no. 3, pp. 80–83, 2006.

[14] Q. S. Zhou, *Detailed Report of the Daping Gold Deposit in Hongjiang City, Hunan Province*, No. 407 Geological Party of the Hunan Bureau of Geology and Mineral Exploration and Development, 2015.

[15] W. G. Tang, *General Report of the Daping Gold Deposit in Hongjiang City, Hunan Province*, No. 407 Geological Party of the Hunan Bureau of Geology and Mineral Exploration and Development, 1987.

[16] G. G. Fu, D. R. Xu, and K. M. Su, "Regularity of mineralization and ore-prospecting criteria of the Daping gold deposit, Hunan Province," *Journal of Earth Sciences and Environment*, vol. 32, no. S1, pp. 7-8, 2010.

[17] J. G. Zhao, "Geological characteristics of Au-deposit and its prospecting foreground at Daping gold mine, Hongjiang," *Hunan Geology*, vol. 20, no. 3, pp. 171–176, 2001.

[18] H. Q. Li, D. H. Wang, F. W. Chen, Y. P. Mei, and H. Cai, "Study on chronology of the Chanziping and Daping gold deposit in Xuefeng Mountains, Hunan Province," *Acta Geologica Sinica*, vol. 82, no. 7, pp. 900–905, 2008.

[19] C. Yang, *Analysis on ore-controlling structure and research on prospecting direction of gold-antimony in Xuefeng arc structure belt, [M.S. thesis]*, Hunan University of Science and Technology, 2012.

[20] X. G. Meng, D. G. Zhu, and X. X. Luo, *Analysis of ore-controlling structures and the evaluation of Au & Sb resources in the middle Xuefeng Mountain area*, Geological Publishing House, Beijing, 1999.

[21] K. M. Su, Z. Z. Xie, and W. G. Song, "Ore-controlling structures of gold deposits in the Xuefeng Mountain area," *Express Information of Mining Industry*, vol. 2006, no. 5, pp. 50–52, 2006.

[22] R. N. Clayton, J. R. O'Neil, and T. K. Mayeda, "Oxygen isotope exchange between quartz and water," *Journal of Geophysical Research*, vol. 77, no. 17, pp. 3057–3067, 1972.

[23] D. L. Hall, S. M. Sterner, and R. J. Bodnar, "Freezing point depression of NaCl-KCl-H_2O solutions," *Economic Geology*, vol. 83, no. 1, pp. 197–202, 1988.

[24] L. Y. Zhang, S. Y. Chen, and S. L. Liao, "Element and metallogenic significance of Jiufangliang gold deposit in Mianluening region, Shanxi Province," *Geological Science and Technology Information*, vol. 36, no. 2, pp. 151–159, 2017.

[25] C. Z. Xi, T. Yang, H. D. Xia, H. J. Deng, and S. G. Wu, "Characteristics of trace elements and REE in Huangjindong gold deposit in northeastern Hunan and their geological significance," *Gold*, vol. 39, no. 2, pp. 17–21, 2018.

[26] H. Ohmoto, "Systematics of sulfur and carbon isotopes in hydrothermal ore deposits," *Economic Geology*, vol. 67, no. 5, pp. 551–578, 1972.

[27] H. Ohmoto and R. O. Rye, "Isotopes of sulfur and carbon," in *Geochemistry of Hydrothermal Ore Deposits*, H. L. Barnes, Ed., pp. 509–567, Wiley, New York, 1979.

[28] L. Cao, Q. F. Duan, S. G. Peng, and Y. Zhou, "Characteristics of fluid inclusions in the Chanziping gold deposit in Xuefeng Mountain and their geological implications," *Geology and Exploration*, vol. 51, no. 2, pp. 213–224, 2015.

[29] Y. W. Han, Z. D. Ma, and H. F. Zhang, *Geochemistry*, vol. 2003, Geological Publishing House, Beijing, 2003.

[30] X. Kong, W. T. Mi, X. Mo, M. T. Xie, G. L. Jiang, and C. L. Fu, "Metallogenic prediction of gold deposits with weighting of evidence based on MRAS in Huaihua area, Hunan Province," *Geophysical and Geochemical Exploration*, vol. 40, no. 3, pp. 467–474, 2016.

[31] X. Kong, W. T. Mi, J. Xin, H. T. Chi, J. Hu, and Z. Y. Yang, "The gold metallogenic prognosis based on the weighting method of evidence in the middle Xuefeng Mountain area," *Computing Techniques for Geophysical and Geochemical Exploration*, vol. 41, no. 6, pp. 832–842, 2019.

[32] H. C. Niu, *Geochemical study on the minerogenetic background and mineralization of gold deposits in the Yiyang-Yuanling region of Hunan province, [Ph.D. thesis]*, Nanjing University, 1991.

[33] S. R. Taylor and S. M. McLennan, "The geochemical evolution of the continental crust," *Reviews of Geophysics*, vol. 33, no. 2, pp. 241–265, 1995.

[34] Q. K. Yang, X. L. Zhang, C. Hua, and P. Y. Xuan, "Geochemical characteristics of trace element of the molybdenite in the Dawangshan tungsten molybdenum polymetallic ore concentration area, Central Jiangxi Province," *Journal of Mineralogy and Petrology*, vol. 38, no. 2, pp. 59–69, 2018.

[35] J. H. Tao, T. Cen, W. G. Long, and W. X. Li, "Mineral chemistry of biotites from the Indosinian weakly peraluminous and strongly peraluminous granites in South China and their constraints on petrogenesis," *Earth Science Frontiers*, vol. 22, no. 2, pp. 64–78, 2015.

[36] D. Y. Bai, N. J. Wu, X. Zhong, P. Y. Jia, X. Xiong, and W. Y. Huang, "Geochronology, petrogenesis and tectonic setting of Indosinian Wawutang granites, southwestern Hunan province," *Geotectonica et Metallogenia*, vol. 40, no. 5, pp. 1075–1091, 2016.

[37] J. H. Li, Y. Q. Zhang, X. B. Xu, H. L. Li, S. W. Dong, and Y. D. Li, "SHRIMP U-Pb dating of zircons from the Baimashan-Longtan super-unit and Wawutang granites in Hunan province and its geological implication," *Journal of Jilin University: Earth Science Edition*, vol. 44, no. 1, pp. 158–175, 2014.

[38] H. Li, *Report of mineral geological survey in Longtan area, Hunan Province*, Internal information of Hunan Institute of Geology Survey, 2017.

[39] N. Y. Hu, Z. Y. Quan, L. Pan, and P. R. Wang, "Deformational characteristics of Xuefeng ARC structural belt and its relationship with Au-deposits," *Geotectonica et Metallogenia*, vol. 22, no. S1, pp. 33–37, 1998.

[40] D. K. Weatherley and R. W. Henley, "Flash vaporization during earthquakes evidenced by gold deposits," *Nature Geoscience*, vol. 6, no. 4, pp. 294–298, 2013.

[41] R. J. Goldfarb, D. I. Groves, and S. Gardoll, "Orogenic gold and geologic time: a global synthesis," *Ore Geology Review*, vol. 18, no. 1, pp. 1–75, 2011.

[42] F. Robert, R. Brommecker, B. T. Boume, P. J. Dobak, and X. Zhou, "Models and exploration methods for Major gold deposit types," *Ore Deposits and Exploration Technology*, pp. 691–711, 2007.

[43] J. W. Mao, G. Q. Xie, Z. H. Zhang et al., "Mesozoic large-scale metallogenic pluses in North China and corresponding geodynamic settings," *Acta Petrologica Sinica*, vol. 21, no. 1, pp. 169–188, 2005.

[44] M. Bonnemaison and E. Marcoux, "Auriferous mineralization in some shear zones: a three stage model of metallogenesis," *Mineralium Deposita*, vol. 25, no. 2, pp. 96–104, 1990.

[45] D. I. Groves, R. J. Goldfarb, M. Gebre-Mariam, S. G. Hagemann, and F. Robert, "Orogenic gold deposits: a proposed classification in the context of their crustal distribution and relationship to other gold deposit types," *Ore Geology Reviews*, vol. 13, no. 1-5, pp. 7–27, 1998.

[46] C. Wang, Y. J. Shao, N. J. Evans et al., "Genesis of Zixi gold deposit in Xuefengshan, Jiangnan Orogen (South China): age, geology and isotopic constraints," *Ore Geology Reviews*, vol. 117, article 103301, 2020.

[47] T. Deng, D. Xu, G. Chi et al., "Geology, geochronology, geochemistry and ore genesis of the Wangu gold deposit in northeastern Hunan Province, Jiangnan Orogen, South China," *Ore Geology Review*, vol. 88, pp. 619–637, 2017.

[48] C. Huang, G. M. Fan, G. L. Jiang, L. Luo, and Z. L. Xu, "Structural ore-controlling characteristics and electron spin resonance dating of the Yanlinsi gold deposit in northeastern Hunan Province," *Geotectonica et Metallogenia*, vol. 36, no. 1, pp. 76–84, 2012.

[49] J. W. Mao, R. Kerrich, H. Y. Li, and Y. H. Li, "High 3He/4He ratios in the Wangu gold deposit, Hunan province, China: implications for mantle fluids along the Tanlu deep fault zone," *Geochemical Journal*, vol. 36, no. 3, pp. 197–208, 2002.

[50] C. Wang, Y. J. Shao, X. Zhang et al., "Metallogenesis of the Hengjiangchong gold deposit in Jiangnan Orogen, South China," *Ore Geology Reviews*, vol. 118, article 103350, 2020.

[51] J. S. Wang, H. J. Wen, C. Li, W. Ding, and J. R. Zhang, "Re–Os isotope dating of arsenopyrite from the quartz vein-type gold deposit, southeastern Guizhou Province, and its geological implications," *Acta Geologica Sinica*, vol. 85, pp. 955–964, 2011.

[52] L. Zhang, L. Q. Yang, D. I. Groves et al., "Geological and isotopic constraints on ore genesis, Huangjindong gold deposit, Jiangnan Orogen, southern China," *Ore Geology Reviews*, vol. 99, pp. 264–281, 2018.

[53] D. Craw, S. J. Windle, and P. V. Angus, "Gold mineralization without quartz veins in a ductile–brittle shear zone, Macraes Mine, Otago Schist, New Zealand," *Mineralium Deposita*, vol. 34, no. 4, pp. 382–394, 1999.

[54] G. J. Davidson and R. R. Large, "Gold metallogeny and the copper-gold association of the Australian proterozoic," *Mineralium Deposita*, vol. 29, no. 3, pp. 208–223, 1994.

[55] B. N. Eisenlohr, D. Groves, and G. A. Partington, "Crustal-scale shear zones and their significance to Archaean gold mineralization in Western Australia," *Mineralium Deposita*, vol. 24, no. 1, pp. 1–8, 1989.

[56] J. L. Ni, J. L. Liu, X. L. Tang, C. Q. Zhao, and Q. D. Zeng, "Evolution of the ductile shear zone of the Paishanlou gold deposits, western Liaoning, China," *Science China: Earth Sciences*, vol. 57, no. 4, pp. 600–613, 2014.

[57] R. W. R. Rutland, M. A. Etheridge, and M. Solomon, "The stratigraphic and tectonic setting of the ore deposits of Australia," *Geology of the mineral deposits of Australia and Papua New Guinea*, vol. 14, pp. 15–26, 1990.

[58] Y. F. Zhu, J. Zhou, and Y. S. Zeng, "The Tianger (Bingdaban) shear zone hosted gold deposit, west Tianshan, NW China: petrographic and geochemical characteristics," *Ore Geology Reviews*, vol. 32, no. 1-2, pp. 337–365, 2007.

[59] No 407 Geol Team, *Periodic Report of Geological Prospecting Achievements of the Daping Gold Deposit in Hunan Province, China*, Hunan Bureau of Geology and Mineral Exploration and Development, 2015.

[60] Z. J. Qiu, H. R. Fan, P. Z. Cong, X. Liu, and K. F. Yang, "Recent progress in the study of ore-forming processes of orogenic gold deposits," *Mineral Deposits*, vol. 34, no. 1, pp. 21–28, 2015.

[61] H. Z. Lu, G. X. Chi, X. Q. Zhu, J. Guha, G. Archambault, and Z. G. Wang, "Geological characteristics and ore forming fluids of orogenic gold deposits," *Geotectonica et Metallogenia*, vol. 42, no. 2, pp. 244–265, 2018.

[62] S. S. Sun and W. F. McDonough, "Chemical and isotope systematics of oceanic basalts: implications for mantle composition and processes," in *Magmatism in Ocean Basins*, A. D. Saunders, Ed., vol. 42, pp. 313–345, Geological Society Publication, 1989.

[63] W. V. Boynton, "Cosmochemistry of the rare earth elements: meteorite studies," in *Rare Earth Element Geochemistry. Amsterdam*, pp. 64–114, Elsevier, 1984.

[64] H. P. Taylor, "Oxygen and hydrogen isotope relationships in hydrothermal mineral deposits," *Geochemistry of Hydrothermal Ore Deposits*, vol. 3, pp. 229–302, 1997.

[65] J. Y. Luo, *Genetic mineralogy and ore prediction of Yixingzhai gold deposit, Fanshi County, Shanxi Province*, vol. 2009, Dissertation of China University of Geosciences (Beijing) for doctoral degree, 2009.

[66] N. X. Peng, Y. J. Shao, Z. F. Liu, and C. Wang, "Metallogenic mechanism of Yixingzhai gold ore field in Fanshi county, Shanxi province: evidences from isotopes and fluid inclusion," *The Chinese Journal of Nonferrous Metals*, vol. 27, no. 2, pp. 305–317, 2017.

[67] C. Wang, Y. Shao, Z. Liu, Q. Liu, and Y. Zhang, "Geology and geochemistry of the Shizitou molybdenum deposit, Jiangxi Province: implications for geodynamic setting and metallogenesis," *Acta Geologica Sinica (English Edition)*, vol. 92, no. 4, pp. 1415–1431, 2018.

[68] X. Luo, "Discussion on the material sources of gold deposits in Precambrian strata in Hunan," *Journal of Guilin Institute of Metallogenic Geology*, vol. 10, pp. 13–25, 1990.

[69] L. Liu, S. Peng, and Y. Wu, "Genetic features forming vein type gold deposits in northeastern Hunan," *Journal of Central South University of Technology (Natural Science)*, vol. 30, pp. 4–7, 1999.

Hindawi
Geofluids
Volume 2022, Article ID 4703957, 11 pages
https://doi.org/10.1155/2022/4703957

Research Article

Study on the Synchronous Instability Mechanism of the Coal Wall and Direct Roof of High Soft Coal Seam

Baojie Fu ,[1,2] Jiawen Li,[1,2] Min Tu ,[1,2] and Ningping Jin[1,2]

[1]*School of Mining Engineering, Anhui University of Science and Technology, Road Taifeng No. 168, Huainan, Anhui 232001, China*
[2]*Key Laboratory of Coal Mine Safety and Efficiently Caving of Ministry of Education, Anhui University of Science and Technology, Huainan, Anhui 232001, China*

Correspondence should be addressed to Baojie Fu; bjfu@aust.edu.cn

Received 4 January 2022; Accepted 13 February 2022; Published 2 March 2022

Academic Editor: Zhijie Wen

The advanced mining stress on a large working face can easily lead to the failure of the roof and coal mass; coal wall spalling and roof caving occur. The degree of coal wall failure and the depth of the plastic fracture zone are closely related to the advanced mining stress. The mechanical analysis model is established, and the stress distribution in the fracture and plastic zone is analyzed by the elastic-plastic theory, and the depth function expressions of two zones are determined. Comparative analysis of the factors affecting mining strength shows that the mining depth, mining height, and strength of coal are the key factors affecting the stability of the coal wall. The A1 coal of Zhangji mine in Huainan is soft and thick, and the direct roof is easily separated by the organic membrane, which is easy to form arc-shaped sliding instability. The increase in the unsupported roof area causes the direct roof caving and reduces its bearing capacity and stiffness. It is unable to provide enough support for the broken block of the overlying key stratum, which makes the broken block reverse rotation and further aggravate the roof fall; the synchronous instability of the coal wall and direct roof is formed.

1. Introduction

A large mining height working face has large stope space, the scope of roof collapse and the movement range of fractured rock strata will be greatly increased, the filling degree of goaf is reduced, and it has an impact on the fracture law and structural characteristics of overburden. In particular, when the roof has multilayer thick and hard rock and one or both sides of the working face are empty, it will lead to abnormal pressure such as spalling and roof caving, which has been proven in the previous mining practice of 4~6 m mining height[1–4]. With the increase in mining height, the depth and frequency of coal wall spalling will undoubtedly be increased, and the leakage of the broken roof will be intensified, which will seriously limit the advancing speed of the working face and form a vicious circle.

The influence of overlying rock structure on the stability of surrounding rock in large mining height has hanged fundamentally, and the surrounding rock control mechanism will also change. Professor Wang Jiachen [5, 6] carried out mechanical analysis and experimental research on the occurrence conditions of "two hard" coal seams, established the elastic thin plate mechanical model of the first roof caving, studied the characteristics of sectional weighting of roof strata in different areas along the length direction of the working face, and analyzed the reasons of roof stratum migration and weighting. Yan et al. [7] established the "short cantilever beam+hinged rock beam" model of a rock layer fracture in a large mining height working face by means of numerical simulation and theoretical analysis. Through field observation, theoretical analysis, and numerical simulation analysis of the large mining height working face, Yan et al. [8, 9] studied the law of mine pressure behavior, the influence range of advanced abutment pressure, and the position of the peak point in the fully mechanized mining face and considered that the basic roof weighting of the fully mechanized mining face with large mining height is more severe than that of the ordinary fully mechanized mining face, and the coal wall spalling and roof caving are more serious, and the hydraulic pressure is more serious; there is a common phenomenon of dynamic load impact on the support. Based on the D-P-Y criterion and limit equilibrium theory of plasticity mechanics, Bo et al. [10, 11] analyzed the width of the plastic failure zone and stress distribution of the coal wall, obtained the calculation method of the width of the plastic failure zone of the coal wall and abutment pressure in front of the working face, and analyzed the failure process and control measures of the roof and wall of "three soft coal seams". Fang et al. [12] established the mechanical model of surrounding rock hydraulic support structure, analyzed the whole process of coal wall deformation-rupture-failure-instability, analyzed the arc sliding instability process of the upper part of the coal wall by the stability coefficient method, and calculated the critical height of coal wall stability. There are mainly four methods [13, 18] to control the stability of the coal wall and roof of the large mining height working face. Change the stress environment of the working face, and appropriately improve the support resistance. Through the coal wall and roof grouting, use an anchor rod (such as bamboo anchor rod) and other means to improve the coal and rock rest cohesive force. A step coal wall mining method reduces the time of coal wall stability maintenance and reduces the mining height. Improve mining technology to speed up the advance, reduce the length of the working face, use the bow mining, improve the speed of the shearer, and reduce the cutting depth and other measures. Based on the elastic-plastic theory, this paper analyzes the stress distribution law of coal and rock mass and the depth of the plastic failure zone under the action of advanced mining stress and defines the main control factors affecting the failure of the coal wall with large mining height. Combined with the occurrence conditions of specific coal seam, the synchronous instability mechanism of the coal wall and roof in the large mining height working face of soft coal is expounded, and the main control measures are proposed.

2. Advanced Mining Stress Distribution Law of the Large Mining Height Working Face

With the mining of the working face, the goaf will be formed; the stress load of the overlying strata gradually transfers to the coal and rock mass around the working face. According to the stress redistribution characteristics, the stress completely acts on the coal and rock mass in front of and on the side of the working face, thus forming a large range of stress concentration in these areas. In general, the stress concentration factor is $k = 2 \sim 4$. Under the influence of the advance pressure, mining stress increasing and reducing area is formed in the coal body and its roof and floor, and they move forward continuously with the mining. According to the total stress-strain curve of coal and rock, its deformation can be divided into three stages: elastic stage, plastic stage, and failure residual stage. When the abutment pressure does not exceed the ultimate bearing capacity of coal, the coal body is in AN elastic state; when the coal mass reaches the yield condition but fails to meet the fracture requirements, the coal mass is in the plastic stage; when the deformation of the coal body reaches the fracture condition, the coal mass is in the fracture state. The fracture zone, plastic zone, elastic zone, and original rock stress zone can be produced in coal mass, as shown in Figure 1.

3. Mechanics Analysis of the Coal Wall of the Large Mining Height Working Face

3.1. Mechanics Analysis of the Coal Wall of Stability. The failure degree of the coal wall and the width of the plastic fracture zone are closely related to the magnitude of mining advance stress. As shown in Figure 2, the mechanical analysis model of the coal wall is established, x_b is the boundary between the broken zone and the plastic zone, and x_p is the boundary between the plastic zone and the elastic zone.

As shown in Figure 2(b), considering the vertical stress σ_y, horizontal resistance P_i, horizontal stress σ_x, and shear stress τ caused by upper and lower boundary dislocation, the microelement equilibrium equation is established:

$$-m(\sigma_x + d\sigma_x) + m\sigma_x + 2\tau dx = 0, \tag{1}$$

where m is the coal thickness.

Shear stress τ caused by upper and lower boundary dislocation is

$$\tau = f d\sigma_y, \tag{2}$$

where f is the friction resistance coefficient of upper and lower boundary dislocation.

Equation (3) can be obtained through [8] and [10]:

$$d\sigma_x = \frac{2f}{m}\sigma_y dx, \tag{3}$$

namely, $\beta = 2f/m$. The above formula is as follows:

$$d\sigma_x = \beta\sigma_y dx. \tag{4}$$

In the broken area ($0 \le x \le x_b$), the medium of coal and rock mass meets the following requirements:

$$\sigma_y^b = K_p\sigma_x^b + \sigma_c^*, \tag{5}$$

where C^* is the medium cohesion in the broken zone and φ is the internal friction angle, namely, $K_p = (1 + \sin\varphi)/(1 - \sin\varphi)$ and $\sigma_c^* = 2C^* \cos\varphi/(1 - \sin\varphi)$.

Equation (5) is substituted into equation (3) to obtain

$$d\sigma_x^b = \beta K_p\sigma_x^b + \beta\sigma_c^*. \tag{6}$$

The general explanation is

$$\sigma_x^b = -\frac{\sigma_c^*}{K_p} + C_1 e^{\beta K_p x}. \tag{7}$$

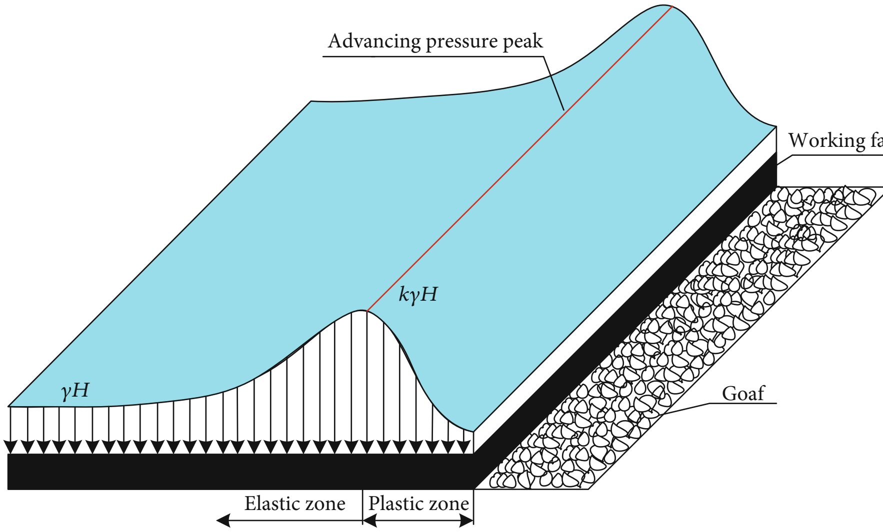

FIGURE 1: Stress distribution of stope.

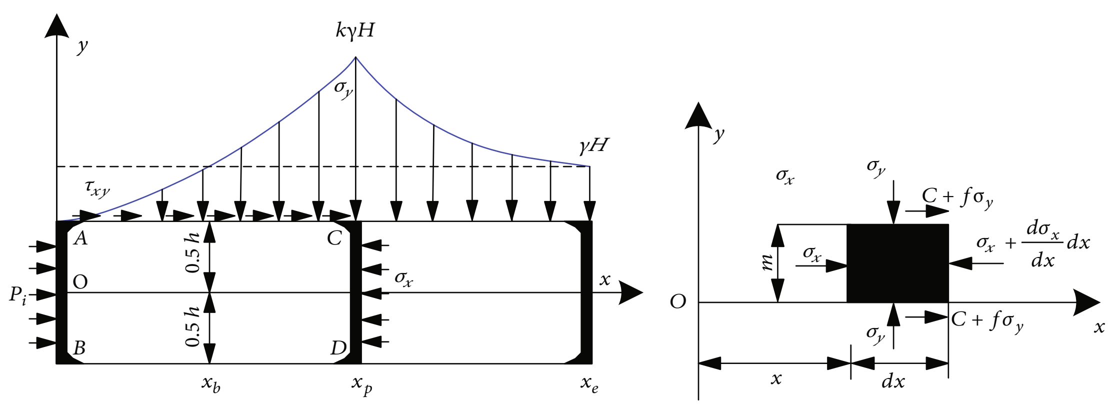

(a) The stress distribution

(b) Mechanical model

FIGURE 2: Stress analysis model of coal mass.

When $x = 0$, $\sigma_x^b|_{x=0} = P_i$, and substitute it into equation (7) to obtain

$$C_1 = P_i + \frac{\sigma_c^*}{K_p}. \tag{8}$$

The stress of coal mass at the edge of the fracture area is

$$\begin{cases} \sigma_x^b = -\dfrac{\sigma_c^*}{K_p} + \left(P_i + \dfrac{\sigma_c^*}{K_p}\right) e^{\beta K_p x}, \\ \sigma_y^b = \dfrac{d\sigma_x}{\beta dx} = K_p \left(P_i + \dfrac{\sigma_c^*}{K_p}\right) e^{\beta K_p x}, \end{cases} \quad (0 \le x \le x_b). \tag{9}$$

In the plastic zone ($x_b \le x \le x_p$), the medium of coal mass meets the following requirements:

$$\sigma_y^p = K_p \sigma_x^p + \sigma_c - M_0 \varepsilon_p, \tag{10}$$

where M_0 is the softening modulus of coal and S_z is the strain gradient of coal in the plastic zone, namely, $S_z = \tan(\alpha)$ and $\varepsilon_p = (S_z/m)(x_p - x)$. α is the sum of deformation angles of the coal roof and floor in the plastic zone.

The above formula is

$$\sigma_y^p = K_p \sigma_x^p + \sigma_c - \frac{M_0 S_z}{m}(x_p - x). \tag{11}$$

Equation (11) is substituted into equation (4) to obtain

$$d\sigma_x^p = \beta K_p \sigma_x^p + \beta \left[\sigma_c - \frac{M_0 S_z}{m}(x_p - x)\right]. \tag{12}$$

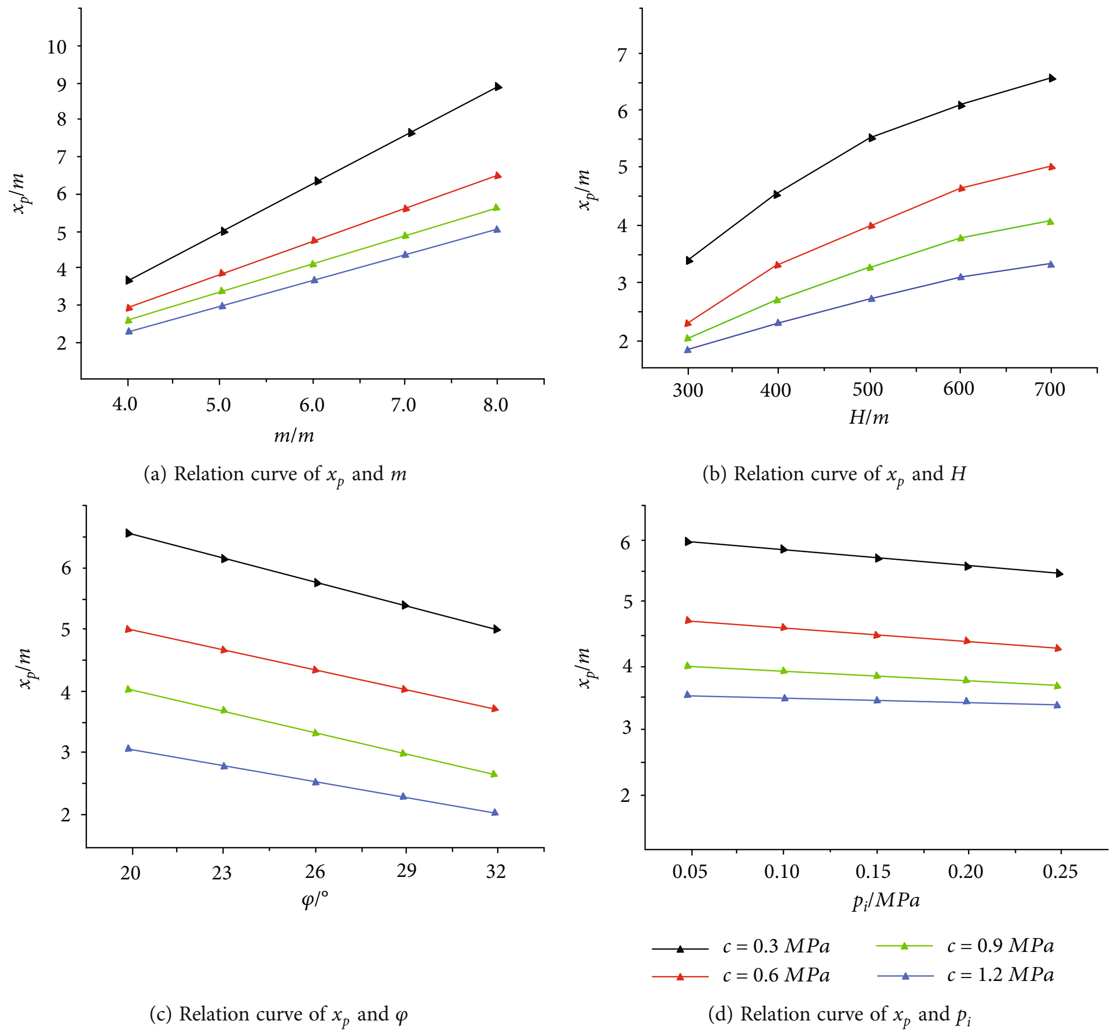

Figure 3: Analysis of influencing factors of x_p.

Therefore, the stress state of coal in the plastic zone can be expressed as

$$\begin{cases} \sigma_x^p = \left(\dfrac{(M_0S_z/m)(x_p - x)}{K_p}\right) - \\ \dfrac{\beta(M_0S_z/m) + \beta^2 K_p \sigma_c}{(\beta K_p)^2} + C_2 e^{\beta K_p x} \quad (x_b \le x \le x_p), \\ \sigma_y^p = -\dfrac{M_0 S_z}{m\beta K_p} + C_2 K_p e^{\beta K_p x}. \end{cases} \tag{13}$$

At the boundary of the plastic and elastic zone ($x = x_p$), the destruction of coal is subject to

$$\sigma_y^p\Big|_{x=x_p} = K_p \sigma_x^p + \sigma_c, \tag{14}$$

where σ_c is the residual strength of coal, namely, $\sigma_c = 2C \cos\varphi/(1 - \sin\varphi)$, and C is the cohesion.

When $x = x_p$, $\sigma_y^p|_{x=x_p} = K\gamma H$, where K is the stress concentration factor and γH is the original rock stress.

Equation (14) is written as

$$C_2 = \frac{(M_0S_z/m\beta K_p) + K\gamma H}{K_p} e^{-\beta K_p x_p}. \tag{15}$$

The stress state of coal in the plastic region can be expressed as

$$\begin{cases} \sigma_x^p = \left(\dfrac{(M_0S_z/m)(x_p - x)}{K_p}\right) - \left(\dfrac{\beta(M_0S_z/m) + \beta^2 K_p \sigma_c}{(\beta K_p)^2}\right) + \\ \left(\dfrac{\beta(M_0S_z/m) + \beta^2 K_p K\gamma H}{(\beta K_p)^2}\right) e^{\beta K_p (x - x_p)} \quad (x_b \le x \le x_p), \\ \sigma_y^p = -\dfrac{M_0 S_z}{m\beta K_p} + \left(\dfrac{(M_0S_z/m) + K_p \beta K\gamma H}{\beta K_p}\right) e^{\beta K_p (x - x_p)}. \end{cases} \tag{16}$$

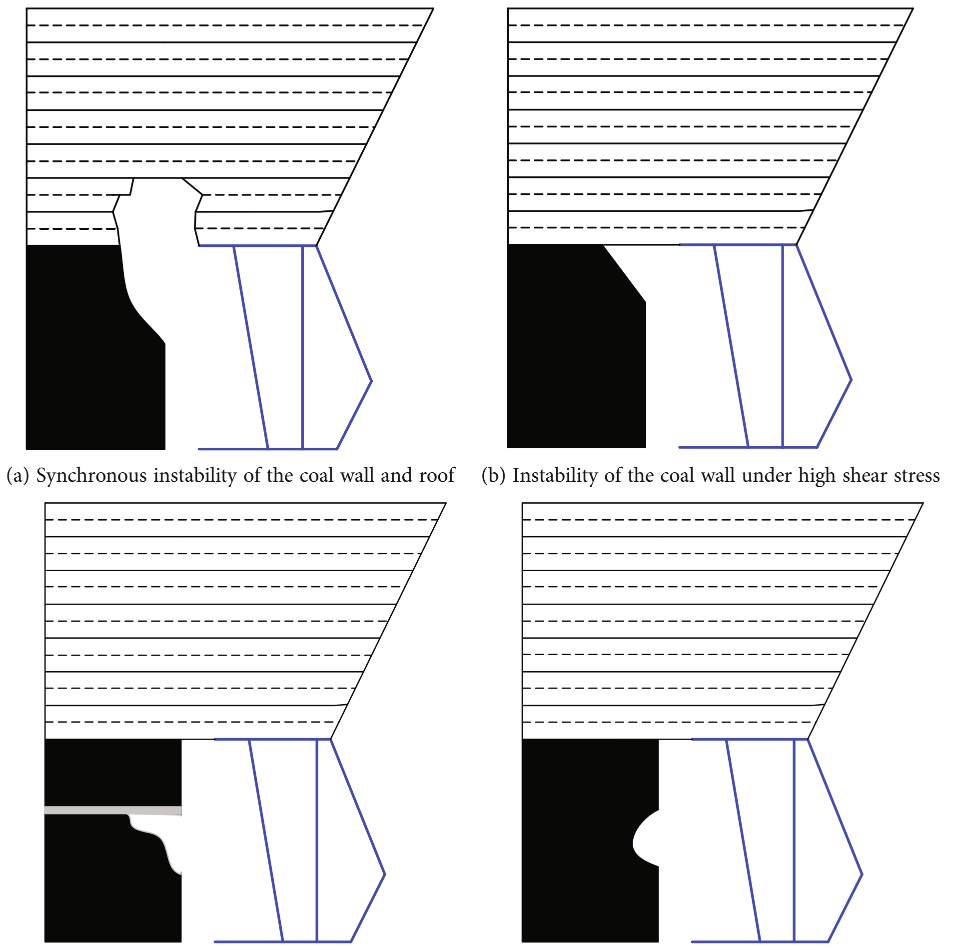

(a) Synchronous instability of the coal wall and roof (b) Instability of the coal wall under high shear stress

(c) Instability of the coal wall affected by gangue (d) Instability of the coal wall caused by tensile cracking

Figure 4: Coal wall spalling type.

When $x = x_b$,

$$\sigma_y^b\Big|_{x=x_b} = K_p \sigma_x^b\Big|_{x=x_b} + \sigma_c - \frac{M_0 S_z}{m}\left(x_p - x_b\right), \tag{17}$$

so

$$K_p\left(P_i + \frac{\sigma_c^*}{K_p}\right)e^{\beta K_p x_b} = K_p\left[-\frac{\sigma_c^*}{K_p} + \left(P_i + \frac{\sigma_c^*}{K_p}\right)e^{\beta K_p x_b}\right] + \sigma_c - \frac{M_0 S_z}{m}\left(x_p - x_b\right). \tag{18}$$

The solution of equation (18) is

$$x_p - x_b = \frac{m\left(\sigma_c - \sigma_c^*\right)}{M_0 S_z}. \tag{19}$$

When $x = x_b$, $\sigma_x^b\big|_{x=x_b} = \sigma_x^p\big|_{x=x_b}$.

$$\begin{aligned} -\frac{\sigma_c^*}{K_p} + \left(P_i + \frac{\sigma_c^*}{K_p}\right)e^{\beta K_p x_b} = {} & \left(\frac{\left(M_0 S_z/m\right)\left(x_p - x_b\right)}{K_p}\right) \\ & - \left(\frac{\beta\left(M_0 S_z/m\right) + \beta^2 K_p \sigma_c}{\left(\beta K_p\right)^2}\right) \\ & + \left(\frac{\beta\left(M_0 S_z/m\right) + \beta^2 K_p K \gamma H}{\left(\beta K_p\right)^2}\right)e^{\beta K_p\left(x_b - x_p\right)}. \end{aligned} \tag{20}$$

Equation (20) is substituted into equation (19) to obtain

$$\begin{aligned} -\frac{\sigma_c^*}{K_p} + \left(P_i + \frac{\sigma_c^*}{K_p}\right)e^{\beta K_p x_b} = {} & \frac{\left(\sigma_c - \sigma_c^*\right)}{K_p} \\ & - \left(\frac{\beta\left(M_0 S_z/m\right) + \beta^2 K_p \sigma_c}{\left(\beta K_p\right)^2}\right) \\ & + \left(\frac{\beta\left(M_0 S_z/m\right) + \beta^2 K_p K \gamma H}{\left(\beta K_p\right)^2}\right)e^{-\frac{m\beta K_p\left(\sigma_c - \sigma_c^*\right)}{M_0 S_z}}. \end{aligned} \tag{21}$$

The depth of the coal broken and plastic zone is expressed as

$$\begin{cases} x_b = \dfrac{1}{\beta K_p} \ln \left[-\left(\dfrac{\beta M_0 S_z}{m(\beta K_p)^2 (P_i + (\sigma_c^*/K_p))} \right) + \left(\dfrac{\beta(M_0 S_z/m) + \beta^2 K_p K \gamma H}{(\beta K_p)^2 (P_i + (\sigma_c^*/K_p))} \right) e^{-\frac{m\beta K_p(\sigma_c - \sigma_c^*)}{M_0 S_z}} \right], \\ x_p = \dfrac{m(\sigma_c - \sigma_c^*)}{M_0 S_z} + \dfrac{1}{\beta K_p} \ln \left[-\left(\dfrac{\beta M_0 S_z}{m(\beta K_p)^2 (P_i + (\sigma_c^*/K_p))} \right) + \left(\dfrac{\beta(M_0 S_z/m) + \beta^2 K_p K \gamma H}{(\beta K_p)^2 (P_i + (\sigma_c^*/K_p))} \right) e^{-\frac{m\beta K_p(\sigma_c - \sigma_c^*)}{M_0 S_z}} \right]. \end{cases} \tag{22}$$

3.2. Case Analysis. The coal mass of group A of Zhangji mine has low strength, the thick roof layer is directly covered with fine sandstone, horizontal bedding is developed, the layer is sandwiched with argillaceous bands, argillaceous inclusions, and organic membrane, and the relevant parameters are taken as follows: $f_b = 0.5$, $n_b = 0.6$ MPa, $f_p = 0.25$, $n_p = 0.24$ MPa, $C^* = 0.2$ MPa, $\varphi = 22.4°$, $M_0 = 0.1$ GPa, $\alpha = 12°$, and $K = 2.3$.

(1) When $H = 500$ m, $P_i = 0.1$ MPa, and $\varphi = 24°$, as shown in Figure 3(a), with the same cohesion, the greater the mining height is, the greater the plastic zone depth is, and the plastic zone depth is basically linearly positively correlated with the mining height

(2) When $m = 8$ m, $P_i = 0.1$ MPa, and $\varphi = 24°$, as shown in Figure 3(b), with the same cohesion, the greater the mining depth is, the greater the plastic zone depth is, and the relationship between the plastic zone depth and the mining depth is approximately hyperbolic, while at the same mining depth, the greater the coal cohesion, the smaller the plastic zone width

(3) When $H = 500$ m, $P_i = 0.1$ MPa, and $m = 8$ m, as shown in Figure 3(c), with the same cohesion, the greater the internal friction angle, the smaller the plastic zone depth, but the plastic zone depth decreases slightly with the increase in the friction angle; at the same internal friction angle, the plastic zone depth decreases with the increase in cohesion, and the reduction amplitude is obvious

(4) When $H = 500$ m, $m = 8$ m, and $\varphi = 24°$, as shown in Figure 3(d), with the same cohesive force, the greater the applied force is, the smaller the depth of plastic zone is. The depth of the plastic zone decreases with the increase in the applied force

The depth of the plastic zone in the coal wall determines the damage degree. The analysis shows that mining depth, mining height, and coal strength have significant influence on the development range of plastic zone. In order to control the instability of surrounding rock in stope, measures such as reducing mining height, grouting reinforcement, and increasing support resistance are adopted in practice.

4. Synchronous Instability Mechanism of the Direct Roof and Coal Wall

4.1. Failure Mode of the Coal Wall. Practice shows that the trace of coal wall spalling is closely related to coal hardness, gangue property, and support strength. If the coal mass is homogeneous, the joints and fissures are not developed, the hardness is small, and there is a large vertical stress acting on the coal wall, which is easy to form the arc-shaped crack to expand to the free surface of the coal wall; then, the synchronous instability as shown in Figure 4(a) is formed. When the strength of coal and direct roof is high, the coal wall is easy to form oblique linear failure trace under the action of roof high pressure, as shown in Figure 4(b). When the coal body is homogeneous and has no influence on the gangue, the joints and fractures are not developed, the integrity is good, the hardness is large, and the support of the coal wall is not timely. The vertical stress causes lateral horizontal displacement of the coal wall, which leads to the failure of the coal wall to break the groove shape, as shown in Figure 4(c). When there are gangues in the coal, the spalling extends or interrupts irregularly at the position of the gangue, thus forming the type as shown in Figure 4(d). Through years of field observation and theoretical research, there are two basic types of coal wall failure: shear and tension, of which (a) and (d) are more than 80%, and type (c) (16%) (a) and (b) belong to shear failure. Type (c) failure is due to a layer of relatively strong rock in the coal seam, and its failure principle is still shear failure. In general, tensile failure often occurs in hard coal seam, and type (d) failure is very rare.

The coal roof of group A in Zhangji mine of Huainan is directly covered with medium fine sandstone, as shown in Figure 5. The horizontal bedding is developed, and there are argillaceous bands in the layer, containing argillaceous inclusions and organic membrane, as shown in Figures 6 and 7. The average thickness of coal seam is 7.2 m, the strength of the coal body is low, and the hardness is 0.8~1. During the mining process, the roof caving and coal wall spalling are serious, and it is difficult to give full play to the supporting role of the bracket. After the coal wall spalling, the unsupported roof area increases. Under the action of the advanced bearing pressure, the roof is easy to leak and fall, which further weakens the support function of the roof. It is difficult to use shearer or air pick to directly crush

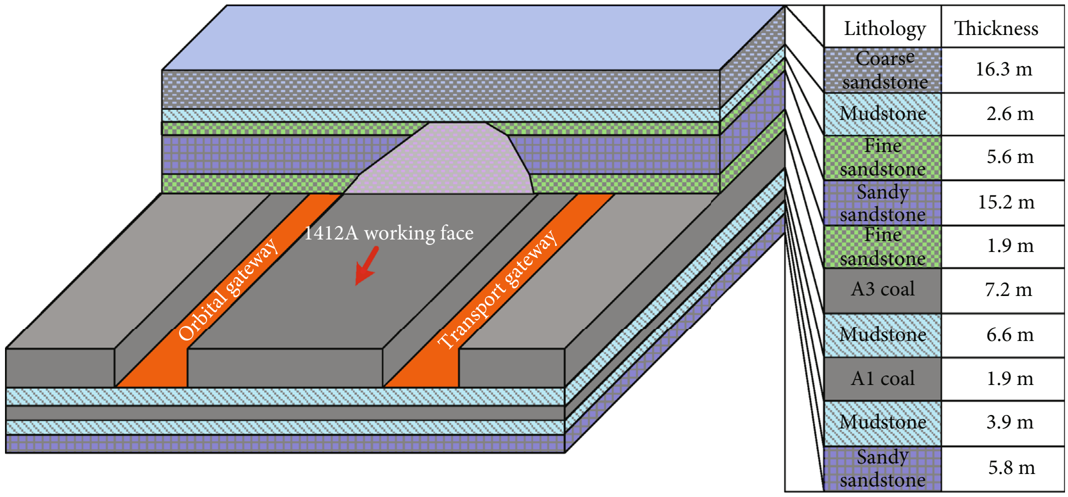

Figure 5: Working face layout and lithology histogram.

Figure 6: The sandstone intercalated with organic membrane.

the gangue due to its large size falling from the roof. It must be treated by drilling and blasting. The influence time is long, which further slows down the pushing progress of the working face, thus forming a vicious circle.

4.2. Synergistic Relationship Between Coal Wall Spalling and Roof Caving. Numerical and similar simulation tests show that the roof of the large mining height working face forms the overburden structure as shown in Figure 8. The stability of block B requires the support to provide supplementary load. The temporary balance of the structure just makes each working procedure of the mining operation successfully completed. Therefore, the stability of the overburden structure is determined by the large resistance of the support, especially for the working face with the mining height of 7~8 m. Due to the insufficient support force, the key blocks are prone to large swing or even sliding instability, which will lead to strong ore pressure appearance.

Due to the effect of advanced mining stress, the coal wall of soft and thick coal seam is prone to spalling, thus increasing the unsupported area. As shown in Figure 9, when the comprehensive roof control measures such as roof reinforcement and pressure relief are not adopted, the weak cohesive layer is separated by an organic membrane and argillaceous inclusion, and the open roof area exceeds the limit of stable span, and the composite layered roof falls in front of the support.

The support force is transmitted through the direct roof to control the change of overburden structure. When the roof caving height is large, the direct roof will be broken and the bearing capacity and stiffness will be reduced. As shown in Figure 10, the direct roof cannot transmit enough support force to the broken block B in this state, resulting in its reverse rotation, and the coal wall will not be able to provide the restraint force too, causing the support movable column to shrink down; it will aggravate the roof caving.

Figure 7: Argillaceous inclusions in sandstone.

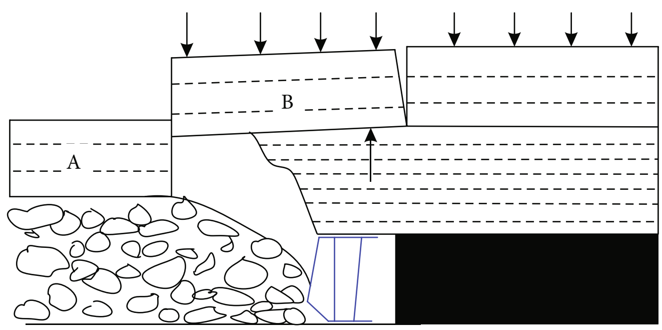

Figure 8: Normal mining.

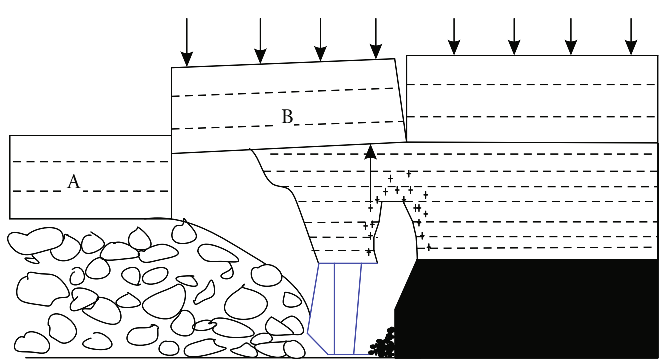

Figure 9: Roof caving caused by coal wall spalling.

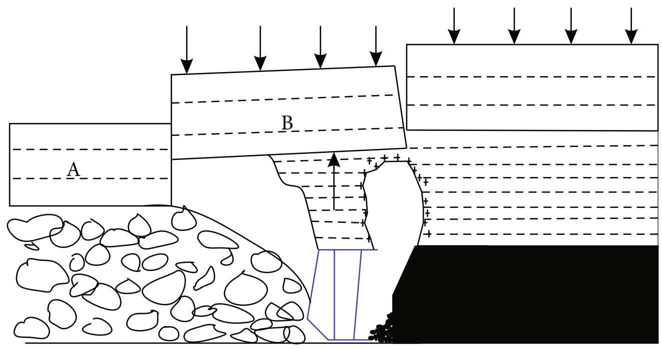

Figure 10: The change of roof structure aggravates the damage.

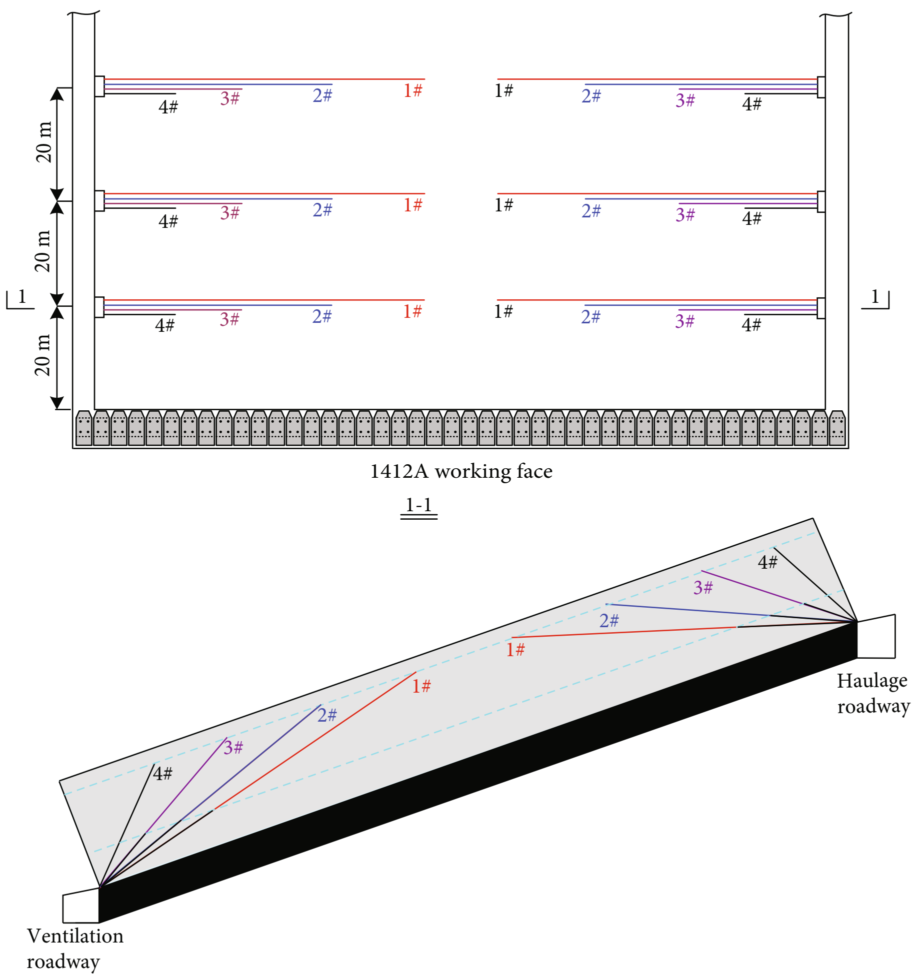

Figure 11: Layout of blasting hole cutting roof.

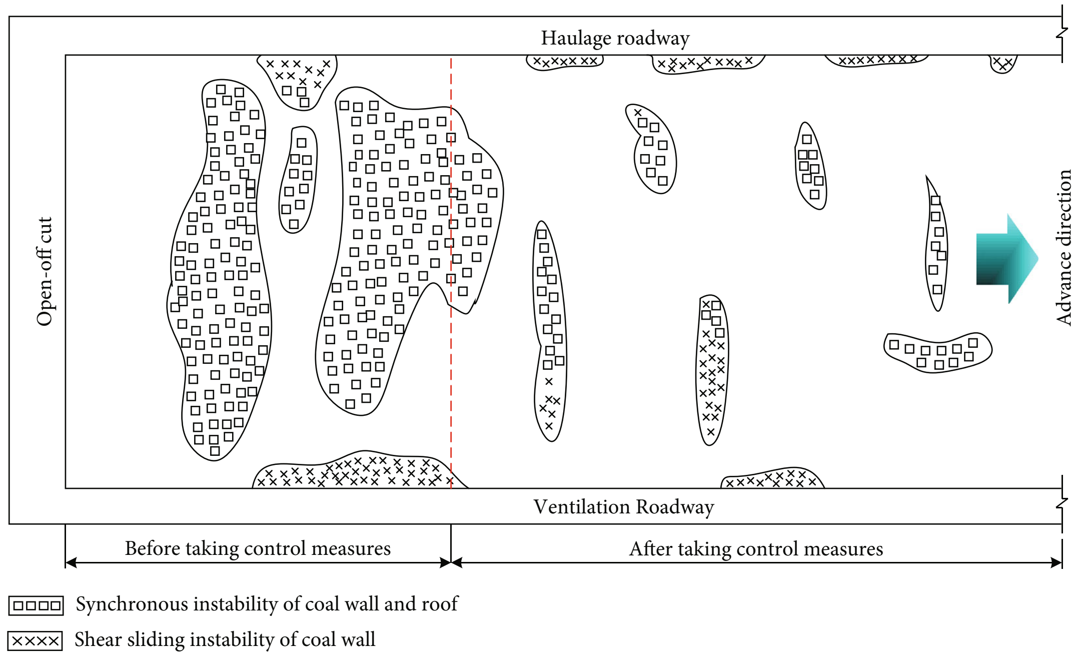

FIGURE 12: Comparison of working face control measures before and after.

5. Control of Coal Wall and Roof Synchronous Instability

In the process of mining in Group A of Zhangji mine, synchronous instability and strong ore pressure appear, which seriously affects the safety of working face. Through theoretical and practical research, the mechanism of surrounding rock instability in stope is expounded, and the comprehensive control measures of "cutting up and placing down" are adopted. Advanced mining stress is the key factor affecting the stability of the coal wall and roof, and the formation of mining stress is directly related to the overburden rock structure. By means of blasting presplitting, the key bearing rock blocks can be broken in advance, thus leading the advanced mining stress to act on the higher strata far away from the stope and weaken the impact on the direct roof and coal wall. According to the maximum bearing capacity of the support, the advance breaking distance is designed to make the hydraulic support effectively control the sinking of the direct roof and avoid the dynamic pressure influence on the coal wall and roof. According to the column chart, the 16.3 m coarse sandstone at the A3 roof is the key layer to control the ore pressure appearance, as shown in Figure 11.

In order to improve the strength and enhance its integrity, polymer materials are injected into the cracks or loose bodies by the pneumatic double liquid synchronous grouting pump, which consolidates and hardens the original broken, loose, and discontinuous rock mass into continuous and complete high-strength rock mass in a short time, so as to repair its defects in structure and improve the mechanical properties of surrounding rock mass. Through the treatment measures of "cutting up and pouring down", the frequency of roof caving and the depth of coal wall spalling are significantly improved, as shown in Figure 12.

6. Conclusion

(1) Based on the elastic-plastic theory, the mechanical model of coal wall stability analysis is established, and the analytical expressions of the stress and plastic zone about P_i, m, f, σ_c^*, C^*, φ, M_0, and S_z are obtained. Combined with mining conditions of A coal in Zhangji mine, it is shown that the mining depth, mining height, and coal cohesion have significant influence on the range of plastic failure zone, which directly determines the damage degree of coal wall spalling

(2) Coal strength of group A is low and easy to slide instability, thus increasing the unsupported space. Due to the influence of the mechanical membrane and argillaceous inclusions, the direct roof is prone to separation damage and then forms the synchronous instability. With the increase in the height of roof fall, the bearing capacity and stiffness of the broken direct roof will decrease, resulting in the reverse rotation of the broken key block, and the coal wall will not be able to provide the binding force at the end of the broken block, which will aggravate the spalling. The key block rotates and sinks, and roof caving is more serious

(3) The comprehensive control measures of "cutting up and injecting down" are adopted to improve the stability of the coal wall and direct roof. According to the maximum bearing capacity of the support, the

16.3 m thick coarse sandstone of A3 roof is pre-cracked with 10~15 m breaking distance from the two roadways, so that the advance mining stress is far away from the surrounding rock of the working face. In order to improve the strength and integrity of the roof, polymer materials are injected into the cracks or loose bodies of coal and rock mass to improve the mechanical properties

Data Availability

Others can access the data supporting the conclusions of the study from this research article. The nature of the data is the laboratory experimental data, the field observation data, and the theoretical calculation data. The laboratory experimental data used to support the findings of this study are included within the article; mainly, the mechanical parameters used to support the findings of this study are available from the corresponding author upon request.

Conflicts of Interest

The authors declare that they have no conflicts of interest.

Acknowledgments

The work presented in this paper is financially supported by the National Natural Science Foundation of China (Nos. 51674007, 52074008, and 52074007). The authors gratefully acknowledge the assistance of the Huainan Mining Group at the Anhui University of Science and Technology for providing access to the mine, data, and physical resources necessary to complete this work.

References

[1] Y. A. N. Shaohong, Y. I. N. Xiwen, G. J. Hu, and Q. M. Liu, "Roof structure of short cantilever-articulated rock beam and calculation of support resistance in full-mechanized face with large mining height [J]," *Journal of China Coal Society*, vol. 36, no. 11, pp. 1816–1820, 2011.

[2] F. Xinqiu, H. Jie, and L. Haichao, "A study of the coal wall fall mechanism in soft coal and its control at a fully-mechanized top-coal caving face," *Journal of China University of Mining Technology*, vol. 38, no. 5, pp. 640–644, 2009.

[3] W. Jiacheng, "Mechanism of the coal wall spalling and the controlling in the very soft coal seam," *Journal of China Coal Society*, vol. 32, no. 8, pp. 785–788, 2007.

[4] W. Jilin, Y. Yong, T. Shihao, and L. I. Bo, "Roof structure characteristics in fully mechanized coalface with large mining height and reasonable loading of support," *Journal of Mining and Safety Engineering*, vol. 31, no. 4, pp. 512–518, 2014.

[5] Y. Yong, T. Shihao, W. Ying, X. T. Ma, and Q. Wu, "Discussion on key problems and countermeasures of fully mechanized mining technology with high mining height," *Coal Science and Technology*, vol. 38, no. 1, pp. 4–8, 2010.

[6] H. Junxiao, L. Huamin, X. Zuoqiang, and W. Wang, "Analysis on setting load and stope control at overlength long face with large mining height in Sihe coal mine," *Coal Technology*, vol. 29, no. 12, pp. 74-75, 2010.

[7] Y. Shaohong, Y. Xiwen, G. J. Hu, and Q. M. Liu, "Roof structure of short cantilever-articulated rock beam and calculation of support resistance in full-mechanized face with large mining height," *Journal of China Coal Society*, vol. 36, no. 11, pp. 1816–1820, 2011.

[8] H. Qingxiang, *Study on roof structure and strata control of long wall mining in shallow seam*, China University of Mining and Technology Press, Xuzhou China, 2000.

[9] W. Guofa, L. Junfeng, and R. Huaiwei, "Design and optimization of high seam-caving coal hydraulic support based on model of support and wall rock coupling," *Journal of China Coal Society*, vol. 36, no. 1, pp. 145–151, 2011.

[10] W. Xuejun, Q. Xuesen, and M. Liqiang, "Research on large mining height technique for thick coal seams," *Journal of Mining and Safety Engineering*, vol. 26, no. 2, pp. 212–216, 2009.

[11] H. Haijin, W. Jian, Z. Yong, and Z. B. Yuan, "The balance structure of main roof and its action to immediate roof in large cutting height workface," *Journal of China Coal Society*, vol. 29, no. 2, pp. 137–141, 2004.

[12] Y. Shaohong and Y. Xiwen, "Discussing about the main theoretical problems of long wall with top coal caving," *Journal of China Coal Society*, vol. 33, no. 5, pp. 481–484, 2008.

[13] W. Jiacheng and W. Zhaohui, "Stability of main roof structure during the first weighting in shallow high-intensity mining face with thin bedrock," *Journal of Mining and Safety Engineering*, vol. 32, no. 2, pp. 175–181, 2015.

[14] W. Jiacheng, Z. Jian, and J. Liuting, "Study on mechanics model of the first cave in main roof for the large cutting height fully mechanized mining under the two hard conditions," *Chinese Journal of Rock Mechanics and Engineering*, vol. 24, pp. 5037–5042, 2005.

[15] H. Guowei and J. Zhongming, "Practice of pressure law and study on the strata behavior regularity of large mining height fully-mechanized face," *Journal of Taiyuan University of Technology*, vol. 37, no. 2, pp. 127–130, 2006.

[16] G. Peiling and J. Zhongming, "Research on influencing factors of tilt for fully-mechanized mining support with large mining height," *Journal of Taiyuan University of Technology*, vol. 32, no. 6, pp. 666–669, 2001.

[17] Y. Bo, M. Xiangrui, Z. Guangming, and G. Zhaoning, "Research on swallow-tailed catastrophe model of coal wall spalling in fully mechanized caving face with great mining height for soft coal seam," *Coal*, vol. 21, no. 1, pp. 1–4, 2012.

[18] Y. Bo, "Study on mechanism and control technology of coal wall spalling in fully mechanized caving face with great mining height of three-soft coal seam," Anhui University of Science and Technology, Anhui China, 2012.

Hindawi
Geofluids
Volume 2022, Article ID 5633861, 10 pages
https://doi.org/10.1155/2022/5633861

Research Article

Mechanism and Control of Rockburst Induced by Draining Spatial Islands and Squaring

Yunhai Cheng,[1,2,3] **Fenghui Li**,[2,3] **Xiufeng Zhang**,[4] **Gangwei Li**,[1,2] **and Le Xu**[5]

[1]*National Engineering Laboratory of Coalmine Backfilling Mining, Shandong University of Science and Technology, Taian 271000, China*
[2]*State Key Laboratory of Mining-Induced Response and Disaster Prevention and Control in Deep Coal Mines, Anhui University of Science and Technology, Huainan 232000, China*
[3]*School of Mining Engineering, Anhui University of Science and Technology, Huainan 232000, China*
[4]*Coal Burst Prevention and Control Research Centre, Yankuang Group Co., Ltd., Zoucheng 273500, China*
[5]*Chahasu Coal Mine, Inner Mongolia Energy Co., Ltd., Inner Mongolia, Ordos 017000, China*

Correspondence should be addressed to Fenghui Li; ahlifenghui@163.com

Received 18 September 2021; Revised 16 December 2021; Accepted 28 January 2022; Published 28 February 2022

Academic Editor: Mohammed Fattah

A small-pillar gob-side roadway showed rockburst appearance during the mining of a gob-side working face located in the Shaanxi-Inner Mongolia mining area. This study examines the 2202 gob-side working face of a coal mine in Inner Mongolia as a case study. A stress evolution model was built for the static-stress spatial islands formed by drainage regions and goafs based on the spatial relationships between drainage regions and goafs. The average microseismic frequency and energy of the high-stress zone of spatial islands were at least 1.37 times of those of other zones, validating the presence of spatial islands. The dynamic and static load effects of working face squaring were obtained based on the evolution of the stope roof as well as changes in microseismic data. Microseismically active zones were advanced to 200 m–300 m on working faces. The rockbursts induced by high static loads and dynamic and static loads formed by spatial islands and squaring were calculated. According to calculation results, the critical stress concentration value under high static loads was 3.27; the critical static stress concentration value under dynamic and static loads was 1.81. The superposition of drainage boundary stress, goaf lateral stress, and lead stress might reach the critical stress concentration under dynamic load disturbances, causing rockbursts. A stress adjustment scheme was established, including overall hydraulic fracturing of the external roof of the drainage region, reduction of stoping speed, and pressure relief of large-diameter boreholes. The stress adjustment scheme was implemented on-site and supplemented by monitoring and early warning methods to safely advance by the first squaring region.

1. Introduction

Rockbursts are one of the most serious dynamic disasters threatening coal mine safety. Existing studies have shown that the primary factors influencing the occurrence of rockbursts include geological factors (such as faults, folds, hard roofs (squared), coal seam attitude, and coal mass properties) as well as mining design factors (such as pillars, working face shapes, and island working faces) [1–14].

In this study, rockburst manifestations were primarily related to working face squaring and spatial island working faces, so we primarily collected and sorted through existing data related to both spatial island working faces and squaring. Cao et al. [15] theoretically examined how the spatial structure and rupture movement of thick and hard overburden of island working faces would affect mine earthquake activities. They held that the large-scale rupture movement of the key strata of a working faces' "T"-shaped overburden space structure was the primary force source of mine earthquake activities as well as provided densified borehole pressure relief in the primary squaring, second squaring, and third squaring regions of working faces. By combining the overburden space structure and mine pressure, Jiang et al. [16] investigated the overburden movement laws of the “103 upper 02 asymmetric island fully mechanized working face” of the Baodian Coal Mine, explored the prediction method for “hard rock fracture-type” mine earthquakes, and identified the “squaring” region of a working face as its primary rockburst hazard region.

Island working faces are generally classified as either plane island working faces (formed by goafs on the two sides of the same coal seam) or spatial island working faces (formed by goafs on the two sides of different coal seams, formed by faults and goafs, or formed by drainage regions and goafs (under investigation in this study)). Many experts and scholars have extensively studied spatial island working faces (formed by two goafs of different coal seams or formed by faults and goafs). Yang et al. [17] proposed putting the rockbursts of island working faces under “classified control” and classified island working faces into six types, that is, island working faces with critical extraction on both sides, island working faces with subcritical extraction on both sides, island working faces with critical extraction on one side, and subcritical extraction on the other side, stereoscopic island working faces formed by goafs of different coal seams, hidden island working faces formed by geological structures, and composite island working faces formed by a geological structure-goaf. Cao et al. [18] examined the dynamic load mechanism of fault slip in the rockburst appearance of an island working face adjacent to a fault on one side and a goaf on the other side and performed a CT-based back analysis on the rockburst hazard of a working face with dynamic early warning. Zhu et al. [19] studied the overall instability type of rockburst in a quasi-island working face formed by fault cutting. Wang et al. [20] investigated the mine pressure manifestations of the 220 quasi-island working face formed by mining of the 3-2 and 4-2 diverged/converged working section of Xiashijie Coal Mine in Tongchuan, finding that the dynamic pressure manifestation of the working face was closely related to periodic weighting and roof activities.

The above scholars have extensively studied island working faces formed by faults and goafs as well as those formed by goafs of different coal seams. This study primarily investigated a type of novel static-stress spatial islands formed by roof drainage regions and goafs. These spatial islands were formed by drainage stress transfer and goaf lateral stress transfer in the sandstone aquifers of the Yan’an Formation and the Zhiluo Formation. The erratic stress anomaly regions formed inside working faces inevitably affect production safety. In particular, the coupling of stress anomaly regions and working face squaring regions produced abnormal pressure manifestations on the gob side of the coupling region. This is an issue worthy of further research. With regard to the obvious dynamic phenomena occurring on the gob side of a spatial island working face, the formation and stress evolution process of the spatial island working face were explored using theoretical analysis as well as on-site monitoring. The force sources behind its rockburst appearance were also analyzed. The mechanism of rockburst induced by high static loads and by dynamic and static loads under the combined action of spatial islands and working face squaring was clarified, and control measures were prepared.

2. Engineering Background

When the 2202 gob-side working face of a coal mine in the Shaanxi-Inner Mongolia mining area was advanced to 200 m–300 m, the gob-side gate road of the working face experienced frequent coal burst and ejection phenomena as well as abnormal pressure manifestations in the yellow area in Figure 1. The 2202 working face had a burial depth of 731.4 m, a dip angle of 0–4, and a coal mass strength of 13.3 MPa and was characterized by simple coal seam structure and small relief. The effects of geological structures (such as faults and folds) were not detected. Table 1 provides the composite columnar section of the 2202 working face. The space above the 2-2 coal seam contains alternating sandy mudstone and medium sandstone. The relative water-rich anomaly regions of the Yan’an Formation and the Zhiluo Formation occur in the roof. The area filled by the red transverse lines is the relative water-rich anomaly region of the Yan’an Formation, 6.87 m away from the 2-2 coal seam. The area filled by the green transverse lines is the relative water-rich anomaly region of the Zhiluo Formation, 58.34 m away from the 2-2 coal seam.

3. Mechanism of Rockburst Induced by Spatial Islands

Island working faces are generally formed by goafs on the two sides caused by production continuity problems. Pillar-type islands are also present and are the result of pillar recycling. As for the spatial islands formed in the 2202 working face in this study, on the one side, there were goafs formed after mining of the 2201 working face. On the other side, there were goaf-like stress transfer regions formed by the relative water-rich anomaly regions of the roof after dewatering, such as 1# and 3# spatial islands in Figure 2. In addition, some spatial islands were formed by drainage regions alone, such as 2# spatial island in Figure 2.

1# spatial island was formed by drainage regions (primarily the drainage region of the Yan’an Formation) and goafs. After dewatering of the sandstone water-rich region of the Yan’an Formation, the support of the upper strata was weakened, and the upper strata settled and deformed. The stress transferred towards the drainage region boundary and superposed with goaf lateral stress, resulting in a unimodal stress distribution. Depending on the effect of the drainage region of the Zhiluo Formation on 1# spatial island, 1# spatial island was divided into two zones, i.e., zone 1 and zone 2. Zone 1 was located below the drainage region of the Zhiluo Formation. The decline in coal seam stress in the drainage region of the Zhiluo Formation lowered the stress level of the spatial island, as illustrated by the profile in Figure 3. Zone 2 was located outside the drainage region of the Zhiluo Formation and raised the stress level of the island working face, as illustrated by the profile in Figure 4.

2# spatial island was formed by the sandstone water-rich region of the Yan’an Formation after dewatering; however, the entire spatial island working face was located below the drainage region of the Zhiluo Formation. As shown in Figure 5, the mine pressure manifestations of the spatial

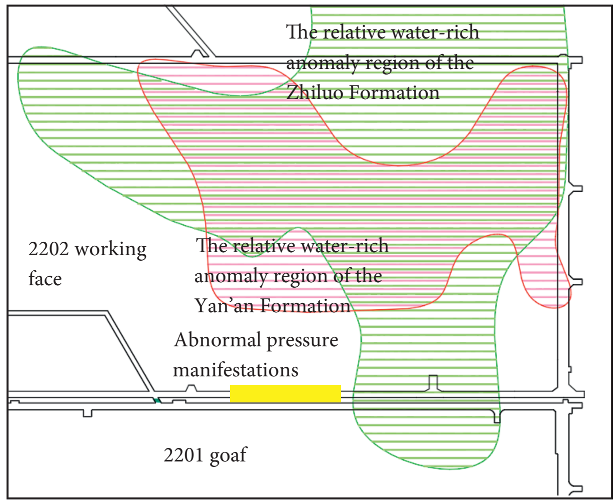

Figure 1: Spatial relationships and rockburst appearance of working faces.

Table 1: Composite columnar section of the 2202 working face.

Strata	Thickness (m)	Comment
Medium fine sandstone	12.91	The relative water-rich anomaly region of the Zhiluo Formation
Sandy mudstone	12.45	
Medium fine sandstone	13.56	
Sandy mudstone	13.90	
Medium fine sandstone	11.56	The relative water-rich anomaly region of the Yan'an Formation
Sandy mudstone	6.87	
2-2 coal seam	6.50	

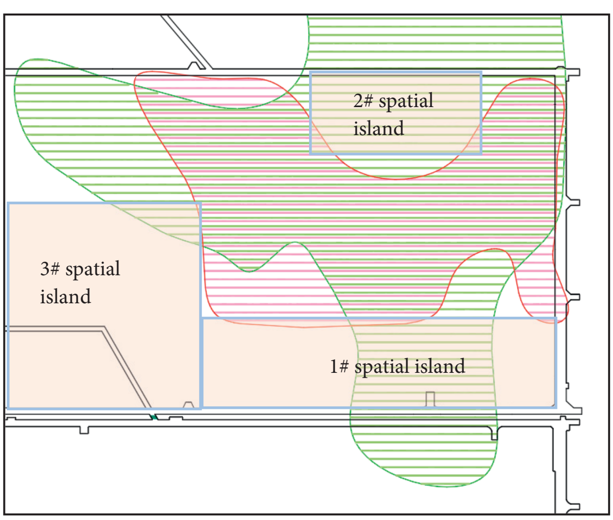

Figure 2: Distribution of spatial island working faces after dewatering.

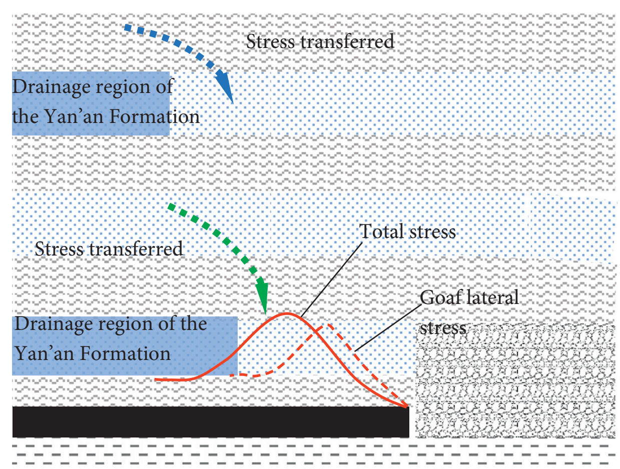

Figure 3: Stress distribution of zone 1 of 1# spatial island.

island, affected by interactions between the sandstone drainage regions of the Yan'an and Zhiluo Formations, were weak.

3# spatial island was formed by the drainage region of the Zhiluo Formation and goafs. The drainage stress transfer of the sandstone water-rich region of the Zhiluo Formation superposed with goaf lateral stress, resulting in bimodal stress distribution as shown in Figure 6. The stress concentration level of 3# spatial island was lower than that of 1# spatial island. 3# spatial island was formed by the drainage region of the Zhiluo Formation and goafs. The drainage stress transfer of the sandstone water-rich region of the Zhiluo Formation superposed with goaf lateral stress, resulting in bimodal stress distribution. The stress concentration level of 3# spatial island was lower than that of 1# spatial island.

The breakage degree of coal-rock mass is related to stress level, and coal-rock mass breakage produces microseismic phenomena. Thus, microseismic energy and frequency can satisfactorily reflect the stress concentration level of coal-rock

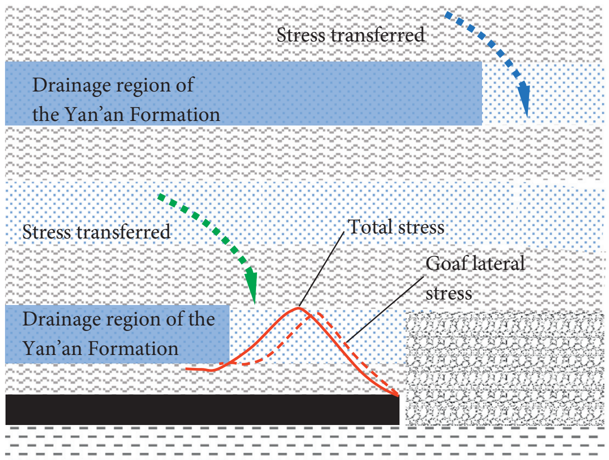

FIGURE 4: Stress distribution of zone 2 of 1# spatial island.

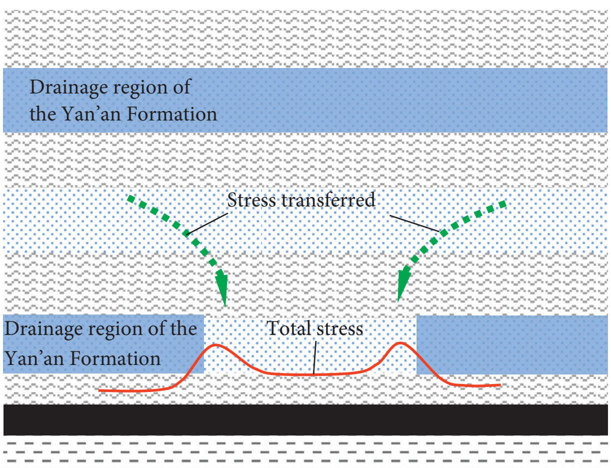

FIGURE 5: Stress distribution of 2# spatial island.

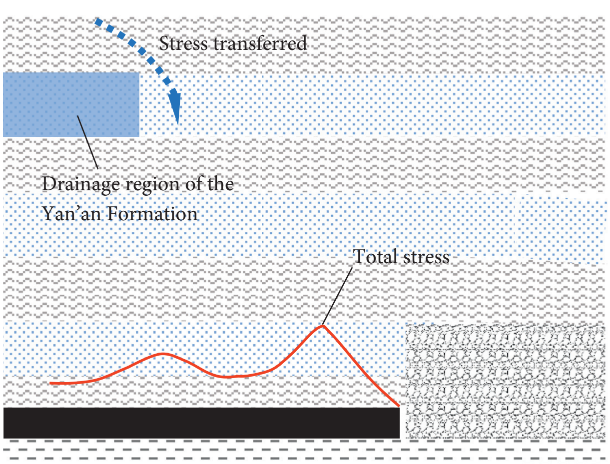

FIGURE 6: Stress distribution of 3# spatial island.

masses. That is, the higher the energy and frequency of microseismic events, the higher the stress concentration level within a coal-rock mass [21]. In this study, the presence of spatial island working faces was validated using "SOS" microseismic monitoring system software monitoring data. All microseismic events from the 2202 working face occurring over cumulative footage of 487 m were collected. Events with an energy level of above 10E3 were screened and projected onto the layout plan of the working face. Figure 7 shows the distribution of microseismic events.

The distribution of microseismic events satisfactorily reflects the stress concentration levels of different regions of the working face. Theoretical analysis in this study revealed that 1# spatial island region had a high-stress concentration level as well as a significant concentration of microseismic events.

1# spatial island region was divided into three zones, that is, zone 1, zone 2, and zone 3. Zone 2 was located below the drainage region of the Zhiluo Formation. Considering the wide scope of 3# spatial island, a zone in 3# spatial island with the same width as 1# spatial island was selected as zone 4 to avoid the effect of goaf distance. The microseismic data (see Figure 8) from the beginning of the 2202 working face to the working face position in Figure 8 were selected. Zone 5 was enclosed by the line from the open-off cut to the working face position in Figure 8 as well as by the two roadways of the working face.

The average frequency of a zone was defined as the ratio of the total microseismic frequency of the zone to its total area, and the average energy of a zone was defined as the ratio of the total microseismic energy of the zone to its total area (the two special events with an energy level of 10E6 were excluded in statistics), as provided in Table 2.

The average frequencies of zones 2 and 3 were 2.04–2.41 times of those of other zones. The average energies of zones 2 and 3 were 1.37–2.04 times of those of other zones. These results validated the presence of 1# spatial island. Zones 4 and 5 had similar average frequencies and average energies, which verified the conclusion that the stress transferred from the drainage region of the Zhiluo Formation was not intensified by superposition with 2201 goaf lateral stress. The average frequency and average energy of zone 2 were 0.92 and 0.78 times of those of zone 3, respectively, which confirmed the protective effect of the drainage region of the Zhiluo Formation for its underlying spatial islands.

4. Mechanism of Rockburst Induced by Squaring Effect

Starting with the open-off cut, goaf area increased linearly as the working face advanced. The squaring position was the dividing line marking the transition from short edge change to long edge change for the goaf. Before squaring, the two long edges of the goaf remained constant, while its two short edges continuously increased. Upon squaring, the short and long edges became equal in length. After squaring, the two short edges of the goaf remained constant, while its two long edges continuously increased. The roof stratum of the coal seam can be regarded as a constantly changing rectangular plate. In this case, identifying the distribution pattern of a coal mass stress under the action of the rectangular plate is of vital significance for clarifying the essence of the dynamic pressure of working face squaring as well as understanding

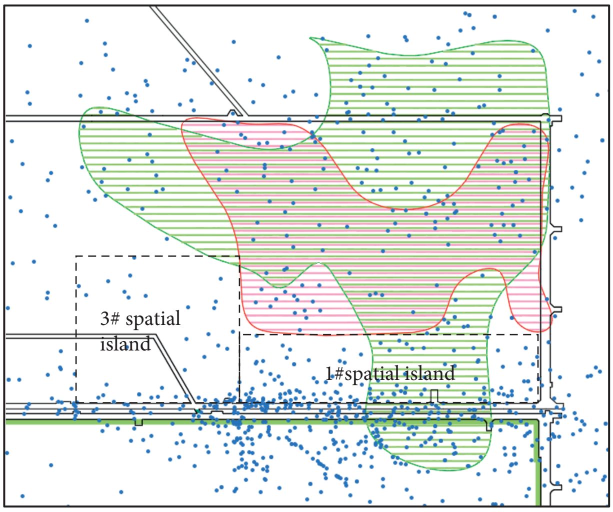

Figure 7: Distribution of microseismic events.

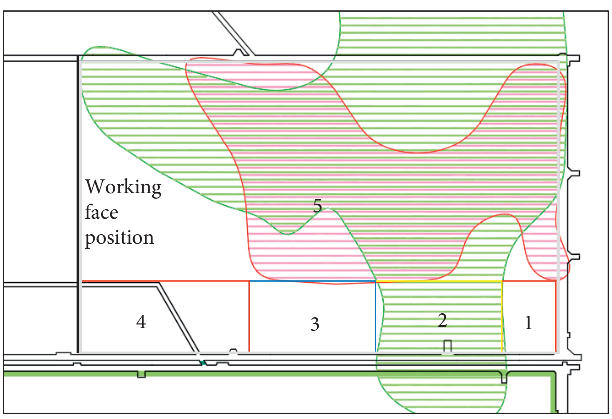

Figure 8: Statistical zoning of microseismic data of spatial islands.

Table 2: Average frequency and energy of each zone.

Zone	Average frequency (event count/1000 m^2)	Average energy (J/m^2)
1	7.34	21.51
2	15.36	29.88
3	16.77	38.46
4	6.94	21.80
5	7.52	18.82

in depth the effect of overburden space structure on the evolution of coal mass stress.

For a rectangular stope, the advance distance and length of the working face are assumed to be a and b, respectively. According to existing studies [22–24], before squaring ($a < b$), the bending moment distribution, coal mass plastic zone, and coal mass stress of the roof rectangular plate all indicate that the long edges of the rectangular plate have a relatively large moment load bearing capacity. The lead abutment stress of the working face increases with its advance.

When advance distance is equal to the length of the working face ($a = b$) [25], the working face was in the squaring stage, and σ_Z reaches its maximum value as shown in Figure 9. Theoretically, the abutment pressure of the stope is highest when the working face advances to "squaring." Clearly, working face squaring commonly produces stress anomaly regions, which can easily trigger the occurrence of rockbursts.

The squaring stage is the formation stage of stope overburden space structure, and the gob-side working face produces an "S"-shaped stope overburden space structure. The initial fracture of high-level strata produces dynamic loads, which commonly causes dynamic disasters in coal seams [27, 28].

When the 2202 working face advanced to 210 m without any significant change in mining velocity, microseismic event count and maximum energy increased rapidly, so the 2202 working face produced a significant squaring effect, using "origin" analysis software to make Figure 10.

5. Mechanism of Rockburst Induced by Spatial Islands and Squaring

5.1. Mechanism of Rockburst Induced by Static Stress. High static load stress is the stress path that leads to the occurrence of rockburst. When the static load reaches the critical rockburst load (i.e., when the static load exceeds 1.5 times of the comprehensive compressive strength of the coal mass), a high rockburst hazard occurs [29, 30].

$$I_c = \frac{\sigma}{\overline{\mu}[\sigma_c]} \geq 1.5, \tag{1}$$

where $\overline{\mu}$ is the average comprehensive compressive coefficient of the coal mass, set as 1–5; (σ_c) is the uniaxial compressive strength of the coal mass.

The 2202 working face had a burial depth of 731.4 m and a gravity stress of

$$\sigma_z = \gamma H = \frac{2.5\,\text{MPa}}{100\,\text{m} \times 731.4\,\text{m}} = 18.285\,\text{MPa}, \tag{2}$$

where σ_z is the gravity stress; γ is the stress gradient, set as 2.5 MPa/100 m; and H is the burial depth of the working face.

The 1# spatial island region demarcated in the 2202 working face is affected by lead abutment pressure, 2201 goaf lateral pressure, drainage boost region, and squaring-induced static load increase. The static load σ_j of the coal mass can be calculated using the following formula:

$$\begin{gathered} \sigma_j = k\sigma_z, \\ \alpha + \beta(\text{or}\,\lambda) + \upsilon \leq k \leq \alpha + \beta + \lambda + \upsilon, \end{gathered} \tag{3}$$

where k is the static load concentration coefficient of 1# spatial island; α is the lead abutment pressure concentration coefficient; β is the lateral pressure concentration coefficient of the 2201 goaf; λ is the stress concentration coefficient of the drainage boost region; and υ is the squaring-induced static load concentration coefficient.

The average comprehensive compressive coefficient $\overline{\mu}$ of the coal mass ranges from 1 to 5 and is set as 1 in the vicinity of roadway surface as well as 3–5 in three-dimensional stress

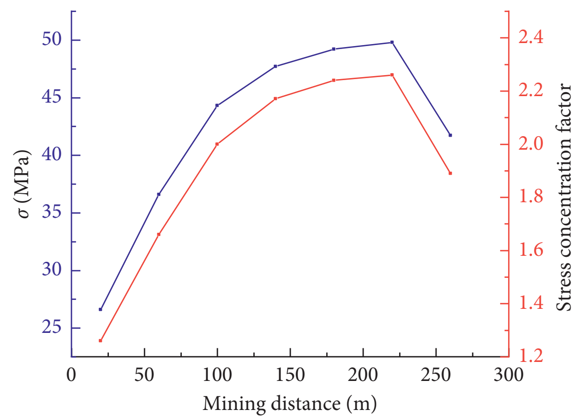

Figure 9: Relationship between advance distance and lead abutment pressure [26].

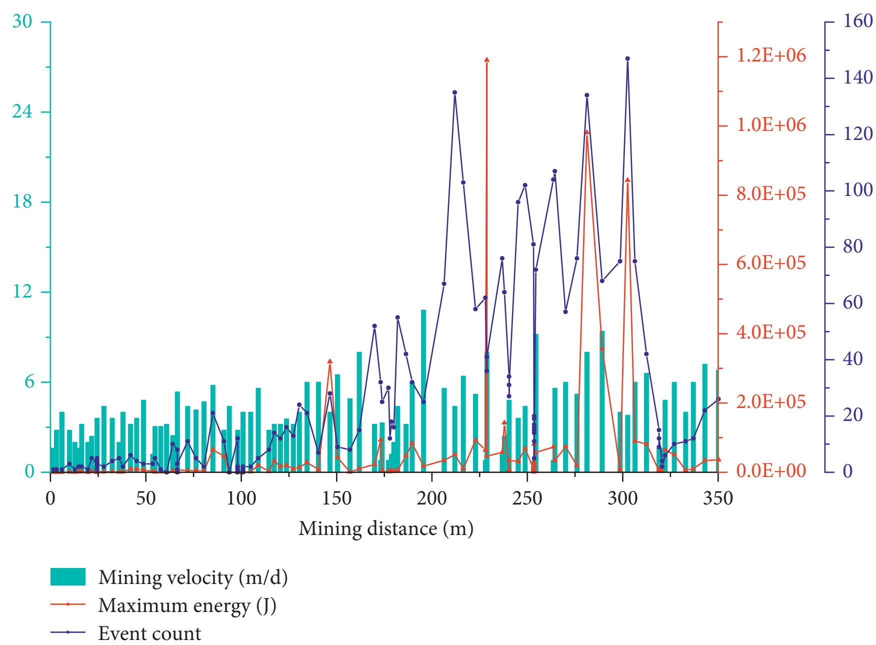

Figure 10: Microseismic energy, event count, and mining velocity curves of the 2202 working face.

state. In this study, 1# spatial island region was 75 m in width, and the width of pressure relief was 20 m. $\overline{\mu}$ was set as 3.

When the static load is equal to or greater than 1.5 times the comprehensive compressive strength of the coal mass, 1# spatial island working face may experience a static load rockburst; that is,

$$k \geq \frac{1.5\overline{\mu}\left[\sigma_c\right]}{\sigma_z} \approx 3.27, \quad (4)$$

and when the superposed sum of the stress concentration coefficients of the lead abutment pressure, 2201 goaf lateral pressure, drainage boost region, and squaring-induced static load increase is equal to or greater than 3.27, spatial island regions may experience static load rockburst.

5.2. Mechanism of Rockburst Induced by Dynamic and Static Loads. When the superposed sum is less than 3.27, the critical static load for rockburst is not reached. When the dynamic load produced by the initial fracture of high-level overburden is transferred to the coal mass, a rockburst may be triggered.

Related studies have revealed that rockbursts are triggered by mine earthquakes or blasting under highly concentrated loads, that is, by superposition of dynamic and static loads [31–35], as expressed by the following formula:

$$\sigma_j + \sigma_d \geq \sigma_b, \quad (5)$$

where σ_j is the static load on the coal-rock mass; σ_d is the dynamic load produced by mine earthquakes or blasting; and σ_b is the ultimate load in case of a rockburst.

The deep coal mass of the working face exists in a triaxial stress state. The comprehensive compressive strength of deep coal mass is far greater than that of roadway surface coal mass, and the critical rockburst load of deep coal mass is also far greater than that of roadway surface coal mass (see Figure 11).

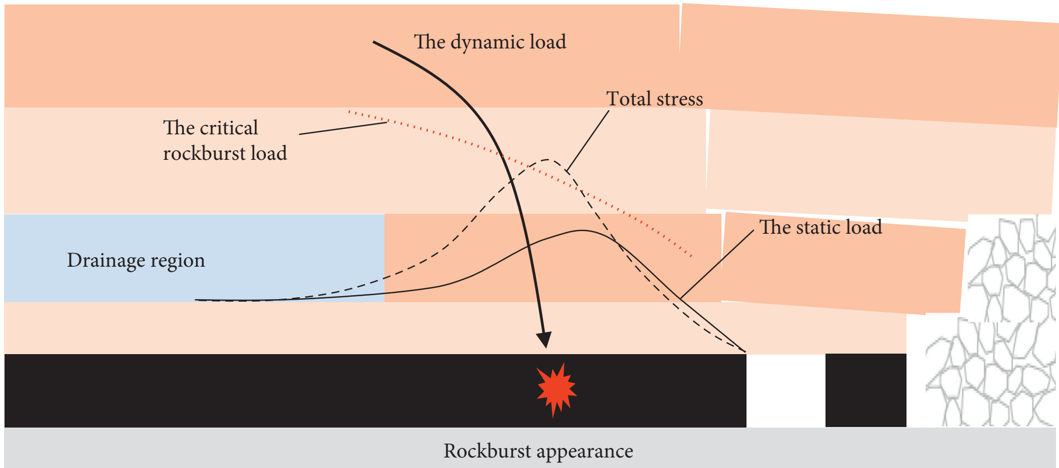

Figure 11: Mechanism of rockburst induced by superposition of dynamic and static loads.

The dynamic load in the abnormal mine pressure manifestation region of 1# spatial island working face is primarily the dynamic load produced during spatial structure formation in the squaring period. Spatial structures are formed by fracturing of high-level rock beams, which produces a dynamic load greater than the first-weighting and periodic-weighting dynamic loads of the working face [28]. In this study, the periodic weighting dynamic load coefficient of the 2202 working face fell within the range of 1.00–1.80. When the dynamic load coefficient in the squaring period was set to 1.80, the static load stress concentration coefficient required by rockburst induced by superposition of dynamic and static loads would be =3.27/1.80≈1.81. Under the combined action of lead abutment pressure, 2201 goaf lateral pressure, drainage boost region, and squaring-induced static load increase, the squaring region was exposed to rockburst induced by the superposition of dynamic and static loads.

6. Rockburst Control Measures

According to the force sources for rockbursts identified in the above analysis, a control scheme was prepared, including overall hydraulic fracturing of the external roof of the drainage region, reduction of stoping speed, and pressure relief of large-diameter boreholes. 2202 working face adopts pressure relief measures such as large-diameter drilling and hydraulic fracturing along the goaf. The number and energy of microseismic events increase obviously during the square period. 4 events with energy above 10E5J were detected by microseismic monitoring system (coal stress, drilling cuttings method does not monitor the data exceeding the standard).

6.1. Overall Hydraulic Fracturing of the External Roof of the Drainage Region. In roof hydraulic fracturing, a directional initial crack was made in the roof, and high-pressure water was continuously injected into the crack, in order to propagate the roof crack until it connected with adjacent cracks and damaged roof integrity [36]. The fracture characteristics and 3D fractal fracture of solid-fluid coupling have been studied [37, 38].

Rockburst in the drainage region was primarily induced by drainage stress transfer, but the transferred stress remained in the working face and affected the safe stoping of the working face. 1# spatial island working face formed because the drainage region transferred stress to a more dangerous area. As a result of roof hydraulic fracturing outside the drainage region, the drainage region and the hydraulic fracturing zone formed an overall regular pressure relief protection layer (see Figure 12), which could reduce static loads in the fracturing zone as well as at the drainage boundary and weaken the fracturing dynamic loads of high-level strata.

6.2. Pressure Relief of Large-Diameter Boreholes (Triaxial Transfer of Stress and Reduction of Static Loads on Roadway Surrounding Rock). In pressure relief of large-diameter boreholes, boreholes distributed at small spacings connected the cracks in coal mass to relieve and transfer coal mass stress. In this way, they modified the mechanical properties of the coal mass and weakened the ability of coal seams to store elastic energy, mitigating rockburst within the coal mass [39].

Large-diameter boreholes formed a pressure relief belt around the roadway and kept coal mass stress away from the roadway (see Figure 13). The comprehensive compressive strength and the critical rockburst load of the deep coal mass were far greater than those of the coal mass near the roadway, mitigating the chance of a rockburst.

6.3. Reduction of Stoping Speed. The aim of reducing stoping speed is to lower lead abutment pressure and reduce the effect of stoping on overburden. Studies have shown that a lower stoping speed leads to smaller peak lead abutment stress and longer distance of peak position from the working face. A low stoping speed can reduce the movement of roof masonry beam structures, lower the level of energy released by their fractures, and weaken the intensity of mine

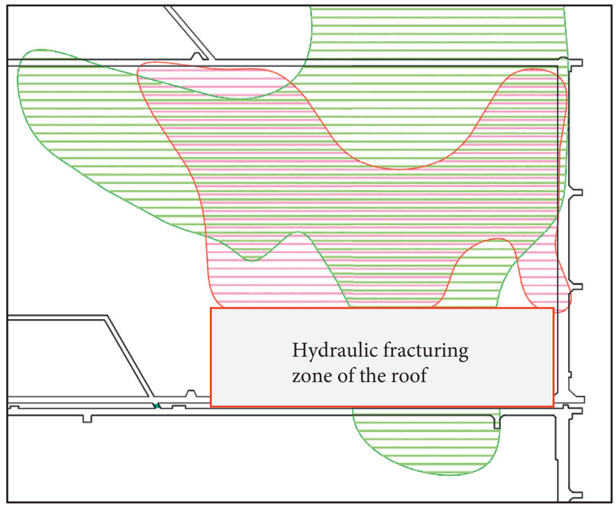

FIGURE 12: Hydraulic fracturing zone of the external roof of the drainage region.

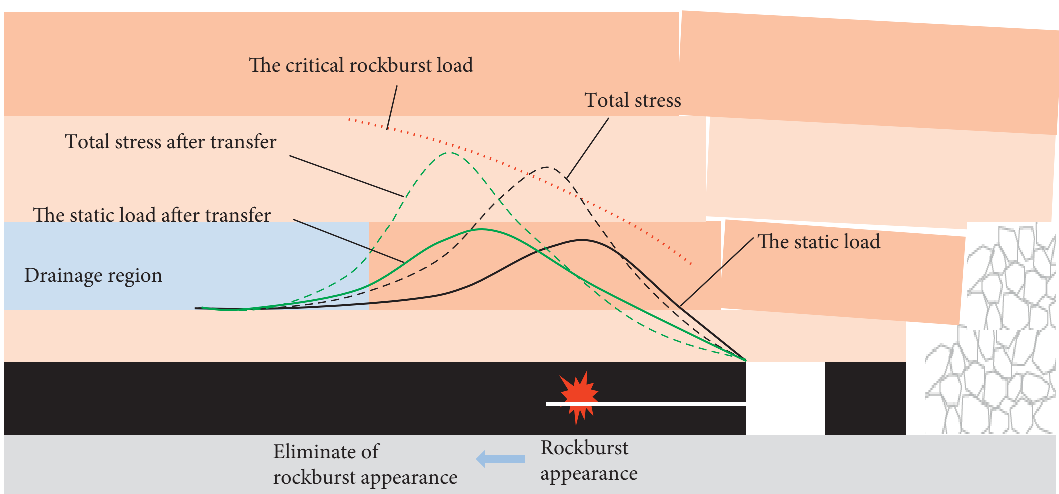

FIGURE 13: Rockburst reduction principle of large-diameter boreholes.

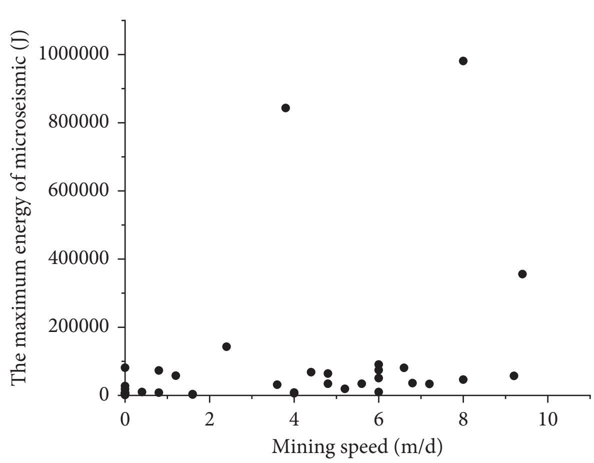

FIGURE 14: Relationship between mining speed and the microseismic maximum energy.

earthquakes. There is a critical stoping speed under specific stoping conditions. After exceeding the critical stoping speed, microseismic energy and major event frequency both increase significantly with increasing stoping speed. In contrast, before reaching the critical stoping speed, microseismic monitoring data are not responsive to stoping speed [40].

In regions facing the rockburst induced by high static loads and dynamic and static loads, properly reducing stoping speed helps to mitigate lead stress concentration on the working face and weaken the intensity of the fracturing dynamic loads of roof strata, thus achieving the goal of rockburst control. In the square period of the working face, the mining speed and the microseismic maximum energy are shown in Figure 14.

The microseismic monitoring system begins to detect large energy events when the mining speed exceeds 3.8 m. This phenomenon verifies the relationship between the mining speed and the intensity of roof movement.

7. Conclusions

With regard to the specific conditions of the 2202 working face, this study explored the static-stress spatial islands formed by roof drainage regions and goafs as well as the squaring effect of the working face and analyzed the dynamic and static load mechanism of the rockburst appearance of the gob-side roadway of the 2202 working face from stoping to squaring stage.

The static load evolution process of drainage regions and goafs under different spatial relationships was analyzed to obtain the stress states of various spatial islands. The drainage region of the Yan'an Formation and 2201 goaf formed 1# spatial island (after initial mining). The average frequency and average energy of 1# spatial island were 2.04–2.41 times and 1.37–2.04 times of those of other zones, respectively. This result validated the presence of spatial islands in the working face.

Based on the evolution of the roof rectangular plate as well as existing studies on numerical simulation, it was found that the lead abutment stress of the squaring region was 1.2 times of that of the nonsquaring region, and high static loads existed in the coal wall in front of the working face during the squaring period. The microseismic frequency and maximum energy of the squaring region of the 2202 working face were both more than three times of those of the nonsquaring region, so there was a significant squaring-induced dynamic loading effect.

Following the theory of rockburst induced by superposition of dynamic and static loads, this study set the critical stress concentration coefficient for rockburst induced by spatial islands and squaring under high static loads as 3.27 and the critical static-stress concentration coefficient for rockburst induced by dynamic and static loads as 1.81. A control scheme was prepared, including overall hydraulic fracturing of the external roof of the drainage region, reduction of stoping speed, and pressure relief of large-diameter boreholes. The first squaring region was advanced safely on-site. There were no spatial islands in the second squaring region, nor were any rockburst observed.

Data Availability

The data used to support the findings of this study are available from the corresponding author upon request.

Conflicts of Interest

The authors declare that there are no conflicts of interest regarding the publication of this paper.

Acknowledgments

This research was supported by the National Natural Science Foundation for Young Scientists of China (Grant no. 52004004).

References

[1] L. P. Dai, Y. S. Pan, Z. H. Li et al., "Quantitative mechanism of roadway rockbursts in deep extra-thick coal seams: theory and case histories," *Tunnelling and Underground Space Technology Incorporating Trenchless Technology Research*, vol. 111, Article ID 103861, 2021.

[2] L. Jiang, P. Kong, P. Zhang et al., "Dynamic analysis of the rock burst potential of a longwall panel intersecting with a fault," *Rock Mechanics and Rock Engineering*, vol. 53, no. 4, pp. 1737–1754, 2020.

[3] J. W. Liu, C. Y. Liu, Q. L. Yao, and G. Si, "The position of hydraulic fracturing to initiate vertical fractures in hard hanging roof for stress relief," *International Journal of Rock Mechanics and Mining Sciences*, vol. 132, Article ID 104328, 2020.

[4] S. Q. He, D. Z. Song, X. Q. He et al., "Coupled mechanism of compression and prying-induced rock burst in steeply inclined coal seams and principles for its prevention," *Tunnelling and Underground Space Technology*, vol. 98, Article ID 103327, 2020.

[5] A. Y. Cao, L. L. Zhu, F. C. Li, M. Dou, Y. L. Zhao, and Z. L. Zhen, "Mechanism of rock burst caused by fracture of key strata during irregular working face mining and its prevention methods," *International Journal of Mining Science and Technology*, vol. 29, no. 6, pp. 889–897, 2019.

[6] W. Z. Cao, J. Q. Shi, S. Durucan, A. Korre, and S. Jamnikar, "Numerical modelling of anomalous microseismicity influenced by lithological heterogeneity in longwall top coal caving mining," *International Journal of Coal Geology*, vol. 216, Article ID 103305, 2019.

[7] G. Wang, S. Gong, L. Dou, W. Cai, X. Yuan, and C. Fan, "Rockburst mechanism and control in coal seam with both syncline and hard strata," *Safety Science*, vol. 115, pp. 320–328, 2019.

[8] H. Wang, R. Shi, C. Lu, Y. Jiang, D. Deng, and D. Zhang, "Investigation of sudden faults instability induced by coal mining," *Safety Science*, vol. 115, pp. 256–264, 2019.

[9] G. Wang, S. Gong, L. Dou, H. Wang, W. Cai, and A. Cao, "Rockburst characteristics in syncline regions and microseismic precursors based on energy density clouds," *Tunnelling and Underground Space Technology*, vol. 81, pp. 83–93, 2018.

[10] S. Zhu, Y. Feng, F. Jiang, and J. Liu, "Mechanism and risk assessment of overall-instability-induced rockbursts in deep island longwall panels," *International Journal of Rock Mechanics and Mining Sciences*, vol. 106, pp. 342–349, 2018.

[11] T.-B. Zhao, W.-Y. Guo, Y.-L. Tan, Y.-C. Yin, L.-S. Cai, and J.-F. Pan, "Case studies of rock bursts under complicated geological conditions during multi-seam mining at a depth of 800 m," *Rock Mechanics and Rock Engineering*, vol. 51, no. 5, pp. 1539–1564, 2018.

[12] J. He, L.-M. Dou, Z.-L. Mu, A.-Y. Cao, and S.-Y. Gong, "Numerical simulation study on hard-thick roof inducing rock burst in coal mine," *Journal of Central South University*, vol. 23, no. 9, pp. 2314–2320, 2016.

[13] A.-Y. Cao, L.-M. Dou, C.-B. Wang, X.-X. Yao, J.-Y. Dong, and Y. Gu, "Microseismic precursory characteristics of rock burst hazard in mining areas near a large residual coal pillar: a case study from Xuzhuang coal mine, Xuzhou, China," *Rock Mechanics and Rock Engineering*, vol. 49, no. 11, pp. 4407–4422, 2016.

[14] J.-C. Wang, F.-X. Jiang, X.-J. Meng, X.-Y. Wang, S.-T. Zhu, and Y. Feng, "Mechanism of rock burst occurrence in specially thick coal seam with rock parting," *Rock Mechanics and Rock Engineering*, vol. 49, no. 5, pp. 1953–1965, 2016.

[15] A. Y. Cao, L. L. Zhu, and F. C. Li, "Characteristics of "T" type overburden structure and dynamic pressure evolution in isolated island working face under thick and hard rock strata," *Journal of China Coal Society*, vol. 39, no. 2, pp. 328–335, 2014.

[16] F. X. Jiang, X. C. Qu, X. H. Ni, F. Q. Wang, and Z. B. Tang, "Case study on the mine earthquake caused by hard rock fracture in Baodian coal mine," *Journal of China Coal Society*, vol. 38, no. S2, pp. 319–324, 2013.

[17] W. L. Yang, Q. D. Wei, X. C. Qu, W. X. Liu, and J. N. Zhang, "Research on classification and application of isolated island working face based on burst prevention," *Journal of Safety Science and Technology*, vol. 14, no. 12, pp. 107–113, 2018.

[18] A. Y. Cao, C. B. Wang, L. M. Dou, Y. Gu, Y. Li, and J. Dong, "Dynamic manifestation mechanism of mining on the island coalface along fault and dynamic pre-warning of seismic waves with seismic tomography," *Journal of Mining and Safety Engineering*, vol. 34, no. 3, pp. 411–417, 2017.

[19] S. T. Zhu, F. X. Jiang, J. H. Liu et al., "Types, occurence mechanism and prevention of overall istability induced rockbursts in China coal mines," *Journal of China Coal Society*, vol. 45, no. 11, pp. 3667–3677, 2020.

[20] S. J. Wang, K. J. Huang, and S. Y. Jin, "Feasibility analysis of the recovery of "Island-like" working face," *Coal Science and Technology*, pp. 1–7, 2020, http://kns.cnki.net/kcms/detail/11.2402.td.20200206.1847.040.html.

[21] D. C. Wang, Q. Wang, S. C. Li et al., "Stress distribution characteristics of deep mine in fully-mechanized sublevel caving face based on microseismic and online stress monitoring system," *Journal of Mining and Safety Engineering*, vol. 32, no. 3, pp. 382–388, 2015.

[22] F. L. He, D. D. Chen, and S. R. Xie, "The kDL effect on the first fracture of main roof with elastic foundation boundary," *Chinese Journal of Rock Mechanics and Engineering*, vol. 36, no. 6, pp. 1384–1399, 2017.

[23] F. L. He, W. R. He, D. D. Chen, S. R. Xie, H. Li, and C. X. He, "First fracture structure characteristics of main roof plate considering elastic-plastic deformation of coal," *Journal of China Coal Society*, vol. 45, no. 8, pp. 2704–2717, 2020.

[24] X. F. Wang and M. Z. Gao, "Mechanical model of fracture mechanism of stope roof for working face with variable length," *Journal of China University of Mining and Technology*, vol. 44, no. 1, pp. 36–45, 2015.

[25] W. L. Zhang, X. C. Qu, C. Li et al., "Fracture analysis of multi-hard roofs based on microseismic monitoring and control techniques for induced rock burst: a case study," *Arabian Journal of Geosciences*, vol. 12, no. 24, p. 784, 2019.

[26] D. Li, F. X. Jiang, C. W. Wang, Z. Tian, and Y. Wang, "Study on the mechanism and prevention technology of "square position" and "stress breakdown effect" inducing rockburst," *Journal of Mining and Safety Engineering*, vol. 35, no. 5, pp. 1014–1021, 2018.

[27] L. H. Kong, Q. X. Qi, F. X. Jiang, and Z. Ouyang, "Abnormal strata stress resulted from goaf square of longwall face based on microseismic monitoring," *Chinese Journal of Rock Mechanics and Engineering*, vol. 31, no. S2, pp. 3889–3896, 2012.

[28] C. W. Wang, F. X. Jiang, Q. G. Sun et al., "The forecasting method of rockburst and the application based on overlying multistate spatial structure theory," *Journal of China Coal Society*, vol. 34, no. 2, pp. 150–155, 2009.

[29] F. X. Jiang, G. Cheng, Y. Feng, C. Wang, and Y. Xu, "Research on coal overall instability of isolated working face with irregular gobs on both sides," *Chinese Journal of Rock Mechanics and Engineering*, vol. 34, no. S2, pp. 4164–4170, 2015.

[30] G. A. Wang, S. T. Zhu, F. X. Jiang et al., "Mechanism of rock burst induced by overall instability of isolated coal and its prevention in large well at thousands-kilometer underground," *Journal of Mining & Safety Engineering*, vol. 36, no. 5, pp. 968–967, 2019.

[31] Z.-L. Li, L.-M. Dou, G.-F. Wang, W. Cai, J. He, and Y.-L. Ding, "Risk evaluation of rock burst through theory of static and dynamic stresses superposition," *Journal of Central South University*, vol. 22, no. 2, pp. 676–683, 2015.

[32] L. M. Dou, J. He, A. Y. Cao, S. Y. Gong, and W. Cai, "Rock burst prevention methods based on theory of dynamic and static combined load induced in coal mine," *Journal of China Coal Society*, vol. 40, no. 7, pp. 1469–1476, 2015.

[33] W. Cai, X. X. Bai, G. Y. Si, W. Cao, S. Gong, and L. Dou, "A monitoring investigation into rock burst mechanism based on the coupled theory of static and dynamic stresses," *Rock Mechanics and Rock Engineering*, vol. 53, no. 12, pp. 5451–5471, 2020.

[34] J. He, L. Dou, S. Gong, J. Li, and Z. Ma, "Rock burst assessment and prediction by dynamic and static stress analysis based on micro-seismic monitoring," *International Journal of Rock Mechanics and Mining Sciences*, vol. 93, pp. 46–53, 2017.

[35] J. Z. Yang and K. G. Zheng, "The mechanism of overburden dynamic disasters and its control technology in top-coal caving in the mining of thick coal seams," *Journal of Mining & Safety Engineering*, vol. 37, no. 4, pp. 750–758, 2020.

[36] H. Kang, H. Lv, F. Gao, X. Meng, and Y. Feng, "Understanding mechanisms of destressing mining-induced stresses using hydraulic fracturing," *International Journal of Coal Geology*, vol. 196, pp. 19–28, 2018.

[37] J. Liu, Y. Xue, Q. Zhang, H. Wang, and S. Wang, "Coupled thermo-hydro-mechanical modelling for geothermal doublet system with 3D fractal fracture," *Applied Thermal Engineering*, vol. 200, Article ID 117716, 2022.

[38] Y. Xue, J. Liu, P. G. Ranjith, X. Liang, and S. Wang, "Investigation of the influence of gas fracturing on fracturing characteristics of coal mass and gas extraction efficiency based on a multi-physical field model," *Journal of Petroleum Science and Engineering*, vol. 206, Article ID 109018, 2021.

[39] S. Zhang, Y. Li, B. Shen, X. Sun, and L. Gao, "Effective evaluation of pressure relief drilling for reducing rock bursts and its application in underground coal mines," *International Journal of Rock Mechanics and Mining Sciences*, vol. 114, pp. 7–16, 2019.

[40] L. F. Feng, L. M. Dou, X. D. Wang et al., "Mechanism of mining advance speed on energy release from hard roof movement," *Journal of China Coal Society*, vol. 44, no. 11, pp. 3329–3339, 2019.

Hindawi
Geofluids
Volume 2021, Article ID 6381549, 11 pages
https://doi.org/10.1155/2021/6381549

Research Article

Experimental Study on Seepage Characteristics of Fractured Rock Mass under Different Stress Conditions

Ma Haifeng ,[1,2] Yao Fanfan ,[2] Niu Xin'gang,[2,3] Guo Jia ,[4] Li Yingming,[2] Yin Zhiqiang ,[2] and Li Chuanming[2]

[1]*State Key Laboratory of Mining Response and Disaster Prevention and Control in Deep Coal Mines (Anhui University of Science and Technology), Huainan, Anhui 232001, China*
[2]*School of Mining Engineering, Anhui University of Science and Technology, Huainan, Anhui 232001, China*
[3]*China Coal Technology and Engineering Group Chongqing Research Institute, Chongqing 400037, China*
[4]*Anhui Academy of Coal Science, Hefei, Anhui 230001, China*

Correspondence should be addressed to Yao Fanfan; 3299531763@qq.com and Guo Jia; kkkguojia@163.com

Received 8 September 2021; Accepted 23 October 2021; Published 20 November 2021

Academic Editor: Zhijie Wen

In order to obtain the mechanical behavior and permeability characteristics of coal under the coupling action of stress and seepage, permeability tests under different confining pressures in the process of deformation and destruction of briquette coal were carried out using the electrohydraulic servo system of rock mechanics. The stress-strain and permeability evolution curves of briquette coal during the whole deformation process were obtained. The mechanical behavior and permeability coefficient evolution response characteristics of briquette coal under stress-seepage coupling are well reflected. Research shows that stress-axial strain curve and the stress-circumferential strain curve have the same change trend, the hoop strain and axial strain effect on the permeability variation law of basic consistent, and the permeability coefficient with the increase of confining pressure and decreases, and the higher the confining pressure, the lower the permeability coefficient, the confining pressure increases rate under the same conditions, and the permeability coefficient corresponding to high confining pressure is far less than that corresponding to low confining pressure. The confining pressure influences the permeability of the briquette by affecting its dilatancy behavior. With the increase of the confining pressure, the permeability of the sample decreases, and the permeability coefficient decreases with the increase of the confining pressure at the initial stage, showing a logarithmic function. After failure, briquette samples show a power function change rule, and the greater the confining pressure is, the more obvious the permeability coefficient decreases.

1. Introduction

In mining engineering, high stress and the coupling effect of karst water pressure and the influence of multiple mining could lead to the structure change of the surrounding rock body, which not only could reduce the mechanical properties of rock itself but also easy to make the surround rock mass permeability changed significantly; rock permeability changed lead to mine water inrush, and mine roadway surrounding rock of roadway was one of the main causes of instability.

The actual underground engineering rock mass exists in a certain stress environment and is subjected to the dual action of external stress and internal stress. The stress state is a major factor affecting the permeability of rock mass [1]. For this reason, many scholars have conducted in-depth research on the evolution law of permeability of underground engineering rock mass with the change of stress. Xu and Yang [2] measured the permeability of sandstone under short-term and long-term compression conditions and analyzed the influence of confining pressure on sandstone strength and failure mode. Hu et al. [3] conducted experimental studies on the mechanical behavior and permeability of saturated sandstone and obtained the evolution law of Biot coefficient and permeability with microcrack propagation. Wang et al. [4] conducted permeability tests on sandstone under different fluid pressures and concluded that the evolution of permeability of rock mass was closely related to the development of microcracks. Jiang et al. [5] conducted a permeability experimental study on brittle rock and concluded that the anisotropic damage of brittle rock is closely related to the change rate of permeability. Based on field investigations and previous tests on physical model, a numerical model of an anaclinal slope using the three-dimension distinct element code software has been built to simulate the failure process of the physical model [6]. The permeability evolution of fractal-based two-dimensional discrete fracture networks during shearing under constant normal stiffness boundary conditions is numerically modeled and analyzed based on a fully coupled hydromechanical model. The effects of fractal dimension, boundary normal stiffness, and hydraulic pressure on the evolutions of mechanical behaviors, aperture distributions, and permeability are quantitatively investigated [7].

In order to understand the seepage mechanism of fractured rocks under stress, the tests on seepage characteristics of fractured rocks under varying confining pressures were carried out, and the law that the flow rate increased with the increase of the seepage pressure gradient and decreased with the increase of the confining pressure was obtained [8]. To study the damage development and permeability change in the process of rock excavation in roadways, the permeability evolution and damage for mudstone material under coupled stress-seepage was analyzed based on the stress-seepage damage coupling model [9]. The change rules of permeability, volumetric strain, and porosity under fluid-solid coupling during coal seam mining were studied based on the numerical model of a Darcy-Forchheimer flow in aquifers [10]. The tests of stress-seepage coupling of fracture of different particle size were carried out using the coupled shear-seepage test system of JAW-600 rock, and the permeability coefficient of quasisandstone increases exponentially with the increase of cranny hydraulic pressure [11]. The permeability of protected coal seam in the process of protective coal seam mining was studied; according to the changes of permeability, the protected coal seam was divided into initial permeability zone, permeability decreasing zone, and permeability increasing zones 1 and 2 [12]. Based on the Drucker-Prager criterion, the rock elastoplastic damage constitutive model was established aiming at the problem of surrounding rock excavation damage zone of tunneling in the rich water region, and the fully implicit return mapping algorithm was adopted to realize the numerical solution [13]. The relation between the anisotropic permeability matrix and effective stress was established, and the deterioration of strength parameters was considered by defining elastoplastic damage variables, and the characteristics of seepage and failure were analyzed by an improved multiphysics coupling model [14]. A stress-seepage-damage coupling model based on the finite element method was developed and first applied in HF in concrete dams, the crack propagation processes of Koyna dam, and a 1 : 40 scaled model dam using the coupling model [15].

The correction model of inertial resistance coefficient and permeability of the goaf was established by introducing the inertial resistance coefficient and shape factor of permeability, and the inertial resistance coefficient shape factor and permeability had good power function relationships with particle size [16]. Qiang et al. used the latest X-ray diffraction, scanning electron microscopy, and mechanical testing methods to analyze the physical, mechanical, and seepage characteristics of the key aquiclude and established the KAS damage state model for the stress-strain-permeability correlation of the composite rock mass and the non-Darcy seepage characteristics of the postpeak fractured rock mass. The research results have a certain guiding significance for the prevention and control of water inrush disasters and the rational development and utilization of coal resources based on KAS [17]. Dong et al. proposed a new coal quality characterization and prediction method for the prediction, early warning, and accurate identification of composite coal and rock dynamic disasters and concluded that the physical characteristics of coal in coal and rock dynamic disasters are between those of gas outburst and rock burst [18]. In order to study the gas outburst prevention theory of the coal seam permeability of the lower protective seam, He et al. put forward the basic hypothesis of the gas-solid coupling model of coal and put forward the permeability increasing coefficient of equivalent layer spacing by numerical simulation, which provides a theoretical basis for the gas drainage technology to prevent coal and gas outburst in the lower protective seam mining [19]. Zhou et al. analyzed the stress sensitivity of permeability and porosity of mudstone, coal, and sandstone based on Langmuir equation by overburden pressure permeability experiment of coal measures reservoir and concluded that the initial permeability and initial porosity of coal are significantly higher than those of mudstone and sandstone, and with the increase of effective stress, the permeability and stress sensitivity coefficients of coal, mudstone, and sandstone decrease in a wavy manner [20]. In order to study the effect of the difference swelling index on the evolution of coal permeability, Chuanzhong et al. established the coal permeability model and proposed the concept of differential swelling index, which theoretically defined the adsorption strain relationship of coal body, fracture, and matrix in equilibrium state, and clarified the effect of differential strain [21]. Zihao et al. studied the influence of effective stress and Klinkenberg effect on shale apparent permeability, used pulse decay permeameter to measure the core of shale formation in situ, and established a multiphysical shale transport model to consider the multiphysical coupling process in shale, to clarify the effect of bedding orientation on apparent permeability [22]. In order to study the unsteady seepage solution of hydraulic fracturing around vertical wells in oil and gas reservoirs, Wu et al. used numerical simulation method to establish the hydraulic fracturing influence model of vertical wells under the condition of unsteady seepage in oil and gas reservoirs and concluded that permeability and hydraulic gradient are the important factors determining whether hydraulic fracturing occurs in the rock [23]. In order to study the height of water flowing fractured zone in thin bedrock and thick clay coal seam, Hao et al. obtained the evolution law of coal reservoir in this area by means of field measurement, theoretical analysis, and numerical simulation, which provided an important theoretical basis for effectively preventing roof water hazards in mines [24]. In the study of permeability of clay-quartz mixture, Lu et al. used NMR and 40°C evaporation test to predict the permeability coefficient of quartz-clay mixture based on Timur-Coates model and obtained a simplified method to predict the permeability coefficient of quartz-clay mixture by NMR [25].

Zhou et al. established the model of the influence of creep deformation and matrix-fracture interaction on the permeability of deep coal and obtained that the permeability decreases with the decrease of pore pressure in the secondary stage and the initial stage of creep by using the fractional derivative transient pulse method and nonlinear least square method [26]. In order to study the permeability law of water-bearing coal seams under the condition of plastic flow, Guo et al. used the transient method to study the permeability changes of water-bearing coal seams and water-free coal seams and concluded that the internal fracture closure rate of water-bearing coals is lower than that of water-free coals, which is conducive to water storage and transportation [27]. Qinghe et al. studied the anisotropic permeability of different ranks of coal under the influence of CO2 adsorption and effective stress, conducted permeability tests under the conditions of cyclic loading and unloading and supercritical CO_2, and concluded that the permeability of coal seams varies with coal ranks, and the permeability is anisotropic, showing that the permeability of parallel layers is greater than that of vertical layers [28]. Haifeng et al. used the method of pore mechanics test for Biot tensor of argillaceous rocks to obtain the gas permeability and elastic properties of clay rock pores and found that gas adsorption-swelling has a greater impact on the migration and mechanical properties of argillaceous rocks in the long-term gas migration process [29]. Ma et al. aimed at the problem of floor water inrush in deep mining of Dongjiahe Coal Mine, through numerical simulation and combining with acoustic emission information of RFPA software and field microseismic monitoring data, the permeability characteristics of fractured rock mass were obtained, which showed that the main direction of permeability changed greatly with the change of surrounding rock pressure when the surrounding rock pressure was different [30]. In the study of permeability damage of coal under cyclic loading, Long and Shimin adopted pulse attenuation method and combined with matrix shrinkage concept to summarize the evolution law of coal permeability and concluded that the evolution of permeability directly controlled the seepage behavior of underground fluid, and the damage of average permeability was affected by loading and unloading paths [31]. Liang et al. studied the creep characteristics and constitutive model of coal. A series of creep experiments were carried out under gas pressure and triaxial compression. It was concluded that the creep deformation characteristics of coal were related to gas pressure and deviatoric stress, and the nonlinear model obtained could accurately describe the whole creep stage of coal [32]. Based on the porosity elasticity theory and uniaxial strain condition, Mathias studied the gas storage coefficient and permeability function of coalbed methane mining, established three analytical models to describe the changes of porosity and permeability, and concluded that without considering the gas adsorption strain, only one of the porosity models can obtain the correct uniaxial strain storage coefficient equation [33]. Yu et al. studied the permeability model of fractured rock mass and derived the formula of fracture permeability in theory and in combination with field experiments and concluded that the proposed permeability evolution description method and model can predict laboratory permeability data [34]. Xiaoyang et al. proposed a simple method of fitting pressure based on fracturing pressure drop under the condition of dynamic leakage coefficient, chose PKN model as the expansion model of hydraulic fracture, predicted the permeability of coal reservoir after fracturing by using the well test theory of water injection well, and concluded that the shape of hydraulic fracture is mainly determined by ground stress [35]. Shuaifeng et al. studied hydraulic fracturing sand-carrying permeability enhancement technology by high-frequency sand-carrying method and obtained that there are three stages in the evolution of cracks, and found that high-pressure fluid "water-sand" injection brings sand into high-frequency cracks, which produces propping force on the crack surface, hinders crack closure, and greatly improves gas permeability [36]. Luo studied the influence of water on the mechanical behavior of rock surrounding hard-rock tunnels [37, 38].

At present, the trend of coal mining into the deep is obvious; the deep coal seam and the surrounding rock of the roadway are in a complex environment, vulnerable to the coupling effect of high stress and high karst water pressure, and then easy to cause significant instability deformation characteristics. Therefore, an in-depth study of the mechanical behavior and permeability response characteristics and evolution law of coal and rock under stress-seepage coupling can provide a certain basic theory and basis for coal and gas outburst, water inrush accident prevention, and control of deep roadway surrounding rock stability control.

2. Experimental Principle and Methods

There are more than 10 kinds of methods for measuring rock permeability in the laboratory, which can be roughly classified into two categories: steady-state method and transient method. Because of steady-state method requires a large number of samples, a long test period, high cost, and confining pressure are not easy to control and other shortcomings. This experiment chooses the transient method to analyze the rock permeability and should pay special attention to when testing sample sealing and axial load is not zero, so the preset first strain value is not zero; confining pressure is greater than the pore pressure; pore pressure is higher than of the confining pressure; the plastic insulation tape and hot shrinkage in the sealed sample will be broken plastic cover test cannot be performed.

2.1. Experimental Principle. The principle of the water permeability test is shown in Figure 1. In the figure, $\sigma 1$ is the axial pressure, $\sigma 3$ is the confining pressure, $p1$ is the water pressure at the upper end of the specimen, and $p2$ is the

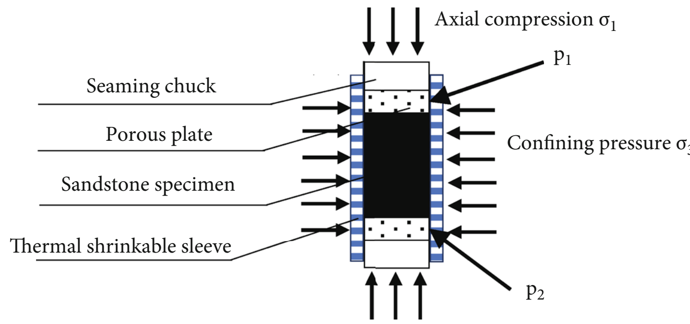

Figure 1: Sketch of permeability experiment principle.

water pressure at the lower end of the specimen. There is a permeable plate at both ends of the specimen, which is a steel plate with many evenly distributed holes The upper part of the permeable plate is the upper pressure head, and the lower part is the lower pressure head. There is a vertical hole in the center, and the plastic insulation belt and the heat-shrinkable plastic sleeve are used to seal the sample for the water flow channel.

In the test, the seepage flow was constant (1 mL/min), and the permeability pressure difference between the two sections changed with the deviatoric stress loading. In the process of specimen deformation and failure, the non-Darcy flow will occur with the expansion and penetration of microcracks. The influence of flow velocity on the calculation of permeability coefficient should be taken into account. In the whole process of the test, the flow velocity through the cross-section of the sample is small (8.5×10^{-6} m/s), so the Darcy steady flow method is adopted to test the permeability coefficient of the sample. That is, the permeability coefficient of the sample is calculated according to the measurement parameters such as the flow rate of the fluid through the sample and the permeability pressure difference between the two ends of the sample. The calculation formula is

$$k = \frac{qL\gamma_w}{\Delta pA} \times 10^{-4}, \tag{1}$$

where k is the permeability coefficient of the sample (cm/s), q is the seepage flow through the sample (mL/s), L is the length of the sample (mm), γ_w is the bulk density of water (kN/m^3), A is the cross-sectional area of the sample (mm^2), and Δp is the permeability pressure difference between the two ends of the sample (MPa).

2.2. Experimental Apparatus. Using MTS815 rock mechanics electrohydraulic servo system in the whole stress and strain in the process of a penetration test, the system has uniaxial compression, triaxial compression, and pore water pressure test, water seepage test, and other functions. The sample size is 50 mm × 100 mm, the maximum confining pressure is 60 MPa, the maximum axial deviatoric stress is 300 MPa, and the maximum pore water pressure is 60 MPa. The deviatoric stress loading can be carried out by controlling the pressure, displacement, and oil pump flow. Axial strain and circumferential strain can be measured simultaneously. The axial strain was measured by two linear displacement sensors (LVDT), and the circumferential strain was measured by a circumferential electronic strain gauge placed in the center of the sample height. The pore water pressure is applied from the bottom of the sample and is also the source of the osmotic pressure difference and seepage water. When the outlet valve connecting the upper end of the sample is opened, the pore water pressure at the upper end of the sample becomes 0. Under the action of the pressure difference between the upper and lower ends, an approximate one-dimensional seepage flow will be formed in the sample.

2.3. Specimen Preparation. The test samples are taken from 1232(1) working faces of the Panyidong Coal Mine in Huainan. The buried depth of the coal seam is about 720 m, the average dip angle is 5°, and the average thickness is 2.3 m. The coal removed from the working face is packed with plastic cloth and sent to the laboratory. The coal is crushed, and the particle size of coal with 60~80 mesh is screened. The briquette is made into briquette samples with a briquette size of Φ50 mm × 100 mm after the briquette mold is prepared on the rigid testing machine of 2000 kN, and the forming stress is stabilized at 100 MPa for 30 minutes. The briquette sample prepared is placed in the oven to dry and stored in the drying oven for test after cooling to room temperature. The prepared briquette samples are shown in Figure 2.

2.4. Experimental Scheme and Procedure. The samples used in the test are taken from no. 11 coal of Panyidong Coal Mine in Huainan. The uniaxial compressive strength of the samples is about 6.5 MPa, and the measured porosity is 12%-20%. Before the penetration test, the samples were immersed in water for 48 h to reach the saturation state, to ensure that the seepage flow in the samples during the test was unidirectional.

The test procedure is as follows:

(1) The sample is sealed with a rubber sleeve to ensure that the oil in the triaxial pressure chamber in the test does not mix with the water in the sample

(2) Apply a preset confining pressure value to the sample

Figure 2: Part of briquette samples.

(3) Apply pore water pressure in a flow-controlled manner. A reasonable water flow rate can ensure that the maximum pore water pressure does not exceed the confining pressure when stable seepage is formed, and the pore water pressure value of the sample after destruction is not lower than the instrument range. The water flow rate used in this test is 1 mL/min

(4) Peak strength of the sample and pressure control (1 MPa/min) is applied to load; after that, the oil pump flow control (0.05 mL/min) is applied to load until the specimen is damaged. The axial pressure is controlled by graded loading. The next load test was carried out after the pore water pressure stabilized at each load level

(5) The confining pressure values were applied in the test. Permeability tests in the process of deformation and failure were carried out on the samples under different confining pressure conditions using 2, 4, 6, and 8 MPa. To reduce the error caused by the difference of samples, three samples were selected for testing under each confining pressure condition. The test scheme is shown in Table 1

Table 1: Test scheme.

Sample number	Sample size		Confining pressure/ MPa
	Diameter/ mm	High/ mm	
ST-2-1	49.6	99.6	
ST-2-2	48.9	100.7	2
ST-2-3	50.3	99.5	
ST-4-1	48.9	99.8	
ST-4-2	49.3	100.5	4
ST-4-3	50.2	99.6	
ST-6-1	49.5	99.7	
ST-6-2	49.8	99.1	6
ST-6-3	49.3	99.3	
ST-8-1	50.3	99.8	
ST-8-2	49.6	100.4	8
ST-8-3	49.7	100.7	

3. Results and Discussion

3.1. Law of Penetration in the Full Stress-Strain Process. Permeability coefficient axial strain curves of samples under different constant confining pressures (2, 4, 6, and 8 MPa) were obtained, limited by length. Only the evolution curve of representative permeability deformation in the deformation and failure of each group of samples is listed here (as shown in Figure 3). Typical permeability test results for samples are presented in Table 2.

To obtain the coal deformation characteristics and permeability evolution response law under the stress-seepage coupling action, the volumetric strain and permeability response characteristics during the whole process of briquette deformation under different confining pressures were analyzed in this paper.

As can be seen from Figure 3 and Table 2, the stress-strain curve shape trend of briquette samples under different confining pressures is the same, and all of them have experienced five stages: nonlinear compaction stage, linear deformation stage, yield stage, strain-softening stage, and residual deformation stage. Under different confining pressures, the curves of permeability coefficient-axial strain are same, and the permeability coefficient of briquette samples has experienced a slow decrease stage, an obvious increase stage, and a steady increase stage.

In the first stage of the stress-strain curve, with the increase of axial compression, the stiffness of briquette samples gradually increases, the curve curves upward, and the initial defects gradually close. This stage is the nonlinear compaction stage. At the same time, due to the decrease of porosity in the sample, the channel for fluid flow becomes narrower, resulting in the decrease of seepage velocity. In the second stage, the stress-strain curves of briquette samples all vary approximately linearly. Under the action of external load, the briquette coal samples are squeezed and staggered among the pulverized coal particles, the cohesion decreases, and the deformation cannot be recovered after unloading. In this stage, the original gap between the pulverized coal particles is filled, and the fluid permeability coefficient continues to decrease. From the third stage, the permeability coefficient of briquette samples changed from a decrease to a sharp increase. With the increase of stress, the shear movement between the briquette particles began to promote the stable crack expansion, the stress-strain curve bent downward, the stiffness decreased, and the briquette entered the yield deformation stage. Under the action of shear movement, pulverized coal particles squeeze and dislocate each other, resulting in a large number of cracks and resulting in a sharp increase in permeability coefficient. In the fourth stage, the briquette samples developed further based on the shear failure, and the bearing capacity began to decline and entered the strain-softening stage. The internal structure of the briquette determined that no stress drop would occur, and the seepage velocity of the briquette increased steadily. In the fifth stage, the axial stress of the briquette remains unchanged, but its axial strain gradually increases, and the coal sample begins to creep and enters the stage of residual deformation. At this point, although the axial stress is unchanged and the specimen is in axial compression, the transverse deformation is constantly expanding, so the seepage velocity is still increasing, but the growth trend is slow.

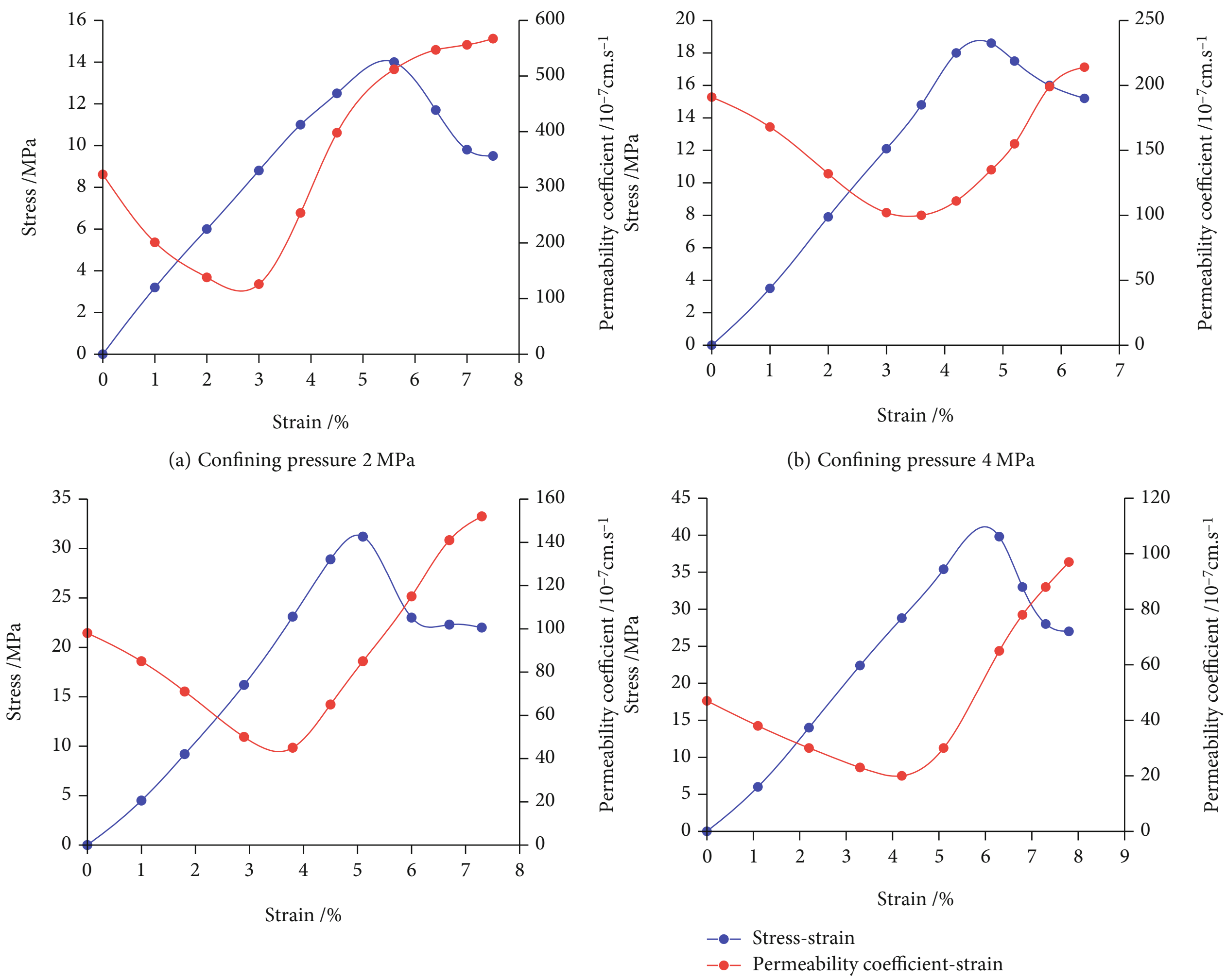

(a) Confining pressure 2 MPa

(b) Confining pressure 4 MPa

(c) Confining pressure 6 MPa

(d) Confining pressure 8 MPa

Figure 3: Variation curve of permeability coefficient during stress-strain process.

Table 2: Results of penetration test.

Sample number	Confining pressure/ MPa	Peak stress/ MPa	Peak strain%	Maximum permeability coefficient/10^{-7} cm·s^{-1}
ST-2-1		15.2	6.2	621
ST-2-2	2	14.0	5.6	567
ST-2-3		16.1	5.9	651
ST-4-1		18.6	4.8	214
ST-4-2	4	19.3	5.2	236
ST-4-3		17.8	4.9	227
ST-6-1		31.2	5.1	152
ST-6-2	6	32.6	5.5	147
ST-6-3		33.7	6.3	161
ST-8-1		39.8	6.3	97
ST-8-2	8	41.3	5.8	94
ST-8-3		40.8	5.7	91

Under different confining pressures, the permeability coefficient-axial strain curve has a similar change rule. With the increase of confining pressure, the permeability coefficient of briquette samples decreases gradually, and the higher the confining pressure, the more obvious the decrease of permeability coefficient is. This is mainly because the higher the confining pressure, the stronger the radial inhibition effect on briquette samples, and then, the crack opening inside the briquette will become smaller, that is, the width of the seepage throat will become narrower, which will lead to a smaller permeability value. The above laws indicate that the confining pressure has a significant effect on the permeability evolution of the briquette.

3.2. Analysis of Seepage Characteristics of Different Hoop Strains. In the process of permeability failure under axial compression, the circum-axial deformation reflects the evolution law of permeability in the process of yield, weakening, and failure from another Angle. The stress-circumferential strain curves and permeability coefficients of the samples under different constant confining pressures (2, 4, 6, and 8 MPa) are shown in Figure 4.

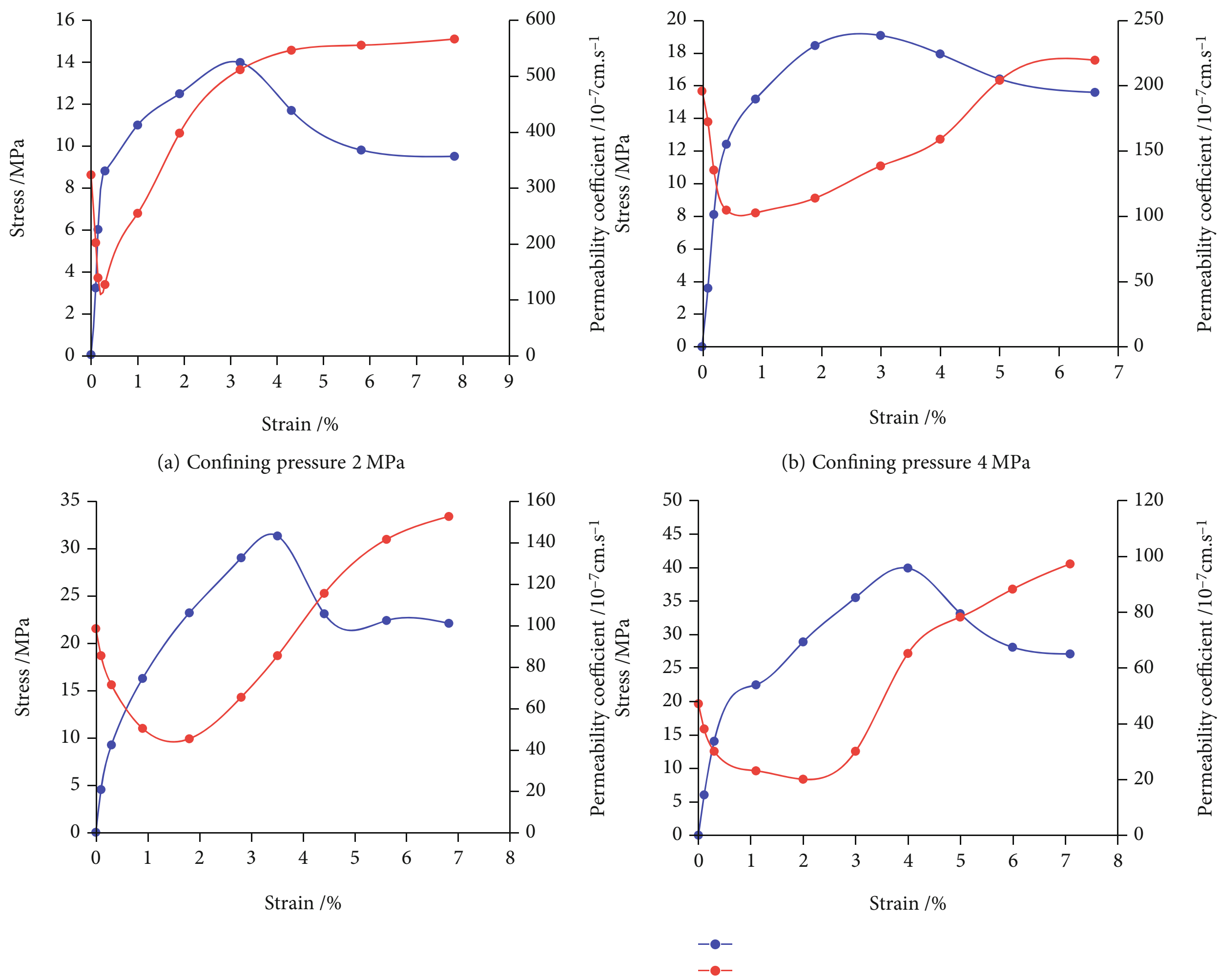

(a) Confining pressure 2 MPa

(b) Confining pressure 4 MPa

(c) Confining pressure 6 MPa

(d) Confining pressure 8 MPa

Figure 4: The relationship curve between hoop strain, permeability coefficient, and stress.

It can be seen from Figure 4 that the stress-circumferential strain curve and the stress-axial strain curve have the same trend of change, but the circumferential deformation more fully reflects the process of specimen yield, weakening, and failure than the axial deformation. In the process of specimen deformation and fracture, the change law of the influence of circum-axial strain and axial strain on permeability is the same, and the change law of permeability coefficient is basically the same. The permeability coefficient decreases with the increase of confining pressure, and the higher the confining pressure, the lower the permeability coefficient. The permeability coefficient corresponding to high confining pressure is far less than that corresponding to low confining pressure.

When the confining pressure is 2 MPa, the initial permeability coefficient is $323 \times 10^{-7}\ \mathrm{cm \cdot s^{-1}}$, and the maximum permeability coefficient after failure is $567 \times 10^{-7}\ \mathrm{cm \cdot s^{-1}}$. When the confining pressure is 4 MPa, the initial permeability coefficient is $191 \times 10^{-7}\ \mathrm{cm \cdot s^{-1}}$, and the maximum permeability coefficient after failure is $214 \times 10^{-7}\ \mathrm{cm \cdot s^{-1}}$. When the confining pressure is 6 MPa, the initial permeability coefficient is $98 \times 10^{-7}\ \mathrm{cm \cdot s^{-1}}$, and the maximum permeability coefficient after failure is $152 \times 10^{-7}\ \mathrm{cm \cdot s^{-1}}$. When the confining pressure is 8 MPa, the initial permeability coefficient is $47 \times 10^{-7}\ \mathrm{cm \cdot s^{-1}}$, and the maximum permeability coefficient after failure is $97 \times 10^{-7}\ \mathrm{cm \cdot s^{-1}}$. When briquette samples are subjected to initial stress, the initial value of permeability coefficient corresponding to the confining pressure of 2 MPa is 6.87 times that corresponding to the confining pressure of 8 MPa. After the briquette sample is damaged, the maximum permeability coefficient corresponding to the confining pressure of 2 MPa is 5.85 times that is corresponding to the confining pressure of 8 MPa.

The circumferential strain in the nonlinear compaction stage and the linear deformation stage is much smaller than the axial strain, and the circumferential strain deviates from the linear state more quickly than the axial strain, and the circumferential strain increases faster in the yield stage. Compared with the axial strain, the circumferential strain at the peak strength is smaller, and the increased range of the circumferential strain from the peak strength to the maximum permeability coefficient is obviously larger than that of the axial strain. The variation law of the circumferential strain is very similar to that of the permeability coefficient. In the nonlinear compaction stage and the linear deformation stage, the circumferential strain increases slowly, the variation range is small, and the permeability coefficient decreases. At the yield stage, the circumferential strain increases rapidly, and the permeability coefficient increases slightly and then sharply. Thus, compared with the axial strain, the permeability coefficient is more sensitive to the change of the circumferential strain.

3.3. Analysis of Permeability Characteristics of Different Confining Pressures. The test results of stress and permeability coefficient of samples in the process of deformation and failure under different confining pressures are shown in Table 3.

Under different confining pressures, the samples show different postpeak variation characteristics. The increase of confining pressure usually results in the axial stress corresponding to the peak stress of the samples changing greatly, and the slope of the post-peak curve gradually decreases. The change of confining pressure also has a strong effect on the dilatancy behavior of the sample. Under the condition of low confining pressure, the brittle failure of samples is accompanied by a large volume expansion. With the increase of confining pressure, the samples show obvious shear failure. The influence of confining pressure on the dilatancy of samples directly results in the difference in the permeability law of samples under different confining pressures. As can be seen from Table 3, (1) with the increase of confining pressure, the peak stress and residual strength increased significantly. (2) Both the initial and maximum values of the permeability coefficient of the sample decreased, and the maximum value of the permeability coefficient increased by 2.44×10^{-4} cm/s compared with the initial value at 2 MPa confining pressure. When the confining pressure increases to 8 MPa, the maximum permeability coefficient only increases by 5.0×10^{-6} cm/s compared with the initial value. It can be seen that the increase of confining pressure makes the increase rate of maximum permeability greatly decrease. It can be seen that the permeability coefficient-strain curve gradually slows down with the increase of confining pressure.

In the process of specimen deformation and failure, the influence of confining pressure on the permeability of the specimen can be analyzed from two stages: first, the pore is the main seepage channel stage before the specimen failure; the second is that the main seepage channel stage is through fracture after specimen failure. The permeability coefficient of briquette samples in the initial stage decreases with the increase of confining pressure, showing a logarithmic function (see Figure 5(a)). The relationship between permeability coefficient and confining pressure in the initial stage is shown in Equation (2). After failure, the permeability coefficient of briquette samples gradually decreases with the increase of confining pressure, presenting a power function (see Figure 5(b)), and the greater the confining pressure, the more obvious the permeability coefficient decreases.

Table 3: Triaxial permeability test results under different confining pressures.

Confining pressure/MPa	Stress/MPa		Permeability coefficient/10^{-7} cm·s^{-1}	
	Peak value	Residual value	Initial value	Maximum
2	14.0	9.5	323	567
4	18.6	15.2	191	214
6	31.2	22.1	98	152
8	39.8	27.1	47	97

The relationship between permeability coefficient and confining pressure is shown in Equation (3).

$$k = 1304.7\sigma_3^{-1.242} \quad R^2 = 0.9916, \tag{2}$$

$$k = -201.4 \ln \sigma_3 + 464.38 \quad R^2 = 0.9984. \tag{3}$$

3.4. Discussion. It is relatively easy to make briquette samples, which are pressed and formed by fine particles. The briquette samples have a standard size, smooth surface, and uniform texture. According to the mechanical characteristics of briquette samples, the total stress-strain curve of briquette samples changes gently, which is different from the existing mechanical characteristics of raw coal samples to some degree. The next step is to study the mechanical characteristics and seepage characteristics of raw coal samples under the coupling action of stress and seepage.

The type of coal samples under the action of stress-seepage coupling of seepage characteristics shows that the permeability of specimen under low confining pressure conditions is greater than the high confining pressure permeability; based on the results, in the coal seam gas extraction in the process, take certain measures, such as hydraulic fracturing, and presplitting blasting, making smoke extracting seam permeability increases advantageous to the coal seam and efficient gas extraction.

4. Penetration Mechanism in the Process of Coal Deformation and Failure

Coal is a highly heterogeneous material with multiple cracks, and its deformation and failure process is essentially a dynamic evolution process of crack initiation, propagation, interaction, and finally, coalescence. The stress state of the coal body has a direct influence on the permeability, which can be theoretically proved by Lious's empirical formula

$$k_f = k_0 e^{-\alpha\sigma}, \tag{4}$$

where k_f is the permeability coefficient of the crack; K_0 is the initial permeability coefficient; α is constant; and σ is the normal stress. The above formula reflects that the relationship between the permeability coefficient and the normal stress is negative exponential. With the increase of the normal stress, the permeability coefficient also increases.

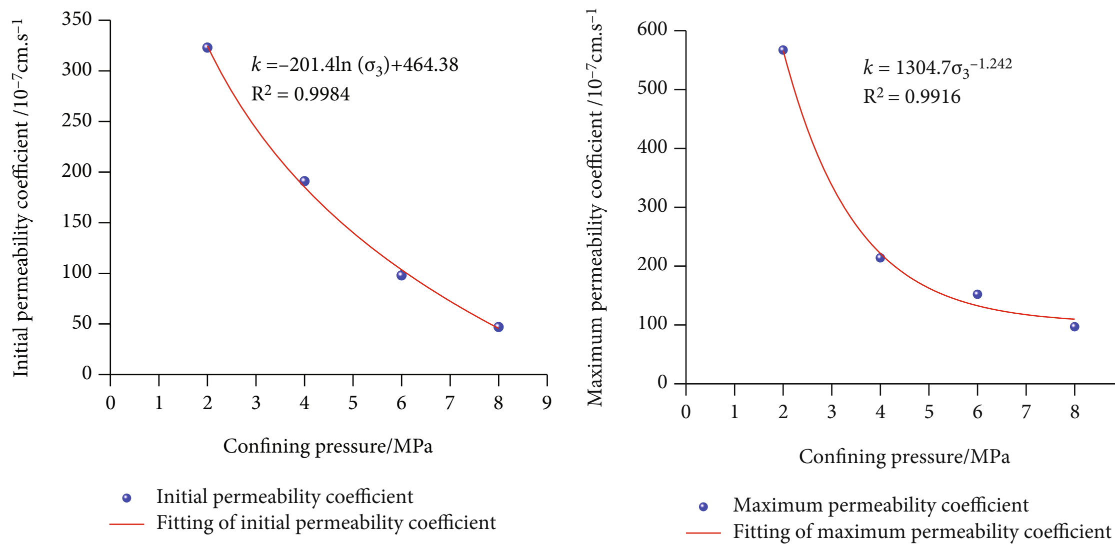

(a) Initial permeability coefficient

(b) Maximum permeability coefficient

Figure 5: The relationship between permeability coefficient and confining pressure.

The influence of the change of stress state on the permeability of briquette can be seen directly from the relationship curves of stress-axial strain, permeability, and stress-circumferential strain-permeability. When the stress-strain of briquette goes through five stages, nonlinear compaction stage, linear deformation stage, yield stage, strain-softening stage, and residual deformation stage, the permeability of briquette corresponding to each stage also changes correspondingly. The prepeak change of the briquette is mainly caused by compression deformation. At this time, the permeability of the briquette is relatively low, and the permeability is the lowest in the linear deformation stage, and the pores and cracks of the sample reach the maximum closure. With the gradual increase of strain, the crack inside the sample expands to reach through, and the briquette material loses its ultimate bearing capacity. In the postpeak stage of briquette, the strain continues to increase, the crack of the sample increases steadily, and the permeability coefficient also increases steadily. In addition, the circumferential strain can reflect the permeability of the sample more sensitively than the axial strain.

In fact, the permeability of coal type and the characteristics of coal itself also involve the concept of microscale seepage properties, such as topological structure characteristics of porous media itself medium and pore and fracture distribution, pore surface roughness, and the distribution of pores and fractures, and a porous media and the relationship between the fluid, such as surface wettability, adsorption and desorption characteristics, saturation distribution, and distribution details between phases.

Besides, in the process of seepage, the maximum permeability coefficient of briquette samples does not appear at the peak of stress-strain, but near its peak value. In short, the study of the seepage mechanism in briquette deformation and failure process has a very important guiding significance for mining engineering and oil and gas field development.

5. Conclusions

(1) The stress-strain of briquette goes through five stages: nonlinear compaction stage, linear deformation stage, yield stage, strain-softening stage, and residual deformation stage. The prepeak change of briquette is mainly caused by compression deformation, and the permeability of briquette is relatively low, and the permeability is the lowest in the linear deformation stage. After entering the yield failure stage, the permeability of the briquette begins to increase with the expansion and penetration of new fractures, and the maximum permeability of the briquette is basically near the peak value of briquette strength. In the residual deformation stage, the new crack increases slowly, and the briquette permeability coefficient changes steadily

(2) The stress-axial strain curve has the same variation trend as the stress-circumferential strain curve, but the circumferential deformation more fully reflects the process of specimen yield, weakening, and failure than the axial deformation. In the process of specimen deformation damage, hoop strain and axial strain effect on the permeability variation law of basic consistent, and the permeability coefficient with the increase of confining pressure and decreases, and the higher the confining pressure, the lower the permeability coefficient, the confining pressure increases rate under the same conditions; high confining pressure corresponding to the permeability coefficient of permeability coefficient is far less than the low confining pressure

(3) Confining pressure affects briquette permeability by affecting briquette expansion behavior. With the increase of the confining pressure, the permeability

of the sample decreases, and the permeability coefficient decreases with the increase of the confining pressure at the initial stage, showing a logarithmic function. After failure, briquette samples show a power function change rule, and the greater the confining pressure is, the more obvious the permeability coefficient decreases

Data Availability

The data used to support the findings of this study are included within the article.

Conflicts of Interest

The authors declare that they have no conflicts of interest.

Acknowledgments

This paper was financially supported by the National Natural Science Foundation (51904010, 51874002, and 51874006) and Anhui Provincial Natural Science Foundation (1808085QE149, 2008085ME142, and 2008085ME147).

References

[1] H. Wang, W. Xu, and J. Zuo, "Compact rock material gas permeability properties," *Physica B*, vol. 449, no. 6, pp. 10–18, 2014.

[2] P. Xu and S. Q. Yang, "Permeability evolution of sandstone under short-term and long-term triaxial compression," *International Journal of Rock Mechanics and Mining Sciences*, vol. 85, no. 5, pp. 152–164, 2016.

[3] D. W. Hu, H. Zhou, F. Zhang, and J. F. Shao, "Evolution of poroelastic properties and permeability in damaged sandstone," *International Journal of Rock Mechanics and Mining Sciences*, vol. 47, no. 6, pp. 962–973, 2010.

[4] H. L. Wang, W. Y. Xu, C. J. Jia, M. Cai, and Q. X. Meng, "Experimental research on permeability evolution with microcrack development in sandstone under different fluid pressures," *Journal of Geotechnical and Geoenvironmental Engineering*, vol. 142, no. 6, article 04016014, 2016.

[5] T. Jiang, J. F. Shao, W. Y. Xu, and C. B. Zhou, "Experimental investigation and micromechanical analysis of damage and permeability variation in brittle rocks," *International Journal of Rock Mechanics and Mining Sciences*, vol. 47, no. 5, pp. 703–713, 2010.

[6] C. Zhu, M. C. He, M. Karakus, X. H. Zhang, and Z. G. Tao, "Numerical simulations of the failure process of anaclinal slope physical model and control mechanism of negative Poisson's ratio cable," *Bulletin of Engineering Geology and the Environment*, vol. 80, no. 4, pp. 3365–3380, 2021.

[7] B. Li, R. Bao, Y. Wang, R. Liu, and C. Zhao, "Permeability evolution of two-dimensional fracture networks during shear under constant normal stiffness boundary conditions," *Rock Mechanics and Rock Engineering*, vol. 54, no. 3, pp. 1–20, 2021.

[8] X. Zhang, H. Chen, C. Yao et al., "Seepage characteristics of triaxial compression-induced fractured rocks under varying confining pressures," *International Journal of Geome Chanics*, vol. 20, no. 9, article 04020160, 2020.

[9] B. Liu, J. Li, Q. Liu, and X. Liu, "Analysis of damage and permeability evolution for mudstone material under coupled stress-seepage," *Materials*, vol. 13, no. 17, p. 3755, 2020.

[10] J. Zhao, L. Bo, C. Juntao, and J. Ning, "Mechanism of seepage-stress fault water inrush and grouting seal," *Arablan Journal of Geosciences*, vol. 13, no. 11, p. 404, 2020.

[11] S. Di, C. Jia, W. Qiao, W. Yu, and K. Li, "Theoretical and experimental investigation of characteristics of single fracture stress-seepage coupling considering microroughness," *Mathematical Pronlems in Engineering*, vol. 2017, article 6431690, pp. 1–12, 2017.

[12] Z. Cheng, H. Pan, Q. Zou et al., "Gas flow characteristics and optimization of gas drainage borehole layout in protective coal seam mining: a case study from the Shaqu coal mine, Shanxi Province, China," *Natural Resources Research*, vol. 30, no. 2, pp. 1481–1493, 2021.

[13] J. Annan, S. Zheng, and S. Wang, "Stress-seepage-damage coupling modelling method for tunnel in rich water region," *Engineeging Computations*, vol. 37, no. 8, pp. 2659–2683, 2020.

[14] W. Wang, Z. Luo, Y. Qin, J. Xiang, L. Wen, and S. Ma, "Multiphysics coupling model of rock mass considering damage and disturbance and its application," *Advances in Civil Engineering*, vol. 2018, 9 pages, 2018.

[15] S. Sha and Z. Guoxin, "Modeling of hydraulic fracture of concrete gravity dams by stress-seepage-damage coupling model," *Mathematical Pronlems in Engineering*, vol. 2017, pp. 1–15, 2017.

[16] Q. Liu, B. Lin, Y. Zhou, and Y. Li, "Permeability and inertial resistance coefficient correction model of broken rocks in coal mine goaf," *Powder Technology*, vol. 384, pp. 247–257, 2021.

[17] Q. Sun, J. Zhang, M. Li, and N. Zhou, "Experimental evaluation of physical, mechanical, and permeability parameters of key aquiclude strata in a typical mining area of China," *Journal of Cleaner Production*, vol. 267, article 122109, 2020.

[18] G. Dong, X. Liang, and Z. Wang, "The properties of a coal body and prediction of compound coal-rock dynamic disasters," *Shock and Vibration*, vol. 2020, Article ID 8830371, 13 pages, 2020.

[19] A. He, H. Fu, B. Huo, and C. Fan, "Permeability enhancement of coal seam by lower protective layer mining for gas outburst prevention," *Shock and Vibration*, vol. 2020, Article ID 8878873, 12 pages, 2020.

[20] D. Zhou, K. Li, H. Wang et al., "Permeability experiments with overburden pressure of coal measure reservoirs and numerical analysis of its stress sensitivity: a case study of Qinshui Basin, China," *Energy Exploration & Exploitation*, vol. 38, no. 5, article 0144598720946495, pp. 1690–1705, 2020.

[21] C. Jiang, Z. Zhao, X. Zhang, J. Liu, D. Elsworth, and G. Cui, "Controlling effects of differential swelling index on evolution of coal permeability," *Journal of Rock Mechanics and Geotechnical Engineering*, vol. 12, no. 3, pp. 461–472, 2020.

[22] L. Zihao, R. Nino, and C. Cheng, "Using pressure pulse decay experiments and a novel multi-physics shale transport model to study the role of Klinkenberg effect and effective stress on the apparent permeability of shales," *Journal of Petroleum Science and Engineering*, vol. 189, p. 107010, 2020.

[23] Y. Wu, Z. Huang, K. Zhao, W. Zeng, Q. Gu, and R. Zhang, "Unsteady seepage solutions for hydraulic fracturing around vertical wellbores in hydrocarbon reservoirs," *International Journal of Hydrogen Energy*, vol. 45, no. 16, pp. 9496–9503, 2020.

[24] H. Fan, L. Wang, Y. Lu, Z. Li, W. Li, and K. Wang, "Height of water-conducting fractured zone in a coal seam overlain by thin bedrock and thick clay layer: a case study from the Sanyuan coal mine in North China," *Environmental Earth Sciences*, vol. 79, no. 6, p. 125, 2020.

[25] Z. Lu, S. Aimin, and W. Wang, "Permeability evaluation of clay-quartz mixtures based on low-field NMR and fractal analysis," *Appliend Scienced-Basel*, vol. 10, no. 5, p. 1585, 2020.

[26] H. W. Zhou and L. Zhang, "Effects of matrix-fracture interaction and creep deformation on permeability evolution of deep coal," *International Journal of Rock Mechanics and Mining Sciences*, vol. 127, p. 104236, 2020.

[27] J. Guo, J. Liu, Q. Li, and Z. Chen, "Study on the Permeability evolution and its formation mechanism of Xiaojihan aquifer coal seam under plastic flow," *Geofluids*, vol. 2020, Article ID 2147503, 16 pages, 2020.

[28] Q. Niu, L. Cao, S. Sang et al., "Study on the anisotropic permeability in different rank coals under influences of supercritical CO_2 adsorption and effective stress and its enlightenment for CO_2 enhance coalbed methane recovery," *Fuel*, vol. 262, p. 116515, 2020.

[29] H. Yuan, F. Agostini, F. Skoczylas, and J. Talandier, "About adsorption effects on the poroelastic properties and gas permeability of COx claystone," *European Journal of Environmental and Civil Engineering*, vol. 24, no. 2, pp. 267–282, 2020.

[30] K. Ma, L. Wang, Y. Peng, L. Long, S. Wang, and T. Chen, "Permeability characteristics of fractured rock mass: a case study of the Dongjiahe coal mine," *Geomatics, Natural Hazards and Risk*, vol. 11, no. 1, pp. 1724–1742, 2020.

[31] F. Long and L. Shimin, "Evaluation of permeability damage for stressed coal with cyclic loading: an experimental study," *Intwrnational Journal of Coal Geology*, vol. 216, article 103338, 2019.

[32] L. Zhang, X. C. Li, J.-X. Gao, Z.-X. An, X.-H. Yang, and B.-S. Nie, "Creep characteristics and constitutive model of coal under triaxial stress and gas pressure," *Energy Science & Engineering*, vol. 8, no. 2, pp. 501–514, 2020.

[33] A. Mathias Simon, "Storage coefficients and permeability functions for coal-bed methane production under uniaxial strain conditions," *Transport in Porous Media*, vol. 130, no. 2, pp. 627–636, 2019.

[34] Z. Yu, C. Wang, and B. Jing, "Permeability model of fractured rock with consideration of elastic-plastic deformation," *Energy Science & Engineering*, vol. 8, no. 2, pp. 441–451, 2020.

[35] X. Zhang, C. Wu, Z. Wang, and D. Xu, "Postfracturing permeability prediction for CBM well with the analysis of fracturing pressure decline," *Energy Science & Engineering*, vol. 7, no. 6, pp. 3111–3123, 2019.

[36] Y. Shuaifeng, M. Haifeng, C. Zhiheng et al., "Permeability enhancement mechanism of sand-carrying hydraulic fracturing in deep mining: a case study of uncovering coal in cross-cut," *Energy Science & Engineering*, vol. 7, no. 5, pp. 1867–1881, 2019.

[37] Y. Luo, "Influence of water on mechanical behavior of surrounding rock in hard-rock tunnels: an experimental simulation," *Engineering Geology*, vol. 277, article 105816, 2020.

[38] Y. Luo, F.-q. Gong, X.-b. Li, and S.-y. Wang, "Experimental simulation investigation of influence of depth on spalling characteristics in circular hard rock tunnel," *Journal of Central South University*, vol. 27, no. 3, pp. 891–910, 2020.

Hindawi
Geofluids
Volume 2021, Article ID 7153015, 11 pages
https://doi.org/10.1155/2021/7153015

Research Article

The Effects of Precrack Angle on the Strength and Failure Characteristics of Sandstone under Uniaxial Compression

Shuai Zhang[1] **Jinhai Xu**[1] **Liang Chen**[1] **Hideki Shimada**[2] **Mingwei Zhang**[3] **and Haiyang He**[1]

[1]*State Key Laboratory of Coal Resources and Safe Mining, China University of Mining and Technology, Xuzhou 221116, China*
[2]*Department of Earth Resources Engineering, Faculty of Engineering, Kyushu University, 744 Motooka, Nishi-ku, Fukuoka 819-0395, Japan*
[3]*State Key Laboratory for Geomechanics and Deep Underground Engineering, China University of Mining and Technology, Xuzhou 221116, China*

Correspondence should be addressed to Jinhai Xu; ts20020122p21@cumt.edu.cn

Received 6 September 2021; Revised 23 September 2021; Accepted 24 September 2021; Published 14 October 2021

Academic Editor: Zhijie Wen

Characterization of the mechanical properties of cracked rock masses is essential for ensuring the long-term stability of the engineering environment. This paper is aimed at studying the relationship between the strength characteristics of specimen and the angle of precrack, as well as the interaction of cracks under uniaxial compression. To this end, two sandstone specimens, distinguished with a single and three precracks, were built using the PFC software. For the former case, both the peak strength and elastic modulus increase to a peak value as the crack angle α gets closer to the forcing (loading) direction. For the latter case, the strength experiences a trend of increasing-maintaining trend as the crack angle α gets closer to the forcing direction, and the elastic moduli are barely affected. For the specimens containing a single precrack, their crack numbers increased approximately in a one-step or two-step stair pattern with increasing axial strain; whereas for the specimens containing three cracks, their crack numbers all showed a multistep growth trend. Furthermore, the failure mode of the specimen is closely related to the precrack angle. However, if the precrack distribution does not affect the original crack propagation path, it will hardly affect the mechanical properties of the specimen.

1. Introduction

Rock is widely distributed on the earth's surface. As a natural material, inevitably, there are defects such as cracks inside the rock which are induced by thermal stress, erosion, earthquakes, human engineering disturbances, etc. [1–3]. As an example, at Hornelen, western Norway, sandstone and conglomerate fill a fault-enclosed basin, about 70×30 km, which is the remains of a once larger basin. The basin sediments are about 100~200 m thick and are of continuous transversal cycles, consisting of beds about 2 m thick. The cracks and joints there caused by the long-time affection of low temperature and ocean erosion have been extremely developed [4–7], as shown in Figure 1. The existence of cracks not only reduces the material strength of the rock but also accelerates the damage process, which poses safety hazards to the construction of slopes and underground projects [2, 5, 7, 8]. Therefore, it is of great significance to study the strength characteristics of cracked specimens and the interaction of multiple cracks within the specimen.

The mechanical properties of defected rock mass have been a hot topic in the field of geotechnical engineering, and rich results have been achieved [2, 9–11]. Differing in the number of predefects, the current researches can be mainly grouped into two categories. The first type of research mainly focuses on rock mass, and the number of precracks reaches hundreds to thousands [5, 6, 12–14]; the second type of research focuses on laboratory specimen, and the number of predefects is generally less than four [15–17].

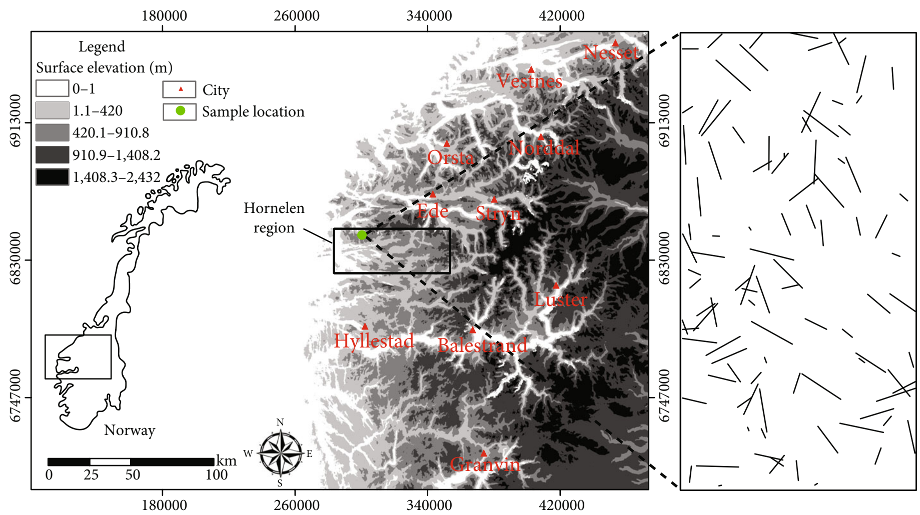

Figure 1: Outcrop map of the natural fracture system in the sandstone at Hornelen Basin, western Norway [5–7].

For the first type of research, due to the large size of the specimen, the current research mainly focuses on the location of rock damage [12], the fracture surface roughness [13, 18], and the specimen heterogeneity [5, 6]. Only a few studies have looked into the strength characteristics of specimens [2]. Shi et al. [2, 7] investigated the correspondence between crack distribution modes and rock mechanical properties, as well as the strength damage theory. However, the number of distributed cracks involved in the above studies is excessive; the crack propagation is thus affected by too many factors. As a result, it is hard to identify the influence of the crack interaction on the strength characteristics of the specimen.

For the second type of research, predefects are mainly made by hydraulic cutting (experiment) or the particle element deleting (numerical simulation). The elastic modulus, compressive strength, shear strength, and failure mode of the specimen were analyzed by changing its shape and size [16, 17], the confining pressure [19], or the angle [20–22] as well as the combination and number of predefects [10, 11]. These researches are of great significance for understanding the mechanical properties of defected rock, although large defects exist in crack prefabrication—the width of the cracks is larger than 2 mm [10, 14]. Therefore, the research object of this research in the strict sense is fissured rock mass rather than the commonly observed cracked rock mass in nature [5, 7]. The mechanical properties of cracked rock mass are obviously not equivalent to that of the fissured rock mass, and the research on cracked specimen is extremely insufficient. Moreover, the current researches on multifissured rock masses only focus on the combinations of fissures and lack a comparative analysis, so it is very hard to understand the specific impact of a fissure on the mechanical properties of a specimen [10, 23, 24].

In this paper, two sets of sandstone specimens differing in containing a single crack and three cracks were built using the PFC software. The relationship between the strength characteristics of the specimen and the angle of the precrack, as well as the interaction of cracks under uniaxial compression, was studied.

2. Numerical Model of Cracked Sandstone Specimen

2.1. Particle Flow Code (PFC). PFC^{2D} software is very convenient in realizing the crack prefabrication and is outstanding in simulating the mechanical properties and failure process of rock and soil medium [23]. Due to these advantages, the PFC^{2D} software was selected for the simulation in this study. The particles and the bonds between particles are used to characterize the medium in the software, where the particles are simulated with rigid body of unit thickness. Two types of bonding effects of rock media suitable for this simulation are selected, namely, contact bond and parallel bond, as shown in Figure 2. The contact bond reflects the normal and tangential interactions (forces) between particles (see Figure 2(a)), while the parallel bond transmits both the force and the moment (see Figure 2(b)). It is widely accepted that these two kinds of bonds both exist in the interior of rock and soil [7], so they are used in this paper.

2.2. Calibration of Sandstone Mesoscopic Parameters. To ensure the credibility of the simulation, it is necessary to determine the model parameters for the simulation. For PFC software, the particles and bonds are used to characterize the medium. Therefore, it is necessary to determine mesoscopic parameters that reflected the physical and mechanical properties of the particles and bonds. Due to the limitation in observation techniques, these parameters can hardly be obtained through laboratory tests. For uniaxial compression simulation with PFC, the "trial and error" method is usually used to calibrate the mesoscopic parameters of the specimen. As shown in Figure 3, m_i is the strength parameter of Hoek-Brown [27]. In this method, the full stress-strain curve and the corresponding failure mode of a representative specimen need to be firstly obtained through

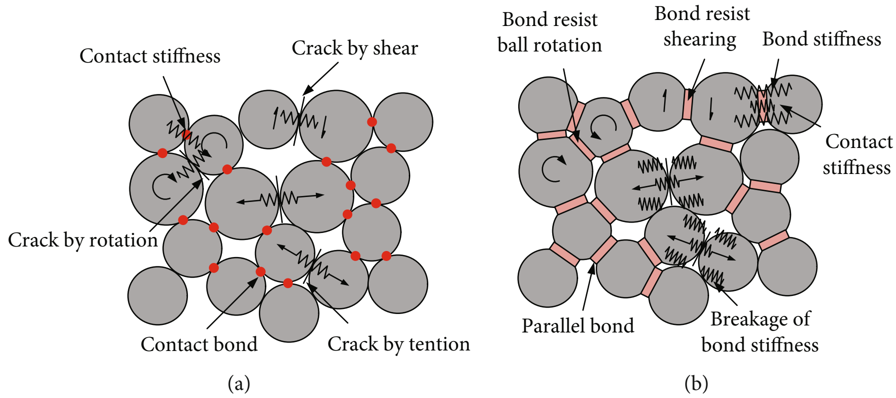

Figure 2: Cohesive model and its micromechanical behavior schematic diagram [7, 25, 26]: (a) contact bonds reflect the normal and tangential interactions (forces) between particles; (b) parallel bonds transmit both the force and the moment.

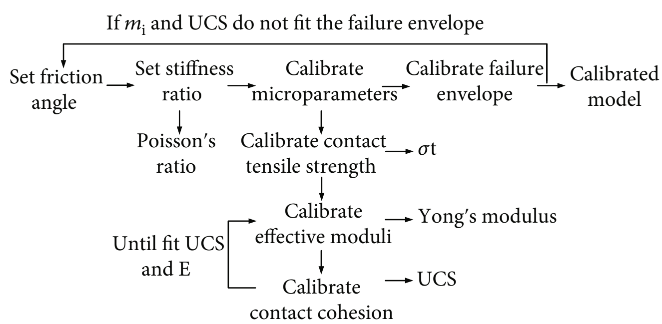

Figure 3: The "trial and error" method parameter checking process of the PFC model [27].

laboratory tests; next, a numerical model is established, and the parameters such as the stiffness, elastic modulus, and the tensile and cohesive strength are adjusted until the numerical curve is roughly consistent with the experimental curve; finally, fine-tune the parameters until the failure mode of the numerical specimen is consistent with that of the experimental specimen [27].

In this paper, the uniaxial compression tests on sandstone specimens were performed by the MTS815 test machine of the State Key Laboratory for Geomechanics and Deep Underground Engineering, China University of Mining and Technology, as shown in Figure 4. The size of the laboratory specimen is 50 mm by 100 mm (diameter and height), and the loading was controlled by displacement with the rate of 0.002 mm/timestep [2].

The intact sandstone model with 31190 particles was established using PFC^{2D} software. The size and loading strategy of the sandstone model are consistent with that of the laboratory test. The parameters of the numerical specimen were calibrated using the "trial and error" method. Model results are compared with the experimental data, showing the stress-strain curve and failure mode of the specimen in Figures 5 and 6, respectively.

Figure 4: MTS815 test machine.

As shown in Figures 5 and 6, the full stress-strain curve and the failure mode of the numerical specimen are qualitatively consistent with that of the experimental specimen. Note that the simulation curves deviate from the experimental ones in the prepeak stage, which is because that there is an obvious compaction stage for the laboratory specimen before the peak. To the best of our knowledge, this stage cannot be simulated by all numerical software including

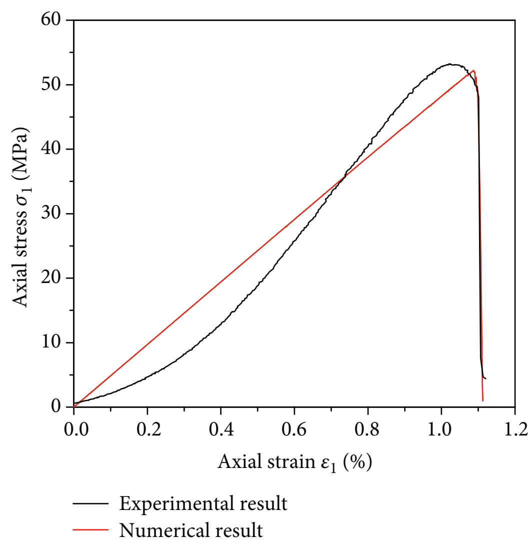

Figure 5: The comparison between the numerical and experimental stress-strain curves of intact sandstone specimens.

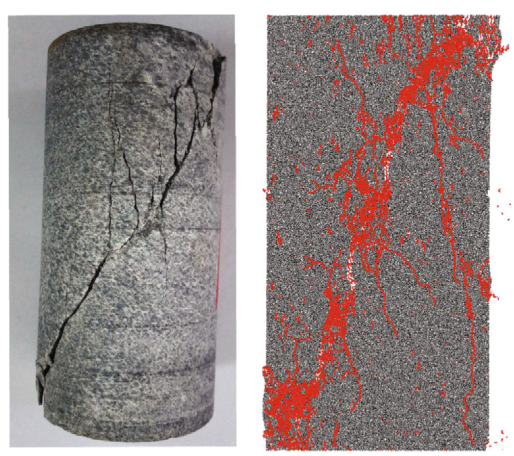

(a) (b)

Figure 6: Failure modes of intact sandstone specimens obtained through simulation and experiment: (a) experimental failure mode; (b) numerical failure mode.

PFC software [2, 14]. Currently, there are two main ways to cope with this problem. The first way is to ensure the consistency of the peak strength and peak strain with that of the actual specimen but might leave a difference in the elastic modulus [7, 28–30]. An alternative method is to ensure the elastic modulus and the peak strength to be consistent with that of the actual specimen but might lead to a significant difference in the peak strain [14].

Considering the study of rock strength to be the priory focus of this research, the first approach was chosen. Furthermore, the relative errors of peak strength and peak strain are 1.7% and 3.8%, respectively. The simulation results qualitatively agree with the experimental results, and the simulation parameters truly reflect the mechanical characteristics of the laboratory specimen.

Table 1: Mesoscopic parameters of the PFC^{2D} medium.

Parameters	Value
Minimum particle size (mm)	0.1
Maximum particle size (mm)	0.3
Density (kg/m^3)	2700
Porosity	0.15
Contact bond modulus (GPa)	0.6
Contact bond stiffness ratio	1.0
Friction coefficient	0.8
Parallel bond tensile strength (MPa)	26.5
Parallel bond cohesion (MPa)	32
Parallel bond friction angle (°)	32.5
Parallel bond modulus (GPa)	8.7
Parallel bond stiffness ratio	1.0

The microscopic parameters of the intact sandstone specimen determined by the “trial and error” method are listed in Table 1.

2.3. Numerical Model of Sandstone Specimen with a Single Crack or Three Precracks. In PFC^{2D}, crack, as a planar and finite-sized discrete element, is characterized by a segment with two vertex object ends. The prefabrication of the crack is realized through the Discrete Fracture Network (DFN). In the DFN module of PFC software, the input parameters to realize the prefabrication of each crack are the length, angle, and center point, with the width of the crack to be insignificant [23, 31–34]. In order to study the relationship between the strength characteristics and the angle of the precrack, as well as the interaction of the cracks, two sets of specimens that contain a single crack and three cracks were established, as shown in Figure 7.

It can be seen from Figure 7(a) that each specimen in the first group contains one precrack, and the angle of the crack is set as 0°, 30°, 60°, 90°, 120°, and 150°, respectively. The lower left corner of the specimen is set as the coordinate origin, and the x and y coordinates of the crack center point are 25 mm and 50 mm, respectively. In the second group, two extra fixed-angle precracks were added on the basis of the specimens in the first group, denoted as precracks ② and ③. For cracks ② and ③, their angles are both 45° and their center points are located at (25 mm, 75 mm) and (25 mm, 25 mm), respectively, as shown in Figure 6(b). In addition, the crack lengths of the precracks in Figure 7 are all 25 mm. The smooth joint model was used to describe the mechanical properties of the crack. The parameters used for the model are listed in Table 2 [2]. It can be seen from the table that the existence of cracks weakens the cohesion on both sides of the crack surface.

3. Simulation Results and Analysis

3.1. Strength Characteristics of the Cracked Sandstone Specimen. The full stress-strain curve of the cracked specimens is shown in Figure 8, and the extracted variation of the strength with the precrack angles is shown in Figure 9.

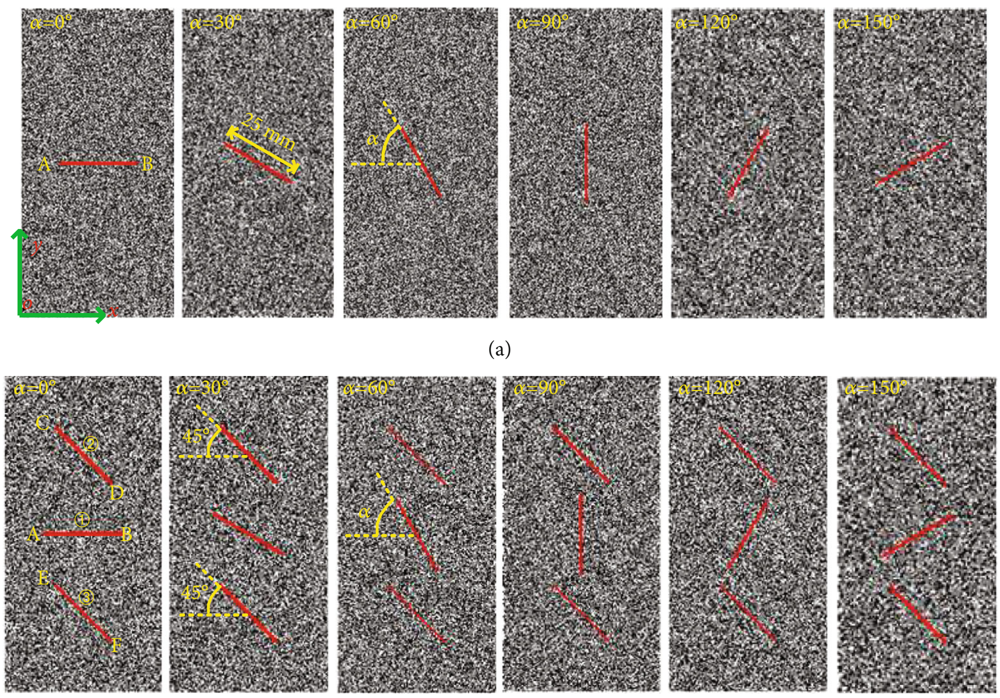

(a)

(b)

Figure 7: Sandstone specimens with a single precrack and three precracks: (a) sandstone specimen with a single precrack; (b) sandstone specimen with three precracks.

Table 2: Mechanical parameters of the smooth joint model [2].

Parameters	Value
Normal stiffness per unit area (GPa)	2
Shear stiffness per unit area (GPa)	2
Friction coefficient	0.35
Tensile strength (Pa)	0
Cohesion (Pa)	0

It can be seen from Figure 8(a) that both the strengths and the elastic moduli of the specimens containing a single crack increase first and then decrease with the increase of the precrack angle. The uniaxial compressive strengths (UCS) of the specimen with the precrack angle of 0°, 30°, 60°, 90°, 120°, and 150° are 21.79 MPa, 26.42 MPa, 33.20 MPa, 49.49 MPa, 40.05 MPa, and 26.47 MPa, respectively, as shown in Figure 9. Theoretically, the specimens with the crack angles of 120° and 60°, as well as the specimens with crack angles of 150° and 30°, are not essentially different, so the elastic moduli of the specimens are almost the same, as shown in Figure 8(a). However, the strengths of the specimens with crack angles of 120° and 60° are quite different, which might be due to the dispersion of the particle and bond distribution inside the specimen [35–37].

The full stress-strain curve and strength value of the specimens with three precracks are shown in Figure 8(b). It can be seen that for the specimen with the precrack angle of 0°, 30°, 60°, 90°, 120°, and 150°, their strengths are 19.6 MPa, 25.4 MPa, 29.3 MPa, 29.1 MPa, 29.10 MPa, and 23.39 MPa, respectively. Compared with the one-crack specimens, the elastic moduli of the specimens change little with the crack angle.

In particular, for the specimens with crack angles of 60°, 90°, and 120°, the difference in their strengths is negligible. Extra uniaxial compression experiments were done on the double-cracked specimens (only including cracks ② and ③, see Figure 9). Results showed that the difference between the strengths of the three precrack specimens and the double-cracked specimen is very small, which indicates that for the specimens with three precracks, the influence of crack ① on the mechanical properties of the specimen can be ignored when the angle of crack ① is in the range of 60° to 120°.

In addition, for both the specimens with a single precrack or three precracks, the smaller the angle between precrack ① and the horizontal direction is, the more fluctuation the full stress-strain curve presents, as shown in Figure 8.

3.2. New Crack Propagation of the Precracked Sandstone Specimen

3.2.1. Initial Crack Propagation. The initial crack propagation of the specimen containing a single precrack is shown in Figure 10. It can be seen that for the specimen with the precrack angle of 0°, new cracks emerge initially in the middle and ends of the precrack, and the development of the new cracks in the middle of the precrack is far quicker than that at the end of the precrack.

For the specimens with the precrack angles of 30° and 60°, new cracks emerge initially at the ends of the precracks,

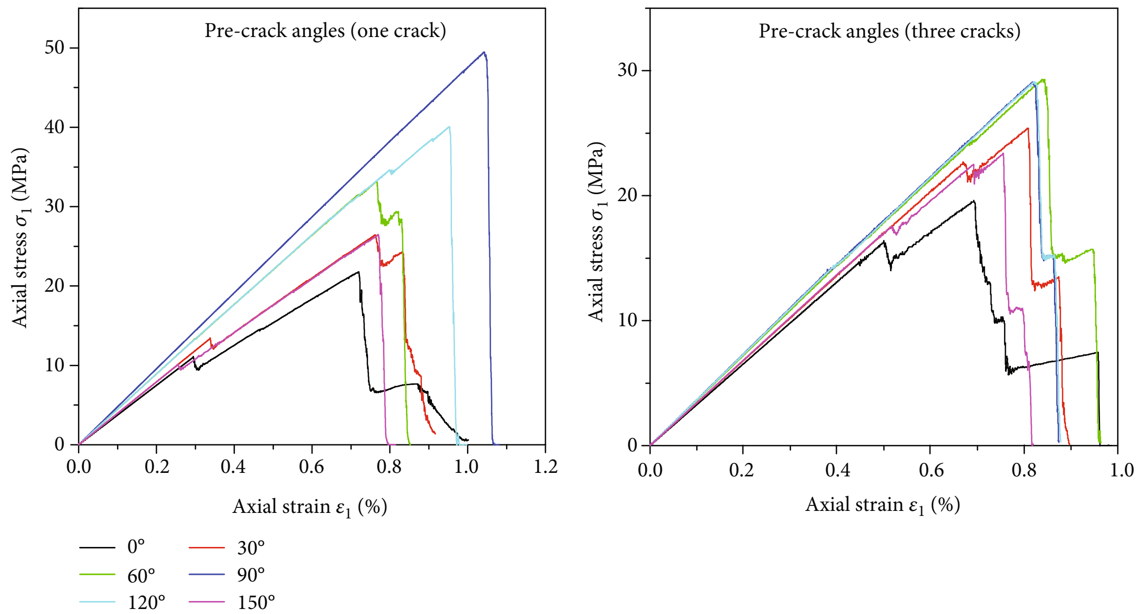

(a) (b)

Figure 8: Complete stress-strain curves of the cracked specimens: (a) complete stress-strain curves of the specimens containing a single precrack; (b) complete stress-strain curves of the specimens containing three precracks.

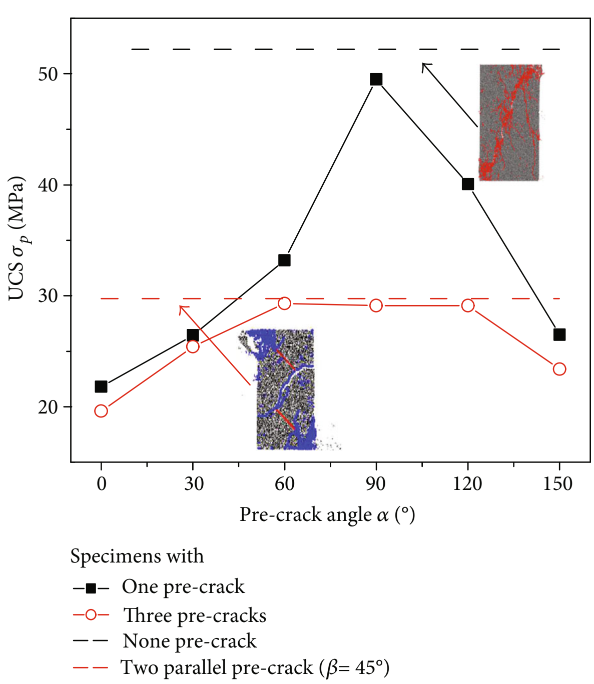

Figure 9: Correspondence between UCS of specimens and precrack angles.

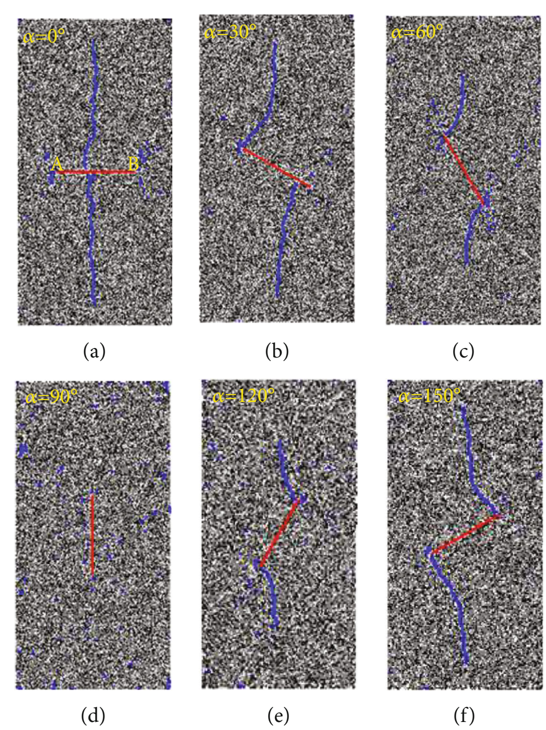

Figure 10: Initial crack propagation of the specimens containing a single precrack.

showing a clear wing expansion. For the specimens with the precrack angle of 90°, new cracks are randomly distributed within the specimen, which indicates that a precrack with the angle of 90° does not cause stress concentration inside the specimen. This is because, under the uniaxial loading condition, the strain and stress distributions of the specimen are uniform on any horizontal section before the specimen is significantly damaged. The crack distribution of the specimens corresponding to Figures 10(e) and 10(f) is symmetrical to the crack distribution of the specimens corresponding to Figures 10(b) and 10(c), respectively, so is the initial crack propagation conditions and thus will not be presented here. Furthermore, it can be clearly seen that as the precrack angle

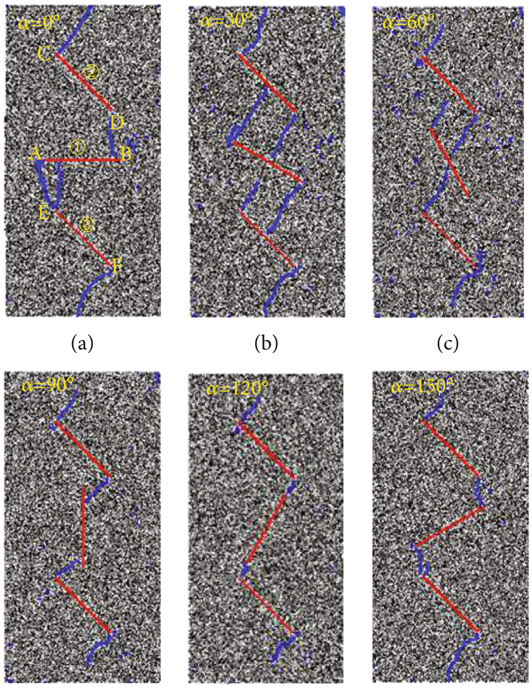

FIGURE 11: Initial crack propagation of the specimens containing three precracks.

increases from 0° to 90°, the temporal development of the new cracks shows a downward trend, as shown in Figure 10.

The initial crack propagation of the specimens containing three precracks is relatively more complicated, as shown in Figure 11. In general, the new cracks are located at the ends of the precracks, whereas the initial crack distributions at the C-end of crack ② and the F-end of crack ③ remain almost unchanged. The change of the angle of crack ① mainly affects the initial crack propagation of crack ①, the D-end of crack ②, and the E-end of crack ③.

When the angles of crack ① are 0°, 120°, and 150°, the ends of crack ① are closer to the D-end of crack ② and the E-end of crack ③. The two ends of crack ① penetrated with the D-end of crack ② and the E-end of crack ③, as shown in Figures 11(a), 11(e), and 11(f). For the specimen with the crack angle of 30° and 60°, the growth of the initial crack at each crack end is less affected by crack ① as the ends of crack ① are far from the ends of crack ② and crack ③, as shown in Figures 11(b) and 11(c).

When the angle of precrack ① is 90°, the internal stress concentration within the specimen is induced by cracks ② and ③. Compared with the one-crack specimen (see Figure 10(e)), the distribution of new cracks in the specimen is no longer uniform, new cracks of precrack ② of crack ③ penetrate through precrack ①, and there is no new crack propagated from the ends of crack ①.

3.2.2. Failure Modes. The final failure modes of specimens containing a single precrack and three precracks are present in Figures 12 and 13. The final failure modes of the speci-

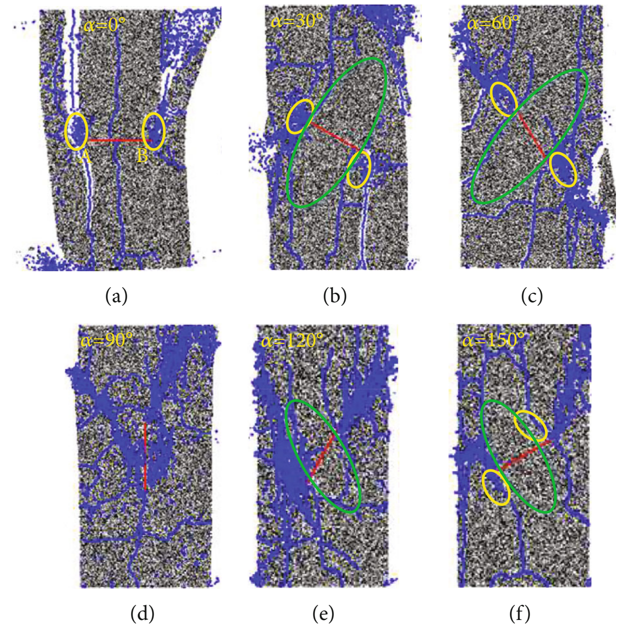

FIGURE 12: Failure mode of the specimens containing a single precrack.

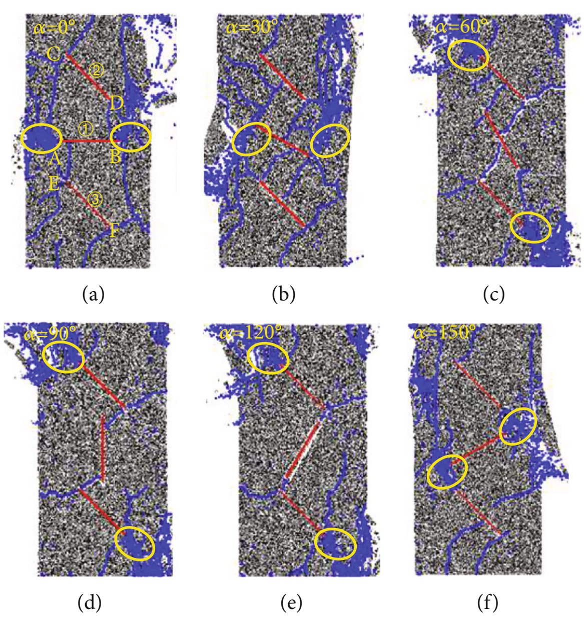

FIGURE 13: Failure mode of the specimens containing three precracks.

mens vary substantially with the change of the precrack angle α.

For the single precrack specimens with 0° crack angle α, the failure mode is mostly the vertical splitting failure. Three vertical cracks extended from the two ends, and the middle of the precrack cut the specimen into strips. Moreover, there are many accumulated cracks located at the ends of the precrack, denoted by the yellow ellipses in Figure 12(a). For the specimens with the crack angles of 30° and 60°, their failures are caused by the gradual expansion of the new cracks along

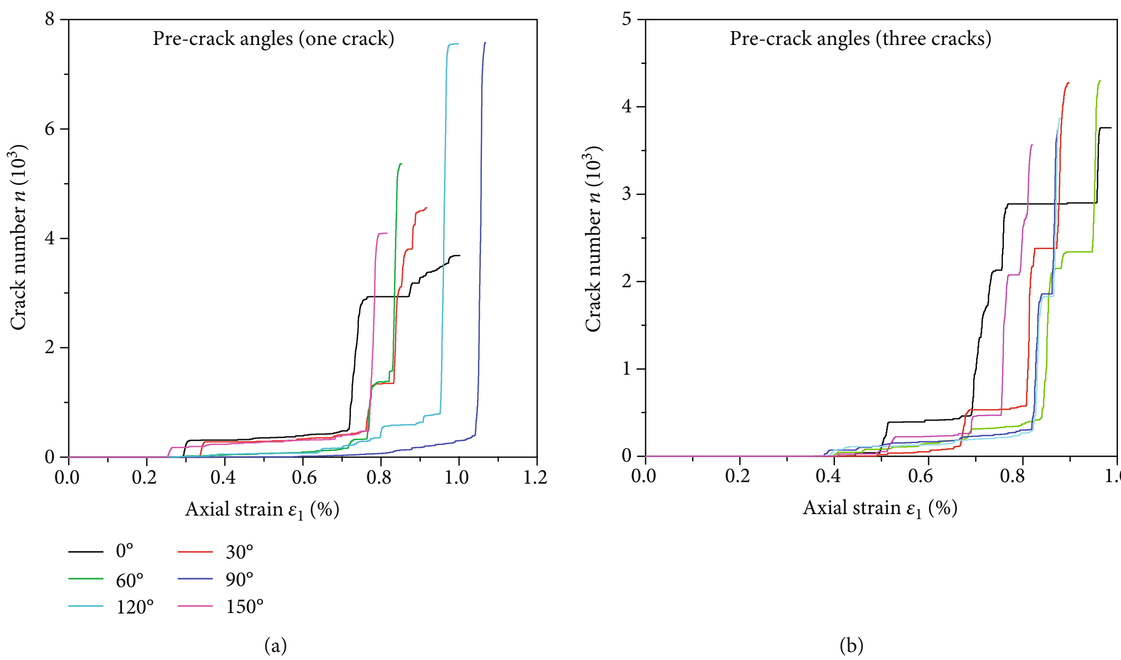

Figure 14: Crack number evolution of the precracked sandstone specimens: (a) crack number evolution of the specimens containing a single precrack; (b) crack number evolution of the specimens containing three precracks.

the ends of the precracks. Quite a few new cracks are closely located at the precrack ends, as highlighted by the yellow ellipses in Figures 12(b) and 12(c). There are few new cracks generated in the vertical direction of the precracks, as shown by the blue ellipses in Figures 12(b) and 12(c). This is agreed with the finding of Shi et al. [2] that nonvertical cracks will form a stress shielding circle with the diameter of its own. For the specimens containing precracks with the angles of 120° and 150°, the failure modes are the same as that of the specimens with the precrack angles of 60° and 30°, respectively, and will not be repeated here. For the specimens with the precrack angle of 90°, the effect of precracks on the failure mode of the specimen is negligible. The failure of the upper right corner of the specimen is very similar to that of the intact specimen (see Figures 6(b) and 12(d)).

For the specimens with three precracks, when the angle of precrack ① is 0°, due to the stress shielding effect of the precracks, there are basically no new cracks that emerged in the area between the adjacent precracks. As shown in Figure 13(a), the ends of the three precracks penetrate through each other, which results in the cutting failure of the specimen [38, 39]. For the specimen with the precrack angle of 30°, the new cracks mainly occurred in the middle of the specimens due to the dense and uniform distribution of the precracks in this area. For the specimen with the precrack angles of 60°, 90°, and 120°, precracks ② and ③ penetrated through precrack ①, and the new cracks mainly concentrated at the C-end of crack ② and the F-end of crack ③. The failure modes of these three specimens are very similar. The failure modes of the specimens with the precrack angles of 150° and 30° are similar, and the concentrated cracks are mainly distributed at the junction of the A-end of crack ① and the D-end of crack ②, as well as the junction of the B-end of crack ① and the E-end of crack ③.

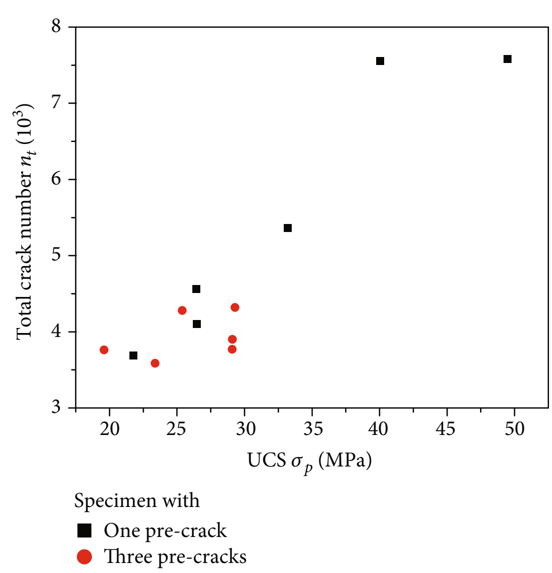

Figure 15: Correspondence between the UCS and the new crack number of the sandstone specimens.

3.3. Crack Number Evolution of the Precracked Sandstone Specimens. New cracks keep emerging in the loading process. The evolution of the number of new cracks (NNC) during loading process is shown in Figure 14. In general, the evolution of NNC exhibits a stair-step tendency, i.e., increases abruptly as the axial strain increases to a

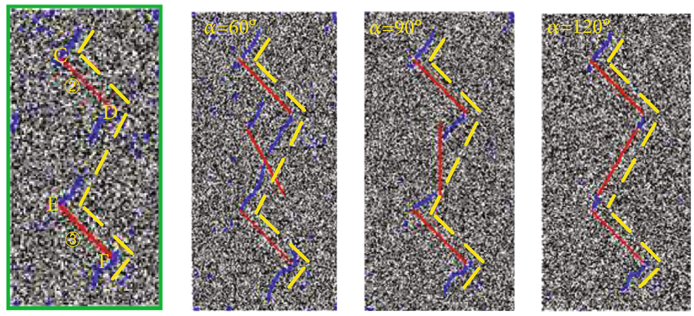

(a) (b) (c) (d)

FIGURE 16: Comparison of the initial crack propagation of double-crack and triple-crack specimens.

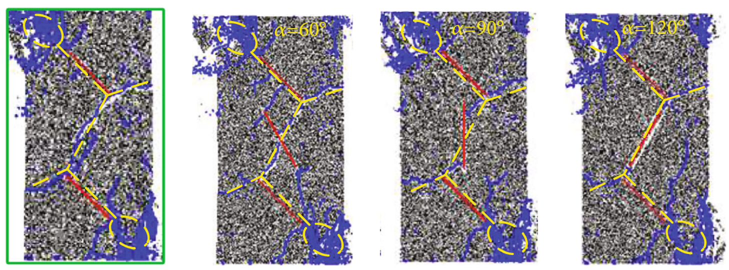

(a) (b) (c) (d)

FIGURE 17: Comparison of the failure mode of double-crack and triple-crack specimens.

certain value. The NNC evolution of single precrack specimens experiences a one-step (corresponding to precrack angles of 90° and 120°) or two-step (corresponding to precrack angles of 0°, 30°, 60°, and 150°) increase. It can be seen from Figure 14(a) that for the specimen containing a single precrack, the number of new cracks approximately increased in one-step stair shape (corresponding to precrack angles of 60°, 90°, and 120°) or two-step stair shape (corresponding to precrack angles of 0°, 30°, and 150°) with the increase of axial strain. Notably, the maximum abrupt increase in NNC occurs at various axial strains for different precrack angles, i.e., increased axial strain value as the precrack angle increased until 90° and declined thereafter. For the specimens with three precracks (see Figure 14(b)), the evolution of NNC shows a multistep growth, which can be attributed to the fluctuations of the full stress-strain curves of the specimens before and after the peak (see Figure 8(b)).

Interestingly, the NNCs corresponding to the final failure of the specimens with three precracks are around 4000 with extremely small deviation. For the specimens with a single precrack, when the crack angles are 0°, 30°, 60°, and 150°, the final NNCs are closer to 4000 as well. However, when the precrack angles are 90° and 120°, the final NNCs are up to 7500. By extracting the final NNC and UCS of the specimens (see Figures 14 and 9), it was found that the final NNC increased with the UCS, as shown in Figure 15.

4. Discussion

The analysis of Figure 9 in Section 3.1 shows that when the angles α of precrack ① are between 60° to 120°, the effect of precrack ① on the mechanical properties of the specimen can be ignored, which is very interesting and worthy of further study.

The initial crack propagation of the double-crack specimen (see Figure 16(a)) and the triple-crack specimens (see Figures 16(b)–16(d)) are shown in Figure 16. The existence of precrack ① inside the three-crack specimens has little effect on the initial crack growth. The D-end of crack ② and the E-end of crack ③ tend to penetrate in both the double-crack and the triple-crack specimens, and crack ① itself, as the penetration path of crack ② and crack ③, only promoted this process, especially for the specimens whose angles of crack ① are 90° and 120°. Therefore, there is very little difference in the crack distribution (including precracks and newly generated cracks, see the yellow dotted lines in Figure 16) inside the specimens, and the bearing structure of the specimens is very similar, as shown in Figure 16.

Figure 17 shows the failure modes of the double-crack specimen (see Figure 17(a)) and the three-crack specimens (see Figures 17(b)–17(d)). The failure modes of the four specimens in Figure 17 are highly similar. There are many newly generated cracks in the upper left and lower right corners of the specimens (see the yellow ellipses in Figure 17). In addition, the Y-shaped expansion fissures in the upper right and lower left corners are symmetrically distributed with respect to the center point of the specimens (see the yellow dotted lines in Figure 17). In summary, the 4 main rock blocks generated after the failure of the specimen in Figure 17 are almost identical.

For a specific loading condition, the existence of cracks may not necessarily weaken the strength characteristics of the specimen. From Figures 9, 16, and 17, it can be found that if the precrack does not affect the original crack propagation path (fracture process), it will hardly affect the mechanical properties of the specimen.

5. Conclusions

In this paper, the relationship between the strength characteristics of the specimen and the angle of the precrack, as well as the interaction of cracks under uniaxial compression, was studied. The two sets of sandstone specimens, respectively, containing a single precrack and three precracks were built using the PFC software, which was to study. The main conclusions are as follows:

(1) For the one-crack specimens, the peak strength and elastic modulus continuously increase as the crack angle α is more aligning with the forcing (loading) direction. For the three-crack specimens, a similar pattern was observed for the strength behavior, i.e., with higher strength as α gets closer to the forcing direction. However, such increase stabilized as the angle between α and forcing direction is smaller than 30°. The elastic modulus of the specimens appears to be unaffected by the angles of precrack

(2) For the specimens containing a single precrack, their crack numbers increased approximately in a one-step or two-step stair pattern with increasing axial strain; whereas for the specimens containing three cracks, their crack numbers all showed a multistep stair growth trend with the axial strain

(3) The failure mode of the specimen is closely related to the precrack angle. However, the existence of cracks may not necessarily weaken the strength characteristics of the specimen. If the precrack does not affect the original crack propagation process (fracture process), it will hardly affect the mechanical properties of the specimen

Data Availability

The data used to support the findings of the study are available from the corresponding author upon request.

Conflicts of Interest

All authors declare that they have no conflict of interest or financial conflicts to disclose.

Acknowledgments

The authors gratefully acknowledge the financial support provided by the Independent Research Project of State Key Laboratory of Coal Resources and Safe Mining, CUMT (Grant Number SKLCRSM001).

References

[1] A. Lenton, K. L. McInnes, and J. G. O'Grady, "Marine projections of warming and ocean acidification in the Australasian region," *Australian Meteorological and Oceanographic Journal*, vol. 65, no. 1, pp. S1–S28, 2015.

[2] H. Shi, L. Song, H. Q. Zhang et al., "Numerical study on mechanical and failure properties of sandstone based on the power-law distribution of pre-crack length," *Geomechanics and Engineering*, vol. 19, no. 5, pp. 421–434, 2019.

[3] J. Y. Wu, M. M. Feng, X. B. Mao et al., "Particle size distribution of aggregate effects on mechanical and structural properties of cemented rockfill: experiments and modeling," *Construction and Building Materials*, vol. 193, pp. 295–311, 2018.

[4] M. Asadi and M. H. Bagheripour, "Numerical and intelligent modeling of triaxial strength of anisotropic jointed rock specimens," *Earth Science Informatics*, vol. 7, no. 3, pp. 165–172, 2014.

[5] Q. H. Lei and K. Gao, "A numerical study of stress variability in heterogeneous fractured rocks," *International Journal of Rock Mechanics and Mining Sciences*, vol. 113, pp. 121–133, 2019.

[6] N. E. Odling, "Scaling and connectivity of joint systems in sandstones from western Norway," *Journal of Structural Geology*, vol. 19, no. 10, pp. 1257–1271, 1997.

[7] H. Shi, H. Q. Zhang, L. Song et al., "Failure characteristics of sandstone specimens with randomly distributed pre-cracks under uniaxial compression," *Environmental Earth Sciences*, vol. 79, no. 9, article 193, 2020.

[8] I. J. Basson and G. Viola, "Structural overview of selected group II kimberlite dyke arrays in South Africa: implications for kimberlite emplacement mechanisms," *South African Journal of Geology*, vol. 106, no. 4, pp. 375–394, 2003.

[9] C. Deng, H. X. Hu, T. L. Zhang, and J. L. Chen, "Rock slope stability analysis and charts based on hybrid online sequential extreme learning machine model," *Earth Science Informatics*, vol. 13, no. 3, pp. 729–746, 2020.

[10] Y. H. Huang, S. Q. Yang, and J. Zhao, "Three-dimensional numerical simulation on triaxial failure mechanical behavior of rock-like specimen containing two unparallel fissures," *Rock Mechanics and Rock Engineering*, vol. 49, no. 12, pp. 4711–4729, 2016.

[11] Y. Q. Zhou, Q. Sheng, N. N. Li, X. Fu, Z. Zhang, and L. Gao, "A constitutive model for rock materials subjected to triaxial cyclic compression," *Mechanics of Materials*, vol. 144, article 103341, 2020.

[12] G. W. Chen, L. Song, and R. R. Zhang, "Modeling acoustic attenuation of discrete stochastic fractured media," *Acta Geodaetica et Geophysica*, vol. 53, no. 4, pp. 679–690, 2018.

[13] P. T. Wang, F. H. Ren, and M. F. Cai, "Mechanical analysis and size effect of rough discrete fractures network model under direct shear tests based on particle flow code," *Journal of China Coal Society*, vol. 43, no. 4, pp. 976–983, 2018.

[14] Z. M. Yang, Y. T. Gao, S. C. Wu, Z. Q. Cheng, and A. B. Jin, "Study of the influence of joint parameters on rock mass strength based on equivalent rock mass technology," *Journal of China University of Mining and Technology*, vol. 47, no. 5, pp. 979–986, 2018.

[15] P. A. Cundall and O. D. L. Strack, "A discrete numerical model for granular assemblies," *Géotechnique*, vol. 29, no. 1, pp. 47–65, 1979.

[16] H. Q. Zhang, S. Nunoo, D. D. Tannant, and S. Y. Wang, "Numerical study of the evolution of cohesion and internal friction in rock during the pre-peak deformation process," *Arabian Journal of Geosciences*, vol. 8, no. 6, pp. 3501–3513, 2015.

[17] H. Q. Zhang, D. D. Tannant, H. W. Jing, S. Nunoo, S. J. Niu, and S. Y. Wang, "Evolution of cohesion and friction angle during microfracture accumulation in rock," *Natural Hazards*, vol. 77, no. 1, pp. 497–510, 2015.

[18] R. Vachon and C. F. Hieronymus, "Mechanical energy balance and apparent fracture toughness for dykes in elastoplastic host rock with large-scale yielding," *Geophysical Journal International*, vol. 219, no. 3, pp. 1786–1804, 2019.

[19] F. S. Ren, T. C. Fang, and X. Z. Cheng, "Study on rock damage and failure depth under particle water-jet coupling impact," *International Journal of Impact Engineering*, vol. 139, article 103504, 2020.

[20] S. Q. Yang, Y. Z. Jiang, W. Y. Xu, and X. Q. Chen, "Experimental investigation on strength and failure behavior of pre-cracked marble under conventional triaxial compression," *International Journal of Solids and Structures*, vol. 45, no. 17, pp. 4796–4819, 2008.

[21] H. Yang, H. Lin, Y. Wang, R. Cao, J. Li, and Y. Zhao, "Investigation of the correlation between crack propagation process and the peak strength for the specimen containing a single pre-existing flaw made of rock-like material," *Archives of Civil and Mechanical Engineering*, vol. 21, no. 2, p. 68, 2021.

[22] C. Zhang, Y. Wang, and T. Jiang, "The propagation mechanism of an oblique straight crack in a rock sample and the effect of osmotic pressure under in-plane biaxial compression," *Arabian Journal of Geosciences*, vol. 13, no. 15, p. 736, 2020.

[23] M. Wang, W. Wan, and Y. L. Zhao, "Experimental study on crack propagation and the coalescence of rock-like materials with two preexisting fissures under biaxial compression," *Bulletin of Engineering Geology and the Environment*, vol. 79, no. 6, pp. 3121–3144, 2020.

[24] C. Q. Zhang, Z. J. Liu, Y. B. Pan, Y. Gao, H. Zhou, and G. Cui, "Influence of amygdale on crack evolution and failure behavior of basalt," *Engineering Fracture Mechanics*, vol. 226, article 106843, 2020.

[25] Itasca Consulting Group Inc, *PFC2D (Particle Flow Code in 2 Dimensions): Version 2018, 5.00.35*, Minneapolis, 2018.

[26] L. X. Xiong, Z. Y. Xu, T. B. Li, and Y. Zhang, "Bonded-particle discrete element modeling of mechanical behaviors of interlayered rock mass under loading and unloading conditions," *Geomechanics and Geophysics for Geo-Energy and Geo-Resources*, vol. 5, no. 1, pp. 1–16, 2019.

[27] U. Castro-Filgueira, L. R. Alejano, J. Arzúa, and D. M. Ivars, "Sensitivity analysis of the micro-parameters used in a PFC analysis towards the mechanical properties of rocks," *Procedia Engineering*, vol. 191, pp. 488–495, 2017.

[28] C. B. Jiang, Z. K. Li, W. S. Wang, Z. Wen, M. Duan, and W. Geng, "Experimental investigation of the mechanical characteristics and energy dissipation of gas-containing coal under incremental tiered cyclic loading," *Geomechanics and Geophysics for Geo-Energy and Geo-Resources*, vol. 7, no. 3, 2021.

[29] S. Mukhopadhyay and S. R. Hallett, "A directed continuum damage mechanics method for modelling composite matrix cracks," *Composites Science and Technology*, vol. 176, pp. 1–8, 2019.

[30] J. Y. Wu, M. M. Feng, B. Y. Yu, and G. S. Han, "The length of pre-existing fissures effects on the mechanical properties of cracked red sandstone and strength design in engineering," *Ultrasonics*, vol. 82, no. 1, pp. 188–199, 2018.

[31] Y. Benveniste, "On the Mori-Tanaka's method in cracked bodies," *Mechanics Research Communications*, vol. 13, no. 4, pp. 193–201, 1986.

[32] K. Wang, F. du, X. Zhang, L. Wang, and C. P. Xin, "Mechanical properties and permeability evolution in gas-bearing coal-rock combination body under triaxial conditions," *Environmental Earth Sciences*, vol. 76, no. 24, 2017.

[33] H. Shi, H. Q. Zhang, and L. Song, "Evolution of sandstone shear strength parameters and its mesoscopic mechanism," *Geomechanics and Engineering*, vol. 20, no. 1, pp. 29–41, 2020.

[34] H. Shi, H. Q. Zhang, L. Song, and Y. Wu, "Variation of strata pressure and axial bolt load at a coal mine face under the effect of a fault," *Archives of Mining Sciences*, vol. 64, no. 2, pp. 351–374, 2019.

[35] L. L. Chen, Z. W. Wang, X. Peng, J. Yang, P. Wu, and H. Lian, "Modeling pressurized fracture propagation with the isogeometric BEM," *Geomechanics and Geophysics for Geo-Energy and Geo-Resources*, vol. 7, no. 3, 2021.

[36] Z. Y. Liao, C. A. Tang, W. M. Yang, and J. B. Zhu, "Three-dimensional numerical investigation of rock plate cracking and failure under impact loading," *Geomechanics and Geophysics for Geo-Energy and Geo-Resources*, vol. 7, no. 2, article 33, 2021.

[37] M. Wang, D. J. Zheng, S. J. Niu, and W. Li, "Large deformation of tunnels in longwall coal mines," *Environmental Earth Sciences*, vol. 78, no. 2, 2019.

[38] K. Eshiet and Y. Sheng, "Influence of rock failure behaviour on predictions in sand production problems," *Environmental Earth Sciences*, vol. 70, no. 3, pp. 1339–1365, 2013.

[39] H. Shi, L. Song, W. L. Chen et al., "New non-destructive method for testing the strength of cement mortar material based on vibration frequency of steel bar: theory and experiment," *Construction and Building Materials*, vol. 262, p. 120931, 2020.

Hindawi
Geofluids
Volume 2021, Article ID 3621040, 12 pages
https://doi.org/10.1155/2021/3621040

Research Article

Study on Influence of Joint Distribution on Surrounding Rock Failure of an Underground Tunnel

Wanrong Liu [1,2] Chao Peng [1] and Baoliang Zhang [1]

[1] School of Architecture & Civil Engineering, Liaocheng University, Liaocheng, Shandong 252059, China
[2] State Key Laboratory of Mining Response and Disaster Prevention and Control in Deep Coal Mine, Anhui University of Science and Technology, Huainan 232001, China

Correspondence should be addressed to Wanrong Liu; wanrongliu1989@163.com

Received 29 August 2021; Accepted 27 September 2021; Published 12 October 2021

Academic Editor: Zhijie Wen

Due to geological structure and artificial disturbance, a large number of joints and fissures are formed in the surrounding rock of an underground tunnel. In order to study the influence of joints on the failure characteristics of tunnels, three test schemes with different joint lengths, joint spacing, and joint positions are designed. The results show that the bearing capacity of the tunnel decreases with the increase in the joint length. With the increase in joint spacing, the bearing capacity of the tunnel decreases first and then increases. The crack propagation law of the three test schemes has experienced four stages: no crack, crack initiation, crack rapid development, and crack gradual reduction. The location of joints has the greatest influence on the failure mode of the tunnel. The crack is most likely to appear at the top of the tunnel and expand along the joint, mainly because it is easy to form tensile stress at the top of the tunnel and compressive stress concentration at the joint tip. Therefore, when excavating the tunnel in the underground space, the influence of joints on the tunnel should be considered. Analyzing the relationship between the tunnel and joints has important practical guiding significance for the control of the surrounding rock of the tunnel. Finally, the failure results of the indoor physical model and numerical model are compared and analyzed. They are in good agreement, which also reflects the rationality of numerical simulation.

1. Introduction

With the development of urban population and economy, the utilization of underground space is increasing day by day, and underground engineering is developing on a large scale. Working in an underground space is mainly aimed at rock mass materials. A large number of joints and fissures are formed in underground rock mass due to geological structure and artificial disturbance. As we all know, joints and fissures as weak planes directly affect the failure characteristics of rock mass. Therefore, when excavating a tunnel in an underground space, it is necessary to consider the influence of joints on the tunnel. Analyzing the position relationship between the tunnel and joints has important practical guiding significance for mastering the failure characteristics of the tunnel and controlling the surrounding rock of the tunnel.

At present, there have been many achievements in the research of jointed rock mass. Yang et al. [1] analyzed the influence of two groups of joints on the failure of rock mass materials by using artificial rock materials. The anisotropy of failure strength of rock mass was obtained. Bahaaddini et al. [2] studied the influence of discontinuous joints on the mechanical parameters of rock mass. The results show that the failure mode of rock mass is mainly determined by the joint direction and step angle, and the joint dip angle is the parameter that has the greatest influence on the properties of rock mass. Lin et al. [3] conducted uniaxial compression tests on physical model samples with different angles of columnar joints and analyzed the strength characteristics and deformation modulus of columnar jointed rock mass. Yang et al. [4, 5] analyzed the failure characteristics and crack propagation law of discontinuous jointed rock mass with holes. The influence law of joints on mechanical properties of rock mass is obtained. In the underground tunnel research, on the one hand, the deformation and failure of surrounding rock are analyzed by using the theory of elastic-plastic mechanics, and the laws of stress and displacement of surrounding rock are studied [6]. Then it provides a theoretical basis for the support control of surrounding rock. On the other hand, the deformation and failure of jointed tunnels are studied. For example, the influence of blasting on the failure of tunnel surrounding rock [7], the damage mechanics, and the elastic-plastic mechanics considering joints are introduced to solve the surrounding rock [8, 9], and the stability of tunnel surrounding rock is studied by the block theory and numerical simulation method [10, 11]. Jia et al. and Wang et al. [12, 13] studied the failure mechanical characteristics of coal and rock mass by an acoustic emission test and analyzed the internal failure process of coal and rock mass by an acoustic emission signal. Jia and Tang [14] used RFPA software to study the effects of layered joint inclination and lateral pressure coefficient on the stability of a jointed rock tunnel. Hu et al. [15] studied the effects of different parameters such as lateral pressure coefficient, joint inclination, and joint spacing on joint parameters and lining performance by experimental and numerical simulation methods. In conclusion, there are few studies on the influence of joint distribution on tunnel failure. There is a lack of systematic research on the damage of joint distribution to the tunnel.

Based on the above research, in this paper, the numerical simulation method is used to systematically study the jointed rock tunnel, three joint distribution schemes are designed, and the effects of different joint distribution forms on the bearing capacity, crack propagation, and failure model of the tunnel are analyzed, respectively. Finally, the numerical simulation results and indoor test results are compared and analyzed. The research content is of great significance for understanding the failure of the tunnel and guiding engineering practice.

2. Test Schemes

2.1. Particle Flow Code (PFC) Theory and Parameter Checking. In order to analyze the influence characteristics of different joint forms on the failure of tunnel surrounding rock, particle flow code (PFC) is used to study it. The basic principles of a discrete element are force displacement law and Newton's second law [16]. PFC provides a PB model to bond dispersion particles. When the external force exceeds the PB bond strength between particles, the bond between particles is destroyed and the bond fracture forms microcracks. A large number of cracks gather and penetrate, resulting in macrodamage of the material. Sandstone is a typical cement material, and the failure of rock is also the place where the bond is weak. The failure process of the whole rock material is similar to that of the PB model. Therefore, the PB model can well realize the simulation analysis of rock materials. Through the built-in fish language, PFC can not only count the number of damaged microcracks but also display whether they are tensile cracks or shear cracks. It can more intuitively reflect the failure characteristics of rock. A particle discrete element has been widely used in many fields since it was proposed. In particular, a large number of research achievements have been made in geotechnical engineering [17–22]. Obtaining particle parameters is the key to PFC simulation. The microscopic parameters of particles do not correspond to the physical parameters completely, but there is a great correlation. The stiffness ratio mainly affects Poisson's ratio of rock materials, the parallel bond tensile strength mainly affects the tensile strength of materials, and the parallel bond cohesive force mainly affects the compressive strength of materials. A contact module of the particle and parallel bond deformation module jointly affect the elastic modulus of the material. Density is basically the actual density of the material. Therefore, the microparameters of PFC rock models are calibrated by simulating the uniaxial compression experiments. At present, the particle parameters are mainly obtained through a trial and error test, and the parameters of the numerical model are continuously adjusted until the numerical simulation results are consistent with the indoor test results. Finally, the indoor test and numerical simulation results are shown in Figure 1, and the particle microparameters are shown in Table 1 [23].

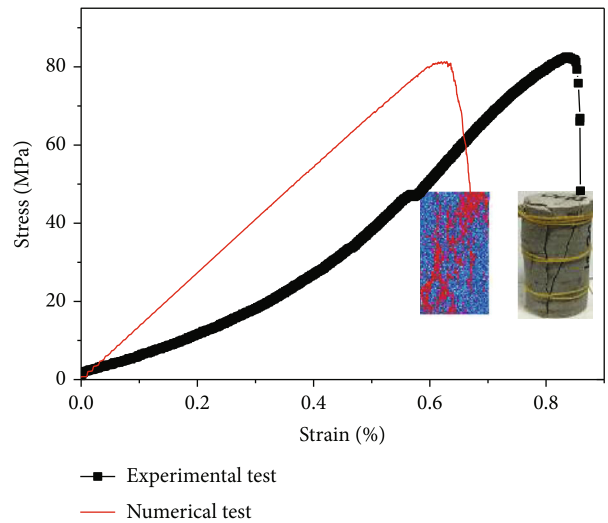

Figure 1: Stress-strain curves of sandstone based on experimental and numerical tests [23].

2.2. Test Schemes. Due to the influence of geological structure and other factors, the distribution of joints in the surrounding rock of the tunnel is complex. In the process of tunnel excavation, the tunnel and joints form different positional relations. In order to systematically explore the influence law of joints on tunnel failure, the influence of three joint distribution modes on tunnel failure is considered. The size of these tunnel models is 200 mm (width) × 200 mm (height). Due to the increase in the model scale, the diameter of particles is appropriately enlarged in order to reduce the amount of computer calculation. The minimum particle diameter is 0.8 mm, and the maximum particle diameter is 1.2 mm. The particle generation process of each model is the same. After the model is generated, the microparameters are given according to Table 1. The excavation of rock mass is completed by deleting particles. The shape of the tunnel is a straight wall semicircular arch, the radius of

Table 1: Microcosmic-mechanical parameters of the model.

Parameter	Value	Parameter	Value
Minimum particle diameter (mm)	0.3	Contact bond gap (mm)	0.05
Maximum particle diameter (mm)	0.5	Density (kg/m^3)	2500
Parallel bond tensile strength (MPa)	22	Contact modulus of the particle (GPa)	10.2
Parallel bond cohesive force (MPa)	56.5	Parallel bond deformation modulus (GPa)	16.2
Stiffness ratio	1.51	Porosity	0.1

Table 2: Mechanical parameters of the joint.

Parameter	Value	Parameter	Value
sj_kn (GPa)	1	sj_fric	30
sj_ks (GPa)	0.5	sj_coh	0
sj_large	1	sj_ten	0

the circular arch of the tunnel is 25 mm, and the size of the straight wall is 50 mm (width) × 25 mm (height). Joints are added after the tunnel excavation, and the joints form different positional relationships with the tunnel. The mechanical parameters of joints are shown in Table 2. The three schemes are different joint lengths, the distance between the joint and the tunnel, and the positional relationship between the joint and the tunnel.

2.2.1. Different Joint Length Models. In order to study the influence of borehole length on the tunnel surrounding rock mass failure, tunnel models with the joint were established (as shown in Figure 2) and the joint lengths are considered 10 mm, 20 mm, 30 mm, 40 mm, and 50 mm, respectively. The joint is located at the foot of the tunnel. And each corresponding model is abbreviated as L-10, L-20, L-30, L-40, and L-50.

2.2.2. Different Spacing between Joints and Tunnel Models. In order to study the influence of joint spacing on tunnel surrounding rock mass failure, tunnel models with different joint spacing were established (as shown in Figure 3) and the spacing is considered 0 mm, 10 mm, 20 mm, 30 mm, 40 mm, and 50 mm, respectively. The joint is located at the foot of the tunnel. The joint length is 20 mm. And each corresponding model is abbreviated as S-10, S-10, S-20, S-30, S-40, and S-50.

2.2.3. Different Joint Location Models. In order to study the influence of double-joint location on the failure characteristics of tunnel surrounding rock mass, numerical models of different locations are established, as shown in Figure 4. Double-joint length is 30 mm. The joints are located in the top and shoulder (T-S), shoulder and waist (S-W), waist and foot (W-F), foot and bottom (F-B), and bottom and top (T-B), respectively.

After the joint tunnel model is built, the compression test is carried out on the model, and the load is applied to the top wall through displacement control to realize the loading of the model. The stress, strain, crack count, and failure mode of the model were monitored during the test.

3. Analysis of Test Results

3.1. Strength Characteristics

3.1.1. Effect of Joint Length on Strength. Figure 5 shows the stress-strain curve of the tunnel model with different joint lengths. It can be seen from the figure that when the tunnel has no joints (intact), the model strength is 52.53 MPa. When the joint length gradually increases from 10 mm to 50 mm, the tunnel model strength is 49.19 MPa, 46.30 MPa, 37.81 MPa, 37.07 MPa, and 33.48 MPa, respectively. With the increase in the joint length, the strength of the tunnel model decreases gradually, and the strength decreases by 6.3%, 11.8%, 28.1%, 29.4%, and 36.3%, respectively. The length of joints has a great influence on the bearing capacity of the tunnel. It is mainly because the joints belong to the weak plane structure, which reduces the bearing capacity of the tunnel. Therefore, during excavation, the tunnel shall avoid passing through long joints as far as possible.

3.1.2. Effect of Spacing between Joints and Tunnel on Strength. Figure 6 shows the stress-strain curve of the tunnel model with different joint spacing. It can be seen from the figure that when the tunnel has no joints (intact), the model strength is 52.53 MPa. When the spacing between joints and tunnel gradually increases from 0 mm to 40 mm, the tunnel model strength is 46.30 MPa, 45.23 MPa, 46.35 MPa, 48.86 MPa, and 51.07 MPa, respectively. With the increase in the spacing between joints and tunnels, the strength of the tunnel model first decreases and then increases, but the strength is still lower than that of the no-joint model. The main reason is that the joint affects the bearing capacity of the tunnel and reduces the strength of the model. With the increase in the spacing between the joint and the tunnel, the impact of the joint on the tunnel decreases until it disappears. Therefore, the tunnel shall keep a certain distance from the joint as far as possible.

3.1.3. Effect of Joint Location on Strength. Figure 7 is stress-strain curves of models with double-joint location in different positions. It can be seen from the figure that when the double joints are located at the top and shoulder of the tunnel, the model strength is 41.42 MPa; when the double joints are located at the shoulder and waist of the tunnel, the model strength is 44.93 MPa; when the double joints are located at the waist and foot of the tunnel, the model strength is 43.23 MPa; when the double joints are located at the foot and bottom of the tunnel, the model strength is 37.82 MPa; and when the double joints are located at the bottom and top of the tunnel, the model strength is 41.22 MPa. With

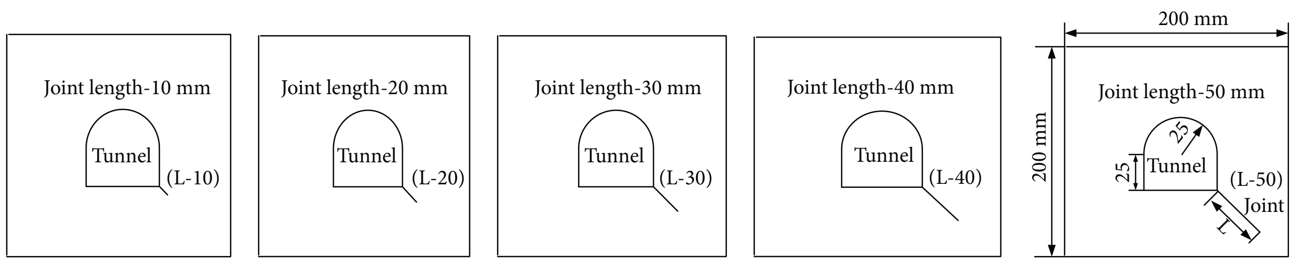

(a) L-10 (b) L-20 (c) L-30 (d) L-40 (e) L-50

Figure 2: Different joint lengths.

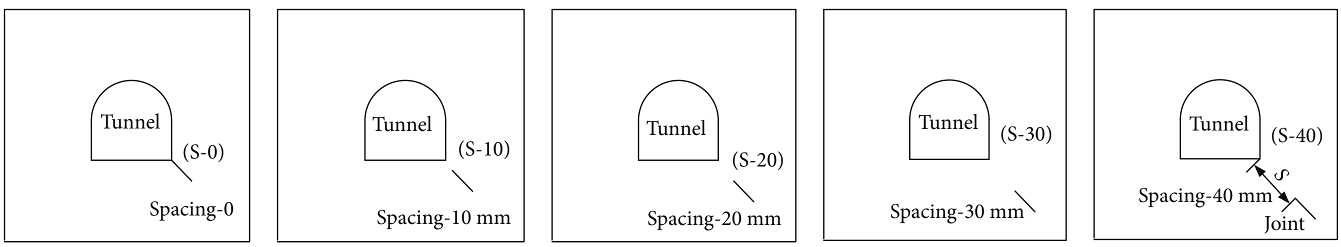

(a) S-10 (b) S-20 (c) S-30 (d) S-40 (e) S-50

Figure 3: Different spacing between joints and tunnel.

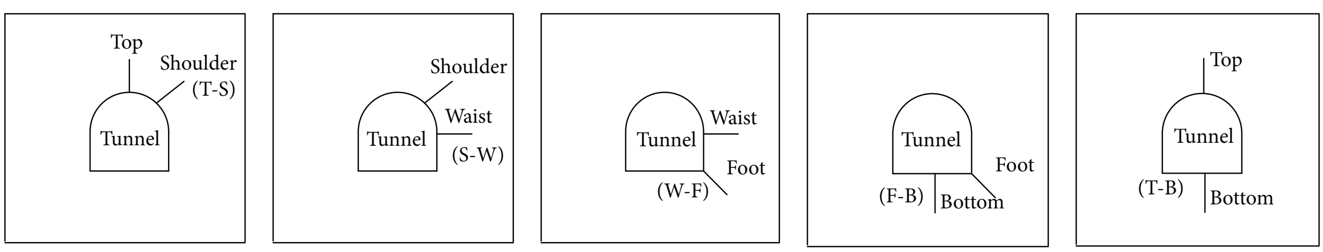

(a) T-S (b) S-W (c) W-F (d) F-B (e) T-B

Figure 4: Double-joint location.

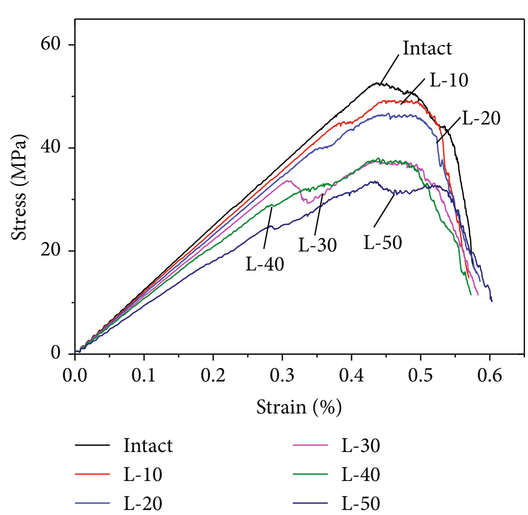

Figure 5: Stress-strain curves of models with different joint lengths.

different joint positions, the bearing capacity of the tunnel is also different. Compared with the jointless model, the bearing capacity of the tunnel is significantly reduced. Except that the bearing capacity is the lowest when the double joint is located at the bottom and foot of the tunnel, there is little difference in the bearing capacity of other models. It is mainly because the tunnel is easy to form stress concentration at the bottom corner, and 45° shear failure is easy to form due to the existence of joints. Therefore, the positional relationship between joints and tunnel should also be considered in the process of tunnel excavation.

3.2. Crack Propagation Characteristics

3.2.1. Influence of Joint Length. Figure 8 shows the stress-crack count curve of models with different joint lengths. It can be seen from Figure 8 that the distribution law of the crack count curve of each model is basically similar. The crack curves have experienced four stages: no crack, crack initiation, crack rapid development, and crack gradual reduction. For the intact model (Figure 8(a)), when the stress is 0-30.1 MPa, there is no crack (the stage of OA). When the stress exceeds 30.1 MPa, the crack begins to initiate and a certain number of cracks appear (the stage of AB). When it is close to the peak stress, the crack begins to develop and expand, and a large number of cracks gather (the stage of BC). The crack accumulation leads to the failure

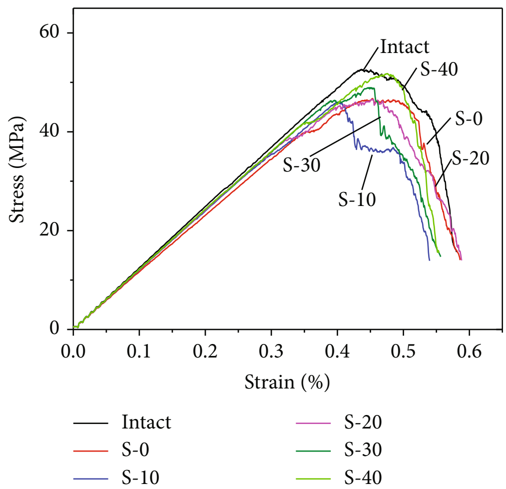

FIGURE 6: Stress-strain curves of models with different spacing between joints and tunnel.

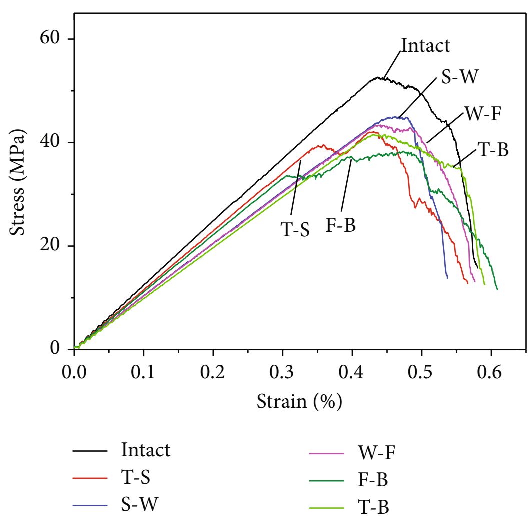

FIGURE 7: Stress-strain curves of models with double-joint location in different positions.

of the tunnel, the bearing capacity of the tunnel decreases, and the crack count also decreases, but a certain crack count is still maintained. Finally, the crack of the sample decreases gradually and the sample is completely destroyed (the stage of CD). For the tunnel model with joint length of 10 mm, the initiation stress is 19.6 MPa. When the strain is 0.4%, there is a small fluctuation in the stress-strain curve at the corresponding position, and the crack count increases sharply at the position of stress fluctuation. For the tunnel model with joint length of 20 mm, the initiation stress is 10.2 MPa. For the tunnel model with joint of 30 mm, the initiation stress is 11.3 MPa. When the strain is 0.33%, the stress fluctuates, mainly because the local bearing capacity decreases after the crack breaks along the joint. For the tunnel model with 40 mm joint, the initiation stress is 10.8 MPa, and for the tunnel model with 50 mm joint, the initiation stress is 10.2 MPa. Joints affect the initiation time of cracks in the surrounding rock of the tunnel. The crack distribution process reflects the failure process of the tunnel.

3.2.2. Influence of Joint Spacing between Joints and Tunnel. Figure 9 shows the stress-crack counts of models with different spacing between joints and tunnel. It can be seen from Figure 9 that the distribution law of the crack count curve is basically the same. The crack curves have experienced four stages: no crack, crack initiation, rapid crack development, and gradual crack reduction. For the jointless model, the curve law is the same as that in Figure 8(a). For the tunnel model with spacing of 0 mm, the initiation stress is 10.2 MPa, and for the tunnel model with spacing of 10 mm, the initiation stress is 20.3 MPa. For the tunnel model with spacing of 20 mm, the initiation stress is 11.8 MPa. For the tunnel model with spacing of 30 mm, the initiation stress is 20.8 MPa. For the tunnel model with spacing of 40 mm, the initiation stress is 11.5 MPa. The crack initiation time of the jointed tunnel is less than that of the no-joint tunnel.

3.2.3. Influence of Double-Joint Locations. Figure 10 shows the stress-crack counts of models with different double-joint locations. The crack distribution curve shows a similar evolution law. The crack curves have experienced a similar evolution process. When the joint is at position T-S, the crack initiation stress of the model is 14.5 MPa, and the crack counting curve has experienced three peaks. The first stress fluctuation occurs before the peak stress, which is mainly due to the crack propagation along the joint direction when the stress reaches a certain strength. The second peak stress appears at the position where the strain is 0.45%, which is mainly due to the accumulation of a large number of cracks and the sharp increase in cracks. The third time appears at the postpeak position. The initiation stress of the model at position S-W, position W-F, position F-B, and position B-T is 14.5 MPa, 12.6 MPa, 13.1 MPa, and 16.7 MPa, respectively. The model with the fastest postpeak stress drop is position S-W, and the total number of cracks is less than that of other models. The maximum crack count appears in the B-T model.

3.3. Failure Mode. The failure mode can reflect the fracture process of the tunnel, and understanding the failure of the tunnel has important guiding significance for the excavation of the tunnel. Therefore, the failure characteristics of the tunnel are analyzed below.

3.3.1. Influence of Joint Length. Figure 11 shows the failure mode of the tunnel with different joint lengths when the strength is 0.95 times the postpeak stress. In the model, the red is the crack distribution, and the black in the lower right corner is the joint. When it is an intact tunnel, the crack first starts to initiate at the top and bottom of the tunnel, and then, the crack extends along the vertical direction. At the same time, a large number of cracks also appear in the lower right corner of the tunnel and gradually penetrate. When the joint length is 10 mm, the crack first starts to sprout at the top of the tunnel and the joint position; then, the top crack extends along the vertical direction, and the crack at the joint extends downward along the vertical direction of the

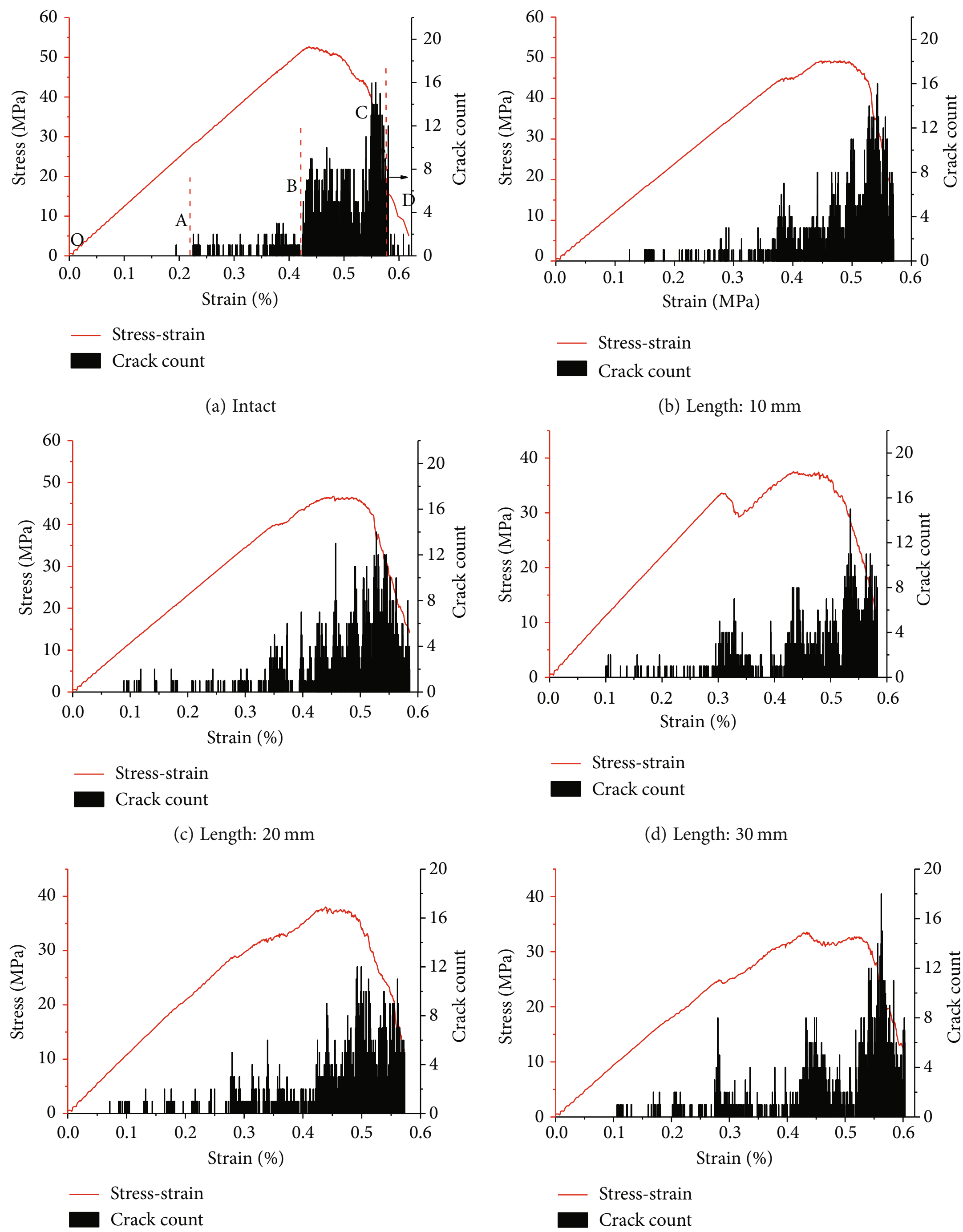

(a) Intact

(b) Length: 10 mm

(c) Length: 20 mm

(d) Length: 30 mm

(e) Length: 40 mm

(f) Length: 50 mm

Figure 8: Stress-crack count curve of models with different joint lengths.

joint. At the same time, there are cracks on the left and right sides of the model. When the joint length is 20 mm, the crack first starts to sprout at the top of the tunnel and the joint position; then, the top crack extends along the vertical direction, and the crack at the joint extends downward along the vertical direction of the joint. At the same time, the crack formed in the lower right corner of the model gradually penetrates with the joint. When the joint length is 30 mm, the crack extends along the top of the tunnel and the joint position. The top crack penetrates the tunnel upward, and an inverted V-shaped crack is formed in the lower right corner. When the joint length is 40 mm, the crack distribution is similar to that when the joint length is 30 mm, but obvious cracks appear in the arch shoulder of the tunnel, and local damage appears in the lower left corner. When the joint length is 50 mm, the crack failure starts to sprout and expand from the spandrel. The tunnel failure is mainly caused by the penetration of the crack and the joint in the

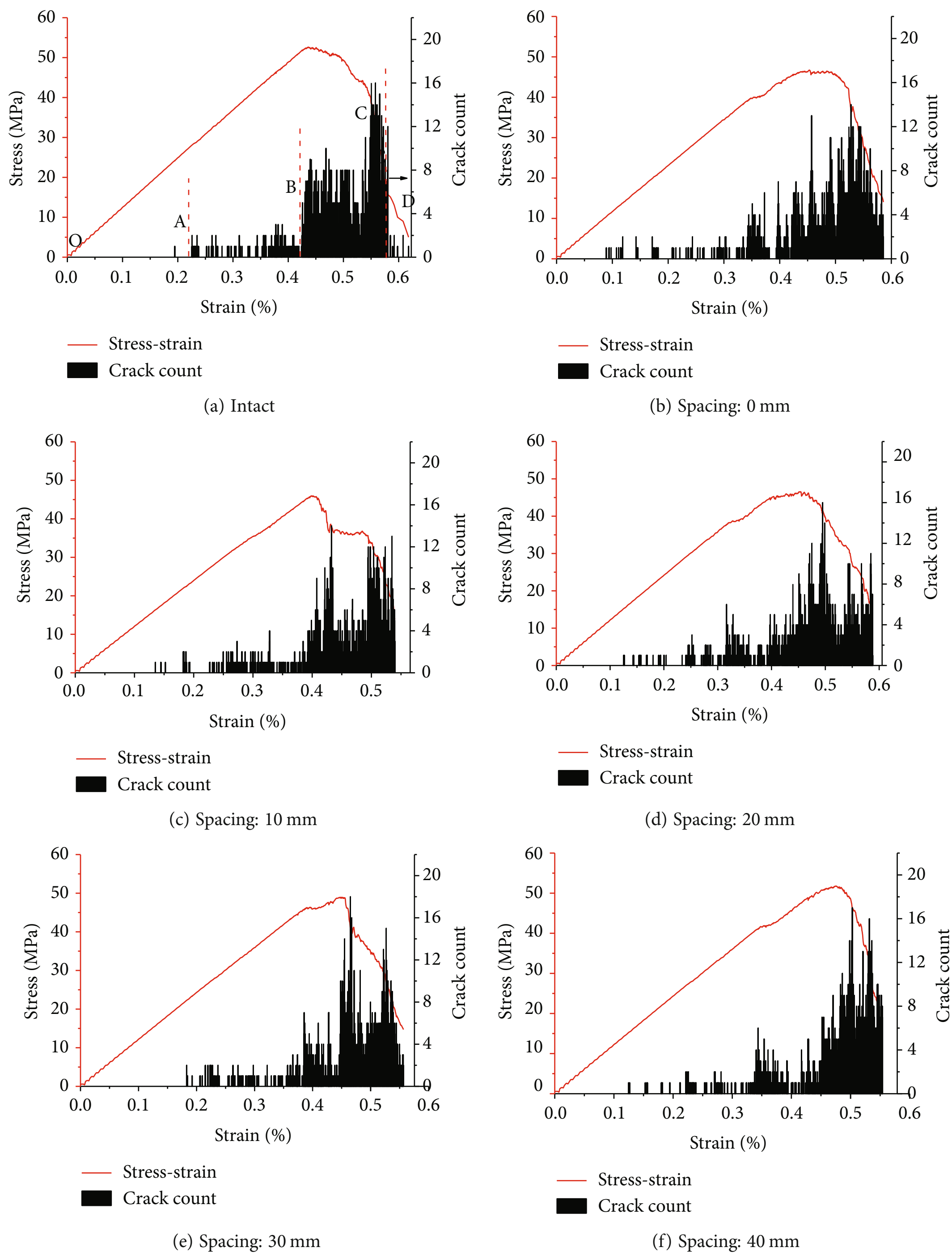

(a) Intact
(b) Spacing: 0 mm
(c) Spacing: 10 mm
(d) Spacing: 20 mm
(e) Spacing: 30 mm
(f) Spacing: 40 mm

FIGURE 9: Stress-crack counts of models with different spacing between joints and tunnel.

lower right corner. With the increase in joint length, the failure of the tunnel is mainly concentrated in the joint position at the lower right corner, which is also the main reason for the decline of the bearing capacity of the tunnel.

3.3.2. Influence of Joint Spacing between Joints and Tunnel. Figure 12 shows the failure modes of the tunnel with different spacing between joints and tunnel. When the spacing S is 0 mm, the failure characteristics are the same as in Figure 11(c). When the spacing S is 10 mm, the crack initiates and expands along the top of the tunnel, and the crack also extends along the lower right corner of the joint to form a through crack, and the rock bridge between the tunnel and the joint is damaged. When the spacing S is 20 mm and 30 mm, some cracks also initiate and expand along the top of the tunnel, the cracks in the lower right corner extend along the joint direction, and the damage is mainly concentrated in the lower right corner. When the spacing S is 40 mm, due to the increase in the spacing between the joint and the tunnel, the crack extends along the vertical direction

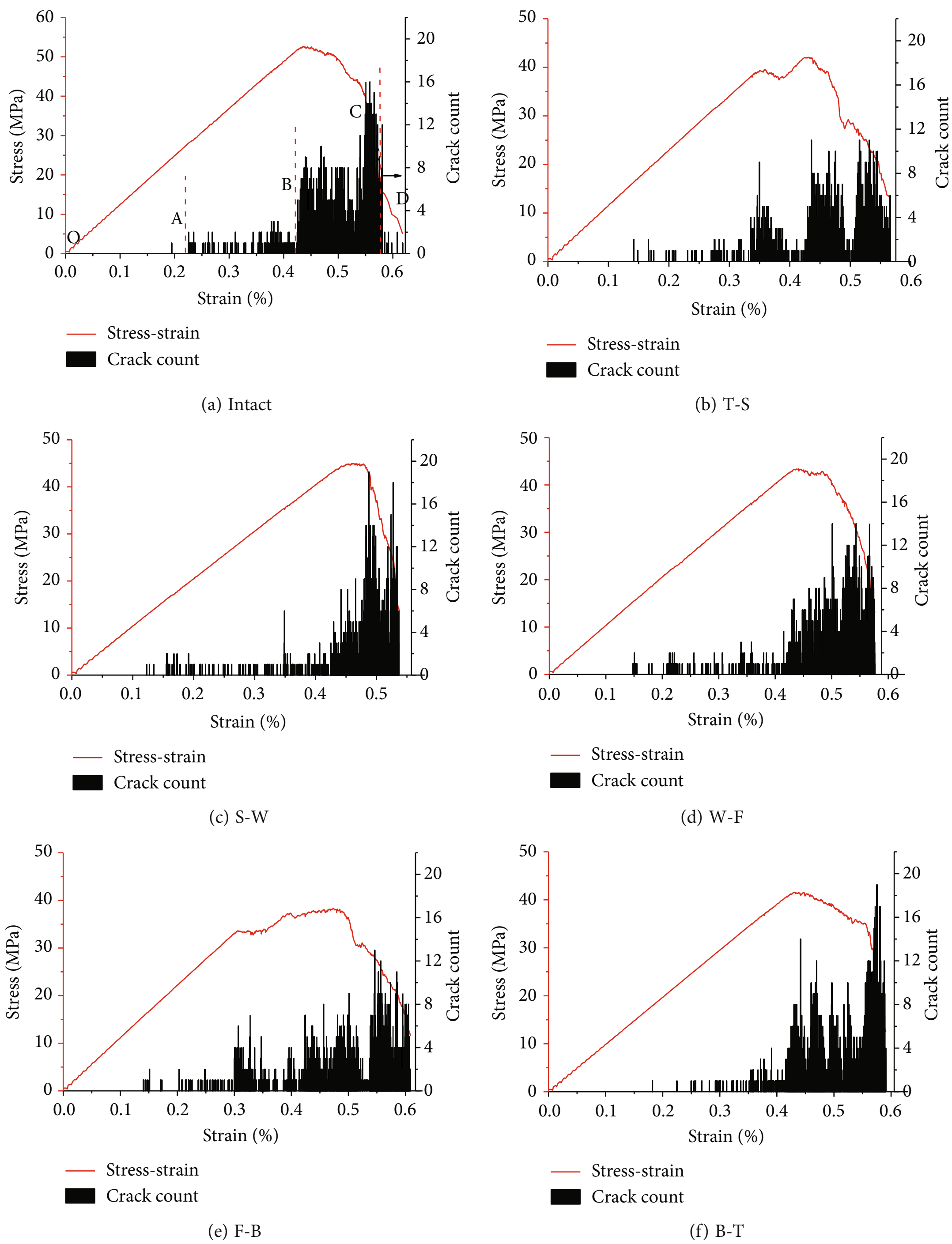

Figure 10: Stress-crack count curve of models with double-joint location.

after initiation at the joint position. The rock bridge between the joint and the tunnel has only a few cracks and is not damaged. The cracks of the whole model are mainly distributed in the upper left corner and near the joint. With the increase in spacing, the influence of joints on the tunnel decreases gradually.

3.3.3. Influence of Double-Joint Locations. Figure 13 shows the failure modes of the tunnel with different double-joint locations. When the double joints are at the position T-S, the crack propagates along the vertical direction of the top joint and the direction of the shoulder joint. Crack propagation also appeared in the lower right corner of the tunnel, mainly because it is easy to form stress concentration at the right foot of the tunnel. When the double joints are located at the position S-W, the crack also propagates along the joint direction of the shoulder and waist, but the crack propagation of the shoulder is obviously stronger than that of the waist, and local failure occurs in the lower left corner of the tunnel. When the double joints are at the position W-

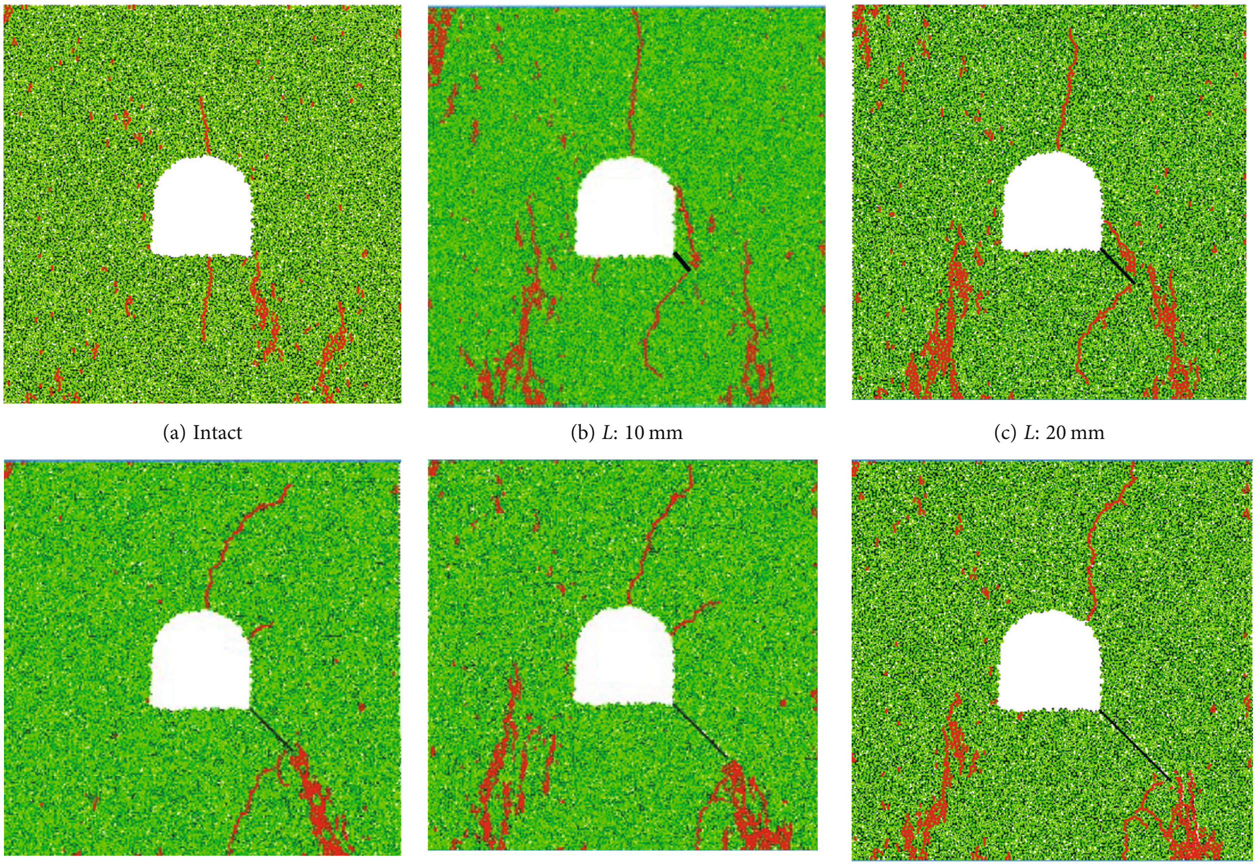

(a) Intact (b) L: 10 mm (c) L: 20 mm

(d) L: 30 mm (e) L: 40 mm (f) L: 50 mm

Figure 11: Failure modes of the tunnel with different joint lengths.

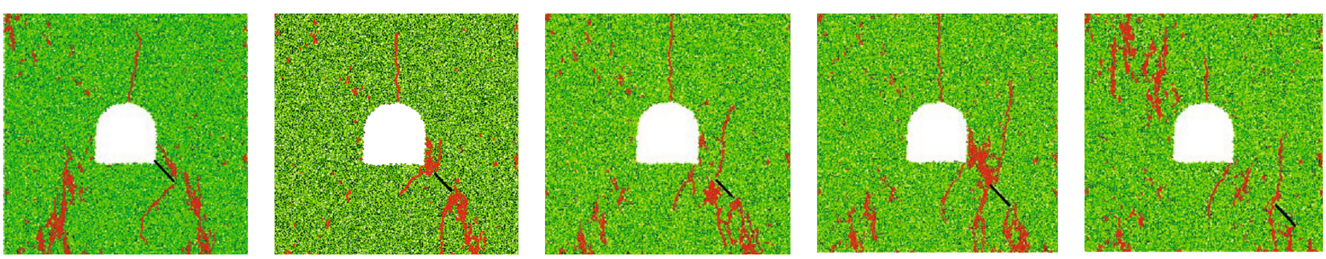

(a) S: 0 mm (b) S: 10 mm (c) S: 20 mm (d) S: 30 mm (e) S: 40 mm

Figure 12: Failure characteristics of the tunnel with different borehole spacing.

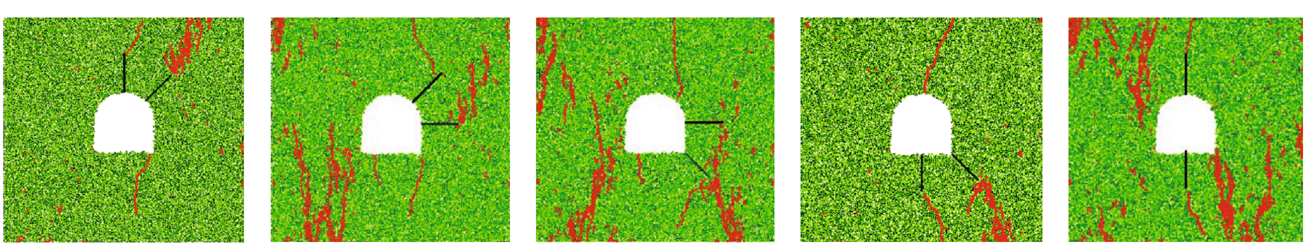

(a) T-S (b) S-W (c) W-F (d) F-B (e) T-B

Figure 13: Failure characteristics of the tunnel with different double-joint locations.

F, the crack extends vertically along the top of the tunnel, and the crack extends to the lower right corner along the joint at the foot. There are few cracks at the arch waist. It can be seen that the joints at the arch waist have little impact on the failure of the tunnel, and there is local failure on the left side of the tunnel. When the double joints are at the

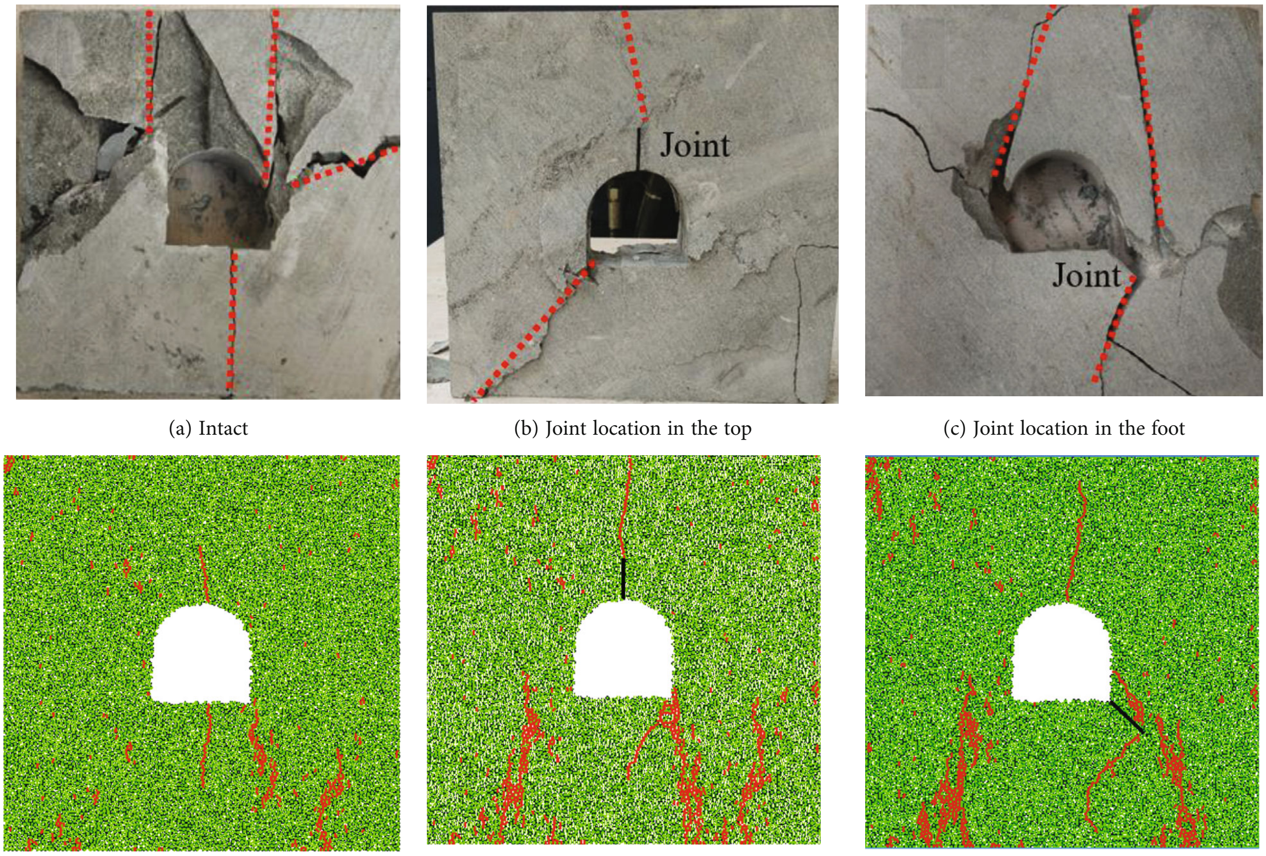

(a) Intact (b) Joint location in the top (c) Joint location in the foot

(d) Intact (e) Joint location in the top (f) Joint location in the foot

Figure 14: Experiment and numerical simulation.

position F-B, the crack extends vertically along the top of the tunnel, along the joint at the arch foot to the lower right corner, and vertically downward along the joint at the bottom. When the double joints are located at position T-B, the crack extends vertically along the top and bottom of the tunnel, and a large number of cracks appear in the local area of the tunnel. It can be seen that the existence of cracks directly affects the failure modes of the tunnel and changes the failure path of the tunnel.

4. Comparison and Discussion

Joints directly affect the failure characteristics of the surrounding rock of the tunnel. In order to further analyze the influence of joint distribution on tunnel surrounding rock, the indoor physical model mechanical test research on the jointed tunnel has been carried out, as shown in Figure 14 [24]. The size of the tunnel model is 200 mm (length) × 200 mm (height) × 50 mm (thickness). The tunnel is straight wall semicircle arch-shaped, and the radius of the semicircular arch and the length of the straight wall are both 25 mm. The joint length is 20 mm. The failure mode after the compression test of the physical model tunnel is shown in Figure 14. Figure 14(a) is the intact tunnel failure mode diagram, and Figure 14(b) is the tunnel failure mode with the joint at the top, and Figure 14(c) is the tunnel failure mode with the joint at the foot. Figures 14(d)–14(f) show the failure modes obtained from the numerical simulation results. It can be seen from the figure that the failure characteristics of both indoor experiments and numerical simulation are in good agreement. For the complete tunnel model, the failure of the tunnel is at the top and bottom, and the cracks mainly expand along the vertical direction. However, the indoor test model has obvious block spalling in the semicircular arch of the tunnel, and cracks extend to the left and right sides. For the tunnel model with joints at the top, the cracks extend vertically upward along the joint direction, and inclined downward cracks appear in the lower left corner, but some cracks also appear in the lower right corner of the numerical model. For the tunnel model with the joint at the foot, the crack first extends along the joint direction in the lower right corner, and an upward extending crack appears at the top of the tunnel. However, for the indoor physical model, the crack also extends vertically along the joint position, and for the numerical model, the crack extends along the lower left corner. The crack of the model is easy to appear at the top of the tunnel and expand along the joint position. It is mainly because it is easy to form tensile stress at the top of the tunnel and compressive stress concentration at the joint tip. Through the comparative analysis, it can be seen that the numerical simulation can better reflect the failure characteristics of the tunnel. It is reasonable to study the influence law of complex joint distribution on the failure of the tunnel by using the numerical simulation method. Nevertheless, there is still a certain deviation between the indoor test results and the numerical simulation, and some factors need to be further considered. For example, the three-dimensional model is used in the physical test, while the numerical simulation is two-dimensional. Considering the running speed of the computer, the particle size in numerical simulation is larger than that of actual sandstone. The discreteness of actual rock failure is much larger than that of numerical simulation samples. Therefore, more influencing factors should be considered in the future research to make it more consistent with the reality.

5. Conclusion

In order to study the influence of joints on the failure characteristics of tunnels, three test schemes with different joint lengths, joint spacing, and joint positions are designed. The conclusions are as follows:

(1) The bearing capacity of the tunnel decreases with the increase in the joint length. The length of joints has a great influence on the bearing capacity of the tunnel. With the increase in joint spacing, the bearing capacity of the tunnel decreases first and then increases. With different joint positions, the bearing capacity of the tunnel is also different. When the double joint is located in B-F, the bearing capacity of the tunnel is the lowest

(2) The distribution law of the crack count curve of each model is basically similar. The crack curves have experienced four stages. In the first stage, the stress is small and there is no crack. In the second stage, cracks appear with the increase in stress. In the third stage, with the further increase in stress, a large number of cracks gather and expand. In the fourth stage, the sample is damaged and the cracks are gradually reduced

(3) With the increase in joint length, the failure of the tunnel is mainly concentrated in the joint position at the lower right corner. With the increase in spacing, the influence of joints on the tunnel decreases gradually. The existence of cracks directly affects the failure modes of the tunnel and changes the failure path of the tunnel. The crack is most likely to appear at the top of the tunnel and expand along the joint. Analyzing the relationship between the tunnel and joints has important practical guiding significance for the control of the surrounding rock of the tunnel

Data Availability

The data used to support the findings of this study are included within the article.

Conflicts of Interest

The authors declare that they have no conflicts of interest.

Acknowledgments

This study was supported by the State Key Laboratory of Mining Response and Disaster Prevention and Control in Deep Coal Mine Research Fund (SKLMRDPC20KF09), Research Project of Undergraduate Teaching Reform in Shandong Province (P2020013), and Research Fund of Liaocheng University (318051703, 318011901, and 318012014).

References

[1] Z. Y. Yang, J. M. Chen, and T. H. Huang, "Effect of joint sets on the strength and deformation of rock mass models," *International Journal of Rock Mechanics and Mining Sciences*, vol. 35, no. 1, pp. 75–84, 1998.

[2] M. Bahaaddini, G. Sharrock, and B. K. Hebblewhite, "Numerical investigation of the effect of joint geometrical parameters on the mechanical properties of a non-persistent jointed rock mass under uniaxial compression," *Computers and Geotechnics*, vol. 49, pp. 206–225, 2013.

[3] Z. Lin, W. Xu, W. Wang et al., "Determination of strength and deformation properties of columnar jointed rock mass using physical model tests," *KSCE Journal of Civil Engineering*, vol. 22, no. 9, pp. 3302–3311, 2018.

[4] X. X. Yang, H. W. Jing, C. A. Tang, and S. Q. Yang, "Effect of parallel joint interaction on mechanical behavior of jointed rock mass models," *International Journal of Rock Mechanics and Mining Sciences*, vol. 92, pp. 40–53, 2017.

[5] S. Q. Yang, P. F. Yin, Y. C. Zhang et al., "Failure behavior and crack evolution mechanism of a non-persistent jointed rock mass containing a circular hole," *International Journal of Rock Mechanics and Mining Sciences*, vol. 114, pp. 101–121, 2019.

[6] A. Singh, K. Seshagiri Rao, and R. Ayothiraman, "A closed-form analytical solution for circular opening in rocks using Drucker–Prager criterion," *Indian Geotechnical Journal*, vol. 49, no. 4, pp. 437–454, 2019.

[7] S. Kuili and V. R. Sastry, "A numerical modelling approach to assess the behaviour of underground cavern subjected to blast loads," *International Journal of Mining Science and Technology*, vol. 28, no. 6, pp. 975–983, 2018.

[8] M. B. Wang and G. Wang, "A stress-displacement solution for a pressure tunnel with impermeable liner in elastic porous media," *Latin American Journal of Solids and Structures*, vol. 9, no. 1, pp. 95–110, 2012.

[9] W. Yang, Q. Zhang, P. G. Ranjith et al., "A damage mechanical model applied to analysis of mechanical properties of jointed rock masses," *Tunnelling and Underground Space Technology*, vol. 84, pp. 113–128, 2019.

[10] C. Jia, Y. Li, M. Lian, and X. Zhou, "Jointed surrounding rock mass stability analysis on an underground cavern in a hydropower station based on the extended key block theory," *Energies*, vol. 10, no. 4, pp. 563–574, 2017.

[11] D. Q. Kong, C. S. Qiao, and G. C. Xue, "Stability evaluation of flat large-span cavern in jointed rock mass," *Arabian Journal of Geosciences*, vol. 13, no. 11, pp. 1–14, 2020.

[12] Z. Jia, H. Xie, R. Zhang et al., "Acoustic emission characteristics and damage evolution of coal at different depths under triaxial compression," *Rock Mechanics and Rock Engineering*, vol. 53, no. 5, pp. 2063–2076, 2020.

[13] X. Wang, Z. Wen, Y. Jiang, and H. Huang, "Experimental study on mechanical and acoustic emission characteristics of

rock-like material under non-uniformly distributed loads," *Rock Mechanics and Rock Engineering*, vol. 51, no. 3, pp. 729–745, 2018.

[14] P. Jia and C. A. Tang, "Numerical study on failure mechanism of tunnel in jointed rock mass," *Tunnelling and Underground Space Technology*, vol. 23, no. 5, pp. 500–507, 2008.

[15] X. Hu, Y. Fang, G. Walton, and C. He, "Experimental analysis of shield TBM tunnel lining mechanical behaviour in an anisotropically-jointed rock mass," *KSCE Journal of Civil Engineering*, vol. 23, no. 6, pp. 2733–2745, 2019.

[16] Itasca Consulting Group, *PFC Users' Manual (Version 5.0)*, Itasca, Minneapolis, MN, USA, 2014.

[17] B. An and D. D. Tannant, "Discrete element method contact model for dynamic simulation of inelastic rock impact," *Computers & Geosciences*, vol. 33, no. 4, pp. 513–521, 2017.

[18] W. Liu, J. K. Liu, and C. Zhu, "Multi-scale effect of acoustic emission characteristics of 3D rock damage," *Arabian Journal of Geosciences*, vol. 12, no. 22, 2019.

[19] S. Pourmand, H. Chakeri, M. Sharghi, and Y. Ozcelik, "Investigation of soil conditioning tests with three-dimensional numerical modeling," *Geotechnical and Geological Engineering*, vol. 36, no. 5, pp. 2869–2879, 2018.

[20] R. Yoshinaka, M. Osada, H. Park, T. Sasaki, and K. Sasaki, "Practical determination of mechanical design parameters of intact rock considering scale effect," *Engineering Geology*, vol. 96, no. 3-4, pp. 173–186, 2018.

[21] U. Castro-Filgueira, L. R. Alejano, J. Arzúa, and D. M. Ivars, "Sensitivity analysis of the micro-parameters used in a PFC analysis towards the mechanical properties of rocks," *Procedia Engineering*, vol. 191, pp. 488–495, 2017.

[22] X. Zhang and L. N. Y. Wong, "Cracking processes in rock-like material containing a single flaw under uniaxial compression: a numerical study based on parallel bonded-particle model approach," *Rock Mechanics and Rock Engineering*, vol. 45, no. 5, pp. 711–737, 2012.

[23] C. Peng and W. Liu, "Study on pressure relief effect of rock mass with different borehole parameters," *Advances in Civil Engineering*, vol. 2021, Article ID 5558673, 15 pages, 2021.

[24] W. Liu, J. Xu, Z. Wang, and C. Peng, "Experimental research on damage characteristics and safety damage threshold of jointed caverns based on acoustic emissions," *Geomechanics and Geophysics for Geo-Energy and Geo-Resources*, vol. 7, no. 3, pp. 1–14, 2021.

Hindawi
Geofluids
Volume 2021, Article ID 2235555, 15 pages
https://doi.org/10.1155/2021/2235555

Research Article

Organic Geochemical Characteristics of Mudstone and Marl from Western Hoh Xil Basin of Tibet

Wentian Mi[1,2,3,4,5] **Xueyuan Qi**[3] **Yan Shang**[6] **Xu Kong**[7] **and Zifu Hu**[3]

[1]*Key Laboratory of Western China's Mineral Resources of Gansu Province, Lanzhou University, Lanzhou 730000, China*
[2]*State Key Laboratory of Oil and Gas Reservoir Geology and Exploitation (Chengdu University of Technology), Chengdu 610059, China*
[3]*School of Mines, Inner Mongolia University of Technology, Hohhot 010051, China*
[4]*Key Laboratory of Geoscience Spatial Information of Land and Resources, Chengdu 610059, China*
[5]*Geomathematics Key Laboratory of Sichuan Province, Chengdu 610059, China*
[6]*Department of Civil Engineering, Ordos Institute of Technology, Ordos 017000, China*
[7]*Department of Geology, Northwest University, Xian 710069, China*

Correspondence should be addressed to Wentian Mi; miwentian1982@imut.edu.cn and Yan Shang; 1142395467@qq.com

Received 8 August 2021; Accepted 18 September 2021; Published 8 October 2021

Academic Editor: Zhijie Wen

The mudstone and marl from western Hoh Xil basin, located in Tibet of the west of China, were deposited in Tertiary lacustrine environment. Investigation of organic geochemistry, sedimentary characteristics, and ^{13}C in kerogen was conducted to analyze the sedimentary environment, biomarkers, paleoclimate, and source of organic matter during deposition. The Cenozoic sedimentary facies of the basin included upper lacustrine facies and lower alluvial fan facies, which belong to Miocene Wudaoliang Formation and Oligocene Yaxicuo Group, respectively. The Miocene marl-sandstone-mudstone from Wudaoliang Formation was analyzed. Maceral composition was dominated by amorphous organic matter. T_{max} values indicated that the mudstones were thermally immature-low maturity with mainly type II and III organic matter, while organic matter in marlite belongs mainly to type I-II$_1$ with low maturity-maturity stage. The biomarkers showed the characteristics of odd-over-even predominance of long-chain n-alkanes, higher proportion of C_{27} sterane in most of the samples, heavy $\delta^{13}C_{org}$ composition, low Pr/Ph ratios (0.11-0.36), and so on. Organic geochemistry indicated that the organic matter originated from bacteria, algae, and higher plants. The rocks were formed in reducing environments with stratified water column and high productivity. The paleoclimate became more humid during depositional stage in the western Hoh Xil basin.

1. Introduction

After years of geological investigation, the Hoh Xil basin was considered to be one of the important targets of hydrocarbon resource exploration for continental basin of Tibetan Plateau. We found two continental facies oil and gas Cenozoic basin belts of Bangong-Nujiang and Jinsha River on Tibetan Plateau. These basins had good prospects for preserving oil and gas resources and exploration potential. The discovery of crude oil from Lunpola basin confirmed that reservoirs of fossil resources occurred in Qinghai-Tibet plateau [1, 2]. And the Hoh Xil basin has been confirmed existing a better prospect for preserving oil and gas too [3–5]. The eastern basin and western basin (Yanghu basin) of Hoh Xil had a conjoined basement, and there existed a unified Hoh Xil basin in Miocene [6–8]. Because of complex tectonism, the geological survey of western basin was very few. Understanding the geological survey of the western Hoh Xil basin (WHXB) is very important to recognize the overall situation of Cenozoic basins on Tibetan Plateau and the plateau lifting. Recently, sedimentary rocks of Wudaoliang Group in Miocene were discovered in WHXB. In this paper, we carried out detailed organic geochemistry investigations of these rocks in WHXB. The pivotal aim is to analyze paleoenvironment and paleoclimatic changes, to give the other geologists more information of Tibet.

2. Geological Setting

Hoh Xil basin is located in north Qiangtang block and the central of Bayankala block, crossing the suture of Jinsha River, and it is the greatest Cenozoic continental basin in Tibet [4, 9]. The western Hoh Xil basin (WHXB), near the eastern basin of Hoh Xil (EHXB), is an uncivilized basin in the central Tibetan Plateau [7, 10, 11] (Figure 1). Because of the harsh geographical environment and high altitude, the geology of the WHXB remains indeterminate. The work focuses on the detrital organic geochemical investigation in WHXB (Figure 1).

The west basin of Hoh Xil is located at an altitude of more than 4000 m with the area of 28,000 km^2, which belongs to the depopulated zone of Tibet province. It is bounded in the south of eastern Kunlun mountains and in the east of the Altyn mountains. The length of WHXB is about 540 km, and the width is about 60 km. In the west, the basin is near to Altyn sinistral strike-slip faults with its south branch. In the north, it is near to Subashi-Muztagh-Whale Lake fault zone, and it is adjacent to the microcontinental block of Kunlun. The south boundary of the basin is Lazhulong-Xijin Ulan-Jinsha fault zone, which is adjacent to the Qiangtang terrane.

The geological investigation revealed that the outcropping strata in WHXB were mainly Devonian, Permian, Triassic, Jurassic, Paleogene, and Neogene. A set of purple continental clastic rocks and carbonate of Cenozoic strata occurred in WHXB too. The Cenozoic sedimentary sequences contain three main parts in these strata of Wudaoliang Group, Fenghuoshan Group, and Yaxicuo Group. At the bottom of EHXB, the Fenghuoshan Group contains sandstone, bioclastic limestone in lacustrine, and fluvial, rounded conglomerate, which obtains the magnetostratigraphic age during the Early Eocene to Early Oligocene (31.3-52.0 Ma) [12]. The Fenghuoshan Group was covered by the Yaxicuo Group (Early Oligocene). The Yaxicuo Group comprises fluvial and playa gypsum, marl, mudstone, and sandstone in Oligocene (23.8-31.3 Ma) [8]. The uncomfortably overlying strata of the uppermost unit (Wudaoliang Group) consist mainly of oil shale, mudstone, and lacustrine marl with biostratigraphical age of basement about ~22 Ma [8]. The clastic rock association of Shapoliang (P01) in WHXB is consistent with the lithologic association of the Yaxicuo Group of Oligocene in EHXB; both of them uncomfortably underlie the volcanic rock of Chabaoma Formation [13]. And lacustrine carbonate of Fengcaogou (P02) in WHXB is consistent with the lithologic association of Wudaoliang Group in EHXB; both of them to belong to Miocene with nearly horizontal occurrence. In the south of EHXB, there is a huge south poured Paleogene thrust system, which is connected with the Tanggula thrust system of south WHXB. Shapoliang (P01) and Fengcaogou (P02) sections were measured at the marginal southeast of the WHXB in the geological survey. Two sections have the relationship of superposing; the profiles have been measured from the core of the syncline to the south part, no bottom. The top of profiles contacts with the Triassic through the fault.

3. Sedimentary Characteristics

Detrital zircon U-Pb isotopic compositions, sedimentary facies, and deformation of Shapoliang and Fengcaogou sections in WHXB are similar with the Oligocene Yaxicuo Formation and Miocene Wudaoliang Group of EHXB, respectively [7]. There are two depositional sequences developed in WHXB, including the lower alluvial fan (Shapoliang section) and upper lacustrine facies (Fengcaogou section), with a total thickness exceeding 1302 m. The Wudaoliang Group comprised crystalline limestone, bioclastic limestone, algal lump limestone, calcarenite, and marl in EHXB with the characteristics of carbonate of a paleolake [4]. The research section of Wudaoliang Group (Fengcaogou section, P02) is located in the southeast part of the WHXB (Figure 2).

In the low part of P02 of Wudaoliang Group, the unit contains gray, yellow-gray, gray-green, and gray-black mudstone and silty mudstone. This unit is sandwiched into maroon thin-middle layer of mudstone, argillaceous siltstone, silty mudstone, and fine sandstone; and some gray-green sheet marl and sandy limestone are outcrop. In the middle part, lithologic column contains the interbedded fine siltstone, mudstone, gray marl, and sandy limestones; this unit was sandwiched into thickness marls (up to 3.0 m). The upper part shows the gray marl, yellow fine sandstone, and brown red silty mudstone with a coarsening-upward sequence from bottom to top, which deposits marl-silty mudstone in the lower part and fine sandstone-siltstone in the upper part (Figure 3). This section presents a sedimentary cycle with coarsening-upward in the overall. Potential organic rocks occur in lower-middle part of Fengcaogou section, which is made up of gray and yellow-gray mudstone, gray-black mudstone, and gray-green marl with a thickness of about 100 m.

The sedimentary environment of Wudaoliang Group belongs to the shallow lacustrine [14]. The Fengcaogou section mainly contains marl, sandstone, siltstone, and mudstone with the thickness of about 205 m. The lithofacies indicate the depositional environment is lacustrine. The massive argillaceous rocks of the Fengcaogou section need suspension in a peaceful water environment. According to characteristics of deposition of profiles, the Fengcaogou section of Wudaoliang Group experienced the evolution of depositional environment by semideep to shallow lake subfacies.

4. Research Methods

4.1. Sample. 20 samples are selected from the Fengcaogou profile in the western Hoh Xil basin. All of the samples were analyzed by geochemical methods. Details of sampling location, lithologic association, and stratigraphic columns are shown in Figure 3. In order to minimize the modern pollutions on surface and the effects of biodegradation and weathering, we used a shovel to collect fresh samples. After the collection of samples from the measured profiles systematically, organic geochemical tests were conducted. There are distinctive heterogeneities in the deposition of lacustrine sedimentary rocks (Table 1). After the evaluation of

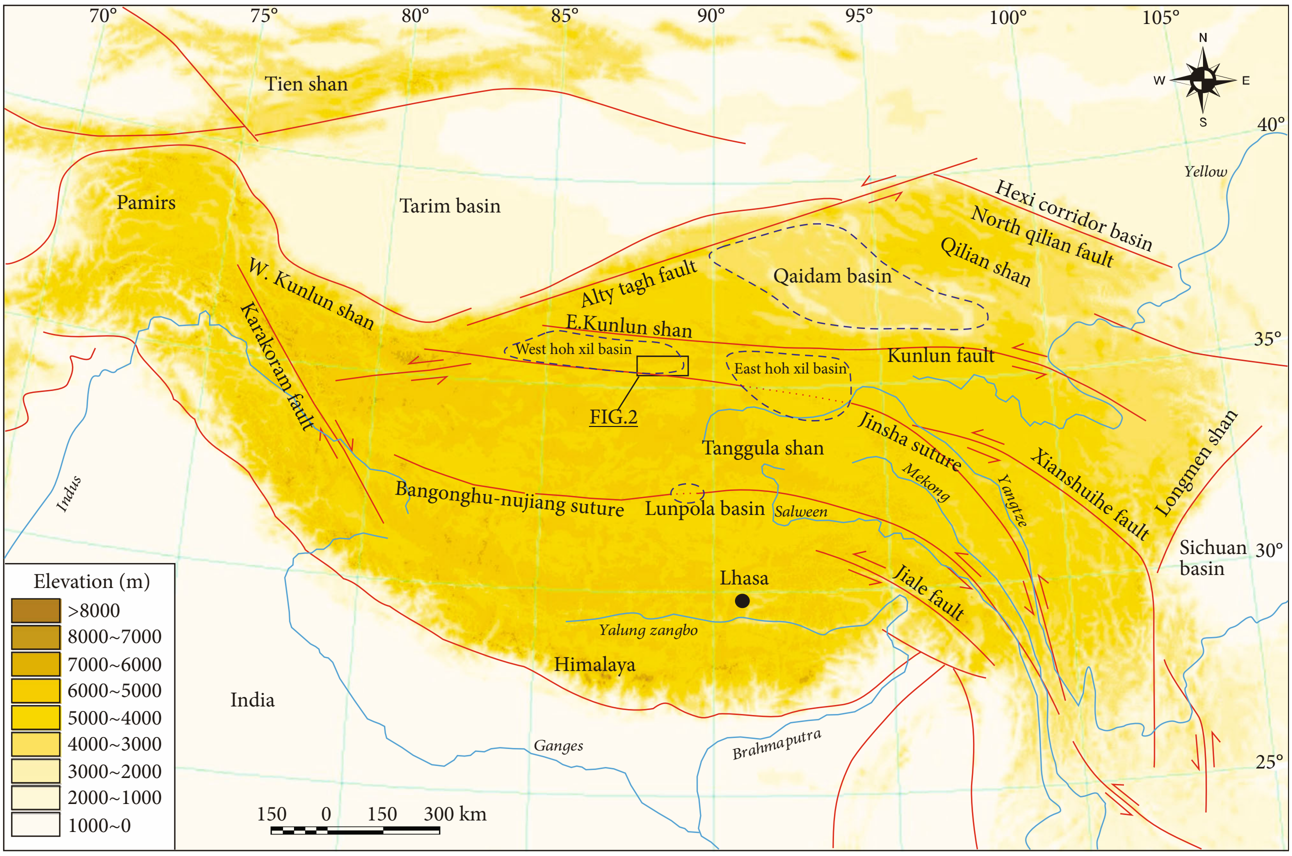

FIGURE 1: Sketch map of structure in the Qinghai-Tibet plateau and Cenozoic sedimentary basins in the north of the Plateau.

Wudaoliang Group samples in the WHXB, gray or yellow-gray mudstones belong to nonpoor organic types of rocks; gray-black mudstones belong to good organic types of rocks; gray-green marl is moderate-good organic types of rocks. The types of organic matter in mudstone belong to types II and III. The types of OM in marl belong to type I-II$_1$.

4.2. Analytical Methods. Some rocks are prepared to the test of organic petrology, Rock-Eval pyrolysis, TOC, and δ^{13}C. Saturated fractions of some samples are tested by the method of GC and GC-MS. Total organic carbon is analyzed using the equipment Leco CS-200 carbon-sulfur. After getting rid of carbonate by hydrochloric acid (HCl), some sample (120 mesh and 100 mg) was raising temperature to 1200°C in the induction furnace. The test of Rock-Eval pyrolysis was conducted on a TOC module-equipped apparatus with Rock-Eval II by strict procedures [15]. In the Soxhlet apparatus, some samples were conducted with chloroform for 72 h. After setting of asphaltenes, through a silica gel alumina column, NSO compounds, saturated hydrocarbons, and aromatic hydrocarbons were isolated from extracts by column chromatography [16].

GC-MS testing of saturated hydrocarbon is conducted using a Finnigan SSQ-7000 spectrometer. This instrument equipped is with DB5-MS fused silica capillary column (0.32 mm ID × 30 m × 0.25 μm film thickness). Carrier gas is helium. The oven is isothermally kept at 35°C in 1 min, then raised to 120°C by 10°C/min, and then increased to 300°C by 3°C/min, keeping this temperature for half an hour. MS is conducted by MID on a source temperature at 200°C with ionization energy of 70 eV. To identify molecular fossils, metastable ion transition for tricyclic terpanes and hopanes (m/z 191) and steranes (m/z 217) was kept an account of a periodic time of 1 s and a residence time for 25 ms per ion [17].

HCI/HF method is applied to 20 samples for kerogen isolation. First, rock fragments were leached in 12 N HCl for getting rid of carbonates in 12 h, and then, keep them clean with distilled water. Second, samples were conducted by hydrofluoric acid to get rid of silicate in 12 h [18]. Third, samples used distilled water for cleaning. Then, samples were again leached with 12 N HCl [18]. Maceral content is conducted by Zeiss Axioskop 2 plus microscope and a point counter for visual evaluating [16]. The test of N, C, H, S, and O was conducted using a FLASH EA-1112 instrument; the accuracy is 0.5% for N and 0.3% for C. The determination of $\delta^{13}C_{kerogen}$ is conducted using the EA Finnigan Delta plus XL mass spectrometer; precision of carbon isotope is ±0.2‰ [19]. Isotopic analyses and GC-MS analyses as well as others analyses were carried out in the Organic Geochemistry Laboratory of Huabei Oilfield Branch Company of PetroChina.

5. Results and Discussion

5.1. Rock-Eval Pyrolysis. Because the weathering has an obvious effect on the sedimentary rocks, the organic carbon of

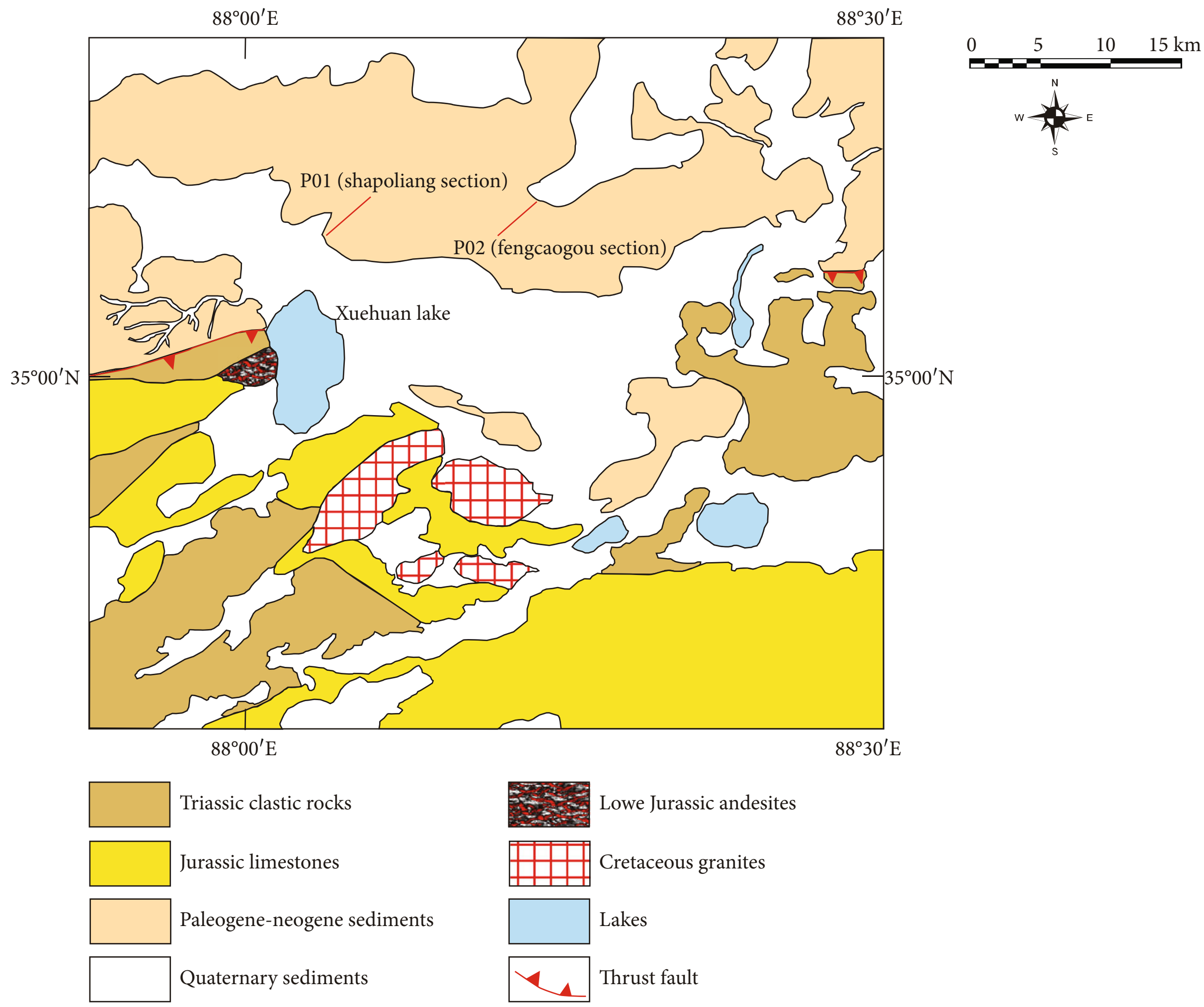

Figure 2: Geological map of study area showing the location of the P02 section.

samples needs recovery. TOC and Rock-Eval data are listed in Table 1. TOC content of Fengcaogou mudstones is in the range of 0.03-1.38 wt.% and an average of 0.19% with most samples > 0.1 wt.%. After the recovery with coefficient of 2.2 [20], the restoration of organic carbon content is in the range of 0.08%~3.04 wt.% and an average of 0.42%. The TOC content of the Fengcaogou marl is in the range of 0.09~0.18 wt.% and an average of 0.14%; after the recovery with coefficient of 1.5 [20], the restoration of organic carbon content is in the range of 0.13%~0.27 wt.% and an average of 0.20%.

Maceral composition of kerogens from the Fengcaogou section is shown in Table 2. Amorphous organic matter exhibits a high abundance ranging from 50% to 90% with an average of 66%. Exinite is in the range of 0~15 wt.% and an average of 4.37%. Vitrinite is in the range of 3~22 wt.% and an average of 16.6%. Inertinite is in the range of 5~31 wt.% and an average of 12.95%. Organic matter of kerogen in mudstone shows the types of mixed II (II_1-II_2), whereas kerogen in marl shows the types of I-II_1.

Rock-Eval S_1 and S_2 are in the change of 0.02-0.24 and 0.06-1.17 mg HC/g rock. S_2 values of marl are in range of 0.09-0.19 mg HC/g rock, compared with 0.06-0.15 mg HC/g rock for mudstone (except P02-5S4) (Table 1). The value of PY changes from 0.09 to 1.41 mg HC/g rock, which can reflect the potential yield and inversion of OM [21]. HI values are not high with the range of 50 to 200 mg HC/g TOC. The HI of marls is higher with the value of 89 to 144 mg HC/g TOC. Ro values change from 0.55 to 0.73. The color of sapropel group in kerogen (yellow) reflects that OM belongs to immature to early mature.

T_{max} of all samples changes from 370°C to 532°C with the average of 437°C (Table 1). In the mudstone, 9 samples of T_{max} values < 435°C indicating a thermally immature stage; 3 samples of T_{max} values change from 435°C to 440°C at low mature stage; 4 samples of T_{max} are between 450°C and 580°C at high mature stage. Organic matter of mudstones is in immaturity-low maturity stage. T_{max} values of marl change from 426 to 447°C; these indicate thermally immature-mature. Difference in thermal maturity of two rocks may depend on the history of burial. The PI (production index) values of all samples are from 0.11 to 0.33. The maturity suggested by PI and T_{max} are not completely consistent, which may be due to the weathering [22].

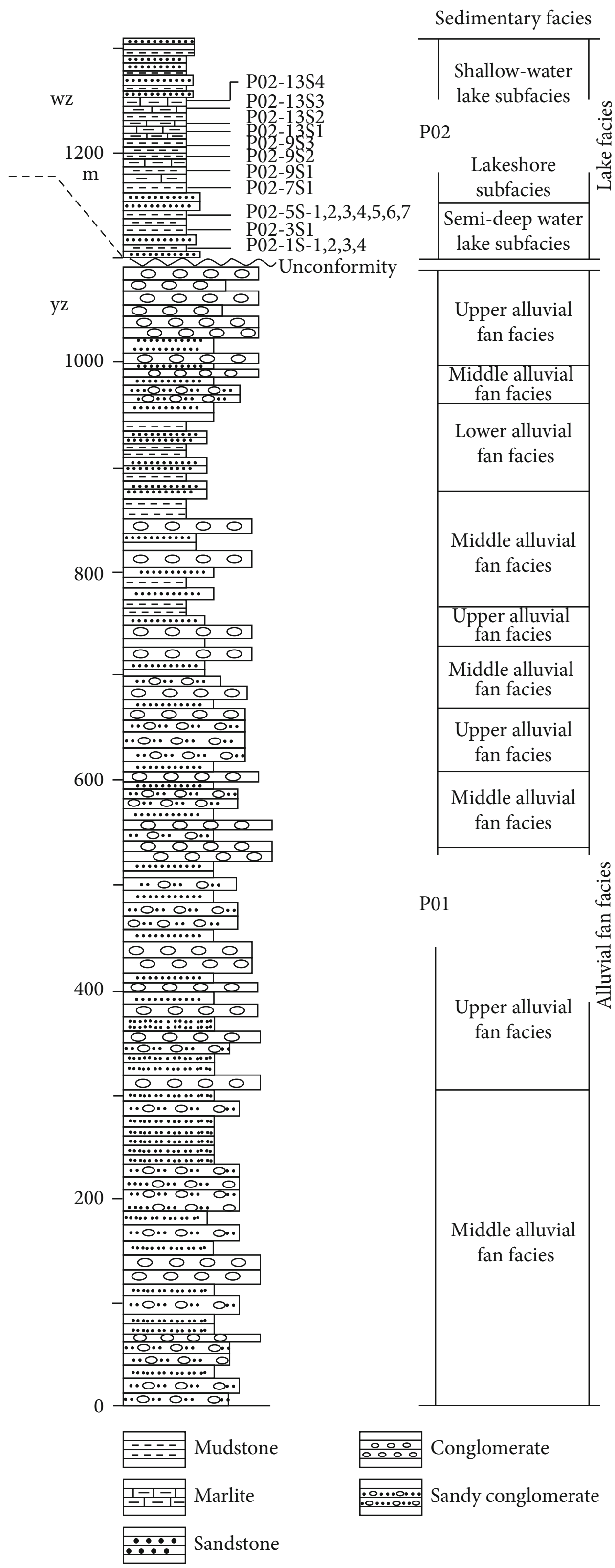

Figure 3: Stratigraphic columns for the Shapoliang-Fengcaogou section of the western Hoh Xil basins. WZ: Wudaoliang Fm.; YZ: Yaxicuo Fm.; P01: Shapoliang section; P02: Fengcaogou section.

5.2. Characteristics of the Element and Kerogen. The characteristics of element can reflect the chemical features of isolated kerogen [23]. And the analysis results of element are shown in Table 2. Variability is marked in the Fengcaogou section. O/C ratios of kerogen change from 0.22 to 0.39; H/C ratios of kerogen change from 0.68 to 1.27 (Table 2). The marl samples of Fengcaogou section have lower O/C ratios (0.22, 0.22, and 0.24) and higher H/C ratios (1.21, 1.25, and 1.27) than the mudstones in this section; mudstones have lower H/C ratios (0.68-0.88) and higher O/C ratios (0.34-0.39). Organic matter of mudstones are mainly types II and III, while organic matter of marl is markedly different (Figure 4), which suggest the probable input of allochthonous OM. And kerogens of type I with lacustrine source are input by AOM and planktonic algae [24].

The variation tendency in different lithology is consistent with kerogen's maceral composition. AOM make up 75-90% kerogen assemblages, together by 1-2% sporinite, 3-15% vitrinite, and 5-10% inertinite for the marl sample (Table 2). The marls contain more hydrogen-rich AOM (75-90%), with much less inertinite and vitrinite (Table 2), which fit well with characteristics of type I-II_1 kerogen.

The kerogen in mudstones is composed of 50-72% AOM, 1-6% sporinite, 12-22% vitrinite, and 9-31% inertinite. There is no appearance of amorphous humic material, indicating little input of land plants [25]. AOM is associated with import sources of bacterial phytoplankton and algae from surface of lacustrine [26]. Taking into account the geochemical characteristics, it could indicate that OM contribution in the marl comes from more algal or bacterial phytoplanktonic sources, while less bacteria and algae contribution in the mudstone could be confirmed. Vitrinite reflectance is used to determine the indicator of maturity. In the mudstones, only one data was obtained (0.58), but the Ro values of marl are 0.55-0.73.

5.3. Biomarkers

5.3.1. Normal Alkanes and Isoprenoids. The gas chromatograms of saturated hydrocarbons separated from Fengcaogou in Wudaoliang Group of WHXB are shown in Figure 5 and results are shown in Table 3. Saturated hydrocarbons of mudstone and marl reveal the dominance of middle to high carbon number molecular; the carbon peak is n-C_{23} (e.g., P02-13S3), n-C_{27}, n-C_{29} (e.g., P02-5S6 and P02-7S1), or n-C_{31} (e.g., P02-3S1). The value of C_{21-}/C_{21+} of Fengcaogou mudstones and marls changes from 0.06 to 0.24; all samples show superiority of long-chain n-alkanes, which indicate terrestrial higher plant-derived n-alkanes [27]. The distributions of n-alkanes in the samples have an odd ($nC_{27,29,31}$)-over-even ($nC_{26,28,30}$) carbon number predominance in the nC_{23} to nC_{31} range (Figure 5). The OEP vary between 1.45 and 6.91, and most of the samples have the CPI values changing from 4 to 1.75. Long-chain n-alkanes (nC_{27} to nC_{31}) are considered coming from terrestrial plant waxes [28]. Thence, predominate of long-chain n-alkanes (e.g., P02-3S1, P02-5S4, P02-5S6, and P02-13S1 besides P02-13S3) can be confused originating from terrestrial plants. But this interpretation is in contradiction with petrographic investigation of kerogens.

TABLE 1: Results of Rock-Eval and TOC analysis and calculated parameters.

Sample no.	Lithology	S_0[a] (mg/g)	S_1[b] (mg/g)	S_2[c] (mg/g)	T_{max}[d] (°C)	PY[e] ($S_1 + S_2$) (mg/g)	PI[f] ($S_1/S_1 + S_2$)	Chloroform bitumen A (%)	HI[g] (mg HC/g TOC)	TOC[h] (wt.%) (restored)
P02-1S1	Gray mudstone	0.04	0.05	0.13	424	0.18	0.27	0.0040	118	0.11 (0.24)
P02-1S2	Yellow-gray mudstone	0.02	0.04	0. 10	391	0.14	0.28	0.0058	71	0.14 (0.31)
P02-1S3	Gray mudstone	0.02	0.04	0.08	399	0.12	0.33	0.0044	160	0.05 (0.10)
P02-1S4	Gray mudstone	0.02	0.04	0.08	368	0.12	0.33	0.0069	133	0.06 (0.12)
P02-3S1	Gray mudstone	0.02	0.03	0.07	438	0.10	0.30	0.0041	175	0.04 (0.08)
P02-5S1	Yellow-gray mudstone	0.02	0.03	0.06	439	0.09	0.33	0.0031	200	0.03 (0.08)
P02-5S2	Gray mudstone	0.02	0.04	0.08	370	0.12	0.33	0.0066	66	0.12 (0.26)
P02-5S3	Gray mudstone	0.02	0.05	0.15	430	0.20	0.25	0.0215	75	0.20 (0.43)
P02-5S4	Gray-black mudstone	0.02	0.24	1.17	428	1.41	0.17	0.0206	84	1.38 (3.04)
P02-5S5	Gray mudstone	0.02	0.04	0.09	434	0.13	0.30	0.0082	56	0.16 (0.35)
P02-5S6	Gray mudstone	0.02	0.04	0.09	438	0.13	0.30	0.0060	53	0.17 (0.37)
P02-5S7	Gray mudstone	0.01	0.03	0.07	380	0.10	0.30	0.0038	70	0.1 (0.22)
P02-7S1	Gray mudstone	0.01	0.02	0.07	524	0.09	0.22	0.0027	87.5	0.08 (0.17)
P02-9S1	Sandy mudstone	0.01	0.03	0.08	532	0.11	0.27	0.0054	53	0.15 (0.33)
P02-9S2	Gray mudstone	0.01	0.03	0.08	522	0.12	0.25	0.0022	50	0.16 (0.35)
P02-9S3	Gray mudstone	0.01	0.03	0.08	472	0.11	0.27	0.0023	73	0.11 (0.24)
P02-13S1	Marl	0.01	0.03	0.13	447	0.16	0.18	0.0037	144	0.09 (0.13)
P02-13S2	Marl	0.01	0.02	0.09	426	0.11	0.18	0.0037	90	0.10 (0.15)
P02-13S3	Marl	0.01	0.02	0.16	446	0.18	0.11	0.0033	89	0.18 (0.27)
P02-13S4	Marl	0.01	0.03	0.19	434	0.22	0.14	0.0048	105	0.18 (0.27)

[a]S_0 = gas hydrocarbons. [b]S_1 = free hydrocarbons. [c]S_2 = pyrolysable hydrocarbons. [d]T_{max} = temperature of maximum S_2. [e]PY = potential yield. [f]PI = productivity index. [g]HI = hydrogen index. [h]TOC = total organic carbon.

Table 2: Elemental and maceral composition and carbon isotope values of kerogens from the Fengcaogou section.

Sample no.	H/C	C/N	O/C	$\delta^{13}C_{PDB}$ (‰)	[a]AOM	Exinite	Vitrinite	Inertinite	Color of sapropel group	Ro (%)	Type
P02-1S1	n.a.	67.8	n.a.	-23.8	65	3	19	13	Yellow		II_2
P02-1S2	n.a.	40.1	n.a.	-23.0	66	3	17	14	Yellow		II_1
P02-1S3	n.a.	n.a.	n.a.	n.a.	55	4	20	21	Yellow		II_2
P02-1S4	n.a.	102.8	n.a.	-24.5	50	13	22	15	Yellow		II_2
P02-3S1	n.a.	n.a.	n.a.	n.a.	60	15	12	13	Yellow		II_1
P02-5S1	n.a.	117.3	n.a.	-25.8	50	6	13	31	Yellow		II_2
P02-5S2	n.a.	39.5	n.a.	-23.7	60	4	15	21	Yellow		II_2
P02-5S3	0.87	27.3	0.31	-25.3	69	3	18	10	Yellow		II_1
P02-5S4	0.88	24.6	0.39	-24.8	72	n.a.	19	9	Brown	0.58.	II_1
P02-5S5	n.a.	40.7	n.a.	-23.8	66	3	20	11	Yellow		II_1
P02-5S6	n.a.	102.9	n.a.	-23.6	67	4	19	10	Yellow		II_1
P02-5S7	n.a.	57.2	n.a.	-23.8	60	1	20	19	Yellow		II_2
P02-7S1	n.a.	12	n.a.	-24.1	66	3	21	10	Yellow		II_1
P02-9S1	0.68	45.9	0.34	-23.7	63	6	21	10	Yellow		II_1
P02-9S2	n.a.	922	n.a.	-23.7	62	6	21	11	Yellow		II_2
P02-9S3	n.a.	46.96	n.a.	-23.9	65	4	20	11	Yellow		II_1
P02-13S1	1.21	33.45	0.24	-21.3	75	1	15	9	Yellow		II_1
P02-13S2	1.25	36.12	0.22	-20.9	76	2	12	10	Yellow	0.59	II_1
P02-13S3	n.a.	31.1	n.a.	-21.9	90	1	3	6	Yellow	0.55	I
P02-13S4	1.27	41.1	0.22	-20.0	89	1	5	5	Yellow	0.73	I

[a]AOM = amorphous organic matter; n.a.: not analyzed.

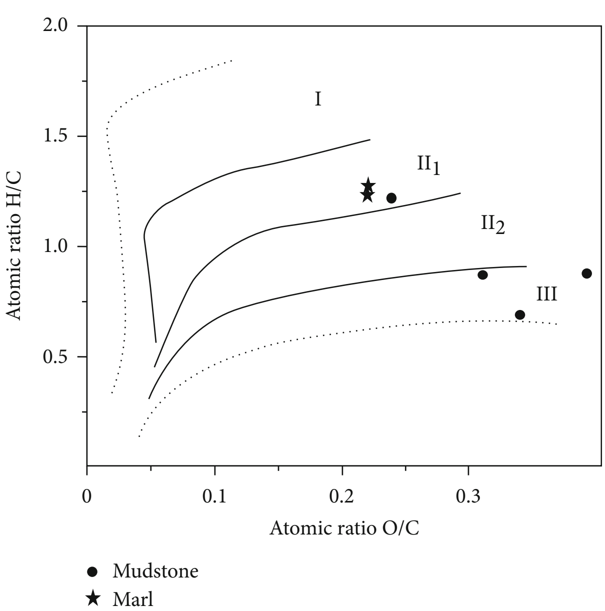

Figure 4: Plot of H/C versus O/C of kerogen from samples of the Fengcaogou section showing organic matter type. I: sapropelic kerogen; II: humic-sapropelic kerogen, sapropelic-humic kerogen; III: humic kerogen.

It has been proved that some nonmarine algae also may be the origin of long-chain n-alkane [29]. Therefore, nonmarine algae and higher plants may be the parent material of long-chain odd n-alkanes together.

The mid molecular weight of n-alkanes (nC_{21} to nC_{25}) is probably considered coming from aquatic macrophytes (predominate of nC_{23} and nC_{25}) and *Sphagnum* [30, 31]. And the intermediate molecular weight of n-alkanes found relative contents in most of the samples, especially in P02-7S1. Because the causation of peat bog was precluded, the source of OM from *Sphagnum* may be excluding and the source of macrophytes leads to the n-alkane patterns. The research shows that the upper strata of Wudaoliang Group (P02) developed a lacustrine sedimentary system. Therefore, n-alkanes of intermediate molecular weight may have originated from macrophytes. By the calculation of $P_{aq} = (C_{23} + C_{25})/(C_{23} + C_{25} + C_{29} + C_{31})$, values of all the samples (averaging 0.42) indicated that the submerged/floating macrophytes were the contributors [30] (Table 3).

Phytane is the dominant acyclic isoprenoid in the samples of WHXB but has a lower peak than n-alkanes in the samples (Figure 5). The oxic/anoxic or the origin of OM is judged frequently by the parameter of pristane/phytane (Pr/Ph) ratio [32]. If phytol side chain of chlorophyll from organic matter was oxidized, it would cause priority to form pristine with high Pr/Ph ratios [33]. The values of Pr/Ph of the mudstone and marl samples are relatively low in WHXB changing from 0.11 to 0.36 (average 0.19) (Table 3). Mudstones from Fengcaogou section exhibit the values of Pr/Ph changing from 0.12 to 0.36. However, Pr/Ph ratios of marl indicate a lower value.

Generally, Pr/Ph > 1 suggests an oxic condition, but Pr/Ph < 1.0 shows anoxic source-rock deposition [34]. However, several studies indicated that the source input and thermal maturation and other factors can affect the Pr/Ph ratios

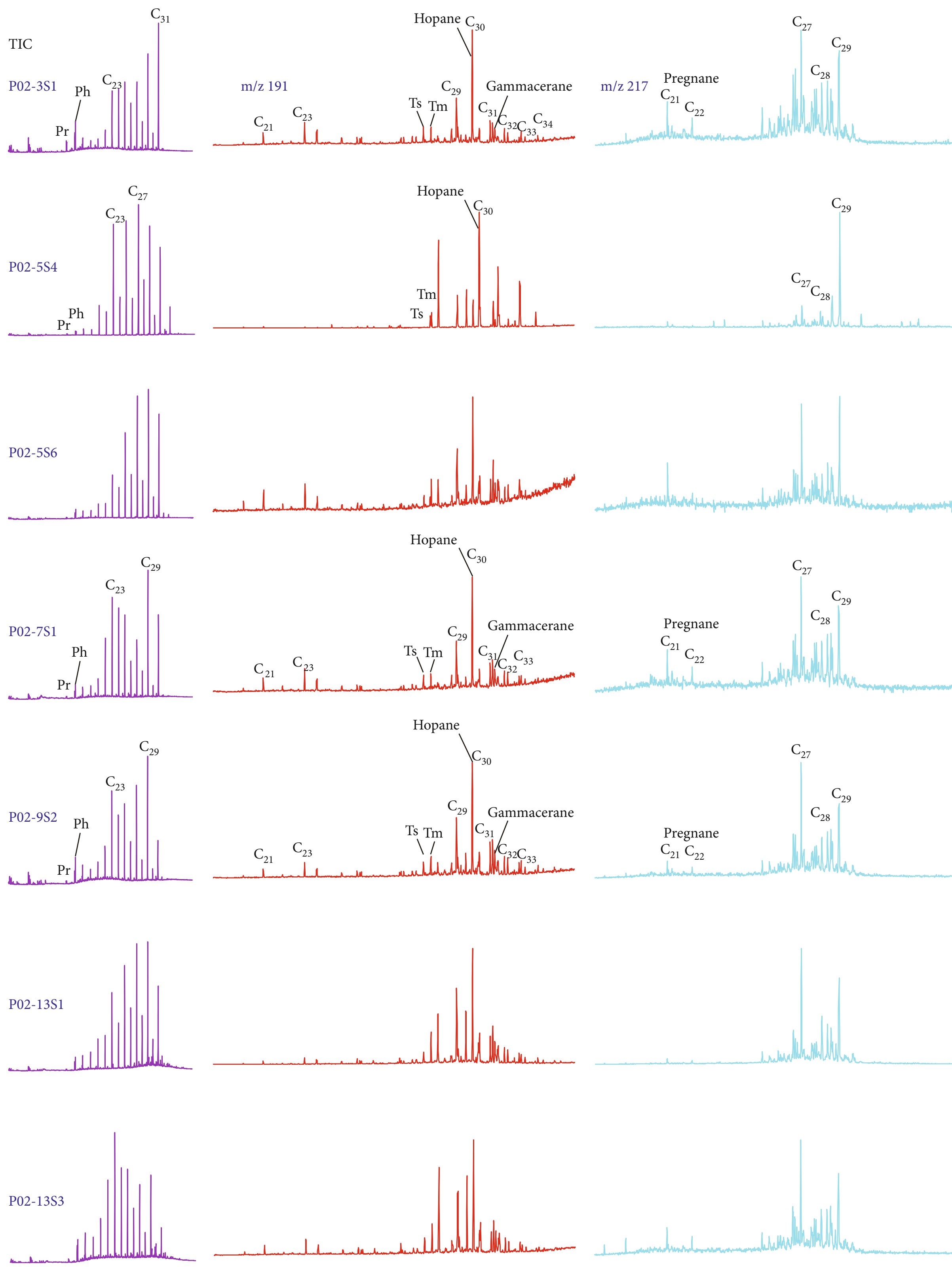

Figure 5: TIC, terpane and sterane mass chromatograms of samples from Fengcaogou in WHXB, Tibet plateau.

[35]. Peters et al. [36] still suggest that Pr/Ph ratios < 0.6 suggest the environmental characteristics of hypersaline and anoxic condition; but Pr/Ph > 3 shows sedimentary environmental characteristics with suboxic to oxic condition. With the mudstone and marl form Fengcaogou, the feature of Pr/Ph ratios can indicate an anoxic probably hypersaline deposited condition in lacustrine environment. Hypersaline environment would cause density stratification of water

Table 3: Basic geochemical data for extracts of samples from the Fengcaogou section in WHXB, Tibet plateau, China.

Sample no	Pr/Ph[a]	nC_{21}^{-}/nC_{22}^{+}	Pr/nC_{17}	Pr/nC_{18}	CPI	Tm/Ts	$C_{30}Hop/C_{29}Mor$	Gammacerane index[b]	P_{aq}[c]	$\alpha\alpha\alpha$-C_{29}·20S/(20S + 20R)	C_{27}%[d]	C_{28}%[e]	C_{29}%[f]
P02-1S1	0.24	0.24	1.08	1.84	2.68	1.63	2.37	0.89	0.89	34.87	42.74	18.32	38.93
P02-1S3	0.24	0.24	1.12	2.08	3.46	1.39	1.94	0.71	0.71	31.66	43.17	18.57	38.26
P02-3S1	0.30	0.12	1.11	1.90	3.10	0.96	2.54	0.68	0.68	38.26	42.41	20.74	36.84
P02-5S2	0.36	0.14	1.25	1.60	3.77	3.49	1.59	0.36	0.36	16.87	29.76	12.82	57.42
P02-5S4	0.35	0.06	0.92	1.11	3.98	21.85	0.85	0.51	0.51	4.61	14.39	6.82	78.79
P02-5S6	0.16	0.06	1.18	1.76	3.38	2.53	1.91	0.58	0.58	26.70	41.74	12.24	46.02
P02-7S1	0.19	0.09	0.91	1.66	2.40	1.16	2.38	0.69	0.69	39.49	46.02	19.01	34.97
P02-9S2	0.12	0.11	1.33	2.07	2.43	1.42	1.97	0.71	0.71	36.43	51.40	15.92	32.69
P02-13S1	0.11	0.10	1.01	1.68	2.44	4.27	1.53	0.68	0.68	30.60	46.63	18.47	34.91
P02-13S3	0.11	0.16	0.90	1.59	1.75	1.91	1.85	0.84	0.84	34.12	48.55	17.02	34.43

[a]Pr/Ph = pristane/phytane ratio. [b]Gammacerane index = gammacerane/(C_{31}(22 S + 22R)/2). [c]$P_{aq} = C_{23} + C_{25}/C_{23} + C_{25} + C_{29} + C_{31}$. [d]$\%C_{27} = \%C_{27}\alpha\alpha\alpha/C_{27}$-$C_{29}\alpha\alpha\alpha$ steranes. [e]$\%C_{28} = \%C_{28}\alpha\alpha\alpha/C_{27}$-$C_{29}\alpha\alpha\alpha$ steranes. [f]$\%C_{29} = \%C_{29}\alpha\alpha\alpha/C_{27}$-$C_{29}\alpha\alpha\alpha$ steranes.

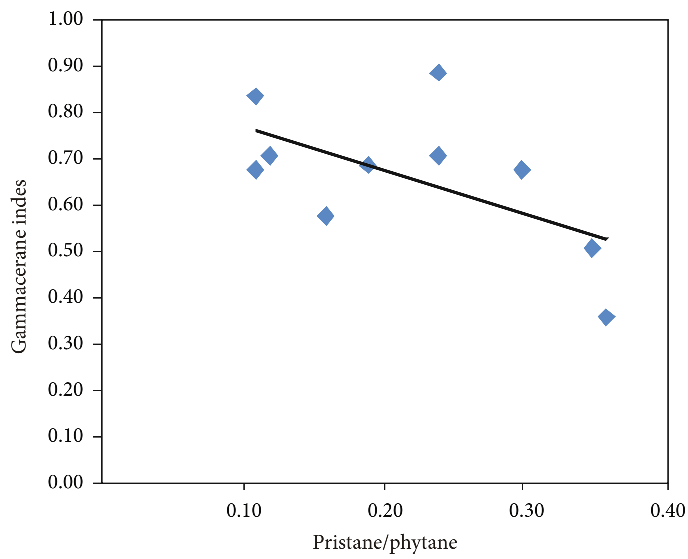

FIGURE 6: Variations in pristane/phytane (Pr/Ph) (redox) and gammacerane index (water salinity stratification) for the samples. For the samples, increased water salinity typically is accompanied by density stratification and reduced oxygen content in bottom waters, which results in lower Pr/Ph.

column increasingly and an anoxic condition at the bottom of the lake. The ratios of Ph/n-C_{18} and Pr/n-C_{17} are shown in Table 3.

5.3.2. Terpanes. Gammacerane first found in bitumen of the Green River shale are detected in both mudstone and marl samples (Figure 5) [37]. The ratio of gammacerane/C_{31} hopane ((22S+22R)/2) changes from 0.36 to 0.89 in Fengcaogou section. The appearance of gammacerane suggests the hypersaline, reducing sedimentary environment [38, 39]. Gammacerane originated from continental and oceanic sedimentary environments with stratified water column [40]. Gammacerane are found in freshwater lacustrine sediments too. In chemocline of stratified water column, there exists tetrahymanol as precursor of gammacerane; tetrahymanol originates from anaerobic ciliates [40]. Because of density-stratified hypersaline water columns, the compounds can get together in the lacustrine environment. The value of $Pr/Ph < 0.5$ is considered associated with hypersaline environment [41]. The relevance of gammacerane indices and Pr/Ph value in Fengcaogou supports the inferred salinity relationship (Figure 6). Therefore, Fengcaogou sedimentary rocks might deposit in hypersaline lacustrine condition. The high salinity was accompanied by anoxic condition in bottom water and water column density stratification.

The relative abundances and distribution pattern of pentacyclic and tricyclic terpanes detected by *m/z* 191 ion chromatograms are listed in Table 2 and Figure 5. Tricyclic terpanes have little content from mudstone and marl and are composed by C_{21}-C_{24} with the peak at C_{23}. In the present studies, it was found that the tricyclic terpanes may originate from some algae or lipids of bacterial membrane [42, 43]. And tricyclic terpanes can be used as parameters of depositional environment. Their relatively low concentrations and the low ratios of tricyclic/pentacyclic terpanes (<0.25) in all samples from the mudstone and marl in WHXB indicate that the biomarkers originate from nonoceanic organism precursor [44, 45].

The primary pentacyclic terpanes with the peak at C_{30} hopanes are detected from the *m/z* 191 fragmentograms, and a lot of homohopanes (C_{31}-C_{35}) are found in most of the samples (Figure 5). Ourisson et al. [46] proposed that homohopanes (C_{31}-C_{35}) originated from bacteriohopanetetrol and other hopanoids of bacteria in chemocline of stratified water column.

5.3.3. Steranes. The regular steranes were detected from extracts of mudstone and marl in WHXB showed by *m/z* 217 mass chromatograms with variable peaks (Figure 5). Most of the samples from profile indicated a higher ratio of C_{27} sterane compared to C_{29} sterane or C_{28} sterane (6.82%-20.74%), while some samples (P02-5S2, P02-5S4, and P02-5S6) have $C_{29} > C_{27}$ sterol distribution (Table 3). The marl is dominated by C_{27} sterane (46.6%–48.5%, averaging 47.59%). Volkman [47] and Peters and Moldowan [48] suggest that C_{29} sterols originate from land higher plants and C_{27} sterols are derived from aquatic algae. Later, Volkman [49] and Volkman et al. [50] suggested that cyanobacteria or microalgae may be the main origin of C_{29} sterols too. Here, the predominance of C_{29} steroids in mudstones of the middle part in the Fengcaogou section shows a proportion contribution of terrestrial plant; however, C_{27} steroids dominant at the lower and upper part of profile may reflect the contribution of algae. With samples from Fengcaogou strata, the explanation of dominant C_{29} steroids is inconsistent with maceral composition and other parameters (hopanoids). Phytane can reflect the contribution of archaebacteria and haloalkaliphilic bacteria [49], and thus, massive phytane in the Fengcaogou samples may originate from bacteria and would not rule out higher plants. Hopanes root from hopane polyols, and hopane polyols are discovered from cyanobacteria or bacterial membranes [29]. All in all, a large number of phytane suggest the contribution of bacteria or higher plants. Associated with other feature of biomarker and petrographic observation, the evidence indicates that the predominance of C_{29} steroids originates from microalgae and bacteria or higher plants. Steranes show the pattern of $C_{27} > C_{28} < C_{29}$, showing complex origination from algae, bacteria, or wax of terrestrial plant [48].

5.4. Analysis of C Isotopes. Lake sediments can provide the effective ancient environmental information. Because the source of organic matter, paleoclimate, atmospheric CO_2 concentration, and water chemistry of lakes is the influencing factors, the explanation of carbon isotopic ratios is a complex problem [51]. The ^{13}C value change could be caused by $_{P}CO_2$, lake surface variation [52], lake trophic status, biological community, obvious climate changes [19], or the diversification of productivity [19, 53].

The mudstones or marls (e.g., P02-13S1) had obviously heavier carbon isotopic composition in kerogen, changing in $\delta^{13}C$ of considerable OM from −20‰ to −25.8‰ with an average of −23.4‰ (Table 2). In Indonesia, a homologous isotopic feature was found in *Pediastrum* and *Botrycoccus* algal shales [54]. Enrichment in ^{13}C of Cenozoic oil shale was found in Australia too [55]. The enrichment in ^{13}C of OM from Cretaceous shales has been found in the northern Tibet plateau with a range of −20.79‰ to −21.78‰ [19].

By analyzing the $^{13}C_{org}$ in 12 sediment cores from lakes, Stuiver [56] found that the low $^{13}C_{org}$ value corresponded to the colder climate during low productivity period and the high $^{13}C_{org}$ value corresponded to the warmer climate with higher productivity in the lake. If the organic productivity was increased in lakes, aquatic plants would increase the absorption of $^{12}CO_2$ selectively. Then, this caused the improvement of concentration of ^{13}C in HCO_3, resulting in the value increasing of $^{13}C_{org}$ of aquatic plant [57]. The closed inland lake in the arid and semiarid area, when the water increased, the biological productivity increased, submerged/floating macrophytes used HCO_3 or dissolved CO_2 as main carbon source, resulting in the increasing of $^{13}C_{org}$; conversely, when there is drought, the value of $^{13}C_{org}$ reduced [58]. Hypersalinity may lead to the heavy isotopic composition in the environment of microbial mats [59], but hypersalinity is not the only causation [19]. High productivity that occurred in microbial/algal mats has been suggested as the cause of abating fractionation of ^{13}C [60]. Therefore, high productivity leads to the enrichment in ^{13}C in the lake ecosystem. OM of mudstones and marls in the Fengcaogou section of the WHXB show different ^{13}C enrichment. The ^{13}C of marl exhibit the values ranging from −20‰ to −21.9‰, whereas the ^{13}C of the mudstone samples exhibit a lighter value ranging from −23‰ to −25.8‰. This indicates the raising of productivity.

Moreover, similar source organisms have been confirmed between mudstones and underlying marl, so the OM in samples should show consistent isotopic trends. However, there is virtually no consistent tendency. OM of mudstone P02-9S suggest no enrichment in ^{13}C relative to marls. Therefore, the enrichment of ^{13}C cannot be triggered by the source organisms. The exuberant productivity with algae and bacteria is the main factor for the enrichment in ^{13}C [61–63].

6. Paleoenvironmental Significances

The evolution of lacustrine paleoenvironment during Oligocene and Miocene of the Hoh Xil basin of has been studied frequently. The lake level fluctuation, lake productivity, geochemical proxies of water, and the feature of organic geochemistry are closely related with tectonic movement and climatic factors [64–67]. The main reason of the formation of carbonate saline lake is the input of outside material continuously in the humid environment with the tendency of wet conditions [68, 69]. In contrast, in the extreme arid climatic conditions, evaporation exceeding precipitation would lead to the concentration of water, with sulfate deposits appearing in saline lake [65]. Major petrological and geochemical factors in sedimentary sequence of Neogene Wudaoliang Group in WHXB suggest the condition of lacustrine water chemistry. Wang [23] reported that Miocene hydrocarbon source rock of Zhuonai Lake in the Hoh Xil basin deposited in a freshwater lake. And paleoclimatic variation from dry to humid caused the transformation of water chemistry, which brought the saline water to fresher water during Oligocene to early Miocene in lakes. There were many tectonic activities, which are accompanied by the uplift of Tibet and paleoclimate and lake ecosystem [70–75]. DeCelles et al. [76] suggested that beneficiation of $\delta^{18}O$ and $\delta^{13}C$ in carbonates of Nima basin indicated strong evaporation and the arid climate during Oligocene. Wu et al. [77] studied the fossils of vegetation; they suggested that there was a dry, warm climate in Oligocene and a wet, cool climate in early Miocene in central Tibetan Plateau. All evidences suggest that in central Tibet exists the development of saline paleolakes and arid climate in Oligocene. In the early Miocene, many evidences show that the climate of central plateau turns to humid. Accompanied with turning of climate during early Miocene time, two paleolakes covered plateau characterized by the Wudaoliang Group with coniferous trees [77]. Wudaoliang Group greatly distributes in HXB during the early Miocene with freshwater lacustrine limestone, which shows that large paleolake exists, the paleolake named "Wudaoliang paleolake." Miocene lacustrine stromatolites were found in Wudaoliang Group in the Hoh Xil basin, which indicated abnormal humid period [78]. Cai et al. [79] suggest that "Wudaoliang paleolake" turns from a playa lake to the freshwater lakes with the precipitation exceeding evaporation in humid climate. Yi et al. [80] indicated that northern Tibetan Plateau climate evolved to enter a humid stage in the early Miocene and paleolake water salinity obviously dropped and reflected water level rise in lower Wudaoliang Formation by using boron concentrations in lacustrine mudstone. Oxygen and isotopes in the Wudaoliang Group showed a humid condition during the lacustrine sedimentary period from (24.1 ± 0.6) Ma to (14.5 ± 0.5) Ma [81]. The above information and organic geochemical investigation indicated that the lacustrine ecosystem was adjusted and updated in the early Miocene characterized by humid condition and productivity improvement.

7. Conclusions

The lacustrine sediment samples from the Miocene Wudaoliang Formation sections of western Hoh Xil basin in Tibetan are studied in order to appraise biologic-source constitution, sedimentary environment, and maturity of organic matter, reconstruct paleolake environment, and deduce paleoclimatic change information.

(1) Organic matter abundance of samples is low, and average organic carbon content of mudstone and marlite is, respectively, 0.19% and 0.14%. Organic matter of mudstones is mainly types II and III and is in immaturity-low maturity stage, while organic matter of marl is mainly type I-II_1 and is in low maturity-maturity stage

(2) The biomarker characteristics indicate that the main sources of the organic matters are algae and bacteria and higher plants. Some of the biomarkers indicate that the sedimentary environment is characterized by the reduced lake conditions and stratified water column

(3) The samples from the Fengcaogou section in the WHXB have obviously heavy C isotopic composition. The enrichment in ^{13}C is caused by elevated productivity

(4) The paleoclimate of the western Hoh Xil basin in early Miocene for depositing mudstone and marl became more humid

Data Availability

The data used to support the findings of this study are included within the article.

Conflicts of Interest

The authors declare that they have no conflicts of interest.

Authors' Contributions

Wentian Mi and Xueyuan Qi equally contributed to the work, and they are joint first authors.

Acknowledgments

This work was supported by the Open Fund of Geomathematics Key Laboratory of Sichuan Province (scsxdz201602), Open Fund of the State Key Laboratory of Oil and Gas Reservoir Geology and Exploitation (Chengdu University of Technology) (PLC20180504), Foundation of Key Laboratory of Western China's Mineral Resources of Gansu Province in Lanzhou University (MRWCGS-2019-01), Natural Science Foundation of Inner Mongolia (2018LH04006, 2019LH04002, and 2020MS04009), and Key Laboratory of Geoscience Spatial Information Technology of Land and Resources, Chengdu University of Technology, China (KLGSIT2016-02).

References

[1] T. Sun, C. S. Wang, Y. Duan, Y. L. Li, and B. Hu, "The organic geochemistry of the Eocene-Oligocene black shales from the Lunpola Basin, central Tibet," *Journal of Asian Earth Sciences*, vol. 79, pp. 468–476, 2014.

[2] C. S. Wang, E. Chang, and S. N. Zhang, "Potential oil and gas-bearing basins of the Qinghai-Tibetan Plateau, China," *International Geological Review*, vol. 39, no. 10, pp. 876–890, 1997.

[3] Z. F. Liu and C. Wang, "Abstract: Oil shale in the Tertiary Hoh Xil basin, northern Qinghai-Tibet Plateau ," *AAPG Bulletin*, vol. 83, p. 1890, 1999.

[4] Z. F. Liu and C. S. Wang, "Facies analysis and depositional systems of Cenozoic sediments in the Hoh Xil basin, Northern Tibet," *Sedimentary Geology*, vol. 140, no. 3-4, pp. 251–270, 2001.

[5] J. Wang, J. Ding, C. S. Wang, and F. W. Tan, *Evaluation and Investigation of the Oil and Gas in the Qinghai-Tibet Plateau*, Geological Publishing House, Beijing, 2009, (in Chinese).

[6] J. Dai, X. Zhao, C. Wang, L. Zhu, Y. Li, and D. Finn, "The vast proto-Tibetan Plateau: new constraints from Paleogene Hoh Xil basin," *Gondwana Research*, vol. 22, no. 2, pp. 434–446, 2012.

[7] Y. L. Li, L. D. Zhu, J. Dai, L. C. Wang, W. G. Yang, and Y. S. Wei, "Sedimentation and deformation of the Yanghu basin and its tectonic implications in the western Hoh Xil, Central Tibet," *Acta Petrologica Sinica*, vol. 29, pp. 1017–1026, 2013, (in Chinese with English abstract).

[8] C. S. Wang, X. X. Zhao, Z. Z. Liu et al., "Constraints on the early uplift history of the Tibetan Plateau," *Proceedings of the National Academy of Sciences of the United States of America*, vol. 105, no. 13, pp. 4987–4992, 2008.

[9] G. T. Pan, J. Ding, D. Yao, and L. Q. Wang, *Guidebook of 1:1500000 Geologic Map of the Qinghai-Xizang (Tibet) Plateau and Adjacent Areas*, Chengdu Cartographic Publishing House, Chengdu, 2004, (in Chinese).

[10] L. Yue, S. Y. Mou, C. X. Zeng, and C. X. Yi, "Age of the Kangtog Formation in the Dinggo-Gyaco area, Qiangtang, northern Tibet, China," *Geological Bulletin of China*, vol. 25, pp. 229–232, 2006, (in Chinese with English abstract).

[11] L. Zhu, C. Wang, H. Zheng, F. Xiang, H. Yi, and D. Liu, "Tectonic and sedimentary evolution of basins in the northeast of Qinghai-Tibet Plateau and their implication for the northward growth of the plateau," *Palaeogeography, Palaeoclimatology, Palaeoecology*, vol. 24, pp. 149–160, 2006.

[12] Z. F. Liu, C. S. Wang, A. Trentesaux et al., "Paleoclimate changes during the Early Oligocene in the Hoh Xil region, northern Tibetan Plateau," *Acta Geologica Sinica*, vol. 77, no. 4, pp. 504–513, 2003.

[13] Y. T. Zhu, Q. X. Jia, H. S. Yi et al., "Two periods of Cenozoic volcanic rocks from Hoh Xil lake area, Qinghai," *Journal of Mineralogy and Petrology*, vol. 25, no. 4, pp. 23–29, 2005, (in Chinese with English abstract).

[14] A. R. Carroll, S. C. Brassell, and S. A. Graham, "Upper Permian lacustrine oil shales, southern Junggar basin, northwest China (1)," *AAPG Bulletin*, vol. 76, p. 1874, 1992.

[15] K. E. Peters, "Guidelines for evaluating petroleum source rock using programmed pyrolysis," *AAPG Bulletin*, vol. 70, pp. 318–329, 1986.

[16] H. I. Petersen, V. Tru, L. H. Nielsen, N. A. Duc, and H. P. Nytoft, "Source rock properties of lacustrine mudstones and coals (Oligocene Dong Ho Formation), onshore Song Hong Basin, northern Vietnam," *Journal of Petroleum Geology*, vol. 28, no. 1, pp. 19–38, 2005.

[17] S. Korkmaz and R. K. Gülbay, "Organic geochemical characteristics and depositional environments of the Jurassic coals in the eastern Taurus of Southern Turkey," *International Journal of Coal Geology*, vol. 70, no. 4, pp. 292–304, 2007.

[18] Z. Han, M. Xu, Y. Li, Y. Wei, and C. Wang, "Paleocene-Eocene potential source rocks in the Avengco Basin, Tibet: organic geochemical characteristics and their implication for the paleoenvironment," *Journal of Asian Earth Sciences*, vol. 93, pp. 60–73, 2014.

[19] X. G. Fu, J. Wang, Y. H. Zeng, Z. X. Li, and Z. J. Wang, "Geochemical and palynological investigation of the Shengli River marine oil shale (China): implications for paleoenvironment and paleoclimate," *International Journal of Coal Geology*, vol. 78, no. 3, pp. 217–224, 2009.

[20] J. F. Zhang, D. L. Wang, J. Z. Qin, and B. Q. Liu, "Study on the weathering correction of surface out crop samples from the Qinghai-Tibet plateau," *Petroleum geology & experiment*, vol. 23, pp. 297–300, 2001, (in Chinese with English abstract).

[21] B. D. Ritts, A. D. Hanson, D. Zinniker, and J. M. Moldowan, "Lower-Middle Jurassic nonmarine source rocks and petroleum systems of the Northern Qaidam Basin, Northwest China1," *AAPG Bulletin*, vol. 83, pp. 1980–2005, 1999.

[22] B. P. Tissot and D. H. Welte, *Petroleum Formation and Occurrence: A New Approach to Oil and Gas Exploration*, Springer-Verlag, Berlin, 1984.

[23] L. Wang, C. Wang, Y. Li, L. Zhu, and Y. Wei, "Sedimentary and organic geochemical investigation of tertiary lacustrine oil shale in the central Tibetan plateau: palaeolimnological and palaeoclimatic significances," *International Journal of Coal Geology*, vol. 86, no. 2-3, pp. 254–265, 2011.

[24] M. R. Talbot, "The origins of lacustrine oil source rocks: evidence from the lakes of tropical Africa," in *Lacustrine Petroleum Source Rocks*, A. J. Fleet, K. Kelts, and M. R. Talbot, Eds., vol. 40, no. 1pp. 29–43, Geological Society London Special Publications, Oxford, 1988.

[25] W. B. Styan and R. M. Bustin, "Petrographyof some fraser river delta peat deposits: coal maceral and microlithotype precursors in temperate-climate peats," *International Journal of Coal Geology*, vol. 2, no. 4, pp. 321–370, 1983.

[26] R. V. Tyson, *Sedimentary Organic Matter: Organic Facies and Palynofacies*, Chapman & Hall, London, 1995.

[27] P. A. Cranwell, "Organic geochemistry of Cam Loch (Sutherland) sediments," *Chemical Geology*, vol. 20, pp. 205–221, 1977.

[28] P. A. Meyers, "Organic geochemical proxies of paleoceanographic, paleolimnologic, and paleoclimatic processes," *Organic geochemistry*, vol. 27, no. 5-6, pp. 213–250, 1997.

[29] A. Riboulleau, J. Schnyder, L. Riquier, V. Lefebvre, F. Baudin, and J. F. Deconinck, "Environmental change during the Early Cretaceous in the Purbeck-type Durlston Bay section (Dorset, Southern England): a biomarker approach," *Organic geochemistry*, vol. 38, no. 11, pp. 1804–1823, 2007.

[30] K. J. Ficken, B. Li, D. L. Swain, and G. Eglinton, "An _n_-alkane proxy for the sedimentary input of submerged/floating freshwater aquatic macrophytes," *Organic geochemistry*, vol. 31, no. 7-8, pp. 745–749, 2000.

[31] C. J. Nott, S. C. Xie, L. A. Avsejs, D. Maddy, F. M. Chambers, and R. P. Evershed, "_n_-Alkane distributions in ombrotrophic mires as indicators of vegetation change related to climatic variation," *Organic geochemistry*, vol. 31, no. 2-3, pp. 231–235, 2000.

[32] J. C. Montero-Serrano, M. Martinez, A. Riboulleau, N. Tribovillard, G. Marquez, and J. V. Gutierrez-Martin, "Assessment of the oil source-rock potential of the Pedregoso Formation (early Miocene) in the Falcon Basin of northwestern Venezuela," *Marine and Petroleum Geology*, vol. 27, no. 5, pp. 1107–1118, 2010.

[33] M. Escobar, G. Márquez, S. Inciarte, J. Rojas, I. Esteves, and G. Malandrino, "The organic geochemistry of oil seeps from the Sierra de Perija eastern foothills, Lake Maracaibo Basin, Venezuela," *Organic Geochemistry*, vol. 42, no. 7, pp. 727–738, 2011.

[34] B. M. Didyk, B. R. T. Simoneit, S. C. Brassell, and G. Eglinton, "Organic geochemical indicators of palaeoenvironmental conditions of sedimentation," *Nature*, vol. 272, no. 5650, pp. 216–222, 1978.

[35] M. P. Koopmans, W. I. C. Rijpstra, M. M. Klapwijk, J. W. de Leeuw, M. D. Lewan, and J. S. S. Damste, "A thermal and chemical degradation approach to decipher pristane and phytane precursors in sedimentary organic matter," *Organic Geochemistry*, vol. 30, pp. 1089–1104, 1999.

[36] K. E. Peters, C. C. Walters, and J. M. Moldowan, *The Biomarker Guide Volume 2; Biomarkers and Isotopes in Petroleum Exploration and Earth History*, University of Cambridge, 2005.

[37] I. R. Hills, E. V. Whitehead, D. E. Anders, J. J. Cummins, and W. E. Robinson, "An optically active triterpane, gammacerane, in Green River, Colorado, oil shale bitumen," *Chemical Communications*, vol. 20, no. 20, pp. 752b–7754, 1966.

[38] J. M. Fu, G. Y. Sheng, P. A. Peng, S. C. Brassell, G. Eglinton, and J. G. Jiang, "Peculiarities of Salt Lake sediments as potential source rocks in China," *Organic Geochemistry*, vol. 10, no. 1-3, pp. 119–126, 1986.

[39] J. M. Moldowan, W. K. Seifert, and E. J. Gallegos, "Relationship between petroleum composition and depositional environment of petroleum source rocks," *AAPG Bulletin*, vol. 69, pp. 1255–1268, 1985.

[40] J. S. Sinninghe Damsté, A. C. T. van Duin, D. Hollander, M. E. L. Kohnen, and J. W. Leeuw, "Early diagenesis of bacteriohopanepolyol derivatives: formation of fossil homohopanoids," *Geochimica et Comsmochimica Acta*, vol. 59, no. 24, pp. 5141–5157, 1995.

[41] H. L. ten Haven, J. W. de Leeuw, J. Rullkötter, and J. S. Sinninghe Damsté, "Restricted utility of the pristane/phytane ratio as a palaeoenvironmental indicator," *Nature*, vol. 330, no. 6149, pp. 641–643, 1987.

[42] F. R. Aquino Neto, J. M. Triguis, D. A. Azevedo, R. Rodrigues, and B. R. T. Simoneit, "Organic geochemistry of geographically unrelated Tasmanites," *Organic Geochemistry*, vol. 18, no. 6, pp. 791–803, 1989.

[43] G. Ourisson, P. Albrecht, and M. Rohmer, "Predictive microbial biochemistry – from molecular fossils to procaryotic membranes," *Trends in Biochemical Sciences*, vol. 7, no. 7, pp. 236–239, 1982.

[44] R. P. Philp and T. D. Gilbert, "Biomarker distributions in Australian oils predominantly derived from terrigenous source material," *Organic Geochemistry*, vol. 10, no. 1-3, pp. 73–84, 1986.

[45] S. C. Zhang, B. M. Zhang, L. Z. Bian, Z. J. Jin, D. R. Wang, and J. F. Chen, "The Xiamaling oil shale generated through Rhdophta over 800 Ma ago," *Science in China Series D: Earth Sciences*, vol. 50, pp. 527–535, 2007.

[46] G. Ourisson, P. Albrecht, and M. Rohmer, "The microbial origin of fossil fuels," *Scientific American*, vol. 251, no. 2, pp. 44–51, 1984.

[47] J. K. Volkman, "A review of sterol markers for marine and terrigenous organic matter," *Organic Geochemistry*, vol. 9, no. 2, pp. 83–99, 1986.

[48] E. K. Peters and M. J. Moldowan, *The Biomarker Guide, Interpreting Molecular Fossils in Petroleum and Ancient Sediment*, Prentice Hall, New Jersey, 1993.

[49] J. K. Volkman, "Biological marker compounds as indicators of the depositional environments of petroleum source rocks," in *Lacustrine Petroleum Source Rocks*, A. J. Fleet, K. Kelts, and M. R. Talbot, Eds., pp. 103–122, Geological Society London Special Publications, Oxford, 1988.

[50] J. K. Volkman, S. M. Barrett, and S. I. Blackburn, "Eustigmatophyte microalgae are potential sources of C_{29} sterols, C_{22}-C_{28} _n_-alcohols and C_{28}-C_{32} _n_-alkyl diols in freshwater environments," *Organic Geochemistry*, vol. 30, no. 5, pp. 307–318, 1999.

[51] F. A. Street-Perrott, K. J. Ficken, Y. Huang, and G. Eglinton, "Late Quaternary changes in carbon cycling on Mt. Kenya, East Africa: an overview of the $\delta^{13}C$ record in lacustrine organic matter," *Quaternary Science Reviews*, vol. 23, no. 7-8, pp. 861–879, 2004.

[52] M. R. Talbot and D. A. Livingstone, "Hydrogen index and carbon isotopes of lacustrine organic matter as lake level indicators," *Palaeogeography,Palaeoclimatology, Palaeoecology*, vol. 70, no. 1-3, pp. 121–137, 1989.

[53] S. Schouten, W. I. C. Rijpstra, M. Kok et al., "Molecular organic tracers of biogeochemical processes in a saline meromictic lake (Ace Lake)," *Geochimica et Cosmochimica Acta*, vol. 65, no. 10, pp. 1629–1640, 2001.

[54] H. H. Williams, M. Fowler, and R. T. Eubank, "Geochemical characteristics of Paleocene and Cretaceous hydrocarbon source basins of Southeast Asia," in *9th offshore South East Asia Conference*, pp. 429–460, Singapore, 1992.

[55] C. J. Boreham, R. E. Summons, Z. Roksandic, L. M. Dowling, and A. C. Hutton, "Chemical, molecular and isotopic differentiation of organic facies in the Tertiary lacustrine Duaringa oil shale deposit, Queensland, Australia," *Organic Geochemistry*, vol. 21, no. 6-7, pp. 685–712, 1994.

[56] M. Stuiver, "Climate versus changes in13C content of the organic component of lake sediments during the Late Quarternary," *Quaternary Research*, vol. 5, no. 2, pp. 251–262, 1975.

[57] N. Nakai, "Carbon isotopic variation and the paleoclimate of sediments from Lake Biwa," *Proceeding of the Japan Academy*, vol. 48, no. 7, pp. 516–521, 1972.

[58] C. Luo, "Stable carbon isotope record of organic matter from the lop-Nur lacustrine sediment in Xinjiang, northwest China," *Quaternary Sciences*, vol. 28, pp. 621–627, 2008, (in Chinese with English abstract).

[59] M. Schidlowski, H. Gorzawski, and I. Dor, "Carbon isotope variations in a solar pond microbial mat: role of environmental gradients as steering variables," *Geochimica et Cosmochimica Acta*, vol. 58, no. 10, pp. 2289–2298, 1994.

[60] S. Schouten, W. A. Hartgers, J. F. Lopez, J. O. Grimalt, and J. S. Sinninghe Damsté, "A molecular isotopic study of ^{13}C-enriched organic matter in evaporitic deposits: recognition of CO_2-limited ecosystems," *Organic Geochemistry*, vol. 32, no. 2, pp. 277–286, 2001.

[61] D. J. Hollander and J. A. McKenzie, "CO_2 control on carbon-isotope fractionation during aqueous photosynthesis: a $_{\text{paleo-pCO2}}$ barometer," *Geology*, vol. 19, no. 9, pp. 929–932, 1991.

[62] E. A. Laws, B. N. Popp, R. R. Bidigare, M. C. Kennicutt, and S. A. Macko, "Dependence of phytoplankton carbon isotopic composition on growth rate and $[CO_2)_{aq}$: theoretical considerations and experimental results," *Geochimica et Cosmochimica Acta*, vol. 59, no. 6, pp. 1131–1138, 1995.

[63] B. N. Popp, E. A. Laws, R. R. Biigare, J. E. Dore, K. L. Hanson, and S. G. Wakeham, "Effect of phytoplankton cell geometry on carbon isotopic fractionation," *Geochimica et Cosmochimica Acta*, vol. 62, no. 1, pp. 69–77, 1998.

[64] E. J. Barron, "Climate and lacustrine petroleum source prediction," in *Lacustrine Basin Exploration—Case Studies and Modern Analogs*, B. J. Katz, Ed., vol. 50, pp. 1–18, AAPG Memoir, 1990.

[65] B. J. Katz, "Controls on distribution of lacustrine source rocks through time and space," in *Lacustrine Basin Exploration—-Case Studies and Modern Analogs*, B. J. Katz, Ed., vol. 50, pp. 61–76, AAPG Memoir, 1990.

[66] D. Lv, Y. Song, L. Shi, Z. Wang, and P. Cong, "The complex transgression and regression history of the northern margin of the Palaeogene Tarim Sea (NW China), and implications for potential hydrocarbon occurrences," *Marine and petroleum geology*, vol. 112, article 104041, pp. 1–17, 2020.

[67] D. Lv, Z. Li, D. Wang et al., "Sedimentary model of coal and shale in the Paleogene Lijiaya Formation of the Huangxian Basin: insight from petrological and geochemical characteristics of coal and shale," *Energy & Fuels*, vol. 33, no. 11, pp. 10442–10456, 2019.

[68] A. M. Alonso-Zarza and J. P. Calvo, "Palustrine sedimentation in an episodically subsiding basin: the Miocene of the northern Teruel Graben (Spain)," *Palaeogeography, Palaeoclimatology, Palaeoecology*, vol. 160, no. 1-2, pp. 1–21, 2000.

[69] C. Arenas and G. Pardo, "Latest Oligocene-Late Miocene lacustrine systems of the north-central part of the Ebro Basin (Spain): sedimentary facies model and palaeogeographic synthesis," *Palaeogeography, Palaeoclimatology, Palaeoecology*, vol. 151, no. 1-3, pp. 127–148, 1999.

[70] G. Dupont-Nivet, C. Hoorn, and M. Konert, "Tibetan uplift prior to the Eocene–Oligocene climate transition: evidence from pollen analysis of the Xining Basin," *Geology*, vol. 36, no. 12, pp. 987–990, 2008.

[71] G. Dupont-Nivet, W. Krijgsman, C. G. Langereis, H. A. Abels, S. Dai, and X. M. Fang, "Tibetan plateau aridification linked to global cooling at the Eocene- Oligocene transition," *Nature*, vol. 445, no. 7128, pp. 635–638, 2007.

[72] N. Harris, "The elevation history of the Tibetan Plateau and its implications for the Asian monsoon," *Palaeogeography, Palaeoclimatology, Palaeoecology*, vol. 241, no. 1, pp. 4–15, 2006.

[73] Z. F. Liu, X. X. Zhao, C. S. Wang, S. Liu, and H. S. Yi, "Magnetostratigraphy of Tertiary sediments from the Hoh Xil basin: implications for the Cenozoic tectonic history of the Tibetan

Plateau," *Geophysical Journal International*, vol. 154, no. 2, pp. 233–252, 2003.

[74] J. P. Pratigya, H. F. Katherine, B. R. David, A. M. Francesca, and S. C. Brian, "Paleoaltimetry of the Tibetan Plateau from _D_/_H_ ratios of lipid biomarkers," *Earth and Planetary Science Letters*, vol. 287, no. 1-2, pp. 64–76, 2009.

[75] M. E. Raymo and W. F. Ruddiman, "Tectonic forcing of Late Cenozoic climate," *Nature*, vol. 359, pp. 117–122, 1992.

[76] P. DeCelles, J. Quade, P. Kapp, M. Fan, D. Dettman, and L. Ding, "High and dry in central Tibet during the Late Oligocene," *Earth Planetary Science Letter*, vol. 253, no. 3-4, pp. 389–401, 2007.

[77] Z. H. Wu, P. J. Barosh, Z. H. Wu, D. G. Hu, X. Zhao, and P. S. Ye, "Vast early Miocene lakes of the central Tibetan Plateau," *Geological Society of America Bulletin*, vol. 120, no. 9-10, pp. 1326–1337, 2008.

[78] H. S. Yi, J. H. Lin, and K. K. Zhou, "The origin of Miocene lacustrine stromatolites in the Hoh Xil area and its paleoclimatic implications," *Journal of Mineralogy and Petrology*, vol. 28, pp. 106–113, 2008, (in Chinese with English abstract).

[79] X. Cai, D. Liu, Q. Wei et al., "Characteristics of north of Tibet ap plateau uplift at Paleocene–Miocene-the evidence from Ke Kexili Basin," *Acta Geologica Sinica*, vol. 82, pp. 194–203, 2008, (in Chinese with English abstract).

[80] H. S. Yi, Z. Q. Shi, Y. T. Zhu, and X. Ma, "Reconstruction of paleo-salinity and lake-level fluctuation history by using boron concentration in lacustrine mudstones," *Journal of Lake Sciences*, vol. 21, no. 1, pp. 77–83, 2009, (in Chinese with English abstract).

[81] Z. H. Wu, Z. H. Wu, D. G. Hu, H. Peng, and Y. L. Zhang, "Carbon and oxygen isotope changes and palaeoclimate cycles recorded by lacustrine deposits of Miocene Wudaoliang Group in northern Tibetan Plateau," *Geology in China*, vol. 36, pp. 966–975, 2009, (in Chinese with English abstract).

Hindawi
Geofluids
Volume 2021, Article ID 8926423, 13 pages
https://doi.org/10.1155/2021/8926423

Research Article

Study on the Reinforcing Effects of the FRP-PCM Method on Tunnel Linings for Dynamic Strengthening

Xiaoshan Wang,[1] Lin Wei,[1] Zaiquan Wang,[1] Yujing Jiang,[2,3] Liming Zhang,[1] Fanzhen Meng,[1] and Yu Cong[1]

[1]College of Science, Qingdao University of Technology, Qingdao, Shandong 266033, China
[2]State Key Laboratory of Mining Disaster Prevention and Control Co-Founded by Shandong Province and the Ministry of Science and Technology, Shandong University of Science and Technology, Qingdao 266590, China
[3]Graduate School of Engineering, Nagasaki University, Nagasaki 852-8521, Japan

Correspondence should be addressed to Xiaoshan Wang; wangxiaoshan@qut.edu.cn

Received 7 September 2021; Accepted 25 September 2021; Published 7 October 2021

Academic Editor: Zhijie Wen

In recent years, fiber-reinforced plastic (FRP) has been widely used in the reinforcement of concrete structure fields due to its favorable properties such as high strength, low weight, easy handling and application, and immunity to corrosion, and the reinforcing effects with FRP grids on tunnel linings should be quantitatively evaluated when the tunnels encounter an earthquake. The aim of the present study is to estimate the reinforcing effects of fiber-reinforced plastic (FRP) grids embedded in Polymer Cement Mortar (PCM) shotcrete (FRP-PCM method) on tunnel linings under the dynamic load. A series of numerical simulations were performed to analyze the reinforcing effects of FRP-PCM method quantitatively, taking into account the impacts of tunnel construction method and cavity location. The results showed that the failure region on lining concrete is improved obviously when the type CII ground is encountered, regardless the influences of construction method and cavity location. With the increment of ground class from CII to DII, the axial stress reduction rate R_σ increases from 13.18% to 48.60% for tunnels constructed by the NATM, while for those tunnels constructed by the NATM, R_σ merely varies from 0.72% to 2.11%. R_σ decreases from 43.35% to 34.80% when a cavity exists on the shoulder of lining, while decreasing from 14.7% to 0.12% when a cavity exists on the crown of lining concrete. All those conclusions could provide valuable guidance for the reinforcing of underground structures.

1. Introduction

Although the dynamic mechanical behavior of underground structures, such as tunnels and underground caverns, is assumed to be better than that of surface structures, some existing tunnels still have been severely damaged by earthquakes in recent years [1–8]. Cracking, spalling, and water leakage occurring during earthquakes would significantly affect the safety of tunnel operation. The repair and reinforcement of existing underground concrete structures has become an import part of civil engineering activities.

A series of methods have been adopted to effectively improve the integrity of concrete structures in existing tunnels, the typical ones of which are grouting reinforcement method, fiber reinforced shotcrete (FRS) method [9–13], carbon fiber sheet (CFS) method [14–16], steel board method [17], and fiber-reinforced plastic (FRP) method [18, 19]. Due to the favorable properties such as high strength, low weight, easy handling and application, and immunity to corrosion, FRP as a strengthening material for the reinforcement concrete (RC) structures has become commonly used in engineering fields. In the reinforcement of mountain tunnel, the FRP grids embedded in Polymer Cement Mortar (FRP-PCM) shotcrete (FRP-PCM method) are typically used. In the FRP-PCM method, the FRP grids are firmly installed on an existing tunnel lining concrete with concrete anchors (see Figure 1(a)). It is noted that the FRP grids should not be damaged during the drilling or

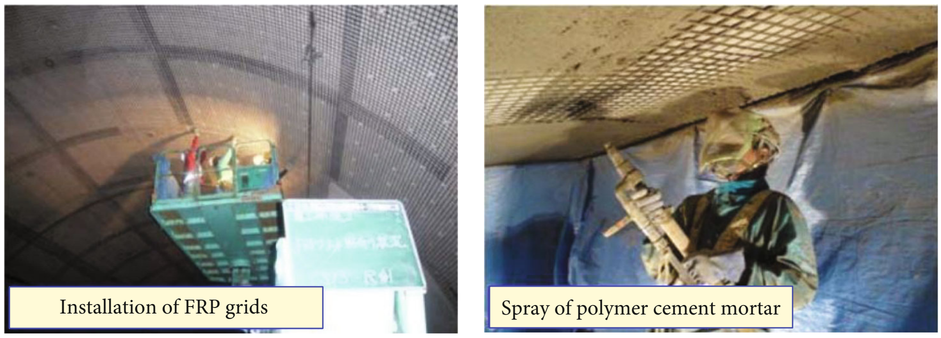

(a) Installation of FRP grids (b) Spray of Polymer Cement Mortar

Figure 1: Reinforcement procedure with the FRP-PCM method.

fastening the anchors. After the installation of FRP grids, the Polymer Cement Mortar (PCM) is sprayed to the surface of FRP grids as shown in Figure 1(b).

In recent years, extensive researches have been carried out to investigate the reinforcing effects of FRP grids under dynamic load. Sheikh and Yau [20] conducted an experimental program in which 12 column specimens were tested under constant axial load and cyclic lateral load to simulate the earthquake loads and found that the strength, ductility, and energy absorption capacity of columns can be improved by utilizing FRP. Zou et al. [21] proposed an optimization technique for the performance-based seismic FRP retrofit design of reinforced concrete (RC) building frames, and the effectiveness of this proposed procedure was discussed and certified by a numerical example. Antoniades et al. [22] conducted cyclic tests on seismically damaged reinforced concrete walls strengthened with FRP reinforcement, and the test results showed that the strength of specimen reinforced by FRP strips increases up to approximately 30% with respect to a conventional repair method. Lam et al. [23] experimentally studied the behaviors of FRP-confined concrete under cyclic compression test, and a number of significant conclusions were drawn, including the existence of an envelope curve and the cumulative effect of loading cycles. Zhou et al. [24] conducted the dynamic three-point bending and axial crushing tests to investigate the dynamic crushing characteristics of unidirectional carbon fiber-reinforced plastic composites, and the results showed that delamination plays a critical role in the dynamic bending deformation. Jerome and Ross [25] numerically simulated the dynamic response of concrete beams that reinforced with a carbon fiber plastic by using the drop-weight impact test, and the numerical results revealed the local displacement behavior of beams when suffering from strong impulse loads.

Despite a large number of researches on the behavior of RC structures reinforcing with FRP were performed, few researches were conducted on the reinforcing effects of the FRP-PCM method on tunnel lining under dynamic load. In the present study, a series of numerical simulations were performed based on the finite difference method (FDM) to quantitatively analyze the reinforcing effects of the FRP-PCM method under dynamic load, taking into account the impacts of tunnel construction method and cavity location, and those analytic results could provide valuable guidance for the reinforcing of underground structures.

2. Numerical Modelling Setup

2.1. Numerical Modelling. The New Austrian Tunneling Method (NATM) and the Fore-piling Method (FM) are the two common methods that have been adopted in tunnelling under shallow or unconsolidated ground (Kitamoto et al., 2004). In the present study, four types of numerical models as shown in Figure 2 are established by utilizing the finite difference method (FDM), and the former two models (see Figures 2(a) and 2(b)) are selected to investigate the effects of construction methods on reinforcing effects of the FRP-PCM method. Since cavities that exist between tunnel lining and surrounding rocks are generally encountered for mountain tunnels constructing with the FM method, a cavity is presumed to exist on the crown (see Figure 2(c)) or at the shoulder (see Figure 2(d)) of the numerical models to investigate the impacts of cavity location on the reinforcing effects. Those cavities cover an angle of 60° and with a thickness of 30 cm. The thickness of shotcrete and secondary lining in the NATM method are set to be 15 cm and 30 cm, respectively, and the lining thickness in the FM method is selected as 45 cm. The reinforcement region with the FRP-PCM method covers an arc length of 180° on the upper wall of tunnel as shown in Figure 3, and the back-filling is conducted to the tunnels with cavities. The tunnel linings are reproduced by the finite element mesh, while the reinforcing effects of the FRP-PCM method are investigated by the liner element [26].

2.2. Boundary Conditions. In order to reduce the computational time and ensure the calculation accuracy, the horizontal distance from the wall of tunnel to the boundary of the main grid model is determined as $2D$ (D is the excavation width of tunnel that is equal to 10 m) based on the precomputation. The dynamic load input is applied at the bottom of the model and normally represented by plane waves propagating upward through the underlying rocks. The free-field boundary conditions are selected during the seismic analysis to minimize the wave reflections, and the lateral boundaries of the main grid are coupled to the free-field grid boundary by a series of viscous dashpots as shown in Figure 4 [26]. By

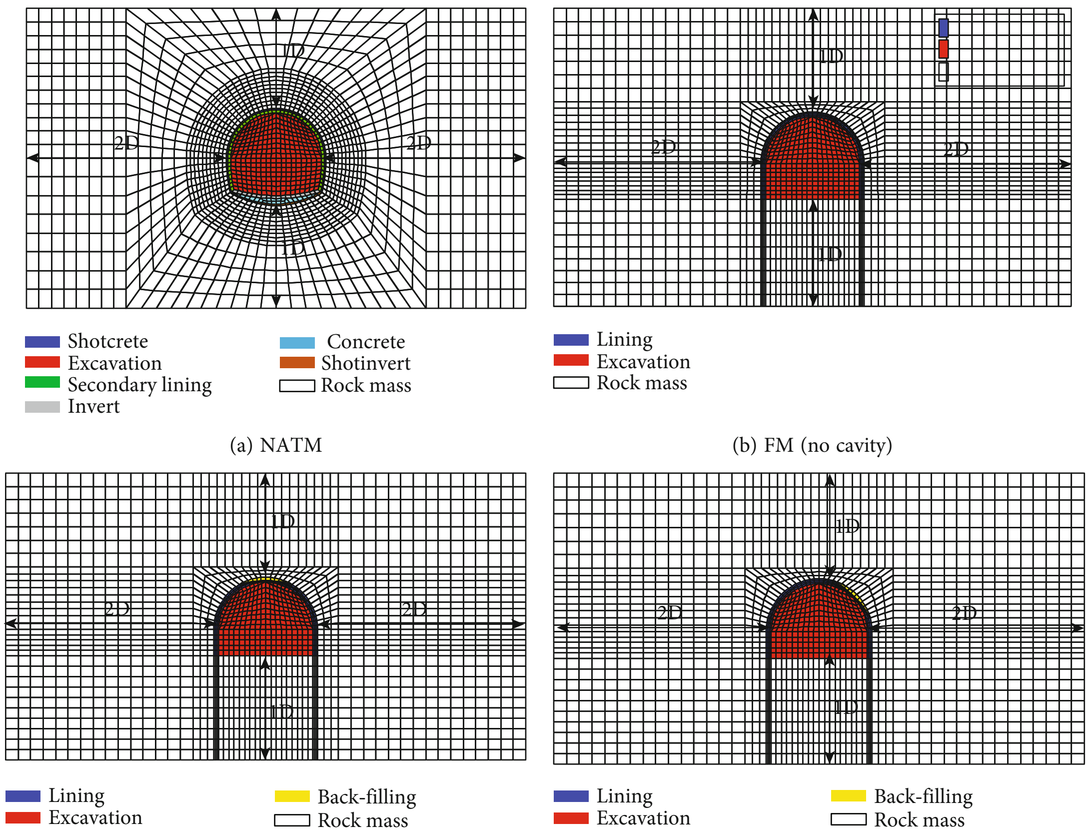

(a) NATM

(b) FM (no cavity)

(c) FM (cavity on the crown)

(d) FM (cavity on the shoulder)

FIGURE 2: Numerical modelling setup.

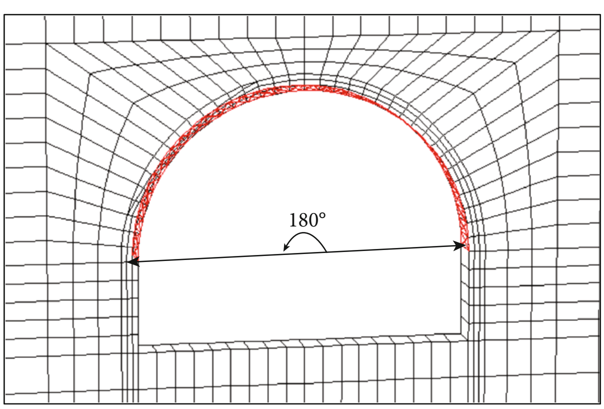

FIGURE 3: Reinforcing region with the FRP-PCM method.

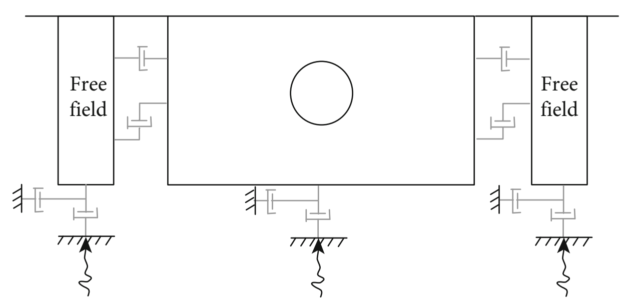

FIGURE 4: Free-field boundary for dynamic analysis.

means of which, plane waves propagating upward surf no distortion at the boundary because the free field grid supplies conditions that are identical to those in an infinite model. Lateral dashpots would not do exercise if the main grid in uniform with no surface structure, since the free field grid performs the same as the main grid, while the dashpots absorb energy in a manner to quiet boundaries if the main grid motion differs from that of the free filed.

2.3. Mechanical Properties. Three types of ground classed as CII, DI, and DII generally encountered in mountain tunnel construction in Japan [27] are selected as the surrounding rocks in the numerical analysis, and the mechanical behaviors of those are listed in Table 1. The urethane material is utilized as the back-filling material due to its quick harden and high strength, and the mechanical properties of back-filling material and lining concrete are also summarized in Table 1. The mechanical behaviors of the interface between the FRP-PCM layer and the concrete layer are obtained based on a series of direct shear tests in our previous study [28], and those values are summarized in Table 2.

2.4. Input Motion. Compared with artificial seismic waves and simple harmonic waves, real seismic wave taken from similar sites is more representative to the real situation when

Table 1: Mechanical behaviors of ground, lining, and back-filling material.

Properties	Ground class				Lining	Back-filling material
	CI	CII	DI	DII		
γ (kN/m^3)	23.5	22.6	21.6	20.6	24	9.8
E (MPa)	1960	980	490	147	24500	12
ν	0.3	0.3	0.35	0.35	0.2	0.13
c (MPa)	1.96	0.98	0.49	0.196	6.99	0.5
φ (deg)	45	40	35	30	40	10
σ_t (MPa)	0.39	0.42	0.19	0.06	3	0.2

Table 2: Mechanical properties of FRP grids and PCM material.

		Elastic modulus (MPa)	Compressive strength (MPa)	Tensile strength (MPa)	Cohesion (MPa)	Internal friction angle (°)	Cross-sectional area of mesh (mm^2)
FRP grid	CR4	1×10^5	—	1400	2.22	17.7	6.6
	CR6						17.5
	CR8						26.4
PCM		2.6×10^4	59.3	4.6			—

a rock foundation is subjected to earthquake loads. In the present study, the input motion is recorded at the observation site of Ojiya City during the M6.8 Chuetsu offshore earthquake happened on July 16, 2007, in Niigata Prefecture, Japan. The distributions of intensities and peak accelerations during the earthquake are shown in Figure 5. Since rock foundations and buildings are easier to damage when they suffer from shear waves, compared with a compression one, the horizontal component motion of ground (see Figure 6) is adopted in the later numerical analysis. The maximum acceleration is observed at about 27.8 s, with a value about 330 Gal. Since the stability of underground tunnel is mainly controlled by the maximum acceleration during the earthquake, in order to reduce the computational time, the input motion at the interval from 20.8 s to 30.8 s is extracted and utilized in the latter numerical analysis.

3. Numerical Results

3.1. Reinforcing Effects for Tunnels Constructed with the NATM. Figure 7 shows the distribution of plastic failure region on lining concrete for tunnels constructed by the NATM. For the unreinforced cases, the plastic failure region first appears at the bottom corner and inner side of the shoulder on lining concrete and gradually expands with the increment of ground class (see Figures 7(a)–(c)). For the type DII ground, the plastic failure region develops at both the inner side and the outer side of lining concrete. After reinforcing with FRP grids, the plastic failure zone on the shoulder diminishes and only can be observed at the bottom corner when the type CII ground is encountered (Figure 7(d)). The plastic failure region at the inner side of the left shoulder decreases greatly when the tunnels surround by the type DI ground (Figure 7(e)).

Tunnel lining deformations are generally governed by both the axial stress parallel to the tunnel wall and the radial stress perpendicular to the tunnel wall. Since the axial stress is approximately two orders of magnitude larger than the radial one, only the variation of axial stress is analyzed in the present study to illustrate the reinforcing effects with the FRP-PCM method. The axial stress distribution on lining concrete for tunnels constructed by the NATM is shown in Figure 8. In those figures, the positive symbol denotes the compression stress, while the negative symbol denotes the tensile stress. Since the input motion is a horizontal shear signal, the maximum tension and compression stresses occur at the left and right shoulder of tunnel lining, respectively. The maximum tension stress can also be observed at the bottom corner of lining concrete due to stress concentration. The maximum tension stresses at the bottom corner or shoulder of lining concrete are 2.77 MPa, 4.73 MPa, and 9.56 MPa, respectively, corresponding to the ground type of CII, DI, and DII (Figures 8(a)–8(c)). After reinforcing with FRP grids, those maximum tension stresses decrease to 2.75 MPa, 4.63 MPa, and 9.53 MPa, respectively (Figures 8(d)–8(f)).

3.2. Reinforcing Effects for Tunnels Constructed with the FM. Figure 9 shows the distribution of plastic failure region on lining concrete for tunnels constructed by the FM. The plastic failure region can be observed at the right inner side of lining concrete as shown in Figure 9(a) for the type CII ground. With the increment of ground class, the strength of surrounding rock reduces, and the plastic failure regions both occur at the left outer side and right inner side of lining concrete (Figures 9(b) and 9(c)). After reinforcing with FRP grids, almost no plastic failure region is observed when the CII ground is encountered (Figure 9(d)), and the plastic failure region decreases obviously when the other two types of ground are encountered (Figures 9(e) and 9(f)).

The axial stress distribution on lining concrete for tunnels constructed by the FM is depicted in Figure 10. Under a horizontal shear load, the maximum tension

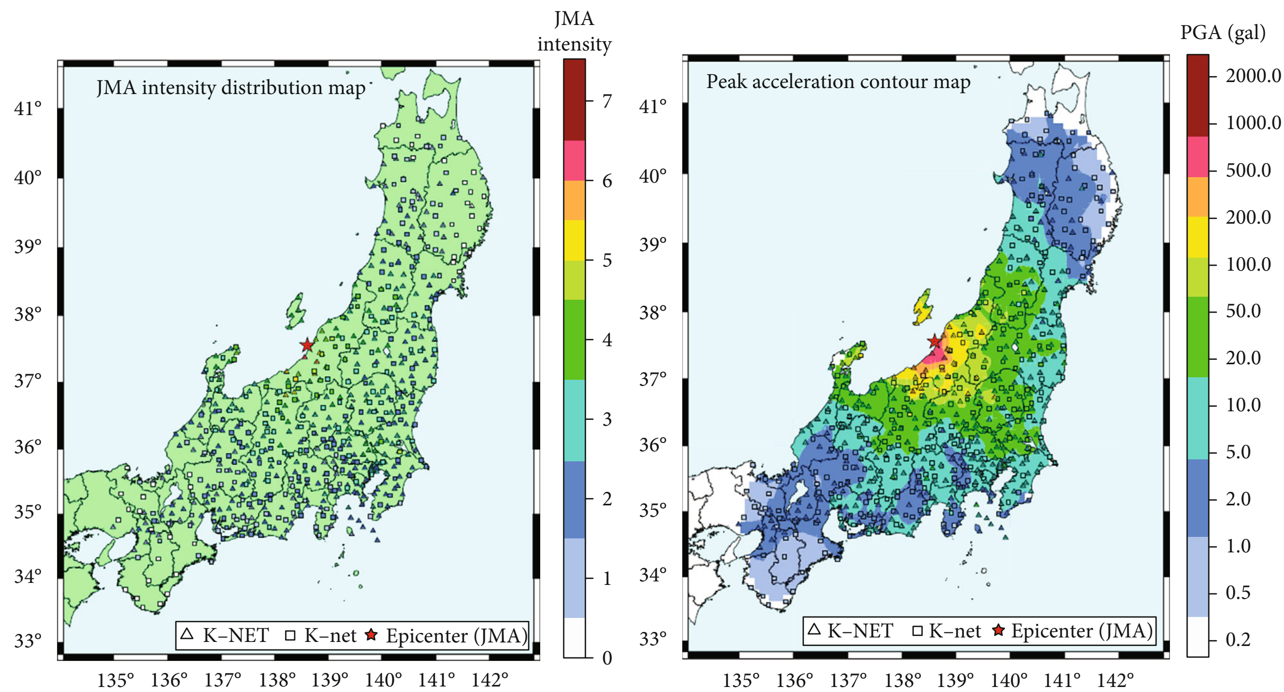

(a) Distribution of intensities

(b) Distribution of peak accelerations

Figure 5: Distributions of intensities and peak accelerations recorded at the observation site of Ojiya City during the M6.8 Chuetsu offshore earthquake happened on July 16, 2007, in Niigata Prefecture, Japan.

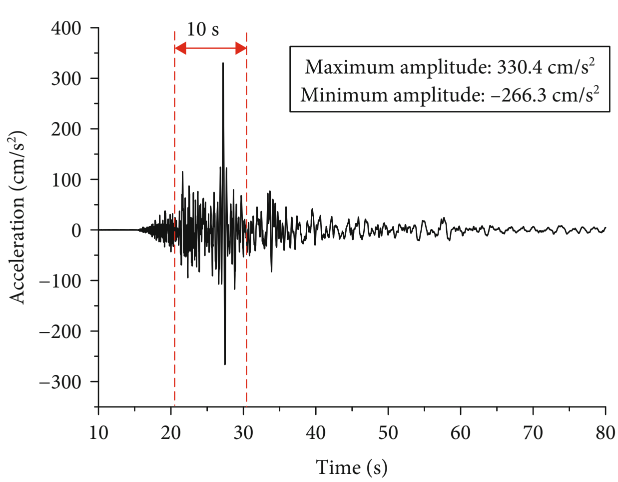

Figure 6: Input motion adopted in the numerical simulations.

and compression stress appear at both sides of the lining shoulder. The maximum tension stress mainly occurs at the left inner side of lining concrete, and the maximum compression one almost can be observed at the right inner of lining concrete. The maximum compression stresses are 2.2 MPa, 8.28 MPa, and 14.16 MPa (Figures 10(a)–10(c)), respectively, corresponding to the type CII, DI, and DII ground. After reinforcing with FRP grid, those compress values decrease to 1.91 MPa, 4.81 MPa, and 7.42 MPa, respectively (Figures 10(d)–10(f)).

3.3. Reinforcing Effects for Tunnels with a Cavity on the Shoulder. The plastic failure region on lining concrete for tunnels with a cavity on the shoulder is shown in Figure 11. Due to the existence of cavity on the shoulder, the flexural rigidity of lining concrete decreases, leading to a larger plastic failure region that appears at the location of cavity. As what mentioned before, the plastic failure region can also be generated at the shoulder of lining concrete due to the application of horizontal shear load. After reinforcing with FRP grids, the plastic failure region on the lining concrete disappears for the type CII ground (Figure 11(d)), and those plastic failure regions decrease dramatically for the other two types of ground (Figures 11(e) and 11(f)).

The axial stress on lining concrete for tunnels with a cavity on the shoulder is plotted in Figure 12. The existence of cavity on the shoulder decreases the bending resistance of lining concrete, and the stress concentration is easy to occur at the thin lining concrete, leading to a great value of axial stress at those locations. The maximum values at the cavity for those three types of ground are 4.90 MPa, 8.10 MPa, and 10.06 MPa (Figures 12(a)–12(c)), respectively, and those values decrease to 2.77 MPa, 4.33 MPa, and 6.56 MPa after reinforcing with FRP grids (Figures 12(d)–12(f)).

3.4. Reinforcing Effects for Tunnels with a Cavity on the Crown. The plastic failure region for tunnels with a cavity on the crown is first observed at the top right shoulder of the lining concrete (Figure 13(a)). With increasing the ground class, the plastic failure region develops and mainly

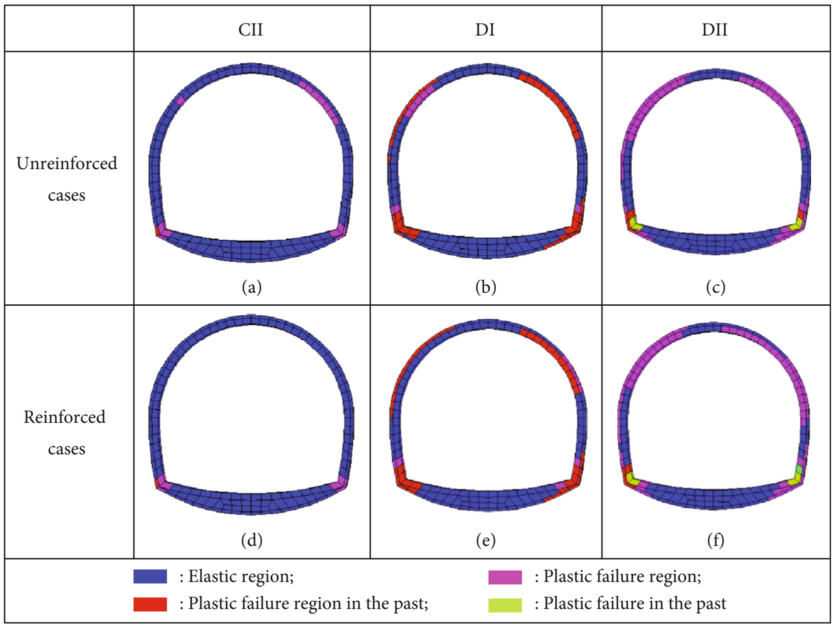

FIGURE 7: Plastic failure region on lining concrete for tunnel constructed by NATM.

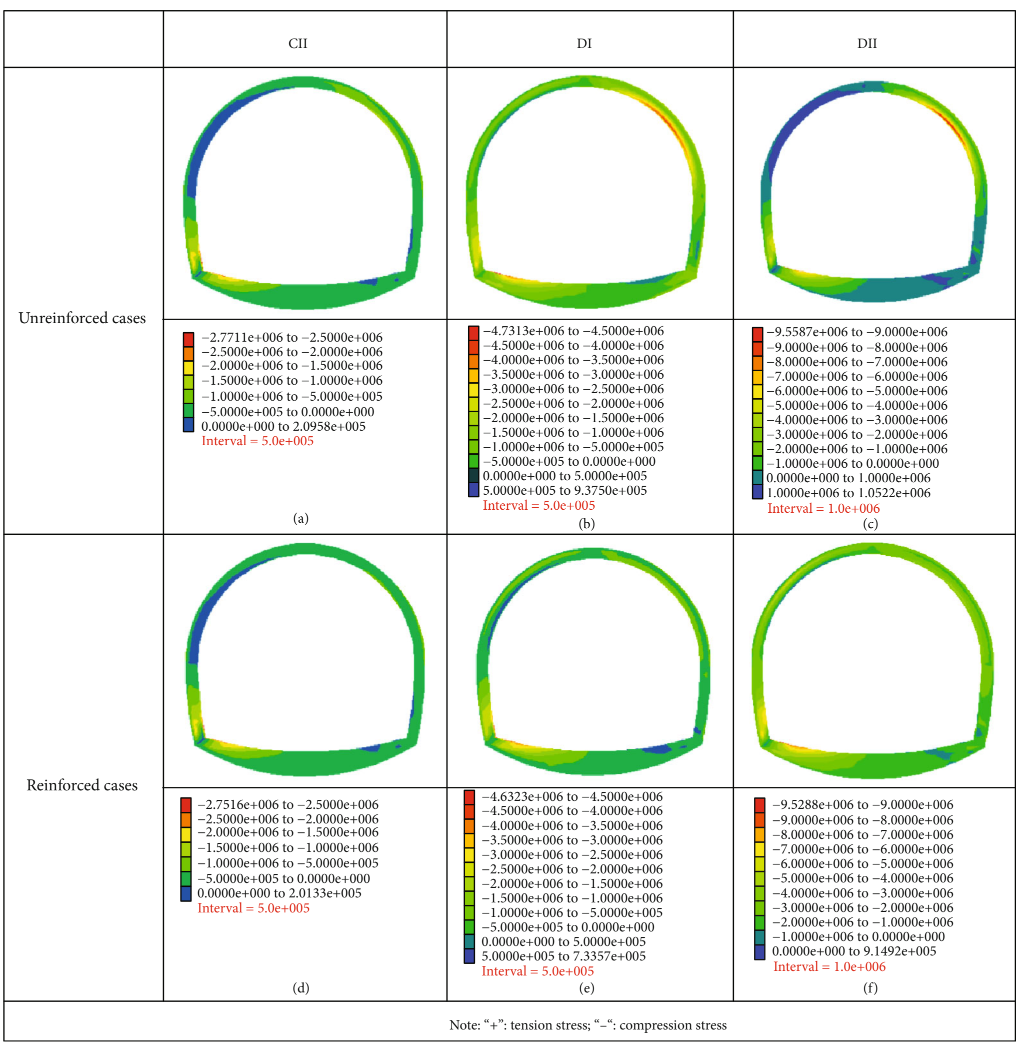

FIGURE 8: Axial stress distribution on lining concrete for tunnel constructed by NATM (unit: Pa).

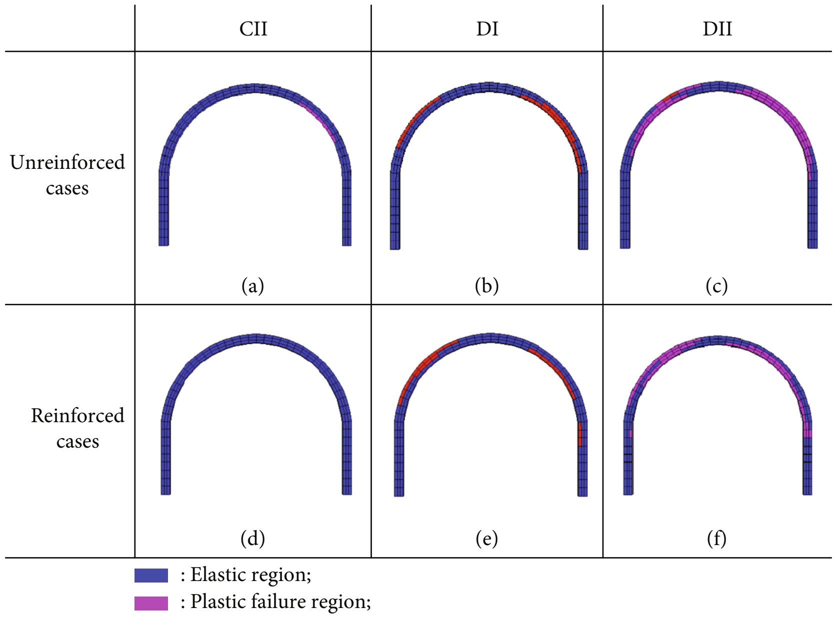

Figure 9: Plastic failure region on lining concrete for tunnel constructed by FM.

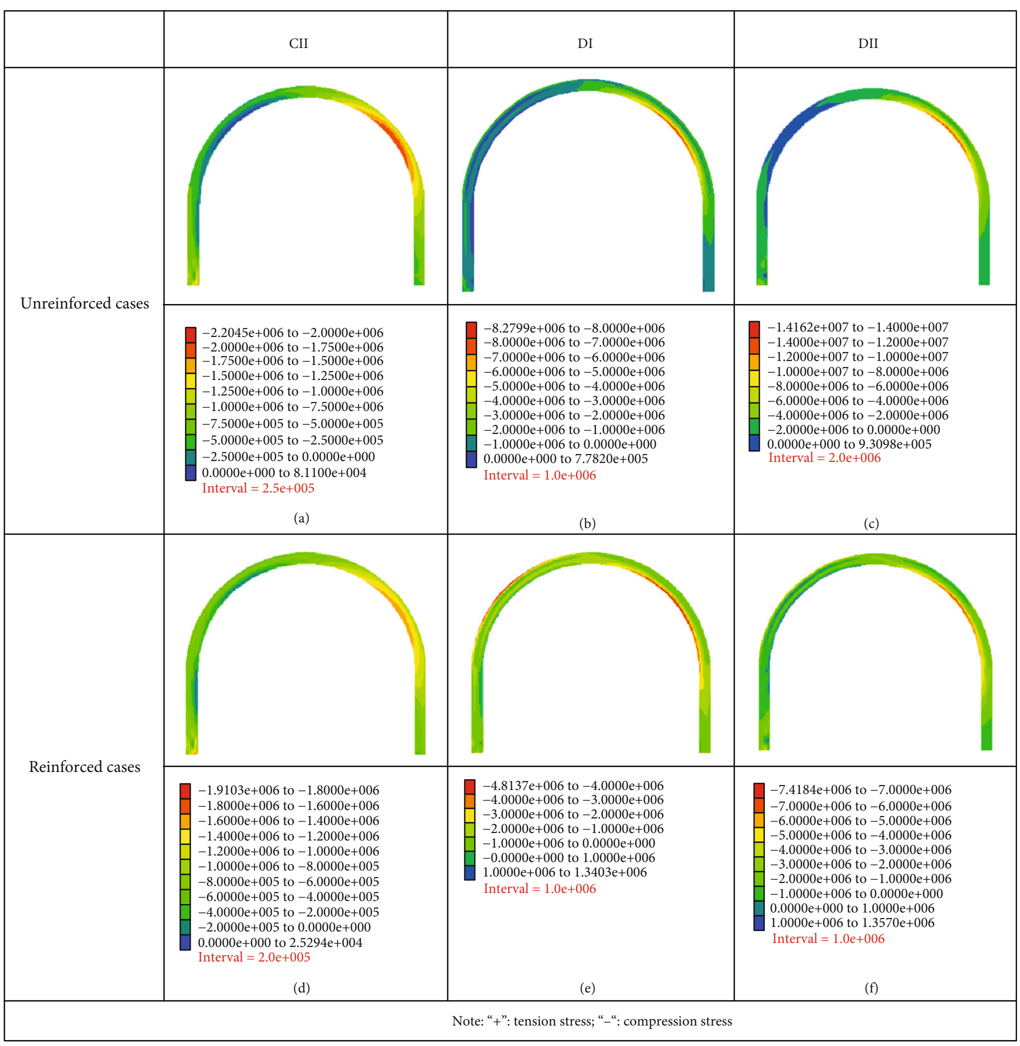

Figure 10: Axial stress distribution on lining concrete for tunnel constructed by FM (unit: Pa).

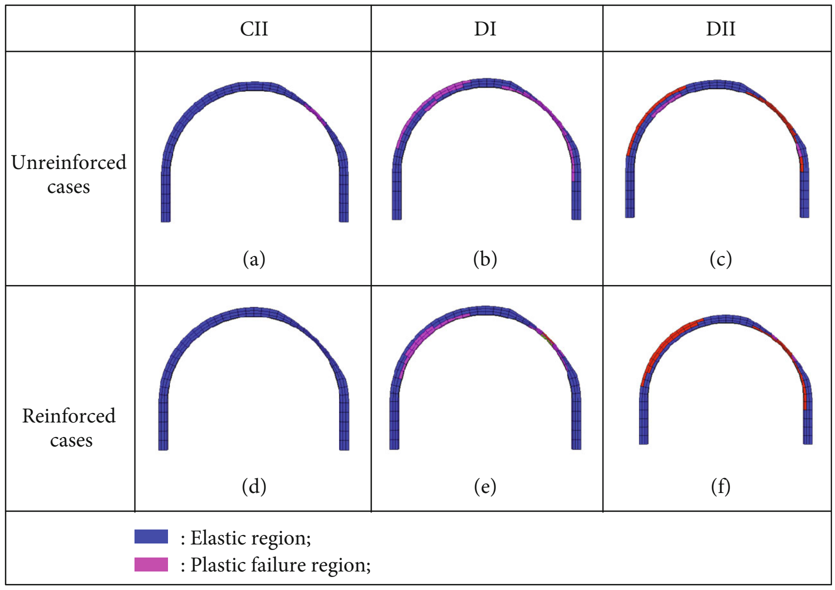

FIGURE 11: Plastic failure region on lining concrete for tunnel with a cavity on the shoulder.

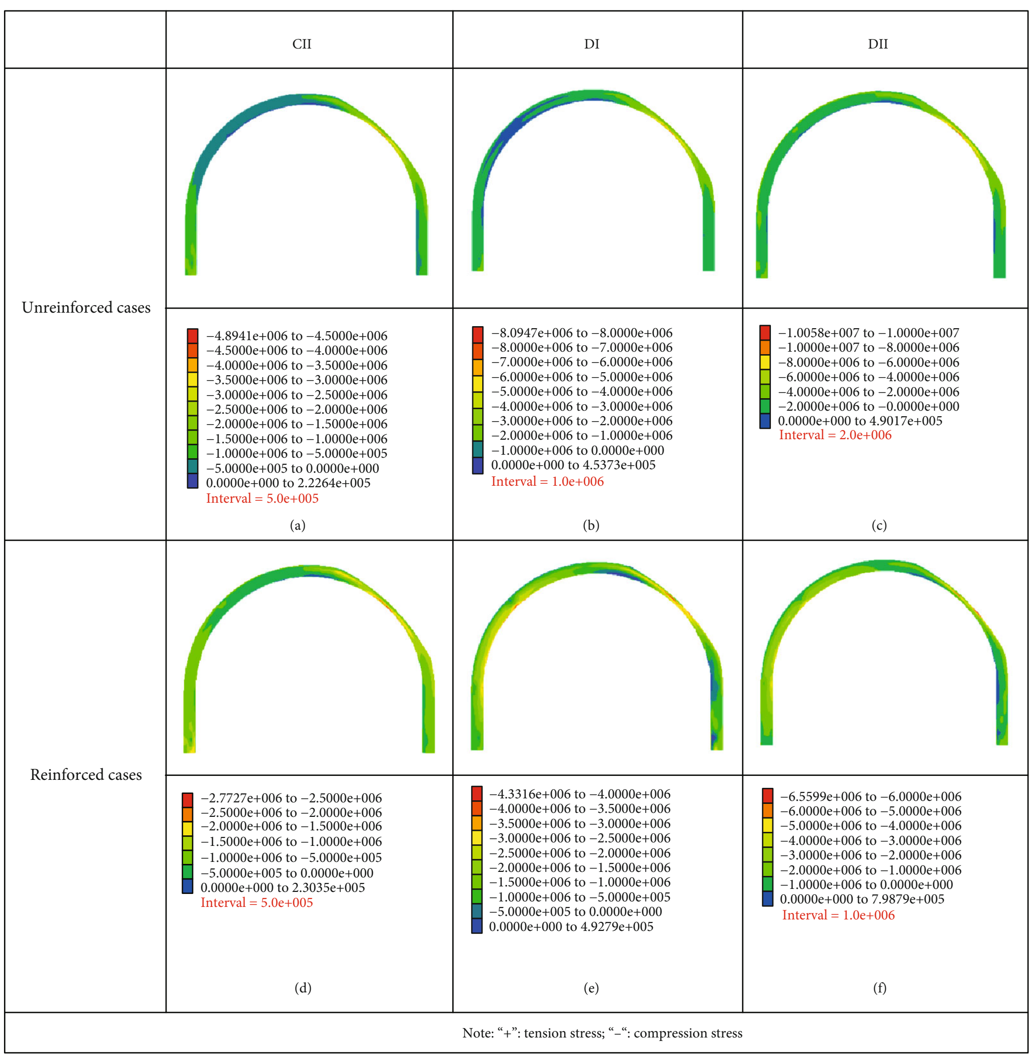

FIGURE 12: Axial stress distribution on lining concrete for tunnel with a cavity on the shoulder (unit: Pa).

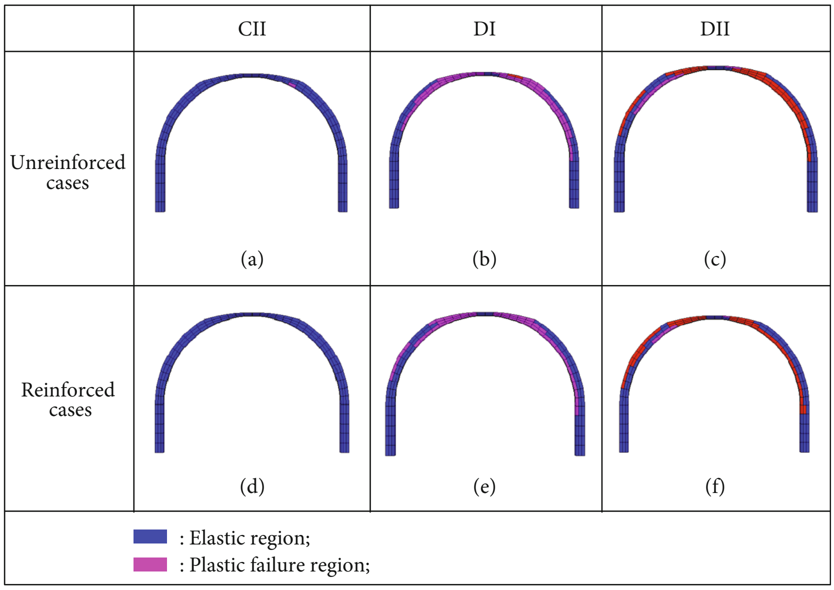

FIGURE 13: Plastic failure region on lining concrete for tunnel with a cavity on the crown.

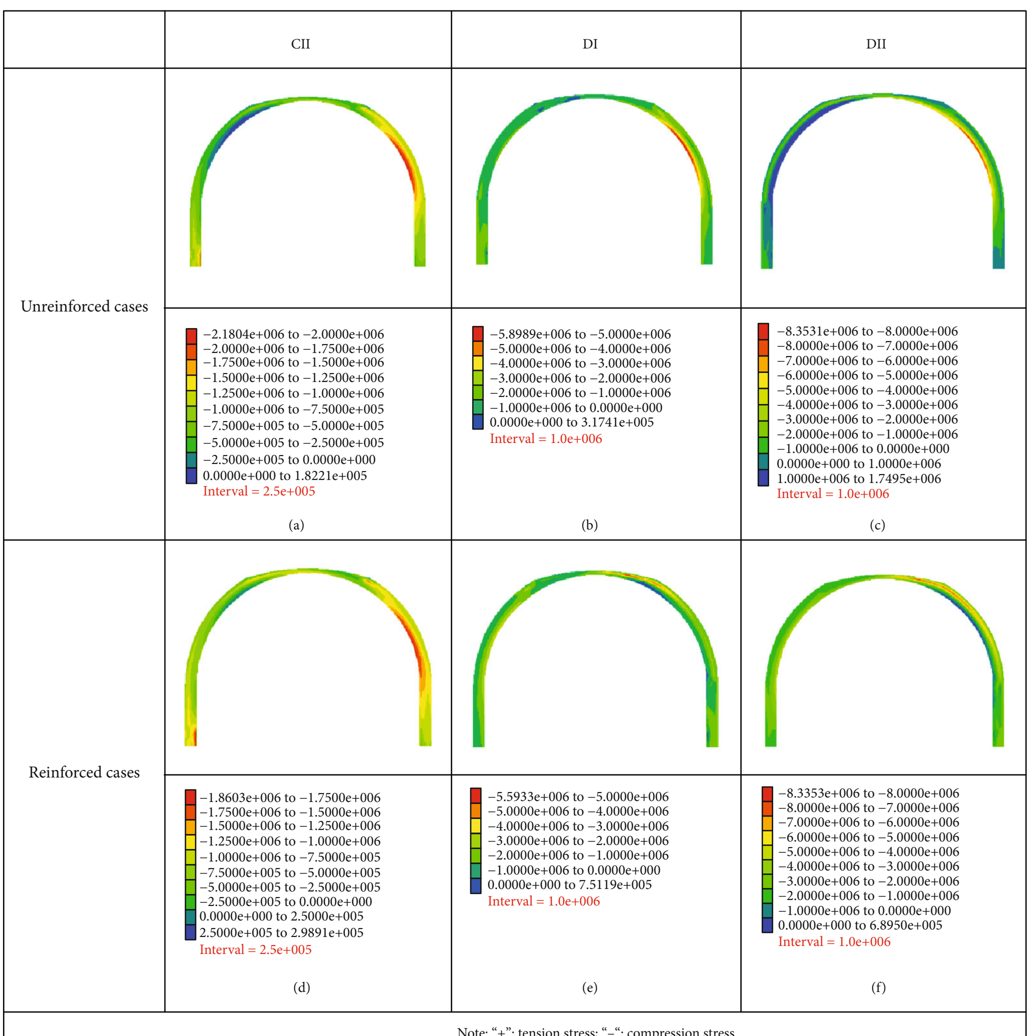

FIGURE 14: Axial stress distribution on lining concrete for tunnel with a cavity on the crown (unit: Pa).

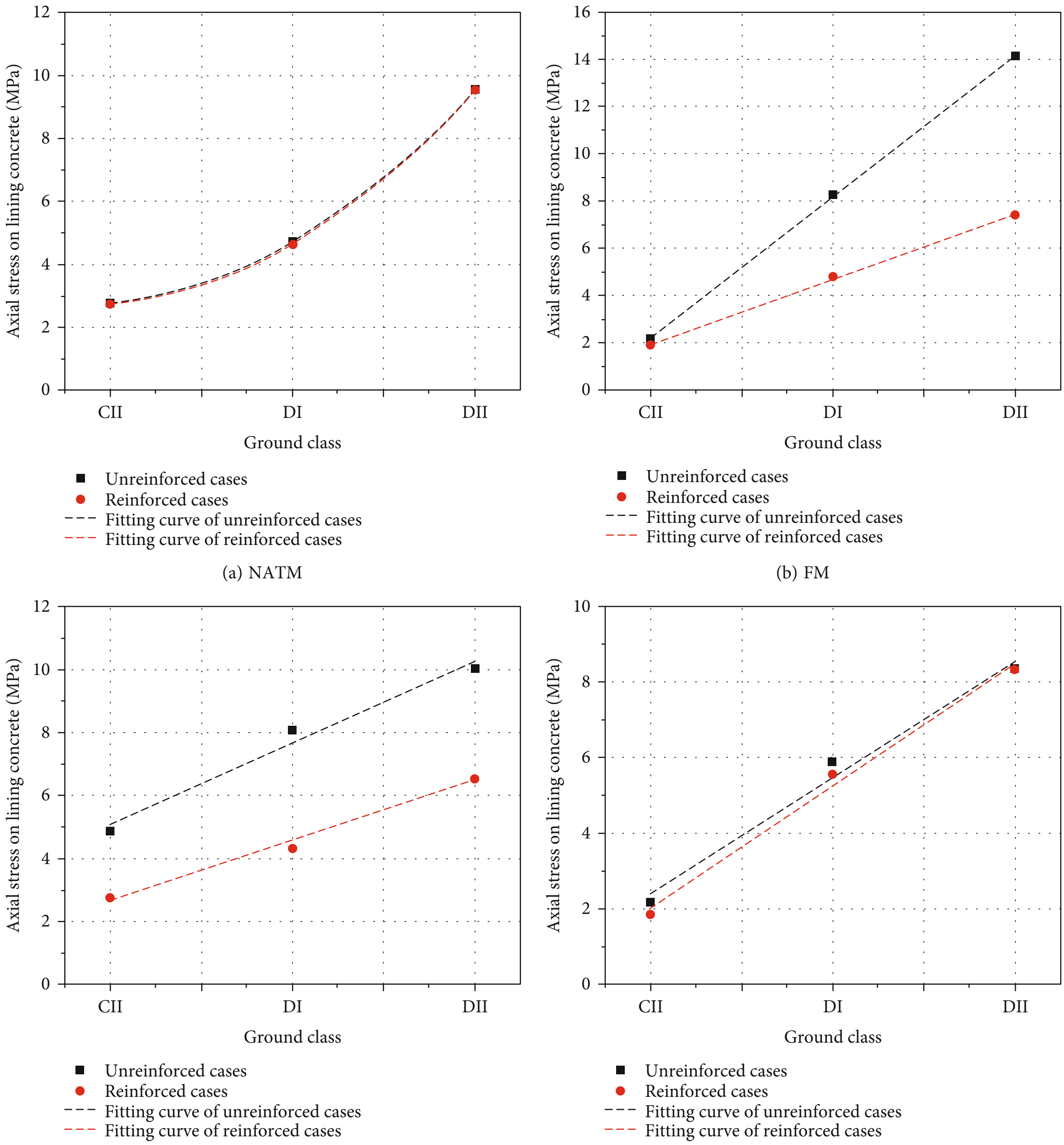

(a) NATM

(b) FM

(c) Cavity on the shoulder

(d) Cavity on the crown

Figure 15: The variation of maximum axial stress on lining concrete.

concentrates at the right inner and left inner sides of lining concrete. The failure region vanishes after reinforcing with FRP grids for the type CII ground (Figure 13(d)) and does not dramatically decrease for the other two types of ground (Figures 13(e) and 13(f)).

The axial stress distribution on the lining concrete for tunnels with a cavity on the crown is shown in Figure 14. The maximum values of compression stress on the right shoulder of lining are 2.08 MPa, 5.89 MPa, and 8.35 MPa, respectively, corresponding to the three types of ground (Figures 9(a)–9(c)). And those values decrease to 1.86 MPa, 5.59 MPa, and 8.34 MPa, respectively (Figures 9(d)–9(f)).

4. Discussion

Figure 15 shows the relationship between the ground class and the maximum axial stress on a lining concrete for the reinforced and unreinforced cases. The maximum axial stress on lining concrete increases with ground class, regardless of the tunnel construction method, existence of cavity,

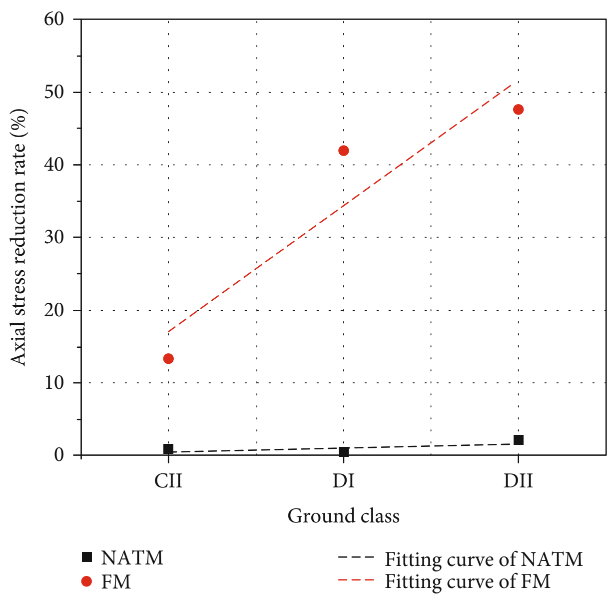

Figure 16: The axial stress reduction rate on lining concrete for tunnels constructed by different methods.

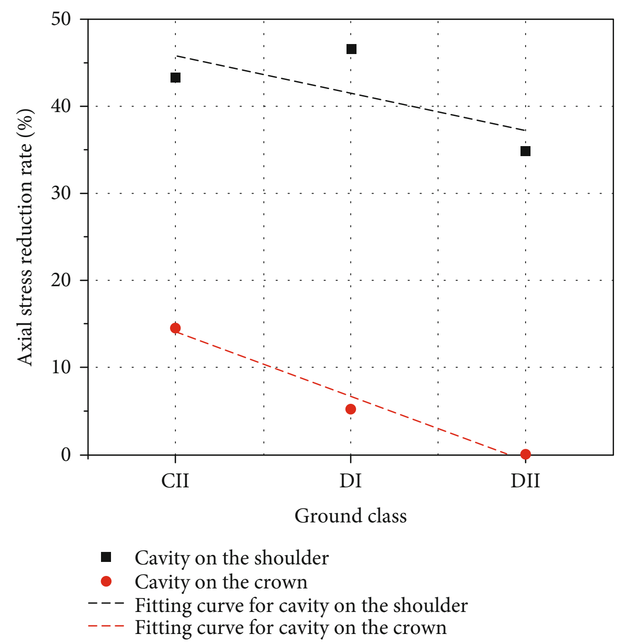

Figure 17: The axial stress reduction rate on lining concrete for tunnels with a cavity.

and reinforcing with FRP grids. However, for tunnels constructed by the NATM, the fitting curves of axial stress for the reinforced one and unreinforced one almost increase nonlinearly, indicating that with decreasing in rock strength, the axial stress on lining concrete increases dramatically (Figure 15(a)). The two fitting curves also show that the axial stress rarely decreases after reinforcing with FRP grids for tunnel constructed by the NATM. The fitting lines of axial stress for tunnel constructed by the FM increase linearly as shown in Figure 15(b). The fitting curves for the reinforced cases and unreinforced cases intersect at the ground class of CII, indicating that the reinforcing effects are not obvious when type CII ground is encountered. With the increment of ground class, stress reduction shows more significant after reinforcing with FRP grids, indicating that better reinforcing effects could be obtained when a weaker surrounding rock is encountered. Although the axial stress on a lining concrete increases with increasing the ground class when a cavity exists on the shoulder of tunnel lining, the slope of fitting curve shows slightly decrement, indicating that the reinforcing effects with FRP grids increase with the increment in ground class (Figure 15(c)). While for those tunnels with a cavity on the crown, the fitting curves almost intersect at the point of the largest ground class (i.e., class DII ground) as shown in Figure 15(d), which demonstrated that the reinforcing effects of the FRP-PCM method are not obvious for a higher class of ground.

In order to investigate the reinforcing effects of the FRP-PCM method quantitatively, an axial reduction rate R_σ defined as follows is calculated:

$$R_\sigma = \frac{\sigma_{nr} - \sigma_r}{\sigma_{nr}} \times 100\%, \quad (1)$$

where σ_{nr} is the axial acting on the unreinforced lining (MPa) and σ_r is the axial stress obtained in the reinforced cases (MPa). Since the axial stress is the principle stress parallel to the tunnel lining, the axial force reduction rate represents the degree of reduction in axial stress after reinforcing with FRP grids.

Figure 16 shows the relationship between axial stress reduction rate and ground class, taking into account the construction method. R_σ increases with the increasing ground class for tunnels constructed by the FM, revealing that the performance of reinforcement is greater when a higher type of ground is encountered. With the increment of ground class from CII to DII, R_σ increases from 13.18% to 48.60%. While for those tunnels constructed by the NATM, R_σ merely varies from 0.72% to 2.11%, which demonstrated that the performance of reinforcement is not obvious.

Figure 17 shows the relationship between the axial stress reduction rate and ground class, taking into account the existence of cavity. R_σ decreases with increasing in ground class, indicating that the performance of reinforcement is weaker when a higher type of ground is encountered. With the increase in ground class from CII to DII, R_σ decreases from 43.35% to 34.80% when a cavity exists on the shoulder of lining, while decreasing from 14.7% to 0.12% when a cavity exists on the crown of lining concrete. The results also demonstrate that the performance of reinforcement is greater when a cavity exists on the shoulder.

5. Conclusions

In the present study, the reinforcing effects of the FRP-PCM method under dynamic load have been investigated based on the numerical analysis, taking into account the tunnel construction method and location of tunnel cavity. In advancing this work, the following conclusions are drawn:

(1) The plastic failure region on lining concrete is improved obviously when the type CII ground is encountered, regardless of the influences of construction methods and cavity locations

(2) For tunnels constructed by the NATM, the axial stress on lining concrete increases dramatically with the increment of ground class, and this axial stress merely changes after reinforcing with FRP grids. While for those tunnels constructed by the FM, the reinforcing effects improve with the increment of ground class

(3) The axial stress on the lining concrete merely varies after reinforcing with FRP grids for tunnels with a cavity on the crown, and a good reinforcing performance is observed for the cases with a cavity on the shoulder, compared with the one with a cavity on the crown

(4) Only the CR8 grids were taken into account during the numerical simulations under seismic load. In the future, various types of FRP grids, such as CR4 and CR6, should be discussed to investigate the reinforcing effects of the FRP-PCM method

(5) With the increment of ground class from CII to DII, R_σ increases from 13.18% to 48.60% for tunnels constructed by the NATM, while for those tunnels constructed by the NATM, R_σ merely varies from 0.72% to 2.11%. R_σ decreases from 43.35% to 34.80% when a cavity exists on the shoulder of lining, while decreasing from 14.7% to 0.12% when a cavity exists on the crown of lining concrete

Data Availability

The original data can be applied if needed.

Conflicts of Interest

The authors declare that there are no conflicts of interest regarding the publication of this article.

Acknowledgments

We gratefully acknowledge the financial support from the National Natural Science Foundation of China under Grant Nos. 51879135, 51808306, and 52179104. This work is also supported by Taishan Scholars Program (2019KJG002 and 2019RKB01083), the Natural Science Foundation of Shandong Province (ZR2019BEE051, ZR2020ME099, and ZR2020MD111), the Foundation of the Key Laboratory of Mining Disaster Prevention and Control (MDPC202010).

References

[1] V. A. Kontogianni and S. C. Stiros, “Earthquakes and seismic faulting: effects on tunnels,” *Turkish Journal of Earth Sciences*, vol. 12, no. 1, pp. 153–156, 2003.

[2] T. D. O’Rourke, S. H. Goh, C. O. Menkiti, and R. J. Mair, “Highway tunnel performance during the 1999 Duzce earthquake,” in *XV International Conference on Soil Mechanics and Geotechnical Engineering*, Istanbul Turkey, August 2001.

[3] Y. Shen, B. Gao, X. Yang, and S. Tao, “Seismic damage mechanism and dynamic deformation characteristic analysis of mountain tunnel after Wenchuan earthquake,” *Engineering Geology*, vol. 180, pp. 85–98, 2014.

[4] T. Suzuki, “Damages of urban tunnels due to the Southern Hyogo earthquake of January 17, 1995 and the evaluation of seismic isolation effect,” in *CD-ROM of the 11WCEE*, Elsevier, Acapulco, Mexico, 1996.

[5] X. Zhang, Y. Jiang, and S. Sugimoto, “Seismic damage assessment of mountain tunnel: a case study on the Tawarayama tunnel due to the 2016 Kumamoto earthquake,” *Tunnelling and underground space technology*, vol. 71, pp. 138–148, 2018.

[6] J. N. Wang and G. A. Munfakh, “Seismic design of tunnels,” *WIT Transactions on the Built Environment*, vol. 57, 2001.

[7] N. Yoshida, “Ungerground and buried structure, earthquake geotechnical engineering,” in *Proceedings of 2nd International Conference on Earthquake Geotechnical Engineering*, Chengdu, China, 1999.

[8] H. Yu, J. Chen, A. Bobet, and Y. Yuan, “Damage observation and assessment of the Longxi tunnel during the Wenchuan earthquake,” *Tunnelling and Underground Space Technology*, vol. 54, pp. 102–116, 2016.

[9] B. Chiaia, A. P. Fantilli, and P. Vallini, “Combining fiber-reinforced concrete with traditional reinforcement in tunnel linings,” *Engineering Structures*, vol. 31, no. 7, pp. 1600–1606, 2009.

[10] A. De la Fuente, P. Pujadas, A. Blanco, and A. Aguado, “Experiences in Barcelona with the use of fibres in segmental linings,” *Tunnelling and Underground Space Technology*, vol. 27, no. 1, pp. 60–71, 2012.

[11] V. Moreira de Alencar Monteiro and F. de Andrade Silva, “The use of the Barcelona test as quality control of fiber reinforced shotcrete for underground mining,” *Construction and building materials*, vol. 262, p. 120719, 2020.

[12] T. Franzén, “Shotcrete for underground support: a state-of-the-art report with focus on steel-fibre reinforcement,” *Tunnelling and Underground Space Technology*, vol. 7, no. 4, pp. 383–391, 1992.

[13] F. Jeng, M. L. Lin, and S. C. Yuan, “Performance of toughness indices for steel fiber reinforced shotcrete,” *Tunnelling and Underground Space Technology*, vol. 17, no. 1, pp. 69–82, 2002.

[14] J. K. Lee and J. H. Lee, “Nondestructive evaluation on damage of carbon fiber sheet reinforced concrete,” *Composite Structures*, vol. 58, no. 1, pp. 139–147, 2002.

[15] K. Miyauchi, *Estimation of strengthening effects with carbon fiber sheet for concrete column*, Japan Concrete Institute, 1997.

[16] C. Nony-Davadie, L. Peltier, Y. Chemisky, B. Surowiec, and F. Meraghni, “Mechanical characterization of anisotropy on a carbon fiber sheet molding compound composite under quasi-static and fatigue loading,” *Journal of Composite Materials*, vol. 53, no. 11, pp. 1437–1457, 2019.

[17] K. Kiriyama, M. Kakizaki, T. Takabayashi, and N. Hirosawa, "Structure and construction examples of tunnel reinforcement method using thin steel panels," *Nippon Steel Technical Report*, vol. 92, pp. 45–50, 2005.

[18] M. A. Erki and S. H. Rizkalla, "FRP reinforcement for concrete structures," *Concrete International Detroit*, vol. 15, pp. 48–52, 1993.

[19] D. A. Hensher, *Fiber-Reinforced-Plastic (FRP) Reinforcement for Concrete Structures: Properties and Applications*, Elsevier Science, 2013.

[20] S. A. Sheikh and G. Yau, "Seismic behavior of concrete columns confined with steel and fiber-reinforced polymers," *ACI Structural Journal*, vol. 99, no. 1, pp. 72–80, 2002.

[21] X. K. Zou, J. G. Teng, L. De Lorenzis, and S. H. Xia, "Optimal performance-based design of FRP jackets for seismic retrofit of reinforced concrete frames," *Composites Part B: Engineering*, vol. 38, no. 5-6, pp. 584–597, 2007.

[22] K. K. Antoniades, T. N. Salonikios, and A. J. Kappos, "Cyclic tests on seismically damaged reinforced concrete walls strengthened using fiber-reinforced polymer reinforcement," *Structural Journal*, vol. 100, no. 4, pp. 510–518, 2003.

[23] L. Lam, J. G. Teng, C. H. Cheung, and Y. XIAO, "FRP-confined concrete under axial cyclic compression," *Cement and Concrete Composites*, vol. 28, no. 10, pp. 949–958, 2006.

[24] G. Zhou, Q. Sun, J. Fenner et al., "Crushing behaviors of unidirectional carbon fiber reinforced plastic composites under dynamic bending and axial crushing loading," *International Journal of Impact Engineering*, vol. 140, 2020.

[25] D. M. Jerome and C. A. Ross, "Simulation of the dynamic response of concrete beams externally reinforced with carbon-fiber reinforced plastic," *Computers & Structures*, vol. 64, no. 5-6, pp. 1129–1153, 1997.

[26] Itasca Consulting Group, Inc, *FLAC3D User's Manual*, 2002.

[27] The Ministry of Public Works Research Institute Tunnel Laboratory, *Document: Prediction and Measures Manuals of Ground Deformation for Tunnel Excavation (Plan)*, 1994.

[28] Y. Jiang, X. Wang, B. Li, Y. Higashi, K. Taniguchi, and K. Ishida, "Estimation of reinforcing effects of FRP-PCM method on degraded tunnel linings," *Soils and Foundations*, vol. 57, no. 3, pp. 327–340, 2017.

Hindawi
Geofluids
Volume 2021, Article ID 9881280, 12 pages
https://doi.org/10.1155/2021/9881280

Research Article

A Study of Support Characteristics of Collaborative Reinforce System of U-Steel Support and Anchored Cable for Roadway under High Dynamic Stress

Qizhou Wang,[1,2] Haiwang Ye,[1,2] Ning Li,[1,2] Xiuwen Chi,[1,2] Wenbing Xie,[3] Dongfang Chen,[1,2] Shengguo Jing,[3] and Tao Lei[1,2]

[1]*Key Laboratory of Hubei Province for Mineral Resources Processing and Environment, Wuhan University of Technology, Wuhan Hubei 430070, China*
[2]*School of Resources and Environmental Engineering, Wuhan University of Technology, Wuhan Hubei 430070, China*
[3]*State Key Laboratory of Coal Resources and Safe Mining, China of Mining and Technology, Xuzhou Jiangsu 221116, China*

Correspondence should be addressed to Ning Li; 13875910191@163.com

Received 12 June 2021; Accepted 3 September 2021; Published 5 October 2021

Academic Editor: Yong-Zheng Wu

This paper presents a comprehensive study of the support effect and characteristics of a collaborative reinforce system of U-steel support and anchored cable (USS-AC) for roadway under high dynamic stress in a coal mine in China. The deformational behavior of the roadway and the load characteristics of reinforcing elements were measured in real time and analyzed. A numerical simulation study has also been conducted to identify the interaction of the reinforcing elements to the surrounding rock under dynamic load. The research results suggest that the stress distribution of roadway surrounding rock could be changed and that residual strength of the surrounding rock near opening could be increased by using USS-AC. Based on the action of anchored cable, the moment distribution of U-steel support is optimized. The load capacity and nondeformability of the U-steel support are promoted. And the global stability of U-steel support is enhanced so as to achieve the goal of high supporting resistance. When the deformation stress of the surrounding rock is higher, the U-steel support deforms as the surrounding rock. The two side beams and the overlapping parts of U-steel support suffer the highest deformation stress. As a result, the anchored cable provides higher reaction force for the previous locations of the U-steel support in order to prevent deformation of support towards to excavation. As an integral structure, the U-steel support is confined to a limited deformation space under the action of anchored cable. The larger deformation is released through sliding motion of the overlapping parts so as to reach the ultimate of high supporting resistance of USS-AC.

1. Introduction

Strata control of roadways developed in soft rock under high in situ stress has become a challenging problem due to increasing mining depth in recent years. It was reported that more than 80% roadways experienced dynamic pressure in the central and eastern China [1, 2]. Numerous research works related to ground support technology for soft rock roadway under high dynamic pressure have been conducted. Among them, active supports of rock bolts or cables have been proposed [3–7]. Besides, a combination of active support of rock bolts and passive support of U-steel has been developed and identified as an effective manner for such geo-conditions [8–10]. For a case study of the -720 south-wing track haulage roadway under dynamic pressure in Renlou Coal Mine in China, U-steel supports, U-steel support wall thickness grouting combination support, and bolting support with wire mesh have failed to decrease the intense deformation of surrounding rock of the roadway. Aiming at such geological condition of soft rock roadways under high-stress, a collaborative reinforce system of U-steel support and anchored cable (USS-AC) was proposed and adopted [9, 10]. The field test indicates that USS-AC is an effective approach to reduce the displacement of the

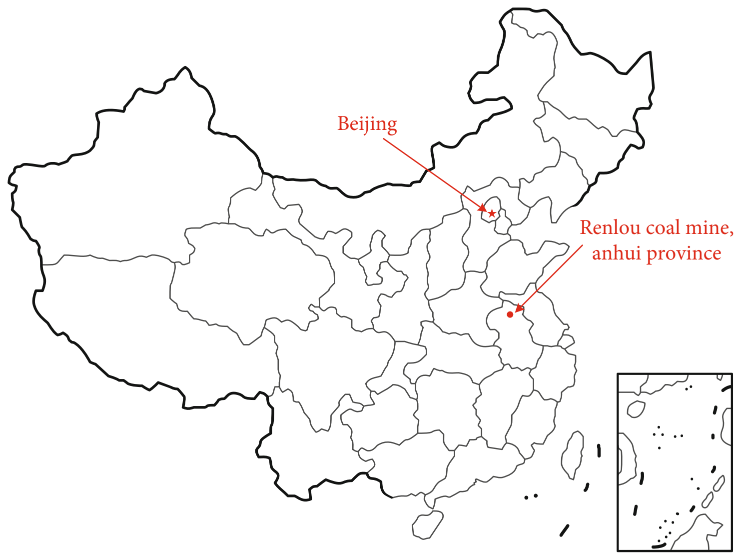

Figure 1: Location of the Renlou Coal Mine.

surrounding rock of the haulage roadway. Load characteristics of U-steel support and anchored cable of USS-AC were analyzed, respectively, by theoretical calculations under static stress [9–15]. However, the transformation law of actual load on U-steel support has not been monitored and obtained with suffering dynamic stress from the beginning to the end of excavation of workface. Therefore, the collaborative interaction between U-steel support and anchored cable of USS-AC could not be described.

For solving the previous issues, optimizing action of stress distribution of surrounding rock under USS-AC and bending moment of U-steel support with collaborative anchored cables were analyzed by a numerical simulation method to reveal the interaction mechanism of USS-AC. Specific parameters of USS-AC were proposed for the field test in Renlou Coal Mine. Meanwhile, actual load of U-steel support and anchored cables respective as well as displacement of surrounding rock of test roadway were monitored by a filed measurement method. The deformation of the surrounding rock and its corelationship to the actual load of USS-AC were disclosed by using of test data. The increasing effect of anchored cables for U-steel support bearing capacity and structural stability was described.

2. Project Overview

The project was at Renlou Coal Mine in the north of Anhui Province of China (Figure 1). The -720 south-wing track haulage roadway was the main channel for pedestrians and ventilation of the mine. The shape of roadway section was a straight wall semicircular arch with a height of 3.9 m and a width of 5.0 m. The roadway with overburden depth 750 m was arranged in the floor strata of coal seam NO.8_2 at a perpendicular distance of 43 m-70 m from coal seam NO.7_2 and 20 m-50 m from coal seam NO.8_2. The relative plane location relationship between the -720 south-wing track haulage roadways with working face II$7_2$14 is given in Figure 2.

The -720 south-wing track haulage roadway was excavated in siltstone and mudstone. The side walls of roadway were mudstone, and the arch roof was siltstone, respectively. The rock of immediate roof was a 2.5 m thick siltstone, which was overlaid by a main roof of fine sandstone with a thickness of 5.0 m.

A combined bolting method, with bolts, cables, and steel bar truss, was conducted in the -720 south-wing track haulage roadway. As shown in Figure 3, the deformation of haulage roadway was insignificant to satisfy the operation requirements without the influence of dynamic pressure of working face II$7_2$14. However, the previous method failed to restrain the deformation of roadway that roof-to-floor convergence reached 0.8 m with the side-to-side convergence up to 1.0 m under excavation of working face. The roadway deformation was so severe that the surrounding rock became loose and broken with a strength reduction. Therefore, in the service period of the roadway, it was severely impacted by dynamic stress due to mining activity of working face II$7_2$14.

3. Functional Mechanism of USS-AC

3.1. Numerical Modelling. USS-AC was divided into two segments. The U-steel support was the primary and basic component to support the loose rock mass near to the excavation of roadway. The second part consisted of anchored cables and joists that linked cables with U-steel supports and transmitted pretension of cables to U-steel supports. The Flac^{2D} model was built to, respectively, analyze a stress distribution law of roadway surrounding rock and a bending moment variation law inside of U-steel.

The numerical model has a length of 80 m and a height of 80 m with element size $0.2\,m \times 0.2\,m$ that Mohr-Coulomb constitutive model in FLAC^{2D} was used to simulate the mechanical behaviors of rocks. The model size and parameters of rocks are illustrated in Figure 4. The normal displacement of the four lateral surfaces and

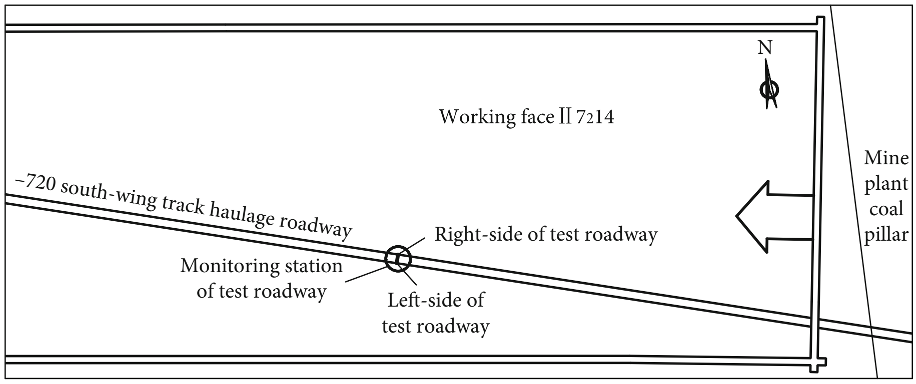

Figure 2: Plane location relationship between -720 south-wing track haulage roadway and working face II7214.

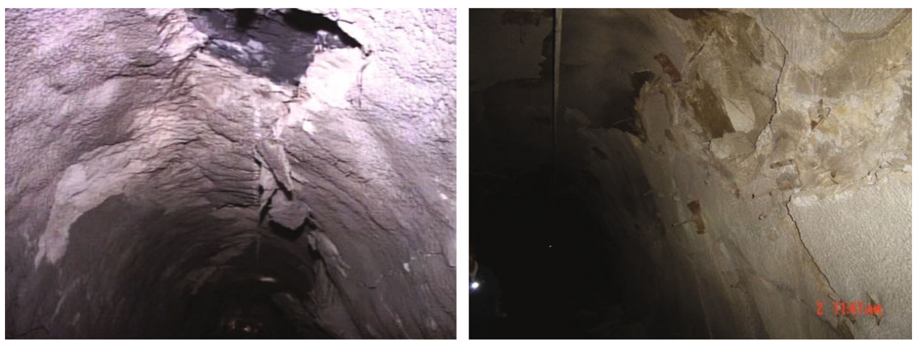

Figure 3: Deformation characteristics of haulage roadway.

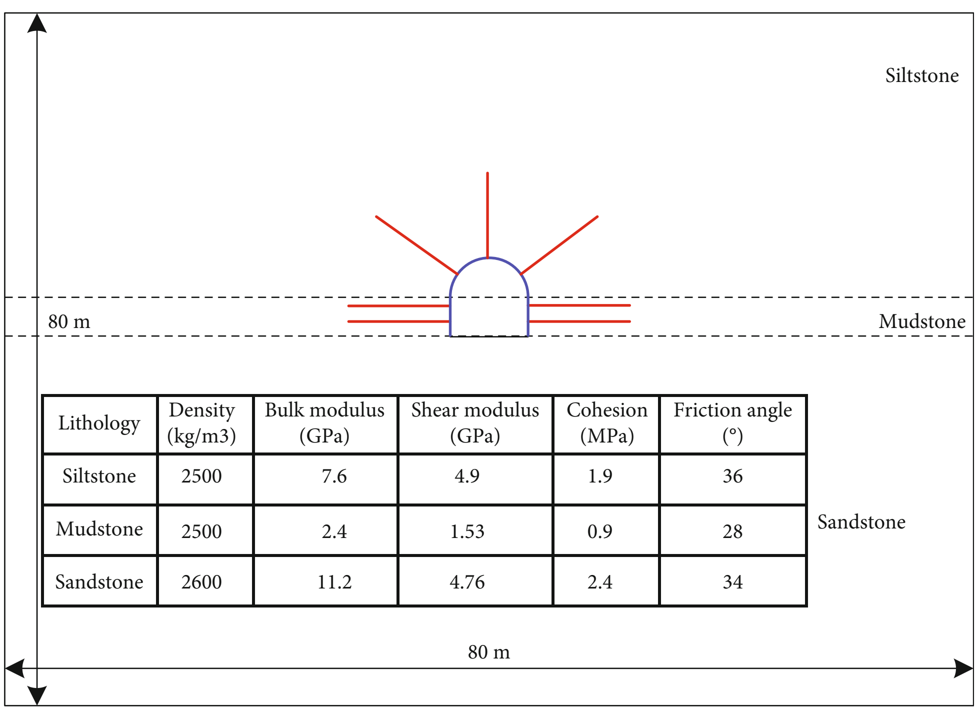

Lithology	Density (kg/m3)	Bulk modulus (GPa)	Shear modulus (GPa)	Cohesion (MPa)	Friction angle (°)
Siltstone	2500	7.6	4.9	1.9	36
Mudstone	2500	2.4	1.53	0.9	28
Sandstone	2600	11.2	4.76	2.4	34

Figure 4: The model size and parameters of rocks.

the bottom surface of the model were fixed to be zero. The stress ($\varepsilon_{zz} = \varepsilon_{xx} = \varepsilon_{yy} = 18\,\mathrm{MPa}$) was applied on the top surface of model to simulate the overburden rock load in the condition of initial stress. A beam unit was adopted to simulate U-steel support. In addition, a cable unit was used to simulate the anchored cable with a length of

6.5 m. And the two support units were linked by slave command in $Flac^{2D}$.

The implementation was divided into three steps: firstly, excavating the roadway region after initial equilibrium of model. And then, support units were set, and the top stress of model was changed into 21.6 MPa to simulate the extra stress due to excavation activity of working face.

3.2. Numerical Modelling Results. Figure 5 shows vertical stress distribution law of the roadway surrounding rock after using two different support ways that U-steel support and USS-AC are adopted, respectively.

It can be seen that the stress condition of the roadway surrounding rock is significantly optimized by using USS-AC. Compared with the roadway using a U-steel support, the development scope of low-stress of the surrounding rock is obviously reduced, while the vertical stress of the surrounding rock near to the excavation space of the roadway is generally increased. According to the research results [3, 16, 17], the residual strength of the rock mass near the excavation space of roadway is greatly increased to enhance the itself-bearing capacity due to increase of confine pressure in broken and fractured rock mass of roadway. Therefore, the confine pressure in fractured zone of test roadway is raised by USS-AC to increase the residual strength of the rock mass in the previous zone.

The load bearing capacity of the rock mass at a deep zone could be used by an active supporting effect of the anchored cable that links the U-steel with the deep rock mass of roadway. On the one hand, the stress concentration zone at the deep part in surrounding rock of the roadway was decreased by more than 50%. The bearing load of the rock mass at the deep part is reduced, and it was kept stable at the same time. On the other hand, the stress in the rock mass at the anchoring end of inside the anchored cable is significantly increased under the function of anchoring to enhance the strength and stiffness of rock mass at the deep part. The support and rock combining bearing structure that has been linked cables with U-steel by joist is formed and affords a large load to provide a higher deformation resistance.

Furthermore, the previous research results [9, 11, 12] showed that the bearing capacity of arch beam on the top of U-steel support is greater than that of side beam. As shown in Figure 6(a), because of poor interaction between U-steel support and surrounding rock near the excavation space of roadway, the load of arch beam is lower even zero in an actual bearing process. However, the overlap part and side beam bear larger load. Therefore, the arch beam of U-steel support is in the condition which bears low actual load and wastes the high resistance to the rock mass. On the contrary, the actual load of side beam is greater than the upper limit of its supporting resistance to create a larger bending moment in the transverse plane of the side beam center line. The load distribution law and bending moment feature of U-steel support generate a phenomenon that side beam is the first place of destruction and losing stability to result in difficultly using the high resistance and great strength of the arch beam.

The bending moment of U-steel support is shown in Figure 6(b) after applying USS-AC. The bending moment of arch beam is changed from 4 N·m to 1.21×10^3 N·m, while that of side beam declines from 7.12×10^4 N·m to 3.64×10^4 N·m. So, the bearing characteristics of U-steel support are optimized to reduce the bending moment of side beam and enlarge that of arch beam owing to anchored cables. The reduction of load difference between the arch beam and side beam is accomplished to reinforce the global stability of U-steel support.

4. The Technology Parameters of USS-AC

According to the geological condition of the -720 south-wing track haulage roadway and excavation arrangement of working face $II7_2 14$ at the Renlou Coal Mine, collaborative supporting technology of USS-AC was adopted in the field test. The specific scheme with supporting parameters is shown in Figure 7.

The parameters of U-steel support are evaluated as follows: the type of U-steel is 36# in Chinese standard. The U-steel support which is assembled by one arch beam on the top and two side beams is set as a main supporting manner with a spacing of 0.5 m. The length of arch beam is 6.13 m and overlapped in its two ends by side beam with a length of 3.54 m for each side. Three suits of locking devices by nuts are used in compressing each overlapping part with a length of 0.54 m.

The cable anchoring parameters are evaluated as follows: the diameter of anchored cable is 17.8 mm with a length of 6 m. Three anchored cables per row are installed in the center line of arch beam and two overlapping parts. Two anchored cables per row are installed in the right side beam with a row spacing of 1 m. One anchored cable per row is installed in the left side beam. The row-to-row distance of anchored cables is 1 m. And all cables are perpendicular to the surface of U-steel. Resin capsules are used to anchor the front part of the cables in the process of installing. The U-steel support is linked with anchored cables by a joist with a length of 0.8 m that is processed by the H-steel. There is a hole with a radius of 0.015 m so that the anchored cables could pass through and preload it on the exterior surface of a joist. Then, pretension loads of 80 kN-100 kN are applied to the cables.

5. Field Monitoring Scheme

A monitoring station was set up in the -720 south-wing track haulage roadway and with a distance of 520 m in advance of working face $II7_2 14$. The convergence of test roadway, actual load of the U-steel support, and load of exterior end of anchored cables were monitored from the beginning of dynamic influence of working face $II7_2 14$ to the end.

5.1. Convergence of Test Roadway. The convergence of test roadway mainly refers to the displacement of the surrounding rock near to the excavation space of the roadway. A datum point was set up at the center of both sides, roof center, and floor center in a cross-section, respectively. At the

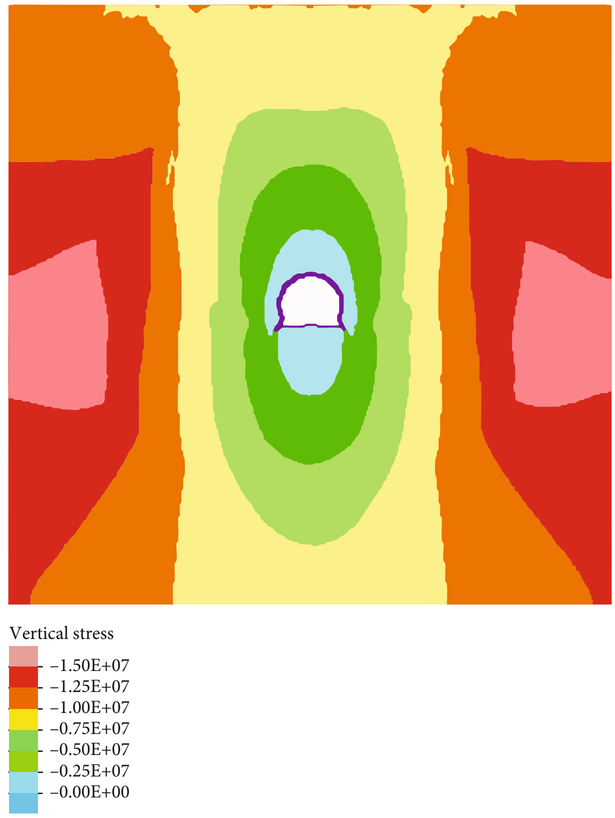

(a) U-steel support

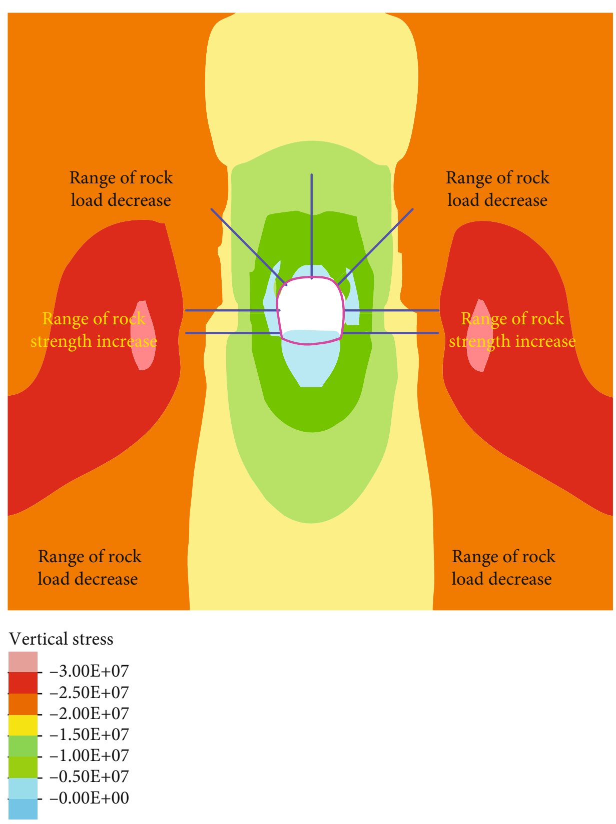

(b) USS-AC

Figure 5: Vertical stress distribution law of roadway surrounding rock with different support methods.

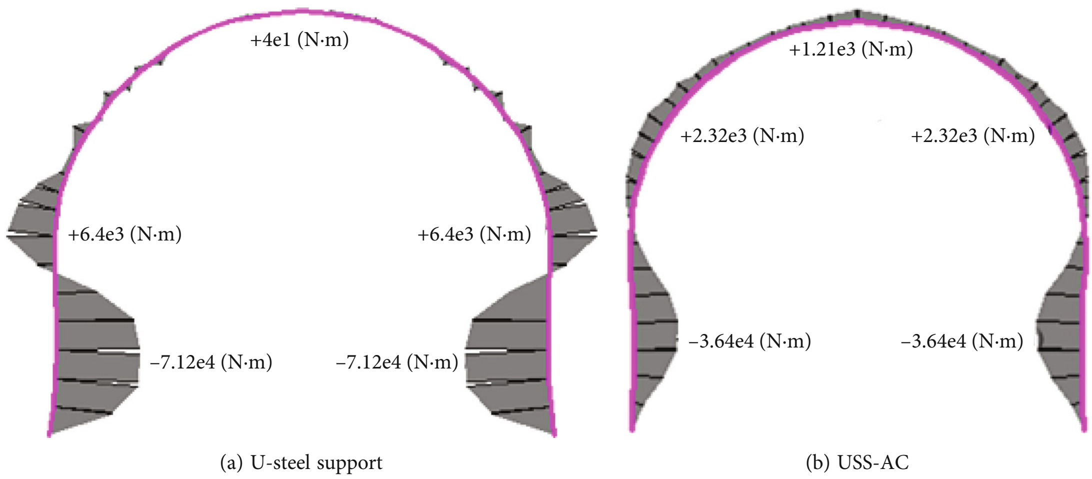

Figure 6: Bending moment distribution law of U-steel support under different support methods.

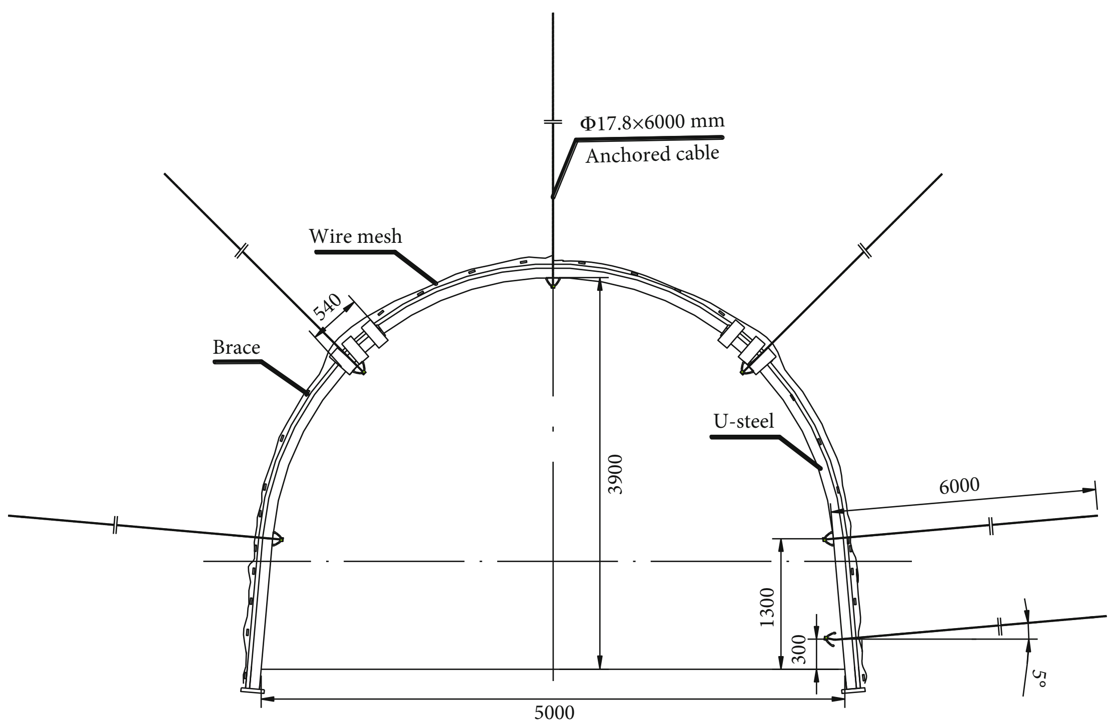

Figure 7: Layout of USS-AC with specific parameters in the case of test roadway.

beginning of monitoring process, the distances between datum points of the roof and floor and between datum points of both sides were measured by a laser distance measuring instrument as the initial value. And then, by subtracting each follow-up monitoring value from the initial value, the distance variation of roof-to-floor and side-to-side was determined and regarded as the convergence of test roadway.

5.2. Actual Load of the U-Steel Support. A hydraulic pressure pillow was adopted to survey the actual load of the U-steel support as shown in Figure 8. Before installing the hydraulic pressure pillow, a flat baseplate needed to be welded on the U-steel support. Further, a cover plate was installed between the hydraulic pressure pillow and the rock mass to ensure the overall contact and guarantee the accuracy of test results. After installation completion, the display value of hydraulic pressure pillow was recorded.

5.3. Actual Load of Anchored Cable. A dynamometer named MGH-30 was adopted to conduct nondestructive monitoring for actual load of exterior end of anchored cable as Figure 9. Because of the supporting resistance of anchored cables applying on the surface of U-steel support by the device of joists, the pressure cells were installed among the joists and the anchorage devices so as to monitor the actual loads of anchored cables. During the operation, a specific number of preload were applied on the exterior end of

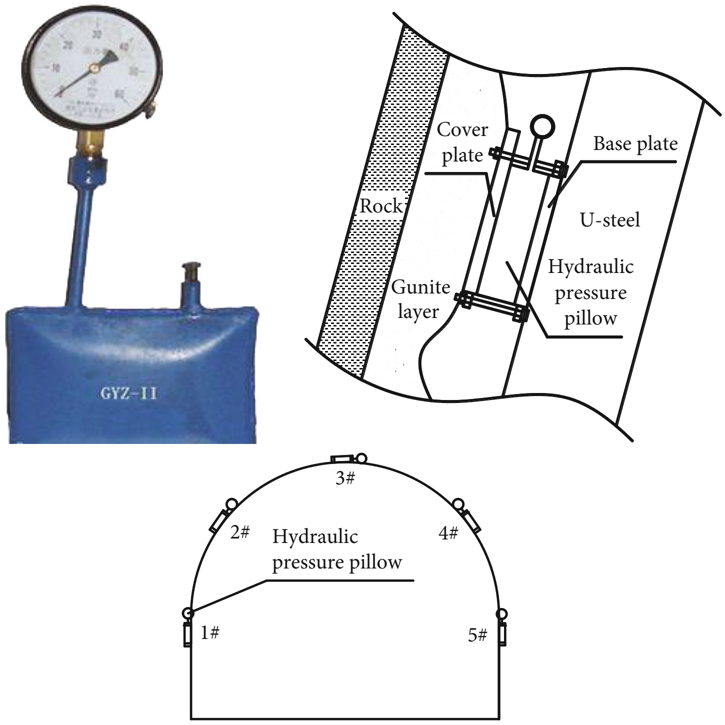

Figure 8: Layout of hydraulic pressure pillow of U-steel support.

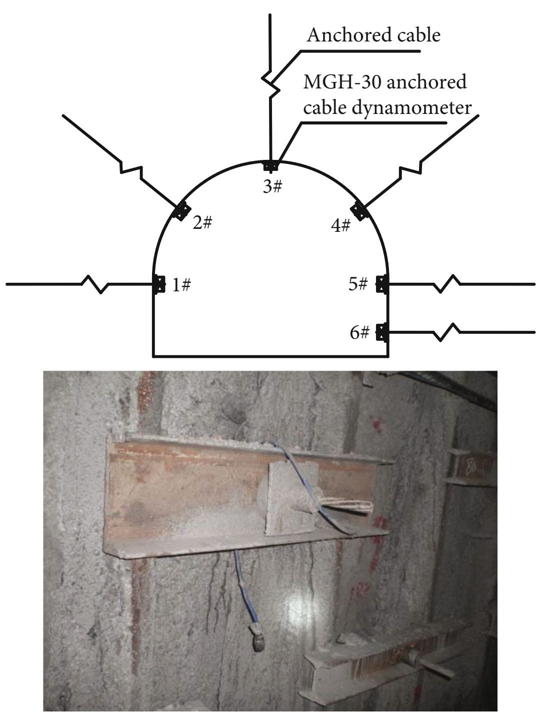

Figure 9: Layout and object diagram of anchored cable dynamometer.

anchored cable and recorded as the initial value. Afterwards, the hydraulic pressure pillows arranged on the U-steel support as well as the load of anchor cables were monitored at regular intervals.

6. Deformation Features of Test Roadway Subjected to Mining-Induced Stresses

The displacement feature of surrounding rock near to the excavation space of roadway was the composite indicator to reflect the stability of test roadway. Figure 10 shows the relationships among developing processes of displacement and its rate with the location of working face $\text{II}7_2 14$ from the beginning influence of the mining-induced stresses to the end. As shown in Figure 10, the negative value of the abscissa refers to the horizontal distance between the monitoring station and working face in the advancing direction of working face, while the positive value refers to the horizontal distance after that the working face has advanced through the monitoring station. The monitoring station is located about 200 m in front of the working face in the initial stage of measurement. And the deformation of roadway is gradually increased in a small rate without subjecting to mining-induced stresses. The deformation rate is 0.5 mm/d with a displacement sum of below 5 mm.

Thereafter, in the reduction process of distance between the monitoring station and working face from 180 m to 139 m, the displacement rate of roadway is converted into 0.3 mm/d with a displacement sum of below 10 mm. However, during the process of distance decreasing from 130 m to 39 m, the displacement rate of side-to-side and roof-to-floor is increased to 1 mm/d and above 0.5 mm/d, respectively. The displacement variation extent of side-to-side was larger than that of roof-to-floor. The main reason lies in that the distance from the upper working face to the monitoring station is large so as that the stress disturbance of side wall of test roadway is bigger than that of roof under

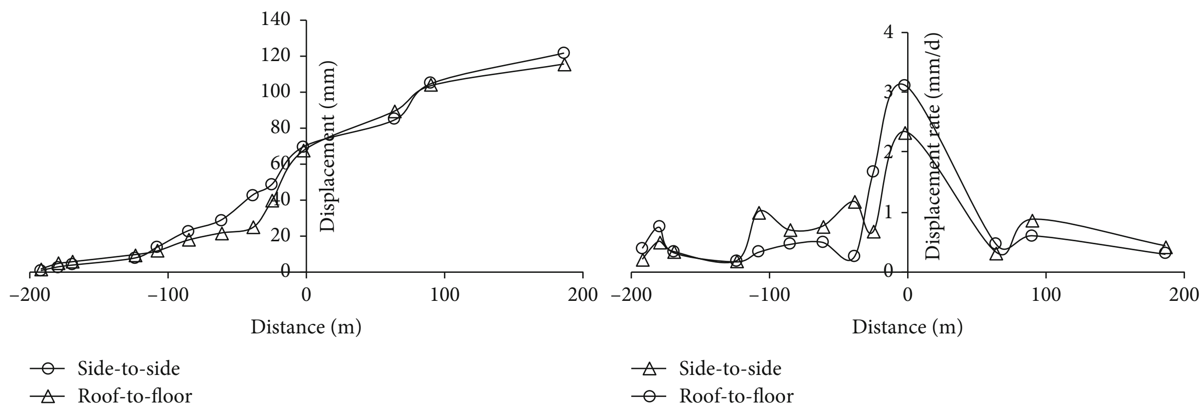

Figure 10: Displacement feature of test roadway subjected to mining-induced stresses.

mining-induced stresses. The integrity and strength of side wall rock are reduced significantly.

When the distance from the monitoring station to the working face is decreased from 39 m to 0 m, the displacement of surrounding rock is suddenly increased. The displacement rate of side-to-side is increased to 2.5 mm/d while that of roof-to-floor is increased to 3.2 mm/d. Although the displacement sum of roof-to-floor and that of side-to-side are approximately equal, the impacting degree of mining-induced stresses on the surrounding rock of roof is larger than that of side wall according to the displacement rate. That is because the working face is located right above the monitoring station so as to generate stronger impact on the roof of roadway. When the location of monitoring station has been advanced by the working face, the surrounding rock of roadway becomes more stable step-by-step along with the gradual increasing of distance between the working face and the monitoring station. Further, the displacement rate is gradually decreased to 0.5 mm/d.

7. Load Feature of USS-AC Subjected to Mining-Induced Stresses

7.1. Actual Load Feature of U-Steel Support. The actual load feature of U-steel support is shown as Figure 11. It can be seen that the variation of actual load is relatively small during the reduction process of distance between the monitoring station and the working face II$7_2$14 from 300 m to 180 m in the advancing direction of working face. The load of left side beam center of U-steel support is about 60 kN, while that of the left overlapping part is about 55 kN. The load, about 30 kN, is observed in the pressure cell installed at the right side beam center, right overlapping part, and arch beam. In sum, the left part of U-steel support including left side beam and left overlapping part suffers larger load than that of other parts. When the monitoring station is 180 m from the working face, the load of the right overlapping part is suddenly increased to 75 kN without significant variation in other segments of support. The loads of both overlapping parts of the U-steel support are gradually increased in the reducing process of distance from 120 m to 110 m; in other words, the load of the left overlapping part and that of right overlapping part varied, 70 kN and 85 kN,

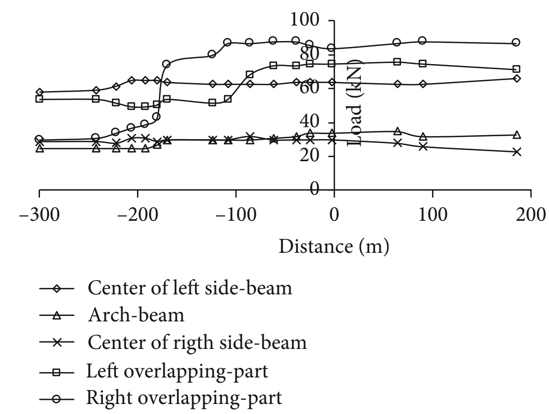

Figure 11: Developing process of actual load of U-steel support.

respectively. At the same time, the loads of other pressure cells of U-steel support were kept constant approximately.

7.2. Actual Load Features of Anchored Cables and USS-AC. The anchored cables directly contacted with the U-steel support via a joist. The supporting resistance of anchored cables is applied on the surface of U-steel support and transformed to the surrounding rock near the excavation of space of test roadway. In other words, the deformation features of U-steel support and sliding value of overlapping parts are reflected by the variation law of load in the exterior end of anchored cables. Meanwhile, the optimization actions of anchored cables on the U-steel support are obtained.

The relationship between the actual loads of USS-AC and convergence of roadway are shown in Figure 12. The developing process of actual loads of USS-AC is displayed undergoing the mining-induced stresses of working face II$7_2$14.

As shown in Figures 12(a) and 12(b), the load of left side beam center of U-steel support is about 60 kN, while that of right side beam center is 30 kN. And the loads of the centers of both side beams are relatively stable under the mining-induced stresses. However, the loads of the anchored cables are increased and larger than those of U-steel support along with the deformation of surrounding rock of roadway. And

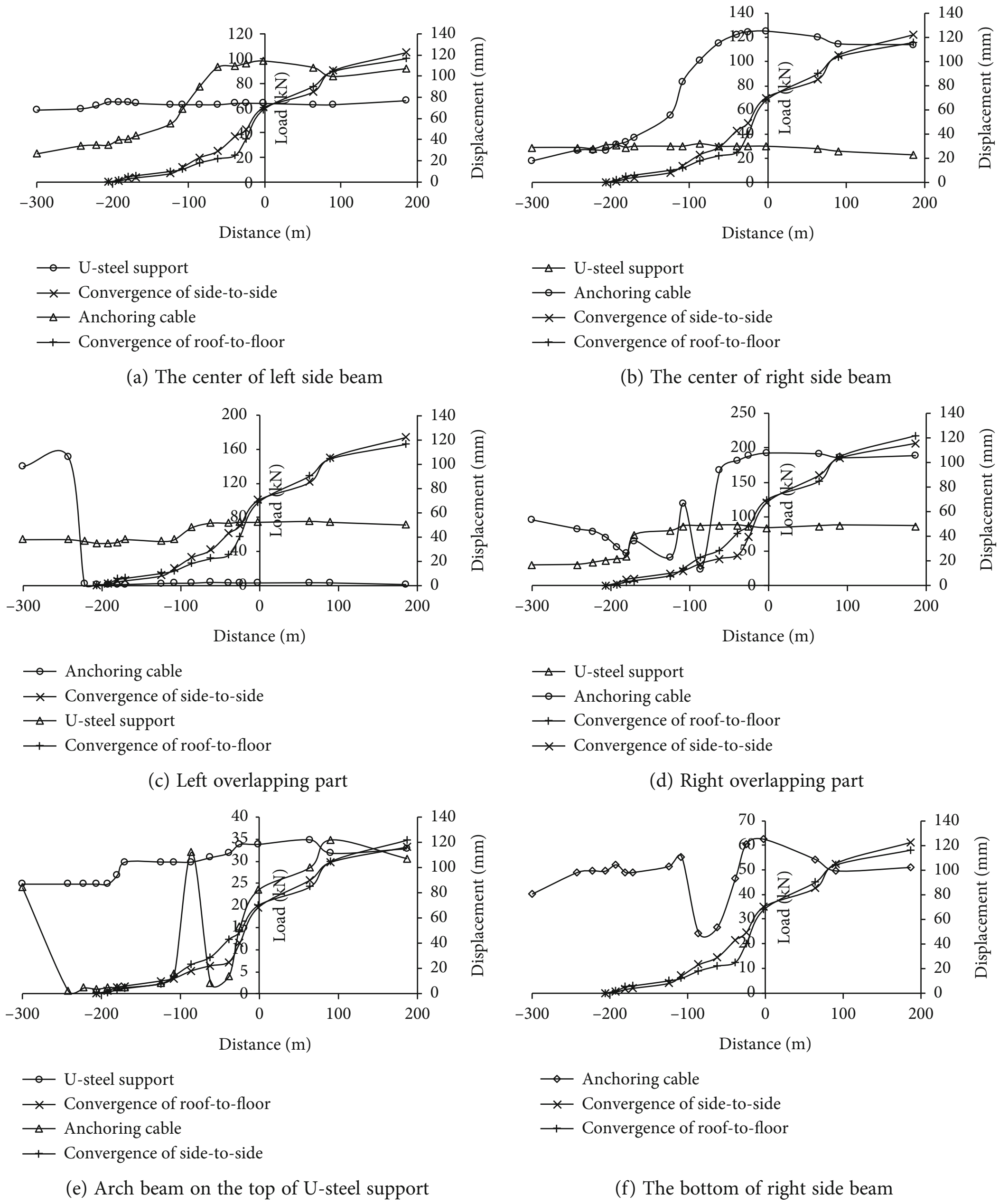

(a) The center of left side beam

(b) The center of right side beam

(c) Left overlapping part

(d) Right overlapping part

(e) Arch beam on the top of U-steel support

(f) The bottom of right side beam

Figure 12: Load development of the U-steel support and anchored cables.

the variation tendencies of load of anchored cables are similar to that of convergence of roadway. The maximum load (98 kN) is observed by a pressure cell installed in the center of the left side beam. Meanwhile, the load of the right side beam center is increased from 20 kN to 125 kN. From the previous phenomenon, both side beams are deformed gradually with the side-to-side convergence to release portion overload of U-steel support. The anchored cables become the main bearing body with their loads rising to restrain the oversize deformation of side beams and keep their loads stable. As a result, the violent deformation of surrounding rock is confined effectively by a combined manner of U-steel and anchored cables.

While the monitoring station is behind the working face in the advancing direction of working face, the loads of anchored cables in both side beams are decreased in a small extent. However, during the increasing to 90 m of distance between monitoring station and working face, the loads of two anchored cables are decreased in a small rate. Afterwards, the loads of cables were kept almost constant.

Figure 12(c) shows the relationship between the load of left overlapping part of U-steel support and that of the anchored cables during the deformation of roadway. The load of left overlapping part is changed from 55 kN to 75 kN at the beginning of influence of mining-induced stresses, and it was stable afterwards. However, the anchored cable is pretensioned with a load of 140 kN in the initial period. And then, the load of anchored cable is suddenly lessened to about zero behind an increased load of 18 kN and keeps below 5 kN. The reason of the phenomenon is analyzed as follows. There is sliding with friction in the left overlapping part to release the sinking movement of arch beam of U-steel support. And the left overlapping part is moved towards to the center of cross-section of roadway. The load of anchored cable is increased up to 158 kN so as to confine the overlapping part without movement. So, bending deflection is generated in the left overlapping part due to continuous deformation of left side beam and arch beam. The symmetry axis of bending deflection is located in the center of the overlapping part. The interval between the support and rock is smaller than that of the initial period result in decreasing the elongation and load of anchored cable in the left overlapping part. After that, there is no obvious increasement of the interval so as the load of anchored cable with a value below 5 kN.

The load developing process of right overlapping part of U-steel support and anchored cable is shown in Figure 12(d). The load of the right overlapping part of U-steel support is gradually increased from below 50 kN to about 80 kN and then tended towards stability. However, the load of the anchored cable is changed in fluctuation to indicate that the sliding and deformation of the right overlapping part is the most evident. From the beginning of load monitoring, there are three decreasing stages due to the declining of interval between support and rock. The reason of that has been explained. The increasing stage is generated after every decreasing stage. And the maximum load of anchored cable (192 kN) is appeared when the working face is located above the monitoring station. The phenomenon is caused by sliding and deformation of the right overlapping part of U-steel support. When the right overlapping part has been sliding, it has generated the movement to the center of roadway cross section and the interval between the support and rock is enlarged. Afterwards, the load of anchored cable is tended to be stable so as that the violent deformation of the right overlapping part of U-steel support is confined.

Figure 12(e) shows the load features of the arch beam and that of the anchored cable. The load of arch beam of U-steel support is constantly increased from 25 kN to about 35 kN. While the monitoring station is behind the working face in the advancing direction of working face, the load of arch beam was kept above 30 kN. However, the load of anchored cable is observed in a tendency with decreasing-increasing-decreasing-increasing stability. In the first stage, the convergence of side-to-side roadway is larger than that of roof-to-floor so as to make the center part of arch beam upward. The interval between it and the rock is smaller than that in the initial situation. So, the load of anchored cable is lessened from the start at 25 kN to below 5 kN. And the load remained at below 5 kN for a long time. When the working face is 90 m in front of the monitoring station, the load of the anchored cable is increased to 35 kN due to the sinking movement of the arch beam. At the same time, it is found that the load of anchored cable installed right overlapping part of the U-steel support is dramatically reduced by comparing with Figure 12(d). And then, it is correct that the bending deflection of the overlapping part of U-steel support is generated by the sinking movement of the arch beam. Afterwards, the load of anchored cable in the arch beam is lessened again, while that of the anchored cable in the right overlapping part of U-steel support is increased. Although there is some sinking of arch beam, the convergence of side-to-side is larger to compress and raise the center of arch beam again. Meanwhile, the raising movement is promoted by the sliding and deformation of right overlapping part of U-steel support. Therefore, the interval of between support and rock is smaller than that in the previous stage result in reducing the load of the anchored cable. In the following stages, the load of the anchored cable is gradually increased to 35 kN with a tendency similar to that of roadway deformation during the variation of distance between monitoring station and working face.

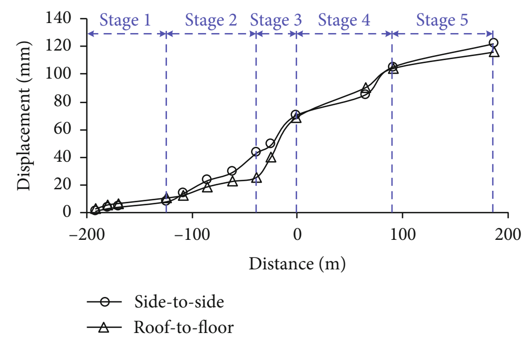

Figure 13: Developing process of deformation of test roadway.

Figure 12(f) shows the relationship between the convergences of roadway with the load of anchored cable installed in the bottom of the right side beam. The load of the anchored cable is gradually increased from 48 kN to 57 kN. When the monitoring station is 90 m in front of the working face, the load of the anchored cable is dropped below 30 kN. Along with a constant increasing of roadway deformation, the load of the anchored cable is increased to the maximum of 63 kN. When the working face is about 90 m in front of the monitoring station, the load of the anchored cable is reduced in a small extent and was kept constant in the following time.

8. Discussions

(1) The stages, extent, and scope of influence of mining-induced stresses: as shown in Figure 13, the deformation of the -720 south-wing track haulage roadway can be divided into 5 stages: stable deformation without mining influence (stage 1), slight deformation under advanced mining influence (stage 2), severely deformation under advanced mining influence (stage 3), slight deformation after mining influence (stage 4), and stable deformation after mining influence (stage 5). The developing process of roadway deformation is also reflected by the load features of USS-AC due to mining-induced stresses. Therefore, according to the space relationship

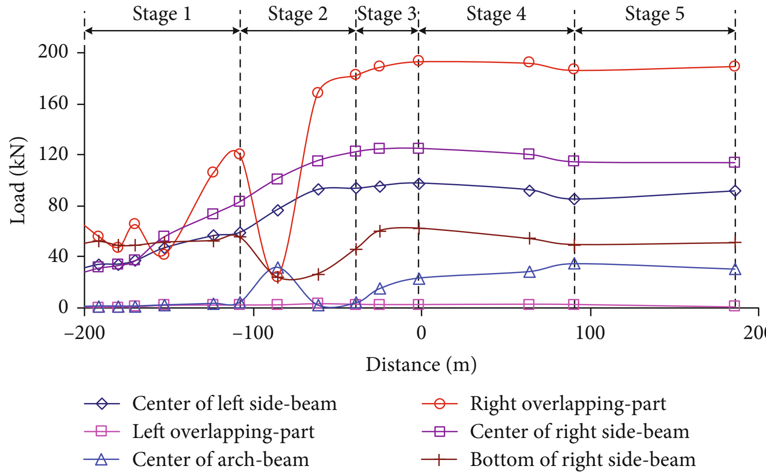

FIGURE 14: Load development of anchored cables.

between test roadway with working face II$7_2$14 and the geological conditions, the scope of advanced abutment pressure caused by the working face is about 140 m. And the influencing scope behind the working face is in a range of 80 m-90 m. The changing law of mining-induced stresses is essential to select the implementing time of extra reinforcing measures of roadway similar to the previous conditions.

(2) The bearing characteristics and implementing locations of anchored cables: in sum, the supporting resistance generated by USS-AC is applied to control the deformation of the -720 south-wing track haulage roadway during the excavation of working face II$7_2$14. The load of U-steel support is kept stable due to the restraining action of the anchored cables. However, the anchored cables installed in the right overlapping part and the center of two side beams are the main bearing bodies with high loads during the stage 3. And in this stage, the convergence of side-to-side of test roadway is larger than that of roof-to-floor. The influencing extent of mining pressure of the side wall of test roadway is heavier than that of the roof. If those anchored cables are removed, the destruction of U-steel support is generated in the right overlapping part and the center of two side beams firstly. Therefore, it can be seen that the anchored cables offer an extra load to optimize the bearing characteristics of U-steel support and increasing the load limit of collaborative reinforce system to confine the deformation of roadway. The changing law of USS-AC loads is significant to select the implementing location of extra reinforcing measures of roadway similar to the previous conditions.

(3) The deformation features and sliding movements of U-steel support: the anchored cables are contacted with U-steel support by joists. The load features of anchored cables are the direct reflection of the deformations or movements of different parts of U-steel support. As shown in Figure 14, in accordance to the cable load, each side beam of the U-steel support is displaced towards the space of test roadway at the 5 stages. The deformation of arch beam on the top is in a procedure of upward-downward-upward-downward. Analyzing the procedure, the upward movement with bending is generated at the center of arch beam because of continuous displacement of both side beams. Afterwards, there is downward movement of the entire arch beam. The deformation of overlapping part which includes sliding movement and bending deformation is related to that of arch beam and side beams. Among it, the bending deformation of overlapping part is produced to lessen the load of anchored cable under the sinking deformation of entire arch beam at the 2nd stage. Meanwhile, when the rock near to the overlapping part and side beam is displaced, there is sliding movement of overlapping part leading to increase the load of anchored cable. The deformation law of different segments of U-steel support is revealed by qualitatively inverse analysis of loads of anchored cables. The results are useful to optimize the installing location of extra anchored cables.

However, there are several issues to be studied as follows: (a) quantitative analysis on the loads relationship between U-steel support and anchored cables by using a theoretical model and (b) building a precisely numerical model of U-steel support and analyzing its response characteristics under various conditions of load.

9. Conclusions

(1) The distribution of stress in the surrounding rock is changed to increasing the residual strength of rock near to the space of roadway by using USS-AC. The extra supporting resistance is supplied by

anchored cables to optimize the moment distribution and enhance the nondeformability and the global stability of the U-steel support. And then, the deformation of roadway is significantly restrained. According to the result of monitoring, both the convergence of side-to-side and that of roof-to-floor are below 120 mm to satisfy the requirement for usefulness of test roadway during the influence process of mining-induced stresses

(2) According to the loads of anchoring cables, the high deformation loads are generated at the right overlapping part and the centers of two side beams undergoing severe mining-induced stresses. And, the anchoring cables are the main bearing bodies with supporting resistance above 100 kN to control the displacement of the right overlapping part and two side beams of U-steel support. Increasing load limit and stiffness of side beams are significant to enhance the bearing ability of arch beam

(3) As an integral structure, the U-steel support is confined to the limited deformation space owing to extra action of anchoring cables. Excessive deformations of arch beam and side beams are released through the sliding movements of overlapping parts of U-steel support so to realize the properties of high resistance and contractibility of the U-steel support

Data Availability

The data is from the project of Renlou Coal Mine in the north of Anhui Province of China.

Conflicts of Interest

The authors declare that they have no conflicts of interest.

Acknowledgments

This study was supported by the National Natural Science Foundation of China (51704218, 51709208, and 51874218) and the National Key R&D Program of China (Grant No. 2019YFC0605304). We are very grateful to the staff of Renlou Coal Mine for the cooperation.

References

[1] H. P. Kang, G. F. Wang, P. F. Jiang et al., "Conception for strata control and intelligent mining technology in deep coal mines with depth more than 1000m," *Journal of China Coal Society*, vol. 43, no. 7, pp. 1789–1800, 2018.

[2] H. P. Kang, P. F. Jiang, J. W. Yang et al., "Roadway soft coal control technology by means of grouting bolts with high pressure-shotcreting in synergy in more than 1000m deep coal mines," *Journal of China Coal Society*, vol. 46, no. 3, pp. 747–762, 2021.

[3] C. J. Hou and P. F. Gou, "Mechanism study on strength enhancement for the rocks surrounding roadway supported by bolt," *Chinese Journal of Rock Mechanics and Engineering*, vol. 19, no. 3, pp. 342–345, 2000.

[4] N. Zhang and M. S. Gao, "High-stress and pretension bolting support of coal roadway and its application," *Journal of China University of Mining and Technology*, vol. 33, no. 5, pp. 524–527, 2004.

[5] H. P. Kang and J. H. Wang, *Rock Bolting Theory and Complete Technology for Coal Roadways*, China Coal Industry Publishing House, Beijing, 2007.

[6] H. P. Kang, J. Lin, Y. Z. Wu, P. Cheng, X. Z. Meng, and S. Ren, "Mechanical performances and compatibility of rock bolt components," *Journal of China Coal Society*, vol. 40, no. 1, pp. 11–23, 2015.

[7] H. P. Kang, P. F. Jiang, B. X. Huang et al., "Roadway strata control technology by means of bolting-modification-destressing in synergy in 1000m deep coal mines," *Journal of China Coal Society*, vol. 45, no. 3, pp. 845–864, 2020.

[8] W. B. Xie, S. G. Jing, T. Wang, Y. K. Ren, and N. Zhang, "Structural stability of U-steel support and its control technology," *Chinese Journal of Rock Mechanics and Engineering*, vol. 29, no. S2, pp. 3743–3748, 2010.

[9] S. G. Jing, *Study on Control Mechanism of Cooperating Support of Support and Anchored Cable in Soft Fragmentized Surrounding Rock Roadway with High Stress [Ph. D. Thesis]*, China University of Mining and Technology, Xuzhou, 2009.

[10] Q. Z. Wang, W. B. Xie, S. G. Jing, L. Zang, and N. Zhang, "Research on U-shape steel frame anchor cable collaborative support mechanism and loading law of roadway under dynamical pressure impact," *Journal of China Coal Society*, vol. 40, no. 2, pp. 301–307, 2015.

[11] C. A. You, "Stability analysis of U-steel yieldable support," *Chinese Journal of Rock Mechanics and Engineering*, vol. 21, no. 11, pp. 1672–1675, 2002.

[12] C. A. You, "Internal force calculation of U-supports considering yielding," *Chinese Journal of Geotechnical Engineering*, vol. 22, no. 5, pp. 604–607, 2000.

[13] J. Z. Liu, N. Zhang, X. G. Zheng, and B. G. Wang, "Research on buckling failure mechanism of U type steel support loaded deviating longitudinally," *Journal of Coal Science & Engineering*, vol. 36, no. 10, pp. 1647–1652, 2011.

[14] C. A. You, *Computing Theory on Steel Support of Roadway*, China Coal Industry Publishing House, Beijing, 2000.

[15] L. Tian, W. B. Xie, S. G. Jing, Y. D. Xing, and J. P. Peng, "Framed timber and anchor coupling collective support technology for fully mechanized top coal mining face crossing over gateway," *Coal Science and Technology*, vol. 39, no. 11, pp. 44–47, 2011.

[16] D. H. Wang, H. R. Guo, H. Zhao, and Y. W. Guo, "Analysis of influences of weak joints and confining pressure on rock-mass strength by numerical simulation," in *Applied Mechanics and Materials*, vol. 438, pp. 607–611, Trans Tech Publications, Ltd., Oct, 2013.

[17] Y. Gan, S. Gan, and X. Zhen, "Study of the influence of joint on the triaxial compression strength," *Science Technology and Engineering*, vol. 12, pp. 9861–9864, 2012.

Hindawi
Geofluids
Volume 2021, Article ID 2530909, 8 pages
https://doi.org/10.1155/2021/2530909

Research Article

Study on Influence of Cavity and Water Mist on Flame Propagation of Gas Explosion in a Pipeline

Shicheng Gu[1,2] **Shujie Yuan**[1,2] **Zhuo Yan**[1,2,3] **and Xiaoxue Xu**[2]

[1]*State Key Laboratory of Mining Response and Disaster Prevention and Control in Deep Coal Mines, Anhui University of Science and Technology, Huainan, Anhui 232001, China*
[2]*School of Safety Science and Engineering, Anhui University of Science and Technology, Huainan, Anhui 232001, China*
[3]*Institute of Energy, Hefei Comprehensive National Science Center, Hefei, Anhui 230031, China*

Correspondence should be addressed to Zhuo Yan; 37571616@qq.com

Received 16 July 2021; Revised 31 August 2021; Accepted 1 September 2021; Published 4 October 2021

Academic Editor: Yong-Zheng Wu

For studying the influence of the cavity and water mist on the flame propagation of gas explosion, a rectangular steel cavity of size of length 80 cm × width 50 cm × height 20 cm was designed. The influence of the cavity and it with water mist on explosion flame propagation in a large circular gas explosion system with a length of 34 m was studied. The change of gas explosion flame in the pipeline was analyzed. The results showed that the intensity and flame propagation velocity increase after the explosion flame passes through the straight pipeline, and the attenuation rates are 4.93% and -2.48%, respectively. After the explosion flame passes through a rectangular cavity of length 80 cm × width 50 cm × height 20 cm, its intensity and propagation speed are inhibited, and the attenuation rates are 66.58% and 45.26%, respectively. After the explosion flame passes through the rectangular cavity of the size of length 80 cm × width 50 cm × height 20 cm with water mist, the intensity and propagation speed are inhibited much more, and the attenuation rates are 85.09% and 65.85%, respectively. The influence of the cavity with water mist on flame attenuation of gas explosion is better than that of the cavity alone. Based on theoretical analysis, it is concluded that the inhibition influence of the cavity on explosion flame propagation is mainly due to repeated reflection of flame in the cavity, which results in the attenuation of its energy. The inhibition influence of water mist is mainly due to its heat absorption by vaporization.

1. Introduction

The gas explosion accident is one of the most destructive accidents in coal mine production in China. Although the safety level of China's coal mining production has been greatly improved in recent years, gas explosion accidents still happen from time to time [1, 2].

The mechanism of gas explosion, its suppression, and mitigation have been studied by many scholars. Yu et al. [3] implemented a comparative experimental research on the explosion flame propagation characteristics of CH_4-air mixture with different volume fractions, by using the self-built small-scale experimental platform. The results indicated that when the methane volume fraction is 9.5%, the wave pressure and explosion flame propagation velocity are the highest. Yu et al., Wen et al., and Yu et al. [4–7] studied the effect of obstacles on the propagation characteristics of gas explosion. Cao et al., Song and Zhang, and Yu et al. [8–14] researched the influence of water mist particle size, spray volume, water mist zone length, and additives on the inhibition influence of water mist in gas explosion suppression by experiments. The results showed that when the particle size of ultrafine water mist is within 10 μm to 15 μm, the inhibition effect of explosion intensity and the methane-air mixture explosion flame propagation velocity is the best. When the concentration of superfine water mist is below 1.5 kg/m^3, its inhibition effect on gas explosion overpressure is not obvious. The water mist reduces the flame temperature largely by absorbing the heat of combustion and rapidly evaporating. Shao et al. [15] found in the experiments that the inhibition effect of a vacuum cavity on gas explosion is related to the volume of the cavity. When the actual volume of the vacuum cavity is larger than the critical volume, it has the inhibition effect on the explosion; otherwise, it enhances explosion propagation to some extent. Wang et al. and Su et al. [16, 17] have concluded through experimental research that ethylene and hydrogen can increase the maximum explosion pressure, laminar combustion rate, and maximum pressure rise rate of methane-air mixture, while it shortens the combustion time. Li et al. and Yan et al. [18, 19] designed rectangular steel cavities with different aspect ratios and installed them in a 36 m long large-scale round pipeline of gas explosion test system. The experiment results showed that the cavity has an inhibition effect on the gas explosion propagation, and the effect of explosion inhibition is related to the volume of the cavities, their aspect ratios, etc. The relationship between the methane explosion peak overpressure attenuation factor y and the aspect ratio x of the cavity is as the following: $y = -1.149\exp(x/10.089) + 2.405$. When the attenuation factor of peak overpressure is 1, the value of the aspect ratio is the critical. When the aspect ratio of the cavity is not more than 1, the cavity has an inhibition effect on the explosion wave overpressure, and the best aspect ratio for inhibition effect is 1/10. When the aspect ratio of the cavity is greater than 1, it enhances the explosion wave overpressure, and the cavity with an aspect ratio of 5/2 has the most enhancing effect on the explosion wave overpressure. Li et al. [20] studied the effects of hydraulic pressure on mechanical behavior, pore size distribution, and permeability.

For the study of gas explosion suppression and its disaster reduction, the small-scale test platforms have been mostly used, but the large-scale test platforms are not much applied. In order to further research the influence of a cavity with water mist on the flame propagation of gas explosion in a large-scale experimental pipeline system, in the paper, theoretical analysis and experimental research were used.

2. Theoretical Analysis of Influence on Gas Explosion Propagation Process

2.1. The Propagation Mechanism of Gas Explosion. The propagation mechanism of gas explosion is the feedback mechanism of the precursor shock wave created by the explosion flame to the heating and compression of the unburned premixed gas. In the process of premixed combustion of a substance, the reaction zone separates the glowing combustion products from the unburned premixed combustibles, as shown in Figure 1 [21]. From the results of combustion, it can be seen that T_0 and C_{A0} of the premixed combustible gas are transformed into T_f and C_{Af} of the reaction products after combustion, and they are separated by combustion wave in space.

According to the combustion theory of premixed flame, the turbulent premixed flame velocity S_T is expressed as the ratio of the volume flow q_v of the combustible premixed gas flowing through the flame to the apparent area A_f of the turbulent flame, as shown in:

$$S_T = \frac{q_v}{A_f}. \tag{1}$$

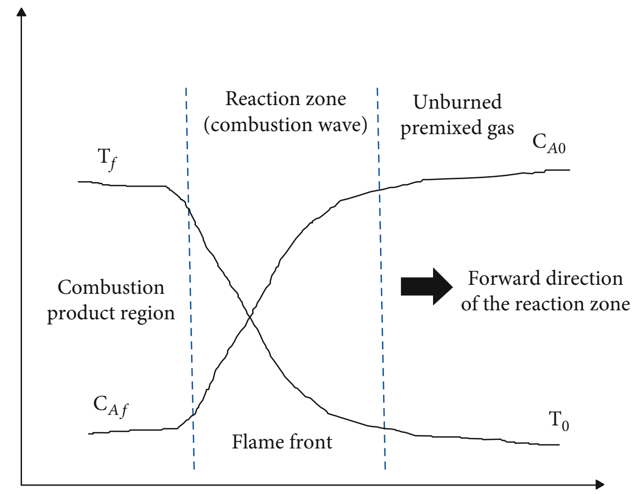

Figure 1: Combustion wave propagation process.

The main reaction of premixed gas/air explosion is shown in the following equation:

$$CH_4 + 2\left(O_2 + \frac{79}{21}N_2\right) = CO_2 + 2H_2O + 7.52N_2. \tag{2}$$

The above chemical reaction formula only expresses the final result of gas explosion. Many studies show that gas explosion is a very intricate chain reaction. When premixed CH_4/air absorbs a certain amount of heat, the molecular chain breaks and turns into free radicals. Then, the free radicals become the reaction activation center. Under the right conditions, the free radicals will continue to decompose, and as the number of free radicals increases, the reaction will become faster and faster, resulting in an explosion.

2.2. Theoretical Analysis of the Effect of Cavity on Flame Propagation of Gas Explosion. It is assumed that the mixture of CH_4 and air is uniform, and relatively static after, the mixture was prepared in the experimental pipeline system. The flame will spread to the two ends, and the periphery of the round pipeline with the ignition source as the detonation center after the mixture is ignited. At this point, the wall of the pipeline will interfere with the flame propagation, and the laminar flame will become turbulent propagation, which will lead to the distortion of the flame front and increase the flame burning speed. After the flame enters the cavity, part of the flame comes out from the cavity to form a primary flame, and the other part of the flame is stirred and mixed in the cavity to form a secondary flame. When the flame passes through the cavity, because of the influence of the cavity disturbance, the primary flame intensity attenuates and the secondary flame intensity increases. However, with the increase of the cavity length, the magnitude of the secondary flame increase decreases, and the time interval of the secondary flame also increases, and the overall attenuation of the flame front is positively correlated with the length of the cavity. Yan et al. [22] studied the mechanism of gas explosion suppression by the cavity by simulating the propagation process of gas explosion shock wave and flame in cavity. According to the method described in reference [22], the mode of the gas explosion flame premixing in the cavity is shown in Figure 2.

2.3. Theoretical Analysis of the Influence of Water Mist on Gas Explosion Propagation. Lentati and Chelliah [23] found through research that the water mist mainly inhibits explosion through physical effect, and its influence through chemical effect is less than 10%. Therefore, in the paper, only its related physical effects were analyzed. The main physical effects of the water mist include heat absorption by vaporization and energy absorption, which mainly effect on the explosion flame. According to the calculation, when the size of the droplet d is less than 200 microns, the spray speed V is less than 30 m/s, the mass concentration Q of water mist is less than 899 g/m^3, and the rate of absorption of flame energy by the droplets is far less than the order of magnitude of the latent heat of vaporization and the sensible heat absorption rate. So the suppression effect of water mist on the flame is mainly based on its heat absorption.

3. Experimental Study

The influence of the cavity and it with water mist on the flame propagation of gas explosion was studied by monitoring the parameters of the explosion flame in the gas explosion experiment system.

3.1. Experimental System. A large-scale gas explosion experiment system with a 34 m-long pipeline is shown in Figure 3. The experiment system consists of five parts: explosion experiment pipeline subsystem, ignition subsystem, gas distribution subsystem, data acquisition and storage subsystem, and explosion suppression subsystem. In the study, the large-scale experimental pipeline system consists of 34 m long circular pipeline and separately installed in it a straight pipe with the length of 50 cm and the diameter of 20 cm, a rectangular steel cavity of length 80 cm × width 50 cm × height 20 cm, or a rectangular steel cavity with length 80 cm × width 50 cm × height 20 cm. The experimental conditions are shown in Table 1. The purpose is to find the influence of the cavity alone or the cavity with water mist on the propagation of gas explosion to provide a reference for studying the suppression of the methane-air mixture explosion.

(1) Explosion experiment pipeline subsystem is made of steel round pipes with a thickness of 0.01 m, diameter of 0.2 m, and compressive strength of 20 MPa, which are connected by flanges and bolts and nuts. The air tightness is guaranteed by rubber gasket between the flange plates. (2) The ignition subsystem is composed of power supply, wire, ignition electrode, and electric fuse. The ignition electrode is installed on the flange plate of the end side of the experiment pipeline system, and the electric fuse is used for ignition. (3) The gas distribution subsystem is composed of methane bottle, connecting pipe, vacuum pump, circulating pump, digital vacuum pressure gauge, and so on. The concentration of methane used in the experiment is not less than 99.9%. (4) The data acquisition and storage subsystem is composed of sensors, computer, high-speed data acquisition units, transmitters, and so on. The flame sensors $F1$, $F2$, $F3$, and $F4$ are CKG100 flame sensors, which are located at 11.200 m from the explosion ignition electrode (30 cm from the entrance of the cavity), 11.250 m from the explosion ignition electrode (25 cm from the entrance of the steel cavity), $(11.700 + X)$ m from the explosion ignition electrode (20 cm from the exit of the steel cavity), and $(11.750 + X)$ m from the ignition electrode (0.250 m from the exit of the steel cavity), respectively, where X is the length of the cavity, and the unit is converted to meters. The acquisition software is DAP7.30 transient signal test and analysis software developed by Chengdu Tester Company. (5) The explosion suppression subsystem is composed of a rectangular steel cavity of the size of 0.8 m × 0.5 m × 0.2 m or the cavity with water mist. The experiment site is shown in Figure 4.

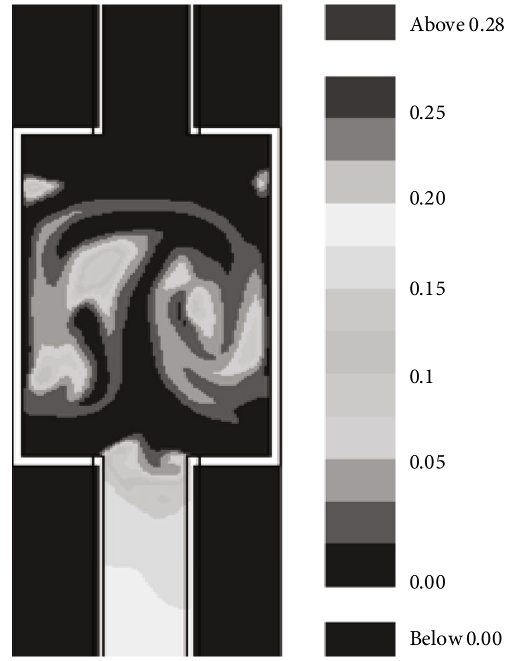

Figure 2: The simulation diagram of secondary flame formation in gas explosion in cavity.

3.2. The Experiment Process. Set up the large-scale gas explosion experiment system as shown in Figure 3. Install the polyethylene diaphragm and the flame sensors $F1$, $F2$, $F3$, and $F4$. The experiment was conducted as follows:

(1) *Check the Air Tightness of the Experiment System.* The ignition electrode was sealed, the experiment system was pumped to -20PV by vacuum pump, and then waited 5-10 min to observe the negative pressure of the experiment system, if there is no change, it shows that the air-tightness of the experiment system is good and the experiment begins

(2) *Install the Ignition Electrode.* Wrap the front end of the ignition electrode around a few fuse so that the two electrodes form a path. Place the fuse-mounted ignition electrode in the position shown in Figure 3

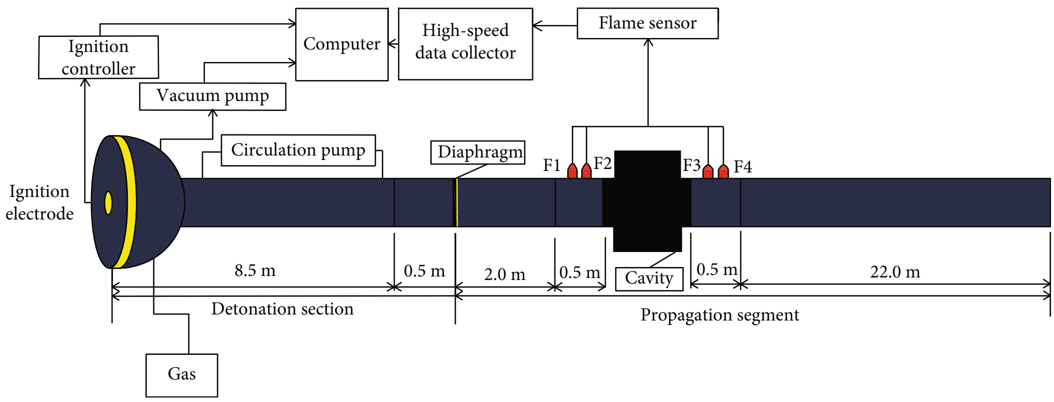

Figure 3: The schematic diagram of gas explosion experiment system.

Table 1: The working conditions in the experiments.

Working condition number	Experimental condition setting
1	A straight pipe with a diameter of 20 cm (straight pipe)
2	Installed a cavity with a length, width, and height of 80 cm × 50 cm × 20 cm
3	Attached with a cavity with a length, width, and height of 80 cm × 50 cm × 20 cm with water mist

Figure 4: The experiment site.

(3) *Gas Distribution*. Dalton partial pressure method was used for gas distribution. First, a vacuum pump was used to vacuum the experimental system to make the system pressure reach −20 PV (the maximum negative pressure of the polyethylene membrane used in the experiment was measured as -25 PV). Then, the experimental system is filled with methane gas with a concentration greater than 99.9%, and stop filling methane gas when the system pressure rises to -10 PV. Open the valve to allow air to enter the experiment system and close the valve when the pressure in the system rises to 0 PV, and a mixture of gas with a methane concentration of 10% was prepared (according to theoretical analysis, the gas concentration of 9.5% is the concentration of the maximum explosion intensity under the experimental conditions) [6]. Because the experiment precision is accurate to 1%, so the concentration of CH_4 in the gas mixture was prepared as 10%

(4) *Premixed the CH_4/Air Mixture*. The specific steps are as follows: when the gas distribution finished, open the circulating pump and circulate the CH_4/air mixture for about 15 minutes, so that the methane gas and the air are fully mixed

(5) *Spray Mist in the Cavity*. 1-2 minutes before detonation, turn on the sprayer. Close the sprayer until the explosion process is complete. The model of high pressure atomizing pump is NS-KL04750. The nozzle is 0.20 mm in diameter, and the spray volume is 0.117-0.155 L/min. The spray direction is from the upper part of the cavity to its lower part

(6) *Detonation and Data Acquisition*. The mixture was ignited by ignition device, and the ignition energy is 10 J. The experimental data were collected and saved by DAP7.30 transient signal test and analysis software, flame sensors, and computer

(7) At the end of the experiment, the exhaust gas in the pipeline was swept by an air compressor

Under experimental conditions 1 or 2, the experiment was implemented according to steps 1-4, 6, and 7. Under experimental conditions 3, the experiment was implemented according to steps 1-7.

3.3. The Experiment Results and Analysis. The explosion flame intensity is defined as the integral value of the flame light signal on the time coordinate axis [22]. The attenuation

Table 2: The results in the experiments.

Working condition number	The flame intensity at $F2$	The flame intensity at $F3$	The explosion flame propagation velocity from $F1$ to $F2$ (m/s)	The explosion flame propagation velocity from $F3$ to $F4$ (m/s)
1	0.07813	0.07428	570.13	584.25
2	0.05134	0.01716	575.00	314.78
3	0.04535	0.00676	573.21	195.75

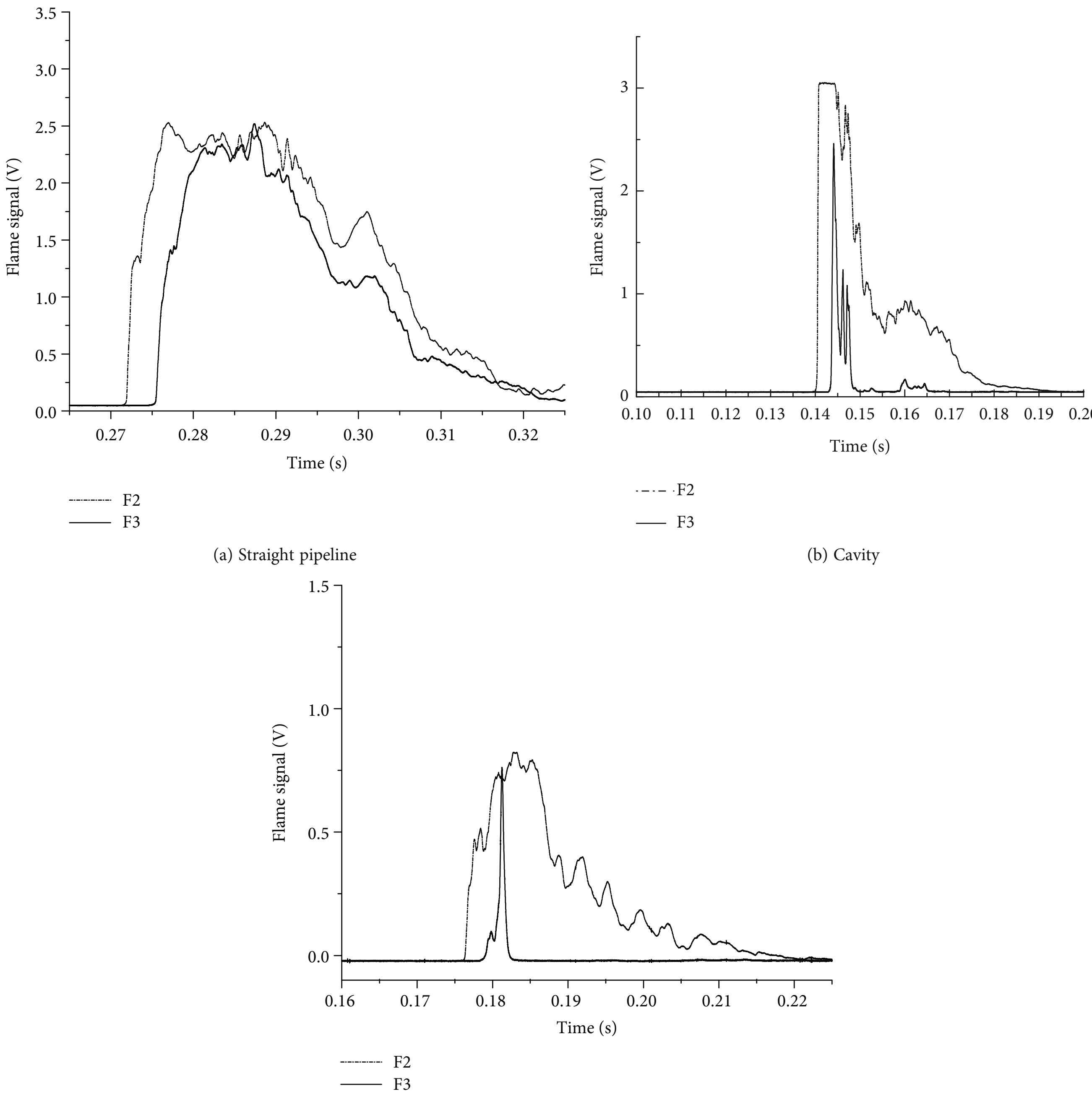

(a) Straight pipeline

(b) Cavity

(c) Cavity with water mist

Figure 5: Explosion flame intensity signal at measuring points $F1$ and $F3$ under different working conditions.

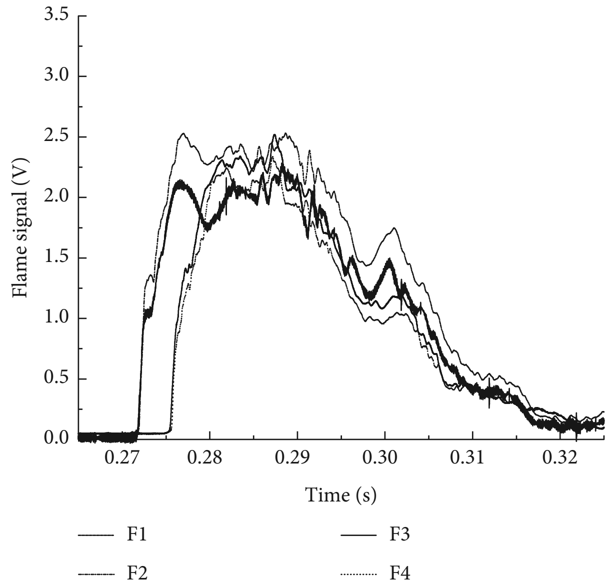

(a) Straight pipe

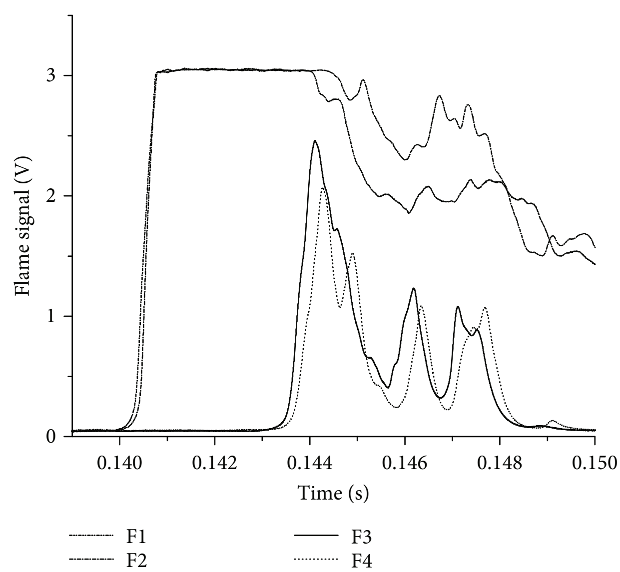

(b) Cavity

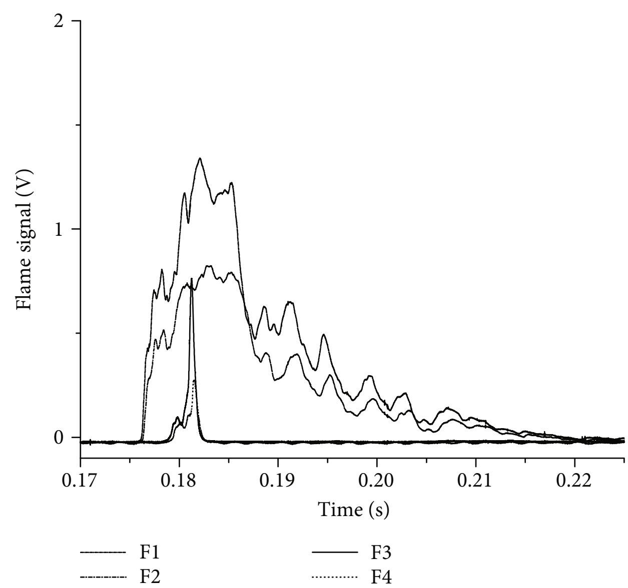

(c) Cavity with water mist

Figure 6: Explosion flame velocity signal information of measuring points $F1$, $F2$, $F3$, and $F4$ under different working conditions.

rate of the flame strength is the ratio of attenuation value ΔS of the flame intensity from $F1$ to $F2$ to the explosion flame intensity at $F1$. The flame propagation velocity is defined as the ratio of the distance S between the two flame sensors to the time interval Δt between signals received by the two sensors, that is, $V_1 = S_{F1-F2}/\Delta t$, $V_2 = S_{F3-F4}/\Delta t$, the attenuation rate of flame speed $\eta_v = (V_1 - V_2)/V_1$. The experimental results are shown in Table 2.

3.3.1. The Variation of Flame Intensity of Gas Explosion under the Three Experiment Conditions. After the mixture gas exploded in the experimental device, the evolution process of the flame at measuring point $F2$ and $F3$ with time is shown in Figure 5. The influence of experiment condition 1 on flame propagation of gas explosion was presented in Figure 5(a). According to Figure 5(a), the flame intensity at $F2$ is 0.07813, and the flame intensity at $F3$ is 0.07428. The attenuation rate of flame intensity from $F2$ to $F3$ is 4.93%. Therefore, the methane explosion flame intensity is enhanced after it passes through the straight pipeline. The influence of experiment condition 2 on flame propagation of gas explosion was shown in Figure 5(b). According to Figure 5(b), the flame intensity at $F2$ and $F3$ is 0.05134 and 0.01716, respectively. The attenuation rate of explosion flame intensity from $F2$ to $F3$ is 66.58%, which indicates that the cavity has a suppression effect on the flame intensity. The influence of experimental condition 3 on flame propagation of gas explosion was presented in Figure 5(c).

According to Figure 5(c), the flame intensity at $F2$ and $F3$ is 0.04535 and 0.00676, respectively. The attenuation rate of flame intensity from $F2$ to $F3$ is 85.09%. The experiment condition 3 has a suppression influence on flame propagation. The cavity with water mist has better effect on inhibition of explosion flame propagation than the cavity alone.

3.3.2. The Variation of Flame Propagation Velocity of Gas Explosion under Three Working Conditions. After the mixture gas exploded in the experimental device, the evolution of the flame at each measuring point $F1$, $F2$, $F3$, and $F4$ is shown in Figure 6. It can be seen from Figure 6(a) that the influence of experimental condition 1 on the explosion flame propagation velocity was explored. The explosion flame propagation velocity $V1$ from $F1$ to $F2$ is 570.13 m/s, and the explosion flame propagation velocity $V2$ from $F3$ to $F4$ is 584.25 m/s. The explosion flame propagation velocity decay rate from $V1$ to $V2$ is -2.48%, so the explosion flame velocity increases after the explosion flame passes through the straight pipe. According to Figure 6(b), the influence of experimental condition 2 on the methane explosion flame propagation speed was explored. The methane explosion flame propagation speed $V1$ from $F1$ to $F2$ is 575.00 m/s, and the explosion flame propagation velocity $V2$ from $F3$ to $F4$ is 314.78 m/s. The explosion flame propagation velocity decay rate from $V1$ to $V2$ is 45.26%. Compared with a pure straight pipe, the cavity has a suppression effect on the methane explosion flame propagation velocity. According to Figure 6(c), the influence of experimental condition 3 on the methane explosion flame propagation speed was explored. The methane explosion flame propagation speed $V1$ from $F1$ to $F2$ is 573.21 m/s, and the methane explosion flame propagation speed $V2$ from $F3$ to $F4$ is 195.75 m/s. The explosion flame propagation velocity decay rate from $V1$ to $V2$ is 65.85%. Compared with the pure straight pipe, the explosion flame propagation velocity is inhibited under the experimental conditions. Compared with experimental condition 1, experimental condition 2 only has a cavity to suppress the methane explosion flame propagation speed. Compared with experimental condition 1, experimental condition of cavity combined with water mist has a stronger suppression effect on the methane explosion flame velocity, and it is better than the restraining effect of only attaching a cavity.

3.4. Analysis of Explosion Suppression by Coeffect of Cavity and Water Mist. After the explosion flame enters the cavity, it expands and dissipates. When it propagates at the outlet, part of the methane explosion flame passes out of the steel cavity, and the other part is blocked by the walls of the cavity and reflected, forming a reverse explosion flame and propagating in the opposite direction. Due to the different reflection angle, part of the reverse explosion flame enters the steel cavity inlet and passes out of the cavity after being superposed. The reverse explosion flame that cannot enter the inlet of the cavity is blocked by the walls of the cavity. The flame is reflected again and propagates toward the outlet. This process is repeated so that the flame disappears as the premixed gas is exhausted. Therefore, the flame of explosion attenuates obviously after passing through the cavity, and the functions of flameout and wave elimination are realized.

The coeffect of cavity and water mist increases the effect of flame suppression because of the reasons such as (1) when the flame enters the cavity, the temperature of the water mist is lower than that of the explosion flame, and heat transfer occurs between water mist and methane explosion flame, resulting in the temperature of the flame decrease. (2) The water mist with high density in the confined space of the cavity can cool down the temperature and isolate the oxygen, so that the enhancement of the secondary flame in the cavity is weakened and the explosion flame is suppressed. (3) As an inert droplet, water can directly interfere with the chemical reaction in the explosion reaction zone, and thus, has the effect of chemical inhibition. The suppression effect of the flame propagation velocity is better because the water mist forms a “water wall” in the cavity, which hinders the explosion flame propagation, thus, resulting in greater inhibition effect on the methane explosion flame propagation speed.

4. Conclusions

(1) The attenuation rate of the explosion flame intensity by using the cavity with the aspect ratio of 5/8 is 66.58%, and the attenuation rate of the flame propagation velocity is 45.26%. The attenuation rates by using the cavity increased by 61.65% and 47.74%, respectively, compared with those in the straight pipelines

(2) The attenuation rate of the methane explosion flame intensity under the coeffect of the cavity with the aspect ratio of 5/8 and the water mist is 85.09%, and the attenuation rate of the flame propagation velocity is 65.85%. The attenuation rates have increased by 80.16% and 68.33%, respectively, compared with those in the straight pipes. The attenuation rates increased by 18.51% and 20.59%, respectively, compared with those by using cavity alone. The suppression effect on the intensity and speed of gas explosion flame by coeffect of the cavity with the aspect ratio of 5/8 and water mist is better than by using the cavity with the aspect ratio of 5/8 alone

(3) The repression effect of the steel cavity on the explosion flame propagation is mainly due to the repeated reflection of the flame in the steel cavity, causing its energy to be attenuated. The repression effect of the water mist is mainly due to its vaporization and heat absorption

Data Availability

The data can be obtained by contacting Zhuo Yan: 37571616@qq.com.

Conflicts of Interest

The authors declare that there is no conflict of interest regarding the publication of this paper.

Acknowledgments

This work was supported by the Education Department of Anhui Province (no. KJ2020A0323), the Institute of Energy, Hefei Comprehensive National Science Center (no. 19KZS203), and the Collaborative Innovation Project of Universities in Anhui Province (no. GXXT-2020-057).

References

[1] Y. -F. Zhu, D.-M. Wang, and D.-L. Li, "Statistics analysis of serious coal mine disasters from 2000 to 2016 in China," *China Energy and Environmental Protection*, vol. 40, pp. 40–43, 2018.

[2] Y.-F. Zhu, D.-M. Wang, and D.-L. Li, "A statistical analysis of coalmine fires and explosions in China," *Process Safety and Environmental Protection*, vol. 121, pp. 357–366, 2019.

[3] M.-G. Yu, J. Kong, and Y. Wang, "Experiment study on explosion characteristic features of the methane-air pre-mixture at different concentrations," *Journal of Safety and Environment*, vol. 14, no. 6, pp. 85–90, 2014.

[4] C.-J. Yu, Y.-X. Tan, and J.-Z. Zhang, "Experimental research on blast characters of methane under obstacle with different distance," *Journal of North University of China (Natural Science Edition)*, vol. 36, no. 2, pp. 188–190,196, 2015.

[5] X.-P. Wen, M.-G. Yu, and W.-T. Ji, "Methane-air explosion characteristics with different obstacle configurations," *International Journal of Mining Science and Technology*, vol. 25, no. 2, pp. 213–218, 2015.

[6] M.-G. Yu, K. Zheng, and T.-X. Chu, "Gas explosion flame propagation over various hollow-square obstacles," *Journal of Natural Gas Science and Engineering*, vol. 30, pp. 221–227, 2016.

[7] M.-G. Yu, X.-F. Yang, and K. Zheng, "Effect of obstacles on explosion characteristics of methane/hydrogen," *Explosion and Shock Waves*, vol. 38, no. 1, pp. 19–27, 2018.

[8] X.-Y. Cao, J.-J. Ren, and M.-S. Bi, "Effect of droplet size on the inhibition of methane/air explosion process by ultrafine water mist," *Journal of China Coal Society*, vol. 42, no. 9, pp. 2376–2384, 2017.

[9] X.-Y. Cao, J.-J. Ren, and M.-S. Bi, "Experimental research on the characteristics of methane/air explosion affected by ultrafine water mist," *Journal of Hazardous Materials*, vol. 324, pp. 489–497, 2017.

[10] Y.-F. Song and Q. Zhang, "Quantitative research on gas explosion inhibition by water mist," *Journal of Hazardous Materials*, vol. 363, pp. 16–25, 2019.

[11] M.-G. Yu, A. An, and H. You, "Experimental study on inhibiting the gas explosion by water spray in tube," *Journal of China Coal Society*, vol. 36, no. 3, pp. 417–422, 2011.

[12] X.-Y. Cao, J.-J. Ren, and Y.-H. Zhou, "Analysis on the enhancement and suppression of methane/air explosions by ultrafine water mist," *Journal of China Coal Society*, vol. 41, no. 7, pp. 1711–1719, 2016.

[13] M.-G. Yu, A. An, and W.-L. Zhao, "On the inhibiting effectiveness of the water mist with additives to the gas explosion," *Journal of Safety and Environment*, vol. 11, no. 4, pp. 149–153, 2011.

[14] X.-Y. Cao, M.-S. Bi, and J.-J. Ren, "Experimental research on explosion suppression affected by ultrafine water mist containing different additives," *Journal of Hazardous Materials*, vol. 368, pp. 613–620, 2019.

[15] H. Shao, S.-G. Jiang, and X.-J. He, "Numerical analysis of factors influencing explosion suppression of a vacuum chamber," *Journal of Loss Prevention in the Process Industries*, vol. 45, pp. 255–263, 2017.

[16] T. Wang, Z.-M. Luo, and H. Wen, "The explosion enhancement of methane-air mixtures by ethylene in a confined chamber," *Energy*, vol. 214, article 119042, 2021.

[17] B. Su, Z.-M. Luo, and T. Wang, "Chemical kinetic behaviors at the chain initiation stage of CH_4/H_2/air mixture," *Journal of Hazardous Materials*, vol. 403, article 123680, 2021.

[18] Z.-Q. Li, C.-M. Mu, and D.-K. Xu, "Influence of cavity length on shock wave propagation of gas explosion," *Journal of Mining and Safety Engineering*, vol. 35, no. 6, pp. 1293–1300, 2018.

[19] Z. Yan, C.-M. Mu, and S.-J. Yuan, "Study on the influence of cavity aspect ratio on the propagation law of gas explosion shock wave," *Journal of China Coal Society*, vol. 45, no. 5, pp. 1803–1811, 2020.

[20] B. Li, R. Bao, Y. Wang, R. Liu, and C. Zhao, "Permeability evolution of two-dimensional fracture networks during shear under constant normal stiffness boundary conditions," *Rock Mechanics and Rock Engineering*, vol. 54, no. 1, pp. 409–428, 2021.

[21] F.-A. Williams, *Combustion Theory*, CRC Press, 2018.

[22] Z. Yan, S.-J. Yuan, and Z. Q. Li, "Study on inhibitory effect of cavity on gas explosion propagation," *Geofluids*, vol. 2021, 9 pages, 2021.

[23] A.-M. Lentati and H.-K. Chelliah, "Physical, thermal, and chemical effects of fine-water droplets in extinguishing counterflow diffusion flames," in *Twenty-Seventh Symposium (International) on Combustion/The Combustion Institute*, pp. 2839–2846, Elsevier, 1998.

Hindawi
Geofluids
Volume 2021, Article ID 2071333, 9 pages
https://doi.org/10.1155/2021/2071333

Research Article

Geological Structure Exploration of Karst Collapse Column and Evaluation of Water Insulation Properties of the Mud Part

Shijian Yu,[1] Jiyang Liu,[1] Peng Bai,[2] Hongtao Xu,[2] Runshan He,[2] Yongshen Wang,[3] and Dawei Yin[1]

[1]*College of Safety and Environmental Engineering, Shandong University of Science and Technology, Qingdao, China 266590*
[2]*Shanxi Shiquan Coal Industry Co., Ltd., Changzhi, China 046020*
[3]*China Huadian Coal Industry Group Co., Ltd., Beijing, China 100035*

Correspondence should be addressed to Dawei Yin; 949251142@qq.com

Received 27 June 2021; Revised 7 September 2021; Accepted 8 September 2021; Published 26 September 2021

Academic Editor: Afshin Davarpanah

In this study, the X5 KCC in Shiquan Coal Mine was investigated by means of controlled source audio magnetotelluric exploration and borehole television. In this way, the subsection geological structure of the KCC was obtained. Next, the geological and electrical characteristics of each part were analyzed, and it is concluded that the development status of the mud part under coal seam floor is the key part to judging whether water inrush will occur during working face recovery under aquifer pressure. Furthermore, the mineral compositions of purplish-red mudstone and lime mudstone were obtained by performing an X-ray diffraction experiment on the KCC interstitial materials. On this basis, the water insulation properties of the mud part were qualitatively evaluated. Finally, the tensile strength of the mud part was obtained by the Brazilian splitting method, and the water insulation ability of the mud part at the periods when the tunneling roadway and the working face passed the KCC was calculated, respectively. The research results boast guiding significance for safe recovery of the working face passing KCCs under aquifer pressure.

1. Introduction

Karst collapse columns (KCCs) are a kind of special depression fault gradually formed in a long geological period under the condition of soluble rock strata and good groundwater dynamics [1]. The explanation for its cause includes the gypsum dissolution collapse theory [2], the gravitational collapse theory [3–5], the hydrothermal genesis theory [6], and the vacuum erosion collapse theory [7]. Generally, the formation of KCCs goes through four stages, namely, the early development stage, the intense development stage, the decline stage, and the death stage [8]. The formation process is controlled by factors such as geological environment, groundwater activity, geological structure, and stratigraphic lithologic combination. The material structure inside a KCC is complex and diverse, and the fabric characteristics of different parts differ obviously [9–11]. From the perspective of water inrush mechanism, a KCC can be divided into four parts, namely, the lower enrockment part, the middle mud part, the upper clast part, and the surrounding rock fracture part [12], and different parts correspond to varying fabric characteristics, water contents, and water conduction (insulation) properties. Water conduction of a KCC is related to the regional sedimentary environment, tectonic evolution, and karst water runoff conditions in the basement during its formation. After its formation, recompaction, cementation, weathering, and activation are the key factors [13–20]. The macroscopic subsection structure and water conduction (insulation) properties of a KCC are the geological basis to determine whether water inrush will occur when the KCC is exposed in the process of mining.

Seismic exploration, as the main method to explore KCCs from the perspective of geological structure, mainly solves the problem of KCC identification [21–25]. Electrical exploration, including the direct current method, the transient electromagnetic method, and the magnetotelluric sounding method, which explores KCCs from the perspective of hydrogeology, mainly solves the problem of KCC water content [26–28]. These geophysical exploration methods interpret KCCs as a whole, without fully considering the characteristics of their subpart geological structure.

In this paper, mining under aquifer pressure when the tunneling roadway and the working face passed the X5 KCC in the 30107 fully mechanized working face of Shiquan Coal Mine was taken as the research background. Firstly, the subsection part geological structure of the X5 KCC was investigated by means of controlled source audio magnetotelluric (CSAMT) exploration and borehole television. Next, the tensile strength of rock in the mud part was obtained through the Brazilian splitting method. Furthermore, the water insulation capacities of the mud part when the tunneling roadway and the mining face passed the KCC were calculated, respectively. The research results provide geological basis for safe mining under aquifer pressure in the 30107 working face.

2. Development Characteristics of KCCs in Shiquan Coal Mine

2.1. Distribution Law of KCCs. Shiquan Coal Mine is located in Shiquan Village, Xiadian Town, 20.00 km west of Xiangyuan County, Changzhi City, Shanxi Province, China. Its maximum north-south length, maximum east-west width, and area are 6.00 km, 2.40 km, and 12.2195 km^2, respectively. The mining coal seam is No. 3 coal seam whose average thickness, mining elevation, and production scale are 6.0 m, +540~+70 m, and 1,200 kt/a, respectively.

Shiquan mine field is located in the east wing of Qinshui compound syncline and the west side of Jinhuo fold fault zone. Under such an influence, the strata belong to monoclinal structure (strike direction nearly south-north, dip direction west-northwest) with an inclination angle of 2°~25°. There are 48 faults and 23 KCCs in the mine field. In the north of the mine field, there are 7 secondary folds, and the strata are undulating. KCCs are usually densely distributed at positions where fractures, underground karst caves, and different tectonic systems are all highly developed. In Shiquan Coal Mine, KCCs are mostly distributed at the turning point of fold axis and near the fault, while they are rarely distributed far away from the fold axis or at positions where fractures are underdeveloped. The 23 identified KCCs are concentrated at or near the turning point of anticline axis.

2.2. Exposure Characteristics of the X5 KCC. The X5 KCC is exposed in the headgate of the 30107 face whose strike length and dip length are 1,530 m and 170 m, respectively. The mining coal seam is No. 3 coal seam whose average thickness is 6.0 m. The elevation of coal seam floor is +425~+530m, and that of Ordovician limestone water level is +636.87~+644.05 m. The 30107 working face is under aquifer pressure. According to the seismic exploration results, the plan shape of X5 KCC is like a dumbbell that is long in two sides and short in the middle, with a long-axis length of about 306 m and a short-axis length of about 75~100 m. The X5 KCC is exposed when the 30107 working face headgate is 530 m from the open-off cut. The exposure length is 98 m, including 78 m of whole rock. It extends into the 30107 working face for a maximum distance of 30 m. The position relationship is shown in Figure 1. The specific conditions of the X5 KCC are as follows.

The designed length of the 30107 headgate is 2,257.48 m. At 1,699 m in the 30107 headgate, the contact zone changes from the coal seam to the KCC. Specifically, the boundary on the lower side appears first, and the upper side lags for 4 m. In the broken zone, there are fine sandstone blocks with a size of over 1 m, small siltstone blocks and mudstone blocks, and the gaps among them are filled with argillaceous material; the accumulation body is dense and slightly wet. At 1,775 m in the 30107 headgate, the contact zone changes from the KCC to the coal seam. Specifically, the change occurs on the upper side first, and the lower side lags for 2 m. Figure 2 displays a longitudinal profile of the X5 KCC. Figure 3 shows a sketch of 30107 headgate passing through the X5 KCC and lithology photos of KCC exposed at different positions of roadway.

According to the classification of KCC structure with reference to literature [12] and the analysis on the actual disclosure situation, the KCC exposed in the 30107 headgate is located in the mudstone slurry water insulation part. Whether the 30107 working face can be safely mined under aquifer pressure depends on the thickness and water insulation ability of the mud part below the floor elevation of the 30107 face.

3. Analysis on the Geological Structure Exploration Results of X5

3.1. Results of Borehole Television Imaging Survey. In the hope of quantitatively determining the fracture development characteristics of the X5 KCC wall fracture part and the mud part, a borehole television imaging survey was conducted. The designed borehole passed through the KCC surrounding rock and the KCC body. The television image at the interface between the KCC surrounding rock and the KCC body is presented in Figure 4. The surrounding rock (siltstone) is an intact dark gray rock mass without developed fractures, indicating that the fractures in the KCC wall are underdeveloped in this part. The television image at the KCC body is illustrated in Figure 5. The KCC body has a pebbled structure, and the gravel is dark gray, grayish white, and brownish red; the gravel diameter ranges from 5 mm to 150 mm; the primary lithology is fine sandstone, and the cementing material is mainly dark gray mudstone, with local brownish red mudstone; the gravel content is about 50%, and no obvious fractures are found. The image suggests that the framework of the KCC fracture zone in this part is formed by the cementation of different-sized fine sandstone blocks, siltstone blocks, and mudstone blocks. The blocks are accumulated densely, resulting in underdeveloped fractures and low permeability. Thus, it is inferred that the KCC body can insulate water well.

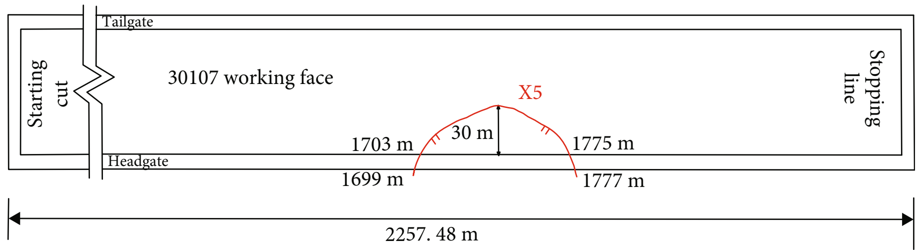

Figure 1: Plane position of the X5 FCC.

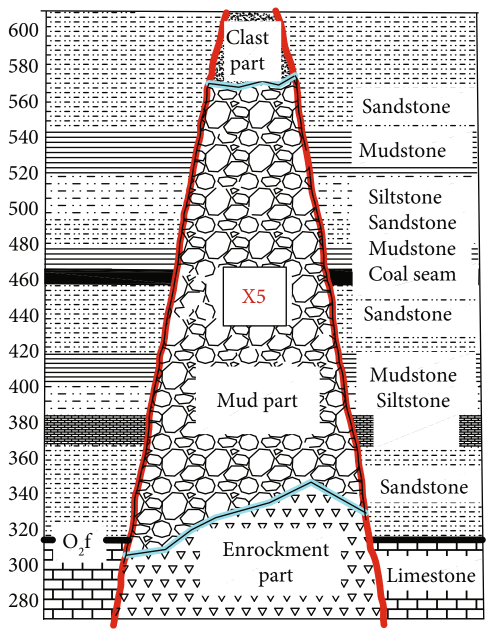

Figure 2: Longitudinal profile of the X5 KCC.

3.2. Results of CSAMT Exploration. To grasp the geological structure of the X5 KCC, the CSAMT geophysical exploration method was adopted. Taking the X5 KCC as the center, eleven 300 m long survey lines were laid along the vertical long axis, with the mesh degree being 10 × 50 m. The layout of survey lines is illustrated in Figure 6.

V8 System 2000.net, the eighth generation of geophysical data acquisition system of Phoenix Geophysical Co., Ltd., was adopted as the exploration equipment. In field observation, the bipolar source (AB = 1200 m) and the side E_x/H_y device were adopted; the measuring mode was scale TM; the measuring electrode distance Mn was 20 m; and the working frequency range is 0.52~5,120 Hz. A total of 38 frequency points were evenly distributed, avoiding 50 Hz, 60 Hz, and their multiple frequency points. The acquisition time for each frequency was longer than 40 s, and the number of single-frequency data stacking was not smaller than 40 times.

3.2.1. Structural Characteristics and Electrical Characteristics of Different Parts of the KCC. With respect to the macro structure, the KCC can be divided into three parts from bottom to top, namely, the enrockment part, the mud part, and the clast part. The electrical characteristics of the three parts differ significantly because of their varying components of filling materials at different heights, water contents, weathering degrees, and cementation degrees.

The enrockment part: located at the lower part of the KCC, the enrockment part was formed in the early stage of KCC formation. The collapse rock blocks were large in volume. Meanwhile, under the action of strong hydrodynamic pressure, fine rock debris and argillaceous material were taken away by the current, and the collapse deposits left were mostly large- and medium-sized rock blocks. This part usually contains some water, and its water content determines its electrical characteristics. When this part is of a large porosity and is filled with water, it shows a reduced resistivity in the transverse direction compared with the KCC surrounding rock strata; otherwise, it shows an increased resistivity.

The mud part: located in the middle of the KCC, the mud part was formed in the middle and late stage of KCC development. The solid materials in this part are the mixture of mud and collapse rock blocks from surrounding rock strata. Under the long-term action of in situ stress, the mixture gradually forms argillaceous cemented conglomerate. Generally speaking, this part of rock and soil mass is densely cemented with a high content of clay particles and low permeability. It neither contains water nor conducts water, belonging to a water insulation part of the KCC. Due to the existence of mudstone cement, it shows a decreased resistivity, compared with the KCC surrounding rock strata. The decrement depends on the content of mudstone cement. The higher the content of mudstone cement is, the more obviously the resistivity decreases.

The clastic part: located at the upper part of the KCC, the clast part is formed in the later stage of KCC development. In this part, rock blocks in the same stratum are arranged continuously, and the rock strata basically maintain continuity. Since the resistivity difference between the Carboniferous Permian upper strata is not large, the resistivity of this part is basically close to that of intact strata of the KCC surrounding rock, and the electrical anomaly characteristics are not obvious. In this part, the area affected by sandstone fracture aquifers and faults contains more water and is characterized by reduced resistivity.

3.2.2. Exploration Results. The resistivity parts of CSAMT sounding inversion on survey lines L3, L6, and L8 are displayed in Figure 7 which clearly reflects the macro geological structure of the X5 KCC, especially that of the water insulation mud part. As revealed by the analysis on the electrical

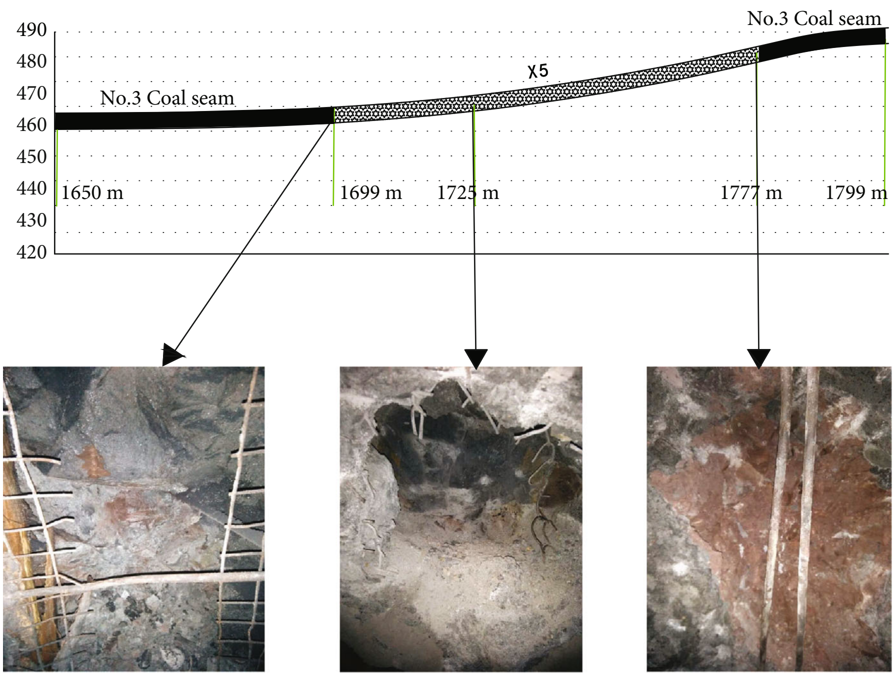

Figure 3: Sketch of 30107 headgate passing through X5 and lithology photos of KCC exposed at different positions of roadway.

characteristics of the three KCC parts, the mud part lies in the elevation ranges of +200~+600 m on the survey line L3, +380~+500 m on the L6 survey line, and +300~+440 m on the L8 survey line. The resistivity of rock mass in the clast part is slightly lower than that of surrounding rock mass, and its development depth is all above the elevation of No. 3 coal seam roof, but the development thickness tends to increase from southwest to northeast. Because of its high content (about 50%) of argillaceous cement, the resistivity of rock mass in the mud part is much lower than that of surrounding rock mass. The mud part below the elevation of No. 3 coal seam floor is thick on both sides and thin in the middle. To be specific, the maximum thicknesses in the southwest (survey line L3), in the middle (survey line L6), and in the northeast (survey line L8, corresponding to the 30107 headgate) are over 200 m, only 60 m, and over 100 m, respectively. The resistivity of rock mass in the enrockment part differs insignificantly from that of surrounding rock mass. It is inferred that the enrockment part has a relatively poor porosity and a low water content, and groundwater there has changed into fine fracture flow or pore seepage.

Based on the results of borehole television survey and CSAMT exploration, for No. 3 coal seam, the X5 KCC belongs to a muddy KCC with underdeveloped fractures on the wall. This type of KCC is filled with mud inside. In the mining process, the working face can advance safely as long as enough distance is kept from the water-containing enrockment part.

4. Evaluation of Water Insulation Properties of the Mud Part

4.1. X-Ray Diffractometry (XRD) Experiment on Interstitial Materials in the X5 KCC

4.1.1. Preparation of Experimental Samples. In the experiment, the purplish-red mudstone and lime mudstone from the interstitial materials in the X5 KCC were taken as the research objects, and the composition test and quantitative analysis were conducted on them with the aid of an XRD analyzer. First, the interstitial mudstone samples collected on site were broken into small particles, and then, the granular mudstone samples were ground into fine powder (generally 200~300 meshes) by using an agate mortar. The ground test samples were sealed in a sealed bag to avoid contact with air. During the experiment, the scanning range was set as 10°~90°, the scanning rate as 4°/min, and the scanning mode as fixed coupling.

4.1.2. Analysis on the Experimental Results. The XRD experiment was performed using the Rigaku D/Max 2500PC XRD instrument. The obtained .raw files were analyzed by Jade software. After interference removal and smoothing of the XRD spectra, the peak fitting conditions were set in accordance with the actual situation of the spectra. After fitting the peaks, qualitative analysis was conducted on the obtained peak parameters. The analysis results can reflect the components contained in the samples (Figure 8).

According to the XRD results, the main components of purplish-red mudstone are quartz, montmorillonite, albite, chlorite, calcite, kaolinite, and hematite and those of lime mudstone are quartz, montmorillonite, kaolinite, albite, and chlorite.

Table 1 shows the quantitative analysis results of XRD spectra. Purplish-red mudstone primarily contains quartz, montmorillonite, albite, chlorite, and calcite, as well as a little kaolinite and hematite. The proportion of quartz in lime mudstone is the highest, reaching 46.41%, while the proportions of montmorillonite, albite, chlorite, and kaolinite

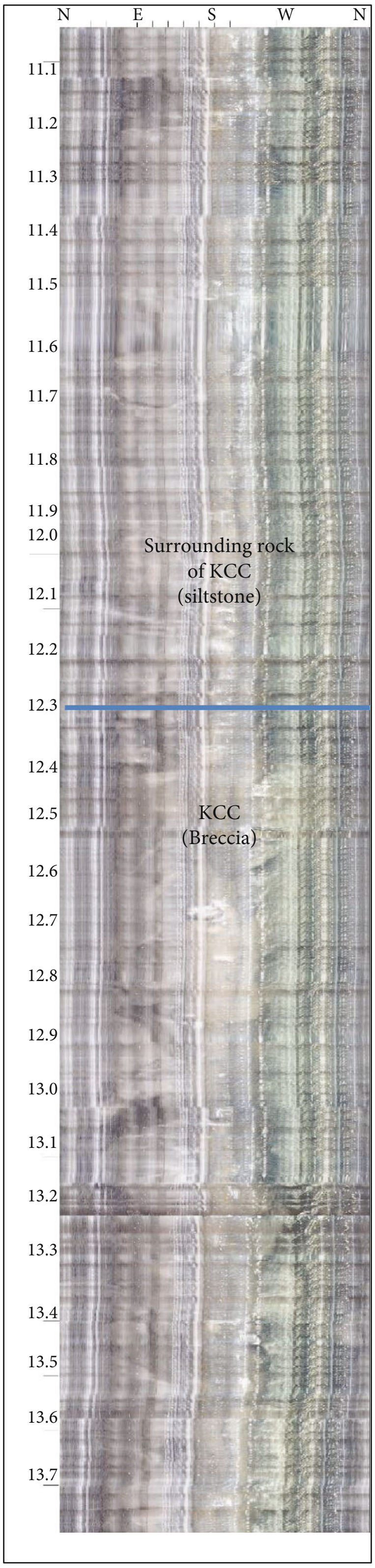

Figure 4: Television image of the interface between KCC surrounding rock and KCC body.

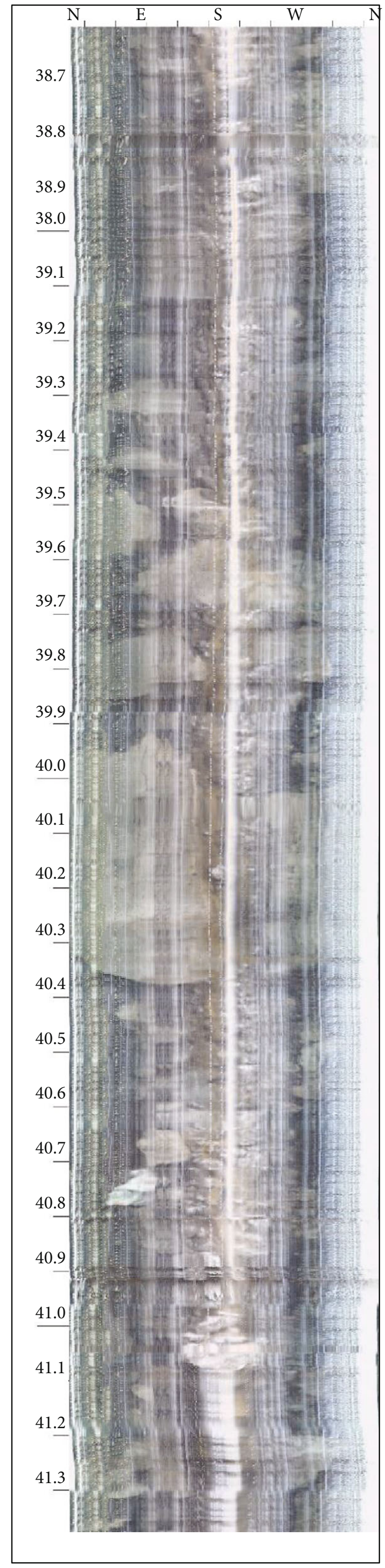

Figure 5: Television image of KCC body.

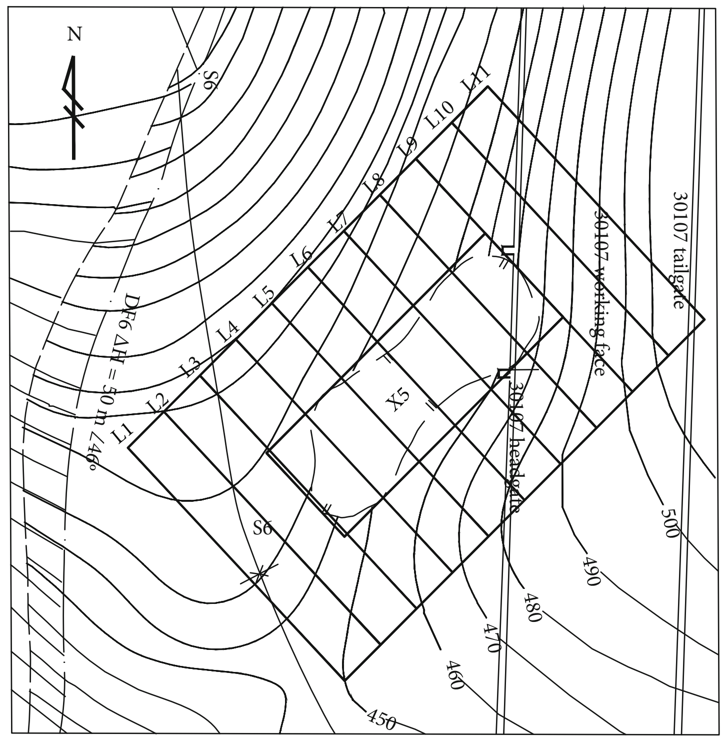

Figure 6: Layout of CSAMT survey lines in the X5 KCC.

resemble. The main components of the two kinds of stone are similar, but the kaolinite content is relatively high in lime mudstone and relatively low in purplish-red mudstone.

The kaolinite, montmorillonite, and chlorite in the interstitial minerals of the above samples belong to clay minerals which are characterized by plasticity, adhesiveness, and volume expansion when getting wet. The following phenomena are found during on-site exposure: the mixture of purplish-red mudstone, lime mudstone, and medium-fine grained sandstone occupies a relatively high proportion. No water seepage occurred throughout the entire disclosure process. The interface between the KCC and the coal seam is densely filled with argillaceous interstitial material, and no water erosion occurred, indicating that the mud part has a strong water insulation ability.

4.2. Uniaxial Tensile Test on the Water Insulation Layer of the Mud Part in the X5 KCC. The Shimazu AG-X250 electronic universal testing machine was used for uniaxial loading. In order to protect the Brazilian splitting test device, the loading adopted the displacement mode and was conducted at the rate of 0.01 mm/s. Table 2 shows the uniaxial tensile test results of X5 specimens.

The average tensile strength of the test specimens K_p = 0.78 MP, the standard variance $s = 0.145$, and the dispersion coefficient of the test results $\mu = s/S_t = 1.8\%$, which demonstrates that the average value of the test results is reliable and effective.

4.3. Evaluation of Water Insulation Ability of the Mud Part. According to *Rules for Coal Mine Water Prevention and Control*, the water insulation ability of tunneling roadway floor is calculated by Equation (1) [29]:

$$p = 2K_p \frac{t^2}{L^2} + \gamma t, \tag{1}$$

where p is the safe water pressure that the floor water insulation layer can bear, MPa; t is the thickness of the water insulation layer, m; L is the roadway width, and its value is 5 m; θ is the average weight of the floor water insulation layer, and its value is 0.022 MN/m^3; K_p is the average tensile strength of the floor water insulation layer, MPa.

The water insulation ability of the mining face is calculated by Equation (2) [29]:

$$P = T_s \times M, \tag{2}$$

where M is the thickness of the floor water insulation layer, M; P is the safe water pressure, MPa; T_s is the critical water inrush coefficient, MPa/m, and its value is 0.06 MPa/m in a tectonically deformed part.

According to the CSAMT exploration results, the water insulation mud part below the 30107 headgate floor is 100 m thick. As can be calculated by Equation (1), the water insulation layer below the X5 KCC of the 30107 face tunnelling roadway floor can bear a maximum aquifer pressure of 626.2 MPa. In addition, according to the elevation (460 m) of No. 3 coal seam floor during the exposure of the X5 KCC in the headgate and the current Ordovician limestone water level (636.87 m) in Shiquan mine field, the water pressure at the bottom of the mud part is calculated to be 2.71 MPa, and the thickness of the water insulation layer is calculated

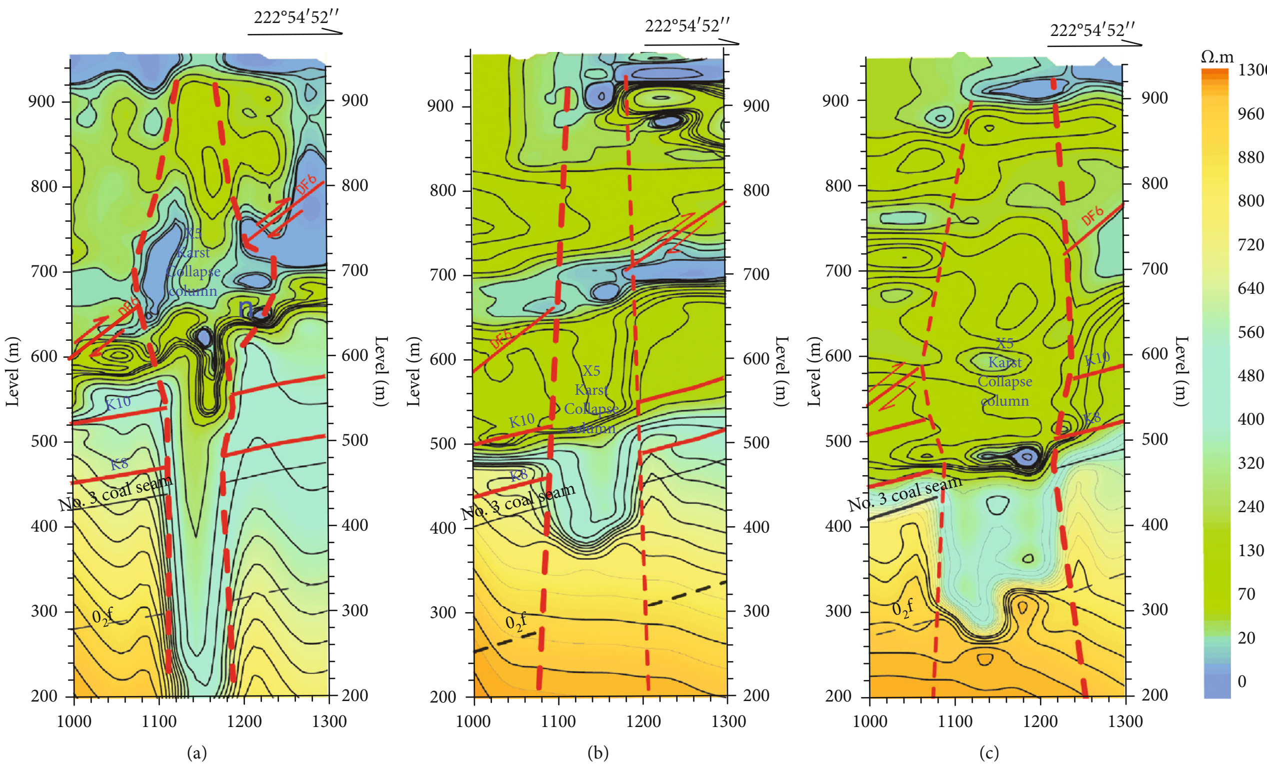

Figure 7: Resistivity part of CSAMT sounding inversion.

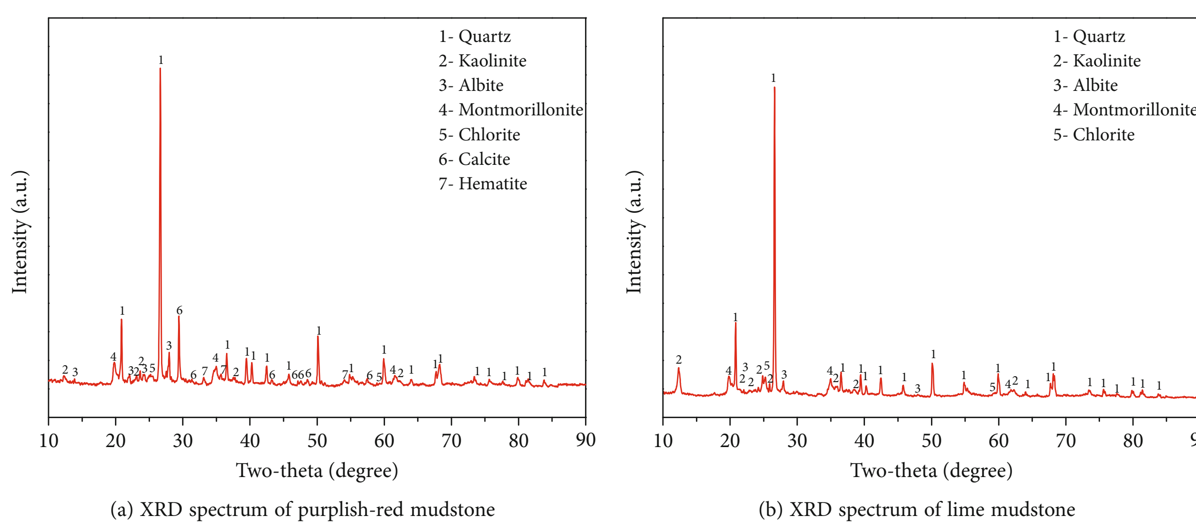

Figure 8: XRD spectra.

to be 45.1 m by Equation (2). Considering the above data, it is judged that the 30107 face can pass the X5 KCC safely without encountering inrush of Ordovician limestone confined water.

5. Discussions

5.1. KCC Occurrence State. Due to the differences in regional geological and hydrogeological conditions, sedimentary environment, and stratigraphic lithologic assemblage, the geological structures of KCCs exhibit significant regional and individual differences. The existence of a mud part is a necessary condition to ensure no water inrush when a working face passes a KCC under aquifer pressure, but it is not a sufficient condition, because whether the working face can advance safely also depends on the thickness and water insulation ability of the mud part below the working face floor. The exploration results of the X5 KCC suggest that the mud part is thick on both sides and thin in the middle. According to the exposure conditions, the KCCs passed

Table 1: Mineral composition of interstitial materials.

Interstitial material	Composition (%) Quartz	Montmorillonite	Kaolinite	Sodium feldspar	Chlorite	Calcite	Hematite	Other
Purplish-red mudstone	41.15	18.67	3.6	15.36	10.41	6.95	1.21	2.65
Grey mudstone	46.41	16.79	13.56	10.72	8.27	—	—	3.25

Table 2: Uniaxial tensile test results of X5 specimens.

Specimen No.	Diameter (mm)	Thickness (mm)	Breaking load (KN)	Tensile strength (MPa)
1	50.16	26.76	1.586	0.752
2	50.02	26.78	1.439	0.684
3	50.22	24.12	1.798	0.945
4	50.58	24.40	1.409	0.727
5	49.96	25.10	1.607	0.816

during the mining of No. 3 coal seam all lie in the mud part, which provides necessary geological conditions for safe recovery of the working face passing KCCs under aquifer pressure.

5.2. Geological Conditions and Genesis of KCC. The KCCs in Shiquan mine field own the geological conditions for the formation of a water insulation mud part. The material basis of a mud part is the formation of dissolvable and decomposable strata, such as mudstone, shale, and argillaceous limestone. After these strata collapse, they can decompose rapidly under the dynamic action of solid-liquid-gas three phases and combine with water to form mud. The formed mud, together with the collapsed surrounding rock strata, compose the solid material of the mud part. The Permian strata in Shiquan mine field (Shanxi Formation and Lower Shihezi Formation in the lower part, Upper Shihezi Formation, and Shiqianfeng Formation in the upper part) are deltaic continental deposits (266~422 m thick) composed of conglomerate, sandstone, siltstone, mudstone, and coal seam. Specifically, Shanxi Formation is mainly composed of black mudstone, dark gray sandy mudstone, siltstone, and gray and gray-white sandstone. Lower Shihezi Formation is composed of gray sandstone interspersed with gray and gray-black mudstone, sandy mudstone, and siltstone; the top is a stable layer of gray green, yellow green, and purple variegated mudstone that contains iron and manganese nodules, commonly known as peach blossom mudstone; the cemented material observed during the exposure of the X5 KCC in the 30107 headgate is just the peach blossom mudstone. Upper Shihezi Formation, which belongs to continental fluvial and lacustrine deposits, is composed of variegated sand and mudstone. Sedimentary characteristics of the Permian strata determine that there is sufficient mudstone slurry to fill the gaps between sandstone blocks and limestone blocks during the formation of KCCs. Under the long-term action of gravity, mudstone slurry material begins to consolidate, solidify, and rheology, gradually forming conglomerate similar to mudstone cement. This is the geological reason why the mud part of the X5 KCC below the elevation of No. 3 coal seam floor is 60~100 m thick. The fabric characteristics (about 50% of argillaceous cement and about 50% of breccia) and the electrical characteristics of the mud part of the KCC developed in Shiquan mine field provide the physical conditions for the accurate classification of the mud part by the electrical exploration method.

6. Conclusions

(1) The KCC in Shiquan mine field has clear subparts in geological structure, and the thickness and water insulation ability of the mud part in the No. 3 coal seam floor are the geological basis for determining whether water inrush will occur when the KCC is exposed in the process of mining

(2) CSAMT exploration and borehole television are effective technical means to divide the geological subparts of the KCC

(3) The interstitial minerals in the mud part are rich in clay minerals such as kaolinite, montmorillonite, and chlorite which are characterized by plasticity, adhesiveness, and volume expansion when getting wet. They are the material basis for the strong water insulation ability of the mud part

(4) Under the sedimentary environment of continental river and lake, dissolvable and decomposable strata, such as mudstone, shale, and argillaceous limestone, are formed in Shiquan mine field, which is the geological reason for the formation of the water insulation mud part. The fabric characteristics of about 50% argillaceous cement and about 50% breccia guarantee the strong water insulation ability of the mud part

Data Availability

The data used to support the findings of this study are included in the article.

Conflicts of Interest

The authors declare that they have no conflicts of interest.

Acknowledgments

This work was supported by the National Science Foundation of China (51904167), the Taishan Scholars Project, the Taishan Scholar Talent Team Support Plan for Advantaged and Unique Discipline Areas, and the SDUST Research Fund (2018TDJH102).

References

[1] S. X. Yin, H. Q. Lian, and D. M. Liu, "70 years of investigation on karst collapse column in North China Coalfield: cause of origin, mechanism and prevention," *Coal Science and Technology*, vol. 47, no. 11, pp. 1–29, 2019.

[2] X. P. Qian, "Formation of gypsum karst collapse column and its hydro - geological significance," *Carsologica Sinica*, vol. 7, no. 4, pp. 70–74, 1988.

[3] R. Wang, "Discussion on the causes and prevention of ground collapse in karst mining area," *Hydrogeology & Engineering Geology*, vol. 26, no. 1, pp. 37–41, 1982.

[4] W. M. Yang and Z. A. Zhou, "Analysis of rock mass structure of karst collapse column," *Journal of Huainan Mining Institute*, vol. 17, no. 2, pp. 1–7, 1997.

[5] B. L. Hu and X. M. Song, "Deep karst cave and collapse column formation mechanism in Huaibei coalfield," *Coal Geology of China*, vol. 9, no. 2, pp. 47–49, 1997.

[6] S. P. Chen, "Discussion on the cause of karst collapse column in Fengfeng area of Hebei Province," *Carsologica Sinica*, vol. 12, no. 3, pp. 52–63, 1993.

[7] W. G. Xu and G. R. Zhao, "The implication of suction action for ground subsidence in karst mining areas," *Geological Review*, vol. 27, no. 2, pp. 86–95, 1981.

[8] Y. J. Li and S. P. Peng, "Classifications and characteristics of karst collapse columns in North China coalfields," *COAL-GEOLOGY& EXPLORATION*, vol. 34, no. 4, pp. 53–57, 2006.

[9] J. G. Zhao, M. T. Guo, and W. S. Li, "Morphological and fabric characteristics of karst collapse pillars in Xishan coalfield," *Journal of China Coal Society*, vol. 45, no. 7, pp. 2389–2398, 2020.

[10] S. X. Yin, Q. Wu, and S. X. Wang, "Studies on characters and forming mechanism of karstic collapse columns at mine area of North China," *Chinese Journal of Rock Mechanics and Engineering*, vol. 23, no. 1, pp. 120–123, 2004.

[11] Z. Q. She, "Characteristics and prediction methods of ancient karst columnar collapse," *Coal Geology & Exploration*, vol. 18, no. 2, pp. 42–45, 1990.

[12] L. Niu, Q. Wu, and B. Li, "Classification of karst collapse columns in North China coalfields based on the generalized model of inside structure of the columns," *Coal Geology & Exploration*, vol. 43, no. 3, pp. 56–60, 2015.

[13] S. X. Yin, Q. Wu, and S. X. Wang, "Water-bearing characteristics and hydro-geological models of karstic collapse pillars in north China," *Journal of Rock Mechanics and Geotechnical Engineering*, vol. 24, no. 1, pp. 77–82, 2005.

[14] W. J. Yu and K. Li, "Deformation mechanism and control technology of surrounding rock in the deep-buried large-span chamber," *Geofluids*, vol. 2020, 22 pages, 2020.

[15] W. J. Yu, G. S. Wu, and B. Pan, "Experimental investigation of the mechanical properties of sandstone–coal–bolt specimens with different angles under conventional triaxial compression," *International Journal of Geomechanics*, vol. 21, no. 6, p. 04021067, 2021.

[16] W. J. Yu, K. Li, and Z. Liu, "Mechanical characteristics and deformation control of surrounding rock in weakly cemented siltstone," *Environmental Earth Sciences*, vol. 80, no. 9, 2021.

[17] D. Ma, J. X. Zhang, and Y. L. Huang, "Reutilization of gangue wastes in underground backfilling mining: overburden aquifer protection," *Chemosphere*, vol. 264, p. 128400, 2021.

[18] H. Wu, D. Ma, and A. J. S. Spearing, "Fracture phenomena and mechanisms of brittle rock with different numbers of openings under uniaxial loading," *Geomechanics and Engineering*, vol. 25, no. 6, pp. 481–493, 2021.

[19] D. Ma, B. K. Sai, and Z. H. Li, "Effect of wetting-drying cycle on hydraulic and mechanical properties of cemented paste backfill of the recycled solid wastes," *Chemosphere*, vol. 282, p. 131163, 2021.

[20] D. Ma, J. J. Wang, and X. Cai, "Effects of height/diameter ratio on failure and damage properties of granite under coupled bending and splitting deformation," *Engineering Fracture Mechanics*, vol. 220, p. 106640, 2019.

[21] S. H. Wu, G. X. Zhou, and S. X. Yang, "Analys is for the seismic response characteristics of collapse column," *Coal Geology & Exploration*, vol. 32, 2004.

[22] J. H. Ning and G. Z. Zhang, "Seismic identification technique and its application of collapse column," *Coal Geology & Exploration*, vol. 33, no. 3, pp. 64–67, 2005.

[23] J. P. Zuo, S. P. Peng, and Y. J. Li, "Investigation of karst collapse based on 3-D seismic technique and DDA method at Xieqiao coal mine, China," *International Journal of Coal Geology*, vol. 78, no. 4, pp. 276–287, 2009.

[24] Q. F. Yin, D. M. Pan, J. C. Yu, and S. D. Liu, "Research on seismic identification technique of coal mine collapse column," *Progress in Geophysics*, vol. 27, no. 5, pp. 2168–2174, 2012.

[25] B. W. Han, X. B. Liu, and Q. Li, "Coalfield subsided column and gob area identification through 3D seismic interpretation," *Coal Geology of China*, vol. 27, no. 9, pp. 67–70, 2015.

[26] J. L. Cheng, F. Li, and S. P. Peng, "Research progress and development direction on advanced detection in mine roadway working face using geophysical methods," *Journal of China Coal Society*, vol. 39, no. 8, pp. 1742–1750, 2014.

[27] G. Q. Xue and J. C. Yu, "New development of TEM research and application in coal mine exploration," *Progress in Geophysics*, vol. 32, no. 1, pp. 319–326, 2017.

[28] J. S. An, Q. X. Sun, and H. Qiu, "Experimental study on underground collapse column by integrated detection technology," *Coal Science and Technology*, vol. 43, no. 10, pp. 144–147, 2015.

[29] State Administration of Coal Mine Safty, *Rules for Coal Mine Water Prevention and Control*, Beijing, China Coal Industry Publishing House, 2018.

Hindawi
Geofluids
Volume 2021, Article ID 1368194, 11 pages
https://doi.org/10.1155/2021/1368194

Research Article

Effect of Fly Ash and Cement on the Engineering Characteristic of Stabilized Subgrade Soil: An Experimental Study

Partab Rai,[1] **Wenge Qiu**,[1] **Huafu Pei**,[2] **Jihui Chen**,[1] **Xufeng Ai**,[1] **Yang Liu**,[1] **and Mahmood Ahmad**[3]

[1]*Key Laboratory of Transportation Tunnel Engineering, Ministry of Education, School of Civil Engineering, Southwest Jiaotong University, Chengdu 610031, China*
[2]*State Key Lab of Coastal and Offshore Engineering, Dalian University of Technology, Dalian 116024, China*
[3]*Department of Civil Engineering, University of Engineering and Technology Peshawar (Bannu Campus), Bannu 28100, Pakistan*

Correspondence should be addressed to Wenge Qiu; qiuwen_qw@163.com

Received 9 May 2021; Accepted 7 August 2021; Published 20 September 2021

Academic Editor: Yong-Zheng Wu

The effectiveness of the use of waste fly ash (FA) and cement (OPC) in the stabilization of subgrade soils and the reasons likely to influence the degree of stabilization were investigated. Incorporating waste fly ash (FA) and cement (OPC) as additives leads to significant environmental and economic contributions to soil stabilization. This study involves laboratory tests to obtain the Atterberg limit, free swell index (FSI), the unconfined compressive strength (UCS), the California bearing ratio (CBR), and the scanning electron microscope (SEM). The test results for the subgrade soil illustrate that the Atterberg limit, plasticity index, and free swell index are decreasing with the addition of different proportions of fly ash and cement, i.e., 0%, 5%, 10%, 15%, and 20% and 0%, 2%, 4%, 6%, and 8%, respectively. The CBR value of untreated soil is 2.91%, while the best CBR value of fly ash and cement mixture treated soil is 10.12% (20% FA+8% OPC), which increases 71.34% from the initial value. The UCS of untreated soil is 86.88 kPa and treated soil with fly ash and cement attains a maximum value of 167.75 kPa (20% FA+8% OPC), i.e., increases by 48.20% from the initial value. The tests result show that the stability of a subgrade soil can be improved by adding fly ash and cement. While effectiveness and usability of waste FA and cement are cost-effective and environmentally friendly alternatives to expansive soil for pavement and any other foundation work in the future.

1. Introduction

Emerging tendency of utilizing waste material in soil strengthening or soil stabilization is operational all over the world in present times. The primary reason behind this trend is the enormous production of fly ash, plastics, rice husk, and other wastes, which are not merely harmful but also leads to deposition problems. Using these wastes in construction work will tremendously reduce this problem. For example, soil stabilization is a technology designed to increase or maintain soil stability and chemical changes to improve its engineering properties [1–4]. More than 500 years ago, the concept of stabilization was pioneered [2, 5]. In ancient Egypt, Greece, and Rome, treated earth roads were used in soil lime mixtures [5, 6]. Stabilization can deal with all kinds of subgrade materials, from expansive clay to granular substances. This allows the establishment of design precedents and the determination of suitable chemical additives and admixture rates to achieve the required engineering performance. At the beginning of the 20th century, around the 1930s, road construction in Europe was paved with stabilized soil [7]. The advantages of the stabilization process include higher resistance values, reduced plasticity, reduced permeability, and reduced thickness of the pavement and a reduction of transport or handling of excavated materials. Stabilization of subgrade soils with mixtures controls possible changes in soil volume and improves soil strength [8].

The soil generally is weak and has not enough stability in heavy loading. This paper is aimed at examining on stabilization of the soil using fly ash activated by cement. Several reinforcement methods can be used to stabilize subgrade materials. These methods include chemical additive stabilization, soil replacement, compaction control, rewetting, humidity, surcharge, and thermal processes [9]. These techniques may have the disadvantage of inadequate performance and high costs. Based on the literature, fly ash and cement are low-cost and effective for soil stabilization [9, 10]. Generally, a pavement is a relatively stable shell built on natural soil to support and distribute a wheel load and provide a good wearing course [11]. These pavements are destroyed at a shorter time due to variations in soil properties and regular application of wheel loads, which can lead to an unsustainable settlement. Further variation in moisture, freeze action, rise, or decrease in the water content of the clay soil leads to further disintegration of the pavement, which leads to a higher cost repair operation [11]. In addition, the use of stabilizing agents in the road and subgrade work with weak soil conditions strengthens other characteristics, such as cohesion, and helps to improve structures or embankments. Eventually, this will lead to a significant decrease in the cost of road maintenance [4, 11]. The stabilization of different admixtures can improve the strength of the soil. Our aim is to work on fly ash and cement as admixtures.

Fly ash is the coal residue of the thermal power plant, which is regarded as a problematic solid waste in the world. The conventional FA treatment technology leads to degradation and pollution of cultivated land [12, 13]. FA consists of an amorphous ferroalumino silicate with a matrix very similar to the soil. The elemental composition of the FA (toxic elements) differs with the type and source of the coal used [14–16]. It is estimated that the annual output of coal ash in the world is about 600 million tons, of which fly ash accounts for about 75-80% of total ash, about 500 million tons [17, 18]. Fly ash can be treated as the fifth largest raw material reserve in the world [19]. As a result, the volume of coal waste (fly ash) generated by industries and thermal power plants is rising worldwide. The disposal of significant amounts of fly ash has become a primary environmental concern [17]. The inclusion of FA to soil can enhance the physicochemical properties as well as soil nutritional character, and the degree of modification depends on soil, and FA properties [16]. An estimated 6,898 MW to generate 5.2 million tons of fly ash per year in Pakistan. Because of the high costs of disposal and environmental protection, the use of FA in the construction and agriculture sector may be a feasible choice [20]. In Pakistan, the ongoing Diamer Basha Dam and the 21 MW Tangir Hydropower Project will use concrete from Ordinary Portland Cement combined with fly ash and other additives [21, 22]. The Frontier Engineering Organisation said, “This reduces thermal loads on the dam and reduces chances of thermal cracking,” according to China Daily News. China-supported projects are scheduled to be completed in 2028 [21]. Besides, the engineering properties of expansive soils such as compaction, strength, hydraulic conductivity, swell potential, free swell index (FSI), and plasticity were determined precisely at 0, 5, 10 15, and 20 percent respectively, in order to investigate the effectiveness of fly ash. Decreased plasticity facet, hydraulic conductivity, and FSI were discerned from the findings due to the rise in the overall maximum dry unit weight [23].

However, cement remains the oldest binding agent since the advent of soil stabilization technology in the 1960s. It can be considered an important stabilizer or hydraulic binder because it can be used on its own to achieve the desired stabilizing effect [24, 25]. Cement reaction is independent of soil minerals, and the primary function is to react to water that may be present in some soil. Almost cement stabilization decreases cohesiveness (plasticity), volume expansion, or compressibility and increases strength. Meanwhile, compared with lime and cement, fly ash has little cementitious property. Therefore, in the presence of a small amount of activator, a chemical reaction may occur to form cementitious compounds, which help improve the strength of subgrade soil [24, 26]. Moreover, many researchers [5, 27–32] have conducted a lot of research on the strength of lime, fly ash and cement, cement, lime fly ash, marble powder, lime rice husk, and their applicability as road and subbase. Since then, many efforts have been made around the world to confirm the treatment mechanism of expansive subgrade soil in highway fields to carry out appropriate pavement design and construction [33–35].

The main contribution of this paper focuses on the influence of fly ash and cement on the stabilization of subgrade soil. Besides, to make the stabilization work more economical than before, and to make use of vast waste raw material fly ash very important, the characteristics investigated in this study include the Atterberg limits, free swell index, optimum moisture content (OMC), maximum dry density (MDD), UCS, CBR, and SEM analysis. Through the experiments in the laboratory, different results are obtained from the tests. These results infer that the strength parameter increases and the Atterberg limit decrease. Finally, their contributions to subgrade soil stabilization are discussed, and the possible uses of stabilization materials are proposed. The structure of the paper is as follows. In Section 2 presents the raw materials, methods, and experimental laboratory processes. In Section 3, results and discussions are given. In Section 4, their comprehensive performance is evaluated, and the concluding remarks are made.

2. Materials and Methods

The primary materials used in this study are soil, fly ash, and Portland cement. This section describes the properties of these materials.

2.1. Soil. In this investigation, subgrade soil samples were collected from the Toll Plaza National Highway in Hyderabad, Pakistan, were obtained from a depth of 0.5 to 1 m from ground level, and had just 5.28% moisture content, which is insignificant in consideration. As per the norm, the soil is classified as A-2-4. This subgrade soil is grey in color. Geographic coordinates, 25°22′12.40″N latitude, 68°13′1.32″E longitude as shown in Figure 1. Besides, according to the specifications, a large number of tests were carried out to determine the engineering properties of soil samples. The results are demonstrated in Section 3.

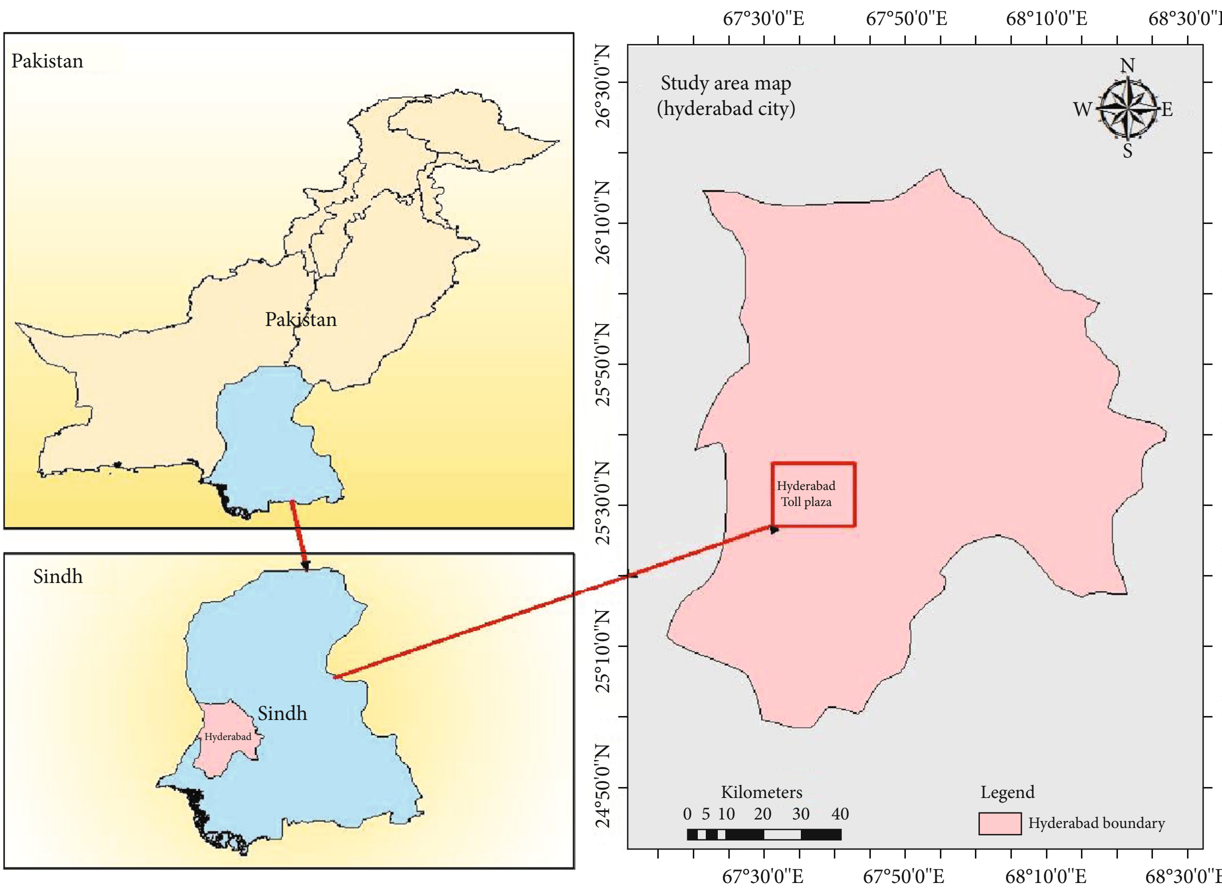

Figure 1: The geographical location of the test site.

2.2. Fly Ash. Class-F fly ash is taken from Jamshoro, Sindh, Pakistan. It was air-dried and pulverized. Fly ash is a waste (by-product) of the Jamshoro coal power plant. Fly ash by itself has tiny cementitious properties compared to cement and lime. Therefore, in the presence of a small amount of activator, a chemical reaction can occur to form cementitious materials conducive to improving the strength and performance of subgrade soil. The chemical composition of fly ash is illustrated in Table 1.

2.3. Cement. Ordinary Portland cement generally used for this study is from the locally available cement market. The essential components of OPC are shown in Table 1.

Table 1: The chemical components of fly ash and OPC.

Components	Class F fly ash	OPC
SiO_2	55.2	61
Al_2O_3	26.8	20.5
Fe_2O_3	12	4
CaO	2	10.5
MgO	2.5	2
SO_3	1.5	2
Fineness (cm^2/g)	—	3110
Ignition loss (%)	—	2.2

2.4. Methodology. Fly ash and cement additives are used as admixtures to blend with the subgrade soil for stabilization. In this study, different proportions of fly ash and cement should be tried until the desired strength is achieved. A reasonable guideline is, to begin with, to use 5% fly ash and 2% cement. Then, appropriate percent increments are added for various trials. In the initial trial, the proportion of activator (cement content) applied to each should be one part of cement and two parts of fly ash, but it can be different according to experience and literature review [6, 23, 35, 36]. After performing some dummy tests, we moved on towards our original sample. It looked tedious in starting because of inadequate techniques in experimental work, but dummy tests helped us understand the procedures of all tests. The methodology used for this research work was to divide samples into two parts: the soils at the natural stage and the second with fly ash and cement mixes. Initial soil tests were performed on samples Figure 2. After which, they were mixed mechanically (physical mixing) with fly ash-cement. The fly ash and cement used for this study were collected from the location in Hyderabad. At the rate of 0%, 5%, 10%, 15%, and 20% fly ash and 0%, 2%, 4%, 6%, and 8% cement by weight. After mixing with mentioned proportion, tests were performed as shown in Figure 2. Finally,

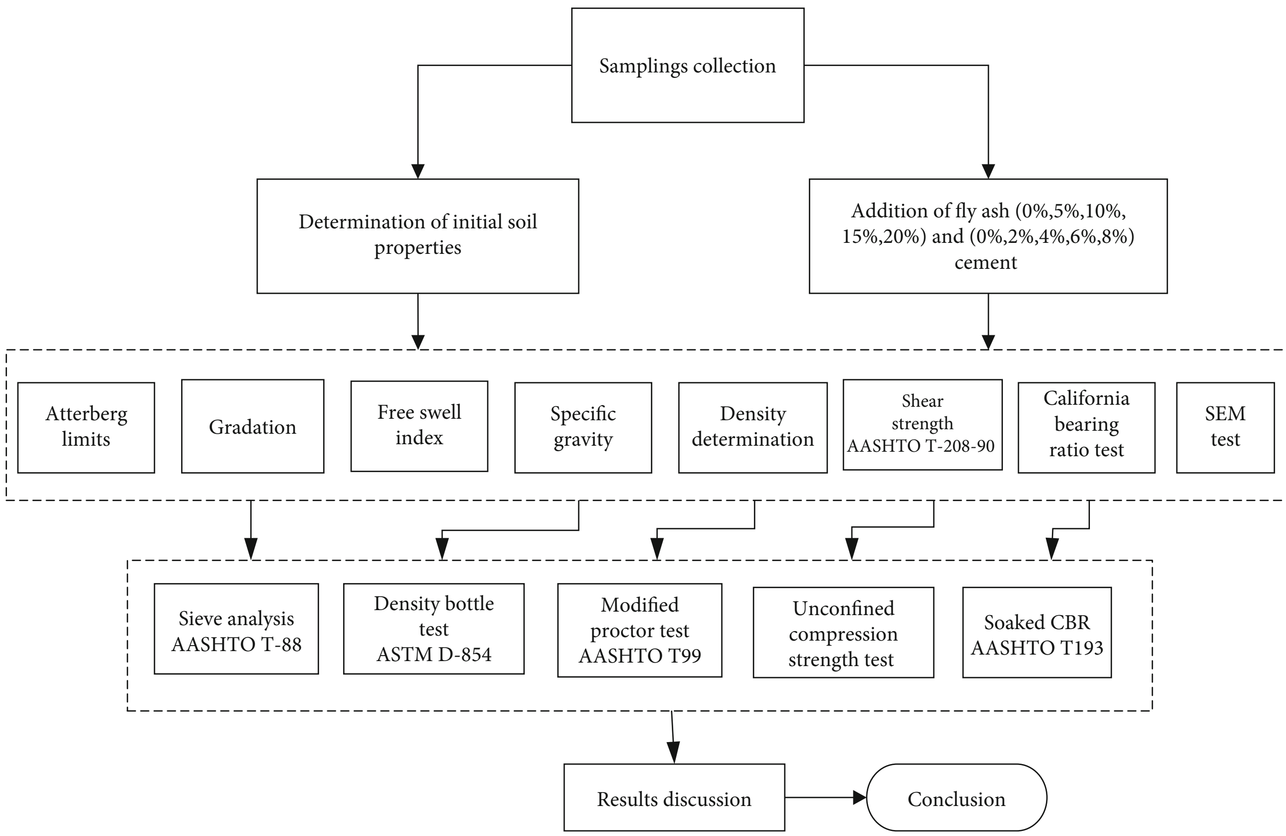

Figure 2: Subgrade soil tests with and without additives.

Table 2: Properties of subgrade soil.

Properties	Obtained value
Moisture content (%)	5.28
Liquid limit (%)	27.5
Plastic limit (%)	17.5
Plasticity index (%)	10
pH	4.03
Specific gravity	2.72
Silt (%)	70.49
Clay (%)	13.76
Sand (%)	15.78
Free swell index (%)	0.410
Dry density (g/cm^3)	2.13
UCS (kPa)	86.88
California bearing ratio	2.91%

comparisons were drawn between soil at a natural state and soil mixed with said proportion.

2.5. Laboratory Experiments Conducted

2.5.1. Liquid Limit (as per AASHTO T-90). Liquid limit is perceived as water content. The precise number 25 blow was given in the standard LL apparatus, which uses a specified number of slotting tools to close standard size grooves on the specimen. The flow curve is represented on a semilogarithmic plot on a logarithmic scale. The water content equal to 25 strokes is decoded from the curve and calibrated to the nearest integer as the soil's liquid limit.

Table 3: Atterberg limits in subgrade soil by adding fly ash and cement.

Mix ratio	PL	LL	Plasticity index
Soil+0% FA+0% OPC	19.5	29.51	10.0
Soil+5% FA+2% OPC	23.905	34.78	10.87
Soil+10% FA+4% OPC	22.58	31.71	9.13
Soil+15% FA+6% OPC	18.98	28.67	9.72

2.5.2. Plastic Limit (as per AASHTO T-91). PL in the fine-grained soil is the water content at which the soil rolled into threads with the smallest diameter of 3 mm, which is expressed as a whole amount extracted from the mean of the PL moisture content.

2.5.3. Modified Proctor Test (as per AASHTO T99). A modified Proctor compaction test is used to evaluate the maximum dry density and optimal moisture content of subgrade soil.

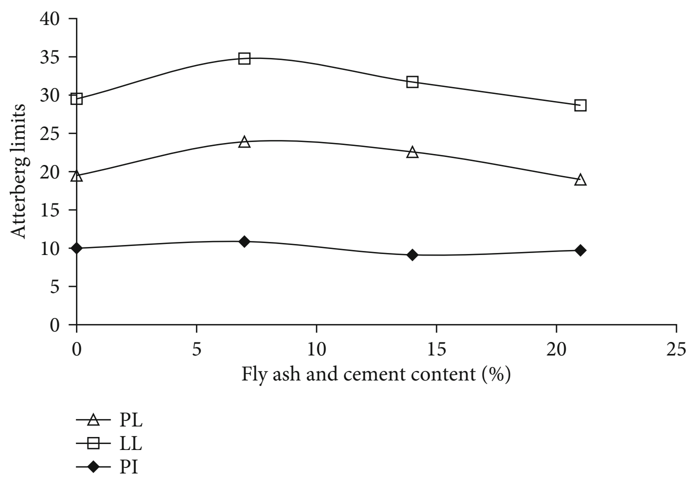

FIGURE 3: Effect of fly ash and cement on PL, LL, and PI.

2.5.4. Free Swell Index (according to IS-2720). The free swelling index is defined as an increase in volume caused by external impediments when soil is submerged in water.

2.5.5. CBR Test (as per AASHTO T-193). CBR is the proportion of the force required per unit area to penetrate the soil with a standard circular piston at a speed of 1.25 mm/min to the corresponding force needed to penetrate the standard substance. Normally, the penetration between 2.5 and 5 millimeter is considered separately, with the ratio at 5 mm being more outrageous than at 2.5 mm, and the ratio at 5 mm is used.

2.5.6. UCS Test (as per AASHTO T-208-90). UCS (q_u) is the load needed per unit area on which a cylindrical sample of a cohesive soil falls in compression.

$$q_u = \frac{P}{A}. \quad (1)$$

3. Results and Discussion

Laboratory experiments were carried out on natural soil samples to evaluate various properties. The test results are illustrated in Table 2.

As shown in Table 2, the primary index properties of expensive subgrade soil without admixtures are demonstrated. The schematic description of these comparisons with admixtures is discussed separately in coming subsections.

3.1. Influence of Fly Ash and Cement on the Engineering Properties of Subgrade Soil. Laboratory experiments were carried out, and the Atterberg limits were found, through which we were able to obtain the liquid limit (LL) and the plastic limit (PL). Through these two limits, we finally get the plasticity index (PI). Fly ash and cement with subgrade soil were extensively examined with the various percentages specified in earlier Section 2, and the results are shown in Table 3.

TABLE 4: Effects by fly ash and cement on the FSI value.

Mix proportion	Free swell index (%)	Degree of expansiveness	Percentage decrease (%)
0% FA+0% OPC	41	High	—
5% FA+2% OPC	34.3	Moderate	16.34
10% FA+4% OPC	26.4	Moderate	35.60
15% FA+6% OPC	20.6	Moderate	49.75
20% FA+8% OPC	12	Low	70.73

Table 3 reveals that with the expansion of fly ash and cement as the supplement of subgrade soil, the plastic limit and the liquid limit of the mixture first increase then decrease, thus paving the road for brittle and stiffer soil. Figure 3 illustrates the variations of LL and PL. It can be seen from the previous results that the increase and decrease of plastic limit value will eventually lead to the decline in the plastic index. The plasticity index value is further reduced by adding fly ash and cement to the subgrade soil, indicating compressibility.

3.2. Influence of Fly Ash and Cement on Free Swell Index (FSI). The change of free expansion index of different percentages of subgrade soil, fly ash, and cement mixture is shown in the table. Therefore, we can say that the addition of fly ash and cement reduces the FSI value, which implies a decrease in the degree of the expansiveness of the blended mixture. The results are presented in Table 4 and Figure 4.

The free soil index is expressed as follows [37]:

$$\text{FSI}\,(\%) = \left(\frac{V_w - V_k}{V_k}\right) \times 100, \quad (2)$$

where V_w and V_k are the volume of soil sample read

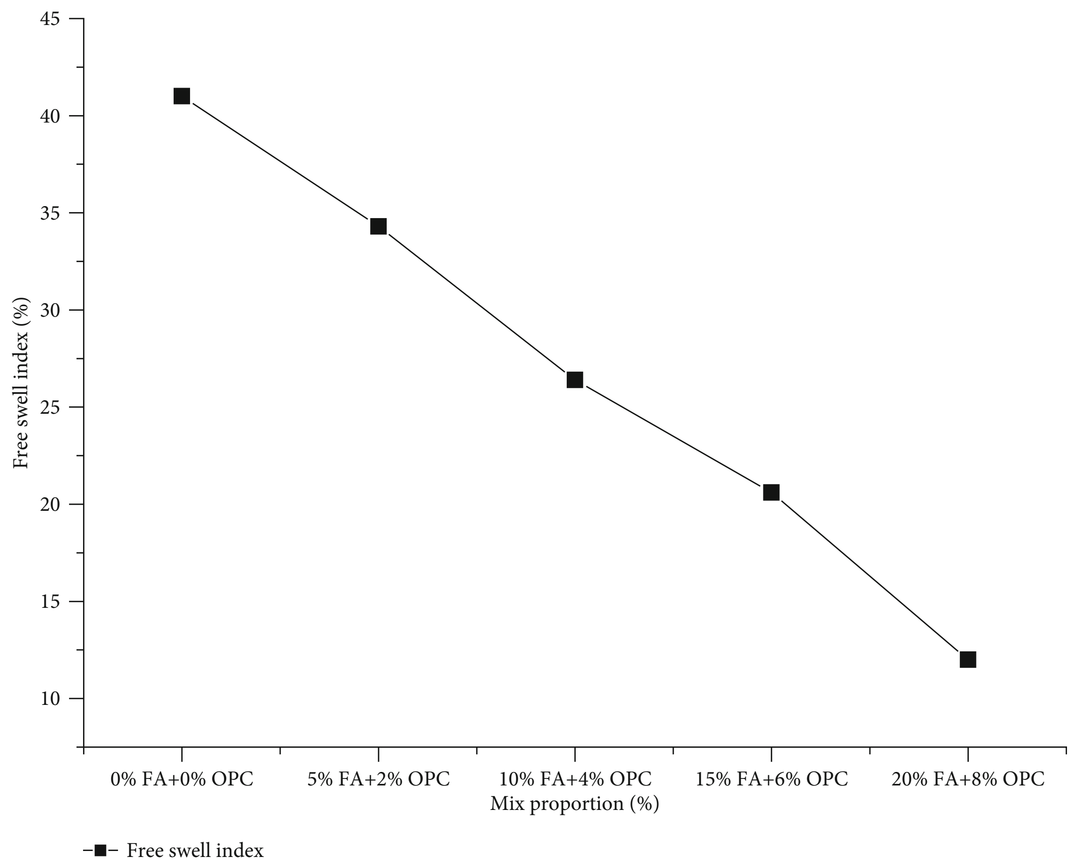

Figure 4: Free swell index for fly ash and cement mixes.

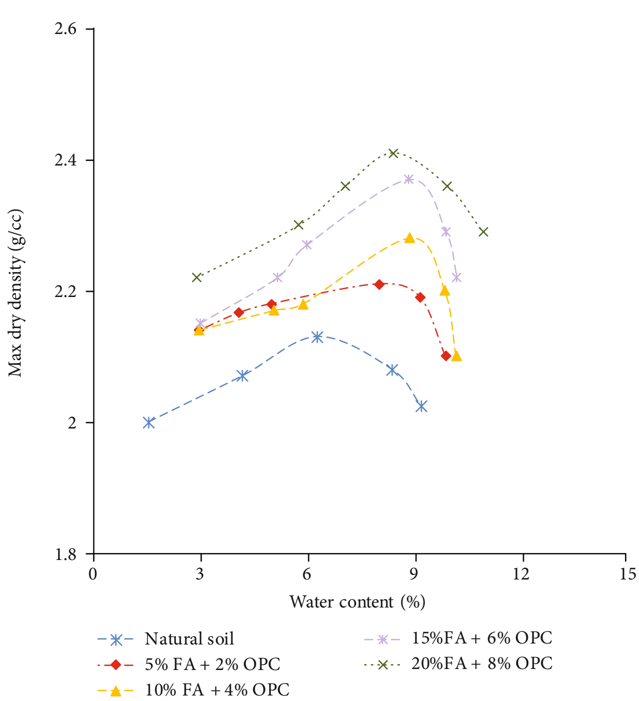

Figure 5: Maximum dry density vs. optimum moisture content for cement and fly ash mixes.

Table 5: The compaction test results.

Mix ratio	Moisture content (%)	Maximum dry density (g/cc)
0% FA+0% OPC	6.31	2.13
5% FA+2% OPC	8.05	2.21
10% FA+4% OPC	8.94	2.28
15% FA+6% OPC	8.89	2.37
20% FA+8% OPC	8.46	2.41

from a graduated cylinder filled with distilled water and kerosene, respectively.

3.3. Influence of Fly Ash and Cement on Compaction Values. Compaction is a method of increasing soil density by using mechanical tools to remove air voids and liquids between soil particles. Standard proctor compaction tests are conducted in the laboratory to determine the optimum moisture content (OMC) of the soil at maximum dry density (MDD). The results are illustrated in Figure 5 and Table 5.

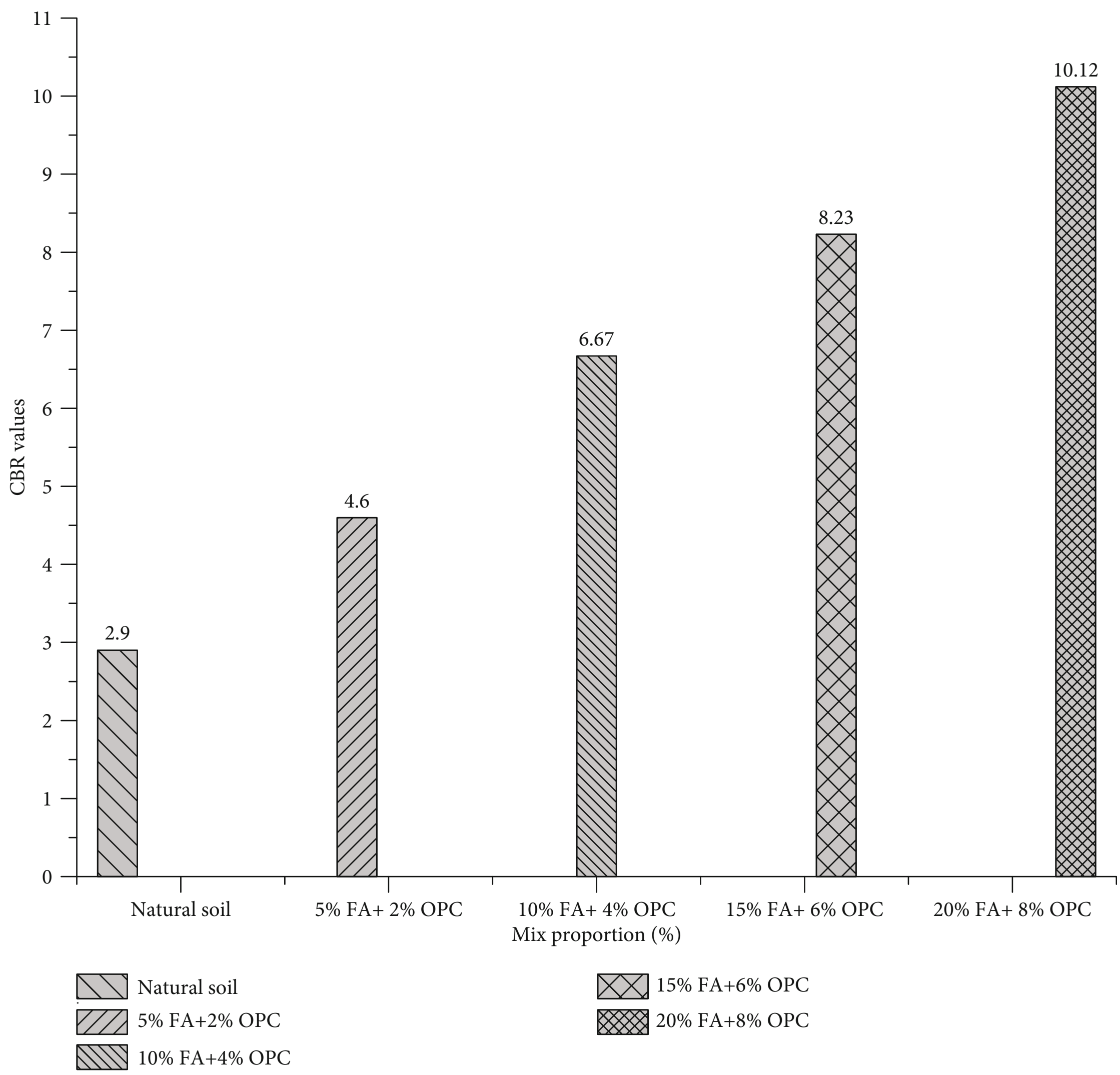

Figure 6: California bearing ratio of fly ash and cement mixture.

Table 6: The effect of adding cement and fly ash on the UCS value.

Mix proportion	1-day UCS (kPa)	7-day UCS (kPa)	14-day UCS (kPa)
Natural soil	86.880	—	—
5% FA+2% OPC	95.314	113.86	123.683
10% FA+4% OPC	105.48	114.85	133.80
15% FA+6% OPC	120.58	136.42	151.515
20% FA+8% OPC	124.47	146.11	167.75

Variance in dry density values is shown in Figure 5. It is inferred that the water content disturbs the density of the soil. As the percentage of water increases, the compacted density tends to decrease until the max dry density is reached, limiting the further inclusion of water to decrease the density. In adding fly ash and cement, the water content increases slightly, which naturally reduces the optimal water content and increases the MDD. Thereof, we can conclude that their maximum dry density is 2.41 in addition to 20% FA and 8% cement (8.46% water).

3.4. Effect of Fly Ash and Cement on California Bearing Ratio. The California bearing ratio (CBR) tests were conducted per the AASHTO code. The mold was a standard CBR with a detachable collar. The test was conducted on samples prepared at the modified Proctor's optimum water content and maximum dry density. Before the test, the soil additive mixture was compacted under the optimum water content and soaked in water for 4 days under the condition of overload weight of 5.72 kg. The results are plotted in Figure 6.

Figure 6 reveals that the CBR value of the initial subgrade soil is 2.9. With the inclusion of fly ash and cement, values are further improved. The optimum percentage of mixture 20% fly ash and 8% cement gives the CBR value 10.12, the best result for subgrade soil. Furthermore, by

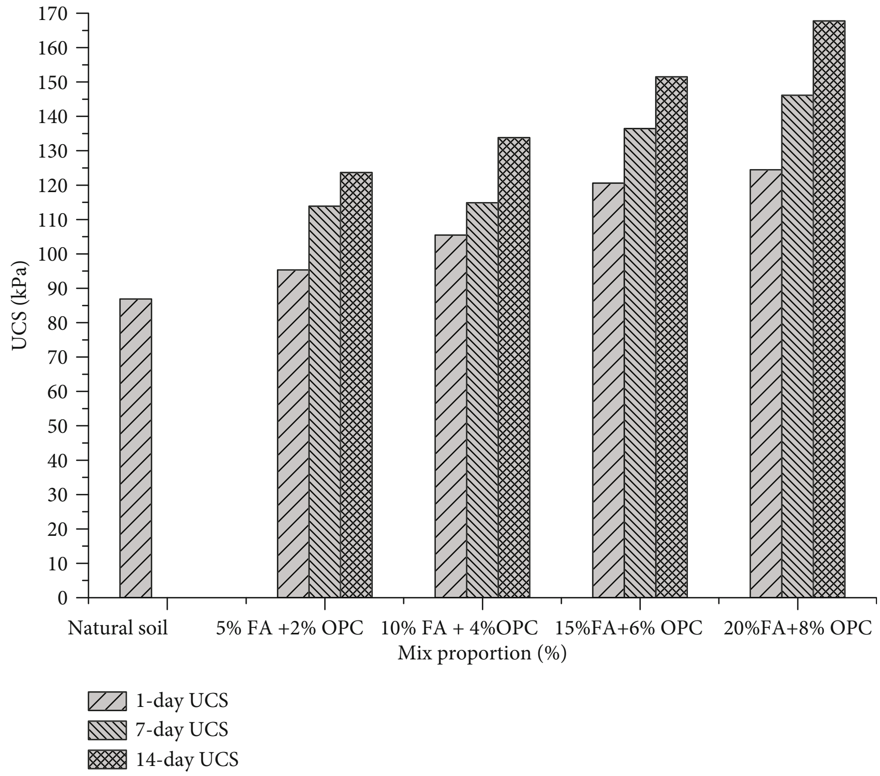

FIGURE 7: Comparison of unconfined compression strength for soil sample with, and without, fly ash and cement mixture.

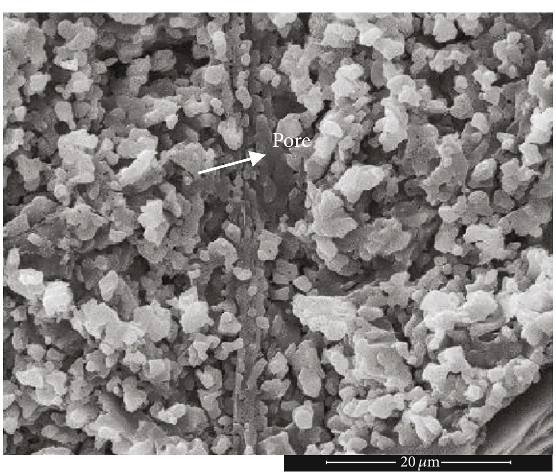

FIGURE 8: SEM image of natural soil.

performing dummy tests, the increase of the mixture supplement will lead to the decrease of CBR value from a dummy test, which indicates the reduction in subgrade strength.

3.5. Influence by Fly Ash and Cement on Unconfined Compressive Strength. Unconfined compressive strength test, referred to as an uniaxial compression test, is a special case of triaxial test. In the triaxial test, the unconfined pressure is zero. The application of the unconfined compression test (UCS) is to quickly estimate or evaluate the unconfined compressive strength of soil with enough cohesion to examine the unconfined state. Unlike fly ash and cement mixtures, the unconfined compressive strength of subgrade soil is arranged in Table 6. This shows that the UCS value differs from the increase in the percentage of fly ash and cement used to calculate the shear strength.

The graph shown in Figure 7 illustrates the distinct compressive strength achieved in 1 days, 7 days, and 14 days by the subgrade soil with differing fly ash and cement proportions. There was a significant rise in soil strength after treatment comparison with natural soil, as shown in Figure 7. The results show that the unconfined compressive strength of undisturbed soil is 86.88 kPa after one day of curing. Furthermore, the values were improved with the addition of additives. The 14-day test findings differ from the 1-day and 7-day test by demonstrating that the compressive strength improves with the inclusion of fly ash and cement. The changes of compressive strength up to a particular amount of different admixtures are required to fill the pores in the soil once the pores are filled, and the soil becomes densified. Further expansion may try to lose soil strength. The pozzolanic cementitious material produced by cement hydration reaction improves the bonding strength of soil particles [36]. The amount of pozzolanic cementitious material increases and hardens with the extension of curing time, which significantly enhances the compressive strength of treated soil. Besides, the maximum UCS value is inferred at 20% fly ash and 8% cement.

3.6. Influence of Fly Ash and Cement on Scanning Electron Microscopy Test (SEM). The micrographs of different scales were obtained to clarify the evaluation of microstructure.

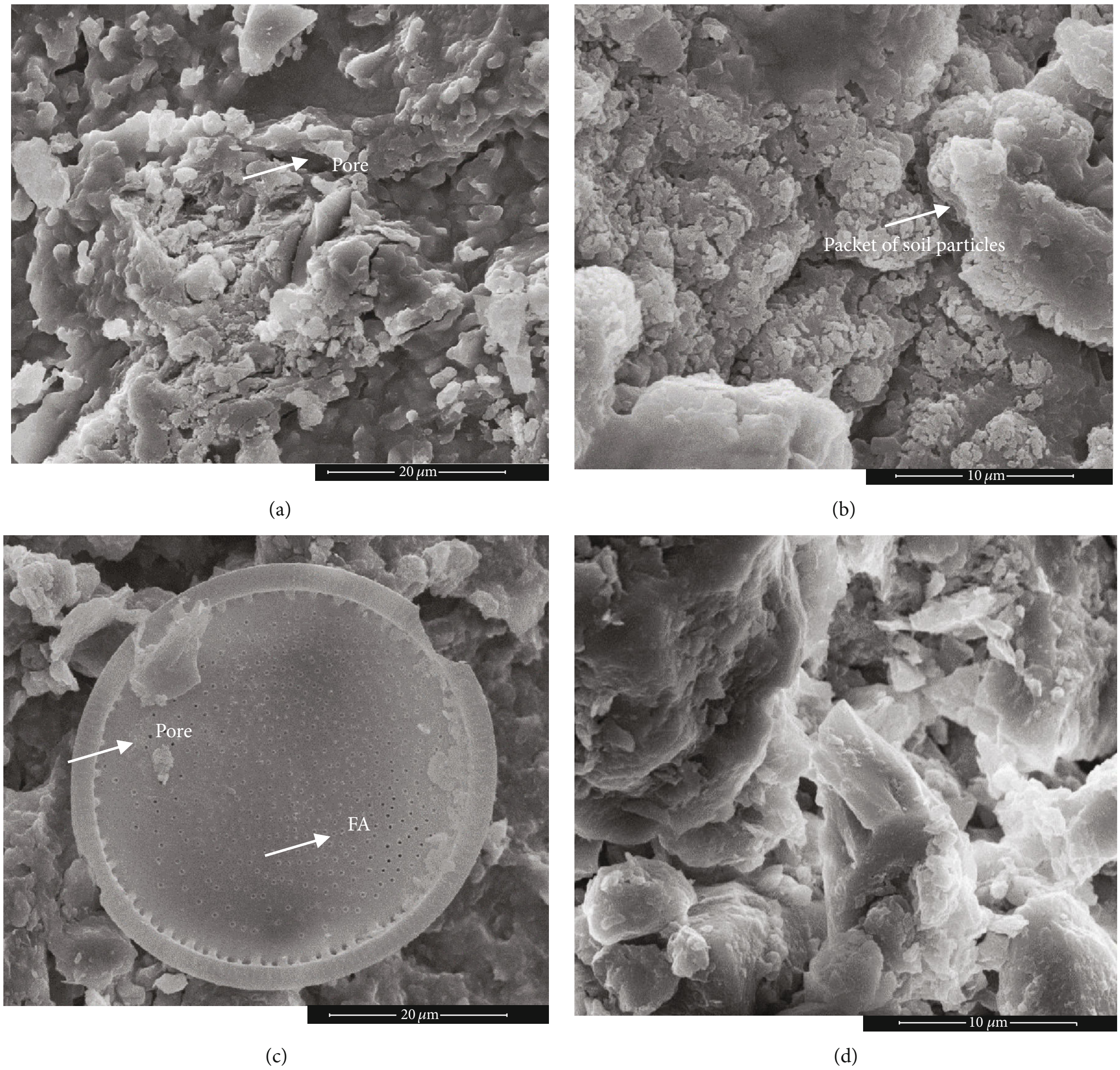

Figure 9: SEM photographs of treated soil containing varying percentages of fly ash and cement mixtures.

The scale of 20, 10 μm was shown in Figures 8 and 9 for natural and treated soil. Figure 9 indicates that the apparent shape of the treated soil particles becomes coarser due to the bonding influence of fly ash and cement binder, where this binder served to attach the fine soil particles to each other, forming broader and larger clusters of photomicrographs.

Figures 9(a) and 9(b) show a closer SEM image of the treated soil. Compared with the untreated soil image Figure 8, new compounds can be identified in the microstructure of treated samples at (a) and (b). It indicates the formation of cementitious products of fly ash and cement.

Figures 9(c) and 9(d) show a micrograph of the soil mixed with bonded 15% fly ash and 6% cement. In this picture, undulating flake particles can be observed. However, the micrograph of the mixed soil shown in image (c) shows that the microstructure of the mixed soil is more dense, compacted, and coherent than that of the untreated soil shown in Figure 8. This confirms the development of cementitious products which are concerned with improving the geotechnical properties of treated soils in this investigation. The image in Figure 9(d) structure shows it. The results showed that the treated soil had fewer pores and highly denser.

4. Conclusions

The study highlighted the stabilization of the problematic subgrade soil with cement and fly ash was investigated, and the effect of the stabilization on the characteristics and geotechnical properties of the subgrade soil were studied. According to the experimental results, the following conclusions can be drawn:

(1) The plastic limit, liquid limit, and plasticity index of the subgrade soil increase first and then decrease with FA and cement content. Meanwhile, the swelling potential of soil also reduces with the inclusion of fly ash and cement. The swelling characteristic, namely, the free swelling index, decreased from

41% to 12%, which is 70.73% lower than the initial value

(2) With the expansion of fly ash and cement content, the optimum moisture content decreases, and the maximum dry bulk density increases. The compaction curve drifts up and to the left as the optimal moisture content is reduced, and the maximum dry unit weight increased with an increase in fly ash and cement content. Adding fly ash and cement can be comparable with the improved compaction effect. Therefore, the subgrade soil becomes more stable

(3) With the increase of fly ash and cement content, the CBR value of soil increases. The CBR value of untreated soil was only 2.9; nevertheless, with the addition of fly ash and cement, the CBR value further increased. The optimum percentage of the mixture (20% fly ash+8% cement) gives the CBR value 10.12, the best result for subgrade soil

(4) Significant increments were observed in the unconfined compressive strength (q_u) of the treated soil. UCS increased with a steady increase in the proportion of fly ash and cement binder and age expansion. UCS of untreated soil is 86.88 kPa after a one-day curing period. However, the maximum UCS of 167.75 kPa, i.e., 20% FA+8% cement, increases to the initial value by 48.20%.

(5) The results show that the microstructure of treated soil samples changes significantly after adding different amounts of fly ash and cement through the understanding of microscopic images. Firstly, the particle size of the natural soil seemed to be larger voids than that of the treated soil. After the additives, a cement gel identical to the structure was observed for fly ash and cement, which covered and bound soil particles to each other. A coherent and compacted soil structure was achieved because of the reduction in the volume of the treated soil

Based on the comprehensive analysis results, it can be concluded that wastes (by-products) such as fly ash and cement can be effectively used in civil engineering construction. Succinctly, due to the large amount of fly ash in Pakistan and the rest of the world, it would be beneficial to utilize large amounts of fly ash. Meanwhile, the use of stabilized soil in this method has the dual advantages of removal removing harmful substances from the environment and, at the same time, the usage of inexpensive construction material for foundations and road networks.

Data Availability

All data generated or analyzed during this study are included in this published article.

Conflicts of Interest

The authors declare that they have no conflict of interest.

Acknowledgments

The authors acknowledge and appreciate the technical support provided by the Mehran University of Engineering and Technology, Jamshoro, Sindh, Pakistan. This research was supported by the "National Natural Science Foundation of China (71942006)" and "Big Data-Driven Structural Disasters Prediction and Maintenance in Hazardous Geological Regions of Subsea Tunnels Grant No. 51991395)".

References

[1] C. C. Ikeagwuani and D. C. Nwonu, "Emerging trends in expansive soil stabilisation: a review," *Journal of Rock Mechanics and Geotechnical Engineering*, vol. 11, no. 2, pp. 423–440, 2019.

[2] A. A. Firoozi, C. Guney Olgun, A. A. Firoozi, and M. S. Baghini, "Fundamentals of soil stabilization," *International Journal of Geo-Engineering*, vol. 8, no. 1, p. 26, 2017.

[3] D. Zhang, A. Ding, T. Li, and X. Wu, "Effects of passivators on *Artemisia selengensis* yield and Cd stabilization in a contaminated soil," *Polish Journal of Environmental Studies*, vol. 30, no. 2, pp. 1903–1912, 2021.

[4] D. Castro-Fresno, D. Movilla-Quesada, Á. Vega-Zamanillo, and M. A. Calzada-Pérez, "Lime stabilization of bentonite sludge from tunnel boring," *Applied Clay Science*, vol. 51, no. 3, pp. 250–257, 2011.

[5] C. McDowell, *Stabilization of Soils with Lime, Lime-Flyash, and Other Lime Reactive Materials*, Highw. Res. Board Bull., 1959, http://onlinepubs.trb.org/Onlinepubs/hrbbulletin/231/231-004.pdf.

[6] P. Indiramma, C. Sudharani, and S. Needhidasan, "Utilization of fly ash and lime to stabilize the expansive soil and to sustain pollution free environment - an experimental study," *Materials Today: Proceedings*, vol. 22, pp. 694–700, 2020.

[7] T. S. Nagaraj and N. Miura, "Soft clay behaviour : analysis and assessment," Brookfield, VT, Rotterdam, 2001, https://www.crcnetbase.com/isbn/9780415889285.

[8] S. D. Khadka, P. W. Jayawickrama, S. Senadheera, and B. Segvic, "Stabilization of highly expansive soils containing sulfate using metakaolin and fly ash based geopolymer modified with lime and gypsum," *Transportation Geotechnics*, vol. 23, article ???, 2020.

[9] A. E. Ramaji, "A review on the soil stabilization using low-cost methods," *Journal of Applied Sciences Research*, vol. 8, no. 4, pp. 2193–2196, 2012.

[10] B. R. Phanikumar and T. V. Nagaraju, "Effect of fly ash and rice husk ash on index and engineering properties of expansive clays," *Geotechnical and Geological Engineering*, vol. 36, no. 6, pp. 3425–3436, 2018.

[11] M. Abu-Farsakh, S. Dhakal, and Q. Chen, "Laboratory characterization of cementitiously treated/stabilized very weak subgrade soil under cyclic loading," *Soils and Foundations*, vol. 55, no. 3, pp. 504–516, 2015.

[12] D. K. Swain, S. K. Rautaray, and B. C. Ghosh, "Alkaline coal fly ash amendments are recommended for improving rice-peanut crops," *Acta Agriculturae Scandinavica, Section B - Plant Soil Science*, vol. 57, no. 3, pp. 201–211, 2007.

[13] C. Marieta, A. Guerrero, and I. Leon, "Municipal solid waste incineration fly ash to produce eco-friendly binders for

sustainable building construction," *Waste Management*, vol. 120, pp. 114–124, 2021.

[14] B. J. Priatmadi, A. R. Saidy, and M. Septiana, "Soil properties and growth performance of rize (Oryza sativa L.) grown in a fly-ash amended soil," *Tropical Wetland Journal*, vol. 1, no. 1, pp. 19–24, 2015.

[15] H. Verma and A. Dubey, "The impact of fly ash application on the carbohydrate content of wheat (Triticum aestivum)," *Journal of Agroecology and Natural Resource Management*, vol. 6, no. 1, pp. 9–12, 2019.

[16] J. J. Camberato, E. D. Vance, and A. V. Someshwar, *Composition and land application of paper manufacturing residuals*, ACS Publications, 1997.

[17] R. C. Joshi and R. P. Lohita, *Fly Ash in Concrete: Production, Properties and Uses*, Taylor & Francis, 1997.

[18] M. Singh and R. Siddique, "Effect of coal bottom ash as partial replacement of sand on workability and strength properties of concrete," *Journal of Cleaner Production*, vol. 112, pp. 620–630, 2016.

[19] A. B. Mukherjee, R. Zevenhoven, P. Bhattacharya, K. S. Sajwan, and R. Kikuchi, "Mercury flow via coal and coal utilization by-products: a global perspective," *Resources, Conservation and Recycling*, vol. 52, no. 4, pp. 571–591, 2008.

[20] V. C. Pandey and N. Singh, "Impact of fly ash incorporation in soil systems," *Agriculture, Ecosystems and Environment*, vol. 136, no. 1–2, pp. 16–27, 2010.

[21] Global Cement staff, "Diamer Basha Dam to use concrete containing fly ash - cement industry news from Global Cement," 2020, 2021, https://www.globalcement.com/news/item/11101-diamer-basha-dam-to-use-concrete-containing-fly-ash.

[22] M. J. Munir, S. M. S. Kazmi, Y.-F. Wu, and I. Patnaikuni, "A literature review on alkali silica reactivity of concrete," *International Journal of Strategic Engineering*, vol. 1, no. 2, pp. 43–62, 2018.

[23] B. R. Phani Kumar and R. S. Sharma, "Effect of fly ash on engineering properties of expansive soils," *Journal of Geotechnical and Geoenvironmental Engineering*, vol. 130, no. 7, pp. 764–767, 2004.

[24] G. Albayrak and U. Albayrak, "Civil Engineering Journal," *Civil Engineering*, vol. 2, no. 10, 2016.

[25] EuroSoilStab, "Design guide: soft soil stabilisation. EuroSoilStab: development of design and construction methods to stabilise soft organic soils," 2002, http://BREbookshop.com.

[26] X. Zhang, W. Li, Z. Tang, X. Wang, and D. Sheng, "Sustainable regenerated binding materials (RBM) utilizing industrial solid wastes for soil and aggregate stabilization," *Journal of Cleaner Production*, vol. 275, p. 122991, 2020.

[27] C. C. Ikeagwuani, I. N. Obeta, and J. C. Agunwamba, "Stabilization of black cotton soil subgrade using sawdust ash and lime," *Soils and Foundations*, vol. 59, no. 1, pp. 162–175, 2019.

[28] P. Rai, H. Pei, F. Meng, and M. Ahmad, "Utilization of marble powder and magnesium phosphate cement for improving the engineering characteristics of soil," *International Journal of Geosynthetics and Ground Engineering*, vol. 6, no. 2, p. ???, 2020.

[29] U Joint Departments of the Army and the Air Force, "Soil stabilization for pavements," in *Tech. Man. No. 5-822-14; Air Force Man. No. 32-1019*, pp. 2–57, University Press of the Pacific, 2004.

[30] J. Muthuramalingam and L. Sing, "Experimental studies on treated sub-base soil with fly ash and cement for sustainable design recommendations," *International Journal of Engineering and Applied Sciences*, vol. 6, no. 8, pp. 331–334, 2012.

[31] C. Fan, B. Wang, and T. Zhang, "Review on cement stabilization/solidification of municipal solid waste incineration fly ash," *Advances in Materials Science and Engineering*, vol. 2018, Article ID 5120649, 7 pages, 2018.

[32] Q. Tang, Y. Liu, F. Gu, and T. Zhou, "Solidification/stabilization of fly ash from a municipal solid waste incineration facility using Portland cement," *Advances in Materials Science and Engineering*, vol. 2016, Article ID 7101243, 10 pages, 2016.

[33] P. Venkara Muthyalu, K. Ramu, and G. V. R. Prasada Raju, "Study on performance of chemically stabilized expansive soil," *International Journal of Advances in Engineering and Technology*, vol. 2, no. 1, pp. 139–148, 2012.

[34] P. Ganapati Naidu, P. V. V. Satyanarayana, C. Sekar Ganja, and K. Durga Rani, "Effect of cement on cement stabilized low plastic graded gravel soils," *Materials Today: Proceedings*, 2021.

[35] N. K. Sharma, S. K. Swain, and U. C. Sahoo, "Stabilization of a clayey soil with fly ash and lime: a micro level investigation," *Geotechnical and Geological Engineering*, vol. 30, no. 5, pp. 1197–1205, 2012.

[36] E. O. Tastan, T. B. Edil, C. H. Benson, and A. H. Aydilek, "Stabilization of organic soils with fly ash," *Journal of Geotechnical and Geoenvironmental Engineering*, vol. 137, no. 9, pp. 819–833, 2011.

[37] W. G. Holtz, "Engineering properties of expansive clays," *Transactions of the American Society of Civil Engineers*, vol. 121, pp. 641–677, 1954.

Hindawi
Geofluids
Volume 2021, Article ID 1968846, 13 pages
https://doi.org/10.1155/2021/1968846

Research Article

Influence of Mine Earthquake Disturbance on the Principal Stress of the Main Roadway near the Goaf and Its Prevention and Control Measures

Penghui Guo,[1] **Jiazhuo Li**,[1,2,3] **Xiqing Hao**,[4] **Heng Cui**,[5] **Lihua Tian**,[4] **Wenhao Xie**,[1] **and Jiaqi Chu**[1]

[1]*School of Mining Engineering, Anhui University of Science and Technology, Huainan, Anhui 232001, China*
[2]*Institute of Energy, Hefei Comprehensive National Science Center, Hefei, Anhui 230031, China*
[3]*School of Mining Engineering, China University of Mining and Technology, Xuzhou 221116, China*
[4]*Gaozhuang Coal Industry Co., Ltd., Zaozhuang Mining Group, Jining, Shandong 277605, China*
[5]*Shandong Energy Zikuang Group, Zibo, Shandong 250014, China*

Correspondence should be addressed to Penghui Guo; gph1996@yeah.net and Jiazhuo Li; jiazhuoli@aust.edu.cn

Received 4 August 2021; Accepted 7 September 2021; Published 16 September 2021

Academic Editor: Bailu Teng

With the reduction and depletion of shallow energy, the mining depth of coal around the world is increasing year by year, and the mining depth of some coal mines in China has reached kilometers. The main roadway near the goaf with the deep high static stress is very easy to be damaged after being disturbed by the mine earthquake. Taking the main roadway in the no. 1 mining area of Gaojiapu coal mine in Binchang mining area, Shaanxi Province, China, as the engineering background, the high-energy mine earthquake monitored by the on-site microseism is equivalently simulated through the dynamic module of FLAC^{3D}, and the spatial-temporal rotation characteristics of the principal stress of roadway surrounding rock under the disturbance of mine earthquake are studied and analyzed and put forward corresponding prevention and control measures. Research shows early stage of mine earthquake disturbance, roadway roof is first affected, and the principal stress of the roof has the trend of deflection to the side of the goaf. In the middle stage of mine earthquake disturbance, the main body of roof principal stress deflects to the side of goaf, and the deflection range is large. In the later stage of mine earthquake disturbance, the principal stress directions in the surrounding rock reverse rotation, and the reverse rotation angle of the principal stress direction in the roof is the largest. Finally, the asymmetric distribution characteristics of principal stress rotation are verified by using the asymmetric deformation phenomenon on both sides of roadway surrounding rock. Based on the rotation characteristics of principal stress under the dual influence of mine earthquake disturbance and goaf, optimize the layout scheme and blasting parameters of blasting pressure relief holes. The transmission direction of principal stress can be changed by blasting pressure relief method; meanwhile, the transmission of principal stress can be blocked; through the comparison of microseismic activity law before and after pressure relief, pressure relief effect is good. The research results can provide a certain reference basis for coal mine roadway pressure relief and reducing disaster conditions.

1. Introduction

Energy and mineral resources are important factors restricting the national economic development of all countries in the world; with the reduction and depletion of shallow resources, the mining depth of coal all over the world is increasing year by year [1–3]. At present, the mining depth of coal mines in China is increasing at the rate of 8~12 m per year; the eastern mine develops at the rate of 100~250 m every ten years; it is estimated that in the next twenty years, many coal mines will enter a depth of 1000~1500 m. With the excavation and construction of underground space entering the deep mining, geological environment has become more complex; it makes the rock mechanics of deep underground engineering become the focus of international research in the field of mining and rock mechanics [4, 5].

After entering deep mining, while bearing high in situ stress, the rock mass experiences strong mining disturbance, and mining disturbance often induces seismicity, which is called mine earthquake [6–9]. With the increase of coal mining depth, underground coal mines are gradually affected by mine earthquakes [10, 11]. Under deep in situ stress, tectonic stress, and engineering disturbance, it causes the whole coal rock system to lose structural stability; engineering disasters such as large deformation failure, collapse, and rock burst occur in the surrounding rock; it not only affects the progress of the whole project but also threatens the life safety of construction personnel [12, 13].

Many scholars have studied the deformation and failure of roadway surrounding rock and its stress field environment. Yang et al. [14] studied the stability of roadway surrounding rock under dynamic disturbance (stress time curve) by using orthogonal test method. Chen et al. [15] believe that mining disturbance changes the size and direction of stress field in roadway surrounding rock, which is the main factor for asymmetric deformation of roadway. Xu et al. [16] studied the stress environment of lower coal seam roadway with the principal stress difference as the measurement index. Yang et al. [17] studied the frequency spectrum characteristics of rockburst vibration wave and the failure law of roadway surrounding rock by using the similar simulation experiment method. Li et al. [18] studied the action of principal stress in different directions by model test and numerical simulation, damage, and failure law of surrounding rock of straight wall arch tunnel. Xie et al. [19] used $FLAC^{3D}$ to simulate the principal stress difference of roadway surrounding rock, the response characteristics of plastic zone, and the evolution law of two groups of principal stress difference under the condition of buried depth of 550~1250 m. Niu et al. [20] with the help of self-developed three-dimensional stress testing elements reveal the true loading and unloading stress path of surrounding rock at different depths of deep roadway and the stress state before and after excavation; the evolution law of the principal stress difference of surrounding rock inside and outside the loose zone is mainly analyzed, and combined with the failure range and mode of surrounding rock, its mechanism is discussed. Li et al. [21] studied the variation law of the direction of the principal stress field of the surrounding rock on the side of the goaf and its influence mechanism on the distribution of plastic zone of surrounding rock along goaf roadway; the mechanism of nonuniform large deformation of deep goaf roadway is revealed. Underground rock mass engineering is usually in a complex triaxial stress state; before the rock mass is excavated, the primary rock stress is in equilibrium. The original stress balance state is destroyed when excavating roadway or mining; under the influence of mining disturbance, the stress in the rock mass is redistributed; extending from the excavation boundary to the interior of surrounding rock, the stress field gradually returns to the original rock equilibrium state [22–24]. The excavation and construction of underground space engineering will not only change the near-field stress of disturbed surrounding rock but also change the direction of stress [25–28]. A large number of geotechnical experiments show that principal stress rotation is a mechanical problem that must be considered in geotechnical engineering [29–31].

Therefore, this paper takes the principal stress closely related to the deformation and failure of rock mass as the starting point; the spatial-temporal rotation law of principal stress direction under mine earthquake disturbance is expounded and put forward effective prevention and control measures; conclusion is verified by the deformation of roadway surrounding rock on-site, and the effect of prevention and control measures is tested by means of on-site microseismic monitoring. The research results can provide a certain reference basis for coal mine roadway pressure relief and reducing disaster conditions.

2. Engineering Geological Background

Gaojiapu coal mine is located in the northwestern part of the Binchang mining area in Shaanxi Province, China; it is the second pair of modern large-scale mines developed and constructed by Shandong Energy Zikuang Group in Binchang mining area, Shaanxi Province. Gaojiapu well field connects with Yangjiaping and Mengcun well fields in the south, extends to the Jinghe River in the north, adjoins Yadian mine in the east, and extends to the border between Shaanxi and Gansu in the west. It is the administrative division of Gaojiapu well field under the jurisdiction of Changwu County in Shaanxi Province, 13 km away from Changwu County; it covers an area of 37.33 hm^2. The east-to-west length is approximately 25.7 km, and the south-to-north width is approximately 16.6 km; the field area is 219.1699 km^2, the geological resource reserves are 970 million tons, and the designed recoverable resource reserve is 470 million tons. The design production capacity of Gaojiapu mine is 5.0 Mt/a, and the service life is 62.5 years; in this mine, 4# coal seam of Jurassic Yanan formation is mainly exploited, and the average burial depth is 960 m; the average thickness of the 4# coal seam in no. 1 mining area is 10 m. The geographical location of Gaojiapu coal mine and the distribution map of surrounding mines are shown in Figure 1.

The main coal roadway in no.1 mining area of Gaojiapu coal mine is located at 4# coal seam, the roadway section shape is straight wall semicircular arch, roadway is 5.8 m wide, the wall is 3 m high, and the arch is 3 m high. The right side of the main roadway is the goaf (three working faces on the right have been mined); use the underground elevation data of the no. 1 mining area of the coal seam to draw the surrounding environment and topographic map of the main roadway (as shown in Figure 2). It can be clearly seen that the main roadway is in the syncline axis; therefore, it is seriously affected by strong tectonic stress.

Figure 1: Geographical location of Gaojiapu coal mine and its surrounding coal mine distribution.

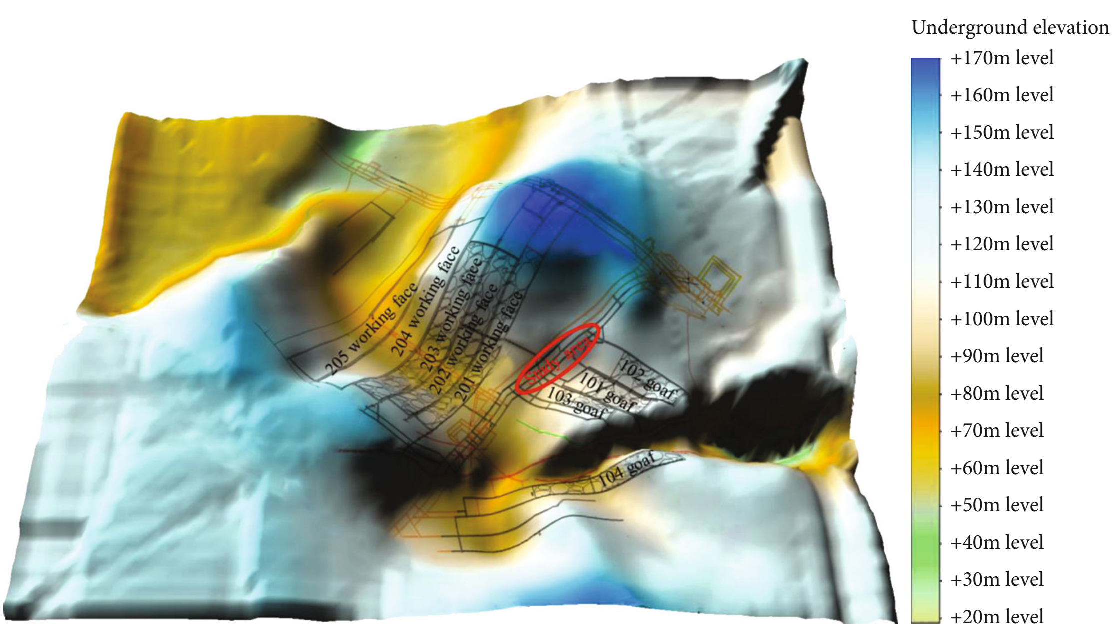

Figure 2: Surrounding environment and terrain of main roadway.

3. Research Methods

3.1. On-Site Mine Earthquake Monitoring. Microseismic monitoring technology is to utilize the microearthquake phenomenon in the process of coal rock mass failure. The seismic wave generated by the internal fracture of coal mass is monitored in real time by setting up microseismic monitoring probe in three-dimensional space around the coal rock mass. Various vibration parameters (vibration energy, vibration frequency, vibration torque, pressure drop, etc.) are determined through the analysis of microseismic events and focal location; on this basis, the stress state and failure of coal and rock mass are judged. Microseismic monitoring technology is considered as the most potential monitoring method for deformation and instability of coal and rock mass [32].

Import the waveform file monitored by the pickup in the microseismic system into the microseismic 3D visualization software (independently developed by Linming Dou team of China University of Mining and Technology), delineate the main roadway area of no. 1 mining area through geological coordinates, and export the data of mine earthquake events in the area, including mine earthquake frequency, energy level, and other information. Then, locate the exported mine seismic data into the mine geological CAD map; the position of the mine shock in the vertical direction can be obtained from the profile chart. On the day of an accident in the main roadway of no. 1 mining area of Gaojiapu coal mine, two large energy events of 10^5~106 J were detected in the area of 20 meters above the roof; the location distribution of mine earthquake focal points is shown in Figure 3.

3.2. Numerical Simulation

3.2.1. Establishment of Numerical Model. Taking the main coal roadway in no. 1 mining area of Gaojiapu coal mine as the simulation object, the numerical model is established by using FLAC^{3D} software; model size is 520 m × 400 m × 100 m, and the model is established as shown in Figure 4. According to the in situ stress measurement report on the mine, the ratio of the maximum horizontal principal stress to the minimum horizontal principal stress is 4.48~5.25, and maximum horizontal principal stress is about 1.61~1.81 times of the vertical principal stress. The in situ stress field is dominated by horizontal stress, it belongs to high-level tectonic stress field; therefore, the influence of principal stress on roadway surrounding rock is mainly considered. The values of physical and mechanical parameters of surrounding rock in the model are listed in Table 1, the Mohr-Coulumb failure criterion was adopted, and the boundary conditions were determined as follows:

(1) The displacement boundary constraint was applied to the model perimeter. The velocities in the x direction at the left and right boundaries, in the y direction at front and rear boundaries, and those in the x, y, and z directions at the bottom boundary were zero

(2) The upper boundary of this model was a free boundary, and a vertical uniformly distributed load was applied to simulate the self-weight load of overlying strata. Given the influence of self-weight of this model, the self-weight load of overlying strata applied was 22.5 MPa

(3) The geostatic stress field was applied to this model, and the gravitational acceleration was taken as 9.81 m/s^2

(4) The average value of lateral pressure coefficient is 1.7; the applied value of lateral stress is 1.7 times of overburden self-weight stress

Because the research object is the main coal roadway in no. 1 mining area, one working face is excavated at one time; as the 104 goaf is far from the main roadway, only three working faces are excavated to simulate the goaf on one side of the main roadway; according to the actual mining sequence of Gaojiapu coal mine, three working faces are excavated in turn and calculated to balance.

3.2.2. Application of Dynamic Load Disturbance. Reference [33] obtained the waveform characteristics of roof fracture and fault activation events through microseismic monitoring; according to the elastic wave theory, any complex stress wave can be obtained by Fourier transform of several simple harmonic waves, that is, simple harmonic is the basic form of downhole complex stress wave. According to reference [34], the duration of vibration recorded by the microseismic monitoring system is only tens of milliseconds when rock burst occurs on-site; generally, there is no effect of multiple rounds of impact in the dynamic load source of rock burst. If the mine earthquake wave is simplified into simple harmonic, the main frequency of mine earthquake is about 10~20 Hz, and the period is 0.05~0.1 s; when the dynamic load time applied in the simulation is about one period, the coal and rock mass will be destroyed. Therefore, the dynamic module in FLAC^{3D} software is used to apply a sinusoidal stress wave 20 m above the roadway to simulate mine earthquake and set the source strength of 48 MPa (equivalent to 10^6 J energy) [35] and frequency of 20 Hz; the action time of dynamic load is 0.1 s, and the dynamic load waveform is shown in Figure 5

3.2.3. Study the Principal Stress Direction through the Equal Angle Stereonet. There is a process of damage development in the failure of coal and rock mass; under the action of stress, there is a certain speed of crack propagation; it takes a certain time for microcracks to propagate from micro to penetration and nucleation to form macrofracture surface. Therefore, under the action of dynamic load, before coal failure, the stress can increase to a higher value in a period of time, showing high strength. On the contrary, inside the coal body, when the superposition of dynamic load and static load makes the principal stress axis rotate, the crack that is not easy to expand under static load can expand and aggravate the damage of coal and rock mass. The damaged coal and rock mass forms a stacked block structure, and its strength has various anisotropy, the principal stress direction rotates under dynamic load, and instability probability of block structure is increased.

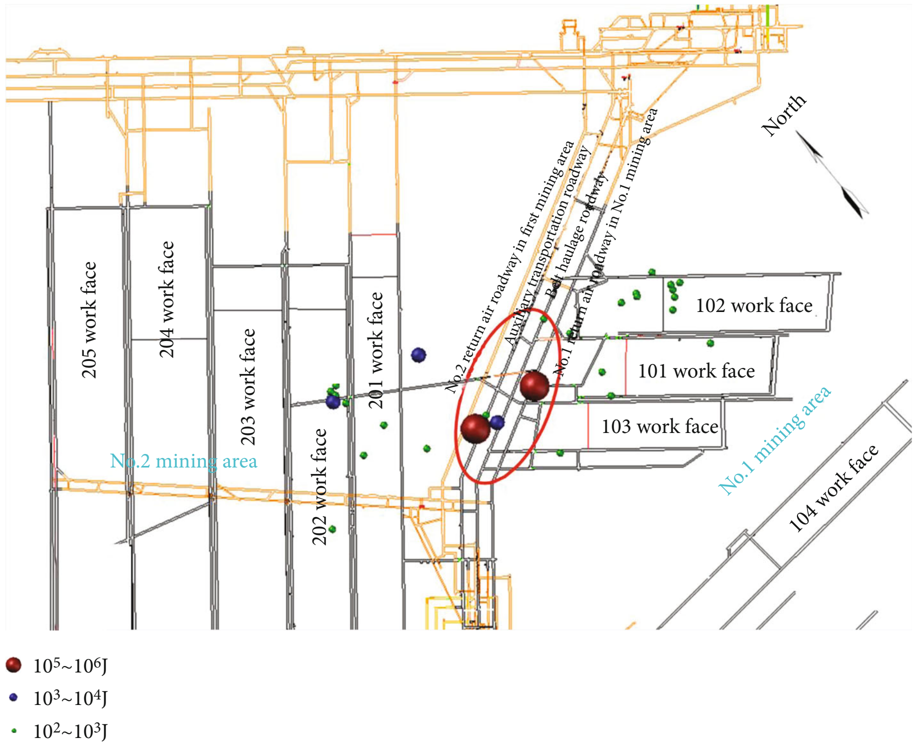

(a)

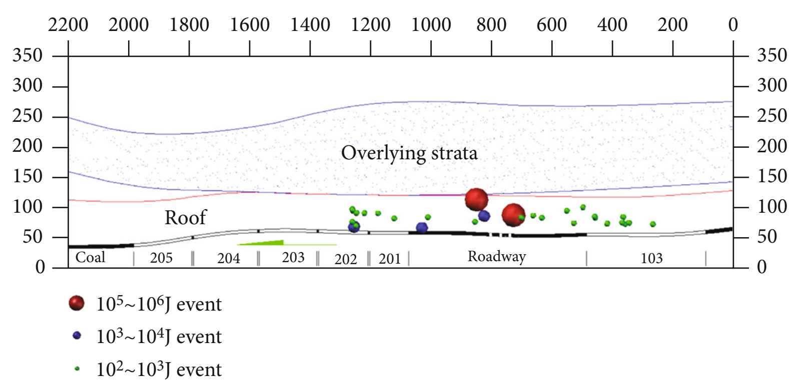

(b)

FIGURE 3: Location distribution of mine earthquake sources monitored by microseism. (a) Plane distribution of mine earthquake; (b) profile distribution of mine earthquake.

Under dynamic load, coal and rock masses show the characteristics of microdamage, decrease of critical static load stress, and increase of macrofailure strength. When the dynamic load fluctuates in the state of "increase-decrease-increase-decrease," the microdamage continues, the macrostress does not increase to the maximum, and coal and rock mass shows damage fatigue failure. Therefore, coal and rock masses are more likely to be damaged under dynamic load. The large-scale coal body contains a large number of joints and fractures. The randomly distributed primary fractures may be formed in the coal forming process or in the later tectonic movement. The existence of fractures leads to the anisotropic mechanical characteristics of coal, that is, the mechanical behavior of coal will change due to the rotation of the direction of principal stress.

Because the three-dimensional principal stress direction is a spatial vector, the evolution law of the principal stress direction of surrounding rock in the mining process cannot be described intuitively and accurately on the plane. Therefore, this paper uses the equal angle stereonet in geological data processing to represent the variation law of azimuth and inclination angle in the direction of principal stress [36].

The equal angle stereonet is composed of a base circle and longitude and latitude grid; the base circle is the stereographic equatorial large circle of the projection sphere, and the longitude and latitude grid is composed of a series of large longitudinal arcs and a series of small latitudinal arcs. The geometric elements (lines and planes) of the three-dimensional space of the object are reflected on the projection plane for research and processing, the spatial plane is

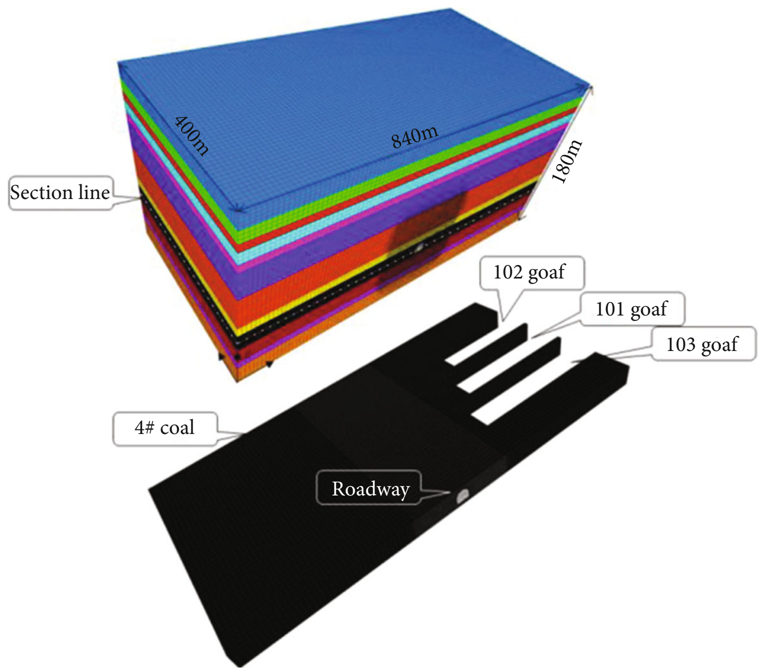

Figure 4: Numerical model of main roadway near goaf in no. 1 mining area of Gaojiapu coal mine.

Table 1: Physical and mechanical parameters of surrounding rock.

Rock formation	Bulk modulus (GPa)	Shear modulus (GPa)	Density (kg·m^{-3})	Cohesion (MPa)	Internal friction angle (°)	Uniaxial tensile strength (MPa)
Mudstone	6.08	3.47	2 480	1.2	30	0.61
Silty sandstone	10.8	8.13	2 460	2.75	38	2.67
Coarse sandstone	12	8	2 700	2.0	45	0.2
Silty sandstone	10.8	8.13	2 460	2.75	38	2.67
Coarse sandstone	12	8	2 700	2.0	45	0.2
Silty sandstone	10.8	8.13	2 460	2.75	38	2.67
Coarse sandstone	12	8	2 700	2.0	45	0.2
Silty sandstone	10.8	8.13	2 460	2.75	38	2.67
4# coal	4.9	2.01	1 380	1.25	32	0.15
Mudstone	6.08	3.47	2 480	1.2	30	0.61
Coarse sandstone	12	8	2 700	2.0	45	0.2
Medium sandstone	11	8.5	2 820	3.2	42	1.29

displayed as an arc on the equal angle stereonet, and spatial straight line is displayed as a point on the equal angle stereonet; position of spatial plane and spatial line is represented by inclination angle/azimuth. The equal angle stereonet is not only a simple and intuitive calculation method, but also an image and comprehensive quantitative graphic method.

The principal stress direction of surrounding rock is a vector, so the inclination angle/azimuth is used to represent the position of this space vector. The inclination angle is defined as the acute angle between the main stress direction and its projection on the *xy* plane. Variation range of the inclination angle is -90°~90°, a positive value indicates that the principal stress direction is above the *xy* plane, and a negative value indicates that the principal stress direction is below the *xy* plane. The azimuth is defined as the angle between the clockwise rotation from the positive direction of the *y*-axis to the projection line of the principal stress direction on the *xy* plane; variation range of the azimuth is 0°~360°.

As shown in Figure 6, on the equal angle stereonet, the projection of the principal stress direction is a point; by

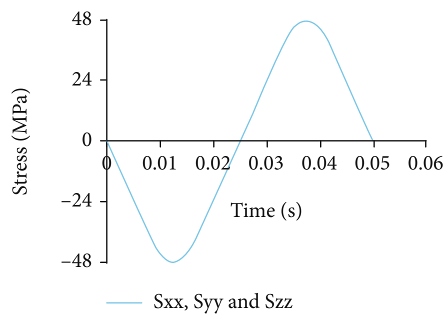

Figure 5: Dynamic stress waveform.

connecting the center of the equal angle stereonet with the projection point and extending it to intersect the equatorial large circle, the reading at the intersection is the azimuth. Rotate the connected straight line to the horizontal along the direction of the acute angle with the horizontal straight line, and the indication of the projection point in the direction of the principal stress at the position on the horizontal straight line is the inclination angle.

4. Result Discussion

4.1. Spatial-Temporal Rotation Characteristics of Principal Stress. Figure 7 shows the equal angle stereonet of the principal stress direction of the surrounding rock of the deep roadway with the action time of the dynamic load.

As can be seen from Figure 7, before dynamic load disturbance, due to the dual influence of high-level tectonic stress and excavation unloading effect, the direction of principal stress in surrounding rock deviates from xy plane (recorded as horizontal plane), but still in a vertical plane parallel to the x-axis (recorded as plane α).

When the dynamic load disturbance is 0.01 s, the dynamic load stress wave does not propagate to the coal seam, so there is no obvious change in the direction of principal stress in the coal seam and floor. The main azimuth of the principal stress in the roof is inclined to the side of the roadway goaf, between 30° and 90°. The inclination angle decreases, between 45° and 90°, deviate from the vertical plane parallel to the y-axis (recorded as plane β).

During dynamic load disturbance of 0.03 s~0.05 s, the azimuth of the roof varies greatly, and the inclination angle is between 45° and 75°. As the dynamic load disturbance stress wave propagates to the roadway floor, the inclination angle of the main stress of the coal seam deflects towards the horizontal plane; the inclination angle and azimuth are reduced; by plane α, directional plane β rotates; the rotation amplitude is close to 90°. The azimuth of the principal stress of the floor does not change obviously, and the inclination angle decreases slightly, but the main body is still inside plane α.

When dynamic load disturbance is 0.07 s~0.09 s, the principal stress of disturbed surrounding rock rotates reversely, the principal stress of the roof faces plane β deflection, and the inclination angle increases obviously. The principal stress of the coal seam deviates from the horizontal plane, the inclination angle and azimuth increase, and by plane β, directional plane α rotates. There is no obvious reverse rotation in the main stress direction of the floor.

4.2. On-Site Investigation. At present, there is no effective monitoring method for the rotation characteristics of principal stress; however, according to the deformation characteristics of surrounding rock, the rotation characteristics of the principal stress direction can be qualitatively analyzed, and the destruction scene of the main roadway in no. 1 mining area of Gaojiapu coal mine is shown in Figure 8.

There are obvious differences in the deformation characteristics of surrounding rock on both sides of the main roadway, the deformation of surrounding rock on the coal side of the roadway is small, and it is mainly horizontal displacement. The deformation of surrounding rock at the side of roadway goaf is large, and the displacement direction has a certain included angle with the horizontal plane; the vertical spatial relationship between the roadway side and the horizontal plane is no longer maintained, and the included angle between the two is reduced to 70°. In Figure 8, the asymmetric characteristics of surrounding rock deformation of roadways on both sides of the working face are caused by the rotation difference in the direction of principal stress. The surrounding rock at the coal side of the roadway is less affected by mining, and the concentration of principal stress is low; the rotation range of principal stress is small, and the failure range of surrounding rock is small. Its deformation is mainly due to the compression effect of high-level tectonic stress, mainly horizontal deformation. The surrounding rock at the side of roadway goaf is highly affected by mining, and the concentration degree of principal stress is high; the rotation range of principal stress is large, and the failure range of surrounding rock is large. Its deformation is mainly due to the plastic flow of roadway surrounding rock caused by the deflection of principal stress.

4.3. Influence of Mine Earthquake Disturbance. The goaf is on the right side of the main roadway in no. 1 mining area of Gaojiapu coal mine (as shown in Figure 9). According to the masonry beam theory, after the main roof is broken, an arc triangular plate “b” is formed at both ends of the working face, and a trapezoidal plate “a” is formed in the middle of the working face. Under the support of solid coal, coal pillar, and goaf gangue, the arc triangular plate and trapezoidal plate form a lateral masonry beam structure along the inclined direction of the working face. The rotation of the rock block on the main roof of the fault forms a strong horizontal extrusion force; it is possible to form a three-hinged arch balance structure under the action of mutual extrusion; the stability of this equilibrium structure will depend on whether the extrusion force at the bite point exceeds the strength limit at the contact surface of the bite point. In this case, as long as the total stress (superposition of static stress and dynamic stress) on the rock block contact surface exceeds the strength limit ($[\sigma]$) at the end of the rock block, it can lead to the rotation of the “masonry beam” structure of the main roof and then deformation and instability.

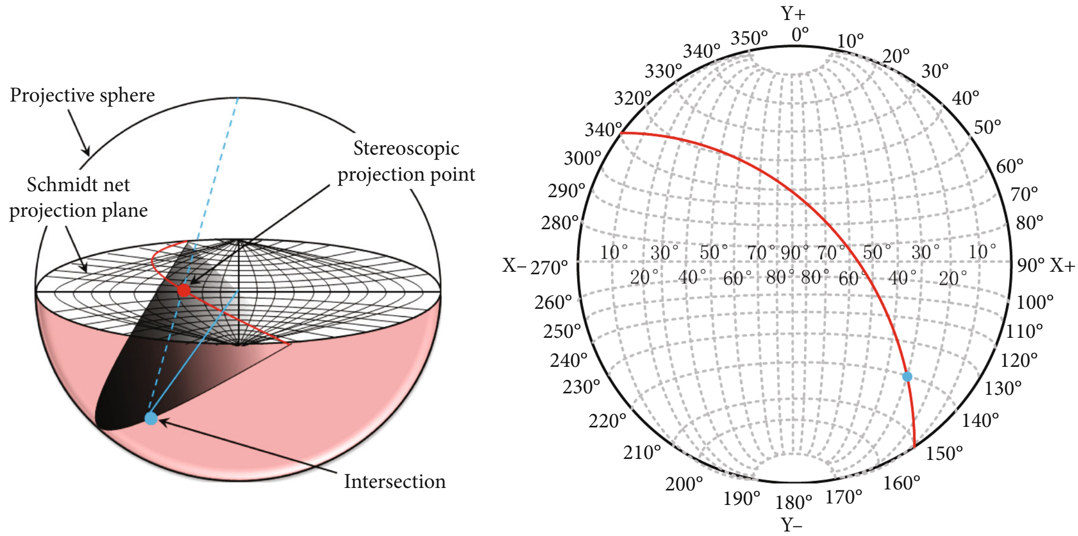

(a) (b)

Figure 6: The equal angle stereonet.

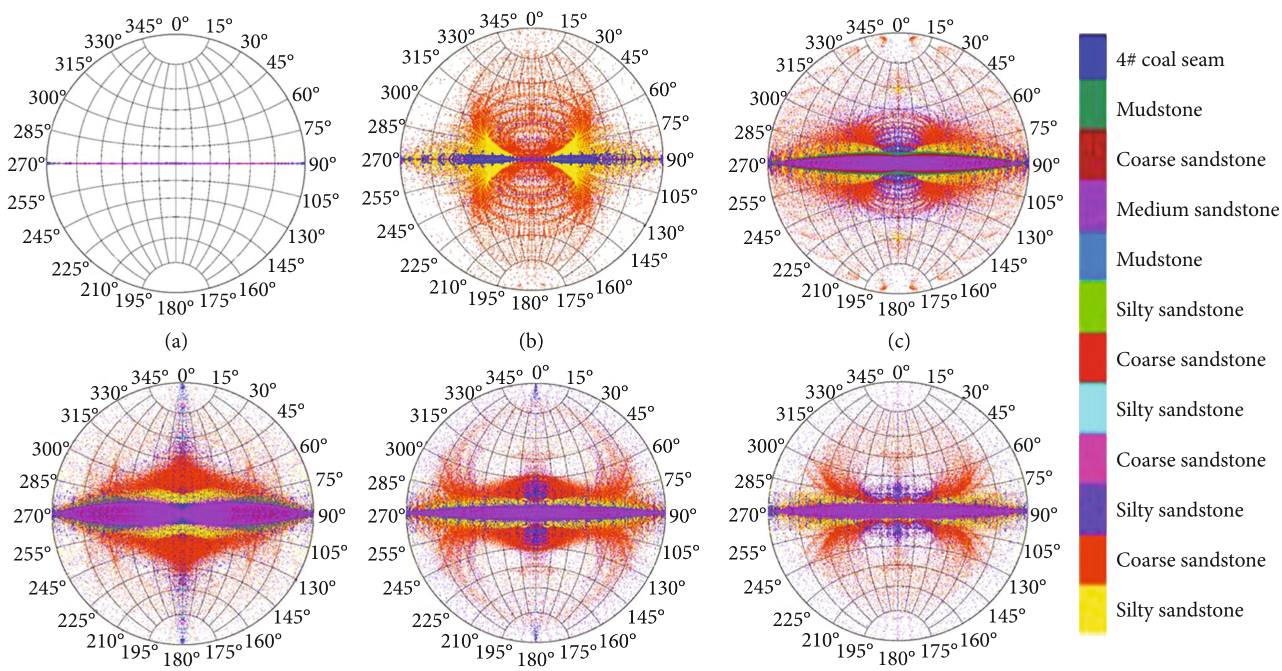

(a) (b) (c) (d) (e) (f)

Figure 7: Evolution track of principal stress direction under dynamic load disturbance. (a) Before dynamic load disturbance; (b) dynamic load disturbance 0.01 s; (c) dynamic load disturbance 0.03 s; (d) dynamic load disturbance 0.05 s; (e) dynamic load disturbance 0.07 s; (f) dynamic load disturbance 0.09 s.

Under the disturbance of mine earthquake, the rotation angle of arc triangular "b" increases, the principal stress direction rotates, eventually loses stability, and slides to the goaf. The principal stress distribution in the top coal on the right side of the green dotted line is always affected by the rotation position of the arc triangular plate "b." The force (F) of mine earthquake disturbance stress wave, arc triangular plate, and overburden collapse rock block on direct roof and lower coal seam, perpendicular to the contact surface between the direct roof and the triangular plate. During the rotation and sinking of the arc triangular plate "b," the direction of the contact surface also changes; therefore, the magnitude and direction of the pressure (F) are related to the rotation angle (θ) of the arc triangle. With the change of the magnitude and direction of roof pressure (F), the stress boundary conditions of direct roof and coal seam

Figure 8: Main roadway destruction site.

change, and it will inevitably affect the magnitude and direction of principal stress in roadway surrounding rock.

5. Pressure Relief Measures

5.1. Optimization of Relevant Parameters for Blasting Pressure Relief. After the roadway is excavated, a free space is formed in the rock mass; it provides space for the deformation of floor rock. The root cause of roadway floor heave are as follows: the vertical stress on the roof is transmitted to the two sides, causing two sides to sink; the sinking of the two sides caused the destruction of the two bottom corners; sinking of the two sides caused the failure of the two bottom corners; floor is squeezed by the secondary horizontal principal stress; the roadway floor expands into the roadway and finally shows floor heave deformation. The problem of floor heave in roadway under high stress environment becomes particularly prominent, high stress leads to the increase of the pressure on the roof and floor of the coal seam, and the clamping effect on the coal seam is more obvious; as the fluidity (ductility) of the coal body increases, the floor heave caused by the subsidence of the two sides will be more serious.

Based on the previous blasting parameters of Gaojiapu coal mine, the blasting construction technical requirements are as follows:

(i) Materials and tools required for blasting construction: $\Phi 60 \times 440 \times 1$ mm blasting cartridge, mine grade III emulsion explosive, synchronous millisecond delay electric detonator, blasting mud, cement, grouting pipe, return pipe, hemp, detonator, detonating cord, blasting busbar, gun rod, insulating tape, etc.; the schematic diagram of blasting hole charging is shown in Figure 10

(ii) Blasting method: FG-500A detonator is used for initiation; millisecond detonate is used for group blasting and single hole detonate

(iii) Blasting parameters and blasting operation process:

(1) Using a blasting cartridge as a carrier for explosives, charge 20 kg

(2) The charging method is positive continuous charging and slowly sent to the hole bottom

(3) Before charging, the residual coal and rock powder in the borehole must be removed. Use PVC gun rod to detect the actual depth of drilling hole and confirm that the drilling depth is normal and meets the requirements of measures; charging can be carried out only after there is no residual coal and rock powder

(4) An operation platform shall be set up before charging, and a 1.2 m high protective fence shall be welded around the platform with waste anchor bolts

(5) Before charging, cut off the blasting barrel at one end of the explosive with a saw blade; one 80 mm long steel wire shall be crossed on both sides of the blasting barrel to prevent the explosive from sliding naturally in the borehole

(6) Index the detonator to the orifice position and then seal the hole (during grouting and hole sealing, the grouting pipe shall be fixed with hemp and blasting mud, and a 0.5 m hole section shall be reserved at the orifice)

(7) When blasting, two detonating cords are connected in parallel with two-millisecond delay electric detonators with the same number at the orifice, seal the joint between detonator and detonating cord with insulating tape, install the detonator and detonating cord, leave a distance of 0.5 m, and then, seal the hole with sealing agent

5.2. Principle of Blasting Pressure Relief. Under the disturbance of mine earthquake, the main stress of roadway surrounding rock deflects to the side of the goaf to form a stress concentration area; the side roof and floor near the goaf of the roadway are seriously damaged. In view of the above problems of roof subsidence and floor heave, the purpose of blasting pressure relief in the roof and floor of the roadway is to reduce the stress concentration, block the transmission of the principal stress in the roof and floor, and reduce the impact of the deflection of the principal stress. The diameter of roof blasting hole is 75 mm, the distance between holes is 5 m, the depth of blasting hole is 40 m, the drilling inclination angle is 60°, and the charge is 20 kg. The diameter of the bottom plate blasting hole is 75 mm, the spacing between holes is 1 m, and the depth of the blasting hole is 12 m until the rock is seen on the floor of the coal seam; the drilling inclination angle is 60°, the charge is 10 kg, and the final hole position of the blasting hole is determined at the peak stress of the floor.

The essence of blasting pressure relief is continuous blasting of multiple blasting holes, and each blasting hole adopts two millisecond detonators; group blasting and single hole detonate create a free surface for the next stage of blasting and make the blasting crack develop in the set direction. By controlling the propagation direction of detonation wave, a continuous weak structural plane is formed in the rock

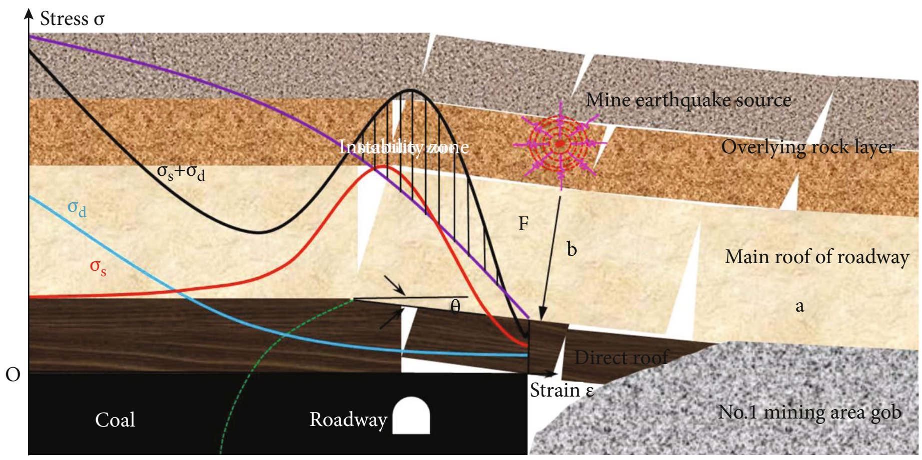

Figure 9: Structure of the side roof in the goaf of main roadway.

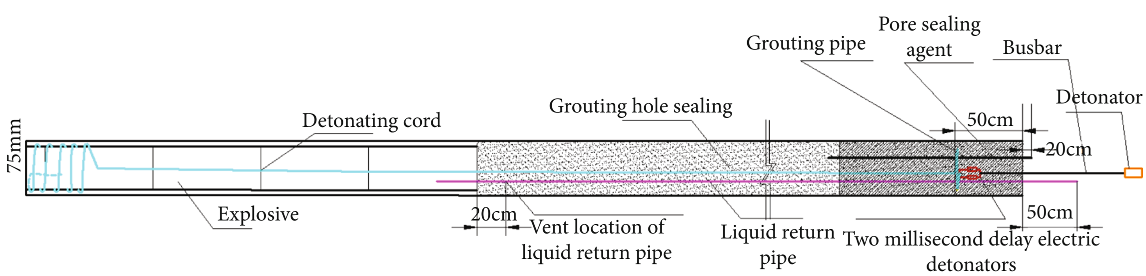

Figure 10: Schematic diagram of blasting hole charging.

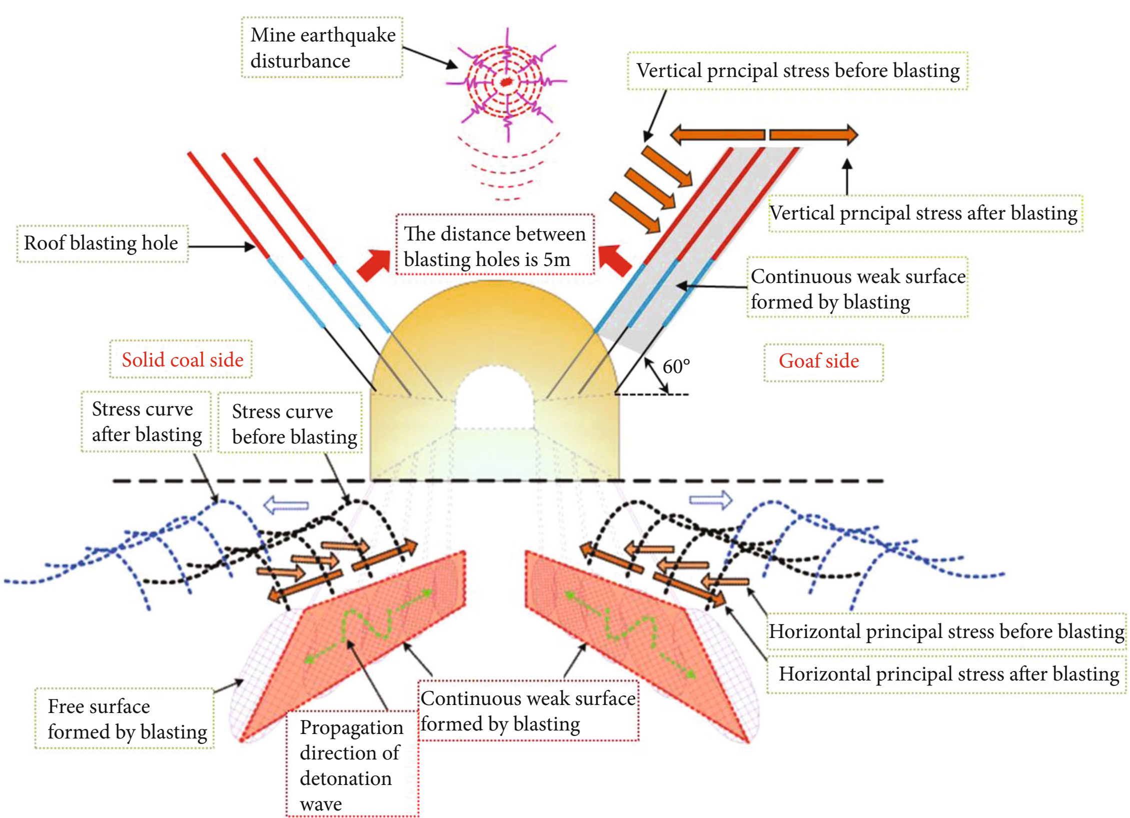

Figure 11: Blasting blocking stress transmission.

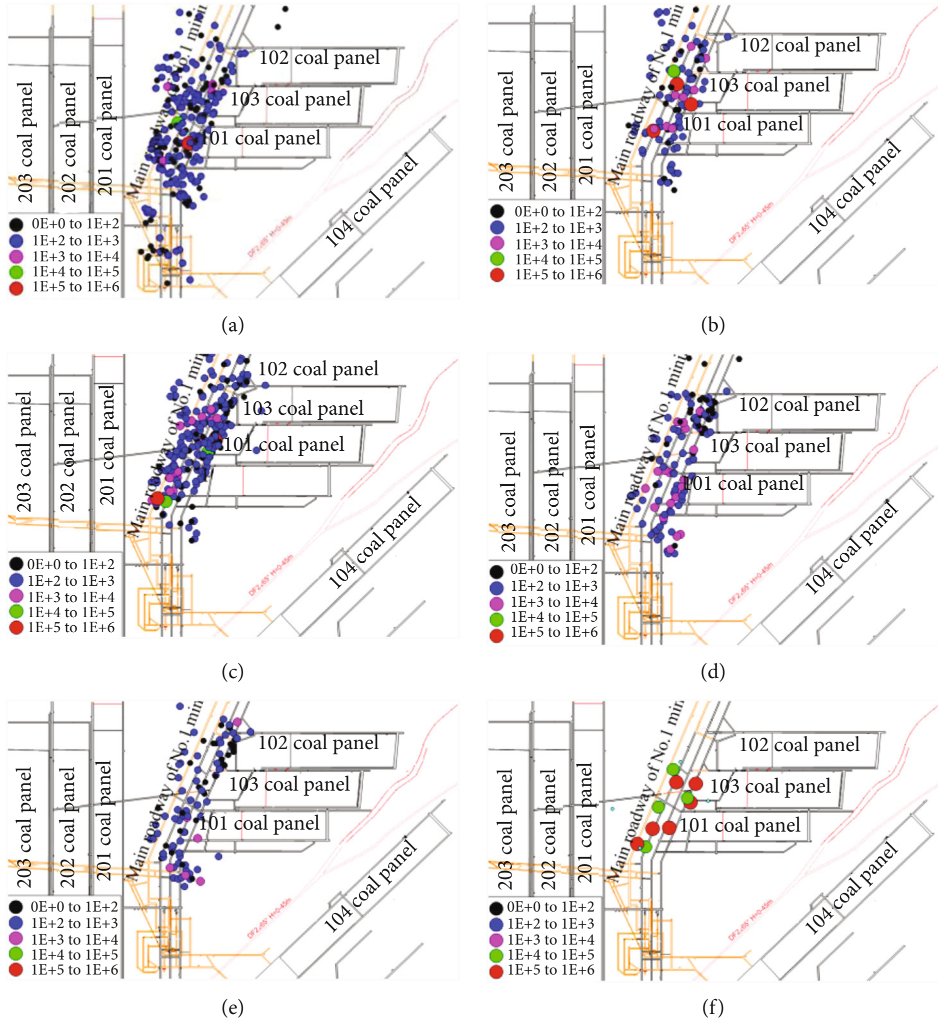

Figure 12: Plane distribution of microseismic events before and after prevention and control of main roadway. (a) August 2017; (b) September 2017; (c) October 2017; (d) November 2017; (e) December 2017; (f) August to December 2017.

layer of roof and floor. The existence of structural plane can change the transmission direction of principal stress so that the principal stress does not deflect to the side of roadway goaf. At the same time, it blocks the transmission of principal stress to the goaf side and floor of the roadway, reduce the horizontal extrusion force on the floor coal and rock mass, and control the serious deformation and floor heave of the goaf side of the roadway (as shown in Figure 11).

5.3. Pressure Relief Effect Test. Microseismic activity can reflect the fracture of coal and rock mass; therefore, the roadway pressure relief effect can be roughly determined based on the change of high-energy microseismic events with time; the significant reduction of high energy events indicates that the pressure relief effect is good.

The main roadway area is selected as the statistical area; after the above blasting scheme is adopted for construction, the prevention and control effect is evaluated through microseismic monitoring. Since the construction protection is carried out in October 2017, August and September 2017 are selected for comparison with November and December 2017; a total of four months are used as the time period for comparison before and after the implementation of pressure relief measures; the plane distribution of microseismic events at this stage is shown in Figure 12.

As can be seen from Figure 12, before the implementation of pressure relief measures (August~September), the total energy of microseismic is larger, and the large energy microseismic events (greater than 10^5 J) are more. During the implementation of pressure relief measures (October), the total number of microseismic events and large energy microseismic events are too many due to the disturbance caused by construction. After the implementation of pressure relief measures (November~December), the total number of microseismic events decreased slightly, it shows that the adopted pressure relief scheme transfers part of the elastic energy stored in coal and rock mass to the deep. There are no large energy microseismic events; it shows that the adopted pressure relief scheme releases the elastic energy stored in coal and rock mass; elastic energy is mostly released in the form of small energy microseismic events (less than 10^4 J); thus, the degree of stress concentration is reduced.

6. Conclusions

The main roadway near the goaf with the deep high static stress is very easy to be damaged after being disturbed by the mine earthquake. Taking the main coal roadway of no. 1 mining area of Gaojiapu coal mine as the engineering background, through numerical simulation and field monitoring methods, the spatial-temporal rotation characteristics of the principal stress of roadway surrounding rock under the disturbance of mine earthquake are studied and analyzed and put forward corresponding prevention and control measures. The research results can provide a certain reference basis for coal mine roadway pressure relief and reducing disaster conditions. The main conclusions of this paper are summarized as follows:

(1) In the early stage of mine earthquake disturbance, the roadway roof is first affected, and the main stress of the roof tends to deflect to the side of the goaf. In the middle stage of mine earthquake disturbance, the main body of roof principal stress deflects to one side of goaf, and the deflection range is large. In the later stage of mine earthquake disturbance, the principal stress direction in the surrounding rock rotates reversely, and the rotation angle of the principal stress direction in the roof is the largest

(2) The asymmetric distribution characteristics of principal stress rotation are verified by using the asymmetric deformation phenomenon on two sides of roadway surrounding rock; based on the rotation characteristics of principal stress under the dual influence of mine earthquake disturbance and goaf, optimize the layout scheme of blasting pressure relief hole and blasting parameters. The transmission direction of principal stress can be changed by blasting; at the same time, it blocks the transmission of principal stress, through the comparison of microseismic activity law before and after pressure relief; the pressure relief effect is good

Data Availability

All data included in this study are available upon request from the corresponding author.

Conflicts of Interest

The authors declare that there are no conflicts of interest regarding the publication of this paper.

Acknowledgments

This research was supported by the National Natural Science Foundation of China (52004004) and China Postdoctoral Science Foundation of China (2019M661991).

References

[1] L. M. Xue, W. J. Zhang, Z. Zheng et al., “Measurement and influential factors of the efficiency of coal resources of China's provinces: based on Bootstrap-DEA and Tobit,” *Energy*, vol. 221, no. 4, p. 119763, 2021.

[2] Y. Zhao, T. H. Yang, H. L. Liu et al., “A path for evaluating the mechanical response of rock masses based on deep mining-induced microseismic data: a case study,” *Tunnelling and Underground Space Technology*, vol. 115, no. 5, 2021.

[3] T. Li, B. G. Yang, Z. Qi, C. J. Gu, Q. Y. Shan, and W. Chen, “Numerical simulation of roof movement and fill strength of coal deep mining,” *Arabian Journal of Geosciences*, vol. 14, no. 8, 2021.

[4] M. C. He, X. J. Lv, and H. H. Jing, “Characters of surrounding rockmass in deep engineering and its non-linear dynamic-mechanical design concept,” *Chinese Journal of Rock Mechanics and Engineering*, vol. 21, no. 8, pp. 1215–1224, 2002.

[5] M. C. He, H. P. Xie, S. P. Peng, and Y. D. Jiang, “Study on rock mechanicsin deep mining engineering,” *Chinese Journal of Rock Mechanics and Engineering*, vol. 24, no. 16, pp. 2803–2813, 2005.

[6] S. M. Hsiung, W. Blake, A. H. Chowdhury, and T. J. Williams, “Effects of mining-induced seismic events on a deep underground mine,” *Pure and Applied Geophysics PAGEOPH*, vol. 139, no. 3-4, pp. 741–762, 1992.

[7] W. Kuhnt, P. Knoll, H. Grosser, and H. J. Behrens, “Seismological models for mining-induced seismic events,” *Pure and Applied Geophysics PAGEOPH*, vol. 129, no. 3-4, pp. 513–521, 1989.

[8] J. A. Vallejos and S. D. McKinnon, “Correlations between mining and seismicity for re-entry protocol development,” *International Journal of Rock Mechanics and Mining Sciences*, vol. 48, no. 4, pp. 616–625, 2011.

[9] W. Cai, L. M. Dou, G. Y. Si, and Y. W. Hu, “Fault-induced coal burst mechanism under mining-induced static and dynamic stresses,” *Engineering*, vol. 7, no. 5, pp. 687–700, 2021.

[10] T. Li, M. F. Cai, and M. Cai, “A review of mining-induced seismicity in China,” *International Journal of Rock Mechanics and Mining Sciences*, vol. 44, no. 8, pp. 1149–1171, 2007.

[11] W. J. Yu, B. Pan, F. Zhang, S. F. Yao, and F. F. Liu, “Deformation characteristics and determination of optimum supporting time of alteration rock mass in deep mine,” *KSCE Journal of Civil Engineering*, vol. 23, no. 11, pp. 4921–4932, 2019.

[12] B. F. Wang, K. M. Sun, B. Liang, and H. B. Chi, “Experimental research on the mechanical character of deep mining rocks in THM coupling condition,” *Energy Sources, Part A: Recovery, Utilization, and Environmental Effects*, vol. 43, no. 13, pp. 1660–1674, 2021.

[13] J. Z. Li, P. H. Guo, A. Y. Yuan, C. Q. Zhu, T. Zhang, and D. H. Chen, “Failure characteristics induced by unloading disturbance and corresponding mechanical mechanism of the coal-seam floor in deep mining,” *Arabian Journal of Geosciences*, vol. 14, no. 12, 2021.

[14] Y. S. Yang, S. J. Wei, and D. M. Zhang, “Influence of rock burst and other disasters on stability of surrounding rock of roadway,” *Geotechnical and Geological Engineering*, vol. 36, no. 3, pp. 1767–1777, 2018.

[15] S. Y. Chen, C. S. Song, Z. B. Guo, Y. Wang, and Y. Wang, “Asymmetric deformation mechanical mechanism and control countermeasure for deep roadway affected by mining,” *Journal of China Coal Society*, vol. 41, no. 1, pp. 246–254, 2016.

[16] L. Xu, H. L. Zhang, D. K. Gen, and B. Li, “Principal stress difference evolution in floor under pillar and roadway layout,”

Journal of Mining & Safety Engineering, vol. 32, no. 3, pp. 478–484, 2015.

[17] Y. S. Yang, S. J. Wei, and S. N. Zhao, "Research on the destructional pattern of surrounding rock of roadway induced by dynamic disturbance," *Geotechnical and Geological Engineering*, vol. 37, no. 5, pp. 4447–4459, 2019.

[18] Y. X. Li, Z. M. Zhu, and J. L. Fan, "Effect of principal stress orientation on stability of surrounding rock of tunnels," *Chinese Journal of Geotechnical Engineering*, vol. 36, no. 10, pp. 1908–1914, 2014.

[19] S. R. Xie, S. J. Li, X. Huang, Y. Y. Sun, J. H. Yang, and S. X. Qiao, "Surrounding rock principal stress difference evolution law and control of gob-side entry driving in deep mine," *Journal of China Coal Society*, vol. 40, no. 10, pp. 2355–2360, 2015.

[20] S. J. Niu, H. W. Jing, and D. F. Yang, "Physical simulation study of principal stress difference evolution law of surrounding rock of deep mine roadways," *Chinese Journal of Rock Mechanics and Engineering*, vol. 31, no. S2, pp. 3811–3820, 2012.

[21] J. Li, N. J. Ma, and Z. W. Ding, "Heterogeneous large deformation mechanism based on change of principal stress direction in deep gob side entry and control," *Journal of Mining & Safety Engineering*, vol. 35, no. 4, pp. 670–676, 2018.

[22] S. Q. Yang, H. W. Jing, and Y. S. Li, *Experimental Investigation on Mechanical Behavior of Coarse Marble Under Six Different Loading Paths Springer US*, Springer US, 2011.

[23] H. P. Xie, H. W. Zhou, J. F. Liu et al., "Mining-induced mechanical behavior in coal seams under different mining layouts," *Journal of China Coal Society*, vol. 36, no. 7, pp. 1067–1074, 2011.

[24] M. G. Qian, P. W. Shi, and X. Z. Zou, *Mining Pressure and Strata Control*, China University of mining and Technology Press, 2003.

[25] Y. Q. Li, Z. M. Zhu, and R. Hu, "Study on the effect of principal stress orientation on tunnel stability," *Journal of Sichuan University(engineering science edition)*, vol. 44, no. S1, pp. 93–98, 2012.

[26] L. B. Guan, *Experimental Study on Effect of Principal Stress Axis Rotation on the Macro-Deformation and Microstructure of Intact Clay*, Zhejiang University, 2010.

[27] D. Jin, *Experimental Study on Effect of Rotation of Principal Stress Orientation on Saturated Sand*, Dalian University of Technology, 2009.

[28] Z. H. Wang, "Numerical simulation research on the influence of buried depth on the stress field of overlying rock in floor roadway," *IOP Conference Series: Earth and Environmental Science*, vol. 787, no. 1, p. 012129, 2021.

[29] M. Barla, "Numerical simulation of the swelling behaviour around tunnels based on special triaxial tests," *Tunnelling and Underground Space Technology*, vol. 23, no. 5, pp. 508–521, 2008.

[30] C. D. Chang and B. Haimson, "True triaxial strength and deformability of the German Continental Deep Drilling Program (KTB) deep hole amphibolite," *Journal of Geophysical Research: Solid Earth (1978–2012)*, vol. 105, no. B8, pp. 18999–19013, 2000.

[31] R. P. Tiwari, K. S. Rao, and R. Seshagiri, "Post failure behaviour of a rock mass under the influence of triaxial and true triaxial confinement," *Engineering Geology*, vol. 84, no. 3-4, pp. 112–129, 2006.

[32] H. He, L. M. Dou, and S. Y. Gong, "Induced impact of key strata in overlying strata," *Chinese Journal of Geotechnical Engineering*, vol. 32, no. 8, pp. 1260–1265, 2010.

[33] X. F. Xu, *Research of Mechanism and Controlling Technology of Floor Burst in Coal Seam Roadway*, China University of Mining and Technology, 2011.

[34] C. P. Lu, *Intensity Weakening Theory for Rockburst of Compound Coal-Rock and Its Application*, China University of Mining and Technology, 2008.

[35] A. N. Li, L. M. Ling, Z. Y. Wang, J. R. Cao, S. W. Wang, and C. H. Shan, "Numerical simulation of rock burst of horizontal sectional mining of near-vertical coal seam under dynamic load," *Coal Engineering*, vol. 50, no. 9, pp. 83–87, 2018.

[36] N. Duan, *Study on Mining-Induced Stress and Energy Evolution of Surrounding Rocks in Deep Mine*, China University of mining and technology, 2016.

Hindawi
Geofluids
Volume 2021, Article ID 5208670, 13 pages
https://doi.org/10.1155/2021/5208670

Research Article

Prevention of Water Inrushes in Deep Coal Mining over the Ordovician Aquifer: A Case Study in the Wutongzhuang Coal Mine of China

Huichao Yin[1,2] **Bin Xu**[3] **Shangxian Yin**[3] **Wuzi Tian**[3] **Hui Yao**[3] **and Haopeng Meng**[3]

[1]*China University of Mining and Technology, Beijing 100083, China*
[2]*Institute of Disaster Prevention, Yanjiao 101601, China*
[3]*North China Institute of Science and Technology, Yanjiao 101601, China*

Correspondence should be addressed to Shangxian Yin; yinshx03@126.com

Received 12 May 2021; Revised 6 August 2021; Accepted 26 August 2021; Published 15 September 2021

Academic Editor: Hualei Zhang

Through field observation and theoretical study, we found that the Hanxing mining area has a typical ternary structure in coal mining under high water pressure of the aquifer. This ternary structure is the Ordovician limestone aquifer-aquiclude including thin limestones-coal seam. Although the aquiclude is considerably thick, there is still a great risk of water burst during mining under water pressure in the deep burial environment. Multidimensional characteristics of floor water inrush in deep mining are summarized in the paper, including water migration upwardly driven by the Ordovician confined water, the planar dispersion of the water inrush channel, the stepped increase of the water inrush intensity, the hysteretic effluent of the water inrush time and the exchange, and adsorption of the water quality. The water inrush mechanism is clarified that the permeability, dilatancy, fracturing, and ascending of the water from the Ordovician limestone aquifer form a planar and divergent flow through the transfer, storage, and transportation of thin limestone aquifers. The corresponding water inrush risk evaluation equation is also proposed. Based on the thickness of the aquiclude, the thickness of the failure zones, and the water inrush coefficient, the floor aquiclude is classified into five categories. While water inrush cannot be completely controlled by the traditional underground floor reinforcement with ultra-thick aquiclude or even zonal grouting, a comprehensive prevention and control concept of the four-dimensional floor water hazard in full time-space domain are proposed. A tridimensional prevention and control model of three-dimensional reticulated exploration, treatment, verification, and supplementation is presented. A full time domain technological quality control process of condition assessment, exploration, remediation, inspection, evaluation, monitoring, and reassurance is formed, and a water disaster prevention method with full time-space tridimensional network in deep coal mining is established. Case study in the Hanxing mining area demonstrates that the proposed methods are highly effective.

1. Introduction and Background

The Ordovician limestone aquifer contains abundant water with very high water pressure. It is deposited in the bottom of coal measure formations and exists in many mining areas in Northern China (Figures 1 and 2). The Ordovician aquifer has caused numerous aquifer water inrush accidents during coal mining. Water inrush from the Ordovician aquifer is one of the major hazards in mining safety [1]. Many studies have been conducted to investigate the mechanism and mitigation methods of water inrushes in this area [2–4]. However, coal mining in those cases was mainly at a shallower depth (<700 m), where the burial depth and water pressure were relatively low, and the water inrush accidents were not very serious. As the mining depth increases in recent years (depth>700 m), in situ stresses and water pressures increase

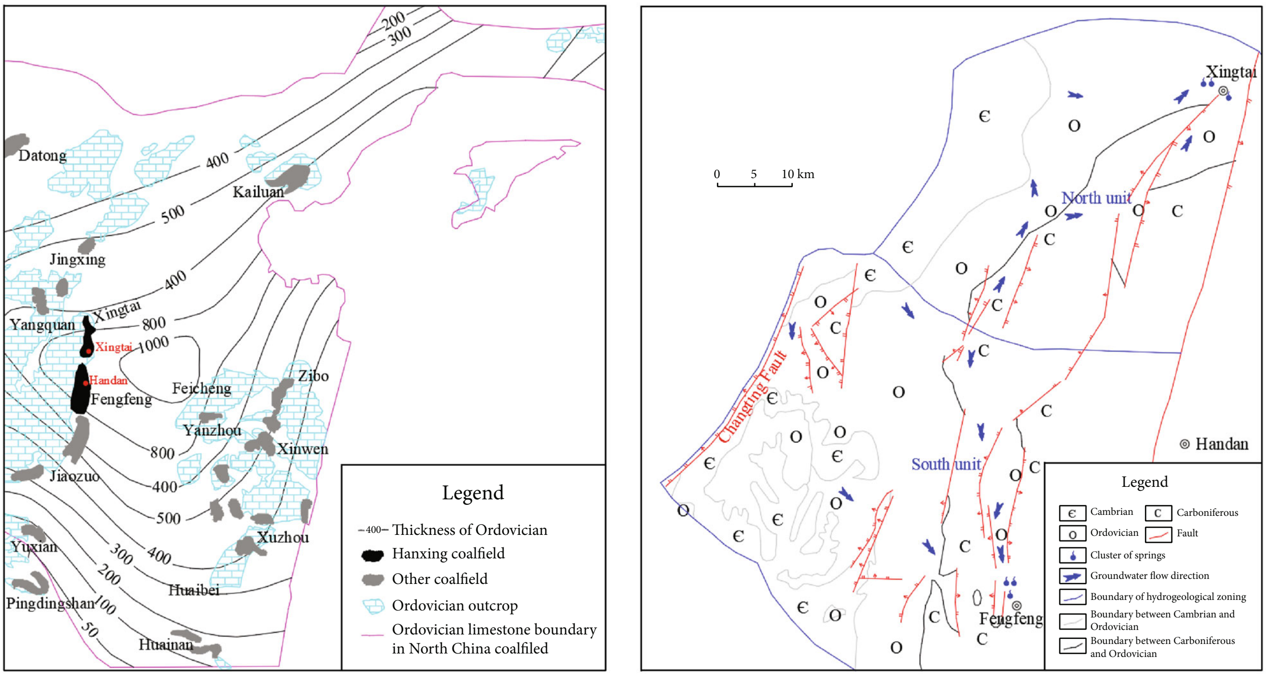

(a) (b)

Figure 1: Map view of location of the Hanxing coalfield and other coalfields in North China coalfield: (a) The Ordovician hydrogeological system in North China and (b) north and south units of the Hanxing area.

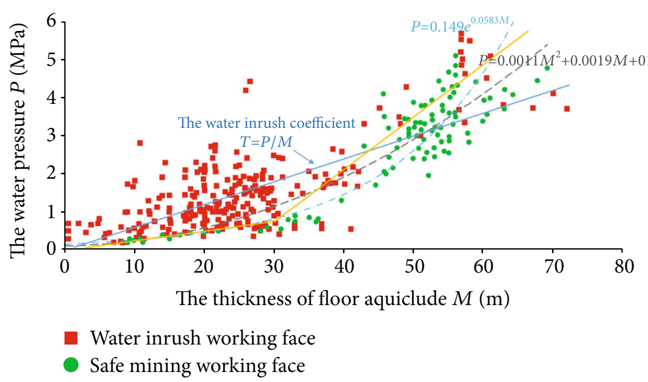

Figure 2: Theoretical and statistical analysis of water pressure and thickness of aquiclude for mining under water pressure.

greatly in the mining area, causing water inrush to become more serious and water disasters more devastated [3–5]. Furthermore, the existing theories and methods of water inrush prevention are not very suitable for this new situation [6–9]. Therefore, it is of critical importance to understand new mechanisms and prevention methods of water inrushes for coal mining at a great depth.

Safe mining under water pressure refers to coal mining over confined aquifers. Since the first water inrush from the Ordovician limestone aquifer occurred in the Kaiping coalfield in 1920 [10], different models for mining under water pressure and predicting water inrushes have been proposed [1]. To date, the development history of mining under water pressure is divided into three stages. The first stage was from the early 1950s to the mid-1980s, in which the system of technologies and theories had been basically formed [11]. Some systematic researches on the main technical measures of drainage and depressurization for confined water or grouting for aquicludes were carried out [12], and the concept of mining under water pressure and the risk evaluation method of water inrush coefficient were put forward. The system of mining under pressure technologies [13], including mining methods and the water control technologies, such as exploration, prevention, and guarantee, had been basically formed, and the theories [14], including water inrush mechanism, safety evaluation, and water inrush prediction, had also been preliminarily constructed. The second stage, from the late 1980s to 2009, was the popularization and application stage of the theory and technology. With the acceleration of mining depth, the mining under water pressure for lower coal seam formations faced the dangerous condition of water inrush coefficient $T > 0.06$ MPa/m, with the frequency of water inrushes increased, the underground treatment of grouting reinforcement of floor aquicludes or thin limestone transformation had been widely applied, and a large number of coal resources had been safely mined [15]. The third stage refers to recent 10 years, in which the regional preact grouting technology for deep mining was developed. The shallow coal resources were exhausted and had to turn to deep mining, facing a more dangerous situation of water inrush coefficient $T > 0.1$ MPa/m, the frequency of floor water inrushes was high, the water influxes were large, and the treatment technology for shallow mining was obviously not suitable for deep mining. With the help of horizontal drilling technology, the regional preact grouting technology tends to mature [6, 7, 9].

With the increasing depth of the coal seam mining, northern China coal fields face various safety issues that are different with those in the shallow mining. In situ stresses, tectonic stresses, water pressure, and temperature continuously increase. Exploitation of deeper coal formations, especially safe mining under water pressure in the deep coal formations, faces new challenges, which is due to the fact that aquifer containment characteristics, water filling regularities of the deep Ordovician limestone karst cavities, main control factors of coal floor water inrush, and water inrush mechanism change fundamentally. The theories and techniques of safe mining under water pressure are also changed profoundly.

The Hanxing mining area consisted of three parts: Fengfeng, Handan, and Xingtai mining areas and is a typical northern China coalfield (Figure 1). It is the main coal production zone in China, with an annual coal production of 7930 tons. The coal and rock formations in this area have a typical ternary tactic model, i.e., the coal seams are above the Ordovician limestone but separated by aquicludes and thin limestones (see Figure 3). The Ordovician limestone aquifer with rich water and high water pressure is a regional main water supply source [16]. However, it also threatens the mining of coal seams by recharging the thin limestone aquifers in the coal measures, i.e., the Benxizu, Daqing, Shanfuqing, and Yeqing limestones from bottom to top. Coal mining may not only cause the water inrush and coal mine flooding but also induce the aquifer water level to drop sharply, affecting water resources and ecological environment [2]. Mines within the area mostly have shifted to deep mining. In this situation, water pressure of the Ordovician limestone can be as high as 10 MPa and water inrush coefficient exceeds 0.1 MPa/m. Based on the national regulations, coal seam cannot be exploited without adopting additional measures. In order to exploit the deep or the lower group of coal formations, zonal preact grouting method is developed on the basis of traditional shallow mine floor reinforcement. Although greatly reducing the risks of water inrushes, it still cannot eliminate the hazard of water inrushes. The main reason is that deep safe mining under water pressure theory has not yet been established nor is the technical system.

2. Water Inrush Prevention Theory of Deep Mining under Water Pressure

Safe mining under water pressure originally means mining safely by taking advantage of natural capability of floor aquiclude for resisting confined aquifer. Because of its simple concept and easy application, the water inrush coefficient method is still widely used in China, and it can be used in either shallow or deep mining, regardless of the conditions of aquicludes. According to related research, this method is only applicable in the condition that the thickness of aquiclude is less than 60-80 m, and the water pressure is less than 4 MPa. In addition, with the great variations in the deep mining environment, the theory and technology of mining under water pressure also need to improve.

2.1. Distinguishing Deep and Shallow Mining for Water Inrush Prediction. According to the current situation of mining, the mining depth in China is set to be 700 to 1500 m. Most of shallow rock masses are in the state of elastic stress, while at the deep depth, rock masses may show large deformation under high crustal stress and mining disturbance. Practice shows that the prediction and evaluation theories, detection method, monitoring tools, and treatment technology used for shallow mining are difficult to achieve effective control of deep water inrush disaster. The risk evaluation method of water inrush, i.e., water inrush coefficient, based on thin plate theory [17], may not be valid in the deep depth. Therefore, the concept of deep mining is proposed from the perspective of mine water inrush prevention and treatment. The surface formed by Eq. (1) in space is defined as the interface between shallow depth and deep depth, with shallow depth above it and deep depth below it. Equation (1) is derived from the formation breakdown pressure in hydraulic fracturing (e.g., [18]):

$$P_0 = 3\sigma_3 - \sigma_1 - P_p + R_m, \tag{1}$$

where σ_3 and σ_1 are the minimum and maximum in situ stresses, P_p is the water pressure of the Ordovician aquifer, and R_m is the tensile strength of the rock.

Due to the relief of the vertical stress after mining, the evaluation criterion by Eq. (1) varies to $P_0 \geq \sigma_3 + R_m$. According to water filling characteristics, the treatment to the floor in deep mining then shifts to large scale grouting from centralized channel treatment, so that the deep water inrush prevention and control method of zonal preact grouting are formed.

2.2. Water Inrush Prediction of the Ordovician Limestone in Shallow Mining. In traditional shallow mining, the thickness of floor aquiclude is generally within 60~80 m, and the confined water pressure is below 3.0 ~ 4.0 MPa. In this condition, the water inrush coefficient method is suitable for evaluating the risk of safe mining under water pressure. According to regulations issued by the Chinese government, the conditions for normal mining under water pressure are that the water inrush coefficient for the floor in the area with geologic structures is generally not greater than 0.06 MPa/m and for the floor in the normal area is not greater than 0.1 MPa/m. The water inrush coefficient can be expressed in the following [2]:

$$T = P/M, \tag{2}$$

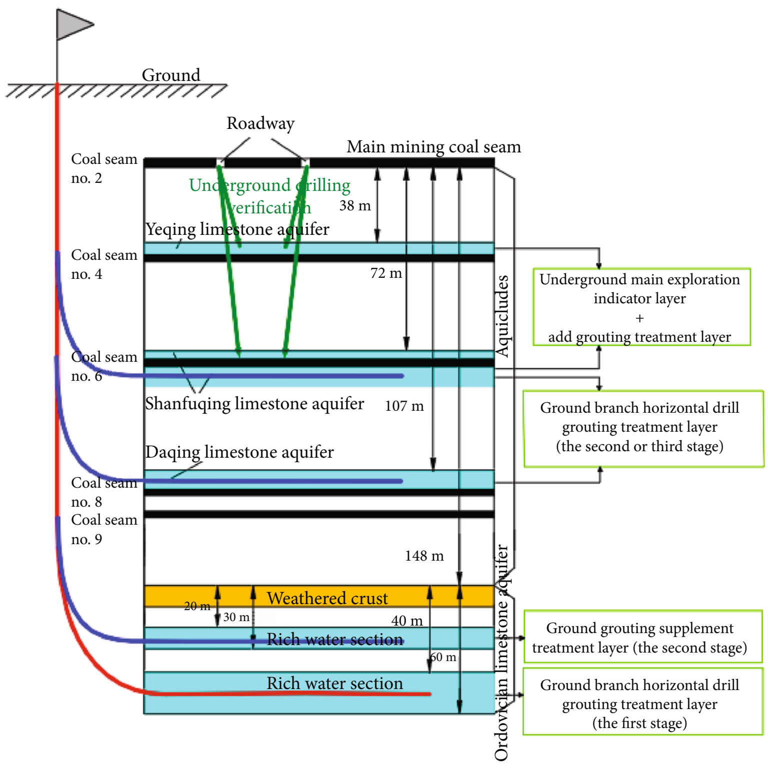

Figure 3: Stratum structural model of the Ordovician limestone and thin limestones under coal seams and grouting treatment of coal seam floor strata for preventing water inrush.

where T is the water inrush coefficient, P is the water pressure, and M is the thickness of the aquicludes.

Based on classical thin plate theory in elastic mechanics, critical water pressure of water inrush (Figure 2, black line) can be expressed as

$$P = 0.0011M^2 + 0.0019M + 0.1. \quad (3)$$

The empirical equation for the critical water pressure of water inrush (Figure 2, light blue line) obtained from the measured data can be written in the following:

$$P = 0.1409e^{0.0583M}. \quad (4)$$

The water inrush coefficient method is also shown in Figure 2 (blue line). Compared with these water inrush prediction methods to the actual water inrush statistical data, each prediction has its limitation. Therefore, a combined method is needed for a good prediction.

In the working faces at shallow and middepth, the characteristics of water inrush from Figure 2 can be summarized as follows:

(1) The working faces could be safely extracted under conditions of confined water pressure less than 2.0 MPa and the thickness of the floor aquiclude more than 35 m, or the pressure less than 1.2 MPa and the thickness more than 20 m

(2) The most prominent feature is that most floor water inrushes occur when the thickness of aquiclude is less than 30 m and the confined water pressure is less than 3.0 MPa

(3) The water inrushes in shallow mining are mostly from the present karst runoff zones or water rich zones, with abundant and low salinity water mainly composed of Ca-HCO_3 or Ca·Mg-HCO_3, and their channels are mainly concentrated water passage in large and medium-sized geologic structures such as paleosinkholes and faults, with huge water quantity

2.3. Water Inrush Characteristics of the Ordovician Limestone in Deep Mining. With the increase of mining depth, the water inrush threat of the confined aquifer in the Ordovician limestone under coal seams becomes increasingly prominent [19–21]. According to statistics, since 1995, 13 cases of water inrush incidents (Table 1) occurred in the Hanxing deep mining area, and they were all caused by water conducting geologic structures and mining-induced fractures.

Large numbers of water inrush cases in deep mining show that there are several characteristics of water inrushes. Water influx increases gradually while the peak values far less than those in the shallow mining, the channels of the influx scattered, and the delayed occurrence of the influx. The water quality of the influx has high salinity with the cations mainly Na^+ or Na^+ and Ca^{2+}. The detailed behaviors of

Table 1: Statistics of water inrushes from coal floor in the Hanxing deep mining area.

No.	Mine	Occurred time (year.month.day)	Occurred sites	Influxes ($m^3 \cdot h^{-1}$)	Pathway types
1	Wutongzhuang mine	1995.12.3	Main and auxiliary shaft connecting roadway	34000	Shaft submergence caused by the Ordovician limestone water inrush through water conducting fault
2	Wutongzhuang mine	2000.5.14	Tunneling of north main return air roadway	160.2	Ordovician limestone water outflow from the floor of fractured zone connected to water conducting paleosinkhole
3	Xingdong mine	2003.4.12	Tunneling of 2903 working face	7000	Driving outflow from the water conducting paleosinkhole
4	Wutongzhuang mine	2004.8.10	Mining of 2101 working face	180	Ordovician limestone water outflow from the floor of fractured zone connected to water conducting fault
5	Lincheng mine	2006.12.16	Mining of 0915 working face	4200	Coal mine submergence by small water conducting fault
6	Jiulong mine	2009.1.8	Mining of 15423 N working face	7200	Ordovician limestone water outflow from the floor of fractured zone connected to paleosinkhole
7	Huangsha mine	2010.1.19	Tunneling of 2124 working face	7200	Ordovician limestone water outflow through small faults connected to large water conducting fault
8	North well of Xingdong mine	2010.11.15	Mining of 92081 working face	1500	Ordovician limestone water outflow from the floor of fractured zone
9	Xingdong mine	2011.4.13	Mining of 2127 working face	125	Ordovician limestone water outflow from fractured zone connected by hidden microfaults
10	Huangsha mine	2011.12.11	Mining of 2106 working face	24000	Ordovician limestone water outflow from the floor of fractured zone connected to a hidden paleosinkhole
11	Wutongzhuang mine	2014.7.25	Mining of 2306 working face	11250	Ordovician limestone water outflow through small faults connected to a hidden paleosinkhole
12	Jiulong mine	2017.1.17	Mining of 15252 N working face	300	Ordovician limestone water outflow from a hidden paleosinkhole
13	Xingdong mine	2018.3.5	Mining of 2228 working face	2649	Ordovician limestone water outflow from a group of faults

the water inrushes in the deep mining are listed in the following:

(1) Water inrush source. The Ordovician limestone is the general source, and the water pressure in the confined aquifer is the driving force. Thin limestones store and accumulate water from the Ordovician aquifer and act as a connecting path. The water with high pressure moves upward from the Ordovician aquifer through fractures to pass the bottom layer of the thin limestone and move to upper layer of the thin limestone till breaking through the coal seam floor and forming water inrush in the mining area

(2) Water inrush channels. The dispersed fracturing zones in the floor, which may connect to the hidden geologic structures, are the main water-conducting channels. For instance, on July 25 of 2014, the mine flooding accident occurred in 2306 working face of the Wutongzhuang mine. The mining depth reached 700 m, the water pressure was as high as 6.5 MPa, and the distance of the mining area to the Ordovician limestone aquifer was 160 m. Water inrush influx in this accident reached as high as 11264 m^3/h. Although the inflow channels were the floor fractured zones, it connected to the Ordovician limestone by a hidden paleosinkhole

(3) Water inrush intensity. As confined water of the Ordovician limestone flows to the floor and continuously fractures the floor rocks, the water-conducting channels increase and more water flows into the channels, and the water inflow presents a step growth trend, eventually forms a water inrush disaster. The water influx generally reaches the peak value through several or even dozens of step growths from a small to a large value (Figure 4) and then stabilizes or decreases depending on the water supply situation of the Ordovician aquifer

(4) Water inrush time. With the initial or periodic mining-induced pressure caused by the collapses of the coal seam roof, the floor deformation and heave appear in the goaf area, and this may cause water inrush. Due to the delay of the floor fracturing process, the water inflow has an obvious delay phenomenon [22, 23]

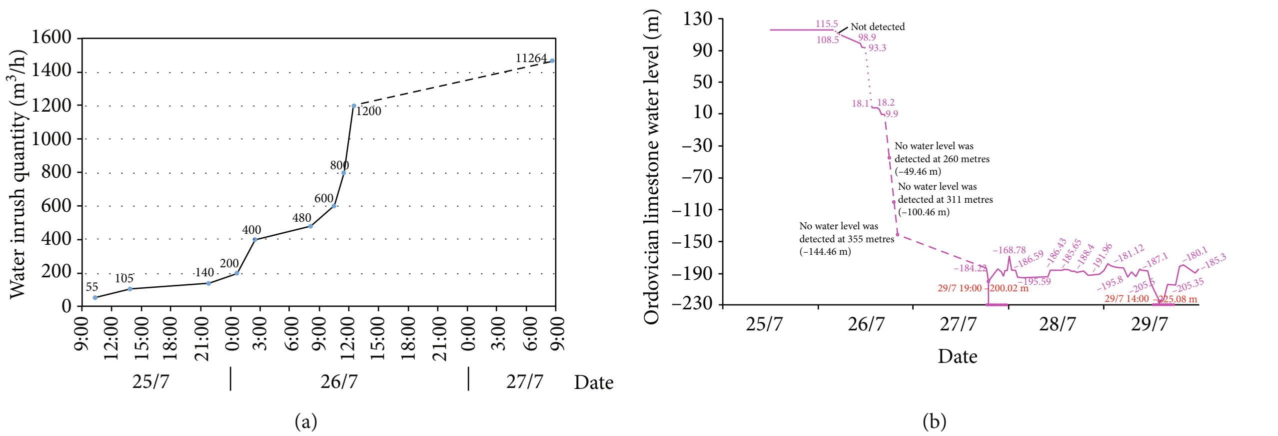

Figure 4: Dynamic variations of water inrush influx (a) and water pressure (water level) (b) in the accident described in the Wutongzhuang mine.

(5) Water inrush source and quality. The water quality of high mineralized water in the deep Ordovician limestone is different from that in the normal limestone, the water gradually changes from Na^+ or Na^+ and Ca^{2+} to Ca^{2+} or $Ca^{2+}$and Na^+ and from $SO_4^{2-}{\cdot}Cl^-$ or $Cl^-{\cdot}SO_4^{2-}$ to HCO^- in the initial stage of influx (Figure 5)

2.4. Water Inrush Mechanism for Deep Mining. The water inrush from the Ordovician aquifer can be assumed as a typical ternary structure model of the Ordovician limestone-thick aquiclude- (or with thin limestone-) coal seam. Due to the equilibrium of stresses of the surrounding rocks and water pressure prior to mining, the confined water in the aquifer ascends to a certain height inside fissures in the floor strata and maintains a static state. Once mining starts in the working face, the vertical stress of the overlying strata is removed in the mined area, causing the floor strata to be almost in a state of two-dimensional stresses. Under the high water pressure, the confined water in the Ordovician limestone seepages, expands, and fractures along fissures in the floor strata and continuously moves upward. After the water intruding into the first layer of thin limestone, the thin limestone is filled by the Ordovician limestone water (Figure 6). The water continues to flow up to the second and then the third layer of thin limestone, till it reaches the mining disturbed zone and failure zone of the coal seam floor and forms water inrush in the mining area (Figure 6).

The water inrush coefficient expressed in Eq. (2) and other equations such as Eqs. (3) and (4) presented in Figure 2 can be applied to estimate water inrush potentials. However, the water inrushes and the coal seam floor failures in deep mining have different behaviors from the shallow mining. Therefore, only using Eqs. (2)–(4) are not sufficient, and different prevention models are needed to be considered, as described in the following sections. In addition, numerical analyses need to be applied to analyze rock failures and water inrush possibilities based on the water inrush mechanism shown in Figure 6.

2.5. The Method of Risk Evaluation in Deep Mining under Water Pressure. Safe mining under water pressure refers to coal mining over aquifers with confined water pressure. Generally speaking, it refers to the mining to achieve the safety goal under natural conditions, i.e., only using the floor aquiclude to resist the aquifer water pressure rather than taking prevention measures to decrease water level by drainage and pressure reduction or local grouting reinforcement. At present, most of coal mines in North China coalfields adopt this method but taking appropriate measures. In deep mining, this method is no longer applicable.

Water inrush from the floor can be divided into two basic mechanisms [24, 25]: microfracturing of thick plate and failure of thin plate (key layer). The thin plate criterion is the ultimate bending moment theory: $M_p \geq M_s$ (M_p stands for actual bending moment, and M_s stands for critical bending moment). The microfracturing of thick plate criterion is a mechanical criterion: $P_0 > 3\sigma_3 - \sigma_1 - P_p + R_m$ (similar to Eq. (1)). According to water inrush mechanism and the statistical data of water inrush cases, the water inrush coefficient method is suitable for the thin plate theory. For the typical ternary structure model of the Ordovician limestone-thick aquiclude coal seam, the thickness of aquiclude is far more than 80 m, and water coefficient is no longer suitable for the risk evaluation of this rock structure model. For thick and ultra-thick aquicludes, theoretically, the holistic breaking the thick plate is impossible to occur. Under the presumption of no straight through structural channel exists, the only way that the Ordovician limestone water can transfer upwards is to ascend through fissured water-conducting fractures. Therefore, $P_0 > 3\sigma_3 - \sigma_1 - P_p + R_m$ can be used to evaluate the water inrush risk of deep Ordovician limestone and thin limestones under the coal floor.

2.6. Prevention Models of Safe Mining under Water Pressure. According to the thickness of aquiclude (M), the failure depth of floor (h_d), height of the water conducting zone from the Ordovician limestone (h_r), and water inrush

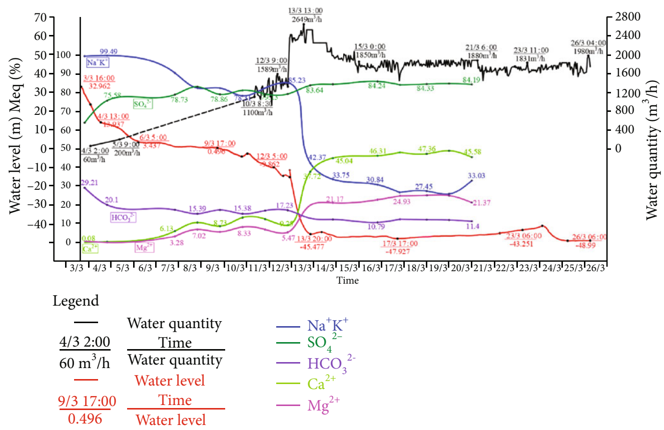

Figure 5: Water quantities and water levels variations before and after water inrush in observation boreholes of 2228 working face in the Xingdong Mine.

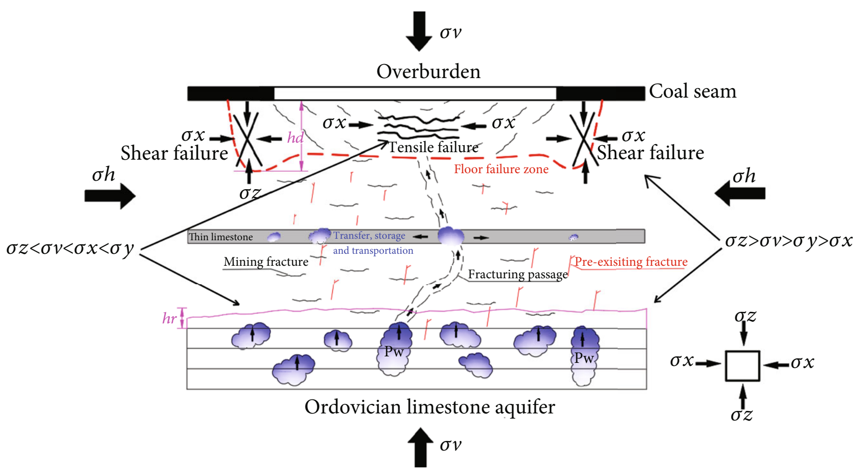

Figure 6: Mechanism of water inrush from the Ordovician limestone and thin limestones in deep mining.

coefficient (T), five categories for the floor aquiclude are classified [26, 27]. They are ultra-thin, thin, medium thick, thick, and ultra-thick aquiclude formations, and five prevention models of safe mining under water pressure are proposed correspondingly (Figure 6).

(1) While $0<M \le h_d + h_r < 30$ m and $T > 0$, the aquiclude is classified as the ultra-thin aquiclude. For this category, as long as mining is under pressure, that is, confined water pressure exists, and water inrush from floor will happen

For this case, grouting should be carried out in the Ordovician limestone aquifer, and the grouting rock selection should mainly meet the condition of $T \le 0.1$ MPa/m and taking into account the water rich property of the Ordovician limestone.

(2) While $h_d + h_r < M \le 80$ m, and $T > 0.06$ MPa/m, it is a thin aquiclude case. According to thin plate theory and statistics of water inrush cases, when the thickness of aquiclude is within 60-80 m, the water inrush coefficient method is suitable for the risk assessment of water inrushes, and the thickness of aquiclude of 80 m is the critical value. In this category, water inrush risk is high

In this category, grouting at the top of the Ordovician limestone aquifer as well as grouting reinforcement in the floor aquiclude should be carried out. The grouting rock layer selection should mainly meet the condition of $T \le 0.1$ MPa/m and also need to consider the water rich property of the Ordovician limestone. The reinforcement of the floor should be selected in the rocks below the floor failure zone.

(3) While $h_d + h_r < M \le 80$ m, and $T \le 0.06$ MPa/m, it is the medium thick aquiclude. In this category, risk of water inrushes is low

In this model, the grouting reinforcement of the floor aquiclude should be adopted, and the grouting layer should be selected in the rocks below the floor failure zone.

(4) While $80\text{ m} < M(h_d + h_r < M)$, and $T > 0.1$ MPa/m, it is classified as thick aquiclude. In this category, although the water inrush risk is relatively high, the

actual possibility of water inrushes is not high, unless large geologic structures exist in the floor

In this case, the key method to prevent water inrushes is to explore and prevent large and medium-sized geologic structures.

(5) While $80\,\mathrm{m} < M\ (h_d + h_r < M)$ and $T \leq 0.1\,\mathrm{MPa/m}$, it is the ultra-thick aquiclude. In this category, the risk of water inrushes and the actual probability of water inrushes are very low, unless large geologic structures exist in the floor

In this case, the key method to prevent water inrushes is also to explore and prevent large and medium-sized geologic structures.

3. A Case Study in the Wutongzhuang Coal Mine

3.1. General Situation. The Wutongzhuang coal mine is located in the southern Fengfeng coalfield, and the studied area is No. 6 Panel of mining area located in the south wing of the mine field, which includes working faces of No. 2601, No. 2602, No. 2603, and No. 2604, while No. 2602 working face is the first one with a strike length of 834 m and dip length of 256 m. The elevation of coal seam floor is -704.3 m ~ -775.5 m, and the buried depth is about 900 m. The coal seam, which has a thickness of 3.7 m, is monoclinic structure, and its inclination is $8^\circ \sim 20^\circ$ with an average of 14°. Normal faults are relatively developed inside the working face, and 5 faults in total are found in the transport roadway and cut-out roadway, with fault displacement of $H = 0.7 \sim 4.2$ m. Comprehensive mechanized full height mining technology is adopted.

The strata in the Fenfeng coalfield are formations in ages of (from old to new) the Paleozoic Cambrian, the Ordovician (water rich confined aquifer), the Carboniferous-Permian (coal measures), the Jurassic, the Paleogene, and the Neogene.

3.2. Treatment Method of Safe Mining of Deep Coal Seam under Water Pressure. On July 25 of 2014, a water inrush accident occurred in No. 2306 working face of the Wutongzhuang mine, and the peak value of water influx reached 11264 m^3/h. Before coal extraction, a large number of drilling exploration and grouting projects were implemented using the shallow underground floor reinforcement technology [28]. The grouting boreholes almost overlaid the whole working face floor. The high density of boreholes and scale of the project was never seen before in the similar situations, but water inrush accident still could not be prevented.

The cause analysis of this accident shows that the water inrush channel was a deep buried paleosinkhole, while the top of the paleosinkhole was more than 100 meters away from the coal seam, and the existing treatment method applied in the shallow mining case is invalid for this case. At that time, the zonal preact grouting method had just been applied to the deep mining with some successful cases achieved. This method had been introduced to complete the No. 6 and No. 8 panel mining area successively. In the treated working faces, the underground exploration of the Yeqing and Shanfuqing limestones was carried out. The results show that there were still many boreholes with large amount of water outflow after coal mining; therefore, the goal of cutting off the hydraulic connection between the Ordovician limestone and thin limestones had not been fully realized. This indicates that the zonal preact grouting method still has some defects.

Therefore, the grouting method in the studied area was to be improved, and the supplementary project was designed. Firstly, the grouting in the Ordovician limestone was changed from single-layer to double-layer grouting, and then grouting in two thin layers of limestone is added. Secondly, different directional drillings for grouting boreholes were designed in different grouting layers, so that an exploration and prevention mode of multilevel three-dimensional networks was formed. This greatly improved the accuracy of exploration and made pale-sinkholes or large and medium-sized faults under control, so that the risk of flooding could be eliminated (Figure 7).

After the completion of the project, verification of geophysical and drilling explorations was carried out again, and numbers of boreholes with water inflow were significantly reduced. In a small number of abnormal boreholes, grouting was supplemented until the abnormality was eliminated. Thus, the deep safe mining with water pressure was realized.

3.3. Technology of Deep Safe Mining under Water Pressure. Water inrush prevention technology in deep mining has been formed based on the successful experience of the Wutongzhuang coal mine and is widely applied in the Yangdong, Jiulong, and Xingdong coal mines, where good results are achieved.

This technology presents an idea of comprehensive water inrush prevention for the aquifers of Ordovician limestone and thin limestones in time and space domains. In the full time domain, this technology integrates all aspects of technical operations and quality control, from evaluation of water inrush, prediction, coal floor exploration, grouting treatment, grouting inspection, to operation monitoring, and quality guarantee. This technology also has the three-dimensional water inrush prevention system of construction, including surface and underground, multilayer and multilevel network treatment, and double target layer inspection in a full space domain (Figure 3).

3.4. Applications in the Wutongzhuang Coal Mine

3.4.1. Assessments of Hydrogeological Conditions. The chemical composition, structures, lithologic combination, and fractures in the Ordovician limestone control its water bearing characteristics. Vertically, the Ordovician limestone can be divided into three formations and eight intervals. Among them, the third formation is located at the top, and its thickness is 103 m with relatively shallow burial and rich water content. After further exploration and evaluation, the layers

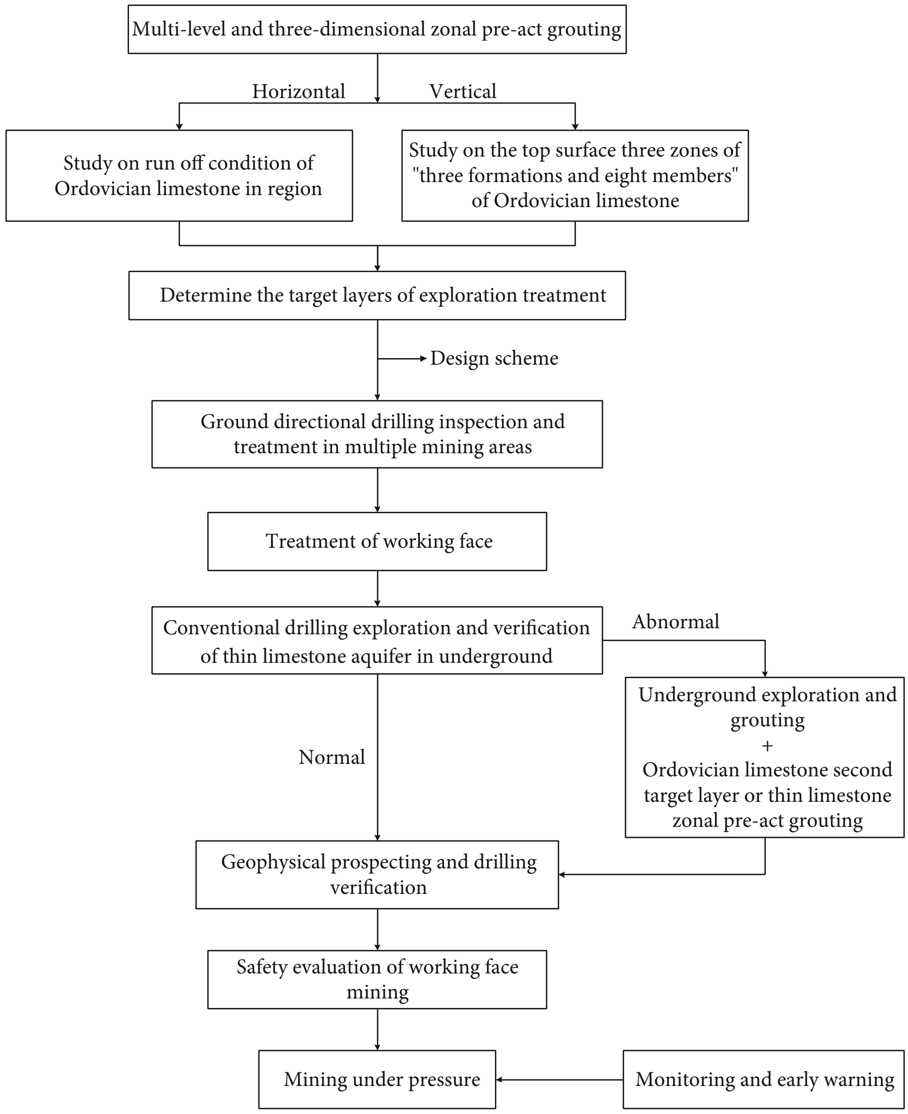

Figure 7: Workflow chart of multilevel and three-dimensional regional treatment mode of water inrush from coal floor in deep mining.

of 40-60 m and 20-30 m below the top surface of the Ordovician limestone contain abundant water, and they are the ideal layers for grouting.

The thin limestone aquifers are heterogeneous, their thicknesses gradually increase from the top to the bottom, and the average thicknesses of the Yeqing, Shanfuqing, and Daqing limestones are 2.5 m (with the maximum of 5.4 m), 5.5 m, and 5-6 m (with the maximum of 10 m), respectively. After evaluation, these three aquifers can all be used as drilling and grouting target layers. And the Yeqing and Shanfuqing can be used as ideal layers for underground verification of the grouting results and supplementary grouting.

3.4.2. Comprehensive Exploration and Treatment in Three-Dimensional Network

(1) The Preact Grouting of Layer from 40 M to 60 M below the Top Surface of the Ordovician Limestone. According to the design, zonal preact borehole grouting was carried out in No. 6 panel, including totally 2 main boreholes and 25 horizontal branch boreholes in the Ordovician limestone (Figure 8), and the branch boreholes were planned and drilled in a fish bone shape (the coss-section is as shown in Figure 7), with a borehole spacing of 50-60 m. A total of drilling distances of the boreholes was 21437 m, which borehole leakage occurred 24 times, with a total of 34845 tons of cement slurry injected. After zonal treatment, karst fissures at the top of the Ordovician limestone aquifer in No. 6 panel were effectively sealed.

(2) Grouting Treatment and Verification in the Yeqing and Shanfu Limestones. Geophysical methods were used to detect No. 2602 working face. According to the detection results, 17 verification holes were designed with a total drilling length of 2337 m (the coss-section is illustrated in Figure 7). However, due to the large amount of water influxes from many boreholes with high water pressure

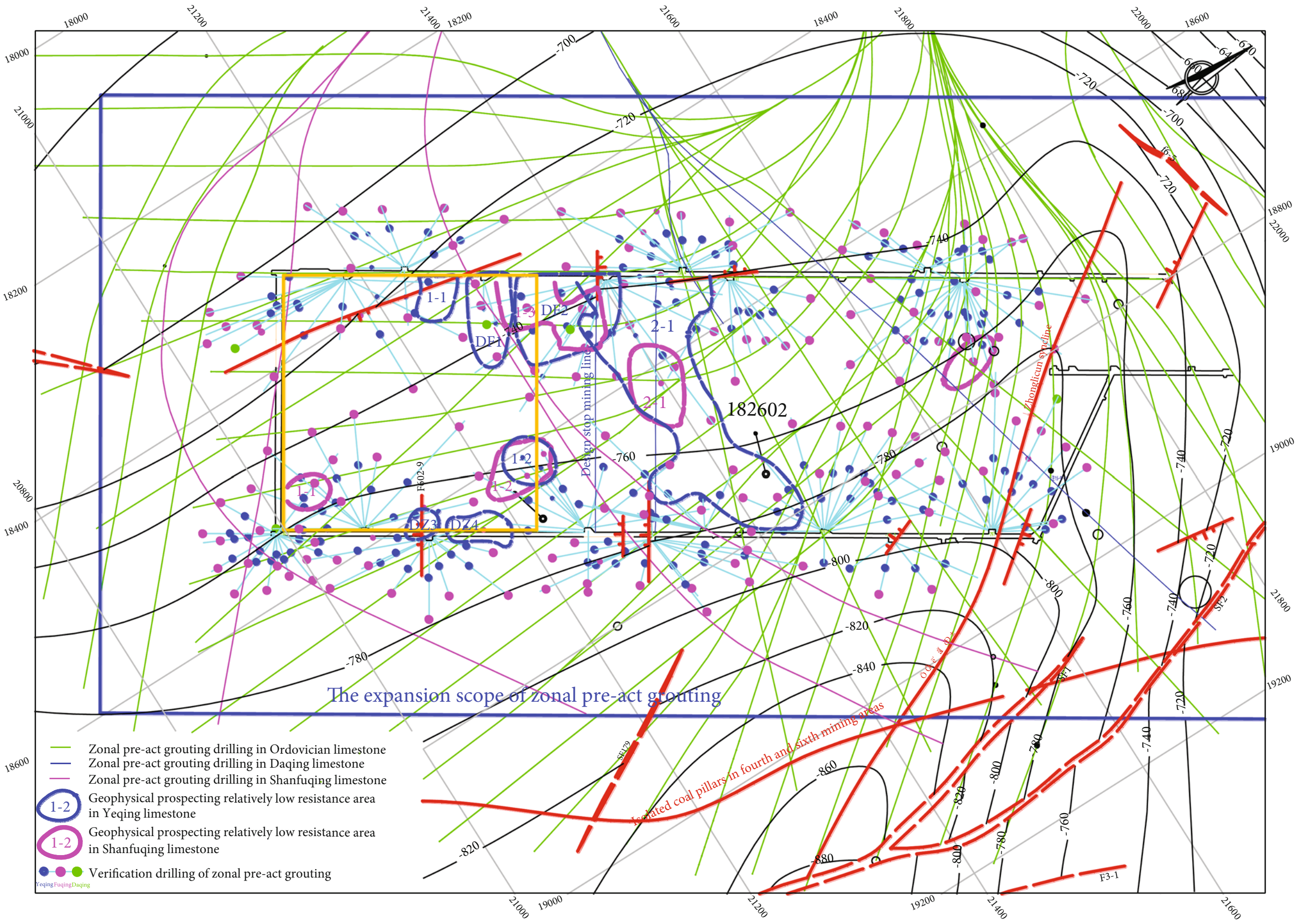

FIGURE 8: Schematic diagram of the exploration and treatment project in No. 2602 working face of the Wutongzhuang mine.

and high water temperature during drilling, additional verification boreholes had to be continuously added. Eventually, 106 boreholes were drilled with a total drilling length of 12671 m and 998.77 tons of cement slurry injected.

The effect of underground verification project was reexamined. In the original design and construction, 70 boreholes were designed to drill through the Yeqing and end in the Shanfuqing limestone. While the aquifers were exposed, most of the boreholes had abnormal water influxes and abnormal temperature, and water sampling in these boreholes showed that these aquifers exhibited water characteristics of the Ordovician limestone. This indicates that the Yeqing and Shanfuqing aquifers were connected to the Ordovician aquifer. When the drilling went through the Yeqing limestone, 57 out of 70 boreholes had water influxes. 15 boreholes had water influxes over $10 m^3/h$, and 3 boreholes had water influxes over 60 m^3/h. The highest water temperature was 45.7°C, and the water pressure was close to the highest level of the Yeqing aquifer. After drilling to the Shanfuqing limestone, 67 out of 70 boreholes had water influxes, 28 boreholes had water inflow over $10 m^3/h$, and 6 boreholes had water inflow over 60 m^3/h. The highest water temperature was 45.9°C, and the water pressure was close to the highest level of the Shanfuqing aquifer.

Comprehensive analysis of the hydrological data of the verification holes and the water discharge test data were conducted. It shows that the Shanfuqing aquifer still received water recharge from the Ordovician limestone, and the vertical recharge of the Ordovician limestone aquifer has not been completely cut off by the treatment project. Hence, it is necessary to further supplement the treatment project.

(3) The Supplemental Grouting to Seal the Top of the Ordovician Limestone and the Daqing and Shanfuqing Thin Limestones. Based on the above grouting treatment, an optimized design for supplemental grouting was given. The layer of 20-30 m below the top of the Ordovician limestone was designed to grout and to cross with the existing grouting layer, i.e., 40-60 m below the top of the Ordovician limestone. And the horizontal branch boreholes in the Daqing and Shanfuqing were designed in a belt-shaped arrangement, forming three-dimensional grouting networks for intensive exploration and treatment. A total of 6 main boreholes and 21 branch boreholes were constructed in the supplementary project, including 16 branch boreholes in the Ordovician limestone, 1 branch borehole in the Daqing limestone, and 4 branch boreholes in the Shanfuqing limestone (Figure 8). A total of 23000.9 m of drilling work were completed, 7066.5 tons of cement injected, and 20 times of borehole leakage occurred. The grouting volume at the

largest leakage point was 1126 tons, and the grouting volume at the other leakage points was less than 1000 tons.

3.4.3. Tests and Assessments of the Treatment Effectiveness

(1) Assessment of the Thin Limestones. Before the treatment, the number of boreholes with water influxes accounted for a large proportion: 69.8% of the total 106 boreholes in the Yeqing, 92.4% in the Shanfuqing, and 100% in the Daqing. After the treatment, it was verified that the number of boreholes with water influxes was very small, the water volume was less than 10 m^3/h, the fissures in the thin limestones were filled, and the hydraulic connection was effectively cut off.

(2) Drilling Verification and Assessment of the Geophysical Abnormal Areas. After the completion of the regional grouting treatment project, 8 abnormal areas with low resistivity delineated by the geophysical method were eliminated, which were verified by underground drilling. Before mining, the water discharge test was carried out in the Yeqing thin limestone and proved that hydraulic connection between thin limestone aquifers was effectively controlled.

(3) The Integrity and Stability of Aquiclude under the Working Face Floor. The distance from coal seam No. 2 to the Yeqing, Shanfuqing, and Daqing limestones and the Ordovician limestone is 37-42 m, 71-76 m, 107 m, and 148 m, respectively. The rock types in the floor strata of the aquiclude are medium fine sandstone, siltstone, shale and mudstone, containing both good plasticity and resistance to seepage of soft rock and good resistance to deformation of the stiff rock. The aquiclude has good stratum integrity in its original state. Through grouting reinforcement, rock strength and stability of the aquifers are also improved.

During tunneling in the working face, a total of 5 faults were exposed, which were all normal faults with displacements of 0.7 to 4.2 m. These faults were all exposed and treated by 7-9 verification holes, and the water resistance of the fault zones was strengthened.

(4) The Risk Assessment of Water Inrush. The water inrush risk of mining under pressure in coal seam No.2 can be assessed by the water inrush coefficient in Eq. (2) according to the national regulations.

After zonal grouting, 60 m rocks in the top of the Ordovician limestone could be considered as the aquiclude as analyzed above. Therefore, water inrush coefficient was changed from 0.072 MPa/m to 0.0536 MPa/m, less than the critical value of 0.1 MPa/m required by the regulations. Hence, the coal mining operations were allowed.

(5) Working Face Water Inflow Prediction. During the extraction of No. 2602 working face, water from sandstone aquifers above coal seam No. 2 and from thin limestone aquifers under coal seam No.2 may enter the goafs of the working face. Using the analogy method and hydrogeological analysis method, the normal water inflow from the roof rocks is 26.5 m^3/h, and water inflow from the Yeqing and Shanfuqing limestones is 60 m^3/h and 35 m^3/h, respectively. The total of inflow is estimated 121.5 m^3/h with a maximum of 240 m^3/h, which belongs to normal water inflow and safely handled by mining operations.

(6) Dewatering Capacity of the Working Face in the No. 6 Panel. There are three dewatering systems in total in the No. 6 panel of the mining area, through examination and verification, and the maximum drainage capacity of system is 600 m^3/h, which is 2.5 times of the maximum water inflow estimated in the above section. The dewatering capacity fully satisfies the requirements.

3.4.4. Monitoring Methods for Safe Coal Extraction

(1) Using the thin limestone aquifers as monitoring indicators, three observation points of boreholes, three long-term observation holes, and dewatering system monitoring points were equipped in upper and lower roadways, respectively, forming a dynamic hydrogeological monitoring system. Monitoring results show that no abnormality occurred during the extraction

(2) 12 monitoring points of microseismic monitoring system and two monitoring substations were installed in upper and lower roadways and cut-out roadway in the working face. During extraction, two abnormalities occurred but were not hydrogeological abnormalities

(3) In the process of extraction, the existing mining pressure monitoring system was used to intently monitor the variation of water inflow during the first and periodic abutment pressures and the time when the length and width of mining face are approximately equal, as a supplemental system to monitor the water inflow from the floor strata

4. Conclusion

Through theoretical study on water inrush mechanisms and prevention methods and a systematic case study, the following conclusions are drawn for deep mining under water pressure:

(1) There are multidimensional characteristics of water inrushes from the coal floor in deep mining, including the water migration upwardly driven by the Ordovician confined water, the planar dispersion of the water inrush channel, the stepped increase of the water inrush inflow, the hysteretic flow of the water inrush time, and the exchange and adsorption of the water quality

(2) The water inrush mechanism is clarified that the permeability, dilatancy, fracturing, and ascending of the water from the Ordovician limestone aquifer form a

planar and divergent flow by the transfer, storage, and transportation of thin limestone aquifers. The corresponding water inrush risk evaluation method is proposed

(3) Based on the thickness of the aquiclude, the failure depth of the floor and the Ordovician limestone water conducted zone height, and the water inrush coefficient, the floor aquiclude is classified into five categories: ultra-thin, thin, medium thick, thick, and ultra-thick aquiclude formations. Five prevention models of safe mining under water pressure are proposed correspondingly

(4) The water disaster prevention method with full time-space tridimensional network in deep coal mining is established. Case study shows that water inrush prevention technologies, including underground large-area grouting and four-dimensional time-space comprehensive water disaster control, can achieve an excellent result

Data Availability

The figure and table data used to support the findings of this study are included within the article.

Conflicts of Interest

The authors declare that they have no conflicts of interest.

Acknowledgments

This paper was partially supported by the National Science Foundation of China (51774136, 51974126) and the Program for Innovative Research Team in University sponsored by Ministry of Education of China (IRT-17R37). The authors thank Mr. Zhang Jincai for his time and his insight for improve this manuscript.

References

[1] Y. Shangxian, L. Huiqing, L. Demin, and Y. Huichao, "70 years of investigation on karst collapse column in North China coalfield: cause of origin, mechanism and prevention," *Coal Science and Technology*, vol. 47, no. 11, pp. 1–29, 2019.

[2] S. Yin and J. Zhang, "Impacts of karst paleo-sinkholes on mining and environment in northern China," *Environmental Geology*, vol. 48, no. 8, pp. 1077–1083, 2005.

[3] S. Yin, J. Zhang, and D. Liu, "A study of mine water inrushes by measurements of in situ stress and rock failures," *Natural Hazards*, vol. 79, no. 3, pp. 1961–1979, 2015.

[4] J. Zhang, "Investigations of water inrushes from aquifers under coal seams," *International Journal of Rock Mechanics and Mining Sciences*, vol. 42, no. 3, pp. 350–360, 2005.

[5] G. Yongqiang, "Water pollution control technology and hydrogeological characteristics of deep mine in Fengfeng mine," *Coal and Chemical Industry*, vol. 41, no. 10, pp. 59–62, 2018.

[6] S. Yin, Y. Wang, and H. C. Yin, "Mechanism and full-time-space prevention and control technology of water inrush from Ordovician and thin limestone in deep mines," *Journal of China Coal Society*, vol. 45, no. 5, pp. 1855–1864, 2020, (in Chinese).

[7] Y. Shangxian, X. Wei, Y. Huichao, and C. Min, "Study on risk assessment method of water inrush from thick floor aquiclude in deep mining," *Coal Science and Technology*, vol. 48, no. 1, pp. 83–89, 2020.

[8] J. W. Zhao, H. W. Zhou, D. J. Xue, T. Su, H. L. Deng, and H. Z. Yang, "Expansion law of seepage path in the concealed structural floor of coal seam in deep confined water," *Journal of China Coal Society*, vol. 44, no. 6, pp. 1836–1845, 2019.

[9] Q. B. Zhao, "Ordovician limestone karst water disaster regional advanced governance technology study and application," *Journal of China Coal Society*, vol. 39, no. 6, pp. 1112–1117, 2014.

[10] G. Liangtao, Y. Guijun, and G. Honglie, *Hydrogeology of coalfields in China*, Coal Industry Publishing House, Beijing, China, 2001.

[11] Hydrogeological Bureau and Research Institute, Ministry of Geology, *Hydrogeological classification of solid ore deposits in China*, Geology Press, Beijing, China, 1959.

[12] S. Jingyi, Liuzhizhong, and L. Xiehuai, *General report on comprehensive control of karst water from Ordovician limestone in North China coal field*, Xi'an Branch of Coal Science Research Institute, Xi'an, 1995.

[13] L. Jinkai, "Characteristics and prevention of Ordovician limestone water inrush in North China coal deposit," *Coal Geology & Exploration*, vol. 5, pp. 38–42, 1981.

[14] M. Wang, "Discussion on water inrush mechanism and prediction method of coal seam floor," *Coal Science and Technology*, vol. 9, pp. 34–39, 1979.

[15] S. Liang and L. Maoquan, "Comprehensive prevention and control of groundwater in Feicheng mining area," *Coal Geology & Exploration*, vol. 2, pp. 45–50, 1986.

[16] S. Yin, Y. Han, Y. Zhang, and J. Zhang, "Depletion control and analysis for groundwater protection and sustainability in the Xingtai region of China," *Environmental Earth Sciences*, vol. 75, no. 18, 2016.

[17] Z. Jincai, Z. Yuzhuo, and L. Tianquan, *Rock Mass Permeability and Coal Mine Water Inrush*, Geological Publishing House, Beijing, China, 1997.

[18] J. Zhang, *Applied Petroleum Geomechanics*, Gulf Professional Publisher of Elsevier, USA, 1st edition, 2019.

[19] S. N. Dong, H. Wang, and W. Z. Zhang, "Judgement criteria with utilization and grouting reconstruction of top Ordovician limestone and floor damage depth in North China coal field," *Journal of China Coal Society*, vol. 44, no. 7, pp. 2216–2226, 2019.

[20] A. Li, *Water Inrush Mechanism and Application of Mining Floor Failure in Confined Water Body of Weibei Coalfield*, China University of Mining and Technology Press, Xuzhou, China, 2015.

[21] Y. P. Liang, B. Li, and Q. L. Zou, "Movement type of the first subordinate key stratum and its influence on strata behavior in the fully mechanized face with large mining height," *Arabian Journal of Geosciences*, vol. 12, no. 2, 2019.

[22] S. L. Liu, W. T. Liu, and D. W. Yin, "Numerical simulation of the lagging water inrush process from insidious fault in coal seam floor," *Geotechnical and Geological Engineering*, vol. 35, no. 3, pp. 1013–1021, 2017.

[23] W. T. Liu and Q. Wu, “Mechanism and numerical simulation technology of lagging water inrush in deep mining,” *Coal Industry Publishing House, Beijing, China*, vol. 2010, pp. 2–5, 2010.

[24] X. X. Meng, W. T. Liu, and D. R. Mu, “Influence Analysis of Mining’s Effect on Failure Characteristics of a Coal Seam Floor with Faults: A Numerical Simulation Case Study in the Zhaolou Coal Mine,” *Mine Water and the Environment*, vol. 37, no. 4, pp. 754–762, 2018.

[25] W. C. Song, Z. Z. Liang, and C. B. Zhao, “Mechanical failure characteristics of mining floor along working face inclination above confined water,” *Journal of Mining & Safety Engineering*, vol. 37, no. 9, pp. 2131–2143, 2018.

[26] J. Sun, L. G. Wang, and Y. Hu, “Mechanical criteria and sensitivity analysis of water inrush through a mining fault above confined aquifers,” *Arabian Journal of Geosciences*, vol. 12, no. 2, p. 4, 2018.

[27] H. T. Xiao, X. L. Wen, W. Q. Zhang, and B. Y. Li, “In situ measurement of floor strata displacements in slice mining,” *Chinese Journal of Geotechnical Engineering-Chinese Edition*, vol. 20, no. 5, pp. 20–338, 2001.

[28] S. Zhang, W. Guo, and Y. Li, “Experimental simulation of water-inrush disaster from the floor of mine and its mechanism investigation,” *Arabian Journal of Geosciences*, vol. 10, no. 22, p. 503, 2017.

Hindawi
Geofluids
Volume 2021, Article ID 3508661, 13 pages
https://doi.org/10.1155/2021/3508661

Research Article

Research on the Reasonable Strengthening Time and Stability of Excavation Unloading Surrounding Rock of High-Stress Rock Mass

Wensong Xu,[1,2] Wentao Xu,[1,2] and Yunhai Cheng[1,2]

[1]*State Key Laboratory of Mining Response and Disaster Prevention and Control in Deep Coal Mines, Anhui University of Science and Technology, Huainan 232001, China*
[2]*School of Mining Engineering, Anhui University of Science and Technology, Huainan 232001, China*

Correspondence should be addressed to Wensong Xu; 359879021@qq.com

Received 27 May 2021; Accepted 25 August 2021; Published 14 September 2021

Academic Editor: Yong-Zheng Wu

This study is aimed at better understanding the deformation and failure mechanism of surrounding rock during excavation unloading of a high-stress rock mass and determining the reasonable reinforcement time for the surrounding rock. To fulfill this aim, true triaxial tests were carried out on different loading and unloading paths during the unilateral unloading of a high-stress rock mass. The variational condition for minimization of plastic complementary energy is obtained, the optimal reinforcement time is determined, and the range of the plastic zone in the surrounding rock reinforced by anchor mesh-cable-grouting is compared and analyzed. The results are as follows: (1) Based on the Mohr-Coulomb yield criterion and the deformation reinforcement theory of surrounding rock, the stable state with the minimum reinforcement force is obtained. (2) After the true triaxial tests on the unilateral unloading of the third principal stress were carried out under different confining pressures, loading continued to be performed. Compared with rock failure without confining pressure, in the conventional uniaxial compression test, the failure of samples is dominated by composite splitting-shear failure; the unilateral unloading stress-concentration failure is a progressive failure process of splitting into plates followed by cutting into blocks and then the ejection of blocks and pieces. (3) The relationship between the time steps of the surrounding rock stability and the excavation distance is obtained. The supporting time can be divided into four stages: presupport stage, bolt reinforcement stage, anchor cable reinforcement stage, and grouting reinforcement stage. (4) In the range of within 5 m behind the tunneling face, the plastic zone of the surrounding rock with support is reduced by 7 m as compared with that with no support. In the range of over 5 m behind the tunneling face, the plastic zone of the roadway floor with support is reduced by 2.6 m as compared with that without support, and the deformation is reduced by 90%. These results can serve as a reference for controlling the behavior of surrounding rock during excavation unloading of high-stress rock masses.

1. Introduction

After roadway/tunnel excavation, the surrounding rock suffers deformation, thus resulting in stress redistribution. In the process of constant stress adjustment, the internal structure of the rock mass changes. With time, the stress in the surrounding rock near the excavated rock mass reaches its critical failure strength, and overall failure occurs [1, 2]. Therefore, understanding the failure characteristics and determining the rational supporting time of surrounding rock near the excavated rock mass can help effectively control the deformation of surrounding rock [3–5].

There have been many studies on the stability of surrounding rock of underground roadways from the perspectives of stress, deformation, energy, etc. using various research methods [6–8]. Wu et al. [9] adopted a variety of research techniques to analyze the zonal deformation and failure characteristics and stress distribution characteristics of the roof, floor, two sides, and four corners of a tilted stratum roadway. Besides, the stability control technology for controlling the nonhomogeneous deformation of the tilted stratum roadway was proposed with engineering verification. Zhang and Han [10] analyzed the magnitude, direction change, and distribution characteristics of crustal stress in mines based on the measured crustal stress data in the mining areas and studied the influence of crustal stress on roadway stability; they provided a reliable basis for the design of a reasonable support structure for roadways. Gou et al. [11] investigated the effect of horizontal tectonic stress on the stability of surrounding rock of a roadway by numerical simulation and showed that with an increase in the horizontal stress, the horizontal stress transfers to the deeper parts of the roadway roof and floor; this causes floor heave and fold failure of the roadway and shear deformation and wedge caving of the roof, with deformation and failure of the roof and floor being greater than that of the two sides of the roadway. Li et al. [12] mainly analyzed the stress distribution, deformation, and failure mechanism of surrounding rock in deep parts by using the elastic-brittle constitutive model and sliding failure theory. Yang et al. [13] showed that the rotation angle of the main roof was the main factor leading to roof deformation; the roof convergence could not be reduced by strengthening the roadway support, and the roof convergence, as well as the fracture direction, could be effectively controlled by increasing the roof cutting height and angle. Yao [14] is of the opinion that the surrounding rock support of a roadway is closely related to the initial stress, excavation mode and progress, surrounding rock grade, etc. Han et al. [15] studied the stress characteristics of rock strata experiencing roof cutting and pressure relief and determined the key parameters of roof cutting height, roof cutting angle, and hole spacing based on the theoretical analysis method of mine ground pressure. They showed that the roof cutting could significantly reduce roadway stress and deformation and improve roadway support and production efficiency. Xu et al. [16, 17] conducted true triaxial tests to study the damage and fracture characteristics of marble under excavation unloading of a high-stress rock mass; they showed that for the excavation unloading surface, the main failure surface is near the free surface as the stress decreases. Dong et al. [18] studied the mechanical characteristics and failure mechanism of surrounding rock during excavation unloading of a deep circular roadway and established the strength criterion and a tension-compression damage model for dynamic unloading to obtain the failure characteristics of the excavation unloading surface. These scholars evaluated the failure characteristics, overall stability, and reasonable support structure of surrounding rock after excavation unloading of roadways from various perspectives; however, they did not propose a reasonable supporting time or specific measures according to the actual situation.

Based on the failure mechanism of the surrounding rock of roadways during excavation unloading, many scholars have put forward reasonable supporting times and supporting modes [19–21]. Su et al. [22] determined the primary support timing through the evolution of safety factors during tunnel excavation. Zhou et al. [23] analyzed the changes of stress in the plastic zone, displacement of the tunnel wall, and support pressure in the tunnel supporting process and proposed a reasonable supporting time for staged tunnel supporting. Sun and Zhang [24] put forward the layer model, obtaining the deformation process and supporting characteristics of the surrounding rock, and studied the synergistic supporting mechanism of the composite supporting layer. Yu [25] studied the space-time evolution of surrounding rock deformation under the disturbance of tunnel excavation and established a three-dimensional mechanical model to study the interaction between tunnel structure and surrounding rock. He also analyzed the supporting effects of various supporting structures and obtained the mechanical characteristics and practicability of composite supporting structures. Dong [26] and Hou et al. [27] mainly summarized three supporting technologies in terms of control technologies: the combined supporting technology with anchor bolt (cable) as the main part supplemented by other technologies, the integrated supporting technology with the integration of anchor bolt, and the combined technology with supports. However, they only analyzed the supporting effect from one aspect or through multiple ways and adopted a single or multiple supporting means for combined support; they, however, did not propose a reasonable supporting time and appropriate supporting mode from the optimal supporting time in different stages of surrounding rock of roadways under excavation unloading. Therefore, building on many previous studies, the reasonable supporting time and stability were explored in this study.

In this study, based on the Mohr-Coulomb yield criterion and the minimum plastic complementary energy, the failure and reinforcement time of surrounding rock were analyzed. True triaxial tests on different loading and unloading paths were conducted to investigate the stress failure characteristics of a rock mass during excavation unloading. Through 3DEC numerical simulation, the optimum supporting time for surrounding rock during excavation unloading at different stages was determined, and on-site verification was conducted.

2. Theoretical Analysis on Surrounding Rock Reinforcement during Excavation Unloading

2.1. Mohr-Coulomb Yield Criterion. According to the method of calculating the safety coefficient of points in surrounding rock based on the Mohr-Coulomb theory, the Mohr-Coulomb yield function is expressed by the principal stress as follows:

$$f(\sigma_1, \sigma_2, \sigma_3) = \frac{1}{2}(\sigma_1 - \sigma_2) - \frac{1}{2}(\sigma_1 + \sigma_3)\sin\varphi - c\cos\varphi, \quad (1)$$

where $\sigma_1, \sigma_2, \sigma_3$ denote the first, second, and third principal stresses, respectively; φ denotes internal friction angle; and c denotes cohesion.

With the elastic theory as the basis, it is considered that yield occurs when the stress value meets certain conditions;

to represent the safety degree of a rock mass, engineering researchers propose the concept of the safety coefficient [22]:

$$F = \frac{H(\chi)}{f(\sigma)}, \quad (2)$$

where H denotes material parameter, which is the function of the internal variable χ of scalar, and F denotes the safety coefficient; $F > 1$ indicates no yield inside the yield surface, $F = 1$ indicates a critical state on the yield surface, and $F < 1$ indicates shear failure outside the yield surface.

According to the Mohr-Coulomb yield criterion, the distance between the stress state at any point in the rock mass and the strength envelope curve is determined (shown in Figure 1).

If the strength envelope curve is translated downward, that is, corresponding to the reserve safety margin, then the safety coefficient based on the Mohr-Coulomb yield criterion is

$$F = \frac{|AC|}{|AB|} = \frac{|AD|\cos\varphi}{|AB|} = \frac{c\cos\varphi + ((\sigma_1+\sigma_3)/2)\sin\varphi}{(\sigma_1-\sigma_3)/2}. \quad (3)$$

2.2. Deformation Reinforcement Theory of Surrounding Rock. It is supposed that for the action on an elastic-plastic structure, the body force is $f = f_i$, the stress boundary is S_σ, and the boundary condition is $T = T_I = \sigma_{ij}n_j$. Then, regarding any given virtual displacement $\delta u = \delta u_i$, the corresponding virtual strain is $\delta\varepsilon_{ij}$. Based on the virtual displacement principle, the following can be obtained:

$$\int_V \delta\varepsilon_{ij}\sigma_{ij}^1 \mathrm{d}V = \int_V \delta u_i f_i \mathrm{d}V + \int_{S_\sigma} \delta u_i T_i \mathrm{d}S. \quad (4)$$

Considering any coordinated equilibrium stress field σ_1 and coordinated stable stress field σ, the difference between them is the plastic stress increment field $\Delta\sigma_p$:

$$\Delta\sigma_p = \sigma_1 - \sigma. \quad (5)$$

Substitute Equation (5) into Equation (4), and through the transposition of terms, the following can be obtained:

$$\int_V \delta\varepsilon_{ij}\sigma_{ij}\mathrm{d}V = \int_V \delta u_i f_i \mathrm{d}V + \int_{S_\sigma} \delta u_i T_i \mathrm{d}S - \int_V \delta\varepsilon_{ij}\Delta\sigma_{ij}^p \mathrm{d}V, \quad (6)$$

$$\Delta\varepsilon^p = \Delta\lambda\frac{\partial f}{\partial\sigma}, \quad (7)$$

$$\Delta\varepsilon^p = C : \Delta\sigma^p = C : (\sigma_1 - \sigma). \quad (8)$$

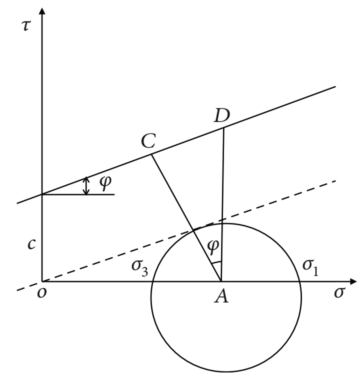

Figure 1: Calculation diagram for the safety coefficient of points based on Mohr-Coulomb theory.

By substituting Equation (8) into Equation (7) and noting that σ is on the yield plane, the final stress state σ can be determined, that is,

$$C : (\sigma_1 - \sigma) = \Delta\lambda\frac{\partial f}{\partial\sigma}, \quad f(\sigma) = 0. \quad (9)$$

Due to the deformation compatibility characteristic of σ_1, it actually represents a certain deformation state. Therefore, Equation (6) can also be expressed as follows: an unstable deformation state can be stabilized by applying reinforcement force. There are many such reinforcement schemes. The stable stress field σ in accordance with the plastic constitutive equation (orthogonal flow rule and consistency condition) is determined as follows: everywhere within $V0$, $\sigma_1 = \sigma$, and σ is determined by using Equation (9) in each point within $V1$. It is clear that the stable stress field σ determined in this way is the stress field closest to the stress field σ_1 in the set S, i.e., L or ΔE is the minimum.

Thus, an important conclusion can be drawn as follows: for a specific rock mass with an unstable deformation structure, the plastic constitutive relation makes the structure approach the nearest stable state, or the plastic constitutive relation makes the structure approach the stable state requiring the minimum reinforcement force. The variational condition for minimizing the plastic complementary energy is

$$\delta(\Delta E) = 0, \delta^2(\Delta E) > 0. \quad (10)$$

For a specific rock mass with unstable deformation structure, it indicates $\delta\sigma_1 \equiv 0$. Due to the positive definiteness of C, the second-order variation of the plastic complementary energy is constantly positive:

$$\delta^2(\Delta E) = \int_V \delta\sigma : C : \delta\sigma \mathrm{d}C > 0. \quad (11)$$

Thus, the following can be obtained:

$$\delta(\Delta E) = -\int_V \delta\sigma : C : (\sigma_1 - \sigma)\mathrm{d}V = -\int_V \delta\sigma : \Delta\varepsilon^p \mathrm{d}V = 0. \quad (12)$$

3. Test Analysis of a High-Stress Rock Mass during Excavation Unloading

Rock masses usually exist in a certain stress environment, and they are in a three-dimensional stress equilibrium state before excavation. In both TMB excavation and borehole-blasting excavation, the original balance is broken, forming a free surface on the rock mass, and the stress state transforms from the original three-dimensional six-sided stress into a three-dimensional five-sided stress, leading to the redistribution of stress in the surrounding rock. Stress concentration occurs in the surrounding rock near the free surface. When the secondary stress exceeds the bearing limit of the surrounding rock, the rock mass suffers failure. Therefore, the use of a unilateral unloading and loading method can more truly reflect the failure state of surrounding rock in practical engineering.

3.1. Test Equipment. The true triaxial disturbance unloading rock test system used in this study (see Figure 2) can expose a surface of the sample to simulate the phenomenon of a free surface occurring after excavation in underground engineering; this is achieved through an independent loading in three mutually vertical directions and sudden unloading in a single surface in the horizontal direction. In the vertical direction (Z) of the system, the maximum load of the loading cylinder is 5000 kN; the disturbance cylinder is installed on the lower beam of the vertical loading frame, with a maximum dynamic load of 500 kN; the maximum loads of the two loading cylinders in the horizontal direction (X, Y) are both 3000 kN; one of the cylinders is a dynamic cylinder, which is used for quick unloading; the loading and unloading are controlled by a fully digital servo controller, which provides the necessary means for determining the stress state of the rock mass when it suffers failure.

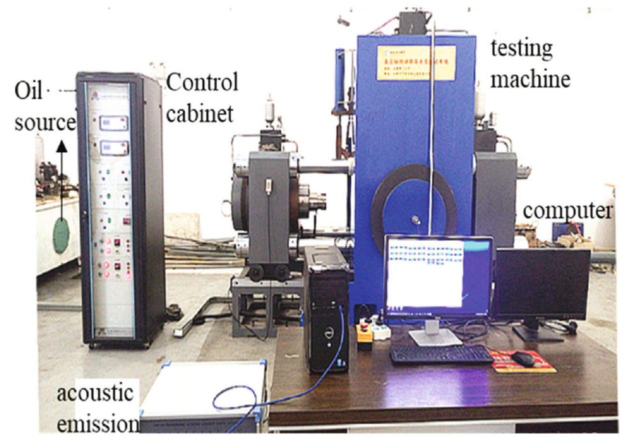

Figure 2: True triaxial disturbance unloading rock test system (Figure 2 is reproduced from Xu et al. [28]).

3.2. Test Scheme. This test mainly simulates the stress-concentration failure test of unilateral unloading under a true triaxial, three-dimensional, and hexahedral stress state. A cuboid marble with good integrity and uniformity was used as the rock sample; it had an initial density of 2758 kg/m^3, a water content of 0.02%, and a size of 100 mm × 100 mm × 200 mm.

3.2.1. Conventional Uniaxial Compression Test. To obtain the conventional compressive strength, deformation parameters, and failure characteristics of the marble, and to serve as a reference for the unilateral unloading and loading tests under true triaxial, three-dimensional, and hexahedral stress states, the confining pressure of sample #1 was designed to be zero in this test (see Table 1). To better observe the variation in the postpeak curve, the deformation mode was used for loading in the test (see Figure 3(a)), with a loading rate of 0.05 mm/min and σ as the stress.

Table 1: Initial stress values.

Sample number	σ_1	σ_2	σ_3
#1	0	0	0
#2	50	5	2.5
#3	50	10	5.0
#4	50	20	10.0
#5	50	30	20.0

3.2.2. Unilateral Unloading Stress-Concentration Failure Test. When simulating deep tunnel excavation, the surrounding rock that is originally in the three-dimensional stress state develops a free surface, and the mutual extrusion of the surrounding rock in the tangential direction intensifies the failure caused by stress concentration. The samples used in this test are numbered from #2 to #5, and the loading was controlled by loading at a loading rate of 0.5 MPa/s. The stress loading path during the test is shown in Figure 3(b). First, in the X, Y, and Z directions, the load is applied at 0.5 MPa/s to the set initial stress level (see Table 1). After reaching the initial stress level, the stress remains unchanged in the Y and Z directions, and transient unloading was performed on a surface in the X direction at a speed of 50 mm/s (see Figure 4(b)). Then, loading was performed in the Z direction at a speed of 0.5 MPa/s until failure.

3.3. Stress-Strain Curve. The stress-strain curve for the true triaxial third principal stress with different confining pressures continuing to be loaded after unilateral unloading is shown in Figure 5. Compared with rock sample #1 without confining pressure failure, the stress-strain curve of the stress-concentration type has the following characteristics: in the case without confining pressure, the peak value is 88 MPa, and with the confining pressure increasing, the peak points increase to 151 MPa, 162 MPa, 200 MPa, and 264 MPa, respectively. The prepeak curve also shows notable yield points. With the increase in the confining pressure, the yield point and the peak point increase, and the slope of the curve between the yield point and the peak point is moderate. The corresponding failure phenomenon is the splitting failure in the free surface and the potential shear failure in

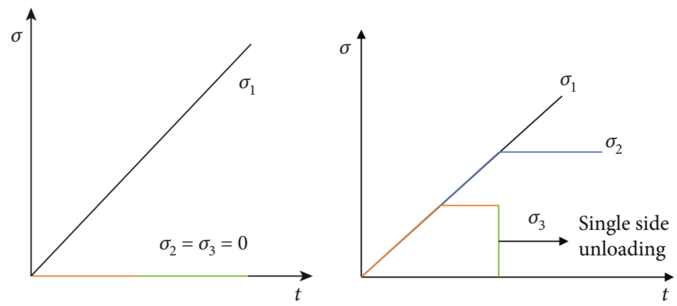

(a)

(b)

FIGURE 3: Test loading and unloading path diagram.

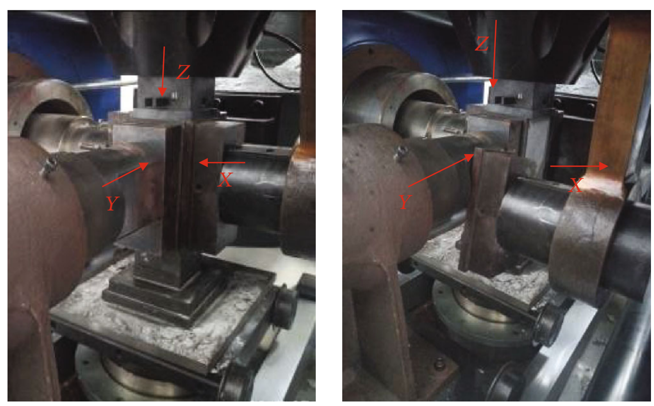

(a) Loading

(b) Unilateral unloading

FIGURE 4: Spatial position of rock samples.

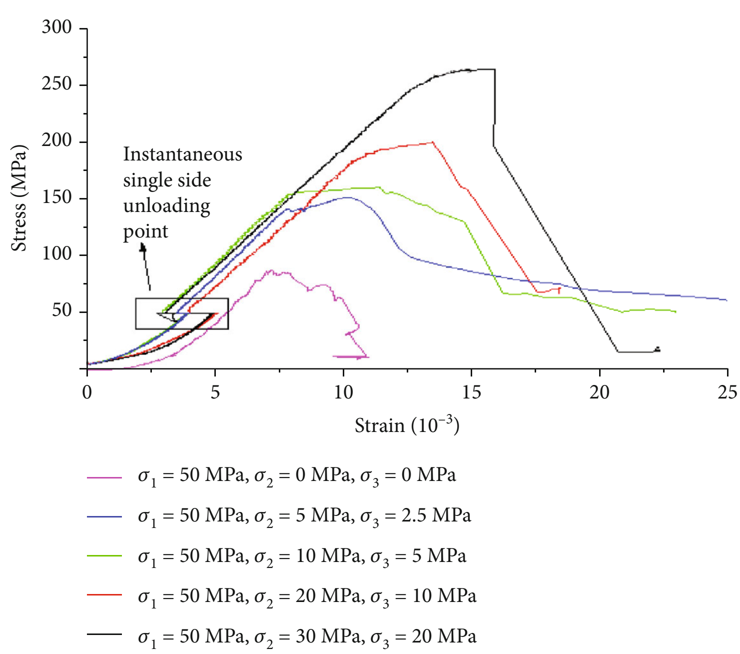

FIGURE 5: Stress-strain curve for stress-concentration failure under unilateral unloading.

the rock mass. The axial strain before the peak is larger than that after the peak, and the postpeak stress after the peak shows a brittle drop. The postpeak stress-strain curve is relatively steep and inclined. When the confining pressure is 30 MPa and 20 MPa, the postpeak curve is the steepest and the postpeak strain is the smallest. This shows that with an increase in the confining pressure, the failure changes from composite tensile-shear failure to splitting failure; with an increase in the confining pressure, the failure of the samples is the most severe, and the intensity of the rock burst is greater.

3.4. Failure Characteristic Analysis

3.4.1. Conventional Uniaxial Compression Test. In conventional uniaxial compression tests, the macroscopic failure type of marble samples is mainly a composite splitting-shear failure (as shown in Figure 6). Because marble is a hard rock and has a relatively high brittleness coefficient, under the condition of no confining pressure, the lenticular angle of the cubic sample experiences a boundary constraint effect. In the failure process, there is a splitting failure surface at the upper part of the rock samples, which is almost parallel to the first principal stress surface. After failure, a peeling surface forms on the rock sample. There is a master shearing surface at the lower part of the rock sample, on which there is a large quantity of scratches and small fragments and powders of the rock sample. This is due to the secondary shear failure caused by stress concentration at resistance to load in the process of shear slip.

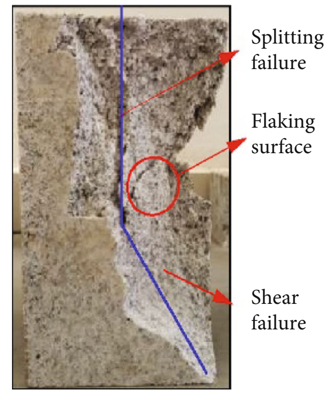

Figure 6: Macroscopic failure diagram for conventional uniaxial compression.

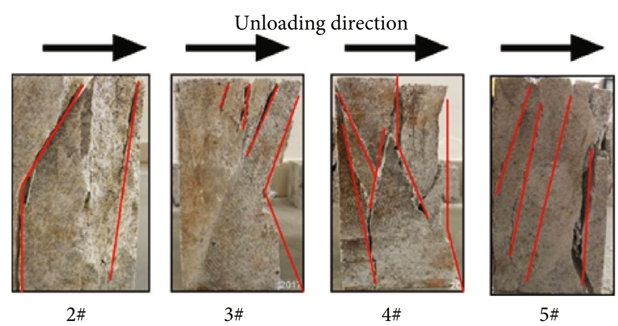

Figure 7: Schematic diagram for unilateral unloading stress concentration macroscopic failure.

3.4.2. Unilateral Unloading Stress-Concentration Failure. After the rock sample is maintained for a certain period of time from triaxial compression to the initial state, rapid unloading is performed on the unilateral third principal stress, and the rock sample is in the stage of microcrack development. The number of microcracks increases, but no macroscopic cracks occur on any of the rock samples. Afterward, loading continues to be performed on σ_1; when it is loaded to 70% of the failure peak, after plate crack and ejection occurs on the #2~#5 rock samples, plate failure occurs on the free surface, with the generation of fine white rock powder. Two larger shear oblique cracks appear inside the rock mass, and a large amount of fine white rock powder appears in the cracks. With the increase in the axial stress, the plate crack width increases, and the rock sample reaches the final failure mode (see Figure 7). The slabby splitting of the rock mass is dominated by a tensile fracture, with a local shear stress. It is a progressive failure process of splitting into plates, followed by cutting into blocks, and then the ejection of blocks and pieces. This indicates that in the unilateral unloading process of σ_3 and σ_2 restricts the lateral expansion of the rock samples under the action of σ_1, leading to the development of rock samples towards the free surface. The continuous deformation causes the rock samples to transform from a state of compression to tension. When the tensile strength is reached, longitudinal cracks running through the rock samples are generated near the unloading surface, and rock plates parallel to the unloading surface form. With the continuous unloading of the unloading surface, the rock slab reaches the critical buckling value, and with the release of excess energy, rock burst failure occurs. The morphology of the rock samples after failure is shown in Figure 7. The #2~#5 rock samples all suffer plate cracks on the free surface, showing the three types of sheet shape, thin-plate shape, and wedge shape. This indicates that tensile failure occurs under true triaxial unilateral unloading conditions with confining pressure. With the increase in the confining pressure, the failure of rock samples shows dual characteristics, with tension failure occurring first followed by compression-shear failure. V-shaped failure pits appear on the free surface, and penetrating shear fractures appear in the areas far away from the free surface. When the confining pressure increases to a certain extent, the rock samples suffer splitting failure, and splitting and penetrating cracks form over the entire rock mass. This shows that in the excavation process of a deeply buried roadway with high crustal stress, the two sides will show an instantaneous "unloading" effect, with instantaneous rebound deformation occurring. With the stress redistribution and stress concentration in local regions, when the tensile strength of the surrounding rock is exceeded, accidents such as plate cracks, rib spalling, and rock bursts will gradually occur on the two sides.

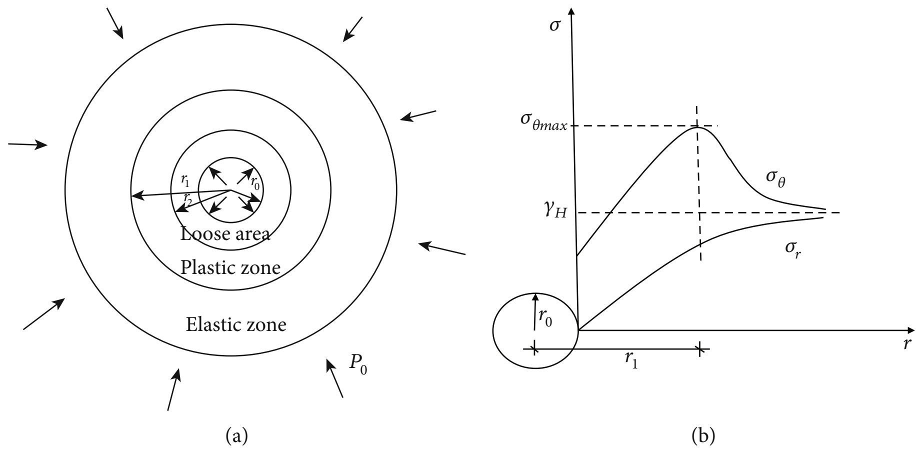

FIGURE 8: Stress distribution in rock mass around the roadway.

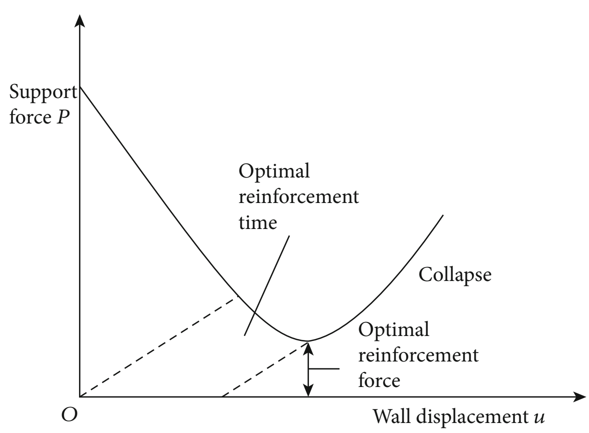

FIGURE 9: Diagram for the reasonable supporting time of surrounding rock.

4. Reasonable Supporting Time for Surrounding Rock of a High-Stress Rock Mass Under Excavation Unloading

After the excavation of a high-stress rock mass, with time, the bearing capacity of the surrounding rock itself decreases, creating a fractured zone with both depth and breadth. The stress concentration is caused by the bearing capacity of the rock mass itself. When the local high stress generated by the stress concentration exceeds the strength of the rock mass, the rock mass will deform towards the excavation surface, thus leading to failure. From the excavation surface to the deep part, it can be divided into three zones: failure zone (completely losing bearing capacity), plastic zone (having certain bearing capacity), and elastic zone (having intrinsic bearing capacity) (as shown in Figure 8). To reduce the range of the failure zone and the plastic zone and reasonably control the deformation of the surrounding rock, it is necessary to support the surrounding rock in a timely manner. According to the basic principle of NATM construction, as shown in Figure 9, selecting the best supporting time is the key after roadway excavation.

The number of time steps is the number of iterative steps calculated through numerical simulation, and it is the number of steps needed to be calculated in the process of establishing the stress balance of surrounding rock. However, the measurement unit used in the actual construction is time. The establishment of the relationship between time and the number of steps facilitates the numerical simulation results to guide the site construction better and more effectively. In the process of numerical simulation, when the displacement field, stress field, and plastic zone do not change with the increase in the time steps, the calculation reaches equilibrium, and the surrounding rock reaches the equilibrium and stable state. In the excavation process of a high-stress rock mass, the effect of each excavation unloading on the displacement field, stress field, and plastic zone is the key factor for guiding the site construction. When the calculation reaches the equilibrium state, it indicates that the effect of excavation unloading ends. According to the displacement curve of the surrounding rock deep in the roof during roadway excavation in numerical simulation, the relationship between the number of time steps required to achieve surrounding rock stability and the excavation distance can be determined through

$$y = 656.4791 + \frac{(50.15365 - 656.4791)}{(1 + \exp((x - 6.5871)/1.81038))} R^2 = 0.99585. \tag{13}$$

4.1. Determination of Reasonable Reinforcement Time. The meaning of reasonable reinforcement time is the time corresponding to maximizing the bearing capacity of the plastic zone without loosening failure occurring. 3DEC was used to conduct numerical simulation on the roadway excavation process to monitor the curves of the change of the convergence quantity and convergence rate of the surrounding rock at the top and sides of the roadway with time, as shown in Figure 10. It basically reflects the movement and

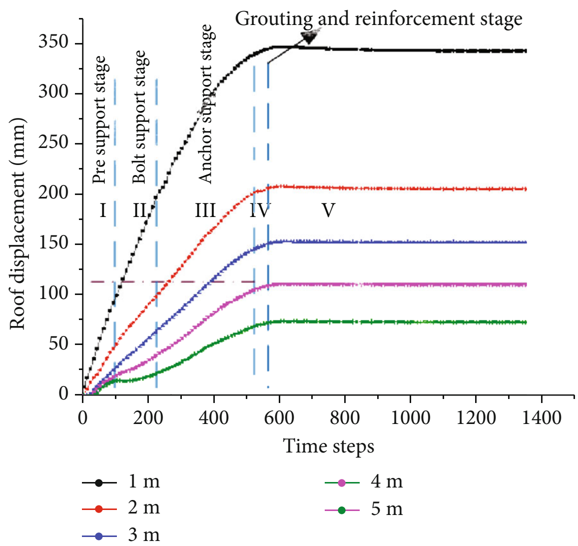

(a) Displacement curve for surrounding rock in deep roadway roof

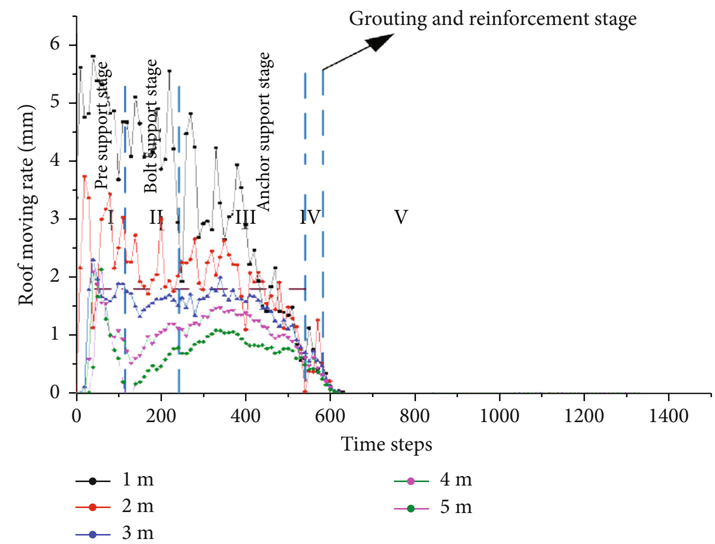

(b) Changing curve for the convergence rate of surrounding rock in deep roadway roof

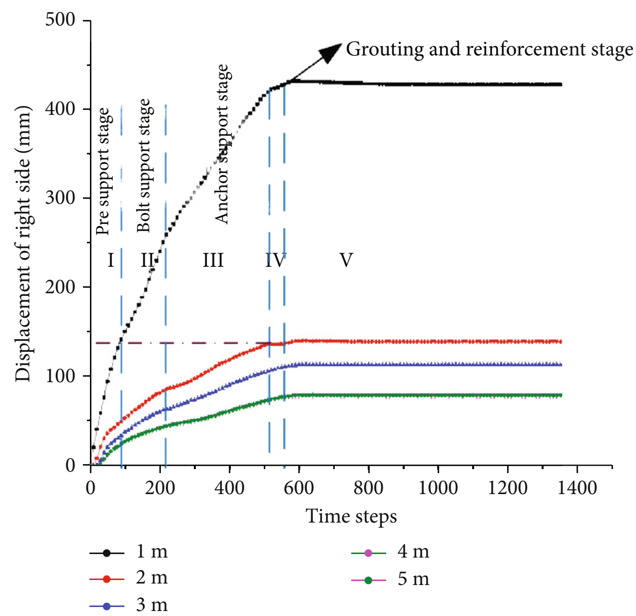

(c) Displacement curve of surrounding rock deep on the right side of the roadway

Figure 10: Continued.

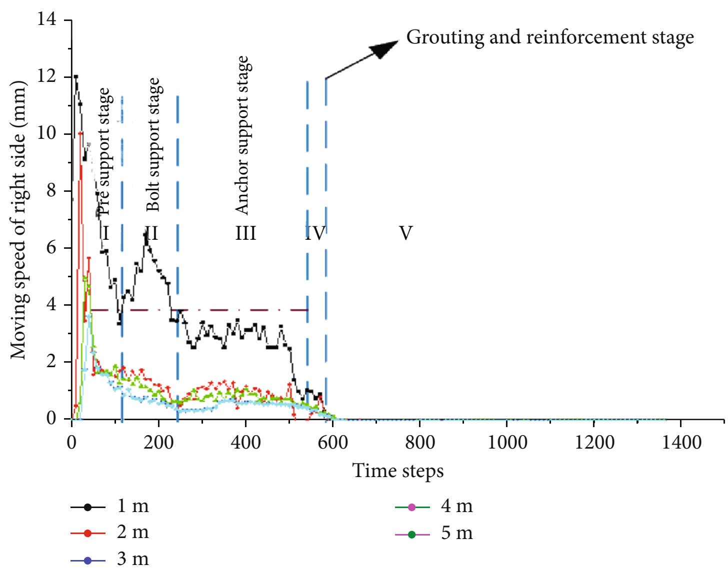

(d) Change curve of the convergence rate of surrounding rock deep on the right side of the roadway

Figure 10: Corresponding curves for the number of time steps and surrounding rock deformation of the roadway.

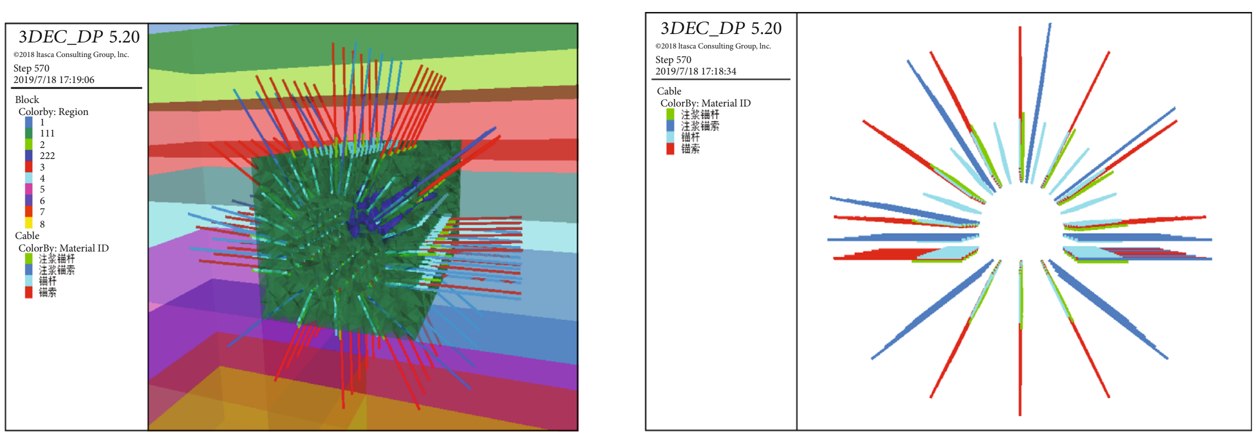

Figure 11: Numerical simulation diagram for support.

deformation of the surrounding rock. Reasonable reinforcement and supporting time should be the corresponding time when the surrounding rock displacement tends to be relatively stable.

As can be seen from Figure 10, due to the influence of roadway excavation, the surrounding rock within 1 m away from the roadway roof is severely deformed and broken into blocks, showing large deformation, and the final deformation reaches 452 mm. Due to the inherent load-bearing capacity of the surrounding rock in the plastic zone, the surrounding rock that is 1 m-4 m away from the roadway roof is subjected to a declining convergence amount and convergence rate from the inner side to the outer side. The convergence amount of the surrounding rock within the range of 4 m to 5 m from the roof is basically the same. Therefore, it can be seen that, in the case with no support, the surrounding rock within 3 m and over 4 m from the roof shows a bed-separation phenomenon. Similar results can be obtained from the curves for convergence amount and convergence rate on the right side.

Analyzing the convergence amount and convergence rate of the surrounding rock at the top and right side of the excavation roadway with high-stress rock mass shows that the deformation of the surrounding rock at the top of the roadway changes dramatically in the first 520 steps of roadway excavation, and the convergence rate of the surrounding rock also shows a sharp change. The convergence amount of the roof tends to be relatively stable after 620 steps. When the number of time steps is 112, 236, and 520, the convergence rates of the surrounding rock of the roof all show the trend of increasing and decreasing, indicating that the plastic zone of the surrounding rock plays its own role of load-bearing during the time steps of 0-112, 192-236, and 482-520; during this time, the convergence rate of displacement decreases. With the increase in the displacement, the rock mass within the plastic zone loses its bearing capacity. The convergence rate of the surrounding rock displacement increases. Similar results can be obtained from the change curves of convergence amount and convergence rate on the right side. Thus, it can be seen that the optimal supporting time can be divided into four stages: (I) presupport stage: controlling the convergence amount of the displacement of the rock mass on the roadway surface to prevent the rock mass on the roadway surface from suffering tensile failure; (II) bolt reinforcement stage: increasing the strength of the plastic zone in the roadway and improving the bearing capacity of the plastic zone; (III) anchor cable reinforcement stage: further increasing the strength of the plastic zone in the roadway, enhancing its inherent bearing capacity, and reducing the deformation of the surrounding rock; and (IV) grouting reinforcement stage: carrying out grouting reinforcement on the rock mass within the plastic zone in the roadway to ensure the long-term stability of the roadway.

4.2. Technical Scheme for Surrounding Rock Reinforcement and Support. After the excavation of a high-stress rock mass, with time, stress concentration will occur in the surrounding rock of the roadway, and stress release will occur within a certain range, making the surrounding rock suddenly suffer severe deformation and failure; this severe deformation and failure will gradually extend to the deeper parts of the surrounding rock.

Anchor bolt (mesh) support plays a positive role in improving the strength and stress state of surrounding rock. The higher prestress can improve the stress state and control the deformation of surrounding rock. The combination of anchor cable and anchor bolt can make the anchorage structure of the anchor bolt hang in the harder and more stable rock strata deep in the surrounding rock. Cement grout plays a bonding role and can penetrate the loose zone to improve the strength of the surrounding rock around a roadway. Therefore, an anchor mesh-cable-grouting reinforcement technology for deep roadways is proposed. The concept is as follows:

(1) The deformation characteristics of high-stress roadways show that their support cannot reach the goal in one step; providing support is a process requiring secondary support or multiple supports

(2) During roadway excavation, the surrounding rock can be permitted to suffer some loose deformation and release some deformation energy accumulated in the surrounding rock, but it is necessary to undertake measures like initial spraying to seal the surrounding rock in time

(3) Anchor bolt-cable support with high strength and high prestress can be carried out on the roadway in a timely manner

(4) According to the monitoring results, after the severe deformation stage of the roadway, grouting reinforcement should be carried out on the surrounding rock of the roadway at the right time to strengthen the surrounding rock and improve its overall bearing capacity

According to the special conditions of the air return cross-hole in the No. 81 mining area of the Xinhu Coal Mine that has a kilometer-deep well, a corresponding support scheme is put forward as follows: Supporting parameters: GM22/2600-490 rebar high-strength anchor bolt is used as anchor bolt; the row spacing between anchor bolts is 800×800 mm, with a rectangular layout; the anchor rod tray is $200 \times 200 \times 10$ mm. Two rolls of the K2950 resin anchoring agent are used for each anchor bolt above the arch camber, and two rolls of the Z2950 resin anchoring agent are used for each anchor bolt at the sides. The anchor cable is prestressed steel strand anchor cable, with a specification of Φ 21.8×7300 mm; two rolls of the Z2950 type and one roll of the K2950 resin anchor agent are used for each anchor cable; the row spacing is set to be 1600×1600 mm; a $300 \times 300 \times 15$ mm anchor tray is used for matching with each anchor cable; and the lockset at the outcrop of the anchor cable is 150~250 mm. Two rolls of the Z2950 resin anchoring agent are used for each anchor bolt on the side. The metal mesh is processed using Φ6.0 mm round steel, with length × width = 2400×900 mm, and mesh of 100×100 mm connected by hook, and with the stubble of 100 mm. The full-face shotcrete is 100 mm thick, and the concrete strength is C20. Grouting anchor bolts are laid out on the full face, and grouting anchor bolts are processed by using $\Phi 25 \times 2800$ mm steel pipe, with the row spacing between them being 1600×1600 mm. At $\ngtr$70 m lagging behind the tunnel face, grouting anchor bolts are set up, and grouting is carried out. P.O42.5-type ordinary Portland cement is used as the cement for grouting, with a water : cement ratio of 1 : 1 and a grouting pressure of 2 MPa. Parameters of the supporting grouting and anchor cable are as follows: a hollow mine anchor cable is used as the anchor cable for grouting, with a specification of $\Phi 22 \times 7000$ mm. The tray of the anchor cable is TPF300 × 300 × 15 mm, and the lockset at the outcrop of the anchor cable is 150~250 mm. 5 anchor bolts are laid out in each row along the roadway, with a row spacing of 2400×2400 mm. Two rolls of the Z2950 resin anchoring agent are used for each anchor cable for the grouting. P.O42.5-type ordinary Portland cement is used as the grouting cement with a water : cement ratio of 1 : 1. At $\ngtr$140 m lagging behind the tunnel face, the grouting anchor cables are set up and grouting is carried out with a grouting pressure of 3 MPa.

4.3. Analysis of the Support Effect of Surrounding Rock. To obtain the deformation, failure, and stress distribution characteristics of the surrounding rock at the roof and floor and the two sides of a high-stress roadway, the mechanical characteristics of the surrounding rock of the roadway were analyzed through 3DEC numerical simulation as shown in Figure 11.

Three-dimensional failure field characteristics of the high-stress surrounding rock during excavation support.

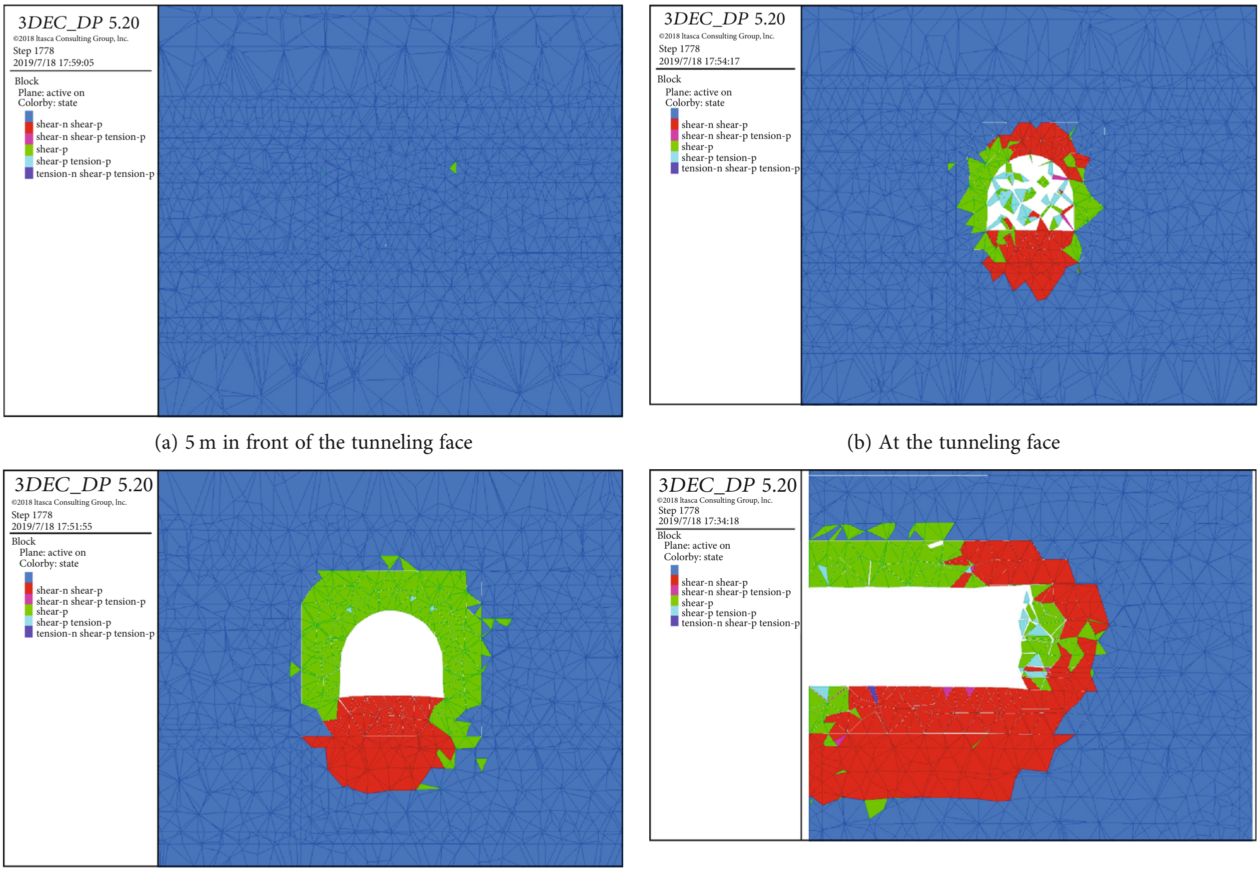

(a) 5 m in front of the tunneling face

(b) At the tunneling face

(c) 5 m behind the tunneling face

(d) Heading direction of tunneling

Figure 12: Diagram for the plastic zone of roadway excavation support.

Figure 12 shows the failure diagrams for the areas 5 m in front of the tunneling face, at the tunneling face, 5 m behind the tunneling face, and the heading direction of tunneling. As can be seen from the figure, although the rock mass 5 m away from the tunneling face has not been excavated, the rock mass suffers failure due to the support factor.

After the roadway is excavated, the surrounding rock suffers failure quickly in a wide range under the action of high stress, but the deformation of the surrounding rock is restricted by the support. In the area within 5 m behind the tunneling face, the plastic zone of the surrounding rock in the entire surrounding rock roadway no longer expands, forming a circular plastic zone with an approximate radius of 2.2 m, which is 7 m smaller than that in the case without support. In the roadway, more than 5 m behind the tunneling face, the plastic zone range at the side no longer expands, but the plastic zone of the floor still continues to expand, and the final plastic zone range of the floor reaches 5.9 m, which is 2.6 m smaller than that in the case without support.

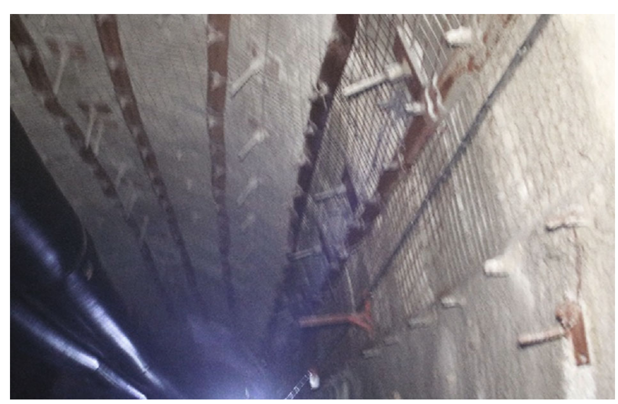

Figure 13: Field support drawing.

4.4. Field Feedback on the Excavation Support Effect of Surrounding Rock. In this study, the deformation and failure characteristics of a high-stress rock mass were obtained through true triaxial tests on different loading paths. According to the deformation reinforcement theory, a composite support scheme of anchor mesh and cable shotcrete +shallow and deep hole grouting is designed and proposed, and the support effect was verified through numerical simulation. Through field practice, with the support field drawing shown in Figure 13, the reliability of the test results was verified, which serves as a reference for related projects.

5. Conclusion

(1) True triaxial tests were carried out to compare and analyze the conventional uniaxial compression test results of a high-stress rock mass and the unilateral unloading stress-concentration failure tests; we obtained the progressive failure process of the surrounding rock, in which the failure characteristics of the rock mass under conventional uniaxial load is a composite splitting-shear failure, while the unilateral unloading stress-concentration failure characteristic follows the process of splitting into plates, followed by cutting into blocks, and then the ejection of blocks and pieces

(2) The roadway tunneling process was simulated through numerical simulation to obtain a reasonable reinforcement time for surrounding rock. It can be divided into four stages, i.e., the presupport stage, the bolt reinforcement stage, the anchor cable reinforcement stage, and the grouting reinforcement stage

(3) Under reasonable support, the plastic zone of the entire surrounding rock forms a circle of approximately 2.2 m, which is 7 m smaller than that without support. The plastic zone at the side no longer expands, but the plastic zone of the base plate still expands, finally reaching 5.9 m, which is 2.6 m smaller than that without support. The deformation is significantly reduced

Data Availability

The datasets generated and analyzed during the current study are available from the corresponding author on reasonable request.

Conflicts of Interest

The authors declared no conflicts of interest.

Acknowledgments

This study was supported by the National Natural Science Youth Fund (52004006) and Talent Fund of AUST (13200013).

References

[1] R. Yang, Z. Ye, L. Yongliang, and L. Weiyu, "Stability analysis and control measures of open roof roadway with hard roof," *Journal of Mining and Safety Engineering*, vol. 37, no. 5, pp. 861–870, 2020.

[2] B. Yingyun, W. H. Ning, and J. M. Jing, "Discrete element study on unloading dynamic failure mechanism of deep jointed rock mass excavation," *Journal of Geotechnical Engineering*, vol. 42, Supplement 2, pp. 196–201, 2020.

[3] S. Yonghua, H. Manchu, and G. Qian, "Rosenblueth method in the evaluation of bolting and shotcrete support system of soft broken surrounding rock," *Journal of Geotechnical Engineering*, vol. 3, pp. 378–382, 2004.

[4] T. Hongming, C. Weizhong, T. Xianjun, W. Hui, and T. Tian, "Study on reasonable support scheme of high ground stress soft rock tunnel," *Journal of Rock Mechanics and Engineering*, vol. 30, no. 12, pp. 2285–2292, 2011.

[5] C. Xiaoping, W. Feipeng, W. Bo, and L. Ziyang, "Experimental study on reasonable support scheme of high ground stress soft rock tunnel," *Journal of railway engineering*, vol. 35, no. 7, pp. 65–71, 2018.

[6] Z. Guangming, X. Wensong, M. Xiangrui, and L. Chongyan, "Instability mechanism of high stress rock mass excavation unloading induced by disturbance," *Acta coalae Sinica*, vol. 45, no. 3, pp. 936–948, 2020.

[7] Z. Xi, L. Shaojun, D. Xu et al., "Study on deformation and stability of surrounding rock during initial excavation of main powerhouse of Shuangjiangkou hydropower station," *Journal of rock mechanics and engineering*, vol. 40, no. 3, pp. 520–532, 2021.

[8] C. Wenzhuo, L. Xibing, Z. Zilong, Y. Haiwang, and W. Hao, "Energy dissipation law of excavation disturbance in high stress hard rock," *Journal of Central South University (NATURAL SCIENCE EDITION)*, vol. 45, no. 8, pp. 2759–2767, 2014.

[9] H. Wu, Z. Nong, W. Wang, and G. Peng, "Deformation characteristics simulation and control technology of deep inclined rock roadway," *Journal of Hunan University of Science and Technology (NATURAL SCIENCE EDITION)*, vol. 28, no. 1, pp. 6–12, 2013.

[10] Z. Baihong, H. Lijun, H. Guilei, and W. Yangning, "Three dimensional in-situ stress measurement and stability study of deep roadway," *Geotechnical Mechanics*, vol. 9, pp. 2547–2550, 2008.

[11] G. Panfeng, W. Sijiang, and Z. Sheng, "Simulation study on tunnel stability under different levels of stress," *Journal of mining and safety engineering*, vol. 27, no. 2, pp. 143–148, 2010.

[12] L. Jie, S. Chunming, X. Hu, C. Wentao, and F. Pengxian, "Analysis of deformation and failure mechanism of surrounding rock of deep roadway," *Geotechnical Mechanics*, vol. 33, Supplement 2, pp. 365–370, 2012.

[13] X. Yang, W. Mao, E. Wang, Y. Sun, J. Wang, and M. He, "Mechanism and control methods of roof deformations in gob-side entry retention by roof cutting under medium-thick coal seams," *Geotechnical and Geological Engineering*, vol. 38, no. 1, pp. 265–282, 2020.

[14] R. Yao, "Study on the relationship between roadway support time and surrounding rock grade," *Mine Pressure and Roof Management*, vol. 4, pp. 11–13, 2003.

[15] Z. Han, Y. Huang, J. Li, S. Zayzay Jr., and H. Gao, "Study on key parameters of roof cutting and pressure release in medium-thickness coal seam," *Geotechnical and Geological Engineering*, vol. 37, no. 4, pp. 3413–3422, 2019.

[16] W. Xu, Z. Guangming, M. Xiangrui, L. Yingming, C. Jinlong, and Gaoliang, "Experimental study on loading and unloading of marble under true triaxial single side unloading," *Journal of Southwest Jiaotong University*, vol. 54, no. 3, pp. 526–534, 2019.

[17] H. Da, Q. Tan, and H. Runqiu, "Mechanism of strain energy transformation process of marble damage and fracture under high stress and strong unloading," *Journal of rock mechanics and engineering*, vol. 31, no. 12, pp. 2483–2493, 2012.

[18] D. Chunliang, Z. Guangming, L. Yingming, M. Xiangrui, L. Xiaoyu, and Z. Liyang, "Mechanical characteristics and failure mechanism of surrounding rock during excavation and unloading of deep circular roadway," *Journal of mining and safety engineering*, vol. 34, no. 3, pp. 511–518, 2017.

[19] A. Li, F. Dai, Y. Liu, H. Du, and R. Jiang, "Dynamic stability evaluation of underground cavern sidewalls against flexural toppling considering excavation-induced damage," *Tunnelling and Underground Space Technology*, vol. 112, p. 103903, 2021.

[20] J. Ruochen, D. Feng, L. Yi, and L. Ang, "Fast marching method for microseismic source location in cavern-containing rockmass: performance analysis and engineering application," *Engineering*, vol. 4, 2021.

[21] A. Li, Y. Liu, F. Dai, K. Liu, and M. Wei, "Continuum analysis of the structurally controlled displacements for large-scale underground caverns in bedded rock masses," *Tunnelling and Underground Space Technology*, vol. 97, p. 103288, 2020.

[22] S. Kai, Z. Yanjun, H. Wu, and Z. Li, "Study on evolution characteristics of safety factor of surrounding rock and selection method of support time during tunnel excavation," *Journal of rock mechanics and engineering*, vol. 38, Supplement 1, pp. 2964–2975, 2019.

[23] Z. Jian, J. Hu, H. Wang, and X.'a. Yang, "Mechanical research on reasonable supporting time of step by step support for deep tunnel," *Engineering mechanics*, vol. 36, no. 12, pp. 145–152, 2019.

[24] S. Yi and Z. D. Li, "Synergism principle of complex tunnel supporting structure system," *Engineering mechanics*, vol. 33, no. 12, pp. 52–62, 2016.

[25] F. Yu, *Study on mechanical properties of interaction system between tunnel support and surrounding rock*, Beijing Jiaotong University, 2017.

[26] D. F. Ting, *Supporting theory and application technology of roadway surrounding rock loose circle*, Coal Industry Press, Beijing, 2001.

[27] H. Chaojiong, G. Lisheng, and G. Panfeng, *Bolt Support of Coal Roadway*, China University of mining and Technology Press, Xuzhou, 1999.

[28] W. Xu, G. Zhao, X. Meng et al., "Effects of unloading rate on energy evolution mechanism in the single-side unloading failure of highly stressed marble," *Advances in Civil Engineering*, vol. 2020, 11 pages, 2020.

Hindawi
Geofluids
Volume 2021, Article ID 8530009, 12 pages
https://doi.org/10.1155/2021/8530009

Research Article

Roof Fracture Characteristics and Strata Behavior Law of Super Large Mining Working Faces

Guozhen Zhao [1,2] Baisheng Zhang [1] Lihong Zhang [3] Chao Liu [1] and Shuai Wang [1]

[1] College of Mining Engineering, Taiyuan University of Technology, Taiyuan, Shanxi, China
[2] Key Laboratory of In-situ Property-Improving Mining of Ministry of Education, Taiyuan University of Technology, Taiyuan, Shanxi, China
[3] State Environmental Protection Key Laboratory of Efficient Utilization Technology of Coal Waste Resources, Institute of Resources and Environmental Engineering, Shanxi University, Taiyuan, Shanxi, China

Correspondence should be addressed to Guozhen Zhao; zgzcumts@163.com

Received 17 July 2021; Accepted 11 August 2021; Published 3 September 2021

Academic Editor: Zhijie Wen

Exploiting the working face in coal mines using a super long mining length and large mining height has become important for intensive production with high yield and high efficiency. The paper develops a roof structure model to analyze the influence of 195 m, 242.4 m, and 376 m working face lengths at large mining height in Wangzhuang Coal Mine in China as the case study. The roof fracture characteristics, migration law, and strata behavior law under different working face lengths are compared and studied by numerical simulation, and the reliability of support selection in the working face at large mining height is analyzed by field measurement statistics. The results show that the roof fracture mode of a super large working face is a successive layered fracture. The length of the working face has little effect on the roof fracture step length, and the fracture step length is positively correlated with the thickness of the rock stratum. The roof subsidence law for a super large working face is different from the intermittent subsidence of the unimodal Gaussian distribution curve of ordinary working faces, which shows the intermittent subsidence of multiple ordinary working faces. The roof periodic weighting of a super large working face, which fluctuates violently within 100 m at both ends, is more drastic than that of an ordinary working face as a whole. Field statistical analysis shows it is more appropriate to choose high-strength support for a super large working face.

1. Introduction

With the rapid growth of the world economy, the market demand for coal continues to increase year by year, and high-yield and highefficiency coal mines are increasingly common [1–5]. After years of development, full-height fully mechanized mining at one time has become an important technology for highyield and highefficiency mining in thick coal seams [6]. In addition to increasing the mining height, increasing the length of the working face has become a new direction for high yield and high efficiency working face mining [7]. It is generally considered that a working face with a length of more than 250 m is a super large face [8]. Lengthening the working face can improve the per unit yield of the working face and simplify the production system and reduce coal loss, which all enhance mine productivity. Super large working face production technology has become a crucial development direction for intensive coal mine production technology [9].

In recent years, research on super large working faces has mainly focused on medium-thick coal seams. In 2002, the average length of longwall working faces in Australia was 227 m, the average annual distance was 2,160 m, and the average yield of working faces was 2.82 million tons [10]. In 2004, the length of some fully mechanized coal mining faces in the United States was close to 300 m, the maximum advancing length was 4,580 m, and the average yield of working faces increased from 1.52 million tons to 3.26 million tons [10]. According to incomplete statistics, there are 11 working faces over 300 m long in the United States and 18 in Germany, with the longest working face of 506 m (coal seam thickness of 1.9 ~ 2.3 m) [11]. Russia, Poland, and other major coal producing countries are also developing super large working faces. In 2007, the first super large working face of 400 m (with an average thickness of 1.7 m) was put into production in China at the Yujialiang Coal Mine in Shendong Mining District of the Shenhua Group [12]. In 2012, the longest face was the 450 m fully mechanized working face (with an average thickness of 2.11 m) at the Halagou Coal Mine in Shendong Mining District [13, 14].

While lengthening working faces, China is also researching very high working faces for thick coal seams. In 2005, Shangwan Coal Mine in Shendong Mining District built the world's first fully mechanized coal mining face a lengthened working face with a large mining height of 300 m and average coal seam thickness of 5.5 m [15]. In 2008, Shangwan Coal Mine completed the design of a lengthened thick working face with a large mining height of 300 m and average coal seam thickness of 5.5 m, which is the world's first fully mechanized mining working face with yield of over 10 million tons [15]. In July 2010, in high gas conditions, the fully mechanized mining technology for large mining height was applied in the Dongsi Panel of the Sihe Coal Mine of the Jincheng Anthracite Coal Mining Group, and a 300 m super large working face was successfully mined with an average thickness of 6.2 m [16].

To sum up, working faces of 300 m length are mainly concentrated in medium-thick coal seams [17], and the thick coal seam mining is difficult; so, the application is relatively less. The increase of face length and mining height will form a larger roof structure, which will exert more load on face supports. Thus, when the length of the working face increases, the roof will present new deformation and loading characteristics, which is a very important and meaningful topic.

This paper systematically compares and studies the roof fracture characteristics and strata behavior of long working faces using field investigation, theoretical analysis, and numerical simulation [18, 19]. The study uses the coal seam occurrence status and mining characteristics of the 3500 Working Face, which has large mining height, in the Wangzhuang Coal Mine in China. The 3500 Working Face is a typical working face with variable sizes. The working face length has experienced three stages: 242.4 m, 195 m, and 376 m, and the average thickness of coal seams is 5.02 m. It is a fully mechanized full-seam large coal mining working face. This working face provides a practical basis for the comparative analysis of the mine pressure behavior law of working faces with different lengths, and therefore, it has vital theoretical and practical value.

2. Case Study Overview

The 3500 Working Face of the Wangzhuang Coal Mine is located in the south of Dongzhang Village in Changzhi, Shanxi Province, China. The mined coal seam is the No. 3 coal seam, in the No. 35 mining area. The average burial depth of the 3500 Working Face is 200 m, and the strike length is 1,066.4 m. The 3500 Working Face is located in the north of the No. 35 mining area, 50 m away from the 3403 Working Face in the east (mined in 2011), three main roadways of Nanyi in the west, the 3401 Working Face and 3402 Working Face and villages in the north, and the 3501 Working Face in the south (mined from 2013 to 2014). It is shown in Figure 1. The length of the working face at the section of 231 m away from the cut of the 3500 Working Face in the original design is 242.4 m, and that at the remaining sections is 195 m. In the north of the original 3500 Working Face, another working face (149.5 m in length and delineated by the prospect entry in the No. 35 Mining Area North) exists, and the net coal pillar size between the working faces is 20 m. To improve the recovery rate of coal resources, the No. 35 Mining Area in the north of the original 3500 Working Face and the original 3500 Working Face has been integrated into one working face for mining. After reintegration, the 3500 Working Face has the shape of a "knife handle," and it is divided into three parts: length of 242.4 m in the first part of the working face in the 231 m section, length of 195 m in the middle part in the 320 m section, and length of 376 m in the remaining part.

The 3500 Working Face uses a comprehensive retreating mechanized coal mining method of longwall full-seam spontaneous caving mining. The No. 3 coal seam mined through the 3500 Working Face has a thickness of 4.20 to 5.50 m (average length of 5.02 m) and a dip angle of 2°–4°. The coal seam roof is mainly composed of carbonaceous mudstone, mudstone, and fine sandstone. The floor is mainly composed of mudstone and fine sandstone. Table 1 summarizes the distribution and the physical and mechanical characteristics of the coal seam and roof strata of the 3500 Working Face.

3. Analyses of Roof Fracture Characteristics of Super Large Working Faces

With the advance from open-off cuts of the working face, the suspended roof length of the goaf continues to increase. Due to the action of mine pressure, every rock stratum on the roof will bend, subside, and become distorted, and when the rock stratum reaches its ultimate strength, it will fracture and cave in [20–24]. Based on the level, thickness, strength, and load of rock strata, the influence of different working face lengths on the roof caving step length is compared and analyzed.

3.1. Calculation of Roof Strata Load. The initial caving step length is the main sign to measure the stability of strata behaviors of the working face. Before calculating the caving step length, it is necessary to calculate the load of each rock stratum. Due to the different thickness and lithology of each stratum, the load on the i stratum is calculated according to the following formula:

$$(q_n)_i = \frac{E_i h_i^3 (\gamma_i h_i + \gamma_{i+1} h_{i+1} + \cdots + \gamma_{i+n} h_{i+n})}{E_i h_i^3 + E_i h_i^3 + \cdots + E_{i+n} h_{i+n}^3}, \quad (1)$$

where $(q_n)_i$ is the load on the i stratum when the n stratum above the i stratum is considered:

$E_i \cdots E_{i+n}$ is the elastic modulus of each stratum.

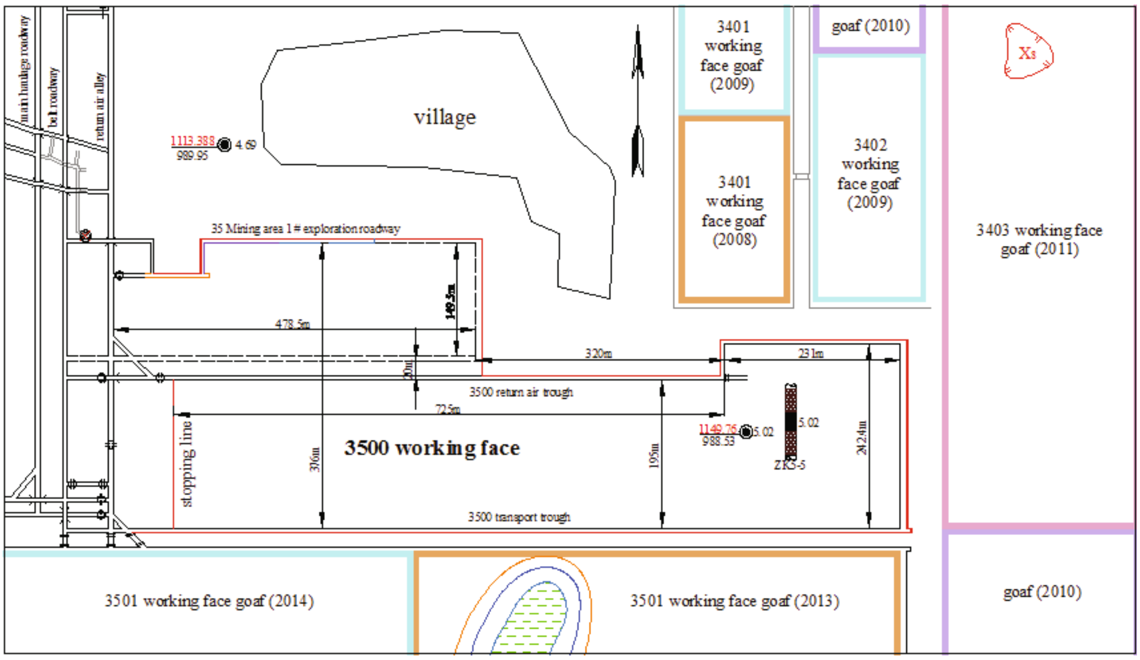

Figure 1: Layout of 3500 Working Face and mining dates of goafs.

Table 1: Distribution and physical and mechanical characteristics of the coal seam and roof strata of 3500 Working Face.

Stratification No.	Roof strata	Thickness (m)	Influence coefficient of stratification and joint fracture	Poisson's ratio	Tensile strength (MPa)	Modulus of elasticity (GPa)	Apparent density (kg/m^3)
15	Fine sandstone	1.18	0.5	0.20	11.64	32.5	2673
14	Mudstone	6.0	0.35	0.22	4.21	14.3	2573
13	Fine sandstone	0.7	0.5	0.20	11.64	32.5	2673
12	Argillaceous sandstone	3.0	0.45	0.24	9.76	19.7	2640
11	Mudstone	8.84	0.35	0.22	4.21	14.3	2573
10	Argillaceous sandstone	0.6	0.45	0.24	9.76	19.7	2640
9	Mudstone	5.22	0.35	0.22	4.21	14.3	2573
8	Argillaceous sandstone	1.5	0.45	0.24	9.76	19.7	2640
7	Fine sandstone	3.7	0.5	0.20	11.64	32.5	2673
6	Mudstone	0.6	0.3	0.24	4.59	14.8	2527
5	Fine sandstone	3.7	0.5	0.20	11.64	32.5	2673
4	Mudstone	1.0	0.35	0.22	4.21	14.3	2573
3	Fine sandstone	4.6	0.5	0.20	11.64	32.5	2673
2	Mudstone	1.4	0.35	0.22	4.21	14.3	2573
1	Carbon mudstone	0.3	0.25	0.24	4.59	14.8	2527
0	No. 3 coal seam	5.02	/	0.33	2.33	6.3	1430

$h_i \cdots h_{i+n}$ is the thickness of each stratum.

$\gamma_i \cdots \gamma_{i+n}$ is the density of each stratum; $i = 1, 2, 3 \cdots$

When $(q_{i+n+1})_i < (q_{i+n})_i$, that is, $(q_{i+n})_i$ as the load applied to the i stratum, the result of equation (1) is used as the load on the i stratum to calculate its caving step length.

The data in Table 1 is put into equation (1), and the load on each stratum is calculated. The calculation results are shown in Table 2.

3.2. Calculation of Caving Step Length of Each Roof Stratum. For super large working face mining, it is difficult to fully

Table 2: Load, initial caving step length, and periodic caving step length of roof of No. 3 coal seam.

Stratification No.	Roof strata	Thickness (m)	Rock stratum load kN	Initial caving step length (m) of each rock stratum with different working face lengths			Periodic caving step length (m) of each rock stratum with different working face lengths		
				195 m	242.4 m	376 m	195 m	242.4 m	376 m
11	Mudstone	8.84	>372.4	36.088	36.070	36.068	14.730	14.722	14.722
10	Argillaceous sandstone	0.6	15.48	18.460	18.460	18.460	7.535	7.535	7.535
9	Mudstone	5.22	149.8	33.594	33.582	33.580	13.712	13.707	13.706
8	Argillaceous sandstone	1.5	39.6	28.861	28.855	28.854	11.780	11.778	11.777
7	Fine sandstone	3.7	133.12	41.6588	41.623	41.619	17.004	16.989	16.987
6	Mudstone	0.6	15.2	12.775	12.775	12.775	5.214	5.214	5.214
5	Fine sandstone	3.7	113.8	45.074	45.020	45.014	18.397	18.376	18.373
4	Mudstone	1.0	25.7	15.531	15.531	15.531	6.339	6.339	6.339
3	Fine sandstone	4.6	203.3	41.911	41.874	41.869	17.106	17.091	17.090
2	Mudstone	1.4	36.0	18.372	18.371	18.371	7.499	7.498	7.498
1	Carbon mudstone	0.3	7.58	9.045	9.0454	9.0454	3.692	3.692	3.692

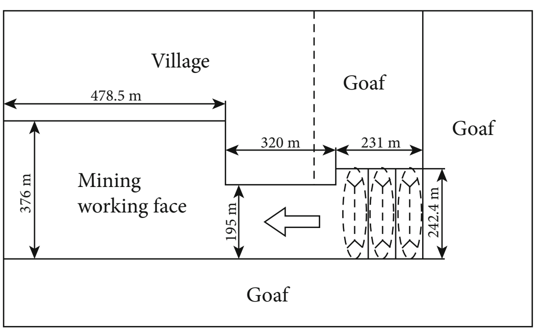

Figure 2: Structure model of 3500 Working Face.

define the problem by solving a single plane problem. Therefore, the roof of the coal seam is regarded as a plate structure, and the initial caving step length and the periodic caving step length of each roof stratum are calculated according to plate theories [25], as shown in Figure 2.

The maximum tensile stress intensity theory is used as the fracture criterion of slope roof fracture:

$$\sigma_1 = \sigma_b, \tag{2}$$

where σ_1 is the maximum tensile stress in the roof, MPa; σ_b is the tensile strength of roof strata, MPa.

The maximum tensile stress of the roof σ_1 is calculated by the following formula:

$$\sigma_1 = \frac{M_{\max} y_{\max}}{I}, \tag{3}$$

where $M_{\max}$ is the maximum bending moment acting on the roof strata, MPa·m; I is the area moment of inertia of roof strata, if the section thickness is h, $I = h^3/12$, the unit is 1; then,

$$M = \frac{\sigma_1 h^2}{6}. \tag{4}$$

Let $l_m = h/(1-\mu^2) \cdot \sqrt{2\sigma_b/q}$, where q is the uniform load of the roof, MPa; μ is Poisson's ratio of the rock stratum.

For the island mining face of the three-sided goaf, if the cut length is 242.4 m, all three sides of the mining face are goafs. According to the theoretical analysis of the plate, the initial caving step length is

$$L = \begin{cases} b \cdot \sqrt[4]{\dfrac{4l_m^2}{15b^2 - 10l_m^2}} & \left(\sqrt{\dfrac{2}{3}}l_m < b < 2\sqrt[4]{\dfrac{10}{225}}l_m\right) \\ \dfrac{b}{2\sqrt{2}l_m} \cdot \sqrt{15b^2 - \sqrt{225b^4 - 160l_m^4}} & \left(b > 2\sqrt[4]{\dfrac{10}{225}}l_m\right) \end{cases}, \tag{5}$$

where b is the length of the working face, m.

For the working face with two adjacent sides mined out and two adjacent sides fixed, if the cut length is 195 m and 376 m, the two adjacent sides of the mining working face are goafs, and the others are unexploited solid coal. According to the theoretical analysis of the plate, the initial caving step length is

$$L = \begin{cases} b \cdot \sqrt[4]{\dfrac{2l_m^2}{3b^2 - 2l_m^2}} & \left(\sqrt{\dfrac{2}{3}}l_m < b < 2\sqrt{\dfrac{2}{3}}l_m\right) \\ \dfrac{b}{2l_m} \cdot \sqrt{3b^2 - \sqrt{9b^4 - 16l_m^4}} & \left(b > 2\sqrt{\dfrac{2}{3}}l_m\right) \end{cases}, \tag{6}$$

where b is the length of the working face, m.

When the working face length of the No. 3 coal seam is 242.4 m, equation (5) is introduced; when the length of No. 3

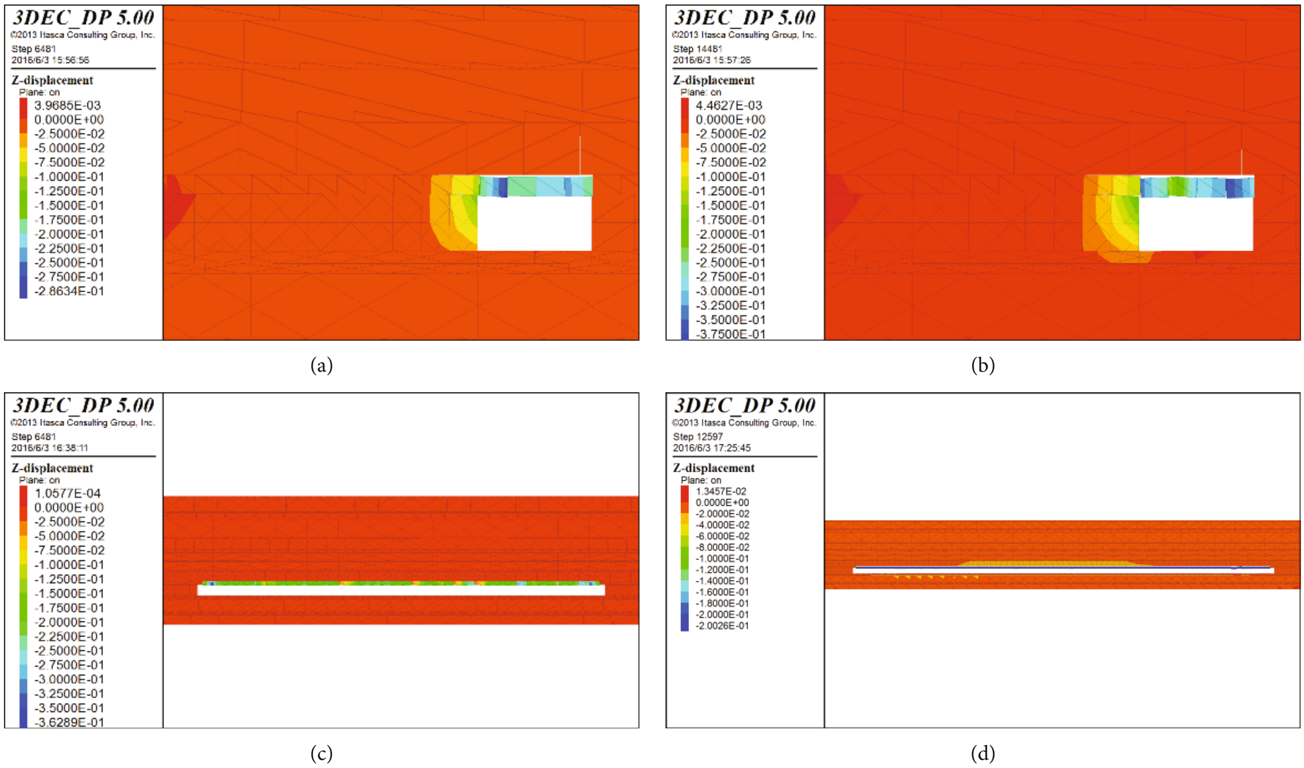

Figure 3: Nephogram of roof strata displacement when advancing to 15 m (unit: m): (a) slice of the 195 m working face in advancing direction, (b) slice of the 376 m working face in advancing direction, (c) lengthwise slice of the 195 m working face, and (d) lengthwise slice of the 376 m working face.

coal seam is 195 m and 376 m, equation (6) is introduced, and the initial caving step length of each roof stratum is calculated according to plate theories, as shown in Table 2. The periodic caving step length of the old roof is often determined by the cantilever fracture of the old roof. According to the calculation of mechanics of materials, the initial caving step length is 2.45 times the periodic caving step length. The calculation results of the periodic caving step length are shown in Table 2.

3.3. Analysis of Fracture Characteristics of Roof Strata. According to the calculation results in Table 2, the fracture characteristics of roof strata are as follows:

(1) The roof caving mode of the goaf of the 3500 Working Face is successive layered caving. When the working face begins to advance from the cut, the first layer of carbonaceous mudstone caves in first, with a caving height of 0.3 m. When the working face continues to advance to 18.4 m, the second mudstone layer caves in, with the roof caving height of 1.7 m. When it advances to 41.9 m, the roof is covered with fine sandstone, and the mudstone on it is fractured. The fractured height of the roof is 7.3 m. After that, the working face advances for three cycles; that is, when the working face advances to 45 m, the fifth layer of fine sandstone is fractured, and the overlying mudstone, fine sandstone, and argillaceous sandstone are fractured along with it, with the fractured height of the roof more than 31 m

(2) The step length of the first caving of the immediate roof of the 3500 Working Face is 12 m. The caving step length of the initial fracture of the main roof is about 35–37 m. The periodic caving step length of the basic roof is 14–15 m

(3) With the increase of the working face length, the roof rock stratum caving step length is basically unchanged. It can be considered that the working face length is in the range of 195 m to 376 m, and the working face length has little influence on the roof caving step length. By comparing the caving step lengths of different rock strata, it can be inferred that the caving step lengths are positively correlated with the thickness of rock strata

4. Study on Strata Behavior Law of Variable-Sized Working Faces through Numerical Simulation

4.1. Construction of Numerical Calculation Models. In the numerical simulation, 3DEC is used to compare and analyze the deformation characteristics, movement law, and stress variation law of the roof in the process of advancing towards working face lengths of 195 m and 376 m [26, 27].

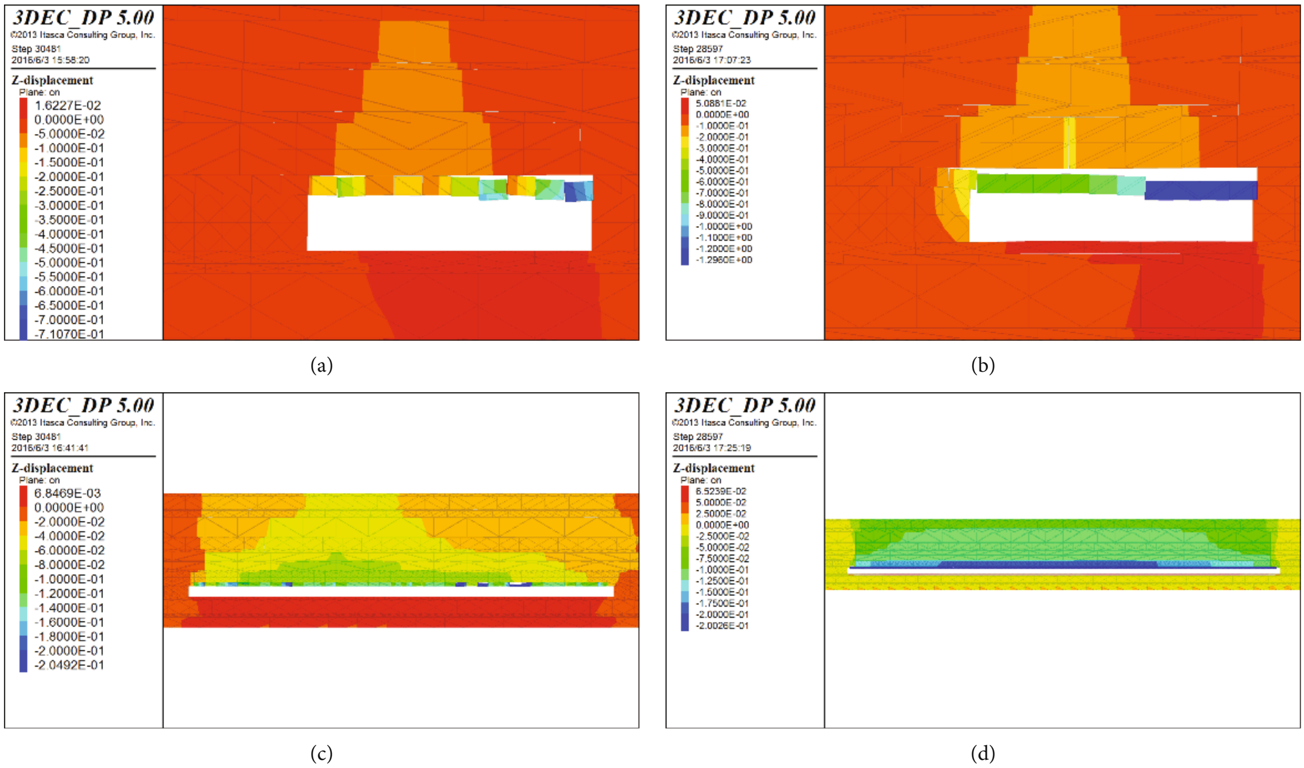

Figure 4: Nephogram of roof strata displacement when advancing to 30 m (unit: m): (a) slice of the 195 m working face in advancing direction, (b) slice of the 376 m working face in advancing direction, (c) lengthwise slice of the 195 m working face, and (d) lengthwise slice of the 376 m working face.

(1) Establishment of the three-dimensional model. Assuming that the dip angle of each stratum in the model is 0 and the thickness is uniform, a three-dimensional calculation model within the study range is established according to the physical and mechanical parameter Table 1 of the roof and floor strata of coal seams. The model size of the 195 m working face is 400 m × 495 m × 61.3 m (length × width × height), with 13,610 deformable blocks which are divided into 334,440 units. The model size of the 376 m working face is 500 m × 676 m × 61.3 m (length × width × height), with 38,916 deformable blocks which are divided into 856,100 units. To analyze the study area more accurately and control the number of blocks within a reasonable range, the model is divided into unequal blocks. In the model, the Mohr-Coulomb constitutive model is adopted for the block, and the Coulomb friction model for the structural plane, with gravity $g = -9.81\ \mathrm{m/s^2}$. The boundary conditions of the model are as follows: the bottom is fixed, the lateral side limits the horizontal displacement, and the upper part uses the stress boundary to simulate the compressive stress of overlying strata on the model

(2) Simulation of working faces and hydraulic support. After the calculation model reaches the initial state before mining, the excavate command of 3DEC software is used to simulate coal cutting. Every time the working face advances 2.5 m at a time, the fill command is used to backfill the goaf formed by coal cutting and to assign a smaller elastic modulus, to simulate the supporting effect of the hydraulic support

(3) Interpretation of the model response. The three-dimensional discrete element method is used for program analysis and calculation, to simulate stratification, fracturing, and caving of rock mass, and judge the state of rock mass and support by integrating the distribution of plastic zones, subsidence amount, and stress

4.2. Deformation Characteristics and Roof Migration Law. As the working face continues to advance, the deformation characteristics and migration laws of the roof under different advancing distances are compared and analyzed, as shown in Figure 3–9.

Figure 3 shows that the first caving step lengths of the immediate roof of the 195 m working face and the 376 m face are almost the same, at 15 m. When the working face advances to 15 m, the displacement of the roof of the 195 m working face is about 100~150 mm, and the whole working face subsides evenly. The displacement of the roof of the 376 m working face is about 180~200 mm, and the middle of the working face largely subsides.

Figure 4 shows that when the working face advances to 30 m, the roof subsidence amount of the 195 m and the 376 m working faces increases, and the subsidence range of

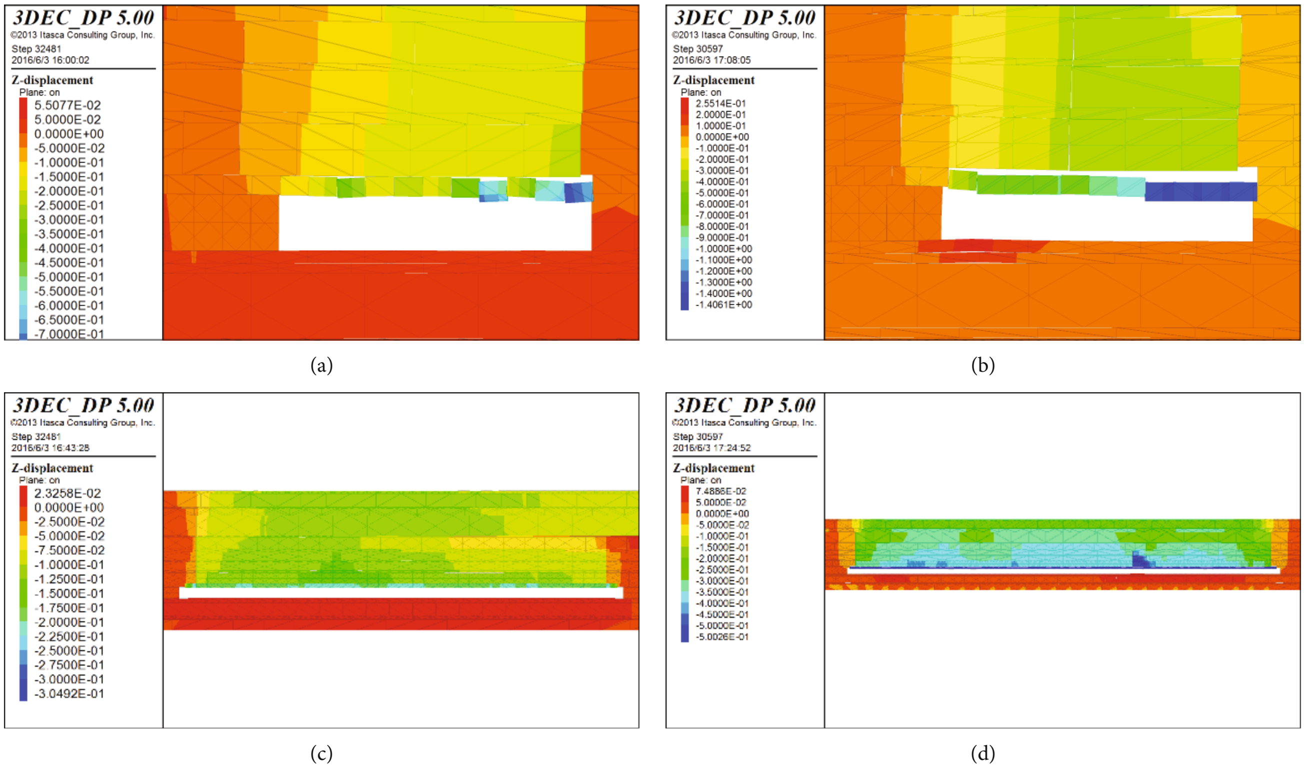

Figure 5: Nephogram of roof strata displacement when advancing to 32.5 m(unit: m): (a) slice of the 195 m working face in advancing direction, (b) slice of the 376 m working face in advancing direction, (c) lengthwise slice of the 195 m working face, and (d) lengthwise slice of the 376 m working face.

the roof extends to the basic roof. At this time, the subsidence curve of the 195 m working face presents an asymmetric Gaussian distribution, in which the central axis deviates slightly to one end of the working face, with roof subsidence of 400~600 mm. The roof subsidence of the 376 m working face is different. The roof of the 376 m working face shows integral subsidence. The initial fracture of the main roof occurs, and the masonry structure [28, 29] is formed, with roof subsidence of about 500~700 mm.

Figure 5 shows that when the working face advances to 32.5 m, the moving range of the roof of the 195 m working face continues to gradually expand, and the basic initial fracture of the main roof occurs, and the masonry structure is formed. The subsidence amount of the roof of the 376 m working face increases in local areas along the lengthwise direction of the working face.

Figure 6 shows that when the working face advances to 35 m, both working faces show obvious subsidence. The difference is that the 195 m working face follows the subsidence rule of the Gaussian distribution curve, while the roof of the 376 m working face shows intermittent subsidence. Because the length of the 376 m working face is about twice that of the 195 m working face, the figure shows intermittent subsidence in two to three intervals. Therefore, it can be inferred that the roof subsidence of a super large working face can be regarded as the combined subsidence of several common working faces.

Figure 7 shows that when the working face advances to 37.5 m, the damage range of the roof of both working faces continues to expand, and the subsidence amount of the roof continues to increase.

Figure 8 shows that the damage range of the roof of both working faces continues to extend to the upper part of the roof. The difference is that the deformation of each part in the lengthwise direction of the 195 m working face is quite different, and the 376 m working face is again characterized by uniform subsidence.

Figure 9 shows that when both working faces advance to 45 m, the displacement and deformation of the roof of the 376 m working face is larger than that of the 195 m working face, and the roof is pressed periodically.

Through the above analysis, it can be concluded that the roof displacement of the 195 m working face follows the subsidence rule of the Gaussian distribution curve, while the roof of the 376 m working face shows intermittent subsidence. Moreover, it can be inferred that the roof subsidence of the super large working face is the combined subsidence of several common working faces.

4.3. Comparison and Analysis of Roof Periodic Weighting Law. Comparison and analysis of the periodic weighting intensity law of both working faces are shown in Figures 10 and 11.

Figure 10 shows that the periodic weighting of the 195 m working face is generally stable, which is high and even in the middle and low at both ends. Within 20 m of both ends, weighting gradually increases from 675 kPa to 800 kPa. Within 20–175 m of the middle of the working face,

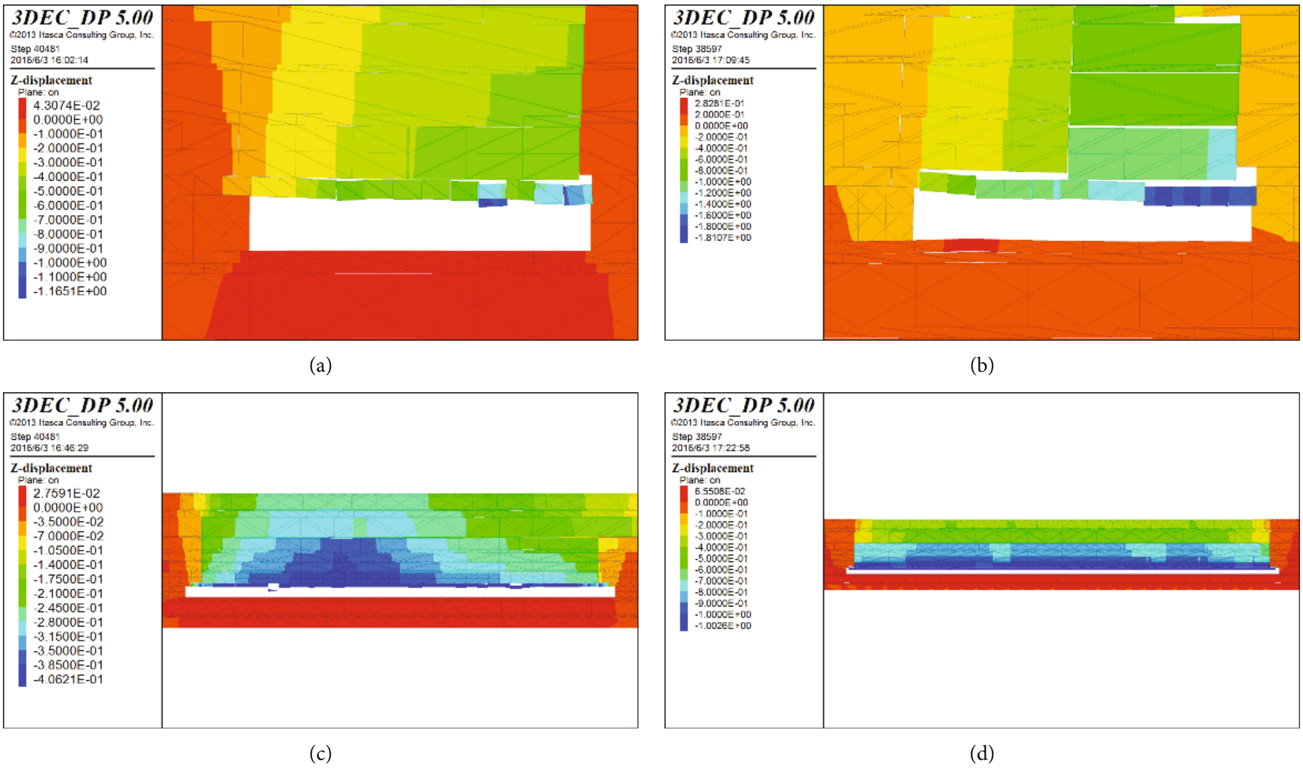

Figure 6: Nephogram of roof strata displacement when advancing to 35 m(unit: m): (a) slice of the 195 m working face in advancing direction, (b) slice of the 376 m working face in advancing direction, (c) lengthwise slice of the 195 m working face, and (d) lengthwise slice of the 376 m working face.

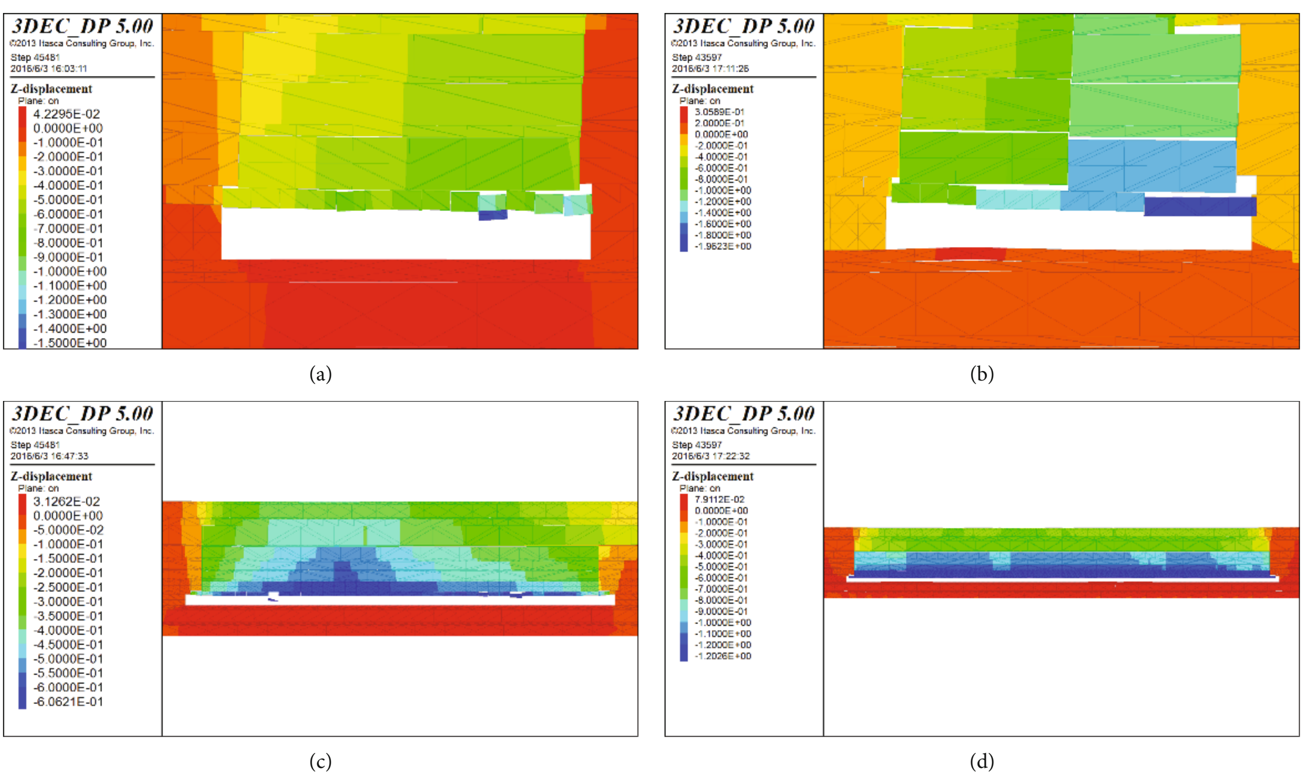

Figure 7: Nephogram of roof strata displacement when advancing to 37.5 m(unit: m): (a) slice of the 195 m working face in advancing direction, (b) slice of the 376 m working face in advancing direction, (c) lengthwise slice of the 195 m working face, and (d) lengthwise slice of the 376 m working face.

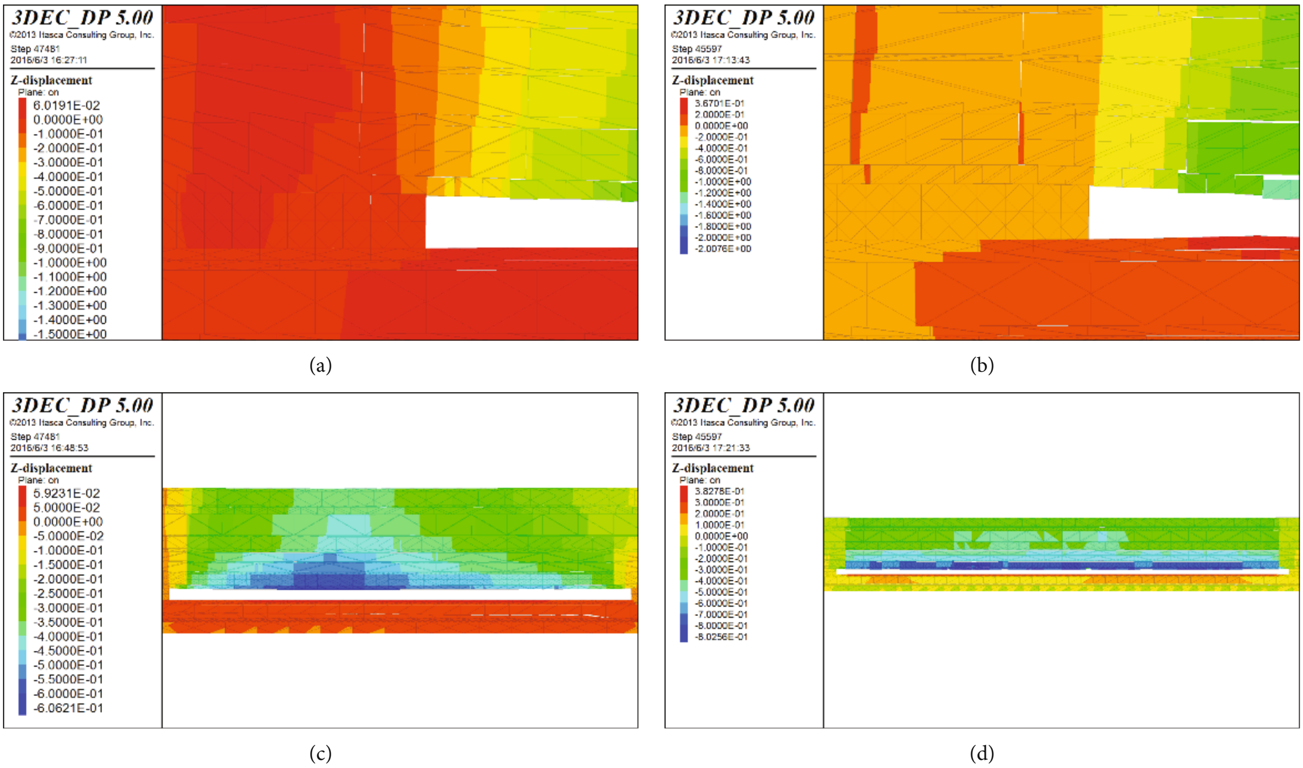

Figure 8: Nephogram of roof strata displacement when advancing to 40 m(unit: m): (a) slice of the 195 m working face in advancing direction, (b) slice of the 376 m working face in advancing direction, (c) lengthwise slice of the 195 m working face, and (d) lengthwise slice of the 376 m working face.

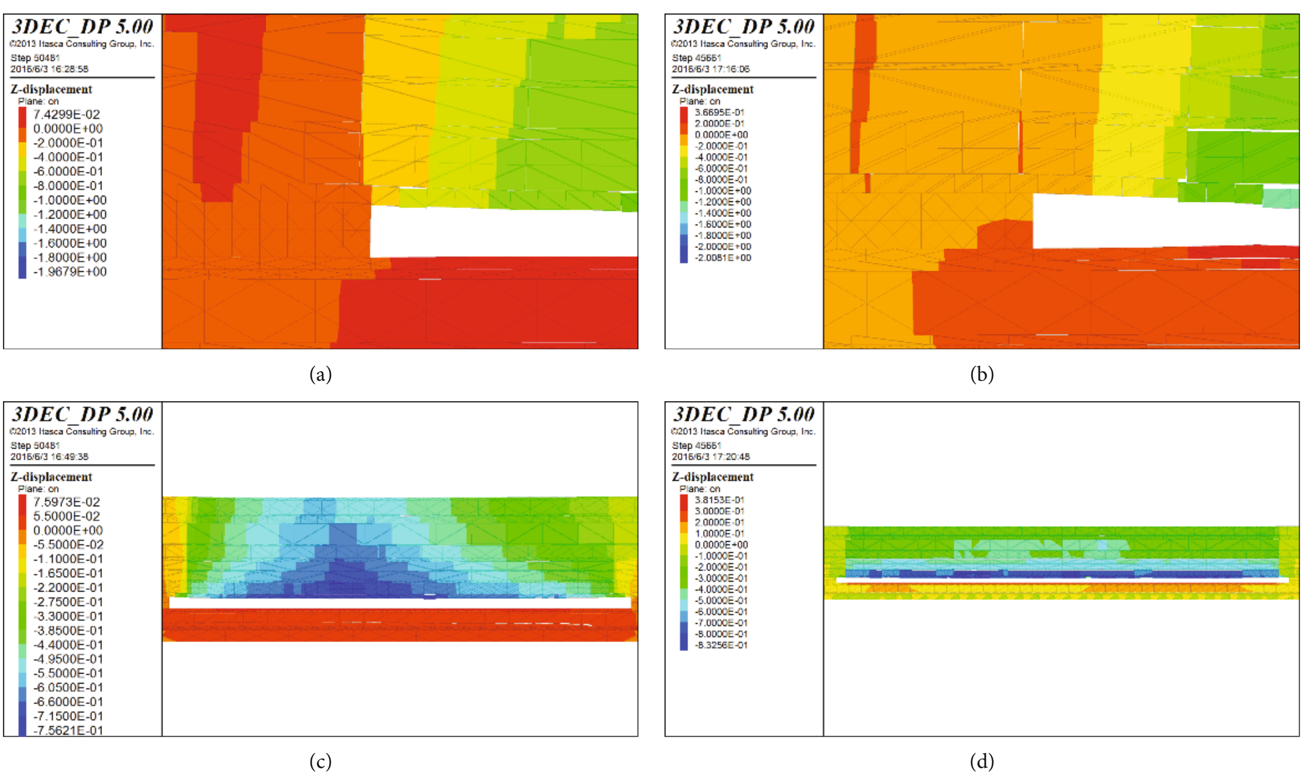

Figure 9: Nephogram of roof strata displacement when advancing to 45 m(unit: m): (a) slice of the 195 m working face in advancing direction, (b) slice of the 376 m working face in advancing direction, (c) lengthwise slice of the 195 m working face, and (d) lengthwise slice of the 376 m working face.

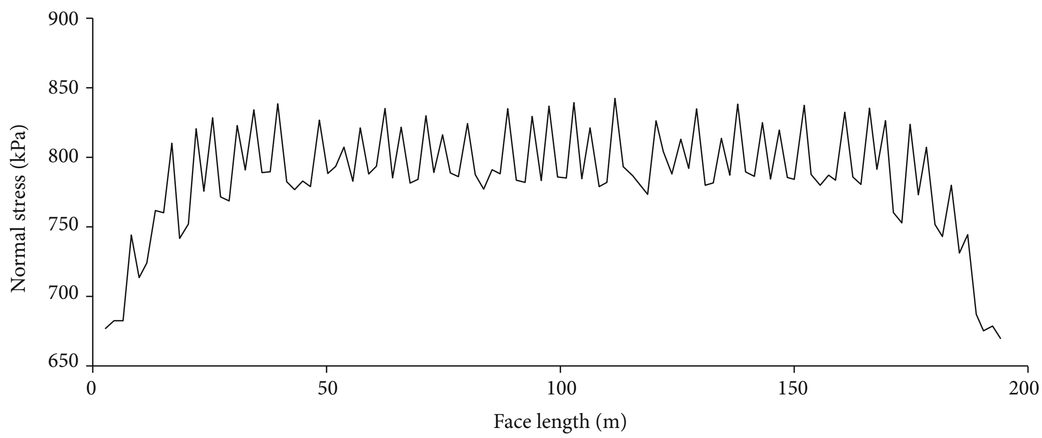

Figure 10: Weighting law of 195 m working face.

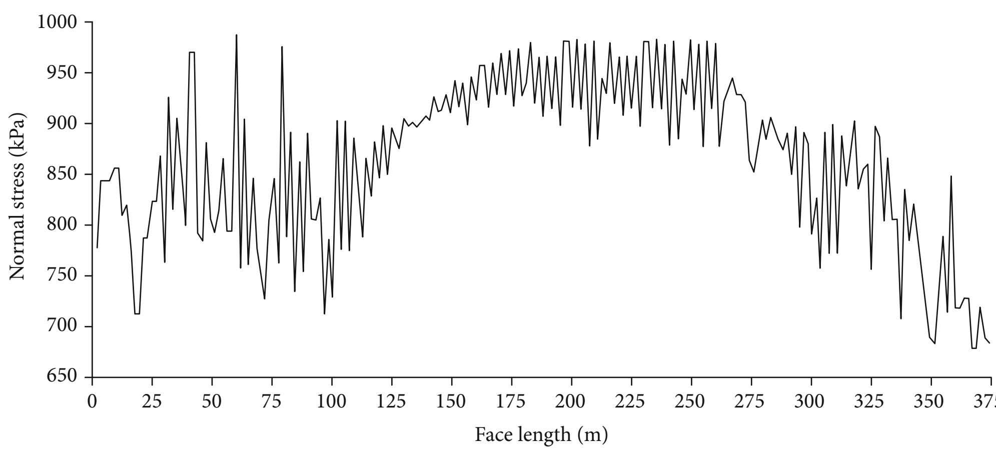

Figure 11: Weighting law of 376 m working face.

weighting is uniformly distributed, remaining basically stable at 800 kPa.

Figure 11 shows that the periodic weighting of the 376 m working face is generally high in the middle of the working face while low at both ends, fluctuating in a small range in the middle but oscillating violently at both ends. Within 100–275 m in the middle of the working face, there is arc fluctuation which is high in the middle and low at both ends, and the average weighting is maintained at 877.80 kPa. The maximum weighting is 985.67 kPa, and the minimum is 676.83 kPa within 100 m from both ends. Weighting oscillation is obvious.

Comparing Figures 10 and 11 shows that the periodic weighting of the 376 m working face is more violent than that of the 195 m working face. The 376 m working face oscillates sharply within 100 m at both ends, while the 195 m working face gradually decreases from the middle of the working face to both ends. The average periodic weighting of the 376 m working face is about 80 kPa higher than that of the 195 m working face. Through the above analysis, it can be concluded that the working resistance of the support needed in a super large working face is greater. Thus, attention should be paid to the intensity of support within 100 m of the end of the face.

Table 3: Statistical results of working resistance of hydraulic support in working faces.

Working face length (m)	Supporting intensity (kPa)	Working resistance of support (kN)
195	880.2	8518.1
242.4	921.4	9136.8
376	991.2	9621.4

5. Measurements and Analysis of Working Resistance of Working Face Support

The 3500 Working Face in the Wangzhuang Coal Mine is monitored and counted in real time, and the supporting strength of hydraulic support with different working face lengths is compared and analyzed. Through theoretical and numerical calculation and analysis, ZY10000/26/55D Two-column Shield Hydraulic Support is selected as the hydraulic support for the 3500 Working Face. Table 3 summarizes the statistics of working resistance for hydraulic support in working faces of three lengths: 195 m, 242.4 m, and 376 m.

The field measurement results show that the measured working resistance of support at 195 m and 242.2 m of working faces is within the rated working resistance range. In the 376 m working face, field measurement exceeded the rated working resistance in 2.76% of statistical cycles, among which the maximum working resistance is 10,049 kN once and 10,098 kN twice. ZY10000/26/55D Hydraulic Support can meet the support requirements of super large working faces.

6. Conclusions

(1) Roof caving in goafs of the super large 3500 Working Face occurs as successive layered caving, with roof fracture height of more than 31 m

(2) With the increase of the working face length, the caving step length of the roof stratum is basically unchanged. Working face length in the range of 195 m to 376 m has little effect on the roof weighting length. By comparing the caving step lengths of different rock strata, it can be inferred that the caving step length is positively correlated with the thickness of the rock stratum

(3) The roof displacement of the 195 m working face follows the subsidence rule of the Gaussian distribution curve, while the roof of the 376 m working face shows intermittent subsidence. Therefore, it can be inferred that the roof subsidence of the super large working face can be regarded as the combined subsidence of several common working faces

(4) The average periodic weighting of the 376 m working face, which is more violent, is about 80 kPa higher than that of the 195 m working face. The 376 m working face is characterized by violent oscillation at both ends and fluctuations within a small range in the middle. Weighting increases gradually within 20 m of the end of the 195 m working face, and the middle of the working face shows uniform weighting

(5) Comparison and analysis of the statistical results of the field working resistance of working faces of 195 m, 242.4 m, and 376 m length confirm that ZY10000/26/55D Hydraulic Support can meet the requirements of super large working faces

Data Availability

The data used to support the findings of the study are available from the corresponding author upon request.

Additional Points

Conflicts of Interest

All authors declare that they have no conflict of interest or financial conflicts to disclose.

Acknowledgments

The authors gratefully acknowledge the financial support provided by the National Natural Science Foundation of China (Grant Number 51904199), the Shanxi Provincial Key Research and Development Program (High-tech Field) Project (201903D121075), Transformation of Scientific and Technological Achievements Programs of Higher Education Institutions in Shanxi (Grant Number JYT2019015), and the Natural Science Foundation for Young Scientists of Shanxi Province (201801D221328).

References

[1] A. Mohammadreza, S. Vahab, and D. Hesam, "Evaluation of plow system performance in long-wall mining method using particle flow code," *International Journal of Coal Science Technology*, vol. 6, no. 4, pp. 518–535, 2019.

[2] S. P. Peng, "Current status and prospects of research on geological assurance system for coal mine safe and high efficient mining," *Journal of China Coal Society*, vol. 45, no. 7, pp. 2331–2345, 2020.

[3] M. G. Qian, J. L. Xu, and J. C. Wang, "Further on the sustainable mining of coal," *Journal of China Coal Society*, vol. 43, no. 1, pp. 1–13, 2018.

[4] J. W. Teng, Y. H. Qiao, and P. H. Song, "Analysis of exploration, potential reserves and high efficient utilization of coal in China," *Chinese Journal of Geophysics*, vol. 59, no. 12, pp. 4633–4653, 2016.

[5] Y. M. Zhang and X. Zhang, "Research on strata-pressure behavior of large mining height at fully mechanized mining face in shallow seam," *Coal Technology*, vol. 35, no. 11, pp. 65–67, 2016.

[6] H. P. Kang, G. Xu, B. M. Wang et al., "Forty years development and prospects of underground coal mining and strata control technologies in China," *Journal of Mining and Strata Control Engineering*, vol. 1, no. 2, pp. 7–39, 2019.

[7] G. F. Wang, J. H. Zhang, Y. J. Xu et al., "Supporting stress characteristics and zonal cooperative control technology of long working face in deep thick coal seam," *Journal of China Coal Society*, vol. 46, no. 3, pp. 763–773, 2021.

[8] X. M. Song, T. F. Gu, and Z. H. Yan, "Effects of increasing working face's length on underground pressure behaviors of mining super-high faces under shallow coal seam," *Chinese Journal of Rock Mechanics and Engineering*, vol. S2, pp. 4007–4012, 2007.

[9] H. P. Kang, G. F. Wang, P. F. Jiang et al., "Conception for strata control and intelligent mining technology in deep coal mines with depth more than 1000m," *Journal of China Coal Society*, vol. 43, no. 7, pp. 1789–1800, 2018.

[10] X. W. Zhang, "Technical research and practice of fully mechanized long working face," *Coal science and technology*, vol. 8, 2007.

[11] Z. Huang, "Thoughts on developing super large mines in China," *Coal Engineering*, vol. 41, no. 9, pp. 5–7, 2009.

[12] W. B. Guo and Y. G. Wang, "The definition of high-intensity mining basedon green coal mining and its index system," *Journal of Mining and Safety Engineering*, vol. 34, no. 4, pp. 616–623, 2017.

[13] L. B. Song and Q. X. Wang, "Study on safety mining technology of China first 450 m ultra long fully mechanized coal mining face," *Coal engineering*, vol. 46, no. 3, 2014.

[14] Q. X. Wang and J. F. Ju, "Study on mine strata pressure behavior law of 450 m ultra long fully-mechanized coal mining face," *Coal Science and Technology*, vol. 42, no. 3, pp. 125–128, 2014.

[15] M. S. Yi, "Selection of mechanized working face length by great height mining under shallow coal-seam in Shendo coal district," *Journal of China Coal Society*, vol. 12, pp. 1253–1257, 2007.

[16] X. D. Li, "Study on the coal pressure appearance rule of large cutting height and super length workface in Sihe coal mine," *Energy and Energy Conservation*, vol. 16, no. 4, pp. 85–87, 2011.

[17] G. F. Wang, F. Liu, X. J. Meng et al., "Research and practice on intelligent coal mine construction (primary stage)," *Coal Science and Technology*, vol. 47, no. 8, 2019.

[18] D. Z. Kong, W. Jiang, Y. Chen, Z. Y. Song, and Z. Q. Ma, "Study of roof stability of the end of working face in upward longwall top coal," *Arabian Journal of Geosciences*, vol. 10, no. 8, p. 185, 2017.

[19] W. R. Liu, "Experimental and numerical study of rock stratum movement characteristics in longwall mining," *Shock and Vibration*, vol. 2019, 2019.

[20] M. Z. Gao, J. Xie, Y. N. Gao et al., "Mechanical behavior of coal under different mining rates: a case study from laboratory experiments to field testing," *International Journal of Mining Science and Technology*, 2021.

[21] B. N. Wang, F. N. Dang, W. Chao, Y. P. Miao, J. Li, and F. Chen, "Surrounding rock deformation and stress evolution in pre-driven longwall recovery rooms at the end of mining stage," *International Journal of Coal Science Technology*, vol. 6, no. 4, pp. 536–546, 2019.

[22] X. Wang, Z. J. Wen, Y. J. Jiang, and H. Huang, "Experimental study on mechanical and acoustic emission characteristics of rock-like material under non-uniformly distributed loads," *Rock Mechanicsand Rock Engineering*, vol. 51, no. 3, pp. 729–745, 2018.

[23] J. C. Wang, S. L. Yang, B. G. Yang et al., "Roof sub-regional fracturing and support resistance distribution in deep longwall face with ultralarge length," *Journal of China Coal Society*, vol. 44, no. 1, pp. 54–63, 2019.

[24] J. L. Zhou and Q. H. Huang, "Stability analysis of key roof layer structure in shallow buried large mining height face," *Chinese Journal of Rock Mechanics and Engineering*, vol. 38, no. 7, pp. 1396–1407, 2019.

[25] K. Yang, Z. Wei, X. L. Chi, A. S. Gao, and Q. Fu, "Fracture criterion of basic roof deformation in fully mechanized mining with large dip angle," *Energy Exploration and Exploitation*, vol. 39, no. 3, pp. 886–902, 2021.

[26] W. Wang, Y. P. Cheng, H. F. Wang, W. Li, and L. Wang, "Coupled disaster-causing mechanisms of strata pressure behavior and abnormal gas emissions in underground coal extraction," *Environmental Earth Sciences*, vol. 74, no. 9, pp. 6717–6735, 2015.

[27] W. F. Yang and X. H. Xia, "Study on mining failure law of the weak and weathered composite roof in a thin bedrock working face," *Journal of Geophysics and Engineering*, vol. 15, no. 6, pp. 2370–2377, 2018.

[28] Y. W. Lan, R. Gao, B. Yu, and X. B. Meng, "In situ studies on the characteristics of strata structures and behaviors in mining of a thick coal seam with hard roofs," *Energies*, vol. 11, no. 9, p. 2470, 2018.

[29] Y. H. Zhao and X. M. Song, "Stability analysis and numerical simulation of hinged arch structure for fractured beam in super-long mining workface under shallow seam," *Rock and Soil Mechanics*, vol. 37, no. 1, pp. 203–209, 2016.

Hindawi
Geofluids
Volume 2021, Article ID 4673152, 13 pages
https://doi.org/10.1155/2021/4673152

Research Article

Research on Optimization of Coal Pressure Relief Borehole Parameters under High-Stress Conditions

Heng Zhang,[1] **Tie Li**,[1] **Zhenhua Ouyang**,[2] **Su Liu**,[3] **and Haiyang Yi**[2]

[1]*School of Civil and Resource Engineering, University of Science and Technology Beijing, Beijing 100083, China*
[2]*School of Safety Regulation, North China Institute of Science and Technology, Hebei 065201, China*
[3]*School of Resources and Civil Engineering, Northeastern University, Shengyang 110819, China*

Correspondence should be addressed to Tie Li; litie@ustb.edu.cn

Received 17 June 2021; Revised 23 July 2021; Accepted 17 August 2021; Published 1 September 2021

Academic Editor: Zhijie Wen

Determining the parameters of boreholes drilled for relieving pressure in coal seams is the key preventing and controlling rock bursts in boreholes of large diameter. In this study, theoretical analysis, numerical simulation, literature research, and other analysis methods are applied to study the angles of elastic energy dissipation and stress transfer, the distribution law of the pressure relief area, and the areas of stress concentration, energy, stress, displacement, and plastic behavior of large-diameter pressure relief boreholes in coal seams under high-stress conditions. The results are then used to evaluate the relationship between large-diameter pressure relief boreholes and the borehole arrangement. The following results are obtained. (1) A large-diameter results in a large amount of elastic energy released by the surrounding coal, low residual elastic energy density, strong interaction between boreholes, large pressure relief range of the borehole, and high pressure relief efficiency. (2) The main evaluation factor of the borehole pressure relief effect is its thickness and stress concentration area; secondary evaluation is based on the areas of energy, displacement, stress, and plastic behavior. (3) Six evaluation index systems are established to evaluate the effects of borehole pressure relief, which are found to be the thicknesses of the borehole pressure relief area and stress concentration area, reduction degree of energy density, percentage of stress reduction, displacement, and penetration degree of the plastic area. (4) It is determined that when the diameters of the pressure relief boreholes are 100, 120, 180, and 200 mm, a single-row borehole arrangement is adopted; a three-pattern borehole arrangement is adopted with diameters of 140 and 160 mm. These research results can provide theoretical support in selecting reasonable borehole arrangements for pressure relief boreholes of different diameters.

1. Introduction

With the increases in coal mining depths in recent years, frequent mine rock burst accidents in coal mines have become major disasters [1–4]. However, large-diameter boreholes drilled in coal seams can effectively relieve the pressure on the seams, thus reducing the occurrence of rock burst accidents [5–8]. Many factors can affect the pressure relief function of boreholes such as mining technology geological factors, hole depth, and borehole aperture [9–11]. For a specific coal seam, considering the small fluctuation of geological factors such as coal seam strength and burial depth, mining technology factors such as mining height and mining method are basically fixed; only the borehole arrangement, angle, depth, diameter, spacing, and other physical factors can be changed. Therefore, determining reasonable borehole parameters for coal pressure relief is the key for preventing rock burst accidents.

Many scholars at home and abroad have conducted abundant research on coal pressure relief boreholes. Li et al. [12] studied the influencing factors of pressure relief boreholes in a high-stress coal roadway and showed that the borehole diameter, spacing, and depth jointly affect the pressure relief effect of the borehole. The research results of Geng et al. [13] showed that the arrangement of pressure relief boreholes has a certain influence on the pressure relief effect and that the effects vary with the borehole arrangement. The research results of LAN [14] showed improved pressure relief effects of boreholes in high-stress areas of coal seams over those in low-stress areas. Jia et al. [15] studied the influence of borehole spacing, diameter, and depth on the strength of samples through laboratory tests and numerical analysis and found that stress release caused by crack propagation and penetration is fundamental for pressure relief in boreholes, with a larger borehole diameter, deeper depth, and smaller spacing showing better pressure relief effects. Yi et al. [16] studied and analyzed the pressure relief effects of large-diameter boreholes in soft and hard coal seams through numerical simulation, with better effects shown in the soft seams. Wang et al. [17] used stress transfer and surrounding rock deformation control effects as direct evaluation indices of the borehole pressure relief effect, categorizing the degree of borehole pressure relief as insufficient, sufficient, or excessive. Then, the dynamic action laws of length, diameter, and spacing of the pressure relief boreholes were applied to determine the stability of rocks surrounding a deep roadway. On the basis of the results, a method for determining the key parameters affecting the pressure relief was proposed. Liu et al. [18] and Zhang et al. [19] used numerical simulation based on Fast Lagrangian Analysis of Continua in Three Dimensions (FLAC3D) to determine that the peak stress of a coal seam can be transferred to deep areas by optimizing the borehole arrangement parameters. Qin [20] studied the stress, energy, and impact tendencies of coal and concluded that the pressure relief effect of large-diameter boreholes can be improved by adjusting the pressure of the coal, dissipating the energy, and reducing the impact properties. Li and Xiong[21] used automatic dynamic incremental nonlinear analysis, ADINA finite element analysis software, to study and evaluate the pressure relief effects of boreholes in stress concentration areas of rock bursts. Zhu et al. [22] put forward a concept based on the energy dissipation index, from which they deduced a quantitative calculation method of antiscour borehole parameters. Shi et al. [23] applied the Mohr strength theory and FLAC3D and determine that varying the borehole spacing and arrangement can significantly reduce large energy vibration occurring in rocks surrounding roadway to greatly reduce the impact risk of coal seams. Li et al. [24] studied the characteristics of the abutment pressure distribution, design scheme of the pressure relief borehole depth, and pressure relief effects in a large coal pillar after mining was conducted on a working face. On the basis of the results, a method was proposed for resolving the dangerous conditions of large coal pillars by controlling the depth and density of the pressure relief borehole, which enabled the transformation of stress distribution in the pillar from “single peak” to “ladle-shaped.” Wang et al. [25] studied the effect of borehole pressure relief from the perspective of energy. Zhai et al. [26] considered that pressure relieved by large-diameter borehole is more effective for stress relief in large areas. Li et al. [27] put forward a method or evaluating pressure relief effects based on the tensile strain value of optical fiber and the pressure relief radius. In their study, the pressure relief process in the borehole was divided into four stages: fracture development, limit equilibrium, hole collapse, and crushing coal compaction. Zhang et al. [28] considered that a greater borehole density results in more energy released from the coal seam and thus better pressure relief effects of the borehole. Ge at al. [29] studied the relationship between different coal strengths and the spacing of pressure relief boreholes and put forth a formula based on the results.

Although such studies on pressure relief boreholes of large diameter in coal bodies are abundant, reasonable arrangement of pressure relief boreholes of various diameters under high-stress conditions has been studied less often. Thus, the present study uses the angles of energy dissipation and stress to evaluate the pressure relief effects of single-row, triple-flower, and double-row borehole arrangement schemes for pressure relief boreholes with varied diameters. The results are then applied to obtain the relationship between the borehole diameter and the arrangement mode. This research will provide certain theoretical support for pressure relief technology of large-diameter boreholes.

2. Mechanism Analysis

2.1. Stress Transfer Mechanism of Pressure Relief Borehole. Pressure relief using large-diameter boreholes is an effective measure for eliminating or reducing the risk of rock burst. After a pressure relief borehole is constructed in coal seam, the stress of the coal seams near the borehole is evaluated. By applying elastic-plastic theoretical analysis, an equation for such stress can be obtained [15, 30]:

$$\begin{cases} \sigma_x = \delta\left(1 - \dfrac{r^2}{l^2}\right), \\ \sigma_y = \delta\left(1 + \dfrac{r^2}{l^2}\right), \\ \tau = 0. \end{cases} \tag{1}$$

Radius of plastic zone R_S [15, 30]:

$$R_S = r\left[\frac{l + c\cot\varphi}{c\cot\varphi}(1 - \sin\varphi)\right]^{(1-\sin\varphi)/(2\sin\varphi)}. \tag{2}$$

In these equations, σ_x, σ_y, τ, and δ are the radial, tangential, shear, and original rock stresses near the borehole, respectively (units: MPa); r is the borehole radius (m); l is the distance between the coal and the borehole center (m); R_S is the radius of the plastic zone (m); c is cohesion in the coal (MPa); and φ is the friction angle in the coal (MPa).

According to Equations (1) and (2), the stress around the borehole is redistributed from the original three-way stress state to the one-way stress state after the pressure relief borehole is arranged in the coal. When the stress of the coal is greater than its uniaxial compressive strength, the coal will be destroyed, and a plastic zone will appear around the borehole. The stress near the borehole is then transferred to a more distant location to form a new high-stress concentration area, and the elastic energy is accumulated locally in the plastic zone radius R_S to form an elastic-plastic region.

With the increase in distance between the coal and the borehole, the stress state of the coal gradually returns to the original rock stress state (as shown in Figure 1).

After the construction of the large-diameter pressure relief borehole in high-stress coal, a new free surface is essentially created on the surface of borehole. The original rock stress at the free surface of the coal changes, and the stress in the area close to the borehole is released. The coal near the borehole contains cracks, and a broken area much larger in diameter than that of the borehole itself is created. When multiple boreholes are continually constructed in the coal, the broken areas connect, resulting in complete fracture of the rock mass along the borehole section. Then, the high-stress concentration area of the surrounding rock support is transferred to deep regions to achieve pressure relief (as shown in Figure 2). The crushing area changes the stress state of the coal seam, which reduces the ability of the coal seam to store destructive energy destructive energy and thus reduces the possibility of rock burst.

2.2. Energy Dissipation Mechanism of Pressure Relief Borehole. A coal unit in a rock mass deformed by external force was selected as the research object of the present study. Assuming that the activity was closed, i.e., the object did not exchange heat with the outside components, the total work performed by the external force is converted into energy U according to the first law of thermodynamics [31].

$$U = U_j + U_\theta. \tag{3}$$

In this equation, U_j is the dissipated energy of the element, and U_θ is the elastic strain energy of the element that can be released.

$$U = \int_0^{\varepsilon_1} \sigma_1 d\varepsilon_1 + \int_0^{\varepsilon_2} \sigma_2 d\varepsilon_2 + \int_0^{\varepsilon_3} \sigma_3 d\varepsilon_3, \tag{4}$$

$$U_j = \frac{1}{2}\sigma_1 \varepsilon_1^e + \frac{1}{2}\sigma_2 \varepsilon_2^e + \frac{1}{2}\sigma_3 \varepsilon_3^e, \tag{5}$$

$$\varepsilon_i^e = \frac{1}{E_i}\left[\sigma_i - v_i\left(\sigma_j + \sigma_k\right)\right]. \tag{6}$$

In Equations (4)–(6), ε_i, ε_i^e, E_i, and v_i are the total strain, total elastic strain, elastic modulus, and Poisson's ratio of the three principal stresses, respectively.

Assuming that the coal is an isotropic medium and that the initial values of E_i and v_i in the three principal stress directions are E_0 and v_0, respectively, Equations (5) and (6) can be obtained, and the elastic strain energy can be released by the coal unit [32].

$$U_j = \frac{1}{2E_0}\left[\sigma_1^2 + \sigma_2^2 + \sigma_3^2 - 2v_0(\sigma_1\sigma_2 + \sigma_1\sigma_3 + \sigma_2\sigma_3)\right]. \tag{7}$$

The change process of coal mechanics is essentially the process of energy dissipation, and that of coal instability is the rapid release process of accumulated elastic strain energy. When the accumulated energy of the coal unit is greater than its ultimate elastic energy, the coal unit will fracture. In the case of fixed coal occurrence and technical mining conditions, a greater amount of elastic strain energy of the coal unit released by the large-diameter pressure relief borehole is related to lower residual elastic strain energy, lower impact risk, and lower possibility of rock burst. Therefore, the effect of borehole pressure relief can be evaluated by the amount of elastic strain energy consumed by the large-diameter pressure relief borehole.

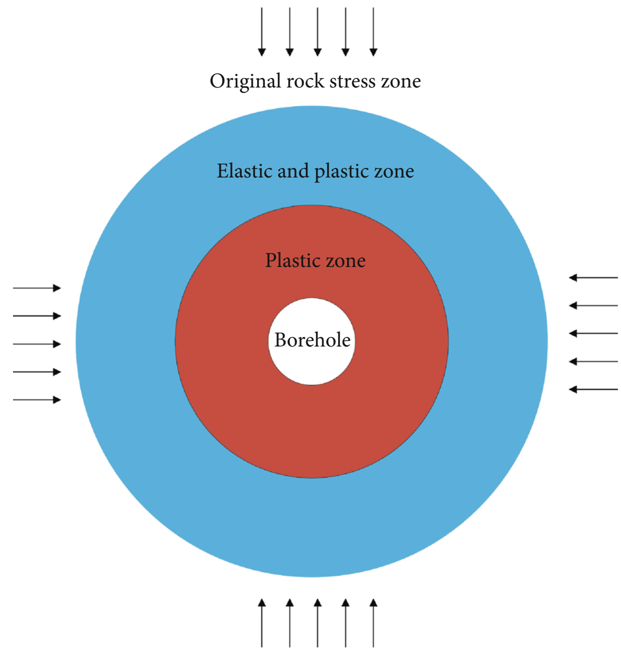

Figure 1: Elastic-plastic zone and stress distribution around a single borehole.

To study the energy release problem of large-diameter pressure relief boreholes in a coal unit, numerical simulation software can be used to calculate the local energy release rate of the coal unit and its elastic release energy [33].

$$\mathrm{LERR}_j = U_{j\,\max} - U_{j\,\min}, \tag{8}$$

$$\mathrm{ERE}_j = \sum_j^m \left(\mathrm{LERR}_j V_j\right). \tag{9}$$

In the above equation, LERR_j is the local energy release rate of the jth coal unit, $U_{j\,\max}$ is the peak elastic strain energy density prior to breakage of the coal of the jth unit, $U_{j\,\min}$ is the valley value of the elastic strain energy density of the jth coal unit after fracturing, ERE_j is the elastic strain energy released by the coal unit, and V_j is the volume of the coal seams in unit J.

From Equation (7), the following can be concluded.

$$U_{j\,\max} = \frac{1}{2E_0}\left[\sigma_{j1}^2 + \sigma_{j2}^2 + \sigma_{j3}^2 - 2v_0\left(\sigma_{j1}\sigma_{j2} + \sigma_{j1}\sigma_{j3} + \sigma_{j2}\sigma_{j3}\right)\right], \tag{10}$$

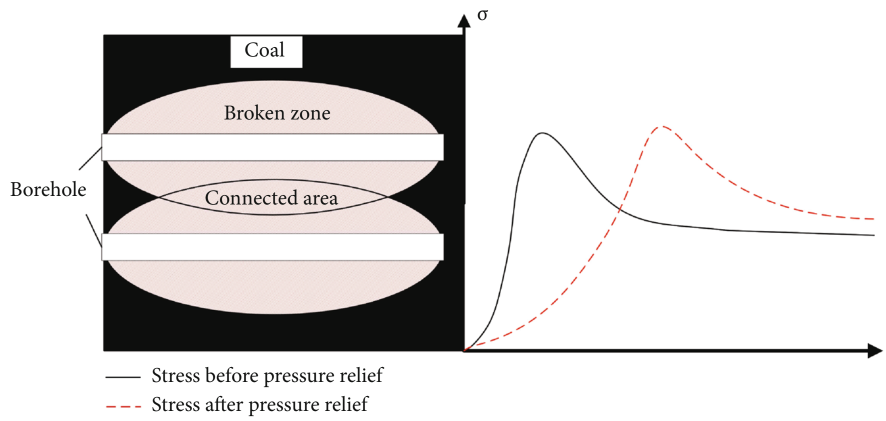

Figure 2: Diagram showing pressure relief in coal borehole.

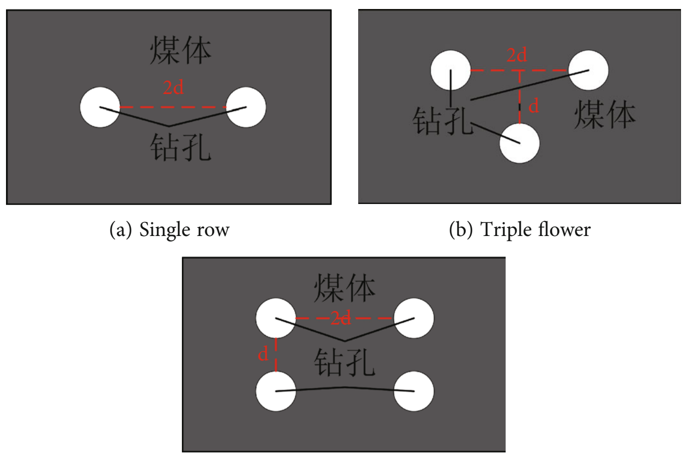

(a) Single row

(b) Triple flower

(c) Double row

Figure 3: Different borehole arrangements.

$$U_{j\,\min} = \frac{1}{2E_0}\left[\sigma_{j1'}^2 + \sigma_{j2'}^2 + \sigma_{j3'}^2 - 2v_0\left(\sigma_{j1'}\sigma_{j2'} + \sigma_{j1'}\sigma_{j3'} + \sigma_{j2'}\sigma_{j3'}\right)\right]. \tag{11}$$

In Equations (4)–(6), σ_{j1}, σ_{j2}, and σ_{j3} are the principal stresses in three directions at the peak elastic strain energy density of the coal element, and $\sigma_{j1'}$, $\sigma_{j2'}$, and $\sigma_{j3'}$ are those at the valley value.

3. Numerical Simulation Scheme and Results

3.1. Modeling and Scheme. To study the different diameters of pressure relief boreholes and to determine the most effective type of borehole arrangement, the Mohr Coulomb model was established by using FLAC3D numerical simulation software. Six types of pressure relief boreholes of varied diameters were selected, and each group of pressure relief borehole was divided into single-row, triple-flower, or and double-row type. The detailed arrangement is shown in Figure 3, with panel (d) showing the borehole spacing. In total, 18 groups of models were used; their size, number of units, number of nodes, and other parameters are shown in Table 1. The top of the model was subjected to a high stress of 45 MPa; the bottom and surrounding parts of the model were fixed; and the top was in free-boundary condition. The mechanical parameters of the coal are shown in Table 2.

3.2. Results Analysis

3.2.1. Arrangement of Single-Diameter Pressure Relief Borehole. The pressure relief borehole of 140 mm in diameter was used as an example for analyzing the thicknesses of the zones of pressure relief, stress concentration, energy density, stress, strain, and plastic behavior near the borehole under the arrangements of single-row, triple-flower, and double-row boreholes. On the basis of the results, the optimal borehole arrangement was obtained.

(1) Thicknesses of Borehole Pressure Relief and Stress Concentration Areas. Figure 4 shows the thickness distribution of the pressure relief and stress concentration areas under different borehole arrangements. The thicknesses of the two areas are closely related to the borehole. Therefore, the thicknesses of the pressure relief area and the stress concentration

Table 1: Parameters of numerical calculation model.

Serial number	Borehole diameter	Borehole arrangement	Model size/M	Number of units	Number of nodes
1	100 mm	Single row	2.3 ∗ 0.5 ∗ 3	15360	23763
2	100 mm	Triple flower	2.5 ∗ 0.5 ∗ 3	18240	28197
3	100 mm	Double row	2.5 ∗ 0.5 ∗ 3	17920	27231
4	120 mm	Single row	2.36 ∗ 0.5 ∗ 3	16340	24856
5	120 mm	Triple flower	2.6 ∗ 0.5 ∗ 3	18240	28917
6	120 mm	Double row	2.6 ∗ 0.5 ∗ 3	17920	27249
7	140 mm	Single row	2.4 ∗ 0.5 ∗ 3	15360	23763
8	140 mm	Triple flower	2.66 ∗ 0.5 ∗ 3	18240	28161
9	140 mm	Double row	2.66 ∗ 0.5 ∗ 3	17920	27195
10	160 mm	Single row	2.44 ∗ 0.5 ∗ 3	15360	23799
11	160 mm	Triple flower	2.72 ∗ 0.5 ∗ 3	20160	31209
12	160 mm	Double row	2.72 ∗ 0.5 ∗ 3	20160	31209
13	180 mm	Single row	2.48 ∗ 0.5 ∗ 3	15360	23787
14	180 mm	Triple flower	2.78 ∗ 0.5 ∗ 3	20160	31179
15	180 mm	Double row	2.78 ∗ 0.5 ∗ 3	23630	37777
16	200 mm	Single row	2.52 ∗ 0.5 ∗ 3	15360	23799
17	200 mm	Triple flower	2.84 ∗ 0.5 ∗ 3	20160	31209
18	200 mm	Double row	2.84 ∗ 0.5 ∗ 3	20160	31209

Table 2: Mechanical parameters of the coal.

Elastic modulus (GPa)	Shear modulus (GPa)	Density (ρ/kg m^3)	Internal friction angle ψ (°)	Tensile strength (MPa)	Cohesive force (MPa)
7.1	4.3	1640	30	5.6	2.1

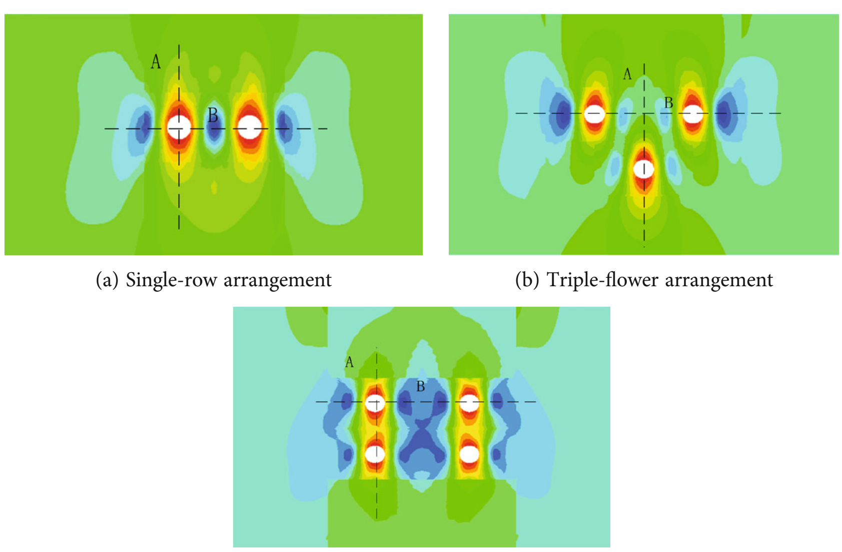

(a) Single-row arrangement

(b) Triple-flower arrangement

(c) Double-row arrangement

Figure 4: Thickness distribution of vertical stress relief zone of the borehole.

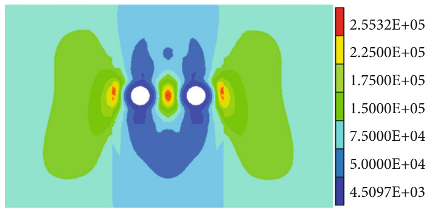

(a) Single-row arrangement

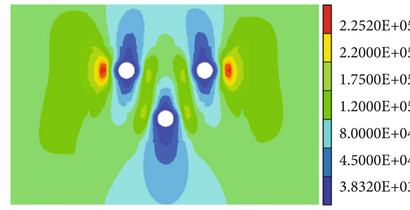

(b) Triple-flower arrangement

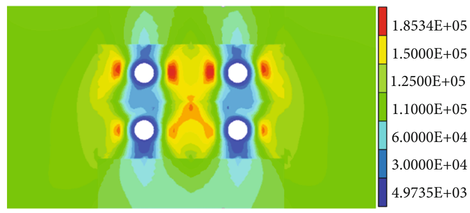

(c) Double-row arrangement

Figure 5: Energy density distribution in the coal unit.

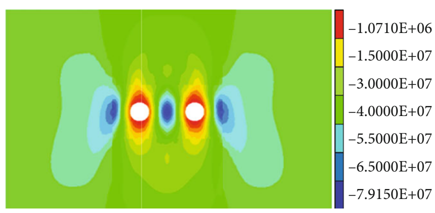

(a) Single-row arrangement

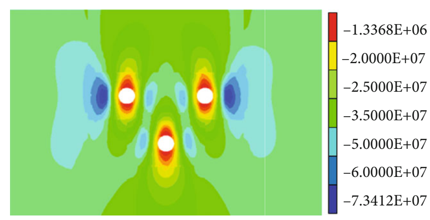

(b) Triple-flower arrangement

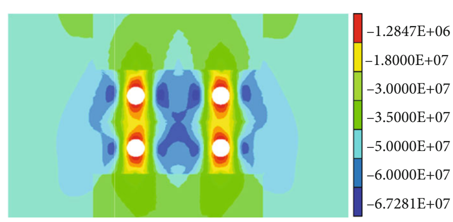

(c) Double-row arrangement

Figure 6: Vertical stress distribution.

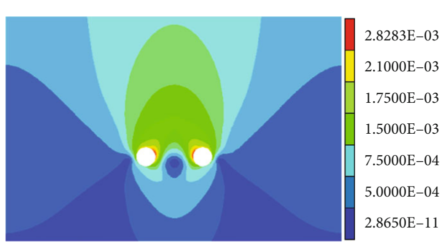

(a) Single-row arrangement

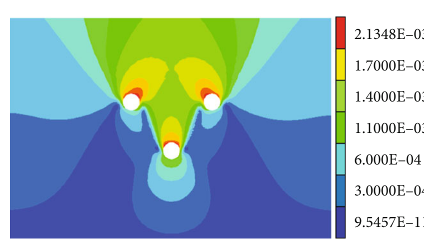

(b) triple-flower arrangement

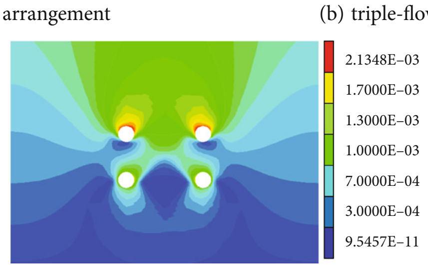

(c) double-row arrangement

Figure 7: Displacement distribution.

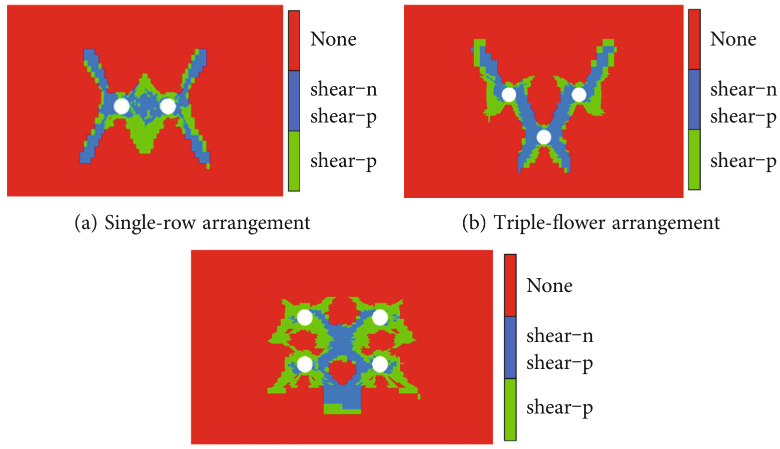

(a) Single-row arrangement

(b) Triple-flower arrangement

(c) Double-row arrangement

Figure 8: Distribution of plastic zone.

area at the dotted lines (a) (along the center of the borehole) and (b) (along the center of the borehole spacing) were statistically analyzed. As shown on the figure, when the pressure relief boreholes were arranged in single-row, triple-flower, and double-row forms the thicknesses of the pressure relief areas along the direction of the dotted line in Figure 4(a) were 1, 1.1, and 1.6 m, respectively, and the thickness of the stress concentration area was 0 m. The thicknesses of pressure relief zones along the direction of the dotted line in Figure 4(b) were 0.56, 0.55, and 0.3 m, and those of the stress concentration zone were 0.11, 0.2, and 0.48 m, respectively. The average thickness of the pressure relief zone of the three different arrangements was 0.78, 0.83, and 0.95 m, and that of stress concentration area was 0.11, 0.2, and 0.48 m, respectively.

The above analysis results demonstrate that the thickness of the pressure relief zone was largest in the double-row arrangement, although this led to the thickest stress concentration zone between boreholes. Under the triple-flower arrangement, the thickness of the pressure relief (stress concentration) zone was larger than (similar to) that in the single row. Therefore, the triple-flower arrangement is the best method for relieving the pressure.

(2) Change in Elastic Energy Density. Figure 5 shows that the initial elastic energy density of coal is about 1×10^5 J/m^3. After the pressure release by the large-diameter borehole, the minimum elastic energy densities around the borehole were 4.5×10^3, 3.8×10^3, and 4.9×10^3 J/m^3 under single-row, triple-flower, and double-row arrangements, respectively. Moreover, the arrangements of single row and double row caused the elastic energy to reaccumulate between boreholes. Therefore, the triple-flower arrangement had the best effect on coal energy release.

(3) Stress Distribution Law. Figure 6 shows that the protorock stress of the coal seam was about 40 MPa. After the construction of large-diameter pressure relief boreholes,

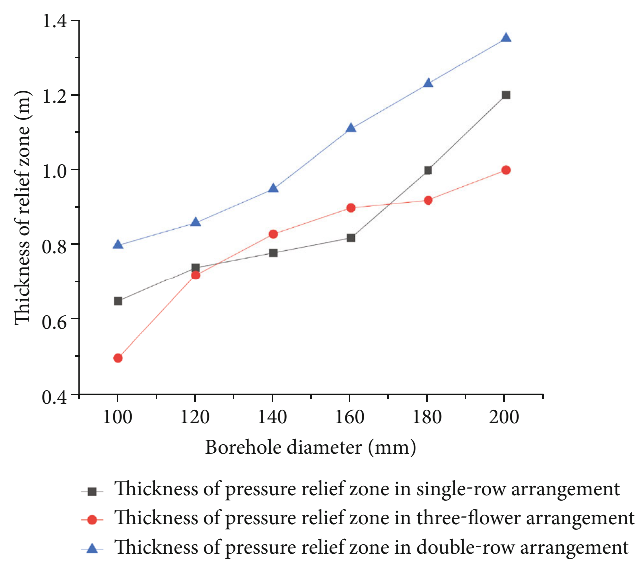

Figure 9: Thickness of pressure relief zone in boreholes with different diameters.

the minimum pressure near the borehole was reduced to about 1, 1.3, and 1.3 MPa under single-row, triple-flower, and double-row arrangements, respectively, and the stress was reduced by about 97%. The three-flowered borehole arrangement resulted in a small stress concentration area between boreholes and smaller stress peak values. Although the stress concentration area between boreholes was also smaller under the single-row arrangement, the peak stress was greater. Moreover, both the stress concentration area and the stress peak value between the boreholes under the double-row arrangement were larger.

(4) Displacement Law. Figure 7 shows that the large-diameter pressure relief boreholes under single-row, triple-flower, and double-row arrangements exhibited maximum displacement of 2.8×10^{-3}, 2.3×10^{-3}, and 2.1×10^{-3} m. It shows that the arrangement of double-row pressure relief

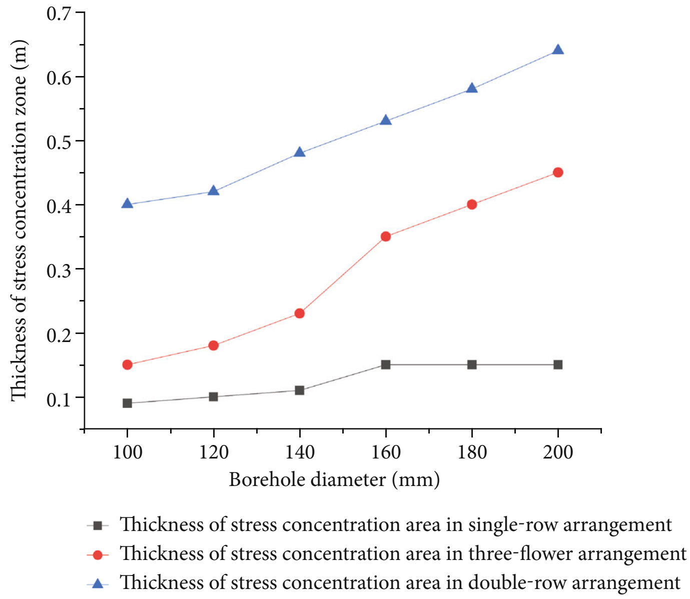

Figure 10: Thickness of stress concentration zone in boreholes with different diameters.

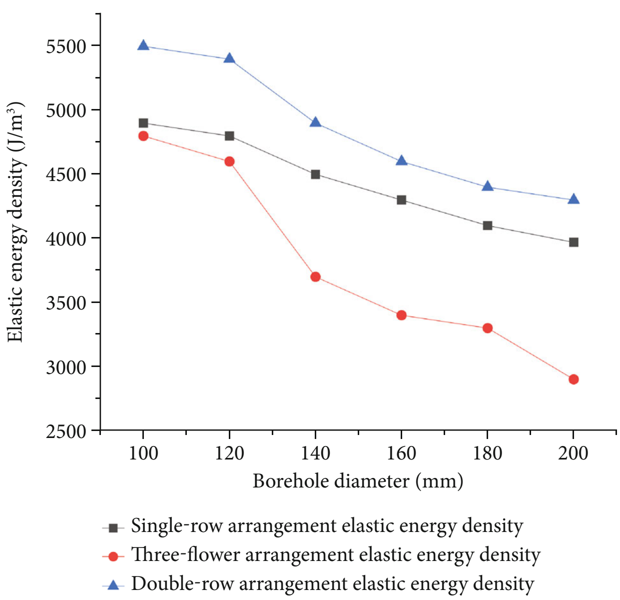

Figure 11: Elastic energy density of boreholes with different diameters.

boreholes has the least impact on the displacement of the coal seam and the effect of controlling the deformation of the roadway is the most significant.

(5) Plastic Zone Expansion. Figure 8 shows that under the different arrangements of large-diameter pressure relief boreholes, the plastic zones of the single-row boreholes expanded and penetrated each other, and an effective pressure relief area was formed between the boreholes. Under the three-flower borehole arrangement, the plastic zones between the boreholes were not connected. Under the double-row borehole arrangement, the plastic zone of the diagonally protruding area between the holes was connected but did not penetrate the horizontal interval of the borehole. Thus, under the three-flower and double-row borehole arrangements, the pressure relief effects of the borehole were not ideal.

The above analysis indicates that according to the angles of stress and energy, when the diameter of the pressure relief borehole was 140 mm, although the single-row and double-row borehole arrangements exhibited the best pressure relief effects in the displacement monitoring and the plastic zone, the boreholes were scattered and had less of a coupling effect as well as easy formation of large stress concentration areas, high peak stress, and large elastic energy density accumulation areas between them. Moreover, when the diameter of the pressure relief borehole was 140 mm, the pressure relief effect was the best under the three-flower borehole arrangement.

3.2.2. Analysis of the Arrangement of Pressure Relief Boreholes with Different Diameters

(1) Thickness of Pressure Relief Zone of Boreholes with Different Diameters. Figure 9 shows that an increase in the diameter of the pressure relief borehole causes the thickness of the pressure relief zone of the borehole to become significantly larger. In the single-row borehole arrangement, the thickness of the pressure relief zone in the boreholes of 100, 120, 180, and 200 mm in diameter was in the middle of the triple-row and double-row arrangements. In the 140 and 160 mm diameter boreholes, the thickness of the pressure relief zone was in the middle of the single-row and triple-flower arrangements.

(2) Thickness of Stress Concentration Area of Boreholes with Different Diameters. Figure 10 shows that as the diameter of the borehole increases, the thickness of the stress

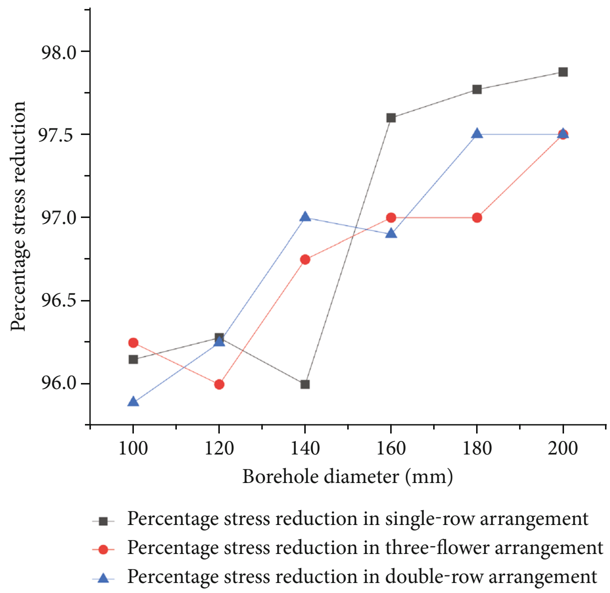

Figure 12: Stress reduction degree in boreholes of different diameter.

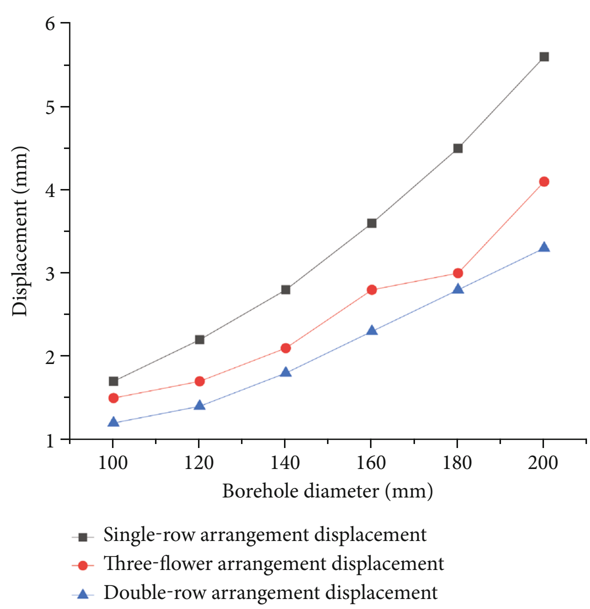

Figure 13: Displacement in boreholes of different diameter.

concentration area also increased, but the thickness of the stress concentration area changed less. In the single-row borehole arrangement, the thickness of the stress concentration area was the smallest. The thickness of the stress concentration area in the three-flower arrangement was in the middle. Under the double-row borehole arrangement, the thickness of the stress concentration area was the largest.

(3) Changes in Elastic Energy Density of Boreholes with Different Diameters. Figure 11 shows that the remaining elastic energy density of the coal seam decreased as the diameter of the pressure relief borehole increased. Under the three-flower borehole arrangement, the residual elastic energy density of the coal seam was the smallest. In the single-row borehole arrangement, the residual elastic energy density of the coal seam was in the middle. Under the double-row borehole arrangement mode, the residual elastic energy density of the coal seam was the largest.

Table 3: Plastic zone connection of pressure relief boreholes with different diameters.

Borehole diameter (mm)	Connection status of the plastic zone of single-row arrangement	Connection status of the plastic zone of three-flower arrangement	Connection status of the plastic zone of double-row arrangement
100	y	n	n
120	y	n	n
140	y	n	n
160	y	n	n
180	y	n	n
200	y	n	n

(4) Stress Distribution Law of Different Diameter Boreholes. Figure 12 shows that as the borehole diameter increased, the coal seam stress decreased more. For the pressure relief borehole 100 mm in diameter under the three-flower arrangement, the coal seam pressure relief degree was the highest, followed by the single-row arrangement and double-row arrangement. In the pressure relief boreholes with diameters of 120, 180, and 200 mm, under the single-row borehole arrangement, the degree of pressure relief for coal was the highest, followed the double-row arrangement and the three-row arrangement. For pressure relief boreholes 140 and 160 mm in diameter, the degree of pressure relief of the coal seam was in the middle when the three-flower arrangement was used.

(5) Displacement Law of Boreholes with Different Diameters. Figure 13 shows that as the borehole diameter increased, the maximum displacement of the coal seam increased. The pressure relief boreholes with different diameters and double-row arrangement had the largest coal displacement. When the three-flower arrangement was used, the coal displacement was the smallest, and the single-row arrangement had middle displacement.

(6) Expansion Law of Plastic Zone of Different Diameter Boreholes. Table 3 shows that when the pressure relief boreholes with different diameters were arranged in a single row, the plastic zone was connected. Under the three-flower and double-row arrangements, the plastic zone was not continuously connected; when the double row was arranged, however, the diagonally protruding area between the boreholes was continuously connected.

Based on the above analysis, reasonable arrangement of six types of pressure relief boreholes with different diameters were studied and analyzed. To obtain the final result conveniently and concisely, six indexes were put forward as the

Table 4: Evaluation of the pressure relief effect of different arrangements of pressure relief boreholes with different diameters.

Evaluation Index	Borehole diameter (mm)																	
	100			120			140			160			180			200		
Borehole arrangement	Single row	Three flower	Double row	Single row	Three flower	Double row	Single row	Three flower	Double row	Single row	Three flower	Double row	Single row	Three flower	Double row	Single row	Three flower	Double row
Pressure relief zone thickness	g	p	e	g	p	e	p	g	e	p	g	e	g	p	e	g	p	e
Thickness of stress concentration area	e	g	p	e	g	p	e	g	p	g	e	p	e	g	p	e	g	p
Energy density reduction degree	g	e	p	g	e	p	g	e	p	g	e	p	g	e	p	g	e	p
Stress reduction percentage	g	e	p	e	p	g	p	g	e	e	g	p	e	p	g	e	g	p
Displacement size	p	g	e	p	g	e	p	g	e	p	g	e	p	g	e	p	g	e
Degree of penetration of plastic zone	e	p	g	e	p	g	e	p	g	e	p	g	e	p	g	e	p	g

evaluation basis: the average thickness of the pressure relief area (along the dotted lines A and B), the average thickness of the stress concentration area (along the dotted lines A and B), the degree of energy density reduction, the percentage of stress reduction, the size of displacement, and the penetration degree of the plastic zone. Among them, the best, middle, and worst pressure relief result of each index of each diameter borehole was regarded as “excellent,” “good,” and “poor,” respectively. The specific evaluation results are shown in Table 4.

From Table 4, it can be concluded that with borehole diameters of 100, 120, 180, and 200 mm, although the thickness of the stress concentration area was excellent when the boreholes are arranged in a double row, the pressure relief area of the borehole was too small and thus poor. Therefore, the single-row arrangement was optimal. When the borehole diameters were 140 and 160 mm, the arrangement mode under the optimal pressure relief effect of the borehole was the three-flower arrangement. Based on the above analysis, when the diameter of the pressure relief borehole is different, the optimal arrangement of the borehole is also different.

4. Theoretical Verification

According to the research results in the literature [34], the pressure relief effects of boreholes were evaluated in the present study under the actual conditions of a mine. To improve the effects of a borehole 200 mm in diameter, three types of borehole arrangement schemes were designed and studied: single-row, three-flower, and square-row arrangements. Through the research and analysis of the thickness and degree of pressure relief area, it was concluded that the proportion of pressure relief area was not different between single-row and three-flower arrangements, although the single-row arrangement showed better effects. In the square-row arrangement, the proportion of the vertical stress concentration area between boreholes was too large owing to the increase in borehole spacing. In terms of the relief effect of vertical stress, the single-row borehole arrangement was the best, followed by the three-flower and square-row arrangements. This is because the boreholes were too scattered, and the mutual coupling effect was small, which can easily form a new stress concentration area.

When the borehole diameter was 200 mm, as shown in Table 4, the single-row borehole arrangement was the optimal solution, which is consistent with the above research results.

5. Discussions

In view of the fact that there is no mature theoretical system for the arrangement of pressure relief boreholes with different diameters of single strength coal under high stress conditions, the current design of the arrangement of pressure relief boreholes is mostly determined according to the combination of field experience and national standards. In this paper, under high stress conditions, a reasonable drilling arrangement for pressure relief boreholes with different diameters of a single strength coal seams is proposed. Its advantages and disadvantages are as follows:

(1) By means of theoretical analysis and numerical simulation, the rational layout of different diameter pressure relief boreholes of single strength coal under high stress condition is studied. The basis of reasonable arrangement of pressure relief boreholes with different diameters of single strength coal under high stress condition is put forward. The evaluation table of pressure relief effect of different diameters and different arrangement of pressure relief boreholes is established. The theory of selecting the arrangement of pressure relief boreholes according to the diameter of boreholes is added, which can provide theoretical guidance for determining the reasonable arrangement of pressure relief boreholes with different diameters in coal mine area

(2) In this paper, the object of study only selected the 6 different diameters of pressure drilling, 18 kinds of model is established, the base also is small and is only a preliminary exploration of a theoretical research direction, although it has certain theoretical guiding significance, but whether it has the broad applicability of different intensity of coal, more research is needed; the theory also needs experts further explore perfect

6. Conclusion

(1) With an increase in the diameter of the pressure relief borehole, the released elastic energy of the coal near the borehole increased; the residual elastic energy density decreased; the coupling between the boreholes was enhanced; the pressure relief range of the borehole increased; and the pressure relief efficiency was improved

(2) Taking the thicknesses of pressure relief and stress concentration zones as the main evaluation basis and the distribution law of elastic energy density, stress, displacement, and plastic zone after the pressure release of the coal seam as the auxiliary evaluation factors, the pressure relief boreholes with different diameters were examined, and a reasonable borehole arrangement was determined

(3) Six evaluation index systems were proposed to evaluate the pressure relief effect: the thickness of the pressure relief zone, thickness of the stress concentration zone, degree of energy density reduction, percentage of stress reduction, displacement, and penetration degree of the plastic zone. It was determined that when the borehole diameters were 100, 120, 180, and 200 mm, the single-row borehole arrangement had the best pressure relief effect. When the borehole diameters were 140 and 160 mm, the three-flower drilling arrangement was best

(4) It is concluded that pressure relief boreholes with different diameters should adopt different borehole arrangement theories. The results of this research provide a reference basis for setting the optimal pressure relief effect in mining areas according to the actual drilling diameter

Data Availability

The data that support the study are included in this paper.

Conflicts of Interest

We declare that we have no conflict of interest.

Acknowledgments

This paper received financial supports from the National Natural Science Foundation of China (grant numbers: 51674016 and 52004090) and the Natural Science Foundation of Hebei Province (grant number: E2020808025).

References

[1] J. Yaodong and Z. Yixin, "State of the art: investigation on mechanism, forecast and control of coal bumps in China," *Chinese Journal of Rock Mechanics and Engineering*, vol. 34, no. 11, pp. 2188–2204, 2015.

[2] Q. Qingxin and P. Yongwei, "Study of bursting liability of coal and rock," *Chinese Journal of Rock Mechanics and Engineering*, vol. 30, no. S1, pp. 2736–2742, 2011.

[3] L. M. Dou, J. He, A. Y. Cao, S. Y. Gong, and W. Cai, "Rock burst prevention methods based on theory of dynamic and static combined load induced in coal mine," *Journal of China Coal Society*, vol. 40, no. 7, pp. 1469–1476, 2015.

[4] F. Jiang, G. Yang, and W. Quande, "Study and prospect on coal mine composite dynamic disaster real-time prewarning platform," *Journal of China Coal Society*, vol. 43, no. 2, pp. 333–339, 2018.

[5] J. F. Pan, Y. Ning, D. B. Mao, H. Lan, T. T. Du, and Y. W. Peng, "Theory of rockburst start-up during coal mining," *Chinese Journal of Rock Mechanics and Engineering*, vol. 31, no. 3, pp. 586–596, 2012.

[6] Y. Sun, G. Li, H. Basarir, A. Karrech, and M. R. Azadi, "Laboratory evaluation of shear strength properties for cement-based grouted coal mass," *Arabian Journal of Geosciences*, vol. 12, no. 22, 2019.

[7] Y. Sun, G. Li, N. Zhang, Q. Chang, J. Xu, and J. Zhang, "Development of ensemble learning models to evaluate the strength of coal-grout materials," *International Journal of Mining Science and Technology*, vol. 31, no. 2, pp. 153–162, 2021.

[8] Y. Sun, G. Li, and J. Zhang, "Investigation on jet grouting support strategy for controlling time-dependent deformation in the roadway," *Energy Science & Engineering*, vol. 8, no. 6, pp. 2151–2158, 2020.

[9] Y. D. Jiang, Y. S. Pan, F. X. Jiang, D. O. U. LM, and Y. Ju, "State of the art review on mechanism and prevention of coal bumps in China," *Journal of China Coal Society*, vol. 39, no. 2, pp. 205–213, 2014.

[10] H. Wu, X. Wang, W. Yu et al., "Analysis of influence law of burial depth on surrounding rock deformation of roadway," *Advances in Civil Engineering*, vol. 2020, 13 pages, 2020.

[11] H. Wu, X. Wang, W. Wang, G. Peng, and Z. Zhang, "Deformation characteristics and mechanism of deep subsize coal pillar of the tilted stratum," *Energy Science & Engineering*, vol. 8, no. 2, pp. 544–561, 2020.

[12] L. Dongyin, D. Zhiguo, and L. Zhiyong, "Numerical simulation analysis on parameters of pressure releasing borehole in high stress seam gateway," *Coal Engineering*, vol. 46, no. 9, 2014.

[13] G. Min-min, M. Zhan-guo, G. Peng, and Z. Guo-wei, "Analysis of the effect on pressure relief by the pressure relieving hole layouts in high stress coal roadway," *Journal of Safety Science and Technology*, vol. 8, no. 11, pp. 5–10, 2012.

[14] Y. W. Lan, P. C. Liu, W. Li, X. H. Chen, Z. Y. Lu, and W. Y. Xing, "The influencing factors of drillhole pressure relief and the regression analysis of destroy radius," *Safety in Coal Mines*, vol. 44, no. 4, 2013.

[15] C. Jia, Y. Jiang, X. Zhang, D. Wang, H. Luan, and C. Wang, "Laboratory and numerical experiments on pressure relief mechanism of large-diameter boreholes," *Chinese Journal of Geotechnical Engineering*, vol. 39, no. 6, pp. 1115–1122, 2017.

[16] E. B. Yi, Z. L. Mu, L. M. Dou, J. G. Ju, L. Xie, and D. L. Xu, "Study on comparison and analysis on pressure releasing effect of boreholes in soft and hard seam," *Coal Science and Technology*, vol. 39, no. 6, pp. 1–5, 2011, 85.

[17] W. Meng, W. Xiangyu, and X. Tongqiang, "Borehole destressing mechanism and determination method of its key parameters in deep roadway," *Journal of China Coal Society*, vol. 42, no. 5, pp. 1138–1145, 2017.

[18] H. G. Liu, Y. N. He, J. H. Xu, and L. J. Han, "Numerical simulation and industrial test of boreholes distressing technology in deep coal tunnel," *Journal of China Coal Society*, vol. 32, no. 1, pp. 33–37, 2007.

[19] Z. Hongwei, L. Yunpeng, C. Ying, Z. Feng, and S. Ling-feng, "Research on bumping prevention scheme optimization of large diameter drilling in isolated area under three hard conditions," *Journal of Safety and Environment*, vol. 17, no. 5, pp. 1823–1827, 2017.

[20] Q. Zi-han, "Study of pressure relief with large diameter drilling hole and results verified," *Journal of Mining And Strata Control Engineering*, vol. 23, no. 4, pp. 77–80, 2018.

[21] L. I. Jinkui and X. Zhenhua, "Numerical simulation of borehole pressure relief to prevent rock burst in roadway," *Journal of Xi'an University of Science and Technology*, vol. 29, no. 4, pp. 424–426+432., 2009.

[22] Z. Si-tao, J. Fu-xing, S. Xian-feng et al., "Energy dissipation index method for determining rockburst prevention drilling parameters," *Rock and Soil Mechanics*, vol. 36, no. 8, pp. 2270–2276, 2015.

[23] S. Qing-wen, C. Hong-ke, L. Da-zhao, P. Jun-feng, X. Yong-xue, and W. Shu-wen, "Study on pressure relief drilling holes layout parameters of roadside in rockburst coal seam," *Journal of Mining And Strata Control Engineering*, vol. 22, no. 6, pp. 74–77, 2017.

[24] D. Li, F. X. Jiang, Y. Chen, D. C. Gai, Y. Wang, and W. B. Wang, "Study on impact mechanism and prevention technology of drainage lane of large coal pillars near deep wells," *Journal of Mining & Safety Engineering*, vol. 36, no. 2, pp. 265–271, 2019.

[25] W. Shu-wen, P. Jun-feng, L. Shao-hong, X. Yong-xue, Y. Lei, and G. Xiao-jin, "Evaluation method for rockburst-preventing effects by drilling based on energy-dissipating rate," *Journal of China Coal Society*, vol. 41, no. S2, pp. 297–304, 2016.

[26] C. Zhai, J. Xu, S. Liu, and L. Qin, "Investigation of the discharge law for drill cuttings used for coal outburst prediction based on different borehole diameters under various side stresses," *Powder Technology*, vol. 325, pp. 396–404, 2018.

[27] Y. Li, H. W. Zhang, J. Han, F. Zhu, and C. Guo, "Time effect of borehole pressure relief based on distributed optical fiber sensing technology," *Journal of China Coal Society*, vol. 42, no. 11, pp. 2834–2841, 2017.

[28] S. Zhang, Y. Li, B. Shen, X. Sun, and L. Gao, "Effective evaluation of pressure relief drilling for reducing rock bursts and its application in underground coal mines," *International Journal of Rock Mechanics and Mining Sciences*, vol. 114, pp. 7–16, 2019.

[29] D. Ge, D. Li, and F. Jiang, "Reasonable pressure-relief borehole spacing in coal of different strength," *Journal of Mining & Safety Engineering*, vol. 37, no. 3, pp. 578–585, 2020.

[30] G. Yong-ge, J. Zhi-xin, M. Xiao-qiang, and Z. Ji-yun, "Effects of hole diameter and arrangement on tunneling surface relief effect," *Coal Technology*, vol. 36, no. 1, pp. 138–140, 2017.

[31] X. Heping, J. Yang, and L. Liyun, "Criteria for strength and structural failure of rocks based on energy dissipation and energy release principles," *Chinese Journal of Rock Mechanics and Engineering*, vol. 24, no. 17, pp. 3003–3010, 2005.

[32] R. Solecki and R. J. Conant, *Advanced mechanics of materials*, Oxford University Press, London, 2003.

[33] G. S. Su, X. T. Feng, Q. Jiang, and G. Q. Chen, "Study on new index of local energy release rate for stability analysis and optimal design of underground rockmass engineering with high geostress," *Chinese Journal of Rock Mechanics and Engineering*, vol. 25, no. 12, pp. 2453–2460, 2006.

[34] W. Shuwen, M. Debing, and R. Yong, "Parameter optimizating of drilling holes for pressure relief," *Journal of Mining And Strata Control Engineering*, vol. 15, no. 5, pp. 14–17, 2010.

Hindawi
Geofluids
Volume 2021, Article ID 3181697, 18 pages
https://doi.org/10.1155/2021/3181697

Research Article

Mechanical Properties and Damage Behavior of Rock-Coal-Rock Combined Samples under Coupled Static and Dynamic Loads

Jinzheng Bai,[1,2] Linming Dou,[1,2] Piotr Małkowski,[3] Jiazhuo Li,[4] Kunyou Zhou,[1,2] and Yanjiang Chai[1,2]

[1]School of Mines, China University of Mining and Technology, Xuzhou 221116, China
[2]State Key Laboratory of Coal Resources and Mine Safety, China University of Mining and Technology, Xuzhou 221116, China
[3]AGH University of Science and Technology, al. Mickiewicza Av. 30, 30-059 Krakow, Poland
[4]State Key Laboratory of Mining Response and Disaster Prevention and Control in Deep Coal Mines, Anhui University of Science and Technology, Huainan 232000, China

Correspondence should be addressed to Linming Dou; lmdou@126.com

Received 4 June 2021; Accepted 9 August 2021; Published 1 September 2021

Academic Editor: Zhijie Wen

This research is aimed at investigating the influence of the coal height ratio on the mechanical properties and damage behavior of rock-coal-rock combined samples (RCRCS) under coupled static and dynamic loads. For this purpose, a uniaxial cyclic dynamic loading experiment with four different coal height ratios of RCRCS was conducted. Mechanical properties, failure modes, and wave velocity evolution of RCRCS were analyzed; the process of rock burst under coupled static and dynamic loads in rock-coal-rock combined structure was discussed. The following research results are obtained. (1) The peak strength of RCRCS under static and dynamic load decreases with the increasing coal height ratio as an inverse proportional function. (2) The loading and unloading modulus remains consistent for the same levels of dynamic load; the coal height ratio of 40% may be the limit for the stable value of modulus. (3) The increase of the coal height in RCRCS leads to a gradual increase of the energy release rate; the cracks develop preferentially in coal and then extend to rock sample. The distribution of AE events and damage is consistent with the distribution of passive wave velocity. The research results provide important scientific bases for the guidance of early warning of rock burst.

1. Introduction

Rock burst is a dynamic disaster in mining engineering with a sudden and violent release of elastic energy accumulated in coal and rock, which poses a significant risk to mine safety [1–3]. The number of coal mines in China with rock burst disasters has been raised from 32 in 1985 to more than 253 in 2019 [4]. For rock bursts in China, some typical features were observed: (1) Accidents are mostly occurred next to gobs or advancing working face [5, 6]. (2) Coal bodies were broken into powder and rushed out several meters, accompanied by the extensive collapse of the overburden strata; the weak floor suddenly rushed uplifted and caused the entire roadway section to be closed instantly [7]. (3) Accidents are mostly controlled by high static stress caused by mining disturbance, complex geological environment, and dynamic stress caused by fault slipping, hard roof breaking, and large-charge roof blasting [8, 9]. Observations showed that the clamping effect of roof-floor surrounding rock on the coal body becomes more significant as the mining depth increases. Rock burst is not caused by a single rock layer or coal seam but by the structural damage of the roof-coal-floor combined system. Therefore, it is of great significance to investigate the interaction mechanism of static load and dynamic disturbance in the process of rock burst [10–12].

In recent years, certain researchers have conducted valuable laboratory experiment investigations on mechanical behaviors of coal-rock combined samples. Petukhov and Linkov [13] first discussed the postpeak failure properties of two-body combined samples composed of rock and coal.

Table 1: Burst tendency index of the 3-3# coal seam and siltstone from Yutian coal mine.

Coal burst tendency index				
Dynamic failure duration (ms)	Elastic strain energy index	Bursting energy index	Uniaxial compressive strength (MPa)	Burst tendency classification
37.60	3.44	20.79	17.82	Strong
Siltstone burst tendency index				
Elastic modulus (GPa)		Bending energy index		Strong
12.20		169.88		

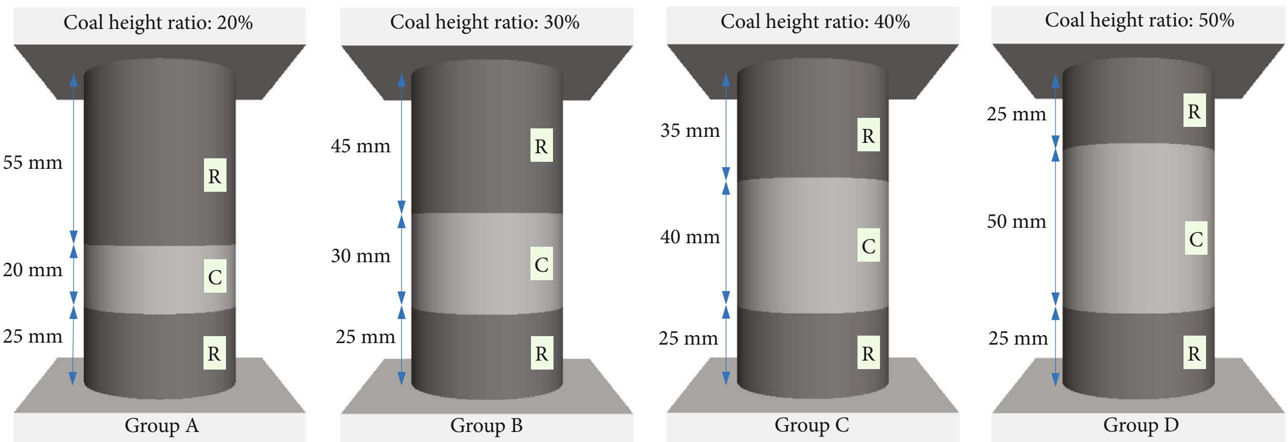

Figure 1: Sketch map of rock-coal-rock combined samples.

Zhao et al. [14] carried out the uniaxial compression test and studied the effect of peak compression strength upon the AE characteristics and P-velocity. Zuo et al. [15] investigated the deformation and failure behavior of rock-coal-rock combined body containing a weak coal interlayer by uniaxial and triaxial tests. Chen et al. [16] analyzed the evolution of internal cracks of coal-rock combined samples based on X-ray computed tomography observations. Zhao et al. [17] established the equivalent homogenous model of coal-rock combined samples and obtained the strength behavior of the combined model composed of different rock mediums and structural plane.

With further in-depth study, researchers are gradually aware that dynamic disturbance functions as an unneglectable external condition among numerous factors that induce rock bursts under deep mining [18, 19]. Zhang et al. [20] studied the energy dissipation characteristics of pure coal samples under multilevel frequency cyclic loading. Gong et al. [21] explored the effect of high loading rate on the mechanical properties of coal-rock combinations. Hu et al. [22] reproduced the cyclic disturbance-induced rock burst in the laboratory using a true triaxial testing system.

However, existing research results mainly focused on the mechanical behavior of coal-rock combined samples under pure static load, while a limited number of studies have been published on the deformation properties and damage behavior of RCRCS under coupled static and dynamic loads. In this study, an experiment of RCRCS with different coal height ratios under coupled static and dynamic loads was conducted. Effects of coal height ratio on mechanical properties, failure mode, and wave velocity evolution of RCRCS are mainly researched in this study. Further, the process of rock burst under coupled static and dynamic loads was discussed, which provides important reference bases for the on-site early warning of rock burst.

2. Methodology

2.1. Sample Preparation. Coal samples used for the experiment were collected from the 3-3# coal seam in Yutian coal mine which is located in Xinjiang Uygur Autonomous Region, China; siltstone samples were collected from the immediate roof of the 3-3# coal seam. According to the Chinese National Standard for Coal Mining Industry, both the coal seam and siltstone layer have an extremely strong burst tendency as shown in Table 1. Numerous researches showed that the coal height ratio has a significant control effect on the mechanical properties of RCRCS [23]. To reflect the clamping effect of roof samples on the coal samples, four sets of samples with different coal heights were prepared for the experiment. Every set had different coal height as shown in Figure 1: group "A"—coal height ratio 20%, group "B"—coal height ratio 30%, group "C"—coal height ratio 30%, and group "D"—coal height ratio 50%. The height of floor siltstone samples was always 25 mm, while the height of roof siltstone samples changed with the coal height.

According to the requirement by the ISRM standard [24], the combined samples were with a diameter of 50 mm and a height of 100 mm. Every part of the RCRCS

Table 2: Physical properties and initial wave velocity of RCRCS.

Coal height ratio (%)	Sample unit	Diameter (mm)	Length (mm)	Mass (g)	Wave velocity (m/s)
	1a1-A1	49.83	100.80	438.6	1828.68
20	1a1-A2	49.96	101.61	421.7	1896.31
	1a1-A3	49.25	100.68	432.8	1912.49
	1a1-B1	49.51	100.04	398.7	1744.27
30	1a1-B2	49.80	101.42	426.8	1738.04
	1a1-B3	49.68	100.47	413.1	1813.16
	1a1-C1	49.51	100.70	422.7	1710.57
40	1a1-C2	49.10	101.50	397.4	1695.36
	1a1-C3	50.04	101.37	438.6	1743.45
	1a1-D1	49.09	101.38	421.7	1566.54
50	1a1-D2	49.29	100.09	403.2	1468.28
	1a1-D3	50.15	100.78	429.3	1347.06

was bonded with super glue; physical properties and initial wave velocity of RCRCS were listed in Table 2.

2.2. Test Device and Measuring System. The tests were carried out in the State Key Laboratory of Coal Resources and Safe Mining of China University of Mining and Technology. The test system is divided into a loading system, an acoustic emission monitoring system, and a high-speed camera system (Figure 2). The 370.50 fatigue-testing machine produced by MTS Corporation in the United States was used to perform multilevel cyclic dynamic load, with a maximum load of 500 kN. The loading system can realize constant amplitude, variable amplitude, and block waveform loading. The PCI-II monitoring system produced by PAC Corporation was applied to capture AE signal features during the test. Eight R15-a sensors were arranged on the surface of the combined sample to be measured through hot melt adhesive to obtain the spatial distribution of AE events. The sampling rate of the system was 2 MHz and the gain of the preamplifier was set as 40 dB. The values of peak definition time (PDT), hit definition time (HDT), and hit lockout time (HLT) were selected as 50 μs, 200 μs, and 300 μs, respectively. The GX-3 high-speed camera system produced by NAC Corporation in Japan was used to capture the deformation and failure characteristics of combined samples in the whole test, which can shoot 2000 frames per second, showing the resolution of 680×480 pixels.

2.3. Test Scheme. The dominant frequency band of a waveform signal of a typical rock burst accident in Yutian coal mine was analyzed. On this basis, the frequency of the applied cyclic dynamic load was determined as 5 Hz by combining with the mechanical properties of the fatigue testing. Relevant research results showed that the strain rate of dynamic load in the coal mine is usually within the range of $10^{-3}\cdot s^{-1}\sim 10^{1}\cdot s^{-1}$ [25], and the strain rate of cyclic dynamic load considered in this paper is about $10^{-2}\cdot s^{-1}$, which meet the above requirements. Therefore, the test results can better reflect the actual situation of rock burst due to external dynamic load disturbance.

The stress-controlled was used in the test, and the loading path was divided into four stages as shown in Figure 3, (I) static load stage: the load reached 10 kN at a rate of 300 N/s from the initial state; (II) hold load stage: the static load remains unchanged for 10 s; (III) cyclic dynamic load stage: the oil source drives the indenter to apply a sinusoidal dynamic load to the samples; (IV) hold load stage: the static load remains unchanged for 10 s. The dynamic load frequency was 5 Hz; the upper and lower load limits are 10 kN in each cyclic dynamic load stage, while 100 cycles were repeated. Afterward, the procedure was repeated in the order of I-II-III-IV until the combined sample was irreversibly damaged; the test was ended.

3. Results

3.1. Strain-Stress Curve. As the most important constitutive relationship in material mechanics, the strain-stress curve can reflect the deformation behavior of the material under a given stress state. Figure 4 illustrates the strain-stress curve of RCRCS with different coal height ratios under coupled static and dynamic loads. To facilitate the analysis, the stress behavior of the pure coal and siltstone sample under static load is drawn for comparison. In addition, from reaching the peak strength to completely losing the load-bearing capacity, both RCRCS and the pure coal sample undergo an obvious yielding stage and fail gradually. However, siltstone samples with higher brittleness have a faster fracture rate and a more violent stress reduction process. The coal height ratio has a key influence on the mechanical properties and failure behavior of RCRCS, which will be analyzed in detail.

The peak strength of the RCRCS with different coal heights under coupled static and dynamic loads is shown in Figure 5. In terms of general rules, the peak stress of RCRCS under coupled static and dynamic loads gradually decreases with the increase of coal height, and higher than the coal samples, lower than the siltstone samples, which is consistent with the conclusions obtained by previous scholars. The relationship between coal height and the peak stress of RCRCS can be described by the inverse proportional function as shown in Equation (1).

$$\sigma_c = 20.6 + \frac{0.57}{h_c}, \tag{1}$$

where σ_c and h_c are peak strength and coal height of RCRCS under coupled static and dynamic loads, respectively.

According to the peak strength of the RCRCS, the $\sigma_c \sim h_c$ curve is divided into three stages. In stage I (coal height ratio between 0–only siltstone was tested and 20%), the peak strength decreases sharply from 77.0 MPa to 23.45 MPa. In stage II (coal height ratio between 20% and 50%), the peak strength experiences a slight decrease from 23.45 MPa to 19.54 MPa. In stage III (coal height ratio between 50% and 100%), the peak strength decreases from 19.54 MPa to 14.59 MPa, which can be defined as a proximate stable trend.

FIGURE 2: Test device and measuring system. (a) MTS Landmark 370.50; (b) PCI-II AE system; (c) NAG GX-3 high-speed camera.

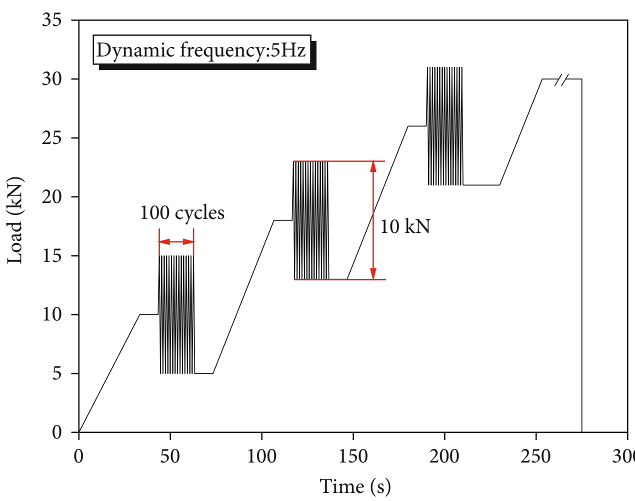

FIGURE 3: Test loading paths under coupled static and dynamic loads.

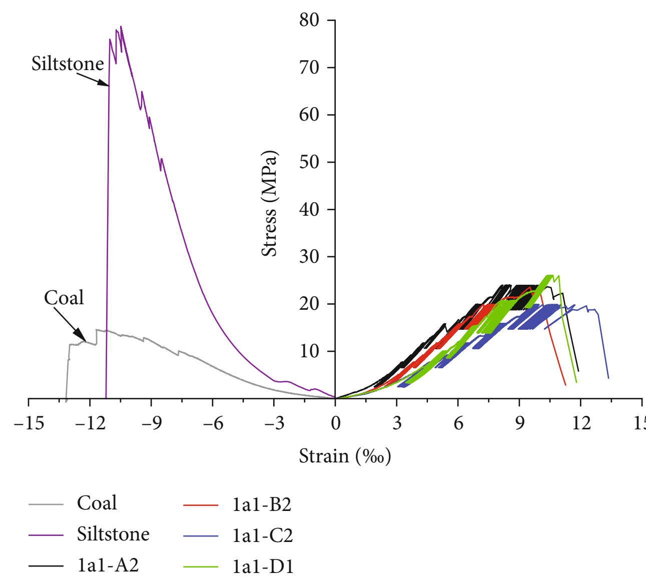

FIGURE 4: Strain-stress curves of siltstone, coal, and RCRCS.

There, it seems that the critical coal height of 20% and 50% have a key effect on the peak strength of RCRCS.

The static load is applied to the top of the combined samples, while the cyclic dynamic load is applied to the bottom. Regardless of static or dynamic load, once the external load reaches the ultimate bearing strength of the coal sample, the entire RCRCS will lose stability. It can be found that the peak strength under coupled static and dynamic loads is closer to that of the pure coal sample. Therefore, it can be considered that the bearing capacity of RCRCS is closer to the coal sample.

3.2. Elastic Modulus of Cyclic Dynamic Load. The research showed that different loading paths significantly affected the process of connection and coalescence of microfractures. Moreover, the evolution trends of microscopic parameters can be characterized based on various macroscopic parameters, such as elastic modulus and Poisson's ratio [26]. Elastic modulus of coal and rocks reflect their ability to resist deformation under the stress condition, which can be determined under a static load in three different ways [27, 28]. In general, the degree of consolidation between material particles increases with increasing stress. However, the evolution laws of the elastic modulus of RCRCS under cyclic dynamic loading are still unclear. In this paper, the loading elastic modulus E_l and unloading elastic modulus E_u in each hysteresis loop were tested, which also meets the recommendations of ISRM; these two moduli can show the effect of dynamic loads on the RCRCS.

The tangential elastic moduli were calculated using Equation (2) and Equation (3), where σ_A, σ_B, and σ_C are the start, middle, and end stress of each strain-stress loop (hysteresis loop), respectively. As shown in Figure 6, ε_A, ε_B, and ε_C are the start, middle, and end strain of each hysteresis

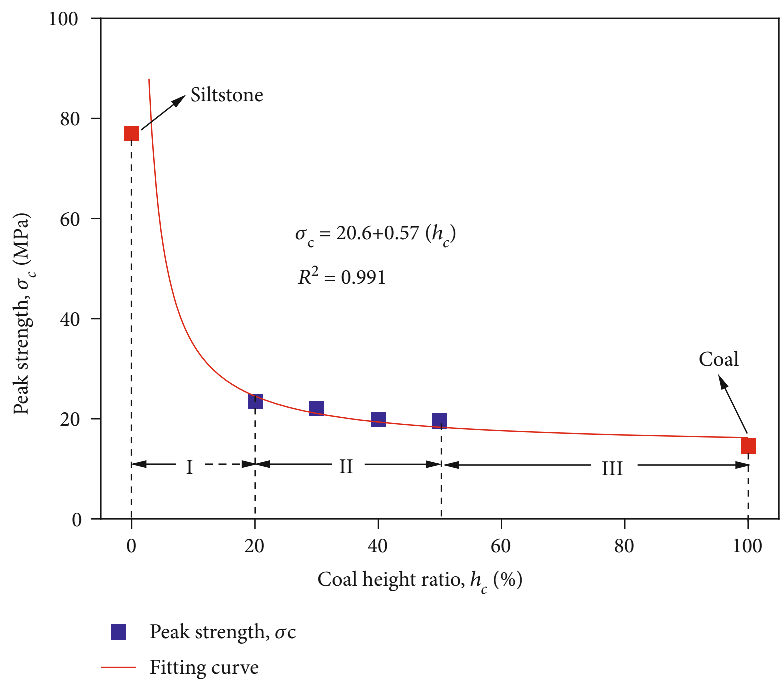

FIGURE 5: Relation between peak strength of RCRCS and coal height ratio.

loop, respectively. The evolution laws of tangential elastic moduli with the number of cycles at each dynamic stress levels were presented in Figure 7.

$$E_l = \frac{\sigma_B - \sigma_A}{\varepsilon_B - \varepsilon_A}, \quad (2)$$

$$E_u = \frac{\sigma_C - \sigma_B}{\varepsilon_C - \varepsilon_B}. \quad (3)$$

As shown in Figure 7(a), the coal height ratio is 20%. The stress in the compaction stage was relatively low, and the microcracks inside the RCRCS were basically closed. Therefore, the tangential elastic modulus in the first cyclic dynamic load level essentially did not change and maintained a relatively stable value. The average loading modulus value is 3.01 GPa, while the average unloading modulus value is 3.02 GPa in level I. Both were between coal samples (2.08 GPa) and siltstone (12.20 GPa) and closer to that of the coal samples. It was found a slightly increasing trend of the E_l and E_u in the second dynamic load level which was induced by the compaction effect. As the continuously strengthened number of loading cycles, the time of occlusion and reconstruction of microfracture surfaces greatly declined, which inhibited the connection and coalescence of the microfracture surfaces. The average loading modulus value is 3.96 GPa, while the average unloading modulus value is 4.08 GPa in the second dynamic load level. In the third cyclic dynamic load level, the E_l and E_u both showed sharply fluctuated. The average loading modulus value is 4.71 GPa, and the average unloading modulus value is 4.99 GPa. Overall, the elastic modulus in the hysteresis loop increased with an increase in the cyclic dynamic stress level, but the value of the increase was decreased.

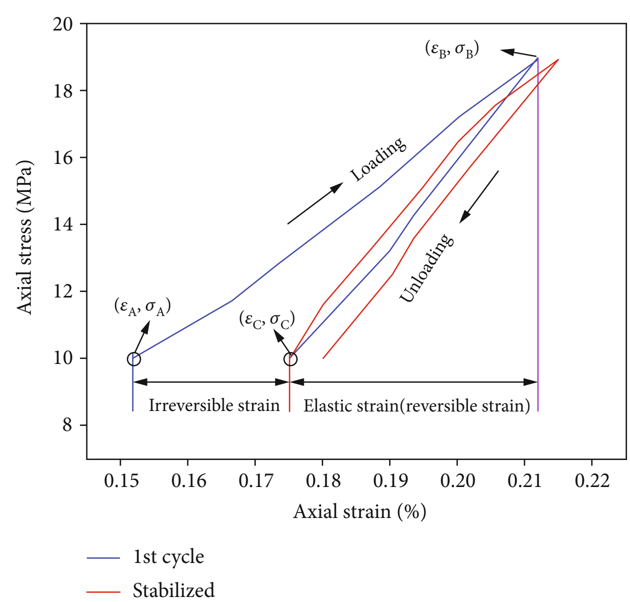

FIGURE 6: Tangential elastic modulus calculation method in each hysteresis loop.

The failure of 1a1-B2 and 1a1-C2 samples occurred in the fourth cyclic dynamic load stage; a slight decrease and fluctuation trends were observed and caused by damage to the RCRCS owing to cyclic loading, which is representative of the progressive damage of macroscopic parameters. It is worth noting that in the 1a1-D2 sample, the coal height ratio is increased to 50%. A slight decreasing trend of the E_l and E_u in level-I and a remarkable decreasing trend near the failure level can be found. As the proportion of coal height ratio increases, the pores, cracks, and discontinuities inside the

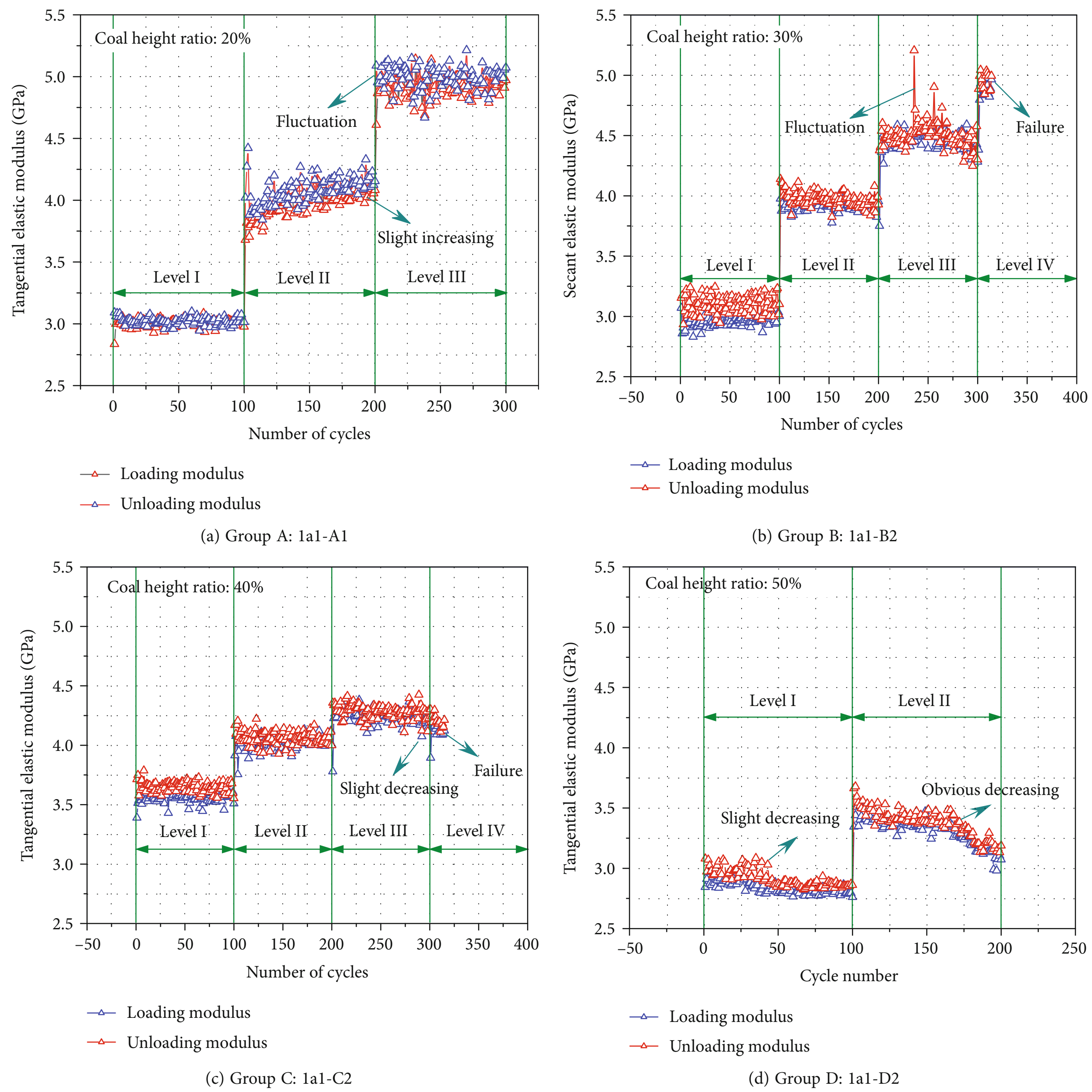

(a) Group A: 1a1-A1

(b) Group B: 1a1-B2

(c) Group C: 1a1-C2

(d) Group D: 1a1-D2

Figure 7: Evolution laws of loading and unloading elastic modulus of RCRCS.

combined structure increase, which further leads to a decrease in the resistance to deformation of the RCRCS. Therefore, the coal height ratio of 40% may be the limit for the stable value of loading and unloading modulus under the dynamic load. For higher coal contribution in the combined samples, it starts cracking under higher loads, and consequent cycles of dynamic loads and modulus values decrease.

In addition, Lei et al. [29] maintained that an increase in the lower stress limit will make the rock harder, while the lower stress limit close to zero will make the rock softer. In this paper, it is also clearly observed that the unloading elastic modulus value is obviously lower than the loading modulus under low-constraint conditions. For the RCRCS which final failure occurred during the dynamic loading level, the two modulus values are basically completely close, indicating that the cyclic dynamic loading caused dense microcrack damage inside the combined sample and reduced the tangential modulus in the hysteresis loop, reflecting the progressive damage characteristics of the RCRCS under the coupled static and dynamic loads.

3.3. The Energy Dissipation. As a quasibrittle material, the RCRCS always exchange energy with the external system under coupled static and dynamic loads. In terms of early warning of rock burst and deeply understanding the fatigue characteristics of rock, energy dissipation has great significance for damage evaluation. For the RCRCS studied in this paper, part of the energy comes from the heat dissipated by conduction, convection, and radiation, and the other part comes from the energy dissipated by the damage of the material itself. Since the thermal energy of RCRCS general remains unchanged under coupled static and dynamic loads, the energy dissipation trend caused by damage is basically the same as the total energy dissipation. So, the total dissipated energy can be represented by the energy dissipation caused by damage. Energy dissipation of a single hysteresis loop is given by Equation (4), where ε_i, ε_{i+1}, σ_i, and σ_{i+1} are the stress and strain data corresponding to the i and $i+1$ hysteretic loop, respectively. The unit of U_i is J/m^3 which represents the dissipated energy per unit volume between two consecutive data points. The cumulative dissipated energy density U_a is given by Equation (5)–Equation (6), which represents the cumulated dissipated energy from the first cycle to the nth cycle.

$$U_i = \sum_{i=1}^{n} \frac{(\varepsilon_{i+1} - \varepsilon_i)(\sigma_{i+1} - \sigma_i)}{2}, \tag{4}$$

$$U_i = \int_{\min}^{\max} U_i = \oint \sigma d\varepsilon, \tag{5}$$

$$U_a = \sum_{i=1}^{n} U_d. \tag{6}$$

Figure 8 shows the accumulated dissipated energy density of the combined samples with different coal heights at each cyclic dynamic load stage. Obviously, the accumulated dissipated energy increases linearly with the number of cycles within the same stress level, while the rate of increase of the dissipated energy remains unchanged.

The increasing rate of dissipated energy density (slope of the curve) gradually increases with the stress level. The final failure of 1a1-A1 and 1a1-D2 samples were both occurred in the static load stage, while 1a1-B2 and 1a1-C2 were both unstable in the fourth cyclic dynamic load stage. There is an obvious abrupt increment of the accumulated dissipated energy density in the last cycle before the final failure, which indicates that the macroscopic instability of the RCRCS that occurs in the cyclic dynamic loading stage is significantly different from that of the static load stage. In this case, the failure is still brittle, but the accumulated energy is consumed and released rapidly and violently. This is also the essential difference between high stress-dominated and cyclic dynamic load disturbance-dominated rock burst.

The rate of energy dissipation can indicate the mechanical response speed of RCRCS under coupled static and dynamic loads. In this paper, we define a new energy dissipation rate index as: dU_a/dN. Figure 9 plots the quantitative relation between the accumulated energy dissipation density rate of the RCRCS with different coal height ratios and cyclic dynamic stress levels. The relationship between accumulated energy dissipation density rate and the dynamic stress level can be well fitted with an exponential function with high consistency <0.9719~1.00>. Besides, it is clear that with the increase of dynamic stress level, the growth of accumulated energy dissipation density rate increases. This demonstrates that under the higher stress level, the effect of cyclic dynamic load accelerates the growth and penetration speed of microcracks in RCRCS, and the rate of energy release also increases. The combined structure is easier to complete the transformation from a steady state to an unsteady state. In addition, with the increases of coal height ratio in RCRCS, the rate of accumulated energy dissipated density increase, which indicated that as the weaker part of RCRCS, the coal body mainly participates in the response to static and dynamic load, and controls the overall stability.

The total amount of energy dissipation refers to the dissipated energy counting from the first cycle to the last cycle up to failure. Previous studies have shown that the total amount of energy dissipated is constant for specific material such as concrete [30]; it is only related to the stress path and stress level. However, this experiment shows another form of the energy dissipation of RCRCS. Figure 10 shows that the total energy dissipation corresponding to different cycles of dynamic times is quite different, indicating that the total dissipated energy could not be a material constant, but a variable related to the total number of cyclic load cycles.

3.4. Spatial Distribution of AE Events and Failure Mode. The AE source location has been widely used to detect the origin and propagation of cracks in various materials, such as concrete [31], rock [32], rock-like material [33], coal [34], and metal [35]. It can realize the continuous visualization of the spatio-temporal evolution law of material damages in the whole loading process. As shown in Figure 11(a), AE event energy (unit: aJ) can be divided into seven grades.

To reflect the internal fracture propagation and damage development of the RCRCS under coupled static and dynamic loads, the load process is sequentially decomposed into the "static + hold load" stage and the "dynamic + hold load" stage. The failure characteristics of the RCRCS under instantaneous dynamic failure are analyzed by capturing the images of the combinations before failure with the high-speed camera. Limited by the article length, to show the influence of different coal height ratios on the failure modes of the combined samples, the biggest (50%) and smallest (20%) coal height ratios in each group are selected to perform the analysis.

The first analysis considers the 1a1-A1 sample of group "A" with a coal height ratio of 20%. Figure 12(a) indicates that the low-energy AE events are initiated in the middle of the coal body of the RCRCS during the initial static load stage, which is mainly due to the closure of primary cracks and pore. The cyclic dynamic load under low stress levels has no obvious effect on the microfracture of RCRCS. With the increase of stress level, the AE events with large energy evolve from coal sample to the roof siltstone. In the second "dynamic + hold load" stage, the growth of AE events is the most obvious, especially the AE events in the roof rock samples began to gather significantly. In the next "static + hold" stage, the development of microfractures in the coal body is almost full, while there are still only a few low-

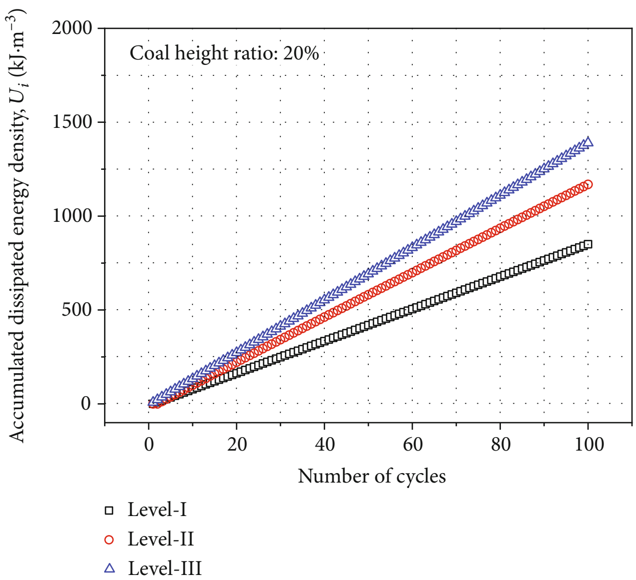

(a) Group A: 1a1-A1

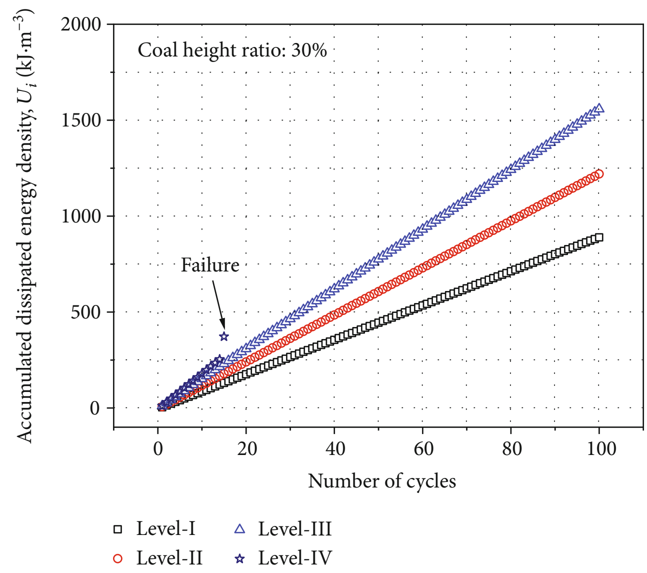

(b) Group B: 1a1-B2

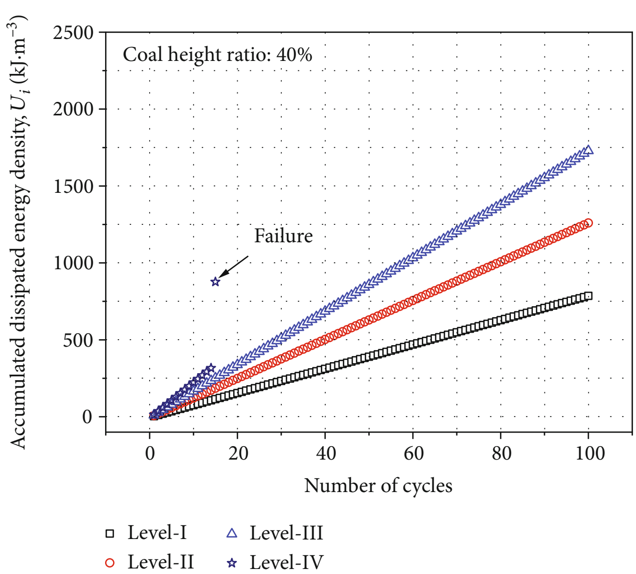

(c) Group C: 1a1-C2

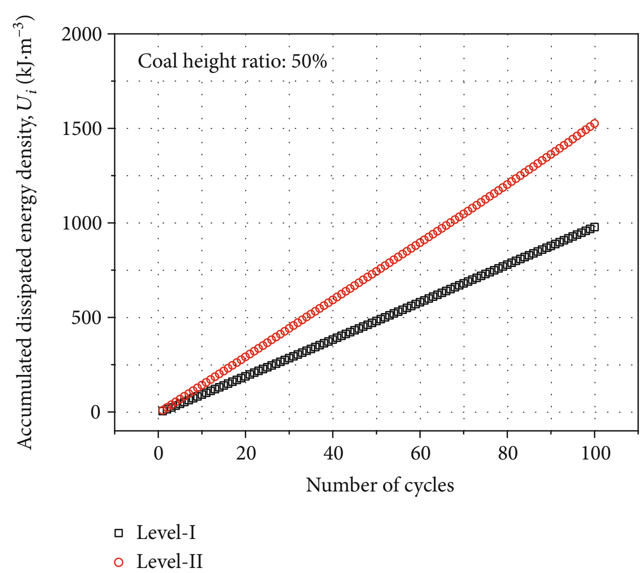

(d) Group D: 1a1-D2

Figure 8: Accumulated dissipated energy density of RCRCS.

energy AE events in the floor rock samples. Until the last "dynamic + hold" load stage, the distribution of AE events in the floor rock sample has been extended to the top end, and the RCRCS structure is close to critical instability. The AE events in the roof rock sample are distributed in a "cone" shape, and the position of its generatrix is the contour where splitting failure occurs, which well corresponds to area A in 1a1-A1 as shown in Figure 12(b). According to the failure process, the coal sample is the first to spray particles, while there is no obvious deformation of the roof and floor siltstone samples. Subsequently, the coal sample showed a visible horizontal volume expansion; the side of the roof rock sample appeared longitudinal splitting failure. A strong impact tendency occurred accompanied by the coal pulver and mass ejection violently.

The second analysis considers the 1a1-D2 sample of group "D" with a coal height ratio of 50%. Figure 13(a) indicates that the AE events are distributed both in the roof, coal, and floor samples in the initial load stress, especially in the interface between the coal and rock samples above and below. The cyclic dynamic load under initial stress levels caused RCRCS to produce a series of low-energy AE energy, different from group "A"; the top and bottom siltstone samples significantly participate in the mechanical response to static and dynamic loads at this time. Subsequent cyclic dynamic load causes the microfractures in the coal body to continue to develop until it reaches a near-destructive state. This indicates that the damage evolution in the RCRCS is not homogenous at the beginning; top and bottom rock parts experience more damage characterized more and

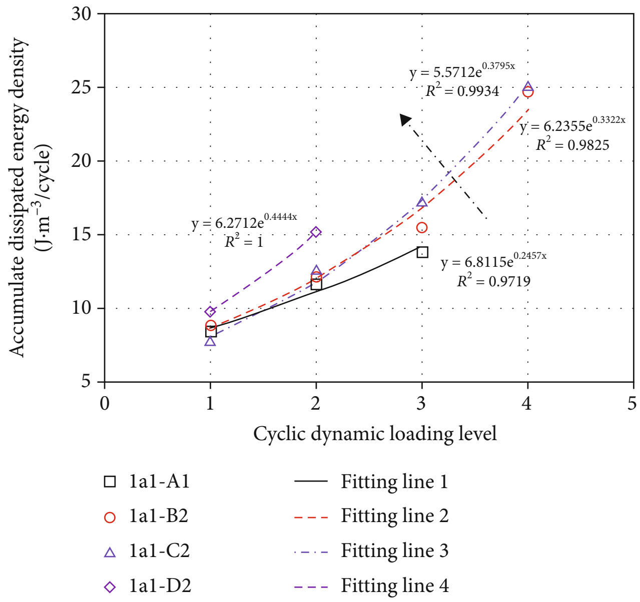

Figure 9: Relation of accumulated energy dissipation density and cyclic dynamic loading level.

stronger AE events. Figure 13(b) documents that the left part of the coal sample burst first out at failure (area B), then the roof siltstone sample showed complete longitudinal splitting failure.

In summary, the damage evolution of RCRCS under coupled static and dynamic loads can be described as follows: (1) When the coal height ratio is small, the damage first initiates in the coal sample, then more and more cracks appear in the roof sample. Finally, the RCRCS was completely destabilized until the macroscopic cracks developed to the top of the roof siltstone sample. (2) When the coal height is large, the damage is distributed both in the roof, floor siltstone and coal samples. The final failure is characterized by the burst failure of the coal sample and the split failure of the siltstone sample, which is consistent with the composite failure pattern of roof-coal-floor described above.

3.5. Distribution of Passive Wave Velocity. Passive velocity tomography is based on the seismic wave velocity of media equaling the result of dividing the length of ray paths by the propagation time of seismic waves from the seismic source to a receiver. In recent years, passive velocity tomography has been extensively used to predict the rock burst hazard in the field [36, 37]. In this part, the wave velocity field is inverted based on the internal wave velocity obtained from the AE source events. Same as the chapter of the spatial distribution of AE events and failure mode, we take 1a1-A1 and 1a1-D2 samples as examples for illustration.

According to the theory of passive velocity tomography, the P-wave velocity variations are linked to the changes of stress. Therefore, the high-velocity zones in tomograms are representing the high-stress zones. In addition, the wave velocity propagation is also related to the physical and mechanical properties of rock and structural properties of the rock mass.

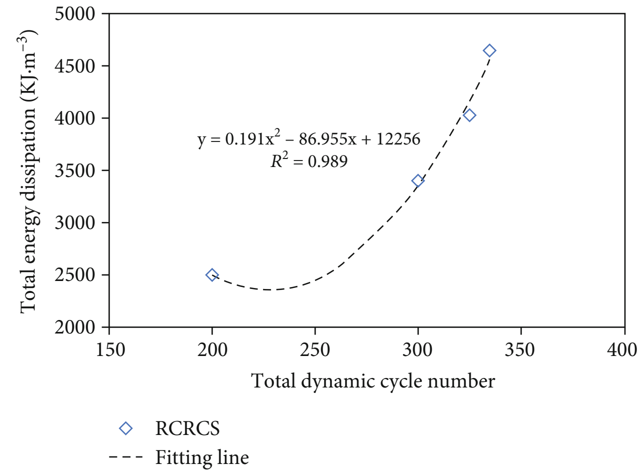

Figure 10: Relation of total amount of energy dissipation and total dynamic cyclic number.

Figure 14(a) indicates that the high-velocity area is mainly concentrated in the middle of the coal and roof siltstone parts in the initial stress level of the 1a1-A1 combined sample, but its concentration is limited. Subsequent cyclic dynamic loads lead to a more concentrated area of wave velocity anomaly, and the degree of concentration is getting higher. Due to the abundant cracks generated inside the RCRCS near the final failure, the strength of the combined structure is reduced and entered a yielding state; the range of high-velocity area is reduced.

Figure 14(b) indicates that the high-velocity area is mainly concentrated in the coal parts of the 1a1-D2 combined sample, while the low-velocity area is scattered around the RCRCS. Due to the high coal body height, it has become the main area that mainly participates in the destruction, and it is also the concentrated area of the high wave velocity abnormal area. The elastic core region is the energy storage region of the RCRCS, which provides the driving force of impact failure in the final failure. The wave velocity distribution is well consistent with the spatial distribution of AE events and failure mode.

4. Discussion

The theoretical model as shown in Figure 15 is established on the basis of the above laboratory experiment results, to deepen the understanding of the impact mechanism of coal-rock mass under coupled static and dynamic loads.

Thanks to the study, it is possible to show the mechanism of rock burst under coupled static and dynamic stresses. Figure 15 plots the energy transfer in the roof-coal-floor systems during the coal burst process under coupled static and dynamic loading. The stress behavior of the surrounding rock is displayed on the left-hand side; the stiffness and strength are both higher than coal. The stress behavior of coal is displayed on the right-hand side, and coal is assumed to be a softening material with nonlinear behavior. In the roof-coal-floor combined system, if the strain $\Delta\varepsilon_2$ is produced in the coal sample under the static load, the corresponding strain will be produced synchronously in the

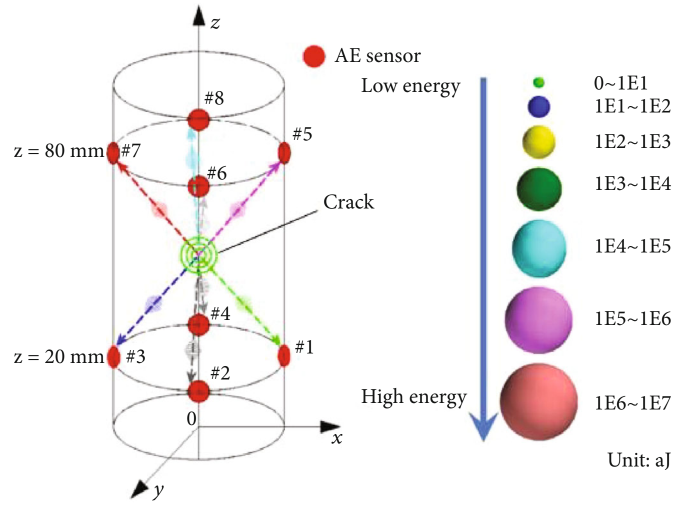

Figure 11: Layout of AE monitoring system and categorization of AE events.

surrounding rock (roof and floor) $\Delta\varepsilon_1$; the relationship between $\Delta\varepsilon_1$ and $\Delta\varepsilon_2$ can be expressed as

$$\Delta\varepsilon_1 = \frac{k_2}{k_1}\Delta\varepsilon_2, \tag{7}$$

where k_1 is the stiffness of surrounding rock and k_2 is the stiffness of coal. Therefore, the total strain of the roof-coal-floor system can be written as

$$\Delta\varepsilon = \Delta\varepsilon_1 + \Delta\varepsilon_2 = \frac{k_1 + k_2}{k_1}\Delta\varepsilon_2. \tag{8}$$

Therefore, the ratio of coal strain to total strain can be written as

$$\frac{\Delta\varepsilon_2}{\Delta\varepsilon} = \frac{1}{1 + (k_2/k_1)}. \tag{9}$$

From Equation (9), if we just consider static load, the process from stability to the instability of coal can be divided into four stages:

(1) Stage AB: both k_1 and k_2 are larger than zero; the coal and surrounding rock are both in the elastic energy storage stage

(2) Stage BD: the coal first enters the inelastic deformation stage. k_1 is still larger than zero, while k_2 gradually decreased to zero at the peak point D. At this time, the coal begins to transform the elastic energy stored into plastic deformation, and the surrounding rock is still in the elastic energy storage stage

(3) Stage DS: the carrying capacity of the coal body gradually loses, and k_2 turns into a negative value. During this process, the roof-coal-floor combined system may undergo an unstable process, when $k_1 + k_2 = 0$, $\Delta\varepsilon_2/\Delta\varepsilon \longrightarrow \infty$. The strain of the roof-coal-floor system expands rapidly in an instant, and the energy accumulated in the coal sample and surrounding rock is released together, which will trigger the overall failure, corresponding to the occurrence of rock burst

(4) Stage SE: the instability of the coal body slows down gradually; the roof-coal-floor system reaches the next stable energetic state, which corresponds to the calm period after the occurrence of the rock burst

When the roof-coal-floor system is subjected to the superposition of external static and dynamic loading stress (σ_s and σ_d), which can be equivalent to a condition that the stiffness of the surrounding rock decreases from k_1 to $k_1^{'}$. In this context, there are two different situations: (1) disturbance dynamic stress: when the cyclic dynamic load is applied under a low-stress level, it is easier to cause the expansion of microcracks inside the RCRCS, accompanied by small fluctuations in the stress value and a series of AE events, but it will not induce impact instability. (2) Impact-derived dynamic stress: when the cyclic dynamic load is applied near the instability, the stress is more likely to evolve along a path in the 1-2-4 direction, rather than the 1-3-D-4. The additional input energy will be larger, and the coal failure process will be more violent. Therefore, the equivalent energy decrease of the stiffness of the surrounding rock will be more remarkable.

5. Conclusions

The mechanical properties and damage behavior mechanisms of RCRCS under coupled static and dynamic loads were investigated in terms of strain-stress curve, loading and unloading modulus, AE events distribution and failure modes, and wave velocity field. Compared with the failure laws of single coal or rock materials, the prediction of the failure of rock-coal-rock is more complex and difficult. After the investigations, the results can be concluded as follows:

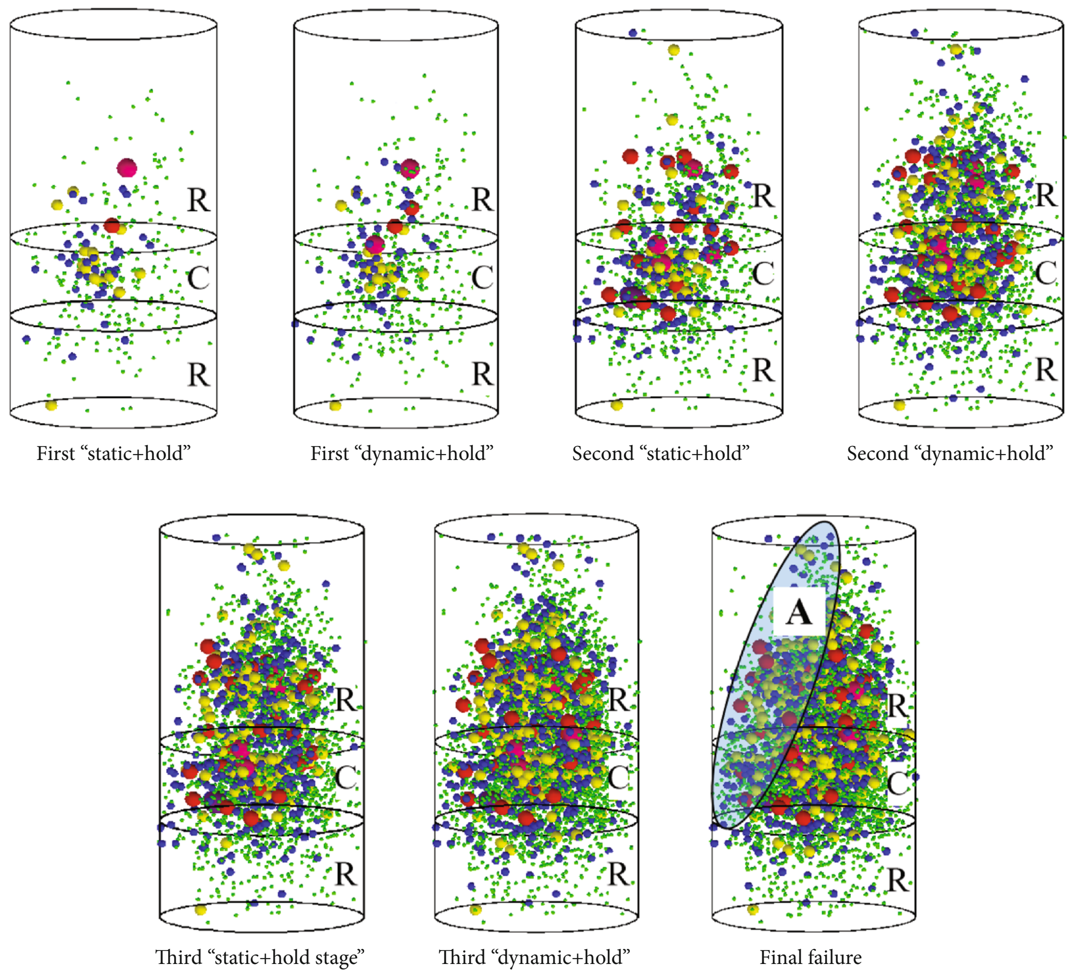

(a)

Figure 12: Continued.

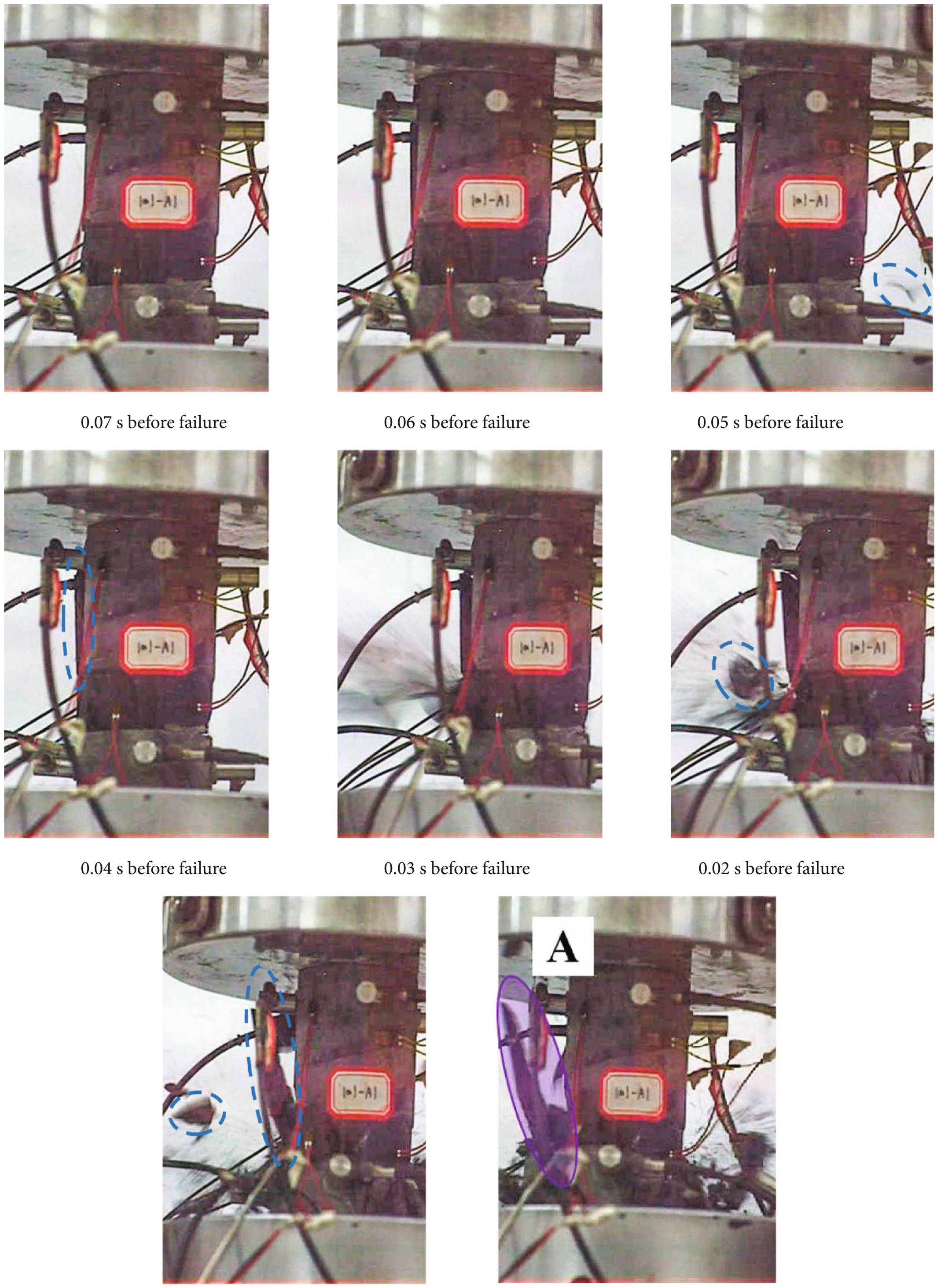

0.07 s before failure

0.06 s before failure

0.05 s before failure

0.04 s before failure

0.03 s before failure

0.02 s before failure

0.01 s before failure

Final failure

(b)

Figure 12: (a) Spatial distribution of AE events for each stress level of the 1a1-A1 specimen. (b) Failure process of 1a1-A1 specimen captured by high-speed camera.

(1) The peak strength of the RCRCS under coupled static and dynamic loads is strongly affected by the coal height. The coal height versus the peak strength curve is divided into three stages, namely, intensive decline stage (0~20%), moderate decrease stage (20~50%), and stable stage (50~100%)

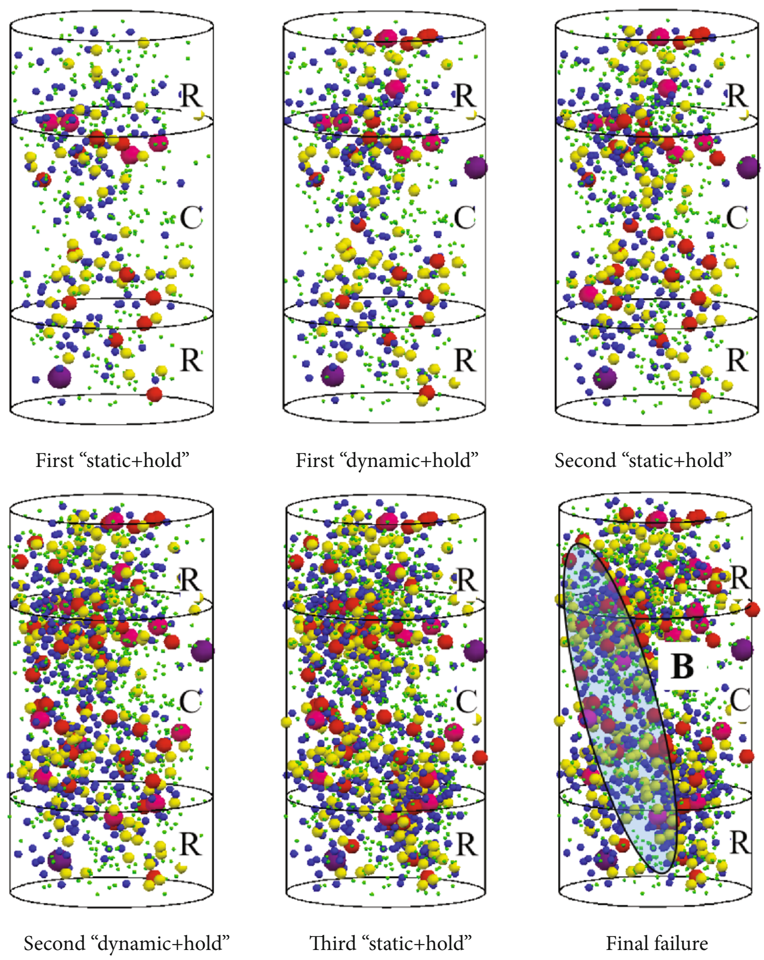

(a)

Figure 13: Continued.

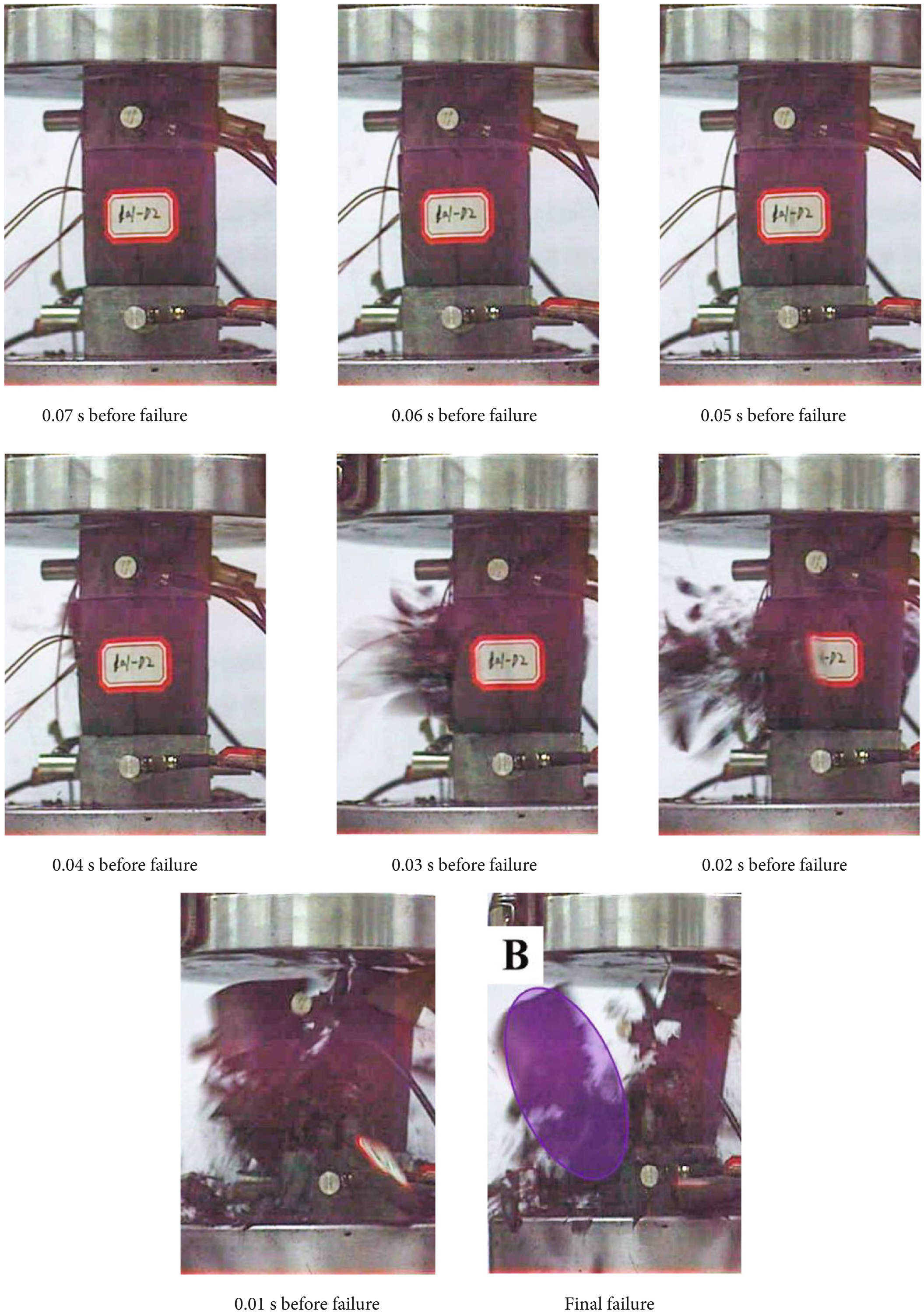

(b)

FIGURE 13: (a) Spatial distribution of AE events for each stress level of the 1a1-D2 specimen. (b) Failure process of 1a1-D2 specimen captured by high-speed camera.

(2) The loading and unloading modulus remain basically consistent for the same levels of dynamic load, while there is a slight decrease at high-stress levels. The coal height ratio of 40% may be the limit for the stable value of modulus values. For higher coal contribution in the combined samples, it starts cracking under higher loads, and consequent cycles of dynamic loads and modulus values decrease.

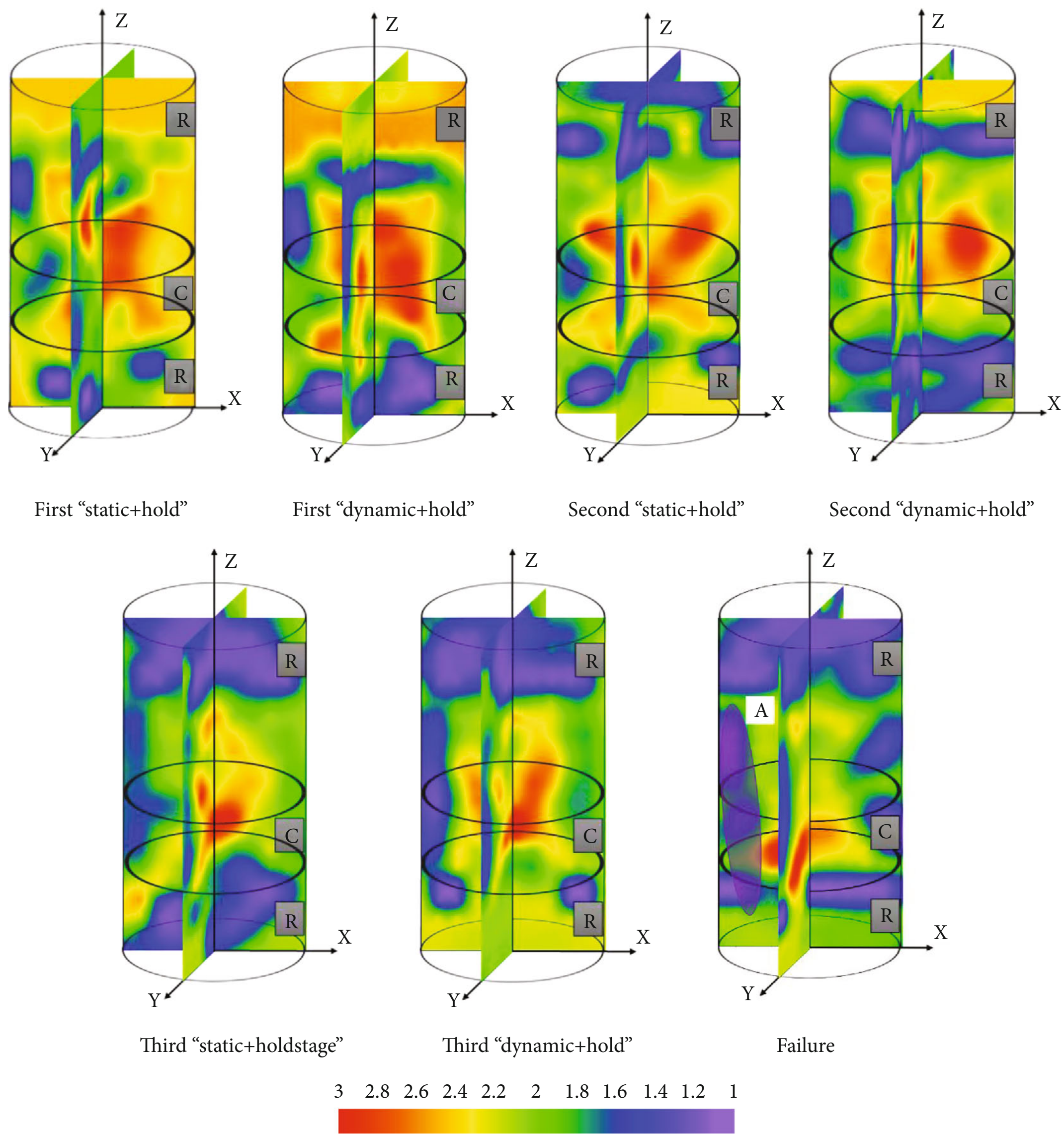

(a) 1a1-A1

Figure 14: Continued.

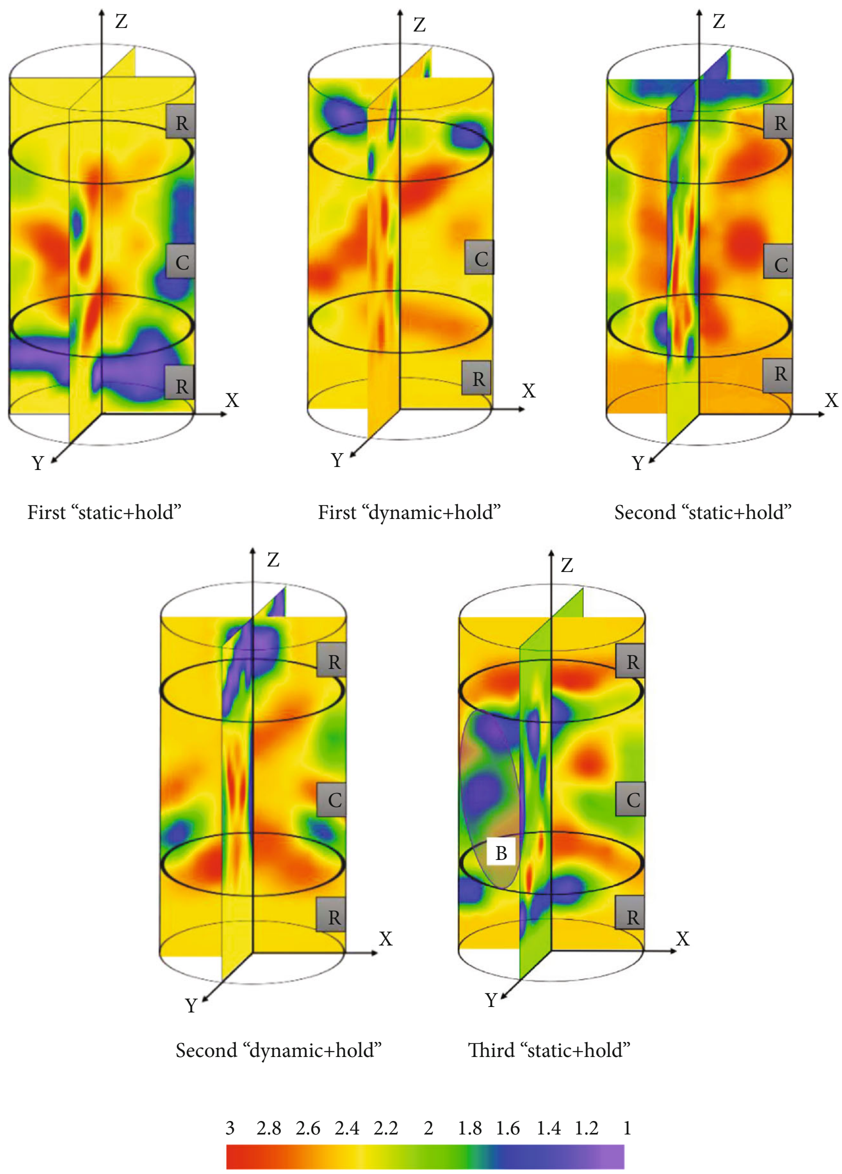

(b) 1a1-D2

FIGURE 14: Acoustic wave velocity distribution.

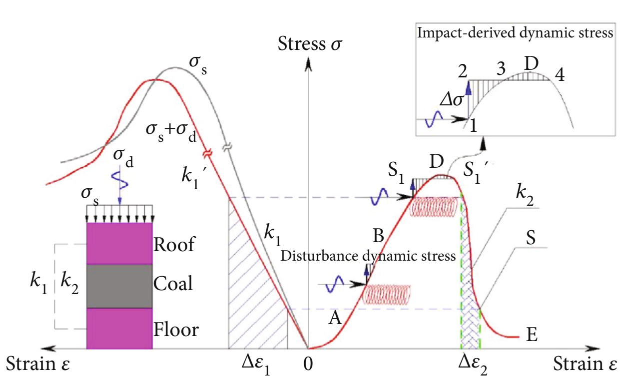

FIGURE 15: Energy transfer in roof-coal-floor system during the coal burst process under coupled static and dynamic loading.

Moreover, the loading and unloading modulus increase with the stress level

(3) When the coal height ratio is 20%, the damage first initiates in the coal sample, then more and more cracks appear in the roof sample. Otherwise, it will be manifested as the combined damage of the ejection damage of the coal body and the splitting of the roof and floor rocks. The results are consistent with the distribution of passive wave velocity

(4) The physical model of RCRCS tested under coupled static and dynamic stresses explains very well the mechanism of rock burst, which takes place in underground mining

Data Availability

The data used to support the findings of this study are available from the corresponding author upon request.

Conflicts of Interest

The authors declare no conflict of interest.

Acknowledgments

The authors are grateful for the financial support from the National Natural Science Foundation of China (Grant nos. 51874292 and 51804303) and Postgraduate Research & Practice Innovation Program of Jiangsu Province (KYCX21_2342).

References

[1] P. K. Kaiser and M. Cai, "Design of rock support system under rockburst condition," *Journal of Rock Mechanics and Geotechnical Engineering*, vol. 4, no. 3, pp. 215–227, 2012.

[2] W. D. Ortlepp and T. R. Stacey, "Rockburst mechanisms in tunnels and shafts," *Tunnelling and Underground Space Technology*, vol. 9, no. 1, pp. 59–65, 1994.

[3] M. Cai, "Principles of rock support in burst-prone ground," *Tunnelling and Underground Space Technology*, vol. 36, pp. 46–56, 2013.

[4] J. R. Cao, L. M. Dou, G. A. Zhu, J. He, S. Wang, and K. Zhou, "Mechanisms of rock burst in horizontal section mining of a steeply inclined extra-thick coal seam and prevention technology," *Energies*, vol. 13, no. 22, p. 6043, 2020.

[5] Y. D. Jiang, Y. X. Zhao, H. W. Wang, and J. Zhu, "A review of mechanism and prevention technologies of coal bumps in China," *Journal of Rock Mechanics and Geotechnical Engineering*, vol. 9, no. 1, pp. 180–194, 2017.

[6] T. Li, M. F. Cai, and M. Cai, "A review of mining-induced seismicity in China," *International Journal of Rock Mechanics and Mining Sciences*, vol. 44, no. 8, pp. 1149–1171, 2007.

[7] Z. J. Wen, X. Wang, Y. L. Tan, H. L. Zhang, W. P. Huang, and Q. H. Li, "A study of rockburst hazard evaluation method in coal mine," *Shock and Vibration*, vol. 2016, Article ID 8740868, 9 pages, 2016.

[8] W. Cai, X. Q. Bai, G. Si, W. Z. Cao, S. Gong, and L. Dou, "A monitoring investigation into rock burst mechanism based on the coupled theory of static and dynamic stresses," *Rock Mechanics and Rock Engineering*, vol. 53, no. 12, pp. 5451–5471, 2020.

[9] Q. Ma, Y. L. Tan, X. S. Liu, Q. H. Gu, and X. B. Li, "Effect of coal thicknesses on energy evolution characteristics of roof rock-coal-floor rock sandwich composite structure and its damage constitutive," *Composites Part B: Engineering*, vol. 198, article 108086, 2020.

[10] M. C. He, F. Q. Ren, and D. Q. Liu, "Rockburst mechanism research and its control," *International Journal of Mining Science & Technology*, vol. 28, no. 5, pp. 829–837, 2018.

[11] W. C. Zhu, Z. H. Li, L. Zhu, and C. A. Tang, "Numerical simulation on rockburst of underground opening triggered by dynamic disturbance," *Tunnelling and Underground Space Technology*, vol. 25, no. 5, pp. 587–599, 2010.

[12] X. S. Liu, Y. L. Tan, J. G. Ning, Y. W. Lu, and Q. F. Gu, "Mechanical properties and damage constitutive model of coal in coal-rock combined body," *International Journal of Rock Mechanics and Mining Sciences*, vol. 110, pp. 140–150, 2018.

[13] I. M. Petukhov and A. M. Linkov, "The theory of post-failure deformations and the problem of stability in rock mechanics," *International Journal of Rock Mechanics and Mining Sciences & Geomechanics Abstracts*, vol. 16, no. 2, pp. 57–76, 1979.

[14] T. B. Zhao, X. B. Gu, W. Y. Guo et al., "Influence of rock strength on the mechanical behavior and P-velocity evolution of coal-rock combination specimen," *Journal of Materials Research and Technology*, vol. 12, no. 1, pp. 1113–1124, 2021.

[15] J. P. Zuo, Z. Wang, H. Zhou, J. Pei, and J. Liu, "Failure behavior of a rock-coal-rock combined body with a weak coal interlayer," *International Journal of Mining Science & Technology*, vol. 23, no. 6, pp. 907–912, 2013.

[16] Y. L. Chen, J. P. Zuo, D. Liu, and Z. Wang, "Deformation failure characteristics of coal–rock combined body under uniaxial compression: experimental and numerical investigations," *Bulletin of Engineering Geology and the Environment*, vol. 78, no. 5, pp. 3449–3464, 2019.

[17] Z. H. Zhao, W. M. Wang, L. H. Wang, and C. Q. Dai, "Compression–shear strength criterion of coal–rock combination model considering interface effect," *Tunnelling and Underground Space Technology*, vol. 47, pp. 193–199, 2015.

[18] J. Li, J. Zhao, S. Y. Gong et al., "Mechanical anisotropy of coal under coupled biaxial static and dynamic loads," *International Journal of Rock Mechanics and Mining Sciences*, vol. 143, no. 3, article 104807, 2021.

[19] F. Q. Gong, J. Y. Yan, X. B. Li, and S. Luo, "A peak-strength strain energy storage index for rock burst proneness of rock materials," *International Journal of Rock Mechanics and Mining Sciences*, vol. 117, pp. 76–89, 2019.

[20] M. Zhang, L. M. Dou, H. Konietzky, Z. Song, and S. Huang, "Cyclic fatigue characteristics of strong burst-prone coal: experimental insights from energy dissipation, hysteresis and micro-seismicity," *International Journal of Fatigue*, vol. 133, article 105429, 2020.

[21] F. Q. Gong, H. Ye, and Y. Luo, "The effect of high loading rate on the behaviour and mechanical properties of coal-rock combined body," *Shock and Vibration*, vol. 2018, Article ID 4374530, 9 pages, 2018.

[22] L. H. Hu, Y. C. Li, X. Liang, C. A. Tang, and L. B. Yan, "Rock damage and energy balance of strainbursts induced by low frequency seismic disturbance at high static stress," *Rock Mechanics and Rock Engineering*, vol. 53, no. 11, pp. 4857–4872, 2020.

[23] H. W. Zhang, Z. J. Wan, Y. Zhang, and D. Wu, "Mechanical properties and failure behavior of composite samples," *Advances in Materials Science and Engineering*, vol. 2018, Article ID 2545127, 16 pages, 2018.

[24] C. E. Fairhurst and J. A. Hudson, "Draft ISRM suggested method for the complete stress-strain curve for intact rock in uniaxial compression," *International Journal of Rock Mechanics and Mining Sciences & Geomechanics Abstracts*, vol. 36, no. 3, pp. 279–289, 1999.

[25] J. He, L. M. Dou, S. Y. Gong, J. Li, and Z. Q. Ma, "Rock burst assessment and prediction by dynamic and static stress analysis based on micro-seismic monitoring," *International Journal of Rock Mechanics and Mining Sciences*, vol. 93, pp. 46–53, 2017.

[26] A. Taheri and F. Tatsuoka, “Small- and large-strain behaviour of a cement-treated soil during various loading histories and testing conditions,” *Acta Geotechnica*, vol. 10, no. 1, pp. 131–155, 2014.

[27] R. Ulusay and J. A. Hudson, *The complete ISRM suggested methods for rock characterization, testing and monitoring: 1974-2006*, International Society for Rock Mechanics: ISRM Turkish National Group, Ankara, Turkey, 2009.

[28] P. Małkowski, Ł. Ostrowski, and J. Brodny, “Analysis of Young's modulus for Carboniferous sedimentary rocks and its relationship with uniaxial compressive strength using different methods of modulus determination,” *Journal of Sustainable Mining*, vol. 17, no. 3, pp. 145–157, 2018.

[29] D. Lei, P. Zhang, J. T. He, P. X. Bai, and F. P. Zhu, “Fatigue life prediction method of concrete based on energy dissipation,” *Construction and Building Materials*, vol. 145, no. 2017, pp. 419–425, 2017.

[30] R. Tepfers, B. Hedberg, and G. Szczekocki, “Absorption of energy in fatigue loading of plain concrete,” *Matériaux et Construction*, vol. 17, no. 1, pp. 59–64, 1984.

[31] R. Vidya Sagar, D. S. Mohit, S. Deepak, and P. R. Desai, “Statistical analysis of acoustic emissions generated during unconfined uniaxial compression of cementitious materials,” *Construction and Building Materials*, vol. 225, no. 20, pp. 692–708, 2019.

[32] M. Naderloo, M. Moosavi, and M. Ahmadi, “Using acoustic emission technique to monitor damage progress around joints in brittle materials,” *Theoretical and Applied Fracture Mechanics*, vol. 104, article 102368, 2019.

[33] X. Wang, Z. J. Wen, Y. J. Jiang, and H. Huang, “Experimental study on mechanical and acoustic emission characteristics of rock-like material under non-uniformly distributed loads,” *Rock Mechanics and Rock Engineering*, vol. 51, no. 3, pp. 729–745, 2018.

[34] L. H. Tan, T. Ren, X. H. Yang, and X. Q. He, “A numerical simulation study on mechanical behaviour of coal with bedding planes under coupled static and dynamic load,” *International Journal of Mining Science and Technology*, vol. 28, no. 5, pp. 791–797, 2018.

[35] P. Sedlak, Y. Hirose, S. A. Khan, M. Enoki, and J. Sikula, “New automatic localization technique of acoustic emission signals in thin metal plates,” *Ultrasonics*, vol. 49, no. 2, pp. 254–262, 2009.

[36] K. Luxbacher, E. Westman, P. Swanson, and M. Karfakis, “Three-dimensional time-lapse velocity tomography of an underground longwall panel,” *International Journal of Rock Mechanics and Mining Sciences*, vol. 45, no. 4, pp. 478–485, 2008.

[37] N. Hosseini, “Evaluation of the rockburst potential in longwall coal mining using passive seismic velocity tomography and image subtraction technique,” *Journal of Seismology*, vol. 21, no. 5, pp. 1101–1110, 2017.

Hindawi
Geofluids
Volume 2021, Article ID 3095690, 13 pages
https://doi.org/10.1155/2021/3095690

Research Article

An Analysis of the Impact of Deviatoric Stress and Spherical Stress on the Stability of Surrounding Rocks in Roadway

Liu Rui [1] **and Zhu Quanjie** [2]

[1] *School of Energy and Mining Engineering, China University of Mining and Technology (Beijing), 100083 Beijing, China*
[2] *School of Emergency Technology and Management, North China Institute of Science and Technology, Beijing 101601, China*

Correspondence should be addressed to Liu Rui; bukaopu999@gmail.com

Received 27 June 2021; Accepted 5 August 2021; Published 31 August 2021

Academic Editor: Hualei Zhang

In this study, a detailed analysis was conducted to evaluate the impacts of the deviatoric stress component and spherical stress component on the stability of surrounding rocks in the roadway via the theoretical analysis and calculation and numerical simulation. Based on the analysis, the distribution laws guiding the main stress differences, plastic zone, convergence of surrounding rocks, and third invariant of stress under various conditions (such as equal spherical stress and unequal deviatoric stress and equal deviatoric stress and unequal spherical stress) were developed, providing an optimization scheme for roadway support misunderstanding under the conditions of high spherical stress field and high deviator stress field. The study further reveals that under the circumstance of the constant spherical stress, the greater the deviatoric stress, the plastic zone range of the surrounding rock of the roadway, the range of tensile deformation of the surrounding rock, the amount of convergence of the surrounding rock, the probability of separation of the roof and floor of the roadway, and the principal stress difference and the main stress, the greater the concentration range of the maximum stress difference is, and the maximum principal stress difference is mainly concentrated in the roof and floor rocks of the roadway, and the greater the deviatoric stress, the greater the probability that the roof and floor rocks of the roadway will be separated, and the maximum principal stress difference is mainly concentrated in the roof and floor rocks of the roadway, the greater the deviator stress, the greater the concentration range of the maximum value of the principal stress difference and the principal stress difference; when the deviator stress is constant, the range of the plastic zone and the maximum principal stress difference concentration range of the surrounding rock of the roadway decrease with the increase of the ball stress, and the principal stress difference, the amount of convergence of the surrounding rock, and the range of tensile deformation increase with the increase of the ball stress. The maximum principal stress difference is mainly concentrated in the roof and floor rocks of the roadway. The principal stress difference increases with the increase of the spherical stress, and the maximum concentration range of the principal stress difference decreases with the increase of the spherical stress. After the method proposed in this paper optimizes the actual roadway support on site, the surrounding rock deformation of the roadway is small and the control is relatively ideal, which basically meets the engineering needs.

1. Introduction

Ground stress has been considered as the fundamental force causing deformations and damages in various underground excavation projects [1, 2] and one of the important bases for designing the support and protection system of the underground projects. Ground stress has been divided into two categories including self-weight stress and horizontal tectonic stress. Therefore, scholars domestically and abroad have invested substantial time and energy in researching the impacts of self-weight stress [3–6] and horizontal tectonic stress [7–10] on the stability of the roadway surrounding rocks.

Based on plastic mechanics, the stress of surrounding rocks can be categorized into spherical stress tensor and deviatoric stress tensor, with the former one deciding the shape changes of the rocks and the latter one dominating the volume changes [11]. Substantial studies have been conducted to explore the distribution laws of spherical stress of roadway surrounding rocks and plastic zone. Ma et al. researched the deviatoric stress field and the distribution law of plastic zone when the roadway surrounding rocks are exposed to uneven stresses [12]. Yu et al. investigated the impacts of deviatoric stress on the plastic zone distribution of roadway surrounding rocks, resulting in the identification of an instability model of the roadway under various lateral pressure coefficients [13]. Xie et al. studied the variance law of deviatoric stress of deep roadway surrounding rocks and proposed asymmetric control technology of surrounding rocks based on various sections [14]. He et al. focused their studies on the structural stress of deep roadway surrounding rocks at high elevation including the damage and the distribution of deviatoric stress, along with corresponding controlling measures [15]. Xu et al. took the superelevation section of a coal mine track in Shanxi as the research object, used UDEC to simulate the deviatoric stress distribution of the surrounding rock of the roadway at different roadway heights, compared the degree of deviatoric stress changes between the roof and floor and the two sides of the roadway, and finally proposed targeted support technology [16]. Luo et al. thoroughly studied the influence of the intermediate principal stress and the rheological properties of the surrounding rock on the displacement of the surrounding rock of the roadway and the plastic zone of the surrounding rock and finally found that ignoring the rheological properties of the rock would overestimate the lithology of the surrounding rock. In control roadway deformation and plastic zone expansion [17], Zhang et al. used the D-P yield criterion to calculate the analytical solutions for the elastoplasticity, plastic zone radius, and displacement of the surrounding rock under bidirectional isobaric conditions and discovered the importance of the intermediate principal stress to the stress distribution of the surrounding rock [18]. According to the D-P yield criterion and the nonassociated flow rule, Chen et al. derived a closed analytical solution for the stress, deformation, and radius of the plastic zone of the surrounding rock of a deep circular roadway under hydrostatic pressure [19].

Scholars have conducted sufficient studies on the deviatoric stress distribution of roadway surrounding rocks and the distribution law of the plastic zone after the roadway excavation. However, limited studies have been performed on the impacts of both spherical stress tensor and deviatoric stress tensor before the roadway excavation on the roadway stability after excavation. Therefore, in this study, a detailed analysis was conducted to evaluate the impacts of deviatoric stress component and spherical stress component on the stability of surrounding rocks in roadway via the theoretical analysis and calculation, numerical simulation, and two sets of loading tests.

2. Loading Plan and Numerical Model

2.1. Loading Plan and the Analysis of Principal Stress Difference of Roadway Surrounding Rock. A plan including two sets of loading tests was proposed to study the impacts of the deviatoric stress component and spherical stress component on the stability of surrounding rocks in the roadway. The detailed loading plan is provided below.

A loading test was performed at a constant spherical stress component ($p = 15$ MPa) and various deviatoric stress components ($q = 2.4$ MPa, 7.2 MPa, 12 MPa, and 16.8 MPa). In other words, during this loading test, constant spherical stress was imposed on the model with different deviatoric stresses.

A loading test was performed at a constant deviatoric stress component ($q = 12$ MPa) and various spherical stress components ($p = 9$ MPa, 12 MPa, 15 MPa, and 18 MPa). In other words, during this loading test, constant deviatoric stress was imposed on the model with different spherical stresses.

$$p = \frac{1}{3}(\sigma_1 + \sigma_2 + \sigma_3), \tag{1}$$

$$q = \frac{1}{\sqrt{2}}\sqrt{(\sigma_1 - \sigma_2)^2 + (\sigma_2 - \sigma_3)^2 + (\sigma_3 - \sigma_1)^2}. \tag{2}$$

Equation (3) can be obtained based on equations (1) and (2) listed above.

$$\begin{Bmatrix} \sigma_1 \\ \sigma_2 \\ \sigma_3 \end{Bmatrix} = \begin{Bmatrix} p \\ p \\ p \end{Bmatrix} + \frac{2}{3}q \begin{Bmatrix} \sin\left(\theta_\sigma + \frac{2}{3}\pi\right) \\ \sin\theta_\sigma \\ \sin\left(\theta_\sigma - \frac{2}{3}\pi\right) \end{Bmatrix}, \tag{3}$$

where p refers to spherical stress, q indicates deviatoric stress, and θ_σ is the loading angle.

A stress space diagram was obtained from equation (3) and illustrated in Figure 1.

The strain increment of the deep surrounding rocks under the plastic strain state demonstrated pure shear deformation with the maximum shear stress dominating the generation of the stratum plastic zone and development [20, 21]. The principal stress difference can reflect the shear stress distribution and the damage in the surrounding rocks [22, 23]. The principal stress difference can be illustrated in

$$\sigma_s = \sigma_1 - \sigma_3. \tag{4}$$

Based on the elasticity theory, the stress of the circular hole in the two-way stress infinite plate is shown in

$$\begin{cases} \sigma_r = \frac{1}{2}(\sigma_v + \sigma_H)\left(1 - \frac{R_0^2}{r^2}\right) - \frac{1}{2}(\sigma_v - \sigma_H)\left(1 - 4\frac{R_0^2}{r^2} + 3\frac{R_0^4}{r^4}\right)\cos 2\theta, \\ \sigma_\theta = \frac{1}{2}(\sigma_v + \sigma_H)\left(1 + \frac{R_0^2}{r^2}\right) + \frac{1}{2}(\sigma_v - \sigma_H)\left(1 + 3\frac{R_0^4}{r^4}\right)\cos 2\theta, \\ \tau_{r\theta} = \frac{1}{2}(\sigma_H - \sigma_v)\left(1 + 2\frac{R_0^2}{r^2} - 3\frac{R_0^4}{r^4}\right)\sin 2\theta, \end{cases} \tag{5}$$

where σ_v refers to the vertical stress in MPa, σ_H indicates

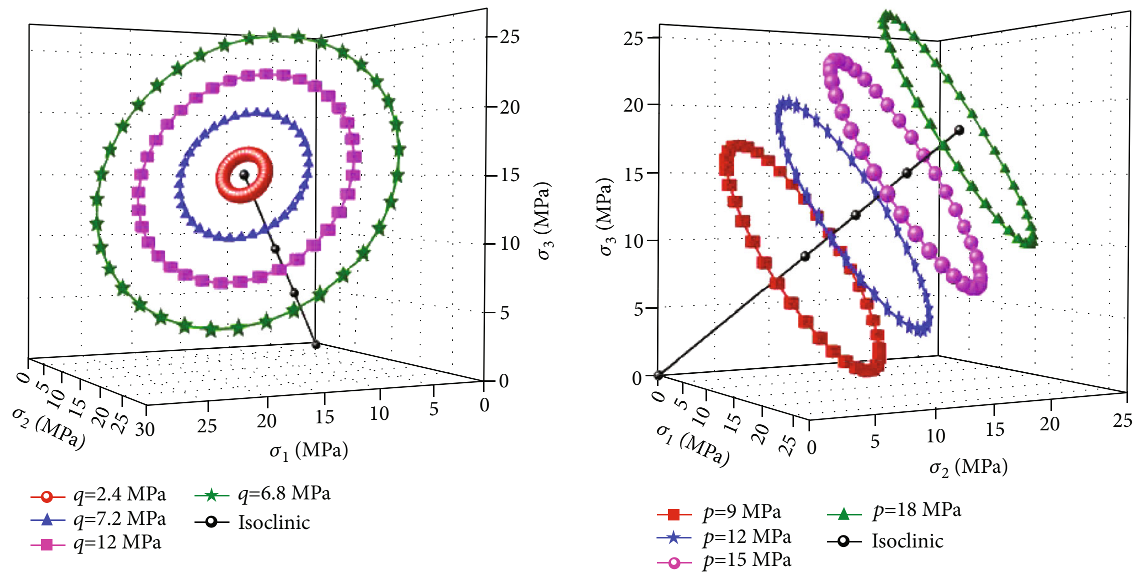

(a) The stress space diagram under the constant deviatoric stress (b) The stress space diagram under the constant spherical stress

Figure 1: The distribution of stress and space.

the horizontal stress in MPa, R_0 is the radius of the circular hole in m, and θ represents the polar angle.

Under the state of the plane strain, the principal stress can be calculated following

$$\sigma_1 = \frac{\sigma_x + \sigma_y}{2} + \sqrt{\left(\frac{\sigma_x + \sigma_y}{2}\right)^2 + \tau_{xy}^2}, \tag{6}$$

$$\sigma_3 = \frac{\sigma_x + \sigma_y}{2} - \sqrt{\left(\frac{\sigma_x + \sigma_y}{2}\right)^2 + \tau_{xy}^2}, \tag{7}$$

where σ_1 refers to the maximum principal stress in MPa and σ_3 indicates the minimum principal stress in MPa. Equations (6) and (7) can be converted into equations (8) and (9) under polar coordinates.

$$\sigma_1 = \frac{1}{2}(\sigma_r + \sigma_\theta) + \frac{1}{2}\sqrt{(\sigma_r - \sigma_\theta)^2 + 4\tau_{r\theta}^2}, \tag{8}$$

$$\sigma_3 = \frac{1}{2}(\sigma_r + \sigma_\theta) - \frac{1}{2}\sqrt{(\sigma_r - \sigma_\theta)^2 + 4\tau_{r\theta}^2}. \tag{9}$$

Considering the roadway as the plane strain allows the overlook of the principal stress, based on equations (3) and (5), equation (10) can be obtained.

$$\begin{Bmatrix} \sigma_H \\ \sigma_v \end{Bmatrix} = \begin{Bmatrix} p \\ p \end{Bmatrix} + \frac{2}{3}q \begin{Bmatrix} \sin\left(\theta_\sigma + \frac{2}{3}\pi\right) \\ \sin\left(\theta_\sigma - \frac{2}{3}\pi\right) \end{Bmatrix}. \tag{10}$$

Under various deviatoric stresses, -10° load was selected for load while -20° load was selected under various spherical stresses. Based on equation (4) to equation (10), the surrounding principal stress differences of the circular hole under various conditions were obtained and presented in Figure 2.

Based on Figure 2, the following results can be obtained. (1) Under constant spherical stress, as the deviatoric stress increases, the principal stress difference on the vertical direction tends to increase accordingly, with the principal stress difference of shallow surrounding rocks greater than that of deep surrounding rocks. Horizontally, the principal stress difference of shallow surrounding rocks decreases as the deviatoric stress increases while the principal stress difference of deep surrounding rocks increases. Overall, the vertical principal stress difference is greater than the horizontal one. (2) Under constant deviatoric stress, as the spherical stress increases, the vertical principal stress difference increases, with the principal stress difference of shallow surrounding rocks greater than that of deep surrounding rocks. Horizontally, the principal stress difference of shallow surrounding rocks increases as the spherical stress increases while the principal stress difference of deep surrounding rocks decreases. Overall, the vertical principal stress difference is greater than the horizontal one.

2.2. Numerical Model and Parameters. A numerical simulation was performed to analyze the impacts of deviatoric stress and spherical stress on the stability of surrounding rocks in the roadway. In the simulation model, the cross section of the roadway was designed in a semicircular arch, with a height of 3500 mm and a width of 4000 mm. The calculation range was set at 50 m × 50 m. The sides and the bottom of the model limited the horizontal and vertical displacements. The rock mass mechanical parameters of each rock stratum are shown in Table 1. Stresses were loaded to the model following the loading plan listed in Section 2.1.

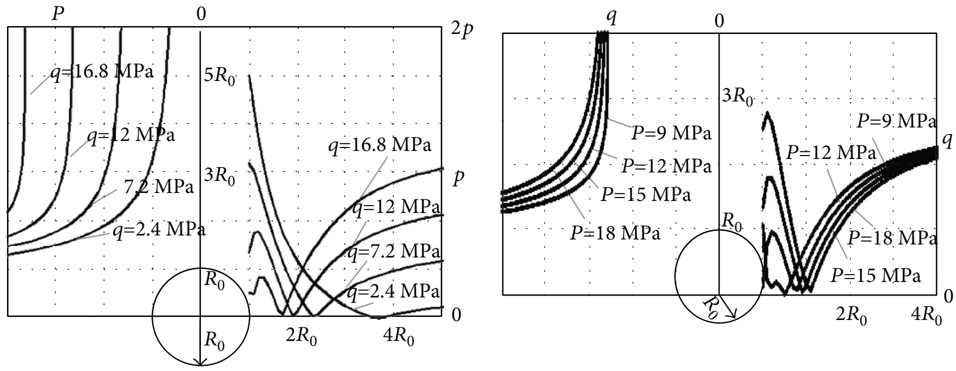

(a) The surrounding principal stress differences of the circular hole under a constant deviatoric stress

(b) The surrounding principal stress differences of the circular hole under a constant spherical stress

Figure 2: The distribution of principal stress difference around circular hole.

Table 1: The rock mass mechanical parameters.

Rock formation	ρ (kg·cm^{-3})	K (GPa)	G (GPa)	Cohesion (MPa)	R_m (MPa)	α (°)
Upper rock mass	2600	8.82	4.63	4.0	2.6	34
Limestone	2800	5.57	4.53	8.4	4.7	38
Argillaceous siltstone	2570	13.4	7.5	2.5	1.8	32
Medium sandstone	2580	3.3	2.5	1.6	1.3	25
Siltstone	2620	7.52	3.1	1.9	1.2	26
Sand shale	2660	5.7	3.4	1.8	1.7	26
Sandy mudstone	2500	3.68	2.15	1.5	1.12	28
Lower rock mass	2695	5.2	4.1	3.3	2.12	35

3. The Test Results under a Constant Spherical Stress

3.1. The Distribution Law of the Principal Stress Difference of the Roadway Surrounding Rocks. With FLAC^{3D}, a cloud diagram shown in Figure 3 was drafted to demonstrate the principal stress difference of the roadway surrounding rocks under constant spherical stress and various deviatoric stresses.

From Figure 3, the following results can be obtained. (1) When $q = 2.4$ MPa, the maximum principal stress difference concentrated within 2 to 5 m range of the roadway surrounding rocks, with maximum principal stress difference observed in the lower stratum of the surrounding rocks. As the deviatoric stress increased, the maximum principal stress difference continued to increase, which is consistent with the trend demonstrated in Figure 2(a), suggesting a higher shear resistance needed in the anchor bolt (cable) installed in the roadway roof in a high deviatoric stress field. (2) As the deviatoric stress increased, the concentration zone of the maximum principal stress in the roadway surrounding rock continued to expand and migrate to the deep layers of rocks, which suggests that longer anchor cables are needed to keep anchor cables fixed to the roof for the purpose of support protection. (3) The deviatoric stress had limited impacts on the principal stress difference of the roadway sides.

3.2. The Variance Law of the Plastic Zone of the Roadway Surrounding Rocks. The distribution of the plastic zone contributes to the identification of the supported depth. The distribution of plastic zone under various deviatoric stresses is demonstrated in Figure 4. The damage depth of the surrounding rock corresponding to the deviatoric stress is shown in Figure 5.

Based on Figures 4 and 5, the following results can be drawn. (1) As the deviatoric stress increases, the plastic zone in the roadway roof grows large, suggesting that longer supporting plates are needed to enhance the stability of the roadway in a high deviatoric stress field, which is consistent with Figure 3. (2) When $q < 16.8$ MPa, the increase of deviatoric stress tends to have limited impacts on the damage of roadway sides. When $q = 16.8$ MPa, the damage of roadway sides increases drastically. Taking Figure 3 into consideration, the maximum principal stress difference concentrates in the lower stratum of the roadway roof. In addition, higher deviatoric stress leads to a larger maximum principal stress difference concentration zone. Therefore, the expansion of the maximum principal stress difference concentration zone is the main cause of the drastic increases in the damage of roadway sides, indicating that proper support and protection are critical to prevent the roadway instability caused by the damage of roadway sides under high deviatoric stress.

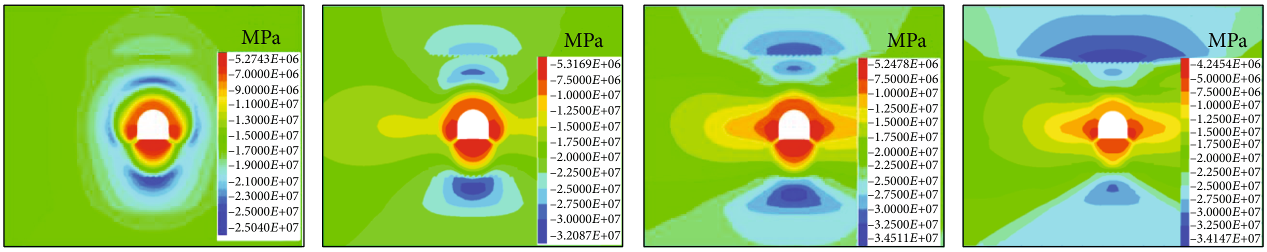

Figure 3: The principal stress difference under different deviatoric stresses.

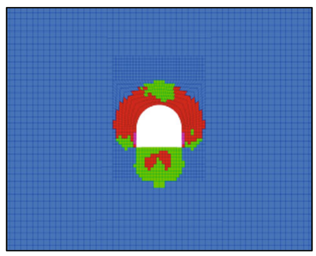

(a) $q = 2.4$ MPa

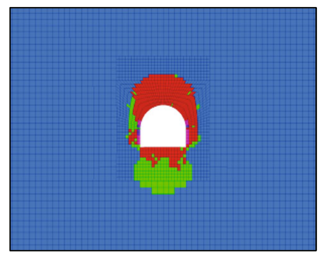

(b) $q = 7.2$ MPa

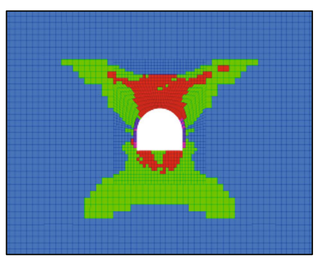

(c) $q = 12$ MPa

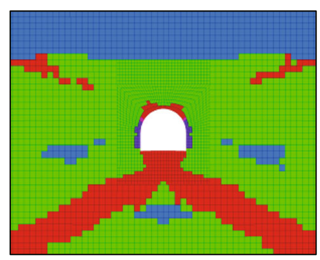

(d) $q = 16.8$ MPa

Figure 4: The distribution of plastic zone under various deviatoric stresses. Blue is no damage, red is raw shear failure, and green is shear failure has occurred.

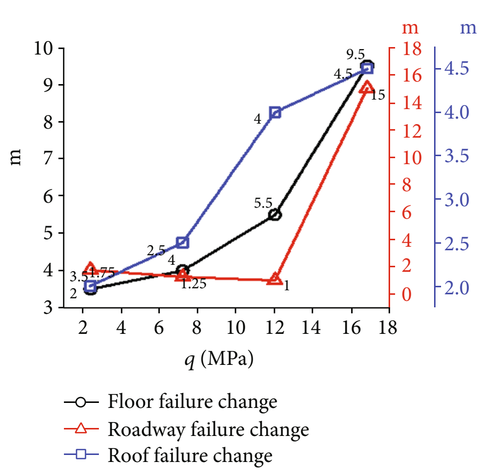

Figure 5: The damage depth of the surrounding rocks corresponding to the deviatoric stress.

3.3. The Deformation Law of the Surrounding Rocks. The deformation degree of the surrounding rocks can reflect the need for ductility of the support system. Under various deviatoric stresses, the deformation of the roadway surrounding rocks from the surface to the depth is demonstrated in Figure 6.

According to Figure 6, (1) the displacement of surrounding rock from shallow to deep decreases in a “logarithmic” pattern, until reaching stability. (2) When $q > 7.2$ MPa, negative displacement was observed at the 3 m of roadway floor in-depth and 2 m of roadway roof, which suggests that in the floor, the deep rock stratum submerges while the shallow ones rise. On the other hand, the deep rock stratum rises while the shallow ones submerge in the roof. The observations suggest that higher deviatoric stress tends to increase the probability of separation in the roadway roof and floor, resulting in a higher possibility of roof collapse and bottom drum. (3) The surface displacement of the roadway can reflect the maximum deformation of the roadway surrounding rocks, the damage of the shallow surrounding rocks, and separation. According to Figure 6, as the deviatoric stress increases, the surface displacement of the roadway increases in a linear pattern. When q increased above 2 MPa, the surface displacement of the roadway decreases, which suggests that when q is higher than 12 MPa, the deep stratum in the roadway roof starts to rise substantially, resulting in a reduced convergence of the surrounding rocks.

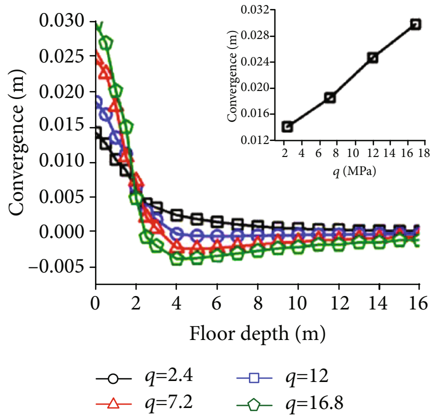

(a) Deformation of surrounding rock of floor

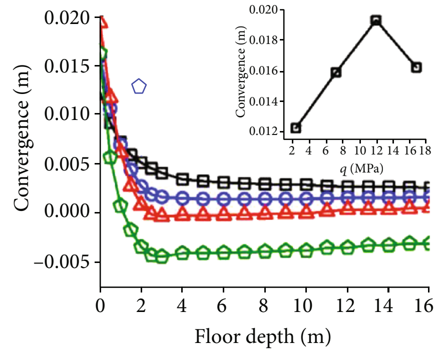

(b) Deformation of roof confining pressure

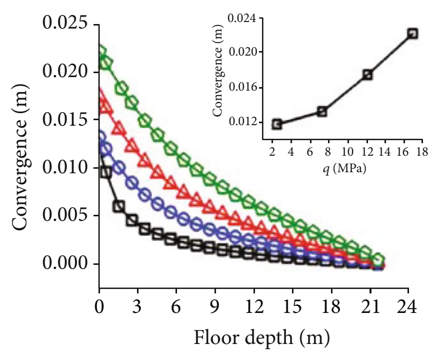

(c) Deformation of surrounding rock of roadside

Figure 6: The convergence of surrounding rocks under various deviatoric stresses.

3.4. The Distribution Law of the Third Invariant of Deviatoric Stress in Surrounding Rocks. The third invariant of deviatoric stress J_3 can be used to identify the deformation type of the surrounding rocks. When $J_3 < 0$, the deformation is categorized as compressive deformation. When $J_3 = 0$, the deformation is considered as planar deformation. When $J_3 > 0$, the deformation is rated as tensile deformation [8]. The third invariant of deviatoric stress J_3 can be a comprehensive index of combining the maximum principal stress, minimum principal stress, and medium principal stress, indicating the deformation type of the surrounding rocks. The third invariant of deviatoric stress J_3 can be expressed in

$$J_3 = \left(\frac{2\sigma_1 - \sigma_2 - \sigma_3}{3}\right)\left(\frac{2\sigma_2 - \sigma_3 - \sigma_1}{3}\right)\left(\frac{2\sigma_3 - \sigma_1 - \sigma_2}{3}\right). \tag{11}$$

A cloud diagram shown in Figure 7 was obtained to demonstrate the third invariant under various deviatoric stresses. According to Figure 7, when $q = 2.4$ MPa, a tensile stress zone was observed within 0.3 to 2.5 m range of the roadway surrounding rocks. As the deviatoric stress increases, the tensile stress zone expands, resulting in a larger tensile stress concentration zone in roadway sides and bottom than the roof. Due to the poor tensile strength of the rocks, high tensile stress can jeopardize the stability of the roadway surrounding rocks. Therefore, a high pretorque value should be adopted to the supporting system of the roadway surrounding rocks in a high deviatoric stress field to enhance the load capacity of the surrounding the rocks in roadway.

4. The Test Results under a Constant Deviatoric Stress

4.1. The Distribution Law of the Principal Stress Difference of the Roadway Surrounding Rocks. A cloud diagram shown in Figure 8 was drafted to demonstrate the principal stress difference of the roadway surrounding rocks under constant deviatoric stress and various spherical stresses.

According to Figure 8, (1) as the spherical stress increases, the maximum principal stress concentration range in the deep surrounding rocks tends to decrease, suggesting that in a high spherical stress field, the layout and installation of the anchor bolts and cables should avoid the principal stress concentration zone for better supporting and stability. (2) As the spherical stress increases, the principal stress difference increases in the surrounding rocks of the roadway bottom, which is consistent with Figure 2(b), demanding a higher shear resistance in the anchor bolts and cables. (3) The spherical stress exerts some influences on the principal stress difference of the shallow surrounding rocks in the roadway sides. However, such influence is limited to the deep surrounding rocks, which is also

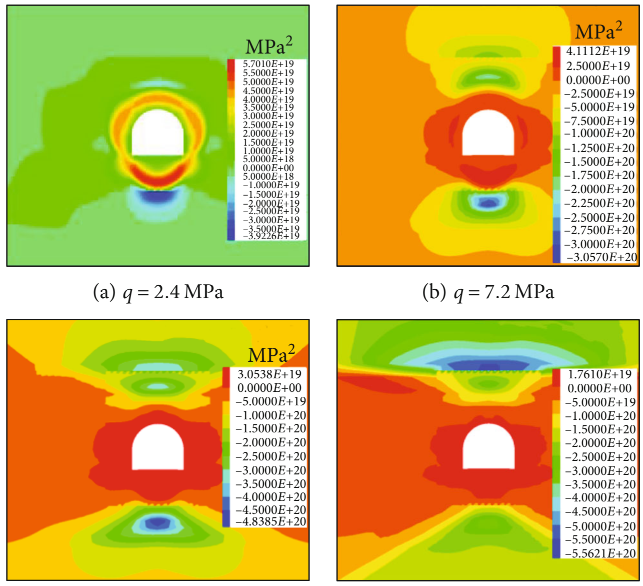

(a) $q = 2.4$ MPa (b) $q = 7.2$ MPa

(c) $q = 12$ MPa (d) $q = 16.8$ MPa

Figure 7: The J_3 distribution under various deviatoric stresses.

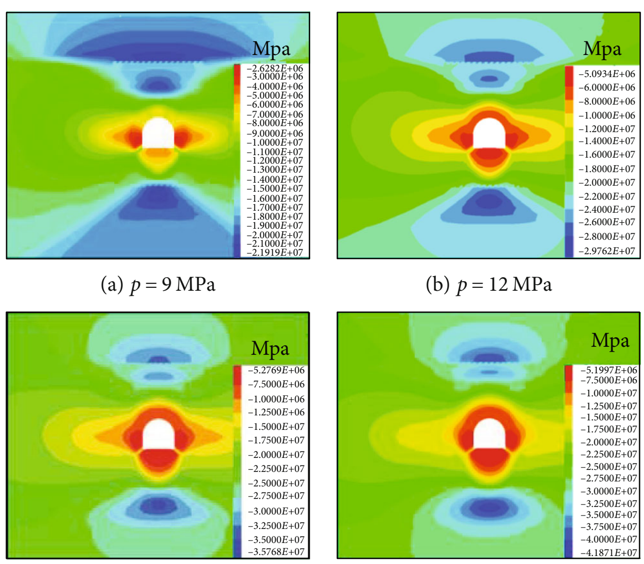

(a) $p = 9$ MPa (b) $p = 12$ MPa

(c) $p = 15$ MPa (d) $p = 18$ MPa

Figure 8: Principal stress difference of the surrounding rocks.

demonstrated in Figure 2(b), resulting in a lower shear resistance requirement to the supporting and protection system of the roadway sides.

4.2. The Deformation Law of the Surrounding Rocks. The distribution of plastic zone under various spherical stresses is demonstrated in Figure 9. The damage depth of the surrounding rock corresponding to the spherical stress is shown in Figure 10.

According to Figures 9 and 10, (1) as the spherical stress increases, the plastic zone of the roadway surrounding rocks tends to decrease due to the increased surrounding pressure on the roadway surrounding rocks under higher spherical stress. In other words, a higher surrounding pressure leads to a higher strength of the surrounding rock and a smaller plastic zone. (2) Under various spherical stresses, the plastic zone of the roadway surrounding rock demonstrates a butterfly shape. The spherical stress only impacts the range of the plastic zone instead of the shape. Comparing with Figure 5 has revealed that the deviatoric stress tends to exert a greater impact on the surrounding rocks of the roadway. (3) The damage depth of the roadway surrounding rocks demonstrates a higher sensitivity to the spherical stress while the damage of the roadway sides is less sensitive.

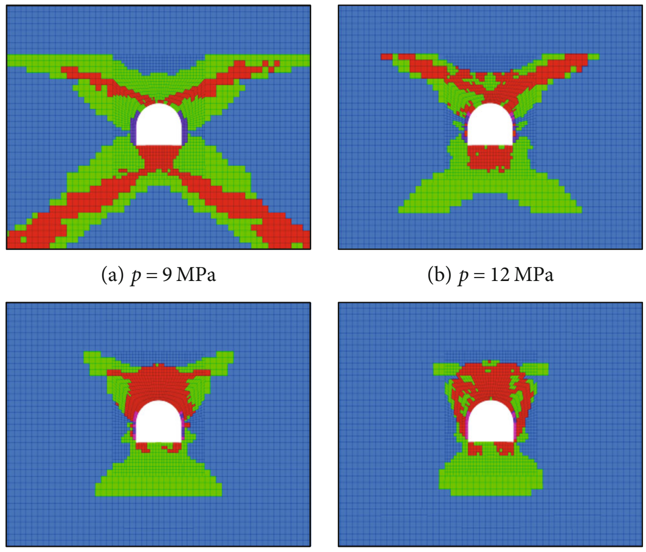

(a) $p = 9$ MPa (b) $p = 12$ MPa

(c) $p = 15$ MPa (d) $p = 18$ MPa

FIGURE 9: The distribution of plastic zone under various spherical stresses.

4.3. The Deformation Law of the Surrounding Rocks. The deformation of the roadway surrounding rocks under various spherical stresses is demonstrated in Figure 11.

According to Figure 11, (1) a threshold depth has been observed in rating the impact of spherical stress on the roadway surrounding rocks. When the spherical stress is higher than the threshold depth, the deformation is limited with a low degree of dispersion associated with the surrounding rock deformation. When the spherical stress is lower than the threshold depth, the deformation is severe with a high degree of dispersion associated with the surrounding rock deformation. (2) Under low spherical stress, the convergences in the deep and shallow surrounding rocks of roadway are negative and positive, respectively. As the spherical stress increases, the convergences from the deep to the shallow surrounding rocks become positive, suggesting that the increase of the spherical stress can lower the probability of the stratum separation. (3) As the spherical stress increases, the convergence value of the roadway surface surrounding rocks follows a linear growth.

4.4. The Distribution Law of the Third Invariant of Deviatoric Stress in Surrounding Rocks. A cloud shown in 12 was developed to demonstrate the distribution of the third invariant of deviatoric stress in the roadway surrounding rocks under various spherical stresses.

According to Figure 12, when $p = 9$ MPa, the roadway surrounding rocks are under pressure as a whole. When $p = 12$ MPa, a tensile stress zone was spotted around the roadway shallow rocks. As the spherical stress increased, multiple tensile stress zones were observed in the roadway sides and surrounding rocks of the roof. In other words, as the spherical stress increases, the tensile stress zone expands in the roadway surrounding rocks, reducing the loading capacity of the surrounding rocks. Therefore, in a high spherical stress environment, a high pretorque value should be

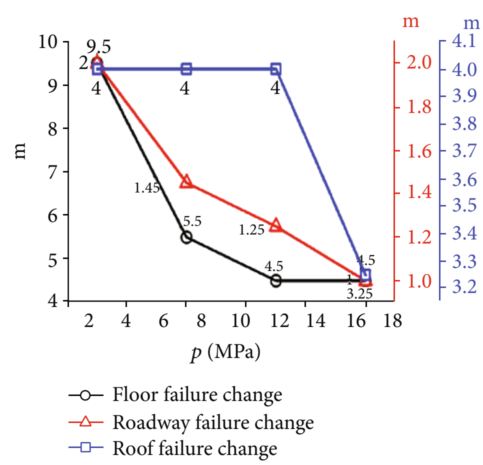

FIGURE 10: The damage depth of the surrounding rocks corresponding to the spherical stress.

adopted to the supporting system of the roadway surrounding rocks to enhance the load capacity of the surrounding rocks in roadway.

5. The Instability Analysis of the Roadway Surrounding Rocks

5.1. The Analysis of the Impact of Deviatoric Stress on the Instability of the Roadway Surrounding Rocks. Taking equation (2) into consideration, the actual deviatoric stress of the roadway surrounding rocks depends on the ratio of three principal stresses instead of the individual value of three principal stresses, which is known as the lateral pressure coefficient. In other words, the deviatoric stress of the roadway surrounding rocks in a deep roadway under high ground stress does not necessarily lead to high deviatoric

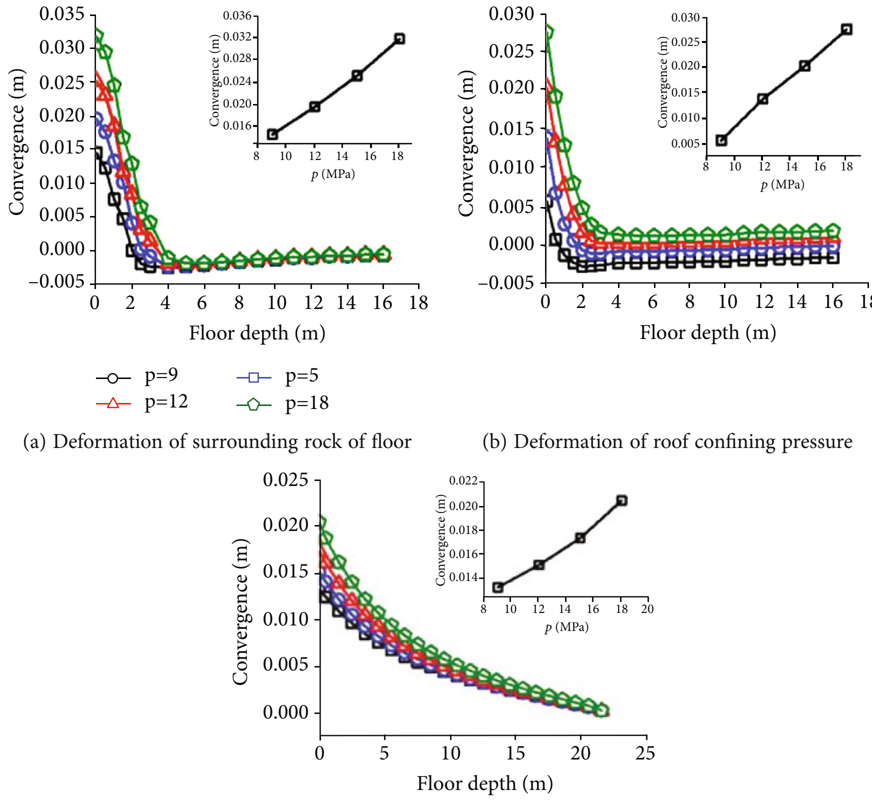

(a) Deformation of surrounding rock of floor

(b) Deformation of roof confining pressure

(c) Deformation of surrounding rock of roadside

Figure 11: The convergence of roadway surrounding rock under various spherical stresses.

stress. The deviatoric stress of the roadway surrounding rocks in a shallow roadway under high ground stress does not necessarily lead to low deviatoric stress either. According to the analysis in Section 3, the deviatoric stress tends to play a critical role in influencing the stability of the roadway surrounding rocks. In fields, many shallow roadways under low stresses tend to experience roof collapse and ground drums, such as the roadway located in the mines of the Shendong area. Therefore, according to the analysis in Section 3 along with the field investigation, some common misunderstandings have been identified to the support and protection system in the shallow surrounding rocks under low stress.

Firstly, according to Figures 4 and 5, the deviatoric stress tends to have a significant impact on the damage range and depth of the roadway surrounding rocks. However, regarding the shallow roadway under high deviatoric stress, the impacts of the stress on the stability of the roadway surrounding rocks are often overlooked during the design of the support and protection system, assuming that due to the shallow location of the roadway, no additional support system is needed, leading to a design of support and protection system shown in Figure 13.

As a result, the support and protection system lacks solid anchor points, accompanied by anchor bolts and cables following the movements of the surrounding rocks.

According to Figure 6 and the analysis in Section 3.3, as the deviatoric stress increases, the convergence of the roadway surrounding rocks increases accordingly, along with potential separation in the roadway roof. Without a strong support system such as a low elongation in anchor bolts and cables, a low support density, and a low strength in the metal protection net, the protection system could risk a total failure, resulting in severe deformation in the roadway sides including roof collapse and floor drums.

According to Figure 7, as the deviatoric stress increases, the tensile deformation continues to expand in the roadway surrounding rocks. Due to the poor tensile strength of the rocks, the expansion of the tensile deformation contributes to the increasing of the plastic zone and decreasing of the roadway stability, which is also reflected in Figure 4. With a low rigid support and protection system, such as a low pretorque value and poor timing for the installation of the support and protection system, a large tensile deformation zone can occur in the surrounding rocks, resulting in the continuous expansion of the plastic zone and severe deformation to the surrounding rocks in a high deviatoric stress environment.

5.2. The Analysis of the Impact of Spherical Stress on the Instability of the Roadway Surrounding Rocks. According to equation (1), the spherical stress value mainly depends on three principal stresses. It is commonly known that a greater depth leads to higher spherical stress. Based on Section 4, the spherical stress exerts a significant impact on the damage range of the roadway surrounding rocks, bearing capacity, and the deformation of the surrounding rocks.

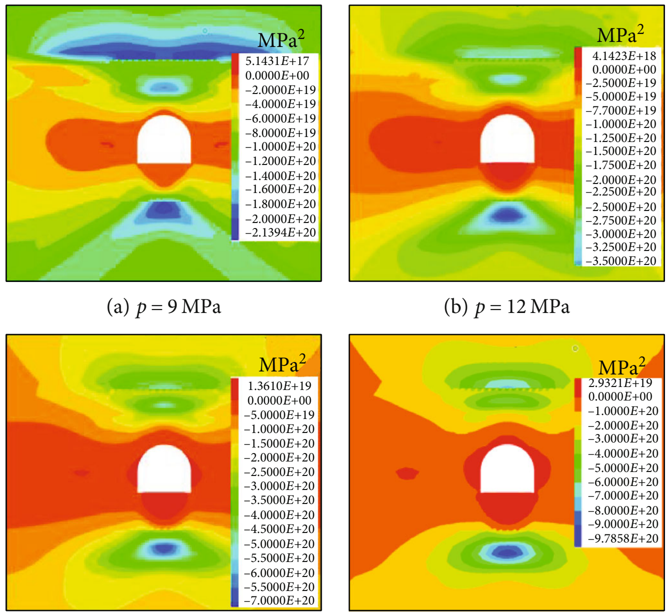

(a) $p = 9$ MPa (b) $p = 12$ MPa

(c) $p = 15$ MPa (d) $p = 18$ MPa

Figure 12: The J_3 distribution under various spherical stresses.

Therefore, according to the analysis in Section 4 and Figure 14 along with the field investigation, some common misunderstandings have been identified to the support and protection system in the shallow surrounding rocks under low stress including increasing the supported depth of the anchor bolts and cables blindingly and lacking specificity in the design of the support system.

In the fields, engineers and designers are misled to believe that a deeper roadway tends to experience more severe damage, resulting in increasing the supported depth blindingly. Based on the analysis in Sections 3 and 4, the damage range of the roadway surrounding rocks increases along with the increase of deviatoric stress and decrease of the spherical stress. As a result, regarding a roadway in an environment featured with high spherical stress and low deviatoric stress, the damage of the surrounding rocks should be limited, eliminating the need of increasing the supported depth. However, the increase of spherical stress tends to lead to the increase in the deformation of the roadway surrounding rocks, principal stress difference, and tensile stress zone, demanding a support system featured with high strength, shear resistance, and contractibility. Therefore, for the deep roadway in an environment featured with high spherical stress and low deviatoric stress, the support system should be improved by increasing the strength, shear resistance, and contractibility instead of the supported depth.

Due to insufficient theoretic guidance, the understandings of the critical factors of the stability of roadway surrounding rocks are limited. For instance, as demonstrated in Figure 9, the damage of the surrounding rocks concentrated in the roadway shoulders and bottom corners instead of the roadway sides. Therefore, the roadway shoulders and bottom corners should be the main protection targets.

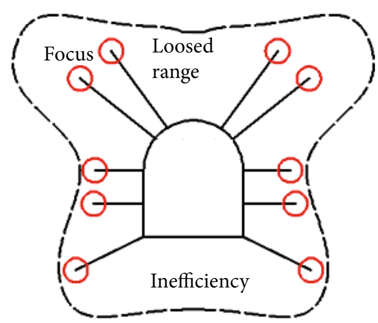

Figure 13: Misled roadway support system under a high deviatoric stress.

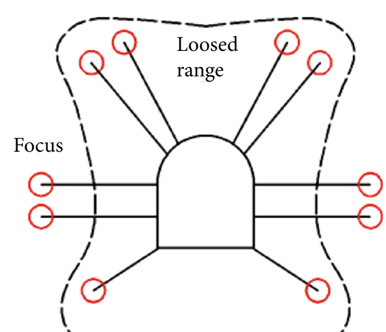

Figure 14: The roadway support misunderstanding under a high spherical stress.

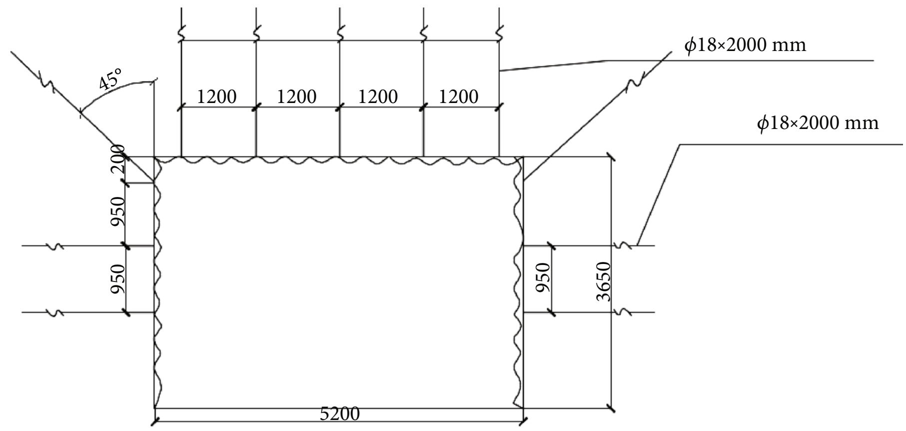

Figure 15: Original supporting plan.

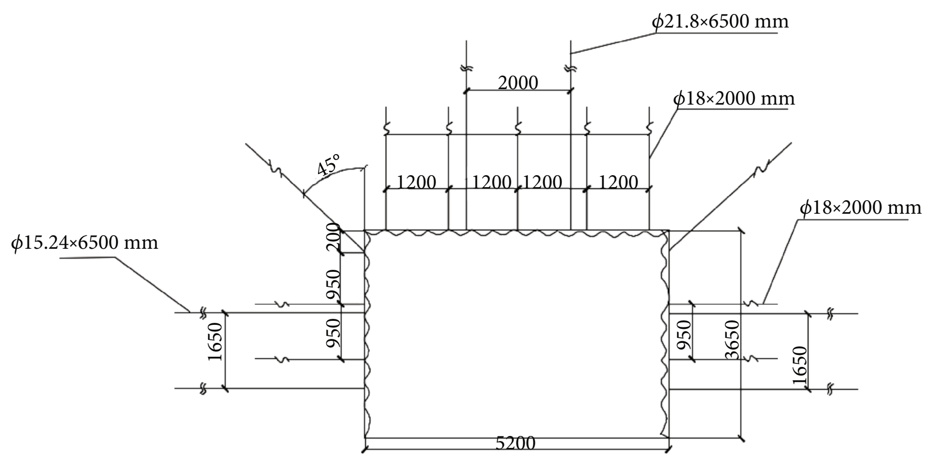

Figure 16: Modified support plan.

6. Engineering Validation

6.1. Project Overview and Maintenance Measures. A mine located in Inner Mongolia was selected for the purpose of engineering validation. The mining focuses on the #3 coal seam with an average thickness of 5 m, categorized as a horizontal coal seam with an average depth of 275 m. Currently, 310 working face is about 300 m away from the stopping mining line. No. 311 working face is featured with a through open cut. The transportation roadway of the No. 311 working face is 230 m away from the No. 310 goaf. Therefore, the No. 311 transportation roadway is not influenced by the mining process. Due to the depth of the #3 coal seam, the limited ground force, and relatively simple geological structure, supports were only added to the transportation roadway roof and sides, as demonstrated in Figure 15. The support system includes steel anchor rods in $\Phi 18\mathrm{mm} \times 2000\,\mathrm{mm}$, arranged in a triangular layout with a row distance of 1200 mm × 1100 mm. Roadway sides were protected with steel anchor rods in $\Phi 18\mathrm{mm} \times 2000\,\mathrm{mm}$, arranged in a flower layout with a row distance of 950 mm × 1100 mm.

After the installation of the support system demonstrated in Figure 15, severe damage was spotted in the roof of the No. 311 transport roadway and roadway sides, with some anchor rod failures, such as migrating with the surrounding rocks, tears in the metal net, and more. Several deep damages concentrated on the roof along with maximum deformation of 200 mm in the bottom, risking roof collapse.

Considering the limited ground force at the location of No. 311 transport roadway and no influence from the mining process, No. 311 transport roadway damage was mainly caused by high deviatoric stress. Following the analysis in Section 3, the deformation of roadway surrounding rocks in a high deviatoric stress field is featured with large damage scale, large roadway surface displacement, potential stratum displacement in the roof, and large tensile stress zone, which were consistent with the deformation of No. 311 transport roadway. In addition, some improper designs were identified in the support plan of No. 311 transport roadway. Therefore, based on the research results, some adjustments were made to the original design plan shown in Figure 16.

Anchor cables can link the load structure of the anchor rods to the deep surrounding rocks, resulting in an interconnected and overlapped network structure in the effective stress zone, resulting in decreasing the tensile stress zone of the surrounding rocks and increasing the stability of the load-bearing structure [24]. Following this concept, the support design of the No. 311 transport roadway was modified as follows. In order to minimize the separation in the roof surrounding rocks and reduce the tensile zone, two additional high-strength and high-elongation prestressed steel strands (dimension of $\Phi 21.8\,\mathrm{mm} \times 6500\,\mathrm{mm}$) were added with a preload no less than120 kN. The distance between two strands was designed at $2000\,\mathrm{mm} \times 3300\,\mathrm{mm}$. Meanwhile, in order to control the roadway deformation and tensile deformation and improve the support efficiency of the anchor rods, two additional high-strength prestressed steel strands were added with a row distance of $1650\,\mathrm{mm} \times 3300$ mm. Besides, an inclined anchor rod was installed at the roadway sides, 15° in contrast with the horizontal direction for the purpose of improving the stability of roadway bottom corners.

6.2. The Analysis of the Modified Support System. Multiple monitoring and detection points were set up to keep track of the roadway surface displacements. The collected data indicated that with the modified support system, the deformation rate of the surrounding rocks was initially maintained at 8~20 mm/d with a higher deformation rate identified in the roadway sides and roof. A total of 4 changes were observed to the roadway sides and roof. The deformation rate demonstrated a downward trend. At day 37, the deformation reached stability, indicating an effective support and protection to the transport roadway.

7. Conclusion

For the principal stress difference distribution of the circular roadway surrounding rocks under various spherical stresses and deviatoric stresses via theoretical analysis, the calculation results were consistent with the numerical simulation.

(1) Under constant spherical stress, the plastic zone, the probability of stratum separation of the roof, the convergence of the surrounding rocks, and the tensile zone increase along with the deviatoric stress. The principal stress difference of the surrounding rocks and the concentration zone of the maximum principal stress difference tends to increase as the deviatoric stress increases

(2) Under constant deviatoric stress, as the spherical stress increases, the plastic zone decreases while the convergence of the surrounding rocks and the tensile zone increases. In addition, higher spherical stress increases the principal stress difference of the surrounding rocks. Meanwhile, the concentration zone of the maximum principal stress difference tends to decrease as the spherical stress increases

(3) Some common misunderstandings about the roadway support in a high spherical stress field and in a high deviatoric stress field were proposed, which was further validated in the field. The field test suggests that the modified support system following the research results can achieve effective protection and support

Data Availability

The data used to support the findings of this study are included within the article.

Conflicts of Interest

The authors declare that they have no conflicts of interest.

Acknowledgments

This research was financially supported by the central government guides local science and technology development fund projects (216Z5401G), Guizhou Province High-Level Innovative Talent Training Program Funding Project ([2019]5675), and Scientific Research Projects of Higher Education Institutions in Hebei Province (Z2020124).

References

[1] M. C. He, H. P. Xie, S. P. Peng, and Y. D. Jiang, “Study on mechanics in deep mining engineering,” *Chinese Journal of Rock Mechanics and Engineering*, vol. 24, no. 16, pp. 2803–2813, 2005.

[2] G. Wang, Y. Guo, P. Wang et al., “A new experimental apparatus for sudden unloading of gas-bearing coal,” *Bulletin of Engineering Geology and the Environment*, vol. 79, no. 2, pp. 857–868, 2020.

[3] Z. J. Wen, E. R. Xing, S. S. Shi, and Y. Jiang, “Overlying strata structural modeling and support applicability analysis for large mining-height stopes,” *Journal of Loss Prevention in the Process Industries*, vol. 57, pp. 94–100, 2019.

[4] K. Wang, Y. Guo, H. Xu, H. Dong, F. Du, and Q. Huang, “Deformation and permeability evolution of coal during axial stress cyclic loading and unloading: an experimental study,” *Geomechanics and Engineering*, vol. 24, no. 6, pp. 519–529, 2021.

[5] J. Chen, W. M. Cheng, G. Wang, H. Li, and Y. Li, “New method of monitoring the transmission range of coal seam water injection and correcting the monitoring results,” *Measurement*, vol. 177, p. 109334, 2021.

[6] J. Chen, W. M. Cheng, and G. Wang, “Simulation of the meso-macro-scale fracture network development law of coal water injection based on a SEM reconstruction fracture COHESIVE model,” *Fuel*, vol. 287, p. 119475, 2021.

[7] X. X. Yang, H. W. Jing, K. F. Chen, and W. L. Wang, “Study on influence law of in-situ stress in deep underground rocks on the size of failure zone in roadway,” *Journal of Mining & Safety Engineering*, vol. 30, no. 4, pp. 495–500, 2013.

[8] Y. F. Sun, “Affects of insitu horizontal stress on stability of surrounding rock roadway,” *Journal of China Coal Society*, vol. 35, no. 6, pp. 891–895, 2010.

[9] P. F. Gou, Z. P. Zhang, and S. J. Wei, "Physical simulation test of damage character of surrounding rock under different levels of the horizontal stress," *Journal of China Coal Society*, vol. 34, no. 10, pp. 1328–1332, 2009.

[10] C. Zhu, M. C. He, M. Karakus, X. Cui, and Z. Tao, "Investigating toppling failure mechanism of anti-dip layered slope due to excavation by physical modelling," *Rock Mechanics and Rock Engineering*, vol. 53, no. 11, pp. 5029–5050, 2020.

[11] F. L. He and G. C. Zhang, "Stability analysis and control of deepunderground roadway subjected to high horizontal tectonic stress," *Journal of China University of Mining & Technology*, vol. 44, no. 3, pp. 466–476, 2015.

[12] X. M. Chen, *Elastoplastic Mechanics*, Science Press, Beijing, 2007.

[13] N. J. Ma, J. Li, and Z. Q. Zhao, "Distribution of the deviatoric stress field and plastic zone in circular roadway surrounding rock," *Journal of China University of Mining & Technology*, vol. 44, no. 2, pp. 206–213, 2015.

[14] W. J. Yu, G. H. Wu, C. Yuan, P. Wang, and S. H. Shao, "Failure characteristics and engineering stability control of roadway," *Journal of China Coal Society*, vol. 42, no. 6, pp. 1408–1419, 2017.

[15] S. R. Xie, S. H. Yue, and D. D. Chen, "Deviatoric stress evolution laws and control of surrounding rock at gob-sideentry retaining in deep backfilling mining," *Journal of China Coal Society*, vol. 43, no. 7, pp. 1837–1846, 2018.

[16] F. L. He and G. C. Zhang, "Stablity analysis and control of deep underground roadways subjected to high horizontal tectonic stress," *Journal of China University of Mining & Technology*, vol. 44, no. 3, pp. 466–476, 2015.

[17] L. Xu, H. K. Wu, B. Li, and T. Q. Xiao, "Stability and control of surrounding rock in ultra-high roadway," *Chinese Journal of Rock Mechanics and Engineering*, vol. 33, no. S2, pp. 3891–3902, 2014.

[18] K. J. Luo, H. L. Dong, and Q. C. Gao, "Deformation division for surrounding rock of circular roadway by considering rheology and the intermediate principal stress," *Journal of China Coal Society*, vol. 42, no. S2, pp. 331–337, 2017.

[19] X. B. Zhang, G. M. Zhao, and X. R. Meng, "Elastoplastic analysis of surrounding rock on circular roadway based on druckerprager yield criterion," *Journal of China Coal Society*, vol. 38, no. S1, pp. 30–37, 2013.

[20] L. Chen, X. B. Mao, M. Li, and Y. L. Chen, "Elastoplastic analysis of cracked surrounding rock in deep roadway based on druckerprager criterion," *Journal of China Coal Society*, vol. 42, no. 2, pp. 484–491, 2017.

[21] Z. J. Wen, S. L. Jing, Y. J. Jiang et al., "Study of the fracture law of overlying strata under water based on the flow- stress-damage model," *Geofluids*, vol. 2019, Article ID 3161852, 12 pages, 2019.

[22] G. T. Yang, *Introduction to Elastoplastic Mechanics*, Tsinghua University Press, Beijing, 2004.

[23] X. Wang, Z. J. Wen, Y. J. Jiang, and H. Huang, "Experimental study on mechanical and acoustic emission characteristics of rock-like material under non-uniformly distributed loads," *Rock Mechanics and Rock Engineering*, vol. 51, no. 3, pp. 729–745, 2018.

[24] F. L. He, X. M. Wang, L. Xu, H. K. Wu, and J. Wang, "Principal stress difference transfer law and support in large-section open-off cut," *Rockand Soil Mechanics*, vol. 35, no. 6, pp. 1703–1710, 2014.

Hindawi
Geofluids
Volume 2021, Article ID 4336163, 9 pages
https://doi.org/10.1155/2021/4336163

WILEY | Hindawi

Review Article

The Integrated Development Strategy of Coastal Industrial Areas and City Based on Underground Space Development

Feng Shao, Pingyang Shi, Yusheng Ding, and Ce Dong

College of Architecture and Urban Planning, Qingdao University of Technology, Qingdao, Shandong 266033, China

Correspondence should be addressed to Feng Shao; 3411376@qq.com

Received 1 June 2021; Revised 7 July 2021; Accepted 13 August 2021; Published 27 August 2021

Academic Editor: Zhijie Wen

As a crucial node of Qingdao's construction of a modern international metropolis, a topnotch marine port, a demonstration zone for local economic and trade cooperation of the Shanghai Cooperation Organization (SCO), and an international shipping trade financial innovation center, the Qingdao Cruise Port warrants transformation to adapt to the future development of Qingdao city. Besides, with the constant increase in the intensity of urban underground space (UUS) development in Qingdao, the organic integration of underground space reconstruction and urban development in the cruise port area must be accentuated. Taking the underground space development project in Qingdao Cruise Port as the background, this study analyzes the multidimensional development and utilization of underground space in the project (the functional distribution of the two-dimensional plane and the stereo integration of the three-dimensional space). In addition, this study explores strategies to promote the organic integration of industrial areas and cities through underground space development. Expanding the research field of UUS, this study provides reference cases for the transformation of old industrial areas in other coastal cities.

1. Introduction

Industrial areas play a vital role in promoting the development of cities. However, with the development of cities, some industrial areas have slowly lost their original functions and are on the verge of being eliminated. Nevertheless, these old industrial areas occupy key geographical locations in cities, which have unique values. Thus, the research on the transformation of old industrial areas has become a hot topic in the architecture field. Meanwhile, to relieve the pressure of urban development, the development of urban underground space (UUS) has been increasingly focused upon because of its advantages of efficient use of land resources, high security, energy conservation, and environmental protection. Developing UUS is a critical way to build green and sustainable cities [1]. At present, people's research on UUS involves underground space planning, underground engineering, and sustainable development. With the development of cities and the transfer of urban industries, some industrial areas have been abandoned. These industrial areas require underground space development. The current research on underground space in industrial areas involves design principles [2], planning strategies [3], technological development [4], and development scale forecast [5]; however, the research on underground space in industrial areas and urban development factors is marginally scarce. Relatively limited research has been conducted on the correlation between the underground space of industrial zones and the elements of urban development. Thus, the exploration of related fields is warranted.

2. Status Quo of Research on Underground Space

2.1. Foreign Research on Underground Space. The Associated Research Centers for Urban Underground Space (ACUUS) conference is an international academic conference on UUS research. The theme of each conference reflects the current international research hotspots in the field of UUS. To date, 17 sessions of the ACUUS conference have been held. Initially, the conference focused on the advantages, structure, form, and development prospects. Later, the theme gradually shifted to the fields of underground space and planning, resources, economy, and environment. As the research progressed in the field, the themes of recent ACUUS conferences focused on the use of underground space development to attain sustainable urban development (Table 1).

2.2. China's Research on Underground Space. China's research on underground space has borrowed significantly from foreign advanced experience. "Comprehensive Utilization of Underground Space" published by a foreign magazine translated by Liantai [6] opened the gate to the research of underground space in China. Subsequently, Bihua [7] and Xu [8] learned a lot from foreign experience and start researching on related fields based on the actual situation in China. However, most research during this period focused on the fields of underground building design and underground space planning, rendering the research field incomprehensive. At the end of the twentieth century, Qihu [9] and Linxu [10] not only further researched underground space planning and design but also keenly captured the key and challenging issues of China's development. In addition, they started combining underground space development with urban development. The development of underground space is a necessary condition for the realization of sustainable urban development. After entering the new century, China's research on UUS has gradually diversified. Yu et al. [11] discussed the overall planning, detailed planning, and planning management process of UUS. Xu et al. [12] discussed the impact of economic factors on the development of underground space, claiming that different stages of economic development exerted different effects on the development of UUS. As the economy continues to improve, the proportion of underground transportation and underground municipal facilities will increase gradually. Hong and Shen [13] combined the evolution process of underground space functions worldwide and the research context of international underground space design theory. The authors proposed forward a requirement for the development of China's underground space (establishment of the discipline of underground architecture) and elucidated two trends therein (the stereo development of buildings, combined development of underground transportation space and urban space). In addition, Zhu et al. [1] summarized China's current planning and management status and examined the corresponding policies and laws for UUS development; they believed China's UUS has a bright future, but further coordination is warranted in planning. In formulating policies and regulations, it is essential to articulate corresponding implementation policies, laws, and regulations in compliance with national conditions. Wang et al. [14] and Ya and Chengli [15] comprehensively analyzed the crowd psychology in the underground space and claimed that people's negative impression of the underground space is objective. The study of crowd psychology in underground space is a crucial means to augment the environmental quality of underground space. Meanwhile, with the continuous furthering of China's green development concept, the use of underground space to assist the green development of society has garnered growing attention, and the research enthusiasm for underground energy systems, underground water storage systems, underground logistics systems, and underground expressways has been increasing every year. Furthermore, the development and research of China's underground space are moving gradually toward world-class standards.

2.3. Limitations in UUS Research

2.3.1. Lack of Research on Urban Fringe Areas. An all-round and multilevel development of cities has created many new urban problems. The research on UUS should be conducted from the perspective of architectural disciplines such as promoting urban development by analyzing and solving practical problems. The current research on UUS still concentrates on the areas of urban pedestrian streets, urban complexes, urban rail transit, and civil air defense engineering; most of these research fields are located in urban central areas, and the pressure on urban land is high. Thus, corresponding research is urgently needed to expand the prospect of UUS development. However, research on the development of underground space in the fringe areas of urban development, such as old industrial areas and historic preservation blocks, is deficient. China's urban development is gradually shifting from incremental construction to stock renewal. Perhaps, research on UUS in low-stress areas could effectively extend the space for urban development, and it has great significance to the realization of urban green and sustainable development.

2.3.2. Lack of Research Related to Urban Development Factors. The pressure on urban development is increasing gradually, and the development and utilization of UUS as one of the critical ways to relieve the pressure of urban development has been broadly recognized and concerned. Currently, the research hotspots of UUS still focus on exploring underground space, underground environment, underground function, and other UUS utilization forms. The research overlooks investigating the elements of UUS that affect urban development, how underground space affects urban development elements, and the complex correlation between underground space and urban development elements. Of note, the discussion on the correlation between urban development factors and UUS development can enable people to find the fundamental "key point" for UUS development to promote urban development, as well as analyze the size of the driving force that promotes urban development during underground space development. Moreover, investigating the correlation between UUS and urban development elements could help people use new research perspectives to analyze underground space, expand the assessment methods of underground space development and utilization, help enhance the overall quality of underground space, and promote sustainable development of cities.

3. Elements of Urban Development

The elements of urban development, including population, economic activities, public resources [16], land [17], and science and technology [18], are the elementary conditions

Table 1: Past conferences of ACUUS.

Session	Time	Location	Conference theme
1	1983	Sydney, Australia	Energy Efficient Buildings with Earth Shelter Protection
2	1986	Minneapolis, United States	Advances in Geotectural Design
3	1988	Shanghai, China	New Developments of Underground Space Use
4	1991	Tokyo, Japan	Urban Underground Utilization
5	1992	Delft, Netherlands	International Conference on Underground Space and Earth Sheltered Structures
6	1995	Paris, France	Underground Space and Urban Planning
7	1997	Montreal, Canada	Underground Space: Indoor Cities of Tomorrow
8	1999	Xi'an, China	Agenda and Prospect of the Underground Space for the Turn of the Century
9	2002	Turin, Italy	Urban Underground Space: A Resource for Cities
10	2005	Moscow, Russia	Underground Space: Economy and Environment
11	2007	Athens, Greece	Underground Space: Expanding the Frontiers
12	2009	Shenzhen, China	Using the Underground of Cities: For a Harmonious and Sustainable Urban Environment
13	2012	Singapore, Singapore	Underground Space Development—Opportunities and Challenges
14	2014	Seoul, Korea	Underground Space: Planning, Administration, and Design Challenges
15	2016	Saint Petersburg, Russia	Underground Urbanisation as a Prerequisite for Sustainable Development
16	2018	Hong Kong, China	Integrated Underground Solutions for Compact Metropolitan Cities
17	2021	Helsinki, Finland (online)	Deep Inspiration

Source: https://www.acuus.org/index.php/past-conferences/complete-list.

affecting urban development and the causes of urban generation, change, and development.

The five elements of urban development, which constitute the urban development model in the form of a pyramid (Figure 1), are the fundamental constituent units of modern urban development and conjointly promote urban development. As the fundamental element of urban development, the population is at the bottom of the pyramid to support the other four elements. Land and economic activities constitute the two core elements of urban development, which provide urban physical activity space and urban economic activity space for the urban population, respectively. In addition, they provide physical construction space and construction funds for public resources. As a crucial element of urban development, public resources inherit the population, land, and economic activities. The factors provide a platform for technological development. As the top element, technology is equally affected by the other four elements and, at the same time, provides feedback on other elements. Technology is progressively becoming a core element influencing urban development. The five elements of a city interact with each other. To accomplish the sustainable development of a city, it is essential to ensure a balanced and stable development among the five elements of population, land, economic activities, infrastructure, and science and technology.

4. Project Overview of Qingdao Cruise Port Starting Area

As a key node of Qingdao's construction of a modern international metropolis, an outstanding marine port, a demonstration zone for local economic and trade cooperation of the Shanghai Cooperation Organization (SCO), and an international shipping trade financial innovation center, the Qingdao Cruise Port warrants transformation to adapt to the future development of Qingdao city. The starting area (Figure 2) project of the cruise port inherits the historical memory of Qingdao and reshapes the physical space of the port area to introduce new industries and new forms of business [19]. In addition, the starting area can provide a new growth engine for the development of Qingdao. Second, the program opened the development process of Qingdao as a world ocean city, acting as a link between the entire cruise port area and the development process of Qingdao.

4.1. Controlled Detailed Planning of the Starting Area. The controlled detailed planning of the project in the starting area transformed the port into commerce, culture, tourism, and parks, while reserving the residential land. In the project, the existing storage facilities will be rebuilt to complete the replacement of commercial, residential, entertainment, and leisure functions in the old industrial zone and then build the Qingdao cultural tourism area as the core of the starting area through new buildings. Besides, the coastal parks will connect cultural and tourist areas, business areas, shopping areas, distribution centers, docks, and residential areas, building a "port-city" integration corridor to connect the city, port, and ocean. In addition, the project will make the "city-port-sea" a connection to bridge the current situation of separation between old industrial areas and urban areas and improve the spatial quality of Qingdao's old urban areas (Figure 3).

5. Underground Space Promotes the Integrated Development of Industrial Zones and Cities

With the change of the urban development mode and the growth of emerging industries, especially the technology

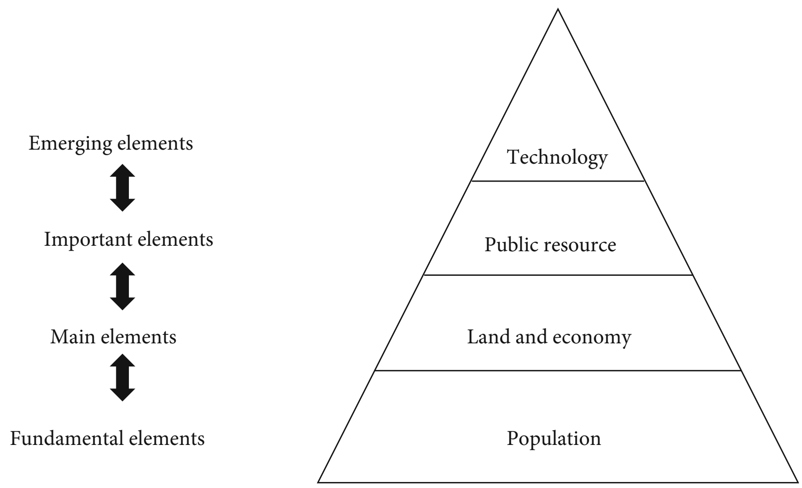

Figure 1: Pyramid of urban development factors (source: self-created).

Figure 2: The rendering of Qingdao Cruise Port starting area (source: from the Internet).

industry, many industrial areas have not fulfilled the requirements of the times, as they are faced with the dilemma of being eliminated and abandoned [20]. The lack of attractiveness of old industrial areas leads to the loss of population in the region, which passively results in the lack of economic activity in this region and decreases the motivation for investment and construction of public resources. The vicious circle of the loss of population, reduction in economic activities, and the lack of public resources results in the continuous decline of the industrial zone. However, the industrial zone has considerable idle land, which can make the positive cycle of attracting population, promoting economic activities, optimizing the allocation of public resources, and attracting high-tech industries through the underground space development; this then aggregates the five elements of population, land, economic activities, public resources, and science and technology to promote the development of the city.

5.1. Create a Vibrant Space Area to Attract the Urban Population and Stimulate Economic Activities. The core of space vitality is people who engage in various activities. The physical space provides people with a place for activities, which certainly affects people's activities [21]. In the overall planning of the underground space of the Qingdao Cruise Port launch area, a large underground pedestrian has been designed. Besides, cultural, entertainment, and commercial functions have been placed on both sides of the pedestrian system, thereby making a multiple plan function to break the traditional monotonous functional organization of the underground space. In addition, the three-dimensional pedestrian system has been used to connect the businesses, subways, and other functions in the three-dimensional space (Figure 4), which will promote the three-dimensional integration of urban, port, underground, and coastal areas, as well as create a systematic and coherent integration of stereo space. Reportedly, the urban vitality space sweeps the attraction of the urban population [22]. Meanwhile, in the underground space plan of the starting area, business centers, distribution centers, subways, exhibitions, culture, entertainment, hotels, and other commercial functions are connected in series through the underground pedestrian system (Figure 5). The connection forms a unified and complete underground commercial facility, stimulating the economic activity to the greatest extent. Underground commerce cannot exist in isolation. Thus, the underground commerce and related functions have been rationally planned in the vertical space, so that underground commerce and related functions on the ground form a synergy to create economies of scale [23].

5.2. Promote Efficient Use of Land. Modern cities are developing in the direction of centralized and intensive use of functions and space; however, the development of cities has not amended the urban environment [24]. As an emerging first-tier city, Qingdao is also fronting the shortage of land resources like other first-tier cities such as Beijing, Shanghai, Guangzhou, and Shenzhen. Through underground space development, multilevel modern urban space can be created to improve urban functions and the environment. In addition, creating a living space full of bright light and green areas on the ground provides residents with a peaceful and comfortable experience, while using underground space to accommodate urban functions [24]. The project advocates the function of underground space in the

(a)

(b)

Figure 3: (a) The current land use map; (b) the land use planning map (source: self-created per the relevant information).

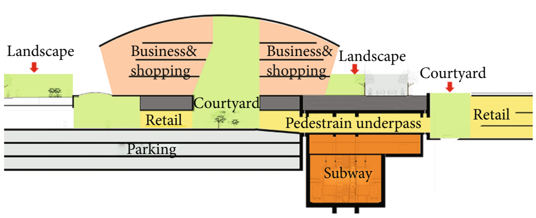

Figure 4: Stereoscopic walking system (source: self-created per the relevant information).

Figure 5: The underground walking system connects each functional node (source: self-created per the relevant information).

vertical commercial space area, such as subways, parking, underground walking area, and integrated pipe gallery (Figure 6), which has increased the development intensity of the unit land space and opened up more development space for the city.

5.3. Provide New Space for the Construction of Public Resources. The development of underground space enables more effective use of urban public resources [24]. Different public resources exert different impacts on urban development. For instance, urban elevated roads affect people's perception of the city, while the landscape will enhance the urban environment, which, in turn, promotes the enhancement of the commercial value around the green space. The development of underground space provides a new construction space for public resources with negative attributes (Figure 7). The development of UUS is the most effective way to increase the land utilization rate, save land resources, ease the density of central cities, and decrease environmental pollution [25]. The municipal integrated pipe gallery in the starting area is buried in the shallow underground space under the urban landscape, reserving a flexible development space to reserve space for urban development. Meanwhile, it provides significant green construction land for the city. By constructing high-quality coastal parks, the city will be a landmark of the Jiaozhou Bay, strengthening the positive role of public resources. In the starting area project, the

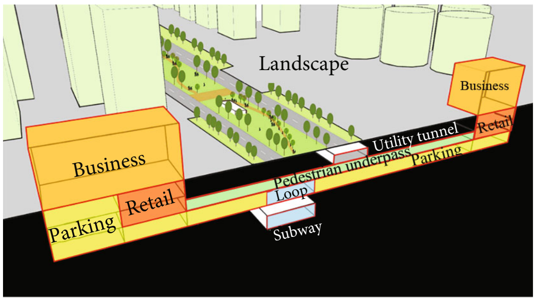

Figure 6: Stereo planning of underground space (source: self-created per the relevant information).

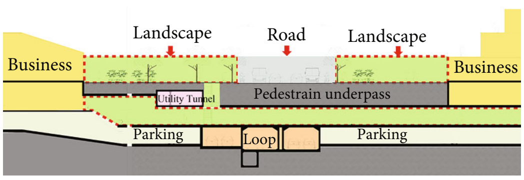

Figure 7: Development form of public resources of underground space (source: self-created per the relevant information).

underground space is comprehensively planned in three dimensions. A regional car loop is built underground to build an efficient and convenient underground train layer. Vehicle leveling and pedestrian leveling are separated in the vertical space to realize the diversion of people and vehicles, passengers and cargo, and arrival and departure transit.

5.4. Provide a New Application Environment for Technological Innovation. High-tech technologies represented by 5G, big data, and artificial intelligence (AI) are becoming one of the main driving forces for urban development. As China's economic development enters "new times," the construction of smart cities supported by technological innovation has been upgraded [26]. While developing the underground space of old industrial buildings and industrial facilities, a combination of parameterization and AI is used to keep the physical environment such as indoor sound, light, and heat in a stable state through computer control; this can ensure a good living environment while avoiding energy waste. In the underground pedestrian system, underground vehicle transportation system, and underground parking, big data combined with 5G technology can be used to broadcast traffic conditions in real time while also effectively forecasting traffic conditions, so that people can plan travel plans reasonably.

6. Strategy of Industrial Transformation and Urban Integrated Development Based on Underground Space Development

Sustainable development should be considered a crucial criterion for the development of underground space [27]. Urban historical and cultural heritage is the foundation of sustainable urban development, a valuable resource for urban development and a key component of the development of the knowledge economy [28]. As an integral part of the historical and cultural heritage of industrial cities, the transformation of industrial areas is the only way to adapt to future urban development; it is also an effective way to preserve urban memory and an urgent task to attain stock renewal. As a special transformation method, the underground space development in the industrial zone has the advantages of increasing land utilization and greening rate, protecting the memory and context of the city, and promoting the three-dimensional development of the city. However, promoting the transformation of industrial areas and urban integrated development per the development of underground space warrants appropriate strategies.

6.1. Development of the Whole Society under the Guidance of Government. The investment in the construction of UUS is substantial [29]. The investment return period of projects is usually longer, and the capital requirements are high. Under typical circumstances, estate developers stay away from such projects. At the moment, it is crucial for the government to lead the development of underground space in the industrial zone by formulating relevant policies and regulations and even acting as the main funder of the project. Through the traction of the government, all parties in the society are gathered for development and construction. In addition, the government should encourage developers to invest in construction independently and provide specific policy support; however, the government should strictly regulate the development and construction plan to ensure the project's quality. Moreover, universities and other scientific research institutions should conduct standardized research on the development standards of underground space in industrial areas. By standardizing the development of underground space in industrial areas, scale effects can be realized and development costs further saved. As the direct participants of development, the public should also present reasonable opinions and suggestions, participate in the development and construction from the first-person perspective, and discuss what type of underground space people need to attain the purpose of enhancing the quality of underground space.

6.2. Demonstration of the Necessity and Feasibility of Underground Space Development in Industrial Areas. Although underground space is a considerable and abundant space resource [30], not all industrial zone transformations need the development of their underground space. Thus, the necessity and feasibility of developing the industrial zone's underground space should be illustrated by demonstrating the project's impact on the city's economy, environment, and humanities. In addition, a comprehensive evaluation should be done to determine whether the industrial zone's underground space needs to be developed and utilized during the transformation. Relevant universities and other scientific research institutions can establish a model of the necessity and feasibility of underground space development by exploring the development of the underground space in industrial areas, economics, environment, and context. Furthermore, the model can be used to determine whether the underground space in industrial areas needs to be developed and realize the standardized development of the underground space.

6.3. Multidimensional Development of the Underground Space in Industrial Areas. The multidimensional development of the underground space in industrial areas has four dimensions. (i) The two-dimensional level includes the reasonable layout of the underground space functions per urban development needs; the integration of commercial areas, walkways, green courtyards, and other functions; and the segregation of pedestrian and vehicle functions. (ii) At the three-dimensional level, the project must make reasonable planning of shallow, medium, and deep underground space in the industrial zone. Of note, the shallow space can be equipped with municipal integrated pipe corridors, underground commerce, and underground parking. The middle space can be equipped with urban underground rail transit, underground garbage treatment facilities, and underground power stations. In deep space, underground strategic safety reserves, such as underground oil and gas depots and underground arsenals, can be arranged [30]. (iii) At the four-dimensional level, owing to the irreversibility of underground space development [30], we should rely on flexible design thinking to build an open underground space structure. Thus, comprehensive urban planning and underground space development and utilization characteristics are needed to enhance the functionality, adaptability, and scalability of the underground space in industrial areas [31] to fulfill the needs of future urban development. (iv) At the five-dimensional level, old industrial areas often play a pivotal role in the development of cities in the past; they constitute the collective memory of people in the area. In the renewal of the old industrial zone, the memory of the place is the site's soul, recording the historical context of the site, witnessing the past and present of the site, and acting as the link between the public and the site [32]. Thus, in the process of underground space development in industrial areas, thinking about the memory of the place is essential. People should make full use of their unique memories and emotions of industrial areas, as only then the value of the place can be realized in a real sense.

6.4. The Underground Space of the Industrial Areas Integrates High-Tech Industries. The old industrial area is representative of the past urban development history, and getting high-tech is representative of the contemporary advanced life. Integrating technology into underground space development in industrial areas can not only fulfill people's diversified needs for life experience but also support the social needs of urban sustainable development [33]. Underground space development of industrial areas actively explores new development directions of technology while utilizing the existing technological research results. In addition, underground space development provides experimental sites for high-tech industries. Of note, utilizing high technologies in underground space development can effectively enhance the quality of space, and the experimental data obtained can better promote technological development. Thus, they should eventually form a mutually promoting coupled development model to realize the parallel development of underground space development and technology. The fusion between the underground space of industrial areas and technology can inevitably create unexpected architectural forms, artistic effects, and experience perception.

7. Conclusions

Underground space development has become a crucial means of activating the vitality of industrial areas and is an integral part of the transformation of industrial areas in the future. Underground space development in the industrial areas can promote the integration of the industrial areas and the city through the organic connection with the urban development elements and then promote the further development of the city.

(1) Underground space development in the starting area reactivates four urban development elements (population, land, economic activities, and public resources), which is of great significance to promote the sustainable development of old urban areas

(2) In the development process of the underground space in the starting area, methods like creating vitality space, enhancing land use efficiency, expanding public resource construction space, and actively using innovative technologies are used, which have reference significance for promoting urban development, endorsing environmental protection, and improving scientific and technological innovation. Moreover, they can be promoted and used in the development of similar projects

(3) The analysis of the underground space project in the starting area can help summarize the development strategy of the integration of the coastal industrial area and the city based on the underground space development; that is, the development of the whole society under the guidance of the government, demonstration on the necessity and feasibility of underground space development in industrial areas, multidimensional development of the underground space in industrial areas, and the underground space of industrial areas integrating high tech

This study has some limitations. First, we only analyzed the underground space development project of the Qingdao Cruise Port starting area from a macro perspective, which lacks the first-person microscopic perspective to analyze the project. Second, the strategies obtained have some limitations. In the future, research in the related fields should be strengthened and constantly explore and innovate to fulfill the needs of the underground space in industrial areas and urban development.

Data Availability

The data used to support the findings of this study are available from the corresponding author upon request.

Conflicts of Interest

The authors declare that they have no conflicts of interest. The authors are employed at the College of Architecture and Urban Planning, Qingdao University of Technology.

References

[1] Z. Hehua, L. Xiao, P. Fangle, L. Xiaojun, and L. Chunyan, "Development strategy on urban underground space planning in China," *Chinese Journal of Engineering Science*, vol. 19, no. 6, pp. 12–17, 2017.

[2] W. Guofu, *Research on the development and utilization strategy of underground space in existing industrial zones from the perspective of urban renewal, [M.S. thesis]*, China University of Mining and Technology, 2020, https://kns.cnki.net/KCMS/detail/detail.Aspx?Dbname=CMFD202101&filename=1020817204.Nh.

[3] W. Yaoyu, "Research on underground space planning strategy in the renewal of urban historical waterfront industrial zone——taking Hangzhou Dacheng north demonstration zone as an example," *Chinese and Foreign Architecture*, no. 6, pp. 102–105, 2020.

[4] J. Xiang, "Prospects for comprehensive planning and renovation technology of underground space in existing urban industrial zones," *Journal of Jiangsu Institute of Architecture and Technology*, no. 1, pp. 1–6, 2019.

[5] Z. Haifeng, *Research on the demand forecast of underground space development in the industrial zone of existing cities, [M.S. thesis]*, China University of Mining and Technology, 2020, https://kns.cnki.net/KCMS/detail/detail.aspx?dbname=CMFD202101&filename=1020817212.nh.

[6] M. Liantai, "Comprehensive utilization of underground space," *Urban Planning*, no. 5, pp. 57–59, 1979.

[7] N. Bihua, "Comprehensive development of underground space in urban design," *Underground Space*, no. 2, 1992.

[8] X. Sishu, "Architectural considerations of underground space," *Underground Space*, no. 5, pp. 54–69, 1982.

[9] Q. Qihu, "Sustainable urban development and underground space development and utilization," *Underground Space*, no. 2, pp. 69–74, 1998.

[10] T. Linxu, "Urban intensive development and underground space development and utilization," *Underground Space*, no. 2, 1998.

[11] S. Yu, P. Fangle, W. Xuan, and Z. Hehua, "Research and practice of urban underground space planning in China," *Chinese Journal of Underground Space and Engineering*, no. S1, pp. 1125–1129, 2006.

[12] X. Hui, L. Xiaozhao, and C. Jing, "Research on the functional ratio of underground space development at different stages," *Chinese Journal of Underground Space and Engineering*, no. 3, pp. 573–580, 2016.

[13] Y. Hong and S. Zhongwei, "Research on the evolution of underground space function and the development process of design theory," *Architectural Journal*, no. 12, pp. 77–82, 2016.

[14] W. Rui, L. Xiaozhao, and W. Jiachen, "Research on the psychological environment influencing factors of underground space workers," *Chinese Journal of Underground Space and Engineering*, no. 1, pp. 1–8, 2019.

[15] F. Ya and X. Chengli, "Challenges and optimization of the psychological environment of urban underground space," *Chinese Journal of Underground Space and Engineering*, no. S2, pp. 499–507, 2019.

[16] Y. Ruiying, *A study on the impact of urban development factors agglomeration on housing prices, [M.S. thesis]*, Chongqing University, 2017, https://kns.cnki.net/KCMS/detail/detail.aspx?dbname=CMFD201801&filename=1017837542.nh.

[17] C. Yan, J. Bo, C. Nanchen, C. Shunli, and L. Zirui, "Urban land use efficiency and new urbanization index selection and system reconstruction," *China Agricultural Resources and Regionalization*, no. 3, pp. 67–75, 2021.

[18] C. Liqiang, "Promoting the construction of people's cities with high quality," *Study Times*, vol. 4, 2021.

[19] W. Kai, "The home port area of cruise ships from the perspective of the common people," *Qingdao Daily*, vol. 13, 2020.

[20] Q. Menghai, *Research on the spatial promotion and reuse strategy of existing urban industrial zones in Foshan City [M.S. thesis]*, South China University of Technology, 2020, https://kns.cnki.net/KCMS/detail/detail.aspx?dbname=CMFD202101&filename=1020332543.nh.

[21] Y. Xu and X. Chen, "Quantitative analysis of spatial vitality and spatial characteristics of urban underground space (UUS) in metro area," *Tunnelling and Undesrground Space Technology*, vol. 111, article 103875, 2021.

[22] Y. Chunxia, L. Chengzhe, and G. Zhuoxing, "The creation of urban characteristics and vitality," *Urban Architecture*, no. 1, pp. 144–150, 2019.

[23] W. Hanbin, *Research on the development strategy of underground space in high-density urban areas, [Ph.D. thesis]*, Tianjin University, 2013, https://kns.cnki.net/KCMS/detail/detail.aspx?dbname=CDFD1214&filename=1014036115.nh.

[24] J. Cui, W. Broere, and L. Dong, "Underground space utilisation for urban renewal," *Tunnelling and Underground Space Technology*, vol. 108, article 103726, 2021.

[25] Q. Qihu, "Welcome climax of urban underground space development in my country," *Chinese Journal of Geotechnical Engineering*, no. 1, 1998.

[26] Z. Yong and L. Shan, "Financial development, technological innovation and smart city construction: an analysis based on the perspective of information development," *Financial Research*, no. 2, pp. 4–15, 2016.

[27] F.-L. Peng, Y.-K. Qiao, S. Sabri, B. Atazadeh, and A. Rajabifard, "A collaborative approach for urban underground space development toward sustainable development goals: critical dimensions and future directions," *Frontiers of Structural and Civil Engineering*, vol. 15, no. 1, pp. 20–45, 2021.

[28] L. Xianjue, *Modern Architectural Theory*, China Construction Industry Press, 2008.

[29] Y. Xinhua, H. Guangyao, W. Qiangxun, and Z. Lei, "Current status and development trend of urban underground space utilization in my country," *Tunnel Construction*, no. 2, pp. 173–188, 2019.

[30] Q. Qihu, "Utilizing underground space to help develop green buildings and green cities," *Tunnel Construction*, no. 11, pp. 1737–1747, 2019.

[31] W. Haibin, "Development and utilization of urban underground space from the perspective of green ecological architecture," *Urban Housing*, no. 4, pp. 20–22, 2019.

[32] Z. Jiali, "*Design and research on the exterior environment renovation of the old industrial zone based on place memory, [M.S. thesis]*," Xi'an University of Architecture and Technology, 2017, https://kns.cnki.net/KCMS/detail/detail.aspx?dbname=CMFD201801&filename=1017736059.nh.

[33] F. Cuixiao and W. Lei, "Analysis of the prospects of science and technology empowering the construction of people's cities in the future," *Zhangjiang Science and Technology Review*, no. 6, pp. 58–61, 2020.

Hindawi
Geofluids
Volume 2021, Article ID 7374363, 10 pages
https://doi.org/10.1155/2021/7374363

Research Article

Numerical Simulation on the Progressive Failure Processes of Foundation Pit Excavation Based on a New Particle Failure Method

Guojin Zhu,[1,2] **Shuyang Yu**,[2] **Yu Ning**,[1] **Xuhua Ren**,[2] **Peng Wei**,[2] **and Yu Wu**[2]

[1]*Power China Kunming Engineering Corporation Limited, Kunming 650051, China*
[2]*College of Water Conservancy and Hydropower, Hohai University, Nanjing 210098, China*

Correspondence should be addressed to Shuyang Yu; yushuyang_hhu@163.com

Received 15 July 2021; Revised 30 July 2021; Accepted 7 August 2021; Published 24 August 2021

Academic Editor: Zhijie Wen

The predictions of failure zone during the foundation excavations will provide important guidance for the safety constructions of engineering structures. Based on this background, the smoothing kernel function in the traditional SPH method has been improved. The failure mark η is introduced into the program to realize the failure characteristics of particles at meso–scale. The "Killing Particle Method" has also been proposed, which can realize the simulations of complex excavation processes. The whole progressive failure processes of the excavation of a foundation pit are numerically simulated and the results show that (1) the failure zone of the excavated foundation pit without retaining walls appears at the corner and then gradually develops into the deep. However, the failure zone of the excavated foundation pit with retaining walls only develops longitudes along the retaining wall. (2) The stiffness of retaining wall has a great impact on the failure zone of foundation pit excavation. The greater the stiffness of retaining wall, the greater the damage degree. (3) The rationality of the proposed method is verified by the comparisons of the simulation results of the proposed method with the ABAQUS numerical examples and the engineering practices. Future research directions should focus on developing the 3D parallel IKSPH programs. The research results can provide some references for the applications of SPH method into predicting the failure zone of foundation pit excavations and ensuring the safety of engineering constructions.

1. Introduction

With the accelerated development of China's economy, the constructions of urban underground space, large-scale water conservancy, and civil engineering projects are becoming the current focus of China, where the safety and stability of foundation pit during the excavation processes have become the main problems [1, 2]. However, due to the complex geological conditions of foundation pit, it is easy to collapse during the processes of excavations. For example, the foundation pit excavation accident that occurred in Suzhou, China, in 2008 caused the destructions of the supporting structure and the damage of construction equipment, as shown in Figure 1(a). The collapse of the foundation pit in the Xiaoshan, Hangzhou in 2008 caused 21 people dead and 24 injured, as shown in Figure 1(b). Therefore, understanding and grasping the failure mechanisms of foundation pit engineering will undoubtedly provide an important guidance for ensuring the safety of engineering constructions and people's lives.

Previous works on the deformation and instability of foundation pit excavations mainly focused on three aspects: (1) experimental studies, (2) theoretical research, and (3) numerical simulation. Experimental studies are regarded as the most important and direct means to obtain the deformation and failure rules of foundation pit excavations, which can be divided into the field test and model test. Field test can directly obtain the deformation laws of actual engineering, but the cost is much. For example, Yang et al. [3] obtained the 3D deformation laws of the foundation pit in Hangzhou based on the monitoring data; Li [4] summarized the general rules of deep foundation pit deformations based on the measured data of the Shanghai subway foundation pit. Model test simplifies the complex and changeable factors of the engineering practice to a certain extent, so that the mechanics law of the whole model can be analyzed comprehensively. For example, Zhang and Qian [5] studied the laws of surface subsidence during the processes of foundation pit excavations under different displacement modes of rigid retaining wall through model test; Xia [6] carried out the model test on the penetration depth of underground diaphragm wall in cohesive soil and conducted a single study on many factors affecting the rebound of pit bottom. However, experimental studies only obtain the macroscopic deformation characteristics, but cannot quantitatively describe the internal mechanisms of excavation failure. Theoretical researches are based on the experimental results and summarize and refine the quantitative mathematical expressions of foundation pit deformation characteristics and failure rules. For example, Jiang [7] derived the analytical formula of pipeline deformation and internal force in the processes of foundation pit excavation by using the elastic foundation beam method; Gao et al. [8] established a lateral displacement prediction model for deep foundation pit excavation based on the combination of weighted first-order local method and trust domain; Zhang et al. [9] proposed a two-stage simplified analysis method for the longitudinal deformation of the adjacent existing tunnel caused by the excavation of double foundation pits based on the Pernak foundation model and analyzed the influence of the excavation of double foundation pits in soft soil on the vertical settlement of the tunnel. However, theoretical research can only obtain the analytical solution of the excavation deformation under simple boundaries and geometric shapes, and complex excavation steps as well as the complex foundation pit shapes will lead to extremely complex mathematical expressions. Meanwhile, previous experimental and theoretical studies on foundation pit excavation rarely paid attention to the progressive failure processes.

Numerical simulation can not only verify the correctness of theoretical studies but also can quantitatively reflect the inherent mechanisms of experimental research, which has been regarded as the “third method” of scientific researches [10, 11]. The finite element method (FEM) was the first method used to study the foundation pit excavation [12–14]; however, FEM has limitations in dealing with excavation failures. Foundation excavation is a progressive failure process which contains the treatments of discontinuous properties such as crack propagation [15]. Therefore, the mesh refinements should be applied to crack tips, and mesh redivisions should also be applied to every step of progressive failure process, which costs huge amounts of computational resources. Meanwhile, for complex crack propagation paths (such as crack intersecting, etc.), the mesh grids will be extremely distorted, leading to the low calculation accuracy or even calculation failure. Different from FEM, the discrete element method gets free from the mesh grids [16, 17], which discretizes the whole computational domain into particles. The interactions of different particles are characterized by the establishments of the contact model between particles,

(a) (b)

Figure 1: Typical foundation pit excavation accidents. (a) Foundation pit collapse accident in Suzhou in 2008. (b) Foundation pit collapse accident in Hangzhou in 2008.

which can be well applied to modeling the progressive failure processes of foundation pit excavation. However, the DEM has many mesoscopic parameters with no actual physical meanings and requires complex parameter calibrations before numerical simulation, which is inconvenient to apply to engineering practice. The newly proposed discontinuous numerical method such as numerical manifold method (NMM) [18, 19], peridynamics (PD) [20, 21], and material point method (MPM) [22, 23], which all have certain applications in the foundation pit excavation, but also have their limitations: the crack tips of NMM must be on the mesh nodes; the bond-based PD method has some theoretical defects which leads to the Poisson’s ratio being constant; the MPM still needs background grids.

In this paper, based on the existing researches, the smoothing kernel function in the traditional SPH method has been improved to realize the failure characteristics of particles, which can reflect the progressive failure processes of the foundation pit during its excavation. Therefore, this method can also be called the Improved Kernel of Smoothed Particle Hydrodynamics (IKSPH). The “Killing Particle Method” has also been put forward to realize the simulations of the complex processes of foundation pit excavation. Based on the engineering practice of foundation excavation in Niulanjiang pumping station, the numerical simulation of progressive failure processes during foundation pit excavation is carried out, and influences of the stiffness of the retaining walls on the failure zone are also discussed. The research results can provide some references for the understandings of internal mechanisms of foundation excavation failure and ensuring the safety of the project.

2. Basic Principles of IKSPH

2.1. Solid Elastic Equations. The total stress tensor $\sigma^{\alpha\beta}$ in IKSPH can be expressed as the combinations of shear stress tensor $\tau^{\alpha\beta}$ and the isotropic stress p, which can be written as:

$$\sigma^{\alpha\beta} = -p\delta^{\alpha\beta} + \tau^{\alpha\beta}, \tag{1}$$

where the isotropic stress p can be expressed as:

$$p = \left(1 - \frac{1}{2}\Gamma\eta\right)p_H + \Gamma\rho e, \tag{2}$$

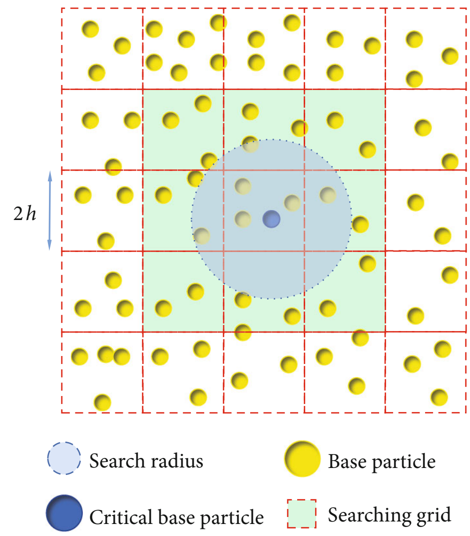

Figure 2: The linked-cell list method.

where p_H is the Hugoniot function, and Γ is the Gruneisen parameter.

The shear stress $\tau^{\alpha\beta}$ is calculated by updating the shear stress rate of every step, which can be written as:

$$\widehat{\tau}_{\alpha\beta} = B\left(\varepsilon^{\alpha\beta} - \frac{1}{3}\delta^{\alpha\beta}\varepsilon^{\gamma\gamma}\right) + \tau^{\alpha\gamma}R^{\beta\gamma} + \tau^{\gamma\beta}R^{\alpha\gamma}, \quad (3)$$

where $\widehat{\tau}$ is the shear stress rate, and the shear stress tensor $\sigma^{\alpha\beta}$ can be calculated by multiplying the shear stress rate $\widehat{\tau}$ and the time step t. B is the shear modulus. $\varepsilon^{\alpha\beta}$ is the strain tensor. δ is the Kronecker delta. $R^{\alpha\beta}$ is the torsion tensor, which can be written as:

$$R^{\alpha\beta} = \frac{1}{2}\left(\frac{\partial v^{\alpha}}{\partial x^{\beta}} - \frac{\partial v^{\beta}}{\partial x^{\alpha}}\right). \quad (4)$$

2.2. Governing Equations. IKSPH assigns to each particle its corresponding physical properties, including density, velocity, energy, and position coordinates. These particles should satisfy the following governing equations:

$$\begin{cases} \dfrac{d\rho_i}{dt} = \displaystyle\sum_{j=1}^{N} m_j v_{ij}^{\beta} \frac{\partial W_{ij,\beta}}{\partial x_i^{\beta}}, \\ \dfrac{dv_i^{\alpha}}{dt} = \displaystyle\sum_{j=1}^{N} m_j \left(\frac{\sigma_i^{\alpha\beta}}{\rho_i^2} + \frac{\sigma_j^{\alpha\beta}}{\rho_j^2} + T_{ij}\right) \frac{\partial W_{ij,\beta}}{\partial x_i^{\beta}}, \\ \dfrac{de_i}{dt} = \dfrac{1}{2}\displaystyle\sum_{j=1}^{N} m_j \left(\frac{\sigma_i^{\alpha\beta}}{\rho_i^2} + \frac{\sigma_j^{\alpha\beta}}{\rho_j^2} + T_{ij}\right) v_{ij}^{\beta} \frac{\partial W_{ij,\beta}}{\partial x_i^{\beta}}, \\ \dfrac{dx_i^{\alpha}}{dt} = v_i^{\alpha}, \end{cases} \quad (5)$$

where ρ is the density of the particle; m is the mass of the particle. v is the velocity tensor of the particle; e is the energy of the particle; x is the position of the particle; T is the artificial viscous term; W is the smoothing kernel function, which can be written as:

$$W(R, h) = \begin{cases} 2/3 - R^2 + 1/2R^3 & 0 \le R \le 1, \\ 1/6(2 - R)^3 & 1 \le R \le 2, \\ 0 & R \ge 2, \end{cases} \quad (6)$$

where h is the smoothing length and R is the radio of average distances between particles and the smoothing length h.

2.3. Particle Pairing Method. Before IKSPH calculation, the first step to be carried out is the pairing between different particles. For example, the smoothing kernel function W in the governing equation (5) is calculated by particle pairing. This is also why IKSPH is different from FEM: the mesh grids in FEM have already been divided in advance, but the particles can move freely in the IKSPH method. While pairing particles in the IKSPH method, the number of paired particles inside the influencing domain should be determined first, and then the position relationship between two different particles can be then calculated.

The direct searching method is the simplest and most direct particle search method, which performs a full pair search by traversing all particles in each time step. We can find that the complexity order of this method is $O(N^2)$, which costs huge amounts of calculation resources when the particle number is relatively large.

The Linked-cell list method has the advantages of high efficiency and low memory saving compared with full-paired searching method and is suitable for parallel computing. The details are as follows: the temporary searching grids are firstly laid onto the computing domain, as shown in Figure 2. The length of the temporary searching grid is defined as the searching radius of the particle, which is 2h in our paper. For 1D, 2D, and 3D problems, the searching grids of any given particle (blue particle in Figure 2 as an example) are 3, 9, and 27 grids adjacent to it. By cycling through each particle, all pairs of particles can be found, whose complexity order is $O(N)$.

2.4. Time Integration. The Leap-frog integrating method is adopted in IKSPH, which has the advantage of low storage required for calculation. Meanwhile, only one optimization estimation is required for each calculation step. Therefore, the density, energy, velocity, and position of each particle can be obtained by cyclic iterations of the following formula:

$$\begin{cases} t = t_0 + \Delta t, \\ \rho_i(t_0 + \Delta t/2) = \rho_i(t_0) + \dfrac{\Delta t}{2} D\rho_i(t_0), \\ e_i(t_0 + \Delta t/2) = e_i(t_0) + \dfrac{\Delta t}{2} De_i(t_0), \\ v_i(t_0 + \Delta t/2) = v_i(t_0) + \dfrac{\Delta t}{2} Dv_i(t_0), \\ x_i(t_0 + \Delta t) = x_i(t_0) + \Delta t \cdot v_i(\Delta t/2). \end{cases} \quad (7)$$

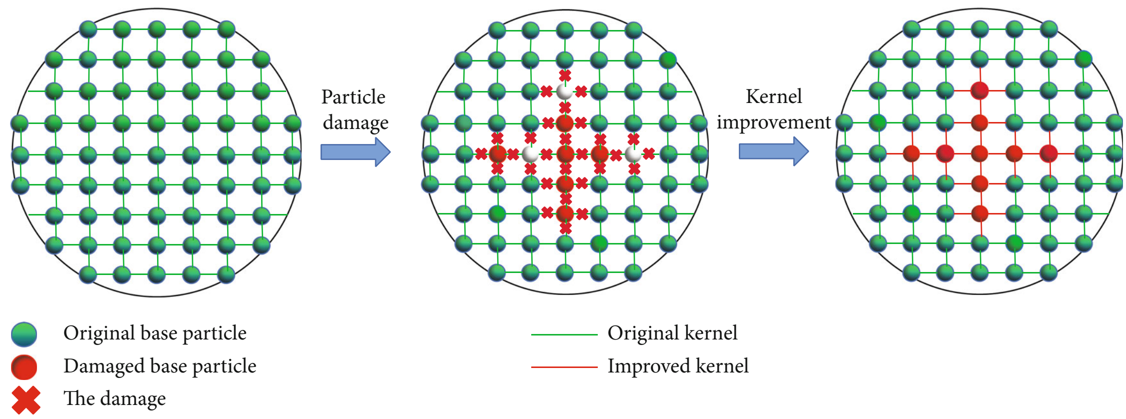

Figure 3: Treatments of particle failure.

In IKSPH, the determination of time step is related to the of material state change process, which can be estimated by the following equation:

$$\Delta t = \min \left(\frac{h}{f}\right)^{1/2}, \tag{8}$$

where f is the average force applied to the particle.

3. Failure Treatments of Particles

3.1. Failure Criteria. There is no unified criterion for soil failure in foundation pit excavation at present. Therefore, the improved Mohr-Coulomb criterion is selected in this section, which has two advantages: (1) the formula form is simple and does not need complex derivations; (2) the parameters are less and easy to access, which can be well applied to the engineering practice. The formula can be written as:

$$\sigma_f = \sigma_t, \tag{9}$$

$$\tau_f = c + \sigma_f \tan \varphi, \tag{10}$$

where σ_f and τ_f are the tensile and shear stress on the failure surface. σ_t is the tensile strength of the particle. c is the cohesion of the particle. φ is the internal friction angle of the particle. While judging whether the particle failure happens, equation (9) is firstly determined, which means that the tensile failure of the particle is easier to happen. When equation (9) is not satisfied, then equation (10) is determined whether the shear failure happens.

3.2. Treatments of Particle Failure. As can be seen from governing equation (5), the derivative of the smoothing kernel function $\partial W_{ij,\beta}/\partial x_i^\beta$ governs the transfer of physical properties between different particles. Therefore, in order to reflect the failure characteristics of particles, the failure mark η is defined. When the particle failure occurs, $\eta = 0$, otherwise, $\eta = 1$, which can be clearly shown in Figure 3. The relationship between the improved smoothing kernel function D and the original smoothing kernel function W can be written as:

$$\frac{\partial D_{ij,\beta}}{\partial \boldsymbol{x}_i^\beta} = \eta_i \cdot \frac{\partial W_{ij,\beta}}{\partial \boldsymbol{x}_i^\beta}. \tag{11}$$

Therefore, the final IKSPH governing equations considering the particle failure can be expressed as:

$$\begin{cases} \dfrac{d\rho_i}{dt} = \displaystyle\sum_{j=1}^{N} m_j v_{ij}^\beta \frac{\partial D_{ij,\beta}}{\partial x_i^\beta}, \\ \dfrac{dv_i^\alpha}{dt} = \displaystyle\sum_{j=1}^{N} m_j \left(\frac{\sigma_i^{\alpha\beta}}{\rho_i^2} + \frac{\sigma_j^{\alpha\beta}}{\rho_j^2} + T_{ij}\right) \frac{\partial D_{ij,\beta}}{\partial x_i^\beta}, \\ \dfrac{de_i}{dt} = \dfrac{1}{2}\displaystyle\sum_{j=1}^{N} m_j \left(\frac{\sigma_i^{\alpha\beta}}{\rho_i^2} + \frac{\sigma_j^{\alpha\beta}}{\rho_j^2} + T_{ij}\right) v_{ij}^\beta \frac{\partial D_{ij,\beta}}{\partial x_i^\beta}, \\ \dfrac{dx_i^\alpha}{dt} = v_i^\alpha. \end{cases} \tag{12}$$

4. Killing Particle Method

To model the excavation processes of the foundation pit, different excavation parts should be grouped. In this section, a particle searching algorithm suitable for the IKSPH method is proposed, which can realize the particle grouping. The details are as follows:

(1) The searching area of the target particles should be determined firstly, as shown in the purple area of Figure 4

(2) The searching points are generated uniformly on the target area (yellow points in Figure 4). The average spacing between searching points should be less than that of real particles, which is set to be 1/2 of the spacing between real particles

(3) For every searching point, a searching radius r_s is assigned. What should be noticed is that r_s should

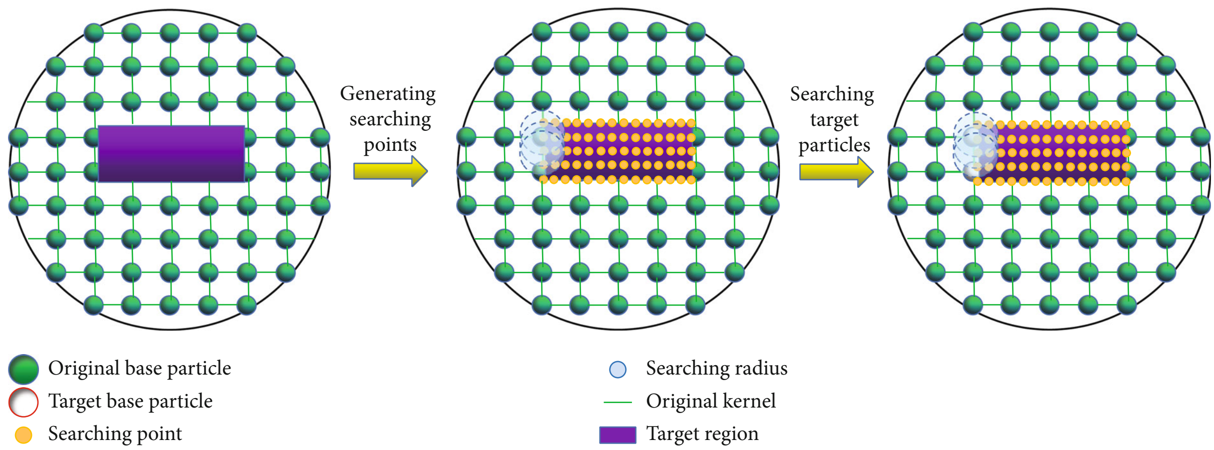

Figure 4: Killing particle method.

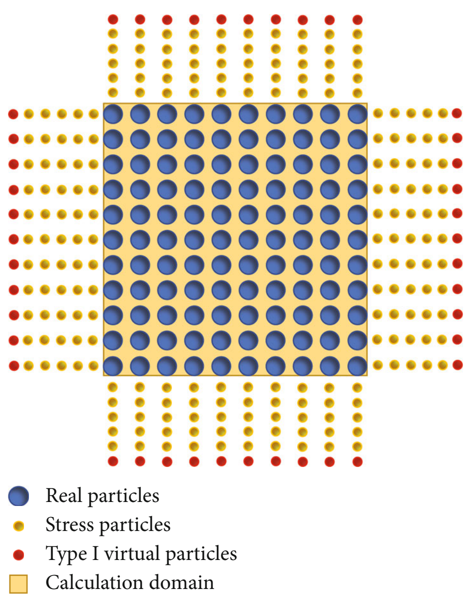

Figure 5: Stress boundaries.

be less than the average spacing of real particles, which is set to be 1/2 of the spacing between real particles

(4) For every real particle covered by the radius of searching points, it is moved to the group of excavation particles. While operating the excavation process, the failure mark η of the excavation part is set to be 0 according to equation (11) to "kill" the particles

5. Stress Boundaries

The stress boundaries adopt the method of stress mapping, and more than 5 layers of "stress particles" are laid outside the solid particles. The "stress particles" shall have the following characteristics, as shown in Figure 5.

(1) "Stress particles" participates in the calculation of internal forces in IKSPH, and the particle density, mass, energy, and positions are updated according to equation (12) in each time step

(2) In every time step, stress is reassigned to the "stress particles," that is, although the "stress particle" participates in the parameter updating of solid particles, its stress changes conform to the preset stress boundary requirements

(3) A layer of "type I virtual particles" with velocity v_inf set to 0 should be laid outside the stress particles

6. Verification of IKSPH Method

In order to verify the proposed IKSPH method, a simple 2D cube model is established. The model size is 1 m × 1 m, and a crack with a length of 0.1 m is prefabricated in the center of the model, the dip angle of which is 45°. The model boundaries are subjected to 1 MPa confining pressure. Figure 6 shows the comparisons between the IKSPH results and the Abaqus results, which shows that compressive stress concentrates at the crack tip. Meanwhile, the maximum principal stress distributions calculated by the IKSPH program are consistent with the Abaqus results, which verify the proposed method.

7. Numerical Models

Based on the engineering practice, the corresponding 2D foundation model is established. The model size is 180 m × 70 m, which is greater than 3 times of the foundation pit depth, as shown in Figure 7. The whole model is divided into 360 × 140 = 50400 particles. Two retaining walls are set on the two sides of the model, and 4 excavation parts are arranged, the depth of which is 3 m, 4.5 m, 4 m, and 3 m, respectively.

The detailed excavation simulation steps are as follows: first, 5000 steps of in situ stress balance are carried out. Then, the excavation steps are operated. The 5000–7000$^{\text{th}}$ steps are the excavation of excavation part 1, the 7000–9000$^{\text{th}}$ steps are the excavation of excavation part 2, the 9000–11000$^{\text{th}}$ steps are the excavation of excavation part 3, and the 11000–13000$^{\text{th}}$ steps are the excavation of excavation part 4.

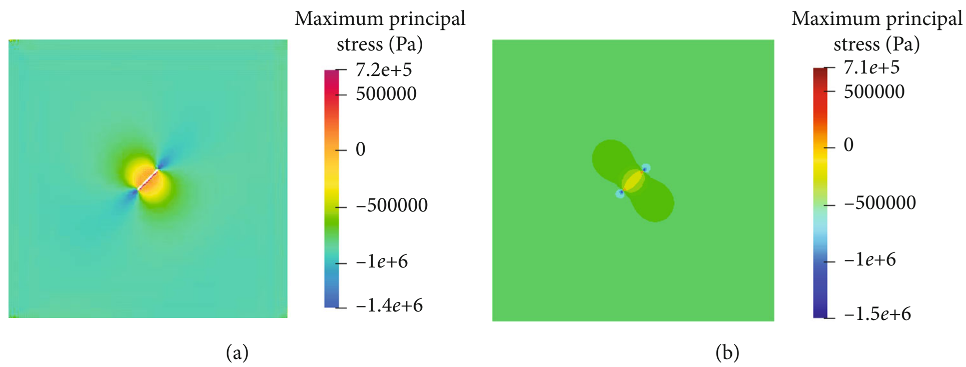

Figure 6: Maximum principal stress distributions calculated by two methods. (a) IKSPH results. (b) Abaqus results.

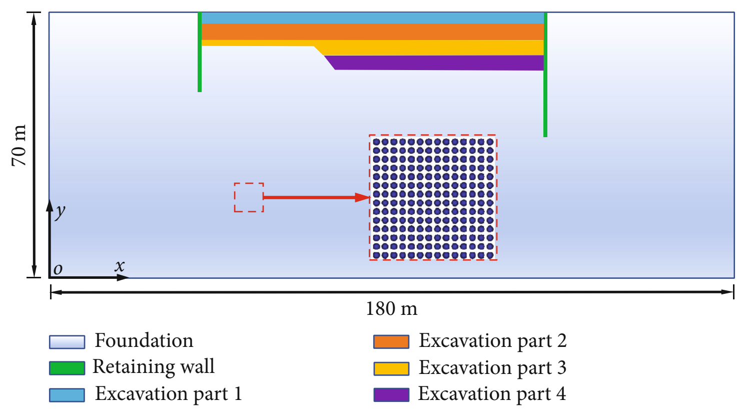

Figure 7: Numerical model of foundation pit excavation.

8. Numerical Results

8.1. Progressive Failure Process of Foundation Pit Excavation. Figure 8 shows the progressive failure process of the foundation pit excavation without retaining walls (Figure 8(a)) and with retaining walls (Figure 8(b)). As can be seen, for the condition without retaining walls, the failure zone firstly appears at the corner of the excavation part 2 and then develops to the deep of the foundation. Meanwhile, after the excavation of the last part, the failure zone appears on the slope surface. For the condition with retaining walls, the failure part of the foundation pit is similar to that of the condition without retaining walls, which appears at the corner of the excavation part 2. What is different is that the failure of the foundation only develops longitudes along the retaining wall, which is due to the fact that the existence of the retaining wall restricts the development trend of the failure zone to the deep. At the same time, after the final excavation, there is no failure particle on the exposed surface of the foundation pit, which is due to the fact that the retaining walls limit the large deformation of the soil, so the disturbance of the soil inside the foundation pit is relatively small, and the foundation pit is stable.

8.2. Influence of Retaining Wall Stiffness on the Failure Zone. To quantitatively characterize the influence of different retaining wall stiffness on the failure zone of foundation pit excavation, the radio of the retaining wall elasticity modulus and the foundation elasticity modulus E_R/E_F is set to be 2, 5, 10, and 20, and corresponding numerical models are established for simulating. Figure 9 shows the failure zone under different conditions. As can be seen, the stiffness of retaining wall does have great impacts on the failure modes of the foundation pit. When the retaining wall stiffness is relatively small, the failure zone is limited to the small range in front of the retaining walls. This is because coordination deformation of retaining wall and foundation is good. However, when the retaining wall stiffness is large, the degree of incongruous deformation increases, and the failure range of soil becomes larger gradually. What should be noticed is that when $E_R/E_F = 20$, a large failure zone appears behind the retaining wall, which indicates that risk of foundation pit instability is increasing under this circumstance.

Figure 10 shows the damage counts under different retaining wall stiffness. As can be seen, with the increasing of E_R/E_F, the damage counts increase accordingly, which means that high stiffness retaining wall will have negative effect on the foundation pit stability.

9. Discussions

9.1. Validation of Numerical Simulation Rationality. Previous studies have rarely focused on the progressive failure process during the foundation pit excavation. In our work, we carried out the numerical simulations on the progressive failure processes of foundation pit excavation for the first time.

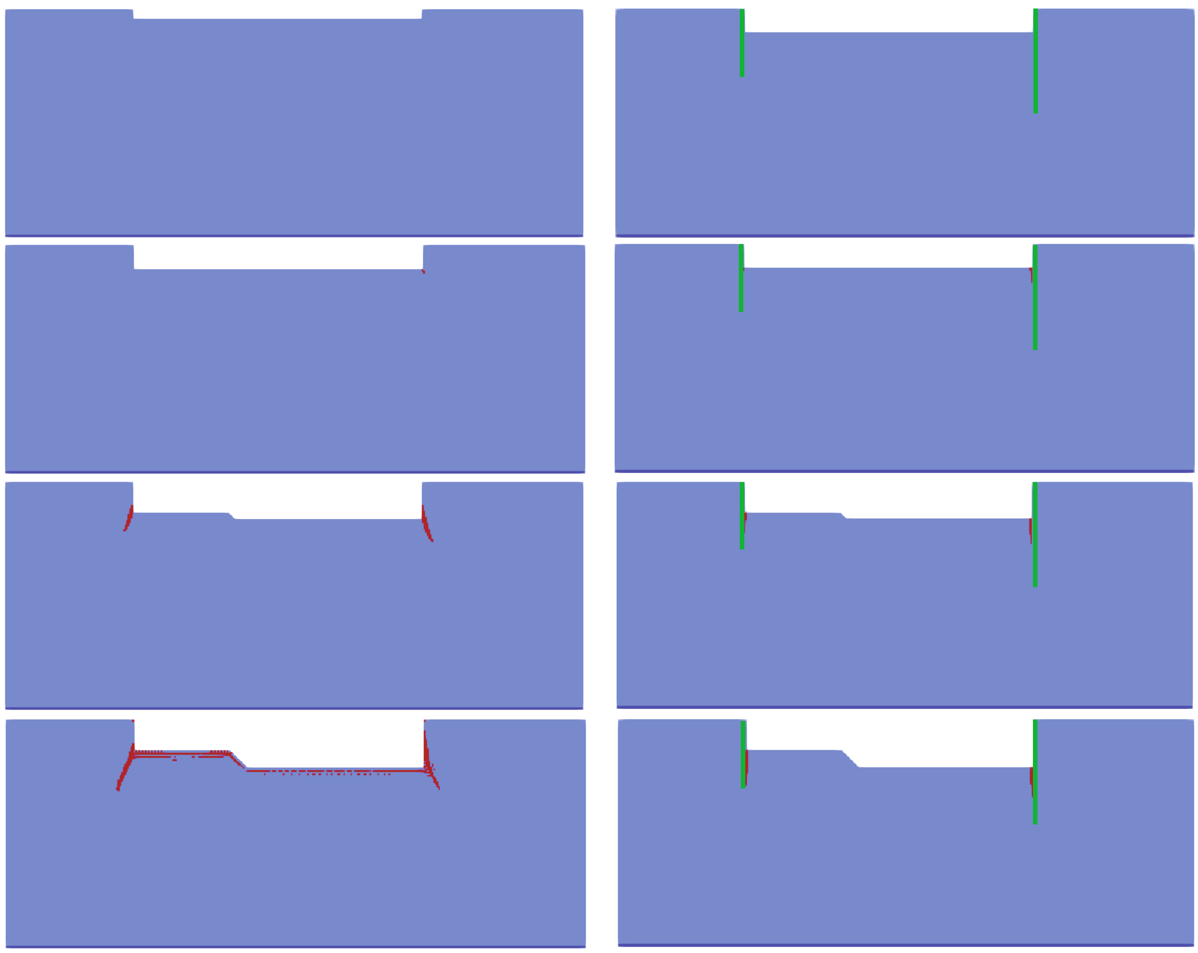

(a) (b)

Figure 8: Progressive failure processes of foundation pit. (a) Numerical model without retaining walls. (b) Numerical model with retaining walls (the green part is the retaining walls).

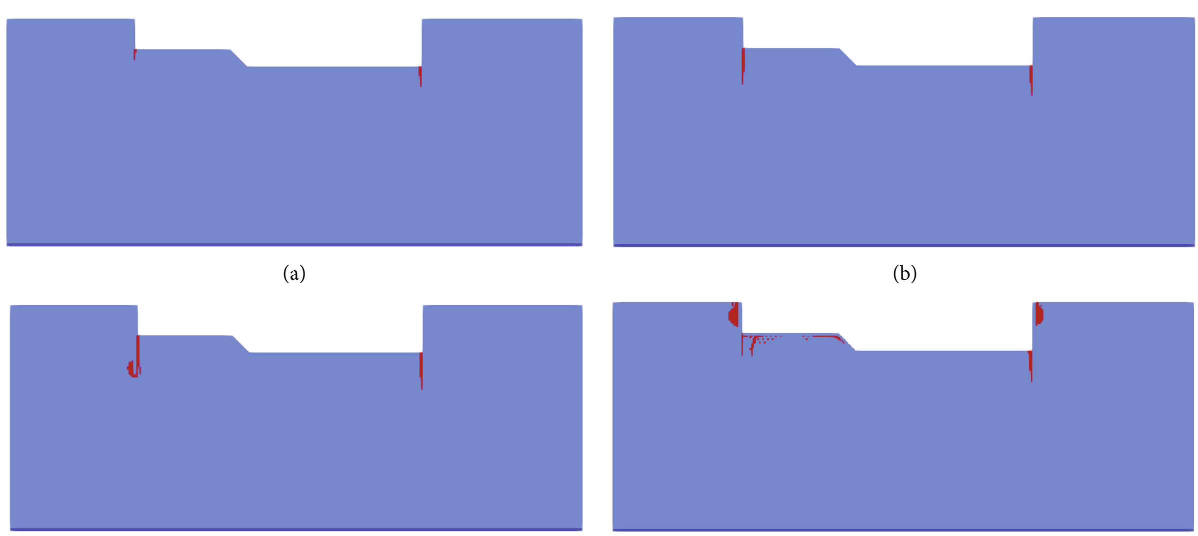

(a) (b) (c) (d)

Figure 9: Failure zone under different retaining wall stiffness. (a) $E_R/E_F = 2$; (b) $E_R/E_F = 5$; (c) $E_R/E_F = 10$; (a) $E_R/E_F = 20$.

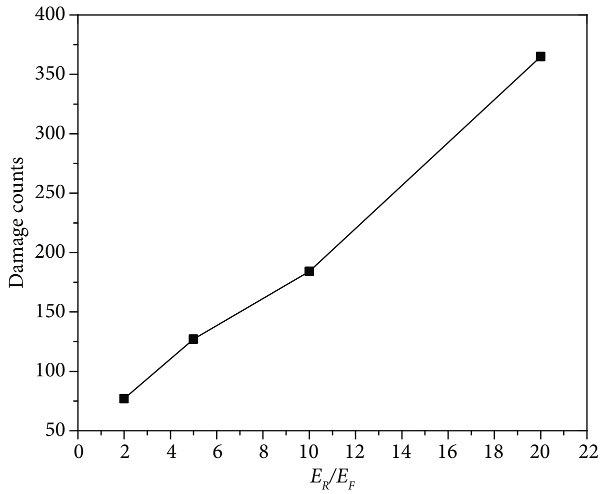

FIGURE 10: Damage counts under different retaining wall stiffness.

(a)

(b)

FIGURE 11: Comparisons of foundation pit failure positions between IKSPH and engineering practice. (a) IKSPH results. (b) Engineering practice positions.

Figure 11 shows the comparisons between the IKSPH results and the engineering practice. As can be seen, the failure positions are all at the corner of the foundation pit, which verifies the proposed method. Figure 12 shows the maximum principal stress distributions and the particle velocity distributions during excavation. We can find that the tensile stress concentrates at the foundation pit corner, meanwhile, the velocity vector deviates at the corners of the foundation pit, indicating

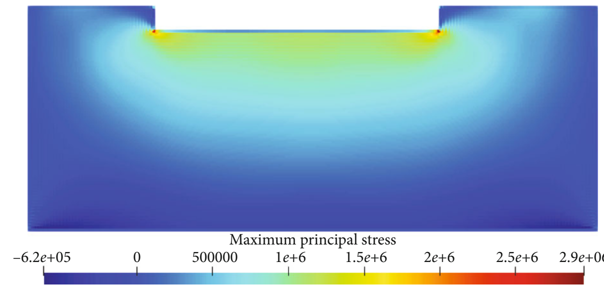

(a)

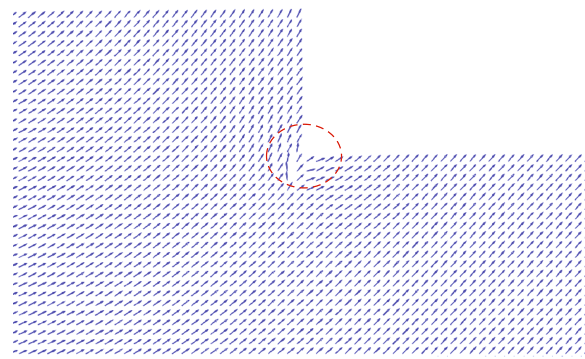

(b)

FIGURE 12: Distributions of maximum principal stress and the particle velocity. (a) Distributions of maximum principal stress. (b) Distributions of particle velocity.

that the failure of the corner is the tensile failure. Therefore, in practical engineering, support should be set at the corner points of the foundation pit to prevent tensile failure.

9.2. Application Prospects of IKSPH in Failure Prediction of Foundation Pit Excavation. In this paper, by improving the smoothing kernel function in the traditional SPH method, we can realize the failure modeling of particles at microscale. Compared with traditional FEM, IKSPH gets free from mesh grids, which can therefore well reflect the large deformation, failure, damage, and other discontinuous characteristics of rock and soil. Meanwhile, compared with DEM, its parameters have definite physical meanings. Therefore, IKSPH has a wide application prospect in rock and soil failure simulation and prediction.

What should be stressed is that this paper only considers the numerical realization of foundation pit excavation under simple circumstances. In practical foundation pit engineering, there are many kinds of supports and the soil properties are different. Therefore, the real construction processes of actual engineering should be taken into consideration in the subsequent research. Meanwhile, the actual foundation pit engineering is a complex 3D problem, and simplifying into a 2D problem will miss lots of useful information. However, the computational efficiency of the 3D IKSPH program is one of the difficult problems in the field of geotechnical simulation. So future research should focus on the development of 3D parallel IKSPH program and its applications in 3D foundation pit excavation simulation.

10. Conclusions

(1) The failure mark η is introduced in this paper, and the smoothing kernel function in the traditional SPH method has been improved, which can realize the simulation of progressive failure process of rock and soil

(2) The "Killing Particle Method" has been put forward to realize the complex excavation processes of foundation pit

(3) The progressive failure processes of the foundation pit are simulated. The failure zone of the excavated foundation pit without retaining walls appears at the corner and then gradually develops into the deep. However, the failure zone of the excavated foundation pit with retaining walls only develops longitudes along the retaining wall

(4) The stiffness of the retaining wall has a great influence on the failure zone of foundation pit excavation. The greater the stiffness of the retaining wall, the greater the damage degree

(5) The numerical simulation results of IKSPH are consistent with the calculation results of commercial software ABAQUS and engineering practice, which verifies the correctness of the proposed method. Meanwhile, future research directions should focus on the development of a 3D parallel IKSPH program

Data Availability

The program data used to support the findings of this study are restricted by Hohai University in order to protect the privacy. Data are available from yushuyang_hhu@163.com for researchers who meet the criteria for access to confidential data.

Conflicts of Interest

None of the authors have any conflicts of interest.

Acknowledgments

We acknowledge the financial supports of the National Natural Science Fund (Grant no. U1765204), "the Fundamental Research Funds for the Central Universities" (B210203078). Meanwhile, the authors greatly wish to express their thanks to Professor Bi Jing, Wuwen Yao, and Yongchuan Yu for their technical supports in the IKSPH programming.

References

[1] G. Wang and Y. Yang, "Effect of cantilever soldier pile foundation excavation closing to an existing composite foundation," *Journal of Central South University*, vol. 20, no. 5, pp. 1384–1396, 2013.

[2] X. Zhang, X. Ou, and J. Yang, "Deformation response of an existing tunnel to upper excavation of foundation pit and associated dewatering," *International Journal of Geomechanics*, vol. 17, no. 4, p. 04016112, 2017.

[3] Y. Yang, A. Hu, and K. Xie, "Analysis of measured characteristics and environmental effects of excavation of a deep foundation pit in soft soil," *Chinese Journal of Civil Engineering*, vol. 44, S2, pp. 90–93, 2011.

[4] Q. Li, *Field Test Study on Deformation Behavior of Deep Foundation Pit in Soft Soil*, Tongji University, 2008.

[5] R. Zhang and J. Qian, "Model test study on ground subsidence induced by displacement of retaining wall of foundation pit," *Rock and Soil Mechanics*, vol. 36, no. 10, pp. 2921–2926, 2015.

[6] M. Xia, "Simulation test of penetration depth of multi-supported diaphragm wall," *Dam observation and geotechnical testing*, vol. 2, pp. 28–36, 1984.

[7] Z. Jiang, "Theoretical analysis of adjacent pipeline deformation caused by excavation of foundation pit," *Journal of Underground Space and Engineering*, vol. 10, no. 2, pp. 362–368, 2014.

[8] H. Gao, D. Huo, and L. Tao, "Lateral displacement prediction of deep foundation pit excavation based on chaos theory and confidence domain," *Journal of Beijing University of Technology*, vol. 2, pp. 136–140, 2005.

[9] Z. Zhang, K. Jiang, and Z. Wang, "Theoretical analysis of longitudinal deformation of existing tunnel induced by excavation of foundation pit considering Pasternak foundation model," *Tunnel construction*, vol. 40, S1, pp. 57–67, 2020.

[10] C. Tang, L. Li, and C. Li, "Stability analysis of geotechnical engineering RFPA strength reduction method," *Chinese Journal of Rock Mechanics and Engineering*, vol. 8, pp. 1522–1530, 2006.

[11] Z. Liang, *Analysis of Rock Failure Process under Three Dimensional Condition and Study on Its Numerical Test Method*, Northeastern University, 2005.

[12] G. Lei, P. Guo, and F. Hua, "Observed performance and FEM-based parametric analysis of a top-down deep excavation in soil-rock composite stratum," *Geofluids*, vol. 2021, 17 pages, 2021.

[13] W. Ye, J. Liu, and H. Fang, "High-performance analysis of the interaction between plate and multi-layered elastic foundation using SBFEM-FEM," *Composite Structures*, vol. 214, pp. 1–11, 2019.

[14] G. Kung and C. Juang, "Evaluation of a simplified small-strain soil model for analysis of excavation-induced movements," *Canadian Geotechnical Journal*, vol. 44, no. 6, pp. 726–736, 2007.

[15] R. Branco, F. Antunes, and J. Costa, "A review on 3D-FE adaptive remeshing techniques for crack growth modelling," *Engineering Fracture Mechanics*, vol. 141, pp. 170–195, 2015.

[16] M. Cai, P. Kaiser, and H. Morioka, "FLAC/PFC coupled numerical simulation of AE in large-scale underground excavations," *International Journal of Rock Mechanics & Mining Sciences*, vol. 44, no. 4, pp. 550–564, 2007.

[17] Y. Meng, "PFC2D simulation on stability of loose deposits slope in highway cutting excavation," *Geotechnical & Geological Engineering*, vol. 35, no. 2, 2016.

[18] Y. Ohnishi, T. Sasaki, and T. Koyama, "Recent insights into analytical precision and modelling of DDA and NMM for practical problems," *Geomechanics and Geoengineering*, vol. 9, no. 2, pp. 97–112, 2014.

[19] S. Miki, T. Sasaki, and T. Koyama, "Development of coupled discontinuous deformation analysis and numerical manifold

method (NMM–DDA)," *International Journal of Computational Methods*, vol. 7, no. 1, pp. 131–150, 2010.

[20] Y. Shou, X. Zhou, and Q. Qian, "Dynamic model of the zonal disintegration of rock surrounding a deep spherical cavity," *International Journal of Geomechanics*, vol. 17, no. 6, 2016.

[21] X. Zhou and Y. Shou, "Numerical simulation of failure of rock-like material subjected to compressive loads using improved peridynamic method," *International Journal of Geomechanics*, vol. 17, no. 3, 2016.

[22] A. Müller and E. Vargas, "Stability analysis of a slope under impact of a rock block using the generalized interpolation material point method (GIMP)," *Landslides*, vol. 16, no. 4, 2019.

[23] D. Zhang, X. Ma, and P. Giguere, "Material point method enhanced by modified gradient of shape function," *Journal of Computational Physics*, vol. 230, no. 16, pp. 6379–6398, 2011.

Hindawi
Geofluids
Volume 2021, Article ID 4141236, 13 pages
https://doi.org/10.1155/2021/4141236

Research Article

Modified Stochastic Petri Net-Based Modeling and Optimization of Emergency Rescue Processes during Coal Mine Accidents

Xiao Li,[1] **Yongkui Shi**,[1] **Zaiyong Wang**,[1,2] **and Wenquan Zhang**[1,2]

[1]*College of Energy and Mining Engineering, Shandong University of Science and Technology, Qingdao 266590, China*
[2]*State Key Laboratory of Strata Intelligent Control and Green Mining Co-founded by Shandong Province and the Ministry of Science and Technology, Qingdao 266590, China*

Correspondence should be addressed to Yongkui Shi; shiyongkui@163.com

Received 25 May 2021; Accepted 24 July 2021; Published 14 August 2021

Academic Editor: Dan Ma

The coal mine accidents seriously affect the safety and efficiency of mining for coal mining enterprises. The reliable emergency rescue (ER) processes are explored to minimize the loss of accidents. This paper introduces the stochastic Petri net (SPN) and Markov chain (MC) models based on the system structure flow to analyze the ER processes of coal mine accidents. In addition, a triangle fuzzy strategy is presented to optimize the SPN model. The "9·28" major water inrush accident in Shanxi Fenxi Zhengsheng Coal Company of China is adopted to evaluate the time performance and accident data of the ER process. The MC model-based steady-state probabilities of the system under various states are used to calculate the average delay time of this system. The triangular fuzzy strategy is used to analyze the change value of the total time in the ER system at the unit transition speed when the firing rate of each transition is changed, which finds the most time-consuming key activities in the ER process. The results show that SPN and MC can reflect the dynamic behaviors of ER process, which provides a reference for the rescue operations of other coal mine accidents. The triangular fuzzy strategy can quickly find out the key activities affecting the ER time, which greatly decreases the calculations generated by analyzing the total time of the system changed at the unit transition speed.

1. Introduction

Coal provides strong supports for the rapid development of the national economy as one of the main energy sources in China. However, frequent safety accidents during coal mining hindered the healthy development of coal mining enterprises. Government and enterprises have tried to change such a passive situation by improving safety management measures and introducing rescue equipment, but the accidents and casualties have not been fundamentally resolved [1–3]. The relevant accident statistics in 2020 show that 122 coal mines accidents occurred in China. Compared with 2019, the death toll caused by coal mine accidents slightly increased. For example, the "1·12" coal dust explosion in Shannxi Baiji Mining Company induced 21 deaths, and the "12·16" coal gas outburst accident in Guizhou Guanglong coal mine resulted in 16 deaths and 1 injury [4]. Therefore, the establishment of an early warning and rapid rescue framework for coal mine accidents is the key point of current works, which would improve the level of emergency rescue (ER) and reduce or even avoid the casualty caused by accidents [5, 6].

To date, several studies have deeply investigated the ER measures of coal mine accidents [7, 8]. The ER communication system can effectively improve the monitoring accuracy and the efficiency of searching dangerous situations [9]. It is found that the emergency stations covering all mining areas are set up underground to provide medical first aid and transportation of injured in the shortest time [10]. In addition, it is significant for rescue to improve the existing refuge chamber and strengthen the escape simulation training [11].

For major coal mine accidents, the core tasks of various ER processes are to construct the mechanism of ER response and strengthen the evaluation of emergency management. It is well known that effective evaluation and optimization of ER processes in coal mines can improve the efficiency of ER and reduce casualties [12, 13]. A Petri net is an important tool to deal with discrete events, and it is widely used in various fields. Petri nets, as a visual tool for modeling and analysis of the system simulation, can accurately simulate the dynamic behavior of the system and analyze the model characteristics through the definition of assumptions. With the application in various complex systems, Petri nets have evolved into many advanced forms such as color networks, stochastic networks, and object networks. Stochastic Petri nets (SPN) based on time have more advantages in describing the dynamic behavior of a system network. Therefore, SPN is used to study the unreasonable problems in the ER process of the coal mines, which can improve the efficiency of ER and increase the survival probability of trapped miners [14–17].

In this paper, based on the "9·28" major water inrush accident, a coal mine ER model is constructed through SPN, and the effectiveness of the model is analyzed. The steady-state probability, the busy rate of the places, and the utilization rate of transitions are calculated and discussed by MC. The triangular fuzzy strategy is used to analyze the change value of the total time in the ER system after changing the firing rate of each transition and find out the key activities affecting the rescue time.

2. Related Work

2.1. Major ER Policies. In 1978, a national meeting about coal mine ER held by the Ministry of Coal Industry of China provided reliable policy supports for the development of coal mine ER. As time goes on, the coal mine ER management system is gradually improved, the ER team is expanded, and the capability of ER is additionally significantly improved. These improvements can be proved by the fact that 34% of 1363 trapped persons were rescued in 2009, and 72% of 306 trapped persons were rescued in 2014 [18]. Since there are still some gaps compared with developed countries, the Chinese government attaches great importance to improve the ER management system and has proposed to establish an emergency management department. It is believed that this measure will encourage the further improvement of ER level in coal mines.

2.2. Structure of the ER Team. The rescue team and the medical team are the two main components of the ER team. So far, China has built 482 coal mine rescue teams, which are distributed all over the country. The medical team is divided into the national and provincial rescue centers and mine enterprise rescue stations [19]. The rescue ability of the rescue team is very important, so it is necessary to strengthen the daily traditional physical training and skill training. The application of high-tech in the field of ER enhances the practical ability of rescue teams and improves the efficiency of rescue work such as the development of a comprehensive simulation training system for ER, which achieves personnel positioning and environmental monitoring [20, 21].

2.3. Introduction of ER Equipment and Communication Technology. The rescue teams are required to equip with a lot of rescue equipment to deal with different types of coal mine accidents. For instance, the large drainage equipment and mining submersible pumps are used to deal with flood disaster, the rapid sealing and spraying machine are used to deal with fire accidents, the positive pressure blower and exhaust fan are used to deal with gas and coal dust explosion accidents, and the light disaster relief drill is used to deal with roof accidents. Besides, life detectors, support vehicles of multifunctional rescue equipment, and detection robots have also been developed. The use of advanced equipment has greatly enhanced the ability of ER and improved the survival possibility of trapped miners [22–24].

With the development of Internet technology, many new communication technologies have been applied to mine ER such as the video communication between the underground and ground and between the accident scene and ER command departments at all levels [25, 26].

3. Research Methodology

At first, SPN was used to describe and analyze the causal relationship between computer system events. After more than a century of development and improvement, SPN has been extensively used in other fields such as finite state machines, communication protocol, synchronous control, production system, and business process. SPN has the characteristics of graphic visualization and mathematical logic, which can describe highly discrete complex systems [27–31].

3.1. Definition of SPN. SPN can simulate and analyze discrete events of the system during an uncertain time. SPN is a seven-tuple directed graph including place, transition, arc, and firing rate [32].

$$\mathrm{SPN} = (P, T, F, K, W, M, \Lambda), \tag{1}$$

(1) $N = (P, T, F)$ refers to a basic network

(2) $K : P \longrightarrow N^{+} \cup \{\omega\}$, K is the capacity of P on SPN, $k = \infty$

(3) $W : F \longrightarrow N^{+}$, W is a weight function of F on N

(4) $M : P \longrightarrow N$ meet a condition $\forall p \in P, M(p) \leq K(p)$, M_0 is the state marking of SPN

(5) $\Lambda : T \longrightarrow R^{+}$ represents firing function, which is quantitatively analyzed by the firing rate

3.2. Basic Relationship. Events $t_i, t_j \in T$ have a sequential relationship on mark M. That is, $M[t_i\rangle M' \wedge -M[t_j\rangle \wedge M'[t_j\rangle$ [33], as shown in Figure 1.

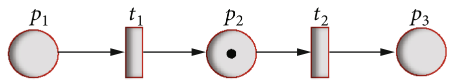

Figure 1: Sequential relationship of an SPN model.

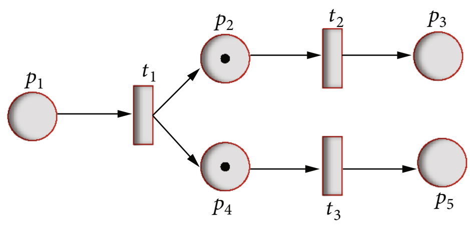

Figure 2: Concurrency relationship of an SPN model.

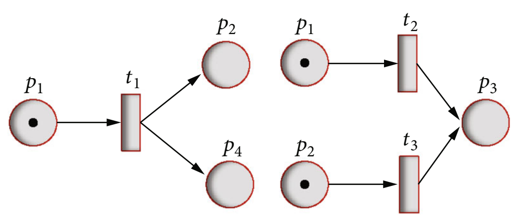

Figure 3: Conflicted relationship of an SPN model.

Events $t_i, t_j \in T$ accept the weight on mark M, resulting in a concurrency relationship, the satisfied relations are as follows:

$$M[\{t_i, t_j\}\rangle \Leftrightarrow \forall p \in P.W(p, t_i) + W(p, t_j) \le M(p) \le K(p) - W(t_i, p) - W(t_j, p),$$

$$M[\{t_i, t_j\}\rangle M' \Leftrightarrow [\{t_i, t_j\}\rangle \wedge \forall p \in P.M'(p) = M(p) + W(t_i, p) + W(t_j, p) - W(p, t_i) - W(p, t_j),$$

as shown in Figure 2.

Events $t_i, t_j \in T$ have a conflicted relationship on mark M [33]. That is,$t_i \ne t_j \wedge M[t_j\rangle \wedge \neg M[\{t_i, t_j\}\rangle$, as shown in Figure 3.

3.3. Model Construction of SPN. The SPN model is shown in Figure 4. $\{p_1, p_2, p_3, p_4, p_5\}$ refers to a set of classical places. $\{t_2, t_2, t_3\}$ refers to a transition set containing time. For example, t_1 represents the time taken from p_1 to p_2 and p_3. After t_1 is fired, p_2 generates two tokens and p_3 generates one token. The number marked on the directed arc indicates the weight. If there is no number, the weight is 1.

The analysis process of the SPN model is as follows: firstly, give place p_1 a token to fire transition t_1, so that place p_2 generates two tokens and place p_3 generates one token. Then, it is judged whether the number of tokens in places p_2 and p_3 meets the condition of firing transition t_2, and if so, place p_4 can be reached. Finally, we judge the condition of firing transition t_3 according to the previous method. If the condition is met, it will reach the termination place p_5, and the process will end.

The implementation steps of using the SPN model to analyze the performance of the ER process for coal mine accidents are as follows [34–36]:

(1) The systematic SPN model is established to verify the validity of the model. Here, T-invariant method is chosen to realize this process. A linear algebraic matrix equation is constructed to determine the performance of the SPN model

$$Cy = (O - I)y = 0, \tag{2}$$

where C refers to the incidence matrix, O refers to the postmatrix, I is the prematrix, and Y is a row vector, representing T-invariant

(2) According to the initial mark M_0 and firing rate λ, the isomorphic Markov chain (MC) is obtained [37]

(3) The MC is studied. Based on the steady-state probability, the system performance is analyzed and evaluated. The steady-state probability in MC is regarded as a row vector $X = (x_1, x_2, \cdots, x_n)$, and the linear equations $XQ = 0$ are listed

$$\begin{aligned} &XQ = 0, \\ &\sum x_i = 1, 1 \le i \le n, \end{aligned} \tag{3}$$

where Q represents the state transition matrix

The linear equations are calculated to obtain the steady-state probability.

$$P[M_i] = x_i (1 \le i \le n), \tag{4}$$

$$Q = [q_{ij}]. \tag{5}$$

For the nondiagonal element q_{ij},

$$q_{ij} = \begin{cases} q_{ij}, \text{when the state } M_i \text{ can reach the state } M_j, \text{the line is marked } q_{ij}, \\ 0, \text{when the states } M_i \text{ can not reach the state } M_j. \end{cases} \tag{6}$$

For the diagonal element q_{ij},

$$q_{ij} = -\Sigma_k q_{ij}, \tag{7}$$

where k refers to the number of states connected to M_i.

$\forall p \in P, \forall i \in N$, $P[M(p) = i]$ is the probability that each p with i marks. The busy probability of place indicator can be calculated using Equation (8).

$$P[M(p) = i] = \Sigma p[M_j]. \tag{8}$$

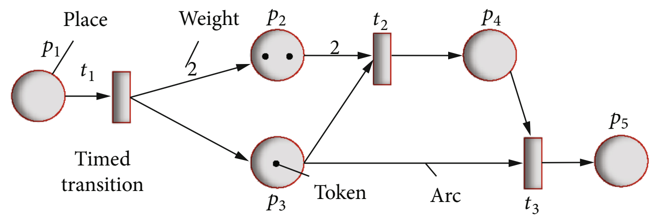

Figure 4: Representation of the SPN model.

The utilization of a transition indicator refers to the sum of all steady-state probability of firing transition t and is calculated as follows:

$$U(t) = \Sigma_{m \in E} P[M]. \tag{9}$$

The token rate of transition indicator represents the average token number of transition flowing into the place p of transition t per unit time. The calculation formula is as follows:

$$R(t, p) = w(t, p) \times U(t) \times \lambda. \tag{10}$$

Suppose $\forall p \in P$, the average token number $\bar{N}$ of the system refers to the average value of marks contained by p_i in any reachable marking graph. The marked average value of the set $p_i \in P$ of a place is the sum of the average value of each place.

$$\bar{N} = \Sigma j \times P[M(p_i) = j]. \tag{11}$$

The average delay time t of the system is the ratio of the average token number $\bar{N}$ and the token rate $R(t, p)$ of transition.

$$\bar{T} = \frac{\bar{N}}{R(t, p)}. \tag{12}$$

3.4. The Optimization Strategy Based on Triangular Fuzzy (TF). The TF is a widely used function of fuzzy mathematics, which is mainly suitable for the situation of insufficient field data and low precision of monitoring instruments. The variables are fuzzified to form a trust interval with the upper and lower limits [38, 39]. Assume that the fuzzy variable is

$$\tilde{E} = (e^-, e, e^+), e^- \le e \le e^+, \tag{13}$$

where e refers to the value of the variable. e^- and e^+ represent the lower and upper limits of fuzzy variables, respectively.

The corresponding triangular membership function is

$$\eta_E = \begin{cases} 0, & x < e^-, \\ \dfrac{x - e^-}{e - e^-}, & e{-}\le x \le e, \\ \dfrac{e^+ - x}{e^+ - e}, & e \le x \le e^+, \\ 0, & x > e^+, \end{cases} \tag{14}$$

where η_E is the membership degree of the fuzzy variable and x is a variable.

The triangular membership function is calculated by using X cut set to obtain a fuzzy interval.

$$\begin{aligned} E^{(a)} &= \left\{\min\left[e^{(a)}\right], \max\left[e^{(a)}\right]\right\} \\ &= \left[e^- + (e - e^-)a, e^+ - (e^+ - e)a\right] \quad a \in [0, 1]. \end{aligned} \tag{15}$$

Optimization steps of the triangular fuzzy are as follows:

(1) The firing rate $\tilde{\lambda} = (\lambda_1, \lambda_2, \cdots, \lambda_n)$ in the SPN model is fuzzified according to different proportions [40]. The fuzzy intervals $[\lambda_i^-, \lambda_i]$ and $[\lambda_i, \lambda_i^+]$ of firing rate λ_i are constructed

(2) a is valued in the interval $[0, 1]$, which meets the rule of increasing step by step. For example, $a = 0, 0.1, 0.2, \cdots, 1$. Substituting different a values into formula (15) to obtain $E_i^{(a)}$. Then, substituting $\lambda' = (\lambda_1, \lambda_2, \cdots \lambda_{i-1}, E_i^a, \lambda_{i+1}, \cdots, \lambda_n)$ into the SPN mode to calculate the interval $[\min_{0\le a\le 1}(\bar{T}_i^a), \max_{0\le a\le 1}(\bar{T}_i^a)](i = 1, 2, \cdots, n)$

(3) The total time of system change under unit transition rate is

$$\delta_i = \left|\frac{\max(T_i^a) - \min(T_i^a)}{\lambda_i^+ - \lambda_i^-}\right| \tag{16}$$

(4) When δ_i is larger than most δ values, it shows that the change of transition has great influences on the average delay time of the system. Therefore, the optimized SPN model can be obtained only by simulating δ_i with a large numerical value

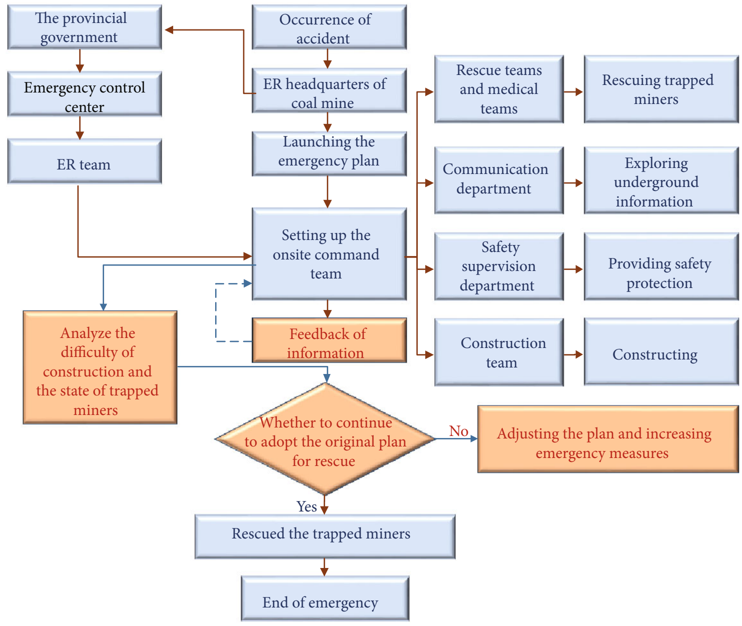

Figure 5: The ER process of the coal mine.

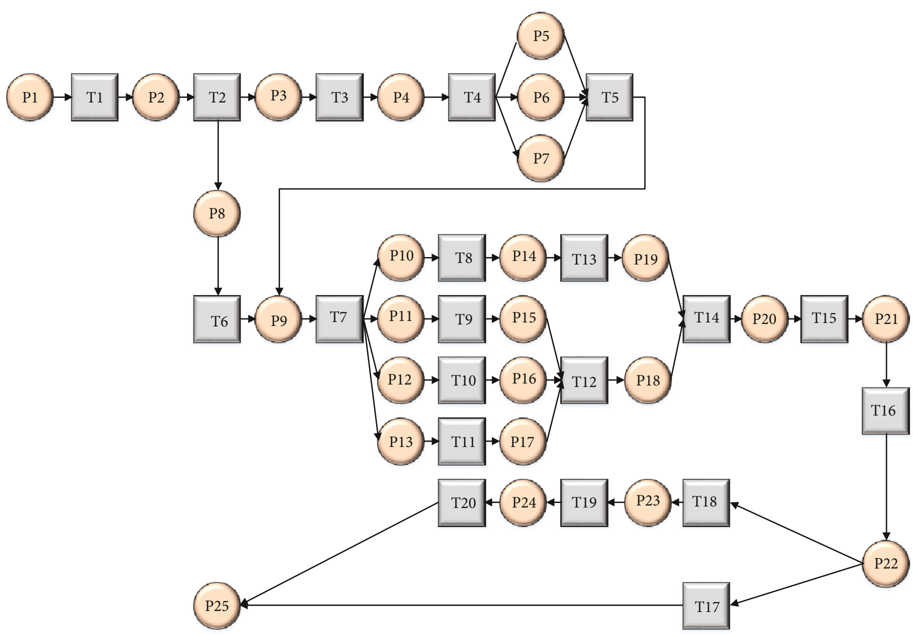

Figure 6: The SPN of ER process during coal mine accident.

4. Case Study

4.1. Case Introduction. The "9·28" major water inrush accident in the Shanxi Fenxi Zhengsheng Coal Company of China is used as a case to validate the proposed model. In this case, the water inrush occurred in the east flank return airflow roadway to the coal mine dispatching room. Though the leader of underground miners executed emergency evacuations immediately, many miners were still trapped for the far distance between the working face and the shaft. According to the guidance of higher authorities, coal mine leaders executed ER plan, set up an ER headquarter, and launched rescue operations. The ER process for this accident is shown in Figure 5.

4.2. Performance Analysis of Water Inrush ER Process Based on SPN Model. Figure 6 shows the SPN model of the ER process. The SPN model combines all the ER activities and points out the relationship among these activities, as shown in Figure 6.

In Figure 6, a place represents the event state and a transition represents the event activity during the ER process. The process includes 25 places and 20 transitions, and their respective definitions are shown in Table 1.

Table 1: Definitions of places and transitions.

	Places		Transitions
P1	Accident occurrence	T1	Reflecting accident information
P2	ER headquarters of coal mine	T2	Reporting the accident to the superior
P3	The provincial government	T3	Issuing rescue command
P4	Emergency control center	T4	Scheduling according to the authority
P5	Experts	T5	Going to the coal mine
P6	Rescue teams and medical teams	T6	Analyzing emergency conditions and making ER plan
P7	Technicians	T7	Allocating resources and organizing team
P8	Implement emergency plan	T8	Starting preparatory work by the communication department
P9	Set up the onsite command team	T9	Starting preparatory work by the rescue teams and medical teams
P10	Communication department	T10	Starting preparatory work by the safety supervision department
P11	Rescue teams and medical teams	T11	Starting preparatory work by the construction team
P12	Safety supervision department	T12	Draining in flooded roadway
P13	Construction team	T13	Exploring information underground
P14	Communications department that finished preparatory work	T14	Finding the location of the trapped miners
P15	The rescue teams and medical teams that finished preparatory work	T15	Reporting to the onsite command team
P16	The safety supervision department that finished preparatory work	T16	Analyzing the difficulty of construction and the state of victims
P17	Construction team that finished preparatory work	T17	Rescuing the trapped miners
P18	Advance of rescue roadway	T18	Adjusting emergency plan and increasing emergency measures
P19	General information	T19	Adding large rescue equipment to join in rescue
P20	Important information	T20	Providing first aid to the victims by rescue teams and medical teams
P21	Information received by the command team		
P22	Judgment of accident grade		
P23	Greater rescue efforts		
P24	Key rescue sections that have been breakthrough		
P25	End of ER		

T-invariant and P-invariant are common methods to analyze the validity of the model. The validity of the model is analyzed by the T-invariant method [41]: $Y_1 = (1, 1, 1, 1, 1, 1, 1, 1, 1, 0, 0, 1, 0, 1, 1, 1, 1, 1, 1, 1, 1)$ and $Y_2 = (1, 1, 1, 1, 1, 1, 1, 1, 0, 1, 1, 1, 1, 1, 1, 1, 1, 1, 1, 1, 1)$.

Y_1 and Y_2 have nonnegative integer solutions. The existence of T-invariant in the SPN model means that the SPN model has the properties of reachability and liveness. In addition, $Y_1 > 0$ and $Y_2 > 0$ mean that the SPN model is bounded which proves that the SPN model is correct and reasonable [42].

5. Results and Discussion

The time parameters that obeyed a certain probability distribution are added in the SPN, and the time of random variables is associated with the transitions. Through the accident investigation, the time consumed in each link of the accident is collected to obtain the average time t of each transition. According to the firing rate formula, the average firing rate of 20 transitions is obtained, and the results are as shown: $\lambda = 1/t = (1/10, 1/5.1/5, 1/20, 1/150, 1/20/1/60, 1/15, 1/15, 1/15, 1/20, 1/170, 1/720, 1/120, 1/5, 1/20, 1/200, 1/10, 1/200, 1/150)$.

5.1. Isomorphic MC. The performances of the SPN and MC models are consistent, and a bounded SPN is equivalent to a finite MC. The structure and performance analysis of the SPN model are integrated into the MC model to obtain the isomorphic MC, which can better analyze the SPN performance. The flow chart of the MC is shown in Figure 7.

According to formulas (4), (8), and (9), the steady-state probability, the busy rate of the places, and the utilization rate of the transitions are calculated, respectively, as shown in Tables 2–4.

In Table 3, the busy rates of places of P9 and P14~P19 are higher, which indicates that the state information of these places cannot be effectively processed and results in the accumulation of information.

The onsite command team (place P9) is composed of coal mine leaders, experts, technicians, rescue team, and medical team, which formulates and adjusts the ER plan according to the onsite situation, and maintains communication with relevant superior departments. Since the experts of research

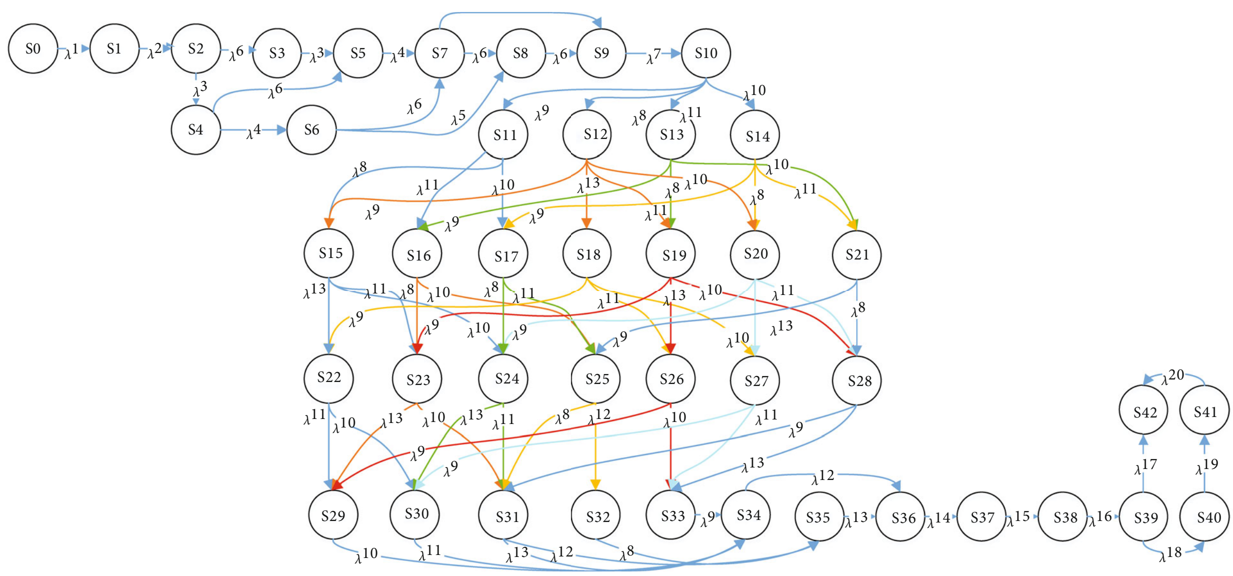

Figure 7: Isomorphic MC equivalents to the SPN model.

Table 2: Steady-state probability.

Steady-state probability	Value	Steady-state probability	Value	Steady-state probability	Value
$P(M_0)$	0.00634	$P(M_{14})$	0.00092	$P(M_{28})$	0.00205
$P(M_1)$	0.00190	$P(M_{15})$	0.00104	$P(M_{29})$	0.00006
$P(M_2)$	0.00254	$P(M_{16})$	0.00066	$P(M_{30})$	0.00016
$P(M_3)$	0.00063	$P(M_{17})$	0.00105	$P(M_{31})$	0.22132
$P(M_4)$	0.00507	$P(M_{18})$	0.00001	$P(M_{32})$	0.00004
$P(M_5)$	0.00761	$P(M_{19})$	0.00065	$P(M_{33})$	0.00006
$P(M_6)$	0.00448	$P(M_{20})$	0.00104	$P(M_{34})$	0.23313
$P(M_7)$	0.09063	$P(M_{21})$	0.00066	$P(M_{35})$	0.22339
$P(M_8)$	0.00060	$P(M_{22})$	0.00002	$P(M_{36})$	0.00634
$P(M_9)$	0.03804	$P(M_{23})$	0.00205	$P(M_{37})$	0.00317
$P(M_{10})$	0.00254	$P(M_{24})$	0.00406	$P(M_{38})$	0.00634
$P(M_{11})$	0.00092	$P(M_{25})$	0.00207	$P(M_{39})$	0.00576
$P(M_{12})$	0.00092	$P(M_{26})$	0.00001	$P(M_{40})$	0.03458
$P(M_{13})$	0.00063	$P(M_{27})$	0.00002	$P(M_{41})$	0.08646

Table 3: The busy rate of the places.

Place	Value	Place	Value
$P[M(p_1) = 1]$	0.00634	$P[M(p_{13}) = 1]$	0.01268
$P[M(p_2) = 1]$	0.00190	$P[M(p_{14}) = 1]$	0.45652
$P[M(p_3) = 1]$	0.00317	$P[M(p_{15}) = 1]$	0.46655
$P[M(p_4) = 1]$	0.01268	$P[M(p_{16}) = 1]$	0.46655
$P[M(p_5) = 1]$	0.09511	$P[M(p_{17}) = 1]$	0.46338
$P[M(p_6) = 1]$	0.09511	$P[M(p_{18}) = 1]$	0.22978
$P[M(p_7) = 1]$	0.09511	$P[M(p_{19}) = 1]$	0.23980
$P[M(p_8) = 1]$	0.01268	$P[M(p_{20}) = 1]$	0.00317
$P[M(p_9) = 1]$	0.17556	$P[M(p_{21}) = 1]$	0.00634
$P[M(p_{10}) = 1]$	0.00951	$P[M(p_{22}) = 1]$	0.00576
$P[M(p_{11}) = 1]$	0.00951	$P[M(p_{23}) = 1]$	0.03458
$P[M(p_{12}) = 1]$	0.00951	$P[M(p_{24}) = 1]$	0.08646

Table 4: Utilization rate of transitions.

Transition	Value	Transition	Value
$U(t_1)$	0.00634	$U(t_{11})$	0.01270
$U(t_2)$	0.00190	$U(t_{12})$	0.45652
$U(t_3)$	0.00317	$U(t_{13})$	0.45652
$U(t_4)$	0.01268	$U(t_{14})$	0.00634
$U(t_5)$	0.09511	$U(t_{15})$	0.00317
$U(t_6)$	0.01269	$U(t_{16})$	0.00634
$U(t_7)$	0.03804	$U(t_{17})$	0.00576
$U(t_8)$	0.00565	$U(t_{18})$	0.00576
$U(t_9)$	0.00951	$U(t_{19})$	0.03458
$U(t_{10})$	0.00951	$U(t_{20})$	0.08646

institutes and universities were in different cities, they cannot arrive at the accident site in time, which caused the waste of the ER time. Therefore, the emergency center should improve work efficiency and optimize deployment time.

After the accident, the busy rate of the places of the P14 and P16 (coal enterprise) is very high. Through deep analysis, it is found that the number of emergency training is less and the rescue work is not proficient enough for employees in the communication department and the safety supervision department. The mine leaders should pay attention to the daily emergency training and strengthen the emergency response awareness of the miners.

The medical rescue team (place P15) includes medical rescue stations of the mining enterprise and medical personnel assisted by other areas. Because the two teams had not trained together before, the cooperation of rescue teams was not good enough, which caused the redundancy of place P15.

The construction team (place P17) mainly includes the rescue team from the provincial mine rescue base and the mine enterprise rescue team. Because many rescue machines are required to be transported, it is very likely that vehicles will be congested and cannot arrive quickly due to the influence of traffic conditions.

Places P18 and P19 are in a synchronized state. Due to the uncertainty of the accident location and the influence of the complex underground environment on the equipment such as life detectors, it is difficult to find the location of the trapped miners for a short time. In the early stage of the rescue, the rescue team can only use drainage equipment to drain the floodwater in the roadway. Therefore, we should increase the number of rescue equipment and use more advanced rescue equipment to deal with ER of coal mine accidents.

It can be seen from Table 4 that the utilization rates of transitions T12 and T13 are much higher than that of the remaining transitions, which indicates that the activities they represented spend more time.

T12 indicates the draining in the flooded roadway. During this process, it is difficult to determine the exact position of the trapped miners, so the ER team can only gradually rescue along the rescue roadway based on the known information and experience. In the flooded roadway, life detectors and other equipment are used to detect the vital signs nearby. This work is difficult because it not only needs to clean up the accumulated water and gravel in the roadway but also needs to stabilize the roadway to ensure its safety, which leads to the total time of T12 is very long.

T13 indicates the exploring information underground. In this process, because the communication staff need to follow the construction team to carry out underground detection and feedback the real-time information to the ER headquarters immediately, which also takes a lot of time.

The average delay time of the system can be calculated according to formulas (10)–(12): $\overline{T} = \bar{N}/R(t,p) = 2.7702/0.0101 = 274.44$ min.

5.2. Optimization Analysis of ER Process. In this process, the SPN model of the emergency rescue process was analyzed, the busy places and high utilization of transitions were identified, and improvement measures were suggested. We changed some transition's time and calculated the corresponding average delay time of the whole ER system.

The method of changing the firing rate of each transition is adopted to optimize the total delay time of the system. When the speed range of the firing rate of each transition is constant, the different decreases of the total delay time have different impacts on the whole ER system. A lot of computations are needed to substitute the firing rate of each transition into the SPN model, so a triangular fuzzy strategy is proposed to optimize the SPN, which greatly simplifies the calculation.

Table 5: Changed value of the total time of the ER system when the transition unit changed.

Transition	Unit value	Sort	Transition	Unit value	Sort
λ_{12}	45889.04	1	λ_{14}	224.91	11
λ_{13}	44605.57	2	λ_{10}	209.04	12
λ_{19}	2702.56	3	λ_{9}	209.04	13
λ_{20}	915.48	4	λ_{17}	155.05	14
λ_{5}	907.76	5	λ_{18}	134.36	15
λ_{7}	460.77	6	λ_{1}	128.00	16
λ_{6}	287.16	7	λ_{3}	71.50	17
λ_{11}	265.23	8	λ_{15}	71.27	18
λ_{4}	238.93	9	λ_{2}	71.00	19
λ_{16}	235.59	10	λ_{8}	36.26	20

Firstly, 5% fuzzy degree is set for each transition to get the fuzzy interval of each transition according to formula (15). Then, the average delay time of the system corresponding to the transition is calculated in the SPN model. Finally, according to formula (16), the change value δ of the total time of the ER system is calculated when each transition unit changes, and the results are shown in Table 5.

Table 5 shows that when the fuzzy degrees of transitions are same, the δ values corresponding to transitions are quite different. The value of δ_{12} corresponding to λ_{12} is 1265 times of δ_8 corresponding to λ_8. Therefore, changing the value of λ_{12} can reduce the total system time more than changing the value of λ_8. In addition, the values of λ_{13},λ_{19},λ_{20}, and λ_5 have the same effect on reducing the total time, so only five parameters need to be changed to optimize the SPN model.

Firstly, it is assumed that only the value of λ_{12} is changed and the remaining values are constant. The results are shown in Figure 8.

Figure 8 shows that when the value of λ_{12} changes from 0 to 0.003, the probability of $P(M_{34}) = (\mathrm{P15, P16, P17, P19})$ is greatly decreased. The probability of $P(M_{31}) = (\mathrm{P14, P15, P16, P17})$ is slightly increased when the value of λ_{12} changes from 0 to 0.0009 but decrease gradually when the value of λ_{12} changes from 0.0009 to 0.003.

With the advancing speed of the rescue roadway in the mining area increases, the communication department will find the location of trapped miners underground faster in the rescue process and promptly report the rescue progress to the ER headquarters of coal mine. The command team masters the latest rescue situation in order to quickly adjust the plan and deploy rescue measures. Therefore, it is necessary to carry out a reasonable allocation of emergency resources and special drainage equipment so that the medical rescue team, the safety supervision department, the construction team, and the communication department can quickly put into the ER work. Meanwhile, the safety supervision department, communication department, and medical rescue team from the mine enterprise must strengthen the daily management and emergency training. The emergency center should request nearby hospitals to allocate medical teams for

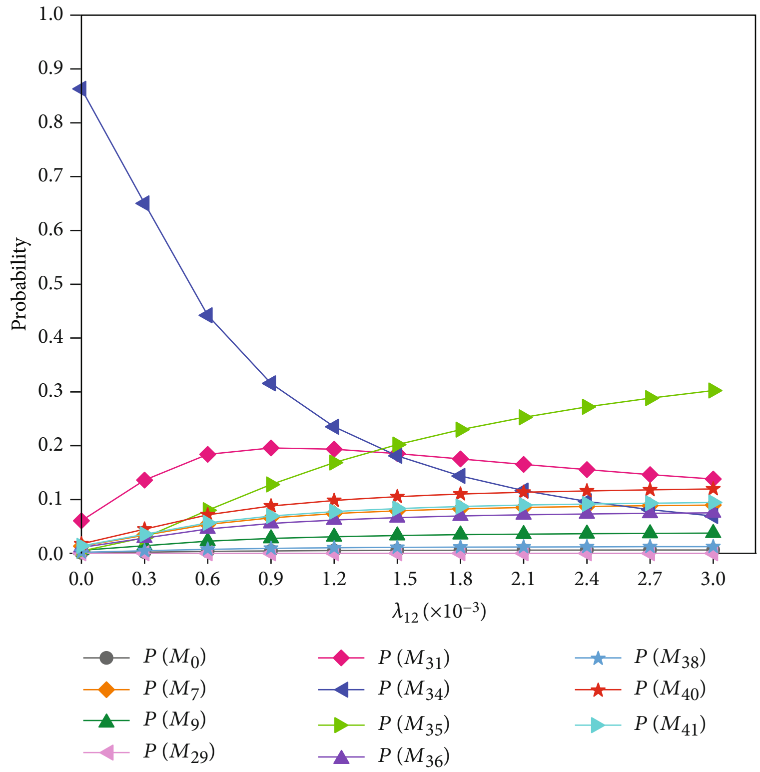

FIGURE 8: Variation of system probability with change in λ_{12}.

support, but it is necessary to ensure that these rescue teams are well trained.

Secondly, it is assumed that only the value of λ_{13} is changed and the remaining values are constant. The results are shown in Figure 9.

Figure 9 shows that when the value of λ_{13} changes from 0 to 0.003, the probability of $P(M_{35}) = (\text{P14}, \text{P18})$ is greatly decreased. The probability of $P(M_{31}) = (\text{P14}, \text{P15}, \text{P16}, \text{P17})$ is slightly increased when the value of λ_{13} changes from 0 to 0.0009, but gradually decreased when the value of λ_{13} changes from 0.0009 to 0.003.

The probability value and variation range of $P(M_{31})$ in Figure 10 is basically consistent with that in Figure 9. This result indicates that if the location information of trapped miners can be grasped as soon as possible, the rescue work of the communications department, rescue teams and medical teams, safety supervision department, and construction team will proceed successfully. With the increase of λ_{13}, the probability value of $P(M_{35})$ gradually decreases from 0.86151 to 0.06308. It means that the communications department works more efficiently, and the rescue roadway advances faster and strives for golden rescue time for trapped miners. Therefore, more detection equipment is needed to expand the range of underground information exploration, to grasp the location information of trapped miners and feedback information to the headquarters faster.

Thirdly, it is assumed that only the value of λ_{19} is changed and the remaining values are constant. The results are shown in Figure 10.

Figure 10 shows that when the value of λ_{19} changes from 0 to 0.01, the probability of $P(M_{40}) = (\text{P23})$ is greatly decreased. The rescue team encountered obstacles in the process of roadway advancement. To solve this problem, the command team immediately adjusted the plan to increase emergency rescue efforts. The most effective way is to mobilize large rescue equipment to remove obstacles in the roadway, which will shorten the rescue time. Therefore, we need to ensure the supply of large-scale rescue equipment to deal with some serious problems in water inrush accidents. The "expanding ER" should also be added to the emergency plan to improve the efficiency of ER.

Fourthly, it is assumed that only the value of λ_{20} is changed and the remaining values are constant. The results are shown in Figure 11.

Figure 11 shows that when the value of λ_{20} changes from 0 to 0.01, the probability of $P(M_{41}) = (\text{P24})$ is greatly decreased. It can be explained that when the rescue speed of the trapped miners is accelerated, the distance between the rescuer and the trapped person is decreased. In this way, if there are some miners in poor health, the rescuer can transport the drugs to the trapped miners by drilling, so that they can get emergency treatment and prevent the deterioration of illness. For this reason, the medical team should prepare all kinds of first-aid medicines in advance to deal with the possible illness of the miners.

Finally, it is assumed that only the value of λ_5 is changed and the remaining values are constant. The results are shown in Figure 12.

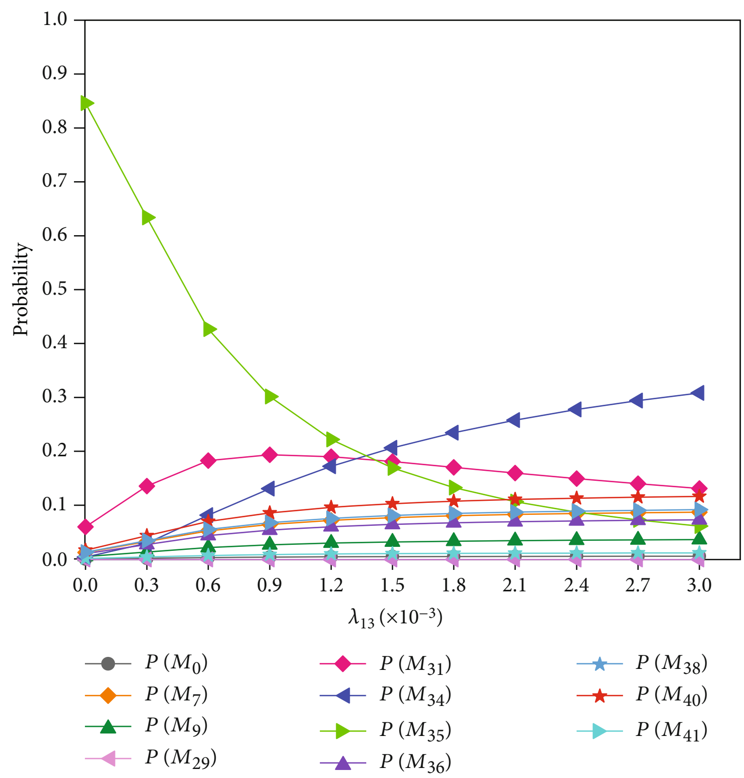

Figure 9: Variation of system probability with change in λ_{13}.

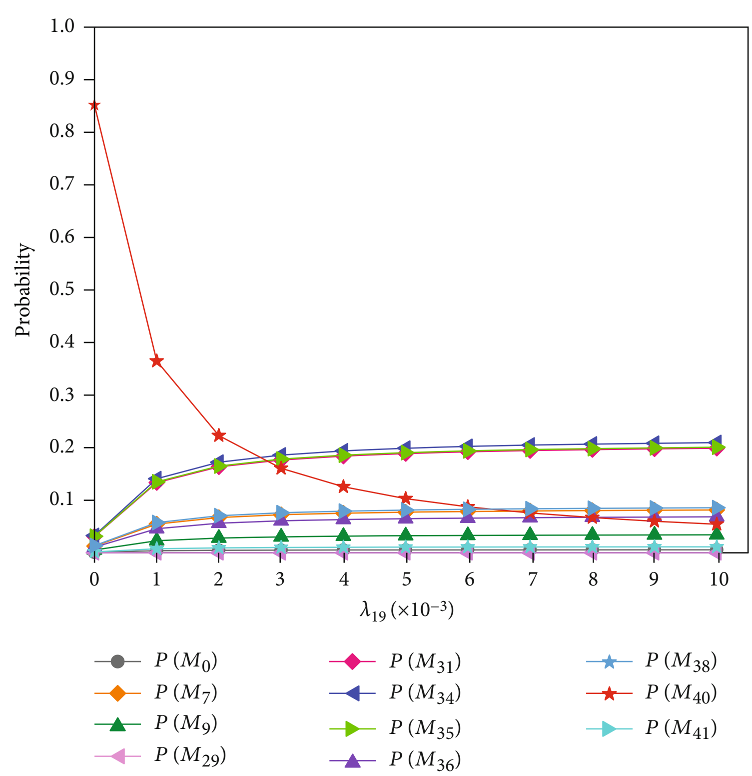

Figure 10: Variation of system probability with change in λ_{19}.

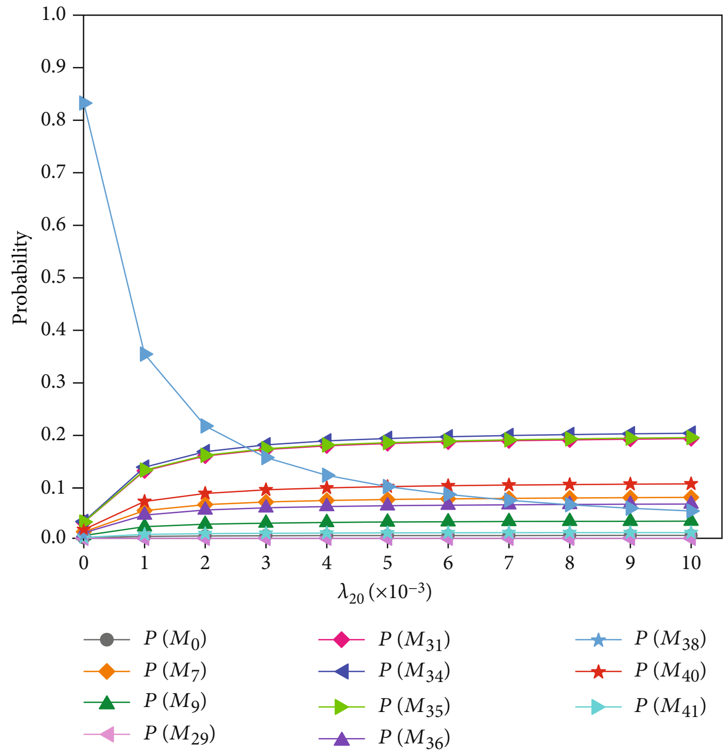

FIGURE 11: Variation of system probability with change in λ_{20}.

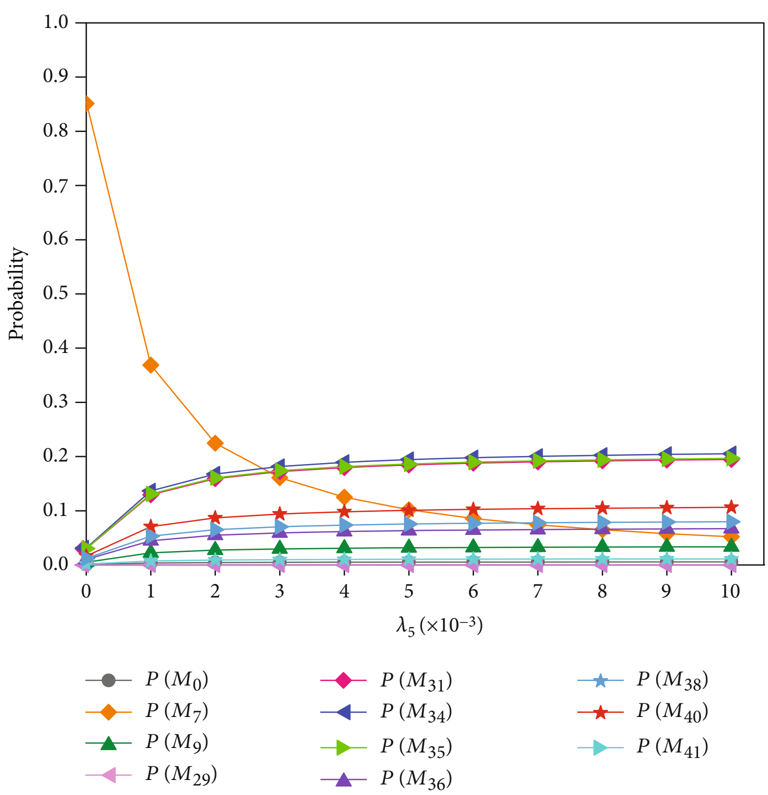

FIGURE 12: Variation of system probability with change in λ_5.

Figure 12 shows that when the value of λ_5 changes from 0 to 0.01, the probability of $P(M_7) = (\mathrm{P5}, \mathrm{P6}, \mathrm{P7}, \mathrm{P9})$ is greatly decreased. It can be explained that if the speeds of the experts, rescue teams, medical teams, and technicians arrive at the accident site are larger, the on-site command team can be set up more quickly. However, because most of the experts are distributed in universities and research institutes, it takes the longest time for them to arrive at the coal mine, which has a great influence on the establishment of the onsite command team. Therefore, the government should provide an emergency green channel for experts to ensure that they can arrive at the accident site faster.

Above all, in the process of ER, coal mining enterprises should be equipped with large rescue equipment to deal with emergencies. When multicooperation is carried out for ER, it is necessary to optimize resource allocation, coordinate internal and external relations, enhance the awareness of cooperation, and organize daily emergency training, which will be better to carry out ER operations.

6. Conclusions and Further Work

6.1. Conclusions. In this paper, a new method is proposed to model and simulate the coal mine ER process based on modified SPN. To validate the correctness of this method, the SPN method is applied to the major water inrush accident in Shanxi Fenxi Zhengsheng Coal Company.

(1) The theoretical method of SPN is adopted to establish the ER process of coal mine and found that busy rates of places P9 and P14~P19 are higher and the utilization rates of translations T12 and T13 are higher. In addition, the problems existing in these places and transitions are analyzed

(2) The triangular fuzzy strategy was introduced into the SPN. The change value of the total time of the ER system is analyzed when each transition changes, which illustrates that the key activities affecting the rescue time

(3) In order to better carry out the ER process, it is suggested that larger rescue equipment should be added, team training should be organized regularly, cooperation should be strengthened, and green channels should be provided for experts

6.2. Further Work

(1) The ER of the coal mine is a very complex process, which can divide many links in more detail, such as organizational structure and emergency supplies. Through this division, a more complete ER process and SPN model can be constructed

(2) When the SPN model is analyzed, it is assumed that the SPN model obeys an exponential distribution. However, this assumption may have some differences with the actual conditions. Therefore, more in-depth researches should be conducted to help us choose a more appropriate probability distribution

(3) Visualization software should be developed for coal mines, which can show the ER process more vividly and give more supports on the ER work using information technology

Data Availability

All data, models, or code generated or used during the study are available from the corresponding author by request.

Conflicts of Interest

The authors declare no conflicts of interest.

Acknowledgments

This work was supported by the National Natural Science Foundation of China (51774199) and the Natural Science Foundation of Shandong Province (ZR2017BEE001).

References

[1] X. S. Zhang, S. S. Li, and X. H. Zhang, "Evaluation of emergency rescue ability based on RS-IPA: evidence from coal mining firms," *Natural Hazards*, vol. 106, no. 3, pp. 1915–1929, 2021.

[2] Z. Wang, Q. Zhang, J. Shao, W. Zhang, X. Wu, and X. Zhu, "New type of similar material for simulating the processes of water inrush from roof bed separation," *ACS Omega*, vol. 5, no. 47, pp. 30405–30415, 2020.

[3] G. Fu, X. Xie, Q. Jia, W. Tong, and Y. Ge, "Accidents analysis and prevention of coal and gas outburst: understanding human errors in accidents," *Process Safety and Environmental Protection*, vol. 134, pp. 1–23, 2020.

[4] T. F. Xu and X. B. Wang, "Statistics and regularity analysis of gas explosion accidents in domestic low-gas coal mines in recent ten years," *Mining safety & Environmental Protection*, vol. 48, no. 3, pp. 126–130, 2021.

[5] G. Zhang, W. Zhang, H. Wang, S. Cao, Y. Wu, and Z. Wang, "Research on arch model and numerical simulation of critical water and sand inrush in coal mine near unconsolidated layers," *Geofluids*, vol. 2020, 12 pages, 2020.

[6] Q. Wu, Z. Du, Y. Zhao, H. Xu, and X. Zhang, "Optimal location of water level sensors for monitoring mine water inrush based on the set covering model," *Scientific reports*, vol. 11, no. 1, 2021.

[7] A. E. Halim and J. F. Brune, "Do refuge chambers represent a good strategy to manage emergencies in underground coal mines?," *Mining Metallurgy & Exploration*, vol. 36, no. 6, pp. 1191–1199, 2019.

[8] Z. F. Hu, "Research on case representation and retrieval of coal mine accidents," in *2013 International Conference on Computational and Information Sciences*, pp. 462–465, 2013.

[9] X. Li, Y. K. Shi, and C. M. Pang, "Evaluation model of coal mine emergency rescue resource allocation based on weight optimization TOPSIS method," in *IOP Conference Series: Earth and Environmental Science*, vol. 651, 2021no. 3.

[10] J. Wang, B. Hu, L. Dong, J. Chang, and W.-P. Wang, "Safety pre-control of stope roof fall accidents using combined event tree and fuzzy numbers in China's underground noncoal mines," *IEEE Access*, vol. 8, pp. 177615–177622, 2020.

[11] T. Phenrat, "Community citizen science for risk management of a spontaneously combusting coal-mine waste heap in Ban

Chaung, Dawei District, Myanmar," *GeoHealth*, vol. 4, no. 6, p. e2020GH000249, 2020.

[12] Y. Liu, Z. Fan, and H. Qi, "Dynamic statistical evaluation of safety emergency management in coal enterprises based on neural network algorithms," *Journal of Intelligent & Fuzzy Systems*, vol. 39, no. 4, pp. 5521–5534, 2020.

[13] Z. He, Q. Wu, L. Wen, and G. Fu, "A process mining approach to improve emergency rescue processes of fatal gas explosion accidents in Chinese coal mines," *Safety Science*, vol. 111, pp. 154–166, 2018.

[14] Y. Zhang, Y. Xie, Y. Zhang, J. Qiu, and S. Wu, "The adoption of deep neural network (DNN) to the prediction of soil liquefaction based on shear wave velocity," *Bulletin of Engineering Geology and the Environment*, vol. 80, no. 6, pp. 5053–5060, 2021.

[15] L. Liu, W. Liu, and Y. Y. Du, "Business process modeling and analysis based on queue logical Petri nets," *International Journal of Software Engineering and Knowledge Engineering*, vol. 29, no. 1, pp. 115–137, 2019.

[16] J. I. Latorre-Biel, D. Ferone, A. A. Juan, and J. Faulin, "Combining simheuristics with Petri nets for solving the stochastic vehicle routing problem with correlated demands," *Expert Systems with Applications*, vol. 168, 2020.

[17] T. Elusakin, M. Shafiee, T. Adedipe, and F. Dinmohammadi, "A stochastic Petri net model for O&M planning of floating offshore wind turbines," *Energies*, vol. 14, no. 4, p. 1134, 2021.

[18] J. Xi, D. Cliff, and Z. Wu, "A comparison of underground coal mine emergency management in China and Australia," *International Journal of Emergency Management*, vol. 13, no. 4, p. 349, 2017.

[19] L. L. Li, *Study on the Secondary Explosion Rule in Disaster Area and Emergency Decision-Making Model of Coal Mine Gas Explosion*, China University of Mining & Technology-Beijing, 2019.

[20] L. Li, D. Guo, Y. Wang, K. Wang, and R. Lian, "Anatomy of mine rescue teams' casualty incidents: a basis for medical emergency preparedness and injury prevention," *Disaster Medicine and Public Health Preparedness*, vol. 13, no. 4, pp. 695–699, 2019.

[21] D. Olave-Rojas and S. Nickel, "Modeling a pre-hospital emergency medical service using hybrid simulation and a machine learning approach," *Simulation Modelling Practice and Theory*, vol. 109, p. 102302, 2021.

[22] Y. Xu, Q. Chang, X. Yan, W. Han, B. Chang, and J. Bai, "Analysis and lessons of a mine water inrush accident resulted from the closed mines," *Arabian Journal of Geosciences*, vol. 13, no. 14, 2020.

[23] X. Zhao, Q. Wang, B. Xie, S. Pan, and M. Ji, "A dynamic rescue route planning method based on 3D network in mine water inrush hazard," *Geomatics, Natural Hazards and Risk*, vol. 10, no. 1, pp. 2387–2407, 2019.

[24] S. N. Nazaretyan and S. S. Nazaretyan, "Assessment of the need for rescue forces during destructive earthquakes (a case study of Armenia)," *Seismic Instruments*, vol. 47, no. 4, pp. 26–42, 2021.

[25] W. Zhang, Z. Wang, X. Zhu, W. Li, B. Gao, and H. Yu, "A risk assessment of a water-sand inrush during coal mining under a loose aquifer based on a factor analysis and the fisher model," *Journal of Hydrologic Engineering*, vol. 25, no. 8, p. 04020033, 2020.

[26] M. Onifade, "Towards an emergency preparedness for self-rescue from underground coal mines," *Process Safety and Environmental Protection*, vol. 149, pp. 946–957, 2021.

[27] Q. Zhang and Z. Y. Wang, *Spatial Prediction of Loose Aquifer Water Abundance Mapping Based on a Hybrid Statistical Learning Approach*, Earth Science Informatics, 2021.

[28] X.-Y. Li, Y. Liu, Y.-H. Lin, L.-H. Xiao, E. Zio, and R. Kang, "A generalized Petri net-based modeling framework for service reliability evaluation and management of cloud data centers," *Reliability Engineering & System Safety*, vol. 207, p. 107381, 2021.

[29] R. M. Cao, L. N. Hao, and Q. Gao, "Modeling and decision-making methods for a class of cyber-physical systems based on modified hybrid stochastic timed Petri net," *IEEE Systems Journal*, vol. 14, no. 4, pp. 4684–4693, 2020.

[30] L. Shi, S. Du, Y. Miao, and S. Lan, "Modeling and performance analysis of satellite network moving target defense system with Petri nets," *Remote Sensing*, vol. 13, no. 7, p. 1262, 2021.

[31] Q. Yu, L. Cai, and X. Tan, "Airport emergency rescue model establishment and performance analysis using colored Petri nets and CPN tools," *International Journal of Aerospace Engineering*, vol. 2018, 8 pages, 2018.

[32] M. K. Molloy, "Performance analysis using stochastic Petri nets," *IEEE Transactions on Computers*, vol. C-31, no. 9, pp. 913–917, 1982.

[33] C. W. Kang, M. Imran, M. Omair, W. Ahmed, M. Ullah, and B. Sarkar, "Stochastic-Petri net modeling and optimization for outdoor patients in building sustainable healthcare system considering staff absenteeism," *Mathematics*, vol. 7, no. 6, p. 499, 2019.

[34] S. Zairi, B. Zouari, H. Rahal, and J. Pradat-Peyre, "A generic generalized stochastic Petri nets model for the performance analysis of FMS considering the resources failures," in *2018 5th International Conference on Control, Decision and Information Technologies*, pp. 737–742, 2018.

[35] A. Finkel and J. Leroux, "Recent and simple algorithms for Petri nets," *Software & Systems Modeling*, vol. 14, no. 2, pp. 719–725, 2015.

[36] J. Hao and W. Pei-an, "An approach for workflow performance evaluation based on discrete stochastic Petri net," in *IEEE International Conference on e-Business Engineering (ICEBE'07)*, pp. 327–330, 2007.

[37] X. M. Dong, "A model of airport security work flow based on petri net," *IOP Conference Series: Materials Science and Engineering*, vol. 242, no. 1, p. 012105, 2017.

[38] X. Li, X. Wang, G. Lang, and H. Yi, "Conflict analysis based on three-way decision for triangular fuzzy information systems," *International Journal of Approximate Reasoning*, vol. 132, pp. 88–106, 2020.

[39] J. Y. Dong, S. P. Wan, and S. M. Chen, "Fuzzy best-worst method based on triangular fuzzy numbers for multi-criteria decision-making," *Information Sciences*, vol. 547, pp. 1080–1104, 2021.

[40] F. Tüysüz and C. Kahraman, "Modeling a flexible manufacturing cell using stochastic Petri nets with fuzzy parameters," *Expert Systems with Applications*, vol. 37, no. 5, pp. 3910–3920, 2009.

[41] H. Sun, J. Liu, Z. Han, and J. Jiang, "Stochastic Petri net based modeling of emergency medical rescue processes during earthquakes," *Journal of Systems Science & Complexity*, vol. 34, no. 3, pp. 1063–1086, 2021.

[42] K. W. G. de Araújo, M. O. de Andrade, R. M. F. Lima, and C. A. L. de Oliveira, "Performance analysis of metropolitan bus rapid transit line via generalized stochastic Petri nets," *Journal of Urban Planning and Development*, vol. 146, no. 1, 2020.

Hindawi
Geofluids
Volume 2021, Article ID 5604642, 9 pages
https://doi.org/10.1155/2021/5604642

Research Article

An Experimental Research on Surrounding Rock Unloading during Solid Coal Roadway Excavation

Hongjun Guo[1,2] **Ming Ji**[3] **Dapeng Liu**[1] **Mengxi Liu**[1] **Gaofeng Li**[1] **and Jingjing Chen**[1]

[1] *Jiangsu Vocational Institute of Architectural Technology, Xuzhou 221116, China*
[2] *State Key Laboratory for Geomechanics & Deep Underground Engineering, China University of Mining & Technology, Xuzhou 221116, China*
[3] *Key Laboratory of Deep Coal Resource Mining, Ministry of Education of China, School of Mines, China University of Mining & Technology, Xuzhou 221116, China*

Correspondence should be addressed to Ming Ji; jiming@cumt.edu.cn

Received 12 May 2021; Accepted 24 July 2021; Published 14 August 2021

Academic Editor: Hualei Zhang

In order to further explore the deformation and failure essence of the deep coal body, based on the characteristics of surrounding rock stress adjustment before and after solid coal roadway excavation, an experiment of unloading confining pressure and loading axial pressure of the coal body was designed and conducted in this study. Based on test results, the failure mechanics and energy characteristics of the coal body were analyzed through experiments. Rapid unloading is considered a key factor contributing to lateral deformation and expansion failure, which exacerbates the deterioration of coal body and reduces the deformation energy storage capacity of coal. On the other hand, the larger loading rate tends to shorten the accumulation time of microcracks and cause damage to the coal body, resulting in strengthening the coal body and improving energy storage. Under the circumstance that the coal body is destroyed, the conversion rates of the internal deformation energy and dissipated energy are more significantly affected by unloading rate. The increasing unloading rate and rapid decreases in the conversion rate of deformation energy make the coal body more vulnerable to damage. Under the same stress conditions, the excavation unloading is more likely to deform, destroy, or even throw the coal than the experiment unloading. In order to reduce or avoid the occurrence of deep roadway excavation accidents, the understanding of the excavation unloading including possible influencing factors and the monitoring of the surrounding rock stress and energy during the excavation disturbance should be strengthened. It can be used as the basis for studying the mechanism of deformation and failure of coal and rock and dynamic disasters in deep mines, as well as the prediction, early warning, prevention, and control of related dynamic disasters.

1. Introduction

With the depletion of coal resources and the deterioration of mining environment, the mine rockburst accidents occurred more frequently than before, posing as a threat to the safe and efficient mining. According to the incomplete statistics of rockburst cases, a total of 85% of the rockburst accidents occurred in the roadway which makes the roadway the main occurrence area of rockburst. In addition, 49% out of roadway rockburst accidents were identified as excavation rockburst with 51% mining rockburst [1–3]. At present, the research on rockburst is mainly focused on mining, centering around the stress environment of large space, high static load, and big disturbance. Comparatively, roadway excavation is a construction process in the environment of small space, featured with low static load and small disturbance. The research on the mechanism of large deformation or rockburst has been limited.

Roadway excavation is defined as an unloading process, which is essentially different from continuous loading failure in mechanical response, action mechanism, and deformation failure characteristics [4–6]. Recently, researchers have done a considerate amount of work on engineering excavation unloading [7–9]. Academician Qian Qihu [10] considered that the zone failure of roadway surrounding rock was led by dynamic unloading caused by excavation, and the practice also confirmed this conclusion. Roadway engineering and even underground engineering are unloading in one direction, and the balance state of triaxial compression is broken, resulting in the deformation and failure of coal and rock. The mechanical and energy characteristics of coal and rock serve as the foundation for studying the system interaction between roadway and surrounding rock. Combined with the specific cases or actual engineering requirements, scholars domestically and abroad have designed a variety of loading and unloading stress paths aiming to explore their mechanical characteristics and energy efficiency mechanism in practical application in a more accurate manner [11].

Wei [2] studied the stress path and failure characteristics of surrounding rock in solid coal roadway excavation by an unloading experiment and numerical simulation method and proposed the excavation rockburst mechanism of high static load+"loading and unloading" stress path transformation of surrounding rock. Feng [12] investigated the deformation and failure characteristics of coal under different stress paths through experiments and established the failure mechanical model for the sides of coal roadway based on the effect of unloading stress. Yao [13] researched the failure mode and law of unloading surrounding rock by theoretical analysis and numerical simulation and carried out on-site monitoring and quality evaluation on the broken range of unloading surrounding rock. Zhu [14] considered that unloading rockburst and creep rockburst are two typical impact forms of extra thick coal seam and explained their occurrence mechanism. Qin et al. [15] discussed the influence of excavation speed on the stress, displacement, and stability of roadway surrounding rock by using numerical software.

Based on the previously conducted research, this study firstly investigated the roadway excavation and surrounding rock stress adjustment and explored the suitable stress paths of loading and unloading for actual engineering. In addition, a number of experimental methods were adopted to investigate the mechanical and energy characteristics of unloading surrounding rock, which lay a foundation for further understanding of deformation, failure, and rockburst of unloading surrounding rock during excavation.

2. An Experimental Analysis on Surrounding Rock Unloading in Roadway Excavation

2.1. Experiment Preparation. The coal sample was selected from the #8 coal seam in the third mining area located in the Xianyang mining zone. The buried depth of the coal seam is nearly 800 m with an average density of 1.4 g/cm^3 and the average uniaxial compressive strength of 22.3 MPa. According to the requirements and standards of the rock mechanics experiment, the sample was processed into a cylinder of Φ 50 mm × H100 mm (Figure 1). In the experiment, multiple systems were adopted including a MTS815.02 electrohydraulic servo rock mechanics experiment system borrowed from China University of Mining and Technology (as shown in Figure 2).

2.2. Experiment Scheme Design. According to the elastic mechanics, after the excavation of a circular roadway, the radial stress of surrounding rock often changes rapidly from the original rock stress p_0 to zero, while the shear stress increases from p_0 to $2\,p_0$. With the increase in the distance from the head-on, the roadway surrounding rock stress is constantly adjusted and gradually reaches equilibrium. The plastic zone (*BC* section) and failure zone (*CD* section) are formed from deep to shallow of the surrounding rock. The variances of the shear stress conform to the stress-strain curve of coal and rock, and the change of the radial stress is not obvious, as shown in Figure 3.

Figure 1: The typical sample specimen.

Figure 2: The MTS 815.02 testing system.

After the excavation of a roadway, the stress changes monitored on the surrounding rock from the depth to the surface stay consistent. The shear stress increases and the radial stress decreases, suggesting that the whole stress adjustment process is to increase shear stress and decrease radial stress. Therefore, the experimental stress path is expanded by unloading confining pressure and loading axial pressure [16] (see Table 1 for details).

At present, the common mining depth in China ranges from 400 to1000 m. In this experiment, a depth of 800 m was selected, resulting in the initial confining pressure at 20 MPa. When the coal sample was placed under a 20 MPa hydrostatic pressure, the sample begun to unload confining

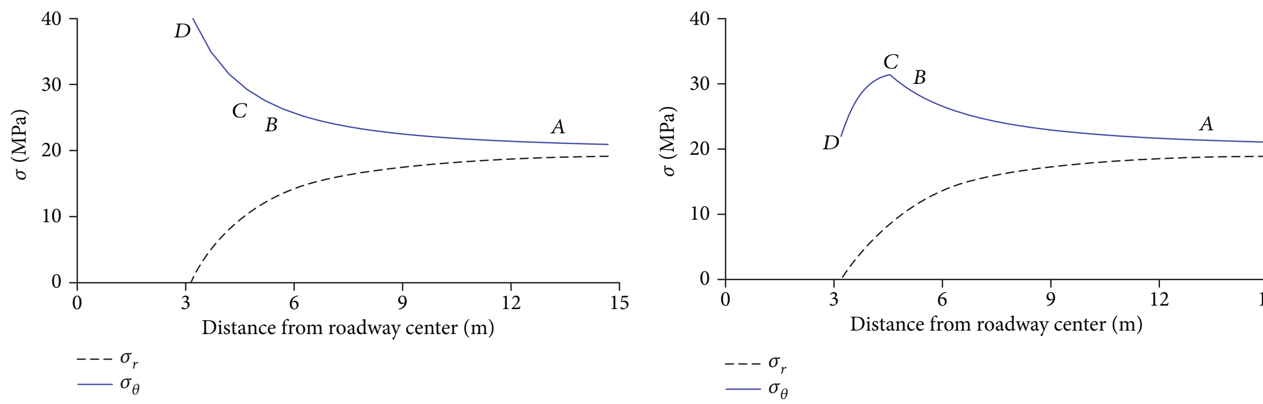

(a) Before stress balance of surrounding rock

(b) After stress balance of surrounding rock

FIGURE 3: Stress distribution in the roadway surrounding rock.

TABLE 1: Summary of the experiment scheme.

Stress path		Engineering correspondence
Unloading confining pressure and loading axial pressure	Unloading rate effect Loading rate effect	Stress adjustment process of surrounding rock unloading in roadway excavation

pressure and increase axial pressure until the coal sample reached failure, as shown in Figure 4. The specific process includes the following. (1) Stress control mode. The confining pressure and axial pressure were loaded alternately at a rate of 5 MPa. Meanwhile, the confining pressure (axial pressure) $\sigma_2 = \sigma_3 = \sigma_1$ was loaded to the predetermined value of 20 MPa at the rate of 0.05 MPa/s. (2) Stress control mode. The confining pressure σ_3 was unloaded at the rate of v_3, with the axial pressure σ_1 loaded at the rate of v_1 until the coal sample reached failure. (3) Displacement control mode. After the coal sample started to fail, the axial pressure was loaded continually with the confining pressure unloading at the rate of 0.001 mm/s to obtain the full stress-strain curve.

2.3. Analysis on Mechanical Properties of Unloading Coal

2.3.1. Unloading Rate Effect. Combined with the unloading rate effect of the unloading confining pressure and loading axial pressure experiment, a stress-strain curve of coal under different unloading rates is shown in Figure 5.

According to Figure 5, with the increase in unloading rate, the confining pressure decreases rapidly from 20 MPa, along with failure strength and axial strain of the coal body. The volume strain demonstrates an increasing trend, with obvious expansion phenomenon. In addition, the changes in the circumferential strain are limited. The relationship among coal strength, unloading rate, and confining pressure during the sample failure is shown in Figure 6.

As indicated in Figure 6, the failure strength of coal decreases with the increase in unloading rate, which indicates that the influence of unloading rate on the failure characteristics of coal is gradually weakening. The rapid unloading leads to dramatic decline of the confining pressure to zero quickly, creating conditions for lateral expansion and pressure relief. Meanwhile, considering that the uniaxial compressive strength is determined lower than the failure strength under high confining pressure, the triaxial loading and unloading experiment is rapidly transformed into a uniaxial loading experiment. Under the circumstance that the unloading rate exceeds a threshold value, the unloading rate actually reflects the uniaxial compression process of coal. Therefore, with the increase in unloading rate, the influence on the failure strength of coal gradually decreases and grows stable. The influence of the unloading rate is significant within the range of 0~0.1 MPa/s. When the coal body fails, the strength and confining pressure follow linear changes suggesting that a higher unloading rate leads to lower confining pressure and the failure strength.

2.3.2. Loading Rate Effect. Based on the test results obtained from the experiment, the stress-strain curve of coal under different loading rates is shown in Figure 7.

According to Figure 7, the failure strength and axial strain of coal increased along with the increase in axial loading rate with limited changes in circumferential strain and volume strain. The relationship among coal strength, loading rate, and confining pressure at the moment of failure is shown in Figure 8.

As indicated in Figure 8, the influence of axial loading on the mechanical properties of coal is significant within the range of 0~0.2 MPa/s. In addition, a higher axial loading rate tends to increase the failure strength of coal suggesting that when the axial pressure was rapidly applied, the failure strength under a certain confining pressure can be reached within a short time. Due to the limited load action time on coal, the crack development inside the rock is limited with nonobvious damage accumulation. Under the circumstance that the bearing limit is exceeded, the main failure crack tends to develop instantly, resulting in failure. Therefore, to

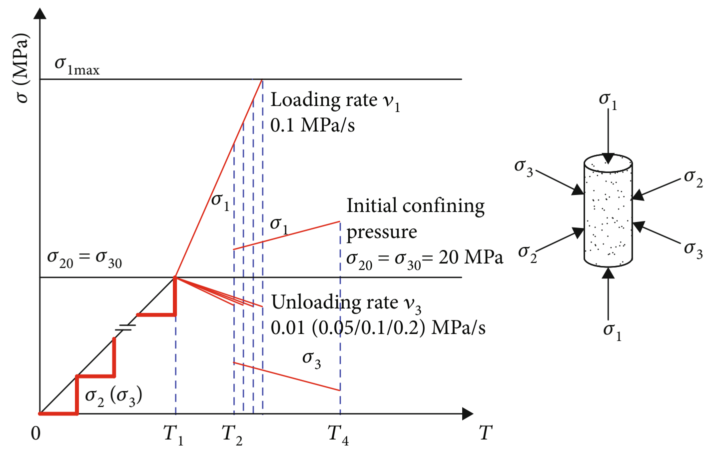

(a) Unloading rate effect

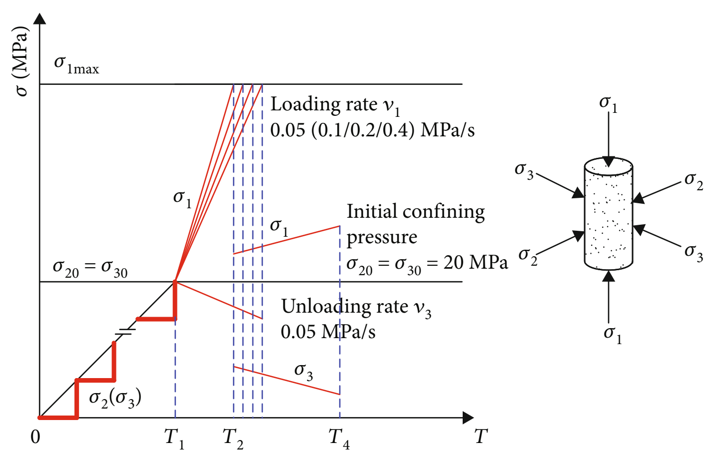

(b) Loading rate effect

FIGURE 4: Schematic diagram of the stress path of unloading confining pressure and loading axial pressure.

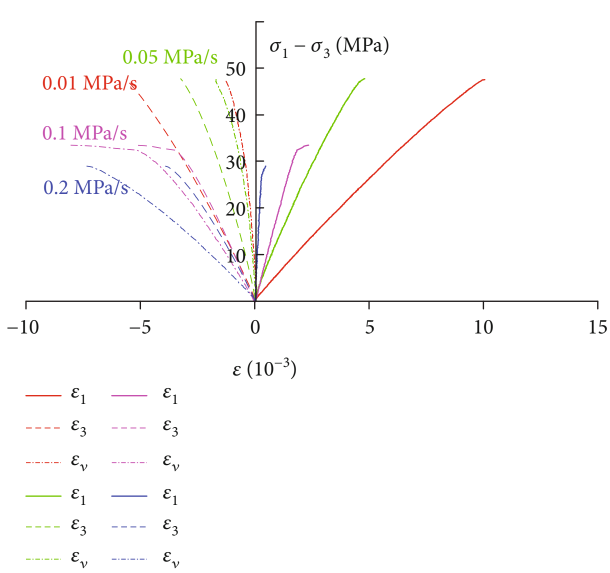

FIGURE 5: The stress-strain curves (unloading rate effect).

a certain extent, the failure strength of coal under corresponding confining pressure is improved by rapidly increasing axial pressure.

2.4. Analysis on Energy Characteristics of Unloading Coal

2.4.1. Unloading Rate Effect. In order to simplify the energy composition and calculation in the coal body during unloading, the following assumptions were made including the following: (1) part of the total work done by the experimental machine is converted into releasable deformation energy and stored in the coal body and (2) the rest of the work done by the experimental machine is converted into dissipative energy to generate cracks, degrade the coal body, or release in other forms [17–22]. The whole process of energy conversion can be expressed as

$$U = U_1 + U_3 = U_e + U_d, \tag{1}$$

where

$$U_1 = \int_0^{\varepsilon_{1(t)}} \sigma_1 d\varepsilon_1,$$
$$U_3 = 2\int_0^{\varepsilon_{3(t)}} \sigma_3 d\varepsilon_3, \tag{2}$$
$$U_e = \frac{1}{2}\sigma_1\varepsilon_1.$$

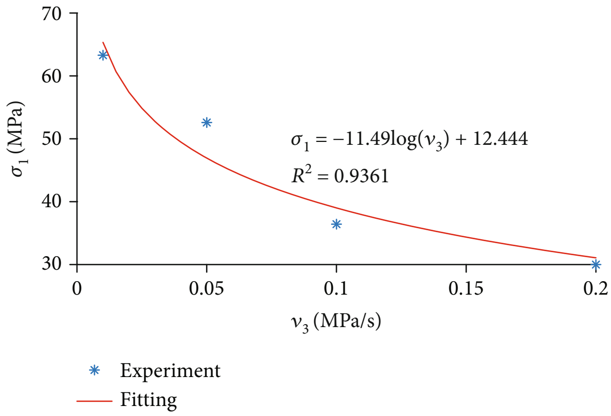

(a) Failure strength and unloading rate

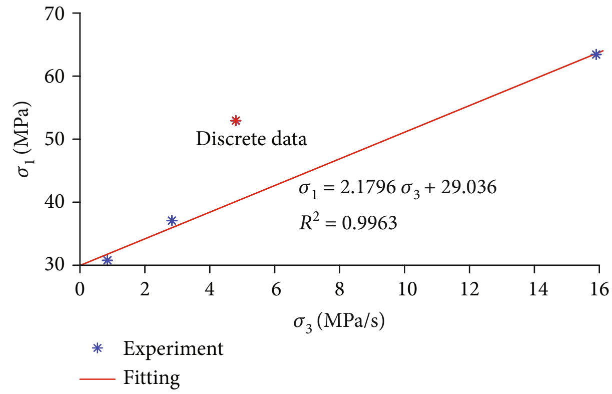

(b) Failure strength and failure confining pressure

FIGURE 6: The relationship among unloading rate, axial pressure, and failure time.

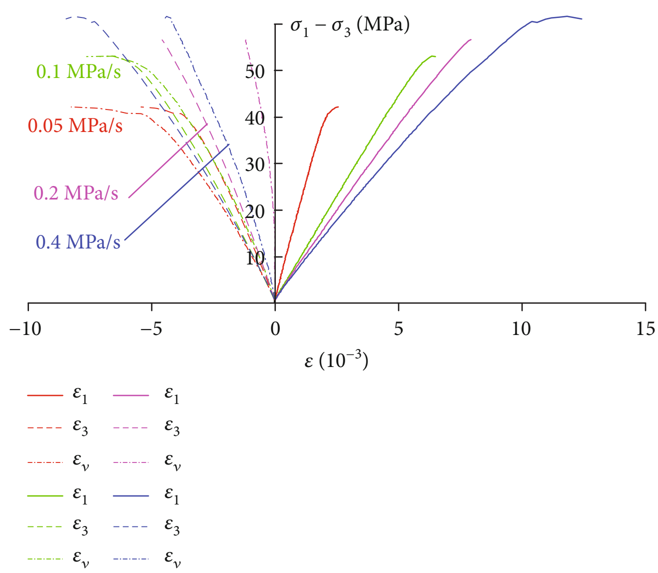

FIGURE 7: The stress-strain curves (loading rate effect).

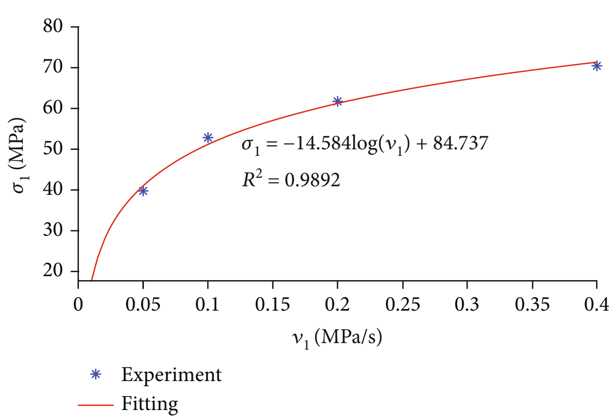

(a) Failure strength and loading rate

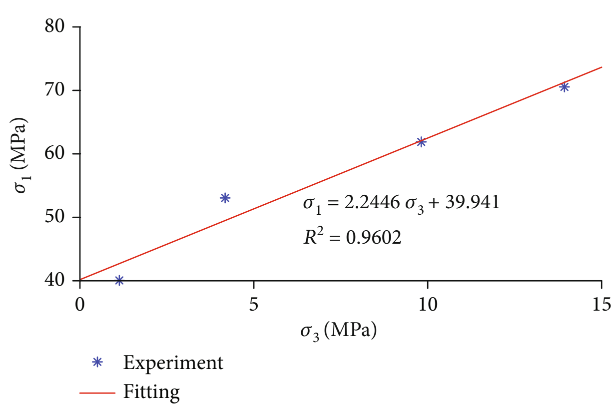

(b) Failure strength and failure confining pressure

FIGURE 8: The relationship among loading rate, axial pressure, and failure time.

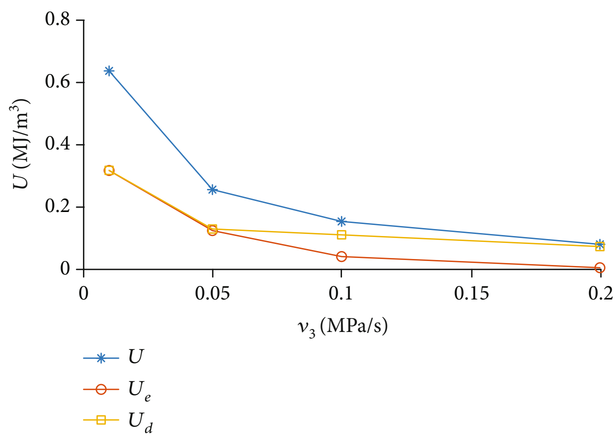

FIGURE 9: The energy-unloading rate curves.

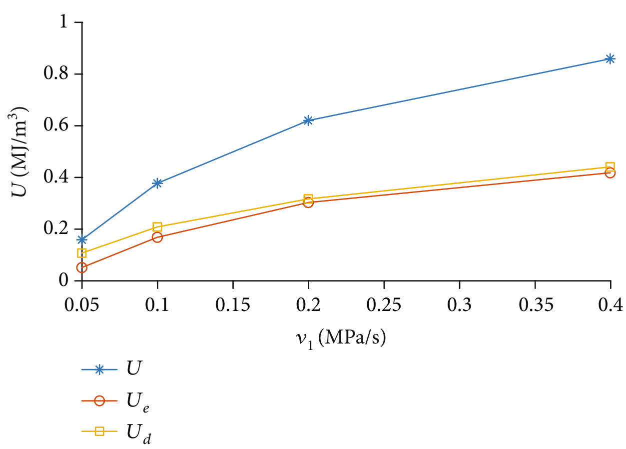

FIGURE 10: The energy-loading rate curves.

The energy of coal failure under different unloading rates is shown in Figure 9.

According to Figure 9, the energy required for coal failure is negatively correlated with the unloading rate, indicating that as the unloading rate increases, the energy required for coal failure tends to decrease in logarithmic form. Meanwhile, the conversion rate of deformation energy also decreases dramatically below 10% at an unloading rate of 0.2 MPa/s, indicating that a higher unloading rate leads to a lower conversion rate of deformation energy. Conversely, a higher conversion rate of dissipated energy can result in early occurrence of coal failure. When the unloading rate can exert a significant impact on the energy and mutual transformation, the unloading rate is below 0.1 MPa/s, with limited impact on the energy change.

2.4.2. Loading Rate Effect. The relationship between the energy and the axial loading rate under the coal failure is shown in Figure 10.

As the axial loading rate increases, the energy required for coal failure increases in a logarithmic form. The increasing failure strength indicates that more energy is absorbed from rapid loading to failure. When the rate is greater than 0.2 MPa/s, the influence becomes more severe. No significant relationship between the transformation rate of deformation energy and the axial loading rate during unloading has been identified. In addition, the experiment suggests that transformation rate is about 20%~30% at the initial stage and 45%~50% at the near failure stage.

To sum up, the axial loading rate tends to shorten the effective accumulation time of microcracks, cause damage in the coal body, and improve the energy storage capacity of coal. Under the event that the axial loading rate varies in the range of 0~0.2 MPa/s, the axial loading rate has a greater influence on the strength and energy storage of coal, while the unloading rate produces the opposite effect. A higher unloading rate leads to a greater inhibition effect on the coal body's lateral deformation which contributes to the lateral expansion failure. The influence is prominent when the axial loading rate changes within the range of 0~0.1 MPa/s.

2.5. Discussion on the Differences between the Excavation Unloading and the Experimental Unloading. Different from the unloading experiment, in the original rock stress environment of three-dimensional compression, the coal body is in a state of pressurized energy storage. During the unloading process of excavation, mutual inhibition between surrounding rocks interacts with each other. The unloading rate will not evolve into a loading form of uniaxial compression, as shown in Figure 11. In actual engineering, the rapid excavation makes the mutual inhibition of surrounding rock weaken rapidly in a certain area, which immediately drops from a high confining pressure state to a low confining pressure stress environment (three-direction five-sided stress state), equivalent to completing the transformation from high initial confining pressure to low initial confining pressure in a short time, reducing the requirements of coal failure. Simultaneously, the shear stress increases synchronously, which intensifies the change of shear-radial stress difference, contributing the stress environment easier to reach the bearing limit of the coal body and creating conditions for the shallow surrounding rock to squeeze out into the free space of the roadway. Since the shallow surrounding rock still has a certain inhibitory effect on the deep surrounding rock, resulting in the coal body in a three-direction six-sided nonisostatic stress state, the crack development in the coal body decreases and gradually evolves into plastic deformation and elastic deformation.

Although the high-energy coal tends to be in a new equilibrium state through energy release in the form of deformation or even failure, various deformations and failures caused by energy release due to excavation unloading and experimental unloading are identified. As shown in Figure 12, r_0 refers to the nominal radius of microunit coal; V_0 and V indicate the volumes before and after energy release stabilizes, respectively, with ω_0 and ω being the internal energy density, respectively; r_1 (excavation unloading) and r_2 (experiment unloading) indicate the maximum nominal radius after deformation; and α refers to the excavation unloading energy release angle.

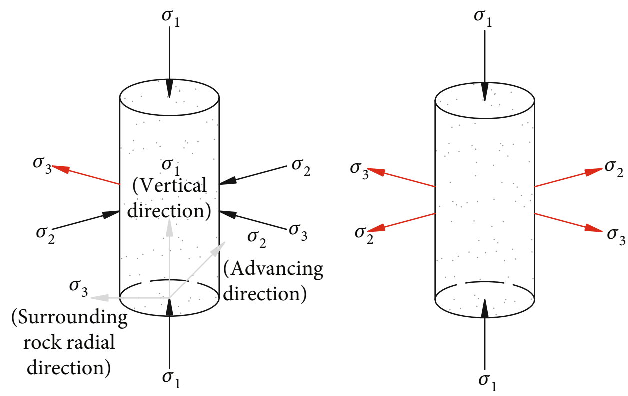

(a) Excavation unloading (b) Experiment unloading

Figure 11: Comparison of excavation unloading and experiment unloading.

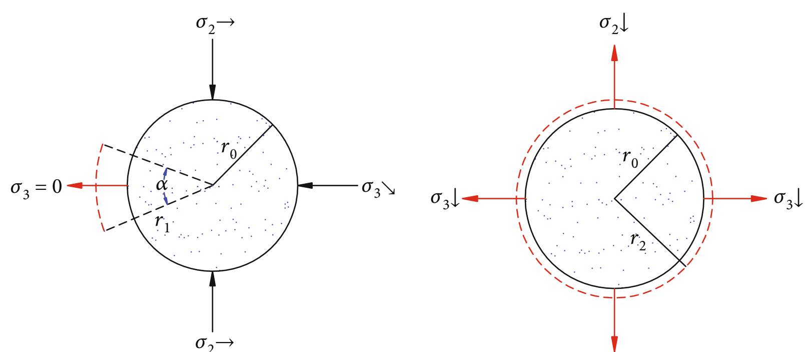

(a) Excavation unloading (b) Experiment unloading

Figure 12: Comparison of excavation unloading and experiment unloading.

According to the law of conservation of energy, then

$$V_0\omega_0 = V\omega. \tag{3}$$

According to equation (3), the expansion volume of microunit coal is provided below:

$$\Delta V = \left(\frac{\omega_0}{\omega} - 1\right)V_0 = \frac{\alpha}{2\pi}\pi\left(r_1^2 - r_0^2\right) = \pi\left(r_2^2 - r_0^2\right). \tag{4}$$

The result of equation (4) is also as follows:

$$\frac{r_1^2 - r_0^2}{r_2^2 - r_0^2} = \frac{2\pi}{\alpha}. \tag{5}$$

From equation (5), the surrounding rock deformation caused by excavation unloading in the actual engineering is much more severe than in the experiment.

Generally speaking, the difference between the excavation unloading and the experiment unloading is similar to that of directional blasting and traditional blasting. Under the premise of given energy, the former one often leads to more obvious deformation in the coal, featured with more damage and a violent process. Therefore, a great deal of attention should be paid to the stress and energy adjustment process of surrounding rock disturbed by excavation in engineering practice for the purpose of minimizing and even avoiding the large deformation or rockburst accident of roadway excavation.

3. Conclusions

Combined with the stress distribution and variation characteristics of surrounding rock before and after roadway excavation, an experiment of unloading confining pressure and loading axial pressure of coal is designed. Based on the experiment, the coal body's failure mechanics and energy characteristics are identified and analyzed. Based on the experiment and data collected, the following conclusions are obtained:

(1) Increasing the axial loading rate can shorten the accumulation time of microcracks and damage and produces a strengthening effect on the coal body. When the axial loading rate ranges within 0~0.2 MPa/s, the axial loading rate tends to have greater influence on the coal body's strength, while the unloading rate provides conditions for lateral

deformation and dilatancy failure (intensifying coal body degradation). The influence of axial loading is prominent when within the range of 0~0.1 MPa/s

(2) Increasing the axial loading rate improves the energy storage capacity of coal, and each energy increases logarithmically while the unloading rate is opposite. When the coal body failed, the transformation rate of deformation energy and dissipated energy is obviously affected by the loading and unloading rate. With the increase in the axial loading rate, the transformation rate of deformation energy approaches 50%. As the unloading rate increases, the transformation rate of deformation energy decreases, resulting in high susceptibility of the coal body to damage

(3) Under the given energy conditions, compared with the experiment unloading, the coal deformation caused by excavation unloading is more obvious, featured with severer damage and a more violent process. According to the experiment and analysis, the stress and energy adjustment process of the surrounding rock disturbed by excavation should be valued by scholars in terms of improving the safety of roadway excavation

Data Availability

The data used to support the findings of the study are available from the corresponding author upon request.

Conflicts of Interest

The authors declare that no conflict regarding the publication of this paper has been identified.

Acknowledgments

This study was supported by the Jiangsu University Natural Science Research Project (20KJB560032, 18KJA560001) and Jiangsu Construction System Science and Technology Project (Guidance) (2020ZD30, 2019ZD080, 2019ZD070, 2018ZD135, 2018ZD146, and 2018ZD170). We thank Xuzhou Yu-Yi (Science and Technology Consulting Service Co., Ltd.) for editing the English text of the draft of this manuscript.

References

[1] Z. Wang, L.-m. Dou, G. Wang et al., "Resisting impact mechanical analysis of an anchored roadway supporting structure under P-wave loading and its application in rock burst prevention," *Arabian Journal of Geosciences*, vol. 11, no. 5, p. 81, 2018.

[2] W. Shen, *Study on Stress Path Variation of Surrounding Rock and Mechanism of Rockburst in Coal Roadway Excavation*, China University of Mining & Technology, Xuzhou, 2018.

[3] D. Linming, C. Tongjun, G. Siyuan, H. He, and S. Zhang, "Rockburst hazard determination by using computed tomography technology in deep workface," *Safety Science*, vol. 50, no. 4, pp. 736–740, 2012.

[4] L. Xibing, C. Wenzhuo, T. Ming, Z. Zhou, and Z. Chen, "Influence of unloading disturbance on adjacent tunnels," *International Journal of Rock Mechanics & Mining Sciences*, vol. 84, pp. 10–24, 2016.

[5] H. Guo, M. Ji, and L. Cao, "Effect of unloading rate on the mechanical properties of siltstone," *Journal of Xi'an Uuniversity of Architecture & Technology (Natural Science Edition)*, vol. 52, no. 6, pp. 860–868, 2020.

[6] C. Yu, Z. Wang, Y. Zheng, F. Xiating, and Z. Liming, "Energy evolution principle of fracture propagation of marble with different unloading stress paths," *Journal of Central South University (Science and Technology)*, vol. 47, no. 9, pp. 3140–3147, 2016.

[7] M. Ji and H. Guo, "Elastic-plastic threshold and rational unloading level of rocks," *Applied Sciences*, vol. 9, article 3164, 2019.

[8] H. Guo, M. Ji, Y. Zhang, and M. Zhang, "Study of mechanical property of rock under uniaxial cyclic loading and unloading," *Advances in Civil Engineering*, vol. 2018, Article ID 1670180, 6 pages, 2018.

[9] D. Zhang, Y. S. Yang, Y. P. Chu, X. Zhang, and Y. G. Xue, "Influence of loading and unloading velocity of confining pressure on strength and permeability characteristics of crystalline sandstone," *Results in Physics*, vol. 9, pp. 1363–1370, 2018.

[10] Q. Qihu and L. Shuchen, "A review of research on zonal disintegration phenomenon in deep rock mass engineering," *Chinese Journal of Rock Mechanics and Engineering*, vol. 27, no. 6, pp. 1278–1284, 2008.

[11] H. Chen, Y. Cheng, T. Ren, H. Zhou, and Q. Liu, "Permeability distribution characteristics of protected coal seams during unloading of the coal body," *International Journal of Rock Mechanics & Mining Sciences*, vol. 71, pp. 105–116, 2014.

[12] F. Youliang, *Study on Rib Breakage Mechanism and Control Technology of Large Cross-Section Coal Roadway for Excavation Unloading*, China University of Mining & Technology, Beijing, 2017.

[13] Y. Jinrui, *Non-Explosive Continuous Mining Theory and Technology Research in Deep Phosphate Mine*, Central South University, Changsha, 2013.

[14] S. Zhu, *Mechanism and Prevention of Rockburst in Extra-Thick Coal Seams Mining*, University of Science and Technology Beijing, Beijing, 2017.

[15] E. Qin, X. Li, Z. He, C. Ma, and C. Wan, "Study on stability of surrounding rock under different tunneling rate in high stress," *Mining and Metallurgical Engineering*, vol. 31, no. 6, pp. 17–20, 2011.

[16] L. Tao, *Siltstone's Mechanical Properties in Different Stress Paths and Research of Unloading Constitutive Model*, China University of Mining & Technology, Xuzhou, 2015.

[17] Z. Zhizhen, *Energy Evolution Mechanism during Rock Deformation and Failure*, China University of Mining & Technology, Xuzhou, 2013.

[18] Z. Zhonghu, R. Lu, and Z. Guoqing, "Analysis on energy transformation for rock in the whole process of deformation and fracture," *Mining Research and Development*, vol. 26, no. 5, pp. 8–11, 2006.

[19] L. Xiangfeng and Y. Wang, "Investigation into law of AE energy accumulation and damage evolution on coal and rock," *Journal of Liaoning Technical University (Natural Science)*, vol. 30, no. 1, pp. 1–4, 2011.

[20] E. Wang, X. He, L. Zhonghui et al., *Electromagnetic Radiation Technology of Coal and Rock and Its Application*, Science Press, Beijing, 2009.

[21] W. Yu, X. Miao, X. Mao, and J. Xu, "Analysis of the heating-up mechanism in the course of the rock ram," *Chinese Journal of Rock Mechanics and Engineering*, vol. 24, no. 9, pp. 1535–1538, 2005.

[22] H. Da and L. Yanrong, "Conversion of strain energy in triaxial unloading tests on marble," *International Journal of Rock Mechanics & Mining Sciences*, vol. 66, pp. 160–168, 2014.

Hindawi
Geofluids
Volume 2021, Article ID 5714547, 12 pages
https://doi.org/10.1155/2021/5714547

Research Article

Characterization of Discontinuity and Mechanical Anisotropy of Shale Based on Continuum Damage Mechanics

Qinglin Shan,[1,2] Peng Yan,[1,2] Hengjie Luan,[1,2] Yujing Jiang,[1,2] and Sunhao Zhang[1,2]

[1]*State Key Laboratory of Mining Disaster Prevention and Control Co-Founded by Shandong Province and the Ministry of Science and Technology, Shandong University of Science and Technology, Qingdao 266590, China*
[2]*College of Energy and Mining Engineering, Shandong University of Science and Technology, Qingdao 266590, China*

Correspondence should be addressed to Peng Yan; yanpeng951202@163.com

Received 16 June 2021; Revised 6 July 2021; Accepted 22 July 2021; Published 14 August 2021

Academic Editor: Afshin Davarpanah

The effect of the bedding structure on the mechanical properties of layered shale was studied by means of experiment and numerical simulation. Based on continuum damage theory and discrete fracture network modeling method (D-DFN), a finite element model describing structural discontinuity and mechanical anisotropy of shale is established. In this model, the degradation process of stiffness and strength of shale after failure is described based on the stress-displacement relationship of elements. In order to distinguish the mechanical properties between the bedding and the matrix, a nonzero initial damage variable is set in bedding elements to show initial lower elastic modulus and strength of bedding elements compared with initially nondamaged matrix elements. The calibration of model parameters is discussed, and the simulation results are compared with the experimental results. The results show that the D-DFN method can effectively simulate the anisotropic characteristics of shale deformation and strength, which verifies the effectiveness of the method.

1. Introduction

As an energy source, oil and gas resources are superior to coal in many aspects such as transportation, heating value, and environmental protection. Therefore, since the 20th century, the proportion of oil and gas in the world energy structure has gradually increased. It is usually used as a strategic material to evaluate, plan, and manage and to formulate special policies and strategies for its development and utilization. At the same time, the problem of resource recovery and reducing environmental pollution during the mining process [1] has been the focus of attention by scholars, and in-depth research has been conducted on the problem of improving recovery, such as carbon dioxide storage [2, 3] and adding nanoparticles to the polymer [4, 5]. In addition, an in-depth understanding of the mechanical properties of rocks also plays an important role in improving the recovery of oil and gas resources in tight reservoirs. Most rock materials show different degrees of anisotropy [6, 7]. During long-term diagenesis, shales develop a large number of discontinuities such as bedding, joints, and cracks through deposition and compaction, leading to structural discontinuity and mechanical anisotropy [8–10]. The results of conventional triaxial compression tests show that shale strength is related not only to confining pressure but also to the angle between maximum principal stress and bedding planes [11]. A reasonable model to describe the structural discontinuity and mechanical anisotropy of shale is meaningful for the design of safety drilling and reservoir treatment in shale oil/gas development. A lot of experiments and theoretical studies have been done by former researchers [12, 13].

[14] carried out compression tests on different kinds of rocks. Tests results showed the effect of bedding plane orientation on the test values of elastic parameters and the yield strengths. [15, 16] found that the anisotropy of shale elastic parameters is significantly affected by the amount of clay and organic content as well as the shale fabric. [17] firstly deduced the analytical solution for the elastic problem of surface loading on transversely isotropic bodies. [18] applied the anisotropic mechanics model to the wellbore stability analysis. The results show that the anisotropy of rock causes an obviously different stress distribution around the wellbore

from that calculated by the isotropic model. [19] established the anisotropic Mises-Schleicher criterion (AMS) by introducing a four-order anisotropic tensor, to describe the failure characteristics of transversely anisotropic rocks under compression or tensile conditions. [20] improved the Cam Clay model to describe the deformation characteristics of shale, as well as the strength weakening process after shale failure, by introducing an orthotropic elasticity and an orthotropic pressure-dependent yield surface. Based on the anisotropic strength criterion of McLamore and Gray for rock and soil, [21, 22] improved the isotropic Drucker-Prager strength criterion as an anisotropic elastoplastic constitutive model for layered rock, which can effectively reflect the deformation and strength characteristics of layered rocks. [23] presented a modified Drucker-Prager yield criterion for the transversely isotropic geomaterials by considering the anisotropy of the friction angle and the dilation angle. [24] introduced an anisotropic parameter into the Hoek-Brown failure criterion and experimentally studied the relation between the anisotropy parameter and the degree of anisotropy. There are many other methods to describe the anisotropic characteristics of material deformation or strength by introducing anisotropic parameters [25–27], which will not be detailed here. With the development of computer technology, a numerical simulation method provides a new way to simulate anisotropic materials. Sainsbury used the 3DEC discrete element code to simulate the anisotropic characteristics of the real rock mass by including the joint elements, and the effects of joints on the rock deformation and strength characteristics were also investigated [28]. [29] established a discrete fracture model to characterize the heterogeneity of shale reservoirs with interlaced distributed natural fractures. In addition to describing the fluid flow in complex fracture networks, the model can also deal with the nonuniform distribution of stress and the anisotropy of the strength caused by the opening and shearing of natural fractures. Therefore, the discrete fracture model provides an alternative way of characterization of shale mechanics. [30] used bonded-particle discrete element modeling with embedded smooth joints to simulate the mechanical behavior of transversely isotropic rock and demonstrate the effectiveness of the new method in modeling the equivalent anisotropic medium.

The above research puts forward different methods to describe anisotropy materials, which have their own characteristics and advantages. The failure criterion established by [19] can reflect the strength characteristics of the transversely anisotropic material. The defect is that massive parameters need to be determined and the rock structural discontinuity cannot be characterized. Crook indirectly characterized strength anisotropy of materials using the method of the equivalent stress, which also has the defect of too many material parameters, while the discrete fracture model provides an effective method that can effectively represent the effect of beddings on rock mechanical and physical properties [29]. In this paper, a continuum damage-based discrete fracture network method (D-DFN) is proposed to describe the structural discontinuity and mechanical anisotropy of laminated shales, where the stiffness and strength evolution of shale after failure are described based on the continuum damage theory, and the discrete fracture network modeling method is used to describe the bedding structure of shales. The model parameters are calibrated by experiment, and the validity of the D-DFN method is proved by comparison between the simulation results and experiment results.

2. Compression Tests on Shales

In this paper, the experimental investigation is performed on Longmaxi shales. This is a silicic, fine-grained, black shale with an average of 21% clay content. During diagenesis of shales, the external force (such as tectonic movement) can cause the opening and propagation of shale joints, forming natural fracture networks [31]. Shown in Figure 1 is the distribution of natural fractures in Longmaxi shales with different scales. At least on the size of Figure 1(b), shales should be described by a discrete fracture network (DFN) model [32]. That is, shales should be considered a combination of the natural fractures and the shale matrices cut by fractures, due to the large differences in mechanical and physical properties between natural fractures and matrices. Even if the rock sample size is reduced to the size of the standard core while the core contains weak interfaces (Figure 1(c)), the results of mechanical tests carried out on this core reflect the combined effect of the interfaces and the matrices. Therefore, a new method is needed to explain conventional mechanical test results carried out on shales.

Standard cores with diameters of 2.5 cm and lengths of 5 cm (Figure 1(c)) are used in the tests. In order to reduce the discreteness of the test results, all the standard cores are taken from the same shale block. The bedding orientation in triaxial tests is denoted by the angle β between the loading direction and the bedding planes (Figure 2). Two sets of core compression tests have been performed to investigate the effects of confining pressure and bedding orientations on rock mechanical properties:

(1) A series of drained triaxial compression tests with the bedding planes orientated normal to the axis of the specimen ($\beta = 90^\circ$) and confining pressures of 0, 10, 20, 30, 40, and 50 MPa

(2) A series of drained triaxial compression tests with confining pressures of 40 MPa and different bedding plane orientations ($\beta = 0^\circ, 30^\circ, 45^\circ, 60^\circ$, and 90°)

The conventional triaxial compression tests with different confining pressures show (Figures 3 and 4) that

(1) the cores mainly show shear failure except at lower confining pressures (0 MPa and 10 MPa) (Figure 3)

(2) with the increase of confining pressure, the elastic modulus of shale is not changed much (average 31 GPa), but the strength of shale is increased evidently (Figure 4)

The conventional triaxial compression tests with different bedding orientations (Figures 5–8) show that

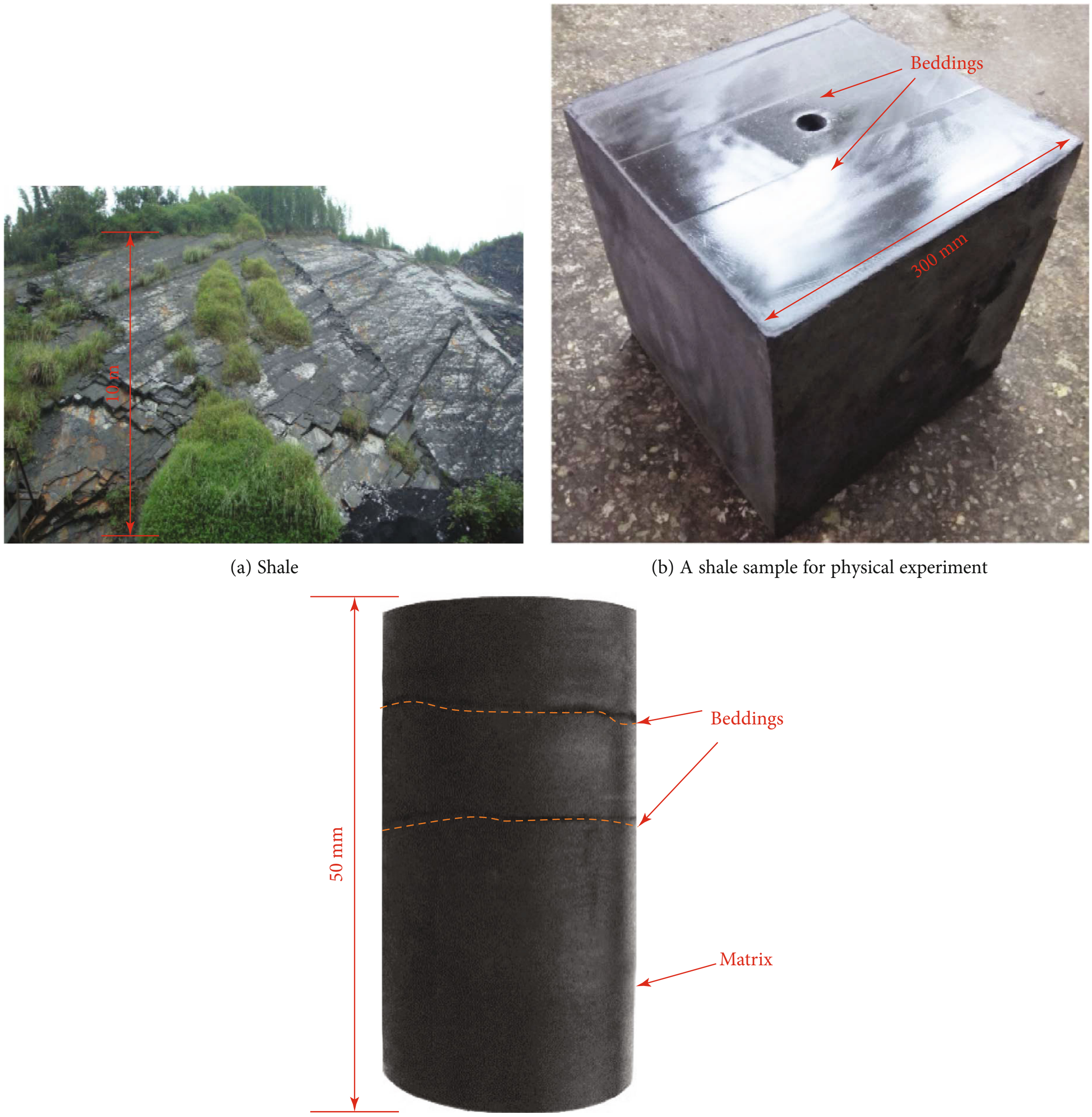

(a) Shale

(b) A shale sample for physical experiment

(c) A standard core with beddings

Figure 1: Distributions of natural fractures in shales [33].

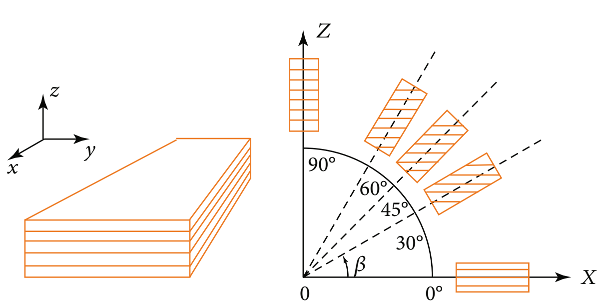

Figure 2: Illustration of coring directions of shale samples.

(1) the cores mainly show shear failure along bedding planes when β equals 30° or 45°. When β is 60°, besides the shear failure along the bedding plane, shear failure also occurs to shale matrices. When β equals 0 or 90°, mainly shear failure occurs to the shale matrix

(2) as β increases from 0 to 90°, the tested elastic modulus decreased (Figure 7). The anisotropic degree of the modulus of elasticity (E_{max}/E_{min}) can be calculated as 1.10. According to Worotnicki's statistics of 200 sets of core compression test results [34], the shale samples of this experiment can be classified as a kind of rock with smaller elastic anisotropy

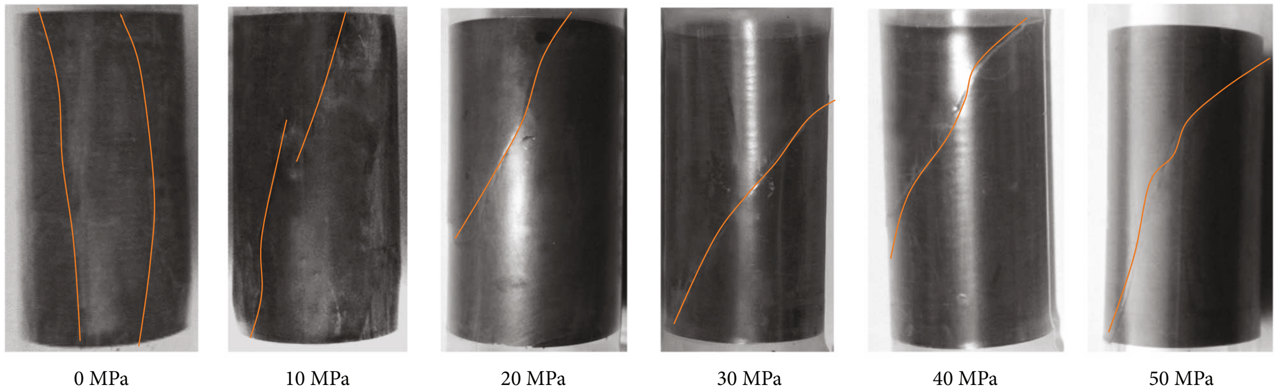

Figure 3: Broken cores after compression with different confining pressures.

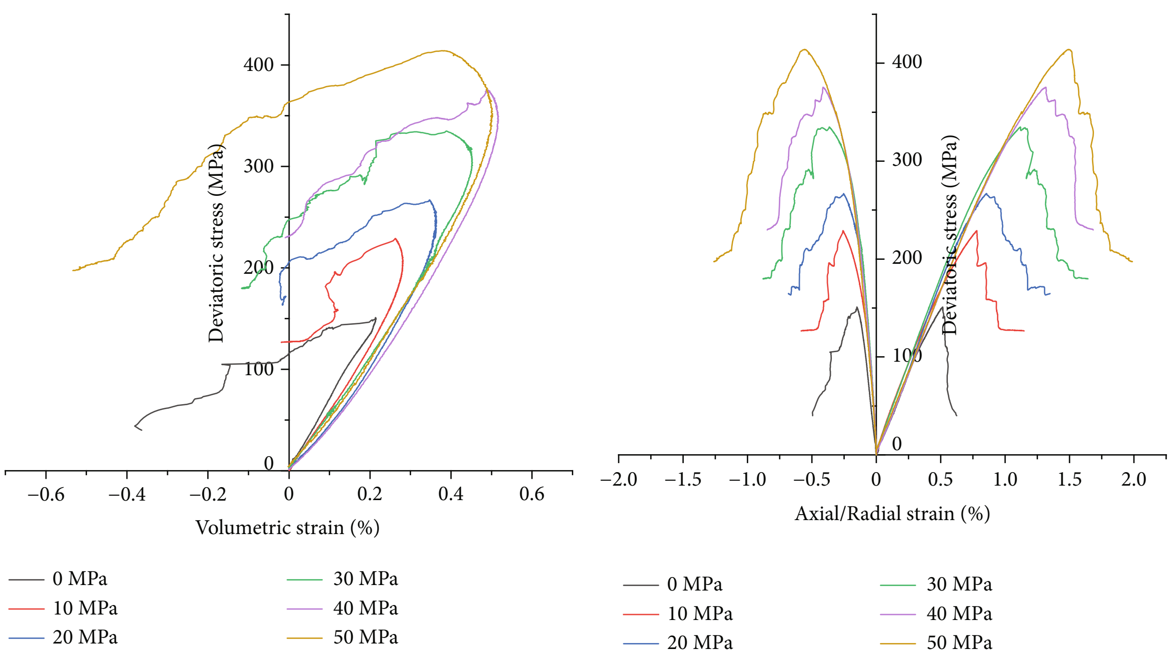

(a) Deviatoric stress-volumetric strain

(b) Deviatoric stress-axial/radial strain

Figure 4: Stress-strain curves of cores under varying confining pressures in triaxial compression tests.

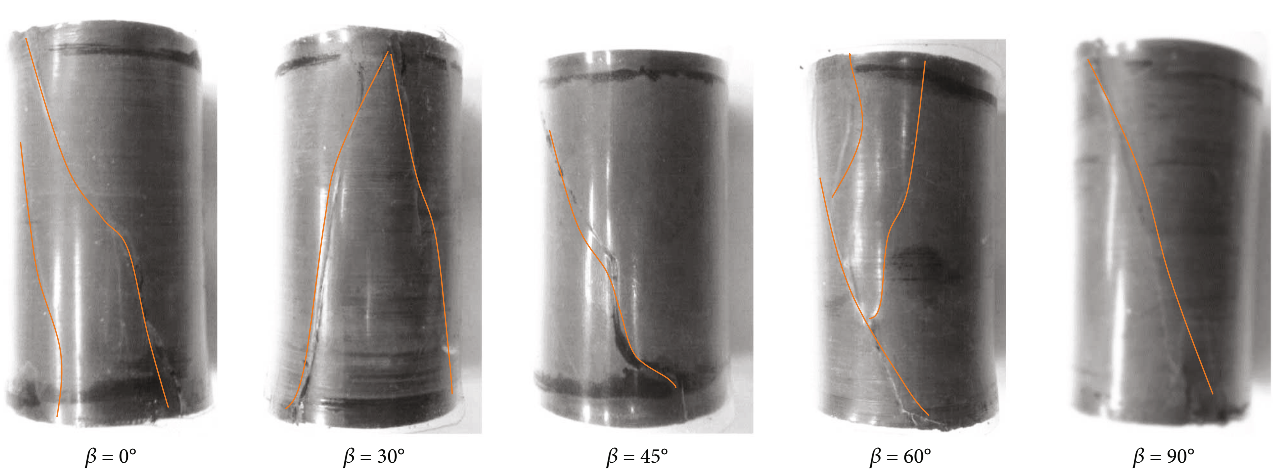

Figure 5: Failure modes of cores after experiments.

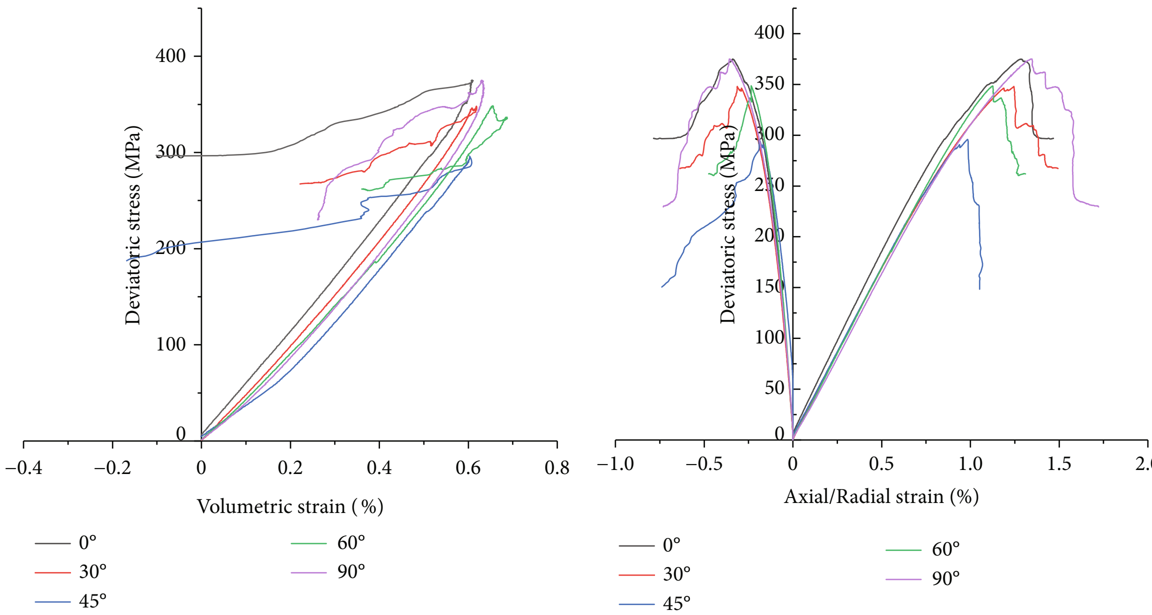

(a) Deviatoric stress-volumetric strain

(b) Deviatoric stress-axial/radial strain

Figure 6: Stress-strain curves of cores with different bedding orientations.

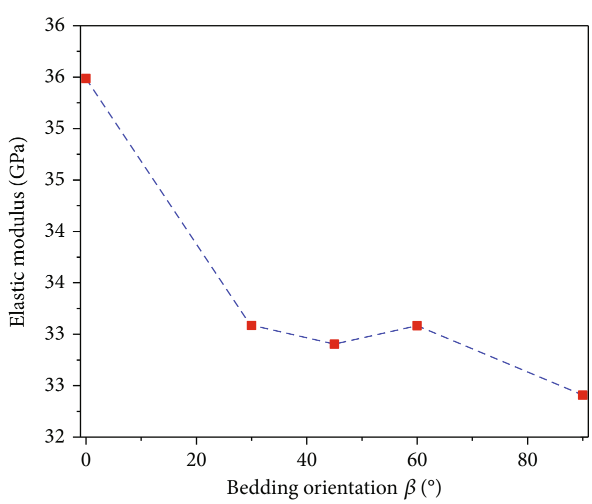

Figure 7: Variation of elastic modulus over β.

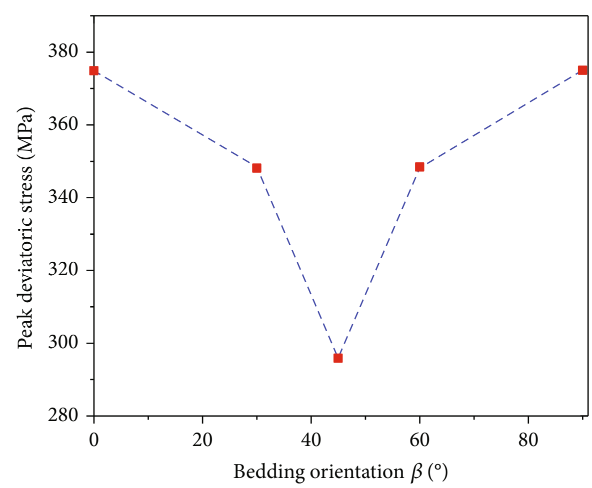

Figure 8: Variation of peak strength over β.

(3) with the increase of β from 0 to 90°, the ultimate deviatoric stress (σ_p) first decreases and then increases, and the minimum value is obtained at 45° (Figure 8). The strength anisotropy ($\sigma_{p\ \max}/\sigma_{p\ \min}$) is calculated to be 1.27. It shows that the strength anisotropy of shale in this experiment is slightly higher than that of elastic modulus due to the bedding structure

3. Simulation Method

In this paper, the mechanical property of shales is studied by combining experimental and numerical methods. Based on current laboratory testing conditions, the following assumptions were made in numerical simulation, as well as for simplified calculation.

(1) The elastic deformation stage before shale failure is described by the anisotropic elastic constitutive model. The damage theory is used to explain the stiffness and strength degradation after shale failure, and the damage evolution process is assumed to be isotropic

(2) The shale bedding structure is described by the discrete fracture network (DFN) modeling method. The mechanical and physical difference between shale beddings and masses was taken into account by setting different initial damage variables to the bedding elements and the matrix elements

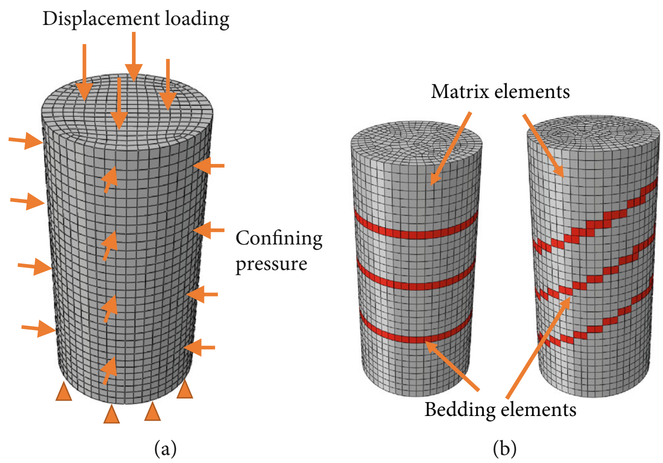

FIGURE 9: Finite element model configuration and load method for triaxial tests.

(Figure 9), where a nonzero initial damage is set to bedding elements to show initial lower elastic modulus and strength of beddings compared with initially nondamaged matrix elements

3.1. Isotropic Elastic Constitutive Model. Because of the geological deposition, shales pose a distinct layered structure, and the transversely isotropic assumption is usually carried out to simplify the calculation. According to the theory of elasticity, the expression of the strain-stress relationship of the orthotropic body is as follows [17]:

$$\begin{Bmatrix} \varepsilon_{11} \\ \varepsilon_{22} \\ \varepsilon_{33} \\ \gamma_{12} \\ \gamma_{13} \\ \gamma_{23} \end{Bmatrix} = \begin{Bmatrix} \frac{1}{E_1} & -\frac{\nu_{21}}{E_2} & -\frac{\nu_{31}}{E_3} & 0 & 0 & 0 \\ -\frac{\nu_{12}}{E_1} & \frac{1}{E_2} & -\frac{\nu_{32}}{E_3} & 0 & 0 & 0 \\ -\frac{\nu_{13}}{E_1} & -\frac{\nu_{23}}{E_2} & \frac{1}{E_3} & 0 & 0 & 0 \\ 0 & 0 & 0 & \frac{1}{G_{12}} & 0 & 0 \\ 0 & 0 & 0 & 0 & \frac{1}{G_{13}} & 0 \\ 0 & 0 & 0 & 0 & 0 & \frac{1}{G_{23}} \end{Bmatrix} \begin{Bmatrix} \sigma_{11} \\ \sigma_{22} \\ \sigma_{33} \\ \sigma_{12} \\ \sigma_{13} \\ \sigma_{23} \end{Bmatrix}. \tag{1}$$

In Equation (1), there are nine independent parameters in the orthotropic model, including Young's modulus, E_1, E_2, and E_3 in three orthogonal directions, three Poisson ratios, ν_{12}, ν_{13}, and ν_{23}, and three shear modulus, G_{12}, G_{13}, and G_{23}.

Assuming that the 1-2 plane is an isotropic plane, then $E_1 = E_2 = E_p$, $\nu_{13} = \nu_{23} = \nu_t$, and $G_{13} = G_{23} = G_t$, in which p and t represent the transverse and normal direction, respectively, and the strain-stress expression of the transversely isotropic body is expressed as follows [18–20]:

$$\begin{Bmatrix} \varepsilon_{11} \\ \varepsilon_{22} \\ \varepsilon_{33} \\ \gamma_{12} \\ \gamma_{13} \\ \gamma_{23} \end{Bmatrix} = \begin{Bmatrix} \frac{1}{E_p} & -\frac{\nu_p}{E_p} & -\frac{\nu_t}{E_t} & 0 & 0 & 0 \\ -\frac{\nu_p}{E_p} & \frac{1}{E_p} & -\frac{\nu_t}{E_t} & 0 & 0 & 0 \\ -\frac{\nu_t}{E_p} & -\frac{\nu_t}{E_p} & \frac{1}{E_t} & 0 & 0 & 0 \\ 0 & 0 & 0 & \frac{1}{G_p} & 0 & 0 \\ 0 & 0 & 0 & 0 & \frac{1}{G_t} & 0 \\ 0 & 0 & 0 & 0 & 0 & \frac{1}{G_t} \end{Bmatrix} \begin{Bmatrix} \sigma_{11} \\ \sigma_{22} \\ \sigma_{33} \\ \sigma_{12} \\ \sigma_{13} \\ \sigma_{23} \end{Bmatrix}, \tag{2}$$

where $G_p = E_p/2(1+\nu_p)$. According to the Saint-Venant principle [35], G_t can be approximated as $G_t = E_p E_t/(E_p + E_t + 2E_p\nu_t)$. Therefore, four parameters are needed for describing the transversely isotropic model of shale, which are E_p, E_t, ν_p, and ν_t.

3.2. Hyperbolic Drucker-Prager Plastic Model. The Drucker-Prager model is widely used to characterize the deformation and strength of geotechnical materials. The yield surface equation can be expressed as a linear relationship between the equivalent stress and the mean stress [36], as shown in Equation (3). In the three-dimensional principal stress space, the shape of the yield surface is an open circular cone. Drucker-Prager of the linear form itself has shortcomings in predicting failure in low confining pressures and tensile failure, which needs to be improved according to specific engineering problems:

$$F = q - p\tan\theta - d = 0, \tag{3}$$

where F is the yield function, q is the equivalent stress, p is the mean stress, and θ and d are the friction angle and cohesion in $p \sim q$ space, respectively.

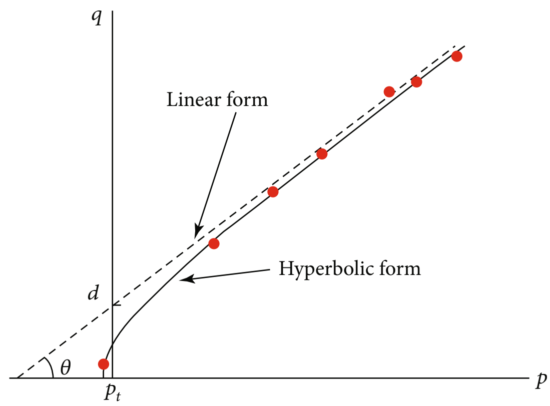

FIGURE 10: Comparison of the linear form and hyperbolic form of Drucker-Prager criterion in the $p \sim q$ plane.

Here, to predict failure of shales under both compression and tension stress, the modified Drucker-Prager criterion of hyperbolic form was employed, which can be expressed as [37]

$$F = \sqrt{(d - p_{t0} \tan \theta)^2 + q^2} - p \tan \theta - d = 0, \tag{4}$$

where p_{t0} is the initial hydrostatic tension strength. Figure 10 shows the comparison of the linear form and hyperbolic form of the Drucker-Prager criterion. Later, it can be found that the curve of hyperbolic form fits the experimental data better.

In the plastic stage, the plastic potential function of shales is defined as

$$G = \sqrt{\left(l \frac{\tan \psi}{\tan \theta}\right)^2 + q^2} - p \tan \psi, \tag{5}$$

where G is the plastic potential function, $l = d - p_{t0} \tan \theta$, and ψ is the dilation angle-related parameter.

The evolution of the plastic flow is defined by a nonassociative flow rule ($\psi \neq \theta$):

$$\dot{\varepsilon}^p = \dot{\lambda} \frac{\partial G}{\partial \sigma}, \tag{6}$$

where ε^p is the plastic strain and λ is the plastic multiplier.

3.3. Damage Constitutive Model. When the stress reaches the peak strength, the shale will soften, exhibiting a transformation from a homogeneous strain field to a heterogeneous strain field with the localized region of intense strain due to the stiffness degradation in the fractured zone. Damage mechanics is often used to describe the failure process of concrete or rock materials [38]. A damage variable D related to plastic deformation is implied in the model to describe the softening stage. To eliminate the effect of element size on the calculation results, the damage variable D is stated by the stress-displacement relationship rather than the stress-strain relationship [39]. Considering the brittle failure characteristics of shale, it is assumed that the relationship between the damage variable and the postfailure equivalent plastic deformation is suited to the first-order exponential decay function (Equation (7)), and the related parameter a can be calibrated by results of the triaxial tests. In order to facilitate programming, the relationship between damage variable and equivalent plastic strain is represented by a piecewise linear function, as shown in Figure 11:

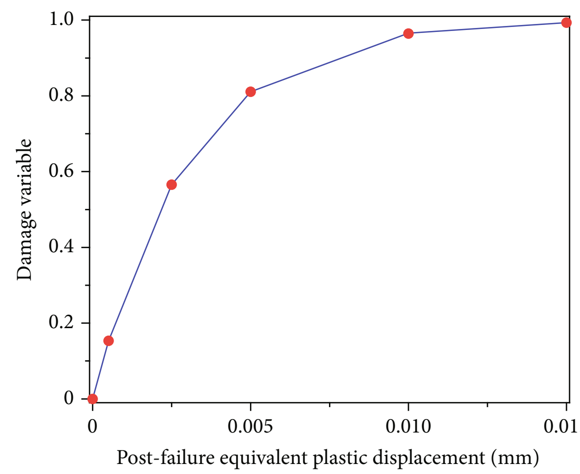

FIGURE 11: Relationship between damage variable and postfailure equivalent plastic displacement.

$$D = \frac{1}{e^{-1/a} - 1} e^{-u_p/a} - \frac{1}{e^{-1/a} - 1}, \tag{7}$$

where e is the base of the natural logarithm, u_p is the postfailure equivalent plastic displacement, and a is the material parameter, which reflects the evolution rate of D with the element deformation.

Since shale is a brittle material, the elastic damage constitutive relation of the element under uniaxial compressive stress and tensile stress can be further simplified, as shown in Figure 12. When the stress of the element satisfies the strength criterion (such as the Drucker and Prager criterion, expressed in Equation (4)), the element begins to fail. In elastic damage mechanics, with the development of damage, the elastic modulus of the element may gradually degrade. The elastic modulus of the damaged element is defined as follows [40]:

$$E = (1 - D)E_0, \tag{8}$$

where D is the damage variable, which is a scaler in this paper; E_0 is the initial elastic modulus; and E is the elastic modulus when the element is damaged.

Tang et al. summarized the elastic damage constitutive model, where the element will be destroyed when the strain of the element exceeds a certain value under tension or compression conditions [40]. Since the description of damage is based on the stress-strain relation, Tang et al.'s modeling results are sensitive to the element size. Therefore, the size of all elements in Tang et al.'s models is uniform and close to the size of rock crystal particles [40]. Hillerborg et al. took

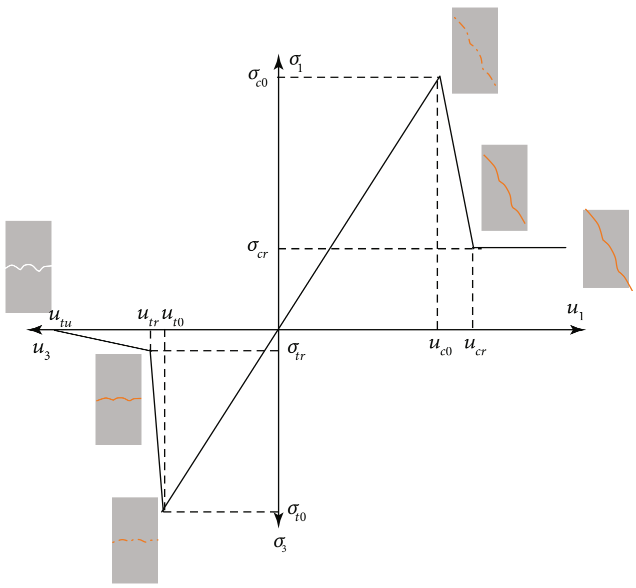

Figure 12: Stress-displacement relationship of an element subject to uniaxial tensile stress (at lower left) and uniaxial compressive stress (at upper right) [33].

Table 1: Elastic parameters of transversely isotropic shale.

E_p (GPa)	E_t (GPa)	G_p (GPa)	G_t (GPa)	ν_p	ν_t
35.49	32.41	14.79	14.01	0.21	0.22

the energy required for fracture opening as a material parameter, based on the theory of brittle fracture mechanics. In such a method, the fracture behavior of elements is described by the stress-displacement relation rather than the stress-strain relation, which can reduce the influence of mesh size on the calculation results [39].

In this paper, the definition of damage variable D is based on the stress-displacement relation. Figure 12 shows the stress-displacement constitutive relation of an element under uniaxial tension and compression conditions.

When an element is subjected to tensile failure, taking the uniaxial tension condition as an example, the expression of the damage variable is as follows:

$$D = \begin{cases} 0, & u_3 \le u_{t0}, \\ \dfrac{u_3 - u_{t0}}{u_{tr} - u_{t0}} \cdot \left(1 - \dfrac{\sigma_{tr}}{\sigma_{t0}}\right), & u_{t0} < u_3 \le u_{tr}, \\ 1 - \dfrac{u_{tu} - u_3}{u_{tu} - u_{tr}} \cdot \dfrac{\sigma_{tr}}{\sigma_{t0}}, & u_{tr} < u_3 \le u_{tu}, \\ 1, \ u_3 > u_{tu}, \end{cases} \tag{9}$$

where u_3 is the elongation of the element under tension stress, which is the product of element strain and element characteristic length l; u_{t0} is the element elongation when the peak stress σ_{t0} is reached; and u_{tr} is the element elongation at the residual stress σ_{tr}. When $u_3 > u_{tu}$, the element is completely damaged and a smeared fracture will be formed in the element.

Table 2: p and q under different test conditions.

p (MPa)	-4.67	49.23	77.67	101.67	133.96	147.54	166.90
q (MPa)	14.10	146.96	202.86	245.02	311.89	322.68	350.72

When a compressive failure occurs to an element, taking the uniaxial compression condition as an example, the expression of the damage variable is as follows:

$$D = \begin{cases} 0, & u_1 \le u_{c0}, \\ \dfrac{u_1 - u_{c0}}{u_{cr} - u_{c0}} \left(1 - \dfrac{\sigma_{cr}}{\sigma_{c0}}\right), & u_{c0} < u_1 \le u_{cr}, \\ 1 - \dfrac{\sigma_{cr}}{\sigma_{c0}}, & u_1 > u_{cr}, \end{cases} \tag{10}$$

where u_1 is the change of element length under compression stress. Other parameters in the equation are defined in Figure 12. Compared with tension failure, the damage cannot reach 1 under compression conditions. That is because rock will shear slide along the broken surface after compression failure, thus maintaining certain residual stress.

4. Calibration of the Numerical Model

The elastic properties can be determined directly from the linear part of the stress-strain relation curves of compression tests on cores with different bedding orientations (Figure 6). The shale studied in the paper is assumed transverse isotropic, and the calibrated elastic parameters are summarized in Table 1.

Compression tests on cores with bedding planes orientated normal to the axis of the specimen ($\beta = 90°$) and different confining pressures (0, 10, 20, 30, 40, and 50 MPa) (Figure 4) are selected to calibrate the parameters in the hyperbolic Drucker-Prager model (Equation (4)). Also, the tension strength (about 14 MPa, obtained from Brazil split tests) is needed to determine the intersection of the failure curve and the horizontal axis (Figure 10). The mean pressures p and respective deviated stresses q at the failure points under different test conditions are collected in Table 2. The yield function [19] is used to fit the data (Figure 13), and the parameters, p_{t0}, d, and θ, are determined as shown in Table 3.

After yielding, there is a hardening stage before shale reaching the peak strength in each test (Figure 4). The hardening behavior can be described by one of the stress-strain curves in Figure 4. The principle is that the hardening curve can represent the average trend of the relationship between the equivalent stress increment and the equivalent plastic strain increment under all confining pressure conditions. Here, we choose the plastic section of the stress-strain curve with confining pressure of 30 MPa to determine the hardening stage.

The simulation model is built using ABAQUS as a platform, and a user subroutine is implemented in the model to

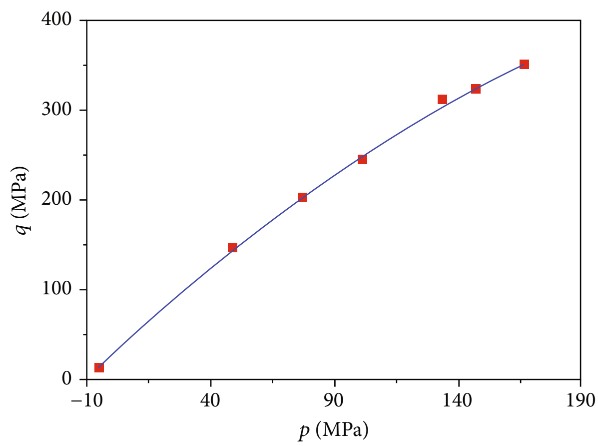

Figure 13: Fitting of the yield surface in the $p \sim q$ plane.

Table 3: Parameters defining yield surface in $p \sim q$ plane.

Parameters	Values
p_{t0} (MPa)	5.05
d (MPa)	88.90
θ (°)	58.98

relate rock element parameters (e.g., elastic modulus and strength) to the damage variable [37]. Figure 14 shows the algorithm flowchart for the ith calculation step.

According to the geometry of the standard rock core, a 3D finite element model discretized by hexahedral elements was developed (Figure 9). In order to take account of computational efficiency and accuracy, the average size of cells is optimized to 1.5 mm, and C3D8R is chosen as the element type. The displacement loading method is adopted (Figure 9(a)).

In order to simulate the influence of weak beddings on shale strength, the finite element model is divided into matrix element sets and bedding element sets (Figure 9(b)). As mentioned before, the mechanical difference between shale beddings and masses was taken into account by setting a nonzero initial damage variable to bedding elements to show initial lower elastic modulus and strength compared with initially nondamaged matrix elements. However, it is difficult to determine the initial damage strength of bedding only by experiment. Here, the paper combines numerical simulation and experiments to solve the problem. Specifically, establishing a core model with β of 30° to simulate, different initial damage variables (such as 0.1, 0.3, 0.5, 0.7, and 0.9) are assigned to the bedding elements every time, and the corresponding stress-strain curves are obtained. Then, the initial damage variable of bedding can be determined by comparing the simulation strength of core with β of 30° to compression test results. Finally, good agreement can be found when the initial damage variable of beddings is set to 0.3. Therefore, the initial damage variable of bedding in all numerical models is set as 0.3 for the shale samples used in this paper. All material parameters are summarized in Table 4.

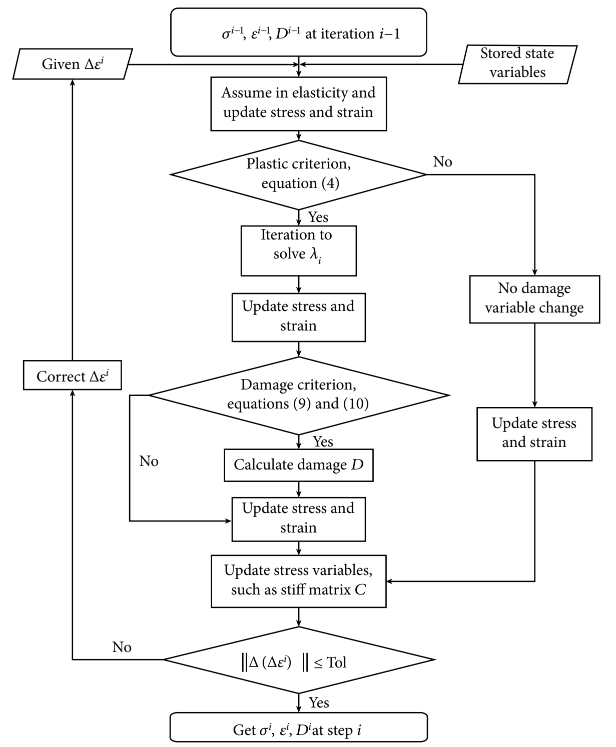

Figure 14: Flowchart for numerical simulation.

Table 4: Material parameters of shale used in the simulations.

Parameter items	Values
The initial out-of-plane elastic modulus (E_t) (GPa)	32.41
The initial in-plane elastic modulus (E_p) (GPa)	35.49
The in-plane Poisson ratio (μ_p)	0.21
The out-of-plane Poisson ratio (μ_t)	0.22
The initial tensile strength (σ_{t0}) (MPa)	14
The residual tensile strength (σ_{tr}) (MPa)	2
The initial compressive strength (σ_{c0}) (MPa)	150
The residual compressive strength (σ_{cr}) (MPa)	30
The fraction angle relative parameter (θ) (°)	58.98
The initial mean tensile strength (p_{t0}) (MPa)	5.05
The dilation angle relative parameter (ψ) (°)	48
The material parameter (a) (mm)	0.003
The initial bedding damage variable (D_0)	0.3

5. Modeling Results

Figure 15 shows the initial and postfailure damage distribution of models with different bedding orientations. It can be found that when β is 30° or 45°, the main failure mode is shearing along bedding planes (Figures 15(b) and 15(c)). When β is 0 or 90°, the shear failure of the matrices is occurring (Figures 15(a) and 15(e)). With β changing from 45° to 60°, the normal stress acting on beddings will increase, resulting in the greater shear strength of bedding planes. When β is 60°, the shear failure will occur both in matrices and along the

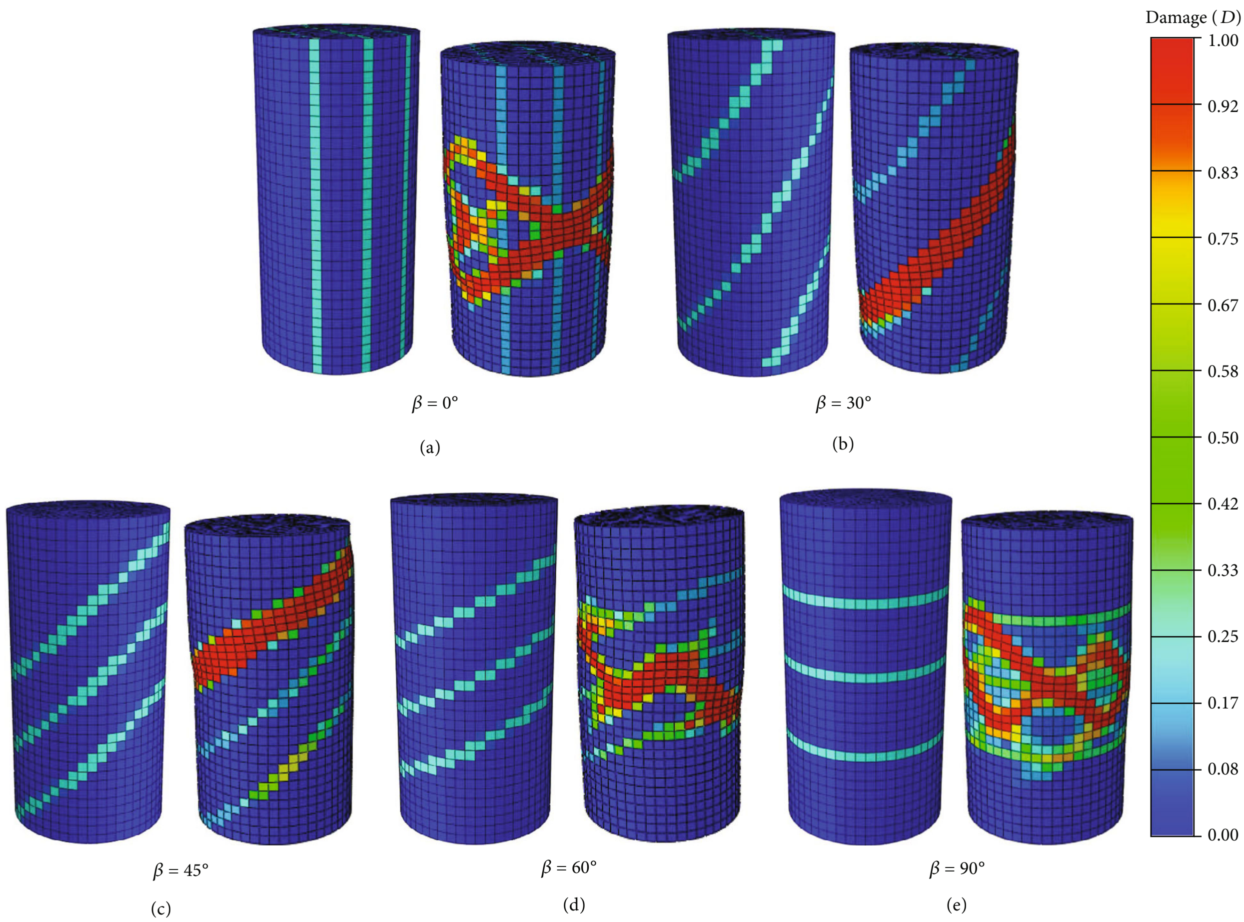

FIGURE 15: Simulations of damage distributions of cores under different bedding orientations.

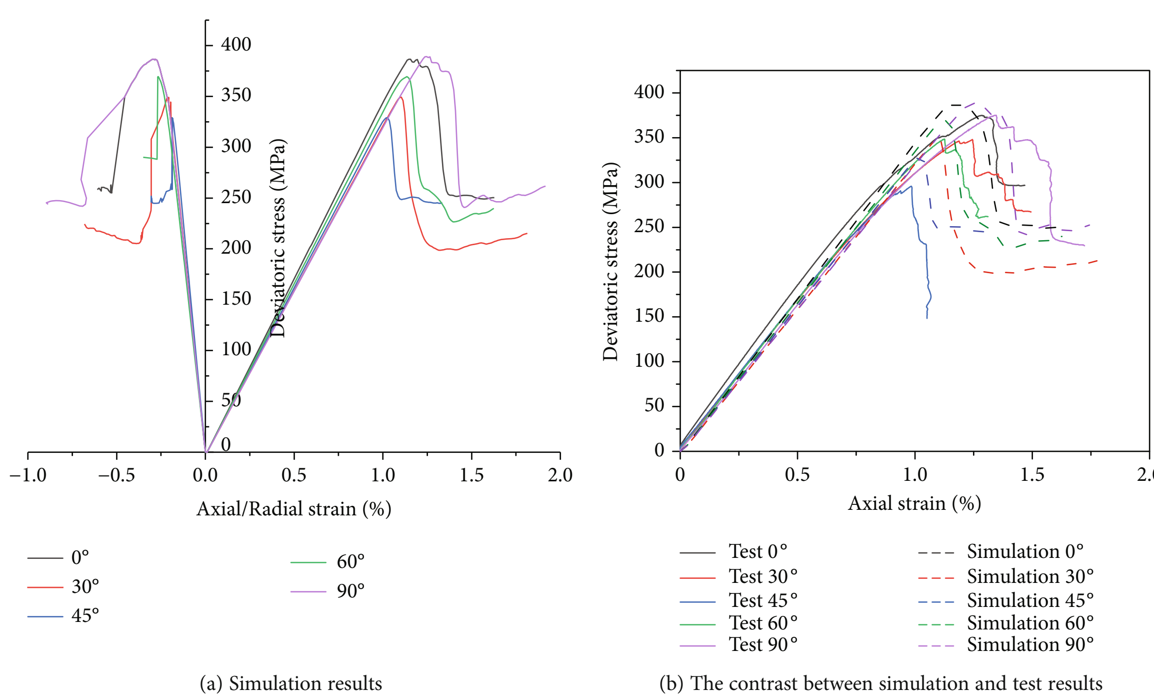

FIGURE 16: Simulation results of stress-strain relationship of cores with different bedding orientations and the contrast with test results.

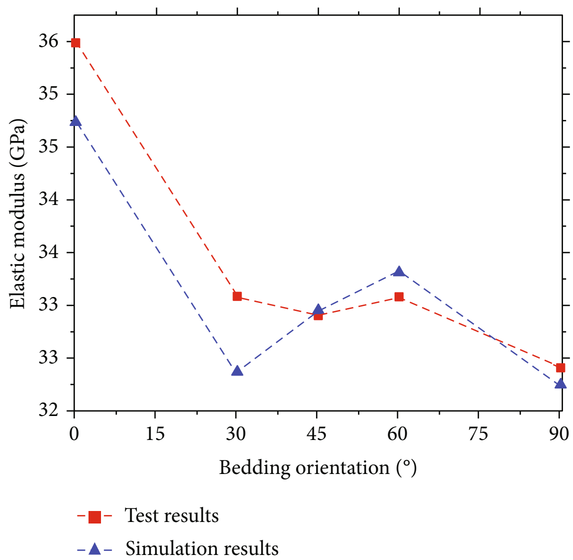

Figure 17: The contrast between simulation and test results on the variation of elastic modulus over β.

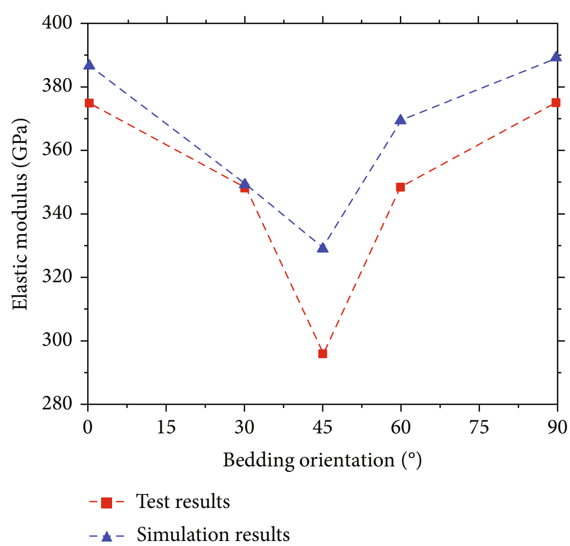

Figure 18: The contrast between simulation and test results on the variation of shale strength over β.

bedding planes (Figure 15(d)). The numerical simulation results are in good agreement with the experimental results (Figure 5).

Figure 16 shows the stress-strain curves obtained from numerical simulations with different bedding orientations. The variation trends of elastic modulus and strength of shale over β are also compared well with the experimental results (Figures 17 and 18). It is proved that the D-DFN model is effective in simulating the mechanical properties of the Longmaxi black shale.

6. Conclusion

In view of the bedding structure of the Longmaxi black shale in Sichuan basin, a finite element model based on continuous damage theory and discrete fracture network modeling method (D-DFN method) is developed to describe the shale's structural discontinuity and the mechanical anisotropy.

In the model, it is assumed that the elastic deformation of shales satisfies the transversely isotropic deformation law. After failure, the isotropic damage model is used to describe the strain softening trend. The discrete fracture modeling method is used to characterize the shale matrices and beddings by setting different initial damage variables to bedding elements and matrix elements. By comparing with the triaxial test results, the validity of the D-DFN method in simulating the deformation and strength anisotropy of the shale is verified.

The model assumes that the strength of the shale matrix is isotropic. Therefore, the D-DFN method proposed in this work is suitable for shale masses with low matrix strength anisotropy. A further study is needed for the characterization of strength anisotropy of shale matrix, to expand the application of the model.

Data Availability

The data used to support the findings of this study are available from the corresponding author upon request.

Conflicts of Interest

The authors declare no conflict of interest.

Acknowledgments

This work is supported by the Shandong Provincial Natural Science Foundation (Nos. ZR2019ZD14 and ZR2020QE120).

References

[1] A. Davarpanah, "Feasible analysis of reusing flowback produced water in the operational performances of oil reservoirs," *Environmental Science and Pollution Research*, vol. 25, no. 35, pp. 35387–35395, 2018.

[2] A. Davarpanah and B. Mirshekari, "Experimental investigation and mathematical modeling of gas diffusivity by carbon dioxide and methane kinetic adsorption," *Industrial & Engineering Chemistry Research*, vol. 58, no. 27, pp. 12392–12400, 2019.

[3] X. Hu, J. Xie, W. Cai, R. Wang, and A. Davarpanah, "Thermodynamic effects of cycling carbon dioxide injectivity in shale reservoirs," *Journal of Petroleum Science and Engineering*, vol. 195, 2020.

[4] A. Davarpanah, "Parametric study of polymer-nanoparticles-assisted injectivity performance for axisymmetric two-phase flow in EOR processes," *Nanomaterials*, vol. 2020, no. 10, p. 1818, 2020.

[5] Y. Hu, Z. Zhao, H. Dong, M. V. Mikhailova, and A. Davarpanah, "Hybrid application of nanoparticles and polymer in enhanced oil recovery processes," *Polymers*, vol. 13, no. 9, p. 1414, 2021.

[6] R. Ghosh and M. Ojha, "Amount of gas hydrate estimated from rock physics analysis based on morphology and intrinsic anisotropy in area B, Krishna Godavari offshore basin,

expedition NGHP-02," *Marine and Petroleum Geology*, vol. 124, no. 1752, p. 104856, 2021.

[7] S. Tao, X. Tang, J. Rutqvist, Q. Liu, and M. Hu, "The influence of stress anisotropy and stress shadow on frost cracking in rock," *Computers and Geotechnics*, vol. 133, no. 4, p. 103967, 2021.

[8] S. L. Chen, B. X. Huang, and D. Li, "Experiment study on the basic law of high-pressure abrasive hydraulic cutting for coal-rock mass," *Journal of Mining and Strata Control Engineering*, vol. 2, no. 4, 2020.

[9] D. L. Wang, B. Y. Hao, and X. Liang, "Slurry diffusion of single fracture based on fluid-solid coupling," *Journal of Mining and Strata Control Engineering*, vol. 3, no. 1, 2021.

[10] B. L. Zhang, B. T. Shen, and J. H. Zhan, "Experimental study of edge-opened cracks propagation in rock-like materials," *Journal of Mining and Strata Control Engineering*, vol. 2, no. 3, pp. 33–35, 2020.

[11] H. Niandou, J. F. Shao, J. P. Henry, and D. Fourmaintraux, "Laboratory investigation of the mechanical behaviour of Tournemire shale," *International Journal of Rock Mechanics & Mining Sciences*, vol. 34, no. 1, pp. 3–16, 1997.

[12] P. P. Mandal, J. Sarout, and R. Rezaee, "Geomechanical appraisal and prospectivity analysis of the Goldwyer shale accounting for stress variation and formation anisotropy," *International Journal of Rock Mechanics and Mining Sciences*, vol. 135, p. 104513, 2020.

[13] H. Shuai, B. Xla, and L. Xiao, "Experimental study on the mechanical properties of bedding planes in shale-Science Direct," *Journal of Natural Gas Science and Engineering*, vol. 76, 2020.

[14] M. E. Chenevert and C. Gatlin, "Mechanical anisotropies of laminated sedimentary rocks," *Society of Petroleum Engineers Journal*, vol. 5, no. 1, pp. 67–77, 1965.

[15] H. Sone and M. Zoback, "Mechanical properties of shale-gas reservoir rocks-part 1: static and dynamic elastic properties and anisotropy," *Geophysics*, vol. 78, no. 5, pp. 381–392, 2013.

[16] H. Sone and M. Zoback, "Mechanical properties of shale-gas reservoir rocks-part 2: ductile creep, brittle strength, and their relation to the elastic modulus," *Geophysics*, vol. 78, no. 5, pp. 393–402, 2013.

[17] S. G. Lekhnitskij, *Theory of the Elasticity of Anisotropic Bodies*, Deformation, 1977.

[18] B. S. Aadnoy, *Modeling of the Stability of Highly Inclined Boreholes in Anisotropic Rock Formations*, Society of Petroleum Engineers, 1987.

[19] O. Cazacu and N. D. Cristescu, "A paraboloid failure surface for transversely isotropic materials," *Mechanics of Materials*, vol. 31, no. 6, pp. 381–393, 1999.

[20] A. J. L. Crook, J. Yu, and S. M. Willson, *Development of an Orthotropic 3D Elastoplastic Material Model for Shale*, Society of Petroleum Engineers, 2002.

[21] H. Xu, *Theoretical and Numerical Modeling of Anisotropic Damage in Rock for Energy Geomechanics*, pp. 736–744, 2014.

[22] H. Xu and C. Arson, "Modeling damage induced by deviatoric stress in rock: theoretical framework," in *Biot Conference on Poromechanics*, pp. 2546–2555, 2013.

[23] W. Y. Wu and G. H. Liu, "A modified Drucker-Prager criterion for transversely isotropic geomaterials and its numerical implementation," *Advanced Materials Research*, vol. 850-851, pp. 115–119, 2013.

[24] M. A. Ismael, H. F. Imam, and Y. El-Shayeb, "A simplified approach to directly consider intact rock anisotropy in Hoek-Brown failure criterion," *Journal of Rock Mechanics and Geotechnical Engineering*, vol. 6, no. 5, pp. 486–492, 2014.

[25] A. Attaia, O. Vorobiev, and S. Walsh, *Implementation of an Anisotropic Mechanical Model for Shale in Geodyn*, Technical Report, 2015.

[26] S. Dineva, *Anisotropy and Non-Linear Effects in SMC Composites*, 2015.

[27] Yuan, *A Non-Coaxial Theory of Plasticity for Soils with an Anisotropic Yield Criterion*, University of Nottingham, 2015.

[28] D. P. Sainsbury, B. L. Sainsbury, and C. G. Limited, *Three-Dimensional Analysis of Pit Slope Stability in Anisotropic Rock Masses*, Slope Stability, 2013.

[29] M. W. Mcclure and R. N. Horne, *Discrete Fracture Network Modeling of Hydraulic Stimulation*, Springer International Publishing, 2013.

[30] B. Park and K. Min, "Bonded-particle discrete element modeling of mechanical behavior of transversely isotropic rock," *International Journal of Rock Mechanics and Mining Sciences*, vol. 76, pp. 243–255, 2015.

[31] J. E. Olson, Q. Yuan, J. Holder, and P. Rijken, *Constraining the Spatial Distribution of Fracture Networks in Naturally Fractured Reservoirs Using Fracture Mechanics and Core Measurements, SPE Annual Technical Conference and Exhibition*, Society of Petroleum Engineers, New Orleans, Louisiana, 2001.

[32] B. H. G. Brady and E. T. Brown, *Rock Mechanics for Underground Mining*, George Allen & Unwin, 1985.

[33] Q. Shan, Y. Jin, P. Tan, and R. Zhang, "Experimental and numerical investigations on the vertical propagation of hydraulic fractures in laminated shales," *Journal of Geophysics and Engineering*, vol. 15, no. 4, pp. 1729–1742, 2018.

[34] G. Worotnicki, *CSIRO Triaxial Stress Measurement Cell*, Rock Testing and Site Characterization, Elsevier, 1995.

[35] B. Saint Venant, "Sur la distribution des élasticités autour de chaque point d'un solide ou d'un milieu de contexture quelconque, particulièrement lorsqu'il est amorphe sans être isotrope," in *Journal de Math*, pp. 257–293, Pures et Appliquées, Tome VIII (2ème série), 1863.

[36] D. C. Drucker and W. Prager, "Soil mechanics and plastic analysis or limit design," *Quarterly of Applied Mathematics*, vol. 10, no. 2, pp. 157–165, 1952.

[37] D. Hibbitt, B. Karlsson, and P. Sorensen, *Abaqus/CAE User's Guide*, ABAQUS, 2013.

[38] J. Lubliner, J. Oliver, S. Oller, and E. Oñate, "A plastic-damage model for concrete," *International Journal of Solids and Structures*, vol. 25, no. 3, pp. 299–326, 1989.

[39] A. Hillerborg, M. Modéer, and P. E. Petersson, "Analysis of crack formation and crack growth in concrete by means of fracture mechanics and finite elements," *Cement & Concrete Research*, vol. 6, no. 6, pp. 773–781, 1976.

[40] C. A. Tang, L. G. Tham, P. Lee, T. H. Yang, and L. C. Li, "Coupled analysis of flow, stress and damage (FSD) in rock failure," *International Journal of Rock Mechanics and Mining Sciences*, vol. 39, no. 4, pp. 477–489, 2002.

Hindawi
Geofluids
Volume 2021, Article ID 4092242, 18 pages
https://doi.org/10.1155/2021/4092242

Research Article

Investigation on the Movement and Fracture Characteristics of an Extra-Thick Hard Roof during Longwall Panel Extraction in the Yima Mining Area, China

Hongwei Wang ,[1,2] Daixin Deng,[1] Ruiming Shi,[1] Guozhen Yang,[1] Shuo Xu,[1] and Yaodong Jiang[1,2]

[1]*School of Mechanics and Civil Engineering, China University of Mining and Technology, Beijing 100083, China*
[2]*State Key Laboratory of Coal Resources and Safe Mining, China University of Mining and Technology, Beijing 100083, China*

Correspondence should be addressed to Hongwei Wang; whw@cumtb.edu.cn

Received 12 May 2021; Accepted 22 July 2021; Published 6 August 2021

Academic Editor: Hualei Zhang

As an extra-thick hard roof is a significant contributing factor to frequently induced sudden roof collapse accidents and coal bursts, this study investigates the relationship between extra-thick hard roof movement and mining-induced stress using physical experiments and numerical simulation methods based on mining activities in a longwall panel in the Yima mining area, Henan province, China. The results suggested that the movement and failure processes of the extra-thick roof could be divided into three main periods: the undisturbed, movement stabilization, and sudden collapse periods. The roof displacement remained essentially unchanged during the undisturbed period. During the movement stabilization period, the displacement gradually increased into the upper roof. However, the extra-thick main roof remained undisturbed until the immediate roof experienced its fourth periodic caving in the physical model. Consequently, the displacement expanded rapidly into the extra-thick main roof during the sudden collapse period and the strain energy was violently released when it accumulated in the extra-thick main roof. Additionally, the mining-induced stress was characterized by a sudden decrease in the gradual increase trend when the extra-thick roof instantly collapsed. The deformation and fracture of the extra-thick roof could cause a sudden decrease in the mining-induced stress and lead to continuous and unstable subsidence pressure exerted on the mining panel and roadway. This significantly contributes to the occurrence of coal bursts.

1. Introduction

An extra-thick hard roof is the strata with large thickness and high strength occurring above a coal seam or a thin immediate roof. Large area movement and unstable fracture of the extra-thick hard roof are significant hazards threatening safe production in coal mines. It will cause extensive damage to the entire stope and is an important factor of inducing typical dynamic disasters such as coal bursts [1–3]. In general, a sudden and violent collapse of the extra-thick hard roof can release masses containing deformation energy and cause coal bursts during longwall panel advancement where machinery and workers assemble.

The frequent extra-thick roof collapse events caused by mining activities have made an important influence on the safety of coal mine production for several years. In November 2011, a severe coal burst resulted in heavy casualties and damaged the roadway section at the 21-221 mining face of the Qianqiu mine in the Yima mining area [4, 5]. Although the accident occurrence was related to the F_{16} thrust fault near the mining panel, the presence of a 550 m thick and hard conglomerate rock above the coal seam was also a key disaster factor. Therefore, dynamic movement evolution of the extra-thick roof is of primary interest in this study.

The deformation and instability of the extra-thick roof are a source of dynamic disasters. Scholars have performed analyses from different perspectives and obtained fruitful results on the extra-thick roof deformation [6–9]. Gao et al. [10] studied the mechanism of ground pressure induced by hard roof instability through physical experiment and field measurement. Zhao et al. [11] introduced the large-sized cantilever beam theory to calculate the caving step distance of the thick and hard roof. Ning et al. [12] investigated dynamic movement and fracturing of the thick and hard roof by microseismic monitoring technology. Shen et al. [13] found the strong influence of the fracture position of a thick hard roof on the roadway. Singh and Singh [14] assessed the effect of basic roof thickness on the strata caving behavior and stated that the caving span of basic roof fall increased linearly with the increase in basic roof thickness. Zhou et al. [15] stated that the solid backfill body is an effective way to control the deformation of hard roof and the hard roof's subsidence decreased as solid backfilling ratio increased. Wang et al. [16] found that overburden pressure induced a fracture in a thick hard roof after initial and periodic instability failure. In addition, extensive field investigation results have been obtained regarding the correlation between the movement of the thick hard roof and roadway failure [17, 18].

Due to the complexity, periodicity, and suddenness of the extra-thick roof collapses, the movement of the extra-thick roof is a significant determinant for underground coal mining activities. To acquire further knowledge of the dynamic movement and fracture of the extra-thick roof, integrated physical experiments and numerical simulations were conducted to study the relationship between displacement and mining-induced stress of the extra-thick roof. Moreover, the mechanism contributing to the sudden occurrence of coal bursts induced by the extra-thick roof collapse in the Yima mining area is introduced.

2. Site Descriptions

The Yima mining area contains several faults and synclines, as shown in Figure 1, and was selected as the principal geological background for this study. The Yima mining area is located south of Yima city, China, and covers five major-producing coal mines, that is, the Gengcun, Yuejin, Yangcun, Changcun, and Qianqiu mines. The number of coal bursts occurring in the last 10 years is also presented in Figure 1.

The 21-221 panel operates with the longwall mining method to extract the no. 2 coal seam with a thickness of 5.59–37.48 m. The generalized stratigraphy and important geotechnical parameters of the 21-221 mining panel in the Qianqiu mine are shown in Table 1. The 21-221 mining panel floor is siltstone with an average thickness of 26 m. The 21-221 mining panel immediate roof is sandstone with an average thickness of 10 m and mudstone with an average thickness of 24 m. The 21-221 mining panel basic roof is a 96.35–580.50 m thick conglomerate with a uniaxial compressive strength (UCS) of 45 MPa measured by uniaxial compression test in the laboratory. Therefore, the basic roof is a typical extra-thick hard rock stratum, which is a characteristic stratigraphic feature of the Yima mining area. Because high overburden stress from extra-thick conglomerate rock acts on coal seams, coal bursts occur routinely in the Qianqiu mine.

3. Physical Experiment of the Movement Characteristics of the Extra-Thick Hard Roof

3.1. Physical Model Construction. In recent years, many investigators have conducted extensive physical geological engineering experiments to summarize the characteristics of ground subsidence, overburden rock displacement behavior, distribution characteristics of mining-induced stress, and even the fault activation process in mining engineering [19–31]. To reproduce the process of extra-thick roof movement through physical experiments, the relationship between the physical model and field prototype must satisfy the similarity law [32–34]. In this study, three principal types of similarity law parameters were considered: the material strength, material geometry, and material density. The similarity parameters C_σ, C_L, and C_ρ are the ratios of material strength, material geometry, and material density between the field prototype and physical model, respectively. In addition, all of these should satisfy the equation $C_\sigma/C_\rho \cdot C_L = 1$. For the similar simulation experiment of mining engineering, when the qualitative analysis model is needed, the geometric similarity ratio of the model should be taken in the range of 50 to 200. As the main purpose of this paper is to explore the deformation and failure mechanism of an extra-thick hard roof, the physical model design should mainly meet the requirements of strength similarity theory. According to the geological conditions of the extra-thick hard roof and the objective conditions of the experiment system, the optimal geometric similarity ratio is determined as 100. Meanwhile according to the maximum loading limit of the physical model and the mechanical parameters of rock strata, the strength similarity ratio is determined as 160. Therefore, the similarity coefficients C_σ, C_L, and C_ρ are considered as 160, 100, and 1.6, respectively. The similarity materials used to simulate rock strata in field prototypes contain fine sand, gypsum, lime, and water, which are widely used as binder and aggregate materials in physical experiments [19, 32–36].

Figure 2 shows that the physical model built on the experimental platform (GDSTM) has dimensions of $150 \times 90 \times 10$ cm. Therefore, the similarity thickness of siltstone, that of coal seam, that of sandstone mudstone, and that of conglomerate rock in this physical model are 5, 5, 10, 24, and 46 cm, respectively. Because the full height mining scheme is adopted in the similar simulation experiment, this paper mainly studies the characteristics of extra-thick hard roof deformation and collapse under the influence of mining. In order to lay a higher hard roof as far as possible in the physical model, the thickness of coal seam is reduced to only 5 cm. Five layers of rock strata with different similarity materials in physical experiment are made with five mixed proportions, as shown in Table 2. The humidity change will cause the strength change of a similar material in physical experiment, resulting in the similarity error of mechanical conditions between the model and the prototype. The drying time of similar materials mainly depends on observation and

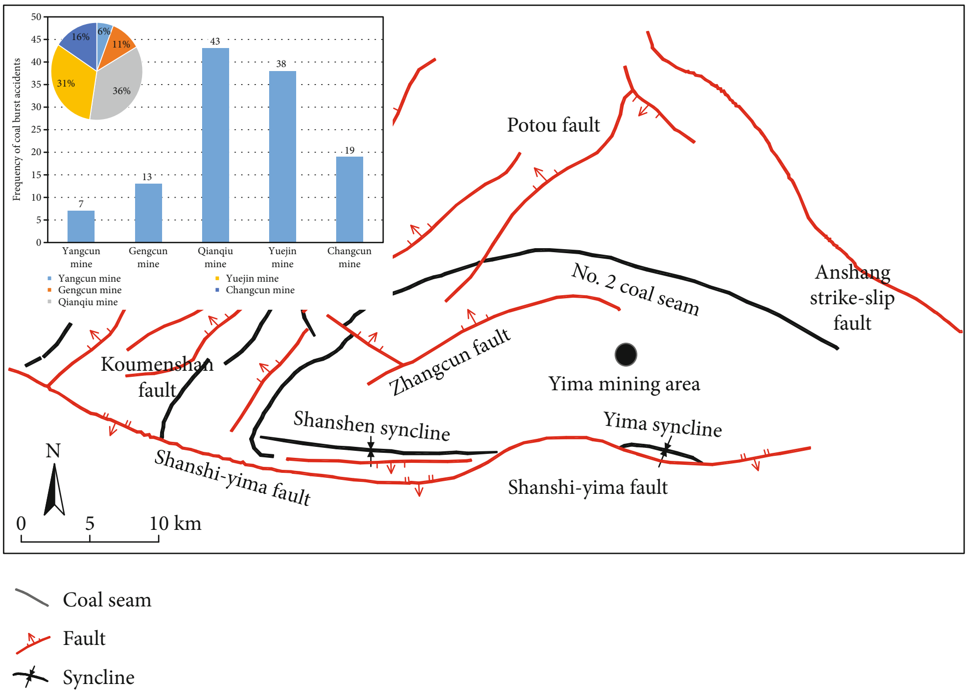

Figure 1: Schematic map of geological structures in the Yima mining area.

Table 1: The generalized stratigraphy and geotechnical parameters.

Rock strata	Thickness (m) Max.	Min.	Mean	Density ($kg.m^{-3}$)	UCS (MPa)
Conglomerate rock	580.50	96.35	550.00	2 700	45
Mudstone	42.20	4.40	24.00	2 170	30
Sandstone	27.00	0.00	10.00	2 200	27
No. 2 coal seam	37.48	5.59	9.60	1 440	16
Siltstone	32.81	0.30	26.00	2 600	30

empirical speculation to determine whether similar materials reach the expected strength. Generally, the drying time of similar materials is 3 to 7 days. The exact drying time depends on the weather conditions during the experiment. The drying time of similar materials is 5 days in this experiment.

The physical model stress boundary conditions in the experiment are loading according to the material strength ratio. The left, right, and top sides of the physical model are loading to 0.13 MPa, 0.13 MPa, and 0.11 MPa, respectively.

3.2. Monitoring Plan and Analysis. Eleven stress sensors were positioned on the extra-thick conglomerate rock, 34 cm away from the coal seam, to monitor the mining-induced stress evolution during the longwall mining process. The horizontal space between the sensors was 10 cm. The digital speckle image correlation technique was utilized to study the displacement evolution of overburden rock during continuous coal seam mining [37–39]. The technique can determine material displacement by following a specific speckle to calculate the movement path between two different pictures [40–43]. The black speckles with a diameter of 1 cm in this study were arranged in an orderly manner on the rock strata surface to monitor the movement characteristics of the extra-thick roof, as shown in Figure 2.

3.3. Test Results. In order to avoid extra-thick hard roof sudden collapse in the preliminary mining process, a coal pillar with a length of 20 m is reserved on the boundary of the on-site 21211 mining face. So, a coal pillar with a length of 20 cm was reserved on the right boundary of the model to reduce the boundary effect. The advancing length of the on-site 21221 mining face is 3 m to 8 m each step according to the field data. The average advancing length is 5 m each step under normal mining conditions. The coal seam was mined 5 cm each step from the right boundary to the left boundary of the physical model.

Figure 3 presented the mining process and roof caving during mining in the test. During the entire mining process in this test, the roof experienced five periodic caving, which showed distinct continuous failure with caving heights of 2, 6, 6, 14, and 36 cm above the goaf. The roof movement process could be divided into three main periods: the undisturbed, movement stabilization, and sudden collapse periods. When the mining face was mined at 35 cm, the roof did not change significantly within a stable state. This stage was the undisturbed period, as shown in Figures 3(a) and 3(b). With the development and connection of cracks in the roof strata, the roof separation phenomenon became increasingly conspicuous. However, the extra-thick roof was essential in the movement stabilization period, as shown in Figures 3(c)–3(g). Meanwhile, the roof progressively sank repeatedly and the roof caving height increased steadily from 2 to 14 cm during this period. The reason for the roof

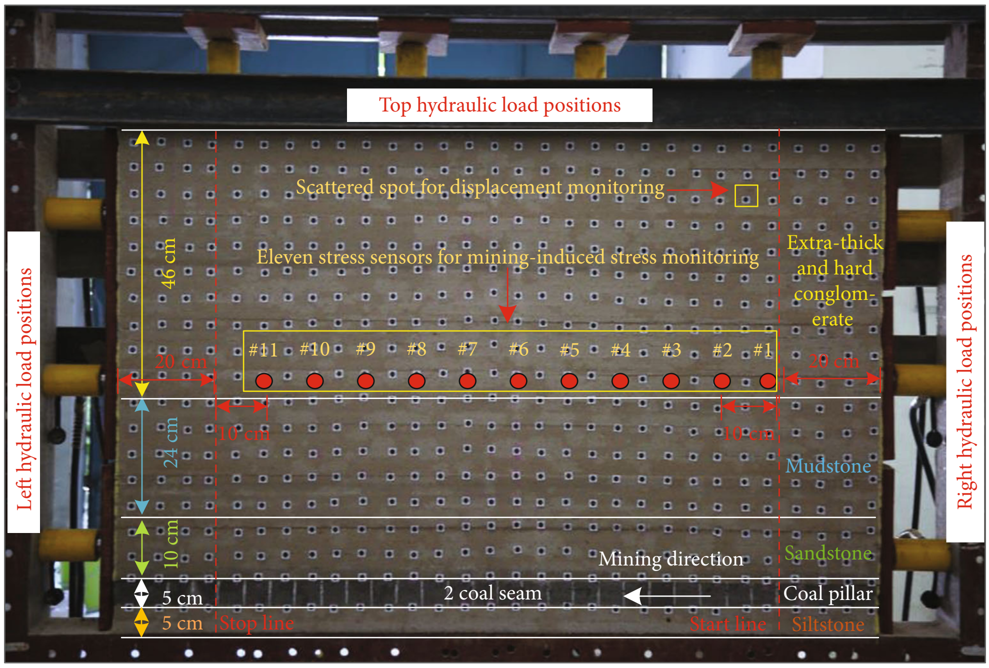

Figure 2: Physical model constructed on the GDSTM and general experimental monitoring plan.

Table 2: Parameters of the similar material.

Rock strata	Fine sand : gypsum : lime : water	UCS of similar material (MPa)	UCS of prototype rock (MPa)
Conglomerate rock	6.0 : 0.5 : 0.5 : 0.6	0.28	44.8
Mudstone	7.0 : 0.4 : 0.6 : 0.7	0.19	30.4
Sandstone	7.0 : 0.5 : 0.5 : 0.7	0.17	27.2
Coal seam	8.0 : 0.6 : 0.4 : 0.8	0.10	16.0
Siltstone	7.0 : 0.4 : 0.6 : 0.7	0.19	30.4

suspension for a long time is that the extra-thick hard roof has great strength and stiffness, which can bear large deformation. Deformation energy is gradually accumulated in the extra-thick hard roof during coal seam mining. The bending and subsidence of hard rock lead to forming the large separation area of the extra-thick hard roof. When the mining face was mined at 110 cm, the roof collapse suddenly expanded into the extra-thick conglomerate in a large area, as shown in Figure 3(h). The roof movement showed an unstable dynamic change in behavior in the sudden collapse period. In this physical experiment, the extra-thick main roof collapse was only observed once when periodic roof caving occurred in the immediate roof. The structural instability of the extra-thick roof was a significant feature of large deformation.

In order to further analyze the spatial structure characteristics of the extra-thick roof in five times the caving state, Figure 4 showed spatial structure distribution of roof caving during advancement of the mining face. The roof caving areas at different stages were distinguished by different color boxes during the experiment process. As the mining face continued advancing and goaf area gradually increased, the caving space was gradually expanded. The development of roof caving was a dynamic process. The characteristic parameters of fractured strata in caving areas were usually the caving height, high-level fractured rock span, low-level fractured rock span, and caving angle, further analyzed in Figure 5.

Low-level and high-level fracture rocks refer to the lowest and the uppermost fracture rock in the roof collapse area, respectively. They can generally describe the spatial range of the roof collapse area. The span of high-level fracture strata is obviously larger than that of low-level fracture strata in the roof collapse area. That is because the roof collapse area expands upward in the mining process of the coal seam. At the first caving, the fracture spans of the low-level and high-level strata were 35 and 32 cm, respectively. The average fracture span of the low-level strata was 20 cm within the next four periodic roof caving. The fracture span of the high-level strata increased steadily except for the third periodic caving, as shown in Figure 5(a). Figure 5(b) shows the minimum and maximum collapse angles of 50° and 56°, respectively. The caving angle showed little fluctuation during the five periodic caving. When the rock strata occur shear failure model, the caving angle between the failure surface and horizontal direction is approximately same under the same lithology condition. The caving angle is closely related to the internal friction angle of the rock stratum. With the advancement of mining faces, the extra-thick roof always

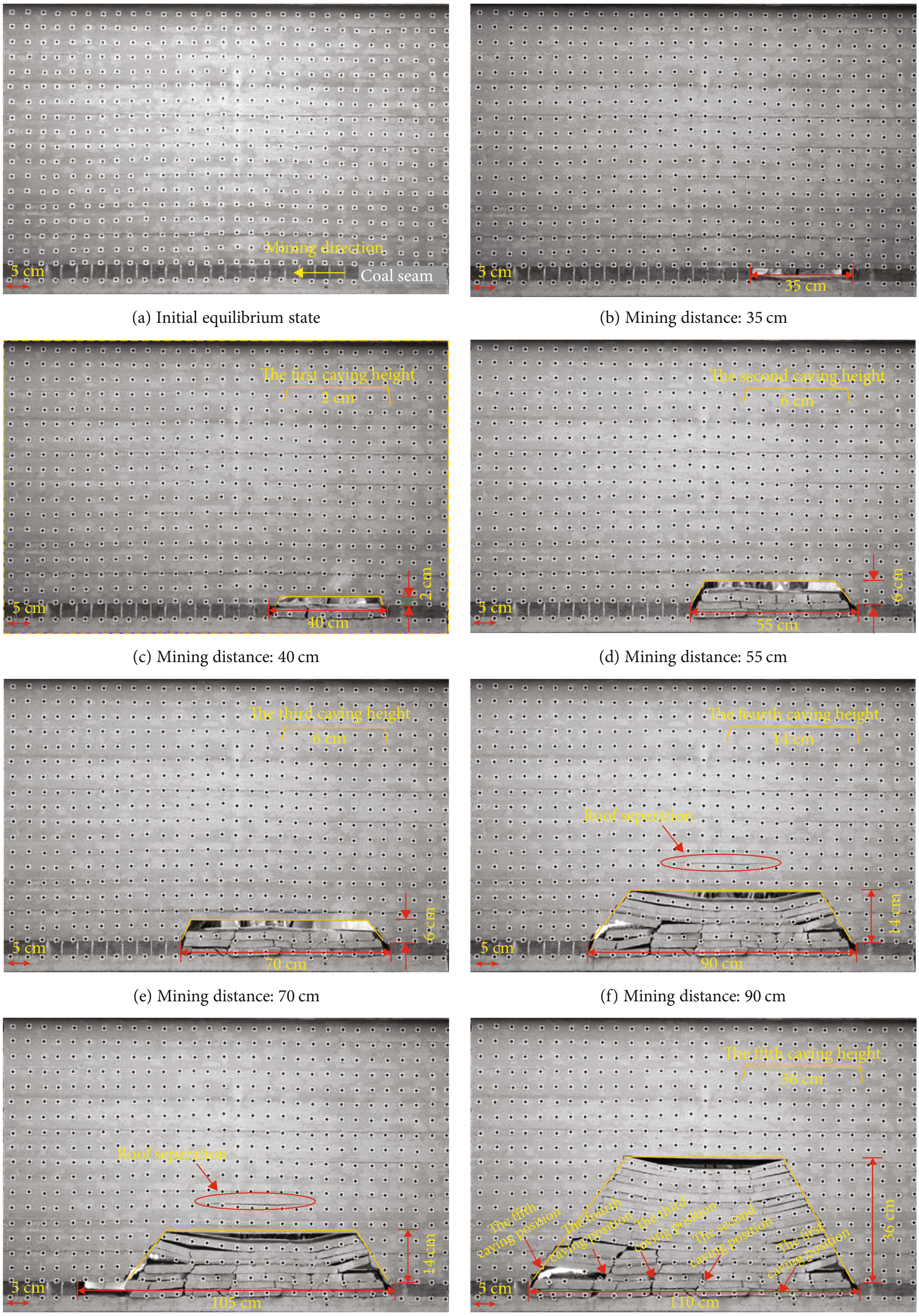

(a) Initial equilibrium state

(b) Mining distance: 35 cm

(c) Mining distance: 40 cm

(d) Mining distance: 55 cm

(e) Mining distance: 70 cm

(f) Mining distance: 90 cm

(g) Mining distance: 105 cm

(h) Mining distance: 110 cm

Figure 3: The movement state of the roof during coal seam mining in the physical model.

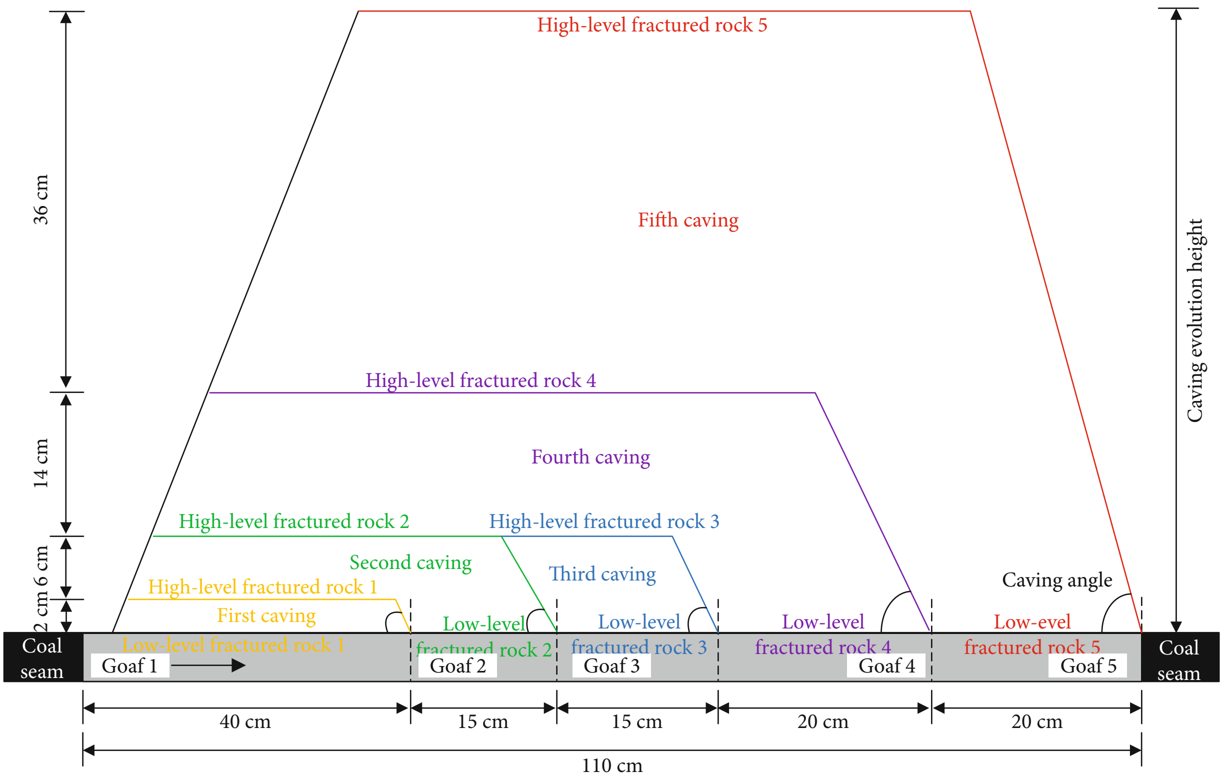

Figure 4: Spatial distribution of roof caving during advancement of the mining face.

experienced change of state alternating between stability and instability after the first roof weighting, and roof pressure release occurred periodically. Because the lithology of low-level strata was mudstone, the breaking span of low-level strata remained stable. However, the lithology of high-level strata was composed of mudstone and extra-thick conglomerates, and the breaking span of high-level strata changed frequently.

The influence of mining disturbance on the extra-thick roof was relatively small in the undisturbed period, and the entire model vertical displacement was zero, as shown in Figure 6(a). During the movement stabilization period, the disturbance effect of continuous mining gradually became obvious. The extra-thick roof experienced five caving in succession and collapsed rock fills in the goaf. The caving strata displacement in the center of the goaf increased to 5.5 cm due to repeated compression. Because of the rock volume expansion, the strata displacement far away from the center of the mining face gradually decreased. In addition, the displacement gradually increased into the upper roof and could be observed only in the immediate roof and the extra-thick roof was not disturbed by the mining activities, as shown in Figures 6(b)–6(e). However, the mining face was mined to a distance of 110 cm in the sudden collapse period and Figure 6(f) shows that the displacement expanded rapidly into the extra-thick roof and the energy accumulated in the hard conglomerate was suddenly released.

With the mining face advancement, the stress balance of the extra-thick roof was broken due to roof collapse. The stress was redistributed to form a new overburden equilibrium structure. Five stress monitoring points marked as #1, #4, #6, #8, and #11 in the extra-thick conglomerate were selected to analyze the characteristics of stress variation, as shown in Figure 7. When the mining face was advanced to a distance from 0 cm to 70 cm, the stress of all monitoring points gradually increased. And the stress of each monitoring point had slightly fluctuated at the same mining distance. When the mining face was advanced to a distance from 75 cm to 110 cm, the stress of 8# monitoring point in extra-thick roof would go through two stages, including sharp increase stage and sharp decrease stage. Therefore, the stress variation and the movement state of the extra-thick roof are combined for integrated analysis. During the undisturbed period, the mining disturbance influence on the extra-thick conglomerate increased. The extra-thick roof stress gradually increased, and the deformation energy slowly accumulated in the extra-thick conglomerate. In the movement stabilization period, the extra-thick conglomerate stress increased to the peak stress. In the sudden collapse period, the extra-thick conglomerate stress dropped suddenly. Because of the extensive deformation energy of the extra-thick conglomerate, the deformation energy was violently released in a sudden manner when the extra-thick conglomerate collapsed over a large area. Therefore, the mining-induced stress was characterized by a sudden decrease in the gradually increasing trend when the extra-thick roof suddenly collapsed.

4. Movement Evolution Characteristics of the Extra-Thick Hard Roof

4.1. Numerical Model. A three-dimensional distinct element code (3DEC) has certain advantages for simulating large

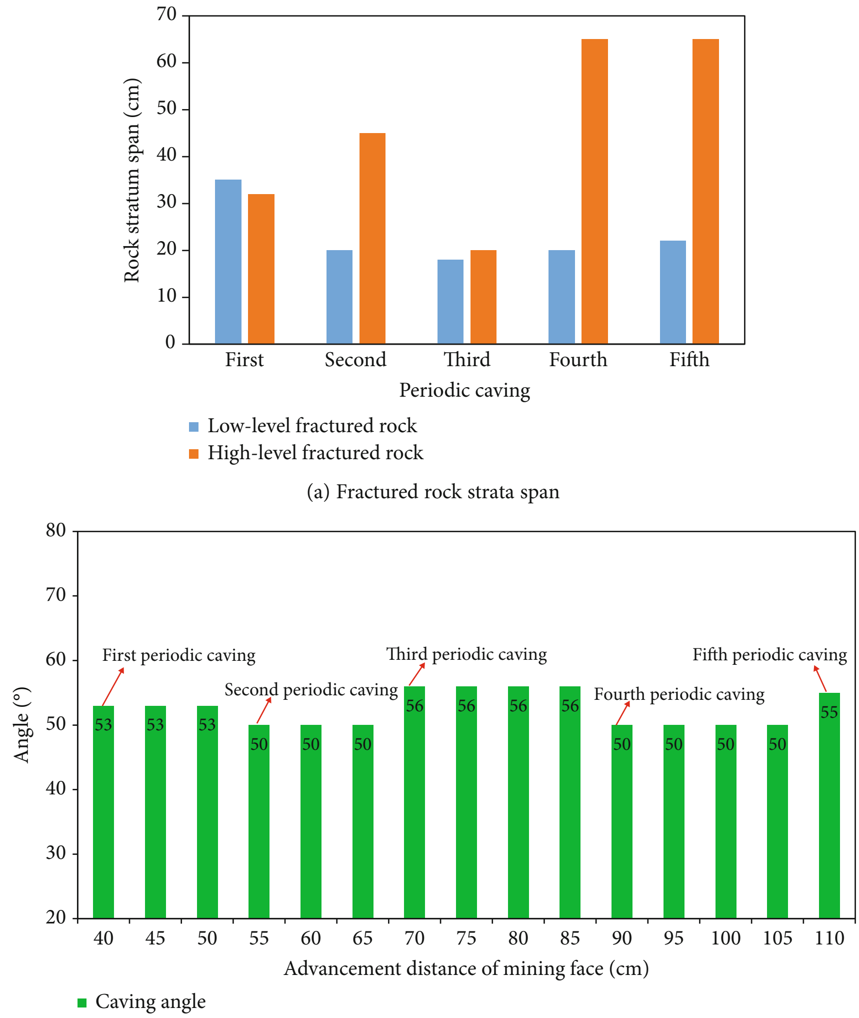

(a) Fractured rock strata span

(b) Fractured rock caving angle

Figure 5: Fractured rock parameters of five periodic caving of extra-thick roof.

movement and large deformation of a massive system under static or dynamic loading of discontinuous medium (such as jointed rock mass). It is suitable for applying to simulate the movement characteristics of an extra-thick roof under the influence of mining disturbance. The material in the 3DEC model was divided into two parts: the rock block as the continuity and the structural plane between rock blocks as the discontinuity. Considering the same physical model dimensions, a geometrical dimension of $150 \times 10 \times 90$ m was established in the 3DEC model, as shown in Figure 8.

Combined with the specific characteristics of each rock stratum, the relevant mechanical parameters of the strata and structure plane between blocks in the numerical mode were shown in Tables 3 and 4, respectively.

They were partially checked after several debugging cycles based on the geological parameters of the 21-221 longwall face. A vertical stress of 20.0 MPa was applied at the top of the numerical model. Because the maximum dominant stress in the 21-221 longwall face is horizontal stress, a horizontal stress of 23.4 MPa was applied to the two-boundary numerical model.

The mining face was mined at a distance of 5 m along the coal seam from the left side to the right side of the numerical model. The entire model advanced 22 times in total, making the total mining distance of 110 m.

4.2. Extra-Thick Roof Collapse Displacement. The displacement and velocity vectors of the extra-thick roof were analyzed to describe the roof movement behavior.

As the mining face advanced to 20 m, there was no obvious extra-thick roof movement but the immediate roof had a triangular shape displacement, as shown in Figure 9(a). As the mining face advanced to 40 m, the immediate roof collapsed under the action of gravity. The main roof, 24 m above the coal seam, exhibited a distinct separation phenomenon, shown in Figure 9(b). The caving area and maximum displacement of the immediate roof gradually increased as the mining face continued advancing. Due to the support of the collapsed rock mass and coal seam to the intact rock stratum, the extra-thick roof was separated from the immediate roof, as shown in Figures 9(c) and 9(d). Bending and subsidence occurred in the extra-thick conglomerate and the roof

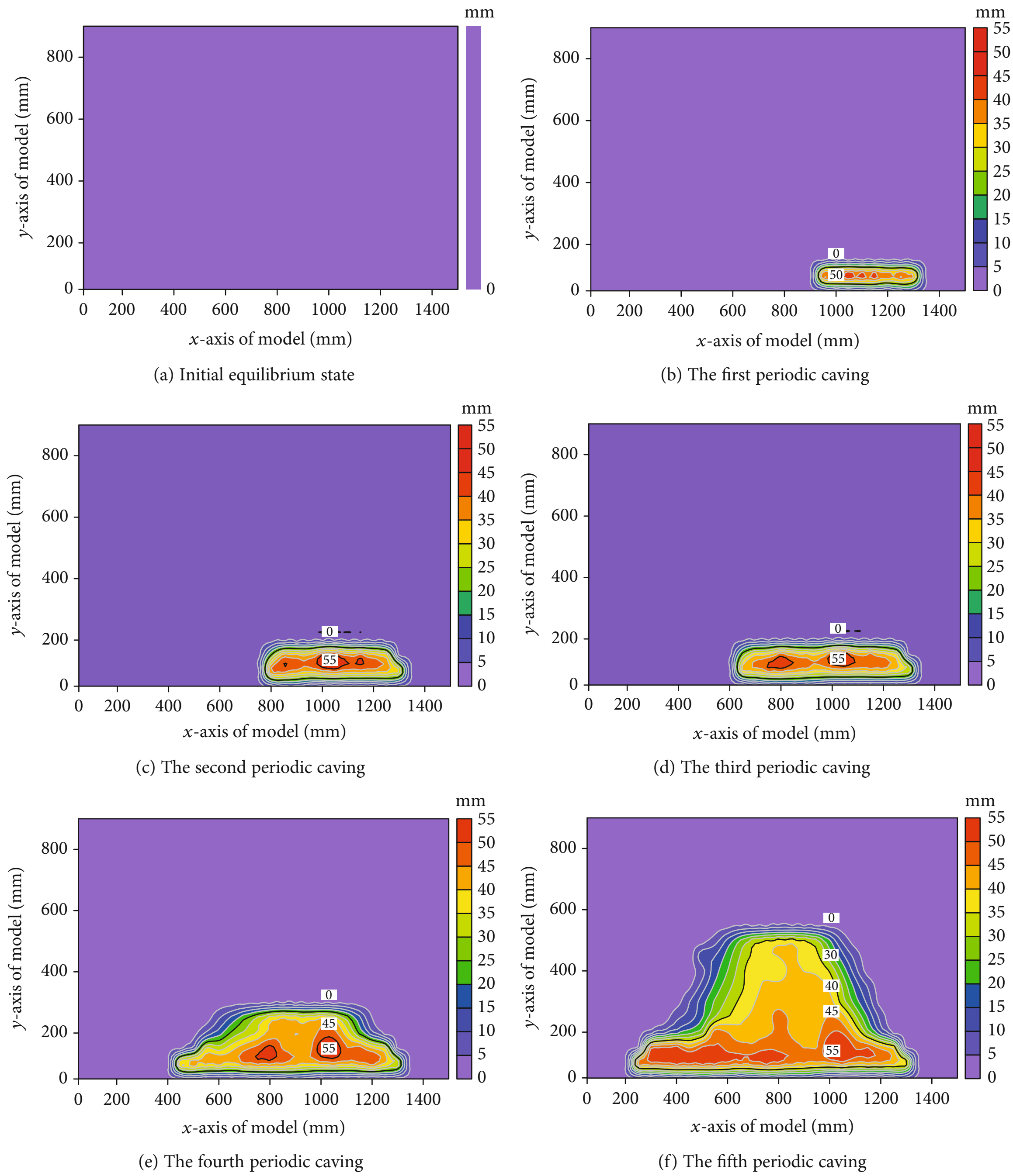

(a) Initial equilibrium state

(b) The first periodic caving

(c) The second periodic caving

(d) The third periodic caving

(e) The fourth periodic caving

(f) The fifth periodic caving

FIGURE 6: Vertical displacement variation of five periodic caving of extra-thick roof.

separation area expanded further, as shown in Figure 9(e). The extra-thick roof moved downward, and the roof displacement increased gradually as the mining face advanced to 110 m, as shown in Figure 9(f). The extra-thick roof collapsed in a large area, which could easily cause coal bursts. Clearly, the broken strata of the extra-thick roof successively progressed through separation, bending subsidence, closing separation, and caving compaction processes.

The rock strata above the mining face began to move down slowly, and the velocity vector appeared at the immediate roof, as shown in Figure 10(a). The extra-thick roof caving in small areas led to stress redistribution, and the velocity vector of the roof enlarged as the mining face advanced to 40 m, as shown in Figure 10(b). As the mining face further was advancing, the collapsed rock strata far away from the mining face entered the compaction state and the velocity vector was essentially zero, as shown in Figures 10(c) and 10(d). In addition, there was a wide range of unstable roofs near the mining face moving to the goaf, and the roof separation gap enlarged. The extra-thick conglomerate had a downward movement trend with a small velocity, as shown in Figure 10(e). It moved further to the goaf, and the velocity vector of the extra-thick conglomerate increased gradually as the mining face advanced to 110 m, as

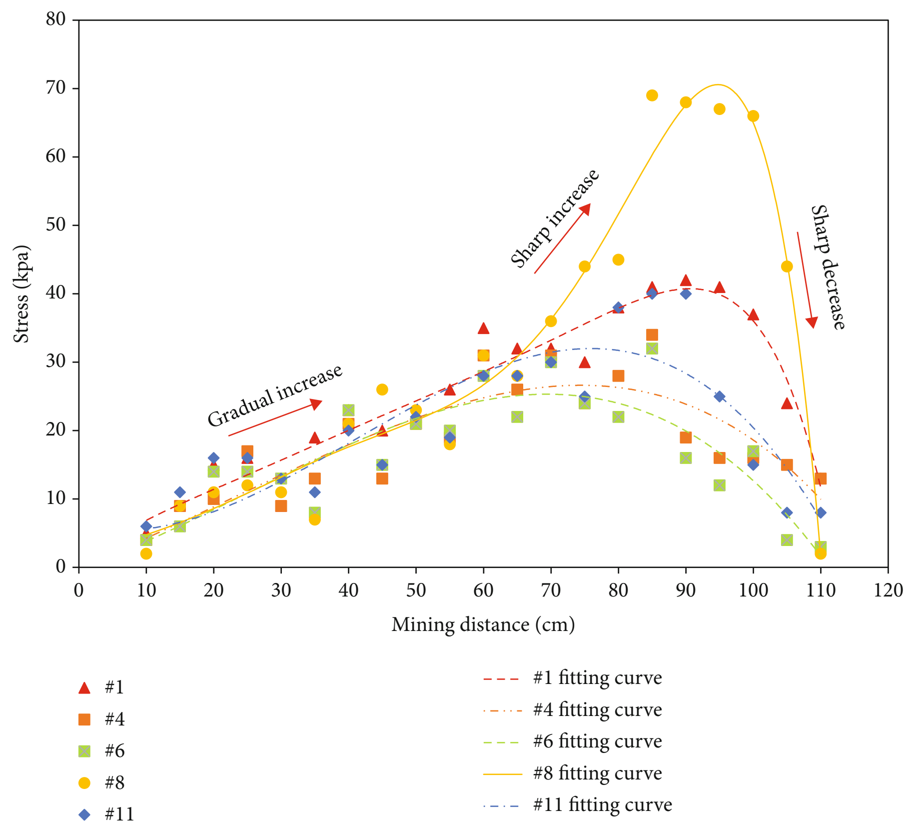

Figure 7: Stress variation detected from stress sensors marked as #1, #4, #6, #8, and #11 during advancement of the mining face.

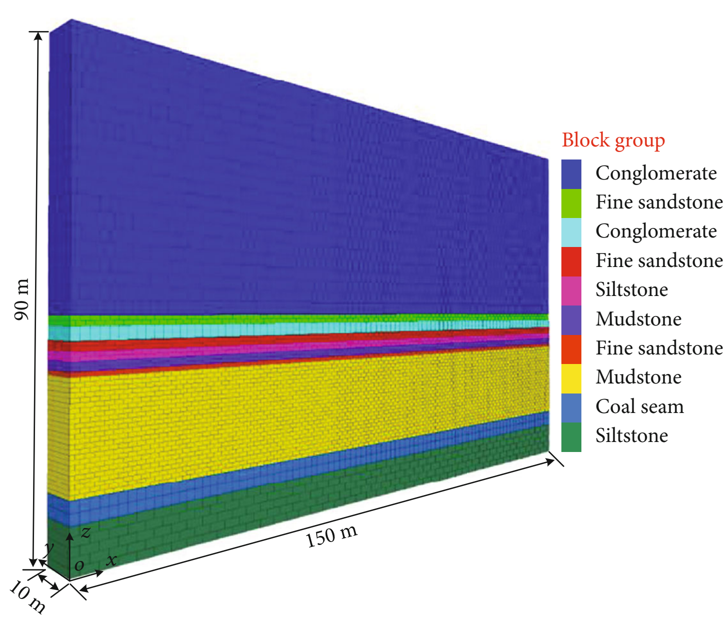

(a) Rock block model

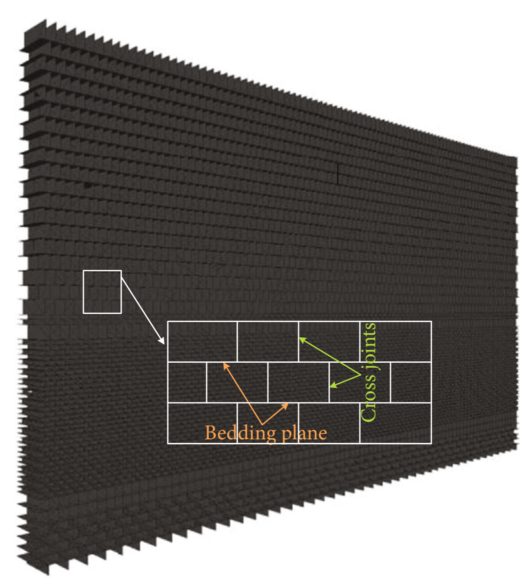

(b) Structure plane between blocks

Figure 8: Schematic diagram of the extra-thick roof in the 3DEC model.

Table 3: Physical and mechanical parameters of rock strata.

Rock strata	Thickness (m)	Density ($kg.m^{-3}$)	Bulk modulus (GPa)	Shear modulus (GPa)	Cohesion (MPa)	Friction angle (°)	Tensile strength (MPa)
Conglomerate	39	2 865	20.33	17.50	11.85	40	10.32
Fine sandstone	2.0	2 873	9.18	8.75	7.51	30	6.65
Conglomerate	3.0	2 865	20.33	17.50	11.85	40	10.32
Fine sandstone	2.0	2 873	9.18	8.75	7.51	30	6.65
Siltstone	2.0	2 707	12.82	10.02	8.97	30	8.65
Mudstone	2.0	2 461	6.11	5.49	4.49	20	4.30
Fine sandstone	1.0	2 873	9.18	8.75	7.51	30	6.65
Mudstone	24	2 461	6.11	5.49	4.49	20	4.30
Coal seam	5.0	1 440	4.67	4.47	3.40	26	3.06
Siltstone	10	2 873	9.18	8.75	7.51	30	6.65

Table 4: Mechanical parameters of structure plane between blocks.

Rock strata	Normal stiffness (GPa)	Shear stiffness (GPa)	Tensile strength (MPa)	Friction angle (°)	Cohesion (MPa)
Conglomerate	12.0	15.0	6.14	10	7.0
Fine sandstone	5.0	5.0	4.10	8	4.5
Conglomerate	12.0	15.0	6.14	10	6.4
Fine sandstone	4.0	5.0	4.10	8	4.5
Siltstone	4.0	4.0	3.61	8	4.4
Mudstone	1.6	4.8	1.30	7	2.2
Fine sandstone	5.0	5.0	4.10	8	5.5
Mudstone	1.6	4.8	1.30	7	2.2
Coal seam	1.4	1.2	1.02	6	1.3
Siltstone	5.0	5.0	4.10	8	4.5

shown in Figure 10(f). Because enormous deformation energy is released by the collapse of the extra-thick conglomerate, the extra-thick roof is in the most dangerous state for mining face safety.

5. Mining-Induced Stress Evolution Characteristics of the Extra-Thick Hard Roof

5.1. Numerical Model. A finite difference program $FLAC^{3D}$ is applied to simulate the mining-induced stress distribution characteristics of an extra-thick hard roof during the advancement of the mining face. By building the appropriate constitutive relation of geological materials in $FLAC^{3D}$, the progressive mining-induced stress evolution of elastic-plastic rock mass is effectively tracked. Combined with the results of physical experiment, the stress evolution of the extra-thick roof in the numerical model was comparatively analyzed.

A numerical model in $FLAC^{3D}$ with 12 stress monitoring points numbered #1–#12 located on extra-thick conglomerate rock was established. The location of the stress monitoring points corresponds to the stress sensor distribution in the physical model to monitor mining-induced stress in the extra-thick conglomerate, as shown in Figure 11. Adjacent stress monitoring points were placed 10 m apart. A vertical stress of 20.0 MPa was applied at the top of the numerical model, and a horizontal stress of 23.4 MPa was applied to the two side boundaries. Moreover, the horizontal boundary displacement was limited and the vertical displacement of the numerical model base was fixed. The physical and mechanical parameters of rock strata in the $FLAC^{3D}$ model after several debugging cycles were used, as shown in Table 5.

5.2. Stress Distribution Characteristics in the Extra-Thick Roof. As the mining face was advancing, the vertical stress in the extra-thick roof was gradually released. The release of vertical stress showed that the absolute value of stress decreased and the release area of vertical stress gradually increased into the upper roof, as shown in Figures 12(a)–12(f). The supportive effect of the original coal seam on the extra-thick roof gradually disappeared. The effect of model top loading and gravity caused bending subsidence of the extra-thick roof. As the mining face advanced to 110 m, the extra-thick roof experienced the largest stress release.

As shown in Figure 13, there were five stages of severe stress change in the extra-thick conglomerate during coal

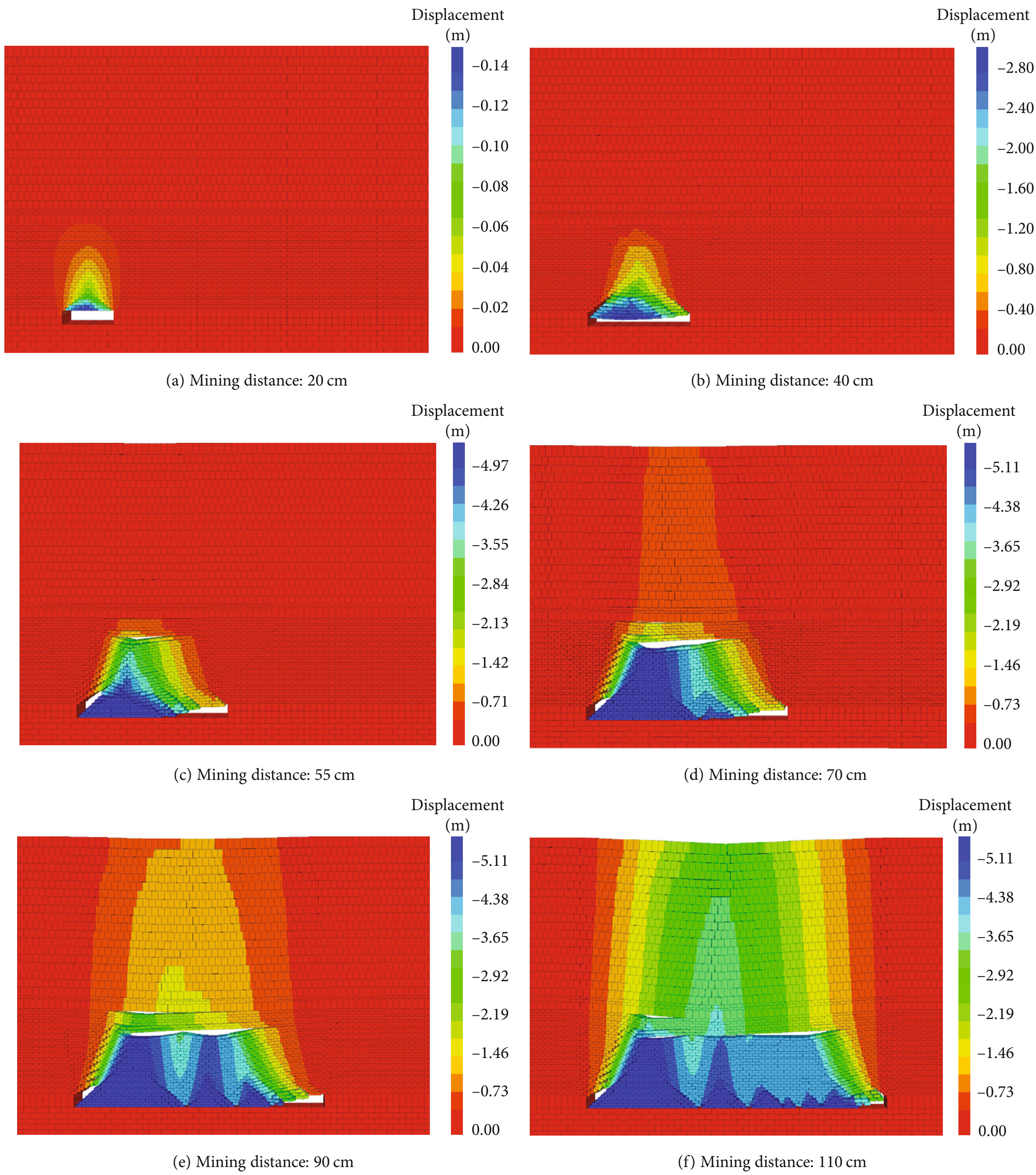

Figure 9: Vertical displacement variation of the roof during the advancement of the mining face.

seam mining. As the mining face advanced to 40, 55, 75, 90, and 110 m in the numerical model, the roof experienced five periodic caving at five mining stages. When the roof collapsed for the fourth time, the response of the extra-thick conglomerate was more intense and the stress of the extra-thick conglomerate was released. When the extra-thick roof collapsed for the fifth time, the stress of the extra-thick conglomerate changed violently and dropped abruptly.

To confirm the reliability of the numerical simulation results, the mining-induced stress obtained from the physical experiment was compared with that obtained from numerical simulation. In this study, the stress change per

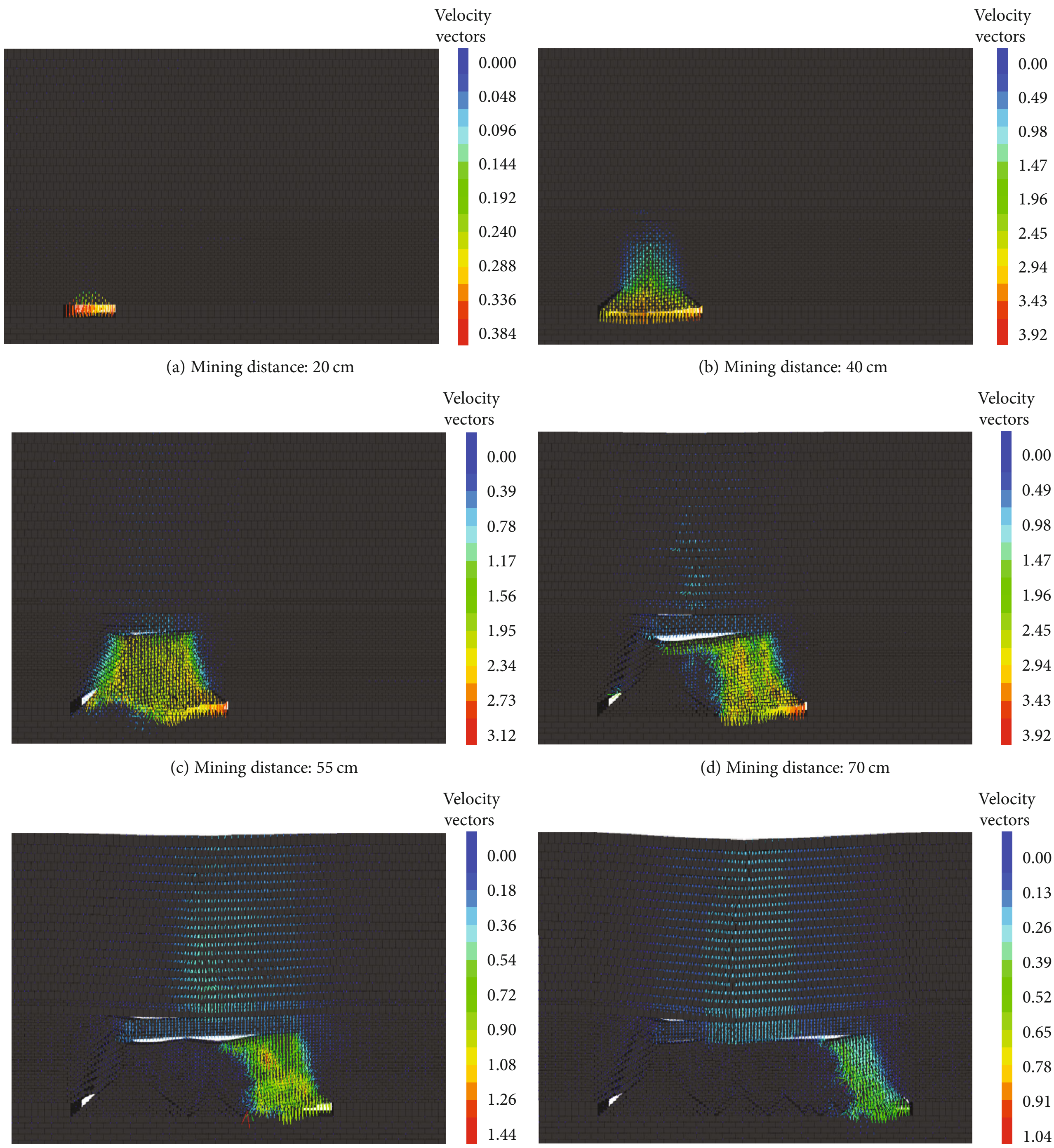

(a) Mining distance: 20 cm

(b) Mining distance: 40 cm

(c) Mining distance: 55 cm

(d) Mining distance: 70 cm

(e) Mining distance: 90 cm

(f) Mining distance: 110 cm

Figure 10: Velocity vector variation of the roof during the advancement of the mining face.

meter of the #8 monitoring point at the same position as the numerical simulation and physical experiment in the mining face advancement was selected for comparative analysis.

Figure 14 showed that the stress change per meter obtained from physical experiments was consistent with that obtained from numerical simulation. In the early stage of coal mining, the stress fluctuation in the extra-thick roof was small. But when the mining face advanced to 110 m, there was a violent fluctuation, indicating that the disturbance of coal mining to extra-thick conglomerate reached its maximum. The fifth caving of the extra-thick roof occurred in the goaf and the stress changed violently; the stress variation behavior at the #8 measuring point at the same position between numerical simulation and physical experiment was basically synchronous.

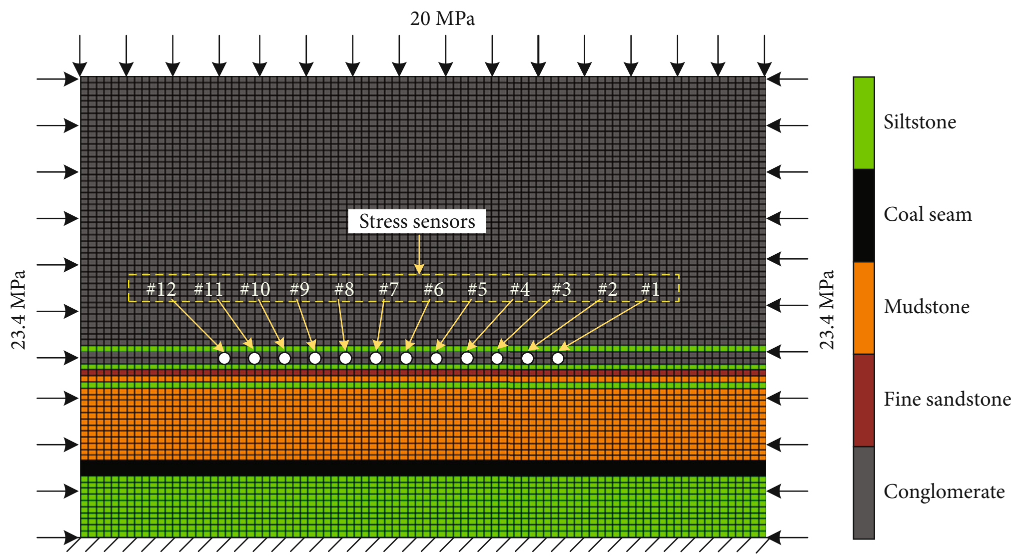

FIGURE 11: Numerical model of the extra-thick roof in FLAC^{3D}.

TABLE 5: Physical and mechanical parameters of rock strata in the FLAC^{3D} model.

Rock strata	Thickness (m)	Density ($kg.m^{-3}$)	Bulk modulus (GPa)	Shear modulus (GPa)	Cohesion (MPa)	Friction angle (°)	Tensile strength (MPa)
Conglomerate	39	2 950	20.94	18.03	12.21	41	10.63
Fine sandstone	2	2 900	9.27	8.84	7.59	31	6.72
Conglomerate	3	2 950	20.94	18.03	12.21	41	10.63
Fine sandstone	2	2 900	9.27	8.84	7.59	31	6.72
Siltstone	2	2 734	12.95	10.12	9.06	30	8.74
Mudstone	2	2 486	6.17	5.54	4.52	22	4.34
Fine sandstone	1	2 900	9.27	8.84	7.59	31	6.72
Mudstone	24	2 486	6.17	5.54	4.52	22	4.34
Coal seam	5	1 440	4.67	4.47	4.40	26	4.06
Siltstone	10	2 734	12.95	10.12	9.06	30	8.74

6. Discussions

According to the displacement and mining-induced stress variation in the extra-thick roof, the following areas should be discussed in greater detail to analyze the dynamic evolution characteristics of deformation and movement of the extra-thick roof.

The extraction of a longwall mining face induced mining-induced changes and extra-thick roof movement above the mining face. The movement and failure processes of an extra-thick roof could be divided into three main periods: the undisturbed, movement stabilization, and sudden collapse periods. Because the mining face advancement distance in the physical experiment was short, the extra-thick roof deformation caused by bending and sinking was relatively small. The mining-induced stress of typical stress sensors was small; therefore, this stage could be categorized as belonging to the undisturbed period. With mining face advancement, the suspended roof length gradually increased and the roof bent and sank under the action of gravity. The bending moment and shearing force at both roof ends gradually increased, leading to roof failure. In addition, the horizontal stress was applied to the left and right boundaries of the physical model and the extra-thick roof collapsed slowly under the action of horizontal pressure. Therefore, this stage was part of the movement stabilization period. Because the main roof was composed of an extra-thick conglomerate, it could sustain a large stress level. Although the roof movement was dynamic in coal mining, an extra-thick roof was not disturbed until the roof reached a certain degree of deformation. The UCS of the extra-thick roof was 45 MPa, and its failure could occur only when the effect of the roof subsidence increased the extra-thick roof stress to the ultimate strength. It broke and caused roof caving in a large area and could easily induce coal bursts. This stage corresponded to the sudden collapse period.

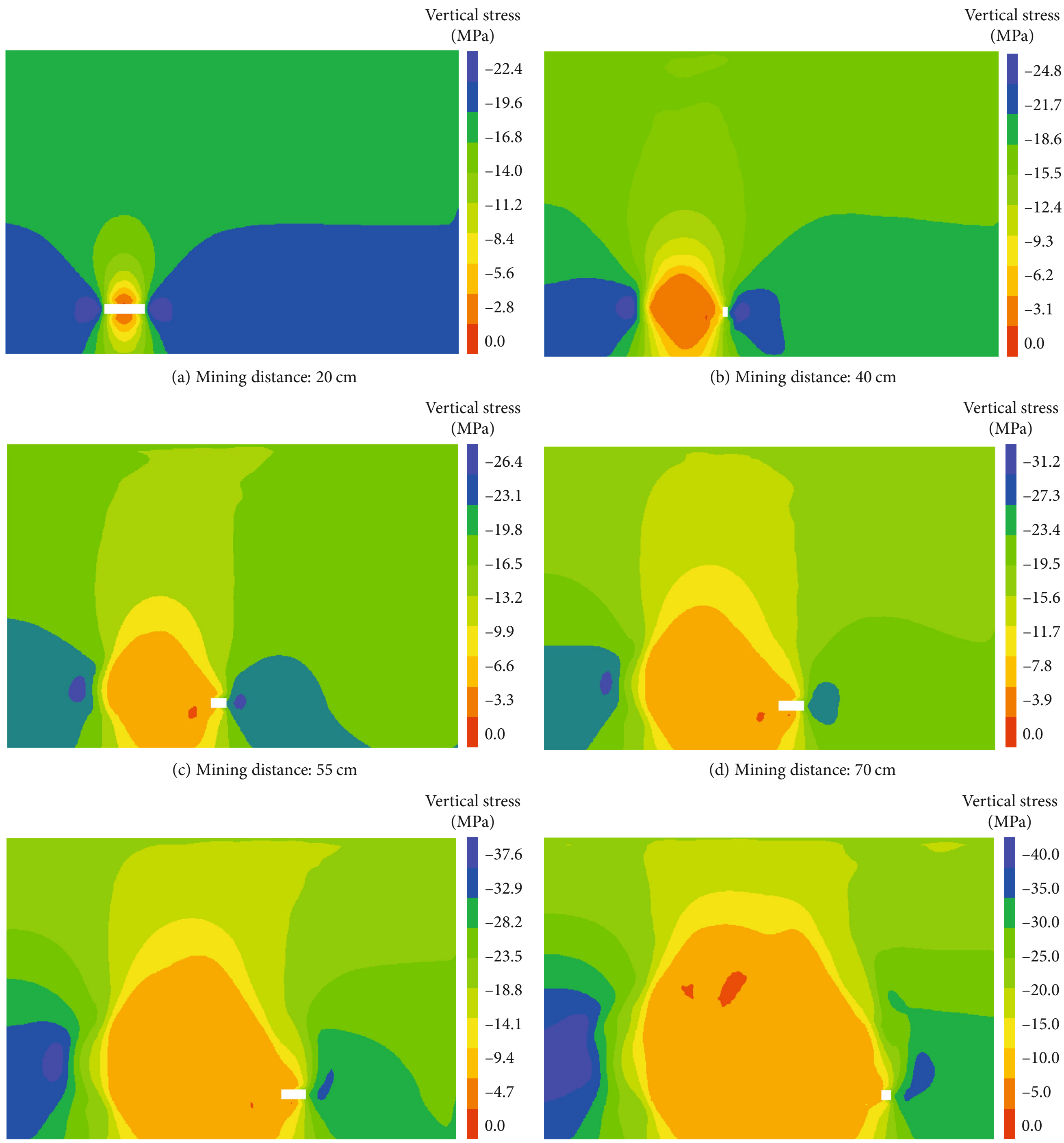

(a) Mining distance: 20 cm

(b) Mining distance: 40 cm

(c) Mining distance: 55 cm

(d) Mining distance: 70 cm

(e) Mining distance: 90 cm

(f) Mining distance: 110 cm

Figure 12: Vertical stress distribution of the extra-thick roof during the advancement of the mining face.

Throughout the mining process, the roof experienced five periodic caving. The displacement and velocity vector of the extra-thick roof increased sharply in this periodic caving, and the collapse height instantly expanded into the entire extra-thick roof. Figures 6 and 9 showed that the results of the displacement and collapse state of the roof in the 3DEC model generally agreed with those in the physical experiment. When the stress monitoring points located on the extra-thick conglomerate were far away from the mining face outside the influence area of the mining disturbance, their stress remained in situ stress. With mining face advancement, the stress gradually increased and extensive deformation energy accumulated by degrees in the extra-thick conglomerates. When the extra-thick conglomerate reached its own ultimate strength, the roof caved for the fifth time and the extra-thick conglomerate stress changed abruptly. Meanwhile, the

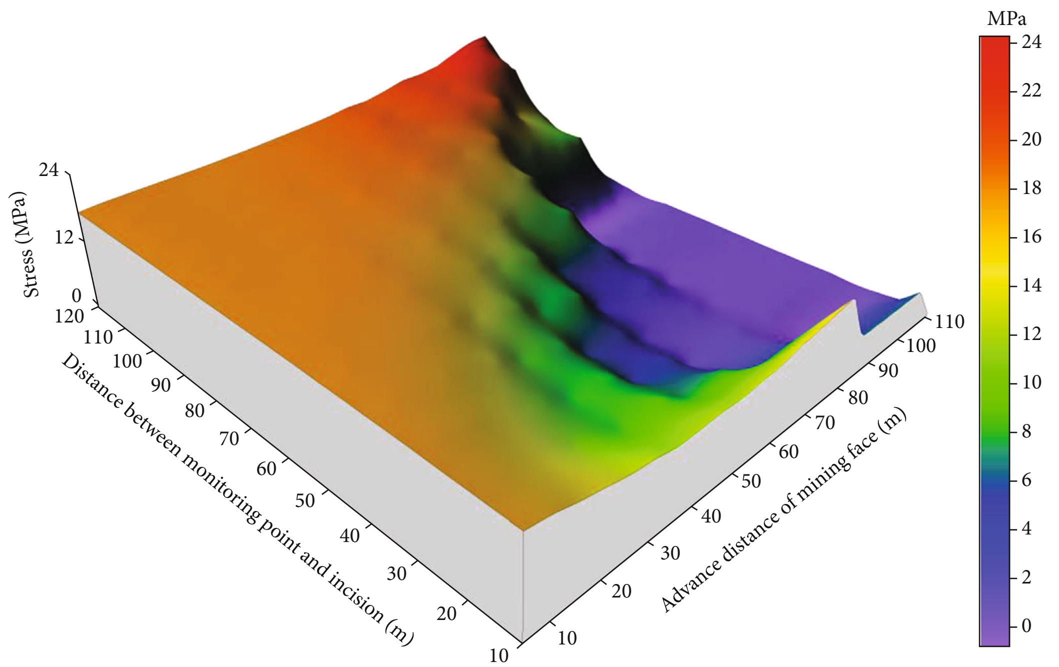

Figure 13: Vertical stress of the extra-thick conglomerate.

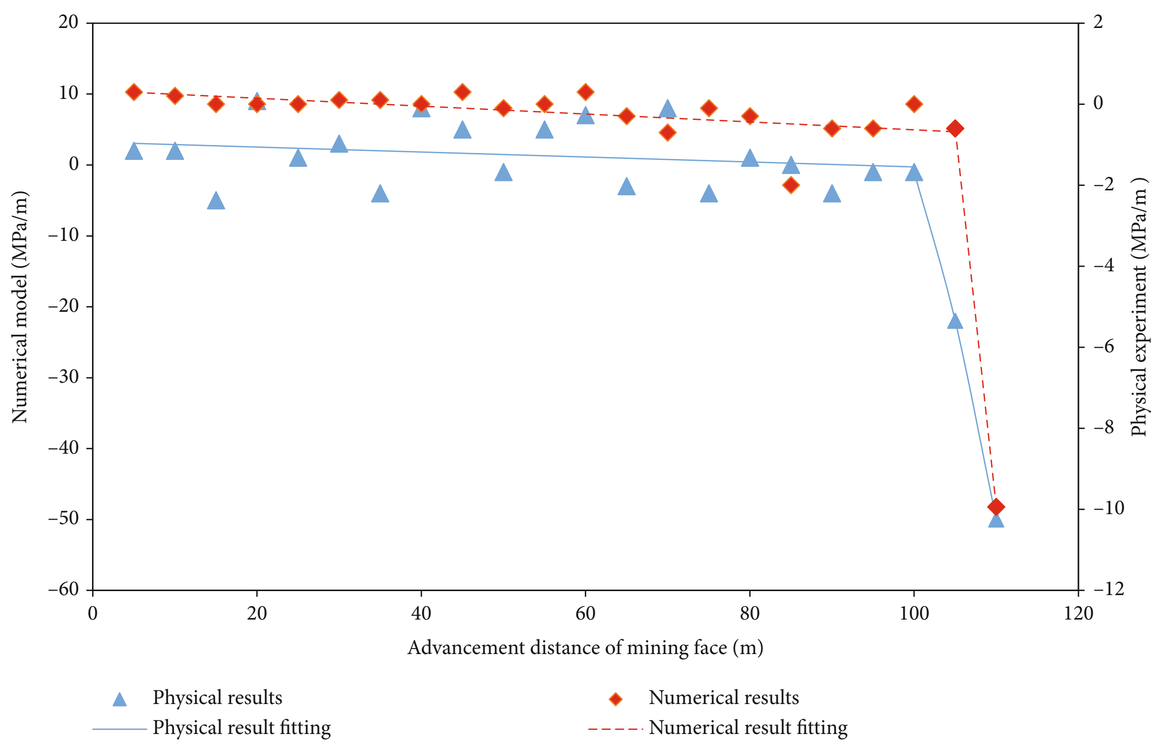

Figure 14: The stress comparison between numerical simulation and physical experiment.

mining-induced stress was characterized by a sudden decrease in the gradually increasing trend when the extra-thick roof suddenly collapsed, as shown in Figures 7 and 13. The stress change characteristics of the #8 measuring point at the same position in both the physical experiment and FLAC^{3D} model were basically synchronous, as shown in Figure 14.

Hence, the deformation and fracture of the extra-thick roof could lead to the continuous and unstable subsidence pressure exerted on the mining face and roadway, which provided a continuous force to the immediate roof, and coal seam and could cause a sudden decrease in the mining-induced stress of the extra-thick roof. This significantly contributed to the occurrence of coal bursts.

7. Conclusions

Numerical simulations and physical experiments were conducted to study the movement and fracture characteristics of the extra-thick roof during coal seam mining. The detailed conclusions are as follows.

(1) The movement and failure processes of the extra-thick roof could be divided into three main periods: the undisturbed, movement stabilization, and sudden collapse periods. The roof displacement essentially did not change during the undisturbed period. During the movement stabilization period, the displacement gradually increased into the upper roof and could be observed only in the immediate roof and the extra-thick roof was not disturbed by the mining activities. However, the displacement expanded rapidly into the extra-thick main roof during the sudden collapse period

(2) Although roof movement is a dynamic process during coal seam mining, the extra-thick main roof was undisturbed until the immediate roof experienced the fourth periodic caving. The UCS of the extra-thick main roof was 45 MPa, and its failure could occur only when the effect of the roof subsidence increased the extra-thick main roof stress to the ultimate strength. Therefore, the strain energy was violently released when it accumulated in the extra-thick roof failure process

(3) The extra-thick main roof collapse was only observed once in the physical experiment when a periodic roof caving occurred in the immediate roof. The displacement and velocity vector of the extra-thick main roof increased sharply in this periodic caving, and the collapse height instantly expanded into the extra-thick main roof. Meanwhile, the mining-induced stress was characterized by a sudden decrease in the gradually increasing trend when the extra-thick main roof suddenly collapsed

(4) As the mining face advanced, the movement and fracture of the extra-thick roof led to a continuous and unstable subsidence pressure exerted on the mining face and roadway. This pressure exertion provided a continuous force to the immediate roof and coal seam. This significantly contributed to the occurrence of coal bursts

Data Availability

All the original data used to support the findings of this study are available from the corresponding author upon request.

Conflicts of Interest

The authors declare that they have no conflicts of interest.

Acknowledgments

This research benefited from the support of the following funds from the Beijing Natural Science Foundation (8202041), National Natural Science Foundation of China (41872205), Yue Qi Young Scholar Project, China University of Mining &Technology, Beijing (2018QN13), the Fundamental Research Funds for the Central Universities (2021YJSLJ10), and the State Key Research Development Program of China (2017YFC0603002 and 2016YFC0801401).

References

[1] Y. D. Jiang, Y. S. Pan, F. X. Jiang, L. M. Dou, and Y. Ju, "State of the art review on mechanism and prevention of coal bumps in China," *Journal of China Coal Society*, vol. 39, no. 2, pp. 205–213, 2014.

[2] L. Yuan, Y. D. Jiang, X. Q. He et al., "Research progress of precise risk accurate identification and monitoring early warning on typical dynamic disasters in coal mine," *Journal of China Coal Society*, vol. 43, no. 2, pp. 306–318, 2018.

[3] Y. D. Jiang and Y. X. Zhao, "State of the art: investigation on mechanism, forecast and control of coal bumps in China," *Chinese Journal of Rock Mechanics and Engineering*, vol. 34, no. 11, pp. 2188–2204, 2015.

[4] H. W. Wang, R. M. Shi, D. X. Deng, Y. D. Jiang, G. Wang, and W. L. Gong, "Characteristic of stress evolution on fault surface and coal bursts mechanism during the extraction of longwall face in Yima mining area, China," *Journal of Structural Geology*, vol. 136, p. 104071, 2020.

[5] H. W. Wang, S. Xue, R. M. Shi, Y. D. Jiang, W. L. Gong, and L. T. Mao, "Investigation of fault displacement evolution during extraction in longwall panel in an underground coal mine," *Rock Mechanics and Rock Engineering*, vol. 53, no. 4, pp. 1809–1826, 2020.

[6] L. R. Alejano, J. Taboada, F. García-Bastante, and P. Rodriguez, "Multi-approach back-analysis of a roof bed collapse in a mining room excavated in stratified rock," *International Journal of Rock Mechanics and Mining Sciences*, vol. 45, no. 6, pp. 899–913, 2008.

[7] M. Tsesarsky, "Deformation mechanisms and stability analysis of undermined sedimentary rocks in the shallow subsurface," *Engineering Geology*, vol. 133-134, pp. 16–29, 2012.

[8] F. Q. Gao, D. Stead, H. P. Kang, and Y. Z. Wu, "Discrete element modelling of deformation and damage of a roadway driven along an unstable goaf – a case study," *International Journal of Coal Geology*, vol. 127, pp. 100–110, 2014.

[9] M. Shabanimashcool and C. C. Li, "Analytical approaches for studying the stability of laminated roof strata," *International Journal of Rock Mechanics and Mining Sciences*, vol. 79, pp. 99–108, 2015.

[10] R. Gao, J. X. Yang, T. J. Kuang, and H. J. Liu, "Investigation on the ground pressure induced by hard roof fracturing at different layers during extra thick coal seam mining," *Geofluids*, vol. 2020, Article ID 8834235, 15 pages, 2020.

[11] T. Zhao, C. Y. Liu, K. Yetilmezsoy, B. S. Zhang, and S. Zhang, "Fractural structure of thick hard roof stratum using long beam theory and numerical modeling," *Environment and Earth Science*, vol. 76, 2017.

[12] J. G. Ning, J. Wang, L. S. Jiang, N. Jiang, X. S. Liu, and J. Q. Jiang, "Fracture analysis of double-layer hard and thick roof and the controlling effect on strata behavior: a case study," *Engineering Failure Analysis*, vol. 81, pp. 117–134, 2017.

[13] W. L. Shen, J. B. Bai, X. Y. Wang, and Y. Yu, "Response and control technology for entry loaded by mining abutment stress of a thick hard roof," *International Journal of Rock Mechanics and Mining Sciences*, vol. 90, pp. 26–34, 2016.

[14] G. S. P. Singh and U. K. Singh, "Numerical modeling study of the effect of some critical parameters on caving behavior of strata and support performance in a longwall working," *Rock Mechanics and Rock Engineering*, vol. 43, no. 4, pp. 475–489, 2010.

[15] N. Zhou, J. X. Zhang, H. Yan, M. Li, and M. Wang, "Deformation behavior of hard roofs in solid backfill coal mining using physical models," *Energies*, vol. 10, no. 4, 2017.

[16] W. Wang, Y. P. Cheng, H. F. Wang, W. Li, and L. Wang, "Coupled disaster-causing mechanisms of strata pressure behavior and abnormal gas emissions in underground coal extraction," *Environmental Earth Sciences*, vol. 74, no. 9, pp. 6717–6735, 2015.

[17] Q. S. Bai, S. H. Tu, F. T. Wang, and C. Zhang, "Field and numerical investigations of gateroad system failure induced by hard roofs in a longwall top coal caving face," *International Journal of Coal Geology*, vol. 173, pp. 176–199, 2017.

[18] J. L. Jia, L. W. Cao, D. J. Zhang, X. W. Chai, S. Q. Liu, and L. Han, "Study on the fracture characteristics of thick-hard limestone roof and its controlling technique," *Environmental Earth Sciences*, vol. 76, no. 17, 2017.

[19] H. W. Wang, Y. D. Jiang, S. Xue et al., "Influence of fault slip on mining-induced pressure and optimization of roadway support design in fault-influenced zone," *Journal of Rock Mechanics and Geotechnical Engineering*, vol. 8, no. 5, pp. 660–671, 2016.

[20] P. Wang, L. S. Jiang, J. Q. Jiang, P. Q. Zheng, and W. Li, "trata behaviors and rock burst-inducing mechanism under the coupling effect of a hard, thick stratum and a normal fault," *International Journal of Geomechanics*, vol. 18, no. 2, pp. 1532–1546, 2018.

[21] Z. B. Cheng, D. Z. Kong, and J. H. Yang, "The breaking characteristics of thick hard roof and determination of support capacity in fully mechanized caving face," *Journal of Mining Science and Technology*, vol. 1, no. 2, pp. 172–180, 2016.

[22] W. L. Gong, Y. Y. Peng, M. C. He, and J. Wang, "Thermal image and spectral characterization of roadway failure process in geologically 45° inclined rocks," *Tunnelling and Underground Space Technology*, vol. 49, pp. 156–173, 2015.

[23] S. Renliang, H. Bo, S. Yongwei, W. Huimin, and F. Xiaolin, "Ground pressure features of roadway under close range goaf in the Xinyu mine," *Journal of Mining Science and Technology*, vol. 1, no. 1, pp. 29–37, 2016.

[24] M. Amini, H. Sarfaraz, and K. Esmaeili, "Stability analysis of slopes with a potential of slide-head-toppling failure," *International Journal of Rock Mechanics and Mining Sciences*, vol. 112, pp. 108–121, 2018.

[25] M. Z. Li, Z. M. Ma, D. L. Xue, and Y. H. Fan, "Research of cumulative energy blasting technology with deep and shallow hole combined in hard roof," *Journal of Mining Science and Technology*, vol. 5, no. 6, pp. 616–623, 2020.

[26] R. Kumar, A. K. Singh, A. K. Mishra, and R. Singh, "Underground mining of thick coal seams," *International Journal of Mining Science and Technology*, vol. 25, no. 6, pp. 885–896, 2015.

[27] H. R. Chen, S. Q. Qin, L. Xue, B. C. Yang, and K. Zhang, "A physical model predicting instability of rock slopes with locked segments along a potential slip surface," *Engineering Geology*, vol. 242, pp. 34–43, 2018.

[28] B. Ghabraie, G. Ren, and J. V. Smith, "Characterising the multi-seam subsidence due to varying mining configuration, insights from physical modelling," *International Journal of Rock Mechanics and Mining Sciences*, vol. 93, pp. 269–279, 2017.

[29] Y. K. Liu, F. B. Zhou, L. Liu, C. Liu, and S. Y. Hu, "An experimental and numerical investigation on the deformation of overlying coal seams above double-seam extraction for controlling coal mine methane emissions," *International Journal of Coal Geology*, vol. 87, no. 2, pp. 139–149, 2011.

[30] H. W. Wang, R. M. Shi, J. Q. Song, Z. Tian, D. X. Deng, and Y. D. Jiang, "Mechanical model for the calculation of stress distribution on fault surface during the underground coal seam mining," *International Journal of Rock Mechanics and Mining Sciences*, vol. 144, p. 104765, 2021.

[31] H. W. Wang, R. M. Shi, C. S. Lu, Y. D. Jiang, D. X. Deng, and D. Q. Zhang, "Investigation of sudden faults instability induced by coal mining," *Safety Science*, vol. 115, pp. 256–264, 2019.

[32] W. L. Gong, J. Wang, and D. Q. Liu, *Infrared Thermography for Geomechanical Model Test*, Science Press, Beijing, 2016.

[33] B. Ghabraie, G. Ren, X. Y. Zhang, and J. Smith, "Physical modelling of subsidence from sequential extraction of partially overlapping longwall panels and study of substrata movement characteristics," *International Journal of Coal Geology*, vol. 140, pp. 71–83, 2015.

[34] W. S. Zhu, Y. Li, S. C. Li, S. G. Wang, and Q. B. Zhang, "Quasi-three-dimensional physical model tests on a cavern complex under high in-situ stresses," *International Journal of Rock Mechanics and Mining Sciences*, vol. 48, no. 2, pp. 199–209, 2010.

[35] M. C. He, X. N. Jia, W. L. Gong, and L. Faramarzi, "Physical modeling of an underground roadway excavation in vertically stratified rock using infrared thermography," *International Journal of Rock Mechanics and Mining Sciences*, vol. 47, no. 7, pp. 1212–1221, 2010.

[36] X. M. Sun, F. Chen, C. Y. Miao et al., "Physical modeling of deformation failure mechanism of surrounding rocks for the deep-buried tunnel in soft rock strata during the excavation," *Tunnelling and Underground Space Technology*, vol. 74, pp. 247–261, 2018.

[37] L. T. Mao, X. X. Zhu, L. Q. An, G. S. Cai, and N. Hao, "Application of digital target marker image correlation method in model experiment," *Journal of Liaoning Technical University (Natural Science)*, vol. 32, no. 10, pp. 1367–1373, 2013.

[38] L. T. Mao, N. Hao, L. Q. An, F. P. Chiang, and H. B. Liu, "3D mapping of carbon dioxide-induced strain in coal using digital volumetric speckle photography technique and X-ray computer tomography," *International Journal of Coal Geology*, vol. 147-148, pp. 115–125, 2015.

[39] Z. Chen, Z. Z. Zhang, L. N. Wang, H. Wang, and S. S. Zhang, "Study on water absorption and pore structure fractal characteristics of slag-based geopolymer," *Journal of Mining Science and Technology*, vol. 6, no. 2, pp. 204–209, 2021.

[40] Q. Lin and J. F. Labuz, "Fracture of sandstone characterized by digital image correlation," *International Journal of Rock Mechanics and Mining Sciences*, vol. 60, pp. 235–245, 2013.

[41] H. Munoz, A. Taheri, and E. K. Chanda, "Pre-Peak and post-peak rock strain characteristics during uniaxial compression by 3D digital image correlation," *Rock Mechanics and Rock Engineering*, vol. 49, no. 7, pp. 2541–2554, 2016.

[42] A. Fakhimi, Q. Lin, and J. F. Labuz, "Insights on rock fracture from digital imaging and numerical modeling," *International Journal of Rock Mechanics and Mining Sciences*, vol. 107, pp. 201–207, 2018.

[43] J. H. Zhao, L. M. Yin, and W. J. Guo, "Stress–seepage coupling of cataclastic rock masses based on digital image technologies," *Rock Mechanics and Rock Engineering*, vol. 51, no. 8, pp. 2355–2372, 2018.

Hindawi
Geofluids
Volume 2021, Article ID 9083547, 8 pages
https://doi.org/10.1155/2021/9083547

Research Article

Operating Environment Assessment of the Coalface in Underground Coal Mining Based on Analytic Hierarchy Process (AHP) and Matter-Element Theory (MET)

Jianghui He,[1] **Shiliang Liu**,[2] **Wenping Li**,[1] **Wei Qiao**,[1] **Zhi Yang**,[3] **and Qiqing Wang**[1]

[1]*School of Resources and Geosciences, China University of Mining & Technology, Xuzhou 221116, China*
[2]*School of Civil Engineering, Shandong University, Jinan 250061, China*
[3]*School of Environment and Spatial Informatics, China University of Mining & Technology, Xuzhou 221116, China*

Correspondence should be addressed to Wenping Li; hjh@cumt.edu.cn

Received 21 June 2021; Accepted 16 July 2021; Published 2 August 2021

Academic Editor: Hualei Zhang

The environmental evaluation of the coalface in underground mining is of great significance to the safety of production and the health of miners. In order to achieve the objective and accurate evaluation of the operating environment of the coalface, the indexes of temperature, humidity, noise, illuminance, dust, harmful gas, and wind speed are selected to construct the environment evaluation index system, and the operating environment evaluation model of the coalface based on analytic hierarchy process (AHP) and matter-element theory (MET) is established. Firstly, the operation environment classification criterion is established; the environment objects, joint domain, and classical domain mater-element are built; and the correlation function is calculated. Secondly, the comprehensive correlation matrix is calculated and the environmental grade is judged. Finally, from the broad point of view, three measures are proposed to improve the operation environment of the coalface: development of the environmental evaluation index monitoring system, improvement on miners' safety awareness, and formulation of regulations and policies for coal mine operation environment. The research results can provide guidelines for miners, coal mining enterprises, and occupational environmental safety departments.

1. Introduction

In the composition of total reserves of primary energy resources, the proportions of coal, oil and natural gas are 94%, 1.71%, and 4.29%, respectively. The characteristics of natural resources in China are rich in coal, less oil, and lack of gas [1]. Since the establishment of the People's Republic of China, the accumulative total production capacity of coal is about 75 billion tons and the proportion of coal in the structure of primary energy production and consumption in China has been maintained at 70% and 60%, which has provided a reliable energy guarantee for the long-term stable and rapid development of the national economy and society. The status of coal as the main energy source in China is difficult to change in the short term. It is estimated that the proportion of coal resources in primary energy will remain 55% in 2030 [2, 3]. Coal resources are mainly derived from underground mining in China. Coalface is the production site of coal and is the key area in the coal mine safety management and environmental monitoring, which is characterized with small working space, many mechanical equipment, poor visual environment, and high temperature. The operating environment of coalface is a general designation for microclimate, harmful gas, dust, and noise within the space of coalface, which affect the working comfort, efficiency, and reliability of the system [4]. With the continuous progress of social civilization, people put more and more demands on the operating environment, and it is particularly important to evaluate the operating environment effectively and accurately.

Scholars have made some contributions on the evaluation for the operating environment of coalface. On the one hand, the coalface operating environment resulting from individual indicators was discussed. Li et al. made an assessment on human thermal comfort based on an uncertain measurement theory [5]. Fu et al. studied the respirable dust pollution in coalface [6]. By means of numerical simulation or experimental research, the movement law of dust in the coalface was researched and the specific dust-proof schemes were proposed [7–10]. Jing et al. evaluated the lighting environment in the fully mechanized coalface based on the light environment index method [11]. Park et al. investigated various heat stress indexes and effective temperature and conducted correlation analysis in order to estimate the thermal environment [12]. Krok presented a model for calculations of the temperature field in electric mine motors with a water cooled frame, which was worked out with the use of modified and improved thermal networks developed by the author for determining the temperature distributions in different types of ac machines [13]. Zhao et al. simulated the thermal environment in the heading face based on the turbulence model, which provided a theoretical and technical basis for coal mine ventilation, cooling, heat harm treatment, and prevention [14]. On the other hand, the comprehensive effect of multiple indicators on the operating environment of coalface in underground mining was also explored. Dey and Pal systematically analyzed the influencing factors of the coalface operating environment [15]. Guan et al. evaluated the coalface operating environment based on the Monte Carlo stochastic simulation [16]. Chen et al. built a multifactor coupling intelligent model of safety evaluation on dynamic environment in coalface based on the kernel principal component analysis and least squares support vector machines [17]. Shi et al. point out the importance of heading's operating environment to work's health and established the evaluating model of the operating environment in the headings using the theory of grey interrelated analysis, which provided new theory bases for supervision and evaluation of the operating environment in the headings of mine [18]. Besides, the fuzzy evaluation theory and analytic hierarchy process (AHP) were also used to classify the working face operating environment [19, 20].

In the above research, the evaluation of individual environmental indicators is specific, but because the operating environment is the result of the interaction of multiple indicators, so the comprehensive evaluation of multiple indicators is more objective. But in the comprehensive evaluation of mult-indexes, different evaluation indexes may be in conflict, and matter-element theory (MET) is a powerful tool to solve the problem of contradiction or incompatibility. MET is the theory of using the matter-element model to solve practical problems. Matter-element is a triplet composed of the matter, the characteristics of the matter, and the value of the matter characteristic, which was recorded as R = (matter, matter characteristic, matter characteristic value). When solving incompatible problems, only when the matter, the characteristics of the matter, and the value of the matter characteristic are considered at the same time can the problem be solved. The main content of MET is to quantitatively describe the variability of matters through the correlation function based on the matter-element model and extension set and then transform the incompatible problem into a compatible problem. For example, when the temperature of a coalface is in the temperature range corresponding to the "comfortable" grade, but the humidity is in the humidity range corresponding to the "uncomfortable" grade, the matter-element model can be used to establish the correlation function to solve the comprehensive correlation degree between the coalface operating environment and each comfort grade. And the final evaluation grade of the coalface operating environment should belong to the comfort grade which has the highest comprehensive correlation with it. To determine the weight of the relevant factors is a necessary step to solve the comprehensive correlation degree, and AHP is an effective method to obtain the weight of the relevant factors. In AHP, the weight of each relevant factor was calculated by the judgment matrix. For this reason, firstly, the indexes of temperature, humidity, noise, illuminance, dust, harmful gas, and wind speed are selected. And then, the environment evaluation model of the coalface based on AHP and MET was established, which was applied to N1228 coalface in Huatai colliery. Finally, three countermeasures to improve the operating environment were discussed in a broad sense.

2. Materials and Methods

2.1. Study Area. Huatai colliery is located in the northeast of the Gangcheng District of Laiwu City, Shandong province, China, as shown in Figure 1(a), which is under the administrative jurisdiction of the Gaozhuang subdistrict office. The geographical coordinates of the mining area are $117°40'06''$ ~$117°45'30''$ in east longitude and $36°09'10''$~$36°12'\ 27''$ in north latitude. In N1228 coalface, the average thickness of coal seam is 4 m, the buried depth is 900 m, and the coalface width is 120 m (Figure 1(b)). The mining method in N1228 coalface is long wall mining. The transverse arrangement of the coal cutter is used in conjunction with the face conveyor and the hydraulic support to form comprehensive mechanized coal mining equipment to complete the coal cutting, coal dropping, and coal loading operation.

2.2. Methods. An environment evaluation model of the coalface based on AHP and MET is established, which the detailed steps are as follows: selecting the operating environment evaluation factors ⟶ classifying the operation environment grade ⟶ building the environment objects, joint domain objects and classical field mater-element ⟶determining correlation function ⟶ determining the weights of evaluation factors ⟶ calculating the comprehensive correlation matrix ⟶ judging the environment grade.

2.2.1. Selecting the Evaluation Factors. Because of the relatively closed space and small space, the underground coalface of a colliery has a completely different environment from that of the ground. Therefore, from the point of view of the factors directly affecting the operating environment of coalface, this

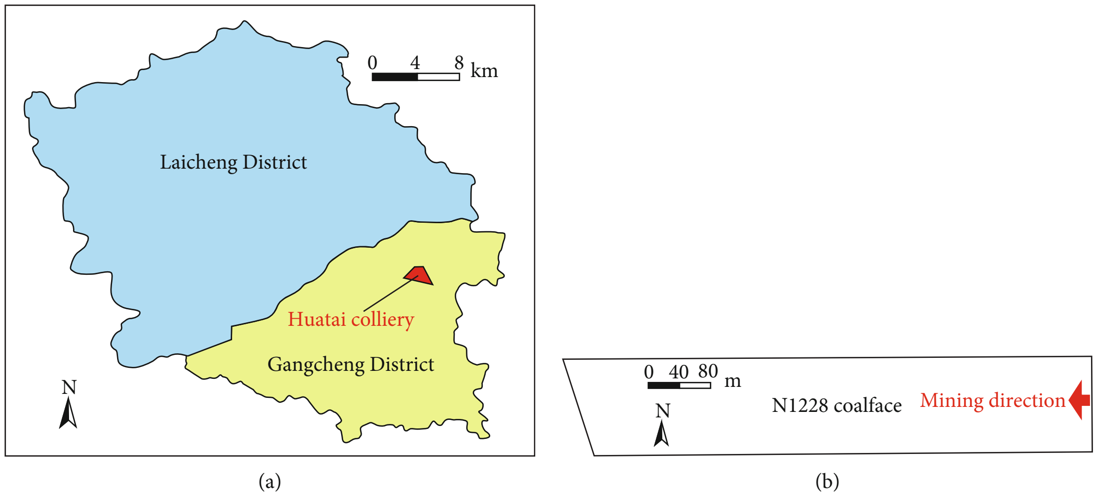

Figure 1: Location of the study area: (a) map of Laiwu City and (b) N1228 coalface.

paper selected seven indexes of temperature, humidity, noise, illuminance, dust, harmful gas, and wind speed.

(1) Temperature. The main heat sources of the coalface are running mechanical equipment and geothermal energy. At present, with the increasing depth of coal mining, more and more mechanical equipment brought about by development of mechanization leads to more and more heating capacity of mechanical equipment. In addition, the temperature of the exposed rock at the coalface will also increase as the mining depth increases. The above two sources make the thermal hazard of coalface more and more prominent, which has become one of the main factors that affect the safety of coal mine production and the health of the workers.

(2) Humidity. Compared with the atmosphere environment, the working face space is closed, and the influence of humidity on the human body is more obvious. When the air humidity is large in the coalface, it can inhibit the evaporation of body heat or accelerate heat conduction, causing the miners to feel uncomfortable. In a worse case, workers work long time in high-humidity areas, which is easy to cause wet arthralgia and seriously affect the health of coal miners.

(3) Noise. The noise in the working face mainly comes from mechanical equipment, such as coal cutter, boring machines, and coal conveyer. Noise affects the workers' vascular system, the nervous system, and the digestive system and can cause irreversible damage to the hearing, even affecting the safety of production and operation efficiency.

(4) Illuminance. Illumination is the intensity of light and the extent of an object's surface lighted, whose unit is lux or lx [21]. Because of the narrow working space in the coalface, if the illumination is not enough and the visibility is low, it is impossible to detect the running state of vehicles or coal cutter and surrounding environment, so workers cannot take measures in advance, which give rise to accidents. If the long-term illumination is not enough, the workers work only by the miner's lamp, which can cause blind spot in the visual center of the eye or lose the ability to see objects directly, that is, the so-called mine blind occupational disease. Therefore, illuminance is an important index in the environment evaluation of the coalface in underground mining.

(5) Dust. In the working face, dust usually refers to solid particles which are explosive and harmful to people's physical health and form dust hazards when they exist in the form of clouds. The dust comes mainly from the operation process, such as drilling, coal cutting, loading, and blasting. The dust hazards in the coal mining face are as follows. On the one hand, the dust has the risk of explosion at the proper concentration; on the other hand, dust will pollute the operating environment, affect the health of the miners, and lead to pneumoconiosis in miners.

(6) Harmful Gas. The harmful gases in the coalface mainly include carbon monoxide (CO), sulfur dioxide (SO_2), and hydrogen sulfide (H_2S). When CO and H_2S are inhaled into the human body, the transport capacity of oxygen in blood or the ability of the tissue to utilize oxygen are impaired, which results in the hypoxia of the tissue. SO_2, a strong irritant gas with colorlessness, acid taste, and well solubility in water, has strong irritation and erosion to the eyes and respiratory tract, which can cause inflammation of the throat and bronchi, respiratory paralysis, and pulmonary edema in severe cases. The safety and hygiene standards in China for the concentration of SO_2, CO, and H_2S are 15 mg/m^3, 30 mg/m^3, and 10 mg/m^3, respectively [22].

The hazard evaluation of a certain harmful gas is measured by index S, where the calculation formula of index S is

$$S = L \cdot \left(\frac{C_i}{M_i}\right), \tag{1}$$

Table 1: Evaluation grade of the operating environment in the coalface.

Factor	Evaluation grade				
	More comfortable	Comfortable	Generally comfortable	Less comfortable	Uncomfortable
Temperature (°C)	20-24	24-26	26-28	28-30	30-45
Humidity (%)	40-50	50-60	60-70	70-80	80-100
Noise (dB)	0-70	70-80	80-90	90-100	100-180
Illumination (lx)	120-300	100-120	80-100	60-80	0-60
Dust (mg/m^3)	0-4	4-6	6-8	8-10	10-30
Harmful gas	0-0.5	0.5-1.0	1.0-1.5	1.5-2.0	2.0-5.0
Wind speed (m/s)	3-4	2-3	1-2	0.5-1	0-0.5

where C_i is the concentration of the ith kind gas, mg/m^3; M_i is the maximum allowable concentration of the ith kind gas, mg/m^3; and L is the weight coefficient of total pulmonary ventilation. When there is a variety of harmful gas, the index of harmful gas can be accumulated.

(7) Wind Speed. In order to ensure the health of the coal miners, to provide appropriate production environment, and to improve work efficiency, ventilation must be carried out at the working face of the colliery. The direct measurement index of ventilation is wind speed. The suitable wind speed can effectively cool and dehumidify in the underground working face, but too high or low wind speed also causes worker's discomfort.

In 1228 coalface, the concentration of SO_2, CO, and H_2S are 4.06 mg/m^3, 0.43 mg/m^3, and 3.35 mg/m^3 by site test, respectively. So, the S value of the harmful gas index was calculated based on formula (1), that is, $S = 1.24$. Moreover, the values of noise, humidity, illumination, wind speed, temperature, and dust concentration are 95 dB, 55%, 77 lx, 0.7 m/s, 29°C, and 6.2 mg/m^3, respectively.

2.2.2. Classifying the Operating Environment Grade. According to the above analysis of environmental factors, from the point of view of human physiological and psychological adaptation to the environment, the operating environment condition of the coalface is divided into 5 grades, that is, more comfortable, comfortable, generally comfortable, less comfortable, and uncomfortable, as shown in Table 1.

2.2.3. Analysis Procedure of AHP and MET. The MET, a cross-disciplinary of thinking science, system science, and mathematics science, is an emerging discipline to study and solve incompatible problems, which have been widely used in the field of natural science and social science in decision-making, management, and evaluation [23].

The name of the matter N, the characteristics of the matter c, and the value of the matter characteristic v are determined, and $R = (N, c, v)$ is used as the basic element to describe the object, which is called matter-element.

A thing has more than one feature, if the object N has n characteristics, such as $c_1, c_2, \cdots c_n$, and corresponding values $v_1, v_2, \cdots v_n$ are described, which can be represented as

$$R(N, c, v) = \begin{bmatrix} N & c_1 & v_1 \\ & c_2 & v_2 \\ & \vdots & \vdots \\ & c_n & v_n \end{bmatrix}, \tag{2}$$

where R is an n-dimensional matter-element, c_i is the matter-element characteristics, and v_i is the value of the matter characteristic.

The operating environment of the coalface is evaluated based on MET, and the steps are as follows:

(1) Determining the Environment Objects. According to the actual situation, to evaluate the characteristics of a certain object, the measured values of multiple characteristics are determined and the corresponding matter-element matrix is established, as shown in

$$R_0(P_0, c, v) = \begin{bmatrix} P_0 & c_1 & v_1 \\ & c_2 & v_2 \\ & \vdots & \vdots \\ & c_n & v_n \end{bmatrix}, \tag{3}$$

where P_0 is the environment objects, c_i is matter-element characteristics, and v_i is the measured value of the matter characteristic.

(2) Determining Classical Field and Joint Domain Mater-Element. The classical field and joint domain mater-element are determined by the operating environment grade, as shown in

$$R_j(N_j, c, v_{ji}) = \begin{bmatrix} N_j & c_1 & v_{j1} \\ & c_2 & v_{j2} \\ & \vdots & \vdots \\ & c_n & v_{jn} \end{bmatrix} = \begin{bmatrix} N_j & c_1 & <a_{j1}, b_{j1}> \\ & c_2 & <a_{j2}, b_{j2}> \\ & \vdots & \vdots \\ & c_n & <a_{jn}, b_{jn}> \end{bmatrix}, \tag{4}$$

$$R_p(N, c, v_{pi}) = \begin{bmatrix} N_p & c_1 & v_{p1} \\ & c_2 & v_{p2} \\ & \vdots & \vdots \\ & c_n & v_{pn} \end{bmatrix} = \begin{bmatrix} N_p & c_1 & <a_{p1}, b_{p1}> \\ & c_2 & <a_{p2}, b_{p2}> \\ & \vdots & \vdots \\ & c_n & <a_{pn}, b_{pn}> \end{bmatrix}. \tag{5}$$

(3) Determining Correlation Function. The correlation function indicates that when the value of the matter-element characteristic is taken as a point on the real axis, the matter-element meets the required range of values, and the value is the correlation degree. The correlation degree $K_j(v_i)$ of each evaluation index v_i about each evaluation grade j is expressed as formula (6).

$$K_j(v_i) = \begin{cases} -\dfrac{\rho(v_i, v_{ji})}{|a_{ji} - b_{ji}|}, v_i \in v_{ji} \\ \dfrac{\rho(v_i, v_{ji})}{\rho(v_i, v_{pi}) - \rho(v_i, v_{ji})}, v_i \notin v_{ji} \end{cases}, \tag{6}$$

where $\rho(v_i, v_{ji}) = |v_i - ((a_{ji} + b_{ji})/2)| - ((b_{ji} - a_{ji})/2) = \begin{cases} a_{ji} - v_i, v_i \le (a_{ji} + b_{ji})/2 \\ v_i - b_{ji}, v_i > (a_{ji} + b_{ji})/2 \end{cases}$,

$$\begin{aligned} \rho(v_i, v_{pi}) &= \left| v_i - \frac{(a_{pi} + b_{pi})}{2} \right| - \frac{(b_{pi} - a_{pi})}{2} \\ &= \begin{cases} a_{pi} - v_i, v_i \le \dfrac{(a_{pi} + b_{pi})}{2}, \\ v_i - b_{pi}, v_i > \dfrac{(a_{pi} + b_{pi})}{2}. \end{cases} \end{aligned} \tag{7}$$

(4) Determining the Weights of Evaluation Factors. AHP is an analytic procedure with a combination of qualitative and quantitative, systematic, and hierarchical analyses. The weight of each factor of the operating environment is determined using AHP, and the steps are as follows:

(1) Building the structure model of AHP

The structure of AHP is shown in Figure 2.

(2) Constructing judgment matrix and calculating eigenvalues and eigenvectors

The judgment matrix is constructed based on the Saaty's $1 \sim 9$ scale scoring method [24] (Table 2), and eigenvalues and eigenvectors are calculated.

(3) Check the consistency of the judgment matrix

Firstly, consistency index CI is calculated, $\mathrm{CI} = (\lambda_{\max} - n)/(n-1)$. Secondly, the corresponding average random consistency index RI is referred in Table 3. Thirdly, consistency ratio CR is calculated, $\mathrm{CR} = \mathrm{CI}/\mathrm{RI}$. When $\mathrm{CR} < 0.1$, the consistency of the judgment matrix is acceptable; otherwise, the judgment matrix is modified.

If the judgment matrix satisfies the consistency test requirement, the normalized eigenvector of the judgment matrix is the weight of each index factor.

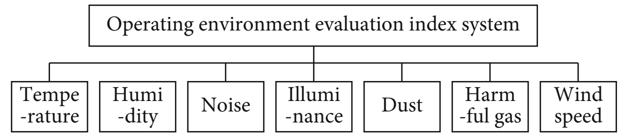

Figure 2: Structure model of AHP

Table 2: Scale meaning from 1 to 9.

Scale	Meaning
1	Equal importance
3	Weak importance
5	Obvious importance
7	Strong importance
9	Absolute importance
2, 4, 6, 8	Represents the intermediate value of the adjacent judgment
Reciprocal	If element i/element $j = a_{ij}$, then if element j/element $i = 1/a_{ij}$

Table 3: Values of average random consistency index RI.

Order	3	4	5	6	7	8	9	10
RI	0.52	0.89	1.12	1.26	1.36	1.41	1.46	1.49

(5) Calculating the comprehensive correlation degree. The comprehensive correlation degree $K_j(P_0)$ is the weighted value of the correlation degree $K_j(v_i)$ of each evaluation index v_i about each evaluation grade j, which is shown in formula (8)

$$K_j(P_0) = \sum_{i=0}^{n} \omega_i \cdot K_j(v_i), \tag{8}$$

where ω_i is the weight of factors and $K_j(P_0)$ is the comprehensive correlation degree.

(6) Judging the environment grade. K_j is used to judge the environment grade, as shown in formula (9)

$$K_j = \max \{K_j(P_0)\}. \tag{9}$$

It is concluded that the corresponding grade of the maximum value of the comprehensive correlation degree is the grade of the environment objects.

3. Results

3.1. Classical Field Mater-Element, Joint Domain Objects, and Environment Objects. The classical field mater-element of the operating environment is shown in

$$R_j\left(N_j, c, v_{ji}\right) = \begin{bmatrix} & N_1 & N_2 & N_3 & N_4 & N_5 \\ c_1 & <20, 24> & <24, 26> & <26, 28> & <28, 30> & <30, 45> \\ c_2 & <40, 50> & <50, 60> & <60, 70> & <70, 80> & <80, 100> \\ c_3 & <0, 70> & <70, 80> & <80, 90> & <90, 100> & <100, 180> \\ c_4 & <120, 300> & <100, 120> & <80, 100> & <60, 80> & <0, 60> \\ c_5 & <0, 4> & <4, 6> & <6, 8> & <8, 10> & <10, 30> \\ c_6 & <0, 0.5> & <0.5, 1.0> & <1.0, 1.5> & <1.5, 2.0> & <2.0, 5.0> \\ c_7 & <3, 4> & <2, 3> & <1, 2> & <0.5, 1> & <0, 0.5> \end{bmatrix}. \tag{10}$$

The joint domain objects and the environment objects mater-element are shown in matrixes (11) and (12), respectively.

$$R_p\left(N, c, v_{pi}\right) = \begin{bmatrix} N_p & c_1 & <20, 45> \\ & c_2 & <40, 100> \\ & c_3 & <0, 180> \\ & c_4 & <0, 300> \\ & c_5 & <0, 30> \\ & c_6 & <0, 5> \\ & c_7 & <0, 4> \end{bmatrix}, \tag{11}$$

$$R_0(P_0, c, v) = \begin{bmatrix} P_0 & c_1 & 29 \\ & c_2 & 55 \\ & c_3 & 95 \\ & c_4 & 77 \\ & c_5 & 6.2 \\ & c_6 & 1.24 \\ & c_7 & 0.7 \end{bmatrix}. \tag{12}$$

3.2. Correlation Degree Matrix. The correlation degree matrix of each evaluation index about each environment grade is as shown in

$$K_j(v_i)_{7\times5} = \begin{bmatrix} 0.5 & 1.5 & 1.25 & -0.5 & 0.0667 \\ 0.5 & -0.5 & 0.5 & 1.5 & 1.25 \\ 0.5 & 1.5 & 0.3571 & -0.5 & 0.0625 \\ 0.15 & 1.15 & 0.2389 & -0.15 & 0.2833 \\ -0.1 & 0.1 & 0.55 & 0.9 & 0.19 \\ -0.48 & 0.48 & 1.48 & 0.52 & 0.2533 \\ 0.3 & 1.3 & 2.3 & -0.4 & 0.4 \end{bmatrix}. \tag{13}$$

3.3. Index Weight. The weights of the operating environment evaluation factors are determined using AHP, as shown in Table 4.

3.4. Comprehensive Correlation Vector and Environment Grade. According to the correlation degree matrix (13) and index weight indexes, the comprehensive correlation vector is calculated using formula (8), as shown in

$$K_j(P_0)_{1\times5} = [-0.0218 \quad 0.7581 \quad 1.172 \quad 0.2291 \quad 0.3023]. \tag{14}$$

It is concluded that the operating environment grade of N1228 coalface in Huatai colliery is "generally comfortable."

4. Discussion

4.1. Development of Environmental Evaluation Index Monitoring System. In Table 4, the weight of the harmful gas is the greatest. Harmful gas is the most important

Table 4: Index weight.

Index	Temperature	Humidity	Noise	Illuminance	Dust	Harmful gas	Wind speed
Weight	0.1194	0.0649	0.0554	0.1398	0.0929	0.3996	0.1281
Rank	4	6	7	2	5	1	3

indicator to the operating environment of the working face, which poses a great threat to the safety of miners' lives. Coalface will continue to advance with coal mining or tunneling activities, and the thickness and dip angle of the coal seam will change or geological structure will appear in the process of advancing, which have the potential to cause impact on the concentration of harmful gases. For this reason, it is necessary to develop a set of reasonable mine environmental monitoring system to monitor the changes in environmental indicators in working face and to protect the health and safety of miners, which can collect and alarm the environment parameter and image data with system stability and short transmission delay.

4.2. Improvement on Miners' Safety Awareness. Safety consciousness is a kind of advanced psychological reflection form of safety production or environment state people have, which can reflect people's understanding of the safety or the environment state in the production activity [25]. Human's safety consciousness has active nature, which regulates production activities and safety operations; conversely, production activities also affect the formation of people's safety consciousness. It is necessary to raise the safety consciousness of miners and ensure the safety of production and the health of miners. Therefore, four methods for improvement on the safety consciousness of miners are put forward.

4.2.1. Raising Workers' Recruitment Requirements. First of all, all candidates are screened by age, educational background, physical examination, and cultural examination, and then, an open reply was made for those who are not allowed to be employed without meeting the standards, which not only solves the problem of low overall quality of workers but also reflects the recruitment of employees open and fair. Secondly, an off-the-job training is made for new workers who can be called formal workers after passing the examination.

4.2.2. Educational Training. Educational training is the key to improve staff safety awareness. In combination with the actual situation of workers, the training of knowledge at different levels and division of labor is adopted. For workers who have different levels of knowledge, the educational level and technical knowledge of workers are divided into three categories: good, medium, and poor, which bring about the difference of the contents and methods of training. Division of labor training refers to the separate training of different types of jobs, and training should have professional characteristics.

4.2.3. Carrying Out Warning Education. Warning education can further improve the effectiveness of safety education training, allowing workers to learn a lot of security experience and strengthen self-protection awareness. There are many ways of warning education, such as the previous coal mine accidents being made into cartoons and posted on the safety bulletin board.

4.3. Formulation of Regulations for Coal Mine Operation Environment. According to the Safety Production Law of People's Republic of China, the Coal Law of People's Republic of China, the Coal Mine Safety Law of People's Republic of China, the Law of People's Republic of China on Prevention and Control of Occupational Diseases, and other relevant laws and regulations, the environmental monitoring regulations of the coal mine working face should have been further formulated, and the environmental level of the working face is divided. In addition, the responsibility of the operation environment is implemented to the individual to ensure the safety of the mine production and the health of the miners. What is more, regulations also need to stipulate that the training time for employees is not less than 10 hours before the job induction, and the regular training time is not less than 5 hours per year during the postperiod.

5. Conclusions

In order to ensure the safety of coal mine safety production and the health of miners, the evaluation method was put forward based on AHP-MET, and the operating environment of N1228 coalface was evaluated. Conclusions are as follows:

(1) The indexes of temperature, humidity, noise, illuminance, dust, harmful gas, and wind speed are selected, and the environment evaluation index system is constructed

(2) The operating environment evaluation model of the coalface based on AHP and MET is established, which was applied to evaluate the operating environment of the N1228 coalface

(3) From the broad point of view, three measures are proposed to improve the operation environment of the coalface: development of environmental evaluation index monitoring system, improvement on miners' safety awareness, and formulation of regulations and policies for coal mine operation environment

Data Availability

All data used during the study and appearing in the submitted article are available from the corresponding author upon request.

Conflicts of Interest

The authors declare that there is no conflict of interest regarding the publication of this paper.

Acknowledgments

This research was jointly supported by the Fundamental Research Funds for the Central Universities (Grant No. 2017XKZD07).

References

[1] H. Gui and L. N. Xu, “Analysis of influencing factors of energy consumption in China based on co integration method,” *China Energy*, vol. 39, pp. 16–19, 2017.

[2] J. S. Zhang, N. Chen, G. Fu, M. W. Yan, and Y. C. Kim, “The safety attitudes of senior managers in the Chinese coal industry,” *International Journal of Environmental Research and Public Health*, vol. 13, no. 11, p. 1147, 2016.

[3] G. R. Li, Y. L. Lei, J. P. Ge, and S. M. Wu, “The empirical relationship between mining industry development and environmental pollution in China,” *International Journal of Environmental Research and Public Health*, vol. 14, no. 3, p. 254, 2017.

[4] S. Z. Long, *Advances in Man-Machine-Environment System Engineering*, Science and Technology Press, Beijing, 1995.

[5] X. B. Li, X. R. Wang, L. J. Dong, and F. F. Sun, “Thermal comfort evaluation for human body in mines based on uncertainty measurement theory,” *Science & Technology Review*, vol. 31, pp. 45–50, 2013.

[6] G. Fu, J. S. Zhang, J. N. Pan, and Y. Z. Li, “Study of long wall top-coal caving face dust pollution status,” *Journal of China Coal Society*, vol. 31, pp. 63–66, 2006.

[7] X. X. Shi, Z. A. Jiang, S. Y. Zhou, and W. Cai, “Experimental study on dust distribution regularity of fully mechanized mining face,” *Journal of China Coal Society*, vol. 33, pp. 1117–1121, 2008.

[8] Z. B. Zhao, H. B. Zhai, and F. Wang, “Numerical simulation and experiment on the dust movement at top caving mining face,” *Transactions of Beijing Institute of Technology*, vol. 28, pp. 1113–1116, 2008.

[9] G. Zhou, W. M. Cheng, L. J. Chen, and W. Nie, “Numerical simulation and its application of dust concentration spatial distribution regularities in fully-mechanized caving face,” *Journal of China Coal Society*, vol. 35, pp. 2094–2099, 2010.

[10] Y. P. Qin, M. M. Zhang, L. J. Cui, and J. Y. Liu, “Numerical simulation of dust migration and study on dust removal modes with the forced ventilation shunt in a fully mechanized workface,” *Journal of University of Science and Technology Beijing*, vol. 33, pp. 790–794, 2011.

[11] G. X. Jing, X. S. Peng, C. Q. Li, and H. Li, “Environmental assessment of fully mechanized excavation face based on light environment index comprehensive evaluation method,” *Safety and Environmental Engineering*, vol. 19, pp. 41–44, 2012.

[12] S. O. Park, J. H. Roh, and K. Jin, “A study on evaluation of thermal environment using heat stress indices for deep coal mine in Korea,” *Annales Medicinae Experimentalis et Biologiae Fenniae*, vol. 24, pp. 166–175, 2014.

[13] R. Krok, “Influence of work environment on thermal state of electric mine motors,” *Archives of Electrical Engineering*, vol. 60, no. 3, pp. 357–370, 2011.

[14] F. J. Zhao, S. Y. Huang, P. W. Shen, and Y. B. Li, “Numerical simulation study on the thermal environment in heading face,” *Journal of Coal Science and Engineering*, vol. 16, no. 3, pp. 272–276, 2010.

[15] N. C. Dey and S. Pal, “A look into miners’ health in prevailing ambience of underground coal mine environment,” *Journal of The Institution of Engineers (India): Series D*, vol. 93, pp. 37–42, 2012.

[16] W. J. Guan, M. Q. Chen, G. He, and Z. G. Zhao, “A model of the environment evaluation for the coal-mining goaf based on the Monte Carlo stochastic simulation,” *Journal of Safety and Environment*, vol. 16, pp. 326–330, 2016.

[17] X. H. Chen, P. F. Lv, and J. X. Zhou, “Safety evaluation model of dynamic environment in working face of mine base on KPCA-LSSVM,” *Journal of Safety Science and Technology*, vol. 12, pp. 34–39, 2016.

[18] S. L. Shi, B. C. Liu, and H. Q. Wang, “Evaluating model of heading’s operating environment and its application,” *Mining and Metallurgical Engineering*, vol. 18, pp. 18–21, 1998.

[19] R. Y. Li and T. J. Li, “Fuzzy evaluation and application of mining face working environment,” *Coal Science & Technology Magazine*, vol. 3, pp. 24–26, 2007.

[20] Y. Chen, X. Y. Wang, Y. Q. Zhao, H. L. Shi, X. M. Liu, and Z. G. Niu, “Quantitative evaluation for the threat degree of a thermal reservoir to deep coal mining,” *Geofluids*, vol. 2020, Article ID 8885633, 15 pages, 2020.

[21] N. Zhi, S. J. Mao, and M. Li, “Enhancement algorithm based on illumination adjustment for non-uniform illuminance video images in coal mine,” *Journal of China Coal Society*, vol. 42, pp. 2190–2197, 2017.

[22] Ministry of Environmental Protection, General Administration of Quality Supervision, Inspection and Quarantine, *Ambient Air Quality Standard*, China Environmental Science Press, Beijing, 2012.

[23] W. Cai, *Matter-Element Model and Its Application*, Science and Technology Press, Beijing, 1994.

[24] A. Ishizaka and A. Labib, “Review of the main developments in the analytic hierarchy process,” *Expert Systems With Applications*, vol. 38, pp. 14336–14345, 2011.

[25] F. W. Guldenmund, “The nature of safety culture: a review of theory and research,” *Safety Science*, vol. 34, no. 1-3, pp. 215–257, 2000.

Hindawi
Geofluids
Volume 2021, Article ID 5667183, 14 pages
https://doi.org/10.1155/2021/5667183

Research Article

Study on Deformation and Failure Characteristics of Surrounding Rock of Overlying Roadway under Upward Mining in the Deep Mine

Teng-Gen Xiong, Ju-Cai Chang, Kai He, Ya-Feng Su, and Chao Qi

School of Mining Engineering, Anhui University of Science and Technology, Huainan, 232001 Anhui, China

Correspondence should be addressed to Ju-Cai Chang; x1216mine@163.com

Received 29 May 2021; Accepted 3 July 2021; Published 28 July 2021

Academic Editor: Zhijie Wen

To study the impact of mining of the lower protective layer on the deformation and failure characteristics of the upper roadway, these characteristics of an 879 gas drainage roadway were studied and analyzed during the mining of the II 1051 working face of the Zhuxianzhuang coal mine using similar simulation experiments and numerical simulation methods. The results indicate that with the continuous excavation of the working face, the range of impact of the mining stress gradually spreads and exceeds the level of the roadway. At the present time, the roadway is in a mining stress-rising area. The two sides of the roadway are sheared, and the roof and floor are under tension–shear composite failure. The floor is the most gravely damaged—the depth of its damage is 2.5 m, and the depths of damage on either side and of the roof are approximately 1–2 m. During the advancing process of the working face, the deformation of the roadway increases slowly at first, then increases sharply, and tends to be stable thereafter. The deformation of the floor is the largest, followed by those of the two sides and the roof; the values are 800, 400, and 300 mm, respectively.

1. Introduction

The depletion of shallow coal resources in China has led to increasing mining depth in various mining areas, and the problems of coal and gas outbursts in coal mines are also increasing. According to the characteristics of "two low and one high" of coal seam gas, several scholars at home and abroad have found that protective seam mining is the most economical and effective method of preventing coal and gas outbursts [1–6]. Although protective seam mining causes the stress redistribution of the protected seam, leading to a sharp drop in the gas pressure, this, in turn, reduces the risk of gas outburst and also causes the movement and deformation of as well as transverse and longitudinal cracks in the overlying strata. It also leads to the formation of stress-reduction and -rise areas. Regardless of whether the roadway is laid on the stress-reduction or -rising area, the stress distribution in the surrounding rock changes [7]. The redistribution of the stress in the surrounding rock promotes the continuous development of cracks in the areas surrounding the roadway, leading to breakage of the surrounding rock and a reduction in the bearing capacity. This further causes deformation in and instability of the roadway, which renders it difficult to maintain.

In view of the deformation and failure characteristics of the overlying strata caused by the mining of the lower protective layer, a significant amount of research has been carried out. Jiao et al. [8], Cao et al. [9], and Bai and Hu [10] studied the movement and deformation characteristics of the overlying strata during the mining process of the lower protective seam. Shun et al. [11] and Xiong et al. [12] analyzed the migration rule of overburden after mining. Wang et al. [13] and Xue et al. [14] formulated a fracture evolution law for the overlying strata following coal mining. Tang et al. [15], Zhang et al. [16], Xu and Han [17], and Zhang et al. [18] analyzed the stress distribution and deformation of the protected layer during the mining process of the lower protective layer. Yang et al. [19] studied the deformation and failure characteristics of the overlying strata, development law of mining stress and fracture, and size of the stress release area. Zhang et al. [20] studied the characteristics of strata failure fracture, fracture evolution, and subsidence deformation in the process of the upward mining of deep coal seams. They further analyzed the relationship between the strata subsidence deformation curve and the strata fracture, fracture development, and stress state. Liu et al. [21] analyzed the law governing the development of overlying strata fractures caused by thin protective seam mining. Huang et al. [22] focused on the comprehensive morphological characteristics of the fracture zone formed by the mining of the lower coal seam and the distribution of the concentrated stress in the surrounding rock. Liu and Chen [23] studied the deformation of coal seam pressure relief, development of mining fracture, protective effect of pressure relief, discharge of pressure relief gas, gas drainage, and outburst prevention and control laws. Qian et al. [24] studied the stress distribution law of the overlying strata with respect to the various support parameters of the upper protective layer and obtained the range of impact of the stress release and concentration areas of the overlying strata.

There have also been several developments in the study of the stability of the overlying roadway owing to the mining of the lower protective layer. Qian et al. [24] used the FLAC numerical simulation software to analyze the effect of upward mining on the stability of the overlying roadway with respect to the various support parameters of the upper protective seam and found that the vertical stress, plastic zone, and displacement of the sidewall on one side of the roadway in the upper protective seam were greater than those on the side near the underlying goaf. Xie et al. [25] studied the impact of the repeated mining of multiple coal seams on the deformation of roof roadways. Wang et al. [26] studied the temporal and spatial evolution laws of the stress and fracture fields in a roof coal roadway after pressure-relief mining in a lower coal seam and found that the superimposed stress formed by the underlying mining and roadway excavation determines the stress distribution and fracture evolution characteristics of the rock surrounding the roadway. Zhang et al. [27] used physical experiments to study the deformation and failure characteristics of the roof roadway in various areas and obtained the similar characteristics of roadways in "three zones": in the collapse zone, the roadway indicated strong roof collapsing and floor bulging; the cracks in the rock surrounding the roadway in the fracture zone were significantly reduced, but the mining damage was still significant; and the deformation and failure of the rock surrounding the roadway in the bending subsidence zone were not evident. Zhou et al. [28] used the UDEC discrete element numerical simulation software to study the failure characteristics of the rock surrounding a coal roadway in the fracture zone and found that the failure was most evident in the roof and floor of the roadway, followed by the failure of the side of the roadway near the working face.

The literature referred to above primarily investigated the deformation and failure characteristics and stress distribution of the overlying strata and coal roadway in the mining process of the lower protective seam. However, little information is available on the deformation and failure law of the rock roadway outside the "three zones" and adjacent to the working face. However, the overlying 879 gas drainage roadway of the II 1051 working face in the Zhuxianzhuang coal mine is located in the rock strata outside the "three zones," which is significantly deformed and damaged by the mining of the working face. Based on the abovementioned conditions, through similar simulation experiments and numerical simulations and considering the overlying 879 gas drainage roadway of the Zhuxianzhuang coal mine II 1051 working face of the Huaibei Mining Group as the engineering background, in this study, the deformation and failure characteristics of the upper roadway during the mining of the lower protective layer are investigated. Further, the law that governs the impact of the deformation and failure characteristics of the overlying strata on similar characteristics of the upper roadway and the instability mechanism of the roadway is summarized.

2. Project Profile

The Zhuxianzhuang mine is located in Suzhou City, Anhui Province, China. The 879 gas drainage roadway, to be studied in this study, is located in the II 5 mining area. The mineable coal seams in the mining area were identified as No. 8 and No. 10 coal. The No. 10 coal seam lies under the No. 8 coal seam, the distance is approximately 78 m, and the coal seam dip angle is approximately 20°. The No. 10 coal seam is used in protective seam mining; the thickness of the coal seam is 0.97–3.2 m, and its structure is relatively simple. The 879 gas drainage roadway is arranged 40–45 m above the roof of the No. 10 coal seam, with a horizontal distance of 5 m from the left coal wall of the working face, serving as gas drainage for the No. 8 coal seam, as depicted in Figure 1(a). The position of the rock surrounding the roadway and the rock properties of the roof and floor of the roadway are depicted in Figure 1(b). According to the geological histogram, it can be seen that the direct bottom of the roadway is made of mudstone, the two sides are made of fine sandstone, and the lithology of the floor is poor. Therefore, under high stress and dynamic load, the floor is more likely to be damaged than either side.

To reduce the amount of roadway excavation required, the 879 gas drainage roadway was used as the main roadway for the eight coal mines. When the lower protective layer was mined, the overlying strata moved and deformed under the impact of mining, the original stress balance state was broken, the coal and rock mass near the working face were destroyed, and the stress on the surrounding rock was redistributed to achieve a new stable state. In the process of relief of pressure from the upper coal seam, the strength of the surrounding rock of the upper roadway was weakened, leading to the fracture and instability of the rock surrounding the roadway, which is difficult to maintain and has a significant impact on the safety of the mine. Therefore, it is necessary to study the characteristics, summarize the mechanism of roadway deformation and failure, and provide guidance for reasonable roadway support design.

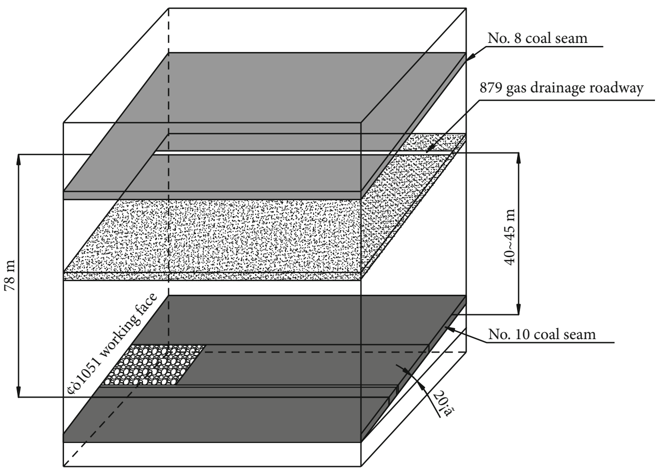

(a)

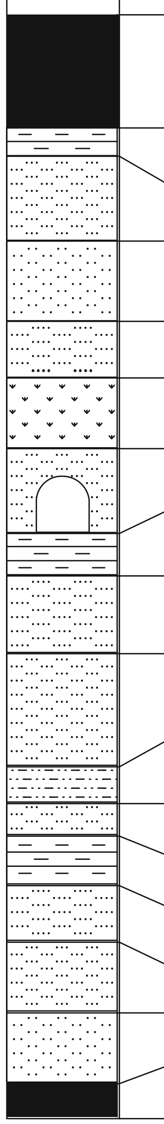

Histogram		Average thickness (m)	Rock name	Rock properties
		8.0	No. 8 coal	It is black, and the upper part is massive, belonging to semibright type
		2.0	Mudstone	It is grayish-black, massive, containing plant fossil fragments
		6.0	Fine sandstone	It is gray or grayish-white, with discontinuous micro oblique bedding
		5.7	Medium sandstone	It is grayish-white, with horizontal microwave bedding.
		4.0	Siltstone	It is dark gray, with horizontal microwave bedding, containing carbon chips
		5.0	Alumine	It is light gray, and the upper part is the pure aluminum, and the lower part contains siderite and purplish-red plaque
		6.0	Fine sandstone	It is gray orbluish-gray, with discontinuous micro-oblique bedding
		3.0	Mudstone	It is light gray, containing argillaceous enclaves and plant fossil fragments
		5.5	Siltstone	It is dark gray, dense, brittle, and fissured, with black mudstone and carbonaceous in the middle
		8.0	Fine sandstone	It is light gray with developed fissures in the middle, a hidden horizontal bedding, and a massive carbonaceous argillaceous belt
		2.6	Sandy mudstone	It is gray, with siderite inclusions, containing carbonized plant debris
		2.3	Fine sandstone	It is grayish-green, dense, with siderite and nodules at the top
		3.5	Mudstone	It is greenish-gray, with a well-developed sliding surface
		4.0	Siltstone	It is blackish-gray, dense, with black argillaceous rock in the middle
		5.0	Fine sandstone	It is gray and massive, and its horizontal bedding is developed
		5.0	Medium sandstone	It is grayish-white, mainly quartz, with argillaceous cementation and fragile.
		2.5	No. 10 coal	It is black and fragmentary, dominated by bright coal

(b)

Figure 1: Comprehensive histogram depicting the spatial location and geology of roadway.

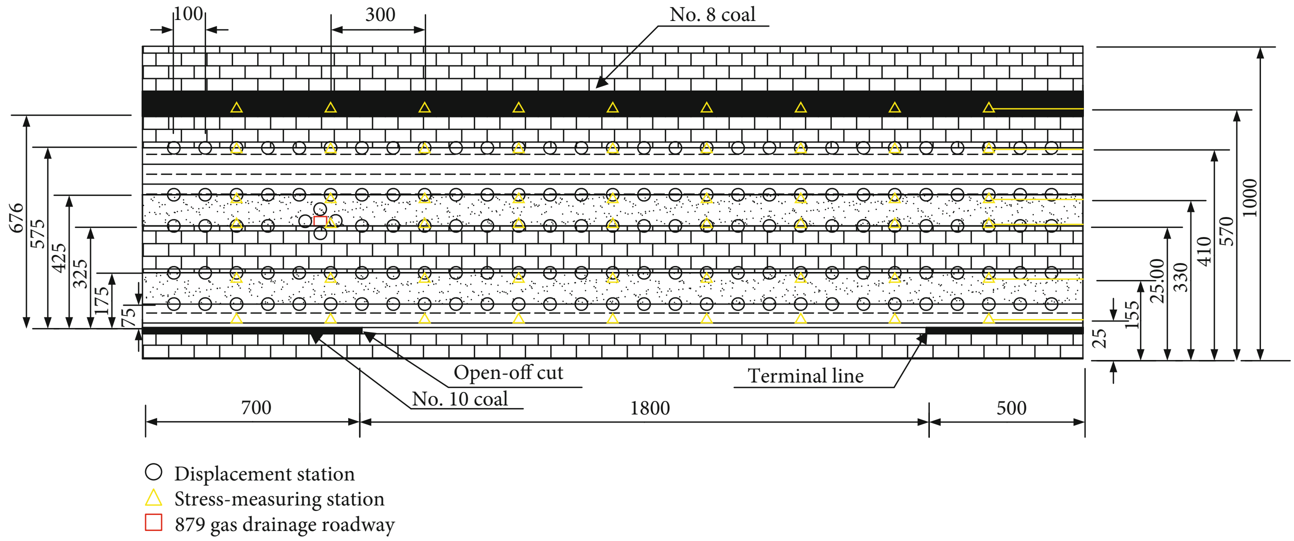

Figure 2: Model sensor layout.

3. Study on Migration and Stress Distribution of Overlying Strata in Upward Mining

3.1. Similar Material Model Design. According to the geological conditions and similarity theory, the geometric similarity ratio was $C_L = 1:100$, bulk density similarity ratio was $C\gamma = 1:1.67$, and stress similarity ratio was $C_\sigma = 1:167$. Therefore, the model size was determined as length × width × height = 3000 mm × 300 mm × 1300 mm, and the mining thickness was determined as 2.5 cm. On either side of the model, 70 and 50 cm boundary coal pillars were set. In the test, fine sand was selected as the aggregate, gypsum powder and lime powder were used as cementing materials, mica powder was used for layered laying between each rock layer, and the remaining weight of the upper part of the model was imposed by an additional counterweight.

3.2. Test Data Monitoring. To monitor the changes in the stress and displacement of the overlying strata and rock surrounding the 879 gas drainage roadway when the model mines the lower protective layer, six stress observation lines were buried from the bottom to top; the distances between the lines and the No. 10 coal roof were 2.5, 15.5, 15.5, 33, 41, 57, and 70 cm. Simultaneously, five displacement-measuring lines were set on the surface of the model. The distances between the measuring lines and the roof of the No. 10 coal seam were 7.5, 17.5, 32.5, 42.5, and 57.5 cm. One measuring point was arranged every 10 cm of the measuring line, and another four displacement-measuring points were arranged around the roadway. The distribution of the measurement points is depicted in Figure 2.

During the test, a BX120-50AA resistance strain gauge and a CM-2B strain gauge were used as the stress acquisition devices to record the stress change in the overlying strata in real time during coal mining. The effect of the equipment connection is depicted in Figure 3.

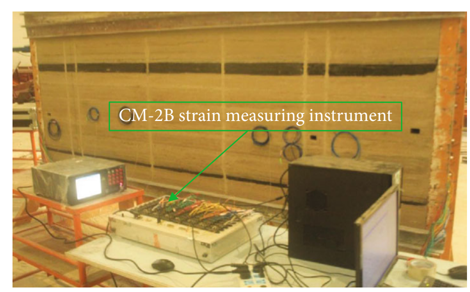

Figure 3: Effect diagram of model observation equipment.

3.3. Analysis of Test Results

3.3.1. Migration Law of Overlying Strata during Mining. In the early stage of mining, the overlying strata moved downward with coal seam mining, and the movement was slow. As the working face was continually excavated, rock fissures developed gradually, rock strata bent and sank, and tensile failure occurred, leading to rock collapse. At this time, the height from which the rocks fell was small, as depicted in Figure 4(a). With continuous mining of the coal seam, the overlying strata also moved toward the goaf. The fissures of the strata developed, the strata broke again, and the falling height increased to 5 m, as depicted in Figure 4(b). When the working face was continually excavated 15 m forward, the main roof was broken periodically, and vertical and horizontal cracks appeared in the front and on the roof of the working face, respectively. At this time, the advancing distance of the working face was 70 m, as illustrated in Figure 4(c). Therefore, the periodic fracture step of the main roof was approximately 15 m.

The continuous excavation of the working face led to increasingly intense movement of the overlying strata, the weak strata collapsed with mining, and the main roof was broken periodically. Owing to the various properties of the strata, bed separation with a length of approximately 300 mm and a height of approximately 10 mm appears among the various strata above the main roof, as depicted

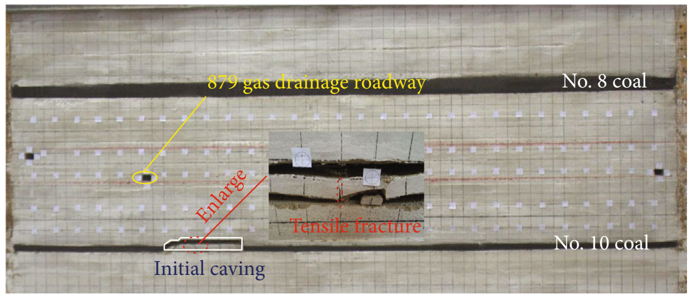

(a) Excavation at 35 m

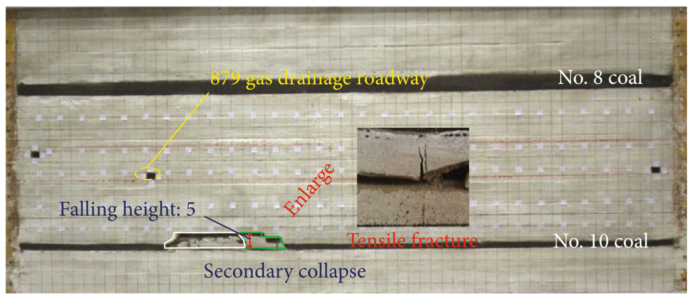

(b) Excavation at 55 m

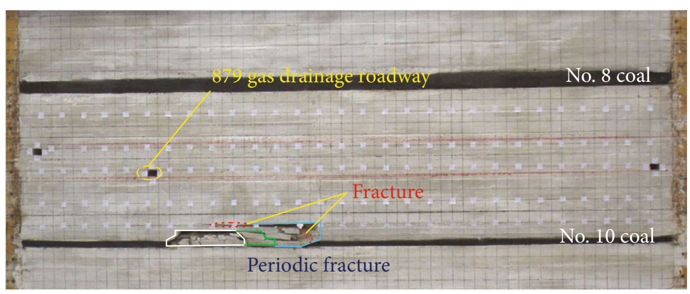

(c) Excavation at 70 m

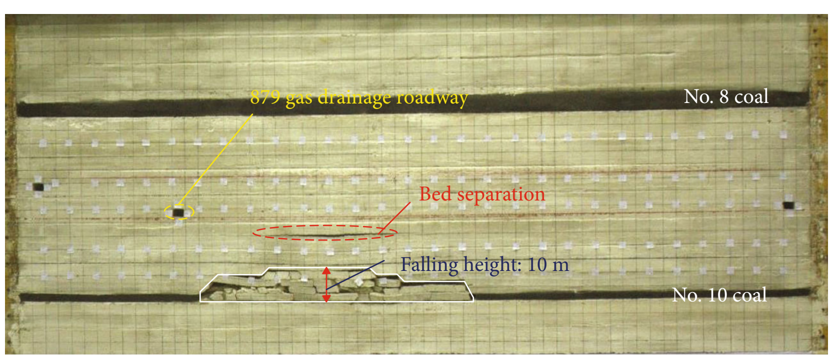

(d) Excavation at 105 m

Figure 4: Continued.

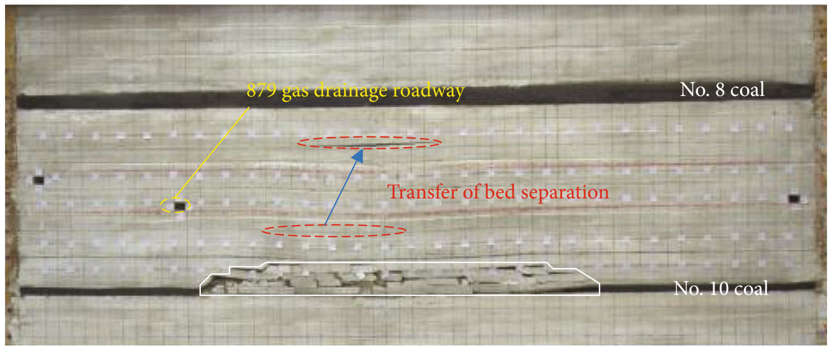

(e) Excavation at 150 m

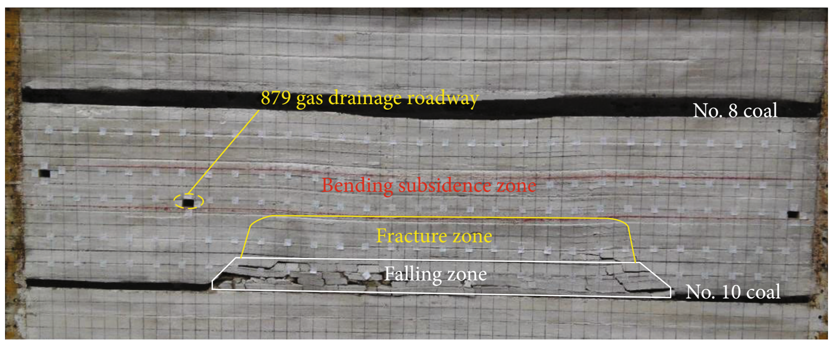

(f) Excavation at 180 m

Figure 4: Movement characteristics of overlying strata during mining.

in Figure 4(d). As the working face was continually excavated further, the overlying strata further bent and sank, and the bed separation gradually closed and developed upward. As depicted in Figure 4(e), the deformation and movement of the strata began to affect the roadway horizon, and the strata moved and deformed toward the goaf, leading to tension in the surrounding rock on the right side of the roadway, causing small vertical tension cracks. When the working face was excavated up to the terminal line, as depicted in Figure 4(f), fissures developed in the rock surrounding the roadway, which exhibited asymmetric characteristics.

3.3.2. Stress Distribution Law of Overlying Strata under Mining. Owing to the mining of the coal seam, the original stress equilibrium state of the overlying strata was broken, the stress was redistributed, and the vertical stress concentration appeared at the coal wall of the working face. In the initial stage of mining, the stress concentration area was small. As depicted in Figures 5 and 6, when the excavation length of the working face was less than 55 m, the stress concentration factor of the rock layer 33 m away from the roof of the working face tended to be 1. The results indicate that when the excavation distance of the working face was less than 55 m, the range of impact of the mining was the largest within 33 m of the roof, and the impact on the strata at 33 m of the roof and above was small. When the excavation length of the working face exceeded 55 m, the scope of impact of the mining expanded. The impact gradually reached and crossed the strata where the roadway was located; the maximum value of the impact was reached on the strata 70 m above the roof, as depicted in Figures 7 and 8.

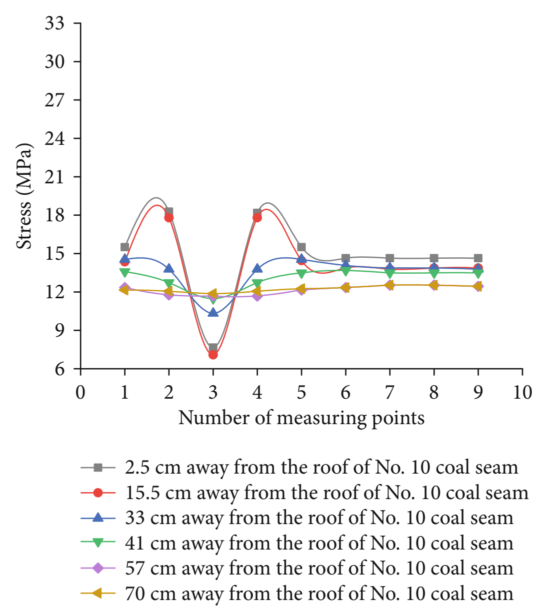

Figure 5: Stress diagram of working face mining at 35 m.

Based on this investigation of overburden migration and stress distribution, the stress distribution during the mining process of the working face was summarized and analyzed. The results obtained from the monitoring and distribution of rock stress were compared with those of the model, and the stress distribution in each layer was determined. The stressed environment of the roof of the 879 gas drainage roadway can be described as follows: After the mining of

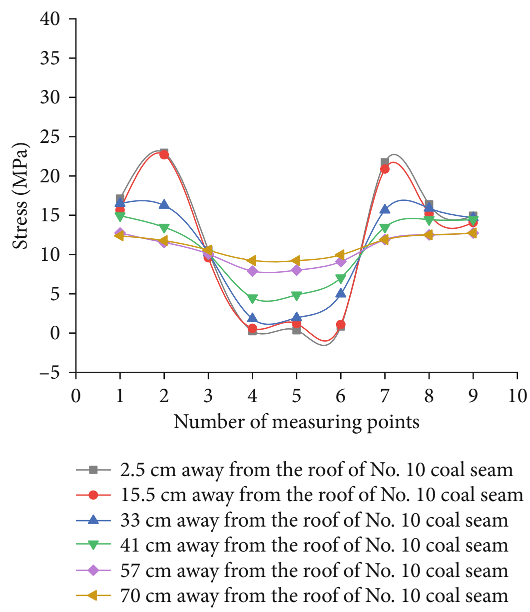

FIGURE 6: Stress diagram of working face mining at 55 m.

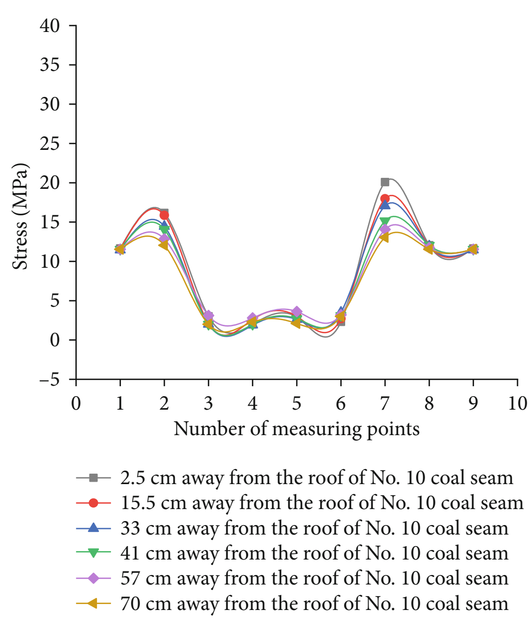

FIGURE 7: Stress diagram of working face mining at 150 m.

the II 1051 working face, the 879 gas drainage roadway in the upper part of the No. 10 coal seam lays in the stress-rising area of the overlying strata formed by mining. As illustrated in Figure 9, the stress concentration factor of the surrounding rock increased, and the roadway was strongly affected by mining. Thus, the roadway was prone to deformation and failure.

4. Numerical Simulation Study on Stability of Upper Roadway under Upward Mining

4.1. Establishment of Numerical Calculation Model. The finite difference numerical simulation software FLAC3D was used

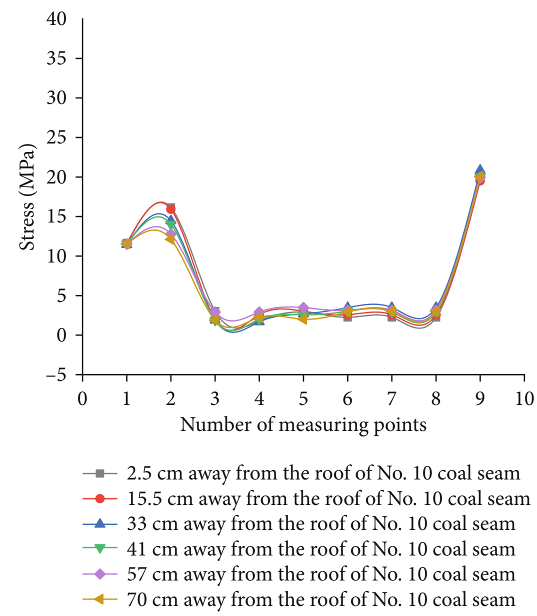

FIGURE 8: Stress diagram of working face mining at 180 m.

to establish the required model based on the actual geological and mining technical conditions of the II 1051 fully mechanized face and the prior establishment of similar models. The model involves the studied coal seam, roadway, and its top and bottom plates. It simulates the dip angle between the coal and rock (20°) and the mining thickness of No. 10 coal seam (2.5 m). The model size is length × width × height = 360 m × 400 m × 320 m, which is divided into 9, 36, and 160 grid units, as depicted in Figure 10. The upper boundary of the model is defined as a free boundary, and the lower and left and right boundaries are defined as single-constraint boundaries to limit their horizontal displacement. The mechanical model adopts the Mohr–Coulomb strain-softening approach to reflect the property that the residual strength gradually decreases with the development of deformation after coal failure. A vertical load corresponding to the actual burial depth of the model was applied to the upper boundary of the model to simulate the stress exerted by the vertical pressure caused by other overlying strata. The physical and mechanical parameters of the model are listed in Table 1.

4.2. Steps in Numerical Simulation

(1) First, the relevant constraints of the model were defined, and the initial equilibrium operation was performed

(2) Second, the excavation balance among the transportation channel, track channel, and upper gas drainage roadway in the II 1051 fully mechanized working face was determined

(3) The working face was excavated step by step, and each excavation was 10 m deep

(4) Finally, comparative analysis and research were conducted on the model after the excavation operation had stabilized

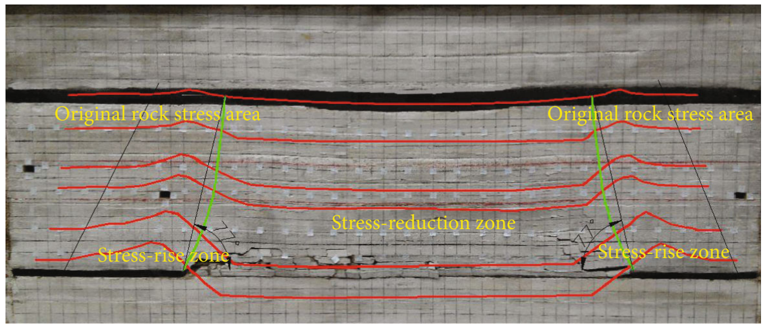

Figure 9: Stress zoning diagram.

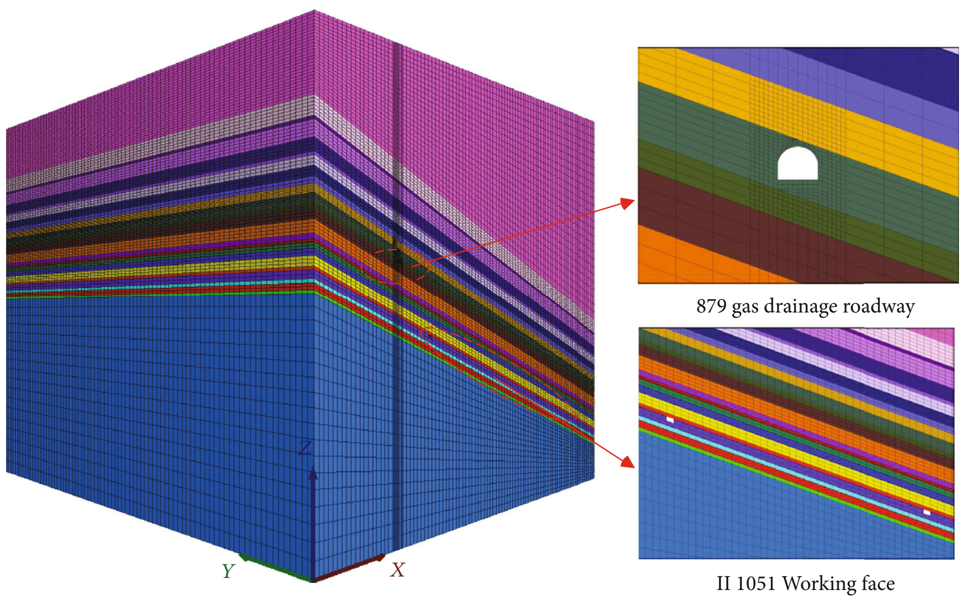

Figure 10: Grid diagram of numerical model.

4.3. Analysis and Discussion of Numerical Simulation Results

4.3.1. Analysis of Characteristics of Failure Field of Rock Surrounding Roadway during Advancing of Working Face. Figure 11 depicts the distribution law of the roadway failure field 120 m from the initial position of the working face at various advancing distances.

As illustrated in Figure 11, in the early stage of the working face mining, the degree and scope of damage of the roadway floor and rock surrounding the roadway on either side were large. With the continuous advancement of the working face, the range of damage of the rock surrounding the roadway gradually increased. When the advancing distance of the working face was less than 60 m, as shown in Figures 11(a) and 11(b), the degree and range of damage of the rock surrounding the roadway remained unchanged. When the advancing distance exceeded 60 m, as shown in Figures 11(c)–11(h), the impact of the mining activities on the surrounding rock on either side of the roadway began to appear, and the degree and scope of damage began to increase. The increase in the range of the scope of damage of the roadway roof was small, and the degree and scope of damage were less than those of the floor and either side. It can be seen from the figure that the two sides of the roadway were damaged primarily by shear, and the damage depth was approximately 1.5–2 m. The roof and floor of the roadway were damaged in the form of shear damage and tension–shear composite damage. The floor damage was the most significant, with a damage depth of 2.5 m, and the roof damage was the least significant, with a damage depth of 1–1.5.

4.3.2. Analysis of Stress Change in Roadway during Advancement of Working Face. To analyze the stress distribution law of the rock surrounding the roadway in mining, the area with the maximum stress concentration on either side of the roadway was selected for data extraction to reflect the maximum stress applied on the roadway. The data in the figure were extracted from 10 to 400 m of the model; the data were taken every 10 m. A total of 40 data points were captured from each survey line, and the data were extracted when the model simulated the excavation of 30, 60, 90, 120, 150, 180, 210, and 240 m. Eight data curves were obtained for each side of the roadway, and the results are presented in Figure 12.

It can be seen from Figure 12 that the continuous advance of the working face led to a gradual increase in

Table 1: Parameters of physical and mechanical properties of the model.

Rock name	Thickness (m)	Bulk (GPa)	Shear (GPa)	Coh. (MPa)	Fric. (°)	σ_{tension} (MPa)	Density (KN/m^3)
Sand-shale interbeds	2	0.13	0.12	0.86	32	0.31	2530
Fine sandstone	4	1.05	0.68	1.28	38	0.52	2873
Siltstone	2.5	0.13	0.12	0.86	32	0.31	2530
No. 10 coal	5	0.25	0.10	0.50	28	0.17	1380
Mudstone	2	0.30	0.17	0.48	26	0.15	2483
Medium sandstone	6	0.55	0.43	1.28	38	0.52	2920
Fine sandstone	4	1.05	0.68	1.28	38	0.52	2873
Siltstone	3.5	0.54	0.41	1.10	34	0.41	2460
Mudstone	2	0.30	0.17	0.48	26	0.15	2483
Fine sandstone	3	1.05	0.68	1.28	38	0.52	2873
Sandy mudstone	8	0.13	0.12	0.86	32	0.31	2530
Fine sandstone	6	1.05	0.68	1.28	38	0.52	2873
Siltstone	3	0.54	0.41	1.10	34	0.41	2460
Mudstone	6	0.30	0.17	0.48	26	0.15	2483
Fine sandstone	5	1.05	0.68	1.28	38	0.52	2873
Alumine	4	0.06	0.04	1.00	32	0.36	2461
Siltstone	6	0.54	0.41	1.10	34	0.41	2460
Medium sandstone	6	0.55	0.43	1.28	38	0.52	2920
Fine sandstone	2	1.05	0.68	1.28	38	0.52	2873
Mudstone	8	0.30	0.17	0.48	26	0.15	2483
No. 8 coal	10	0.25	0.10	0.50	28	0.17	1380
Fine sandstone	2	1.05	0.68	1.28	38	0.52	2873
Mudstone	12	0.30	0.17	0.48	26	0.15	2483

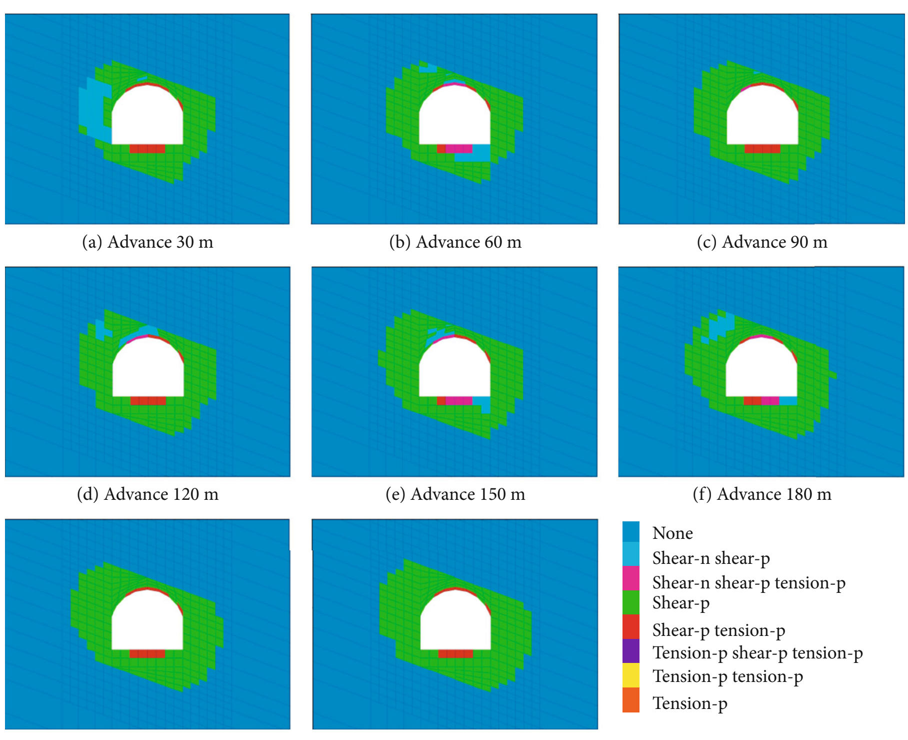

Figure 11: Distribution of characteristics of failure field of the surrounding rock at various positions from the working face.

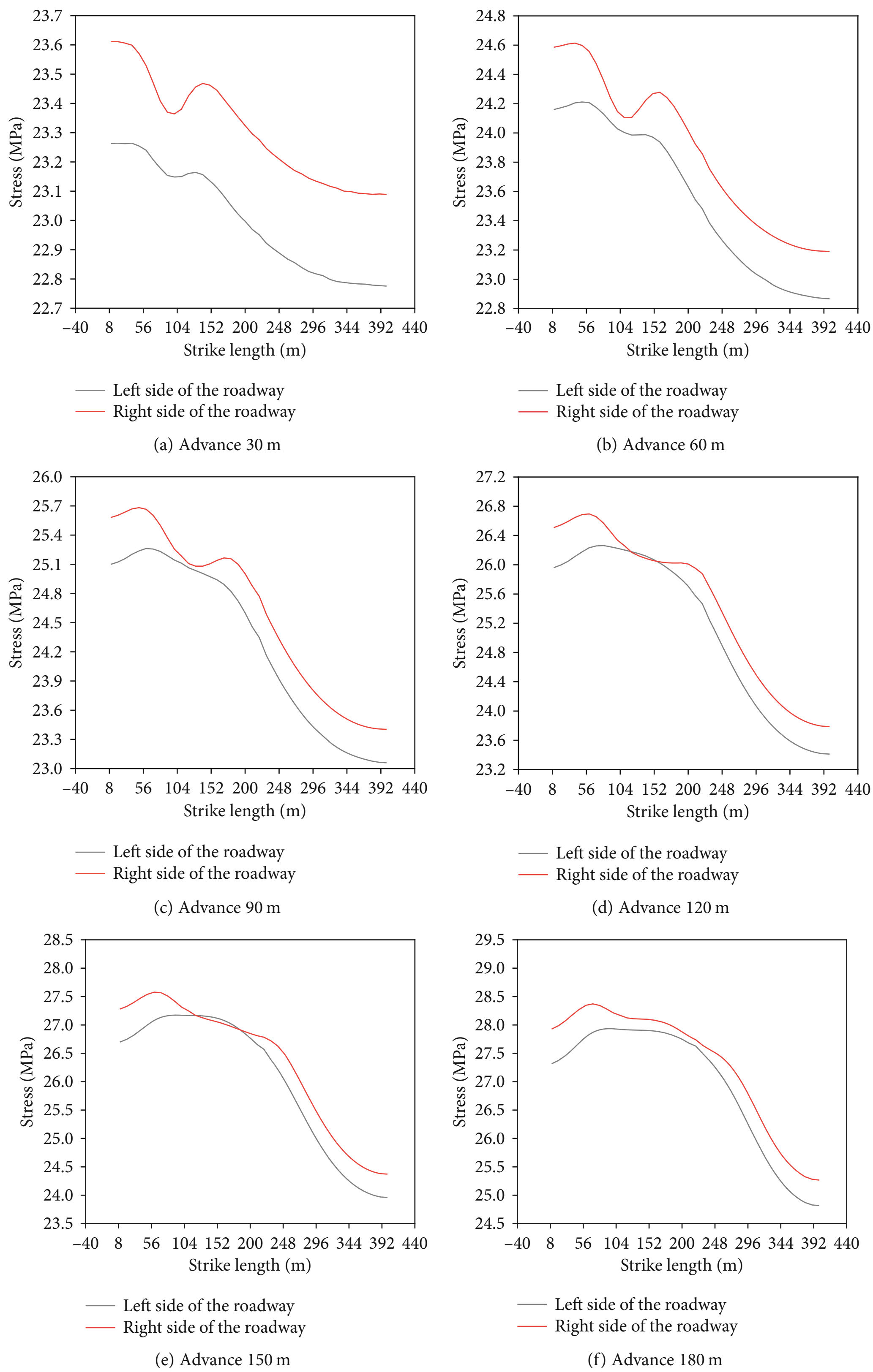

Figure 12: Continued.

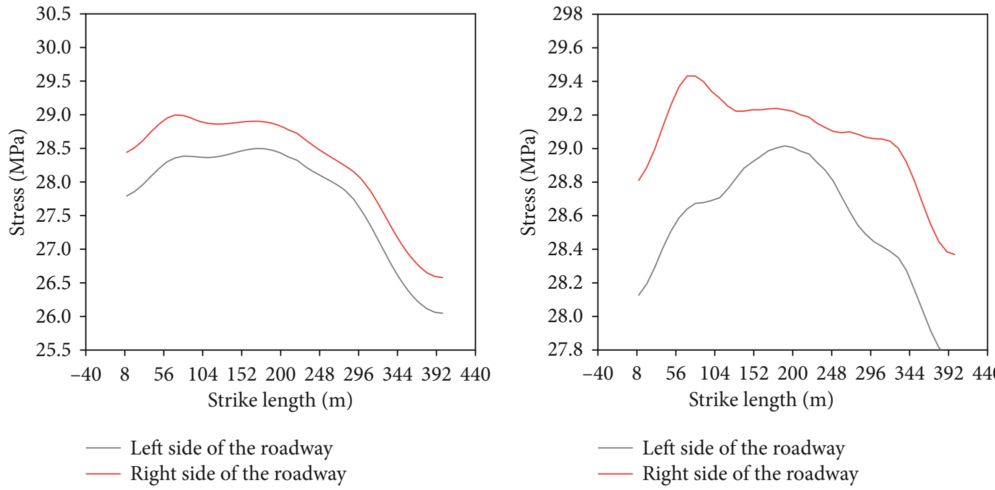

(g) Advance 210 m

(h) Advance 240 m

FIGURE 12: Vertical stress distribution on either side of roadway along strike under different advancing distance.

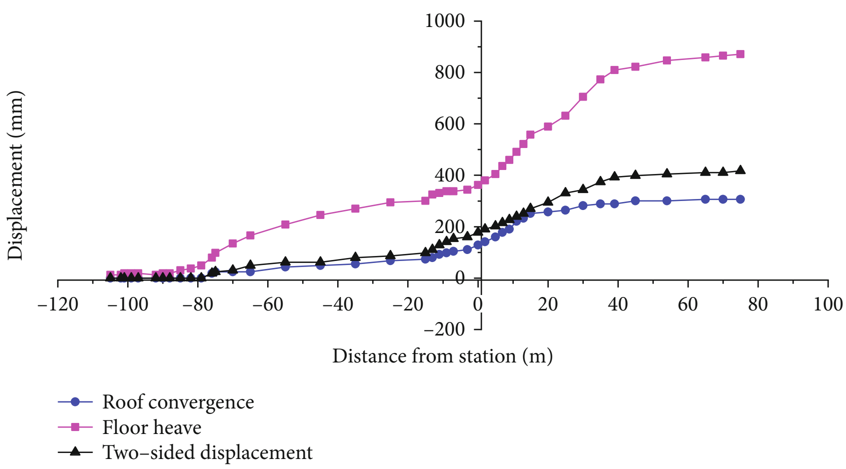

FIGURE 13: Deformation of roadway at various advancing distances.

the degree of stress concentration on either side of the roadway. The roadway was located in the mining abutment pressure-rising area, which also corresponded to similar simulation results; the degree of stress concentration on the right side of the roadway near the working face was greater than that of the left side. When the advancing distance of the working face was less than 60 m, as shown in Figures 12(a) and 12(b), the stress on the rock surrounding the roadway exhibited no apparent change. At this time, the impact of mining did not affect the strata of the roadway. When the advancing distance of the working face was more than 60 m, as shown in Figures 12(c)–12(h), the stress on the surrounding rock began to increase, and the roadway was definitely affected by mining.

4.4. Reasons for Deformation and Failure Characteristics and Instability of Roadway. The natural caving method was used to manage the roof during the excavation process of the II 1051 working face. With the advance of the working face, the overlying strata moved continuously, forming “three zones” above the working face: the falling zone, fracture zone, and bending subsidence zone. With the increase in the falling height and the development of fractures, the bending subsidence of the overlying strata intensified. Because the upper roadway floor consisted of mudstone, the lithology was poor and was affected by the bending subsidence of the overlying strata; the floor is subjected to shear and tensile failures. With the continuous advancement of the working face, the impact of mining gradually affected the roadway horizon, stress concentration occurred on either side, and the damage gradually developed from the floor to either side, which led to aggravation of damage to the sides, primarily in the form of shear failure. Aggravation of the failure of the floor and either side led to breaking of the equilibrium state of the rock surrounding the roadway, which further caused subsidence of the roof. After the failure of the roof, the entire surrounding rock gradually became unstable, which further increased the scope of the floor failure and finally led to an increase in the failure of the entire surrounding rock field.

5. Measurement and Analysis of Roadway Deformation

To determine the deformation characteristics and stability time of the roadway, the displacement observation station was set at an appropriate position in the roadway. To determine the appropriate roadway support technology and support time, the cross point method was used to observe the deformation of the roadway in the process of mining. The observation started in early June and ended in December. A measuring point was selected and set to 0. A negative value indicates a distance near the measuring point, and a positive value indicates a distance away from the measuring point. By processing the observation data, the deformation curves exhibited in Figure 13 were obtained for the roadway roof subsidence, floor heave, and two sides.

As presented in Figure 13, with the advance of the II 1051 working face, the trend of roadway roof subsidence, floor heave, and either side moving closer was roughly the same. When the II 1051 working face was advanced to 60 m away from the measuring station, the impact of mining on the roadway was weak, and the deformation of the roadway was small. This conclusion was consistent with the results of the numerical simulations. When the working face was 20 m away from the measuring station, the speed of deformation of the roadway increased sharply. At this time, the roof subsidence, floor displacement, and two-sided approach were 60, 300, and 90 mm, respectively. When the working face was pushed over the measuring station for 40 m, the deformation rate of the roadway began to slow down, and the deformation of the roadway tended to be stable. At this time, the roof subsidence, floor subsidence, and two-sided approach were 300, 800, and 400 mm, respectively. From the field measurement data, it can be seen that the 879 gas drainage roadway was affected by the mining of the lower working face, and the roadway deformation, particularly the floor heave, was evident. Therefore, floor heave control should be considered when selecting a roadway support scheme.

6. Conclusion

We studied and analyzed the deformation and failure characteristics of the overlying strata to understand the law that governs their impact on similar characteristics of the upper roadway and the instability mechanism of the roadway during the mining of the lower protective seam. For this purpose, the similarity simulation experiments and numerical simulations were used.

(1) At the initial stage of mining, the movement and deformation of the overlying strata had little impact on the upper roadway. When the working face was excavated at more than 55 m, the movement and deformation of the overlying strata began to spread to the roadway, and the surrounding rocks on either side of the roadway began to produce asymmetrically distributed microcracks. With the continuous excavation of the working face, the range of impact of the mining stress also expanded. When the excavation reached the terminal line, that is, the working face was connected, the area impacted by the mining stress extended to 70 m above the roof roadway of the working face. At this time, the roadway lays in the mining stress-rising area, and the stress concentration factor of the surrounding rock increased

(2) Affected by the mining of the lower working face, the degree of damage of the surrounding rock of the roadway was intensified, and the two sides produced shear damage. The roof and floor appeared in the form of composite tension-shear damage, and the degree of damage to the floor was greater. The depth of the final damage to the floor was 2.5 m, and the depth of damage to either side and the roof of the roadway was 1–2 m. With the continuous advancement of the lower working face, the degree of concentration of stress on the surrounding rock gradually increased, and that on the right side of the roadway near the working face was greater than that on the left side

(3) With the advancement of the working face, the trends of roadway roof subsidence, floor heave, and either side of the roadway moving closer were roughly the same, indicating a dynamic trend of increasing slowly first, then increasing sharply, and finally becoming stable. Here, the floor deformation (800 mm) was the largest, followed by that of the two sides (400 mm), and the roof deformation was the smallest (300 mm). Therefore, floor heave control should be considered in the selection of the roadway support scheme

Data Availability

The experimental test data used to support the findings of this study are available from the corresponding author upon request.

Conflicts of Interest

The authors declare that there are no conflicts of interest regarding the publication of this article.

Authors' Contributions

Teng-Gen Xiong contributed to the conceptualization, methodology, and writing—original draft. Ju-Cai Chang contributed to the conceptualization, writing—review and editing, and funding acquisition. Kai He contributed to the formal analysis. Ya-Feng Su contributed to the resources. Chao Qi contributed to the visualization.

Acknowledgments

This work was supported by the National Natural Science Foundation of China (nos. 51774009 and 51874006), the Key Research and Development Projects in Anhui Province (no. 202004a07020045), the Colleges and Universities under

Natural Science Foundation of Anhui (no. KJ2019A0134), and the Graduate Innovation Foundation of Anhui University of Science and Technology (no. 2020CX2011).

References

[1] J.-y. Jiang, Y.-p. Cheng, P. Zhang, K. Jin, J. Cui, and H. du, "CBM drainage engineering challenges and the technology of mining protective coal seam in the Dalong Mine, Tiefa Basin, China," *Journal of Natural Gas Science and Engineering*, vol. 24, pp. 412–424, 2015.

[2] R. Zhang, Y. Cheng, and L. Yuan, "Study on the stress relief and permeability increase in a special low-permeability thick coal seam to stimulate gas drainage," *Energy Sources, Part A: Recovery, Utilization, and Environmental Effects*, vol. 42, no. 8, pp. 1001–1013, 2020.

[3] Q. Tu and Y. Cheng, "Stress evolution and coal seam deformation through the mining of a remote upper protective layer," *Energy Sources, Part A: Recovery, Utilization, and Environmental Effects*, vol. 41, no. 3, pp. 1–11, 2018.

[4] L.-g. Wang, Z.-f. Wang, S.-r. Xu, W. Zhou, and J. Wu, "A field investigation of the deformation of protected coal and its application for CBM extraction in the Qinglong coalmine in China," *Journal of Natural Gas Science and Engineering*, vol. 27, pp. 367–373, 2015.

[5] K. Jin, Y.-p. Cheng, W. Wang, H. Liu, Z. Liu, and H. Zhang, "Evaluation of the remote lower protective seam mining for coal mine gas control: a typical case study from the Zhuxianzhuang Coal Mine, Huaibei Coalfield, China," *Journal of Natural Gas Science and Engineering*, vol. 33, pp. 44–55, 2016.

[6] F. Yang, Z. Ge, J. Chen, L. Cheng, H. Lei, and L. Zou, "A comprehensive gas extraction system coupling high-level suction roadway and boreholes for gas disaster prevention in closely-spaced multiple coal seams," *Energy Sources, Part A: Recovery, Utilization, and Environmental Effects*, pp. 1–14, 2020.

[7] C. Wang, N. Zhang, G.-c. Li, X.-l. Xu, D.-y. Qian, and N.-c. Zhang, "Control principles for roadway roof stabilization in different zones during ascending mining, China," *Journal of China University of Mining and Technology*, vol. 41, no. 4, pp. 543–550, 2012.

[8] Z.-h. Jiao, G.-m. Tao, H. Wang, and Z.-g. Lu, "Overburden strata movement and fissure evolution in lower protective layer in Jincheng mining district, China," *Journal of Mining and Safety Engineering*, vol. 34, no. 1, pp. 85–90, 2017.

[9] Z.-y. Cao, X.-q. He, E.-y. Wang, and B. Kong, "Protection scope and gas extraction of the low-protective layer in a thin coal seam: lessons from the DaHe coalfield, China," *Geosciences Journal*, vol. 22, no. 3, pp. 487–499, 2018.

[10] Y.-s. Bai and Y.-q. Hu, "Overlying strata movement of below protective seam," *Journal of Coastal Research*, vol. 83, no. 10083, pp. 193–198, 2018.

[11] L. Shun, X.-h. Li, Y.-x. Mao, and C.-j. Li, "Time-domain characteristics of overlying strata failure under condition of longwall ascending mining," *International Journal of Mining Science and Technology*, vol. 23, no. 2, pp. 216–220, 2013.

[12] Z.-q. Xiong, C. Wang, N.-c. Zhang, and G.-m. Tao, "A field investigation for overlying strata behaviour study during protective seam longwall overmining," *Arabian Journal of Geosciences*, vol. 8, no. 10, pp. 7797–7809, 2015.

[13] C. Wang, N.-c. Zhang, Y.-f. Han, Z.-q. Xiong, and D.-y. Qian, "Experiment research on overburden mining-induced fracture evolution and its fractal characteristics in ascending mining," *Arabian Journal of Geosciences*, vol. 8, no. 1, pp. 13–21, 2015.

[14] J.-h. Xue, H.-p. Wang, W. Zhou, B. Ren, C.-r. Duan, and D.-s. Deng, "Experimental research on overlying strata movement and fracture evolution in pillarless stress-relief mining," *International Journal of Coal Science & Technology*, vol. 2, no. 1, pp. 38–45, 2015.

[15] J.-x. Tang, Y.-l. Li, Y.-j. Jia, and L. L. Sun, "Study on zoning of overburden strata and roadway deformation of ascending mining in thin coal seam," *Sustainable Development of Natural Resources*, vol. 616-618, pp. 505–509, 2013.

[16] H.-t. Zhang, Z.-h. Wen, B.-h. Yao, and X.-q. Chen, "Numerical simulation on stress evolution and deformation of overlying coal seam in lower protective layer mining," *Alexandria Engineering Journal*, vol. 59, no. 5, pp. 3623–3633, 2020.

[17] N.-z. Xu and L. Han, "Pressure-relief effect of coal rock body of long distance lower protective seam mined based on FLAC3D," *Journal of Coal Science and Engineering*, vol. 16, no. 4, pp. 341–346, 2010.

[18] H. Zhang, B. Jin, B. Huo, F. Zhu, X. Fu, and Y. Lu, "Analysis on pressure relief and deformation of overlying rock-coal as lower protective seam mine in Changping mine, China," *Journal of Liaoning Technical University (Natural Science Edition)*, vol. 35, no. 3, pp. 225–230, 2016.

[19] K. Yang, X. He, L.-t. Dou, W.-j. Liu, L. Sun, and H.-s. Ye, "Experimental investigation into stress-relief characteristics with upward large height and upward mining under hard thick roof," *International Journal of Coal Science & Technology*, vol. 2, no. 1, pp. 91–96, 2015.

[20] X.-y. Zhang, Q.-h. Ren, M. Tu, and Y.-c. Dou, "Fracture evolution characteristics of surrounding rock during ascending mining of closer coal seam in Panyidong Coal Mine, China," *Journal of Mining and Safety Engineering*, vol. 33, no. 2, pp. 191–198, 2016.

[21] A.-x. Liu, T. Shi-hao, F.-t. Wang, Y. Yuan, C. Zhang, and Y.-w. Zhang, "Numerical simulation of pressure relief rule of upper and lower protected coal-seam in thin-protective-seam mining," *Disaster Advances*, vol. 6, pp. 16–25, 2013.

[22] W.-p. Huang, W.-b. Xing, Y.-s. Zheng, and C. Li, "Reasonable layout of roadways for upward mining technology of close coal seams, China," *Chinese Journal of Rock Mechanics and Engineering*, vol. 36, no. 12, pp. 3028–3039, 2017.

[23] H.-b. Liu and Y.-p. Cheng, "The elimination of coal and gas outburst disasters by long distance lower protective seam mining combined with stress-relief gas extraction in the Huaibei coal mine area," *Journal of Natural Gas Science and Engineering*, vol. 27, pp. 346–353, 2015.

[24] D. Qian, H. Shimada, T. Sasaoka, S. Wahyudi, and P. Pongpanya, "Stability of roadway in upper seam of deep multiple rich gas coal seams through ascending stress-relief mining," *Memoirs of the Faculty of Engineering, Kyushu University*, vol. 75, no. 2, pp. 59–80, 2015.

[25] J.-l. Xie, J.-l. Xu, F. Wang, J.-k. Guo, and D.-l. Liu, "Deformation effect of lateral roof roadway in close coal seams after repeated mining," *International Journal of Mining Science and Technology*, vol. 24, no. 5, pp. 597–601, 2014.

[26] W. Cheng, Z.-s. Du, N.-c. Zhang, and D.-y. Qian, "Study on surrounding rock control for mining roadway of the overlying protected seam in ascending de-stressed mining, China," *Journal of Mining and Safety Engineering*, vol. 29, no. 2, pp. 220–225, 2012.

[27] N. Zhang, L. Yuan, W. Cheng, J.-g. Han, and X.-l. Hu, "Deformation characteristics and stability analysis of roof roadway in destressed mining, China," *Journal of China Coal Society*, vol. 36, no. 11, pp. 1784–1789, 2011.

[28] Z. Zhou, C.-Q. Zhu, and Q.-F. Li, "Failure mechanism and stability control of roof roadway in fractured zone, China," *Journal of the China Coal Society*, vol. 42, no. 6, pp. 1400–1407, 2017.

Hindawi
Geofluids
Volume 2021, Article ID 6838092, 12 pages
https://doi.org/10.1155/2021/6838092

Research Article

Experimental Study of the Influence of Moisture Content on the Mechanical Properties and Energy Storage Characteristics of Coal

Nan Liu [1,2], Chuanming Li [1,2], Ruimin Feng [3], Xin Xia [1,2], and Xiang Gao [1,2]

[1] *School of Mining Engineering, Anhui University of Science and Technology, Huainan 232001, China*
[2] *Key Laboratory of Coal Mine Safety and Efficiently Caving of Ministry of Education, Anhui University of Science and Technology, Huainan 232001, China*
[3] *Department of Civil Engineering, University of Arkansas, 4190 Bell Engineering Center, Fayetteville, AR 72701, USA*

Correspondence should be addressed to Chuanming Li; chuanmingli@126.com

Received 31 May 2021; Accepted 1 July 2021; Published 24 July 2021

Academic Editor: Zhijie Wen

Rock burst occurs frequently as coal mining depth goes deeper, which seriously impacts the safety production of underground coal mines. Coal seam water injection is a technique commonly used to prevent and control such accidents. Moisture content is a critical factor tightly related to rock burst; however, an in-depth insight is required to discover their relationship. In this study, the influence of moisture content on the mechanical properties of coal and rock burst tendency is explored via multiple measurement techniques: uniaxial compression test, cyclic loading/unloading test, and acoustic emission (AE) test. These tests were performed on coal samples using the MTS-816 rock mechanics servo testing machine and AE system. The testing results showed that with the increase in moisture content, the peak strength and elastic modulus of each coal sample are reduced while the peak strain increases. The duration of the elastic deformation phase in the complete stress-strain curves of coal samples is shortened. As the moisture content increases, the area of hysteretic loop and elastic energy index W_{ET} of each coal sample are reduced, and the impact energy index K_{E} is negatively correlated with the moisture content, whereas dynamic failure time is positively correlated with the moisture content, but this variation trend is gradually mitigated with the continuous increase of moisture content. The failure of the coal sample is accompanied by the sharp increase in the AE ring-down count, whose peak value lags behind the peak stress, and the ring-down count is still generated after the coal sample reached the peak stress. With the increase in moisture content, the failure mode of the coal sample is gradually inclined to tensile failure. The above test results manifested that the strength of the coal sample is weakened to some extent after holding moisture, the accumulative elastic energy is reduced in case of coal failure, and thus, coal and rock burst tendency can be alleviated. The study results can provide a theoretical reference for studying the fracture instability of moisture-bearing coal and prevention of coal and rock burst by the water injection technique.

1. Introduction

As underground coal mining gradually goes deeper, rock burst has become a dynamic disaster seriously threatening the coal mine safety production [1–3]. As an important index used to measure the possibility of rock burst occurrence, the burst tendency of coal is affected by various factors, among which moisture content is a highly significant influencing factor [4]. Coal seam water injection is a common technique for preventing and controlling rock burst [5]. Therefore, studying the influence laws of moisture content on the mechanical properties of coal and its burst tendency will be of great theoretical and practical significance.

Many researchers have studied the influence of moisture content on the mechanical properties of coal body, mainly concentrating on the compressive strength [6–10], the tensile strength [10–14], and the physical properties under triaxial tests [15–18]. Based on a widely accepted viewpoint, a piece of coal, if containing water, will go through creep damage, which also damages coal strength [19, 20]. Auxiliary monitoring means are generally adopted by many scholars to indirectly reflect the strength loss relation of coal [21, 22].

Acoustic emission (AE), a mature technique to monitor sample failure process, can reflect the precursor information of compression-induced fracture instability of coal on the basis of the AE signal [23], and the peak value of AE ring-down count appears nearby the peak stress, making it applicable to geotechnical engineering, such as coal mining, slope, tunnel, and bridge [24, 25]. AE signal has a favorable corresponding relationship with the complete stress-strain curve of coal [26–29]. The increase in the moisture content of coal will repress the occurrence of AE events [30–32], and meanwhile, the load-carrying induced failure of moisture-containing coal-rock mass is usually accompanied by the changes in its internal structure and physicochemical properties, as well as the energy released in forms of AE, recovery of elastic energy, and so on [33, 34].

Most of the abovementioned studies have been focused on the influence laws of moisture content in coal on its mechanical properties, which has, to a great extent, deepened the understanding of fracture instability characteristics of moisture-containing coal samples, but the influence of high moisture content on the mechanical properties and burst tendency of coal has been rarely involved. Therefore, studying the influence of high moisture content on the mechanical properties and burst tendency of coal under waterlogging effect will be of great pertinence and significant research value.

Figure 1: Ready condition of the coal sample.

Figure 2: Some coal samples after processing.

2. Introduction of Test

2.1. Testing Equipment and Sample Preparation. The testing system used in this study was mainly composed of two setups. The MTS-816 rock mechanics servo testing machine was used for the uniaxial compression and cyclic loading/unloading, and the DS5 AE system was employed to monitor the AE data in the load-carrying process of coal samples. The AE system was equipped with a probe to acquire signals, which was bonded onto the surface of the coal pillar using a coupling agent and mighty adhesive tape. Based on the past testing experience, the sampling frequency of the amplifier was set to 40 dB, with a threshold value of 50 dB. The MTS-816 rock mechanics servo testing machine consisted of a loading/unloading subsystem and automatic data acquisition subsystem, which can be conveniently operated via the computer. Meanwhile, the testing process can be manually intervened, and the control mode, test parameters, and test procedures can also be altered. Figure 1 pictorially shows the ready condition of the coal sample.

To reduce the measurement errors induced by sample preparation, a few coal samples were collected from the same place and taken to the laboratory, followed by the coring, cutting, and grinding procedures. Ultimately, they were processed into cylindrical samples with a diameter of 50 mm and a height of 100 mm. The coal samples were numbered as a1-a9 and b1-b9, where a1-a9 were used to perform the mechanical property test and AE test under uniaxial compression, and b1-b9 were used to test the energy evolution characteristics under cyclic loading. The pictures of the well-prepared coal samples are shown in Figure 2.

2.2. Testing Program and Process. Before the test was started, all coal samples were soaked in water to study their water absorption laws. Firstly, the mass of each sample was weighed and calculated, it was then soaked in water until reaching the prescribed mass, and meanwhile, the time needed by the sample to reach the prescribed moisture content was recorded. Lastly, it was maintained in a closed container for 24 h, and the test was finally commenced. The moisture content ω is calculated by Formula (1), and the results are listed in Table 1.

$$\omega = \frac{M_1 - M_2}{M_2} * 100\%. \quad (1)$$

The uniaxial compression test and cyclic loading/unloading tests were carried out in accordance with the standard of the China National Coal Association (GB/T 25217.2-2010). In the uniaxial compression test, the stress loading was applied using MTS-816 on each coal sample at a rate of 0.5 MPa/s. In the cyclic loading/unloading test, the load was applied to each sample at a rate of 0.5 MPa/s until reaching 75%–85% of average uniaxial strength, and then, it was unloaded to 5% of uniaxial strength at the same rate, and thereafter, the coal sample was cyclically loaded and unloaded in this way. The maximum strength

Table 1: Mechanical parameters of some coal samples.

Preloading condition	No.	Moisture content	Preloading condition	No.	Moisture content
	a1	16%		b1	16%
	a2	17%		b2	17%
	a3	17%		b3	18%
	a4	18%		b4	18%
Uniaxial compression test	a5	19%	Loading/unloading test	b5	19%
	a6	20%		b6	21%
	a7	21%		b7	22%
	a8	22%		b8	23%
	a9	25%		b9	25%

value of cyclic loading each time was 5% greater than the maximum strength value at the previous loading stage until the coal failure. During the testing process, the MTS-816 was synchronously operated with the AE system, where the MTS-816 system automatically acquired data, recorded the stress, strain, and time, and drew the stress-strain curves, and the AE system realized the automatic acquisition of the event number.

3. Analysis of Test Results

3.1. Effects on Mechanical Properties of Coal Samples. The complete stress-strain curves of several coal samples are shown in Figure 3. Each curve can be divided into five phases: fracture compaction, elastic, yield, failure, and postpeak phases. Once the loading got started, the complete stress-strain curve was obviously bent, and as the moisture content increased, the slope of the curve was obviously reduced, namely, the duration of the elastic deformation phase was shortened and that of the plastic zone in the postpeak phase was lengthened, and the overall curve was inclined to rightward offset, that is, the possibility of plastic failure was increased. The moisture state significantly led to the mechanical damage of coal samples.

The influences of different moisture contents on the peak strength and peak strain of coal samples are shown in Figure 4. Peak strain, referring to the strain of the coal sample in case of peak stress, denotes the deformation degree of the coal sample when experiencing a failure. As shown in the figure, the peak strength of the coal sample has a negative linear correlation with the moisture content, and the peak strain shows a positive linear correlation with the moisture content. As the moisture content increases from 16% to 25%, the compressive strength declines from 4.28 MPa to 1.71 MPa, with the decreasing amplitude approaching 60%. When the peak strain increases from 0.01168 to 0.01736, the increasing amplitude is approximately 32%. Therefore, the coal samples with high moisture content showed more obvious plastic failure characteristics. A possible reason is that after containing water molecules, the enhanced plastic ability of coal particles lengthens the fracture compaction phase and weakens the friction coefficient and cohesion between internal coal particles [35],

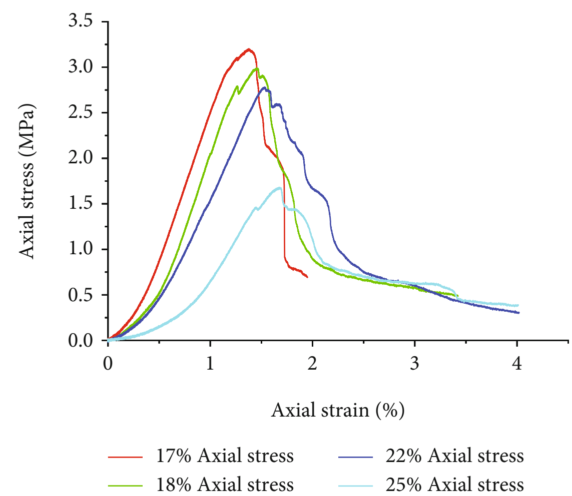

Figure 3: Complete stress-strain curves of coal samples with different moisture contents.

further indicating that the higher moisture content leads to the lower peak strength, the higher peak strain, and the more obvious coal "softening."

Elastic modulus reflects the coal-rock deformation resistance in the elastic deformation phase. Based on the linear relationship between stress and strain in the elastic deformation phase, the elastic modulus of coal and rock [36] can be calculated by

$$E = \frac{\sigma_2 - \sigma_1}{\mu_2 - \mu_1}, \tag{2}$$

where σ is the stress at one point on the complete stress-strain curve, MPa; μ is the corresponding strain of the complete stress-strain curve.

Figure 5 and Table 2 show that the elastic modulus of coal presents a declining trend with the increase in moisture content, showing an overall negative correlation. The elastic moduli of most samples are roughly 0.35 GPa, possibly because the high moisture content in the coal sample leads to an internal crack closure and tremendous friction

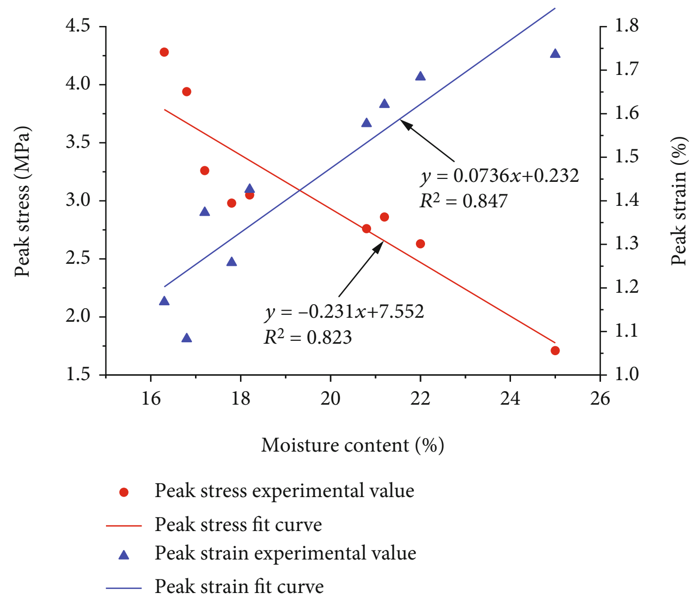

Figure 4: Influence curves of peak stress and peak strain of coal samples with different moisture contents.

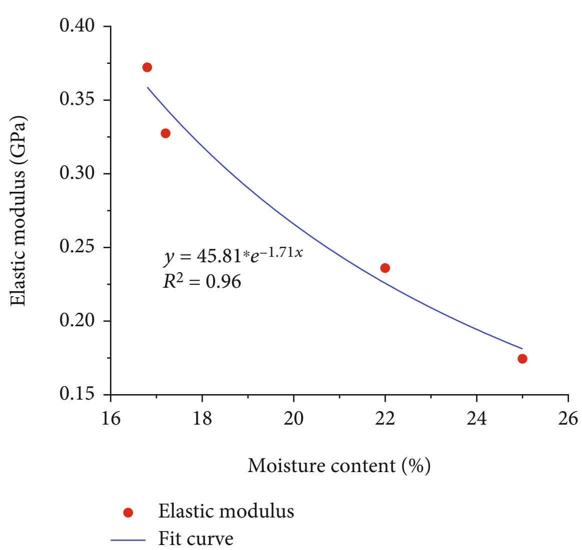

Figure 5: Influence curve of moisture content on elastic modulus of the coal sample.

coefficient, which makes it difficult for the fracture surface to slide during failure [37].

Under hydraulic pressure, the elastic modulus of the coal sample will also be reduced, and the relation is as follows [38]:

$$E = c - dp, \tag{3}$$

where c and d are coefficients and p is the hydrostatic pressure.

From Formula (3) and Figure 5, it can be known that elastic modulus will decline more obviously under high hydraulic pressure. Therefore, coal is prone to deformation and even failure under high moisture content and high hydraulic pressure.

3.2. Energy Evolution Characteristics of Coal Samples. The primary cause for a dynamic disaster is energy release [39]. Rock loading/unloading is a process of energy accumulation, dissipation, and release, and the annular region enclosed by the loading curve segment of the coal sample and the unloading curve segment formed in the previous cycle is a hysteretic loop [40, 41].

Based on the energy conservation law and thermodynamics, the mechanical energy of the MTS-816 rock mechanics servo testing machine can be largely divided into two parts: internal elastic strain energy temporarily stored and plastic strain energy. The relationship between those two can be expressed by Formula (4) as follows:

$$U = U_1 + U_2 = \sum_{i=1}^{n} \frac{1}{2} (\sigma_{i+1} + \sigma_i) \times (\varepsilon_{i+1} - \varepsilon_i), \tag{4}$$

$$\begin{aligned} U_1 &= \int_a^b \sigma d\varepsilon, \\ U_2 &= \int_b^c \sigma d\varepsilon, \end{aligned} \tag{5}$$

where U is the total energy generated by the work done by the external load to the rock sample, being the area under the ith loading curve; U_1 is the plastic strain energy, being the area of the hysteretic loop in the ith cycle; and U_2 is the elastic strain energy, being the area under the ith unloading curve. σ_i and ε_i are the corresponding stress and strain values at each point on the stress-strain curve.

Table 2: Mechanical parameters of some coal samples.

Loading condition	No.	Moisture content	Loading rate	Elasticity modulus (GPa)	Peak strength (MPa)
Uniaxial compression failure	a2	17%	0.5 MPa/s	0.3722	3.94
	a4	18%		0.3274	3.05
	a8	22%		0.2361	2.63
	a9	25%		0.1744	1.71

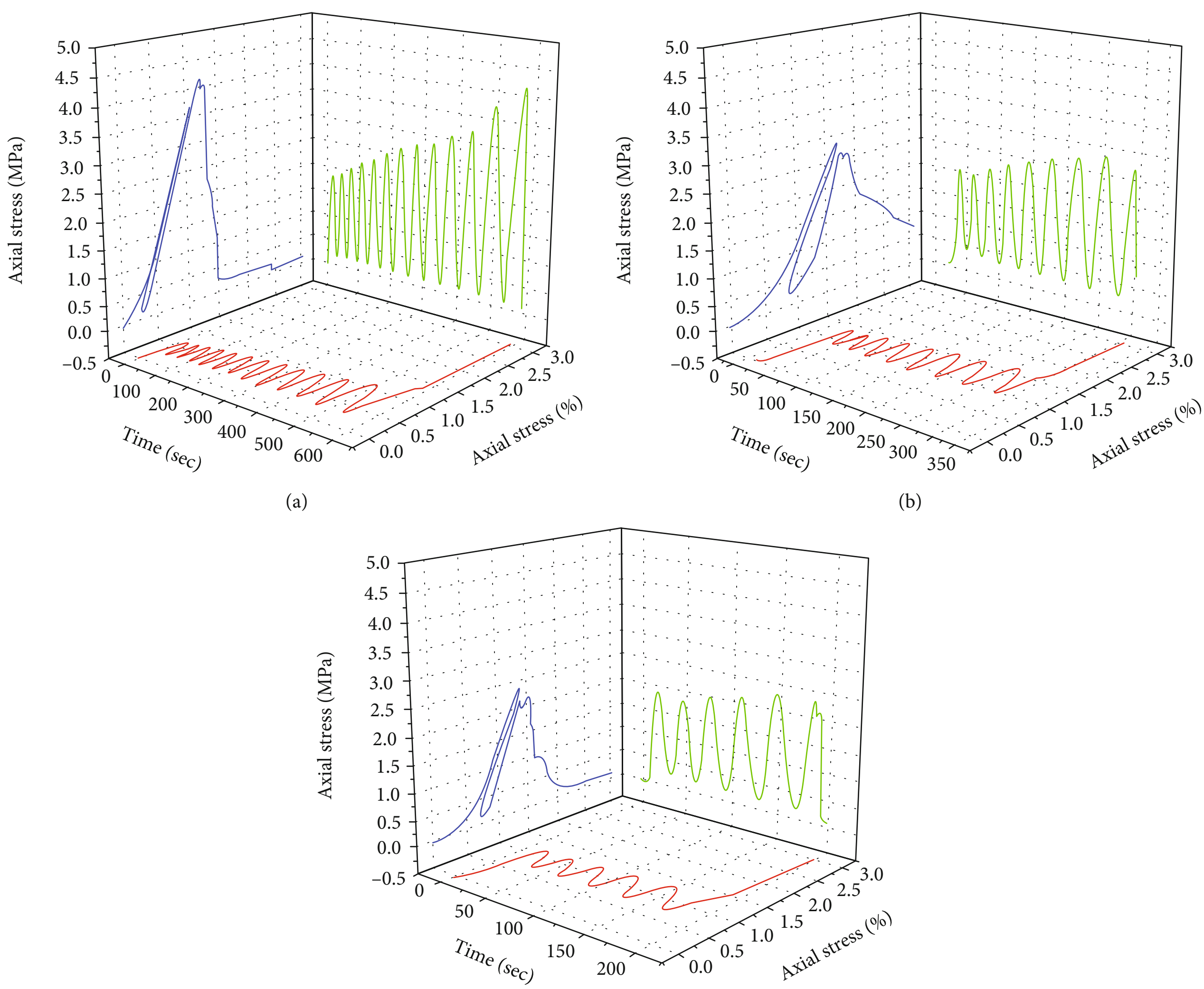

Figure 6: Cyclic loading/unloading curves of coal samples with different moisture contents ((a) 18%; (b) 21%; (c) 25%).

Table 3: Calculation results of cyclic loading energy of coal samples.

Loading mode	No.	Moisture content	Number of cyclic stages before failure	Total strain energy U	Area of hysteretic loop U_1 /J·m^{-3}	Recoverable strain energy U_2
Cyclic loading/unloading	b3	18%	12	2.95441	0.39274	2.56167
	b6	21%	8	2.42494	0.44268	1.98226
	b9	25%	5	2.00783	0.54268	1.46515

Table 4: Classification of burst tendency of coal.

	Type Burst tendency	Type I No	Type II Weak	Type III Strong
Index	Dynamic failure time/ms	$D_T > 500$	$50 < D_T \le 500$	$D_T \le 50$
	Elastic energy index	$W_{ET} < 2$	$2 \le W_{ET} < 5$	$W_{ET} \ge 5$
	Impact energy index	$K_E < 1.5$	$1.5 \le K_E < 5$	$K_E \ge 5$
	Uniaxial compressive strength (MPa)	$R_C < 7$	$7 \le R_C < 14$	$R_C \ge 14$

The cyclic loading/unloading images of the coal samples with moisture contents of 18%, 21%, and 25% were selected as an example demonstration. As shown in Figure 6 and Table 3, the unloading curve of the coal sample was slightly lower than the loading curve, and the total strain energy presents a declining trend. For each coal sample in this test, the area of the hysteretic loop was gradually enlarged with the increase in moisture content, indicating that the dissipated energy gradually increases. The peak stresses failing three coal samples are 3.112 MPa, 2.663 MPa, and 2.315 MPa, after the 13-stage, 9-stage, and 6-stage cyclic loading, respectively. The peak stress leading to the failure of the coal sample under the cyclic loading/unloading is not much different from the peak stress of the coal sample with the same moisture content under the uniaxial compression. A possible reason is that the overall strength of coal samples with high moisture contents is partially low, and thus, the change laws of peak strength under different loading modes can be hardly distinguished.

According to the PRC National Standard (GB/T 25217.2-2010), the dynamic failure time D_T means the duration from peak strength to complete specimen failure in the uniaxial compression test. The impact energy index K_E refers to the accumulative deformation energy before the peak value leading to the sample failure, and the deformation energy consumed after the peak value is reached in the uniaxial compression test. The elastic energy, an index used to measure the burst tendency of coal-rock mass, is the ratio of the elastic energy to the plastic strain energy in the cyclic loading/unloading test: the greater the W_{ET} value, the smaller the energy dissipated in the specimen loading process, namely, the stronger the release of kinetic energy will be.

$$W_{ET} = \frac{U_2}{U_1}, \tag{6}$$

where U_1 is the plastic strain energy, being the area of the hysteretic loop in the ith cycle; and U_2 is the elastic strain energy, being the area under the ith unloading curve.

According to the PRC National Standard (GB/T 25217.2-2010), the coal samples in this test showed a weak burst tendency. The burst tendency of coal was divided into three types on the basis of the related indexes, as listed in Table 4. When four indexes were contradictory, the classification could be implemented using the fuzzy

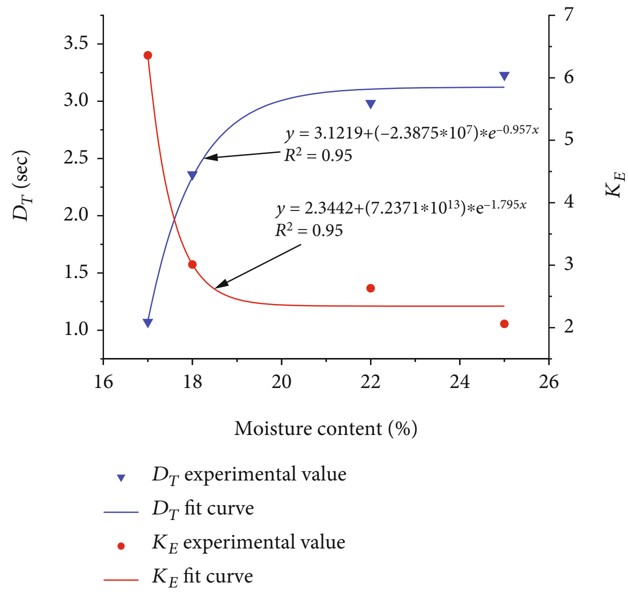

Figure 7: Fitted curves of dynamic failure time and impact energy index of coal samples with different moisture contents.

comprehensive evaluation method. With the increase in moisture content, the elastic energy index W_{ET} is reduced from 6.52256 (strong impact) to 2.69984 (weak impact), impact energy index K_E from 6.36 (strong impact) to 2.06 (weak impact), uniaxial compressive strength σ from 3.94 (weak impact) to 1.71 (no impact), and dynamic failure time D_T from 64.3 ms (weak impact) to 193.34 ms (weak impact). Fundamentally, the burst tendency of the coal sample is reduced after containing moisture. Higher moisture content contributed to more obvious reduction amplitude, further indicating that the coal sample with a high moisture content experiences a failure by absorbing less energy, thus mitigating its burst tendency. Given this, the feasibility and theoretical reasonability of coal seam water injection in the prevention and control of rock burst are verified through the test.

Figure 7 and Table 5 reveal that as the moisture content increases, the dynamic failure time is gradually lengthened, and they have a positive correlation, whereas the impact energy index is negatively correlated with the moisture content, possibly because the water molecules change the structure and connection type of particles inside the coal sample. Unloading cannot be timely realized in case of

Table 5: Test values of burst tendency of some coal samples.

Loading condition	No.	Moisture content	Dynamic failure time D_T (ms)	Impact energy index K_E	Elastic energy index W_{ET}
Uniaxial compression failure	a2	17%	64.3	6.36	—
	a4	18%	141.6	3.01	—
	a8	22%	179.1	2.63	—
	a9	25%	193.34	2.06	—
Cyclic loading/unloading	b3	18%	—	—	6.52256
	b6	21%	—	—	4.47789
	b9	25%	—	—	2.69984

failure of the coal sample with high moisture content, the potential energy accumulated inside it fails to be timely dissipated, and thus, long unloading time is needed. The peak stress inducing the sample failure and elasticity energy W_{ET} were gradually reduced with the increase in moisture content, indicating that the existence of water can reduce the elastic limit of the coal sample, soften the rock, and easily lead to deformation and failure of the coal sample. However, as the moisture content continuously increases, the weakening effect of water on coal strength is gradually alleviated, while the coal with a high moisture content would maintain a certain strength.

Based on the data acquired by the DS5 AE system, the AE energy count and ring-down count of some coal samples were selected in this study. Accumulative energy—energy of mathematical meaning—reflects the intensity of the relative energy of the AE signal, and it is calculated as the area under the detection envelop line of the AE signal; ring-down count reflects the number of AE events, and it has a certain corresponding relation with the internal damage degree of rock material [42, 43].

From the ring-down count and stress-strain curves as shown in Figure 8, the peak value of AE ring-down count appears nearby the peak stress. In the initial compaction phase, the early stage AE signal of the coal sample was obviously weak due to the softening and lubricating effects of water, and almost no AE signal is generated; in the elastic and yield phases, the AE signal of each sample is obviously enhanced; in case of coal failure, microcracks can be intuitively observed, accompanied by the sharp increase in AE ring-down count. The peak value of AE ring-down count lags behind the peak stress, and the ring-down count is still generated after the coal sample reaches the peak stress. However, under an excessively high moisture content, the lag time is shortened, indicating, again, that under an extremely high moisture content in the coal sample, the generation of AE events in the sample is weakened, namely, the ability of water molecules to change the internal structure of the coal sample is limited.

By analyzing the accumulative energy and stress-strain curves in Figure 8, each coal sample experiences a slow increase in energy in the initial phase, and the sharp increase in energy can be obviously observed before the coal failure. As natural soaking is adopted to treat the coal samples, the bonding ability between coal particles is degraded due to the action of moisture, and the energy needed by the coal sample to reach the peak stress is reduced. The accumulative energy in case of coal failure presents a gradual declining trend, demonstrating that the coal sample with a higher moisture content absorbs less energy when going through a failure. As shown in Figure 8(b), the accumulative energy is still increasing after the peak stress, because after the coal sample reaches the peak stress, the AE probe fails to be fixed around the sample. As the test proceeds, a slight collision takes place between the probe and the wall surface of the coal pillar. The curves in Figure 8(c) are not continuously changed with the implementation of this test, because the coal sample is already completely damaged during the loading process, the AE probe falls off, and thus the complete data cannot be acquired.

The moisture content has a bearing on the form of coal failure in addition to its strength. As shown in Figure 9, the failure modes of coal samples are analyzed. The coal samples mainly experience tensile fracture failure, and meanwhile, a small number of shear cracks are generated. By comparing the crack development in Figure 10, the red line represents macrocrack. With the increase in moisture content, the coal failure form gradually tends to be a tensile failure, and as for their morphological characteristics, they are run through by tensile cracks. These cracks are fully developed, and the fragment shedding phenomenon occurs to some coal samples in case of failure. The tensile cracks are not obvious in the coal sample with the moisture content of 16%, possibly because the coal sample experiences a failure under the insufficient development of the tensile fracture failure.

4. Conclusions

The mechanical properties, energy storage characteristics, and failure modes of moisture-containing coal samples are analyzed through the uniaxial compression test, loading/unloading test, and AE test. Ultimately, the following conclusions were drawn:

(1) As the moisture content increases, the duration of the elastic phase in the loading-induced coal failure is shortened, while the duration of the plastic zone in

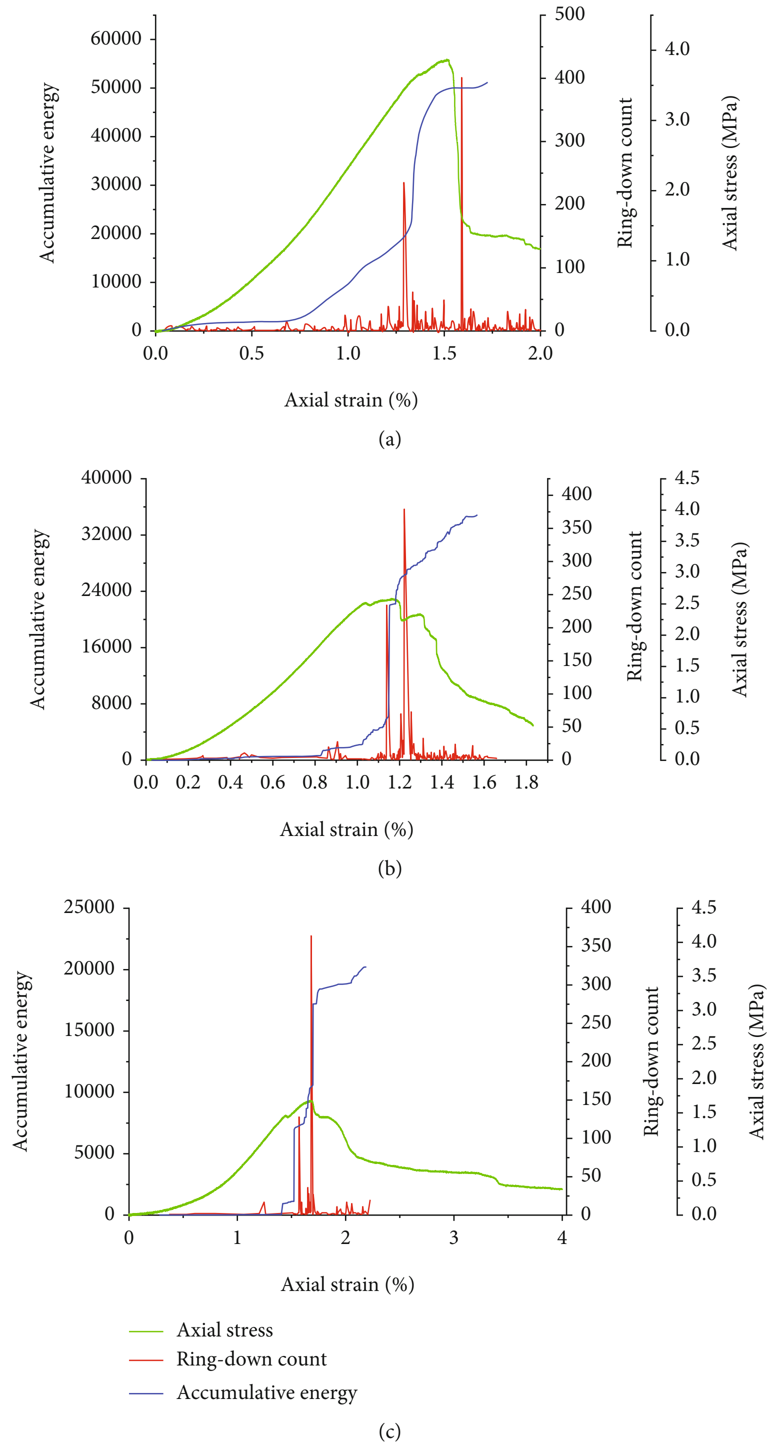

Figure 8: Stress-strain-accumulative energy-ring-down count curves under different moisture contents ((a) 17%; (b) 21%; (c) 25%).

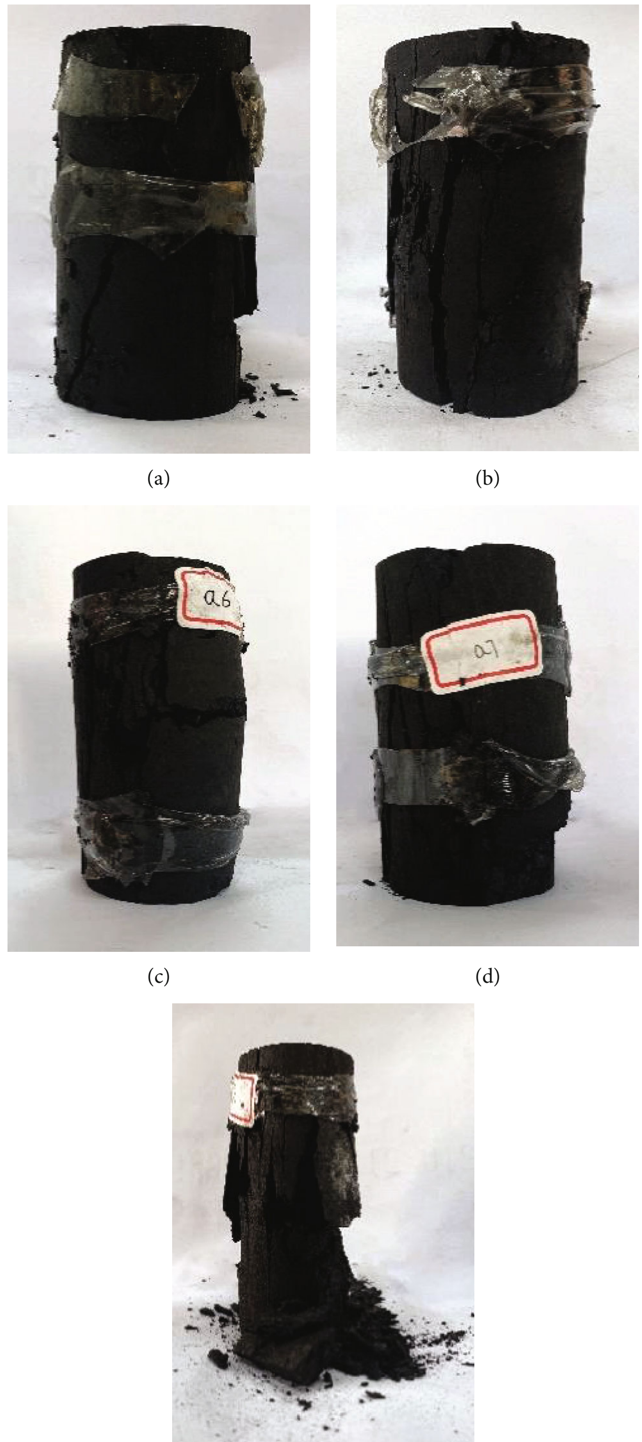

(a) (b) (c) (d) (e)

Figure 9: Broken states of coal samples with different moisture contents ((a) 16%; (b) 17%; (c) 20%; (d) 21%; (e) 25%).

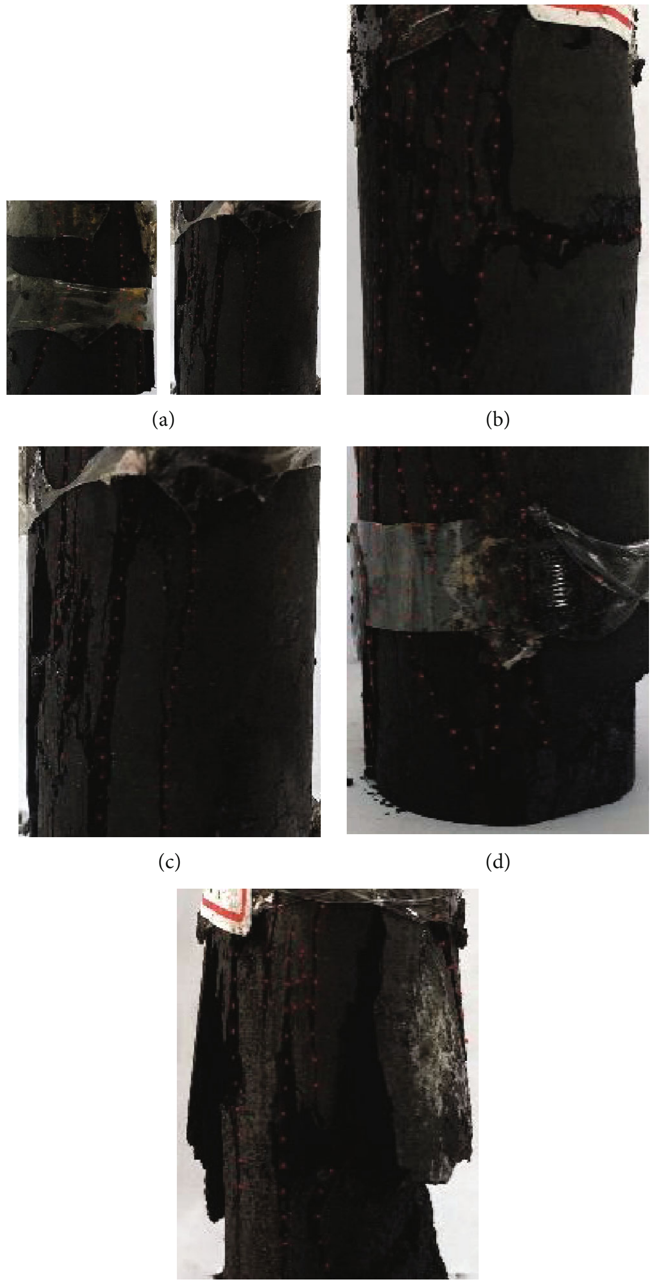

(a) (b) (c) (d) (e)

Figure 10: Local images of the broken states of coal samples with different moisture contents ((a) 16%; (b) 17%; (c) 20%; (d) 21%; (e) 25%).

the postpeak phase is lengthened. The higher moisture content leads to the lower peak strength and elastic modulus of coal, and the more obvious coal "softening"

(2) The peak stress leading to coal failure, area of the hysteretic loop, and elastic energy index W_{ET} decline with the increase in moisture content. The impact energy index K_{E} is negatively correlated with the moisture content, and the dynamic failure time D_T positively correlates with the moisture content, but as the moisture content continues to increase, this variation trend is gradually mitigated, indicating that when the coal sample goes through a failure after containing moisture, the accumulative elastic energy is reduced, so is the burst tendency. However, when the moisture content approaches the saturated state, the weakening effect of water on coal strength is gradually mitigated, and the coal sample with a high moisture content retains a certain strength

(3) The number of AE events shows an excellent corresponding relation with the complete stress-strain laws of coal samples. The coal failure is accompanied

by the sharp increase in AE ring-down count, which lags behind the peak stress, and is still generated after the coal sample reaches the peak stress. The tensile failure is a dominant failure mode of the coal sample, along with a small quantity of shear failure. With the increase in moisture content, the failure mode is gradually inclined to tensile failure, and the fragment shedding phenomenon occurs to some coal samples in case of failure

Data Availability

All data generated or analyzed during this study are included in this published article.

Conflicts of Interest

The authors declare no conflict of interest.

Authors' Contributions

Chuanming Li and Nan Liu designed the experiments; Nan Liu, Xin Xia, and Xiang Gao carried out the experiments; Nan Liu and Chuanming Li analyzed the experimental results; Nan Liu and Ruimin Feng wrote the manuscript.

Acknowledgments

This research was supported by the Anhui Provincial Natural Science Foundation (2008085ME147) and open foundation from the Key Laboratory of Coal Mine Safety and Efficiently Caving of Ministry of Education (JYBSYS2018102).

References

[1] H. Y. Li, Y. L. Mo, and Z. X. Sun, "Research status and prospect of coal bumps prevention and control technology," *Coal Science and Technology*, vol. 47, no. 1, pp. 62–68, 2019.

[2] Y. S. Pan and L. P. Dai, "Theoretical formula of rock burst in coal mines," *Journal of China Coal Society*, vol. 46, no. 3, pp. 789–799, 2021.

[3] D. X. Zhang, W. Y. Guo, C. W. Zang et al., "A new burst evaluation index of coal–rock combination specimen considering rebound and damage effects of rock," *Geomatics, Natural Hazards and Risk*, vol. 11, no. 1, pp. 984–999, 2020.

[4] H. C. Zhou, C. Z. Jia, and H. F. Jiang, "Influence of water injection on impact tendency of hard rock," *Inner Mongolia Coal Economy*, vol. 4, no. 10, pp. 127–147, 2018.

[5] B. Liang, M. Tian, and J. G. Wang, "Effect of different water contents on bursting potential of hard coal seam," *Journal of Water Resources & Water Engineering*, vol. 25, no. 1, pp. 100–102, 2014.

[6] C. X. Wan, "Effect of different moisture state on coal bursting tendency," *Opencast Mining Technology*, vol. 4, no. 2, pp. 31–35, 2015.

[7] C. B. Jiang, M. K. Duan, G. Z. Yin, G. P. Wu, and H. Yu, "Loading-unloading experiments of coal containing gas under the condition of different moisture contents," *Journal of China Coal Society*, vol. 41, no. 9, pp. 2230–2237, 2016.

[8] Z. L. Zhou, X. Cai, Y. Zhao, L. Chen, C. Xiong, and X. B. Li, "Strength characteristics of dry and saturated rock at different strain rates," *Transactions of Nonferrous Metals Society of China*, vol. 26, no. 7, pp. 1919–1925, 2016.

[9] H. R. Li, R. Shen, D. Li et al., "Acoustic emission multi-parameter analysis of dry and saturated sandstone with cracks under uniaxial compression," *Energies*, vol. 12, no. 10, p. 1959, 2019.

[10] Z. L. Zhou, X. Cai, W. Cao, X. Li, and C. Xiong, "Influence of water content on mechanical properties of rock in both saturation and drying processes," *Rock Mechanics and Rock Engineering*, vol. 49, no. 8, pp. 3009–3025, 2016.

[11] Z. A. Erguler and R. Ulusay, "Water-induced variations in mechanical properties of clay-bearing rocks," *International Journal of Rock Mechanics and Mining Sciences*, vol. 46, no. 2, pp. 355–370, 2009.

[12] C. M. Li, N. Liu, and W. R. Liu, "Experimental investigation of mechanical behavior of sandstone with different moisture contents using the acoustic emission technique," *Advances in Civil Engineering*, vol. 2020, Article ID 8877921, 10 pages, 2020.

[13] H. Karakul and R. Ulusay, "Empirical correlations for predicting strength properties of rocks from P-wave velocity under different degrees of saturation," *Rock Mechanics and Rock Engineering*, vol. 46, no. 5, pp. 981–999, 2013.

[14] C. Tang, Q. Yao, Z. Li, Y. Zhang, and M. Ju, "Experimental study of shear failure and crack propagation in water-bearing coal samples," *Energy Science & Engineering*, vol. 7, no. 5, pp. 2193–2204, 2019.

[15] Z. Li and D. J. Reddish, "The effect of groundwater recharge on broken rocks," *International Journal of Rock Mechanics and Mining Sciences*, vol. 41, pp. 280–285, 2004.

[16] J. D. Jiang and J. Xu, "Investigation of energy mechanism and acoustic emission characteristics of mudstone with different moisture contents," *Shock and Vibration*, vol. 2018, Article ID 2129639, 11 pages, 2018.

[17] D. Y. Li, L. N. Y. Wong, G. Liu, and X. Zhang, "Influence of water content and anisotropy on the strength and deformability of low porosity meta-sedimentary rocks under triaxial compression," *Engineering Geology*, vol. 126, pp. 46–66, 2012.

[18] X. T. Feng, Y. H. Gao, X. W. Zhang, Z. Wang, Y. Zhang, and Q. Han, "Evolution of the mechanical and strength parameters of hard rocks in the true triaxial cyclic loading and unloading tests," *International Journal of Rock Mechanics and Mining Sciences*, vol. 131, p. 104349, 2020.

[19] R. Qian, G. Feng, J. Guo, P. Wang, and H. Jiang, "Effects of water-soaking height on the deformation and failure of coal in uniaxial compression," *Applied Sciences*, vol. 9, no. 20, p. 4370, 2019.

[20] G. Cheng, C. Tang, L. Li, X. Chuai, T. Yang, and L. Wei, "Micro-fracture precursors of water flow channels induced by coal mining: a case study," *Mine Water and the Environment*, vol. 40, no. 2, pp. 398–414, 2021.

[21] Z. Chong, X. Li, J. Lu, T. Chen, J. Zhang, and X. Chen, "Numerical investigation of acoustic emission events of argillaceous sandstones under confining pressure," *Mathematical Problems in Engineering*, vol. 2017, Article ID 7676417, 16 pages, 2017.

[22] L. Yu, Q. Yao, X. Li, W. Wang, H. Han, and M. Zhang, "Experimental study of failure characteristics and fissure propagation in hydrous siltstone," *Arabian Journal of Geosciences*, vol. 13, no. 13, 2020.

[23] The Japanese Society for Non Destructive Inspection, *Practical Acoustic Emission Testing*, Springer, Tokyo, Japan, 2016.

[24] L. I. Tian-bin, C. H. Zi-quan, C. H. Guo-qing, M. Chun-chi, T. Ou-ling, and W. Min-jie, "An experimental study of energy mechanism of sandstone with different moisture contents," *Rock and Soil Mechanics*, vol. 36, no. S2, pp. 229–236, 2015.

[25] H. Q. Wu, F. Y. Ren, and D. Xia, "Damage deformation and acoustic emission characteristics of raw coal under different moisture contents," *Tehnički vjesnik*, vol. 27, no. 4, 2020.

[26] Y. A. O. Qiang-ling, L. I. Xue-hua, H. E. Li-hui, and Z. H. O. U. Jian, "Strength deterioration and acoustic emission characteristics of water-bearing sandstone in uniaxial compressive experiment," *Journal of Mining & Safety Engineering*, vol. 30, no. 5, pp. 717–722, 2013.

[27] C. J. Chen, Y. J. Zhao, S. L. Guo, L. Zhao, and Y. T. Pan, "Experimental study on acoustic emission characteristics of coal with different moisture content," *Safety in Coal Mines*, vol. 49, no. 5, 2018.

[28] X. D. Li, *Study on acoustic emission test and impact tendency in the failure process of coal rock sample, [M.S. thesis]*, China University of Mining and Technology, 2020.

[29] V. Rudajev, J. Vilhelm, and T. Lokajíček, "Laboratory studies of acoustic emission prior to uniaxial compressive rock failure," *International Journal of Rock Mechanics and Mining Sciences*, vol. 37, no. 4, 2000.

[30] P. Zhang, Z. P. Meng, K. Zhang, and S. Jiang, "Impact of coal ranks and confining pressures on coal strength, permeability, and acoustic emission," *International Journal of Geomechanics*, vol. 20, no. 8, article 04020135, 2020.

[31] X. Fu, Y.-X. Ban, Q. Xie, R. A. Abdullah, and J. Duan, "Time delay mechanism of the Kaiser effect in sandstone under uniaxial compressive stress conditions," *Rock Mechanics and Rock Engineering*, vol. 54, no. 3, pp. 1091–1108, 2021.

[32] Q. L. Yao, W. N. Wang, L. Zhu, Z. Xia, C. Tang, and X. Wang, "Effects of moisture conditions on mechanical properties and AE and IR characteristics in coal–rock combinations," *Arabian Journal of Geosciences*, vol. 13, no. 14, 2020.

[33] F. K. Xiao, "Analysis on warning signs of damage of coal samples with different water contents and relevant damage evolution based on acoustic emission and infrared characterization," *Infrared Physics and Technology*, vol. 97, pp. 287–299, 2019.

[34] R. S. Yang, Y. Li, D. Guo, L. Yao, T. Yang, and T. Li, "Failure mechanism and control technology of water-immersed roadway in high- stress and soft rock in a deep mine," *International Journal of Mining Science and Technology*, vol. 27, no. 2, pp. 245–252, 2017.

[35] T. Teng and P. Gong, "Experimental and theoretical study on the compression characteristics of dry/water-saturated sandstone under different deformation rates," *Arabian Journal of Geosciences*, vol. 13, no. 13, 2020.

[36] C. Z. Cen, Y. F. Jiang, and C. J. Jiang, "Experiment and analysis about the change of elasticity modulus of coal with different water contained," *Value Engineering*, vol. 34, no. 24, pp. 154-155, 2015.

[37] E. Eberhardt, D. Stead, B. Stimpson, and R. S. Read, "Identifying crack initiation and propagation thresholds in brittle rock," *NRC Research Press Ottawa, Canada*, vol. 35, no. 2, 1998.

[38] Z. P. Meng, J. N. Pan, L. L. Liu, G. X. Meng, and Z. H. Zhao, "Influence of moisture contents on mechanical properties of sedimentary rock and its bursting potential," *Chinese Journal of Rock Mechanics and Engineering*, vol. 28, no. S1, pp. 2637–2643, 2009.

[39] C. J. Wu, T. Qin, Z. W. Liu, and G. Liu, "Study on mechanical properties and energy evolution law of coal samples with different impact tendency," *China Mining Magazine*, vol. 30, no. 2, pp. 160–166, 2021.

[40] C. Li, N. Liu, W. Liu, and R. Feng, "Study on characteristics of energy storage and acoustic emission of rock under different moisture content," *Sustainability*, vol. 13, no. 3, p. 1041, 2021.

[41] W. Cai, L. Dou, G. Si, A. Cao, J. He, and S. Liu, "A principal component analysis/fuzzy comprehensive evaluation model for coal burst liability assessment," *International Journal of Rock Mechanics and Mining Sciences*, vol. 81, pp. 62–69, 2016.

[42] D. Xia, T. Yang, T. Xu, P. Wang, and Y. Zhao, "Experimental study on AE properties during the damage process of water-saturated rock specimens based on time effect," *Journal of China Coal Society*, vol. 40, no. S2, pp. 337–345, 2015.

[43] C. Grosse and M. Ohtsu, *Acoustic Emission Testing*, Springer, 2008.